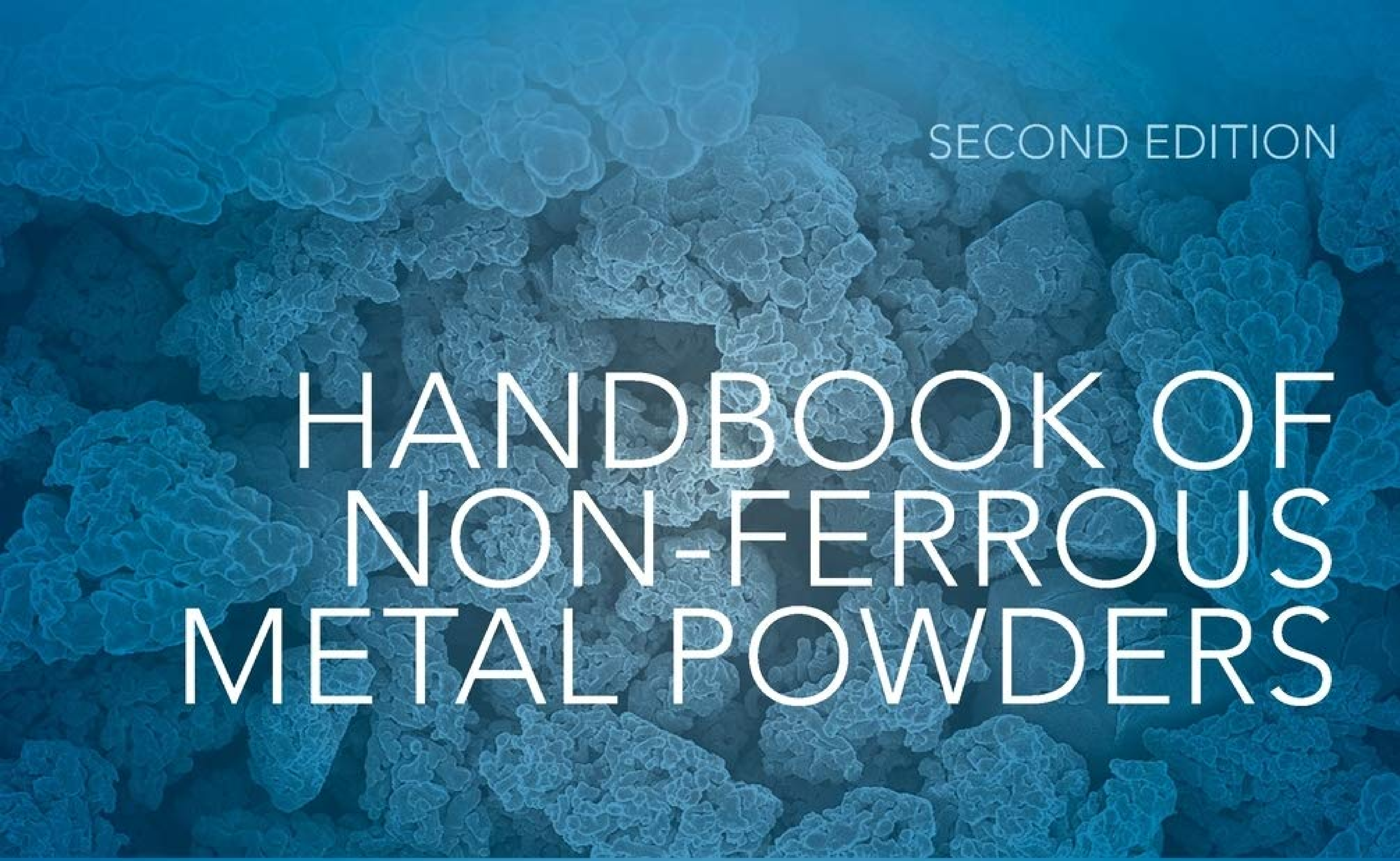

SECOND EDITION

HANDBOOK OF NON-FERROUS METAL POWDERS

TECHNOLOGIES AND APPLICATIONS

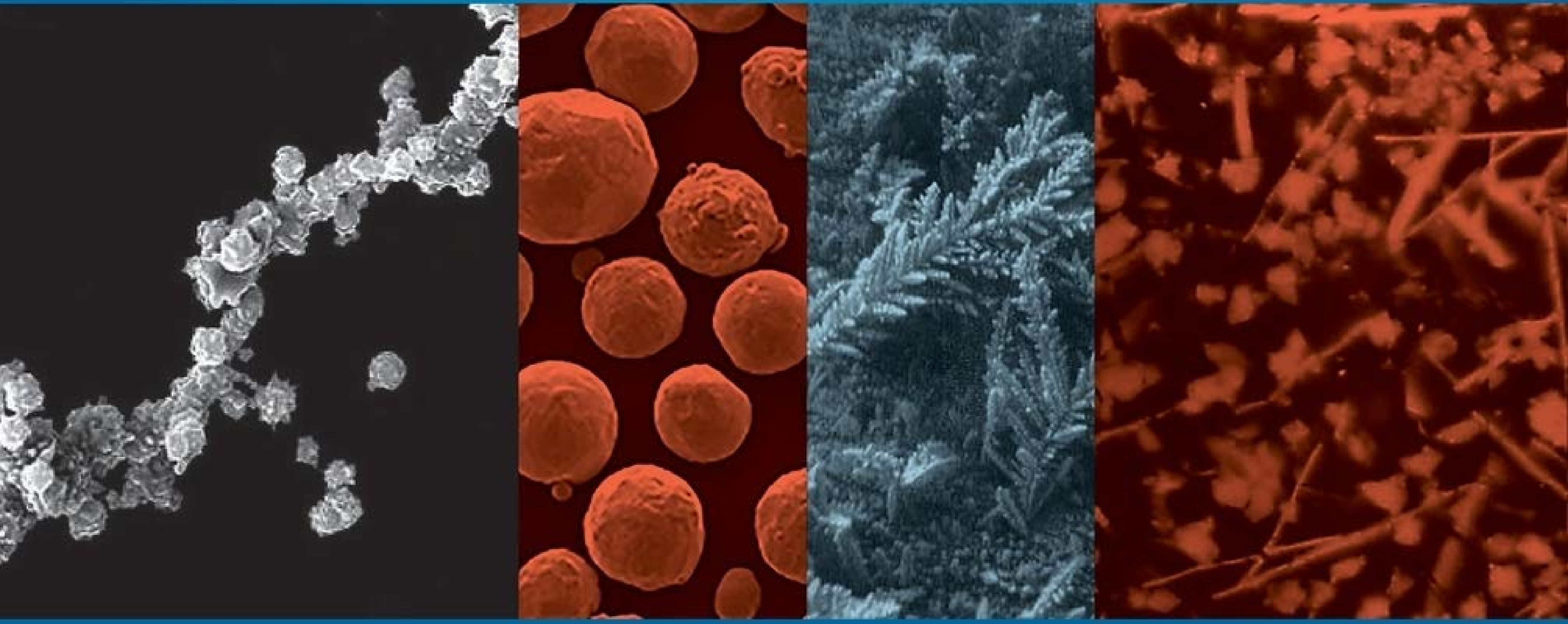

Edited by
OLEG D. NEIKOV

ELSEVIER

Handbook of Non-Ferrous Metal Powders

Handbook of Non-Ferrous Metal Powders

Technologies and Applications

Second Edition

Oleg D. Neikov

Stanislav S. Naboychenko

Nikolay A. Yefimov

ELSEVIER

Elsevier
Radarweg 29, PO Box 211, 1000 AE Amsterdam, Netherlands
The Boulevard, Langford Lane, Kidlington, Oxford OX5 1GB, United Kingdom
50 Hampshire Street, 5th Floor, Cambridge, MA 02139, United States

© 2019 Elsevier Ltd. All rights reserved.

No part of this publication may be reproduced or transmitted in any form or by any means, electronic or mechanical, including photocopying, recording, or any information storage and retrieval system, without permission in writing from the publisher. Details on how to seek permission, further information about the Publisher's permissions policies and our arrangements with organizations such as the Copyright Clearance Center and the Copyright Licensing Agency, can be found at our website: www.elsevier.com/permissions.

This book and the individual contributions contained in it are protected under copyright by the Publisher (other than as may be noted herein).

Notices
Knowledge and best practice in this field are constantly changing. As new research and experience broaden our understanding, changes in research methods, professional practices, or medical treatment may become necessary.

Practitioners and researchers must always rely on their own experience and knowledge in evaluating and using any information, methods, compounds, or experiments described herein. In using such information or methods they should be mindful of their own safety and the safety of others, including parties for whom they have a professional responsibility.

To the fullest extent of the law, neither the Publisher nor the authors, contributors, or editors, assume any liability for any injury and/or damage to persons or property as a matter of products liability, negligence or otherwise, or from any use or operation of any methods, products, instructions, or ideas contained in the material herein.

Library of Congress Cataloging-in-Publication Data
A catalog record for this book is available from the Library of Congress

British Library Cataloguing-in-Publication Data
A catalogue record for this book is available from the British Library

ISBN: 978-0-08-100543-9

For information on all Elsevier publications
visit our website at https://www.elsevier.com/books-and-journals

ELSEVIER
Book Aid International
Working together
to grow libraries in
developing countries
www.elsevier.com • www.bookaid.org

Publisher: Matthew Deans
Acquisition Editor: Christina Gifford
Editorial Project: Andrae Akeh
Production Project Manager: Kamesh Ramajogi
Cover Designer: Greg Harris

Typeset by SPi Global, India

Acknowledgments

The Editor would like to acknowledge the assistance and participation of the following individuals without whose assistance this second edition would not have been possible

Igor Dyakov, Institute Scientifique de Service Public

Alexander V. Krajnikov, Inst. For Problems of Mater. Science

Yuly V. Milman, Inst. For Problems of Mater. Science

Ivan Neikov, Consultant

Pavel B. Rabin, Uralelectrodin

Anatoliy V. Sameljuk, Inst. For Problems of Mater. Science

Oleksandr A. Shcheretskyi, Physico Technological Inst. of Metals and Alloys

Valeriy G. Tokhtuev, Rolling Department IPMS

Galina I. Vasilieva, Inst. For Problems of Mater. Science

Vitaliy S. Voropaev, Rolling Department IPMS

Natalya P. Zakharova, IPMS section: Physical Material Science and Physics of Strength

Foreword

This second edition of the Handbook of Nonferrous Metal Powders is a completely revised and updated work written and reviewed by the leading experts in this area. First created in 2008, this book covers the fundamentals of the main methods of nonferrous metal powder production, including mechanical methods, chemical and electrolytic methods, and physical-chemical. In addition to in-depth articles on powder production, testing, and characterization, the book expands coverage on the secondary operations, the safety engineering in the production of powders, and advanced areas of nanopowders, composites, and additive manufacturing processes.

Based on feedback from users and reviewers, the revised book has been reorganized for better perception. New chapters have been created, including *Production of aluminum alloy powders, Powders for composites, Powders for additive manufacturing processes,* and *Powders with quasicrystalline structure*.

Elsevier is grateful for the work of volunteer editors, authors, and reviewers who devoted their time and expertise to develop a reference publication of the highest technical editorial quality.

Introduction

Oleg D. Neikov
Frantsevich Institute for Problems of Materials Science (IPMS), Kiev, Ukraine

Nonferrous powder production methods are multifarious and numerous. These techniques allow the manufacture of a wide spectrum of metal powders designed to meet the requirements of a variety of applications. Various powder production processes allow precise control of the powders' chemical composition and physical characteristics to obtain prescribed attributes for the features of different applications.

The ratio of nonferrous powder to ferrous powder shipments (expressed in tonnage) is about one to four. But in market value terms, aluminum, silver, and zinc are all close to the value of iron powders [1, 2]. This is illustrated by data about worldwide yields of metal powder manufactured by all processes [2]. Fig. 1 shows the price in $/kg of powder, its volume in t/yr, and its total market value in millions of dollars (log scale).

BASIC METHODS OF POWDER PRODUCTION

Nonferrous powders are produced by mechanical, chemical, and electrochemical methods. Mechanical methods include the comminution of solids and atomization of melts. The comminution of solid metals and alloys is carried out by machining, milling (in impact mills, ball mills, vibration mills, stream mills, and edge-runner mills), and using attritors. General chemical methods include reduction methods, precipitation from solution, hydrometallurgical processing in leach autoclaves, the carbonyl process, and the hydride/dehydride process. Electrolytic methods include electrolysis of aqueous solutions, melt electrolysis, and the cementing process (Table 1).

The shape and size of particles depend on the method of powder production and may vary widely. In Fig. 2, common particle shapes produced by different methods as depicted in ISO 3252 are shown.

Atomization is the most universal method used that allows powder production over a wide range of compositions and in a wide variety of particle sizes, from 1 μm to a few mm. While ferrous powders are currently produced by the water atomization of liquid steel, nonferrous powder production methods are multifarious and numerous. Chemical and electrolytic methods are widely used for producing high-purity nonferrous powders. One basic nanopowder production method is extraction from the gaseous phase.

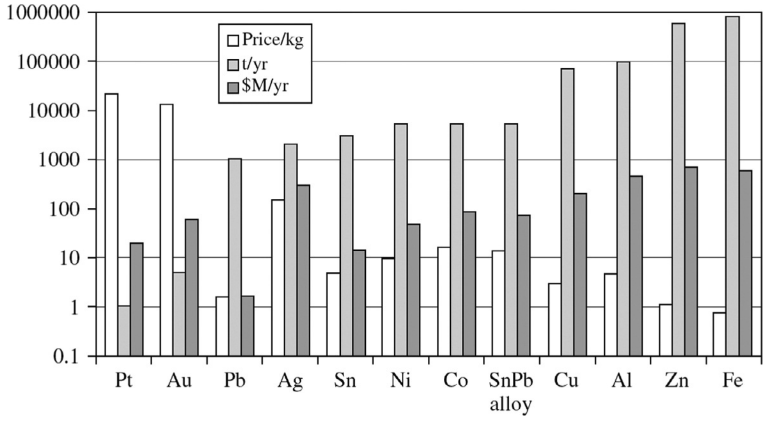

FIG. 1 Yield and value of metal powders.

TABLE 1 Basic Methods of Non-Ferrous Metals Powder Production

			Characteristic of Powder Particles	
Method of Production	**Processing Character**	**Material**	**Mean Mass Diameter (δ_m), μm**	**Shape**
Mechanical methods				
Dispersion of solids	Machining	Brass, bronze, Mg, Al, Cu	3×10^3–10^3	Chips
	Hammer mills	Sinter cakes	5×10^3–50	Angular, irregular
	Ball, rod, and pebble mills, self-grinding	Bronze, Al, Ag, Ti, Ni, Cr	5×10^3–10	Scaly, flake
	Mill rolls and bowl mills	The same	10^4–20	Irregular, scaly
	Vibratory mills	Metals, alloys	10–0.2	Scaly
	Attritors	Metals, alloys	15–0.1	Scaly
	Stream mills	Mo, Be, tungsten alloys	40–1.0	Irregular
Dispersion of melts	Water granulation	Metals, alloys	5×10^3–10^3	Spherical, irregular
	Water atomization	Metals, alloys	2×10^3–1.0	Irregular
	Gas atomization	Metals, alloys	500–10	Spherical, irregular
	Centrifugal atomization	Al alloys, Be alloys, Mg, Mo, Ni alloys	150–50	Spherical, irregular
	Rotating electrode process	Ti alloys, Ni alloys	300–150	Spheroidal Irregular, angular
Chemical and electrolytic methods				
Reduction metal oxides	Oxide reduction by reducing atmospheres	Ni, Co, Cu, W, Mo	300–20	Spongy, granular, (conglomerates)
	Precipitation from solution	Ti, W, Precious metals	100–1, nano size	Irregular, angular
	Hydrogenation, dehydrogenation	Ti, Zr, Hf	200–20	Spongy, irregular, angular
	Hydrometallurgical processing in leach autoclaves	Ni, Co, Cu, Precious metals	70–10	Spongy, granular, briquettes
	Metallothermy	Tantalum, niobium, magnesium, titanium, thorium, zirconium, vanadium	300–20	Acicular, spongy
	Carbothermy	Aluminum, magnesium, iron, niobium, tungsten	400–0.1	Angular, nodular
Electrolysis	Electrolysis of aqueous solutions	Copper, tin, lead, zinc, nickel	400–0.1	Dendritic
	Electrolysis from melts	Aluminum, magnesium, titanium, tantalum, niobium, vanadium, zirconium	400–10	Dendritic
Physical-chemical methods				
Gas phase precipitation	Evaporation and condensation	Zn, Mg, Ti, Ag, Cd, Bi	Ultrafine, Nano size	Conglomerate of particles, clusters
Carbonyl-process	Chemical precipitation, evaporation and codensation	Ni, Co, W, Mo	300–2	Acicular, granular

TABLE 1 Basic Methods of Non-Ferrous Metals Powder Production—cont'd

Method of Production	Processing Character	Material	Characteristic of Powder Particles	
			Mean Mass Diameter (δ_m), μm	Shape
Other methods				
Mechanical alloying	Ball milling	Metals, alloys	Ultrafine, nano size	Agglomerate of particles, clusters
Spray granulation	Fluidized bed spray granulator	Al, Co, Pyrophoric Rare Earths	5×10^3–10^3	Spherical

Comminution of most solid metals is significantly limited due to their ductility. Nevertheless, milling in high-energy apparatus, such as attritors, finds wide application for mechanically alloying powders. Some basic physical and chemical methods of nanopowder and ultrafine powder production are discussed in Chapters 3, 5, and 9.

Mechanical alloying is a simple and efficacious technique for synthesizing both equilibrium and nonequilibrium phases of commercially and scientifically advantageous materials obtained from initial elemental powders. The exclusive advantages of mechanical alloying consist in the possibility of the synthesis of unique alloys that are not accessible by other technique, because mechanical alloying is a completely solid-state process and, therefore, limitations specified by state diagram do not request here. Mechanical alloying is realized by means of high-energy ball milling technique.

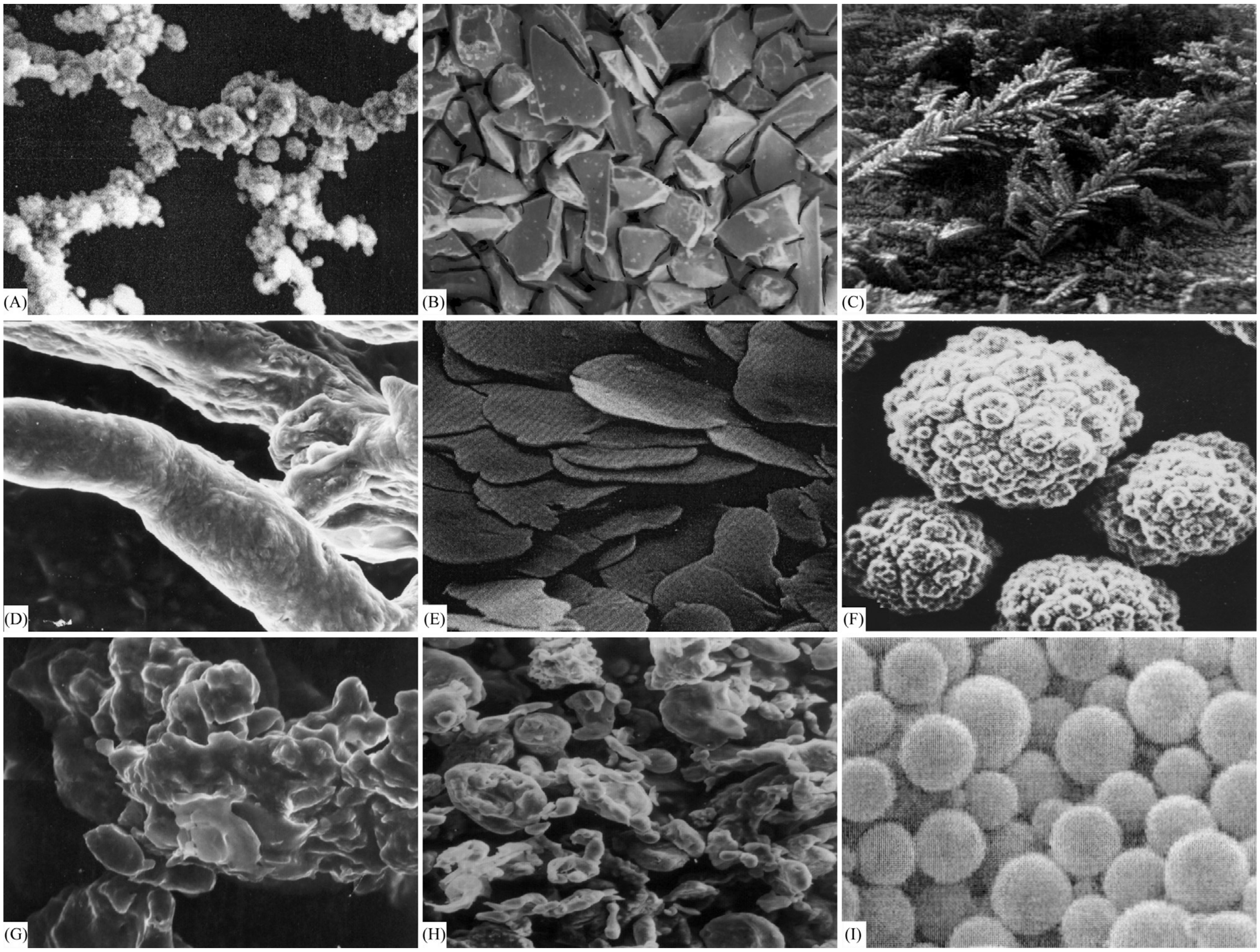

FIG. 2 Characteristic particle shapes: (A) Acicular powder particles; (B) Angular powder particles; (C) Dendritic powder particles; (D) Fibrous powder particles; (E) Flaky powder particles; (F) Granular powder particles; (G) Irregular powder particles; (H) Nodular powder particles; (I) Spheroidal powder particles.

Water-atomized powder-based aluminum alloys with nanoquasicrystalline phases display high mechanical properties and heat-resistance at both room and elevated temperatures [3]. Their high strength results from the high hardness and high Young's modulus of alloys with quasicrystalline phases. Low thermal conductivity combines herein with a thermal expansion coefficient approximate to the thermal expansion coefficient for nickel-, aluminum-and iron-based structural materials.

Additive manufacturing (AM) technologies fabricate models by fusing, sintering, or polymerizing materials in predetermined layers without tools. AM enables the manufacture of complex geometries, including detailed internal parts that are essentially impossible to manufacture using machining and molding processes, because AM does not require predetermined tool paths, draft angles, under cuts. [4] In AM, a model's layers are formed by combining computer-aided design (CAD) data with professional software. In powder-bed-based additive manufacturing, the choice of powder is crucial for the performance and cost of the built parts, for a number of reasons. In general, the powders require high apparent densities to achieve maximum density when deposited in packed beds. Chemical composition and the presence of impurities in the powder translate into the final material and its properties. The particle size distribution and morphology determine the powder's flowability and packing density. Chapter 13 contains discussion of the aspects of powders for additive manufacturing processes.

Grapheme oxide composite powders offer the perfect layer structure of two-dimensional (2D) sp2-hybridized carbon atoms; graphene has been extensively investigated in recent years due to its outstanding properties, such as high Young's modulus, high fracture strength, and excellent thermal conductivity [5]. Due to these excellent mechanical properties and high specific surface area, graphene is expected to be an ideal reinforcement phase interacting with a metal matrix, even in a small concentration. The production technique using grapheme oxide composite powders is considered in Chapter 12.

Powder particle size is a dominant characteristic of a metal powder designated for subsequent use in PM. The application of the powder determines the required size range. In Fig. 3, the length of the segment lines approximately shows these application regions in terms of powder size. A rising number of PM applications require submicron powders produced by chemical and physical methods. Powder applications embraces particle sizes ranging from a few nanometers to granules millimeters in size. The main problems in the production and processing of metallic nanopowders are caused by their high reactivity, explosibility (due to high specific area), and agglomeration of particles. In Chapter 9, "Nanopowders," a novel method for manufacturing semi-products directly from metal vapor, omitting the production of nanopowder in powdered form, is discussed.

Powder characterization and testing described in the Chapter 1 is key to the evaluation of powder production, and precedes the description and discussion of powder manufacturing methods. The main test methods and specific testing

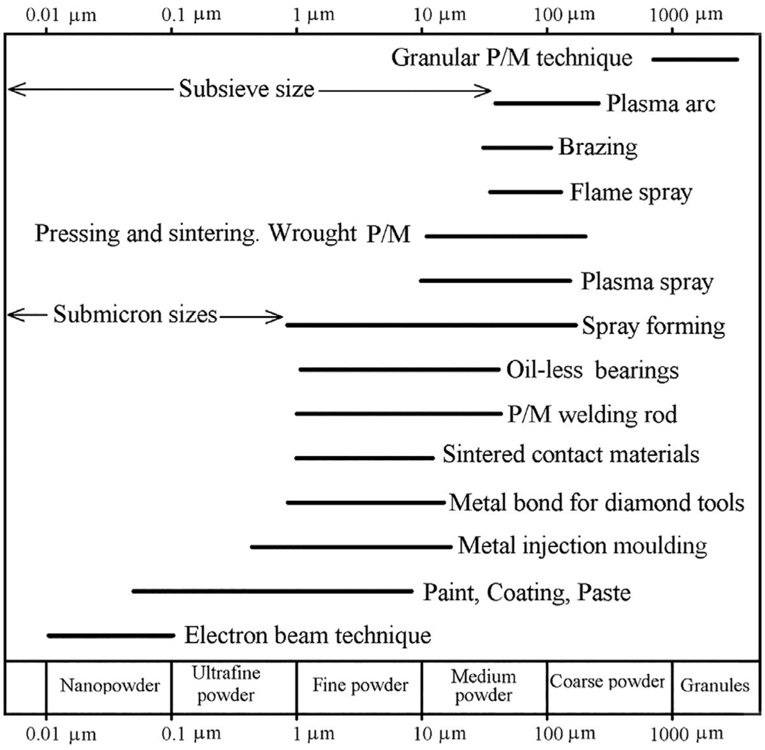

FIG. 3 Ranges of particle size suitable for different applications of non-ferrous powders.

procedures that characterize powders' physical properties, such as particle size distribution, particle shape, and surface area, are shown. Each of these parameters may have an important effect on the physical and mechanical behavior of powders produced for manufacturing PM products. Bulk properties of powders are also examined in this chapter. Finally, test methods for determination of compressibility (a key factor in reaching high part density) are given.

The fundamentals of the main methods of nonferrous metal powder production, including mechanical, chemical, electrolytic, and physical–chemical methods, are described and discussed in Section B.

Chapter 14 describes techniques used for secondary operations such as dehydrogenation, powder passivation, powder classification according to size, mixing, dosage, and packing.

Production methods and techniques for aluminum and aluminum-alloy powders, magnesium and magnesium-based powders, titanium and titanium-alloy powders, copper and copper-based powders, zinc, cadmium, and their alloy powders, nickel, cobalt, and their alloy powders, refractory metal powders, rare metal powders, noble metal powders, and many other nonferrous metal powders are described and discussed in Section C.

Chapter 27 contains the description and discussion of production safety engineering techniques and environmental protection.

REFERENCES

[1] Williams B. Powder metallurgy—a global market review. In: International powder metallurgy directory & yearbook. 13th ed. 1:2008/2009. p. 5–11.

[2] Dunkley JJ. Atomization of metals—craft or science? In: Publ. Universitat Bremen Vol. 1, Edited by: Bauckhage K, Fritsching U, Uhlenwinkel V, Leatham A, editors. Proceedings of 2nd international conference on spray deposition and melt forming, vol 1, Bremen (Germany): Universität Bremen; 2003. p. 1–3–11.

[3] Pedrazzini S, Galano M, Audebert F, et al. Strengthening mechanisms in an Al-Fe-Cr-Ti nano-quasicrystalline alloy and composites. Mat Sci Eng A 2016;672:175–83.

[4] DebRoy T, et al. Additive manufacturing of metallic components—process, structure and properties. Prog Mater Sci 2018;92:112–224.

[5] Wang HD, Kurata K, Fukunaga T, Zhang X, Takamatsu H. Width dependent intrinsic thermal conductivity of suspended monolayer graphene. Int J Heat Mass Transf 2017;105:76–80.

Chapter 1

Powder Characterization and Testing

Oleg D. Neikov and Nicholas A. Yefimov
Frantsevich Institute for Problems of Materials Science (IPMS), Kiev, Ukraine

Chapter Outline

Introduction 3
Sampling of Powders 4
- Weight of Sample 6

Particle Image Analysis 6
- Size Measurements 7
- Particle Shape 7

Particle Size Distribution Analysis 8
- Optical Microscopy 8
- Metallographic Microscopy 10
- Scanning Electron Microscopy 10
- Transmission Electron Microscopy 10
- Sieve Analyses 11
- Classification in a Gravitational Field 13
- Classification in Centrifugal Field 16
- Classification in Inertia Force Field 18
- Counting and Sizing of Particles by Indirect Measures 18
- Coulter Counter 21
- Regularities of Granulometric Composition 22

Techniques of Chemical Analysis for Powders 26
- Microanalysis Methods 27
- Surface Analysis 30
- Bulk Analysis 33

Surface Area and Porosity of Powders 38
- Gas Adsorption 39
- Permeametry 41
- Pycnometry 42
- Porosimetry 43

Bulk Properties of Powders 47
- Bulk Flow Parameters 47
- Cohesive Strength 47
- Frictional Properties 48
- Bulk Density 49
- Tap Density 52
- Flow Rate 54
- Sliding at Impact Point 54
- Segregation of Particles 54
- Trajectory Effect 54
- Screening Model (Also Called Sifting Phenomenon) 54
- Fluidization 55
- Angle of Repose 55
- Multiaimed Powder Tester FT4 57

Compressibility and Compactibility of Metal Powders 57
- Compressibility 57
- Green Strength 58

Apparatuses for Powder Analysis 59
References 61

INTRODUCTION

Apparent density, tap density, angle of repose, flow rate, compressibility, and green strength are referred to as the physical-technological properties of powders. These properties for a certain powder composition may depend on granulometric composition, particle shape, particle morphology, specific surface, moisture content, etc. The knowledge of technological parameters coupled with the physical properties enables the evaluation of the behavior of powder during processing that is accomplished by their consolidation. The procedures are described in standards recommended to determine the technological properties of powders in delivery conditions.

To evaluate powder properties, standard monitoring methods are used. The standard demands of the International Standards Organization (ISO) are the basis for the development of regional, national, and branch standards. Usually, in contrast to ISO, a feature of these standards is the fact that they contain additional or refined specifications. Appendix A at the end of the book contains a list of the standard methods of powder characterization and testing.

Obtaining reliable powder samples is of vital importance for getting the genuine data of chemical composition and the physical and technological properties of a given powder. To obtain a representative powder sample for analysis, it is necessary to follow the principles of sampling described below.

Handbook of Non-Ferrous Metal Powders. https://doi.org/10.1016/B978-0-08-100543-9.00001-4
© 2019 Elsevier Ltd. All rights reserved.

SAMPLING OF POWDERS

The sampling arrangement and the subsequent partition of the selected samples needed for tests are regulated by ISO 3954. An analogous standard functions in North America (ASTM Standard B215) and in the United States (MPIF Standard 01). Generally, two methods are used for obtaining samples of metal powders for subsequent testing. The first method is based on the *gold rules of sampling,* to sample take-off while the powder is in motion. A general rule in this method is that the whole of the powder stream should be taken for many short increments of time as opposed to a single part of the stream being taken permanently. This may be done when blenders or storage tanks are being fed by screw or belt conveyors. The position for collecting the increments is where the powder falls in a stream from the end of the conveyer. Different devices are used for sampling flowing powder streams, such as the point samplers, stream sampling ladles, and traverse cutters. A rotary sample divider for free-flowing powders conforms to the golden rules of sampling; this is shown in Fig. 1.1. Several versions of this device were designed for dusty powders as well as some for cohesive powders [1].

The second method is used for sampling stored nonflowing materials: powders already packaged in containers. They may be stored in small containers such as drums or bags, or in large containers such as trucks or railway wagons. Several of these containers should be selected systematically or, preferably, using a table of random numbers. The standard recommends the number of samples depending on the total number of containers (Table 1.1). Sampling accuracy is provided by means of a sampling spear. The MPIF Standard 01 recommends the use of the keystone sampler that consists of two coaxial tubes, outer and inner, closed from the bottom and with windows in the sides. The bottom part of the sampler is provided with a screw and the portion from above is supplied by a handle. In the closed position, the sampler is inserted into the powder at a point of 70% of the distance from the center of the cross-section to the periphery and straight down to the bottom of the container. The sampler is twisted to the open position, allowing powder to flow into the sampler tube. After filling the sampler, the tube is closed and the sampler is removed from the container.

In sampling from trucks and wagons, it is recommended that eight samples be extracted [1]. No increment should be taken less than 300 mm below the surface in order to avoid sampling from the surface layer, in which segregation can occur due to vibration (Fig. 1.2).

In the standard, the following sample types, represented in the sampling scheme in Fig. 1.3, are distinguished. In the standard, the sequent terms are defined:

- Lot—a definite quantity of powder processed or produced under uniform conditions.
- Increment—a quantity of powder obtained by a sampling device at one time from a single lot.
- Gross sample—a quantity of powder, adequate for the tests to be performed, consisting of all the increments taken from a single lot.
- Composite sample—the blended entire gross sample.

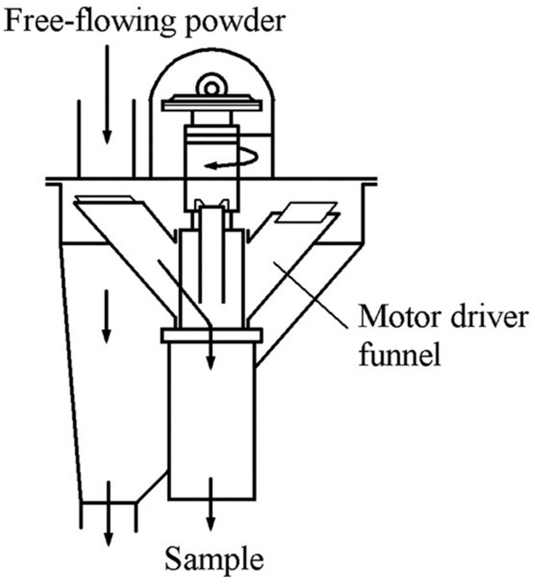

FIG. 1.1 Rotary sample divider.

TABLE 1.1 Recommended Number of Containers to Be Selected From a Packaged Lot

Number of Containers in Lot	Number of Containers to Be Selected
1–5	All
6–11	5
12–20	6
21–35	7
36–60	8
61–99	9
100–149	10
150–199	11
200–299	12
300–399	13
More than 400	13+1 per 100 additional containers

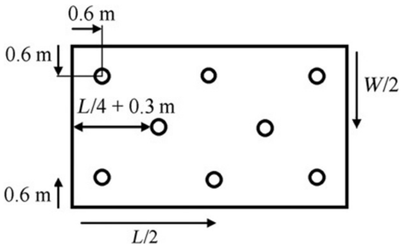
0.6 m
0.6 m
W/2
L/4 + 0.3 m
0.6 m
L/2

FIG. 1.2 Sampling points for a truck or a wagon.

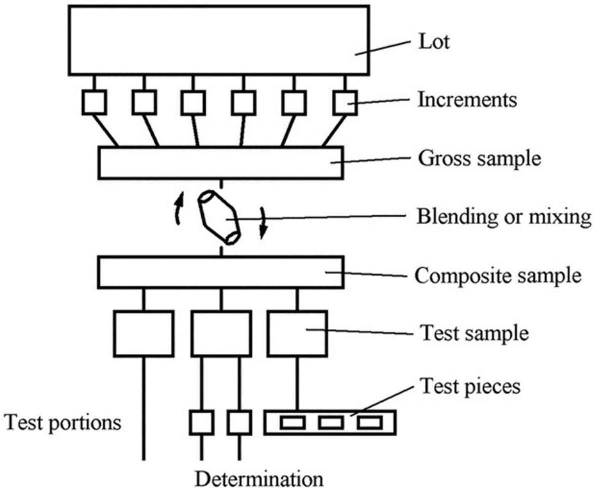
Lot
Increments
Gross sample
Blending or mixing
Composite sample
Test sample
Test pieces
Test portions
Determination

FIG. 1.3 Sampling scheme.

- Test sample—a quantity of powder taken from the composite sample for determination of a single property or for preparing the test pieces. It should normally be taken by splitting the composite sample.
- Test portion—a defined quantity of powder drawn from the test sample, on which the test is performed or from which test pieces are produced.

At least three increments shall be taken for each lot of powder. The actual number depends on the size of the lot and the powder involved and shall be agreed upon by the parties involved.

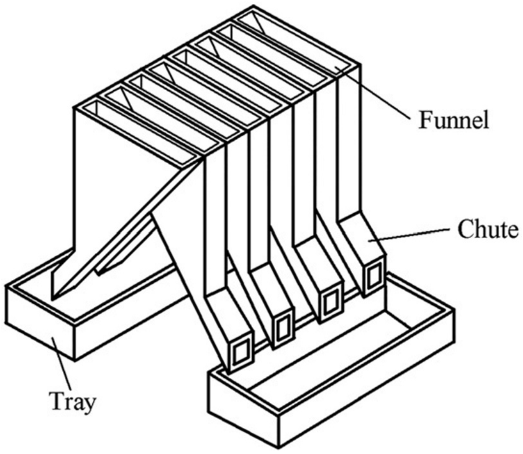

FIG. 1.4 Sample splitter.

The gross sample is often too large to be handled easily and may have to be reduced to a more opportune weight. Several methods are used for sample reduction:

- *Scoop sampling* consists of plunging a scoop into the powder and selecting a sample. Such samples may not be representative from the bulk because the sample is taken from the surface, and the sampling device does not pass through the whole heap.
- *Conical pouring and quartering* consists of pouring the powder into a heap on a flat horizontal surface and dividing by a cross-shaped cutter. The powder from two opposite portions is integrated in the common sample that in one turn is divided into four parts for subsequent testing.
- *Chute splitting* is adopted for sample division. The chute splitter consists of funnels located along the bottom, forming two lines of chutes that separately feed two trays placed on either side of the chutes (Fig. 1.4).

All above methods are simple and therefore popular, owing to the fact that samplers contain no moving parts and are inexpensive.

The reliability of selected methods was examined using binary mixtures of coarse and fine sand (60:40 ratio) [2]. It was deduced that the standard deviations amounted to 6.81 and 5.14, respectively, for the quartering and scoop sampling methods, respectively. Consequently, little confidence can be placed in the first two techniques. For the chute slitting method and rotary sample divider, the standard deviations amounted to 1.01% and 0.146%, respectively. Hence, the rotary sample divider is better than all the other methods.

Weight of Sample

The limiting (minimum) weight of the gross sample may be calculated using the following simple formula:

$$M_s = \frac{1}{2}\left(\frac{\rho}{\sigma_i^2}\right)\left(\frac{100}{w_1} - 2\right)d_1^3 \times 10^3$$

where M_s is the limiting weight in grams, ρ is the powder density in g/cm^3, σ_i^2 is the variance of the tolerated sample error, w_1 is the fractional mass of the coarsest size class being sampled in wt.%, and d_1^3 is the arithmetic mean of the cubes of the extreme diameter in the size class in cubic centimeters. This equation is applicable when the coarsest class is less than 50% of the total sample.

ISO 3082:2009 recommends a minimum incremental mass depending on the maximum particle size in millimeters. According to this standard, the minimum mass of increment with maximum particle size of 10–0 mm amounts is 0.3 kg.

PARTICLE IMAGE ANALYSIS

Particle image analysis includes measurements of particle size, particle shape characterization, morphological analysis, and surface chemistry analysis. Light microscopy is a very precise method of particle image analysis and allows the observation and measurement of individual particles. Scanning electron microscope and transmission electron microscopy make

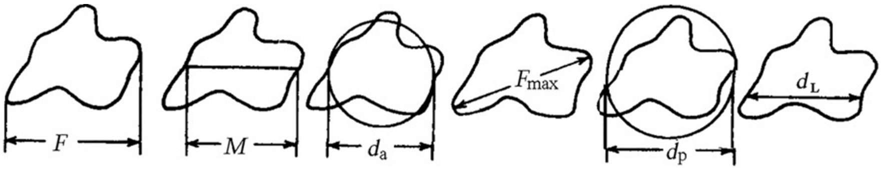

FIG. 1.5 Measuring of irregular particles.

possible the particle image analysis of nano- and smaller particles. However, some of the analyzing techniques used are more art than science. At the same time, the basic principles of sampling, preparation, and measurement permit a precise count to be made with the thorough conception of the essence of the observable particles. The details of using optical microscopy for particle sizing are included in ASTM Standard E 20.

Size Measurements

These measurements consist of the determination of particle sizes, which are used to classify the two-dimensional particle images in terms of an equivalent spherical particle. Accepted particle measurements shown in Fig. 1.5 include:

- d_F, the maximum length of the particle measured in a fixed position (also called Feret's diameter, F).
- d_M, the length of the line that bisects the area of the particle image, all particles being measured in the same direction (called Martin's diameter, M).
- d_a (project area diameter), the diameter of a circle with the same area as the two-dimensional image of the particle.
- F_{max} (the longest diameter), the maximum diameter of each particle, no set direction.
- d_p (perimeter diameter), the diameter of a circle having the same circumference as the perimeter of the particle.
- d_L (maximum horizontal intercept), the length of the longest line that can be drawn through the particle in a fixed direction.

The first three diameters are related to one another by the expression $d_M < d_a < d_F$. The ratio d_F/d_M is used as a shape function, which is equal to 1.0 for spherical particles and increases in magnitude as particle shape becomes more irregular. The projected area diameter, d_a, gives the best evaluation of the accurate cross-sectional area of the particle.

The sampling techniques are described at the beginning of this chapter.

The following methods are also common measurements of experiencing the size of irregular particles:

- *Surface diameter* is the diameter of the sphere having the same surface area as the particle.
- *Specific surface diameter* is the diameter of the sphere having the same ratio of external surface area to volume as the particle.
- *Stokes' diameter* is the diameter of the sphere having the same terminal velocity as the particle.
- *Volume diameter* is the diameter of the sphere having the same volume as the particle.

Particle Shape

Particle shape characterization draws attention from many fields of PM technology. It is desirable to adjust particle shape to improve the quality of PM materials (see Chapter 13). Advances in computer- and image-processing techniques have made it possible.

Photomicrographs of several types of loose powders described in the ISO Standard 3252 (see Appendix A) are shown in Fig. 2 in the Introduction to this book.

The British Standards Institute has prepared a standard glossary of terms for use in the description of the appearance of powder grains (British Standards 2955 Glossary of Terms Relating to Powders):

- *Acicular*: needle-shaped.
- *Angular*: sharp-edged or roughly polyhedral shaped. (Polyhedral derives from poly, meaning many. Therefore, polyhedral is understood to be a geometric shape having many faces, each of which can act as a base.)
- *Crystalline*: a geometric shape freely developed in liquid.
- *Dendritic*: a branched crystalline shape.
- *Fibrous*: regularly or irregularly threadlike.
- *Flaky*: no normal definition in the British Standards. (It is assumed that a flaky fine particle is recognizable.)

- *Lamellar*: plate-like.
- *Granular*: approximately equidimensional but irregularly shaped.
- *Irregular*: lacking any symmetry.
- *Modular*: rounded, irregularly shaped.
- *Spherical*: globular shaped.

Various shape terms have been proposed quantitatively to represent particle shape. Early systems tended to measure one specific feature of a particle.

There are known conventional shape factors [2], including the three ratios: elongation factor (x), bulkiness factor (y), and surface factor (z). A rectangle of minimum area is drawn around the cross-section of a particle (particle projection). The ratio of the rectangle side length permits the calculation of a particle's elongation factor:

$$x = \frac{a}{b}$$

where a and b are side lengths of the rectangle.

The ratio of the area (A) of the projected particle to the area of the enveloping rectangle of minimum area ($a \times b$) indicates the bulkiness factor of the particle:

$$y = \frac{A}{a \times b}$$

Thus, the cross-sectional area of the particle is correlated with some of its linear dimensions.

To characterize the surface configuration by surface factor, which is an essential factor of shape, the surface of the respective particle should be compared with the surface of a sphere of equivalent volume or a cross-section should be compared with that of the particle:

$$z = \frac{c^2}{12.6A}$$

where c is the perimeter of the projection profile of the particles. For a spherical particle, $z = 1$, and for particles of other shape, $z < 1$.

Although the three ratios (x, y and z) do not permit the exact characterization of particle shape, they are nevertheless descriptive.

PARTICLE SIZE DISTRIBUTION ANALYSIS

The classification process is used to determine particle size distribution or to separate certain particle sizes from a distribution. Generally, along with the sieve analysis and direct counting and sizing of particles by microscopy, there are numerous powder classification techniques based on the movement of the suspended particles in a fluid under the action of a force field, which is created by gravity, centrifugal, or inertia forces. The fluid is usually air or water. The classifiers may be distinguished depending on the stream direction: counterflow equilibrium and cross-flow separation.

Optical Microscopy

Optical microscopy allows the counting and sizing of particles from 100 to 0.5 μm in size. The depth of field of an optical microscope is about 10 μm at 100 magnification and 0.5 μm at 1000 magnification. This requires the specimen powders to be placed in one plane and eliminates the wide particle size range by using automatic counting devices. Another limitation is that, owing to the small number of particles usually counted, only the field of view can be characterized, not the representative lot from which the specimen was obtained.

Preparation techniques of slides for optical microscopy depend on the type of powder, the particle size range, and particle composition. Solicitude must be taken to prevent segregation of particle sizes and to obviate the formation of agglomerates.

When a permanent slide is not required and the powder develops good flow characteristics, slides can be prepared by applying dry powder onto the slide with a brush.

In conditions that require shearing action to disperse the powder, a dispersing fluid such as cedar oil or glycerol can be used. The simplest technique involves placing a drop of the dispersing fluid on a glass slide and placing a small amount of powder onto the drop. This sample is then fixed by a cover slip.

Obtaining permanent slides consists of preparation of thin films that can be produced by dissolving collodion in butyl acetate, Canada balsam in xylene, and polystyrene in xylene. Films are formed from a 0.5% solution directly on the glass slide. After the films dry, the powder is applied by spraying on the surface. The particles sink into the medium, forming a permanent slide.

A filar micrometer eyepiece is used for direct measuring of particle sizes in an optical microscope. This eyepiece contains a dial and a movable cross hair that is operated by a calibrated knob. During measuring, a particle is moved so that one side touches one of the fixed mesh markings while the cross hair is moved to touch the other side of the particle. The difference between the two readings is the particle diameter, d_F, that is, the maximum length of the particle measured in a fixed position, also known as the Feret's diameter [1]. This is a time-consuming technique. Eyepiece graticules are usually used to shorten the time required for particle size measurement.

A typical example of eyepiece graticules is given in British Standard 3406 (Fig. 1.6), showing seven circles in a root-2 progression of sizes and five different geometric areas. A similar eyepiece graticule is used in the Russian Federation Standard 23402. The last presents a disk comparator with 10 circles and Vigdorchik's denumerably measuring scale with 20 geometric areas [3]. These stencils are etched on glass disks that are positioned in the back focal plane of the microscope ocular and are thus in the same focal plane as the particle images. Feret's diameter, project area diameter (d_a), or perimeter diameter (d_p) (see Fig. 1.5) are measured expediently with graticules.

Many appliances of semiautomatic and automatic techniques are available to shorten the time required to fulfill a particle size analysis. Most semiautomatic devices record the number of particles in a preset size range. The particle count can be completed by particle photographs or by work directly within the optical microscope. The former consists in the adjustable light spot analyzers using a circle of light projected onto a photograph. The diameter of the circle is adjusted by a diaphragm, then transferred to a bank of registers to record the diameter according to the diaphragm setting. Each particle on the photograph is passed under the light spot, which is adjusted to measure the projected area diameter or the perimeter diameter. When a transparent electronic graticule is used as a plastic sheet on which various size circles have been drawn, under each circle, an electrical contact is connected to a bank register. With every contact, the register records one number. The latter uses a similar recording mechanism, but works directly within the optical microscope applied by recording the micrometer eyepiece.

Automatic techniques allow counting large numbers of particles directly within the microscopy. The main trouble in using this technique is recognizing the particles because of their contiguity and overlap. Spot scanning and slit scanning devices find an application in particle size measurements. Spot scanning devices use the moving spot from a cathode ray tube, which is projected through the microscope onto the specimen. When the spot meets with a particle, the light beam is interrupted, and a photocell records the particle. The slit scanning method projects the microscope image onto a slit. The slide is mechanically scanned, and the signal produced as the particle images pass the slit is recorded. The width of the slit can be varied to eliminate coincidence and overlap.

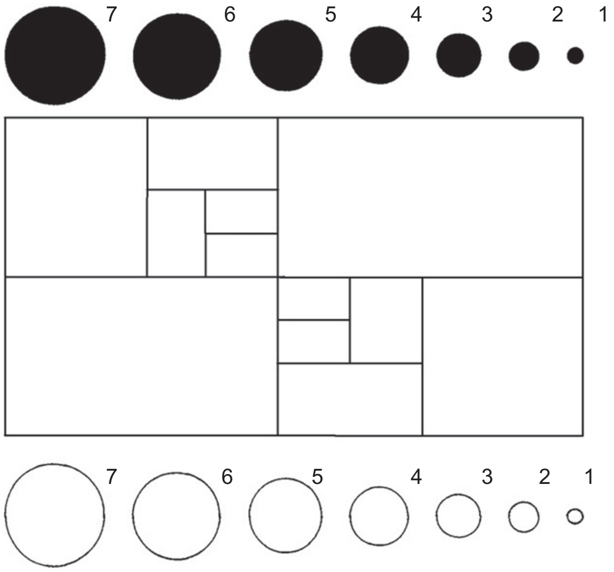

FIG. 1.6 The British Standard eyepiece graticule for particle diameters measuring in an optical microscope.

Metallographic Microscopy

The requirement for the metallographic optical microscopes used for analyzing powders is that they create the image by a transmission principle. In contrast to a traditional optical microscope, the light is passed through the aperture and onto a polished sample surface. The light is usually modified using polarizers, apertures, lightfields, darkfields, and other lenses and filters. These different lighting effects allow us to perform dissimilar types of surface analyses.

Metallographic optical microscopy allows, along with common particle size measurement and powder particle size distribution performed by the optical microscope, various investigations, including powder particle surface and pore morphology, grain structure and grain size analysis of metals and their alloys, and thin film characterization. Another common use is coating thickness measurement and multilayered powder metallurgy (PM) materials. Metallographic microscopy also plays a significant role in failure analysis investigations of the PM works. A corrosive etchant preferentially attacks grain boundaries on a polished metal surface, making them more defined.

It is important to properly prepare slides to prevent the segregation of particle sizes and the formation of agglomerates. The powder sample is placed on a glass plate that may locate each particle separately to allow use of the automatic image analysis at the study of particle shape or size. Separate powder particles are poured by resin or molded in a special plastic. Subsequently, the resulting compact sample is polished. The mechanical, chemical-mechanical, and electrochemical methods of polishing are applied. The etching is used for identifying the microstructure of powders.

Modern microscopes are equipped with digital cameras and computers with a special program for powder analysis.

Scanning Electron Microscopy

Conventional SEM possesses a resolution of about 10 nm and enables very low magnification (about 10 ×) up to 50,000 ×. It consequently allows us to count particles ranging in size from 1 mm to 0.1 μm. However, the count particle size of a sample with polydisperse granulometric composition has to fulfill by various magnifications. The powder sample preparation for counting particles consists of placing a small amount of powder on the substrate on the condition that coincidence and the overlap of particles are eliminated. The substrate must possess a smooth surface. Therefore, a glass slide is acceptable. However, when energy-dispersive X-ray spectrometry (EDS, referred to as EDXA) is to be performed for particle analysis, a carbon or polystyrene surface is preferred. The smooth substrate as the glass and contains no elements that may binder EDXA is made by placing a polystyrene pellet on a glass slide and heating it up to it softening. A second glass slide is then placed over the first, and they are pressed together until the pellet is formed in a thin disk; after that, the slides are removed. The substrates for SEM must be conductive. Therefore, glass or plastic substrate surfaces must be coated with evaporated metal or carbon film. This coating is fulfilled after the particles have been placed on the surface.

The ready sample is placed in the scanning electron microscope with the surface normal to the electron beam so that the magnification, which changes with working distance, will be constant on all areas of the viewing screen. Particle counting can be done directly from the viewing screen, from photographs, or by using an automatic image analyzer.

Transmission Electron Microscopy

A transmission electron microscope can be used for counting particles in the range of 0.001–5 μm in diameter. Particles are usually not counted directly from the viewing screen of the TEM, and counts are made from photographs.

The substrate films on which powders can be placed must be thinner than 100 nm because the electron beam is easily absorbed and less thin films are completely opaque. The carbon films on which powders can be placed for counting are usually used. The technique for producing the flat smooth carbon films consists of the evaporation of carbon in a vacuum unit and the subsequent precipitation of carbon vapor, which is generated onto the mica surface to a thickness of about 10 nm. The mica slide covered by the carbon film is then removed from the vacuum and slowly dipped into a cup of distilled water. The carbon film floats off the mica onto the water surface, where it is picked up on an electron microscope grid.

Powders are dispersed on the surface of support films by injection from an aspirator or a drop of aqueous suspension to dry. So far as carbon films are hydrophobic, the use of an aqueous suspension requires that they be rendered hydrophilic by treatment with a thin solution of albumen. Exposure to reactive oxygen must be done at a very low setting (4 W) for several seconds so that the carbon film will not be destroyed.

Ethylene glycol is a suitable dispersing agent for some samples that are difficult to disperse. A small amount of powder is added to a few drops of this viscous liquid on a glass slide and mulled until a good dispersion is achieved. Then a carbon substrate grid is touched to the thin liquid film, which sticks to the grid. The grid is placed in a vacuum chamber and exhausted for a few minutes, during which time the ethylene glycol sublimates and particles are left on the carbon substrate.

The TEM enables the measurement of particle thicknesses by "shadowing" particle dispersions in which the particles are found on a substrate and are not embedded in a plastic film. This technique consists of evaporating a small amount of metal placed at an angle to the substrate surface in a vacuum unit. The fused metal coats the substrate surface, including particles in a line-of-sight fashion, leaving a "shadow" fusion behind the particles. The magnitudes of the angle to the substrate and shadow length allow the calculation of the particle height.

Sieve Analyses

Sieve analysis is the method most widely used in the PM industry for determination of particle size distribution of metal powders larger than 5 μm. Wire cloth sieves woven in a square mesh pattern from phosphor bronze or stainless steel wires are mounted in 75 or 200 mm stainless steel or brass rings. A series of sieves is selected that covers the full range of particle sizes present in a powder. The sieving unit with sieve series where sieves are stacked in order, with the largest mesh size at the top and a pan at the bottom on a shaker with rotary and tapping action, is shown in Fig. 1.7.

A sieve series according to international and national standards is represented in Table 1.2. The standard sieve series is specified in ISO Standards 565 and 3310/1, the American Society for Testing and Materials (ASTM) standard E 11, and the RU standard GOST 3584. These standards are similar and include the following requirements:

- Mechanical sieve shakers combining a rotary motion and tapping action.
- Test specimen size of $\sim$100 g nominal weight for metal powders with an apparent density $>1.50\,\text{g/cm}^3$ and 50 g test specimen for lower apparent density powders.
- Mechanical sieve shaking for 15 min or another specified time.
- Weighing powder retained on each sieve and in the bottom pan to the nearest 0.1 g and totaling all weights.
- Calculating and reporting the percentages of each sieve fraction to the nearest 0.1%.

The ISO sieve series is based on the principle of a fixed ratio between the sieve openings with the selection of the row of preferable numbers, with the denominator of $\sqrt[20]{10} \approx 1.12$ (R 20) for supplementary sizes and the selection of the each third number from row numbers for principal sizes (R 20/3 $\approx$ 1.4).

ISO standard 4497 has been established for the sieve analysis of metal powders. Analogous standards are used in North America (ASTM Standard B 214), the United States (MPIF Standard 05), and the RU (GOST 18318-94).

The main sieving problems are:

- In the case of an overloaded sieve surface, the weight of the oversized and near-mesh powder tends to retard the particles finer than mesh opening the pass through the openings.
- Sieve opening clogging, when near-mesh oversized particles become entrapped in the openings. If brushing fails to remove the particles, an ultrasonic wash with a wetting agent must be used to eliminate them.
- Irregularly shaped particles are able to pass through sieve openings in a certain orientation only. Usually vibrating and shaking are sufficient to change the orientation of particles.

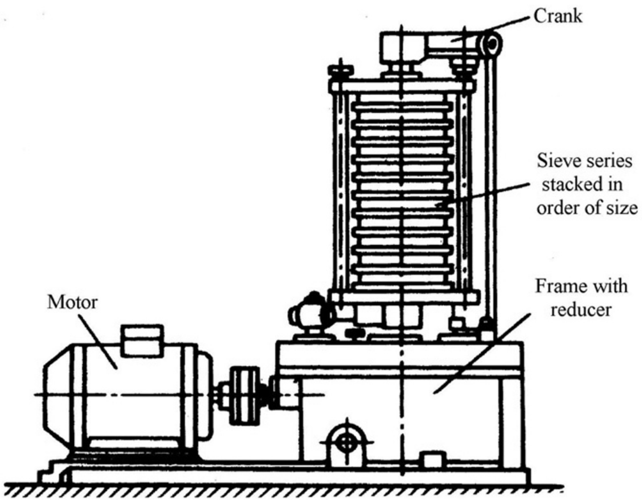

FIG. 1.7 Sieving classifier.

TABLE 1.2 Standard Sieve Series

ISO 565 and 3310/1					British Standard	
Principal Sizes (R 20/3)	**Supplementary Sizes (R 20)**	**DIN 4178**	**ASTM E11**	**RU GOST 3584**	**Sieve Designation**	
µm	**µm**	**µm**	**µm**	**mm**	**µm**	**mesh**
1000[a]	1000[a]	1000[a]	1000[a]	1.00	1000	16
	900	900				
	800	800	850	0.80	850	18
710	710	710	710		710	22
	630	630		0.63		
	560	560	600		600	25
500	500	500	500	0.50	500	30
	450	450				
	400	400	425	0.40		36
355	355	355	355		355	44
	315	315		0.315		
	280	280	300		300	52
250	250	250	250	0.250	250	60
	224	224				
	200	200	212	0.200	212	70
180	180	180	180		180	85
	160	160		0.160		
	140	140	150		150	100
125	125	125	125	0.125	125	120
	112	112				
	100	100	106	0.100		
90	90	90	90	0.090	90	170
	80	80		0.080		
	71	71	75	0.071	75	200
63	63	63	63	0.063	63	240
	56			0.056		
	50	50	53	0.050	53	300
45	45	45	45	0.045	45	350
	40	40		0.040		
	36	36	38		38	400
	32	32	32			
	28	28				
	25	25	25			
	22	22				
	20	20				

[a] *The beginning of sieve series is 125 mm. The range up to 1000 is not presented here.*

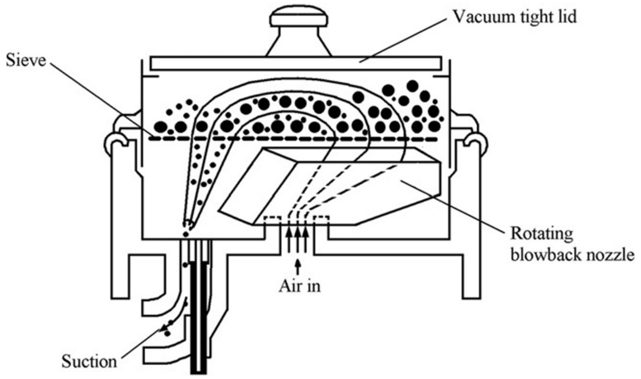

FIG. 1.8 Micromesh jet siever.

- Damaged sieves may have stretched and distorted the mesh openings or may be torn. A microscope should be used to examine sieves regularly. Epoxy has been used to repair minor damage.
- Electrostatic charges may cause fine particles to adhere to each other, forming an agglomerate of particles. Fine particles also can adhere to larger particles. The use of sieving aids, such as commercial antistatic agents, may lessen the agglomeration.

Micromesh sieves have an advantage in comparison with wire cloth sieves, but they are more expensive. The micromesh sieves are manufactured by photo-etching and electrodeposition techniques. This method makes it possible to produce flat sheets of electrodeposited nickel with precise square openings. This thin gauze is supported by a coarser square-etched grid of nickel-plated cupronickel. The ASTM E 11-87 specification claims a maximum deviation of only ±2.0 μm for sieves ranging from 125 to 5 μm.

Irrespective of sieve types, for sieves finer than 45 μm (325 mesh), most dry sieving techniques are insufficient. For these finer size sieves, a jet type sieve can be used, such as the Alpine production (Fig. 1.8). This device uses an exhaust coupled with a rotating blowback nozzle. Fine particles are suctioned through the mesh while the blowback nozzle redistributes the powder sample on the sieve surface, thus disintegrating agglomerates and purging the mesh openings. The sieving operation is rapid and permits sieving down to 10 μm.

Sieve Analysis Variations

Sieve analysis is the prevalent method of measuring particle size while variations among results for different sieving tests of the same material are common. For example [4], statistical treatment of dry sieving tests of silica sand samples shows the number of variables for each variation source (4 batches, 88 samples, 2 sieve stacks, 2 sieving machines, and 4 operators) and the average variation (in percent) each source contributed to the total variation. Sampling (19.4%), sampling reduction (33.5%), and sieve stocks (29.9%) contributed most of the total variation. The contribution of sieving machines and operators to the total variation were 11.4% and 5.8%, respectively. Therefore, to minimize variations in sieve analysis, it is necessary to reduce or identify the sources of variation in sampling, sample reduction, sieve stocks, sieving machines, and operators.

Classification in a Gravitational Field

Sedimentation Methods

Sedimentation methods are based on the classifying of metal powders depending on the settling rate under gravity of particles situated in a fluid. This determination is based on Stokes's law of fluid dynamics by laminar current. That states that the resistance frictional force F_r on a spherical particle moving through a fluid at a constant velocity is proportional to the product of the velocity, v, the fluid viscosity η, and the diameter of the sphere, D:

$$F_r = -3\pi\eta D v \tag{1.1}$$

The Stokes equation is a relationship between settling velocity, v_{st}, and particle diameter:

$$v_{st} = \frac{(\rho_s - \rho_f) g D^2}{18\eta} \tag{1.2}$$

where ρ_s is the solid density, ρ_f is the fluid density, and g is the gravitational acceleration.

Measuring this velocity, v_{st}, is possible with the help of the Stokes equation (Eq. 1.2) to determine the diameter, D, of settling particles:

$$D = \sqrt{\frac{18\eta v_{st}}{g(\rho_s - \rho_f)}} \tag{1.3}$$

To ensure valid results, convection currents must be eliminated in the suspending fluid, and the relative rate of motion between the fluid and powder particles must be slow enough to guarantee a laminar flow. The application area of the Stokes law is limited to both large and fine particle sizes. However, these limits may be applied to the sufficiently great particle size range in air, $0.1 - 100\,\mu\text{m}$, by corresponding amendments in Eq. (1.1) [3,5]. As particle size decreases below 0.1 μm, this method becomes unreliable because of the Brownian motion of the particles, but in liquids particle sizes down to 0.1 μm can be determined. The upper limit in air is about 100 μm. Particles of more than 100 μm cause the display of medium inertia forces, which are not taken into account by the Stokes equation. The method is not suitable if particle shape strongly differs from the spherical for powders, which cannot be dispersed, or for agglomerated powders. The suspension must be diluted enough to ensure independent motion to the maximum particle concentration even to 1 vol.% of particles in the suspension. Compositions of dispersion liquids used for sedimentation analysis are given in Table 1.3.

TABLE 1.3 Liquids for Preparation of Suspensions

Powder	Liquid for Suspension	Dispersion Stabilizer
Aluminum	Water with pH value amount 3–4; Cy, Cye, isopropanol, vegetable oil	ST of 0.1 wt.%; Sfa ОП-7 of 0.075 g/L
Boron carbide	WD; butanol/ethanol	SP of 0.5 g/L
Bronze	Cy, Cye	SP of 0.5 g/L
Chrome	WD, butanol, kerosene	SPP of 0.001–0.002 mol/L
Cobalt	EA, *n*-butanol	SP of 0.5 g/L
Copper	WD, ethanol, acetone, Cyl, *n*-butanol, isoamyl, EA, water/glycerin in ratio 1:1	SP of 0.5 g/L
Lead	Cy, Cye, acetone, *n*-butanol	SP of 0.5 g/L
Magnesium	EA, *n*-butanol	SP of 0.5 g/L
Manganese	Cye, isobutanol	SP of 0.5 g/L
Molybdenum	EA, acetone, WD, water/glycerin, water/glycol	Sodium hexametaphosphate of 0.1 g/L
Nickel	Water/glycerin, EA, *n*-butanol/acetone, Cye	Alkyl polysulfonate of 0.1 g/L
Silver	Water/glycerin, EA	…
Tantalum	Cy, Cye	…
Tin	WD, *n*-butanol, isobutanol	Alkyl sulfonate of 0.1 g/L
Titanium	WD, Cye	SSP of 0.5 g/L
Tungsten	WD, water/glycerin, Ethanol, *n*-butanol	Alkyl polysulfonate of 0.1 g/L Sodium hexametaphosphate of 0.1 g/L
Tungsten carbide	Water/glycerin	Sodium polyphosphate
	WD	Alkyl polysulfonate
Zinc	Kerosene, EA, Cy, butanol	…
Zirconium	Isobutanol, methanol	Hydrochloric acid 0.01 g/L

Abbreviations: *Cy*, cyclohexanol; *Cye*, cyclohexanone; *EA*, ethyl alcohol; *NS*, naphtha soap; *SC*, sodium carbonate; *Sfa*, surfactant; *SP*, sodium phosphate (Na_3PO_4); *SPP*, sodium pyrophosphate ($Na_4P_2O_7 \cdot 10H_2O$); *ST*, sodium tartrate; *WD*, water distillate.

Among the number of sedimentation methods available, only a few are usually used for metal powders. Devices based on the method of accumulation of the deposition from the suspension that were popular in the past find an application in the present, too. Turbidimetry methods are widely used to determine the particle size distribution of refractory metal powders, such as tungsten and molybdenum. The micromerographs find a use in determining the particle size of subsieve metal powders.

Accumulation of Sediment

The method of accumulating the deposit from a suspension consists of the calculation of the cumulative weight of the powder settled from the fixed high suspension column h as a function of time. The construction of a curve of distribution function is shown in Fig. 1.9. In the initial period, the increment sediment mass m is a linear function of the time τ.

$$m = k\tau$$

where k is proportion coefficient or corner line coefficient (tangent of corner α_1, see Fig. 1.9).

On completion of the initial period, the increment sediment mass on the sediment pan starts to diminish because all particles of the largest size have by then settled from the suspension. The increment sediment mass on the pan will continue to slow down as the sedimentation of the particles of fixed sizes is completed. The function of sediment accumulation $m = f(\tau)$ in this period is graphically described by a smooth curve asymptotically approaching the straight line, $m_{\max}$, which represents the maximum of mass sediment that can accumulate on the pan. The increment rate of the sediment $dm/d\tau$ constitutes the angle of slope of the tangent to the curve of sediment accumulation at the point corresponding to the time τ.

Because the sediment mass on the pan at the time τ_i (see Fig. 1.9) is depicted by the segment projection on the ordinate line $A\tau_i$ (of the length $0m_i$), the tangent traced to this point of the curve divides this projection into two parts: a segment m_iR_I equal to τ_i $(dm/d\tau)$ that represents the mass of particles for which the settling rate is not higher than h/τ_i, and a segment $0R_I$, that constitutes the mass of particles for which the settling rate is not lower than h/τ_i, and therefore they had completely settled from the suspension in the column h at time τ_i. Accordingly, the ratio of $0R_I$ to $0m_{\max}$ represents the fraction of particles that have completely settled from the suspension.

Fig. 1.10 shows a schematic diagram of a typical device based on the method of accumulation of the sediment from a suspension.

One serious disadvantage of the gravitational sedimentation techniques is the excessively long precipitation time for particles smaller than 5 μm. The centrifuging process can greatly accelerate the rate of settling [1].

Micromerograph

The method of accumulation of the sediment suspended in air powder is used in a micrograph apparatus for particle size distribution analysis. A typical micromerograph contains a sediment chamber in the form of a vertical aluminum tube with an inside diameter of 100 mm and a height of 2.5 m. The pan, located at the bottom of the chamber, receives the sediment

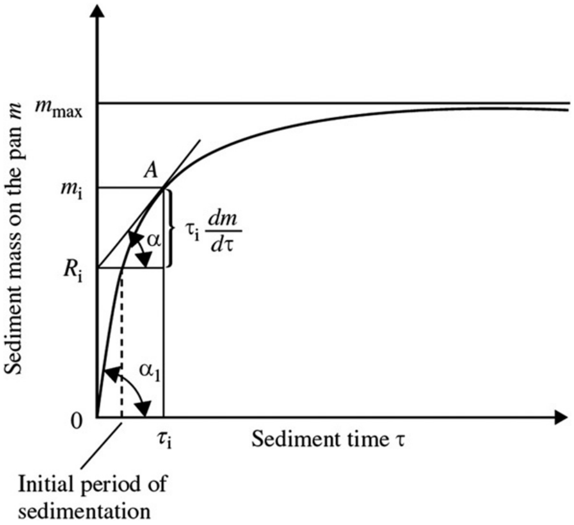
Sediment mass on the pan m
$m_{\max}$
m_i
R_i
A
α
$\tau_i \frac{dm}{d\tau}$
α_1
0
τ_i
Sediment time τ
Initial period of sedimentation

FIG. 1.9 Construction of a curve of distribution function.

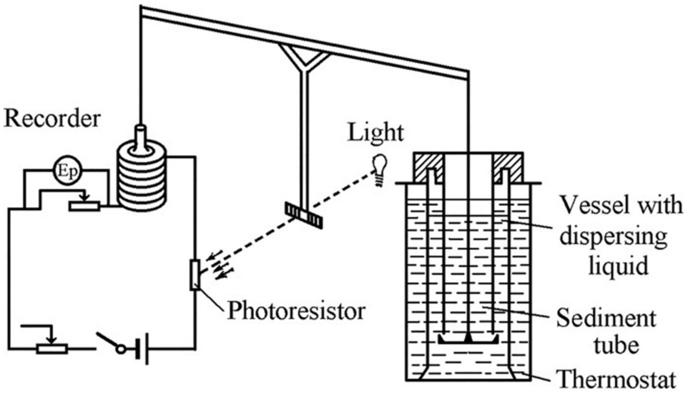
Recorder
Ep
Light
Vessel with dispersing liquid
Photoresistor
Sediment tube
Thermostat

FIG. 1.10 Liquid sedimentograph.

weight. Particle size distribution, being the first derivative of the function of sediment accumulation, is calculated based on the obtained function $m = f(\tau)$ (see Fig. 1.9) and Eq. (1.3). This device allows the determination of particle size distribution in the range of 2–100 μm.

Method of Weight Samples

This method of particle size measurement, known as the pipette method, is based on Stokes law (Eq. 1.1). The pipette method consists of taking consecutive suspension samples of a certain volume from a given depth, h, at time, τ_x. The powder weight in suspension samples is determined after evaporation. Thus, in the pipette method the residual weight of the suspended powder at the fixed time is defined and, on the basis of the function $m = f(\tau)$ and Eq. (1.3), the particle size distribution is calculated. However, in the pipette method, the residual weight of the suspended powder is defined directly in contrast to turbidimetry, where an indirect method for its measurement is used. Fig. 1.11 shows a schematic diagram of typical pipette devices. In practice, for the determination of particle size distribution, the Andreasen's pipette is still used.

Classification in Centrifugal Field

The fluid is usually air or water. The classifiers may be distinguished depending on the stream direction: counterflow equilibrium and cross-flow separation. The classifiers such as elutriators, zig-zag classifiers, and Bahco centrifugal classifiers are related to the counterflow equilibrium devices [2].

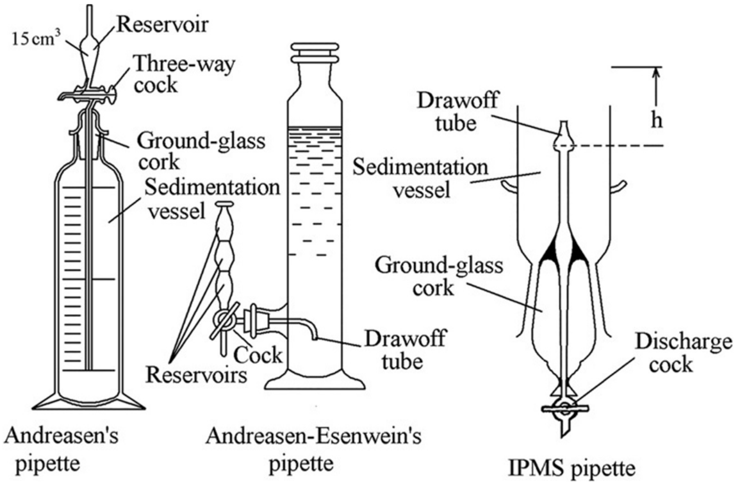
15 cm³
Reservoir
Three-way cock
Ground-glass cork
Sedimentation vessel
Reservoirs
Cock
Drawoff tube
Sedimentation vessel
Drawoff tube
h
Ground-glass cork
Discharge cock
Andreasen's pipette
Andreasen-Esenwein's pipette
IPMS pipette

FIG. 1.11 Pipette devices.

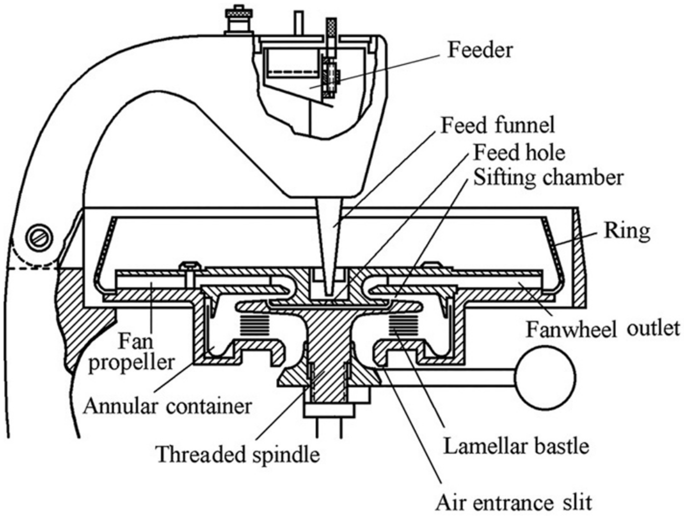
Feeder
Feed funnel
Feed hole
Sifting chamber
Ring
Fanwheel outlet
Fan propeller
Annular container
Threaded spindle
Lamellar bastle
Air entrance slit

FIG. 1.12 Schematic draft of the Bahco classifier.

Bahco Classifier

The Bahco classifier is a counterflow centrifugal classifier (Fig. 1.12). This instrument can be graded in the size range from 5 to 100 μm, but this method yields the most accurate and reliable results in a size range between 1 and 30 μm. For the samples, 5–10 g of powder are required.

A sample of powder dosed from a feed funnel goes through the central orifice and then the annular slot enters the separation chamber, where the powder particles get under the influence of incipient centrifugal force because of the chamber's rotation and the opposite aerodynamic force of air current. Dividing into two size fractions takes place on the border size of particles, for which these forces appear equal. The size fraction with particles finer than the border size is gone by the air current from the separation chamber, and the coarse material is accumulated in the annular container. On the difference between the mass of powder entered into the separator and the settling mass in the annular container, the mass of the fanned fraction is determined. The airflow rate and the dynamic pressure of airflow in the separation chamber are regulated by varying the opening size of the entrance slit, through which air enters the device. The number of consecutive order separations and their conditions are chosen subject to powder properties, required number, and size fraction.

Cyclone Classifier

The cyclone classifier is related to cross-flow separation devices. The overall view of a cyclone classifier contains three sequentially positioned cyclones, as illustrated in Fig. 1.13.

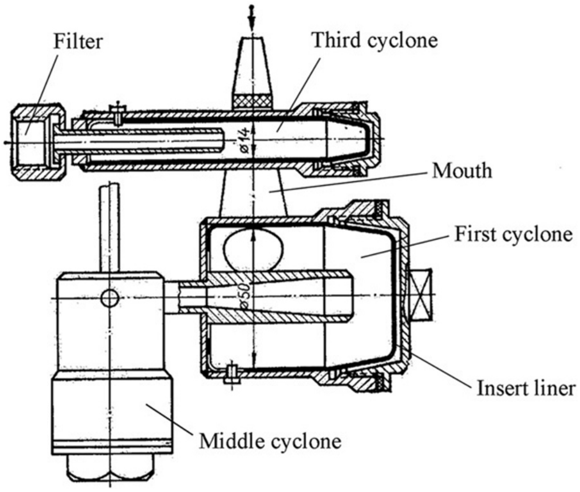
Filter
Third cyclone
ø14
Mouth
First cyclone
ø50
Insert liner
Middle cyclone

FIG. 1.13 Cyclone classifier.

A suspended solid in air is fed into the first, with a maximal diameter cyclone. An insert liner is introduced into every cyclone for comfort of unloading the separated powder fractions. The second cyclone is in the middle diameter. For residual particle collection, after the cyclone with the least diameter, a fine air cleaning filter is foreseen. The analysis results are submitted graphically in a coordinate grid of logarithmic normal distribution and characterized by two parameters: the median diameter, δ_{50}, and the mass percentage of all particles with a diameter less than 2 δ_{50}.

Classification in Inertia Force Field

Precipitation of the suspended particles in the inertia force field occurs in impactors. In this device, the suspended particles are passed through a nozzle and made to interact normally with a plane surface. The resulting particle trajectories can be calculated using the equation of motion of a particle in a flow field. Above a certain size of particle, termed the cut size, particles will strike the surface with the potential for collection. Particles smaller than the cut size will follow the flow of air, not touching the surface. By reducing the nozzle diameter for the identical airflow, the impact velocity increases and the cut size is reduced. Thus, multiple impact stages in cascade impactors allow one instrument to collect the particles of various sizes. By weighing or otherwise estimating (microscopy) the weight of particles on each surface, a size distribution can be measured. The Andersen impactor is typical of these (Fig. 1.14).

Impactors usually suffer from errors in that the particles rebound from the current collection surfaces and are recollected in later stages. To minimize the rebound, the surface must be adhesive. Agglomeration is another source of probable errors. The agglomerates will be collected as if they were large particles. Upon impact, however, they may mechanically disperse into their smaller components on the collection surface. Impactors are generally used for particle sizes in excess of 1 μm with cyclone or sedimentation prestages for sizes greater than 10 μm.

Counting and Sizing of Particles by Indirect Measures

Fisher Subsieve Sizer

The Fisher subsieve sizer (FSSS) is a common industrial method for particle size measurements in the range of 0.2–50 μm. This sizer is a simple, inexpensive device that measures the flow of air through a packed powder bed but does not measure particle size or surface area. From this measurement, average particle size and porosity are determined from a chart that is an integral part of the instrument. Consequently, analysis results cover a Fisher "number" rather than a size. The FSSS is therefore used especially for process control purposes where only relative values are required. Fig. 1.15 shows a schematic of this method.

For conversion of the permeability to a powder surface area, the Kozeny-Carman equation was used, which is usually written in the following way:

$$\frac{\Delta p}{L} = \frac{k S_v^2 (1-\varepsilon)^2 \eta u}{\varepsilon^3} \tag{1.4}$$

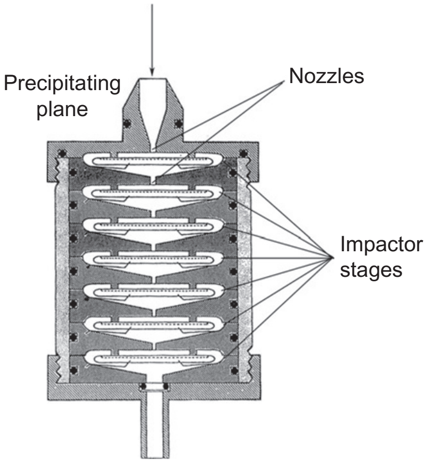

FIG. 1.14 Andersen impactor.

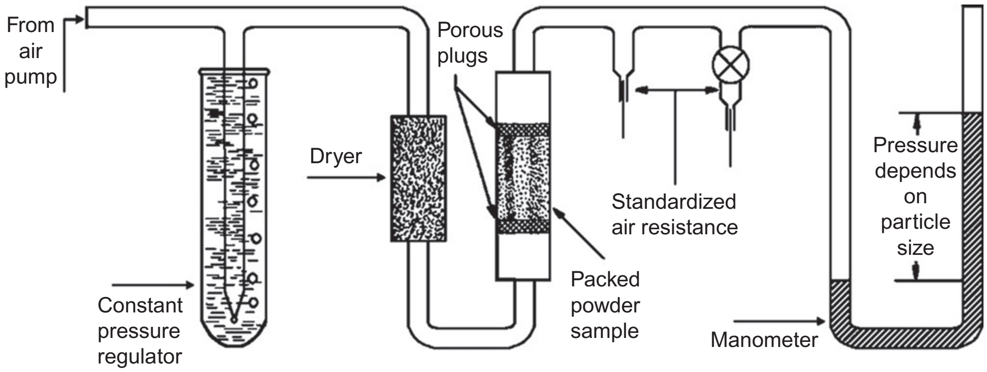
From air pump
Porous plugs
Dryer
Standardized air resistance
Pressure depends on particle size
Packed powder sample
Constant pressure regulator
Manometer

FIG. 1.15 Schematic diagram of Fisher subsieve sized.

where Δp is the pressure drop, Pa; L is the powder bed thickness, m; k equals 5 is the Kozeny constant; S_v is the surface area per unit volume of powder, m^2/m^3; ε is the porosity of the powder bad; η is the viscosity, Pa s; and u is the fluid velocity, m/s.

Conversion of the measured permeability to a specific surface is accomplished by the Kozeny-Carman equation, Eq. (1.4), with transformed symbols:

$$K = \frac{E^3}{(1-E^2)BS_w^2\rho^2} \tag{1.5}$$

and

$$E = \frac{V_{\text{bed}} - V_{\text{powder}}}{V_{\text{bed}}}$$

where K is the permeability of the powder bed; E is porosity of the powder bed; V is the volume, cm^3; ρ is the true, or absolute, density of the powder material, g/cm^3; S_W is the specific surface based on the particle weight, cm^2/g; and B is the constant.

Thus, Eq. 1.5 is a function of the three variables: powder bed thickness, specific surface, and particle density. However, the density on its own account cannot, apparently, influence the permeability, but its role is in a relationship with average surface particle diameter (d_m), also known as the Sauter mean diameter, calculation:

$$d_m = 6/\rho S_w \tag{1.6}$$

Conversion of the equation (Eq. 1.5) subject to the relationship (Eq. 1.6) results in the reduction of the variable number up to real two. Permeability, therefore, depends on the porosity, particle shape, surface morphology, particle size, particle size distribution, and method of powder bed compaction. Comparison of results from the FSSS with those from other specific surface and size distribution techniques may show no agreement and should not be performed. If particles are packed differently and exhibit the same porosity but with different pore structure, this relationship may not be derived while two powders of the same chemical composition with different particle size distribution may be given the same Fisher subsieve numbers.

When particle shape, size, and distribution are essentially the same and do not vary significantly from one production batch to another, the Fisher subsieve analysis provides adequate comparisons for the quality control process. The main limitations include constant sample packing and instrument calibration.

The same principle of air permeability by flow through a packed bed of powder is used in the Subsieve Auto Sizer. This instrument performs an automated conversion of the pressure drop into a mean particle size with electronic recordings of particle size measurement limits of 0.2–75 µm and porosity limits of 0.3–0.9.

ASTM B 330 Standard and TSO 10070 contains calibration and operating instructions for Fisher subsieve analysis. Standard ASTM C 721, "Average Particle Size of Alumina and Silica Powders by Air Permeability," also contains guidelines. These guidelines are on the FSSS instruction manual [6].

Turbidimetry

The turbidimeter is standardized in ASTM B 430. Fig. 1.16 shows a schematic diagram of a typical light turbidimeter. A sample of powder dispersed in a liquid is filled into a glass cell. A collimated beam of light passes through the cell

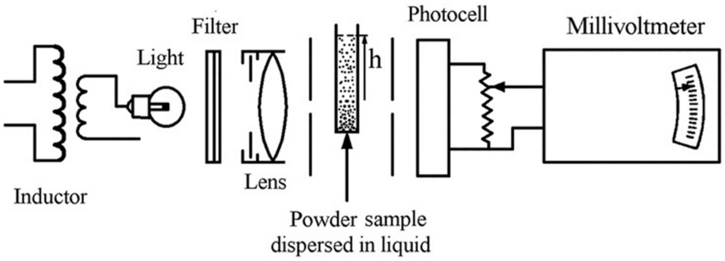

FIG. 1.16 Schematic diagram of light turbidimeter.

at a level of a certain height of the vertical suspension column, h. The intensity of the light beam is determined by the current generated in a photocell and is measured by a recording millivoltmeter. The determination of the particle size distribution is based on the effect of attenuation of the light beam intensity proportionally to the projected area of the suspended particles, and consequently proportional to the square of the particle diameter. As the suspension settles, the projected area of the particles in the suspension decreases, and the intensity of the light beam increases.

The information obtained consists of the residual weight of the suspended powder. Accordingly, the sediment accumulation after a given time, τ_x, allows the calculation of the particle size distribution on the basis of the function $m = f(\tau)$ (see Fig. 1.9 and Eq. 1.3). The particle sizes are presented here by their projected diameters (diameter of a circle equivalent to a particle projected area).

When X-rays are used to determine particle size distribution of a particle suspension, the attenuation of the X-ray beam intensity is proportional to the mass of the powder particles in contrast to their projected area in white light.

Light Scattering

Light-scattering measurements are based on the Mie theory [7]. Fig. 1.17 represents schematically the principle of laser light scattering. Light-scattering intensity obtained from the Mie theory is described by the following equation:

$$K(\theta, m, D) = \frac{\lambda^2}{8\pi^2 R^2}[i(\theta m) + i(\theta, m, D)] \tag{1.7}$$

where $\pi D/\lambda$ is the size parameter, D is the particle diameter, λ is the incident light wavelength, R is the radial distance, $m = \mu_1/\mu_2$ is the refractive index of the particle, and μ_2 is the refractive index of the dispersing medium. The parameters λ and R are defined by the design of the instrument and are constant. Refractive indices (μ_1 and μ_2) in many cases are found in standard reference literature. In rare cases of newly developed materials or mixed dispersed systems, these values can be determined experimentally.

The light-scattering method is capable of providing particle size analysis in a broad range of particle sizes in a rapid fashion; it is also easy. These instruments are sensitive to determining subtle differences in size distributions that are not reflected in a change of the median size of distribution. These subtle changes can be correlated to a change of the process variations. Therefore, this is an important characteristic of the generated data and can be used in process control.

A typical recent device for laser light-scattering measurement consists of a light source, particle dispersion and delivery systems, a detector to measure the light-scattering specimen, and a computer to control the system and to define the particle size distribution. Previous versions of laser particle analyzers were only capable of measuring the scattering pattern at small angles, lower than 20 degrees, and were limited to measuring particles coarser than 1.0 μm. Modern instruments collect scattering data at larger angles. This allows accurate measuring of particles of 2.0 μm down to 0.02 μm. Particles in a parallel laser beam deflect the light at a fixed angle that depends on the particle diameter. A lens focuses the scattered light in a ring on the sensor that is mounted in the focal plane of the lens, whereas undiffracted light converges at the focal point on the optical axis. A certain scattering angle is allocated to each individual particle size. The energy distribution measured in the sensor elements that are arranged radially and symmetrically is evaluated, and the particle size distribution is calculated.

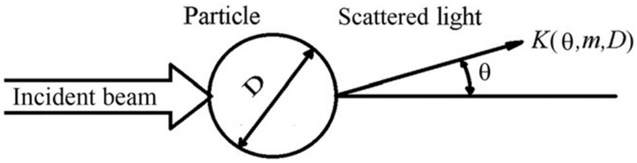

FIG. 1.17 Laser scattering principle.

The major difficulty in accurate, reproducible particle size measuring is the dispersion. In previous instruments, the analyzer usually did not envisage this need. It was accepted that the dispersion would be performed external to the instrument particle analyzers. This, however, did not provide the stable dispersion and was not handy. Recent instruments, such as the laser particle sizer "Analysette 22" (produced by Fritsch), are supplied with liquid and dry dispersing units. These two techniques give comparable results. For the liquid process, a mixture of liquids for suspension preparation is selected for sedimentation analyses, depending on the powder material composition (see Table 1.3). Usually, an ultrasonic bath is used for the dispersion. The amount of sample required is approximately 0.2–1.0 g. The dispersing unit for dry samples processes the agglomerates by means of mechanical forces. A vibratory feeder meters the amount of sample supplied.

The popular tendency has been to incorporate a centrifugal pumping system. This type of pump provides sufficient power to pump particles even 2.0 mm in size around the system in a uniform condition. In this system, the ultrasonic probe is placed directly into the stream of the flowing liquid. The rapid flow rate and its position immediately in front of the cell where the laser beam is focused make it possible to analyze even strongly agglomerating samples. These accessories have extended the range of samples that these instruments can analyze. Similar systems are incorporated into all newer devices.

There is also another tendency consisting of total removal of the pumping module from the system. This option is suitable only for smaller particles; larger particles tend to become sediment below the laser beam. This approach is useful for analyzing particles in obnoxious fluids. It minimizes the use of the solvent and simplifies moving the sample.

The popularity in the last decades of laser light scattering as a method of particle size analysis has led to the development of new capabilities. The analysis has been automated and the reproducibility and repeatability have been improved. Currently, several companies are producing such advanced apparatuses. The Bluewave analyzer of Microtrac GmbH (Krefeld, Germany) provides particle size analysis for a diverse range of applications by utilizing the Mie theory for spherical particles and the modified Mie calculations for nonspherical particles. The measurement capability range is from 0.01 to 2000 μm. Similar devices are produced by Angstrom Advanced Inc. (Stoughton, MA, USA), HORIBA Scientific (Kyoto, Japan), Malvern Instruments (Malvern, UK), etc.

Unified Scatter Technique

This instrument is an advanced light-scattering technique. The apparatus known as the TRI-LASER system (Microtrac Sizer) is equipped with a three-laser arrangement. It produces scattered light through an angular range from very close to 0 degrees up to 160 degrees. The established geometrical configuration of detectors renders it possible to convert scattered light flux into signals that are directly proportional to particle volume. These signals can be easily converted into a volume (mass) particle size distribution using a high-resolution iterative deconvolution algorithm. Detailed information about the above technique is contained in an article of Freud et al., called, "Unified scatter technique for full-range particle size measurement," provided by Microtrac, Inc., September 2008.

Coulter Counter

The Coulter principle was discovered by W. Coulter in 1940, though US Patent 2,656,508 was not awarded until October 20, 1953. This method patented for blood cell counting has found widespread use in various branches of techniques. The Coulter principle is used for particles in liquids only.

The Coulter principle consists of passing the suspended particles once through the orifice in the electric field of known characteristics; in the issue the momentary changes in impedance give rise to voltage pulses, the heights of which are proportional to volume (consequently, to volume diameter) of the particle traversing the orifice. These pulses are amplified, sized, counted, and expressed as a size distribution. Size ranges from 0.4 to 1600 μm are typical. While the Coulter principle can be implemented in a variety of designs, there are two that have become the most commercially relevant. These include an *aperture format* and a *flow cell format*.

The aperture format is used in most commercial Coulter counters. In this setup, an orifice of defined size is created in a jewel disk using special manufacturing processes. The resulting aperture is then embedded in the wall of a glass tube. Fig. 1.18 shows the aperture format principle. Particles are dispersed in an electrolyte and the glass tube with an orifice of known sizes is inserted into the suspension vessel. By placing an electrode both inside and outside the tube and initiating the flow of an electrical current through the orifice, an electric field of known characteristics becomes a sensing zone. At the start of the experiment, the electric field is turned on and the pump begins to draw the suspension through the aperture. The resulting data are derived, as described above.

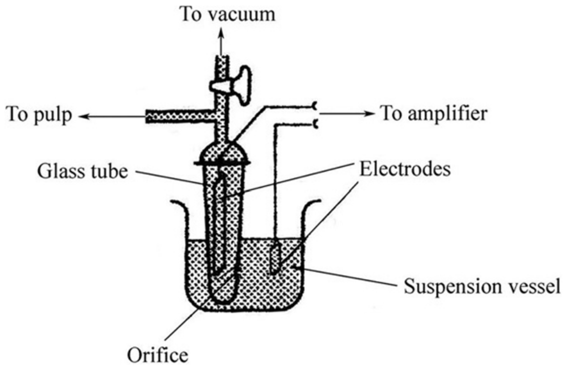

FIG. 1.18 Coulter counter aperture format principle.

Several apertures/tubes have to be used to achieve defined size range detection. This is because each orifice can sense particles from 2% to 60% of the orifice diameter. The advantage of the Coulter principle is that it can be used to measure both mass and particle counting distribution of particle size, and in addition as a volume diameter is one typical size representation, this agrees closely with most sedimentation analysis.

In the *Flow Cell Format,* electrodes are embedded at either end of a flow channel and the electric field is applied through the channel. This format has several advantages as opposed to the aperture format. This arrangement allows for continuous sample analysis whereas the aperture format is a single-batch format. Further, the use of a flow cell lends itself to the addition of a sheath flow, which keeps particles centered in the middle of the flow channel. This allows measurements to be performed simultaneously, such as probing the object with a laser. The major disadvantages of the flow cell format are that it is much more expensive to manufacture and is typically fixed to one channel width, whereas the aperture format offers a wide variety of aperture sizes.

Regularities of Granulometric Composition

The percentage of fractions obtained as a result of analyzing the granulometric composition is conveniently presented in the form of a step-like graph (histogram). Particle sizes are plotted (at a uniform or nonuniform scale) as abscissas and relative fraction contents, that is, percentages of each fraction, as ordinates.

In practice, the ranges of separate fractions are usually taken to be nonequal without a strict adherence to this condition. As a consequence, while constructing the histograms of weight distribution throughout particle sizes, the relative contents of fractions plotted on the ordinate are counted by dividing the weight percentage of each fraction by its range (difference in the limiting sizes in the fraction). The histogram gives a vivid presentation of powder disperse composition, and the correctness of the presentation increases with narrowing the range limits. In Fig. 1.19 the influence of the sizes of fraction range on the form of histograms is seen.

In constructing the diagrams, it should be borne in mind that the ranges of separate fractions are usually taken to be nonequal. This is caused by technical conditions of analyzing as well as by the fact that, for a complete powder characteristic, the range of fractions should be increased with a particle size increase. Indeed, the surface area of a particle of 1 μm in diameter is four times lower than the surface area of a particle of 2 μm in diameter, whereas for particles of 10 and 11 μm in diameter, the difference in their surface areas is only 20%, and for particles of 100 and 101 μm in diameter, it is as small as 2%. As powder properties significantly depend on their surface area, in the ranges coarser than 10 μm, a difference of 1–2 μm has a very small effect on particle properties and the separation into such small ranges is in this case nonexpedient. Therefore, an increase of fraction ranges in geometrical series with the growth of particle size seems to be justified. In the case of technological processes with high requirements regarding the purity of the environment, the particle concentration (number basis) as a measurable parameter is usually used.

In practice, the ranges of separate fractions are usually taken to be nonequal without a strict adherence to this condition. Therefore, while constructing the histograms of weight distribution throughout particle sizes, the relative contents of fractions plotted on the ordinate are counted by dividing the weight percentage of each fraction by its range (difference in the limiting sizes in the fraction). The histogram gives a vivid presentation of powder disperse composition and the correctness of the presentation increases with narrowing the range limits.

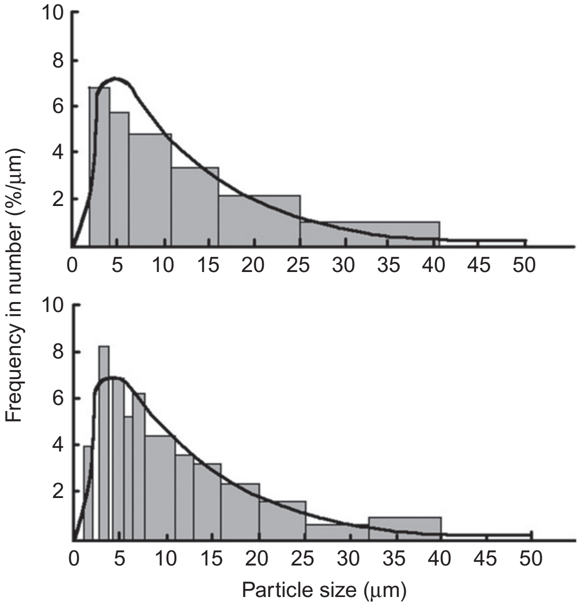

FIG. 1.19 Histograms and size frequency curves of the two identical powder specimens by different particle size ranges.

There are known theoretical and empirical formulas expressing distribution functions [3,8]. Among the formulas stated below, lognormal distribution is proved theoretically while the Rosin-Rammler distribution is deduced on the basis of use of mathematical statistics to milling products.

Normal Distribution

The normal, or Gaussian, distribution is defined as

$$\frac{dD}{d\delta}=\frac{1}{\sigma\sqrt{2\pi}}\exp\left(-\frac{\left(\delta-\overline{\delta}\right)^2}{2\sigma^2}\right) \tag{1.8}$$

where D is the undersize, percent; δ is the current particle diameter; and $\overline{\delta}$ is the mean diameter defined by

$$\overline{\delta}=\int_{-\infty}^{\infty}\delta dD$$

and σ is the standard deviation expressing the dispersion of the distribution,

$$\sigma^2=\int_{-\infty}^{\infty}\left(\delta-\overline{\delta}\right)^2 dD$$

Eq. (1.8) represents a bell-shaped curve centered at $\delta=\overline{\delta}$. In the practical measurement of particle sizes, $\overline{\delta}$ and σ can be calculated as

$$\overline{\delta}=\frac{\sum n_i\sigma_i}{N}$$

$$\sigma=\left(\frac{\sum n_i\left(\delta_i-\overline{\delta}\right)}{N}\right)^{1/2}$$

where n_i is the number of particles having diameter δ_i and N is the total particle number. $\overline{\delta}$ also coincides to the number median diameter at $D=0.5$.

Lognormal Distribution

The lognormal distribution is accomplished if in normal Gaussian distribution the argument as real value of particle diameter to substitute by its logarithm. The validity of the lognormal distribution law when the solid materials are exposed to a long-term mechanical comminution is theoretically proved by Kolmokhorov [3]. Applicability of this law for many kinds of powders and dust is corroborated by series experimental investigations [3,9].

The lognormal distribution function by submitting $\ln\delta_{50}$ and $\ln\sigma$, respectively, for $\overline{\delta}$ and σ in Eq. (1.8) takes the form:

$$\frac{dD}{d(\ln\delta)} = \frac{1}{\sqrt{2\pi}\,\ln\sigma}\exp\left(-\frac{(\ln\delta - \ln\delta_{50})}{2\ln^2\sigma}\right).$$

This distribution function can be converted to the following cumulative mass basis distribution:

$$D = \frac{100}{\sqrt{2\pi}\,\ln\sigma}\int_{-\infty}^{\ln\delta}\exp\left[-\frac{(\ln\delta - \ln\delta_{50})^2}{2\delta^2}\right]d\ln\delta \tag{1.9}$$

where δ_{50} is the median mass diameter and $\ln\delta$ is the standard deviation of log diameters from their mean magnitude.

The integral contained in Eq. (1.9) cannot be expressed via elementary functions. Therefore, it is transformed to a function of new argument t:

$$t = (\ln\delta - \ln\delta_{50})\ln\sigma. \tag{1.10}$$

Argument t is called as a normally normalized distributed magnitude. Its middle magnitude is nought. The cumulative mass basis distribution function (Eq. 1.9) is given by the above substitute as follows:

$$D(\delta) = F(t) = \left(\frac{\ln\delta - \ln\delta_{50}}{\ln\delta}\right) = \frac{100}{\sqrt{2\pi}}\int_{-\infty}^{\ln\delta}\exp\left[-\frac{t^2}{2}\right]dt,$$

called normalized function of normal distribution with limits of variation from 0% to 100%.

It is convenient to represent the lognormal distribution graphically on the lognormal probabilistic coordinate grid, that is, in such a rectangular coordinate system where the logarithm diameters are plotted on an abscissa axis (while δ real values are written down), and t magnitudes are plotted on an ordinate axis (while the values of $F(t)$ function are written down). The t magnitudes that answer to the given function $F(t)$ values are found from tables in the mathematical reference books. A lognormal distribution graph drawn on that coordinate grid will appear by straight line so far as will be expressed the dependence t on $\ln\delta$, which according to Eq. (1.10) is linear (Fig. 1.20), while a density distribution of particle size represents a bell-shaped curve centered at $\delta = \delta_{50}$ (Fig. 1.21). These graphs are constructed by the size analysis data (Table 1.4).

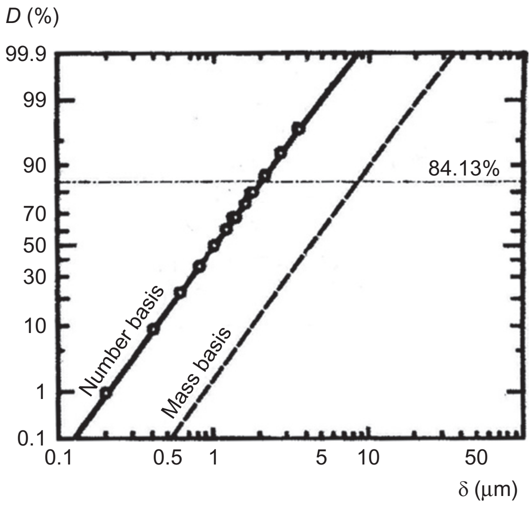

FIG. 1.20 Cumulative distribution of particle size in lognormal probabilistic coordinate grid constructed by data in Table 1.4.

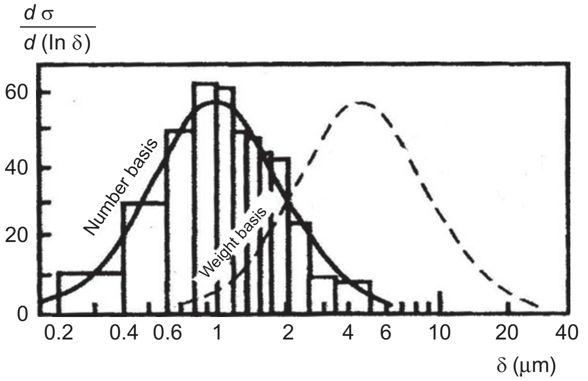

FIG. 1.21 Density distribution of particle size in log scale.

TABLE 1.4 Example of Particle Size Distribution Data

Size Interval (µm)	Number Measured (ΔN)	Size Range ($\Delta\delta$, µm)	Mean of Size Interval ($\delta_{a.m}$)	$\frac{100\Delta N}{N}$ (%)	Cumulative Distribution (%)
0 – 0.2	10	0.2	0.1	5	1
0.2 – 0.4	80	0.2	0.3	40	9
0.4 – 0.6	132	0.2	9.5	66	22.2
0.6 – 0.8	142	0.2	0.7	71	36.4
0.8 – 1.0	138	0.2	0.9	69	50.2
1.0 – 1.2	112	0.2	1.1	56	61.4
1.2 – 1.4	75	0.2	1.3	37.5	68.9
1.4 – 1.6	65	0.2	1.5	32.5	75.4
1.6 – 1.8	52	0.2	1.7	26	80.6
1.8 – 2.1	65	0.3	1.95	21.7	87.1
2.1 – 2.7	62	0.6	2.4	10.3	93.3
2.7 – 3.6	32	0.9	3.15	3.6	96.5
3.6 – 5.1	35	1.5	4.35	2.3	100

Note: $\sum \Delta N = N = 1000$.
From Kousaka Y., Endo Y. Particle size. In: Powder technology handbook. 2nd ed. Marcel Dekker, Inc.; 1997.

The conversion from mass ($\delta_{50(M)}$) to number median diameter ($\delta_{50(N)}$) is made [3] by the following equation if the distribution obeys the lognormal form:

$$\ln\left(\delta_{50(N)}\right) = \ln\left(\delta_{50(M)}\right) - 3(\ln\sigma)^2$$

Therefore, the particle number distribution function is represented by a straight shift with respect to particle mass distribution upward on a line space equal to $3\ln\sigma$ and to the left on a line space equal to $3\ln^2\sigma$ (Fig. 1.20).

The angular coefficient of the above straight line is equal to:

$$tg\alpha = \frac{1}{\ln\sigma} \tag{1.11}$$

where α is the angle between the straight line and the positive direction of the abscissa axis.

The more polydisperse powder, the larger the dispersion and standard deviation line of its distribution curve, and therefore the less angle α (Eq. 1.11). The nearer to vertical a distribution line in the lognormal probabilistic coordinate grid, the more narrow the distribution, that is, the more homogeneous under particle sizes is a powder under investigation.

Rosin-Rammler Distribution

The authors, Rosin and Rammler, in consideration of the size distribution of products of a milling as a statistical population, found that the cumulative distribution curves by sieve analysis data can be expressed by the equation

$$D(\delta) = 100[1 - \exp(-b\delta^a)] \tag{1.12}$$

where b and a are constant

From Eq. (1.12), it is followed that the mass density distribution by particle sizes $f(\delta)$ is described by the formula

$$\varphi(\delta) = 100a\delta^{\mathrm{a}-1}\exp(-b\delta^a) \tag{1.13}$$

Bennet [3] suggested to intake in the Rosin-Rammler formula a new parameter δ_e in expression $b = \frac{1}{\delta_\mathrm{e}^\mathrm{a}}$. Then Eq. 1.12 takes on the form:

$$D(\delta) = 100\exp\left(1 - \left(\frac{\delta}{\delta_\mathrm{e}}\right)^a\right) \tag{1.14}$$

Accordingly

$$R(\delta) = 100\exp\left(-\left(\frac{\delta}{\delta_\mathrm{e}}\right)^a\right) \tag{1.15}$$

where R is the remains.

By $\delta = \delta_\mathrm{e}$

$$R = 100\mathrm{e}^{-1} \approx 36.8\%$$

$$D = 100\left(1 - \mathrm{e}^{-1}\right) \approx 63.2\%.$$

Thus, the δ_e by its physical meaning corresponds to such a diameter by which a mass of particles greater than δ_e amounts to 36.8% and less 63.2%.

Index a in Eqs. (1.12), (1.14), and (1.15) characterizes the breadth of a distribution, that is, the degree of uniformity of a powder according to particle sizes: the larger the a, the narrower the particle size range.

For practical application of the Rosin-Rammler formula, the exponential equation (Eq. 1.14) is twice found in the logarithm:

$$\lg\left(\lg\frac{100}{R}\right) = a\lg\delta + C$$

where $C = \lg(\lg e) - a\ \lg\delta_\mathrm{e}$

This equation circumscribes a straight line in $\lg\left(\lg\frac{100}{R}\right)$, $\lg\delta$, that is, in the log-log grid.

TECHNIQUES OF CHEMICAL ANALYSIS FOR POWDERS

Chemical analysis of powders is carried out for quantitative and qualitative information. This is a complicated process with difficulties that can arise in the selection of the appropriate instrument and the correct interpretation of the results. The chart in Fig. 1.22 can be used for the selection of the appropriate analytical technique.

Atomic absorption spectroscopy (AAS), atomic emission spectrometry (AES), and inductively coupled plasma optical emission spectroscopy (ICP-OES) are widely employed for the chemical analysis of metal powders. AAS can detect the element content in parts per billion (ppb), but analyzes one element at a time. ICP-OES has a lower resolution, typically of 0.2–0.5 wt.% for dissolved elements; however, the analysis ensures quantitative data for 20 or more elements simultaneously.

X-ray fluorescence allows the same broad element determination as ICP-OES; however, the material can be analyzed in a bulk solid condition. For trace analyses, this method has a lower resolution limit of approximately 100 ppm. The scanning electron microscopy (SEM) equipped with an energy-dispersive spectroscopy (EDS) system can ensure a qualitative analysis of a metal particle. The microprobe analysis is regarded as a microchemical analysis because of the small sample volume used to obtain the data.

Auger electron spectroscopy (AES), ion-scattering spectroscopy, and X-ray photoelectron spectroscopy (XPS) can be used for surface analysis. The last is also known as electron spectroscopy for chemical analysis. Higher sensitivities are

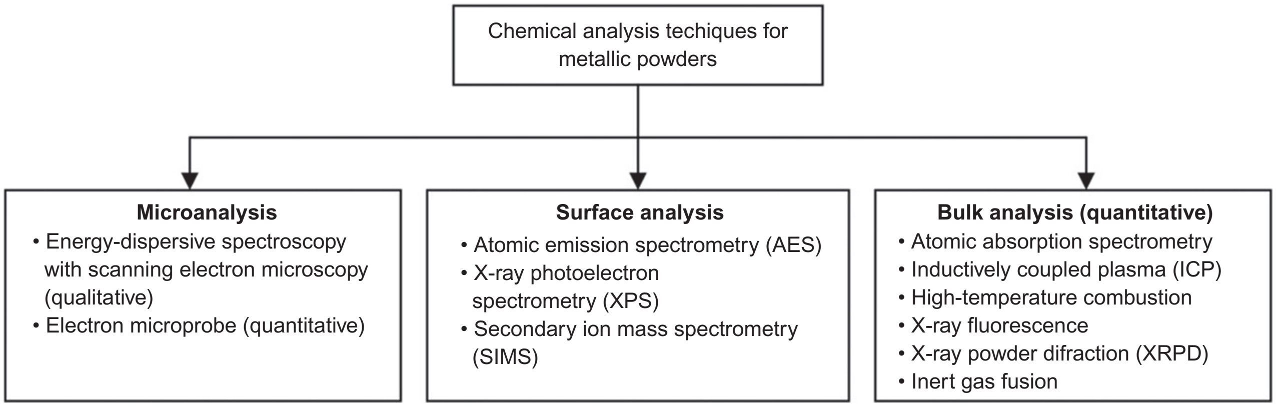
Chemical analysis techiques for metallic powders
Microanalysis
• Energy-dispersive spectroscopy with scanning electron microscopy (qualitative)
• Electron microprobe (quantitative)
Surface analysis
• Atomic emission spectrometry (AES)
• X-ray photoelectron spectrometry (XPS)
• Secondary ion mass spectrometry (SIMS)
Bulk analysis (quantitative)
• Atomic absorption spectrometry
• Inductively coupled plasma (ICP)
• High-temperature combustion
• X-ray fluorescence
• X-ray powder difraction (XRPD)
• Inert gas fusion

FIG. 1.22 Basic chemical analysis techniques for metallic powders.

achievable by the use of the secondary ion mass spectrometry (SIMS). Microanalysis is also done with some SIMS techniques that can be used to measure composition and trace impurity levels as a function of depth, ensuring a detection limit in the ppb to ppm range for many elements.

X-ray diffraction analysis is one of the few methods that is available for a quantitative determination of the amount of phases existing in a powder sample. It should be remembered that the sensitivity of the X-ray diffraction technique in revealing the phase strongly depends on the phase chemical composition and lattice type and is, in general, of about 3–5 vol.%. X-ray diffractometers are widely used for this purpose, though the photographic technique can have better sensitivity. The sensitivity can be strongly increased by using synchrotron radiation.

To obtain specific information for a particular phase in the powder (size and shape of phase particles, crystallographic orientation, etc.) as well as to detect phases existing in a small amount, the transmission electron microscopy should be employed. Thin foils of about 0.2 μm in thickness are obtained from individual particles by microtome technique, most often with a fine diamond cutter [10]. In general, some defects are introduced into the foil in the cutting process, but for phase analysis it is quite allowable.

Microanalysis Methods

Microanalysis combines location-specific structural and composition analysis in one operation. Thus, microanalysis provides information concerning specimen composition on a microscopic scale; therefore, microanalysis processes relate to both chemical analysis and microscopy. Microanalysis usually involves the use of a scanning electron microscope to perform chemical analysis of micron-sized areas of a surface. The scanning electron microscope in this role is termed an electron probe microanalyzer.

Several techniques, including AES, secondary ion mass spectroscopy (SIMS), XPS (also known as electron spectroscopy for chemical analysis), and ion-scattering spectroscopy, are used for elemental analysis of a surface. Higher sensitivity is achievable by using SIMS, whose instruments also perform chemical analysis. Surface analysis has various applications in problem solving related to both particle powders and powder compacts, including powder consolidation, oxidation, adhesion, corrosion, wear, lubrication, catalysis, and fracture conditions in which consequent properties are determined by the composition at the surface of the fracture.

Scanning Electron Microscopy

Due to the small scale of metal powders, surface analysis is connected with a difficult problem. Therefore, microfocused electron beam techniques are the only solution for this. As an apparatus for surface analysis, the primary applications of the scanning electron microscope are to provide high-resolution and depth-of-field images of the specimen, and chemical analysis of the micron-sized area. Actually, modern SEM provides the imaging of surface features to 10–100,000 ×, and resolution of features down to 3–100 nm, depending on the sample. The microscope, equipped with a backscattered detector, allows the observation of grain boundaries on unetched surfaces, the evaluation of the crystallographic orientations of grains down to 2–10 μm in size, and imaging of the second phases on unetched surfaces when the second phase has a different average atomic number. This allows the evaluation of individual grains, precipitated phases, and dendrites while also identifying the chemistry of features down to micron sizes on the particle surface and the evaluation of chemical

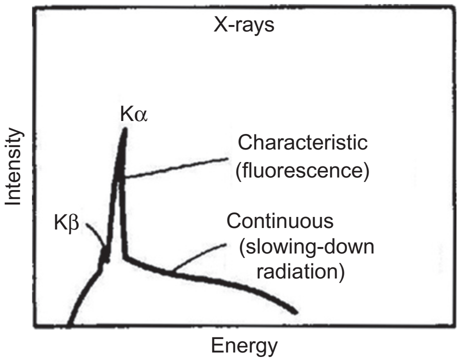

FIG. 1.23 The energy distribution of emitted X-ray signals generated by the electron beam.

composition gradients on the surface over distances approaching 1 μm. In addition to the secondary electron detector (including the detection of backscattered electrons), most scanning electron microscopes are equipped with an X-ray detector.

For optimum choice and use of electron beam instruments, it is necessary to understand at least general notions on the nature of the signal generation by the electron beam interaction with a specimen surface. Electrons and X-rays are emitted from the solid surface by an electron beam impacting with it. The emitted characteristic X-ray is shown in Fig. 1.23. Electromagnetic radiation, known as cathodoluminescence, of lower energies than X-rays, which is not shown in Fig. 1.23, is also emitted. Basically, three types of electrons are generated by the electron beam: secondary, Auger, and backscattered (Fig. 1.24). Elastically scattered electrons arise with substantially the same energy as the beam energy. Inelastically scattered electrons arise with a spectrum of energies lower than the beam energy. Plasmon and interband transition scattered electrons are scattered by interactions that produce a plasmon oscillation of the electrons in the sample material or a transition of sample electrons between different energy levels. Comparison of Fig. 1.24A and B shows that the energies of the secondary and Auger electrons are invariable, but the energy values of backscattered electrons are shifted as the original beam energy is changed.

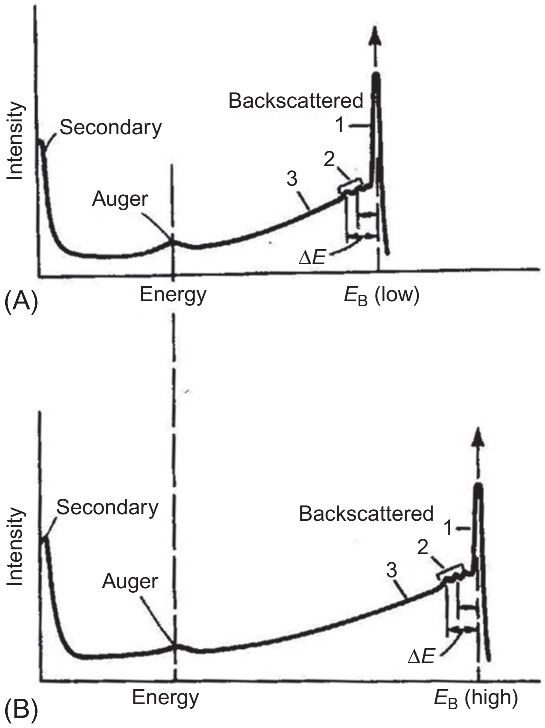

FIG. 1.24 The energy distribution of emitted electrons at (A) low beam energy (around 1 keV) and (B) at higher beam energy (around 5 keV): 1——Elastically scattered; 2——Plasmon and interband transition scattered; and 3——Inelastically scattered.

Samples for analysis can be solid or liquid with a low vapor pressure greater than 0.13 Pa (∼10^{-3} torr). Sample size is limited by the scanning electron microscope available. Usually, samples of 15–20 cm size can be placed in a microscope, but areas on samples that can be examined without repositioning are limited to approximately 4–8 cm. Sample preparation by standard metallographic polishing and etching techniques is acceptable for electrically conducting materials. Nonconducting materials are usually coated with a thin layer of carbon, gold, or gold alloy. Samples should be electrically grounded to the holder. Powder samples are sprayed on an electrically conducting film, such as a silver paint that has been thoroughly dried. Samples should be free from high vapor pressure liquids, such as water, organic cleaning solutions, and remnant oil-base films.

Electron Probe X-Ray Microanalysis

This technique is based on the measurement of characteristic X-rays emitted from a microscopic part of a specimen bombarded by a beam of accelerated electrons. These apparatuses are often termed electron microprobes. Commercial electron microprobes were available before the scanning electron microscope. Recent EPMA models, which provide structural resolution nearly equivalent to the less conventional scanning electron microscope, are usually better in their function as an electron microanalyzer and include an optical system that enables imaging of the sample in situ at approximately 400 ×. They are, however, generally more expensive than a scanning electron microscope equipped with an equivalent X-ray analyzer.

The energy of the electron beam to keep the reactive volume within one or a few micrometers is typically between 10 and 20 keV. X-ray spectra can be obtained for all elements except hydrogen. The EPMA feature is the possibility of local analysis of a small region on the specimen surface limited by the electron beam of less than 1 μm in diameter. The sensitivity of EPMA is moderate, being in most cases much poorer than that of secondary ion mass spectrometry. Two types of X-ray spectrometers are used for EPMA measurements: the energy-dispersive spectrometer (EDS) and the modification wavelength-dispersive spectrometer (WDS).

Energy-Dispersive Spectrometry

Energy-dispersive X-ray spectroscopy, sometimes called energy-dispersive X-ray analysis or energy-dispersive X-ray microanalysis, is based on the measurement of the energy of characteristic X-ray emissions of excited specimens under study. To stimulate the emission, a high-energy beam of charged particles such as electrons or protons, or a beam of X-rays, is focused into the observable specimen. At rest, an atom within the sample contains a ground state (or unexcited electrons) in discrete energy levels or electron shells bound to the nucleus. The incident beam may excite an electron in an inner shell, ejecting it from the shell, while creating an electron hole that is filled by an electron from a higher-energy shell. The difference in energy between the higher-energy shell and the lower-energy shell may be released in the form of an X-ray. The number and energy of the X-rays emitted from a specimen can be measured by an energy-dispersive spectrometer that allows us to define the elemental composition of the specimen.

The EDS apparatus includes four primary components: the excitative source (electron beam or X-ray beam), the X-ray detector, the pulse processor, and the analyzer. An excitative electron beam is used in electron microscopes, scanning electron microscopes, and scanning transmission electron microscopes. The X-ray beam excitation is used in X-ray fluorescence spectrometers. A detector is used to convert X-ray energy into voltage signals; this information is sent to a pulse processor, which measures the signals and passes them onto an analyzer for data display and analysis. The most common detector now is the Si(Li) detector cooled to cryogenic temperatures with liquid nitrogen; however, newer systems are often equipped with silicon drift detectors with Peltier cooling systems.

Wavelength-Dispersive X-Ray Spectroscopy

Wevelength-dispersive X-ray spectroscopy (WDS) differs from EDS in the change of charge carriers in the detection device. In WDS, only one element can be analyzed at a time while EDS gathers a spectrum of all elements, within limits, of a sample. Sensitivity is 100 ppm (0.01 wt.%) with X-ray measurement by wavelength-dispersive spectrometry; 1000 ppm is typical with X-ray measurement by energy-dispersive spectrometry. Poorer sensitivity occurs for light elements in a heavy matrix. The number and energy of the X-rays emitted from a specimen can be measured by an energy-dispersive spectrometer. As the energy of the X-rays is characteristic of the difference in energy between the two shells, and of the atomic structure of the element from which they were emitted, this makes it possible to define the elemental composition of the specimen. Additional information about the WDS detector is contained in "X-Ray Fluorescence Spectrometry" section.

Table 1.5 contains an overview of the scanning electron beam instruments. The scanning transmission electron microscope and the scanning Auger microscope regarding top surface analysis are compared. The scanning transmission

TABLE 1.5 Comparison of Scanning Electron Beam Instruments

Instrument	Features Testing	Minimum Areas		Annotations
		Surface Pictures	Microchemical Analysis	
Scanning electron microscope	Surface picture above ~500 × on polished and etched samples; at all magnifications on high depth-of-field surfaces; accuracy and sensitivity of microchemical analysis	4 – 5 nm (conventional scanning electron microscope) 2 – 3 nm (in-lens)	1 – 3 μm (EDS and/or WDS)	Can be equipped by a WDS X-ray detector for maximized sensitivity and light-element analysis. WDS: elements with $Z > 4$. EDS: elements with $Z > 10$
Scanning transmission electron microscope	Small area of microanalysis of thin films; small area diffraction	2 – 3 mm (SEM mode, in-lens)	5 – 30 nm (EDS)	Samples must be thinned; generically functions as a transmission electron microscope; allows chemical analysis of particles characterized by transmission electron microscope observation
Scanning Auger microscope	Chemical analysis of surface monolayers made by in situ fracturing, and low-Z elements on surfaces cleaned by in situ ion etching	~100 nm (Auger) 10 nm (SEM mode)	~100 nm (Auger) 1 – 3 μm (EDS)	Requires ultra high vacuum and careful sample surface preparation
Electron microprobe	Surface pictures above 400 ×; quantitative analysis particles with diameter not less than approximately 1–2 μm; detection limits ~100 ppm, and at a lateral spatial resolution of approximately 1 μm	Elemental compositional mapping of same millimeters areas	~1 μm, depending on electron beam diameter	Qualitative and quantitative elemental analysis of elements with $Z \geq 11$; qualitative analysis for light metals from $Z = 5$ to $Z = 10$; sensitivity by WDS is 100 ppm, 1000 ppm by EDS; generally more expensive than an SEM equipped with equivalent X-ray analyzers

microscope enables direct probing through the sample while with the scanning Auger microscope, the surface films are probed by ion spattering. In general, these instruments are multifunctional.

To correctly interpret the physical meaning of the various signals used in scanning electron beam instruments, it is important to know the region below the surface from which the signals arise (Table 1.6). For instance, it is not possible to quantitatively analyze the particles with diameters less than ~1 μm using the electron probe microanalyzer while these particles show themselves to be bulky on the scanning electron microscope screen. It is important to realize that the X-ray sample size and shape vary with the electron beam voltage and the sample atomic number.

Surface Analysis

Several techniques, including AES, secondary ion mass spectroscopy (SIMS), XPS (also known as electron spectroscopy for chemical analysis), and ion-scattering spectroscopy, are used for elemental analysis of the surface. Higher sensitivity is achievable by using SIMS. Microanalysis is also performed with some SIMS instrumentation. Surface analysis has various applications in solving problems related to oxidation, adhesion, corrosion, wear, lubrication, catalysis, and fracture of both powder particles and powder compacts, in which resultant properties are determined by the composition at the surface of the solid.

Auger Electron Spectroscopy

The Auger effect was discovered independently by both Lise Meitner and Pierre Auger in the 1920s. The discovery was primarily reported by Meitner in the journal *Zeitschrift für Physik* in 1922. Since 1953, AES has become a practical and

TABLE 1.6 Comparison of Signals Used in Scanning Electron Beam Instruments

Signal Type	Type Variety	Energy	Source	Use
X-ray	Characteristic (fluorescent)	Discrete values; different for each element: Cu $K\alpha = \sim 8000\,\text{eV}$; Si $K\alpha = \sim 1800\,\text{eV}$	Interband transitions: $L \rightarrow K = K\alpha$, $M \rightarrow K = K\beta$; $K\alpha$: lose K electron, $L \rightarrow K$, photon ejects	Chemical analysis from micron areas in SEM, STEM, and SAM
Electron	Auger	Discrete values; different for each element; range: $100-1500\,\text{eV}$; Si $LMM = \sim 100\,\text{eV}$; Cu $LMM = \sim 900\,\text{eV}$	Interband transitions; LMM: lose L electron, $M \rightarrow L$, M electron ejects	Monolayer surface analysis in SAM
	Backscattered (elastic)	Essentially same as beam energy	Beam electron scattered back after elastic collision	Atomic number contrast, channeling contrast, channeling patterns, and magnetic contrast in SEM
	Backscattered (inelastic)	Energies less than beam energy	Beam electron scattered back after inelastic collision	Atomic number contrast, channeling contrast, channeling patterns, and magnetic contrast in SEM
	Backscattered (plasmon and interband transition interactions)	$1-1000\,\text{eV}$ less than beam energy	Beam electron scattered back after collision producing plasmon oscillations or interband transition	Surface analysis in SAM; light-elements analysis in STEM
	Secondary	$\sim 5\,\text{eV}$	Loosely bound electron scattered from surface	Main signal for image formation in SEM

SAM, scanning Auger microscopy; *SEM*, scanning electron microscopy; *STEM*, scanning transmission electron microscopy.

straightforward characterization technique for probing chemical and compositional surface environments. It has found applications in metallurgy, gas-phase chemistry, and throughout the microelectronics industry.

The Auger effect is an electron transition process resulting from the inter- and intrastate transitions of electrons in an excited atom when electrons, ions, photons, or neutral atoms interacts with an atom with an energy exceeding that necessary to remove an inner-shell electron (K, L, M) from the atom. The interaction process leaves the atom in an excited state with a core hole that is a missing inner-shell electron. These excited atoms are unstable and the vacancy is filled immediately by an electron from a higher energy level. The energy thus disengaged is either emitted as a photon (X-ray fluorescence) or transferred to another outer-shell electron, which is emitted (called the Auger electron) if the energy is quite enough (called the Auger transition).

In AES, the powder sample to be analyzed is bombarded with electrons. When an incident electron strikes a K-core-level electron with sufficient energy to free it, the atom is left in a singly ionized state with a core-level electron vacancy. If the atom is near the surface, both the incident electron and the core-level electron are emitted from the sample as backscattered electrons, with energies below approximately 25 eV. The single ionized atom undergoes an electron rearrangement to achieve a more stable energy configuration, where an outer-shell electron fills the core-level vacancy and the Auger electron is emitted from the sample. These stroke events occur up to 3 nm in depth under the surface, which allows the compositional analysis of the surface for all elements except hydrogen and helium because the energy of the Auger electrons is different for each element. Auger analysis has some advantages for the analysis of light elements because the probability for Auger emission exceeds that for X-ray emission as the atomic number decreases.

AES instrumentation typically includes an electron gun for primary electron excitation of the sample, an electron spectrometer for energy analysis of secondary electrons, a secondary electron detector for secondary electron imaging, an ion gun for sputter removal of atoms from the sample surface, and a stage for sample manipulation.

Detection sensitivity for most elements is from 0.1 to 1.0 at.%. The accuracy of quantitative analysis is limited to ±30% of the element present when calculated using published elemental sensitivity factors. Better quantification (±10%) is possible by using standards that closely resemble the sample. Samples can be solid materials with relatively low vapor pressures at room temperature, less than 10^{-8} torr. Higher vapor pressure materials can be handled by sample cooling or by applying a thin film onto a conductive substrate. Uneven and rough surface of powders make the correct conversion of peak heights into atomic concentrations unachievable. Sample size can be individual powder particles as small as 1 μm in diameter. The maximum sample size depends on the specific device.

X-Ray Photoelectron Spectroscopy

XPS is a quantitative spectroscopic technique that analyzes the average surface chemistry of a sample up to a depth of approximately 5 nm. This technique quantitatively measures the elemental composition, atomic concentrations, and chemical states of elements present at a sample surface. XPS can detect all elements with an atomic number greater than 3, therefore hydrogen and helium. XPS uses X-rays to remove an electron from a core level to the Fermi (1s) level. Knowing the photon energy and measuring the kinetic energy with the electron spectrometer enable the direct determination of the binding energy of electrons, which is individual and can be used to identify concrete elements.

A typical XPS apparatus contains an ion gun as the X-ray source, an electron energy analyzer, an electron multiplier, a pulse-counting detector, and a computer system. An ultrahigh vacuum system up to 10^{-10} torr is required for measurements. For good resolution during profiling, the ion beam must be defocused over a surface area of approximately 10 mm^2 (0.15 in.^{2}) because photoelectrons are collected from a surface area of several square millimeters during analysis.

XRS surface sensitivity is comparable to other surface analysis methods, but analysis time is slow. The requirement for ultrahigh vacuum conditions necessitates long-continued vacuum pumpdown before analysis. Sequential qualitative analysis is performed in 5–10 min; quantitative analysis requires 1 h to several hours, depending on the information necessary.

Secondary Ion Mass Spectrometry

The principle of SIMS consists of ion bombardment directed at the sample surface in a high or ultrahigh vacuum environment. The transfer of momentum from the impinging primary ions to the sample surface affects the sputtering of surface atoms and molecules. Some of the sputtering corpuscles are ejected with positive or negative charges, which are termed secondary ions. The secondary ions are then mass analyzed using a double-focusing mass spectrometer or an energy-filtered quadrupole mass spectrometer. This method allows getting a variety of information about the surface, subsurface, or bulk composition of the sample. If the rate of sputtering is high, the intensity of peaks in the mass spectrum can be continuously recorded to provide an in-depth concentration profile of the near-surface region. At very high sputtering rates, trace element or impurity analysis in the bulk is possible.

Fig. 1.25 illustrates an example of SIMS together with an XPS analysis of element depth distribution on particle surfaces. An O_2^+ primary beam was used to record positive secondary ions while both O_2^+ and C^+ primary beams were used for

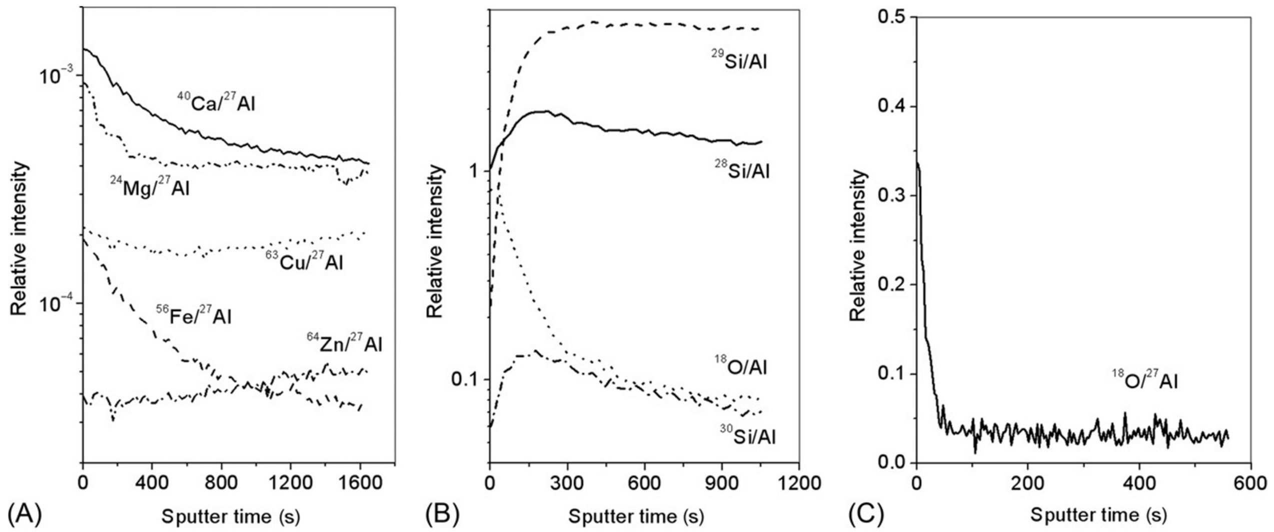

FIG. 1.25 Typical depth profiles for: (A) Mg, Ca, Cu, Zn, and Fe ions normalized to Al (primary O_2^+ and secondary positive ions), (B) Si and ^{18}O ions normalized to Al (primary Cs^+ and secondary negative ions), and (C) $^{18}O/^{27}Al$ (primary O_2^+ and secondary negative ions).

analysis of negative secondary ions. The powder surface was scanned ranging from $35 \times 35\,\mu m^2$ to $50 \times 50\,\mu m^2$ with focused oxygen or cesium ion beams over an area. The spot size of the primary ion beam was approximately 3 μm. A mass resolution of $m/\Delta m = 300$ was used for all measurements.

Typical profiles of some elements are shown in Fig. 1.25. Only Mg exhibits a pronounced enrichment of subsurface layers. Both Zn and Cu are distributed more or less homogeneously with some deviations from an ideal plane profile. Main metallic impurities, Fe and Ca, are typically enriched in the subsurface, as is seen from Fig. 1.25A. The average thickness of the surface oxide film as well as the widths of the observed Mg, Fe, and Ca segregation zones are estimated on the basis of the available depth profiles and respective ion sputter rate data. These thicknesses are taken to be proportional to the sputtering times required for a 50% drop in the element profiles [10,11]. The average thickness of the surface oxide usually varies from 4 to 10 nm. The widths of Mg, Ca, and Fe enrichment layers range between 30 and 70 nm.

Typically, a secondary ion mass spectrometer consists of the primary ion gun generating the primary ion beam; a primary ion column, accelerating and focusing the beam onto the sample; a high vacuum sample chamber holding the sample and the secondary ion extraction lens; a mass analyzer separating the ions according to their mass to charge; and a ratio ion detection unit. A high vacuum with pressures below 10^{-4} Pa (roughly 10^{-6} torr) is needed to ensure that secondary ions do not collide with background gases on their way to the detector. It also prevents surface contamination by adsorption of background gas particles during measurement.

Three basic types of ion guns are employed. In one, ions of gaseous elements are usually generated with duoplasmatrons or by electron ionization, for instance noble gases ($^{40}Ar^+$, Xe^+), oxygen ($^{16}O^-$, $^{16}O_2^+$, $^{16}O_2^-$), or even ionized molecules such as SF_5^+ (generated from SF_6) or C_{60}^+ (fullerene). This type of ion gun is easy to operate and generates roughly focused but high current ion beams. A second source type, the surface ionization source, generates $^{133}Cs^+$ primary ions. Depending on the gun design, fine focus or high current can be obtained. A third source type, the liquid metal ion gun (LMIG), operates with metals or metallic alloys, which are liquid at room temperature or slightly above. The LMIG provides a tightly focused ion beam (<50 nm) with moderate intensity and is additionally able to generate short-pulsed ion beams. It is therefore commonly used in static SIMS devices. The choice of the ion species and ion gun, respectively, depends on the required current (pulsed or continuous), the required beam dimensions of the primary ion beam, and the sample that is to be analyzed. Oxygen primary ions are often used to investigate electropositive elements due to an increase of the generation probability of positive secondary ions while cesium primary ions often are used when electronegative elements are being investigated. For short-pulsed ion beams in static SIMS, LMIGs are most often deployed for analysis; they can be combined with either an oxygen gun or a cesium gun during elemental depth profiling, or with a C_{60}^+ or gas cluster ion source during molecular depth profiling.

Depending on the SIMS type, there are three basic analyzers available: sector, quadrupole, and time-of-flight. A sector field mass spectrometer uses a combination of an electrostatic analyzer and a magnetic analyzer to separate the secondary ions by their mass-to-charge ratio. A quadrupole mass analyzer separates the masses by resonant electric fields, which allow only the selected masses to pass through. The time-of-flight mass analyzer separates the ions in a field-free drift path according to their velocity. It is the only analyzer type able to detect all generated secondary ions simultaneously, and is the standard analyzer for static SIMS instruments.

A comparison summary of surface analytical techniques is given in Table 1.7, based on data published in *Material Characterization,* Volume 10, *ASM Handbook.* The Auger electrons are collected from sample depths of 0.5–3 nm below the surface, depending on their energy. The Auger electron energies are relatively subambient, therefore only those electrons near the sample surface can free themselves without additional energy consumption. The inelastic backscattered electrons arise from a volume approximately one-half the depth of the scattered electron range.

Bulk Analysis

Many methods are available to determine the chemical composition of powders. A brief description of methods used in powder analysis is presented below.

X-Ray Powder Diffraction

This technique allows making various investigations, including qualitative and quantitative phase identification and analysis, determination of crystallinity, lattice-parameter determinations, high-temperature studies, thin film characterization, analysis of crystal structure, determination of crystallite size, and the mean lattice microstrains. Owing to the relatively high sensitivity and rapidity of XRPD analysis, all these characteristics can be determined sufficiently rapidly.

TABLE 1.7 Comparison Summary of Surface Analytical Techniques

Parameters	Auger Electron Spectroscopy	X-Ray Photoelectron Spectroscopy	Secondary Ion Mass Spectroscopy	Ion-Scattering Spectroscopy
Fundamentals	Emission of Auger electrons by electron transition effect	Emission of photoelectrons by core-level excitation	Sputtering of surface atoms by ion beam	Elastic ion backscattering
Sensor	~1–30 keV electrons	X-ray, photons	~1–3 keV ions	~0.5–3 keV ions
Signal	Derivative of electron emission energy	Electron current vs electron binding energy	Ion current vs mass	Ion current vs energy
Elements detected	All except H and He	All except H	All	All except H and He
Sensitivity, in general	Variable	Variable	Variable	High
Sensitivity, low atomic number	High	High	High	Low
Spectral shift due to chemical bonding	Yes	Yes	No	Generally no
Molecular information	Moderately effective	Yes	Usually no	Not effective
Quantitative analysis	Yes	Yes	No	Yes
Observable materials	Excellent for metals, damaging to polymers	Good for metals and polymers	Good for metals and polymers	Good for metals and polymers
Analysis, depth from the surface	<2 nm	~1–3 nm	Monolayer	Monolayer
Depth-profiling analysis vs sputtering	Simultaneous or sequential	Usually sequential	Usually sequential	Usually sequential

The physical basis of XRPD analysis is diffraction as a result of X-rays passing through a three-dimensional crystalline lattice of the material. Origination of X-ray diffraction occurs according to the Wulf-Bragg's law. The angular position, θ, of the diffracted X-ray beam depends on the spacing, d, between planes of atoms in a crystalline phase and on the X-ray wavelength, λ:

$$2d\sin\theta = n\lambda.$$

While the θ angle is changed, the conditions of Wulf-Bragg's law are alternately satisfied for the various plane systems in a polycrystalline material. This causes the appearance of the diffraction peaks (X-ray lines) on the X-ray pattern. Each of these diffraction peaks is characterized by a specific interplanar spacing d and intensity I.

Phase identification using XRPD is based on the unique pattern produced by every phase. Pointed peaks are obtained from crystalline and quasicrystalline phases, and a nonlinear pattern (halo) results from the amorphous phase. A diffraction pattern is usually recorded using film, analog, or digital methods. In such conditions, the final data can be displayed as a graph or intensity as a function of diffraction angle 2θ. Many modern automated powder diffractometers are capable of providing further data processing, including peak finding, a tabular listing of peak intensity compared to interplanar spacing, and other computer utilities.

Qualitative identification can be accomplished by pattern-recognition methods that include established manual techniques and the newer methods that use computers. All these methods make use of the database maintained by the JCPDS International Centre for Diffraction Data (Joint Committee on Powder Diffraction Methods, International Centre for Diffraction Data, Swarthmore, PA).

The quantitative determination of crystalline or quasicrystalline phase concentration using XRPD is based on an analysis of the intensity and shape of the X-ray lines. The total content of amorphous phases is determined according to the intensity of the nonlinear pattern (halo).

For the determination of the phase amount in the sample in the case of known phases, graphs constructed based on X-ray patterns of standard mixtures as well as the Rietveld method can be used. Quantitative XRPD phase analysis is used to adjust the data obtained by other methods.

Another solved task using XRPD is the determination of independently diffracting region sizes that coherently diffract the X-ray beam. These small crystalline regions are termed crystallites. For some powders, the crystallite size is the same as the size of the whole powder particles.

Generally, an XRPD characterization of a substance consists of placing a powder sample in a collimated monochromatic X-ray beam. In XRPD analysis, samples are usually a fine powder fraction (ordinarily less than 50 μm in size). However, X-ray lines became fuzzy with powder particle sizes less than 100 nm. Therefore, the size limitation is important because most applications of powder diffractions calculate using X-ray signals from a statistical sample of crystallites.

Consolidated specimens, such as PM articles, will appropriately have crystallites small enough to be useful for diffraction analysis, although they can appear to have considerably larger particle sizes. This occurs because the particles in a specimen can comprise one or more independently diffracting regions that coherently diffract the X-ray beam.

XRPD techniques require some specimen preparation. This can involve crushing the specimen to fit into a glass capillary tube, rolling it into a very thin rod shape for the Debye-Scherrer camera, spreading it as a thin layer on a specimen holder, etc.

Inert Gas Fusion

This method is used to determine the quantitative content of oxygen, nitrogen, and hydrogen in materials. Gases introduced into the material are quantitatively determined using inert gas fusion. Inert gas fusion reverses the physical and chemical bonding between the gases and metals to dissociate the gases and sweep them from the fusion area with an inert carrier gas. Because the gas/metal bonds are formed over a wide temperature range, bonds can be broken only by heating the sample above the highest temperature at which the gas/metal bonding occurred. The required powder sample mass is usually 2 g or less, depending on the material type and the expected amount of gases present. Special precautions are required for metals with low boiling points. Materials with stabile nitrides or oxides require the addition of fluxes. The method is destructive of the material.

X-Ray Fluorescence Spectrometry

X-ray fluorescence spectroscopy (XRF) is based on the excitation of atoms of the material under study by an X-ray beam, resulting in the secondary fluorescent emission. X-ray fluorescence intensity directly depends on the concentration of every element in the specimens. Spectra analysis allows determining the specimen's elemental composition.

Information about the source and energy of the fluorescent signal is contained in Table 1.6. The X-ray tube with Rh-anode is a widespread device in this technique field. However, in certain cases, other materials may be preferable (e.g., Mo, Cr, Au, etc.). Generally, XRF is used to determine the concentrations of elements from beryllium ($Z=4$) to uranium ($Z=92$) in the range from ppm fractions to 100% with accuracy of 10^{-7}–10^{-6} g. Usually, the sample weight is 0.1 g.

Two types of X-ray spectrometers—the energy-dispersive spectrometer (EDS) and its modification wavelength-dispersive spectrometer (WDS)—are used by XRF analysis for decomposition of the fluorescent radiation in the spectra. These spectrometers are equipped with the scanning electron beam instruments (Table 1.6) and EPMA apparatus. Additional information about these detectors is contained above, in "Electron Probe X-Ray Microanalysis" section.

In WDS spectrometers, the selection of the different wavelengths corresponding to the investigated elements is used for the spectrum decomposition. For this purpose, the crystal monochromators (analyzers) with the crystal planes parallel to the surface and with the interlayer distance d are used. When the radiation with wavelength λ is directed on the crystal at the angle θ, the diffraction occurs only if the distances passed by the photons reflected from the adjacent crystal planes differ on an integer number n of wavelength λ. With the change of the angle θ by rotation of the crystal relative to the radiation current, the diffraction will be occur sequentially for different wavelengths, according to Wulf-Bragg's law:

$$2d\sin\theta = n\lambda$$

The angular position (θ) of the crystal is determined depending on the wavelength, which is necessary to separate from the spectrum to analyze the desired element.

Single crystals such as germanium (Ge111) and lithium fluoride (LiF200/220/440) are ideal analyzers (crystal monochromators) for the radiation of many elements. Multilayer synthetic coatings are used to increase the sensitivity by analysis of the light elements.

In WDS, for relatively long wavelengths (light elements), the gas-filled proportional detectors (flowing or sealed) are used. Their effect is based on the gas ionization by radiation and the measurement of electrical impulses passed through the ionized gas. For shorter wavelengths (heavy elements), the scintillation detectors are used. Their operations are based on the registration by photo-detector the light flashes arising when X-rays are collided with scintillator (NaI/Tl) and measurement of electrical impulses formed by a photomultiplier.

In sequential action WDS (with a *scanning channel*), the measurements are carried out by successive selection of each of the characteristic X-ray lines of any number of elements by means of the mobile crystal monochromator and precision goniometer. In simultaneous action WDS (with *fixed channels*), the intensity of the characteristic radiation of elements is measured simultaneously by using multiple turned *fixed channels* located around the sample. In fact, each channel is a separate spectrometer with a crystal monochromator and a detector turned to accept a certain wavelength of one element.

In EDS the whole energy range of secondary (characteristic) radiation from the specimen is registered simultaneously. The resulting spectrum corresponds to a dependence of the intensity on the element's radiation energy. This is achieved by the element-wise decomposition of the energy current of characteristic X-ray emissions from the excited specimen.

In EDS spectrometers, the semiconductor solid-state detectors (Si or Ge) based on the inner ionization of the semiconductor are used. During the analysis by the Peltier effect or by liquid nitrogen, the cooling of the detector is mandatory. Voltage up to several kV is applied to the semiconductor crystal, and it provides the gathering of all the charges formed in the detector's inner volume. The electric pulse arises, and it is further amplified and recorded by the counting electronics.

The spectrum processing by the mathematical processing programs enables providing the quantitative and qualitative (semiquantitative) analysis. In modern XRF spectrometers, the amplifiers and pulse analyzers allow us to accomplish the elemental composition measurement of a specimen in less than 2 s with satisfactory statistical error.

Inductively Coupled Plasma Atomic Emission Spectroscopy

The ICP-AES is an analytical technique based on the principles of atomic spectroscopy for the determination of more than 70 elements with detection limits in the parts per billion to parts per million range. In theory, the technique allows us to analyze all elements except argon. The samples can be introduced as liquids, solids, or gases. In practice, favorable analytical results are obtained for approximately 70 elements, with detection limits usually reaching the ppb level; most samples are introduced in liquid form as aqueous solutions. The inductive coupled plasma is the excitation source for atomic emission spectroscopy. Argon plasma operates at atmospheric pressure and is kept by inductive coupling to a radio frequency so that the standard frequency of operation is of 27.17 MHz or, less commonly, 40.68 MHz (the frequencies permitted by the Federal Communications Commission for scientific and medical instrumentation). The resulting plasma is a highly ionized gas with temperatures of about 10,000 K. The ICP provides the capability of simultaneous multielement analysis for as many as 60 elements in 1–2 min. The precision and accuracy are of the order of 1%.

Atomic Adsorption Spectrometry

AAS is commonly used for the analysis of relatively low concentrations of approximately 70 metallic elements in solution samples.

Three types of AAS exist (Fig. 1.26) [12]. Several features are common to all three techniques:

- Flame atomic emission spectrometry (AES) (Fig. 1.26A), where hot flame gases, to produce the desired signal, must thermally excite a significant fraction of the free atoms produced by dissociation in the atomizer from the ground-state level to one or more electronically excited states. AES usually necessitates scanning the monochromator completely over the analytical spectral line to obtain the background signal values necessary for the calculation of a correct response.
- Flame atomic absorption spectrometry (Fig. 1.26B), where the radiation from a lamp emitting a discrete wavelength of light that has an energy corresponding to the difference in energies between the ground state and an excited state of the analyzed element is passed through the atomizer. Free analyzed atoms within the atomizer absorb source-lamp light at wavelengths within their absorption profiles. In contrast to AES, the ground-state (not excited state) atomic population is observed. The source light not absorbed in the atomizer passes through the monochromator to the light detector and the data reduction/display system of the spectrometer outputs an absorbance response directly proportional to the concentration of the analyzed atoms in the sample solution.
- Flame atomic fluorescence spectrometry (AFS) (Fig. 1.26C) is an emission method based on an external light beam to excite analyte atoms radiatively. The absorption of light from the light source composes a higher count of excited-state atoms in the atomizer than that predicted by the Boltzmann equation at that temperature. Therefore, the absolute sizes of

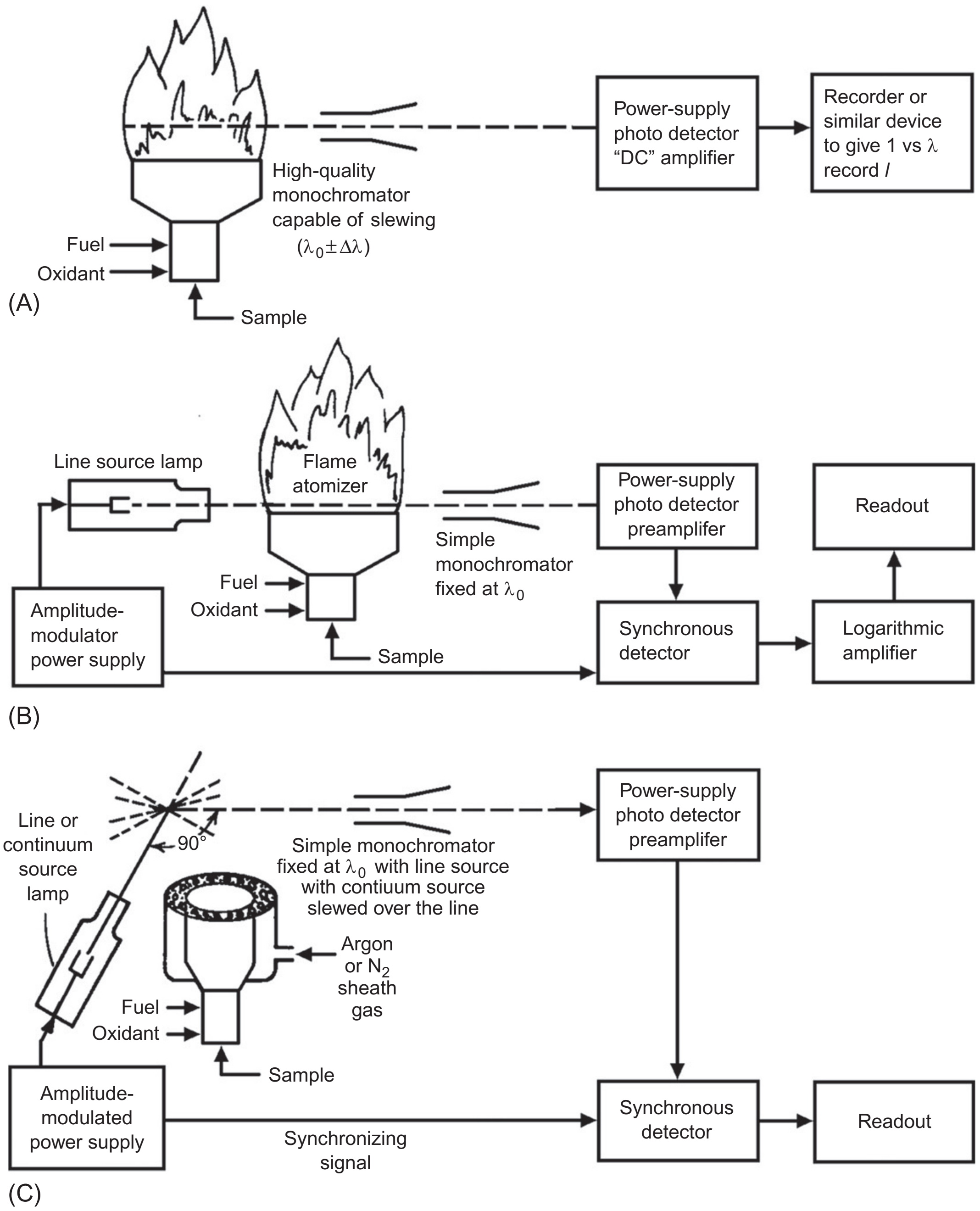
Power-supply photo detector "DC" amplifier
Recorder or similar device to give 1 vs λ record *I*
High-quality monochromator capable of slewing ($\lambda_0 \pm \Delta\lambda$)
Fuel
Oxidant
(A)
Sample
Line source lamp
Flame atomizer
Power-supply photo detector preamplifer
Readout
Simple monochromator fixed at λ_0
Fuel
Oxidant
Amplitude-modulator power supply
Sample
Synchronous detector
Logarithmic amplifier
(B)
Line or continuum source lamp
90°
Power-supply photo detector preamplifer
Simple monochromator fixed at λ_0 with line source with contiuum source slewed over the line
Argon or N_2 sheath gas
Fuel
Oxidant
Sample
Amplitude-modulated power supply
Synchronizing signal
Synchronous detector
Readout
(C)

FIG. 1.26 Comparison of (A) flame atomic emission spectrometry (AES), (B) flame atomic absorption spectrometry (AAS), and (C) flame atomic fluorescence spectrometry (AFS).

the atomic emission signals detected are larger than those seen in AES analysis performed with the same concentration of analyzed atoms within the atomizer. AFS has two major sources of error. The first is chemical scavenging or deexcitation (termed quenching) of the nonequilibrium excited-state analyzed atom population before a useful light signal can be emitted. The second source of error is a scatter of the exacting radiation by particulate matter within the atomizer. For example, some refractory metals, such as zirconium and uranium, if present in high concentration in the sample, have a tendency to be incompletely dissociated or gasified in conventional atomizers.

The sensitivity of AAS is characterized by the magnitude of the atomic absorbance signal expected when a 1 ppm solution of the element is continuously aspirated into a flame atomizer or introduced as a discrete 25 μL aliquot into a graphite furnace. On the whole, the AAS method has been one of the most widely used techniques of trace element analysis.

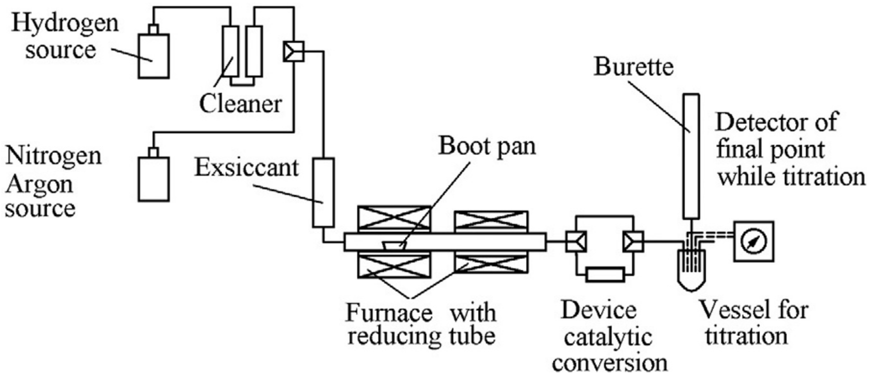
Hydrogen source
Cleaner
Nitrogen Argon source
Exsiccant
Boot pan
Burette
Detector of final point while titration
Furnace with reducing tube
Device catalytic conversion
Vessel for titration

FIG. 1.27 Flowchart of apparatus for oxygen content determination.

The capabilities of the contiguous techniques can be summarized as follows:

- Optical microscopy: provides superior image quality on relatively flat samples at less than 300–400 ×.
- X-ray diffraction: provides bulk crystallographic information.
- SEM: minimum area for surface pictures of 4–5 nm (conventional scanning microscope), and for microchemical analysis of 1–3 μm (energy-dispersive spectrometry and/or wavelength-dispersive spectrometry).
- Scanning transmission electron microscopy: minimum area for surface pictures of 2–3 nm (SEM mode, in-lens), and for microchemical analysis of 5–30 nm (energy-dispersive spectrometry).
- Auger electron microscopy: minimum area for surface pictures of ≈100 nm (Auger), and of 10 nm (SEM mode), and for microchemical analysis of ≈100 nm (Auger), of 1–3 μm (energy-dispersive spectrometry).
- Transmission electron microscopy: provides information from within the volume of material such as dislocation images, small angle boundary distribution, and vacancy clusters. The conventional resolution is of about 1–2 nm. A superior resolution requires very thin samples.

Determination of Oxygen Content by Reduction Methods

The methods for the determination of oxygen content by reduction in hydrogen are laid down in ISO Standard 4491. They include determination of loss of mass on hydrogen reduction (ISO 4491-2:1997), determination of reducible oxygen (ISO 4491-3:1997), and determination of total oxygen by reduction-extraction (ISO 4491-4:19889). Analogous standards function are in the RUS GOST 29006-91, GOST 27417-87, and GOST 18897-73 (see Appendix A).

Standard ISO 4491-3:1997 establishes the technique for the determination of the oxygen content reduced by hydrogen in metallic powders that contain from 0.05 to 3 wt.% of oxygen. This technique is applicable to powders of elemental metals and alloys. It cannot be used for powders containing a binder but can be extended over powders containing carbon by using a special catalytic device.

The principle of the process is in reducing a powder sample in the stream of pure dry hydrogen at a given temperature. The water formed by reduction is absorbed by methanol and titrated by Karl Fisher's reagent. In the case of analyzing powders containing carbon, a conversion of carbon monoxide and dioxide in methane with a nickel catalyst is carried out.

The reduction is performed in an apparatus equipped with a reducing tube with a closed end, or in an apparatus with a running reducing tube with an open end (Fig. 1.27). A weighed powder sample is from 1 to 5 g, depending on the oxygen content. The temperature and the optimum duration of the reduction are determined for each type of powder. Thus, the temperature for reducing oxides in nickel and cobalt powders is 900 ± 20 K with a duration of 20 min, and for molybdenum and tungsten oxides, it is 1100 ± 20 K.

SURFACE AREA AND POROSITY OF POWDERS

The surface area in a quadratic degree strongly depends on the powder particle size and not so strongly on the morphology and open porosity. At the same time, all these characteristics are significant factors for understanding and controlling product properties and processing behavior.

Various techniques can be used to determine these characteristics. However, the results of various test methods can differ owing to their inherent features. Mainly, the following methods to determine powder surface area, porosity, and density are used: gas adsorption method, permeametry, pycnometry, and mercury porosimetry.

Gas Adsorption

The gas adsorption technique is based on the Brunauer-Emmett-Teller (BET) model included in the determination of the amount of gas that is adsorbed on the surface of the sample at low temperatures [13]. The specific surface area (m^2/g) defined by this method comprises the outward as well as the internal (open pores) surface area. However, the surface area of closed pores cannot be determined because of its inaccessibility for adsorbing gas molecules.

Brunauer, Emmett, and Teller extended Langmuir's kinetic monolayer physical adsorption theory (1916) to a multilayer adsorption theory (1938). For convenience of chart creation, the BET relationship is entered in the following form:

$$\frac{p}{V(p_0-p)}=\frac{1}{V_\mathrm{m}C}+\frac{C-1}{V_\mathrm{m}C}\frac{p}{p_0}. \tag{1.16}$$

The BET relationship is significantly complicated in the case where the number of adsorbed layers is limited:

$$\frac{V}{V_\mathrm{m}}=\frac{C\frac{p}{p_0}}{1-\frac{p}{p_0}}\frac{1-(n+1)\left(\frac{p}{p_0}\right)^n+n\left(\frac{p}{p_0}\right)^{n+1}}{1+(C-1)\left(\frac{p}{p_0}\right)-C\left(\frac{p}{p_0}\right)^{n+1}} \tag{1.17}$$

where V_m is the monolayer capacity; V is the adsorbed amount of gas in the actual experiment, measured as a function of equilibrium adsorbate pressure, p; p_0 is the saturation pressure of the adsorbate at the corresponding temperature of the adsorption measurement; p/p_0 is often referred to as the relative pressure; and the parameters C and n are parts of the BET conception. The parameter C is:

$$C\approx \exp\left(\frac{q_1-q_\mathrm{c}}{RT}\right)$$

where the parameters q, R, and T are the heat of adsorption, gas constant, and temperature, respectively.

Due to the complexity of Eq. (1.17), it is seldom used in practice. Calculations are simplified by graphical construction. A diagram of $p/(V_\mathrm{m}(p_0-p))$ dependence on p/p_0 in accordance with Eq. (1.16) generally gives a straight line in the range of $p/p_0=0.06$–0.3. The amount of gas adsorbed in a monomolecular layer, V_m, is determined from the slope of this line and its intercept with the ordinate axis. The total surface of the sample can then be calculated based on the specific size of the adsorbing molecule. It should also be taken into account that the value of C is rather sensitive to errors in the measurement and it can vary by 50% or more depending on how accurately the data points are taken and which data points are omitted in the calculation.

An isotherm of nitrogen adsorption on the metallic powder surface of a typical gibbous shape of its initial part is illustrated in Fig. 1.28. The initial supposition is that the process of the formation of the first adsorption layer on the surface of the powder sample is finished at point B of the beginning of the rectilinear section BC of the isotherm. A comparison of the

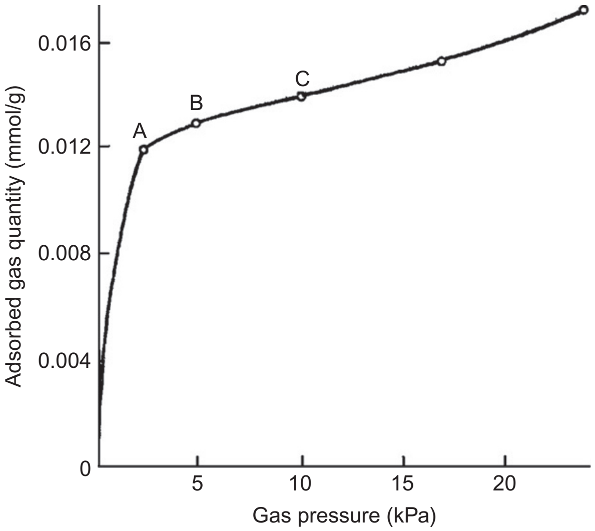

FIG. 1.28 Adsorption nitrogen isotherm on metallic powder surface at 78 K.

values of monomolecular coatings by low temperature nitrogen adsorption (78 K) for different particulate materials calculated by the BET (V_m) technique and with the help of point B (V_b) in most cases shows a satisfactory coincidence: the average value of the ratio V_b/V_m equals 0.97 and varies between 0.65 and 1.3. The results of investigations by the technique of low temperature (78 K) nitrogen adsorption of other authors for different metallic powders have shown the V_b/V_m ratio to lie between 0.9 and 1.04 [14].

The determination of the specific surface of metallic powders from 0.1 to 500 m^2/g is standardized in RUS by the thermal desorption of argon (Appendix A, GOST 23401-90). The essence of the adsorption/desorption technique is in the determination of the amount of argon adsorbed on the surface of the adsorbent from the argon-helium mixture of a predetermined concentration at liquid nitrogen temperature and its subsequent desorption into the same mixture on increasing the temperature to 293 K. A maximum diversity between two parallel determinations does not exceed 20% for adsorbents with the specific surface from 0.1 to 10 m^2/g and 10% for adsorbents with the specific surface of 10 m^2/g and higher.

Gas adsorption/desorption methods can also be used to study the pore size distribution in the sample. Pores of up to 100 or 200 nm in size can be determined. The method is based on the capillary condensation, which means that a gas will condense into a liquid phase below its saturation point when it is confined in small pores. The fundamental relation between relative pressure and pore size is described by the Kelvin equation:

$$\ln\left(\frac{P}{P_0}\right) = -\left(\frac{2\gamma_{1v}V_1}{RTr}\right)$$

where γ_{1v} is the interfacial tension of the liquid-gas interface, V_1 is the molar volume of the liquid-gas phase, and other symbols are the gas constant, R, temperature, T, and radius of curvature of the liquid-gas interface, r. The adsorption/desorption isotherm shows a hysteresis and the relative pressure range where the hysteresis appears provides the information about the pore size. The explanation and analysis of the hysteresis effect in more detail, including the information about network and connectivity effects of the pore system in a sample, are described in several manuals [15,16].

For the determination of the specific surface area, various gases can be used. Usually, nitrogen or argon is used. The use of krypton or argon as the adsorbent improves the accuracy of measuring low specific surface areas.

The apparatus for the determination of the specific surface area originally developed by Emmett is shown in Fig. 1.29. Commercial instruments are now completely automated. In these devices, instead of the burette-type mechanism to

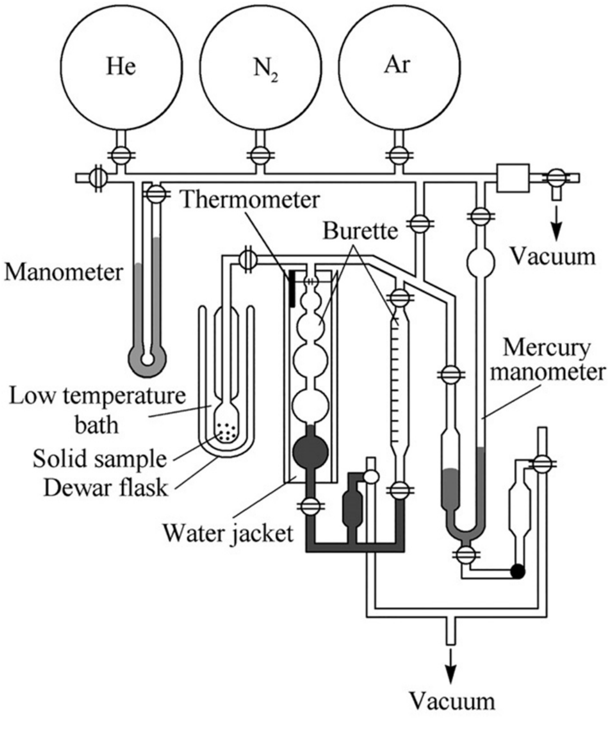

FIG. 1.29 BET apparatus for specific surface area determination.

measure the adsorbed gas volume, very precise pressure transducers are used to calculate the adsorbed amount from the known volume of a calibration chamber and the pressure drop that happens when the valve between the sample and calibration chamber is opened. Further details are described in several manuals [15–17].

Permeametry

Among the indirect methods for the determination of the powder specific surface, methods based on measuring the gas permeability of the powder have gained ground. The quickness of the analysis and the simplicity of the apparatus design have led to a wide usage of this method in industry.

Noteworthy is that, in all cases, the measured quantity is the resistance to fluid flow through a compact powder layer. In this way, the outer particle surface without regard to their roughness and blind pores is determined, therefore the value of the permeability specific surface area (S_h) is even less than one determined by BET (S_{BET}).

The Kozeny-Carman equation is the widely used basis for all permeametry modifications. It expresses a connection between the pressure drop across the powder layer (Δp), the velocity of fluid flow (v), and parameters characterizing the powder layer including the permeable porosity (ε_v), the viscosity of fluid (η), the layer thickness (l), the average length of the path through the powder layer (l_0), and the density of powder material (ρ_p). It has the following form:

$$S_h^2 = \frac{l^2}{2\eta v l_0^2 \rho_p^2} \frac{\Delta p}{l} \frac{\varepsilon_v^2}{(1-\varepsilon_v)^3} \tag{1.18}$$

The method for the determination of the specific surface of metallic powders by means of measuring the powder layer air penetrability is laid down in ISO 10070. An analogous standard, GOST 23401-90, functions in the RUS.

The value of the specific surface of powder, of which the permeable porosity is known, is determined by measuring volumetric flow (q) and the pressure drop of a dry gas (air as a rule) passing through the powder layer in laminar mode (Δp). It is calculated by the equation:

$$S_h = \sqrt{\frac{\varepsilon_p^3 A \Delta p}{5.0(1-\varepsilon_p)^2 q \eta l \rho_p}}$$

where A is the section area (m^2), Δp (Pa), q (m^3/s), η (kg/(m·s)), and ρ_p (kg/m^3) are as mentioned above (Eq. 1.18).

The equivalent diameter of a spheroidal particle may be calculated as a diameter of the nonporous spheroidal particle having the same specific surface area as the particles of the investigated powder (measured by the same method).

Commercial permeametry is applicable for powders with specific surface area and particle size in a range of 70–20,000 cm^2/g and of 0.5–50 μm, respectively [18,19].

Several designs of permeametry apparatus are used. These instruments can be classified into two groups, depending on whether the mass flow of the gas across the powder layer is constant or changing. The apparatus developed by Lea and Nurse [20] and Tovarov [3] (Fig. 1.30) refers to the first group.

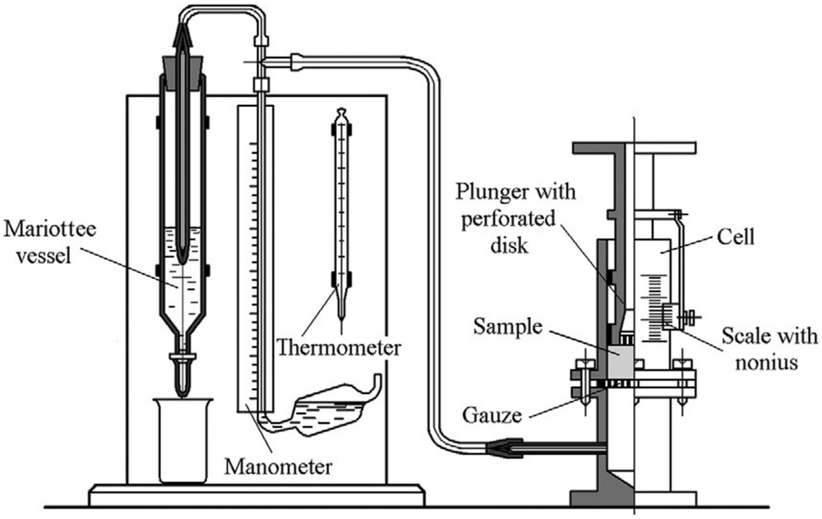

FIG. 1.30 Tovarov's apparatus.

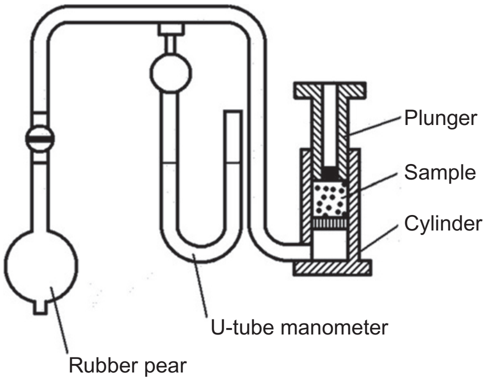

FIG. 1.31 ADΠ apparatus for specific surface area determination.

The Lea and Nurse apparatus was modified by Gooden and Smith by means of an addition of a self-calculating diagram that allows the direct readout of the specific surface. The commercial version of their modification is known as the Fisher subsieve sizer (Fig. 1.15) [19].

The instruments of the second group are simplified in comparison with the first. The Blaine permeameter [17] IICX and ADII designs (Fig. 1.31) [3] represent this type of apparatus. A variable pressure technique is used. Like this, a hand-operated pump in the form of a rubber pear is used in ADII apparatus.

A typical sample occupies a volume of about 5 cm^3 and, depending on its apparent density, is from 5 to 20 g in weight.

The ADII apparatus consists of a cylinder (pan) with a perforated bottom, under which there is a connecting pipe for connecting the cylinder to the manometer. A hollow plunger is inserted into the cylinder, a circle of filter paper is put into the cylinder, and a powder sample weighed to within ±0.01 g is added. The sample is coated with a circle of filter paper and is densified by a plunger. The height of the sample layer is measured by means of the points indicated on the plunger, then the plunger is removed and, by means of a rubber pear, the underpressure under the false bottom measured by the manometer is created. The underpressure gradually decreases due to air penetration through a layer. A stopwatch fixes the duration.

Using the empirical formula, the powder specific surface (S, cm^2/g) is calculated:

$$S = k\frac{M\sqrt{t}}{P}$$

where k is the device constant (determined by a reference specimen); M is the coefficient found from the table for measured layer height and air temperature; t is the time of a manometric liquid lowering between two readings, s; and P is the sample weight, g.

The specific surface determined by such a method characterizes the external surface of a powder without taking into account a relief of particle surface, porosity, etc.

In the advanced design of the device, the evacuation with vibration at a frequency of 50 Hz is applied that prevents aggregation of particles and provides the stacking of particles with the porosity within the limits of 0.4–0.8. It increases the accuracy and reproducibility of the measurement.

Pycnometry

Pycnometry is used for the determination of the true density of PM materials. Density is one of the most important properties of metallic powders.

In addition to its use in measuring the true density of a powder, pycnometry can also be used to discriminate among different crystalline phases or grades of materials, different alloys, compositions, or prior treatments. Pycnometry allows information to be obtained on the porosity of a material if the sample volume is known as well. Then the pore volume can be calculated as the difference between the bulk volume and the specific volume.

Archimedes' law is the basis for definition of the true density by means of the displacement principle. These can be measured using either liquid or gas pycnometry. In liquid pycnometry, the volume displacement is measured directly, as liquids are incompressible. The inability of the liquid to permeate pores, chemical reaction or adsorption onto the particle surface, and wetting or interfacial tension problems lead to errors in density measurement. In these cases, the gas pycnometry has an advantage over the liquid one.

Powder density defined by liquid pycnometry is calculated by the following expression:

$$\rho_\mathrm{p} = \frac{m_2 - m_1}{V_\mathrm{P} - V_\mathrm{L}}$$

where m_2 is the weight of the pycnometer bottle with the powder and the liquid (g), m_1 is the weight of the bottle with the liquid (g), V_L is the liquid volume in the pycnometer (mL), and V_P is the volume of the liquid with submerged powder in the bottle (mL).

In gas pycnometry, the volume displacement is measured indirectly from the pressure/volume relationship of the gas under controlled conditions. Gas pycnometry requires the use of high-purity, dry, inert, nonadsorbed gases such as argon, neon, dry nitrogen, dry air, or helium. Of these, helium is recommended because it can penetrate into pores as small as 0.1 nm and behaves like an ideal gas.

In commercial pycnometers, the powder sample is first conditioned to remove contaminants that fill or occlude pores and influence in such a way the surface characteristics. This is achieved by the exhaustion of the system and heating it to elevated temperatures, followed by a purging with an inert gas. A typical commercial gas pycnometer is a helium-filled sample system consisting of the sample cell, the calibrated reference cell, the vessel with a gas such as helium, the pressure transducer, and the connecting pipes with flow control valves. This system is in "zero" condition if it achieves the environmental pressure and temperature. At this point, the sample cell and the reference cell are isolated from each other and from the system by closed valves [21]. In the process of measuring, the gas is fed by opening the valves first into the reference cell. It then enters the sample cell where a given pressure value is established. Before the measurement in the sample cell starts, a pressure p_2 is established that exceeds the ambient pressure by 100 kPa, then the pressure is elevated to the p_3 value. The state of the system can be characterized by the equations:

$$pV = nRT$$

for the sample cell and

$$pV_\mathrm{R} = n_\mathrm{R}RT$$

for the calibrated reference cell and, when a solid sample of the volume V_S is placed in the sample cell

$$p(V - V_\mathrm{S}) = n_1RT$$

where p is the ambient pressure; V is the volume of the sealed empty sample cell; V_R is the volume of the calibrated reference cell; n is the amount of the gas (moles) in the sample cell volume at a pressure p; n_1R is the amount of the gas (moles) in the reference cell volume at a pressure p; n_1 is the amount of the gas (moles) occupying the remaining volume in the sample cell at a pressure p; R is the universal gas constant; and T is the ambient temperature.

Omitting the intermediate computations that characterize the changes of the gas state in the sample cell at a pressure of p_2 and the following pressure elevation, the expression is deduced for the gas volume V_S that penetrated into the pores at a pressure of p_3 (working equation):

$$V_\mathrm{S} = V + V_\mathrm{R}/[1 - (p_2/p_3)].$$

In recent years, the gas pycnometer has been further improved by means of a more accurate pressure transducer, a better temperature control, and automation. Modern pycnometers can now reach an accuracy of 0.01% [21].

Porosimetry

Mercury and gas porosimetry are mutually complementary techniques with the former covering a much wider pore size range, from 0.3 mm to 3.5 nm, and the latter applicable to pores of 0.2 μm and smaller in size [22]. Mercury porosimetry consists of the step-by-step intrusion of mercury into an evacuated porous medium at increasing pressures followed by extrusion as the pressure is lowered.

Mercury porosimetry is based on the capillary rise phenomenon in which surplus pressure is required to cause a nonwetting liquid to enter a narrow capillary. The pressure difference across the interface is described by the equation of Laplace (1806) and Young (1855), and its peculiarity is such that the pressure is lower if the contact angle (Fig. 1.32) is greater than 90 degrees or higher if θ is smaller than 90 degrees. In the case of a capillary circular in cross-section

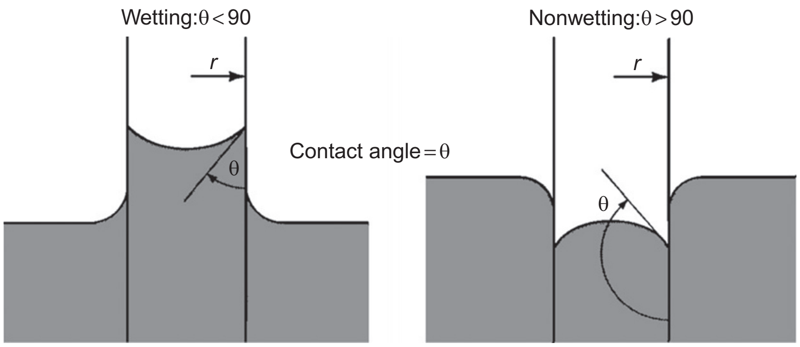

FIG. 1.32 Contact angle (θ) of a liquid in capillary.

and not too large in radius, the mercury meniscus will be approximately hemispherical. The curvature of the meniscus can be functionally related to the radius of the capillary that is given by the Young-Laplace-Washburn equation (1921):

$$\Delta p = \gamma_{1v}\left(\frac{1}{r_1}+\frac{1}{r_2}\right) = \frac{2\gamma_{1v}}{r_p}\cos\theta \tag{1.19}$$

where Δp is the pressure drop across the interface, η_{1v} is the surface tension of the liquid (for mercury, 0.485 N/m), r_1 and r_2 are mutually perpendicular radii of a surface segment, r_p is the capillary radius, and θ is the angle of the contact between the liquid and the capillary walls (Fig. 1.32).

Every mercury porosimeter contains a penetrometer unit into which the sample is placed. It is then evacuated to a given vacuum level before the sample cell is filled with mercury. The increasing pressure forces the mercury to penetrate into the largest pores in the sample. The amount of mercury penetrating into the sample is recorded at each pressure point respective to the pore size. The first reading is usually carried out at a pressure of 3 kPa, though a reading at a pressure of 0.07 kPa is possible [22]. The pressure is increased up to a final pressure of 400 MPa. Commercial units work either in a consecutive discrete or in a continuous mode. In the former, the pressure is increased in steps and the system is allowed to stabilize at each pressure point before the next step. In the case of the continuous mode, the pressure is increased continuously at a given rate.

As is obvious (Eq. 1.19), two parameters play the most important role in the determination of pore size from the accurately measured applied pressure: the contact angle, θ, and the surface tension, .η_{1v} The pressure is usually measured with an electronic pressure transducer or with a Heise-Bourdon manometer used in older manual units.

Various methods are available to determine the contact angle. Usually the sessile drop mode is used. A drop of mercury is placed on the flat surface of the sample and the resulting contact angle is observed visually and usually measured in its shadowgraph on a screen [23]. The contact angle depends on the drop size (Fig. 1.33). The same technique can be used to measure the contact angle in transparent capillaries. In the case of nontransparent capillaries, to obtain a shadowgraph such techniques as X-ray and ultrasonic flow detection can be employed. It is necessary to take into account the difference between microscopic and macroscopic measurement of the contact angle under conditions of wetting and nonwetting [24].

A simplified formula can be used when the maximum height of the drop, $h_{\max}$, is determined:

$$\cos\theta = 1 - \frac{\rho g h_{\max}^2}{2\eta_{1v}}$$

where g is the acceleration of gravity and ρ is the density of the liquid.

The Wilhelmy plate method [25], based on the effect of contact angle hysteresis for emersion and immersion, is also known. Surface roughness or a change in surface composition during contact with mercury can explain the presence of this difference. No surface roughness effects manifest themselves below pore size of about 100 nm.

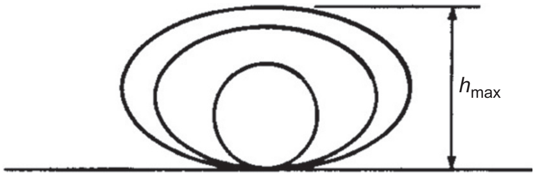

FIG. 1.33 Change of mercury-drop shape on size.

TABLE 1.8 Contact Angle Between Mercury and Select PM Nonferrous Materials

Powder	Angle (Degrees)
Aluminum	140
Cooper	116
Zinc	133
Tungsten carbide	121
Tungsten	135

Another technique consists of pressing a powder compact onto a disk with a well-defined hole. Mercury is now placed on the face plane of this disk and the contact angle can be calculated from the required pressure to force the mercury through this cylindrical pore, with the size measured directly.

The contact angle, θ, is frequently supposed to be equal to 130 or 140 degrees. This assumption is perhaps the largest source of error. The contact angles of mercury with various materials may significantly differ. Contact angle values between mercury and select PM nonferrous metals [26] are shown in Table 1.8.

Samples of such metals as zinc, silver, and lead can react with mercury. This can strongly change the nonwetting behavior of mercury with the sample. In this case, using a protective film, for example, of stearic acid formed on the pore surface can prevent this reaction. Moreover, for some reactive metals such as aluminum, their natural oxide layer on the surface ensures sufficient protection.

Surface Tension of Mercury

The purity of mercury strongly influences the surface tension. Mercury is very sensitive to contamination and, probably for this reason, the evaluations of its surface tension values in earlier publications showed a lack of reproducibility. The effect of temperature is minimal because the temperature coefficient of the surface tension of mercury is only of $2.1 \times 10^{-4}\,\mathrm{N/(m\,K)}$.

Another error is caused by very small radii of pore surface curvature. The following correction has been suggested by Kloubek [27]:

$$\eta_{\mathrm{corr}} = \eta - 2.66 \times 10^{-4}\,\Delta p.$$

For $\Delta p = 200\,\mathrm{MPa}$, the correction term gives an error of 12%.

Restrictions and Limitation

The principal limitations of the results obtainable by mercury porosimetry are the following:

- The extent of the pore volume filled with mercury is limited by a maximum pressure. In such conditions, mercury cannot penetrate into very small pores.
- Contrary to the former, the penetration into very large pores is limited by the height of the sample, which determines a minimum pressure. Consequently, very large pores may remain unfilled.
- In the process of porosity measurement, mercury not only penetrates into pores, but it also fills the space between particles that distorts the results obtained for the true volume of coarse pores.

Detailed discussions about restrictions and limitations of mercury porosimetry can be found in a series of works [28,29].

Surface Area Determination

The surface area of a sample is calculated from mercury porosimetry measurements under a supposition of specific pore geometry. Many publications show a relatively good correlation between surface area values derived from mercury porosimetry measurements and corresponding nitrogen adsorption BET values (Table 1.9) [15,26].

The value of the specific surface area is often used to calculate the contact angle of mercury on the sample material by modifying the contact angle while the surface area computed from mercury porosimetry measurements correlates with the values determined from nitrogen adsorption data.

TABLE 1.9 Comparison of Surface Area Measurements With Nitrogen Adsorption and Mercury Porosimetry

	Surface Area (m^2/g)	
Sample	**N_2 Adsorption**	**Hg Porosimetry**
Aluminum dust	1.14	1.35
Boron nitride	20.0	19.6
Copper powder	0.49	0.34
Silver iodide	0.53	0.48
Tungsten powder	0.10	0.11
Zinc dust	0.32	0.34

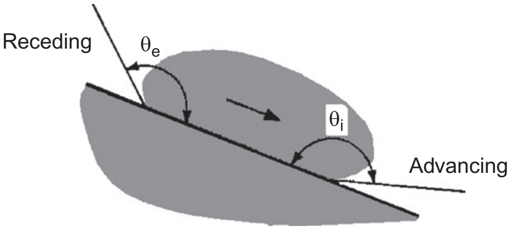

FIG. 1.34 Contact advancing (θ_i) and receding (θ_e) angles.

Hysteresis and Detained Mercury

The interpretation of the penetration data from mercury porosimetry measurements has been mostly neglected because the interpretation was vague. Generally, three theories are used to explain the hysteresis between the intrusion and extrusion curves in mercury porosimetry measurements: contact angle hysteresis, ink-bottle theory, and the connectivity model [29].

Numerous data of contact angle hysteresis indicate different values for advancing and receding contact angles (Fig. 1.34). This model does not offer any explanation for the penetrated mercury that can remain in the sample pores after complete depressurization.

The ink-bottle model describes the condition in which mercury enters and leaves pores. It shows how some mercury remains trapped in the sample pores. However, for most samples, the ink-bottle theory prognosticates a much larger amount of mercury remaining in samples than that obtained in actual measurements.

The connectivity model represents a network of pores. In the regular network model, a porous medium is presented in the form of a regular two-dimensional or three-dimensional grid, the sites of which are connected by pores of a constant section. The main characteristics of the grid are obtained experimentally. The peculiarities of a real porous solid in its grid model are taken into account by the selection of the place of the principal pores volume concentration (in connections or in sites of the grid), the amount and succession of the connections, the size of elements, and their combination. This model probably describes the real condition better. However, in spite of a relatively large number of works in the field of mercury penetrability in porous media, the hysteresis problem remains unsolved to the present day.

ASTM standards D 4284 [30] and C 493 [31] contain the recommendations for procedures accomplishing the mercury intrusion porometry.

Bubble Test of Pore Size

The essence of this method consists of measuring the pressure necessary for the appearance of the first air bubble on the surface of the sample completely saturated by a liquid to determine the maximum pore size, and in measuring a pressure that corresponds to the beginning of air bubble discharge on the total sample surface to determine the average pore size. Ethyl alcohol is used as a liquid for sample saturation.

The ISO 4003 standard establishes the recommendations for the procedures accomplishing the method of bubble test of pore size. There is also an analogous RU standard (GOST 26849-86) (see Appendix A).

BULK PROPERTIES OF POWDERS

Apparent density, tap density, angle of repose, and flow rate are the main attributes that characterize bulk properties of powders. For accurate determination of these properties, a knowledge of the problems of powder movement plays an important part in powder processing. Thus, the flow of metal powders in bins, hoppers, feeders, and conveyors as well as filling a die cavity is not always reliable or uniform. This often results in the press having to operate at pressing cycle times and wasted product due to composition or apparent density variations. A powder may form a stable arch or a hollow, particle segregation may happen, resulting in unacceptable variations in bulk density of the powder delivered to the feed shoe, or the powder may flow uncontrollably.

Bulk Flow Parameters

There are two virtual movement types that can occur in a bin: funnel flow and mass flow, which are shown in Fig. 1.35.

In funnel flow, an active flow channel is formed above the outlet with nonflowing powder at the periphery. As the level of powder in the bin decreases, layers of nonflowing powder may not slide into the flowing channel, which can result in the formation of stable hollows. Along with this, funnel flow can cause powder caking, forming first in nonflowing powder and increasing the extent of sifting segregation.

In mass flow, all the powder is in motion. Powder from the center as well as the periphery moves toward the outlet. Mass flow hoppers provide the flow sequence, eliminate the stagnation of powder, reduce sifting segregation, and provide a steady discharge with a consistent bulk density and flow that is continuous and well controlled. Conditions for the attainment of mass flow are accomplished by means of making the hopper walls smooth and steep as well as the outlet sufficiently large to prevent arching.

Having the information about bulk properties of powders, engineers can optimize the selection of storage and handling equipment. These same properties can be used to modify prevalent processes to correct flow problems. The following bulk solids handling properties are relevant to constitutive flow behavior: cohesive strength and frictional.

Cohesive Strength

When the powders are placed in bins, hoppers or containers, the consolidation pressures range in position from zero at the surface to relatively large values at increasing depth within the vessels. If a powder acquires a cohesive strength because of the pressures applied to it, an arch or hollow can form. An arch is a stable obstruction that forms over the point of narrowed cross-section of the vessel. The arch supports the rest of the content vessel, hindering discharge. A hollow (called also a rathole) is a stable pipe or vertical cavity that connects with the outlet. Powder is left in stagnant zones that remain in their place until an external force is applied to destroy them.

The cohesive strength can be measured as a function of the applied consolidation pressure on a Jenike apparatus [32], shown in Fig. 1.36 and accepted in ASTM D 6128 Standard [33]. The bottom of the cover and the inside of the base are roughened to increase friction with the powder under test. The base and the ring are filled with the powder being tested, and a vertical load is applied to the cover. A horizontal shearing force that acts on the section of contact between the ring and the base is transferred from the bracket to the ring through a loading pin. The standard shear cell is 95 mm in inside diameter.

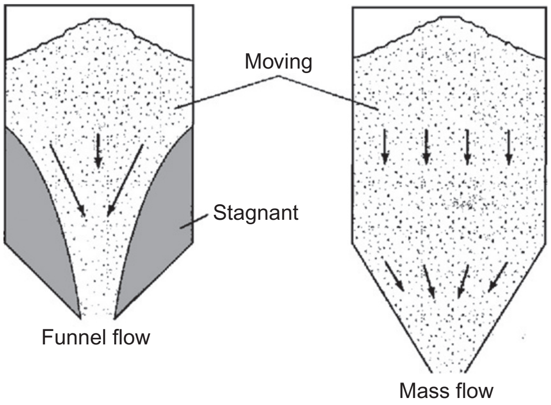

FIG. 1.35 Two move types of powder that can develop in the bin: funnel flow and mass flow.

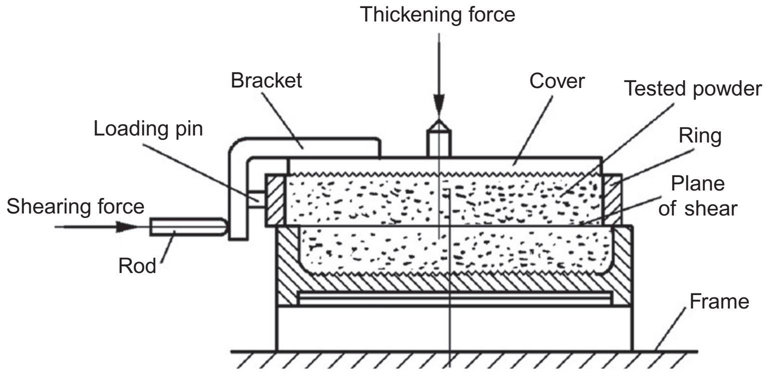

FIG. 1.36 Jenike shear cell in initial offset shearing position.

The present shear tester is equipped with a shear cell, a gravity vertical loading system, and an electronic shearing force applicator with a shearing rate of 2.54 mm/min. This arrangement produces a permanent record of the stress-strain relationship.

Shear testing is a two-step process that consists of consolidation (also called preshear) and shear. The consolidation is realized by the specimen flowing under given stresses until a steady state is reached or closely approached. Measurement of the shear stress σ_{40} consists of obtaining its dependence on the pressure normal stress σ_p in yield locus. The determination of one yield locus requires the measurement of three to five points of the locus. For each point, the specimen is first consolidated and then sheared. The value of shear normal stress typically ranges between 25% and 80% of the preshear normal stress σ_p.

The flow condition of a powder is used for a variety of engineering decisions, for example, to design an optimal outlet assembly to prevent the formation of cohesive arches and ratholes. Details can be found in the book by Jenike [32].

Moisture, particle size, and shape, long-term storage at rest in vessels, and some chemical additives influence the cohesiveness of the bulk powder.

Typically, cohesiveness rises as moisture content increases, but not in direct proportion. Hygroscopic materials can suffer significant increases during exposure to humid air. As a rule, the finer the powder, the more cohesive the powder and the more difficult it is to handle. Dendritic, flaky, or fiber particles are more cohesive than those that are spherical.

When a powder is kept in a bin or hopper for a period without moving, it can become more cohesive and difficult to handle. Such cohesion may result from settling and compaction, crystallization, adhesive bonding, and agglomeration.

In some cases, adding a small amount of a chemical additive such as calcium, lithium, or zinc stearate can make a cohesive powder flow more easily.

Frictional Properties

Both internal and external friction values can be determined by measuring cohesive strength with a shear tester (Fig. 1.37) such as the Jenike shear cell. Internal friction is conditioned by solid particles moving against each other and is

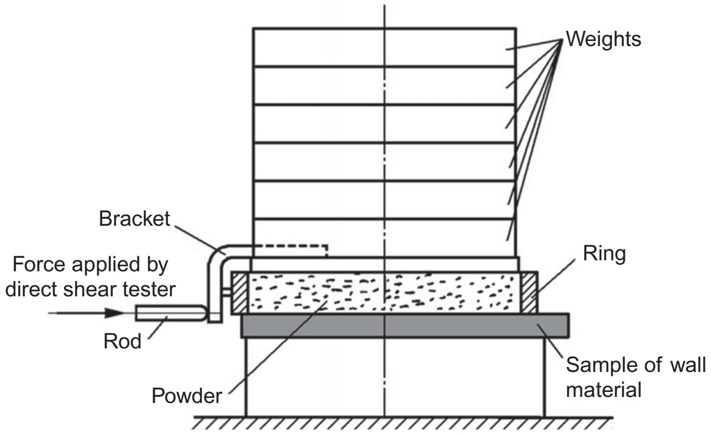

FIG. 1.37 Shear cell used in measuring wall friction properties.

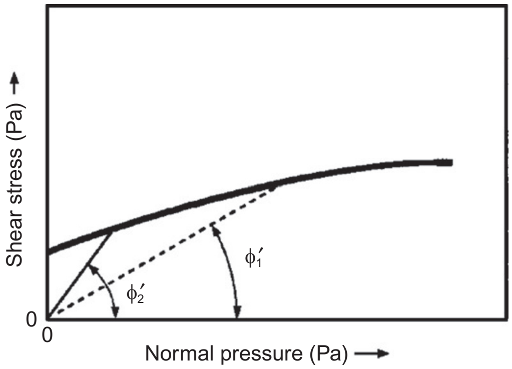

FIG. 1.38 Typical results of the wall friction properties measuring by means of shear cell test setup shown in Fig. 1.37 to determine wall friction angle.

characterized by the angle of internal friction and the effective angle of internal friction. External friction is characterized by the wall friction angle or coefficient of sliding friction. The higher the coefficient of sliding friction, the steeper the hopper walls that are necessary for mass powder flow.

In the shear cell (Fig. 1.37), a sample of wall material is placed on a disk so that the top surface of the wall material is the horizontal section of the force measuring stem. The ring is placed over the wall material sample and filled with the powder. After the excess powder is scraped off, a cover is placed over the powder. A vertical force is applied to the cover by means of weight disks. This force creates a vertical pressure σ_w in the powder. Several (usually up to six) 0.5 or 1 kg weights are placed directly on top of the cover of the shear cell to give the largest required normal pressure σ_w. The stem is moved. When the shear stress τ_w is leveled off with recording its value, one weight is removed. Thus, sequentially removing away the weights, the τ_w is determined for every magnitude of σ_w.

Characteristic results of the test for wall friction angle determination in the shear tester are shown in Fig. 1.38. Typically, as vertical pressure increases, the wall friction angle decreases.

The pressure, moisture, particle size and shape, long-term storage at rest in vessels, and wall surface condition influence both the internal and external friction values of metal powders.

Typically, as the consolidating pressure increases, the effective angle of friction decreases. Similarly, the coefficient of sliding friction often decreases as the pressure acting normal to the plate increases. When a powder is kept in a bin or a hopper for a period without moving, many powders experience an increase in friction between the particles and the wall surface.

Fine powders and those with a wide range of particle sizes are usually more frictional than coarse powders or those with a narrow particle size distribution. Dendritic, flaky, or fiber particles are more frictional than roundish ones. An increase of moisture content in many powders leads to an increase in their friction.

The wall surface condition can appreciably manifest itself in sliding powders along it. Thus, smooth surfaces are typically less frictional. Values of both internal friction angle and wall friction angle are required to design chutes, mass flow hoppers, and other vessels.

Bulk Density

The term powder bulk density includes its apparent density and top density that differ from one another in their effect on the compressibility of powder samples. This is one of the fundamental properties of a powder.

Apparent Density

The apparent density of metal powder is the weight of a unit volume of loose powder expressed in grams per cubic centimeter. This characteristic determines the actual volume allocated by a mass of loose powder that directly defines the processing parameters such as the design of consolidation tooling and the range of the press motions required to pack and compact the loose powder.

Apparent density of a metal powder strongly depends on the particle size. Usually, it decreases with decreasing particle size. Table 1.10 shows the influence of particle size on the apparent density for several nonferrous powders.

Apparent density decreases as the particle shape becomes more irregular, decreases with increasing surface roughness, and depends on particle size distribution. In the case of powders with a wide range of particle sizes, the apparent density increases because the space between coarse particles is filled with smaller particles.

TABLE 1.10 Influence of Particle Size and Particle Shape on Apparent Density for Several Nonferrous Metal Powders

Material	Manufacture Method	Particle Diameter (μm)	Specific Surface Fisher (m^2/g)	Particle Shape	Apparent Density (g/cm^3)	Source
Aluminum	Granulation	500–2500	…	Needle	1.4	ECKA
Aluminum	Grinding	1000–2000	…	Irregular to semispherical	1.3	ECKA
		500 max	…	Irregular to semispherical	0.8–1.2	ECKA
		150 max	…	Irregular to semispherical	0.8–1.2	ECKA
Aluminum	Air atomization	160 max	…	Irregular	1.0	ECKA
		18[a]	…	Irregular	1.07	[34]
		15.5[a]	…	Irregular	0.98	[34]
		6.0[b]	0.6	Irregular	0.60	ECKA
Copper	Air atomization	500 max	…	Irregular	5.2	ECKA
		315 max	…	Irregular	5.1	ECKA
	Water atomization	315 max	…	Irregular	4.2	ECKA
	Air atomization	160 max	…	Irregular	5.0	ECKA
	Water atomization	100 max	…	Irregular	4.2	ECKA
	Air atomization	63 max	…	Irregular	4.7	ECKA
		45 max	…	Irregular	4.4	ECKA
	Grinding	…	0.3	Flake	1.1	ECKA
		…	0.4	Flake	1.1	ECKA
		…	1.0	Flake	0.8	ECKA
	Electrodeposition	63 max	0.23	Dendritic	0.7	ECKA
Zinc	Air atomization	315 max	…	Irregular	3.0	ECKA
		45 max	…	Irregular		
Tin	Gas atomization	200 max	…	Teardrop shaped	4.0	ESKA
		63 max	…	Teardrop shaped	3.7	ESKA
		40 max	…	Teardrop shaped	3.5	ESKA
		32 max	…	Teardrop shaped	2.2	ESKA
		8[b]	0.25	Teardrop shaped	2.0	ESKA
Nickel	Carbonyl	3.2[a]	…	Acicular	0.61	[34]
		3.8[a]	…	Acicular	1.87	[34]
		4.1[a]	…	Acicular	2.10	[34]
Nickel	Precipitation	3.5[a]	…	Roundish	1.81	[34]
		4.4[a]	…	Roundish	2.09	[34]
		8.0[a]	…	Roundish	2.60	[34]

[a] *Average particle diameter.*
[b] *Median mass diameter.*
ESKA, ECKA Granules Company.

Funnel Method

The most prevalent method for the determination of apparent density of metal powders uses the Hall funnel illustrated in Fig. 1.39. The ISO 3923/1 standard establishes recommendations for using this method with the application of the Hall funnel (Fig. 1.39). An analogous standard functions in the RU (GOST 19440-94-86) (see Appendix A). Both ASTM B 212 and MPIF Standard 04 describe this method of using the Hall funnel. Both ASTM B 417 and MPIF Standard 28 provide for the Carney funnel. This funnel differs in the design of the discharge opening (Fig. 1.39). The orifice diameters amount to 2.5 and 5 mm, respectively. The equipment assembly for the determination of the apparent density is shown in Fig. 1.40.

Apparent density measurements are carried out by pouring powder into the funnel from which it flows into the 25 cm^3 density cup. After filling the cup, the funnel is moved away and the excess powder is leveled off using a spatula. The apparent density in grams per cubic centimeter is then defined by weighing the powder in the cup in grams and dividing by 25 cm^3.

For powders that do not flow freely, the Carney funnel is used. The larger opening allows a greater variety of powders to flow. If the powder does not flow readily, its flow can be stimulated by poking a wire up and down in the orifice without entering the density cup.

Scott Volumeter

This method is used for powders that do not flow freely through a Carney funnel. In the Scott volumeter, the bulk condition of the powder is obtained by filling the density cup as a result of passing the gravitational powder jet through a system of

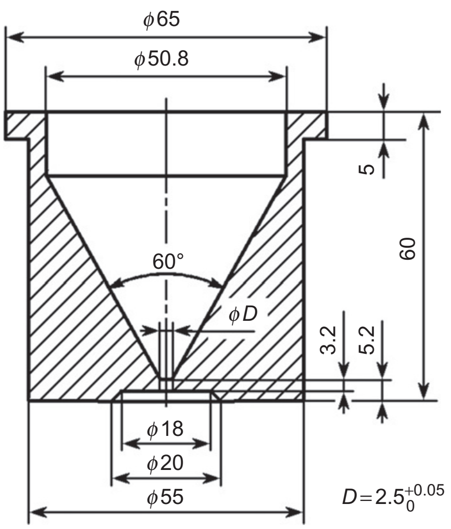

FIG. 1.39 Hall funnel.

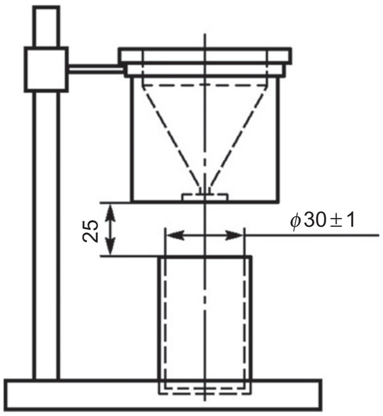

FIG. 1.40 Equipment assembly for apparent density determination.

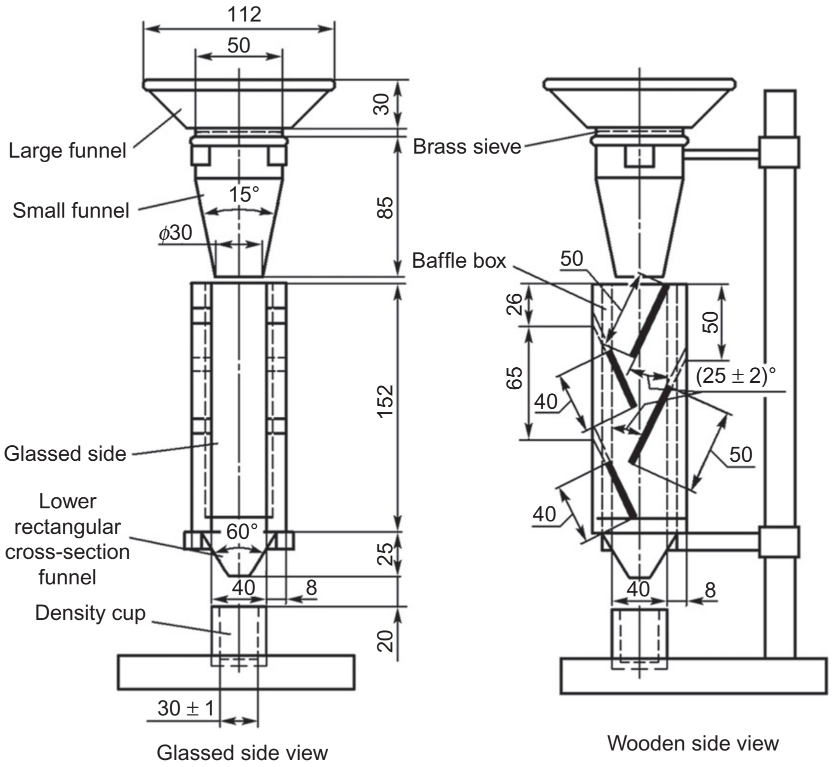

Glassed side view

Wooden side view

FIG. 1.41 Scott volumeter.

inclined plates of the volumeter. As shown in Fig. 1.41, the apparatus consists of a large funnel with a metallic screen and a smaller funnel that has a straight stem directing the powder into the baffle box. The latter with glass sides and two wooden sides contains a series of glass baffle plates and a funnel at the bottom to direct the powder into the density cup.

Pouring the test specimen carefully into the funnel begins the operating procedure. Ultrafine powders may require a light brushing with a synthetic brush to stimulate the powder to flow through the screen into the funnel. The powder is permitted to stream into the density cup until it completely fills and overflows the circumference of the cup. The excess powder should be removed from the cup by passing a spatula blade in flat contact with the top of the cup. The powder weight is determined accurately to 0.05 g. The density of the powder is given in grams per cubic centimeter if a metric cup is used, or grams per cubic inch if a nonmetric cup is used.

Tap Density

The method for the determination of tap density, which is defined as the density of a powder when the volume container is tapped or vibrated under specified conditions, is established by ISO 3953. This method in accordance with ISO 3953 is accepted in the ASTM B 527, MPIF 46, GOST 25279-93, and MILSTD-1233 standards (see Appendix A).

Tap density is a function of particle size distribution, particle shape, and surface roughness. It is always higher than the free-flow apparent density.

A graduated glass cylinder with a volume of 100 mL and a multiplying factor of 0.2 mL (or a smaller graduated cylinder may be used for high-density powders) is used for tap density measurement. The amount of the powder for tap density testing is shown in Table 1.11. If mechanical tapping is used, the filled cylinder is placed in the mechanical apparatus, which operates until no further decrease in volume of the powder is observed (Fig. 1.42). The amplitude of tapping or vibrating must be of 3 mm and frequency shall be from 100 to 300 impulses per minute. In both the latter or hand tapping, care must be taken to exclude loosening the surface layers of the sample during the procedure. The tap density in grams per cubic centimeter is then defined by weighing the powder in the cylinder in grams and dividing by the volume of the tapped powder in cubic centimeters. The results should be obtained with accuracy not worse than ±0.1 g/cm^3.

The amount of increase from apparent to tap density depends to a great extent on particle shape and particle size. Usually, the lower the apparent density, the higher the percentage increase in density on tapping.

TABLE 1.11 Typical Tap Density in Comparison With Apparent Density of Nonferrous Powders

Powder	Particle Size (μm)	Apparent Density (g/cm^3)	Particle Size (μm)	Tap Density (g/cm^3)	Increase (%)
Aluminum [34]	6.00[a]	0.60[b]	5.05[a]	1.30	117
Cobalt [35]	99.6 wt.% <40 μm	1.8	99.6 wt.% <40 μm	3.0	67
Copper [36][c]: Spherical	…	4.5	…	5.3	18
Irregular	…	0.4	…	0.7	35
Flake	…	0.4	…	0.7	75
Nickel [34,37]	3.0[a]	1.0	3.0[a]	1.9	90
Tin [34][b]	8.0[d]	2.0	2.45[a]	3.15	57
Tungsten fine [34,38]	3.27[a]	2.16	1.15[a]	4.45	106

[a] *Fisher subsieve size.*
[b] *ESKA Metal Powders.*
[c] *Particle size distribution is the same for apparent and tap density.*
[d] *Mass median particle size measured by means of laser granulometer.*

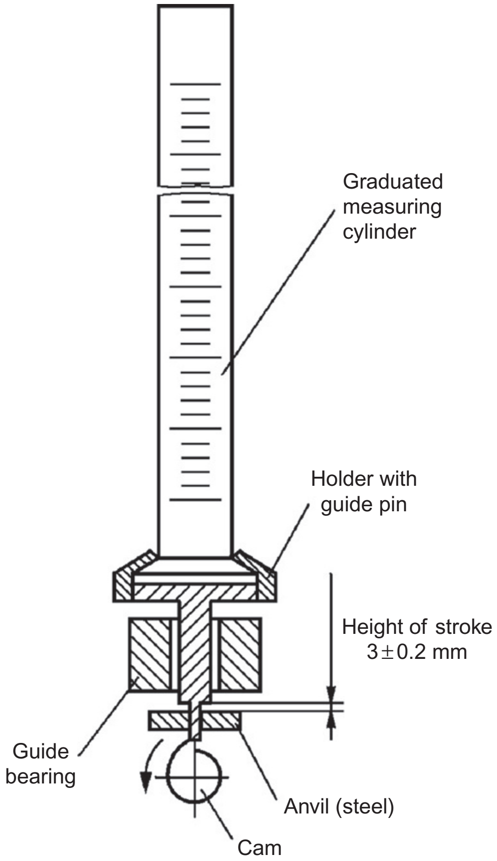
Graduated measuring cylinder
Holder with guide pin
Height of stroke 3±0.2 mm
Guide bearing
Anvil (steel)
Cam

FIG. 1.42 Diagram of tapping apparatus.

Flow Rate

Flow rate is the time required for a powder sample of a standard weight (50 g) to flow gravitationally under atmospheric conditions through the Hall funnel into the cup. A determination of the flow rate of the powder is important in high-volume manufacturing, which depends on rapid, uniform, and consistent filling of the die. Poor flow characteristics cause slow and nonuniform press feeding and even difficulty in filling the die cavity. In modern automatic presses, the die cavity shall be filled with a certain constant amount of the powder in about 1 s.

ISO 4490 establishes the method of flow rate determination of metallic powders by means of the Hall funnel. The description of this method is also contained in the ASTM B 213, MPIF 03, and GOST 2089975 standards (see Appendix A). The Japanese standard JIS 7-2502-1966 and the German standard 82–96 are standards equivalent to ISO 4490. The funnel with a calibrated orifice of 2.5 mm in diameter is made of aluminum alloy 6061-T6 with a smooth finish to minimize wall friction.

The test procedure consists of the following. A dry sample of 50 g in weight is poured into the funnel, the orifice of which is covered by the operator's finger. The stopwatch is started when the fingertip is removed and is stopped when the last powder leaves the funnel. The flow rate (s/50 g) of the sample is expressed as the time in seconds necessary for 50 g in weight of the powder to flow through the orifice. A powder that does not flow through the 2.5 mm orifice of a Hall funnel is classed as nonfree-flowing powder.

The Hall funnel is calibrated using a standard powder (150-mesh Turkish corundum) that has a flow rate of 40.0 s/50 g in the standard funnel. Real funnels can give somewhat different values of the flow rate of this powder due to peculiarities of their manufacture; this value is usually stamped on the funnel. Calibration with Ballotini solid glass spheres with particle size ranges of 0.090–0.102 and 0.065–0.090 mm in diameter has flow rates of 35.6 and 33.4 s/50 g, respectively.

Sliding at Impact Point

The chute angle and the roughness of the chute surface at the point of impact are the key factors in chute design. Optimum is the chute angle that does not facilitate an accelerated movement of powder in the chute with the transformation of the constrained moving to the free one, which is accompanied by a transition into the suspension state of dust powder fractions (mainly of particles smaller than 50 μm in size) and by increasing particle segregation in the reservoir filled with the powder. All the factors affecting frictional properties can influence the optimum chute angle.

Segregation of Particles

A uniformity of the mixture is very important in achieving high-quality PM manufacture. In the case where a particulate material is represented by both a polydisperse powder and a mixture of powders differing in their physical-chemical properties, segregation results in the heterogeneity of the particle size distribution as well as of the physical-chemical properties. This requires not only a proper mixing, but also suitable storing, feeding, and transporting of powders.

Three phenomena have been identified as the primary cause of most segregation problems in metallic powders. They are the simple segregation mechanisms under gravity considered below.

Trajectory Effect

While pouring the powder by the chute onto the pile, particles are separated in size. The frictional drag on particles moving on a pile surface is higher for finer particles than for coarser particles. This results in a concentration of finer particles nearer to the end of the chute while coarser particles come to rest at a much greater distance to the base of the pile (Fig. 1.43).

Screening Model (Also Called Sifting Phenomenon)

This effect occurs when finer particles move through a matrix of coarser particles. The screening effect occurs in typical PM processes connected with filling of different volumes. In these processes, an impingement effect is also revealed when, under the impact of falling coarser particles, the pile of finer particles becomes more dense and that causes the slope angle of the upper part of the pile to become higher that the angle of repose (see Fig. 1.43).

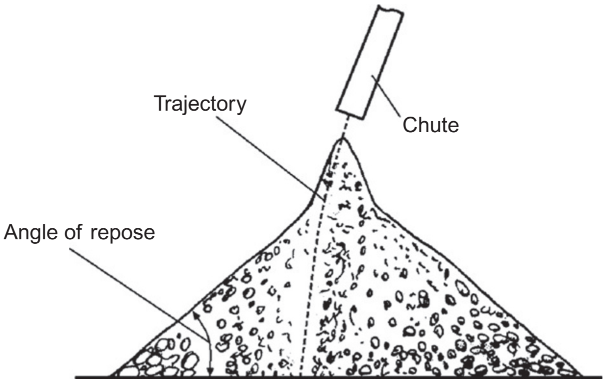

FIG. 1.43 Trajectory effect segregation of particles.

Fluidization

Fine particles retain the ability to remain in suspension for a long time whereas coarser particles settle first (according to their sedimentation rate). This results in a vertical segregation of particles within the powder layer. If the powder is segregated by air entrainment, fine particles will be located close to the top of the bottom-poured container. Air currents can carry the airborne fine and light particles away from a fill point to certain parts of a bin, such as toward vents and dust collectors.

Using the following data can help to influence the powder segregation during the production of PM parts:

- The more cohesive a powder, the less probable its segregation. Therefore, for some materials, the opportunity for segregation can be reduced by adding binders. This causes fine particles to stick to coarse ones and makes the powder less free flowing. However, an additive must be optimized to avoid the possibility of reducing to zero the powder flow in the chute.
- The type of the displacement device can appreciably influence the segregation tendency of powders. It is significant that funnel flow patterns strengthen segregation while a mass flow pattern tends to minimize such problems.
- Trajectory effect segregation is most likely to occur when the powder has a wide particle size distribution and when there is interparticle motion during operation. Usually, particles greater than about 100 μm in diameter are most subject to trajectory effect segregation. If most of the particles are smaller than 100 μm, the segregation by fluidization and particle entrainment is more probable.

Angle of Repose

The angle of repose is related to interparticle friction and the flowability of powders. It is not standardized. Several methods are used to measure this parameter. However, it is necessary to have in mind that the reliability of measuring the ultimate angle of repose depends on the measuring method used. Therefore, the measuring method should be carefully selected so that it best represents the property to be quantified.

A popular method for the determination of the angle of repose consists of the calculation of the tangent of the angle as the ratio of the height to the mean base radius of the powder heap. This powder cone is formed by means of carefully pouring the powder through a funnel. It can be formed as a fixed height cone, as a fixed base cone, or by using a circular method (Fig. 1.44) measuring the angle.

The following methods have also found a use for measuring the angle of repose [39]:

- *Titling table*, where a rectangular box filled with powder is tilted until the contents begin to slide.
- *Rotating cylinder*, where a sealed hollow cylinder half full of powder is rotated until the powder surface shows its maximum angle with the horizontal. This angle is the angle of repose.
- *Ledge method*, where the powder is initially charged into a rectangular box (see Fig. 1.44). A slot at the base of one vertical wall is closed by a board. The closure board is then removed to allow the material to flow slowly through the narrow slot. The angle with the horizontal plane of the surface of the powder equilibrium when the flow stops is calculated as the angle of repose.
- *Crater method* (called also the discharge method [40]), where a circular tube is placed vertically on a plate with an orifice in the center (Fig. 1.45). The height of the remaining powder against the wall of the tube is measured at eight equidistant points around the circumference to determine the angle of repose [41].

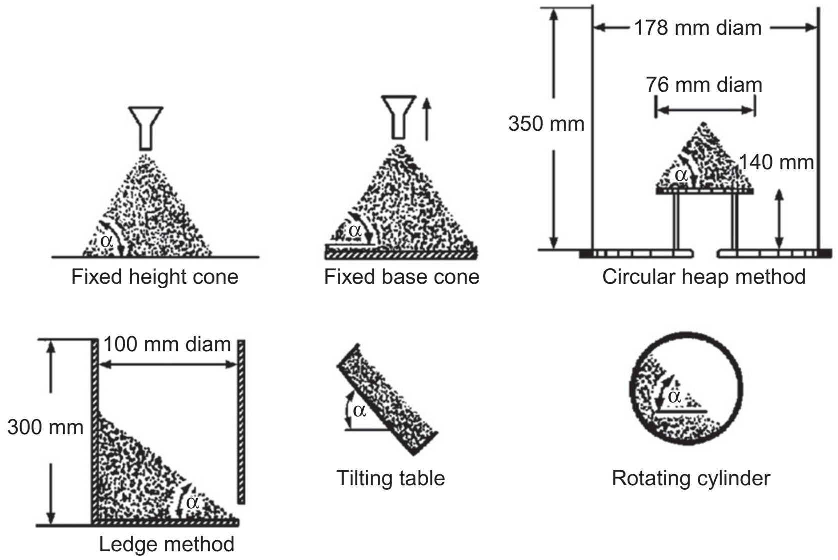
α
Fixed height cone
Fixed base cone
350 mm
178 mm diam
76 mm diam
140 mm
Circular heap method
100 mm diam
300 mm
Ledge method
Tilting table
Rotating cylinder

FIG. 1.44 Six methods used to measure the angle of repose.

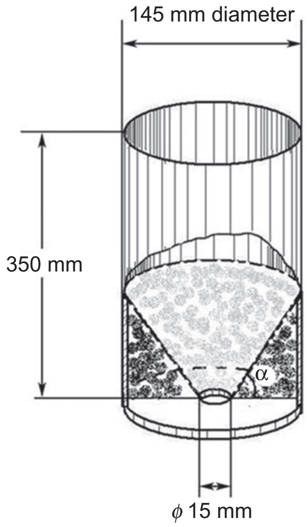
145 mm diameter
350 mm
α
ϕ 15 mm

FIG. 1.45 Crater method used to measure the angle of repose.

- *Dynamic angle of repose* is determined in the apparatus consisting of a drum with a roughened internal surface that is half filled with powder and slowly rotated around its horizontal axis. Within a certain range of rotation speeds (usually from 2.5 to 6 rpm), the surface of the powder in the drum comes to a sufficiently steady condition. The maximum angle of bed inclination just before slump occurs is designated as the dynamic angle of repose [34].

Factors Influencing on Angle of Repose

There are internal and external factors affecting the angle of repose. Internal factors include particle size, particle shape, and cohesiveness. Generally, coarser particles have higher angles of repose. However, very fine particles may reveal cohesiveness owing to the electrostatic effect, which increases the angle of repose. Typically, spherical particles have smaller angles of repose than irregularly shaped ones, owing to spherical particles having a greater tendency to roll.

External factors include the method of measurement and the presence of other components, including moisture. The effect of the measuring method is discussed in detail above. It is significant that the ledge and crater methods give a higher angle of repose than that obtained from the heap formation methods. The angle of repose of loose dry powder increases by compacting as well as by introducing moisture.

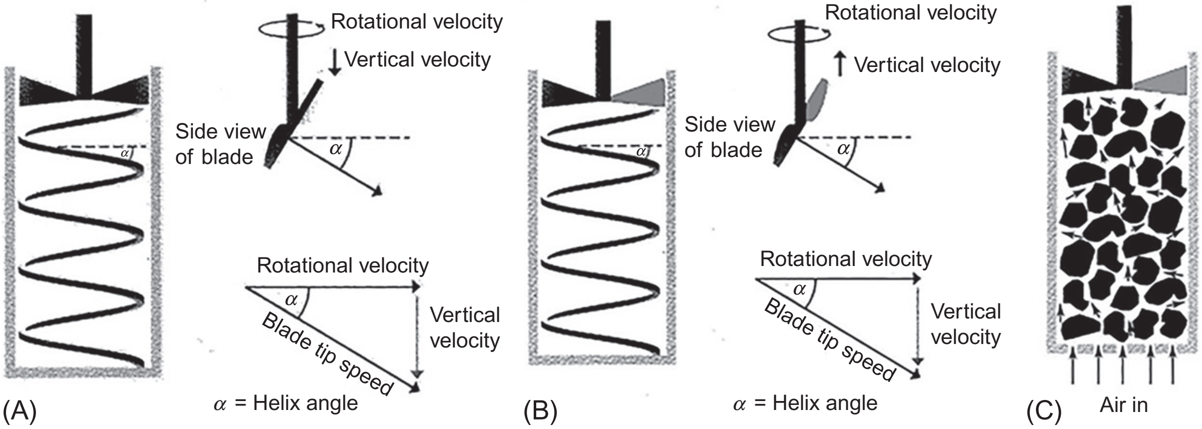

FIG. 1.46 Schematic drawing of the FT4 device: downward move (A); upward move (B); and air permeability testing (C).

Multiaimed Powder Tester FT4

The FT4 powder rheometer, also known as *Freeman Technology* [42,43], is based on the torque and force signals measured as the blade is rotated and moves through the powder (Fig. 1.46). Force measurements are converted into energy to determine the total energy consumed or work done during the downward and upward traverse. It is supposed that the more difficult it is to move the blade because the particles resist motion, the harder it is to get the powder to flow. This parameter is used as a key in the assessment of powder flowability and is called *basic flow energy*. The sizes of FT4 equipment assembly ordinarily are a 48 mm diameter blade and a 160 mL powder sample contained in a 50 mm borosilicate test vessel.

Powder flowability by FT4 is characterized by dimensionless parameters: flow rate index (FRI) and flow function (FF). But, there is no information about correlation between both above parameters and basic flow energy. The powders by flowability are classified as *not flowing* ($FF < 1$)*, easy flowing* ($4 < FF < 10$)*, and free flowing* ($FF > 10$).

The measurements of bulk density, permeability, and compressibility is fulfilled by the FT4 by means of conventional techniques. Bulk property characterizations include bulk density measurements on conditioned, tapped, and consolidated powders; permeability (pressure drop at fixed air throughput) as a function of varying bulk pressure; and compressibility of a powder bulk as a function of external pressure.

COMPRESSIBILITY AND COMPACTIBILITY OF METAL POWDERS

Compressibility and compactibility define the ability to form unsintered (green) compacts by die pressing of powders. Generally, the compressibility is quantified as the value of the compacting pressure required to ensure a specified green density of the sample. Therefore, the compressibility of the powder is an important factor in the design of pressing equipment. It is usually expressed in terms of green density. The compressibility is also measured by the compression ratio, which is the ratio of the green density to the apparent density of the powder.

The compactibility is evaluated by the green strength of a powder compact and relates to the sample complexity, fragility, and the ability of the compact to be ejected from the die. The relation between the compressibility and the compactibility is complex because some factors can improve one of them to the detriment of the other. Thus, particles of a spherical shape generally have a higher compressibility. In contrast, an increase of particle surface area, which can be achieved by increasing the particle surface irregularity, usually increases the green strength. At the same time, such factors as increasing the compaction pressure and the temperature have competing effects on the compressibility and the green strength. These factors promote intense particle movement and deformation, which are the bases to improve mechanical interlocking.

Compressibility

Characteristic compressibility data for gas-atomized aluminum powder and electrolytic copper powder are shown in Fig. 1.47 as a functional dependence of the percentage of the theoretical density on the compacting pressure [44].

Lubricants are used to promote the ejection of the compacted samples from the die. At higher compacting pressures, lubricants reduce the green density, owing to the fact that they are taken up by the available pores. There are two lubrication techniques. One method consists of mixing a dry lubricant such as zinc stearate, amide wax, and stearic acid with the

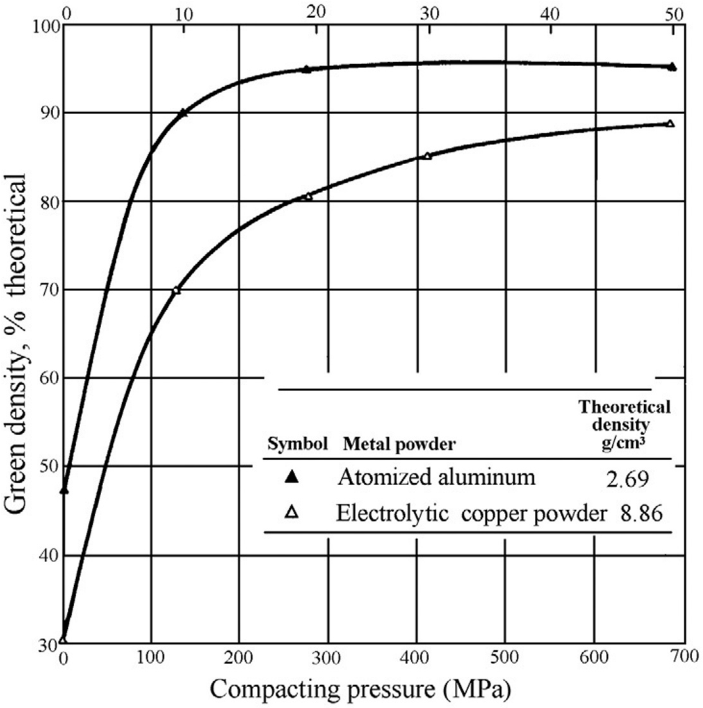

FIG. 1.47 Compressibility curves for gas-atomized aluminum powder and electrolytic copper powder.

metallic powder. By the other method, the die walls and punches are greased by the lubricants. In the case of the powder lubrication method, the lubricant addition may range from 0.5 to 1.5 wt.%. With the wall lubrication, a solid lubricant, for example, 100 g zinc stearate, is mixed with a volatile organic liquid, 1.0 L methyl chloroform. This mix is either painted or sprayed on the tooling. The organic liquid evaporates, leaving a thin film of dry lubricant on the working surface of the die cavity and punches.

ISO 3927, "Metallic Powders Excluding Powders for Hardmetals—Determination of Compactibility (Compressibility) in Uniaxial Compression," establishes the method for compressibility. The description of this method is also contained in ASTM B331, MPIF 45, and GOST 25290-90 standards (see Appendix A).

For pressing, dies of tool steel hard metal are used, one of them for cylindrical and the other for rectangular compacts. The cylindrical die shall ensure the manufacture of compacts of 20–26 mm in diameter and with the height-to-diameter ratio of 0.8–1.0, and the rectangular die shall ensure the manufacture of compacts in the form of plates of $30 \times 12\ \text{mm}^2$ in size and of 5–7 mm in thickness. The shaping is carried out in a press with loading to 500 kN, which is controlled for a uniform growth with a rate not higher than 50 kN/s. To construct the curve of powder compressibility at repeated pressing, loadings of 200, 400, 500, 600, and 800 MPa are used. If the compressibility at a single pressing is needed, it is measured at one of the above pressure values.

After pressing, the green samples are weighed to ±1 mg, and their sizes are measured by a micrometer to ±1 μm. The compressibility (ρ_p) that is determined by the density of the pressed sample is calculated by the formula:

$$\rho_p = \frac{m}{V}$$

where ρ_p is the compressibility, g/cm^3; m is the weight of the green compact, g; and V is the volume of the green compact, cm^3.

Green Strength

Necessary and sufficient mechanical strength of a cold-pressed green specimen allows the ejection of the green specimen from the die and its transfer to the sintering furnace or die head without breakage. This is particularly important for thin-walled specimens, thin sections of large parts, and finned specimens. The strength of green compacts depends mainly on mechanical interpenetration of superficial irregularities of particles, which is favored by plastic deformation during pressing. Therefore, spherical particles show the lowest degree of mechanical strength because of low initial surface contact

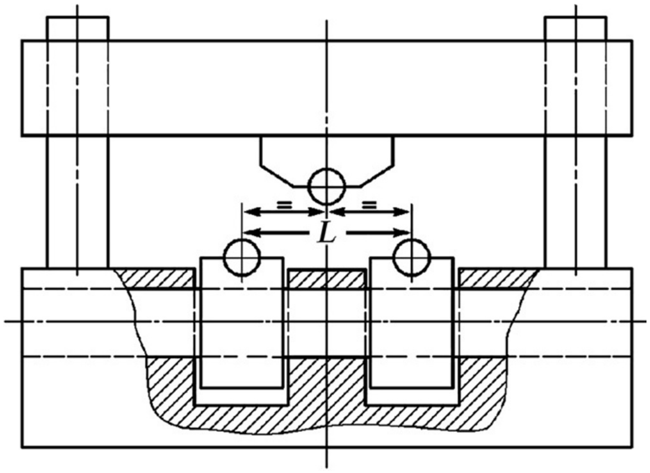

FIG. 1.48 Device for testing of green strength of an unsintered compact.

between neighboring particles. Green strength is also decreased when oxidation and contamination of particle surfaces and the amount of adsorbed gases increase.

Standard test methods to determine green strength of an unsintered compact are specified in ISO 3995, "Metallic Powders—Determination of Green Strength by Transverse Rupture of Rectangular Compacts." The description of this method is also contained in the ASTM B312, MPIF 15, and GOST 25282-93 standards (see Appendix A).

The main point of the method consists of the determination of the bending stress of green samples of a rectangular section by means of the action on the sample of a uniformly growing load up to fracture. The strength is determined as the stress calculated by the bending equation that is necessary to crack the rectangular billet installed on the two supports along the edges and subjected to the load imposed in the center. An example of the device for testing the sample strength is shown in Fig. 1.48.

For the test, samples of not less than 30 mm in length, 10–13 mm in width, and 5.5–6.5 mm in thickness are used. The load is increased with a constant rate until the sample fails (not quicker than 10 s). The strength of the nonsintered material is calculated by the formula:

$$S = \frac{3PL}{2t^2W}$$

where S is the green strength, MPa; P is the force at the instant of the destruction, N; L is the distance between the supports, mm; t is the thickness of the specimen, mm; and W is the width of the specimen cross-section, mm.

For most applications, green strength values of 5.0–6.0 MPa or higher allow us to preserve the condition during the handling of green specimens. Lower green strength may cause horizontal lamination in the specimen. Specimens with sharp contours or thin sections, or specimens made from a blend of several powders in which some of the components detract from the overall strength of the specimen, require higher green strength characteristics.

APPARATUSES FOR POWDER ANALYSIS

Several advanced designs of apparatus for powder analysis have been developed in recent years. These include the particle size techniques as well as surface area, porosity, and density measurements. Table 1.12 contains a list of some of these devices.

The new generation SediGraph III 5120 Particle Size Analyzer with advanced instrumentation from Micromeritics Instrument Corporation (SIC) provides accurate and reproducible particle size measurements in the diameter range of 300 to 0.1 μm. Scanning the sedimentation cell from bottom to top permits an accurate inventory of particles while minimizing the time required for the sedimentation of fine particles. In the Microtrac S3500 particle size analyzer, the implementation of modifying the Mie equation by the use of the three laser arrangements allows us to measure nonspherical particles in size ranging from 2800 to 0.02 μm. The laser particle sizer Analysette 22 Comfort from Fritsch GmbH is a versatile instrument for the determination of the size distribution of suspensions, emulsions, and powders. The usable inverse Fourier optics provide measurement of particle size distribution with a very high resolution. Also, with the computer-controlled location of the measuring cell (max. 310 positions) in the convergent beam between laser and sensor, it is possible to utilize up to 310 measurement signals for the calculation. The Multisizer 4 Coulter Counter provides size

TABLE 1.12 Apparatus for Powder Analysis

Apparatus	Principle of Operations	Measurement Range	Measuring Time. Accuracy	Source
Particle size analysis techniques				
SediGraph III PLUS particle size analyzer Addition by Master Tech 052 Autosampler	It is based on sedimentation theory and the absorption of X-radiation Designed to increase throughput, repeatability, and reproducibility; up to 18 samples can be prepared to transfer to the analysis system	Particle size ranging from 300 to 0.1 μm equivalent to spherical diameter	Runs up to 18 samples unattended in 15 min max	MIC
Microtrac S3500 particle size analyzer	Modified Mie equation for nonspherical particles due to the three laser arrangements generating scattered light in wide range degrees and the geometrical configuration specific of nonlinear detectors	Particle size ranging from 2800 to 0.02 μm	10–30 s	Microtrac Inc.
Saturn Digisizer 5205	The digital reproducing of a pattern is obtained as a result of laser light scattering. The resulting information is then processed on the basis of Mie theory. The sample handling system maintains a homogenous and representative suspension flowing	Particle size ranging from 2500 μm to 40 nm	Approx. 10 s	MIC
Laser Particle Sizer Analysette 22 NanoTec Plus	The laser diffraction method for particle size determination based on Mie theory is utilized. A module system for appropriate wet and dry dispersion is developed	Particle size ranging from 2000 to 0.01 μm	5 − 10 s	Fr
Multisizer 4 Coulter Counter	Coulter principle consists in the occurrence of voltage pulse proportional to the volume of the particle through passing the aperture into electrolyte, in which electric current flows	Particle size ranging from 1600 to 0.4 μm	10 − 90 s	Beckman Coulter, Inc.
Surface area, porosity, and density measurements				
TriStar 3000	Surface area determination and porosimetry are based on the technique of gas adsorption	Measures surface area are as low as 0.01 m^2/g	Runs three BET 5-point samples in approx. 20 min	MIC
ASAP 2020	Surface area and porosimetry analyzer uses the gas sorption technique	Surface area down to 0.0005 m^2/g Pore diameters: 3.5–5000 Å Micropore volumes: 0.0001 cc/g	Ramp up to 20°C/min to 800°C 10°C/min to 1000°C 5 °C/min to 1100°C	MIC
FlowSorb III	The FlowSorb III measures surface area using the flowing gas method, which involves the continuous flow of an adsorptive and inert gas mixture over the sample at atmospheric pressure	Surface area measurable in the range 0.01 to over 1000 m^2/g	Reproducibility is better than 0.5%	MIC
AutoPore IV 9500	Porosity of material is characterized by various levels of a sample immersed in mercury	Capability to measure pore diameters from 0.003 to 1100 μm	Collects resolution data: better than 0.1 μL for mercury intrusion and extrusion volumes	MIC
MultiVolume Pycnometer 1305	Method utilized a principle of gas pycnometry where volume displacement is determined from the pressure/volume relationship of a gas, preferably helium, under controlled conditions	Range of sample volumes: from 0.5 to 150 cm^3	Accuracy: ±0.1% to 0.2%	MIC

Fr, Fritsch GmbH; *MIC*, Micromeritics Instrument Corporation.

distribution in number, volume, and surface area in one measurement with an overall sizing range of 1600 to 0.2 µm. The TriStar 3000 gas adsorption analyzer from SIC is a fully automated surface area and porosimetry analyzer, providing three BET surface area measurements simultaneously in approximately 20 min. The AutoPore IV 9500 Series from SIC characterizes a material's porosity by applying various levels of pressure to a sample immersed in mercury; this instrument is applied over a capillary diameter range from 360 to 0.003 µm.

The operating details and special features of these devices can be found in the respective brochures available from the manufacturers.

REFERENCES

[1] Allen T. Sampling and classification of powders. In: ASM handbook, vol. 7. ASM International Publishers; 1998. p. 205–21.
[2] Allen T. Particle size measurements. 4th ed. London: Chapman and Hall Publishers; 1990.
[3] Kouzov PA. Fundamentals of particle-size analysis of industrial dusts and particulate materials. Leningrad: Himiy Publishers; 1987 [in Russian].
[4] Cowley SD, Moris SJ. Understanding and minimizing variation sources in dry sieving tests. Powder Bulk Eng 1991;Feb:34–41.
[5] Fuks NA. Mechanics of aerosols. Moscow: AN SSSR Publisher; 1955.
[6] Fisher sub sieve sizer instructions manual. Pittsburgh, PA: Fisher Scientific Co.
[7] Mie G. Beiträge zur Optik trüber Medien. Ann Phys 1908;25:377–445.
[8] Rose HE. Eine Studie über das Problem der Korngrössen-messung. Chem Ing Tech 1959;31(3):183–91.
[9] Dankley JJ. Atomization. In: ASM Handbook, vol. 7. ASM International Publishers; 1998. p. 35–52.
[10] Shimizu K, Brown GM, Kobayashi K, Skeldon P, Thompson GE, Wood GC. Ultramicrotomy—a route towards the enhanced understanding of the corrosion and filming behavior of aluminum and its alloys. Corros Sci 1988;40(7):1049–72.
[11] Krajnikov AV, Gastel M, Orter HM, Likutin VV. Surface chemistry of water atomised aluminium alloy powders. Appl Surf Sci 2002;191:26–43.
[12] Iacocca R. Bulk and surface characterization of powders. In: ASM handbook, vol. 7. ASM International Publishers; 1998. p. 222–33.
[13] Brunauer S, Emmett PH, Teller E. Adsorption of gases in multimolecular layers. J Am Chem Soc 1938;60:309–19.
[14] Panichkina VV, Uvarova IV. Testing methods of dispersity and specific surface area of metallic powders. Kiev: Naukova Dumka Publishers; 1973 [in Russian].
[15] Gregg SJ, Sing KSW. Adsorption, surface area and porosity. London: Academic Press Publishers; 1982.
[16] Lowell S, Shields JE. Powder surface area and porosity. London: Chapman and Hall Publishers; 1991.
[17] Allen T. Particle size measurement. vol. 2, London: Chapman and Hall Publishers; 1997.
[18] Callis CF, Irani RR. Miscellaneous techniques, particle size: measurements, interpretation, and application. New York: John Wiley and Sons Publishers; 1963.
[19] Method for Determination of Average Particle Size of Metal Powders Using the Fisher Subsieve Sizer. In: MPIF Standard 32. Princeton: MPIF Publishers; 2003. p. 45–7.
[20] Heinzer PJ. Permeametry. In: ASM handbook, vol. 7. ASM International Publishers; 1998. p. 277–8.
[21] Heinzer PJ. Pycnometry. In: ASM handbook, vol. 7. ASM International Publishers; 1998. p. 278–80.
[22] AutoPore 1V Operator's Manual. Micrometrics; 2004.
[23] Naidich YV, Perevertailo VM, Lavrinenko IA, Kolesnichenko GA, Zhuravlev VS. Surface properties of melts and solids and their usage in material science. Kiev: Naukova Dumka Publisher; 1991 [in Russian].
[24] Good RJ, Mikhail RS. The contact angle in mercury intrusion porosimetry. Powder Tech 1981;29:53–62.
[25] Hiemenz PC, Rajagopalan R. Principles of colloid and surface chemistry. New York: Marcel Dekker Publisher; 1997.
[26] Rootare HM. A review of mercury porosimetry. Advanced techniques in powder metallurgy. Perspectives in powder metallurgy, vol. 5. Plenum Press Publisher; 1970.
[27] Kloubek J. Hysteresis in porosimetry. Powder Technol 1981;29(1):63–73.
[28] Plachenov TG, Kolesencev SD. Porosimetry. Leningrad: Himiya Publishers; 1988 [in Russian].
[29] Giesche H. Mercury porosimetry. In: ASM handbook, vol. 7. ASM International Publishers; 1998. p. 280–6.
[30] ASTM standard D 4284. Pore volume distribution of catalysts by mercury intrusion porosimetry. In: Annual book of ASTM standards, vol. 5.03. ASTM International Publishers; 2003.
[31] ASTM standard C 493. Bulk density and porosity of granular refractory materials by mercury intrusion porosimetry. In: Annual book of ASTM standards, vol. 15.01. ASTM International Publishers; 2003.
[32] Jenike AW. Storage and flow of solids. Bull Univ Utah 1964;53(26):1–198.
[33] ASTM standard D 6128. Standard shear testing method for bulk solids using the Jenike shear cell. ASTM Publishers; 1977.
[34] Carson JW. Bulk properties of powders. In: ASM handbook, vol. 7. ASM International Publishers; 1998. p. 287–301.
[35] Freeman G. Production of cobalt-base powders. In: ASM handbook, vol. 7. ASM International Publishers; 1998. p. 179–81.
[36] Poster AR, editor. Handbook of metal powders. Reinhold Publisher; 1966.
[37] Tundermann JH. Production of nickel-base powders. In: ASM handbook, vol. 7. ASM International Publishers; 1998. p. 167–71.
[38] Lux B, Zeiler B. Production of tungsten and tungsten carbide powders. In: ASM handbook, vol. 7. ASM International Publishers; 1998. p. 189–201.

[39] Brown RL, Richards JC. Principles of powder mechanics. Oxford: Pergamon Press Publisher; 1977.
[40] Yokoyama T. Fluidity of powder. Powder technology handbook. New York, Basel: Marcel Dekker, Inc.; 1997. p. 413–25.
[41] Herein H, Brimacombe JK, Watkinson AP. The modeling of transverse solids motion in rotary kilns. Metall Trans B 1983;14:191–205.
[42] Freeman R, Xiaowei F. Characterisation of powder bulk, dynamic flow and shear properties in relation to die filling. Powder Metall 2008; 51(3):196–201.
[43] Freeman T, Brockbank K, Sabatier J. Characterising powder flow properties—the need for a multivariate approach. Powder and Grain 2017. EPJ Web of Conferences 2017;140(03008):1–4. https://doi.org/10.1051/epjconf/201714003008.
[44] Lumpman S. Compressibility and compactibility of metal powders. ASM handbook, vol. 7. ASM International Publishers; 2015. p. 171–8.

Chapter 2

Mechanical Crushing and Grinding

Oleg D. Neikov
Frantsevich Institute for Problems of Materials Science (IPMS), Kiev, Ukraine

Chapter Outline

Introduction 65
Mechanism of the Ductile Metal Deformation 66
Regularities of Milling 68
  Impact Process by Colliding Balls 68
  Grindability 70
  Temperature Rise During Milling 72
Crushing and Grinding Equipment 74
  Crushers 74
  Grinding Techniques 75
  Medium Agitating Mills 81
  Jet Mills 85
  Other High-Energy Milling Methods 85
References 89

INTRODUCTION

Comminution is the oldest mechanical operation for the size reduction of solid materials and is an important step in many processes where raw materials are converted into intermediate or final products. It is the most widely used method of powder production for hard metals and oxide powders. The secondary grinding of spongy cakes of reduced oxide and electrolytic or atomized powders is the most conventional milling process; hammer crushers and rod mills are used for this purpose. Depending on the degree to which the material is sintered, every primary particle size distribution is re-established during grinding, or larger agglomerates are produced.

Demand for fine or ultrafine particles is increasing in many kinds of industries, particularly in solid-state alloying or high-energy milling. The energy efficiency of comminution is very low while the energy required for comminution increases with a decrease in produced particle size.

The main purposes of grinding include:

- Particle size reduction.
- Particle size growth.
- Particle shape change (to flake shape).
- Agglomeration.
- Mechanical alloying (solid-state alloying).
- Blending of two or more materials or mixed phases.
- Modifying or changing of properties of a material (density, flowability, or work hardening).

The grinding process disintegrates, deforms, or cold welds the impacted particles. Grinding also may produce polymorphic transformation [1]. The specific effect that grinding has on a powder depends on its physical and chemical properties, the grinding conditions, and the vacuum, gaseous, or liquid environment in which the operation is performed.

Four types of forces act on particulate material during grinding: impact, attrition, shear, and compression. Impact is the instantaneous striking of one object by another; both objects may be moving or one may be stationary. Attrition is the producing of particles by the rubbing action between two bodies, or wear debris. Shear consists of cutting or cleaving particles and usually is combined with other types of forces. Shear contributes to breaking particles into separate pieces with a minimum fine yield. Compression is the slow application of compressive forces to a solid. This type of grinding action is realized in jaw crushers, predominantly when the material is hard and nonductile.

Handbook of Non-Ferrous Metal Powders. https://doi.org/10.1016/B978-0-08-100543-9.00002-6
© 2019 Elsevier Ltd. All rights reserved.

Design and process advancement was originally based on empirical and semiempirical data. The fundamental research of grinding ductile metals is missing, although much is known phenomenologically about the process.

Breaking occurs in hard, brittle materials with minimal particle deformation and agglomeration due to welding. Deformation, cold welding, and breaking happen in varying degrees with both hard and ductile materials.

MECHANISM OF THE DUCTILE METAL DEFORMATION

Existent theoretical views on crushing and grinding patterns are based on the process of multiphase disintegration of a solid. Such a model acts on the promise that the disintegration process of the solid passes through several phases:

- Accumulation of defects leading to local concentration of strains.
- Formation of the embryonic microcracks, that is, the rupture of continuous crystal lattice in several cells.
- Development and joining of embryonic microcracks down to the formation of the main disruption crack.
- Disruption of a solid into several parts.

Let us discuss these disruption process stages in more detail.

The dislocations, incipient from unequal atom numbers in neighboring lattice planes, are a main type of crystal lattice defect that defines the strengthening properties of a solid. Odd atoms in a structure remain without a chemical bond. In that case, a defect of structure, that is, a dislocation, occurs (Fig. 2.1).

The action of an external load can displace this defect from one part of a crystal to another. Finally, if on the path of motion the obstacles do not meet, the dislocation appears on the surface where a step in one atom is formed. To such unimpeded displacement of dislocations (in extremely schematic form), a ductile deformation mechanism is represented.

By the imposition of a deforming load to a solid in which there are braking centers of dislocations, the accumulation of dislocations is observed by obstructions interfering with their motion. In these locations, high local stresses appear, which can turn out to be sufficient for the integration of some of the dislocations and the formation of an embryonic microcrack (Fig. 2.2). At that stage, the stresses in materials directly adjoining the microcrack boundaries are decreased and elastic

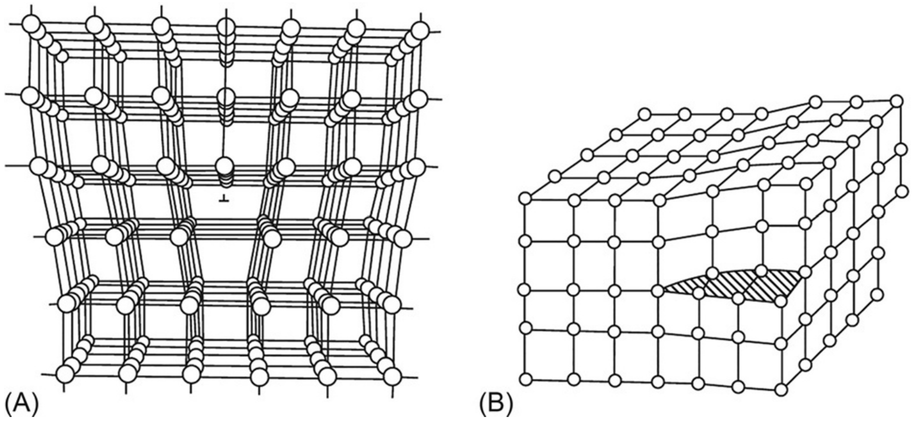

FIG. 2.1 Scheme of (A) linear and (B) helical dislocations in crystal lattice.

FIG. 2.2 Confluence of dislocations with formation of the embryonic microcrack at (A) two and (B) three dislocations.

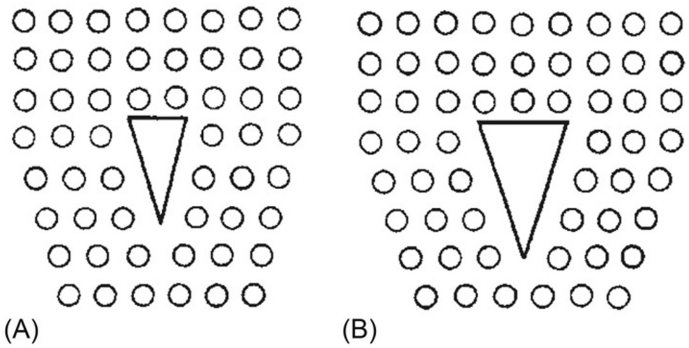

energy is released. The value of the latter is approximately proportional to the square of the crack length or its penetration depth into the crystal. Energy, which is needed for forming two new surfaces, is proportional to crack length in the first power. Thus, a small crack, for its growth, must consume more surface energy than released energy due to the relaxation of the stresses that designate its stability.

However, if a crack affected by applied stress begins to develop, the condition of the process is changed. With a growth in crack size, the released energy is increased rapidly because it's proportional to the second power of the crack length. At a definite critical crack length, the crack begins to release more energy than it consumes. Then, an abrupt change occurs and the crack can propagate in the body of the metal at high speed and is ramified, forming a break surface.

The conception about breaking as a process and its subsequent growth arose because the usually observed ultimate strength values, from 10 to 1000 MPa, differ markedly from theoretical data calculated at the strength of interatomic bonding, amounts from 10 to 100 GPa. The application of compressive forces to solids can significantly increase the durability of solids by prevention of the development of microcracks. Therefore, the slow application of compressive forces to solids accounts for the high power consumption and low efficiency of this technique. The microcracks can readily develop under the influence of tensile and shear stresses.

In the development phase of microcracks, the adsorption of surfactants has great importance. Their penetration into the microcrack mouth weakens interatomic bonding and facilitates crack propagation while adsorption on newly formed surfaces prevents its closing (the Rehbinder effect [2,3]). However, the observance of a number of conditions is necessary for the appearance of the Rehbinder effect. First, the action of the surfactant becomes apparent when a solid is in the stressed state. Environmental high pressure promotes penetration of the surfactant into embryonic microcracks. The optimum temperature in the range 373–423 K is also a requisite condition while the intensive thermal fluctuations that occur above a certain limit may result in the dissipation of dislocation clusters and the stabilization of microcracks [4].

The mechanisms of the Rehbinder effect, called the adsorption-induced reduction of the strength of solids (AIRS) [3], are based on the existence of the relation between the free energy of a surface, which is formed as a result of the fracture of a solid, and the strength of the solid. In an idealized case of microscopic brittle fracture, this relation is quantitatively determined by the well-known Griffith's relation (Eq. 2.1), according to [5]:

$$\sigma_s = A\left(\frac{E\gamma_s}{L_s}\right)^{1/2} \tag{2.1}$$

where σ_s is the ultimate strength (fracture stress), A is the numerical constant, E is the Young modulus,γ_s is the surface free energy per unit area, and L_S is the length of an initial surface crack.

According to Eq. (2.1), the strength reduction corresponds to the surface energy drop resulting from the adsorption of environment components on the fractured surface (i.e., when a solid is fractured in contact with a surface active environment). Together with the Gibbs adsorption relation [6], which relates to changing the surface free energy to the adsorption value, Eq. (2.1) represents the simplest thermodynamic interpretation of the adsorption-induced reduction of strength [7].

When the fracture has a quasielastic character, that is, the characteristic size of a plastic zone is much smaller than the size of a crack, the residual plastic deformation and, on the whole, the irreversible structural rearrangements are localized in a thin layer at the fractured surface. Such a condition allows [8,9], without essential changes in the Griffiths approach, to modify Eq. (2.1) by replacing the surface free energy by the specific work of fracture W_f as:

$$\sigma_s = \text{const}\left(\frac{EW_f}{L_s}\right)^{1/2} \tag{2.2}$$

Correspondence (Eq. 2.2), known as the Griffith-Irwin-Orovan's relation, underlies the concept of quasibrittle fracture, which is applicable, although with different accuracies, to a very broad spectrum of materials and external conditions. The specific work of the fracture in Eq. (2.2) may be presented as the sum:

$$W_f = \gamma_s + W_p \tag{2.3}$$

where the work of plastic deformation W_p comprises dissipative losses. Usually, for structural materials, work W_p is noticeably greater than surface energy γ_s.

Griffith's and Griffith-Irwin-Orovan's relations are applicable to macroscopic cracks. In this case, the contribution of the long-range surface forces to the energy balance of the fracture can be, in most cases, ignored [10,11]. When the crack propagation occurs in a nanosized region, the role of the surface forces can appear to be essential.

Malkin, based on fundamental regularities and contemporary concepts of the mechanisms for the AIRS [3], reported that a reduction in the strength characteristics of solids under the influence of an adsorption active external environment is a widespread phenomenon, which is observed for solid-environment systems with various structures and chemical compositions. As the author reported [3], the AIRS is characterized by a pronounced chemical selectivity and sensitivity to the structure of a solid as well as the test conditions and peculiarity of the fracture under the conditions of AIRS is the non-chemical interaction between a solid and an environment along internal surfaces of a crack.

Despite great advances in the investigation of AIRS, the level achieved in understanding the mechanisms for the fracture of solids in contact with an adsorption active environment cannot be recognized as satisfactory. Many important aspects of AIRS, including estimating the roles of hydrodynamic, diffusion, and capillary-osmotic phenomena, remain to be studied.

Differently, the Griffith's relation (Eq. 2.1) is modified in the work [12]. The general form of the fracture equation for modes of leading that result in catastrophic failure is represented as:

$$\sigma_c = A\left(\frac{\gamma E}{c(1-\mu^2)}\right)^{1/2} \tag{2.4}$$

where σ_c is the stress at which a crack propagates depending on the size of the crack; A is the numerical constant that depends on crack geometry and its location, mode of loading, and dimensions of the particle (for example, A is $\sqrt{2/\pi}$ for the slit crack in an infinite sleet); c is the size of crack; E is the Young modulus; μ is the Poisson's ratio; and γ is the surface energy of the milled substance. Thus, measured strength depends on the crack size, elastic properties, and surface energy. For brittle materials, γ is between 10^2 and 10^3 mJ/cm^2.

The stress σ for fracture of a particle is represented [12] by:

$$\sigma = \sqrt{\frac{2Er}{L}}$$

where L is the length of the crack and r is the radius of the crack tip.

REGULARITIES OF MILLING

Impact Process by Colliding Balls

A model of impact process at the moment of collision, by which the particles are trapped between two colliding balls within a space occupied by a suspended, dispersed, or mass of powder particles, is shown in Fig. 2.3.

This effect is typical in dry and wet milling operations that use colliding devices such as tumbling, vibratory, planetary, and attrition ball mills. The number of particles within the incremental volume subjected to impact compression stress may range from one to a multitude, depending on the average particle size and the radius of the ball or curved surfaces contacting the trapped incremental volume.

The number of particles trapped between two balls on impact in an unconnected powder mass increases as the ratio of the ball diameter D to the particle diameter d increases. At the high ratios of D/d encountered in the milling of fine particles (less 150 μm), the trapped volume consists of particles within the microvolume BB′DD′ (see Fig. 2.3). Outside this incremental volume, the seeming (apparent) density of the powder sharply decreases to the density of the agitated unconnected particulate material, or suspension in the case of wet milling.

The amount of powder trapped and the size of the trapped volume depends on many factors, along with ratios of D/d, including particle size, apparent density of the particle cloud, the presence of slurry and its concentration and viscosity, air or gas pressure within the mill, surface roughness of the balls, velocity of the balls, and kinetic energy of the balls at the instant of collision.

In the gaseous atmosphere prior to impact, the majority of particles, mainly of a lesser size, are ejected as the balls approach each other (Fig 2.4A), while the remaining fraction becomes trapped and compacted between the decelerating balls at the moment of collision (Fig 2.4B). If the impacting force is sufficient, the trapped incremental volume of powder is compacted to an agglomerate particle (Fig. 2.4C), which is released when elastic energy impels the balls apart.

If bonding by welding or adhesion occurs between contacting surfaces and bonding forces are sufficient, the agglomerate does not break apart. Similarly, particles may bond to the surfaces of the balls, which may become coated with the powder. If the compressive impact forces exerted by the balls and particles are sufficient, particles are fractured (see Fig. 2.4D) or compacted (see Fig. 2.4C) within a critical zone of diameter X_c and thickness t, within the boundaries of BB′ and DD′ (see Fig. 2.3). The initial zone of compaction theoretically does not exceed AA′EE′. The density of the

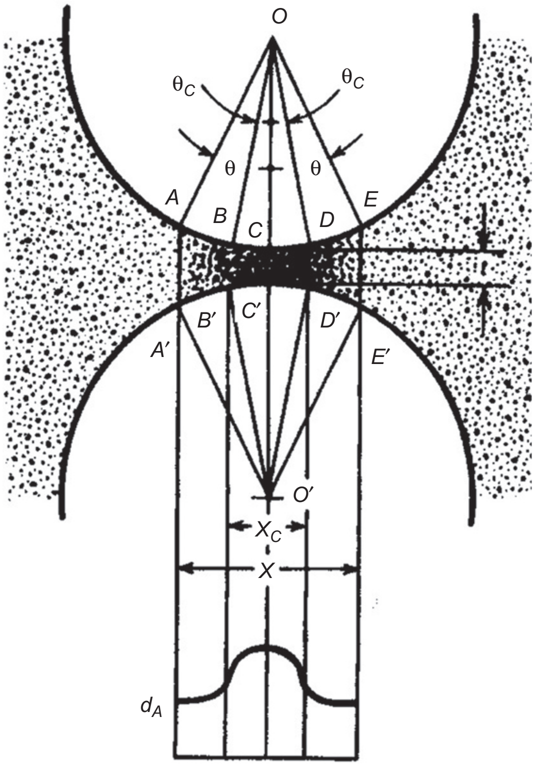

FIG. 2.3 Model of impact act at a moment of maximum impacting force, illustrating the formation of a microcompact. *(Source: Koch CC. Milling of brittle and ductile materials. In: ASM Handbook, Vol. 7. ASM International Publishers; 1998, pp. 53–66.)*

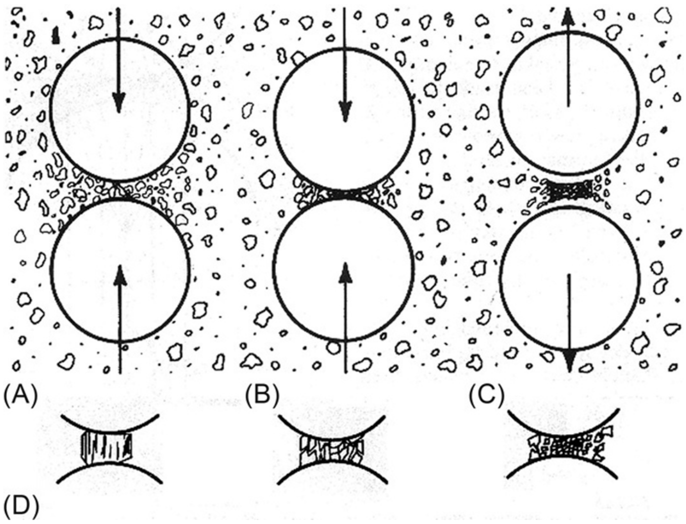

FIG. 2.4 Model of process trapping an incremental volume of ductile powder between two balls, including (A) series of balls coming together, (B) impact event, (C) release of agglomerate by elastic energy, and (D) brittle single particle.

trapped bed of particles varies from the maximum at the point CC′ to the density of the unconnected agitated powder outside the two A–A′ and E–E′ boundaries.

Fragmentation is similar to impact compacting of a radially unrestricted micropowder compact. Compaction begins with a powder mass that is characterized by relatively large spaces between particles compared to the particle size.

The first stage of compaction represents rearrangement of the particles. Particles slide past one another with a minimum of deformation and fracture, producing some fines, especially from brittle, unevenly shaped particles. During this stage, flowability is reduced and void spaces are partially filled with fine particles. Particle shape plays a significant part in this stage. Spherical particles, having the greatest flowability and the least friction, are almost totally ejected from between colliding balls; flake or irregular particles, having the greatest frictional resistance to flow, tend to be retained between the nearing balls.

During the second stage, plastic deformation and cold welding have major effects on comminution for ductile materials. For hard and brittle metallic materials, plastic deformation and welding have little effect on comminution. Most metals become harder during the second stage, which increases deformation resistance.

The closing, or third stage of compaction, involving particle fracture results in further deformation and/or fragmentation of the particles. The microcompacts range from very small for slightly ductile materials to relatively large for highly ductile metal powders, depending on the strength of the bonds between particles, which in turn depends on factors such as characteristics of the bonding surfaces, impact force, oxide films, and temperature.

During grinding, a major part of the energy input is expended on various internal processes that do not contribute to particle fragmentation. As grinding proceeds into the ultrafine region, the fracturing mode varies and conditions that were insignificant when particles were relatively large become controlling factors.

If the particle deforms plastically, fracture is difficult to induce and the probability that stress will occur is reduced further. As fragments decrease in size, the tendency to aggregate increases and fracture resistance increases. Particle fineness approaches a limit as grinding continues and maximum energy is expended. Generally, as batch comminution proceeds over an extended time, the mean applied stress needed for particle failure increases while the magnitude of local stresses available to initiate fracture decreases. Fig. 2.5 illustrates the crushing of a single ductile metal powder particle between impacting balls.

Typical changes in ductile metal powder particle morphology during milling are shown in Fig. 2.6. These occur during wet milling of gas-atomized, cobalt-base alloy powders due to the following processes: microforging, fracture, agglomeration, and deagglomeration.

Microforging is the predominant process during initial grinding as a result of compression shape forming of ductile metal particles by impact from the milling medium (see Fig. 2.5).

After a certain period of grinding, separate particles deform to the state that cracks initiate, propagate, and ultimately fracture the particles. Particles formed from irregular or spongy particles contain fissures and cracks that facilitate compression, fatigue failure, and fragmentation, compared to the smooth, relatively nonporous spheroidal particles formed by atomization. Some friable metals (such as antimony, bismuth, silicon, manganese, and chromium) and brittle intermetallic alloys (for example, copper-aluminum, aluminum-magnesium, copper-tin, nickel-iron, nickel-zirconium, and phosphorus-copper) can be milled easily.

Agglomeration of particles may appear by welding, mechanical joining of spongy or rough surfaces, or autoadhesion. Autoadhesion is the molecular interaction of particles themselves, characterized by van der Waals forces.

Deagglomeration is a process that breaks up agglomerates formed by autoadhesion without further disintegration of the separate powder particles.

Grindability

When a metal is plastically deformed by cold working, most of the mechanical energy of the deformation process is converted in the heat. However, a small amount (approximately 5%) is conserved in the metal, thereby raising its internal energy. The energy connected with permanent lattice strain or cold work is minimal for hard, brittle particles, but can be large for ductile materials. The energy expended to overcome the friction between particles is translated to heat and fulfills no useful work in grinding.

If the temperature of the powder rises above a certain level, the cold-processed metal particles may undergo recovery and recrystallization. Heat is generated by particle deformation and by elastic deformation of the metal grinding balls and grinding chamber. Generally, the temperature rises during severe cold working, abruptly falls just before cold work attains saturation levels, and then slowly decreases after extended milling time. Water-jacketed milling chambers usually are required for large, high-energy vibratory and attrition mills that reach temperatures above 473 K.

Grindability characterizes the comminution efficiency of a grinding technique and is determined by a strictly defined mode. Usually one of the two following methods is used:

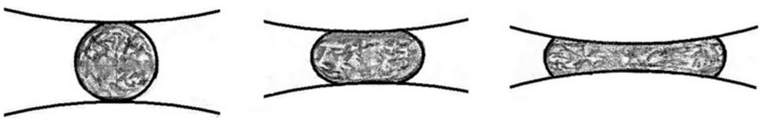

FIG. 2.5 Geometrical parameters involving an impact between two grinding balls of the single ductile metal powder particle.

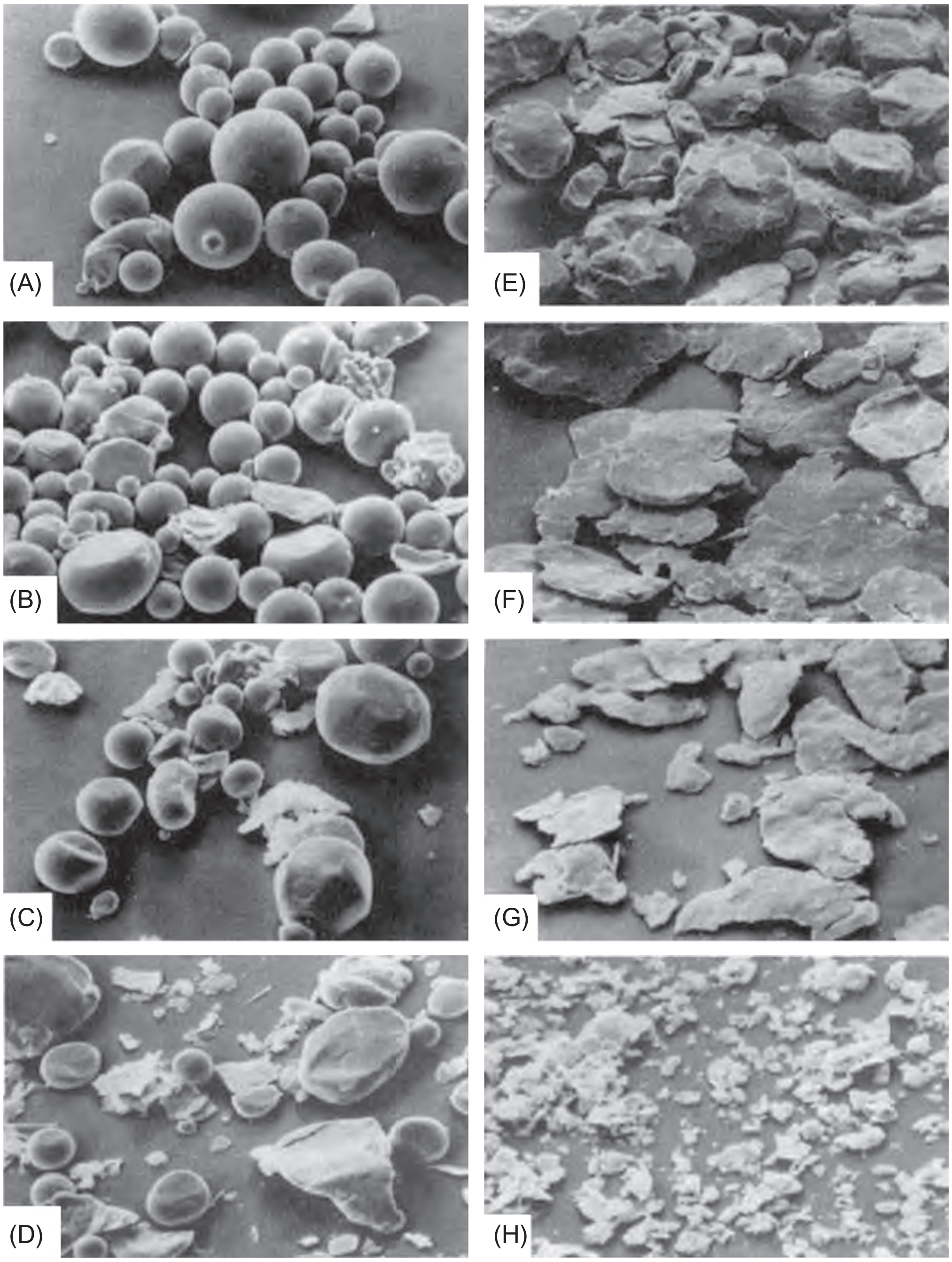

FIG. 2.6 Scanning electron micrographs of stellite 21 cobalt base alloy powder, wet milled in ethyl alcohol with an aluminum nitrate grinding aid. (A) As produced gas atomized powder; (B) after 1 h grinding; (C) after 2 h; (D) after 4 h. (E) after 8; (F) after16 h; (G) after 32 h; (H) after 64 h. *(Source: Koch CC. Milling of brittle and ductile materials. In: ASM Handbook, Vol. 7. ASM International Publishers; 1998, pp. 53–66.)*

Hardgrove Grindability Index (ASTM D409 Standard)

Grindability is an important factor for the characteristic of the brittle raw materials by the design the mills. As grindability depends on many unknown factors, hardgrove grindability index (HGI) is determined empirically using a sample mill, according to the following procedure. The device to measure the hardgrove grindability consists of a top rotating ring with eight balls of 1 in. (25.4 mm) diameter. A load of 64 ± 0.5 lb. (29.5 ± 0.23 Kg) is applied on the top rotating ring. The HGI is defined as:

$$\mathrm{HGI} = 13 + 6.9w$$

where w (g) is the mass of ground product finer than 74 μm.

The smaller the HGI, the harder and less grindable the raw material.

Bong's Work Index (JIS M4002 Standard)

Bong's Work Index is used in Bong's law of comminution energy. It states that the total work useful in breakage is inversely proportional to the length of the formed crack tips and directly proportional to the square root of the formed surface:

$$W = W_{\mathrm{i}}\left(\frac{10}{\sqrt{d_{\mathrm{p}}}} - \frac{10}{\sqrt{d_{\mathrm{f}}}}\right) = C'_{\mathrm{B}}\left(S_{\mathrm{p}}^{0.5} - S_{\mathrm{f}}^{0.5}\right)$$

where W is the specific energy expenditure in kilowatt-hours per ton and d_{p} and d_{f} are the particle size in microns at which 80% of the corresponding product and feed passes through the sieve; C'_{B} is a constant depending on the characteristics of materials; and S_{p} and S_{f} are the specific surface areas of product and initial feed, respectively. W_{i} is called Bond's Work Index in kilowatt-hours per ton. It is given by the empirical equation:

$$W_{\mathrm{i}} = \frac{1.1 \times 44.5}{P_1^{0.23} G_{\mathrm{b.p}}^{0.82}\left(\frac{10}{\sqrt{d_{\mathrm{p}}}} - \frac{10}{\sqrt{d_{\mathrm{f}}}}\right)}$$

where P_1 is the sieve opening in microns for the grindability test, $G_{\mathrm{b.p.}}$ (g/rev) is the ball mill grindability, d_{p} is the product particle size in microns (80% of product finer than size P_1 passes) and d_{f} is the initial feed size in microns (80% of feed passes). A standard ball mill is 305 mm in internal diameter and 305 mm in internal length charged with 285 balls, as tabulated in Table 2.1. The lowest limit of the total mass of balls is 19.5 Kg. The mill is rotated at 70 rev/min. The process is continued until the net mass of undersize produced by revolution becomes a constant $G_{\mathrm{b.p}}$ in the above equation.

In fine grinding, when P is smaller than 70 μm, the Work Index W_{i} is multiplied by a factor f to account for the increased work input. The factor f is found from the following empirical equation:

$$f = \frac{P + 10.3}{1.145P}$$

The Work Index is an important factor in designing comminution processes and has been widely used.

Temperature Rise During Milling

The temperature rise during milling is mainly due to ball-to-ball, ball-to-powder, and ball-to-wall collisions as well as frictional effects. The overall temperature rise of the powders during milling can be due to more than one cause. First, the intense mechanical deformation due to kinetic energy of the grinding media (balls) raises the temperature of the powder. Thus, the higher the energy (milling speed, relative velocity of the balls, time of milling, size of the grinding balls, ball-to-powder weight ratio, etc.), the higher the temperature rise. Second, it is possible that exothermic processes occurring during the milling process cause the powder particles to ignite and generate additional heat [13].

It has been reported that >90% (different values have been quoted by different investigators) of the mechanical energy imparted to the powders during milling is transformed into heat [14], raising the temperature of the powder.

Bhattacharya and Arzt [15] calculated the contact temperature of the powder compact surfaces, considering that head-on collisions occur during collisions between two grinding media. Therefore, the calculated value will be the upper bound

TABLE 2.1 Set of Steel Balls for Test by Bond's Work Index

Diameter (mm)	Number of Balls
36.5	43
30.2	67
25.4	10
19.1	71
15.9	94
Total	285

of the temperature rise. In arriving at these values, the authors have assumed that the time of impact, $\Delta\tau$, could be approximated using Hertz's theory of elastic impact [16,17], and the energy flux at the compact surface is uniform over the entire contact area and is constant for times less than $\Delta\tau$. They have also assumed in their calculations only a small fraction, β, of the kinetic energy

$$E = {}^{1}\!/_{2} m v^2,$$

where m is the mass and v is the relative velocity of the balls, is utilized in plastically deforming the powder, that is, the expended plastic energy, $U_\mathrm{p} = \beta E$. By taking the appropriate heat transfer conditions into consideration, the authors [15] calculated the temperature rise, ΔT, as

$$\Delta T = \frac{2q_2\Delta\tau}{\rho c t_0} + \frac{q_2 t_0}{2\kappa}\left[\frac{1}{3} - \frac{2}{\pi^2}\sum_{n=1}^{\infty}\frac{(-1)^n}{n^2}\exp\left(-\frac{4n^2\pi^2\alpha\Delta\tau}{t_0^2}\right)\cos n\pi\right] \tag{2.5}$$

where

$$q_2 = \frac{\delta Q}{\pi r_0^2 \Delta\tau}$$

and Q represents the average quantity of heat arising from the total deformation process over a time interval $\Delta\tau$, δ is the heat yield transfer into the powder compact, κ is the thermal conductivity of the powder, t_0 is the thickness of the powder sheet between two colliding balls at a moment of maximum impacting force (Fig. 2.7), r_0 is the radius of the powder compact, and α is the thermal diffusivity.

Such as, assuming that niobium powder is milled using stainless steel balls and that the powder compact has a thickness of $t_0 = 100\,\mu\mathrm{m}$ and a radius $r_0 = 263\,\mu\mathrm{m}$, the maximal temperature rise ΔT reached at the time of contact surface at a moment of maximum impacting force calculated according to [15] at $\beta = 0.03$ by $v = 6$ m/s and 8 m/s is 496 and 669 K, respectively, and at $\beta = 0.09$ by $v = 6$ m/s and 8 m/s is 941 and 1460 K, respectively.

The temperature rises calculated and estimated above using theoretical models on the basis of heat build up owing to kinetic energy of the collisions of balls [15] or microstructural changes [18] are not accurate or reliable due to the assumptions made, some of which may not be substantiated. Therefore, only experimental investigations may give reasonable and accurate values for the rise in temperature. However, experimental measurements are not easy and they measure only the bulk temperature of the wall of a mill, not the instantaneous temperature at the time of impact.

Some investigators have reported very large temperature rises. The experimentally measured bulk temperature rise in different alloy systems and milling conditions is in the range 323–489 K [17], and more commonly it is about 373–390 K. A maximal temperature of 373–488 K was recorded [19] by milling Ni-base superalloy in an attritor. It should be realized that this is the macroscopic temperature rise, even though it is recognized that local (microscopic) temperatures can be very high, often exceeding the melting points of some component metals [20].

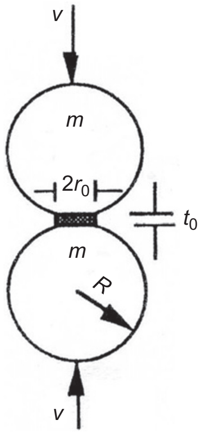

FIG. 2.7 Geometrical parameters involving an impact between two grinding balls and the powder compact.

CRUSHING AND GRINDING EQUIPMENT

A major objective of comminution is to liberate minerals for concentration processes. Another objective is to manufacture powder with particles of required sizes. Comminution processes generally consist of several stages in series. Various types of crushing and grinding equipment have been used industrially for these objectives.

Crushers

Crushers are widely used as a primary stage to produce the particulate product finer than about 50–100 mm. They are classified as jaw, gyratory, and cone crushers based on compression, cutter mill based on shear, and hammer crusher based on impact.

A *jaw crusher* consists essentially of two crushing plates, inclined to each other forming a horizontal opening by their lower borders. Material is crushed between a fixed and a movable plate by reciprocating pressure until the crushed product becomes small enough to pass through the gap between the crushing plates. Jaw crushers find a wide application for brittle materials. For example, they are used for comminution of porous copper cake. A Fritsch jaw crusher with maximal feed size 95 mm, final fineness (depends on gap setting) 0.3–15 mm, and maximal continuous throughput 250 Kg/h is shown in Fig. 2.8.

A *gyratory crusher* includes a solid cone set on a revolving shaft and placed within a hollow body, which has conical or vertical sloping sides. Material is crushed when the crushing surfaces approach each other and the crushed products fall through the discharging opening.

Hammer crushers are used either as a one-step primary crusher or as a secondary crusher for products from a primary crusher. They are widely used for crushing hard metal scrap for different hard metal recycling processes. Pivoted hammers are pendulous, mounted on the horizontal axes symmetrically located along the perimeter of a rotor. Crushing takes place by the impact of material pieces with the high speed moving hammers and by contact with breaker plates. A cylindrical grating or screen is placed beneath the rotor. Materials are reduced to a size small enough to pass through the openings of the grating or screen. The size of the product can be regulated by changing the spacing of the grate bars or the opening of the screen.

The feature of the hammer crushers is the appearance of elevated pressure of air in the discharging unit of the crusher and underpressure in the zone around the shaft close to the inside surface of the body side walls. Thus, the hammer crushers also act as high-pressure, forced-draught fans. This may lead to environmental pollution and product losses in fine powder fractions. A design for a hammer crusher (Fig. 2.9) essentially allows a decrease of the elevated pressure of air in the crusher discharging unit [5]. The A-zone beneath the screen is communicated through the hollow ribs and openings in the body side

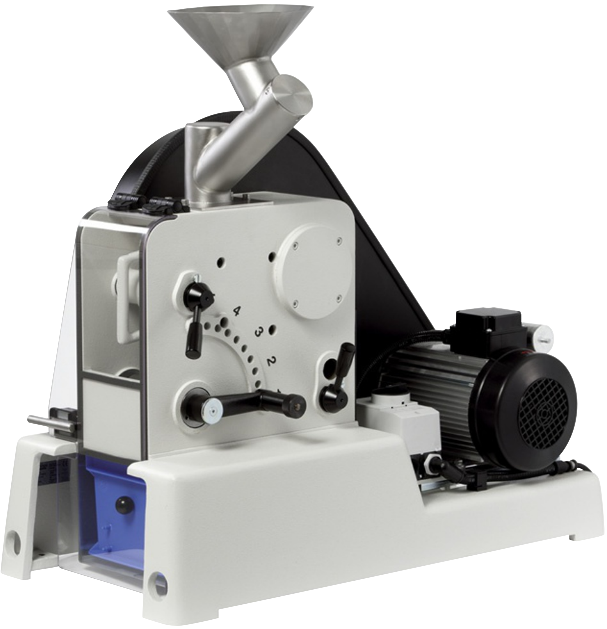

FIG. 2.8 Jaw crusher.

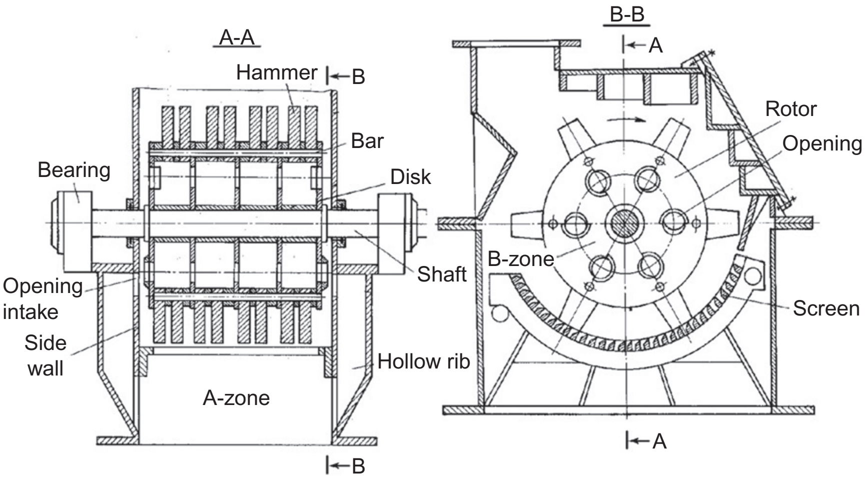

FIG. 2.9 Hammer crusher.

walls with the B-zone around the shaft close to the inside surface of body side walls. As a result, the circulation of suspended matter in the gas between A and B zones is established and the high pressure of air in the discharging unit of crusher is reduced.

Grinding Techniques

In ball-medium types, the grinding energy is transferred to materials through such media as balls, rods, and pebbles by moving the mill body. Based on the mode of motion of the mill body, ball-medium mills are classified as tumbling ball mills, vibration mills, and planetary mills.

Grinding Kinetics

The mathematical descriptions of grinding kinetics of mineral materials [22] are known. Gal'chuk and Rud [23] made an attempt to apply the above kinetic equations of the mineral grinding process to the metal powder grinding. The application possibility of Gundermann's equation, Tovarov's modified formula, and Razumov's equation [21] to the description of the grinding kinetics of metal powders has been analyzed [23].

The calculations by Razumov's equation have given the best approach to the experimental data. This equation is represented as follows:

$$R = \frac{R_0 p}{(e^{kpt} + p)}$$

where R is the coarse particle size fraction content at the t instant, R_0 is the initial content of coarse particles fraction, the parameter p characterizes the properties of the material that is being grinded, and parameter k characterizes the grinding technique. These parameters were defined using R_1 and R_2 values at t_1 and t_2 instants for each. The calculations of the p and k parameters were calculated for each particle size fraction separately.

As the authors [22] reported, the difference between the calculations by Razumov's equation and the experimental data by ball-bearing waste grinding was lower than 1%.

Tumbling Ball Mills

Tumbling ball mills or ball mills are most widely used in both wet and dry systems, in batch and continuous operations, and on small and large scales.

Grinding elements in ball mills travel at different velocities. Therefore, collision force, direction, and kinetic energy between two or more elements vary greatly within the ball charge. Frictional wear or rubbing forces act on the particles as well as collision energy. These forces are derived from the rotational motion of the balls and the movement of particles within the mill and contact zones of colliding balls.

By the rotation of the mill body, due to friction between the mill wall and balls, the latter rise in the direction of rotation until a helix angle does not exceed the angle of repose, whereupon the balls roll down. Increasing the rotation rate leads to

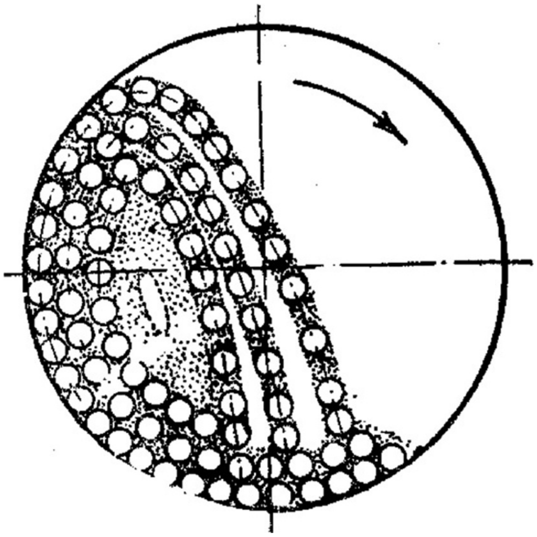

FIG. 2.10 Displacement of balls in mill.

the growth of the centrifugal force and the helix angle increases, correspondingly, until the component of the weight strength of balls becomes larger than the centrifugal force. From this moment, the balls are beginning to fall down, describing certain parabolic curves during the fall (Fig. 2.10).

With the further increase of rotation rate, the centrifugal force may become so large that balls will turn together with the mill body without falling down. The critical speed n (rpm) when the balls remain attached to the wall with the aid of centrifugal force is:

$$n = \frac{42.3}{\sqrt{D_m}}$$

where D_m is the mill diameter in meters. The optimum rotational speed is usually set at 65%–80% of the critical speed. These data are approximate and may not be valid for metal particles that tend to agglomerate by welding.

The minimal magnitude of the ball size is calculated in millimeters from the equation:

$$d_{b.min} = 10 d_{b.max} \sqrt[3]{\frac{\sigma^2}{0.128 E \rho_b D}}$$

where $d_{b.max}$ is the maximum size of the feed (mm), σ is the compression strength (MPa), E is the modulus of elasticity (MPa), ρ_b is the density of material of balls (kg/m^3), and D is the inner diameter of the mill body (m).

Generally, a maximum allowed ball size is situated in the range from $D/18$ to $D/24$.

The degree of filling the mill with balls also influences the productivity of the mill and milling efficiency. With excessive filling, the rising balls collide with falling ones. Generally, filling the mill by balls must not exceed 30%–35% of its volume.

The productivity of ball mills depends on the drum diameter and the relation of ∫drum diameter and length. The optimum ratio between length L and diameter D, L:D, is usually accepted in the range 1.56–1.64. The mill productivity also depends on many other factors, including the physical-chemical properties of the feed material, the filling of the mill by balls and their sizes, the armor surface shape, the speed of rotation, the milling fineness, and the timely moving off of the ground product.

It is possible to make an approximate calculation of the capacity of a ball mill with uneven armor by means of the equation:

$$N = \left(0.104 D^3 L \rho_{b.ap} \varphi^{0.88} + 0.1 L n\right) \frac{1}{\eta_1 \eta_2}$$

where D is the drum diameter, L is the drum length, $\rho_{b.ap}$ is the apparent density of the balls, φ is the degree of filling of the mill by balls, n is the revolutions per minute, and η_1, and η_2 are coefficients of efficiency of electric engine and drive, respectively.

A feature of ball mills is their high specific energy consumption. A mill filled with balls, working idle, consumes approximately as much energy as at full-scale capacity, that is, during the grinding of material. Therefore, it is most disadvantageous to use a ball mill at less than full capacity.

Ball mills have the following advantages:

- Universality and high capacity.
- Permanence of a prescribed milling fineness by certain capacity over long periods of time (with periodical addition of balls for compensation of their wear).
- Reliability and safety, simplicity of servicing.

Shortcomings of ball mills:

- Unhandiness and large weight.
- Grinding high specific energy consumption; energy is mainly consumed on the wear of balls and wall armor, friction, heating of material, etc.
- Loud noise during working.

Depending on the form of the body, ball mills are differentiated as cylindrical, tubular, and conical.

Depending on the discharging method, they are also differentiated as:

- Mills with free discharge of ground product through a hollow trunnion.
- Mills with discharge along the length of the drum through a cylindrical sieve.
- Mills with an external separation system in which a prepared product is separated from the undermilled powder in separators outside the mill drum.

Milling time in tumbler mills is longer to accomplish the same level of blending achieved in the attrition or vibratory mill, but the overall productivity is substantially greater. Tumbler mills usually are used to pulverize or flake metals, using a grinding aid or lubricant to prevent cold welding agglomeration and to minimize oxidation [23].

Cylindrical Ball Mills differ usually in steel drum design (Fig. 2.11), which is lined inside by armor slabs that have dissimilar sizes and form a rough inside surface. Due to such juts, the impact force of falling balls is strengthened. The initial material is fed into the mill by a screw feeder located in a hollow trunnion; the ground product is discharged through the opposite hollow trunnion.

Cylindrical screen ball mills have a drum with spiral curved plates with longitudinal slits between them. The ground product passes into these slits and then through a cylindrical sieve and is discharged via the unloading funnel of the mill body.

Conical Ball Mills differ in mill body construction, which is composed of two cones and a short cylindrical part located between them (Fig. 2.12). Such a ball mill body is expedient because efficiency is appreciably increased. Peripheral velocity along the conical drum scales down in the direction from the cylindrical part to the discharge outlet; the helix angle of balls is decreased and, consequently, so is their kinetic energy. The size of the disintegrated particles also decreases as the discharge outlet is approached and the energy used decreases. In a conical mill, most big balls take up a position in the deeper, cylindrical part of the body; thus, the size of the balls scales down in the direction of the discharge outlet.

For emptying, the conical mill is installed with a slope from bearing to one. In wet grinding, emptying is realized by the decantation principle, that is, by means of unloading through one of two trunnions.

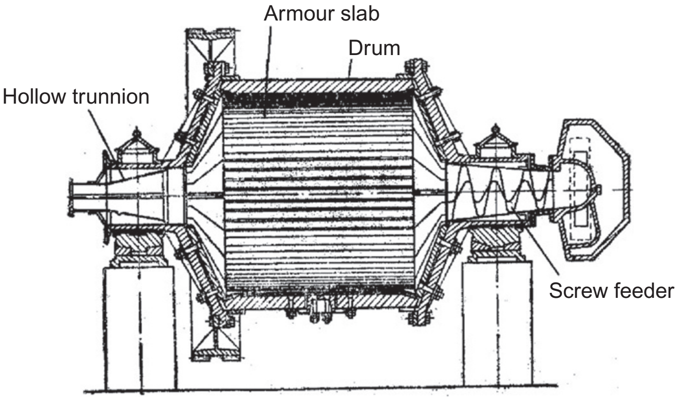

FIG. 2.11 Cylindrical ball mill.

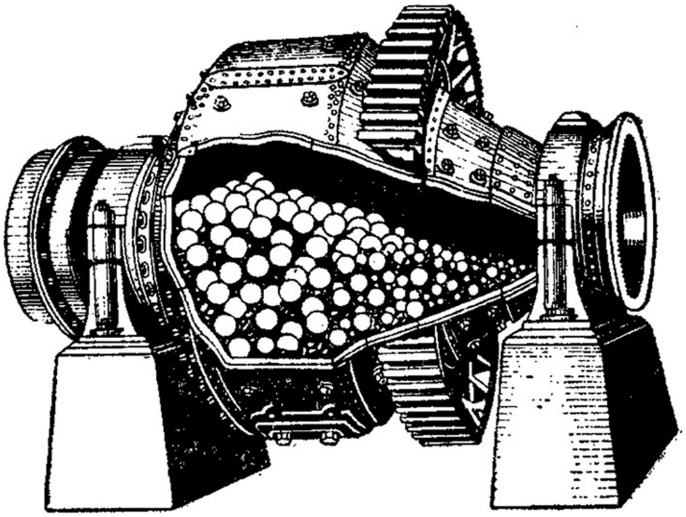

FIG. 2.12 Conical ball mill.

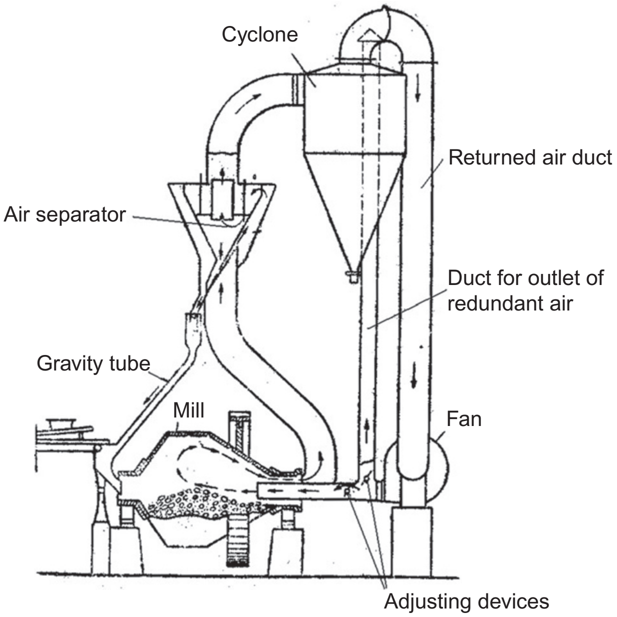

FIG. 2.13 Conical ball mill supplied by air separator, working in a closed cycle.

With dry grinding, these mills often work in a closed cycle. A scheme of the conical ball mill supplied with an air separator is shown in Fig. 2.13. Air is fed to the mill by means of a fan. Carried off by air currents, the product arrives at the air separator, from which the coarse particles are returned by gravity via a tube into the mill. The finished product is trapped in a cyclone while the air is returned in the fan.

Rod Mills

For fine grinding, rod mills are also used. In these, the rods are 40–80 mm in diameter and play a part in the grinding media. In such mills, the contacts between grinding rods and materials occur along a line, not at separate points as in ball grinding. Furthermore, coarse particles prevent the fine ones from welding together; consequently, a more homogeneous product is produced.

Cylindrical Grinding Elements Mill

The RETSCH XRD-Mill McCrone was developed for the preparation of samples for subsequent x-ray diffraction (XRD) analysis. The 125 mL grinding vessel is filled with an ordered array of 48 identical cylindrical grinding elements, available in agate, zirconium oxide, or corundum. A typical sample volume is between 2 and 4 mL. During operation, the vessel's circular motion causes a gentle grinding of the samples via friction. The result is a short grinding time the sample from ≤ 0.5 mm to the low μm-range (typically <10 μm) reducing with almost a narrow particle size distribution and crystal lattice entirely preservation during grinding operation.

Planetary Mills

A planetary mill consists of a revolving base disk and rotating mill pots, as shown in Fig. 2.14. Materials are ground by the large centrifugal force generated during revolution and rotation. The intensity of acceleration can be increased up to $150g$ on the scale of the gravitational acceleration. Thus, the pot containing the grinding media rotates about two separate parallel axes. A planetary arm of radius R_p is centered at a point about which it rotates at angular velocity, ω_{pl}. The pot with radius r_p rotates (usually in the direction opposite to the planetary arm) with angular velocity ω_p.

Planetary ball mills have often been used for research studies.

Typically, the commercially available Fritsch Pulverisette P-5 four-station planetary ball mill has been used (Fig. 2.15). Grinding pots and balls are available in several different materials, including agate, silicon nitride, sintered corundum, zirconia, chrome steel, chrome-nickel steel, tungsten carbide, and plastic polyamide.

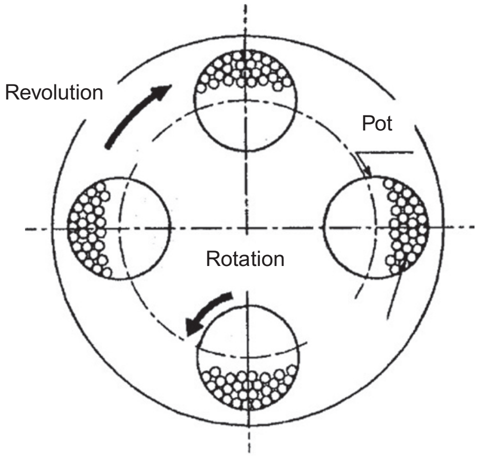

FIG. 2.14 Schematic drawing of a planetary ball mill.

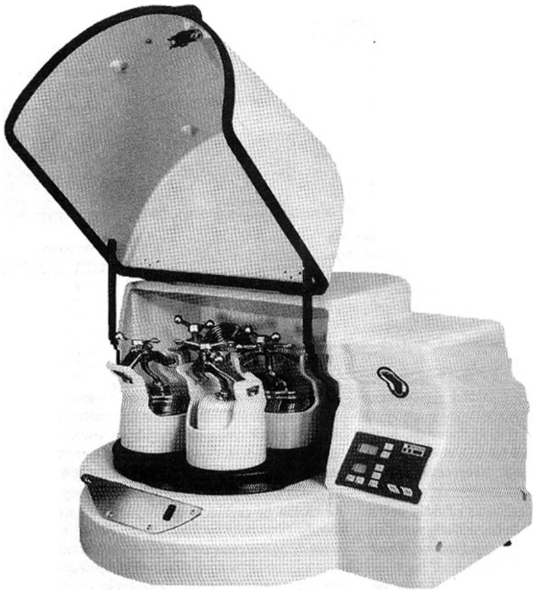

FIG. 2.15 Fritsch planetary ball mill Pulverisette 5 with four bowl fasteners.

Vibratory Ball Mills

In the vibratory tube mill, the oscillatory motion of the balls is used. The trajectories of the balls and particles is determined by many factors, including vibrational speed, amplitude, and curvature of the mill chamber side walls. The balls gyrate around the chamber wall, sometimes traveling horizontally in a spiral trajectory. Balls also revolve at different rates and directions, causing substantial shearing action, which is desirable in blending operations.

Impact forces acting on powders in a vibratory mill are a function of the rate of milling, the amplitude of vibration, and the mass of the milling medium. High-energy milling forces can be obtained by using high vibrational frequencies and small amplitudes of vibration.

Large production mills operate at relatively low vibrational frequencies and high amplitude, for example, 1000–1500 rpm and up to 12 mm while a laboratory mill [12] operates at 3300 rpm with a 2 mm amplitude, reaching a maximum acceleration rate of 12.2*g*.

The vibratory ball mill is also an excellent means of producing solid-state alloyed and dispersion strengthened metals. Fig. 2.16 shows the pilot- and production-sized cascade two-stage vibratory mills. The material passes sequentially through two grinding steps. In large tube mills, the vibratory motion of the medium decreases from the chamber walls to the center of the mill tube; consequently, the grinding effect is less at the center of the mill than adjacent to the chamber walls. Efficient operation is obtained at a ball fill of 60%–80% of the volume of the mill chamber for tubes about 500 mm in diameter, with 100% fill of the volume between the balls.

In vibratory mills, the grinding medium receives rapid impulses at a rate proportional to the vibrational frequency of the mill. Impact forces acting on the powder exceed shearing and friction forces. Vibratory mills utilize smaller grinding media because of higher impact forces, frequencies, and acceleration.

The rate of processing in a vibratory mill is proportional to the diameter of the balls and their density, proportional to the cube of the frequency of vibration, while not significantly affected by chamber diameter. The rate of processing increases as the amount of powder in the mill decreases and is greater with balls than cylinders or other shapes, but rods provide the more homogeneous product.

Vibrating Grinders

Vibrating grinders are also called cone inertia crushers (KID) [4]. The principal constructional diagram of a KID is shown in Fig. 2.17.

The grinder consists of a body with a conical inner surface in which is arranged an internal moving milling cone. The two cones form the milling chamber. On the axle of the internal moving milling cone, an unbalanced vibrator is fitted, driven through a flexible transmission. During vibrator rotation, centrifugal force is generated, leading the internal cone to roll along the inner cone surface of the grinder body without clearance if a material that is being grinded is absent in the milling chamber or on this material layer. Such inner cone varying movement is possible owing to the absence in these

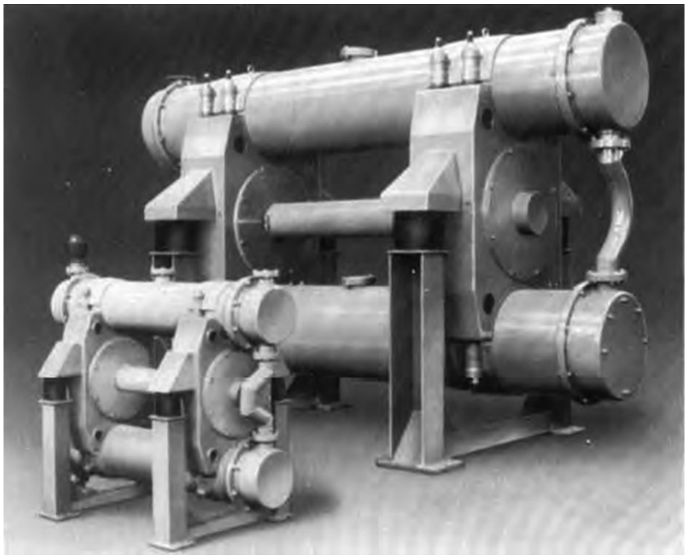

FIG. 2.16 The pilot- and production-size cascade two-stage vibratory mills.

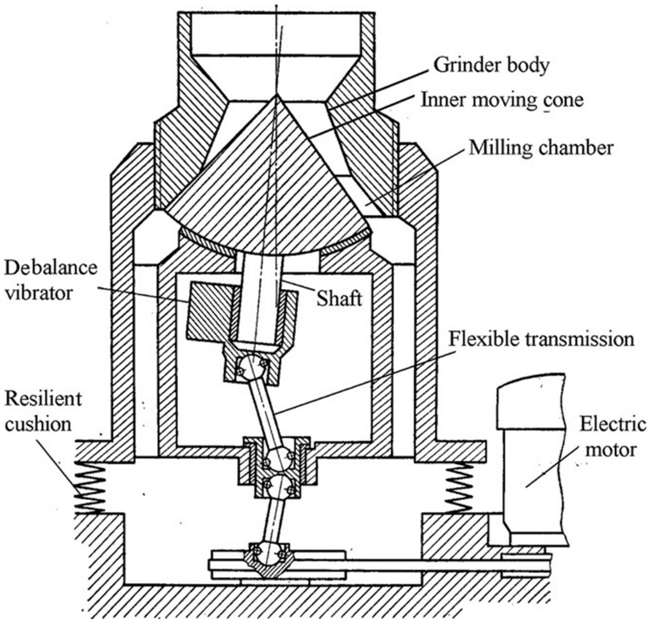

FIG. 2.17 Principal constructional diagram of the cone inertia crusher (KID). *(Source: Revnivcev VI, et al. Vibrating disintegration of solid materials. Moscow: Nedra; 1992 [in Russian].)*

machines of kinematic limitation of inner cone amplitude. KID does not have a discharging gap as do ordinary cone crushers; therefore, the diametric annular between cones is received by coincidence of their axes.

The idea of using the vibrator drive of the cone crusher appeared as long ago as 1925 (US Patent 1,553,333) and then its later versions—German Patent 679,800 (1952), Austrian Patent 200,598 (1957), and Japanese Patent 1256 (1972)—were published. The first experimental KID specimens were created in Russia in the early 1950s. Subsequently, in the various branches of industry in the Soviet Union, KIDs with a capacity from 1 to 300 t/h were produced. The manufacture of KIDs under license from Soviet Union was developed in Japan in 1981.

The basic KID feature—the absence of rigid kinematic bonding between the cones—allows the inner moving cone to change its amplitude, depending on the variation of grindable material resistance, or to stop if a large nongrindable body is encountered. This is not detrimental and does not lead to stopping the debalance. Another KID feature is the nature of the crushing force. In KID, the crushing force is the sum of the centrifugal force of debalance and the inner cone by its gyrating movement. Such force is determined by mechanics and does not depend on the properties of the processed material. This characteristic in combination with the resilient isolation of KID from the foundation allows a two-fold increase in the inner cone vibration frequency.

The vibrating grinder KID-60 is shown in Fig. 2.18. It can be adjusted to yield powder finer than 71 μm or coarser powder with almost complete absence of minus 71 μm powder (Table 2.2).

Technical characteristics of the main KID dimension-types are given in Table 2.3.

Medium Agitating Mills

In this technique, a large number of small grinding media are agitated by impellers, screws, or disks in a chamber. Breakage occurs mainly by the collision of the media. There are designs of the mill with a vertical or horizontal rotating shaft with wet or dry systems (Fig. 2.19).

The medium agitating mill is one of the most efficient devices for micronizing materials and has been in regular use for the production of fine particles and mechanical alloying processes. A typical stirred mill with a vertical rotating shaft and horizontal arms is shown in Fig. 2.20. This stirring action causes a differential movement between balls and the material being milled, thus a substantially higher degree of surface contact than is achieved in tumbling or vibratory mills is ensured. Milling takes place by impact and shear forces. The rotating charge of balls and milling product form a whirl where the milling product is impacted by balls moving in various trajectories.

The attrition mill agitator rotates at speeds ranging from 60 rpm for production units to 300 rpm for laboratory units and uses media that range from 3 to 6 mm while ball mills use large grinding media, usually 12 mm or larger, and run at low

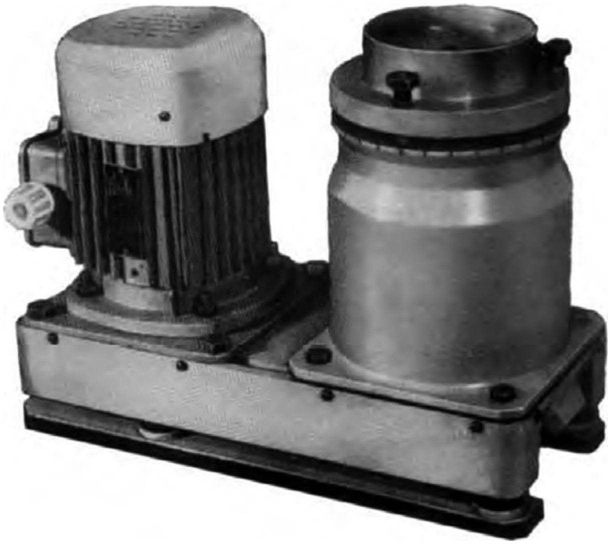

FIG. 2.18 Vibrating grinder KID-60.

TABLE 2.2 Attributes of Vibrating Grinder KID-60

Parameter	Unit	Magnitude
Piece of feedstock	mm	max 6
Productivity depending on particle sizes of obtained product		
Up to 71 µm	kg/h	3
Up to 100 µm	kg/h	5
Up to 0.5 µm	kg/h	10
Up to 1.0 µm	kg/h	20
Capacity of motor	kW	0.55
Vibrational frequency	rpm	2800, 2300 and 1900
Overall dimension	mm	370 × 160 × 300
Weight	kg	25

rotational speeds of 10–50 rpm. Power input to attrition mills is used to agitate the medium, not to rotate or vibrate heavy drums. Therefore, specific energy consumption of attrition mills is significantly less than with ball mills. Table 2.4 offers a comparison of grinding mills by rotational velocity. In the attrition grinding process, grinding time is related to medium diameter and agitator speeds [12], within given limits, as:

$$t = \frac{kd}{\sqrt{n}}$$

where t is grinding time required to reach a certain medium particle size; k is a constant that varies with the suspension being processed and the type of medium and mill being used; d is the diameter of the grinding medium; and n is shaft movement, in rpm.

Attrittion mills are classified as batch-, continuous-, or circulation-type mills. In the batch mill, material is loaded into the chamber and ground until the desired dispersion and particle size are achieved. Chamber walls are jacketed so that either hot or cold water can be circulated to control and maintain the temperature of the charging. The batch attrition mills can process high-density material, such as tungsten carbide, as well as viscous materials. They are also suitable for dry grinding and for producing dispersion-strengthened metals by means of mechanical alloying.

TABLE 2.3 Technical Characteristics of Main Cone Inertia Crushers (KID) Dimension-Types

Parameters	Unit	KID Dimension-Types						
		KID-100	**KID-200**	**KID-300**	**KID-450**	**KID-600**	**KID-900**	**KID-1200**
Productivity on output	t/h	0.03	0.16	2	7	25	45	80
Piece size of a feedstock, max	mm	10	35	20	30	50	70	80
Particle size in product, max	mm	0.3	1	2	3	5	6	8
Installed capacity	kW	1	5.5	11	30	75	160	250
Overall dimensions								
Depth	mm	400	920	1300	1400	2170	3115	3800
Width	mm	210	365	800	1000	1280	1970	2500
Height	mm	350	755	1450	1650	2170	2290	3000
Weight	t	0.06	0.32	2	4	7.5	17	30

Source: Revnivcev VI, Denisov HA, Zarogatsky LP, Turkin, VJ. Vibrating disintegration of solid materials. Moscow: Nedra; 1992 [in Russian]

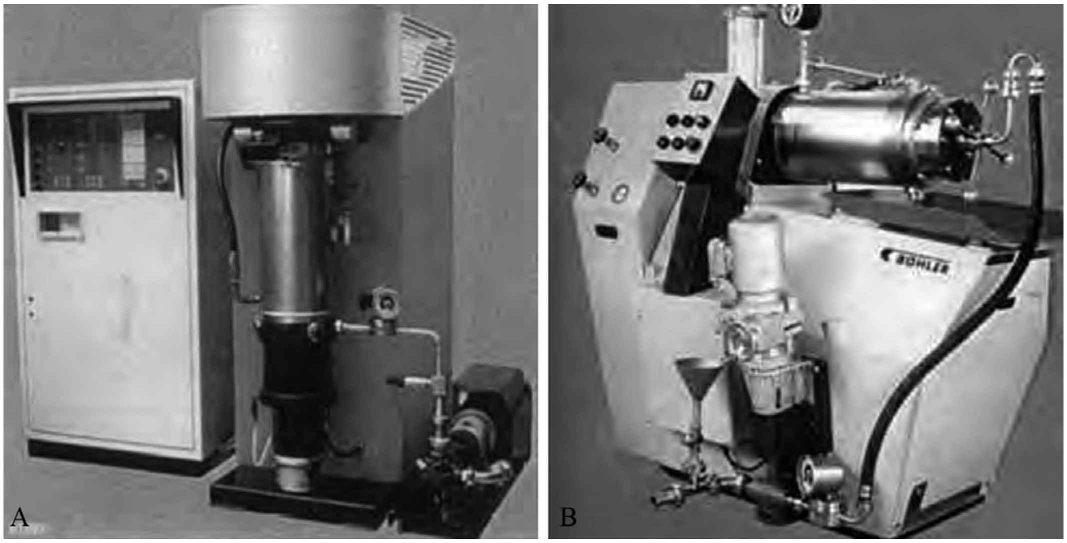

FIG. 2.19 Attrition mill designs with (A) vertical or (B) horizontal rotating shaft.

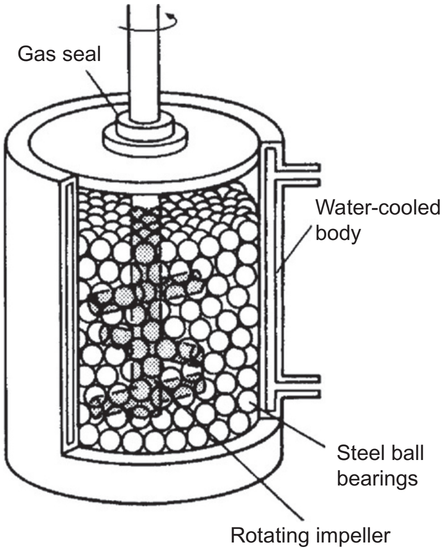

FIG. 2.20 Schematic drawing of an attrition ball mill.

TABLE 2.4 Comparison of Grinding Mills

Mill Type	Media Size (mm)	Revolutions per Minute	Arm Tip Speed (m/min)
Tumbling ball mill	10 mm and larger	10–50	n/a
Planetary mill	0.1–40	50–1100[a]	n/a
Attritor [24]	3–10	50–350	600–1000
High speed attritor [24]	0.5–3	320–1700	2500–3000

[a] *Rotational speed of main disk.*

Continuous attrition mills, more appropriate for large production output, consist of a tall, jacketed chamber through which previously prepared slurry is pumped in at the bottom and discharged at the top. Grids located at the bottom and top retain the grinding medium, as shown in Fig. 2.21.

The circulation grinding system comprises an attrition mill and a large holding tank, generally 10 times the volume of the grinding unit. The attrition mill contains grids that restrain the medium while the slurry passes through. Usually, the contents of the holding tank are passed through the system at a rate of 10 times per hour. The slurry can be monitored continuously and processing is stopped when the desired particle size dispersion is achieved.

Dry milling can provide reduced transportation costs compared to wet grinding because 50% of the gross weight is liquid in many wet slurry processes. Because the removal of the liquid from a wet grinding process involves not only another process step but also requires large amounts of energy, dry grinding can provide reduced energy costs. Another advantage is the elimination of waste liquid disposal.

Attrition mills find application for hard materials such as carbides and hard metals where conventional tumbling and vibratory ball mills are less efficient. The principal advantages of attrition mills for mixing and blending tungsten carbide with cobalt as binder metal cutting tool powders include a short milling time, the production of fine particle size (submicron sizes), and the enhanced coating of cobalt onto the surface of tungsten carbide particles [25]. Attrition mills effectively grind metals in inert atmospheres, such as in solid state or mechanical alloying.

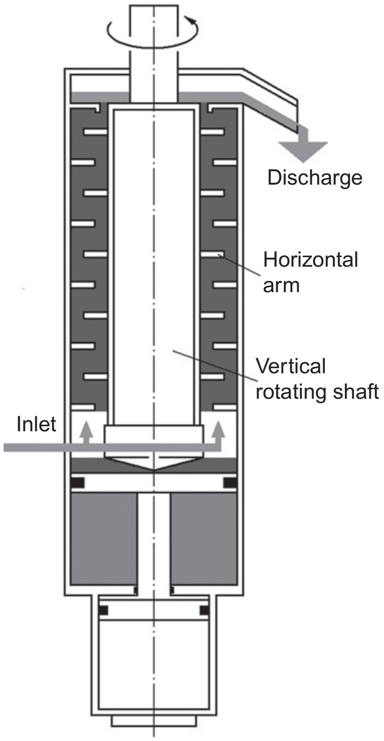

FIG. 2.21 Schematic drawing of continuous attrition mill.

Jet Mills

The jet mill, also called the fluid-energy mill, is based on a cold stream impact process in which the materials are disintegrated by the collision of a particle with a particle, a stationary target, or a wall of the containing chamber. The collision energy is generated by a high-speed jet flow.

Fluid energy mills may be classified in terms of the mill action. In a fluidized bed jet mill, schematically illustrated in Fig. 2.22, the grinding energy is created by gas streams from horizontal grinding air nozzles. Particles in the fluidized bed created by the gas streams are accelerated toward the center mill chamber, colliding with slower moving particles. The particles' laden air transports the particles to the classifier. Coarse particles are separated by the classifier and returned into the mill. The particle-to-particle milling system prevents wear of the internal mill components. The supersonic nozzles are made of cemented tungsten carbide, but other wear-resistant materials or products being comminuted can be used to make these parts.

Commercial jet mills are available from the NETZSCH-Feinmahltechnik Company (Table 2.5). The CGS 50 fluidized bed jet mill is shown in Fig. 2.23. These jet mills allow finenesses ranging from $d_{97} = 3\ \mu m$ to $d_{99} = 50\ \mu m$ (Table 2.6). The adjustment of the desired fineness is carried out by a dynamic air classifier integrated into the housing.

In another type of mill, two streams convey particles at high velocity into a chamber where they collide. Rapidly expanding gases emerging from the nozzle create a cooling effect by adiabatic expansion. This effect is greater than the heat generated in the process. Thus, the process operates at well below room temperature. For example [12], a compressor operating at $56\,m^3$/min and 6.9 MPa is used.

The cold stream impact process is used to disintegrate hard, abrasive, relatively expensive materials such as tungsten carbide, tungsten alloys, molybdenum, beryllium, and other alloys. The process rapidly reduces an initial particulate material of particles 3 mm or smaller to micron size. Process advantages include simplicity, a low operating temperature that prevents oxidation, and the ability to retain high purity and particle size control over the material being ground. The cold stream process generally produces a relatively oxide-free powder. Most atomized powders have a slight oxide film on the surface of the particles. The cold stream process leads to the removal of this oxide film and thus improves the properties of the powder. During processing, this brittle oxide film is stripped from the metal surface and broken up into fine dust. The lower density and smaller particle size of the latter facilitate its separation from the metal particles by air classification.

Other High-energy Milling Methods

Vibratory, attrition, and large-diameter tumbling mills may be classified as high-energy ball mills and, as such, may be used effectively in solid-state or mechanical alloying processes. Fluid energy mills are also related to high-energy mills.

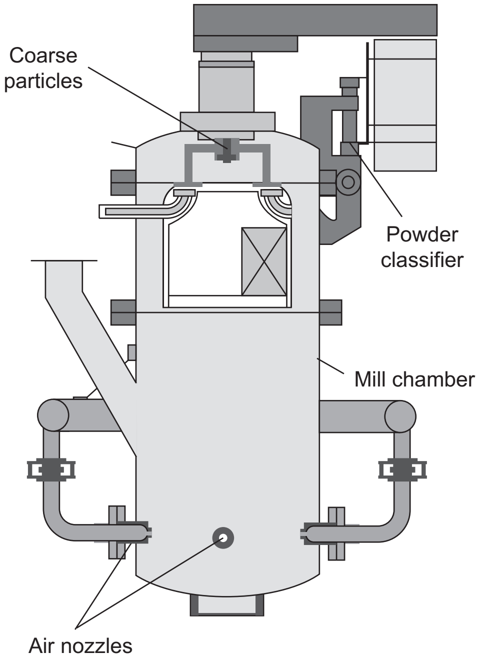

FIG. 2.22 Schematic drawing of fluidized bed jet mill.

TABLE 2.5 Technical Characteristics of NETZSCH Fluidized Bed Jet Mills

Parameter	Unit	CGS 32	CGS 50	CGS 71	CGS 100	CGS 120	CGS 150	CGS 180
Throughput coefficient	…	0.35	1	2	4	6	9	12
Air consumption[a]	m^3/h	330	960	1920	3860	5770	8930	11,660
Number of jets	number	3	3	3	3	4	4	4
Jet diameter	mm	5.0	8.5	12.0	17.0	18.0	22.4	25.6
Milling chamber diameter[b]	mm	350	600	800	1200	1500	1800	2100
Classifying apparatus power, max	kWt	4	7.5	15	30	45	75	90
Classifying apparatus rpm, max	rpm	7000	5100	3600	2300	2200	1700	1400
Final fineness[c]	μm	2.5–70	2.5 – 80	3–85	3.5–90	4–90	5–90	5–90
Overall dimensions								
Width	mm	1000	1450	1800	2140	3300	3600	4200
Depth	mm	1000	1450	1800	2340	3300	3600	4200
Height	mm	1575	2270	2880	3930	5000	7000	7700
Weight	kg	680	1200	3000	5400	12,500	2400	2900

[a] *Compressed gas under 0.8 MPa at RT temperature.*

[b] *Outside diameter.*

[c] *Data of the limestone milling (with 2.7 Kg/L density).*

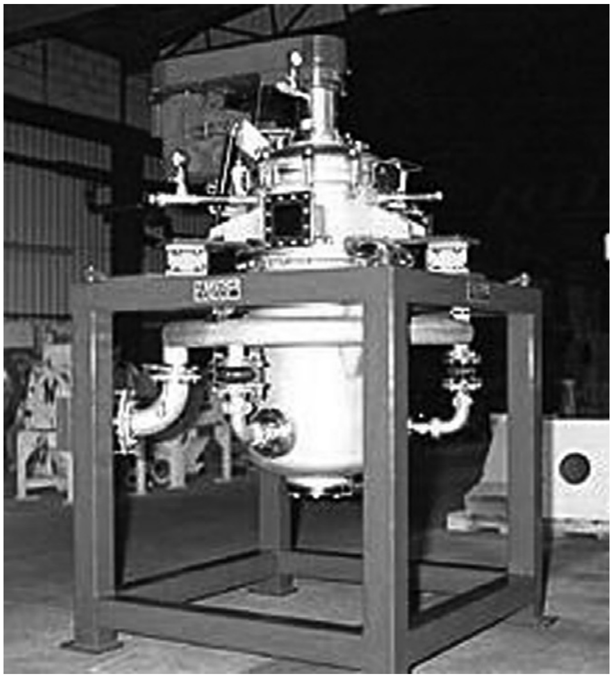

FIG. 2.23 CGS 50 fluidized bed jet mill commercially available from NETZSCH-Feinmahltechnik.

TABLE 2.6 Final Fineness (μm) of Product Milled by Bed Jet Mill

Product	Dispersibility (μm)	Fluidized Bed Jet Dimension-Type				Productivity (kg/h)
		CGS 10	CGS 16	CGS 50	CGS 71	
Cobalt	d_{97}			10		200
Cobalt oxygen	d_{99}				5.8	700
Cobalt-lithium oxygen	d_{99}			6		700
Graphite	d_{97}			3.76		13.5
Hard materials	d_{97}			2.75		137
Molybdenum	d_{99}		34			32
Molybdenum disulfide	d_{99}			3.5		45
Neodymium-iron-boron	d_{97}	4–40				5
Ruthenium	d_{99}		50			40
Silicon oxide	d_{90}				9.8	360
Tungsten carbide	d_{99}			3		66

Many commercially available high-energy, laboratory-scale mills have been developed and used for research as a result of the sharp rise in interest in the last 20 years in the use of mechanical milling/alloying for the production of metastable materials such as amorphous alloys, quasicrystalline materials, metastable crystalline phases, and nanostructured materials. These mills process small quantities of powder and, in some cases, are more energy efficient than larger industrial mills. Planetary ball mills have often been used for research studies. Frequently, the various commercially available types of Fritch Pulverisette planetary mills are used (Table 2.7). A Vario-planetary mill Pulverisette 4 with wide variable grinding conditions is an advanced mill for mechanical activation and mechanical alloying for different materials.

TABLE 2.7 Technical Characteristics of Fritsch Pulverisette Planetary Mills

Parameter	Unit	Planetary Mill Types			
		Pulverisette 4	Pulverisette 5/4	Pulverisette 6	Pulverisette 7[a]
Grinding process	…	Dry/wet	Dry/wet	Dry/wet	Dry/wet
Grinding tools					
Grinding bowls	ml	12, 45, 80, 250, 500	80, 250, 500	80, 250, 500	20, 45, 80
Grinding balls	Ø mm	0.1–40	0.1–40	0.1–40	0.1–20
Rotational speed of main disk	rpm	0–400	50–400	100–650	100–1100
Centrifugal acceleration	g	22	22	29	95
Input power	W	6000	1600	1100	1100
Max. feed size, depending on the feed stock	mm	10	10	10	10
Max. sample quantity	ml	450	900	225	70
Final fineness	μm	<1	<1	<1	<1
Typical grinding time	min	4	4	4	3

Continued

TABLE 2.7 Technical Characteristics of Fritsch Pulverisette Planetary Mills—cont'd

		Planetary Mill Types			
Parameter	**Unit**	**Pulverisette 4**	**Pulverisette 5/4**	**Pulverisette 6**	**Pulverisette 7**
Bowl number		2	4	1	2
Overall dimension					
Width	mm	600	580	370	400
Depth	mm	800	670	530	580
Height	mm	1100	570	500	360
Weight	kg	320	120	63	44
Physical properties of the sample material[b]		H, Md—H, S, Br, T, M	H, Md—H, S, Br, M	H, Md—H, S, Br, M	H, Md—H, Br, M

[a] *Pulverisette 7 premium.*
[b] *H, hard; Md—H, medium-hard; S, soft; Br, brittle; T, tough; M, moist.*

A mill often used in research, especially in the United States, is the Model 8000 shaker mill of Spex [26]. This high-energy ball mill agitates the charge of the powder and grinding medium in three mutually perpendicular directions at approximately 1200 rpm. Ball velocities in such shaker mills are high, about 5 m/s. The Glenmills Ultra centrifugal mill, the Laboratory jet mill, the Covington Engineering bead mills, the Hwa Maw Machine bead and planetary mills, and the Fritsch Vibratory micro mill Pulverisette 0 are also used in research investigations.

There are several other examples of specially designed mills for experimental investigations. These include the experimental ball mill designed by Calka and the coauthors [25], which can change the milling action from predominantly impact to mainly shearing by changing the placement of strong permanent magnets, which are external to the vial. A disintegrator installation for fine grinding of metals and alloys, which are liable to form explosive airborne dust, has also been designed [27]. The coupled counter-rotation reinforced by hard alloy rotors is located in a chamber with a controlled inert gas atmosphere. The step-less regulation of the rotor speed in a wide range up to 15,000 rpm allows the investigation of the grinding process and mechanical activation condition. The explosion-proof disintegrator technique is described in more detail in Section E, "Safety engineering in the production of powders."

Netzsch–Feinmahltechnik attritors are both horizontal and vertical, and they include industrial as well as laboratory mills. The Netzsch LMZ horizontal-type attritor permits the production of ultrafine and nanopowders. The Super Misuni NEV-MA-8 from Nisshin Giken (Fig. 2.24) has been a popular milling unit with several Japanese researchers. This technique has some special features, such as s variety of selections for milling energy (up to a speed of 1600 rpm), a variety of selections for atmospheres (vacuum or any flowing gas), the ability to control the temperature of milling from very low temperatures of 83 K up to a high temperature of 573 K, and in situ observation of the grinding medium during milling.

Production and laboratory attritor mills of both batch and circulation types from Union Process are commercially available. The Zoz Simoloyer horizontal attritor mills have been developed for both laboratory and pilot plant powder quantities [28–30].

High-energy ball milling has been employed to synthesize metastable structures analogous to other nonequilibrium processing methods such as rapid solidification and physical vapor deposition. However, the initial phase in the case of mechanical alloying is generally a crystalline solid or solids rather than liquid or vapor. The thermodynamics and kinetic factors that govern metastable phase formation can be very different. The more detailed mechanical alloying technique is described in Chapter 3.

Fig. 2.25 shows the possibilities (with certain approaching) of typical size reduction equipment for grinding a material of a given feed size to a desired product size when the purpose is comminution of a hard and/or brittle metal or ceramic material.

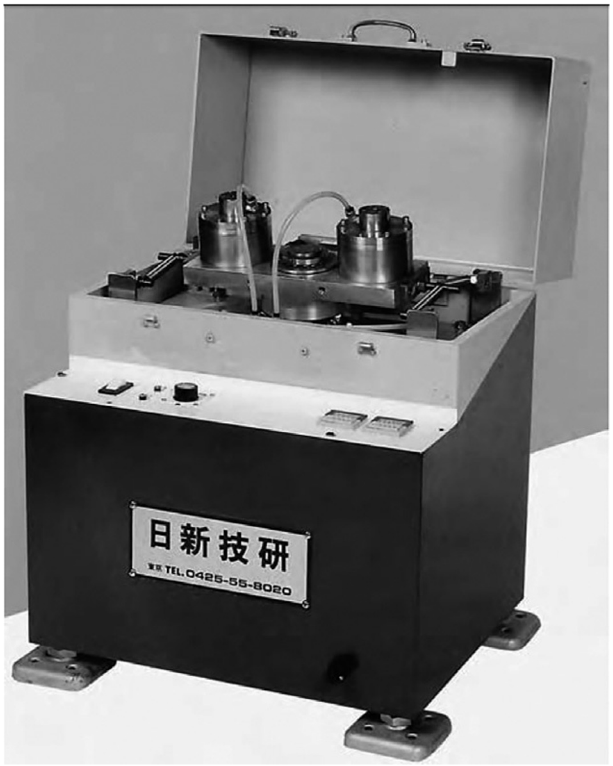

FIG. 2.24 Super Misuni NEV-MA-8 mill.

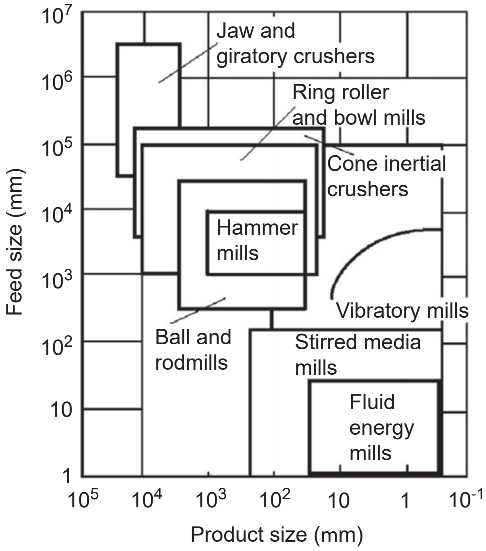

FIG. 2.25 Possibilities of typical size reduction equipment for grinding a material of a given feed size to a desired product size.

REFERENCES

[1] Senna M, Kuno H. Polymorphic transformation of PbO by isothermal wet ball-milling. J Am Ceram Soc 1971;54(5).

[2] Rehbinder PA. Surface energy changings effect on cleavability, hardness and other properties of crystals. In: VI Congress of russian physicists. Moscow: OGIZ; 1928. p. 29–35 [in Russian].

[3] Malkin AI. Regularities and mechanisms of the Rehbinder's effect. Colloid J 2012;74(2):223–38. https://doi.org/10.1134/S1061933X12020068.

[4] Revnivcev VI, Denisov HA, Zarogatsky LP, Turkin VJ. Vibrating disintegration of solid materials. Moscow: Nedra; 1992 [in Russian].

[5] Griffith AA. The phenomena of rupture and flow in solids. Philos Trans R Soc Ser A Lond 1921;221:163–98.

[6] The Collected Works of J. W. Gibbs. Gibbs, vol. 1. New Haven: Yale Univ. Press, 1948.

[7] Rehbinder PA, Shchukin ED. Surface phenomena in solids during deformation and fracture processes. In: Davison SG, editor. Progress in surface science. vol. 3, Part 2. Pergamon Press, Inc; 1973. p. 97–188.

[8] Orowan E. The fatique of glass under stress. Nature 1944;(3906):341–3.

[9] Cherepanov GP. Brittle fracture mechanics. Moscow: Nauka; 1974 [in Russian].

[10] Wiederhorn SM, Fuller ER. Effect of surface forces on subcritical crack growth in glass. J Am Ceram Soc 1989;72(2):248–51.

[11] Lawn BR. Interfacial forces and fundamental nature of brittle cracks. Appl Phys Lett 1985;47(8):809–11.

[12] Koch CC. Milling of brittle and ductile materials. In: ASM handbook, vol. 7. ASM International Publishers; 1998. p. 53–66.

[13] Takacs L. Self-sustaining reactions induced by ball milling. Prog Mater Sci 2002;47:355–414.

[14] Pustov LY, et al. Experimental measurement and theoretical computation of milling and intensity and temperature for the purpose of mechanical alloying kinetics description. Mater Sci Forum 2001;360–2:373–8.

[15] Bhattacharya AK, Arzt E. Temperature rise during mechanical alloying. Scr Metall 1992;27:749–54.

[16] Johnson KL. Contact mechanics. Cambridge, UK: Cambridge University Press; 1985.

[17] Suryanarayana C. Mechanical alloying and milling. New York: Marsel Dekker; 2004.

[18] Davis RM, McDermott B, Koch CC. Mechanical alloying of brittle materials. Metall Trans 1988;19A:2867–74.

[19] Borzov AB, YaE K. Method for measurement of temperature in attritor during mechanical alloying. In: deBarbadillo JJ, et al., editors. Mechanical alloying for structural applications. Materials Park, OH: ASM International; 1993. p. S1–4.

[20] Ermakov AE, Yurchikov EE, Barinov VA. Phys Met Metallogr 1981;52(6):50–8.

[21] Soviet Union Patent 1,242,233, Dec 1984.

[22] Belenko LF. Features of grinding in dram mills. Moscow: Nedra; 1984 [in Russian].

[23] Galchuk TN, Rud VD. Kinetics of ball-mill grinding of powders produced from bearing-production waste. Powder Metall Metal Ceram 2011;50 (5–6):262–7.

[24] Schilling R, n.d.. Media milling advances. <http://www.unionprocess.com/tech_papers/mm_advances.pdf> [Accessed 31 July 2018].

[25] Calka A, Radlinski. Universal high performance ball-milling device and its application for mechanical alloying. Mater Sci Eng A 1991;134:1350–3.

[26] Model 8000 shaker mill, n.d.. SPEX Sample Prep. <//www.spexsampleprep.com/about-us/contact-us> [Accessed 31 January 2018].

[27] Soviet Union Patent 1,044,328, June 1981.

[28] Zoz H, et al. Mechanical alloying of Ti-24Al11Nb (at %) using the Simoloyer. Metall 1996;59(9):575–9.

[29] Zoz H, Reichardt R, Ernst D. Simoloyer CM100s, semi-continuously mechanical alloying in a production scale using cycle operation – Part II. Metall 1998;51(9):521–7.

[30] HV-Simoloyer, n.d.. Zoz GmbH. http://gmbh.zoz.de/?page_id=1248 [Accessed 31 December 2017].

Chapter 3

Mechanical Alloying

Oleg D. Neikov
Frantsevich Institute for Problems of Materials Science (IPMS), Kiev, Ukraine

Chapter Outline

Introduction 91
Mechanical Alloying Process 92
  Process Control Agent 92
Further Processing 94
Milling Equipment 94
  Planetary Ball Mills 94
  Shaker Mills 96
  Attritors 97
  Other Laboratory Mills Used for Mechanical Alloying 100
  Commercial Mills 101
  Selection of Grinding Medium 102
Mechanical Alloying Fundamentals 104
Oxide Dispersion-Strengthened Alloys 107
Contact Displacement Reactions 108
Powder Contamination 109
Applications 112
  Nickel-Base Alloys 112
  Cobalt-Base Alloys 113
  Aluminum-Base Alloys 113
  Copper-Base Alloys 119
Safety Engineering 119
References 121

INTRODUCTION

Mechanical alloying is a completely solid-state processing technique; phase diagram regularities do not act here. This process permits the synthesis of novel alloys that is not possible by any other technique. Mechanical alloying (MA) is usually a dry, high-energy milling process that has been employed to manufacture a variety of commercially advanced materials. This technique was developed in the mid-1960s by John Benjamin and his colleagues at the International Nickel Company (INCO), mainly to combine the advantages of precipitation strengthening and oxide-dispersion hardening (ODS) in some nickel- and iron-based superalloys for gas turbine applications [1,2]. Subsequently, it was realized that MA can also be used to synthesize a variety of both equilibrium and nonequilibrium materials at room temperature, starting from blended elemental powders. This technique has attracted the attention of a large number of researchers during the past 30–35 years. This technique is also capable of synthesizing a variety of equilibrium and nonequilibrium alloy phases starting from prealloyed powders. Mechanical alloying is presently one of the most popular nonequilibrium processing techniques.

The process consists of repeated welding-fracturing-welding of a mixture of powder particles in a high-energy ball mill. The powder particles are trapped between the colliding balls during the milling and undergo deformation, welding, or fracture, depending on the mechanical behavior of the powder components. The process is used to produce a variety of materials and alloys: supersaturated solid solutions, amorphous materials, intermetallic compounds, and metal-matrix composites.

The MA stages with two ductile metal powders can be schematized in the following way. First, the particles undergo deformation and their morphology changes from the initial to a flattened one. In the following stage, the welding mechanism predominates, which produces equiaxed particle formation. At this stage, oriented welding lines are observed. Then, welding and fracture mechanisms reach equilibrium and the formation of particles with randomly oriented welding lines predominates. The final stage is characterized by the steady-state process in which the microstructural refinement can continue but the particle size and size distribution remain approximately stable.

The main characteristics of mechanical alloying can be summarized as:

- Production of a fine dispersion of second phase particles.
- Extension of solid solubility limits.
- Refinement of grain sizes down to the nanometer range.

Handbook of Non-Ferrous Metal Powders. https://doi.org/10.1016/B978-0-08-100543-9.00003-8
© 2019 Elsevier Ltd. All rights reserved.

- Synthesis of novel crystalline and quasicrystalline structures.
- Development of amorphous phases.
- Promotion of chemical reactions at low temperatures.
- Scalable process.

Several terms in the literature are used to designate the processing of powders in high-energy mills [3]. Mechanical alloying is the process where mixtures of powders of different metals or alloys/compounds are milled together. In this process, material transformation is accomplished to obtain a homogeneous alloy. While milling of a homogeneous composition of powders, such as pure metal, intermetallic, or prealloyed powders, is usually called mechanical milling (MM), the term mechanical grinding (MG) is also used as a synonym of MM. However, in this article, the term MA as a fixed notion term is used to include both MA and MM.

MECHANICAL ALLOYING PROCESS

The MA process starts with mixing powders in the given proportion and charging the powder into the mill, along with the grinding medium. This mixture is then milled for the required time until the final state is reached. This state occurs when the composition of every powder particle is the same as the proportion of the elements in the starting powder mixture. Sometimes the powder is milled either to form metastable phases or to achieve certain desired properties. The obtained powder is further consolidated into the bulk shape and heat-processed to achieve the specified microstructure and properties.

The raw materials used for MA are widely available as commercially pure powders with particle sizes usually up to 200 μm. At the same time, the powder particle size is not especially crucial. If it should be smaller than the grinding ball size, the powder particle size decreases exponentially with time and reaches a small value after a few minutes of milling. These powders include many kinds of pure metals, master alloys, prealloyed powders, and refractory compounds. The oxygen content of commercially pure metal powders generally ranges from 0.05–0.2 wt%. Therefore, if it is relevant to phase formation, it becomes important to choose the appropriate purity of the powder. It is significant because, as a rule, the nature and amount of impurities in the system determine the character of the final phase formation and the chemical constitution of the alloy. Dispersion-strengthened materials usually contain additions of oxides, carbides, or nitrides. Oxides are the most common addition and such alloys are known as oxide-strengthened (ODS) materials. MA allows the production of novel alloys by milling of ductile-ductile, ductile-brittle, and fully brittle powder mixtures.

Process Control Agent

For MA process control, a process control agent (PCA) is introduced into the powder mixture, especially when the latter involves a substantial fraction of a ductile component. The PCAs are ordinary organic compounds that act as surfactant agents. They are adsorbed onto the surface of the powder particles and minimize contact between particles, thereby inhibiting agglomeration.

In the development phase of microcracks in solids, the adsorption of surfactants has great importance. Their penetration into the microcrack mouth weakens the interatomic bonding, which facilitates the dissemination of cracks while adsorption on a newly formed surface prevents the closing (Rehbinder's effect). This effect was discovered by P·Rehbinder in 1928 [4]. The molecular nature of Rehbinder's effect consists of the facilitation of rupture and reconstruction of the intermolecular (interatomic) bonding in solids over active adsorption and, moreover, enough movable extrinsic molecules (atoms and ions) [5]. More details on Rehbinder's effect can be found in Chapter 2.

A wide range of PCAs has been used in practice. They are mostly organic compounds in the range from 0.3–4 wt% of the total powder charge and include stearic acid ($CH_3(CH_2)_{16}COOH$), hexane (C_6H_{14}), oxalic acid ($(COOH)_2 \cdot H_2O$), methanol, ethanol, acetone, isopropyl alcohol, heptane, Norcowax-22 DSP, octane, toluene, trichlorotrifluoroethane, organosilicon compounds, etc. Alumina, aluminum nitrate, graphite, and sodium chloride have also been used as PCAs [6,7]. A selective listing of the PCAs used in different investigations is presented in Table 3.1.

In addition, other uncommon PCAs such as sodium1.2-bis (dodecyl carbonyl)ethane-1-sulfonate, lithium-1,2-bisdodecyloxycarbonylsul-fasuccinate, didodecyl dimethyl ammonium acetate (DDAA), didodecyl dimethyl ammonium bromide (DDAB), trichlorotrifluoroethane, and others such as polyethylene glycol, oxalic acid, boric acid, and borax have also been used [6]. Most of these compounds have low melting and boiling points, and consequently they either melt or evaporate during milling, owing to the temperature increase. Furthermore, they decompose during milling, interacting with the powder and forming interstitial compounds. These get incorporated in the form of inclusions and/or dispersoids into the powder particles during milling. Thus, hydrocarbons containing hydrogen and carbon, and carbohydrates containing

TABLE 3.1 Process Control Agents Used in Different Investigations

Process Control Agent	Chemical Formula	Quantity (wt%)	Reference
Alcohol	…	…	[8]
Benzene	C_6H_6	…	[9]
C wax	$H_{35}C_{17}CONHC_2H_4NHCOC_{17}H_{35}$	1.5	[10]
Didodecyl dimethyl ammonium acetate	$C_{28}H_{59}NO_2$	…	[11]
Dodecane	$CH_3(CH_2)_{10}CH_3$	…	[6]
Ethanol	C_2H_5OH	4.0	[12]
Ethyl acetate	$CH_3CO_2C_2H_5$	…	[13]
Ethylenebis distearamide Nopco Wax–22 DSP	$C_2H_2{\cdot}2(C_{18}H_{36}ON)$	2.0	[6]
Heptane	$CH_3(CH_2)5CH_3$	0.5	[14]
Methanol	CH_3OH	1.0	[15]
		3.0	[6]
		4.0	[16]
Ostane	$CH_3(CH_2)6CH_3$	1.0	[17]
Polyethylene glycol	$HO(CH_2CH_2)_nOH$	0.5–2.0	[18]
Sodium chloride	NaCl	2.0	[19]
Acid	$CH_3(CH_2)_{16}COOH$	1.0	[20]
		0.5–3.0	[18]
		4.0	[21]
Toluene	$C_6H_5CH_3$		[22]

hydrogen, carbon, and oxygen, are likely to introduce carbon and/or oxygen into the powder particles, resulting in the formation of carbides and oxides that are uniformly dispersed in the matrix. These are not necessarily harmful to the alloy system because they can contribute to dispersion strengthening of the material, resulting in increased strength and higher hardness. The hydrogen subsequently escapes as a gas or is absorbed into the metal lattice on heating or sintering, even though hydrogen gas primarily serves as a surfactant and does not usually participate in the alloying process. In some other cases, hydrogen assists in embrittling the powders and consequently finer particles could be produced.

Reactive metals such as aluminum, titanium, and zirconium, when milled in the presence of air, can gather substantial amounts of oxygen and nitrogen and effect phase changes, including the formation of new phases [23]. Completely non-oxidized finely milled powders may self-ignite when contacting the air [24]. Some metals, such as aluminum, nickel, and copper, react with certain alcohols during milling to form complex metalloorganic compounds. Thus, aluminum reacts with isopropyl alcohol. Other metals such as titanium and zirconium can react explosively with chlorinated fluids such as carbon tetrachloride. Therefore, chlorinated fluids should never be used with reactive metals. Reactive milling (milling of metal powders in the presence of reactive solids/liquids/gases causing a chemical reaction to occur) has also been used to synthesize metal oxides, carbides, and nitrides [25]. Thus, the milling of titanium in a nitrogen atmosphere has produced titanium nitride; several other nitrides have also been produced in a similar way. Milling of aluminum with carbon, or by the use of PCA containing carbon, produced aluminum carbide ($A_{14}C_3$), which appears dispersed inside the aluminum matrix and improves the properties of the alloy. The carbide in this case is only partially formed during milling; further heat treatment is required to accomplish the reaction of carbon with aluminum. The milling of tungsten with carbon (graphite) has produced tungsten carbide.

Use of a PCA ordinarily introduces some impurities into the powder. Therefore, to produce a high-purity alloy, use of a PCA should be eschewed. Generally, the choice of a PCA for milling depends on the nature of the powder being milled and the final product specification.

FURTHER PROCESSING

The further processing of mechanical alloying powders implies mechanical and heat treatment, consolidation, microcapsulation, coatings or plating of powders, and additive manufacturing. Here, the aim isn't to describe the above processing technologies. Their nomenclature is enumerated for definition of demands to the powders in connection with the processing type.

All the consolidation methods generally used in powder metallurgy processes can also be used for mechanically alloyed powders. At the same time, with mechanically alloyed condition features, where the powder particles are smaller in size than those used in conventional powder metallurgy operations, some special precautions are needed. Conventional consolidation of powder to full density through processes such as hot extrusion and hot isostatic pressing normally requires the use of high pressures and high temperatures for extended periods of time.

The most common method of MA powder consolidation is hot compaction followed by hot extrusion, or by direct hot extrusion at temperatures greater than half the melting point, consequently at temperatures considerably lower than those used for conventional powders, in order to minimize MA powder activity. For example, while conventional γ-TiAl powders are hot isostatic pressed at about 1373 K, mechanical alloyed γ-TiAl powders can be consolidated to full density by hot isostatic pressing at about 1023 K [6].

The consolidation methods used for mechanically alloyed powders, both on laboratory and industrial scales, include plasma-activated sintering, electrodischarge compaction, CeraCon processing, and explosive forming. These processes could be used if their application does not lead to the loss of metastable effects, such as the crystallization of the amorphous phase in the powder.

MA powder contamination is still a matter of concern by consolidation, particularly when homogenization of the product phase and formation of new active interfaces are important. As an example, these could include hydrogen storage alloys, composite materials, and modification of drugs. Consolidation of the powder is involved in these cases, and care should be taken not to introduce additional contamination into this process. Alternatively, one could use this technique to produce advanced materials that show high tolerance to gas content. One could also consider using the MA technique to synthesize materials that could be used in the powder form without the need for consolidation. Such applications include catalysts, paints, pigments, fertilizers, solder components, and carbides for inclusion as hardening phases and the like.

MILLING EQUIPMENT

Tumbling ball mills, planetary mills, attritors, and vibratory (shaker) mills are widely used for laboratory investigations of mechanical alloying processes. Attritors and ball mills are commercially available for MA and are much larger in size than such types of mills in laboratory use. The former are different in capacity and efficiency of milling while having additional arrangements for cooling, heating, etc.

Planetary Ball Mills

Planetary ball mills have often been used for research studies, in particular by European investigators. These planetary mills are manufactured by Fritsch GmbH in Germany and marketed by Gilson Co. in the United States, Fritsch Beijing Scientific Instruments in China, and Fritsch Asia Pacific. A Vario-planetary mill Pulverisette 4 with infinitely variable grinding conditions is the perfect mill for mechanical alloying and activation. It is equipped with two bowls (Fig. 3.1). The bowls are arranged on a rotating support disk and a special drive mechanism causes them to rotate around their own axes. The centrifugal force produced by the bowls rotating around their axes and by the rotating support disc acts on the bowl contents, consisting of material to be milled and grinding balls. Because the bowls and the supporting disk rotate in opposite directions (Fig. 3.2), the centrifugal forces alternately act in like and opposite directions. This results in the grinding balls running down the inside wall of the bowl, stimulating the friction effect followed by the impact effect when the material being ground and the grinding balls lift off and travel freely through the inner area of the bowl and collide against the opposing inside wall.

In the Vario-planetary Pulverisette 4 mill, the rotational speeds of the grinding bowls and supporting disk can be adjusted completely independently of each other in contrast to standard planetary mills. By changing the transmission ratio, it is possible to accomplish mechanical alloying as well as mechanical activation. The performance features of the Pulverisette 4 are:

- Free selectable controlled rotation speed for the grinding bowls and supporting disk.
- Programming of the grinding parameters by PC software.

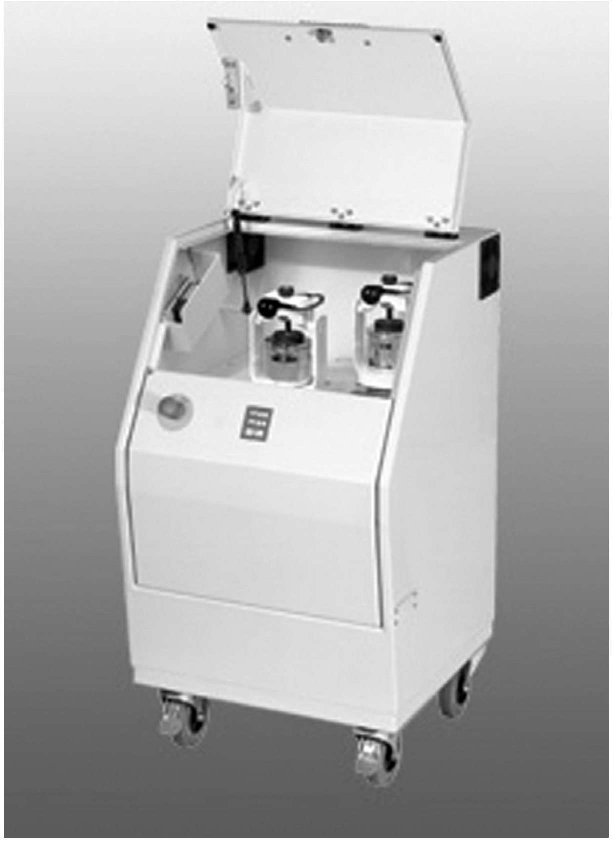

FIG. 3.1 Vario-planetary mill Pulverisette 4.

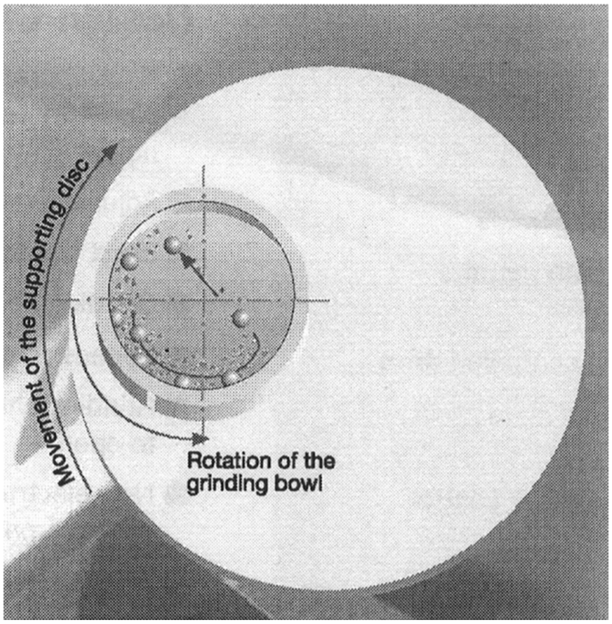
Movement of the supporting disc
Rotation of the grinding bowl

FIG. 3.2 Schematic depiction of the ball motion inside the bowl of a planetary mill.

- Reversing option to improve the milling results.
- Real-time display of the speeds to monitor the milling process.

Grinding bowls and balls are available in several different materials: agate, hard metal tungsten carbide, stainless steel, silicon oxide, zirconium oxide, and sintered corundum. The mills are provided by grinding balls with diameter sizes of 5, 10, 15, 20, and 30 mm. Additional technical attributes of Fritsch planetary mills are given in Chapter 2.

Retsch does a series of planetary ball mills for soft, hard, brittle, and fibrous materials. The technical characteristics of Retsch planetary mills are summarized in Table 3.2.

TABLE 3.2 Technical Characteristics of Retsch Planetary Mills

		Planetary Mill Types			
Parameter	**Unit**	**PM 100**	**PM 100CM**	**PM 200**	**PM 400**
Grinding process	…	Dry/wet	Dry/wet	Dry/wet	Dry/wet
Size reduction principle	…	Impact, friction	Impact, friction	Impact, friction	Impact, friction
Material feed size	mm	<10	<4	<10	<10
Final fineness	µm	<1 µm, for colloidal grinding <0.1 µm	<1 µm, for colloidal grinding <0.1 µm	<1 µm, for colloidal grinding <0.1 µm	<1 µm, for colloidal grinding <0.1 µm
Batch size/feed quantity	ml	Max. 1 × 220 mL, max.2 × 20 mL with stacked jars	Max. 1 × 220 mL, max. 2 × 20 mL with stacked jars	Max. 1 × 50 mL	Max. 4 × 220 mL, max. 8 × 20 mL with stacked jars
Sun wheel speed	min^{-1}	100–650	100–650	100–650	300–400
g Force	*g*	33.3	33.3	37.1	26.8
Material of grinding tools[a]	…	HS, S-S, TC, A, SAO, Si_3N_4, ZrO_2	HS, S-S, TC, A, SAO, Si_3N_4, ZrO_2	HS, S-S, TC, A, SAO, Si_3N_4, ZrO_2	HS, S-S, TC, A, SAO, Si_3N_4, ZrO_2
Drive power	W	750	750	750	1500
Power consumption	W	≈1250	≈1250	≈1250	≈2100
Width × height × depth closed	mm	630 × 468 × 415	630 × 468 × 415	630 × 468 × 415	836 × 1220 (1900) × 780
Net weight	kg	≈86	≈86	≈72	≈290
Sample material[b]	…	S, H, Br, F	S, H, Br, F	S, H, Br, F	S, H, Br, F
Applications[c]	…	Gr, Mix, Ho, MA, CM	Gr, Mix, Ho, MA, CM	Gr, Mix, Ho, MA, CM	Gr, Mix, Ho, MA, CM

[a] HS, *hardened steel;* S-S, *stainless steel;* TC, *tungsten carbide;* A, *agate;* SAO, *sintered aluminum oxide.*
[b] S, *soft;* H, *hard;* Br, *brittle;* F, *fibrous.*
[c] Gr, *grinding;* Mix, *mixing;* Ho, *homogenizing;* MA, *mechanical alloying;* CM, *colloidal milling.*

Shaker Mills

SPEX mill (SPEX SamplePrep Mixer/Mill), a shaker type mill, is another popular mill that is often used in research, especially in the United States. It mills about 10–20 g of the powder at a time and is most commonly used for laboratory investigations. The common kind of the mill has one bowl containing the sample and grinding balls, attached in the clamp and swung energetically. These mills can be considered as the high-energy variety. On a level with planetary mills, SPEX mills are the most commonly used, and most of the research on the fundamental aspects of MA has been carried out using some version of these mills.

The shaking motion is combined with lateral movements of the ends of the bowl so that it appears to be tracing a figure of 8. Thus, the charge of powder and balls is agitated in three mutually perpendicular directions at approximately 1200 rpm. With each swing of the bowl, the balls impact against the sample and the end of the bowl, both milling and mixing the sample. Due to ≈ 5 cm amplitude and the high agitating rate of the bowl and grinding balls, the ball velocities are high and, consequently, the force of the ball impact is very large. A variety of bowl materials is available for the SPEX mills, including alumina, agate, hardened steel, silicon nitride, stainless steel, tungsten carbide, zirconia, plastic, and methacrylate. A typical example of a tungsten carbide vial, gasket, and grinding balls of the SPEX mill is shown in Fig. 3.3.

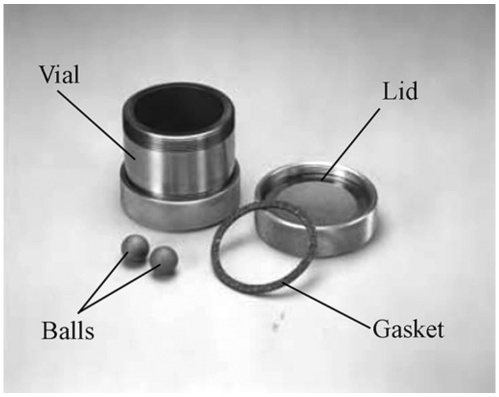

FIG. 3.3 Tungsten carbide vial, gasket, and grinding balls of SPEX mill.

Attritors

The main feature that makes the attritor more efficient in comparison with other mills is that its power input is used directly for agitating the media to achieve grinding, not to rotating or vibrating a large, heavy tank in addition to the grinding media.

Attritors of different sizes and capacities are available (from batch size of parts of a liter for the laboratory to batch sizes of hundreds of liters for commercial attritors). A vertical attritor is shown in diagram form in Fig. 3.4. The powder to be milled is placed in a stationary chamber (tank) with the grinding medium. This mixture is then agitated by a vertical shaft with horizontal arms, rotating at a speed from 60 to 350 rpm. An attritor in horizontal performance is schematically represented in Fig. 3.5. As was reported [26], the mill utilizes specially designed delta discs that provide directed and uniform media distribution throughout the mill chamber while simultaneously providing greater random media motion and improved milling. The use a small grinding media, in a range from 0.5–2 mm, in horizontal attritors allows increasing the rpm up to 1700 and the tip speed up to 916 m/s, respectively.

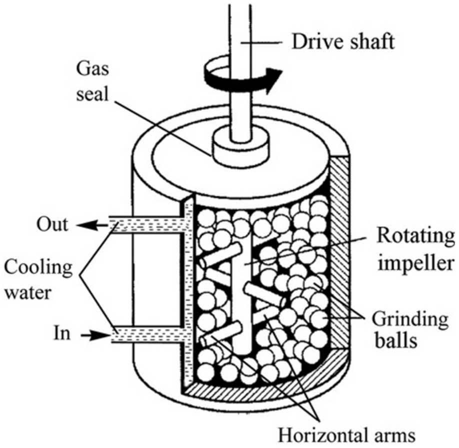

FIG. 3.4 The diagram of a vertical attritor with rotating impeller.

FIG. 3.5 Schematical image of an attritor in horizontal performance.

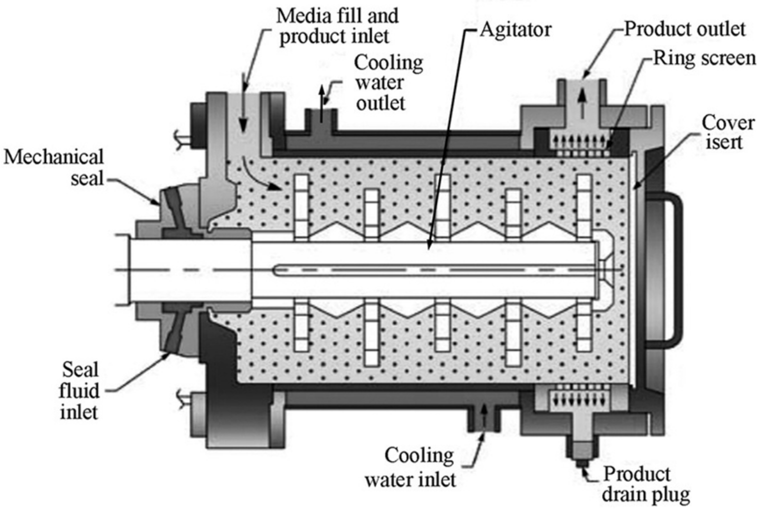

TABLE 3.3 Technical Characteristics of Netzsch Attritor Dimension Types

Technical Data	Unit	Attritor Dimension Types			
Laboratory batch mills					
Machine type		PE 075	PE 5	PR 01	PR 1
Drive	kW	0.25	2.5	0.25	2
Speed	rpm	233–2100	400–1500	71–530	80–400
Batch size	L	0.15–0.3	2–2.5	0.15–0.3	2
Commercial batch mills					
Machine type		PRK 17 S	PRK 32 S	PRK 102 S	PRK 201 S
Tank volume	L	115	250	490	720
Drive	kW	14/15	22/24	55/58	75/84

A wide range of laboratory and commercial attritors is available from the NETZSCH-Feinmahltechnik, Union Process, and Zoz GmbH companies. The grinding tanks of attritors produced by Union Process are available in stainless steel or stainless steel coated inside with alumina, silicon carbide, zirconia, rubber, or polyurethane. A variety of grinding media is also available, including alumina, zirconium, zirconium silicate, stainless steel, chrome steel, tungsten carbide, silicon carbide, silicon nitride, sialon, mullite, steatite ceramic, glass, and flint-stones. NETZSCH laboratory attritors are available in batch sizes from 0.15–2 L (see Table 3.3). Union Process laboratory attritors of S-1 model series (Fig. 3.6) are designed for a tank capacity from 5.7–9.5 L, a media volume from 3.8–5.7 L, a media milling size from 2.34 mm (1/8 in.) to 7.0 (3/8 in.), and running from 100 to 500 rpm [27].

High-energy attritors called “simoloyers” have been developed by Zoz Maschinenbau GmbH. A laboratory attritor in a horizontal performance simoloyer CM01-051 is shown in Fig. 3.7. Its impeller arms have a typical shape (Fig. 3.8) [28]. The process parameters depend on the alloy composition. Thus, mechanical alloying of $Ti_{65}Al_{24}Nb_{11}$ alloy is accomplished by the following milling conditions: powder components with milling balls of 5.1 mm diameter are processed in an argon atmosphere in a water-cooled tank by an impeller run up to 1300 rpm, a weight of powder charge of 130 g, and a powder-to-ball weight ratio of 1 to 10.

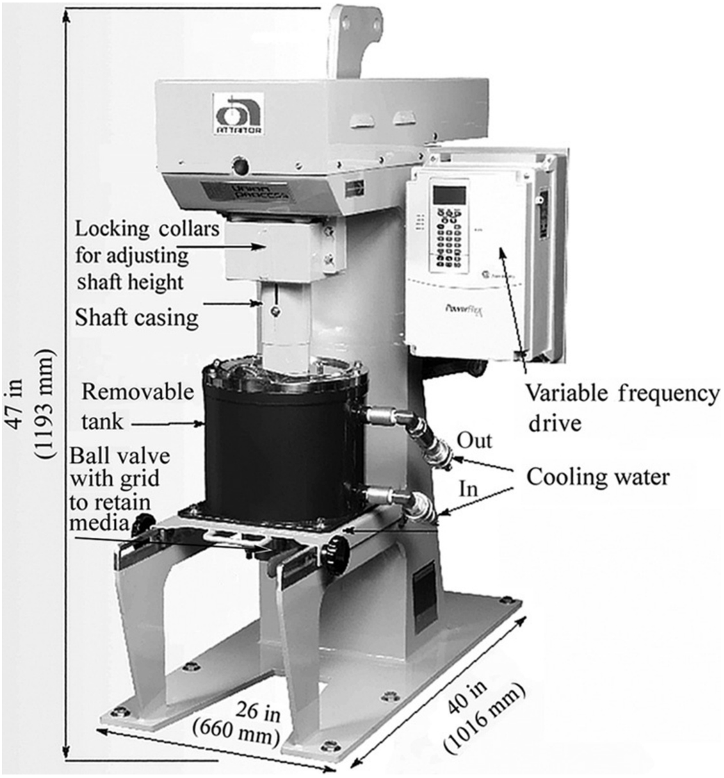
47 in
(1193 mm)
Locking collars
for adjusting
shaft height
Shaft casing
Removable
tank
Ball valve
with grid
to retain
media
Variable frequency
drive
Out
In
Cooling water
26 in
(660 mm)
40 in
(1016 mm)

FIG. 3.6 Union Process laboratory attritor of the S-1 model series. *(Courtesy of Union Process Incorporated.)*

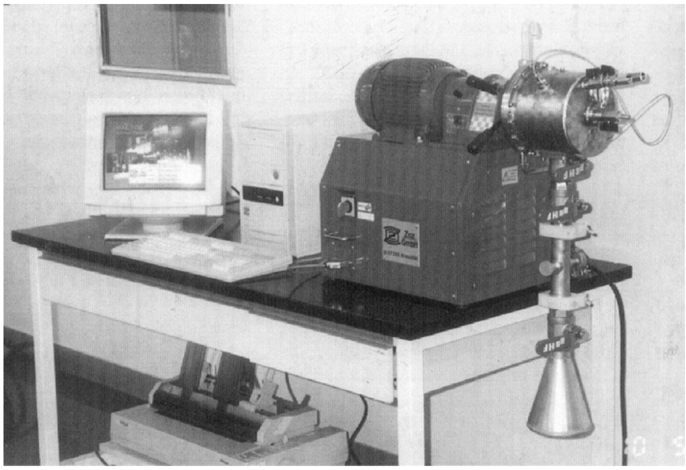

FIG. 3.7 Laboratory Simoloyer attritor in horizontal performance. *(Source: Zoz H, et al. Mechanical alloying of Ti-24Al11Nb (at%) using the Simoloyer. Metall 1996; 50 (9): 575–9.)*

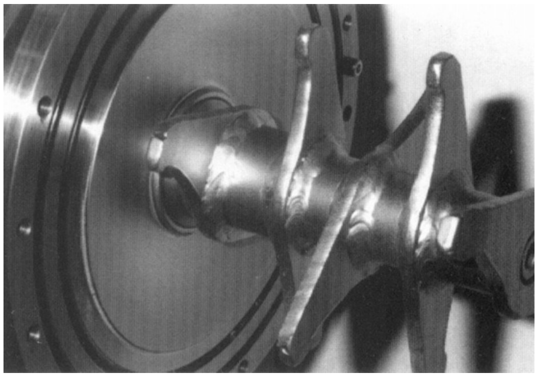

FIG. 3.8 Impeller of a laboratory Simoloyer attritor.

Other Laboratory Mills Used for Mechanical Alloying

Along with the FRITZSCH, NETZSCH, and Union Process laboratory mills and the SPEX shaker mill widely used for investigations of mechanical alloying and mechanical milling, other apparatuses have also been designed for these specific purposes. Some of these mills are described below.

HE (high-energy) mill is a type of vibratory ball mill (Fig. 3.9) with high impact velocities of up to 4 m/s, high impact frequency of the balls with the container walls of 20 Hz, and grinding media up to a 10-kg ball charge [6]. The container motion has a fixed amplitude of 30 mm. The work cycle can be programmed with a resolution of 1 min and a total milling time of up to 4 days. The container could be filled with different types of gases under controlled pressure. Bakker and colleagues [29] used a mill in which a single hardened steel ball with a diameter of 60 mm was kept in motion by a vibrating frame on which the container was mounted.

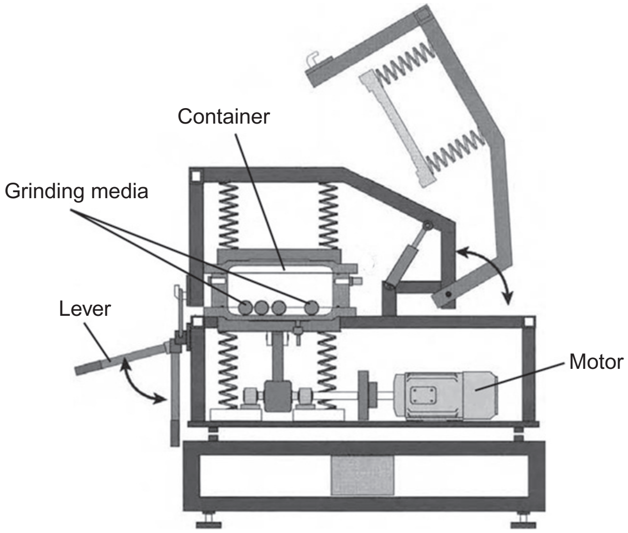

FIG. 3.9 Laboratory HE (high-energy) vibratory ball mill.

Pochet et al. developed a similar mill, although it used a driving magnetic field (Fig. 3.10) [30]. The bowl is made of stainless steel with a hardened steel bottom, the central part of which consists of a tungsten carbide disk of 20 mm diameter. This mill has low efficiency because the moving amplitude of the ball is very small and therefore has a long repetition time, and the specimen gets milled only during the collisions. On the other hand, the shaker mills, for example, the SPEX mills, have a much higher efficiency. However, in the SPEX mills, due to friction between the grinding balls and with the inner surface of the container walls, the sample contamination is higher.

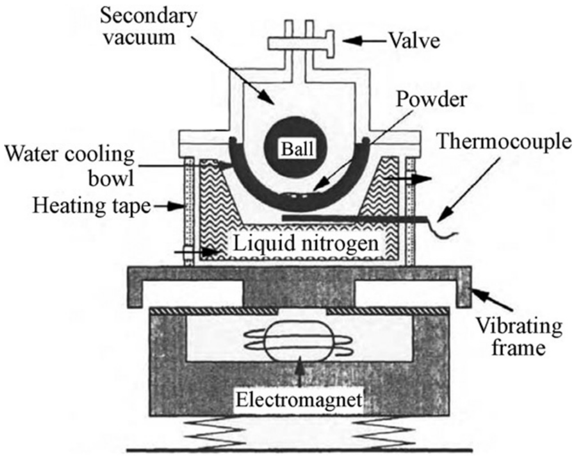

FIG. 3.10 Laboratory ball mill set in vertical vibration by a magnetic field.

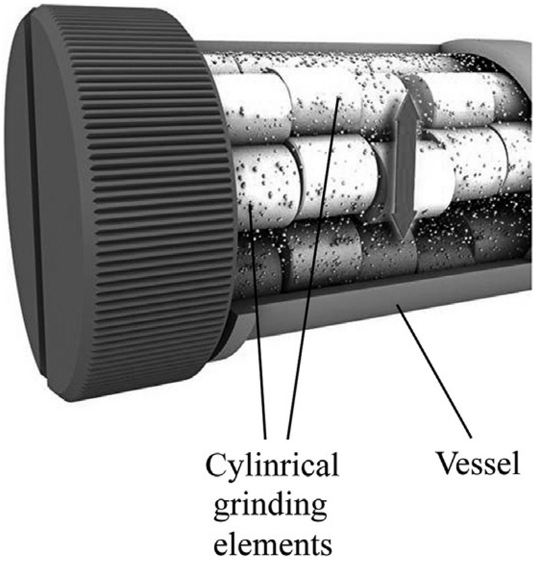

FIG. 3.11 Mill with vibratory grinding elements.

Vertical rod mill. To overcome some of the above-mentioned problems, Szymanski et al. [30] designed a friction-free mechanical grinder. This mill consists of seven steel rods (10mm in diameter and 100mm in height) arranged in a hexagonal motif with one rod in the center. These rods stand in a vertical position between a pair of parallel horizontal steel anvils separated by a distance of 116mm. The device moves up and down with an amplitude of 3.5mm and a frequency of 25Hz. Powders milled in this device have a low contamination level. Therefore, this mill corresponds to the vertical rod mill in comparison with the common horizontal rod mills.

Mill with vibratory grinding elements. In this design, the cylindrical grinding elements are stringed on the vibrating rods (Fig. 3.11). Due to such construction, wall scuffing is prevented and the uniform distribution of the grinding element in the vessel volume is organized. As a result, the milling efficiency is increased by less contamination.

The Uni-Ball mill from Australian Scientific Instruments Fyshwick is another type of mill where it is possible to control the nature and magnitude of the ball impact by controlling the magnetic field strength with the help of adjustable magnets. The introduction of permanent magnets generates a magnetic field, which acts on the ferromagnetic balls used for milling. By adjusting the distance between the balls and the magnet, the impact energy can be varied. Thus, one can choose the desired impact energy depending on the requirement and the materials to be milled. Also, changing the positions of the magnets can alter the type of energy transferred to the powder, allowing one to obtain impact or shear modes or a combination of both. Atmosphere composition, pressure, and temperature within the mill chamber are controlled. Precision control of milling energy by properly adjusting the position, quantity, and proximity of the magnets around the mill chamber allows the selection of the impact energy, the shear force and the proportion of these [6].

Calka and Wexler [31] modified the Uni-Ball mill to achieve milling modes involving impact or shearing of hardened curved surfaces on particles under a controlled electric discharge within a controlled atmosphere. As reviewed, the effects of low-frequency and high-voltage electrical impulses during milling were shown to be very efficient in synthesizing intermetallics, promoting reduction reactions, and forming nitride phases of several different metals not possible by conventional milling under regular impact mode.

Commercial Mills

Commercial tumbling ball mills for mechanical alloying are much larger in size than the mills described above and can process from several 100kg to up to 1 tonne at a time. The milling time increases with a decrease in the specific energy of the mill. Thus, a process that takes only a few minutes in a planetary mill can take hours in attritors and several days in commercial tumbling ball mills. Commercial batch NETZSCH attritors (Fig. 3.12) used industrially today are available in sizes from 115 to 720L (Table 3.3).

The attritors can be operated in both continuous and batch-processing applications. In the continuous operation, a material is fed uninterruptedly into the tank at the top. It then migrates through the agitating bed where it is processed to a desired particle size and is discharged through metering bar grids at the bottom of the tank. In the batch mode, material is charged into the mill, ground for a predetermined time, then discharged through grids at the bottom of the tank. Union

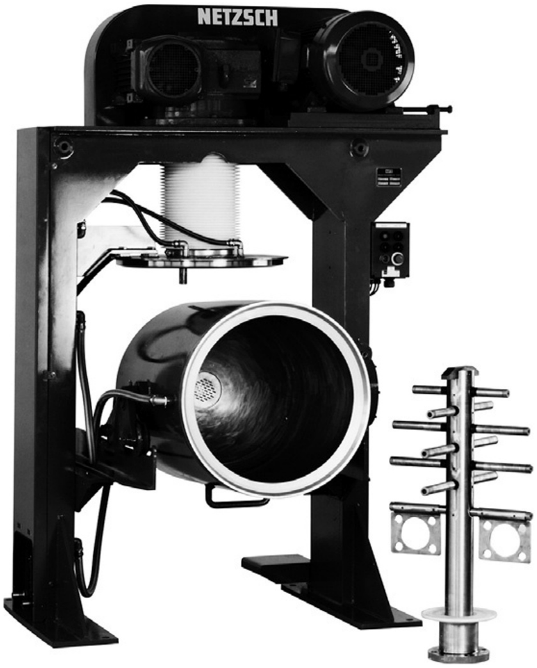

FIG. 3.12 Commercial batch NETZSCH attritor PRK 52 S. *(Courtesy of NETZSCH Inc.)*

Process SD dry grind attritors are commercially available in material capacity sizes from 7.5–11.3 to 285–470 L and by media value sizes from 19 to 700 L, respectively [32]. They are used in MA technology, specifically to make dispersion-strengthened metals. The SD-50 dry grind attritor of 57–95 L material capacity sizes by 140 L media value sizes is illustrated in Fig. 3.13. The high-speed attritor (HSA) is generally used in a continuous mode. The material is charged into the mill at the top and is discharged from the bottom under centrifugal force. The initial particle size (generally about 40 μm) of materials is led into the machine and the micron-sized final product is desired.

The circulation systems are wet systems and consist of a holding tank that is generally 10 times the size of the attritor. One of the essential requirements of the system is the high circulation rate by means of a slurry pump. The entire capacity of the holding tank are passed through the attritor at least once every 7–8 min.

Almost 25 years ago, a tendency to decrease the grinding media sizes for the purpose of decreasing the milled powder particle sizes was observed on the basis that small media in comparison with larger sizes transfers more energy into the milling process due to its greater specific surface [26,33,34]. In agitator bead mills, this principle is realized. There are grinding machines for ultra-fine processing of solids in liquids. In bead mills the area of application covers the particle size range from 200 μm (max. 500 μm) down to the nanometer range with a comminution factor down to 1:10,000 (200 μm → 20 nm). Small media is generally defined as 3 down to 0.25 mm, and finer. Recently, the bead mill technology found a use in such powder metallurgy nomenclature as coatings, including magnetic coatings, and ceramics. The new NETZSCH Alpha modular machine, the advanced disk grinding system, Discus, the Zeta system with optimized grinding media separation, and the peg system, Macro, are commercial available in wide material capacity size ranges [35]. For the present, the available data search regarding the application of bead mill techniques in MA has been not succeeded. But the outlook for bead mills in MA technology has not been ruled out. The bead mill application range is extensive and the variety of tasks extremely diverse.

Selection of Grinding Medium

In general, high-density media give better results. This is because the kinetic energy of the balls is higher and consequentl, ay higher amount of energy is transferred to the milled powder. The media should be denser than the powder being ground. Also, highly viscous materials require media with a higher density to prevent floating.

Because smaller media cannot break up large particles, the initial grinding media should be larger than the powder particle size. It is preferable to use a mixture of different sizes of balls rather than one size. A mixture of different sizes of grinding balls helps to improve the efficiency of the attritor. In the final state, the grinding media should be smaller when very fine particles are desired. Therefore, the smaller the grinding medium, the smaller the final particle size.

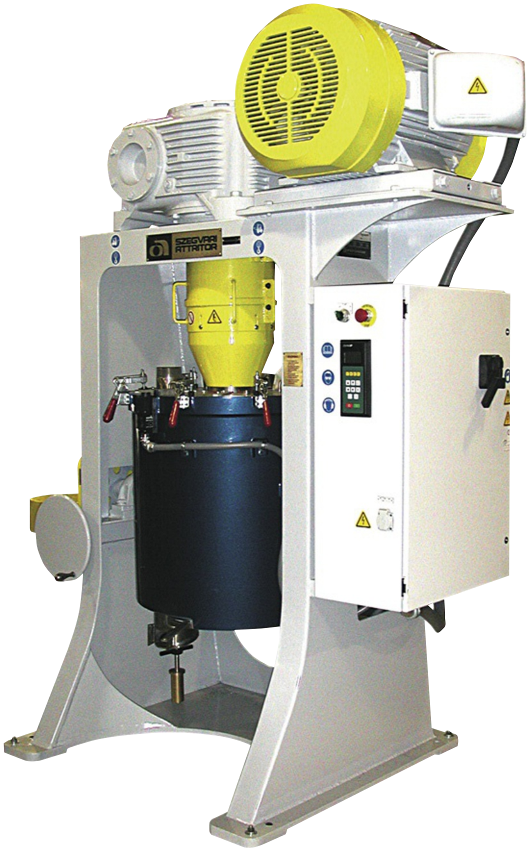

FIG. 3.13 Union Process SD dry grind attritor SD-50. *(Courtesy of Union Process Inc.)*

Regarding media hardness, the harder the media, the lesser the powder contamination, and consequently the medium lasts longer. However, if the medium is brittle, then the edges of the medium may be chipped off, becoming incorporated into the milled powder and contaminating it. However, if the media is magnetic in nature and the powder is not, then the material resulting from the wear of the grinding medium may be separated by magnetic means.

Contamination could be a serious consideration because material resulting from the wear of the media affects the product and may contaminate it. Therefore, it should be removed by a magnetic separator, chemicals, or sintering.

Costly media that are two to three times more expensive may last considerably longer. These may well be worth the extra cost over the long run. Table 3.4 presents the different types of grinding media available for MA or MM purposes and their properties.

TABLE 3.4 Properties of the Different Grinding Media Available for Mechanical Alloying and Mechanical Milling

Material	Density (g/cm^3)	Abrasion Resistance	Material to be Ground
Agate (99.9% SO_2)	2.65	Good	Soft to medium hard samples
Silicon nitride (90% Si_3N_4)	3.1	Extremely good	Abrasive sample, iron-free grinding
Sintered corundum (99.7% Al_2O_3)	>3.8	Fairly good	Medium-hard as well as fibrous samples
Sintered corundum-2 (85%–90% Al_2O_3)	>3.8	Fairly good	Medium-hard as well as fibrous samples
Stainless steel (12.5%–14.5% Cr + 1% Ni)	7.8	Fairly good	Medium-hard as well as fibrous samples
Tungsten carbide (93.2% WC + 6% Co)	14.7	Very good	Hard, abrasive samples
Zirconium oxide (94.8% ZrO_2)	5.7	Very good	Fibrous as well as abrasive samples

TABLE 3.5 Comparing the Different Mill Types Used for Mechanical MA Technology

	Device			
Parameter	**Planetary Mill**	**Attritor SD Model**	**High Speed Attritor HSA Model**	**Tumbling Ball Mill**
Maximal total volume (L)	8	1090	320	20,000
Maximal diameter (m)	0.2	0.74	0.36	3
Maximal relative velocity (m/s)	5	4.5–5.1	…	<5
Media size (mm)	5–30	3–9	0.5–3	12 and larger
Revolutions per minute	100–800	60–350	320–1700	10–50
Tip speed (rpm)	…	185–305	770–910	…

Table 3.5 compares the different devices (planetary ball mill, attritors, and a conventional ball mill) regarding their sizes and capacities.

MECHANICAL ALLOYING FUNDAMENTALS

For the realization of a chemical reaction between solids, which are able to interact due to thermodynamic considerations, it is necessary to satisfy at least two conditions. These are bringing them together at an acting distance of interatomic forces, and imparting to the atoms sufficient excess energy for the redistribution of electron density, by which a chemical conversion is accomplished. Realization of the first condition is not as complicated as the latter. The average energy density transmitted to matter, as a rule, is much less than the energy of the interatomic bonds. Therefore, the concentration factor of the former in local points amounts to a quantity sufficient for the fulfillment of the second condition to become of primary importance.

There are several approaches to an explanation of the mechanism of mechanical alloying [25,36]. One theory, which is called "thermal," reckons that the activation of chemical processes is provided by heat caused by friction and collision of particles with the grinding medium and with each other [37]. In the second approach, "dislocation," it is reckoned that the activation occurs at the expense of the energy of exit dislocations on particle surfaces by plastic deformation of particles that are being ground [38]. In the third approach, the activation of chemical processes is connected with the "trip out" of resilient energy at the distraction of a solid and with the formation of short-lived active centers [39–43]. The presence of numerous effects, such as luminescence, emission of electrons and other charged particles, the appearance of electric charges on the surface, and the "evaporation" of crystal lattice components, leads to the creation of the "deformation" model. The above models, without exception, complement each other.

The evolutional course of the MA process, following modification of the shape and powder particle structures, occurs in the following way. During high-energy milling, the powder particles are repeatedly flattened, fractured, and rewelded. Whenever two steel balls collide, some powder is trapped between them. This plastically deforms the powder particles, creates new surfaces, and enables the particles to weld together, which leads to an increase in particle size. In the early stages of milling, the particles are soft (in conditions when either ductile-ductile or ductile-brittle material combinations are used) and their tendency to weld together and form large particles is high. A widened range of particle sizes develops in this early stage. A microphotograph (Fig. 3.14) illustrates both widened particles and their agglomerates in an A1-30 at.% Mg powder sample mechanically alloyed for 2 h [6].

The composite particles at this stage have a typical layered structure consisting of various combinations of the initial components. With continued deformation, the particles become work-hardened and fracture by a fatigue failure mechanism and/or by the fragmentation of fragile flakes. At this stage, the inclination to fracture predominates over cold welding. Due to the continued impact of grinding balls, the structure of particles is steadily refined while the particle size continues to be the same. As a result, the interlayer space decreases while the number of layers in a particle increases. The rate of the internal structure refinement of the particles is roughly logarithmic with processing time while the initial size of the particles is relatively unimportant [2,3].

Milling for a certain length of time leads to a steady-state equilibrium when a balance is reached between the rate of welding, which tends to increase the average particle size, and the rate of fracturing, which tends to decrease the average

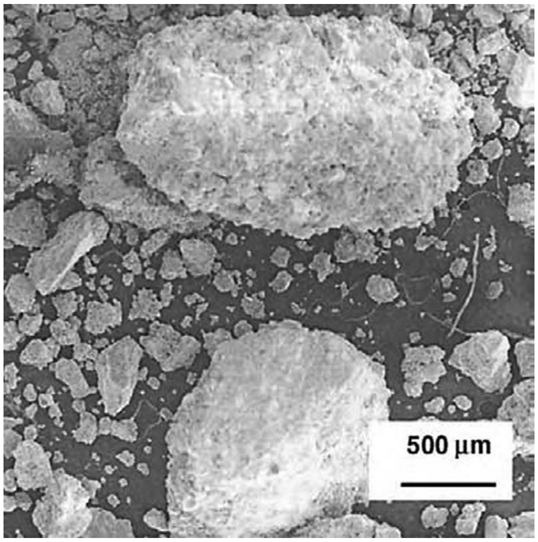

FIG. 3.14 Widened condition of particle sizes in an A1-30 at.% Mg powder sample mechanically alloyed for 2h.

composite particle size. At this stage, generally each particle contains substantially all of the initial ingredients in the proportion in which they were mixed together, and the particles attain saturation hardness. The particle size distribution at this stage is narrow because particles larger than average are reduced in size at the same rate as fragments smaller than average grow through agglomeration of smaller particles [44]. The average particle size obtained at this stage depends on the relative ease with which agglomerates can be formed by cold welding and the fracture strength of composite particles and the resistance of particles to deformation. At this stage, the particles consist of convoluted lamellae. Due to the increased amount of cold working, the crystal defects such as dislocations, vacancies, stacking faults, and an increased number of grain boundaries introduced in particles increase with time. The impact of the ball-ball, ball-powder, and ball-wall collisions also causes a rise in the powder temperature and this further facilitates diffusion. Alloy formation (either stable or metastable phases) occurs due to the combined effect of all these factors. Microstructural refinement continues to take place at this stage, and the oxide dispersion becomes more uniform.

At the final stage, the lamellae become finer and more convoluted, and the composition of the individual powder particles approaches that of the overall composition of the starting blend. The lamellar spacing and dispersoid spacing is <1 µm, and the microhardness of the particles attains a saturation level, due to the accumulation of strain energy. Further processing will not improve the distribution of the dispersoids, and the compositions of the individual powders are now equivalent to the starting powder blend. This is called the steady state.

Three feasible combinations of metals and alloys in MA technology are considered: (1) ductile-ductile, (2) ductile-brittle, and (3) brittle-brittle.

Ductile-ductile is the ideal combination of materials for MA. From the start, a small quantity of the powder, usually one or two particle thicknesses, also gets welded onto the ball surfaces. This coating of the powder on the grinding medium is advantageous because it prevents excessive wear of the grinding medium. In the next stage, these flattened particles get cold welded together and form a composite lamellar structure of the constituent metals. With increasing MA time, the composite powder particles get work hardened, the hardness increases, and the particles get fragmented, resulting in particles with more equiaxed dimensions. With further milling, the elemental lamellae of the welded layer and both the coarse and fine powders become convoluted rather than being linear (Fig. 3.15). This is due to the random welding together of equiaxed powder particles without any particular preference to the orientation with which they weld. Alloying begins to occur at this removed from the grinding input into the process and the work hardening rate of the material being processed [45].

Alloying begins to occur at this stage due to the combination of decreased diffusion distances (interlamellar spacing), increased lattice defect density, and any heating that may have occurred during the milling operation. The hardness and particle size tend to reach a saturation value at this stage. With further milling, real alloying occurs at the atomic level, resulting in the formation of solid solutions, intermetallics, or even amorphous phases. As was considered [45], the rate of structural refinement depends on the rate of mechanical energy input into the process and the work hardening rate of the material being processed.

Ductile-brittle is a category of traditional ODS alloys because the brittle oxide particles are dispersed in a ductile matrix. The microstructural evolution in this type of system was described in the work [46]. In the initial stages of milling, the

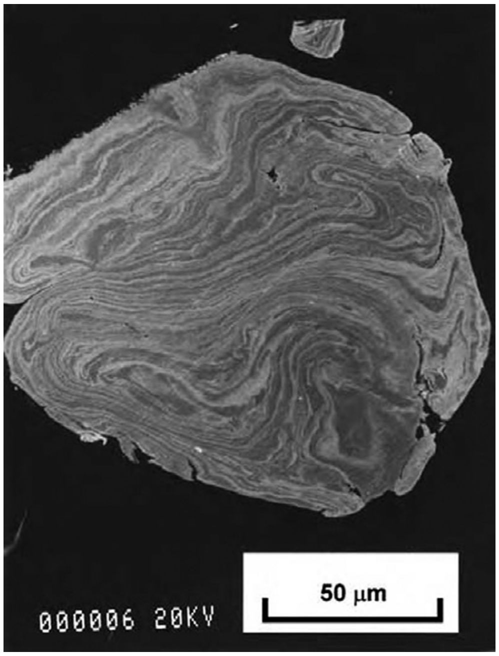

FIG. 3.15 Scanning electron micrograph of the convoluted lamellar structure obtained during milling of a ductile-ductile component system (Ag-Cu).

ductile metal powder particles get flattened by the ball-powder-ball collisions whereas the brittle oxide or intermetallic particles get fragmented. These fragmented brittle particles tend to become occluded by the ductile constituents and trapped in the ductile particles. The brittle constituent is closely spaced along the interlamellar spacings. With further milling, the ductile powder particles get work hardened, and the lamellae get convoluted and refined. The composition of the individual particles converges toward the overall composition of the starting powder blend. With continued milling, the lamellae get further refined, the interlamellar spacing decreases, and the brittle particles get uniformly dispersed in the ductile matrix in an ODS alloy. A typical transmission electron micrograph showing the dispersion of Er_2O_3 in a mechanically milled α_2-titanium aluminide matrix is shown in Fig. 3.16.

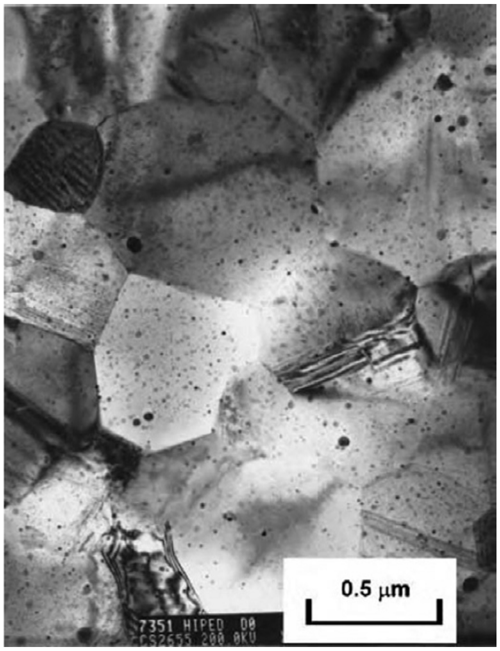

FIG. 3.16 Transmission electron micrograph showing a uniform dispersion of Er_2O_3 particles in a mechanically alloyed α_2-titanium aluminide alloy matrix.

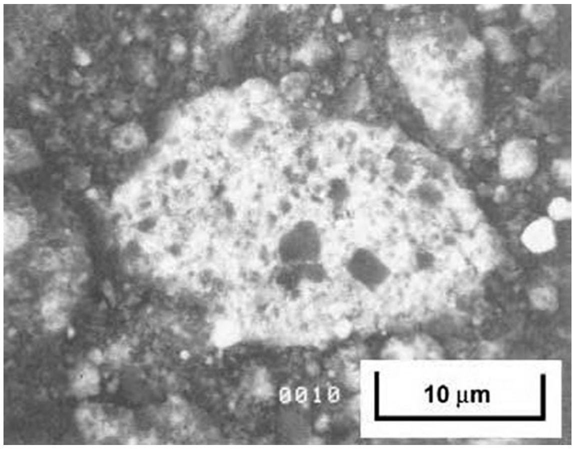

FIG. 3.17 Scanning electron micrograph showing that the harder Si particles are incorporated in a softer Ge matrix after mechanical alloying of the Si-Ge powder mix for 12h.

In *brittle-brittle* component systems, during milling, the harder (more brittle) component gets fragmented and embedded in the softer (less brittle) component. Thus, in the brittle-brittle component system Si-Ge and Mn-Bi [47], the harder Si particles are embedded in the softer Ge matrix (Fig. 3.17). Possible mechanisms that may contribute to material transfer during milling of brittle components may include plastic deformation, which is made possible by the following: local temperature rise, microdeformation in defect-free volumes, surface deformation, and/or a hydrostatic stress state in the powders during milling [47].

OXIDE DISPERSION-STRENGTHENED ALLOYS

The main use of MA of nonferrous metals has been in the present-day development of commercial oxide dispersion-strengthened (ODS) nickel-, copper-, and aluminum-base alloys. The feature of these materials is elevated temperature strength, which is derived from several mechanisms. First, their structure is characterized by uniform dispersion with a spacing of about 100nm by very fine (from 5 to 50nm) oxide particles of stable oxides such as alumina (Al_2O_3), titania (TiO_2), thoria (ThO_2), yttria (Y_2O_3), lanthana (La_2O_3), and beryllia (BeO). This dispersion inhibits dislocation motion in the metal matrix and increases the resistance of the alloy to creep deformation. Another function of the dispersoid particles is to inhibit the recovery and recrystallization processes. Second, the homogeneous distribution of alloying elements due to MA gives both the solid-solution strengthened and precipitation-hardened alloys more stability at elevated temperatures and improvement in properties. Mechanically alloyed materials also have high oxidation and hot corrosion resistance.

The production of ODS alloys on a commercial scale uses as raw materials elemental powders, crushed master alloy (intermetallic) powders, and prealloyed powders. Yttria powder as well as other oxide powders with narrow ranges of crystallite size (preferably when the crystallite size is below 30nm) and metal powders are mixed together to form a bulk feedstock. These mixtures are charged into large tumbling ball mills or attritors with steel balls. During milling, an equilibrium powder particle size distribution is established until each individual particle achieves the alloying constituents in the given proportions. The mechanically alloyed powder from the mill is then filled into stainless steel containers. Then the powder is consolidated at elevated temperatures, usually by either extrusion or hot isostatic pressing (HIP). In most cases, extrusion is preferred because it is less expensive then HIP. The former is accomplished in the following way. The powder is loaded into mild steel extrusion cans with characteristic sizes up to 300mm in diameter and 900mm in length and containing up to 280kg. The batch is held for several hours in a furnace at the extrusion temperature, during which time homogenization of the powder and complete alloying occur if that has not already been accomplished during milling. Extrusion is done in commercial presses at temperatures, ratios, and speeds that are independent variables, depending on the properties of the material.

The consolidated mechanically alloyed billets are worked to a final shape such as sheet, plate, rod, bar, tube, etc., using typical hot-working techniques such as extrusion and hot rolling.

CONTACT DISPLACEMENT REACTIONS

Contact displacement reactions (cementation) in solutions are well known. The electrolytic nature of these is described in "Contact displacement method (Cementation)" in Chapter 8. Electrolytically precipitated powder is produced by the displacement of one metal from the solution due to the conjugated dissolution of the other metal.

The mechanical activation of solids to cause chemical reactions has been used for nearly a century [36]. A revival in this activity arose in 1989 when it was discovered that MA can be used as a refining process [2]. This was done by showing that pure metallic copper can be synthesized as a result of ball milling copper oxide and calcium together at room temperature. Numerous metals, including Zn, Ti, Zr, Ta, Gd, Er, Sm, V, W, and some intermetallics, for example, $SmCo_5$, can now be synthesized directly from oxides or chlorides. The general equations for the displacement reactions of the metal oxides as well as chlorides may be represented as:

$$\mathrm{MO} + \mathrm{R} \rightarrow \mathrm{M} + \mathrm{RO}$$

$$\mathrm{MCl} + \mathrm{R} \rightarrow \mathrm{M} + \mathrm{RCl}$$

where a metal oxide (MO) or metal chloride (MCl) is reduced by a reductant (R) to the metal (M).

The displacement reactions realized by MA are characterized by a large negative free energy conversion at room temperature and are therefore thermodynamically practicable at room temperature. At the same time, commercial operations by pyrometallurgical techniques are conducted at elevated temperatures to overcome the kinetic barriers and achieve sufficiently high reaction rates.

Mechanical alloying can provide the means to increase the reaction kinetics of the displacement reactions because the repetitive fracturing and welding of powder particles increases the area of contact between the particles and allows newly formed surfaces to come into contact many times. Due to this, the reaction proceeds without diffusion through the product layer. Parallel with this, the high surface defects caused during MA accelerate the diffusion process. As a result, these reactions will now occur at room temperature. In the case where a reaction cannot occur at room temperature, the particle surface refinement and consequent reduction in diffusion distance can considerably reduce the reaction temperature.

Two different reaction kinetics (depending on milling conditions) have been distinguished [6,48]. The reaction can extend to a very small volume during each collision between the grinding media, leading to a gradual conversion. Alternatively, when the reaction enthalpy is high enough, a self-propagating combustion reaction can be initiated. Such reactions require a critical milling time for the combustion reaction to be ignited. If the temperature of the powder is recorded during MA, a sudden increase in temperature at a critical time indicates combustion. Measurements of the ignition time and temperature provide a means of characterizing the structural and chemical evolution during MA as well as preventing the risk of explosion.

The displacement reaction products normally consist of two phases – the metal or a compound and the oxide or chloride, subject to reductant. The by-product phase can be easily removed if the metal particles are embedded in a continuous matrix. Removal of the by-product is achieved by leaching the product mixture in a dilute acid or hot water, or by vacuum distillation. The use of carbon or hydrogen as the reductant leads to the formation of gaseous carbon dioxide or water vapor as the by-product and avoids the need for leaching and distillation.

The mechanically driven displacement reaction shows a number of advantages over conventional metal processing techniques:

- The mechanically driven displacement reaction allows the direct formation of powder product without first having to manufacture the bulk alloy and then convert it to powder.
- It enables the reduction of a number of oxides and halides to pure metals at room temperature, which ensures energy savings.
- If a number of components are reduced simultaneously, it is possible to produce an alloy without first having to convert the oxides to pure metals and then to the desired alloy.

Thus, a number of high-temperature conventional technical processes can be combined into one single-room temperature process with the potential for considerable cost savings.

The typical chemical reactions by the mechanical alloying technique are summarized in Table 3.6. These are characterized by a large negative free energy change and are therefore thermodynamically feasible at room temperature.

Process parameters, including ball-to powder weight ratio (BPR), ball diameter, milling temperature, use of a process control agent, and relative proportion of the reactant phases, play an important role in the nature and amount of product

TABLE 3.6 Chemical Reactions by Mechanical Alloying

Reaction[a]	Mill Type	BRP[b]	% Excess Reductant	ΔH (kJ)	Ignition Time (min)	Ref.
$CoCl_2+2Na \rightarrow Co+2NaCl$	SPEX 8000	3:1	25	−495	20	[49]
$3CuO+2Al \rightarrow 3Cu+Al_2O_3$	SPEX 8000	33:1	10	−1197	15	[48]
$CuO+Ca \rightarrow Cu+CaO$	SPEX 8000	3:1	…	−473	6.5	[50]
$CuO+Mn \rightarrow Cu+MnO$	SPEX 8000	3:1	10	−231	43	[48]
$NiCl_2+2Na \rightarrow Ni+2NaCl$	SPEX 8000	3:1	50	−507	42	[49]
$3NiO+3Al \rightarrow Ni_3Al+Al_2O_3$ (<1 h)	SPEX 8000	>7:1	…	…	…	[51]
$3PbS+2Al \rightarrow 3Pb+Al_2S_3$	SPEX 8000	13:1	…	−267	…	[52]
$3TiO_2+4Al+3C \rightarrow 3TiC+2Al_2O_3$ (7 h)	SPEX 8000	>7:1	…	−1038	…	[51]
$TiO_2+2Ca+C \rightarrow TiC+2CaO$	Fritsch P5	7.5:1	20	−510	…	[53]
$3V_2O_5+10Al \rightarrow 6V+5Al_2O_3$	SPEX 8000	7:1	10	−3727	…	[54]
$3ZnS+2Al \rightarrow 3Zn+Al_2S_3$	SPEX 8000	13:1	…	−107	…	[52]

[a] *By starting room temperature of the components.*
[b] *Ball-to-powder weight ratio.*

phases obtained by the displacement reactions; these need to be optimized for the best yields. Normally, about 10%–15% stoichiometric excess of the reductant has been used in most of the investigations conducted so far. This excess reductant is used partly to compensate for the surface oxidation of the reactive reductant powder particles.

Among the inhibition of interparticle welding during collisions, acceleration of the powder comminution, and decreasing the particle size, a process control agent (PCA) is used in a few specific instances, such as suppressing a self-propagating combustion reaction. For example, when CuO was ball milled with reactive metals in the absence of any PCA, a self-propagating combustion reaction occurred after an incubation period [6,48]. When toluene was used as a PCA, the reduction of CuO proceeded in a controlled manner and reached completion in about 24 h [48]. The use of a PCA acts likes an additive (diluent) and either delays or completely suppresses the combustion event.

The required time for the reduction reaction decreases with an increase in the ball-to-powder weight ratio. For example, the time required to form Ti during the reduction of $TiCl_4$ with Mg at 293 K was 48 h at a BPR of 3:1 while it was only 18 h at a BPR of 12:1 [6]. As reported, the ignition temperature T_{ig} decreased with increasing milling time, suggesting that the reaction kinetics become faster during milling. Furthermore, the rate of decrease of T_{ig} increased with increasing BPR, and this is related to the decrease in particle size. The values of the ignition time t_{ig} also decreased with increasing BPR. Both of these effects are related to the average frequency of collisions that increases with increasing BPR. It has also been reported that the combustion reaction did not occur when small grinding media (1 and 3 g balls) were used, but it occurred when large (8 g) balls were used.

POWDER CONTAMINATION

A most important problem in the MA process is the impurities that get into the powder particles during milling, contaminating them. Because of the small size of the particles, their surface area is large, which promotes contamination of the powders. The magnitude of contamination depends on the milling medium, the time of milling, the intensity of milling, the atmosphere in which the powder is milled, and the difference in strength to hardness of the powder. As is well known, from 1 to 4 wt% of iron has been found as normally present in most of the powders milled with the steel grinding medium while amounts as large as 7 wt% (20 at.%) iron in a tungsten-carbon mixture milled for 310 h and 13 wt% (33 at.%) iron in pure tungsten milled for 50 h in a SPEX mill [6] have also been found.

The origins of contamination of metal powders can be the chemical purity of the initial powders, the milling equipment (milling container and grinding medium), the milling atmosphere, and the process control agents (PCA) added to the powders. Contamination is characterized by Suryanarayana [6] as: contamination from milling equipment is mainly substitutional and that from the milling atmosphere is, in essence, interstitial in nature while contamination from chemical purity can be either substitutional or interstitial in nature, and the PCA additions lead to interstitial contamination. The interstitial impurities oxygen and nitrogen are deleterious to reactive metals such as titanium and zirconium and the presence of these impurities leads to a change in the constitution of the alloys [55,56].

Experimentally determined levels of nonferrous metal powder contamination during milling of different types of powder compositions are summarized in Table 3.7. The type of mill, the ball-to-powder weight ratio, and milling time employed are also listed because these parameters determine the magnitude of contamination. The major impurities listed are oxygen and nitrogen, mainly from the atmosphere and/or PCAs used, and iron from the steel grinding medium and the steel container. The levels of carbon, chromium, and other metallic impurities are also listed in some cases, whenever reported.

The level of contamination can be different under different processing conditions and is dependent on the type of mill, the intensity of milling, the nature of the powder, the nature of the grinding medium and tank, the ambient atmosphere, etc.

Several attempts have been made to minimize powder contamination during mechanical alloying. The following ways to minimize powder contamination are known:

- Using the same material for the mill body (tank) and grinding medium as the powder being milled.
- The grinding medium and tank should be harder and stronger than the powder being milled.
- Preventing the outside atmosphere leaking into the mill by using a controlled milling atmosphere.
- Proper cleaning of the tank that was previously used for another powder.
- Optimization of the milling process.

The first way is of restricted use because it is difficult in many cases due to the nonavailability of the special grinding media and tanks. The problem is becoming more and more complicated because the MA technique is being applied to a variety of materials, including metals, alloys, ceramics, polymers, and composites. It is impossible to get tanks and grinding media of all these types of materials. But it is possible to find another solution using a thin adherent coating on the internal surface of the tank of the material to be milled. Independently of the above, a simple rule that must be followed to minimize contamination is that the tank and grinding medium should be harder/stronger than the powder being milled.

The problem of the milling atmosphere is also important. It has been observed [6] that when the tank is not properly sealed, the atmosphere surrounding the tank, usually air, leaks into the tank and contaminates the powder. So, when reactive metal such as titanium and zirconium is milled in incompletely sealed containers, the powders are contaminated with nitrogen and oxygen. Flushing with argon does not remove oxygen and nitrogen absorbed on the internal surfaces.

Attempts have been made to improve the tank-sealing integrity to prevent the surrounding atmosphere leaking in. It has been reported [56] that the use of a high-purity argon (99.998%) milling atmosphere and improvements in the sealing quality resulted in the processing of high-quality titanium alloy powder with <100 ppm oxygen and 15 ppm nitrogen. However, this technique may not be economically viable and therefore may not be acceptable on a commercial scale.

Attempts to minimize the powder contamination by means of milling process optimization are known. Such a method for minimizing the powder contamination during ball milling was recently described [77]. Because the optimum milling conditions ensuring a minimum of contamination are different from the conditions for maximum productivity for a specified quality of the powder being milled, the authors propose a solution for achieving a compromise between the targets mentioned above.

Summarizing the foregoing about the state of the problem of powder contamination during milling, it is noted that claims have been made in the literature for the superiority of certain mills and practices over others, but systematic investigations on milling the same powder under identical conditions in different mills and evaluating the contamination levels have not been undertaken. Therefore, the regularity of these data is an important aspect of improvement in increasing the purity of the mechanically alloyed powders.

TABLE 3.7 Powder Contamination During Mechanical Alloying

Composition[a]	Mill Type	Milling Medium	BPR	Milling Time (h)	Contamination Level (at%)			Ref.
					Oxygen	Nitrogen	Iron	
Al-20Cu-15Fe	Planetary ball mill	Hardened steel	10:1	300	…	…	1.2	[57]
Al-5Fe-5Nd	High speed shaker mill	Steel	…	240	…	…	9	[58]
Al-12Ti	Attritor	Steel	…	400	27.4	22.6	0.07	[59]
Al-12T	Attritor	Steel	…	1300	36.5	16.3	0.11	[59]
Al-Ti	Planetary ball mill	Hardened steel	60:1	120	…	…	1.5 add 0.3 Cr	[60]
$Cu_{44}Nb_{42}Sn_{14}$	Lab. ball mill	WC-Co	50:1	24	13.5	2.4	…	[61]
Cu-50Zr	SPEX 8000	440C SS	10:1	13	3.3	…	0.25	[62]
Mo-66.7Si	Planetary ball mill	Tempered steel	…	48	…	…	10.5	[63]
Nb-25Ge	SPEX 8000	…	…	13	10	…	1.5	[64]
Ni-25Al	SPEX 8000	…	…	40	…	…	4	[65]
Ni-40Nb	SPEX 8000	521,000 steel	3:1	14 (air)	13.4	2.1	2.3	[66]
Ni-40Nb	SPEX 8000	521,000 steel	3:1	11 (helium)	2.0	1.9	5.1	[66]
Ni-Zr	Fritsch planetary mill P5	SS	30:1	10 (nitrogen)	…	…	12	[67]
Ru-50Al	SPEX 8000	Hardened steel	10:1	35	…	…	15	[68]
Ta-30Al	Rod mill	SS	36:1	400	…	…	5	[69]
Ti-5Al	SPEX 8000	Hardened steel	10:1	30	21	33	…	[70]
Ti-50Al	SPEX 8000	Hardened steel	10:1	70	10	26	…	[70]
Ti-60Al	Fritsch planetary mill P5	…	10:1	70	6.7	7.4	…	[71]
Ti-20Cu-24Ni-4Si-2B	SPEX 8000	Hardened steel	5:1	24	2.9	…	0.35	[72]
Ti-37.5Si	SPEX 8000	Hardened steel	5:1	24	4.4	1.8	…	[73]
W-C	Ball mill	Hardened steel	30:1	310	…	…	20	[74]
W-30Ni	SPEX 8000	Hardened steel	11:1	60	…	…	50	[75]
W-40Ni	SPEX 8000	Hardened steel	11:1	60	…	…	40	[75]
Zr-30Cu-10Al-5Ni	Retsch PM 4000 planetary ball mill	Hardened steel	14:1	100–200	1.5–2.0	…	0.5	[76]

[a] *All alloy compositions are expressed in atomic percent.*

APPLICATIONS

The main industrial applications of mechanically alloyed materials are in thermal processing, power engineering, glass processing, aerospace, and other industries. These applications are based on the ability of MA to synthesize materials with metastable phases, such as supersaturated solid solutions, nonequilibrium crystalline or quasicrystalline intermediate phases, and amorphous alloys [3,43,78].

Comparison of the ability to produce metastable phases by MA with the results of rapid solidification shows differences in the nature of the mechanisms by which metastable phases form as well in processing techniques. For example, solid solutions have been obtained in the full composition range in the Cu-Co, Cu-Fe, and AlSb-InSb systems by MA, but not by rapid solidification. The formation of metastable intermediate phases and amorphous alloys also differs in various systems using the two techniques. For example, the formation of an amorphous phase in the titanium-aluminum system by MA is realizable while it is not possible by rapid solidification [79]. An important difference between these methods is that whereas amorphous phases form in the vicinity of eutectic compositions by rapid solidification, they form near the equiatomic composition by MA. A transmission electron micrograph illustrating the difference for mechanically alloyed material and rapidly solidified alloy in the matrix grain size, and the size and distribution of dispersoids is shown in Fig. 3.18 [6,79]. The rapidly solidified Ti_3Al phase alloy was added by 2 wt% Er and then hot isostatic pressed at 1123 K. The mechanically alloyed $Ti_{61}Al_{25}Nb_{10}V_3Mo_1$ material was also added by 2 wt% Er and then hot isostatic pressed at a higher 1273 K temperature. In comparison to the rapidly solidified alloy, the mechanically alloyed material shows a finer matrix grain size, more uniform distribution, the absence of large dispersoids at grain boundaries, and the absence of dispersoid-free zones near the grain boundaries [6].

The major MA developments in the dispersion strengthened nickel-, aluminum-, and copper-base alloys are considered below.

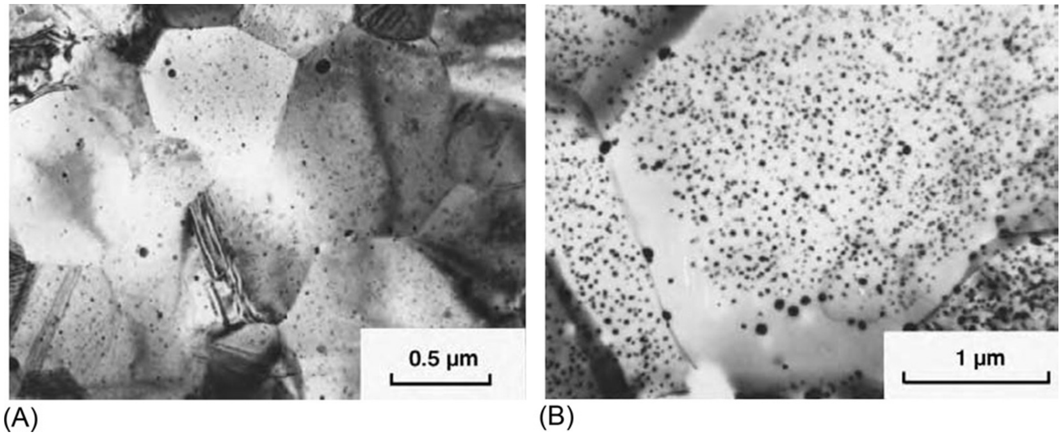

FIG. 3.18 Transmission electron micrographs of two polished metallographic sections showing the difference in the matrix grain size and the size and distribution of dispersoids. (A) Rapidly solidified and hot isostatic pressed at 1123 K. (B) Mechanically alloyed and hot isostatic pressed at 1273 K. *(Source: Suryanarayana C. Mechanical alloying and milling. New York: Marsel Dekker; 2004.)*

Nickel-Base Alloys

Compositions of several grades of the mechanically alloyed nickel-base superalloys are given in Table 3.8. The term “superalloy” is employed to characterize the materials with high strength at high temperatures that are used principally in turbine engines for aircraft and power generation.

The oxide dispersion-strengthened alloys are intended for applications in a wide variety of industries. The Special Metals Corporation used MA for a few of the most specialized alloys [85]. The MA nickel-base superalloys are intended mainly for gas turbine engine components and sheet for use in oxidizing/corrosive atmospheres. Thus, the largest use of MA 754 is as vanes and bands for aircraft gas turbine engines. It is also used for the brazed nozzle guide vane and band assemblies in aero engines. The principal advantages of the alloy for these applications are thermal fatigue resistance, a high melting point, and long-term creep strength. The alloy MA 758 is intended for a number of industrial applications where its high chromium content makes it resistant to extreme temperatures. This alloy was used in the glass industry for high-temperature components requiring both elevated temperature strength and resistance to extremely corrosive molten glass.

TABLE 3.8 Nominal Compositions (wt%) of Mechanically Alloyed Nickel-Base Superalloys

	Trade Grade (Source)					
	MA 754	MA 757	MA 758	MA 760	MA 6000	TMO-2
Elements	[80,81]	[81]	[82]	[80,81]	[83,84]	[80,81]
Aluminum	0.3	4.0	0.3	6.0	4.5	4.2
Boron	…	…	…	…	0.01	…
Carbon	0.05	…	0.05	…	0.05	…
Cobalt	…	…	…	…	…	9.7
Chromium	20	16	30	20	15	6.0
Iron	1.0	…	…	…	…	…
Molybdenum	…	…	…	2.0	2.0	2.0
Tungsten	…	…	…	3.5	4.0	12.4
Tantalum	…	…	…	…	2.0	4.7
Titanium	0.5	0.5	0.5	…	2.5	0.8
Yttrium oxide	0.6	0.6	0.6	0.95	1.1	1.1
Zirconium	…	…	…	…	0.15	…
Nickel	Bal	Bal	Bal	Bal	Bal	Bal

A large diameter and the thin wall tubing of alloy MA 754 has been produced and evaluated for radiant tube applications. Alloy MA 758 has been used as tubing in heat exchangers and process equipment operating at very high temperatures. Because of its complex composition, the alloy MA 6000 has excellent resistance to oxidation and sulfidation. It was used for first- and second-stage advanced gas turbine vanes and blades machined from a solid bar.

Data about room temperature and elevated temperature mechanical properties of commercial oxide dispersion-strengthened nickel-base superalloys are given in “Production of Nickel and Nickel-alloy powders” (Chapter 21).

Cobalt-Base Alloys

The cobalt-base alloys are the current materials for application in oral and orthopedic surgery [86]. The biomaterial alloys must demonstrate the most useful balance of strength, fatigue, and wear along with resistance to corrosion in order to be useful to replace a body part. A surgical implant such as a dental implant must meet biological requirements for joint replacement. The Co-Cr-Mo-C system alloys answer hereby conditions.

Sánchez-De Jesús et al. [87] synthesized a biomedical Co-27Cr-6Mo-0.25C alloy by mechanical alloying. This alloy represents one of the current materials of choice for cast and wrought metallic implants based on >40 years of clinical application in oral and orthopedic surgery [86]; it has become standardized [88]. Its status as a metallic material of choice results from its high strength and corrosion resistance.

The MA process was carried out at room temperature in a shaker mill using hardened steel balls of 12.7 mm in diameter and a vessel as the milling media with 1:8 as the ball/powder weight ratio. An update of the authors’ process consists of mechanical alloying of a Cr-Mo-C blend for 7 h, followed by the addition of Co and an additional milling time of 3 h. The final particle’s median diameter was about 28 μm. As milling time is increased, the particle size decreases, but prolonged milling time increases the previous 0.5% weight contamination by iron.

Aluminum-Base Alloys

Through the presence of durable surface oxide film, the initial aluminum powder during processing in a high-energy mill is easily granulated. Thus, it has been reported [43] that at the end of 5 min milling in a vibratory ball mill, the powder becomes lamellar. An increase in the specific surface of particles as a result of shape change leads to disruption of the oxide layer continuity and the appearance of fresh surfaces. During this stage, cold welding dominates over fracture. Then, during processing in the range from 5 to 20 min, fracture prevails, leading to an appreciable decrease in lamellar particle size. They range from 100 to 200 μm in two directions with thickness at most 4–5 μm. Further processing has no perceptible influence on the particle thickness, but decreases particle size in two other directions, resulting in a steep decrease of apparent density from the initial 1.1–1.3 to 0.4–0.6 g/cm^3 at the end of 20 min milling. Along with the comminution process, a reverse process takes place, including agglomeration and cold welding of metallic aluminum on one hand and oxide splinters and products of interaction between oxides and adsorbed gases on the other hand. This process prevails after 30 min, which leads to an increase of granules and apparent density (Fig. 3.19). The latter reaches a maximum of 1.3–1.4 g/cm^3 after processing for 2 h, and does not change significantly upon further processing.

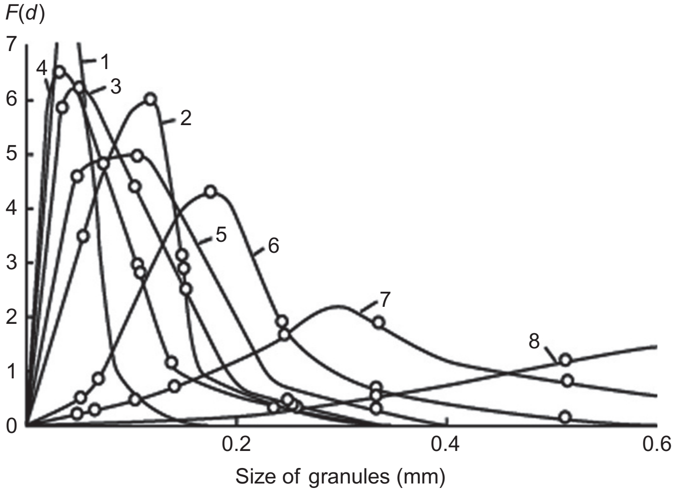

FIG. 3.19 Change of aluminum granule size distribution during mechanical alloying processing at the end of: (1) 0 min, (2) 5 min, (3) 10 min, (4) 20 min, (5) 30 min, (6) 40 min, (7) 60 min, and (8) 90 min. *(Source: Vitjaz PA, Lovshenko FG, Lovshenko GF. Mechanical alloyed alloys based on aluminium and copper. Minsk (Byelorussia): Byelorusskaja Nauka; 1998.)*

An increase of milling time above 30 min changes the shape of particles, altering them from lamellar to a fission-fragment shape. Adhesion processes lead to agglomeration of particles as well as attachment of fragments to the grinding balls. By ball collisions, the particles are welded layer-wise on the particle incrustations due to the action of the normal strength component while the tangential strength component causes the breakup of the incrustations. After 1 h, a dynamic balance is stabilized, at which approximately 10 wt% of the charge is found on the balls.

Under multiple plastic deformation action, the granules assume a shape that is nearly spheroidal. Simultaneously, the structure of composition is also transformed (Fig. 3.20). At the first granulation stage, the structure of granules is characterized by pronounced lamination. During further processing, the thickness of layers is continuously decreased and the gradual homogenization of composition occurs. However, in granulated aluminum and in aluminum-base compositions obtained without surfactant, typical lamination is observed after long-continued processing. Increasing the processing time up to 6–8 h leads to growth up to 2 mm in average size of the granules and a dynamic balance between welding and the destruction of granules is established.

Mechanical alloying of aluminum alloys of various compositions generally brings an increase of granule hardness. Table 3.9 contains the data about microhardness of granulated compositions obtained by mechanical alloying of aluminum with various elements and their oxides.

Here it is shown that strengthening does not depend on the initial hardness of the alloying component, but rather on the kinetics of the mechanochemical reactions that determine the formation of the strengthening phases. Thus, a correlation is observed between the Gibbs function oxidation-reduction reaction values and the hardness of the compositions. The latter increases with a decreasing ΔG value.

It is typical that aluminum milling with an aqua addition as well as its processing in carbon dioxide or sodium superoxide leads to significantly greater strengthening in comparison with mechanical alloying with oxides Cr_2O_3, TiO_2, and ZrO_2, which have high hardness and a low value of Gibbs function of oxidation-reduction reaction. Mechanical alloying with oxides such as CuO, Co_3O_4, MoO_3, and V_2O_5 is more advantageous. The characteristics of room- and elevated-temperature mechanical properties for mechanically alloyed aluminum of various compositions are summarized in Table 3.10.

The IncoMAP AL-9052 alloy has a density 5% less than that of a conventional age-hardening aluminum alloy of comparable strength, such as Alloy 2024. Therefore, its combination of light weight, high strength, and corrosion resistance

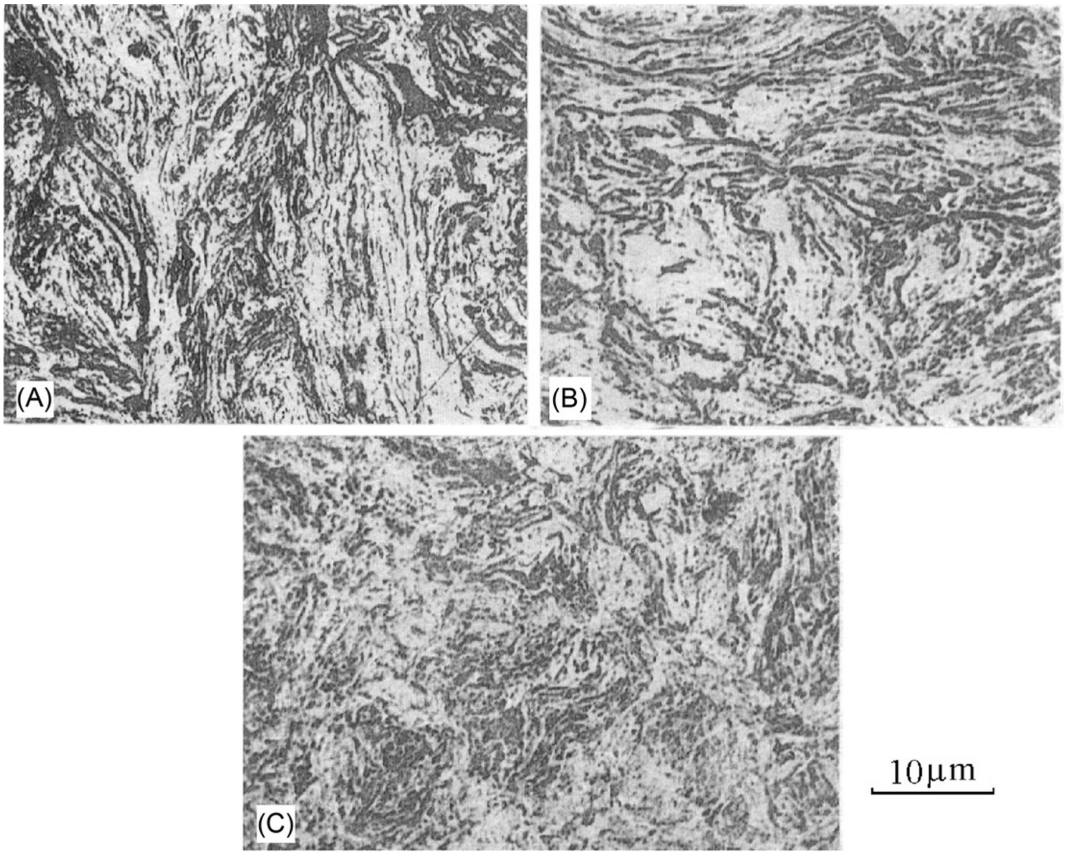

FIG. 3.20 Microstructure of granules obtained by processing of aluminum powder in a vibratory ball mill at the end of: (A) 1 h, (B) 4 h, and (C) 8 h. *(Courtesy of Institute of Mechanical Engineering of the NAS of Belorus.)*

is useful for aerospace applications. The addition of lithium to mechanically alloyed aluminum alloys produces an ultra-lightweight alloy, IncoMAP AL-905XL. Its density is lower and its stiffness 10% greater than the age-hardening 7075-T73 alloy of comparable strength. The excellent combination of properties makes this alloy useful for airframe applications [6,91].

Increasing the alloying component content leads generally to an appreciable increase in the durability of the semifinished products. However, their plasticity ductility is decreased down to the lower limit admissible for construction materials. Thus, the introduction of a 9.14 wt% molybdenum trioxide together with 5 wt% magnesium in an aluminum-base MA composition resulted in increasing the ultimate tensile strength of the rod to 660 MPa with 2% elongation in comparison with an alloy without molybdenum trioxide addition—580 MPa and 5%, respectively (see Table 3.10). Highly alloyed compositions retain sufficient high mechanical properties up to 573 K.

The largest tensile strength values are achieved by alloying with organic compounds: 700–770 MPa. Organic compounds of different groups were used: oxalic acid (COOH·COOH), carbamide ($HN_2 \cdot CO \cdot NH_2$), dinitrotoluene ($CH_2 \cdot C_6H_3(NO_2)_2$), 1,5-diphenylinecarbazide ($C_{13}H_{14}N_4O$), and others. Thus, organic compounds successfully serve as donors of the elements for hardening phases such as Al_4C_3, AlN, Al_2O_3, etc.

Due to their high elasticity coefficient and oxidation resistance, the Al_3Nb intermetallic compounds are suitable for high-temperature structural materials such as those used in aerospace, gas turbines, etc. The Al_3Nb alloy has a comparatively low density (4.54 g/cm^3), which is lower than that of the comparable advanced Ni_3Al-based compound (7.6 g/cm^3). However, it is difficult to fabricate the alloy by conventional methods due to the large difference in melting point between Al and Nb. Furthermore, due to intrinsic brittleness, Al_3Nb ingots crack during solidification. It is reported [92] that some of these problems can be overcome by MA. The relationships between MA processing parameters and the structural characteristics of Al_3Nb nanocrystalline powders are described. The homogeneous Al_3Nb powder particles were obtained by means of ball milling using 3 wt% stearic acid as PSA.

Recently, high-strength aluminum-titanium alloys have been developed using MA by dispersing nanometer- or submicron-sized Al_3Ti intermetallic particles (in addition to the Al_2O_3 and Al_4C_3 dispersoids by the addition of PCAs)

TABLE 3.9 Microhardness of Granulated Compositions Obtained by Mechanical Alloying of Aluminum With Various Elements and Their Oxides

Alloying Component			Microhardness of Granulated Composition (MPa)	
Substance	**Content (wt%)**	**Gibbs Function of Oxide Formation $-\Delta G_T$ (kJ/mol at)**	**Without Surfactant**	**With 0.5 wt% Surfactant**
Without alloying component		…	720	850
Al_2O_3	14.83	527	950	1150
B	4.0	…	1150	1600
B_2O_3	4.42	395	950	1500
CO_2	4.19	197	1400	1550
Co	5.0	…	1000	1100
Co_3O_4	11.47	189	1300	1550
Cr	5.0	…	1150	1250
Cr_2O_3	9.6	350	1100	1350
Cu	5.0	…	1200	1300
CuO	6.26	128	1350	1500
Fe	5.0	…	1000	1150
Fe_2O_3	5.0	247	1150	1350
La	5.0	…	1100	1250
Li	5.0	…	1300	1550
Mn	5.0	…	1050	1200
MnO_2	8.28	233	1200	1450
MoO_3	9.14	226	1250	1550
Ni	5.0	…	1050	1150
NiO	10.50	215	1300	1400
NO_2	4.38	103	1450	1600
Pb	10.0	…	650	750
SiO_2	10.25	413	1050	1350
Ti	5.0	…	950	1100
TiO_2	7.62	445	950	1250
ZnO	15.5	317	1050	1300
Zr	5.0	…	1150	1300
ZrO_2	14.83	514	950	1200

(Source: Vitjaz PA, Lovshenko FG, Lovshenko GF. Mechanical alloyed alloys based on aluminium and copper. Minsk (Byelorussia): Byelorusskaja Nauka; 1998.)

in an aluminum matrix. Similar approaches could be used to develop high-strength alloys in other systems. High mechanical properties where achieved in the Al-10Ti alloy obtained by MA [92]. A mixture of aluminum and 10 wt% titanium powders were attrition milled in the presence of 1.5 wt% wax. After 10 h milling time, about 9 wt% Ti was dissolved in aluminum. The powder prepared in this way showed a Vickers microhardness of 192 HV.

TABLE 3.10 Mechanical Properties of Mechanically Alloyed Al-Mg System Alloys

Alloyed Component				Mechanical Properties			
Substance	Content (wt%)	Mg conten (wt%)	Temperature (K)	Hardness (MPa)	UTS (MPa)[a]	Elongation (%)	Reference
Al-Mg[b]		5.0	RT[c]	1550	580	5	[43]
			473	700	290	23	
			623	250	100	10	
			673	150	70	9	
NO_2	4.4	5.0	RT	1650	650	2	[43]
			473	1100	370	16	
			623	650	200	21	
			673	550	160	19	
			773	…	100	12	
CO_2	4.2	5.0	RT	1650	670	2	[43]
			473	1100	360	15	
			623	600	190	19	
			673	550	150	16	
			773	…	100	8	
MoO_3	9.14	5.0	RT	1700	680	2	[43]
			473	1150	380	12	
			623	900	210	16	
			773	…	120	10	
V_2O_5	6.93	5.0	RT	1650	580	3	[43]
			473	1150	350	15	
			623	800	180	17	
			673	650	140	14	
			773	…	90	11	
B_2O_3	4.42	5.0	RT	1650	630	2	[43]
			473	1200	340	17	
			623	800	170	19	
			673	600	120	14	
			773	…	70	10	
SiO_2	5.78	5.0	RT	1400	500	3	[43]
			473	1000	300	19	
			623	700	160	14	
			673	500	120	12	
			773	…	60	8	
ZrO_2	12.5	5.0	RT	1650	660	2	[43]
			473	1200	370	16	
			623	900	200	18	
			673	700	160	15	
			773	…	110	9	

Continued

TABLE 3.10 Mechanical Properties of Mechanically Alloyed Al-Mg System Alloys—cont'd

Alloyed Component				Mechanical Properties			
Substance	Content (wt%)	Mg conten (wt%)	Temperature (K)	Hardness (MPa)	UTS (MPa)	Elongation (%)	Reference
Al_2O_3	6.5	5.0	RT	1500	520	4	[43]
			473	1050	310	22	
			623	600	130	23	
			673	450	100	17	
			773	…	60	10	
CH_4ON_2	2.5	2.0	RT	…	720	2	[43]
			473	…	420	8	
			623	…	310	15	
			673	…	240	12	
$C_7 H_6 (NO_2)_2$	2.5	2.0	RT	…	770	2	[43]
			473	…	480	8	
			623	…	360	14	
			673	…	260	10	
			773	…	190	8	
$C_{13} H_{14} N_4 O$	2.5	2.0	RT	…	760	2	[43]
			473	…	480	7	
			623	…	370	15	
			673	…	270	11	
			773	…	190	9	
$C_{10} H_{10} ON_2$	2.5	2.0	RT	…	750	2	[43]
			473	…	470	8	
			623	…	360	14	
			673	…	250	11	
Al-Mg-Li- O-C[d]			RT	…	510	10	[89]
4.0Mg-0.75O-1.0C-balanceAl[e]			RT	…	450	13	
4.0Mg-1.3 Li-0.6O-1.1C-balanceAl[f]			RT	…	520	9	[90]

[a] *Ultimate tensile strength.*
[b] *Without alloyed component.*
[c] *Room temperrasture.*
[d] *Commercial production grade: MAP Al-Mg-Li-O-C.*
[e] *Commercial production grade: MAP alloy 9052Al.*
[f] *Commercial production grade: IncoMAPalloy AL-905XL.*

Copper-Base Alloys

The fundamentals of the formation of phase composition, structure, and properties of mechanically alloyed aluminum alloys are also typical for the MA copper alloy. One of the features of copper composition formation that differentiates them from aluminum is their high tendency toward granulation. This is caused by the absence of a durable oxide film on the powder particle surfaces. It is reported [43] that MA processing in a vibratory mill can be done using the following conditions: acceleration of milling bodies in the range from 100 to 150 m/s^2, 70%–80% of the mill volume occupied by the balls, the ratio of the balls to charge volumes must be 7–10, the temperature must not exceed 353 K, and the processing duration ranges from 6 to 10 h. The properties of the main granulated compositions are presented in Table 3.11.

The apparent density ranges from 4.5–5.5 g/cm^3 at the end of 20–30 min processing. The structure of the majority of the granulated copper compositions is homogeneous (Fig. 3.21). Grain size does not exceed 10th quantums of a micron. Depending on the nature of the main phase transformations during MA processing of the alloys, it is possible to recognize three groups. The main phase change in the first group of alloys is the formation of solid solutions; in the second, the formation of compounds. The third group includes systems that do not have a fundamental phase change.

Electrical applications are the main areas served by MA copper alloys. Notable are the electrodes for welding and electroerosion processes, where costs can be reduced and productivity increased by the longer life of the electrodes [93].

The Cu-Fe-Co alloys are considered to be alloys that possess useful magnetic properties and can be used in very different fields as hard magnets [94–97]. In the work [94], the starting material was a metal powder mixture comprising copper, iron, and cobalt at a mass ratio of 50:25:25. The alloyed component selected to be added in 1, 3, and 10 wt% was α-alumina with a particle size around 1 μm. The milling set used was a ball-milling Fritsch Pulverissette 6 with 10 mm diameter balls and a 250 mL capacity bowl, both made of stainless steel. The ball-to-powder mass ratio was 16:1. The MA process was fulfilled by different milling times: 3, 8, 10, and 16 h.

As the authors reported [94], the initially coercive field value, H_c, and electroerosion maximum energy product, BH_{max}, increased rapidly until 3 h of milling time, followed by an abrupt decrease and finally a more slow and continuous decrease in H_c and BH_{max} because the crystallite size decreased. Additions of alumina in the Cu-Fe-Co powder enhanced the H_c and BH_{max}, but with alumina content higher than 3%, they increase slightly—the former from 8,326,666 to 8,637,051 A/m and the latter from 186,086 to 194,391 J/m^2.

López et al. studied the structural, magnetic, and mechanical properties of the $Cu_{90}Co_{10}$ and $Cu_{85}Co_{10}Ni_5$ alloys performed by mechanical alloying for different milling times [98]. The elemental powders (Cu, Co, and Ni powders with purity over 99.5% and particle sizes of Cu <146 μm, Co <81 μm, and Ni <38 μm) were milled in a RETSCH planetary ball mill operated at 200 rpm using stainless steel containers (500 cm^3) and 20 mm balls with a ball-to-powder weight ratio of 10:1. Containers were loaded under an argon atmosphere with the stoichiometric powder mixture, adding 3 vol% ethylene glycol to the powder blends to prevent agglomeration of powders. Mechanical alloying was carried out for milling times of 30, 45, and 60 h.

As the authors reviewed [98], a superparamagnetic behavior was observed in the as-milled $Cu_{85}Co_{10}Ni_5$ alloy. With consolidation (pressing and sintering at 973 K for 1 h), the $Cu_{85}Co_{10}Ni_5$ alloy achieved a coercive field of 19.4 kA/m. The presence of Co as the precipitated magnetic particles was corroborated by the soft magnetic behavior of the sintered alloy. The iron impurities from the mechanical alloying process would be related with cobalt in the as-milled and sintered states. The authors [98] explained that the effect of nickel on the $Cu_{95-x}Co_xNi_5$ system is that the Ni content inhibits (Cu-Co) phase segregation during annealing at high temperatures, leading to a structure with reduced Co particle precipitation into a homogeneous Cu-Ni strengthened solid-solution matrix, as evidenced by the 441 MPa hardness.

SAFETY ENGINEERING

Because of the very small particle sizes and the large surface area of mechanically alloyed powders, they are highly reactive and can be pyrophoric as well as cause health problems when inhaled. Therefore, mechanically alloyed powders should be handled with caution and care. Safety hazards are accentuated in the mechanically alloyed powders due to the increased stress and strain, temperature, and chemical reactivity. During the MA processes, some phenomena occur irrespective of the nature of the final product phase. There is evolution of heat. Another phenomenon that occurs is gas evolution. Gases may be produced during milling due to the decomposition of the process control agents, vaporization and/or sublimation of a deliberately added component, or chemical reactions among the components. Most commonly the gas is oxygen, but other gases, such as chlorine, nitrogen, carbon monoxide, and carbon dioxide, may also be vigorous oxidants. These effects could increase the pressure in the milling container and the temperature of alloyed powders. The presence of combustible MA powders and an oxidant environment, combined with an ignition source, is the necessary condition for fires and explosions.

TABLE 3.11 Properties of Granulated Copper-Base Compositions Obtained by Processing in Vibratory Ball Mill and MA Copper-Base Alloys

		Properties of Granulated Compositions			Properties of MA Alloys			
Alloyed Components and Their Contents (wt%)	Duration of Mechanical Alloying (h)	Granule Shape	Average Size of Granules (mm)	Micro-Hardness (MPa)	Hardness (MPa)	Ultimate Tensile Strength (MPa)	Elongation (%)	Electrical Resistivity ($10^{-8}\Omega\cdot$m)
Al (1.00)	6	Lamellar	0.6	2700	2250	850	6	4.453
Al (5.00)	6	Angular	0.6	3100	2750	1060	3	4.976
Be (0.50)	6	Lamellar	1.1	2300	2200	810	6	4.338
Be (1.50)	…	…	…	…	2900	1120	3	6.043
Be (2.00)	6	Angular	0.4	3100	…	…	…	…
Mo (5.00)	6	Spheroidal	0.4	2300	…	…	…	…
Nb (5.00)	6	Lamellar	1.1	3200	2650	990	3	2.386
Al(0.80), CuO (3.56)	8	Angular	0.3	2600	2600	1040	3	2.350
Al (0.80),CH_4ON_2 (0.44)	8	Angular	0.3	2900	2650	1130	2	2.383
Be(0.40), CuO (3.56)	8	Angular	0.3	2600	2400	980	3	2.413
Al (0.80), C (0.30)	8	Lamellar	1.1	2400	2300	830	6	4.338
Zr (2.00), C (0.30)	8	Lamellar	1.0	2700	2450	970	4	2.452
Nb (5.00)	6	Lamellar	1.1	3200	2650	990	3	2.386
Al_2 O_3 (1.88)	…	…	…	…	2300	760	2	2.452

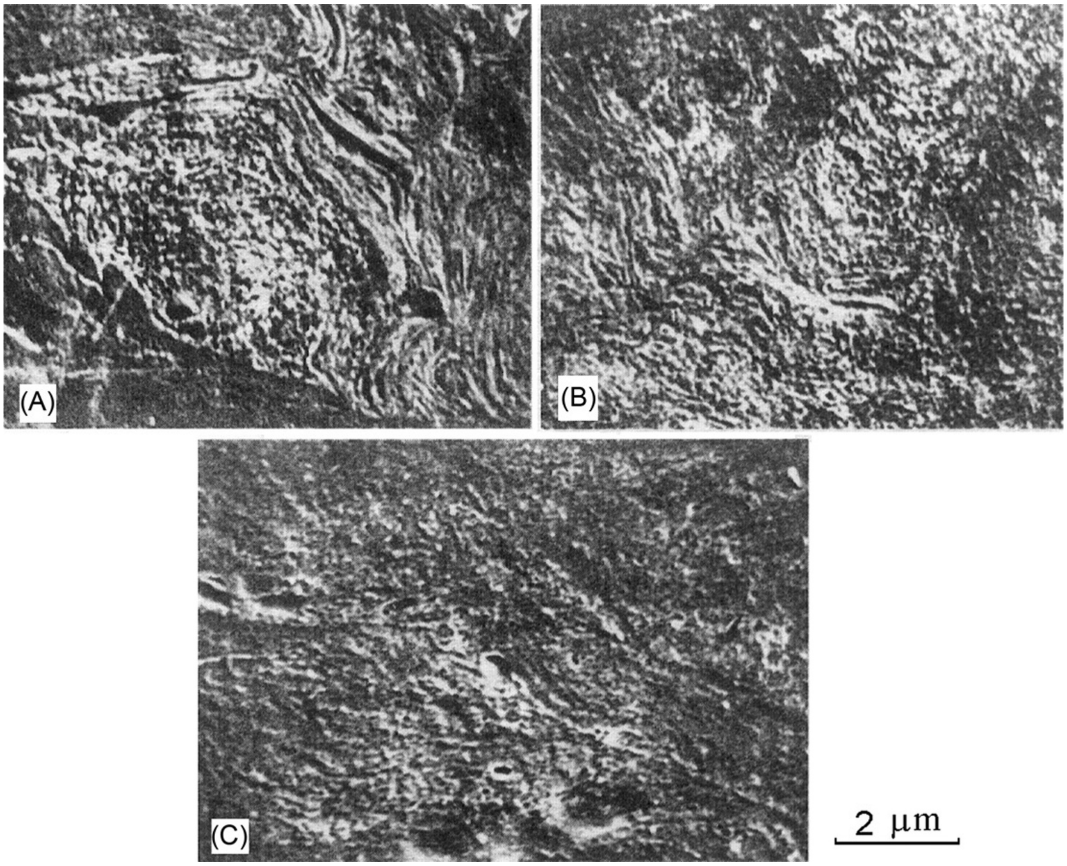

FIG. 3.21 Microstructure of granules obtained by processing of copper alloy powders in vibratory ball mill at the end of 8 h milling time: (A) Cu-0.4Be-3.56CuO; (B) Cu-0.5Al; and (C) Cu-20Zn.

The large enthalpy changes associated with the chemical reactions are responsible for the occurrence of the combustion reaction. If the temperature generated during the milling process (due to ball-to-ball and ball-to-powder collisions), T_c, is higher than the ignition temperature, T_{ig}, then the combustion reaction can occur. The time at which the T_{ig} and T_c intersect is the critical milling time, t_{ig}, at which ignition would occur. It is quite clear that up to the milling time t_{ig}, intermixing the particles, particle refinement, and accumulation of lattice defects occur and these appear to favor the combustion reaction. Furthermore, room temperature aging was found to significantly accelerate the beginning of combustion due to substantially reducing the overall milling time [99,100]. It is also important that due to the effect of process variables on the reaction during MA, the ignition of the combustion reactions, as was observed [53], is strongly dependent on the milling intensity. Therefore, the ignition temperature also decreased with mechanical activation. The ignition temperature of 1100–1300 K for the CuO + Mg reaction decreased to 400–450 K with mechanical activation [101]. The addition of diluents, for example, Al_2O_3, to Ni-Al mixtures during milling changed the spontaneous reactions to gradual reactions [53].

Out of caution, the powder container should not be opened after milling immediately before temperature and pressure normalization to avoid an abrupt oxidation of the powders and, under certain conditions, an ignition and explosion. Further, such reactive powder processing must be fulfilled in a protective atmosphere. The safety engineering technique is described in more detail in Chapter 27. An important source of information is also the National Fire Protection Association (NFPA) (https://catalog.nfpa.org/Codes-and-Standards-C3322.aspx).

REFERENCES

[1] Benjamin JS. Mechanical alloying. Sci Am 1976;234(5):40–8.
[2] Suryanarayana C. Mechanical alloying and milling. Prog Mater Sci 2001;46:1–184.
[3] Suryanarayana C. Bibliography on mechanical alloying and milling. England: Cambridge International Science Cambridge; 1995.
[4] Rehbinder PA. Surface energy changings effect on cleavability, hardness and other properties of crystals. In: VI congress of Russian physicists. Moscow: OGIZ; 1928. p. 29–35 [in Russian].

[5] Rehbinder PA, Shchukin ED. Surface phenomena in solids during deformation and fracture processes. In: Davison SG, editor. Progress in surface science. vol. 3 (Part 2). Pergamon Press, Inc.; 1973. p. 97–188.
[6] Suryanarayana C. Mechanical alloying and milling. New York: Marsel Dekker; 2004.
[7] Soviet Union Patent 1,436,341, July 1988.
[8] Schneider M, Pischang K, Worch H, Fritsche G, Klimanek P. Investigation of passive layer properties on nanocrystalline nickel by electrochemical impedance spectroscopy. Mater Sci Forum 2000;343–346:873–9.
[9] Lee W, Kwun SI. The effects of process control agents on mechanical alloying mechanisms in the Ti-Al system. J Alloys Compd 1996;240:193–9.
[10] Rodriguez JA, Gallardo JM, Herrera EJ. Structure and properties of attrition-milled aluminium powder. J Mater Sci 1997;32:3535–9.
[11] Millet P, Calka A, Ninham BW. Reduction of ilmenite by surfactant-assisted mechanochemical treatment. J Mater Sci Lett 1994;13:1428–9.
[12] Huang B, Ishihara KN, Shingu PH. Metastable phases of Al–Fe system by mechanical alloying. Mater Sci Eng A 1997;A231:72–9.
[13] Lu L, Lai MO, Wu CF, Breach C. Influence of mechanical alloying on precipitation in aluminium alloy. Mater Sci Forum 1999;312−314:357–62.
[14] Suzuki TS, Nagumo M. Synthesis of TiAl-$Al_2Ti_4C_2$ composite reaction milling mater. Sci Forum 1995;179–181:189–94.
[15] Arce Estrada EM, Diaz De la Torre S, Lorez Hirata VM, Cabaňas-Moreno JG. Electrochemical characterization of Co-Cu mechanical alloys. Mater Sci Forum 1996;225–227:807–12.
[16] Kobayashi KF, Tachibana N, Shingu PH. Formation of amorphous AI-Cr alloys by mechanical alloying of elemental aluminium and chromium powders. J Mater Sci 1990;25:801–4.
[17] Fair GH, Wood JV. Mechanical alloying of iron-aluminium intermetallics. Powder Metall 1993;36(2):123–8.
[18] Zhang YF, Lu L, Yap SM. Prediction of the amount of PCA for mechanical milling. J Mater Process Technol 1999;89–90:260–5.
[19] Hida M, Asai K, Takemoto Y, Sakakibara A. Solid solubility in nanocrystalline Ti/Mg and Mg/Ti composites powder produced by mechanical alloying. Mater Sci Forum 1997;235–238:187–92.
[20] Wolski K, Le Caër G, Delcroix P, Fillit R, Thevenot F, Le Coze J. Influence of milling conditions on the FeAl intermetallic formation by mechanical alloying. Mater Sci Eng A 1996;A207:97–104.
[21] Lu L, Zhang YF. Prediction of the amount of PCA for mechanical milling. J Alloys Compd 1999;290:279–83.
[22] Chattopadhyay PP, Pabi SK, Manna I. A metastable allotropic transformation in Nb induced by planetary ball milling. Mater Sci Eng A 2001;A304–306:424–8.
[23] Masters K, editor. Spray drying handbook. 4th ed. New York: Halstead Press; 1985.
[24] Alekseev AG, Neikov OD. The explosion risk of metal powders. Staub Reinhaltung der Luft 1990;50:245–50.
[25] Avvakumov EG. Mechanical methods of activation of chemical processes. Novosibirsk: Nauka; 1986 [in Russian].
[26] Schilling R, Media milling advances. http://www.unionprocess.com/tech_papers/mm_advances.pdf [Accessed 31 July 2018].
[27] Laboratory grinding attritors, http://www.unionprocess.com/laboratory-grinding-attritors.html, 2017. [Accessed 31 July 2018].
[28] Zoz H, et al. Mechanical alloying of Ti-24Al11Nb (at%) using the Simoloyer. Metall 1996;50(9):575–9.
[29] Bakker H, Zhou GF, Yang H. Mechanically driven disorder and phase transformation in alloys. Prog Mater Sci 1995;39:159–241.
[30] Szymanski K, Zaleski P, Recko K, Waliszewski J. Friction-free mechanical grinder. Mater Sci Forum 1997;235–238:223–30.
[31] Calka A, Wexler D. Electrical discharge assisted ball milling: a promising materials synthesis and processing method. Mater Sci Forum 2002;386–388(Jan):125–34.
[32] Dry grinding attritors, http://www.unionprocess.com/pdf/DryGrindingAttritors/index.html [Accessed 31 July 2018].
[33] Ye J, Han BQ, Shoenung JM. Mechanical behaviour of an Al–matrix composite reinforced with nanocrystalline Al-coated B_4C particulates. Philos Magazine Lett 2006;86(11):721–32.
[34] Siegel RW.n.d. Ceramic nanopowders. Rensselaer Polytechnic Institute. http://www.wtec.org/ioyoia/iWGN. Research Director [Downloaded 10 June 2008].
[35] NETZSCH agitator bead mills. www.netzsch-grinding.com/en/products-solutions/wet-grinding/netzsch [Accessed 31 October 2017].
[36] Heinicke G. Tribochemistry. Berlin: Academie-Verlag; 1984.
[37] Bowden FP, Tabor D. The friction and lubrication of solids. Oxford: The Clarendon Press; 1964.
[38] Schradar R, Stadter W, Octtel H. Untersuchungen an mechanisch aktivirten. XIII festkörperstruktur und katalishe verhalten von nickel-pulver. Z Phys Chem 1972;249:87–100.
[39] Streletskiy AN, et al. Regularities of mechanochemical synthesis of the complicated oxides in Pb-$Fe_2O_:$-Nb_2O_5 system. In: Proceedings of the mechanical synthesis in inorganic chemistry. Novosibirsk; 1991. p. 66–83 [in Russian].
[40] Butjagin PY. Initial active centres in mechanochemical reactions. VChO imeni DI Mendeleeva 1973;18:90–5 [in Russian].
[41] Butjagin PY, Bystrikov AV. About initiation chemical reactions by destruction of solids. In: Proc. of V. All-Union Symp. for mechano-emission and mechanochemistry of solids. Tallin (Estonia), Part 1; 1977. p. 63–78 [in Russian].
[42] Clemens BM. Solid-state reaction and structure in compositionally modulated zirconium-nickel and titanium-nickel films. Phys Rev B 1986;33 (11):7615–26.
[43] Vitjaz PA, Lovshenko FG, Lovshenko GF. Mechanical alloyed alloys based on aluminium and copper. Minsk (Byelorussia): Byelorusskaja Nauka; 1998.
[44] Lee PY, Yang JL, Lin HM. Amorphization behaviour in mechanically alloyed Ni–Ta powders. J Mater Sci 1998;33:235–9.
[45] Benjamin JS, Volin TE. The mechanism of mechanical alloying. Metall Trans A 1974;5:1929–34.
[46] Benjamin JS. Mechanical alloying—a perspective. Metal Powder Rep 1990;45:122–7.
[47] Davis RM, McDermott B, Koch CC. Mechanical alloying of brittle materials. Metall Trans A 1988;A19:2867–74.

[48] Schaffer GB, McCormick PG. Displacement reactions during mechanical alloying. Metall Trans A 1990;21A:2789–94.

[49] Ding J, Tsuzuki T, McCormick PG, Street R. Ultrafine Co and Ni particles prepared by mechanochemical processing. J Phys D Appl Phys 1996;29 (9):2365.

[50] Schaffer GB, McCormick PG. Reduction of metal oxides by mechanical alloying. Appl Phys Lett 1989;55:45–6.

[51] Tomasi R, Pallone EMJA, Botta FWJ. Reactivity in high-energy ball milling induced self-sustaining reactions. Mater Sci Forum 1999;312–314:333–8.

[52] Matteazzi P, Le Caër G. Mechanically activated room temperature reduction of sulphides. Mater Sci Eng A 1992;A156:229–37.

[53] Kudaka K, Iizumi K, Izumi H, Sasaki T. Synthesis of titanium carbide and titanium diboride by mechanochemical displacement reaction. J Mater Sci Lett 2001;20:1619–22.

[54] Yang H, McCormick PG. Mechanochemical reduction of V_2O_5. J Solid State Chem 1994;110:136–41.

[55] Chen GH, Suryanarayana C, Froes FH. Structure of mechanically alloyed Ti-Al-Nb powders. Metallurgical Mater Trans A 1995;26(6):1379–87.

[56] Goodwin PS, Ward-Close CM. Contamination control in the mechanical alloying of nanocrystalline intermetallic compound based alloys. Mater Sci Forum 1995;179/181:411–8.

[57] Zhang FX, Wang WK. Amorphization of AI-Cu-Fe quasicrystalline alloys by mechanical milling. J Alloys Compd 1996;240:256–60.

[58] Cardoso KR, Garcia-Escorial A, Botta WJ, Lieblich M. Crystallization of $Al_{90}Fe_5Nd_5$ amorphous alloy. Mater Sci Forum 2001;360–362:161–6.

[59] Saji S, Abe S, Matsumoto K. Formation process of amorphous phase during mechanical alloying for Al-6 and -12 at% mixed powders. Mater Sci Forum 1992;88–90:367–74.

[60] Fan GJ, Gao WN, Quan MX, Hu ZQ. Preparation and thermal stability of supersaturated nanocrystalline Al-Ti alloys. Mater Lett 1995;23:33–7.

[61] Inoue A, Kimura HM, Matsuki K, Masumoto T. Preparation of new amorphous Cu-Nb-Sn alloys by mechanical alloying of elemental copper, niobium and tin powders. J Mater Sci Lett 1987;6:979–81.

[62] Jang JSC, Koch CC. The glass transition temperature in amorphous $Cu_{1-x}Zr_x$ by mechanical alloying/milling. Scripta Metall 1989;23(10):1805.

[63] Gaffet E, Malhouroux-Gaffet N. Nanocrystalline $MoSi_2$ phase formation induced by mechanically activated annealing. J Alloys Compd 1994;205:27–34.

[64] Kenik EA, Bayuzick RJ, Kim MS, Koch CC. Microstructural evolution in mechanically alloyed Nb-25at%Ge. Scripta Metall 1987;21:1137–42.

[65] Cardellini F, Contini V, Mazzone G. Ordering kinetics of disordered Ni_3Al synthesized by mechanical alloying. Scripta Metall Mater 1995;32:641–6.

[66] Koch CC, Cavin OB, McKamey CG, Scarbrough JO. Preparation of “amorphous” $Ni_{60}Nb_{40}$ by mechanical alloying. Appl Phys Lett 1983;43:1017–9.

[67] Aoki K, Memezawa A, Masumoto T. Atmosphere effects of the amorphization reaction in NiZr by ball milling. J Mater Res 1993;8(2):307–13.

[68] Liu KW, Müklich F, Birringer R. Synthesis of nano-RuAl by mechanical alloying. Intermetallics 2001;9:81–8.

[69] El-Eskandarany MS, Aoki K, Suzuki K. Rod milling for solid-state formation of $Al_{30}Ta_{70}$ amorphous alloy powder. J Less Common Metals 1990;167:113–8.

[70] Guo W, Martelli S, Padella F, et al. F.C.C. metastable phase induced in the Ti-Al system by mechanical alloying of pure elemental powders. Mater Sci Forum 1992;88–90:139–46.

[71] Guo W, Iasonna A, Magini M, Martelli S, Padella F. Synthesis of amorphous and metastable $Ti_{40}AI_{60}$ alloys by mechanical alloying of elemental powders. J Mater Sci 1994;29:2436–44.

[72] Zhang LC, Xu J. Formation of glassy $Ti_{50}Cu_{20}Ni_{24}Si_4B_2$.alloy by high energy ball milling. Mater Sci Forum 2002;386–388:47–52.

[73] Counihan PJ, Crawford A, Thadhani NN. Influence of dynamic densification on nanostructure formation in Ti_5Si_3 intermetallic alloy and its bulk properties. Mater Sci Eng A 1999;A267:26–35.

[74] Wang GM, Campbell SJ, Calka A, Kaczmarek WA. Synthesis and structural evolution of tungsten carbide prepared by ball milling. J Mater Sci 1997;32:1461–7.

[75] Courtney TH, Wang Z. Grinding media wear during mechanical alloying of Ni-W alloys in a SPEX mill. Scripta Metall Mater 1992;27:777–82.

[76] Deledda S, Eckert J, Schultz L. Nanocrystalline CaO and ZrO as a second phase in amorphous Zr-Cu-Al-Ni matrix composites. Mater Sci Forum 2001;360–362:85–90.

[77] Spârchez Z. Chicinas I. Method for minimising the powders contamination during the ball milling process. In: Proceedings of 2005 powder metallurgy European congress, Prague (Czech Republic): European powder metallurgy association, UK, vol. 1; 2005. p. 107–12.

[78] Koch CC. Mechanical milling and alloying. In: Proceedings: materials science and technology—a comprehensive treatment. Weinheim, Germany: VCH; 1991. p. 193–245.

[79] Suryanarayana C. Mechanical alloying. In: ASM handbook, vol. 7. Materials Park, Ohio: ASM International Publishers; 1998. p. 80–90.

[80] Gilman P, Benjamin JS. Nickel- and iron-based dispersion strengthened alloys. In: ASM handbook, vol. 7. Materials Park, Ohio: ASM International Publishers; 1985. p. 722.

[81] Inconel Alloy MA 754, Alloy Dig., ASM International; 1990.

[82] Inconel Alloy MA 758, Alloy Dig., Rev. May 1996. ASM International; 1990.

[83] Pettit FS, Meier GH. Oxidation and hot corrosion of superalloys. In: Proceedings of Fifth International Symposium on Superalloys. The Metallurgical Society; 1984. p. 651–87.

[84] Inconel Alloy MA 6000, Alloy Dig., Rev. July 1983. ASM International; 1980.

[85] Special Metals Corporation. http://www.nasdaq.com/markets/ipos/company/special-metals-corp-5798-8262 [Accessed 31 January 2018].

[86] Bhat SV. Biomaterials. Boston/Dordrecht/London: Kluwer Academic Publishers; 2002.

[87] Sánchez-De Jesús F, Betancourt JA, Torres-Villaseñor G, Bolarín-Miró AM. Structure and properties of a biomedical Co-Cr-Mo-C alloy produced by mechanical alloying. In: Proceedings of PM 2010 world congress, Florence. Compiled by European powder metallurgy association, Bellstone Shrewsbury, UK, vol. 1; 2010. p. 217–23.

[88] ISO 58342-4, (E). Implants for surgery, metallic materials. Part 4. Cobalt-chromium-molybdenum casting alloy; 1996.

[89] Murakami Y. Aluminum-based alloys. Mater Sci Technol 1996;8:213–76.

[90] Buhl H, editor. Advanced aerospace materials. Berlin: Springer-Verlag Publishers; 1992.

[91] IncoMAP alloy AL-905. Aluminium alloys by mechanical alloying. Aircr Eng Aeros Technol 1987; 59 (6), p. 20,https://doi.org/10.1080/10426914.2015.1037904 [Accessed 31 January 2018].

[92] Gallardo JM, Rodrigues JA, Herrera EJ. Structure and properties of attrition-milled aluminium-10% titanium powder. In: Proceedings of 1998 powder metallurgy world congress, Granada. Compiled by European powder metallurgy association, UK, vol. 1; 1998. p. 378–83.

[93] Hofmockel M, Neubing H-C. ECKA Discup—new high performance PM-copper materials process, properties and applications. In: Proceedings of PM 2004 world congress, Vienna. Compiled by European powder metallurgy association, Bellstone Shrewsbury, UK, vol. 1; 2004. p. 231–6.

[94] Llorca-Isern NC, Artieda-Guzmán CN, Porras-Mateu N, Roca A. Structural and magnetic properties of nanocrystalline Cu-Fe-Co-Al_2O_3 composite powders processed by mechanical alloying. In: Proceedings of PM 2010 world congress, Florence. Compiled by European powder metallurgy association, Bellstone Shrewsbury, UK, vol. 1; 2010. p. 159–66.

[95] Anderson KR, Groza JR, Dreshfield RL, Ellis DL. High-performance dispersion-strengthened Cu-8Cr-4Nb alloy. Metall Mater Trans 1995;26A (September):2197–206.

[96] López M, Corredor D, Ramam K, Jiménez J, Ruano O. Performance of new dispersion-precipitation strengthened copper-ceramic materials made by mechanical alloying. Phys Stat Sol 2007;4(11):4248–53. https://doi.org/10.1002/pssc.200675940.

[97] López M, Jiménez JA, Corredor D. Precipitation strengthened high strength-conductivity copper alloys containing ZrC ceramics. Composites 2007;38(Part A):272–9, http://www.elsevier.com/locate/compositesa.

[98] López M, Núñez V, Koduri R, Gómez ME, Jiménez J, Reyes D. Soft magnetic Cu-Co-Ni composite materials produced by mechanical alloying, cold compaction, and sintering. In: Proceedings of PM 2010 world congress, Florence. Compiled by European powder metallurgy association, Bellstone Shrewsbury, UK, vol. 1; 2010. p. 187–94.

[99] Schaffer GB, McCormick PG. Anomalous combustion effects during mechanical alloying. Metall Trans A 1991;A22:3019–24.

[100] Takacs L. Self-sustaining reactions induced by ball milling. Mater Sci Forum 2002;47:355–414.

[101] Torosyan AR, Baghdasaryan VS, et al. Diamond synthesis by mechanical induced detonation. Mater Sci Forum 2002;386–388:229–34.

Chapter 4

Atomization and Granulation

Oleg D. Neikov
Frantsevich Institute for Problems of Materials Science (IPMS), Kiev, Ukraine

Chapter Outline

Introduction 125
Water Atomization 128
  Water Atomization Technique 128
  Atomization Mechanism 132
  Powder Characteristics 134
  Particle Size Distribution 135
Oil Atomization 142
Gas Atomization 143
  Gas-Atomizing Units 144
  Process Parameters 148
  Models of Gas Atomization 149
  Gas-Atomized Powders 158
  Other Gas-Atomization Methods 162
  Vacuum-Dynamic Atomization 167
Centrifugal Atomization 167
  Models of Centrifugal Atomization 167
  Centrifugal Atomization Methods 169
Other Methods 173
  Impact Atomization 173
  Vibrating Electrode Atomization 173
  Melt Drop Orifice Technique 173
  Roller Atomization 175
  Plasma Atomization Process 175
  Explosive Atomization 176
Granulation 177
  Spray Granulation 177
  Spray Drying 178
  Control of Powder Properties 178
  Water Granulation 179
  Applications 179
References 181
Further Reading 185

INTRODUCTION

Because of the ease with which a liquid can be broken up into fine droplets, atomization has become the prevailing mode of powder production of nonferrous metals and their alloys [1]. Atomization allows the manufacture of rapidly solidified metal alloys. The use of rapid solidification of melts to produce new structural and other materials with a complex of properties unachievable by traditional metallurgy is not only a very popular subject of investigation, but also finds a wide industrial application nowadays.

The basic types of atomization processes include (Fig. 4.1):

- Jet atomization of the melt, where a liquid metal is dispersed into droplets by the impingement of high-pressure jets of gas, water, or oil (Fig. 4.1A and B) and plasma torch atomization (Fig. 4.1C).
- Melt spinning centrifugal atomization, where a liquid stream is dispersed into droplets, flakes, or ribbons by the centrifugal force effect of a rotating disc, spinning cup, or spinning roller (Fig. 4.1D).
- Rotating of a consumable electrode (Fig. 4.1E).
- Plasma-transferred arc (Fig. 4.1F).
- Disintegration of liquid metal (Fig. 4.1G).
- Impact atomization of a liquid stream (Fig. 4.1H).
- Ultrasonic atomization, where a liquid metal film is subjected to ultrasonic vibration (Fig. 4.1I).
- Impulse atomization, where impulses are mechanically applied to the melt (Fig. 4.1J).
- Vacuum atomization, where heavily saturated molten metal with a gas is atomized in the vacuum (Fig. 4.1K).
- Drop explosion (Fig. 4.1L).

Handbook of Non-Ferrous Metal Powders. https://doi.org/10.1016/B978-0-08-100543-9.00004-X
© 2019 Elsevier Ltd. All rights reserved.

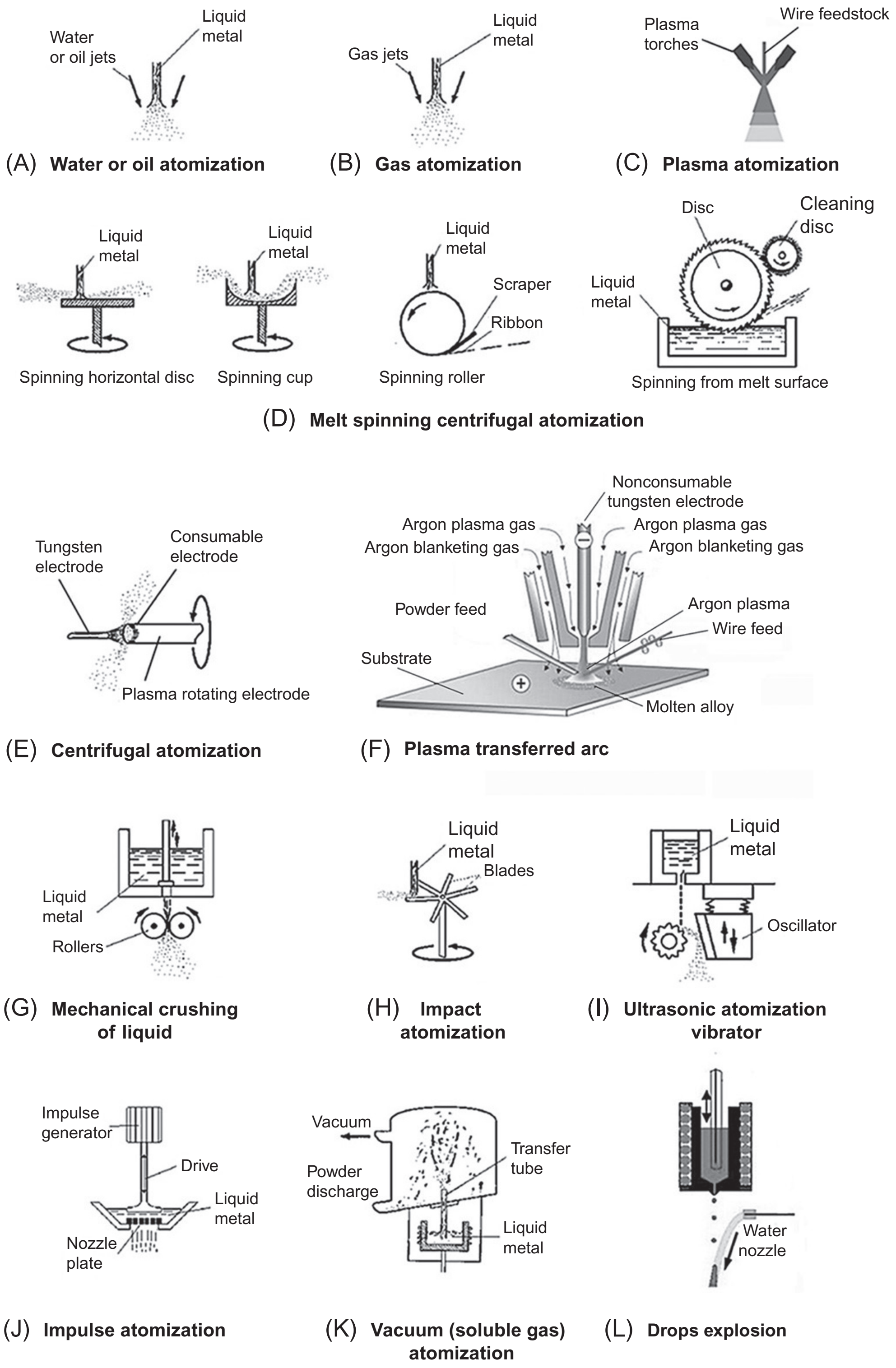
Water
or oil jets
Liquid
metal
Gas jets
Liquid
metal
Plasma
torches
Wire feedstock
Liquid
metal
Liquid
metal
Liquid
metal
Scraper
Ribbon
Disc
Cleaning
disc
Liquid
metal
Spinning horizontal disc
Spinning cup
Spinning roller
Spinning from melt surface
Tungsten
electrode
Consumable
electrode
Plasma rotating electrode
Nonconsumable
tungsten electrode
Argon plasma gas
Argon blanketing gas
Argon plasma gas
Argon blanketing gas
Powder feed
Argon plasma
Wire feed
Substrate
Molten alloy
Liquid
metal
Rollers
Liquid
metal
Blades
Liquid
metal
Oscillator
Impulse
generator
Drive
Liquid
metal
Nozzle
plate
Vacuum
Powder
discharge
Transfer
tube
Liquid
metal
Water
nozzle

(A) **Water or oil atomization** (B) **Gas atomization** (C) **Plasma atomization**

(D) **Melt spinning centrifugal atomization**

(E) **Centrifugal atomization** (F) **Plasma transferred arc**

(G) **Mechanical crushing of liquid** (H) **Impact atomization** (I) **Ultrasonic atomization vibrator**

(J) **Impulse atomization** (K) **Vacuum (soluble gas) atomization** (L) **Drops explosion**

FIG. 4.1 Schematic drawing of atomization processes.

Particle size distribution is one of the most important parameters of powders. The particle size distribution of atomized powders generally follows the lognormal law. This signifies that the particle size distributions form straight or nearly straight lines on the log-probability paper (Fig. 4.2).

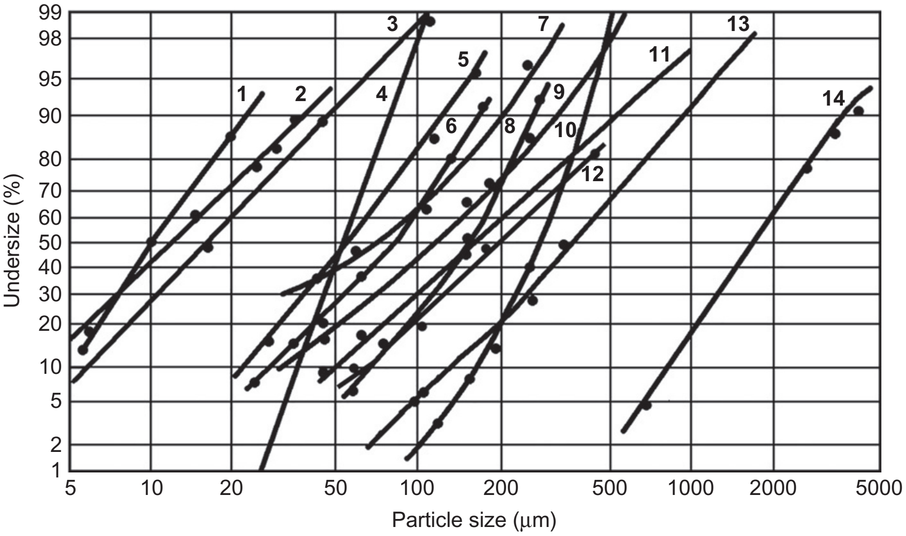

FIG. 4.2 Typical particle size distribution of atomized powders:

Curve No.	Powder	Median Mass Diameter (d_m), μm	Geometric Standard Deviation (σ_g)	References
1	Copper, hot-gas atomized at 4.5 MPa in nitrogen at 500°C	10	2.0	[2]
2	Copper, water atomized at 54 MPa	12.5	2.4	[3]
3	Zinc, gas atomized at 2 MPa	16	2.1	[3]
4	67Pb-33Sn ultrasonically atomized	64	1.31	[3]
5	44.85Al-13.7Fe-28.55Cu-12.9Cr, water atomized at 10 MPa	55	1.83	A*
6	43Al-40Cu17Fe, argon atomized at 0.6 MPa	87	2.48	A*
7	60Pb-40Sn solder, gas atomized at 0.8 MPa	70	2.5	[3]
8	Aluminum, water atomized at 4.8 MPa	150	2.0	A*
9	Bronze, air atomized at 0.5 MPa	120	2.33	[3]
10	Zinc, centrifugally atomized	270	1.4	[3]
11	Zinc, water atomized at 5.5 MPa	170	2.58	[3]
12	Aluminum, water atomized at 2.0 MPa	168.8	2.0	[4]
13	Copper shot, water atomized at 2.0 MPa	280	2.1	[3]
14	Phosphor shot, water atomized at 0.05 MPa	1950	1.9	[3]

A*, author's data.

Granulation of a melt is realized by means of free fall into cold liquid, usually water. During the free fall and by impact with the water surface, the melt stream is broken up into droplets, which then solidify. The melt is caused to flow through a nozzle plate (Fig. 4.1J) in order to obtain granules of a pellet shape. Particulate materials coarser than 1 mm in diameter are conventionally referred to as granules (see Introduction). Thus, several types of conventional atomization processes are useful for granule production.

WATER ATOMIZATION

Water atomization (WA) is used for commercial production of copper, copper alloys, nickel-base alloys, and zinc powders. Water-atomized precious metals are used in dental techniques, sintered electrical contacts, and brazing pastes. WA is less expensive than other methods of atomization. It allows the production of powders within wide yield limits from 1 to 500 kg/min for a single nozzle. The main limitation of WA is powder purity, especially for metals and alloys inclined to oxidation. However, owing to the higher cooling rate of the melt by WA, the average thickness of surface oxides is similar to that in gas-atomized powders. This is realized, in particular, in water-atomized aluminum alloys [5] (discussed in chapter 16 in this book).

Water Atomization Technique

The major components of a conventional water-atomization system are a melting unit, a tundish, an atomizing chamber, a water pumping/recycling system, and the dewatering and drying units. A flow diagram of the typical WA process for copper and copper alloy powder production is shown in chapter 19.

Conventional installations usually operate with water pressure in the range of 5–20 MPa, producing the powders with mass median particle sizes of 30–150 μm. Significantly higher water pressures of 50–150 MPa are used to manufacture finer powders with mass median particle sizes of 1–20 μm. These powders are used for the injection molding process, binders in diamond tools, sintered bearings, paints, coatings, and pastes.

Generally, water atomizer designs are based on "V" configurations with some nozzles (at the minimum two) located symmetrically about the axis of the liquid metal stream (Fig. 4.3).

A representation of the overall processing stages in water atomization is shown in Fig. 4.3. The associated melting process variables include the charge ingredients, atmosphere, and superheat of the melt; the associated atomization stage variables are nozzle diameter, metal stream length, density of metal, surface tension of the melt, viscosity of the melt, water pressure, jet geometry, and apex angle; key variables in the particle solidification stage are the melting point, droplet size, heat transfer, quenching medium, temperature of suspended solid in atomization chamber, and flight path. Basic water-jet configurations are shown in Fig. 4.4.

Typical range of operating conditions in water atomization are as follows [3]:

- Metal flow rate (single nozzle), 1–90 kg/min.
- Water flow rate, 20–380 L/min.

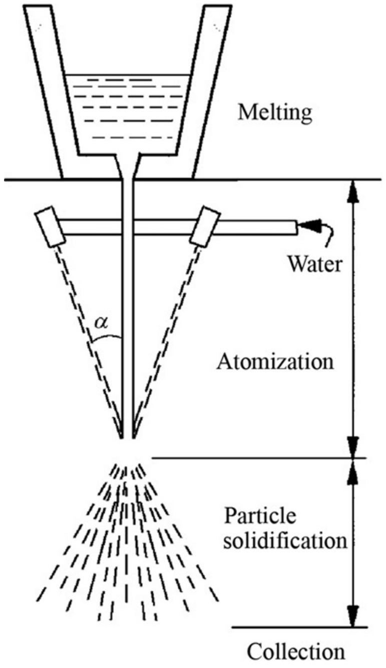

FIG. 4.3 Stages in water atomization.

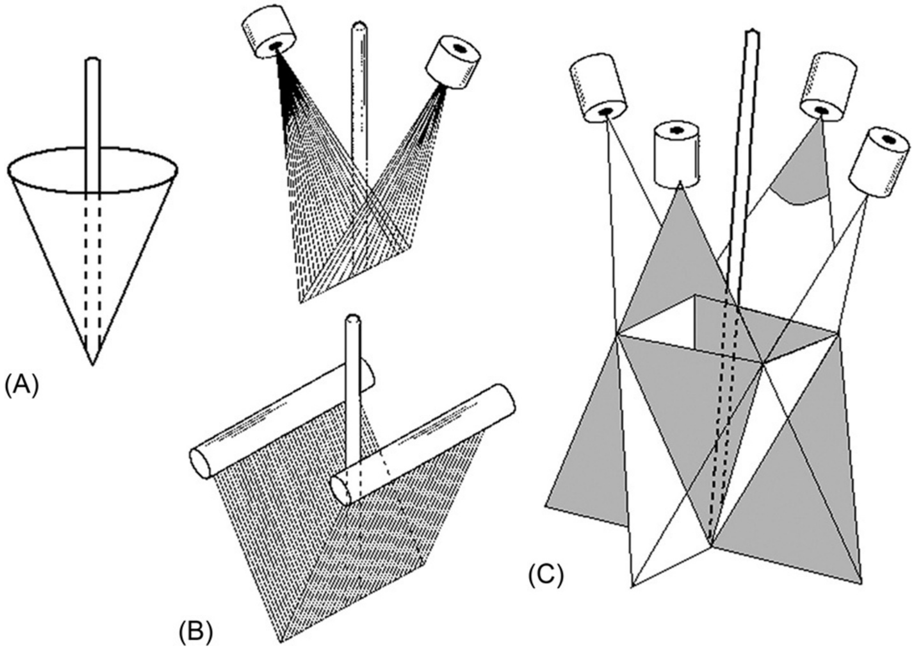

FIG. 4.4 Water jet configurations: (A) annular jet; (B) open V-jets; (C) closed V-jets.

TABLE 4.1 Properties of Several Water-Atomized Powders

	Operating Parameters				Powder Properties		
Alloy	Metal Flow (M) (kg/min)	Water Flow (W) (L/min)	W/M Ratio	Water Pressure (MPa)	Median Diameter *r* (μm)	Apparent Density (g/mL)	Oxygen (ppm)
Ag[a]	18	100	5.5	50	21	3.4[b]	—
Al-5Zn-3Mg-0.49Fe[c]	6.5	90	13.8	10	60	0.9[d]	—
Al-1.3Fe-1.5Cr[c]	7.0	90	12.8	15	45	0.98[d]	600
Cu-5Cr[a]	27	180	6.7	20	24	3.18[b]	—
Co[a]	27	180	6.7	20	29	3.28[b]	—
Au-2Cu[a]	7	40	5.7	13.7	88	—	—
Ag-22Cu-3Zn[a]	9	42	4.7	17.2	72	3.95[b]	110
Ni-B-Si[a]	24	160	6.7	17.2	51	4.26[b]	—

[a] *All data from V-jet atomizer with 40–50 degrees apex angle, nitrogen purged [3].*
[b] *Apparent density for fractions under size 250 μm [3].*
[c] *IPMS atomizer equipped with eight discrete nozzles (details might find below, in this article) (IPMS).*
[d] *Apparent density for fractions under size 63 μm (IPMS).*

- Water velocity (at nozzle exit), 10–500 m/s.
- Water pressure (at exit or in manifold), 5–150 MPa.
- Metal superheat, 75–170 (above melting point).

Commercial WA plants typically operate with water flow to metal flow ratios between 2/1 and 15/1. Table 4.1 shows the operating conditions for specific powders and their properties.

Atomizers

The atomizers play the main role in ensuring the efficiency of the disintegration of a liquid metal stream. In the literature on atomization, the terms nozzles and jets are often used interchangeably. However, the jet is the stream of liquid or gas that flows out from the nozzle whereas the nozzle is one part of the atomizer. As far as possible, the use of these terms throughout the book is consistent with these definitions.

Though numerous patents for the atomizer design have been filed, only a few types of atomizers are used in most commercial water-atomization units. Atomizer design in most commercial water-atomization units is a variant of either V-jet nozzles (Fig. 4.4) or annular cone-jet nozzles that are concentric with the metal stream. Annular ring nozzles are utilized in some large-capacity plants, but are rarely used elsewhere because they are less flexible and difficult to make than designs based on V-nozzle configurations with two or more discrete openings located symmetrically about the axis defined by the metal stream.

The liquid metal stream typically falls a certain distance (usually about 15–25 cm) before meeting the water jets. A partial vacuum is often created above the impingement point where the water and gas/air sucked by the water streams can disrupt the liquid metal before it actually meets the water jets [6].

A swirl water atomizer for fine powder production has been developed [7]. Fig. 4.5 shows a schematic of high pressure water atomization by “free fall” design and a swirl water jet. This unit allows the production of bronze (Cu-10 mass% Sn) powder with median particle size 7.5 μm and apparent density 2.8 g/cm^3 by water pressure of 83.3 MPa.

Fig. 4.6 shows the effect of the jet configuration apex angle (θ) on the median diameter of swirl water-atomized copper powder (δ_{50}) [8]. The water jets are generated at water pressure 90 MPa with flow rate 5 L/s on the jet swirl angle, ω = 0.2 rad

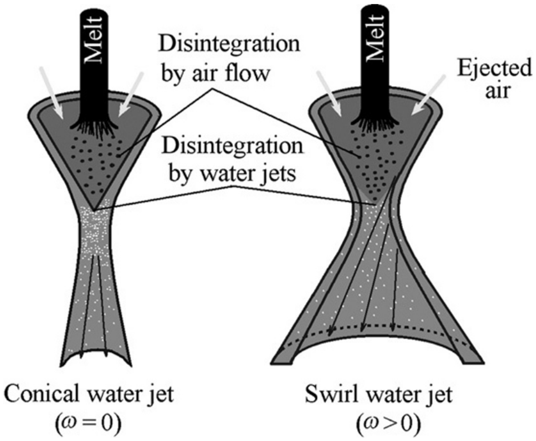
Melt
Disintegration by air flow
Melt
Ejected air
Disintegration by water jets
Conical water jet ($\omega = 0$)
Swirl water jet ($\omega > 0$)

FIG. 4.5 High-pressure water atomization using conical swirl water jet.

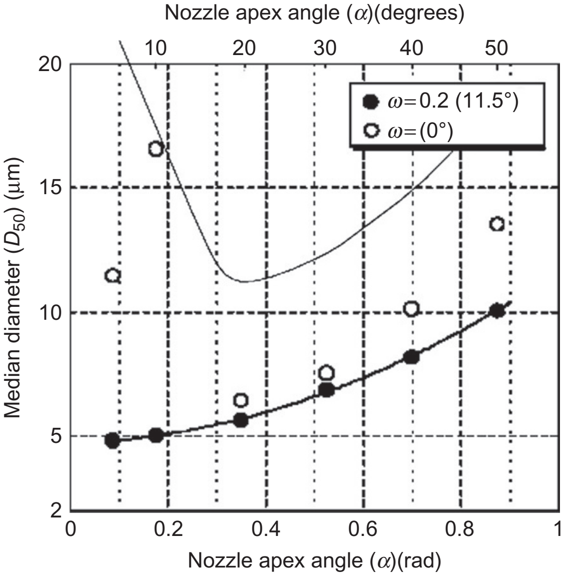

FIG. 4.6 Dependence of powder median diameter on jet apex angle of conical swirl water jet atomizer.

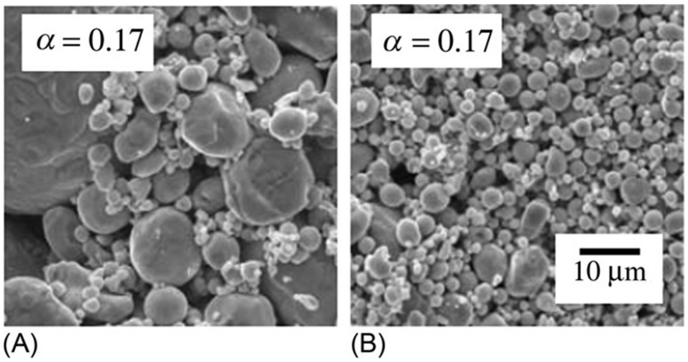
α = 0.17
α = 0.17
10 μm
(A)
(B)

FIG. 4.7 SEM micrographs of copper powders produced by the high-pressure water atomization using conical swirl water jet with apex angle 0.17 rad (≈9.7 degrees) and jet swirl angle, ω = 0 (A), that is, common cone water jet configuration, and ω≈50 degrees (B), accordingly.

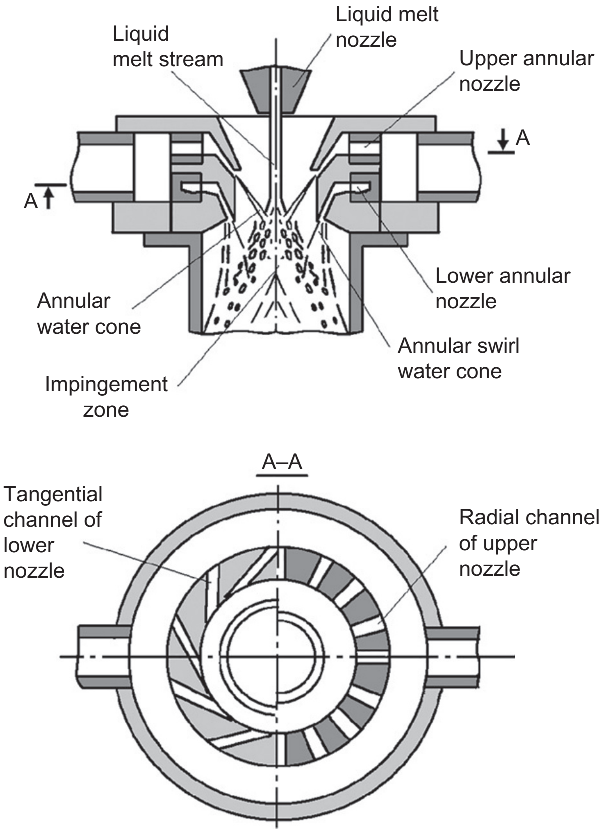
Liquid melt stream
Liquid melt nozzle
Upper annular nozzle
A
A
Lower annular nozzle
Annular water cone
Annular swirl water cone
Impingement zone
A–A
Tangential channel of lower nozzle
Radial channel of upper nozzle

FIG. 4.8 Atomizer with binary water cone configuration.

(≈11.5 degrees) and ω = 0.0 rad (0.0 degrees), that is, the usual conical jet configuration. For ω = 0.0 rad, δ_{50} of common conical jet configuration atomized powders decreases with decreasing θ down to 0.35 rad, but as θ becomes <0.35 rad, δ_{50} increases abruptly with decreasing θ while, by swirl jet configuration for ω = 0.2 rad, δ_{50} keeps decreasing with θ decreasing. As can be seen from dependences of δ_{50} on θ in ranges from θ = 0.35 to θ = 0.87 rad, δ_{50} for swirl jet configuration is less on one order of magnitude in comparison with the common conical jet configuration. Via the latter, there are many coarse particles with wide size distribution (Fig. 4.7). The particles are spherical or drip-shaped, but with increasing θ up to 0.87 (≈50 degrees), the powders become irregular in shape. In the former, there are few irregular aggregates. Almost all particles were spherical and particle sizes decreased with θ decreasing.

Applications for such ultrafine powders include the MIM, sintered filters, conductive pastes, and corrosion-resistant paints.

In atomization installations using an atomizer with a binary water cone configuration (Fig. 4.8) [9], a second convergent water cone performing angular motion relative to the melt stream axis affects the atomized melt droplets. The lower annular

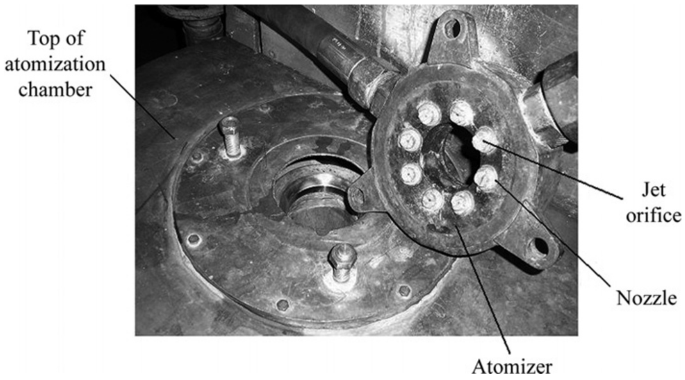

FIG. 4.9 IPMS atomizer equipped with eight discrete nozzles. *Courtesy of IPMS.*

nozzle is provided with tangential channels at 27–29 degrees that create a swirl jet configuration. The apex angle of the upper nozzle ranges from 54 to 58 degrees and the lower one ranges from 36 to 40 degrees. The liquid melt outflow orifice is 9 mm.

The IPMS atomizer is equipped with eight discrete nozzles located symmetrically about the axis defined by the metal stream (Fig. 4.9). Four nozzles create a closed V-jet configuration and disintegrate the metal stream upon meeting the atomizing fluid. A second closed V-jet configuration is created by means of four nozzles that impinge on the melt stream at a more acute apex angle than the former. Thus, they meet the melt droplets after the impingement point.

Atomization Mechanism

The water-atomization process is distinguished by a high density of the energy carrier, a high cooling rate, and steam formation in the contact zone between water and melt. High water density $\rho_w \approx 10^3 \rho_{air}$ leads to an essential increase of impulse linear momentum ($p = mv$) and kinetic energy $\left(E_k = \frac{mv^2}{2}\right)$ of the energy carrier.

Steam film originating around a drop decreases the heat transfer from drop to surroundings; if the film is disrupted and the contact of melt with water is provided, the cooling rate is appreciably accelerated. The high density of the energy carrier preserves the high velocity of water jets over a long distance that allows a wide range of positional relationships of melt streams and water jets while simplifying the design of hydraulic atomizers.

Liquid metal drops are disintegrated by superheated compressed steam, which is formed on the melt contact surface with water. The breakdown force of the steam film on the melt drop depends on the physical conditions in the contact zone: temperature and density of steam as well as water pressure and volume.

Grandzol and Tallmadge first proposed a mechanism of liquid melt drop formation under impact from the exploding water-steam packet rather than shear for water atomization [10]. This model reflects the dispersed nature of the water and an inverse proportionality between particle size and the normal velocity component of the water, with respect to the metal stream axis. Grandzol and Tallmadge represent the dependence of the mass median particle size (δ_m) on the water drop velocity (v_w) such that:

$$\delta_m = \frac{A}{v_w} = \frac{14{,}900}{v_w}\left(\frac{1}{n}\right)^{1/3} \tag{4.1}$$

where A is a constant, δ_m is in μm, v_w is in m/s, and n is the number of metal droplets formed from the disintegration of one water droplet. In this equation, water flow rate, water pressure, momentum and energy, jet length, and metal flow are not primary parameters influencing δ_m; they do, however, affect particle size by influencing water-jet velocities and the number of water droplets. Impingements during atomization can also influence particle size, particle size distribution, and particle shape [11].

From subsequent experimental observations on the influence of the angle between the metal stream axis and the water jet axis on δ_m, it was concluded that the velocity component of the water normal to the liquid metal stream, rather than the velocity component parallel to the liquid metal stream, is the dominant parameter in controlling δ_m [12]. Thus, the refined model [13] gives a relation between δ_m and v_w of:

$$\delta_m = \frac{B}{v_w}\sin\alpha \tag{4.2}$$

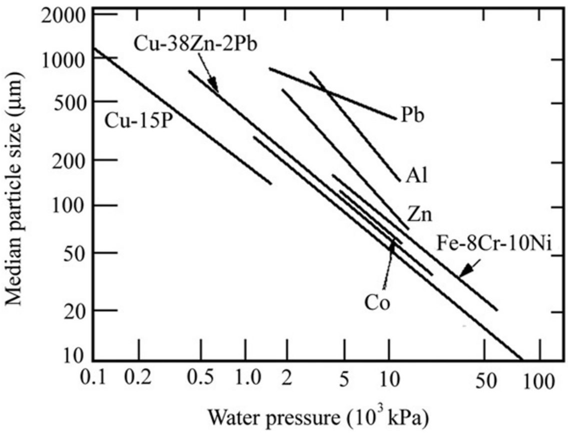

FIG. 4.10 Particle size of water-atomized metals as function of water-atomized pressure.

where δ_m is in μm, v_w is in m/s, α is the angle (in degrees) between the axis of the metal stream and the water jets, and B is a constant. The value of B in conditions of [13] is 2750.

The relation between δ_m and water pressure (p_w) for various metal powders [14] is shown in Fig. 4.10.

Based on the straight log-log plots in Fig. 4.10, the relationship between δ_m and p_w can be expressed as:

$$\delta_m = K p_w^{-m} \tag{4.3}$$

where K and m are constants for the given material and atomization unit. For atomizer modification with two nozzles, when δ_m is in μm, the parameter m is typically in the range 0.6–0.8 for water pressure and from 0.1 to 50 MPa [3].

The values of K are almost one order of magnitude higher for aluminum and zinc than for copper. In practice, this means that for two alloys water atomized under identical operating conditions, δ_m can vary by a factor of about 6. The value K evidently depends strongly on the physical and chemical properties of the molten alloy, in particular viscosity and surface tension. Modification of the surface tension by the atmosphere (steam) to allow the formation of oxides is also expected to be important in terms of disintegration of the molten metal stream.

Increasing the melt superheat reduced δ_m in water atomization, primarily through the effect of temperature on viscosity and surface tension. For example, for zinc, an increase in superheat from 100 to 300 K reduces δ_m from 150 to 100 μm [14]. Similarly, in a cobalt-base alloy, increasing the superheat by about 150 K leads to a decrease in δ_m of about 13.5% [3]. In addition to its effect on particle size, superheat is used as an operating variable to prevent freezing of the alloy in the exit nozzle of the tundish; simultaneously, the superheating leads to an increase of the melt flow rate through the tundish orifice, due to decreasing of melt viscosity.

The apex angle also influences particle size. With the apex angle increasing, the velocity component normal to the metal stream increases. It is shown [13, 15] that δ_m decreases with an increasing angle between the axis of the water jet nozzle and the liquid stream. Grandzol and Tallmadge represent this dependence in the form:

$$\delta_m = \frac{1}{v_w \sin\alpha}$$

However, there is a practical limit to the magnitude of the apex angle. Above about 50 degrees, flow of the molten metal from the orifice of the tundish is impeded by the upward thrust of water, and the incidence of metal freeze-up at higher axis angles, especially at higher pressures (Fig. 4.11). To decrease attenuation in water pressure, a short water-jet length is preferred, but again there are practical limits. It is normally found that using the apex angle to control fineness leads to dangerously unstable conditions. It is better to select a good stable setup with a full shutdown of melt and spray toward the jets and tundish, and then provide the necessary pressure to achieve the desired particle size.

Based on the droplet formation model [16] as the break up of the liquid microjets by instability wavelength and experimental data, Ternovoy [17] derived a semiempirical formula for powder mass median diameter δ_m calculation. The δ_m magnitude is determined subject to all main parameters influencing one, in contrast to Eqs. (4.1)–(4.3) involving the one or two parameters. Ternovoy's formula is represented in the form:

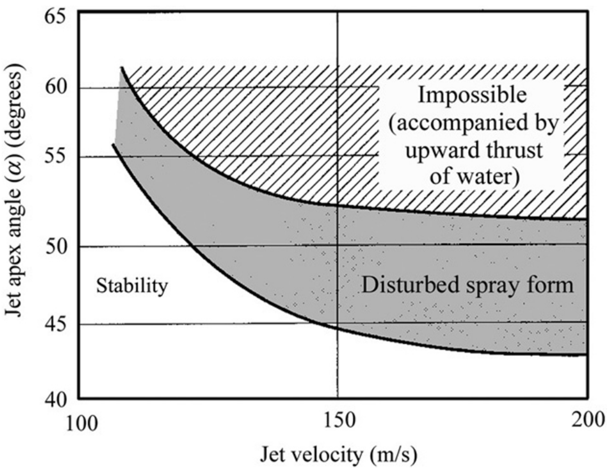

FIG. 4.11 Effect of jet apex angle on stability of water atomization at various water velocities.

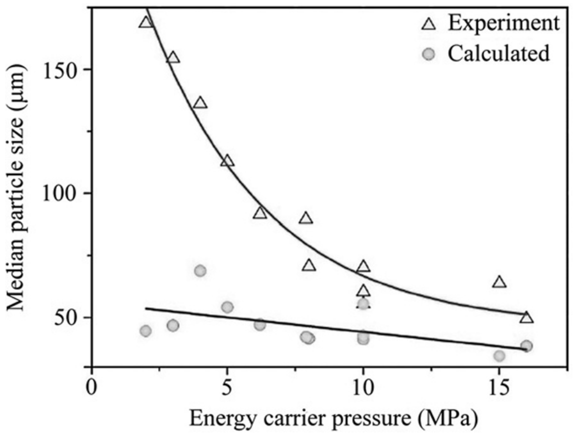

FIG. 4.12 The dependence of powder median diameter on energy carrier pressure by 1273 K temperature.

$$\delta_{\mathrm{m}} = 4.97\frac{G_{\mathrm{Me}}^{1.24}}{G_{\mathrm{w}}^{0.3}}\frac{v_{\mathrm{Me}}^{0.35}}{\gamma_{\mathrm{Me}}^{0.15}D_{\mathrm{c}}^{1.03}\rho_{\mathrm{Me}}^{0.56}\rho_{\mathrm{w}}^{0.25}\nu_{\mathrm{w}}^{0.07}\nu_{\mathrm{w}}^{0.96}(\sin\alpha)^{0.96}} \tag{4.4}$$

where G_{Me} is the melt mass flow (kg/s), v_{w} is the water jet velocity (m/s), G_{w} is the water mass flow (kg/s), ν_{Me} is the kinematic viscosity of the liquid metal ($\mathrm{m^2/s}$), ρ_{Me} is the density of the liquid metal ($\mathrm{kg/m^3}$), γ_{Me} is the surface tension of the liquid metal (N/m), D_{c} is the liquid metal squirt diameter (m), ρ_{w} is the water density ($\mathrm{kg/m^3}$), ν_{w} is the kinematic viscosity of the water ($\mathrm{m^2/s}$), and α is the jet's apex angle.

The experimental and calculated dependence curves of the powder mass median diameter magnitudes on powder pressure in the 2.0–16.0 MPa range by 1273 K temperature, according to study [4], are shown in Fig. 4.12. The calculations are made with Eq. (4.4). The process parameters and physical quantities by median diameter calculation were in the following range: G_{Me} (0.033–0.1 kg/s), G_{w} (1.33–3.2 kg/s), ν_{Me} (7.52×10^{-7}–12.3×10^{-7} $\mathrm{m^2/s}$), v_{w} (97–137 m/s), ρ_{Me} (2235–2357 $\mathrm{kg/m^3}$), and ν_{w} (1.4×10^{-6} $\mathrm{m^2/s}$).

The calculated median diameter volumes are similar to actual sizes by high-pressure volumes (Fig. 4.12). The difference is grown by decreasing the water pressure, and at 2.0 MPa the calculated particle sizes are diminished three times less than in the actual values.

Powder Characteristics

Particles of water-atomized powder generally have an irregular shape with a pronounced uneven surface as compared with gas-atomized powders. For high-yield, low-cost production, and safely engineering, water atomization usually is preferred over gas atomization, providing powder characteristics are compatible with the application.

Particle Size Distribution

Generally, water-atomized powders exhibits lognormal size distribution. Typical data for a range of metals and alloys and for differing operating conditions in water atomization are shown in Fig. 4.13. Deviations from linearity using log normal-probability coordinates usually indicate operational instability, sampling errors, or loss of fines. Minimum values of standard deviations (σ) are normally in the range 1.8–2.3, with some alloys on the low end of this range, for example, Cr-Ni-Mo and Fe-Si. For aluminum alloys (Fig. 4.14) and the alloys that contain aluminum and chromium, which form refractory oxides, the values of σ are typically higher, namely 2.0–3.0. The standard deviation is calculated by:

$$\sigma = \frac{\delta_{84.1}}{\delta_{50}} = \frac{\delta_{50}}{\delta_{15.9}} \tag{4.5}$$

where δ_{50}, $\delta_{84.1}$, and $\delta_{15.9}$ correspond to the particle sizes at the 50%, 84.1%, and 15.9% cumulative weight percent levels, respectively. Thus, the main influence on standard deviation, once a good and stable atomizing jet set-up is ensured, appears to be melt chemistry.

The large effect of the atmosphere is observed in work [18]. In fact, it is confirmed [3] that if copper is atomized with a large dissolved oxygen content, the powder is much finer. Thus, the large difference between nitrogen and air atmosphere may be due to this effect. Similarly, the chemistry may be directly influencing standard deviation. The generally lower values of standard deviation at lower metal flow rates reflect the importance of collisions in broadening the size distributions. Fig. 4.15 illustrates the effect of pouring temperature for water-atomized aluminum and copper powders [4, 6]. The influence of the discharged melt temperature elevation on the atomized powder granulometric composition is characterized by the increase in powder dispersibility. The powder median size decreased from close to 90 μm up to nearly 40 μm by the discharged melt temperature elevation from 963 to 1273 K by the 14 MPa water jet pressure. This is explained by increasing the temperature head and heat flow density and, as result, the heat transfer coefficient expansion, and on the other hand increasing the liquid metal disintegration efficiency due to the surface tension decrease.

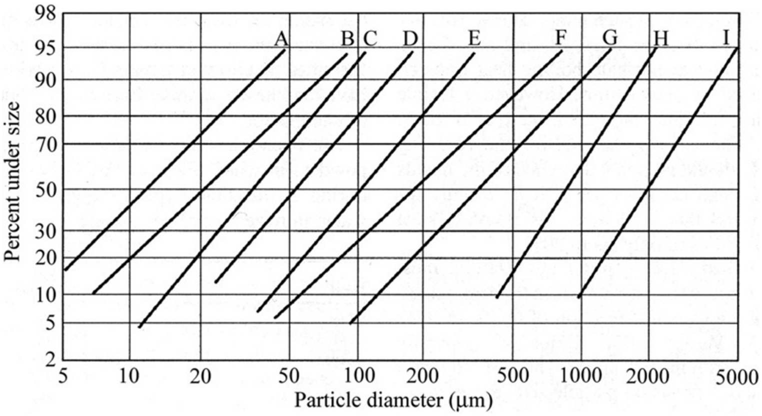

FIG. 4.13 Typical water-atomized particle mass size distribution.

	Alloy and Water Pressure	δ_{50}	σ
A	Copper atomized at 54 MPa	12	2.40
	18Cr-10Ni-2.5Mo stainless steel atomized at 50 MPa	20	2.40
C	Fe-15Si atomized at 20 MPa	40	1.70
D	M2 high-speed steel atomized at 140 MPa	55	2.11
E	Fe-45Si for welding electrodes atomized at 4 MPa	100	1.70
F	Zinc for alkaline manganese batteries atomized at 5.5 MPa	180	2.34
G	Copper shot atomized at 2.0 MPa	400	2.30
H	15% phosphor copper shoot atomized at 0.15	800	1.76
I	15% phosphor copper shoot atomized at 0.05	2000	1.75

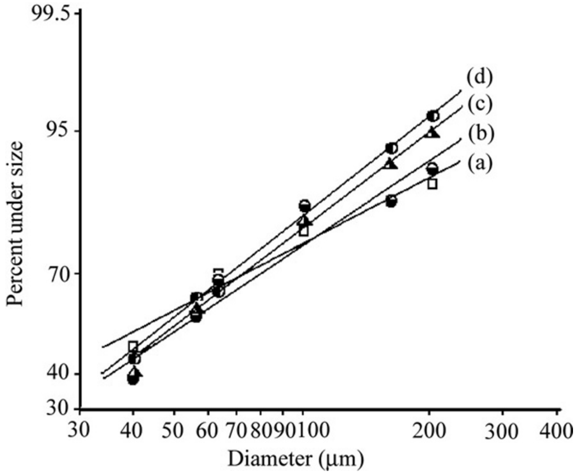

FIG. 4.14 Typical particle mass size distribution of water-atomized aluminum alloys:

	Alloy and Water Pressure	δ_{50}	σ
(a)	$Al_{94}Fe_{2.0}Cr_{2.0}Ti_{2.0}$ alloy atomized at 15 MPa	40.5	2.96
(b)	$Al_{94}Fe_{2.5}Cr_{2.5}Ti_{0.7}Zr_{0.3}$ alloy atomized at 15 MPa	46	2.83
(c)	$Al_{94}Fe_{4.1}Cr_{1.3}Zr_{0.6}$ alloy atomized at 15 MPa	43	2.51
(d)	$Al_{94}Fe_{4.1}Cr_{1.3}$ $Ti_{0.47}Zr_{0.13}$ alloy atomized at 15 MPa	42	2.5

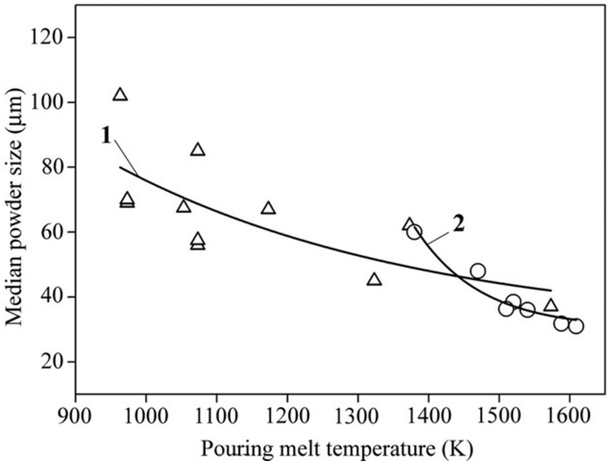

FIG. 4.15 Effect of pouring temperature on distribution of water-atomized aluminum and copper powder. (1) aluminum powder (metal stream diameter 7 mm, water flow 5 kg/s, water pressure 14 MPa), air atmosphere; (2) copper powder (metal stream diameter 4 mm, water flow 5.3 kg/s, water pressure 13.2 MPa, atmosphere nitrogen).

It is appropriate to mention here that each commercial water atomization unit has its own feature operating characteristics. However, well-established proprietary empirical relations give a high degree of predictability in terms of operating conditions and powder properties, in particular, particle size.

Particle Shape

The shape of water-atomized powder particles can vary appreciably. Most water-atomized powders are somewhat irregular in shape. Certain alloys can be produced with a spherical or near-spherical shape, exhibiting apparent densities about 50% of theoretical while others can be sponge-like and extremely irregular in shape, in which case apparent densities are as low as 10%–15% of theoretical.

During melt atomization, the irregular liquid metal drops under action of the surface tension forces tend to a spherical shape, the surface of which is minimal for a certain volume that corresponds to minimum free energy. At that, in prognostication of the particle shape, a determining index is the ratio of spheroidization time τ_{sph} and cooling time τ_{cool}:

$$\varepsilon = \frac{\tau_{sph}}{\tau_{cool}} \tag{4.6}$$

The melt drop cooling time τ_{cool} from the discharged melt temperature t_m up to liquidus temperature t_{liq} is expressed [19] by:

$$\tau_{cool} = d\frac{c_m \rho_m}{6\alpha} \ln \frac{t_m - t_w}{t_{liq} - t_w} \tag{4.7}$$

where d is the drop diameter (m), c_m is the heat capacity of the liquid metal (J/(kg K)), ρ_m is the density of the liquid metal (kg/m^3), α is the heat transfer coefficient (W/(m^2 K)), t_m is the initial temperature of the drop (K), t_{liq} is the liquidus temperature (K), and t_w is the water temperature in the meeting point with the drop (K).

The formula for spheroidization time definition [19] is:

$$\tau_{sph} = \frac{3\pi^2 \mu}{4V\sigma}\left(r_{str}^4 - r_{dr}^4\right) \tag{4.8}$$

where μ is the dynamic viscosity of the liquid metal (Pa s), σ is the surface tension of the liquid metal (N/m), V is the drop volume (m^3), r_{str} is the strand radius before transformation to drops (m), and r_{dr} is the particle radius after transformation to drop (m).

The melt strand radius formula, which was presented by authors [20] with reference to work [21], is described as:

$$r_{str} = 0.82 d^{1.09} \sigma^{0.09} \nu^{-0.18} \rho_m^{-0.09}$$

where ν is the kinematic viscosity (m^2/s) and ρ_m is the density of the liquid metal (kg/m^3).

The definition of the heat transfer coefficient is an involved problem in the calculations of the melt drop cooling time. A heat exchange by melt metal drop cooling is the heat transfer process by water boiling. This process is very complicated and possesses a chaotic character even at a constant heat supply in stationary conditions [22]. Analytical process descriptions are presently absent. The experiment and theory of similarity with the dimensional analysis have a decisive role here.

The heat-exchange process of the melt atomization by high-pressure water jets is complicated by the transience of the liquid drop cooling process and the variable heat current. The picture of heat emission in the moment of drop origination and subsequent cooling is possible to see (Fig. 4.16). In the beginning, because of a very high temperature head Δt and heat current q, exceeding the first q_{cr1} and second q_{cr2} critical heat current density, the heat emission occurs in the film boiling conditions. A drop is enveloped by steam film, considerably reducing the intensity of the boiling heat transfer; then, after

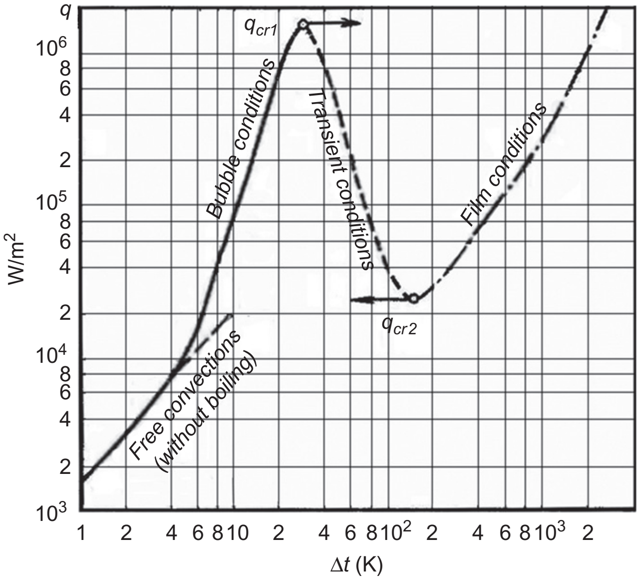

FIG. 4.16 Heat exchange process of the melt atomization by high-pressure water jets.

overcoming $q_{cr2,}$ the cooling rate grows; water begins periodically contacting the drop surface, and the greatest cooling rate is reached in the final cooling stage–bubble boiling conditions, that is, chiefly already after drop consolidation. With such unstable conditions of heat exchange, it is possible to operate only with average heat transfer coefficient values for all cooling drop stages.

The empirical formulas of heat transfer coefficient definition are known for different boiling conditions [22, 23]. However, they are reached by boiling on the body surfaces of cylindrical shapes and plates at atmospheric pressure, that is, for conditions very distant from the heat exchange by high-pressure water atomization of the melt.

The heat transfer coefficient calculated values for well-developed bubble boiling conditions by empirical formulas [23] exceed by 2–3 orders of magnitude the current actual values and the calculated values for film boiling conditions by empirical formulas [22, 23], and exceed by 1.5–2 orders of magnitudes the current actual values. For example, the calculation by Bramley's [23] advanced formula (Eq. 4.9) for the case of an 11.4 μm aluminum melt drop cooling by 963 K pouring melt temperature and 10 MPa water pressure gave a result of $\alpha = 10^6$ W/(m^2 K). The above-mentioned formula is expressed as:

$$\alpha = 2.7\sqrt{\lambda_2 \varphi r \rho_2 w / \Delta t d} \tag{4.9}$$

where λ_2 is the heat conductivity of the steam (W/(m K)); r is the heat of vaporization (J/kg); ρ_2 is the steam density (kg/m^3); w is the velocity of the water jet in the meeting moment with the melt stream (m/s); Δt is the temperature head, assignable as the temperature differential of the melt drop (t_s) and water (t_w) in the meeting point with the drop disconnected by the steam film (K); c_2 is the heat capacity of the steam by the saturation line temperature, J/(kg K); d is the drop size (m); and $\varphi = 1 + c_2\Delta t/2r$. The parameter magnitudes by the calculation are the following: $\lambda_2 = 5.55 \times 10^{-2}$ W/(m K); $r = 1.5 \times 10^6$ J/kg; $\varphi = 1.736$; $\rho_2 = 36$ kg/m^3; $w = 119$ m/s; $c_2 = 5.45 \times 10^3$ J/(kg K); and $\Delta t = 405$ K.

Thus, the prerequisites [19, 24] about the possibility that the film-bubble heat emission conditions occur in the 923–973 K temperature range and in connection with this, the increasing of heat emission had not been confirmed by study in work [4].

More reliable cooling time data can be gathered using a method for cooling rate definition based on the particle structure [4]. Thus, the cooling rate of melts is estimated with the use of the dendrite parameter, which is equal to the average size of the nondendrite grain [25]. The analysis of the dendrite structure allows one to estimate the cooling rate by the equation:

$$v = (\alpha/\delta)^{1/n}, \tag{4.10}$$

where δ is the measured nondendrite grain in μm; v is the cooling rate in K/s; and a and n are constants for aluminum alloys $a = 100$. A value of n is taken in the interval 0.25–0.5 depending on the grain shape, $n = 1/3$ for equiaxed grains (chapter 16 contains details of the analysis of the droplet cooling rate).

Then the average size of the heat transfer coefficient is defined according to the formula (Eq. 4.7). It is used for definition of the heat transfer coefficient values by the various drop sizes at various discharged melt temperatures and water pressures:

$$\alpha = d\frac{c_m \rho_m}{6\tau_{cool}} \ln\frac{t_m - t_w}{t_{liq} - t_w}$$

The dependence of the heat transfer coefficient on the heat flow density in the 953–1273 K temperature range by aluminum water atomization is shown in Fig. 4.17 [4]. The heat transfer coefficient varies from the 10^4 to 5.2×10^4 W/(m^2·K) range, when the heat flow density is increased from 10^7 to 4×10^7 W/m^2 by 10–14 MPa energy carrier pressure. Such heat transfer coefficient values range with ±5.5% abmodality, can be considered, is not great, whereas the transience of liquid drop cooling process and variable heat current and as well that the cooled particles had various sizes, shape and morphology.

It is significant that the lowest heat transfer coefficient values were reached for large-dimension particles. It can be explained by the more irregular shape and uneven surface of coarse particles, contributing to the steam film rupture and abruption from its particle surface, which results in the abrupt heat dissipation decreasing.

The spheroidization time (τ_{sph}) was calculated via a formula (Eq. 4.8) added by the correction, taking into account the energy carrier density (ρ_w) in the ratio form of the energy carrier density to steam density (ρ_{stm}). That is more reasonable in film boiling conditions than how air density was accepted before. The formula (4.4) with the correction coefficient is written as:

$$\tau_{sph} = \frac{3\pi^2 \mu \rho_w}{4V\sigma\rho_{stm}}\left(r_{str}^4 - r_{dr}^4\right)$$

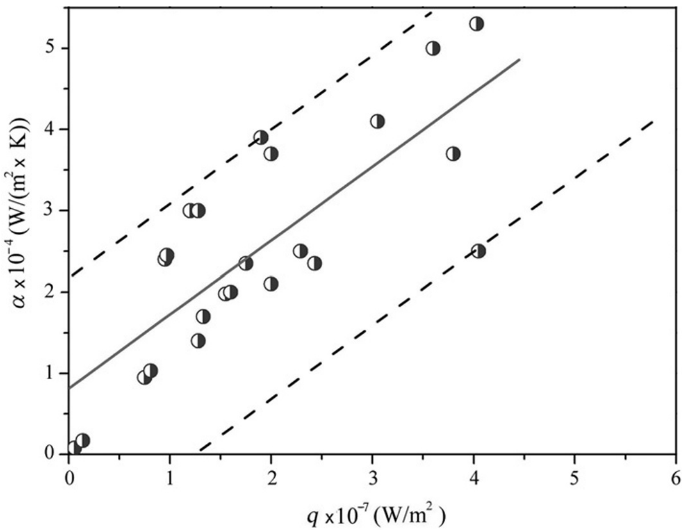

FIG. 4.17 The dependence of the heat transfer coefficient on the heat flow density by the 10–14 MPa energy carrier pressure range.

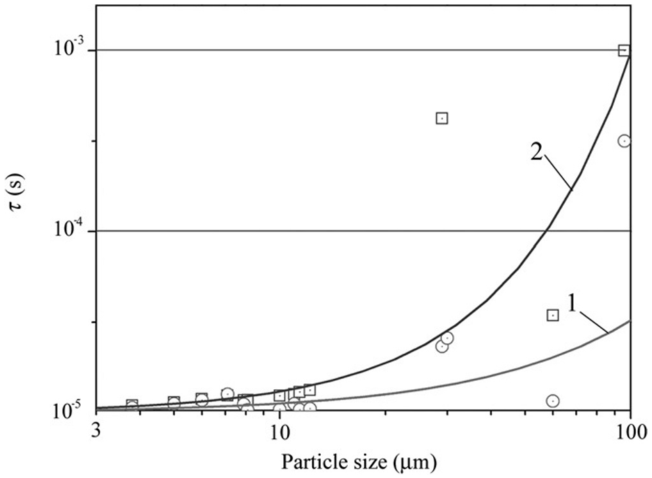

FIG. 4.18 Comparison of (1) $\tau_{cool} = f_1(d)$ and (2) $\tau_{sph} = f_2(d)$ dependences for powders made by water pressure in 3–15 MPa range and melt pouring temperature in 960–1620 K range.

The cooling time (τ_{cool}) of the drops up to liquidus temperature is calculated by their cooling rates defined by the experimental dendrite parameter values, according to the above-mentioned method [24] by Eq. (4.10).

The dependence of cooling time on particle size ($\tau_{cool} = f_1(d)$) and the dependence of spheroidization time on the particle size ($\tau_{sph} = f_2(d)$) are presented in Fig. 4.18. The approximation curves of these dependences are approached with each other in the course of particle size decreasing and flow together when τ_{sph} is being diminished up to τ_{cool} of the particle's results in particle spheroidization. It occurs with the 5–7 μm drops and smaller dimensions.

Micrographs of the water-atomized aluminum powders, made by melt atomization at 1273 K and pouring temperature in the pressure range from 2.0 to 16 MPa, are shown in Fig. 4.19. Characteristically, the influence of energy carrier pressure magnitude over the particle shape and morphology is not affected notedly as both for particles larger 50 μm (Fig. 4.17A and B), when $\tau_{sph} > \tau_{liq}$, and lesser sizes particles (Fig. 4.19C and D), when spheroidization time is less, than their cooling time.

The influence of the pouring melt temperature in the 963–1273 K range by 10–14 MPa energy carrier pressure is not observed on the surface relief and shape of the particles, similar to sizes as large as 50 μm (Fig. 4.20A and B) and as small as 20 μm (Fig. 4.20C and D).

Therefore, particles larger than 50 μm have an irregular shape and uneven surface that increases with the particle size growth. In particles <30–20 μm and with further diminishing of the sizes, the surface irregularities are smoothed and complete spheroidization of the 7–5 μm particles occurs. Thus, the melt drop size is a determinative parameter in the

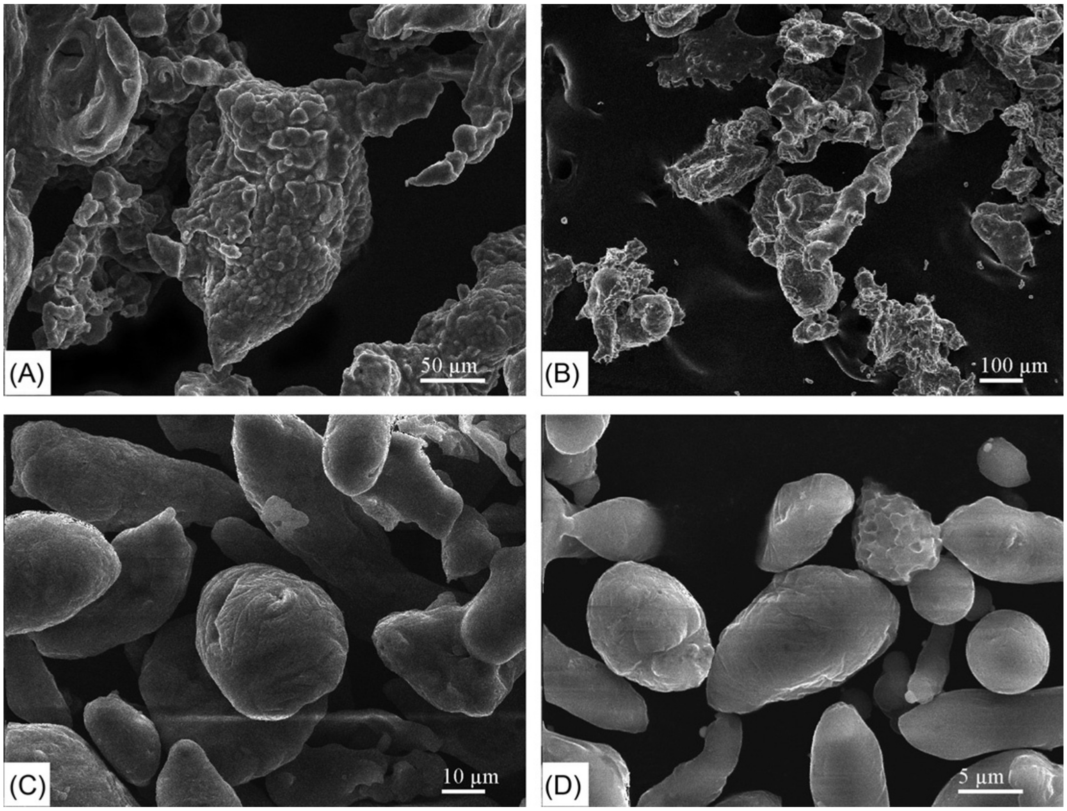

FIG. 4.19 Characteristic shape and morphology of the particles similar in sizes: (A, B) larger 50 μm, (C, D) less 20 μm, made at 1273 K pouring melt temperature and various energy carrier pressure: (A) 3 MPa, (B) 16 MPa, (C) 2 MPa, (D) 6.2 MPa.

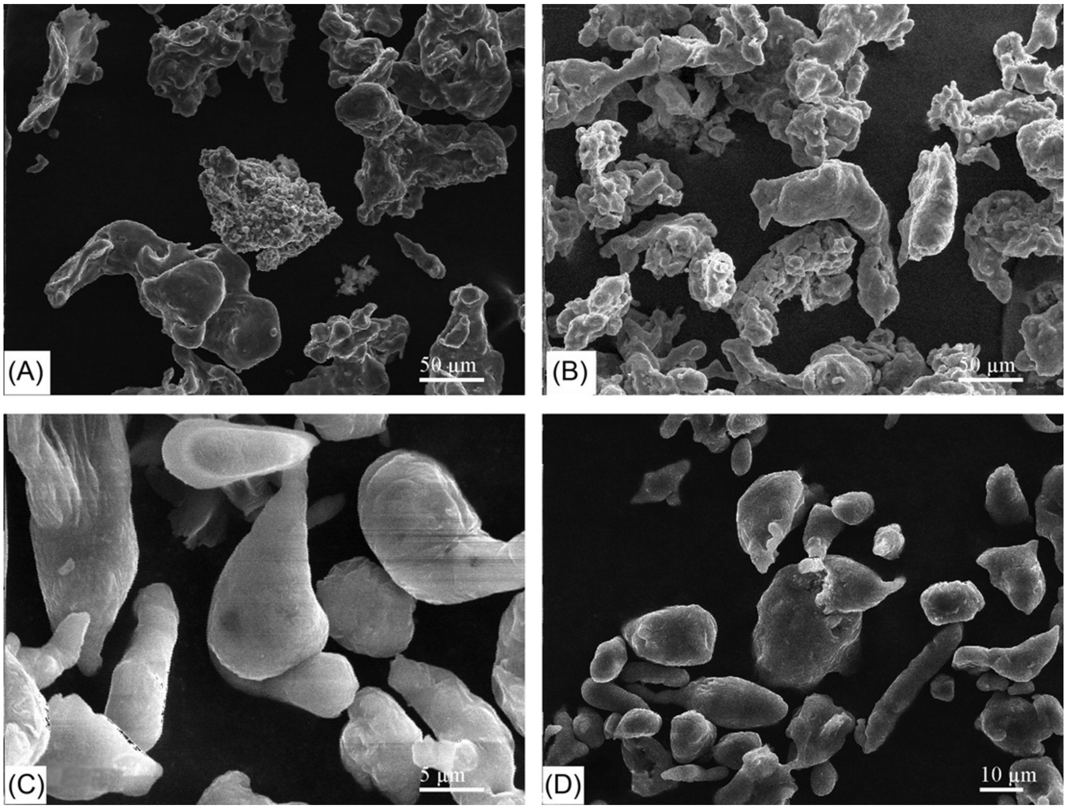

FIG. 4.20 Characteristic shape and morphology of the particles similar in sizes: (A, B) larger 50 μm, (C, D) less 20 μm, made by 10–14 MPa energy carrier pressure and at various pouring melt temperature: (A) 963 K, (B, C) 1273 K, (D) 1273 K.

independent shaping of the current energy pressure range and the pouring melt temperature range while the granulometric composition greatly depends on the energy current pressure and discharged melt temperature.

Lawley [13] summarized that the estimated spheroidization time for a 100 μm diameter droplet to be in the range from 0.1 to 10 μs, depending on the magnitude of surface tension forces. Freezing (solidification) times are of the order of 50–750 μs for elevated temperature aluminum alloys by a pouring melt temperature 1520–1573 K. Thus, solidification times are near to or less than the spheroidization times and water-atomized particles are therefore predicted to be predominantly irregular in shape.

The formation of an oxide film on the surface of the droplet before it is in free fall and able to spheroidize can drastically affect particle shape. Elements that form refractory oxides prevent spheroidization by producing an oxide film with sufficient strength to oppose the forces of surface tension.

Thus, in terms of particle shape, droplets with very short freezing times tend to be more irregular and in turn are associated with low apparent densities. Accordingly, the longer freezing times characteristic of high melting point elements or alloys result in a more spherical particle shape.

Surface Morphology and Internal Structure

Water-atomized powders, along with their irregular shape, typically show a rough surface morphology and are honeycombed. This characteristic is illustrated in water-atomized Al-6.0Zn-0.3Mg-0.3Zr-0.5Mn high strength alloy (Fig. 4.21) and Al-5.0Fe-5.0Cr-2.0Ti-1.0Zr elevated temperature alloy (Fig. 4.22). Their morphology is similar to one of aluminum powders similar in size (Figs. 4.19A and 4.20A). The combination of irregular shape, surface roughness, and porosity is an important feature of water-atomized powders because green strength is enhanced by the mechanical interpenetration of irregular powders during die pressing.

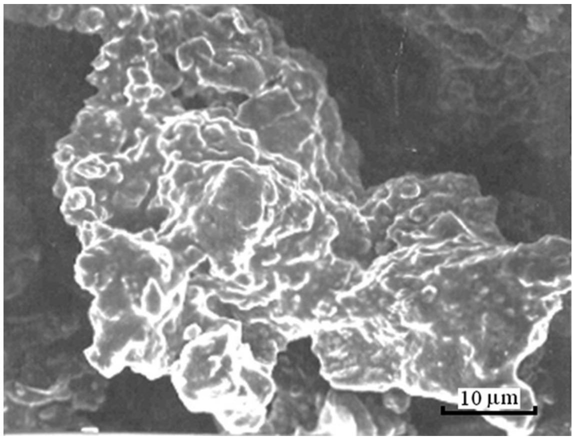

FIG. 4.21 SEM micrograph of water-atomized powder of Al-6.0Zn-0.3Mg-0.3Zr-0.5Mn high-strength alloy.

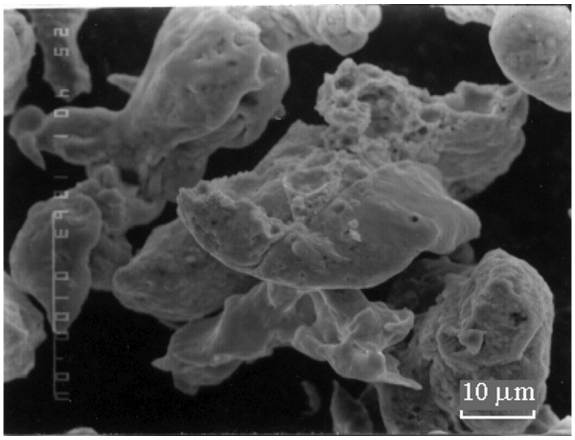

FIG. 4.22 SEM micrograph of water-atomized powder of Al-5.0Fe-5.0Cr-2.0Ti-1.0Zr elevated temperature alloy. Superheat 200 K; diameter of gravity melt stream 7.0 mm.

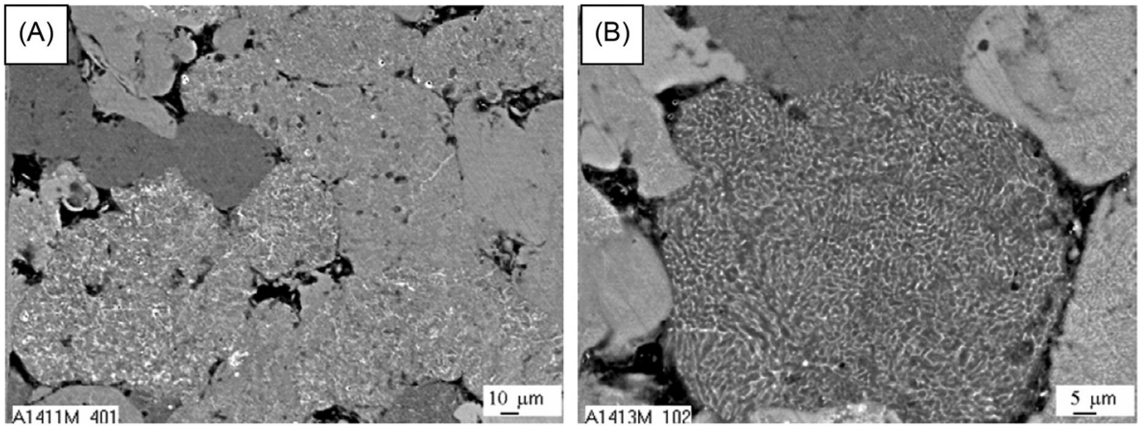

FIG. 4.23 Microstructures of two typical metallographic sections of water-atomized powder particles of Al-Fe-Ce alloy in backscattering electrons with lower (A) and higher (B) magnifications.

Individual particles or even different grains within a powder particle differ in microstructure (Fig. 4.23A). This is caused by differences in solidification behaviors of the solidifying fronts growing into the melt and of primary intermetallic phases distributed in the melt. Most particles exhibit a cellular or nondendritic-like structure with an arm spacing of a few hundred nanometers in colonies a few microns in diameter (Fig. 4.23B). Some other grains show a coarser background network structure where coarse primary intermetallics act as separate growth centers.

In addition to a nondendritic structure, some other areas of individual particles show subdendritic and cellular structures. Such observations can be explained by a significant intensification of the nucleation during crystallization by a deep super cooling of the melt. The nondendritic and subdendritic cell sizes are different for different particles. For example, the calculated cell size values shown in Fig. 4.23B range from 1.2 to 0.94 μm that, in accordance with Eq. (4.10) corresponds to cooling rates from 0.83· to 1.7 K/μs.

Powder Purity

Deoxidation of the melt plays an important role in the atomization process. The oxygen content of water-atomized powder is a function of the free energy of the reaction of the metal with water vapor and also of the reaction kinetics. For many water-atomized powders, oxygen levels are in the range 1000–4000 ppm by weight. The importance of the kinetic effect is exemplified by the appropriate oxygen levels in aluminum or high silicon alloys. In these alloys, a protective oxide film arises on the particle surface, which prevents or retards further oxidation. The surface oxide of water-atomized powders is nonuniform in thickness. Therefore, with water-atomized powders, three-dimensional film islets with a typical thickness of 30–40 monolayers usually cover 30%–70% of the particle surface. The rest is covered by a thin oxide film of three to eight monolayers [26]. Table 4.2 gives the characteristic properties of water-atomized powders, including oxygen content.

The increase of oxygen content can be accommodated by modifying the atomization conditions. For example, the use of inhibitors in combination with the control of the hydrogen ion level and suspension temperature during the atomization process can lead to a decrease in the oxygen content to the level of gas-atomized powders [27]. The Au-Ni brazing alloys normally have oxygen contain about 200 ppm. By using inert purging gases in the melting process, the oxygen level is reduced to 150 ppm. Further reductions in the oxygen level to 100 and 40–50 ppm can be achieved by deionized water or by the addition of alcohol to the water. The use of antifoaming agents in the atomizing water can further reduce oxidation and increase the cooling rate [15].

OIL ATOMIZATION

The oil-atomization process should avoid the problem of powder oxidation. In the early 1980s, Sumitomo Metals developed the oil-atomization process for the commercial production of relatively high carbon (0.4 wt%) steel [15]. Oil-atomized powders resembled water-atomized powder in particle size. Their densities are intermediate between water- and gas-atomized powders as the cooling rate is slower and the oxidation much less. However, carbon pickup occurs to an extent depending on metal temperature and the carbide-forming tendency of the melt [28].

TABLE 4.2 Characteristic Properties of Water-atomized Powders

Metal Alloys	Mass Median Particle Size (δ_m) (μm)	Standard Deviation σ_g	Apparent Density (g/mL)	Oxygen Content (ppm)
Ag	37	2.16	3.76	—
Ag-28Cu	32	2.3	3.37	285
Ag-25Sn-5Cu-1Zn	35	2.40	5.11	260
Al-3.92Fe-3.65Cr-3.3Ti[a]	40.5	2.96	1.07	—
Au	130	2.69	7.82	—
Au-20Ni	62	2.9	—	57
Bi	79	3.33	3.58	—
Cd	185	2.00	1.29	—
Cu	46	2.30	3.48	350
Cu	90	2.40	5.07	397
Cu-0.3Mg	31	2.51	2.01	1105
Ni	100	2.10	4.50	645
Ni-5Al	34	2.29	2.85	710
Ni-Cr-B-Si	51	1.69	4.26	—
Pt-10Rb	250	2.80	12.3	—
Sn	160	2.19	1.48	314
Sn	90	2.19	1.23	620
Zn	58	2.05	1.82	—

[a] *IPMS data.*
Lawley A. Atomization. Princeton: Metal Powder Industries Federation Publishers; 2003.

GAS ATOMIZATION

Gas atomization (GA) is the process in which the liquid metal is dispersed by a high-velocity jet of air, nitrogen, argon, or helium. Gas atomization is used for the commercial production of powders of copper, copper alloys, aluminum and its alloys, magnesium, zinc, titanium, titanium alloys, nickel-base alloys, cobalt-base alloys, lead, tin, solder, precious metals, refractory metals, beryllium, etc.

Gas atomization differs substantially from water atomization. The gas-to-metal ratio is the dominant factor in controlling particle size while the pressure of the medium is dominated by water atomization. This fundamental difference is easily explained. In the case of gases, increases in pressure above 0.1 MPa, at which sonic velocity is reached, give very small increments in gas velocity. In contrast, to reach sonic velocity with a water jet, a pressure of nearly 40 MPa is needed and the velocity increases uniformly as the square root of the pressure. Moreover, gas atomization takes place by the action of a continuum on another while in water atomization, a stream of droplets in an entrained gas flow acts on a continuum. Therefore, the density of the water medium is about a thousand times higher than typical gases, giving much greater impact.

Air atomization is used for aluminum, copper, brass, and zinc powder production. Inert gases are used when the oxygen content must be kept low or when atomizing reactive metals such as superalloys and titanium. The worldwide annual tonnage of inert gas-atomized metal powders is much less than for water-atomized powders. The relationship between the shipments of ferrous and nonferrous powders is about 4 to 1. However, in market value terms, aluminum, silver, and zinc are all close to the value of iron powders [1, 29].

Gas-Atomizing Units

Gas-atomizing units exist in a much wider range of designs than water atomizers. The earliest gas atomization was with steam, patented in 1872 by Marriott of Huddersfield. The very simplest design of the atomizer is to let a metal stream fall onto a horizontal gas jet, and this has been used for zinc powder production. The earliest scientific worker in this field seems to have been Professor Hall, founder of the Metals Disintegrating *Co*. His patent in the late 1920s [30] represents a kind of close-coupled atomizer for aluminum atomization. The basic design shown in this patent is still in use and has yet to be improved in any radical manner. A similar unit developed by VAMI is shown in Fig. 4.24. The atomizing gas is delivered through an annular orifice around the nozzle at the converging angle. The gas flow creates the suction (ejection) effect at the tip of the nozzle that draws the molten metal into the nozzle. The amount of gas delivered by the nozzle is controlled by the size of the air gap and the pressure and temperature of the gas. The rate of metal flow and resultant powder particle size are influenced by the aspirating force, the nozzle metal orifice diameter, and the vertical distance between the nozzle and the molten metal level.

This atomizer design aims to contact the liquid metal stream with the gas is at or close to the gas jet exit plane where the highest jet velocities exist. It leads to an efficient break-up of the liquid, resulting in finer powders, and is the preferred method for aluminum and other low melting point metals. It can be operated vertically upward or downward or in the horizontal position. Careful design of the atomizer is required, however, to avoid the freezing of the metal by the gas jet, which can lead to solidification at the nozzle tip.

Many gas atomizer designs are known. They are classified as free fall, confined or closed nozzles (Fig. 4.25), and internal mixing. The closed nozzle designs are also called close-coupled nozzle designs. For free gas atomization (Fig. 4.25A), the key process variables are similar to those of water atomization (Fig. 4.3). In this atomizer, the liquid metal issues in the form of a stream from a tundish and falls 100–200 mm by gravity. Then it is atomized either by means of a discrete or an annular directed at the point of meeting with the metal stream. This method is easy to operate but is not suitable for making fine powders. In the "internal mixing prefilming" atomizer type, the gas and liquid metal are mixed together before expanding into the atomizing chamber [31].

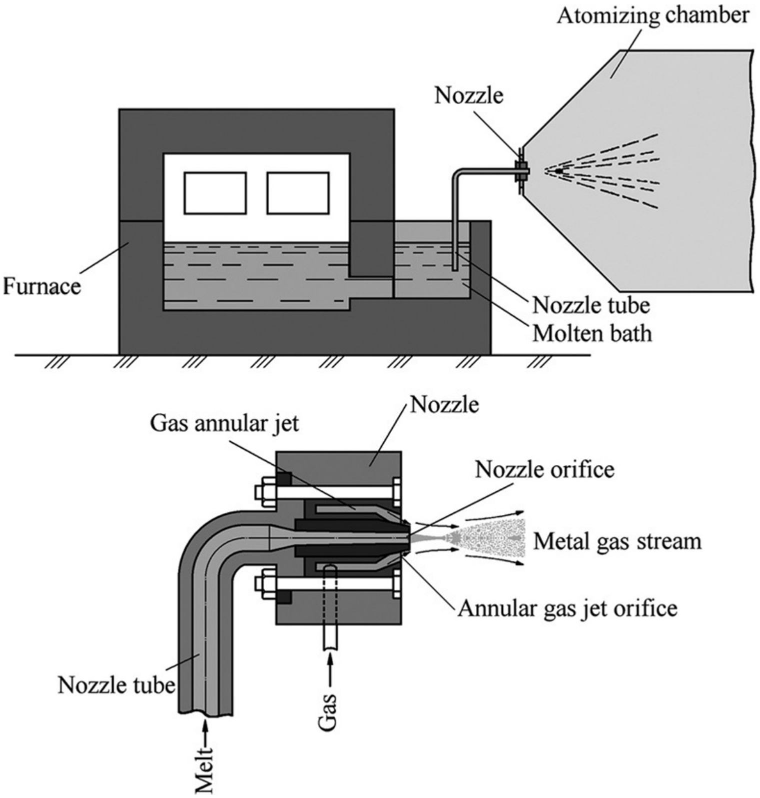

FIG. 4.24 VAMI ejection nozzle design with horizontally molten metal stream.

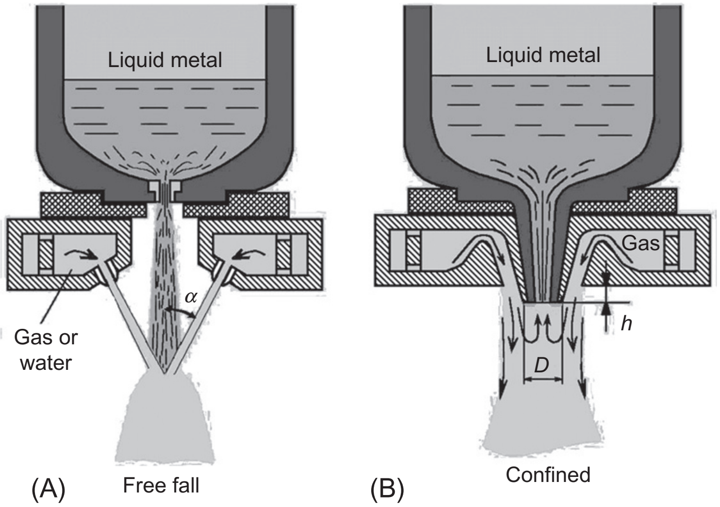

FIG. 4.25 Atomizer designs of two types: (A) free-fall design (gas or water) and (B) confined-nozzle design (only gas). Design characteristics: α, angle formed by free-falling molten metal and atomizing medium jet; *D*, diameter of confined molten metal nozzle end; *h*, protrusion length of metal nozzle.

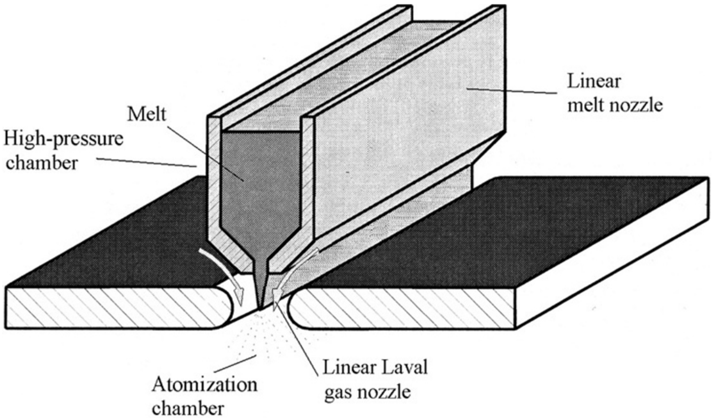

FIG. 4.26 Simplified drawing of the WIDEFL0W confined linear nozzle design.

Confined Nozzle Designs

This nozzle design (Fig. 4.25B) make it possible to increase the yield of median particle size powder (40–60 μm) by maximizing the gas velocity and density at the meeting with the metal stream [32]. However, the use of these units can cause the freezing of the molten metal at the end of the tundish nozzle, which immediately stops the atomizing. Along with this, the interaction of the gas stream with the nozzle tip can form either underpressure or positive pressure, varying from an underpressure that can significantly increase melt flow rate to an inverse pressure sufficient to stop it and blow gas into the tundish. Thus, great care is needed in setting up closed nozzles and control during atomization.

The WIDEFLOW gas atomizer based on the confined nozzle principle is illustrated in linear modification (Fig. 4.26) [33]. This atomizer involves two chambers, a high-pressure chamber (autoclave) containing melting and pouring units, and a low-pressure atomization chamber divided by a linear Laval gas nozzle. The pressure difference between the two chambers forces the gas-accelerated flow through the converging linear Laval nozzle to sonic velocity, when the pressure ratio exceeds the critical value. The kinetic energy of ultrahigh velocity gas flow is transferred efficiently to the atomization of the thin melt film. Schulz reported that by using nitrogen or argon, the mean particle diameters of about 10 μm can be achieved with pressures of 2.0–2.5 MPa [34].

Prefilming Nozzle Design

In several confined designs, the circulation created by the gas flowing up the side of the tundish nozzle caused due to suction force action, the molten metal to spread across the face of the ceramic nozzle to its edge, where it is sheared by the flowing gas [35]. These nozzle designs are referred to as "prefilming" (Fig. 4.27A) and are quite widely used.

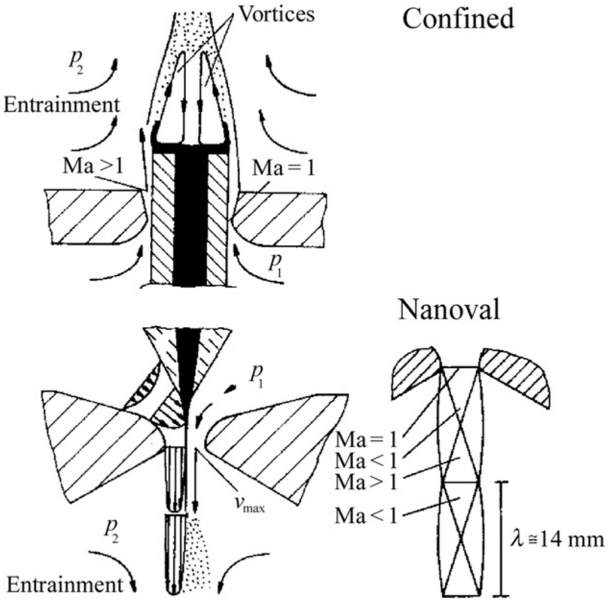

FIG. 4.27 Schematic of prefilming nozzle design (A) and Nanoval design (B). Ma is the Mach number.

The regime when a thin film is formed on the melt nozzle top is the preferred operating regime for producing fine powders. When the metal flow rate is too high, the filming effect is partially lost, and some of the metal is entrained into the low-velocity wake [36]. Such a regime leads to coarser powders and to the formation of undesirable flakes in the powder. The low pressure (suction, aspiration) created at the nozzle tip is a useful feature of the prefilming nozzle design. It is employed to draw the liquid metal into the melt nozzle from the crucible in up-draught operation, as mentioned above. Additionally, the presence of suction at a point of contact between the gas and liquid avoids the potentially hazardous blowback effects observed in free fall nozzle designs for certain jet geometries.

At the same time, by air atomization a sudden stoppage or decrease of flow rate can lead to ignition or explosion of the suspended solid powder in the case of active metals or alloys. The level of suction created by a nozzle is found to be extremely sensitive to nozzle geometry, atomizing gas nature, and operating gas pressure.

Nanoval Nozzle Design

In the Nanoval nozzle design [37], a metal melt stream is broken up by the action of friction forces between the atomization gas and the liquid (Fig. 4.27B). Because the metal stream is always kept very thin and is delivered directly to the throat of the nozzle, this design is capable of producing very fine powders. The comparison of mean particle sizes by Nanoval and the conventional confined nozzle design represented in the form of mass median diameter dependence on specific gas momentum is shown in Fig. 4.28.

Pressure-Swirl Hybrid Prefilming Atomizer

This atomizer combines pressure-swirl atomization and ring-gas atomization. In the first stage, a film is generated followed by gas jet atomization in the second step [38]. The pressure-swirl-metal chamber, atomization chamber, and gas-recirculation system are the main components of the powder atomization unit. Fig. 4.29 [39] schematically shows a pressure-swirl-atomizer. Due to overpressure, the molten metal flows tangentially into the swirl chamber, leaves it through a small cylindrical hole (D_L), and forms a swivelling hollow cone film of molten metal. The film is subsequently atomized by the gas jets through the orifices (D_G).

Spherical tin powders with median diameter 10–20 μm and standard deviation below 2 were obtained by superheating to 373 K, gas (nitrogen) pressure 1.0 MPa, gas-to-metal ratio of 1.3, and with a melt flow rate between 160 and 190 kg/h.

Prefilming Hybrid Atomizer

This atomizer has been developed for viscous melt atomization [40]. Viscous melts, such as oxidized metals or slags, have a comparably high viscosity. The prefilming hybrid atomizer is shown in Fig. 4.30. Their local flow regimes are to be

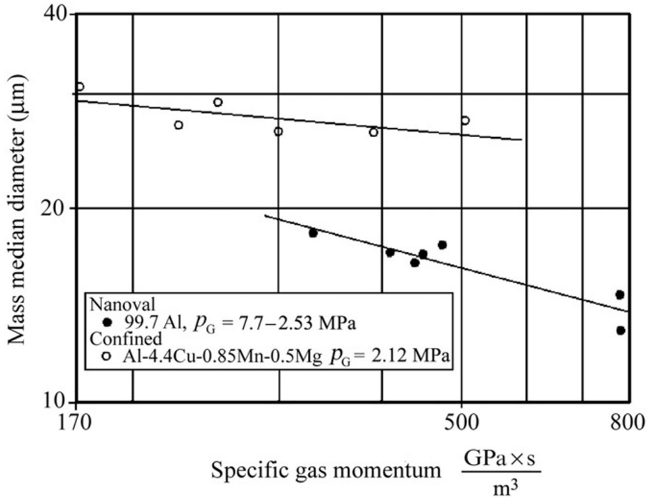

FIG. 4.28 Comparison of mean particle sizes by Nanoval and conventional confined atomizing nozzle designs.

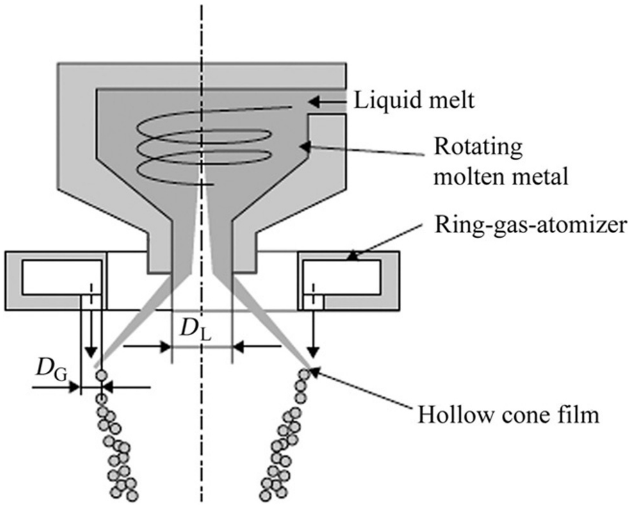
Liquid melt
Rotating
molten metal
Ring-gas-atomizer
D_L
D_G
Hollow cone film

FIG. 4.29 Pressure-swirl hybrid prefilming atomizer.

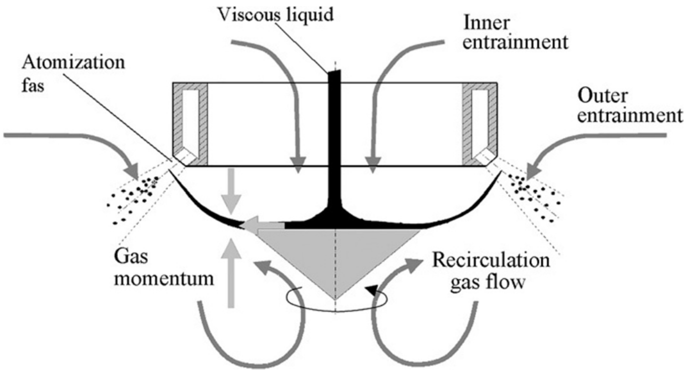
Viscous liquid
Inner
entrainment
Atomization
fas
Outer
entrainment
Gas
momentum
Recirculation
gas flow

FIG. 4.30 Prefilming hybrid atomizer for viscous melt atomization. *Czisch C, Fritsching U. Atomizer design for viscous-melt atomization. Mater Sci Eng A 2008;477(1–2): 21–5.*

distinguished by the difference from where the ambient gas interacts with the atomization gas. The inner entrainment reaches the atomization area through the atomizer's liquid stream passage. The outer entrainment reaches the atomization area directly and the recirculation gas flow reaches the atomization area from below the rotary disc. The aim of the prefilming hybrid design is to generate a maximum recirculation momentum so that the film is transported closer to the external mixing atomizer gas outlet.

Process Parameters

In conventional gas atomization processes, the atomization pressures are typically in the range 0.5–4 MPa, and gas velocities in the nozzles range from Mach 1 to 3. However, in free-fall atomizers, gas velocities in the impingement zone usually have fallen to 50–150 m/s (for air or nitrogen). Typically, gas-atomized powders are usually spherical with a lognormal size distribution. Average particle sizes are usually in the range 10–300 μm with a standard deviation of about 2; oxygen content is about 100 ppm. Prealloyed alloys are commonly made by inert gas atomization. The worldwide annual tonnage of inert gas-atomized powder is much less than that of water-atomized powders, probably amounting to >50,000 tons per year. Metal feed rates are lower than in water atomization, and the melt batch is smaller. However, the tonnage of air-atomized powders, especially zinc and aluminum as well as copper, tin, lead, and copper alloys, probably exceeds 400,000 tons per year [29]. Air atomizers operate continuously for many hours or around the clock. Multinozzle units are often used to boost the yield on aluminum and zinc.

In conventional inert gas or air atomization, typical metal flow rates through single orifice nozzles range from about 1 to 90 kg/min. The capability of plants varies from very little laboratory units to immense plant such as the ANVAL Atomizer 1 (Fig. 4.31), which is the biggest inert gas atomizer and was designed for producing large tonnages of superalloys and other alloy powders. Melting takes place in two 5.5-ton induction furnaces. Plasma-heated tundish is used. Due to the height of the tower, powder with up to a 1 mm particle size can de produced. Very fine powder can also be produced for applications such as MIM.

In conventional atomizers, the typical gas flow rate ranges from 1 to 50 m^3/min at pressure ranges of 350 kPa to 4 MPa. The superheating of molten metal (the temperature differential between the melting point and the temperature at which the molten metal is atomized) is generally about 75–150 K. In gas atomization with inert gas, the cost of gas consumption is significant, and a means of circulation to promote gas reuse is desirable, especially in large-scale facilities.

In practice, for a given gas nozzle design and size, the mean particle size is controlled by the pressure of the atomizing medium and the melt flow rate. For all nozzles, the velocity of the gas usually "chokes" at sonic velocity (about 300 m/s for nitrogen and argon) in the narrowest region of the nozzle if the upstream gas pressure is at least 1.9 times the external pressure [3].

Therefore, the amount of gas flow (Q) depends on gas pressure, temperature, and nozzle area. For ideal conditions and zero velocity on the entrance side of the nozzle, gas flow can be expressed as:

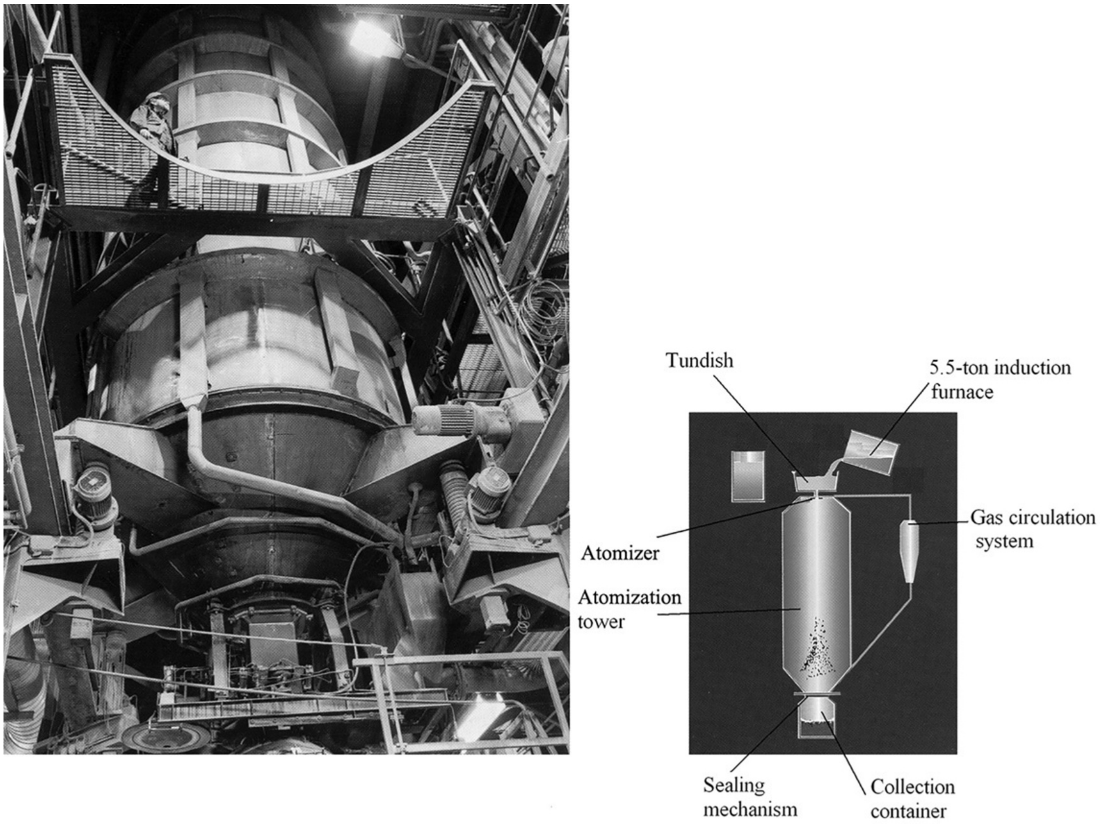

FIG. 4.31 ANVAL atomizer 1. *Courtesy of ANVAL.*

$$Q = \omega\left(\frac{2}{k+1}\right)^{\frac{k+1}{2(k-1)}} \frac{p\sqrt{2g}}{\sqrt{RT}} \tag{4.11}$$

where ω is the cross section of gas nozzle at exit; k equals C_p/C_v, is the ratio of specific heat at constant pressure and volume, correspondingly; p is the gas pressure in the reservoir; T is the temperature in the gas reservoir; R is the gas constant; and g is the acceleration due to gravity. For nitrogen $k = 1.4$, Eq. (4.11) takes on the form with the dimension of quantity (g/s):

$$Q = 4 \times 10^6 \frac{ap}{\sqrt{T}}$$

Comparisons based on how much powder surface is generated per unit volume of gas spent can be used for evaluation of the gas efficiency. This criterion accounts for higher gas consumption requirements when higher gas pressures are applied in producing finer powders. Confined nozzle designs in comparison with consumption ones give higher efficiencies at a comparable gas-to-metal ratio [41]. A simple equation of median particle size dependence on gas/metal ratios can be used:

$$\delta_m = \frac{k}{\sqrt{G/M}}$$

where k is a constant for the process and G/M is the gas/metal ratio, which is variously measured in kg/kg or cubic meters of gas per metal mass (m^3/kg). The source [32] involves typical values of k for confined nozzle designs.

Models of Gas Atomization

Superheated metal melts may be considered as Newtonian fluids; in this connection, their interaction with a gas jet is expressed by criterial dependences. The most empirical formulations for definition of an average particle size in real atomization systems use the aerodynamic Weber number:

$$We = \frac{\rho_g v_g^2 d_0}{\sigma_m}$$

This criterion represents the balance of the break-up force, related to gas kinetic energy through the gas density, ρ_g, and v_g^2, that is resisted by melt surface tension, σ_m, acting over a specific melt stream diameter, d_o.

Generally in each model of droplet formation, a stability criterion involves the Weber number of the liquid metal. The first attempt to develop a model of a three-step droplet formation process seems to have been made by Dombrowski and Johns [42]. Proposed mechanisms of droplet formation involve:

- The initiation of a sinuous wave that rapidly increases in amplitude.
- Detachment of the wave from the layer of the liquid to became a ligament whose dimensions depend on the wave length λ at disintegration on wave number k_w (i.e., $2\pi/k_w$).
- Breakdown of ligaments into droplets (Fig. 4.32).

In Bradley's mathematical model, known as the capillary wave model [43, 44], the liquid is considered to be a horizontal infinitely deep phase, initially unmoving and being swept by a compressible gas phase with a uniform velocity parallel to the liquid surface. The Rayleigh instability was invoked for the break up of the ligament into spherical drops. In the first stage of the atomization process, the critical wave number k_{max} with the fastest-growing amplitude is determined from the quadratic equation in k and includes a dependence on the kinematic viscosity of the liquid, the densities of the gas and liquid phases, the liquid/gas interfacial energy that opposes the growth of the wave, and the Mach number M of the atomizing gas.

In the second stage of atomization, Bradley suggested that the ligament diameter D is related to the wavelength λ_{max}, that is, $2\pi/k_{max}$ by linear dependence:

$$D = \varepsilon\lambda_{max} = \frac{2\pi\varepsilon}{k_{max}}$$

where the parameter ε (of the order of 0.25) was defined in earlier studies on the air atomization of water.

The resultant droplet diameter δ is expressed as:

$$\delta = \frac{2.95\sigma_m}{L\rho_g v_g^2}$$

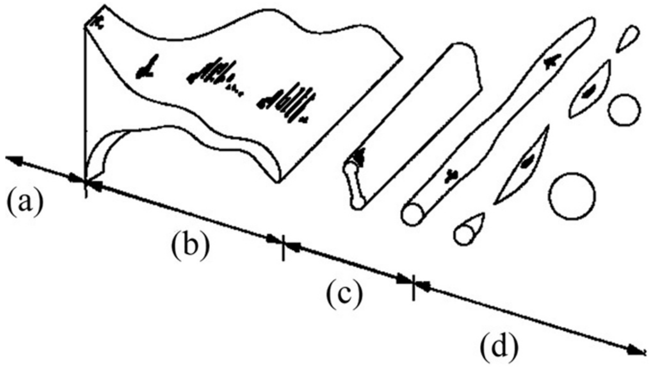

FIG. 4.32 Model for the disintegration of a liquid sheet by a high velocity jet of gas: (a) stable sheet; (b) growth of waves in sheet; (c) ligament formation; (d) ligament breakdown.

where σ_m is the liquid surface tension (N/m), ρ_g is the density of the gas (kg/m^3), v_g is the sonic gas velocity (m/s), L is a dimensionless parameter, the function of the Mach number M and knowing the value of M during gas atomization; and L can be defined by [45].

A comparison of the experimental data of See and Johnston to Bradley's predictions for the nitrogen atomization of lead sees that the model gives agreement approximately within a factor of 2 [46]. As at present design, Bradley's model does not give any indication of the origin of the spread in powder production by gas atomization.

The other often-cited models are the capillary and acceleration wave models of Ingebo [47]. Here, the Reynolds number is an important part of the Ingebo expressions for both capillary and acceleration wave break up. The Reynolds number

$$Re_L = \frac{\rho_L (v_g - v_L)^2 d_0}{\mu_L}$$

contains the dimensionless balance of gas kinetic energy through $(v_g - v_L)^2$, as related to the dynamic viscosity, μ_L, in the melt with a density, ρ_L, in the melt stream diameter, d_o.

The resulting Ingebo equation is:

$$\frac{d_0}{\delta_m} = c_0 (WeRe_L)^m$$

where c_0 and m are adjustable constants; for area $WeRe_L > 10^6$ $c_0 = 0.027$ and $m = 0.4$, then

$$\delta_m = 37 d_0 [WeRe]^{-0.4}$$

A modified capillary wave model in melt atomization was applied in several works [48, 49]. Ternovoy with colleagues [48] considered the atomization of a free melt stream by an annular gas jet with a hollow cone of metal formation. The instability wavelength λ_f with the fastest growing amplitude in the metal film was defined in accordance with [16]

$$\lambda_f = \frac{1.5\gamma}{\rho_g v_g^2}$$

where γ is the specific surface energy of a melt, ρ_g is the gas density, and v_g is the gas velocity at the exit of the melt nozzle.

The droplet formation is considered as a break up of the melt microjets by instability wavelength $\lambda_{\mu j}$ with the fastest-growing amplitude in metal microjets and is described in accordance with [16] by the expression:

$$\lambda_{\mu j} \approx 4\pi \left(\frac{\nu_m^2 \rho_m \delta_{\mu j}^3}{8\gamma} \right)^{1/4}$$

where ν_m is the kinematic viscosity of a melt, ρ_m is the melt density, and $\delta_{\mu j}$ is the diameter of the microjet.

The resulting semiempirical formula for the droplet diameter definition is:

$$\delta_m = \frac{1.88 \nu_m^{0.4} \rho_m^{0.2} d_m^{1.26}}{\gamma^{0.026} \rho_g^{0.17} R_{tr}^{0.63} v_g^{0.34}} \left(\frac{gh\rho_m + \Delta p}{gh\rho_m - 2\Delta p} \right) \left(\frac{G_m}{G_g} \right)^{0.3}$$

where d_m is the melt jet diameter at the exit of the melt nozzle, R_{tr} is the film opening radius in the position of toroidal thickening on its periphery, g is the acceleration of gravity, h is the melt height in the tundish, Δp is the pressure differential between the furnace chamber and the exit of the melt nozzle, G_m is the melt mass flow, and G_g is the gas mass flow.

More recently, improved flow visualization techniques used to study melt atomization dynamics do not confirm the formation of a film hollow cone in the conditions of atomization of a free melt stream by an annular gas jet [50]. Through that, the authors [49] obtained the tolerable convergence of median particle size values calculated on the suggested formula with measures for argon or argon/helium mixture atomization by a confined jet.

The pressure-swirl atomization principle allows forming the film metal hollow cone, as shown in Fig. 4.29. Here, a conical film of melt created by the pressure swirl nozzle and shaped by centrifugal forces is atomized by high-velocity gas jets. The physical model of such a combined atomization process was represented in the work [51]. These are considered the stages of the atomization process (Fig. 4.33):

1. Transmission of an instability wave in a film across and along the velocity vector owing to oscillation processes caused by external and internal factors. The instability wavelength λ_f with the fastest growing amplitude in a metal film was introduced in accordance with Ref. [16]. Depending on the physical properties of the liquid and gas, two schemes are suggested: a thickening of a film in toroidal form in accordance with the wavelength (Fig. 4.33A) and when a film is just bending (Fig. 4.33B).
2. Formation of a liquid torus on the peripherals of a film as a result of transmission of a longitudinal wave with the fastest growing amplitude.
3. Transmission of the instability of the toroidal peripheral area.
4. All previous stages coincide with the above-described model [49] while the final stage differs because it consists of secondary atomization of previously broken-up film ligaments (torus or drops in dependence on atomization conditions) under the action of a high gas pressure jet.

The thin film represents a surface for efficient disintegration in order to achieve fine particle sizes and narrow size distribution using low specific gas consumption.

On the basis of this model, a formula for the definition of particle diameter was suggested:

$$\delta = k\varphi^{0.46}\frac{\nu_m^{0.17}\rho_m^{0.08}\sigma^{0.38}d^{0.92}}{R_f^{0.46}\rho_g^{0.46}v_g^{0.92}} \tag{4.12}$$

where k is the coefficient of the nozzle geometry; φ is the unfilled coefficient for the melt nozzle orifice of d diameter; ν_m is the kinematic viscosity of a melt; ρ_m is the density of a melt; σ is the surface tension of the melt; R_f is the radius of the film at the point of break up; and ρ_g and v_g are the density and velocity of a gas stimulating the film atomization.

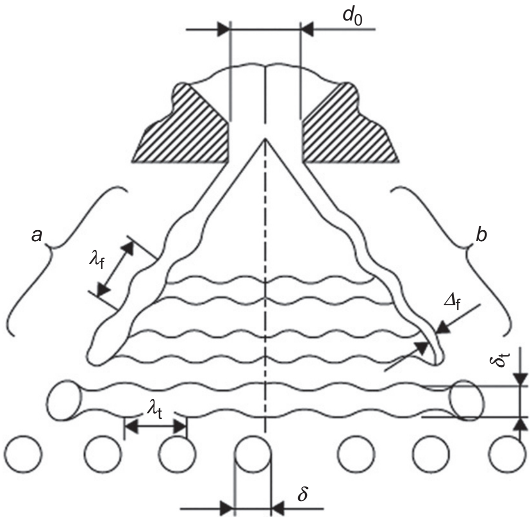

FIG. 4.33 Model of the pressure-swirl atomization process: d_0 is the melt metal nozzle orifice diameter, Δ_f is the film thickness in zone of impingement with secondary atomization gas jet, δ_t is the diameter of max torus cross section in zone of impingement with secondary atomization gas jet, λ_f is the wavelength of film instability, λ_t is the wavelength of in liquid torus, and δ is the atomized particle diameter. *Lagutkin S, Uhlenwinkel V, Achelis L, Pulbere S, Sheikhaliev S. Centrifugal—gas atomization: preliminary investigation of the method. In: Proceedings PM 2004 World Congress. Wien, Austria: EPMA; 2004. p. 71–6.*

TABLE 4.3 Tin Powder Properties Produced by Means of the Pressure-Swirl Atomization Process.

Oxygen Content in the Atomization Chamber (ppm)	Melt Temperature (K)	Melt Pressure (MPa)	Melt Flow Rate (kg/h)	Gas Pressure (MPa)	Gas Flow Rate (m^3/kg)	Mass Median Diameter (μm)	Standard Deviation (δ_{84}/δ_{50})
<100	563	0.7	180	0.7	109	33.5	1.85
100	563	0.7	180	0.7	109	22.8	1.6
300	563	0.7	180	0.7	109	22.1	1.6
500	563	0.7	180	0.7	109	24.6	1.6

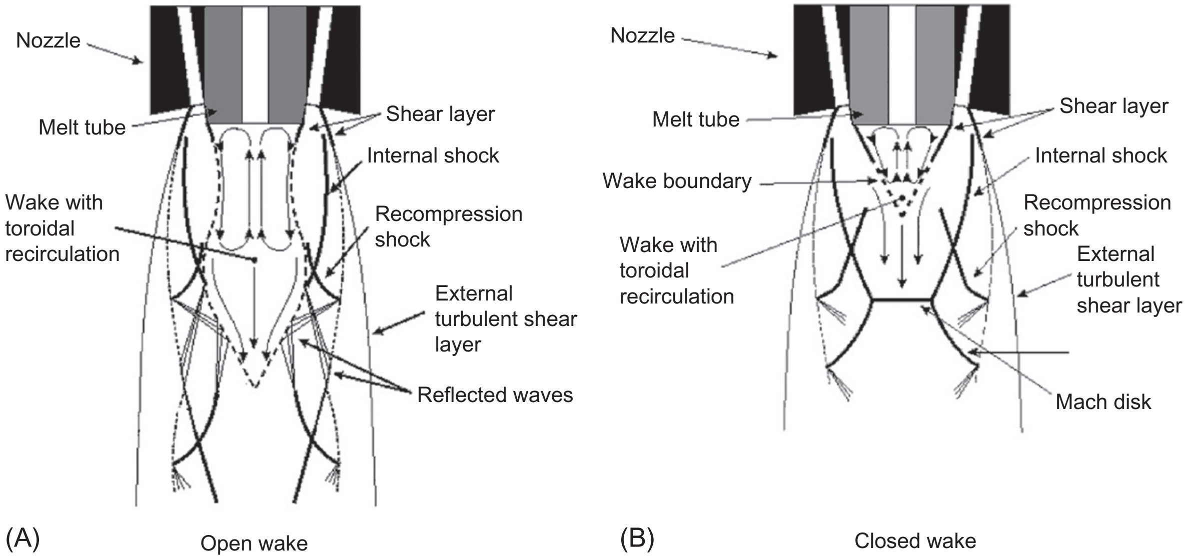
Nozzle
Melt tube
Shear layer
Internal shock
Wake with toroidal recirculation
Recompression shock
External turbulent shear layer
Reflected waves
(A)
Open wake
Nozzle
Melt tube
Shear layer
Internal shock
Wake boundary
Recompression shock
Wake with toroidal recirculation
External turbulent shear layer
Mach disk
(B)
Closed wake

FIG. 4.34 Schematic of (A), open-wake and, (B) closed-wake gas flow patterns in close-coupled gas atomization. *Anderson IE, Terpsta RI, Figliola R. Gas recirculation flow in the melt feeding zone of a close-coupled gas atomization nozzle: modelling and measurement. In: Proceedings of 2nd international conference on spray deposition and melt atomization, vol. 2. Bremen: Bremen Universität; 2003. p. 19–30.*

The estimation of the mass median diameter, offered by Eq. (4.12), shows sufficient comparability between the calculated and experimental values for tin, tin-lead solder (61Sn-39Pb), and copper alloy (Cu-15Sn-5Pb-4Ni) in experiments by gas/metal ratio values in the range from 0.15 to 0.35 m^3/kg [51]. An effect of oxygen content on powder properties was revealed (Table 4.3).

Traditionally, gas atomization by means of close-coupled nozzles is believed to involve the formation of a melt film at the nozzle edge [35], as shown in Fig. 4.27A. Fine particles are thought to form as a result of the primary breakup of the melt film upon its interaction with the supersonic gas flow at the nozzle edge. Further, even if low melt flow conditions that favor filming are used, it has been suggested that secondary breakup still plays an important role in determining particle size.

More recently, a microsecond-exposure spark schlieren technique allow us to visualize the melt atomization process along with the atomizing gas flow features, providing a look at the fluid dynamic interactions during atomization [50]. These experiments indicated more complex atomization behavior, including a primary breakup stage close to the nozzle tip followed by a finer secondary breakup stage where the coarse droplets are disintegrated under high shear into fine powder. Therefore, several authors [52, 53] have discussed the apparent dominance of secondary atomization and break-up mechanisms in most studies of close-coupled gas atomization.

The increased understanding of the atomization process shows new ways to approach the problem of particle size control and atomization efficiency. In this connection, in close-coupled gas atomization there is considered a description of the two gas flow situations that are termed the open wake condition [53, 54], as shown in Fig. 4.34A, and the closed wake condition in Fig. 4.34B. Where the sketches are of a central cross-section and may apply to either a discrete jet nozzle ensemble or an annular slit nozzle with the same melt tube arrangement.

A more complicated gas flow situation has often been developed purposefully for the production of high yields of fine droplets where the shear wall gas flow is interrupted by a Mach shock disc. The Mach shock disc can appear during high-pressure operation of either an annular slit [54] or a discrete jet [55]. The wake closure effect and its associated Mach shock can present an additional kind of atomization energy coupling.

The pressure value on the liquid metal nozzle tip is an important parameter in close-coupled gas atomization. The pressure formation on the melt nozzle tip in dependence on gas pressure is shown in Fig. 4.35.

A pulsatile gas-atomization model based on the close-coupled atomization kinetics advances the understanding of the atomization process fundamentals [56–59]. The model reveals that melt flow rate is determined by the time-averaged stagnation pressure formed in front of the melt orifice. This stagnation front dictates the behavior of the melt exiting the melt orifice and how it interacts with the atomizing gas.

As illustrated in Figs. 4.34 and 4.35, the rapidly flowing gas passing around the melt tip can produce an overambient or subambient pressure region in front of the delivery tube orifice that is often known as the aspiration base pressure. Ting [59] reported that seven 22.7 kg batches of an Ni-based alloy were atomized. Prior to atomizing each batch, the gas-only aspiration profile of the atomizer nozzle was measured with a digital pressure transducer to determine the manifold pressure at which wake closure occurred. The aspiration measurements discovered the existence of an abrupt transition zone between open-wake and wake-closure conditions (Fig. 4.36). The tests indicated that this transition pressure, named the wake-closure pressure (hereafter known as WCP), developed around 4.93–4.95 MPa (715–718 psi).

For each atomization batch of the Ni-based alloys, the atomization gas pressure in the nozzle manifold was selectively tuned to atomize at pressures either above or below the WCP. Batches that were atomized below WCP had shallow gas-only aspiration of 0.25 atm. (3.7 psi) below atmosphere pressure while batches atomized above WCP had deep gas-only aspiration of 0.58 atm. (8.5 psi) below atmosphere. The atomization pressure was monitored, and the particle size distribution was vibratory screened and sonically sieved to obtain the particle size distribution above and below 45 μm, respectively.

The gas-to-melt ratio, atomizing pressure, median diameter δ_{50}, and standard deviations (δ_{84}/δ_{50}) are presented in Table 4.4. Produced powders in a close-wake regime showed considerably finer median δ_{50} particle size than those atomized at pressures below WCP (in open-wake condition). The median particle size from L1270 atomized at 0.017 MPa (3 psi) above WCP was 42% (or 26.5 μm) smaller than that of L1271 atomized at 0.034 MPa (5 psi) below WCP. The 60% longer gas atomization run time, associated with a slower average melt flow rate, resulted in the particle refinement in L1270. This atomization run had a 64% greater gas-to-metal ratio (GMR) than L1271 (Table 4.1). It was also interesting to note that atomizing at pressures above WCP showed a resulting mean average 23% improvement in particle size standard deviation ($^{\delta_{84}}/_{\delta_{50}}$) when compared to atomization below WCP, giving rise to a narrower particle size distribution. The observed particle yields above and below WCP in melt atomization are due to changes in the atomization gas dynamics when the melt is introduced.

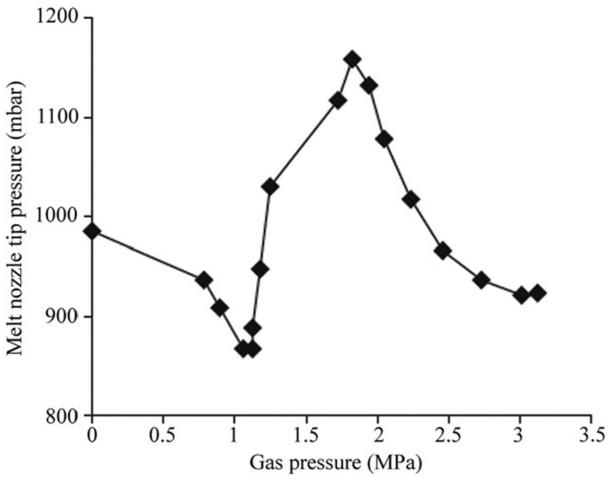

FIG. 4.35 The pressure formation on the melt nozzle tip in dependence on gas pressure in close-coupled slotted nozzle design (by the constant protrusion length 10 mm).

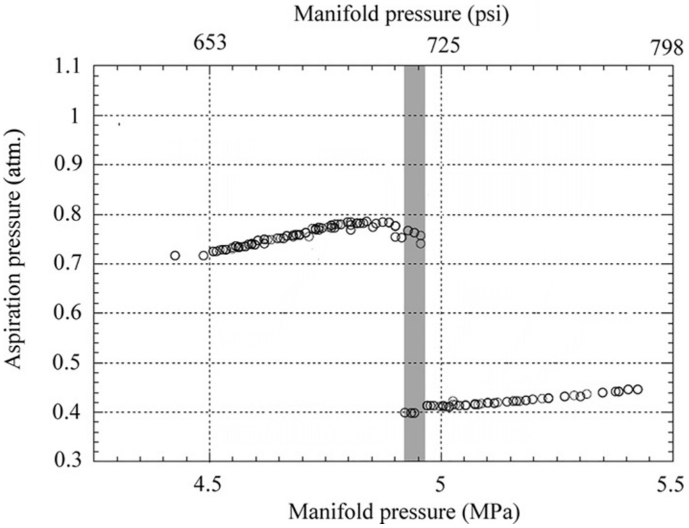

FIG. 4.36 Gas-only aspiration pressure measurements at the melt orifice. Shaded area shows the WCP location. *Reproduced with modification from Ting J. The close-coupled gas atomization: a quantitative analysis of the dynamic pressures of the pulsative atomization process. In: Compiled by Russell A, Chernenkoff W, Brian J. Proceedings of 2014 powder metallurgy world congress. Orlando, FL: Metal Powder Industries Federation; 2014: p. 02-76–84.*

TABLE 4.4 Atomization Parameters and Results for a Nickel-Based Alloy Produced Near the WCP

Batch Number	GMR	Atomizing Pressure (MPa)	δ_{50} (μm)	δ_{84}/δ_{50}
L 1267	1.77	4.48	68	3.16
L 1271	2.48	4.89	63.5	3.38
L 1270	4.06	4.96	37	2.61

The aspiration pressure being the force of the total recirculating gas flow on the melt discharge orifice area, the proposed model [57, 60] suggests that it is possible to determine a stagnation pressure in the wake front of the atomizer nozzle, hence providing a way to regulate the atomization process. According to this model, the majority of the gas masses enter the wake through the stagnation front and exit along the circumferential edge of the melt tip base. In Fig. 4.37A below WCP (in open-wake condition), the recirculating gas enters the wake via Point 1 (stagnation front) and exits the edge of the melt tip, as depicted. The turbulent boundary that separates the recirculation zone (inside) from the atomization gas stream (outside) has been identified as the "sonic line" [57]. In the two-phase flow interaction between the melt and the gas, the gas-only feature at below WCP creates the aspiration pressure that draws the melt into the wake, causing it to enlarge and allowing the stagnation pressure at Point 1 to quickly and easily be drawn to the melt orifice. The reverse gas flow against the melt orifice then temporarily arrests the melt flow (Fig. 4.37B). As the recirculation is devoid of melt, the aspiration pressure is formed once again to draw the melt down the tundish nozzle.

In the computational fluid dynamic study by Ting and Anderson [58], using the modeling, they showed that the stagnation pressure (Point 1) at the primary wake front was twice its magnitude before WCP (Fig. 4.37A) when compared to after WCP (Point 2) (Fig. 4.37C). Subsequently, the smaller new primary recirculation zone (above WCP) with the smaller stagnation pressure Point 2 generates a lower orifice pressure than that at Point 1 (below WCP). From the modeling [57, 59], two stagnation pressure points are formed downstream of the Mach disc (depicted as Points 3 and 4 in Fig. 4.37C). Above WCP, the magnitude of the stagnation pressure at Point 4 is 1.28 times greater than that at Point 1 below WCP. This is important because it is this stagnation pressure Point 4 that is the primary pressure that causes the melt to slow in above-WCP atomization, and making melt flow slower than in open-wake atomization.

In the two-fluid flow closed-wake condition, the melt flowing from the delivery tube orifice acts as a moving boundary that can disrupt the stability of the closed-wake structure by displacing the internal shock (Fig. 4.37C). In this state, the Mach disc vanishes (Fig. 4.37C) and the stagnation pressure from the secondary recirculation zone rushes into the "opened" primary recirculation zone, pushing upward against the melt orifice and temporarily arresting the melt flow. As the melt flow is indented in the pour tube and short halted by the strong upstream gas flow from stagnation Point 4 (Fig. 4.37E), the gas dynamic is the reestablishment of the Mach shock structures as the recirculation is devoid of melt. The deep aspiration

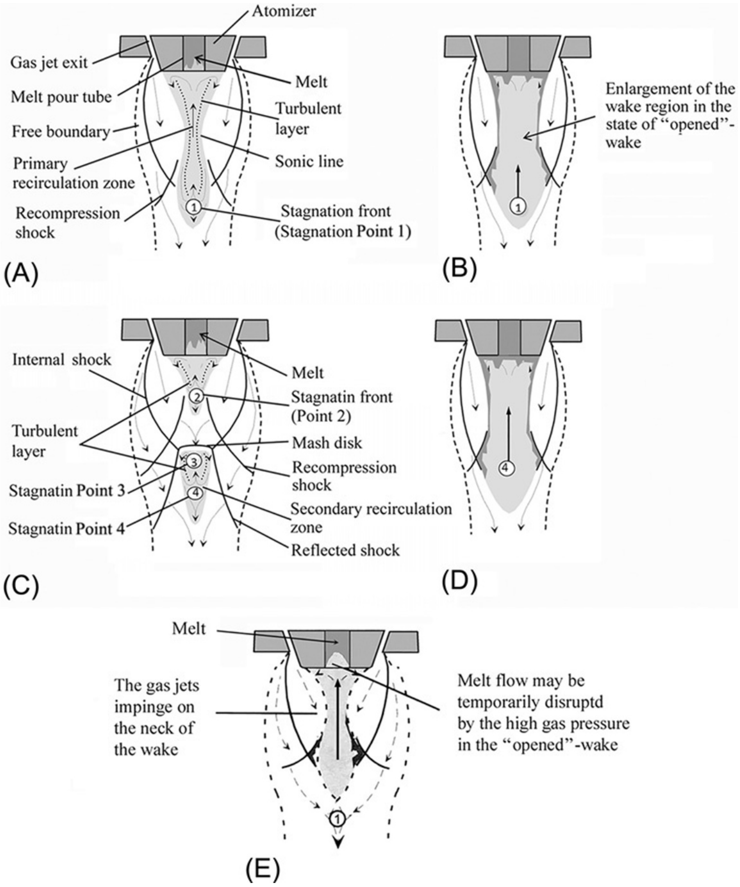
Atomizer
Gas jet exit
Melt pour tube
Free boundary
Primary recirculation zone
Recompression shock
Melt
Turbulent layer
Sonic line
Stagnation front (Stagnation Point 1)
1
(A)
Enlargement of the wake region in the state of "opened"-wake
1
(B)
Internal shock
Turbulent layer
Stagnatin Point 3
Stagnatin Point 4
Melt
Stagnatin front (Point 2)
Mash disk
Recompression shock
Secondary recirculation zone
Reflected shock
2
3
4
(C)
4
(D)
Melt
The gas jets impinge on the neck of the wake
Melt flow may be temporarily disruptd by the high gas pressure in the "opened"-wake
1
(E)

FIG. 4.37 The phase flow interaction by the pulsatile atomization model below (A, B) and above (C, D, E) WCP. *Reproduced with modification from Ting J, Peretti MW, Eisen WB. The effect of wake-closure phenomenon on gas atomization performance. Mat Sci Eng 2002;A326:110–21; Ting J. The close-coupled gas atomization: a quantitative analysis of the dynamic pressures of the pulsative atomization process. In: Compiled by Russell A, Chernenkoff W, Brian J. Proceedings of 2014 powder metallurgy world congress. Orlando, FL: Metal Powder Industries Federation; 2014: p. 02-76–84.*

pressure of the reestablished closed-wake condition strongly draws the melt down the ceramic pour tube to once again resume the melt flow (Fig. 4.37D). When operating at above WCP, this whole intermittent melt atomization process would repeat itself, pulsating between Fig. 4.37C and Fig. 4.37E. Thus, own domination the pulsatile atomization model had derived thanks to such atomization cyclicity.

It is necessary to note that the wake-closure phenomenon is highly sensitive to atomizer and melt pour tube geometry. It possesses a hysteresis-type aspiration behavior that suggests that there is an energy of formation associated with the wake-closure structure.

Rieken et al. [61] developed the enhanced closed-wake nozzle (named ECW) containing an interior ring of 30 jets with 0.74 mm diameter and a gas flow apex angle of 45 degrees equally spaced around 11.15 mm annulus, similar to the DJ-HPGA nozzle type [62]. It also contains an additional second concentric ring of 60 jets with 0.74 mm diameter and gas flow apex angle of 90 degrees equally spaced around a 21.92 mm annulus (Fig. 4.38). The ECW geometry was selected to create an identical gas flow focal point between the two rings of jets while the exterior ring of jets contains twice the cross-sectional area compared to the interior jets**.** The two rings of jets in the ECW nozzle are hermetically isolated (during operation) and supplied from independent gas manifolds, allowing significant experimental design flexibility (e.-g., independent manifold pressures and/or differing atomization gas types).

According to the work [61], three gas nozzle configurations were engineered and tested using a high temperature alloy to develop atomizer parameters to maximize powder yield in the 20–75 μm range. The comparison between close-coupled atomizers with close-wake and enhanced closed-wake nozzles showed the 20–70 μm fraction yield up to 68% and 74%, respectively.

Lampa and Fritsching [63] discussed the effect of spray parameters on the large-scale fluctuations of gas and droplets in confined sprays investigated experimentally and numerically. In numerical simulations, the relevant fluctuating scales have been resolved with large-eddy-simulation (LES) [64]. In the experimental part adopted from the work [65], twin-fluid nozzles in a confined environment have been analyzed with planar Particle-Image-Velocimetry (PIV) to yield the velocity of the gas and the discrete phase. The transient behavior of the spray process including the spray flow structures in

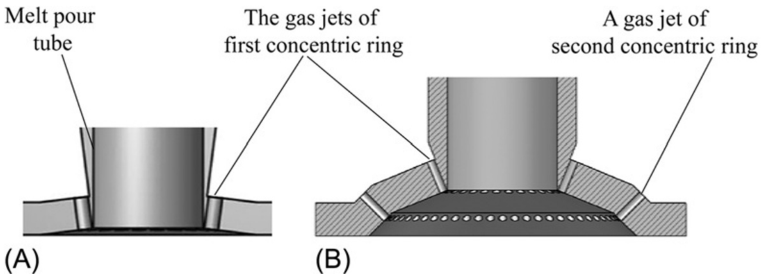
Melt pour tube
The gas jets of first concentric ring
A gas jet of second concentric ring
(A)
(B)

FIG. 4.38 Schematic representation of the two close-coupled atomizer gas nozzles: (A) closed-wake and (B) enhanced closed-wake (ECW).

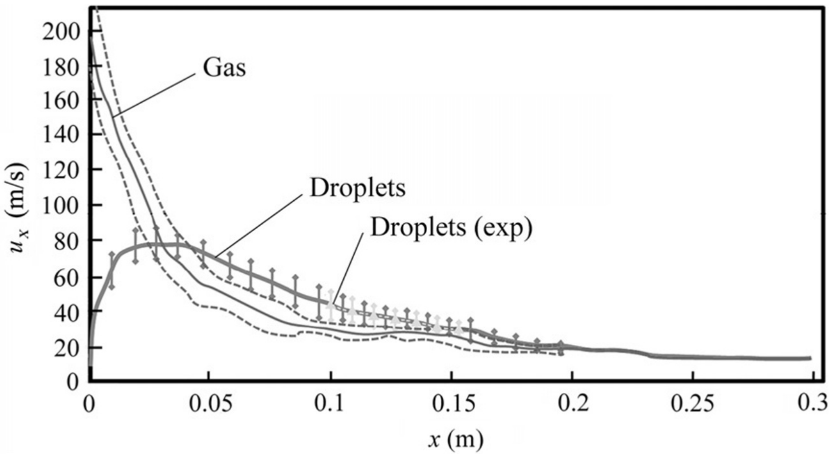

FIG. 4.39 Axial gas and droplet velocity on spray axis (LES) and validation with experimental droplet velocity (PIV, $p=0.5$ MPa). The *error bars* and *dashed lines* indicate the upper and lower RMS values of the velocity component. *Reproduced with modification from Lampa A, Fritsching U. Spray structure and propagation in confined atomization processes. In: Uhlenvinkel V, Fritsching U, Ellendt, Mädler, editors. Proceedings of 5th international conference on spray of spray deposition and melt atomization. Bremen, Germany: Universität Bremen; 2013. p. 1–14.*

dependency from the spray chamber design was discovered by LESs. For the validation of the LES spray simulation, the numerical results have been compared with PIV measurements in the distance range 100–157 mm in the stream-wise direction. The distribution of axial gas and droplet velocity on the spray axis (LES) and experimental droplet velocity (PIV) presented in Fig. 4.39 shows in principle good agreement with the measured data, through the authors reported [63] that generally the mean absolute droplet velocity is higher than the mean absolute gas velocity in this region of the spray.

Studies based on water-spray modeling of the close-coupled atomization [66] showed that a combination of gas pressure, nozzle insert angles, and extension can lead to melt film back flow, a so called "lick back." Fig. 4.40 is a schematic of the cross-section of an annulus-type nozzle showing the normal path for the melt and the melt path taken that defines full lick back situations. As mentioned above, lick back can appear as a result of atomizer design features. Other factors may also lead to lick back, such as gas pressure regime, surface tension of the melt, and the melt reaction with the insert's surface. If the melt makes contact with the inner annulus, the nozzle will be destroyed.

Strauss [66] reported the study of nozzles with a three-nozzle tip angle (Fig. 4.41) and at two atomization pressure levels (arbitrarily low and high). Additional tests were performed with the insert recessed and protruding from its normal placement in the atomization nozzle.

Fig. 4.42 shows three typical atomization conditions: (a) partial, (b) total, and (c) and without lick back. In the case of the matched angle configuration, the low-pressure level shows total lick back. The high-pressure level shows partial lick back. In this case, increasing the pressure decreases the extent of lick back. When the nozzle jet angle is less than the nozzle insert angle, total lick back is at both pressure levels. In the case where the nozzle jet angle is greater than that of the insert, lick back does not occur at the low-pressure level and only partial lick back occurs at the high-pressure level. Among the compared nozzle insert placements, the atomization nozzle with a greater angle in a protruding placement appeared more preferable.

Outside the design of the attributes of the atomization nozzle and nozzle insert, there are other factors that may lead to or cause lick back. Along with the gas pressure, the surface tension effect may be related to another extrinsic factor connected to the lick back occurrence. Strauss also reported [66] the tests using water, acetone, and isopropyl alcohol as the atomized fluid by pressure ramped slowly to determine the onset pressure of lick back. These tests showed that the onset of lick back occurred 0.1 MPa (~15 psi) lower in pressure for acetone and isopropyl alcohol than for water. The surface tensions of these fluids are 5–20 times lower than those of molten metals. On the basis of surface tension dependence data from varied

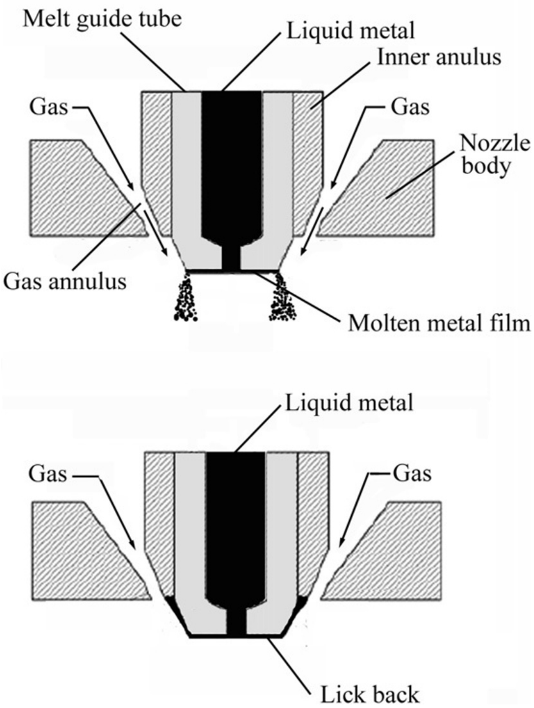
Melt guide tube
Liquid metal
Inner anulus
Gas
Gas
Nozzle body
Gas annulus
Molten metal film
Liquid metal
Gas
Gas
Lick back

FIG. 4.40 Molten metal film formation for normal and lick back modes.

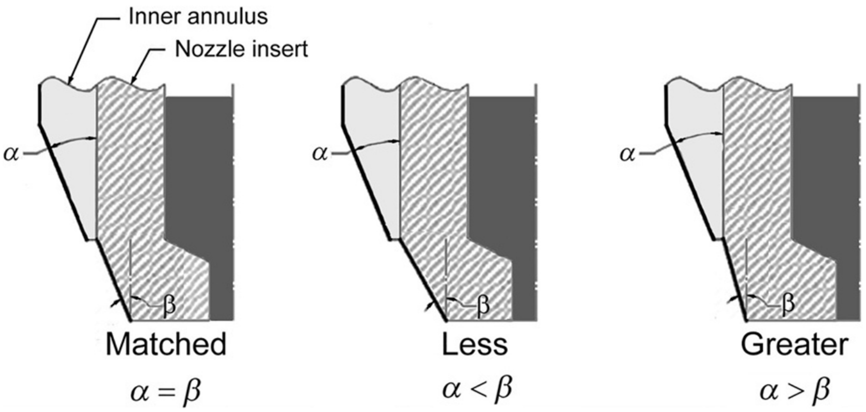
Inner annulus
Nozzle insert
α
β
Matched
$\alpha = \beta$
α
β
Less
$\alpha < \beta$
α
β
Greater
$\alpha > \beta$

FIG. 4.41 Schematic of the angle matching between the nozzle jet and nozzle insert.

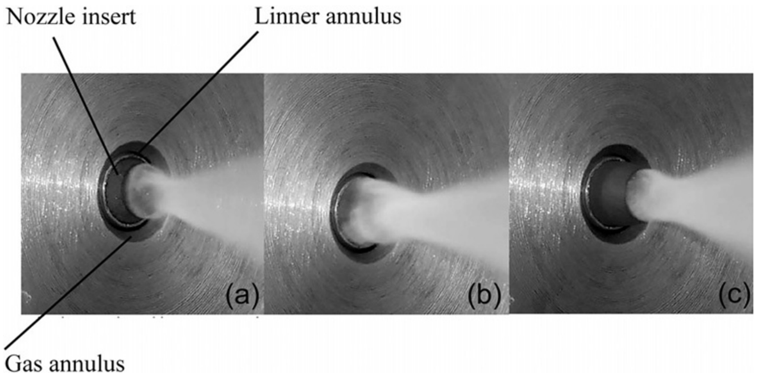
Nozzle insert
Linner annulus
Gas annulus
(a)
(b)
(c)

FIG. 4.42 Configuration of atomization plume: (A) the angles of the nozzle jet and nozzle insert are matched, at high pressure; (B) the angle of the nozzle jet is less than the insert angle, at high gas pressure; (C) the angle of the nozzle jet is greater than the insert angle, the nozzle is in a protruding placement, at low gas pressure. *Reproduced with modification from Strauss JT. Lick back in close-coupled atomization: a phenomenological study. In: Compiled by Russell A. Chernenkoff W, Brian J. Proceedings of 2014 Powder Metallurgy World Congress, Orlando, FL: Metal Powder Industries Federation; 2014: p. 02-38–45.*

factors, the author concluded that, while surface tension may not be the primary driving force for lick back, it is certainly plausible that it can affect the occurrence of lick back. Slight changes in alloys, insert materials, impurities, and oxygen content may possibly be enough to cause lick back that is otherwise simply explained by random occurrences.

In the paper [67], Mullis and Dunkley discussed using acoustic techniques [68, 69] for study of the pulsation phenomena during close-coupled gas atomization of a metal melt. The gas atomizer studied uses a gas delivery nozzle of the annular slit type with the melt delivery nozzle having an included apex angle of 30 degrees, a tip diameter of 9 mm, and a central bore for the melt feed of 5 mm. The atomizer was operating with nitrogen gas at a gas inlet pressure of 2.4 MPa. The melt and gas flow rates were 0.25 and 0.35 kg/s, respectively, and a typical batch atomization takes about 15 min, wherein some 200 kg of metal was atomized. During the run recorded, the gas was preheated to an inlet temperature of 673 K, wherein the jet exit temperature upon ideal expansion will be 190 K. made an audio recording during gas atomization.

The authors found that there is strong absorption of frequencies in the 1–8 kHz range. These frequencies are characteristic of the resonance of droplets with 150–600 μm diameters and may be indicative of the dynamics of the initial breakup of melt ligaments. During atomization, it was found that there are considerable low frequency (<30 Hz) fluctuations in the intensity of the acoustic emissions. In the judgment of the authors, this may be related to atomizer pulsation and the quasiperiodic low-frequency variation in the melt volume instantaneously at the atomizer tip (see Fig. 4.37).

According to Ref. [67], in contrast with high speed imaging, acoustic recording is inexpensive and can be set up at a distance of about 1 m from the atomizer without the need for direct line-of-sight of the melt plume. Moreover, the equipment is much more robust than precision optics, needs no careful alignment, and produces a data stream of a size that would make real-time processing feasible.

Gas-Atomized Powders

Particle Size, Size Distribution, Shape, and Surface Morphology

There is a comprehensive literature base on gas atomization in terms of the effect of operating conditions on powder properties [6, 15, 70, 71].

One of the most important single parameters controlling particle size in gas atomization is specific gas consumption. It can be expressed as a mass ratio of gas-to-metal flow or as the ratio of gas volume to metal mass. Data for several metals and alloys conform to an equation of the form:

$$\delta_{\mathrm{m}} = KF^{-1/2}$$

where K is a constant and F is the specific gas consumption in m^3/kg. The value of K is a function of nozzle design and alloy properties [15].

Specific gas consumption is also an important process parameter in controlling δ_{m} in ultrasonic gas atomization [46, 72]. For an aluminum alloy at a fixed atomizing gas pressure, median diameter value can be varied from ~250 to below 50 μm when the mass flow ratio of gas to metal increases from 0.3 to 2.0. A decrease in δ_{m} is also predicted with increasing gas pressure.

Gas-atomized powders generally have a lognormal size distribution with standard deviation normally around $\sigma = 2.0 \pm 0.3$. The values of σ generally decrease as δ_{m} decreases and most data show an empirical relation of the form [70, 73]:

$$\sigma = a\delta_{\mathrm{m}}^{b}$$

where a and b are constants.

Lubanska [73], by comparing the literature on gas-atomized metal powders and by using a relationship developed by Wigg [74], derived an empirical equation for the average particle size (δ_{m}). In dimensionless form, Lubanska's formula is:

$$\frac{\delta_{\mathrm{m}}}{d_0} = K\left[\frac{\nu_{\mathrm{m}}}{\nu_{\mathrm{g}}}\frac{1}{We}\left(1 + \frac{M}{A}\right)\right]^{1/2} \tag{4.13}$$

where We is the Weber number; δ_{m} is the mass median particle diameter; d_0 is the diameter of the metal stream; ν_{m} is the kinematic viscosity of liquid metal; ν_{g} is the kinematic viscosity of the atomizing medium; M/A is the ratio of gas-to-metal mass flow rates; and K is a constant.

Data from the source [73] for various metals are depicted graphically on a log/log scale in Fig. 4.43 and show consistent agreement with experimental data.

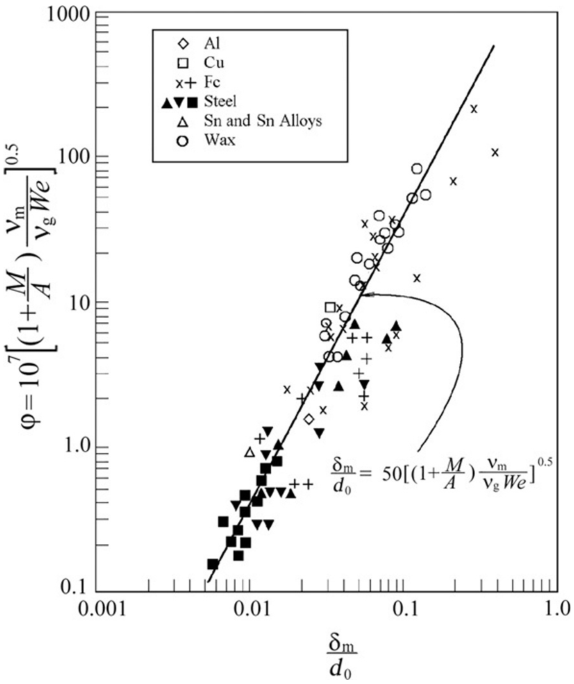

FIG. 4.43 Lubanska correlation (Eq. 4.13) for air atomization.

Various other empirical equations have been published. Miller and Giles [13] have analyzed the atomization of a variety of metals and concluded that acceleration wave break up predominates at a high gas velocity. They define a modified Weber number and correlate it to material properties and the ratio of gas-to-metal mass flow rates. The functional (dimensionless) form of relation was obtained from experiments.

Some empirical relationships can be transformed in terms of physical models for droplet formation. That referred to as maximum stability criterion, for instance, gives maximum drop size as a function of surface tension of the liquid metal (σ), gas density (ρ_g), and velocity (v) of the atomizing medium as:

$$\delta_{\text{crit}} = \frac{\sigma}{\rho_g v^2}$$

This equation applies to the breakup of ligaments [46]. Secondary disintegration into particles smaller than δ_{crit} occurs only if the dynamic pressure due to the gas stream velocity exceeds the restarting force of surface tension. Owing primarily to the higher surface tension of liquid metals, energy requirements and, therefore, gas pressures used for atomizing metals is typically between 0.35 and 2.75 MPa.

Similar to water atomization, commercial gas-atomization units exhibit nonuniform operating characteristics. Proprietary empirical relations have been established between operating conditions, material properties, and powder characteristics, in particular median particle size and standard deviation. Beddov [75] has annotated several of these empirical relations for gas atomization.

The majority of inert gas-atomized powders are spherical or nearly spherical in shape. However, in reality, "satelliting" may be formed when small particles are attached to larger particles (Fig. 4.44). Their collision probability is increased with small particle yield growth and/or by the circulation of gas within the atomizing chamber that lifts finer particles back into the spray plume, where they collide with larger, still partly molten particles [76].

In the absence of impurity effects and surface oxide films, particle shape is controlled by the relative magnitudes of the times for solidification and spheroidization, provided the residence time of the particle in the suspended solid state in the gas is greater than either of these times. Models of both phenomena are given in Ref. [77].

In the model for solidification time in gas atomization, it was assumed that the molten droplets did not undercool, that the relative velocity between the gas phase and the particle is constant, and that convective heat transfer is dominant. Then, the total solidification time τ_{sol} (in seconds) [46, 77] is expressed by:

$$\tau_{\text{sol}} = \frac{\delta_m \rho_m}{6h_g}\left[\left(c_p\right)_m \ln\left(\frac{t_{\text{in}} - t_g}{t_m - t_g}\right) + \left(\frac{\Delta H_m}{t_m - t_g}\right)\right]$$

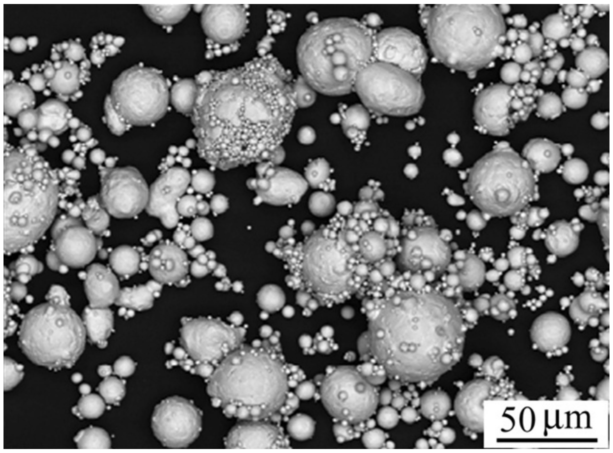

FIG. 4.44 Argon gas atomized Cu-10Sn alloy.

where δ_m is the mass median particle diameter (m); h_g is the convective heat transfer coefficient of the gas (W/(m^2 K)); ρ_m is the density of the liquid metal (kg/m^3); $(c_p)_m$ is the heat capacity of the liquid metal (J/(kg K)); t_{in} is the initial temperature of the particle (K); t_g is the gas temperature (K); t_m is the melting point of the metal/liquidus temperature for alloys (K); and ΔH_m is the latent heat of fusion of the metal (J/kg).

The value of h_g is given by:

$$h_g = \frac{k_g}{\delta_m}\left(2.0 + 0.6Re^{0.5}Pr^{0.33}\right)$$

where k_g is the thermal conductivity of the gas (W/(m K)); Re is the Reynolds number relative to the particle; and Pr is the Prandtl number for the gas.

Under the influence of surface tension forces alone, the time for spheroidization τ_{sph} is expressed by:

$$\tau_{sph} = \frac{3\pi^2\mu_m}{4V\sigma_m}\left(r^4 - r_{tr}^4\right) \tag{4.14}$$

where μ_m is the dynamic viscosity of the liquid metal (Pa s); V is the particle volume (m^3); σ_m is the surface tension of the liquid metal (N/m); r is the radius of the spheroidized droplet (m); and r_{tr} is the metal liquid trickle radius before transformation to spherical droplets (m).

A more detailed and general model to estimate the time for spheroidization of a droplet has been given by Rao and Tallmadge [78]. Lawley [13] notes that their predicted spheroidization times are not significantly different from those given by Eq. (4.14).

Based on these models, See and Johnston [46] have calculated the times for spheroidization and solidification of a range of droplet sizes (149–420 μm) for tin. Spheroidization times ($<2\times10^{-5}$ s) are several orders of magnitude lower than the times required for solidification so that only spherical particles should be produced in gas atomization, if there are no factors that hinder this transformation. The presence of ligament-shaped particles of Sn, particularly at small particle size fractions, is attributed to the presence of an oxide layer (SnO_2) that opposes the action of the surface tension.

The surface of gas-atomized powders is generally smooth. The particle surfaces frequently exhibit a cellular or dendritic morphology, subject to cooling rate during solidification of the droplets. When reactive elements are prealloyed with the base elements, some surface oxidation can occur during gas atomization.

The spherical shape and smooth surface inhibit the development of green strength in cold compaction. In addition, prealloying before atomization increases particle hardness and strength, which reduces compressibility. These inherent limitations of gas-atomized powders have stimulated development of elevated temperature consolidation processes to achieve high density; examples include hot extrusion and hot pressing. A change in particle shape toward nonsphericity is possible by means of an increase of cooling rate via decreased particle size. There is also the possibility of adding elements that alter the surface tension values (Li, Mg, Si, Ca, Mn, etc.).

The relatively high cooling rates intrinsic to gas atomization result in fine-scale microstructures. In NiAl and Ni_3Al powders, sonic gas atomized using nitrogen either dendritic or equiaxed structures depending on the particle size and consequently on the cooling rate were disclosed [79]. The $Al_{82}Ni_{10}Y_8$ alloy powder produced at a close-coupled nozzle

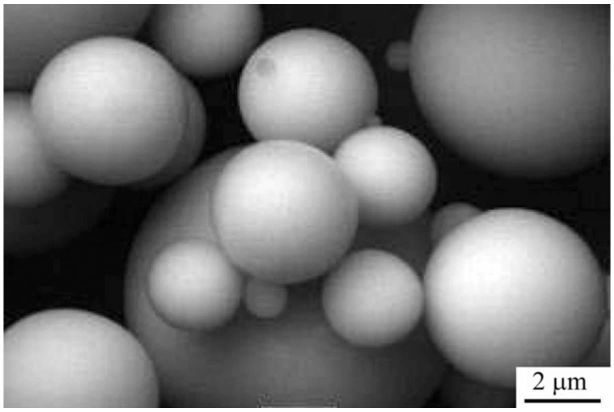

FIG. 4.45 Surface morphology of $Al_{82}Ni_{10}Y_8$ alloy powder with particle diameter below 15 μm. *Liu Y, Guo Sh, Huang B, Liu Z, Du Y. Densification behaviour of Al-Ni-Y powder containing amorphous and nanocrystalline phases. In: Proceedings PM2004 world congress, vol. 1. Wien, Austria: European Powder Metallurgy Association; 2004. p. 425–30.*

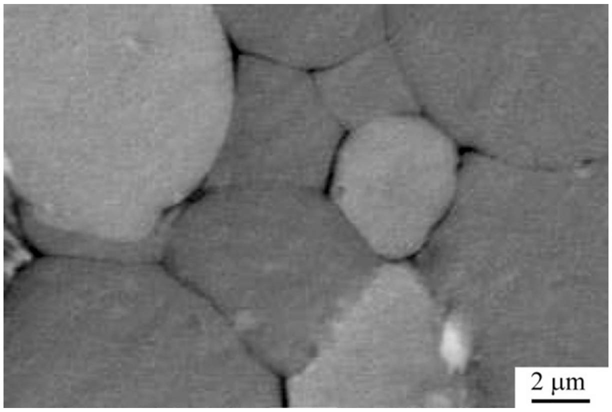

FIG. 4.46 SEM microstructure of $Al_{82}Ni_{10}Y_8$ alloy powder with particle diameter below 15 μm. *Liu Y, Guo Sh, Huang B, Liu Z, Du Y. Densification behaviour of Al-Ni-Y powder containing amorphous and nanocrystalline phases. In: Proceedings PM2004 world congress, vol. 1. Wien, Austria: European Powder Metallurgy Association; 2004. p. 425–30.*

atomizer unit at 3.03 MPa argon jet pressure has perfectly spherical and smooth particles (Fig. 4.45). In particles of several micrometers, the dendritic and cellular microstructures were not detected and they tend to be amorphous (Fig. 4.46).

Internal pores can be present in gas-atomized powder and may be detrimental in several respects. The effect of closed porosity leads to reduced apparent density, causes gas bubbling in thermal spray deposits, and gives rise to uncontrolled dimensional change during sintering. Internal pores are of the most concern in superalloy powders atomized with argon. The argon in the pores is insoluble in the alloy and this gives rise to the phenomenon of thermally induced porosity following densification by hot isostatic pressing with an attendant decrease in mechanical properties. From the study [80], it is concluded that internal closed porosity is a common phenomenon in gas atomization and that its extent increases with increasing particle size. A major source of internal porosity is gas entrapment, especially when the gas is insoluble in the solid powder particles.

Powder Cleanliness

Impurity control is of paramount importance for high-performance applications. Powder cleanliness is a major concern with atomized speciality alloys. These alloys are frequently used in applications with exacting combinations of strength, ductility, toughness, and fatigue resistance. In these conditions, there are nonmetallic inclusions in the powder that limit performance when the powder is consolidated. Inclusions may be introduced during melting and inert gas atomization; their source is the refractory tundish or pouring nozzle used in conventional gas atomization. The inclusions act as sites of stress concentration and can result in the initiation of fatigue cracks. This effect is of prime concern in components for aircraft engine applications.

Using a practicable induction melting technique, it is possible to closely replicate the composition of the melt stock in the resulting gas-atomized powder. Thus, speciality alloys based on aluminum, copper, nickel, cobalt, and titanium can be gas atomized to exacting compositional specifications. A partial loss of elements with a high vapor pressure or reactive elements can be quantitatively compensated for during melting prior to atomization. Primary sources of intermediate impurities are initial charge impurities, the melting atmosphere, the atomizing gas, and refractory ceramics (crucible, tundish, and tundish nozzle). In the case of the most critical superalloys, a bottom-pouring electroslag remelting furnace that discharges using a ceramic-free pouring nozzle to minimize all possibility of inclusion capture [81] has been developed. In the EIGA (Electrode Induction Melting Gas Atomization) process [82], prealloyed rods as an electrode are inductively melted without crucible. The metal liquid droplets from the electrode fall into atomization nozzle design and are atomized with inert gas jet. The EIGA process was used for titanium and niobium alloy powder production [83] and can also be applied to other alloys. Process developments in the EIGA technique [84] allow this process to be realized crucible- and ceramic-free, with larger electrode diameters up to 61 mm and increased melt flow rates of 26.4 kg/h. The optimized technique was applied for the atomization of pure Ti, Ti-6Al-7Nb, and gamma- TiAl based Ti-46Al-9Nb alloy powders. The oxygen level of the Ti-6Al-7Nb rod was about 1800 ppm; for the argon atomized powder, fraction <20 μm, the oxygen content increases to 2300 ppm. The TiAl rod had an oxygen level of 560 ppm; for powder fraction 63–90 μm, this level was maintained.

The control of the interstitial level is very important, particularly in titanium alloys, titanium aluminides, and beryllium. The control of interstitial levels in titanium alloys and aluminides is particularly important because ductility is very sensitive to carbon, oxygen, nitrogen, and hydrogen impurities. Typical interstitial impurity contents of gas-atomized gamma titanium aluminide, alpha two titanium aluminide, and alpha titanium alloy powders are given by Lawley [13] and Yolton [85]. There is, in the main, no increase in carbon, nitrogen, and hydrogen over the starting material during atomization. The increase in oxygen content from the starting material to the <500 μm powder is typically 200 ppm [46, 85]. Nitrogen content appears to be independent of particle size but the oxygen content shows an increase from 800 ppm in <500 μm powder to 1020 ppm in <45 μm powder due to the large increase in surface area. In helium-atomized beryllium powder, it is possible to keep the oxide content to a relatively low level [13, 86].

Other Gas-Atomization Methods

Internal Mixing Nozzles

In an internal mixing atomizer, gas and liquid metal are mixed under pressure, and expansion and atomization occur at the nozzle exit into the chamber [87]. As shown in Fig. 4.47, the gas enters with high velocity through tangential inlets into a nozzle to which the liquid metal flows axially and is carried by the rotational gas flow in film form on the inner surface of the nozzle walls to the outlet in the bottom. The narrowing of the lower nozzle part forces the gas to accelerate so that the liquid film becomes thinner. At the outlet, the film breaks into small droplets. Concerning its working principle, this nozzle design is termed a prefilming spin nozzle. The lab melt feeding unit allowed the control of melt flow rates between 0.4 and

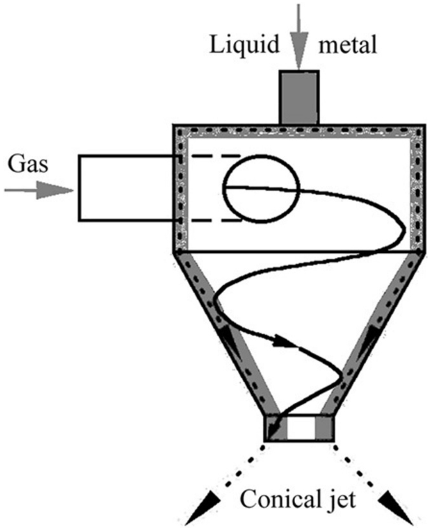

FIG. 4.47 Principle of the internal mixing nozzle.

5 mL/min for temperatures up to 473 K. The atomization conditions were as follows: atomizing gas was argon, gas pressure max 0.6 MPa, and initial metal was 62Bi-38Sn (weight). Its physical data were as follows: melting point 417 K, viscosity 2.2 MPa s at 473 K, surface tension 0.41 N/m at 423 K, and density 8.7 g/m^3. The average particle diameters range from 14 to 25 μm. The pressure swirl hybrid-prefilming atomizer, described in Fig. 4.29, contains an internal mixing nozzle in combination with a ring gas atomizer.

The fundamental disadvantage of the internal mixing technique is the engineering difficulty of arranging to pressurize the melt to the same pressure as the gas. There are also problems with erosion of the ceramic nozzles employed because of the metal velocity. Normally only 1–3 m/s in a pouring nozzle could be expected to rise to the same order of magnitude as the gas velocities, that is, possibly about 100 m/s. Thus, applications are so far very limited.

Soluble Gas Atomization Process

The soluble gas-atomization process is also known as vacuum atomization (see Fig. 4.1K). This process [88] is based on the rapid expansion of gas-saturated molten metal, resulting in a fine atomization of molten droplets that forms as the dissolved gas, usually hydrogen or an argon hydrogen mixture, is suddenly released in an evacuated powder collection tank (Fig. 4.48). The droplets solidify at a rate of about 1000 K/s. The powder collection tank is cooled under vacuum while the powder is sealed and then backfilled with an inert gas. This technique is capable of atomization up to 1000 kg of superalloy in one fusion and produces spherical powder. This process has been employed on a commercial scale for LC Astroloy, MERL 76, and IN-100 production.

Ultrasonic Gas Atomization

Lierke and Griesshammeer seem to have been the first to report the experimental production of metal powders by ultrasonic atomization in 1967 [89]. Later, they achieved atomization of silver [90]. Many experimental studies have been carried out to evaluate particle size distributions. There are differences between low- (20–100 kHz) and high-frequency (up to 3 MHz) atomizers. Analytical studies work on two assumptions: either the breakup mechanism results from growing instabilities in a capillary wave pattern created at the surface of the liquid film, or it derives from cavitational phenomena [91].

According to capillary-wave hypothesis (Fig. 4.49), a thin layer of a liquid wetting the surface of a solid resonator that vibrates vertically to its surface plan forms a chessboard-like pattern of stationary capillary waves. This occurs when the vibration amplitude exceeds a threshold value. On further increase of the amplitude, ligament breakup of the liquid follows and droplets are hurled from the crests of the capillary waves. The key parameter is λ, the capillary wavelength.

Rayleigh [92] stated that

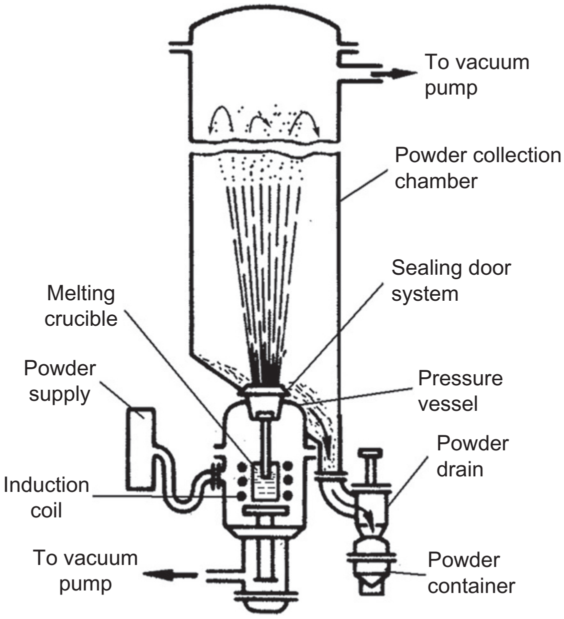

FIG. 4.48 Soluble gas atomization system.

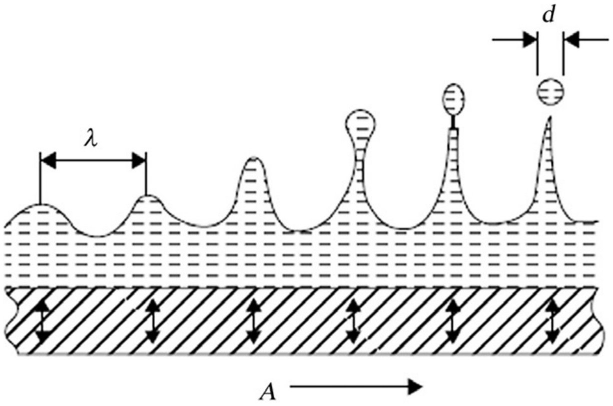

FIG. 4.49 Cappillary wave atomization model.

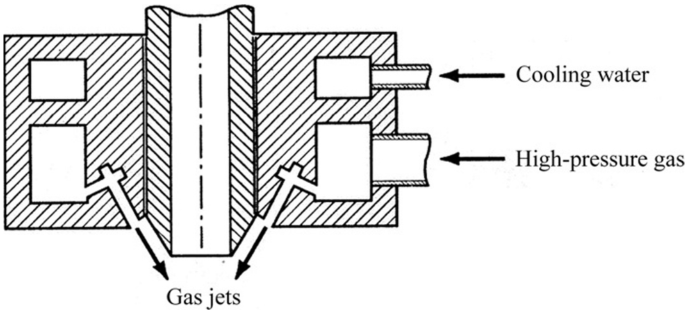

FIG. 4.50 Confined ultrasonic atomizer.

$$\lambda = \left(\frac{2\pi\sigma}{\rho\nu^2}\right)^{1/3}$$

where σ is the liquid surface tension; ρ is the liquid density; and ν is the oscillation frequency. If the oscillation frequency in the liquid is half that in the solid resonator, then

$$\lambda = \left(\frac{8\pi\sigma}{\rho f^2}\right)^{1/3}$$

where f is the ultrasonic frequency.

Later, Ruthardt and Lierke [90] measured particle diameter amounting to 0.25 λ for silver.

Theoretical predictions based on the capillary-wave hypothesis are numerous and essentially apply to low frequency, low flow rate atomizers whereas cavitation is supposed to occur at higher regimes [91, 93]. Yule [94, 95] has shown that capillary-wave atomization is not as orderly as foreseen theoretically. As an alternative, Dumouchel and Boyaval [96] used the maximum entropy formalism (MEF) to model size distribution. A detailed description of the MEF can be found in Kapur's paper [97]. In general, the MEF is a mathematical tool for the elaboration of probability distributions.

A confined ultrasonic atomizer is presented in Fig. 4.50. The ultrasonic designs use the Hartman tube principle to apply high-frequency pulsation to the gas stream, with gas exit velocities reported to be Mach 2–2.5 and the major pulsation frequency at about 100,000 Hz. The HEV's ultrasonic atomization unit includes an induction melting unit, atomizer, transducer, transfer tube, and tubular resonator [98]. Classification of the pneumoacoustic atomizers, the development of new devices, and procedures for ultrasonic gas atomization are given in the work [99, 100].

On HEV's (University of Applied Sciences of Western Switzerland) ultrasonic atomizer [98], a magnesium alloy, AZ63, and pure silver were atomized at 20 kHz. The atomizer, the induction melting unit, the transfer tube, the transducer, and the tubular resonator are the principal parts of HEV's ultrasonic atomizer. Experimental results show a spheroidal particle shape (Fig. 4.51); the powder fraction <50 μm yields are about 65 and 71 vol% for magnesium alloy and silver powders, respectively.

Sono-Tek's founder, Dr. Harvey Berger, was the inventor of ultrasonic atomization technology, commercializing his patented invention in the late 1970s [101]. Early applications were the development of ultrasonic nozzles for use in home

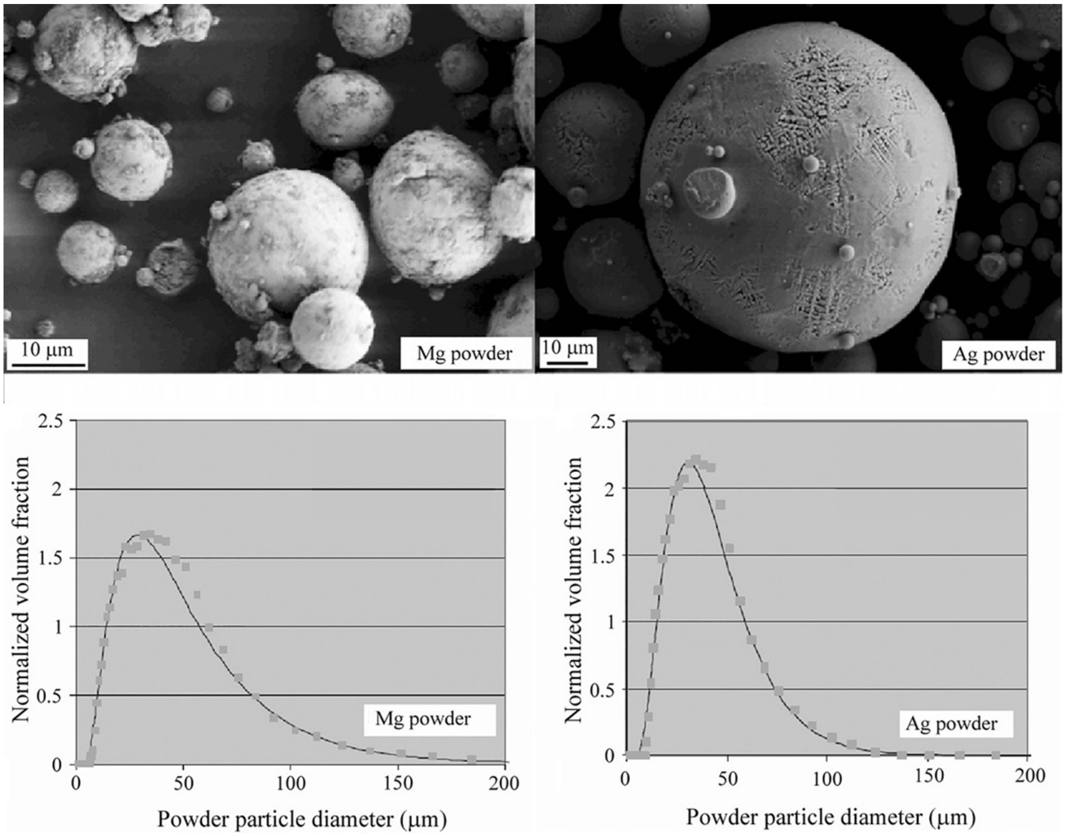

FIG. 4.51 Scanning electron micrographs of the ultrasonic atomized magnesium alloy and silver powders, and their size distribution. *Reproduced with modification from Caccioppoli G, Clausen B, Bonjour Ch, Hofman H. Ultrasonic atomization of metallic melts: modelling and case studies. In: Proceedings of PM2004 world congress, vol. 1. Shrewsbury, UK: European Powder Metallurgy Association; 2004. p. 59–64.*

heating oil burners and liquid fuel burners in portable power generation equipment. Currently, commercially available ultrasonic nozzles [102] have found wide application for molten metals atomization, especially when a precise particle size, such as for solder powder, is required.

Hot Gas Atomization

In practice, the hot-gas process has been partly motivated by an appreciation of the fact that it allowed the production of finer powders, and partly by the fact that it reduced or avoided the problems of nozzle freezing when processing lower melting point alloys (e.g., Li, Sn, Bi, Cd, Pb, Zn, and Al). This allows the use of smaller nozzles and pouring rates, which in turn allows convenient continuous production as well as the production of finer powders than is possible at higher melt flow rates.

The effect of gas temperature on particle size by constant gas mass flow is shown in Fig. 4.52. These data are the result of computation [103] based on dependence of the decrease in the median size of the powder on the square root of gas absolute temperature. In this case, a gas temperature to 473 K reduces the size by 11% and 673 K by 19%. The effect of gas temperature on gas consumption for constant particle size is shown in Fig. 4.53.

A calculation of the economic effect in the case of steel powder production [103] shows that going from 293 K to 473 K reduces costs by 16% and 673 K by 34% (this calculation assumes a gas cost of 0.14 €/m^3 for nitrogen and an electricity cost for heating of 0.14 €/kWh). Heating gas to 473 K or even 673 K is not very demanding technically while reaching 1273 K is far more difficult. Besides that, savings from going from 772 to 1273 K are only a further 18%.

Hot-gas atomization was applied for the production of inexpensive copper powder for metal injection molding where powder costs currently form a high component part [2]. The powder with median diameter about 10 µm was produced by the following process parameters: pouring temperature 1673 K (melting point 1356 K) and atomization gas temperature 773 K. In the study [104], Zr-based ($Zr_{48}Cu_{36}Ag_8Al_8$) glassy powders are formed through both ambient and high temperatures up to 571 K inert gas atomization at various melt flow rates. Particles atomized under an ambient temperature were

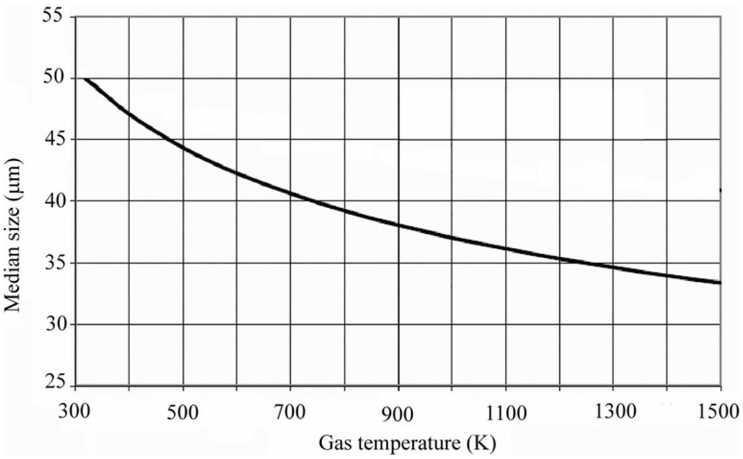

FIG. 4.52 Effect of gas temperature on particle size. *Reproduced with modification from Dunkley JJ. Hot gas atomization—economic and engineering aspects. In: Proceedings PM2004 world, vol. 1. Wien, Austria: European Powder Metallurgy Association; 2004. p. 13–8.*

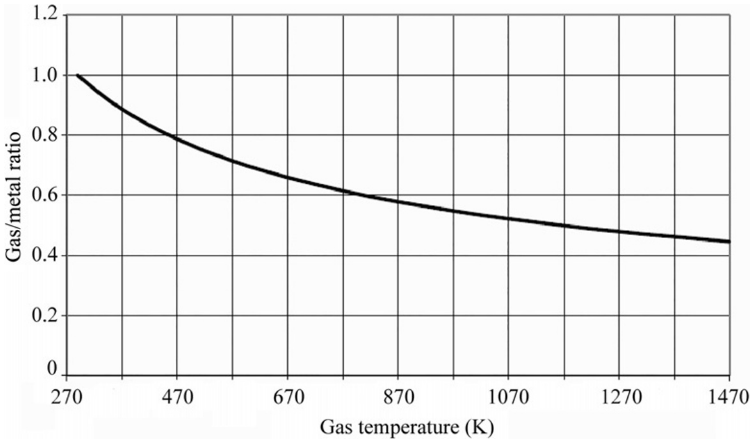

FIG. 4.53 Effect of gas temperature on gas consumption for constant particle size. *Dunkley JJ. Hot gas atomization—economic and engineering aspects. In: Proceedings PM2004 world, vol. 1. Wien, Austria: European Powder Metallurgy Association; 2004. p. 13–8.*

fully amorphous up to a particle size class of 90 μm for glass-forming alloys. It was confirmed that the smaller the particle diameter, the higher the amorphous fraction formed. However, the use of hot gas has not shown a great impact on the Zr-based glass-forming alloy regarding the mass median particle diameter δ_{50} and geometric standard deviation with a free-fall atomizer. Because of the small amount of fine powders generated with a free-fall atomizer (the amount of amorphous powder below 90 μm is in this study <20%), the closed-coupled atomizer offers advantages over the free-fall atomizer with regards to a higher output of fine and amorphous powders. Hot-gas atomization results in a higher output of fine powders, a smaller mass median particle diameter, a smaller gas-to-melt flow ratio (GMR), and constant amorphous fraction but to a lower sphericity.

However, hot-gas atomization leads to an increase in the time needed for solidification rather than to a decrease in median diameter, and that necessitates an increase in the size of the atomizer chamber.

Liquefied Gas Atomization

The atomization of melts with liquefied and cryogenic gases seems to have been developed in 1988 [105]. The so-termed liquefied gas atomization (LGA) is, in principle, similar to the well-established WA technique and results in comparable or even higher cooling rates than WA. During LGA, no oxidation occurs between the atomizing fluid and melt. Materials exhibiting high sensitivity to oxidation have been atomized via LGA, such as the rare earth NdFeB [106] and NiLa or special solder alloys. Starting with atomizing arrangements similar to WA (free-fall design), the technique has been further developed for the use of confined nozzles, similar or identical to the one used for GA.

Two identical inert gas-atomization units at ATZ-EVUS, a laboratory unit up to 30 kg and a pilot unit of 100 kg per batch, have been used for GA and LGA powder production [107]. Melting is done by inductive heating. The melt orifice diameters range from 1.7 to 4 mm, the melt superheat temperatures are typically 100–200 K, and the atomizing pressures range from 1.0–25 MPa. Liquefied gas after cooling to cryogenic temperatures flows to the atomizer when the flow of the superheated melt begins. The mass median diameters range from 30 to 80 μm for NdFeB alloy, copper, and Sn-37Pb alloy. The cooling rate achieved is $>10^6$ K/s in the above laboratory size unit by melt flow rates up to 20 kg/min [106].

No commercial operator is known to use this method. More detailed data, including powder characteristics, economic effect, and safety engineering aspects, are necessary to evaluate the liquefied gas-atomization process.

Vacuum-Dynamic Atomization

This method is based on the use of the energy of two contrary rotating gas flows (Fig. 4.54) with the initiation of a tornado result (USSR Patent 1,082,566, Jan., 1984). However, the evaluations of vacuum level and the rapid expansion of gas-saturated molten metal are not known.

CENTRIFUGAL ATOMIZATION

Models of Centrifugal Atomization

According to the studies of Hinze [108], Tanasawa [109], Champagne and Angers [110, 111], and Halada [112] in centrifugal atomization, there are three basic droplet formation modes. These models conform to the rotating electrode process and are shown in Fig. 4.55. Their analysis is applicable to centrifugal atomization in general.

The direct drop formation (DDF) mode occurs at relatively small rotating speeds and small rates of liquid supply. In this mode, a lot of protuberances grow under the balance between centrifugal force and surface tension. When surface tension is lower than the centrifugal force, droplets are separated and ejected from the protuberances. The major part of every protuberance forms the main drops in large sizes. Its tail usually becomes satellites. Therefore, the typical powder size distribution in this mode has two peaks with equal numbers of large and small droplets.

The ligament formation (LF) mode occurs when the rate of supply of molten metal at the periphery of the electrode increases. Here the protuberances develop a larger amplitude than in the DDP mode before the Rayleigh instability breaks up the elongated ligaments. Droplet size increases and, though still bimodal, the weight fraction of the small and large droplets becomes similar as the liquid supply rate increases.

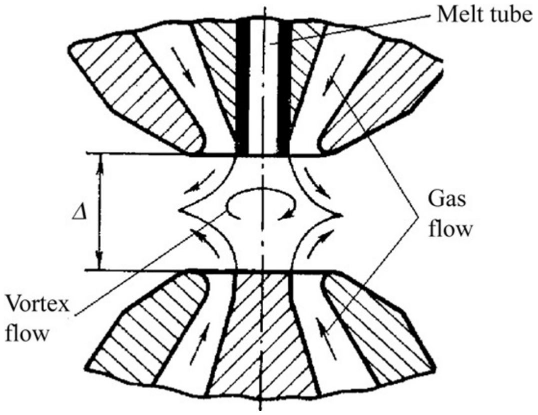

FIG. 4.54 Vacuum-dynamic atomization.

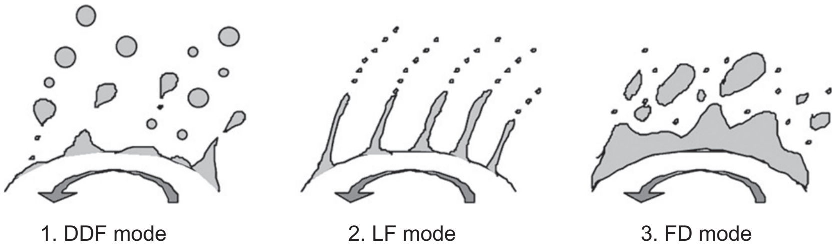

FIG. 4.55 Three disintegration modes in centrifugal atomization.

When the liquid flow rates are very high, ligaments become unstable and the disintegration mode changes gradually to formation disintegration (FD). The transition conditions among these modes have been studied experimentally in a broad range: $10^3 < We < 10^7$ and $10^2 < Re < 10^6$ by Masumoto [113]. The condition range for metal centrifugal atomization is Weber number 10^4–10^5 and Reynolds number 10^5–10^6.

Champagne and Angers [110, 111] observed that, for various metals (e.g., Al, Cu, and Zn), the final droplet shape seen in the DDF mode is spherical. In the LF mode a more ellipsoidal shape is formed. Champagne and Angers [110, 111] discovered that the ratio of two parameters determines the transitions from the DDF to the LF and the LF to the FD modes:

$$X = \frac{\left(\dfrac{Q\omega^{0.60}}{D^{0.68}}\right)}{\left(\dfrac{\sigma^{0,88}}{\eta_L^{0.17}\rho_L^{0.71}}\right)}$$

where Q is the liquid supply rate ($\mathrm{m^3/s}$); ϖ is the angular velocity of the anode (rad/s); D is the anode diameter (m); σ is the surface tension (N/m); η_L is the dynamic liquid metal viscosity (Pa s); and ρ_L is the density of the liquid ($\mathrm{kg/m^3}$).

The numerator includes only process variables while the denominator includes only the material variables. Using the above units for the process and material variables, the DDF to LF mode change occurs when $X = 0.07$. The second mode change to FD mode occurs when $X = 1.33$. These relations are plotted in Fig. 4.56. Thus, an increase in melting rate and angular velocity and a decrease in rotating anode diameter favor a transition from the DDF to the LF mode, and finally to the FD mode. Close agreement exists between model predictions of the transitions in atomization modes for various metals (Fig. 4.55).

Centrifugal atomization generally leads to a narrower spread in particle size than does gas atomization. The analysis of centrifugal atomization developed by Champagne and Angers allows for a quantitative prediction of mean particle diameter in the direct droplet formation mode. In its present form, the model gives no indication of the extent of droplet sizes. The median particle size δ_{50} for the rotating electrode process is approximately defined [114] by

$$\delta_{50} = \frac{K}{\omega\sqrt{D}}$$

where K is a constant for a given alloy for a limited range of arc power.

In a simple model [115] that considers force balance between centrifugal force and surface tension forces, the particle size is expressed as:

$$\delta_{50} = \sqrt{\frac{A\sigma}{\rho_m \omega^2 R}} \tag{4.15}$$

where ω is the angular velocity (rad/s) of the rotating disc (or the electrode); R is the radius of the atomizer (or electrode) (m); ρ_m is the liquid density ($\mathrm{kg/m^3}$); and σ is the surface tension (N/m). A is a constant with value 6 in the elementary case (spheroidal particle shape).

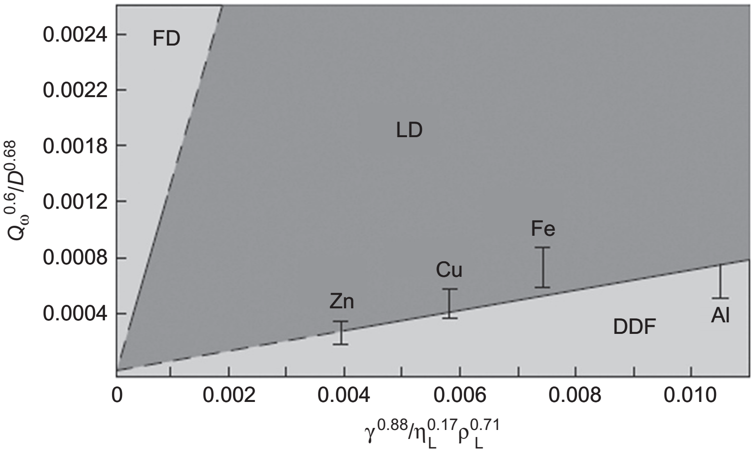

FIG. 4.56 Atomization mechanism domains in centrifugal atomization. *Lawley A. Atomization. Princeton: Metal Powder Industries Federation Publishers; 2003.*

Actual powder sizes are coarser then those predicted [91], which may be explained by the influence of viscosity, particularly at higher speeds. In effect, the molten film is "slipping" on the disc surface, making its speed less than the peripheral speed of the disc. If a term that is counteracting the centrifugal acceleration and that includes both the viscosity and the speed at the rim of the disc is added to the basic model (Eq. 4.15), the following relationship is suggested by Tornberg [41]:

$$\delta_{50} = \sqrt{\frac{A\sigma}{\rho_m \omega^2 R\left(1 - (\omega R)^n \eta\right)}}$$

where the constant $A = 4.8$ and the exponent $n = 0.93$.

Centrifugal Atomization Methods

There are several different types of the centrifugal atomization process (Fig. 4.1), which are discussed. In general, centrifugal atomization methods are far more energy efficient than gas and water atomization, where only about 1% of the jet energy is used in the disintegration of the metal stream [13]. In contrast, the energy used in centrifugal methods is low as it all goes into the acceleration of the metal droplets instead of into the atomizing fluid, as in the case of the two-fluid techniques. Centrifugal atomization also generally leads to a narrower spread in particle size than does gas atomization (see Fig. 4.2), with σ_g as low as about 1.4 in some cases.

As the process depends on the solution to the problem of finding a compatible material for the spinning disc or cup, the applications that have been and are currently used on a significant industrial scale are quite distinct. They are selected in order of ascending melting point of alloy.

Spinning Disc Atomization

Solder powder for electronic applications has a very demanding specification: it must be perfectly spherical and satellite-free, it must be very low in oxygen content (~100 ppm), and it must have a very narrow size distribution. Attempts to make this product with inert gas atomization have practically ceased as yields are as little as 5% and the avoidance of satellites is very difficult.

In the United States, Europe, and Japan, there are many producers using spinning disc methods to make this product. This is possible because a steel disc is well wetted by ordinary Sn63Pb37 solder and is not very quickly eroded. A disc with a diameter of 40–100 mm running at speeds of 30,000–60,000 rpm can produce this material with good yields of 30%–70% and at rates of 50–100 kg/h.

When used with higher melting point metals, it is difficult to run at the level of speeds that are used on solder because of the need to increase the plant diameter. However, there are markets for coarser powders of zinc (alkaline batteries), aluminum (chemical), and magnesium (flares) that are made by this process. In all cases, the cup is 100–200 mm diameter, running at moderately high speeds from 3000 to 10,000 rpm. The chamber size needed is very large, up to 12 m in diameter, but productivity can be very high. Battery applications commonly require −600+100 μm zinc powder. Using a 5 kW spinning cup, 98% can be achieved at outputs of several tons per hour and with compressed air costs.

Course aluminum powder is also produced in this way, but because of the large size of plant needed to freeze large droplets, it is done in open air, which produces a needle-shaped powder. In this case, a perforated steel or cast iron cup is used to make a series of streams of metal, which break up into needles due to the oxide film on them. Production is probably thousands of tons per year.

The spinning cup water granulation process [116] allows an increase in the cooling rate and a notable decrease of the size of plant, owing to cooling the molten droplets in water. Thus, the chiller chamber size is only 1.2–1.5 m in diameter in comparison with 12 m in diameter in the open-air granulation. chapter 16 includes more detailed information about this technique.

Sheikhaliev et al. studied the influence of melt flow rate, melt feeding modes, and environment properties on the quality of the finished solder powder [117]. Experiments were carried out on Sn-39Pb and Sn-3Cu solder alloys in the plant using both melt feeding by a free fall 1–2 mm diameter melt stream and a prefilming nozzle generating a hollow cone melt film (Fig. 4.57). This nozzle function on the centrifugal effect is named the "pressure-centrifugal-atomizer" (PCA).

A scanning electron micrograph of the spinning disc atomized Sn-3Cu solder by free-fall melt feeding is represented in Fig. 4.58. The particles are spherical, satellite-free, and narrow in size.

Table 4.5 contains the data that characterize an effect of atomization conditions on the solder powder particle size. Powder produced by a PCA atomizer had a finer particle size distribution in comparison with one made by free-fall melt

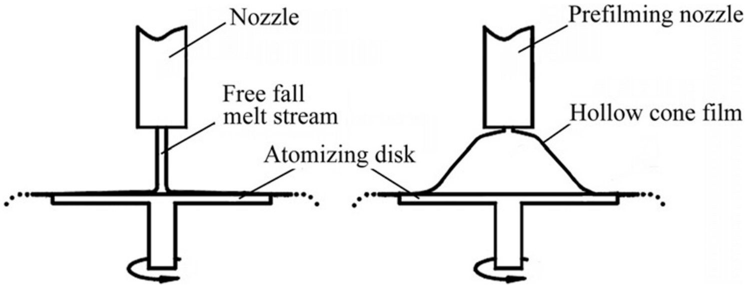

FIG. 4.57 Schemes of melt feeding on spinning atomizing disc.

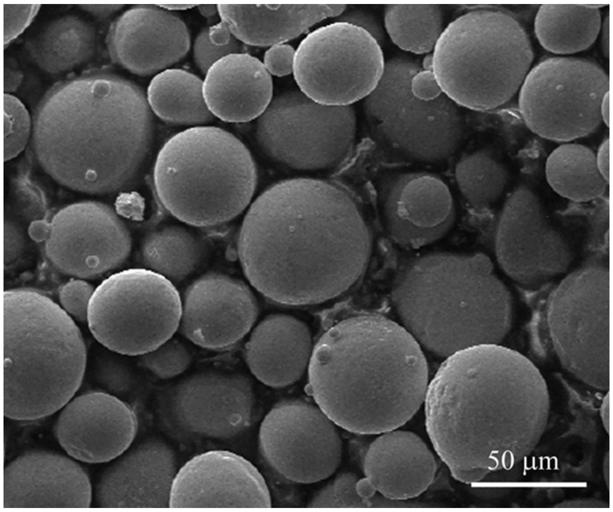

FIG. 4.58 Scanning electron micrograph of Sn-3Cu solder powder made by free fall melt feeding on spinning atomizing disc.

TABLE 4.5 Effect of Atomization Conditions on the Solder Powder Particle Size

Melt Feeding Mode	Gas Type	Gas Density (kg/m^3)	Rotation Speed (rpm)	Melt Flow (kg/h)	W_g/W_m, (W/W)	Particle Size δ_{50} (μm)	Particle Size σ_g
Free fall	Nitrogen	1.25	50,000	60	—	60	—
Prefilming nozzle	Nitrogen	1.25	50,000	60	—	25	—
Free fall	Nitrogen	1.25	40,000	20	—	25.9	1.6
Free fall	Nitrogen	1.25	40,000	40	—	39	2.5
Free fall	Nitrogen	1.25	40,000	60	285/600	78	—
Free fall	Helium	0.18	60,000	40	110/—	—	—
—	Argon	1.8	40,000	—	365/—	—	—
—	Nitrogen[a]	0.1	60,000	—	80/—	—	—

[a] *At pressure of 10^3 Pa;* W_g*—consumption power by free running in gas environment;* W_m*—consumption power by melt atomization;* σ_g*—geometric standard deviation.*

feeding mode. The authors [117] reported that the thickness of the PCA hollow cone melt film formed by contact with the disc becomes about 15 μm; therefore, it will need less energy for atomization along with finer powder forming. Decreasing the melt flow rate from 40 to 20 kg/h results in increasing a finer particle yield, and particle size distribution becomes more narrowly describable by decreasing σ_g from 2.5 to 1.6. As is also seen, using a lighter gas allowed the production of finer powder. A powder made in a helium atmosphere had a granulometric composition with 38 μm median diameter while the powder manufactured in nitrogen had one with $\delta_g = 76\,\mu\text{m}$. The authors also reported the calculation of consumption power by free running in various gas environments and consumption power by melt atomization.

Rapid Solidification Rate Process

The rapid solidification rate (RSR) process is another design of a centrifugal disc or cup atomization, which was developed for superalloy powder production. To overcome the problems of the material in handling high melting and aggressive alloys, the process [118] employs a high-speed, water-cooled rotating disc (20,000–50,000 rpm), which breaks up the molten metal stream. To enhance solidification rates, the resulting droplets are then struck by high-pressure helium gas as they leave the periphery of the rotating disc. Powders produced by the RSR process are spherical, satellite-free, and have smooth surfaces. Particle sizes are usually below about 200 μm with a mass median particle diameter $< 90\,\mu\text{m}$ and a low standard deviation in the range 1.4–1.6.

RSR facilities currently in use incorporate closed-loop helium recirculation. Based on Ni-base alloys, the largest unit has a melt capacity of about 900 kg with an atomization chamber close to 5 m in diameter. In the intermediate size unit, melt sizes are 135 kg with an atomization chamber of about 2.3 m in diameter. Production rates can be varied between 0.05 and 0.3 kg/s for Ni-base alloys. Typically, RSR droplets smaller than 100 μm in diameter cool at rates of about 10^5 K/s. Apart from these operating variables, the superheat of the melt has a strong influence on particle size and hence the particle cooling rate. More detailed data can be found in chapters 15 and 16.

Melt Spinning Roller Technique

At present, the maximum melt cooling rate has been achieved under heat abstraction from a melt by means of a contact with metallic substrate. The main conditions for the advance of the high melt cooling rate due to heat conductivity are the following:

- Minimal loss of heat during carrying from furnace to cooling point.
- Minimal melt thickness in the line of the heat sink.
- High heat conductivity of freezing metallic material (substrate).
- Sufficiently high melting point of the substrate.
- Good heat contact (first of all, cleanness of the substrate surface) of the freezing and cooling materials.

As freezing material, pure copper or its alloys (e.g., beryllium bronze) mostly serve. For good heat contact, the substrate surface is thoroughly polished. The most advanced method of obtaining particles (ribbons, flakes) by means of their freezing on a substrate is the spinning roller technique [116]. A liquid metal stream (Fig. 4.59) collides with the surface of a rapidly rotating roller and wets it. At the contact point, a liquid metal bath is formed. The moving roller surface expands the bath into a ribbon, which begins to move with the same velocity as that of the roller surface. The solidified ribbon is released from the roller under the action of centrifugal force.

The cooling rate of liquid metals achieves 10^5–10^7 K/s, depending on ribbon thickness, which is changed from 20 to 80 μm; the roller circumferential speed is ~30 m/s [115] and output of the Al alloy 4–6 kg/min.

The phenomenon of heightened solubility by such cooling rates becomes possible. Thus, for example in aluminum alloy ribbons, an increase of the nonequilibrium solubility of scandium up to 2 wt% was achieved [119]. Alloying of aluminum with scandium leads to hardnesses of 950, 1200, and 1800 MPa for scandium concentrations of 0.6, 1.0, and 2.0 wt%, respectively (significantly higher than the maximum hardness achieved for aluminum alloys by traditional technology, i.e., 800 MPa).

At the plant shown in Fig. 4.60, a flaky magnesium powder is manufactured [120]. A $Mg_{97}Zn_1Y_2$ alloy was melted by high-frequency induction heating in an argon atmosphere and a flaky powder was produced by spinning roller atomization. In the experiments, the distance between the melt nozzle end and copper roller surface was 0.3, 15, and 30 mm while the roller circumferential speed was 30, 40, and 50 m/s, respectively. As a result, the flaky powders ranged from 20 to 65 μm and the Vickers hardness from 104 to 134, depending on the experimental conditions produced.

FIG. 4.59 Aluminum alloy ribbon obtaining on melt spinning roller. *Courtesy of IPMS*.

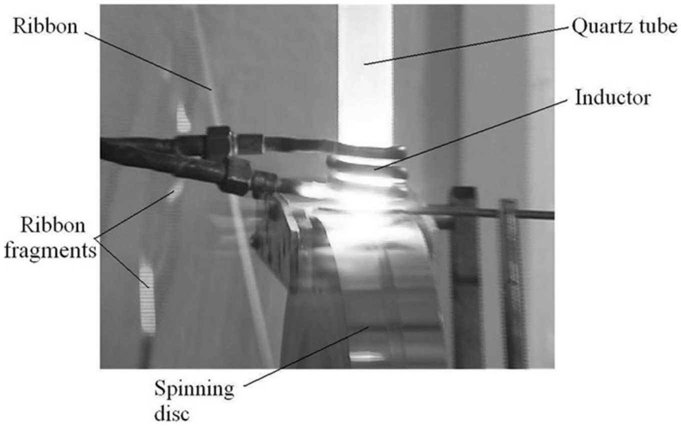

FIG. 4.60 The diagram of flaky powder production by melt spinning roller technique.

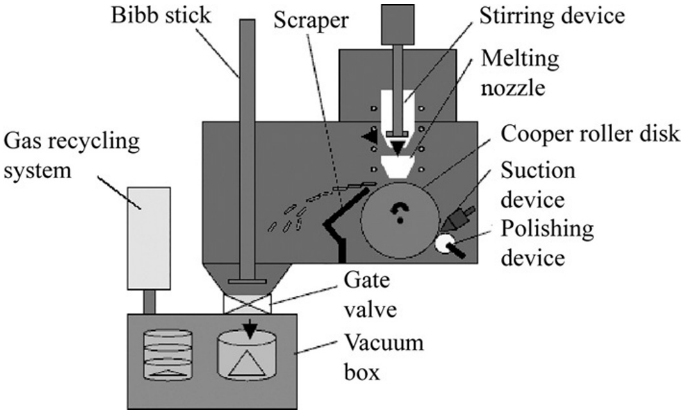

The melt spinning roller technique is widely used in laboratory studies. A closed processing system in an inert gas atmosphere (O_2, $H_2O < 0.5$ ppm) is employed for high reactivity metals [121]. The details of this processing system realizing a single-roller melt spinning method are described in the article [122].

Rotating Electrode Atomization

In the rotating-electrode process (REP), one end of a metal bar is melted while it is rotated around its longitudinal axis (Fig. 4.1E). The molten metal is ejected by centrifugal force in the form of droplets from the periphery of the bar. The REP process was developed by Nuclear Metals, Inc. and patented [123, 124].

In the original process, the consumable rotating bar is the anode of direct current power circuit and the permanent (non-melted) stationary cathode is either a cooled tungsten-tipped device or a transferred-arc plasma torch. When the latter mode is used to melt the end of the rotating anode, the atomization process is termed the "plasma rotating electrode process" (PREP). A chamber of 2440 mm in diameter is used with the circular section oriented. Anode rotational speeds are normally 1570 rad/s. Melting of the anode is carried out in an inert atmosphere. Helium gas enhances both arc stability and the convective cooling efficiency of the atomized droplets.

Powder particles produced by REP and PREP are spherical with smooth, high-quality surfaces. The particle size range is typically from 50 to 400 μm with a mass median particle size around 200 μm [13]. Particle cooling rates are lower than in water or gas atomization. From secondary dendrite arm spacing measurements, the cooling rate is $\leq 10^2$ K/s, depending on the gas condition in the chamber and the particle size.

However, a major drawback is the mechanical limitations on rotational speed, which limit the minimum median particle size to about 50–150 μm [3]. Also, the cost of making a high-quality bar of metal is very significant while productivity is low and energy consumption high compared with other techniques.

OTHER METHODS

Impact Atomization

Impact atomization was developed [125] for producing rapidly solidified particulates. In this method, a molten alloy and volatile liquid coolant are fed simultaneously to a rapidly rotating impeller. As the molten alloy is atomized, the coolant vaporizes; the necessary heat of vaporization of the coolant is taken from the droplets as they solidify. Patents covering this process were issued to the Dow Corning Corporation [126, 127]. Powders have been prepared from a variety of stainless steels, nickel, copper, and a glass-forming alloy [125]. Coolants used included water, liquid ammonia, methanol, and hexane at flow rates from 60 to 200 L/min, depending on the heat of solidification of the alloy, the heat of evaporation of the coolant, the degree of superheat, and the molten metal feed rate.

This process has been used in Argentina where, since 1997, two commercial plants have been operating using induction melting furnaces with 80 and 500 kg capacity, respectively [128]. Both plants include furnaces, tundishes, rotating impellers, atomization tanks with water, reservoirs of circulating water, and pumps feeding circulating water to the impeller. The speeds of impeller rotation are from 2000 to 3500 rpm depending on alloy type, required particle size distribution, and powder apparent density values. The commercial bronze (Cu-5Sn-5Zn-5Pb) powder contains the size fraction $\leq$44 μm up to 26 wt% and the size fraction $\geq$147 μm max 20 wt%. For the 2.2–2.5 t/h atomized powder yield, a 10 kW belted drive is used.

Vibrating Electrode Atomization

Powder is atomized at the molten end of a vibrating consumable electrode in rod form that is continuously fed between rollers into an atomization chamber. A water-cooled rotating electrode of copper or graphite is located opposite the end of the consumable electrode. The rollers are attached to an electrodynamic oscillator, which transfers vibration to the rod electrode. Thus, the electrode forms a resonant rod with one free and one fixed end. Atomization takes place in an inert atmosphere when the arc is struck between the rotating electrode and the vibrating end of the rod electrode.

In the facility described in the literature [129], currents between 600 and 1200 A were generated at a potential between 30 and 60 V. Electrode vibration frequencies up to 500 Hz were evaluated. Powder particles are spherical with mass median sizes typically in the range 300–500 μm. The vibrating rod diameter range is 1–4 mm and the feed rate 1.7–4.3 m/min. Disadvantages of the vibrating electrode atomization are that particles are coarse, productivity is low, and cost is high.

Melt Drop Orifice Technique

There are several types of such a technique, which include impulse atomization (IA), the melt drop vibrating orifice method, and the pulsated orifice ejection method.

Impulse Atomization Method

A schematic of the process is shown in Fig. 4.1J. This unit includes the impulse generator, the mechanical drive, a tundish, and a nozzle plate complete with orifices [130]. There are two modes of impulse atomization operation: the first (gravity impulse mode) is the generation of monosized granules larger than 1 mm in diameter, and the second (impulse mode) is the atomization of droplets with a narrow size distribution $<$1 mm up to 150–180 μm. In the impulse mode of operation, by varying the plunger acceleration, orifice size, orifice shape, melt superheat temperature, and gas atmosphere type, the powder particle size, distribution, shape, and microstructure can be controlled to the required specifications. In gravity impulse mode, the melt stream free falls out through the orifice and impulses are applied to generate millimeter-sized droplets. The powders have been produced in an experimental tower 0.5 m in diameter and 4 m height. In the atomization chamber, the quiescent gas atmosphere into which the melt has been atomized includes helium, nitrogen, argon, and air. The nozzle plate contains $>$500 orifices. Standard refractory materials are used for the tundish, plunger, and orifice plate. There are no temperature limitations to the use of impulse atomization, provided an appropriate refractory material is available for use. For example, a nickel-aluminum alloy was atomized at 1873 K.

Table 4.6 includes a summary of the materials and range of particle size data reported in Ref. [130]. The powders have a narrow particle size distribution; the geometric standard deviation is in the 1.1–1.6 range, typically 1.4, for the impulse mode.

In the impulse mode of operation, mass flow rates of 225 kg/h have been attained in pilot scale tests with, to date, 2.5 h of continuous operation with zinc. This corresponds to a mass throughput of 7300 kg/(m^2 h) based on the area of orifices in the

TABLE 4.6 Powders and Granules Produced Using Impulse Atomization Method

Metal or Alloy	Atomization Mode	Average Particle Sizes	
		Unit	Value
Aluminum	Impulse mode	μm	310
Aluminum	Gravity impulse mode	mm	2–10
Al-(5–24 wt%)Cu alloys	Impulse mode	μm	250–710
Al 6061 alloy and Al 6111 alloys	Impulse mode	μm	250–850
Al 357 alloy	Impulse mode	μm	560–700
Al-(0.1–8.0 wt%)Fe alloys	Impulse mode	μm	400
Al-(10–24 wt%)Sr alloys	Impulse mode	μm	1000
Al-Al_2O_3 composite powders (5–20 vol% of 35 μm reinforcement)	Impulse mode	μm	1000
Copper	Impulse mode	μm	200–1400
Bronze 90/10 and bronze 94/6	Impulse mode	μm	180–720
Pb-(10–12 wt%)Sn alloys	Impulse mode	μm	200–1000
Magnesium	Impulse mode	μm	850–1000
Magnesium	Gravity impulse mode	mm	2 and 4
Mg-9Al-1Zr alloy	Impulse mode	μm	850–1000
AZ91D alloy	Impulse mode	μm	850
Knife alloy	Impulse mode	μm	1000
90Ni-10Al alloy	Impulse mode	μm	350
34Ti-45Cu-1Zr-8Ni alloy	Impulse mode	μm	350
Zinc	Impulse mode	μm	150
Zn-500 ppm Pb	Impulse mode	μm	250

nozzle plate, while the mass throughput for aluminum ranges in these experiments from 2000 to 3000 kg/(m^2 h). The mass flow rate attained with the gravity impulse mode was 15 kg/h for 2 mm magnesium granules. Alcoa has developed a forecast model for the conversion cost of a commercial gravity impulse unit [130].

In the work [131], a thermal model of melt droplet cooling coupled with the temperature of the primary phase in the impulse atomization system is considered. It is based on in situ measurements of droplet size, velocity, and temperature during moving of droplets with subsequent solidification.

Melt Drop Vibrating Orifice Method

In this method, molten metal contained in a pressurized crucible is subjected to vibratory oscillations. Forcing the metal through a nozzle at the bottom of the crucible and into a vacuum or inert gas chamber causes it to form a jet and break up into uniform droplets. The technique has been demonstrated with aluminum, beryllium, copper, lead, and some superalloys [132] and has been proposed for solder [133]. The technique was in limited industrial use in the 1990s, making precision solder balls for electronics with sizes in the range 500–1000 μm. It is limited as production is related to the square of particle size and nozzle blockage is a problem for orifices in the 200–20 μm range.

Pulsated Orifice Ejection Method

This method is intended for the production of monosized spherical particles [134]. Fig. 4.61 shows a schematic diagram of a pulsated orifice ejection method. A piezoelectric actuator was used as a driving device of a metal diaphragm, in which the

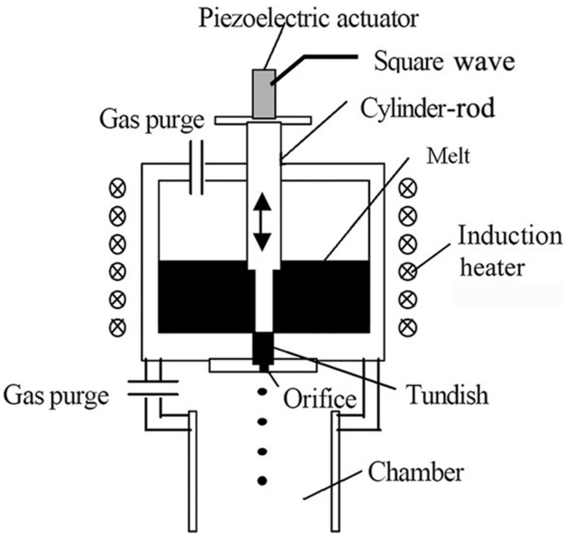

FIG. 4.61 Schematic illustration of pulsated orifice ejection apparatus.

maximum displacement was 14.7 μm and the frequency was 69 kHz. Rectangular waves were generated by a function generator for controlling the output waveform of a power amplifier. A hole about 0.2 mm in diameter, as an orifice, was machined at the center of the bottom of the tundish. Each pressure pulse produced one melt droplet. The apparatus allows the preparation of particles having a very narrow particle size distribution with size deviation <2% of mean particle size. It has been found that the pulsated orifice ejection method is applicable for preparing monosized particles of various metals and alloys. For example, the monosized Sn-3.5 wt%Ag powder with mean particle size of 187 μm with 0.8% deviation was demonstrated.

Roller Atomization

In roller atomization, a molten metal stream is fed between rapidly rotating twin rollers (Fig. 4.1G). Its feature is that little conductive heat transfer between the liquid metal and the rolls takes place [135]. This distinguishes roller atomization from the spinning roller in which rapidly solidified ribbons or flaky particles are produced. Epoxy and phenolic resin coatings on the rolls were found to satisfy the heat transfer requirements for temperatures below 573 K because of poor thermal stability. Epoxy/alumina roll coatings have been used for the atomization of higher melting point metals and alloys. The original atomization facility consisted of a pair of 150 mm diameter rolls contrarotated at speeds up to 1250 rad/s with a roll gap in the range 50–100 μm. The process has been used to atomize a range of metals including lead, tin, aluminum, and copper at metal flow rates up to 6 kg/min. The particle shapes can be irregular, acicular, spheroidal, or flaky, depending on the operating conditions and the metal properties. The spheroidal particles are relatively coarse; mass median particle diameters for Sn powder are in the range 250–680 μm. Primary operating variables are roll speed, roll gap, metal flow rate, metal stream velocity, and metal superheat.

Plasma Atomization Process

This process (Fig. 4.1C) was developed to produce fine spherical titanium powder using titanium wire as the starting material [136]. The wire is fed into the apex of three plasma torches, where it is melted and atomized in an argon atmosphere. Droplets are then cooled during flight in the argon atmosphere with a cooling rate in the range 10^2–10^3 K/s and then solidify, forming spherical powder particles. Spherical titanium and Ti-6Al-4V alloy powders with diameters from 5 to 150–250 μm have been produced commercially in four grades, differing as to particle sizes. The oxygen content depends on particle size and is in the range 0.1–0.3 wt%. The flow rate varies depending on particle size up to 150 kg/day [137]. PyroGenesis proposes the use of plasma-atomized titanium powders for producing porous filters, applications in injection molding and thermal spray processes, and biomedical applications.

Explosive Atomization

Electrical Explosion of Wires Technology

Electrical explosion of wires technology (EEW) is a process of explosive destruction of a metal wire under the action of great density current of 10^6–10^9 A/cm^2 [138]. EEW is characterized by the following peculiarities: time of explosion is 10^{-5}–10^{-8} s; temperature at the moment of explosion can reach a value more than 10^4 K and pressure $\sim 10^9$ Pa; and velocity of the product recession is from 1 to 5 km/s. The material of the wire transmutes into particles of nanosized range (10–100 nm) in accordance with certain conditions. The process can be carried out either in a gas or liquid environment. More detailed EEW data can be found in chapter 9.

Steam Explosion method

The atomization of melt by means of the steam explosion (CANOPUS) method allows, according to the data [139], an achievable cooling rate of the melt of 10^8 K/s. This method was achieved on a laboratory installation. Molten metal held in a crucible flows out through a small orifice in the base, drop by drop, at a set time interval. The drop of melt entering the stream of cooled water (or water salt solutions) causes an explosive formation of steam and results in melt atomization (Fig. 4.62). For the production of the $Al_{89}Fe_{11}$ alloy, the cooling liquid used was a 25% water solution of calcium chloride. Powder particle sizes obtained were in the range of 30–400 μm. However, no commercial operator is known to use this technique.

Flame Spray Pyrolysis

The synthesis of nanoparticles by flame spray pyrolysis (FSP) is a newer but already well-developed process in terms of product diversity. Many elements of the periodic table can be turned into oxides, salts, or even metal nanoparticles in laboratory-scale reactors with production rates of a few grams per hour [140–143]. In these reactors, low-cost metallic precursors (e.g., hexamethyldisiloxane) dissolved in a liquid fuel (e.g., xylene) are supplied into a two-substance nozzle. Pure oxygen is utilized as the dispersion gas and atomizes the liquid precursor in fine droplets with a mass median diameter of ~10 μm. Flamelets feed by a mixture of methane and oxygen allow a permanent ignition of the spray. Droplet evaporation, nucleation, cluster formation, coalescence, and finally agglomeration of product nanoparticles are determined as respective process steps in FSP. The combustion of organic solvents and precursors causes a huge release of thermal energy with temperature > 2300 K within the flame.

It is supposed that correlation between product quality (particle size, purity, etc.) and production rate can be considered as a trade-off in large-scale production facilities [144]. For industrial large-scale nanoparticle production via FSP, a new precursor atomization concept consisting of a combination of a liquid hollow cone (pressure swirl nozzle) and a dispersion gas nozzle (discrete jet nozzle) was presented [145]. Experiments were done under nonburning conditions with water and compressed air to gain impressions of the spray pattern and nozzle functionality (Fig. 4.63). Based on the experimental data

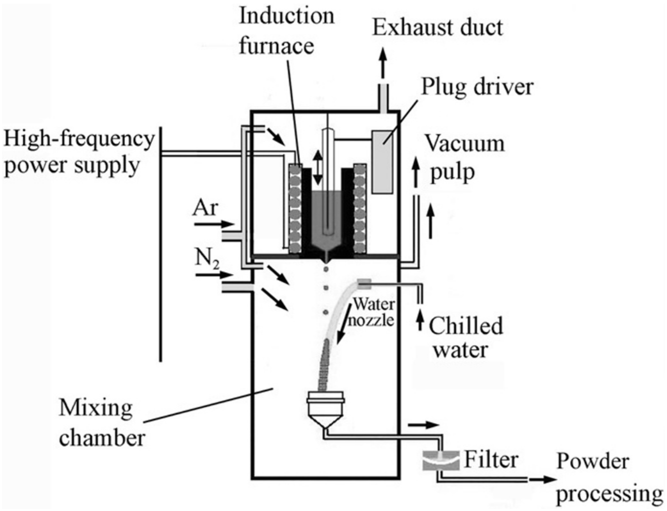

FIG. 4.62 Schematic of steam explosion CANOPUS experimental installation.

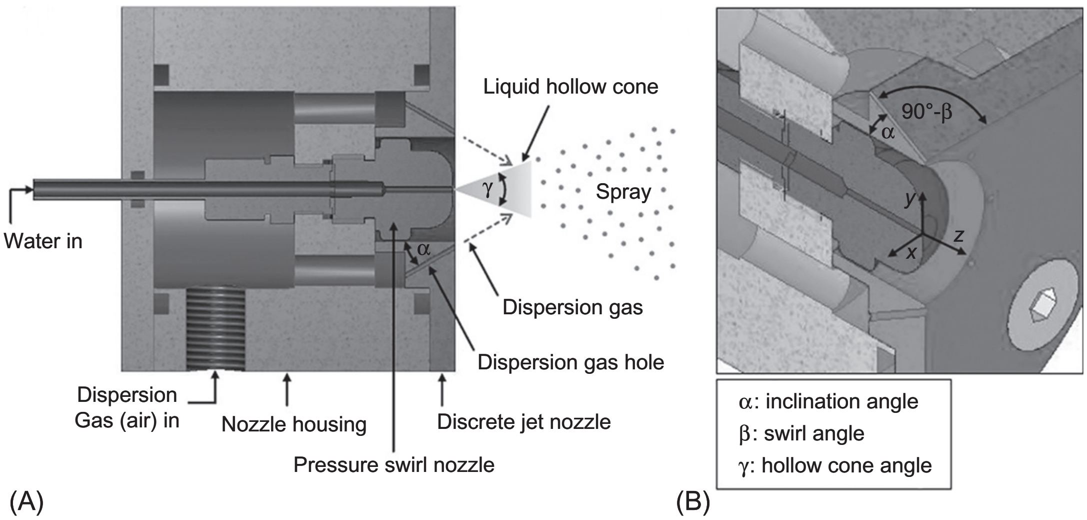

FIG. 4.63 Liquid hollow cone nozzle (pressure swirl nozzle) adapted with custom-made dispersion gas nozzle (discrete jet nozzle); view onto cross-sectional plane (A) and cross-sectional plane as well as sectional plane under inclination angle α to illustrate swirl angle β (B). *Courtesy of Universität Bremen.*

in terms of mass median droplet diameter δ_{50} and spray angle, a combination of the pressure swirl nozzle (γ) and the discrete jet nozzle (number of holes/ α/δ) as $\gamma = 70$ degrees and 8/30°/15° was optimized.

GRANULATION

Granulation is a term that is used to define two dissimilar processes. In one definition, granulation is defined as the production of metal by the atomization of molten metal. These processes have been discussed above. The other definition is the most commonly used spray drying and spray granulation techniques. Granulation is the purposeful agglomeration of fine particles into larger clusters to improve certain powder properties. For example, bulk powders characteristically have low density, do not readily flow, are dusty, and have low thermal conductivity. When properly granulated, the same powder pours easily, exhibits a high and uniform bulk density, does not “dust,” and more efficiently transfers thermal energy.

Spray Granulation

The basic method for making granules in a fluidized bed can be by the combination of the hot gaseous fluidized bed and a two-fluid spray nozzle. A binding liquid or solution is spread onto a bed surface of fluidized particles or is sprayed directly into the bed (Fig. 4.64). It tends to show that, compared to seed particles, larger spray droplets generally result in the formation of agglomerates, which is influenced by the variation of operating conditions. In relation to granule growth of simultaneous coating and agglomeration in a hot fluidized bed, the size distribution and growth rate of granules under continuous operation can be derived from the material balance of the bed particles. Granule size increases as the fraction of the bed exposed to the binding liquid is reduced and the spray nozzles are adjusted to give coarser droplets. Increasing the intensity of bed agitation (with higher velocity) decreases the size of granules. There is an upper limit on granule size because of the tendency of the powder bed to defluidize. However, spray granulation can form larger granules than are usually possible by spray drying because of a longer residence time.

Both spray granulation and spray drying are scalable technologies and provides the means for producing bulk quantities of nanophase composite powders at a low manufacturing cost.

A direct current plasma-heated fluidized bed was applied to the granulation of spheroidal alloy grains from metal powder mixtures [146]. From a mixture of aluminum powder (74–88 and 125–149 μm) and iron powder (149–210 μm), alloy grains from 1 to 5 mm in diameter were produced. The grains exhibited a dense homogeneous core and a porous nonhomogeneous shell structure. A fluidized bed process facilitates the production of contamination-free pyrophoric rare earths and abrasive ceramic powders [147]. The production of exactly limited particle fractions is an important process for rare earths (Sm-Co, Nd-Fe-B) and ceramic oxides (oxides, carbides, nitrides, and borides) products.

FIG. 4.64 Fluidized bed spray granulator.

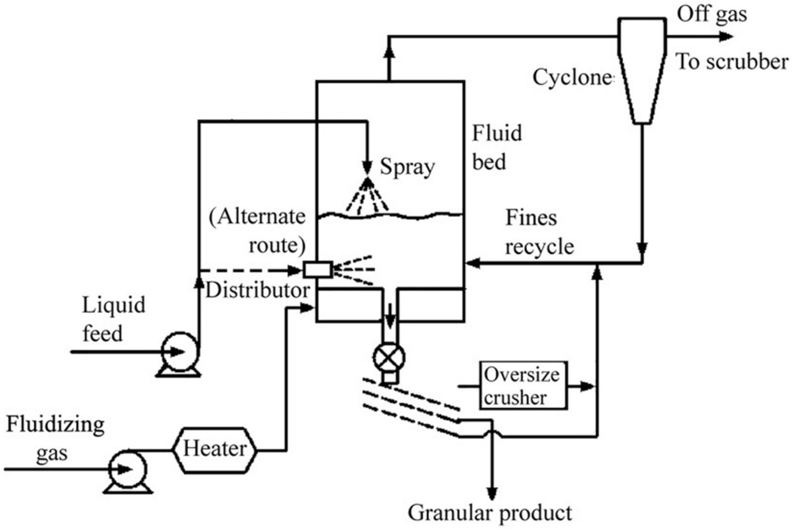

Spray Drying

Spray drying is a powder production process in which a slurry or a solution is atomized into droplets in a chamber through which heated gases, usually air, are passed. A typical spray dryer utilizes a disc atomized with cocurrent air flow. This process is described in chapter 14. Spray drying offers several advantages over other powder-processing techniques, particularly in applications requiring agglomerates for subsequent pressing and sintering operations. Spray drying also is one of the most economical ways of drying slurries.

Control of Powder Properties

Most of the applications of spray drying in the PM industry require the formation of free-flowing agglomerates, including the powder injection molding process. Many of these powders are used for producing pressed parts. Therefore, the agglomerate size distribution and bulk density are the two most important properties of spray-dried powders. Agglomeration is achieved by using a binder.

Agglomerate size distribution is a function of atomization conditions and properties of slurry. Commonly, a lower solid content yields a finer average agglomerate size. The maximum attainable solid content varies with the material, but usually can be increased by using deflocculating or suspending agents.

Bulk density is a function of the solid content of the slurry additives. Lower bulk densities are generally achieved from slurries with low solid contents. Also, excessive inlet temperatures can cause lower bulk densities. Rapid evaporation of the liquids causes the partially dried droplets to expand rapidly, thus decreasing density. Introduction of frothing agents may draw air into the slurry, which also leads to lower bulk densities. Typically, frothing agents are not added in PM applications.

The moisture content of a powder can be controlled by the inlet and outlet temperature of the spray dryer in conjunction with the slurry feed rate. Moisture levels below 0.1% are possible. For a given airflow and inlet temperature, outlet temperature is controlled by the rate of slurry feed and the solid content. With a higher percentages of solids, less water will be evaporated, which leads to higher throughput of dry product.

*Binders for agglomeration***.** Suitable binder materials must be homogeneously dispersed (preferably soluble) in the liquid introduced to form the slurry. When dry, binders must form a coating and/or adhere to the material being agglomerated. They must impart the required strength and crush resistance to the granule for subsequent handling. In addition to the liquids, solids, and binders used to formulate a slurry, various other additives may be necessary. Table 4.7 includes typical components of spray-dried slurries.

Plasticizers may be used with binding materials that are hard and that tend to crack during drying. Suspending agents may be needed to prevent solids from settling within the slurry. Deflocculating agents aid the formation of slurries by preventing the agglomeration of fine particles. Wetting agents also may be used to retain suspended-solid condition. Some slurries have a tendency to foam during mixing. Antifoaming agents or defoamers may be used to control this action. Chemical activators also may be used as additives to aid in subsequent sintering or processing of powders.

TABLE 4.7 Binders for Agglomeration of Spray Drying Slurries

Binder Classification	Binder
Organic binders	Polyvinyl alcohol, gum arabic, other natural gums, carboxy-methyl cellulose salts, polyvinyl acetate, methyl cellulose, ethyl cellulose, polyvinyl butyral dispersions, protein colloids, acrylic resin emulsion, ethylene oxide polymers, water-soluble phenolics, lignin sulfonates, propylene glycol alginates, flour, starches
Inorganic binders	Sodium silicate, boric acid, borax, carbonates, nitrates, oxylates, oxychlorides
Plasticizers	Glycerine, ethylene glycol, triethylene glycol, dibutyl phthalate, ethanolamines, propylene glycol, glycenol monochlorhydrin, polyoxyethylene arylether
Deflocculating agents	Sodium hexametaphosphate, sodium molybdenate, tetrasodium pyrophosphate, ammonium citrate, ammonium oxalate, ammonium tartrate, ammonium chloride, monoethylamine
Wetting agents	Synthetic detergents, alkylaryl sulfonates, alkylaryl sulfates, soaps

Water Granulation

Water granulation is a process for producing metal granules by pouring molten metals through a screen into water or by agitating molten metals into droplets with subsequent water quenching. Granulation of liquid metal offers a simple technique for solidification of metals, but pouring liquid metal into water has always been regarded as hazardous. In order to prevent a steam explosion as ignition and explosion of reactive metals like aluminum a large water tank must be used.

An improved technique called the "spinning water atomization process" (SWAP) was used for manufacturing rapidly solidified magnesium alloy granules [148]. In SWAP installation, the outlet molten through nozzle plug in crucible bottom is dispersed by gas atomizer. Molten metal particles entered in the rotatable water stream on the inner surface of chamber walls are rapidly crystallized. The magnesium alloy (6.01AI-0.26Mn-2.09Ca-0.038Si-0.004Cu-0.002Fe-0.007Zn-Mg Bal/mass%) granules are $1-5$ mm size. It was previously verified that the coarse Mg powders of these sizes were noncombustible. Added data about SWAP process can be found in chapter 17.

The spinning cup water granulation process [116] allows an increase of the cooling rate and a notable decrease of the size of plant, owing to cooling the molten granules in water. Thus, the chiller chamber size is only 1.2–1.5 m in diameter in comparison with 12 m in diameter in open-air granulation. A spinning cup water granulator, which was used in VILS, is shown in Fig. 4.65. The cup with apertures in the walls is made from ceramics, which are nonwettable by aluminum while possessing high resistance and low heat conductivity. The rotating disc sets the water in the atomizing chamber in rotation and under centrifugal force, the water is thrown away to the atomizing chamber walls and flows down to the overflow apertures. Thus, a mobile layer of water is formed on the inner surface housing walls. The liquid metal flows onto the rotating cup and is subjected to centrifugal force in the cup wall apertures in the form of droplets, with such droplets being force cooled by contact with the annular wall of water. The solidified granules are carried from the atomizing chamber together with the cooling water through the suspended granule discharge.

The following conventional atomization processes are used to atomize slurries for spray drying:

- Melt drop orifice atomization.
- Centrifugal (rotating disc) atomization.
- Two fluid jets atomization.

Table 4.8 includes data about the size ranges of powders produced by the above atomization processes. As shown, the largest agglomerate sizes (600 μm) are achieved by melt drop orifice atomization. However, recently this agglomerate size level has been raised to 2 and 4 mm by using the impulse atomization method [130].

Applications

Spray-drying applications include the production of cemented carbides, mineral processing, the production of oxide-dispersion-strengthened alloys, and the production of powders for thermal spraying applications.

Closed-cycle spray drying is required for most cemented carbide powders because the binders that are used are soluble only in volatile organic fluids. The nitrogen drying gas that is used in the spray drying of cemented carbides is heated to

FIG. 4.65 Schematic of spinning cup water granulator.

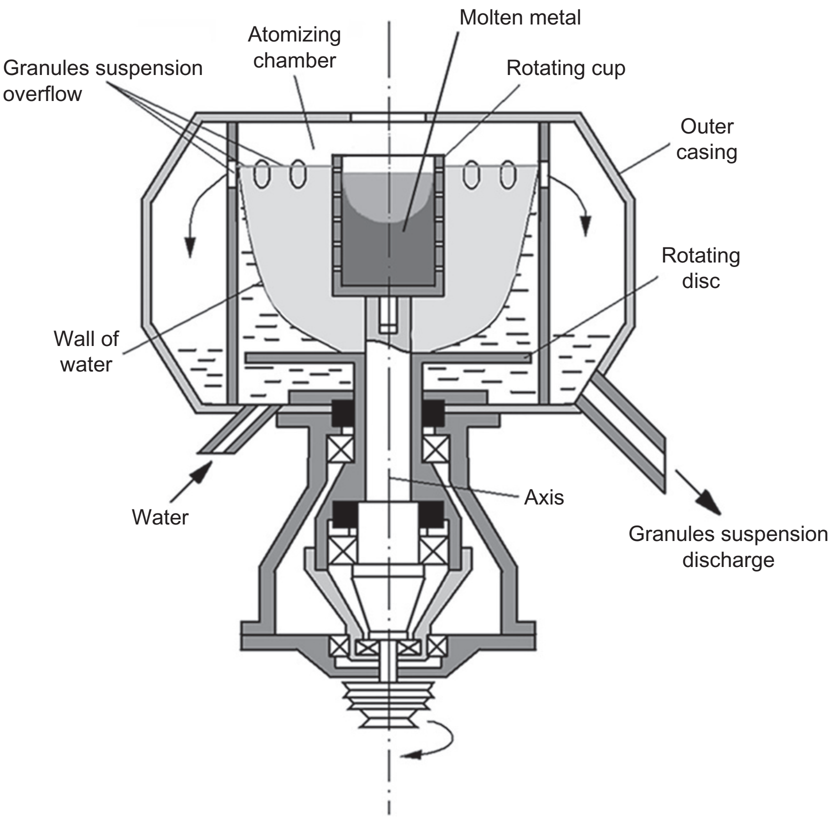
Atomizing chamber
Molten metal
Granules suspension overflow
Rotating cup
Outer casing
Rotating disc
Wall of water
Water
Axis
Granules suspension discharge

TABLE 4.8 The Size Ranges of Powders Produced by Several Atomization Processes

Atomization Method	Average Agglomerate Size (μm)
Centrifugal atomization (rotating disc)	
High speed	25–100
Medium speed	50–200
Low speed	100–300
Melt drop orifice atomization	
High pressure	25–100
Medium pressure	50–200
Low pressure	100–300
Very low pressure	200–600
Two fluid jets atomization	
High pressure	10–50
Medium pressure	25–100
Low pressure	50–200

348–373 K. Viscosity of milled slurries is sometimes modified with stabilizers such as stearic acid (0.3–0.5 wt%). Pressures for melt drop orifice atomization range from 590 to 1470 kPa. A more detailed description of this is given in chapter 23.

Multicomponent oxide powders for plasma spraying is an other area of spray drying. The concept of multicomponent powders consists of two steps. The first step is the agglomeration of the starting powder by the drying process. The second step involves plasma densification [149, 150]. The plasma-densified powder obtained has a spheroidal smooth surface, a high density, and a porosity approaching zero. Experience in this technique concerning the plasma densification of metals, metallic hard materials, and ceramics shows that the multicomponent powder concept is practicable for nearly all materials. It has been shown that coatings of plasma-densified powders show better resistance to wear than coatings of agglomerated powders.

Amastan Technologies [151] developed a powder densification/spheroidization microwave-based plasma process that improves powder flowability while increasing particle density, overall powder tap density, and purity. Its main features include axial injection of feedstock into an axisymmetric hot zone with a high and uniform profile plasma temperature, laminar gas flows, and high heating rates. The hot zone is electrode-free, which eliminates the presence of contaminants in the final product. This technique is capable for the production of uniform diameter, dense, and spherical powder particles. These droplets undergo rapid pyrolysis, followed by melting and then solidification in one step. This rapid processing could be of interest to the coating industry and other PM technologies as well, especially when uniformly sized and dense powder particles are desired.

REFERENCES

[1] Dunkley JJ. Atomization of metals—craft or science? In: Proceedings of 2nd international conference on spray deposition and melt atomization. Bremen Universität; 2003. p. 3–11.

[2] Hopkins WG. Hot gas atomization. In: European congress and exhibition on powder metallurgy, vol. 4. European Powder Metallurgy Association; 2001. p. 194–200.

[3] Dunkley JJ. Atomization. In: ASM handbook, vol. 7. ASM International Publishers; 1998. p. 35–52.

[4] Neikov OD, et al. Effect of atomization parameters on the physical properties of water atomized aluminum powders. In: Compiled by Russell A, Chernenkoff W, Brian J. Proceedings of 2014 powder metallurgy world congress. Orlando, FL, USA: Metal Powder Industries Federation; 2014, p. 02-85–94.

[5] Neikov OD, Vasilieva GI, Sameljuk AV, Krajnikov AV. Water atomized aluminum alloy powders. Mater Sci Eng A 2004;383:7–13.

[6] Seki Y, Takigava H, Kawai N. Effect of atomization variables on powder characteristics. Met Powder Rep 1990;38–40.

[7] Kikukawa M, Matsunaga S, Inaba T, Iwatsu O, Takeda T. Development of spherical fine powders by high-pressure water atomization using swirl water jet. In: Proceedings of 2000 powder metallurgy world congress. Kyoto: Japan Society of Powder and Powder Metallurgy; 2000. p. 363–6.

[8] Terai S, Kikukava M, Inaba T, Koyata T. Development of spherical fine powders by high-pressure water atomization using swirl water jet. In: Proceedings of 2006 powder metallurgy world congress. Korean Powder Metallurgy Institute; 2006. p. 18–9.

[9] Russian Federation Patent 1,812,731. May 1990.

[10] Grandzol RJ, Tallmadge JA. Water jet atomization of molten steel. Am Inst Chem Eng J 1973;19(6):1149–58.

[11] Klar E, Fesko J. On the particle shape of atomized metal powders. Prog Powder Metall 1981;37:47–66.

[12] Grandzol RJ, Tallmadge JA. Effect of jet angle of water atomization. Int J Powder Metall Powder Technol 1975;11(2):103–16.

[13] Lawley A. Atomization. Princeton: Metal Powder Industries Federation Publishers; 2003.

[14] Dunkley JJ. The production of metal powders by water atomization. Powder Metall Int 1978;10(1):38–41.

[15] Small S, Bruce TJ. The comparison of characteristics of water and inert gas atomized powders. Int J Powder Metall 1968;4(3):7–17.

[16] Levich VG. Physicochemical hydrodynamics. Moscow: Phizmatgiz Publishers; 1958 [in Russian].

[17] Ternovoy YF, Kudyevskiy SS, Pashetneva NR. Engineering accounts of technological processes of melt metals atomization. Zaporozhye, Ukraine: Zaporozhskoy Inzhenernoy Academiy Publisher; 2005 [in Russian].

[18] Yule AJ, Dunkley JJ. Atomization of melts. Oxford: Oxford University Press Publishers; 1994.

[19] Nichiporenko OS. Shaping of powder particles during the atomization of a melt with water. Powder Metall Met Ceram 1976;15(9):665–9.

[20] Ternovoy YF. Theoretical bases of metal melt atomization processes. Zaporozhye, Ukraine: Zaporozhskoy Inzhenernoy Academiy Publisher; 2008 [in Russian].

[21] Grant NJ. The scope and trends of developments in rapid solidification technology. In: Rapidly quenched metals proceedings of the fifth international conference on rapidly quenched metals 1, Wurzburg, Germany, 1984. Elsevier Science Publishers; 1985. p. 3–34.

[22] Mikheev MA, Mikheeva IM. Bases of heat transfer. Moscow: Energyja; 2010 [in Russian].

[23] Kutateladze SS. Bases of theoretics of heat transfer. Athomizdat: Moscow; 2014 [in Russian].

[24] Bechke KV, Sanin AF. Structure and properties of water-atomized aluminum powder alloy. Powder Metall Met Ceram 2010;49(5):266–71.

[25] Dobatkin VI, Elagin VI, Fedorov VM. Rapidly solidified aluminum alloys. Moscow: All-Russian Institute of Light Alloys Publishers; 1995 [in Russian].

[26] Neikov OD, Krajnikov AV, Milman YV, Thompson G, Sameljuk AV, Sirko AI, Chaykina NG. Advanced PM aluminium alloys produced by new rapid solidification technology. In: Proceedings PM2004 world congress, vol. 1. Shrewsbury, UK: European Powder Metallurgy Association; 2004. p. 237–42.

[27] Neikov OD, Milman YV, Sirko AI, Sameljuk AV, Krajnikov AV. Elevated temperature aluminium alloys produced by water atomization. Mater Sci Eng A 2008;477(1–2):80–5.

[28] Dunkley JJ. An assessment of atomization with hydrocarbon. Met Powder Rep 1992;22–3.

[29] Williams B. Powder metallurgy—a global market review. In: International Powder Metallurgy Directory & Yearbook. 12th ed., vol. 1; 2012/2013. p. 5–16.

[30] US Patent 1,659,291, 1917, Feb. 1928.

[31] Wiggers H, Koster S, Walzel P. Experiments to liquid metal atomization with a new prefilming nozzle. In: Proceedings of international conference on spray deposition and melt forming. Bremen Universität; 2000. p. 569–78.

[32] Dunkley JJ. Atomization of metal powders in powder metallurgy. Institute of Metals Publishers; 1991.

[33] US Patent 6,481, 638, Nov 2002.

[34] Schulz G. Concepts for a continuous operation of a WIDEFLOW gas atomizer. In: Proceedings of 2nd international conference on spray deposition and melt atomization, vol. 2. Bremen Universität; 2003. p. 59–66.

[35] Ünal A. Flow separation and liquid rundown in a gas atomization process. Metall Trans B 1989;20B(10):613–21.

[36] Ünal A. Influence of nozzle geometry in gas atomization of rapidly solidified aluminium alloy. Mater Sci Technol 1988;4:909–15.

[37] Stobik M. Nanoval atomizing—superior flow design for finer powder. In: Proceedings of international conference on spray deposition and melt atomization. Bremen Universität; 2000. p. 511–20.

[38] Germany Patent DE 102 37 213.6, August 2002.

[39] Achelis L, Uhlenwinkel V. Characterization of metal powders generated by pressure-gas-atomizer. Mater Sci Eng A 2008;447(1–2):15–20.

[40] Czisch C, Fritsching U. Atomizer design for viscous-melt atomization. Mater Sci Eng A 2008;477(1–2):21–5.

[41] Tornberg C. Gas efficiency in different atomization system. In: Proceedings powder production and spray forming, vol. 2. Metal Powder Industries Federation; 1992. p. 127–35.

[42] Dombrowski N, Johns WR. The aerodynamic instability and disintegration of viscous liquid sheets. Chem Eng Sci 1963;18:203–14.

[43] Bradley D. On the atomization of a liquid by high velocity gases: I. J Phys D Appl Phys 1973;6:1724–36.

[44] Bradley D. On the atomization of a liquid by high velocity gases: II. J Phys D Appl Phys 1973;6:2267–72.

[45] Allen T. Particle size measurement. 3rd ed. Chapman and Hall Publishers; 1981.

[46] See JB, Johnston GH. Interactions between nitrogen jets and liquid lead and tin streams. Powder Technol 1978;21:119–25.

[47] Ingebo RD. Capillary and acceleration wave breakup of liquid lets in axial-flow airstreams. In: NASA Technical Paper. National Aeronautics and Space Administration, Scientific Technical Information Branch; 1981. p. 1791.

[48] Sheichaliev SM, Sharonov IV, Karpov MP. Centrifugal-hydraulic method of powder production. Sov Powder Metall Met Ceram 1989;6:16–21 [in Russian].

[49] Ternovoy YF, Pashetneva NN, Manegin YV. Physicomathematical model of the process of gas spraying of the melt jet. Sov Powder Metall Met Ceram 1992;3:11–5 [in Russian].

[50] Mates SP, Biancaniello FS, Ridder SD. An alternative view of close-coupled gas atomization of liquid metals. In: Proceedings of 2002 world congress of PM and particulate materials, vol. 3. Princeton, NJ: Metal Powder Industries Federation; 2002. p. 178–87.

[51] Lagutkin S, Uhlenwinkel V, Achelis L, Pulbere S, Sheikhaliev S. Centrifugal Gas atomization: preliminary investigation of the method. In: Proceedings PM 2004 World Congress. Wien (Austria): EPMA; 2004. p. 71–6.

[52] Ünal A. Effect of processing variables on particle size in gas atomization of rapidly solidified aluminium powders. Mater Sci Technol 1987;3:1029–39.

[53] Mates SP, Ridder SD, Biancaniello FS. Comparison of the supersonic length and dynamic pressure characteristics of discrete-jet and annular close-coupled nozzles used to produce fine metal powders. In: Proceedings liquid metal atomization: fundamentals and practice. Warrendale, PA: The Minerals, Metals and Materials Society; 2000. p. 71–81.

[54] Ting J, Peretti MW, Eisen WB. Control of fine powder production and melt flow rate using gas dynamics. In: Proceedings of world congress of PM and particulate materials, vol. 2. Princeton, NJ: Metal Powder Industries Federation; 2000. p. 27–40.

[55] Anderson IE, Terpsta RI, Figliola R. Gas recirculation flow in the melt feeding zone of a close-coupled gas atomization nozzle: modelling and measurement. In: Proceedings of 2nd international conference on spray deposition and melt atomization, vol. 2. Bremen: Bremen Universität; 2003. p. 19–30.

[56] Mi J, Figliola RS, Anderson IE. A numerical investigation of gas flow effects on high pressure gas atomization due to melt tip geometry variation. Metall Mat Trans B 1997;28B(10):935–41.

[57] Ting J, Peretti MW, Eisen WB. The effect of wake-closure phenomenon on gas atomization performance. Mat Sci Eng 2002;A326:110–21.

[58] Ting J, Anderson IE. A computational fluid dynamic (CFD) investigation of the wake closure phenomenon. Mat Sci Eng 2004;A379:264–76.

[59] Ting J. The close-coupled gas atomization: a quantitative analysis of the dynamic pressures of the pulsative atomization process. In: Compiled by Russell A, Chernenkoff W, Brian J. Proceedings of 2014 powder metallurgy world congress. Orlando, FL: Metal Powder Industries Federation; 2014: p. 02-76–84.

[60] Ting J, Peretti MW, Eisen WB. Control of fine powder production and melt flow rate using gas dynamics. In: Ferguson H, Whychell DT, editors. Advances in powder metallurgy & particulate materials, vol. 2. Princeton, NJ: APMI-MPIF; 2000. p. 27–40.

[61] Rieken JR, Heidloff AJ, Anderson IE, Mullis A. Development of close-coupled gas atomization process for fine metal powder production. In: Compiled by Russell A, Chernenkoff W, Brian J. Proceedings of 2014 powder metallurgy world congress. Orlando, FL: Metal Powder Industries Federation; 2014: p. 02-54–60.

[62] Anderson IE, Figliola RS, Morton H. Flow mechanisms in high pressure atomization. Mat Sci Eng 1991;A148:101–14.

[63] Lampa A, Fritsching U. Spray structure and propagation in confined atomization processes. In: Uhlenvinkel V, Fritsching U, Ellendt M, editors. Proceedings of 5th international conference on spray of spray deposition and melt atomization. Bremen, Germany: Universität Bremen; 2013. p. 1–14.

[64] Bouffanais R. Advances and challenges of applied large-eddy simulation. Comput Fluids 2010;39(5):735–8.

[65] Li D, et al. Direct numerical simulation of a particle-laden low Reynolds number turbulent round jet. Int J Multiphase Flow 2011;37(6):539–54.

[66] Strauss JT. Lick back in close-coupled atomization: a phenomenological study. In: Compiled by Russell A, Chernenkoff W, Brian J. Proceedings of 2014 powder metallurgy world congress. Orlando, FL: Metal Powder Industries Federation; 2014: p. 02-38–45.

[67] Mullis AM, Dunkley JJ. Analysis of acoustic emissions from gas atomisation. In: Compiled by European powder metallurgy association, Bellstone Shrewsbury, UK. Proceedings of PM 2016 world congress, Hamburg, Germany; 2016. p. 1–7.

[68] Motaman S, Mullis AM, Cochrane RF, Borman DJ. Numerical and experimental investigations of the effect of melt delivery nozzle design on the open- to closed-wake transition in closed-coupled gas atomization. Metall Mater Trans B 2015;46:1990–2004. https://doi.org/10.1007/s11663-015-0346-6.

[69] Gowid S, Dixon R, Ghani S. A novel robust automated FFT-based segmentation and features selection algorithm for acoustic emission condition based monitoring. Appl Acoust 2015;88:66–74.

[70] Klar E, Shafer WM. High-pressure gas atomization of metals. Powder Metallurgy for High-Performance Applications. Syracuse, NY: Syracuse University Press; 1972.

[71] Anderson IE, Filial R, Teresa RI, Rau S, Rauscher B. Progress in experimental analysis of gas atomization process physics. In: Proceedings of world congress of PM and particulate materials, vol. vol. 3. Princeton, NJ: Metal Powder Industries Federation: 2002. p. 150–62.

[72] Rai G, Lavernia E, Grant NJ. Powder size distribution in ultrasonic gas atomization. J Met 1985;37(8):22–9.

[73] Lubanska H. Correlation of spray ring data for gas atomization of liquid metals. J Met 1970;22(2):45–9.

[74] Wigg LD. Drop-size prediction for twin-fluid atomizers. J Inst Fuel 1964;500–5.

[75] Beddov JK. The production of metal powders by atomization. Philadelphia: Heyden Press Publishers; 1978.

[76] Dunkley JJ, Telford B. Control of "satellite" particles in gas atomization. In: Proceedings of world congress of PM and particulate materials, vol. 3. Princeton, NJ: Metal Powder Industries Federation; 2002. p. 103–10.

[77] Nichiporenko OS. On the effect of blast energy on the formation process of melt drops during atomization. Soviet Powder Metall Ceram 1974;6:1–7 [in Russian].

[78] Rao P, Tallmadge JA. Change of shape of metal droplets in quench atomization. In: Proceedings of 1971 powder metallurgy conference. New York: Metal Powder Industries Federation; 1972. p. 251–8.

[79] Zambon A, Badan B, Ramous E. Gas atomization of nickel aluminides powders. In: Proceedings PM1998 world congress, vol. 1. United Kingdom: European Powder Metallurgy Association; 1998. p. 173–8.

[80] L'Estrada L, Hallén H, Ljunggren R. Internal porosity of gas atomized powders. In: Proceedings modern developments in powder metallurgy, vol. 20. Princeton, NJ: Metal Powder Industries Federation; 1988. p. 187–95.

[81] US Patent 5,310,165, May, 1994.

[82] German Patent DE 4,102,101 Al, 1991.

[83] Pleier S, Hohmann M, Goy W, Schaub B. Actual improvements of ceramic-free metal powder production. In: Proceedings PM2004 world congress, vol. 1. Wien, Austria: European Powder Metallurgy Association; 2004. p. 89–90.

[84] Gerling R, Schimansky FP. Crucible- and ceramic-free melting and atomization of Ti-based alloys. In: Proceedings PM 2004 world congress, vol. 1. Wien, Austria: European Powder Metallurgy Association; 2004. p. 77–82.

[85] Yolton CF. Gas atomized titanium and titanium aluminide alloys. In: P/M in aerospace and defence technologies. Princeton, NJ: Metal Powder Industries Federation; 1989. p. 128–36.

[86] Babun AV, Neklyudov IM, Azhazha VM, Kovtun KV, Vasiliev AA, Bobylev GG. Beryllium powder metallurgy: developments of the National Scientific Centre "Kharkov Physicotechnical Institute". Powder Metall Met Ceram 2006;(3/4):118–25.

[87] Wiggers H, Köster S, Walzel P. Experiments to liquid metal atomization with a new prefilming nozzle. In: Proceedings of SDMA 2000 international conference on spray deposition and melt atomization, vol. 2. Bremen: Bremen Universität; 2000. p. 569–78.

[88] Reichman S, Chang DS. Superalloys II. John Wiley & Sons Publishers; 1987.

[89] Lierke EG, Griesshammer G. The formation of metal powders by ultrasonic atomization of molten metal. Ultrasonics 1967;5:224–8.

[90] Ruthardt R, Lierke EG. A new ultrasonic atomization technique for the production of metal powder. In: Proceedings modern developments in powder metallurgy, vol. 12. Princeton, NJ: Metal Powder Industries Federation; 1980. p. 105–11.

[91] Rajan R, Pandit AB. Correlation to predict droplet size in ultrasonic atomization. Ultrasonics 2001;39:235–55.

[92] Rayleigh JWS. The theory of sound. vol. 2. New York: Dover Publishers; 1945.

[93] Barreras F, Amaveda H, Lozano A. Transient high-frequency ultrasonic water atomization. Exp Fluids 2002;33:405–13.

[94] Yule AJ, Al-Suleimani Y. On droplet formation form capillary waves on a vibrating surface. In: Proceedings of the Royal Society. London; 2000. p. 1069–85.

[95] Al-Suleimani Y, Yule AJ. A CFD prediction of wave development and droplet production on surface under ultrasonic excitation. In: Proceedings ILASS-Europe 2002; 2002. p. 9–11.

[96] Dumouchel C, Boyaval S. Use of the maximum entropy formalism to determine drop size distribution characteristics. Part Part Syst Charact 1999;16:177–84.

[97] Kapur JN. Twenty-fife years of maximum entropy principle. J Math Phys Sci 1983;17:103–56.

[98] Caccioppoli G, Clausen B, Bonjour C, Hofman H. Ultrasonic atomization of metallic melts: modelling and case studies. In: Proceedings of PM2004 world congress, vol. 1. Shrewsbury, UK: European Powder Metallurgy Association; 2004. p. 59–64.

[99] Sparchez Z. Development of new procedures and devices for ultrasonic gas atomization of metallic melts using specific methods of engineering creativity. In: Proceedings of PM2004 world congress, vol. 1. Wien, Austria: European Powder Metallurgy Association; 2004. p. 25–32.

[100] Eskin GI, Eskin DG. Ultrasonic treatment of light alloy melts. 2nd ed. CRC Press; 2014.

[101] Ultrasonic atomization technology. <http://www.sono-tek.com/ultrasonic-nozzle-technologyes> [accessed 31.01.18].

[102] MoltenMist technology for solder paste manufacturers. <http://www.sono-tek.com/moltenmist/>; [accessed 31.01.18].

[103] Dunkley JJ. Hot gas atomization—economic and engineering aspects. In: Proceedings PM2004 world, vol. 1. Wien, Austria: European Powder Metallurgy Association; 2004. p. 13–8.

[104] Ciftcia N, Ellendta N, Mädlera L, Uhlenwinkel V. Impact of hot gas atomization on glass forming alloys. In: Compiled by European powder metallurgy association, Bellstone Shrewsbury, UK. Proceedings of PM 2016 world congress, Hamburg, Germany; 2016. p. 1–7.

[105] Bergmann HW, Vetter J, Cai Q. Die Erzeugung von Metallpulvern durch Verdüung ihrer Schmelzen mit flüssigen Gasen. Steels Met Mag 1988;26 (10):985–1003.

[106] Wolf G, Nöth M, Schubert, Martin VE, Bergmann HW. Production and characterization of liquid gas atomized hard magnetic NdFeB alloy powders for bonded isotropic magnets. In: Proceedings of the powder metallurgy world congress, vol. 3. 1994. p. 1745–53.

[107] Wolf G, Lang A, Bergmann HW. Investigations on melt atomization with gas and liquefied cryogenic gas. In: Proceedings of international conference on spray deposition and melt forming. Bremen, Germany: Bremen Universität; 2000. p. 535–47.

[108] Hinze H, Milborn H. Atomization of liquids by means of rotating cup. J Appl Mech 1950;17(2):145–53.

[109] Tanasawa Y, Miyasaka Y, Umehara M. On the filamentation of liquid by means of rotating discs. J Jpn Mech Soc 1959;25(156):879–97.

[110] Champagne B, Angers R. Fabrication of powder by rotating electrode process. Int J Powder Metall Powder Technol 1980;16(4):359–64.

[111] Champagne B, Angers R. REP atomization mechanism. Powder Metall Int 1984;16(3):125–8.

[112] Halada K, Suga H. Theoretical investigation on parameters of centrifugal atomization of metal powder. Powder Powder Metall 1990;37(4):492–9 [in Japanese].

[113] Matsumoto S, Saito K, Takashima Y. Disintegration modes of centrifugal atomization. J Eng Japan 1974;7(1):13–5.

[114] Angers R, Dube C, Tremblay R. Inverted disk centrifugal atomization of 2024. Int J Powder Metall 1994;30(44):429–34.

[115] Dunkley JJ, Aderhold D. Centrifugal atomization of metal powders. In: Proceedings of international conference on spray deposition and melt forming. Bremen, Germany: Bremen Universität; 2006. p. 1−−6.

[116] Bondarev BI, Shmakov YV. Technology of rapidly solidified Al alloy production. Moscow: All-Russian Institute of Light Alloys Publishers; 1997 [in Russian].

[117] Sheikhaliev S, Moscvitin V, Zibin V, Sheikhalieva Z, Dunkley JJ. Characterization of metal powder production by a pressure-centrifugal-atomizer. In: Proceedings of 2nd international conference on spray deposition and melt atomization. Bremen, Germany: Bremen Universität; 2009. p. 3–11.

[118] US Patent 4,343,750, August 10, 1982.

[119] Pan SV, Slypenyuk OM, Kuprin VV, Milman YV, Troy Tacke V. Influence of scandium concentration on structure peculiarities and hardness of the rapidly-quenched Al–Sc alloys. Met Phys Adv Technol 1999;18:452–5.

[120] Hitoshi O, Takashi O, Nobuyki I, Motonori N. Development of safe production system for Mg-Zn-Re rapidly solidified powders. In: Proceedings of PM2004 world congress, vol. 1. Wien, Austria: European Powder Metallurgy Association; 2004. p. 111–5.

[121] Kawamura Y, Inoue A. Rapidly solidified powder metallurgy $Mg_{97}Zn_1Y_2$ alloys with tensile yield strength of 610 MPa and elongation of 5%. In: Kaplan HI, editor. Magnesium technology. TMS (The Minerals, Metals & Materials Society); 2002. p. 2002.

[122] Kawamura Y, Inoue A, Masumoto T. Mechanical properties of amorphous alloy compacts prepared by a closed processing system. Scripta Metall Mater 1993;29:25–30.

[123] US Patent 3,099,041, July, 1963.

[124] US Patent 3,802,816, April, 1974.

[125] Liles DT, Deleeuw DC. Rapid solidification via centrifugal atomization with a volatile liquid coolant. In: Das SK, Kear BH, Adam CM, editors. Proceedings rapidly solidified crystalline alloys. Warrendale, PA: The Metallurgical Society; 1985. p. 285–90.

[126] US Patent 4,347,199, August, 1985.

[127] US Patent 4,419,060, December, 1983.

[128] Naida YI, Stepanchuk AN, Naida AY. Industrial production of copper alloys powders using impact atomization method. Powder Metall Met Ceram 2006;(1/2):112–7.

[129] Matei G, Bicsak E, Huppmann WJ, Claussen N. Atomization of metal powders using the vibrating electrode method. In: Proceedings modern development in powder metallurgy, vol. 9. Metal Powder Industries Federation; 1977. p. 153–60.

[130] Henein H. Impulse atomization: as innovative approach for the generation of powders and spray deposits. In: Proceedings of 2nd international conference on spray deposition and melt atomization, vol. 1. Bremen: Bremen Universität; 2003. p. 31–9.

[131] Khatibi PD, Henein H. In-situ measurement of droplet size, velocity and temperature in a drop tube-impulse system. In: Uhlenvinkel V, Fritsching U, Ellendt M, editors. Proceedings of 5th international conference on spray of spray deposition and melt atomization. Bremen, Germany: Universität Bremen; 2013. p. 1–13.

[132] Aldinger F, Linck L, Claussen N. A melt drop technique for the production of high-purity metal powder. Mod Dev P/M 1977;9:141–51.

[133] Yim P, et al. Production and characterisation of mono-sized Sn38Pb alloy balls. Int Metall Powder Technol 1996;32(2):155–64.

[134] Kawasaki A, Watanebe R. Preparation of monosized spherical particles of metals and alloys by POEM process. In: Proceedings of 2002 world congress of PM and particulate materials, vol. 3. Princeton, NJ: Metal Powder Ind. Fed; 2002. p. 96–102.

[135] Singer ARE, Roche AD, Day L. Atomization of liquid metals using twin roller technique. Powder Metall 1980;(2):81–5.

[136] Smagorinski ME, Tsantrizos PG. Production of spherical titanium powder by plasma atomization. In: Proceedings of 2002 world congress of PM and particulate materials, vol. 3. Orlando, FL: Metal Powder Industries Federation; 2002. p. 248–60.

[137] Advanced powders & coatings. Division of Raymor Industries Inc. <www.raymor.com>. [accessed 31.01.18].

[138] Teoh WY, Amal R, Madler L. Flame spray pyrolysis: an enabling technology for nanoparticles design and fabrication. Nanoscale 2010;2 (8):1324–47.

[139] Furuya M, Arai T. Innovative ultra rapid cooling and atomizing process utilizing vapor explosion and production of new functional powders. Compiled by European powder metallurgy association, Bellstone Shrewsbury, UK. In: Proceedings of PM 2010 world congress, Florence, vol. 1. 2010. p. 33–8.

[140] Wegner K, et al. Pilot plants for industrial nanoparticle production by flame spray pyrolysis. Kona Powder Part J 2011;29:251–65.

[141] Meierhofer F, et al. Investigation of atomization concepts for large-scale nanoparticle production by flame spray pyrolysis (FSP). In: Uhlenvinkel V, Fritsching U, Ellendt M, editors. Proceedings of 5th international conference on spray of spray deposition and melt atomization. Bremen, Germany: Universität Bremen; 2013. p. 1–13.

[142] Mueller R, Jossen R, Pratsinis SE, Watson M, Akhtar MK. Zirconia nanoparticles made in spray flames at high production rates. J Am Ceram Soc 2004;87(2):197–202.

[143] Mädler L, Kammler HK, Mueller R, Pratsinis SE. Controlled synthesis of nanostructured particles by flame spray pyrolysis. J Aerosol Sci 2002;33 (2):369–89.

[144] Wegner K, et al. Pilot plants for industrial nanoparticle production by flame spray pyrolysis. Kona Powder Part J 2011;29:251–65.

[145] Meierhofer F, et al. Investigation of atomization concepts for large-scale nanoparticle production by flame spray pyrolysis (FSP). In: Uhlenvinkel V, Fritsching U, Ellendt M, editors. Proceedings of 5th international conference on spray of spray deposition and melt atomization. Bremen, Germany: Universität Bremen; 2013. p. 1–13.

[146] Tsukada M, Goto K, Yamamoto RH, Horio M. Metal powder granulation in a plasma-spouted/fluidized bed. Powder Technol 1995;82(3):347–53.

[147] Prem H, Eddington DJ. Contamination-free processing of pyrophoric rare earths and abrasive ceramic powders. Powder Handl Process 1989;1 (1):101–7.

[148] Jones T, Kondoh K. Ballistic analysis of new military grade magnesium alloys for armor applications, Magnesium technology. TMS (The Minerals, Metals and Materials Society); 2011. p. 425–30.

[149] Luo P, Strutt PR, Xiao TD. Synthesis of chromium silicide–silicon carbide composite powders. Mater Sci Eng B 1993;17(1–3):126–30.

[150] Lugscheider E, Loch M, Suk HG. Powder technology—state of the art. In: Proceedings of thermal spray: int. advances in coatings technology. ASM international; 1992. p. 552–9.

[151] Hadidi K, Redjdal M. Powder densification and spheroidization using an axisymmetric microwave generated plasma. In: Conference paper of Aeromat 25 conference and exposition American Society for Metals. 2014. <https://www.researchgate.net/publication/267901747_Powder_Densification_and_Spheroidization> [accessed 31.01.18].

FURTHER READING

[152] Levis GC, et al. Atomization of liquids in high velocity gas streams. Ind Eng Chem 1948;40(1):67–74.

[153] Ünal R. Effect of the pressure formation at the tip of the melt delivery tube in close-coupled nozzles in gas atomization process. In: Proceedings of 2006 powder metallurgy world congress. Busan, Korea: Korean Powder Metallurgy Institute; 2006. p. 562–3.

[154] Liu Y, Guo S, Huang B, Liu Z, Du Y. Densification behaviour of Al-Ni-Y powder containing amorphous and nanocrystalline phases. In: Proceedings PM2004 world congress, vol. 1. Wien, Austria: European Powder Metallurgy Association; 2004. p. 425–30.

[155] Capes CE. Particle size enlargement. In: Handbook of powder technology. Elsevier Scientific Publishers; 1980.

Chapter 5

Gas-Phase Method of Metal Powder Production☆

Irina V. Frishberg

Institute of Metallurgy, Ural Branch of the Russian Academy of Science, Yekaterinburg, Russia

Chapter Outline

Introduction 187
Theoretical Basis of the Gas-Phase Method 187
Mechanisms of Powder Formation During Vapor Condensation 189
Peculiarities of the Formation of Alloy Powders 193
Controlling Principles of the Condensation Process 194
Powder Production and Application of Gas-Phase Processes 194
  Physical Vapor Deposition (PVD) Process 195
  Properties of Powders and Areas of Their Usage 196
  Chemical Vapor Deposition (CVD) Process 197
  Health and Environment Protection 198
References 199

INTRODUCTION

The theory and technique of obtaining particulate precipitates from metals or their compound vapors are the essence of the gas-phase method [1,2]. Two types of gas-phase precipitation, physical vapor deposition (PVD) and chemical vapor deposition (CVD), are known. In the former, the powder is formed as a result of evaporation of a metal followed by condensation of its vapor; the second one involves chemical interactions (see Chapter 20). These techniques are usually called inert gas condensation (IGC) and chemical vapor reaction (CVR), respectively. The gas-phase methods are universal and sufficiently economical. They are versatile and allow the manufacturing of powders with targeted properties. The technique is applicable for producing powders from volatile metals such as zinc, cadmium, lead, magnesium, tin, copper, and their alloys as well as from a variety of metals capable of forming volatile halides, carbonyls, and metal organic compounds. Inert gas condensation methods are available for the production of nanopowders.

The process of powder formation comprises three stages:

1. Vaporization, either by evaporating the metal or by its chemical interaction with the components of the gas phase.
2. Feeding the vapor into the zone of condensation (decomposition).
3. Formation of solid particles by condensing or decomposing the gaseous chemical compounds (nucleation and growth of a new condensed phase).

In the case of physical condensation, the temperature of the vapor source is higher than that of the powder formation zone; in most cases of chemical precipitation it is vice versa.

THEORETICAL BASIS OF THE GAS-PHASE METHOD

Temperature (T) and pressure (p) are the principal thermodynamic characteristics of the process. The evaporation and precipitation take place at T_1 and p_1 (zone 1) and at T_2 and p_2 (zone 2), respectively. Under the equilibrium conditions, the phase rule is observed in each zone:

☆ Expanded and updated by O.D. Neikov.

Handbook of Non-Ferrous Metal Powders. https://doi.org/10.1016/B978-0-08-100543-9.00005-1
© 2019 Elsevier Ltd. All rights reserved.

$$G = N - \varphi + 2 \tag{5.1}$$

where G, φ, and N are the number of components, phases, and degrees of freedom, respectively.

In the first zone, the vapor of a pure metal consists of a single component and the system possesses two degrees of freedom (the system is bivariant); T and p change independently, and no formation of a new phase takes place. In the second zone, a new liquid or solid phase is precipitated from the vapor. As a result, the number of degrees of freedom decreases to one, the system becomes monovariant, and changing T automatically leads to changes in p, according to the dependence of equilibrium vapor pressure (p_e) on T known for each substance. Changing T to the value at which the liquid phase begins to solidify or the solid phase begins to melt makes the system invariant: it exists only at one temperature and one pressure—the so-called "triple point." Adding a new component brings in a new independent variable, namely the composition, and the system now acquires one more degree of freedom. The phase rule is observed when there is dissociation of a compound or interaction between several solids during evaporation. In this case, the "reaction pressure" characterizes the system. In the case of the condensed phases, the system is also monovariant.

The formation of a new condensed phase in zone 2 is a consequence of a certain degree of vapor supersaturation (S) occurring either due to decreasing the vapor temperature or to its decomposition:

$$S = \frac{p_1(T_1)}{p_e(T_2)} \tag{5.2}$$

where T and p are bound by the correlation of the Clausius-Clapeyron equation $p_e(T) = p_0\exp(-E/T)$ with $E = Q/R$; Q is the molar heat of evaporation; and R is the universal gas constant. The value of S depends on the degree of the vapor saturation; $S = 1.0$ for saturated vapors, $S > 1.0$ for super-saturated vapors, and $S < 1.0$ for nonsaturated vapors.

Eq. (5.3) gives the probability of the development of a new phase nucleus in a unit volume of the supersaturated vapor

$$J = Ke^{-\Delta G/kT} \tag{5.3}$$

where K is a coefficient; k is the Boltzmann constant; and $\Delta G = 16\pi M^2\sigma^3/3\rho^2 \times k^2T^2\ln^2 S$ displays the work of the formation of a condensed phase nucleus (M is the molecular mass of the vapor, σ is the surface tension of the nucleus drop, and ρ is the vapor density).

The physical state of the new phase can be controlled via the degree of vapor supersaturation, $S = p_1(T_1)/p_2(T_2)$, to yield either a monolith or a disperse phase. With $S > 1$, the vapor is supersaturated and is ready for condensation, a quite definite critical value of the degree of supersaturation existing for each substance. The critical supersaturation S_{cr} generated in zone 2 (for metals $S_{cr} > 10^{20}$) is instantaneously realized in building up complexes of vapor molecules – clusters that grow to the critical nuclei of the new condensed phase having its own structure.

In the case of chemical precipitation from the gas phase, an analogous parameter exists, S_{cr} that connects the vapor pressure of the substance in the gas phase with the equilibrium vapor pressure of the metal.

The Hertz-Knudsen equation (Eq. 5.4) describes the rate of substance evaporation and vapor condensation:

$$J = \frac{\alpha(p - p_e)}{(2\pi MRT)^{0.5}} \tag{5.4}$$

where α is either the coefficient of evaporation depending on the nature of the substance and on the properties of the surface or, in the case of precipitation from vapor, the coefficient of condensation (the portion in the total flux of the vapor molecules condensing under given conditions) [3].

The value of the coefficient of evaporation is close to unity in the case of a clean surface of evaporation while the condensation coefficient varies from 10^{-6} to 1.0. In the case when the evaporation-condensation process strongly depends on the total pressure, Eq. (5.5) assumes the form of a simple Langmuir diffusion equation:

$$J = \frac{\alpha D(p - p_e)}{L\Delta T} \tag{5.5}$$

where D is the diffusion coefficient; Δ is the mean free path of the vapor molecules; and L is the thickness of the diffusion layer adjacent to the surface of evaporation or condensation. Eq. (5.5) describes the rate of transfer of vapor molecules when that rate is determined by molecular diffusion [4].

MECHANISMS OF POWDER FORMATION DURING VAPOR CONDENSATION

The following conditions are necessary for the condensation of metallic vapor and the formation of a particulate phase:

1. High supersaturation of the vapor sufficient to trigger simultaneous and multiple formation of nucleation centers.
2. The presence of a neutral gas acting as a medium preventing the coagulation and growth of particles due to diffusion. The presence of foreign inclusions, ions, and chemically active compounds in the neutral gas promotes the nucleation. Forced or natural circulation of the gas ensures the transfer of the condensation heat like the particles and contributes to a variety of forms of their growth.

The formation of powders calls for a molecular-viscous or a viscous flow state of the gas medium (Knudsen number $Kn < 0.01$ and the pressure between 0.01 Pa and 100 kPa). Decreasing the temperature of powder particles, removing the particles from the zone of condensation, passivation of the surface, and dilution of the vapor add to the stability of the disperse system and enable control of particle growth.

The condensation of the metallic vapor and the formation of powder can take place on a cooled surface (a heterophase process), in the bulk gas volume (a homophase process), and as a mixed homoheterophase process as well. The interval of the vapor supersaturation of 10^4–10^8 is assumed as a boundary between the first and second processes. At supersaturation values below 10^4, the formation of the powder occurs on the surface whereas at values above 10^8, it occurs in the volume; within this interval, a mixed process often takes place.

The formation and properties of the particulate system depend on the heat and mass transfer in the condensation zone. The driving force of the process, that is, the temperature difference between the initial and the final state of the vapor, results from the joint effect of the boundary conditions and the heat evolution during condensation.

Powder formation on a cooled surface (a heterophase process) takes place as a mass growth of crystalline particles, which are nucleated on macroscopic defects of the surface. First, there is formed a multiplicity of little “islands” growing perpendicularly to the substrate along the *C*-axis of the crystals. The islands are shaped as prisms and pyramids of up to 10–20 μm. Then, a second front of crystals is formed with crystals having a *C*-axis parallel to the substrate, and dominant particles are precipitated, intergrowing each other. The new generation of more fine particles replenishes theirs. The density and thickness of the precipitate depend on the growth conditions. The precipitate remains particulate until its relative density does not exceed 30% of the solid. The particle size distribution varies from fractions of microns to several millimeters while the particles are in the shape dendrites or platelets, sometimes with a monocrystalline structure.

The heterophase process is characterized by a high rate of heat and mass transfer interactions, specific thermo-hydrodynamic phenomena occurring on the boundary of the gaseous and particulate phases, and the formation of intermediate particulate structures.

Different conditions can lead to the formation of powder in the volume (a homophase process), among them adiabatic expansion of the gas medium in the condensation chamber; supercooling of the gas layer adjacent to the intensely cooled surface; feeding cold neutral gas into the vapors; and the presence of chemically active substances able to interact with the gas.

In real processes, almost all the above conditions are present. The particles grow mainly by coagulation, coalescing in the gas flow and precipitating onto cooled surfaces under the influence of thermo- and diffusion-phoretic forces [5,6].

The shape, structure, and size of powder particles depend on the gas dynamics and the heat and mass transfer in the gas phase. At gas temperatures exceeding 0.7 of the metal melting point, particles mostly take a spherical shape, and their formation occurs according to the solid-liquid-solid mode. At temperatures below that value, faceted crystalline shapes appear (prisms, pyramids, and more complex shapes) according to the vapor-crystal mode, with the particles sometimes having a monocrystalline structure. The lower the pressure and vapor concentration, the finer the size of the particles formed. Varying the methods and conditions of condensation allows the production of powders with particle sizes ranging from 0.01 to 50 μm.

Three major types of volume condensation of metallic vapor are of practical interest and can be singled out:

(1) Diffusion condensation when zones 1 and 2 are combined and evaporation occurs over the open surface of the melted metal.
(2) Condensation in flame when zone 1 and zone 2 are separated and the vapor enters zone 2 through an orifice, condensing by the action of convection currents.
(3) Condensation in a vapor jet.

The condensation type is specified by the values of the parameters involved in the equation (Eq. 5.6):

$$J = A/p_{\mathrm{vg}}, \tag{5.6}$$

TABLE 5.1 The Condensation Parameters

The Condensation Type	Partial Pressure of the Metal Vapor, p_i	The Degree Indicator, *n*	The Evaporation/Condensation rate, *J*,kg/(m^2·s)	The Gas Feeding Rate, *v*, m/s	The Value of the Reynolds number (*Re*)	The Value of the Richardson Number Criterion for the Stability of the Flow (*Ri*)
Diffusion	$<< p_{vg}$	1	≤0.001	…	…	…
In-flame	$\leq p_{vg}$	2–4	0.001–0,1	1–5	<30	>1
In-jet	$\geq p_{vg}$	4–15	0.1–1.0	5–15	500–1000	<1

Note: p_{vg} is the total vapor-gas pressure; *n* is degree of vapor saturation values; $Re = \frac{\rho u L}{\mu}$ $Ri = \frac{g\beta(T_{hot} - T_m)}{u^2}$ where ρ is the density of the fluid; *u* is the characteristic velocity of the fluid; *L* is the characteristic length; μ is the kinematic viscosity; *g* is the gravitational acceleration; T_{hot} is the wall temperature; and T_m is the average temperature value.

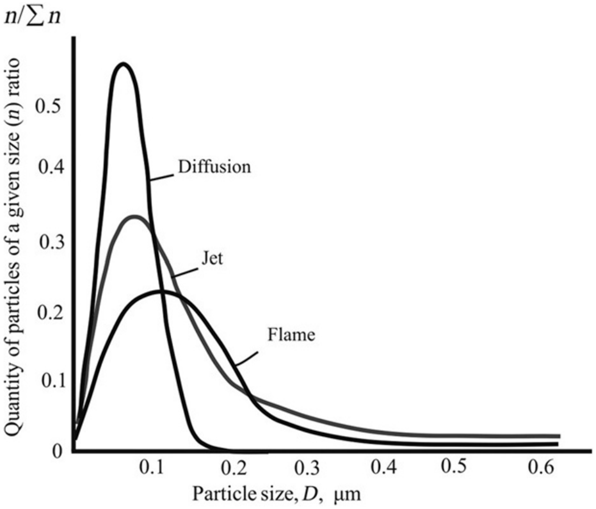

FIG. 5.1 Particle size number basis distribution of copper powder in diffusion, jet, and flame condensation regimes.

that describes the relation between the rate of evaporation (condensation), *J*, and the total pressure of the vapor-gas medium, p_{vg} (see Table 5.1). In the last two cases, the values of the current temperature along the jet (flame) axis are inversely proportional to the apparatus length.

The jet (flame) exhibits three zones: the metallic vapor zone (near the jet inlet), the vapor condensation zone, and the aerosol zone. The jet parameters and linear dimensions of the apparatus determine the ratio between zones.

The powder particle size distribution at volume condensation is determined by the rate and mechanism of the growth of condensation nuclei. Particle size distributions in diffusion, flame, and jet modes do not differ substantially, as is shown in Fig. 5.1.

A dominant feature in the diffusion regime is that powder particles increase in size, owing to the vapor condensing on them. Particle size distribution is close to normal while in the flame, the distribution is lognormal. Particle growth is controlled by Brownian coagulation on the free-molecular model. Powder formation in the jet occupies an intermediate position.

The crystal morphology of particles depends on the growth conditions, the properties of the metal, and on the rate of heat and mass transfer processes in the gas medium. Spherical particles form, for the most part, by the vapor-liquid-solid mode and are typical of low-melting metals (tin, zinc, cadmium, and lead). Faceted crystalline forms are produced by the vapor-solid mode (manganese) [5,7].

At certain combinations of the process parameters (surface temperature, volume geometry and dimensions, amount of vapor and gas, etc.), the formation of powder in the bulk may be accompanied by the growth of particles on the cooled surface. Powders obtained by a mixed process are bimodal and contain particles of mixed shapes and structures, including faceted, spherical, and poly- and monocrystalline. Their dimensions range from tens of nanometers to several millimeters. Ultrafine particles are formed in the bulk while large ones are formed on the surface. Like the heterophase process, the process conditions control the powder granulometric composition and the maximum particle size.

The rate of the metal powder formation obeys the equation (Eq. 5.7):

$$W = KF\rho X^{n+1} \tag{5.7}$$

where F is the geometric factor determining the mass flow to a unit of the volume section; n is the order of the reaction; $X = p_v/p$; p_v is the partial pressure of the vapor in the mixture with a total pressure of p; and ρ is defined as

$$\rho = \frac{X}{X + (1 - X)M_g/M_v} \tag{5.8}$$

M_g and M_v are molecular weights of the gas and vapor, respectively; K is the process rate constant.

Typical constant values are $K < 0.3$ and $n = 1/2$ for volume condensation; $K > 0.6$ and $n > 1$ for surface condensation; and $0.3 < K < 0.6$ and $n = 1/2$ for the mixed process. The latter value of the parameter n is specific to chemical chain reactions with a quadratic breakage of chains. Parallel to these reactions, the neutral gas initiates the process at $p < 1$ kPa and inhibits it at higher pressures.

During volume condensation, the empirical activation energy values turn out to be lower than the corresponding calculated theoretical values, whereas at surface condensation, on the contrary, they are higher than the theoretical values; in the case of a mixed process, the values almost coincide.

In the process of condensation of metal vapors, the vapor-solid phase transition is accompanied by a rise in temperature due to the release of the internal heat of crystallization ΔH_c, the value of which for metals is significantly high (kJ/kg): Zn–1884; Mn–4618; Mg–5652; and Al–9211. Empirical equations exist, displaying the interrelations of the basic dimensionless criteria of heat transfer (*Nu*), mass flow (*Re*), peculiarities of the gaseous medium (*Pr*, *Sc* and *Le* criteria), and of the vapor-solid phase transition process (Kutateladze criterion) [8].

Intensive heat and mass transfer interactions occurring at the gas-solid boundary, at the front of the growth of the particulate phase, lead to superheating the adjacent gas layer that, in turn, results in a considerable difference between theoretical and empirical values of the coefficients of heat and mass transfer.

The mechanism of heat and mass transfer processes, for example, for the heterophase process of powder formation, can be assumed to be the following. In the gas phase, convective streams and turbulent flows taking place at the growth front of the disperse precipitate enable the heat transfer so that the average temperature of the gas near the boundary becomes higher than the temperature of the metal powder particles. In the boundary region, a temperature gradient arises, growing as the dilution of the medium and the rate of condensation increase (see Fig. 5.2).

If T_g is the temperature of the gas of the phase boundary, $p_v(T_g)$ is the equilibrium vapor pressure in the mixture, and T_c, $p_v(T_c)$ are the temperature and the equilibrium vapor pressure at the front of crystal growth, respectively, then the driving force of the mass transfer depends on $\Delta T_1 = (T_g - T_c)$ and $\Delta p = p_v(T_g) - p_v(T_c)$. In this case, the gas temperature in the layer

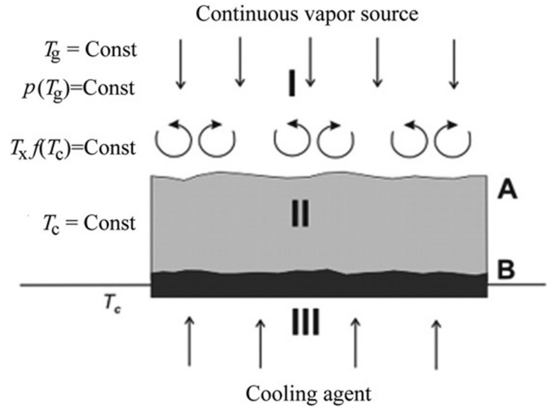

FIG. 5.2 Scheme of heat-and mass transfer during crystallization: I is the gas solution region; II is crystal deposit; and III is cooling agent. Designation of the parameters: T_g is the gas temperature; p is the gas pressure. At the boundary A between II and I: T_x is the gas temperature; T_c is the crystal temperature; and the vapor pressure is $p = f(T_c)$. The temperature of the condensation surface B equals T_c.

FIG. 5.3 The general criteria interrelations for (A) heterophase, (B) homophase, and (C) heterohomophase processes: I and II are the first and the second series of experiments; *ec* is eliminated thermoconvection; *ecg* is eliminated thermoconvection and varying geometry of the condensation volume; *fc* is free convection; *fcu* is free convection in an unlimited volume; Mg-Ar is condensation of magnesium vapor in argon; and Zn-He is condensation of zinc vapor in helium.

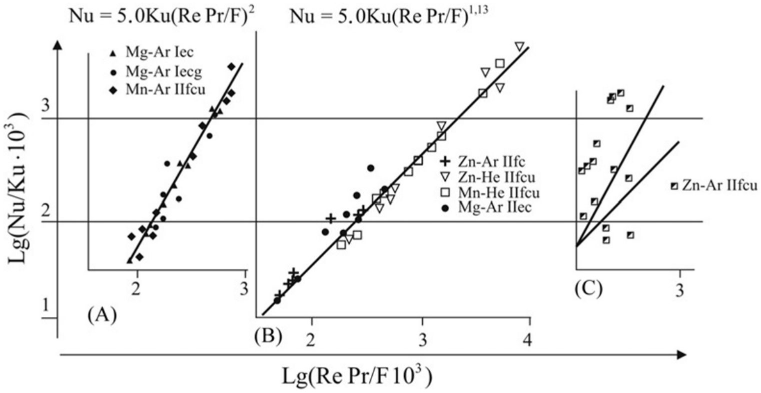

adjacent to the front of the crystal growth is $T_x > T_c$ and the driving force for the heat transfer is $\Delta T_2 = (T_g - T_x)$. The total heat flow through the phase boundary from the first region into the second is given by

$$\alpha \Delta T_1 = \Delta H W + W c_p \left[\frac{1}{X \mu p_v} - 1 \right] \Delta T_2 \tag{5.9}$$

The first member of Eq. (5.9) represents the heat of the phase transition; the second one is the physical heat of the gas at the total coefficient of heat exchange α, where the equation for the mixture flow is replaced by the relations:

$$\frac{WM}{XM_V} \quad \text{and} \quad \mu p_v = \frac{M_v}{M_v X + M_g (1 - X)};$$

the rest of symbol meanings are given above (Eqs. 5.7 and 5.8).

An analogous equation (Eq. 5.10) for heat and mass transfer at vapor condensation follows from the assumed transfer model:

$$\alpha = \beta K c_p Le^{2/3} \sigma \tag{5.10}$$

or

$$\alpha = W c_p Ku \tag{5.11}$$

where β is the mass transfer coefficient; K is the Ackerman's process rate correction [9]; c_p is the specific heat capacity of the vapor-gas mixture; Le is the Lewis criterion for the vapor-gas mixture; σ is a dimensionless parameter displaying the effect of the thermohydrodynamic interactions at the phase boundary; $Ku = \Delta H / c_p T_m$, is the Kutateladze phase transition criterion; and T_m is the average temperature value;

$$\sigma = \frac{\Delta p_{\Delta T_1}}{\Delta p_{\Delta T_2}}$$

where $\Delta p_{\Delta T_1}$ is the difference of partial pressures at T_g and T_c temperatures; and $\Delta p_{\Delta T_2}$ is difference of partial pressures at T_g and T_x temperatures.

General criterion equations (Eqs. 5.12 and 5.13) displaying the interrelations of the basic criteria were obtained by processing the empirical data for condensation of metal vapors in various conditions (Fig. 5.3):

$$Nu = AKu(RePr/F)^B \tag{5.12}$$

where F is the geometrical criterion, reflecting the effect of the geometry of the condensation volume; and A and B are empirical constants, calculated as 0.6 and 0.5 for homophase processes, and as 1.1 and 2.0 for heterophase processes, respectively.

In the case of forced convection at a flow rate of 0.001–0.1 m/s, the above equation assumes the form of

$$Nu = A \frac{M_V}{M_g} \left(\frac{RePr}{F} \right)^B \tag{5.13}$$

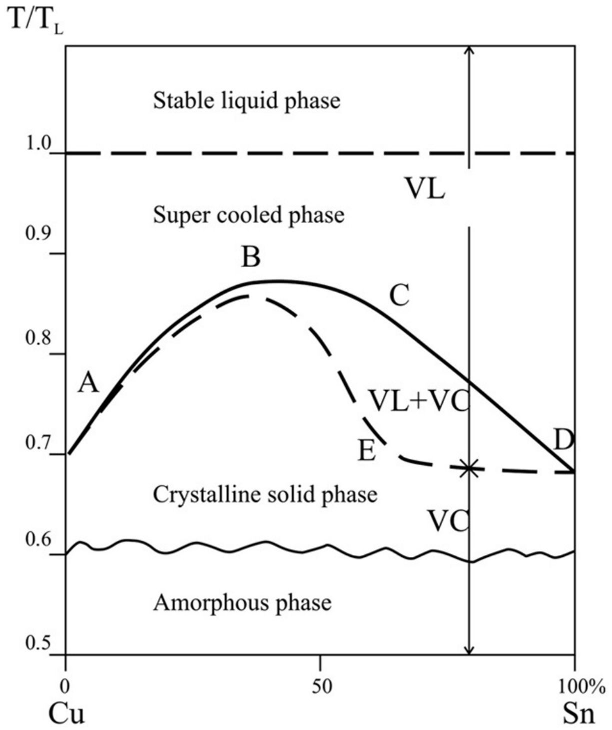

FIG. 5.4 Phase equilibrium diagram of the copper–tin alloy: VL is the vapor-liquid; VC is the crystal-crystal; ABCDE is the transitory (intermediate) region: and T_L is the temperature of the liquidus (the boundary between the vapor and liquid phases).

PECULIARITIES OF THE FORMATION OF ALLOY POWDERS

If the vapor-gas mixture contains several metals at a given stoichiometric ratio, a powder of the corresponding alloy is produced. This can normally be achieved either by evaporating an alloy of required composition, by evaporation of the components of the alloy separately from independent sources, or by coprecipitation of powders produced by decomposition of a mixture of metal-containing gaseous compounds.

The composition and properties of the final powder depend mostly on the type of the corresponding phase diagram. The formation of a mixture of particles of individual components is a feature of eutectic alloys with the mixing energy $U > 0$ (Pb – Sb). For the alloys with the cigar-shaped phase diagram with $U = 0$ (Bi–Sb, Mg – Cd), a joint condensation of metals takes place on common nuclei, and the resulting powder consists of particles of the alloy. In the case of metals forming congruent and incongruent melting of the compounds with $U < 0$ (Cd – Sb, Pb – Bi), the powder often comprises particles of intermetallic compounds.

The formation of alloy powders displays peculiarities associated with their phase diagram. The latter determines the composition and structure of the surface layer of the evaporating melt and, therefore, the properties of powders. In cases where the alloy constituents form no chemical compounds, the knowledge of the phase diagram suffices to predict those properties. For alloys displaying strong particle interaction whose components form a number of intermetallic compounds, vapor and melt composition dependent on the temperature and pressure values obey the Vrevsky laws. It has been found for such alloys that S_{cr} approaches unity due to the presence of ready cluster groups (condensation nuclei) in the vapor.

The rate J of evaporation (condensation) of an n-component alloy obeys the equation:

$$J = \sum_{1}^{n} J_i(a_i b_i)$$

where a is the activity of the alloy component and b is the mole fraction of clusters in the vapor. The latter can be evaluated correctly enough from the model of ideal associated solutions.

Fig. 5.4 shows the phase equilibrium diagram in the condensation process of a copper-tin alloy.

Using the temperature as a control parameter enables the production of either spherical ("super cooled phase," Fig. 5.5A), faceted crystalline particles (region "crystalline solid phase," Fig. 5.5B), or amorphous powder (Fig. 5.5C) [7].

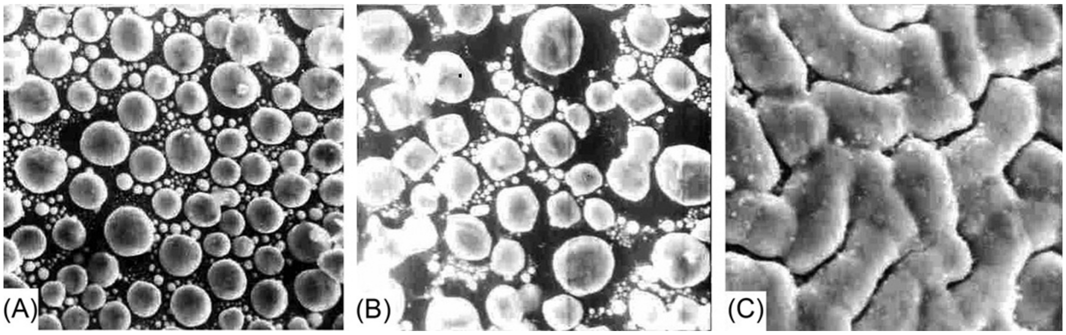

FIG. 5.5 Micrographs of the copper-tin alloy powders obtained in the condensation process in several regions of the phase equilibrium diagram (see figure): (A), VL, vapor-liquid ×1200; (B), VC, crystal-crystal ×2500; (C), ABCDE ×500.

CONTROLLING PRINCIPLES OF THE CONDENSATION PROCESS

The theoretical concepts given above form a foundation for the development of the basic IGC technology for production of metal powders. The condensation process is carried out by one of three modes, depending of the targeted powder properties:

- In the bulk of the condensation zone at the starting supersaturation degree of the vapor $S_{cr} > 10^6$.
- On a cooled surface placed in the condensation zone at $S_{cr} < 10^6$.
- In a mixed process, simultaneously in the volume and on the cooled surface. In the absence of thermoconvection, the temperature gradients can be evaluated using the equation

$$T = T_2(T_2 - T_1)\frac{e^{\mathrm{B}} - 1}{e^{\mathrm{b}} - 1}$$

with $b = \frac{Q_v C_v (r_2 - r_1)}{\lambda 2\pi r_1 r_2 (1 - \cos\alpha)}$ and $B = \frac{b r_1}{r}$.

where b and B are distances between the vapor source and the powder receiver with crossing angle α; Q_v and C_v are the flow and the specific heat capacity of the vapor; r_1, r_2 are the radii of a cell at the source and the receiver levels; r is the radius of the cell when the latter has the shape of a sphere; and λ is the heat conductivity coefficient.

The concentration and vapor supersaturation gradients are determined by differential equations representing the interrelations of the parameters of the vapor-gas medium (density, viscosity, partial pressure, etc.) and the geometrical characteristics of the condensation volume (shape, linear dimensions, distance from the vapor source to the crystallization surface, etc.).

The control of the powder dispersivity is realized through the residence time of the powder in the condensation zone and by selecting appropriate values of the condensation parameters. Quick cooling of the vapor and a short residence time in the condensation zone result in the formation of fine and ultrafine powders while full or partial condensation on the cooled surface gives more coarse powders with the particle size in the range from several microns to several millimeters.

In the case of bulk condensation, the control of the shape and structure of particles is realized through selecting such boundary conditions and the rate of heat transfer, which can provide the condensation process going in either vapor-solid or vapor-liquid-solid mode. In the first case, faceted monocrystalline particles are formed while, in the other case, particles of a spherical shape and semicrystalline structure are formed. In the case of condensation on the surface, particles of faceted shapes and of mono-or polycrystalline structure prevail.

Steady boundary conditions and permanent geometrical parameters of the condensation zone provide stable quality characteristics of the powder. The criterion equations (Eqs. 5.12 and 5.13) are helpful for designing the equipment and selecting the process parameters.

POWDER PRODUCTION AND APPLICATION OF GAS-PHASE PROCESSES

The gas-phase methods find wide application for the manufacture of semiproducts directly from metal vapor, by omittance the operation of nanopowder obtaining. The simultaneous evaporation of several materials, mixing their vapor flows, followed by condensation on a substrate and subsequent thermomechanical treatment, make it possible to design materials with unique properties.

Physical Vapor Deposition (PVD) Process

The PVD process includes melting the metal; producing a vapor; feeding the vapor into the zone of condensation; condensing the vapor into powder either in the free space or on a cooled surface (in a static or moving gas medium); and accumulating the powder in the cold part of the volume. The process is carried out in the presence of a neutral gas, sometimes with the addition of an oxidant or, on the contrary, of a passivating agent.

In the PVD process installations, a source material is transformed from a solid to a gaseous state by the technique, which may be divided into two physical process groups: evaporation and physical sputtering [10]. The evaporation is realized by means of resistance or induction furnaces, electron beams, low-voltage arcs, hollow cathodes, or laser beam heating. The processes can be carried out with additional ionization or without, in a reactant gas medium or without, and with bias voltage or without [11,12]. Diode or magnetron sputtering is used by direct current or rf current in the reactant gas medium or without, with bias voltage or without, or with additional modification of the magnetic field or without [13–15].

A zinc powder of high purity is manufactured in plate-type rectifying columns. The zinc vapor is fed via vapor pipes into one or several large tanks with water-cooled walls that act as condensers. A neutral gas is fed into the column. The lower part of the column is equipped with a bunker for accumulation of the powder and with an appliance for its discharge. The discharged powder is subjected to classification. Typically, the output of columns and condensers is within the range of 200–400 kg/h; the rejected fractions are normally recycled. The temperature of the column controls the powder quality (see also Chapter 20).

There are different types of equipment for the laboratory and pilot plant scale intended for the production of powders by the evaporation-condensation method. As a rule, an apparatus is fitted with an induction or resistance heated evaporator and moving cooled surfaces (drum, belt, or disc) for vapor condensation. Sometimes a common volume is used both for evaporation and condensation. The nature of the metal governs the process. The manufacturing of volatile metal powders (zinc, magnesium, cadmium, lead) calls for atmospheric pressure while aluminum and copper powders are produced at a considerably reduced pressure of a neutral gas. The lower the pressure, the lower the evaporator temperature.

One of the installations for zinc powder manufacturing is shown in Fig. 5.6. A vertical apparatus of $>10\,\mathrm{m}^3$ in volume equipped with a sealed water-cooled evaporated chamber consists of several sections, each up to 1 m high, made so as to permit the regulation of the volume of the condensation zone.

Each of the sections includes a 100 kW inductor and a graphite crucible with a capacity of up to 300 kg of molten zinc. The design of the crucible facilitates feeding nitrogen into the condensation zone. The zinc vapors are directed by the nitrogen flow toward a rotating water-cooled drum condenser. The powder deposited on the drum surface is cut away with a special blade and dropped into a bunker. The unit operates at the evaporator temperature of 923–1073 K in rarefied atmosphere at 3–20 kPa. The unit yield is 10–15 kg/h of ultrafine zinc.

A modular type apparatus named “Tuman” (trade name “Fog”) was developed at the Institute of Metallurgy, Ural Branch of the Russian Academy of Science. It can feature either combined or separate zones of evaporation and condensation and is less sophisticated in design and easier in operation in comparison with the above installation.

The Tuman unit (Fig. 5.7) has an annual output of 120 tons of zinc powder. Electric power consumption is up to 40 kW; the operational cycle of 25 days is followed by a one-day stop for maintenance. The machine is easy to operate and to

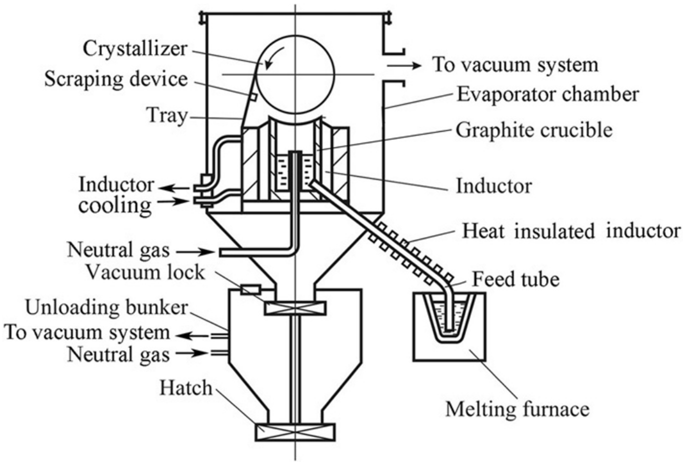

FIG. 5.6 An apparatus for the production of ultrafine powders.

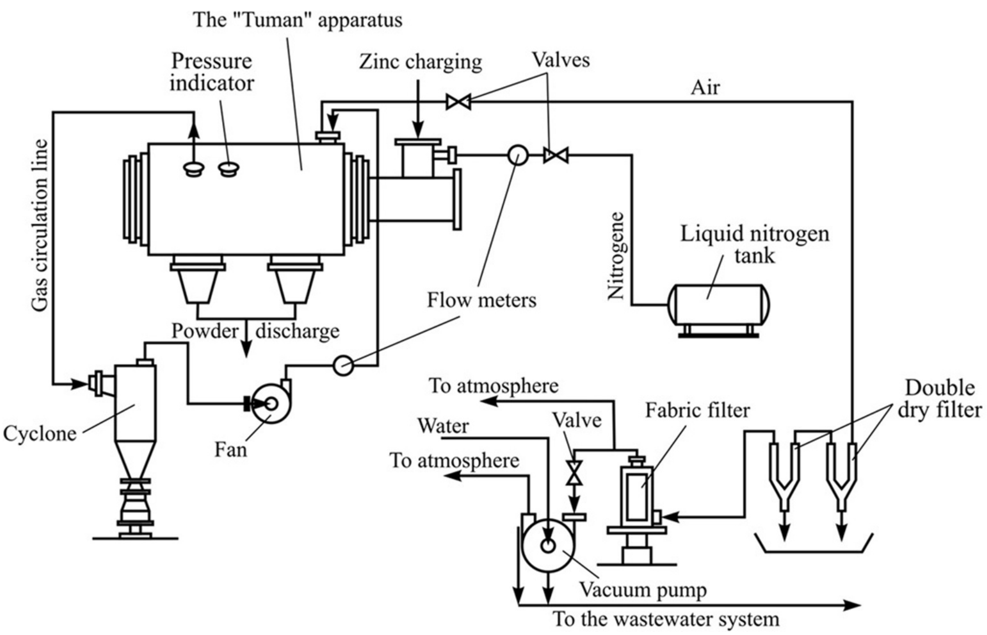
The "Tuman" apparatus
Pressure indicator
Zinc charging
Valves
Air
Gas circulation line
Nitrogene
Liquid nitrogen tank
Flow meters
Powder discharge
Cyclone
Fan
To atmosphere
Water
Valve
Fabric filter
Double dry filter
To atmosphere
Vacuum pump
To the wastewater system

FIG. 5.7 The schematic drawing of the "Tuman" ("Fog") unit.

TABLE 5.2 Specification of Metal Powders Produced by the PVD Technique

The Powder Mark (as Given by the Manufacturer)	Active Metal Content, % (min)	Bulk Density (g/cm^3)	Specific Surface (m^2/g)	Average Particle Size (μm)
Zinc powder PZHD	96.0	1.4–2.0	0.1–0.6	4–12
Copper powder PCND	99.98	0.4–1.3	8.0–12.0	0.1–0.3
Bronze powder PBND	Cu 89.0–98.0; Sn 1.0–10.0 (typical)	0.3–1.2	3.0–8.0	0.1–0.2
Lead powder PLHD	94.0–95.0	1.8–3.6	...	0.5–3.0

convert from the production of one type of powder to another. The controllable process ensures the production of metal powders with a targeted particle size in the micron, submicron, and nanometer ranges with high product yields.

Commercial scale Tuman units are in use at the VMP R&D Company's plant in Yekaterinburg (Russia) for manufacturing fine and ultrafine powders of nonferrous metals and alloys (Table 5.2) (see also Chapter 20).

Properties of Powders and Areas of their Usage

Powders produced by the evaporation-condensation process may be divided into two categories according to their particle size: ultrafine (micron and submicron) and nanosized powders, with the categories differing radically in their chemical and physical properties. The nanopowders display higher activity due to their high specific surface area and a peculiar "nonequilibrium" structure of particles (see Fig. 5.8 and Table 5.1). This makes them fit for such specific fields as the production of rocket fuel, catalysts, heat absorbents, and microelectronics. The properties of ultrafine powders are more ordinary, and the range of their application is much wider, from pigments for paints and varnishes to items of powder metallurgy. Nanopowders of copper and its alloys have an average particle size of 100–200 nm. Areas of applications of these powders are considered in more detail in Chapter 19.

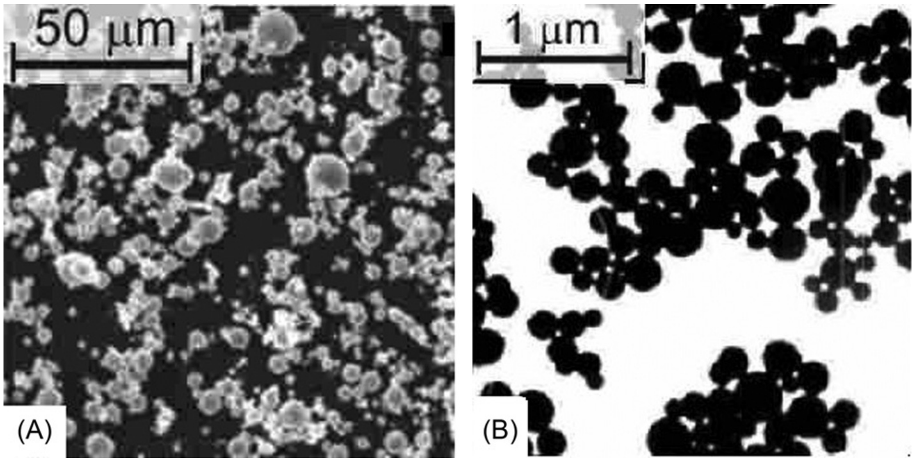

FIG. 5.8 Micrographs of fine (A) and ultrafine (B) powders produced by the PVD technique.

Chemical Vapor Deposition (CVD) Process

CVD is practiced in a variety of formats. These processes generally differ in the means by which chemical reactions are initiated. Those classified by operating pressure:

- Atmospheric pressure CVD (APCVD)-CVD at atmospheric pressure.
- Low-pressure CVD (LPCVD)-CVD at subatmospheric pressures. Reduced pressures tend to reduce unwanted gas-phase reactions and improve film uniformity across the wafer.
- Ultrahigh vacuum CVD (UHVCVD)-CVD at very low pressure, typically below 10^{-6} Pa ($\sim 10^{-8}$ torr). Note that in other fields, a lower division between high and ultrahigh vacuum is common, often 10^{-7} Pa.

Most modern CVD processes are either LPCVD or UHVCVD.

Those classified by the physical characteristics of vapor:

- Aerosol-assisted CVD (AACVD)-CVD in which the precursors are transported to the substrate by means of a liquid/gas aerosol, which can be generated ultrasonically. This technique is suitable for use with nonvolatile precursors.
- Direct liquid injection CVD (DLICVD)-CVD in which the precursors are in liquid form (liquid or solid dissolved in a convenient solvent). Liquid solutions are injected in a vaporization chamber toward injectors. The precursor vapors are then transported to the substrate, as in classical CVD. This technique is suitable for use on liquid or solid precursors. High growth rates can be reached using this technique.

Plasma methods (also cooled plasma processing):

- Microwave plasma-assisted CVD (MPCVD).
- Plasma-Enhanced CVD (PECVD)-CVD that utilizes plasma to enhance the chemical reaction rates of the precursors. PECVD processing allows deposition at lower temperatures, which is often critical in the manufacture of semicon ductors. The lower temperatures also allow for the deposition of organic coatings, such as plasma polymers, that have been used for nanoparticle surface functionalization.
- Remote plasma-enhanced CVD (RPECVD)—similar to PECVD except that the wafer substrate is not directly in the plasma discharge region. Removing the wafer from the plasma region allows processing temperatures down to room temperature.

In typical CVD, the substrate is exposed to one or more volatile precursors in possession of high vapor pressure by low temperatures (373–673 K), such as chlorides and organometallic compounds, which react and/or decompose on the sub strate surface to produce the desired deposit. Frequently, volatile by-products are also produced, which are removed by gas flow through the reaction chamber.

CVD for tungsten is achieved from tungsten hexafluoride (WF_6), which may be deposited in two ways:

$$WF_6 \rightarrow W + 3F_2$$

$$WF_6 + 3H_2 \rightarrow W + 6HF$$

Other metals, especially aluminum and copper, can be deposited by CVD. Cu(hfac)$_2$ is acceptable as a precursor for copper CVD [14]. Copper is typically deposited by electroplating. The precursors for copper chemical vapor deposition are discussed in the work [16]. Aluminum can be deposited from triisobutylaluminum (TIBAL) and related organoaluminum compounds.

CVD for titanium, nickel, and refractory metals, including molybdenum, tantalum, niobium, and rhenium, is widely used [17–19]. These metals can form useful silicides when deposited onto silicon. Mo, Ta, and Ti are deposited by LPCVD from their pentachlorides. Nickel, molybdenum, and tungsten can be deposited at low temperatures from their carbonyl precursors. In general, for an arbitrary metal M, the chloride deposition reaction is as follows:

$$2MCl_5 + 5H_2 \rightarrow 2M + 10HCl$$

whereas the carbonyl decomposition reaction can happen spontaneously under thermal treatment or acoustic cavitation and is as follows:

$$M(CO)_n \rightarrow M + nCO$$

The decomposition of metal carbonyls is often violently precipitated by moisture or air, where oxygen reacts with the metal precursor to form a metal or metal oxide along with carbon dioxide.

Niobium(V) oxide layers can be produced by the thermal decomposition of niobium(V) ethoxide with the loss of diethyl ether [20,21], according to the equation:

$$2Nb(OC_2H_5)_5 \rightarrow Nb_2O_5 + 5C_2H_5OC_2H_5$$

Chemical reactions of the CVD processes occur in the immediate vicinity or on the surface of an under-treatment article at temperatures up to 1373 K, what bounds CVD application for materials, such as high-speed steel, which properties are lost consequently of the tempering (Fig. 5.9).

Recently, PECVD modification was developed permitting the decrease of the coating temperature up to temperatures lower than 773 K [22]. In fact, this method corresponds to a combination of two basal methods of gas-phase precipitation, so far as in this CVD modification the coating occurs in the plasma medium, such as by PVD. A layout view of the PECVD parallel plate reactor is represented in Fig. 5.10.

Both the gas-phase methods CVD and PVD are used for wear-resistant and thermostable covering. Microfabrication processes widely use CVD to deposit materials in various forms, including monocrystalline, polycrystalline, amorphous, and epitaxial. These materials include silicon (SiO_2, germanium, carbide, nitride, oxynitride), carbon (fiber, nanofibers, nanotubes, diamond and graphene), fluorocarbons, filaments, tungsten, titanium nitride, and various high-*k* dielectrics.

Health and Environment Protection

The safety system for the plants operating the evaporation-condensation-based processes must include, apart from the conventional topics relating to the high-temperature and vacuum processes, the issues meeting safety requirements for the flammable and explosive materials. In terms of environmental protection and health, special measures are required such

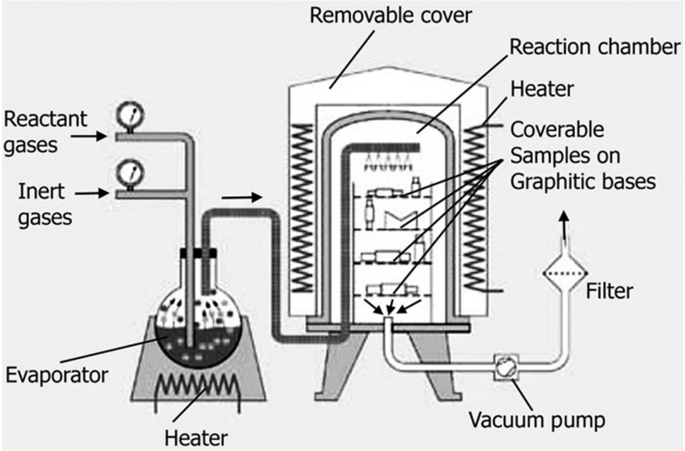

FIG. 5.9 The schematic drawing of the installation for deposition by the CVD technique.

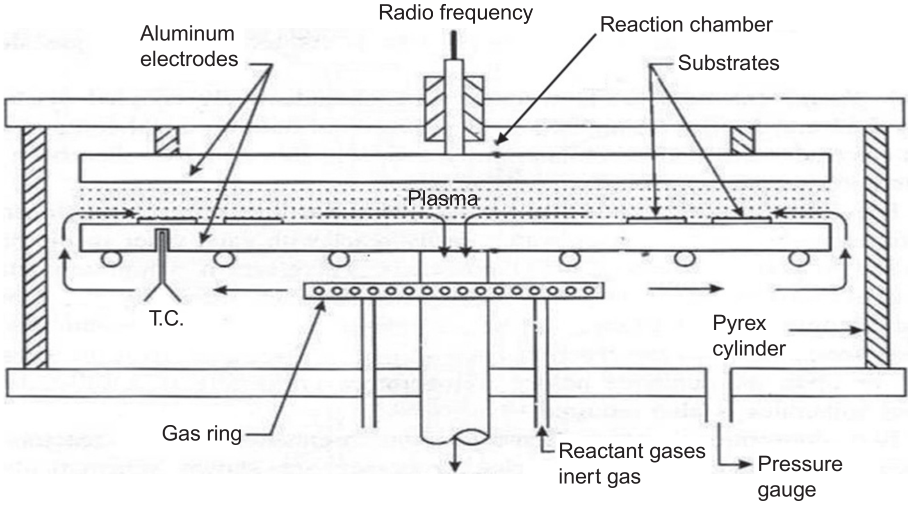

FIG. 5.10 Parallel-plate reactor of the plasma-enhanced CVD process.

as the neutralization of gas and water effluents, cleaning the working areas, providing the workers with the necessary individual protection gear, etc. More specific requirements are described in the chapters dealing with the production of powders of individual metals.

REFERENCES

[1] Frishberg IV, Kvater LI, Kuz'min BP, Gribovskii SV. The gas-phase method of preparing powders. Moscow: Nauka Publishers; 1978 [In Russian].
[2] Naboychenko SS, editor. Handbook of NonFerrous Metal Powders. Moscow: Metallurgia Publishers; 1997 [in Russian].
[3] Brock JR. The dynamics of ultrafine particles: a survey. J Aerosol Sci 1979;10(2):192–5.
[4] Hirsh D, Pound G. Evaporation and condensation. Moscow: Metallurgya Publishers; 1966 [in Russian].
[5] Subbotina OY, Kishkoparov NV, Frishberg IV. Genesis of ultrafine metal powders built on their particle size distribution. In: Proceedings of the 5th All-Russian Conf. on Physical Chemistry of Ultra Disperse Systems, Part. Vol. 1. Yekaterinburg (Russia): Publ. the Ural Branch of the Russian Academy of Sciences; 2001. p. 53–7 [in Russian].
[6] Subbotina OY, Kishkoparov NV, Frishberg IV. Mechanism and kinetics of coagulation of ultrafine metal particles formed at an IGC process. In: Proceedings of the 5th All-Russian Conference on Physical Chemistry of Ultra Disperse Systems, Part 1. Yekaterinburg (Russia): Publ. the Ural Branch of the Russian Academy of Sciences; 2001. p. 58–63 [in Russian].
[7] Frishberg IV. Gas-phase metallurgy: from an idea to the commercial manufacturing of fine metal powders and products based thereon. In: Proceedings of the EuroPM 1997 International Conference. Munich: Publ. EPMA; 1998. p. 252–4.
[8] Kutateladzhe SS. The heat transfer by condensation and boiling. Moscow–Leningrad: Mashgiz Publ; 1952 [in Russian].
[9] Ackerman G. Wärmeübergang und molekuläre stoffübertragung im gleichen feld bei grossen temperatur- und partialdruck-differenzen. VDJ-Forschungsh 1937;382:1–16.
[10] Fuller L. Physical vapor deposition–evaporation and sputtering. Webpage (26 Nov 2013): <http://people.rit.edu/lffeee/PVD_Recipes.pdf> [Accessed 31 October 2017].
[11] Harsha KSS. Principles of physical vapor deposition of thin films. Great Britain: Elsevier; 2006.
[12] Movchan BA. Inorganic materials and coatings produced by EBPED. Surf Eng 2006;22(1):35–46.
[13] Sigmund P. Mechanisms and theory of physical sputtering by particle impact. Nucl Instrum Meth Phys Res 1987;27:l–20.
[14] Kuzmichev AI. Magnetron sputtering systems. Kiev (Ukraine): Avers; 2008 [in Russian].
[15] Behrisch R. Sputtering by particle bombardment: experiments and computer calculations from threshold to mev energies. Eckstein W., editor. Berlin: Springer; 2007.
[16] BuFaroosha M. Precursors for copper chemical vapor deposition. Dr dissertation, B.S. United Arab Emirates University, 2002.
[17] Fortini AJ. Low-cost, high-performance refractory metal alloys for rocket engines. In: Proceedings of the 9th Tungsten, refractory & hardmaterials conference. Orlando (FL, U.S.A.): Metal Powder Industries Federation; 2014. p. 537–43.
[18] ATI Wah Chang. Technical data sheet C-103 niobium properties and products. Overview the requirement for high-performance. 2017 <http://www.industrycortex.com/datasheets/profile/2482808.pdf>.
[19] Tuffias R, Brockmeyer J, Fortini A, Williams B, Duffy A, Kaplan R. Engineering issues of iridium/rhenium rocket engines revisited. In: Proceedings of the 35th AIAA/ASME/SAE/ASEE joint propulsion conference. Los Angeles (U.S.A.): American Institute of Aeronautics and Astronautics, Reston, VA; 1999. p. 1–7.

[20] Maruyama T, Konodawa T. Electrochromic properties of niobium oxide thin films prepared by chemical vapor deposition. J Electrochem Soc 1994;141(10):2868–71. https://doi.org/10.1149/1.2059247.

[21] Rahtu A. Atomic layer deposition of high permittivity oxides: film growth and in situ studies. Academic dissertation. University of Helsinki 2002. ISBN 952-10-0646-3.

[22] Cardenas P. and Tung D. Plasma enhanced chemical vapor deposition (DECVD). <http://www.ece.umd.edu/class/enee416.F2007/GroupActivities/Presentation5.pdf>; 2007 [Accessed 31 January 2018].

Chapter 6

Carbonyl Method of Metal Powder Production☆

Irina V. Frishberg
Institute of Metallurgy, Ural Branch of the Russian Academy of Science, Yekaterinburg, Russia

Chapter Outline

Introduction 201
Preparation of Metal Carbonyls 201
  Theoretical Basis of the Synthesis 202
  Preparation of the Starting Materials for Carbonyl Production 204
  Synthesis of Carbonyls 205
  Extraction, Purification and Separation of Carbonyls 205
Manufacture of Powders by Thermal Decomposition of Metal Carbonyls 206
  Physicochemical Basis of the Process 206
  The Technique of Powder Manufacture 207
  Manufacture of Composite Powders 208
Properties and Applications of the Metal Carbonyl Powders 208
Health and Environmental Protection Measures in the Carbonyl Industry 209
References 210

INTRODUCTION

The carbonyl method is one of the most widely used methods of chemical deposition [1–5]. Physical and chemical techniques of gas-phase manufacturing of metal powders have a common theoretical basis. A chemical reaction may answer for the formation of the metal vapor; its precipitation may occur because of simple condensation. At the same time, the evaporation-condensation processes also involve chemical interactions.

The process of chemical vapor deposition (CVD), mainly of high purity refractory metals, requires reagents able to vaporize without decomposition, form a sufficient concentration of the vapor of the metal-containing compound, and giving, upon decomposition of the latter and deposition of the metal, only gaseous and chemically inert substances.

The decomposition of metal-containing compounds takes place as a result of a heat impact (plasma discharge, laser radiation). For chemical deposition, reducing agents are used, for example, hydrogen for deposition of tungsten from halides (see Chapter 23) and zinc or magnesium vapors for a quick deposition of titanium, zirconium, and beryllium from their halides. Using hydrogen lowers the process temperature. When a metal is used as a reducing agent, its quantity must strictly correspond to the stoichiometry of the reaction to prevent its coprecipitation and appearance in the powder. A lowered pressure serves the same result.

The method of chemical deposition from the gas phase is universal. It enables the manufacture of powders of a very high purity of the majority of refractory metals with targeted chemical composition, particle size, and shape; it also introduces necessary additives.

PREPARATION OF METAL CARBONYLS

The carbonyl method basis consists of the treatment of metal-containing materials with carbon monoxide at elevated pressures and temperatures followed by thermal decomposition of the metal carbonyls with deposition of the metal as a powder, and recycling of the carbon monoxide according to the scheme:

☆ Expanded and updated by O.D. Neikov.

Handbook of Non-Ferrous Metal Powders. https://doi.org/10.1016/B978-0-08-100543-9.00006-3
© 2019 Elsevier Ltd. All rights reserved.

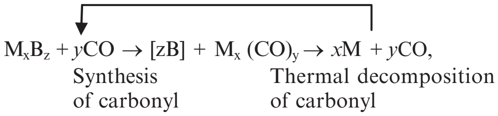

$$\underset{\text{Synthesis of carbonyl}}{M_xB_z + y\text{CO} \rightarrow [zB] + M_x(\text{CO})_y} \underset{\text{Thermal decomposition of carbonyl}}{\rightarrow xM + y\text{CO},}$$

where B is the "ballast" matters (oxygen, salt residue, impurities, etc.); x, y, and z are the coefficients, the values of which depend on the nature of the metal; and $M_x(CO)_y$ is the carbonyl of the metal M.

The flow sheet of the synthesis and decomposition of carbonyls is shown in Fig. 6.1.

The carbonyl process is used for manufacturing powders of nonferrous metals of VI, VII, and VIII groups of the periodic table (nickel, partly tungsten, molybdenum, cobalt, and some platinum group metals). Characteristic features of this process are low raw material and energy consumption, versatility of raw materials, high yield and purity of powders produced, and the possibility of completely automated operation. The technique affords control of particle size, shape, and structure. It makes possible the production of metallic films, coatings, filamentary crystals, and composite materials.

One of the shortcomings of the method is that it is applicable to only a limited range of metals. Other shortcomings include the toxicity of the materials, the high pressures involved in the process, the necessity of environmental control, and the health and safety measures.

Theoretical Basis of the Synthesis

Metal carbonyls are volatile and low-melting compounds of the $M_x(CO)_y$ type that decompose upon heating into carbon monoxide and metal, their properties being conditioned by the structure of the carbonyl molecules and the type of chemical bonds in them. In the molecules of metal carbonyls, CO groups are bound to the atom of a metal via carbon atoms. The electron pair of the carbon atom is transferred to the metal atom with the formation of a σ-bond, and the α-electrons of the metal are transferred to vacant antibonding π^*-orbitals of CO (π-bond). The metal coordinates of such a number of CO groups as to complete its electron shell up to the one of the located behind it noble gas. It is assumed that CO donates two electrons, and the metal is in the zero oxidation state (in the neutral metal carbonyls).

The metal carbonyls may be mononuclear and polynuclear. In the polynuclear carbonyls, the metal atoms are bound to each other directly and in many cases also via bridging CO groups. The formula of carbonyls is determined according to the equations:

$$G - \frac{(xm + 2y)}{x} = x - 1 \tag{6.1}$$

and

$$y = \frac{x}{2}(G - m - x + 1) \tag{6.2}$$

where m is the metal atomic number; G is the atomic number of the nearest located behind noble gas; and x and y are the coefficients, the values of which depend on the nature of the metal.

Some properties of metal carbonyls are given in Table 6.1.

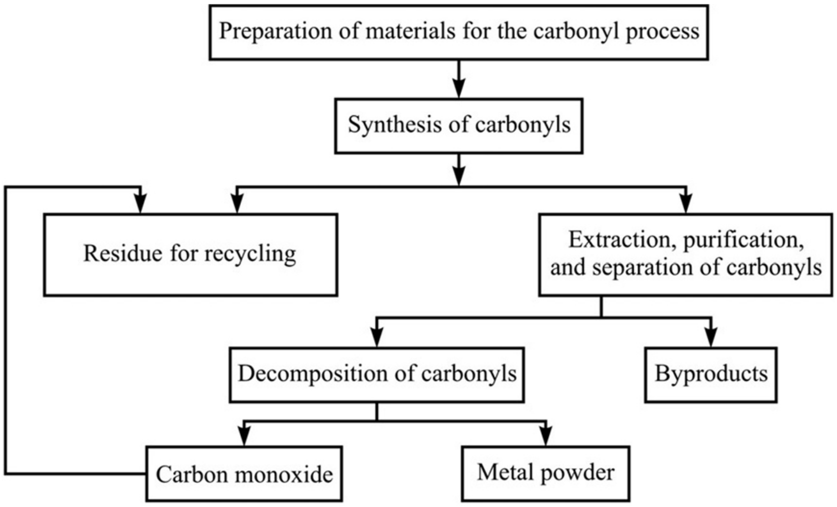

Preparation of materials for the carbonyl process
Synthesis of carbonyls
Residue for recycling
Extraction, purification, and separation of carbonyls
Decomposition of carbonyls
Byproducts
Carbon monoxide
Metal powder

FIG. 6.1 The flow sheet of the carbonyl process.

TABLE 6.1 Properties of Metal Carbonyls

Carbonyl	Physical State	Color	Temperature (K)				Density at 293 K (kg/m^3)	Reaction With Air	Solvents of Carbonyls
			Evaporation (sublimation)	Boiling	Melting	Decomposition			
Group V of Periodic Table									
$V(CO)_6$	Solid	Blue-green	313	…	…	343	…	Yes	Ethers, pyridine, toluene, benzene
Group VI									
$Cr(CO)_6$	Solid	Colorless	303	426	420	360–503	1.77	No	Chloroform, ethers, benzene, alcohols
$Mo(CO)_6$	Solid	Colorless	313	428	421	403–673	1.96	No	Ethers, benzene
$W(CO)_6$	Solid	Colorless	323	448	442	413–773	2.65	No	Chloroform, ethers, alcohols
Group VII									
$Mn_2(CO)_{10}$	Solid	Golden-yellow	323	p*	427	383–573	1.81	Weak	Ethers, organic solvents
$Tc_2(CO)_{10}$	Solid	Colorless	323	…	432	333–343	–	No	Ether, acetone
Group VIII									
$Fe(CO)_6$	Liquid	Light-yellow	373	376	253 (freezing)	333–523	1.47	No	Petrol, benzene, ethers
$So(CO)_5$	Liquid	Colorless	…	…	258 (freezing)	…	…-	–	Benzene (weakly)
$Os_3(CO)_{12}$	Solid	Light-yellow	403	…	497	…	…	No	Benzene (weakly)
$Co_2 (CO)_8$	Solid	Orange	318	P	324	298–325	1.82	Yes	Petrol, benzene, alcohols
$Co_4(CO)_{12}$	Solid	Dark green	…	P	…	333	…	Yes	Pentene, benzene
$Rh_2(CO)_8$	Solid	Orange-yellow	–	P	349	…	…	Yes	Organic solvents
$[Rh(CO)_3]_x$	Solid	Brown -red	…	…	…	473	…	No	Benzene (weakly)
$Rh_6(CO)_{15}$	Solid	Black	…	…	…	493	…-	Yes	Organic solvents (weakly)
$Ir_2(CO)_8$	Solid	Greenish-yellow	433	…	…	373–433	…	Yes	Ethers, CCl_4
$Ni(CO)_4$[a]	Liquid	Colorless	303	316	248 (freezing)	333–473	1.31	No	Ethers, benzene, alcohols, acetone
$[Pt(CO)_2]_x$	Solid	Dark red	…	P	…	483	3.55	Yes	Ketones, aniline, pyridine, alcohols

[a] *Properties of nickel carbonyl vapor: the density is 5.98 (in provided that air = 1.0) at 299 K; the pressure is 400 mm Hg at 280 K.*
p—Decomposes below boiling point.*

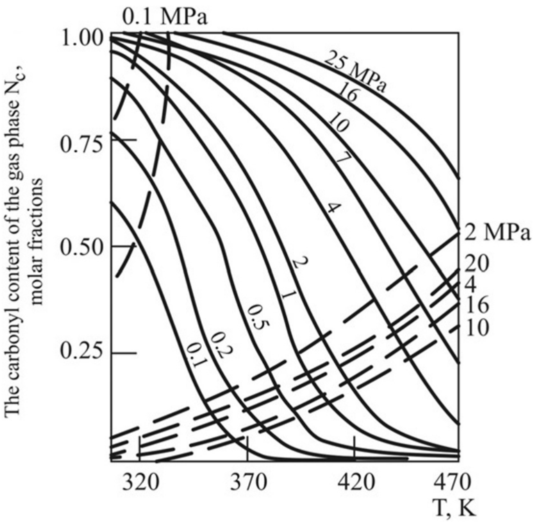

FIG. 6.2 The equilibrium content of nickel carbonyl in the gas phase as a function of the synthesis temperature under reaction (Eq. 6.3). Dashed lines divide the regions of condensed and gaseous state of the carbonyl.

Metal carbonyls form upon a reaction of the metal in its active state with carbon monoxide, according to the reversible reaction:

$$x\mathrm{M} + y\mathrm{CO} \leftrightarrow \mathrm{M}_x(\mathrm{CO})_y \tag{6.3}$$

The reaction is exothermic and is accompanied by a decrease in the number of moles of the products formed compared to the starting materials. Therefore, the process requires high pressures and moderate temperatures (Fig. 6.2).

The synthesis of carbonyls takes place at the gas-solid boundary and goes through the following stages: carbon monoxide diffusion from the gas phase toward the solid surface that has cracks and pores; the formation of an absorbed layer of CO on the surface; the chemical reaction of CO with the metal in this layer with the initial formation of sub-carbonyls, followed by the formation of the $M_x(CO)_y$ molecule; and diffusion of metal carbonyl molecules from the solid surface into the gas phase. The reaction rate is, as a rule, limited by the diffusion of the gaseous compounds. Activation of the solid surface accelerates the synthesis reaction.

Metal carbonyls are obtained by a direct reaction of carbon monoxide with free metals, according to the reaction (Eq. 6.1) or by the reaction of carbon monoxide with metal compounds in the presence of reducing agents such as H_2, Zn, Mg, Na, aluminum-organic compounds, and complex metal hydrides, for example:

$$\mathrm{Ni_3S_2} + 4\mathrm{Cu} + 12\mathrm{CO} \rightarrow 3\mathrm{Ni(CO)_4} + 2\mathrm{Cu_2S}$$

The latter method is widely employed in practice due to available and low metal comprising raw materials.

Another known technique is carbonyl formation carried out in aqueous media or organic solvents:

$$2\mathrm{MoCl_5} + 5\mathrm{Zn} + 12\mathrm{CO} \xrightarrow{\text{ether, dichloroethane}} 2\mathrm{Mo(CO)_6} + 5\mathrm{ZnCl_2}$$

$$\mathrm{WCl_6} + 3\mathrm{Zn} + 6\mathrm{CO} \xrightarrow{\text{ether}} \mathrm{W(CO)_6} + 3\mathrm{ZnCl_2}$$

In the process of synthesis of carbonyls of metals belonging to groups VI–VIII, a selective extraction of the metal from starting raw materials takes place while all the elements of the groups I–V except vanadium do not form carbonyls.

Preparation of the Starting Materials for Carbonyl Production

Carbonyls of cobalt and nickel are obtained either by direct reaction with pure metal or with metal-containing compounds. Thus, various oxidized and sulfide materials such as scrap metal, alloys based on Ni-Fe-Cu, Ni-Fe-Cu-S, and Ni-Cu-S systems, etc., are in use as starting materials for the commercial production of nickel carbonyl. To produce tungsten and molybdenum carbonyls, chlorides of these metals obtained from ore concentrates are used.

The reactivity of the starting materials depends on their structure, degree of defects, and chemical composition; it increases with the growth of surface area accessible for the chemical interaction. Therefore, a disintegration of the starting materials to the optimal particle size in the range from 10 to 25 mm is preferable. Technological operations of crushing, granulating, or briquetting the starting materials, including the simultaneous addition of sulfur and oxidation, quenching, treatment with abrasives, etc., are used for this purpose.

Impurities can act either as inhibitors or as catalysts of the synthesis. Thus, copper, mercury, iron, sulfur, selenium, phosphorus, and some other elements increase the rate of carbonyl formation of nickel-containing materials while carbon, silicon, and chromium act conversely. The catalytic effect of impurities depends on their content and usually has a maximum, for example, for copper and for sulfur it equals ≈3% and 3%–8%, respectively.

In order to increase the metal content in the starting material and to intensify the reaction, raw materials are subjected to a pretreatment using the techniques of pyro- and hydrometallurgy, described in the chapters relating to the individual metals.

Synthesis of Carbonyls

The synthesis of most of carbonyls is carried out at carbon monoxide pressures in the range of 0.1–20 MPa and at temperatures of 320–550 K. The main parameters of the process are pressure, temperature, the flow rate of the gas stream, and the processing time. An increase in carbon monoxide pressure results in a higher stability of the carbonyls that allows the reaction temperature to increase and, accordingly, the process rate and the yield of the carbonyls (Fig. 6.2). However, the use of expensive high-pressure equipment involves an increase in both capital outlays and operational costs. The higher the reactivity of the starting material, the lower the optimal value of the synthesis pressure.

The yield of carbonyl depends on the temperature, growing with the rise in temperature up to the point where thermal decomposition of the carbonyl begins. A further rise of the temperature results in lowering the yield of the product. The intensity of heat and mass transfer in the reactor depends on the flow rate of the gas stream. Increasing the flow rate allows the use of a lower operating pressure of CO, or, at a given pressure, enlarges the output. The processing time determines the average rate of the process and the attainable extraction ratio of the metal.

The synthesis of carbonyls is performed in a hermetic vertical or horizontal reactor with cold walls cooled naturally or by external cooling means. The close contact and interaction of material with gas are attained by their countercurrent and the rotation of the reactor body or special mechanical devices. The reactors are usually provided with charging and unloading devices for preventing dust loss. There are continuous or batch reactors. The use of reactors with fluidized beds is quite promising (Chapter 21 contains a more detailed description of the reactor designs).

Carbonyl production in aqueous media is carried out in autoclaves equipped with stirring devices or in column reactors of a scrubber type. Pumps are used for the transportation of the reagents. The favorable features of these techniques are the continuity of the process and ease of control.

Extraction, Purification and Separation of Carbonyls

As a rule, the gas-vapor mixture of metal carbonyl with carbon monoxide coming out from a synthesis reactor contains admixtures including: carbonyls of elements relational to groups close to the base metal; ingress of water (up to 0.5%) out of the gas-holder; oil from compressors and pumps; and chlorine- and sulfur-containing compounds introduced by pretreatment of the raw materials. To eliminate the admixtures from the vapor-gas mixture, the carbonyls are liquefied by condensation at a pressure of 2–7 MPa. The purification of liquid carbonyls to a significant degree of purity is carried out in rectification columns by a conventional technology at atmospheric pressure. This technique is applicable to purification of nickel carbonyl containing 2%–3% max of iron carbonyl. Tungsten and molybdenum carbonyls are purified by steam distillation followed by alkaline washing to remove traces of chlorides.

If two or more carbonyls are formed in the synthesis process in comparable quantities, their purification and especially separation become more difficult. Thus, despite different volatilities of nickel, iron, and cobalt carbonyls, there are no means to prevent their decomposition when their mixture is separated at atmospheric pressure. The problem consists of sophisticated and expensive methods of separation such as rectification under pressure, fractional condensation, or some other special method. Therefore, in the commercial production of nickel, either starting materials with low iron content are used or mixed iron-nickel powders are produced. In processing tungsten-molybdenum raw materials where full separation of $W(CO)_6$ and $Mo(CO)_6$ is practically impossible, a preliminary separation of the metal chlorides is performed.

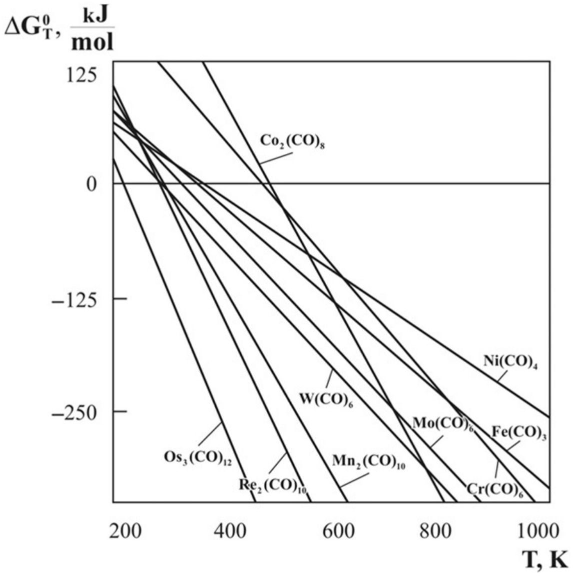

FIG. 6.3 Dependence ΔG^0_T on temperature for the reaction of thermal decomposition of metal carbonyls.

MANUFACTURE OF POWDERS BY THERMAL DECOMPOSITION OF METAL CARBONYLS

Physicochemical Basis of the Process

Thermal decomposition of metal carbonyls is an endothermic process, and according to the reaction (Eq. 6.3), it proceeds with the increase of the amount of the formed substance moles; therefore, the low pressures and high temperatures are expedient. According to the thermodynamic calculations (Fig. 6.3), trinuclear carbonyls are most prone and mononuclear ones are least prone to thermal decomposition.

The nucleation and growth of the new phase can proceed either heterogeneously on a prepared surface or in the gas volume. In the first case a metal coating and in the second case a metal powder arises.

The decomposition of the metal carbonyls proceeds stepwise, starting with the formation of unstable primary subcarbonyls and followed by splitting off the carbon monoxide molecules off to release the metal atoms. The latter by integration form nuclei of powder particles. The particles, the dimensions of which reach 4–20 nm, continue to grow due to thermal decomposition of the remained carbonyl vapor on their surface. At high concentrations of carbonyl in the gas phase, the fragments of the carbonyl can aggregate, and this process is accompanied by a partial splitting off of the CO group according to the scheme:

$$M_a(CO)_i + M_b(CO)_j \rightarrow M_{a+b}(CO)_{i+j-k} + k\mathrm{CO} \tag{6.4}$$

These aggregates act as the nuclei of the new phase. The process of nucleation depends on the kinetics of the reaction (Eq. 6.4), in the course of which the aggregates transform into metal particles with CO molecules sorbed onto their surface. Sintering and coagulation of the particles also contribute to their growth.

Side reactions of decomposition of the carbonyls lead to the formation of carbon, metal oxides, and carbides:

$$\left.\begin{array}{l} CO \leftrightarrow 0.5CO_2 + 0.5C \\ 2M + CO \leftrightarrow MO + MC \\ M + CO \leftrightarrow MO + C \\ M + 2CO \leftrightarrow MC + CO_2 \end{array}\right\} \tag{6.5}$$

These reactions are typical for all the metals except the refractory metals.

The impurities influence the shape and structure of powder particles. The decomposition of CO according to (Eq. 6.5) results in a laminated "onion"-type structure of particles of carbonyl powders.

The carbon and oxygen content of the powders depends on the nature of the metal and on the process parameters. Side reactions have practically no influence on the properties of the metal powder. However, an exception must be made for metals, which do not form stable carbides, are slowly oxidized, and can affect as weak catalysts of the reaction of CO disproportionation (for example, nickel). The influence of the side reactions is considerably higher for tungsten and molybdenum. Oxidation of the metal by carbon dioxide can take place when the latter is present in a considerable amount. The admixture of the iron carbonyl $Fe(CO)_5$ in the amount of 1%–2% catalyzed the decomposition of the carbon monoxide.

The higher the process temperature, the lower the thermodynamic probability of the formation of carbides, oxides, and other admixtures. Therefore, the decomposition process should be carried out at a maximal allowable temperature to ensure the purity of the metals produced.

The Technique of Powder Manufacture

The decomposition of carbonyls is performed at carbon monoxide pressures close to atmospheric and at temperatures depending on the metal: 470–670K for nickel, 620–1470K for tungsten and molybdenum, and 420–520K for cobalt. The reaction is carried out in a vertical column with external heating and filled with carbon monoxide. Carbonyl vapors from the evaporator are fed into the column. The greater part of the carbonyl decomposes in the upper section of the column; the growth and sintering of the particles formed take place in the middle and lower sections. The particles are initially suspended in the gas, and then precipitate and fall into a bunker. In some cases, forced circulation of carbon monoxide is applied.

The main process parameters are the temperature in the sections of the apparatus, the concentration of the carbonyl vapor at the entrance and its feed rate, the volume flow rate of the gases, and the presence of seeds. The temperature is the most important parameter controlling the powder particle shape and size. The higher the temperature in the top section of the apparatus, the more centers of nucleation of the metal arise, and the finer the size of powder particles.

Raise the temperature from the top to the lower part of the apparatus intensifies the circulation of the reaction gas. The metal particles, which are being formed, repeatedly move with respect to apparatus height and particle residence time within the apparatus increases. The result is an increase of particle size.

Diluting the carbonyl vapor with an inert gas or carbon monoxide leads to the formation of finer powders and vice versa, increasing the vapor concentration leads to an increase of the particle size. The higher the gas volume flow rate, the shorter the residence time of the particles in the apparatus; accordingly, the finer powder is produced, and vice versa.

There are two basic modes of powder production in commercial usage:

(1) A moderate rate of carbonyl is fed at a comparatively low temperature in order to stimulate the formation of a relatively small number of coarse primary particles and to obtain “heavy” powders (with high bulk density).
(2) A high feed rate at a high temperature leading to the formation of a large number of small primary particles prone to coagulation into aggregates that results in the formation of “light” powders (with low bulk density).

In order to obtain fine and almost monodisperse powder, carbonyl vapors undergo decomposition by mixing immediately with a large volume of hot inert gas, followed by quenching the aerosol formed by diluting and cooling.

To increase the productivity of carbonyl decomposition, the nucleus seeds (metallic aerosol, solid particles) or appropriate chemical agents (oxygen, halogens, ammonia, HCl or HNO_3 vapors, chlorides or bromides of arsenic, boron, silicon, titanium, etc.) are introduced. The presence of these agents stimulates the transformation of carbonyls into oxides or other metal compounds used as crystallization nuclei.

The parameters of heat and mass transfer and, accordingly, the design of the apparatus influence the powder properties and process productivity. Heating or cooling of the apparatus sections as well as heating the introduced inert gas are used. To prevent metal deposition on the walls of the apparatus as well as to increase the process productivity, the gas flow is turbulent, stimulated either with a stirrer or with a tangential inlet of the gas. Adding to the height of the apparatus by lessening its diameter results in coarser powder. Placing a broad tube along the axis of the reactor decreases the free section and ensures the uniformity of powder particle size, etc. Feeding the carbonyl into the apparatus through spraying devices makes it more widely dispersed, the reaction volume is used more evenly, and the powder is more uniform.

The details of the carbonyl process for such metals as Ni, Co, W, and Mo are given in the corresponding sections.

A process, submitted in [6], comprises processing at atmospheric pressure and an effective temperature with hydrogen in the presence of chloride anion the nickel source including nickel chloride in admixture with nickel carbonate ore to produce resultant nickel and subsequent reacting the carbon monoxide with the resultant nickel to produce the $Ni(CO)_4$.

A number of special methods for the decomposition of carbonyls are known. Ultraviolet and pulsed laser radiation, acoustic vibrations, and a magnetic field can be used for the manufacture of finely dispersed homogenous powders. In this process, a magnetic field below the Curie point results in a domain structure of the ferromagnetic particles formed.

In the plasma process, the reaction is carried out in highly ionized argon at a temperature of 4800–5300 K. Under those conditions, the number of nucleation centers increases sharply, and the dilution of the carbonyl vapors by the inert gas prevents coagulation of the particles. The result is the formation of submicron powders.

Manufacture of Composite Powders

The methods of producing composite powders by the carbonyl process are based either on the mutual solubility of metal carbonyls or on their ability to dissolve compounds prone to dissociation. Iron-nickel (permalloy) powders containing from 5% to 50% of nickel can be manufactured by simultaneous decomposition of a mixture of liquid iron and nickel carbonyls; the addition of cobalt and molybdenum is also possible.

Another method is based on the decomposition of a metal carbonyl on the surface of the introduced "seeds" (dispersed particles of metals, nonmetals, or oxides, carbides, sulfides, silicates of metals, and their mixtures). In this case, a metal film encapsulates both single particles and agglomerates of particles having different properties. The process is carried out in a fluidized bed. The intense mixing of the particles results in a uniform thickness of the metal coatings obtained. The deposition of a metal coating onto the particles imparts corrosion protection and electrical conductivity while increasing heat conductivity.

PROPERTIES AND APPLICATIONS OF THE METAL CARBONYL POWDERS

The size of carbonyl powder particles varies in a broad range from 0.5 to 20 μm. The features of these powders are high specific surface and considerable defects of crystalline structure; they are more active as compared to the powders manufactured by other techniques. However, these powders are not pyrophoric due to adsorbed carbon monoxide that passivates the particle surface. The particle shape is close to spherical. Sometimes particles have a laminated "onion" structure that imparts specific electromagnetic properties to the material. Carbonyl powders can contain 1–3% of carbon and oxygen (that is equivalent to about 30% of metallic compounds) while the amount of other impurities does not exceed 1×10^{-3}%. Both typical spherically shaped nickel powders produced through a carbonyl process are shown in Fig. 6.4A with a spiky morphology and in Fig. 6.4B with a mottled surface.

The powders can be subjected to additional treatments with the purpose of bringing them into accordance with the requirements relating to the purity and the particle size. Mechanical methods (crushing, mixing, sieving, separating, and trapping) and thermal treatment are in use. The latter may cause changes in the crystalline structure of particles, thus enabling production of powders with specified properties, for example, light powders with coarse and porous particles. It can also cause an increase in the metal content of the powder up to 99.96% due to of the elimination of carbon and oxygen.

Carbonyl powders of metals, alloys, and composites are used for manufacturing pure malleable metals, precision alloys, and various solid and porous items (parts, strips, rods, filters, etc.) as well as in electric and radio engineering, mechanical engineering, automation, and other areas. Detailed characteristics of powders are given for each metal in corresponding chapters of Section 4.

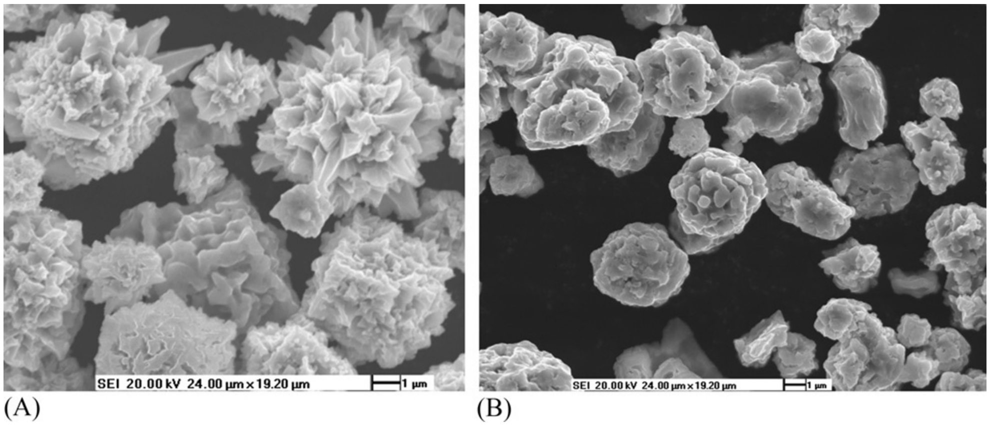
SEI 20.00 kV 24.00 μm × 19.20 μm
1 μm
(A)
SEI 20.00 kV 24.00 μm × 19.20 μm
1 μm
(B)

FIG. 6.4 SEM images of typical spherically shaped nickel powders produced by the carbonyl processes: (A) Nickel powder Grade AH50 with a spiky morphology, with Ni content 99.8% min and apparent density 2.1–2.4 g/cm^3; (B) Nickel powder Grade AH410 with a mottled surface, with Ni content 99.8% min and apparent density 4.1–4.4 g/cm^3. *Courtesy: HUNTER Chemical LLC, PA, USA.*

HEALTH AND ENVIRONMENTAL PROTECTION MEASURES IN THE CARBONYL INDUSTRY

The carbonyl process involves considerable danger such as increased flammability and explosiveness of the materials used, high toxicity, and high pressures employed in the process. Major health hazards are potentially fatal if inhaled, allergic reactions, cancer hazard. Physical hazards may include an explosion if exposed to shock, friction or heating; finely divided materials may explode spontaneously; extremely flammable liquid and vapor; vapor may cause a fire flash; liquid may decompose violently on heating; or possible decomposition on contact with air [7,8].

The mixture of nickel carbonyl and air or oxygen may ignite or explode. With its flammable and reactive nature, nickel carbonyl is classified as *serious* with a hazard rating of 3 by maximal ones 4 accordingly to the UA National Fire Protection Association (NFPA) [7–9]. Therefore, sources of ignition are prohibited while nonsparking equipment and tools and explosion-proof electrical equipment and fittings must be used. Metal containers involving the transfer of nickel carbonyl should be grounded and bonded.

The combustibility and explosive values of nickel carbonyl are characterized by the following: the flash point is 253 K; the autoignition temperature is 473 K, and the lower flammable limit in air is 2 vol%. The flammability class according to OSHA is 1B [8,9].

Toxic carbon monoxide can be responsible for acute and chronic poisoning in the manufacturing process. Under the legislation on 'Health and Safety' in the European PM industry the long- and short (15-min reference period)- term workplace exposure limits (WELs) for carbon monoxide in the workplace atmosphere are 35 mg/m^{3}and 232 mg/m^3, respectively [10]. The long term WELs for carbon monoxide in workplace atmosphere is of 20 mg/m^3 according to Legislation on 'Health and Safety' in the RUS Standard [11].

Metal carbonyls are toxic, with volatile ones such as nickel carbonyl being particularly dangerous. Nickel carbonyl is carcinogenic as well as flammable and reactive. Nickel carbonyl irritates and burns the skin and eyes. The WELs of the nickel carbonyl in the workplace atmosphere averaged over an eight-hour work shift under legislation in the United States, called *permissible exposure limits* (PEL), is 0.001 ppm. Exposure to 2 ppm ($\approx$2.5 mg/m^3) is immediately dangerous for life and health [8]. The WELs of the carbonyls in the workplace atmosphere under the CIS Standard are (in mg/m^3): $Ni(CO)_4$, 0.0005 ($\approx$0.0004 ppm); $Co_2(CO)_8$, 0.01; $Mo(CO)_6$, 1.0; and $W(CO)_6$, 2.0 [11].

The powders are also toxic, especially the nickel powder that affects the breathing organs; they are also carcinogenic. The long-term WELs of the powders in the air (mg/m^3) are Ni, 0.05; Co, 0.5; Mo metal, 0.5; and W, 6.0 [11].

Implementation of enclosed operations, local exhaust ventilation, and general ventilation must be made to ensure the workplace exposure limit.

The industrial equipment for the carbonyl process must pass strict controls for gas tightness. All equipment and pipe work must be purged with an inert gas prior to feeding in the toxic and explosive compounds with the object of checking their gas-tightness as well as eliminating oxygen. When feeding in the carbon monoxide at operating pressures, control of its content in the air. The shop floors must be equipped with automatic analysis and alarm appliances for control of the presence of carbonyl vapors and carbon monoxide in the air. In all dangerous areas, personnel must wear protective breathing masks. Rubber-impregnated suits, rubber boots, gloves, and gas masks are a must for the personnel involved in handling liquid carbonyls.

The methods of determining small concentrations of carbonyls in the air are based on absorption, decomposition, or chemosorption of carbonyls by using various chemical reagents, combined with instrumental methods of analysis (colorimetric, gas chromatography, spectral analysis, etc.). The method for determining the carbonyl content in water is based on the volatility of carbonyls and consists in their being purged from the aqueous solution using nitrogen, followed by chemosorption from the gas phase using porous active materials and chemical reagents.

Liquid carbonyls must be poured only into special tanks under a water layer. Special gas-tight vessels must be used for the transportation of carbonyls and carbonyl-contaminated wastes to the place of disposal, according to local regulations. Solid wastes of carbonization fit for recycling and further processing undergo a pretreatment with oxidizing agents.

Nickel carbonyl must be stored to avoid heat, flames, sparks, and other sources of ignition. Nickel carbonyl is incompatible with halogens, oxidizing materials, and halocarbons. Therefore, avoid contact with oxidizing agents (such as perhlorates, peroxides, permangamates, chlorates, nitrates, chlorine, bromine, and fluorine), strong acids (such as hydrochloric, sulfuric, and nitric), dinitrogen tetraoxide, and tetrachloropropadiene because violent reactions may occur.

The major environment protection requirements relate to the technology for purification of the atmospheric ventilation discharges from toxic compounds and preventing the contamination of surface water according to Surface Water Standards & Guidance. The carbonyls can be present in considerable amounts in liquid waste due to their solubility in the water employed in the production process. Contaminated effluents, especially from the rectification unit, may have a dangerous impact on the human body, mainly via inhalation. The limits of the concentration of carbonyls in aqueous media must be evaluated in accordance with local environmental regulations.

Purification of ventilation discharges from carbonyls is complicated by their small concentration. The traditional way of air decontamination consists of thermal treatment or oxidation by using various agents (oxygen, chlorine, gaseous hydrogen chloride, phosphorus, etc.) on active porous materials (activated carbon, silicate absorbents, dry aluminum oxide, etc.). In a high frequency electric discharge, the molecules of carbonyls are destroyed and oxidized by ozone. The degree of air decontamination reaches 97%–99%.

The method of decontamination of carbonyl-containing water to a concentration below that of the admissible concentration limit [12,13] consists of purging the carbonyls by nitrogen, followed by passing water through the columns filled with activated carbon. The gas after purging is directed into the ventilation system and subjected to decontamination together with other gaseous discharges.

Health hazard information, including acute health effects, chronic health effects, cancer hazards, reproduction hazards, medical testing, mixed exposures, and conditions made worse by exposure, is contained in [9–11].

REFERENCES

[1] Naboychenko SS, editor. Handbook of nonferrous metal powders. Moscow: Metallurgia Publishers; 1997 [in Russian].

[2] Mnukhin AS, Shvartsman RA, Zaitsev AY. Synthesis of nickel tetra carbonyl at average pressure. Tsvetnaya Metallurgiya Publ 1998;2:64–6 [in Russian].

[3] Syrkin VG. CVD-process. Moscow: Nauka; 2001 [in Russian].

[4] Biketova LV, Kozyrev VF, Mnukhin AS. Carbonyl nickel powders for manufacturing of batteries. Tsvetnaya Metallurgiya 2001;2:73–5 [in Russian].

[5] Lascelles K, Morgan LG, Nicholls D, Beyersmann D. Nickel Compounds. In: Ullmann's Encyclopedia of Industrial Chemistry. Wiley-VCH; 2005. p. 17–235.

[6] Process for production nickel carbonyl, nickel powder and use thereof. Canadian Patent Application 2012, No: CA 2461624.

[7] MATENSON TRI-GAS, Inc. Material savety data shift. Nickel carbonyl. Revision date: Dec 11 2008. https://www.mathesongas.com/pdfs/msds/MATH0059.pdf [Accessed 31 January 2018].

[8] US New Jersey Department of Health and Senior Services. Hazardous Substance Sheet. Nickel carbonyl. Revision: February 2001. http://nj.gov/health/eoh/rtkweb/documents/fs/1343.pdf [Accessed 31 January 2018].

[9] UA National Fire Protection Association. Codes & Standards.

[10] EH40-Update to EH40/2005 Workplace Exposure Limits. 2nd ed., Published 2011 (as consolidated with amendments, December 2011).

[11] CIS Standard GOST 12.1.005–88.

[12] Sanitary Regulations and Standards of surface waters from pollution. SanPiN 4630–88 (in Russian).

[13] Surface Water Standards & Guidance. EPA United States Environmental Protection Agency. https://www.epa.gov/wqs-tech/federal-water-quality-standards-requirements May 16, 2017.

Chapter 7

Reduction Methods of Powder Production

Stanislav S. Naboychenko
Ural Federal University (UrFU), Yekaterinburg, Russia

Chapter Outline

Solid-Phase Reduction of Metal Oxides and Salts **211**
Theory of the Process 211
Kinetics and Mechanism of the Process 212
Feedstock and Reagent Reducers 215
Powder Production **218**
Push Type Furnaces 218
Drum Furnaces 219
Conveyor Furnaces 219
Fluidized Bed Furnaces 219
Safety Engineering **220**
Metallothermy **221**
Chemical Reduction **221**
Chemical Precipitation from Solutions 221
Thermodynamic Peculiarities of Metal Chemical Reduction 221
Kinetics of Solid-Phase Formation in Solution 223
Application of Chemically Reduced Powders and Sols 225
Autoclave Precipitation of Metal Powders **225**
Theory of Autoclave Metal Ions Reduction 226
Hydrodynamics 227
Parameters and Components of the Process 227
Autoclave Processing of Hydroxide and Metal Carbonate Pulps 229
Autoclave Precipitation of Metal Powders from Organic Phases 230
Equipment 230
Safety Engineering 231
References **231**

SOLID-PHASE REDUCTION OF METAL OXIDES AND SALTS

In the solid-phase reduction process, metal oxides or metal salts (carbonates, halides, oxalates, and formates) are treated by a reducing agent at temperatures below their melting point. Oxide-reduced powders characteristically exhibit the presence of pores within powder particles and thus are called sponge powders. This sponginess is controlled by the number and size of the pores and accounts for the high green strength as well as the good compactibility and sinterability of such powders. Typically, high reduction temperatures (higher than 60% of the melting point, T_m) facilitate the formation of large intraparticle pores and therefore powders of a specific surface that are required for high compressibility. Parallel with these, elevated temperatures may cause excessive sintering and agglomeration, which cause difficulties with the disintegration of the sintered cake. Low reduction temperatures lead to the production of powders with fine pores, large specific surface areas, and high green strength. But extremely low reduction temperatures ($<0.3T_m$) can readily produce pyrophoric powders.

For metals with very high melting points, such as tungsten and molybdenum, oxide reduction is a benefit partly for economic reasons. Thus, for molybdenum trioxide, because of its high vapor pressure, the reduction is accomplished in two stages to control particle size. The first step, the reduction of molybdenum trioxide to molybdenum dioxide, is carried out at a temperature between 1146 and 1246 K. The second step, the reduction of molybdenum dioxide to molybdenum monoxide, is carried out at around 1446–1646 K.

In contrast to atomized powders, where oxides usually are concentrated on the surface of the particles, oxide-reduced powders, at least when freshly reduced or stabilized against tarnishing, contain most of their residual oxide within the particles.

Theory of the Process [1,2]

The thermodynamics of metal oxide reduction by hydrogen or carbon monoxide are determined based on the analysis of the generalized reaction:

Handbook of Non-Ferrous Metal Powders. https://doi.org/10.1016/B978-0-08-100543-9.00007-5
© 2019 Elsevier Ltd. All rights reserved.

$$\frac{1}{y}M_xO_y + H_2(CO) \leftrightarrow \frac{x}{y}M + H_2O(CO_2)$$

The latter is analyzed as a set of oxide dissociation reactions

$$M_xO_y \leftrightarrow xM + \frac{y}{2}O_2$$

and gaseous reducer combustion:

$$xB + \frac{y}{2}O_2 \leftrightarrow B_xO_y$$

Below, the corresponding equations for the dependence of the equilibrium constant on the temperature for the reactions of hydrogen combustion ($2H_2 + O_2 \rightarrow 2H_2O$) are given:

$$\lg K_{eq} = \frac{12\,543}{T} - 0.473 \lg T - 3.6 \times 10^{-4}T + 8.1 \times 10^{-6}T^2 - 0.865$$

and carbon monoxide combustion ($CO + 0.5O_2 \leftrightarrow CO_2$):

$$\lg K_{eq} = \frac{14\,250}{T} - 2.65 \lg T - 0.08 \times 10^{-3}T + 100T^{-0.5} - 15.4$$

This process is possible only if the partial pressure of the reducing gas is higher than its equilibrium value typical for the reduction of the oxide of the given metal. An opposite development of the reaction is possible in the case of low concentration of the reducing gas or high concentration of its oxidation products. The reduction system is a three-component and three-phased one (oxide, metal, gas), therefore there are two degrees of freedom. The equilibrium constant (K) of the reduction reaction is determined by the ratio of partial pressures of the reducing gas and the product of its oxidation. The equilibrium gas composition is determined by its pressure and temperature. Only temperature influences the equilibrium constant (K) at low pressures of the gas; therefore, the reaction proceeds without changing the number of gas moles. If the reaction constant is $K \leq 1.0$, the oxides are difficult to reduce and vice versa. The stronger the metal bond with oxygen, the higher the oxide formation heat and the more positive the thermal effect of its reduction reaction.

The utilization factor of the gaseous reducer ($\eta\%$) is determined by the equilibrium constant of the reaction

$$\eta = \frac{K}{1+K} \cdot 100$$

and can never achieve 100%. The lower the value of the equilibrium constant, the higher the hydrogen consumption; the utilization factor of hydrogen increases with its dehumidification.

The partial pressure of the metal in the gas phase enters into the equation for the reaction equilibrium constant by the reduction of metal compounds with high vapor pressure. The decrease of the total pressure and the increase of temperature and reducing gas concentration facilitate the development of similar processes. If the equilibrium metal pressure is higher than its saturated vapor pressures, the production of metal by condensation is possible. If the reduction reaction is endothermic, the opposite reaction (i.e., oxidation by carbon dioxide or water vapor) is possible during the cooling of the gaseous mixture together with the condensation of metal vapors. The formation of oxides on metal particle surfaces is possible in the presence of oxidizers in the gaseous phase. This complicates the coalescence of metal particles.

Kinetics and Mechanism of the Process

Reduction processes are developed in accordance with the Baykov principle on the consecutive transformations of all chemical compounds formed in the given system. The reactions of indirect reduction are special cases of topochemical reactions; they proceed on the interphase boundary [3].

The kinetics of solid-phase reduction depend on the process parameters (temperature, pressure, reducer type, and mass transfer conditions) as well as on the physical and chemical properties of the initial raw material (structure defects, dispersivity, and specific surface). According to the adsorption-autocatalytic theory, the main stages of the process are:

1. Supply of a gaseous reducer to the surface of the processed material.
2. Adsorption of the reducing gas molecules on active centers of the solid surface.
3. Recombination of the reducing gas molecule under the influence of crystal lattice forces that is accomplished by the formation of an activated form at the atomic level.

4. Diffusion of reducing gas atoms through pores and cracks along the defects of the crystals lattice, and filling of electron vacancies.
5. Chemical interaction (electron interchange, nucleation, and growth of metallic phase crystals); the latter accelerates the adsorption and dissociation of molecules and provides the autocatalytic nature of further reduction due to high surface activity.
6. Desorption of gaseous oxidation products of the reducer through the layer of the metallic phase.
7. Diffusion of ions of metal and oxygen; electron transfer inside the crystalline phase.

The supply of the reducing gas (an act of external diffusion) in conditions of its excess consumption, purity, and optimal feed rate does not retard the process. The process rate limited by the adsorption stage depends on the pressure of the reducing gas (p_{g}) and is described by one of the following equations:

$$\nu = k\frac{bp_{\mathrm{g}}}{1+bp_{\mathrm{g}}}$$

$$\nu = k\cdot p_{\mathrm{g}}^{n}$$

where k is the rate constant; and b and n are experimental coefficients, which usually are not higher than 1.0.

For reversible reactions:

$$\nu = k\frac{p_{\mathrm{g}} - p_{\mathrm{g}}^{1}}{p_{\mathrm{pr}}^{n}}$$

where p_{g} and p_{pr} are partial pressures of the reducing gas and reaction product; and p_{g}^{1} is the equilibrium pressure of the reducing gas.

Reducing gas comes to the reaction zone in accordance with laws of internal diffusion and its supply is increased with the growth of the gas pressure and the lowering of the temperature. Adsorption of the reducing gas molecule is accompanied by the transmission of electrons in the oxide lattice. Adsorption mechanisms are different for oxides of hole (p-type) semiconductors with cation vacancies (Cu_2O, NiO) and electronic (n-type) semiconductors (ZnO, CdO and Ti_2O) with cations in interstitial spaces or with vacancies in the oxygen lattice. Owing to its insignificant affinity to electrons, hydrogen is a donor in the case of adsorption of its molecule on the oxide surface; in this case, a positive charge containing H^+ ions arises.

As the process develops, a metallic phase layer is formed that complicates diffusion conditions and decelerates the reduction rate. The negative influence of the metallic film is weaker when hydrogen is used because its molecule size is smaller than that of carbon monoxide while the diffusion coefficient is larger ($D_{H_2} = 3.74\ D_{CO}$). The elevated activity of hydrogen especially appears in the region of lower temperature. Diffusion of metal ions and electrons to the boundary layer accomplishes the metallic phase nuclei:

$$n\mathrm{M}^{2+} + 2n\mathrm{e}^{-} \leftrightarrow n\mathrm{M} \rightarrow (\mathrm{M})_{n}$$

A chemical reaction includes three sequential stages: chemisorption of a reducing gas molecule on the reaction surface; separation of an oxygen ion from the oxide lattice and its interaction with activated atoms (molecules) of the reducer that is completed by metallic phase formation; and adsorption of gaseous products of the reduction.

In the beginning stage, the reduction develops slowly due to different rates of reducing gas chemisorption at centers of the oxide surface, which differ by their activity. In the beginning stage for p-type semiconductors, all holes are involved and adsorbed H_{abi}^{+} ions are formed:

$$\mathrm{H}_{2(\mathrm{g})} \leftrightarrow 2\mathrm{H}_{\mathrm{adi}}^{+}\left(\mathrm{M}_{\beta}^{2-}\right)$$

The free electrons are formed in the boundary layer:

$$0.5\,\mathrm{H}_2(\mathrm{g}) \leftrightarrow \mathrm{H}_{\mathrm{adi}}^{+} + \mathrm{e}$$

Reduction develops with the filling of cation vacancies M_{β}^{2-}

$$2\mathrm{H}_{\mathrm{adi}}^{+} + \mathrm{MO} + \mathrm{M}_{\beta}^{2-} \leftrightarrow \mathrm{H_2O_g} + \mathrm{M}$$

and further with electron usage:

$$2H^{+}_{adi} + MO + 2e \leftrightarrow H_2O_g + M$$

For *n*-type semiconductors, the reduction process includes the following stages:

- Chemisorption of hydrogen and ionization of atoms:

$$H_{2(g)} \leftrightarrow H_{2adi} \leftrightarrow 2H_{adi} \leftrightarrow 2H^{+}_{adi} + 2e$$

- Connection of free electrons by metal oxide ions.
- Elimination of oxygen with formation of vacancies on the surface.

$$H_{2(g)} \leftrightarrow H_2O_g + O^{2+}_{\beta} + 2e$$

and collection of holes on a metal oxide surface.

- Metal ion formation in interstitial spaces of (*x*) lattice.

$$H_{2(g)} + MO \leftrightarrow H_2O + M^{2+}(x) + 2e$$

In the case of a multistage mechanism of the reduction process, which includes a series parallel formation of the lower oxides, the reaction rate is determined by the lowest rate among these stages. A zonality process of an autocatalytic type is observed, specified by the different catalytic activity of the formed phases.

Transformation of the lattice of the higher metal oxide into the lattice of the lower oxide or metal lattice occurs in accordance with the principle of phase structure succession. With decreasing temperature, the induction period becomes longer and the speed of interphase boundary movement decreases. Metal ions as well as oxygen atoms can take part in diffusion stages; the limiting stage is determined by the ratio of their diffusion rates. The diffusion is carried out through crystal lattice volume and along the grain boundaries.

In real conditions, due to the use of elevated temperatures, the rate of crystal chemical transformation is much higher than the rate of reducer supply or the elimination of gaseous reaction products, that is, the reduction process flows in the diffusion area.

Rostovtsev [4] suggested a kinetic equation, which described the diffusion-kinetics range of the reduction process:

$$\tau = \frac{q}{\Delta N}\left[\begin{array}{l} \dfrac{1}{k}\ln\dfrac{e^{S}(S-1)+e^{-S}(S+1)}{e^{S\cdot\xi}(S\cdot\xi-1)+e^{-S\cdot\xi}(S\cdot\xi+1)} \\ +\dfrac{R^2}{D_{2e}}\left(\dfrac{1-\xi^2}{2}-\dfrac{1-\xi^3}{3}\right)+\dfrac{4R^2\left(1-\xi^3\right)}{3D_{1e}\left(\sqrt{Re}+4\right)} \end{array}\right]$$

where τ is the reduction duration, s; q is the gas mass necessary for full reduction of $1\,\mathrm{cm}^3$ of raw material, mole/cm^3; R is the radius of a spherical piece, cm; ΔN is the reducer excess over its equilibrium concentration; k is the constant of the crystal transformation rate; $S = R\sqrt{k/D_{1e}}$ is the dimensionless simulation criterion; D_{1e} and D_{2e} are the coefficients of internal diffusion in volumes of an initial material particle and a particle after reduction, mol/(cm s); ξ is the dimensionless parameter; $\xi = (1-\omega)^{1/3}$, where ω is the reduction degree, in unity fraction; and Re is the Reynolds's criterion.

As the criterion S decreases, the process shifts to the kinetics area; in the transition area S ranges from 10 to 50; diffusion limits become determinative at high values of this criterion.

The following guidelines are useful for metal powder production practice:

- Some impurities contained in the gaseous reducer can be adsorbed on active surface centers more rapidly and capably, thereby reducing the front of the productive reaction. Therefore, it is necessary to use pure gases with prior drying.
- Increasing particle surface and dispersivity, decreasing the thickness of the material layer, and enhancing mass transfer conditions (increasing the active concentration and speed of the reducing gas, and layer stirring) are required for process acceleration by its behavior in the diffusion area.
- Temperature monitoring, excluding submelting of particles of newly reduced metal and retaining the gas-permeability of the treated layer.
- The oxide reduction rate increases in the presence of a number of impurities in the basic material. The degree of oxide structure disorder increases by substitution of the matrix phase cation particles, for example, by selenium and tellurium cations. This leads to a number of vacancies and holes in *p*-type oxide-semiconductors increase that simplifies ion diffusion, accelerates chemisorption of the reducing gas, makes easier crystal transformations.

- Oxides of alkali metals interact with microimpurities (sulfur, phosphorus, and arsenic) with their transfer into water-soluble compounds, which are eliminated in the process of cake washing that increases the powder purity.
- The size of powder particles significantly depends on the initial product dispersivity.
- Powder particle size appreciably depends on the reduction temperature; the finer powders are produced by the reduction of chemically precipitated salts at a moderate temperature (573–773 K), heightened reducer consumption, and limited duration.
- To increase the gas permeability layer as well as exclude powder sintering and grain coarsening, it is useful to granulate the charge by the injection of 1%–3% binders (alcohols, organic acids, or chlorides of alkali-earth metals), which then are sublimated at reduction temperatures.
- Powder purity greatly depends on the composition of the basic raw material, as only impurities forming volatile compounds (C, As, S, O, and Cl^-) can be eliminated in the reduction process.

Feedstock and Reagent Reducers

Reducers are gaseous (hydrogen, carbon monoxide, converted natural gas, and dissociated ammonia), solid (graphite, charcoal, and other carbon-bearing reagents with limited content of sulfur, phosphorus, and arsenic), or combined reducers (for example, carbon monoxide and charcoal). The gases are produced in dedicated plants and oxygen and water vapor are removed.

Hydrogen is the most effective reducer. Four industrial methods of hydrogen production (conversion of natural gas and electrolysis of aqueous solutions) are well known and readily available commercially: A, by electrolysis of aqueous solutions; B, by the iron-steam method and by the interaction of ferroslag with the alkaline solution; C, by chloride electrolysis; and D, by steam conversion of hydrocarbon gases (Table 7.1).

Hydrogen is purified from oxygen in vertical furnaces filled with a catalyst (copper sponge, chromium-nickel powder, or an iron-nickel-copper mixture at 673–723 K. The dehydration is carried out in columns filled by silica gel and cement; the residual moisture content is not higher than 20 mg/m^3, which corresponds to a dew point about 228 K. Silica gel is periodically regenerated at 450 K. Deeper dehydration of hydrogen, giving a residual content of 2–4 mg/m^3 and removal of carbon dioxide, is achieved by passing the gas through columns with granulated potassium hydroxide. To exclude the formation of explosive mixtures, gas is supplied with a surplus to the stoichiometry (the efficiency is below 15%–20%), therefore the discharge gases are burned or directed to regeneration. The latter provides cleaning from dust, moisture, and oxygen. Methods of diffusion separation on palladium-containing membranes and of short-cycled adsorption under a pressure with blowing off adsorbent regeneration are used in case of need to free hydrogen from CH_4, CO, H_2S and N_2 and producing particularly pure hydrogen. The former is implemented for devices with low capacity while the latter is for devices with hydrogen consumption amounts of 1000 m^3/h and higher.

TABLE 7.1 Physical and Chemical Properties of Technical Hydrogen

	Brand					
			C		D	
Properties	**A**	**B**	**1**	**2**	**1**	**2**
Chemical composition						
Hydrogen content, vol%, min	99.8	98	98.5	97.5	97.5	95
Impurties: vol%, max						
Oxygen	0.2	0.3	0.3	0.5	0.2	0.2
Carbon monoxide	–	0.3	0.2	0.3	0.5	1.2
Carbon dioxide	–	0.5	9.2	0.3	0.5	1.0
Water steam content (298 K, 0.1 MPa) (g/m^3)	25	25	25	25	25	25
Max: transportation via gas conduits and storage in rubber-textile gasholders						

The kind of adsorption under pressure technology, called “pressure swing adsorption (PSA),” has become state-of-the-art technology for the production of high purity H_2 (99.995+%) from a feed gas containing 60%–90% H_2. It is used for >85% of global hydrogen production [5–8].

The basic principle of an H_2 PSA process for these applications is relatively simple. The bulk and dilute impurities present in the feed gas are adsorbed by passing through a column packed with one or more adsorbents in order to produce the pure H_2 product gas at feed pressure. The impurities are then desorbed by lowering their superincumbent partial pressures inside the column in order to produce an impurity-rich gas. Though simple in principle, a practical PSA process can be complex, consisting of the adsorption and the desorption steps in conjunction with a variety of complementary steps that are designed to improve the H_2 product’s purity and recovery, and to reduce the adsorbent units. Thus, a PSA process involves a series of sequential nonisothermal, nonisobaric, and unsteady-state steps operated in a cyclic steady-state fashion using multiple parallel adsorption columns.

The two most commonly used gas sources for H_2 production are steam-methane-reformer off gas (SMROG) after it has been further treated in a water-gas-shift (WGS) reactor, and refinery off gases (ROG) from various sources. The most frequently used H_2 PSA processes are used for the production of high-purity H_2 from the natural gas. A popular design called the polybed process contains nine sequential steps, described by Sircar [5]. The adsorbers are packed with a layer of activated carbon in the feed end and a layer of zeolite in the product end. The process was originally used to produce high-purity H_2 at high H_2 recovery from SMROG.

Fig. 7.1 is a schematic box diagram for the most commonly used steam methane reforming (SMR)–water-gas shift (WGS)–PSA route of H_2 production [6,9]. Steam and natural gas in the ratio of 2.5–6.0 react ($CH_4+H_2O \leftrightarrow CO+3H_2$) at a high temperature (1023–1173 K) and pressure (0.4–3.0 MPa) over a nickel catalyst. In an endothermic SMR reactor, the effluent gas comprising (in vol%) (70–72)H_2, (6%–8%)CH_4, (8–10)CO, and (10–14)CO_2 (dry basis) is cooled to 573–673 K (steam-produced) and subjected to the exothermic WGS reaction ($CO+H_2O \leftrightarrow CO_2+H_2$), cooled again, and purified in a multicolumn PSA unit. The H_2 product contains 99.999 H_2 (<15 ppm CO_x) and the H_2 recovery volume from the PSA unit is typically 70%–95%. The PSA waste gas is recycled as fuel to the reformer, with fresh natural gas providing the balance of the fuel.

Elseviers et al. [7] reported that the current generation of polybed PSA systems is characterized by advancement induced by the availability of improved computational capabilities of personal computers and advanced adsorption simulation programs. A new generation of ultrahigh performance adsorbents allows further reduction in the installed adsorbent volume per ton of hydrogen recovered without sacrificing purity or recovery.

According to Linde’s group comp. Data [8], the capacities range from a few hundred Nm^3/h to large-scale plants with >400,000 Nm^3/h that are commercially available. The hydrogen product meets every purity requirement up to 99.9999 mol

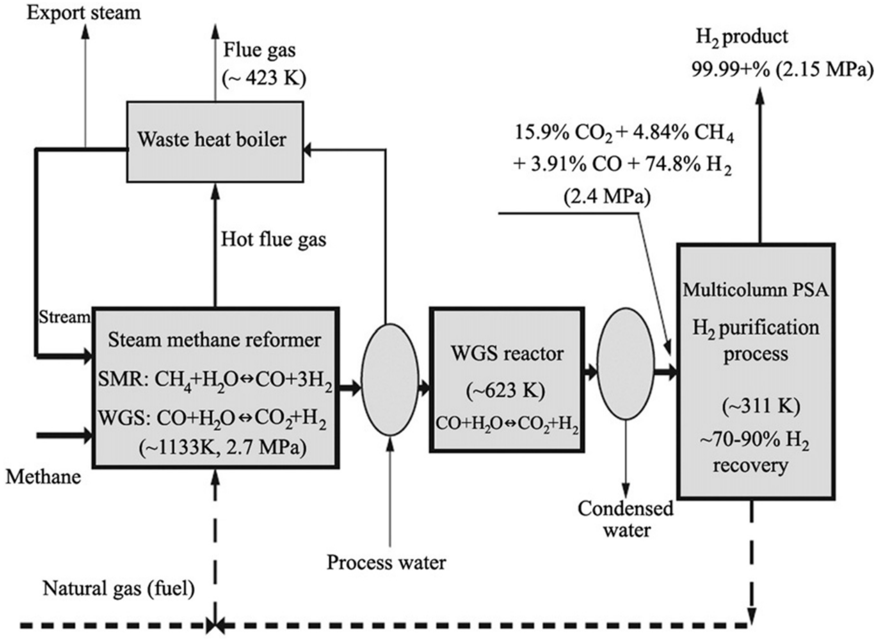
Export steam
Flue gas
(~ 423 K)
Waste heat boiler
Hot flue gas
Stream
Steam methane reformer
SMR: $CH_4+H_2O \leftrightarrow CO+3H_2$
WGS: $CO+H_2O \leftrightarrow CO_2+H_2$
(~1133K, 2.7 MPa)
Methane
Natural gas (fuel)
Process water
WGS reactor
(~623 K)
$CO+H_2O \leftrightarrow CO_2+H_2$
Condensed water
15.9% CO_2 + 4.84% CH_4 + 3.91% CO + 74.8% H_2 (2.4 MPa)
H_2 product
99.99+% (2.15 MPa)
Multicolumn PSA
H_2 purification process
(~311 K)
~70-90% H_2 recovery

FIG. 7.1 Conventional steam methane reforming (SMR) route for hydrogen production.

%. Final desorption and regeneration is performed at the lowest pressure of the PSA sequence. Highly pure hydrogen obtained from an adsorber in the provided purge step is used to purge the desorbed impurities into the tail gas system. Before restarting adsorption, the regenerated adsorber is pressurized again. This is accomplished in the pressure equalization step by using pure hydrogen from adsorbers presently under depressurization.

Hydrogen is an explosive gas that requires special permissions according to safety measures. When choosing structural steels to manufacture devices that operate in hydrogen atmospheres, it is necessary to take into account that the formation of volatile hydrides with impurities contained in the steel (sulfur, phosphorus, and carbon) is possible at high temperatures. Recrystallization of the metal structure and a decrease of strength properties are possible during long-term operation.

Endothermic gas is produced by incomplete combustion ($\alpha = 0.25$–0.3) of the natural gas at 1300 K. It has the following composition: 38–40 vol% H_2, 18–20 vol% CO, 1–2 vol% CO_2, balance N_2; the dew point is in the range of 268–273 K. Exothermic gas is produced by means of combustion of the natural gas with somewhat higher air consumption.

Dissociated ammonia is produced from liquid ammonia by means of its vaporization, heating and dissociation, cooling, and drying. The gas has the following composition: 75 vol% H_2 and 25 vol% N_2; dew point is in the range of 213–230 K without afterburning, and with afterburning, 4–20 vol% H_2 and nitrogen balance.

Converted natural gas is produced by processing of natural gas by steam at 1170–1370 K over a catalyst. A volume of 4 m^3 of reaction gas is produced from 1 m^3 of natural gas. Conversion furnaces with a capacity of 1000 m^3/h are used for the process. The gas has the following composition: 75–76 vol% H_2, 22–23 vol% CO, 1–2 vol% CO_2, 1–1.5 vol% H_2O, 1.5 vol % N_2, max, and 0.4 vol% CH_4; the dew point is 293 K.

The furnace is purged by nitrogen before the introduction of the explosive and combustible gases into the furnace and in the case of the formation of a neutral atmosphere or as a reagent for nitration of refractory metals and alloys. Nitrogen is produced by cryogenic separation of air; its properties are given in Table 7.2. Nitrogen costs about three times less than hydrogen. Argon is used as a neutral atmosphere in the production of extreme purity metals.

In industrial practice, coke, anthracite culm, charcoal, and carbon black are used among the solid reducers. Coke is produced by means of heat treatment of special coals or petroleum. It is an effective reducer, comprising 93–98 vol% carbon and up to 5 vol% hydrogen in the form of hydrocarbons. However, depending on the composition of the initial raw material, coke includes up to 2%–4% sulfur and 0.5%–1.0% ash, that is, impurities, which lower the quality of the metal powder produced. Anthracite culm is produced by means of anthracite heat treatment. It contains up to 75% active carbon, but also a considerable amount of ash (10%–20%) and sulfur (3%–3.5%). Charcoal is the solid reducing agent with the lowest sulfur content, but it has a high ash content (2%–2.5%) and is also high in volatile matter (17%–20%).

Carbon black is an ultrafine product of hydrocarbon heat treatment: its chemical activity is determined by its large specific surface (up to 15–18 m^2/g). Lampblack is produced by the combustion of liquid petroleum products in wick burners with air deficiency at 1470 K. It contains 0.1% ash and 0.5% moisture maximum. Gas black is produced by the combustion of natural gas with an air deficit. It contains 0.06% ash and 2.5% moisture, maximum.

TABLE 7.2 Commercially Available Nitrogen

		Gaseous and Liquid Nitrogen			
		Grades			
Properties	**Technical Gaseous Nitrogen**	**Extra Pure**	**I grade**	**II grade**	**III grade**
Chemical composition					
Nitrogen content (vol%, min)	99.994	99.996	99.6	99	97
Impurities content (vol% max)					
Oxygen	0.005	0.001	0.4	1.0	3.0
Water (293 K, 0.1 MPa)	0.005	0.005	0.07	…	…
Hydrogen	…	0.001	…	…	…
CO, CO_2, C_nH_m, total	–	0.001	…	…	…
Dew point (0.1 MPa), K	210	210	230	…	…

When coal-based solid reducers are used, it is necessary take the following into account:

- Process parameters depend significantly on purity, porosity, dispersity, and surplus concentration of the reducer.
- In the case of an excess of the reducer and high temperature (especially up to 1470K), there is a high probability of carbon monoxide formation by oxidation of carbon by the carbon dioxide generated.
- The kinetics of carbon monoxide formation determine the rate of the total reduction process.
- The carbon monoxide yield increases by lower pressure (the reaction proceeds with the increase of molar volumes).
- Decomposition of carbon monoxide with solid-phase formation (soot carbon) is possible in a catalyst's presence (for example, just formed powders of the iron subgroup).

Gaseous reducers are preferable to solid-phase ones because they are more active and contaminate the powder to a lesser degree. Hydrogen has the greatest commercial importance for metal powder production.

POWDER PRODUCTION

The flow sheet of powder production by solid-phase reduction of metal compounds includes three main stages: preparation of the raw material (blending, milling, drying, and degreasing), reduction, and powder processing (milling, classification, and mixing). Preparation of the raw material may also include an oxidation process of the metallic part, as in the copper-oxide process for the manufacture of a typical starting material for both the red cuprous oxide, Cu_2O, and the black cupric oxide, CuO, for producing pure copper powder. The oxidation of air atomized, water-atomized, or shotted copper leads to a radical change in powder particle shape and thus enhances the control of various engineering properties of powders. More detailed information is found in Section D, which is devoted to the methods of individual nonferrous metal powder production.

For producing PM alloys and composites, the initial components are thoroughly mixed in the required proportion and finely milled if necessary. More homogeneous mixtures are produced by chemical precipitation. Solid-phase reduction is carried out in electrical muffle furnaces of discontinuous or continuous operation. Furnaces of continuous operation (drum, push type, conveyor, and walking beam) are the most popular. These are productive, mechanized devices with moderate energy consumption, but they are more complicated in design and in operation compared to furnaces of discontinuous operation.

Push Type Furnaces

The furnaces (Fig. 7.2) have metallic, water-cooled housing lined internally with layers of fire brick. The metal-oxide powder is filled into flat metal boats, which are loaded and unloaded automatically. This results in a static powder layer throughout the whole reduction process. Several heating zones along the furnace length are maintained. Typical reduction temperatures range from 873 to 1373K.

The water vapor formed during reduction is carried away by the reducer gas flow. The flow of reaction gas is usually in the countercurrent direction. By variation of reduction parameters such as temperature and powder layer thickness, the particle size can be controlled over a wide interval. For instance, in the case of tungsten powder, the particle sizes can be controlled in the range between 0.1 and 100 μm. The operation of the furnace is complicated by fast wear of the guides used for boat movement and by the danger of their jamming.

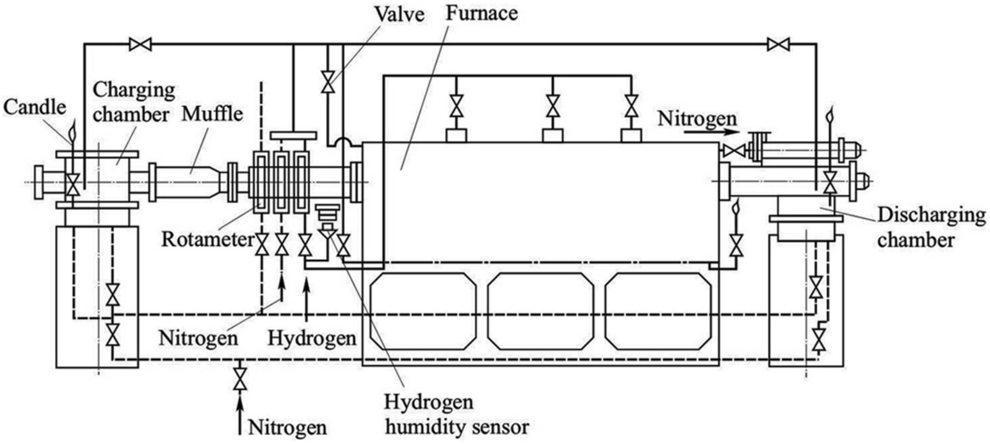

FIG. 7.2 Tying scheme for push-type furnace working on hydrogen.

Drum Furnaces

This type of furnace, called also a rotary furnace, is convenient for use in automatic lines. The metal oxide is directly introduced into the rotating furnace tube. As a consequence, there is no static but a dynamic powder layer. The depth of the layer is influenced by the feed rate, rotational speed, incline, and lifters inside the tube. The temperature range is comparable to that of push-type furnaces and the hydrogen flow direction is also, in most cases, countercurrent. As regards changes of particle size of the metal powder produced, the rotary furnace is not as flexible as the push-type furnace. They have high heat efficiency and easy pressurization while providing heat uniformity and good contact of the material with the reaction gas. But there is a danger of material nodulizing and adhering to the internal wall of the muffle (in cases of wet material processing and local submelting). In addition to these, there is appreciable erosive wear, additional energy consumption (for the rotator drive), more complicated pressurization of powder charging and discharging units, and increased dust formation.

Conveyor Furnaces

These continuous furnaces are used for chemical-thermal treatment and sintering of powders at temperatures not higher than 1423 K. The furnace operation controls some properties, particularly particle size and shape, apparent density, and green strength of the powder production. For example, roasting of air-atomized, water-atomized, or shotted copper is accomplished in belt conveyor furnaces. In commercial practice, oxidation or roasting copper powder is normally done in air at temperatures above 923 K. Reduction of the copper oxide thus produced is generally accomplished in a continuous belt furnace.

In a typical operation, the powder is transferred into the charge bin of a stainless steel mesh belt electric furnace. To prevent the powder from falling through the belt, a continuous sheet of high wet-strength paper covers the belt and then the powder is loaded onto the paper. A roller compresses the powder to improve heat transfer. As it enters the furnace, the paper burns, but not before the powder has sintered sufficiently to prevent it from falling through the belt. The gas enters the furnace from the discharge end and, because it is refrigerated, aids the cooling of the powder cake. By varying the furnace temperature between 753 and 1033 K and the time of exposure, considerable variation can be made in the content of fines, apparent density, and shape. To exclude powder oxidation, it is cooled down to 300–330 K in a reducing gas atmosphere and on completion of the furnace operation, the cake is broken and is ready for grinding. The reliability of the furnace operation is determined by the lifetime of the conveyor belt, which is operated in conditions of elevated temperatures, mechanical loads, and a corrosive environment.

Fluidized Bed Furnaces

The reduction process is accelerated 3–4 times when using fluidized bed furnaces due to increasing the contact area between the powder and the gas-reducer. However, the reduction operations are more difficult to control than reduction in a conveyor furnace. Along with this, dust entrainment and reducing gas consumption enlarge and, as a consequence, the cost of purification and regeneration of the forming gas phase increases.

When using calcium carbide or hydride as the solid reducer, the initial material is thoroughly dried and ball milled together with the reducer to <100 μm particle size. It is then thoroughly blended and processed in the furnace at a required temperature that provides the reduction of the metal or metal compound oxides. A dispersing agent (calcium oxide or sodium chloride) is injected to decrease the agglomeration of metallic particles. Discharge of the resulting cake is fulfilled by a water jet (with simultaneous cooling and removal of excess calcium compounds). The pulp is processed in hydrocyclones for lime separation, acidulated by hydrochloric acid, and then washed free from the calcium chloride formed. The powder is then dewatered in a centrifuge and dried in a nonoxidizing atmosphere.

The extra pure metal powders are produced by reacting low-boiling metal halides (MH) (chlorides and fluorides of molybdenum, rhenium, tungsten, tantalum, and niobium) by hydrogen (Fig. 7.3). A mixture of hydrogen and inert gas, usually argon (in ratio H_2 to Ar–1.5 to 2.0), is supplied in the amount that provides a stable fluidized bed in the furnace. Hydrogen consumption exceeds the theoretically required H_2 to MH ratio several times; therefore, waste gases are regenerated in order to utilize both the hydrogen and hydrogen chloride (hydrogen fluoride) that are returned to the technological process. The total degree of reduction achieves 98–99%; the precipitation takes place on seed particles 10–50 μm in size, which are produced by fine powder milling. Particle sizes of the powder produced range from 200 to 500 μm; the particles are spherical and the grain texture is dense.

Reduction processes are significantly accelerated and the produced powder is distinguished by ultrafine dispersity (30–70 nm) by using low-temperature plasma. Hydrogen or convertible natural gas is used as a reducer.

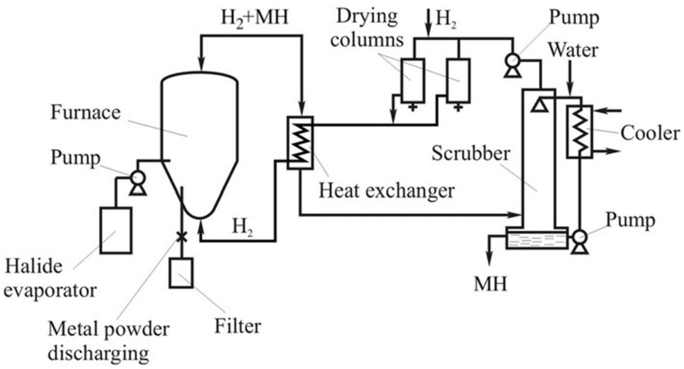

FIG. 7.3 Scheme of device circuit for halide metal (MH) reduction by hydrogen in a fluidized bed furnace.

SAFETY ENGINEERING

The main hazards in metal powder production by reduction processes are dust formation, thermal and electrical action, and explosion risk.

The building is constructed in conformity with the standards of technical design (discussed in Chapter 27). The standards cover adequate ventilation, explosion-proof lighting, lightning protection, and additional safety exits [10].

Safety-critical conditions for operation are the following:

- Good working order of the equipment (explosion-proof and fire-proof design, gas tightness, earthing, protective cover of rotating units, and performance of local ventilation according to standard requirements).
- Safe methods of process conducted by experienced personnel (mechanization, remote tests and control, correct application of personnel protection and firefighting means, dust handling, hygiene and sanitary precautions, and so on).
- Maintenance of design specifications concerning thermal and water supply, the arrangement of freight flow and the usage of leak-tight packages for powders, acoustic and light alarms, and warning labels.

The explosive data of burning gases mixed with air are shown in Table 7.3 [11,12]. Design, installation, and gas tubing operation have to meet regulations for installation and safe operation for combustible, toxic, and condensed gases [11]. The European Development Centre, in Sheffield, the United Kingdom, has Material Safety Data Sheets (MSDS) for industrial gases and gas mixtures available in published form [13].

Reaction gas is supplied either directly to the cold furnace or after purging with inert gas. Gas pressure ranges from 0.1–0.2 MPa; an acoustic alarm is activated if it fails.

TABLE 7.3 Combustion Data of Burning Gases Mixed With Air

	Combustion Limits, vol%		
Gas	Lower	Upper	T_B (K)
Ammonia	14.0	33.0	1053
Butane	1.5	8.5	748–823
Carbon oxide	12.5	74.2	913–926
Hydrogen	4.0	74.2	853–863
Methane	5.0	15.0	923–978
Propane	2.4	9.5	791
Exogas*	17.5	87.5	…
Endogas*	8.5	80	…

Ignition temperature (T_B) depends on gas composition.

The furnaces are equipped with special chambers with double doors from the charging and discharging sides to prevent the ingress of atmospheric air. Automatic temperature control is provided. The temperature shall not exceed 318 K on the external surface of the thermal insulation of furnace screens.

Before the arrangement of fuel spray, the absence of flap while inflame (test-tube trial) and flame combustion stability are controlled. In the case of a sudden failure of the gas supply and fuel spray disappearance, it is immediately necessary to close the output gas fitting and stop the furnace charging and discharging processes. The line of gas supply to the furnace is blocked quickly in the case of gas inflammation.

The speed of gas movement through the suction tubes is chosen to prevent dust precipitation in them. The gases are freed from dust in devices equipped with explosive valves. During furnace repair, access inside is permitted only after cutting off all services, cooling below 313 K with a constant rate, blowing by steam or inert gas that contains 4 vol% O_2 maximum, and water washing of precipitated powder if necessary.

METALLOTHERMY

This process is the reduction of oxides and salts of metal by another metal that has a greater affinity for the metalloid included in the composition of the initial compound. Calcium, magnesium, aluminum, and sodium are mostly used for the reduction. The reducer is chosen according to its activity, availability, volatility, inability to form compounds with the produced metallic powder, and the ease with which it can be removed from the final product. Calcium hydrides or carbides are kinds of reducers. Metallothermy excludes metal powder contamination by carbon. It is very important for the production of precise materials and units made of them. However, the more complicated the reduction reaction, the more probable the contamination of the powder by the metal reducer.

The metallothermy reaction equilibrium is determined by the equality, for example, of oxygen pressures by dissociation of the initial metal oxide and the produced oxide of the metal reducer. The metallothermy process proceeds in autogenous mode if the heat of the reaction is not <2300 kJ per 1 kg of the reaction mixture. In metallothermic reduction, a cake is usually produced; its finishing to commercial powder requires the usage of milling, screening, and uniform mixing.

CHEMICAL REDUCTION

Chemical Precipitation from Solutions

Chemical precipitation of metal as a powder is an oxidation-reduction reaction, which can proceed in an aqueous as well nonaqueous medium [14]. Chemical precipitation from an aqueous medium permits production of all metals capable of coexistence with water: cadmium, thallium, cobalt, nickel, tin, lead, bismuth, rhenium, indium, copper, and noble metals. However, thermodynamically possible reactions are often impracticable due to their extremely low rate affected by great kinetic difficulties of the reaction.

Thermodynamic Peculiarities of Metal Chemical Reduction

The electromotive force of the oxidation-reduction reaction is determined by the difference of oxidizer (Table 7.4) and reducer (Table 7.5) potentials. Values of oxidation-reduction potentials in real systems as a rule differ from standard values given in tables, according to component activities in the solution and pH of the medium.

To form a fine, highly dispersed product of reduction, it is necessary to provide a maximum difference of oxidation-reduction potentials of the reduced metal and the reducer. The ligands forming complexes with reduced metal ions are introduced into the solution to prevent metal hydroxides forming in the alkaline medium.

Metal reduction is possible thermodynamically if the oxidation-reduction potentials of the metal and the reducer are within the zone of their stability (shaded area I, II in Fig. 7.4, with the example of chemical precipitation of nickel). Soluble complexes of nickel are formed in the presence of ligands (citrate-ions) at $pH = 7$, and so the zone of nickel chemical precipitation is significantly expanded (I). Therefore, the nickel precipitation by means of formaldehyde becomes possible (Fig. 7.3, zone II).

Thermodynamic data allow the determination of a principal possibility of oxidation-reduction reaction performance, but do not provide any information concerning the rate of the process.

TABLE 7.4 Standard Oxidation-Reduction Potentials of Some Metals in Aqueous Solutions at 298 K

Electrode Reaction	Potential *E* (V(nhe))
$Ni^{2+}+2e=Ni$	−0.23
$[Ni(NH_3)_6]^{2+}+2e=Ni+6NH_3$	−0.476
$Co^{2+}+2e=Co$	−0.277
$Cu^{2+}+2e=Cu$	+0.337
$[CuOOH]^{+}+2e=Cu+HCOO^{-}$	+0.285
$[CuCH_3COO]+2e=Cu+CH_3COO$	+0.276
$[Cu(NH_3)_4]^{2+}+2e=Cu+4NH_3$	−0.05
$[Cu(NH_3)_2]^{+}+e=Cu+2NH_3$	−0.11
$Ag^{+}+e=Ag$	+0.799
$[AgNH_3]^{+}+e=Ag+NH_3$	+0.603
$[AgCH_3COO]^{+}+e=Ag+CH_3COO^{-}$	+0.643
$[AgCHCO]^{+}+e=Ag+HCOO^{-}$	+0.502
$[Ag(NH_3)_2]^{+}+e=Ag+2NH_3$	+0.373
$AgCN+e=Ag+CN^{-}$	−0.04
$[Ag(CN)_3]^{2-}+e=Ag+3CN^{-}$	−0.51
$Au^{+}+e=Au$	+1.692
$[AgCl_2]^{-}+e=Au+2Cl^{-}$	+1.154
$[AgCl_4]^{-}+3e=Au+4Cl^{-}$	+1.002

TABLE 7.5 Oxidation-Reduction Potentials of Reducers in Aqueous Solutions [7]

Electrode Reaction	Potential *E*, V(nhe)
$H_2PO_2^{-} + 3OH^{-} = HPO_3^{2-} + 2H_2O+2e$	−0.31–0.09 pH
$HPO_3^{2-} + 3OH^{-} = PO_4^{3-} + 2H_2O+2e$	+0.14–0.09 pH
$H_3PO_2^{-} + H_2O=H_3PO_3+2H^{+} + 2e$	−0.499–0.06 pH
$H_3PO_2^{-} + H_2O = H_2PO_3^{-} + 3H^{+} + 2e$	−0.446–0.09 pH
$H_2PO_2^{-} + H_2O = HPO_3^{2-} + 3H^{+} + 2e$	−0.323–0.09 pH
$H_2PO_2^{-}+ 2H^{+} + e=2H_2O+P$ (red form)	−0.248–0.12 pH
$HCHO +3OH=HCOO +2H_2O+2e$	+0.19–0.09 pH
$HCHO + H_2O=HCOOH^{-}+2H^{+} + 2e$	+0.056–0.06 pH
$2HCHO+4OH=2HCOO+2H_2O+2e$	+0.32–0.12 pH
$BH_4^{-} +8OH = BH_2^{-} + 6H_2O+8e$	−0.45–0.06 pH
$N_2H_4+4OH=N_2+4H_2O+4e$	−0.31–0.06 pH
$N_2H_4+2OH=2NH_2OH+2e$	+1.57–0.06 pH
$N_2H_5^{+} = N_2+5H^{+} + 4e$	−0.23–0.075 pH
$NH_2OH+7OH=NO_3^{-}+5H_2O+6e$	+0.683–0.07 pH
$2NH_2OH+4OH=N_2O+5H_2O+4e$	−0.21–0.06 pH

TABLE 7.5 Oxidation-Reduction Potentials of Reducers in Aqueous Solutions—cont'd

Electrode Reaction	Potential *E*, V(nhe)
$S_2O_4^{2-} + 4OH = 2SO_3^{2-} + 2H_2O + 2e$	+0.56–0.12 pH
$SO_3^{2-} + 2OH = SO_4^{2-} + H_2O + 2e$	−0.09–0.06 pH
$S_2O_3^{2-} + 6OH^- = 2SO_3^{2-} + 3H_2O + 4e$	+0.69–0.09 pH
$HSnO_2^- + H_2O + 3OH^- = Sn(OH)_6^{2-} + 2e$	+0.33–0.09 pH
$Ti^{3+} = Ti^{4+} + e$	−0.04
$Sn^{2+} = Sn^{4+} + 2e$	+0.151
$Cr^{2+} = Cr^{3+} + e$	+0.41
$Fe^{2+} = Fe^{3+} + e$	+0.771
$V^{2+} = V^{3+} + e$	−0.25
$R_2NHBH_3 + 3H_2O = R_2H_2N^+ + H_3BO_3 + 5H^+ + 6e$	E[a] −0.05 pH

[a] *E is dependent on nature of* R.

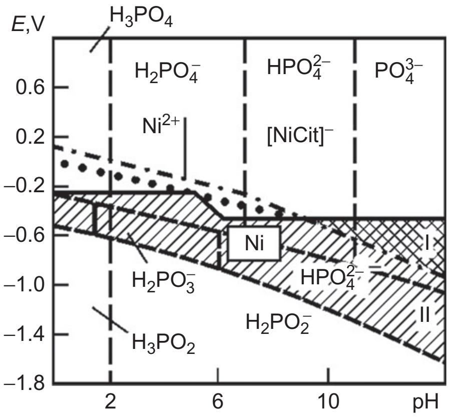

FIG. 7.4 Dependence of potential on pH: upper dashed line is balance of HPO_3^{2-}/PO_4^{3-}; point line is $2H^+/H_2$; solid line corresponds to Ni^{2+}/Ni (left part) and $[NiCit]^-/Ni$ (right part); upper dotted line corresponds to $H_2PO_2^-/HPO_3^{2-}$; lower dotted line corresponds to $H_3PO_2/H_2PO_3^-$ (left part) and $H_2PO_2^-/H_2PO_3^-$ (right part).

Kinetics of Solid-Phase Formation in Solution

The rate of metal chemical reduction from solutions is determined by kinetic factors, by a constant process rate, and the duration of the induction period. The slow reaction in the initial stage depends on the formation of stable particles of solid phase, which show an autocatalytic effect in the following stages. During the initial stage, the reaction proceeds by successive coarsening of nonstable fine particles of the solid product. For example, the crystallization of silver nuclei is performed step by step through the formation of successively coarsening clusters:

$$Ag^+ + Red \leftrightarrow Ag_1 + Red^+$$

$$Ag_1 + Ag^+ \leftrightarrow Ag_2^+$$

$$Ag_2^+ + Red \leftrightarrow Ag_2 + Red^+$$

$$Ag_m + Ag_n = Ag_{m+n}$$

where Red is the nucleus of reductant.

Clusters containing a small number of atoms are thermodynamically nonstable (the oxidation-reduction potential of atomic silver is 1.8 V (nhe) instead 0.799 V for the metallic silver phase). Metal particles become stable in the reaction

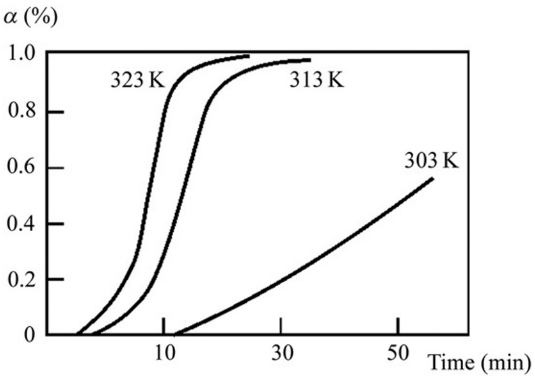

FIG. 7.5 Kinetic curves of Cu (II) reduction by formaldehyde.

medium after achieving 1–5 nm particle size. Assuming the number of growing metal particles to be unchanged after the induction period and the particles to have a spherical shape, the rate of their growth is constant and proportional to the surface S:

$$\frac{d\alpha}{dt} = k_1 S = k_2 S^{2/3}$$

where α is the reduced metal yield in the fractional part of unity; and k_1 and k_2 are the constants of reaction rate.

The integral form of the equation, which describes the initial sections of reaction kinetic curves (Fig. 7.5), is

$$\alpha = kt^3$$

where k is the integration constant and t is the duration of reaction.

In the case of diffusion control of metal reduction, the rate of particle growth is proportional to its radius and is described by the equation

$$\alpha = kt^{3/2}$$

where k is the rate constant (its value for temperature ranges from 313 to 323 K amounts to 1.66–1.67).

In the general case of stage formation of crystallization centers, the equation of kinetics of the metal crystallization process from liquid melt is developed:

$$\alpha = 1 - \exp\left(-kt^{\mathrm{n}}\right)$$

which after series expansion is reduced to $\alpha = kt^n$ and describes the reduction of metal ions (copper and silver) from aqueous solutions by various reducers, and 'n' can vary from 1.5 to 10. The initial stages of the reduction reaction are followed by the period when the process rate depends not only on the value of the particle surface, but on the concentration of ions of the metal ($C_{\mathrm{M}^{n+}}$) and reducer (C_{Red})

$$\frac{d\alpha}{dt} = kC^{\mathrm{a}}_{\mathrm{M}^{\mathrm{n}+}} C^{\mathrm{b}}_{\mathrm{Red}} S$$

where α is the reduced metal yield as the fraction of unity, and 'a' and 'b' are constants.

In the case of reducer excess in the solution, the following proportion

$$kt_1 = 0.5\ \ln\left(\frac{1+\alpha^{1/3}+\alpha^{2/3}}{\left(1-\alpha^{1/3}\right)^2}\right) + \sqrt{3}\mathrm{arctg}\left(\frac{2\alpha^{1/3}+1}{\sqrt{3}}\right)$$

describes the kinetic reduction curves for some metals rather well; copper is reduced by formaldehyde; tellurium is reduced by hydrazine; silver is reduced by ascorbic acid and hydroquinone, etc.

By chemical reduction, metals can be produced as sols or powders depending on the chosen method. Particle shape and size are controlled by the nucleation rate. In the case of sol formation, the reduction is controlled by the formation of new metal nuclei; the rate of the development of these nuclei is small. In the case of powder production, the conditions for nucleation are less favorable, but the rate of particle growth is appreciable. Also, aggregation of fine particles into larger agglomerates takes place.

A momentary formation of finely divided reduction product is realized at large values of the difference of chemical reagent's oxidation-reduction potentials and in the absence of the autocatalytic effect of the newly formed surface of metallic particles. Metallic colloids are usually formed at the maximum allowable concentration of the reducer and rather low concentration of metal ions. Ligands and protective colloids are introduced into the solution for stabilization of metal sols. Sols of various metals in borohydride solution are produced at elevated temperature and in the presence of a protective colloid (for example, gelatin). In such a way, sols of Ag, Au, Pd, Os, Rh, Pt, Cu, Sn, Tl, Te, Co(B), and Ni(B) can be synthesized. In the case of noncomplex metal ions, sols are homogeneous and superfine. In the case of the reduction of complexes, the degree of sol homogeneity decreases with the growth of their strength.

The growth rate and size of powder particles are controlled by changing the nature and concentration of the reducer, the concentration of precipitated metal ions, the solution temperature, and the concentration of complexing agents or surfactant. Monodisperse powders are formed during cooling by thorough and intensive stirring of the reaction medium. To reduce particle size, the solution temperature is decreased and complexing agents and surfactants are introduced.

Application of Chemically Reduced Powders and Sols

Metal powders and sols are used as catalysts in many organic reactions. The catalyst's activity increases by deposition on a carrier. Monodisperse powders with uniform distribution of the catalyst on the surface are produced by applying chemically reduced metal sols on the carrier particle surface. There are several methods of sol deposition:

- A metal colloid is precipitated by a chemical method and a metallized dispersed carrier is produced in a brief contact of the metal colloid with the carrier particles as a result of colloid adsorption. The method is possible if the rate of colloid adsorption is higher than its aggregation rate.
- Colloid production directly in the presence of the carrier is preferable. Carrier particles impregnated by a salt of reducible metal are put into the reducer solution and colloid metal particles are formed on the carrier surface. $Al(OH)_3$, TiO_2, Si, MgO, $CaCO_3$, ZrO, and carbon fiber material are used as carriers.
- Selective precipitation of chemically reduced metal on the carrier is performed by preliminary activation of the carrier surface by microcrystals of silver or palladium. Subject to conditions of preliminary activation and precipitation, it is possible to produce particles with controlled dispersivity, differing by thermal stability in relation.

AUTOCLAVE PRECIPITATION OF METAL POWDERS

This method includes processing of a metal salt solution (solutions of metal hydroxide or carbonate pulp are rather rare) by a reagent-reducer at elevated temperatures and pressures [1,2]. The autoclave scheme for hydrogen reduction is shown in Fig. 7.6. Some companies use the autoclave method to produce nickel, cobalt, and copper powders. The processing of laterite deposits of nickel and cobalt ore high in iron is accomplished through pressure leaching with sulfuric acid in Moa, Cuba. The nickel and cobalt sulfide concentrates so produced are the principal feed to the Sherritt International Refinery in Fort Saskatchewan, Alberta, Canada. The Sherritt refining process includes leaching at elevated temperature and pressure in the leach autoclaves. The Sherritt process is adaptable to handle a wide variety of different feedstocks. It has been adopted by Western Mining Corporation in a refinery at Kwinana, Western Australia. The Sherritt nickel and cobalt refining processes are further discussed in Chapters 21 and 22.

Organic reagents (glucose, formaldehyde, hydrazine, etc.) are used as reducers, but they contaminate the final solution and powder by their dissociation products. Gaseous precipitators, that is, sulfur oxide, carbon monoxide, and hydrogen are more effective. Hydrogen is the most widely used gaseous reducer; it is an effective, readily available reagent that does not contaminate the solution.

According to the experience of autoclave plants, hydrogen is produced by natural gas conversion. Possible impurities (CO_2, CO, H_2O and H_2S) lead to decreasing hydrogen activity, increasing total pressure in the autoclave, contaminating the metal powder, and the formation of carbonate ions in the ammonia media. This fact increases ammonia consumption and changes the molar ratio NH_3 (free) and $(NH_4)_2CO_3$, which is a kinetically important parameter.

Sulfur dioxide is a well-known reagent, but it is toxic, has limited critical parameters, and leads to the accumulation of sulfuric acid in the solution and powder contamination. This reagent, like carbon monoxide, is rather useful for precipitation of metal powders from alkaline and ammonium media. However, carbon monoxide possesses some shortcomings: it is toxic, explosive, difficult to synthesize, and expensive as well as changes the acid-basic equilibrium.

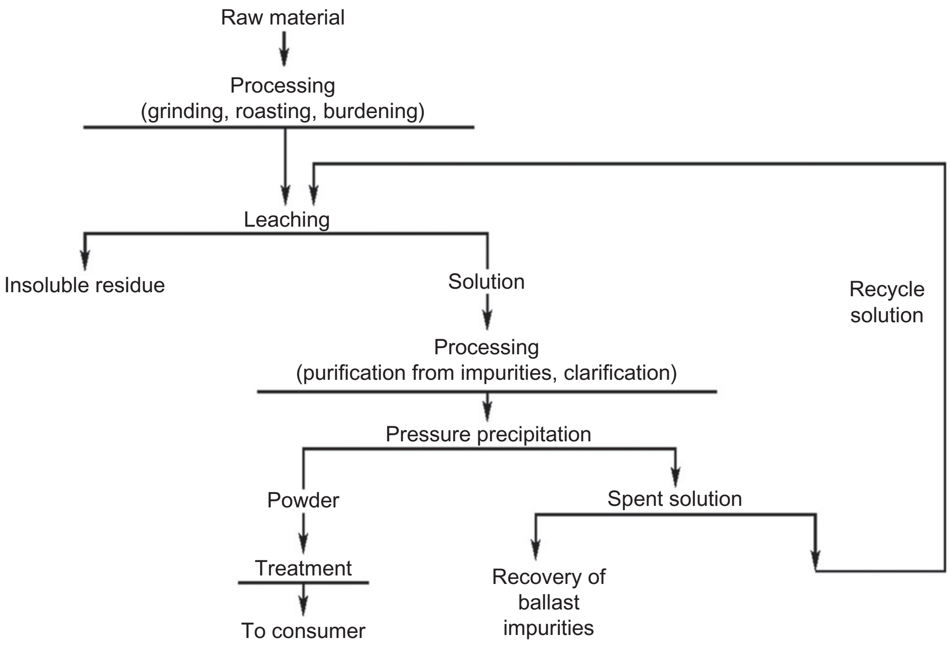
Raw material
Processing
(grinding, roasting, burdening)
Leaching
Insoluble residue
Solution
Recycle
solution
Processing
(purification from impurities, clarification)
Pressure precipitation
Powder
Spent solution
Treatment
Recovery of
ballast
impurities
To consumer

FIG. 7.6 Flowsheet for metal powder production by the autoclave method.

Theory of Autoclave Metal Ions Reduction

The reaction of metal ion reduction by hydrogen

$$M^{n+} + \frac{n}{2}H_2 \rightarrow M + nH^+$$

will proceed to the right until the hydrogen potential (E_{H_2}) is more electronegative than the potential of the metal ion (E_M^{n+1}). The limiting degree of metal ion reduction is achieved at the moment when $E_{H_2} = E_M^{n+1}$.

The moving strength of the summary reaction is defined by the difference of potential boundary phases M^{n+}/M and H^+/H_2. These potentials are determined per the Nernst equation [15]:

$$E_{M^{n+}/M} = E^0_{M^{n+}/M} + \frac{RT}{nF}\ln\left(a_{M^{n+}}\right) \tag{7.1}$$

where $E^0_{M^{n+}/M}$ is the standard potential of this boundary phase (standard conditions: $T = 298\,K$, activity of metal ions in solution g-ion/L); n is the metal ion charge; R is the universal gas constant; T is the temperature; F is the Faraday constant; is the activity factor for M^{n+}; and $C_{M^{n+}}$ is the concentration of metal ions.

For hydrogen, as its standard potential is zero by definition, the boundary potential is connected with hydrogen-ion activity (a_{H^+}) in the following manner:

$$E_{H^+/H} = 0 + \frac{RT}{2F}\ln\left(\frac{\left(a_{H^+}\right)^2}{p_{H_2}}\right) = \frac{RT}{F}\ln\left(a_{H^+}\right) - \frac{RT}{2F}\ln\left(p_{H_2}\right)$$

where p_{H_2} is the hydrogen gas pressure.

The substitution of a negative logarithm of hydrogen-ion activity by the conventional symbol pH gives:

$$E_{H^+/H} = -\frac{2.303RT}{F}\left(\mathrm{pH} + \frac{1}{2}\lg\left(p_{H_2}\right)\right) \tag{7.2}$$

The equilibrium activity $a_{M^{n+}}$ and concentration of metal ions in the solution are calculated by means of joint decision of Eqs. (7.1) and (7.2). The intermediate transformations lead to the equation:

$$\lg\left(a_{M^{n+}}\right) = -n \cdot \mathrm{pH} - \frac{n}{2}\lg\left(p_{H_2}\right) - \frac{nF \cdot E^T_{M^{n+}}}{2.303 \cdot RT}$$

where is the standard potential for metal with correction with respect to temperature T.

This equation is acceptable for conditions in dilute solutions (with ion concentration below 0.1 mol/L), in which the activity factor for M^{n+} is near 1.0.

In concentrated solutions, it is necessary to take into account the bond of the activity factor for M^n with the ionic force of solution and, after that, calculate the equilibrium concentration of metal ions $C_{M^{n+}}$.

$$\lg(C_{M^{n+}}) = -n \cdot \mathrm{pH} - \frac{n}{2}\lg(p_{H_2}) - \frac{nF \cdot E^{T}_{M^{n+}}}{2.303 \cdot RT} - \lg(f_{M^{n+}})$$

The values of activity factors are given in the reference literature; for sulfate media the following equation is valid:

$$f_{M^{n+}} = 0.056(\lg \mu)^2 + 0.016$$

where μ is the ionic force of solution equal to $\frac{1}{2}\sum n_i^2 \cdot c_i$; c_i is the concentration of ith ions, g mol/L.

To denote X, the share of reduced metal ions (M^{n+1}), the degree of its reduction is calculated according to the equation:

$$E^{0}_{M^{n+}/M} - \frac{0.0592}{n}\lg(1 - X) = 0.05921 \cdot \lg n \cdot X.$$

As the influence of pH is most significant, the alkali solutions are preferable for the precipitation of electronegative metals. In the presence of ammonia and other complex ligands, metal ions and complex ions with a different number of addenda are in the solution. For this case, the potential of the metal ion (E_{M_K}) is calculated as follows:

$$E_{M_K} = E_{M^{n+}/M} - \frac{RT}{nF} \ln \sum_{0}^{m} \beta_i \cdot a^{i}_{i_{\mathrm{free}}}$$

where $E_{M^{n+}/M}$ is the potential of the metal ion in the solution with the same concentration without complex ligands; i is the number of addenda in the complex; β_i is the stability constant of the complex that contains i complexing groups; $a^{i}_{i_{\mathrm{free}}}$ is the efficiency of excess complexing ligands; and m is the coordination number.

The pH value of the ammonia solution containing free ammonia and ammonium salt is calculated as:

$$\mathrm{pH} = pK^2\beta + \lg a_{NH_3\,\mathrm{free}} + \lg\frac{a_{NH_4^+} \cdot a_{OH^-}}{a_{NH_4OH}} - \lg a_{NH_4^+}.$$

The concentration of free ammonia in the solution is determined by pH-potentiometric titration.

Thermodynamically, the reduction of many metal ions by hydrogen is possible already at 298 K and $p_{H_2} = 0.1$ MPa. However, the implementation is first determined by kinetic factors. The rate of autoclave precipitation of metals is defined by hydrodynamics, pressure of the gas reducer, temperature, and solution (pulp) composition.

Hydrodynamics

Effective saturation of the liquid phase by the reaction gas and uniform density of the formed pulp with minimal energy consumption are achieved by sufficiently intensive stirring. Mechanical mixers that provide mass exchange by means of configuration-aerated units or rotation intensity are used; the latter is limited by the increasing energy consumption of mixer drives, the complexity of tightening units for their inlet into the reactor, and intensive foaming. Aeration units are more effective, but they lose the effect of the presence of powder surface deposits.

Parameters and Components of the Process

Reaction Gas Pressure

When the gas pressure is increased, the concentration of dissolved gas diluted in the pulp proportionally increases, and that accelerates the process. Critical pressures are limited by design reasons, the extra cost for gas compression, and the complexity and danger of plant servicing. The partial pressures of reducing gas vary between 0.05 and 3.0 MPa.

Temperature

The use of a higher temperature is particularly justified by effective aeration, but it involves a greater consumption of energy, more risk of corrosion, and greater pressure in the autoclave, especially if volatile reagents such as ammonia are used. Also, the composition of the solution may change because of hydrolysis, the sintering of powder particles, and the decreasing solubility of the salts. Furthermore, the operation of equipment is more difficult. Usually the precipitation is performed in the temperature range from 400 to 500 K.

Solution Composition

Ammonia, sulfuric acid, hydrochloric acid, and organic media are used; attention is increased to the processing of metal hydroxide pulps. Process rate and powder yield per unit volume increase with the growth of precipitable metal content on the condition that a reducing gas deficit is avoided. The upper limit is determined by solution stability (restricted solubility and metal salt hydrolysis); the rheological properties of pulps and the effectiveness of total mass exchange become limiting factors in pulp processing. The lower limit is determined by economic indexes of the process.

Free acid in the solution complicates the corrosion condition and decelerates the rate of reducing gas molecule activation. A minimal acidity sufficient for hydrolysis prevention at elevated temperatures and introducing buffering salts (ammonia salts and alkali metal salts are preferable) are recommended. When using ammonia media, the concentration of free ammonia is chosen, taking into account the provision of the stability of diamine complexes of the $(M(NH_3)_m)^{n+}$ type, where $m = 2.2$–2.5. In the case of ammonia excess, the total pressure in the autoclave and the loss of gas vapor mixture are increased.

Depending on the initial raw composition, the solutions used for autoclave precipitation contain various impurities, especially when using acid closed-circuit technologies with respect to the solution. With organic ammonia-based solvents, which provide highly selective leaching, the problem of coprecipitation of metallic impurities arises (for example, in nickel powder production-cobalt and copper coprecipitation). Therefore, a prior solution purification is required.

Accumulated impurities cause increased reducing gas consumption, change the solution properties (kinematic viscosity, solubility, and pH), and lead to powder contamination. To exclude the ingress of suspended solids, the initial solution must be thoroughly filtered.

During metal precipitation, the process of ion reduction is developed by a homogeneous mechanism of reacting gas activation. The ions with alternating valence play a significant part. They can accelerate the process or oxidize the intermediate ions formed with lower valence of the precipitated metal while causing an increase of reaction gas consumption and a lengthening of the precipitation process.

Some impurity anions form insoluble compounds with metal ions, which are reduced to intermediate valences. For example, the formed copper halides are insoluble, contaminating copper powder and decreasing its yield.

Seed

The effect of introduced dispersed solid substances (similar powder, graphite, carbides, borides, etc.) appears during the metal precipitation process, the mechanism of which obeys the regularities of heterogeneous catalysis per reducing gas molecule activation (for example, under hydrogen precipitation of nickel and cobalt). Introduction of a seed not only accelerates the process but also helps to control particle size and cover seed particles with a precipitated metal layer to obtain composite powders. The autoclave cladding technique provides the treatment of materials with different particle size, layer thickness control, and a high rate and absence of toxic emissions.

Surfactants

Insignificant additions of organic substances (polyacrylic salts, anthraquinone, and its derivatives) eliminate powder deposits on the autoclave's inside surface; influence the powder dispersity, shape, and texture of powder particles; provide uniform covering of the precipitated metal on the surface of inert seeds; and accelerate the process. But then, the surfactants introduced and the products of their destruction contaminate the powder with carbon.

Polyacrylamide (PAA) surfactant (0.4 g/L) introduced into the initial solution of the autoclave cupper powder production prevents the skull formation on the inner surface wall of the reactor and increases the metal yield. An 80–85 wt% minimum copper yield was obtained in the following conditions: initial copper concentration of 1.0–1.2 wt%, $(NH_4)_2SO_4$ of 1.2–1.5 wt%, sulfuric acid up to 0.15–0.25 wt%, at 408–418 K temperature, and under 2.5–2.8 MPa pressure. While in the autoclave process without PAA, a significant part of the powder (up to 20%–30% of the copper mass yield) precipitates on the inner surface wall of the reactor. However, the effect is reached by the surfactants content COO^- carboxyl group and along with this, they must be polymeric and stable up to 673–700 K.

The mechanism of the antiskull effect in the presence of the carboxyl containing surfactant may be described in the following way:

1. During dissolution of polymer compounds due to micelle formation, a high dispersity two-phase system is formed.
2. In weak acidity copper solutions, carboxyl compounds of the surfactant form a complex with copper ions. Due to the development of chemisorption processes, a micelle structure of dissolved surfactant promotes the appearance of numerous centers with high copper content that accelerate the formation of cupric ions by interaction with hydrogen.
3. The appearance of a metallic phase by autoclave copper precipitation proceeds through a phase of cupric ion formation with their further disproportionation; the formation rate and cupric concentration are proportional to the initial copper concentration.

Therefore, the conditions for nucleation and particle formation of copper directly in the solution volume are created; consequently, the depositions on the reactor inner surface wall are reduced.

Autoclave Processing of Hydroxide and Metal Carbonate Pulps

In general, the method of autoclave precipitation of metal powder includes the following stages:

- Gas dissolution and saturation of the aqueous phase by it.
- Adsorption of the gas on the seed surface and its activation with the formation of the intermediate metal hydride (heterolytic mechanism):

$$\mathrm{MX_{n-1}^{m-n} + H_2 \leftrightarrow MX_{n-1}H^{m-n} + H^+ + X^-}$$

- Gas activation by metal ions with alternating valence (homolytical mechanism):

$$\mathrm{2MX_{n}^{m-n} + H_2 \leftrightarrow 2MH^{m+} + 2nX^-}$$

- Electrochemical reaction of metal ion reduction.
- Reaction products transfer to solution volume.

Hydroxides or carbonates of metals are semiproducts of their extraction from low-grade raw materials or are formed during neutralization of technological overflow solutions. Direct autoclave processing of pulps provides a greater volume of powder and is useful for the production of powders with special properties (catalytically active powders, powders with narrow size distribution, powders with roundish shape particles, and ultrafine powders). Solid-phase composition and morphology, temperature, hydrogen pressure, catalyst consumption, and metal content in the aqueous phase are the main factors influencing the choice of pulp processing parameters.

So far as by hydrothermal conditions, the basic metal carbonate undergoes destruction and is transformed into metal hydroxide; the theoretical positions are considered using hydroxide as an example.

The summary reaction $\mathrm{M(OH)_2 + H_2 \rightarrow M + H_2O}$ consists of two subreactions:

$$\mathrm{M^{2+} + 2e \rightarrow M^0}, E_1^0 \text{ and } \mathrm{2H^+ + 2e \rightarrow H_2}, E_2^0$$

The difference in potential for them is the following:

$$\Delta E = E_1^0 - E_2^0 - 2.303\frac{RT}{2F}\left(2\lg K_\mathrm{W} - \lg Lp_{\mathrm{M(OH)_2}}\right)$$

where $K_\mathrm{W} = [\mathrm{H^+}][\mathrm{OH^-}]$; and $Lp_{\mathrm{M(OH)_2}}$ is the solubility product of $\mathrm{M(OH)_2}$ and $Lp_{\mathrm{M(OH)_2}} = [\mathrm{M^{2+}}][\mathrm{OH^-}]^2$.

Temperature, dissolved hydrogen concentration, and metal hydroxide solubility are the characteristic parameters of this system.

The process is carried out at a temperature range of 470–520 K, $p_{\mathrm{H_2}} = 2-3\,\mathrm{MPa}$ over 1–1.5 h using pulps that contain 25%–40% of solid phase. The powder properties depend on the pulp composition, shape, and size of solid phase particles and process parameters. The contents of carbon dioxide and ammonia influence the value of apparent density; the powder particle size depends on metal concentration, temperature, and hydrogen pressure.

If semiproducts are used, then, for pure powder production, it is useful to dissolve them to purify the solution and to produce secondary carbonate after solution redistillation.

Autoclave Precipitation of Metal Powders from Organic Phases

This method of powder production allows producing ultrafine powders with a developed surface and widening the choice of raw material base by implication of low-grade raw material, which can be processed by a leaching-extraction process. This method has been developed for the production of nickel, cobalt, copper, and noble metal powders.

The organic phase should be thermally stable with low solubility in water and be quantitatively regenerated during autoclave processing. Carboxylic acids and derivatives on their base and chelate compounds relate to similar reagents. Tertiary carboxylic acid $(CH_3)_3CCOOH$ is most thermally stable up to temperatures of 520–570 K. It is used in a mixture with diluent in the ratio of 1 to 2.

The advantages of autoclave metal precipitation from organometallic phases are their noncorrosiveness to stainless steels; significant decreasing of total pressure in the unit (lower than vapor pressure, below 0.5 MPa at 570 K); prevention of particle flocculation; property features of powder (roundish shape of particles, and fine particle sizes within several micrometers); organic phase regeneration; and a more compact flow diagram of powder production in an extraction-precipitation cycle.

But commercial application is restricted by the limited choice of available reagents that are stable at 348–483 K; their unavoidable partial destruction and contamination of the powder by carbon, sulfur, and phosphorus; fire risk; difficulties in separation of produced powder pulp; and the high power consumption of the process (owing to lean per metal solutions and elevated temperatures).

Equipment

For hydrogen precipitation of metals, the vertical and horizontal autoclaves with mechanical stirring are used; the latter type is predominantly used for scale production. The autoclave body is made of carbon steel clad inside with a corrosion-proof material: stainless steels or high alloyed steels by processing of ammonia, organic media, and pulp of metal hydroxides and titanium by processing of sulfurous and chloride media).

The autoclaves are equipped with a hatch for inside inspection and maintenance, fittings for installation of gauges for process characteristics control (thermocouples and pressure gauges), safety fittings (explosive valve, check valve), and tubing for the supply of solution, gas feeding, and discharge of the products produced. Gases and the initial solution are supplied from the top into the autoclave; powder pulp is discharged through a dipping tube. The diagrammatic pattern for a horizontal autoclave is shown in Fig. 7.7.

Autoclaves for powder precipitation work parallel in periodic mode. Continuous mode is also possible, but it is complicated because of the possibility of autoclave "obliteration," the risk of hydrogen leakages, and the complexity of unit operation for solution supply and especially for powder pulp discharge. Also, there is difficulty with control of the particle size and powder particle density. The load to stirrers drives is controlled, especially at the end of the process when pulp density increases and is quickly laminated. Overheating and shutdown of the stirrer is an emergency situation. Stirrer drives are equipped by guard relay actuators for thermal protection. Autoclaves are shut down regularly for inspection and maintenance with particular attention paid to the condition of the protective cladding and the welds.

Self-evaporators are capacitive devices with a conical bottom, which are equipped with a fitting for transfer of the solution and release of the gas-vapor phase. They are made of a corrosion-proof material (like the autoclave) and operate at atmospheric pressure. One self-evaporator is connected with two or three autoclaves as the duration of powder pulp processing and discharge is much smaller than the duration of the powder producing cycle in the autoclave. A double-pipe heat exchanger is the most popular type; it is manufactured from high-alloyed steel or titanium. Heat transfer efficiency

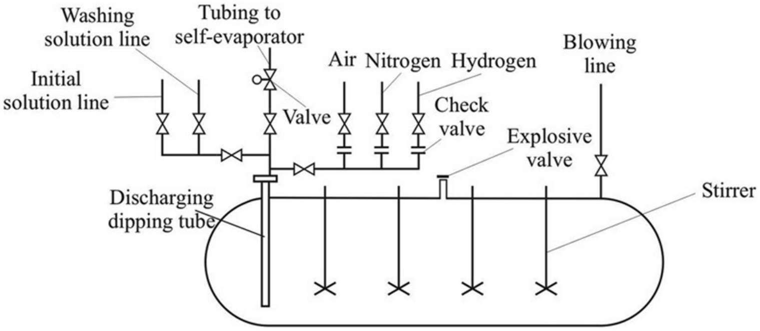

FIG. 7.7 Diagrammatic scheme for hydrogen reduction in an autoclave.

deteriorates in the long run due to the precipitation of basic salts of metals and calcium sulfate. The rate of deposit formation depends on solution composition and temperature. Alkaline salts and sulfate deposits are dissolved by the spent solution and by nitric acid, respectively.

Centrifugal pumps are used for transmission of the solutions; their supply into vessels operating under pressure is carried out by pumps of a plunger type. The amount of the solution supplied is controlled by the duration of pump operation and by prior measurement of the solution supply rate.

Discharging units of the autoclaves, the self-evaporator, and the line for powder pulp transportation are subject to strong erosion, so they should be changed periodically. Discharging lines are designed with the minimum number of elbows. Relief valves are changed from time to time.

The equipment used for powder treatment (drying, screening, mixing and stirring, milling, and packing) typical for powder metallurgy is described in Chapter 14.

Safety Engineering

Autoclaves for reduction are located in a separate building with easy dropping cover and big window openings [10]. The hydrogen content in the atmosphere in the building is controlled continuously [10–13].

The process gases are supplied into the autoclave via the separate gas tubing; the line for each gas has two faucets and a check valve allowing unused lines to switch off. The hydrogen pressure lines are controlled according to rules [16]. The whole system, including autoclaves, is purged with nitrogen ($p = 0.11$ MPa) before hydrogen or air is let in. The gas-vapor mixture is continuously blown away from self-evaporators to eliminate hydrogen accumulation to critical concentration. Oxygen content in the gaseous phase after venting of equipment shall not exceed 2%. Hydrogen-containing gases from the autoclave and the self-evaporator are passed through a drip pan and released via a chimney out of the building area. Welding works have to be performed only after equipment shutdown, its purging, and ventilation of the building with continuous monitoring of the hydrogen content in the air.

Autoclave operation must be largely automated and be carried out by remote control. Control valves, electric drives of autoclaves stirrers, ventilation systems, and pumps must have explosion-proof performance. Intermittent inspection, monitoring, high maintenance culture, and personnel experience are required.

REFERENCES

[1] Kiparisov SS, Padalko OV. Equipment in powder metallurgical enterprises. Metallurgy: Moscow; 1988.
[2] Kakovsky IA, Naboychenko SS. Thermodynamics and kinetics of hydrometallurgical processes. Alma-Ata: Nauka; 1986.
[3] Chopra KL. Thin film solar cells. New York, London: Plenum Press; 1983.
[4] Naboychenko SS, editor. Handbook of NonFerrous Metal Powders. Moscow: Metallurgia Publishers; 1997 (in Russian).
[5] Sircar S. Pressure swing adsorption technology for hydrogen purification. In: Zhou L, editor. Adsorption. World Scientific; 2006. p. 29–45.
[6] Li B, He G, Jiang X, Dai Y, Ruan X. Pressure swing adsorption/membrane hybrid processes for hydrogen purification with a high recovery. Frontiers of Chemical Science and Engineering 2016;10(2):255–64.
[7] Elseviers W, Hassett PF, Navarre JL, Whysall M. 50 Years of PSA technology for H_2 purification, Des Plaines, IL: UOP LLC, A Honeywell Company UOP LLC; 2016.1–5. [other] https://www.uop.com/?document=psa-50-paper&download=1.
[8] US New Jersey Department of Health and Senior Services. Hazardous Substance Sheet. Hydrogen. Revision: July 2016. < http://nj.gov/health/eoh/rtkweb/documents/fs/1343.pdf> [Accessed 31 January 2018].
[9] Leiby SM. Options for refinery hydrogen. Menlo Park, CA: Process Economics Program, SRI International; February 1994 Report No. 212.
[10] Determination of explosion-proof and fire-safe categories of rooms and buildings. 2017. < http://www.nj.gov/health/eoh/rtkweb/documents/fs/1010.pdf > [Accessed 30 December 2017]
[11] Baratov AN, Korolychenko AJ, editors. Fire- and explosion-proof of matters and materials and means for their quenching. Moscow: Chimia; 1990.
[12] Guide to EU legislation and "Health and Safety" in the European PM industry. Shrewsbury: EPMA Publisher; 2009.
[13] Regulation for installation and safe operation for combustible, toxic and condensed gases. BOC Gases. European Development Centre, UK. <//www.boconline.co.uk/en/about_the_linde_group/about-boc/index.html>.
[14] Sviridov VV, Vorob'eva TN, Gaevskaja TV, Stepanova LI. Chemical deposition of metals from aqueous solutions. Minsk: Minsk University Publishing; 1987.
[15] Uhlig HH, Winston RR, Viley A. Corrosion and corrosion control. New York: John Wiley & Sons; 1985.
[16] PRXAIR. Hydrogen, compressed safety data sheet P-4604. Revision data: Oct 15, 2016. <http://www.boconline.co.uk/internet.lg.lg.gbr/en/images/tg-8360-hydrogen-v1.3410_84488.pdf>

Chapter 8

Electrochemical Methods of Metal Powder Production[☆]

Irina B. Murashova
Ural State Technical University, Yekaterinburg, Russia

Chapter Outline

Introduction 235
Physical and Chemical Principles of Electrolytic Crystallization of Dendrite Deposits 236
Electrolysis of Aqueous Solutions 240
  Copper Precipitation in Industrial Electrolysis 245
  Reduction from Solution Through Film of Surfactants 248
  Special Methods of Production of Metal Powders Recovered From Spent Solutions 250
  Production of Metal Multicomponent Alloy Powders 252
  Powder Production Using the Method of Zone Electrochemistry 254
Contact Displacement Method (Cementation) 254
Production of Powders by Electrolysis from Melts 258
Amalgam Metallurgy Method 263
Workplace Atmospheres Safety 267
References 268

NOMENCLATURE AND SYMBOLS

A	cross-section of N nuclei formed on the boundary solution-mercury, m^2
C_0	bulk concentration of discharging metal ions in the solution, mol/m^3
C_{SAA}	bulk surfactant concentration
C_2; $C_{2,0}$	instant and initial concentrations of discharging ions in the solution, mol/m^3
C	instant ion concentration of dissolving metal, mol/m^3
Ce_k	cathode current efficiency
Ce_a	anode current efficiency
Ce_{ins}	current efficiency in the cells with insoluble anodes
D	diffusion coefficient, m^2/s
DLA	mechanism of diffusion-limited aggregation of metal particles
E	electrode potential, V
E_{eq}	the equilibrium potential on the interfacial boundary $Me|Me^{z+}$, V
$E^0_{M_1}$, $E^0_{M_2}$	standard potentials, a_{st} is standard activity equal to 1000 mol/m^3
E^0_{loc}	local standard potential (depends on curvature radii of the surface)
F	Faraday constant, A s/mol, A h/mol
I	current load on the electrolyzer, A
I_{ins}	current load on the electrolyzer with insoluble anodes, A
$I(t)$	current changing in galvanodynamic electrolysis by linear mode, A
I_{M_2}	current of metal M_2 reduction per unit area of the growth front, A/m^2
I_{TAH}	reduction current of metal M_2 on tangential spreading film per unit area of initial electrode surface, A/m^2
I_{M_1}	dissolution current of M_1 in areas free from the precipitated metal per unit area of the initial electrode surface, A/m^2
K	rate constant for the contact displacement reaction of the first order, s^{-1}, Eq. (8.33)
K	empirical rate constant for elongation of silver dendrites electrodeposited from the melts $m/(sV^n)$, Table 8.9
K'	empirical united rate constant for accumulation of ions-cementator $M_1^{z\dagger}$ in solution, s^{-1}, Eq. (8.34)
$K_{dep} = i/i_{lim}$	depletion factor

[☆] Expanded and updated by O.D. Neikov.

Handbook of Non-Ferrous Metal Powders. https://doi.org/10.1016/B978-0-08-100543-9.00008-7
© 2019 Elsevier Ltd. All rights reserved.

$K_{\text{dep-eff}}$	effective depletion factor–quotient of current density on the surface of the growth front to $i_{\lim}$
N	dendrite distribution density on area unit of dendrite deposit growth front, m^{-2}
N_0	number of columns per unit electrode surface formed as a result of electrolytic precipitator contactwith the solution, m^{-2}, the compact growth block of a radius r and a height h is spread over the surface
R	universal constant, J/(vol·K)
S	electrode surface, m^2
S_{μ}	thermodynamic criterion for stability of the flat growth front stability, Ohm·m
S_E	field criterion for stability of the flat growth front stability, V/m
S_w	specific volume surface of dendrite deposit, m^2/m^3
T	temperature, K
V	molar volume of the metal, m^3/mol
V_{Σ}	electrolyte volume in n electrolyzers, m^3
ΔC	electrolyte oscillation of electrolyte concentration in bath, mol/m^3, kg/dm^3
ΔE_{all}	the effect of depolarization, shift of the equilibrium potential of the jth metal component to more positive values, V
a_{M}^{z+}	activity of metal ions in the solution, mol/dm^3
$a_{M(Hg)}$	metal activity in amalgam, mol/dm^3
dQ_j	quantity of electricity consumed to reduce the metal on the deposit growth front within the time interval dt_j
dr_{tip_j}	time period corresponding to one of m intervals when r_{tip} changes on dr_{tip}, s
d_0	initial diameter of cylindric cathode, m
h	height of growth block, m
i	current density or current per unit area of initial electrode surface, A/m^2
i_k	kinetic current density controlled by slow charge transfer through interfacial boundary, A/m^2, at settled potential i_k may be calculated as $i_k = i_0 \exp\left(-\frac{\alpha zF}{RT}(\eta)\right)$, where $\eta = E - E_{eq}$
i_0	exchange current density on equilibrium interfacial boundary Me|Me^{z+}, A/m^2
i_0^{st}	standard exchange current density, A m/mol
i_{0,M_1}	exchange current density for metal M_1, A/m^2
I_{0,M_2}	exchange current density for metal M_2, A/m^2
$i_{\lim}$	limit current density, A/m^2, Eq. (8.1)
i_{limsph}	limit current density of the spherical diffusion equation (8.5) when dendrite height exceeds the diffusion layer thickness, A/m^2
$i_{H,1}$	current density of hydrogen emission on M_1 surface which is free from M_2 deposit, A/m^2
$i_{H,2}$	current density of hydrogen discharge on M_1 surface formed as a result of contact displacement, A/m^2
i_{0,H_1}	exchange current density of hydrogen emission on M_1 surface, A/m^2
i_{0,H_2}	exchange current density for hydrogen emission on M_1 surface, A/m^2
i_{0,M_1}	exchange current density for metal-precipitator M_1, A/m^2
i_{0,M_2}	exchange current density for crystallizing metal M_2, A/m^2
i_{tip}	current density on tips of growing dendrites, A/m^2, calculated according to Eq. (8.4)
m	number of equal intervals dr_{top_J}, in which the interval of the tip radius change for the period of dendrite growth, t, is divided
m	constant for the given metal (Table 8.10) for calculation of the particle size distribution in accordance with Gauss law
n	quantity of electrolyzers with soluble anodes
n_{ins}	quantity of electrolyzers with insoluble anodes, which are necessary to keep material balance in batch
q	electrochemical equivalent, A s/mol; A h/mol
r	radius of compact film spreading over the surface during contact displacement, m
r_{tip}	radius of dendrite tip, m
t	time, s, h
t_k	a number of cation transfers (the share of ion conductivity among a summary solution conductivity)
t_{cor}	period between corrections of electrolyte concentration, h
y	dendrite length; the height of dendrite layer on electrode, m
z, z_j	metal ion charge
1000	standard concentration, mol/m^3
α, α_j	transfer factor for reaction on interfacial boundary
α_2 and $(1 - \alpha_j)$	apparent transfer factors for cathode and anode reactions
$\alpha_{r_{\text{tipj}}}$	share of the dendrite deposit with the tip radius $r_{\text{tip},j}$ at any moment of electrolysis
β	rate of current rise in galvanodynamic electrolysis, A/h
δ	thickness of the diffusion layer, m

γ	specific surface energy of interface boundary, J/m^2
η	overpotential, $\eta = E - E_{eq}$, V
ν	rate of dendrite elongation at overvoltage η, cm/s
ρ_s	solution resistivity, Ohm·m
ρ_{dep}	deposit resistivity, Ohm·m
τ	transient time interval, s

INTRODUCTION

Electrochemical methods (Fig. 8.1) are used for the production of powders with particle sizes ranging from a few nanometers (by the method of zone electrochemistry) to several millimeters (electrolysis of melts) [1].

The main qualities of these powders are purity, the dendritic shape of particles (Fig. 8.2), and good compressibility.

Electrochemical methods make feasible control crystallization (shape and size of powder particles) by selecting the process parameters: concentration of the metal and hydrogen ion exponent pH of the electrolyte, cathode potential, current density, temperature and rate of circulation of the electrolyte, type and size of the anode and cathode and their distance from each other, type and quantity of addition agents, and conditions of removing deposits at the electrodes. The use of some techniques (permanent anodes, electrochemical reduction from the solid phase, electrodes with highly developed surface) enables us to utilize production waste and to achieve complete recovery of the metal as powder. Electrolytic powder alloys do not require chemical homogenization; moreover, some alloys are produced only by the electrochemical method. Nanoparticles display a unique catalytic activity.

Electrolysis of aqueous solutions is used for scale production of copper, nickel, cobalt, cadmium, zinc, and silver powders. This method is differentiated by the electrodeposition properties: the first method, namely "direct deposition"

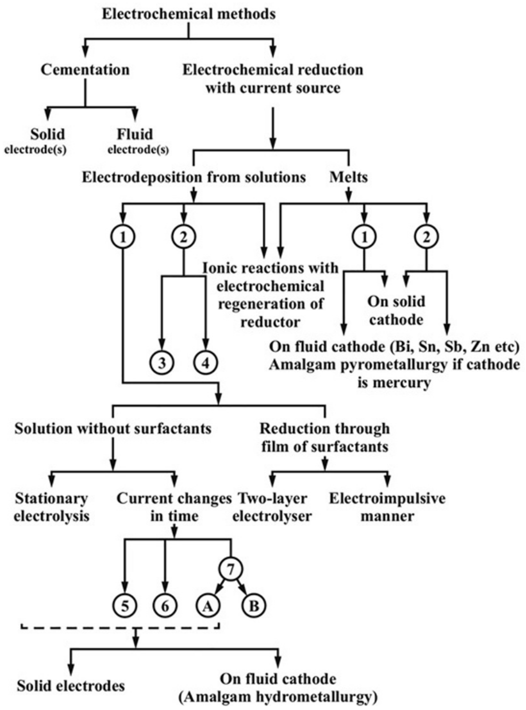
Electrochemical methods
Cementation
Electrochemical reduction with current source
Solid electrode(s)
Fluid electrode(s)
Electrodeposition from solutions
Melts
1
2
Ionic reactions with electrochemical regeneration of reductor
1
2
On solid cathode
3
4
On fluid cathode (Bi, Sn, Sb, Zn etc) Amalgam pyrometallurgy if cathode is mercury
Solution without surfactants
Reduction through film of surfactants
Stationary electrolysis
Current changes in time
Two-layer electrolyser
Electroimpulsive manner
7
5
6
A
B
Solid electrodes
On fluid cathode (Amalgam hydrometallurgy)

FIG. 8.1 Methods of producing metal powders by electrolysis of metals: 1, with nonpermanent anodes; 2, with permanent anodes; 3, on smooth electrodes; 4, on electrodes with developed surface and heightened transient factor; 5, galvodynamic electrolysis; 6, controlled potential electrolysis; 7, impulse electrolysis: (A) current impulses; (B) current impulses alternated with ultrasonic impulses (zone electrochemistry).

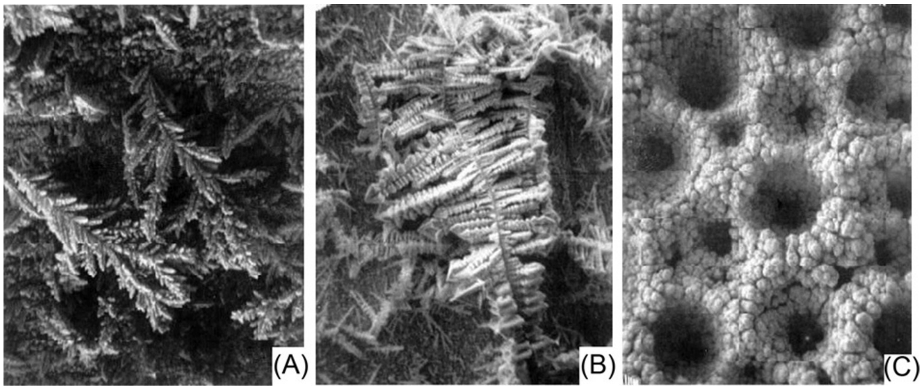

FIG. 8.2 Scanning electron micrographs of electrolytic dendrite deposits on the cathode in the water solution: (A) copper, (B) lead, (C) nickel.

of a friable or spongy deposit that can easily be disintegrated mechanically into fine particles, and the second method, called "brittle process" deposition of a dense, smooth, brittle layer that can be ground into powder [2]. Both deposition types are achieved by controlling the suitable composition and operating conditions. Such metals as nickel and cobalt are characterized by a high electrolytic polarization while forming deposits that can form brittle layers.

A great number of metal powders are manufactured by electrolysis of melts. The possibilities of making a wide list of metal powders are provided by amalgam metallurgy.

PHYSICAL AND CHEMICAL PRINCIPLES OF ELECTROLYTIC CRYSTALLIZATION OF DENDRITE DEPOSITS

In the course of electrolysis, the metal is crystallized in dendrites due to the disturbed stability of the flat front of growth of the newly formed metallic phase particles that occurs by positive values of the thermodynamic criterion S_μ or the field criterion S_E (Table 8.1) [3]. The trend of the transition to a dendritic deposit may be evaluated with the help of comparative computing of the criterion values when new electrolysis conditions are used.

In many cases, metal deposition is controlled by material transfer toward the phase boundary. The maximum rate of such an electrochemical reaction is characterized by limited current density (i_{lim}, A/m^2):

$$i_{\text{lim}} = \frac{zFDC_0}{(1 - t_k)\delta} \tag{8.1}$$

where z is the number of electrons in the cathode process; F is the Faraday constant (96.485 kJ per volt equivalent or 26,8 A·h/mol); D is the diffusion coefficient, m^2/s ($\sim 10^{-9}$); C_0 is the concentration of discharging metal ions in the solution, mol/m^3; t_k is the number of cations transfer (0,4–0,6); and δ is the thickness of the diffusion layer, m ($\approx 10^{-4}$).

As a rule, the resistivity of the solution ρ_s is considerably higher than the resistivity of the deposit ρ_{dep}. Therefore, during electric precipitation, the metal surface is gradually covered by deposits that build up in the form of dendrites. The more the stability of the flat growth front is disturbed, the higher the crystal branching, the thinner the dendrites, and the smaller the curvature radius of their tips r_{tip}. Dendrite growth is favored by a low concentration of ions in the solution, diffusion limitations, and low polarizability (crystallization from noncomplex solutions free from surfactants).

The structure of particles of the dendritic deposit depends on the nucleation mechanism and the dynamics of the dendrite growth (Table 8.2). The deposit type does not always directly determine the morphological characteristics of the particles. Both sponges and electrolytic powders can include two- or three-dimensional fernlike dendrites. Different nucleation and growth mechanisms define different particle sizes (<10 μm in sponge). Strands produced in deep passivation conditions of the cathode surface by surfactants differ in dimension and property anisotropy. The particle structure is influenced by the degree and character of the cathode overvoltage. If the diffusion constituent prevails, sharply cut ribbed dendrites of various twinning degrees are formed. An increase in the transition overvoltage share (for copper up to 70%) results in the crystallization of smooth spheroidal spherulite-globules.

TABLE 8.1 Criteria of the Stability of Growth Flat Front[a]

Electrochemical Precipitation	Equation for S_{μ}, S_E	Condition at Failure of Growth Flat Front $S_{\mu} > 0$; $S_E > 0$
Thermodynamic criterion		
From specific melt	$zF \cdot i \cdot (\rho_s - \rho_{dep})$	$\rho_s > \rho_{dep}$
From melted down solution or melt	$zF \cdot \left[\frac{RT}{zFDC_0 \cdot (1 - i/i_{lim})}\right] + \rho_s - \rho_{dep}$	$\rho_s + \frac{RT}{(zF)^2 DC_0(1 - i/i_{lim})} > \rho_{dep}$
From complex electrolyte	$\frac{RT}{zF} \cdot \left(\frac{1}{D_{MX} \cdot C_{MX}} + \frac{m^2}{D_X \cdot C_X}\right) + zFi\left(\rho_s - \rho_{dep}\right)$	$\frac{RT}{(zF)^2} \cdot \left(\frac{1}{D_{MX} \cdot C_{MX}} + \frac{m^2}{D_X \cdot C_X}\right) + \rho_s > \rho_{dep}$
Diffusion saturation	$RT\left[\left(\frac{d\ln(C)}{dx}\right)_s - \left(\frac{d\ln(C_c)}{dx}\right)_{dep}\right] + zFi\left(\rho_s - \rho_{dep}\right)$	$D_C C_C > D_P C_P$
Field stability criterion of growth flat front		
From specific melt	$\left(\rho_s - \rho_{dep}\right) \cdot i - \frac{d\beta}{dx} i + \frac{dE_l^0}{dx}$	$\frac{d\eta_a}{dx} < \rho_s i$ at $\frac{d\eta}{dx} = 0$
From melted down solution or melt	$-\frac{d}{dx}(\eta_a - E_l^0) + \left[\frac{RT}{(zF)^2 DC_0(1 - i/i_{lim})} - \rho_{dep}\right] \cdot i$	$S_E > 0$

[a] *Designation:* i, *A/m^2 is the current density;* ρ_s, Ω m *is the resistivity of solution;* ρ_{dep}, Ω m *is the resistivity of deposit;* i_{lim}, *A/m^2 is the limit current density;* m *is the number of ligands in the complex ion* MX_m; C_x, *mol/m^3 is the concentration of ligands;* C_C, *mol/m^3 is the concentration of precipitated metal in the alloy;* η, V *is the activated component of overvoltage;* β, Ω m^2 (β = dη/di) *is the polarizability of the process;* E_1^0, V *is the local value of standard potential.*

TABLE 8.2 Types of Dendrite Deposits, Peculiarities of Their Nucleation, and Morphology.

Deposit	Nucleation Mechanism	Surface Morphology
Sponge	Slow nucleation at limited mass transfer. Passivation of cathode base, decreasing of number of growth active places	Fibers, fern dendrites
Threads	Competitive layer growth of tips and passivation of side surface due to the absorption of SAA or different crystallography of cutting	Needles, fibers, whiskers
Branched dendrites	Crystallization in the condition of spherical diffusion ions transfer to the tips: (1) accelerated crystallization of faces with the highest indexes; (2) twinning; (3) dislocation pyramids; (4) three-dimensional nucleation at limited mass transfer	Needles, two and three dimensional dendrites; globular outgrowth

Subsieve dendritic particles (up to 1–10 µm) are obtained by electrolysis in a two-layered cell and by the chemical reduction from solutions. Big, well-faceted dendrites of 50 µm–100 mm are crystallized from the melts. Particles of 5–200 µm are produced by electrolysis of aqueous solutions.

Diffusion limitations are provided by a high depletion factor $K_{dep} = i/i_{lim}$, named so by Pomosov ($K_{dep} = 5$, 10 and higher) [4]. In the course of the growth of dendrite deposit, the electrochemical reaction is forced out to the dendrite tips while the electrical crystallization is localized in the thin upper layer, which forms a growth front. The extension of the cathode size (including the dendrite deposit layer) results in decreasing the effective depletion factor $K_{dep\text{-}eff}$ (the ratio of the dimension current density to the limit current density) in the galvanostatic electrolysis.

An anisotropic shape of dendritic particles is connected with the difference between the electrolytic crystallization rate at the tips (i_{tip}) and on the rest of the deposit surface and is determined by the dynamics of their elongation [5] because

$$i_{tip} = \frac{dy}{dt} \cdot \frac{zF}{V} \tag{8.2}$$

where y, m is the dendrite length at a time t, s and V, m^3/mol is the molar volume of the metal.

Dendrite growth dynamics completely depend on the conditions of the electrolysis as well as the potentiostatic and galvanostatic conditions. In the potentiostatic condition [5], dendrite length increases linearly during the period of their visible growth ($r_{tip}/y \langle 10^{-3}$).

$$y = \frac{zF}{V} i_{\text{tip}}(t - t_{\text{i}}) \tag{8.3}$$

where t_{i} is the period of dendrite nucleation; i_{tip} is determined by the ratio (4), and r_{tip} is the dendrite tip radius.

$$i_{\text{tip}} = \frac{i_{\text{limsph}} \cdot i_{\text{k}}}{i_{\text{limsph}} + i_{\text{k}}} \tag{8.4}$$

where i_{k} is the current kinetic density determined in accordance with electrochemical laws [6] by the exchange current density i_0 and the set overvoltage η or the potential ($\eta = E\text{–}E_{\text{eq}}$).

If dendrite height exceeds the diffusion layer thickness, then the maximum current of the spherical diffusion is calculated as the following:

$$i_{\text{lim.sph}} = \frac{zFDC_0}{r_{\text{tip}}} \tag{8.5}$$

The tip shape that is closest to parabolic can be approximated by a semisphere with the radius r_{tip}. The value of r_{tip} depends on the set overvoltage and is connected with the exchange current density for the given metal which, in turn, varies with the concentration of discharging metal ions $C_{0,}$ according to the law

$$i_0 = i_0^{st} \cdot C_0^{1-\alpha} \cdot 1000^{\alpha} \tag{8.6}$$

where i_0^{st} is the standard exchange current density, A m/mol, and C_0 and α are determined above in the list of designations.

Thus, the dendrite growth rate is defined by the overvoltage value η, the nature (i_0^{st}, α), and the concentration C_0 of discharging ions. In practice, the linear dendrite growth is preceded by the period of roughening and developing the primary surface unevenness (t_{i}) that increases with the electrolyte dilution and the decrease of the applied overvoltage.

In potentiostatic conditions, uniform dendrite growth is determined by the establishment of a constant curvature radius of the dendrite tips that is correlated with the applied overvoltage. The spherical diffusion rate determined by the surface curvature radius (6) is low on flatter tips while very sharp tips remain unstable. Their equilibrium potential $E_{\text{eq,tip}}$ is shifted to the area of negative values by the amount of $2\gamma V/(zFr_{\text{tip}})$, so that the effective overvoltage at the tip ($E\text{–}E_{\text{eq,tip}}$) turns out to be too low to provide quick growth. Here, y is the surface energy of the "metal-solution" boundary ($\approx$0.15 J/mol).

Such electrolysis conditions provide for the crystallization of the dendrite deposit's uniform structure during long-term electrolysis. At that, the size and morphological characteristics of dendrites are determined and regulated by the value of the applied overvoltage. This prospective way to obtain dendritic deposits of uniform and regulated structure is not implemented currently due to a lack of industrial potentiostats.

Because in galvanostatic electrolysis the set current is many times higher than the limit current, hydrogen is formed at the cathode together with the metals that do not possess a high exchange current (in precipitation from an aqueous solution). If hydrogen is not coreduced together with the metal, then the change of the dendrite length within an interval t on a cylindrical electrode with a diameter d_0 is described in the wing way, neglecting the height of the initial surface unevenness [7]:

$$y^2 + d_0 y = \frac{V}{zF} \frac{d_0 K_{\text{dep}} i_{\text{lim}}}{2\pi N r_{\text{tip}}^2} t \tag{8.7}$$

where N is the density of dendrite tip distribution on the front of the dendrite deposit growth (10^8–$10^{11}\,\text{m}^{-2}$). The dendrite growth rate in these electrolysis conditions decreases in the course of time in accordance with Eq. (8.7). At high values of t, the growth rate decreases in proportion to the ratio $1/\sqrt{t}$:

$$\frac{dy}{dt} \approx \frac{1}{2} \sqrt{\frac{V d_0 K_{\text{dep}} i_{\text{lim}}}{zF 2\pi r_{\text{tip}}^2 N}} \frac{1}{\sqrt{t}} \tag{8.8}$$

Due to a decrease of i_{tip}, metal precipitation rates become alike in all directions, the dendrite tip curvature radius increases, the particle shape is gradually roughened, and crystal spherulites are formed. During the process of dendrite deposit growth, the effective depletion factor decreases to unity, diffusion limits of the growth front are cancelled, the potential is shifted to the area of more positive values, the uniform overgrowing of the spherulites begins (Fig. 8.3), and, finally, a continuous metal layer cover is formed. The duration of diffusion limits application for the deposit growth front grows together with the increase of the set depletion factor and is determined by the electrode dimensions. For example, on a cylindrical electrode this period grows together with the rod diameter enlargement.

Uniform dendritic deposits can be obtained in galvanostatic electrolysis too, when the deposit growth front area is constant. For instance, in the aqueous solution together with the dendrite layer growth, the current load must be increased.

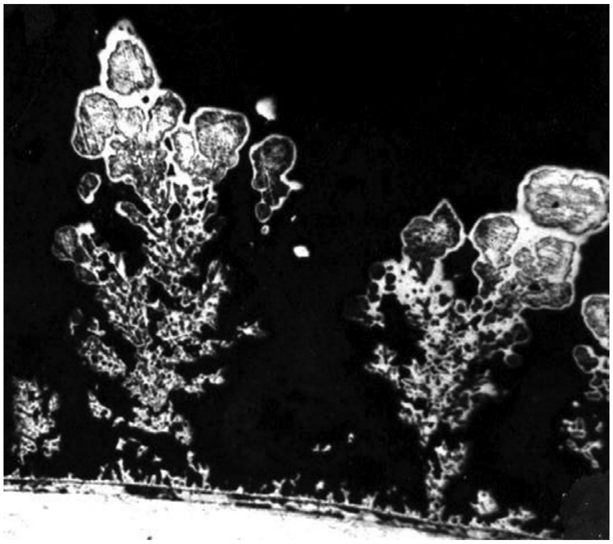

FIG. 8.3 Cross-section of the loose copper deposit on the *v* cathode with a diameter of 1.5 mm.

Then, the initial current value and its rates of increase will determine the structural and technological parameters of the powder [1]. In melts, lifting of the cathode covered with deposit from the cell should be done simultaneously with switching on the current. Solidifying melt preserves a bundle of dendritic strands. If the cathode lifting rate and the dendrite elongation rate are matched, the process in the electrolyte continues on the constant deposit growth front area [8]. The value of the set current and the cathode lifting rate determine the properties of the strands in the dendritic bundle [9].

Simulation of the electrolytic dendrite deposit growth is meant for the description of a relation between powder technological properties and electrolyte composition and electrolysis conditions. In the course of processing, after electrolysis the powder properties (particle size distribution, apparent density, and specific surface) are significantly changed depending on drying, milling, and screening conditions. However, the basis of particle structure is formed in the electrolysis stage. While simulating the process, it is assumed that the key structural parameters are the dendrite tip curvature radius $\mathrm{r_{tip}}$ and the dendrite distribution density on a unit area of the dendrite deposit growth front N, m^{-2} [1].

The distribution of the obtained dendritic deposit over the dendrite tip radii is a prototype of electrolysis product distribution by particle size. The average density of tip distribution on the growth front characterizes a dendritic form of the loose deposit and is proportional to the reciprocal apparent density of the powder. The share of the dendrite deposit with the tip radius $r_{\mathrm{tip_j}}$ at any moment of electrolysis is $\alpha_{\mathrm{r_{tipj}}}$:

$$\alpha_{\mathrm{r_{tip_j}}} = \frac{\Delta Q_{\mathrm{j}}}{\sum\limits_{\mathrm{n}} \Delta Q_{\mathrm{j}}} \tag{8.9}$$

where n is the number of equal intervals, and ΔQ_j is the quantity of electricity consumed to reduce the metal on the deposit growth front within the time interval Δt_j. The calculated result of such distribution is determined by dendrite growth dynamics, although, to be more correct, it is determined by two dependences: changes with the time of the dendrite tip radius $r_{\mathrm{tip}}(t)$ and the metal reduction current on the tips $I_{\mathrm{tip}}(t)$ necessary to calculate every corresponding charge dQ_{j}. Preliminary calculation of dendrite growth dynamics is performed for galvanostatic conditions [1]. Such calculation is necessary to evaluate powder structural characteristics a priori. The process is described by a system of differential equations based on the following main principles: the laws of electrochemical kinetics (for metal reduction and for the accompanying production of hydrogen) as well as the principle of charge balance on the electrode equipotential surface. The set current is distributed between metal ion discharge on the dendrite tips that creates the deposit growth front and hydrogen that reduces around the entire metal surface. The suggested equation system is solved by the Runge-Kutta method that enables the relationships $r_{\mathrm{tip}}(t)$ and $I_{\mathrm{tip}}(t)$, required to calculate the distribution that correlates with the results of the particle size distribution analysis [10], to be obtained. Trends of maximum shifting along the curves of tip radius distribution by size show (Fig. 8.4) that the average powder particle size increases with the decrease of the set current and the growth of the metal ion concentration in the solution as well as the decrease of the exchange current of the reduced metal and the increase of the hydrogen exchange current.

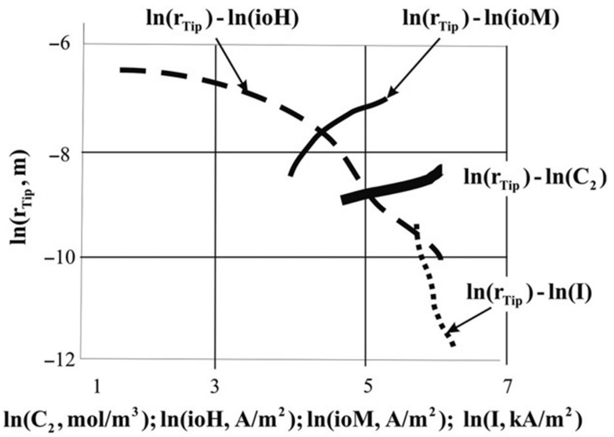

FIG. 8.4 Trend of variation of predominant radii for dendrite tips of dendrite deposit depending on the parameters of galvanostatic electrolysis (model calculation): (8.1) C_2, mol/m^3; (2) i_{oH}, A/m^2; (3) i_{oM}, A/m^2; (4) I, A.

The use of activation control or ohmic control instead of transfer control can result in a radical change of the type of dendrite deposit that is weakly connected with the degree of diffusion limitations. Another kind of control (for example, activation or ohmic control) instead of a transport one can result in a radical change of the mode of the dendrite deposit. In such cases, the deposit structure is controlled by other technological parameters, for example, a change of discharge activation parameters (introduction of surfactants, complexing ligands) or an increase of electrolyte conductivity.

Electrolytic dendrite deposits produced under the diffusion control conditions possess fractal properties so that the structural characteristic of such deposits is the value of the fractal dimension D. The process can be described by stochastic models based on diffusion-limited aggregation (DLA) [11]. The deposit fractal properties are lost at the cancellation of transfer control of the process. This phenomenon is observed in the process of the development of the dendrite deposit growth front ($K_{dep} \rightarrow 1$).

Nanopowders are produced under the condition of the enforced removal of metal nuclei that develop within the period of short-term current impulses from the cathode surface [12]. In this case, the shape of the particles formed is close to spherical and the average particle size is of the order of 5–15 nm [13]. In the process of prolonged electrolysis under such conditions, one can get dendrite clusters, and the mechanism of their format is explained by the diffusion-limited aggregation.

ELECTROLYSIS OF AQUEOUS SOLUTIONS

Electrical precipitation of metal as a loose dendritic deposit is performed from diluted solutions under a high current density. The possibility of powder precipitation on the cathode from an aqueous solution is defined by the relation of electrochemical parameters of metal and hydrogen. Intensive emission of hydrogen is observed for the majority of metals (except mercury) by potential ranging from (−1) V to (−1.2) V. This range determines the area within which metals can be precipitated from the aqueous solution on the cathode with appropriate current efficiency. Taking into account the polarizability, the most electrically negative metal that is precipitated from the aqueous solution as a dendritic deposit is zinc. The use of a mercury electrode allows extending the range of metals precipitated from the aqueous solution. The electrolysis on a solid cathode is accomplished usually at low temperature (290–330 K) with a relatively low specific power consumption (1.6–10 kW h/kg). The crystallized deposit either falls off due to shaking or is brushed off from the cathode, subject to the nature of the precipitated metal. The anode current density on the soluble anodes is usually lower than the cathode one to avoid passivation. The powder deposit is removed from the electrolyzer and dehydrated; it is then washed, stabilized with surfactants to protect it from oxidation, milled, screened, blended, mixed, and packed. An alternative technological treatment of powder includes washing, drying, sintering in a reducing atmosphere, milling, and screening. In this case, the powder is characterized by higher apparent density and flowability, but has a lower corrosion resistance owing to the destruction of stabilizing layers while sintering.

All the factors that contribute to the destabilization of the flat growth front result in comminution of powder particles. The stability is disturbed ($S_\mu > 0$; $S_E > 0$, Table 8.1) in the case of deep diffusion limitations ($i >> i_{lim}$). In conditions of diffusion control, the depletion factor K_{dep} is the key parameter that determines particle dispersity in fixed intervals of their precipitation on the cathode. If K_{dep} becomes higher, the average particle size and apparent powder density decrease, but particle branching is enhanced. Elevation of K_{dep} is achieved either by a higher current density or a decrease of the limit current density i_{lim} (by lowering the concentration C_0, decreasing the diffusion factor D due to lowering the temperature, and the addition of other electrolytes to the solution that results in lowering t_k). A decrease of current density and an increase of i_{lim} (growth of C_0, higher temperature, and accelerated circulation) cause the coarsening of powder particles. The transition parameters of electrochemical reaction (current changing, transfer coefficient) regulated by complexing for current metal and surfactant additives significantly influence the powder particle properties (see Fig. 8.4). The decrease of exchange current after the introduction of complexing ligands or surfactants into the solution increases the polarization of the process and, consequently, the stability of flat front growth, that is, it leads to the formation of coarser particles with simpler shape and the production of powder with higher apparent density and flowability. The passivation of the electrode surface is possible due to the formation of sparingly soluble basic salts and hydroxides, and an intensive evolution of hydrogen.

Escaping together with metal hydrogen stirs the cathode layer, making the diffusion layer thinner and facilitating the dendrite coarsening (lowering K_{dep} due to i_{lim} elevation). The increase of the hydrogen ion exponent pH of the cathode layer by escaping hydrogen can cause the passivation that facilitates the three-dimensional nucleation and the formation of more ramified dendrites. At the same time, the increased polarization due to the discharge on the passive surface facilitates its equalization and initiates the growth of spherulitic crystals.

After energizing, the sediment is formed within the transient time interval τ and, at the end of this interval, the metal ion concentration C at the cathode surface decreases from the original value C_0 to zero:

$$\tau = \pi D\left(\frac{zFC_0}{2i}\right)^2 \tag{8.10}$$

Then, the dendrites can crystallize in two ways depending on the ratio of equilibrium potentials and the exchange currents of the metal and hydrogen: either by means of the cathode process (discharge of metal ions) or by a combined reduction of metal and hydrogen ions. The noble metals with the equilibrium potentials are much more positive than the ones of hydrogen as well as metals with high overvoltage of hydrogen release on them (lead, cadmium, tin from simple electrolytes) are related to the first group. The dynamics of dendrite growth in the first group are described by Eqs. (8.2), (8.6), and (8.7). An intensive dendrite growth rapidly removes diffusion difficulties on the growth front. The starting crystallization of massive needles and clusters requires a decrease in the time interval of deposit growth to shake it off often or to brush it off from the cathode automatically.

The second group comprises the remainder of the metals as well as metals of the first group precipitated from solutions of complex compounds or in the presence of surfactants. In these cases, dendrite deposit growth is accompanied by hydrogen release, the dendrites grow more slowly, and the cathode potential is determined by the current density of hydrogen reduction until the condition of dendrite growth $K_{\text{dep.eff}} > 1$ is reached. The removal of diffusion limitations from the growth front is accompanied by a considerable shift of potential to the more positive area. Powder properties may be regulated thus by means of the selection of the successful electrolysis conditions.

The trends of different distribution of the dendrite deposit in dendrite radii of dendrite tips under new electrolysis conditions are equal for electrolytic crystallization of all metals (see Fig. 8.4). A coarsening of electrolytic powder particles is expected to follow the increase in metal ion concentration in the solution when the set current and the metal exchange current are decreased and hydrogen is released more easily. However, a combination of electrochemical parameters of metal and hydrogen provides a wide range of such changes.

Electrical crystallization of the structurally uniform deposit that grows with a constant rate is provided with potentiostatic electrolysis. However, the galvanodynamic mode with a linear change of current in time is more technically simpler:

$$I(t) = I_{\text{init}} + \beta t \tag{8.11}$$

where I_{init} is the initial current, A and β is the rate of current change, A/h.

By selection of the values of I_{init} and β, a prolonged crystallization of dendrites with required properties is achieved. Here the value of the cathode overvoltage is a reference parameter of the stability of electrical crystallization conditions. The process may be enhanced by agitation of the solution by fine air bubbles sparging without turbulization of the cathode layer. An increased share of transient overvoltage causes a simplification of particle shape and an increase of powder apparent density.

The impulse mode of electrolysis is elaborated to affect the particle structure directly and enables a change of particle size distribution and powder particle shape, depending on the amplitude and duration of the impulse.

Constant electrolyte composition is one of the main conditions of process stability and of permanent powder quality. The requirements for the electrolyte are the following: absence of impurities able to coreduce together with the metal; high conductivity to reduce the specific power consumption; a minimum rate of hydrogen release that decreases cathode current efficiency; and the lowest possibility of chemical dissolving of the precipitated metal.

Soluble anodes are manufactured from refined metal and the solution is prepared from pure reagents. Potentiostatic conditions allow selective recovery of powders of different metals from multicomponent electrolytes. The necessary conductivity of the electrolyte is imparted by salts, alkali, or acid. The concentration of the latter is selected according to the current efficiency because it decreases at high acidity. Approximately neutral electrolytes should be prepared with a sufficient buffer capacity to avoid quick increasing of the pH of the cathode layer and connected with this cathode contamination due to hydrate formation.

The current efficiency of the dendrite deposit is always <100% because of the following reasons:

- Accompanying escaping hydrogen.
- Interaction of cathode and anode products if insoluble anodes are used.
- Reduction of metal ion only to intermediate valency.
- Chemical dissolving, especially when powder falls down from the cathode.

The following measures contribute to the increase of the current efficiency:

- Maintenance of optimal parameters of electrolysis (metal ion concentration, background, current density, agitation mode).
- Installation of a diaphragm if permanent anodes are used.
- Extension of the interval of cathode deposit growth.
- Rapid powder removal of the electrolyte and its washing to reduce secondary dissolution.

Measures to increase the current efficiency should be balanced with their effect on powder dispersivity and powder particle shape. During increasing current density, the current efficiency passes through a maximum. At first, the proportion of current for dendrite deposit precipitation increases due to a decrease of the quantity of the compact precipitate and multibranch dendrites formed if current densities are comparable with the limit density. An accelerated hydrogen release decreases the cathode current efficiency Ce_k and leads to stirring the electrode layer that conduces to decelerate Ce_k near to the maximum. A further growth of the current density is accompanied by hydrogen effervescence and an abrupt decrease of current efficiency. When temperature and metal ion concentration in the solution increase, the current efficiency grows and powder particles coarsen.

The anode current efficiency in the case of soluble anodes is, as a rule, higher than the cathode yield.

and can exceed 100%, taking into account the chemical dissolution of the metal. In a number of electrochemical systems, anode passivation and decreasing of anode current efficiency are possible. To align current efficiencies, depassivators (for example hydrochloric acid in nickel powder production) are introduced in solution.

The inequality of cathode and anode current efficiencies changes the electrolyte composition. Metal ions are gradually accumulated; a saturation by gas of the solution close to the cathode and a growth of the concentration of metal ions in the near-anode space lead to electrolyte separation into layers. More dense solution from the near-anode space sinks to the bottom of the electrolyzer while in its upper part, the solution with a lowered concentration accumulates. This effect is overcome by a periodic withdrawal of a part of the electrolyte respectively with the introduction of a fresh correction solution or the introduction of insoluble anodes.

Denoting the electrolyte volume in n-cells as V_Σ, m^3, the current load as I, A, the electrochemical equivalent of precipitated metal as q, kg/A h, and the permissible fluctuation of metal ion concentration as ΔC, kg/m^3, it is possible to calculate the duration of the period between corrections t_{cor}, h (without consideration of electrolyte leakage and water evaporation):

$$t_{cor} = \frac{V_\Sigma \Delta C}{nIq(Ce_a - Ce_k)} \tag{8.12}$$

where Ce_a and Ce_k represent anode and cathode current efficiencies, respectively.

The required quantity of cells with insoluble anodes (n_{ins}), by current load on them I_{ins}, A and current efficiency Ce_{ins}, for the circuit consisting of n electrolyzing cells with soluble anodes, is calculated in the following way:

$$n_{ins} = n\frac{I}{I_{ins}}\frac{Ce_a - Ce_k}{Ce_{ins}} \tag{8.13}$$

If such a cell is one in the series, then its current load will be:

$$I_{ins} = nI\frac{Ce_a - Ce_k}{Ce_{ins}} \tag{8.14}$$

Electrolyte circulation (approximately 0.4 L/(A·h) with a 12% difference in anode Ce_a and cathode Ce_c current efficiencies) is necessary to prevent electrolyte layering.

Electrolytic cells of box type with plain (disk) or cylindrical cathodes (bars or in the form of a drum) are used by water-solution treatment. In electrolytic cells, devices of electrolyte input and output are provided. Powder is removed in the form of sludge through the bottom union. The electrolyte temperature is maintained using heat exchangers installed in the circulation scheme.

The type of device depends upon the duration of precipitate buildup and the strength of its binding with the cathode. Shaking off the friable precipitate (Fig. 8.5A) or cutting it off (Fig. 8.5B–C) is applied. Several types of shaking devices for powder removal from bar cathodes are known. Using the electroimpulse method, high-voltage current is for a short time passed through dischargers installed inside the cylindrical cathode bars. When using the pneumatic shaking device, the cathode rods are preliminarily lifted up over the bus bar. Then fluctuations are transferred by a pneumatic vibrator through a support frame to the group of cathodes supported by it at one shoulder. After shaking off powder from the rods, the frame is lowered and the cathode shoulder again nests on the bus bar.

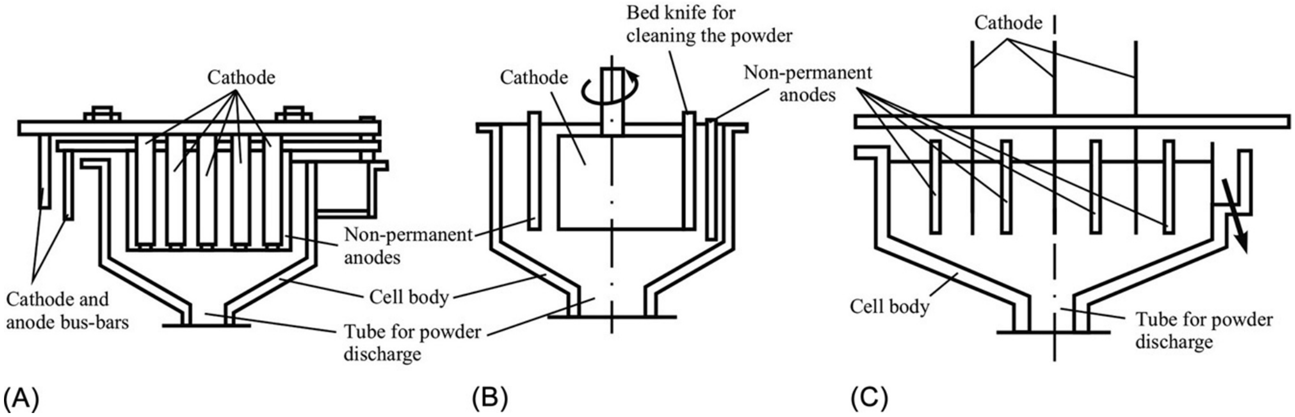
Cathode
Cathode and anode bus-bars
Non-permanent anodes
Cell body
Tube for powder discharge
Bed knife for cleaning the powder
Cathode
Non-permanent anodes
Cathode
Cell body
Tube for powder discharge
(A)
(B)
(C)

FIG. 8.5 Basic types of electrolyzers with (A) rod, (B) cylinder, and (C) disk cathodes.

In the cells with disk cathodes, a quick shifting of cathode sections in the air, automatic powder cleansing from the cathode, and powder washout into the collector are provided. Cathodes are placed between anodes and are made in the form of sections; they are fixed on the shaft and are able to rotate independently around its axis. When a cathode goes from solution, each section of it is separated from others and, using a mechanism, is quickly transferred to a chamber where the powder is cut from the cathode with a knife and flushed with water into the collector.

The bath for collection of the powder from the cylindrical cathodes is installed on a platform moved in the vertical plane by a screw using a drive (Fig. 8.6). After the cathode recurrent interval deposit growth, the programmable logic controller (PLC) has switched the electrode and the electromagnet feed off. The cathode is drive-rotated through an adapter and cathode holder. The scrubber approaches the cathode and cleanses the deposit formed, which falls down into the collector. Then the PLC switches on current on the electrodes and in the electromagnet circuit.

If a duct cathode is used, the electrolyte is supplied into it under pressure through a fitting. The electrolyte is released through holes and falls onto plates. It is reflected from them and flows along the cathode surface. In this process, ultrasonic fluctuations with a frequency of 100 kHz arise in the solution. Metal powder precipitates on the cathode. Then, it is taken off the cathode by solution jets and ultrasonic vibrations and removed into the collector in the form of a sludge.

To intensify the process of electrolysis and to simplify powder discharge, the electrolyte is fed by impulses of 5–300 s with a periodicity of 1–100 h from below the apparatus under an angle of 5–75 degrees to the horizontal with speeds in a range under 200 cm/s (the range under 10 cm/s is preferable), depending on the quantity and the granulometric composition of the precipitated particles.

If a vibrating ribbed cathode is used, the process of powder precipitation is accelerated 50–100 times (the amplitude is 0.8 mm and the frequency is 100 Hz). Cavitation arises close to the ribbed surface of the cathode and this intensifies electrolyte stirring and facilitates powder fall from the cathode.

Impulse gas feeding through holes of a hollow cathode (Fig. 8.7) significantly accelerates powder precipitation. The holes are placed between ring angular flanges. As the powder accumulates, the gas is supplied into the hollow cathode through a special device. The bubbles formed accelerate the separation of the precipitate that falls into the basket.

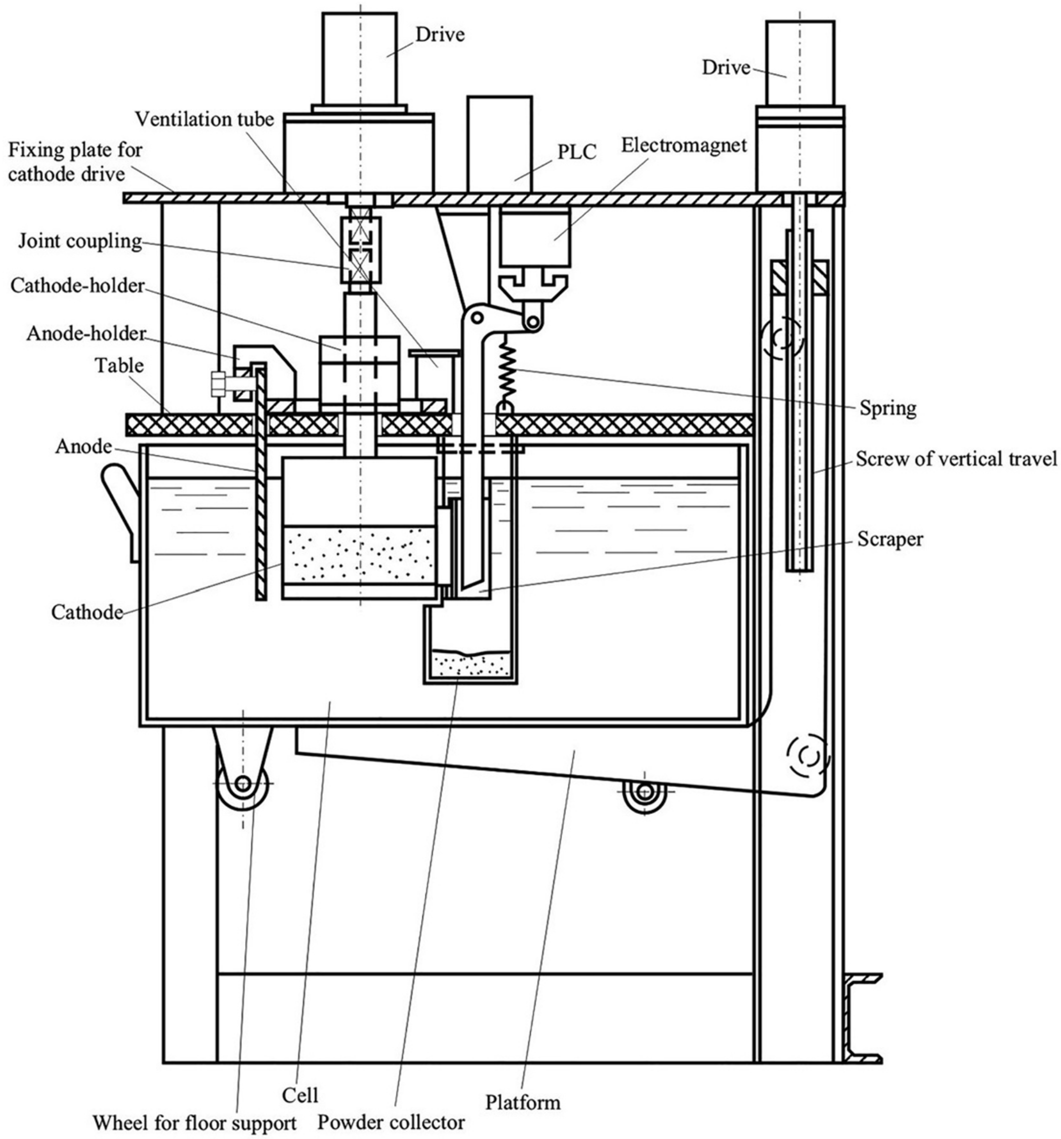
Drive
Drive
Ventilation tube
Fixing plate for cathode drive
PLC
Electromagnet
Joint coupling
Cathode-holder
Anode-holder
Table
Spring
Anode
Screw of vertical travel
Scraper
Cathode
Cell
Platform
Wheel for floor support
Powder collector

FIG. 8.6 Cell with cylindrical cathode and automatic powder take off from the cathode.

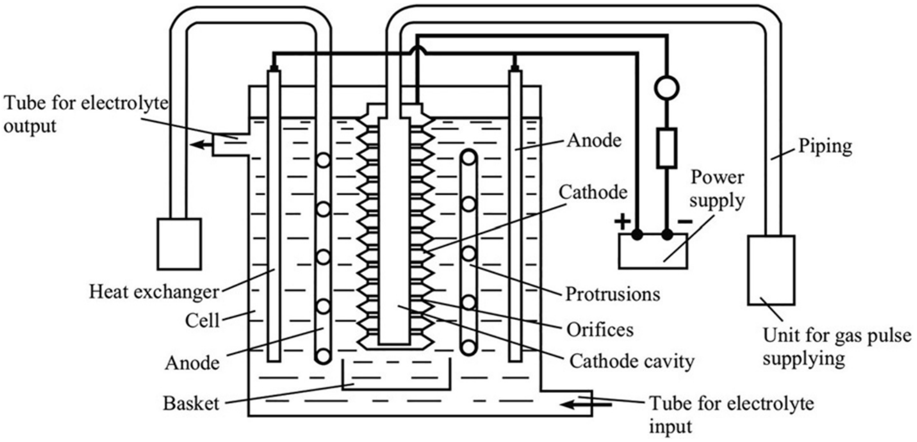
Tube for electrolyte output
Anode
Piping
Cathode
Power supply
+
−
Heat exchanger
Protrusions
Cell
Orifices
Unit for gas pulse supplying
Anode
Cathode cavity
Basket
Tube for electrolyte input

FIG. 8.7 Electrolyzer with gas pulse supply to the cathode to take off powder.

Copper Precipitation in Industrial Electrolysis

Galvanostatic Conditions

In terms of manufacturing, the galvanostatic conditions versus the potentiostatic [14] ones more easily yield to organization and monitoring. Therefore, in the industry, electrolytic copper powders are commonly produced in galvanostatic conditions. One of the major demands for industrial-scale electrolysis is the ability to obtain copper powder with a homogeneous structure. However, the structure of dendritic copper powder is known to vary during galvanostatic electrolysis. Rapid elongation of thin-branched dendrites in the initial growth stage gradually slows down, involving the crystallization of dense globular tips at the growth front [1]; the tips can form a continuous metal crust when grow together. The crusting effect makes periodic removal of the dendritic deposit from the cathode impossible, disables the cathode assembly (because the deposit crust has to be cut down manually), and increases the specific power consumption in the production of copper powder. To prevent this, it is necessary to optimize the periods when the deposit is removed from the cathode.

The authors [15] discuss the model, described by Eq. (8.7), for analyzing the dynamics of structural changes in the dendritic copper deposit using video-recorded data on its formation in situ in the commercial electrolytic cell of the Uralélektromed Joint Stock Company. Eq. (8.7), by starting the diameter value of the electrode ($d_0 + 2yo$), looks like the following:

$$d_0y + y^2 - \left(d_0yo + yo^2\right) = \frac{V}{zF}\frac{d_0K_{\text{dep}}i_{\text{lim}}}{2\pi Nr_{\text{tip}}^2}t$$

The transfer of results obtained from laboratory research on the continuous electrolysis process to industrial production is difficult. The known method of full-scale experiment consists of periodically removing the cathode bar from a cell section, followed by photographing the deposits formed. However, this method is inadequate because pauses disrupt the kinetics of the electrolysis process. An advanced control method that could be used on an industrial scale utilizes a video recording of the copper deposit growth [15]. This technique, with simultaneous recording of time history cathode overstrain, provides the possibility of improving electrolysis efficiency and controlling the conditions for optimal results.

A schematic illustrating the installation of a continuous electrolysis process on a commercial scale with a submersible web camera is shown in Fig. 8.8.

Formation of dendritic copper sediment is accompanied by the release of hydrogen:

$$\left.\begin{array}{l} \mathrm{Cu}^{2+} + 2\bar{e} = \mathrm{Cu} \\ 2\mathrm{H}^{+} + 2\bar{e} = \mathrm{H}_2 \end{array}\right\}$$

Hydrogen is especially intensively emitted after energizing, as can be seen in Fig. 8.9. The solid and dashed lines are routes of hydrogen gas moving along the cathode rod. There are also individual bubbles that are mainly small. After 5 min, the bubbles form a thick "fog" (Fig. 8.10B) but the release of hydrogen is appreciably decreased 30 min after energizing (Fig. 8.10D).

The intensive gas flow mixes the near-electrode space, thus abruptly increasing the limiting current density. The rapid gas release ceases quite soon and changes into periodic liberation of quite large bubbles from the growing dendritic deposit. The successively measured diameter of the electrode with the growing deposit allows determining the dependence of the length y of dendrites on time t as follows: $y = 0.5(d - d_0)$. The dendrites of the friable growing deposit elongate with time at a slowing rate with gradually decreasing cathode overpotential $\eta = E_{\text{Eq.}} - E$, where E and $E_{\text{Eq.}}$ are the cathode potentials under current and in equilibrium, respectively (Fig. 8.11).

Osipova et al. [15] reported that the structural parameter Nr_{tip}^2 of the cathode deposit after energizing at first slightly changes during electrolysis and then rapidly increases. So long as this parameter depends on the squared radius (in contrast to linear dependence between Nr_{tip}^2 and the density of growing tips on an area unit of dendrite deposit growth front N), it increases with the tip radius, that is, the coarsening of particles. The variation of structural parameter Nr_{tip}^2 values during crystallization of the dendritic deposit in commercial production of PMS-1 copper powder is shown in Fig. 8.12. This leads to a conclusion that in these conditions, it is unreasonable to crystallize the deposit on the cathode after electrolysis for 6000 s (100 min) because it will have coarser fractions and will be less homogeneous even if not covered by a dense crust of spherulites (Fig. 8.13).

Potentiostatic Conditions

The deposition period without formation of dense built-up deposits may be established by analyzing the dynamics of deposit growth and the variation in cathode overpotential [1,16]. Pomosov [17] was the first to calculate the voltage across

FIG. 8.8 Schematic of installation of the electrolysis process with continuous control on an industrial electrolyzer.

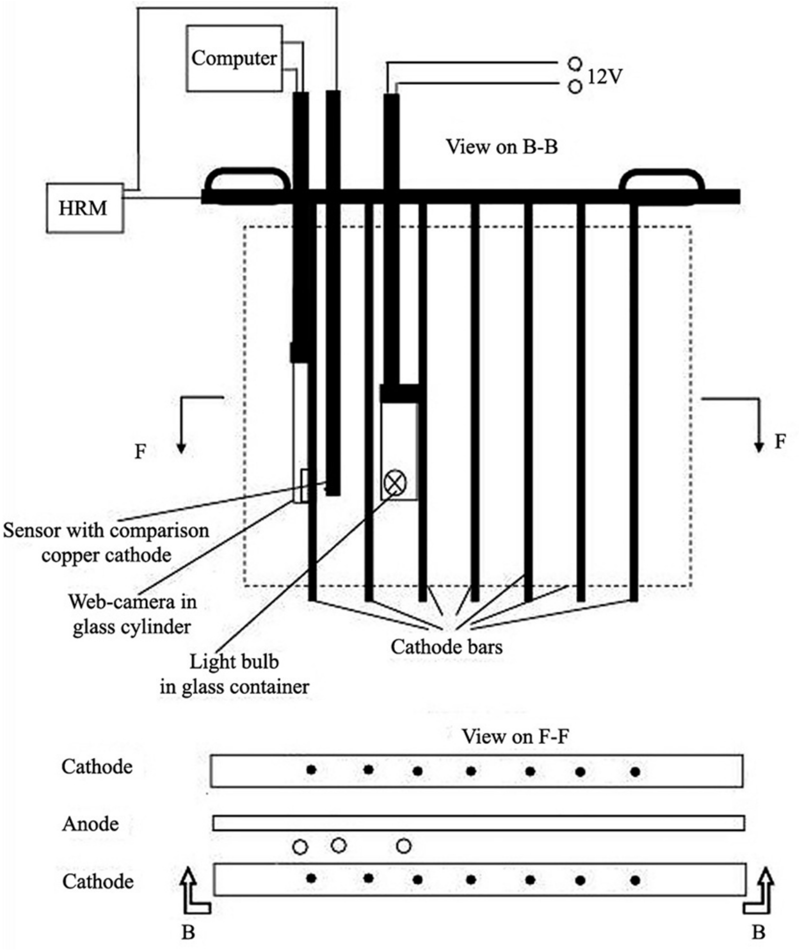
Computer
12V
View on B-B
HRM
F
F
Sensor with comparison copper cathode
Web-camera in glass cylinder
Light bulb in glass container
Cathode bars
View on F-F
Cathode
Anode
Cathode
B
B

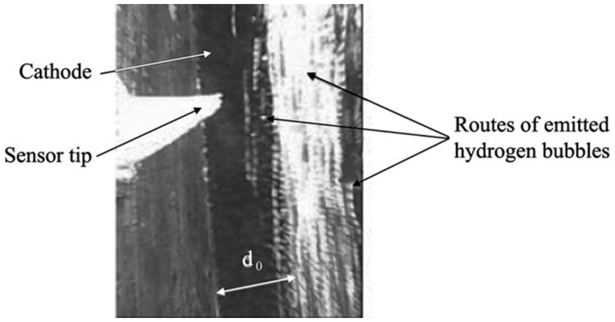
Cathode
Sensor tip
Routes of emitted hydrogen bubbles
d_0

FIG. 8.9 Fragment of cathode rod immediately after energizing.

FIG. 8.10 Formation process of dendritic deposit layer of PMS-1 copper powder: still frames from a video record of the growth of deposit for PMS-1 powder, taken at 0 (A), 1 (B), 5 (C), 30 (D), 60 (E), and 120 (F) min after process beginning.

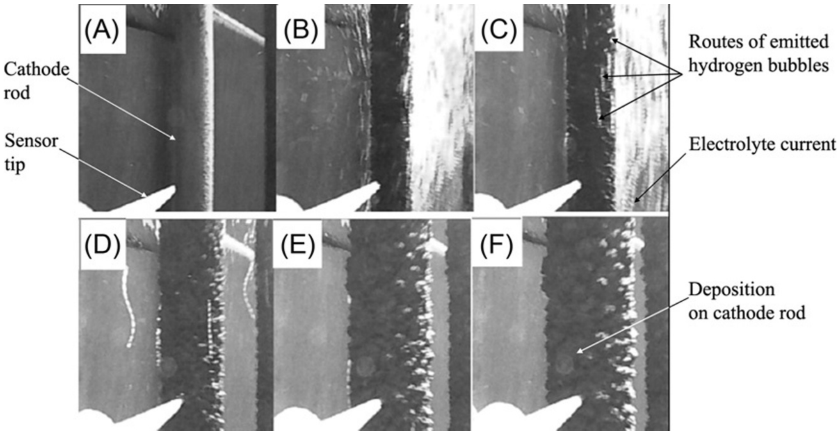
(A)
(B)
(C)
Cathode rod
Sensor tip
Routes of emitted hydrogen bubbles
Electrolyte current
(D)
(E)
(F)
Deposition on cathode rod

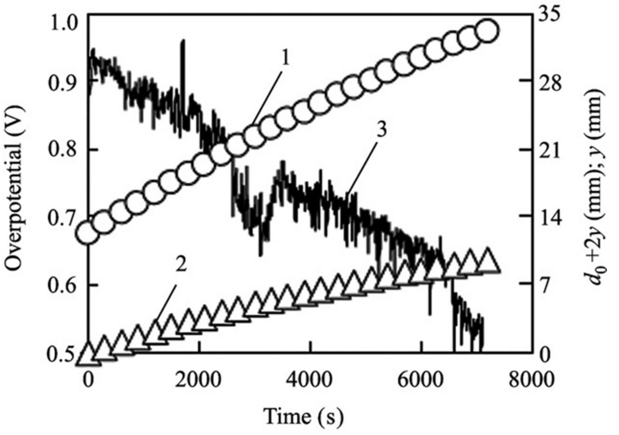

FIG. 8.11 Dependence of the electrode diameter with friable deposit (1), height of the dendritic layer (2), and cathode overpotential (3) on the deposition time.

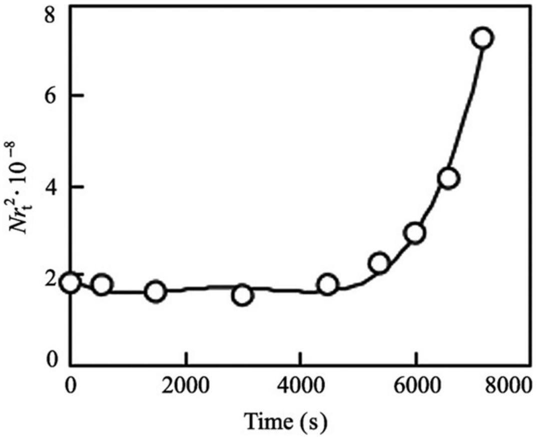

FIG. 8.12 Dependence of structural parameter Nr_{tip}^2 on the deposition time during crystallization of the dendritic deposit by commercial production of PMS-1 copper powder.

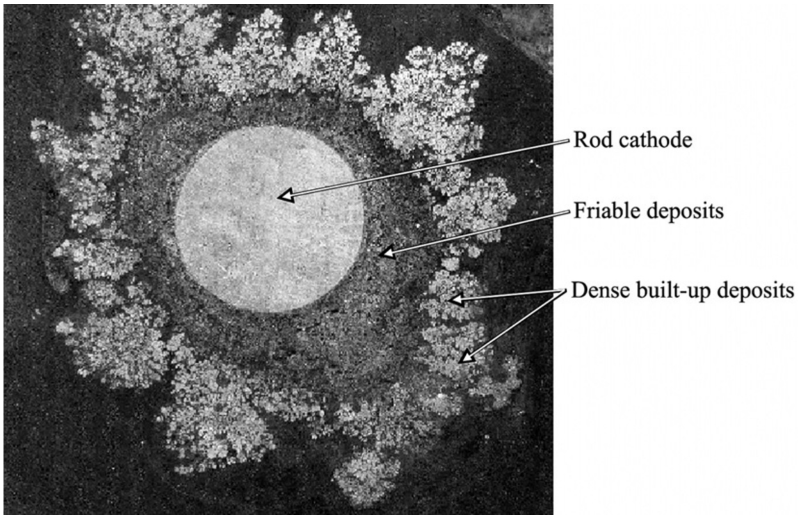

FIG. 8.13 Metallographic cross-section of industrial rod cathode with friable deposits and dense, built-up deposits.

TABLE 8.3 Composition and Properties of Electrolyte and the Kinetic Parameters of Manufactured PMS11 and PML0 Powders

Parameter	Unit	Trademark of Powder	
		PMS11	PML0
Concentration of copper ions (Cu^{2+})	g/L	12–13	9–10
Concentration of sulfuric acid	g/L	155–165	155–165
Temperature	K	323	323
Molar volume of copper	m^3/mol	7.154×10^{-6}	7.154×10^{-6}
Conductivity	S/m	85	80
Current density limiting	A/m^2	270	150
Exchange current density	A/m^2	17	12
Transfer factor	nondim	0.535	0.286
Deposit growth period	s	7200	3600

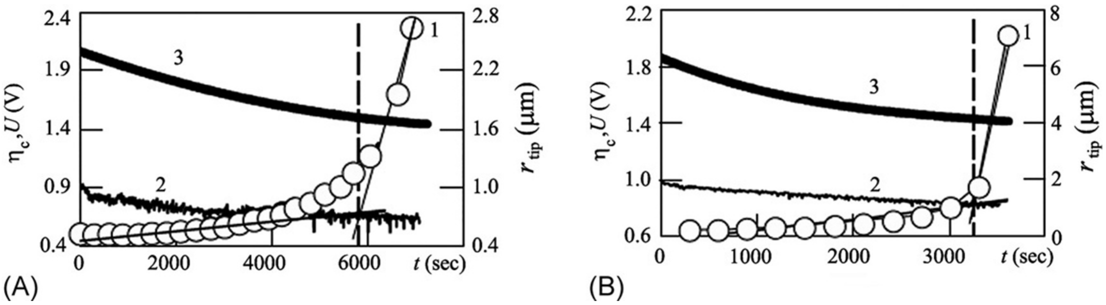

FIG. 8.14 Dependence of radius of dendrite tip r_{tip} (1), cathode overpotential η_c (2), and potential across the cell U (3) on the deposition time, for powders PMS11 (A) and PML0 (B).

the cell for the production of copper powder. He determined the average voltage drop across an electrolytic cell with flat cathodes and an initial cathode current density of 1200 A/m^2. The limiting cathode overpotential (0.55–0.59 V), below which compact copper crystallizes at the growth front, was determined in laboratory conditions using potentiostatic chronoamperometry [16].

Osipova et al. [18] studied the variation of the voltage across a commercial electrolytic cell for the production of PMS11 and PML0 powders to determine the period of their growth during which no crystallization of dense globular aggregates of cathode scrap occurs. Electrolysis was carried out in hopper-type cells with the following characteristics: distance between like electrodes of 150 mm; initial diameter of cathode rod, $d_0 = 12$ mm; initial average thickness of anode, $h = 15$ mm; total working surface area of cathode, 3.8 m^2; total working surface area of anode, 30 m^2; and current capacity, 1200 A. The composition and properties of electrolyte and the kinetic parameters of manufactured PMS11 and PML0 powders are shown in Table 8.3.

The authors [18] reported that the critical time points for the function $r_{tip}(t)$ after which deposits begin to grow intensively had been identified: 5900 s for PMS11 and 3300 c for PML0 (Fig. 8.14). The contribution of cathode overpotential into the voltage balance is 49% for PMS11 and 56% for PML0. The time of increase in the radius of particles had been used to determine the cell voltage, after which external actions are needed to keep the deposit homogeneous without the formation of dense globules of cathode scrap. A procedure for the calculation of the voltage across a commercial electrolytic cell from the time history of the cathode overpotential and interelectrode distance for PMS11 and PML0 copper powders has been proposed.

Reduction from Solution Through Film of Surfactants

Metal particles with a grain size of 0.1–10 μm are produced by electric precipitation in a bath with a two-layer electrolyte. The cathode is a rotating metal drum or disk. The bottom electrolyte layer is an aqueous solution of a salt of the precipitated metal; the upper layer is an organic liquid (toluene, as a rule) that contains surfactants (oleic, palmitic, myristic and other acids) in the amount of 0.5%–12%. Electric crystallization of fine whiskers, strands, and elongated dendrites arises when the electrode passes through the water solution. The particles formed during cathode rotation pass into the layer of the organic liquid, from which they are extracted by organic sol filtration or by centrifugation. The powder is rinsed by hot water, then it is washed free from residual organic substances by a mixture of water with spirit or acetone and dried under vacuum at room temperature. The obtained powders do not need surfactant stabilization against oxidization.

In the process of crystallization of ultrafine elongated whiskers and strands precipitated from the two-layer bath, several stages are distinguished:

- Formation of a strong passive layer on the electrode surface.
- Metal ions discharge through the absorbing film by overcoming a high potential barrier.
- Development of three-dimensional nuclei on the electrode surface.
- Development of crystals inside the thin passive layer of the organic liquid.
- Growth of dendrites outside the film in the aqueous phase.

Under conditions of increased concentration of metal ions in the water phase, the discharge through the film of organic liquid occurs with overcoming a high energy barrier and is controlled by the parameters of the changing reaction. When diluted solutions of the water phase are used, diffusion factors control dendrite growth rate and qualitative links between particle structure and mass transfer parameters remain the same: particle size decreases when water solution is diluted, current density is increased, and temperature is reduced. Surfactants influence the electrocrystallization process: whiskers and needles of constant section are formed due to the localization of electroprecipitation on their end surface, as crystal side faces are blocked by the layer of absorbed particles of the surfactant. The process is controlled by surfactant diffusion because of continuous nucleation and movement of growth steps with competing surfactant absorption.

In the case of precipitation from solutions saturated by surfactants, the value of the current density on the strand end is practically close to constant. According to Krichmar [1], if it is a small value and linear approximation of the absorption isotherm curve $X = G \cdot C_{\mathrm{SAA}}$ (X is the surfactant concentration, G is the coefficient of proportionality for the linear part of the isotherm curve of Lengmoure) is taken, the rate of the process speed on the strand end is proportional to the surfactant concentration in the solution independently of its radius:

$$i \approx A\sqrt{C_{\mathrm{SAA}}} \tag{8.15}$$

Introducing into the water layer a surfactant other than oleic acid that is usually present in the organic phase in the amount of 2–5 kg/m^3 is inadvisable as it can reduce dendrite wettability by the organic liquid and make difficult their transfer to the upper bath layer. As a result of the double effect (change of the proportion of organic phase components and variation of the electrolysis parameter), the composition of the absorbed surfactant layer is controlled and particles not only of a certain structure but also modified by oleic acid and oligomer are produced. Epoxy and organic-silicon compounds are used as oligomers. Thermal treatment in hydrogen of the so-produced powders improves their properties and increases powder resistance to oxidization.

Current efficiency of ultrafine disperse precipitation goes through a maximum with growing current density, decreasing at too high current densities due to intense hydrogen emission. An excess quantity of the acid added to the water phase to increase its electric conductivity leads to prevailing hydrogen discharge and reduces the current efficiency.

In alkaline media, an excessive increase of pH causes the formation of hydrates and a passivation of the electrode surface. A growth of metal ion concentration in the water layer leads to an increase of the current efficiency of the disperse precipitate. In electrolyzers, to produce metal organic sol, devices for continuous removal of the disperse phase are provided (Fig. 8.15). Through holes in the inner pipe, the organic sol gradually goes outside through the hollow shaft. The boundary between water and nonwater layers shall be on the level of the upper line of the shaft. To reduce the particle size of the organic sol, water-cooled hollow disks connected into a whole unit by the pipe are used (Fig. 8.15). Particulate anodes in the form of containers made of mesh material are filled with metal chips. Laminar movement of the electrolyte around the cathode necessary for process intensification is provided by the oscillatory motion of the cathode shaft.

A promising method for production of ultrafine metal powders is based on the use of emulsion devices with fixed electrodes. The method of a running magnetic field is proposed for production of ultrafine powders with the participation of nonequiaxed ferromagnetic particles (Fig. 8.16). Coaxially located electrodes are placed inside an inductor that creates the running magnetic field. Ferromagnetic particles in the running magnetic field come into intense motion and agitate the electrolyte with the organic liquid. In the formed “oil-water” emulsion, metal particles and the inner surface of the device are wetted with the organic liquid containing the surfactant. Ferromagnetic bodies are covered by a casing (for example,

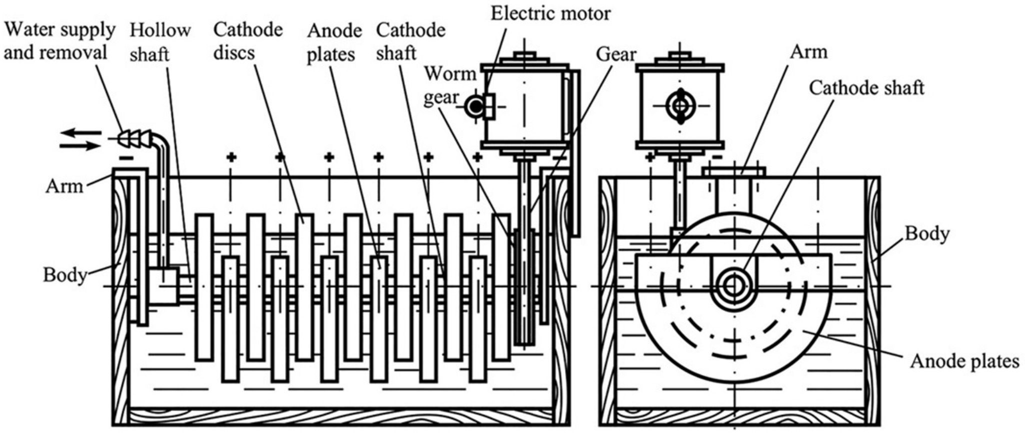
Water supply and removal
Hollow shaft
Cathode discs
Anode plates
Cathode shaft
Electric motor
Worm gear
Gear
Arm
Cathode shaft
Arm
Body
Body
Anode plates

FIG. 8.15 Electrolyzer with cooled cathodes and fluctuating motion of the cathode shaft.

FIG. 8.16 Unit for electrolytic production of ferromagnetic metals and alloys: (A) cross-section of electrode cell with cooling jacket; (B) longitudinal section of electrolyzer with cooling jacket in the inductor of an alternating running magnetic field.

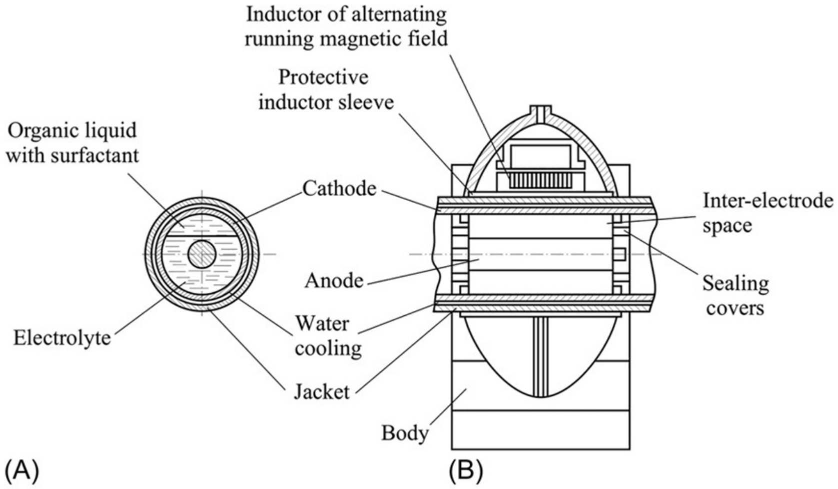
Inductor of alternating running magnetic field
Protective inductor sleeve
Organic liquid with surfactant
Cathode
Inter-electrode space
Anode
Sealing covers
Electrolyte
Water cooling
Jacket
Body
(A)
(B)

fluoroplast) insoluble in the aqueous medium and organic liquid. Thus, ferromagnetic bodies that intensify the stirring efficiency of the near-electrode space do not participate in the electrode process themselves. Metal ions contained in the solution are reduced on the cathode.

Special Methods of Production of Metal Powders Recovered from Spent Solutions

High-efficiency methods of metal recovery from dilute solutions are based on the application of electrodes with a developed surface together with an increase of the mass transfer coefficient that is achieved under respective hydrodynamic conditions in the electrolyzer. Metal electroprecipitation under such conditions occurs with the formation of powder.

Eco-Cell

In the Eco-cell process (Ecological Engineering Ltd. company design), a cathode in the form of a horizontally rotating cylinder (Fig. 8.17) is used. The cathode is fixed on the shaft and surrounded by the coaxially located anode. An ion-change membrane is located between cathode and anode sections at a distance of approximately 10 mm from the cathode. The powder is scrubbed from the cathode and removed by solution flow. Current connection is carried out by a sliding contact. The intensification is reached by the turbulence of liquid flow conditions, even at low speeds of cathode rotation, and this allows a significant increase of the current density. Thus, for metal recovery from solutions with concentrations of $<1\,\text{kg/m}^3$, a cathode current density of 2–4 kA/m^2 can be used. The electrolyte is pumped through the cell at a predetermined speed. The metal is precipitated in the form of powder by simultaneous hydrogen emission. Gas is separated from the

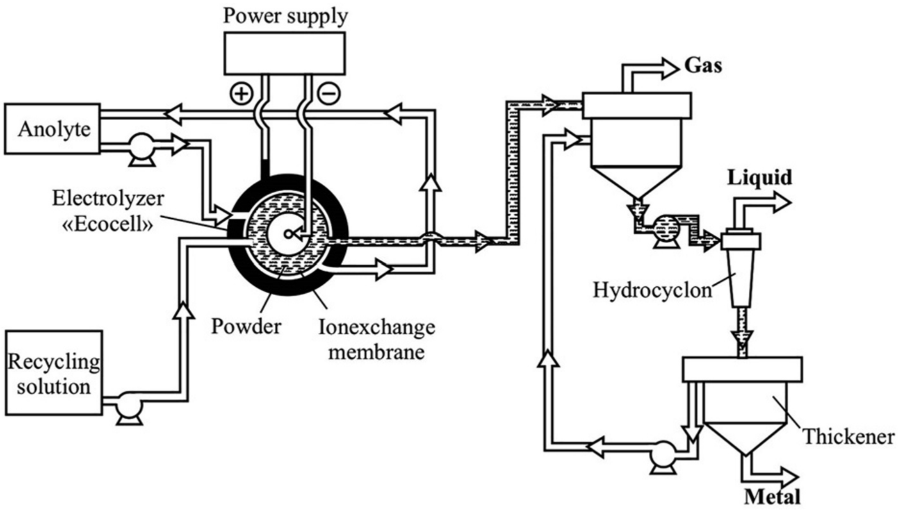

FIG. 8.17 Plant Eco-cell.

TABLE 8.4 Parameters of Selective Metal Extraction («Eco-cell» Process)

Extracted Metal	Composition of Origin Solution (kg/m^3)	Final Concentration of Metal 10^3 (kg/m^3)
Silver	1.5 Ag; 0.9 Cu; 9.5 HNO_3	20 Ag
Copper	Cu/Zn (1:1); 147 H_2SO_4	10 Cu
Copper	Cu/Ni (1:1); 147 H_2SO_4	20 Cu
Silver, copper	Cyanide electrolyte pH 4; 0.02 Ag; 0.02 Cu	1.4 Ag; 3.0 Cu

three-phase mixture in the gas separator; the powder is extracted using a hydrocyclone or other type of thickener. Using the Eco-cell plant, it is possible to produce from solutions zinc, silver, manganese, cobalt, rhenium, rhodium, cadmium, palladium, indium, nickel, tin, iridium, platinum, gold, lead, and rare-earth metals in the form of powder.

Series installation of several chambers with each of them working at a certain cathode potential allows a selective recovery of different metals from solutions (Table 8.4).

Pump-Cell

The process is activated due to the high mass transfer coefficient in the interelectrode space of two electrodes, the anode being rotated at a high speed and the cathode being fixed (Fig. 8.18). In another variant, a bipolar electrode mounted on the ceramic axis is used. Dendrite particles up to 100 μm in size are removed from the interdisk space by electrolyte flow. The precipitation is carried out from solutions that contain up to 1 kg/m^3 of metal with a current density of 10 kA/m^2.

Electrolyzer With a Rotating Cylindrical Layer of Particles

The electrolyzer with a rotating cylindrical layer of particles consists of two concentric perforated nonconducting cylinders (Fig. 8.19A) and between them, conducting particles and cathodes are located. Two concentric metal mesh cylinders form anodes. The cathode cylinders are continuously rotated so that conducting balls or particles interspaced inside them are interfused. The electrolyte circulates through the electrolyzer. The metal is precipitated in the form of dendrites on the conducting particles inside the cathode cylinders and continuously crumbles into the bottom part of the electrolyzer, where it is periodically removed into the collector. The thickness of the compact layer on conducting cathode particles is <0.01 mm.

In the electrolyzer with hammering rods (Fig. 8.19B), the cathode consists of separate metallic rods with the ends sliding freely along ring-shaped metallic guides. The anode is in the form of two mesh cylinders located concentrically regarding

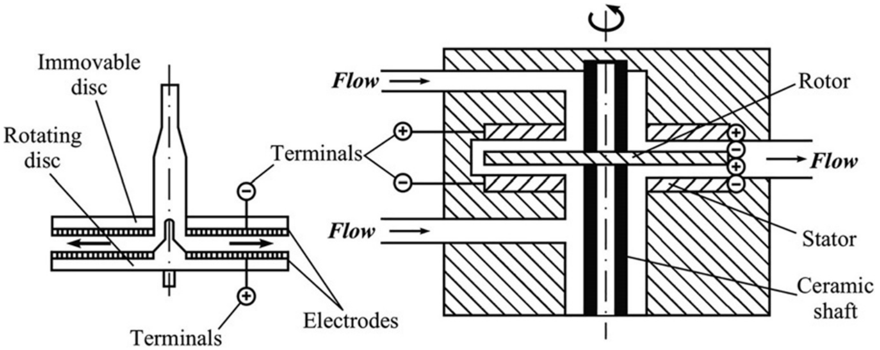
Immovable disc
Rotating disc
Terminals
Terminals
Electrodes
Flow
Flow
Flow
Rotor
Stator
Ceramic shaft

FIG. 8.18 Scheme of the electrolyzer pump cell.

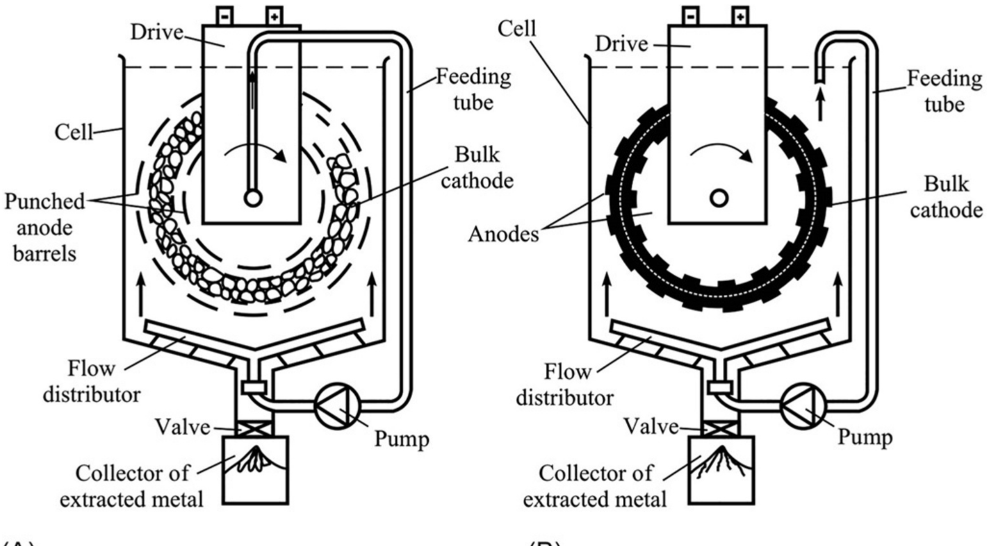
Drive
Cell
Feeding tube
Bulk cathode
Punched anode barrels
Flow distributor
Valve
Pump
Collector of extracted metal
Cell
Drive
Feeding tube
Bulk cathode
Anodes
Flow distributor
Valve
Pump
Collector of extracted metal

(A) (B)

FIG. 8.19 Electrolyzers: (A) with rotating cylindrical layer, (B) with striking bulk cathode.

the cathode ring. The electrolyte is continuously pumped. The powder crumbles and is removed into the collector through the lock valve.

Both electrolyzers with a moving particle layer are designed for cadmium recovery from solutions containing cyanide. Metal precipitates on the cathode in the form of powder and cyanide ions oxidize on the anode to carbon dioxide. The cathode current efficiency starts to decrease significantly when the metal concentration reaches $10^{-3}\,\mathrm{kg/m^3}$. Using the above-mentioned method, gold is recovered from solutions up to a final concentration of $10^{-4}\,\mathrm{kg/m^3}$, silver is recovered from the cyanide complex with a concentration of $5\,\mathrm{kg/m^3}$ (down to $2 \times 10^{-3}\,\mathrm{kg/m^3}$). This method is also applied to recover metals of the platinum group, copper, nickel, and zinc. A moving layer of steel balls 4.5 mm in diameter covered by an 18 μm copper layer is used for copper recovery from the sulfate solutions. The balls fill up to 35% of the drum volume [1].

Production of Metal Multicomponent Alloy Powders

The condition for the precipitation of metal alloy powders is the equality of discharge potentials of metal ions on dendrite tips. The electrocrystallization of the dendrite deposit proceeds under diffusion control and is located at the tips of growing dendrites. The conditions of mixed electrochemical kinetics with a semispherical character of diffusion are realized:

$$E_{\mathrm{j}} = E_{\mathrm{eq,\,j}} - \frac{RT}{\alpha_{\mathrm{j}} z_{\mathrm{j}} F} \ln \frac{i_{\mathrm{tip,\,j}}}{i_{0,\,\mathrm{j}}} + \frac{RT}{\alpha_{\mathrm{j}} z_{\mathrm{j}} F} \ln \left(1 - \frac{i_{\mathrm{tip,\,j}}}{i_{\mathrm{lim.sp.j}}} \right) - \frac{2\gamma V}{z_{\mathrm{j}} F r_{\mathrm{tip}}} \tag{8.16}$$

where j is the number of the alloy component.

The content of the component in the alloy is proportional to the current density of its reduction at the growing front $i_{\text{tip}} \cdot 2\pi r_{\text{tip}}^2 N$, where N and r_{tip} are the density of location and the radius of alloy dendrite tips, respectively. For a two-component alloy:

$$\left(\frac{C_1}{C_2}\right)_{\text{Alloy}} = \frac{i_{\text{tip},1}}{i_{\text{tip},2}} \tag{8.17}$$

So far, diffusion limitations are not released from the growing front, the current densities on tips $i_{\text{tip,j}}$ are comparable with limit currents of spherical diffusion $i_{\text{tip,j}} \approx i_{\text{lim,sph,j}}$ with the values proportional to the concentration of the components in the solution $C_{\text{sol},j}$, mol/m^3,

$$i_{\text{lim.sph.,j}} = \frac{z_j F D_j C_{\text{sol,j}} y}{\delta r_{\text{tip}}} \tag{8.18}$$

The combination of Eqs. (8.17) and (8.18) gives the following:

$$\left(\frac{C_1}{C_2}\right)_{\text{alloy}} = \frac{z_1 D_1}{z_2 D_2}\left(\frac{C_1}{C_2}\right)_{\text{sol}} \tag{8.19}$$

In aqueous solutions, the effective diffusion factors for different ions are close to each other, so that for $z_1 = z_2$ the proportionality coefficient $z_1 D_1 / z_2 D_2$ is close to one.

During electrolysis, the depth of diffusion limitations on the growth front of the dendrite deposit is gradually decreased while the potential shifts to the field of more positive values. In this case, the alloy component with a more electronegative potential may prove to be under conditions of activation discharge control; then the linear connection between $(C_1/C_2)_{\text{alloy}}$ and $(C_1/C_2)_{\text{sol}}$ is violated and alloy composition depends upon the time of discontinuous precipitate accumulation on the cathode.

To provide diffusion control, alloys are precipitated from dilute solutions (the total concentration of metal salts is not higher than 0.2 mol/L) of simple electrolytes. The proportion of metal ions in the solution corresponds to their proportion in the alloy and a constant value of $(C_1/C_2)_{\text{sol}}$ provides the stability of the alloy composition. If the difference between the equilibrium potentials of alloy components is too high (of the order of 1 V) then the electrochemical characteristics of metals (E_{eq}, i_0, c_x) may be juxtaposed by the complexing. Meanwhile, it is important to support pH values for the stabilization of the ion composition of complex compounds as well as to avoid a decrease of alloy current efficiency.

The methods of supporting constant solution composition depend on the nature of the anode reaction. When using insoluble anodes, it is necessary to make up the loss of reducing components in the electrolyte while an accumulation of ballast salts in the electrolyte is possible. If the soluble anodes are used, a periodical correction of electrolyte composition is required because of the difference of cathode and anode current efficiencies and uncontrolled current distribution between soluble anodes.

The most reliable method is the application of combined anodes (Fig. 8.20) with independent adjustment of current in the circuit of each anode. The proportion between currents of soluble anodes shall correspond to the proportion of cathode currents of the reduction of alloy components and the part of the current passing though the insoluble anode shall be equal to 1.0 Ce_{all}, where Ce_{all} is the current efficiency.

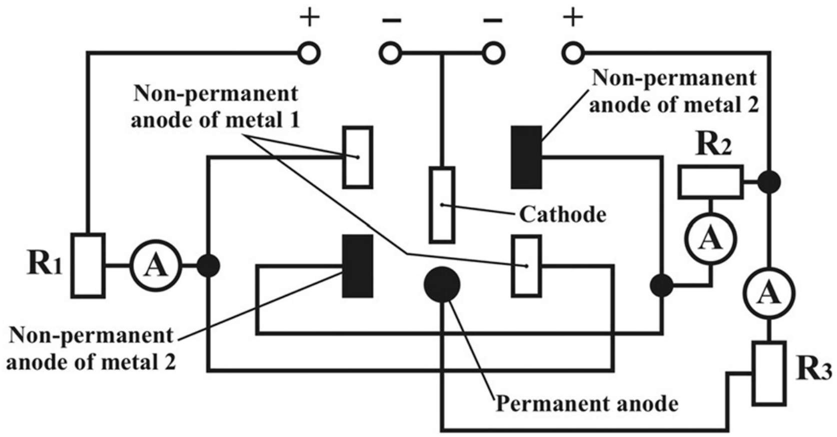
+
–
–
+
Non-permanent anode of metal 1
Non-permanent anode of metal 2
R2
Cathode
A
R1
A
A
Non-permanent anode of metal 2
R3
Permanent anode

FIG. 8.20 Electrical circuit to connect the electrolyzer with combined anodes (R, rectifiers; A, ammeters; K, rheostats).

Alloy components can interact with each other with the formation of chemical compounds. A change of the partial mole Gibbs energy by the entrance of the *j*-metal into the alloy ΔG is expressed in the effect of depolarization, that is, a shift of the equilibrium potential of the *j*-th metal component to more positive values:

$$\Delta E_{\text{all}} = \frac{\Delta G}{zF} \tag{8.20}$$

The kinetics of electrochemical reduction of metal ions depend on the nature and the character of the cathode surface that changes for each metal during alloy formation in comparison with individual discharge. If diffusion limitations on the growth front are released for any component, these effects are manifested in the change of alloy composition in comparison with one calculated according to Eq. (8.19).

Dispersivity, grain-size distribution, and the apparent density of alloy powder depend on the total concentration of metal ions and on the parameters of electrolysis (current density, temperature, hydrogen ion exponent, stirring mode), as in the case of precipitation of a single component powder. The dispersivity of powders from multicomponent alloys increases, their apparent density lowers, and the flowability deteriorates with growing depletion factor K_{dep} and vice versa.

Powder Production Using the Method of Zone Electrochemistry

The method is based on a combination of zone chemistry and electrochemistry, and this allows the.

manufacture of nanopowders because of the following effects:

- Substance transportation to the reaction zone is uninterrupted.
- Electrode surface is cleaned and degassed.
- The rate of the electrochemical process is increased.

The idea of the method is that, after each electrochemical impulse of constant current, during which metal nuclei form on the electrode surface, an ultrasonic (zone) impulse follows, the energy of which is located in the reaction zone. It separates nuclei from the cathode surface and throws them into the solution.

In this method, the characteristics of impulse and zone electrolysis (interval between ultrasonic impulses, parameters of cathode-sample electrode, capacity of ultrasonic impulse) are added to the traditional factors that determine particle size and shape (solution composition, current density, electrolysis duration).

As under other electrolysis modes, the dominating particle size decreases with the growth of current impulse amplitude, with the dilution of the solution, when the time period between ultrasonic impulses is reduced, and noticeably depends on their wattage. If the energy of ultrasonic impulses is low, then metal clusters formed on the cathode-sample electrode are not able to overcome the adhesion forces and strip the deposit from the electrode into the solution. The clusters remaining on the surface affect every subsequent current impulse so that the nanoparticle yield is lowered. If the impulse energy is excessive, the temperature goes up immediately in the reaction zone. This leads to the disappearance of the transport control and to undesirable particle aggregation.

By means of zone electrochemistry, dendrite clusters consisting of branches like pearl necklaces can also be produced. Such formations are obtained if the zone electrolysis is lengthy. One of the mechanisms of the formation of such structures is similar to the model of diffusion-limited aggregation. According to another model, particles suspended in the solution after contact with the cathode get a negative charge and act as a part of the cathode. The dependence of particle quality on a large number of parameters leads to especially high requirements to determine the range of their optimum values to provide a high yield of particles of the prescribed shape and size.

CONTACT DISPLACEMENT METHOD (CEMENTATION)

Electrolytically precipitated powder may be produced by the displacement of one metal M_2 from the solution due to the conjugated dissolution of other metal M_1.

$$z_1 M_2^{z_2^+} + z_2 M_1 \xrightarrow{z_1 z_2 e} z_1 M_2 + z_2 M_1^{z_1^+} \tag{8.21}$$

To provide a high rate of this heterogeneous reaction, a large area of the cementing metal (precipitator) is provided by using it in the form of powder, chips, and lumps and the intensity of the solution flow is increased. Complete deposition of the precipitated metal is attained by the excess of the cementing metal. After electrolytic precipitation, the solution is washed from the product and the precipitator surplus is eliminated (by acid solution treatment, by magnetic separation, etc.).

The possibility of spontaneous proceeding of the process is estimated by the decrease of Gibbs free energy $-\Delta G = zF(E^{+}–E^{-})$, where E^{+} and E^{-} are respective equilibrium potentials. The contact displacement is thermodynamically possible if the initial potential of the reduction reaction of the precipitated metal M_1 is more positive than the initial potential of the oxidation reaction of the cementing metal M_2. Completeness of the precipitation is defined by equilibrium, according to Nernst's equation:

$$E_{M_1} = E_{M_2} = E^0_{M_1} + \frac{RT}{z_1F}\ln\left(\frac{a_{M_1}^{z_1^+}}{a_{st}}\right) = E^0_{M_2} + \frac{RT}{z_2F}\ln\left(\frac{a_{M_2}^{z_2^+}}{a_{st}}\right) \quad (8.22)$$

where $E^0_{M_1}$ and $E^0_{M_2}$ are standard potentials, and a_{st} is standard activity equal to 1000 mol/m^3. The equilibrium ratio $a_{M_2}^{z_2^+}/a_{M_1}^{z_1^+}$ is calculated from the given expression. The thermodynamical completeness of the precipitation is shown in Table 8.5. Actually, the process is complicated by difficulties in kinetics of the reactions of both cathode reduction and anode dissolution.

The basis of electrolytic precipitation is corrosion (Fig. 8.21). The contact displacement potential E is set up where the cathode current I_c and the anode current I_a are equal. During electrolytic precipitation, the solution concentration and the state of the precipitator surface are modified, which leads to a change of polarization curve behavior as well as of the potential and electrolytic precipitation rate. As simple solutions at high initial potential difference E_2 and E_1 are used, the metal M_2 is reduced by diffusion control with dendrite formation and accompanied by hydrogen evolution.

Metal is located on the tips of growing dendrites with tip location density at the growth front N (m^{-2}) and tip radius r_{tip}, and this process proceeds at current density i_{tip} (A/m^2) with current I_{M_2} per unit of area:

$$I_{M_2} = i_{tip} \cdot 2\pi N r_{tip}^2 \quad (8.23)$$

Around N_0 ccolumns formed as a result of electrolytic precipitator contact with solution, the compact growth block of a radius r and a height h is spread over a surface:

TABLE 8.5 Parity for Equilibrium Activities for Precipitated Metal (M_2) and Precipitator (M_1)

		Standard Potential of Metal ($B_{(NVE)}$)		
Precipitator M_1	**Precipitated Metal M_2**	**Precipitator**	**Precipitated**	**Equilibrium Ratio, $a_{M_2}^{z_2^+}/a_{M_1}^{z_1^+}$**
Zinc	Copper	−0.763	0.34	$1.0 \cdot 10^{-38}$
Zinc	Nickel	−0.763	−0.23	$6.0 \cdot 10^{-19}$
Iron	Copper	−0.44	0.34	$1.3 \cdot 10^{-27}$
Copper	Copper	−0.22	0.34	$2.0 \cdot 10^{-20}$

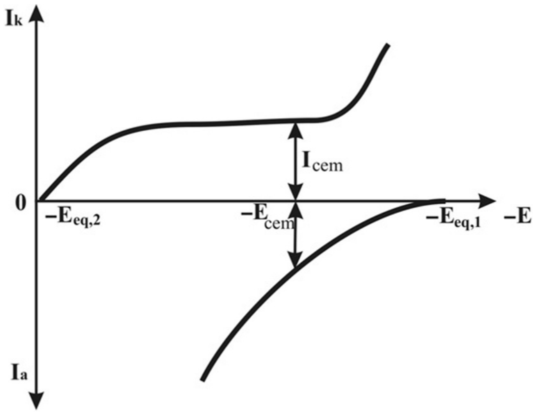

FIG. 8.21 Polarization chart of contact displacement process.

$$I_{\mathrm{TAN}} = i_{\mathrm{TAN}}\,2\pi N_0 rh \tag{8.24}$$

The precipitable metal M_1 is dissolved in areas free from the precipitated metal $(1 - N_0\pi r^2)$:

$$I_{\mathrm{M}_1} = \left(1 - N_0\pi r^2\right) \tag{8.25}$$

The formed dendrite deposit has a volumetric specific surface S_{w}. Hydrogen is reduced both in precipitable metal M_1 areas free from dendrites with the rate $i_{\mathrm{H},1}$ and on developed surfaces of the precipitated metal with the rate $i_{\mathrm{H},2}$.

$$I_{\mathrm{H}} = i_{\mathrm{H},2} \cdot S_{\mathrm{w}} \cdot y + i_{\mathrm{H},1} \cdot \left(1 - N_0\pi r^2\right) \tag{8.26}$$

The dendrite growth rate and the expansion rate of areas covered by the precipitated metal are described by Faraday's law in differential form:

$$\frac{dy}{dt} = \frac{V}{z_2F} i_{\mathrm{tip}}, \quad \frac{dr}{dt} = \frac{V}{z_2F} i_{\mathrm{TAN}} \tag{8.27}$$

where V, $\mathrm{m^3/mol}$ is the mole volume of the precipitated metal. The precipitation rate of the metal on the growth front is determined by mixed kinetics: lineal by tangential growth on the surface and spherical diffusion on the tips [4]. The latter is described by the following equation:

$$i_{\mathrm{tip}} = i_{0,\mathrm{M}_2}\left(1 - \frac{i_{\mathrm{tip}}}{i_{\mathrm{sph}}}\right) \cdot \exp\left[-\frac{\alpha_2 z_2 F}{RT}\left(E - E_{\mathrm{eq},2}\right)\right] \tag{8.28}$$

On the area of the tangentially spread film, the metal is precipitated during diffusion control, as the effective value of the diffusion layer for the film is increased up to the value $\delta + y$ in advance of the dendrite deposit over a distance y:

$$i_{\mathrm{TAN}} = \frac{i_{\mathrm{lim}}\delta}{\delta + y} \tag{8.29}$$

The cementing metal dissolves according to the mechanism of delayed ionization:

$$i_1 = i_{0,\mathrm{M}_1} \cdot \exp\left[\frac{(1-\alpha_1)z_1F}{RT}\left(E - E_{\mathrm{eq},1}\right)\right] \tag{8.30}$$

The hydrogen emission rate is determined by its exchange current on the metal that is connected with the parameters of the kinetic equation as well as by its equilibrium potential $E_{\mathrm{eq,H}}$:

$$\begin{gathered} i_{\mathrm{H}_1} = i_{0,\mathrm{H}_1} \cdot \exp\left[-\frac{\alpha_{\mathrm{H1}}F}{RT}\left(E - E_{\mathrm{eq,H}}\right)\right]; \\ i_{\mathrm{H}_2} = i_{0,\mathrm{H}_2} \cdot \exp\left[-\frac{\alpha_{\mathrm{H2}}F}{RT}\left(E - E_{\mathrm{eq,H}}\right)\right] \end{gathered} \tag{8.31}$$

where i_{H_1}, i_{H_2} are current densities of hydrogen discharge on the metals M_1 and M_2, respectively; $i_{0,\,\mathrm{H}_1}$, $i_{0,\,\mathrm{H}_2}$ are exchange current densities for hydrogen on these metals; and α_{H1}, α_{H2} are the transfer factors for hydrogen on these metals.

The charge balance in this process is retained:

$$i_{\mathrm{tip}} 2\pi N r_{\mathrm{tip}}^2 + i_{\mathrm{TAN}}\,2\pi N rh + i_{\mathrm{H}_2} S_{\mathrm{w}} y + i^{\mathrm{H}_1}\left(1 - N\pi r^2\right) = i_1\left(1 - N\pi r^2\right) \tag{8.32}$$

The dynamics of the electrocrystallization of the dendrite deposit are calculated by the solution of the system of differential equations that describes the behavior in the time of its structural characteristics (y, r, r_{tip}) and of the potential. These equations are derived according to Faraday's law (Eq. 8.27), the relations of electrochemical kinetics (Eqs. 8.28–8.31), the charge balance on the unit area of the electrode (Eq. 8.32), and the conditions of its equipotential surface. It is solved numerically by the Runge-Kutta method. In the case where an electrochemical system that excludes joint hydrogen reduction is used, this process is ignored [7].

As all surface of the cementing metal is covered by the tangential film of the precipitate, the anode current density increases and the electrode potential becomes more positive. When $N_0\pi r^2$ reaches unity, the anode current density tends to infinity, the anode current decreases down to zero, and the electrode potential sharply shifts to more positive values (Figs. 8.22 and 8.23). Later, the electrolytic precipitation process continues with a negligibly small rate only through pores of the precipitated metal layer.

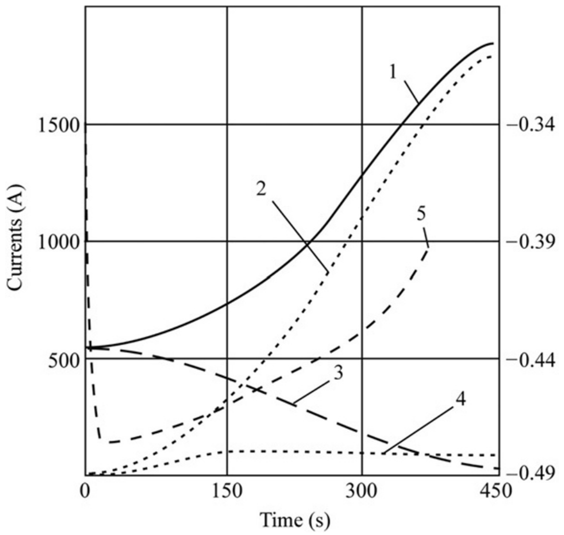

FIG. 8.22 Current distribution per time and variation of precipitation potential (model calculation):1 is the summary cementation current; 2 is the metal reduction current on the deposit growth front; 3 is the current of hydrogen reduction on the metal precipitator; 4 is the current of the distribution of tangential film; and 5 is the potential alteration.

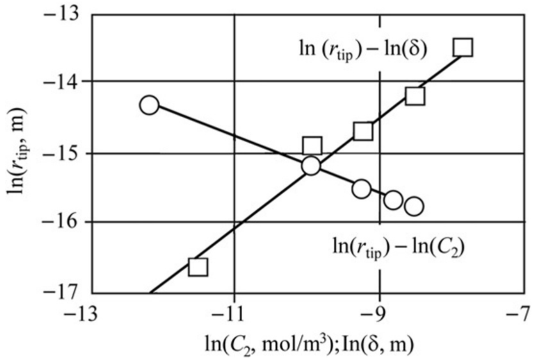

FIG. 8.23 Trend of variation of predominate radii ($r_{\text{tip}_{\max}}$) for dendrite tips of dendrite deposit depending on the parameters of the cementation process: C_2, metal ions concentration, mol/cm^3; δ, thickness of diffusion layer, m.

The solution of this task makes it possible to observe the behavior in the time domain of the dendrite tip radius and the current of metal M_2 reduction on the tips of the growth front. This makes it possible to evaluate the distribution of the dendrite deposit over tip radii at various conditions of electrolytic precipitation (Eq. 8.5). As seen from these calculations, the higher the concentration of reducing metal ions in the solution, the larger the average dendrite tip radius (Fig. 8.23). It increases also with the decrease of exchange currents of the metal M_2 and the precipitator. The average size of cementing powder particles is changed in this direction, too. Besides, the longer the process, the larger the particles.

The diffusion control of the process absolute at the moment of metal M_1 contact with the solution of the more electropositive component is reduced during electrolytic precipitation and can be changed for activation control. This causes difficulties in direct analytic description of the electrolytic precipitation. Besides, anode and cathode surfaces continuously change in the process of contact displacement. Numerical simulation seems to be the only possible method of adequate description.

All factors contributing to the instability of the flat growth front (see Table 8.1) lead to the acceleration of dendrite growth, the refining of produced particles, and the increase of the powder specific surface. This is observed in the cases of dilute solutions, the decrease of complexing ligand concentrations, the reduction of electrolyte conductivity, and the lowering of the cathode reaction polarizability. On the contrary, the extent of difficulties at the stage of the discharge and the acceleration of ion diffusion to the phase boundary leads to particle coarsening, an increase of their apparent density, and a decrease of the powder specific surface. Passivation of cathode areas by surfactants and hydroxides prevents the metal reduction and decreases the rate of electrolytic precipitation (Tables 8.6–8.8). Halogen anions and chloride ions, in particular, enhance powder dispersivity and the formation of dendrite particles.

TABLE 8.6 Drum Rotating Velocity Effect on Intensity of Copper Precipitation with Iron and Powder Properties.

Process Parameters	Unit	Drum Rotation Velocity (rpm)					
		0	10	20	30	40	50
Average rate of precipitation	kg/(m^{2}h)	0.21	0.29	0.37	0.40	0.43	0.18
Average particle size	μm	100	115	131	139	148	165
Apparent density	kg/m^3	1540	1800	2150	2660	2900	3140
Specific surface	m^2/kg	60.0	57.1	53.2	40.0	38.0	33.0

TABLE 8.7 Precipitation Parameters Depending on Duration Between Shaking of Iron Plates in the Solution $CuSO_4$

Process Parameters	Unit	Duration of Deposit Growth (min)				
		5	15	60	90	120
Average rate of precipitation	kg/(m^{2}h)	0.47	0.39	0.31	0.28	0.21
Average particle size	μm	65	81	89	94	100
Apparent density	kg/m^3	2910	2450	2000	1810	1540
Specific surface	(m^2/kg)	60.0	52.0	58.0	49.5	48.1

If both processes take place on the unchangeable equal surface of the cathodes S_k and the anodes S_a ($S_k = S_a = S$) and the displaced metal is reduced at the limit current, the solution depletion by ions of the discharging metal M_2 is described by the first-order equation of the reaction rate with rate constant K:

$$\text{In}\,\frac{C_2^0}{C_2} = Kt \tag{8.33}$$

where C_2^0 is the initial concentration of the solution.

The cases of delayed discharge of cathode and anode reaction are described most completely by the Rotinyan-Heifez equation [1].

$$-\frac{dC_1}{dt} = K^{'} C_2 \frac{x(1-\alpha_1)}{\alpha_2 - (1-\alpha_1)} \tag{8.34}$$

where x is the reaction order by ions of the reducing metal; α_2 and $(1 - \alpha_1)$ are the apparent transfer factors of cathode and anode reactions; and K' is the combined rate constant that takes into account complexing ligand concentrations in the solution, their reaction order, the relations of the surfaces of the anode and cathode reactions, and electrolyte volume.

A chemical treatment of the product is most effective for cleaning the produced powder from precipitator residues. Sometimes such treatment is conducted in an inert atmosphere to prevent the produced powder from oxidation, or magnetic separation is applied.

PRODUCTION OF POWDERS BY ELECTROLYSIS FROM MELTS

Electrolysis from melts is used for producing electronegative metal powders. Their precipitation from water solutions is noneffective because of intensive hydrogen emission. High values of rate constants of electrochemical processes at high temperatures cause an insignificant polarizability and, as a result, the flat growth front becomes unstable long before the achievement of the limit current density.

TABLE 8.8 Temperature Influence on Copper Cementation Rate With Iron and on Powder Properties

		Variation of Process Parameters for Different Solutions and Temperatures (K)										
		0.4 mol/l $\mathrm{CuS0_4}$				1.0 mol/l $\mathrm{CuS0_4}$			0.4 mol/l $\mathrm{CuS0_4}$ + 1.0 mol/l $\mathrm{CuS0_4}$			
Process parameters	**Unit**	**298**	**318**	**338**	**358**	**318**	**338**	**358**	**298**	**318**	**338**	**358**
Average rate of precipitation	kg/(m^2h)	0.21	0.76	1.04	1.26	1.91	2.34	3.62	0.30	0.38	0.68	0.65
Average particle size (μm)	μm	100	79	68	62	187	91	81	135	165	183	200
Apparent density	kg/m^3	1540	1280	810	560	1890	1760	1600	2030	2580	3000	3710
Specific surface	m^2/kg	60.0	78.1	93.1	140.0	38.0	61.0	99.8	60.0	54.3	48.6	42.0

TABLE 8.9 Equation Parameters for the Growth of Silver Dendrites

Silver Concentration (mass%)	Temperature (K)	Direction of Growth	$K \times 10^5$ cm/(s·mV)	*n*
Nitrate melt				
1	498	⟨112⟩	0.59	1.34
1	573	<112>	0.62	1.41
10	498	⟨110⟩	0.33	1.46
10	573	<112>	0.98	1.38
100	498	<110>	1.2	1.50
100	573	<112>	7.6	1.45
Chloride melt				
2	673	<112>	1.4	1.47
10	628	<112>	2.6	1.50
10	673	<112>	4.3	1.48
10	628	<112>	5.4	1.47

As a rule, metals from melts are crystallized in dendritic form. To prevent the electrolyte from the absorption of moisture and metal oxidation at high gas temperatures, the dendrite deposit is discharged from the electrolyzer in the form of solid dispersed bulk metal together with electrolyte salts. Further treatment of the powder consists of separation of powder and electrolyte by mechanical milling, air separation, salt leaching, or vacuum distillation of the electrolyte. High electric conductivity of salt electrolytes allows the use of high current densities that provide high efficiency of the process of metal takeoff and high current efficiency because of the absence of cathode hydrogen emission.

All the factors that lead to positive values of S_μ and S_E criteria (see Table 8.1) lead to the formation of small dendrites, and vice versa, the higher the metal salt concentration and temperature, the larger the electrolysis duration and the lower the current density, the coarser are the powder particles formed. A passivation of growing surfaces by impurities, especially by nonmetallic inclusions and by oxygen in particular, plays a significant role in the dendrite structure. The passivation facilitates the increase of the nucleation rate of new crystallization centers and dendrite refining. At the same time, the increase of charge polarization on the passivated surface tends to make it smooth so that crystals lose a strict faceting and look like spherolytes. The rate of dendrite elongation in melts is high due to high current density at the tip that achieves hundreds of amperes per square centimeter.

At controlled potential conditions, the experimental dependence for silver dendrite elongation v in the overvoltage interval of 5–60 mV is the following:

$$v = K\eta^{n} \tag{8.35}$$

where K and n are growth parameters (Table 8.9).

At high cathode current densities, fine crystals of secondary powders are formed due to metal reduction by subions of precipitated basic metals. When selecting the solvent salt, it is necessary to take into account the possibility of achieving a lower electrolysis temperature and a higher thermodynamic stability than the reduced metal compound. As a rule, equimolecular mixtures of metal chlorides ($NaCl+KCl$, $KCl+LiCl$, $NaCl+KCl+MgCl_2$, chloride and fluoride salts of metals) are used. The decomposition voltage of each electrolyte component is defined by the equation:

$$E = -\frac{\Delta G}{zF}$$

where ΔG is a modification of Gibbs free energy at the formation of a given compound.

It is necessary to supply periodically or continuously the salt of the precipitated metal to the electrolyte and to add solvent salts carried away by the discharged cathode deposit. Metals and conductive metal-like compounds (carbides, nitrides, oxycarbides, carbonitrides) are used as soluble anodes.

The following factors can cause a decrease of powder yield in relation to current:

- Chemical dissolution of precipitated metal interaction with the solvent.
- Disproportionation reaction accompanied by the formation of low-valency ions.
- Reaction of reversed oxidation of metal in the anode area as a result of its convection or diffusion transfer.
- Recombination of the products of cathode and anode processes.
- Reduction of metals with more negative potential.

The following measures promote the increase of powder yield with current efficiency:

- Addition to the electrolyte of salts with cations having more negative potential and decreasing metal solubility in the electrolyte.
- Separation of anode and cathode areas by a diaphragm.
- Maintenance of temperature and current density at the optimum level.

As the temperature rises, current efficiency passes through a maximum. An excessive temperature increase intensifies chemical dissolution and facilitates the diffusion and convection transfer of active substances to the anode area. At low temperatures, the maximum process rate defined by the limit current density is decreased. Thus, the lower the temperature, the lower the melt electroconductivity and the larger the specific power consumption.

The current efficiency increases when current density increases to $i_{\lim}$; then a growth of the part of the accompanying metals with more negative potential takes place. Anode passivation starts. All these processes decrease the current efficiency (powder yield). At high anode current density, the cation oxidation reactions are possible, for example:

$$\mathrm{Ti} - 2\mathrm{e} = \mathrm{Ti}^{2\pm}, \quad \mathrm{Ti}^{2+} - \mathrm{e} = \mathrm{Ti}^{3+}$$

At a "critical" current density, there is the possibility of an "anode effect" (abundant gassing on the anode that leads to reducing the contact of the electrolyte with the anode, spark formation, and an increase of the resistance, especially when the electrode is wetted poorly by an electrolyte), which is undesirable. To increase the "critical" current density, the surfactants improving anode wettability, the chlorides of basic metal, and the oxides of the reduced metal (if oxygen is permissible in the melt) are injected into the electrolyte. If the metal oxide is considered to be an electroactive substance, the anode effect is permitted to appear with a certain regularity as the index of the oxide concentration factor in the melt.

The parameters of producing disperse precipitates of various metals are generally the same; normally sodium chloride or its eutectics with potassium chloride are used. The melt contains 10%–20% of metal chlorides (usually between 3% and 7% calculated for the metal). The electrolysis temperature is between 970 and 1140 K; a high cathode current density of 5–15 kA/m^2 is supported; and anode current density does not exceed 4 kA/m^2.

High densities of metal exchange current in molten media cause a rapid increase of the area of the precipitate growth front and cancel the diffusion control. This causes a corresponding coarsening of dendrite crystals during electrolysis and the deposition of the product in the form of large powder particles.

Statistical models that relate the average particle size (r_{av}) with current density and metal concentration (C, mass%) are true under the following conditions: current density of $i = 5$–34 kA/m^2, temperature of 1000–1020 K, metal concentration of 2%–8% (in mass), the background is the equimolar mixture KCl–NaCl; and precipitation time is 2 h. According to the experimental data, the average size of powder particles obtained by electrolysis was calculated:

$$r_{av} = \sum \alpha_j \cdot r_j \tag{8.36}$$

where $r_j = 0.5 \cdot (r_{j-1} + r_{j+1})$, α_j is the total mass share of powder particles of j-th fraction in the total powder mass.

The following statistical ratio between the average particle size and electrolysis conditions is valid for metals indicated in Table 8.10:

TABLE 8.10 Parameters to Calculate the Powder Particle Size Distribution

Metal	a	b	α_0	m
Copper	1030	0.18	0.37 ± 0.015	$6.8 + 0.10$
Iron	200	0.10	0.39 ± 0.01	6.7 ± 0.65
Manganese	205	0.10	0.36 ± 0.01	6.5 ± 0.60
Titanium	172	0.10	0.39 ± 0.02	7.3 ± 0.03
Tungsten	81	0.34	0.32 ± 0.01	6.7 ± 0.03

$$r_{\mathrm{av}} = a\left(\frac{C}{i}\right)^{\mathrm{b}} \tag{8.37}$$

The values of constants a and b are presented for various metals in Table 8.10.

The ratio (38) can be used to estimate the average size of powder particles in new conditions referred to the interval mentioned above. Particles are distributed regarding the average size under the Gauss law. The fraction of particles of the size r_{j} with the accuracy of ±20% can be calculated by the equation:

$$\alpha_{\mathrm{j}} = \alpha_0 \cdot \exp\left(-m^2 \Delta r_{\mathrm{j}}^2\right) \tag{8.38}$$

where α_0 and m are constants for the given metal (see Table 8.10). By calculating the values of α_{j} for a number of values Δr_{j} (deviations from the average value r_{av}), the curve of the powder particle size distribution is obtained. The values exp. $(-m^2 \Delta r_{\mathrm{j}}^2)$ are obtained when using the function $\phi(mx) = 2/\sqrt{\pi} \cdot e^{-m^2 x^2}$, which is tabulated.

In this case it is simpler to calculate the α_{j} value by the formula:

$$\alpha_{\mathrm{j}} = 0.885\alpha_0 \varphi(m\Delta r) \tag{8.39}$$

Calculations of formulas (Eqs. 8.38–8.40) are based on the following dimensionalities: $[i]$ A/cm^2; $[c]$ mass%; $[r_{\mathrm{av}}]$ μm.

By simulating the dendrite crystallization from the melt, the growth front on the cylinder end can be presented in the form of a hemisphere with radius $r_0 + y$ that increases over the course of time (Fig. 8.24A). For the set current (I) at a dendrite arrangement density on the growth front N, the differential equation for dendrite elongation (Eq. 8.40) can be obtained and, after separation of variables and integration, Eq. (8.41) for the dependence of the dendrite.

length y on the time t (Fig. 8.24) is obtained:

$$\frac{dy}{dt} = \frac{V}{zF} \cdot \frac{I}{4\pi^2 (r_0 + y)^2 r_{\mathrm{tip}}^2 N} \tag{8.40}$$

$$r_0^2 y + r_0 \cdot y^2 + \frac{1}{3} \cdot y^3 = \frac{V}{zF} \cdot \frac{I}{4\pi^2 r_{\mathrm{tip}}^2 \cdot N} t \tag{8.41}$$

The dendrite growth rate decreases in time and leads to a nonhomogeneous structure of the product. But, at any moment, dendrites can be lengthened linearly (see Fig. 8.24B) by the selection of the cathode lifting speed equal to the dendrite growth rate. In this case, constant precipitation conditions are maintained on the growth front and, consequently, a homogeneous dendrite precipitate will be obtained. Structural characteristics of the dendrite precipitate are defined by the set current value and the speed of cathode lifting [1,7].

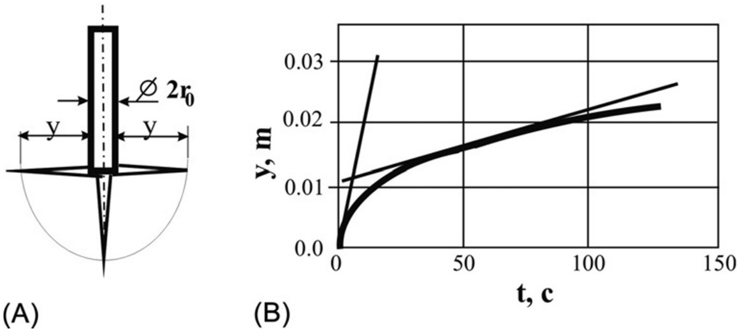

FIG. 8.24 Formation of the hemispherical front by dendrites at the end of cylindrical electrode (a) and dynamic of its elongation (b) $r_0 = 2$ mm, $I = 2$ A; $r_{\mathrm{tip}} = 2 \times 10^{-6}$ m; $N = 3 \times 10^7$ m^{-2}; $V = 9.55 \times 10^{-6}$ m^3/mol.

The electrolyzer with soluble anodes and immovable cathodes is a vessel with anodes and cathode core and an inlet for inert gas injection. The graphite sleeve in the electrolyzer fulfills simultaneously the function of anode current supply in the cell with the diaphragm. A design of an electrolyzer with the transfer of the cathode precipitate to a water-cooled chamber is known (Fig. 8.25). The electrolyzer with the precipitate cut under the electrolyte layer allows the discharge of precipitate without lifting the cathode. The precipitate, cut by a knife, falls into a basket that moves under each cathode in turn. Then the precipitate goes to the chamber for collection and cooling. The slime together with the electrolyte is passed through metal-ceramic filters.

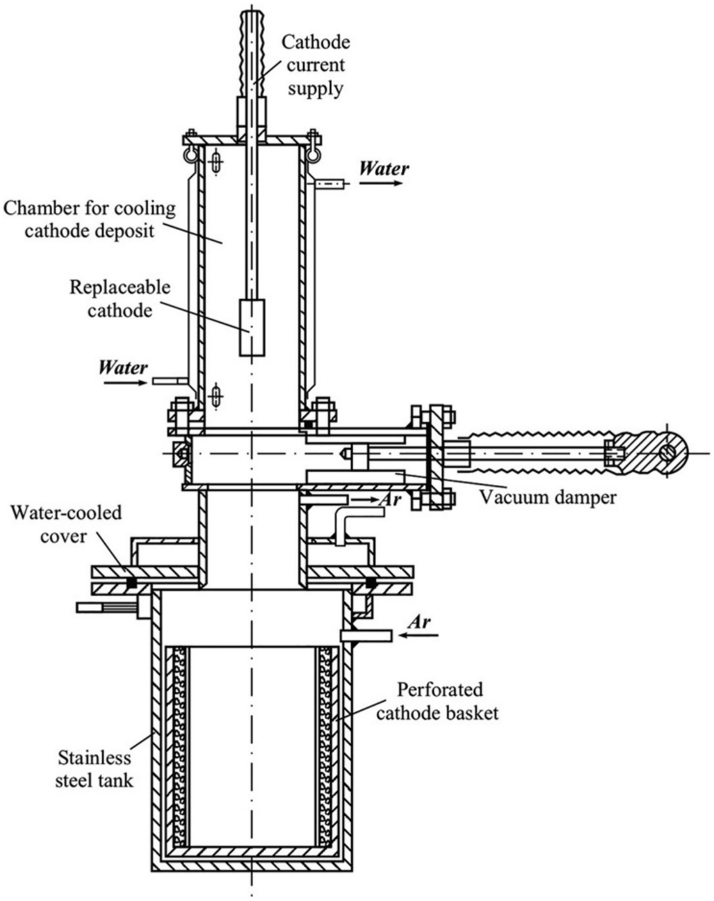
Cathode
current
supply
Water
Chamber for cooling
cathode deposit
Replaceable
cathode
Water
Vacuum damper
Ar
Water-cooled
cover
Ar
Perforated
cathode basket
Stainless
steel tank

FIG. 8.25 Scheme of the electrolyzer for electrolytic refining of tungsten.

AMALGAM METALLURGY METHOD

Dendrites are crystallized in a mercury electrode as a result of the formation of oversaturated amalgams after achieving the metal solubility limit in mercury (Table 8.11). The stability of mercury and amalgam depends upon the nature of anions in the solution (Table 8.12). The metal is precipitated either by electrolysis on the liquid mercury cathode or by amalgam cementation of a more negative metal (Fig. 8.20).

When the metal is precipitated in the form of amalgam, continual use as the anode means that more positive impurities are left in the amalgam anode and more negative impurities remain in the solution. The Volta series for amalgams differs from that for pure metals and depends upon the amalgam phase composition. The following presented for a single-phase amalgam Nernst equation is of the form:

$$E = E^0_{\mathrm{M(Hg)}} + \frac{RT}{zF}\mathrm{In}\frac{a_{\mathrm{M}^{z+}}}{a_{\mathrm{M(Hg)}}} \tag{8.42}$$

where $E^0_{\mathrm{M(Hg)}}$ is the amalgam standard potential that differs from the standard potential of pure metal; $a_{\mathrm{M(Hg)}}$ is the metal activity in amalgam, and $a_{\mathrm{M}^{z+}}$ is the activity of metal ions in the solution. The standard potential of the amalgam is connected with the standard potential of pure metal (see Table 8.12) by the following relation:

$$E^0_{\mathrm{M(Hg)}} = E^0_{\mathrm{M}} + \frac{RT}{zF}\mathrm{In}\left(a^{\mathrm{sat}}_{\mathrm{M(Hg)}}\right) - E_{\mathrm{s}} \tag{8.43}$$

where $a^{\mathrm{sat}}_{\mathrm{M(Hg)}}$ is the metal activity in its saturated amalgam,

$$E_{\mathrm{s}} = -\frac{\Delta G^0}{zF} + \frac{RT}{zF}\mathrm{In}\left(a^{\mathrm{sat}}_{\mathrm{Hg}}\right)^{\mathrm{y}} \tag{8.44}$$

TABLE 8.11 **Metal Solubility in Mercury (%(at))**

	Temperature (K)			
Metal	**298**	**373**	**473**	**623**
Indium	70.3	83.7	N/s	N/s
Thallium	43.7	56.1	76.9	N/s
Cadmium	10.1	31.9	66.7	N/s
Zinc	6.4	22.0	44.1	81.87
Lead	1.9	17.9	63.1	N/s
Bismuth	1.6	25.0	68.9	N/s
Tin	1.2	29.8	83.8	N/s
Gallium	3.6	6.8	43.5	N/s
Magnesium	3.0	9.07	22.31	28.1
Ruthenium	0.694			
Gold	0.13	0.60	2.47	26.18
Silver	0.078	0.41	1.75	10.86
Rhodium	0.012			
Aluminum	0.015	0.089	0.5	3.0
Palladium	0.012			
Uranium	0.0031	0.025	0.18	1.11
Neodymium	0.0099	0.045	0.21	0.22
Gadolinium	0.00487	$5.53\cdot10^{-2}$	0.22	2.87
Samarium	0.00644	$5.53\cdot10^{-3}$	0.21	0.82
Magnesium	0.00371	$4.62\cdot10^{-2}$	0.32	2.24
Niobium	0.002	N/a	N/a	N/a
Iridium	0.001	The same	The same	The same
Thorium	0.00136	$4.5\cdot10^{-3}$	0.011	0.052
Silicon	0.007	$3.71\cdot10^{-2}$		
Copper	0.00742	$3.71\cdot10^{-3}$	0.18	0.94
Vanadium	0.00022	N/a	N/a	N/a
Nickel	$1.52\cdot10^{-5}$	$1.7\cdot10^{-4}$	N/a	0.0123
Molybdenum	$4\cdot10^{-5}$	N/a	The same	N/a
Tungsten	$1\cdot10^{-5}$	N/a	N/a	N/a
Titanium	$2.05\cdot10^{-3}$	$9.2\cdot10^{-5}$	$6.15\cdot10^{-4}$	$7.12\cdot10^{-3}$
Zirconium	$2.25\cdot10^{-6}$	$1.86\cdot10^{-5}$	$1.85\cdot10^{-4}$	$9.21\cdot10^{-4}$
Chromium	$6.19\cdot10^{-7}$	$4.58\cdot10^{-6}$	$2.27\cdot10^{-6}$	$9.1\cdot10^{-5}$

N/s, nonsoluble; N/a, nonavailable.

TABLE 8.12 Values of Standard Potentials of Mercury in Various Media, V (nve)

Reaction	Potential
$H_2+2OH^-=H_2O+H_2O+2e$	0.926
$2Hg + SO_4^{2-} = Hg_2SO_4+2e$	0.615
$2Hg + CrO_4^- = Hg_2CrO_4 + 2e$	0.41
$2Hg + 2IO_2^- = Hg_2\ (IO_3)_2+2e$	0.394
$2Hg +2Cl^-= Hg_2Cl_2 + 2e$	0.268
$Hg+4Cl^-=HgCl_4^{2-}+2e$	0.48
$2Hg+2Br^-= Hg_2Br_2 + 2e$	0.139
$Hg+4Br^-=HgBr_4^{2-}+2e$	0.21
$2Hg+2CNS^-= Hg_2(CNS)_2 + 2e$	0.22
$2Hg+2OH^-=Hg_2O + H_2O+2e$	0.123
$2Hg +2I^-= Hg_2I_2 + 2e$	0.041
$Hg+4I^-=HgI_4^{2-}+2e$	0.04
$Hg+4(CN)^-=Hg(CN)_4^{2-}+2e$	−0.37
$Hg+S^{2-}=HgS+2e$	−0.70

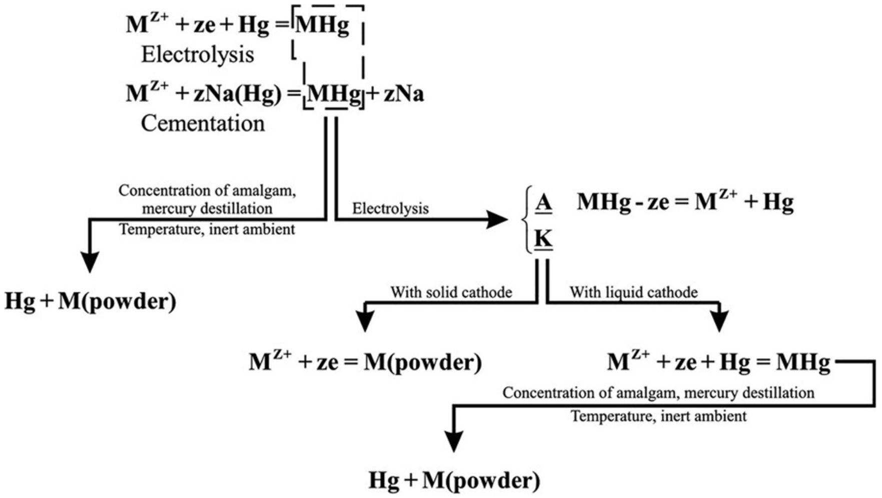
M^{Z+} + ze + Hg = MHg
Electrolysis
M^{Z+} + zNa(Hg) = MHg + zNa
Cementation
Concentration of amalgam, mercury destillation
Temperature, inert ambient
Electrolysis
A
K
MHg - ze = M^{Z+} + Hg
Hg + M(powder)
With solid cathode
With liquid cathode
M^{Z+} + ze = M(powder)
M^{Z+} + ze + Hg = MHg
Concentration of amalgam, mercury destillation
Temperature, inert ambient
Hg + M(powder)

FIG. 8.26 Modes of producing metal powders in amalgam metallurgy.

ΔG^0 is the change of Gibbs free energy for the process of formation of the solid phase that is in equilibrium with the amalgam liquid phase, a_{Hg}^{sat} is the mercury activity in the saturated amalgam, and y is the number of mercury moles for one metal mole in the amalgam solid phase.

In surface layers of the mercury, a supersaturated solution of metal being reduced is formed and conditions for homogeneous crystallization of metal nuclei of a size defined by the degree of amalgam oversaturation are created. Nuclei crystallization leads to amalgam depletion by metal atoms near the newly formed surface; reduced particles flow through the "solution mercury" phase boundary. This flow is determined by the set current density. Dendrites are crystallized under conditions of substance diffusion delivery through the amalgam layer to the surface of growing crystals.

The rate of dendrite lengthening is defined by current density on the boundary "solution mercury" by the number of nuclei N, m^{-2}, formed and their cross-section A, m^2, (for Co about $5\,nm^2$):

$$\frac{dy}{dt} = \frac{V}{zF}\frac{I}{N \cdot A} \tag{8.45}$$

where V is the value of the metal mole volume.

Factors increasing particle flow (increase of the current density, growth of temperature, mixing of mercury and solution) cause dendrite coarsening. Amalgams are formed by electrolysis and metals are precipitated on solid cathodes in cells with rotating disk anodes (Fig. 8.27). Steel amalgamated plates fitted on a slowly rotating shaft serve as anodes and feed new portions of the amalgam to the upper space containing the electrolyte.

FIG. 8.27 Electrolyzer cell with rotating disk anodes.

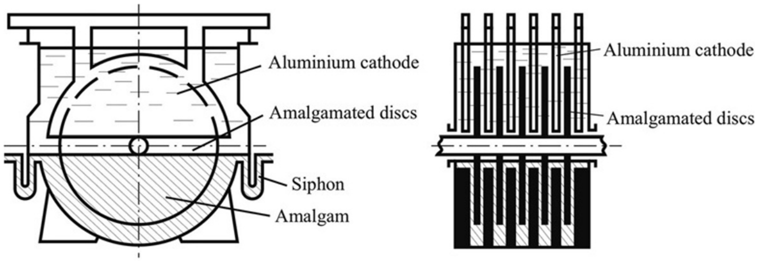
Aluminium cathode
Amalgamated discs
Siphon
Amalgam
Aluminium cathode
Amalgamated discs

Electrolyzers with amalgam bipolar electrodes are used to produce high-purity powders (Fig. 8.28). The electrolyzer consists of a series of concatenated isolated cells separated by a vertical partition that does not touch the bottom. To exclude electrolyte ingress into the next cell, a plate from an easily amalgamated metal hardly soluble in mercury is inserted in the slot in the bottom part of the partition.

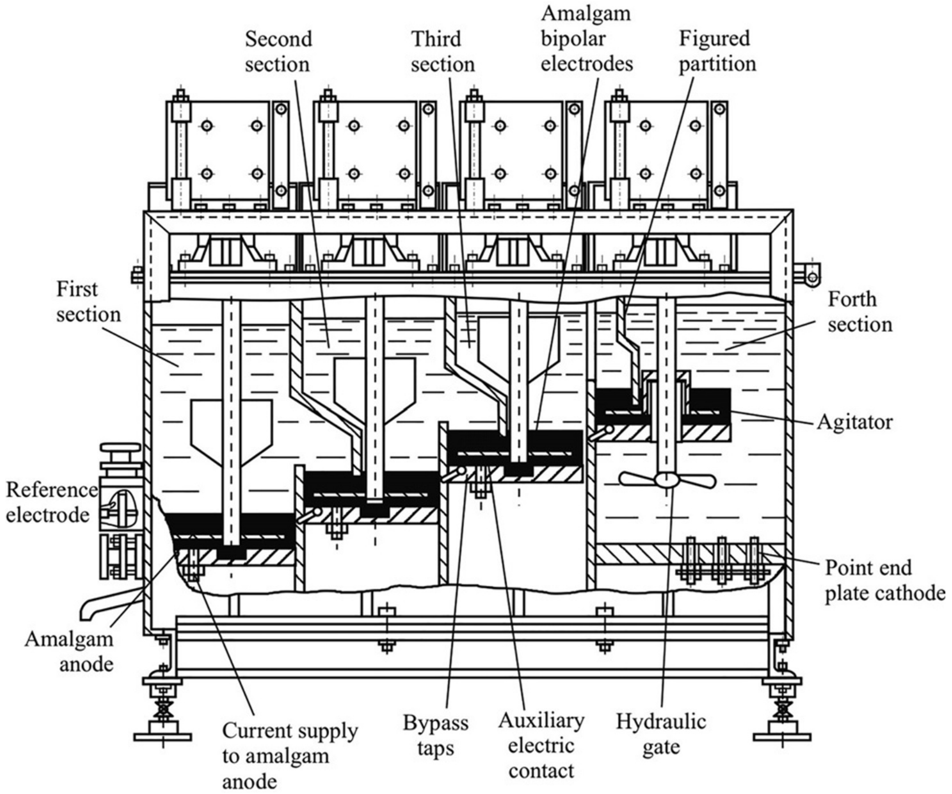
Second section
Third section
Amalgam bipolar electrodes
Figured partition
First section
Forth section
Agitator
Reference electrode
Point end plate cathode
Amalgam anode
Current supply to amalgam anode
Bypass taps
Auxiliary electric contact
Hydraulic gate

FIG. 8.28 Industrial electrolyzer with cascade bipolar amalgam electrodes.

For contact displacement (cementation) by amalgams, there are in use units in which amalgams and solution are strongly mixed with an agitator. Drum precipitating devices are used to recover metals from flowing solutions. These units operate in the conditions of countercurrent flow of amalgam by means of centrifugal or magnetic pumps.

Fine powders of copper, gold, silver, cobalt, niobium, molybdenum, chromium, vanadium, tantalum, zirconium, hafnium, and other metals hardly soluble in mercury are produced by precipitation from an aqueous organic medium on a rotating cathode (Fig. 8.29).

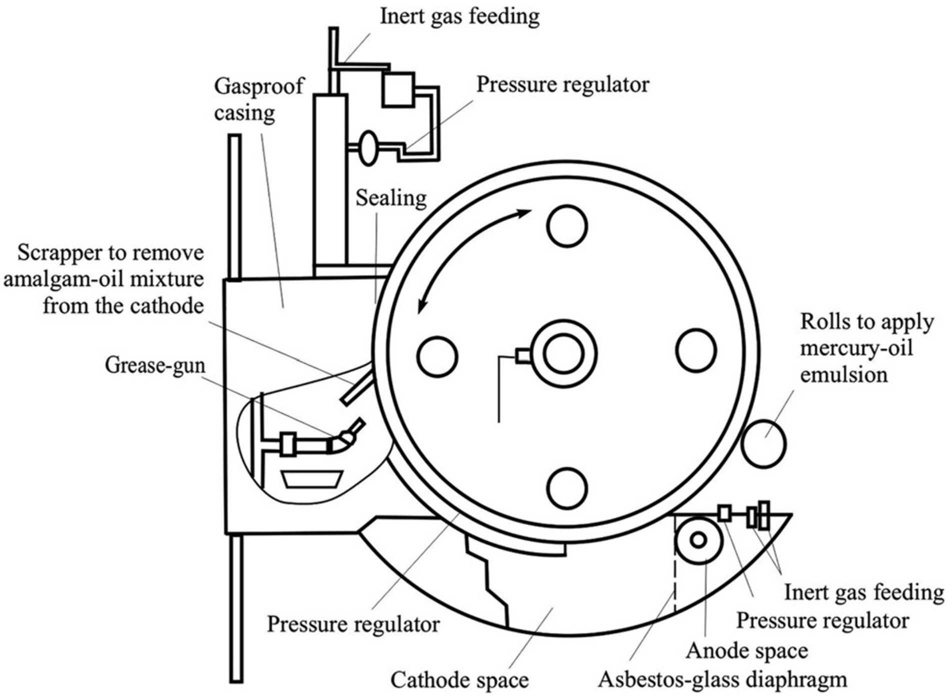

FIG. 8.29 Electrolyzer for producing fine metal powders.

An oily solvent film with mercury dispersed in it is applied to the cathode surface with a roller. The electrolysis takes place in an inert atmosphere; the gas is supplied separately to the anode and cathode areas separated by a diaphragm. The cathode deposit is removed from the cathode by a scraper after oil is applied to the cathode surface with a grease gun.

The amalgam is filtered in a nutsch filter or filter press and treated in a distillation furnace. The amalgam is moved into the furnace by a screw conveyer. Inert gas or hydrogen is supplied by countercurrent flow and carries mercury fumes to a cooler. In the predistillation zone, a temperature of 670–770 K is maintained while 870 K is the baking temperature. Dendrites are separated from mercury by heating under vacuum or in an inert gas atmosphere. When using amalgam as the anode together with a solid (liquid) cathode, a supersaturated solution is formed and fine dendrites are then separated from mercury by a subsequent process (see Fig. 8.26).

WORKPLACE ATMOSPHERES SAFETY

Metallic mercury is a highly toxic agent. Elemental mercury and inorganic compounds in liquid and vapor conditions have an effect when they are inhaled and adsorbed through the skin. Contact irritates the eyes, nose, throat, and lungs. Represented exposure can cause mercury poisoning with tremors, personality changes, damage to the kidneys, and gum problems. The workplace exposure limits established by EH40-Update to EH40/2005 Workplace Exposure Limits [19], New Jersey Department of Health-State (NJDOH) [20] and GOST 12.1.005–88 of the RUS Occupational Safety Standards System [21] are given in Table 8.13.

Mercury reacts with acetylene to form explosive acetylene. Mercury can form explosive compounds with ammonia and will explode when mixed with chlorine dioxide, oxidizing agents (such as perchlorates, pereoxides, permanganates, chlorates, nitrates, chlorine, bromine, and fluorine), strong acids (such as hydrochloric, sulfuric, and nitric), and methylazide. Mercury is not compatible with combustible materials (such as aluminum and copper), calcium, sodium carbide, amines, lithium, and rubidium.

If mercury is spilled or leaked, it is necessary to fulfill in turn the following [22]:

- Evacuate personnel and secure and control entrance to the area.
- Eliminate all ignition sources.
- Cover with a sulfur compound to keep from vaporizing and collect with a charcoal filter vacuum by special apparatus for the clean up of mercury spills (do not use a regular vacuum).
- Use zinc or copper flakes and a flashlight to check for remaining mercury after clean up.
- Ventilate and wash areas of spill or leak (not wash into sever).

TABLE 8.13 Workplace Expose Limits of Mercury Elemental and Inorganic Compounds

Substance	CAS Registry Number	Hazard Rating Key	Workplace Expose Limit (mg/m)		References
			Long-Term Exposure Limit (8 h TWA[a] Reference Period)	Short-Term Exposure Limit (15 min Reference Period)	
Mercury and divalent inorganic compounds including mercuric oxide and mercuric chloride (measured as mercury)			0.02		[19]
Mercury, elemental, and inorganic compounds	7439–97-6	3[b]	0.1 0.05[c]	0.1	OSHA[d] [20] NIOSH[e] [20]
Mercury metallic	7439–97-6	I[f]	0.005	0.01	[21]
Mercury inorganic compounds (measured mercury)		I	0.05	0.2	[21]
Mercuric oxide	21,908–53-2	3	0.1 0.1[c]	0.05	OSHA [20] NIOSH [20]
Mercuric sulfate	7783–35-9	3	0.1 0.1[c]	0.05	OSHA [20] NIOSH [20]

[a] *TWA is the Total weight average.*
[b] *Hazard rating key (0–minimal, 1–slight, 2–moderate, 3–serious, 4–severe).*
[c] *Averaged over an 10-h workshift.*
[d] *OSHA is abbreviation of 'Occupational Safety and Health Administration'.*
[e] *NIOSH is an abbreviation of National Institute for Occupational Safety and Health.*
[f] *Severe hazard according to [21].*

Implementation of enclosed operations, local exhaust ventilation, and general ventilation must proceed from the requirements of ensuring the workplace exposure limit. Store in lightly closed containers in a cool, well-ventilated area.

REFERENCES

[1] Naboychenko SS, editor. Handbook of nonferrous metal powders. Moscow: Metallurgia Publishers; 1997 [in Russian].

[2] Taubenblat PW. Chemical and electrolytic methods of powder production. In: Eisen WB, Ferguson BL, German RM, editors. ASM Handbook, 7. ASM International Publishers; 1998. p. 67–71.

[3] Baraboshkin AN. Electrolytic crystallisation of metals from melt salts. Moscow: Nauka Publisher; 1976 [in Russian].

[4] Nichiporenko OS, Pomosov AV, Naboychenho SS. The powders of copper and of its alloys. In: Zelikman AN, Korshunov BG, editors. Metallurgy of rare metals. Moscow: Metallurgiya Publisher; 1988 [in Russian].

[5] Despic AR, Popov KI. The modern aspects of Electrochemistry, 7. New York: Plenum Press; 1972. p. 199–313.

[6] Newman JS. Electrochemical systems. Inglwood Cliff (NJ): Prentice-Hall Inc.; 1973.

[7] Murashova IB, Pomosov AV. Crystallisation of metals as dendrites. In: Itogi nauki, 31. Moscow: VINITI Publisher; 1989. p. 55–110 [in Russian].

[8] Ivanovsky LE, Rozanov IG, Zotin IV, Khramov AP. Metal dendrite deposits production by electrolysis of ion melts and their application. Melts 1997;2:51–69 [in Russian].

[9] Murashova IB, Khramov AP, Zotin IV, Zaikov YP, Zyryanov VG. Electrocrystallization of fibrous silver deposits from nitrate melts. Experience and modeling. J Min Metal 2003;39(1–2):137–47.

[10] Murashova IB, Ostarkova GV, Burchanova NG. Modelling structural changes in the deposit during galvanostatic electrolysis and contact deposition of metals. Electrochemistry 2002;38(3):284–9 [in Russian].

[11] Mason TJ. Practical sonochemistry. Chichester (UK): Ellis Horwood Publishers; 1991.

[12] Mandelbrot BB. Fractal geometry of nature. San Francisco: Freeman; 1983.

[13] Qiu XF, Xu JZ, Zhu JM, Zhu JJ, Xu S, Chen HY. Controllable synthesis of palladium nanoparticles via a simple sonoelectrochemical method. J Mater Res 2003;18(6):1399–404.

[14] Ali GAM, Yusoff MM, Ng YH, Lim HN, Chong KF. Potentiostatic and galvanostatic electrodeposition of manganese oxide for supercapacitor application: a comparison study. Current Applied Physics 2015;15(10):1143–7.

[15] Osipova ML, Murashova IB, Savel'ev AM. Formation of dendritic copper deposit under industrial electrolysis. Powder Metallurgy and Metal Ceramics 2010;49(5–6):253–9.

[16] Sokolovskaya EE, Murashova IB, A. B. Lebed, Osipova ML. Determining the longest possible period of growth of electrolytic copper deposit between its removals from the cathode. Tsvet Met. 2010; 1: 36–9 [in Russian].

[17] Pomosov AV. Balance of electrolytic cell voltages and possibilities for decreasing the specific consumption of electricity in the production of copper powder. Zh Prikl Khim 1959;32(7):1626–9.

[18] Osipova ML, Savel'ev AM, Osipov DL. Dependence of electrolytic cell voltage on the structure of cathode deposition of PMS11 and PML0 powders. Powder Metallurgy and Metal Ceramics 2013;(32 (3–4)):119–25.

[19] EH40-Update to EH40/2005 Workplace Exposure Limits. second ed., 2011 (as consolidated with amendments, December 2011).

[20] US New Jersey Department of Health and Senior Services. Hazardous Substance Sheet. Mercury elemental and inorganic compounds. Revision: February; 2001.

[21] Occupational Safety Standards System. General sanitary requirements for working zone air. GOST 12.1.005–88 [in Russian].

[22] Mercury Safety Sanitary Requirements. SanPIN 4607–88. Russian National Standards. <http://www.russian-national-standards.com/russian-sanitary-norms.html.>.

Chapter 9

Nanopowders

Oleg D. Neikov and Nicholas A. Yefimov
Frantsevich Institute for Problems of Materials Science (IPMS), Kiev, Ukraine

Chapter Outline

Introduction 271
Features of Nanoparticles 272
  Structural Characteristic 272
  Thermodynamic Data 273
  Mechanical Properties 274
  Electromagnetic Properties 274
  Optical Properties 274
Testing of Nanopowders 275
  Testing of Nanopowder Structures and Chemistry 275
  Instrumental Indentation 276
Production Methods 278
  Condensation Technique 278
  Chemical Precipitation From Solution 282
  Spray Conversion Method 285
  Plasmachemical Synthesis 286
  High-Energy Disintegration 289
Nanopowder Passivation 292
  Nanopowder Chemical Passivation 293
  Microencapsulation of Nanoparticles 293
Powder Processing Methods 294
Safety Aspects of Nanopowders Production 295
Applications 296
  Vapor Deposition in Vacuum 297
  Cemented Carbides 300
  Fiber-Reinforced Material 302
  Gradient Materials 302
  Nanopowder-Polymer Composites 303
  Thin Film Technique 304
  Semiconductors 305
  Electrical Storage Systems 306
  Miniaturized Systems 307
References 307

INTRODUCTION

Currently, it is the convention to consider several kinds of nanomaterials. Under conditions, they can be denoted as consolidated objects, nanosemiconductors, nanoporous structures, numerous nanotubular objects, nanopolymers, catalysts, and supramolecular structures [1]. Here, however, we are concerned with their use as powders. The general rule is that the size of the basic structural components (crystallites, phases, pores, particles, and molecular ensembles) does not exceed 100 nm. Such traditional materials as dispersion-strengthened alloys, the structure of which includes ultrafine- and nanoparticles, occupying usually only some 5–10 vol%, as well as wrought metals and alloys, in which assemblies and local nonoriented areas are small, but the original coarse grain size remains, do not come into category of nanomaterials.

It is necessary to note several terminological peculiarities. The terms with the “nano” prefix such as nanotechnology, nanochemistry, nanoscience, etc., have wide dissemination. In the American literature [2], the nanotechnology concept is accepted as the ability to create and use the materials, devices, and systems in which structural elements have sizes ranging from 1 to 100 nm. The nanoscience is science about low-sized matter, that is, an aggregate of knowledge about the properties of substances and the effects on the nanometer scale.

The nanoparticles—that are low-sized hard substances, the geometrical size of which ranges from 1 to 100 nm, are generally called nanoparticles. At the same time, the particles in the range from 1 μm to 400 nm are conventionally defined as “submicron particles” [3]. Therefore, the lower range is compared with the wavelength of visible light (its lower limit is about 400 nm). For powders with a particle size <1 μm, the name “ultrafine” is often used. Under the ASTM Standard (Standard Terminology of Powder Metallurgy. Designation: B243–13), a powder consisting of particles typically <100 nm in size is determined to be a nanopowder. The nanopowder and nanoparticle concepts are in many respects overlapping. But certainly, it is necessary to bear in mind the possible separate nature of the former and the necessarily aggregated state of the latter (the powder that is an aggregate of the separate hard small particles ranging from 0.001 to1000 μm).

Handbook of Non-Ferrous Metal Powders. https://doi.org/10.1016/B978-0-08-100543-9.00009-9
© 2019 Elsevier Ltd. All rights reserved.

The fundamental importance of the low-sized objects was underscored in 1959 by Nobel Prize Winner Richard Feynman in a lecture (Feynman, R.P. "There is plenty of room at the bottom." In Miniaturization. New York: Reinhold, 1961, which later became famous. Feynman told the audience about fantastical perspectives with the creation of materials on the atomic or molecular level. He also showed that the necessity will arise to create an absolutely new class of operative and measuring apparatus required for handling such small, nanosized objects.

The apparatus predicted by Feynman appeared only in 1980 (scanning tunnel and atomic power microscopes and other devices). At the same time, considerable progress in computer techniques had been made that allowed the simulation of the material characteristics on the nanoscale. In the traditional technological approach, which is termed "top-down," the fine and ultrafine objects are created (miniaturization) from large ones (for example, by means of comminution). The second approach, termed "bottom out," which is popularized in organic chemistry and chemistry of high-molecular composition, is based on the submicron erection of the material with given composition and structure, followed by an increase in its size.

Starting with the pioneering work of Gleiter and colleagues [4,5], the interest in nanomaterials has grown steadily. Because of their unique properties, the nanomaterials occupy key positions in state-of-the-art materials science. The nanotechnology and nanomaterial information grows greatly, including articles in journals (Nanotechnology, UK; Journal of Cluster Science including Nanostructured Materials, The Netherlands; Journal of Metastable and Nanocrystalline Materials, Switzerland; Journal of Computational and Theoretical Nanoscience, United States; Journal of Nanoparticle Research, The Netherlands; Journal of Nanoscience and Nanotechnology, United States; Materials Science of Nanostructures, Ukraine; International Journal of Nanoscience, Singapore; Journal of Aerosol Science, United States; Composites and nanostructures, Russia; Nanomaterials and Nanostructures, Russia; Nanostructures and Nanoobjects, Germany; Nano Today, Singapore; Applied Nanoscience, Germany). Also included are the proceedings of numerous conferences and annual symposia, patents, and monographs.

As *nanowerk* reported [http://www.nanowerk.com/nanotechnology/nanotechnology_periodicals.php], >200 academic journals dedicated themselves wholly or primarily to nanoscience and nanotechnology.

According to *nanowerk* data [http://www.nanowerk.com/nanotechnology/research/nanotechnology_links.php], >1300 university departments, labs, and research groups are operating in the field of nanoscience and nanotechnology.

In this chapter, the main attention is focused on the production of ultrafine and nanopowders and their application in the particulate condition and consolidated state.

FEATURES OF NANOPARTICLES

By the micronization of solid particles, the specific surface area increases generally in reversal square-law proportion to the particle size. Therefore, when the particle of 1 μm is micronized to 10 nm, the specific surface area becomes 10,000 times greater. As the increase in the specific surface area directly influence such properties as the reaction rates of the particles, it is one of the major reasons for the unique properties of the nanoparticles different from the bulk material together with the change in the surface properties of the particles itself. The fraction of the atoms or the molecules located at the surface on the particles plays a great role because they are more active than those inside the solid particles because of the free hand, which leads to easy bonding with the contacting materials and causes various changes in particle properties. In the work [6], the relationship between the particle size and the fraction of the number of atoms located at the particle surface with an assumption of atomic distance of 0.2 nm are given. It is indicated that the fraction of surface atoms of a 20 μm cubic particle is only 0.006%, but it increases to 0.6% for a 200 nm particle. It is then estimated that almost half the atoms are situated at the surface of a 2 nm particle.

The nanoparticles have various unique features in the morphological/structural properties, thermal properties, electromagnetic properties, optical properties, and mechanical properties.

Structural Characteristic

Increasing powder dispersity leads to a change of material structure parameters. According to data [7], the variation of the specific surface of aluminum powder in the 8.0–19.0 m^2/g range results in the following changes of the lattice: the lattice constant, a, increases from 0.40515 to 0.40518 nm; decreasing of the structure density from 0.20% to 0.18%; increasing of the displacement of atoms from equilibrium position from 1.38% to 3.78%; and decreasing of the dislocation density from 21.5×10^{14} to $7.7 \times 10^{14}\,m^{-2}$. The authors [7] are of the opinion that the increasing of the potential energy of aluminum nanoparticles from 0.6 to 1.2 kJ occurs by reason of decreasing of aluminum structure density up to 0.12%–0.21%. Thus, the structure-energy state of aluminum nanoparticles corresponds to heating up to 343 K that might appreciably influence chemical reaction kinetics.

Thermodynamic Data

In general, it is known that the temperature of phase transformation depends on the particle size [8–11]. Usually, this is described as

$$T_{\text{melt-nano}} = T_{\text{melt-bulk}} - \frac{a}{d}, \tag{9.1}$$

where $T_{\text{melt-nano}}$ is the transformation temperature of nanoparticles; $T_{\text{melt-bulk}}$ is the transformation temperature of bulk material; a is a constant value depending on the entropy of transformation and the difference of the surface energy in both phases [8]; and d is the particle diameter. The same description, as proved for phase transformations, was corroborated for the enthalpy of phase transformations.

As typical examples, experimental results obtained for aluminum particles were given by Eckert [9], for tin particles by Lai et al. [10], or by Suresh and Mayo [11] on zirconia particles doped by yttrium. The range of particle sizes where Eq. 9.1 is valid is limited in the range of both larger and lower particle sizes [12,13]. Castro et al. [14] have discussed the lower limit of particle sizes. Experimental results illustrate this. Fig. 9.1 displays the dependence of the melting temperature of gold nanoparticles on their sizes. These experimental data may be separated into two ranges: a first, which follows Eq. 9.1, and a separated second lower about 4 nm, which does not obey Eq. 9.1.

The numerical simulation of individual metallic nanoparticles was developed by Wen and Song [15]. This work, based on molecular dynamic (MD) simulations, examines the size-dependent properties of individual nanoparticles, the sintering and agglomeration of metallic nanoparticles, the oxidation of nanoparticles in the presence of oxygen, and the heating and cooling of passivated core-shell nanoparticles.

To reveal the influence of particle size, different-sized aluminum nanoparticles were simulated. As is reported [15], the result shows a strong size-dependent melting temperature, which is due to the increased fraction of loosely bounded surface atoms at reduced dimension. The size-dependent, MD-simulated melting temperatures are compared with a few other experimental and simulation results [16,17]. In Fig. 9.2, it is shown that compatible results are obtained, with a maximum

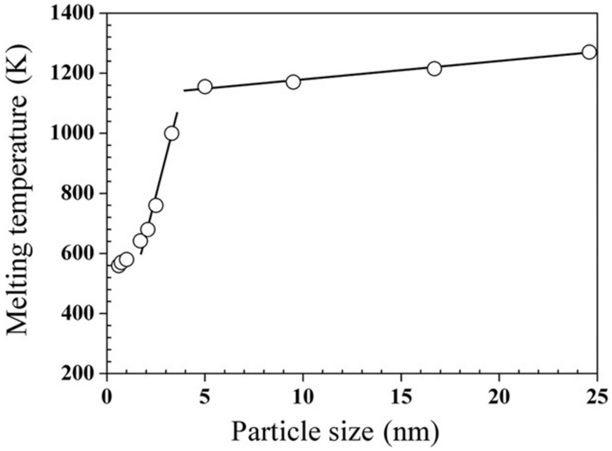

FIG. 9.1 Experimental and fitted data for the melting temperature of gold nanoparticles.

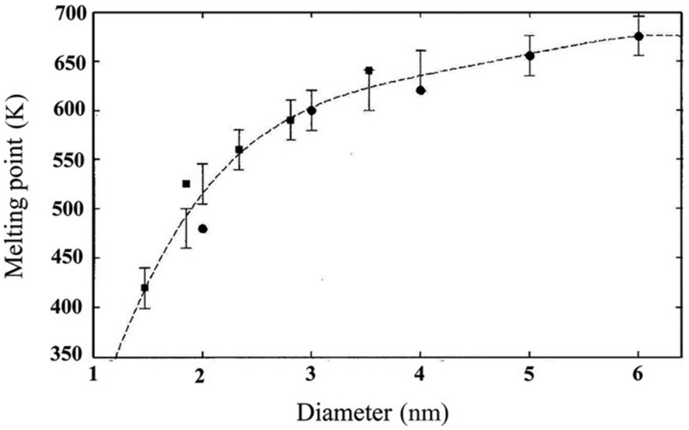

FIG. 9.2 Comparison of MD-simulated melting temperatures with the experimental melting point data of an Al particle.

difference of 25%. For nickel particles, the calculated melting temperature decreases, defined as the melting temperature of particles regarding the bulk value, are 0.7 and 0.5 for 3.52 and 1.76 nm nickel particles, respectively, from Cao et al. [18] while the MD-simulated results are 0.75 and 0.55, respectively, based on the surface melting temperature [15].

Mechanical Properties

It is known that the hardness of the crystalline materials generally increases with the decreasing crystalline size, and that the mechanical strength of the materials considerably increases by micronizing the structure of the metal and ceramic material or composing them in the nano range [6,19]. Furthermore, with the ceramic material having a crystalline size less than several hundred nanometers, the unique super-plastic phenomenon is seen so that it is extended several to several thousand times from the original size at the elevated temperature over 50% of the melting point [20], which may provide the possibility of forming and processing of ceramic-like metallic materials.

Fundamentals of metal alloy nanostructure formation and the technique for their creation are discussed in the powder production methods and production of nonferrous metal powder chapters in the present book.

Electromagnetic Properties

The nanoparticles are used as the raw material for a number of electronic devices. The electric properties and particle size of these nanoparticles play a great role in the improvement of the product performance. As an example, the minimum particle size to keep the ferroelectric property (critical size) differs depending upon the kind and composition of the materials. According to [6], the data of various kinds of materials varies from 7 nm for $PbTiO_3$ to 317 nm for Ba-Pb-Ti composite. The Curie point [21] is defined as the point changing from the ferroelectric material to the paraelectric phase. As for the Curie point, some equations have been proposed for its estimation [22].

As ferromagnetic particles become very small less than about 1 μm and finer they show a superparamagnetic property. Although the individual particles are ferromagnetic with the single magnetic domain structure, the particles collectively behave as a paramagnetic. It is magnetized as a whole in the same direction of the external magnetic field but the magnetization disappears by the thermal fluctuation when the external magnetic field is taken away. The time for disappearing of magnetization depends upon the particle size, namely, the magnetization of the material responds promptly with the external magnetic field as a paramagnetic when the particles are small enough, but it decreases gradually as the particle size becomes larger.

Optical Properties

The nanoparticles of a specified size range absorb the light with a characteristic wavelength as the plasmon absorption caused by the plasma oscillation of the electrons and the transmitted light with a different color depending upon the kind of metal and particle size are obtained [23].

It is shown the plasmon absorption of silver nanoparticles, where the spectral absorption intensity differs depending upon the particle size [24]. In the case of gold nanoparticles, it is reported that the maximum light absorption wavelength is 525 nm for the particles of 15 nm, but it is enlarged by about 50 nm for 45 nm particles. In this way, these gold and silver nanoparticles show the color phenomena with splendid tinting strength, color saturation, and transparency compared with the conventional pigments for the paint in the submicron size. Also, the tinting strength per unit volume of silver nanoparticles becomes about 100 times higher than that of organic pigments.

Toda [25] used the band model [21] for an analysis of the optical property of nanoparticles, including metallic, insulator, and semiconductor nanoparticles. The author [25] reports that conduction bands of a metal (conductor) are partially filled with electrons; no gap exists in electronic excitation. Conducted electrons in metal form a kind of plasma state, and the intraband transition of conduction electrons is described as the collective motion of free electrons. The oscillation of electrons by this collective motion is referred to as plasma oscillation and this oscillatory wave is referred to as a plasmon. The contribution of a conduction electron is interpreted using the classical Drude model [26,27]. The effect of surface plasmons is manifested brightly in nanoparticles with a large surface fraction. Recently, metal nanoparticle systems have been attracting attention because of their enhanced nonlinear optics properties by the single electronic electrical conduction phenomenon. The nonlinear optical effect originates from nonlinear polarization that is proportional to the power of order. Therefore, a nonlinear optical effect can be implemented at high efficiency by reinforcing a local field remarkably by surface plasmons.

TESTING OF NANOPOWDERS

Techniques of chemical analysis and bulk properties of nanopowders, including particle size distribution, density, flow rate, surface area and porosity, angle of repose, etc., are in general similar to study powders analysis, defined in Chapter 1. However, the resolution of the apparatuses for nanosized powder testing must be higher in comparison with microsized powder analysis. Therefore, in addition to the content in Chapter 1 of nanopowder testing, the scanning tunneling microscopy, atomic force microscopy, and instrumental indentation are considered here.

Testing of Nanopowder Structures and Chemistry

Methods of microanalysis, surface analysis, and bulk analysis both of micro- and nanopowders are described in Chapter 1. These methods for testing nanopowders apply the following techniques: scanning electron microscopy (SEM), transmission electron microscopy (TEM), electron probe X-ray microanalysis (EPMA), energy dispersive spectrometry (EDS), wavelength dispersive X-ray spectrometry (WDS), auger electron spectroscopy (AES), X-ray photoelectron spectroscopy (XPS), secondary ion mass spectroscopy (SIMS), X-ray powder diffraction (XRPD), X-ray fluorescence spectrometry, inductively coupled plasma atomic emission spectroscopy (ICP-AES), atomic adsorption spectroscopy (AAS), etc.

Additional testing capabilities of nanoscale powders have appeared with the development of the scanning probe microscopy (SPM) technique: scanning tunneling microscopy, atomic force microscopy, and magnetic force microscopy. In general, the SPM provides a three-dimensional image of the surface (topography) with high resolution. The information obtained by SPM methods based on the results of the probe and the sample interaction, which is used by a feedback system for fixing the probe-sample distance during scanning. The subnanometer resolution of 10^{-2} nm is achieved.

In a scanning tunneling microscope [28], during scanning the needle (probe) moves along the sample surface, the tunneling current is kept stable due to the feedback action, and registration of the tracking loop varies depending on the surface topography. These changes are recorded, and on their basis the map of heights is constructed. Another technique is based on the movement of the needle at a fixed height above the sample surface. In this case, the change of the tunneling current is fixed, and on the basis of this information, the topography surface is constructed. The resolution is up to 0.01 nm.

Atomic-force microscopy (AFM) or scanning-force microscopy (SFM) is a type of scanning probe microscopy (SPM) with demonstrated resolution on the order of fractions of a nanometer, >1000 times better than the optical diffraction limit [28,29]. Piezoelectric elements that facilitate very small but accurate and precise movements on (electronic) command enable very precise scanning. The AFM can be operated in a number of modes, depending on the application. In general, possible imaging modes are divided into static (also called *contact*) modes and a variety of dynamic (*noncontact or* "*tapping*") modes where the flexible console (cantilever) is oscillated at a given frequency. The typical configuration of a drive that moves sample and stage in connection with deflection and motion of the probe by AFM testing is shown in Fig. 9.3. Thus, it shows the drive attached to the sample, but the drive can also be attached to the tip or independent drives can be attached to both because it is the relative displacement of the sample and tip that is connected to controller and plotter, the both latter of which are not shown in Fig. 9.3.

In *contact AFM* mode, the probe (sharp needle looks) attached to a cantilever is moved across the surface of the sample and the contours of the surface are measured, either using the deflection of the cantilever directly or, more commonly, using the feedback signal required to keep the cantilever at a constant position. The probe is made from various materials

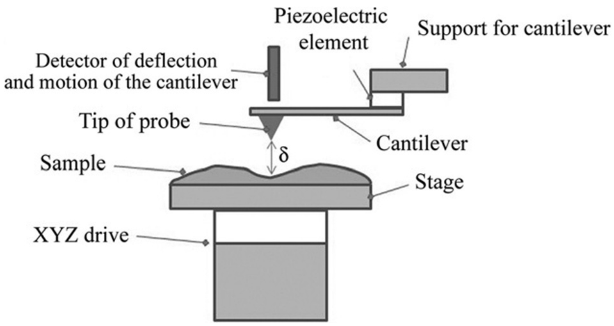

FIG. 9.3 Typical configuration of a drive that moves sample and stage in x, y, and z directions in connection with deflection and motion of the probe, by AFM testing.

(e.g., silicon or silicon nitride) with a radius of curvature of 10 nm for silicon and 20–60 nm for silicon nitride. In contrast to the scanning tunneling microscope, in the atomic force microscope both conductive and nonconductive objects can be investigated.

In *tapping* mode, the cantilever is driven to oscillate up and down at or near its resonance frequency. This oscillation is commonly achieved with a small piezo element in the cantilever holder. The amplitude of this oscillation usually varies from several nm to 200 nm. This amplitude is used as the parameter that goes into the electronic servomechanism that controls the height of the cantilever above the sample. The servo adjusts the height to maintain a set cantilever oscillation amplitude as the cantilever is scanned over the sample. A tapping AFM image is therefore produced by imaging the force of the intermittent contacts of the probe tip with the sample surface. Although the peak forces applied during the contacting part of the oscillation can be much higher than typically used in contact mode, tapping mode generally lessens the damage done to the surface and the tip compared to the amount done in contact mode.

In *noncontact AFM* mode, the tip of the cantilever does not contact the sample surface. The cantilever is instead oscillated at either its resonant frequency (frequency modulation) or just above (amplitude modulation) where the amplitude of oscillation is typically a few nanometers (<10 nm) down to a few picometers. Measuring the tip-to-sample distance at each (x, y) data point allows the scanning software to construct a topographic image of the sample surface.

The scanning probe microscopy is produced by many companies, in particular: Asylum Research, an Oxford instruments company (Goleta, California, United States); Agilent Technologies, Inc., (Folsom, California, United States); JEOL Ltd. (Tokyo, Japan); Nikon Corporation (Tokyo, Japan); JEOL Inc. (Peabody, Massachusetts, United States); Shimadzy Corp. (Kyolto, Japan); WITek GmbH (Germany), etc.

Instrumental Indentation

Instrumental indentation performs a special role be the only one of its kind possibility to study capability of the powder particles to deformation and evaluation of the local strength and plasticity of separate particles with the exception of a compaction and consequently cold working of the particles. This method, introduced in 1992 for measuring the hardness and elastic modulus by instrumented indentation techniques [30], has been widely adopted and used in the characterization of mechanical behavior of materials at small scales. Films with characteristic dimensions of the order 1 μm are now routinely measured. With good technique, the method can be used to characterize, at least in a comparative sense, the properties of films as thin as a few nanometers [31].

In an indentation test, a hard tip is pressed into a sample. The tip can be sharp or spherical. After the tip is removed, an impression is left. The hardness is defined as the indentation load divided by the projected area of impression. Moreover, by means of instrumental indentation testers, the indentation load and indentation depth can be continuously and simultaneously measured. Many models have been developed to extract the material properties from the recorded indentation load-depth curve, including the elastic modulus, yield stress, strain hardening coefficient, residual stress, fracture toughness, etc. The indenters commonly used for nanoparticle indentation are listed in the Table 9.1. A diagram of the Berkovich indenter geometry is presented in Fig. 9.4.

A schematic illustration of the unloading process, showing parameters characterizing the contact area, and a schematic representation of a typical data set obtained with a Berkovich indenter, are presented in Fig. 9.5A and B, respectively. In the latter, the parameter P designates the load and h the displacement relative to the initial undeformed surface. Deformation during loading is assumed to be both elastic and plastic in nature. During unloading, it is assumed that only the elastic displacements are recovered; it is the elastic nature of the unloading curve. However, finite element simulations have shown that reverse plastic deformation is usually negligible [32].

The procedure used to measure hardness, H, and elastic modulus, E, is based on the unloading processes shown schematically in Fig. 9.5A and B, The hardness is evaluated [30] by the equation:

$$H = \frac{P_{\max}}{A},$$

where $P_{\max}$ is the maximum applied load and A is the contact area of the indentation, at the maximum load. The reduced Young's modulus, E_{eff}, is determined (e.g., [30,33]) from the equation:

$$E_{\text{eff}} = \frac{\sqrt{\pi}}{2\beta}\frac{1}{\sqrt{A}}\frac{1}{S},$$

TABLE 9.1 Indenters Used for Nanoparticle Indentation

Characteristics of Indenters	Indenter Types				
	Berkovich	Vickers	Cube Corner	Cone (Angle ψ)	Sphere (Radius r)
Shape	Triangular pyramid	Tetrahedral pyramid	Triangular pyramid with perpendicular faces	Conical	Spherical
Applications[a]	B-M, T-Fil, S-T, Sep-Part, W-T, Im	B-M, Fil, Fo, S-T, W-T	T-Fil, S-T, Fr-T, W-T, Im	B-M, T-Fil, S-T, W-T, Sep-Part, Mod, Im	B-M, Fil Sep-Part
Available as traceable standard	Yes	Yes	Yes	No	No
Centerline to face angle (θ), degree	65.3	68	35.26	–	–
Projected contact area[b]	$3h_c^2$	$3h_c^2(\mathrm{tg}\theta)^2$	$3h_c^2(\mathrm{tg}\theta)^2$	$\pi h_c^2\left(tg\frac{\psi}{2}\psi\right)^2$	$2\pi r h_c$
Intercept factor	0.75	0.75	0.75	0.72	0.75
Geometry correction factor	1.034	1.012	1.034	1.000	1.000

[a] *B-M, bulk materials; T-Fil, thin films; S-T, scratch testing; W-T, wear testing; Im, Imaging; Fil, films; Fo, foils.*
[b] h_c*, the depth along which contact is made between the indenter and material, see Fig. 9.5.*
Fr-T, *fracture toughness;* Mod, *modeling;* Sep-Part, *separate particles.*

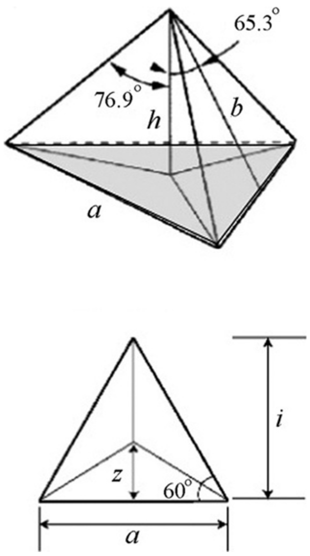

FIG. 9.4 (Upper image) Diagram of Berkovich indenter geometry; (Lower image) Projected area.

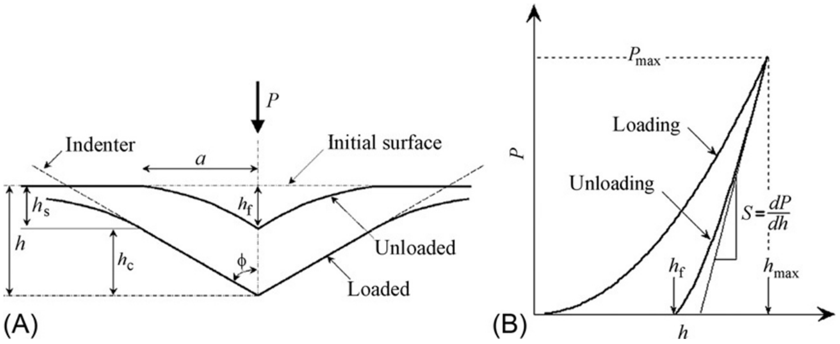

FIG. 9.5 Schematic presentation of indentation load–displacement data showing measured parameters.

where β is the geometrical correction factor for the indenter geometry and S is the elastic unloading stiffness, $S = \mathrm{d}P/\mathrm{d}h$. The specimen's Young's modulus, E, is obtained using the equation:

$$\frac{1}{E_{\mathrm{eff}}} = \frac{1-\nu^2}{E} + \frac{1-\nu_{\mathrm{i}}^2}{E_{\mathrm{i}}},$$

where the reduced Young's modulus takes into account the fact that elastic displacements occur in both the specimen, with Young's modulus E and Poisson's ratio ν, and the indenter, with elastic constants E_{i} and ν_{i}.

Several important changes to the method that improve its accuracy and extend its field of application were made. These changes have been developed both through experience in testing a large number of materials and by improvements to testing equipment and techniques [31,34]. For example, the measurement of contact stiffness by dynamic techniques allows for the continuous measurement of properties as a function of depth and also facilitates more accurate identification of the point of first surface contact.

A transmission electron microscope combined with a specimen holder capable of applying a force on the nanoparticle and a camera capable of recording the events enables the nanoindentation of nanoparticles with observing and recording deformation events at various scales as they occur in real time. The authors [35] showed the existence of both diffraction contrast and phase contrast in in situ TEM nanoindentation experiments on silver nanoparticles with diameters below 50 nm. Evidence of the presence of dislocations was observed during deformation, but upon unloading dislocations disappeared.

PRODUCTION METHODS

Several methods are available for the production of ultrafine powders used for manufacturing nanomaterials. Conventionally, they can be subdivided into chemical and physical. However, such subdivision remains greatly tentative. Thus, chemical reactions take a large part, for example, by evaporation in reacting gas media, while many chemical methods are based on the physical phenomena (such as low-temperature plasma, laser emission, and others). The most typical methods of obtaining ultrafine powders are the following:

- Evaporation and condensation in a vacuum or inert gas.
- Gas-phase method of reacting in a gaseous medium.
- High-energy disintegration (high-energy comminution, detonation gun spray process, and electrical explosion).
- Plasma spray process.
- Mechanochemical method.
- Electrochemical precipitation.
- Chemical precipitation from solution.
- Self-propagating high-temperature process.
- Thermal decomposition.

One of the basic processes is inert gas condensation (IGC). With IGC, high-quality powders with low chemical impurities from precursor materials and low amounts of oxides or nitrides from the production process can be produced. Other processes, such as flame reduction or plasma reduction, use the decomposition and reduction of metal in a gas flame or plasma. The chemical vapor reaction (CVR) process uses the reaction of metal chlorides and hydrogen in a hot wall reactor. A wet-chemical approach in which the nanoparticles are produced by gelation, precipitation, and hydrothermal treatment is used in the so-called sol-gel processes. Electrical explosion of wires (EEW) is one of the high-energy disintegration processes. Some of these methods of producing ultrafine and nanopowders are considered in more detail below.

Condensation Technique

The process of powder formation comprises three stages:

1. Vaporization, either by evaporating the metal or by its chemical interaction with the components of a gas phase.
2. Feeding the vapor into the zone of condensation (decomposition).
3. Formation of solid particles by condensing or decomposing the gaseous chemical compounds (nucleation and growth of a new condensed phase).

In the case of physical condensation, the temperature of the vapor source is higher than that of the powder formation zone; in most cases of chemical precipitation, it is vice versa.

The following conditions are necessary for the condensation of metallic vapor and the formation of a particulate phase: high supersaturation of the vapor sufficient to trigger simultaneous and multiple formation of nucleation centers, and the presence of a neutral gas acting as a medium preventing the coagulation and growth of particles due to diffusion, or evaporation in a vacuum and following physical vapor deposition.

The presence of foreign inclusions, ions, and chemically active compounds in the neutral gas promotes nucleation. Forced or natural circulation of the gas ensures the transfer of the condensation heat and of the particulate matter and contributes to a variety of modes of their growth.

Temperature (T) and pressure (p) are the principal thermodynamic characteristics of the process. The evaporation and precipitation take place at T_1 and p_1 (zone evaporation) and at T_2 and p_2 (zone precipitation), respectively.

Under the equilibrium conditions, the phase rule is observed in each zone:

$$G = N - \varphi + 2$$

where G, φ, and N are the number of components, phases, and degrees of freedom, respectively.

Homogeneous and heterogeneous nucleations are distinguished. The former represents the volumetrical condensation. Realizing the evaporation in an inert gas over a deposition surface, it is possible to provoke heterogeneous nucleation, for which the nucleation energy barrier is much lower in comparison with the volumetrical condensation.

By changing the system of supersaturation (by increasing or lowering vapor pressure, varying, for example, the process temperature), it is possible to adjust the critical nucleus size and obtain the required powder particle size.

Detailed information on the theoretical basis of the gas-phase method and the mechanism of powder formation during vapor condensation can be found in Chapter 5.

The inert gas condensation (IGC) is realized by evaporating and condensing a suitable material in a vacuum chamber filled with low-pressure inert gas (e.g., 100 Pa helium) [36]. The evaporation of the material is performed by electron beam or magnetron sputtering laser, either in a resistance or induction furnace. The vapor forms particles homogeneously due to collisions with the cold inert gas. The particle fog condenses on cooled substrates (crystallizers) that are inserted into the vacuum chamber.

Fig. 9.6 shows the scheme of a well-known installation utilizing an induction furnace for the metal evaporation. A nitrogen stream directs the zinc vapor to the rotating crystallizer. The particles form a flaky powder layer on the cooling crystallizer surface that is removed continuously by a scraper. The operating conditions for producing zinc nanopowders are as follows: the melt temperature in the induction furnace ranges from 923 to 1073 K, the pressure of nitrogen from 3 to 20 kPa, and the powder yield in the range from 10 to 15 kg/h.

Fig. 9.7 shows the scheme of equipment used on the lab scale by the Fraunhofer Institute (IFAM) for the production of precious metal nanopowders with a rate of about 1–2 kg per day [37]. The particles are transported to and deposited on cooled surfaces due to free thermal convention (Fig. 9.7A). By this scheme it is difficult to achieve real control of the powder deposition process resulting, for example, in a rather low output of usable powder material. A closed-loop gas flow design, as outlined in Fig. 9.7B has improved on the above concept and may operate at a higher level of gas pressure (ranging from 2 to 5 kPa). The condensed silver particles coagulate within the gas flow, forming highly porous (spongy)

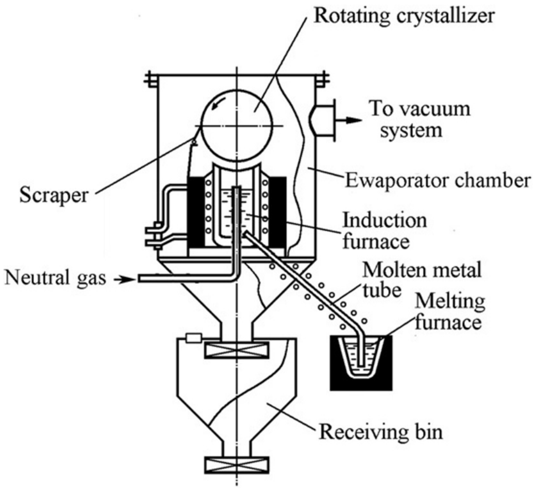

FIG. 9.6 Scheme of equipment to produce metallic nanopowders by the inert gas condensation process.

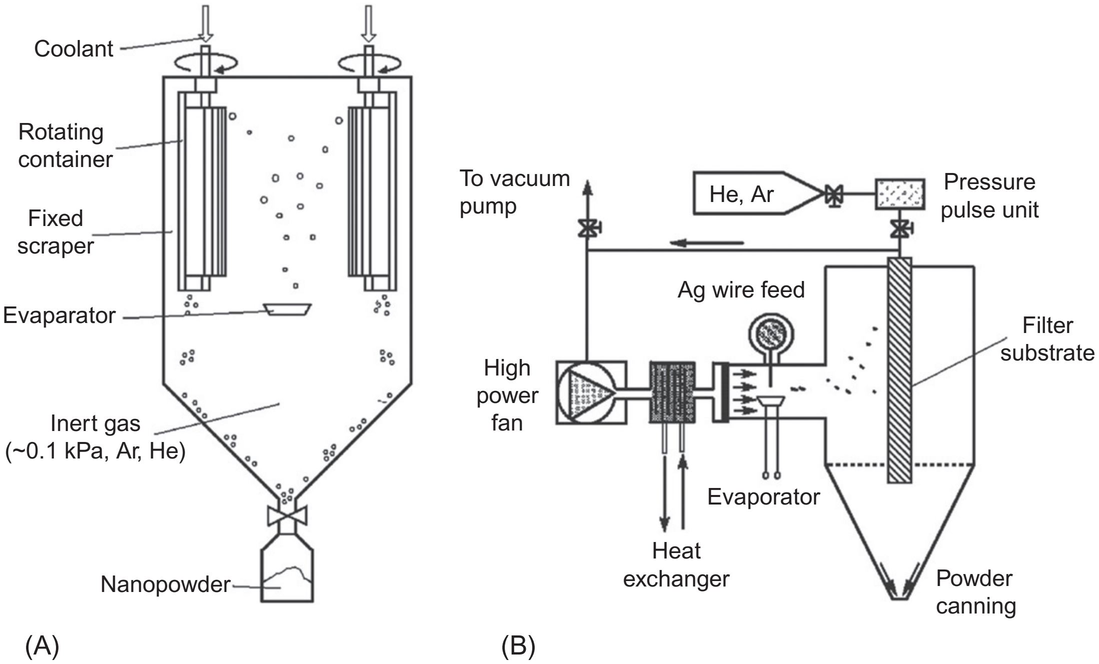
Coolant
Rotating container
Fixed scraper
Evaparator
Inert gas (~0.1 kPa, Ar, He)
Nanopowder
(A)
To vacuum pump
He, Ar
Pressure pulse unit
Ag wire feed
Filter substrate
High power fan
Evaporator
Heat exchanger
Powder canning
(B)

FIG. 9.7 Draft of two different variants of the inert gas condensation process: (A) purely convective powder transport and thermophoretic deposition on cooled surfaces followed by mechanical stripping off of the powder deposits; (B) nanoparticles are transported to the filter substrate by enforced gas flow. Powder removal is realized by means of pressurized backflow pulses.

aggregates that deposit as a fluffy layer on a filter substrate. By using back-flow pressure pulses, the powder is easily removed. The excess inert gas volume thereby introduced into the system is pumped off within a few seconds. Thus the process basically runs at a constant background pressure.

The main problem in the production and processing of metallic nanopowders is high reactivity, explosibility because of a very high specific area, and an agglomeration of particles.

In the Gleiter's installation, the ultrafine powder obtained in the atmosphere of the evacuated inert gas is combined with vacuum compacting [4]. Condensed on the cooled rotating cylinder, surface powder particles are taken away by a scraper and collected in a press mold of the preliminary pressing, under pressure up to 1 GPa (Fig. 9.8), then the green compact is repressed at higher pressures (3–5 GPa).

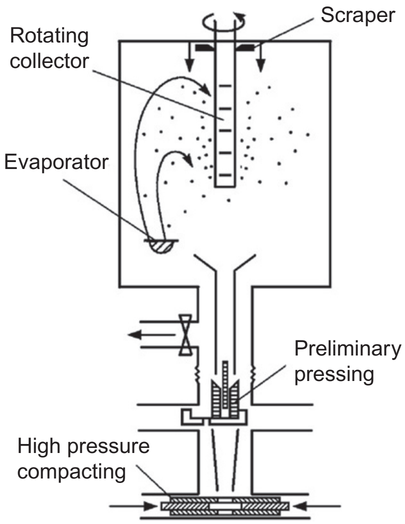
Rotating collector
Scraper
Evaporator
Preliminary pressing
High pressure compacting

FIG. 9.8 Scheme of Gleiter's installation. *(Source: Gleiter H. Nanocrystalline materials. Prog Mater Sci. 1989; 33: 223–315.)*

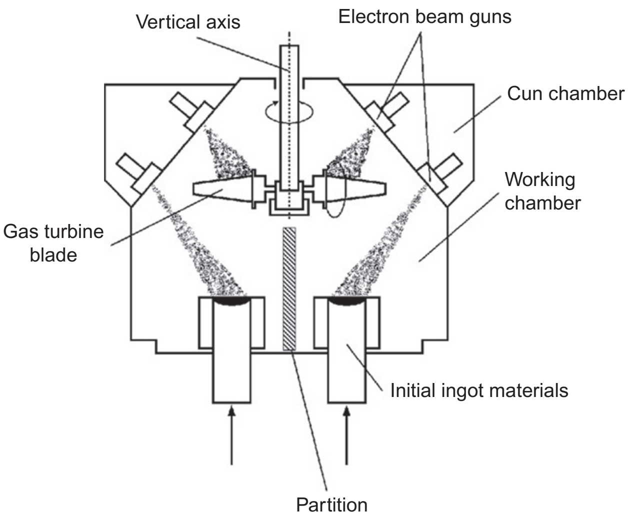

FIG. 9.9 Scheme of microlayered material deposition on gas turbine blades. *(Courtesy of EBPVD.)*

A schematic figure of a technology for the manufacture of semiproducts directly from metal vapor, without the operation of producing nanopowder, is shown in Fig. 9.9 [38]. The simultaneous evaporation of several materials, mixing their vapor flows, followed by condensation on a substrate and subsequent thermomechanical treatment allows the construction of materials with unique properties.

In a high vacuum, molecular evaporation from an open surface takes place at a rate that can be determined by the Langmuir formula [39] or the Hertz-Knudsen equation [40]. The latter is:

$$\frac{1}{A}\frac{dN}{dt}=q=\frac{\alpha p N_A}{\sqrt{2\pi MRT}},$$

where A is the surface area, m^2; N is the number of material vapor (gas) molecules; q is the current of the gas molecules evaporating from 1 m^2 in 1 s, m$^{-2}\cdot$s^{-1}; α is the sticking coefficient of the gas molecules onto the surface, $0 \leq \alpha \leq 1$; p is the equilibrium pressure of material vapor at a given temperature, Pa; M is the molar mass, kg·mol^{-1}, T is the evaporation temperature, K; N_A is the Avagadro constant, mol^{-1}; and R is the gas constant, J·mol^{-1}K^{-1}. Experimental values of vapor pressures and evaporation rates of the elements and inorganic compounds are given in publications [41,42].

At the beginning of the 1960s, the EO Paton Electric Welding Institute started systematic research and equipment development of electron beam evaporation followed by physical vapor deposition in a vacuum (EBPVD) to produce thick films (1–2 mm) and bulk condensates of inorganic materials with preset structure and properties [43].

The electron beam evaporation of materials in a vacuum differs from other methods in such conditions, namely, thermal and ion plasma, primarily by its versatility, technological flexibility, and cost effectiveness. During the collision of flying electrons with the solid surface, their kinetic energy is consumed in heating, secondary emission, and in excitation of X-ray radiation. The main part of the kinetic energy of the electrons on their collision with a solid surface is transformed into thermal energy in a thin subsurface layer of 1–2 μm thickness. At a voltage of 20–25 kV and a beam current of several amperes, energy losses for X-ray radiation excitation are about 0.1% of the total power of the electron beam. X-ray radiation arising in the above voltage range has a low penetrability and is completely absorbed by the chamber's metal walls, which are several millimeters thick. Energy losses for the excitation of the secondary emission (really true secondary emission and reflected electrons) are about 15%. Here, in heating by an electron beam, the heat source is located in the working chamber (see Fig. 9.9), and provides the maximum complete transformation of the electric energy into thermal energy [43].

Modern electron guns of 50–100 kW power enable the evaporation of metallic materials at high enough rates, approximately 10^{-2} g/cm^2 s. For evaporation of a 70 mm diameter ingot, the rate of vapor flow condensation on a flat stationary substrate located above the liquid pool surface at 300 mm distance can be up to 30–50 μm per minute for metals and alloys and 15–20 μm per minute for ceramics (i.e., oxides, carbides, and borides).

Similar to alloys, pure metals are evaporated as individual atoms. For most alloys, however, the composition of the vapor phase is not equivalent to the average ingot alloy composition. Alloy fractionation occurs, namely, condensate layers beside the condensation surface, and contains maximum amounts of volatile components. Condensates of multicomponent metallic materials of a composition homogeneous across their thickness are produced, using various evaporation techniques, including evaporation of individual alloy components from independent sources.

Evaporation of compounds (e.g., oxides, carbides, borides, etc.) is, as a rule, accompanied by a change of the initial molecules. Many refractory compounds are characterized by dissociation of initial molecules with the formation of gaseous products, for instance: O, Al, AlO_3, and Al_2O form during Al_2O_3 evaporation. Results of the analysis of the thermal dissociation of compounds are generalized [41,44]. Producing condensates by direct evaporation from one source without any change of the initial composition of the compounds is possible only under the condition that dissociation products have practically the same volatility, that is, a harmonized "congruent" evaporation of the compounds is required. Refractory oxides (i.e., Al_2O_3, Y_2O_3, ZrO_2, and MgO), carbides (i.e., TiC, ZrC, and NbC), and borides (i.e., TiB_2 and ZrB_2) can be evaporated from water-cooled copper crucibles using electron-beam heating with practically no change in the composition.

A number of compounds, for instance, WC, SiC, TiN, AlN, and ZrN, cannot be deposited by direct evaporation because they decompose on heating, forming products with markedly different volatilities. Such compounds can be produced in the form of condensates by component evaporation from two independent sources (i.e., WC and SiC) or using the so-called reactive evaporation, bleeding the appropriate gas into the working chamber, and vapor flow ionization [41].

Fig. 9.10 shows the schematics of electron beam evaporation of material A from one and A and B from two sources, and subsequent vapor flow condensation on flat surfaces. The condensation surfaces can also be cylindrical or have a more complex shape and can be stationary (Fig. 9.10(A)) or make certain movements in space, using an appropriate feed mechanism for motion transfer (Fig. 9.10(B)). The schematic (Fig. 9.10(B)) corresponds to the technological process of deposition of a two-component material AB, for instance, WC or SiC, on a flat surface in the form of a circle rotating about a vertical axis. Substrate rotation is required to produce a uniform composition across the condensate thickness.

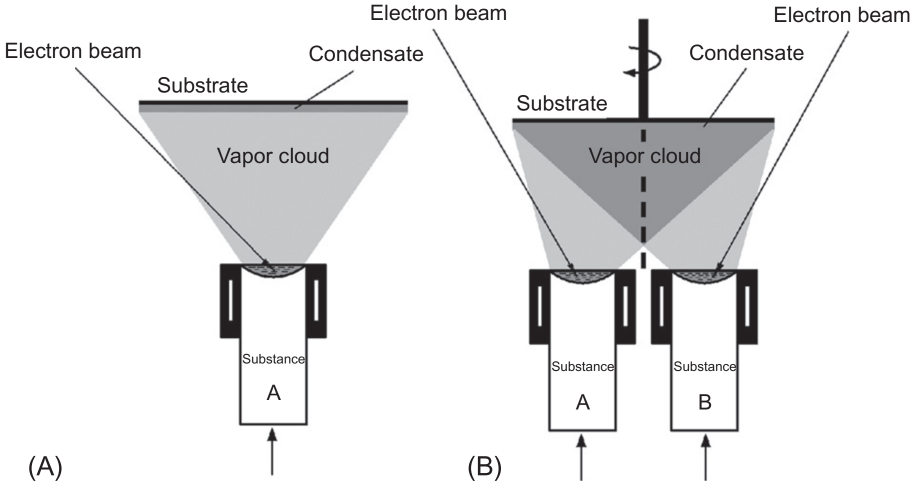

FIG. 9.10 Material evaporation process following by condensation: (A) from one source; (B) from two sources. *(Courtesy of EBPVD.)*

It should be noted that such a technological process could be easily transformed during production of multilayer condensates of A/B type by placing a partition between the sources (Fig. 9.9). At a constant rate of evaporation of substances A and B, the substrate rotation rate will be a simple and reliable process parameter for adjustment of the thicknesses of alternate layers. Laboratory and production units, developed by the EO Paton Institute, have three or four independent evaporators (water-cooled crucibles) and corresponding electron beam guns for evaporation of three to four materials by a preset program [43].

However, with regard to simplicity and cost effectiveness of the deposition process, the technology variants of evaporation from one source of mixtures of dissimilar materials, prepared in the form of special tablets or composite ingots, are particularly interesting.

Chemical Precipitation From Solution

Ultrafine copper powders find wide application for microelectronic components, multilayer ceramic capacitors (MLCCs), and μ-metal injection molding (μ-MIM).

μ-MIM is an advanced method of metal injection molding, using sub-μm-sized metal powders and very fine molds to produce extremely small three-dimensional structures with very high resolution, sharp edges, and outstanding aspect ratios while the cheap and well-established method of injection molding is applied.

Based on the design criteria of microelectronic components, the sub-μm particle size of metal powders used is one key component, as, for example, the internal electrodes in MLCCs are only about 1–2 μm in thickness. Theses layers are manufactured by screen printing of metal paste, a technique widely used in electronic components manufacture [45].

Therefore, products such as ceramic capacitors and μ-MIM parts need to use sub-μm-sized metal powders to assure the requirements defined by their dimensional design. It is consequently essential to characterize the particle size not only by means of distribution in general, but also to find a method to characterize the biggest particles present in such powders. For example, ceramic capacitor manufacturing normally defines values of $d_{100} < 1.5\,\mu m$ or even $d_{100} < 1.0\,\mu m$.

Industrial consumption of sub-μm powders in quantities of tons/month as well as the cost aspect emphasize that the wet chemical process of powder production by precipitation from solution is able to fulfill these requirements in a competitive and economical way.

This process is in principle shown in Fig. 9.11. By precise selection of process parameters, including concentrations, temperatures, negative logarithm of hydrogen-ion activity (pH) value, and time, it is possible to control and adjust properties such as particle size, apparent density, specific surface, and overall morphology to customer requirements.

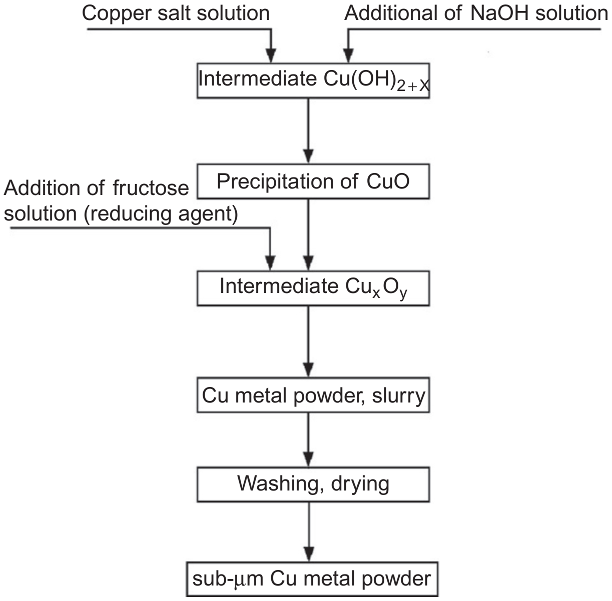

FIG. 9.11 Process flow sheet for the wet chemical production of copper powder.

Nanosized copper powder produced by the wet chemical precipitation process on a lab-scale is shown in Fig. 9.12.

The wet chemical precipitation process can be controlled in such a way as to adjust properties such as particle size; it is also able to produce agglomerated as well as nonagglomerated powders (Fig. 9.13). The latter are best suited for metal pastes used for the screen-printing deposition of thin layers.

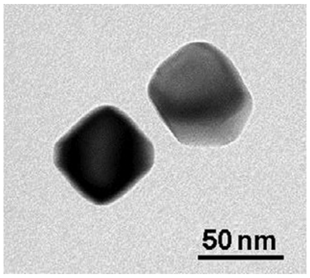

FIG. 9.12 Transmission electron micrograph of nanosized copper powder, produced by wet chemical precipitation process in lab-scale. *(Source: Huenert R. Ultrafine copper powder. In: Proceedings of 2002 Powder Metallurgy World Congress, Princeton, MPIF Publishers, New Jersey, U.S.A., 2002, Vol. 10: pp. 1–11.)*

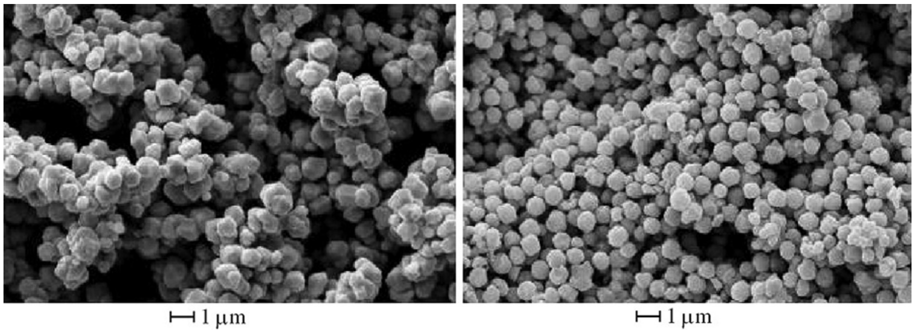

FIG. 9.13 Copper powders of different particle size and morphology produced by wet chemical precipitation from copper salt solution: (Left image) agglomerated powder grade, (Right image) nonagglomerated powder grade. *(Modified from Huenert R. Ultrafine copper powder. In: Proceedings of 2002 Powder Metallurgy World Congress, Princeton, MPIF Publishers, New Jersey, U.S.A., 2002, Vol. 10: pp. 1–11.)*

It is well known that for a given cobalt content, the hardness of WC-Co cemented carbides can be increased by decreasing the WC mean particle size. The classical ways of production of WC, described in Chapter 23, allow the production a WC particle size ranging from 0.5 to 20 μm. During the production of ultrafine powders, 0.3–1 μm, starting for instance with WO_3, the formation of $W_{18}O_{49}$, should be skipped over, and the two main reduction steps $WO_3 \rightarrow WO_2$, and $WO_2 \rightarrow W$ should take place in the lowest possible humidity environment [46]. The formation of ultrafine powders is favored by:

- Decreasing the amount of tungsten oxide in the boats.
- Increasing the hydrogen flow rate.
- Decreasing the passing through rate of the boats.
- Decreasing the reduction temperature below 1673 K.
- Having a smooth temperature gradient in the furnace.
- Using hydrogen with the lowest dew point.
- Using a two-step reduction process.

In the production of ultrafine and nanopowders, the carburization temperature must be kept in the range of 1023–1273 K. For such powder production, special ultrafine cobalt powders are needed because the conventional ones, ranging from 1 to 3 μm, are too coarse.

Pastor et al. developed a process for the production of cobalt powder based on the reduction at 483 K of cobaltous hydroxide by a mixture of ethylene- and de-ethylene glycol [47]. This powder, named "polyol cobalt," is characterized by a spherical shape, narrow particle size distribution, and nonagglomerated particles (Figs. 9.14 and 9.15).

Replacement of the conventional "hydrogen-reduced cobalt" by polyol cobalt greatly improves the microstructure of the sintered product and allows a decrease of the milling (mixing) time by half, a decrease in the sintering temperature, and even the avoidance of HIP of low cobalt content grades.

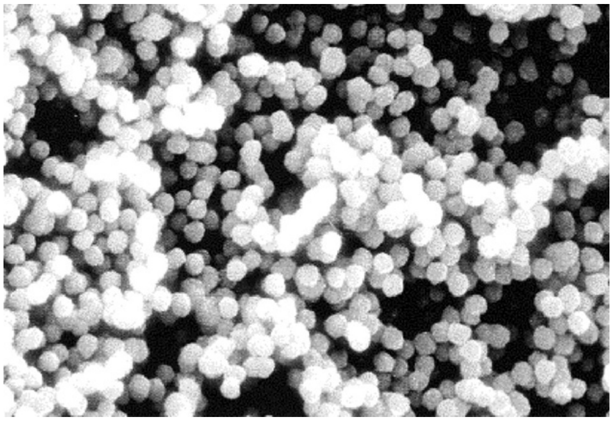

FIG. 9.14 SEM micrograph of polyol cobalt powder. *(Modified from Pastor H. Developments in tungsten carbide-cobalt cemented carbides. In: International Powder Metallurgy Directory & Yearbook, 12th ed. 2006/2007: pp. 99–108.)*

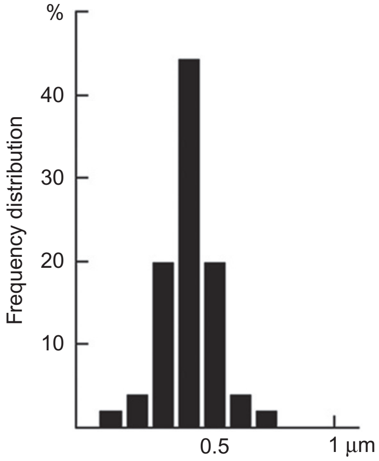

FIG. 9.15 Polyol powder particle size distribution. *(Modified from Pastor H. Developments in tungsten carbide-cobalt cemented carbides. In: International Powder Metallurgy Directory & Yearbook, 12th ed. 2006/2007: pp. 99–108.)*

The nanostructured WC-Co cermets starting from water-soluble precursor compounds have the advantage that the cobalt can be mixed homogeneously with tungsten at the molecular level, the Co to W can be varied over a large range, and additional constituents (Ti, Ta) or grain growth inhibitors (Cr, V) can be introduced homogeneously at the same time.

It is a three-step process:

1. Preparation and mixing of the starting reactants
   - Cobalt *tris*-ethylenediamine tungstate, obtained by a reaction between an aqueous solution of $CoCl_2$ and a solution of H_2WO_4 in ethylene diamine [48,49].
   - Ammonium metatungstate or ammonium paratungstate (APT) + cobalt salt + ammonia (aqueous solution, pH 7) precipitating: $(NH_4)_8[H_2Co_2W_{11}O_{40}]\cdot H_2O$, [50–52].
   - APT + cobalt salt + Cr(Cl O_4) and VCl_3 (grain growth inhibitors) [53].
2. Fixed bed or spray drying (873–973 K) of the resulting precursor to a chemically homogeneous mixture of oxides.
3. Classical or fluid-bed thermochemical conversion (973–1273 K, H_2, CH_4, $CO + CO_2$) of the dried mixture into the desired nanoscale (20–50 nm WC powder) composite WC-Co powder.

Nanosized platinum particles are very active and commercially important as catalysts. One method of production of platinum powder with a size of about 30 nm is the reduction of chloroplatinic acid with sodium borohydride. The reduction process can be written as:

$$H_2PtCl_6 + NaBH_4 + 3H_2O \rightarrow Pt_{(s)} + H_3BO_3 + 5HCl + NaCl + 2H_{2(g)}$$

An organic protective agent such as poly (vinylpyrrolidone) is commonly added to prevent coagulation of these ultrafine platinum particles.

Spray Conversion Method

With the advent of closed-cycle systems, the production of cemented carbides by spray drying increased considerably in the 1980s. Spray conversion processing is a versatile technology that can be applied to a variety of metal-metal systems (e.g., W-Cu) [46,47,54,55].

The nitrogen drying gas that is used in spray drying is heated to 348–473 K, depending on the milling liquid used. The solid content of the slurry varies from 75% to 80%. Pressures for single-fluid nozzle atomization range from 590 to 1500 kPa.

The process of making WC-Co nanopowders consists of synthesizing a liquid solution, spray drying, hydrogen reduction and carburization for the purpose of the refinement, and homogeneous distribution of WC particles and cobalt binder (Fig. 9.16).

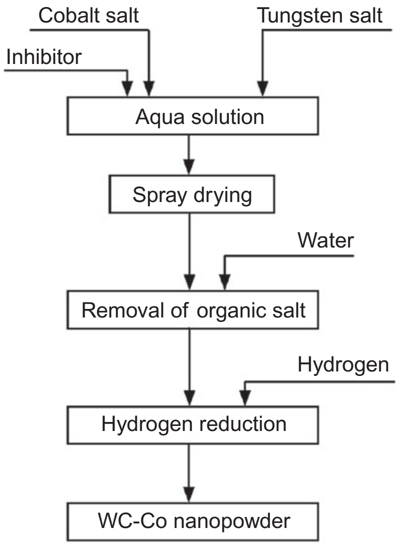
Cobalt salt
Tungsten salt
Inhibitor
Aqua solution
Spray drying
Water
Removal of organic salt
Hydrogen
Hydrogen reduction
WC-Co nanopowder

FIG. 9.16 Spray conversion process for production of tungsten carbide–cobalt nanopowders.

Plasmachemical Synthesis

Plasmachemical synthesis realized at temperatures of 6000–8000 K allows a high supersaturation level and a high reaction and condensation process rates. The arc plasmatrons as well as high- and plasma-microwave generators are used. The former is more efficient; however, the latter ensures the production of fine and pure powders. The diagram of such an installation is shown in Fig. 9.17.

As the initial product, metal chlorides, metal powders, and silicon- and metal-organic compounds are used. Plasmachemical powders of nitrides, metal oxides, and other compounds are manufactured.

The plasmachemical technique provides for the production of refractory metal ultrafine powders (W, Mo, Ni), compounds (TiN, AlN, Al_2O_3, SiC, Si_2N_4, Ti(C, N), and others), and composite material types such as Si_3N_4 + SiC, TiB_2 + TiN, and others. Due to the features of plasmachemical synthesis (nonisothermal process, coagulation of particles, and others), the particle size distribution range is, in most cases, rather wide.

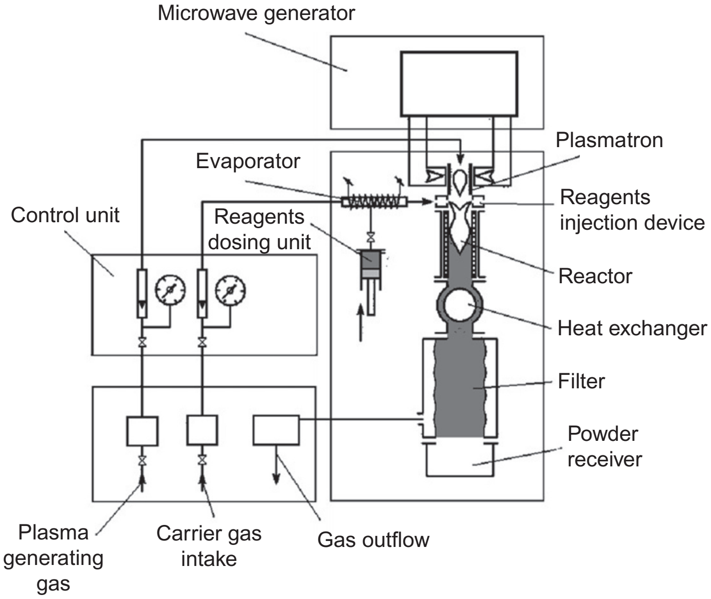
Microwave generator
Plasmatron
Evaporator
Reagents injection device
Control unit
Reagents dosing unit
Reactor
Heat exchanger
Filter
Powder receiver
Plasma generating gas
Carrier gas intake
Gas outflow

FIG. 9.17 Flowchart of plasmachemical synthesis installation. *(Modified from V.N. Troizkiy, Production of ultrafine powders in plasma microwave discharge, In: Proceedings of the plasma microwave generators: Physics, technique, and application, Energoatomizdat, Moscow, 1988, pp. 175–221, [in Russian].)*

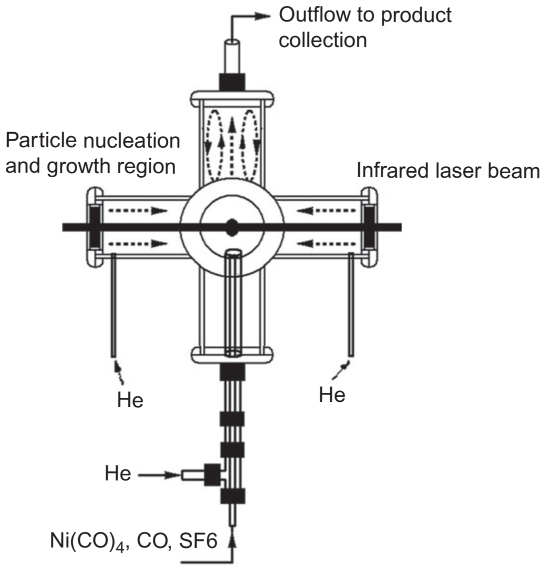
Outflow to product collection
Particle nucleation and growth region
Infrared laser beam
He
He
He
$Ni(CO)_4$, CO, SF6

FIG. 9.18 Schematic drawing of the lab laser pyrolysis reactor for nickel nanopowder production. *(Modified from Miessler GL, Tarr DA. Inorganic chemistry. 3rd ed. Pearson/Prentice Hall Publisher; 2010.)*

Laser pyrolysis has been developed for the production of nickel nanopowders [56]. A schematic drawing of the lab laser pyrolysis reactor is shown in Fig. 9.18.

This process makes possible the production of nickel particles by laser-driven decomposition of a nickel precursor, such as nickel carbonyl (NiCO). Here, an infrared laser rapidly heats a dilute mixture of nickel carbonyl and a photosensitizer in a carrier gas to decompose the precursor and initiate particle nucleation. The photosensitizer is selected from the group consisting of sulfur hexafluoride, ethylene, silicon tetrafluoride, and ammonia. Nickel carbonyl was generated in situ from activated nickel powder and carbon monoxide at room temperature. During the synthesis process, laser heating allows for rapid cooling of the freshly nucleated particles by mixing with unheated gas. By varying the precursor flow rate, laser energy, and unheated gas flow rate to change the residence time, precursor concentration, and reaction temperature, the average particle size can be controlled over a range of primary diameters from 5 to 50 nm. Fig. 9.19 illustrates the nickel nanoparticle average size versus the carbon monoxide flow rate.

Such powders are of growing interest in the development of nanostructured magnetic materials, motivated by the potential of these materials in a broad range of applications, including data storage, biomedicine, and telecommunications.

The plasma arc installation mainly consists of the vacuum chamber, tungsten cathode, copper anode, gas flow system, and electric power supply. The flowchart of the plasma arc process is shown in Fig. 9.20.

The plasma arc discharge process is used for the synthesis of ultrafine zirconium-based alloy powder [57]. Such powders are of particular interest in hydrogen storage and gas absorption applications. The $Zr_{57}V_{36}Fe_7$ bulk alloy was used as a raw material. The vacuum chamber was evacuated down to 10^{-5} Torr and then backfilled with the hydrogen/argon

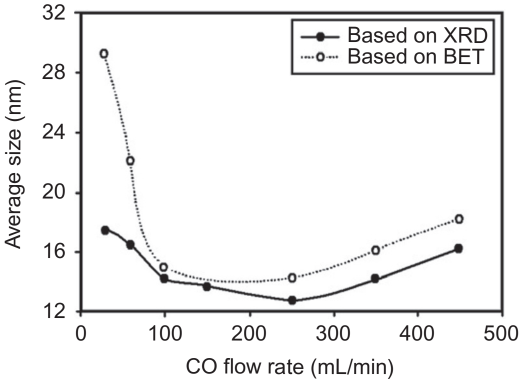

FIG. 9.19 Nickel nanoparticle average sizes versus carbon monoxide flow rate.

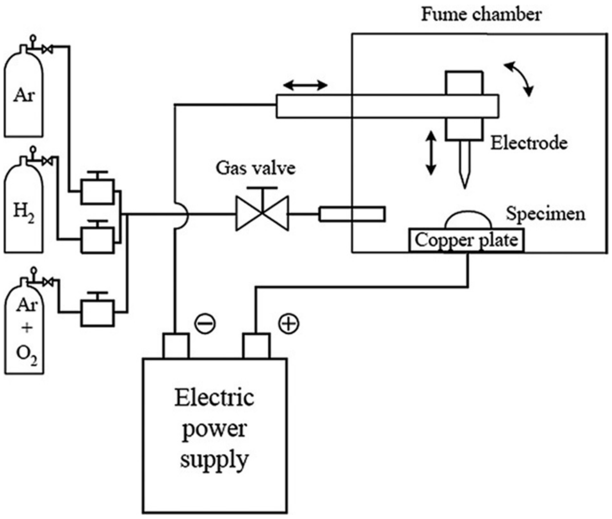

FIG. 9.20 Flowchart of plasma arc process for synthesis of ultrafine zirconium-based alloy powder. *(Modified from Lee Gil-Geun, Park Je-Shin, Kim Won-Baek. Synthesis of ultrafine Zr based alloy powder by plasma arc discharge process. In: Proceedings of 2006 Powder Metallurgy World Congress, Publ. Korean Powder Metallurgy Institute, Busan, Korea, 2006: pp. 505–506.)*

mixture gas to 300–550 Torr. The arc plasma was then initiated between the tungsten cathode and the bulk alloy on the copper anode using an arc current 140 A and an arc voltage of 21–25 V. The mixture ratio of the hydrogen to argon was changed from 4 to 6 to equal volumes.

The chemical composition of the synthesized powder strongly depends on the volume content of hydrogen in the synthesis atmosphere. The chemical composition of the synthesized powder approaches that of the raw material with increasing hydrogen—up to 50% hydrogen atmosphere. The synthesized powder has an average particle size of 50 nm.

By means of the plasma technique, nanoscale metal oxide powders are produced on a commercial scale [58]. A high-resolution TEM image of cerium oxide is shown in Fig. 9.21. Particle size distribution of this powder is illustrated in Fig. 9.22.

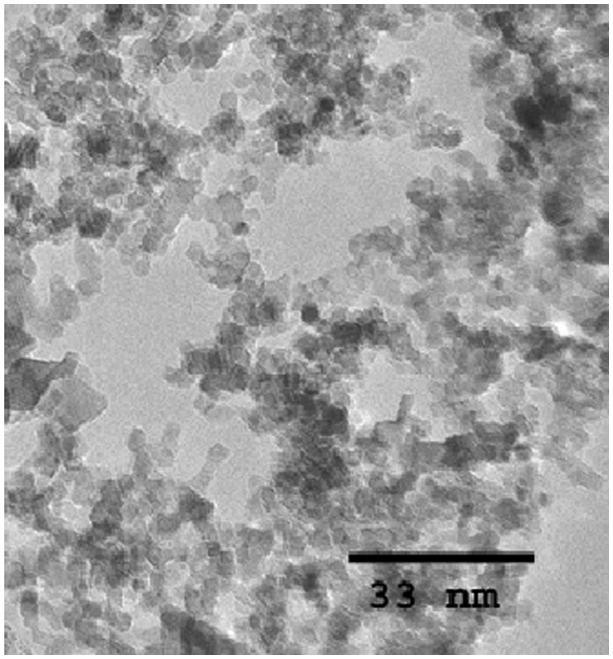

FIG. 9.21 Transition electron microscopy image of cerium oxide powder particles. *(Modified from NanoProducts Corporation, Colorado, USA, www.siclists.com/colorado/longmont/Nanoproducts-Corporation.)*

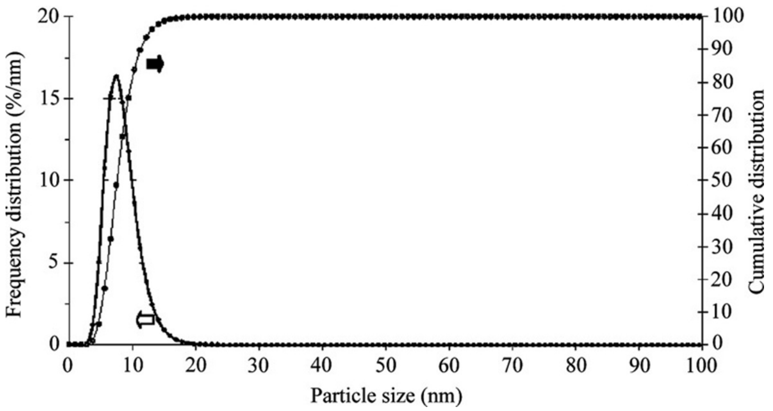

FIG. 9.22 Cerium oxide nanopowder particle size distribution. *(Modified from NanoProducts Corporation, Colorado, USA, www.siclists.com/colorado/longmont/Nanoproducts-Corporation.)*

High-Energy Disintegration

High-Energy Comminution

The lower limit of the particle size of powders produced by high-pressure gas or water atomization is between 1 and 5 μm. Examples are the trademark product FLQT5 of aluminum atomized powder with medium diameter 2 ± 1 μm or the trademark of silver atomized powder with average diameter 1.2 μm [59].

Vibratory, attrition, jet, planetary, and large-diameter tumbler mills may be classified as high-energy mills.

The agglomerated particles of nanosized WO_2 and W to WC powder, generated by direct carburization, were crushed by a jet mill [60]. This ensured disintegration of the agglomerated particles and led to a decrease of the average particle size of powders, separated in a bag filter, from 72 to 61 nm and increased specific surface area from 5.28 to 6.28 m^2/g.

Commercial jet mills are available from the NETZSCH-Feinmahltechnik Company. A fluidized bed jet mill CGS 16, which is able to realize the finest jet milling in the existing CGS series, is shown in Fig. 9.23. The product to be milled is fed through a double flap valve and inlet into the milling chamber above the milling nozzles (Fig. 9.24). The material is formed in the bottom of the milling chamber on a fluidized bed by the gas stream from the milling nozzles. Particles from the fluidized bed are drawn into the gas stream and accelerated with increasing velocity toward the center of the chamber. The milling gas, laden with ground particles, rises centrally to the classifier wheel, which is driven by a controlled variable speed motor. Coarse particles are rejected by the classifier wheel and return directly to the fluidized bed. Fine particles together with worked-out gas leave by the fines outlet and are separated sequentially in a cyclone and filter. The CGS 16 mills hard materials down to median particle size $d_{50} = 0.8\,\mu m$ with a powder yield of 4.5 kg/h.

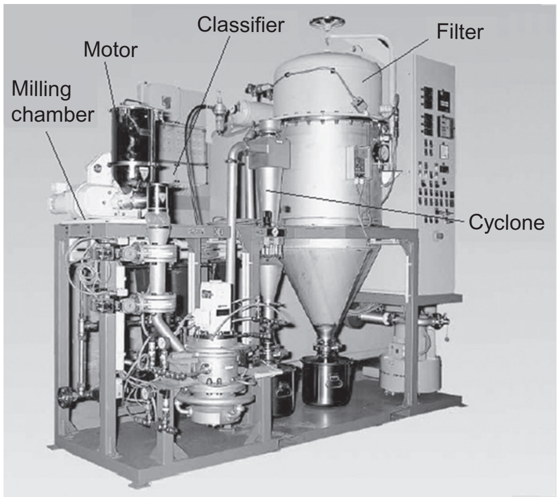

FIG. 9.23 Model CGS 16 fluidized bed jet mill. *(Courtesy of NETZSCH-Feinmahltechnik Company.)*

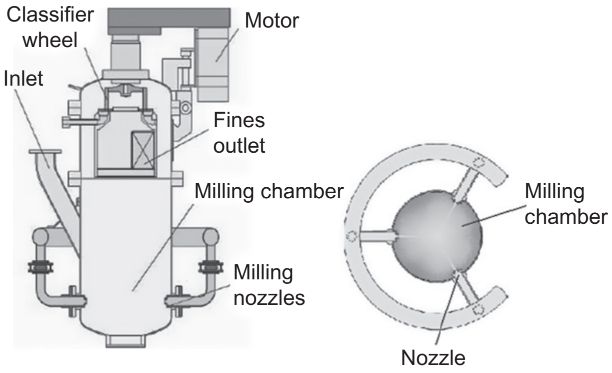

FIG. 9.24 Draft of a fluidized bed jet mill.

To produce composition materials of the TiN-AlN system, the initial raw materials consist of titanium hydride and aluminum powder with specific surface 1.5 and 2.1 m^2/g, respectively. They are treated in a planetary mill where mechanical activation accelerates the nitriding process, which takes place in liquid nitrogen [61]. The processing was fulfilled with 1440 promptness per minute in liquid nitrogen. The proportions of the ingredients correspond to the equilibrium for the reaction:

$$3TiH_2 + Al + 2N_2 = 3TiN + AlN + 3H_2$$

The specific surface of the product amounts to 2.8, 4.39, 6.16, and 9.49 m^2/g as a result of milling for 10, 30, 40, and 60 min, respectively. The average particle size was 160 nm. The mechanical activation accelerates the nitriding process.

Some bulk alloys are easily crushed to fine powder in a hydrogen atmosphere. The Nb-Ti alloys are examples of this kind [62]. These alloys were hydrogenated by a gas-solid thermal reaction system. They were placed in a furnace containing high-purity hydrogen gas and annealed at 1473 K for 3 h, followed by furnace cooling to room temperature. The hydrogenated Nb-Ti alloys are brittle and friable in comparison with the original alloys. The hydrogenated $Nb_{94}Ti_6$ powders milled in a planetary ball mill with tungsten-carbide balls in the air for 60 min at room temperature have an average particle size of 2.3 μm while by milling at a temperature lower than 203 K, the average particle size is <1 μm with better uniformity.

Porous compact structures of pure niobium and niobium alloys such as Nb-Ti and Nb-N are widely used as a metal substrate for electrolytic capacitors, which realize a large electrical capacity in a surface layer of niobium pentoxide. Here, the porous compacts are generally produced from powders. One of the ways to improve the performance is to employ powders having a finer particle size under 1 μm and higher impurity so as to increase the relative surface area of porous compacts with solid niobium pentoxide layers.

Ultrasonic milling was used for obtaining a tungsten heavy alloy [63]. This process uses ultrasonic cavitation, which leads to the violent collapse of macroscopic bubbles, producing extremely high energy densities [64]. This energy source can be used to produce nanopowders free of impurities. The design of the interface structure of tungsten heavy alloys such as 93 W-4.9Ni-2.1Fe is essential for property improvement. In particular, it is necessary to reduce particle sizes, to homogenize the powder mixture, and to maintain purity in order to reinforce interface strength. Previously, mechanical alloying in an attritor was used, but this resulted in deterioration of the properties of the powder as a result of the pick up of impurities.

In an ultrasonic milling process [63] with WO_3, NiO, and Fe_2O_3 as source materials, powders were mixed together to give a 93 W-4.9Ni-2.1Fe composition using a turbular mixer. The mixture was milled in an ultrasonic bath for 50 and 100 h. After drying at 353 K, the powder was sieved. The mean particle size of samples after 50 and 100 h was measured as 500 and 400 nm, respectively. Particle size distribution of the 100 h sample is narrower and the mean size of agglomerates is smaller. The mixture was then reduced at 1073 K in a hydrogen atmosphere for 1 h.

The mechanical alloying process makes it possible to obtain nanopowders of metals, metal oxides, complex oxides, and others. Therefore, the nanosize products are synthesized by reductive reactions and as some of them are exothermic reactions, it is necessary to depress the thermal elevation. For this purpose, it can be done by mixing a dilute agent in the starting materials, followed by a grinding operation. As Ding reported [65], NaCl plays a significant role as a dilute agent in the case of the formation of Ni nanoparticles obtained from a mixture of $NiCl_2$ and Na, as given by the following equation:

$$NiCl_2 + 2Na + 1.5NaCl \rightarrow Ni + 3.5NaCl$$

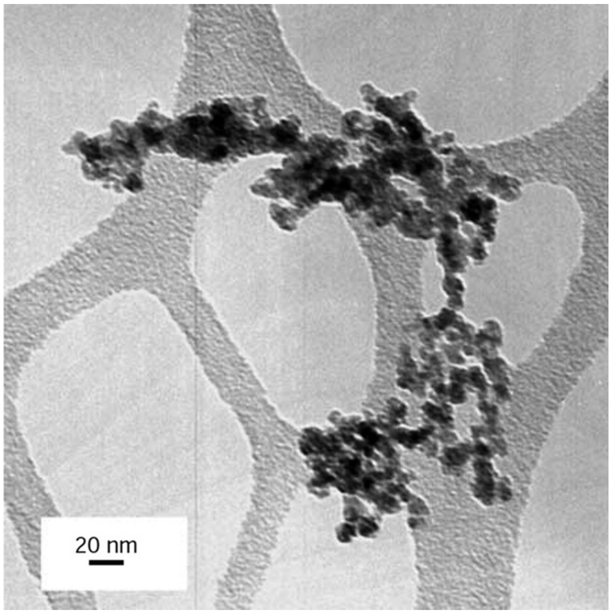

FIG. 9.25 TEM image of Ni nanoparticles obtained by the mechanical alloying process.

The dilute agent plays a role of dispersion to prevent aggregation caused by grinding, besides the depression of thermal elevation. As a result, well-dispersive nanoparticles can be separated by washing chloride out from the product with solvent. A TEM photo of the obtained nickel nanoparticles is shown in Fig. 9.25 [65]. From this figure, it is seen that fine and well-dispersive particles of 5–10 nm in sizes are recovered.

Electrical Explosion

Electrical explosion of wires technology (EEW) is a process of explosive destruction of a metal wire under the action of a great density current of 10^6–10^9 A cm^{-2} [66,67]. EEW is characterized by the following peculiarities: time of explosion is 10^{-5}–10^{-8} s; temperature at the moment of explosion can reach more than 10^4K and a pressure $\sim 10^9$ Pa; and the velocity of product recession is from 1 to 5 km/s. Material of the wire transmutes into particles of nanosized range (10–100 nm) in accordance with certain conditions. The process can be carried out either in a gas or liquid environment.

According to [66], low energy consumption (<10 kWh/kg) is due to the direct heating of the wire by electric current without heat carriers and due to the high heating rate ($>10^7$ K/s) that provides adiabatic conditions of energy transmission to the wire. The yield of nanopowders on the basis of aluminum is 50 g/h and on the basis of tungsten is 300 g/h under production using one set. The energy content of EEW depends on the type of metal, which determines the current of the discharge process in the electrical circuit and the amount of energy stored in the circuit. Metals can be conventionally divided into three groups: metals with high electrical conductivity (Al, Cu, Ag, Sn, etc.); metals with low electrical conductivity (Fe, Ni, etc.); and metals with ionization energy less than bond energy (W, Mo, etc.).

The principal diagram of the experimental installation for producing electroexplosive powders in ambient gas is shown in Fig. 9.26 [67]. The installation operates as follows. A high-voltage generator is used for switching a high-voltage pulse to the wire. The wire is wound on the reel in a wire supply unit. The installation is previously evacuated by means of a vacuum system and filled up with argon by a gas supply system. The former and latter are isolated from the installation by means of valves V1 and V2. A centrifugal fan is turned on and provides gas circulation along the installation loop: reactor → separator → filter → fan → cooler → reactor. After the wire feeding mechanism is turned on, the wire is fed to the reactor. In the process of its movement inside the reactor, the wire step-by-step closes the circuit between high-voltage and low-voltage electrodes. The discharger is activated and a high-voltage pulse is applied to the wire; the wire explodes. The obtained gas suspension passes from reactor to separator, which separates particles $>0.5\,\mu$m, and then to the filter. The filter removes nanoparticles from the gas flow and they gravitate to the container. Purified gas passes through the fan to the cooler, where its temperature decreases to approximately 278 K and then returns to the reactor.

The process is repeated with a frequency of 1.0 Hz and higher. When the container is filled with nanopowder, excessive gas pressure is decreased to atmospheric pressure and the valve V3 closes. The container is removed and packed in a sealed container for further operations.

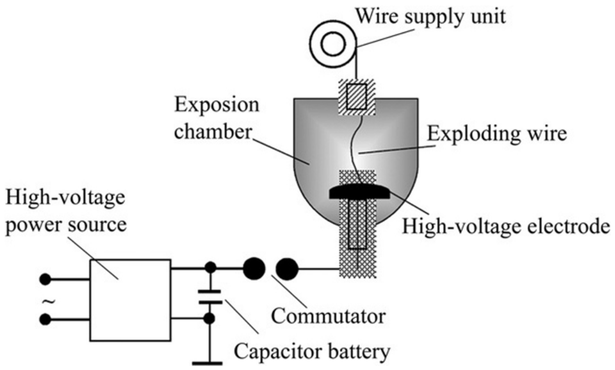

FIG. 9.26 Diagram of the experimental installation for producing electroexplosive powders in a gas medium.

The authors [68] have indicated the EEW process parameters that determine the average size of Al nanoparticles as follows: EEW energy content E/E_S (E is the energy delivered to the wire; E_S, is the energy of metal sublimation); wire diameter, d_0; gas medium pressure, p; and gas medium temperature, T.

The study [67] of Al powders produced at different gas temperatures in a container (Fig. 9.26) showed that the average size of nanoparticles depends on the temperature of the gas medium, by invariable all other EEW parameters. Thus, if the specific surface of Al powder at gas temperature $T = 318.8\,K$ is $15\,m^2/g$, then at $T = 298.2\,K$ it will comprise 19.5 $m^2\ g^{-1}$.

The characteristic spherical particle shape of aluminum and tungsten nanopowders produced by the EEW method is shown in Fig. 9.27 [69]. They are polydisperse with wide size distribution in the range from 5 up to 1000 nm.

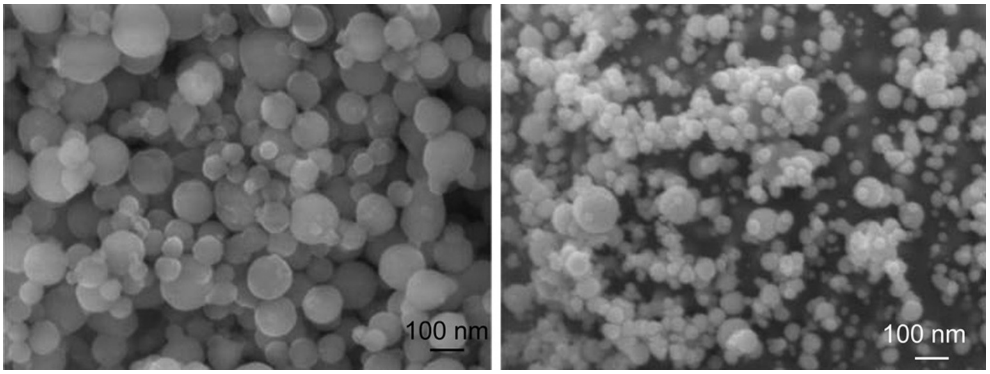

FIG. 9.27 SEM micrographs of aluminum (left image) and tungsten (right image) nanopowders produced by the electrical explosion wire process.

Nazarenko and Ilyin reported [66] that the nanopowders obtaining by electrical explosion of aluminum wires in water and copper wires in industrial oil were produced. The main product of aluminum EEW in water at the energy input e in 0.6–0.9 E_s range is $Al(OH)_3$ (E_s is the sublimation energy of the wire material). The rise of energy input in the wire to 1.8 E_s results in obtaining high temperature modification γ-Al_2O_3 and a transformation ratio with hydrogen formation up to about 100%. Copper nanopowder in the result of the EEW decreased the industrial oil friction constant up to 40%.

The specific surface area of the aluminum oxide powder produced by EEW in water at $E/E_s = 1.5$ was 36.3 m^2/g by average particle size of 33 nm.

According to the generalization [70] about the EEW nanopowder yield, subject to process parameters, it is in one installation between 50 and 200 g/h with a particle size ranging from 50 to 100 nm by consumed power 25–50 kWh/kg. Depending on the atmosphere, the particles may be metallic (in neutral atmospheres), oxide, or nitride.

NANOPOWDER PASSIVATION

All metallic nanopowders (Al, Cu, Co, etc.) made by any of the existing methods (condensation technique, plasmochemical synthesis, electrical explosion of wires, mechanochemistry, etc.) are highly pyrophoric, and surface passivation procedure for particles is required. After synthesis, nanopowders exposed to air can ignite as a result of heating caused by metal oxidation by components of air oxygen. Various passivation means are used in order to reduce the pyrophoricity of nanopowders, all of which can be classified as chemical passivation and microencapsulation methods.

Nanopowder Chemical Passivation

Passivation by oxygen-containing atmosphere (air, in particular) is partial oxidation resulting in widespread oxide film formation and is one of the simplest methods [71,72]. In this method, an oxide film is formed on the particle surface, which protects the metallic phase from contact with the environment. On the other hand, a major part of the existing technology of metal powder processing is tailored for a certain (usually low) content of oxide phases. Thus, the oxide layers are formed during the slow aluminum oxidation by air. In fact, this method of passivation can be considered, whereas a water vapor contained in air, as a process including the reactions:

$$2\mathrm{Al(s)} + 3/2\mathrm{O_2(g)} \rightarrow \mathrm{Al_2O_3(s)}$$

$$2\mathrm{Al(s)} + 3\mathrm{H_2O(g)} \rightarrow \mathrm{Al_2O_3(s)} + 3\mathrm{H_2\ (g)}$$

It is generally known that the water vapor always present in air is more reactive to passivating agents than oxygen.

The oxide layers may have different thickness and chemical compositions, depending on the powder production and passivation methods [72,73]. For aluminum, according to the works [74,75], this thickness is about 8–10 nm on the surface of the 50–1000 nm particles (Fig. 9.28). The reaction until this thickness is achieved occurs by chemical kinetics not hindered by diffusion.

The nanosize fraction of electroexplosive powder particles separated in a container (see Fig. 9.26) directly after the wire explosion does not conglutinate when the process is realized at argon with a slightly higher pressure than the atmospheric one. In these conditions, nanoparticles have an adsorbed argon gas on their surface that does not allow the particles to contact and prevents them from sintering in the first minutes after synthesis [71]. Aluminum nanoparticles are exposed to the oxidation of their surface by slow reaction with about 0.1 vol% air concentration for 72 h during the passivation process.

Simultaneously, it is necessary to set optimal parameters of the passivation process in order to preserve the chemical activity of nanopowders.

Microencapsulation of Nanoparticles

Microencapsulation is fulfilled by substantially covering the particle surface with organic and polymers agents [72,73,76,77]. Protective coatings were represented by organic substances of low molecular weight that were capable of forming a hydrophobic protective layer on the surface of metal nanoparticles. These are stearic acid, 8-hydroxyquinoline, glyoxal, and the polymers polyethylene glycol adipate (PEGA), vinylidene difluoride copolymer, and hexafluoropropylene (Viton), in combination with a mono ether.

Nanopowders produced by plasma-based technology were passivated with an S2-80/120 petroleum solvent adsorbed on their surface [67]. The produced powders, even being exposed to a pressure of 3 MPa and a temperature of 293 K in a pure oxygen atmosphere for 24 h, did not demonstrate any increase in their weight. Depending on the parameters of the mode, metal powders produced by this process have specific surface 6–15 m^2/g.

Gromov et al. [73] reported the results of the complex investigation of the aluminum nanoparticles produced by EEW technology and passivated in different medias. Gaseous, liquid, and solid passivative reagents were investigated. The

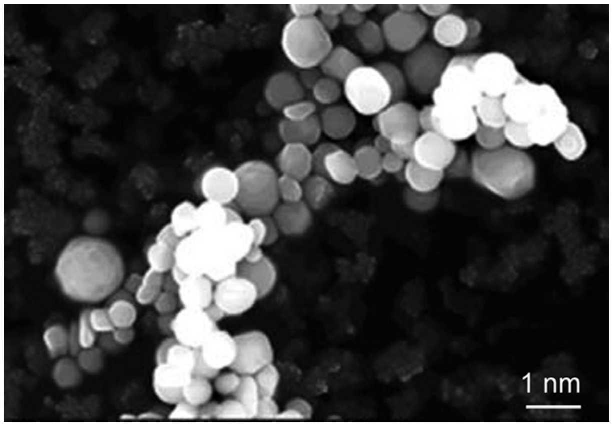

FIG. 9.28 SEM micrograph of electroexplosive aluminum powder particles with surface covered by oxide film.

samples passivated by boron, air, and CO_2 had the best characteristics. Thus, coating Al nanoparticles with organic compounds at the rate of 0.5%–3% creates a protective layer on the surface of Al nanoparticles, which prevents interaction between aluminum nanoparticles and water vapors and increases the oxidation rate of nanoparticles in the process of heating. However, organic layers covering the nanoparticles did not provide total protection from the oxidation that followed. Therefore, oxide layers were found on the nanoparticles below the organic layers.

The particles of aluminum as well as other metal nanoparticles are passivated, as a rule, with oxide layers having an amorphous or crystal structure. The oxide layers are formed on the aluminum particles at slow oxidation by air during the passivation process. The layers may have different thickness and chemical compositions depending on the powder production and passivation methods. Spherical aluminum nanoparticles have amorphous oxide layers that crystallize at the defined thickness (7–8 nm) during the storage period of 2–3 years at room temperature in air. The metal content in the powder substantially reduces (up to 30–50 wt%) with aluminum particle size decreasing up to ~30 nm.

POWDER PROCESSING METHODS

The powder processing methods such as classification, blending, thermal treatment, and compaction are complicated with nanodispersed metallic systems due to their high surface activities. In many cases, new approaches are required. While the influence of the free surface and interfacial energies in the micrometer scale is limited to the well-known powder metallurgy phenomena of driving forces for sintering, wetting behavior, and grain growth, on moving to the nanometer scale, even characteristics that generally are considered to be constant will change. Thus, as was considered above, the melting temperature may be lowered by hundreds of degrees and the lattice parameter decreases while the vapor pressure over the solid surface strongly increases if the particle size is as small as 10 nm [78]. With the decreasing particle size, the proportion of atoms located in surfaces or interfaces increases and the surface and grain boundary diffusion with coefficients 10^3 to 10^4 times higher than those of volume diffusion [79] become dominant in thermally activated processes. The important factors for the properties of nanostructured materials are the interactions between lattice defects and interfaces or surfaces as well as dimensional electric and magnetic effects. Fundamentals on this matter are given in [80,81].

Without arrangements specified during powder production, a strong agglomeration of powder particles can take place, owing to surface diffusion. To prevent agglomeration, particles may be introduced into a liquid before they come into contact. The interactions between powder particles and the environment can also be minimized by coating procedures included in the powder production process [82].

Densification by compaction is difficult, even for ductile metals, when the particles become very small and their hardness increases. At particles sizes of 50–100 nm, dislocation mechanisms are still active to enable plastic deformation. Smaller particles are dislocation-free and the image forces counteract dislocations to penetrate into particles [82]. Higher densities are achieved at elevated temperatures during compaction [83]. The relative density data of Ni and Si_2N_4 powders of various particle size pressed at 1 GPa are given in Table 9.2 [84]. They illustrate the aforesaid: the ductile nickel powders and brittle silicon nitride powders in the ultrafine state are pressed equally.

Higher densities are achieved at elevated temperatures during compaction [80]. The biggest problem, however, is connected with grain growth if dense and nanostructured materials have to be obtained by free sintering. Grain growth in the nanostructure can be reduced, at least to a certain extent, by multiphase alloy design and pressure sintering at lower

TABLE 9.2 The Relative Density Data of the Ni and Si_3N_4 From Various Particle Size Powders Pressed at 1 GPa.

	Conventional Pressing		Hydrostatic Pressing	
Particle Sizes (μm)	Ni	Si_3N_4	Ni	Si_3N_4
50	0.82	…	0.86	…
5	0.73	…	0.77	…
1.1	…	0.64	…	0.69
0.05	0.58	0.54	0.68	0.60
0.015–0,017	0.49	0.47	0.61	0.50

temperatures. For example, sintering of titanium nitride powders with an initial average particle size 60 nm at temperature ranges from 573 to 1073 K and pressing pressure 7.7 GPa gives compacts with low porosity (below 3%–5%), while by conventional sintering without high pressure, the porosity ranges from 10% to 12% [85].

SAFETY ASPECTS OF NANOPOWDERS PRODUCTION

The peculiarities of the structural characteristics, surface properties, and thermodynamic data of nanopowders result in some effects not observed for bigger size powders [74,75,86–92]. These features have a relationship to:

- Self-ignition and thermal explosions in air, oxygen, or other reactive gas environments.
- Substantially decreased ignition temperatures and energies.
- Sharply rising combustion velocities.
- The possibility of deflagration.

Lerner and coauthors [91] represented the results of the risk criteria of electroexplosive nanopowders by their handling and transportation. These results included nanopowders of Al-(Ar), Al-(N_2), Cu-(Ar), Cu-(CO_2), Ni-(Ar), and Zn-(Ar), (given in brackets is the gas in which the electric explosion process was realized). All nanopowders were initially passivated by a slow 72 h subject to air and Al-(Ar), followed by exposure to water at 293 K.

The fire hazard test was fulfilled by placing metal powder samples in a layer into a furnace at 773 K under air or oxygen. Al-(Ar), Al-(N_2), Ni-(Ar), and Zn-(Ar) ignited and were classified as combustible while with Cu-(Ar) and Cu-(CO_2), no burning occurred in the layer condition and they were classified as hardly combustible. Whereas all suspended above powders in air, including copper powders, where ignited.

The interaction between Al-(N_2), which contains AlN around 40%, and distilled water results in gassing (hydrogen and ammonia) started after 2 h with intensity up to 106.6 L/(kg·h). Nanopowders of such aluminum nitride composition (Al(N_2)) exhibit a higher hazard and lower induction time compared to Al nanopowder.

Electrostatic discharges (ESD) are the widespread origin of ignitions and explosions of nanopowders during their handling and transportation. A person's body is also a source of electric discharges. According to [91], the average energy that a person's body can keep is around 78×10^{-3} J.

The authors [91] tested Al-(Ar) nanopowders, coated by palmitic acid, after storage at different times in air. Table 9.3 contains the testing results from the data in which it is obvious that an ESD from a person's body can ignite nanopowders. On the other part, the suspended powder in air or oxygen is dramatically more sensitivity toward electrostatic discharges. For example, the minimum ignition energy of a suspended airborne 44 μn particle size 55Al-50Cu alloy powder is 100 mJ (see Chapter 27, Table 27.6).

The hazardous materials storage and tranportation regulations are intergovernmental or of one's own country, such as ISO - ISO Standards - ICS 13.300: Protection against dangerous goods; GOST12.1.044-89: Occupational safety standards system. Fire and explosion hazard of substances and materials. Nomenclature of indices and methods of their determination; GOST 19433-88: Dangerous goods; Classification and marking; U.S. Department of Transportation: The hazardous materials regulations.

TABLE 9.3 Combustibility of Electroexplosive Nanopowders by Electric Discharge

Powder	Time of Storage (Days)	Active Metal (%)	Number of Test	h^a (mm)	Capacitance of Capacitor (pF)	U^b (kV)	W^c (10^3J)	Source
Al-(Ar)	5	92	12	1	340	4.4	3.276	[91]
Al-(Ar)	5	92	10	0	340	4.53	3.488	[91]
Al-(Ar)	30	86	10	0	1100	4.83	12.830	[91]
L-ALEX[d]	20	96	21	0	227	3.13	1.110	[91,92]

[a] *The distance electrode end to powder surface.*
[b] *The voltage of electric discharge.*
[c] *The energy of electric discharge.*
[d] *The trade name of electroexplosive nanopowder.*

Lerner and coauthors [91] reported that polymer capacities are not perfect in the prevention of air penetration and mechanical strength. They suggested that, for minimization of interaction products of metal reaction with water vapors and oxygen packing for nanosized unpassivated metal powders, the hermetically sealed glass or metal capacities are used. While for storage of passivated metals, bilayer polyethilene film sacks are applied. For storage and transportation of aluminum passivated nanosized powders, the sacks of metallized polymer for prevention of static electricity accumulation are recommended [91].

Chapter 27 contains the safety engineering in the production of powders and more detailed data of dangerous and harmful manufacturing factors.

APPLICATIONS

At present, there are a number of application fields of nanopowders and numerous potential applications in advanced engineering and technology. Some of these are nanocomposites, coatings, catalysts, magnetic recording materials, electrically conductive inks and pastes, power engineering, chemical industry, renewable energy, biotechnologies, and environmental control [1,3,93,94]. Commercial scale production of inorganic nanoparticles, composed by Tsuzuki [95], is shown in Fig. 9.29.

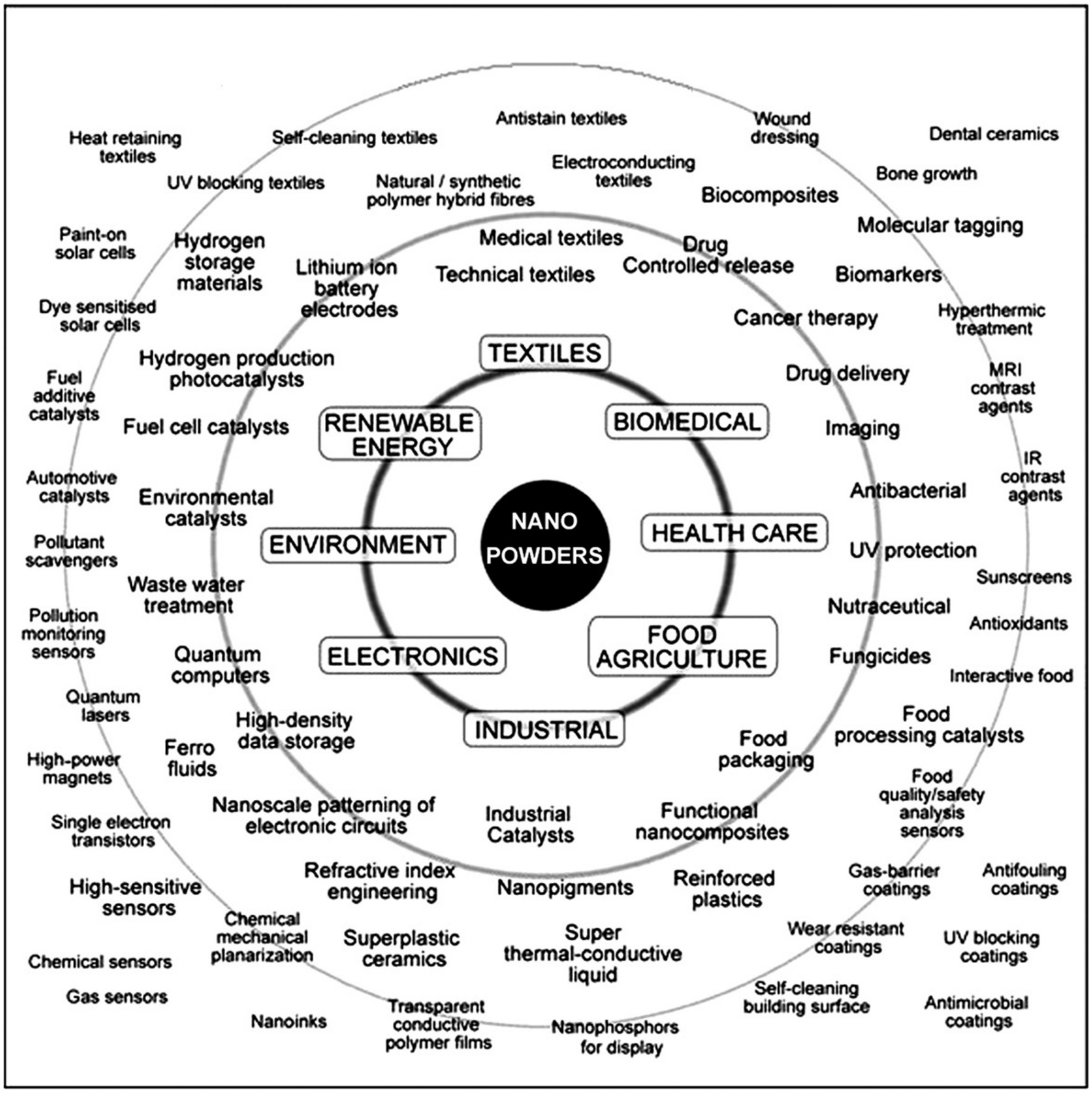
NANO POWDERS
TEXTILES
BIOMEDICAL
HEALTH CARE
FOOD AGRICULTURE
INDUSTRIAL
ELECTRONICS
ENVIRONMENT
RENEWABLE ENERGY
Heat retaining textiles
Self-cleaning textiles
Antistain textiles
Wound dressing
Dental ceramics
UV blocking textiles
Natural / synthetic polymer hybrid fibres
Electroconducting textiles
Biocomposites
Bone growth
Molecular tagging
Medical textiles
Technical textiles
Drug Controlled release
Biomarkers
Cancer therapy
Hyperthermic treatment
Drug delivery
MRI contrast agents
Imaging
IR contrast agents
Antibacterial
UV protection
Sunscreens
Nutraceutical
Antioxidants
Fungicides
Interactive food
Food processing catalysts
Food packaging
Food quality/safety analysis sensors
Functional nanocomposites
Industrial Catalysts
Gas-barrier coatings
Antifouling coatings
Reinforced plastics
Nanopigments
Wear resistant coatings
UV blocking coatings
Super thermal-conductive liquid
Self-cleaning building surface
Antimicrobial coatings
Nanophosphors for display
Transparent conductive polymer films
Superplastic ceramics
Refractive index engineering
Chemical mechanical planarization
Nanoinks
Gas sensors
Chemical sensors
High-sensitive sensors
Single electron transistors
Nanoscale patterning of electronic circuits
High-power magnets
Ferro fluids
High-density data storage
Quantum lasers
Quantum computers
Pollution monitoring sensors
Waste water treatment
Pollutant scavengers
Environmental catalysts
Automotive catalysts
Fuel cell catalysts
Fuel additive catalysts
Hydrogen production photocatalysts
Dye sensitised solar cells
Paint-on solar cells
Hydrogen storage materials
Lithium ion battery electrodes

FIG. 9.29 Commercial scale production of inorganic nanoparticles. *(Modified from T. Tsuzuki, Commercial scale production of inorganic nanoparticles, Int J of Nanotechnology 6 (5/6) (2009) 567–568.)*

Vapor Deposition in Vacuum

At present, one of the prevailing methods to produce nanopowders in a controlled way is the gas-phase technique.

Due to the high reactivity of nanosized metal powders, the main problem is prevention of oxidation or nitriding during processing or storage. As nanopowders are used or processed in suspension, agglomeration is also a quality issue because of the need of deagglomeration of the powders. Both parameters, the pickup of gaseous impurities and agglomeration, increase with decreasing particle size. Therefore, for nanopowders, the development of technologies that combine production and processing is essential. Just such a principle was used in Gleiter's lab installation [4] and was used in recent commercial units [93]. While the inert gas condensation process (IGS) was in the beginning used only in fundamental studies [1,3,96,97], tonnage quantities of nanopowders are now being produced [93,98–100].

The general views of the laboratory electron beam installation UE-209 and all-purpose installation UE-204 of the International Center for Electron Beam Technology (ICEBT) of the EO Paton Electric Welding Institute are presented in Fig. 9.30.

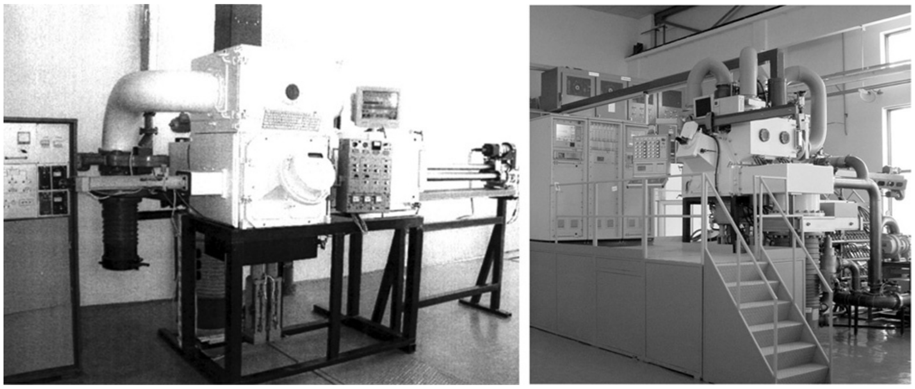

FIG. 9.30 Electron beam installations: laboratory UE-209 (A) and all-purpose UE-204 (B) of the International Center for Electron Beam Technology (ICEBT) used for electron beam evaporation and following physical vapor deposition in vacuum and the manufacture of various materials and components. *(Courtesy of ICEBT.)*

Table 9.4 contains the technical characteristics of ICEBT electron beam installation [101]. Condensed materials by these installations can be manufactured in the following structures:

- Relatively thin (from 10 to 150 μm) coatings on finished products.
- Thick (up to 1 mm) structural coatings with the function of a load-carrying structural element.
- Condensates in the form of foil, sheet, or even individual bulk intermediate products up to 3–5 mm thick for subsequent thermoplastic treatment.
- Wide size range, including nanosized powders.

TABLE 9.4 Technical Characteristics of ICEBT Electron Beam Plants

		Electron Beam Plant Type			
Technical data	**Unit**	**Laboratory Plant, UE-209**	**All-Purpose, Plant, UE-204**	**All-Purpose, Plant, UE-208**	**All-Purpose, Plant, UE-204 P**
Working chamber dimensions	mm	600 × 600 × 500	1000 × 1000 × 800	1000 × 980 × 640	1000 × 980 × 640
Dimensions of load chamber	mm	…	700 × 410 × 480	800 × 500 × 500	800 × 500 × 500
Plant dimensions: length, width, height	mm	1500 × 900 × 2500	4800 × 2570 × 3800	4800 × 2750 × 3000	5100 × 2600 × 3000
Number of electron beam guns		4	6	4	2
Electron beam gun parameters: power	kW	40	60	60	60 or 40
accelerating voltage	kV	20	20	20	20

Continued

TABLE 9.4 Technical Characteristics of ICEBT Electron Beam Plants—cont'd

		Electron Beam Plant Type			
Technical data	**Unit**	**Laboratory Plant, UE-209**	**All-Purpose, Plant, UE-204**	**All-Purpose, Plant, UE-208**	**All-Purpose, Plant, UE-204 P**
High-voltage source power	kV	120	250	200	…
Number of evaporators		4	5	3	2
Dimensions of evaporation ingots: diameter, length	mm	50, 200	70, 300	70, 250	70, 300
Dimensions of surfaces on which condensation is performed, not higher					
Flat, circular: diameter	mm	150	400	280	…
Flat, rectangular	mm	…	…	…	500 × 280
cylindrical: diameter, length	mm	150, 200	280, 400	280, 500	280, 500

ICEBT, International Center for Electron Beam Technology.

Fig. 9.9 shows the scheme of the installation in the process of microlaminate coating forming on the rotating blade of a gas turbine. Electron beam guns located in the gun chambers isolated from the working chamber perform the evaporation of the initial ingot materials. The two upper guns heat the substrate to the required temperature. The partition prevents mixing the vapor flows formed in the left and right parts of the working chamber and the substrate rotation provides the formation of a microlaminate condensate [38].

The typical distribution of the main elements in the coating cross-section, produced by successive evaporation of the CrAlY alloy ingot, is shown in Fig. 9.31 [102]. In the evaporation of the NiCrAl alloy, chromium is the first to evaporate and it forms a chromium-rich layer (55 wt% Cr) 4–5 μm thick on the bed coat surface. Then, as the insert evaporates, NiAl intermetallic with 5%Cr forms an approximately 10 μm thick layer. The second bond coat consists of two layers: a chromium-rich layer and then an NiAl intermetallic layer.

Fig. 9.32 gives typical data of ultimate strength (a) and microhardness (b) of two-phase Fe-Cu, C-Cu, and Mo-Cu condensates, produced by deposition from two independent sources at substrate temperatures of 873, 1123, and 1223 K.

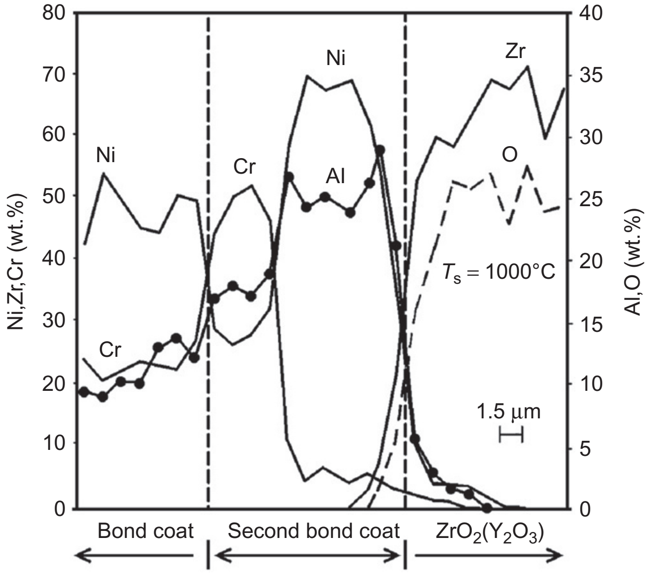

FIG. 9.31 Element distributions across the coating thickness produced by evaporation of the CrAlY alloy. *(Modified from Movchan AB. Functionally graded EB PVD coatings. Surf Coat Technol. 2002; 149: 252–262.)*

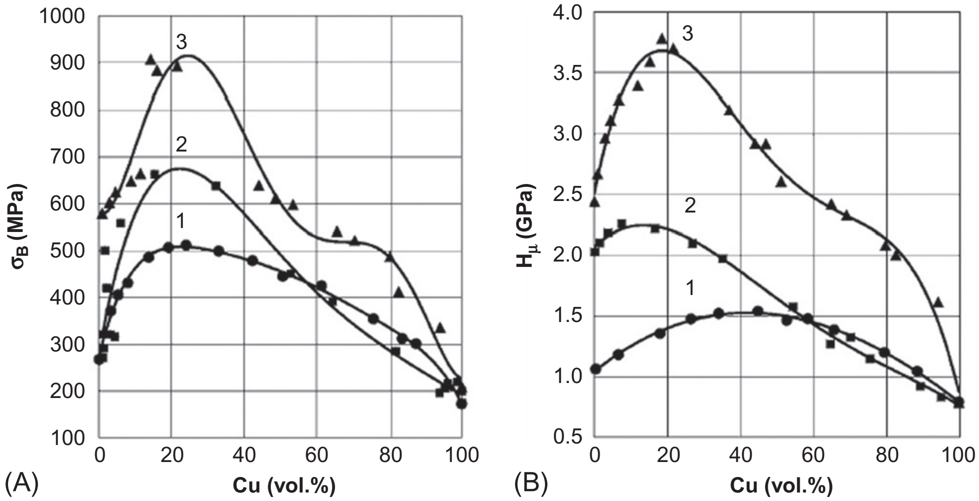

FIG. 9.32 Ultimate strength (A) and microhardness (B) of two-phase Fe-Cu (1), Cr-Cu (2), and Mo-Cu (3) condensates, depending on copper volume concentration. *(Modified from Movchan BA. Inorganic materials and coatings produced by EBPED. Surf Eng. 2006; 22(1): 35−46.)*

Because the structural coatings have a greater thickness as compared to normal protective coatings, they can perform the function of the bearing members. The bimetal structure in which the second layer is produced by the electron beam physical vapor deposition (EBPVD) method is the simplest example of structural coating. Some experience is available on the application of structural coatings for producing channeled components. First, precise casting or machining is used to make semi-products with open channels. Then the channels are filled with a salt mask and structural coatings are deposited on the surface of the masked channels. Next, the afore-named component is heated to a temperature above the condensation one. Salt filler evaporates to empty the channels. Fig. 9.33 shows the blade and vane blanks with channels, produced

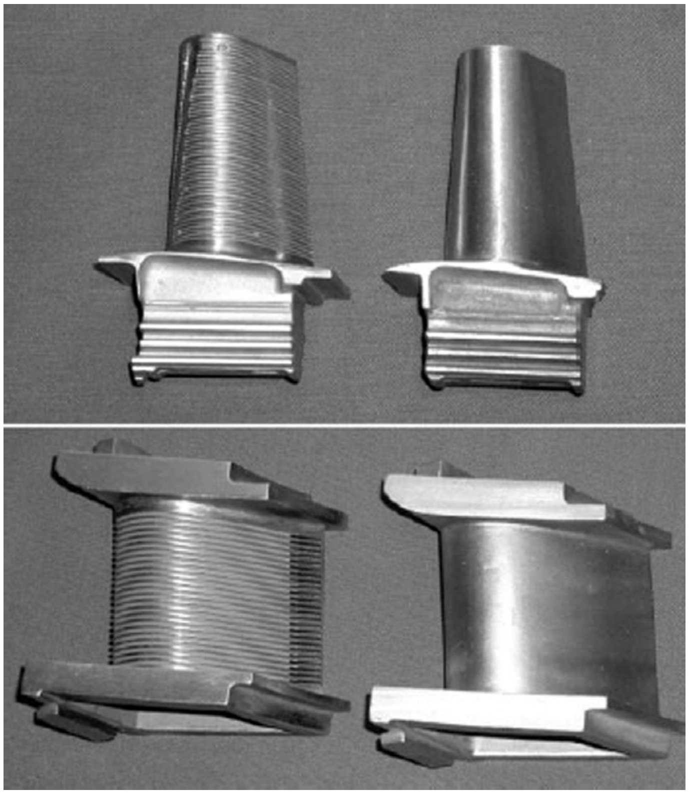

FIG. 9.33 Channel blade and vane with channels, produced by precision casting, before (*left*) and after (*right*) deposition of the about 0.7 mm structural coating. *(Courtesy of ICEBT.)*

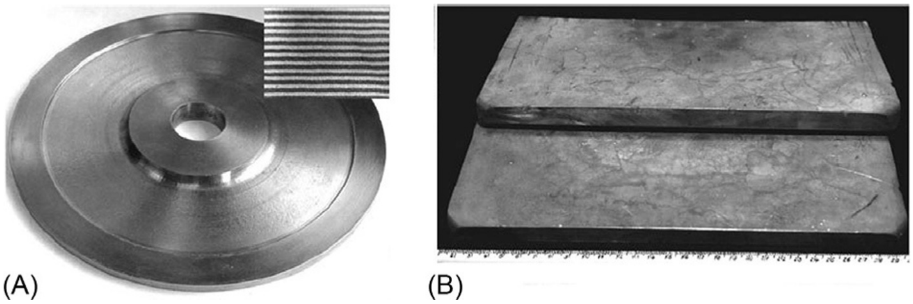

FIG. 9.34 (A) 220 mm diameter and 15 mm thickness disk, composed of 10,000 alternating TiAl/Ti microlayers; (B) 300 × 80 × 16 mm strips of Cu-Cr-Nb alloy. *(Courtesy of ICEBT.)*

by precise casting, before (on the left) and after (on the right) deposition of the 0.7 mm structural coating. Fig. 9.34 shows examples of a disc and billets produced by the EBPVD process [43].

At present, the following examples of existing and currently developed practical applications of vapor phase technologies are [43]:

- Protective and structural coatings on gas turbine blades for various purposes.
- Solid oxide fuel cells.
- Superhard coatings on tools for material processing.
- Catalysts in the form of graded coatings on an appropriate surface (e.g., wire and strip, etc.).
- Materials and coatings with special physical properties (e.g., optical, electric, magnetic, etc.).
- Biomaterials and biocoatings.

Because of their high reactivity, ultrafine powders are provided with a passivating surface layer to aid handling and incorporation into the final product. The commercial ultrafine aluminum powder is passivated with an oxide layer <5 nm thick. The powder particles have a spherical shape, a controlled size distribution in the range 100 ± 50 nm, and a high surface area-to-volume ratio ranging from 25 to 30 m^2/g [100,103]; the application area of this aluminum nanosize powder is propellants and explosions. Nano Technology, Daejeon, Korea [100] along with aluminum manufactures copper, zinc, cobalt, tungsten, and silver nanpowders.

The global market for the physical vapor deposition (PVD) industry, including equipment, materials, and services, was worth roughly $19 billion in 2013. The market is expected to increase to $26.4 billion in 2019 by a compound annual growth rate (CAGR) of 5.5% for the period from 2014 to 2019 [104]. According to this forecast, the microelectronics industry, encompassing semiconductors, components, and flat-panel displays, remains the largest market segment with data storage representing the fastest-growing sector.

Nonconsolidated nanopowders find a wide application due to their special catalytic, optical, biological, electrical, and magnetic properties. A broad spectrum of metal oxide nanopowders is produced for various purposes [93], including antimicrobial (wood preservation, marine antifouling, textile fibers, thermoplastics, and permanent coatings), catalysts (environmental catalysts and fuel cells), performance coatings (abrasion-resistant coatings), personal care, and polishing (glass polishing and semiconductor polishing).

Cemented Carbides

The discovery that a reduction of the carbide particle size results in considerable improvement in hardness and wear as well as strength makes further grain refinement down to real nanostructures [46,105,106]. Along with this, the preparation of a homogeneous microstructure and the reduction of the size of crack-initiating defects in parallel with the carbide grain size are important. Characteristic compositions of carbide powders with particle sizes below 200 nm are adduced in Table 9.5.

The greatest challenge is grain coarsening during sintering. The reduction of the sintering temperature appears to be the important factor. Two ways appear to be possible to reduce grain coarsening:

- Adjustment of a favorable initial state for sintering with a homogeneous distribution of the cobalt phase and homogeneous packing of the carbide particles in order to avoid local densification during sintering connected with the formation of large pores; extensive densification during solid-state sintering.
- Densification at low temperatures using pressure-assisted sintering (hot pressing, HIP).

TABLE 9.5 Characteristic Compositions of Cemented Carbide Powders

Property	Unit	Compositions of Cemented Carbide Powders by Different Cobalt Concentration				
Elements of nominal composition						
Cobalt	wt%	6	8	9	10	12
Tungsten	wt%	85–94	85–94	85–94	85–94	85–94
Total carbon	wt%	5.85–5.95	5.75–5.85	5.72–5.82	5.65–5.75	5.55–5.65
Impurities max						
Aluminum	ppm	20	20	20	20	20
Calcium	ppm	10	10	10	10	10
Copper	ppm	40	40	40	40	40
Iron	ppm	5	5	5	5	5
Magnesium	ppm	4	4	4	4	4
Manganese	ppm	4	4	4	4	4
Molybdenum	ppm	10	10	10	10	10
Nickel	ppm	80	80	80	80	80
Lead	ppm	2	2	2	2	2
Potassium	ppm	1	1	1	1	1
Silicon	ppm	…	…	…	…	…
Sodium	ppm	7	7	7	7	7
Sulfur	ppm	40	40	40	40	40
Oxygen	wt%	…	…	…	…	…
Zinc	ppm	…	…	…	…	…
Particle sizes	µm	<0.2	<0.2	<0.2	<0.2	<0.2
Apparent density	g/cm^3	≤1.95	≤1.80	≤1.70	≤1.65	≤1.50

Several processes have been developed for the production of nanostructured cemented carbides, such as the Nanodyne Process [106–109], mechanochemical synthesis [110], gas phase carburization [105], or high-energy milling.

Xueming and Gang [111] reported about a nanostructured WC-Co alloy prepared by mechanical alloying, which was accomplished in the following way. Mixtures of elemental powders (tungsten, graphite, and cobalt with a particle size smaller than 75 µm) are milled under argon in a planetary ball mill. The particle size decreases to 16 nm after 20 h and to 11 nm after 100 h of milling.

The integrated mechanical and thermal activation process [112] consists of high-energy milling of a mixture of WO_3 + CaO + graphite. The milled powder is subsequently subjected to reduction and carburization at 1273 K in argon.

High-purity nanosized WC-Co powders with a mean WC particle size of 60 nm and a cobalt content of 11 wt% can be prepared from $CoWO_4$ by a two-step process: hydrogen-plasma reduction giving W-Co powders around 40 nm and carburization at low temperatures (823–1223 K) in a CO + H_2 atmosphere [113].

The problem of grain growth preventing sintering of ultrafine and nanometric WC-Co powders has often been solved in recent decades by adding grain growth inhibitors (mainly VC, Cr_3C_2, and TaC).

In the work [114], the grain growth process during the sintering of nanosized WC-Co powders is considered as consisting of an initial slow stage I, a rapid grain growth stage II, and a latter stage III. In the initial stages (I and II), grain growth takes place during heat up while the latter stage of grain growth occurs after the isothermal holding temperature is reached. The authors of the work [115] report that the key challenge to the production of bulk nanocrystalline cemented tungsten carbide materials is to control the rapid grain growth during the early stage of sintering.

A specific class of solid-solution grain growth inhibitor alloys, which are solid solutions of VC and Cr_3C_2 in a Co-rich matrix, has been developed [116]. These alloys form multicomponent liquids at temperatures as low as 1473 K, so that the inhibitor carbide phase can be dispersed in the Co-rich liquid phase at a lower temperature than is common. Thus ultrafine and nanosized grades can be sintered to full density at 1523 K, resulting in a finer microstructure with high magnetic coercivity; this leads to higher hardness and toughness.

The ultrafine- and nanometric-grained tungsten-cobalt cemented carbides exceed the classical fine-grained WC-Co in wear resistance, by identical toughness. They are finding increasing application, including about 35% of the total cemented carbide production, in wear parts, round tools, end mills, drills, helical cutters, chipless forming tools, circular shearing and cutting blades for paper and plastics, dental tools, and microdrills for the electronic industry.

Fiber-Reinforced Material

Tungsten is the main candidate material for the first wall of a fusion reactor as it is steady against erosion by hydrogen isotopes, has the highest melting point of chemical elements, and shows good behavior under neutron irradiation [117]. One major disadvantage of tungsten is its brittleness below the ductile-to-brittle transition temperature, which ranges from 400 to 700 K [118], depending on the preparation history of the material. To eliminate the issue of brittleness by using tungsten, different composite approaches are investigated. One example is tungsten laminates that consist of a stack of tungsten foils, which are assembled as a layer composite [119]. Tungsten fiber-reinforced tungsten (W_f/W), as another example, utilizes fiber reinforcement and comprises a pure tungsten matrix and an interface layer around a W_f fiber [119,120]. It is considered that W_f/W incorporates an extrinsic toughening mechanism that enables energy dissipation, which leads to a reduction in stress peaks at crack tips and therefore cracks can be stopped. Accordingly, even in the brittle regime, this material allows for a certain tolerance toward cracking and damage in general in comparison to conventional tungsten.

The chemical vapor infiltration (CVI) process is a conventional method of fiber-reinforced tungsten material fabrication. Zhang et al. described this technology and techniques of microdrill design [121]. Thus, fiber-reinforced material with tungsten carbide nanorods (with diameters between 2 and 40 nm and a length to diameter ratio of 10 to 1000) is produced by a chemical vapor transport process carried out in a continuous flow reactor, using a support metal catalyst—a carrier tungsten carbide coated with a metal catalyst (Co/P)—as well as a volatile species source (tungsten oxide) and a carbon source (carbon black). Iodine acts as the transport reagent. The powder thus obtained (WC nanorods + Co) is mixed with paraffin wax or stearate-based lubricants, formed by extrusion (which facilitates the directional arrangement of the tungsten carbide nanorods), and hot pressed in a hydrogen ammonia atmosphere. As a result of the nanorods' parallel orientation, the contact area between the rods is considerably decreased while in the radial direction, the characteristics of this fiber-reinforced material are strengthened.

Jasper et al. developed a method of hot isostatic pressing (HIP) for making the fiber-reinforced tungsten materials [122].

A W_f/W material was composed of commercially available tungsten fibers, coated with an interface layer and integrated into a tungsten matrix. Different materials and material combinations were investigated as an interface material, for example, copper, carbon, and ceramics such as erbia and zirconia [123]. In this work, erbium oxide (Er_2O_3) as the interface material was used and is deposited onto the fiber surface in a magnetron sputter device. The samples were hot isostatic pressed in an argon atmosphere at 200 MPa for 4 h. Carbon heating filaments were used to achieve the desired temperatures of 1873, 1973, and 2173 K. The samples prepared at 1873 and 1973 K exhibited a density of 99% of the theoretical density of tungsten or higher. In the 2173 K case, the density amounted to 97.73% only.

Gradient Materials

Since the late 1960s, hundreds of patents and papers have been published on PVD and CVD coating of the surface of cutting inserts by a variety of functionally different materials [46]. This shows the considerable success of the coated cutting tools. But, nearly simultaneously, many attempts have been made to create and develop cemented carbides with a combination of different layers that complement the properties of each other, for instance, by reciprocal cosintering, common gradual pressing, sputtering, or electrophoretic deposition of different compositions [124].

Closed-die plastic working and extrusion of aluminum alloy-based gradient materials have been investigated [125]. The gradient materials were manufactured from powder mixes of aluminum and Al-17Si-5Fe-3Cu-1.1 Mg-0.6Zr alloy. In specimens, the alloy concentration range was from 0% to 100%, by a 20% interval. Specimens were made as two-parallel layers and core-coat type. The former was produced by the close-die cold compaction of powder mixes. Then, so-prepared green compacts were densified in dies in near isothermal conditions of 763 K, at pressure up to 200 MPa. The latter was made by hot compaction of a preform as a coat ring from aluminum alloy powder around an aluminum powder core in isothermal conditions of tool and material of 763 K and 120 MPa pressure with the following hot extrusion at 753 K by 4.11 and 13.32 extrusion rate. Extruded specimens were annealed at 753 K for 0.5 h, then cooled in water and aged at 453 K. The authors [125] reported that compression strength ranged from 470 to 800 MPa, subject to powder composition, the construction of the specimens and extrusion parameters. There was a pronounced anisotropy of compressive strength. Tested perpendicular to the gradient, it was approximately double the value when testing parallel to the gradient.

Nanopowder-Polymer Composites

Metallic filling powders in polymers play an important role in the realization of electrical conductive adhesives, radio frequency shielding polymers, or magnetic polymeric layers. In most cases, the use of high-aspect ratio fibers and flake is advantageous.

Polymer-matrix composites, composite nanoparticles, and microsphere composite nanoparticles are some of the main types of nanopowder polimer composites, playing a main role concerning the property modification of polymers and applications.

Polymer-Matrix Composites

Polymer-matrix composites are the classical type of a nanocomposite, where—in the ideal case—separate nanoparticles are uniformly dispersed in a polymer matrix. In reality, agglomerated nanoparticles can be formed in a polymer matrix. For the control of aggregation and the dispersion behavior of fine particles in suspension, physical and mechanical methods such as the ultrasonic and milling methods and chemical surface modification are generally used.

Chemical methods use chemical reactions in a liquid environment to generate nanocomposites. The result may be either nanocomposite particles or compact nanocomposite material. Comprehensive reviews on the variety of chemical synthesis methods are given by Caseri [126] and Althues et al. [127].

In colloidal process conditions, for further nanoparticle agglomeration prevention, there are two types of general surface modification methods, as Kamiya summarized [128]. One is the adsorption of surfactants on the nanoparticle surface after nanoparticle synthesis. In this case, a multistep procedure that involves particle synthesis, drying, and dispersing of obtained agglomerated particles is required. Another is the in situ modification process, which introduces surfactant compounds on the nanoparticle surface during the particle synthesis procedure. Thus, the surfactant in the synthesis solution controls the particle growth and attaches to the particle surface at the same procedure of the former method, and consequently separate nanoparticles can be obtained.

Composite Nanoparticles

Composite nanoparticles as core/shell nanoparticles or surface-modified nanoparticles are considered [129] as a special type of nanocomposite. When these nanoparticles contain an inorganic core and an organic shell, they are named hybrid nanoparticles. In this case, the inorganic core may be a metal or a metal oxide, and the organic shell either a polymerized monomer, a chromophore, a detergent or surfactant, carbon, or some organic molecule. Particles of this type, consisting of a metaloxide core and a polymerizable organic shell, were reported in the mid to late 1990s by Vollath [130,131], synthesized in a microwave plasma reactor by gas-phase synthesis. This concept allows the design of new functional materials with novel or modified magnetic, optical, electronic, or biological properties. In most of the cases, the change of the feature correlates with the filler load.

Microsphere Composite Nanoparticles

This type of composite is characterized by larger spheres, themselves composed of a nanocomposite. Thus, ceramic or metallic nanoparticles in a polymer matrix are spheroidal, encapsulated by an organic compound. Microsphere composites are reported from several authors. The ceramic part in most described cases is magnetic with an application focus in biology or magnetic resonance. Mangeney et al. reported about the bioreactivity of magnetic Fe_2O_3-PS/polypyrrole core/shell particles [132]. Magnetic encapsulated polymer nanocomposites were prepared by Jeon et al. [133]. Another method was presented by Zhang et al. [134]. This research group developed Sn-nanoparticles encapsulated in hollow carbon spheres for application in lithium-ion batteries.

Physical methods are mainly gas-phase methods that are able to synthesize both functional and encapsulated nanoparticles, also called also "hybrid core/shell nanoparticles." Their common feature is that they apply energy to transform chemical compounds (precursor and gas) into inorganic nanoparticles, and by a subsequent coating step, organic compounds are grafted on the nanoparticle surface for coating, encapsulation, or surface functionalization. The application of microwaves for plasma generation is a versatile approach for the gas-phase synthesis of hybrid core/shell nanoparticles. The microwave plasma synthesis of hybrid core/shell nanoparticles is characterized in more detail in Chapter 12.

The physical vapor deposition (PVD) process may be used for nanopowder polymer composites [43]. Coming back to the process sequence in Fig. 9.10, it should be noted that if one of the evaporated metals, A or B, is to be replaced by a polymer, a variant of the nanopowder polymer will be obtained.

Thin Film Technique

The manufacture of films with a variety of makeup in a nonporous state is possible in a wide range of particle sizes, beginning at 1–2 nm and higher. PVD methods as well as chemical vapor deposition (CVD), electrical explosion, ion deposition, and others are used. Excitation of the voltaic arc in a nitrogen- or carbon-bearing atmosphere is one of the most widespread ion deposition technology variants; metallic cathodes are used as metal ion sources. The electric arc evaporation is a highly productive process but is accompanied by formation of a dripping metal phase. The magnetron variant of ion-plasma deposition, in which a target (cathode) is atomized by means of gas discharge ion-plasma bombardment, is free from the above imperfection. The transversal magnetostatic field localizes the plasma at the atomized target surface and increases the atomization efficiency. By magnetron deposition, the substrate temperatures are moderate (below 373–473 K), which widens the opportunities for nanograin and amorphous thin films. But spraying yields are sometimes less than by the electric arc evaporation.

Nanograin films represent a diamagnetic (as copper) or paramagnetic (as rhenium) matrix with nanoparticle inclusions of ferromagnetic metal (cobalt, iron, and nickel) [85,135]. The devices for information recording (recording heads, magnetic carriers, disks, etc.) are an important field of application of the magnetic nanomaterials. Lightness in reproducibility, stability in storage, high recording density, and low cost are only some of the demands required of these systems. The giant magnetic resistance (GMR) manifestations in multilayer magnetic/nonmagnetic films such as Fe/Cr, Co/Cu, etc., have proved to be very useful for efficient recording of information [136]. Various makeups of nanostructure Co-Cu films obtained by electrolytic precipitation were studied [137–139]. Multilayer films of Nb/Fe and Nb/Gd systems consisting of ferromagnetic and superconducting layers are also considered a promising area for electronics and measurement technology.

The vapor-deposited nanosized quasicrystalline films of various alloys are discussed by Dubois [140]. A technique of deposition of a film from the vapor phase called the flash evaporation method was used. This method produces a pulse of vapor by instant overheating of a grain of the alloy positioned on the surface of a tungsten or platinum filament. For Al-Cu-Fe alloys that melt at a low enough temperature, the films are usually amorphous when precipitated on a substrate at room temperature but may also be obtained in situ as a single-phase quasicrystal if the substrate is preheated above about 623 K. Magnetron sputtering produces essentially the same kind of films, but with a much more pronounced shift of the film composition with respect to that of the target. Such a target containing a variety of Al-Cu-Fe phases was used to prepare Al-Cu-Fe films. Whereas as-deposited films were amorphous, annealing at 473, 673, and 573 K, producing partial crystallization with an increasing fraction of microcrystalline approximant crystals. The films that annealed for 2 h at 1023 K were fully icosahedral [141].

The laser ablation of Al-Pd-Mn targets means that atoms, or groups of atoms, are ejected out of a target into the vapor phase under the impact of an intense laser beam pulsed at nanosecond periods. A thin film forms at a reasonable growth rate upon collecting these atoms onto a substrate that may be kept at a temperature varying between that of liquid nitrogen and up to 573 K.

Another way to prepare quasicrystalline films proceeds along the growth of a multilayer of the individual constituents followed by a heat treatment that leads to a homogeneous material by diffusion of the compositions. Initially, the layers are produced by sequential evaporation of the atoms, using one or another of the techniques mentioned above (flash evaporation, laser ablation, and sputtering) [141,142]. Hence, the overall composition of the sandwich is imposed by the thickness of the individual layers.

Thin layers of thickness below 500 nm were prepared using this technique. Encapsulation of the multilayer between a sapphire substrate and a covering alumina layer protects the sample from unwanted oxidation and warrants a good definition of its geometry, necessary for precise measurements of electron transport properties. According to [140], a systematic study of the transformations taking place in five-layer stackings, that is, Al-Cu-Fe-Cu-Al and Al-Fe-Cu-Fe-Al, showed that this was not the case and that the icosahedral quasicrystal forms after annealing up to about 973 K. Observation of electron transport in thin film samples showed that the conduction in the presence of a magnetic field becomes anisotropic.

This anisotropy is detected with a sample of 12.5 nm in total thickness whereas a 25 nm specimen does not show this effect. These sandwiches were used extensively for magnetoconductivity measurements.

Under the heading of "energy savings," two potential applications of quasicrystalline materials are implied [140]. The first one, thermal barrier coatings, takes advantage of a combination of the low thermal conductivity of quasicrystals, the enhanced ductility at high temperature, and the thermal expansion coefficient, rather identical to that of metallic alloys, in order to increase the thermal gradient from surface to the bulk of mechanical parts submitted to a heat source. This in turn allows either increasing the thermodynamic efficiency of a combustion engine or limiting heat losses. The other application revolves around a reduction of the power dissipated through friction and ultimately wear at the surface of moving parts put into contact. Substantial hardness and lowered solid-solid adhesion are the two properties of quasicrystals that support this application. Although studied to a rather detailed technical standpoint, neither of these two applications seems to have significantly approached the market, probably because more efficient solutions may be found with other materials.

Semiconductors

With decreasing the size of semiconductor materials to nanoscale, their physical and chemical properties change drastically, resulting in unique properties due to their large surface area. Currently, semiconductor nanomaterials and devices are still in the research stage, but they are promising for applications in many fields, such as solar cells, nanoscale electronic devices, light-emitting nano devices, laser technology, waveguides, chemicals, and biosensors [3,143].

One of these application fields is bright phosphors because displays and lighting with high luminance, ultrafine resolution, and low-energy consumption are required. In this field, ceramic phosphors doped with rare earth ions and transition metal ions have been mainly researched and developed so far, due to the fact that those ceramic phosphors are highly stable. Therefore, much attention is directed to nanoparticles of group II–VI semiconductors such as CdTe and ZnSe because they emit bright photoluminescence (PL) whose wavelength depends on the particle size.

The research and development of glass phosphors showed various fluorescent colors with improved long-term stability by incorporating semiconductor nanoparticles [3]. Semiconductor nanoparticles also find applications in fluorescent markers for biological tissues and materials from a living body [144]. The position and movement of a virus and various materials bound to the semiconductor nanoparticles can be monitored by luminescence.

Classifications of Semiconductor Nanostructures

Classifications of semiconductor nanostructures proceed from that of nanocrystalline materials, as the electrons are confined to regions having one, two, or three dimensions when the relative dimension is comparable with the de Broglie wavelength. For a semiconductor such as CdSe, the de Broglie wavelength of free electrons is around 10 nm. The nanostructures of semiconductor crystals having the z direction below this critical value (thin film, layer structure, quantum well) are defined as two-dimensional nanostructures. When the dimension both in the x and z direction is below this critical value (linear chain structure, quantum wire), the nanostructures are defined as one dimensional and when the y direction is also below this threshold (cluster, colloid, nanocrystal, quantum dot) it is referred to as zero dimensional. Objects having either an overall size in the nonnanometric range (mainly in the micrometer or millimeter range), but displaying nanometric features (such as nanosized confinement spaces) or resulting from the periodic arrangement and assembly of nanosized building blocks, can be classified as three-dimensional nanosystems.

Quantum Confinement Effects

Quantum confinement effects describe electrons in terms of energy levels, potential wells, valence bands, conduction bands, and electron energy band gaps. The quantum confinement effect is observed when the size of the particle is too small to be comparable to the wavelength of the electron. Obviously, the confinement of an electron and hole in nanocrystals significantly depends on the material properties, namely, on the Bohr radius a_B. These effects take place in bigger nanocrystals and depend on the material properties, namely, on the Bohr radius $a_B = 2.34$ nm and a_B of about 10 nm, which would have Cd-related compounds such as CdTe, CdZnTe, and CdTeSe [143].

There is a general rule that the bandgap of group II–VI semiconductors becomes narrower as the constituent atoms become heavier. In the case of nanoparticles with diameters of ca. 2–10 nm, the bandgap is increased due to the quantum size effect compared with the bulk semiconductor, and it leads to various fluorescent colors reflecting small differences in the particle size.

Aqueous Solution Method

The aqueous solution method (also called the "wet chemical method") and the *sol-gel* method are commonly used for syntheses of highly photoluminescent semiconductor nanoparticles. When the semiconductor nanoparticles are coated with sulfur- and phosphor-containing surfactants, the PL efficiency improves.

Highly photoluminescent nanoparticles can be synthesized in organic solutions [145] and aqueous solutions [146]. However, the organic solution route uses reactions of explosive materials at high temperatures that need complex, expensive apparatuses and devices, and the synthesized nanoparticles tend to lose their PL quickly when contacting water. On the other hand, the uncoated nanoparticles have many surface defects, which cause nonradiative deactivation after excitation. Along with this, such nanoparticles easily agglomerate, and the agglomeration causes imperfect chemical bonds between nanoparticles. The coating with surfactants decreases the number of surface defects on the nanoparticles and suppresses the agglomeration of the nanoparticles. Various surfactants are used, such as thioglycerol, thioglycole acid, etc.

Sol-Gel Method

Three forms—bulk, small bead, and a thin film–of well-solidified glass phosphors were prepared by a sol-gel method using water-dispersible semiconductor nanoparticles [3].

Sol-gel-derived bulk glass phosphors incorporating semiconductor nanoparticles were prepared by hydrolysis of alkoxysilane in solutions mixed with aqueous solutions of semiconductor nanoparticles [147,148]. Alkoxysilane, having an amino group, adsorbs surfactants on the surface of nanoparticles that suppresses the agglomeration of the nanoparticles and leads to bright glass phosphors. The authors [3] reported that it was possible to incorporate CdTe nanoparticles up to a concentration of about 2×10^{-4} mol/L in the bulk glass. The obtained bulk glass phosphors showed PL spectra similar to those of the aqueous solutions of nanoparticles, and exhibited PL efficiencies higher than 40%. These glass phosphors retained PL efficiencies of higher than 30% even after 6 months of preparation, demonstrating superior long-term stability [147,148].

Small glass bead phosphors incorporating semiconductor nanoparticles were prepared by the sol-gel reaction in the small space inside inverse micelles [149]. The agglomeration of nanoparticles is suppressed by involving water-dispersible semiconductor nanoparticles in the individual inverse micelle. The PL efficiencies of the green- and red-emitting small glass beads incorporating CdTe nanoparticles reached 27% and 65%, respectively. These values were the same as those of the initial aqueous solutions of the nanoparticles.

Glass film phosphors incorporating highly concentrated semiconductor nanoparticles can be prepared by a layer-by-layer (LbL) self-assembly method. In this method, alkoxysilanes such as 3-aminopropyltrimethoxysilane and 3-mercaptopropyltrimethoxysilane (MPS) are used to link the layers of nanoparticles. A glass substrate coated with APS or MPS is dipped in an aqueous solution of nanoparticles and then in a toluene solution of APS or MPS. By repeating these dip-coating processes, glass film phosphors having an alternating layered structure of nanoparticle layers and glass layers were obtained [150]. The glass film phosphors prepared were used to incorporate semiconductor nanoparticles at very high concentrations around 0.01 mol/L. According to the authors data, it was possible to prepare glass film phosphors incorporating red- and green-emitting CdTe nanoparticles and blue-emitting ZnSe nanoparticles. The PL efficiency of the red-emitting glass film phosphor was estimated to be about 24%.

The semiconductor nanoparticles are synthesized by colloidal methods, hydrolysis treatment, gas phase technique (included phase evaporation), etc.

Application of heterogeneous structures with multilayers as AlGaAs/GaAs in semiconductor lasers has allowed a considerable decrease in the threshold currents, used more short radiation waves, and improved other field-performance factors in fast optical fiber communication systems. The conversion to nanostructures with quantum wires and dots leads to still more considerable effects (further decrease of the threshold current, increased temperature stability, and others) important for lasers, optical modulators, detectors, and emitters, working in the far-infrared region. The semiconductor nanostructures are very promising for solar energy conversion systems. Thus the advance in the creation of heterogeneous structures with quantum wires and dots will make possible improvements to the performance of current and future techniques.

Electrical Storage Systems

In the last decade the development of electrical storage systems such as primary and secondary batteries has gained worldwide significance for portable electronic devices as well as for hybrid or full-electric vehicles [151,152]. Especially the future development of large-scale lithium-ion-batteries toward a powerful and safe storage system with huge energy density and specific power will enable a sustainable individual mobility [151].

Besides the low viscous, organic solvent-based electrolytes, which are dangerous from flammability, polymer-gels, solid polymers, and polymer composites can be found as electrolytes in lithium-ion batteries, mostly in small-sized devices such as mobile phones. These electrolytes possess enhanced safety due to an improved protection against leakage, no internal shorting, reduced combustibility, and better freedom of design [153]. Three different types of polymer-based electrolytes have been developed: solvent-free polymer electrolytes, gel polymer electrolytes, and polymer composite electrolytes [154,155].

Miniaturized Systems

Miniaturization of advanced techniques defines the specifications of components used to design and produce, for example, highly integrated printed circuit boards (PCB) for PCs and cell phones. All these advanced PCBs each use hundreds of capacitors—so-called MLCCs (multilayer ceramic capacitor)—that contain components with ultrafine metal powders. A modern cell phone for example, contains about 300–500 MLCCs and perfected electronics used in modern cars consume about 5000 MLCCs per car. To keep the units small in size, these capacitors are all typically not >1.2 mm in thickness, although they have a quite complicated internal laminate structure consisting of several hundreds of layers; most advanced MLCCs already have >1000 layers [151].

Another application requiring the use of ultrafine metal powders is μ-MIM, an advanced kind of metal injection molding (MIM) able to produce μm-sized three-dimensional structures with high resolution as a low-cost mass product.

A lot of work is going on in the field of microelectromechanical and nanoelectromechanical (<100 nm) systems that finds application in superminiature sensors, electric motors, transformers, valves, shutters, etc. Currently, there are already pilot models of microelectric motors with a rotor size about 1 mm and rotor speed up to 40,000 rpm.

REFERENCES

[1] Andrievski RA. Nanomaterials: conceptions and up-to-date problems. Russ Chem Journal 2002;XLVI(5):50–6 [in Russian].

[2] Roco MC, Williams RS, Alivisatos P. Nanotechnology research directions: IWGN Workshop report. Vision for Nanotechnology R&D in the next decade. On behalf of NSTS/CT/IWGN, Dorbrecht-Boston-London: Kluwer Academic Publishers; 1999.

[3] Hosokawa M, Nogi K, Naito M, Yokoyama T. Nanoparticle technology handbook. Elsevier; 2014.

[4] Gleiter H. Nanocrystalline materials. Prog Mater Sci 1989;33:223–315.

[5] Birringer R, Gleiter H, Klein HP, Marquard P. Nanocrystalline materials: an approach to the novel solid structure with gas-like disorder. Phys Lett 1984;102:365–9.

[6] Yokoyama T, et al. Basic properties and measuring methods of nanoparticles. In: Hosokawa M, Nogi K, Naito M, Yokoyama T, editors. Nanoparticle technology handbook. Elsevier; 2014. p. 5–48.

[7] Il'in AP, Korshunov AV, Perevezenceva DO, Tolbanova LO. Diagnostics of nanopowders and nanomaterials. Tomsk: Tomsk Polytechnic University; 2008.

[8] Vollath D. Nanomaterials–An introduction to synthesis, properties, and applications. Weinheim: Wiley-VCH Verlag GmbH; 2008.

[9] Eckert J, Holzer JC, Ahn CC, Fu Z, Johnson WL. Melting behavior of nanocrystalline aluminum powders. Nanostruct Mater 1993;2:407–13.

[10] Lai SL, Guo JY, Petrova V, Ramanath G, Allen LH. Size-dependent melting properties of small thin particles: nanocalorimetric measurements. Phys Rev Lett 1996;77:99–102.

[11] Suresh A, Mayo MJ, Porter WD, Rawn CJ. Crystallite and grain-size-dependent phase transformations in yttria-doped zirconia. J Am Ceram Soc 2004;86:360–2.

[12] Chang J, Johnson E. Surface and bulk melting of small metal clusters. Philos Mag 2005;85:3617–27.

[13] Coombes CJ. The melting of small particles of lead and indium. J Phys F 1972;2:441–9.

[14] Castro T, Reifenberger R, Choi E, Andres RP. Size-dependent melting temperature of individual nanometer-sized metallic clusters. Phys Rev B 1990;42:8548–56.

[15] Wen DS, Song PX. Numerical simulation of individual metallic nanoparticles. In: Gromov A, Teipel U, editors. Metal nanopowders. Wiley; 2014. p. 25–66.

[16] Alavi S, Thompson DL. Molecular dynamics simulations of the melting of aluminum nanoparticles. J Phys Chem A 2006;110:1518–23.

[17] Zhurkin EE, Hautier G, Hou M. Stress distribution and mechanical properties of free and assembled Ni_3Al nanoclusters. Phys Rev B 2006;73:94–108.

[18] Cao LF, Xu GF, Xie D, et al. Thermal stability of Fe, Co, Ni metal nanoparticles. Phys Status Solidi B 2006;243:2745–55.

[19] Neikov OD, YuV M, Sirko AI, Ivashchenko RK, Zakharova NP. Advanced high-strength nanostructured Al-Mg alloys produced by new rapid solidification technology. In: Compiled by European Powder Metallurgy Association Proceedings of PM 2010 World Congress. Florence, 4; 2010. p. 25–32.

[20] Wakai F, et al. A superplastic covalent crystal composite. Nature 1990;344(29):421–3.

[21] Miessler GL, Tarr DA. Inorganic chemistry. 3rd ed. Pearson/Prentice Hall Publisher; 2010.

[22] Ishikawa K, Yoshikawa K, Okada N. Size effect on the ferroelectric phase transition in $PbTi0_3$ ultrafine particles. Phys Rev B 1988;37(10):5852–5.

[23] Yokoyama T. Size effect and properties of nanoparticles. In: Hosokawa M, Nogi K, Naito M, Yokoyama T, editors. Nanoparticle technology handbook. Elsevier; 2014. p. 5–10.

[24] Sato S, Asai N, Yonese M. Formation of colloidal silver in the presence of a nonionic surfactant, Surfynol 465. Colloid Polym Sci 1996;274:889–93.

[25] Toda K. Optical property of nanoparticle. In: Hosokawa M, Nogi K, Naito M, Yokoyama T, editors. Nanoparticle technology handbook. Elsevier; 2014. p. 45–8.

[26] Dressel M, Scheffler M. Verifying the Drude response. Ann Phys 2006;15(7–8):535–44.

[27] Drude model parameters to fit the dielectric function of free electron metals including plasma frequencies and damping constants for Ag, Al, Au, Cu, K, Na, Pt. www.wave-scattering.com/drudefit.ht [Accessed 30 July 2016].

[28] Bryant PJ, Miller RG, Yang R. Scanning tunneling and atomic-force microscopy combined. Appl Phys Lett 1988;52(26):2233–5.

[29] Giessibl FJ. Advances in atomic force microscopy. Rev Mod Phys 2003;75(3):949–83.

[30] Pharr GM, Oliver WC, Brotzen FR. On the generality of the relationship among contact stiffness, contact area, and elastic modulus during indentation. J Mater Res 1992;7(3):613–7.

[31] Oliver WC, Pharr GM. Measurement of hardness and elastic modulus by instrumented indentation: advances in understanding and refinements to methodology. J Mater Res 2004;19(1):3–18.

[32] Pharr GM, Bolshakov A. Understanding nanoindentation unloading curves. J Mater Res 2002;17:2660–71.

[33] Sneddon IN. The relation between load and penetration in the axisymmetric Boussinesq problem for a punch of arbitrary profile. Int J Eng Sci 1965;3:47–56.

[34] Taljat B, Zacharia T, Pharr GM. Pile-up behavior of spherical indentation in engineering materials, In: Moody NR, Gerberich WW, Burnham N, Bake SP, editors. Fundamentals of nano-indentation and nanotribology. Mater. Res. Soc. Symp. Proc., vol. 522, Warrendale, PA; 1998. p. 33–8.

[35] Carltona CE, Ferreira PJ. In situ TEM nanoindentation of nanoparticles. Micron 2012;43:1134–9.

[36] Eifert H. Metallic nanopowders. In: ASM handbook. vol. 7. ASM International Publishers; 1998. p. 77–9.

[37] Günther B. Schäfer. In: Proceedings of 1998 Powder Metallurgy World Congress, Granada1:Shrewsbury, UK: European Powder Metallurgy Association Publishers; 1998. p. 567–72.

[38] Movchan BA. EB-PVD Technology in the gas turbine industry: present and future. J Metals Mine Mater Soc 1996;48:40–5.

[39] Langmuir I. The vapor pressure of metallic tungsten. Phys Rev 1913;2(5):329–42.

[40] Kolasinski KW. Surface science: Foundations of catalysis and nanoscience. 3rd ed. New York: John Wiley & Sons; 2012.

[41] Maissel L, Gland R, editors. Handbook of thin film technology, Volume 1. New York: McGraw Hill Company Publishers; 1970.

[42] Nesmiyanov AN. Vapour pressure of chemical elements. Moscow: AN USSR Publishing House; 1961 [in Russian].

[43] Movchan BA. Inorganic materials and coatings produced by EBPED. Surf Eng 2006;22(1):35–46.

[44] Kulikov IS. Thermal dissociation of compounds. Moscow: Metallurgia Publ. House; 1969 [in Russian].

[45] Huenert R. Ultrafine copper powder. In: Proceedings of 2002 Powder Metallurgy World Congress, Princeton, MPIF Publishers, New Jersey, U.S.A. Vol. 10, 2002. p. 1–11.

[46] Pastor H. Developments in tungsten carbide-cobalt cemented carbides. In: International powder metallurgy directory & yearbook. 12th ed; 2006/2007. p. 99–108.

[47] Pastor H, et al. New spherical mono-dispersed and nonagglomerated cobalt powder. In: Proceedings of Int. Conf. on Advanced in Hard Materials Production. Publ. EPMA, Shrewsbury; 1992. p. 6-1–6-11.

[48] US Patent 5,338,330, Aug. 16, 1994.

[49] US Patent 5,352,269, Oct. 4, 1994.

[50] Intern. Pat. WO 96/03239, Feb. 8, 1996.

[51] Intern. Pat. WO 96/14952, May 23, 1996.

[52] Wahlberg S. Nano-structured hard material composites by molecular engineering. 1. Synthesis from soluble tungsten salts. Nanostruct Mater 1997;9:105–8.

[53] Intern. Pat. WO 96 14962, Feb. 8, 1996.

[54] Spray drying and granulation. In: ASM Handbook, vol. 7. ASM International Publishers; 1998. p. 91 – 6.

[55] Troizkiy VN. Production of ultrafine powders in plasma microwave discharge. In: Proceedings plasma microwave generators: Physics, technique, and application. Moscow: Energoatomizdat; 1988. p. 175–221 [in Russian].

[56] US Patent 20,060,225,534, Oct. 12, 2006.

[57] Lee G-G, Je-Shin P, Won-Baek K. Synthesis of ultrafine Zr based alloy powder by plasma arc discharge process. In: Proceedings of 2006 Powder Metallurgy World Congress. Busan, Korea: Publ. Korean Powder Metallurgy Institute; 2006. p. 505–6.

[58] NanoProducts Corporation, Colorado, USA, www.siclists.com/colorado/longmont/Nanoproducts-Corporation.

[59] Nippon Atomized Metal Powder Corporation, Japan, <//www.atomize.co.jp/product_e/index.html>.

[60] Yamonato Y, Mizukami M. Development of nano-sized WC powder for hardmetal. In: Proceedings of 2006 Powder Metallurgy World Congress. Busan, Korea: Publ. Korean Powder Metallurgy Institute; 2006. p. 427–8.

[61] Krushinskaya LA, et al. Production of ultrafine Ti–AlN powders. Mater Sci Nanostruct 2006;1:3–8 [in Russian].

[62] Semboshi S, Masahashi N, Kono TJ, Hanada S. Powder fabrication of Nb–Ti alloys using hydrogenation process. In: Proceedings of 2006 Powder Metallurgy World Congress, Busan, Korea: Publ. Korean Powder Metallurgy Institute; 2006. p. 250–1.

[63] Lee C-W, Lee S-C, Lee J-S. Synthesis of nanocomposite powder for tungsten heavy alloy by hydrogen reduction of ultrasonic-milled oxide nanopowders. In: Proceedings of 2006 Powder Metallurgy World CongressBusan, Korea: Publ. Korean Powder Metallurgy Institute; 2006. p. 507–8.

[64] Suslick KS, Price GJ. Applications of ultrasound to materials chemistry. Annu Rev Mater Sci 1999;24:295–326.
[65] Ding J, Tsuzuki T, McCormick PG. Microstructural evolution of Ni-NaCl mixtures during mechanochemical reaction and mechanical milling. J Mater Sci 1999;34:5293–8.
[66] Nazarenko OB, Ilyin AP. Nanopowders production by electrical explosion of wires: environmental applications. In: Proceedings of the 3rd Environmental Physics Conference. Aswan (Egypt); 2008. p. 135–40.
[67] Lerner M, Vorozhtsov A, Guseinov S, Storozhenko P. Metal Nanopowders Production. In: Gromov A, Teipel U, editors. Metal nanopowders. Weinheim (DEU): Wiley-VCH; 2014. p. 81–106.
[68] Lefrancois A, LeGallic C. Expertise of nanometric aluminum powder on the detonation efficiency of explosives. In: Proceedings of the 32nd International Annual Conference of ICT. Karlsruhe (Germany): Fraunhofer-Institut für Chemische Technologie; 2001. July 3–6. pp. 36-1.
[69] Nazarenko OB, et al. Electroexplosive nanometals. In: Gromov A, Teipel U, editors. Metal nanopowders. Weinheim (DEU): Wiley-VCH; 2014. p. 67–78.
[70] Kotov YA. Nanopowders derivable with using of target heating by impulse technique. Adv Mat 2003;4:79–81 [in Russian].
[71] Kwon YS, Gromov A, Ilyin AP, Rim GH. Passivation process for superfine aluminum powders obtained by electrical explosion of wires. Appl Surf Sci 2003;211:57–67.
[72] Jouet RJ, Carney JR, Granholm RH, Sandusky HW, Warren AD. Preparation and reactivity analysis of novel perfluoroalkyl coated aluminium nanocomposites. Mater Sci Technol 2006;22(4):422–9.
[73] Gromov A, Il'in A, Teipel U, Pautova J. Passivation of metal nanopowders. In: Gromov A, Teipel U, editors. Metal nanopowders. Weinheim (DEU): Wiley-VCH; 2014. p. 133–51.
[74] Eisenreich N, Fietzek H, Juez-Lorenzo M, Kolarik V, Koleczko A, Weiser V. On the mechanism of low temperature oxidation for aluminum particles down to the nanoscale. Propellants Explos Pyrotech 2004;29(3):137–45.
[75] Eisenreich N, Fietzek H, Juez-Lorenzo M, Kolarik V, Weiser V, Koleczko A. Influence of nano-particle size on the oxidation behaviour of Al, Fe, and Cu. Mater High Temp 2005;22(3/4):329–33.
[76] Kwon YS, Gromov AA, Strokova JI. Passivation of the surface of aluminum nanopowders by protective coatings of the different chemical origin. Appl Surf Sci 2007;253:5558–64.
[77] Sossi A, et al. Combustion of HTPB-based solid fuels loaded with coated nanoaluminum. Combust Sci Technol 2013;185(1):17–36.
[78] Geguzin JE. Physik des sinterns. Leipzig: Deutscher Verlag für Grundstoffindustrie Publishers; 1973.
[79] Kolobov YP. Grain boundary diffusion and properties of nanostructured materials. Novosibirsk: Nauka Publishers; 2001 [in Russian].
[80] Morris DG. Mechanical behaviour of nanostructured materials. Zürich: Trans Tech Publications; 1998.
[81] Ajayan PM, et al. Nanocomposite science and technology. Weinheim (DEU): Wiley-VCH; 2003.
[82] Siegel RW, Hu E, Rocco MC. Nanostructure science and technology–A worldwide study. Maryland: WTEC, Loyola College Publishers; 1999.
[83] Sanders PG, Youngdahl CJ, Weertman JR. The strength of nanocrystalline metals with and without flaws. Mater Sci Eng A 1999;234–6:77–82.
[84] Andrievski RA. Powder material science. Moscow: Metallurgia Publishers; 1991 [in Russian].
[85] Andrievski RA, Ragulya AV. Nanostructure materials. Moscow: Academia Publishers; 2005 [in Russian].
[86] Ivanov YF, et al. Productions of ultra-fine powders and their use in high energetic compositions. Propellants Explos Pyrotech 2003;28:319.
[87] Weiser V, Kelzenberg S, Eisenreich N. Influence of the metal particle size on the ignition of energetic materials. Propellants Explos. Pyrotech 2001;26:284–9.
[88] Trunov MA, Schoenitz M, Dreizin EL. Effect of polymorphic phase transformations in alumina layer on ignition of aluminium particles. Combust Theor Model 2006;10:603.
[89] Tulis AJ, Sumida WK, Dillon J, Comeyne W, Heberlein DC. Submicron aluminum particle size influence on detonation of dispersed fuel-oxidizer powders. Arch Comb 1998;18(1–4):157–64.
[90] Jones DEG, et al. Hazard characterization of aluminum nanopowder compositions. Propellants Explos Pyrotech 2003;28:120–31.
[91] Lerner M, Vorozhtsov A, Eisenreich N. Safety aspects of metal nanopowders. In: Gromov A, Teipel U, editors. Metal nanopowders. Weinheim (DEU): Wiley-VCH; 2014. p. 153–62.
[92] Tepper F, Lerner MI, Gimley DS. Metallic nanopowders. In: Lyshevski SE, editor. Dekker Encyclopedia of nanosience and nanotechnology4:New York: Marsel Dekker Inc.; 2014. p. 2491–502.
[93] Nanowerk. Available from: http://www.nanowerk.com/nanotechnology-applications.php; [Accessed 30 August 2016.
[94] Altavilla C, Ciliberto E. Inorganic nanoparticles. Boca Raton (FL, USA): CRC Press; 2011.
[95] Tsuzuki T. Commercial scale production of inorganic nanoparticles. Int J of Nanotechnology 2009;6(5/6):567–8.
[96] Frishberg IV, Kvater LI, Kuz'min BP, Gribovskii SV. The gas-phase method of preparing powders. Moscow: Nauka Publishers; 1978 (in Russian).
[97] Naboychenko SS, editor. Handbook of non-ferrous metal powders. Moscow: Metallurgia Publishers; 1997 (in Russian).
[98] Frishberg IV, Subbotina OY, et al. New Russian zinc-rich materials. Promyshlennaya Okraska 2003;1:8–15 (in Russian).
[99] Nanostructured & Amorphous Matertials, Inc. Los Alamos, NM, USA. http://www.nanoamor.com/our_technology; [Accessed 30 August 2016].
[100] Nano Technology Inc. Daejeon, Korea. http://nanocorp.en.ec21.com/company_info.html; [Accessed 30 August 2016].
[101] International center for electron beam technology. http://www.paton-icebt.kiev.ua/index.php?n=equip.
[102] Movchan AB. Functionally graded EB PVD coatings. Surf Coat Technol 2002;149:252–62.
[103] QinetiQ Nanomaterials Ltd. https://www.qinetiq.com/Pages/default.aspx.
[104] bccResearch. Physical Vapor Deposition (PVD): Global Markets. Report Code: MFG015F: September 2014.
[105] Gille G. et al. Submicron and ultrafine grained hard metals for microdrills and metal cutting inserts. In: Proceedings of 15th International Plansee Seminar. Publ. Plansee Holding AG, 2001, Vol. 2: p. 782–816.

[106] Fridrichs K, Moertl K. Development of new types of carbides with ultrafine and even finer tungsten carbide powders. In: Proceedings of 2002 Powder Metallurgy World Congress, Princeton, MPIF Publishers, New Jersey, USA, 6; 2002. p. 1–11.

[107] Sun L, Jia CC, Cao RJ, Lin CG. Effects of Cr3C2 additions on the densification, grain growth and properties of ultrafine WC-11Co composites by spark plasma sintering. Int J Refract Met Hard Mater 2008;26(4):357–61, http://www.hindawi.com/journals/jnm/2014/640750/. Accessed 30 August 2016.

[108] Çalışkan H, et al. Wear behavior and cutting performance of nanostructured hard coatings on cemented carbide cutting tools in hard milling. Tribology International 2013;62:215–32.

[109] Ren X, Miao H, Peng Z. A review of cemented carbides for rock drilling: An old but still tough challenge in geo-engineering. Int J Refract Met Hard Mater 2013;39:61–77.

[110] Al-Aqeeli N, Saheb N, Laoui T, Mohammad K. The synthesis of nanostructured WC-based hardmetals using mechanical alloying and their direct consolidation. J Nanomater 2014; 16 pages, https://doi.org/10.1155/2014/640750. Accessed 30 August 2016.

[111] Xueming MA, Gang JI. Nanostructured WC-Co alloy prepared by mechanical alloying. J Alloys Compd 1996;245:L30–2.

[112] Ban ZG, Shaw LL. On the reaction sequence of WC-Co formation using an integrated mechanical and thermal activation process. Acta Mater 2001;49(15):2933–9.

[113] Fu L, Cao LH, Fan YS. Two-step synthesis of nanostructured WC-Co powders. Scr Mater 2001;44(7):1061–8.

[114] Wang X, Fang ZZ, Sohn HY. Grain growth during the early stage of sintering of nanosized WC-Co powder. Int J Refract Met Hard Mater 2008; 26(3):232–41.

[115] Fang ZZ, et al. Synthesis, sintering, and mechanical properties of nanocrystalline cemented tungsten carbide—a review. Int J Refract Met Hard Mater 2009;27(2):288–99.

[116] Sadangi RK, et al. Liquid phase sintering aids for nanograin and micrograin WC-Co. In: Proceedings advances in powder metallurgy & particulate materials. Princeton, USA: Cemented Carbides. Publ. MPIF; 1999. p. 10/15–22.

[117] Lässer R, et al. Structural materials for DEMO: the EU development, strategy, testing and modelling. Fusion Eng Des 2007;82:511–20.

[118] Bolt H, et al. Plasma facing and high heat flux materials-needs for ITER and beyond. J Nucl Mater 2002;307–311:43–52.

[119] Reiser J, et al. Tungsten foil laminate for structural divertor applications—basics and outlook. J Nucl Mater 2012;423:1–8.

[120] Riesch J, et al. Enhanced toughness and stable crack propagation in a novel tungsten fibre-reinforced tungsten composite produced by chemical vapour infiltration. Phys Scr 2014;159:1–9.

[121] Zhang L, et al. WC nanorod reinforced cemented carbide material and technology design for PCB micro drill. Powder Metall Sci Technol Briefs 2001;3(4):8–11.

[122] Jasper B, Coenen BJ, Riesch J, Höschen T, Bram M, Linsmeier C. Powder metallurgical tungsten fiber-reinforced tungsten. Mater Sci Forum 2015;825–826:125–33.

[123] Du J. A feasibility study of tungsten-fiber-reinforced tungsten composites with engineered interfaces. Ph.D. Thesis, Technische Universität München; 2011.

[124] Spasil J. Functionally gradient materials in the cemented carbide field creation and application. In: Proceedings of 14th International Plansee Seminar. Publ. Plansee Holding AG. 2; 1997. p. 338–51.

[125] Szczepanik S. Processing of PM aluminium alloy based gradient materials. Arch Civil and Mech Eng 2012;12(4):413–7.

[126] Caseri WR. Nanocomposites of polymers and inorganic particles: preparation, structure and properties. Mater Sci Technol 2006;22:807–17.

[127] Althues H, Henle J, Kaskel S. Functional inorganic nanofillers for transparent polymers. Chem Soc Rev 2007;36:1454–65.

[128] Kamiya H. Introduction of nanoparticle dispersion and aggregation behavior. In: Hosokawa M, Nogi K, Naito M, Yokoyama T, editors. Nanoparticle technology handbook. Elsevier; 2014. p. 115–9.

[129] Hanemann T, Szabó DV. Polymer-nanoparticle composites: from synthesis to modern applications. Materials 2010;3:3468–517. https://doi.org/10.3390/ma3063468.

[130] Vollath D, Szabó DV, Seith B. Verfahren zur Herstellung von Partikeln mit einem Kern und einer Hülle. German patent DE 196 38 60 CI, 1996.

[131] Vollath D, Szabó DV. Coated nanoparticles: a new way to improved nanocomposites. J Nanopart Res 1999;1:235–42.

[132] Mangeney C, et al. Magnetic Fe_2O_3-polysyrene/PPy core/shell particles: bioreactivity and self-assembly. Langmuir 2007;23:10940–9.

[133] Jeon BS, et al. Controlled aggregates of magnetic nanoparticles for highly sensitive MR contrast agent. J Nanosci Nanotechnol 2009;9:7118–22.

[134] Zhang WM, et al. Tin nanoparticles encapsulated in elastic hollow carbon spheres for high-performance anode material in lithium-ion batteries. Adv Mater 2008;20:1160–5.

[135] Fedosyuk VM. Nanogranular electrodeposit magnet: cobalt alloys. In: Encyclopedia of nanoscience and nanotechnology, Vol. 2. American Scientific Publishers; 2004. p. 895–918.

[136] Mizuseci H, Kikuchi K, Tanaka K. Modeling of magnetic multivalued recording in granular materials. Japan J Appl Phys, B 1996;37(4):2155–8.

[137] Fedosyuk VM, Kasyutich OI, Blythe HJ. Composition and annealing influence on the superparamagnetizm of granular Cu-Co films. J Magn Mater 1996;156:77–8.

[138] Fedosyuk VM, Blythe HJ. Magnetic of electrodeposited inhomogenious alloyed CuCo films. Phys Status Solidi A 1994;146(2):k13–7.

[139] Fedosyuk VM. Magnetic and magnetoresistive properties of granulated films in the Co-Cu system. Mater Sci Nanostruct 2005;2–6:3–11 [in Russian].

[140] Dubois JM. Useful quasicrystals. Singapore: World Scientific Publishing Co; 2005.

[141] Ding Y, Northwood DO, Alpas AT. Fabrication by magnetron sputtering of Al-Cu-Fe quasicrystalline films for tribological applications. Surf Coating Techn 1997;96:140–7.

[142] Ichikawa N, et al. Preparation of Al-Pd-Mn quasicrystal films by laser ablation method. Jpn J Appl Phys 1994;33:L736–8 Volume 33/2 (5B).

[143] Surech S. Semiconductor nanomaterials, methods and applications. Nanosci Nanotechnol 2013;3(3):62–74, http://article.sapub.org/10.5923.j.nn.20130303.06.html.

[144] Bruchez M, Moronne M, Gin P, Weiss S, Alivisatos AP. Semiconductor nanocrystals as fluorescent biological labels. Science 1998;281:2013–6, www.sciencemag.org.

[145] Dabbousi BO, et al. (CdSe)ZnS core-shell quantum dots: synthesis and characterization of a size series of highly luminescent nanocrystallites. J Phys Chem B 1997;101:9463–75.

[146] Rogach AL, et al. Synthesis and characterization of thiol-stabilized CdTe nanocrystals. Phys Chem 1996;100:1772–8.

[147] Li CL, Murase N. Synthesis of highly luminescent glasses incorporating CdTe nanocrystals through sol-gel processing. Langmuir 2004;20(1):1–4.

[148] Li CL, Ando M, Murase N. Preparation and characterization of glass embedding of photoluminescent CdTe nanosrystals. J Non Cryst Solids 2004;342:32–8.

[149] Selvan ST, Li CL, Ando M, Murase N. Formation of luminescent CdTe-silica nanoparticles through an inverse microemulsion technique. Chem Lett 2004;33:434–5. http://www.journal.csj.jp/doi/pdf/10.1246/cl.2004.434.

[150] Yang P, Li CL, Murase N. Highly photoluminescent multilayer QD-glass films prepared by LbL self-assembly. Langmuir 2005;21:8913–7.

[151] Multilayered ceramic chip capacitors, World Market, Technology and Opportunities: 2015–2020. Cary (North Carolina): Paumanok Publications, Inc.Kazunori O, editor. Lithium ion rechargeable batteries. Weinheim (Germany): Wiley-VCH; 2008.

[152] Pistoia G, editor. Lithium-ion batteries. Advances and applications. Elsevier; 2014.

[153] Van Schalkwijk WA, Scrosati B. Advances in lithium-ion batteries. New York: Kluwer Academic/Plenum Publishers; 2002.

[154] Stephan AM. Review on gel polymer electrolytes for lithium batteries. Eur Polym J 2006;42:21–42.

[155] Liu HK, Wang GX, Guo ZP, Wang JZ, Konstantinov K. The impact of nanomaterials on Li-ion rechargeable batteries. J New Mat Electrochem Syst 2007;10:101–4.

Chapter 10

Powders With Quasicrystalline Structure

Nicholas A. Yefimov
Frantsevich Institute for Problems of Materials Science (IPMS), Kiev, Ukraine

Chapter Outline

Discovery and Structure of Quasicrystalline Materials 313
  Properties and Application of QC Materials 313
Manufacturing Technique of QC Powders 314
  Mechanical Alloying 314
  Vaporization by Laser Beam 315
  Crushing of Ingots 315
  Centrifugal Atomization 316
  Gas-Atomized Powders 317
  Water-Atomized Powders 318
References 320
Further Reading 321

DISCOVERY AND STRUCTURE OF QUASICRYSTALLINE MATERIALS

Quasicrystals (QC) are solids (generally, there are intermetallic phases) that possess a unique crystallographic structure characterized by long-range aperiodic order and crystallographically forbidden rotational symmetries. Accordingly, they exhibit five-fold, seven-fold, eight-fold, 10-fold, 12-fold, 15-fold, etc., rotational symmetries and a quasiperiodic translational order. For the discovery of quasicrystals, D. Shahtman was awarded the Nobel Prize in Chemistry in 2011. QCs were discovered in a rapidly solidified $Al_{0.86}Mn_{0.14}$ alloy in 1984 [1]. The material was obtained after rapid solidification from the liquid state at a cooling rate up to 1 million degrees per second. The samples of such alloys dissipated the electron beam and formed a clear diffraction pattern with a five-fold symmetry (Fig. 10.1). Many scientists consider the discovery of QC (along with metallic glasses, high-temperature superconductors, and nanocrystalline materials) as the most important achievements of material science in the 20th century.

Despite the relatively recent discovery, QCs gradually keep their place among the materials with a wide range of unique properties that are used in industry.

The structure of the QC is based on the icosahedron geometric figure, unlike most crystals, which have structures based on simple geometric figures such as a cube, tetrahedron, and octahedron. However, the icosahedron has the axis of the fifth order and the complete filling of space by these figures is impossible. In addition, the icosahedron that consists of 13 atoms, one of which is situated in the center and 12 of which are located above the sphere surface, is imperfect because there are small clearances between the 12 atoms on the surface. The addition of new atoms increases the imperfection. Therefore, the QCs usually are formed by icosahedral clusters with agglutinant atoms between them. It is shown that the structure of the icosahedral QC is formed by clusters of about 1.0nm in dimension (0.9nm in the case of Al-Pd-Mn [2]). The models of such clusters consist of 51 atoms for Al- Pd—Mn [3] and 33 atoms for Al-Cu-Fe [4].

Soon after the discovery of the icosahedral QC structure, the decagonal QC structure with a 10th-order symmetry axis was found in 1985 [5]. The octagonal QC with eighth-order symmetry axes and the dodecagonal QC with 12th-order symmetry axes also exist. The Al-based QCs are the most known and studied; however, the QCs also exist on V, Nb, Mn, Zn, Ti, Zr, Mg and other metal base. The majority of the discovered QCs are manufactured by rapid crystallization and are metastable. Currently more than 200 metastable QCs are known. A number of stable QC phases (in systems of Al-Cu-Fe, Al-Pd-Mn, Al-Cu-Co, Al-Co-Ni, and other alloys) also exist and are presented in equilibrium diagrams; they can be manufactured by the slow cooling rate of the melt [6,7].

Properties and Application of QC Materials

The electronic structure of a QC is usually characterized by the neighborhood of the Fermi surface to a minimum on the curve of the density states. In connection with this, the QC interatomic bonds have a mainly covalent character that accounts

Handbook of Non-Ferrous Metal Powders. https://doi.org/10.1016/B978-0-08-100543-9.00010-5
© 2019 Elsevier Ltd. All rights reserved.

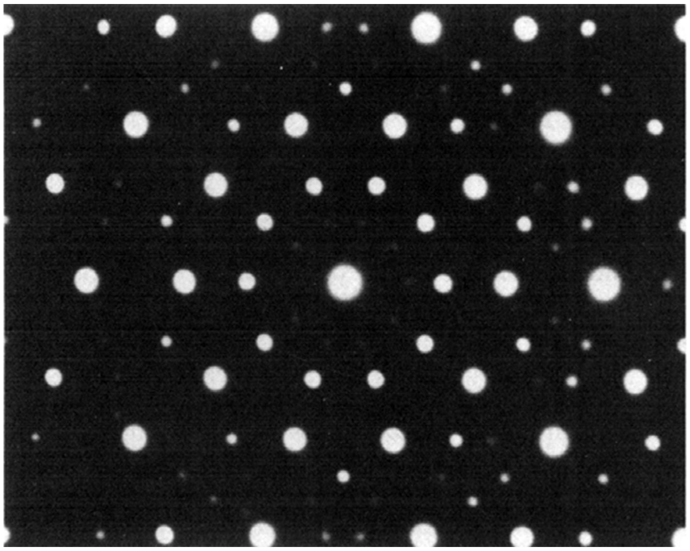

FIG. 10.1 Electron diffraction pattern of five-fold symmetry from the rapidly solidified alloy Al_6Mn.

for the existence in QCs of a wide energetic pseudogap. Accordingly, a small number of free electrons causes their low electric and thermal conductivity. This sets conditions for the specific and unique nature of the QC's physical and chemical properties. Thus, in annealed Al-Cu-Fe quasicrystals, the specific electric resistance achieves by the temperature 0.4 K the value of $\rho_{0.4K} = 0.01\ \Omega$ cm that is the level of the electric resistivity of semiconductors. In contrast to the usual conditions of crystals, the electric resistivity of OC by the increase of temperature is decreased; for example, for Al-Cu-Fe and Al-Pd-Mn quasicrystals, the ratio values ρ_{4K}/ρ_{100K} in the range of ~2–3 (where ρ_{4K} and ρ_{300K} are the electric resistivity at temperature 4 K and 300 K, respectively) are typical [8]. The thermal conductivity of the Al-Cu-Fe quasicrystals is of 1–3 $\mathrm{W\,m^{-1}\,K^{-1}}$ that is on the level of the thermal conductivity of oxide ceramics ZrO_2 [9].

The high level of mechanical properties and deformation characteristics of QCs single them out into a special class of materials. Direct study of the QC's deformed structure by transmission electron microscopy (TEM) shows that the deformation of QCs has a dislocation character [10,11]. Dislocations in the QCs have the phonon and phason components of distortions. Phason defects can move only by diffusion. That, along with a high value of Peierls stress (that is inherent in covalent crystals), results in a high value of yield strength and hardness. The hardness of different QCs is in the range of 4–11 GPa, and Young's modulus is within 80–200 GPa due to the high level of binding forces in the QC. However, the fracture toughness of QC is $K_{1c} = 0.5–1.5\ \mathrm{MPa\,m^{1/2}}$, which is close to the fracture toughness of silicon and a number of ceramic materials.

The unique properties of QC materials make possible a wide application of QCs in different industries. The main directions of application of QC materials are shown in Table 10.1.

MANUFACTURING TECHNIQUE OF QC POWDERS

Mechanical Alloying

Mechanical alloying is a technique to synthesize both equilibrium and nonequilibrium phases of materials starting from elemental powders. Mechanical alloying is a completely solid-state processing technique and therefore limitations imposed by the phase diagrams do not function here. More detailed information of mechanical alloying is contained in Chapter 3.

QC powders have been synthesized by mechanical alloying since 1989 [12,13]. The value of the interdiffusion coefficient determines the time formation of the QC phase. For example, the formation of the icosahedral phase in the Mg-Al-Zn system requires only 3–10 min [14], whereas in the Ti-Zr-Ni system it requires approximately 2 h [15], which is associated with a lower diffusion rates of elements in the system Ti-Zr-Ni. The types of powders with icosahedral QC structure and the conditions for their making are summarized in Table 10.2. In some cases, the subsequent annealing is required to form the QC structure in powders with an amorphous or nanocrystalline structure.

Recently, the synthesis of the decagonal QC phase in the Al–Cu–Cr system by the mechanical alloying technique has been reported [16]. This phase has grains with a faceted shape. The above composition is in the range of 71–73 at.% Al, 11–12 at.% Cu, and 15–18 at.% Cr.

TABLE 10.1 Application Area of QC Materials

Areas of Application	Properties	QC Composition
Thermal barriers (aviation turbine and turbine generators, diesel engines, automotive industry)	Low thermal conductivity	Al-Cu-Fe, Al-Co-Cr-Fe
Disperse-reinforcing particles in aluminum alloys, steels, and composites	Hardness and high mechanical properties at elevated temperatures	Al-Fe-Cr, Al-Cu-Fe, martensite aging steels
Accumulation of hydrogen	The high adsorption capacity for hydrogen	QC on Ti base
Selective light absorbers	The absorption of light radiation of certain wavelengths	Al-Cu-Fe, Al-Cu-Fe-Cr;
Nonburn coating for chemical reactors, kitchen utensils, and others.	Corrosion resistance, high hardness, low surface energy (no sticking)	Al-Cu-Fe-Cr
Coatings for tools	Wear resistance, low coefficient of friction	Al-B-Cu-Fe, Al-Pd-Mn
Catalysts in chemical reactions	The catalytic activity	Al-Pd, Al-Pd-B Al-Pd-Fe, Al-Pd-Mn, Al-Pd-Cr, Al-Cu-Fe, Al-Cu-Co, Al-Pd-Co

Vaporization by Laser Beam

A technique for manufacturing powders containing an icosahedral phase by evaporating by laser beam of ribbons from Al-Cu-Fe and Al-Pd-Mn system alloys of 50 μm in thickness is described in the work [17]. The laser with the $\lambda = 248$ nm wavelength was used. Targets of 2.5 cm in diameter were placed in a vacuum chamber filled by high purity argon at a pressure of 10 mmHg. The laser beam was focused on a spot of 0.5–1 mm in diameter on the surface of a rotating target. Pulses of 20 ns duration were emitted with a frequency of 10 Hz. The pulse energy (about 50 mJ/pulse) remained constant on this level during all experiments. Evaporated powders were collected in the nylon filter of the vacuum system. Powder produced by laser evaporation had a flake shape, a 10–20 μm size range, and a superfine grain structure.

The initial alloy was made from a mixture of high-purity Al, Cu, and Fe in accordance with the composition $Al_{62}Cu_{25.5}Fe_{12.5}$ and following evaporation-condensation in the argon atmosphere. Studying the manufactured powder had shown the presence of the icosahedral QC phase with an admixture of the crystalline β phase. The powders of the $Al_{70}Pd_{21}Mn_9$ alloy containing the QC phase were also produced by this technique [18].

Crushing of Ingots

For the laboratory investigation of the QC alloys' properties, the small ingots (50–100 g) were manufactured by melting in a high-frequency furnace in an argon environment followed by the melt pouring into the cooled copper crucible. The samples of several mm in diameter and of several cm in length were formed by drawing the melt. The crystallization rate of 10 mm in diameter samples was about 250 K/s. Thus, the ingots of 47 alloys based on Al-Cu-Fe, Al-Co-Fe, Al-Co-Ni, and other systems were produced. Such ingots contain, as a rule, several phases, and the QC phase in them was elevated by 24 h annealing at 1085 K that allowed the increase of the QC phase content in the ingot up to 95% [19]. The ingot obtained in an induction furnace under an argon protective atmosphere was crushed to produce a powder with a size in the range 20–50 μm, which was used later for sintering under uniaxial pressure [20].

Evidently, producing powders by crushing such ingots on an industrial scale is not expedient. In work [20], the QC powders were produced by comminution of the 5 kg ingots (50 mm diameter) and the coatings from these powders were investigated. Crushing was carried out in a mechanical agate mortar. Shevchukov et al. [16] reported the technology for production from 100 kg melt the 2 kg Al-Cu-Fe ingots contain 95 wt% of QC phase. The ingots are crushed in a tumbling ball mill with steel balls. This technology can be a base for commercial production of QC alloys by crushing ingots.

A typical powder particle image of a crushed QC ingot is shown in Fig. 10.2. Along with elongated particles and particles with sharp edges, the powder contains many particles of a polyhedral shape. Evidently, it is due to a high degree of symmetry in the icosahedral phase.

TABLE 10.2 Icosahedral QC Phases Formed after Mechanical Alloying and Rapid Solidification

Chemical Composition	Type of Mill	Ball-to-Powder Ratio	Milling Intensity	Milling Time (h)	Subsequent Annealing	Ref.
$Al_{65}Cu_{20}Co_{15}$	Fritch P5	15:1	–	55	873 K, 1 h	17
Al-Cu-Cr	Fritch P5	15:1	–	–	–	17
$Al_{70}Cu_{20}Fe_{10}$	Fritch P5	10:1	–	40	–	18
$Al_{65}Cu_{20}Fe_{15}$	Fritch P7	15:1	–	15	–	19
$Al_{65}Cu_{20}Fe_{15}$	AGO-2 U	15:1	–	15	823 K	20
Al_{70-x} (Cu, Fe)$_{30+x}$	Fritch P5	10:1	–	20–30	–	21
$Al_{65}Cu_{20}Mn_{15}$	Fritch P5	15:1	–	90	–	19
$Al_{65}Cu_{20}Mn_{15}Ge_{25}$	Fritch	20:1	450–650 rpm	66	–	22
$Al_{75}Cu_{15}V_{10}$	Fritch P5/P7	15:1	–	–	723 K, 1 h	23
$Al_{92}Mn_6Ce_2$	Fritch P5	13:1	300 rpm	700	–	23
$Al_{91}Mn_7Fe_2$	Fritch P5	13:1	300 rpm	700	–	23
$Al_{50}Mn_{20}Ge_{30}$	Fritch	20:1	45–650 rpm	47	–	24
$Al_{50}Mn_{20}Si_{20}Ge_{10}$	Fritch	20:1	45–650 rpm	80	–	24
$Al_{70}Pd_{20}Mn_{10}$	Fritch P7	15:1	–	30	–	25
$Mg_{32}Cu_8Al_4$	Planetary	–	900 rpm	–	–	13
Mg-Al-Pd	Planetary mill	40:1	150 G	4	–	26
Mg_{32} (Al, Zn)$_{49}$	Fritch	–	600 m/s^2	10 min	–	15
$Mg_3Zn_{5\text{-}x}Al_x$ ($x = 2$–4)	Planetary mill	40:1	900 rpm	–	–	13
$Mg_{44}Al_{15}Zn_{41}$	Planetary ball mill	–	600 m/s^2	30 min	–	27
$Ti_{56}Ni_{18}Fe_{10}Si_{16}$	SPEX 8000	6:1	–		1023 K, 30 min	28
$Ti_{45}Zr_{38}Ni_{17}$	Fritch P7	8:1	9.5	–	828 K	29
$Ti_{45}Zr_{38}Ni_{17}$	AGO-2	20:1	400 m/s^2	2	–	16

Centrifugal Atomization

This technique is an intermediate between laboratory and commercial production ones. The centrifugal atomization was used [21] for manufacturing Al-Cu-Fe powder with a QC component. The several hundreds grams ingot previously melted in an induction furnace in argon environment was remelted in a crucible placed in the center of the atomization chamber in a helium atmosphere. After achieving the pouring temperature (exceeding the melting point up to 200 K), the crucible's bottom drain aperture was opened, and the jet melt fell on the disk rotating with a speed of 30,000 rpm. The melt spread over the disk under centrifugal force is atomized with a generation of fine melt droplets, which are solidified during their flight to the chamber walls. However, the melt cooling rate by centrifugal atomization does not exceed 10^3 K/s. Therefore, the QC phase content in powder was comparatively small (about 30%). Further powder annealing did not bring it to the one-phase condition.

The powders of AI-Mn, Al-Cr, and AI-Mn-Cr system alloys with the QC phase were made using an apparatus in which the molten alloy was first atomized into small droplets by a nozzle atomizer, then the droplets collided with a high-speed rotating disc, and finally were atomized. Therefore, the droplets were rapidly solidified. The calculated cooling rate was in the 10^5–10^7 K/s range [22].

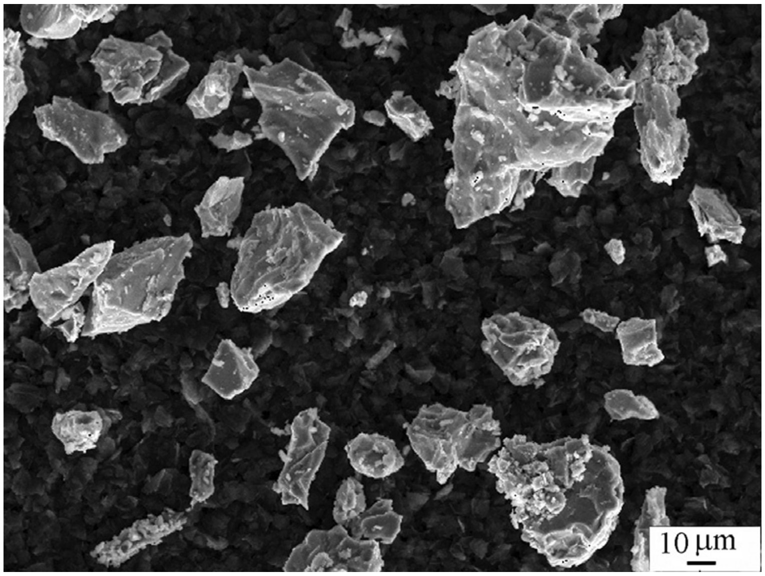

FIG. 10.2 SEM micrograph of $Al_{63}Cu_{25}Fe_{12}$ alloy powder produced by crushing ingots.

Gas-Atomized Powders

At present, gas atomization (GA) is the main commercial production method of aluminum and aluminum alloys and is described in the Ref. [23]. The cooling rate by GA achieves 10^5 K/s, which is about three orders higher than the cooling rate of ingot in a water-cooled copper mold. A high solidification rate provides fineness structure and a more homogeneous composition in powders.

The technique of manufacturing QC Al-Cu-Fe alloys by inert GA is presented in the patent [24]. As reported [25], in Al-Cu-Fe powder produced by GA, an x-ray investigation reveals two phases: the icosahedral QC phase and the cubic crystalline (β). Very small crystals of the crystalline λ-phase are revealed only by TEM investigation. Inert GA protects the surface of powder particles from strong oxidation. Thus, in the $Al_{63}Cu_{25}Fe_{12}$ powder produced by argon atomization, the content of oxygen varied from 0.205 to 0.065 wt% for powder size fractions of 0–25 μm and 75–106 μm, respectively [24]. The oxygen content determined by the Leco 12 technique of melting in an inert gas showed it lowering with the increase of particle size due to reducing the specific surface of particles. The part of the QC phase in these fractions varied from 69% to 55% because the solidification rate in fine particles is higher.

In comparison with ingot-crushed powders, which have an irregular splinter particle shape, GA powders have a spherical shape. The spherical QC powders, produced by GA of the $Al_{65}Cu_{20}Cr_{15}$ [25] alloy, are shown in Fig. 10.3.

For coatings, subject to size fractions of QC GA powders, different types of plasma torches are used. For the coating by the 10–25 μm size fraction, minitorches are used. For the size fraction 25–45 μm or even 45–75 μm, conventional torches are used. Small particles below 10 μm in diameter are not used because they evaporate in the high temperature plasma while the particles with size above 75 μm do not stay long enough within the flame to reach full melting [26].

The $Al_{65}Cu_{20}Fe_{15}$ QC spherical shape powder with a median diameter of 17.4 μm was made by argon atomization using Rayleigh-plateau forces in primary mode [26]. The Nanoval system, which used an atomizer with a Laval nozzle, was applied. Powder consisted of the icosahedral QC phase dendrites and a small amount of Al(Cu, Fe) cubic phase in the interdendritic areas.

The French firm CRISTOME (Coating solutions Saint-Gobain) manufactures gas-atomized QC powders. Commercially available powders include CRISTOME A_1 ($Al_{71}Fe_{8.7}Cr_{10.6}Cu_{9.7}$), CRISTOME F_1 (Al_{59} $Fe_{12.4}$ $Cu_{25.5}$ B_3), and CRISTOME BT_1 ($Al_{71.3}Fe_{8.1}Co_{12.8}Cr_{7.8}$) [27]. The main properties of CRISTOME QC powders are summarized in Table 10.3.

The new application of gas-atomized QC Al-Cu-Fe-B alloy powders was conductive to a commercial development of polymer-matrix composites reinforced with QC particles [28]. The process is based on selective laser sintering (SLS), which is one of the three-dimensional additive manufacturing technologies used in the mechanical industries. For example, the intake manifold from the polyamide composite reinforced by QC particles was made by SLS [29].

As reported [30–33], the gas atomized Al-Fe-Cr alloy powders strengthened by nanoquasicrystalline particles are produced. Various gases are used for atomization: helium [31]; nitrogen [32] under 0.45 and 0.5 MPa pressure, respectively; and argon [30] under 9.8 MPa pressure. Argon was used for the atomization of a number of Al-Fe-Cr-Nb system alloys [33].

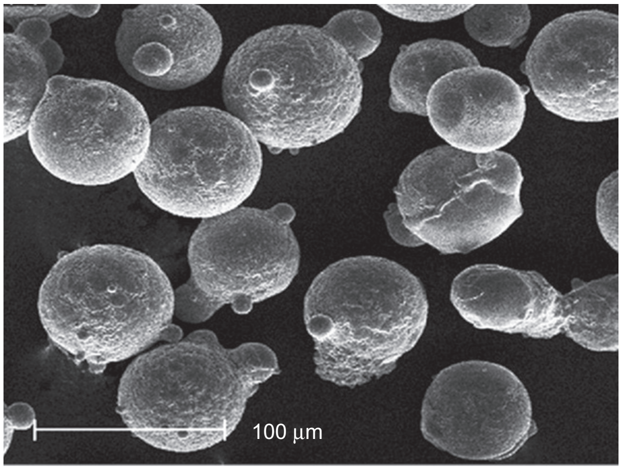

FIG. 10.3 SEM micrograph of 61–74 µm fraction of QC $Al_{65}Cu_{20}Cr_{15}$ powder, produced by argon atomization.

TABLE 10.3 Main Properties of CRISTOME Quasicrystalline Powders

Compositions (at.%)	**Al_{71} $Fe_{8.7}$ $Cr_{10.6}$ $Cu_{9.7}$**	**Al_{59} $Fe_{12.4}$ $Cu_{25.5}$ B_3**	**$Al_{71.3}$ $Fe_{8.1}$ $Co_{12.8}$ $Cr_{7.8}$**
Solidus, K	1163	1069	1364
Liquidus, K	1309	1343	1393
Thermal conductivity (W/mK)			
20 K	2	3	2
300 K	3.2		
800 K	6	7.5	5
Thermal diffusivity (mm^2/s)			
20 K	0.80	1	1.45
300 K	1.10		
800 K	2.39		
Electrical resistivity (µΩ cm)	600		400
Thermal dilatation coefficient ($\times 10^{-6}$ K^{-1})	15.5–18.6	15.4–23.5	13.7–15
Density (g/cm^3)	3.99	4.72	4.09

Water-Atomized Powders

A well-known technique of melt atomization by jets of high-pressure water (WA) enables increasing the melt cooling on a single order in comparison with GA. This process is widely used for producing powders of ferrous metals and some nonferrous metals (e.g., copper and alloys on its base, nickel, nickel alloys). However, this process was not applied to manufacturing aluminum and aluminum alloy powders for two main reasons: First, due to the explosion hazard that arises from the emanation of hydrogen as a result of powder interaction with water, and, second, for fear of powder oxidation and the deterioration of powder properties. The problem of powder quality and safety of the WA atomization process to produce Al alloy powders has been recently solved at the Institute for Problems of Materials Science (Kiev, Ukraine) [34]. The developed solution has been realized in the form of a pilot plant and is based on the following technical innovations: using for atomization water with the properties of a weak electrolyte, monitoring its temperature and hydrogen index, the hydraulic classification of powders in particle size, a contact-convection drying process with a high drying efficiency for drying chemically active substances, and preventing powder oxidation and thermal self-ignitions.

WA-atomized powders have an irregular shape and uneven surfaces (Fig. 10.4). As follows from direct TEM observations, the surface oxide of water-atomized powders is nonuniform in its thickness. Coarse surface oxide islands, with a typical thickness of 30–40 monolayers, cover 30%–70% of the particle's surface. The rest is covered with a thin oxide film of about 2 to a maximum of 5–6 monolayers [35]. The cooling rate of melt is 10^6 K/s and higher, which is necessary for obtaining QC phases.

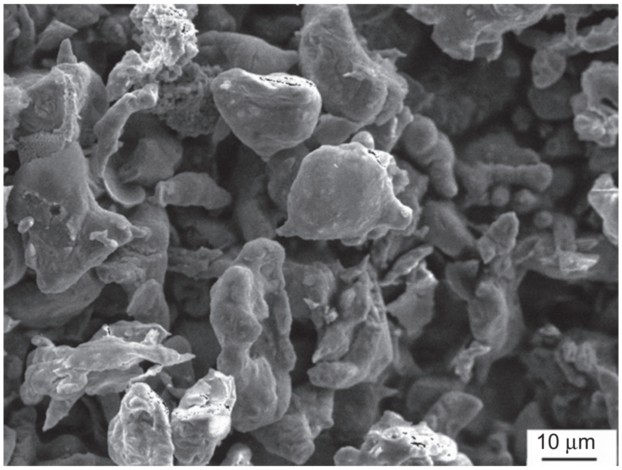

FIG. 10.4 SEM micrograph of 40–63 μm fraction of QC $Al_{63}Cu_{25}Fe_{12}$ powder, produced by water atomization.

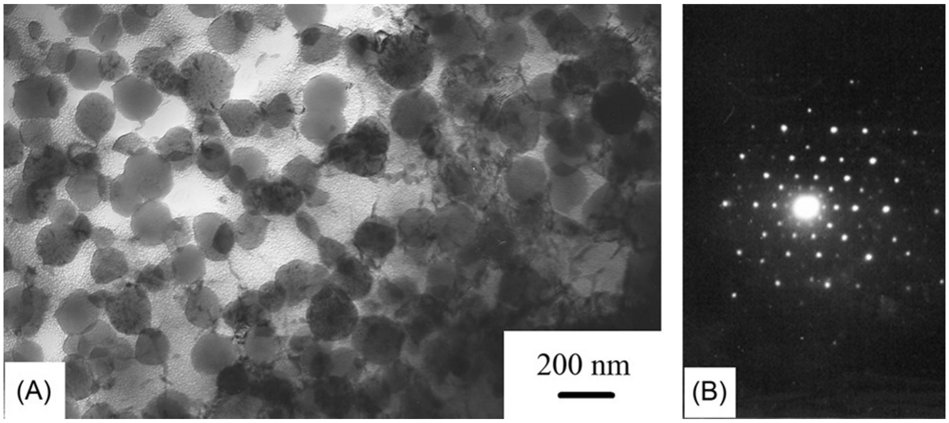

FIG. 10.5 TEM image of water-atomized $Al_{96}Fe_{2.5}Cr_{2.5}Ti_1$ alloy powder (A) and electron diffraction pattern of five-fold symmetry from a quasicrystalline particle (B).

A polygonal cell structure of the Al matrix with a cell size of 500 nm and nanoquasicrystalline strengthening particles with a size of 200–300 nm is observed in the $Al_{96}Fe_{2.5}Cr_{2.5}Ti_1$ alloy, obtained by extrusion of water-atomized powder (Fig. 10.5A) [36]. The TEM image illustrates an electron diffraction pattern of five-fold symmetry from the QC particle (Fig. 10.5B).

Among wrought aluminum alloys, the Al-Fe-Cr alloys based on the WA powders possess uniquely high mechanical properties both at room and elevated temperatures (Table 10.4). Such high strength ensues due to a high hardness and high Young modulus of the QC while plasticity is provided by the special deformation treatment of nanoquasicrystals.

The QC based on WA powders technique used for manufacturing $Al_{63}Cu_{25}Fe_{12}$ powder [37] results in obtaining two-phase powder (QC + crystalline β) (Fig. 10.6A), following conversion to the QC phase by vacuum annealing at 973 K over 2 h (Fig. 10.6B). For producing $Al_{64}Cu_{25}Fe_{12}$ powder aluminum A5 (99.95%), cathodic copper (99.99%) and iron "Armco" (99.92%) were used. The charge composition consists of (43Al-40.1Cu-16.9Fe) wt%. The overheating of pouring temperature was 200–250 K. The 6 mm melt stream flowing from the crucible was atomized by water jets under 100 MPa pressure. Dried powders were separated by sieving into the following size fractions: 0–63, 63–100, 100–160, 160–200, and >200 μm.

QC Al-Cu-Fe coatings, especially with additional alloying, have low thermal conductivity (1.65–2.42 $W\,m^{-1}\,K^{-1}$) combined with the thermal expansion coefficient (14.5×10^{-6}–$18.5 \times 10^{-6}\,K^{-1}$ at a temperature of 373–973 K) approximate to the thermal expansion coefficient for structural materials of nickel, aluminum, and iron base. Therefore, one can recommend them for use as thermal barriers for gas turbines, internal combustion engines, etc.

Water-atomized QC Al-Cu-Fe system powders were also used to produce the surface-hardened composite layers on an aluminum alloy by ultrasonic impact processing [38].

TABLE 10.4 Mechanical Properties of Extruded Rods from Al-Fe-Cr WA Powders With Nanoquasicrystalline Strengthening

	Test Temperature					
	293 K			573 K		
Chemical Compositions (at. %)	[a]YS (MPa)	[b]UTS (MPa)	[c]El (%)	YS (MPa)	UTS (MPa)	El (%)
$Al_{96}Fe_3Cr_3$	485	542	7.0	283	297	3.5
$Al_{96}Fe_{2.5}Cr_{2.5}Ti_1$	546	585	8.4	328	345	3.9
$Al_{96}Fe_{2.5}Cr_{2.5}Ti_{0.5}Zr_{0.5}$	648	677	7.0	331	351	1.8

[a] *Yield strength.*
[b] *Ultimate tensile strength.*
[c] *Elongation.*

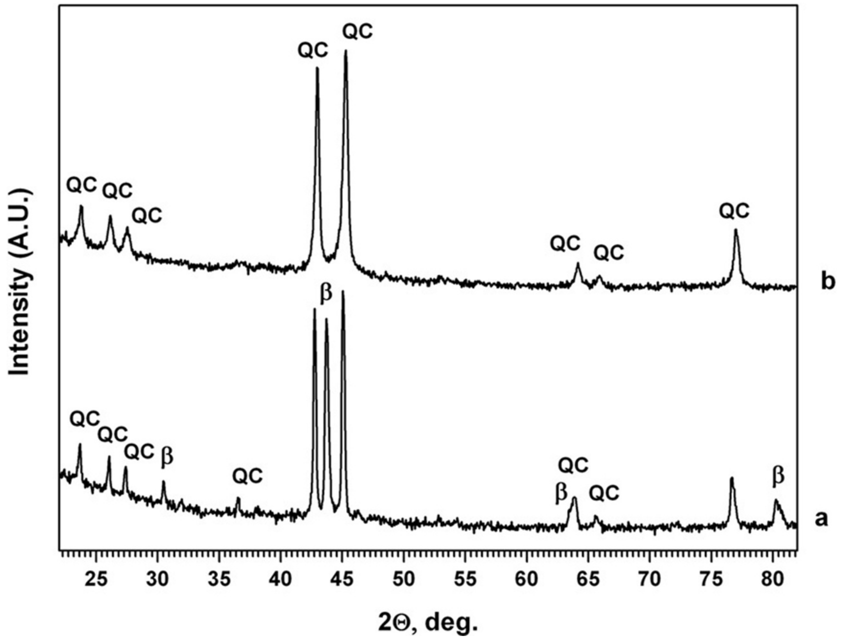

FIG. 10.6 X-ray patterns of water-atomized $Al_{63}Cu_{25}Fe_{12}$ powder of 40–63 μm fraction before (a) and after (b) vacuum annealing at 973 K over 2 h.

REFERENCES

[1] Shechtman D, Blech I, Gratias D, Cahn JW. Metallic phase with long-range Orientational order and no translational symmetry. Phys Rev Lett 1984;53:1951–3.

[2] Ebert P, Feuerbacher M, Tamura N, Wollgarten M, Urban K. Evidence for a cluster-based structure of AlPdMn single quasicrystals. Phys Rev Lett 1996;77(18):3827–30.

[3] Feuerbacher M, Metzmacher C, Wollgarten M, Baufeld B, Bartsch M, Messerschmidt U, Urban K. The plasticity of icosahedral Quasicrystals. Mat Sci Eng A 1997;233(1–2):103–10.

[4] Katz A, Gratias D. Chemical order and local configurations in AlCuFe-type icosahedral phase. In: Janot C, Mosseri R, editors. Proceedings of the 5th International Conference on Quasicrystals; 1995 May 22–26; Avignon, France, Singapore: World Scientific; 1995. p. 164–7.

[5] Bendersky L. Quasicrystal with one-dimensional translational symmetry and a tenfold rotation axis. Phys Rev Lett 1985;54(14):1461–5.

[6] Dubois JM. New prospects from potential applications of quasicrystalline materials. Mat Sci Eng A 2000;294–296:4–9.

[7] Dong C, Perrot A, Dubois JM, Belin E. Hume-Rothery phases with constant e/a value and their related electronic properties in Al-Cu-Fe(-Cr) Quasicrystalline systems. Mater Sci Forum 1994;150–151:403–16.

[8] Berger C, Mayou D, Cyrot-Lackmann F. “Anti” Metallic Properties of Quasicrystals. In: Janot C, Mosseri R, editors. Proceedings of the 5th International Conference on Quasicrystals; 1995 *May 22–26;* Avignon, France, Singapore: World Scientific; 1995. p. 423–30.

[9] Tritt TM, editor. Thermal Conductivity Theory, Properties and Applications. Springer; 2004.

[10] Brunner D, Plachke D, Carstanjen H. The strain-softening phenomenon of icosahedral Al-Pd-Mn single quasicrystals. Mat Sci Eng A 2000;294–296:773–6.

[11] Takeuchi S, Suzuki T, Asao T. Effect of plastic deformation on the electrical conductivity in single-quasicrystals of icosahedral Al-Pd-Mn. In: Takeuchi S, Fujiwara T, editors. Proceedings of the 6th International Conference on Quasicrystals; 1997 May 26–30; Tokyo, Japan, Singapore: World Scientific; 1997. p. 545–8.

[12] Eckert J, Schultz L, Urban K. Formation of quasicrystals by mechanical alloying. Appl Phys Lett 1989;55:117–9.

[13] Ivanov EY, Konstanchuk IG, Bokhonov BD, Boldyrev VV. Mechanochemical synthesis of icosahedral phases in Mg-Zn-Al and Mg-Cu-Al alloys. Reactiv Solids 1989;7:167–72.

[14] Bokhonov B, Konstanchuk I, Ivanov E, Boldyrev VV. Stage formation of quasi-crystals during mechanical treatment of the cubic Frank-Kasper phase $Mg_{32}(Zn, Al)_{49}$. J Alloys Compd 1992;187(1):207–14.

[15] Konstanchuk IG, Ivanov EY, Bokhonov BB, Boldyrev VV. Hydriding properties of mechanically alloyed icosahedral phase $Ti_{45}Zr_{38}Ni_{17}$. J Alloys Compd 2001;319(1–2):290–5.

[16] Shevchukov AP, Sviridova TA, Kaloshkin SD, Tcherdyntsev VV, Gorshenkov MV, Churyukanova MN, et al. Decagonal quasicrystalline phase quasicrystalline phase in as-cast and mechanically alloyed Al–Cu–Cr alloys. J Alloys Compd 2014;586:391–4.

[17] Srinivas V, Barua P, Murty BS. On icosahedral phase formation in mechanically alloyed $Al_{70}Cu_{20}Fe_{10}$. Mater Sci Eng A 2000;294–296:65–7.

[18] Nicula R, Jianu A, Grigoriu C, Barfels T, Burkel E. Laser ablation synthesis of Al-based icosahedral powders. Mat Sci Eng A 2000;294–296:86–9.

[19] Giacometti E, Guyot P, Baluc N, Bonneville J. Plastic behavior of icosahedral Al-Cu-Fe quasicrystals: experiment and modeling. Mat Sci Eng A 2001;319–321:429–33.

[20] Dubois JM, Belin-Ferré E. Wetting and adhesion properties of quasicrystals and complex metallic alloys. Appl Adhes Sci 2015;3(28):1–16.

[21] Michot G. Production of icosahedral Al-Cu-Fe powders by centrifugal atomization method. In: Janot C, Mosseri R, editors. Proceedings of the 5th International Conference on Quasicrystals; 1995 May 22–26; Avignon, France, Singapore: World Scientific; 1995. p. 794–7.

[22] Zhenhua C, Yun W, Duosan Z, Xiangyang J. Preparation and consolidation of Al-based alloy quasicrystalline powders. Scripta Met 1990;24:599–604.

[23] Naboychenko SS, editor. Nonferrous metal powders handbook. Moscow: Metallurgya; 1997 [in Russian].

[24] Method of making quasicrystal alloy powder, protective coatings and articles, United States patent US 5433978. 1995 Jul 18.

[25] Sordelet DJ, Kim JS, Besser MF. Dry Sliding of polygrained quasicrystalline and crystalline Al-Cu-Fe alloys. In: Dubois JM, Tiel PA, Tsai AP, Urban K, editors. Quasicrystals, 553. Warrendale, PA: MRS Symposium; 1999. p. 459–71.

[26] Dubois JM. Useful quasicrystals. Singapore: World Scientific Publishing Co. Pte. Ltd; 2005.

[27] Available from: http://www.coatingsolutions.saint-gobain.com.

[28] Kenzari S, Bonina D, Degiovanni A, Dubois JM, Fournée V. Quasicrystal-polymer composites for additive manufacturing technology. Acta Phys Polonica A 2014;126(2):449–52.

[29] Kenzari S, Bonina D, Dubois JM, Fournée V. Quasicrystal–polymer composites for selective laser sintering technology. Mat Des 2012;35:691–5.

[30] Kimura H, Inoue A, Sasamori K. Microstructure and mechanical properties of P/M Al-V-Fe and Al-Fe-M-Ti (M = V, Cr, Mn) alloys containing dispersed Quasicrystalline particles. Mater Trans JIM 2000;41(11):1550–4.

[31] Garcia-Escorial A, Natale E, Cremaschi VJ, Todd I, Lieblich M. Microstructural transformation of quasicrystalline AlFeCrTi extruded bars upon long thermal treatments. J Alloys Compd 2015;643:199–203.

[32] Vojtěcha D, Michalcová A, Pruša F, Dáma K, Šedá P. Properties of the thermally stable $Al_{95}Cr_{3.1}Fe_{1.1}Ti_{0.8}$ alloy prepared by cold-compression at ultra-high pressure and by hot-extrusion. Mater Charact 2012;66:83–92.

[33] Audebert F, Galano M, Triveco Rios C, Kasama H, Peres M, Kiminami C, et al. Nanoquasicrystalline Al–Fe–Cr–Nb alloys produced by powder metallurgy. J Alloys Compd 2013;577:650–7.

[34] Neikov OD, Krajnikov OV, Milman YuV, Vasyl'ieva HI, Sirko OI, Tokhtuiev VH. Method for production of semi-finished products of aluminium alloys. UA Patent 66588, 2005 Sept 15 [in Russian].

[35] Krajnikov AV, Gastel M, Ortner HM, Likutin VV. Surface chemistry of water atomised aluminium alloy powders. Appl Surf Sci 2002;191:26–43.

[36] Milman YV, Sirko AI, Iefimov MO, Neikov OD, Sharovsky AO, Zakharova NP. High-strength aluminum alloys reinforced by nanosize quasicrystalline particles for elevated temperature application. High Temp Mater Processes 2006;25(1–2):19–29.

[37] Iefimov MO, Lotsko DV, Milman YV, Borisova AL, Chugunova SI, Neikov OD. Structure and high-temperature properties of the alloyed quasicrystalline Al-Cu-Fe powders and thermal-sprayed coatings from them. High Temp Mater Processes 2006;25(1–2):31–8.

[38] Mordyuk BN, Prokopenko GI, Milman YV, Iefimov MO, Grinkevych KE, Sameljuk AV, Tkachenko IV. Wear assessment of composite surface layers in Al–6Mg alloy reinforced with AlCuFe quasicrystalline particles: Effects of particle size, microstructure and hardness. Wear 2014;319:84–95.

FURTHER READING

[39] Bokhonov BB, Ivanov EY, Tolochko BP, Sharaphutdinov MP. In situ study of structural transformations of $Mg_{44}Al_{15}Zn_{41}$ quasicrystals under heating. Mater Sci Eng A 2000;278:236–41.

[40] Takasaki A, Han CH, Furuya Y, Kelton KF. Synthesis of amorphous and quasicrystal phases by mechanical alloying in Ti45Zr38Ni17 powder mixtures and their hydrogenation. Philos Mag Lett 2002;82:353–61.

[41] Lityńska-Dobrzyńska L, Dutkiewicz J, Stan-Głowińska K, Wajda W, Dembinski L, Langlade C, et al. Characterization of aluminium matrix composites reinforced by Al–Cu–Fe quasicrystalline particles. J Alloys Compd 2015;643:114–8.

[42] Yamasaki M, Nagaishi Y, Kawamura Y. Inhibition of Al grain coarsening by quasicrystalline icosahedral phase in the rapidly solidified powder metallurgy Al–Fe–Ti–Cr alloy. Scr Mater 2007;56:785–8.

Chapter 11

Porous Powders and Metallic Foams

Oleg D. Neikov
Frantsevich Institute for Problems of Materials Science (IPMS), Kiev, Ukraine

Chapter Outline

Introduction 323
Porous Powder 323
  Material Selection 324
  Powder Preparation 324
  Compaction Methods 325
  Sintering 326
  Mechanical Properties 326
  Applications 326
Metallic Foams 328
  Closed-Cell Metallic Foams 330
  Foaming Agents 334
  Open-Cell Metallic Foams 336
  Materials 338
References 346

INTRODUCTION

Porous and cellular powder metallurgy (PM) materials find a wide variety of applications. Using similar techniques and manufacturing equipment as structural PM components, porous and cellular PM materials are commonly sintered to densities between 25% and 85% of theoretical mean density (TMD) while structural PM parts are typically 85%–99.9% of TMD. These designed materials provide specialized production for applications such as filters, self-lubricating bearings, battery electrodes, flow-control devices and flow restrictors, shock absorbing materials, floating structures, boundary layer control, cushioning, damping, insulation, and many other applications. Highly porous materials have a high stiffness combined with a very low specific weight due to very high porosities. Because of this, cellular materials frequently occur as constructional materials.

There is no established porous powder terminology. Thus "cellular metals" were regarded by Banhart [1] as the most general term, referring to a metallic body in which any kind of gaseous void is dispersed while the "porous metals" are a special type of cellular metal that is usually round and isolated from other pores. The metal foams are considered a special class of cellular metals that originates from liquid-metal foams and have round cells, or polyhedral closed cells, which are separated from each other by thin films.

Cellular metals and metallic foams by Lefebvre et al. [2] are identified as metals with pores deliberately integrated into their structure. Also, the cellular metals or porous metals terms are general expressions referring to metals having a large volume of porosities while the terms foamed metal or metallic foams apply to porous metals produced with processes where foaming take place. Besides, the term "metal sponge" refers to highly porous materials with complex and interconnected porosity where the porosity cannot be subdivided into well-defined cells.

In the current chapter, the terms "porous" and "cellular metals" in accordance with ISO 13314: 2011 Standard [3] are accepted. Under this standard, the terms "cellular metals" and "metallic foams" are identified.

POROUS POWDER

Selection of the production method is decisive for determining the final mechanical properties and porous characteristics of the porous product. It is based on the powder characteristics and type of porosity required by the application. The preparation of the powders, the use of additives, the compaction methods, and the sintering conditions must be closely controlled to produce uniform and repeatable porous characteristics.

Handbook of Non-Ferrous Metal Powders. https://doi.org/10.1016/B978-0-08-100543-9.00011-7
© 2019 Elsevier Ltd. All rights reserved.

Material Selection

A wide variety of PM materials can be selected, depending on application requirements and economics. The porosity is determined by the particle size distribution, particle shape, powder surface morphology, and other powder characteristics that are dependent on the material production technique. Because the powder characteristics are one of the major factors in determining the porous material properties of the finished product, reproducible powder characteristics and manufacturing methods are critical to the production of a consistent product.

Bronze, nickel, and nickel base alloys are the most common porous PM materials. Other nonferrous metals such as aluminum, copper, gold, niobium, silver, tantalum, titanium, and zirconium are fabricated into porous materials from powder [4].

The size distribution of particles can be a direct result of the powder production process or can be altered by classification techniques or additional processing [5].

Bronze powders containing of 89%–90% Cu, 10%–11% Sn, and 0.1%–0.5% P are the most common materials for porous bronze PM parts such as filters and self-lubricating bearings. A small addition of phosphorous improves mechanical strength [6]. More information on bronze PM products can be found in Chapter 19.

Bearings can be manufactured from premixed elemental powder or prealloyed powders. Air or inert gas atomization of prealloyed 89/11 or 90/10 bronze yields spherical particles that can be processed to low densities by gravity sintering, as illustrated in Fig. 11.1 [7]. Bronze particles were also made by coating atom-sated copper powder with tin with a size range of 45–100 μm, depending on the powder type. Rounded particles are made by cutting tin-coated copper wire with a composition of 93%–97% Cu and 3–7 Sn [8].

The filamentary chain-type nickel powders produced by carbonyl decomposition with very fine particle size and narrow size distribution are possible using the porous PM process. This process can result in uniform pore material after processing, as shown in Fig. 11.2. Components with higher porosity and finer pore sizes are produced by applying very low compaction pressures of <7 MPa [9].

Powder Preparation

After the material is selected, powder preparation begins with the separation of the desired size distribution. Depending on the kind of secondary processing, commercial powders are available with either wide or narrow particle size distributions. The porous product manufacturers produce powders with narrow size distributions by removing oversized and undersized particles or by adding a screen to obtain another narrow size distribution. Vibratory or ultrasonic sieve screening methods are used for particles >20 μm while other methods such as air classification or centrifugal separation are used for particles <20 μm.

The porous PM products manufactured from narrow particle size distribution powders have better reproducibility and uniformity of the final porosity.

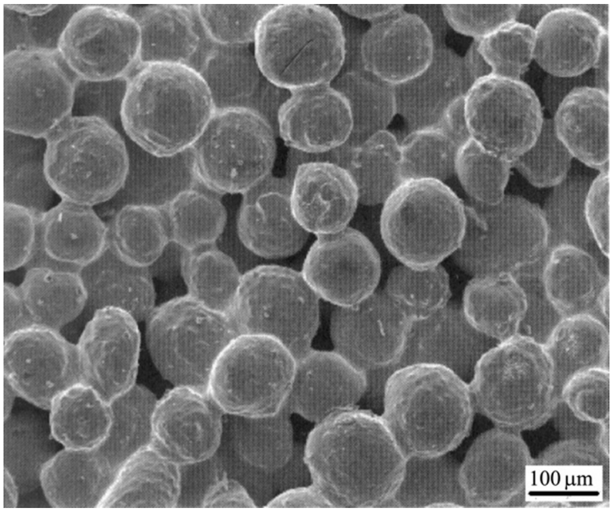

FIG. 11.1 Bronze particles gravity sintered to 64% density. *(Modified from M. Eisemann, R. Morgan, Porous powder metallurgy technology, In: Article in ASM handbook, vol. 7, ASM International Publishers, Materials Park, OH, 2015, pp. 799–805.)*

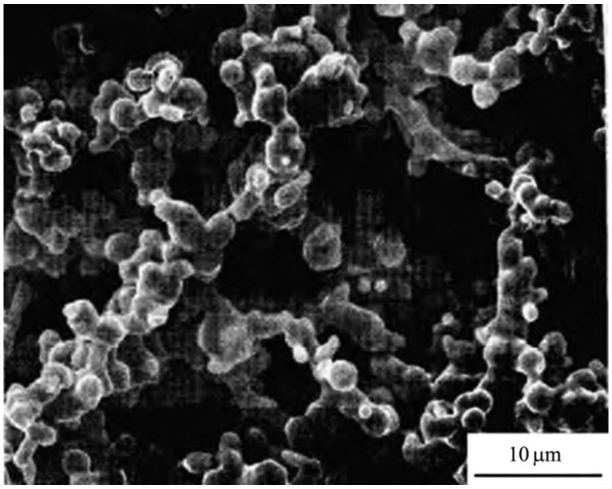

FIG. 11.2 Carbonyl nickel powder particles with a size range of 2–4 μm compacted and sintered to 35% density. *(Modified from M. Eisemann, R. Morgan, Porous powder metallurgy technology, In: Article in ASM handbook, vol. 7, ASM International Publishers, Materials Park, OH, 2015, pp. 799–805.)*

When the desired particle size distribution is obtained, the powder must be thoroughly blended prior to use in order to avoid segregation and to maximize homogeneity. However, excessive blending can modify the powder characteristics as a result of the formation of additional fine powder particles or by changing the particle surface. The apparent and tap densities of the powder's narrow cuts are measured to control tight specifications because these characteristics regulate further processing steps such as powder flow and die filling. Additives such as pore formers, lubricants, or binders are precisely mixed with powder when it is required during processing [10,11].

The powder cleanliness requirements must be carefully controlled to avoid contamination with outside materials during powder preparation and further processing. The use of porous materials with contamination from elements such as iron, carbon, sulfur, and others can lead to a significant reduction in the mechanical properties and corrosion resistance of porous materials when used in an aggressive environment. Other trace impurities such as oxygen, alumina, silica, and nitrogen can also influence the final mechanical properties.

Compaction Methods

Compaction and further sintering are usually required to produce porous materials from prepared powders in order to achieve the best combination of mechanical strength and porosity. Lower density and higher permeability parts from metals such as nickel and nickel-based alloy materials can be made by a gravity sintering process without compaction of the powders when the application does not require high strength levels.

Die compaction, isostatic pressing, and roll compaction technique are commonly used for the production of porous materials. These processes increase the green strength of the parts by cold welding of the particles with each other at contact areas due to plastic deformation.

Die compaction and sintering are the most common methods of improving mechanical properties while achieving the lowest density part in order to maximize porosity and permeability. Minimum green operation strength can be obtained by using lower compaction forces in the range of 70–210 MPa. By comparison, higher-density structural PM components require compaction pressures of 420–840 MPa [12]. Porous components with 20%–50% green densities usually have minimal green strength and require careful handling. Waxes and stearates are commonly added to the powder to reduce die-wall friction and tool wear.

Isostatic compaction is a common method of compaction for manufacturing semiproducts such as tubes that have a length-to-diameter ratio >3 to 1. The isostatic technique can produce porous components with more uniform density than can die compaction [13,14]. The wet-bag cold isostatic pressing (CIP) process uses pressure ranging from 3.5 to 550 MPa applied to tooling [15]. Other near-net shapes such as cones, funnels, and tubes with splines can be manufactured by CIP [16]. Hot isostatic pressing (HIP) that combines the CIP and sintering in one step is used in applications where complex shapes are needed or when a material has low green strength for handling.

Roll compaction of porous nickel sheet materials has been commonly used in the production of battery materials [17,18]. Nickel and other powders are rolled to a thickness ranging from 0.13 to 3.8 mm and widths up to 1 m, depending

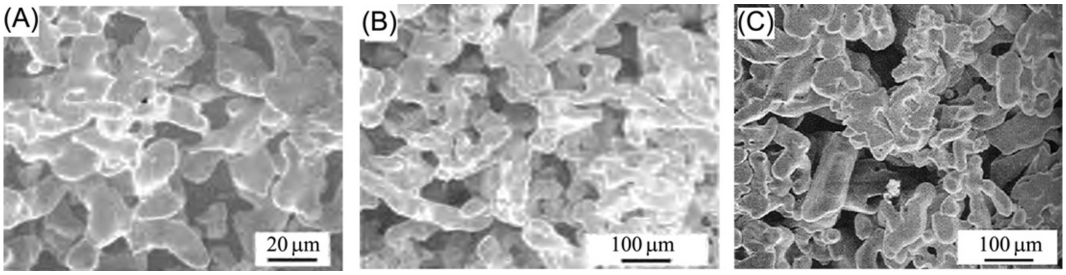

FIG. 11.3 Scanning electron micrograph of (A) titanium powder produced by calcium reduction method, (B) and (C) the microstructure of the rolled plates with 30% and 50% theoretical density, correspondingly.

on the green strength and requirements of the application. Titanium porous plates and foils were manufactured by rolling a billet compacted from powders produced by the calcium reduction method [19]. Detailed information on the calcium reduction method can be found in Chapter 18. A scanning electron micrograph of titanium powder produced by calcium reduction method is shown in Fig. 11.3A. The Fig. 11.3B and C illustrate the microstructure of the rolled plates with 30% and 50% theoretical density, respectively. Powder particles are welded to each other with a honeycomb-like structure and connected pore formation.

The rolled sheet can be directly fed into a sintering furnace to minimize handling operations in certain high-volume applications. Shapes or patterns can often be designed into the rolls, or components can be stamped from the finished porous sheet. Roll compaction is used to produce an economical, uniform density material with tight dimensional tolerances.

Other forming methods used to obtain porous metal components include metal injection molding [20], centrifugal slurry casting [21], extrusion, gravity filling of shaped molds, direct typing method [22], laser deposition by direct typing [23], and wet powder spraying [24]. Complicated shapes and lower-density components are formed using pore formers such as water and/or thermoplastic binders that allow adequate handling strength. Removal of the additives prior to sintering is ordinarily realized in the preheat zone of the furnace or in a separate controlled baking process. Metal spraying can create a controlled porous structure with or without former additives by spraying molten metal onto a base material to combine compaction and sintering processes [25].

Sintering

Sintering of porous metal is a crucial balance between maximizing material properties and maximizing the open porosity and permeability. However, permeability and material properties such as strength and ductility are usually inversely related and the area in which the optimum compromise is obtained is quite small. Sintering temperature is selected depending on the material type, the powder particle size distribution, and the powder particle shape. Sintering is ordinarily done at 70%–90% of the material melting temperature. Finer powder particles require a lower sintering temperature because the surface energy driving force to initiate bond growth is much higher than for the coarser particles. Sintering at too high a temperature also leads to the formation of large pores.

Mechanical Properties

The mechanical properties of porous materials are highly dependent on the porosity and processing method. Table 11.1 contains typical values for tensile strength, elongation, and shear strength of 90 wt% copper/10 wt% tin bronze discs as a function of density and filter grade. Mechanical properties increase significantly as the pore size and the percentage of porosity decrease.

Applications

Filtration, battery electrodes, self-lubricated bearings, and flow control are the largest commercial applications of the porous PM materials. Filtration and separation technology applications are the largest market for porous PM materials. Many industrial applications require fine filtration capability, excellent mechanical properties, and corrosion resistance, especially at elevated temperatures and high pressures. Various porous materials and design for the filters are used for gas cleaning by filtration.

TABLE 11.1 Typical Mechanical Properties of Bronze 90%Cu/10%Sn

Material	Filter Grade (μm)[a]	Density (%)	Minimum UTS (MPa)[b]	Elongation (%)	Shear Strength (MPa)[c]
Bronze	10	75	48	8	130
	20	68	41	6	110
	40	62	35	4	100
	90	57	28	3	75
	150	54	21	2	40
	250	52	14	2	30

[a] *Filter grades in micrometers as estimated by the bubble-point test method [20,21].*
[b] *Ultimate tensile strength.*
[c] *Shear strength is the punching force divided by the sheared edge area per DIN standard V 30910 [22].*

Advanced porous sintered metal is developed for diesel soot filtration [26]. The demand for a flexible porous sheet material with excellent properties needs the combination of metal powder and fully dense metal. Porous parts that are only based on powder with high porosity could not achieve good vibration resistance. Besides, weldability of highly porous materials does not meet the demands for a lifetime of welded connections. Therefore, latticed metal is selected for the matrix material. Water-atomized powder is preferable to reach the best filtration efficiencies.

Fig. 11.4 shows the main process steps from the metallic powder to the manufactured article. By varying powder particle size, binder, and additive content, one can adjust some properties of the filter material adapted to the demands of customers. The scanning micrographs (Fig. 11.5) give a view of the porous material: the surface of the porous (A) and the interconnection between metal powder and the metallic lattice (B). In the latter, one can obviously see the lattice fragments.

Sintered metal porous filters are characterized by the following: thickness is 0.38 mm, porosity is 45%, area weight is 1700 g/m^2, mean pore size is 10 μm, and air permeability amounts to 100 m^3/(m^2 h) by hydraulic resistance 200 Pa. The view of the Jetfilter for passenger cars, based on the above filter material, is shown in Fig. 11.6A with its entrance in Fig. 11.6B. The 60 filter pockets are placed symmetrically for a filter in a cylindrical casing with a 150 mm diameter. By selecting 250 mm for the length of the filter, a surface of 1.8 m^2 · is obtained. This size is enough for diesel engines up to a 2-L cylinder and ensures gas cleaning from soot without replacement during running at 100,000–120,000 km.

Two-layer porous powder material is developed for highly effective separation of mechanical impurities and water from petroleum products [27]. The substrate is made from sintered bronze or titanium powder with a thickness of 3–4 mm. The second layer, with average pore sizes of 20–22 μm, is made from fluoroplastic powder. The degree of cleaning from oil, water drops, and moisture in the first layer and second layer is not <97% and 99.3%, respectively.

Over the last decades, intermetallic compounds such as NiAl as well as Ni-based alloys, for example, Inconel, have been developed to serve under extreme conditions demanding excellent high-temperature stability and oxidation/corrosion resistance. For many applications such as high-temperature filtration porous structures, diesel soot traps, and catalyst carriers, these materials are required.

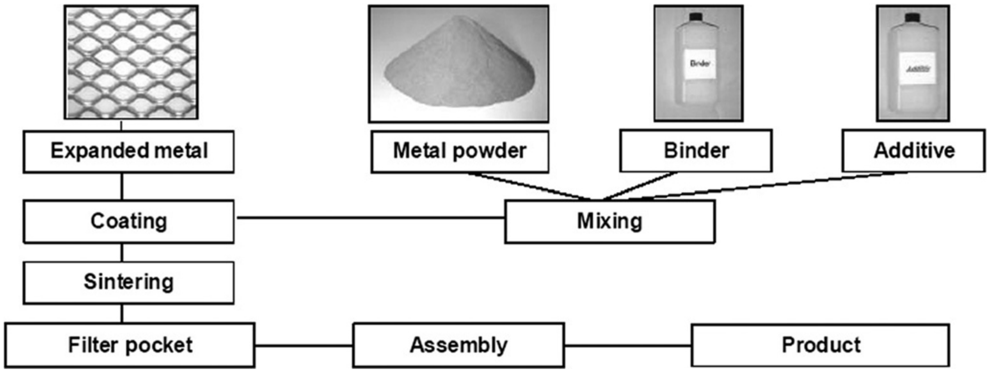

FIG. 11.4 Main process steps from the metallic powder to the manufactured filter.

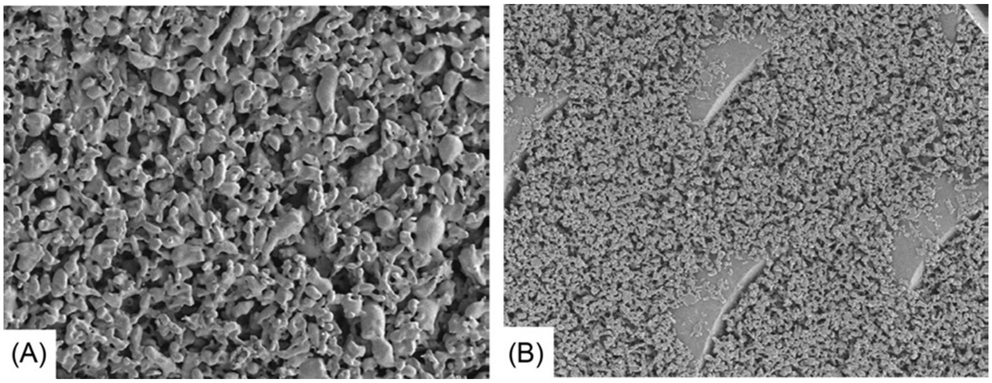

FIG. 11.5 Scanning micrographs of porous material: (A) the surface of the porous material and (B) the interconnection between metal powder and the metallic lattice. *(Modified from S. Steigert, Porous sintered metal for soot filtration. In: Compiled by European Powder Metallurgy Association (Bellstone Shrewsbury, UK). Proceedings of 2004 Powder Metallurgy World Congress, Vienna, vol. 4, 2004, pp. 195–200.)*

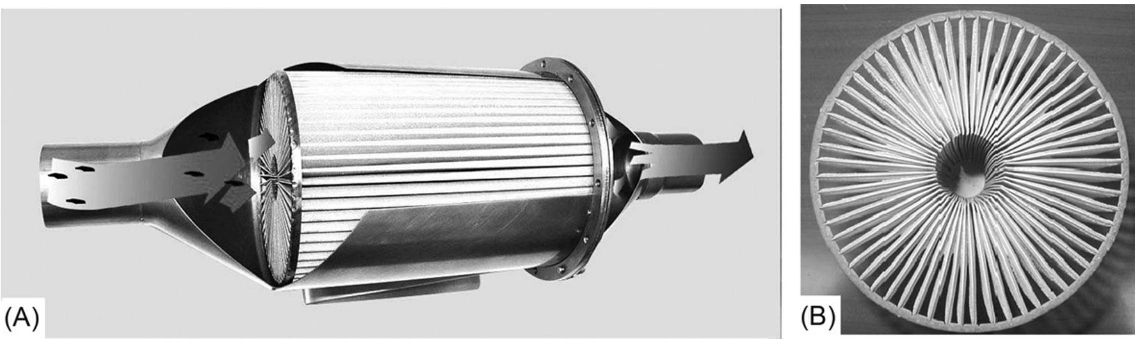

FIG. 11.6 Jetfilter for passenger cars: (A), general view of jetfilter and (B) jetfilter entrance.

Laminar flow control devices using porous PM flow throttles [4,7] are more accurate and reliable than other volumetric flow-restricting devices such as orifices and micrometering valves that operate at higher fluid velocities. Porous PM materials are less susceptible to contamination and blockage because there are hundreds of fine jets instead of a single orifice.

Several application fields of porous PM materials demand the extremely high internal surface area and porosity available [7,14,18,19]. For example, the conductivity of the electrodes for alkaline batteries and fuel cells can be significantly increased by a large contact area with the reaction fluid. Biomedical implants use the large surface area to allow tissue growth into the porous structure to ensure good joint attachment.

In the gas-liquid contacting processes, flowing gas through a fine-grade, porous PM material with a high surface area produces tiny bubbles that result in a high-efficiency transfer contact of the gas to the liquid [4]. Conventional drilled pipe spargers produce larger bubbles that do not dissolve and react as well as the finer bubbles generated by porous metals. Simultaneously, finer pore materials prevent the liquid from penetrating back into the pores at lower internal pressures.

Boundary layer control devices such as flotation bars and vacuum hold down plates are highly specialized applications [4]. A boundary layer of air in order to eliminate contact turning of thin films, tapes, or webs can be formed on the outside surface of a fine-porosity tube when the inside cavity is pressurized.

The major application areas of porous PM materials are summarized in Table 11.2. As is shown, many specialized applications have been developed to take advantage of the unique characteristics of porous materials.

Thus, the application of porous powder metallurgy technology is rapidly developing as a cost-effective, commercially viable technique that offers diverse solutions to technical challenges. The powder characteristics are key factors in determining the porous material properties of the finished product. Therefore, the powder selection and manufacture methods are critical to produce a consistent product.

METALLIC FOAMS

In contrast to any other porous metal materials, metal foams are characterized by a very low specific weight. Using PM technology, density values ranging between 0.5 and 1 g/cm^3 are usually obtained. These diapason values can be widened

TABLE 11.2 Major Application Areas of Porous PM Materials

Filtration/separation technology		
Analysis instruments	Food and beverage	Polymer processing
Gas/liquid chromatography	Cooking oil, corn syrup	Caustic/sizing recovery
Gas sampling	Juice/sugar clarification	Gel dehydration
Sensor protection	Removal of yeast from beer	Polymer fibers
Chemical processing	Mineral processing/concentration	Power generation
Catalyst recovery	Catalyst manufacturing	Condensate aqua
Gases and liquids processing	Coal, silica, silicon, and metal oxides	Fossil fuel waste and flue gases
Fluid-bed reactor product and electrolytes	Metal sulphides	Radioactive material refining
Chemicals	Petrochemical industry	Semiconductor
Acids, solvents, and inks	Flue gases	Bulk gas delivery systems
Adhesives and greases	Fluid cracking catalysts	Particle removal process gas
Precipitates, solutions, and salts	Slurry oils	Purifier media retainers
Fluid power	Pharmaceutical	Other filter areas
Pneumatic equipment	Autoclave vent filters	Aircraft and marine fuel
Protect hydraulic valves	Oxygen filters	Automotive diesel soot filters and oil burners
Water separation in air lines	Process steams	Paper, pulp, and incinerators
Reservoirs and capillary attraction		
Applicators	Heat sinks	Microelectronics packaging
Atomizers	Insulating components in furnace constructions	Printer ink reservoirs
Die-wall lubrication	Liquid wicks, evaporation	Self-lubricating bearings
Heat exchangers	Microelectronics satellites for cooling devices	Transpiration cooling
Dampening		
Exhaust silencers/mufflers	Microphone frequency	Sound attenuation
Flame arresters/quenching	Pressure equalization	Telephone transmitters
Hearing aids	Pressure snubbers	Vibration reduction
Flow control devices		
Calibrated leaks	Flow rate timing devices	Vacuum delay valves
Gas and liquid metering	Flow restrictors	Vents and breathers
Surface area devices		
Batteries	Cathode dispensers	Fuel cells
Biomedical implant/prosthesis	Electrodes	Ionizers

Continued

TABLE 11.2 Major Application Areas of Porous PM Materials—cont'd

Gas-liquid contacting		
Aerators	Bubblers	Spargers
Agitation of liquids	Carbonators	Chlorine and oxygen bleaching
Bioremediation	Enhances chemical reactions	Hydrogen ion exponent control
Oxygenation, fish farming	Fermentation	Oxygen and volatile stripping
Steam injectors/heat transfer	Hydrogenation	Water/oil separation
Boundary layer control		
Air bearings	Friction reduction	Polymer fiber cooling
Flotation devices	Material handling/transport	Turning bars for film/webs
Fluidizer plates for fluid bed	Mold release	Vacuum plates

down to 0.2 g/cm^3 and up to 2.0 g/cm^3. In the case of closed porosity, aluminum foam floats on water. Because of these features, cellular materials are frequently used as constructional materials. Cellular materials find wide use for damping, cushioning, insulating, filtering, construction, and in many other applications.

Closed-Cell Metallic Foams

Production methods are distinguished first between molten metal or metal powder of the liquid material state. A second difference is the gas source used for creating porosity. Third, foaming can be instantaneous, or an intermediate product is created that can be foamed in a later stage (delayed foaming). Fig. 11.7 contains an overview of the main methods available for metal foam making.

Foaming of Melts With Blowing Agents (Alporas)

In this process with the trade name *Alporas,* the foaming agent is introduced directly into the melt. Shinko Wire Company, Amagasaki, Japan, has been producing n this way since 1986 with a production volume up to 1000 kg/day [1].

In the first step, about 1.5 wt% calcium metal is added to an aluminum melt at 953 K (Fig. 11.8). The melt is stirred for several minutes, during which its viscosity continuously increases by a factor of up to five because of the formation

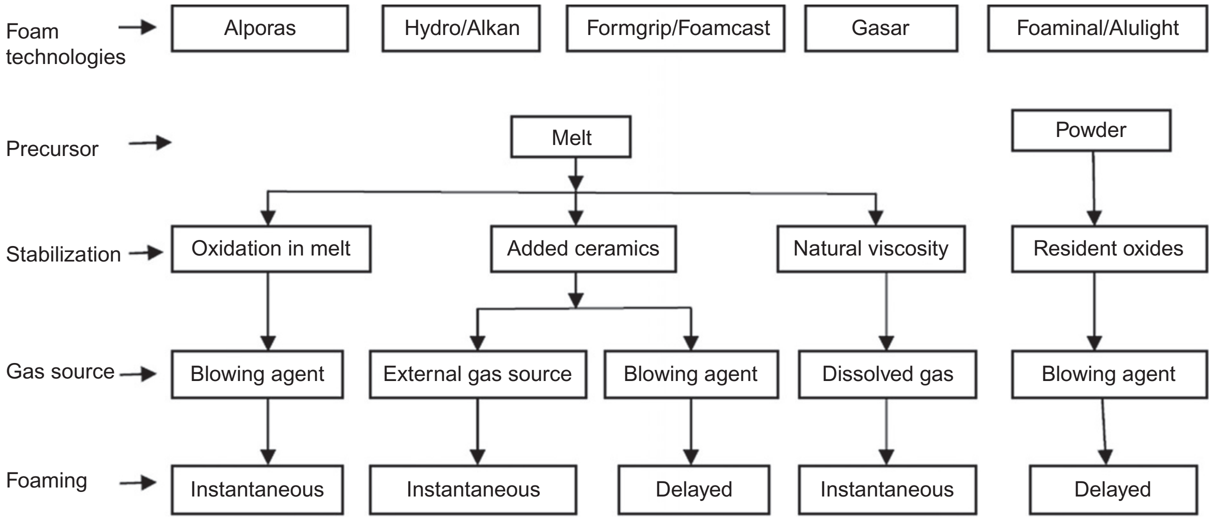
Foam technologies
Alporas
Hydro/Alkan
Formgrip/Foamcast
Gasar
Foaminal/Alulight
Precursor
Melt
Powder
Stabilization
Oxidation in melt
Added ceramics
Natural viscosity
Resident oxides
Gas source
Blowing agent
External gas source
Blowing agent
Dissolved gas
Blowing agent
Foaming
Instantaneous
Instantaneous
Delayed
Instantaneous
Delayed

FIG. 11.7 Overview of main methods available for metal foam making.

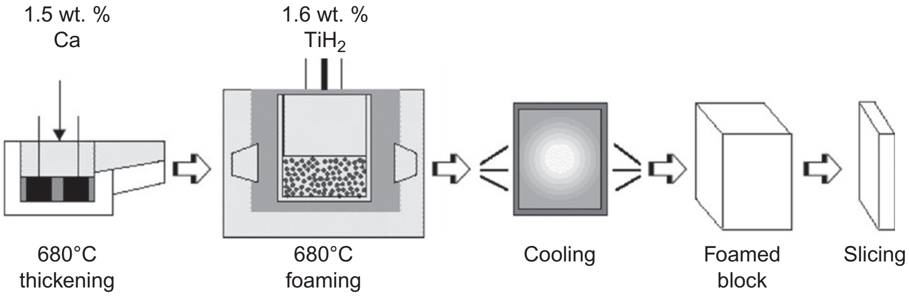

FIG. 11.8 Flowsheet of the foaming of melt with blowing agent process (*Alporas*).

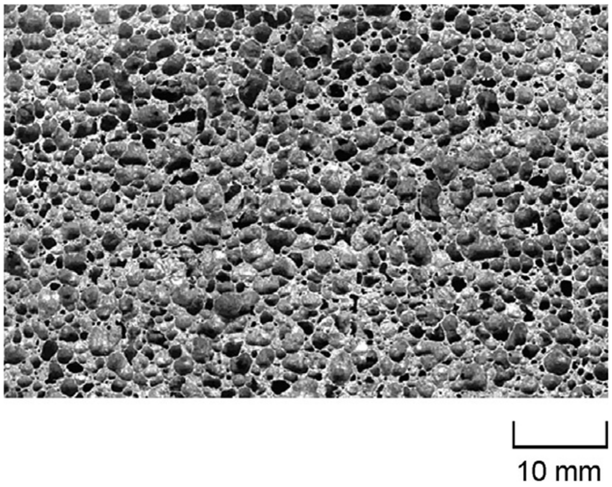

FIG. 11.9 The metallic foam structure. *(Courtesy of Southeast University, China.)*

of calcium oxide (CaO), calcium-aluminum oxide ($CaAl_2O_4$), or perhaps even Al_4Ca intermetallics, which thicken the liquid metal.

After the viscosity has reached the desired value, titanium hydride (TiH_2) is added (typically 1.6wt%), used as a blowing agent by the generation of hydrogen gas in the hot viscous liquid. The melt soon starts to expand slowly and gradually fills the foaming vessel. The foaming takes place at constant pressure. After cooling the vessel below the alloy melting point, the liquid foam turns into solid aluminum foam and can be taken out of the mold for further processing. The entire foaming process can last 15min for a typical batch (2050mm × 650mm × 450mm). The foams produced in this way seem to excel in homogeneity (Fig. 11.9). Typical densities after cutting off the sides of the cast foam blocks are between 0.18 and 0.24 g/cm^3, with the average pore size ranging from 2 to 10mm.

Foaming of Melts by Gas Injection (Hydro/Alcan)

This method with the trade name *Hydro/Alcan* is being used by the Cymat Aluminium Corporation in Canada [28]. The producible metal foam is called Cymat's Stabilized Aluminum Foam (SAF). In this process, shown schematically in Fig. 11.10, silicon carbide, aluminum oxide, or magnesium oxide particles are used to enhance the viscosity of the melt. Therefore, the first step comprises the preparation of an aluminum melt containing one of these substances, making it a metal-matrix composite (MMC). This step requires scrupulous mixing techniques to ensure a uniform distribution of particles.

The melt is foamed in a second step by injecting gases (air, nitrogen, or argon) into it using specially designed rotating impellers or vibrating nozzles. These generate very fine gas bubbles in the melt and distribute them uniformly. The resultant viscous mixture of bubbles and metal melt floats up and is gone on a conveyer belt where it becomes cool and hard. Because ceramic particles are in the melt, the foam is relatively stable. The resulting solid foam is, in principle, as long as desired, as wide as the vessel containing the liquid metal allows it, and typically 100mm thick. The volume fraction of the reinforcing particles typically ranges from 10% to 20% with a mean particle size from 5 to 20 μm. The choice of particle size and content has been carried out empirically. The densities of aluminum foams produced this way range from 0.069 to

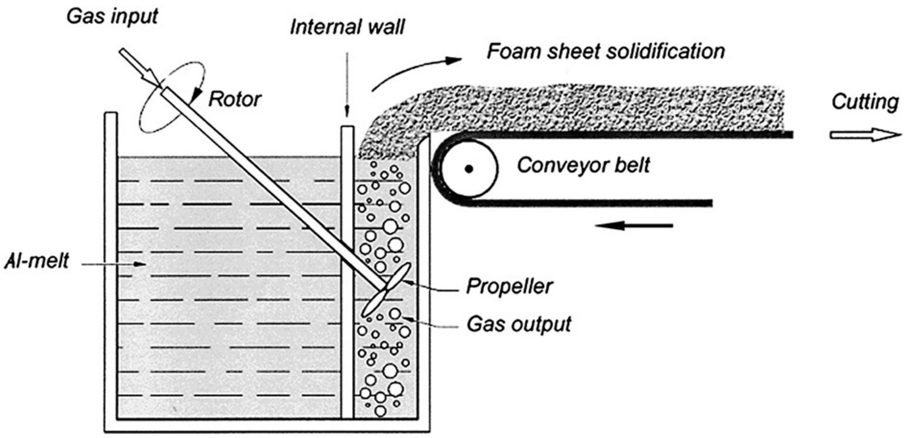

FIG. 11.10 Flowchart of the foaming of melt by the gas injection process (*Hydro/Alcan*).

0.54 g/cm^3, average pore sizes from 25 μm down to 3 μm, and wall thicknesses from 50 to 85 μm. The average cell size is inversely related both to the average cell wall thickness and to the density, and it can be influenced by adjusting the gas flow, the impeller speed, the nozzle vibration frequency, and other parameters.

The slabs usually have a gradient in density, pore size, and pore elongation in the issue of gravitationally induced drainage. Besides, the shearing forces of the conveyor belt lead to diagonally distorted cells in the final product, which becomes isotropic. The foamed material is either used with a closed outer surface (its state upon coming out of the casting machine) or is cut into the required shape after foaming. However, the high content of ceramic particles can make machining of MMC foams difficult.

Advantages of the direct-foaming process include the capability for continuous production of a large volume of foam and the low densities that can be achieved [1]. MMC foams are, therefore, probably less expensive than other cellular metallic materials. A possible disadvantage of the direct-foaming process is the eventual necessity for cutting the foam, thereby opening the cells.

Foaming of Ingots Containing Blowing Agents (Formgrip/Foamcast)

The process name "Formgrip" is an abbreviation of *foaming of reinforced metals by gas release in precursors*. This process consists of the incorporation of titanium-hydride particles directly into an aluminum melt. To avoid untimely hydrogen evolution, the melt has to be either quickly cooled down below its melting point after mixing or the blowing agent has to be passivated to prevent it from releasing gas before solidification. The current technique, also called "Foamcast," was carried out in a die-casting machine, when the powdered titanium-hydride was injected into the die simultaneously with the melt. Normal casting alloys without ceramic additives were used. The current route requires that TiH_2 powders be subjected to a cycle of heat treatments that forms an oxide barrier on each particle and delays decomposition. The powders are then added to a melt and can be cooled at comparatively slow rates after stirring. Melts containing silicon carbide are used to obtain stable foams. The foaming process can be influenced by varying heating rates and final foaming temperatures, thus allowing for the production of a variety of different pore structures [1], as is shown in Fig. 11.11.

Solid-Gas Eutectic Solidification (Gasar)

This process with the trade name *Gasar* (a Russian abbreviation meaning "gas-reinforced") uses the fact that some liquid metals form a eutectic system with hydrogen gas [29]. If one of these metals is melted in a hydrogen atmosphere under high pressure (up to 5 MPa), the result is a homogeneous melt charged with hydrogen. If the temperature is lowered, the melt will eventually undergo a eutectic transition to a heterogeneous two-phase system (solid + gas). As the melt is solidified, gas pores precipitate and are entrapped in the metal. The pore size and shape depend on the hydrogen content, the pressure magnitude, the direction and rate of heat removal, and the chemical composition of the melt. Generally, largely elongated pores oriented in the direction of solidification are formed (Fig. 11.12). Pore diameters range from 10 μm to 10 mm, pore lengths from 100 μm to 300 mm, and porosities from 5% to 75%. The pore size distribution is nonuniform. Pores may be conical or even corrugated.

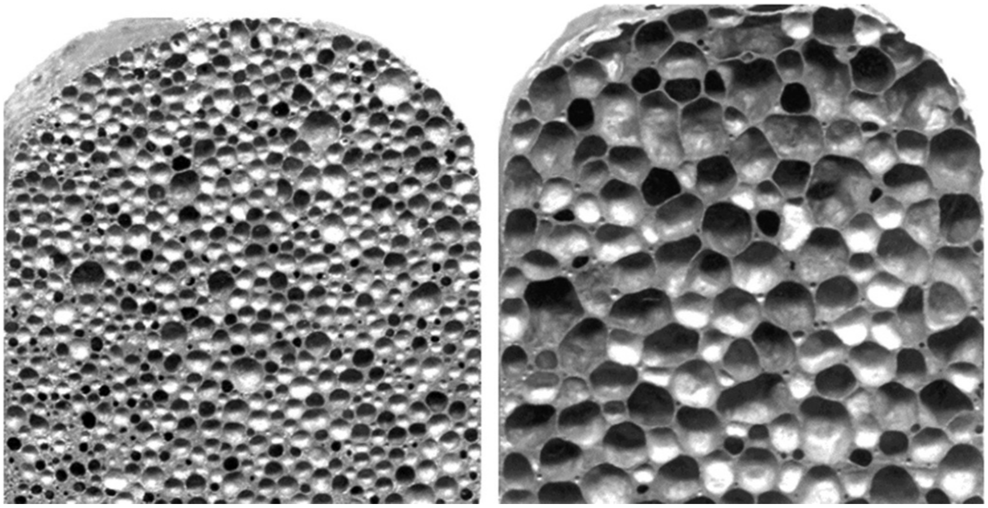

FIG. 11.11 Two samples of aluminum/silicon-carbide foam derived by different process conditions.

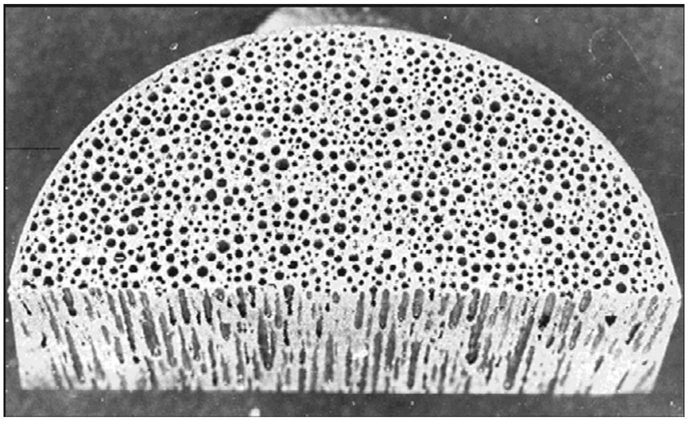

FIG. 11.12 Gasar process metallic foam sample showing largely elongated pores. *(Modified from V. Shapovalov, in: D.S. Schwartz, et al. (Eds.), Porous and cellular materials for structural applications, vol. 521, MRS, Warrendale, PA, 1998.)*

Foaming of Powder Compacts (Foaminal/Alulight)

In this process, foamed metal is prepared from metal powders. The names "Foam-in-Al" and the Austrian company "Alulight" have been used for this process trade name. The production process begins with the mixing of metal powders (elementary metal powders, alloy powders, or metal powder blends) with a blowing agent, after which the mix is compacted to semifinished product condition. Any compaction technique such as uniaxial or isostatic compression, rod extrusion, or powder rolling can be used in which the blowing agent is introduced into the metal matrix without any appreciable residual open porosity. The precursor has to be manufactured very carefully because residual porosity or other defects will appear as negative results in further processing. The next step is heat treatment at temperatures near the melting point of the matrix material. The blowing agent, which is homogeneously distributed within the dense metallic matrix, decomposes and the released gas forces the melting precursor material to expand, forming its highly porous structure. The time needed for full expansion depends on the temperature and size of the precursor and ranges from a few seconds to several minutes. The method is not restricted to aluminum and its alloys; tin, zinc, brass, lead, gold, and some other metals and alloys can also be foamed with appropriate blowing agents and process parameters.

Sandwich panels consisting of a foamed metal core and two metal face sheets can be easily obtained by bonding the face sheets to a piece of foam by means of adhesives. Alternatively, if pure metallic bonding is required, metal sheets (aluminum or steel) are roll clad to a sheet of foam metal [30]. The resulting composite can be deformed in an optional step, for example, deep drawing. The final heat treatment, in which only the foamable core expands and the face sheets remain dense, brings sandwich structures such as the product shown in Fig. 11.13.

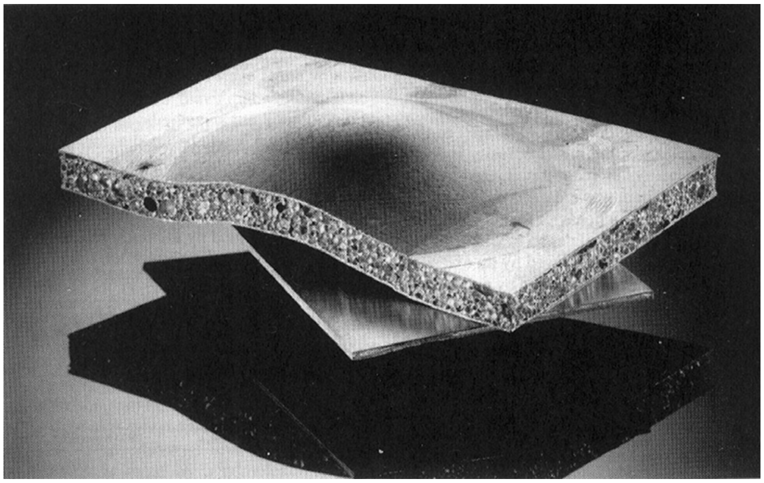

FIG. 11.13 Sandwich component with a porous aluminum foam core and steel face sheets (Article of Studiumgesellschaft Stahlanwendungen, Germany).

Foaming Agents

Titanium hydride (TiH_2) is a popular foaming agent because of its decomposition temperature, which is close to the melting temperature of aluminum and aluminum alloys. However, TiH_2 is expensive and dangerous to handle. Calcium carbonate ($CaCO_3$) is a promising alternative foaming agent, which was listed as one of the appropriate foaming agents along with zirconium hydride and titanium hydride [31,32]. A coating technique with dispersion of $CaCO_3$ in aluminum melts has been proposed by researchers in Japan [33]. In the last decade, the theme of calcium carbonate in a foaming agent role has attracted the attention of many researchers [34–39].

The decomposition of TiH_2 study [40] showed that the decomposition (reaction 11.1) starts at around 693 K and continues up to 1073 K. Most of the hydrogen gas was released from 773 to 973 K.

$$TiH_{2(s)} = Ti_{(s)} + H_{2(g)} \tag{11.1}$$

The decomposition of $CaCO_3$ is usually described by reaction (11.2):

$$\begin{aligned} &CaCO_{3(s)} = CaO_{(s)} + CO_{2(g)} \\ &\Delta G^o = 161 - 0.137T\,\text{kJ} \end{aligned} \tag{11.2}$$

Theoretically, under normal atmospheric pressure, the thermal decomposition of pure $CaCO_3$ is thermodynamically favorable only at temperatures above 1173 K. Nevertheless, in the real system, chemical conversion occurs at the interface of $CaCO_3$ powder and the aluminum semisolid or liquid. The Gergely et al. [34] studies of the $CaCO_3$ powders indicate that they undergo thermal decomposition above about 923 K and this becomes rapid at about 1023 K.

Therefore, in order to have a notion about the real foaming process, additional chemical reactions should be also considered, which are reported in Ref [34]:

$$\begin{aligned} &2Al_{(l)} + 3CO_{2(g)} = Al_2O_{3(s)} + 3CO_{(g)} \\ &{}^*\Delta G^o = -840 + 0.066T\,\text{kJ} \end{aligned} \tag{11.3}$$

$$\begin{aligned} &8Al_{(l)} + 3CO_{2(g)} = 2Al_2O_{3(g)} + Al_4C_{3(s)} \\ &\Delta G^o = -2440 + 0.741T\,\text{kJ} \end{aligned} \tag{11.4}$$

$$\begin{aligned} &6Al_{(l)} + 3CO_{(g)} = Al_2O_{3(s)} + Al_4C_{3(s)} \\ &\Delta G^o = -1600 + 0.674T\,\text{kJ} \end{aligned} \tag{11.5}$$

$$\begin{aligned} &2Al_{(l)} + 3CaCO_{3(s)} = Al_2O_{3(s)} + 3CaO_{(s)} + 3CO_{(g)} \\ &\Delta G^o = -300 - 0.417T\,\text{kJ} \end{aligned} \tag{11.6}$$

In addition, if the melt contains magnesium as the alloying element, MgO and $MgAl_2O_4$ solid phases are also formed, according to reactions (11.7) and (11.8):

$$\begin{aligned} &Mg_{(l)} + CO_{2(g)} = MgO_{(s)} + CO_{(g)} \\ &\Delta G^o = -321 + 0.037\text{T kJ} \end{aligned} \tag{11.7}$$

$$2Al_{(l)} + Mg_{(l)} + 4CO_{2(g)} = MgAl_2O_{4(s)} + 4CO_{(g)}$$
$$\Delta G^o = -1181 + 0.077T \text{ kJ} \tag{11.8}$$

Reactions (11.3)–(11.8) are all thermodynamically favorable at an over temperature range but can only occur at the solid-liquid interface, at a small number of points adjacent to foaming agent particles at the surface of a cell. This brings an undesirable decorating or coating the surface of the cells with solid material during the foaming process.

It was ascertained by Gergely et al. [34] that foams produced using coarse $CaCO_3$ powder (crushed limestone) have lower porosities and coarser cells than those produced using finer, synthetic powder. It seems likely, by the authors' opinion, that this is predominantly due to there being fewer gas nucleation points during foaming with coarser powder while with very fine powder, there may be difficulties in dispersing it effectively in the melt and avoiding agglomeration. Oxides of aluminum and magnesium (when Mg is present in the alloy), likely the spinel $MgAl_2O_4$, are generated during decomposition of the $CaCO_3$ and the associated reaction with the melt. These oxides form on the inner surfaces of the cells created during foaming and they apparently conduce to stabilize the cells against coarsening and coalescence. They also inhibit the migration of ceramic particles to these surfaces.

Closed cell aluminum foam samples were prepared in the work [35], using parallel PM and melt routes, accordingly. The Foaminal/Alulight and Formgrip/Foamcast techniques, under their trade names (Fig. 11.7), modified by introduction of foamable precursors with $CaCO_3$. Precursors obtained by the melt route were machined and additionally cold isostatically pressed in order to improve their density. In all cases, the resulting precursors consisted of an aluminum matrix containing various fractions (3, 5, 7, and 12 wt%) of uniformly dispersed $CaCO_3$ powders of various average particle size ($d_{50} = 38, 72$, and 120 μm). Precursors were foamed by inserting them into a cylindrical stainless steel mold and placing them in a preheated batch furnace at 1023 K for 10 min. Subject to $CaCO_3$ content and its particle size, the porosity, density, and average pore size of foams by the PM and melt routes are in the following ranges: 77.4%–84.4%, 0.42–0.61 g/cm^3, 0.5–1.2 mm and 63.3%–70.7%, 0.79–0.99 g/cm^3, and 0.7–1.5 mm, accordingly.

TiH_2, magnesium hydroxide ($MgOH_2$), magnesium carbonate hydroxide ($4MgCO_3{\cdot}Mg(OH)_2{\cdot}5H_2O$), magnesium carbonate ($MgCO_3$), dolomite ($CaMg(CO_3)_2$), and calcium carbonate ($CaCO_3$) were investigated as foaming agents for the Al-Si-Cu alloy by the PM route [36]. Air-atomized AlSiCu powder containing mass fractions of Si (10.8%) and Cu (2.4%) was used to make the precursor. The powder was sieved through a 150 mm mesh before use. In addition to (1)–(8) reactions, the following possible reactions are listed:

$$\begin{gathered} Mg(OH)_{2(s)} = MgO_{(s)} + H_2O_{(g)} \\ 4MgCO_3 \cdot Mg(OH)_2 \cdot 5H_2O_{(s)} = 4MgCO_{3(s)} + MgO_{(s)} + 6H_2O_{(g)} \end{gathered} \tag{11.9}$$

$$4MgCO_{3(s)} = 4MgO_{(s)} + 4CO_{2(g)} \tag{11.10}$$

$$MgCO_{3(s)} = MgO_{(s)} + CO_{2(g)} \tag{11.11}$$

$$\begin{gathered} CaMg(CO_3)_{2(s)} = CaCO_{3(s)} + MgO_{(s)} + CO_{2(g)} \\ CaCO_{3(s)} = CaO_{(s)} + CO_{2(g)} \end{gathered} \tag{11.12}$$

In these reactions, TiH_2 isolates hydrogen (H_2), $MgOH_2$ isolates water vapor (H_2O), and $4MgCO_3{\cdot}Mg(OH)_2{\cdot}5H_2O_{(s)}$ isolates H_2O and CO_2 while $MgCO_3$, $CaMg(CO_3)_2$, and $CaCO_3$ isolate CO_2.

Precursors were formed by hot extrusion at 623 K with extrusion ratio 18 using a mixture of the AlSiCu and foaming agent powders. AlSiCu melting starts at 793 K and continues up to 853 K. The liquidus temperature of the AlSiCu alloy is 80 K lower than that of pure aluminum. Consequently, it is necessary for the foaming agent to decompose between 793 and 853 K when using AlSiCu as the matrix. The decomposition temperature of TiH_2 is within the melting temperature range of AlSiCu, which indicates that TiH_2 is a suitable foaming agent of AlSiCu. In contrast, most $Mg(OH)_2$ decomposes between 633 and 753 K while the release of H_2O occurs before AlSiCu begins melting. During the decomposition of $4MgCO_3{\cdot}Mg(OH)_2{\cdot}5H_2O_{(s)}$, H_2O is released from ambient temperature to 613 K, and then CO_2 is released by the decomposition of $MgCO_3$ from 613 to 833 K. Before AlSiCu begins to melt, H_2O is released. $MgCO_3$ decomposes from 793 to 993 K, which is close to the melting temperature range of AlSiCu. The decomposition of both TiH_2 and $4MgCO_3{\cdot}Mg(OH)_2{\cdot}5H_2O$ began at a low temperature. These foaming agents have released more than half of their decomposition gas before AlSiCu begins to melt. The released gas breaks the extruded aluminum powder boundary because the solid phase has a higher strength than the solid-liquid phase, and broken cells combine and grow in the extrusion direction. At a high temperature, the TiH_2 foam forms a coarse and rounded cell structure because the cell structures expanded by H_2 are easily combined and deformed to reduce the surface energy of the cell wall. The $4MgCO_3{\cdot}Mg(OH)_2{\cdot}5H_2O$ foam grows as a torn cell structure because the oxidizing gases H_2O and CO_2 are released by $4MgCO_3{\cdot}Mg(OH)_2{\cdot}5H_2O$ decomposition. This stabilizes the cell wall by

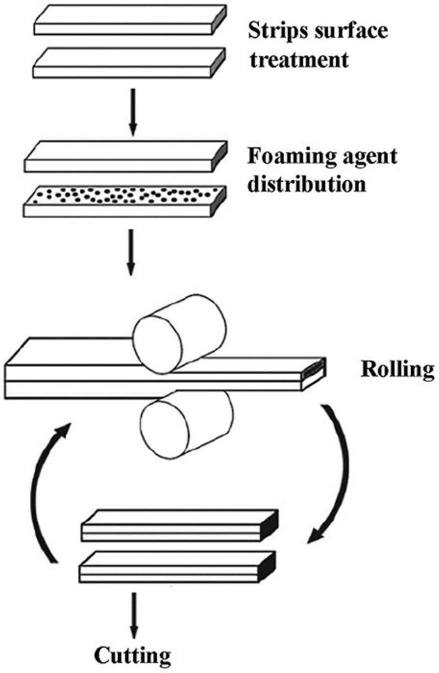

FIG. 11.14 Production steps of accumulative roll bonding process.

oxidization, which prevents the cell from becoming connected and spherical, and leads to the coarse-torn cell structure. To support this, it has been reported that the carbonate foam oxidizes and stabilizes the cell wall. $MgCO_3$ and $CaMg(CO_3)_2$ have higher decomposition temperatures than TiH_2 and $4MgCO_3{\cdot}Mg(OH)_2{\cdot}5H_2O$, and only $<1\%$ of the decomposition gas has been released when AlSiCu starts melting. Most of the decomposition gas is released while AlSiCu melting is well under way, which reduces the flow stress of AlSiCu. These cells do not have torn fibrous aluminum powder boundaries, and their structures could be flat or spherical. Even after expansion, the shape and homogeneity of the cell structure are maintained because of the stability of the cell wall. Therefore, $MgCO_3$ is a suitable foaming agent of AlSiCu. A carbonate foaming agent $CaCO_3$ that begins decomposing at 993 K after the matrix has melted is required for the formation of metal foams with a fine and homogenous cell structure by the PM route, the authors of the work [36] conclude. $MgCO_3$ and $CaMg(CO_3)_2$ were selected as the suitable foaming agents of AlSiCu. The $CaMg(CO_3)_2$ foam had a specific gravity of 1.19 and a homogeneous, fine, and spherical cell structure.

The accumulative roll bonding (ARB) process is based on the decomposition of foaming agent $CaCO_3$ pressurized in aluminum strips. In the work [37], a commercial aluminum 1050 sheet with initial 5 mm thickness was used as the initial matrix material. It was cold rolled into a 3 mm thick sheet. The aluminum sheet was then cut into $30 \times 150\,mm^2$ strips and annealed at 623 K for 1 h in order to eliminate any strain hardening due to primary cold rolling. The sequence of the production steps is schematically shown in Fig. 11.14. $CaCO_3$ powder with 0.5 wt% in the sample and a particle size $<15\,\mu m$ was uniformly distributed between two stacked strips, the surface of which was previously treated to eliminate surface contamination and to increase the roughness of surfaces to get an excellent bonding between layers. The two strips were then fixed and fastened together. The derived sandwich was heated at 473 K for 5 min to provide higher strength bonding followed by rolling. The procedures were repeated up to six passes. The thickness and length of composite at the end of this process were 3 mm and 300 mm, respectively. The resultant strip was halved and annealed at 473 K for 10 min to achieve a good bonding after the first pass. The halved strips were stacked again over each other without adding any further blowing agent.

As was ascertained by Fathi et al. [37], calcium carbonate layers are about 22, 12, and 7 μm thick after the first, second and third rolling cycle, respectively. The resultant strip, 300 mm long and 3 mm thick, was cut into samples with 20 × 10 mm dimensions for further foaming treatment. Maximum porosity up to 55% is obtained by the optimum foaming condition at 973 K and 8 min aging time.

Open-Cell Metallic Foams

Open-cell metallic foams are not as stiff as closed-cell metallic foams, but they have characteristics that can be exploited in multifunctional load supporting and heat transfer applications because of the ability to flow fluids readily through the heated structure. They also have a high surface area to volume ratio and can be used as high-temperature supports for catalysts and electrodes in electrochemical cells. The synthesis of open-cell metal foams can be accomplished by investment casting using an open-cell mold [41], electrolytic deposition [42–44], chemical [45] or physical [46,47] vapor deposition on polymer templates, and the PM route [48]. The as-deposited structures are subjected to a low-temperature thermal treatment during which the parent polymer template is thermally decomposed. This is usually followed by a high temperature sintering treatment to densify the ligaments. These methods result in foams with cell sizes ranging from 100 mm to 5 mm and relative densities from 0.01 to 0.15.

The electrolytic deposition process involves the dissolution of one electrode (an anode) and the deposition of this metal on a second electrode (the polymer template cathode). Because polymer-based foams are nonconductive, they must be made electrically conductive by either sputtering or ionic deposition. The metal foam is then created by the subsequent electrolytic deposition of elemental Ni or Cu. Metal foams produced by this method are manufactured for use in Ni-Cd and Ni-metal hydride batteries and catalytic devices. A major limitation of deposition processes is that deposition is limited to a few metallic elements. Along with this, nonuniform deposition may occur due to uneven field distribution over irregular shaped objects.

Chemical vapor deposition (CVD) of a metal carbonyl gas has also been used to manufacture metal foams [45,46]. Pure (>99 wt% Ni) metal foams are manufactured by thermal decomposition of $Ni(CO_4)$ gas. Refractory metal foams (i.e., Zr, Nb, Hf, Ta, W, and Re) produced by chemical vapor infiltration (CVI) are manufactured by Ultramet Advanced Materials (United States) and Recemat International (The Netherlands) under the trade names Ultrametal and Recemat. Potential applications include thermal insulation, lightweight nozzle flaps for advanced turbine engines, aircraft wing and fuselage structures, and catalytic filtration devices. However, vapor decomposition of the least-expensive chemical precursors occurs at high temperatures where the thermal stability of the polymer template must be taken into consideration. The need to use toxic, low decomposition temperature chemical precursors results in a costly process that is difficult to implement in an environmentally satisfactory practice.

Physical vapor deposition (PVD) techniques including metal spray deposition, thermal evaporation, reactive sputtering, and arc-vapor deposition have also been used to manufacture metal foams [46,47]. The advantages of these techniques are the ability to deposit most metal elements and many of their alloys and to even create foams with multilayered or functionally graded metal ligaments. However, because these processes operate in high vacuum (10^{-5}–10^{-9} Torr), they coat only the surfaces that are in the line-of-sight of the vapor source. This is likely to result in uneven coating of the polymer template, depending on the cell size. In addition, low deposition rates (<2 mm/min), low material utilization factors, and difficulties in maintaining stoichiometry for alloys whose constituents possess widely varying vapor pressures can impose constraints upon the use of conventional PVD techniques for the low cost synthesis of metal foams.

The application of an electron beam-directed vapor deposition approach for synthesizing open-cell metal alloy foams was explored in the work [49]. A schematic illustration of such is shown in Fig. 11.15. The system used for deposition consisted of a 60 kV/10 kW axial electron beam gun and a He carrier gas jet. For the deposition, cylindrical samples were used (25.4 mm in length and 12.7 mm in diameter) as the deposition template. They consisted of open-cell, reticulated polyurethane foams with a pore size of approximately 0.85 mm (30 pores/in. nominal). The polymer foam was positioned 70 mm from the nozzle and 50 mm from the vapor source. The polymer foam template was rotated about its cylindrical axis at approximately 1 revolution/min and also translated axially through the vapor flux region to promote uniform deposition and complete infiltration. The intermediate process pressures were of 0.07 Torr.

After deposition, the polymer template was removed by a thermal decomposition step. The resulting carbon remains potentially contaminate the metal foam. Among explored various decomposition approaches, in one where metal-coated polymer templates were rapidly exposed (less than about 5 s) to a temperature at least 873 K (in air), the complete removal of the polymer core with minimal carbon residue resulted. This process caused the gaseous oxidation products to form a large internal pressure and created burst holes in the metal layer. After thermal decomposition, the samples were pressureless sintered, which consisted of heating the samples at a rate of 10 K/min up to 1420 K, holding for 12 h followed by furnace cooling at approximately 25 K/min in vacuum (approximately 10–5 Torr). In all cases, the mass of the liquid-phase sintering agent added was <5% of the mass of the deposited metal foam.

An Inconel alloy 625 nickel-based superalloy of nominal composition Ni-21.3Cr-8.8Mo-3.9 Nb-0.13Al-0.19Ti wt% was used for deposition. The morphology of the directed vapor-deposited foam and the polymer template used for its synthesis is shown in Fig. 11.16. It can be seen in Fig. 11.16A that the reticulated polymer foam template had cusp-shaped solid ligaments with triangular cross-sections. The as-deposited metal foam therefore had hollow ligaments with cusp-shaped triangular interior voids, as seen in Fig. 11.16B.

The resultant ultralightweight metal foams consisted of a three-dimensional open cell and a reticulated structure possessing hollow triangular ligaments with relative densities <3%.

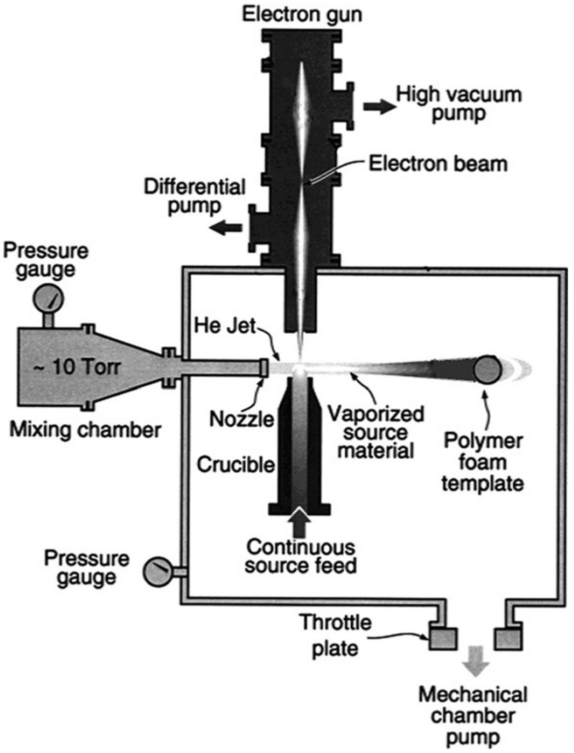

FIG. 11.15 Schematic diagram of the processing chamber showing the introduction of a carrier gas flow into the chamber through a nozzle that transports the evaporated source material through the polymer template. *(Modified from D.T. Queheillalt, D.D. Hass, D.J. Sypeck, H.N. Wadley, Synthesis of open-cell metal foams by templated directed vapor deposition, J Mater Res 16 (4) (2001) 1028–1035.)*

In the patented technique [50,51], the conversion of nickel foams into advanced high temperature-stable alloy foams is based on the diffusion process. NiAl, NiAlCr, Monel, and NiFeCr were synthesized [52]. The nickel foam is continuously unwound, coated first with a binder solution using a spraying technique and then with a high alloyed powder. Afterward, the foam is cut into sheets of the desired size. The following heat treatment includes a debindering and sintering step in which the elements from the powder diffuse into the foam struts and ensure a homogeneous alloy foam composition. This technology is profitable and suitable for a large-scale production. Weissgaerber et al. presented the results of the synthesis, thermoelectric properties, and the production of supercapacitor prototypes based on the IN625 foam. Calculations of the energy density have shown that values of about 10 Wh/kg are feasible. This is a promising value because the energy densities of state-of-the-art supercapacitors are less 5 Wh/kg [53].

Materials

The selection of the material structure is generally determined by the end application. Closed-cell materials provide good mechanical properties and are mostly used in structural, loadbearing applications. In contrast, open-cell foams are mostly used in functional applications where loadbearing capability is not the primary aim. The open-cell materials remain the most important commercial applications for the production of filters, gas-flow controlling devices, batteries, biomedical implants, and bearings.

Materials for Structural Applications

The main R&D areas in the last two decades have been centered on the investigation of foaming and stabilization mechanisms, the development of new foaming agents, the optimization of the fabrication processes, and the reduction of the fabrication costs. Some researchers are directed toward understanding in more detail the complexities of foaming. Indeed, it is still not completely understood how metallic films are formed within liquid metal foams and how foams are stabilized. Because foams are complex mixtures of solid, liquid, and gaseous phases, their study is challenging, both experimentally and theoretically. Single liquid metallic films have been used to help understand the properties of the cell walls and better understand foaming and stabilization [54]. X-ray imaging techniques have also been utilized to reveal the inner volume of

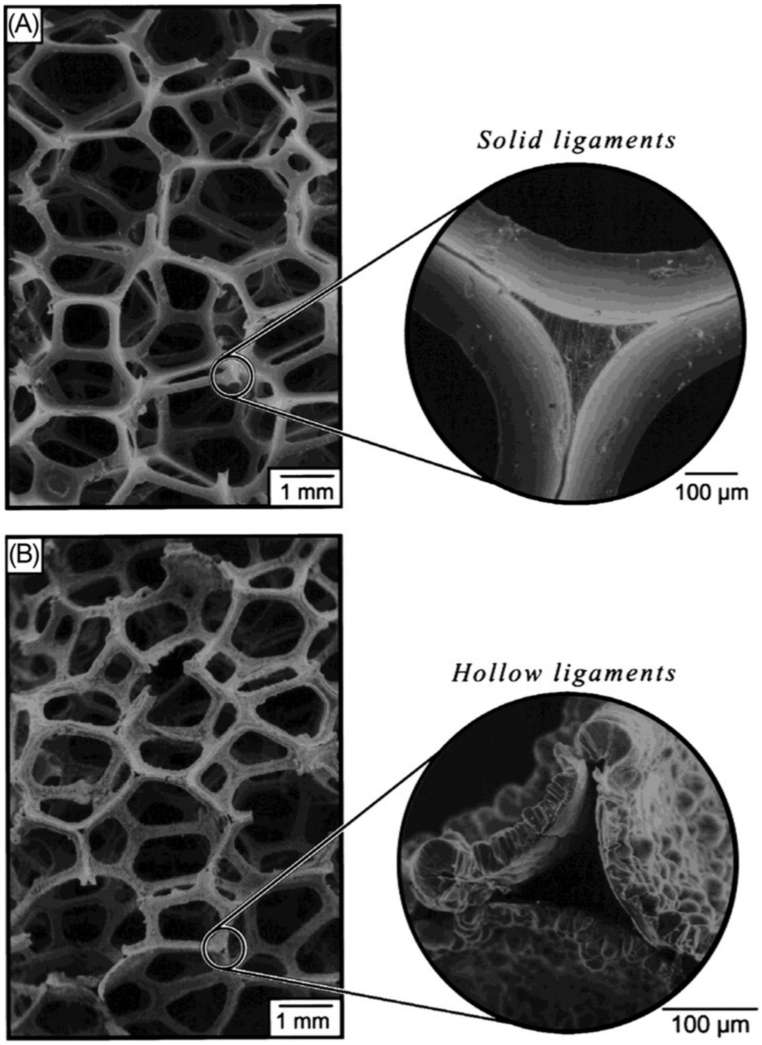

FIG. 11.16 The morphology of the directed vapor-deposited foam and the polymer template used for its synthesis: (A) polymer foam template; (B) vapor deposited metal foam.

expanding foam and to measure some structural parameters, such as the rupture time of individual films [55]. Observation of metallic foams in other spectral ranges was also found to yield useful information. An optical technique has been used for the contactless imaging of expanding metal foams in three dimensions by placing the sample on a rotating plate inside a furnace [56]. The temperature distribution in the expanding aluminum foam was recorded in situ using an array of microbolometers operating in the far infrared regime and was integrated in a commercial thermal camera [57].

The work [58] presents the results of a systematic study on the evaluation of foamability by using an alternative mixture of carbonates with molten aluminum. Foams were obtained by varying the carbonate content and the mixing and the foaming time, both in single- and double-step processes. In addition, low amounts of TiH_2 in combination with these carbonates was also tested. The experimental results suggest that it should be possible to obtain foams with a similar quality and lower cost than other commercialized products, although further improvement is still needed.

Byakova et al. have studied the influence of impurities of cell wall material on mechanical properties of closed-cell Al-foams by different foaming agent and process rotes [59]. Several kinds of Al-foams have been produced with pure Al by the Alporas route and the PM route, all performed either with a conventional TiH_2 foaming agent or $CaCO_3$ as an alternative. The mechanical characteristics of impurities induced by processing, all of which were presented in one or another kind of Al-foam, have been determined in indentation experiments. The discrepancy of the real strength properties with a calculation for the idealized model of a defect-free cellular structure [60,61] the authors [59] put down mainly to the impurities of cell walls. The damaged behavior of these impurities affects the micromechanism of deformation and favors either plastic buckling or brittle failure of the cell walls. The presence of low ductile $Al+Al_3Ti+Al_4Ca$ eutectic domains and brittle particles/layers of Al_3Ti, fine $CaCO_3/CaO$ particles, Al_2O_3 oxide network, and, especially, residues of partially reacted TiH_2 results in reducing the compressive strength to values close to or even below those of open-cell foams of the same relative density. In the current work, the aluminum foams show characteristics for closed-cell foams subjected to deformation in an initial linear elasticity regime before general yielding (yield stress, σ_y), followed by a relatively long and well-defined "plateau" regime, which is typically associated with cell collapse, accompanied by densification of the cell wall material. Table 11.3 contains "plateau" strength magnitudes for hydride and carbonate kinds of aluminum foams. Further, it is evident that compressive stress decreases as relative density decreases.

Foam stabilization can be achieved by adding ceramic particles into the metallic melt, which adhere to the gas/metal interfaces during foaming and prevent pore coalescence. The Alcan process described above uses liquid metal matrix composites (MMCs) containing 10–20vol% particles (typically 10μm silicon carbide or alumina particles) into which a blowing gas is injected. However, the high particle content makes the solid foams very brittle and hard to machine. Replacement of the large particles in the MMCs by nanometric particles is a solution to overcome this problem. Using nanoparticles, melts can be foamed at much lower particle loading. Indeed, 5% of 70-nm SiC particles dispersed ultrasonically in the melt were shown to be sufficient to stabilized aluminum foams [62]. Particles formed in situ by chemical reactions have also been used with success for the same purpose. As an example, 4wt% of TiC particles (200–1000nm) formed in situ in liquid aluminum resulted in stable aluminum alloy foams [63]. The fact that metal foam manufactured from powders includes many processing steps has been one of the motivations of work focusing on integrating various steps into one. High-pressure molding of structural foams was proposed in that direction. The process consists of injecting an aluminum alloy melt into a die-casting machine together with the blowing agent MgH_2 and allowing the controlled foaming of the components inside the die [64]. Structural foam components with a closed outer surface can be manufactured using this method.

Metallic hollow sphere structures (MHS) are a new kind of cellular metal. This technique insures the controlled manufacturing of single cells to single MHS and makes reproducible the structure of the tailored components. An electrodeposition of various metals such as nickel, cobalt, and copper on spherical substrates has been realized. An impediment with this method is that there are a limited number of metals that can be deposited on carrier surfaces by electrolysis, which limits the use of this technology.

A PM process clears the way for these advantages [65]. An organic sphere substrate, mostly foamed polystyrene, has been used as a cell-forming undercoat. Fluidized deposition is provided with these foamed substrates and, by means of a nozzle system, a metal powder-binder suspension is atomized onto the outside of the styrofoam spheres [66]. Binder and styrofoam cores are removed by a subsequent heat treatment. Using the developed PM process for MHS, a wide range of powder material can be used for their production. There are several options to consolidate single hollow spheres to an MHS component, including sintering, brazing, and adhesive bonding [67]. Fig. 11.17 shows an overview of the spray coating process.

The MHS technology is suitable for a wide range of materials. A broad cell size spectrum of 0.5–10mm is possible while the cell size distribution is very narrow. The cell wall thickness can be varied from approximately 20μm to 1mm. The wall can be sintered fully dense as well as porous [68]. Composites structures have also been developed with hollow spheres for structural applications [69]. A process to produce hollow Cu_2O and NiO nanoparticles via the oxidation of Cu and Ni nanoparticles has also been presented [70]. Hollow and spherical particles of 125–500μm size of NiCrSiB powders obtained through argon gas atomization were used. The metallic foam structure was obtained by sintering the hollow particles in a

TABLE 11.3 **Compressive Strength Magnitudes for Hydride and Carbonate Kinds of Aluminum Foams**

Process Route	Processing Additions	ρ/ρ_s	"Plateau" Stress (MPa)
Alparas	1wt%Ca+2wt%TiH_2	0.22	2.4–2.9
		0.07	0.3–1.0
PM	2wt%TiH_2	0.08	0.2–0.5
Alparas	1wt%Ca+2wt%$CaCO_3$	0.21	1.4–2.0
		0.28	3.8–4.0
PM	2wt%$CaCO_3$	0.3	0.8–0.9

ρ and ρ_s, correspond the density of foam and solid, respectively.

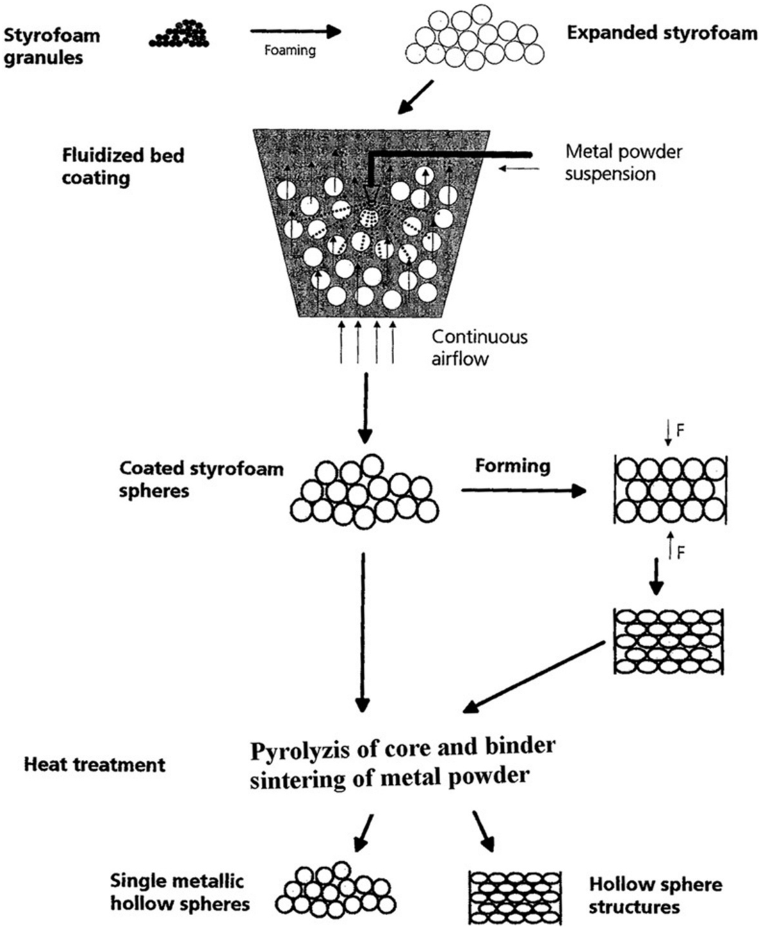
Styrofoam granules
Foaming
Expanded styrofoam
Fluidized bed coating
Metal powder suspension
Continuous airflow
Coated styrofoam spheres
Forming
F
F
Heat treatment
Pyrolyzis of core and binder sintering of metal powder
Single metallic hollow spheres
Hollow sphere structures

FIG. 11.17 Flowchart of the spray coating process.

vacuum, 10–5 Torr at 1223 K. To shape the macroporous open-cell network inside the structure, space holders were used. Thus, biporous metallic foams were obtained with closed cells due to hollow particles and open cells formed by the space holders [71].

Combining metal foams with other materials offers a unique opportunity to tailor material properties. The simplest approach is to fill hollow sections with foam or to produce sandwich structures with a metal foam core and a variety of face sheets. As an example, the process for sandwich foam production by using the diffusion welding technique, described in work [71], consists of making an aluminum foam precursor from an aluminum and TiH_2 powder extrusion mixture at 983 K, placing the precursor between the Al-4.5Cu-0.5Mg alloy plates, and joining at 0.1 MPa and 903 K with 60 min aging. The potential for improvements is still large as demonstrated by the combination of aluminum foam and glass-fiber reinforced polymer composites and aluminum alloy sheets or by composites containing aluminum foam spheres bonded together with a polymeric adhesive [2]. A related approach is to deposit a high-strength coating on the struts of a foam, as demonstrated with nanocrystalline Ni-W coated aluminum foams showing improvements in strength and energy absorption [72].

Using the PM route, Koshita and Ishijima developed for a heat exchanger highly porous open-cell aluminum foams [48]. An equivalent weight of Al powders with median particle size 6 μm and 2 wt% of binder aqueous solution were mixed to obtain Al powder slurry. To prepare a sintering precursor, urethane foam was immersed in the Al powder slurry, extra slurry was removed, and the obtained wet precursor was dried in hot air. Decomposition was achieved in a nitrogen atmosphere by heating from room temperature to 773 K and maintaining the temperature for 120 min. The Al foam was sintered in a vacuum. Fig. 11.18 shows an SEM image of sintered Al foam with different pore sizes.

The synthesized Al foam possesses an open-cell structure with features akin to urethane foam (template) and porosity exceeding 90%. Fig. 11.19 shows a cross-section SEM image of the frame in Al foam by 10 ppi urethane foam. It shows a triangular shape enclosing a hollow structure with the same shape. This hollow structure is a product of the original urethane foam. The Al layer is approximately 70–90 μm thick, and has dense organization.

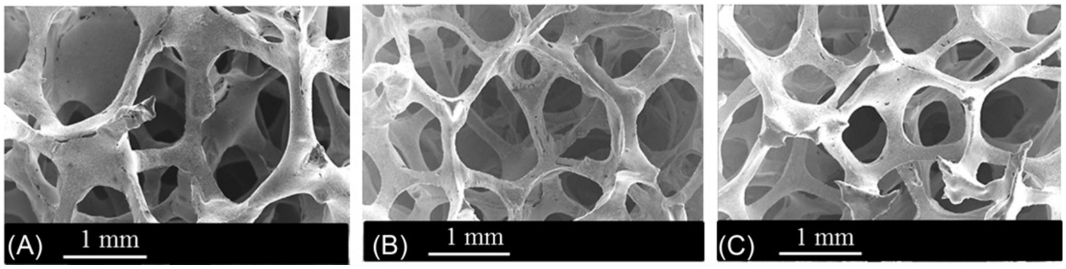

FIG. 11.18 SEM images of sintered Al foam with different pore sizes:

Fig.	(A)	(B)	(C)
Pore size of used urethane foam (ppi, pore per inch)	6	10	20
Porosity (%)	93	93	92

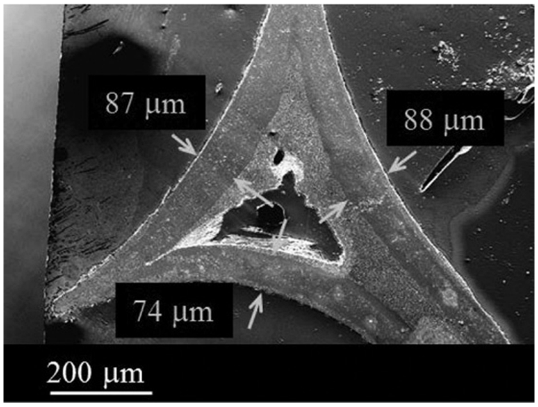

FIG. 11.19 SEM image cross-section of the Al foam frame by 10 ppi urethane foam. *(Modified from H. Koshita, Z. Ishijima, Development of highly porous aluminum with an open-cell structure, In: Compiled by Russell A, Chernenkoff W, Brian J. proceedings of 2014 Powder Metallurgy World Congress, Orlando (FL, USA): Metal Powder Industries , Federation 2014, p. 09-209–14.)*

Along with using low cost foaming agents as compared to expensive TiH_2, another cost reduction strategy is to use chip waste, for example, from machining, as a replacement for the expensive aluminum alloy powders. Chips are mixed with ceramic additives and foaming agent, then densified by compressive torsion processing or thixocasting [38], after which the compacted materials are foamed in the usual manner. An open question remains, however, as to whether the need for more expensive compaction techniques contradicts the material cost-saving issue.

Materials for Functional Applications

High temperature resistant-materials. High temperature-resistant materials such as intermetallic compounds NiAl and Ni-based alloys, for example, Inconel, over the last decades have been developed to serve under extreme conditions demanding excellent high-temperature stability and oxidation/corrosion resistance. For many applications such as high-temperature filtration porous structures, diesel soot traps, and catalyst carriers, these materials are required but are not yet commonly available. A technique has been developed that is suitable to produce large amounts of NiAl- and Inconel alloy-based foams with different porosities. This process starts from pure nickel foam, which is homogeneously coated and subsequently transformed into the desired material by heat treatment [73]. The first step of the manufacturing process involves coating the nickel foam with a binder solution. The foam is then coated with the desired powder (50 wt% for manufacturing NiAl-foam). During the subsequent sintering step, the final composition of the foam and its specific surface area and porosity can be tailored as desired. The process also allows coating the base substrate with multiphase composite powders and is consequently also suitable for manufacturing complex alloy compositions. Fig. 11.20 illustrates a comparison of the individual states of the coating from the base foam to the reacted NiAl final product.

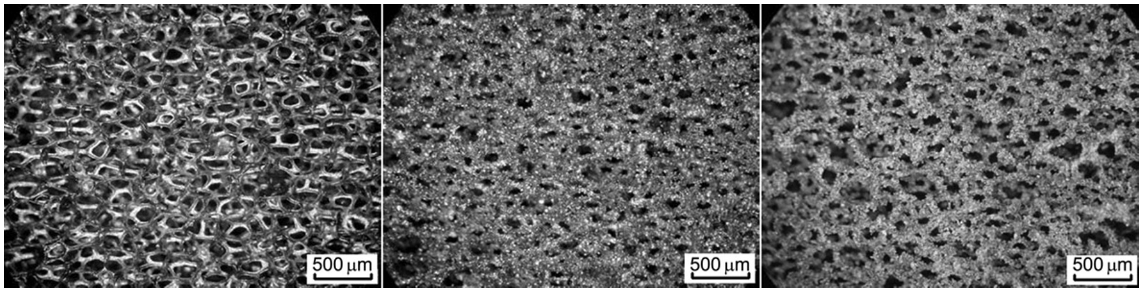

FIG. 11.20 Comparison of the processing states (from left to right: Ni base foam, coated foam, sintered NiAl foam).

So long as the efficiency of the engine is affected by the pressure drop at the exhaust, materials with good permeability are required. Metallic foams with good corrosion resistance at temperatures up to 873 − 1073 K, especially NiCrAl-based alloys, are being considered for these applications. Walther et al. developed a process to produce high temperature-resistant Fe-Ni-Cr-Al foams using the deposition and transient liquid phase sintering of fine prealloyed particles onto thin, commercially available nickel foam strips [74]. Filters are produced either by coiling the foam strip or by sintering the sheets in stacks. Long-term stability, provided by a protective layer consisting of α-alumina on the surface, was shown at temperatures up to 1223 K. Compared to the state-of-the-art wall-flow filters, the regeneration of the foam filters occurs faster and at lower temperatures because of the improved soot-filter wall contact provided by the turbulent gas flow. A route proposed to enhance the chemical stability of the material was to depose TiN on the surface using chemical vapor infiltration (CVI) processes. Casting replication of an oxide space-holder has also been demonstrated to create sponges from an oxidation-resistant Ni-Mo-Cr alloy developed for fuel cell interconnects [75].

For replacing molybdenum usable in high temperature stress conditions by a less expensive material, the Fraunhofer Institutes IFAM-DD and IKTS in cooperation with H.C. Starck Hermsdorf GmbH developed a lightweight molybdenum foam for heat insulation applications, using the low heat conductivities of about 1%–5% of the basic dense material. Network-like structures with porosities up to 95% and cell sizes of 0.8–1.2 mm where synthesized [68]. In comparison to the conventional heat shielding plates, the temperatures at the cold zones only show differences of about 2% when the molybdenum foam heat insulation was used. Simultaneously, the heat insulation package mass was reduced four times. In the same way, metal hollow spheres (MHS) can be used in thermal insulation applications, especially in a high-temperature environment. The heat conductivity values of the material range between 0.5 and 2 W/(m K) [68].

Biomaterials. The PM technology found application at the end of the 1960s to overcome problems with bone cement. Porous coatings, also used in the past, are now extensively used in various orthopedic applications. Research has recently switched from thin porous bead coatings, sintered mesh, and thermal-sprayed rough coatings to metallic foams and these materials have been used in the development of various new and improved treatments (e.g., bone augmentation, graft-free vertebra fusion for the treatment of degenerative disk diseases). Levine reviewed some uses of metallic foams in joint replacements in [76] while Schiefer et al. presented the development of porous titanium for the production of dental implants in [77].

In the last decade, net-shape manufacturing of porous titanium has attended increasing interest in the biomedical community due to its high potential for several implant applications such as spine implants used in the case of complete replacement of vertebrae disc, the acetabular cup of hip implants, and dental implants with porous coatings as well as filler material in the case of large bone defects [78–80]. The space holder method has become a well-established method for manufacturing such implants. Usually, the method consists of pressing compacts of Ti powder and space holder mixtures with subsequent machining to net shape in the unsintered state (green state), followed by space holder removal and sintering. Compaction pressures up to 400 MPa enable the formation of a stable and compact network of Ti particles during pressing. In the work [80], Trancer et al. make a comparison between NaCl and KCl as spacer materials and infer that NaCl powders with melting temperature of 1074 K were preferentially used as a spacer material while KCl powders with spherical morphology are advantageous for metal injection molding processing and load transfer of the compressing load to the titanium particles during compaction, in contrast to cubic NaCl. Along with this, KCl has a slightly higher solubility in water when compared to NaCl.

Open and interconnected porosity was reached through the PM route presented in the work [81] by obtaining titanium foams consisting of a total interconnected porosity of about 53% and a pore entrance diameter of about 178 μm of macroporosity. The implants were obtained by pressing a 65 vol% of NaCl of about 300–600 μm, and 35 vol% Ti (with an average size of 200 μm) mix with an addition of 15 wt% of ethilenglycol (acting as a binder for homogenizing the mix), at 300 MPa to get an overdimensional green part (an 8% shrinkage is expected after sintering). The space holder is removed using a continuous washing cycle of distilled water up to match a stable conductivity near the distilled water. Then a final sinter step is carried out at 1623 K during 4 h under high vacuum conditions ($<5\cdot10^{-4}$ mbar). In addition, an alkali bioactive surface treatment was applied in order to obtain a better mechanical match to tissue with attractive surfaces bone cell growth.

Properties of Materials

Mechanical Properties. There are several models based on the idealized representation of a defect-free cellular structure. Among them, the most famous scaling laws applied for describing mechanical properties are summarized in [60]. A schematic stress-strain curve for foam in uniaxial compression is shown in Fig. 11.21. Initial linear elasticity is followed by a roughly constant stress plateau that continues up to large strains, beyond which the stress increases dramatically. As the stress increases, the cells begin to collapse at a roughly constant load by elastic buckling, yielding, or fracture, depending on the nature of the cell wall material. Once all the cells have collapsed, further deformation presses opposing cell walls against each other, increasing the stress sharply: This final regime is referred to as densification.

For open-cell foams made of elastic-plastic materials, dimensional arguments give the plastic collapse stress, σ_{pl}, relative to the yield strength of the solid cell edge material, σ_{pl}^* as:

$$\frac{\sigma_{pl}^*}{\sigma_{ys}} = C_3\left(\frac{\rho^*}{\rho_s}\right)^{3/2}$$

where the constant C_3 is related to the cell geometry and $\frac{\rho^*}{\rho_s}$ is the relative density. For a wide range of foams the constant above, C_3, is roughly about 3.

For closed-cell foams, yielding of the stretched cell faces contributes to their strength so that the additional term on the right side appears in the relation for the plastic collapse stress:

$$\frac{\sigma_{pl}^*}{\sigma_{ys}} = C_3\left(\frac{\rho^*}{\rho_s}\right)^{3/2} + C_3'\left(\frac{\rho^*}{\rho_s}\right) \tag{11.13}$$

Finite element analysis of a tetrakaidecahedral unit with flat faces gives a slightly different relation [61].

$$\frac{\sigma_{pl}^*}{\sigma_{ys}} = 0.33\left(\frac{\rho^*}{\rho_s}\right)^{3/2} + 0.44\left(\frac{\rho^*}{\rho_s}\right) \tag{11.14}$$

Sintering of aluminum closed-cell foams at elevated temperature shows [82] that the plastic collapse stress, σ_{pl} obeys the Eqs. (11.13), (11.14) in the temperature range 1373–1673 K but with modified coefficient values: at 1373 K $\frac{\sigma_{pl}{}^*}{\sigma_{ys}} = 0.57\left(\frac{\rho^*}{\rho_s}\right)^{3/2} - 0.06$; at 1400 K $\frac{\sigma_{pl}{}^*}{\sigma_{ys}} = 0.68\left(\frac{\rho^*}{\rho_s}\right)^{3/2} - 0.07$.

In situ X-ray tomography has been used for correlation with mechanical properties and deformation mechanisms. This method could clarify the deformation mechanisms of aluminum foams under monotonic or cyclic loading with lateral constraint [83]. It was also applied to hollow-sphere foams so as to determine the main deformation mechanisms and compare with the results of finite element modeling (FEM) calculations [84]. FEM was also applied to investigate the effects of open-cell metallic foam irregularity on deformation behavior and energy absorption during impact loading [85]. Another advanced imaging technique—digital image correlation—was utilized for foams cycled under tension/compression loading or uniaxial tensile loading to capture localized deformation (crush or tensile bands), cell wall fracture, and global foam failure [86].

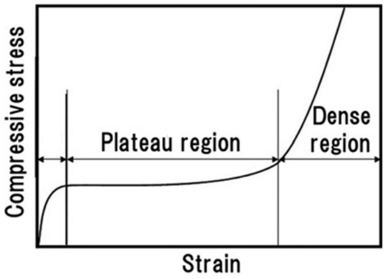

FIG. 11.21 A schematic stress-strain curve for metallic foam.

Acoustic Properties. Sound, pressure, and vibration-dampening components find wide industrial applications [4,67]. Porosity acts as an acoustical impedance and dampens certain sound frequencies while others pass through. A pressure pulsation in a fluid delivery system is also dampened by reducing the fluid rate when it passes through the small interconnected channels. The pressure gauges are equipped with porous metal antivibrators to dampen the vibration or pressure fluctuation.

Investigations of the sound absorption of sintered 316 L foam metal showed that MHS structures reveal a significantly higher sound dissipation up to 1000 Hz compared to glass wool. The sound level could be reduced by about 10–15 dB [68]. Compared with the state-of-the-art mufflers, a significant weight reduction (up to 25%) and a simpler assembling of the whole muffler can be pointed out. The main parameters on sound absorption are the diameter of the spheres and the structural density. Smaller diameters of the spheres and a lower structural density lead to a more pronounced sound dissipation. Because of the low thermal conductivity of the MHS structures, additional thermal insulation materials of the muffler can be omitted.

When the acoustic properties can be combined with other characteristics of the metallic foams (i.e., thermal and chemical stability, mechanical properties), metallic foam mufflers become more attractive than common sound absorbers such as mineral wool or polymer foams. The budgets associated with sound management being generally low, metallic foams will find applications when substantial improvements are observed or when the combination of the properties of the metallic foams represents an important benefit (i.e., standard sound absorbers are generally much cheaper than most metallic foams).

Energy Absorption. Energy absorption is one of the most promising application areas of the metal foams. For instance, the German automotive supplier Karmann suggests that sandwiches containing an aluminum foam core and aluminum face sheets be used in the bulkhead and the rear seat wall of convertible cars. The components are up to 10 times stiffer compared to the conventional steel parts used in the past and weigh 30%–50% less. Steel is also used for sandwich face sheets. Subsequent deep drawing allows a three-dimensional structure to be produced (Fig. 11.13).

The energy absorption behavior of foamed materials is determined as the efficiency η. For the given strain, this parameter is defined as a ratio of the actual absorbed energy to the energy that would be absorbed by an ideal absorber.

The determination of the elastic modulus of foamed metals should not be done in the convenient way, that is, by evaluation of the slope in the elastic part of the stress-strain curve. The typical elastic modulus dependence on apparent density is obtained for foamed Al-12Si [87]. It was investigated using the vibrational bending test. A straight line would be expected in a double-log plot of the foam modulus versus density. Increasing density from 0.7 to 2.5 g/cm^3 leads to growth of the elastic modulus from 7 to 55 GPa.

Damping is strongest in foams with the lowest densities. It is known that any kind of porosity enhances damping due to the stress concentration, what is called mode conversion around pores. Another mechanism is of a macroscopic source. The cell walls of metallic foams sometimes contain cracks and holes that may either originate from the gas released during the foaming process or from the contraction of the foamed body by cooling after foaming. These defects may give rise to an extra frictional contribution caused by the relative movement of the crack or hole walls with respect to each other. Integrally, it is also well established that PM materials have higher damping capacities than cast ones.

Thermal Properties. Metallic foams are conductive, permeable, and have a high surface area. This combination of properties makes them attractive for various thermal applications (heat exchangers, heat sink, heat pipes). Heat exchanges and conduction in metallic foams are uniquely complex. Heat exchange efficiency is affected by the conductivity of the foam, the heat exchange between the foam and the surrounding fluid, and the pressure drop in the foam. These characteristics are all affected by various structural parameters (density, pore size distribution, cell connectivity, tortuosity, strut size, geometry, cell wall and ligament structures, surface roughness, etc.) that are difficult to measure and integrate. In various research centers, the characterization and modeling of heat transfer and thermal exchanges in metal foams with various structures are being fulfilled [88–91].

Permeability. Permeability is an important property for complex applications such as thermal applications, filtration, electrochemistry, acoustic absorption, and porous implants. A review of Lefebre et al. [2] showed that classical models such as Darcy's or Forchheimer's do not appropriately describe the pressure drop in the porous solid, especially at high fluid velocity. It was shown that the pressure drop cannot be normalized by the material thickness because entrance and exit effects can significantly affect the pressure drop. Accordingly, new models should be developed and the methods to measure permeability should be reevaluated, especially when the material thickness is small and the fluid velocity high. The effect of surface modification and wettability on the permeability of Fe-Cr-Al fiber mats shows that the material's wettability significantly affects the permeability of the materials. This demonstrated that controlling the interaction forces between the porous media and working fluid may be used to control the pressure drop in the porous media. The effect of a perforation on the pressure drop and gas diffusion in metallic foams demonstrated that gas diffuses from the perforation into the foam and perforations can be used to reduce the pressure drop while giving access to the internal surface of the foam.

TABLE 11.4 Major Application Areas of Metallic Foams

Electrodes for NiMH and NiCd Batteries	Structure Car Components
High temperature resistant materials: NiAl and Ni-based alloys, e.g., Inconel	Flat Alpares panels and aluminum sheets for various applications in mechanical engineering and transport industry
Diesel particulate filters	Elevated temperature structures
Diesel oxidation catalysts	Vibration damping girder for milling and cutting machines
Encapsulating of noise sources	Energy absorption car components
Buoys, life buoys	Crash elements for cars
Porous coatings in various orthopedic applications	Floating structures
	Heat exchangers
Various implant applications, comprise complete replacement of vertebrae disc, coxofemoral joint. Dental implants with porous coating. Filler material for large bone defects	Heat sink and heat pipes

Applications

Aluminum foam is currently produced by a number of companies worldwide, such as Shinko Wire (Japan), Gleich (Germany), Alantum (Korea), Alulight (Austria), Degussa AG, Applied Light-Weight Materials (Germany), Alcoa (United States), Metafoam (Canada), etc. It is, however, sometimes difficult to assess how sustainable a commercial activity is because precise information about production volumes and markets is not available.

Electrodes for NiMH and NiCd batteries are probably the largest industrial applications of metallic foams nowadays. Another important commercial application of metallic foams is the production of biomedical implants. Porous coatings (sintered beads and meshes) have been used with success for the last 20 years in orthopedic applications and most orthopedic implant manufacturers are using these coatings on many of their implants. The companies are now developing metallic foams to improve the performance of their implants and to develop implants for new and improved surgical treatments (for example, bone augmentation, graft-free vertebra fusion for the treatment of degenerative disk diseases). Major orthopedic implant manufacturers are now bringing these materials into the market (Zimmer Biomet, Tritanium from Stryker, Regenerex from Biomet). The major application areas of metallic foam materials are summarized in Table 11.4.

REFERENCES

[1] Banhart J. Manufacturing routes for metallic foams. JOM 2000;52(12):22–7.

[2] Lefebvre LP, Banhart J, Dunand DC, editors. Porous metals and metallic foams. Pennsylvania: DEStech Pub; 2008.

[3] ISO 13314: 2011 Mechanical testing of metals – Ductility testing – Compression test for porous and cellular metals.

[4] Porous Metal Products Overview, Mott Brochure PMOVER, 2010.

[5] Fan X, Guo J, Dignard N, Normand C. Tekna Plasma Systems Inc., Sherbrooke, Quebec, Canada Document Download, Product code: ZCP2003ITSC1075.

[6] Peissker E. Metal powders. Norddeutsche Affinerie, Hamburg: Brillant-Offset Publ; 1986.

[7] Eisemann M, Morgan R. Porous powder metallurgy technology. In: Article in ASM handbook. vol. 7. Materials Park, OH: ASM International Publishers; 2015. p. 799–805.

[8] Bronze filter powders, a Cu powder international brochure. Materials Park, OH: Acu Powder International Publishers; 1997.

[9] Bagshaw N, Barnes M, Evans J. The properties of porous nickel produced by pressing and sintering. Powder Metall 1967;10(4):13–31.

[10] Porous Metal Council. Porous metal design guidebook. Princeton, NJ: Metal Powder Industries Federation Publishers; 1980.

[11] Porous Metal Design Guidebook. MPIF Website. http://www.mpif.org/.

[12] German R. Particle packing characteristics. Princeton, NJ: Metal Powder Industries Federation Publishers; 1989.

[13] Albano-Muller L. Filter elements of highly porous sintered metals. Powder Metall Int 1982;14:73–9.

[14] Savich VV, Pilinevich LP, Tumilovich MV. Comparison of porous materials properties made from sponge titanium powders produced by different methods. In: Compiled by European Powder Metallurgy Association, (Bellstone Shrewsbury, UK) proceedings of 2004 Powder Metallurgy World Congress, Vienna, vol. 4, 2004. p. 157–62.

[15] Price PE. Cold isostatic pressing. In: Article in ASM handbook. vol. 7. Materials Park, OH: ASM International Publishers; 1998. p. 382–8.

[16] Lenel F. Powder metallurgy–principles and applications. Princeton, NJ: Metal Powder Industries Federation Publishers; 1980.

[17] Tracey V. The roll-compaction of metal powders. Powder Metall 1969;12(24):598–612.

[18] Williams N, Tracey V. Porous nickel for alkaline battery and fuel cell electrodes: production by roll-compaction. Int J Powder Metall 1968; 4(2):47–62.

[19] Moxson V, Senkov ON, Froes FH. Production and applications of low cost titanium powders. In: Compiled by European Powder Metallurgy Association, (Bellstone Shrewsbury, UK) proceedings of 1998 Powder Metallurgy World Congress, vol. 1; 1998. p. 274–9.

[20] Neumann P, Amhold V, Heiburg K, Rohlig R. Porous metal products with special properties. In: In: Proceedings of Powder Metal Materials Colloquium. Soc. Franc. De Metal. Et de Mater. Public; 1992. pp. 4-1 to 4-6.

[21] Koehler P. Seamless porous metal article and method of making, U.S. Patent No 4,828,930, 1989.

[22] Andersen O, Studnitzky T, Bauer J. Direct typing–a new method for the production of cellular P/M parts. In: Compiled by European Powder Metallurgy Association, (Bellstone Shrewsbury, UK) proceedings of 2004 Powder Metallurgy World Congress, Vienna, vol. 4, 2004. p. 189–94.

[23] Mahamood RM, Akinlabi ET, Shukla M, Pityana S. Characterizing the effect of processing parameters on the porosity of laser deposited titanium alloy powder. In: Proceedings of the international multi conference of engineers and computer scientists Vol II, IMECS 2014, March 12 – 4, 2014, Hong Kong; 2014.

[24] Bram M, Buchkremer HP, Stöver D. Development of porous composite membranes for microfiltration devices. In: Compiled by European Powder Metallurgy Association, (Bellstone Shrewsbury, UK) proceedings of 2004 Powder Metallurgy World Congress, Vienna, vol. 4, 2004, p. 183–8.

[25] Porous Metal Design Guidebook, Porous Metal Council. Princeton, NJ: Metal Powder Industries Federation Publishers; 2005.

[26] Steigert S. Porous sintered metal for soot filtration. In: Compiled by European Powder Metallurgy Association, (Bellstone Shrewsbury, UK) proceedings of 2004 Powder Metallurgy World Congress, Vienna, vol. 4, 2004. p. 195–200.

[27] Savich VV, Pilinevich LP, Tumilovich MV, Petracov AV. Effectiveness of application of porous powder materials for separation of water from petroleum products. In: Compiled by European Powder Metallurgy Association, (Bellstone Shrewsbury, UK) proceedings of 2004 Powder Metallurgy World Congress, Vienna, vol. 4, 2004. p. 163–7.

[28] Esholt P. In: In: Banhart J, Ashby MF, Fleck NA, editors. Metal foams and porous metal structures. Bremen: MIT-Verlag; 1999. p. 133.

[29] Shapovalov V. In: In: Schwartz DS, et al., editors. Porous and cellular materials for structural applications. vol. 521. Warrendale, PA: MRS; 1998.

[30] Seeliger W. In: In: Banhart J, Ashby MF, Fleck NA, editors. Metal foams and porous metal structures. Bremen: MIT-Verlag; 1999. p. 29.

[31] Elliott JC. Method of producing metal foam. US Patent No. 2,751,289 June 19, 1956.

[32] Allen BC, Mote MW, Sabroff AM. Method of making foamed metal. US Patent No. 3,087,807, April 30, 1963.

[33] Nakamura, Gnyloskurenko SV, Sakamoto K, Byakova AV, Ishikawa R. Development of new foaming agent for metal foam. Mater Trans Jpn Inst Metals 2002;43:1191–6.

[34] Gergely V, Curran DC, Clyne TW. The FOAMCARP process: foaming of aluminium MMCs by the chalk-aluminium reaction in precursors. Comp Sci Technol 2003;63:2301–10.

[35] Kevorkijan V. Low cost aluminum cost foams made by $CaCO_3$ particulates. Assoc Metal Eng Serbia 2010;16(3):205–19.

[36] Koizumi T, Kido K, Kita K, Mikado K, Gnyloskurenko S, Nakamura T. Foaming agents for powder metallurgy production of aluminum foam. Mater Trans Jpn Inst Metals 2011;52(4):728–33.

[37] Fathi H, Emadoddin E, Habibolahzadeh A. Manufacture of aluminum closed-cell foam by ARB process using $CaCO_3$ as the blowing agent. Iran J Mater Sci Eng 2012;9(3):40–8.

[38] Haesche M, Lehmhus D, Weise J, Wichmann M, CIM M. Carbonates as foaming agent in chip-based aluminium foam precursor. J Mater Sci Technol 2010;26(9):845–50.

[39] Praveen Kumar TN, Venkateswaran S, Seetharamu S. Effect of grain size of calcium carbonate foaming agent on physical properties of eutectic-Si alloy closed cell foam. Trans Indian Inst Met 2015;68(Suppl. 1):109–12.

[40] Kadoi K, Babcsan N, Nakae H. Heat treatment of TiH_2 powder to control decomposition phenomenon for aluminium foam fabrication by melt route. Mater Trans Jpn Inst Metals 2009;50(4):727–33.

[41] Walz DD. Method of making an inorganic reticulated foam structure. U.S. Patent 3 616 841 (2 November 1971).

[42] Brannan JR, Bean AS, Vaccaro AJ, Stewart JJ. Continuous electroplating of conductive foams. U.S. Patent 4 978 431 (18 December 1990).

[43] Brannan JR, Vaccaro AJ, Healy JP. High density, high capacity battery electrode. U.S. Patent 5 374 491 (20 December 1994).

[44] Vaccaro AJ, Gregg JS, Gibbons DW, Brannan JR, Pohto GR, Hinden J.M. Continuously electroplated foam of improved weight distribution. U.S. Patent 5 804 053 (8 September 1998).

[45] Babjak J, Ettel VA, Paserin V. Method of forming nickel foam. U.S. Patent 4 957 543 (18 September 1990).

[46] Perugini G, Marcaccioli E. Process for the preparation of metallic and/or metal-ceramic and/or ceramic sponges. U.S. Patent 4 076 888 (28 February 1978).

[47] Pinkhasov E. Method of making open pore structures. U.S. Patent 5 011 638 (30 April 1991).

[48] Koshita H, Ishijima Z. Development of highly porous aluminum with an open-cell structure. In: Compiled by Russell A, Chernenkoff W, Brian J. proceedings of 2014 Powder Metallurgy World Congress, Orlando (FL, USA): Metal Powder Industries Federation; 2014. p. 09-209–14.

[49] Queheillalt DT, Hass DD, Sypeck DJ, Wadley HN. Synthesis of open-cell metal foams by templated directed vapor deposition. J Mater Res 2001; 16(4):1028–35.

[50] Böhm A, Walther G, Naumann D. German Patent, DE 103 46 281 B4, 2006, World Patent, WO 2005/037467 A2, 2005.

[51] Walther G, Böhm A, Weißgärber T, Böhm H-D, Engelmann B, Naumann D. German patent, DE 103 16 929 B3, 2005, European patent EP 1 620 370 B1, 2006.

[52] Walther G, Klöden B, Kieback B. A new PM process for manufacturing of alloyed foams for high temperature applications. In: Compiled by European Powder Metallurgy Association, Bellstone Shrewsbury, UK, Proceedings of PM 2010 World Congress, Florence, vol. 4, 2010. p. 109–16.

[53] Weissgaerber T, Pacheco V, Recknagel C, Walther G, Klöden B, Kieback B. Advanced PM technologies to manufacture thermoelectric materials and supercapacitors. In: Compiled by Russell A, Chernenkoff W, Brian J. Proceedings of 2014 Powder Metallurgy World Congress, Orlando (FL, USA): Metal Powder Industries Federation; 2014. p. 09.208–14.

[54] Garcia-Moreno F, Rack A, Helfen L, et al. Fast processes in liquid metal foams investigated by high-speed synchrotron x-ray microradioscopy. Appl Phys Lett 2008;92:134104-1 – 3.

[55] Rodriguez-Perez MA, Solórzano E, De Saja JA, García-Moreno F. The Time-uncoupled aluminium free-expansion: intrinsic anisotropy by foaming under conventional conditions. In: Lefebvre LP, Banhart J, Dunand DC, editors. Porous metals and metallic foams. Pennsylvania: DEStech Pub; 2008. p. 75–8.

[56] Solórzano E, Rodriguez-Perez MA, et al. Aluminium foaming monitored by far-infrared thermography: temperature gradients and bubble rupture. In: Lefebvre LP, Banhart J, Dunand DC, editors. Porous metals and metallic foams. Pennsylvania: DEStech Pub; 2008. p. 79–82.

[57] Lefebvre L-P, Banhart J, Dunand DC. Porous metals and metallic foams: current status and recent developments. Adv Eng Mater 2008;775–87.

[58] Lázaro J,Solórzano E,Rodríguez-Pérez AM. Alternative carbonates to produce aluminium foams via melt route Procedia Materials Science, vol. 4, 2014 8th international conference on porous metals and metallic foams: 275–280.

[59] Byakova A, Gnyloskurenko S, Nakamura T. The role of foaming agent and processing route in the mechanical performance of fabricated aluminum foams. Metals 2012;2:95–112.

[60] Gibson LJ. Mechanical behavior of metallic foam. Annu Rev Mater Sci 2000;30:191–227.

[61] Simone AE, Gibson LJ. The effect of cell face and corrugations on the stiffness and strength of metallic foams. Acta Mater 1998;46:3929–35.

[62] Brothers AH, Banhart J. Verfahren zur Herstellung eines Metallmatrix-Nanoverbundwerkstoffes, Metallmatrix-Nanoverbundwerkstoff und seine Anwendung; 2007, German Patent Application DE 10 2007 044 565.4.

[63] Babcsán N, Murty BS, Vinod Kumar GS, García Moreno F, Banhart J. New foam stabilizing additive for aluminium. In: Lefebvre LP, Banhart J, Dunand DC, editors. Porous metals and metallic foams. Pennsylvania: DEStech Pub; 2008. p. 27–30.

[64] Wiehler H, Heinl P, Körner C, Singer RF. High pressure integral foam moulding of aluminium. In: Lefebvre LP, Banhart J, Dunand DC, editors. Porous metals and metallic foams. Pennsylvania: DEStech Pub; 2008. p. 15–8.

[65] Jaeckel M. Verfahren zum Herstellen von metallisctn oder keramischen hohlkugeln. European Patent EP 0 300543, Patentblatt 89/04.

[66] Waag U, Schneider L, Löthman P, Stephani G, Kieback B. Metallic hollow spheres–a new product. In: Proceedings of 2000 Powder Metallurgy World Congress. Publ. Japan Society of Powder and Powder Metallurgy; 2000. p. 510–4.

[67] Waag U, Stephani G, Färber J, Venghaus H, Bingel G. Cellular structures based on metallic hollow spheres–mechanical and acoustical properties. In: Compiled by European Powder Metallurgy Association proceedings of PM 2010 World Congress, Florence 2010, vol. 4, 2004. p. 143–8.

[68] Stephani G, Andersen O, Quadbeck P, Kieback B. Cellular metals for functional applications–an overview. In: Compiled by European Powder Metallurgy Association, (Bellstone Shrewsbury, UK) proceedings of PM 2010 World Congress, Florence, vol. 4, 2010. p. 95–102.

[69] Rabiei A, Vendra L. Elastic and plastic behavior of composite metal foams under compressive loading. In: Lefebvre LP, Banhart J, Dunand DC, editors. Porous metals and metallic foams. Pennsylvania: DEStech Pub; 2008. p. 387–90.

[70] Lhuissier P, Fivel M, Salvo L, Brechet Y. Constitutive equation for the compression of metallic Hollow Spheres Foam. In: Lefebvre LP, Banhart J, Dunand DC, editors. Porous metals and metallic foams. Pennsylvania: DEStech Pub; 2008. p. 395–8.

[71] Jumate N, Vida-Simiti I, Thalmaier G, Bruj E, Nemes D. Preliminary research on bi-porous metallic foams from Ni-based metal alloy powders. In: Compiled by European Powder Metallurgy Association, (Bellstone Shrewsbury, UK) proceedings of PM 2010 World Congress, Florence, vol. 4; 2010. p. 173–9.

[72] Boonyongmaneerat Y, Schuh CA, Dunand DC. Mechanical properties of reticulated aluminum foams with electrodeposited Ni–W coatings. Scr Mater 2008;59:336–9.

[73] Böhm A, Walther G, Naumann D, Croset M, Bartout JD, Bienvenu Y. Preparation and properties of high temperature stable NiAl and Inconel-based foams. In: Compiled by European Powder Metallurgy Association, (Bellstone Shrewsbury, UK) proceedings of 2004 Powder Metallurgy World Congress, Vienna, vol. 4; 2004. p. 101–5.

[74] Walther G, Klöden B, Weissgärber T, Kieback B, Böhm A, Naumann D, Saberi S, Timberg L. A new class of high temperature and corrosion resistant nickel-based open-cell foams. In: Lefebvre LP, Banhart J, Dunand DC, editors. Porous metals and metallic foams. Pennsylvania: DEStech Pub; 2008. p. 125–8.

[75] Boonyongmaneerat Y, Dunand DC. Ni-Mo-Cr foams processed by casting replication of sodium aluminate preforms. Adv Eng Mater 2008;10:379–83.

[76] Levine BA. New era in porous metals: applications in orthopaedics. In: Lefebvre LP, Banhart J, Dunand DC, editors. Porous metals and metallic foams. Pennsylvania: DEStech Pub; 2008. p. 251–4.

[77] Schiefer H, Bram M, Buchkremer H-P, Stöver D. Porous titanium for dental implant applications. In: Lefebvre LP, Banhart J, Dunand DC, editors. Porous metals and metallic foams. Pennsylvania: DEStech Pub; 2008. p. 259–62.

[78] Takemoto M, Fujibayashi S, Neo M, Suzuki J, Kokubo T, Nakamura T. Mechanical properties and osteoconductivity of porous bioactive titanium. Biomaterials 2005;26:6014–23.

[79] Cysne Barbosa AP, Bram M, Buchkremer HP, Stöver D. Fabrication of titanium implants with a gradient in porosity by 2-component-MIM. PIM Int 2012;6(1):69–73.

[80] Tuncer N, Bram M, Buchkremer HP. Effects of production method and space holder material on microstructure of porous titanium, Proceeding of the PM2012 (Basel). PM BIO: 348–356.

[81] Caparrós C, Molmeneu M, Ortiz-Hernandez M, Punset M, Gil FJ. Advance in open cell titanium for biomedical application. In: Compiled by Russell A. Chernenkoff W, Brian J. Proceedings of 2014 Powder Metallurgy World Congress, Orlando (FL, U.S.A.), Metal Powder Industries Federation; 2014. p. 09.216–24.

[82] Tuncer N, Maire E, Salvo L, Gursoy Arslan G. Investigation of PM parameters effect on architecture of titanium foams using x-ray microtomography. In: Compiled by European Powder Metallurgy Association proceedings of PM 2010 World Congress, Florence, vol. 4, 2010. p. 125–30.

[83] Mukherjee M, García-Moreno F, Banhart J, Kolluri M, Ramamurty U. Deformation mechanisms in constrained monotonic and cyclic compressive loading of Al foam. In: Lefebvre LP, Banhart J, Dunand DC, editors. Porous metals and metallic foams. Pennsylvania: DEStech Pub; 2008. p. 347–50.

[84] Fallet A, Salvo L, Brechet Y. Metallic hollow spheres foam: structure and mechanics. In: Lefebvre LP, Banhart J, Dunand DC, editors. Porous metals and metallic foams. Pennsylvania: DEStech Pub; 2008. p. 343–6.

[85] Borovinšek M, Ren Z. Effects of cell irregularity on the impact behavior of open-cell foams. In: Lefebvre LP, Banhart J, Dunand DC, editors. Porous metals and metallic foams. Pennsylvania: DEStech Pub; 2008. p. 371–4.

[86] Issen KA, Smith CJ, Black ML, Morrison DJ. Inhomogeneous deformation and fracture of aluminum foam under uniaxial tension. In: Lefebvre LP, Banhart J, Dunand DC, editors. Porous metals and metallic foams. Pennsylvania: DEStech Pub; 2008. p. 355–8.

[87] Banhart J, Baumeister J, Weber M. Metallic foam. In: ASM handbook. vol. 7. Materials Park, OH: ASM International Publishers; 1998. p. 1043–7.

[88] Reutter O, Sauerhering J, Fend T, Pitz-Paal R, Angel S. Characterization of heat and momentum transfer in sintered metal foams. In: Lefebvre LP, Banhart J, Dunand DC, editors. Porous metals and metallic foams. Pennsylvania: DEStech Pub; 2008. p. 489–92.

[89] Berg A, Baumeister J, Rausch G, Busse M, Schnabel L, Bauer J. Application of aluminium sponges in the adsorption refrigeration engineering. In: Lefebvre LP, Banhart J, Dunand DC, editors. Porous metals and metallic foams. Pennsylvania: DEStech Pub; 2008. p. 493–6.

[90] Solórzano E, Escudero J, Lázaro J, Rodriguez-Perez MA, De Saja JA. Critical cooling velocities maps for thermal hardening treatments in aluminium foams: density characterization, finite elements analysis, experimental validation and final results. In: Lefebvre LP, Banhart J, Dunand DC, editors. Porous metals and metallic foams. Pennsylvania: DEStech Pub; 2008. p. 505–8.

[91] Suzuki A, Kitazono K. Design of anisotropic metal foams for thermal. In: Lefebvre LP, Banhart J, Dunand DC, editors. Porous metals and metallic foams. Pennsylvania: DEStech Pub; 2008. p. 517–20.

Chapter 12

Powders for Composites

Oleg D. Neikov
Frantsevich Institute for Problems of Materials Science (IPMS), Kiev, Ukraine

Chapter Outline

Introduction 351
Manufacture of Composite Powders 351
Nickel-Clad Aluminum Powders 351
Aluminum-Based Composite Powders 352
Copper-Based Composite Powders 353
Titanium-Based Composite Powders 355
Refractory-Based Composite Powders 355
Zinc-Rich Composite Powders 355
Carbon Nanotube-Reinforced Metal Composite Powders 357
Graphene-Oxide Composite Powders 360
Manufacture of Composites 363
Composite Manufacturing Methods 363
Aluminum-Based Composite 363
Copper-Based Composite 364
Refractory Metal and Carbide-Based Composites 366
References 368
Further Reading 372

INTRODUCTION

A composite is a complete content powder, every particle of which consists of the macrovolumes of a few components differing by chemical composition. The production methods of composite powders are divided into two groups: direct manufacturing (primary methods) and modification of existing powders (derived methods). Methods of the first group provide the powder particle formation in the course of the process, such as atomization, mechanical alloying, the gas-phase method, the solid-phase reduction of metal oxides and salts, etc. (Fig. 12.1A). Cladding and conglomeration relate to the second group. Figure 12.1B illustrates a conglomeration of clad particles. The combination of these two composite particle fashions allows making hybrid structures (Fig. 12.1C–E). The PM composite materials can be produced either from powders composed of a mono constituent part or a composite.

MANUFACTURE OF COMPOSITE POWDERS

Nickel-Clad Aluminum Powders

Composite materials are a special class of aluminum powder materials that include powders of aluminum and its alloys or mixtures of such powders with powders of other compounds, clad by nickel.

The production technology of the specified composite materials developed by the Norilsk Nickel Concern [1] consists of coating powder particles of aluminum and its alloys with metallic nickel by the carbonyl process, that is, by the decomposition of nickel tetra carbonyl vapor on the surface of the powder suspended in the vibro-fluidized bed:

$$\mathrm{Ni(CO)_4 + Al \xrightarrow{450-520K} AlNi + 4CO}$$

Depending on the chosen technological parameters of the process and the material base, three main structural types of powder compositions are formed:

- Clad powders, where particles of the base material are surrounded by a compact nickel coating.
- Conglomerated powders, where fine particles of the base material are conglomerated on the metallic nickel bundle.
- Capsulated powders, where particles of a different composition, structure, and property are coated with a single nickel casing.

Handbook of Non-Ferrous Metal Powders. https://doi.org/10.1016/B978-0-08-100543-9.00012-9
© 2019 Elsevier Ltd. All rights reserved.

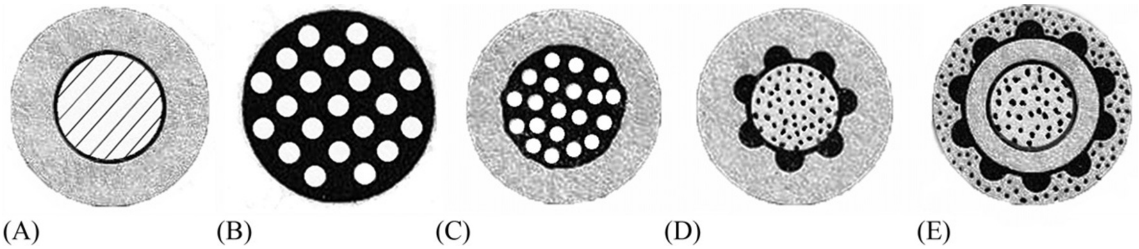

FIG. 12.1 Particle ctructures of composite powders: clad particle (A); conglomerate of clad particles (B); hybrid structure of particles (C), (D), (E).

It is possible to form compositions that are combinations of the three above types. Thus, it is obviously possible to create a wide range of complex multicomponent compositions possessing a complex of predetermined physicotechnological properties.

Composite powder materials metallized by nickel are subdivided into three main groups:

- Metal-metal and metal-carbide compositions intended to increase the wear resistance and corrosion resistance of plasma coatings.
- Thermal reacting metal-metal and metal-metal-oxide compositions used for coating wearproof, heat-resistant, and heat-shielding coatings.
- Metal-solid lubricant and metal-carbide-solid lubricant compositions used for antifriction coatings.

Nickel introduction into the makeup of clad, conglomerated, and encapsulated compositions by the following thermal spraying provides:

- Protection of the basic material of the coating against interaction with the plasma jet and oxidation.
- More uniform distribution of components in the coating due to the absence of segregation.
- Interaction of separate components with the formation of solid solutions, intermetallics, etc.
- Directed course of exothermic reactions that facilitates powder heating and improvement of coating quality.
- Creation of essentially new phases and structural components in the coating.
- Coarsening of fine powders that essentially expands the nomenclature of powders for spraying.
- Increase of fluidity, productivity of spraying, and the use factor of powder.
- Formation of essentially new multilayered powder compositions.
- Increase of durability, density, and heat conductivity of coatings.

The low temperature of the process, the precise dosing of the nickel, the complete absence of a liquid phase, the lack of waste, and the fact that no additional processing such as drying, filtration, or regeneration of solutions is required are the main advantages of the chosen method for producing composite powder materials in comparison with many liquid-phase and gas-phase processes.

Chapter 15 contains data from the typical physical properties of nickel-clad aluminum powders.

Aluminum-Based Composite Powders

The one-step in situ production of aluminum matrix composite powders has been realized by means of mechanical alloying (MA). The composite material powders were manufactured by simultaneously mixing the elemental powders in the appropriate percentages to obtain the aluminum alloy matrix and the selected carbides. In this case, the elemental powders used for the aluminum alloy were aluminum, copper, silicon, and magnesium. Two different carbides were used as reinforcement for the composite material as VC and TiC [2].

Numerous aluminum alloys are manufactured by MA [3], including alloys from the 6xxx [4] and 7xxx [5] series. Aluminum matrix composite powders that have been reinforced with SiC and Al_2O_3 [6–8] have been obtained in order to improve the wear behavior of the aluminum alloy matrix. More recent studies have considered the possibility of adding intermetallics, which is potentially successful because of their hardness and compatibility with the matrix [9–11].

Aluminum alloys based on gas- and water-atomized powders can be reinforced with Al_2O_3 by hot extrusion. Fig. 12.2 illustrates typical water-atomized aluminum alloy powder particles with a size less than 25 μm.

The paper [12] analyzes the mechanical behavior and microstructure of some Al-Mg base alloys. The Al_2O_3 oxide films on the water-atomized powder surface are comminuted during hot extrusion into ultrafine particles that are disposed, as TEM local X-ray spectrometry analysis showed, along the boundaries of fibers and cells (Fig. 12.3). The presence of nanoparticles in the composite structure hinders the growth and confluence of fibers and cells that prevent the recrystallization.

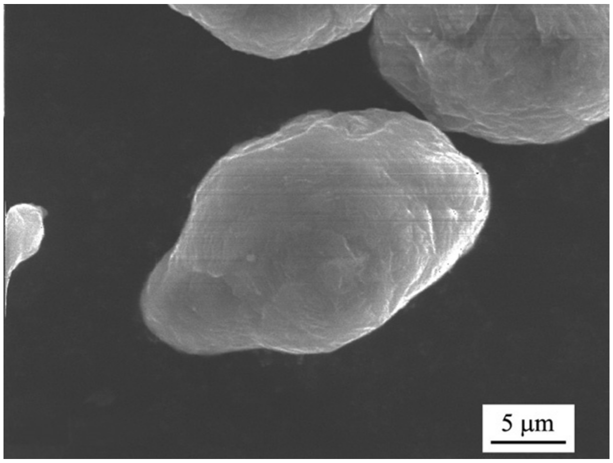

FIG. 12.2 Typical morphology of water-atomized aluminum alloy powder particles with a size less than 25 µm.

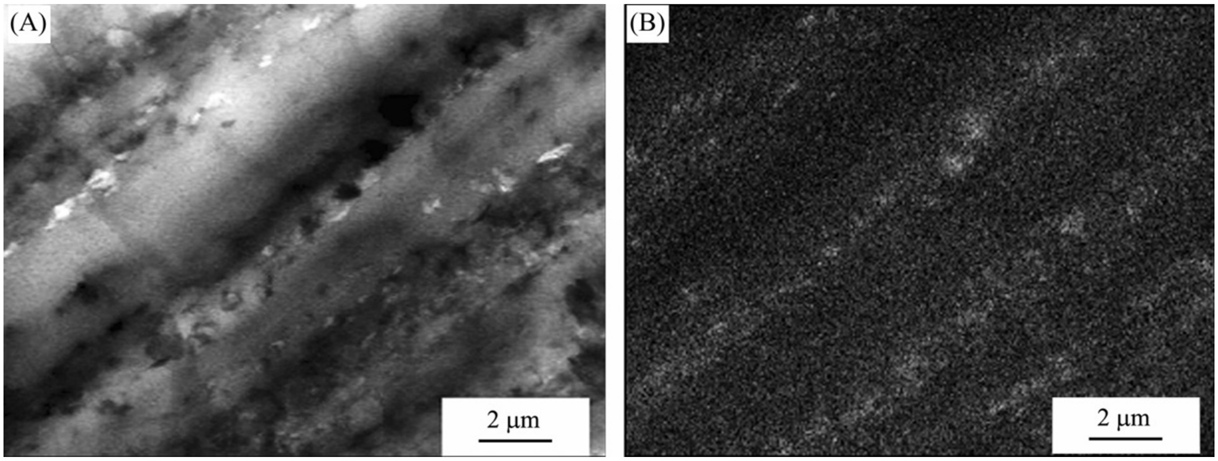

FIG. 12.3 Microstructure of the Al–5Mg–0.3Sc–0.15Zr–0.2Cr powder alloy (A) and distribution of Mg-Kα (B) elements; the black-colored spots correspond to the alumina particles in the metal composite powder.

Chapter 15 contains data about the tensile mechanical properties of aluminum alloys reinforced with alumina by hot extrusion.

Boron carbide (B_4C) is one of the hardest and lightest materials and thus a candidate for reinforcing light ductile metals. However, owing to the poor wettability of B_4C with the molten Al alloys, it is difficult to produce dense Al–B_4C composites by liquid-phase approaches. It has been reported that Al requires a temperature as high as 1373 K in order to wet the B_4C surface completely. Processing at such high temperatures leads to the formation of a series of components by chemical reactions between these two phases [13,14]. Ye et al. [15,16] have optimized the cryomilling technique for processing composite powders that consist of particulate B_4C reinforcement in different aluminum matrices. It has been reported that Al–B_4C composites prepared by consolidation of the cryomilled powder particles exhibited better wear resistance [17] and improved mechanical properties [18] when compared to the unreinforced alloys. The effect of interfacial debonding on the mechanical properties of Al–B_4C composites consolidated by different thermomechanical techniques was reported in another study [19]. However, in the aforementioned studies, cryomilling was used to prepare the Al–B_4C composite powders by using micrometer-sized B_4C particles. Nanosized boron carbide particles can be produced from commercially available boron carbide particles and mechanically alloyed with Al6061 to synthesize the corresponding nanocomposite powdery [20].

Copper-Based Composite Powders

The copper reinforcement with ceramic particles such as TiC and NbC increases the microhardness of composites and maintains the microhardness at elevated temperatures [21]. There are some publications focused on the production of pure

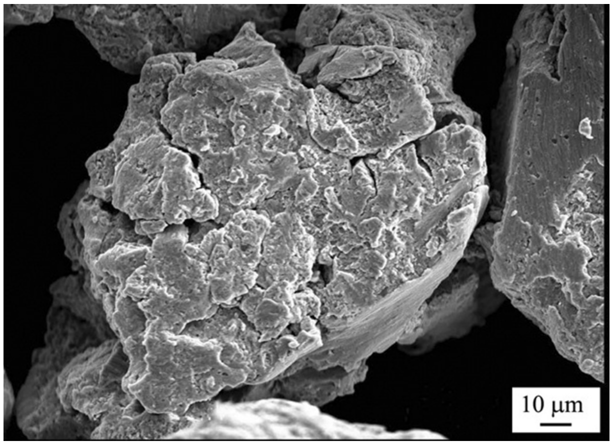

FIG. 12.4 SEM micrographs of the Cu-Fe-Co with 3 wt%Al_2O_3 composite powder particles after high-energy ball milling. *Modified from Llorca-Isern N, Artieda-Guzmán C, Porras-Mateu N, Roca-Vallmajor A. Structural and magnetic properties of nanocrystalline Cu–Fe–Co–Al2O3 composite powders processed by mechanical alloying. In: Compiled by European powder metallurgy association proceedings of PM 2010 world congress, Florence (Italy). vol. 2. 2010. p. 256–63.*

Cu matrix nanocomposites such as Cu–Al_2O_3 [22,23], Cu–MgO [24], Cu–TiB_2 [25], Cu–ZnO [26], and Cu–MnO [27], using an MA method. Very few methods used copper alloy as the matrix (Cu(Mo)), yet it seems that the presence of a nanocrystalline Cu(Mo) alloy as a matrix and the homogenous distribution of Al_2O_3 reinforcements can be helpful in achieving better mechanical properties in a nanocomposite.

The mechanochemical reduction of copper oxide with different reductants such as Fe, Al, Ti, Ca, Ni, and C has already been studied [28,29]. The products were usually a mixture of copper with dispersed oxide particles, that is, copper matrix composites. When this process is combined with mechanical milling (reactive milling), nanostructured composites with a uniform distribution of reinforcement particles are synthesized.

The Cu-Fe-Co/Al_2O_3 composite powders were made by PM processing of an elemental components mix [30]. The reaction stages and resulting magnetic properties were analyzed in order to determine the influence of the ceramic powder on the process and properties, compared to the metallic system. Al_2O_3 interacts with the metallic dissolution of Fe and Co atoms in Cu, resulting in a barrier to the progress of the atomic diffusion. It has been shown that a 3% Al_2O_3 is a barrier to the plastic deformation, resulting in increased fragility of the material so that this composite powder becomes brittle (Fig. 12.4).

The cross section of composite powder (CuFeCo + 10 wt% Al_2O_3) processed by high-energy ball milling is shown in Fig. 12.5. The alumina of different size particles can be seen as dark spots embedded within the metallic matrix.

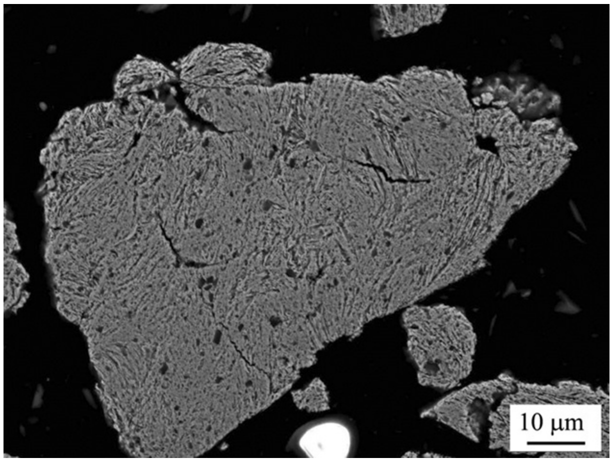

FIG. 12.5 SEM BCE cross-section of composite powder (CuFeCo + 10 wt% Al_2O_3) processed by high-energy ball milling.

Titanium-Based Composite Powders

Many reinforcements are used in titanium matrix composites (TiMCs), including SiC, Al_2O_3, TiO_2, TiC, TiB, TiB_2, and rare earth oxides. In addition, elements of rare earth added to the TiMCs can greatly increase the strength of the matrix alloy at high temperatures. Rare earth oxide is produced from the rare earth element and solid-solution oxygen in a matrix alloy [31].

Titanium alloys are the metallic biomaterials that are most commonly used for medical implants, owing to their good biocompatibility, high chemical stability in the physiological environment, and excellent mechanical properties. Therefore, effort has been devoted to synthesizing titanium alloy-hydroxyapatite (Ti6Al4V/HA) composites. Plasma spraying is the most popular technique for adding a coating of HA to the titanium substrate. Thian et al. [32] studied the formation of Ti-6Al-4V/HA composite powders using a technique called the "ceramic slurry approach," which was employed to produce ti6al4V/Ha composite powders that have a surface layer consisting of a biocompatible hydroxyapatite (HA) while the inner core consists of mechanically strong Ti-6Al-4V.

Several studies represent nanometer-scale reinforcements as potential materials for the production of metal matrix composites (MMCs). A few works present titanium MMCs (TiMMCs) strengthened with nanocarbon reinforcements. Montealegre et al. [33] studied the behavior of TiMCs reinforced with nanocarbon materials, CNTs, and nanodiamonds (NDs), which were produced via powder metallurgy under different processing conditions. It was shown that TiMCs with a well-distributed and small reinforcing phase presented the best flexural strength (1473 MPa for TiMCs with NDs hot pressed at 1173 K, compared to 400 MPa for a titanium pure matrix) [34].

Joshi et al. [35] studied a titanium composite powder ($Ti–TiO_2$) produced by in situ metal oxidation during the MA process. Begin-Colin et al. [36] obtained metal-ceramic composite powders of Al_2O_3–Ti by MA using TiO_2 and Al as raw materials. These are both examples of TiMC powders.

Refractory-Based Composite Powders

A wide variety of refractory materials is available. These materials can be classified in three general families of refractories in terms of their chemical composition:

- Oxide refractories.
- Nonoxide refractories.
- Composite refractories.

Tungsten and molybdenum are two refractory metals that are especially attractive for high-temperature applications in industries such as consumer electronics, aerospace, telecommunications, medicine, and defense, owing to their excellent heat resistance. Their high melting temperatures, however, make it extremely difficult to process the materials by melting and casting. Therefore, tungsten- and molybdenum-based alloys and composites are produced by a powder metallurgical method, followed by minor machining or grinding, if necessary.

An important refractory metal-based composite is the W–Cu system, which has superior thermal management properties and a high microwave absorption capacity. It is predominantly used for heavy-duty electrical contacts and arcing resistant electrodes. Tungsten-copper alloy powders are used in many fields due to the high electric and thermal conductivities of copper and the high melting point of tungsten. Good thermal and electrical conductivity and a low thermal expansion coefficient contribute to making these composites advanced engineering materials. However, because the W–Cu system exhibits mutual insolubility, W–Cu powder compacts have a bad sintering capacity, even when using liquid-phase sintering at above the melting point of the Cu phase. Therefore, it has been reported that W–Cu composite powders can be produced by ball milling [37], oxide coreduction [38], a freeze-drying technique [39], mechanochemical methods [40], and MA [41,42]. However, only a few reports are available on the synthesis of W–Cu composite powders through chemical routes [43,44]. Compared to MA processes, chemical synthetic approaches have the advantage of better control of particle size, shape, and distribution through adjustment of the reaction parameters [45].

Zinc-Rich Composite Powders

In recent years, the organic/inorganic zinc-rich coatings have been widely used to protect metal structures against corrosion in marine and industrial environments [46–48]. In a zinc-rich coating, there is continuous contact between the metal particles. However, the weakness of this coating is the faster oxidation rate of zinc particles. This can be responsible for the fast sacrificial property reduction of the coating. The metal particles' contact will be significantly reduced at longer exposure times because of zinc oxides/hydroxides creation in the coating porosities. The corrosion products can fill the coating porosities and reduce the coating cathodic protection ability [49–51]. Therefore, the coating shows more barrier properties instead of sacrificial properties. Different factors, that is, zinc dust content and morphology, can influence the sacrificial protection and, therefore, the service life duration of a zinc-rich coating [49]. In recent years, attempts have been made to produce zinc-rich coatings with a longer cathodic protection duration. Decrease the zinc content of the zinc-rich coating without reducing its cathodic protection properties has also been attempted. The effects of size and shape of the zinc particles on the anticorrosive performance of the zinc-rich coating has been studied by Kalendova [49] and Jagtap et al. [52].

Park et al. [53] investigated the effects of zinc particles' surface modification on their sacrificial properties. They showed that surface modification of the zinc particles is an important factor that can influence its sacrificial properties. The dissolution rate of zinc particles can be significantly reduced after surface modification. This can result in the increase of the service life of the coating.

The effects of lamellar aluminum and micaceous iron oxide (MIO) pigments on the anticorrosion properties of an epoxy zinc-rich coating were studied [54]. Epoxy zinc-rich coatings containing 70% wt/wt spherical Zn particles, 60% wt/wt Zn + 10% wt/wt MIO, and 60% wt/wt Zn + 10% w/w Al were prepared. Pigments including zinc, aluminum, and MIO were used in the zinc-rich coating formulations. The aluminum pigment used in this study was in the form of paste, including 65% wt/wt aluminum pigment, 4% w/w stearic acid, and 31% wt/wt white spirit solvent. The epoxy zinc-rich coatings were prepared using epoxy resin of Epiran-01. The solid content and density of the epoxy resin were 75% and 1.099 g/cm^3, respectively. The SEM micrographs of different zinc-rich coatings before and after a salt spray test are shown in Fig. 12.6. Results show that Zn particles are appropriately in contact with each other (Fig. 12.6A). The lamellar Al particles are appropriately oriented at the surface, parallel to the metal substrate (Fig. 12.6C). The MIO is also a lamellar-type pigment, which can be oriented at the surface of the zinc-rich coating. The MIO particles could increase barrier properties

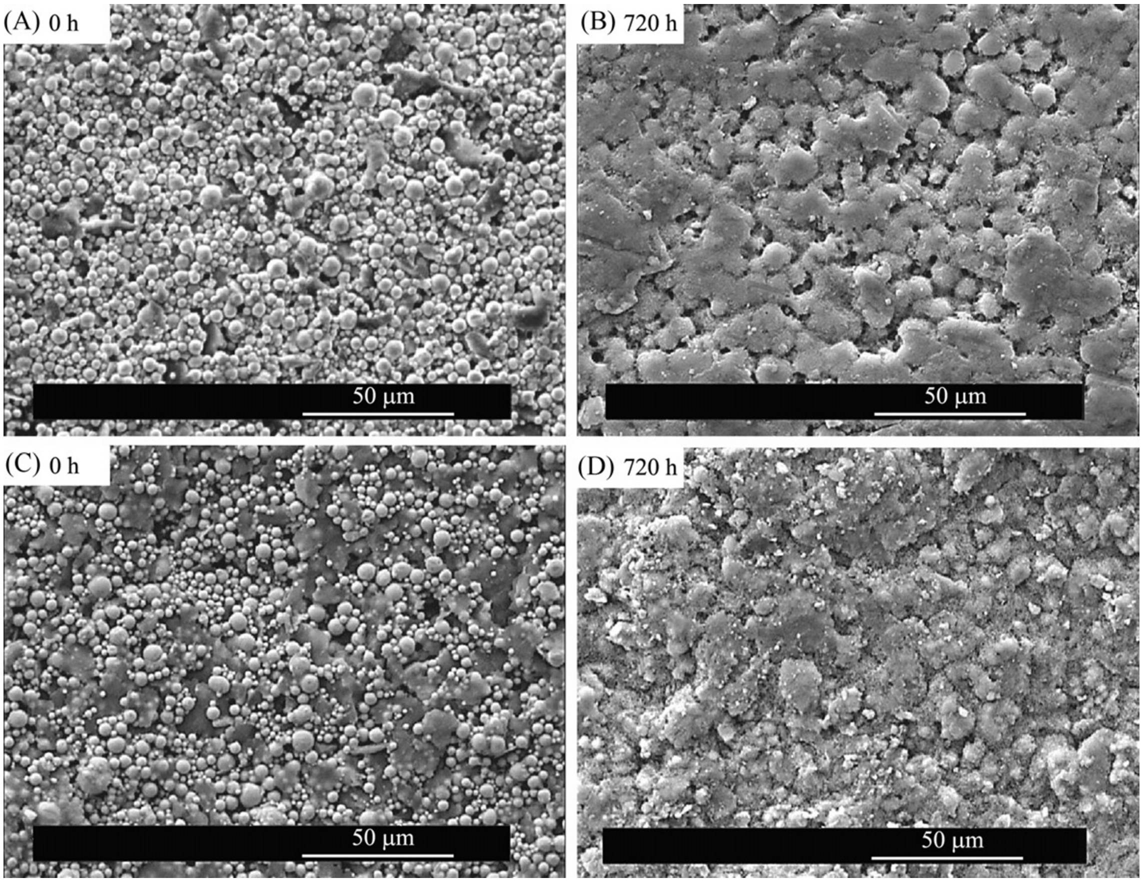

FIG. 12.6 SEM micrographs of the epoxy zinc-rich paints: 70% wt/wt zinc particles without pigments (A), (B); 60% wt/wt zinc particles with 10% wt/wt aluminum pigment (C), (D); before (A), (C) and after (B), (D) exposure to the salt spray test. *Modified from Ramezanzadeh B, Arman SY, Mehdipour M. Anticorrosion properties of an epoxy zinc-rich composite coating reinforced with zinc, aluminum, and iron oxide pigments. J Coat Technol Res 2014;11(5):727–37 (Accessed 9 February 2018).*

of the zinc-rich coating due to their lamellar shape. It can be seen (Fig. 12.6D) that the surface morphology of the zinc-rich coatings significantly changed after the salt spray test. As a result of electrolyte diffusion into the zinc-rich coating matrix, an oxide layer composed of zinc and aluminum oxide/hydroxides formed on the surface of the coatings.

The authors [54] reported that micaceous iron oxide particles could enhance the cathodic protection duration of the zinc-rich coating by enhancing its barrier properties and reducing the zinc particles oxidation rate. It was also shown that Al particles reduced zinc-rich coating sacrificial behavior at short immersion times and increased it at long immersion times. Unlike MIO particles, Al particles behaved both as a barrier and a sacrificial pigment.

Liu L et al. [55] reported that the types and additional dose of zinc in the zinc-rich coating have a significant impact on the character of the coating. Two types of zinc powders and the content of zinc were researched. It was revealed that the flaky zinc coating is better than the spherical zinc coating on corrosion performance, and the performance of the coating will be the best only when the solid content of zinc is reasonable. The results also show that the optimal solid content of flaky zinc is 62.5%, 60%, and 60.5% in the inorganic zinc-rich coating, epoxy zinc-rich coating, and vinyl resin zinc-rich coating, respectively.

In order to develop coatings with higher corrosion resistance and lower pigment content, several series of coatings were designed and manufactured employing lamellar Zn (Al) pigments mixed with a silicone-acrylate, emulsion-modified inorganic silicate vehicle, and then were evaluated by conventional methods as well as the electrochemical method [56]. The results indicated that the pigment contents were reduced to approximate 25 mass% with lamellar Zn or (Zn and Al) pigments as a substitute for spherical Zn pigments, and pigment mixtures were homogeneously dispersed due to a silicone-acrylate emulsion moistening modification. Furthermore, the optimal coating had good coating properties (adhesion grade: one), acid resistance (lower mass losses), and anticorrosive performance (improved corrosion potential and anodic passivation). The experimental results indicated that the modified lamellar Zn (Al) coating was suitable for large-scale spread and application on protecting steel structures in a hostile environment.

Carbon Nanotube-Reinforced Metal Composite Powders

Recently, carbon nanotubes (CNTs) have attracted great attention for strengthening metal matrix composites (MMCs) due to their low density ($2.1\,\mathrm{g{\cdot}cm^{-3}}$), high tensile strength (~10 GPa), high Young's modulus (~1 TPa), and excellent thermal/electrical conductivities [57]. Because pristine CNTs are prone to being easily tangled, acid treatment is widely employed to modify their surfaces [58]. The surface of acid-treated CNTs (ATCNTs) is coated with an abundance of hydrophilic groups; this results in ATCNTs being negatively charged and stably suspended in a solvent [58]. Moreover, ATCNTs could remain remarkably stable thermally with intrinsic strength as reinforcements, even though certain disorders are present on their outer walls [59].

The dispersion of CNTs by high-energy ball milling for the production of metal matrix composites is applied. Pérez-Bustamante et al. [60] studied the effects of milling time and CNT concentration on the hardness of CNT/Al2024 composites produced by MA. They observed not only a homogeneous dispersion of CNTs but also needle-shaped aluminum carbide (Al_4C_3) crystals in the aluminum alloy matrix, resulting in a significant improvement in the hardness as a function of the CNT content. Esawi et al. [61] investigated the influences of CNT content, morphology, and diameter on the mechanical properties of CNT-reinforced Al composites. They observed enhancements of up to 50% in tensile strength and 23% in stiffness compared with pure Al. In addition, smaller diameter CNTs were more difficult to disperse with increasing CNT content and had a relatively larger effective interfacial contact area with the Al matrix, which in turn affected the tensile properties and hardness of the composites.

Pérez-Bustamante et al. [62,63] researched the microstructural and mechanical characterization of aluminum-based nanocomposites produced using multiwalled carbon nanotube MWCNT dispersion by mechanical milling, followed by sintering and hot extrusion. Fig. 12.7 shows SEM micrographs of the as-prepared MWCNTs. From these figures, a diameter of ~40–100 nm and a length of ~10 μm can be observed.

A characteristic of the Al–1.0 wt% MWCNTs composite is illustrated in Fig. 12.8. The contrast corresponds to bent contours, grain boundaries, dislocations, and MWCNTs dispersed into an aluminum matrix.

They observed that yield strength, maximum strength, and microhardness values of the composites were considerably higher than those of pure aluminum. The most important strengthening mechanisms of Al–CNT nanocomposites were strengthening by nanofiber dispersion and aluminum-carbide precipitation.

The effects of CNT concentration on the micromorphologies and laser absorption properties of CNT/AlSi10Mg composite powders produced by high-energy ball milling were studied [64]. Multi-walled CNTs (purity >90%, 30–50 nm in diameter, and 10–20 μm in length) and AlSi10Mg (99.7% purity, −200 mesh) were used in the present investigation. The main chemical composition of the AlSi10Mg powder in wt% was 0.06Cu-0.623Mg-0.08Fe-(<0.24)other-Al(balance).

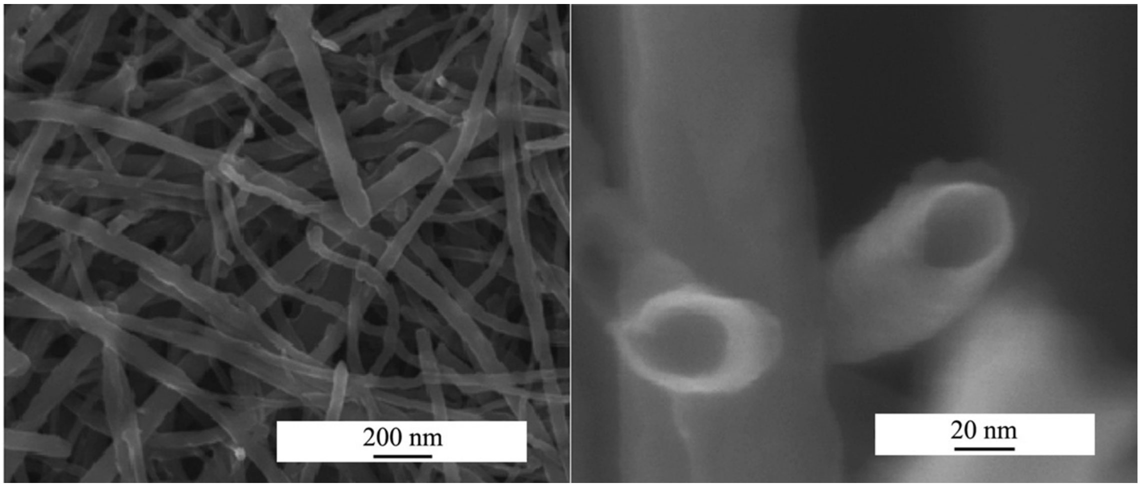

FIG. 12.7 SEM BCE images from CNTs at varying magnifications. *(Modified from Pérez-Bustamante R, et al. Microstructural characterization of Al-MWCNT composites produced by mechanical milling and hot extrusion. J Alloys Compd 2010; 495:399–402.)*

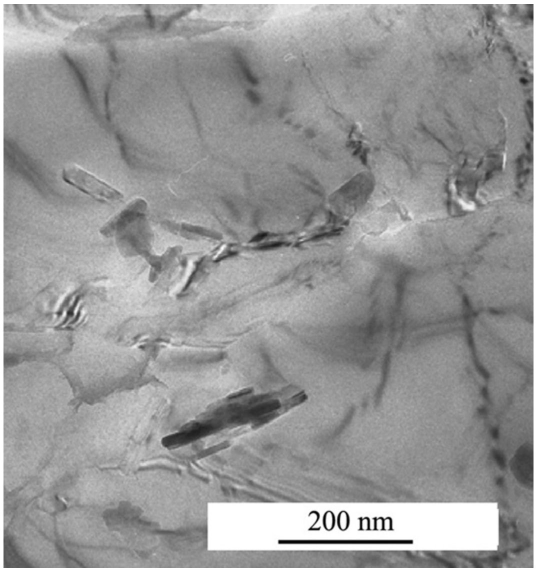

FIG. 12.8 Bright field TEM image of an Al-MWCNTs composite containing 1.0 wt% of MWCNTs.

The scanning electron microscope images of the composite powders with different CNT contents are shown in Fig. 12.9. For these tests with a ball-milling speed of 600 r/min and a milling time of 2 h in all instances, the mean particle size (median diameter) from 54 μm by 0.5 wt% CNT content decreased to 22.9 μm with the addition of 1.5 wt% CNT (Fig. 12.9B). Because the CNTs were uniformly dispersed in the AlSi10Mg matrix and contributed to the grinding process, the agglomeration of the AlSi10Mg powder was hindered. After increasing the CNT concentration, the AlSi10Mg powders changed from granule- to flake-like shapes. The CNTs penetrated into the powders, resulting in the plastic deformation of the AlSi10Mg powders under the strong collisions and impacts by the ball. Consequently, flaky powders could be observed in the milling process. In addition, the mean particle sizes gradually increased up to 48.8 μm with the addition of 2.5 wt% CNT (Fig. 12.9D), which was due to the fracturing of large particles and the cold welding of small particles.

Wang et al. [64] reported the following:

(1) With increases in milling rotational speed and time, the micromorphologies of the composite powders gradually changed from flake-like to granule-like and the average particle sizes of the composite powders sharply decreased. Moreover, the intensities of the Al and Si peaks for the composite powders initially decreased before increasing in comparison with the raw AlSi10Mg powders, and the main constituents of the composite powders were Al, Si, Al_4C_3, and an Al_2Cu intermetallic compound when the ball milling time was 2 h.

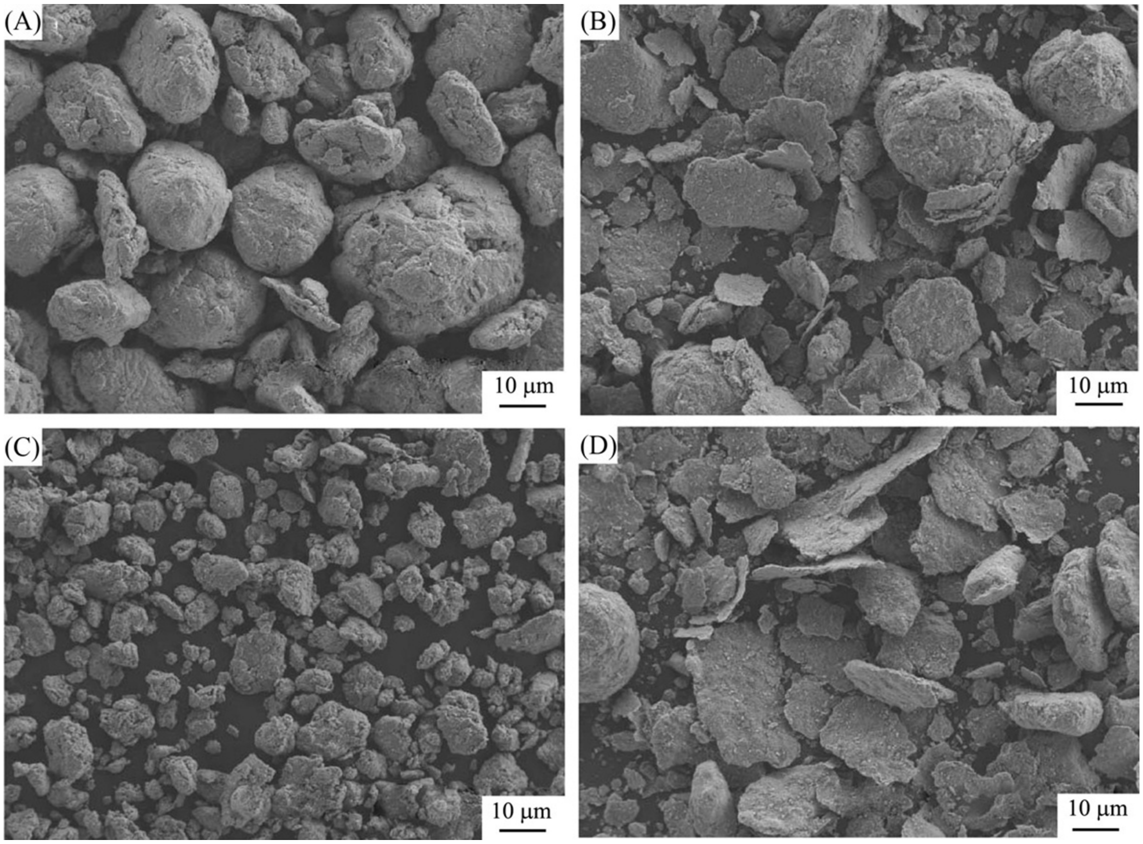

FIG. 12.9 SEM images of the composite powders with different contents of CNTs: (A) 0.5 wt%; (B) 1.0 wt%; (C) 1.5 wt%; (D) 2.5 wt%. *Modified from Wang L, Liu Y Wei W, An X, Zhang T, Pu Y. Preparation of CNT/AlSi10Mg composite powders by high-energy ball milling and their physical properties. Int J Miner Metall Mater 2016;23(3):330–8.*

(2) With the addition of 1.5 wt% CNTs, the mean particle size decreased to a minimum value, and uniform dispersion of CNTs in the AlSi10Mg powders was achieved. However, with further increases in CNT concentration, the AlSi10Mg powders changed from granule- to flake-like shapes and the mean particle sizes gradually increased.

(3) The DSC curve for the composite powders containing 2.5 wt% CNTs had both an endothermic peak and an exothermic peak, and the exothermic peak may have been associated with the reaction peak between CNTs and Al.

(4) Laser absorption values of the composite powders gradually increased with the increase of CNT concentration. Moreover, the spectra displayed characteristic absorption peaks at a wavelength of approximately 826 nm.

It is known that by synthesis of CNT-reinforced Al MMCs, the elevated temperatures reached during processing commonly resulted in the formation of carbides and aluminum grain growth. One method of preventing the heat-induced changes in the powders during milling is the use of cryogenic techniques. The low temperatures accelerate grain refinement and allow for further reduction in grain size as compared to room temperature milling, due to the increased brittleness of the material and the reduced grain growth [65–67]. Therefore, cryogenic milling conditions are believed to reduce processing times, to yield finer grain structures, and to lower the risk of temperature-induced changes during processing, as compared to conventional ball-milling techniques. Cryogenic milling refers to milling at very low, normally 100 K, temperatures; however, the grinding method and milling media can vary. Lee et al. [68] studied the milling behavior of CNTs at low temperatures using an agitator-applied ball mill and found that, due to their rigid and inflexible shapes at cryogenic conditions, CNTs were opened and shortened.

Woo et al. [69] synthesized the CNT-reinforced aluminum composite powders by cryogenic milling. The effects of different milling parameters and CNT contents on the structural characteristics and mechanical properties of the resulting composite powders were studied. They reported that with increasing CNT content, both powder particle size and size range generally decreased. The mean particle sizes of the 5 and 10 wt% CNT–Al MMC powders are in the range of 18.2–44.4 μm. It was observed that the microscale dispersion of CNTs gradually progressed with milling time while extensive milling

(~90 min) led to tube damage. Furthermore, for the same total milling time, the shorter cycle times and larger number of cycles are more efficient in reducing grain size and increasing hardness, independent of CNT content.

Detailed information on powder morphology and the dispersion and structural integrity of the CNTs is crucial for many powder consolidation methods, particularly cold spray, which is increasingly utilized to fabricate metal-based nanocomposites. While all the produced composite powders exhibited particle sizes suitable for spray applications, it was found that with increasing CNT content, the average particle size decreased and the size distribution narrowed. The dispersion of CNTs improved with milling time and helped to maintain a small Al grain size during cryogenic milling. Although extensive milling allowed for substantial grain size reduction, the process caused notable CNT degradation, leading to a deterioration of the mechanical properties of the resulting composite.

Graphene-Oxide Composite Powders

As the perfect layer structure of two-dimensional (2D) sp2-hybridized carbon atoms, graphene has been extensively investigated in recent years due to its outstanding properties, such as a high Young's modulus, high fracture strength, and excellent thermal conductivity [70–74]. Due to these excellent mechanical properties and high specific surface area, graphene is expected to be an ideal reinforcement phase interacting with the metal matrix, even in a small concentration. Wang et al. [75] have fabricated aluminum composites reinforced with graphene nanosheets (GNS/Al composite) through a feasible methodology based on flake powder metallurgy, and found that 0.30 wt% GNSs give rise to 62% enhancement over pure Al. However, Bartolucci et al. [76] investigated the mechanical properties of 0.1 wt% GNSs/Al composite through ball milling followed by hot isostatic pressing and hot extrusion, and obtained a remarkable decrease in tensile strength and elongation for 0.1 wt% GNS/Al composite compared with pure aluminum.

Reduced graphene oxide (GO) reinforced 7075 Al matrix composites were made by electrostatic self-assembly and powder metallurgy mode on a laboratory scale [77]. This process includes the following procedure stages:

- Preparation of GO aqueous dispersion. To strip the as-received graphite oxides having a particle size of 5 μm with 99% purity into GO nanaosheets with a structure of several layers, the graphite oxide was added to deionized water and then by ultrasonication treated for 2 h to obtain a brown dispersion with no residual sediment. A 1-mg/mL content GO aqueous dispersion was finally prepared. The thickness of the GO nanosheets was ~5 nm, consisting of no more than five ~1 nm thickness monolayers.
- Modifying 7075 Al powders with cetyl trimethyl ammonium bromide (CTAB). A CTAB aqueous solution (0.8 wt%) was magnetically stirred for 2 h, filtered, and then rinsed with deionized water to obtain the CTAB-modified 7075 Al powders.
- Adsorption of GO onto the 7075 Al powders. A powder slurry was prepared by adding CTAB-modified 7075 Al powders into deionized water. The GO aqueous suspended matter was added drop by drop. The mixed slurry was magnetically stirred until the color changed to transparent, and was then filtered and rinsed to obtain the composite powders. The composite powders were finally vacuum dried at 343 K for 8 h.
- CTAB removal and reduced graphene oxide (rGO) reinforced 7075 Al rGO/7075 Al composites fabrication. No particular heating treatment was used to remove the CTAB and reduce the GO because the sintering temperature (833 K) was high enough to achieve the purpose. The green billets (30 mm in diameter and 40 mm in height) were prepared by compacting the composite powders under 140 MPa at room temperature. Subsequently, the green billets were heated in a vacuum furnace at 833 K for 2 h, followed by hot pressing under 70 MPa for 10 min to ensure the density. After that, slabs with cross-sections 12 mm in width and 4 mm in thickness were obtained by hot extrusion at 723 K. The conditions of 14.7 extrusion ratio and 1 mm/s ram speed were adhered to. Subsequently, the slabs were solution treated in a resistance furnace at 743 K for 2 h, followed by water quenching, and then aged at 393 K for 24 h. The contents of rGO in the composites were 0.15, 0.30, and 0.50 wt%, respectively. For comparison, a 7075 Al sample was also prepared using the same method without adding GO.

Sun et al [77] reported that the Vickers hardness of rGO/7075 Al composites increases with the increase in rGO content. Compared with 7075 Al, the composites all show higher tensile properties. The yield strength and the ultimate tensile strength both reach the peak values for rGO/7075 Al composite with 0.30 wt% rGO addition. The yield strength and ultimate tensile strength of 0.30 rGO/7075 Al are increased by 15.6% and 11.7% compared with 7075 Al. With rGO content reaching 0.50 wt%, however, the excessive addition of rGO gives rise to a weakening in the enhancement of the tensile properties compared with the 0.30 rGO/Al composite, due to the increasing amounts of brittle Al_4C_3.

Various types of metal sulfides have been actively studied as suitable candidates for anode materials to be used in lithium-ion batteries (LIBs) because of their high theoretical capacity and low cost [78–81]. The materials should have spherical shapes, microscale sizes, and narrow size distributions to obtain highly efficient anode layers for use in LIBs. Recently, spherical-like metal oxide-reduced graphene-oxide (RGO) composite powders were prepared by one-pot spray pyrolysis [82,83]. A droplet containing graphene-oxide sheets and metal salt formed by an ultrasonic nebulizer was directly turned into a metal oxide-RGO composite powder by drying and decomposition inside a reactor maintained at temperatures above 873 K. The spherical-like metal oxide-RGO composite powders had excellent electrochemical properties for application as anode materials in LIBs [82,83].

Nanostructured zinc sulfide (ZnS) semiconductors have been employed in various devices such as photocatalysts, solar cells, light-emitting diodes, lasers, and sensors [84–92]. In addition, composite materials with graphene nanosheets have been studied to improve the properties of ZnS nanomaterials [88–91]. ZnS-graphene composite materials are mainly prepared by hydrothermal and solvothermal methods. Yu et al. prepared super-photoactive ZnS graphene nanocomposites by a solvothermal method [90].

In a study [93], a one-pot method for synthesizing spherical-like metal sulfide-RGO composite powders by spray pyrolysis was considered (a spray pyrolysis technique is described in Chapter 4). The formation mechanism of the ZnS–RGO composite powder, which was selected as the first target material, was investigated. The ZnS–RGO composite powder with superior electrochemical properties was synthesized by complete sulfidation (by the one-pot method) of ZnO nanocrystals spread on RGO powders by hydrogen sulfide gas formed by thiourea decomposition. The electrochemical properties of the ZnS–RGO composite powder were compared to those of a ZnO–RGO composite, bare ZnS, and bare ZnO powders prepared by the same process.

The formation mechanism of the spherical-like ZnS–RGO composite powders by one-pot spray pyrolysis includes the following stages:

- The droplets with a size of several microns containing graphene-oxide sheets, zinc chloride, and thiourea were formed by an ultrasonic atomizer. In this study, zinc chloride was selected as the zinc source material because it formed a stable colloidal solution with graphene-oxide sheets. Droplet drying produced a crumpled zinc chloride-thiourea-graphene oxide composite powder as an intermediate product in the region near the reactor entrance. The mole ratio of zinc chloride and thiourea dissolved in the spray solution was 1:10.
- The formation of hydrogen sulfide gas by thiourea decomposition maintained a reducing atmosphere within the reactor, which was heated at 1173 K. The thermal decomposition of zinc chloride and graphene oxide under the reducing atmosphere resulted in a crumpled RGO ball decorated with zinc nanocrystals.
- Rapid sulfidation of zinc metal into zinc sulfide by hydrogen sulfide gas produced a spherical-like ZnS–RGO composite powder with a crumpled structure. Therefore, ZnS nanocrystals were uniformly distributed all over the spherical-like ZnS–RGO composite powder.

The morphologies of the ZnS–RGO composite powders prepared by one-pot spray pyrolysis are shown in Fig. 12.10. The powder particles look like crumpled spheres with a size of approximately 1 μm.

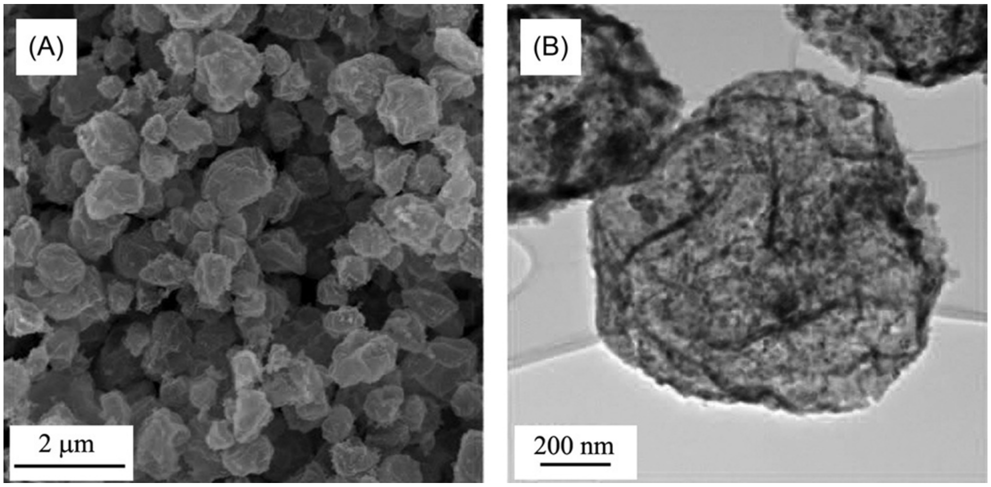

FIG. 12.10 SEM images of the ZnS-RGO composite powders by various magnifications. *Modified from Ref Park GD, Choi SH, Lee JK, Kang YC. One-pot method for synthesizing spherical-like metal sulfide-reduced graphene oxide composite powders with superior electrochemical properties for lithium-ion batteries. Chemistry 2014;20(38):12183–9.*

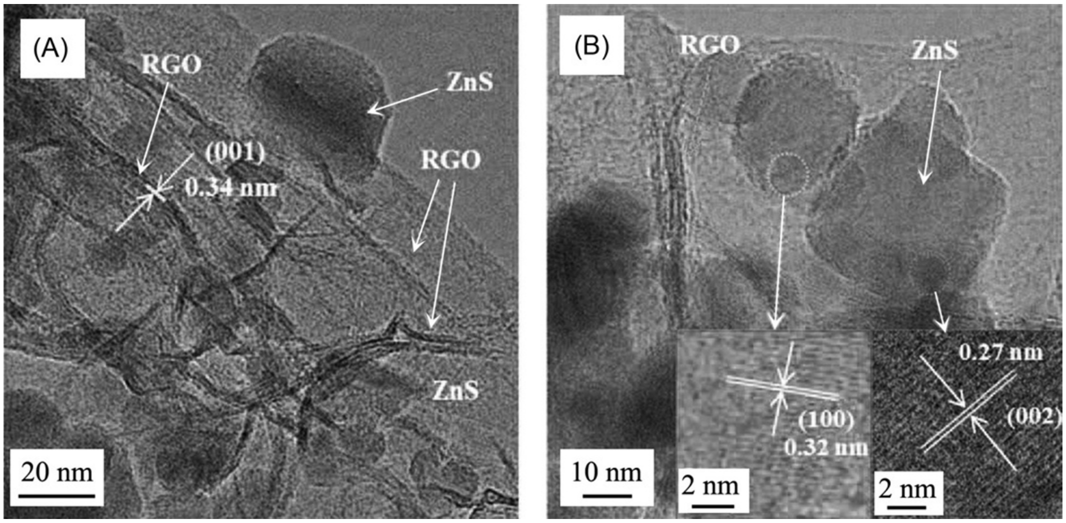

FIG. 12.11 TEM images of the ZnS-RGO composite powders by various magnifications. *(Modified from Park GD, Choi SH, Lee JK, Kang YC. One-pot method for synthesizing spherical-like metal sulfide-reduced graphene oxide composite powders with superior electrochemical properties for lithium-ion batteries. Chemistry 2014; 20(38):12183–9.)*

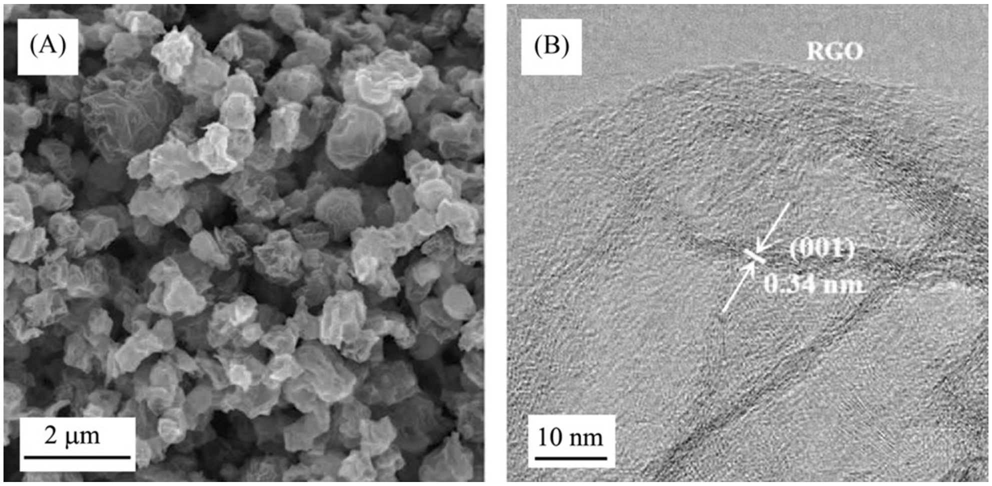

FIG. 12.12 Morphology images of the ZnO–RGO composite powders: (A) by SEM, (B) by TEM. *Modified from Park GD, Choi SH, Lee JK, Kang YC. One-pot method for synthesizing spherical-like metal sulfide-reduced graphene oxide composite powders with superior electrochemical properties for lithium-ion batteries. Chemistry 2014;20(38):12183–9.*

The TEM image shown in Fig. 12.11A depicts ZnS nanocrystals with a size below 20 nm dispersed on an RGO composed of a few layers. Crystal growth occurred during the formation of ZnS through the Zn intermediate by the sulfidation process. The high-resolution TEM image shown in Fig. 12.11B reveals clear lattice fringes with spacings of 0.27 and 0.32 nm that can be indexed to the (002) and (100) planes of **the** cubic and hexagonal ZnS, respectively.

The morphology of the spherical-like ZnO–RGO composite powders prepared by one-pot spray pyrolysis from the spray solution without thiourea is shown in Fig. 12.12A. The TEM image of the composite powder (Fig. 12.12B) shows that its morphology is different from that of the ZnS–RGO composite powders shown in Fig. 12.11. The ZnO nanocrystals dispersed on RGO layers could not be clearly observed in the high-resolution TEM images shown in Fig. 12.12B because of their ultrafine sizes (less than a few nanometers). The mean size of the ZnO nanocrystals shown in Fig. 12.12B was lower than that of the ZnS nanocrystals shown in Fig. 12.11B.

Park et al. [93] reported that the highly conductive ZnS– and ZnO–RGO composite powders with ultrafine crystallite sizes and high structural stabilities showed better electrochemical properties than the bare ZnS and bare ZnO powders. In particular, the ZnS–RGO composite powders with low charge-transfer resistance and high lithium-ion diffusion rate showed superior electrochemical properties, even at a high current density of 4000 $mA \cdot g^{-1}$.

Directed Energy Deposition (DED) and Powder Bed Fusion (PBF) are used. A further distinction is provided as a function of the primary heat source: the nomenclature for laser (L), electron beam (EB), plasma arc (PA), and gas metal arc (GMA) heat sources as PBF-L, PBF-EB, DED-L, DED-EB, DED-PA, and DED-GMA is used.

A metal matrix composite (MMC) is a composite material with at least two constituent parts, one necessarily being a metal and the other may be a different metal or another material, such as a ceramic or organic compound. When at least three materials are present, it is called a hybrid composite.

MANUFACTURE OF COMPOSITES

Composite Manufacturing Methods

In general, composite powders are similar in their mechanical properties to many bare ones. Therefore, the powder shaping and compaction conventional methods are also admissible for composite powders while the methods used to manufacture composite contact materials can be classified into three major categories:

- Conventional PM processes for producing composites that cannot be conventionally alloyed.
- Internal oxidation processes for producing silver-base composites with dispersed oxides.
- Hybrid consolidation, which is a combination of the internal composition with or without a binder to impart green strength, followed by pressing and sintering into a skeleton of required oxidation and PM consolidation processes.

Powder Metallurgy Methods

Metal powder or carbide powder is first blended to the desired shape. Silver or copper is then infiltrated into the pores of the skeleton. This method produces the composites, generally 97% or more of theoretical density. After infiltration, the contact sometimes is chemically or electrochemically etched so that only pure silver appears on the surface.

Press-Sinter-Extrude. The blended powder of the final composition is pressed into an ingot and sintered. The ingot then is extruded into wires, slabs, or other desired shapes. Material made by this method is usually fully dense and is used mostly for silver-base composites. Direct extrusion and direct rolling of the initial powder for manufacturing silver-base composite is also used.

Internal Oxidation

In this process, a silver alloy first is fused into ingots, which are rolled into strips or fabricated further into the finished product form. The silver alloy material is then heated from 1073 to 1173 K (in the case of silver-cadmium alloy) in air or oxygen so that the oxygen diffuses into the alloy and forms Cd0 particles dispersed in the silver matrix. Upon completion of the oxidation, the material displays a microstructure of CdO particles embedded in a silver matrix. The size of the CdO particles and the uniformity of their dispersion are dependent on the temperature and the partial pressure of oxygen.

Hybrid Consolidation Nanotube (CNT)

Hybrid consolidation methods are used to produce a finer average oxide size and a more uniform distribution of cadmium oxide particles in the matrix of the Ag-CdO composite. These methods include preoxidized-press-sinter-extrude and coprecipitation.

The preoxidized-press-sinter-extrude process combines the oxidation and press-sinter-extrude processes. Commercially, it is called a preoxidized process. Alloys are reduced to small particles in the shape of flakes, slugs, or shredded foil. These particles are oxidized and then consolidated by the press-sinter-extrude process. Material made by this method is more uniform than the same material made by conventional internal oxidation. The Ag-CdO particulates are made by comminution of the Ag-CdO wire or water atomization of molten silver-cadmium alloy.

Coprecipitation. The silver and CdO powders are conventionally blended or mechanically mixed in nitric acid. Compounds of silver and cadmium coprecipitate from the solution when the pH value of the solution is changed by adding ether hydroxide or carbonate solutions. During subsequent calcination at approximately 773 K, the compound mixture decomposes to a condition of silver and CdO. Contacts are consolidated from this mixture by conventional PM methods.

Aluminum-Based Composite

There are many studies of the mechanical properties and dry sliding wear behaviors of aluminum metal composites (AMCs) reinforced with various particulates such as SiC, Al_2O_3, silica sand, boron, TiC, MgO, and Si_3N_4 [94,95]. It was observed that the reinforcement material improved the metal yield strength and the ultimate tensile strength. However, AMC ductility declines significantly with a higher concentration of ceramic particles. To prevent this reduction in composite ductility, it can be produced as lightweight components cast-formed from metal matrix nanocomposites with a uniform distribution of reinforcement [96–99].

The Al–TiO_2 nanocomposites with various amounts of titanium oxide were studied [100]. In this study, pure aluminum powders with a diameter of 15 μm were used as a matrix. Titanium dioxide (TiO_2) particles were used as reinforcement, with an average diameter of 50 nm. Pure aluminum powders were mixed with the ceramic particles to prepare composites with about (0.5, 1.5, 2.5, 3.5, and 4.5) vol% reinforcement; mixing was done by ball milling. The powder mixtures were compressed at room temperature for 6 min under a pressure of 104 N/cm^2. Green compacts were sintered at 723 K under argon gas. The authors [100] reported that the addition of nano TiO_2 particles to the Al matrix composites increased the tensile strength of the alloy in the range of 198–250 MPa at room temperature along with an increase in the TiO_2 particles' volume fraction from 0.5 to 4.5 vol%. The nanoparticles protect the surface, so the wear resistance is enhanced. It was found that the addition of nanoparticles to the matrix alloy increases the hardness as the nano TiO_2 particles act as obstacles for the dislocation motion.

In the work [101], the Al–Al_4C_3 composites were obtained by a hot-pressing method. The introduction of nanodiamond into aluminum nanopowder in the amount of 10 wt% leads to the formation of 15 wt% of aluminum carbide during hot pressing. It is found that composite materials with the diamond content of 10 wt% in the initial powder mixture have the microhardness 150 HV while the similarly hot-pressed aluminum powder without reinforcing particles shows a hardness of 75 HV. The mechanical properties of an Al–Al_4C_3 composite material at elevated test temperatures exceed those of commercial casting aluminum alloys.

In the work [101], the Al–Al_4C_3 composites are produced by a hot-pressing method. It was shown that hot pressing of the powder mixture of the Al nanodiamond leads to the formation of a fine dispersed aluminum carbide phase with an average grain size of 150 nm. It was found that aluminum carbide in composite materials remains stable within the temperatures up to 573 K. The linear thermal expansion coefficient of the Al–Al_4C_3 composites significantly differs from the tabular data of the CTE for "pure" aluminum. It is reported that at room temperature, the ultimate tensile strength and yield strength are 580 and 330 MPa, respectively. A significant decrease of the compressive strength and yield strength is recorded at 523 K.

An aluminum-based composite by repetitive press roll bonding (RPRB), which is a process of severe plastic deformation (SPD) that combines accumulative press bonding with the rolling process, was considered [102]. Aluminum as a matrix material and alumina nanofiber as a reinforcement were used. In this process, alumina nanofibers of 7 nm diameter and 50 nm length are uniformly dispersed between two aluminum AA1070 sheets (3 × 16 cm with 3 mm thickness). The process comprises three pressing stages. The first pressing carried out without lubrication at 435 MPa pressure resulted in a volume reduction equal to 50%, and to 4 × 20 cm with 1.5 mm thickness samples size, accordingly. In the second stage, the pressure is made in the condition "forth and back" for obtaining a uniform grain. In the third stage, rolling "forth and back" was done without lubrication at 623 K. Pramono et al. [102] reported that the addition of Al_2O_3 in AA1070 by the RPRB process increases the mechanical properties, although not significantly, but retains the grain uniformity up to 623 K. Uniformity of grain and interphase bonding by the APB (accumulative roll bonding) process [103] requires a cycle up to 14–16 times. It can be replaced with one cycle by the RPRB process.

Copper-Based Composite

Over the last several decades, there has been considerable interest in the use of copper-based metal matrix composites (MMCs). For many applications, pure Cu cannot be used because of its low strength. Therefore, improvement in the properties of copper has become essential for its use in cutting-edge technological applications. Copper at the nanoscale becomes more useful because copper nanoparticles have a high surface area and a small size.

The improvement of the mechanical properties of copper is important for its use in a larger number of fields. Composite materials offer several applications in the aerospace, automotive, and shipbuilding industries as they have certain advantages over other conventional metals. Metal matrix composites (MMCs) combine both metallic properties, such as toughness and ductility, and ceramic properties, such as elastic modulus and high strength, which endow shear strength, providing service at high temperatures. Copper has high thermal conductivity and is used as a structural material for cooling. In order to increase its high temperature properties, different reinforcements are being used.

Copper-graphite composites are widely known as a material for sliding electrical contacts, due to high thermal and electrical conductivities close to pure copper and a low friction coefficient caused by the graphite lubricating ability [104–106]. At the same time, in recent years a number of studies have been devoted to copper-based composites reinforced with carbon nanostructures-nanotubes (CNTs) or fibers (CNFs) [107–111]. The homogeneity of the reinforcing component distribution and good interfacial bonding are key points for the improvement of the mechanical and tribological properties. The carbon nanostructures were coated with Ni [107,112] or Cu [108].

The copper-based composite reinforced with carbon nanostructure materials produced by the chemical vapor deposition (CVD) method was studied [113]. A copper metal powder of 99 % purity with an average particle size of 2–5 µm was used as the matrix. For the synthesis of carbon nanomaterials, the reactor was heated to the 973–1213 K temperature range in an argon atmosphere. After 5 min, argon was replaced by hydrogen for a 5 min reduction. The growth of CNFs was conducted in an acetylene-hydrogen and an ethylene-hydrogen atmosphere with a varying carbon/hydrogen ratio. After 20 min, the acetylene-hydrogen gas mixture was replaced by argon and the crucible was cooled to room temperature. In order to fabricate the compact composites of preassigned composition, the produced powders were mechanically mixed with a certain amount of pure copper powder. The powder mixtures were cold pressed at 500–600 MPa using a cylindrical mold with a diameter of 8 mm. The sintering was carried out at 1223 K during 2 h in an H_2 atmosphere. For comparison, pure Cu and Cu-graphite powders were consolidated under the same conditions. The final annealing was carried out at 693 K, also for one hour in a hydrogen atmosphere. Fig. 12.13 illustrates the microstructures of the sintered samples of copper-based composites reinforced with carbon nanostructures. As is seen, the matrix copper grain sizes are, on average, 10 µm-sized matrix grains (similar to a pure copper sample) and there are very rough carbon inclusions (Fig. 12.13A). The Cu-CNF composite contains finer grains (around 4 µm) with homogeneously dispersed carbon (Fig. 12.13B). Due to the even distribution of CNF dispersion in the matrix, the grain growth is restrained during sintering. In the case of Cu-graphene, it was observed that the grains of size 6–8 µm elongated in the rolling direction with fine carbon layers located between (Fig. 12.13C). The plastic deformation of the copper particles during rolling resulted in a disruption of less plastic graphene layers attached to the particle surfaces; therefore, graphene only partially blocked growth of the Cu grains.

As reported [113], any carbon additions to copper led to a hardening of the composite and a decrease in the ductility compared to pure copper. The best results were obtained for the Cu-CNF composite; this material showed a 1.7-time increase in hardness compared to pure copper. Copper hardened by graphene showed only a 39% increase in HB with a significant ductility decrease (Table 12.1).

The work [114] studies the effect of the process parameters for the production of copper-based bearing composite materials doped with nickel and molybdenum, with CaF_2 additions (DN5M3KF9) as a solid lubricant, on the structurization and

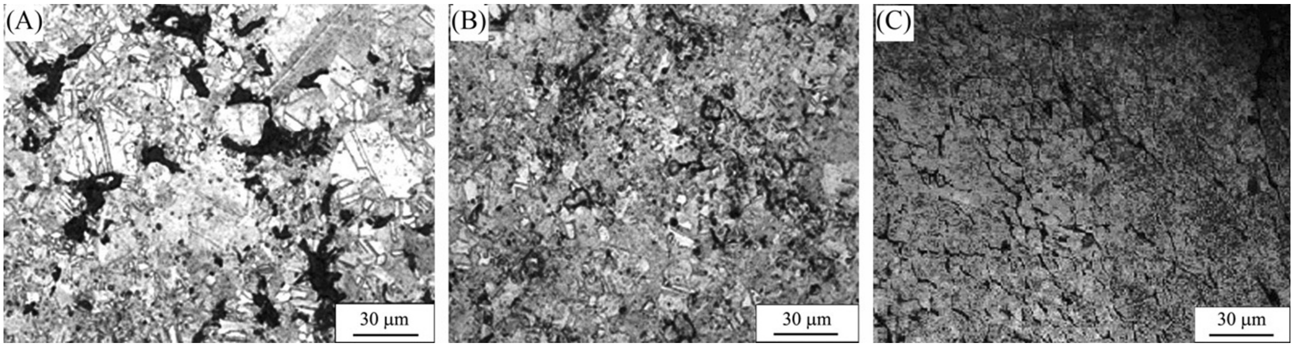

FIG. 12.13 SEM of the sintered samples of copper-based composites reinforced with carbon nanostructures: (A) Cu-(9vol%) graphite; (B) Cu-(9vol%) CNFs; (C) Cu-(9vol%) graphene.

TABLE 12.1 Mechanical Properties of Copper-Based Composite Reinforced With Carbon Nanostructures

Material	HB	Elongation (%)
Cu	35	55
Cu-(9vol%) graphite	38	19
Cu-(9vol%) CNFs	60	38
Cu-(9vol%) graphene	48	9

HB, Brinell hardness measured by a hardness tester Zwick/Roell ZHU by using 2.5 mm steel ball at the load of 62.5 kg; Elongation measurements were carried out using a tensile machine IR-5040-5 with a maximum load of 5 kN.

tribotechnical properties at high-speed friction (bearings perform at a sliding speed of 6 m/s and a pressure up to 38.5 MPa in air). The study focused on the distribution of CaF_2 in the composite with a Cu–Ni–Mo matrix. It is shown that the solid lubricant is evenly distributed over the contact surfaces as it piles up over the entire friction area during high-speed friction. It is established that the tribofilms formed in the presence of the CaF_2 solid lubricant are capable of high wear resistance of copper-based materials.

The mechanical and tribological properties of hot-pressed, copper-based composites containing different amounts of graphene nanosheets (GNSs) are compared with those of copper-graphite (Gr) composites fabricated by the same method [115]. The results showed that the Cu–GNSs composites possess higher relative density, microhardness, wear resistance, and bending strength compared to Cu–Gr composites with the same volume fraction of GNSs and Gr. It was confirmed that the optimal volume fraction of GNSs to the copper matrix composites is 7.5%.

Two copper-based composites containing Al_2O_3 micro- and nanosized particles are produced, one by mechanical alloying and another by mechanical alloying and internal oxidation [116]. It was reported that the addition of nanosized Al_2O_3 particles considerably increases **the** hardness of the Cu-nano-Al_2O_3 composite and improves the wear resistance to a significant extent while also reducing the coefficient of friction. The favorable distribution of nanosized Al_2O_3 particles combined with the pinning effect on grain growth [117] reduced the deformation of the matrix during the sliding process. Reduced deformation of the material together with the high hardness of the nanosized Al_2O_3 particles ensured the wear resistance of this material, which was much higher (more than two orders of magnitude) than the wear resistance of the copper-micro Al_2O_3 composite.

Refractory Metal and Carbide-Based Composites

A high melting point and hardness but poor electrical and thermal conductivity and poor oxidation resistance distinguish refractory metals and their carbides. In pure elemental form, refractory metals perform well under low-current conditions. Creation of a composite can compensate for these obstacles. Thus, the development of composite contact materials involving silver or copper with tungsten or molybdenum or their carbides has resulted in materials that can withstand higher currents and more arcing than other contact materials. The refractory metal content can vary from 10% to 90%. Owing to the fact that silver and copper do not fuse with molybdenum, tungsten, or their carbides, PM processes are required in manufacturing. Depending on the composition, refractory metals containing silver or copper contact materials are usually made by pressing and sintering or by the press-sinter-infiltrate method. Most infiltrated composite contacts use silver as the infiltrant because of its excellent electrical and thermal conductivities as well as its superb oxidation resistance. The copper infiltrant, which costs less but has very poor corrosion resistance, is used for composites that operate in a noncorrosive environment such as oil, vacuum, or inert atmospheres. The characteristic tungsten base and molybdenum-silver composites are shown in Chapter 23.

Few works of additive manufacturing (AM) for refractory metal and carbide-based composites have been reported so far. Within the study [118], the limitations of AM of hard metals were investigated. Pötschke et al. [118] reported that either powder bed-based techniques such as binder jetting or suspension-based techniques such as thermoplastic three-dimensional printing can be used. To avoid pores, cracks, and local inhomogeneity of the chemical compositions found in both selective laser melting and the electron beam melting technique, two-step (printing and sintering) AM techniques are preferable. Thus, the implementation of AM in the field of hard metals would enhance the possibility of producing complex shaped parts that cannot be produced by conventional means while also producing parts within hours instead of days because of the tool-free production technology.

The creation of a MoTiAl-based composite with acid-treated carbon nanotubes (ATCNTs) by laser powder bed fusion (PBF) is discussed [119]. A novel method to fabricate an Al_2O_3-nanoparticle/metal composite for PBF by using ATSNTs as the agent during heteroagglomeration was developed. Due to acid treatment, the negatively charged ATSNTs bridged positively charged Al_2O_3 and MoTiAl powders utilizing electrostatic attraction. It made individual Al_2O_3 nanoparticles uniformly coat the surface of MoTiAl without agglomeration (called heteroagglomeration). In this study, an Mo-based alloy of composition (in mass percents) Mo-33Ti-13Al was used. The MoTiAl powders were fabricated via conventional arc melting followed by mechanical milling and sieving. Commercially available Al_2O_3 nanoparticles had a purity of 99.9%. Pristine CNTs with a diameter of 2–15 nm and 20–110 nm were applied. The ATCNTs were prepared in an ultrasonic acidic mixture of 61%HNO_3 and 97%H_2SO_4 (1:3, V/V) at 323 K for 4 h. Fig. 12.14 shows the morphology of the 5%Al_2O_3-0.15%ATCNT/MoTiAl composite powder via SEM. The uniform dispersion of Al_2O_3 is observed (see white particles on the MoTiAl particle surface (Fig. 12.14B). By such covering, the MoTiAl powders remain in their original state shape, particle size, and distribution.

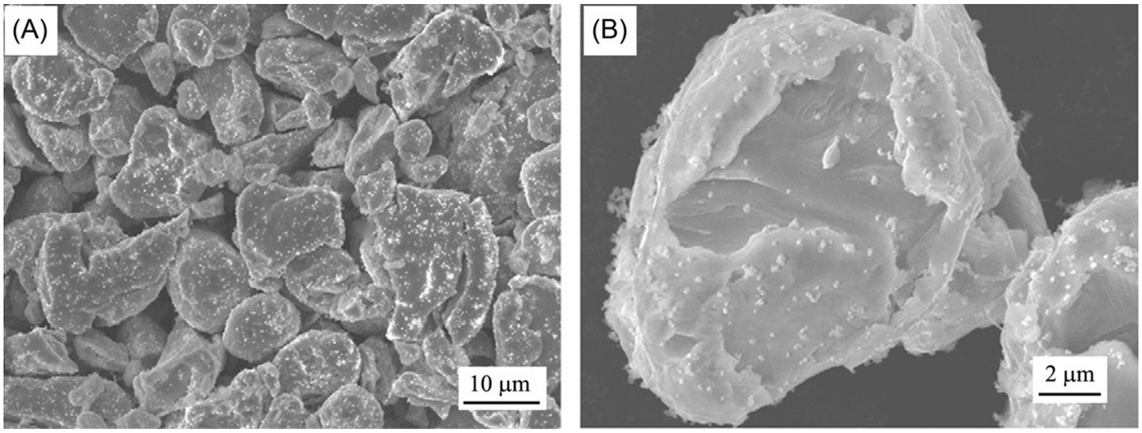

FIG. 12.14 SEM images of 5%Al_2O_3-0.15%ATCNT/MoTiAl composite powder at various magnifications.

The bulk samples were produced on a laser PBF installation (Fig. 12.15) that was equipped with a fiber laser source. The optimized laser PBF parameters (laser power of 20.6 W; scanning speed of 10 mm^{-1} by spot diameter of 45 μm; hatch distance of 100 μm; layer thickness of 25 μm) were utilized for fabricating the row composite.

The electron images of a PBF-processed 5%Al_2O_3-0.15%ATCNT/MoTiAl composite are shown in Fig. 12.16. Zhou et al. [118] under EPMA mapping and SEM-EDS analysis revealed that the black spots in Fig. 12.16 consist of elemental oxygen and aluminum that should correspond to Al_2O_3.

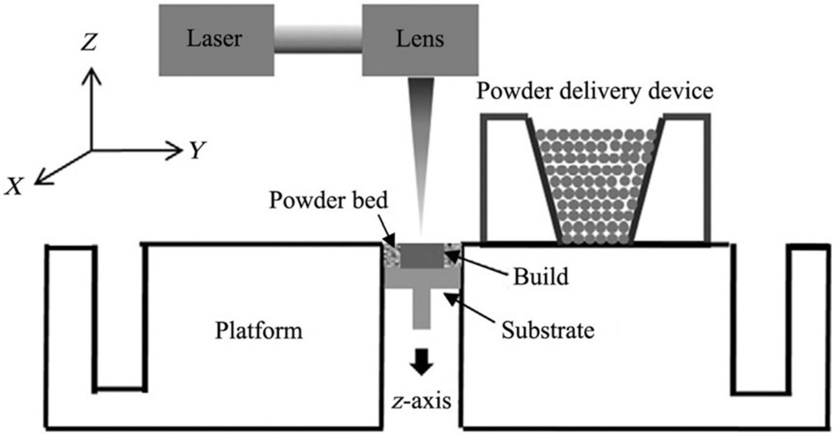
Z
Y
X
Laser
Lens
Powder delivery device
Powder bed
Build
Substrate
Platform
z-axis

FIG. 12.15 Schematic diagram of laser powder bed fusion installation.

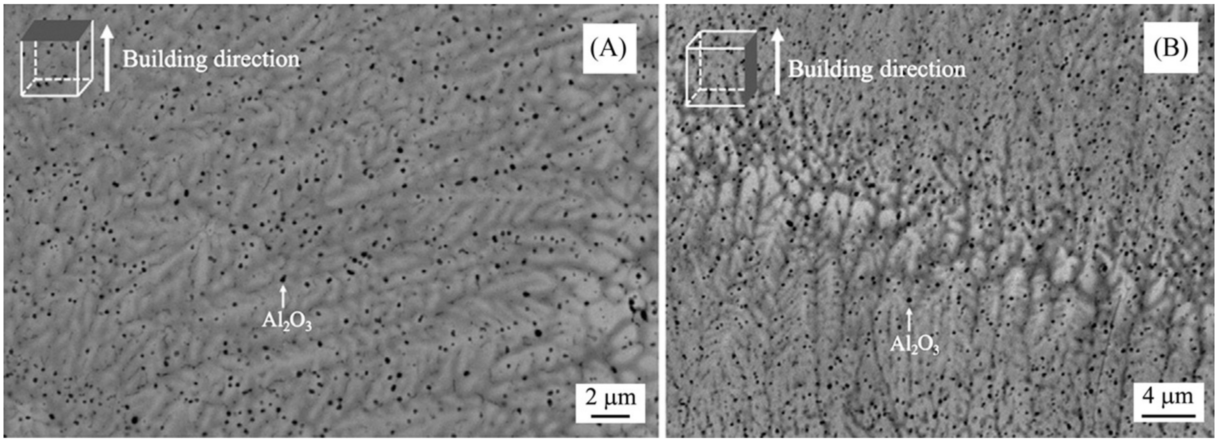
Building direction
(A)
Al_2O_3
2 μm
Building direction
(B)
Al_2O_3
4 μm

FIG. 12.16 SEM-BSE (backscattered electron) of (A) transversal and (B) longitudinal cross-section of a PBF-produced 5%Al_2O_3-0.15%ATCNT/MoTiAl composite.

TABLE 12.2 Vickers Hardnesses of PBF-Processed Pure MoTiAl, 5%Al_2O_3-0.15%ATCNT/MoTiAl and 15%Al_2O_3-0.46% ATCNT/MoTiAl Composites in the Transversal and Longitudinal Cross-Sections

	Vickers Hardness[a]	
Material	Transversal Cross-Section	Longitudinal Cross-Section
MoTiAl	453–523.5	436–523
5%Al_2O_3-0.15%ATCNT/MoTiAl	600–645.5	592.2–627
15%Al_2O_3-0.46%ATCNT/MoTiAl	600–678	606.3–631.4

[a] *Vickers hardnesses measuring by FISCERSCOPE HM200 microhardness tester; the indenter continuously loaded to the peak load of 0.588 N in 60 s and unloaded after a holding time of 30 s.*

The Vickers hardnesses of PBF-processed pure MoTiAl and Al_2O_3-ATCNT/MoTiAl composite are shown in Table 12.2. The average values of Vickers hardnesses of pure MoTiAl are 487.2 and 479.7 in the transversal and longitudinal cross-section, respectively. The average values of Vickers hardnesses of 5%Al_2O_3-0.15%ATCNT/MoTiAl composite were 622.1 and 609.6 in the transversal and longitudinal cross-sections, respectively. The enhancement of Vickers hardnesses should be mostly attributed to the well-dispersed Al_2O_3 nanoparticles, which had the load-bearing capability to suppress the dislocation motion and plastic deformation of the MoTiAl matrix. However, the 15%Al_2O_3 concentration is the hardness growth threshold due to aggregation of Al_2O_3 particles.

REFERENCES

[1] Naboychenko SS, editor. Handbook of non-ferrous metal powders. Moscow: Metallurgia Publishers; 1997 [in Russian].

[2] Ruiz-Navas EM, Fogagnolo JB, Velasco F, Ruiz-Prieto JM, Froyen L. One step production of aluminum matrix composite powders by mechanical alloying. Composites 2006;37:2114–20.

[3] Li L, Lai M. Mechanical alloying. Boston: Kluwer Academic Publishers; 1998.

[4] Mukai T, Ishikawa K. J Jpn Soc Powder Powder Metall 1995;42:180–4.

[5] Polkin IS, Borzov AB. New materials produced by mechanical alloying. Adv Perform Mater 1995;2:99–109.

[6] Faure JF, Brune G. New PM aluminum alloys for wear and sliding applications. Met Powder Rep 1987;42:101–3.

[7] Bhadury A, Gopinathan V, Ramakrishnan P, Miodownik AP. Microstructural changes in a mechanically alloyed Al–6.2Zn–2.5Mg–1Cu alloy (7010) with and without particulate SiC reinforcement. Metall Mater Trans A 1996;27:3718–26.

[8] Ravikiran A, Surappa MK. Oscillations in coefficient of friction during dry sliding of A356 Al–30% wt SiCp MMC against steel. Scr Mater 1997;36:95–8.

[9] González-Carrasco JL, García-Cano F, Caruana G, Liebich M. Aluminum/Ni_3Al composites processed by powder metallurgy. Mater Sci Eng 1994;183:5–8.

[10] Torralba JM, da Costa CE, Cambronero LEG, Ruiz-Prieto JM. PM aluminum composite reinforced with Ni_3Al. Key Eng Mater 1997;127–131:929–36.

[11] Adamiak M, Fogagnolo JB, Ruiz Navas EM, Dobrzanski LA, Torralba JM. Mechanically milled AA6061/(Ti_3Al)P MMC reinforced with intermetallics—the structure and properties. J Mater Process Technol 2004;155–6:2002–6.

[12] Milman YV, et al. Structure and properties of Al–Mg alloys depending on scandium and zirconium additions and production methods. Powder Metall Met Ceram 2010;49(7-8):429–37.

[13] Shorowordi KM, Laoui T, Haseeb ASMA, Celis JP, Froyen L. Microstructure and interface characteristics of B_4C, SiC and Al_2O_3 reinforced Al matrix composites: a comparative study. J Mater Process Technol 2003;142:738–43.

[14] Lee BS, Kang S. Low-temperature processing of B_4C–Al composites via infiltration technique. Mater Chem Phys 2001;67:249–55.

[15] Ye JC, He JH, Schoenung JM. Cryomilling for the fabrication of a particulate B_4C reinforced Al nanocomposite: part I. Effects of process conditions on structure. Metall Mater Trans A 2006;37:3099–109.

[16] Ye JC, Lee Z, Ahn B, He JH, Nutt SR, Schoenung JM. Cryomilling for the fabrication of a particulate B_4C reinforced Al nanocomposite: part II. Mechanisms for microstructural evolution. Metall Mater Trans A 2006;37:3111–7.

[17] Tang F, Wu XL, Ge SR, Ye JC, Zhu H, Hagiwara M, Schoenung JM. Dry sliding friction and wear properties of B_4C particulate-reinforced Al-5083 matrix composites. Wear 2008;264:555–61.

[18] Ye JC, Han BQ, Schoenung JM. Mechanical behavior of an Al–matrix composite reinforced with nanocrystalline Al-coated B_4C particulates. Philos Mag Lett 2006;86:721–32.

[19] Zhang H, Chen MW, Ramesh KT, Ye J, Schoenung JM, Chin ESC. Tensile behavior and dynamic failure of aluminum 6092/B_4C composites. Mater Sci Eng 2006;433:70–82.

[20] Khakbiz M, Akhlaghi F. Synthesis and structural characterization of Al–B_4C nano-composite powders by mechanical alloying. J Alloys Compd 2009;479:334–41.

[21] Hussain Z, Othmana R, Longa BD, Umemotob M. Synthesis of copper–niobium carbide composite powder by in situ processing. J Alloys Compd 2008;464:185–9.

[22] Wu JM, Li ZZ. Nanostructured composite obtained by mechanically driven reduction reaction of CuO and Al powder mixture. J Alloys Compd 2000;299:9–16.

[23] Ying DY, Zhang DL. Processing of Cu–Al_2O_3 metal matrix nanocomposite materials by using high energy ball milling. Mater Sci Eng 2000;286:152–6.

[24] Mulas G, Varga M, Bertoti I, Molnar A, Cocco G, Szepvolgyi J. $Cu_{40}Mg_{60}$ and Cu–MgO powders prepared by ball-milling: characterization and catalytic tests. Mater Sci Eng 1999;267:193–9.

[25] Dong SJ, Zhou Y, Shi YW, Chang BH. Formation of a TiB_2-reinforced copper-based composite by mechanical alloying and hot pressing. Metall Mater Trans A 2002;33A:1275–80.

[26] Castricum HL, Bakker H, Poels EK. Oxidation and reduction in copper/zinc oxides by mechanical milling. Mater Sci Eng 2001;304–6:418–23.

[27] Sheibani S, Khakbiza M, Omidib M. In situ preparation of Cu–MnO nanocomposite powder through mechanochemical synthesis. J Alloys Compd 2009;477:683–7.

[28] Schaffer GB, McCormick PG. Anomalous combustion effects during mechanical alloying. Metall Trans A 1991;22(12):3019–24.

[29] Sheibani S, Ataie A, Heshmati-Manesh S, Khayati GR. Structural evolution in nano-crystalline Cu synthesized by high energy ball milling. Mater Lett 2007;61:3204–7.

[30] Llorca-Isern N, Artieda-Guzmán C, Porras-Mateu N, Roca-Vallmajor A. Structural and magnetic properties of nanocrystalline Cu–Fe–Co–Al_2O_3 composite powders processed by mechanical alloying. In: Compiled by European powder metallurgy association proceedings of PM 2010 world congress, Florence (Italy), vol. 2; 2010. p. 256–63.

[31] Zhang GJ, Ando M, Yang JF, Ohji T, Kanzaki S. Boron carbide and nitride as reactants for in situ synthesis of boride-containing ceramic composites. J Eur Ceram Soc 2004;24:171–8.

[32] Thian ES, Khor KA, Loh NH, Tor SB. Processing of HA-coated Ti-6Al-4V by a ceramic slurry approach: an in vitro study. Biomaterials 2001;22:1225–32.

[33] Montealegre I, Neubauer E, Angerer P, Danninger H, Torralba JM. Influence of nano-reinforcements on the mechanical properties and microstructure of titanium matrix composites. Compos Sci Technol 2011;71:1154–62.

[34] Kondoh K, Threrujirapapong T, Imai H, Umeda J, Fugetsu B. Characteristics of powder metallurgy pure titanium matrix composite reinforced with multi-wall carbon nanotubes. Compos Sci Technol 2009;69:1077–81.

[35] Joshi PB, Marathe GR, Murti NSS, Kaushik VK, Ramakrishnan P. Reactive synthesis of titanium matrix composite powders. Mater Lett 2002;56:322–8.

[36] Begin-Colin S, de Araujo Pontes LR, Le Caer G, Pianelli A, Mocellin A, Matteazzi P. Tkacova K, editor. Synthesis of metal-ceramic composite powders (Al_2O_3-Ti) by mechanical alloying. In: Proceedings international conference mechanochemistry, Kosice (Slovakia); 1993.

[37] Gaffet E, Louison C, Harmelin M, Faudot F. Metastable phase transformations induced by ball-milling in the Cu–W system. Mater Sci Eng 1991;134:1380–4.

[38] Gusmano G, Bianco A, Polini R. Chemical synthesis and sintering behavior of highly dispersed W/Cu composite powders. J Mater Sci 2001;36:901–7.

[39] Xi X, Xu X, Nie Z, He S, Wang W, Yi J, Tieyong Z. Preparation of W–Cu nano-composite powder using a freeze-drying technique. Int J Refract Met Hard Mater 2010;28:301–4.

[40] Kim DG, Kim GS, Oh ST, Kim YD. The initial stage of sintering for the W–Cu nanocomposite powder prepared from W–CuO mixture. Mater Lett 2004;58:578–81.

[41] Doré F, Martin CL, Allibert CH. Apparent viscosity of W–Cu powder compacts during sintering. Mater Sci Eng 2004;383:390–8.

[42] Alam SN. Synthesis and characterization of W–Cu nanocomposites developed by mechanical alloying. Mater Sci Eng 2006;433:161–8.

[43] Ardestani M, Rezaie HR, Arabi H, Razavizadeh H. The effect of sintering temperature on densification of nanoscale dispersed W\20–40wt.% Cu composite powders. Int J Refract Met Hard Mater 2009;27:862–7.

[44] Hashempour M, Rezaie HR, Razavizadeh H, Salehi MT, Mehrjoo H, Ardestani M. Investigation on fabrication of W\Cu nanocomposite via a thermochemical coprecipitation method and its consolidation behavior. J Nanopart Res 2010;11:57–66.

[45] Liorca-Isem N, Artieda-Guzman. 9-Metal-based composite powders. In: Advances in powder metallurgy. 2013. p. 241–72.

[46] Schaefe K, Miszczyk A. Improvement of electrochemical action of zinc-rich paints by addition of nanoparticulate zinc. Corros Sci 2013;66:380–91.

[47] Pereyra AM, Giudice CA, Herrera LK, Echeverría F, Castaño JG. Tripigmented anticorrosive coatings based on lamellar zinc as inhibitor. Surf Coat Int 2006;89(B3):245–9.

[48] Pereyra AM, Giudice CA. Shaped for performance: the combination of lamellar zinc and mica improves the efficiency of zinc-rich primers. Eur Coat J 2007;9:40–5.

[49] Kalendova A. Effects of particle sizes and shapes of zinc metal on the properties of anticorrosive coatings. Prog Org Coat 2003;46(4):324–32.

[50] Shreepathi S, Bajaj P, Mallik BP. Electrochemical impedance spectroscopy investigations of epoxy zinc rich coatings: role of Zn content on corrosion protection mechanism. Electrochim Acta 2010;55:5129–34.

[51] Meroufel A, Deslouis C, Touzain S. Electrochemical and anticorrosion performances of zinc-rich and polyaniline powder coatings. Electrochim Acta 2008;53:2331–8.

[52] Jagtap RN, Nambiar R, Hassan SZ, Malshe VC. Active power for life and residual life of the zinc rich primer coatings with electrical measurement. Prog Org Coat 2007;58:253–8.

[53] Park JH, Yun TH, Kima KY, Song YK, Park JM. The improvement of anticorrosion properties of zinc-rich organic coating by incorporating surface-modified zinc particle. Prog Org Coat 2012;74:25–35.

[54] Ramenzanzadeh B, Arman SV, Mehdipour M. Anticorrosion properties of an epoxy zinc-rich composite coating reinforced with zinc, aluminum, and iron oxide pigments. J Coat Technol Res 2014;11(5):727–37 (Accessed 9 February 2018).

[55] Liu L, et al. Preparation and research on anticorrosion zinc-rich coating of hydraulic metal structure. In: Yu L, Guo W, Sun M, He J, editors. Advanced materials research. 2013. p. 887–91. https://doi.org/10.4028/www.scientific.net/AMR.785-786.887.

[56] Zhang L, et al. Anti-corrosion performance of waterborne Zn-rich coating with modified silicon-based vehicle and lamellar Zn (Al) pigments. Prog Nat Sci Mater Int 2012;22(4):326–33.

[57] Popov VN. Carbon nanotubes: properties and application. Mater Sci Eng R 2004;43:61–102.

[58] Zhou W, Sasaki S, Kawasaki A. Effective control of nanodefects in multiwalled carbon nanotubes by acid treatment. Carbon 2014;78:121–9.

[59] Zhou W, Yamaguchi T, Kikuchi K, Nomura N, Kawasaki A. Effectively enhanced load transfer by interfacial reactions in multi-walled carbon nanotube reinforced Al matrix composites. Acta Mater 2017;15(2):369–76.

[60] Pérez-Bustamante R, et al. Effect of milling time and CNT concentration on hardness of CNT/Al2024 composites produced by mechanical alloying. Mater Charact 2013;75:13–9.

[61] Esawi AMK, Morsi K, Sayed A, Taher M, Lanka. The influence of carbon nanotube (CNT) morphology and diameter on the processing and properties of CNT-reinforced aluminum composites. Compos A 2011;42(3):234–43.

[62] Pérez-Bustamante R, et al. Microstructural characterization of Al-MWCNT composites produced by mechanical milling and hot extrusion. J Alloys Compd 2010;495:399–402.

[63] Pérez-Bustamante R, et al. Microstructural and mechanical characterization of Al-MWCNT composites produced by mechanical milling. Mater Sci Eng A 2009;502(1–2):159–63.

[64] Wang L, Liu Y, Wei W, An X, Zhang T, Pu Y. Preparation of CNT/AlSi10Mg composite powders by high-energy ball milling and their physical properties. Int J Miner Metall Mater 2016;23(3):330–8.

[65] Lavernia E, Han B, Schoenung J. Cryomilled nanostructured materials: processing and properties. Mater Sci Eng A 2008;493(1):207–14.

[66] Han B, Ye J, Tang F, Schoenung J, Lavernia E. Processing and behavior of nanostructured metallic alloys and composites by cryomilling. J Mater Sci 2007;42(5):1660–72.

[67] Witkin D, Lavernia EJ. Synthesis and mechanical behavior of nanostructured materials via cryomilling. Prog Mater Sci 2006;51(1):1–60.

[68] Lee J, et al. Short carbon nanotubes produced by cryogenic crushing. Carbon 2006;44(14):2984–9.

[69] Woo DJ, Hooper JP, Osswald S, Bottolfson BA. Low temperature synthesis of carbon nanotube-reinforced aluminum metal composite powders using cryogenic milling. J Mater Res 2014;29(22):2644–56.

[70] Bolotin KI, et al. Ultrahigh electron mobility in suspended graphene. Solid State Commun 2008;146:351–5.

[71] Seiner H, et al. Elastic properties of silicon nitride ceramics reinforced with graphene nanofillers. Mater Des 2015;87(Dec):675–80.

[72] Wang HD, Kurata K, Fukunaga T, Zhang X, Takamatsu H. Width dependent intrinsic thermal conductivity of suspended monolayer graphene. Int J Heat Mass Transf 2017;105:76–80.

[73] Won JM, Son MY, Seo J-H, Kang YC. Electrochemical properties of WO_3-reduced graphene oxide composite powders prepared by one-pot spray pyrolysis process. J Alloys Compd B 2016;688(Dec):647–53.

[74] Park GD, Kim JH, Park S-K, Kang YC. $MoSe_2$ embedded CNT-reduced graphene oxide composite microsphere with superior sodium ion storage and electrocatalytic hydrogen evolution performances. ASC Appl Mater Interfaces 2017;9(12):10673–83.

[75] Wang JY, et al. Reinforcement with graphene nanosheets in aluminum matrix composites. Scr Mater 2012;66:594–7.

[76] Bartolucci SF, et al. Graphene-aluminum nanocomposites. Mater Sci Eng A 2011;528:7933–7.

[77] Sun Y, et al. Reduced graphene oxide reinforced 7075 Al matrix composites: powder synthesis and mechanical properties. Metals 2017; 7(499):1–14.

[78] Xu C, et al. Controlled soft-template synthesis of Ultrathin C@FeS nanosheets with high-lithium storage performance. ACS Nano 2012; 6(6):4713–21.

[79] Choi SH, Kang YC. Synthesis for yolk-shell-structured metal sulfide powders with excellent electrochemical performances for lithium-ion batteries. Small 2014;10:474–8.

[80] Son MY, Choi JH, Kang YC. J. Electrochemical properties of bare nickel sulfide and nickel sulfide–carbon composites prepared by one-pot spray pyrolysis as anode materials for lithium secondary batteries. Power Sources 2014;251:480–7.

[81] Stephenson T, Li Z, Olsen B, Mitlin D. Lithium ion battery applications of molybdenum disulfide (MoS2) nanocomposites. Energy Environ Sci 2014;7:209–31.

[82] Choi SH, Kang YC. Crumpled graphene-molybdenum oxide composite powders: preparation and application in lithium-ion batteries. ChemSusChem 2014;7:523–8.

[83] Choi SH, Kang YC. Balls by an aerosol process for lithium-ion battery cathode material. Chem Eur J 2014;20:6294–9.

[84] Chen ZG, et al. Field emission and cathodoluminescence of ZnS hexagonal pyramids of zinc blende structured single crystals. Adv Funct Mater 2009;19:484–90.

[85] Pan S, Liu XH. ZnS-graphene nanocomposite: synthesis, characterization and optical properties. J Solid State Chem 2012;191:51–6.

[86] Bodo B, Singha R, Das SC. Structural and optical properties of chemically synthesized ZnS nanostructures. Int J Appl Phys Math 2012;2:287–9.

[87] Yao WT, Yu SH, Wu QS. From mesostructured wurtzite ZnS nanowire/amine nanocomposites to ZnS nanowires exhibiting quantum size effects: a mild-solution chemistry approach. Adv Funct Mater 2007;17:623–31.

[88] Patil BN, Acharya SA. Preparation of ZnS-graphene nanocomposite and its photocatalytic behavior for dye degradation. Adv Mater Lett 2014;5:113–6.

[89] Li C, Jiang D, Zhang LL, Xia JF, Li Q. Controlled synthesis of ZnS quantum dots and ZnS quantum flakes with graphene as a template. Langmuir 2012;28:9729–34.

[90] Yu LH, Ruan H, Zheng Y, Li DZ. Nanotechnology 2013;24:375601–11.

[91] Shen XY, Mu DB, Chen S, Wu B, Wu F. Enhanced electrochemical performance of ZnO-loaded/porous carbon composite as anode materials for lithium ion batteries. ACS Appl Mater Interfaces 2013;5:3118–25.

[92] US Patent 201503185544 A1. Method for forming a reduced graphene oxide/metal sulfide composite and its use as an anode for batteries.

[93] Park GD, Choi SH, Lee JK, Kang YC. One-pot method for synthesizing spherical-like metal sulfide-reduced graphene oxide composite powders with superior electrochemical properties for lithium-ion batteries. Chemistry 2014;20(38):12183–9.

[94] Sannino AP, Rack HJ. Dry sliding wear of discontinuously reinforced aluminum composite: review and discussion. Wear 1995;189:1–19.

[95] Groza JR. Sintering of nanocrystalline powders. Int J Powder Metall 1999;35:59–66.

[96] Mazahery A, Shabani MO. Plasticity and microstructure of A356 matrix nano composites. J King Saud Univ Eng Sci 2013;25:41–8, https://www.sciencedirect.com/science/article/pii/S1018363911000869.

[97] Habibnejad-Korayem M, Mahmudi R, Poole WJ. Enhanced properties of Mg-based nano-composites reinforced with Al_2O_3 nano-particles. Mater Sci Eng A 2009;519:198–203.

[98] Kwok JKM, Lim SC. High speed tribological properties of Al/SiC composites: I. Frictional and wear rate characteristics. Compos Sci Technol 1999;59:55–63.

[99] Riveiro A, et al. Experimental study on the CO2 laser cutting of carbon fiber reinforced plastic composite. Compos A Appl Sci Manuf 2012; 43(8):1400–9. https://doi.org/10.1016/j.compositesa.2012.02.012 (Accessed 28 February 2018).

[100] Nassar AE, Nassar EE. Properties of aluminum matrix nano composites prepared by powder metallurgy processing. J King Saud Univ Eng Sci 2017;29(3):295–9.

[101] Vorozhtsov S, Khrustalyov A, Kulkov A. Synthesis and properties of aluminum-based composite materials for high operating temperatures. In: Advanced materials with hierarchical structure for new technologies and reliable structures. Tomsk: AIP Publishing; 2016 Conference Paper (PDF Available) November 2016, p. 020230-1–4. https://doi.org/10.1063/1.4966524, https://www.researchgate.net/309894732_Synthesis_and_properties_of_aluminum-ba. Jan 1, 2018-Full-text (Accessed 15 August 2018).

[102] Pramono A, Kollo L, Veinthal R. Aluminum based composite by novelty process: repetitive press roll bonding (RPRB). Proc Chem 2015;16:473–9.

[103] Amirkhanloua S, Ketabchi M, Parvin N, Khorsand S, Bahrami R. Accumulative press bonding; a novel manufacturing process of nanostructured metal matrix composites. Mater Des 2013;51:367–74.

[104] Kovácik J, Emmer S, Bielekc J, Kelesi L. Effect of composition on friction coefficient of Cu–graphite composites. Wear 2008;265:417–21.

[105] Rajkumar K, Aravindan S. Tribological behavior of microwave processed copper–nanographite composites. Tribol Int 2013;57:282–96.

[106] Sarmadi H, Kokabi AH, Seyed Reihani SM. Friction and wear performance of copper–graphite surface composites fabricated by friction stir processing (FSP). Wear 2013;304:1–12, https://www.sciencedirect.com/science/article/pii/S0043164813002652.

[107] Chen X, et al. Preparation and properties of Cu matrix composite reinforced by carbon nanotubes. Trans Nonferrous Metals Soc China 2005; 15(2):314–8.

[108] Lina CB, Chang ZC, Tunga YH, Ko YY. Manufacturing and tribological properties of copper matrix/carbon nanotubes composites. Wear 2011;270:382–94.

[109] Daoush WM, Lim BK, Mo CB, Nam DH, Hong SH. Electrical and mechanical properties of carbon nanotube reinforced copper nanocomposites fabricated by electroless deposition process. Mater Sci Eng A 2009;513:247–53.

[110] Arai S, Endo M. Carbon nanofiber-copper composite powder prepared by electrodeposition. Electrochem Commun 2003;5:797–9.

[111] Guiderdoni C, et al. The preparation of carbon nanotube (CNT)/copper composites and the effect of the number of CNT walls on their hardness, friction and wear properties. Carbon 2013;58:185–97.

[112] Tu JP, Yang YX, Wang LW, Ma XC, Zhang XB. Tribological properties of carbon-nanotube reinforced copper composites. Tribol Lett 2001; 10(4):225–8.

[113] Koltsova T, Larionova T, Fadin Y, Tolochko O. Copper-based composite materials reinforced with carbon nanostructures materials. Mater Sci (Medžiagotyra) 2015;21(3):354–8.

[114] Konopka K, Rolk TA, Gavich AP, Yu VY, Mazan T. Effect of CaF_2 surface layers on the friction behavior of copper-based composite. Powder Metall Met Ceram 2012;51(5/6):363–7.

[115] Li J, Zhang L, Xiao J, Zhou K. Sliding wear behavior of copper-based composites reinforced with graphene nanosheets and graphite. Trans Nonferrous Metals Soc China 2015;25(10):3354–62.

[116] Vencl A, Rajkovic V, Zivic F. Friction and wear properties of copper-based composites reinforced with microand nano-sized Al_2O_3 particles. In: Proceedings of the 8th international conference on tribology. Sinaia: ART; 2014. p. 357–64.

[117] Chen D, Choneim T, Kulkarni Y. Effect of pinning particles on grain boundary motion from interface random walk. Appl Phys Lett 2017;111:161606-1–5. https://doi.org/10.1063/1.4986294.

[118] Pötschke J, Berger C, Richter H-J, Scheithauer U, Weingarten S. Additive manufacturing of hardmetals. In: Proceedings of PM 2017 Euro Congress, Milan (Italy). Shrewsbury, UK: European powder metallurgy association; 2017. p. 1–6.

[119] Zhou W, Sun X, Kikuchi K, et al. Carbon nanotubes as a unique agent to fabricate nanoceramic/metal composite powders for additive manufacturing. Mater Des 2018;137:276–85.

FURTHER READING

[120] Larionova T. Copper-based composite materials reinforced with carbon nanostructures. Mater Sci 2015;213(3). https://doi.org/10.5755/j01.ms.21.3.7348.

Chapter 13

Powders for Additive Manufacturing Processing

Oleg D. Neikov
Frantsevich Institute for Problems of Materials Science (IPMS), Kiev, Ukraine

Chapter Outline

Introduction 373
Principles of AM 374
  Rapid Prototyping 374
  Selective Laser Melting (SLM) 375
Direct Energy Deposition (DED) and Powder Bed Fusion (PBF) AM Processes 375
Powders for AM 376
  Powder Characterization and Testing 377
  Powder Properties 381
Applications of AM 384
  Aluminum and Magnesium Alloys 384
  Titanium Alloys 387
  Nickel Base Alloys 392
Conclusion 395
References 395
Further Reading 399

INTRODUCTION

For selection of powders as well their creation, there is necessary the conception about conditions of powder utilization and technical specification. Powder properties vary during manufacturing processes. By understanding and controlling these, the final material properties for different applications can be improved and become more reliable. The principles of additive manufacturing (AM) are considered in this chapter.

AM is a general term for all technologies that produce parts by the layer addition of material at the micron level to achieve the required shape, besides the metal removal technique, which is traditionally a subtractive process [1–5]. During the research period, the layer-by-layer manufacturing terminology has been standardized by the American Society for Testing and Materials (ASTM) committee F42 on additive layer technologies. The AM processes fall into two categories defined by the ASTM Standard F2792 [6] as directed energy deposition (DED) and powder bed fusion (PBF). A further distinction is provided as a function of the primary heat source: the nomenclature for laser (L), electron beam (EB), plasma arc (PA), and gas metal arc (GMA) heat sources as PBF-L, PBF-EB, DED-L, DED-EB, DED-PA, and DED-GMA is used [5]. PBF includes all processes where focused energy (electron beam or laser beam) is used to selectively melt or sinter a layer of a powder bed. DED encompasses all processes where focused energy generates a melt pool into which feedstock is deposited. This process can use a laser or an arc ore-beam heat source. The feedstock used can be either powder or wire.

Considerable advances over the past 20 years in AM metal processing technology, including reliable industrial lasers at a lower cost, inexpensive high-performance computing hardware and software, and metal powder feedstock technology have enabled AM to become a state-of-the-art processing method. It has now reached a critical acceptance level, as evidenced by the rapid growth in sales of commercial systems. AM metal technology, developed in laboratories, universities, and research institutes, is now being used and adopted by industry. Now, a more thorough understanding of the feedstock materials, processes, structures, properties, and performances are desirable to produce defect-free, structurally sound, and reliable AM parts.

In the beginning, AM technologies were restricted because of the commonly accepted method of rapid prototyping (RP) for the production of parts and prototypes. Advancement in the material, process, and system hardware showed that the parts could be manufactured with an adequate mechanical property for further applications. This allowed the production of end-use models with layer additive technologies, so rapid manufacturing (RM) was adopted, which distinguished the functional nature of the models produced from the prior RP parts and prototypes. Recently, AM has been generally used and RM and RP are only used to illustrate the particular application of AM technologies.

Handbook of Non-Ferrous Metal Powders. https://doi.org/10.1016/B978-0-08-100543-9.00013-0
© 2019 Elsevier Ltd. All rights reserved.

PRINCIPLES OF AM

AM technologies fabricate models by fusing, sintering, or polymerization of materials in predetermined layers with no need of tools. AM makes possible the manufacture of complex geometries including internal part details that are not possible to manufacture using machining and molding processes because the AM process does not require predetermined tool paths, draft angles, and under cuts.

In AM, the layers of a model are formed by slicing computer-aided design (CAD) data with professional software. All AM systems work on the same principle; however, layer thickness depends upon parameters, the machine being used, and the thickness of the layer range from 10 to 200 μm. Layers are clearly visible on the part surface in AM operation, which controls the quality of the final product. The relation between thickness of layer and surface orientation is known as the staircase effect. However, the thinner the layer, the longer the processing time and the higher the part resolution (Fig. 13.1).

Layers in AM are built up at the top of the previous one in a z axis. After a layer gets processed, the work platform is dropped down by the single layer thickness in the z axis and the fresh material layer is recoated differently for a number of other methods. In a resin-based system, a traversing edge flattens the resin while in a powder-based system, the deposited powder is spread using aroller or wiper. In some systems, the required material is deposited through a nozzle because the recoating time is even longer than the layer processing time. For that reason, multiple parts are being built together in the time of a single material recoating build. Different software is available to position and orient parts so that the maximum number of parts can be built together. Available software includes VISCAM RP and Smart Space, used in MAGICS.

Rapid Prototyping

In 1987, stereolithography (SLA) was the first rapid prototyping (RP) technique developed by 3D Systems. SLA builds a single layer at a time by tracing the beam of the laser on the vat of liquid UV curable photo polymer resin. UV light strikes the surface of the polymer resin and solidifies the single layer of resin; when one layer is cured, the built platform is dropped down by a single-layer thickness. A resin-filled blade sweeps over the cross-section and fills it with fresh material for further curing at the top of the previous layer; the process continues until the model is produced.

Selective laser sintering (SLS) uses powdered materials (Fig. 13.1). This is one of the system's major advantages, that a part could be built in any fusible powdered material. SLS technology was developed at the University of Texas, and then commercialized in 1993 by a company named DTM. In 2001, DTM was bought out by the 3D Systems company. This technology works by selectively sintering fine powder materials directly using an infrared (IR) laser from computer-aided design (CAD). Numbers of thermoplastic materials are processed in SLS [7]. However, as compared to traditional casts, the part had poor mechanical properties, so the material required postprocessing to form dense models. Therefore, it was very difficult to control the part accuracy because of introduced stresses in the processing stage. With the combination of EOS GmbH and Electrolux, a special alloy powder was developed, which did not develop shrinkage distortions.

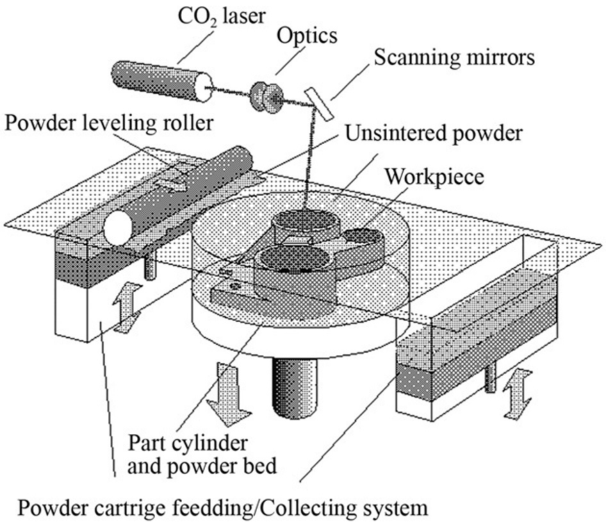

FIG. 13.1 Schematic diagram of powder bed sintering by a laser heat source.

Selective Laser Melting (SLM)

A selective laser melting machine was first introduced by Fockele and Schwarze (F&S) of Germany in 1999 with the support of the Fraunhofer Institute of Laser Technology. That was the steel powder-based SLM machine. In 2004, the first SLM machine, called the Realizer 250 SLM, was released commercially after F&S joined up with MTT (MCP Tooling Technologies). In 2005, a high-resolution machine named the SLM Realizer 100 was released.

Since the release of the MCP Realizer SLM, other manufacturers such as Concept Laser and EOS released machines with a different process, called laser curing and direct metal laser sintering, respectively. Concept Laser (GmbH) first released the M3 Liner and M1 Cusing in 2001, then later released another machine called the M2 Cusing to produce reactive materials such as titanium and aluminum alloys. EOS released a machine called the EOSINT M 270 DMLS in 2003 and termed it the most common machine for direct metal fabrication. In 2008, a new version of SLM was released by MTT called SLM 250 and SLM 125.

Basic Principles of SLM

SLM is a powder-based additive manufacturing process that permits attaining three-dimensional (3D) functional parts from CAD data. SLM follows the same process route as SLS, where complete melting of the powder occurs instead of sintering or partial melting [4]. The process begins with the deposition of a thin layer of powder thickness ranging from 50 to 75 μm across a substrate platform. A high-power fiber laser scans the powder surface, then the generated heat melts the powder particles and forms a molten pool. Once the layer has been scanned, the platform drops down by a single-layer thickness in the z axis and the fresh layer of powder is deposited. The process is repeated until the entire build is completed. Loose powders are removed once the fully dense part is complete. SLM parts must be completed in an inert gas atmosphere such as argon to remove oxygen from the building chamber. The substrate is removed from the build chamber once the process completes and the supports are removed carefully.

DIRECT ENERGY DEPOSITION (DED) AND POWDER BED FUSION (PBF) AM PROCESSES

The characteristic designs of the MA categorized according to the ASTM Standard F2792, as defined above, are illustrated in Fig. 13.2.

Fig. 13.2A shows direct energy deposition (DED-L) with powder used as the feedstock material [7–11]. DED-L typically supplies the feeding of powder into the molten pool created by the laser beam to deposit the material layer-by-layer upon a substrate plate. A shielding gas such as argon is used to protect the molten metal from oxidation and to carry the powder stream into the molten pool. DED-EB (Fig. 13.2B) uses an electron beam to create a deposit by feeding commercial filler wire into the molten pool. In DED-PA or DED-GMA, an electric arc is used as the heat source with filler wires as the feedstock material to fusion welding [12–14]. In all these DED processes, three-dimensional (3D) parts are fabricated in a layer-by-layer manner following the input of a digitized geometry from a computer aided design (CAD) file. The distance between the focused beam and the build surface is maintained by synchronized multiaxis movement of the fixture that holds the substrate and the heat source during layer-by-layer deposition. After the deposition process, the made part is removed from the substrate by machining and often requires a finishing operation to achieve the desired surface quality.

The ultrasonic additive manufacturing (UAM) process [15,16] involves joining metallic sheets together by use of ultrasonic vibrations under a contact normal force, as shown schematically in Fig. 13.2C. Metal sheets are softened by the heat generated by ultrasonic vibration and joined in a solid state. In UAM, the feedstock is supplied as a rolled sheet or foil, typically in the thickness range of 0.5–1.0 mm. Thus, this sheet lamination process uses the stacking of precision-cut metal sheets into two-dimensional (2D) part slices from a 3D object [17]. After stacking, these sheets are either adhesively joined or metallurgically bonded using brazing, diffusion bonding [18], laser welding [19], resistance welding [20], or ultrasonic consolidation. A key feature of sheet lamination hardware is the order in which sheets are applied and cut/machined. Sheets may be either cut to the specified geometry prior to adhesion or machined postadhesion. Some of the advantages of the sheet lamination process include low geometric distortion (the original metal sheets retain their properties), ease of making large-scale (0.5 m × 0.8 m × 0.5 m) parts, relatively good surface finish, and low cost. However, sheet lamination does have some limitations. Adhesively joined parts may not work well in shear and tensile loading conditions. Geometric accuracy in the *z*-direction is difficult to obtain due to swelling effects. Finally, anisotropic properties are prevalent in sheet lamination builds due to the type of joining processes.

Fig. 13.2D shows powder bed fusion with a laser beam heat source (PBF-L) [21,22]. During the process, a thin layer of metal powder is distributed evenly across the build chamber by a roller. The laser moves across the powder and, as it moves, fuses the powder level of the part’s cross-section. As the powder in the above level shape of the part is being produced, a

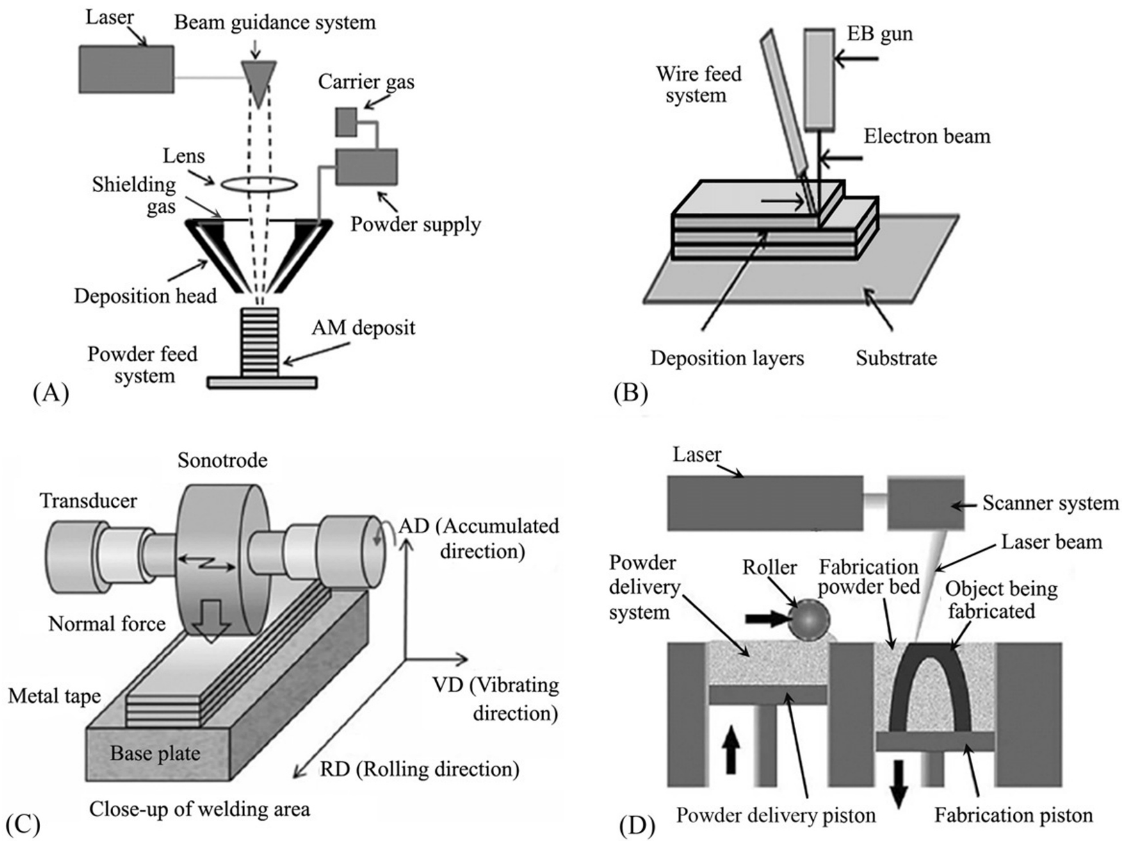
Laser
Beam guidance system
Carrier gas
Lens
Shielding gas
Powder supply
Deposition head
AM deposit
Powder feed system
(A)
EB gun
Wire feed system
Electron beam
Deposition layers
Substrate
(B)
Sonotrode
Transducer
AD (Accumulated direction)
Normal force
Metal tape
VD (Vibrating direction)
Base plate
RD (Rolling direction)
Close-up of welding area
(C)
Laser
Scanner system
Laser beam
Powder delivery system
Roller
Fabrication powder bed
Object being fabricated
Powder delivery piston
Fabrication piston
(D)

FIG. 13.2 Schematic view of (A) DED-L, (B) DED-EB, (C) ultrasonic additive manufacturing (UAM) process, and (D) PBF-L.

next layer of powder is then spread over the top of the previous layer and the next cross-section of the part is produced. During and after the building, the part is surrounded by unagglomerated powder. This excess powder encases the object in the printing process, providing support for complex geometries.

It is obvious that in these processes, the physical characteristics of the powder play an important role in transporting the powder to the bed and the particle packing within the bed. A number of characteristics of the powder, such as particle size, shape, surface area, and packing density, play a role in the formation of the powder bed.

The packing density of the powder bed influences the sintered density as well as mechanical and physical properties of the final part.

A comparison of the DED and PBF-based AM techniques is shown in Table 13.1. As stated above, AM processes with alloy powder as the feedstock material are commonly used to fabricate very complicated components with a sufficiently good surface finish. However, the fabrication process is very slow and the powder feedstock is expensive [5]. Wire and metallic sheet-based AM processes are fast but lack dimensional accuracy and result in defects and poor surface finish, especially for parts with complex shapes. In summary, several variants of AM techniques have evolved to manufacture parts with complex internal features and external contours as well as work with alloys that are difficult to cast and process thermomechanically and hard to machine.

POWDERS FOR AM

The delivery of the feedstock material depends on the specific AM process. In the DED-L process, the alloy powder is fed coaxially with the laser beam by a set of nozzles. In PBF-based AM processes, solid powders are often reused to avoid waste that can result in poor surface finish and mechanical properties of the final part, as discussed in a later section. In contrast to the powder-based AM processes, the DED-GMA technique is similar to filler wire-based fusion welding processes. Gas metal arc welding processes, especially with a short-circuiting mode of metal transfer, are commonly used for the DED-GMA process because of lower arc power compared to other modes of metal transfer. For deposition of titanium alloys, a plasma arc (DED-PA) is also attempted as the heat source with titanium filler wire to avoid arc instability [13].

TABLE 13.1 Characteristics of Direct Energy Deposition (DED) and Powder Bed Fusion (PBF) Additive Manufacturing Processes

Process	**DED**			**PBF**	
Feedstock	**Powder**	**Wire**		**Powder**	
Nomenclature	DED-L	DED-EB	DED-PA/DED-GMA	PBF-L	PBF-EB
Heat source	Laser	*E*-beam	Electric arc	Laser	E-beam
Feature size/ beam diameter (μm)	380	16,000	…	75–100	100–200
Power (W)	100–3000	500–2000	1000–3000	50–1000	
Nominal powder size fraction (μm)	20–200	…	…	10–45	45–106
Layer thickness (μm)	250	3000	…	10–50	50
Speed (mm/s)	5–20	1–10	5–15	10–1000	
Max feed rate (g/s)	0.1–1.0	0.1–2.0	0.2–2.8	…	
Max build size (mm × mm × mm)	2000 × 1500 × 750	2000 × 1500 × 750	5000 × 3000 × 1000	500 × 280 × 320	
Production time	High	Medium	Low	High	
Dimensional accuracy (mm)	0.5–1.0	1.0–1.5	…	0.04–0.2	
Surface roughness (μm)	4–10	8–15	Needs machining	7–20	
Postprocessing	HIP and surface grinding are seldom required	Surface grinding and machining is required to achieve better finishing	Machining is essential to produce final parts	HIP is rarely required to reduce porosity	
References	[5,7–11,23,24]	[2,11,24–26]	[12–14]	[11,24,27,28]	

Commercial abundance and low price of the filler wire compared to alloy powders make the DED-GMA or PA processes less expensive. In UAM, the feedstock is supplied as rolled sheet or foil, typically in the thickness range of 0.5–1.0 mm [15,16]. The AM processes are also characterized by their production times, the maximum size of the component that can be fabricated, the ability to produce intricate parts, and the product qualities such as defects and dimensional accuracy. The production time of the powder-based AM processes is high due to the limitations of the powder-feeding rate, the scanning speed, and low layer thickness. In contrast, filler wires allow relatively higher mass flow (deposition) rate in wire-based processes. As a result, the powder-based processes are considered suitable for relatively smaller parts and the wire-based processes are considered suitable for the fabrication of large-size components typically heavier than 10 kg.

The qualities of the feedstock materials depend on their manufacturing process. The alloy powders for AM are mainly made in the following ways: gas atomization (GA), centrifugal atomization, plasma rotating electrode process (PREP), and water atomization (WA). All these methods are described in Chapter 4.

Powder Characterization and Testing

The qualities of the additively manufactured parts are significantly influenced by the characteristics of the feedstock materials [29,30]. These characteristics include the shape, size distribution, surface morphology, composition, and flowability of the powders [24]. X-ray and computed tomography (CT) are used to examine the shape and surface morphology of the powder particles [31].

Determining the properties of powder used in an AM system is a necessary condition for the industry to be able to find select powder and produce consistent parts with known and predictable properties. Table 13.2 summarizes the influences of the powder particle and possible defects during the AM build up process and in the manufactured part. This information emphasizes the need for high-quality powders and reliable processes for powder handling, storage, and transport conditions.

The powders used for AM are usually characterized by conventional methods. The powders' particle size distribution according to ISO 4497 sieve analysis is used. Also, the laser diffraction method (ISO 13320 Standard) for particle size analysis is employed. Flowability is characterized for 50 g of powder by means of a calibrated funnel with a 2.54 mm diameter (Hall flowmeter, DIN ISO 4490). Apparent density is determined by the funnel method (DIN ISO 3923/1). Tap density is measured on a Scott volumeter according to DIN ISO 3953. Density of solids is measured using an AccuPyc 1340 gas pycnometer with helium. Chapter 1 includes the description of these methods, such as the chemical composition analysis, interstitial impurities determination, and imaging performing of surface and structure powders.

One of the peculiarities of AM technology is the need for processes where comparably small amounts of powders are used to create thin powder layers, and where powders are more or less dynamically moved over the build area. More precisely, the evaluation is focusing on AM processes where the powder layers are created by a ruler or a rotating cylinder (Fig. 13.2) and where the powder is taken from a powder reservoir. In such a situation, the powders have a comparably high free surface and can be aerated to some degree, depending on the speed of the coating device. Therefore, powder flowability plays a particular role here.

For bulk powders, the ring shear cell tester (Fig. 13.3) according to ASTM D6773 [46] is often used and industrial standards get insight into powder properties such as powder flowability, compressive strength, powder compressibility, consolidation time, internal and wall friction, and bulk density. Schulze discussed the fundamentals of the flow properties of powders [47,48].

The angle of repose, defined in ISO-4490/ASTM B213 [49,50], is a principle where powder flows freely through a funnel onto a plate and the slope angle of the developed cone to the base plate is the angle of repose; it is considered a measure for powder flowability. This method is also recommended by ASTM as the characterization method for metal powders for AM [51].

The Hausner ratio (HR), defined as the ratio between the tapped and bulk density [52], is a common technique that's widely used. The measurement of powder density (apparent/bulk and tap density) is described in ASTM D7481–09 [53]. Because of the fact that tapped density is highly dependent on the amount of tapping [54] and that powders often do not reach stable density values within a reasonable number of tapping cycles [55], measuring bulk and tap powder densities is comparably far away from the situation in a powder bed-based AM process [56]. Therefore, as it is necessary to apply a flowability characterization method allowing the comparison of as different powders as possible, HR is not considered to be adequate for application in AM.

Spierings et al. showed a possibility to distinguish quantitatively between good flowable powders and powders that show insufficient flowability for AM using the revolution powder analyzer [36].

The revolution powder analyzer works according to Fig. 13.4. It consists of a rotating drum with an inner diameter of 100 mm and a width of 35 mm, covered on both sides with transparent glass. A camera records pictures of the rotating drum (0–200 min^{-1}) before a backlight. As the powder occupies a certain area, the record is a black-and-white picture of the powder and avalanches, respectively, within the drum. Two different tests are applied: a fluidization test and a flowability test. The fluidization cycle is used to put the powder into a normalized condition where the effects of consolidation and handling are removed.

Measurable parameters comprise the avalanche angle (α_P) and avalanche surface fractal (ψ_P). The authors [36] discussed the measurement of the avalanche angle as a methodology, which is nearer to powder bed-based AM (SLS, SLM) than the other techniques. It typically consists of a rotating transparent drum filled with a certain amount of powder and a camera in front of a backlight. The camera records pictures of the powder-free surface and the cross-sectional area of powder inside the drum (Fig. 13.4). The pictures can be analyzed for different values associated with powder flowability [57]. The avalanche surface fractal is a measure of the fractal dimension of the surface profile [58]. Fig. 13.5 illustrates the cumulative magnitude distribution of the avalanche angle for gas-atomized nickel powders with a size distribution describable by a median diameter in the 18–35 μm range. It shows the avalanche angle values generally in the 58–72 degree range.

Slotwinsky et al. [31] reported the results of systematic studies carried out on two different powder materials used for additive manufacturing: stainless steel and cobalt chrome. An extensive array of characterization techniques was applied to these two powders, in both virgin and recycled states. The physical techniques included laser diffraction particle size analysis, X-ray computed tomography for size and shape analysis, and optical and scanning electron microscopy.

TABLE 13.2 Powder Characteristics and Their Influence on the Additive Manufacturing Process

Powder Characteristics	Description	Influence on Process and Product
Particle size distribution	Maximum particle size determines optimal powder layer thickness [32] Balanced particle size distribution has a positive effect on packing density, due to small particles filling the small voids [33], and powder compactibility [34] Small particles are light and get easily thrown out of the process zone, furthermore due to their surface to volume ratio they are more likely to inflame or explode if making contact with reactive gas [32] Small particle size and narrow particle size distribution leads to uniformity in the melt pool, and results in a higher part density [32,33] Powder bed density influences the resulting heat transportation and thus the heat balance [32]	*Process*: Optimal powder layer thickness, heat balance of the powder bed, consistency in melt pool, packing density, compactibility, dispersing *Product*: Density
Plowability	Affects the layer deposition and layer quality (e.g., homogeneous layers) [35,36]	*Process*: Layer deposition
Reflectivity, absorptivity	Laser energy is absorbed (absorptivity) or reflected in the process chamber (reflectivity) by the powder bed [32] Absorptivity of a powder depends on the wavelength of the laser and the condition of the powder bed [32] High reflectivity of the powder bed (>91% for aluminum) requires an increase in laser power [37–39]	*Process*: Variations in energy input, required laser power, and wavelength
Thermal conductivity	High thermal conductivity increases the required laser power [38,39], which leads to a rapid dissipation of heat away from the melt pool [37]	*Process*: Required laser power, melt pool temperature
Oxidation	Oxides form during the process (oxygen level 0.1 to 0.2%) [37] Theory: most predominant factor controlling the flowability is the amount of surface oxides on particle surface Rupture of the oxide layer of small powder particles is more difficult [40]	*Process*: Obstacle for effective melting, adherent thin oxide films on molten aluminum reduce wettability *Product*: Involved oxide: region of weakening
Humidity, hydrogen	Single or multiple molecular layers can form on the particle surface, leading to hydrogen bonding [41] Increased interparticular forces lead to a decrease in flowability [33,41,42] and the metal microstructure of the part [5] On the particle surface and in the powder material can lead to hydrogen porosity [43,44]	*Process*: Powder flowability *Product*: Metal microstructure, hydrogen pores
Particle shape, morphology	Typical powder defects are irregular shapes e.g., elongated particles, satellites, hollow or porous particles [31,44] Affects flowability [33], spherical particle morphology is beneficial for powder flowability and helps to form uniform powder layers [43] Excessive amounts of large pores or pores with entrapped gas can affect material properties [44] Stacking density is a function of the powder morphology [32] Surface roughness affects the absorptivity [32]	*Process*: Powder flowability *Product*: Layer deposition, absorptivity
Surface oxide of powder particles	Nonuniform in thickness of particles surface oxide (from 30 to 40 up to three monolayers, in case water-atomized powder of aluminum alloys), therefore melting temperature increases [45]	*Process*: High temperature strengthening phase *Product*: Mechanical properties

Adapted from Dietrich S, Wunderer M, Huissel A, Zaeh MF. A new approach for a flexible powder production for additive manufacturing. Proc Manuf 2016;6:88–95.

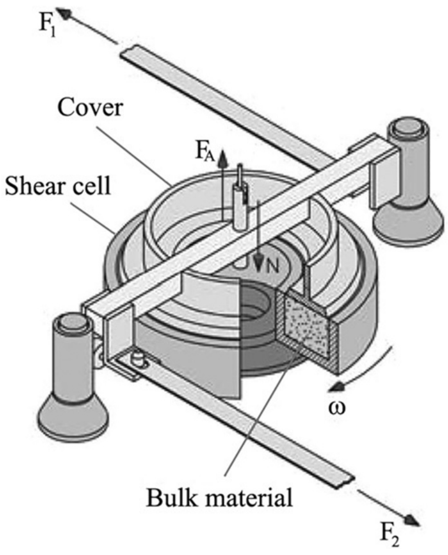
F_1
Cover
F_A
Shear cell
N
ω
Bulk material
F_2

FIG. 13.3 Ring shear cell tester.

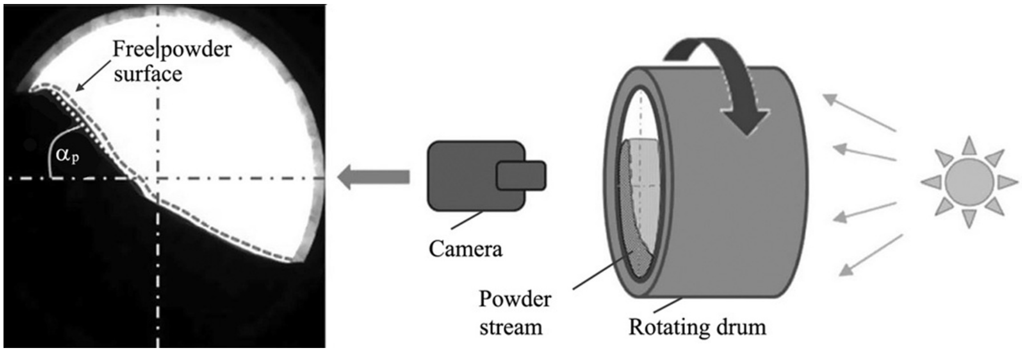
Free powder surface
α_p
Camera
Powder stream
Rotating drum

FIG. 13.4 Schematic of the revolution powder analyzer principle.

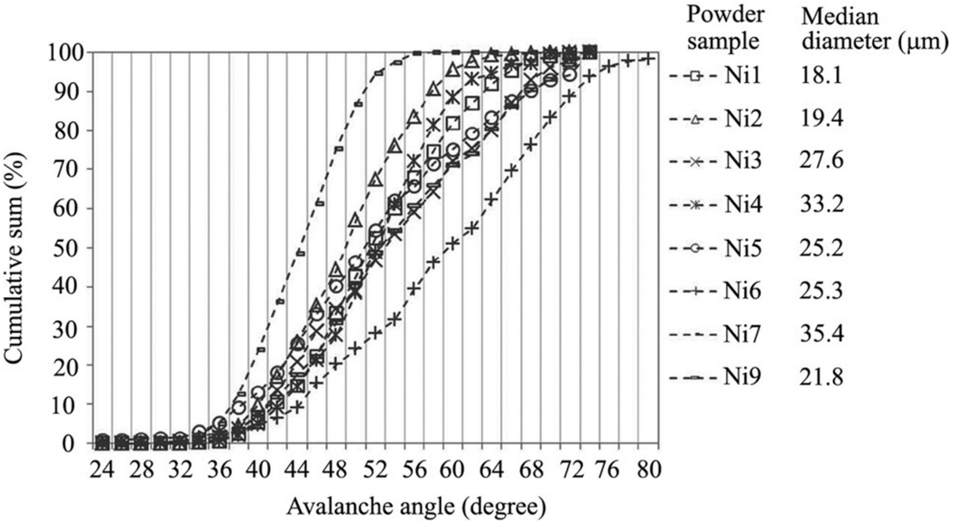

FIG. 13.5 Cumulative size distribution of the avalanche angle (α_p) for nickel powder.

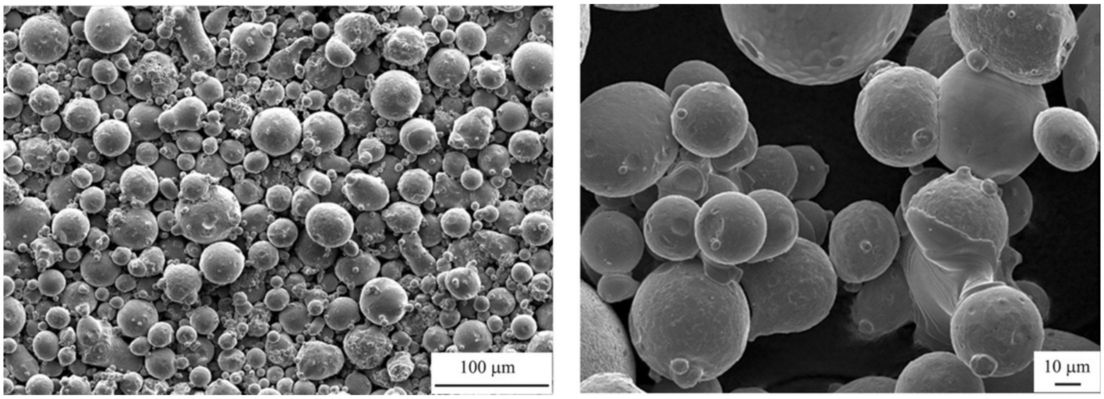

FIG. 13.6 SEM micrographs of gas-atomized CoCr powder particles by various magnification. *Modified from Slotwinski JA, Garboczi EJ, Stutzman PE, Ferraris CF, Watson SS, Peltz MA. Characterization of metal powders used for additive manufacturing. J Res Natl Inst Stan 2014;119:460–93.*

Techniques sensitive to structure and chemistry, including X-ray diffraction, energy dispersive analytical X-ray analysis using the X-rays generated during scanning electron microscopy, and X-ray photoelectron spectroscopy were also employed. The results of these analyses show how virgin powder changes after being exposed to and recycled from one or more direct metal laser sintering of AM build cycles. Fig. 13.6 illustrates the shape and surface morphology of particles of gas-atomized CoCr powders.

Powder Properties

Mainly the AM equipment manufacturer supplies the powders for selective laser melting (SLM) and electron beam melting (EBM). Using the material Ti-6Al-4V as an example, Kirchner et al. [59] determined the properties of such powders provided by several equipment manufacturers for (SLM) and (EBM) as well as changes of their properties after multiple reuse cycles. The SLM machines employed within this study were an EOS Eosint M270, a Concept Laser M2 cusing, and a SLM Solutions 250HL. EBM studies were performed on an Arcam A2X machine.

Table 13.3 contains the analysis data of four Ti-6Al-4V powders provided by manufacturers of SLM and EBM machines: EOS Titanium Ti64 with a nominal particle size of 20–45 μm, Concept Laser rematitan CLM (15–45 μm), SLM Solutions Ti-6Al-4V (20–63 μm), and Arcam (45–105 μm). It also comprises custom-specified Ti-6Al-4V powders

TABLE 13.3 Properties of Ti-6Al-4V Powders Provided by Manufacturers EOS, Consept Laser, SLM Solutions and Arcam and Properties of Custom Specified Ti-6Al-4V Powders

Parameters	Unit	Equipment Manufacturers				Custom Specified Powders	
		EOS	Concept Laser	SLM Solution	Arcam	SLM	EBM
δ_{10}	μm	21.9	20.2	28.2	51.4	32.8	52.9
δ_{50}	μm	31.9	29.8	36.6	73.2	44.1	73.7
δ_{90}	μm	46.3	43.7	49.2	107.8	62.5	104.6
Flowability	s	39.3	53.2w	31.7	21.8	31.4	28.3
Apparent density	g/cm^3	2.46	2.54	2.45	2.59	2.32	2.37
Tap density	g/cm^3	2.83	2.83	2.73	2.81	2.64	2.70
Al content	wt%	6.49	6.38	6.37	5.75	…	6.42
V content	wt%	4.09	3.91	3.90	3.97	…	4.20
Fe content	wt%	0.24	0.22	0.22	0.21	…	0.22
O content	wt%	0.188	0.147	0.143	0.116	0.119	0.118
N content	wt%	0.010	0.009	0.016	0.017	0.005	0.005

Adapted from Kirchner A, Klöden B, Weißgärber T, Kieback B. Powders for additive manufacturing. In: Compiled by European Powder Metallurgy Association, (Bellstone Shrewsbury, UK) Proceedings of PM 2016 World Congress. Hamburg (Germany); 2016: p. 1–5.

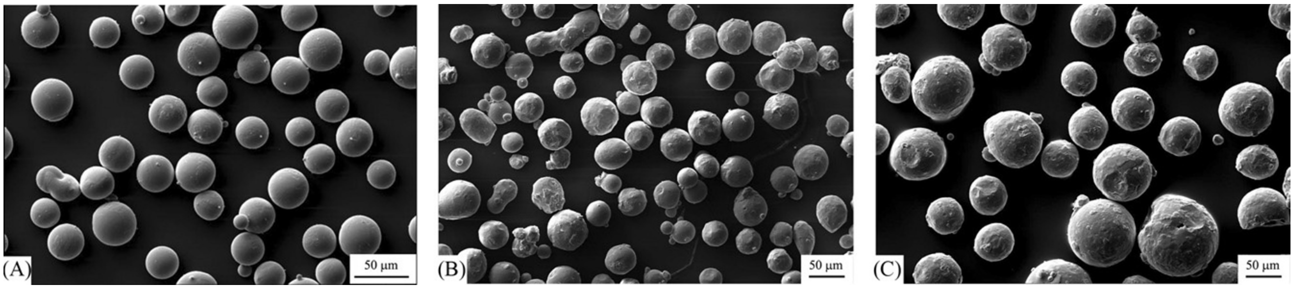

FIG. 13.7 SEM micrographs of (A) SLM Solution Ti-6Al-4V powder provided by AM equipment manufacturer, and (B) SLM and (C) EBM custom specified Ti-6Al-4V powders.

that were fabricated by electrode induction-melting gas atomization using argon by TLS Technik Bitterfeld (GmbH&Co. Spezialpulver KG) and supplied in two nominal fractions of 20–63 µm (SLM) and 40–120 µm (EBM).

Among the SLM powders, the Concept Laser powder is the finest with a median diameter δ_{50} of 29.8 µm. The coarsest is the custom-specified powder with a median δ_{50} of 44.1 µm. An electron microscopy image provided by an AM equipment manufacturer of powders (Fig. 13.7A) shows a highly spherical shape with very few satellites. Both the SLM (Fig. 13.7B) and the EBM (Fig. 13.7C) custom-specified powder are less spherical than that provided by manufacturers of powders. This affects both apparent and tap density, which are slightly reduced.

The finest powder from SLM Solutions exhibits the lowest flowability at 53.2 s while the coarsest powders from SLM Solution and the customer specified exhibit the highest flowability of the SLM powders at 31.7 and 31.4 s, respectively. In comparison, the EBM powder provided by Arcam is characterized by a larger particle size because the fine powder fraction is linked to process instabilities. Consequently, flowability as well as apparent and tap density are higher than those of the SLM powders.

The authors reported [59] that, after processing virgin SLM powder on an SLM Solutions machine, a number of insignificant changes in powder properties were detected. While the median particle size stayed practically constant, the number of particles smaller than 30 µm was reduced over the first three cycles. Flowability was increased continuously such that after six cycles, flow time was reduced to 28.6 s. While the effect on apparent density was negligible, tap density increased to a level of 2.73 g/cm^3. A moderate increase in impurities was detected. The oxygen content rose to 0.138% within six cycles at an average rate of 0.003%/cycle.

In a work [60], the production of powders for AM by thermal spraying is considered. The process of thermal spraying is similar to the gas atomization process, due to the use of a gas flow for melt atomization; however, it is more compact. There are many process variations, which are listed in DIN EN 657:2005-06, according to their energy sources or spraying consumables [61]. The process that is most preferable for powder production is arc spraying. Arc spraying is a wire-based process that transfers the heat of the arc directly into the material (Fig. 13.8) [62]. The particle velocity and process

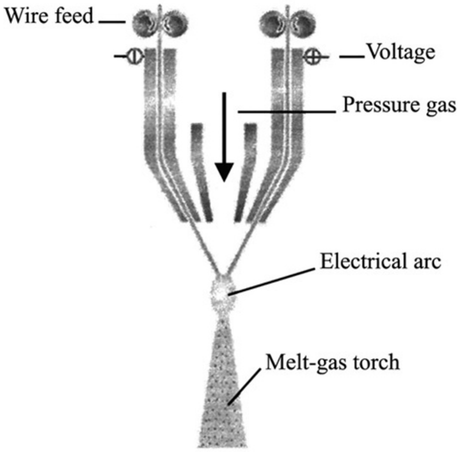

FIG. 13.8 Schematic diagram of the arc spraying process.

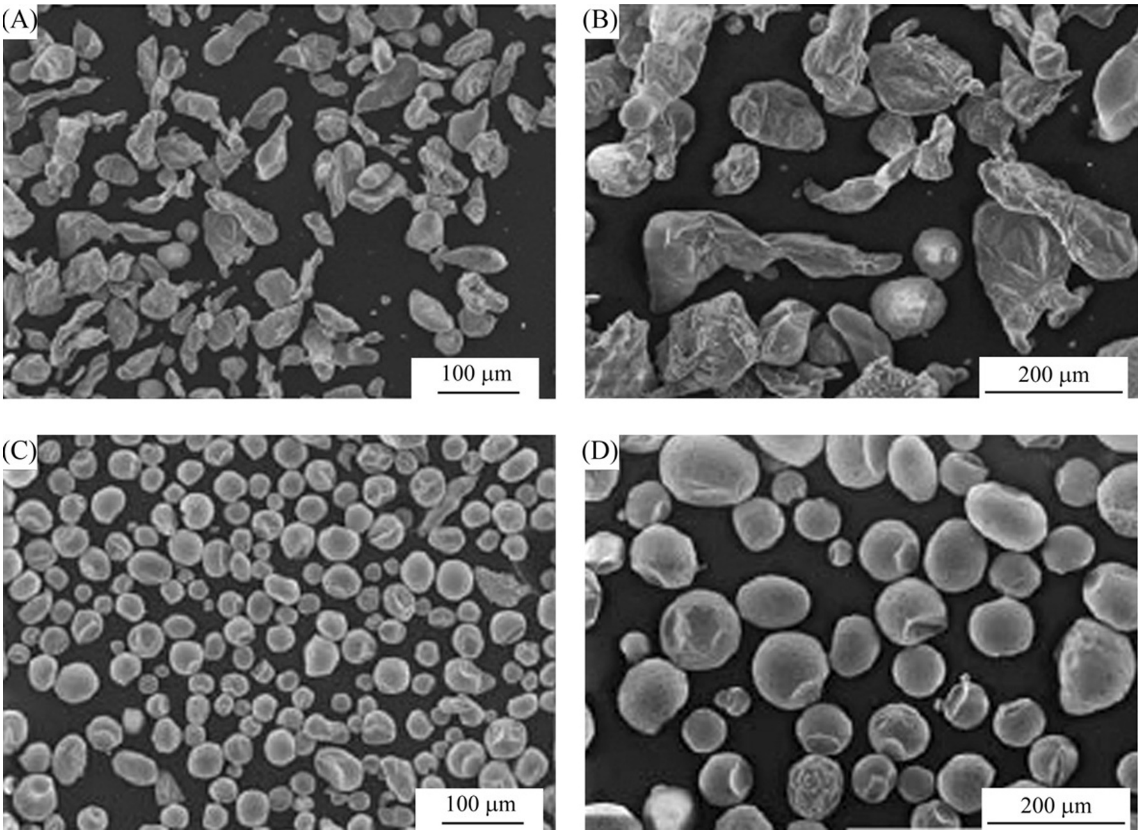

FIG. 13.9 SEM images of various magnifications of AlSi5Mg powders by (A, B) air, and (C, D) argon arc spraying. *Modified from Dietrich S, Wunderer M, Huissel A, Zaeh MF. A new approach for a flexible powder production for additive manufacturing. Proc Manuf 2016;6:88–95.*

temperature are lower compared to plasma spraying and reach about 3970–4970 K and 100–150 m/s, depending on the process parameters. The aluminum powder yield is about 6–8 kg per hour.

The aluminum alloy AlSi5Mg with a wire diameter of 1.6 mm was processed with common spray parameters for coatings, consisting of a voltage of 28 V, an amperage of 100 A, and a process gas pressure of 0.28 MPa (40 psi). In order to produce particles for AM, the usage of low voltage, low amperage, and high process gas pressure generally led the way to the production of small particle sizes under 63 μm, which are favorable for AM. Compressed air ($O_2 \approx 21$ vol.%) and argon 4.6 ($O_2 \leq 4 \times 10^{-4}$ vol.%) were used as the atomizer medium. Fig. 13.9 illustrates SEM images of particles produced by the use of air (Fig. 13.9 A–B) and argon (Fig. 13.9C–D) as the atomization medium. The particle shape of the air-atomized powder particles is irregular. The argon-atomized powder particles show a more spheroidal shape. Occasionally, rounded oblong (nodular) particles are present. The particle surface is considerably smoother.

Characteristics of powders produced by gas atomization (GA), rotary atomization (RA) and the plasma rotating electrode process (PREP) are compared in the work [24]. Fig. 13.10 illustrates surface morphology, shape, and the laminated object manufacturing (LOM) cross-section of powder particles.

The majority of GA powders are spherical or near spherical in shape and with satellites (Fig. 13.10A). As is known, “satelliting” may be formed when small particles are attached to larger particles. Their collision probability is increased with small particles yield growth and/or by the circulation of gas within the atomizing chamber that lifts finer particles back into the spray plume, where they collide with larger, still partly molten particles [63]. Along with near spherical, RA powder particles are oblong in shape (Fig. 13.10C). Almost all PREP powder particles are spheroidical (Fig. 13.10E). Porosity is common for certain production techniques, such as gas atomization (Fig. 13.10B), that entrap inert gas during production. The PREP powder particles do not contain such pores (Fig. 13.10F). The entrapped gas can be transferred to the part, due to rapid solidification, and results in powder-induced porosity in the fabricated material. These pores are spherical, resulting from the vapor pressure of the entrapped gas.

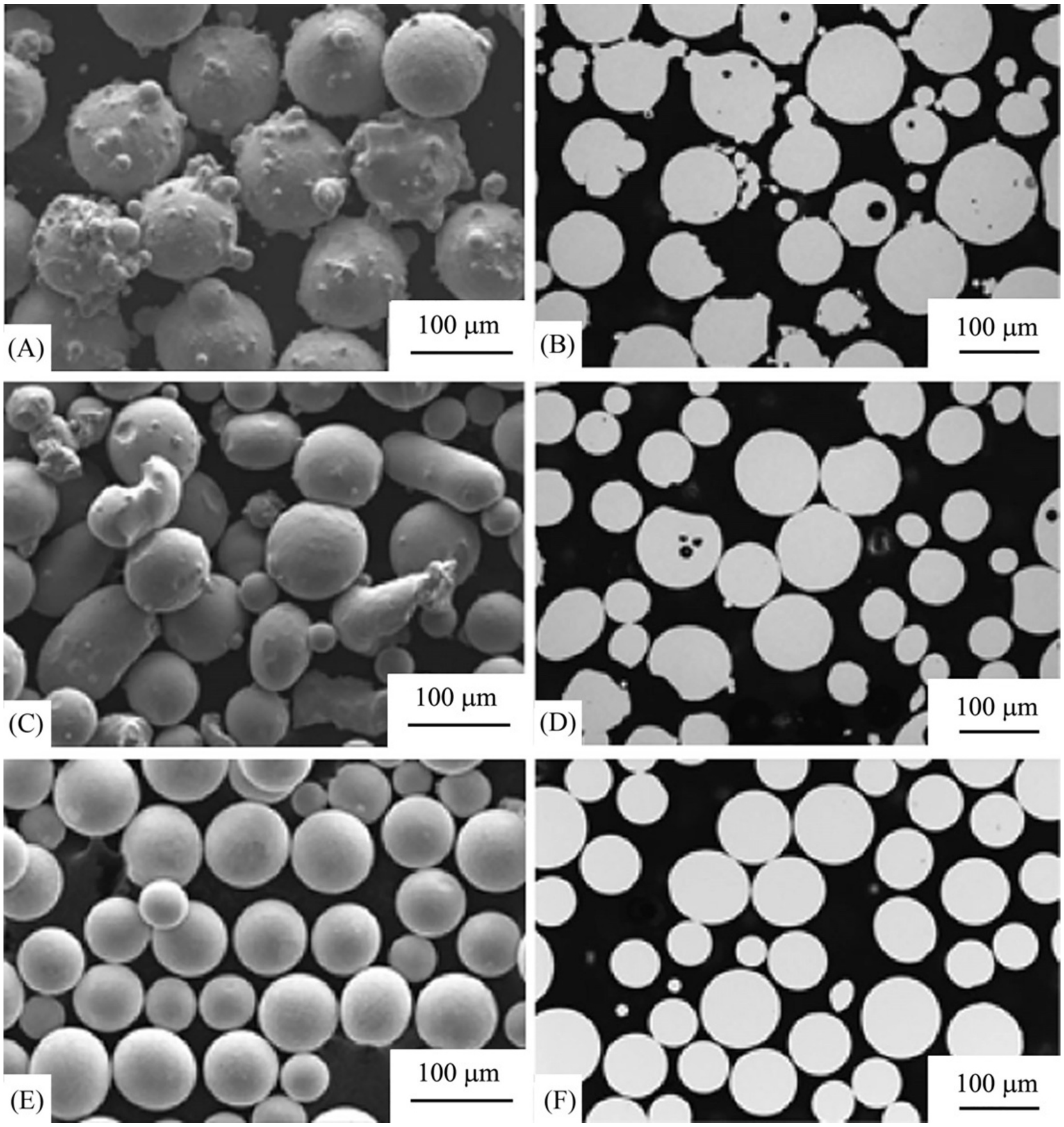

FIG. 13.10 SEM micrographs of (A), (C), (E) surface morphology and (B), (D), (F) LOM cross-section of Inconel 718 powders made by (A, B) GA; (C, D) RA; (E, F) PREP. *Modified from Sames WJ, Medin F, Peter WH, S. S. Babu SS, Dehoff RR. Effect of process control and powder quality on Inconel 718 produced using electron beam melting. In: 8th International Symposium on Superalloy 718 and Derivatives. Pittsburgh (PA, USA); 2014. p. 409–23.*

APPLICATIONS OF AM

Aluminum and Magnesium Alloys

In order to achieve high levels of mechanical properties in built parts, it is important to guarantee reproducible and high-quality powder production, storage, and processing. Aluminum alloy powders produced and handled under dry conditions would be expected to be covered by a passive Al_2O_3 layer a few nanometers thick (see Chapter 16). However, in humid conditions, water reacts with the alumina layer, leading to AlOOH generation. Finally, the hydroxide is reduced by aluminum, generating hydrogen bubbles at the metal/oxide interface. As soon as the hydrogen pressure in the gas bubbles exceeds the oxide's tensile strength, the passive layer is destroyed, exposing fresh reactive metal and further promoting surface layer formation.

The most commonly studied Al alloy in AM is AlSi10Mg. Two different atomized powder grades of Al-7.0Si-0.6Mg and Al-10Si-0.45Mg alloys were investigated in the study [64]. These powders were produced by electrode induction melting gas atomization with an inert gas as the atomizing medium. All atomized powders were separated by air and then sieved to give a particle size distribution between 20 and 63 µm. The oxygen content was 500 ppm max. Fig. 13.11

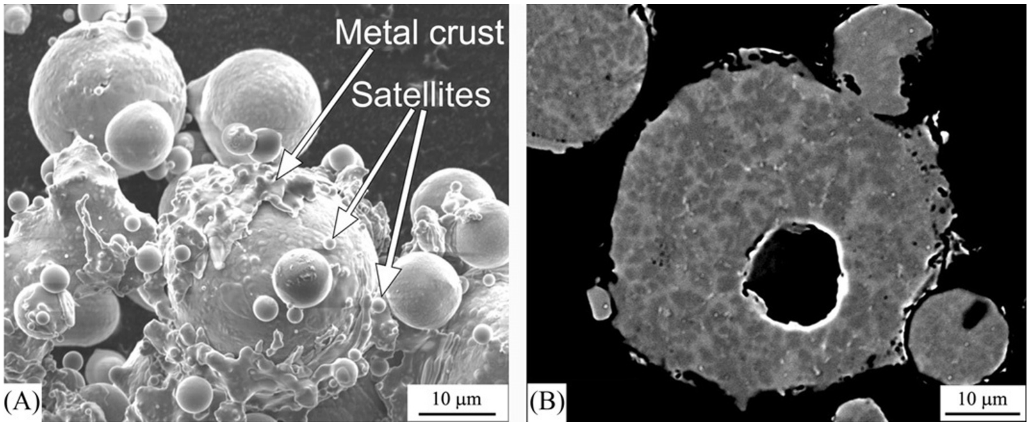

FIG. 13.11 Typical gas atomized Al-Si-Mg alloy powder: (A) surface morphology; (B) polished cross-section. *Modified from Tang M, Pistorius PC, Narra S, Beuth JL. Rapid solidification: Selective laser melting of AlSi10Mg. JOM 2016; 68(3): 1–7.* https://doi.org/10.1007/s11837-015-1763-3.

illustrates typical features of the metal powder. While the powder particles appear generally spherical (Fig. 13.11A), they differ from ideal sphericity in two main ways: smaller satellite particles are attached to large particles, and "metal crust" is observed. Some particles contain internal pores (Fig. 13.11B), likely entrapped atomizing gas. These can affect part quality; satellites and crusts are likely to affect the spreading behavior of the powder, and entrapped gas would contribute to part porosity if the gas did not escape from the melt pool before solidification.

Powder aging due to handling and laser beam machining (LBM) process simulation was assessed using a climate chamber comprising containers equipped with a moisture barrier. A salt solution in the container provides a nearly constant value of the moisture content for defined temperatures. To create defined moisture levels, potassium chloride and magnesium chloride were used for the aging investigations. The final powder characteristic assessed was flowability measured with a revolution powder analyzer (see Fig. 13.4). For the increasing humidity, the avalanche angle and time increased significantly. This can be related to a higher agglomeration rate caused by the higher moisture content and hydrogen bond. Due to the high number of fine particles, this powder material is sensitive to agglomeration. The average avalanche angle decreases slightly from the condition where the powder was only dried from the starting condition without exposure to a higher humidity. The results of this investigation showed that the average avalanche time is more sensitive to moisture than the average avalanche angle. From these tests, the authors concluded that there is a potential to dry the powder and, consequently, recondition the flowability. Drying the powder was also expected to reduce the agglomeration rate and achieve a higher bulk density in the deposited powder.

The laser powder bed processing of aluminum-based powder faces challenges related to a number of its physical characteristics, such as high reflectivity, high thermal conductivity, and low powder flowability. From the broad range of available aluminum alloys, the Al-10Si-0.45Mg alloy has emerged as the most attractive for AM processing because of its high fluidity in the molten state and its narrow solidification range due to its near-eutectic composition. The extremely high cooling rates that arise during laser powder bed processing near 10^6 K/s [65] allow the creation of fine and new microstructures and hence unique mechanical properties. The relationship that had been used for the definition of the cooling rate was as follows:

$$\mathrm{v} = \left(\frac{43.2}{\lambda}\right)^{1/0.324}$$

where v is the cooling rate in K/s and λ is the cell size in μm.

Cell sizes were measured from backscattered electron images of polished planes that were perpendicular to the laser traveling direction and contained the building direction. Care was taken to minimize distortion of the measured cell sizes by stereological effects. For built parts, the presence of a few small spherical gas pores allowed direct comparison of the apparent cell size on a polishing plane with the actual cell size visible at the surface of the pore; an example is shown in Fig. 13.12. Arrows are shown spanning the width of three and four cell spacings on the polished surface. Cells are also visible within a gas pore, allowing measurement of cell size with less stereological uncertainty.

Published data [66] showed that high strength could be achieved by the introduction of transition metals, such as nickel, to rapidly solidified Al—Si alloys. An EOSINT M270 Xtended system was used to build the samples. This system uses an

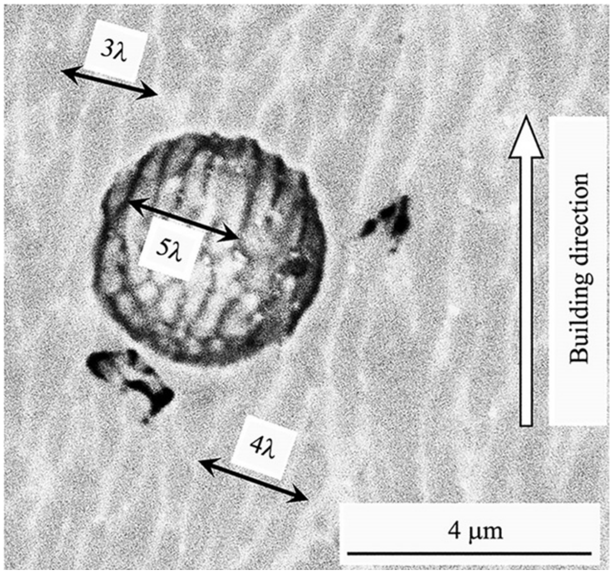

FIG. 13.12 Backscattered electron image of polished cross-section of built part. *Modified from Tang M, Pistorius PC, Narra S, Beuth JL. Rapid solidification: Selective laser melting of AlSi10Mg. JOM 2016; 68(3): 1–7. https://doi.org/10.1007/s11837-015-1763-3.*

argon atmosphere with oxygen content lower than 0.1% and a ytterbium fiber laser with a power up to 200 W to melt thin layers of metal powder. An Al-10Si-0.45Mg gas-atomized powder was mixed with a spherical pure nickel powder. The nominal chemical compositions of the powder batches are the following (in wt%): (8.5–10.5)Si, (0.18–0.42)Mg, 5.1Ni, ≤0.55Fe, <0.45Mn, ≤0.15Ti, <0.05Cu, reminder Al. The mixing ratio for the Al-Si-Ni material was chosen to obtain a chemical composition close to the ternary eutectic (840 K at 4.9 wt% Ni and 10.98 wt% Si). Vickers hardness tests, on the samples built with the optimized parameters, showed that the introduction of nickel into the alloy strongly increased the hardness level, from around 136 HV (1.334 GPa) to 180 HV (1.765 GPa).

The low evaporation temperature and melting point of magnesium, coupled with its high vapor pressure, make it challenging to the AM process. The magnesium powder, used in both powder bed fusion and directed energy deposition processes, must be passivized during production to allow for safe handling. The resulting stable magnesium oxide layer on the surface of powder inhibits the wetting process and, therefore, influences the processing conditions.

The paper [67] reported on a study of AM-, via both laser powder bed fusion and directed energy deposition, of the Magnesium Elektron powder grade, Elektron MAP+43, which was specifically developed for AM processing.

Directed energy deposition studies used a gas-atomized spherical Elektron MAP+43 powder ($\delta_{10} = 50\,\mu m$, $\delta_{50} = 83\,\mu m$, $\delta_{90} = 133\,\mu m$). The deposition experiments were performed on a custom-fabricated deposition system with build dimensions of up to 1000 mm L × 300 mm W × 450 mm H. The power source was a ytterbium fiber laser with a wavelength ranging from 1070 to 1100 nm. Powder was delivered using a custom-designed, four-nozzle system. The substrate was placed approximately 10 mm from the nozzles. At this location, the laser beam was in a defocused position and had a measured beam diameter of approximately 4 mm. The process parameters investigated included varying the laser power between 1750 and 2250 W, travel speed between 0.85 and 1.27 cm/s, nozzle gas flow between 100 and 200 L/min, and layer height step between 0.038 and 0.1 cm. The powder flow rate was set at 5 g/min and the chamber oxygen level was between 80 and 110 ppm. The best results were obtained using a laser power of 2250 W with a scan speed of 1.06 cm/s and an overlap of 0.20 cm. Under these conditions, an optimum combination of small grain size (8 µm), small pore volume (0.70%), and high as-deposited microhardness (81 HV) was obtained.

Laser powder bed fusion investigations were performed on an SLM 125HL machine with a 100 W fiber laser and a focus diameter of 70 µm, using gas-atomized Elektron MAP 43 powder with a particle size distribution $\delta_{10} = 22.5\,\mu m$, $\delta_{50} = 31\,\mu m$ and $\delta_{90} = 45\,\mu m$. A 50 × 50 × 50 mm^3 build volume was used along with high purity Ar as the shielding gas. Parameter studies on varying laser power, scan speed, and hatch distance were performed with the goal of obtaining high as-deposited density (>99%). The laser power was varied between 20 and 100 W, the scan speed between 200 and 10,000 mm/s, and a layer thickness of 50 µm was used. Pore-free samples achieved a yield strength of 194 MPa, an ultimate strength of 312 MPa, and elongation of up to 14%. These values are superior to the Elektron MAP 43 strength obtained via DED and better than typical values for cast WE43.

Electron beam welding (EBW) was employed in joining the thin-walled containers, showing the feasibility of EBW to overcome the size limitation issue [68]. Thin-walled containers were fabricated from a prealloyed AlSi10Mg powder (particle size in the range of 25–45 μm) utilizing an EOSINT- M280 system equipped with a 250 × 250 × 300 mm building platform and 400 W CW Yb-fiber laser. The containers were built under an argon atmosphere in the vertical direction. Container dimensions were 50 mm in height, 47 mm in outer diameter, and 3 mm in wall thickness. Both the thickness of the base and flange were 5 mm and the boss thickness was 7 mm. The containers were cut in three orthogonal reference planes, each further cut into three more specimens, allowing each section to be sampled from three regions of the container (top, middle, and bottom).

In the study [69], the influence of SLM process parameters on the size of the trusses inside the BCC lattice structure was investigated. The median size of the particles of metal powder was 40.7 μm, the mean size was 41.4 μm, and standard deviation was 12.9 μm. In comparison with standard process parameters used for volumetric components, the best result is reached with process parameters with a much higher scanning speed. Structures with a laser power of 350 W and a laser speed of 3000 mm/s achieves better accuracy and geometry stability of the truss diameter while material porosity is kept under 1% (internal density 99.3%). It was found that the size of the trusses increases with rising laser power and decreases with higher laser speed.

Table 13.4 shows the ultimate tensile strength and ductility values in additively manufactured AlSi10Mg that are generally higher than or equal to as-cast and high-pressure, die-cast AlSi10Mg, which can be attributed to the fine microstructures seen in AM samples [65,73,84–86].

As mentioned above, AM-induced defects have a dramatic impact on mechanical properties. Aboulkhair et al. [87] studied the link between pore shape and scanning speed in AlSi10Mg deposited using PBF-L. It was shown that at speeds higher than 500 mm/s with a laser power of 100 W, a lack of fusion porosity and unfused particles were present while below this speed, spherical porosity was more prominent. A relative density of 99.77 ± 0.08% was achieved with a laser scanning speed of 500 mm/s, a hatch spacing of 50 mm, a laser power of 100 W, a layer thickness of 40 mm, and a presinter scan strategy.

AM technology requires low heat inputs within a narrow range to effectively process magnesium alloys. Thus far, there has been minimal research on magnesium and its alloys made by AM due to the difficulty in processing. However, there have been studies on optimizing AM processing parameters for the fabrication of Mg alloys by AM. Ng et al. [88] performed optimization of the deposition of magnesium using PBF-L by studying the behavior of 20 mm long single tracks. They studied the impact of varying energy density (from 1.27 to 7.84 10^9 J/m^2) as well as the impact of using a continuous versus a pulsed laser heat input. For both continuous and pulsed laser, the grain size grew from 2.3–4.9 μm with increasing energy density. However, the hardness decreased from 88.7 to 66.2 HV when using a continuous laser, and 96.9–68.3 HV when using a pulsed laser input with increasing energy density. Zhang et al. [89] used PBF-L to manufacture Mg9wt%Al, whose as-deposited microstructure contained magnesium, $Mg_{17}Al_{12}$, and MgO. They achieved relative densities of up to 82% using a laser power of 15 W and scan speed of 20 mm/s. Hardness values reached 75 HV compared to 60 HV of the as-cast AZ91 alloy.

Titanium Alloys

Titanium alloys have been widely studied in the field of AM due to their high strength-to-weight ratio and corrosion resistance. Many investigations of Ti-6Al-4V focus on the direct relations between mechanical properties and either processing parameters or microstructure. Important factors include process parameters, build geometry, and size and surrounding conditions. Zhao et al. [90] showed that the part size had an obvious influence on the microstructure and mechanical properties of EBM samples but less so for SLM samples of Ti-6Al-4V. In particular, small samples (on the order of 1.7 mm in diameter), had approximately 20% higher strength and 80% lower ductility compared to larger samples (on the order of 7 mm in diameter). Both SLM and EBM samples possessed higher strength and better ductility in the vertical orientation than those in the horizontal orientation. The tensile strength of SLM samples was significantly greater than that of EBM samples whereas the ductility was much lower. Due to the pores contained in samples, the fatigue strength of both EBM and SLM samples was lower than those of the cast and annealed alloys. However, hot isostatic pressing (HIP) significantly increased the fatigue limit the s of both SLM and EBM samples to above 550 MPa by closing the pores.

By means of variations in processing parameters in powder bed fusion using electron beam melting, Hrabe et al. [91] found that increased energy input led to a larger melt pool size, which resulted in a lower temperature gradient and therefore increased a lath thickness and prior-ß grain size. The increases in microstructural features with these processing parameter variations led to decreased yield strength, ultimate tensile strength, and hardness. Vertically oriented parts were found to have a considerably lower percent elongation (30% change) compared to horizontally oriented parts, which was attributed to differences in tensile axis orientation in relation to the direction of elongated prior-β grains and microstructural texture

TABLE 13.4 Processing Parameters and Mechanical Properties of Aluminum Alloys Fabricated by AM Compared to Their Traditionally Processed Counterparts

Alloy	P (W)	v (mm/s)	H (J/mm)	Post treatment	Orient.	E (GPa)	YS (MPa)	UTS (MPa)	El (%)	HV	Ref
Powder bed fusion											
AlSi10Mg	250	500	0.50	As-built	Long.		250	350	2.5	145	[70]
					Transv.		240	280	1.2		
AlSi10Mg	250	500	0.50	T6[a]	Long.		295	350	6.5	118	[70]
					Transv.	285	340	4.9			
AlSi10Mg				As-built	Long.	75 ± 10	270 ± 10	460 ± 20	9 ± 2	119 ± 5	[71]
					Transv.	70 ± 10	240 ± 10	460 ± 20	6 ± 2		
				2 h/573 K	Long.	70 ± 10	230 ± 15	345 ± 10	12 ± 2		
					Transv.	60 ± 10	230 ± 15	350 ± 10	11 ± 2		
AlSi10Mg	200	1400	0.14	As-built	Long.	68 ± 3		391 ± 6	5.5 ± 0.4	127	[72]
					Transv.			396 ± 8	3.47 ± 0.64		
AlSi10Mg	200	1400	0.14	As-built	Long.	68 ± 3		396 ± 8	3.5 ± 0.6	136 ± 9	[73]
				6 h/448 K	Transv.	66 ± 3		399 ± 7	3.3 ± 0.4	152 ± 5	
AlSi10Mg	195	800	0.24	2 h/573 K	Long.		252 ± 11	348 ± 5	6.6 ± 0.3	105 ± 2	[74]
					Transv.		240 ± 5	347 ± 6	5.1 ± 0.3	108 ± 1	
AlSi10Mg	195	800	0.24	2 h/573 K	Long.	73 ± 1	243 ± 7	330 ± 3	6.2 ± 0.3	105 ± 2	[75]
					Transv.	72 ± 1	231 ± 3	329 ± 2	4.1 ± 0.2	108 ± 3	
AlSi10Mg	400	1000	0.40	2 h/573 K	Long.		182 ± 5	282 ± 5	25.2 ± 1		[76]
					Transv.		184 ± 5	288 ± 5	18.3 ± 1		
AlSi12	320	1455	0.22	As-built	Transv.		260	375	2.8		[33]
				6 h/473 K	Transv.		260	340	2.4		
				6 h/573 K	Transv.		170	275	5.0		
				6 h/623 K	Transv.		120	190	9.2		
				6 h/673 K	Transv.		100	155	15.0		
				6 h/773 K	Transv.		95	140	13.0		

AlSi12	350	930	0.38	As-built	Transv.		396.3 ± 3.4	202.2 ± 4.3	4.38 ± 0.16		[77]
				513 K	Transv.		361.1 ± 4.5	201.5 ± 3.7	4.05 ± 0.15		
AlSi12	350	930	0.38	As-built	Transv.	78.7 ± 2.3	220.5 ± 9.5	418.9 ± 9.6	3.91 ± 0.27		[78]
				473 K	Transv.	76.5 ± 1.8	218.0 ± 9.5	372.39 ± 2.8	3.41 ± 0.16		
Al-Sc-Mg	195			4 h/598 K	Long.		515	530	15	177	[79]
brand[b]					Transv.		500	525	13		
Al-Cu-Mg	200	83.3	2.40		Transv.		276.2 ± 4.1	402.4 ± 9.5	6 ± 1.4	111	[80]
Wire-fed											
ER2319[c]					Long.		114	253	18.3	68.3	[81]
					Transv.		106	258	15.6		
Traditionally cast processed											
AlSi10Mg				HPDC		71	160–185	300–350	3–5	95–105	[82]
				HRDC-T6		71	285–330	330–365	3.5	130	
AlSi12				Die-cast			130	290	35[d]	80	[83]

[a] *Signified the solution treatment at 798 K for 6 h, water quenching and subsequent aging at 338 K for 7 h.*
[b] *Scalmalloy: Al-0.66Sc-4.5Mg-0.37Zr-0.51Mn-0.064 impurities.*
[c] *Nominal content of ER2319 alloy: Al-6.3Cu-0.3Mn-0.18Zr-0.15Ti-0.1V; HPDC is the high pressure die cast.*
[d] *% in 50 mm.*

P is the laser power; *v* is the scanning speed; *H* is the linear heat input; *ρ* is the density; *E* is the elastic modulus; *YS* is the yield strength; *UTS* is the ultimate tensile strength; *HV* is the Vickers hardness; *El* is the elongation; *Long.* is the orientation in longitudinal direction; *Transv.* is the orientation in transverce direction.
Adapted from DebRoy T, et al. Additive manufacturing of metallic components—process, structure and properties. Progr Mater Sci 2018;92:112–224.

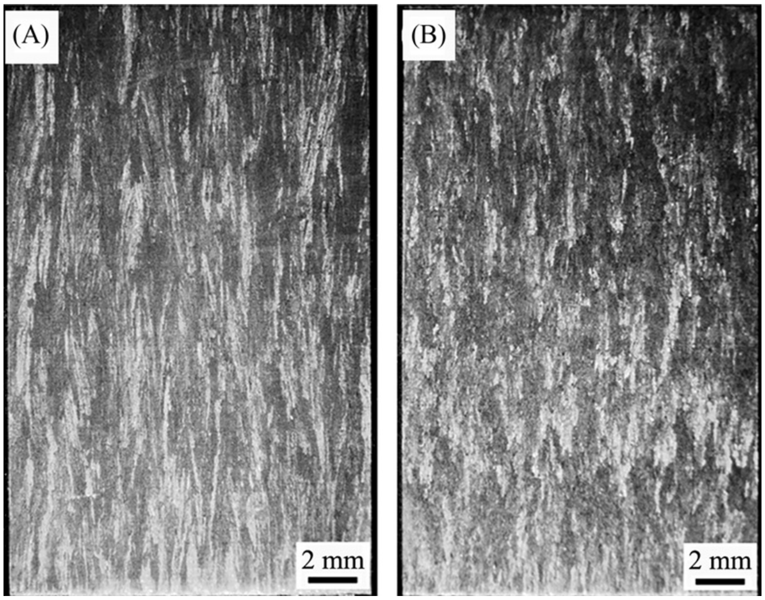

FIG. 13.13 Optical microscope images of (A) *x*-oriented part and (B) *y*-oriented part showing prior-ß grain structure. The *y*-oriented part has a smaller prior-ß grain size.

for EBM Ti-6Al-4V. Fig. 13.13 illustrates images of (A) *x*-oriented part and (B) *y*-oriented part showing prior-ß grain structure. The *y*-oriented part has a smaller prior-ß grain size.

In the study [92], a metal 3D printer based on DED-L, which can fabricate relatively large-sized components up to ~1 m, was developed. The process was optimized for fabricating Ti-6Al-4V parts. For this, various samples were fabricated by changing the laser power from 600 to 800 W, the feeding rate from 9.6 to 12.0 g/min, and the scan speed from 240 to 360 mm/min. In addition to the powder feeding flow of 4 L/min, the argon shielding gas was ejected at 20 L/min to protect the molten pool. The oxygen content was maintained at <3000 ppm throughout the experiment. The spot size of the laser beam was fixed at 1.9 mm. A spherical prealloyed Ti-6Al-4V powder grade 23 with diameter under 150 μm ($\delta_{10} = 49$ μm, $\delta_{50} = 83$ μm and $\delta_{90} = 139$ μm) was employed in this work. The mechanical properties of longitudinal specimens were achieved: the yield strength (YS) 950 ± 2 MPa, ultimate tensile strength (UTS) 1025 ± 10 MPa, and elongation 12 ± 1%. The specimens possess columnar microstructures with small-sized grains (Fig. 13.14).

The study [93] the dependence of tensile mechanical properties and the microstructure of AM Ti-6Al-4V parts fabricated by PBF-L on orientation, distance from the build platform, annealing time, and temperature results in conclusion that the tensile properties are greater in the conditions when porosity is lower. At great length, with 0.15% average porosity in the material, the differences between the mechanical properties of the parts fabricated from different locations and distances from the build platform are mainly related to the porosity, with variations in the microstructures being of secondary importance. The porosity of samples in the middle of the build plate (0.25 vol%) was more than twice as high as that in samples on the edge of the build plate (0.09 vol%). Additionally, it was found that nonspherical lack-of-fusion pores, which often contain partially melted particles, were more detrimental to the mechanical properties in the as-built, transverse direction than in the longitudinal direction because the long axis of these pores is oriented in the longitudinal direction. As a result, vertical, or transverse samples, had 28% lower elongation than horizontal, or longitudinal, samples.

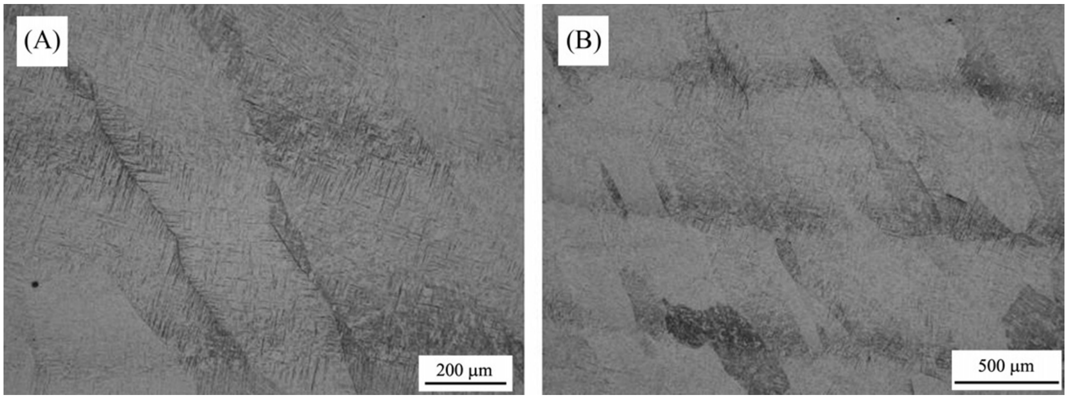

FIG. 13.14 Microstructures of the 3D printed sample made of Ti-6Al-4V: (A) lamella structure and (B) columnar structure.

TABLE 13.5 Mechanical Properties of As-Deposited Ti-6Al-4V Parts Fabricated by AM Compared to Cast and Annealed Ti-6Al-4V

AM System	*P* (W)	*v* (mm/s)	H (J/mm)	Orient.	*E* (GPa)	YS(MPa)	UTS(MPa)	El (%)	HV	Ref.
Powder bed fusion–laser heat source										
Realizer PBF-L	200	1000	0.20	Long. Transv.		1220 1200	1150 1300	6 6 ± 1		[91]
Renishaw AM250	157	225	0.70	Long. Transv.	115 ± 6 119 ± 7	978 ± 5 967 ± 10	1143 ± 6 1117 ± 3	11.8 ± 0.5 8.9 ± 0.4		[94]
Powder bed fusion–electron beam heat source										
Arcam A1	50–3500	3000	0.70	Long.		783 ± 15	833 ± 22	2.7 ± 0.4		[95]
				Transv.		812 ± 12	851 ± 19	3.6 ± 0.9		
Arcam A2	7000	1000	7.0	Long.		890 ± 5	970	12 ± 1.2		[96]
				Transv.		880 ± 10	950 ± 5	14 ± 1.2		
Arcam S12				Long.		982.9 ± 5.7	1029.7 ± 7.0	12.2 ± 0.8	372.0 ± 7.2	[93]
				Transv.		9841 ± 8.5	1032.9 ± 12.9	9.0 ± 0.26	367.6 ± 8.3	
Arcam A2				Long.		1006	1066	15		[97]
				Transv.		1001	1073	11		
Arcam Q10				Long. Transv.		973 1051	1032 1116	15 12		[97]
Directed energy deposition–powder feedstock										
Custom-built	2000	10.6	189	Long Transv.	115 ± 5 113 ± 5	961 ± 40 916 ± 34	1072 ± 33 1032 ± 31	17 ± 4 19 ± 4		[8]
Custom-built	800	6.0		Long. Transv.		1038 1011	1113 1086	7.3 11.3		[92]
Directed energy deposition–wire feedstock										
Custom-built	3500			Long. Transv.		960 ± 70 860 ± 10	1060 ± 70 935 ± 15	4 ± 0.8 9.6 ± 1.2		[96]
Custom-built	2625	7.5	350	Long. Transv.		818 ± 30 792 ± 15	895 ± 40 870 ± 20	4 ± 1 11 ± 3.5	355 ± 28	[98]
Custom-built	2192.3	10	438	Long. Transv.		880 ± 30 860 ± 10	965 ± 15 935 ± 20	8 ± 2 17 ± 3.5	341 ± 15	[98]
EOS[a] DMLS	170	1250	0.14	Long. Transv.		1099 1162	1186 1260	8.47 8.07		[99]
Traditionally fabricated										
Cast – typical						896	1000	8	200	[100]
Annealed – typical						855	930	12	202	[101]

[a] *EOS DMLS System–Tool-less AM Company.*

P is the laser power; v is the scanning speed; H is the linear heat input; ρ is the density; E is the elastic modulus; YS is the yield strength; UTS is the ultimate tensile strength; HV is the Vickers hardness; El is the elongation; Long. is the orientation in longitudinal direction; Transv. is the orientation in transverse direction.

Adapted from DebRoy T, et al. Additive manufacturing of metallic components—process, structure and properties. Progr Mater Sci 2018;92:112–224.

Mechanical properties of as-deposited Ti-6Al-4V parts fabricated by AM compared to cast and annealed Ti-6Al-4V are presented in Table 13.5.

Nickel Base Alloys

Ni-base alloys, including Inconel 625, Inconel 718, and Invar 36, and Ni-base superalloys Inconel 718 and Inconel 625, are employed in the AM technique. These alloys are widely used, primarily in turbine engines for aircraft and power generation due to their high strengths at elevated temperatures. The different types of AM processes, including PBF-L, PBF-EB, DED-L, and DED-PA, are applied.

Observations of EBM and SLM fabrication of Ni-base and Co-base superalloys have demonstrated the development of columnar precipitates formed within the micron-sized melt pools along with textured, columnar grains in the fcc matrix [102,103]. In these studies, EBM fabrication involved connected melt pools measuring 2–3 μm while SLM fabrication involved melt pool dimensions ~1 μm. EBM scanning differs from SLM scanning in fundamental ways, which include the energy absorption and deposition within the additively formed powder bed layers, beam focus, and scan spacing as well as powder bed preheat scanning and multiple or remelt scanning. These thermokinetic phenomena can influence precipitate or other phase development and transformation in complex ways, which differ notably from more conventional thermoprocessing. Strondl et al. [104] observed γ''-Ni_3Nb (bct) precipitate columns in alloy 718 fabricated by EBM while Amato et al. [105] observed similar precipitate columns formed in alloy 718 fabricated by SLM.

Inconel 625 cylinders were manufactured by electron beam melting (EBM) and selective laser melting (SLM) and compared [105]. EBM cylinders were built in the *Z*-axis direction (parallel to the build direction), and SLM cylinders were built in the XY-axis (perpendicular to build direction) and Z-axis directions. The authors reported that EBM-fabricated components contained columnar plates of γ'' (Ni3Nb) precipitates while SLM components contained columnar arrays of fine γ'' nanoparticles. The EBM-fabricated and HIPed samples and SLM-fabricated and HIPed samples exhibited equiaxed grains, but both components contained complex arrays of dissimilar precipitates. Both the Vickers microindentation hardness (HV) and Rockwell C-scale hardness (HRC) increased significantly on comparing Z-axis component fabrication by EBM versus SLM. Correspondingly, there is a significant increase on comparing SLM Z-axis fabrication with XY-axis fabrication: HV 3.4 GPa versus 4.2 GPa. In contrast to EBM Z-axis fabrication, SLM Z-axis fabrication increases even more notably: HV 2.7 GPa to 4.2 GPa. Microstructures and precipitation features developed during HIPing of the EBM and SLM-fabricated alloy 625 were examined along with the resulting mechanical properties to characterize the associated and comparative microstructures and microstructural architectures represented by columnar precipitate arrays.

The metallurgy of selected metal and alloy components fabricated by additive metallurgy using EBM is presented for a range of examples, including Ni-base super alloy systems of Inconel 625, 718, and Rene 142, and niobium [106]. Precursor and prealloyed powders are preheated and selectively melted using a range of EBM process parameters, including beam scan strategies, beam current variations, and cooling rate features. Microstructures and residual mechanical properties are discussed for selected systems in contrast to more conventional wrought and cast products.

Shishkovsky, et al. [107] synthesized the functionally graded system composed of the nickel-chrome superalloy matrix reinforced by NiTi intermetallic phases by the DED process. Amdy 625 and Ti 2 powders produced by TLS Technik GmbH were used. The Amdy 625 had the following composition, in wt%: 21.5Cr-2.5Fe-9.0Mo-3.7(Nd + Ta)-Ni balance. The particle size distribution was the following (by volume): $\delta_{10} = 42.6\,\mu m$, $\delta_{50} = 66.4\,\mu m$ and $\delta_{90} = 94.85\,\mu m$. Powders Amdy 625 and TiGd2 were mixed in ratio 1:1 and 1:3 during direct metal deposition by Trumpf DMD505. The experiments were carried out on a Trumpf DMD505 industrial-scale laser DMD machine. The beam spot diameter increased linearly from 3.6–5 mm as the laser power varies from 2 to 5 kW. The powder is applied to the workpiece via the nozzle with a stream of Ar and He gas mixtures (9:1).

Microhardness testing results for 3D functionally graded cladded samples are shown as a whole. NiCr + Ti = 1:1 has higher microhardness on a 550–600 $HV_{0.1}$ level, than the liable to cracks 1:3 system about 500–550 $HV_{0,1}$, accordingly.

The authors concluded that the NiCr superalloy enriched by titanium is a suitable material for relatively low temperature of approximately 1448 K joining or repairing of turbine blades because it contains the same components as typical turbine blades and vanes without foreign elements to lower the melting point of the repaired material or adversely affect the mechanical properties of the repaired component. It was shown that under the 3D layerwise laser cladding in the NiCr-Ti system, the formation of the $Ti_{50}Ni_{50\text{-}x}Cr_x$ intermetallides was observed.

Invar 36 (Fe-36 wt% Ni alloy) is well known for its low coefficient of thermal expansion (CTE) below its Curie temperature (503 K) and excellent mechanical properties in a cryogenic environment [108,109]. Due to these features, it has been widely used as highly reliable and high-precision materials in components where high dimensional stability is

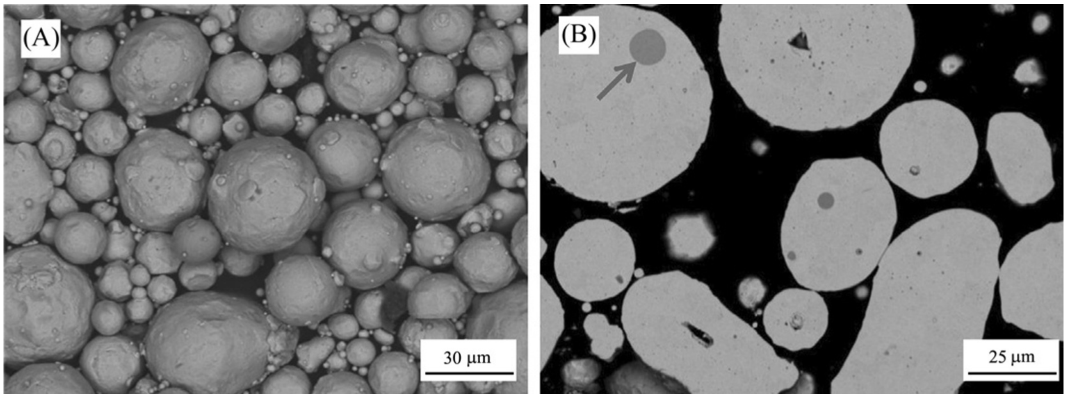

FIG. 13.15 Morphology and powder particle size distribution (A), cross section of as-received Invar 36 powder particles (B).

required. The applications include space equipment, precision instruments, clocks, seismic creep gauges, television shadow-mask frames, valves in motors, liquefied natural gas storage tanks, and antimagnetic watches.

Invar 36 samples were fabricated by selective laser melting [110]. The material used in this study was gas-atomized Invar 36 powder supplied by TLS Technik in the size range of 25–50 μm. A Concept Laser M2 Cusing SLM system that employs an Nd:YAG laser with a wave length of 1075 nm, a maximum laser output power of 400 W, and a maximum laser scanning speed of 4300 mm/s was used to prepare 10 × 10 × 10 mm cubes and 70 × 10 × 10 mm blocks for characterization to understand the influence of laser scanning speed and sample size on porosity development. The samples were fabricated at a constant laser power of 400 W but with different laser scanning speeds ranging from 1800 mm/s up to 4300 mm/s. Fig. 13.15A shows the morphology and powder particle size distribution while Fig. 13.15B illustrates the cross-section of the as-received Invar 36 powder. The powder section reveals the presence of pores within a few particles, probably due to gas entrapment during atomization.

Dependence on the porosity of the as-SLMed small cubic samples and elongated blocks on the laser scanning speed at a fixed laser power (400 W) shows (Fig. 13.16) that the porosity levels in the both the cubic and elongated block samples are generally low when the laser scanning speeds are below 3200 mm/s (<0.5% in area fraction). However, above 3200 mm/s, the samples show a pronounced increase in porosity (0.7–1.8%). However, at 3200 mm/s, the elongated sample was found to show much higher porosity (0.75%) than its small cubic counterpart (0.25%).

Increased scanning speed also led to increasingly irregular-shaped laser scanned tracks together with an increased number of pores on sample surfaces and keyhole features within the samples, all indicative of increasingly unstable melt flow behavior. Heat treatment did not change the microstructure significantly while HIPing closed the majority of pores but also caused a pronounced coarsening of α precipitates, especially those located at grain boundaries during subsequent slow cooling. With the presence of elongated pores, the vertically built samples were found to show much lower elongation than horizontally built samples while in the absence of pores, their ductility has been significantly improved but their tensile strengths are still lower than the latter.

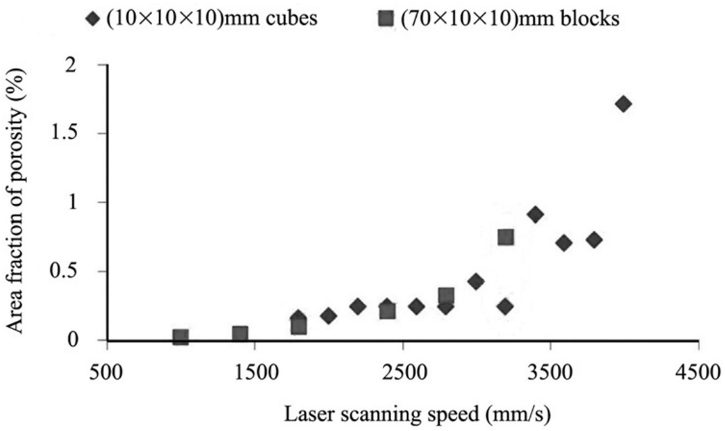

FIG. 13.16 Dependence of the porosity of the as-selective laser melted small cubic samples and elongated blocks on the laser scanning speed at a fixed laser power (400 W). *Modified from Qiu CL, Adkins NJE, Attallah MM. Selective laser melting of Invar 36: microstructure and properties. Acta Mater 2016;103:382–95.*

TABLE 13.6 Mechanical Properties of Ni-Base Alloys Fabricated by AM Compared to Traditionally Processed Counterparts

Alloy	P (W)	v (mm/s)	H (J/mm)	Post treatment	Orient.	E (GPa)	YS (MPa)	UTS (MPa)	El (%)	HV	Ref
Powder bed fusion–laser heat source											
Invar 36	400	1800–4300	0.22	As-built	Long.		400	535	14		[110]
					Transv.		340	455	30		
				HT	Long.		311	447	32		
Inconel 625	200	800–1200	0.25	HIP	Long Transv.		380 360	900 880	58 58	347 296	[111]
Inconel 625	50	130	0.38	As-built.	Long. Transv.	202.24 ± 4.12 140.66 ± 8.67	800 ± 20 1070 ± 60	1030 ± 50 720 ± 30	8–10 8–10		[112]
Haynes 230	200	450–1200	0.44	As-built	Long. Transv.	205 ± 4 152 ± 1	798 ± 5 656 ± 4	1102 ± 6 941 ± 2	28 ± 1 32 ± 3		[113]
Powder bed fusion–electron beam heat source											
Inconel 625	1800	10,000	0.18	As-built HIP	Transv. Transv.		410 330	750 770	44 69	224	[111]
Directed energy deposition–powder feedstock											
Inconel 718				As-built HT	Long. Long.		650 1257	1000 1436	38%[a] 13%[a]		[114]
				HT + HIP	Long.		1155	1380	20.4%[a]		
Inconel 718	2350	8	294	As-built HT	Long. Long.		590 1133	845 1240	11 9		[30]
Directed energy deposition–wire feedstock											
Inconel 625		5		As-built	Long. Transv.	180		722 ± 50 684 ± 23	42.27 ± 2.4 40.13 ± 3.7		[115]
Inconel 718		5		As-built	Long. Long.	154 ± 1 163	473 ± 6 666	828 ± 8 1022	28 ± 2 26.1		[116] [117]
				HT	Long.	24.1	947	1242	23.5		
Traditional technique											
Inconel 718	Cast–typical Hardened						483–552 759–828	759–862 862–931	6–10 3–5	170[b] 435	[118]
Inconel 625	Cast–typical Annealed–typical						310–380 430	587–655 940	25–30 51.5	266[b] 145[c]	[120 – 122]
Invar 36	CastVtypical AnnealedVtypical						265 260	483 470	44 37	131	[119]

[a] *Reduction in area.*
[b] *Max.*
[c] *Min.*
P is the laser power; v is the scanning speed; H is the linear heat input; ρ is the density; E *is* the elastic modulus; YS is the yield strength; UTS is the ultimate tensile strength; HV is the Vickers hardness; El is the elongation; Long. is the orientation in longitudinal direction; Transv. is the orientation in transverce direction.

The mechanical properties of Ni-base alloys fabricated by AM compared to traditionally processed counterparts are considered in Table 13.6.

CONCLUSION

AM processes are now increasingly used in the aerospace, automotive, and medical industries because of many unique attributes, particularly for producing value-added components that could not be made easily by conventional processing. The growing volume of sales of commercial AM equipment indicates a deeper market penetration in the future. There are several factors acting together for this growth. These include the continuing improvements of computational hardware and software, more affordable equipment such as lasers, improvements in automation, and the valuable knowledge base of both metallurgy and fusion welding. However, several scientific and technological issues now affect AM product quality and cost, including the prevalence of defects in parts such as porosity, the lack of fusion voids, poor surface finish, distortion, and residual stresses.

Whereas mechanical properties of parts produced by AM are in many cases comparable with their conventionally processed counterparts, properties can vary with process parameters as well as locally within a part. Controlling mechanical properties of parts will require greater understanding of both the AM process and the evolution of the microstructure under complex thermal cycles. Furthermore, greater market penetration of AM will require an increased level of standardization and control to attain repeatable processes to produce parts with consistent properties.

In powder bed-based AM, the choice of powder is crucial for the performance and cost of the built parts for a number of reasons. The chemical composition and the presence of impurities in the powder translate into the final material and its properties. The particle size distribution and morphology determine the powder flowability and packing density. These quantities control the powder processability that includes the feeding behavior, density, uniformity, and roughness of the raked layer as well as the necessary process parameters to achieve dense parts. Ultimately, mechanical properties, surface quality, and productivity are influenced by the powder quality.

In general, these powders require high apparent densities to achieve maximum density when deposited in packed beds. In addition, the flow of the powders is critical when these powders are dispensed from equipment that builds the prototype part. For the finer SLM powders, the Hall flowmeter might not be the most suitable characterization method. Alternative tests such as rheological measurements in a ring shear cell or measurement of the avalanche angle in a revolution powder analyzer deserve attention [36].

Depending on a variety of factors such as type of process, machine make, material, and part geometry, the cost of powder ranks among the top three expenses in AM today [120,121]. Powder prices are expected to fall once alternatives to the powders supplied by the machine manufacturers are established and the economies of bulk production are realized.

Presently, extensive activity in powder metrology and standardization is ongoing. The focus is to characterize the powders supplied by the SLM and EBM equipment manufacturers in order to extract the quantities necessary for a custom powder specification. Custom powders mast be examined with regard to their suitability for the SLM and EBM processes as well as changes to their properties after multiple reuse cycles. Mainly, subtle changes in the powder properties after multiple reuse cycles occur. Because these “aging” effects depend on many factors such as machine type, build geometry, and processing specifics, they may not be readily applicable to every powder bed-based AM process and need to be checked individually.

Many unique technical capabilities such as tool-less, design-driven, and onsite manufacturing of customized parts as well as building highly complex components in one step soon after conceptualization provide unprecedented business advantages for AM. As a result, there has been a growing recognition of its importance in the engineering and research communities as well as governmental funding agencies.

REFERENCES

[1] Chua CK, Leond KF. 3D Printing and additive manufacturing. 4th ed. Singapore: World Scientific Publishing Co; 2014.
[2] Hegab HA. Design for additive manufacturing of composite materials and potential alloys: a review. Manufacturing Rev 2016;3(11):1–17.
[3] Dutta B, Froes FH. The additive manufacturing (AM) of titanium alloys. Metal Powder Report 2017;72(2):96–106.
[4] U.S. Patent 9718129 B2, Aug 1, 2017.
[5] DebRoy T, et al. Additive manufacturing of metallic components—process, structure and properties. Progr Mater Sci 2018;92:112–224.
[6] Standard terminology for additive manufacturing technologies. ASTM Int 2013; F2792–12a.
[7] Imran MK, et al. Direct metal deposition (DMD) of H13 tool steel on copper alloy substrate: evolution of mechanical properties. Mater Sci Eng A 2011;528(9):3342–9.

[8] Keist JS, Palmer TA. Role of geometry on properties of additively manufactured Ti-6Al-4V structures fabricated using laser based directed energy deposition. Mater Des 2016;106:482–94.
[9] Ma MM, Wang ZM, Zeng XY. Effect of energy input on microstructural evolution of direct laser fabrication IN718 alloy. Mater Charact 2015;106:420–7.
[10] Shah K, Pinkerton AJ, Salman A, Li I. Effects of melt pool variables and process parameters in laser direct metal deposition of aerospace alloys. Mater Manuf Process 2010;25(12):1372–80.
[11] Wang T, Zhu YY, Zhang SQ, Tang HB, Wang HM. Grain morphology evolution of titanium alloy components during laser melting deposition additive manufacturing. J Alloy Comp 2015;632:505–13.
[12] Ding DH, Pan ZX, Cuiuri D, Li HJ. Wire-feed additive manufacturing of metal components: technologies, developments and future interests. Int J Adv Manuf Technol 2015;81(1–4):465–81.
[13] Williams SW, et al. Wire plus arc additive manufacturing. Mater Sci Tech 2016;32(7):641–7.
[14] Xiong J, Lei YY, Chen H, Zhang GJ. Fabrication of inclined thin-walled parts in multi-layer single-pass GMAW-based additive manufacturing with flat position deposition. J Mater Process Technol 2017;240:397–403.
[15] Dehoff RR, Babu SS. Characterization of interfacial microstructures in 3003 aluminum alloy blocks fabricated by ultrasonic additive manufacturing. Acta Mater 2010;58(13):4305–15.
[16] Ram CDJ, Robinson C, Yang Y, Stucker BE. Use of ultrasonic consolidation for fabrication of multi-material structures. Rapid Prototyp J 2007;13 (4):226–35.
[17] Levy GN, Schindel R, Kruth JP. Rapid manufacturing and rapid tooling with layer manufacturing (LM) technologies, state of the art and future perspectives. CIRP Ann Manuf Technol 2003;52:589–609.
[18] Yi S, Liu F, Zhang J, Xiong S. Study of the key technologies of LOM for functional metal parts. J Mater Process Technol 2004;150:175–81.
[19] Thomas H, Anja T, Steffen N, Eckhard B. Recent developments in metal laminated tooling by multiple laser processing. Rapid Prototyping J 2003;9:24–9.
[20] Xu B, et al. Research on micro-electric resistance slip welding of copper electrode during the fabrication of 3D metal micro-mold. J Mater Process Technol 2013;213:2174–83.
[21] Mower TM, Long MJ. Mechanical behavior of additive manufactured, powder-bed laser-fused materials. Mater Sci Mater A 2016;651:198–213.
[22] Schade CT, Murphy TF, Walton C. Development of atomized powders for additive manufacturing. In: Proceedings of 2014 World Congress of PM & Particulate Mater. Orlando (USA): Metal Powder Ind Fed; 2014. p. 02-15-25.
[23] Riza SH, Masood SH, Wen CE, Ruan D, Xu SQ. Dynamic behaviour of high strength steel parts developed through laser assisted direct metal deposition. Mater Des 2014;64:650–9.
[24] Sames WJ, List FA, Pannala S, Dehoff RR, Babu SS. The metallurgy and processing science of metal additive manufacturing. Int Mater Rev 2016;61(5):315–60. https://doi.org/10.1080/09506608.2015.1116649.
[25] Baufeld B, Brandl E, van der Biest O. Wire based additive layer manufacturing: Comparison of microstructure and mechanical properties of Ti-6Al-4V components fabricated by laser-beam deposition and shaped metal deposition. J Mater Process Technol 2011;211(6):1146–58.
[26] Brandl E, Schoberth A, Leyens C. Morphology, microstructure, and hardness of titanium (Ti-6Al-4V) blocks deposited by wire-feed additive layer manufacturing (ALM). Mater Sci Eng A 2012;532:295–307.
[27] Jamshidinia M, Sadek A, Wang W, Kelly S. Additive manufacturing of steel alloys using laser powder-bed fusion. Adv Mater Process 2015;173 (1):20–4.
[28] Khairallah SA, Anderson AT, Rubenchik A, King WE. Laser powder-bed fusion additive manufacturing: physics of complex melt flow and formation mechanisms of pores, spatter, and denudation zones. Acta Mater 2016;108:36–45.
[29] Karlsson J, Snis A, Engqvist H, Lausmaa J. Characterization and comparison of materials produced by Electron beam melting (EBM) of two different Ti-6Al-4V powder fractions. J Mater Process Technol 2013;213(12):2109–18.
[30] Zhao XM, Chen J, Lin X, Huang WD. Study on microstructure and mechanical properties of laser rapid forming Inconel 718. Mater Sci Eng A 2008;478(1–2):119–24.
[31] Slotwinski JA, Garboczi EJ, Stutzman PE, Ferraris CF, Watson SS, Peltz MA. Characterization of metal powders used for additive manufacturing. J Res Natl Inst Stan 2014;119:460–93.
[32] Van Elsen M. Complexity of selective laser melting: a new optimisation approach. Heverlee: Katholieke Universiteit Leuven; 2007.
[33] Prashanth KG, et al. Microstructure and mechanical properties of Al-12Si produced by selective laser melting: effect of heat treatment. Mater Sci Eng A 2014;590:153–60.
[34] Cai Z, Wang R, Peng C, Zhang C. Effect of particle size on microstructure and cold compaction of gas-atomized hypereutectic Al-Si alloy powder. Metall Mater Trans 2015;46:824–30.
[35] Kempen K, et al., Process optimization and microstructural analysis for selective laser melting of $AlSi_{10}Mg$, 2011. <ps://sffsymposium.engr.utexas.edu/Manuscripts/2011/2011-37-Kempen.pdf> [accessed Aug. 2018].
[36] Spierings AB, Voegtlin M, Bauer T, Wegener K. Powder flowability characterization methodology for powder-bed-based metal additive manufacturing. Progr Addit Manuf 2015;1–12.
[37] Louvis E, Fox P, Sutcliffe CJ. Selective laser melting of aluminium components. J Mater Process Technol 2011;211:275–84.
[38] Gu DD, Meiners W, Wissenbach K, Poprawe R. Laser additive manufacturing of metallic components: materials, processes and mechanisms. Int Mater Rev 2013;57:133–64.

[39] Aboulkhair NT, Maskery I, Tuck C, Ashcroft I, Everitt NM. On the formation of $AlSi_{10}Mg$ single tracks and layers in selective laser melting: microstructure and nanomechanical properties. J Mater Proc Technol 2016;230:88–98.
[40] Olakanmi EO, Dolgano KW, Cochrane R. Laser sintering of blended Al-Si powders. Rapid Prototyp J 2012;18:109–19.
[41] Schulze D. Pulver und schüttgüter: fließeigenschaften und handhabung. Berlin: Springer Vieweg; 2016.
[42] Hebert RJ. Viewpoint: Metallurgical aspects of powder bed metal additive manufacturing. J Mater Sci 2016;51:1165–75.
[43] Weingarten C, Buchbinder D, Pirch N, et al. Formation and reduction of hydrogen porosity during selective laser melting of $AlSi_{10}Mg$. J Mater Process Technol 2015;221:112–20.
[44] Zhang B, Li Y, Bai Q. Defect formation mechanisms in selective laser melting: a review. Chin J Mech Eng 2017;30:515–27.
[45] Krajnikov AV, Gastel M, Ortner HM, Likutin VV. Surface chemistry of water atomized aluminium alloy powders. Appl Surf Sci 2002;191:26–42.
[46] ASTM International. ASTM D6773–08, Standard shear test method for bulk solids using the schulze ring shear tester. West Conshohocken, PA: ASTM International; 2008.
[47] Schulze D. Flow properties of powders and bulk solids. <http://www.dietmar-schulze.com/grdle1.pdf.> [Accessed 12.1.2018].
[48] Schulze D. Flow properties of powders for equipment designs. 2015. <http://Flow_properties_of_powders_for_equipment_design_Copenhagen_Dietmar_Schulze_14012015%20(3).pdf> [accessed Aug 2018].
[49] International Standardization Organization. ISO 4490: 2014—Metallic powders—Determination of flow rate by means of a calibrated funnel (Hall flowmeter). ISO; 2014.
[50] ASTM_International. ASTM B213–13: standard test methods for flow rate of metal powders using the hall flowmeter funnel. ASTM_International, West Conshohocken, PA; 2013.
[51] ASTM_International. ASTM F3049–14: Standard guide for characterizing properties of metal powders used for additive manufacturing processes. ASTM_International, West Conshohocken, PA; 2014.
[52] Hausner HH. Powder characteristics and their effect on powder processing. Powder Technol 1981;30(1):3–8. https://doi.org/10.1016/0032-5910(81)85021-8.
[53] ASTM_International (2009) ASTM D7481–09, standard test methods for determining loose and tapped bulk densities of powders using a graduated cylinder. ASTM_International, West Conshohocken, PA.
[54] Rastogi S, et al. Survey of characterization techniques of dry ultrafine coals and their relationships to transport, handling and storage. Powder Technol 1993;74(1):47–59. https://doi.org/10.1016/0032-5910(93)80007-W.
[55] Miyajima T, Yamamoto K-I, Sugimoto M. Effect of particle shape on packing properties during tapping. Adv Powder Technol 2001;12(1):117–34. https://doi.org/10.1163/156855201745001.
[56] Abdullah EC, Geldart D. The use of bulk density measurements as flowability indicators. Powder Technol 1999 1999;102(2):151–65.
[57] Soh JLP, Liew CV, Heng PWS. New indices to characterize powder flow based on their avalanching behavior. Pharm Dev Technol 2006; 11(1):93–102. https://doi.org/10.1080/10837450500464123.
[58] Allen M, Brown GJ, Miles NJ. Measurement of boundary fractal dimensions: review of current techniques. Powder Technol 1995;84(1):1–14. https://doi.org/10.1016/0032-5910(94)02967-S.
[59] Kirchner A, Klöden B, Weißgärber T, Kieback B. Powders for additive manufacturing. In: Compiled by European Powder Metallurgy Association, (Bellstone Shrewsbury, UK) Proceedings of PM 2016 World Congress. Hamburg (Germany); 2016: p. 1–5.
[60] Dietrich S, Wunderer M, Huissel A, Zaeh MF. A new approach for a flexible powder production for additive manufacturing. Proc Manuf 2016;6:88–95.
[61] ASM Handbook Volume 5A—Thermal spray technology: ASM International. https://www.youtube.com/watch?v=kH3jJ1tpCDg; 2013.
[62] Boronenkov V, Korobov Y. Fundamentals of arc spraying. Cham: Springer International Publishing; 2016. https://doi.org/10.1007/978-3-319-22306-3_1.
[63] Dunkley JJ, Telford B. Control of "satellite" particles in gas atomization. In: Proceedings of World Congress of PM and Particulate Materials. 3: Princeton (NJ): Publ. Metal Powder Ind. Fed; 2002. p. 103–10.
[64] Bauer D, et al. Investigations on aging behaviour of aluminum powders during a lifetime simulation for the LBM Process. In: Compiled by European Powder Metallurgy Association, (Bellstone Shrewsbury, UK) Proceedings of PM 2016 World Congress. Hamburg (Germany); 2016: p. 1–6.
[65] Tang M, Pistorius PC, Narra S, Beuth JL. Rapid solidification: Selective laser melting of AlSi10Mg. JOM 2016;68(3):1–7. https://doi.org/10.1007/s11837-015-1763-3.
[66] Aversa A, et al. Microstructural and mechanical properties of Al-Si-Ni alloy produced by direct metal laser sintering. In: Compiled by European Powder Metallurgy Association, (Bellstone Shrewsbury, UK) Proceedings of PM 2016 World Congress. Hamburg (Germany); 2016: p. 1–6.
[67] Tandon R, et al. Additive manufacturing of magnesium alloy Powders: investigations into process development using Elektron®MAP+43 via laser powder bed fusion and directed energy deposition. In: Compiled by European Powder Metallurgy Association, (Bellstone Shrewsbury, UK) Proceedings of PM 2016 World Congress. Hamburg (Germany); 2016: p. 1–6.
[68] Rosenthal I, et al. Additive manufacturing by selective laser melting (AM-SLM) of thin-walled AlSi10Mg containers: structural characterization and electron beam welding (EBM). In: Compiled by European Powder Metallurgy Association, (Bellstone Shrewsbury, UK) Proceedings of PM 2016 World Congress. Hamburg (Germany); 2016: p. 1–6.
[69] Vrana R, Koutny D, Palousek D, Zikmund T. Influence of selective laser melting process parameters on impact resistance of lattice structure made from AlSi10Mg. In: Compiled by European Powder Metallurgy Association, (Bellstone Shrewsbury, UK) Proceedings of PM 2016 World Congress. Hamburg (Germany); 2016: p. 1–6.

[70] Buchbinder D. Generative fertigung von aluminiumbauteilen für die serienproduktion. In: AluGenerativ Abschlussbericht BMBF 01RIO639A-D. 2010.
[71] Material data sheet: EOS aluminium AlSi10Mg for EOSINT M 270. EOS; http://gpiprototype.com/images/PDF/EOS_Aluminium_AlSi10Mg_en.pdf. [browsed January 2018].
[72] Kempen K, Thijs L, Van Humbeeck J, Kruth J-P. Mechanical properties of AlSi10Mg produced by selective laser melting. Phys Proc 2012;39:439–46.
[73] Kempen K, Thijs L, Van Humbeeck J, Kruth J-P. Processing AlSi10Mg by selective laser melting: Parameter optimization and material characterization. Mater Sci Tech 2015;31(8):917–23.
[74] Manfredi D, Calignano F, Ambrosio EP, Krishnan M, Canali R, Biamino S, et al. Direct metal laser sintering: an additive manufacturing technology ready to produce lightweight structural parts for robotic applications. Metall Ital 2013;10:15–24.
[75] Manfredi D, Calignano F, Krishnan M, Canali R, Ambrosio EP, Atzeni E. From powders to dense metal parts: characterization of a commercial AlSiMg alloy processed through direct metal laser sintering. Materials 2013;6(3):856–69.
[76] Rosenthal I, Stern A, Frage N. Strain rate sensitivity and fracture mechanism of AlSi10Mg parts produced by selective laser melting. Mater Sci Eng A 2017;682:509–17.
[77] Siddique S, Imran M, Wycisk E, Emmelmann C, Walther F. Influence of process-induced microstructure and imperfections on mechanical properties of AlSi12 processed by selective laser melting. J Mater Process Technol 2015;221:205–13.
[78] Siddique S, Wycisk E, Frieling G, Emmelmann C, Walther F. Microstructural and mechanical properties of selective laser melted Al 4047. Appl Mech Mater 2015;753–754:485–90.
[79] Schmidtke K, Palm F, Hawkins A, Emmelmann C. Process and mechanical properties: Applicability of a scandium modified Al-alloy for laser additive manufacturing. Phys Proc 2011;12:369–74.
[80] Zhang H, Zhu HH, Qi T, Hu ZH, Zeng XY. Selective laser melting of high strength Al-Cu-Mg alloys: processing, microstructure and mechanical properties. Mater Sci Eng A 2016;656:47–54.
[81] Gu J, Cong B, Ding J, Williams SW, Zhai Y. Wire+arc additive manufacturing of aluminium. In: Solid freeform fabrication proceedings. 2014. p. 451–8.
[82] Lumley R. Technical data sheets for heat treated aluminium high pressure die castings. CSIRO Light Metals Flagship, 2008.
[83] Aluminum A413. Die casting alloy, DYNACAST. https://www.dynacast.com/a413>. browsed January 2018.
[84] Thijs L, Kempen K, Kruth JP, Van Humbeeck J. Fine-structured aluminium products with controllable texture by selective laser melting of pre-alloyed AlSi10Mg powder. Acta Mater 2013;61(5):1809–19.
[85] Tang M, Pistorius PC. Oxides, porosity and fatigue performance of AlSi10Mg parts produced by selective laser melting. Int J Fatigue 2017;94:192–201.
[86] Read N, Wang W, Essa K, Attallah MM. Selective laser melting of AlSi10Mg alloy: Process optimization and mechanical properties development. Mater Des 2015;65:417–24.
[87] Aboulkhair NT, Everitt NM, Ashcroft I, Tuck C. Reducing porosity in AlSi10Mg parts processed by selective laser melting. Addit Manuf 2014;1:77–86.
[88] Ng CC, Savalani MM, Lau ML, Man HC. Microstructure and mechanical properties of selective laser melted magnesium. Appl Surf Sci 2011; 257(17):7447–54.
[89] Zhang BC, Liao HL, Coddet C. Effects of processing parameters on properties of selective laser melting Mg-9%Al powder mixture. Mater Des 2012;34:753–8.
[90] Zhao XL, Li SJ, Zhang M, Liu YD, Sercombe TB, Wang SG, et al. Comparison of the microstructures and mechanical properties of Ti-6Al-4V fabricated by selective laser melting and electron beam melting. Mater Des 2016;95:21–31.
[91] Hrabe N, Quinn T. Effects of processing on microstructure and mechanical properties of a titanium alloy (Ti-6Al-4V) fabricated using electron beam melting (EBM), part 2: Energy input, orientation, and location. Mater Sci Eng A 2013;573:271–7.
[92] Jeong W, Kang M-G, Kim D, Kwon Y-S. Development of a metal 3D printer using laser powder deposition and process optimization for fabricating titanium alloy parts. In: Compiled by European Powder Metallurgy Association, (Bellstone Shrewsbury, UK) Proceedings of PM 2016 world congress. Hamburg (Germany); 2016: p. 1–6.
[93] Galarraga H, Lados DA, Dehoff RR, Kirka MM, Nandwana P. Effects of the microstructure and porosity on properties of Ti-6Al-4V ELI alloy fabricated by electron beam melting (EBM). Addit Manuf 2016;10:47–57.
[94] Simonelli M, Tse YY, Tuck C. Effect of the build orientation on the mechanical properties and fracture modes of SLM Ti–6Al–4V. Mater Sci Eng A 2014;616:1–11.
[95] Edwards P, O'Conner A, Ramulu M. Electron beam additive manufacturing of titanium components: properties and performance. J Manuf Sci Eng 2013;135(6).
[96] Brandl E, Leyens C, Palm F. Mechanical properties of additive manufactured Ti-6Al-4V using wire and powder based processes. In: IOP conference series: materials science and engineering. 2011. 012004.
[97] Zhai YW, Galarraga H, Lados DA. Microstructure evolution, tensile properties, and fatigue damage mechanisms in Ti-6Al-4V alloys fabricated by two additive manufacturing techniques. Proc Eng 2015;114:658–66.
[98] Brandl E, Baufeld B, Leyens C, Gault R. Additive manufactured Ti-6Al-4V using welding wire: Comparison of laser and arc beam deposition and evaluation with respect to aerospace material specifications. Phys Proc 2010;5:595–606.

[99] Palanivel S, Dutt AK, Faierson EJ, Mishra RS. Spatially dependent properties in a laser additive manufactured Ti-6Al-4V component. Mater Sci Eng A 2016;654:39–52.
[100] Donachie MJ. Titanium: a technical guide. 2nd ed. ASM international; 2000. https://books.google.lu/books?id=HgzukknbNGAC>.
[101] SSd R, Adabo GL, Henriques GEP, Nóbilo MAA. Vickers hardness of cast commercially pure titanium and Ti-6Al-4V alloy submitted to heat treatments. Braz Dent J 2006;17(2):126–9.
[102] Gaytan SM, et al. Comparison of microstructures and mechanical properties for solid and mesh cobalt-base alloy prototypes fabricated by electron beam melting. Metall Mater Trans 2010;41A:3310–27.
[103] Murr LE, et al. Fabrication of metal and alloy components by additive manufacturing: examples of 3D materials science. J Mater Res Tech 2012; 1(1):42–54.
[104] Strondl A, Fischer R. Investigations of MX and γ'/γ'' precipitates in the nickel-based superalloy 718 produced by electron beam melting. Mater Sci Eng 2008;480A:138–47.
[105] Amato KN, et al. Microstructures and mechanical behavior of Inconel 718 fabricated by selective laser melting. Acta Mater 2012;60(5):2229–39.
[106] Murr LE. Metallurgy of additive manufacturing: examples from electron beam melting. Addit Manuf January 2015;2015(5):40–53.
[107] Shishkovsky I, Kakovkina N, Jacquier M. Direct metal deposition of functional graded structures in NiCr-Ti system. In: Compiled by European Powder Metallurgy Association, (Shrewsbury, UK) Proceedings of PM 2017 Euro Congress. Milan (Italy); 2016: p. 1–6.
[108] Zhao Y, Wu AP, Yao W, Wang ZM, Sato YS. Microstructure and mechanical properties of Nd:YAG laser welded Invar 36 alloy. Mater Sci Forum 2011;675–677:739–42.
[109] Park WS, Chun MS, Han MS, Kim MH, Lee JM. Comparative study on mechanical behavior of low temperature application materials for ships and offshore structures: Part I—Experimental investigations. Mater Sci Eng A 2011;528:5790–803.
[110] Qiu CL, Adkins NJE, Attallah MM. Selective laser melting of Invar 36: microstructure and properties. Acta Mater 2016;103:382–95.
[111] Amato K, et al. Comparison of microstructures and properties for a Ni-base superalloy (alloy 625) fabricated by electron beam melting. J Mater Sci Res 2012;1(2):3–41.
[112] Yadroitsev I, Thivillon L, Bertrand P, Smurov I. Strategy of manufacturing components with designed internal structure by selective laser melting of metallic powder. Appl Surf Sci 2007;254(4):980–3.
[113] Bauer T, Dawson K, Spierings A, Wegener K. Microstructure and mechanical characterization of SLM processed Haynes 230. In: Solid freeform symposium; 2015.
[114] Blackwell PL. The mechanical and microstructural characteristics of laser-deposited IN718. J Mater Process Technol 2005;170(1–2):240–6.
[115] Wang JF, Sun QJ, Wang H, Liu JP, Feng JC. Effect of location on microstructure and mechanical properties of additive layer manufactured Inconel 625 using gas tungsten arc welding. Mater Sci Eng A 2016;676:395–405.
[116] Baufeld B. Mechanical properties of Inconel 718 parts manufactured by shaped metal deposition (SMD). J Mater Eng Perform 2012;21(7):1416–21.
[117] Bird RK, Hibberd J. Tensile properties and microstructure of Inconel 718 fabricated with electron beam freeform fabrication (EBF3). VA, USA: Hampton; 2009.
[118] Materials-alloys poured. American Casting Company; 2017.
[119] Frantz EL. Nonferrous alloys and special purpose materials. ASM International; 1990.
[120] Kianian B. Wohlers Report 2017: 3D Printing and additive manufacturing state of the industry, Annual Worldwide Progress Report: Chapters titles: The Middle East, and other countries. Fort Collins (CO, USA): Wohlers Associates; 2017.
[121] Baumers M, et al. The cost of additive manufacturing: machine productivity, economies of scale and technology-push. Technol Forecast Social Change 2016;102:193–201.

FURTHER READING

[122] Sames WJ, Medin F, Peter WH, Babu SS, Dehoff RR. Effect of process control and powder quality on Inconel 718 produced using electron beam melting. In: 8th International Symposium on Superalloy 718 and Derivatives. Pittsburgh (PA, USA); 2014. p. 409–23.
[123] Nickel-based super alloy Inconel 625-properties and applications by united performance alloys. AZO Materials; 2017. <https://www.azom.com/article.aspx?ArticleID=446>1.
[124] Donachie MJ. Superalloys-source book. Metals Park (OH): American Society for Metals; 2017. http://www.waterstonesmarketplace.com/Superalloys-Source-Book-Matthew-J-Donachie/book/6462141>.

Chapter 14

Processing of Powders and Processing Equipment

Oleg D. Neikov
Frantsevich Institute for Problems of Materials Science (IPMS), Kiev, Ukraine

Chapter Outline

Introduction 403
Dehydration 403
  Thickening in Cyclones 405
  Conical and Cylindrical Thickeners 407
  Filtration 408
  Centrifugation 410
  Cartridge Vacuum Filter 411
  Rotary Disk Filter 412
  Filter Press 413
Thermal Drying 413
  Introductory Conceptions 413
  Drying Characteristic Curve 414
  Drying Rate 415
  Dryer Selection and Design 415
  Pneumatic Convective Dryer 416
  Spray Drying 419
  Convective Dryer With Fluidized Bed 421
  Shaker Dryer 422
  Drum Contact Dryer 423
  Vacuum Dryers 424
Powder Classification by Size 424
  Sieving Methods 426
  Sieving Apparatus 428
  Round Vibrating Sifters 429
  Air-assisted Sieving Machine 431
  Air Separation 432
  Hydraulic Classification 433
Mixing 435
  Powder Mixers 436
  Mechanism of Powder Mixing 440
Passivation Techniques 442
  Passivation Methods 444
Powder Spheroidization by Thermal Plasma Processes 446
Proportioning, Packaging, and Interstage Transport 449
  Proportioning 449
  Packaging 451
  Interstage Transport 452
References 454
Further Reading 455

INTRODUCTION

The precursor powder processing generally involves the following processes before consolidation:

- Dehydration and drying to fixing the required moisture content limit.
- Powder classification by particle size.
- Preparation of the mixtures of elemental powders with master alloys, prealloys, or hybrid alloys.
- Powder spheroidization.
- Powder passivation.
- Proportioning.

These processes along with passivation methods, microcupsulation, interstage transport facilities, and powder packaging are considered in this chapter.

DEHYDRATION

In the production of nonferrous metal and alloy powders, the technological processes and procedures effected in an aqueous environment, either aqueous acidic or alkaline solutions (atomization and granulation of melts, methods of obtaining

Handbook of Non-Ferrous Metal Powders. https://doi.org/10.1016/B978-0-08-100543-9.00014-2
© 2019 Elsevier Ltd. All rights reserved.

powders from solutions, and electrochemical methods) are popularized. Residual moisture content in the powders is usually at the most 0.1 wt.%.

The moisture content (or humidity content) w^0 is the ratio of moisture mass in a product W to the mass of the absolute dry product G_d

$$w^0 = \frac{W}{G_\mathrm{d}} 100\% \tag{14.1}$$

A moisture concept w is also used because usually not all moisture is taken away:

$$w = \frac{W}{G_\mathrm{d} + W} = \frac{w^0}{1 + w^0}$$

When the moisture content is small $w^0 \ll 1$, a value of $1 + w^0 \approx 1$ and the values w and w^0 practically do not differ.

There can be distinguish the overall moisture content w^0, the moisture content of air-dry material w^a, and the surface moisture content w^s, determined by the difference:

$$w^\mathrm{s} = w^0 - w^\mathrm{a}$$

and, consequently,

$$w^0 = \mathrm{w}^\mathrm{a} + w^\mathrm{s}$$

Depending on the physicochemical mechanisms of material bonds with water, the free, capillary, adsorption, and chemical moisture bonds are distinguished. The free (gravitational) moisture fills the spaces between the particles and can move relative to the solid particles under the action of gravity. The capillary moisture is in particle pores, cracks, and spaces between fine particles, kept by capillary forces arising on the boundaries of solid, liquid, and gaseous phases. The capillary moisture volume depends on the porosity of the material.

The adsorption moisture, in the form of a hydrated film, is kept on the surface of particles by adsorption forces. The adsorption moisture in turn is subdivided into hygroscopic and adhesion moisture. The hygroscopic moisture is condensed on the solid surface in the form of a film represented by water molecule layers retained by adsorption forces. The adsorption moisture is represented by water molecules layers, located above the hygroscopic moisture and bound less fast to the surface of solid particles because this bond is determined by the second orientation of the water molecules and hydration by adsorbed ions. Chemically bounded moisture is differentiated in constitutional (OH^-, H^+, H_2O^+) and crystallization (contained in crystallohydrate) forms.

Depending on the amount and form of the moisture, there are various dehydration methods. According to the water content, the powders are classified as water-bearing, wet, moist, air-dry, and dry. The water-bearing powders are a mechanical mixture of solid with water and possessing liquid mobility (as pulps and suspensions). The water-atomized melts, products of electrolysis, chemical precipitation, discharges by wet milling, overflows, spills, and the like are in this category. The moisture of these products is characterized by the ratio of solid to liquid (S:L) in mass units.

The quantities that characterize the pulp or suspension are connected by the following correlations. The volumes of solid V_1 and liquid V_2 phases in kg of pulp are:

$$V_1 = S/\rho_1; V_2 = 1 - S/\rho_1$$

where ρ_1 is the density of solid, kg/m^3 and S is a mass content of the solid in pulp per 1 m^3.

The solid volume-part concentration:

$$c_{1_\mathrm{v}} = \frac{1}{1 + n}$$

where n is the volume ratio, L_V to S_V.

Then the solid mass concentration in the pulp or suspension is

$$c_{1_\mathrm{m}} = c_{1_\mathrm{V}} \rho_1$$

where ρ_1 is the mass density of the solid, kg/m^3.

Such water-bearing powders are usually dehydrated in thickeners, settling basins, and sumps; previously, they were thickened in hydrocyclones.

Wet powders include gravitational moisture partially, capillary and adsorptive moisture.

Moist powders do not contain gravitational moisture, but include adsorptive moisture and some capillary moisture.

TABLE 14.1 Dehydration Methods

Method name	Apparatus	Initial Product	*L:S*, Volume Ratio	
		Method Essence	Initial	Final
Inertial precipitation	Hydrocyclones	Pulp Inertia precipitation	10–12	2–4
Gravity sedimentation	Cylindrical and other thickeners	Pulp Gravity sedimentation	10–12	2–4
Centrifugation	Filtrate centrifuges	Pulp; thickened product Separation under action of centrifugal forces	0.5–12	6%–15%[a]
	Precipitated centrifuges	Pulp Separation under action of centrifugal forces	5–15	5%–10%[a]
Filtration of slurries	Plate filters, cartridge filters	Pulp Filtration through porous partitions under pressure	5–15	20%–30%[a]
Filtration of thickened products	Vacuum filters, cartridge filters	Thickened product Filtration through porous partitions under vacuum	2–4	8%–15%[a]
Thermal drying[b]	Drum dryers, pneumatic conveying dryers, vibrating dryers, vacuum dryers, fluidized bed dryers	Moist product	8%–15%	up to 0.1%[a]

[a] *Aqua content in mas.%.*
[b] *heat-mass exchange by thermal drying: convection and conduction (drum dryers); convection (pneumatic conveying dryers and fluidized bed dryers); convention, conduction, and radiation (vibrating dryers); conduction (vacuum dryers).*

The air-dry products are the dusts entrapped in dry cyclones and filters from dust-laden aspiration gases. They contain only hydroscopic moisture. Dry powders are obtained by means of moisture evaporation from wet powders during thermal drying.

The basic dehydration methods of powders are listed in Table 14.1. Commonly, the powders are dehydrated in three stages with first, their thickening, followed by moisture receding from the thickened product by mechanical methods and drying. The dehydration of sludge (waste of technological processes) is done in two or three stages. Ordinarily, the thickened product from the settling tank is dehydrated on a filter press. The overflow is subjected sequentially to purification in cartridge and sand filters.

Thickening in Cyclones

The hydrocyclones of cast and welded design lined by cast ceramic or rubber for wear prevention of the walls are shown in Figs. 14.1 and 14.2.

The necessary pulp pressure on entry into the hydrocyclone ranges from 0.03 to 0.25 MPa and is applied by a sand pump. If the desired capacity is not accomplished by one hydrocyclone, battery cyclones are used in which hydrocyclones are turned in parallel operation.

A calculation of hydrocyclones includes the definition of the diameter D_c and throughput Q_c on pulp at a given maximal size of solid particles δ_{max} in overflow, and pressure at entry in cyclone:

$$D_c = 0.121 \times 10^{-2} \left(\frac{D_f}{D_{ov}}\right)^2 \delta_{max}^2 (\rho_1 - \rho_2)\sqrt{p_{en}}, \quad \text{m}, \tag{14.2}$$

$$Q_c = 0.94 D_f D_{ov} \sqrt{H}, \quad \text{m}^3/\text{s} \tag{14.3}$$

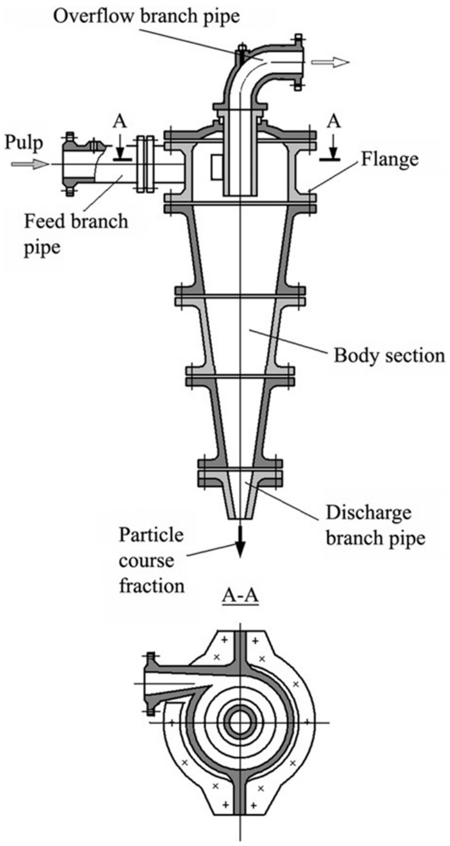
Overflow branch pipe
A
A
Pulp
Flange
Feed branch pipe
Body section
Discharge branch pipe
Particle course fraction
A-A

FIG. 14.1 Hydrocyclone of cast design lined with cast ceramic or rubber.

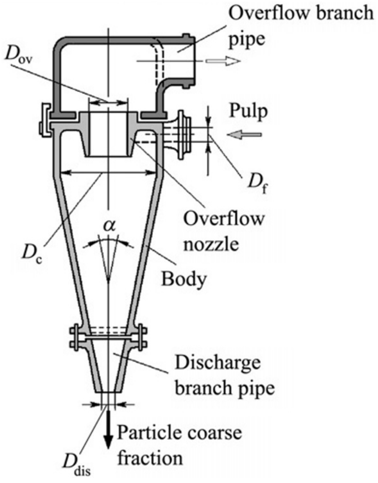
Overflow branch pipe
D_{ov}
Pulp
D_f
Overflow nozzle
α
D_c
Body
Discharge branch pipe
Particle coarse fraction
D_{dis}

FIG. 14.2 Hydrocyclone of welded design.

where D_f (see Figs. 14.1 and 14.2) is the diameter of the feed branch pipe, m; D_{ov} is the diameter of the overflow branch pipe, m; p_{en} is the pressure at entry to the cyclone, MPa; D_{dis} is the diameter of the discharge hole, m; δ_{max} is the maximum size of solid particles in overflow, mm; ρ_1, ρ_2 are the mass densities of solid and liquid, respectively, kg/m^3; and H is the water pressure at the entry to the cyclone, mm column of water.

Sequence calculation:

- The diameter of the hydrocyclone D_c is defined according to Eq. (14.2) by the ratio D_{dis}/D_{ov} values in ranges from 0.3 to 0.6 and is chosen to the nearest lesser diameter of a standard hydrocyclone (Table 14.2).
- The throughput of the hydrocyclone is defined according to Eq. (14.3).
- The check on unit load at the discharge opening, accepted in ranges from 0.5 to 2.0 t/h per 1 cm^2 of discharge opening cross-sectional area.
- The required number of hydrocyclones on a given pulp yield subjected to thickening is defined.

Detailed calculation of hydrocyclones (determination of their sizes, throughput, particle sizes in overflow, and their contents in the initial slurry and overflow) can be found in Ref [1]. Table 14.2 includes the main parameters of the standard series of hydrocyclones up to 360 mm in diameter.

Conical and Cylindrical Thickeners

A typical scheme of thickener is shown in Fig. 14.3. In such an apparatus, an initial pulp is fed via the vertical pipe into the thickener. The solid phase is deposited in the conical section, the clarified water rises and is discharged into the annular chute. The thickened product is discharged continuously through orifices or by means of periodical action valves.

The capacity G (t/h) of conical thickeners is calculated from following equation:

$$G = \frac{1.76 w D_{con}^2}{\left[n_{st} - \nu n_f + (1-\nu)\rho_1^{-1}\right]}$$

TABLE 14.2 Hydrocyclone Characteristics[a, b]

Parameter	Unit	Standard (in RUS classification)					
		HC-25	HC-50	HC-75	HC-150	HC-250	HC-360
Diameter D_c	mm	25	50	75	150	250	360
Cone angle α_{con}	degrees	10	10	10	10	10	10
Equivalent diameter of feed aperture $D_f^{(a)}$	mm	6	12	17; 32	40	65	90
Diameter of overflow branch pipe D_{ov}	mm	7	13	22	40; 50	80	115
Diameter of the discharge opening D_{dis}	mm	4; 6; 8	6; 8; 12	8; 12; 17	12;17; 24; 34	24; 34; 48; 75	35; 48; 75; 96
Pressure at entry in cyclone p_{en}	MPa	0.01–0.2	0.01–0.2	0.01–0.2	0.03–0.25	0.03–0.25	0.03–0.25
Throughput per feed with solid content up to 40% by pressure 0.1 MPa $Q^{(b)}$	m^3/h	0.7	2.5	5	15; 20	50	95
Maximal size of solid particles in overflow δ_{max}	µm	10	10	10–60	28–95	37–135	44–180
Overall dimensions, max							
Length	mm	120	230	300	500	600	700
Breadth	mm	70	100	350	450	650	750
Height	mm	200	400	600	1100	1400	1900
Mass	kg	2	6	20	100	220	400

(a) $D_f = \sqrt{\frac{4bh}{\pi}}$, where b and h are sizes of feed aperture (mm).

(b) *If pressure* p_{en} *differs from 0.1 MPa, the throughput is corrected by multiplication on* $\sqrt{10p_{en}}$.

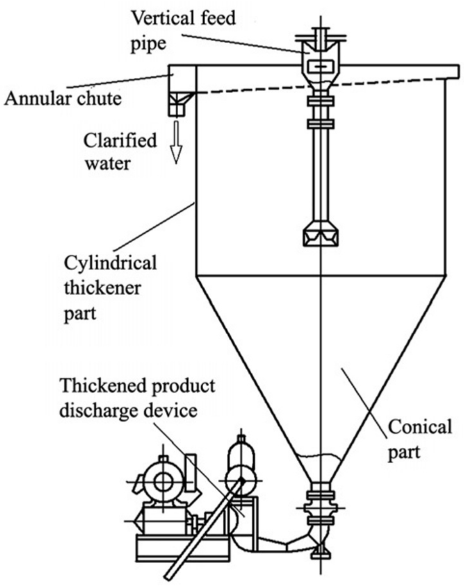
Vertical feed pipe
Annular chute
Clarified water
Cylindrical thickener part
Thickened product discharge device
Conical part

FIG. 14.3 Cylindrical thickener.

where w is the sedimentation rate of the boundary size particles, mm/s; D_{con} is the cone diameter, m; n_{st} and n_{f} are the dilution (L:S) in initial and thickened material; v is the solid in thickened material yield, part of one; and ρ_1 is the mass density of solid, t/m^3.

By calculation of cylindrical thickeners, the sedimentation surface is defined, starting from the initial pulp yield (G, t/h), (L:S) rates in initial pulp (n_{st}), and thickened product (n_{f}), subject to gravity sedimentation of boundary size particles w, m/h. Then the thickener specific surface is equal to

$$\bar{f} = \frac{n_{\text{st}} - n_{\text{f}}}{k w \rho_{\text{ov}}}$$

where k is the thickener surface use coefficient, usually $k = 0.75$ and ρ_{ov} the overflow mass density, t/m^3.

The total sedimentation surface

$$F_s = \bar{f}\,G$$

then the thickener diameter

$$D_{\text{cyl}} = \sqrt{1.27 f \bar{G} + D_{\text{feed}}^2}$$

where D_{feed} is diameter of feeding pipe, m.

Filtration

Filtration is a process for separation of solids from the slurry by means of a porous medium that retains the solids and allows the liquid to pass. The operations are divided into two broad categories: "cake" and "depth" filtration. From the viewpoint of a driving force, cake filtration is moreover divided into pressure, vacuum, gravity, and centrifugal operations. In cake filtration, particles contained in the slurry are retained in an incipient layer on the porous medium surface while the fluid passes through it. In depth filtration, particles are captured within complex pore structures of the filter medium and the cake is not formed on the medium surface. The first particles can enter the medium and, with very dilute slurries, there can be a time lag before a cake begins to form. Smaller particles enter the medium whereas larger particles bridge the openings and start the buildup of a surface layer. Depth filtration is generally used to remove small quantities of fine particles. In practice, cake filtration is mainly employed in industry.

The equation of flow through porous media is based on Darcy's law that can be expressed in the form

$$\frac{dp_{\text{L}}}{dx} = \frac{\mu}{K_{\text{p}}} u \tag{14.4}$$

where dp_L/dx is the hydraulic pressure gradient; μ is the viscosity of the liquid; K_p is the permeability; and u is the apparent liquid velocity relative to the solids. This velocity is expressed as the volumetric flow rate per unit area, which is defined by

$$u = q - \frac{\theta}{1-\theta} r = q - er$$

where q is the apparent flow rate of liquid; θ is the local porosity; r is the apparent migration rate of solid particles; and e is the local void ratio. In filtration, it is usual to use the volume v of dry solids per unit area instead of the distance x from the medium surface. Hence, the incremental volume dv is given as

$$dv = (1-\theta)\,dx \tag{14.5}$$

Substituting Eq. (14.5) into Eq. (14.4) gives

$$\frac{dp_L}{dv} = \frac{\mu u}{K_p(1-\theta)} \tag{14.6}$$

While suspended solids are deposited during cake filtration, liquid flows through the interstices of the cake in the direction of decreasing hydraulic pressure (Fig. 14.4). The solids forming the cake are compact and relatively dry at the filter medium whereas the surface layer is in a slurry and wet condition. So the porosity is minimum at the point of contact between the cake and the filter medium when $v = 0$ and maximum at the cake surface ($v = v_0$) where the liquid enters.

On the assumption that the inertial forces are negligible, the force balance can be written

$$p_L + p_s = 0 \tag{14.7}$$

where p_s is the local cake compressive pressure. Eq. (14.7) and Fig. 14.4 show that the cake compressive pressure increases as the hydraulic pressure decreases.

It is basically assumed in compressible cake filtration theory that the local porosity and flow resistance are unique functions of the cake compressive pressure. The flow resistance α is related to the porosity ε as in Eq. (14.8):

$$\alpha = \frac{kS_0^2(1-\varepsilon)}{p_s\varepsilon^3} \tag{14.8}$$

where k is Kozeny's constant and S_0 is the effective specific surface of the solids.

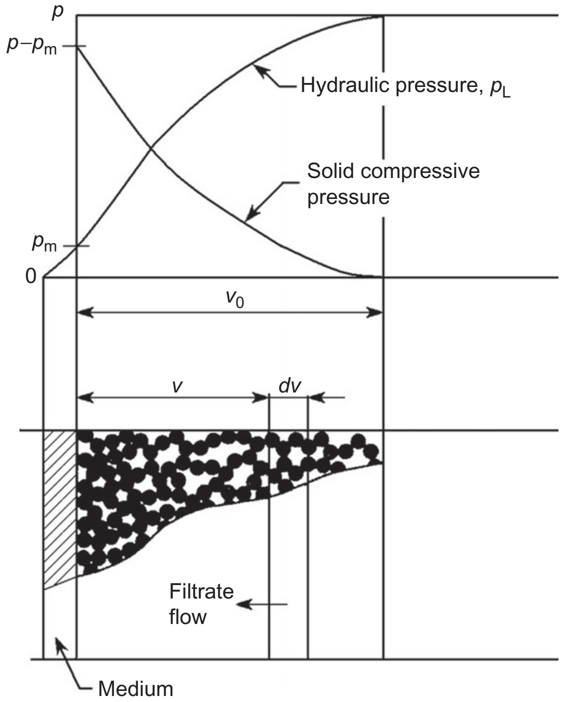

FIG. 14.4 Schematic diagram of compressible filter cake. *(Modified from Shirato M, Murase T, Iritani E. Filtration in the chemical process industry. In: Matteson MJ, Orr C, editors. Filtration, principles and practices. 2nd ed. New York: Marcel Dekker, Inc.; 1987. p. 299–423).*

Cake filtration processes are classified according to the variations of both the pressure and flow rate with time into the following kinds: (a) constant pressure filtration (by means of compressed gas maintained at a constant pressure, or a vacuum pump), (b) constant rate filtration (positive displacement pumps are employed), and (c) variable pressure and variable rate filtration (the use of a centrifugal pump results in the rate varying with the back pressure on the pump).

In practice, the original parameters for selection of the apparatus performance include specific loading per dry sediment, q_f, t/(m^2·h), filtration rate, u_f, m/h, and drag during filtration, Δp, kPa. The drag during slurry (pulp) filtering, Δp, comprises the drag of the filter cake and the filtering medium

$$\Delta p = p_\delta h + p_m, \text{kPa}$$

where p_δ is the average specific drag of the unit thickness of the filter cake layer, kPa/m; h is the thickness of the filter cake layer, m; and p_m is the drag of the material of the filtering medium, kPa.

The values of p_δ and p_{fm} are estimated experimentally on a laboratory filtering apparatus at the adjusted values of the filtration rate. The specific loadings, q_f, t/(m^2·h) of atomized powders of copper, lead, and zinc (and their alloys) are adopted as 0.1–0.2; 0.1–0.2; and 0.2–0.4, respectively.

A wide variety of filtration equipment is commercially available. The operating principles and important features of typical filtration equipment in nonferrous powder production conditions are described here.

Centrifugation

To dehydrate products in the metallic powder production industry, filtering centrifuges find a use. The centrifugal settling is accomplished in centrifuges that include bowls of cylindrical or conical form with screen walls that rotate at high speed around their own axes. The product to be dehydrated (pulp) is fed into the bowl, which involves the pulp rotational movement. The water present in the pulp is filtered under the action of centrifugal forces through the compressible filter cake settled upon the inner surface of the bowl wall and on the porous screen itself. The liquid phase passing through the screen is normally called the filtrate. Centrifuges with screen bowl walls are called filtering in contrast to settling centrifuges that have a solid wall.

Calculation of the centrifugal effect is restricted to the measurement of the rate of centrifugal filtering. At $Re < 1$, the rate of filtration, u_f is determined by Darcy's law:

$$u_f = k\rho_2 2\omega^2 (R - 0.5h)$$

where k is the coefficient of filtration determined either experimentally or using Kozeny's formula:

$$k = \frac{0.2\theta^2}{S_0^2(1-\theta)\mu}, \quad \text{m}^2/(\text{Pa}\cdot\text{s})$$

θ is the average porosity of the filter cake; S_0 is the volumetric specific surface of the solids, m^{-1}; μ is the viscosity of liquid, Pa·s (at 293 K the viscosity of water $\mu = 1.002$ mPa·s); ρ_2 is the density of liquid, kg/m^3; ω is the angular speed of rotation, c^{-1}; R is the radius of rotation circle, m; h is the thickness of filter cake layer in m; and Re is the Reynolds number, determined from the formula

$$\text{Re} = \frac{\rho_2 u_f d_p}{\mu}$$

where d_p is the diameter of the pore in the filter cake.

Calculated value, u_f, and area of filtration, F_f (of screened surface of centrifuge walls), are determined starting from the required yield of dehydrated product. The F_f, R, and u_f parameters are used for selecting the desired centrifuge type.

Powders of copper and its alloys are produced using filtering centrifuges with the following performance: rotary drum internal diameter 1200 mm; the greatest number of rpms is 980; the greatest separation factor 640; and shaft rotational speed 333–1000 rpm. As filtering material, a volumetric 300 mesh wire grid made from stainless steel as per CIS Standard GOST 3187-76 is used. Operating conditions are periodic, with a stopping interval for wet material feeding and manual removal of the filter cake from the walls. With the initial value of L:S = 10, residual moisture after dehydration ranges between 4% and 8%.

In an improved machine, removable filtering bags are used followed by unloading normally. In another model, the centrifugal machine includes a bottom-unloading scraper. The material enters the rotary drum from the top. Under centrifugal force, the liquid passes through the filtering medium and is discharged out of the machine and the solid is left in the rotary

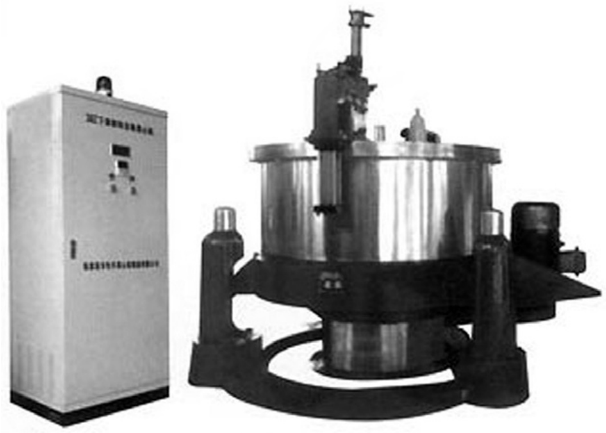

FIG. 14.5 LD/SD series settling hanging-bag centrifuge. *(From Info of Jiangsu Peony Centrifuge Manufacturing Co. in China (www.Mudancentrifuge.cn).)*

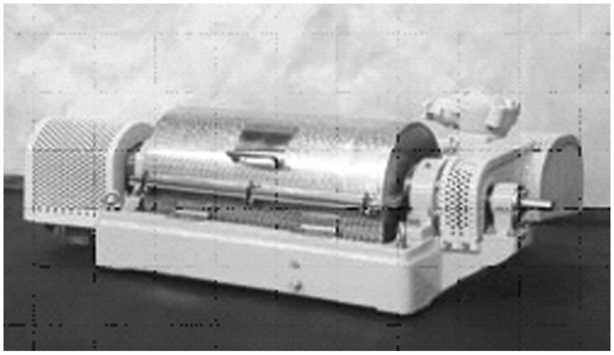

FIG. 14.6 OGSh series automatic and continuous operated, horizontal performance, and equipped by scraper scroll-type for continuous removal of the precipitate cake settling centrifuge. *(Courtesy of JSC Sumy Frunze NPO Company in Ukraine.)*

drum. When the rotary speed falls, the scraper scrapes the solid material, which is discharged from the bottom of the machine (Fig. 14.5).

A more upgraded filtering as well as settling centrifuge has automatic and continuous operation, equipped by a scraper scroll-type for continuous removal of the precipitated cake (Fig. 14.6). Such centrifuges have maximum rotational speed of 6000 rpm, separation factor up to 4000, and a ratio of basket operating length to internal diameter max 3:1.

Cartridge Vacuum Filter

Vacuum filters of the batch type designed by the Design Bureau of IPMS (Fig. 14.7) have filtering elements of cylindrical form made of sintered porous materials. The general filtering area of each filter element is 0.6 m^2. The filter elements are arranged horizontally in the lower portion of the receiving bin with a 30 mm gap relative to the bottom. One end of the cylindrical filter element is blanked off and the second end is connected to the manifold of the vacuum system via a branch pipe. The slurry or thickened product is charged into a receiving bin and the vacuum pump is switched on. With the removal of the moisture from the material, the powder layer is densified and retains the fine particles, decreasing the breakthrough of particles into the filtrate and protecting the filter elements against blinding. The sucked-off condensed moisture (filtrate) is collected by a drop catcher, trickles down into a container, and is then returned to the recycled water supply. The dehydration procedure takes 10–20 min, depending on the powder properties and water content. With the initial ratio L to S in ranges from 2 to 4 in the thickened pulp supplied to the receiving bin, the residual content of moisture will be 8–15 wt.%. When the residual moisture content reaches the required level, the vacuum pump is stopped; the receiving bin is tilted by a rotary device and the moist material discharged.

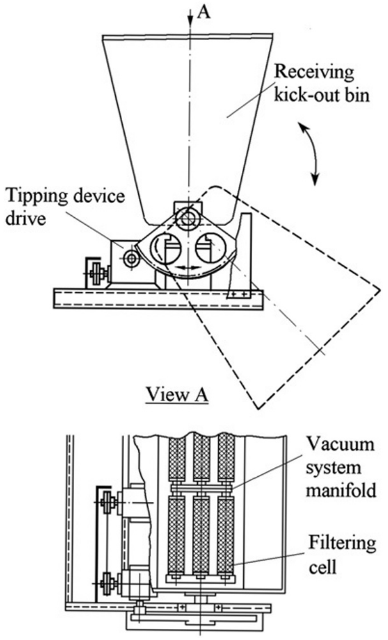
A
Receiving kick-out bin
Tipping device drive
View A
Vacuum system manifold
Filtering cell

FIG. 14.7 Cartridge vacuum filter.

Rotary Disk Filter

Disk vacuum filters (also called "rotary drum filters") are designed for filtering suspensions containing particles that settle mainly at a rate less than 18 mm/s. The process of filtering is continuous. The operation of this filter is schematically shown in Fig. 14.8. The slurry is supplied via a pipeline to a bath containing sunken disks in the form of hollow chambers (filter cells) with perforated surfaces wrapped with a filter material. The slurry excess is poured down into a chute to receive overflowed slurry. The filter cake is removed from the filter cell surface by scrapers. A distributor head is intended for leading away the filtrate and exhaust air and feeding air to blow the filter cake layer off. The filter is equipped with a variable speed gear that allows variation of the number of revolutions of the shaft between 10 and 80 revolutions per hour. When rotating, the disk passes the following zones per each rotation:

1. Formation of the filter cake and exhaust of the filtrate.
2. Drying the filter cake.
3. "Dead" zone.
4. Blowing the filter cake away.

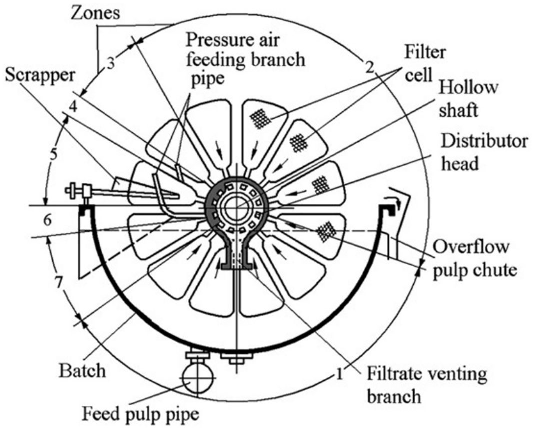
Zones
Pressure air feeding branch pipe
Filter cell
Hollow shaft
Distributor head
Scrapper
3
2
4
5
6
7
Overflow pulp chute
Batch
1
Filtrate venting branch
Feed pulp pipe

FIG. 14.8 Rotary disc filter.

5. Removing the filter cake.
6. Blowing through and cleaning the filter.
7. "Dead" zone.

Filter Press

The dehydration of poor-pressing suspensions, which may include fine slurries from sedimentation tanks, is performed using apparatus operating under pressure–filter presses. There are various designs of filter presses: chambers, plate-and-frame, sheets, and disks.

For dehydration of slurries accumulated in the settling tanks, a simple design plate-and-frame type filter press can be used, having manual or electromechanical drive of the clamping device (Fig. 14.9). The filter is composed of vertically arranged alternating plates and frames, which are connected and tightened by screw or hydraulic ram, formatting the chambers and making a gasket of the filter cloth.

The slurry feed is introduced into the chambers under a pressure of 0.5–1.0 MPa. The liquid passes through the filter medium, which, in turn, retains the solids. The filtrate is removed at a discharge outlet. Completion of the cake formation is controlled by the filtering time, the decrease in the rate of the feed, and on a rise in back pressure. Once the frames are full of cake, filtration is stopped and a wash liquid is applied if the solids are to be recovered. The yield per dehydration of slurries ranges from 7.5 to 15 kg/(m^2 h); residual moisture in the filter cake amounts to 19–25 wt.%.

In the other filter press design of sampling action filtering, it is composed of a series of horizontal filter plates that are lifted and sealed by the clutch and the filter cloth in the form of a continuous tape-extending zigzag between the filter plates that can eliminate the step of preliminary thickening of the pulp and automate the dehydration procedure. When discharging the filter cake, the filter cloth is relocated by the drive of the tape feed. The filter cake is discharged from two sides of the tape simultaneously. The cloth is washed in the regeneration chamber. The feeding pressure of the pulp is maximum 1.2 MPa. The suspension contains from 10 to 500 kg/m^3 of solid phase. Filtering conditions for filter presses are determined by an experiment for each type of suspension. The use of filter presse's for suspensions containing coarse particles is not recommended because of siltation of the inlet collecting manifold and the channels that feed the suspension.

THERMAL DRYING

Introductory Conceptions

Thermal drying is a process for the dehydration of moist products based on moisture evaporation by heating. The heat for evaporation is transferred to the material, which is dried, either by heated hot gas or smoke fumes–fuel combustion products (convective heat transfer), or from a hot surface by contact with the material. The heat may also be applied by radiation and high-frequency currents.

In drying techniques, the following forms of moisture in the material being dried are differentiated: free, absorbed, excess, and moisture equilibrium.

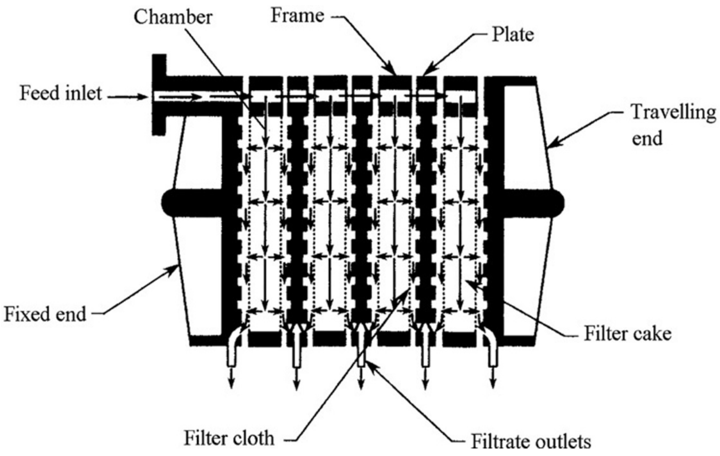

FIG. 14.9 Plate-and-frame type filter press.

The free moisture is the difference between total moisture and maximum adsorbed moisture. The adsorbed moisture (w_a) is the moisture adsorbed on the powder surface, which is dependent on the hygroscopic property of the material and the moisture content of the environment.

The excess moisture is the free and partly adsorbed moisture, which can be removed from the material by means of evaporation in dry conditions. The moisture equilibrium (w_{eq}) is the difference between the total and excess moisture.

Heated air, smoke fumes, or their mixture, with some volume of aqueous vapor called a drying agent, may be a medium receiving evaporable moisture from the material that is being dried.

In air drying, it is also necessary to avoid heating the powder to a temperature that will cause it to oxidize. The amount of water that can be received by the drying agent depends on the content of the water therein and on the gas temperature and pressure. The moist gas pressure may be represented as

$$p_h = p_{p-d} + p_{aq-v}$$

where $p_{p\text{-}d}$ and $p_{aq\text{-}v}$ are the partial pressure of dry gas (air) and water vapor, respectively.

A saturated gas is one that contains the maximum amount of moisture that it can hold at the given temperature and pressure.

There are used two types of (mean) water content: dry-basis water content (w) (kg water per kg dry material) and wet-basic water content (w^*) (kg water per kg wet material). The former is much more easy to use for calculation than the latter:

$$w = \frac{w^*}{1 - w^*}$$

$$w^* = \frac{w}{1 + w}$$

Drying Characteristic Curve

In the conditions when a wet nonhydroscopic particulate material is being held in a hot airstream of constant temperature, moisture, and velocity, the water content w and the material temperature t^m change with time drying, as shown in Fig. 14.10. The drying process after preheating consists of the following two periods: (I) constant drying rate period and (II) decreasing drying rate period.

During the preheating period, heat is transferred to the material on heating from an initial temperature t_1^m to wet-bulb temperature t_w with the moisture evaporation. This drying period is usually small in comparison with other drying periods. After preheating, there is a constant drying rate period (BC) when free water exists on the surface of the material and the material temperature t^m remains constant and is equal to the wet-bulb temperature of the hot air, t_w. This period continues until the water content becomes the critical value w_{cr}. During period II, there is no free water on the surface. As evaporation takes place from the surface and proceeds throughout the bulk by diffusion of vapor in the material, the drying rate decreases with time until, finally, drying ends at the equilibrium water content w_{eq}. Hot-air heat is consumed for heating up the material as well as for water evaporation and the temperature rises from t_w until it finally reaches the hot air temperature t_a.

The shapes of drying characteristic curves are individual for each solid material, but commonly changing average humidity content with time has the form represented in Fig. 14.10.

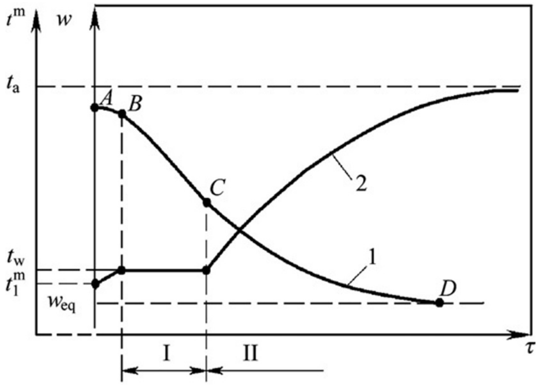

FIG. 14.10 Drying characteristic curve (1) and heating curve (2) of materials for two periods: (I), constant drying rate period and (II), decreasing drying rate period.

Drying Rate

During the constant drying rate period, the drying rate R is apparently equal to the evaporation rate of the free water surface:

$$R_c = \frac{G}{S}\frac{dw}{d\tau} = k(H_{\mathrm{m}} - H)$$

where G is the mass of dry material, kg; S is the drying area of material, m^2; w is the dry-basis water content (kg water/kg dry material); k is the film mass transfer coefficient, kg/(m^2·h); H is the moisture content (kg water/kg dry air); H_{m} is the moisture content of saturated air at t^{m} (kg water/kg dry air); and τ is the drying time, h.

When the heat is supplied from the hot air only, the material temperature t^{m} is equal to the wet-bulb temperature of the air t_{w}.

The decreasing drying rate R_{d} is strongly affected by the material properties and drying method. This drying rate can be estimated [2] by

$$R_d = \rho_{\mathrm{s}}\delta_{\mathrm{s}}r_{\mathrm{w}}\frac{dw}{d\tau}\left[1 + \left(\frac{c}{r_{\mathrm{w}}}\right)\frac{dt_{\mathrm{s}}}{d\tau}\right] \tag{14.9}$$

where ρ_{s} is the density of solid (kg/m^3); δ_{s} is the modified radius of particles (m); c is the specific heat of the material (kJ/(kg K)); and t_{s} is the temperature of particles.

Eq. (14.9) is a fundamental equation of drying kinetics but, to use it, it is necessary to know the water content dependence on drying time. It is possible to obtain this dependence by a solution of differential equations of system of heat and mass transfers, which is a very difficult task. Approximate answers to the equation simplify a problem. Thus, Lykov [3] proposes a different method, replacing the decreasing drying rate curve by a straight line, results in fluctuation the reduced critical moisture content, w_{cr} (point 'C' in diagram (Fig. 14.10)). Then, the decreasing drying rate period can be described as

$$-\frac{dw}{d\tau} = K\left(w - w_{\mathrm{eq}}\right) \tag{14.10}$$

where K is the proportionality coefficient, called the drying coefficient; w_{eq} is the reduced moisture content.

If the drying condition dependent part is only singled out, the drying coefficient may be represented by:

$$K = \kappa R_{\mathrm{c}}$$

where κ is the relative drying coefficient; R_{c} is the drying rate during the constant drying rate period (period BC in Fig. 14.10).

As it should be from Eq. (14.10), K is the slope ratio of the straight line, which is determined in the following way:

$$K = \frac{R_{\mathrm{c}}}{\left(w_{\mathrm{eq}} - w\right)} = \kappa R_{\mathrm{c}}$$

Integration of Eq. (14.10) gives

$$\frac{\left(w - w_{\mathrm{eq}}\right)}{\left(w_{cr} - w_{\mathrm{eq}}\right)} = \exp\left(-\kappa R_{\mathrm{c}}\tau\right)$$

Taking the logarithm of the last expression permits us to obtain the approximate equation of the drying rate curve

$$\lg\left(w - w_{\mathrm{eq}}\right) = \lg\left(w - w_{cr}\right) - \frac{1}{2.3\kappa R_{\mathrm{c}}\tau}$$

Knowing the drying coefficient, it is possible to define the decreasing drying time, and so for the relative drying coefficient determination in practical terms, simple dependence is used

$$\kappa = \frac{1.8}{w}$$

Dryer Selection and Design

Many types of dryers have been developed and operated. First, dryers should be selected based on the size and shape of the powder particles, water content, the production rate, and the mode of drying operation. Then, the properties of the material (e.g., chemical activity, behavior at elevated temperatures, and stickiness) are taken into consideration when the selection of dryer type is made. Finally, the volume of the dryer selected should be estimated.

For dryers receiving convective heat from hot air, the rate of heat transfer q is given approximately in batch operation by:

$$q = h_v V (t - t_m)$$

in continuous operation by

$$q = h_v V (t - t_m)_{lm}$$

For those of the conductive heating type,

$$q = U_k A_k V (t_k - t_m)$$

where h_v is the volumetric heat transfer coefficient, kJ/m^3·h·K); V is the volume of the dryer, m^3; t is the hot air temperature, K; t_m is the material temperature, K; $(t - t_m)_{lm}$ is the logarithmic mean of the temperature differences between the hot air and the material at the material inlet and outlet; U_k is the overall heat transfer coefficient, kJ/(h·K·m^2); A_k is the heating area of the material by conduction, m^2; and t_k is the temperature of the heat source, K.

Pneumatic Convective Dryer

In pneumatic convective dryers, the drying is accomplished during transport by heat-carrying gases as a consequence of convective heat transfer. The apparatus consists of an upright directed tube where drying takes place in an upward suspended solid current (Fig. 14.11). Such dryers are named “tube dryers.” Powder time in the drying zone amounts to several seconds. The upward suspended solid current velocity must be larger than the maximum size of the particle in the powder fractions subject to drying (usually in the range from 15 to 40 m/s).

A drying active regime is provided under the conditions of nonstationary interaction of phases along all drying conduits. Thus, there are rational reasons to design the tube dryers with a variable diameter (with widening), while the permanent

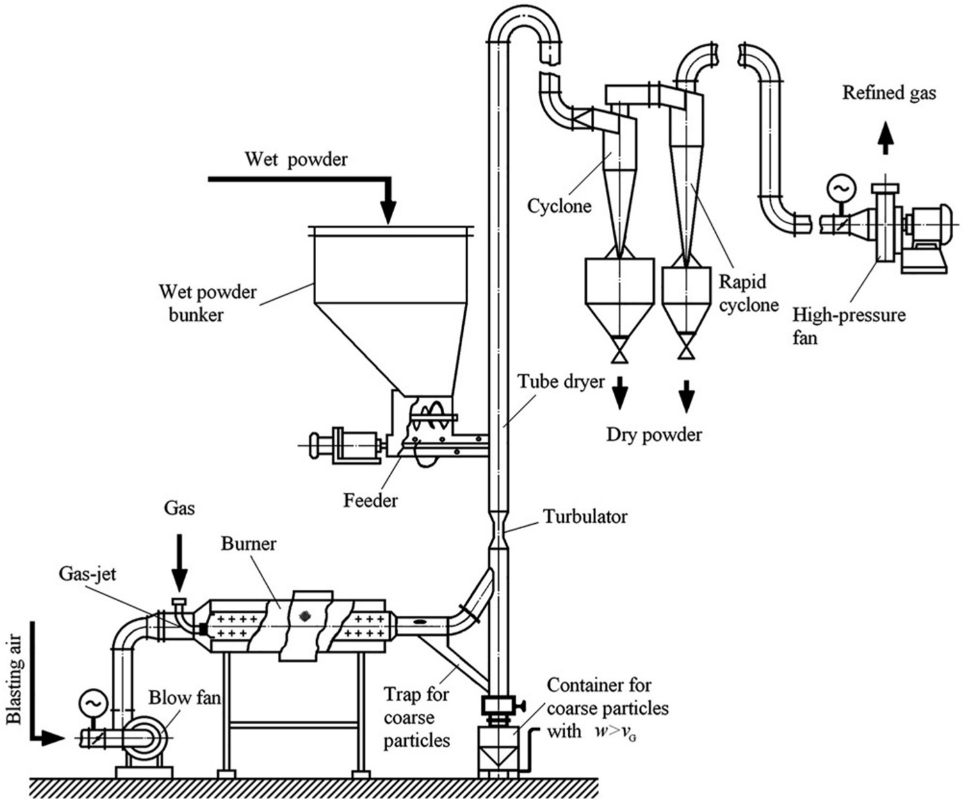
Refined gas
Wet powder
Cyclone
Wet powder bunker
Rapid cyclone
High-pressure fan
Tube dryer
Dry powder
Feeder
Gas
Turbulator
Burner
Gas-jet
Blasting air
Blow fan
Trap for coarse particles
Container for coarse particles with $w > v_G$

FIG. 14.11 Pneumatic convective dryer.

diameter rectilinear divisions must not be taken as acceleration divisions. Calculation methods of pneumatic convective dryers are described in Refs [4, 5]. A simple and sufficiently reliable calculation method is given below.

1. For calculation of thermal conductivity α between gas and particles before the ratio is defined according to [6]:

   $$Nu = 0.4Fe^{0.9}$$

   where Nu is the Nusselt number and Fe is the Fedorov's criterion (it is also named Kirpichev's criterion)

   $$Fe = \overline{d}_{\mathrm{f}}\sqrt{\frac{4g(\rho_1 - \rho_2)}{3\nu^2\rho_2}}$$

   where $\overline{d}_{\mathrm{f}}$ is the average surface equivalent diameter, m; g is the acceleration of gravity, m/s^2; ρ_1 and ρ_2 are the mass density of solid particles and gas, respectively, kg/m^3; and ν is the kinematic viscosity (at average temperature), m^2/s. So the average diameter of particles in order of particle number and particle mass are, respectively $\overline{d}_{\mathrm{eq}.n} = \sqrt{\frac{\sum n_i d^2_{\mathrm{eq}.i}}{\sum n_i}}$, and $\overline{d}_{\mathrm{eq}.m} = \sqrt{\frac{\sum \frac{m_i}{d_{\mathrm{eq}.m,i}}}{\sum \frac{m_i}{d^3_{\mathrm{eq}.m,i}}}}$ where $d_{eq.1}$, $d_{\mathrm{eq}.2}$, …. $d_{\mathrm{eq}.n}$, are irregular shape particle diameters modified to spherical shape; and $n_1, n_2, \ldots. n_n$, and $m_1, m_2 \ldots. m_n$ are their share to total particle number and mass of these particles, respectively.

2. Thermal conductivity

   $$\alpha = Nu\lambda/d_{\mathrm{eq}}$$

   where λ is heat conduction coefficient, W/(m·K).

3. Summarized surface of particles, passing trough the dryer during 1 h

   $$\Sigma F_{\mathrm{p}} = 6G_1/\left(d_{\mathrm{eq}} \cdot \rho_1\right)$$

   where G_1 is the material flow rate, kg/h.

4. Drying duration in seconds

   $$\tau = 3600Q/\alpha\, \Sigma F_{\mathrm{p}} \Delta t_{\mathrm{av}}$$

   where Q is the heat consumption on particle heating and moisture evaporation, and Δt_{av} is the average difference of temperatures between the gas and powder particles, K.

5. The hover rate defined by a graphic approach [7] is widely used. The ψRe_w^2 complex value is defined by Eq. (14.11):

   $$\psi\,\mathrm{Re}_{\mathrm{w}}^2 = \frac{4}{3}Ar \tag{14.11}$$

   where $\mathrm{Re}_w = \frac{wl}{\nu}$ is the Reynolds number; w is the hover speed of particles; v is the gas kinematic viscosity; l is the characteristic particle size, in this case $l = 1.5\Omega_{\mathrm{p}}/F_{\mathrm{p}}$; Ω_{p} is the particle volume; and F_{p} is the particle surface; $Ar = \frac{g(\rho_1 - \rho_2)l^3}{\rho_2 \nu^2}$ is the Archimedes number; $\psi = \frac{2g(\rho_1 - \rho_2)\Omega_{\mathrm{p}}}{w^2\rho_2 F_{\mathrm{p}}}$ is the aerodynamic resistance coefficient or in criteria form $\psi = \frac{4Ar}{3\mathrm{Re}_{\mathrm{w}}^2}$. According to the calculation of the Re_{w}^2 value by Eq. (14.11), the Re_{w} magnitude is found from the nomographic (Fig. 14.12) followed by the definition of maximum particle size hover speed.

6. The influence of particle shapes is taken into account by means of a dynamic shape coefficient χ_{D} determined by the ratio of particle resistance force R_{p} to volume equivalent sphere one R_{sp} at relative velocity:

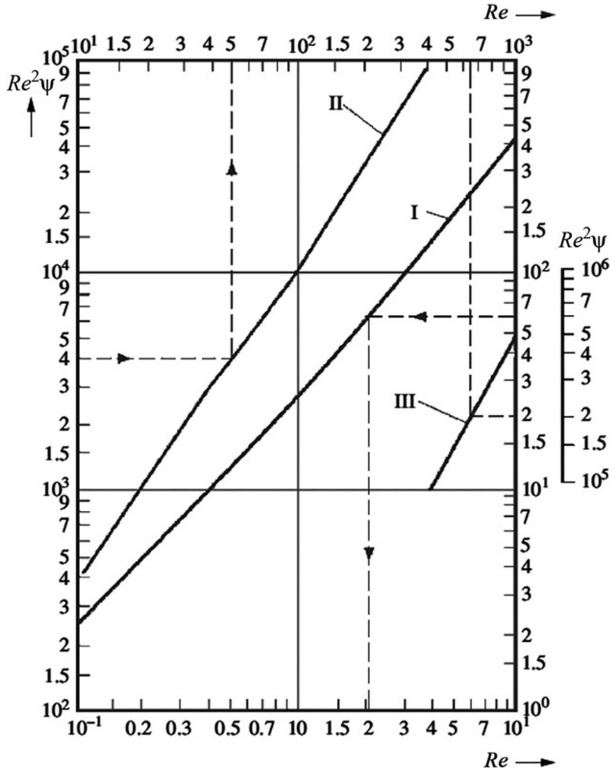

FIG. 14.12 Nomographic for Re_w definition using calculated ψRe_w^2 values (use sequence of nomographic is shown by arrows; the curve I corresponds to right and lower scales in ranges ψRe_w^2 values from 3 to 400, the curve II corresponds to left and upper scales in ranges ψRe_w^2 values from 400 to 100,000, and curve III corresponds to additional scale in area ≥100,000.

$$\chi_D = \frac{R_p}{R_{sp}} = \frac{4\psi_p s_p}{\psi_{sp}\pi d_{sp}^2}$$

where ψ_p and ψ_{sp} are the aerodynamic resistance coefficients of the real particle and volume equivalent sphere, and s_p is the particle's midlength section.

A method of the coefficient χ definition and its values are given in source [7]. Table 14.3 includes the magnitudes of χ_w, χ_D, and ψ for typical geometrical shape particles. Here, $\chi_w = w/w_{eq}$, that is, the ratio of real shape particle sedimentation rate to volume equivalent sphere one.

7. The gas velocity in a tube dryer vG is 1.3–1.5 times more than the hover rate of the largest sized particle.

The vertical tube part length of the tube dryer amounts to $l_{t\text{-}d} = \tau(v_G - w)$.

The diameter of the vertical tube:

TABLE 14.3 Magnitudes of χ_w, χ_D, and ψ for Typical Geometrical Shape Particles

Particle Shape	χ_w	χ_D	ψ
Spherical	1.0	1.0	0.5
Roundish	0.74	1.83	0.915
Angular	0.635	2.48	1.24
Oblong	0.56	3.18	1.59
Lamellar	0.392	6.50	3.25

$$D_{\text{tub}} = \sqrt{\frac{L_G}{0.785 v_G}}$$

where L_G is gas consumption moving in the vertical tube, m^3/s, and v_G is gas velocity, m/s.

Spray Drying

Spray drying is a process in which a slurry or a solution is atomized into droplets in a chamber through which heated gases, usually air, are passed. A typical spray dryer using a disc atomizer with cocurrent air flow is represented in Fig. 14.13.

Spray drying is a continuous rather than a batch process that allows close control of particle size, apparent density, and moisture content. Particles have a very short exposure time. Residence time within the dryer chamber usually ranges from 2 to 20 s, depending on dryer size and mixing scheme (cocurrent, countercurrent, or mixed flow). Therefore, heat-sensitive materials can be spray dried. Lubricating additives can be added for subsequent processing.

Spray drying also has several advantages over other powder processing techniques, particularly in applications requiring agglomerates for subsequent pressing and sintering operations.

The atomized droplets dry rapidly due to their high surface-to-volume ratio. Coarse dried solids fall to the chamber bottom and are continuously collected (see Fig. 14.13). The finer particles are separated by cyclone and ultrafine particles are collected by bag filter. Droplet-air mixing in spray dryers is determined by the location of the air disperser and the atomizer, resulting in the given relative directions of the cooler air current and atomized droplets stream formation.

Cocurrent conditions exist when the atomizing device is located near the hot air disperser at the top of the dryer (see Fig. 14.13). In cocurrent drying, the maximum temperature to which larger dried particles are exposed is approximately 10°C less than the outlet temperature of the dryer. This is explained by the evaporative cooling effect that occurs when the liquid leaves the droplet while passing through the heated zone. Finer particles, which dry more quickly, reach temperatures approaching those of the inlet gas. In cocurrent conditions, the settling rate of particles is determined by their hover rate and drying agent velocity.

The spray dryers work also in countercurrent or mixed-flow conditions. However, cocurrent drying is mostly used because it allows drying at high temperatures without overheating of materials.

In countercurrent conditions, the settling rate is less. When the atomizing device is placed at the top of the chamber and the air disperser is located at the bottom, immediately after formation, the droplets contact cool humid air while, as their moisture content decreases, they are exposed to increasingly hotter air. When the slurry is introduced from the bottom and gas from the top of the dryer, droplets dry both in their upward and downward movement. Therefore, narrower, shorter dryer chambers can be used. However, if partially dried products cannot be exposed to overheating, both modes of countercurrent spray drying may not be applicable.

Mixed-flow conditions are a combination of cocurrent and countercurrent air flow. This type is commonly used in fountain-type dryers, where a nozzle atomizer is located at the base of the drying chamber and the air disperser is placed at the top of the chamber (Fig. 14.14).

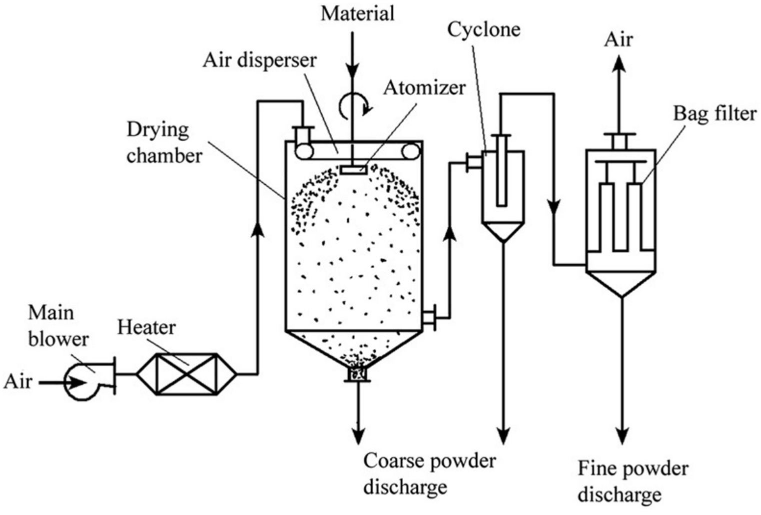

FIG. 14.13 Spray dryer with cocurrent air flow.

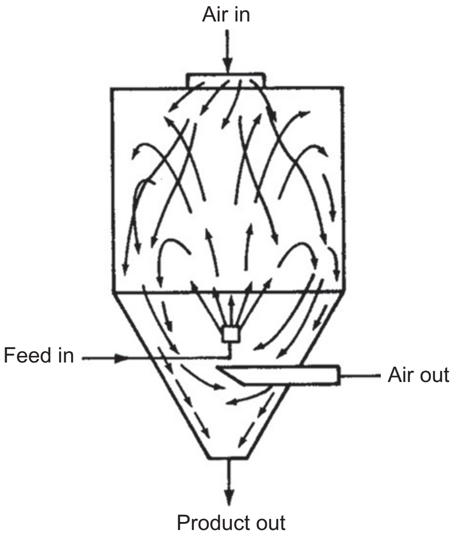

FIG. 14.14 Mixed-flow type of spray dryer.

For fine particles, precipitation and decrease of carryover of the air rate in the chamber (per its total cross-section) commonly does not exceed 0.3–0.5 m/s. However, even by such rates, the carryover is considerable and it is necessary to provide for collection of suspended fine particles.

Zirconia-toughened alumina (ZTA) composites have raised great interest in the orthopedic field [1], being particularly suitable for the production of femoral heads due to their biocompatibility and excellent room-temperature mechanical properties such as strength, toughness, and wear resistance [2,3,8]. However, the performance of ZTA composites is deeply affected by their microstructural features [4–7]. Indeed, a good dispersion of zirconia in the alumina matrix is a key issue to produce reliable biomedical devices with the required mechanical behavior that are free from low-temperature degradation (LTD), as zirconia aggregates can lead to localized aging phenomena [7,9,10].

The alumina-10 vol % ZrO_2 (AZ) composite powders prepared by using two different methods were investigated [11]. In the first method (called PM-AZ), the composite slurry was produced by powder mixing of commercially available raw oxides. In the second one (called SM-AZ), a commercial α-alumina powder was submitted to a surface modification process by using an aqueous solution of a zirconium salt. In the latter process, nanocrystalline tetragonal zirconia grains directly crystallized on the alumina particle surface under controlled thermal treatments, forming a composite powder used to prepare the slurries to spray dry.

In the PM-AZ route, Al_2O_3-10 vol% ZrO_2 aqueous suspensions at three different solid contents (50, 63, and 75 wt.%) were prepared and dispersed by ball milling, performed using high-purity alumina balls in a plastic jar for 24 h. The suspension pH was adjusted to 4.5. In the SM-AZ route, the technique consists on the addition of a suitable amount of zirconium chloride aqueous solution to a well-dispersed alumina suspension. The alumina powders was dispersed by ball milling for about 12 h at a pH value of about 3.5. The obtained slurry, made of a mixture of alumina particles and metal salts, was spray dried and then calcined at 873 K for 1 h, under air, to promote by-product burnout and to induce the crystallization of zirconia nanograins on the surface of the α-alumina particles. In this process, any zirconia phase stabilizer was added because the tetragonal phase was retained at room temperature due to the ultrafine size of the zirconia particles. After this thermal treatment, tetragonal ZrO_2 particles of about 10–20 nm were observed. The specific surface area of the calcined powder was $15 \pm 0.5\,m^2/g$, consequently slightly higher than the starting nano α-alumina one [12]. Fig. 14.15 illustrates (A) the PM-AZ granules obtained by spray drying at pH 8, and (B) granules obtained by spray-drying SM-AZ suspensions destabilized at pH 6.5, with 3 wt.% PEG 4000.

Naglieri et al. [11] reported that the highly dense and homogeneous ZTA materials were produced by both the processing routes through careful control and optimization of the process parameters.

There are numerous companies producing the spray-drying plants for metal and ceramic powder processing, such as LPW Technology Ltd (United Kingdom), Power Processing and Technology, (United States), DORST Technologies (Germany), Fujisaki Electric Spray Company (Japan), etc. DORSET Technologies produces spray-drying plants in a wide size range of water evaporation capacity (17 types): from Type D 20 of 10 kg/h to Type D 8000 of 8000 kg/h water evaporation capacity. Characteristic parameters of Fujisaki Electric spray-drying technology are shown in Table 14.4.

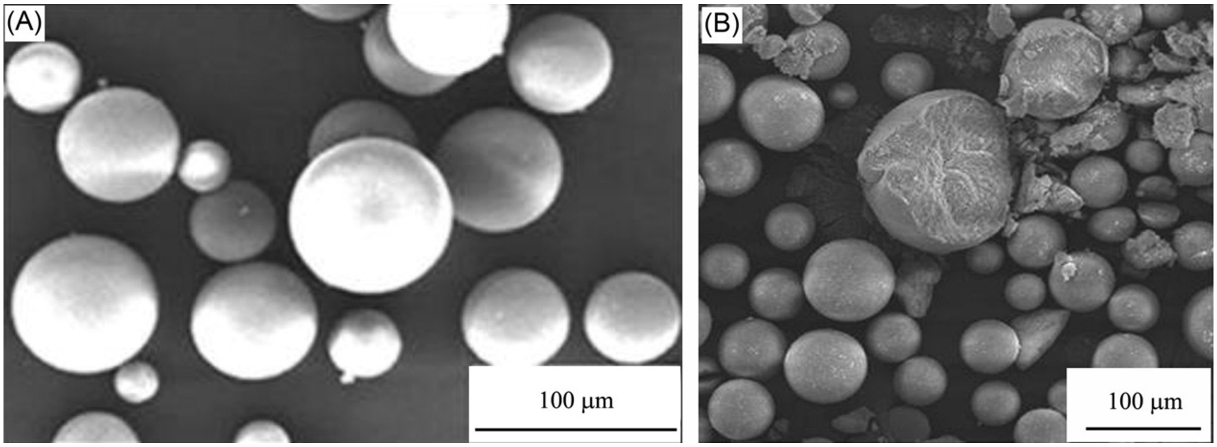

FIG. 14.15 SEM images of (A) PM-AZ granules obtained by spray drying at pH 8 solution and (B) granules obtained by spray drying SM-AZ suspensions destabilized at pH 6.5, with 3 wt.% PEG 4000.

TABLE 14.4 Chracteristic Parameters of Fujisaki Electric Spray-Drying Technology

	Spray Dryer Type			
Process Parameters	**MMSD**[a]	**Other Spray Dryer**		
Nozzle type	Four fluid nozzle	Two fluid nozzle	Pressure nozzle	Rotary atomizer
Droplet particle size, µm	Fine particles	Fine particles	Coarse particles	Coarse particles
	5 – 15	5 – 30	0 – 150	10 – 100
Atomization uniformity	Even	Uneven	Slightly uneven	Even
Energy currier of atomization	Compressed gas	Compressed gas	Pressurizing pump	Motor
Atomization energy consumption	High	High	Low	Low
Liquid processing capacity per nozzle	High	Low	Medium	High
Capacity for droplet size control	High	Conditions apply	Condition apply	High
Countermeasure against viscosity change	Gas pressure	Gas pressure	Fluid pressure	Revolution
Ability to spray high-viscosity liquids	Great	Mediocre	Incapable	Mediocre
Maintainability	High	High	Medium	Conditions apply
Spray angle, degree	180	Under 30	Under 60	180
Spray shape	Hollow cone	Hollow cone fine	Full cone fine	Hollow cone

[a] *MMSD is the abbreviation of Micro Mist Spray Dryer.*

Convective Dryer With Fluidized Bed

Convective dryers with fluidized beds have been widely used because of their high drying efficiency, resulting from intensive heat-mass exchange in the fluidized bed. The volume heat exchange coefficient related to a fluidized bed amounts to approximately 5–10 kW/(m^3·K) while, for drum dryers, per total volume attains not more than 0.5 kW/(m^3·K). In fluidized bed installations, it is possible simultaneously to carry out several processes: drying and burning, drying and particle size classification, drying and granulation, etc. However, these dryers have disadvantages, too: high energy consumption, low process rate under fine powder drying conditions, abrasion of the powder particles and dust fraction formation results, and carryover of ultrafine particle fractions.

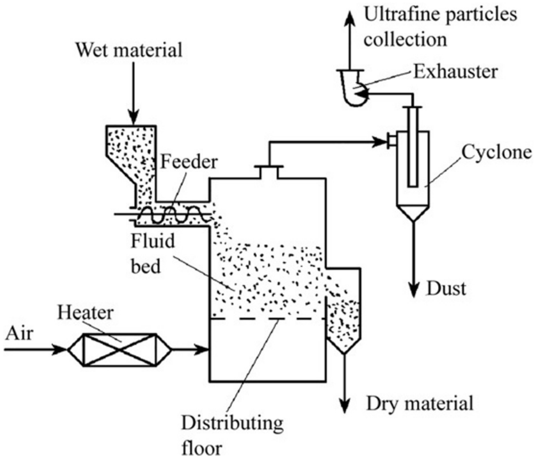
Ultrafine particles collection
Wet material
Exhauster
Cyclone
Feeder
Fluid bed
Dust
Heater
Air
Dry material
Distributing floor

FIG. 14.16 Single-stage continuously working dryer with fluidized bed.

The dryers with fluidized bed designs are multifarious. Single-stage continuously working dryers are most widespread (Fig. 14.16). In dryers with a cylindrical chamber, a drying irregularity is observed, resulting from variation of dwelling time of particles in the fluidized bed chamber. In order to increase the drying uniformity, the dryers with a dilative upward section are used. Due to decreased air rate, the carryover of fine particles is decreased and the drying uniformity is increased.

Shaker Dryer

In a vertical shaker dryer, the powder is moved on a vibrofluidized bed and is heated via convective and conductive heat [13]. A continuous operation dryer, SVT-0.5 (Fig. 14.17), consists of an upright tube with a lift helical chute wound around one heat insulated casing, vibroexciters, and an elastic suspension. The chute with a vertical tube forms a freely oscillating

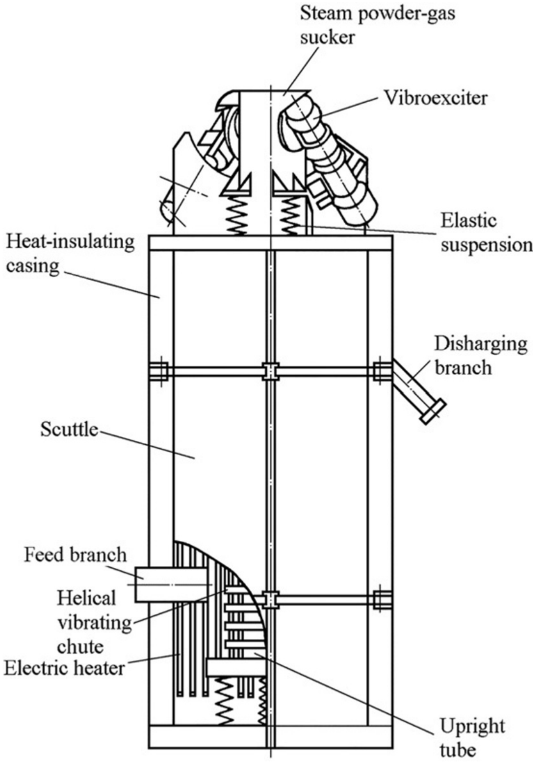
Steam powder-gas sucker
Vibroexciter
Elastic suspension
Heat-insulating casing
Disharging branch
Scuttle
Feed branch
Helical vibrating chute
Electric heater
Upright tube

FIG. 14.17 Continuous operation vertical shaker dryer, SVT-0.5.

above-resonance vibration system. The casing has doors that open externally. The inner surfaces of the doors have attached electrical heaters. The unit is supplied by loading and unloading branches attached inside the casing, and by a branch to carry away the vapor-dust-gas mixture. The air is sucked in through openings in the casing, passes via built-in channels in the casing, goes up, and then flows around the spiral chute with the material, which is dried and sucked away, together with the evaporated moisture through the branch. The material lifting combined with drying favors a space-saving arrangement of the dryer and adjacent units of the processing system.

The dryer throughput in terms of evaporating moisture amounts to 80 kg/h; the duration of the material held in the dryer can be varied from 3 to 8 min by means of the oscillation amplitude from 2 to 5.2 mm at a frequency of 16.6 Hz; and the volume of vapor-gas mixture to be exhausted from the dryer should not be above 1500 m^3/h. The height of lifting of the material from the loading level to the unloading level is 2.0 m. The working components adjacent to the material being dried are made from corrosion-resistant steel; the installed power of the tubular electric heaters is 120 kW. The heating power is regulated by switching on a certain number of heater segments.

For atomized bronze powder, Cu-5Sn-5Zn-5Pb with a particle fraction finer than 150 μm, inclusive after centrifugation to a water content up to 7%–8%, and initial temperature of 293 K, there are the following drying conditions in a shaker dryer: holding period of the powder in the dryer amounts to 6 min, temperature of the dry powder as unloaded from the dryer is 398 K, throughput of the dried powder is 400 kg/h, and the power of the operating segments of heaters is 60 kW.

The drying process can be performed by preliminary warmed gas (air) in the heater with a supply to a shaker dryer. This scheme excludes zone localized overheating of the powder in the dryer.

Drum Contact Dryer

There are convection as well as contact drum dryers in use. Here, combustion products of natural gas are used as the drying agent. A drum dryer consists of a welded cylinder with two bands supported by radial-bearing rollers. Drum axial rotation is performed through a toothed hoop attached to the drum and made into toothing with the drive gear. One side of the drum adjoins a firebox with a mixing chamber and a loading device while the other has an unloading chamber for dried material. The combustion gas, because of the decreased content of oxygen, also plays the role of a protective atmosphere and prevents oxidation of powder during drying. Heat rate on drying under the contact heat mass exchange is higher than that of a convection one. Conduction units are justified when drying ultrafine powders for the avoidance of their carryover with combustion gas. The design and calculation of a convective drum dryer are given in Refs. [1,2].

Among the known designs of contact drum dryers, the unit [10] exhibits essential advantages. Because of the connection of the vapor outlet tube (Fig. 14.18) to the charging point of the drum with the moist powder, the counterflow of the air-vapor mixture current and material occurs along the longitudinal axis of the drum (Fig. 14.19). As a result, the maximum flow rate of the air-vapor mixture occurs in the feeding part of the drum, where the material is still wet and its particles are in a bound state and dynamic interaction with the flow of air-vapor current does not lead to carryover of powder. In the discharging part of the drum, the air current is completely absent and powder carryover does not occur, despite the fact that the

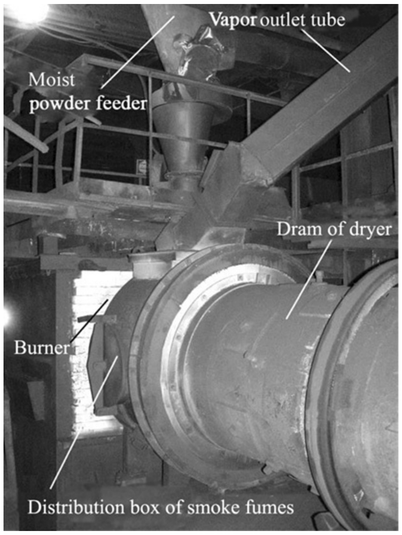

FIG. 14.18 Overview of drum-conducted dryer.

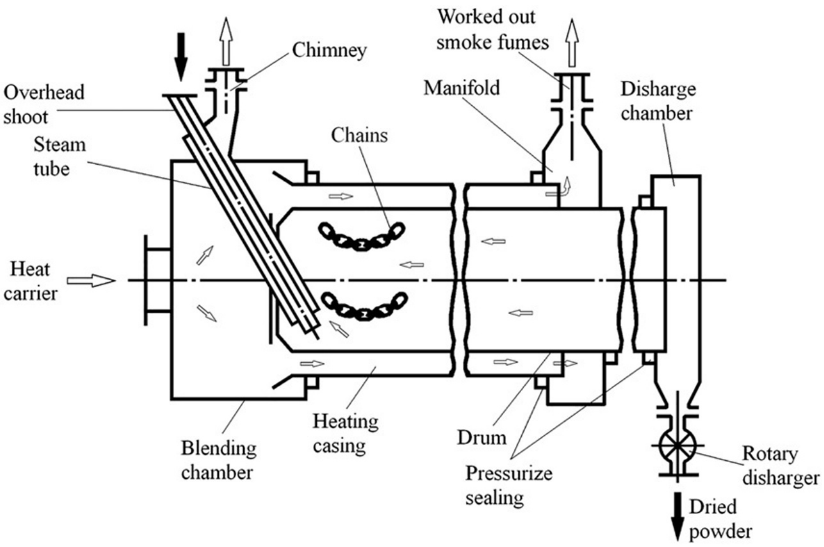

FIG. 14.19 Schematic diagram of conducted drum with counterflow of the air-vapor mixture current and dried material.

material is dry in the discharging part. The material takes up the heat not only from the warmed inner drum surface, but also from the air vapor current, thus accelerating the drying process, in contrast with conventional concurrent conditions when the maximum flow rate of the air-vapor mixture is the discharging point of the drum.

Vacuum Dryers

A shelf vacuum batch dryer is a simple type of the contact batch operation dryers. Such dryers are manufactured with shelves of areas 4.5, 16, and 33 m^2 by the Progress Berdichev machine-building plant (http://www.bozhur.com/progress.htm). It is a horizontal cylindrical apparatus with two pivoting butt lids. The apparatus has inside mounted shelves made in the form of heated plates. Dryers having areas of 4.5 and 16 m^2 are heated by steam. The residual pressure inside the dryer is 2.63 kPa; the maximum temperature of the plate wall is 423 K; and the pressure of the heat carrier in the plates is 0.4 MPa.

Shelf vacuum dryers are a contact apparatus of batch operation; they are used for drying heat-sensitive materials (for instance, magnesium and titanium powders). However, they are inefficient and ineffective, inasmuch as drying takes place in a motionless layer, in the presence of bad conductive heat gaps between particles and between the layer and give out warmth plates. They are used in small-capacity manufacture with a wide assortment of products.

The drying rate increases in hoe-type vacuum dryers as a result of mixing by slowly revolving a horizontal stirring rod with paddles (Fig. 14.20). Parallel with this, they do not need the manual charging and unloading of material like shelf vacuum batch dryers.

The hoe-type vacuum dryer with batch operation has a cylindrical body with a steam jacket. The reversing motor means automatic changes every 5–6 minutes. Thus, during drying a material moves from the middle to the ends of the dryer body and back. The freely rolling rods between the paddles assist the destruction of lumps and additional mixing of materials. The dryer is connected to a steam condenser and vacuum pump.

POWDER CLASSIFICATION BY SIZE

Particle size and size distribution have a significant effect on the behavior during processing. Therefore, to a considerable extent, they govern the properties of the final products made from powders.

In the technological processes commonly used, powders have a wide range of size and need to be adjusted before use. Usually the powders are classified by size, dosed in a given ratio, and blended. Classification by size can be achieved either by a screen on a subdividing partition or by fluid forces. The fluid is usually water or air, and the field force may involve gravity, centrifugal, or Coriolis force. Hydroclassification in moving or motionless liquid media and dry classification in gas flows are used.

The main technological characteristics of the classification process are the efficiency of division size fractions by a size separation process. In evaluation of separation processes, the following parameters are used: the weights of the feed (M),

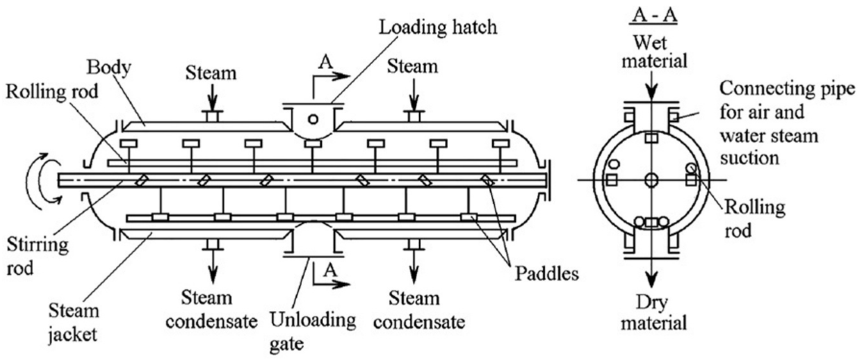
Loading hatch
Body
Steam
A
Steam
Rolling rod
Stirring rod
Steam jacket
Steam condensate
Unloading gate
A
Steam condensate
Paddles
A - A
Wet material
Connecting pipe for air and water steam suction
Rolling rod
Dry material

FIG. 14.20 Hoe-type vacuum dryer.

coarse stream (M_R), and fine stream (M_U); the cumulative fraction undersize of feed, $F(x)$, coarse stream, $F_R(x)$, and fine stream, $F_U(x)$; and x is particle size. Then:

$$M = M_R + M_U \tag{14.12}$$

The total fine efficiency

$$E_U = \frac{M_U}{M} \tag{14.13}$$

and the total coarse efficiency

$$E_R = \frac{M_R}{M} \tag{14.14}$$

so that $E_R + E_U = 1$. However, total efficiency does not enable us to determine the effectiveness of a classification process because it only defines how much of the feed ends up in one or the other of two outlet streams, not how much of the desired material arrives at the correct outlet stream. To discover this, it is necessary to determine the grade efficiency.

Thus, the grade efficiency at size x is a ratio of the desired material in a product of size x to the amount of desired material of size x in the feed. Therefore coarse grade efficiency at size x may be defined as:

$$M_R(x) = \frac{M_R}{M} \frac{dF_R(x)}{dF(x)}$$

and taking into consideration Eq. (14.14)

$$M_R(x) = E_R \frac{dF_R(x)}{dF(x)}$$

Similarly, the fine grade efficiency is defined as:

$$M_U(x) = E_U \frac{dF_U(x)}{dF(x)} \tag{14.15}$$

Consequently, from Eqs. (14.12), (14.13), (14.15)

$$M_U(x) = 1 - M_R\,(x)$$

However, generally these ratios do not define the sharpness of the cut, and it is important to know the amount of fines in the coarse and the amount of coarse in the fines.

For these cases, the evaluation of the effectiveness of a separation process for the fine yield is defined by the ratio of the weight fine fraction in the fine stream to the one in the feed stream. Some of the fine fraction remains in the coarse stream. The amount of the fine particle content in the coarse stream c_R depends on the efficiency of the separation process and the content of fine fraction in the feed stream c:

$$c_R = \frac{100(c - E_R)}{(100 - E_R)}$$

Sieving Methods

Sieving consists of placing a powder on a sieve containing openings of a fixed size and agitating the sieve. A variety of sieve apertures is commercially available, ranging in size from about 20 µm to millimeters for woven wire sieves, down to 5 µm or less for electroformed sieves, and greater than 1 mm for punched plate sieves. In powder manufacture, sieves with apertures smaller than 40 µm generally are not used because of their very low capacity. The sieves in spread-spectrum aperture sizes are commonly used for particle-size distribution analysis.

Sieves are often referred to by their mesh size, which is the number of wires per linear inch. The American Society for Testing Materials Standards range from 635 mesh (20 µm) to 5 mesh (125 mm). The apertures for the 400 mesh are 37.5 µm; hence, the wire thickness is 26 µm and the percentage of open area is 35. Table 14.5 includes the data about sieve aperture sizes in accordance with international and national Standards.

TABLE 14.5 Aperture Sieve Sizes in Accordance With International and National Standards

International ISO 566 (TBL. 2): 1983		American ASTM E 11-87		Tyler STD SCRN 1910		British BS 410 1986	CIS GOST 3584	German DIN 4188: 1977		
Nominal Opening mm/µm		Alt. US Std. inch/mesh		Equivalent inch/mesh		Aperture BS mesh	mm	mm/µm		DIN No 2E
26.50	mm	1.06	inch	1.05	inch			4.00	mm	
25.00	…	1.00	…		…			2.00	…	3E
22.40	…	7/8	…	0,883	…			1.50	…	4
19.00	…	3/4	…	0.742	…			1.20	…	5
16.00	…	5/8	…	0.624	…			1.00	…	6
13.20	…	0.530	…	0.525	…			750	µm	8
12.50	…	1/2	…		…			600	…	10
11.20	…	7/16	…	0.441	…			500	…	12
9.50	…	3/8	…	0.371				430	…	14
8.00	…	5/16	…	2.5	mesh			400	…	16
6.70	…	0.265	…	3	…			340	…	18E
	…				…			300	…	20
5.60	…	3.5	mesh	3.5	…			250	…	24
4.75	…	4	…	4	…	3		200	…	30
4.00	…	5	…	5	…	3.5		170	…	35E
3.35	…	6	…	6	…	4		150	…	40
2.80	…	7	…	7	…	5		120	…	50
2.36	…	8	…	8	…	6		100	…	60
	…		…		…	7		90	…	70
2.00	…	10	…	9	…		2.00	75	…	80
1.70	…	12	…	10	…	8		67	…	90E
1.40	…	14	…	12	…	10		60	…	100
1.18	…	16	…	14	…	12		56	…	110
1.00	…	18	…	16	…	14	1.00	50	…	120

TABLE 14.5 Aperture Sieve Sizes in Accordance With International and National Standards—cont'd

International ISO 566 (TBL. 2): 1983		American ASTM E 11-87		Tyler STD SCRN 1910		British BS 410 1986	CIS GOST 3584	German DIN 4188: 1977		
Nominal Opening mm/μm		Alt. US Std. inch/mesh		Equivalent inch/mesh		Aperture BS mesh	mm	mm/μm		DIN No 2E
			…		…	16		36	…	130
					…			25	…	200
850	……	20	…	20	…					
710	μm	25	…	24	…	18	0.710	French		
600	…	30	…	28	…	22		AFNOR NFX11-50: 1970		
500	…	35	…	32	…	25	0.500	mm/μm		TAMIS
425	…	40	…	35	…	30		5.00	mm	38
355	…	45	…	42	…	36	0.355	4.00		37
						44		3.15		36
300		50		48	…			2.50		35
250	…	60	…	60	…	52	0.250	2.00		34
212	…	70	…	65	…	60		1.60		33
180	…	80	…	80	…	72	0.180	1.25		32
	…					85		1.00		31
150		100	…	100	…			800	μm	30
125	…	120	…	115	…	100	0.125	630		29
106	…	140	…	150	…	120		500		28
90	…	170	…	170	…	150	0.090	400		27
75	…	200	…	200	…	170		315		26
63	…	230	…	250	…	200	0.063	250		25
53	…	270	…	270	…	240		200		24
45	…	325	…	325	…	300	0.045	160		23
						350		125		22
38		400	…	400				100		20
32	…	450	…			400		80		21
25	…	500	…			440		63		19
20	…	635	…					50		18
								40		17

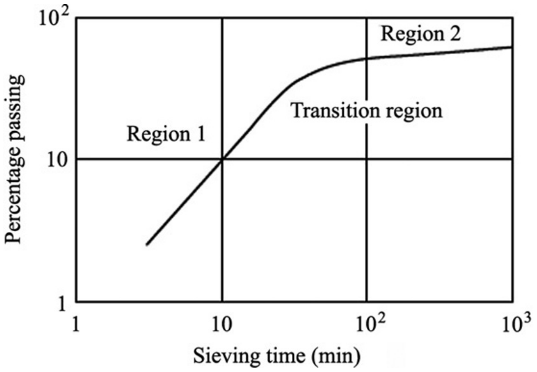

FIG. 14.21 The rate of sieving process.

Fractionation by sieving is a function of two dimensions of particles only, maximum breadth and maximum thickness, because, unless the particles are excessively elongated, the length does not affect the passage of particles through the sieve apertures. The particles much smaller in size than the sieve aperture pass through more rapidly, and larger particles pass through more slowly. The final particle that can pass through will pass through the largest opening when its two smaller dimensions are in the preferred direction. Thus, the sieving process can be divided into two regions with a transition region in between: an initial region that relates to the passage of particles much finer than the mesh apertures, and a second region that relates to the passage of near-mesh size particles (Fig. 14.21). Here the time-weight curve is plotted on log-probability paper. Near-mesh particles are defined as particles that will pass through the apertures in only a limited way, and the ultimate particle is the one that will pass only through the largest aperture in only one orientation. In practice, there is no end point to a sieving operation because this is defined in an accidental method.

The continuous rate method is fundamentally more accurate than the time method and is used in powder manufacture processing. For that, ensuring a uniform rate of powder feeding to the screening surface is the main requirement.

Sieving Apparatus

Selection of a proper sieve surface is very important. Fine sieves are usually woven with phosphor bronze wire, medium sieves with brass, and coarse sieves with stainless steel. Heavy-duty sieves are often made of perforated plate, giving size to circular apertures.

The sieving apparatus can be classified into five main categories: grizzly screens, revolving screens, vibrating screens, sifters, and air-assisted screening machines. Grizzly screens are used generally for separating material of 50 mm and coarser size while revolving screens or trommel screens are primarily used for separations of particulate material greater than 1 mm in size. The screening machine consists usually of a cylindrical frame equipped with a wire cloth or perforated plate. The material to be screened is delivered at the upper end and the oversize is discharged from the lower end. The screens rotate at a relatively low speed of 15–20 rpm. Such screens have been replaced largely by vibrating screens.

Vibrating sieves, whose sieving surface vibrates perpendicularly to its surface with a frequency greater than 600 rpm, are useful for fine powders as well as coarse powders. There are a large variety of commercially available vibrating sieves, but they can be divided basically into two main types: mechanically vibrated sieves and electrically vibrated sieves.

The most important factors for the selection of vibrating sieves are amplitude and frequency. The centrifugal effect k is characterized by the formula

$$k = \frac{r\omega^2}{2g}$$

where r is the amplitude (in m), $\omega = 2\pi n$, n is the frequency (in rpm)/60, and g is the acceleration of gravity.

If the centrifugal effect is too small, the near aperture size particles will stick in the sieve apertures. The appropriate vibrating action not only keeps a feed materials moving on the sieve but more importantly, it also serves to reduce blinding.

Fig. 14.22 shows a schematically typical sieving surfaces of sifters. Sifters are characterized by low-speed (300–400 rpm), large-amplitude (up to 50 mm) vibration in a plane essentially parallel to the sieving surface. Sifters are usually used for material of 30–400 μm or more in particle size. Most gyratory sifters have an additional auxiliary vibration.

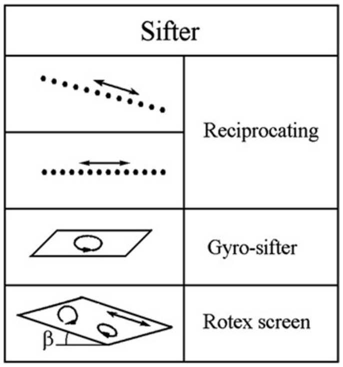

FIG. 14.22 Motion of sieve surface of sifters.

The relationship between 50% separation volume and sieving length may be obtained using Gaudin's theory. According to this probability theory, the passage probability P of particles of size δ_p through an aperture of size a in the sieve surface is given by

$$P = \frac{(a-\delta_p)^2}{a^2} = \left(1 - \frac{\delta_p}{a}\right)^2$$

Introducing the concept of the number of passage trials i, the oversized fraction of particles after i trails, η_i, which is the partial separation efficiency, is expressed by

$$\eta_i = (1-\delta_p)^i = \left[1 - \left(\frac{a-\delta_p}{a}\right)^2\right]^i \tag{14.16}$$

If i is sufficiently large, Eq. (14.16) is written approximately as

$$\ln \eta_i = -i\left(\frac{a-\delta_p}{a}\right)^2 \tag{14.17}$$

Hence, the particle size at 50 percentage separation efficiency, δ_{p50}, is derived, substituting $\delta_p = 0.5$ into Eq. (14.17):

$$\delta_{p50} = a - \frac{0.832a}{\sqrt{i}} \tag{14.18}$$

Round Vibrating Sifters

A two-deck vibrating sifter is shown in Fig. 14.23. The sifter consists of a set of cylindrical sidewalls with sieving surfaces that are assembled using bow connections. The lower sidewall has a conical form bottom and is assembled on a frame by means of flexible ties. Rotation from the motor to the vibroexcitor shaft is transmitted via a V-belt drive. The loading and unloading branches are equipped with rubber sleeve gaskets to seal joints to branches of an initial material feeding device and classified product chutes. Provision is made to operate at rotational rate of 23.7 and 29.5 Hz. Adjustment is also provided for oscillation amplitude by varying the angle between the axes of debalances. The vibrosieve is equipped with points for sampling from the powder flow in the unloading branches for periodic control of sieving efficiency. The vibrosieve is soundless; the impermeability of joints is provided by air or an inert gas pressurization up to 2 kPa within the working area of the sifter.

The area of each of two sieving sidewalls is 0.56 m^2 with an outer diameter of sidewalls of 900 mm. The sifter can yield three fractions. The vibrosieve is equipped with screening meshes with openings 1.0; 0.315; 0.16; 0.1; and 0.05 mm. The throughput when sifting, for instance, an atomized bronze powder in terms of passing for the –0.16 class is 3.2 t/h. The efficiency of sizing $E = 90\%–95\%$. Table 14.6 contains approximate values of the throughput of these sifters. The throughput, factors E and c_R (Eq. 14.18), are determined experimentally on a material subjected to sizing.

A Russell Finex sifter is shown in Fig. 14.24. The sifters (Russell Finex ECO separator) are commercially available in six sizes: 24 in (609.6 mm), 30 in (762 mm), 40 in (1016), 48 in (1219 mm, 60 in (1524 mm), and 72 in (1828.8 mm). These

FIG. 14.23 Two-deck vibrating sifter of 900 mm size.

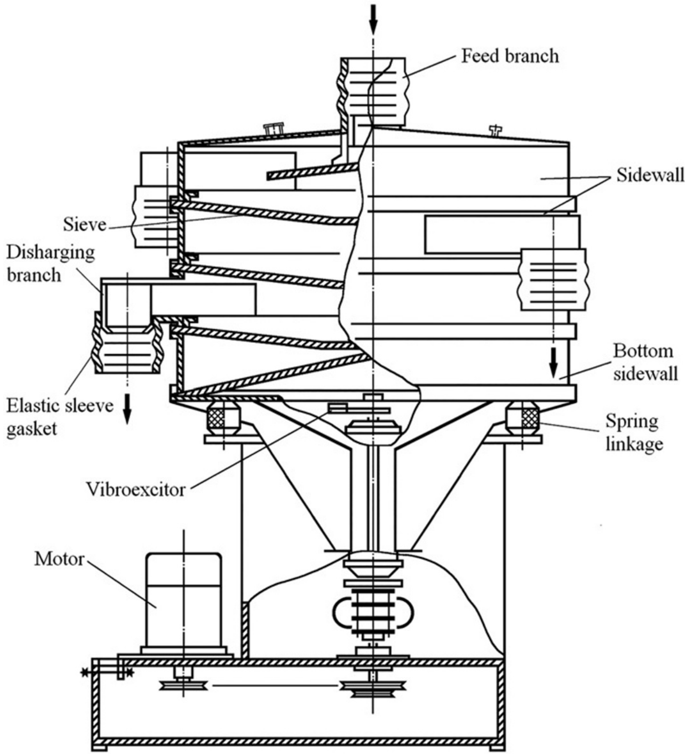
Feed branch
Sidewall
Sieve
Disharging branch
Bottom sidewall
Elastic sleeve gasket
Spring linkage
Vibroexcitor
Motor

TABLE 14.6 Throughput of Two-Deck Vibrating Sifters

Sieve Aperture Sizes, mm		Throughput, m^3/h	
Upper Deck	Under Deck	SV2-0.6[a]	SV2-0.9[b]
2	0.63	0.3	0.7
2	0.315	0.3	0.7
1	0.315	0.2	0.5
1	0.16	0.2	0.50.3
0.63	0.16	0.1	0.3
0.63	0.1	0.1	0.1
0.315	0.1	0.04	0.1
0.315	0.063	0.04	0.02
0.16	0.045	0.01	0.02
0.1	0.045	0.01	

[a] *Deck 600 mm in diameter.*
[b] *Deck 900 mm in diameter.*

can be used in potentially explosive gaseous or dusty environments. There is also a vibrosonic system that eliminates the blinding and blocking of the apertures, allowing accurate separation down to 20 µm.

Preliminary separation of coarse fractions, for example of the water-atomized powder, can be carried out on a hydraulic sizing screen. Such a flat screen [1] is equipped with a shaker. The usable area of one sieve is 0.75 m^2, tilt angle 40–50

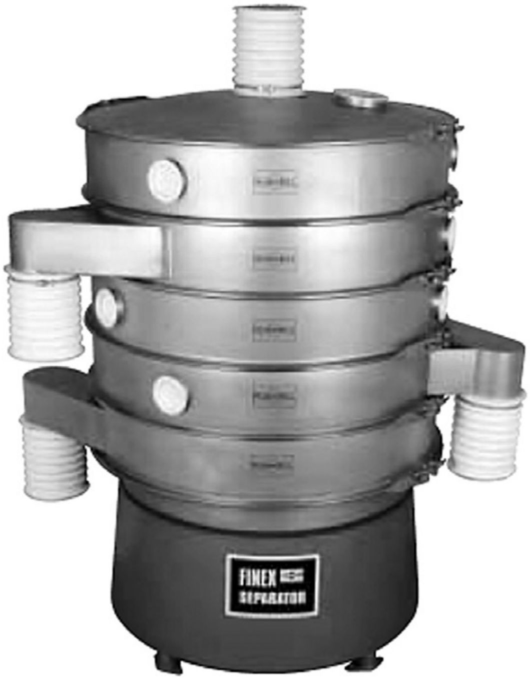
FINEX
SEPARATOR

FIG. 14.24 Russel Finex ECO separator. *Courtesy of RusselFinex Inc.*

degrees, slot size 0.09–1.0 mm, throughput of one segment (depending on the slot size) per solid is 10–30 t/h, and per pulp flow 20–40 m^3/h.

Air-assisted Sieving Machine

An air-assisted sieving machine is schematically shown in Fig. 14.25. It has been predominantly used for fine powders. The stream of air accelerates the passage of fine particles through the sieve and removes the blinding particles in the apertures of the sieve.

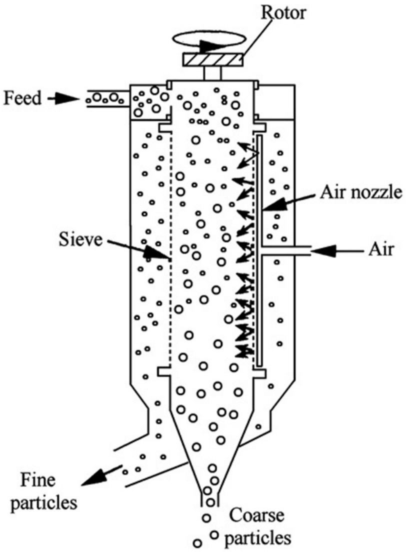
Rotor
Feed
Air nozzle
Sieve
Air
Fine particles
Coarse particles

FIG. 14.25 Schematic drawing of air-assisted sieving machine.

Air Separation

In general, air classification is used for small particles where effective sieving is not applicable. The particle size range for air classification is mostly between a few and 150 μm but, recently, classification of submicrometer particles has been possible.

In air classification, particles are separated by their difference in settling velocity or displaced distance, which depends on the size, shape, and density of particles and the types of forces applied to the particles. Such forces may be drag force, gravitational force, centrifugal force, Coriolis force, inertial force, electrostatic force, magnetic force, impaction force, adhesion force, etc.

In air classifiers, a material is usually separated into two classes: coarser and finer. If more classes are needed, classification is performed in sequence using several apparatuses. Air classifiers are divided into three groups, depending on the particle separation mechanism:

- The relationship between the settling velocity of particles due to the gravitational or centrifugal force and the velocity of airflow.
- The displacement of particles traversing the airflow.
- Others.

The gravitational mechanism is used in a classifier with powder deflector sloping shelves (Fig. 14.26). The powder passes through a bin with gates and is blown by the countercurrent gas flow. Coarse particles discharge through the discharging penstock while the suspended solid of finer particles is aspirated to the cyclone. The powder classification is adjusted by varying the gas flow rate and by positioning the deflector sloping shelves, the inclination angle of which is varied using special rods.

As air classification is accomplished by the difference in particle trajectories, the mechanism of any air classification can be investigated by solving the equation of particle motion numerically with the initial conditions of the particle and fluid flow in the classification zone.

Centrifugal classification is the most commonly used in air classification. The centrifugal force easily attains a force a few hundred times greater than gravitational force and the force strength can be controlled by the rotational speed. The centrifugal air classification is applicable to particles ranging in size from submicron to several tens of micrometers. There exists an equilibrium point, the position at which the radial velocity of a certain size of particle equals the inward air velocity. Particles larger than the equilibrium size move outward and are separated as coarse particles while the smaller particles, classified as fine particles, are caught by the collector.

Centrifugal air classifiers are used usually in combination with comminutors in a closed loop [1]. Centrifugal force is created either by airflow in cyclone-type classifiers, or by mechanical revolution in air separators. There are many centrifugal classifiers, for instance: Micron separator, Turbo classifier, Classiel (O-sepa), and Turboplex classifier [8], the characteristics of which are given in Table 14.7.

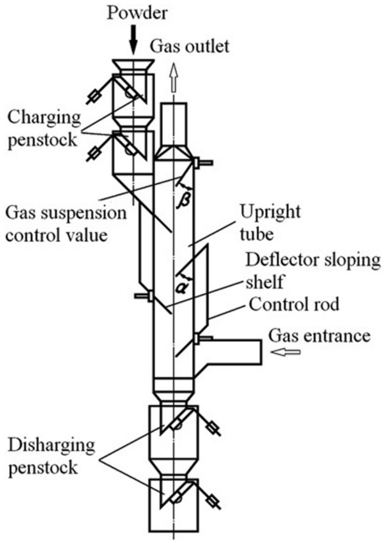

FIG. 14.26 Air gravitational classifier with powder deflector sloping shelves.

TABLE 14.7 Characteristics of Centrifugal Air Classifiers

Type of Classifier	Cut Size (μm)	Throughput (kg/h)	Rotor Speed (rpm)	Power (kW)
Micron separator	5–150	150–12,000	200–2,300	0.75–37
Turbo classifier	0.5–150	150–24,000	700–12,000	1.5–70
Turdoplex	2–180	40–36,000	120–22,000	1–45
Classiel	3–400	200–300,000	75–8,400	4–400

Modified from Shirato M, Murase T, Iritani E. Filtration in the chemical process industry. In: Matteson MJ, Orr C, editors. Filtration, principles and practices. 2nd ed. New York: Marcel Dekker, Inc.; 1987. p. 299 – 423.

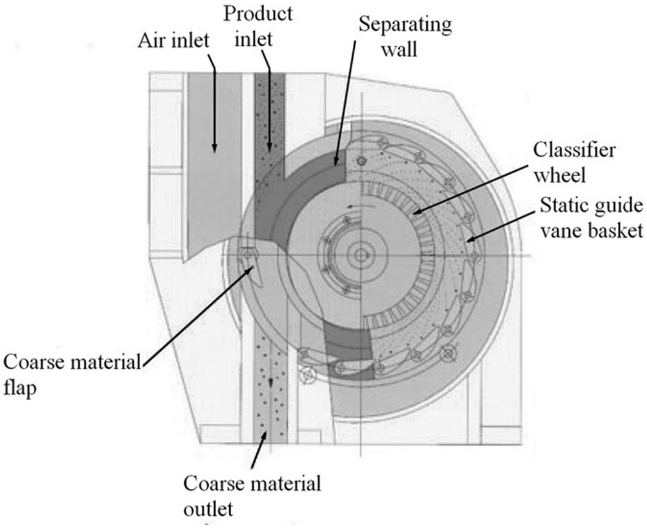

FIG. 14.27 Schematic function of NETZSCH-CONDUX Fine Classifier CFS/HD-S. *(Courtesy of NETZSCH-CONDUX Mahltechnik GmbH.)*

The schematic function of the NETZSCH-CONDUX Fine Classifier CFS/HD-S is shown in Fig. 14.27. The necessary air that disperses the feed product through many adjustable guide vane slots and then leads it to the classifier wheel is fed via the air inlet. The classifier wheel separates coarse and fine particles. The fine particles are discharged via the hollow shaft. Coarse ones are rejected by the wheel and are discharged through the screw-shaped machine housing and via the coarse material outlet at the bottom. The discharge of coarse material can be adjusted by the position of the coarse material flap and so the cleanliness of the coarse material can be influenced.

Air classification cannot be used for potentially explosive powders such as aluminum and aluminum alloys, magnesium, titanium, etc. Explosion-proof conditions can be ensured by means of inert atmospheres but that leads to a considerable price increase of the process. In general, air classifiers are inferior to hydraulic classifiers in terms of efficiency and accuracy of separation [14].

Hydraulic Classification

Hydraulic classification of powders is based on the difference in the different size particle settling rates in a liquid medium in a gravitational field. Fig. 14.28 illustrates the relationship between the size of the spherical particles and their settling velocity. In contrast to air classification where, to prevent cohesion of particles a low concentration of particles 0.003–0.3 vol% in the gaseous medium is maintained, hydraulic classification can be performed under much higher solids concentrations. In fact, classification is fulfilled typically in the range 30–40 vol% in a wet closed circuit grinding processes. The hydraulic classification process is normally performed with a cut size in the range of 200 – 1 μm.

Two principles are used: (i) separation in the flow, the direction of which coincides with that of the main active forces or oppositely directed, and (ii) separation in the flow directed angularly to them. The first principle is used by gravity classifiers, the second one by centrifugal classifiers (with separation in the field of centrifugal forces). Table 14.8 lists the major types of hydraulic classifiers that are useful for wet powder metallurgy processing.

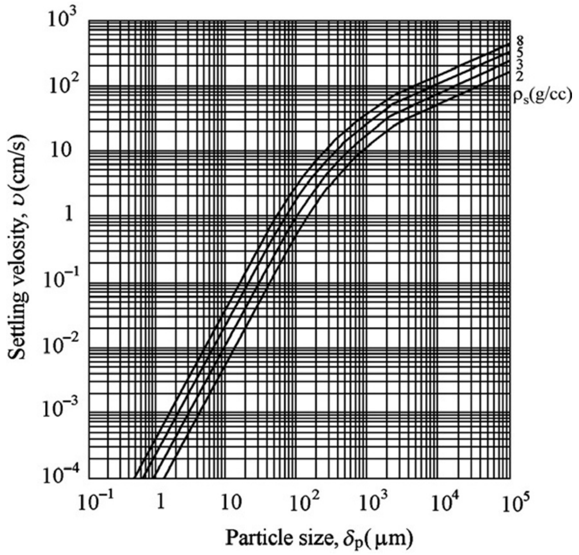

FIG. 14.28 The relationship between the size of the spherical particles and their settling velocity in water (288 K).

TABLE 14.8 Hydraulic Classifiers

Classification Technique	Type	Approximate Range of Cut Size (μm)	Features
Gravity classifiers			
Settling reservoirs	Settling cone[a]	100–1000	Simple structure; used mainly for coarse range
	Spitzkasten (multicones)	50–200	
	Settling reservoir with siphon discharge	20–200	Suitable for wide particle size
	Hydroseparator		
Mechanical classifiers	Spiral classifier		Usable for high density; medium to coarse range
	Drag classifier		
Centrifugal classifiers			
Hydrocyclone	Hydrocyclone (ordinary type)	3–200	High throughput; fine to medium size range; requires slurry pump
	Multicyclone		
Centrifuge	Solid-bowl centrifuge (decanter type)	0.5–30	
	Disc centrifuge (de Laval type)		Very fine to medium size range

[a] *Settling cone is described in subsection "Dehydration" in this section, where its use as thickener is shown.*

Gravity settling reservoirs represent the simplest type of hydraulic classifier. Except for the hydroseparator, which is a modification of gravity thickeners, most gravity settling reservoirs are used for coarse size particle separation. The gravity classifier is used for separation of off-sized fractions from water-atomized powders. A classifier having a siphon unloading in comparison with a bottom outlet ensures a higher accuracy of classification (Fig. 14.29). The classifier comprises a cylindrical tank; the pulp is fed through a branch pipe and the discharge drains into a concentric overflow chute. Water is also fed

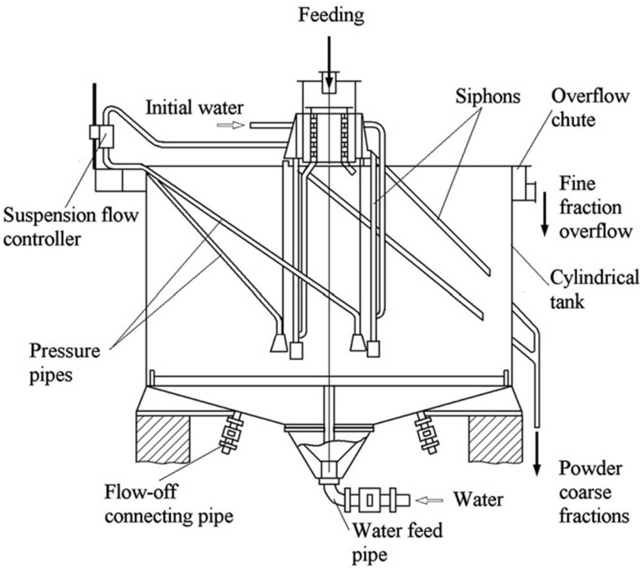

FIG. 14.29 Gravity classifier with siphon unloading.

from the bottom via a tube to produce a suspended layer of particles. Coarse particles reaching the lower part of the tank are removed by siphons. The suspension flow rate is adjusted by valves connected to pressure pipes. The latter are sensors of the pulp density in the medium part of the tank. At the start of the classifier work, the siphons are actuated by water supply to their lower part via pipes.

Hydrocyclones are extremely simple equipment with no moving parts except for rare modifications. The typical hydrocyclones are shown in the subsection "Dehydration," in this chapter, where their use as thickeners is described. The applications of hydrocyclones for classification by size of water-atomized aluminum alloy powders are described in Chapter 16.

Hydrocyclones are manufactured in the size range 10–1200 mm in the diameter of the cylindrical part D_c (see Fig. 14.2). Because the throughput of the hydrocyclone is reduced in proportion to the square of the unit size, very small cyclones are frequently fabricated in the form of batteries. Based on consideration of fluid mechanical efficiency, the optimum parameters of the hydrocyclones have been derived [15] as follows:

$$\frac{L}{D_c}=5,\ \frac{D_{ov}}{D_c}=0.34,\ \frac{D_f}{D_c}=0.38,\ \frac{L_0}{D_c}=0.4$$

where D_{ov} is the diameter of the overflow nozzle; D_f is the inlet diameter (or the equivalent diameter of the inlet); L is the complete length; and L_0 is the length of the cylindrical part.

In the centrifuge, in contrast to hydrocyclones, a forced vortex prevails, which is characterized by constant angular velocity over the whole radius of the slurry pool in which centrifugal settling of particles occurs. Centrifugal classifiers are commonly classified into two types of designs: solid bowl and disc (or de Laval type). According to the design features, solid bowl centrifuges can achieve coarse to ultrafine separation while disc centrifuges are intended basically for very fine separation. The typical separation size ranges from 5 to 200 μm and from 0.2 to 10 μm, respectively.

MIXING

Powder mixing is an operation to prepare a homogeneous mixture from two or more powder ingredients with, if necessary, some liquid additions. Mixing is sometimes confused with blending, which is much the same technique but is used for mixing batches of powder of the same nominal composition, but differ in particle size or production lot. In mixing, the powders being combined are different in composition. Premixing is an operation to make a powder system composed of two or more ingredients with binders, which are mixed and bonded together to avoid segregation in handling. The bulk chemical composition might be the same as that found in wrought metallurgy but, at the particle level, there will be distinct differences. For example, bronze is made both as a prealloyed powder but also as a premixed powder. For a 90% copper and 10% tin bronze, the premixed material will consist of the proper ratio of pure copper and pure tin particles, but no bronze particle will be present [15].

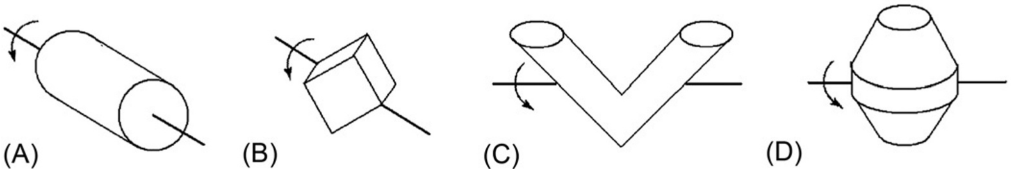

FIG. 14.30 Schematic image of typical rotary vessel mixers: rotary cylinder with horizontal axis of rotation (A); cubic vessel type (B); V vessel type (C); double cones vessel type (D).

Powder Mixers

Mixing is achieved in a mechanical device that rotates or in a stationary vessel with agitators, a vibration unit, gravity motionless, etc. A few simple design rotary vessel mixers are schematically illustrated in Fig. 14.30. Each revolves around some central axis, which, in many cases, might also have a central intensifier bar with blades that spin at a high velocity to disrupt the particles during a tumbling motion. Most mixers split and recombine the powders to create new interfaces and to remove segregation and stratification. However, these same devices also can induce segregation of powders based on differences in particle size, particle shape, or density [16].

Table 14.9 comprises a classification of various powder mixers, based on the mode by which the powders are set in motion. The table also shows rough ranges of powder properties appropriate to each type of mixer.

Rotary Vessel Type

Although the rate of mixing is slow, a good final degree of mixing can be achieved. Powders to be mixed are charged up to 30%–50% of the vessel volume. The rotational speed is set at 50%–80% of the critical rotational speed, n_{cr}, given by

$$n_{cr} = \frac{0.498}{\sqrt{R_{max}}} \left(s^{-1}\right)$$

where R_{max} (m) is the maximum rotation radius of the mixer. For mixing powders with poor flowability and large differences in particle densities and diameters, various types of guide plates or other internals are installed in the rotating vessel.

The double cone mixer of the batch operation contains a body constructed from two cone bottoms with the apex angle at 90 degrees, having loading and unloading hatches equipped with sealed gates. Pivots of the body are mounted on the supports and connected with a reduction gear to the drive. Commercially available double-cone mixers have geometric volumes of 1.6 and 2.5 m^3, filled with components to be mixed up to 0.63 and 1.0 m^3, respectively. The throughput of the 1.6 m^3 mixer is 0.3 m^3/h. The work cycle includes the component loading (14 min), mixing (20 min), and mixture unloading (4 min). The mixer is powered by a 15 kW primary drive and a 0.75 kW secondary drive. Rotational speed of the primary drive is 20.5 rpm and of the secondary drive is 0.96 rpm. The throughput of the 2.5 m^3 mixer amounts to 0.5 m^3/h.

The mixing efficiency of double-cone mixers is somewhat lower than vibrating toroidal ones; therefore, the mixing procedure requires a longer time. The joints of the loading and unloading hatches, together with the corresponding loading device and the receiving finite mixture device, must be thoroughly made and reliably operating to be able to localize dust escape and lead dust to the exhaust system.

The Matson IBC batch blender allows mixing directly within the intermediate bulk container (IBC). An IBC with powder to be mixed is located in a revolving frame and clamped by means of a holding-down device in an asymmetric axis of the rotation position (Fig. 14.31).

Stationary Vessel Type

Stationary vessel mixers with mechanical agitation are shown in Fig. 14.32. In stationary vessels using mechanical agitation, large amounts of powders can be handled in a small space. Specialized atmospheres as well as normal temperatures and pressures are accessible for multipurpose operations. The mixers of ribbon type (Fig. 14.32A) are preferentially used for preparing mixtures of components noticeably differing in bulk density and their contents in the mixture. Some types of stationary vessel mixtures can be used in both batch and continuous mode.

The vibrating toroidal mixer of a batchwise operation (Fig. 14.33) [17] consists of a toroidal chamber made of stainless steel, with loading and unloading hatches, a vibroexcitor, and elastic supports. The tightness of joints between the loading hatch and the loading device branch tube and similarly between the mixture unloading device and the chute branch tube is achieved by means of corrugated elastic sleeve gaskets.

TABLE 14.9 Classification of Powder Mixers and Ranges of Their Use

Classification	Techniques and Design Characteristics	Mixer[a]	Operation		Typical Powder Properties								Differences in Ingredients Properties		Abrasive	Water Content	
					Range of Particle Size (mm)				Flowability Angle of Repose (degrees)								
			Batchwise	Continuous	Over 1.0	1.0–0.1	0.1–0.01	Under 0.01	Under 35	35–45	Over 45	Cohesive	Small	Large		Dry	Wet
Rotary vessel	Horizontal axis of rotation	Horizontal cylinder (14.30A)	○	○	○	○	●		○	●			○		○	○	
		Double cones (14.30D)	○		○	○	●		○	●			○		○	○	
		V-type (14.30C)	○		○	○	●		○	●			○		○	○	
		Cubic (14.30B)	○		○	○	●		○	●			○	●	○	○	
		Continuous V-type		○	○	○	●		○	●			○		○	○	
Stationary vessel	Horizontal axis of rotation	Ribbon agitator (14.32A)	○	○	○	○	○	○	○	○			○			○	●
		Screw agitator	○	○	○	○	○	○	○	○	○	○	○	●		○	○
		Rod or pin agitator	○	○	○	○	○	○	○	○	○	○	○	○		○	○
		Double-axle paddles agitator	○	○	○	○	○	○	○	○	○	○	○	○		○	○
	Vertical axis of rotation	Ribbon agitator	○	○	○	○	○	○	○	○	○		○	○		○	○
		Screw in cone agitator (14.32B)	○		○	○	○	○	○	○	○		○	●		○	○
		High-speed agitator (14.32C)	○		○	○	○		○	○	●		○	○		○	○
		Rotating disc agitator		○	○	○	●		○	●			○			○	
		Muller agitator	○	○	○	○	○	○	○	○	○	○	○	○		○	○

Continued

TABLE 14.9 Classification of Powder Mixers and Ranges of Their Use—cont'd

Classification	Techniques and Design Characteristics	Mixer[a]	Operation		Typical Powder Properties								Differences in Ingredients Properties		Abrasive	Water Content	
					Range of Particle Size (mm)				Flowability Angle of Repose (degrees)								
			Batchwise	Continuous	Over 1.0	1.0–0.1	0.1–0.01	Under 0.01	Under 35	35–45	Over 45	Cohesive	Small	Large		Dry	Wet
	Vibration	Vibratory toroidal mixer (14.33)	○		○	○	○	○	○	○	○	○	○	●		○	
		Vibratory mill	○	○	○	○	○		○	○	○		○	●		○	
		Sieve		○	○	○	●		○	●			○		○	○	
	Gas flow	Moving other fluidized bed (14.32D)	○		○	○			○	●			○		○	○	
	Gravity	Falling under gravity action (14.32E)		○	○	○			○				○		○	○	
Complex	Internals in rotating vessel	Horizontal cylinder	○	○	○	○	○		○	○	●		○	●		○	○
		V-type	○		○	○	○		○	○	●		○	●		○	○
		Double cones	○		○	○	○		○	○	●		○	●		○	○
	Gas flow and mechanical agitation		○	○	○	○	●		○	○			○		○	○	
	Vibration and mechanical agitation (14.32F)		○	○	○	○	○	●	○	○	○	●	○	●	○	○	○

○, suitable; ●, usable. [a]*The number and symbol of figure, illustrating a mixer.*

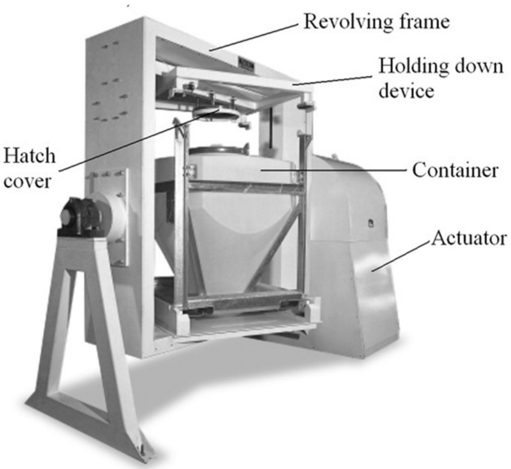

FIG. 14.31 Matson IBC batch blender. *Courtesy of the MATSON Company.*

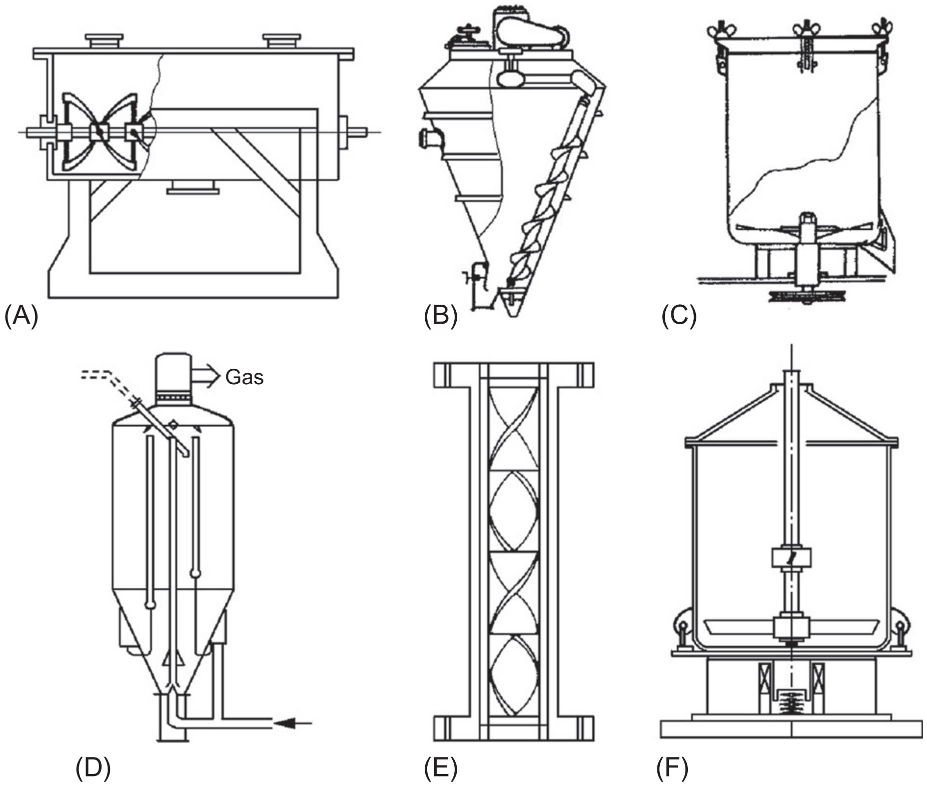

FIG. 14.32 Typical examples of stationary vessel and complex type mixers: rotary vessel with horizontal axis of rotation (A); stationary vessel with vertical axis of rotation (B); stationary vessel with vertical axis of high speed rotation (C); stationary vessel with mixing by gas flow action (D); stationary vessel with mixing by gravity action (E); complex mixing action by vibration and mechanical agitation 9 (F).

The volume of the mixing chamber is 0.7 m^3, the maximum weight of the loaded material occupying not more than 85% of the volume is 1400 kg; the time of mixing is 10–20 min; the vibration parameters on the outer diameter are vertical amplitude 1–3 mm and horizontal 1–2.5 mm; and the oscillation frequency 24.2 Hz. Efficient mixing is achieved by an intense corkscrew movement of powders in the toroidal chamber. The coefficient of heterogeneity varies from 1.5% to 3.0% and should be corrected for specific materials.

The stationary vessel mixers using gas-flow agitation are applied primarily for batch mode mixing. Powders to be mixed can be charged to more than 70% of the vessel volume. Additional equipment, including blowers, dust collectors, and pressure regulators, is necessary so that the system as a whole usually becomes rather large.

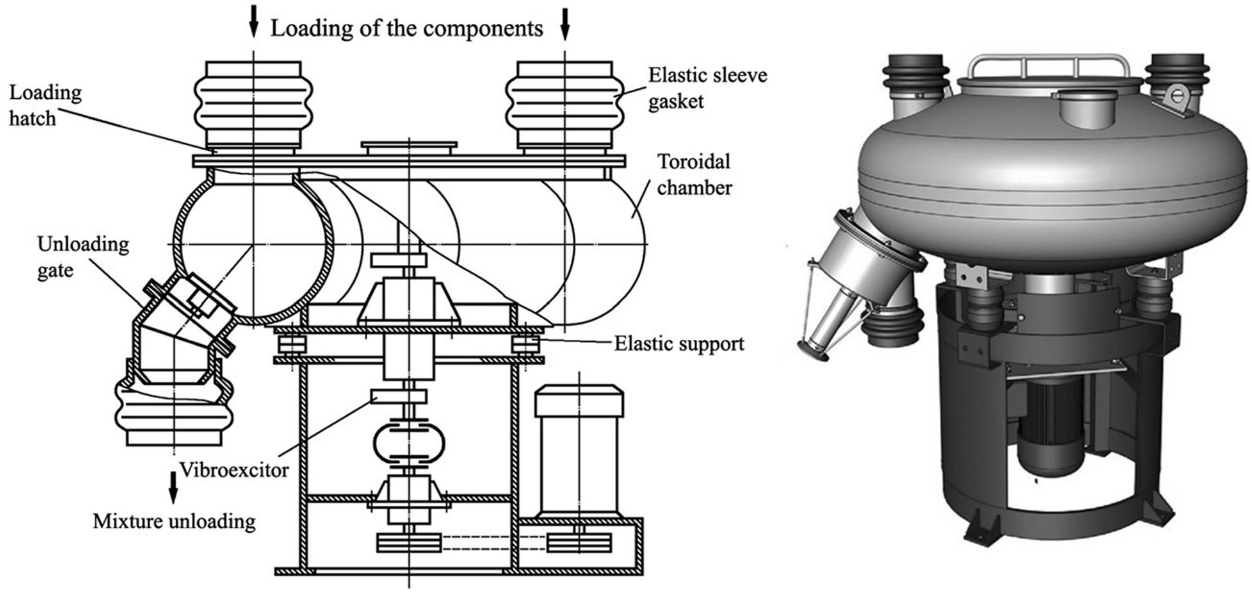

FIG. 14.33 Vibrating toroidal mixer, of batchwise operation. *(Courtesy of Consit Production Company.)*

In a stationary vessel with free gravity falling powders, the flow of powders is repeatedly divided and united to improve mixing and the degree of mixing can be adjusted by the number of repetitions.

Complex Type and Others

Several combinations of mechanisms are possible for powder mixing. Mechanical agitation can be fulfilled in addition to agitation by gas flow. Vibratory motion can also be added to stationary vessel mixers (see Fig. 14.32F). All these types are to make the powder motion in mixers as free as possible from the force of gravity, improving the rate of mixing and extending the application of mixers to powders having rather large differences in physical properties.

Mechanism of Powder Mixing

Three types of particle motion are generally responsible for mixing of powders: convective mixing, shear mixing, and diffusive mixing.

Convective Mixing

A circulating flow of powders is generally affected by the rotational motion of a mixer vessel, an agitating impeller such as a ribbon or a paddle, or gas flow and vibratory motion. The circulating flow gives rise to convective mixing and contributes mainly to a microscopic mixing of bulk powder mixtures. Though the rate of mixing by this mechanism is rather high, its contribution to the microscopic mixing is unexpected. Convective mixing is beneficial for batch mode operation but gives unfavorable effects for continuous mode mixing.

Shear Mixing

The momentum exchange of powder particles having different velocities leads to shear mixing. The velocity distribution develops around the agitating device and the vessel walls due to the compression and extension of bulk powders. It also developed in the powder layer in rotary vessel mixers, in gas-flow mixers at blowing openings, and in suspended solids in vibratory mixers. Shear mixing can improve semimicroscopic mixing and be favorable in both batch and continuous operation.

Diffusive Mixing

Diffusive mixing is caused by random motion. The rate of mixing by this mechanism is low compared with convective mixing, but diffusive mixing is essential for microscopic homogenization.

During powder mixing, all of the above three mechanisms take place together.

Statistical Analysis of the Mixing

Analytical determination of the standard deviation of a mixture is described as a statistical measure of how much the concentration of one constituent in a sample varies from the true concentration that characterizes the entire mixture. A statistical mixture of a typical two-component PM mix depends on the component mass ratio, the average component masses, the standard deviations of the component particle mass distributions, and the sample size [18]. If the percentage of the component in a batch is X, and the percentage found in a spot sample is X_i, then the difference is $(X-X_\mathrm{i})$. The average of all the X_i readings could approach the value of X if enough samples are checked; the average of all the plus and minus variation of $(X-X_\mathrm{i})$ would approach 0. To obtain a measure of the overall sample–the significance of all the spot samples–the statistical variance and standard deviation are computed. The biased variance can be expressed:

$$\sigma_\mathrm{s}^2=\frac{\sum_{i=1}^{n}(X-X_i)^2}{n}$$

where σ_s^2 is the biased sample variance; σ_s is the biased standard deviation; i is the spot sample number; X_i is the spot sample measurement; X is the actual content of the ingredient; and n is the spot numbers.

To compensate for the increased uncertainty that entails by using very few spot samples, the unbiased variance is used. The difference is that n–1 is placed in the denominator instead of n. The expression then becomes:

$$\sigma_\mathrm{s}^2=\frac{\sum_{i=1}^{n}(X-X_i)^2}{n-1}$$

The degree of homogeneity (the degree of mixedness, M) for a powder mixture can be estimated by evaluating the magnitude of variance of the samples:

$$M=\frac{\sigma_0^2-\sigma_\mathrm{s}^2}{\sigma_0^2-\sigma_\mathrm{r}^2}$$

where σ_0^2 is the variance for the initial segregated mixtureand σ_r^2 is the variance anticipated for perfectly mixed random samples.

The final variance for a fully mixed, randomly sampled system should approach zero, that is, $\sigma_\mathrm{r}^2=0$ in the ideal. This gives a simplified form of M:

$$M=1-\frac{\sigma_\mathrm{s}^2}{\sigma_0^2}$$

Usually the homogeneity improves rapidly with initial mixing, but over time a steady-state homogeneity is attained that is less than unity; the maximum mixture homogeneity occurs when the rate of mixing equals the rate of segregation.

Powder mixing is accomplished in a mixer where the three mechanisms described above take place simultaneously. The characteristic curve of mixing is the chart of the degree of mixing M against the mixing time t. Fig. 14.34 illustrates a schematic example of a similar curve where the standard deviation σ (on a logarithmic scale) shows the degree of mixing M against the mixing time t (on the linear scale).

Generally, convective mixing is dominant in the initial stage (I) and the mixing proceeds steadily by both the convective and shear mechanisms in the intermediate stage (II). In the final stage (III), the effect of diffusive mixing appears and the dynamic equilibrium between mixing and segregation is reached. The degree of mixedness at this state is called the final degree of mixing, M_∞. The characteristic curve of mixing is useful for the evaluation performance of mixers. Various powder mixers show a variety of patterns in the characteristic curve of mixing. The value of M_∞ is also influenced perceptibly by operating conditions and powder properties.

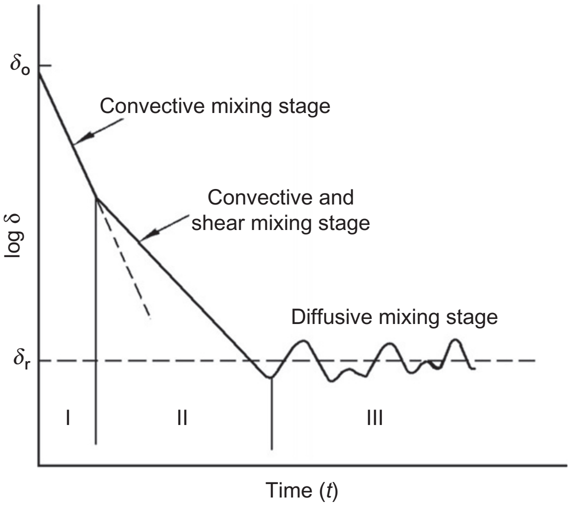

FIG. 14.34 Schematic presentation of characteristic curve of the mixing process.

PASSIVATION TECHNIQUES

Oleg D. Neikov, Irina B. Murashova

For most metals, their condition in humid air is thermodynamically unstable. The property of metals to transform from the metallic state to another is characterized by the free energy decrease during the oxidation reaction.

In Table 14.10, the nonferrous metals are listed in descending order of the negative normal electrode potential followed by increasing of the positive one. This series is divided by hydrogen (–0.414 and 0.000 V) and oxygen (+0.815 and +1.23 V) equilibrium potential values on five metal groups different to their thermodynamical stability.

In a humid and oxygen presence, very few metals from the fourth and fifth groups could be considered thermodynamically stable. More information about the thermodynamic stability of metals can be obtained based on analysis of the metal potential-hydrogen ion exponent (pH) diagram.

Recent conceptions about corrosion processes are founded on electrochemical theory. Corrosion processes, which occur on a metal surface, have been more extensively studied and various processes for protection against corrosion of cast metal have been developed. At the same time, the powders, due to their large specific surface, are more vulnerable to corrosive action. The corrosion resistance of metals and alloys is characterized not only by thermodynamic stability but, to a greater extent, by process kinetics, that is, its real rate

In accordance with an approximate scheme of the corrosion element work in case of linear dependence between the electrode reaction rate and potential, the expression for the corrosion rate can be given as:

$$u = K\frac{E_c^b - E_a^b}{\dfrac{P_c}{S_c} + \dfrac{P_a}{S_a} + R}$$

where K is the conversion factor; $(E_c^b - E_a^b)$ is the difference between starting potentials of cathode and anode parts of a corrosion element; P_c and P_a are, respectively, the specific cathode and anode polarizability (dE/dI) by the corrosion current I; S_c and S_a are the areas of cathode and anode parts respectively of the corrodent metal; and R is the ohmic resistance of the powder-liquid system.

Generally, the E_c^b and E_a^b values are determined experimentally or for evaluation of the corrosion motive force, the values of equilibrium potential of depolarizator (E_c^{eq}) cathode reduction and anode reaction of metal solution (E_a^{eq}), calculated via Nernst's equation, are used (see Chapter 8). The value $(E_c^{eq} - E_a^{eq})$ is proportional to the change of free energy of the system and characterizes the extent of its thermodynamic instability. The denominator represents the summarized kinetic inhibition of cathode and anode processes, taking into account the ohmic resistance and ratio of the area of the electrode parts. The large surface of powders promotes their instability; therefore the anticorrosion effect during their production and processing is aimed at increasing polarizability of the cathode and anode processes and items on the rise of medium ohmic resistance.

Recent simulation of electrochemical process kinetics using computers allows the corrosion rate to be evaluated more accurately by the calculation of corrosion potential E_{cor} and corrosion current I equal for cathode and anode processes.

TABLE 14.10 Common Thermodynamic Characteristic of Corrosion Resistance of Metals and Their Normal Electrode Potential

Group	Common Characteristic of Corrosion Resistance	Electrode Reaction[a]	Potential, E^0, V at 25°C
1	Metals with elevated thermodynamic instability (corrosion is virtual even in neutral aquatic environment free from oxidants)	Cs—e	–3.02
		Rb—e	–2.99
		Ba—e	–2.90
		La—3e	–2.52
		Mg—2e	–2.37
		Be—2e	–1.85
		Hf—3e	–1.70
		Al—3e	–1.66
		Ti—2e	–1.60
		Zr—4e	–1.63
		Ti—3e	–1.21
		V—2E	–1.18
		Nb—3e	–1.1
		Zn—2e	–0.782
		Cr—3e	–0.74
2	Metals are thermodynamically instabile, inconvertible in neutral environment durante absentia of oxygen; they can corrode in acid medium durante absentia of oxygen too	Cd—2e	–0.402
		Ti—3e	–0.336
		Co—2e	–0.227
		Ni—2e	–0.250
		Mo—3e	–0.200
		Sn—2e	–0.136
		Pb—2e	–0.126
		W—3e	–0.110
3	Metals of intermediate thermodynamic instability (in durante absentia of oxidants they are resistant in acid and neutral environments).	Bi—3e	+0.226
		Sb—3e	+0.240
		Cu—2e	+0.337
		Ag—e	+0.799
		Rh—3e	+0.800
4	High-stability metals (they are corroded in neutral environmental in the oxygen presence and in acid environmental in the oxidants presence)	Pd—2e	+0.987
		Ir—3e	+1.000
		Pt—2e	+1.190
5	Full-stability metals (they are resistant in acid environmental in the oxygen presence; they are not dissolved in complex compounds in the oxidant's presence)	Au—3e	+1.500
		Au—e	+1.700

[a] *Electrode reactions* $M \leftrightarrow M^{ne} \pm ne$ *are written summarily* $M - ne$.

The anode metal dissolution is described by the equation of retarded discharge (Eq. 14.19) while the cathode process mechanism, depending on the medium hydrogen ion exponent, is characterized by the kinetics of hydrogen emission (Eq. 14.20, acid medium) or limit diffusion current of oxygen solution reduction (Eq. 14.21, neutral and alkaline solutions):

$$\frac{I}{S_\mathrm{a}} = i_\mathrm{ex}^\mathrm{M} \exp \frac{(1-\alpha_\mathrm{M})zF}{RT}\left(E_\mathrm{cor} - E_\mathrm{eq}^\mathrm{M}\right) \tag{14.19}$$

$$\frac{I}{S_\mathrm{c}} = i_\mathrm{ex}^\mathrm{H} \exp\left(-\frac{\alpha_\mathrm{H}F}{RT}\left(E_\mathrm{cor} + \frac{2.303RT}{F}pH\right)\right) \tag{14.20}$$

$$\frac{I}{S_\mathrm{c}} = \frac{4FD_{\mathrm{O}_2}C_{\mathrm{O}_2}}{\delta} \tag{14.21}$$

where i_ex^M and i_ex^H, (A/m^2) are the exchange current density of metal and hydrogen during reduction; a_M and α_H, are the transport coefficients for metal and hydrogen; F is the Faraday constant (C/mol); R (J/mol K) is the absolute gas constant; T (K) is the temperature; D_{O_2} (m^2/s) is the oxygen diffusion coefficient in corrosion medium; C_{O_2} (mol/m^2) is the oxygen solubility in the medium at respective temperature; and δ is the thickness of the diffused layer (about 100 μm). The values of i_ex, α, D, and C are given in the reference literature [19]. A joint resolution of Eqs. (14.19), (14.20) or Eqs. (14.20), (14.21) depending on the medium is carried out in one of the mathematical application packages (for example, MathCAD) and the unknowns, current, and corrosion potential are found.

Passivation Methods

Passivating techniques are based on the following principles: reduction of the degree of thermodynamic instability, inhibition of cathodic processes, and rising of ohmic resistance of the system. These may be implemented in the following ways.

- A decreased thermodynamic instability of a metal can be achieved via alloying, protection of powder surface by an insulated coating, or by processing and storage of a product in an inert atmosphere. Alloying is restricted by the purity requirements of powders to their technological characteristics and economic considerations. For instance, the thermodynamic stability can be increased by alloying copper with gold and nickel with copper.

  The powder surface insulation is possible by coating with polymer films, encapsulation of powders, forming oxide films, nitriding of surface, and by applying greases.

  The thermodynamic stability of powders of aluminum, titanium, zirconium, niobium, and other metals can be enhanced by nitriding their surface. Electromechanical passivity is attained through the formation of insoluble corrosion products on a reactive surface.

  Depending on the metal type, as inert atmospheres, nitrogen, argon, helium, and other gases or gas mixtures not containing oxidants can be used, or with depleted content.

  To this group of powder-passivating methods, we can also add air medium drying (using silica gels, aluminogels, and other moisture absorbing agents).
- The inhibition of cathode processes is achieved by the elimination of cathode contaminants from an alloy by introduction of additives that step up the cathode process overvoltage.

  The stability of zinc, aluminum, and magnesium is improved with an increase in their purity. The stability of commercial zinc can be improved by cadmium introduction while that of magnesium by the introduction of manganese. The use of these techniques in the production of commercial powders is restricted by technological requirements and economics.
- The inhibition of anode processes is achieved via alloying by introduction of cathode additives or cations into solution to reduce the overvoltage of cathode processes as well as by introduction of oxidizers or anode inhibitors into the corrosive medium or by a protective coating. Thus, the passivity is enhanced by alloying nickel with chromium and titanium with small additions of palladium. The cathode process overvoltage is decreased by the addition of chromates, nitrates, phosphates, and perrhenates into the solution.

  Zinc chromate and other anode inhibitors are added to a paint film or grease.
- No special actions are undertaken as a rule to reduce electrical conduction of the solution to increase ohmic resistance. This is contributed by the creation of hydrophobic layers and poor conductive films on the powder particle surfaces.

  The techniques of the first group are of the greatest significance for passivation.

Hydrophobization

The work of a corrosion element implies the transfer of charges between the cathode and anode in a liquid phase. A powder that possesses a developed surface adsorbs air moisture in which other gas ingredients of air have been dissolved and a current-conductive electrolyte is formed; otherwise electrochemical corrosion is not possible. The existing methods of air drying (use of silica gels, aluminogels, etc.) are only valid for a limited period of time and require a reliable sealing for packages in which to store powders. On the other hand, imparting of hydrophobic properties to the surface of metal particles prevents formation of a moisture film and can practically prevent corrosion [14,15]. The hydrophobization of the metal powder surface is performed by treating powders with an aqueous solution of surfactant and organic compounds of fatty and aromatic series. Soda soap is an efficient stabilizer of copper powder against corrosion; the corrosion resistance of the powder as treated with stabilizing soap solution increases by 10–80 times (Table 14.11).

TABLE 14.11 Methods of Copper Powder Stabilization

Stabilizing Component of Solution	Unit	Concentration	Corrosion Resistance Increase Degree[a]	Wettability	Hydrophobization Operation
Stabilizing after electrolysis					
Without stabilizing	…	…	1.0	+ [b]	
Laundry soap	wt%	0.01	81.0	– [b]	The powder rinsed out after electrolysis is washed with inhibitor solution – washed out the excess of stabilizing solution–moisture removed by centrifuge–drying in hot air current
Soapnaphtha	wt%	0.05	…	–	
Benzothiazole	wt%	0.01	9.8	–	
Benzothiazole	wt%	0.06	57.8	–	
Glue	wt%	0.01	4.1	+	
Glue	wt%	0.05	9.0	+	
Gelatine	wt%	0.01	3.5	+	
Gelatine	wt%	0.02	8.0	+	
Gelatine	wt%	0.05	12.0	+	
Beta–naphtoquinoline	wt%	0.02	9.3	+	
Polyethylene polyamine	g/L	0.2–0.5	6.6	+	
Polyethyleneimine	g/L	1.0	6.4	+	
Benzothiazole	g/L	0.12–5.0	…	–	Dipping of powder in hot benzothiazole solution; airing
Stabilizing during electrolysis process					
Polyvinyl alcohol	g/L	0.2	4.44	…	Introduction of a surfactant into electrolyte
Gelatine	g/L	0.2	4.4	…	
Polyvinylpyrrolidinone	g/L	0.2	9.0		
Polyethylene polyamine	g/L	0.2–0.5	3.7	…	
Polyethyleneimine	g/L	1.0	5.8	…	
Stabilizing during drying in the fluidized bed					
Benzothiazole	..	…	2.2	…	Introduction of a saturated inhibitor vapour in hot air

[a] *The action of each stabilizing matter is evaluated in comparison with conditions durante absentia of one, which is taken for unit.*
[b] *Plus and minus indicate wettable and nonwettable, respectively.*

The powder as rinsed out after electrolysis, treated with an inhibiter solution, washed with fresh water, dehydrated by a centrifuge, and then dried in a current of hot air. To produce powders with retained hydrophilic properties, the powder is treated with gelatine or another surfactant (see Table 14.11) that prevents powder oxidation after the electrolysis treatment operations when the access of oxygen to the metal is enhanced through a thin moisture film (interoperation protection). Stabilizing surfactants can also be used directly at the electrolysis stage (see Table 14.11), which increases the interoperation protection. The effect of surfactant appears directly on the electrolysis kinetics and thus, on the properties of the powders produced. For instance, electrolysis conducted in the presence of polyvinylpyrrolidone leads to an increased content of fractions having a particle size between 45 and 71 μm.

When electrolytic copper powder is sintered in hydrogen with further milling, its corrosion resistance is decreased by the removal of the stabilizing film during annealing. In that case, the powder can be treated immediately as milled in an organic solvent containing fatty acids.

Volatile inhibitors when added to hot gases allow simplification of the stabilization process by combining it with drying (see Table 14.11). However, such a stabilization method has not found commercial application.

Copper powders produced by atomization are prone to oxidation during the metal drop cooling. Surface hydrophobization of a molten metal is impossible; however, the use of water with added laundry soap in the receiving tank increases the stability of the powder against oxidation.

Nitriding and Oxide Formation

An ultrafine electrolytic powder containing 41.1% Cu, 1.8% Ni, 4.0% Al balance, and iron in its freshly produced state is pyrophoric; it can be passivated by producing an oxide or nitride film on its surface.

Nitriding is performed using ammonia which, mixed with a reducing gas, is introduced at the end of the recovery annealing of powders at 573–673 K. The flow rate of the nitrogen-containing compound is at least 20 vol% of the reducing gas. Nitriding treatment for 15 min forms a nitride film on the powder surface. When titanium is nitrided, a layer of nitrogen solution formed in α-titanium plays the role of the protective film.

The oxide formation on the ultrafine powder surface can be achieved in the following way. After the recovery annealing is complete, the reducing gas is cut off and the powder is cooled down to room temperature in argon containing about 0.02% of oxygen [20].

Microencapsulation

Microencapsulation implies the application of polymer films either on the surface of each powder particle or granule. The following microencapsulation methods are known [21]: physical-chemical methods (in water medium, in organic liquids media); chemical methods with the use of polymers, polycondensation, and polymerization; and physical methods (via vapor condensation, extrusion, microcapsulaton in a fluidized bed).

As film-forming material, the powder microencapsulation via vapor condensation uses a metal that is vaporized in a vacuum and condensed on the cold powder surface.

During extrusion, a thin viscous film is formed on a small diameter screen perforated surface and the particles to be encapsulated are forced through this perforated surface. Centrifuges of specific design are used for this extrusion.

Microencapsulation in a fluidized bed is accomplished via formation of a fluidized bed of particles with spraying by a solution or suspension of a film-forming material.

The aluminum powder of APV grade (in the Russian classification) is microencapsulated with a film forming composition based on a silicon organic liquid [22] with the formation of aggregates consisting of fine, 5–20 μm particles bonded to coarser ones. The presence of zones being blocked with a microfilm produces the effect on powder oxidation conditions in the low-temperature range. Thus, the temperature of onset oxidation for the microencapsulated powder of aluminum APV (APV-M) is 90 degrees higher than for common APV (Fig. 14.35A). Oxidation kinetics with heating of APV jointly with APV-M (Fig. 14.35B) show an endothermic effect (374.5 J/g).

Along with the decrease of dust formation when handling powders in processing steps, the microencapsulation also reduces the fire/explosion hazard [23].

POWDER SPHEROIDIZATION BY THERMAL PLASMA PROCESSES

A convenient way to produce spherical metal particles is to remelt irregularly shaped particles at high temperatures and solidify the droplets by rapid quenching. This can be done by using thermal plasmas, which are characterized by their extremely high temperatures (3000–10,000 K) and rapid heating and cooling rates (approx. 10^6 K/s) under oxidizing,

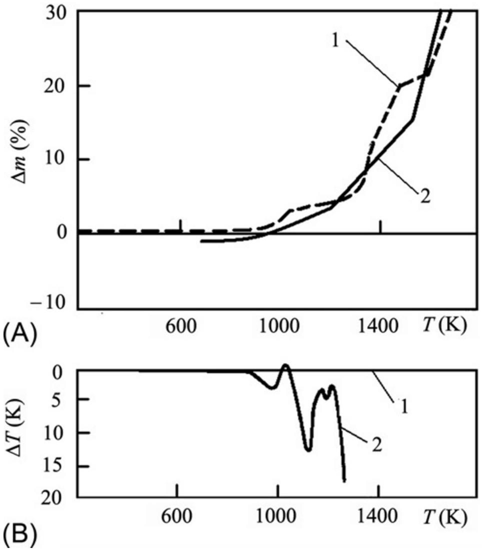

FIG. 14.35 Mass increase of powder specimens during heating with rate 10 degree per minute (A) and thermogram (B) of synchronous oxidation of initial (1) and microcapsulated (2) powders: (1), APV; (2), APV-M.

reducing, or inert conditions. Plasma is a partially or fully ionized gas in a condition of quasineutrality. Thermal plasmas used for particle spheroidization are generally produced by devices such as radio frequency (RF) inductively coupled discharges and direct current (DC) arc plasma torches. Although various plasma methods can be used, RF induction plasmas are the preferred method for the spheroidization and densification of particles. This is due to the longer residence time in the plasma and the lower possibility of contamination caused by electrode erosion. The residence times commonly employed for particle melting in RF plasmas range from 5 to 20 ms [24]. DC arc plasma torches, although not regularly used for spheroidization, are also an option.

A schematic of a typical RF induction plasma device is illustrated in Fig. 14.36. Various RF induction plasma systems are available; several research studies have utilized those available from Tekna Systems. Most of these studies have used the Tekna PL 50 torch, which can be operated at various frequencies (0.3, 2, or 3 MHz) and power inputs (30, 40, 50, and 100 kW). For spheroidization, argon or argon/hydrogen is used as the plasma gas [25]. The use of the Tekna PL 035LS torch has also been reported [26].

There are two types of direct current (DC) torches, these being nontransferred and transferred arc torches. In nontransferred arc DC torches, the electrodes between which the arc is created are inside the body of the torch itself. The plasma gas moves through the arc and is ionized to form the plasma jet. In Fig. 14.37, a typical configuration for a nontransferred arc plasma torch is shown.

In Table 14.12, the decrease in impurity levels and increase in the flow rate are indicated for titanium powder with spheroidization treated by a Tekna torch operated at 50 kW using argon plasma [27].

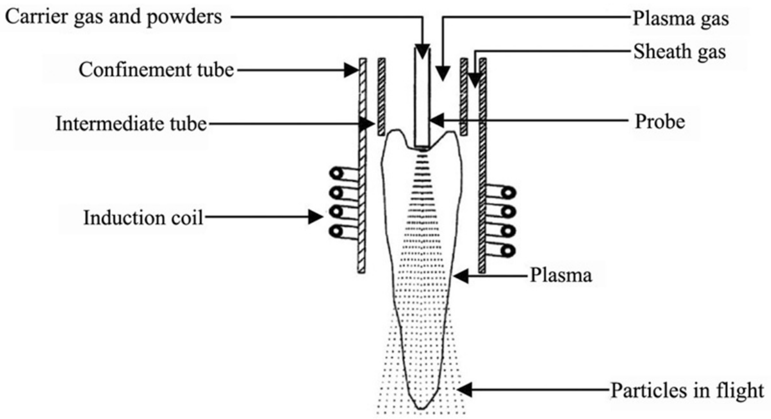

FIG. 14.36 Radio frequency (RF) induction plasma device.

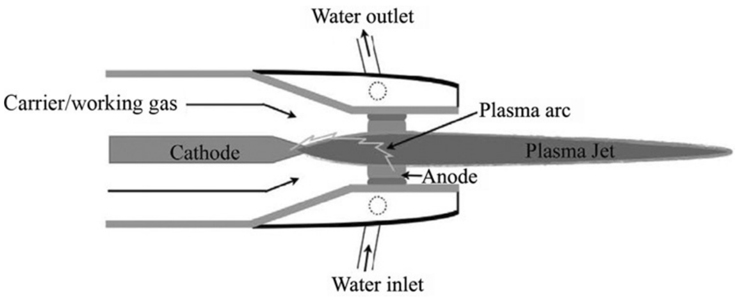

FIG. 14.37 Nontransferred arc plasma torch.

TABLE 14.12 Spheroidization of Titanium Powder by the Tokla Argon Plasma Torch

Properties	Unit	Before Plasma Treatment	After Plasma Treatment
Tap density	g/cm^3	1.0	2.0
Production rate at 100 kW	kg/h	…	10
Particle size	mesh μm	−140 +400 40 − 100	−140 +400 40 − 100
Hall flow test	s/50g	No flow	37
Trace			
[O]	ppm	2050	1800
[C]	ppm	160	120
[H]	ppm	166	114
[N]	ppm	90	90
[Cl]	ppm	1200	360
[Al]	ppm	80	58

In the work [28], the melting and spheroidization of titanium powders were studied. Argon gas was used as the plasma gas. There was informed that the residence times of particles in the plasma region range from 5 to 20 ms, therefore this is usually sufficient, so far as 7–8 ms is required for heating and melting of titanium or zirconium metal particles in the 30 μm size range at 3500 K. In this study, the melting and spheriodization of titanium powders was investigated by the DC non-transferred arc and RF induction plasma methods. Bissell et al. reported [28] that in this study, SEM images indicated that the powder could be spheroidized by an RF thermal plasma using argon gas without significantly increasing impurity levels. Various powder fractions were tested. Only the <75 μm and 75 − 125 μm fractions could be spheroidized; the larger fractions (125 − 250 μm and 250 − 425 μm) were not affected by the plasma treatment. SEM and optical microscope images also showed that titanium powder could be effectively spheroidized by DC thermal plasma using nitrogen gas. In this instance, the powder was used as received and not sieved into fractions. The particles changed color, indicating surface contamination by nitrogen. It is, however, expected that spheroidization without contamination will be possible by DC thermal plasma treatment using argon gas at a gas m temperature near 6200 K.

The nickel-based powders were spheroidized by inductively coupled plasma (ICP) technology [29]. This process is developed by the induction plasma Tekna system. The system consists of a standard Tekna inductively coupled plasma torch (Model PN) placed on top of a water-cooled stainless steel chamber (Fig. 14.36). The feed material is injected axially into the center of the discharge using a water-cooled injection probe with an appropriate amount of carrier/diluent gas. As the individual particles of the feed material are heated and melted in the plasma, they form perfectly spherical dense molten metal droplets, which cool and solidify as they drop by gravity to the bottom of the processing chamber. A scrap Haynes 230 powder, recovered from a laser cladding process, was spheroidized. Fig. 14.38 illustrates the improvement in morphology (more spherical shape and smooth surface of particles) by laser treatment.

Vert et al. reported [29] that Tekna's ICP technology improves the availability for production and recycling of nickel-based powders in the particle size range of −250 +5 μm with tailored morphological and chemical properties (Table 14.13).

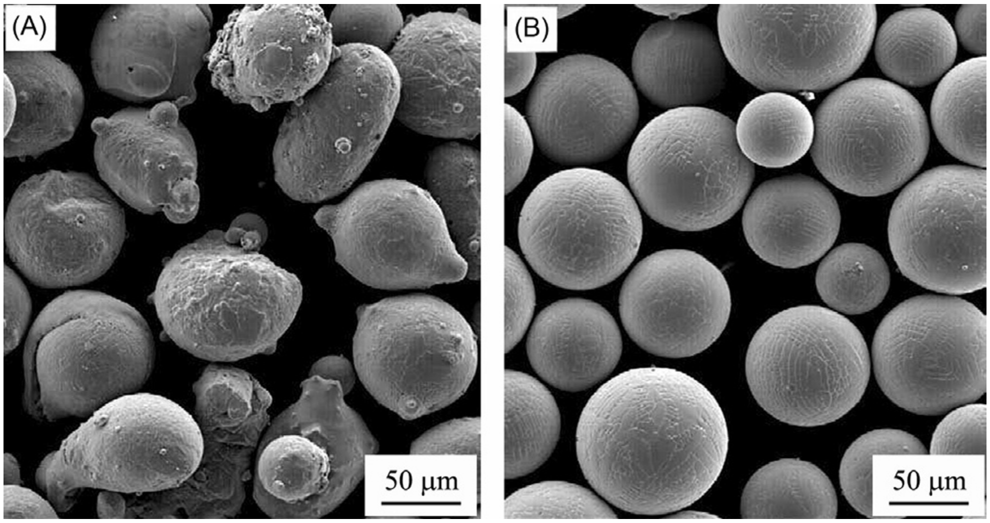

FIG. 14.38 SEM micrographs of Haynes 230 nickel alloy powders: (A) scrap from a laser cladding process; (B) recovered by inductively coupled plasma (ICP) technology. *(From Vert R, Pontone R, Boulos MI. Induction plasma technology applied to powder spheroidization, densification and recycling. In: Compiled by European Powder Metallurgy Association, (Bellstone Shrewsbury, UK) Proceedings of PM 2016 World Congress. Hamburg (Germany); 2016: p. 1–5.)*

TABLE 14.13 Properties of Haynes 230 Nickel-Based Alloy Scrap Powders Treated by Inductively Coupled Plasma (ICP) Tekna's Technology

			Plasma Processing	
Properties	Unit	Scrap Powder	Low Feed Rate	Medium Flow Rate
Apparent density	g/cm^3	5.08	5.45	5.43
Tap density	g/cm^3	5.57	5.92	5.90
Hall flow	s/50g	13.1	10.7	10.9
Oxygen	ppm	1067	160	246
δ_{10}	μm	46.6	49.0	48.0
δ_{90}	μm	89.3	93.4	91.7

δ_{10} is the 10 wt.% cumulative part in ≤particle size range; δ_{90} is the 90 wt.% cumulative part in ≤particle size range.

PROPORTIONING, PACKAGING, AND INTERSTAGE TRANSPORT

Proportioning

Proportioning of a material may be continuous performed by means of feeders, or intermittent by feeding material in batches of preset weight or volume. Continuous uniform material feeding with a given flow rate is required, for instance, during drying and sizing of powders.

Powder feeders play an important role in powder processing such as feeding raw materials or discharging product materials from a storage vessel. The powder load to be treated in the process depends on the accuracy of feeders.

The static and dynamic characteristics of feeders depend on powder properties such as particle size, shape, internal friction coefficient, and powder flowability. They also depend on the operating conditions, including temperature and pressure in the process.

Moreover, feeders are always associated with feed hoppers and their design might affect the function of feeders. If the feed hopper is not well designed, the flow mode in the hopper will be an unfavorable one, called funnel flow and arch formation.

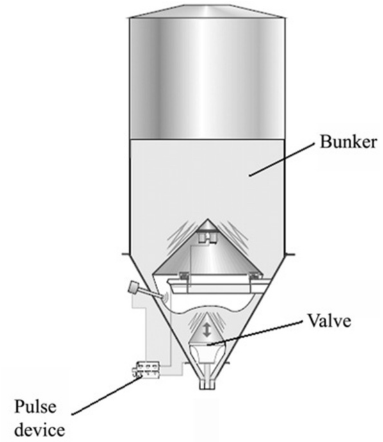

FIG. 14.39 The lower discharger valve that lifts and vibrates to discharge product in either conditions or pulse mode. *Courtesy of MATCON Company*.

Unstable flow is caused by poor feeder selection or inappropriate hopper design. An unstable flow with bridging will also be caused by a variation in powder properties or operating conditions. The wall surface can be coated with ultrahigh molecular weight materials so as to reduce these problems. Suitable vibrators can also be utilized for this purpose. Granulation, drying, or encapsulation can also decrease the friction so that the powder flow can be changed from the funnel flow mode to the mass flow mode, even for a hopper having a large wall angle.

The pulp or slurry is supplied in batches for dehydration in an apparatus of gravitational settling (batch operation) or of filtering (vacuum filters of sampling action). Batch feeding is produced by filling containers (packages) with commodity powder, mixed with other components, and when components have to be delivered for passivation and microencapsulation of powders.

The feeder-activator design provides the powder outflow from the bunker (or storage) through an annular slot between the face plane of the discharge branch pipe and feeder cone. As a result of vibrating the powder, outflow occurs in a fluidized state. Such a design helps to prevent arching. To prevent arch formation in large silo/hoppers, MATCON developed a design of a lower discharger valve that lifts and vibrates to discharge the product in either continuous or pulse mode (Fig. 14.39).

The feeder intended for supplying a wet material is shown in Fig. 14.40. It comprises a horizontal shaft with turning arms, which prevent adhering of wet material to the work element and allow the feeding rate to be adjusted. An agitator mounted in the discharge mouth of the feed bin eliminates arch formation and mouth occlusion with wet material. The maximum throughput is 0.8 m^3/h.

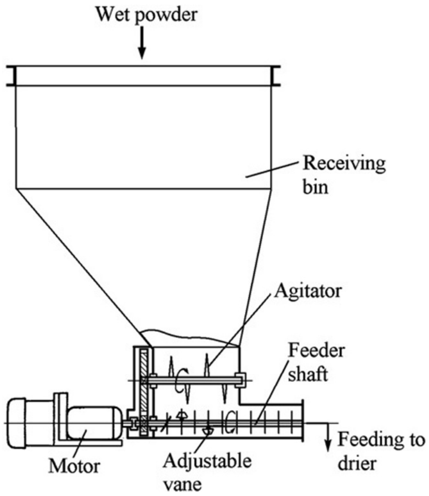

FIG. 14.40 Screw feeder for feeding of wet powders.

Various feeder types have been developed by the Thayer Company [30], including the screw feeder for slurry as well as for dry powder feeding and bell feeders for dry particulate materials. The former are produced in a feed rate range from 0.113 to 27 kg/h (0.25 – 60 lbs/h) by apparent density of powder 0.8 kg/L (MSF model) up to 9 – 4536 kg/h (20 – 10,000 lbs/h) PF-S-4 model.

The required precision of the feed rate magnitude is defined by technological process characteristics. For example, the feed rate of wet powder to drying does not require high volume precision while the additive manufacturing process requires high exact ones. In the work [31], the wheel feeder and newly developed disk feeder were compared by the direct metal deposition process of additive manufacturing technology. It was concluded that the disc feeder had fewer inconsistencies than the wheel feeder and that the former had a better performance metric over the wheel feeder system.

For proportioning the powder discharge, the automatic dosing machines are used. Several companies produce such machines available for proportioning metallic powders and granules. Thus, the MOM company (France) manufactures semiautomatic powder filling machines in a large dose range of dry products (powder, grains, fragments): 10mg to 60kg, up to 10 units per minute. The DOSA Company (Italy) produces high-speed dosing machines by the Auger dosing system for powder, granules, and milled product dosing.

Packaging

There is a variety of apparatuses for proportioning and packaging powders. However, they are designed for handling foods, detergents, dyes, etc. These apparatuses are, however, nonusable for metal powder handling because of the higher density and higher volume containers of the latter. On the other hand, there are completely automated units for proportioning and packaging of iron powders. However, these are very complicated and costly machines and their use is only justified at high production volume.

The Design Bureau of IPMS has developed simpler units for proportioning and packaging of powders. Their capacities correspond to production lines with a value up to 3 t/h. Two types of units have been developed to batch powders: weight batching and volume batching.

For volume batching, the powder is charged into polyethylene packages of 15 and 20 L inserted into steel barrels of the same volume. The package is weighed using an electronic scale and the weight recorded. It is then placed in a vessel. The orifice for charging is then welded, the chamber depressurized, and the packed package is passed to the finished products storage area. The throughput of the unit is 30 packages per hour.

The unit proportioning the powder by weight is completed by commercial equipment, including weight batcher, rotary table, and vacuum pump (Fig. 14.41). The polyethylene bag is introduced into a cartridge of the packaging mechanism of the turntable (Fig. 14.4A–C). Then the package, as was programmed, gradually takes positions to complete the following operations: filling with powder, vibrating densification with simultaneous partial welding of the loading package orifice, air

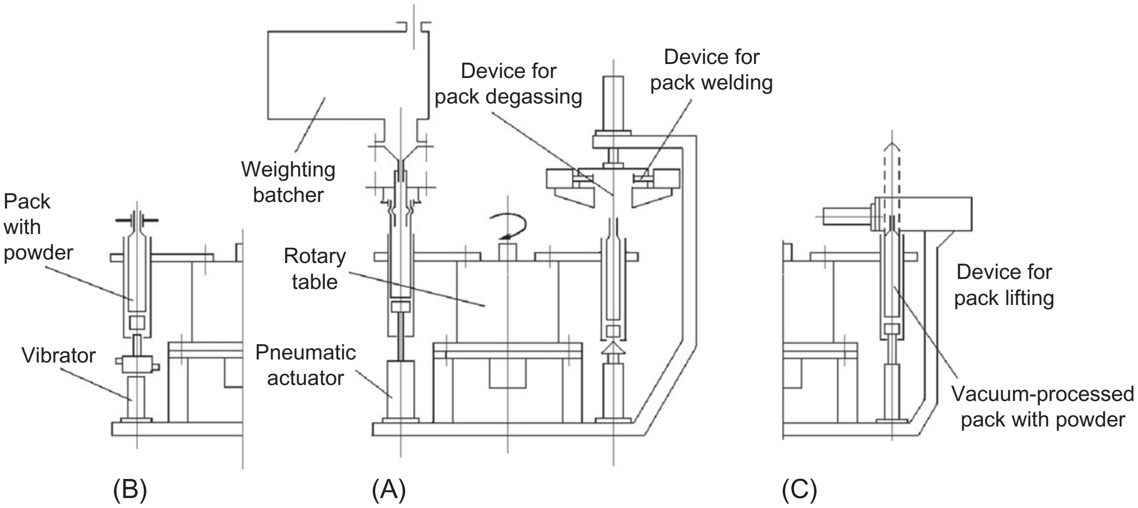

FIG. 14.41 The unit for proportioning the powder by weight, fulfilling the operation in the following positions: (A) filling bag with powder; (B) vibrating densification with simultaneous partial bag welding; (C) vacuumization, final bag welding, and unloading.

extraction and final welding of the package loading orifice of the package, and unloading. Loading batch of powder is maximum 20 kg; maximum throughput of the unit is 30 packages per hour.

Interstage Transport

The type of the interstage transport chosen depends on the physical and mechanical properties of the material; assembling of processing equipment; production process management; and power of the production line.

Transportation of dry mixtures is done in special charge cans by material handling equipment (bridge cranes, electrical loaders fed via cables, crane jibs, telpher loaders, swing jib cranes), electric loaders, and roller tables. The type of material handling equipment is chosen, taking into account the weight and height of the load to be lifted, material flow volume, load-displacement range, room geometry, and category of fire/explosion safety.

The pulp is pumped by gravel pumps. Common types in the CIS countries are pumps that provide a pulp flow rate up to 63 m^3/h at a pressure of 22.5 m of water.

There are continuous and discontinuous interstage transports for powders. The discontinuous container transport is used for handling relatively small quantities. Advantages of such a transport type are that compact placing of processing equipment is achievable, interoperation relations become simpler, and mechanical material loss is reduced. Container volume is chosen, taking into consideration the quantity of the powder to be processed during one shift. Containers can be simultaneously operated as storage (silos).

A container [32] is designed to ensure the tightness of joints to the loading and unloading devices. The container housing has a mounted bypass tube to exhaust the dust-laden air, which is forced from the filling tank to the upper portion of the container as its content decreases. Detailed information on this container design can be found in the subsection, "Definition of the local exhaust capacity," in Chapter 27.

The containers equipped with a cone valve system for joining to the receiving hopper during powder unloading are shown in Fig. 14.42. Such containers produced by the MATCON Company are commercially available.

Containers with a bottom fitting in spitzkasten form (Fig. 14.43) provide a uniform settling of the powder throughout the horizontal cross-sections during its unloading from the container, thus preventing powder segregation.

The conveyors (belt conveyors, vibrating conveyors, vertical spiral vibrating conveyors, spiral conveyors, and worm conveyors), bucket elevators, and pneumatic transports are used as continuous types of transport.

Belt conveyors are used either for displacement of powders in a horizontal plane or for low height lifting. The angle of inclination of a conveyor should be lower than the angle of friction of powder on the belt surface. Belt conveyors are favored when the loading sequence is in a straight line, for instance, when the melt is atomized in a horizontal chamber.

Belt conveyors can be set up at a steep angle of 60 degrees when wet powders are displaced, unloaded, for instance, from a dehydrating apparatus. The wet powder on a conveyor-loaded side is pressed by the belt of another conveyor moving synchronously with the former.

Vibrating conveyors are used for the transport of powders in a horizontal plane, for example, when the loading is performed at several points from hopper sections. Dustproof performance and simplicity of design are advantages of vibrating conveyors. Vibrating conveyors contain a load-carrying element in the form of a tube mounted via elastic elements on a fixed frame. As the vibroexciter, a debalanced two-shaft vibrator or two electromechanical vibrators are used. The jump

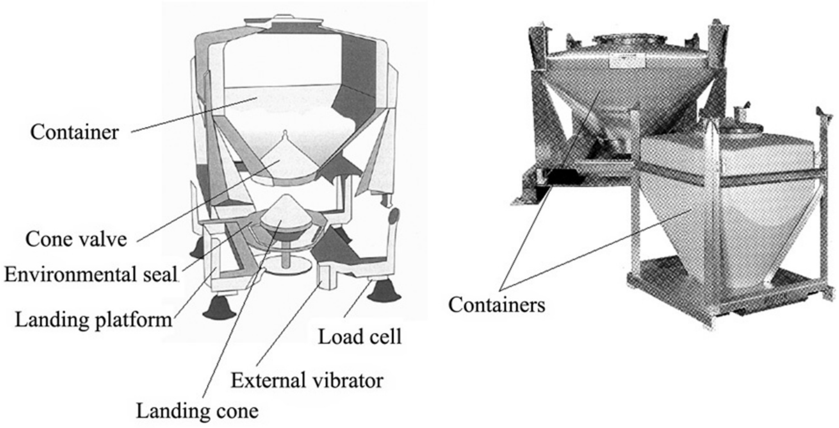

FIG. 14.42 Container equipped by cone valve system. *Courtesy of the MATCON Company.*

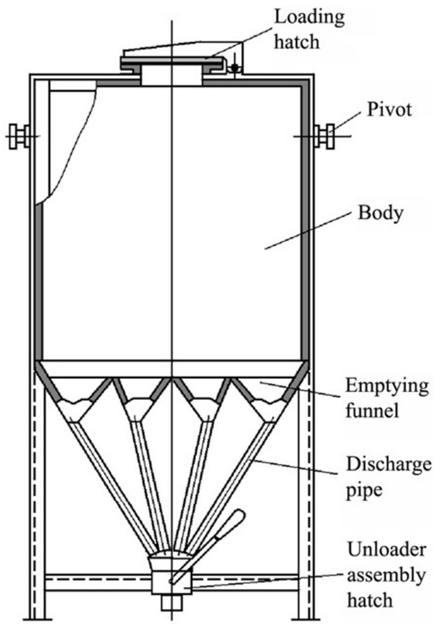

FIG. 14.43 Container with bottom fulfilling in spitzkasten form for marketable powder.

joints of overloads are tightened using elastic rubber gaskets. Throughput amounts to 6.0 t/h, and the length of transportation is 2.5–5.0 m.

A vertical vibrating conveyor is a conveying column with an inside spiral chute connected to supports by means of elastic ties and equipped with vibroexciters. The tightness of the loading and unloading subassemblies is reached via elastic corrugated rubber gaskets. The conveyor KVV-0.5 has a column of 500 mm external diameter; a lifting height of 5.0 m; and a throughput maximum 1.5 m^3/h apparent volume at a ratio of the chute filling of 0.6–0.8. An upgraded design of the conveyor has vibroexciters mounted on the top of the column. A dustproof construction of the conveyor excludes dust emission. The vertical vibrating conveyor is a rather costly machine.

Vertical bucket elevators can also be used. However, their operation is accompanied by increased dust emission.

For transportation of a relatively small quantity of powders, inclined spiral conveyors are convenient to use (Fig. 14.44). The powder is delivered to a transfer bin equipped with a gate. In a tube, a lift helix is rotated, the upper end of which is connected to the electric motor shaft while the lower end is free. The powder passes to the tube through a feed slot in the bin and is carried away by the lift helix and unloaded through a discharge branch pipe. The conveyor may, if required, be equipped with a water cooler, coaxially attached to the lift pipe; the feed and lead away water through nipples are provided. The spiral rotates with 1000 R/h speed. Volumetric throughput is 0.2 m^3/h apparent volume of powder; the height of lifting is 4.0 m.

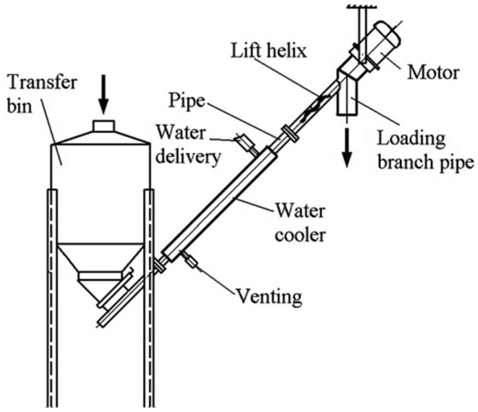

FIG. 14.44 Spiral conveyor.

Pneumatic transport of powder is able to lift a powder, if required, to as much as 8–10 m in height, or to convey it to long ranges, especially by a cascade assembly of equipment. Recommendations relative to the design and calculation of transport systems are given in [33]. The use of a pressurized pneumatic transport is preferred.

Pneumatic transport is used in pneumatic dryers (see Fig. 14.11), in which the powder is conveyed suspended in a gas while its movement is provided by a high-pressure exhauster.

REFERENCES

[1] Bogdanova OS, Olevsky VA, editors. Handbook for enriching of ores. In: Preparatory processes. 2nd ed. Moscow: Nedra; 1982 [in Russian].

[2] Dytnerskiy YI. Processes and apparatuses of chemical technology. 3rd ed. Moscow: Chimija Publishers; 2002 [in Russian].

[3] Lykov MV. Drying in chemical industry. Moscow: Chimija Publishers; 1976 [in Russian].

[4] Yurenjeva VN, Lebedeva PD, editors. Thermotechnical Handbook. 2nd ed. Moscow: Energija Publishers; 1976 [in Russian].

[5] Sazhin VS. Technique of drying. Moscow: Energija Publishers; 1984 [in Russian].

[6] Gorbis ZR. Heat exchange and hydrodynamics of disperse through streams. Moscow: Energija Publishers; 1970 [in Russian].

[7] Neikov OD, Logachev IN. Aspiration and air dedusting during manufacture of powders. Moscow: Metallurgija Publishers; 1986 [in Russian].

[8] Shirato M, Murase T, Iritani E. Filtration in the chemical process industry. In: Matteson MJ, Orr C, editors. Filtration, principles and practices. 2nd ed. New York: Marcel Dekker, Inc; 1987. p. 299–423.

[9] Deville S, et al. Low-temperature ageing of zirconia-toughened alumina ceramics and its implication in biomedical implants. J Eur Ceram Soc 2003;23:2975–82.

[10] Morita Y, Nakata K, Ikeuchi K. Wear properties of zirconia/alumina combination for joint prostheses. Wear 2003;254:147–53.

[11] Naglieri V, et al. Optimized slurries for spray drying: different approaches to obtain homogeneous and deformable alumina-zirconia granules. Materials 2013;6:5382–97. https://doi.org/10.3390/ma61.

[12] Kern F, Palmero P. Microstructure and mechanical properties of alumina 5 vol % zirconia nanocomposites prepared by powder coating and powder mixing routes. Ceram Int 2013;39:673–82.

[13] Brodskiy YA, Bazikov VI, Zubkov IV, Krylov AI, Stepanenko VD. Vibratory dryers for chemical industry. Chem Oil Gas Eng 2006;10:7–10.

[14] Barskiy MD. Fractionating of powders. Moscow: Nedra Publishers; 1980 [in Russian].

[15] Bradley D. The hydrocyclone. New York: Pergamon Press Publishers; 1965.

[16] German RM. A-Z of powder metallurgy. Oxford: Elsevier Advanced Technology Publisher; 2005.

[17] Troitskiy VN, Brodsky YA. Application of vibratory mixers in powder metallurgy. Powder Metall Met Ceram 1989;1:91–4.

[18] Schatt W, editor. Pulvermetallurgie Sinter und Verbundwerkstoffe. Leipzig: VEB Deutscher Verlag für Grundstoffindustrie; 1979.

[19] Perry JH. Chemical engineers' handbook. McGRAW-HILL BOOK Company Publishers; 1969.

[20] Zhelibo EP, MYa G, Pol'shin ÉV. Effect of annealing on the composition, structure, and magnetic properties of very fine iron and iron-cobalt alloy powders. Powder Metall Met Ceram 1989;28(10):739–42.

[21] Solodovnikov VD. The type of the in-process transport is chosen in dependence on physical and mechanical properties of a material; Microcapsulation. Moscow: Chemija Publishers; 1980 [in Russian].

[22] Burykin AA, Neikov OD, Rabin PB, Sharova LS. Microencapsulation of metallic powders for prevention of explosions and dust emissions during their production and processing I. Study of the morphology and oxidation kinetics of microcapsulated powders. Powder Metall Met Ceram 1991;30 (6):527–30.

[23] Neikov OD, Rabin PB, Vasiliyeva GI. Microcapsulated aluminium powders. Mater Sci Forum 1997;242:219–22.

[24] Gignard NM. Experimental optimization of the spheroidization of metallic and ceramic powders with induction plasma. Thesis, Sherbrooke (Quebec, Canada): National Library of Canada; 1998 [Accessed 15 March 2018].

[25] Jiang X, Boulos M. 2006. Induction plasma spheroidization of tungsten and molybdenum powder. Trans Nonferrous Met Soc China 2006;16:13–7.

[26] Károly Z, Szépvölgyi J. Plasma spheroidization of ceramic particles. Chem Eng Process 2005;44:221–4. Available from: János Szépvölgyi, 02 February 2018.

[27] Boulos M, Heberlein J, Fauchais P. Thermal plasma processes, fundamentals and applications. In: Short course. Pretoria (South Africa): University of Pretoria, 28-29 October. 2011; 2011, https://www.researchgate.net/publication/291417167_Titanium_and_zirconium_metal_powder_spheroidization_by_thermal_plasma_processes. Accessed 12 March 2018.

[28] Bissett H, van der Walt IJ, Havanga JL, Nel JT. Titanium and zirconium metal powder spheroidization by thermal plasma processes. J. SAIMM 2015; 115(10): 937 – 42. DOI: 10.17159/2411-9717/2015/v115n10a6. [Accessed 14 March 2018].

[29] Vert R, Pontone R, Boulos MI. Induction plasma technology applied to powder spheroidization, densification and recycling. In: Compiled by European Powder Metallurgy Association, (Bellstone Shrewsbury, UK) Proceedings of PM 2016 World Congress. Hamburg (Germany); 2016. p. 1–5.

[30] Thayer Company (Pembroke, MA). http://www.thayerscale.com/our-company/.

[31] Bitragunta VS, Sparcs T, Liou F. Performance metric for powder feeder systems in additive manufacturing. Rolla, MO: Missouri University of Science and Technology; 2015, https://sffsymposium.engr.utexas.edu/sites/default/files/2015/2015-38-Bitragunta.pdf. Accessed 15 March 2018.

[32] USSR Patent 1,126,508, July, 1983.

[33] Spivakovskiy AO, Dijachkov VK. Transporting machines. Moscow: Mashinostroenie Publishers; 1983 [in Russian].

FURTHER READING

[34] Chevalier J, Gremillard L. Ceramics for medical application: a picture for the next 20 years. J Eur Ceram Soc 2009;29:1245–55.

[35] USSR Patent 1,017, 891, November, 1981.

[36] Neikov OD, Kolesnichenko YuV. Tokhtuyev VG. Drying of water atomized iron powders. Powder Metall Metal Ceram 2015;54(5–6):364–73.

[37] Usol'tseva EE, Pomosov AV. Electrodeposition of fine copper powders in the presence of organic additions. Sov Powder Metall Met Ceram 1983;22 (8):610–3.

[38] Nichiporenko OS, Pomosov AV, Naboychenko SS. Powders of copper and copper alloys. Moscow: Metallurgija Publishers; 1986 [in Russian].

Chapter 15

Production of Aluminum Powders☆

Victor G. Gopienko

All-Russian Aluminum-Magnesium Institute, Saint Petersburg, Russia

Chapter Outline

Introduction 459
Gas Atomization of Aluminum Powder 460
Production of Aluminum Granules 465
Production of Flakes, Pigments, and Pastes 468
Nickel-Clad Aluminum Powders 474
  Properties of Nickel-Clad Aluminum Powders 474
Aluminum Scrap Recycling 474
  Waste Aluminum Foil Recycling 474
  Processing of Recycled Aluminum to Granules 477
The Main Application Fields for Aluminum Powders 477
References 480

INTRODUCTION

Aluminum and aluminum alloy powders are manufactured almost exclusively by gas atomization. Compressed air is used as the atomizing gas for most applications. Inert gases (nitrogen, argon, and helium) have found application in special cases. Currently, the annual world production of aluminum powders amounts to 100,000 metric tons [1] while the productive capacity is estimated to be approximately twice that [2]. A large part of this capacity is in North America and Russia. North American metal shipments in short tons in 1995–2015 (Fig. 15.1) show the tendency of the dynamics of aluminum powder production up to 2013, and stabilization in 2014–15, at the level of 40,000 tons [3].

The ranges of aluminum powder applications are of great variety. They include aluminothermic reduction in metallurgy, chemical processes, explosives, rocket fuels, pyrotechnics, thermite welding, additives for gas generation in aerocrete production, pharmaceuticals, and pigments for paints and inks.

These are the following basic kinds of powder products from aluminum:

- Powders: particles with a size from a few microns to 1.0 mm (usually, not >0.5 mm) of spherical, oval, drop-like, irregular, fragmental, or dendritic shape.
- Flakes: scaly (lamellar) particles with a thickness smaller than 1.0 μm and linear sizes 50–200 μm. Particles are usually coated with a thin layer of stearin, aluminum stearate, paraffin, or other fats, the content of which is 0.2%–4.0%.
- Pastes: compositions of flake particles (65%–75%) and a liquid phase (water, hydrocarbons).
- Granules (grit): particles with a size larger then 0.5–1.0 mm of spherical, oval, drop-like, disc-shaped, needle, or irregular shape.

Known methods of aluminum powder production can be divided into two basic groups:

- Physicochemical methods: electrolytic sedimentation from solutions or melts; reduction (or thermal decomposition) of aluminum compounds; and evaporation and condensation of the metal from a vapor phase.
- Physicomechanical methods, that is, without basic changes of chemical and phase structure of the initial material: mechanical crushing of aluminum, fragile alloys of chips, foil; atomization of melts.

Along with the main commercial gas-atomization technique, the following methods for aluminum powder manufacture are known:

- *Crushing* of fragile aluminum alloys (Al—Ni, Al—Mg, Al—Si) in ball mills or other crushing devices (particle shape is fragmental).

☆Expanded and updated by O.D. Neikov.

Handbook of Non-Ferrous Metal Powders. https://doi.org/10.1016/B978-0-08-100543-9.00015-4
© 2019 Elsevier Ltd. All rights reserved.

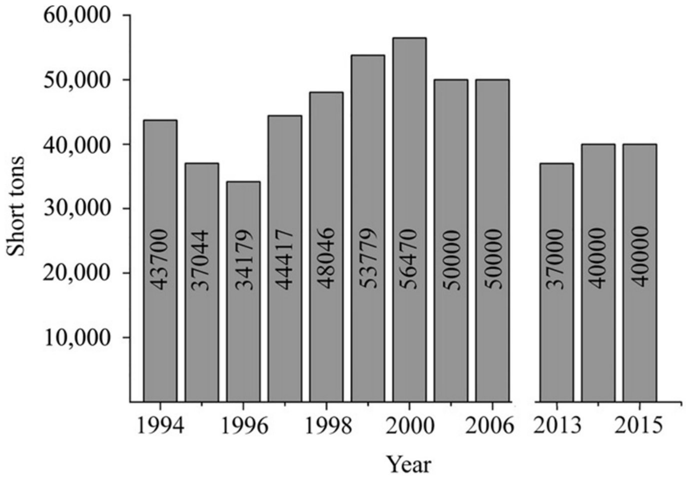

FIG. 15.1 North American aluminum powder shipments in short tons in 1994–2015. *From Williams B. Powder metallurgy—a global market review. In: International powder metallurgy directory & yearbook, 12th ed.; 2006/2007. p. 5–16, MPIF2016(5)* www.mpif.org.

- *Dry grinding* of aluminum powder or foil in the presence of surfactants in a protective gas atmosphere with monitored content of oxygen (production of pigment, pyrotechnic, and clumpy powders).
- *Grinding of aluminum particles* in a liquid phase (hydrocarbons, water) containing surfactants (stearin) and other additives (production of pastes). Pastes can also be manufactured by mixing the powder with hydrocarbons or aqueous solutions with special additives.
- *Granulation*: free casting of the melt into a cooling medium through ground apertures of the melting pot (crucible); the size of the granules is of 4–20 mm (the shape is disk-shaped).
- *Centrifugal atomization* of the melt through lateral apertures of the punched walls of a rotating glass, from a flat disk surface, edges of a cone glass, etc. The molten metal forms droplets that solidify in the cooling gas medium or in water. Plants for centrifugal atomization of the melt are mainly used to manufacture granules with a grain size of >0.5 mm in size or coarse fractions of powders larger than 100 μm in size. Centrifugal atomization is usually carried out through apertures of the rotating punched vessel (glass). Designs of plants with centrifugal atomization are used in Russia and Ukraine [4].
- *Disintegration of solid metal* at hot brittleness temperature; the size of granules is 5–20 mm, and their shape is irregular.
- *Lumping of fine foil scrap* into round granules of 3–6 mm in size.

The characteristics of aluminum powders produced by various methods are given in Table 15.1.

GAS ATOMIZATION OF ALUMINUM POWDER

Atomization of melts by compressed gases or liquids provides for the manufacture of powders of aluminum and its alloys in a wide range of sizes from 1–2 μm to 1–2 mm with particle shape varying from spherical to drop-like to irregular. Uniformity of composition and fine microstructure of powder particles are achieved by atomization of aluminum alloys due to a high cooling rate of 10^4–10^6 K/s [5–7].

The greatest development and industrial application for producing metal powders by melt atomization by compressed gases use the following basic types of plants:

- Vertically upward aspirating plants, such as operated by Alcoa [2], allow the production of powders with the widest range of particle sizes.
- Horizontal aspirating installations, where the melt jet and atomizing torch are directed horizontally or obliquely to the horizon. The ejection feed of the melt for atomization of aluminum, magnesium, and their alloys is used at aluminum mills in Russia while a feed under pressure was utilized at the Kluchevskoy ferroalloy mill in Russia and a siphon feed was used at the Ekkart-Werke in Germany [4].
- Vertical installations, where a free flow stream of the liquid melt is atomized into droplets by impingement of high-pressure jets of gas or oil. They are used mainly to produce powders of heavy metals and alloys (iron, copper, complex alloys based on iron). In some cases, plants of such type are also used for producing light metals and alloys, including aluminum [4].

TABLE 15.1 Characteristics of Aluminum Powders [4]

Type of Powder, Method of Production	Shape of Particles	Mass Medium Particle Size (μm)	Density (g/cm^3)		Al_2O_3 (wt%)	Al Content (wt%)
			Apparent	Tap Density		
Powders produced by:						
Air	Oval with rough surface shape, irregular	50–200	0.73–1.24	1.15–1.25	0.1–1.0	99.5
Inert gas atomization	Spheroidal	45–100	0.5–1.4	0. 90–1.70	0.1–1.7	99.5
Ultrafine powders produced by condensation from gas medium	Spheroidal	0.2–0.5	…	…	…	>99
Powders produced by grinding fragile alloys of Al—Mg, Al—Ni, Al—Si systems	Fission-fragment	40–2000	…	…	…	70–90
Flakes produced by dry grinding:						
Fine	Flaky	45	0.27–0.41	0.41–0,68	2–21	96–98
Coarse	Plate-shaped	150–1170	0.22	0.36	1	>99.5
Cloddy (for SAP)	Lump of flaky particles	210	1.08–1.21	1.35–1.49	6–14	The rest
Granules produced by melt atomization	Oval, tear-shaped, irregular, acicular	500–5000	1.8–1.5	1.6–1.8	…	87–99.5
Granules produced by free melt casting into the water or cooled surface	Disc-shaped	500–20,000	1.5–1.7	…	…	87–99.9
Paste produced by grinding in the fluid of liquid hydrocarbon	Flaky	45	…	…	2–20	…

Numerous other variants of constructive design of the basic types of plants for atomization of molten metals and alloys listed above are known.

A scheme of the Alcoa process based on the vertically upward aspirating principle is shown in Fig. 15.2 [8]. The molten metal is supplied from the holding or melting furnace to the atomizing tundish. The liquid is drawn from the tundish through a delivery tube into the atomizing nozzle. This is attained owing to the suction (aspiration) effect arising at the nozzle end by the flow of the high-pressure atomizing gas in the nozzle. Meeting with the high velocity gas jet, the liquid metal is broken up into droplets that are carried along by the gas flow and quenched by the gaseous cooling atmosphere in the chiller chamber. The particles formed together with the cooling air pass into the collection system that consists of two sets of cyclones. The powder collected in the cyclones is then transported in an inert gas atmosphere to the screens and packing station under inert gas.

However, this process requires careful adjustment and maintenance. An expected stopping or decreasing of the delivery of the cooling air in the chiller chamber causes an increase of the airborne dust concentration of aluminum powder over the level, which forms an explosive mixture. Generally, the technology of producing gas-atomized aluminum powders is a potentially explosive process and special safety measures are required that considerably increase the manufacturing cost. These safety measures, such as those accomplished by Alcoa, comprise cooled air supplied for the melt atomization in the chiller chamber; the carrying out under inert gas of all powder movement, including screening for separating into size

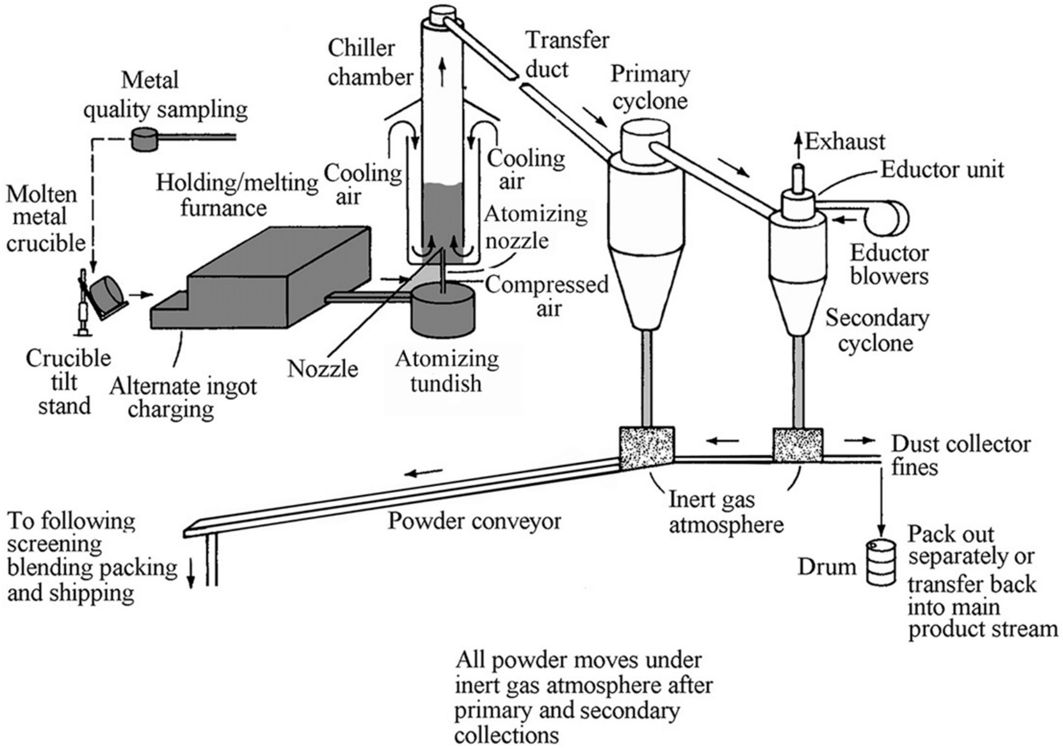
Metal quality sampling
Chiller chamber
Transfer duct
Primary cyclone
Exhaust
Eductor unit
Molten metal crucible
Holding/melting furnace
Cooling air
Cooling air
Atomizing nozzle
Eductor blowers
Compressed air
Secondary cyclone
Crucible tilt stand
Alternate ingot charging
Nozzle
Atomizing tundish
Dust collector fines
Inert gas atmosphere
To following screening blending packing and shipping
Powder conveyor
Drum
Pack out separately or transfer back into main product stream
All powder moves under inert gas atmosphere after primary and secondary collections

FIG. 15.2 Schematic of the Alcoa process for atomizing aluminum powder.

fractions and packing into drums; and, in addition, using sensitive systems controlling a low concentration of powder in the gas and the pressure rise.

Plants of the horizontal type have the following advantages:

- Impossibility of melt ingress into the dust-precipitating system in the case of a bath fracture.
- Relative ease of monitoring of the atomization process.
- Increase of safety due to the division of stages and devices of atomizing (melting bath, atomizer) and primary classification (atomizing chamber, cyclones).

The disadvantage of such plants is the amount of the area occupied, which is greater than for other types because a large part of the plant is in a horizontal plane.

Plants of a vertical type with top-down atomization are more compact and occupy a smaller production space. However, in this case the danger connected with an opportunity of melt inrush into the atomizing chamber is increased, the atomization process is more difficult to control, and a large chiller height is necessary for supply of solidification of the molten particle stream. The main characteristics of the explosion risks of the powders are shown in Table 15.2 [4].

The properties of typical commercial aluminum powders are given in Table 15.3.

Plants of the granulation type are lesser dangerously explosive and have a higher efficiency. However, they are not suitable for producing highly dispersed powders. The horizontal aspirating circuit of gas-atomized powder production (Fig. 15.3) most widely used in Russia includes the high compressed gas (air or inert gas) atomization systems and powder separation.

Devices with dry separation of atomization products (in cyclones, multicyclones, bag filters) and with melt atomization into a liquid medium (hydrocarbons or aqueous solutions) are used. In the latter case, higher cooling rates are achieved. A disadvantage of atomization into a liquid is the necessity of powder drying and regeneration of the coolant and received powders can be contaminated with carbon (in the case of the atomization into liquid hydrocarbons), oxygen, and hydrogen (in the case of water atomization or gas atomization into water). The high activity of aluminum powders limits the opportunities of using devices for water atomization of aluminum and its alloys.

The results of studying the influence of gas-atomization parameters on aluminum powder particle size are considered in the work [9]. The schematic diagram of an installation at the RUSAL PM manufacturing plant, where the investigations were fulfilled, is presented in Fig. 15.4. Atomization is performed by the ejection nozzle design under 3.0 MPa nitrogen pressure. Gaseous nitrogen heated by passing through a heater is supplied to the atomizer.

TABLE 15.2 Explosion Risk Characteristics

Type of Powder	Composition, Content (wt%)	Powder Particles Size (μm)	Explosion Risk Characteristics			
			LCIL (g/m^3)	p_{max} (MPa)	v_{max} (MPa/s)	τ_{in} (s)
Al	99.95Al	160 max 50 max	60 47	0.43 0.56	6.6 7.7	0.10 0.05
AD-33 (in Russian Federation classification)	1.3(Zn+Mg)-0.3Cu-0.5Si-0.14 Mn Al—balance	160 max 50 max	80 58	0.39 0.43	4.3 5.6	0.15 0.1
Al-Cr-Fe	90.5Al-8Cr-1.5Fe	63 max 50 max	101 84	0.43 0.49	2.0 4.0	0.3 0.1

LCIL: the low concentration ignition limit; p_{max}: the maximal explosion pressure; v_{max}: the maximal velocity of its growth; τ_{in}: the induction period (the time from the start of igniter to the ignition moment of the powder suspension).

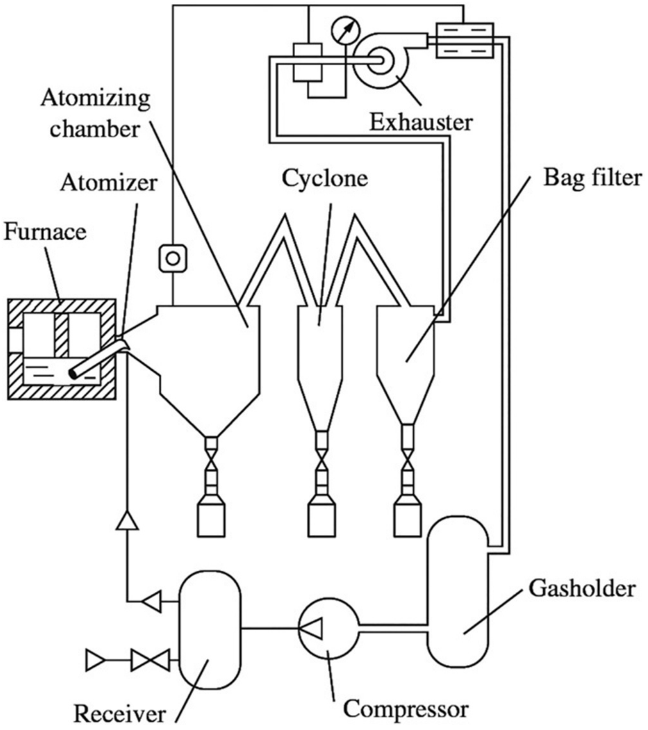

FIG. 15.3 Schematic diagram of a gas-atomization plant.

The atomizing gas is delivered through an annular orifice around the nozzle at the converging angle (Fig. 15.5). The gas flow creates the suction (ejection) effect at the tip of the nozzle that draws the molten metal from the tundish into the nozzle. In contrast of close coupled gas atomization [10] (see also Chapter 4), in present nozzle design the intake liquid metal stream is atomized by converging annular gas jet. The spraying torch is cooled by nitrogen entering from the cooling ring and the forming spray precipitated in a bottom part of the atomization chamber, which is not shown in Fig. 15.4. The amount of gas delivered by the nozzle is controlled by the heated gas tube valve.

According to data [10], the variation of atomization parameters in the following range: 1153–1253 K liquid melt temperature (T_m), 873–973 K nitrogen temperature (T_n), and 0.17–0.21 m^3/s nitrogen consumption (Q) showed that the optimum is achieved by $T_m = 1253$ K, $T_n = 933$ K, $Q = 0.17$ m^3/s condition. The optimum criterion was the maximal yield of powder particle fraction <10 μm, which in the above condition was 21.3% by 21.2 μm median diameter.

TABLE 15.3 Properties of Typical Commercial Atomized Aluminum Powders

Type of Powder	Chemical and Physical Properties											Source
	Composition (wt%)					Apparent Density (g/cm^3)	Sieve Analysis (wt%), Sieve Size (μm)					
	Al (min)	Fe	Si	Each	Total		+250	+160	+100	+45	–45	
Atomized powders Typical	99.7	0.25[a]	0.15[a]	0.05[b]	0.15[b]	0.8–1.3	Median diameter within 5–150 μm					[2]
High-purity atomized powders Minimum Typical	99.97 99.976	0.007	0.008		0.009	0.8–1.3	Median diameter within 5–150 μm					[2]
AL-180[c]	99.99–99.999						Inquire					AEE
Atomized aluminum powders	99.4	0.4	0.3			0.95–1.05	0	0	5–15	55–65	35–45	PM
AL-111, Coarse aluminum powder	99.7						−50 + 100 mech					AEE
AL-104, Spherical aluminum powder	99.9						1–3 μm					AEE
GY-FLT	99.0	0.2[b]	0.1[b]	0.27[b]		0.9	1–1000 μm					Xjalp
Pigmentary aluminum powder[d]	Bal	0.5	0.4	4.06[e]			0	0	…	0.8		RUSAL

[a] *Fe + Si of 0.30 wt% max.*

[b] *Max.*

[c] *Aluminum sputtering targets;* RUSAL, *Russian Federation Aluminum Company;* PM, *Pometon;* AEE, *Atlantic Equipment Engineers, Division of Micron Metals, Inc.;* Xjalp, *Xinji Guangyuan Metal Powder Co. Ltd.*

[d] *Gas (nitrogen + 6 wt% oxygen) atomized powders are ground in ball mills with greasy additives.*

[e] *Including 3.8% greasy additives.*

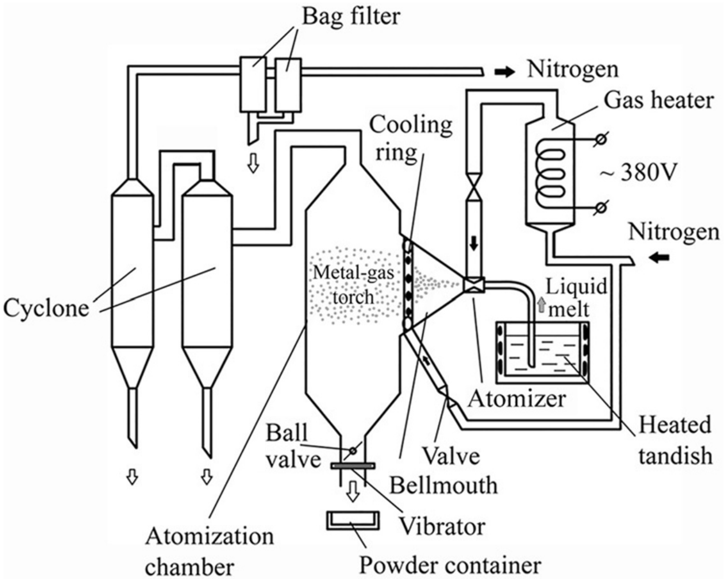
Bag filter
Nitrogen
Gas heater
Cooling ring
~380V
Nitrogen
Metal-gas torch
Liquid melt
Cyclone
Atomizer
Heated tandish
Ball valve
Valve
Bellmouth
Vibrator
Atomization chamber
Powder container

FIG. 15.4 Gas-atomization installation with ejection nozzle design at RUSAL PM manufacturing plant.

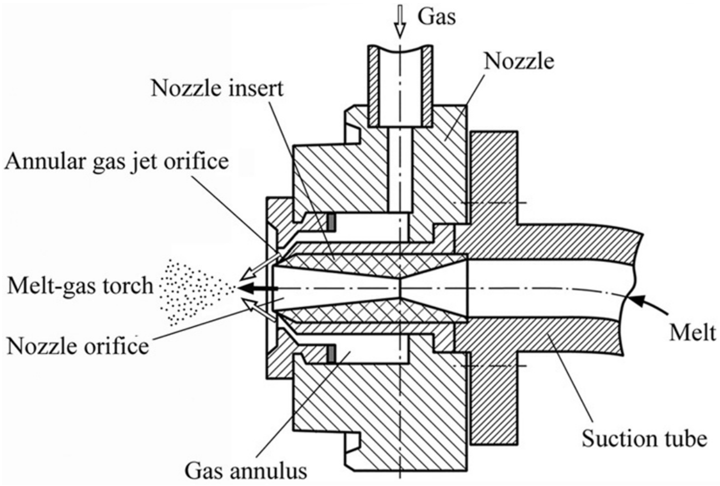
Gas
Nozzle
Nozzle insert
Annular gas jet orifice
Melt-gas torch
Nozzle orifice
Melt
Suction tube
Gas annulus

FIG. 15.5 Ejection gas atomizer.

The typical chemical analyses and physical properties of atomized aluminum powders are shown in Table 15.3.

Water atomization is not used commercially for aluminum and its alloys for fear of the explosion risk of the atomization process due to rapid hydrogen emission during powder-water interaction and the high reactivity of aluminum that can cause heavy oxidation of the surface of water-atomized powders.

In contrast to the traditional opinion, recent studies have shown that water atomization under optimized conditions could be used for the production of high-quality aluminum alloy powders [11,12]. This technique is discussed in Chapter 16.

PRODUCTION OF ALUMINUM GRANULES

According to the properties and application fields, granules are a transition link between powders and ingots; the precise border between powders and granules in the range of particle size from 0.1 to 1.0 mm is practically absent. In some cases, powders can be successfully replaced by granulated aluminum and its alloys, in particular in the chemical industry and in the production of steel and ferroalloys, chromium, etc.

The advantages of granules in comparison with powders are their higher profitability and the lower explosion risk, both of the production process and the product itself. This simplifies the organization of manufacture and use of such products.

The largest consumers of granules from primary and secondary aluminum are ferroalloy and steel works. The consumption of granules has increased with a corresponding decrease in the consumption of pig aluminum or powders.

In recent years, the technology for melted aluminum granulation has mainly developed in the direction of an increase of granule uniformity in size, reduction of their oxide and gas content, and a possibility of regulation by the coarseness, granule shape, and microstructure of granulated alloys. Four basic circuits of granulation technique allowing the manufacture of aluminum granules of various grain size, shape, and hardening degree are used. The basic technological schemes of granulation that are used in Russia are given in Table 15.4 and Fig. 15.6.

The scheme in Fig. 15.6A, circuit I (pouring into the water through a tundish with apertures in the bottom), is used in the enterprises of the aluminum industry and ferrous metallurgy plants. Granules of aluminum of high and technical purity as well as granulated aluminum alloys are manufactured. Mechanized lines with productivity up to 10,000 tons per year working under circuit I are used in the Volgograd Aluminum plant of the RUSAL company in Russia [4] to produce granules with a size of 5–20 mm from high-purity aluminum (for gallium cementation from aluminate solutions) and granules from secondary aluminum with high iron content (for processing pig iron and steel). In this circuit, the reduction of the granule size is achieved by vibration of the pouring bowls. The plant is completely mechanized and provides a continuous technological process from melting of the metal to discharging the commodity product classified by granule size.

Granules manufactured by centrifugal atomization of the melt into water, circuit II (Fig. 15.6B), are used in powder metallurgy. The cooling rate of granules is close to that for gas-atomized powders. The inhibition of diffusion and fixing of high-temperature structure allow a two- to three-fold increase in the level of allowable impurities in alloys without a decrease in the mechanical and corrosion properties of the material, that is, to use effectively low-grade metal. In some cases, impurities traditionally considered as harmful, such as iron, form fine intermetallic phases that provide good elevated temperature strength and other mechanical properties.

The scheme in Fig. 15.6C, circuit III, provides cooling of atomized particles in a gas atmosphere. In this process, needle-shaped (in air), drop-shaped, or spherical (in inert atmosphere or under protection of a particle surface by flux) granules are produced.

The technological circuit IV (pouring to a cooled surface, Fig. 15.6D) eliminates the contact of granules with water and the subsequent drying process. Despite the seeming simplicity in this circuit, there are serious difficulties connected with the necessity of fast heat removal from solidifying granules. As a rule, the productivity of such plants is of the order of 100–300 kg/h. Drop casting is carried out from the punched tube (funnel) radially placed over a water-cooled metal disk rotating in a horizontal plane. The granules, which have solidified on the disk, are cleaned off in the receiver, where they are led to sieving and packing. Instead of a rotating disk, a moving belt can be used. Plants of this type are used by the firms Ekkart-Werke (Germany) and Pechiney (France).

Under industrial conditions, there are plants with units that generate electromagnetic oscillations acting on the melt stream, which has allowed a reduction of granule size up to 2–10 mm [4].

In centrifugal atomization, centrifugal force breaks up the molten metal as a spray of droplets, which then solidify as powder particles. The circuits for centrifugal melt atomization (Table 15.4, circuits II and III) produce granules of various shape and size (from 0.1 up to 5 mm) with a high crystallization rate. In all cases, the cup is 100–200 mm diameter, running at moderately high speeds from 3000 to 10,000 rpm. The cooling rate estimated by calculation and experiment for the above circuits, I, II, III, and IV, is within 100–200, 100–500, 10^3–10^4, and 10^2–10^3 K/s, respectively.

Granulated alloys of the aluminum-silicon system have been developed based on cheaper electrothermal silumin manufactured by direct reduction from ores that essentially expand the raw-material base of the aluminum industry. Cooling of the melt at a high rate in the process of granulation has allowed an increase in the content of silicon in the alloy up to 35%, thereby providing its precision properties [4].

New designs of the spinning cup have allowed the organization of the metal pouring from the cup channels as a torch that has ensured the production of a finer product and has created an opportunity to carry out "dry" atomization (the circuit VI, Fig. 15.6C). The size of the basic fraction of granules is decreased from 2.0–2.5 to 1.0–1.5 mm.

By an increase of speed rotation of the spinning cup, the centrifugal technology is capable of ensuring production granules of 0.1–0.8 mm in size. The physical properties of the granules so produced do not differ significantly from those of gas-atomized powders but they are distinguished by greater uniformity of granulometric composition and by the absence of dust fractions.

In aluminothermic processes, the application of granules with a specific surface of 200–400 cm^2/g up to 1 mm in size produced by melt centrifuging are the most effective. Granules from 0.2 up to 2.0 mm in size are most effective for steel deoxidation. Coarse granules of a spherical shape of 1–5 mm in size are most suitable for the production of heat-conducting components for electric motors. Granules of spherical shape of 0.4–0.8 mm in size are used in the chemical industry in

TABLE 15.4 Characteristic of the Main Circuits of the Granulation Technique

Technological Circuit	Characteristic of Granules			Circuit Characteristic		Application Field of Granules	Device Productivity (t/h)
	Size (mm)	Shape	Particle Weight (g)	Advantage	Disadvantages		
I. Free or vibration pouring with cooling in a liquid; drying, classification	3–20	Disk-shaped, nodular	0.5–1.5	Stability of shape and size	Contact with liquid: necessity of drying; low cooling rate	Gallium cementation from aluminate solutions, ligatures, steel deoxidation, chemical industry	0.2–1.0
II. Melt centrifugal atomization with cooling in a liquid; drying; classification	0.2–2.0	Spindle-shaped, drop-like, nodular	0.002–0.05	Ease of size and structure regulation, high rate of cooling	Contact with liquid, drying of granules is necessary	Powder metallurgy, pigments, deoxidation, aluminothermy	0.6–2.5
III. Melt centrifugal atomization with cooling in gas medium; classification	0.2–2.0 thick 3–10 length	Acicular, fibrous, spindle-shaped, peteliform	0.002–0.006	No contact with liquid, no drying of granules	Large size of a collecting chamber (8 m in diameter), intensive heat mode, low rate of cooling	Aluminothermy, deoxidizers, powder metallurgy, ligatures, pigments	0.6–1.0
IV. Free or vibration pouring with cooling on a cold surface	5–40	Hemisphere, petaliform	0.5–1.5	No contact with liquid, no drying; high speed of cooling	The shape of granules are a disadvantage for compacting	Gallium cementation, chemical industry, semiproduct for grinding, ligatures, steel deoxidation, sheet rolling, pigments	0.1–2.0

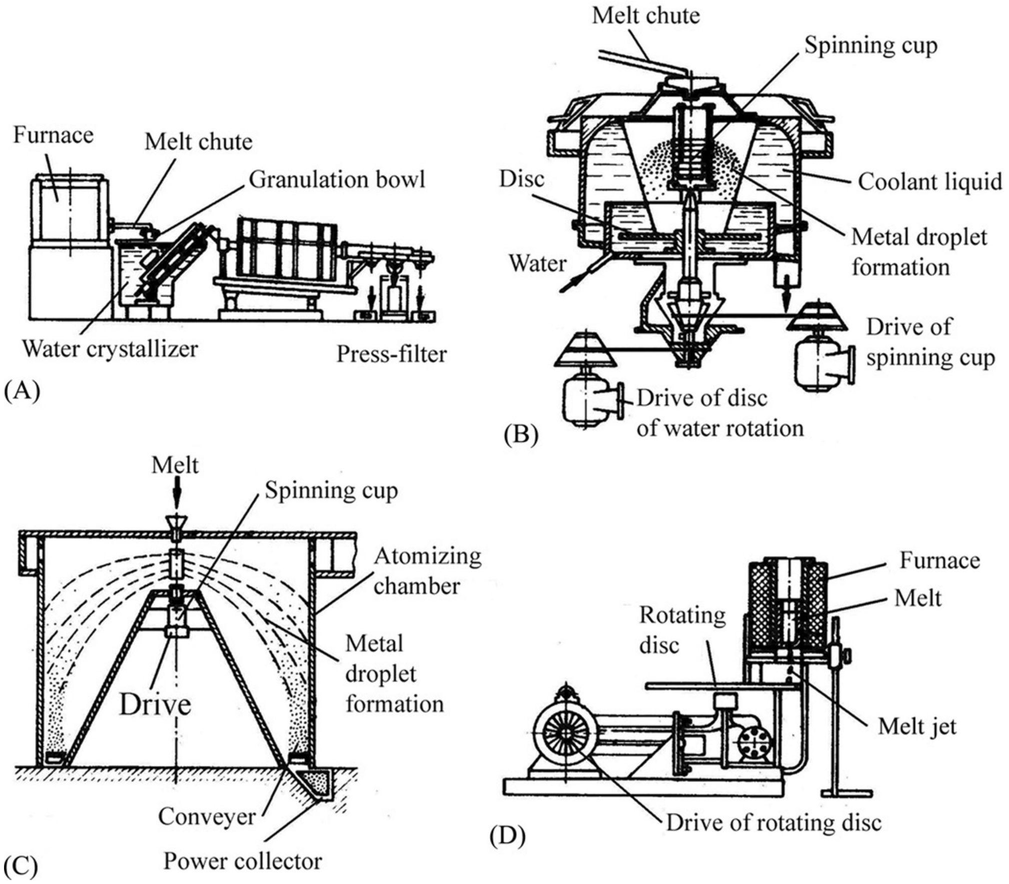
Furnace
Melt chute
Granulation bowl
Water crystallizer
Press-filter
(A)
Melt chute
Spinning cup
Disc
Coolant liquid
Water
Metal droplet formation
Drive of spinning cup
Drive of disc of water rotation
(B)
Melt
Spinning cup
Atomizing chamber
Metal droplet formation
Drive
Conveyer
Power collector
(C)
Furnace
Melt
Rotating disc
Melt jet
Drive of rotating disc
(D)

FIG. 15.6 Technique circuits of the aluminum granulation: (A) scheme of the device for production of granules by the method of free casting into a liquid (water); (B) scheme of the device for granule centrifugal atomization with cooling in a liquid; (C) scheme of the device for centrifugal atomization with cooling in gas atmosphere; and (D) scheme of the device for aluminum granulation with cooling on a cold surface.

fluidized bed devices. Granules of 7–20 mm in size from high purity aluminum are used in hydrometallurgical processes (for example, cementation of gallium from aluminate solutions).

Nowadays, master alloys and modifiers are one of the most promising areas for using granules 5–20 mm in size. An advantage of granules in comparison with master alloys in the form of ingots or bars is the fine microstructure of the material. This provides a large number of crystallization centers while modifying the alloys and providing a heredity of structure as well as the simplicity of batching and introduction of granules into the melt.

There are numerous application fields of aluminum granules in the areas of powder metallurgy due to satisfactory properties of the products produced from low-grade aluminum and the unique properties of highly alloyed granulated alloys. The basic kinds of aluminum granules, which are produced commercially, are given in Table 15.5.

Impulse atomization is capable of producing droplets of controlled size having a relatively narrow distribution and a predictable cooling rate [13]. The scheme of the process, shown in Fig. 15.7, consists of an impulse generator, a mechanical driver, a tundish, and a nozzle plate with orifices. The impulses generate monodisperse droplets that free fall out of the orifices. The quiescent gas atmosphere, into which melts have been atomized, may be helium, nitrogen, argon, or air. By varying the plunger acceleration, orifice size, orifice shape, melt temperature, and gas atmosphere, the granule size and size distribution, shape, and microstructure can be manipulated to the required specifications. Using this method, aluminum monodisperse granules from 2 to 10 mm in size are produced.

PRODUCTION OF FLAKES, PIGMENTS, AND PASTES

Aluminum flakes, pastes, or powders from fragile alloys, such as Al–Mg, Al–Ni, Al–Si, and others are produced by this method. For producing flakes, aluminum stock material (powder, foil) is crushed in a protective gas atmosphere (dry scheme) or in a liquid (wet scheme).

TABLE 15.5 Aluminum Granules and Pellets

	Sieve Residue (wt%) (max) on Sieve With Aperture (mm)			Chemical Composition (wt%)										
				Al (wt%), min	Admixtures (wt%), max									
Brand	**7**	**15**	**20**		**Mg**	**Si**	**Fe**	**Mn**	**Cu**	**Zn**	**Ni**	**Sn**	**Applications**	**Source**
AGHF	95.0	0.3		99.0		0.03	0.01		0.005		0.006		For cementation of gallium from aluminum solutions, as a chemical reagent etc	RUSAL
AL-110	0.297–0.841 mm (20–50 mesh)			99.7									Alloys, industrial-general	AEE
AG	95.0	5.0	0.3	96.0	1.0	0.6	3.0	0.5	0.3	0.5		0.3	In the metallurgical industry for deoxidization, modification of cast iron and steel	RUSAL
AL-130, pellets	6.35–12.7 mm (1/4″ – 1/2″)			99.99									Alloys, industrial-general	AEE
Granule 4121	0.25–2.0; max 5 wt% >2.0 mm; max 2 wt %< 0.25 mm												Shot peening, shot blasting	SA

RUSAL, Russian Federation Aluminum Company; *AEE*, Atlantic Equipment Engineers, Division of Micron Metals, Inc.; *SA*, produced by Sun Ark Aluminum Industries.

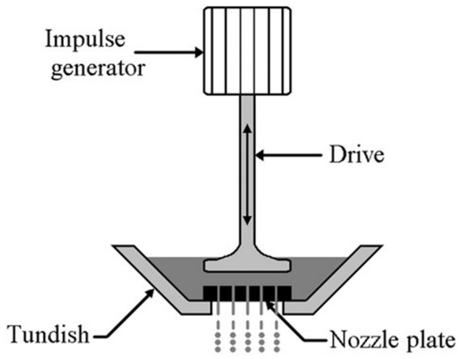

FIG. 15.7 Schematic of the impulse atomization process.

The basis of the technology for producing aluminum fine is the process of plastic deformation that provides the manufacture of particles in the form of thin flakes or leaflets. To prevent aluminum particles welding together and to reduce the friction between them and the milling balls, thus reducing the work required for deformation, stearin or another surfactant, in amounts from 0.3% to 4.0%, are added to the charge. Dry milling is carried out in a leak-tight mill working in a closed cycle in an atmosphere of nitrogen with the content of oxygen from 3% to 8%; the latter is necessary for the formation of a protective oxide film on the particle surface. At an oxygen content higher than 8%, an ignition inside the milling system is possible, and at an oxygen content lower than 2%, self-ignition of the discharged powder is possible.

The scheme for the production of pigment (PAP marks), pyrotechnic (PP marks) flakes, and lumpy flakes for sintering (AΠC marks, in Russian classification) is shown in Fig. 15.8. The main characteristics of aluminum flakes and lumpy aluminum flakes are presented in Table 15.6. Particles of aluminum lumpy flake are uniformly oxidized from the surface in the grinding process and agglomerated to the apparent density 0.9 g/cm^3 minimum. According to Russian GOST 10096–76, AΠC marks contain 6%–17% $A1_30_3$ [14].

The process of AΠC lumpy flake production consists of two stages. In the first stage, aluminum stock material is ground in the presence of 0.5–1.2 wt% of fats. The flakes produced have a lamellar particle shape no more than 80 μm in size; the apparent density does not exceed 0.2 g/cm^3. On decreasing the content of the fatty additive to 0.5%, a further oxidation (second stage) and cold welding of the aluminum particles takes place. Conglomerates (lumps) of fine particles with apparent density 1.0–1.4 g/cm^3 are formed. The sizes of particles aggregated during balling are basically of 300–500 μm but can achieve 1000 μm.

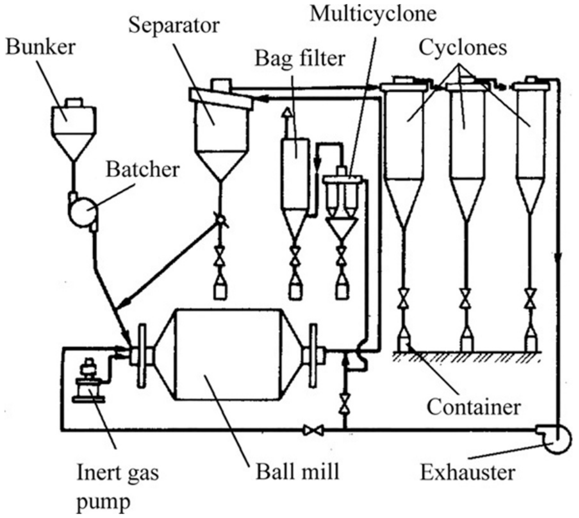

FIG. 15.8 Schematic diagram of the pneumoseparation grinding installation.

TABLE 15.6 Aluminum Flakes and Lumpy Flakes

Trade Name	Particle Size (μm) (max)	Covering Ability for Water Surface (cm^2/g) (min)	Apparent Density, (g/cm^3) (min)	Composition, wt%								Applications
						Impurities, wt% (max)						
				Al	Al$_2$O$_3$	Mg	Si	Fe	Cu	Zn	Fat Additives (max)	
Aluminum flakes												
PAP-1[a]	80	700	0.3	90	…	0.01	0.4	0.5	0.05	…	3.8	Production of paints, enamels, resin glues. As a gas developing agent to produce aerocrete is used in aircraft building, machine-building, instrument-making, polygraphic branch of industry. Production of explosives and pyrotechnic components
PAP-2[a]	45	1000	0.2	85	…	0.01	0.4	0.5	0.05	…	3.8	
PP-1	160	…	0.3	97	…	…	0.4	0.5	0.08(Cu +Zn)		0.8	
PP-2	100	…	0.4	95	…	…	0.4	0.5	0.08(Cu +Zn)		0.8	
PP-3	63	…	0.5	93	…	…	0.4	0.5	0.08(Cu +Zn)		0.8	
TA 3700 G[b]	62[c]	8000	0.17	96								Autoclaved aerated concrete (AAC), light weight concrete (LWC). Feedstock for chemical reactions, fuel cells and batteries, exothermic applications, binder agent for master alloy briquetting, drain cleaners, thermal and electrical conductivity enhancement in plastics, granular alternative for highly reflective roofing applications
K-109[d]	600 × 600 × 25 (length × width ×thickness)		0.47	99								
Aluminum lumpy flakes												
AПC-1A	315	…	0.9	Balance	6–8	…	0.25	0.20	…		…	Production of elevated temperature material SAP-1, capillary pipes and foil with the thickness from 0.3 to 0.1 mm resisting at 350–500°C. Production of profiled semiproduct. Production of semiproduct from SAP-2 with heat resistance higher by 15%–20% than SAP-1. Production of the semiproduct from the most heat-resisting material SAP-3
AПC-16	1000	…	1.0	Balance	6–8	…	0.25	0.25	…		…	
AПC-2	1000	…	1.0	Balance	9–12	…	0.25	0.30	…		…	
AПC-3	1000	…	1.0	Balance	13–17	…	0.25	0.30	…		…	

[a] *PAP-1 and PAP-2 produced for varnish-and-paint industry have the leafing of 80% min.*
[b] *Swedish Carlfors Bruk Company.*
[c] *δ_{50}—median diameter.*
[d] *Transmet Corporation.*

The charge of the fatty additive is increased with the increase of $A1_2O_3$ content in the final product:

(Al_2O_3), wt%	6–11	11–17
Charge of the additive, wt%	0.6	0.6–0.9

Pastes are manufactured with petroleum-based or aqueous liquid phases. With the former, the aluminum flake content is of the order of 65% with 33% of volatile liquids such as white spirit, and 2% of fatty material (stearin acid). By the degree of fineness at grinding and the area of water coating (1.5–3.0 m^2/g) on a mass unit, such paste considerably surpasses PAP-2—the finest aluminum flakes produced by dry grinding. Wet grinding is less explosive than the dry process of aluminum flake production.

The technological scheme that provides an opportunity of simultaneous or consecutive production of aluminum powders, flakes, and pastes includes the steps of initial material preparation, grinding, thickening, homogenizing, and casing (Fig. 15.9).

For the production of paste, aluminum powder manufactured by atomization, or scrap foil $<50\,\mu m$ in thickness, liquid hydrocarbons (white spirit, xylene, toluene, etc.) and fatty additives (stearin and oleic acids, etc.) are used. Mixed material is ground in ball mills in one or several stages depending on the size of the initial aluminum particles and the required degree of particle fineness in the manufactured paste. The slurry from the mills is separated in a filter press, a drum-type filter, or in a centrifuge.

Aluminum pastes are more convenient in use and in transportation because of the absence of dusting, greater bulk weight, etc. Mixing the paste with a lacquer gives a paint, which has high moisture resistance and durability, high reflectivity, and heat resistance. Leafing and nonleafing aluminum pastes are produced. Aluminum particles of the leafing paste rise to the surface of the varnish film and arrange themselves parallel to the surface, which imparts a metallic shine and high reflectivity, complicates the penetration of moisture, and increases the stability of the coating. Aluminum particles of nonleafing paste settle in the bottom part of the varnish film, providing a polychromatic effect. Roof coatings comprise the largest market for nonleafing aluminum paste. The largest market for leafing aluminum paste is for automotive coatings.

Special application fields of aluminum paste are polygraphy, powder metallurgy, and the production of aerocrete.

Firms produce a multitude of aluminum pastes different in floating, granulometric composition, solvent, and special additives. Characteristics of the aluminum pastes produced in Russia are presented in Table 15.7.

There are two processes for aqueous aluminum paste. In the first process, aluminum flakes are mixed with an aqueous solution containing phosphate ions, glycols aryl alkyl sulfonates, carbohydrates, polyatomic spirits, etc., as an inhibitor. Such technology is mastered both at factories producing aluminum flakes and at some factories producing aerocrete. In

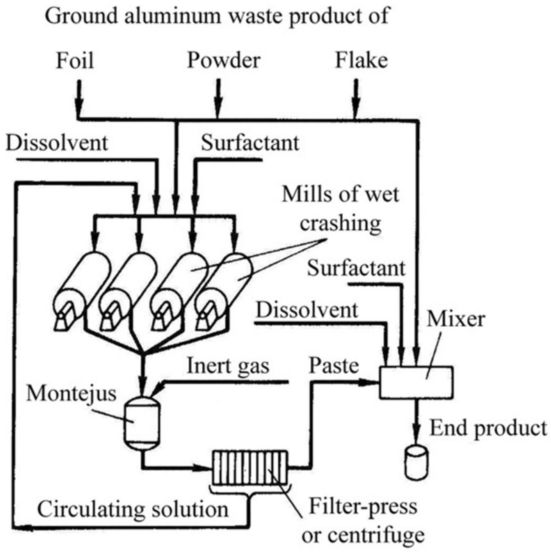

FIG. 15.9 Schematic diagram of manufacture of the aluminum pastes.

TABLE 15.7 Aluminum Pastes

Trade Name	Particle Size (μm) (max)	Covering Capacity on Water Surface (m^2/g) (min)	Leafing (wt%) (min)	Substances Soluble in Organic Solvents (wt%) (max)	Impurities (Fe, Si, Cu, Zn) total (wt%) (max)	Al (wt%)	Application
Leafing aluminum pastes							
B-1	80	1.6	65	3.0	1.0	Balance	Finish paints with metallic shine
B-2	45	2.0	75	4.0	1.2		
B-3	45	2.4	73	4.0	1.2		
Nonleafing aluminum pastes							
H-1 H-2	80 45	– –	– –	3.0 4.0	1.2 1.2	Balance	
H-3	45	–	–	4.0	1.2		Priming coat protective paints
Special aluminum pastes							
C-1	80	0.7	65	3.0	1.2	Balance	Hammer enamels
C-2	45	1.7	75	3.5	1.2		
C-3	45	1.7	–	4.0	1.3		
MAΠ	160	1.3–1.7	50	3.5	1.0		Thermoregulating coatings
ΠD	80	2.0	30.0	3.5	1.0		Slushing paints and enamels
ΠDA	80	2.0	30.0	3.5	1.0		Paints and enamels in aerosol packing
GLS-70[a]	≤70 μm (≥95%)					80 minimum	Autoclave aerated concrete (AAC)
Silver lucule 9008[b]	−45 μm	2.5	75	2–4		Balance	Exterior coatings, heat-resistant paint, anticorrosive

[a] *Produced by Xinji Guangyuan Metal Powder Co., Ltd.;*
[b] *Produced by Sun Ark Aluminum Industries (P) Ltd.*

the second process, foil waste is ground in an aqueous solution containing fatty acids and inhibitors (salts of phosphoric and boric acids and colloid substances: albumin, casein, gelatin, glue, or arabic gum). Grinding is carried out at the lowest possible temperature of 283–323 K.

Water aluminum pastes containing 50%–65% of aluminum particles are fire- and explosion-proof, convenient to use, and the content of the active metal keeps the properties stable for a long time. They are used as a gas-forming agent to produce aerocrete, in the production of paints, in the structure of water-filled explosives, and in powder metallurgy.

The same technique is used for producing a water paste containing 20 wt% $A1_2O_3$. This paste is thickened, dried, and ground to a powder state. Thus, a “heavy” powder with the apparent density above 1.2 g/cm^3 suitable for use in PM is manufactured.

NICKEL-CLAD ALUMINUM POWDERS

A special class of aluminum powder materials is composite materials, which include powders of aluminum and its alloys or mixtures of such powders with powders of other compounds clad by nickel.

The production technology of the specified composite materials developed by the Norilsk Nickel Concern consists of coating powder particles of aluminum and its alloys with metallic nickel by the carbonyl process, that is, by the decomposition of nickel tetra carbonyl vapor on the surface of the powder suspended in the vibrofluidized bed:

$$\mathrm{Ni(CO)_4 + Al \xrightarrow{450-520K} AlNi + 4CO}$$

Properties of Nickel-Clad Aluminum Powders

- Powder composition, wt%: 4–23 A1; 96–77 Ni.
- Powder properties
  - Thickness of the nickel coating on a particle of aluminum: from one to tens of microns.
  - Shape of particles: close to spherical.
  - Flow rate: 10–40 s/50 g.
  - Apparent density: 2.5–5.1 g/cm^3 (depending on the content of nickel).
  - The size of particles: 50–100 μm.
- Properties of plasma coatings:
  - Microhardness: 4.0–8.0 GPa.
  - Porosity: 3%–10%.
  - Strength of adhesion to the substrate: 30–38 MPa.
  - Exothermal effect while spraying of coatings comes at 898 K due to the reaction heat of the synthesis of the nickel-aluminum intermetallic in isothermal conditions.
  - Thickness of the coating layer that excludes peeling from the substrate: on steel-3: 1.0 mm; on steel-45: 0.8 mm; on D16T alloy: 3.0 mm (The steel brands are given in Russian classification).
- Purpose: spraying of an intermediate layer on steels, cast irons, aluminum, and titanium alloys, etc.
- The addition data about nickel-clad powders are contained in Chapter 12.

ALUMINUM SCRAP RECYCLING

Waste Aluminum Foil Recycling

The great significance of recycling is for environmental and economic aspects of saving material and energy. Especially, the recycling of aluminum scrap is important because the production of aluminum requires a lot of energy. Almost 100% of the use of foil waste products is achieved by their processing to aluminum powders (grit), flakes, or paste.

The technology of foil processing is quite simple: crushing in cutting units such as the ones used for comminution of paper and plastic with subsequent use as the raw material for the production of aluminum flakes (dry crushing) or pastes (wet crushing). After grinding in mills (ball, jet-type, etc.), disintegrators, and the like, the crushed flat particles of foil become rounded in shape, forming a special kind of powder product named “grit.” Grit has a wide application in the chemical industry as a reducing agent or gasifier, and in other industries as well.

Aluminum flake powders have been widely used in fingerprint detection, aerated concrete, as a paint component for automobile and industrial applications, an additive for ink, and explosives due to their metallic color, glossy appearance, and good adherence. The aluminum flake powders of mean size 20–45 mm and water covering area of 4000–30,000 cm^2/g are mainly used in the industry. In the paste manufacturing industry for paints and inks, flake powders are produced by the wet ball-milling process of gas-atomized aluminum powder. The wet ball milling is performed in an inorganic solvent such as mineral spirits.

A study for producing aluminum flake powder from aluminum foil scrap by dry ball milling under a gaseous argon with a small percentage of oxygen was carried out [15]. Aluminum foil scrap of thickness 6.5 mm, width 8 mm, and purity 99.4 wt% was used as the initial milling material. The mill drum was filled with argon gas containing 8 vol% oxygen, which slightly reacts with the surface of the aluminum powder, preventing the explosion of the milled fine powder after exposure

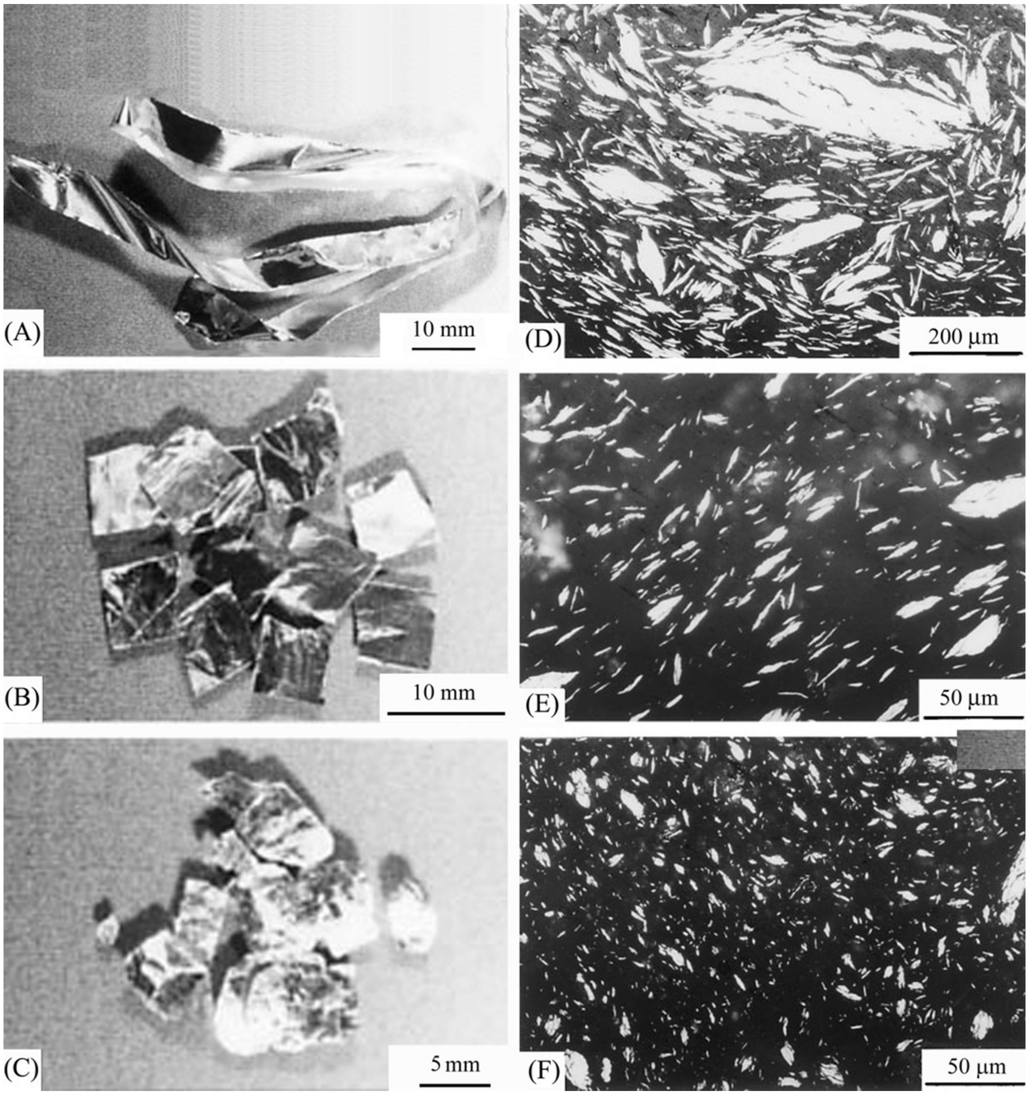

FIG. 15.10 Optical micrographs of aluminum flake powder during making from foil scrap for different milling times: (A) foil scrap with a thickness of 0.65 mm; (B) cut foil of 6 × 7 mm; (C) foil ball milled for 5 h; (D) flake powder ball milled for 10 h; (E) 20 h, and (F) 25 h. *(From Hong SH, Lee DW, Kim BK. Manufacturing of aluminum flake powder from foil scrap by dry ball milling process. J Mater Process Technol 2000;100:105–9.)*

in air. The content of stearic acid was varied from 1.5 to 5 wt% in order to check the effect of the level of stearic acid. The milling was performed for 45 h at a rotational speed of 120 rpm.

Optical micrographs of aluminum flake powder during manufacture from foil scrap for different milling times are presented in Fig. 15.10. During the milling of the cut foil (6.5 × 6 × 8 mm) using steel balls of diameter 16 mm for 5 h, the foil was microforged by the falling of the balls and deformed plastically into an elongated shape. Most of the aluminum foil is transformed into coarse flake powder by milling for up to 10 h (Fig. 15.10D). As shown in Fig. 15.10E, coarse flake powder is transformed into smaller flake powder with a single layer, or a laminated form occurs with crack nucleation and growth in the laminated flake powder after milling for 15 or 20 h. As the milling time increases up to 25 h, the powders are work-hardened and fragmented into fine flake powder, as shown in Fig. 15.10F.

A larger amount of stearic acid reduces friction between the foil and the balls and vial wall, thus giving less milling efficiency and a 3 wt% of stearic acid as the additive being verified as the optimum content. The variation of the mean powder size with the cooling of the milling material by an intermediate stop during the milling of aluminum foil for 25 h was examined. The powder milled continuously for 25 h shows 62 µm mean size, but the powder, which was milled with three intermediate stops (10, 15, and 20 h, respectively) during milling for 25 h, has a mean size of 14 µm. This result was interpreted by the elevated temperature behavior of the prolonged continuous milling process, thus the milled

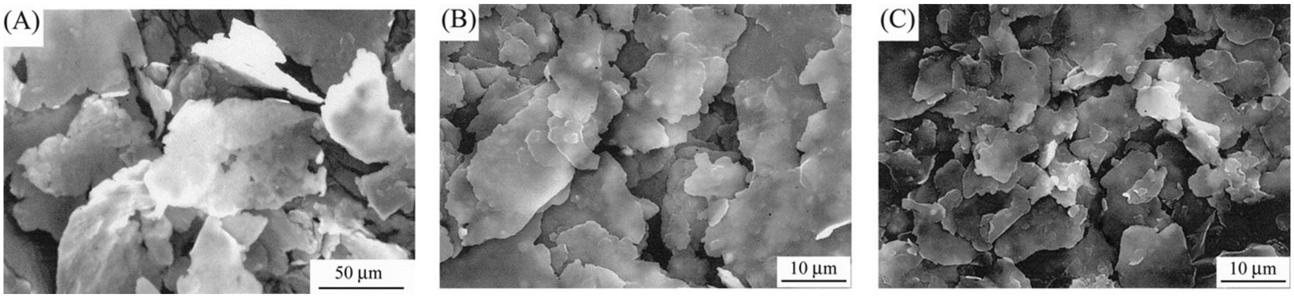

FIG. 15.11 SEM micrographs of aluminum flake powder wet milled for 30 h with foils having different initial thickness: (A) 60 μm, (B) 16 μm, and (C) 6.5 μm. *(Modified from: Hong SH, Kim BK. Fabrication of aluminum flake powder from foil scrap by a wet ball milling process. Materials Letters 2001; 51 (Issue 2, October): 139–43.)*

aluminum powder became more ductile, leading to the agglomeration of incipient particles by welding and autoadhesion. The intermediate stops lead to decreased temperature and less ductility. However, such techniques decrease the powder output and increase the power consumption.

The aluminum flake powder produced by the dry ball milling of aluminum foil scrap can be used in fingerprint detection or to aerate concrete.

Wet ball milling is used mainly in the paste manufacturing industry for paints and inks, in which milling is fulfilled in an inorganic solvent. The fabrication of aluminum flake powder by the wet ball milling of aluminum foil scraps and the effect of related factors were studied in the work [16]. The aluminum foil scraps of various thickness (6.5, 16, 60, and 120 μm), 8 mm in width, and a purity of 99.4 wt% were used as the initial milling material. The milling was performed for 60 h under a rotation speed of 120 rpm. In the capacity of inorganic solvent, the mineral spirits was used. The main variable parameters in the wet ball-milling process were the initial foil thickness 6.5, 16, 60, and 120 μm, the content of oleic acid in the 0%–5% range, the weight ratio of mineral spirits to foil in the 0.5–3.0 range, and a ball sizes of 16 and 4.8 mm. Oleic acid of 2–3 wt% as the additive and a weight ratio of 1.0–3.0 of mineral spirits to foil were evaluated as the range of optimum content. Fig. 15.11 shows aluminum flake powders prepared by milling of foil scraps with different initial foil thickness for 30 h. In comparison to the foil scrap with an initial thickness 60 mm, the one with 6.5 mm in thickness was milled to a finer flake powder.

Hong et al. reported [16] that the water-covering area of flake powder is increased with milling time due to the increase of the specific surface area of milled powder. Flake thickness of powder is decreased continuously by milling up to 30 h. For the foil of 6.5 mm in thickness, as milling time increases to 30 h, the aspect ratio of flake powder is increased to the maximum due to a high degree of flake. After milling for 60 h, flake powder is fragmented into fine powder with a low degree of flake. As the content of oleic acid increases from 1.5% to 5%, the mean size of powder milled for 30 h is decreased drastically due to the prevention of coagulation, as shown in Fig. 15.12.

For the mineral spirit content below 50%, foil scrap with an initial thickness of 6.5 μm was not milled because of the sliding motion of balls coated by oleic acid. As the weight ratio of mineral spirit to foil increases over 100%, foils were milled to powders with a mean powder size of 15–20 μm. After milling for 30 h, the content of mineral spirits in aluminum paste was controlled at 35% below by vacuum drying for pigment application.

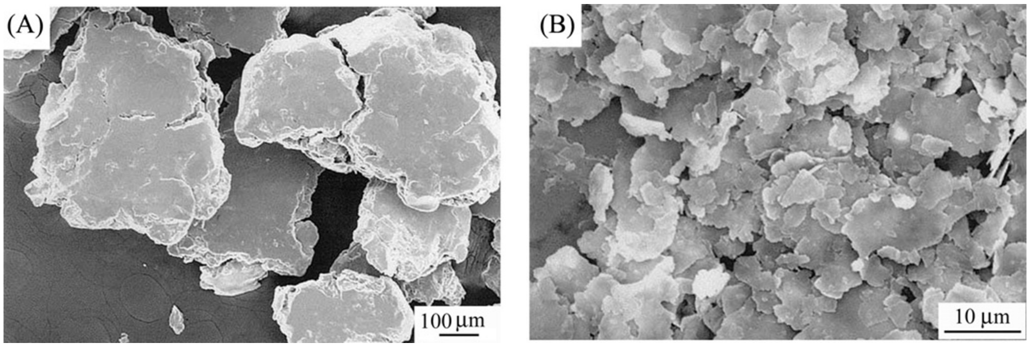

FIG. 15.12 SEM micrographs of aluminum flake powder wet milled for 30 h: (A) without and (B) with 5 wt% oleic acid content.

Processing of Recycled Aluminum to Granules

In recent years, the processing of aluminum scrap (mainly chips and used drink cans) has attracted increasing attention. Aluminum scrap has a complex chemical composition based on aluminum (>90%). Magnesium, zinc, silicon, iron, etc., are the main impurities. Sources of impurities are the composition of the alloy for producing drink cans (mainly, Al–Mg alloy containing up to 3%–4% Mg) and mechanical impurities that enter into the scrap due to inefficient sorting, classification, and storage of the scrap.

Nowadays, all over the world, the main method of processing aluminum scrap is remelting in units of various types. The melt is usually cast into ingots. In some cases, the melt is granulated or gas atomized to produce powder of recycled aluminum (for example, APV powders in Russia). These remelting-casting technologies are rather power consuming.

Processing of aluminum scrap to powders and granules is an alternative to remelting scrap to produce ingots. The advantage of this technology is that it is a simpler and cheaper process of producing granules from recycled aluminum. The size of granules is easily regulated by the adjustment of grinders and varies from 1 to 10 mm. Such granules are used more effectively than ingots in ferrous metallurgy for steel deoxidation.

THE MAIN APPLICATION FIELDS FOR ALUMINUM POWDERS

Powders and flakes of aluminum are ingredients of many industrial explosives used in the mining industry (ammonal, rock ammonites). As a high-energy carrier, aluminum essentially raises the heat of the explosive transformation and the efficiency of the blasting operations. Powders such as PA, pyrotechnic flakes of PP marks, powders from secondary aluminum such as APV, PA-VV, etc., (in RUS classification) are the most widely used.

The aluminum is used to increase the energy and raise the flame temperature in rocket propellants. Aluminized explosives have been used in various formulations since the beginning of the 20th century. It is incorporated in explosives to enhance air blast, increase bubble energies in underwater weapons, raise reaction temperatures, and create incendiary effects [17–19]. Nanometric aluminum powder has recently become available in quantities large enough for introduction into energetic materials and small-scale performance testing. The most widely known product is the ultrafine aluminum powder “Alex,” which comprises spherical particles of 100–200 nm size.

Various plastic-bonded explosives (PBXs) and trinitrotoluene (TNT)-based formulations have been developed to compare ultrafine and conventional micron-sized aluminum [20]. Explosive performance was determined by velocity of detonation (VOD) measurements and plate dent depth tests. The study was also complemented by air-blast tests to evaluate the difference in energy release in the far field. Brousseau et al. reported [20] that it was found that for PBX compositions, no significant differences were observed between formulations containing micron-sized and nanometric aluminum. For mixes of TNT and aluminum, an improvement was noted in the velocity of detonation and in plate dent depths using ultrafine aluminum. Aquarium tests were carried out on TNT/Al blends to confirm the improvement observed, to evaluate the relative performance of the different sizes of aluminum, and to qualify the behavior of the aluminum in such an explosive. No increase of pressure was found in aquarium tests. However, the expansion of the gases appears faster for TNT-type formulations containing nanometric aluminum.

In the study of the acceleration ability of high explosives by aluminum nanopowder additives, Davydov and Gubin [21] used two types of powders. The first was obtained by exploding wires in a nitrogen atmosphere. The particle size ranged from 50 to 300 nm. The content of active Al was approximately 89%. The second powder, made by the plasmochemical method, was passivated with a 2% silicone coating. This powder has an amorphous and, hence, more permeable oxide film and possesses an extremely high chemical activity. The content of active Al was approximately 87%. The study, similarly to the work [20], showed that the introduction of various Al additives into high explosives reduces the detonation pressure while raising the temperature of the detonation products. The authors [21] explained this phenomenon by the following main features of the behavior of metallic particles in the composition of high explosives during their detonation:

- The difference in the shock compressibility of the high explosives and the metal additive should probably lead to the creation of zones of increased pressure due to shock wave reflection from the metal particles, which manifests itself in the known sensitizing effect of metal additives.
- During shock wave loading, due to differences in the physical and mechanical properties of Al and Al oxide, the destruction of the latter occurs.
- Due to differences in the shock compressibility of high explosives material, Al, and its oxide, a high explosives decomposing material behind the detonation complex shock front flows around Al particles. As a result, the oxide peels off the surface of Al particles, thereby ensuring the supply of oxidizer to the particle surface and the removal of the reaction products.

Two compositions of aluminized explosives were developed for an investigation of the effects of boron powder on the air blast properties [22]. These had the following mass compositions: 35% of metal powders, 20% of ammonium perchlorate (AP), 36% of hexogen (RDX), and 9% of wax $(CH_2)n$ and other additives (including 1% graphite). Charges of 500 g of the aluminized explosives were prepared and studied. Their trinitrotoluene (TNT) equivalences were calculated according to the experimental data and the explosion law.

The authors reported [22] that the highest surface temperatures of the fireballs of these aluminized explosives were up to 1870 K, which was higher than that of the TNT charge. In the region of the highest surface temperature above 970 K, the duration for the composition RDX/Al/AP was about 232 ms (2.73 times more than TNT) while RDX/Al/B/AP (by 25wt% Al/10wt%B ratio) was about 360 ms. The fireballs obtained from the explosion of these aluminized explosives had larger dimensions than that of TNT. Therefore, for the two compositions, RDX/Al/B/AP had a higher surface temperature, a longer duration of the explosion fireball, and when the surface temperature was above 1273 K, it had larger fireball dimensions than the other composition**.** The authors [22,23] considered that aluminum and boron powders act as inert additives in the reaction zone. The secondary oxidation reactions of aluminum and boron with the expanding detonation products contribute to late-time effects, such as the air blast shock wave, postdetonation fireballs, and detonation temperature**.**

In ferrous metallurgy, aluminum powders (granules) are used as a reducing agent. Introduction of 0.1%–1.5% of aluminum groats into the melt of iron completely releases it from the oxide (II) and thereby provides the production of a dense casting without blowholes. Aluminum powders are also used for heating the riser part of the ingot in the casting of ferrous metals. A mixture of oxides and aluminum powders, tamped around the sprue opening and the riser, which "ignites" from the melt and during burning, provides cast metal in the liquid state for a long time. This allows, in the time of the melt solidification following by decreasing of its volume, adding melt to the mold and avoiding the formation of shrinkage cavities in casings.

Aluminothermic reduction of refractory metal oxides is used in the production of ferromolybdenum, ferroniobium, ferrotungsten, etc.

The thermite mix containing 75% Fe_2O_3 and 25% Al provides a burning temperature up to 2773 K.

In the chemical industry, aluminum powders and granules are active reducers as they rapidly react in aqueous solutions of acids or alkaline media with the emission of hydrogen: 1.0 kg of aluminum powders gives 1240 L of hydrogen. They are applied in the production of aluminum alkyls, polymerization of ethyls, for production of antidetonants, tetraethyl lead, etc.

Aluminum powders are used for coating steel products by the methods of spray deposition, flame or plasma spraying, and thermal diffusion. Aluminum powders and pastes are used as a paint and protective pigment in compositions of various paints, varnishes, and enamels. The paints obtained have a beautiful silvery color while protecting products from moisture, heat, and light.

The American Society for Testing and Materials (ASTM) has enacted specifications for aluminum flake pigments (ASTM D 962, Part 28) [24]. The standard lining paste (ASTM D 962, type 2 class A) is used for structural steel coatings.

Aluminum-based sintered materials are distinguished in good pressing and sintering ability of powders, manufacturing efficiency, high strength, and good corrosion resistance.

In Russia, a range of Al-based powders is produced such as lumpy powder АПС, powders of high-purity aluminum (PA-VCh), of technical-purity aluminum such as PA, aluminum groats AKP, and powders of SAS alloys (Al–Si). These materials are destined for PM production in machine building and electrical engineering as well as in the nuclear, electronics, and other industries.

Porous aluminum shows the promise of heat sink cooling materials due to its unique combining of high heat conductivity with small mass density. In the case of using a boiling cooling system for heat removal from the electronic equipment, harnessing latent heat with refrigerant, the advantage of the system is that it does not require a water pump and extra power source, which are necessary equipment for a forced water-cooling system. For better performance of the ebullient cooling system, it is important to boil refrigerant efficiently on the surface of the boiling heat transfer. Recently, applying porous aluminum for the boiling heat transfer surface has been widely reported [25,26]. In the work [27], a three-dimensional structure with porous aluminum is discussed. The product making comprises the following major steps. First, pure aluminum powders ($\delta_{50} = 6\,\mu m$, purity 99.7%) are mixed with a polyvinyl alcohol water solution and some reagents are added to make an aluminum powder slurry. Next, the slurry is coated on urethane form and dried by hot air. This green body was heat-treated by using a vacuum heat-treatment furnace and then sintered in a vacuum. Fig. 15.13 shows SEM images of the porous aluminum sample: in initial condition (left) and after etch and ultrasonic treatment (right). The latter shows the 0.5–2 μm size particles on the sintering surface. The result showed the boiling heat transfer coefficient of the etched and ultrasonic treated sample reached the highest value, $16\,kW/(m^2 \cdot K)$. In contrast, the boiling heat transfer coefficient of the ingot machined sample showed an even configuration amount of $7.5\,kW/(m^2 \cdot K)$.

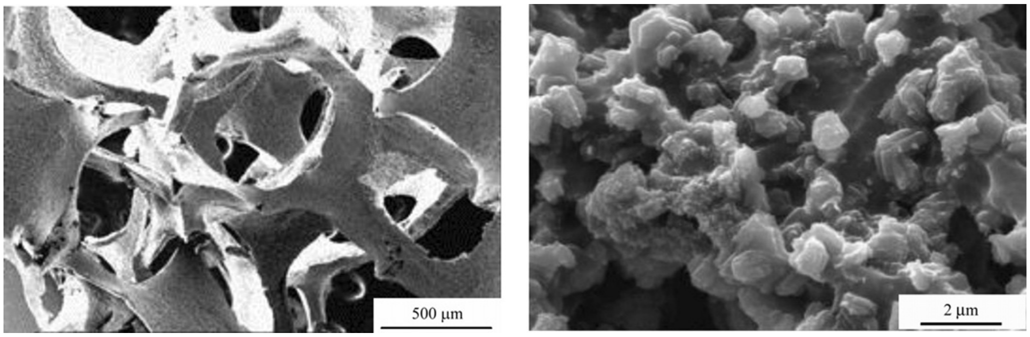

FIG. 15.13 SEM images of porous aluminum sample: in initial condition (*left*) and after etch and ultrasonic treatment (*right*).

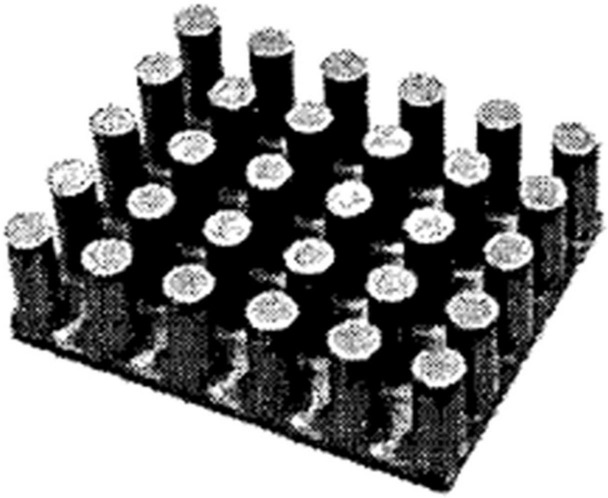

FIG. 15.14 Fin heat sink produced by powder injection molding (PIM) process.

Tan and Ma considered [28,29] the making of aluminum components by powder injection molding (PIM) for heat sink application. The authors reported [28] that the thermal conductivity of a fin heat sink (Fig. 15.14) produced by the PIM process in comparison with a machined square pin in the same setup is about 30% higher, accordingly 180 W/(m·K) and 135 W/(m·K).

Aluminum powders, flake pigments, pastes, paints, and granules are applied in:

- Production of high density refractory materials (to increase the thermal resistance and mechanical strength of the refractory material).
- Production of porous adsorption materials for cryogenic equipment.
- Production of a welding wire and cutting emulsions.

Aluminum powders are added to rubber to produce automobile tires with the purpose of increasing the heat conductivity of the protective rubber and to improve the operating conditions for the inside tire surface. An addition of powders to plastics improves their mechanical properties, increases their wear resistance, and imparts special properties (electric conductivity, heat conductivity, etc.).

Aluminum powder is applied as a filler material in plastics such as epoxy, polyester, and phenolic resins. In particular, powder aluminum is used in the preparation of so-called "cold solders" (fillers), which are used for filling of hollows, cracks, and seams on the surface of a metal. >50% of the content of the cold solder is aluminum powder, which is mixed with the resin and hardener. Aluminum powder is used as a lubricant in producing ceramic details by the method of dry pressing for the reduction of the wear in molds, the obtaining of high-density compacts, and the reduction of the pressing force.

REFERENCES

[1] Dunkley JJ. Atomization of metals—craft or science? Bauckhage K, Fritsching U, Uhlenwinkel V, Leatham A, editors. In: Proceedings of 2nd international conference on spray deposition and melt atomization. Bremen Universität; 2003. p. 3–11.
[2] Unal A, Leon DD, Gurganus TB, Hildeman GJ. Production of aluminum and aluminum-alloy powder. In: Eisen WB, Ferguson BL, German RM, editors. ASM handbook. vol. 7. ASM International Publishers; 1998. p. 148–9.
[3] Williams B. Powder metallurgy—a global market review. In: International powder metallurgy directory & yearbook. 12th ed.; 2006/2007. p. 5–16.
[4] Naboychenko SS, editor. Nonferrous metal powders. Handbook. Moscow: Metullurgiya; 1997 [in Russian].
[5] Dobatkin VI, Elagin VI, Fedorov VM. Rapidly solidified aluminum alloys. Moscow: All-Russian Institute of Light Alloys Publ.; 1995 [in Russian].
[6] Dunkley JJ. Atomization. In: Eisen WB, Ferguson BL, German RM, editors. ASM handbook. vol. 7. ASM International Publishers; 1998. p. 35–52.
[7] Lawley A. Atomization. Metal Powder Industries Federation: Princeton; 2003.
[8] Ünal A. Production of rapidly solidified aluminum alloy powders by gas atomization and their applications. Powder Metall 1990;33(1):53–64.
[9] Arkhipov VA, et al. Influence of operational parameters and design of the ejection nozzle on characteristics of finely dispersed aluminum powder: part I. Influence of operational parameters of the nozzle. Russ J NonFerr Met 2016;57(2):131–4.
[10] Ting J. The close-coupled gas atomization: a quantitative analysis of the dynamic pressures of the pulsatile atomization process. In: Chernenkoff RA, James WB, editors. Proceedings of 2014 powder metallurgy World Congress. Orlando: Metal Powder Industries Federation; 2014. p. 02-76–84.
[11] Neikov OD, Krajnikov AV. Surface chemistry of water-atomized high-alloyed Al-Zn-Mg-Cu base powders. In: Proceedings of the powder metallurgy world congress & exhibition, Granada (Spain); 1998. p. 123–8.
[12] Neikov OD. Nonferrous powder production: manufacturing methods and properties of copper, aluminum, titanium and nickel powders. Powder Metall Rev 2014;3(2):65–87.
[13] Henein H. Impulse atomization: an innovative approach for the generation of powders and spray deposits. Bauckhage K, Fritsching U, Uhlenwinkel V, Leatham A, editors. In: Proceedings of 2nd international conference on spray deposition and melt forming, vol. 1. Bremen: Universitat Bremen; 2003. p. 1-3–1-11.
[14] GOST 10096-76, Standard CIS Aluminum flake pigments [in Russian].
[15] Hong SH, Lee DW, Kim BK. Manufacturing of aluminum flake powder from foil scrap by dry ball milling process. J Mater Process Technol 2000;100:105–9.
[16] Hong SH, Kim BK. Fabrication of aluminum flake powder from foil scrap by a wet ball milling process. Mater Lett 2001;51(2):139–43.
[17] Brousseau P, Anderson CJ. Nanometric aluminum in explosives. Prop Explos Pyrotech 2002;27(5):300–30.
[18] Wildegger-Gaissmaier AE. Aspects of thermobaric weaponry. Mil Technol 2004;28(6):125–6.
[19] Yen NH, Wang LY. Reactive metals in explosives. Prop Explos Pyrotech 2012;37(2):143–55.
[20] Brousseau P, et al. Detonation properties of explosives containing nanometric aluminum powder. In: Proceedings of powder, 12th international detonation symposium, San Diego (California); 2002.
[21] Davydov VY, Gubin AS. Acceleration ability of high explosives and their mixtures with fuel additives. 2. Activated and ultrafine aluminum powders. Russ J Phys Chem B 2011;5(4):610–5.
[22] Chen Y, et al. Experimental study of the explosion of aluminized explosives in air. Cent Eur J Energ Mater 2016;13(1):117–34.
[23] Manner VW, et al. The role of aluminum in the detonation and post-detonation expansion of selected cast HMX-based explosives. Prop Explos Pyrotech 2012;37(2):198–206.
[24] ASTM Standard D 962, Aluminum pigment, powder and paste, for paint.
[25] Lee CY, Bhuiya MMH, Kim KJ. Pool boiling heat transfer with nano-porous surface. Int J Heat Mass Transf 2010;53:4274–9.
[26] Kim DE, et al. Review of boiling heat transfer enhancement of micro/nanostructured surfaces. Exp Thermal Fluid Sci 2015;66:173–96.
[27] Oshiyama N, et al. Development of porous aluminum for boiling heat transfer surface. In: Proceedings of PM 2016 world congress, Hamburg (Germany). Bellstone Shrewsbury, UK: European Powder Metallurgy Association; 2016. p. 1–6.
[28] Tan LK, Ma J. Characterisation of powder injection molded aluminum (aluMIM). In: Proceedings of the 2003 international conference on powder metallurgy & particulate materials. Las Vegas, NV: ASM International; 2003. p. 282–8 [Part 8].
[29] Tan LK, Ma J. Performance of powder injection molding (PIM) heat sink. In: Proceedings of inter society conference on thermal phenomena; 2004. p. 451–4. 0-7803-8357-5/04/r520.00 02004 IEEE.

Chapter 16

Production of Aluminum Alloy Powders

Oleg D. Neikov
Frantsevich Institute for Problems of Materials Science (IPMS), Kiev, Ukraine

Chapter Outline

Introduction 481
Mechanical Alloying 482
Rapid Solidification Process 487
Centrifugal Atomization 493
  RSR Process 493
  Spinning Cup Water Granulation Process 494
Gas Atomization 497
Melt Spinning Technique 503
Water Atomization 505
Recycling of Secondary Aluminum 511
Elevated Temperature Aluminum Alloys 513
Al-Mg System Alloys 516
Al-Zn-Mg System Alloys 516
Spray Forming 521
Other Technologies 526
References 527
Further Reading 531

INTRODUCTION

The unique combinations of properties provided by aluminum and its alloys make aluminum one of the most versatile, economical, and attractive metallic materials for a broad range of uses—from soft, highly ductile wrapping foil to the most demanding engineering applications. Aluminum alloys are second only to steels in use as structural metals.

It is convenient to divide aluminum alloys, produced by conventional techniques, into two major categories: wrought compositions and cast compositions. A further differentiation for each category is based on the primary mechanism property development. Many alloys respond to thermal treatment based on phase solubility. These treatments include solution heat treatment, quenching, and precipitation, or age, hardening. For either casting or wrought alloys, such alloys are described as heat-treatable. A large number of other wrought compositions are based instead on work hardening through mechanical reduction, usually in combination with various annealing procedures for property development. These alloys are referred to as work hardening. Some casting alloys are essentially not heat treatable and are used only in as-cast or in thermally modified conditions unrelated to solution or precipitation effects. Cast and wrought alloy nomenclatures have been developed. The Aluminum Association system is the most widely recognized by United Aluminum [1]. Aluminum alloys for sheet products are identified by a four-digit numerical system that is administered by the Aluminum Association. The alloys are conveniently divided into eight groups based on their principal alloying element. The first digit identifies the alloy group, as shown in Table 16.1.

The last two digits in the 1xxx group correspond with the two digits after the decimal, which indicate the minimum aluminum content. For example, the aluminum content of the 1060 alloy is 99.60% minimum while the1100 alloy is 99.00% minimum. The last two digits of the other groups are sequential numbers issued by the Aluminum Association to ensure each alloy is uniquely identified. The second digit in all the groups indicates a minor modification of the basic alloy. For instance, the 5252 alloy is the second modification of the 5052 alloy.

Emerging powder metallurgy (PM) processes, such as rapid solidification, mechanical alloying, and spray forming, create powders that upon subsequent consolidation provide significant improvements in room and elevated temperature strength, fracture toughness, fatigue life, and corrosion resistance. The real advantage of PM processing is in the production of new alloys and composites with metallurgical structures and compositions that cannot be produced by ingot metallurgy. Rapid solidification extends the solubility of alloying elements, particularly transition and rare earth elements, and refines the structure of the intermetallic phases responsible for improved mechanical properties. Mechanical alloying (MA) is a dry, high-energy milling process producing dispersions of insoluble oxides and carbides that stabilize the microstructure, leading to high strength at elevated temperatures in the consolidated materials. By blending the alloy powder with a

Handbook of Non-Ferrous Metal Powders. https://doi.org/10.1016/B978-0-08-100543-9.00016-6
© 2019 Elsevier Ltd. All rights reserved.

TABLE 16.1 Subdivision of Aluminum Alloys for Sheet Products Subject to Principal Alloying Element

Alloy Group	Principal Alloying Element	Property Features
1 × × ×	Unalloyed aluminum	Purity of 99.0% min
2 × × ×	Copper	Heat treatable alloys
3 × × ×	Manganese	
4 × × ×	Silicon	Low melting alloys
5 × × ×	Magnesium	
6 × × ×	Magnesium and silicon	Heat treatable alloys
7 × × ×	Zinc	Heat treatable alloys
8 × × ×	Other elements	

strengthening phase, discontinuously reinforced aluminum-matrix composites containing insoluble dispersoids (oxides and carbides), particulates, whiskers, or fibers are produced for high-performance structural applications [2–5]. Table 16.2 contains the chemical composition of aluminum PM alloys, including dispersion-strengthened composites.

The discontinuously reinforced aluminum-matrix composites are generally isotropic and less costly in comparison with continuous fiber-reinforced aluminum-matrix composites. Silicon carbide or alumina particle-reinforced aluminum composites have higher stiffness and, principally, higher wear resistance in comparison with the unreinforced aluminum alloys. The PM route for producing the discontinuously reinforced composites involves blending elemental or prealloyed powder with the reinforcement, followed by canning, vacuum degassing, and some form of consolidation, such as hot pressing or hot isostatic pressing (HIP), into a billet that is subsequently rolled, forged, or extruded.

MECHANICAL ALLOYING

This technique is used for fabricating oxide dispersion-strengthened alloys and discontinuously reinforced composites. High-energy ball milling results in mechanical alloying of pure metal powder and alloying components. During this process, intimate alloying by repeated welding, fracturing, and rewelding takes place. A more detailed discussion of mechanical alloying can be found in Chapter 3.

In the case of aluminum alloys, carbon derived from process contribution agents and incorporated into the processed powder reacts with aluminum to form very fine carbides. These carbides and the fine oxide particles derived from the breakup of surface films on the initial powder particles create a dispersion that effects the fine-grained microstructure. This processing technique promotes the problem solution of low solubility according to the phase diagram or the possibility of forming a low-melting equilibrium or nonequilibrium phases. Thus, a metastable supersaturating can be achieved in systems such as aluminum-iron, aluminum-nickel, aluminum-copper, aluminum-titanium, and aluminum-chromium. Another potential of MA is the generation of amorphous alloys that, following controlled crystallization, can create nanometer-scale microstructures [6].

Aluminum-based composites with 5 and 10 vol% MA956 (Fe-20Cr-4.5Al-0.5Ti-0.5Y_2O_3 (wt%)) were produced by mechanical alloying [7]. Commercial pure aluminum powder (99.5%) supplied by ALCOA with particle sizes smaller than 100 μm was blended with 5 and 10 vol% of MA956 alloy powder produced by INCO Alloys International. The milling was carried out in a high-energy Pulverisette planetary ball mill at 200 rpm with a ball-to-powder weight ratio of 20:1 under an argon atmosphere.

Micrographs shown in Fig. 16.1 present the morphological evolution of powder with milling time, which is the typical observed in MA. In the early stages of milling, until 2.5 h, the events of plastic deformation and cold welding prevail. The tendency at this stage is that the flake-like particles resulting from the severe plastic deformation, weld together to form large particles. As the deformation progresses, the particles harden and the tendency to fracture predominates over cold welding, resulting in the refining of particle size, which can be observed by comparison to the micrographs of Fig. 16.1A from powders milled for 20 h and of Fig. 16.1B after milling over 50 h. According to data [7], the median diameter of powders after 50 h milling results in 97 μm for a composite with 5 vol% MA956 and 37 μm for the one with 10 vol% MA956.

TABLE 16.2 Nominal Chemical Composition on Aluminum PM Alloys and Dispersion-Strengthened Composites

Alloy Designation	Nominal Mass Elemental Composition																			
	Be	C	Ce	Co	Cr	Cu	Fe	Li	Mg	Mn	Mo	O	Ni	Si	Ti	V	Zn	Zr	Al	(L)
Al-Cr-X	…	…	…	…	5.0	…	…	…	…	1.0	…	…	…	…		…	…	2.0	bal	…
Al-Ti-X	…	…	3.0	…	…	…	…	…	…	…	…	…	…	…	3.0	…	…	…	bal	…
Al-Be-X	22.6	…	…	…	…	…	…	10.8	…	…	…	…	…	…	…	…	…	…	bal	…
7090	…	…	…	1.5	…	1.0	…	…	2.5	…	…	0.35	…	…	…	…	8.0	…	bal	…
7091	…	…	…	0.4	…	1.5	…	…	2.5	…	…	…	…	…	…	…	6.5	…	bal	…
X7090	…	…	…	1.0–1.9	…	0.6–1.3	0.15	…	2–3	…	…	…	…	0.12	…	…	7	…	bal	…
X7091	…	…	…	0.2–0.6	…	1.1–1.8	0.15	…	1–3	…	…	…	…	0.12	…	…	5.8–7.1	…	bal	…
X7093	…	…		…	…	1.5	…	…	2.2	…	…	…	0.1	…	…	…	9.0	0.14	bal	…
8009	…	…	…	…	…	…	8.5	…	…	…	…	…	…	2.4	…	1.3	…	…	bal	…
X8019	…	…	4.0	…	…	…	8.3	…	…	…	…	…	…	…	…	…	…	…	bal	…
CZ42	…	…	6.0	…	…	…	7.0	…	…	…	…	…	…	…	…	…	…	…	bal	…
Al-Fe-Ni	…	…	…	…	…	…	8	…	…	…	…	…	1.7	…	…	…	…	…	bal	…
Al-Fe-Mo	…	…	…	…	…	…	8.0	…	…	…	2.0	…	…	…	…	…	…	…	bal	…
Al-Fe-V	…	…	…	…	–	…	10.5	…	…	…	…	…	…	…	…	2.5	…	…	bal	…
Al-Fe-Ni-Co	…	…	…	6.0	…	…	5.0	…	…	…	…	…	3.0	…	…	…	…	…	bal	…
Al-Fe-Mo-V	…	…	…	…	…	…	8	…	…	…	2	…	…	…	…	1	…	…	bal	…
Al-Fe-Mo-V-Zr	…	…	…	…		…	8.0	…		…	2.0	…	…	…	…	2.0	…	1.0	bal	…
Al-Fe-Cr-V-Si	…	…	…	…	3.86	…	8.29	…	…	…	…	…	…	2.31	…	1.19	…	…	bal	…
Al-Fe-Ti-V-Si	…	…	…	…	…	…	8.31	…	…	…	…	…	…	2.31	3.57	1.2	…	…	bal	…
FVS-0812	…	…	…	…	…	…	8.5	…	…	…	…	…	…	1.7	…	1.3	…	…	bal	…

Continued

TABLE 16.2 Nominal Chemical Composition on Aluminum PM Alloys and Dispersion-Strengthened Composites—cont'd

Alloy Designation	Nominal Mass Elemental Composition																			
	Be	C	Ce	Co	Cr	Cu	Fe	Li	Mg	Mn	Mo	O	Ni	Si	Ti	V	Zn	Zr	Al	(L)
RAE 72	…	…	…	…	7.5	…	1.2	…	…	…	…	…	…	…	…	…	…	…	bal	…
Al-Li-Cu	…	…	…	…	…	2–3.5	…	2.5–3.2	0.5	0.6	…	…	…	…	…	…	…	…	bal	…
Al-Mn-Ni	…	…	…	…	…	…	…	…	…	3–8	…	…	1.5–7.0	…	…	…	…	…	bal	…
Al-Mn-Co	…	…	…	1.6–6.5	…	…	…	…	…	3–8	…	…	…	…	…	…	…	…	bal	…
Al-Ni-Co				2–5	…	…	…	…	…	…	…	…	2–5	…	…	…	…	…	bal	…
601AB	…	…	…	…	…	0.25	…	…	1.0	…	…	…	…	0.6	…	…	…	…	bal	1.5
201AB	…	…	…	…	…	4.4	…	…	0.5	…	…	…	…	0.8	…	…	…	…	bal	1.5
602AB	…	…	…	…	…	…	…	…	0.6	…	…	…	…	0.4	…	…	…	…	bal	1.5
202AB	…	…	…	…	…	4.0	…	…	…	…	…	…	…	…	…	…	…	…	. bal	1.5
MD-22	…	…	…	…	…	2.0	…	…	1.0	…	…	…	…	0.3	…	…	…	…	bal	1.5
MD-24	…	…	…	…	…	4.4	…	…	0.5	…	…	…	…	0.9	…	…	…	…	bal	1.5
MD-69	…	…	…	…	…	0.25	…	…	1.0	…	…	…	…	0.6	…	…	…	…	bal	1.5
MD-76	…	…	…	…	…	1.6	…	…	2.5	…	…	…	…	…	…	…	…	…	bal	1.5
Dispersion-strengthened composites																				
Al-C	…	3.0	…	…	…	…	…	…	…	…	…	…	…	…	…	…	…	…	bal	…
Al-Cu-C	…	1.5	…	…	…	1.0	…	…	…	…	…	…	…	…	…	…	…	…	bal	…
Al-Mg-Co	…	1.5	…	…	…	…	…	…	2.0	…	…	…	…	…	…	…	…	…	bal	…
Dispal2	…	2.0	…	…	…	…	…	…	…	…	…	1.0	…	…	…	…	…	…	bal	…
7090	…	…	…	1.5	…	1.0	…	…	2.5	…	…	0.35	…	…	…	…	8.0	…	bal	…
Al-Fe-Ce	…	…	3.5	…	…	…	8.0	…	…	…	…	0.35	…	…	…	…	…	…	bal	…
Al-Fe-Co	…	…	…	2–7	…	…	3–8	….	…	…	…	0.35	…	…	…	…	…	…	bal	…

Al-Fe-Cr	…	…	…	…	1.5	…	8.5	…	…	…	…	0.35	…	…	…	…	…	…	bal	…
XAP001	…	0.4	…	…	…	…	0.2	…	…	…	…	6.0 (ox)	…	0.08	…	…	…	…	bal	…
XAPOO2	…	0.19	…	…	…	…	0.28	…	…	…	…	8.0 (ox)	…	…	…	…	…	…	bal	…
XAP004	…	0.39	…	…	…	…	0.29	…	…	…	…	14.0 (ox)	…	0.1	…	…	…	…	bal	…
IN9021	…	1.2	…	…	…	4.0	…	…	1.5	…	…	0.75	…	…	…	…	…	…	bal	…
IN9051	…	0.7	…		…	…	…	…	4.0	…	…	1.4	…	…	…	…	…	…	bal	…
IN9052	…	1.0	…	…	…	…	…	…	4.0	…	…	0.4	…	…	…	…	…	…	bal	…
905XL	…	1.1	…	…	…	…	…	1.3	4.0	…	…	0.4	…	…	…	…	…	…	bal	…

L, lubricant; 601AB, 201AB, 602AB, 202AB, MD-22, MD-24, MD-69, and MD-76 grades are commercially available aluminum powder alloy compositions consist of blends of atomized aluminum powders mixed with powders of alloying chemicals; *ox*, oxide.

Source: Buhl H, (ed.). Advanced aerospace materials. Berlin, Heildelberg: Springer-Verlag Publishers;1992, Aluminum and aluminum alloys. In: ASM speciality handbook. Metals Park (OH, USA):ASM International Publishers; 1993, Jung TK, Sung TJ, Kim MS, Kim WY. A comparative study of mechanical property in Al-8Fe-2Mo-2V-1Zr bulk alloys fabricated from an atomized powder and melt spun ribbon. In: Proceedings of 2006 Powder Metallurgy World Congress. Busan (Korea): Korean Powder Metallurgy Institute; 2006. p. 1105–6, and Genkava T, Yamasaki M, Kavamura Y. Microstructure and mechanical properties of rapidly solidified powder metallurgy Al-Fe-V-Si-X. In: Proceedings of 2006 Powder Metallurgy World Congress. Busan (Korea): Korean Powder Metallurgy Institute; 2006. p. 1123–4.

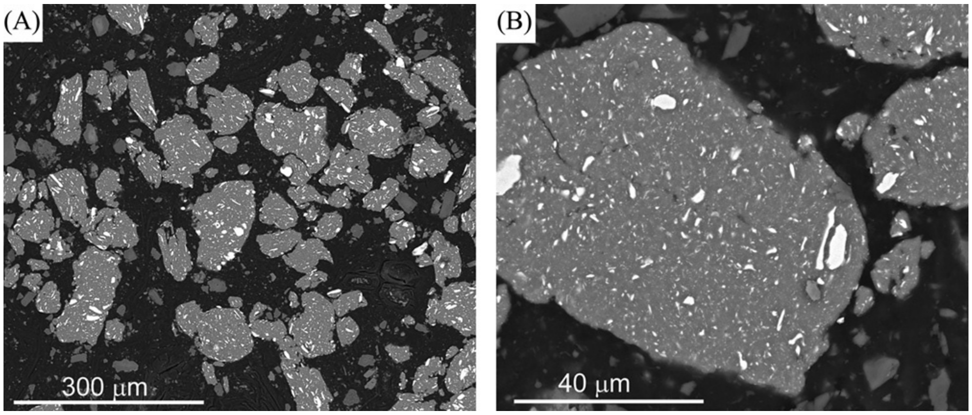

FIG. 16.1 SEM micrographs obtained by back scattered electrons of Al-10 vol% MA956 powder milled for (A) 20h and (B) 50h. *Source: Gomes LACMoutinho et al. Production of MA956 alloy reinforced aluminum matrix composites by mechanical alloying. Materials Researches 2015; 18(2).*

It is visible that a fine and homogeneous dispersion of the MA956 reinforcement particles is obtained after 20h of milling (Fig. 16.1A). The presence of high hard particles into the Al soft matrix gives rise to a high rate of formation of geometrically necessary dislocations near the particles and to large local strain gradients. The density of such dislocations is proportional to the strain gradient, that is, the amount of plastic strain divided by the microstructural scale over which this gradient is created [8]. The increase in volume fraction (to 10vol%) of the reinforcement phase, the MA956 alloy, decreases the interparticle spacing, increasing the dislocation density and therefore the work hardening rate of the aluminum matrix. As a result, the fracture process is started earlier when the reinforcing volume is higher. This high density of dislocations is also a strong driving force for faster substructure generation, and contributes to the grain refinement process [8,9].

Gomes et al. [7] reported that a heat treatment at 693K of 10vol% MA956 resulted in a partial reaction between the matrix and reinforcement particles while at 843K, the extension of the reaction was overall, with formation in both cases of intermetallic phases rich in aluminum.

The stability of the reinforcement phase is more important if the matrix is an age-hardenable aluminum alloy, therefore a solution heat treatment step would be necessary, which normally takes place at temperatures of about 773K. Torres et al. [10] have studied the stability of aluminum and aluminum alloys reinforced by the intermetallic phase Ni_3Al and showed that when the unalloyed Al was used, the composite was thermally stable at 573K up to 1000h. Above this temperature, dissolution of Ni_3Al occurred with the formation of an outer Al_3Ni layer and an intermediate Al_3Ni_2. However, when the composite matrix was an alloy such as AA6061, the reaction product contained alloying elements such as Si and Mg, and as a consequence, the age hardenability of the alloy was lost because of the depletion of solute elements in the matrix during the solution treatment. The mechanical properties of the AA2124 aluminum alloy reinforced with several intermetallic particles such as Ni_3Al, Cr_3Si and $MoSi_2$ were found to be directly related to the thermal stability of the composites during processing and subsequent thermal treatment [11].

The IncoMAP alloy Al-9052 has a specific density that is 5% less than that of a conventional age-hardenable aluminum alloy of comparable strength, such as 2024 [12], and its combination of light weight, high strength, and corrosion resistance makes it advantageous in aerospace applications.

In the work [13], MA is used to prepare composite powders of 7010 Al from elemental powder with or without SiC particulates. The addition of SiC improves the mechanical properties. The mechanically alloyed composites had higher modulus but lower strength values than the matrix at room temperature. However, at temperatures above 473K, they exhibited higher tensile strength than the matrix.

Using elemental powders as starting materials, nanocrystalline Al-4.9Fe-4.9Ni alloy powders were prepared by MA [14]. Ultimate tensile strength at room temperature of a consolidated semiproduct achieves 650MPa while the yield strength remained above 280MPa at 573K.

It is typical that aluminum milling with aqua addition as well its processing in a carbon dioxide or sodium peroxide medium gives significantly greater strengthening in comparison with mechanical alloying with oxides, Cr_2O_3, TiO_2, and ZrO_2, having high hardness and a low value of the Gibbs function of redox reaction. Mechanical alloying with oxides that have higher values of Gibb's energy formation, such as CuO, Co_3O_4, MoO_3, and V_2O_5, is more advantageous.

The largest value of ultimate tensile strength was achieved in (Al-Mg) alloying compound surfactant materials, alloying by organic compounds [15]. These organic compounds belong to various classes, including oxalic acid ($C_2H_2O_4$), carbamide ($H_2N{\cdot}CO{\cdot}NH_2$), dinitrotoluene $CH_3{\cdot}C_6H_3(NO_2)_2$, 1.5-diphenylcarbazide ($C_{13}H_{14}N_4O$), and 3-methyl-1-phenyl-2-pyrazoline-5-one ($C_{10}H_{10}N_2O$) (Table 16.3).

TABLE 16.3 Alloying Addition Nature Dependence on Phase Composition and Mechanical Properties of Al-Mg-Alloying Compound-Surfactant Alloys

Alloying Addition		Phase Composition	Mechanical Properties		
Matter	Content (wt%)		Hardness (MPa)	UTS (MPa)	El (%)
$Cu(OH)_2$	9.08	Al, Al_2Cu,, Al_4Cu_9, Al_3Mg_2, Al_2O_3, MgO, Al_4C_3	1700	610	3
$Co(OH)_2$	6.82	Al, Al_5Co_2, Al_3Mg_2, Al_2O_3, MgO, Al_4C_3	1750	630	3
$Ni(OH)_3$	6.81	Al, Al_3Ni, Al_3Mg_2, Al_2O_3, MgO, Al_4C_3	1700	630	3
$Fe(OH)_3$	6.61	Al, Al_3Fe, Al_3Mg_2, Al_2O_3, MgO, $MgO{\cdot}Al_2O_3$, Al_4C_3	1700	620	3
LiOH	4.45	Al, Al_3Mg_2, Al_2O_3, MgO, $MgO{\cdot}Al_2O_3$, Al_4C_3	1650	640	4
$CuCO_3$	7.66	Al, Al_3Cu, Al_4Cu_9, Al_3Mg_2, Al_2O_3, MgO, Al_4C_3	1700	610	3
$Co(NO_3)_2{\cdot}3H_2O$	4.51	Al, Al_3Co_2, Al_3Mg_2, Al_2O_3, MgO, AlN, Al_4C_3	1800	660	2
$Ni(NO_3)_2{\cdot}6H_2O$	4.51	Al, Al_3Ni, Al_3Mg_2, Al_2O_3, MgO, AlN, Al_4C_3	1850	670	2
$Fe(NO_3)_2{\cdot}6H_2O$	4.43	Al, Al_3Fe, Al_3Mg_2, Al_2O_3, MgO, $MgO{\cdot}Al_2O_3$, AlN, Al_4C_3	1750	650	2
$H_2N{\cdot}CO{\cdot}NH_2$	2.50	Al, Al_2O_3, MgO, AlN, Al_4C_3	1900	720	2
$CH_3{\cdot}C_6H_3(NO_2)_2$	2.50	Al, Al_2O_3, MgO, AlN, Al_4C_3	2200	770	2
$C_{13}H_{14}N_4O$	2.50	Al, Al_2O_3, MgO, AlN, Al_4C_3	2200	760	2
$C_{10}H_{10}N_2O$	2.50	Al, Al_2O_3, MgO, AlN, Al_4C_3	2300	750	2

Source: Vitjaz PA, Lovshenko FG, Lovshenko GF. Mechanical alloyed alloys based on aluminum and copper. Minsk: Belaruskaja Nauka Publishers; 1998 [in Russian], Russian Federation Patent 2,001,715, Jan. 1991, Russian Federation Patent 2,000,882, Jul. 1991.

The alloys produced have a microcrystalline structure with grain sizes less than 0.4 µm. The sizes of the main strengthening phases, MgO, $MgO{\cdot}Al_2O_3$, Al_4C_3, and AlN, do not exceed 5 nm. The microcrystalline structure with ultrafine and nanosized main strengthening phases determines the high degree of strengthening. The MA alloys produced are heat-resistant (Table 16.4). They stand the test up to 773 K. Dependence of the ultimate tensile strength on the testing temperatures in the temperature ranges studied is near linear while the elongation is a curve with a maximum at 523–623 K.

RAPID SOLIDIFICATION PROCESS

Rapid solidification is a metastable process that results in a significant undercooling of the molten metal, leading to a refinement of microstructural features and constitutional effects such as the extension of solubility limits, the synthesis of novel crystalline phases, and the formation of metallic glasses [12,16–18].

Currently, gas atomization and centrifugal atomization methods for rapid solidified aluminum alloy powder production are most extended and commercially available [19–24]. One of the centrifugal atomization processes, which is used for this purpose, is spinning cup atomization [22–24]. In all cases, the cup is 80–200 mm diameter, running at moderately high speeds from 3000 to 10,000 rpm. Solidification of the molten particles in a gaseous medium requires a very large chiller chamber, up to 12 m in diameter.

Spinning disc atomization is another form of centrifugal atomization [23], where a molten metal stream collides with a rapidly moving metal substrate surface such as a rotating disc rim. In this case, material in the form of a ribbon is obtained. By melt extraction through melt atomization using a rotating disc that touches the melt surface, a product in the form of a flake is obtained. The material, in the form of a thin ribbon, flake, or wire, is rapid cooled by heat conduction through the metal substrate, followed by a grinding or chopping operation to the particulate state. Additional information on spinning disc atomization and melt extraction can be found in Chapter 4.

TABLE 16.4 Mechanical Properties of Aluminum Alloys Mixed With Organic Compounds

Alloying Addition				Mechanical Properties	
Matter	Content (wt%)	Magnesium Content (wt%)	Testing Temperature (K)	UTS (MPa)	Elongation (%)
$H_2N{\cdot}CO{\cdot}NH_2$	2.5	2.0	293	720	2
			473	420	8
			573	310	15
			673	240	12
			773	170	10
$CH_3{\cdot}C_6H_3(NO_2)_2$	2.5	2.0	293	770	2
			473	480	8
			573	360	14
			673	260	10
			773	190	8
$C_{13}H_{14}N_4O$	2.5	2.0	293	760	2
			473	480	7
			573	370	15
			673	270	11
			773	190	9
$C_{10}H_{10}N_2O$	2.5	2.0	20	750	2
			200	470	8
			300	360	14
			400	250	11
			500	180	9

Source: Vitjaz PA, Lovshenko FG, Lovshenko GF. Mechanical alloyed alloys based on aluminum and copper. Minsk: Belaruskaja Nauka Publishers; 1998 [in Russian].

The dendritic structure is a primary form in rapid solidification alloys, up to a cooling rate of 10^5–10^6 K/s. An important milestone in the study of dendritic structure was the discovery at the end of the 1940s of the hyperbolic dependence of the space between the second order dendrite branches on the solidification rate [25,26]. Such a characteristic has a physical meaning as a determinative to a first approximation value of the separation diffusion volume by crystallization and is expressed by the hyperbolic equation

$$v = \left(\frac{A}{d}\right)^{1/n} \tag{16.1}$$

where d is the measured dendrite parameter in μm, v is the cooling rate in K/s, and A and n are constants [27]. Constant A connected with alloy properties increases as the coefficient of diffusion rises and the alloying degree decreases. For high-strength aluminum alloys, $A = 100$, the constant n value is in the interval 0.25–0.5, depending on the grain shape. In particular, $n = 1/3$ for equiaxed grains.

The dendrite parameter is determined by means of calculation of average dendrite cell area in the metallographic section of powder particles. The square root of this area gives the dendrite parameter, which is unambiguously dependent on the solidification rate [18]. The dependence of dendritic branching on the cooling rate is shown in Fig. 16.2 [28]. A characteristic dendritic structure is observed in a 200 μm particle (Fig. 16.2A); its dendritic parameter is equal to 2.8 μm, which according to Eq. (16.1), corresponds to a cooling rate of approximately 4.5×10^4 K/s. For a 90 μm particle

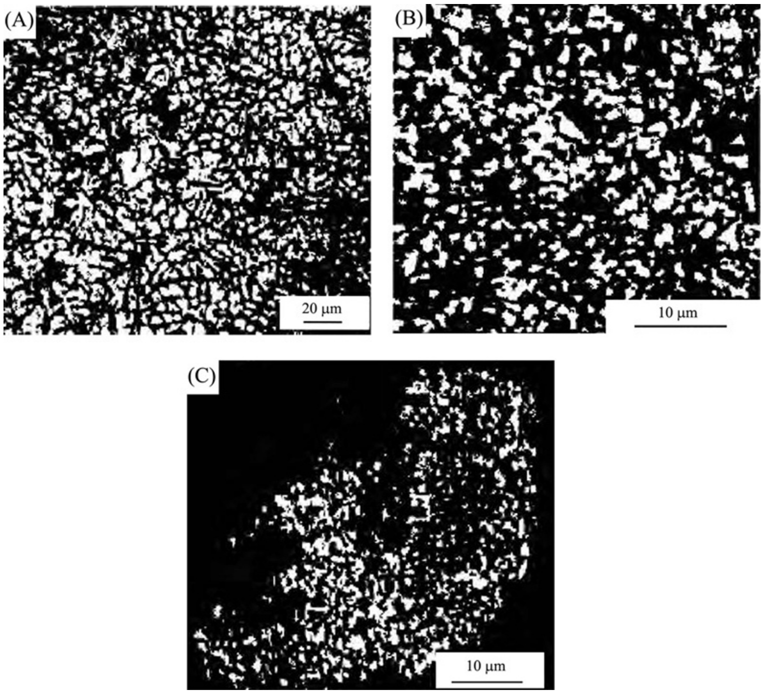

FIG. 16.2 Structure of Al-9.5Zn-3.0Mg-1.2Cu alloy powder particles of various sizes with projected diameter equal to (A), 200 μm; (B), 90 μm; and (C), 50 μm.

(Fig. 16.2B), the dendritic parameter is 1.57 μm, and the corresponding cooling rate is 2.5×10^5 K/s. The microcrystalline structure of a 50 μm particle (Fig. 16.2C) is characterized by the dendritic parameter of 1.0 μm, which corresponds to the cooling rate of 10^6 K/s. The formation of nondendritic grains with increasing cooling rate can be explained by increased supercooling and by a significant intensification of the nucleation, respectively.

The approximate evaluation of the dendritic parameter dependence on the cooling rate during crystallization of aluminum alloys was made by Dobatkin [18] (Table 16.5). Nondendritic grain sizes ranging from 0.02 to 0.05 μm (which correspond to a calculated cooling rate of 10^{10}–10^{11} K/s) were discovered and studied by Belocerkovcev, Barabanenkov, and Pavlenko. The 10–20 μm flakes of Al-6wt%Zr alloy were obtained by means of drop firing on a copper substrate after melt heating up to a temperature exceeding the liquidus temperature by 323–373 K.

TABLE 16.5 Correspondence Between Dendritic Parameter and Cooling Rate During Crystallization of Aluminum Alloys

Cooling Rate (K/s)	Dendritic Parameter (μm)	Solidification Conditions
0.001	1000	Casting big ingot into the casting molds
1	100	Continuous casting of ingots
1000	10	Big granules
10^6	1	Fine granules and flakes
10^9	0.1	Ultrafine flakes
10^{12}	0.01	Crystallization of flakes with initial deep undercooling[a]
10^{15}	0.001	It is not obtained experimentally

[a] *Nondendritic grain.*

At a high cooling rate, along with dendritic structure, the nondendritic structure is formed without physical means of action on the melt while by still higher cooling rates, only nondendritic structures may be obtained [18]. The probability of increasing the nondendritic grain by high cooling rates can be explained by a deep precrystallization undercooling and drastic intensification of the nucleation. Here it is necessary to note that initial undercooling, which determines the intensification of the nucleation increase, does not control the following crystallization process in consequence of temperature increasing (recalescence) on the first stage of alloy solidification. The deep undercooling can repress the crystallization process and lead to the formation of metallic glass.

Even at relatively low cooling rates, nondendritic structures can be obtained by introducing a conditioning agent and applying ultrasonics. Some conditioning agents such as scandium allow nondendritic structures to occur without ultrasonic assistance. Nondendritic structure of ingots, granules, powders, and flakes are shown in Fig. 16.3.

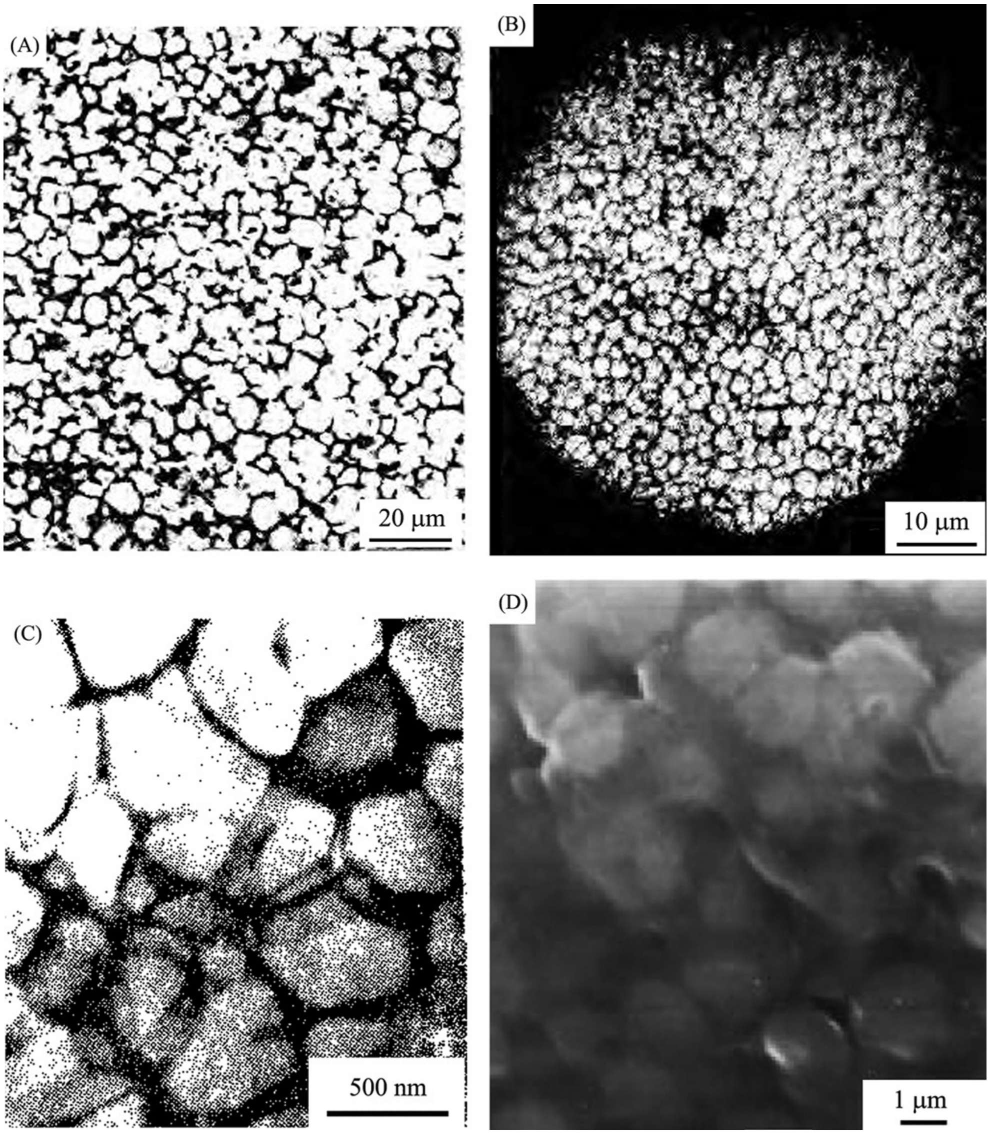

FIG. 16.3 Non-dendritic structure of (A), ingots; (B), granules; and (C) flakes of D16 alloy (in Russian grading analogous 2024 US grade) (Source: Ref. [18]); (D), powder particles of Al-5Fe-5.0Cr-2Ti alloy (Source Ref. [29]).

Dobatkin and his colleagues at the All-Russian Light Alloys Institute (VILS) [30] showed that it is possible to obtain a nondendritic structure whatever the cooling rate and that the grain size will not be dependent on factors other than cooling rate. Grain size refinement is achieved only by a cooling rate increase and therefore the dendritic parameter curve is a lower boundary grain size depending on the cooling rate (Fig. 16.4).

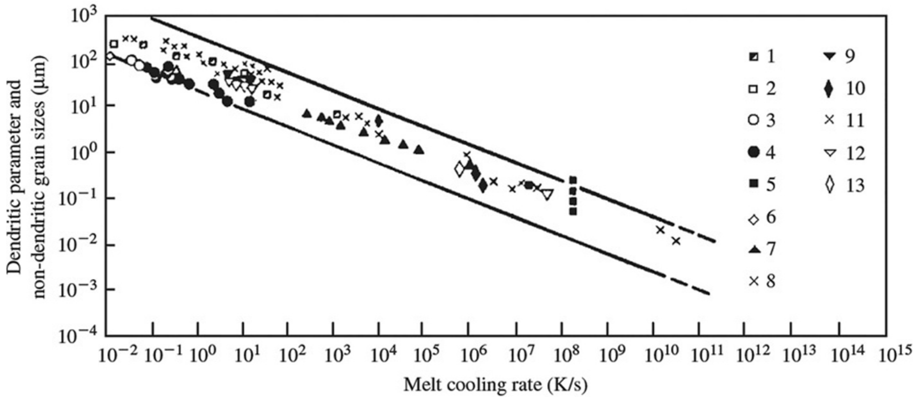

FIG. 16.4 Dependence of non-dendritic grain size (11–13) and dendritic parameter (1–10) on melt cooling rate for aluminum alloys (1–8, 11), magnesium alloys (9, 12), and nickel elevated temperature alloys (1, 13). *From Eskin GI. Non-dendritic crystallization of light alloys. Technol Light Alloys 2000;2:17–25 [in Russian].*

In ingots of various size and shape of aluminum and magnesium alloys, the nondendritic structure was obtained at the expense of nucleation intensification by means of modifiers in combination with ultrasonic (cavitational) treatment. In granules, the nondendritic structure was obtained by ultrasonic atomization with a cavitational effect on the melt before solidification and in flakes in response to deep precrystallization undercooling.

The phenomenon of heightened solubility by rapid crystallization is known as anomalous supersaturation [31]. Experimental data of attainable supersaturation in alloys of some duplex systems for ingots, granules of 1–3 mm diameter, and flakes, and the maximum solubility in solid solution according to equilibrium diagram are presented in Table 16.6.

TABLE 16.6 Content of Alloying Elements in Solid Solution of Binary Aluminum Alloys

		Content of Alloying Elements in Solid Solution (wt%)		
Second Component	Maximum Solubility Under Equilibrium Diagram (wt%)	In Ingots by $v_{cool} = 1\,K/s$	In Granules by $v_{cool} = 10^3–10^4\,K/s$	In Flakes by $v_{cool} = 10^5–10^6\,K/s$
Copper	5.7 [32]	2.0 [18]	…	33 [18]
Magnesium	17.4 [32]	3.0 [18]	…	34–38 [18]
Manganese	1.4 [32]	1.0 [18]	4.5 [18]	14.5 [18]
Zirconium	0.28 [32]	0.11 [18]	2.0 [18]	4.0 [18]
	…	…	1.2 [33]	…
Chromium	0.77 [32]	0.2 [18]	2.0 [14]	5.8 [18]
				5.7 [28]
Titanium	0.28 [32]	0.1 [14]	1.0 [18]	2.5 [18]
Vanadium	0.37 [31]	…	1.0 [18]	1.2 [34]
Molybdenum	0.2 [31]	…	0.6 [18]	1.0 [18]
Germanium	7.2 [32]	…	…	17.3 [18]
Iron	0.052 [31]	0.03 [18]	…	0.17 [18]
				0.2 [34]
Silicon	1.65 [32]	0.5 [18]	…	10.7 [18]
				11 [35]
Tungsten	0.22 [31]	…	1.2 [18]	…

For the eutectic systems with limited confined solubility, peritectic systems, and systems with one or several chemical compounds, the metastable diagrams differ from the equilibrium ones. This is illustrated by reference to the aluminum-manganese system in the metastable equilibrium diagram in Fig. 16.5 [36].

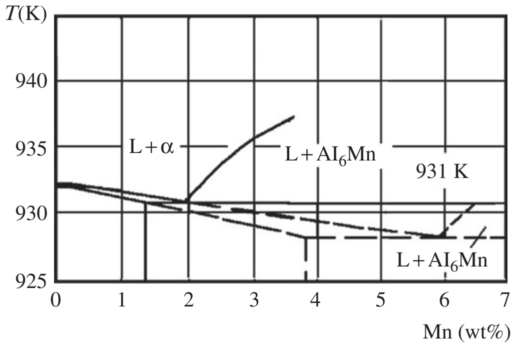

FIG. 16.5 Scheme of metastable equilibrium diagram of Al-Mn system (dotted line). *From Dobatkin VI, Elagin VI, Fedorov VM. Rapidly solidified aluminum alloys. Moscow: All-Russian Institute of Light Alloys Publishers; 1995 [in Russian].*

Depending on cooling rate, the location of the eutectic horizontal is changed but, in all cases, the liquidus and solidus lines of the equilibrium diagram are in continuation in the second component (manganese in this case) direction of the equilibrium system liquidus and solidus lines. Thus it is possible to make at least two conclusions. First of all, at high cooling rates in hypereutectic alloys, one can prevent the formation of a primary crystal's second component or its compound and obtain a quasieutectic or even quasihypoeutectic alloy structure. Second, the content of the second component in a solid solution may be increased in comparison with maximum solubility as in the equilibrium diagram and solid solution obtained by crystallization as in the equilibrium diagram have a eutectic structure.

In peritectic systems, by rapid cooling, the liquidus and solidus lines can also be continued in the second component direction. In this case, the liquidus and solidus lines are continued, not downward as in eutectic systems (Fig. 16.5), but upward, as shown in Fig. 16.6 for the Al-Zr system [18].

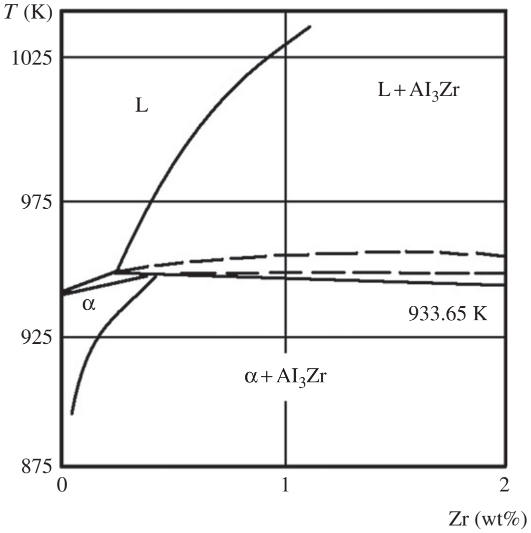

FIG. 16.6 Scheme of metastable equilibrium diagram of Al-Zr system (dotted line). *From Dobatkin VI, Elagin VI, Fedorov VM. Rapidly solidified aluminum alloys. Moscow: All-Russian Institute of Light Alloys Publishers; 1995 [in Russian].*

The higher the melt cooling rate (and the attainable overcooling as a result), the greater becomes the concentration at which solidification is as the solid solution type. The concentration area in which alloys without second component primary crystals and peritectic reaction products can be obtained is also widened.

For alloys of peritectic systems, with a rise in the cooling rate, the change from the primary intermetallic compound crystallization area directly to the solid solution crystallization area is observed, which can be explained by suppression of the peritectic reaction (Fig. 16.7).

The content curve of the supersaturated solid solution usually has a remarkable bend in the cooling rate range from 10^3 to 10^6 K/s. This bend is related also to beginning precipitation of the second component crystals and the existence of nonequilibrium eutectics.

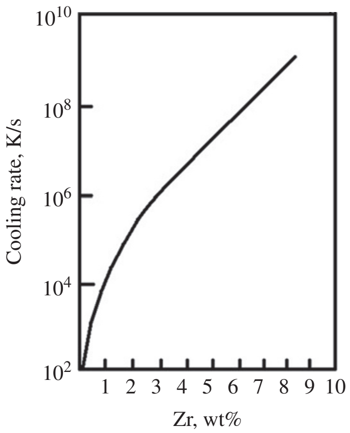

FIG. 16.7 Phase diagram of Al-Zr system.

Two very important features of metastable diagrams—widening of the solid solution area and the displacement of the start of the second component primary crystal emission—are confirmed for complicated aluminum alloys. Property changes resulting from the aging of supersaturated solid solutions include an increase of hardness and strength, which can significantly exceed those of the primary solid solutions.

Consequently, the metastable crystallization effect allows the creation of alloys with strength, heat resistance, and other property levels unattainable in alloys produced by conventional technology.

CENTRIFUGAL ATOMIZATION

RSR Process

The mode of centrifugal atomization is the rapid solidification rate (RSR) process. The RSR process has been described by Cox et al [37], Paterson [38], and Anderson [39]. The first RSR unit operated in late 1977, producing IN-100 powder in a pilot plant and patents were issued in 1978 [21] and 1982 [40]. The latter patented plant is shown in Fig. 16.8.

The metal alloy is normally vacuum induction melted. When the desired level of superheat is reached, the system is backfilled with helium. The pressure head of liquid metal in the tundish, the area of the nozzle, and the pressure difference

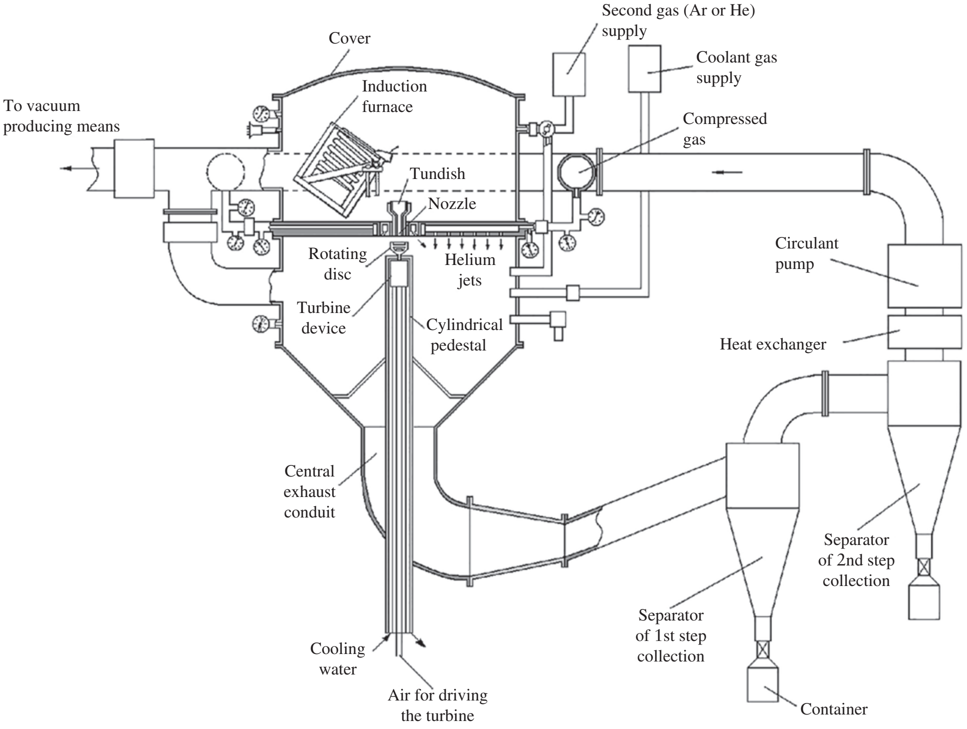
Second gas (Ar or He) supply
Cover
Coolant gas supply
To vacuum producing means
Induction furnace
Compressed gas
Tundish
Nozzle
Circulant pump
Rotating disc
Helium jets
Turbine device
Cylindrical pedestal
Heat exchanger
Central exhaust conduit
Separator of 2nd step collection
Separator of 1st step collection
Cooling water
Air for driving the turbine
Container

FIG. 16.8 Schematic of spinning disc atomization.

between the upper chamber and lower chamber are controlled to obtain the desired flow rate of liquid metal through the nozzle. The liquid metal flows through the nozzle and onto the rotating disc, or atomizer rotor. The surface onto which the liquid metal flows imparts kinetic energy to it, the metal being flung from the edge of the rotor in the form of droplets, ligaments, or sheets, depending on the speed of the rotating disc, the flow rate of the liquid metal through the nozzle, the atomizer rotor geometry, and the fluid properties of the liquid metal. Such particles are rapidly cooled convectively by contact with the annular curtain of cooling helium jets directed downward from the nozzle plate. The powder particles are carried from the lower chamber by a cooling stream and deposited in containers according to particle size. The RSR plant incorporates closed-loop helium recirculation.

Total gas mass flow amounts to 0.9 kg/s while a nozzle diameter of 4 mm was used to deliver a molten alloy at a mass flow rate of 0.15 kg/s. A speed of 18,000 rpm has been used with an atomizer fulfilled as a cup having an 82.5 mm inner diameter to produce metal particles in the range from 10 to 50 μm in diameter. In such conditions, the mean cooling rates are evaluated in a range of 10^5 K/s. To obtain these cooling rates with particle sizes up to 75 μm, it is necessary that a high thermal conductivity gas, such as helium, be used.

Parallel with nickel-base superalloys, the RSR process has been used to produce specialty aluminum alloys, beryllium alloys, molybdenum, titanium alloys, and silicide powders.

This technique allows the production of narrow size distribution powders and is used commercially to manufacture plasma-spraying powders where size ranges such as −150 +53 or −100 +38 μm are needed. But, the uncontrolled geometry of the scull on the rotating disc, and the problems of out-of-balance forces, degrade the size distribution greatly compared with that achieved with lower-melting metals where the cup or disc has precise geometry. It also results in heavy maintenance costs on the spinning cup assembly. The use of huge volumes of expensive helium is another drawback. As a result of these disadvantages, gas atomization has continued to dominate the production of higher-melting alloy powders. Therefore, Pratt and Whitney, the main producer of RSR powder, remained the only operator in the 1990s, and the few attempts that have been made to develop similar devices elsewhere have not been productive. Production was less than 1000 tons/year, according to data [41].

Spinning Cup Water Granulation Process

Generally, the spinning cup granulation process is carried out in open air because of the large size of the plant needed to freeze coarse particles. In this case, a perforated steel or cast iron cup is used to make a series of streams of metal, which break up into needles due to the oxide film on them. Production is considerable, probably thousands of tons per year [41].

The spinning cup water granulation process [22] allows an increase of the cooling rate and a notable decrease of the size of the plant, owing to cooling the molten granules in water. Thus, the chiller chamber size is only 1.2–1.5 m in diameter in comparison with the 12 m diameter one in open-air granulation. A spinning cup water granulator, which was used in VILS, is shown in Fig. 4.65 (Chapter 4). The flow diagram of the spinning cup granulation process with cooling of molten drops in water is shown in Fig. 16.9. The solidified granules are carried from the atomizing chamber together with cooling water through the overflow apertures.

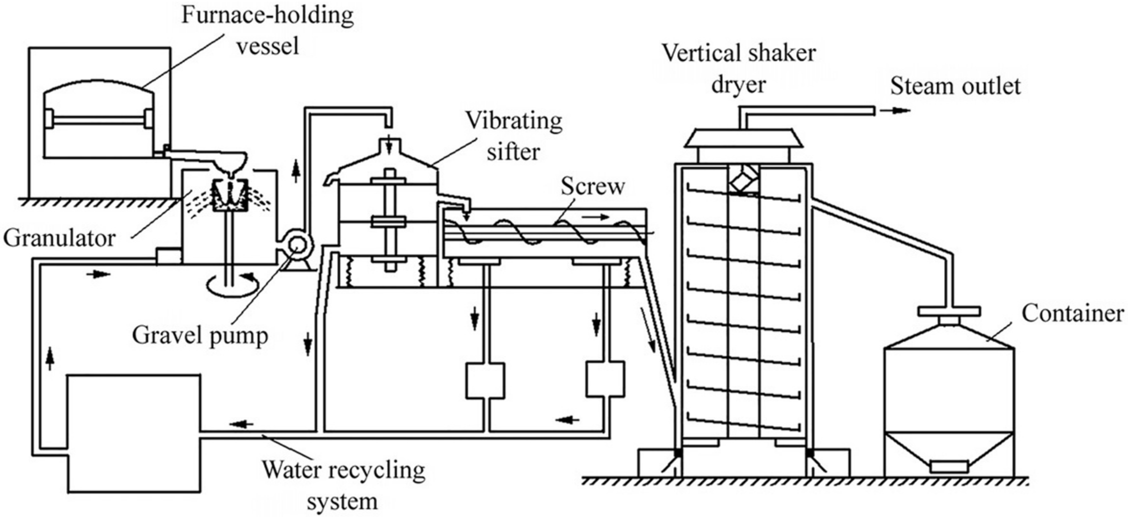

FIG. 16.9 Flowchart of the spinning cup water granulation process.

TABLE 16.7 Dependence of Calculated Heat-Transfer Coefficient α_d on Cooling Medium

Cooling Medium	Design Equation	α_d (W/(mK))	Explanation
Air	$\alpha_m = \frac{Nu\lambda}{d_p}$	396	$Nu = 2 + 0.6Re^{0.5}Pr^{0.33}$; λ is coefficient of heat conductivity; d_p is diameter of drop; Re is Reynolds' number, $Re = \frac{wd_p}{v_a}$; w is drop velocity relatively to gas medium; ν_g is kinematic viscosity; Pr is Prandtl number, $Pr = \frac{\nu_g}{a_g}$; a_g is thermal diffusivity; $w = 5$ m/s
Steam jacket	$\alpha_j = \frac{2\pi\lambda_s}{d_p(1 - d_p/d_j)}$	803	λ_g is heat conductivity; d_p and d_j are diameters of drop and steam jacket, accordingly
Water	$\alpha = \frac{\rho r q_{cr}}{3(t_{cr} - t_w)\tau_{cr}}$	11,200	q_{cr} is crystallization heat; t_w is water temperature; τ_{cr} is crystallization time; ρ is metal density; t_{cr} is metal crystallization temperature; r is drop radius

Modified from Bondarev BI, Shmakov YuV. Technology of rapidly solidified Al alloy production. Moscow: All-Russian Institute of Light Alloys Publishers;1997 [in Russian].

The cooling rate of the particles in air is considerably lower than those in water because of differences of the heat transfer process (Table 16.7). Therefore the flight time of particles before coming into contact with the water must be kept a short as possible. This is achieved by reducing the air space in the atomizing chamber and increasing the velocity of the molten droplets.

The dependence of granule fraction yield on cup rotary speed for the Al-(1.4–2.0)Mn-(0.8–1.2)Cr-(0.5–0.9)Zr-(0.4–0.8)Ti-(0.4–0.8)V alloy is shown in Fig. 16.10.

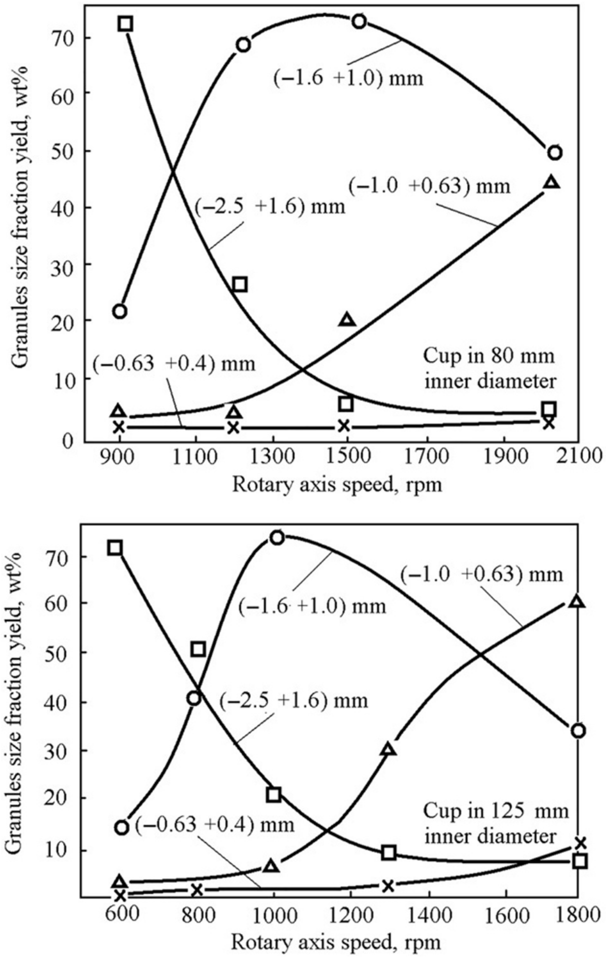

FIG. 16.10 Dependence of granule fraction yield on cup rotary speed for 01419 alloy (in Russian grading). *Source: Bondarev BI, Shmakov YuV. Technology of rapidly solidified Al alloy production. Moscow: All-Russian Institute of Light Alloys Publishers;1997 [in Russian].*

TABLE 16.8 Main Parameters of the Spinning Cup Granulation Process

Atomizer	Cup Inner Diameter (mm)	Aperture Size (mm)	Cup Rotary Speed (rpm)	Molten Mass Flow Rate (kg/h)
Breaking up from cup lip	150	…	600–2700	100–300
Cup with apertures	80–150	1.2–3.0	600–10000	100–600
Cup with slits	125–150	1.0–1.5	600–1000	100–600

Source: Bondarev BI, Shmakov YuV. Technology of rapidly solidified Al alloy production. Moscow: All-Russian Institute of Light Alloys Publishers;1997 [in Russian].

The main parameters of the spinning cup granulation process in ranges in which the investigations in VILS were carried out are given in Table 16.8. The conditions of the granulation process for (−2.0 +0.5) mm granule fraction yield were optimized:

- For high strength Al-Zn-Mg-Cu base alloys slotted or with an apertures cup 125 mm in diameter; a cup speed of 1000 rpm; a mass flow rate of molten alloy ranging from 170 to 250 kg/h; and the temperature of the liquid metal on pouring ranges from 1273 to 1323 K.
- For elevated temperature alloys with apertures cup 80 mm in diameter; a cup speed of 1500 rpm; a mass flow rate of molten alloy in the range from 140 to 150 kg/h; and the temperature of liquid metal on pouring ranging from 1473 to 1523 K.

The spinning cup granulation process with cooling of molten drops in water enables the cooling rates of granules in ranges from 10^3 to 10^4 K/s to be achieved. This process is explosion-proof (owing to the absence of ultrafine and fine particles) and easy to operate.

In comparison with gas-atomized powders cooled in a technical nitrogen gas medium, the spinning cup granules cooled in water are lower oxidized (Table 16.9) because of a high cooling rate and a lesser specific surface of the latter.

TABLE 16.9 Influence of Cooling Medium on Surface Properties of Rapid Solidified Particles

Cooling Medium			Characteristics of Powders and Granules			
	Aqua and Oxygen Content					
Composition	Aqua (wt%)	Oxygen (vol%)	Diameter (μm)	Oxygen Content (wt%)	Adsorbed Water Content (wt%)	Oxide Film Thickness (nm)
Helium, high purity	Max 0.002	Max 0.002	50–350	0.01	Max 0.001·	3–4
Argon, highest grade	<0.0009	Max 0.0007	50–350	0.005	Max 0.001	3–4
Nitrogen, technical	0.09	Max 0.5	50–350	0.1–0.4	Max 0.01	3–5
Centrifugation in air, cooling in water	<100	<2	500–2000	0.05	Max 0.01	3–5

Modified from Bondarev BI, Shmakov YuV. Technology of rapidly solidified Al alloy production. Moscow: All-Russian Institute of Light Alloys Publishers;1997 [in Russian].

The granulation technique followed by granule degassing and subsequent consolidation is applied for manufacturing alloys for various applications, including high strength, high strength weldability, and elevated temperature aluminum alloys [18,22]. The total residual concentration of water and hydrogen should not exceed 0.3 ppm to provide sufficient quality of dense billets, including such important characteristics as plasticity, low-cycle fatigue, and rate of crack propagation. Typical mechanical properties of high strength, high strength weldability, and elevated temperature aluminum alloys on the basis of granules solidified in water are given in Table 16.19.

For comparison, the properties of ingot alloys similar in composition and function are included in Table 16.10. As may be seen, the high strength and weldable granular alloys show significantly better tensile properties than the ingot-based material. The semiproducts of elevated temperature alloy 01419 are inferior at room temperature in strength characteristics

TABLE 16.10 Mechanical Properties of Aluminum Alloy Semiproducts Made From Water-Atomized Granules

Alloy	Alloy Composition (wt%)	Semiproduct	Condition Strengthening	Temperature (K)	Mechanical Properties		
					UTL (MPa)	YS (MPa)	El (%)
High-strength alloys							
01969	Al-(8–9)Zn-(2–3)Mg-(1–1.5)Cu-(1.15–2.4)T/M	Sheet in 2 mm thickness	T1	RT	670	640	10
		Rod in 5 mm diameter	T1	RT	690	660	6
01959	Al-(6–7)Zn-(1.8–2.5)Mg-(0.8–1.4)Cu-(0.8–2.15)T/M	Sheet in 2 mm thickness	T1	RT	580	490	8
		Rod in 5 mm diameter	T1	RT	620	580	11
B95pch[a]	Al-6Zn-2.3Mg-1.7Cu-0.4Mn-0.17Cr	Sheet in 2 mm thickness	T1	RT	510	420	10
High-strength weldability alloys							
01949	Al-(4.5–5.5)Zn-(2.5–3.5)Mg-(0.1–0.4)Mn-(0.4–0.8)Cr-(0.4–0.8)Zr-(0.1–0.3)Ti	Sheet	T6	RT	590 500 (w)	500	10
1201[b]	Al-(4.0–5.0)Zn-(1.0–1.8)Mg-(0.2–0.7)Mn-(0.06–0.2)Cr-(0.08–0.2)Zr-(0.01–0.06)Ti-0.1Cu-0.4Fe-0.35Si	Sheet	T2	RT	410 280 (w)	330	10
Elevated temperature alloys							
01419	Al-(1.8–2.2)Mn-(0.8–1.2)Cr-(0.4–0.8)Zr-(0.4–0.8)Ti-(0.4–0.8)V-max 0.3Fe-max 0.3Si	Extruded semiproducts	…	RT	340	310	15
			…	523	150	130	20
			1000 h expose	523	100	…	…
			…	573	110	90	21
			1000 h expose	623	50	…	…
AK4–1[c]	Al-(1.9–2.5)Cu-(1.4–1.8)Mg-(0.8–1.3)Ni-(0.8–1.3)Fe-(<0.3)Zn-(<35)Si-(<0.2)Mn	Extruded semiproducts	…	RT	420	360	7
			…	523	130	90	25
			1000 h expose	523	60	…	…
			…	623	50	40	
			1000 h expose	623	30	…	…

[a] B95pch is ingot alloy (in Russian grading analogous 7050 US grade).
[b] 1201 is ingot alloy in Russian grading.
[c] AK4–1 is ingot alloy in Russian grade, RM is room temperature.

to the semiproducts of the AK4–1 conventional alloy, but at elevated temperatures they are 1.5–2 times better in strength, particularly greep-rupture strength.

The VILS granular technique enables the following to be produced [22]:

- Billets with mass up to 350 kg up to 500 × 650 mm in size.
- Extruded semiproducts: rods from 10 to 200 mm in size, structural shapes from 0.8 to 130 cm^2 in cross-section area, tubes from 20 to 200 mm in diameter with wall thickness from 1.5 to 20 mm.
- Rolled semiproducts: sheets from 0.8 to 6 mm in thickness with width up to 1000 mm and length up to 3000 mm.
- Stamped semiproducts: pistons, coupler links, impellers, and others in mass from 0.5 to 40 kg.

GAS ATOMIZATION

For aluminum and its alloys, gas atomization (GA) is widely used in industry [45–47]. The conventional process provides cooling rates up to 10^5 K/s. However, the GA technology is a dangerous process and special safety measures are required, which considerably raises the manufacturing costs.

Because of the high affinity of the aluminum for oxygen, precautions should be taken to elude generation of a suspended solid and to avoid ignition sources such as electrical sparks and electrostatic charges [48]. National Fire Prevention Association (NFPA) Standard 654 provides guidance on the prevention of fire and dust explosion [49]. Along with this, the conventional PM process requires the addition of a lubricant to the aluminum powder, which tends to provide a coating of organic material and makes aluminum powders stick together, making them less receptive to forming a suspended solid.

Atomization processes can be grouped by the method of melting the feedstock, with or without the use of a crucible (Fig. 16.11), and by the type and geometry of the nozzle used. When the material is melted in a crucible, inductive heating or a plasma torch are used. Subsequently, the melt is led through the nozzle into the atomization chamber. The most common atomizer types are the free-fall nozzle, the close-coupled nozzle, and the De Laval nozzle described in Chapter 4.

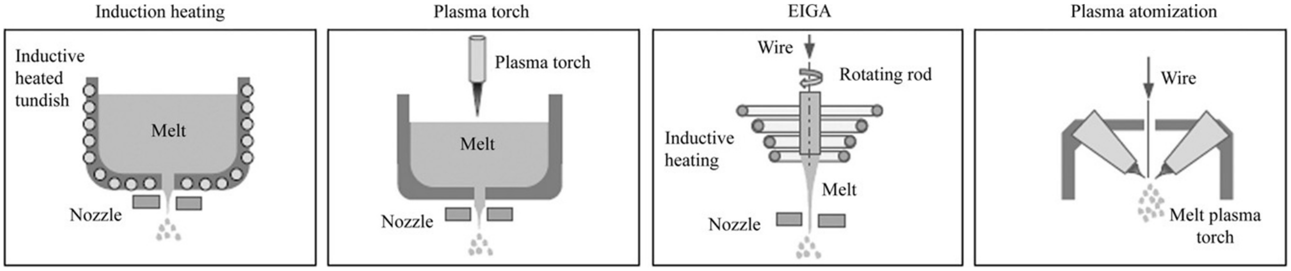

FIG. 16.11 Schematic of melting methods for gas atomization.

In the EIGA (Electrode Induction Melting Gas Atomization) process and in the plasma atomization process, the material is not melted in a crucible and therefore contaminations by ceramic material or remains of foreign material from earlier process batches should not arise. In the EIGA process, the metal is melted from an induction-heated rod, from which the liquid metal drops into the atomization nozzle without any contact with the surrounding parts. In the plasma-atomization process, a wire with a diameter of 3 mm is melted using three plasma torches [50] and directly atomized, using the heat and kinetic energy of the plasma. From this process, particles from 5 to 250 μm with a particularly spherical shape are obtained.

Gas atomization is the most widely used method for compacting grade of aluminum alloy powders. This technique is similar to gas atomization of aluminum powder and is described in Chapter 15.

Various master alloys and molding-grade powders are available. Pure aluminum metal powder may be combined with other additives such as zinc, copper, magnesium, silicon, and zirconium to form special alloy compositions. Some common aluminum alloys are presented in Table 16.11.

Aluminum powders are highly compressible, therefore high dense green compact is achievable. Aluminum PM green parts can be sintered in protective furnace atmospheres such as pure hydrogen, nitrogen with a hydrogen mix, dissociated ammonia, or vacuum. However, nitrogen atmosphere is preferable for aluminum sintering [56–58]. As Schaffer and Huo discussed [51], nitrogen can play a role in the reduction of aluminum oxide because of the formation of aluminum nitride. On these grounds, sintering in nitrogen is even more effective than in argon or vacuum. Along with this, hydrogen may show a negative effect on the sintering of aluminum alloys [52]. One possible cause is that hydrogen hinders the formation of aluminum nitride by reacting with oxygen and forming water vapor.

Typical mechanical properties for some of the more common PM aluminum alloys produced by commercial manufacturing processes are shown in Table 16.12.

The most conventional aluminum PM alloys exhibit low tensile ductility in the range of 0%–5%. The recent Alumix developments [53] allow improved tensile ductility and strength of same conventional aluminum alloys. A number of the enhanced materials that exhibit such characteristics are listed in Table 16.13.

The enhanced Alumix 123 is reached by optimizing alloy composition and by studying the influence of the raw material components. In a similar way, modified Alumix 321 was optimized. Due to the low alloy content of that grade, it is used for parts requiring increased corrosion resistance. Other advantages include higher ductility and higher thermal conductivity; however, the disadvantage of this alloy is low mechanical strength. Optimization of this alloy was to maintain the good corrosion resistance, ductility, and thermal conductivity but improve the low strength. Basically, increasing the sinter activity is also for that grade, similar to Alumix 123, resulting in a higher shrinkage during sintering and subsequently a less porous microstructure. Modified Alumix 231 exhibits an increase in ductility and strength of the sintered parts with outstanding wear resistance. A continuous isostatic pressure sintering process, combined with sizing (CISIZE), produces aluminum alloys with finely dispersed Si particles having elevated ductility [54].

TABLE 16.11 Nominal compositions for accepted PM aluminum alloys employed in commercial manufacturing

Denomination		Composition (wt%)					
ASTM	Modification	Al	Cu	Mg	Si	Zn	Others[a]
A-1050		bal					
A-2014	AMPAL[b]: AMB2712; ECKA[c]: Alumix 123; Obsolete ALCOA[d]: 201AB	bal	3.8–5.0	0.2–1.2	0.5–1.2		1.5
A-2214	Obsolete ALCOA: 202AB	bal	3.8–4.2				1.5
A-2314	Obsolete MD-22 VILS[e]: AK4-1	bal bal	1.8–2.2 2.2	0.8–1.2 1.6	0.3 0.35		1.5 2.0
A-4032	AMPAL: AMB40XX ECKA: Alumix 231	bal bal	0.8–3.5 2.4–2.8	0.4–1.2 0.5–0.8	6–15 14–16		1.5 1.5
A-5106		bal	0.1–0.5	0.8–1.2	0.2–		1.5
A-6061	AMPAL: AMB6711; ECKA: Alumix 321 Obsolete ALCOA: 601AB; MD-69	bal	0.0–0.4	0.8–1.2	0.4–0.9		1.5
A-6002	Obsolete ALCOA 602AB	bal		0.4–0.8	0.2–0.6		1.5
A-7075	AMPAL: AMB777X ECKA: Alumix 431 VILS: 01959	bal bal bal	0.7–1.7 1.5–2.0 0.8–1.4	2.0–3.0 2.2–2.8 1.8–2.5	0.0–0.6	6.0–8.0 5.6–6.4 6.0–7.0	1.5 12.5 0.8–2.15

[a] *Value contains the combined content of admixed lubricant, typical impurities (oxygen, nitrogen, iron, etc.), and any additions for improving sintering characteristic and mechanical fulfilment.*
[b] *Ampal Inc.*
[c] *ECKA granules.*
[d] *Alcoa corporation*
[e] *All-Russian Institute of Light Alloys.*
Source: Dobatkin VI, Elagin VI, Fedorov VM. Rapidly solidified aluminum alloys. Moscow: All-Russian Institute of Light Alloys Publishers; 1995 [in Russian] and Lall Ch, Bishop P. Conventional powder metallurgy aluminum alloys. In: ASM handbook, vol. 7. ASM International Publishers; 2015. p. 581–90

Different approaches have been used to enhance the high-strength potential of that Zn containing Al-alloys of 7xxx series. First attempts by using elemental blends resulted in some difficulties with Zn evaporation during sintering and in distortion of the sintered parts. In order to overcome those difficulties, special blends were developed utilizing atomized Al prealloyed powders. This approach reduced the Zn evaporation and minimized distortion of the sintered parts. Mais et al. reported [55] that Alumix 431 grade offers a high-strength potential, especially when applying a heat treatment according toT6 conditions.

The rapid cooling rate of the aluminum alloys allows obtaining significant effects from alloying by nonsoluble or slightly soluble refractory components in aluminum. This opens opportunities for creation of the new PM constructional alloys with elevated durability on the base of Al-Cu-Mg, Al-Zn-Mg-Cu, and Al-Mg-Si systems by increased alloying with the transition metals (TM). Along with the heat treatment effect of these alloys, their heightened strength is characterized by two strengthening mechanisms:

- Dispersion hardening connected with precipitation of the strengthening phases under formation by copper, magnesium, zinc, and silicon consequently of quenching and aging the specimens.
- Dispersion hardening connected with formation of anomalously oversaturated solid solutions of the TM in aluminum during crystallization of melt drops with the TM aluminide precipitation by the following powder treatment or with immediate formation by crystallization of a disperse intermetallic phase, such as Al_3Fe, Al_3Zr, etc.

The deformable, heat-hardenable, weldable Al-Zn-Mg system alloys have a favorable combination of mechanical properties along with corrosion resistance and manufacturability (good weldability, formability, and heat treatability). The supplementary possibilities of improving the properties of these alloys by scandium addition were discovered at the beginning of the 1980s [56,57]. Scandium is a powerful modifier of aluminum alloys that renders possible the formation of grain structure without inner dendrite morphology with grain size determinate by the cooling rate during crystallization [18]. Fig. 16.12 illustrates the microstructure of the Al-Zn-Mg type 1970 (Russian classification) aluminum alloy ingots poured by a cooling rate about 125 K/s. The specimen comprising 0.2 wt% Sc (Fig. 16.12B) possesses a grain structure with average

TABLE 16.12 Typical Mechanical Properties for Common PM Aluminum Alloys Produced by Commercial Manufacturing Processes

Alloy	Compaction Pressure (MPa)	Green Strength (MPa)	Density		Temper	Yield strength (MPa)	UTS (MPa)	Elongation (%)	Hardness
			Green % (g/cm^3)	Sintered % (g/cm^3)					
A-2014	110	4.2	85 (2.36)	91 (2.53)	T1[a]	145	169	2	60HRE
					T4	179	210	3	70 HRE
					T6	248	24	<1	80 HRE
	180	8.3	90 (2.50)	93 (2.58)	T1	170	201	3	70 HRE
					T4	205	245	3	75 HRE
					T6	322	323	<1	85 HRE
	413	13.8	95 (2.64)	97 (2.70)	T1	181	209	3	70 HRE
					T4	214	262	5	80 HRE
					T6	327	332	2	90 HRE
A-2214	180	5.4	90 (2.49)	92.4 (2.56)	T1	75	160	10	55 HRE
					T4	119	194	8	70 HRE
					T6	147	227	7	45 HRE
A-4032	600	13	91.8(2.46)	98.5 (2.64)	T1	206	206	1	40 HRE
					T6	330	339	<1	83 HRE
A-6061	96	3.1	85 (2.29)	91.1 (2.45)	T1	48	110	6	55 HRE
					T4	96	141	5	80 HRE
					T6	176	183	1	70 HRE
	165	6.6	90 (2.42)	93.7 (2.52)	T1	88	139	5	60 HRE
					T4	114	172	5	80 HRE
					T6	221	232	2	75 HRE
	345	10.4	95 (2.55)	96 (2.58)	T1	94	145	6	65 HRE
					T4	117	176	6	85 HRE
					T6	230	238	2	80 HRE
A-6002	165	6.6	90 (2.42)	93 (2.55)	T1	59	121	9	55 HRE
					T4	62	121	7	65 HRE
					T6	169	179	2	55 HRE

	345	10.4	95 (2.55)	96 (2.58)	T1	62	131	9	55 HRE
					T4	65	134	10	70 HRE
					T6	172	186	3	65 HRE
A-7075	200	4.5	80.6 (2.27)	97.7 (2.75)	T1	221	241	2	55 HRE
					T6	463	499	1	87 HRE
	400	7.0	88.6 (2.49)	97.7 (2.75)	T1	279	323	1	67 HRE
					T6	473	497	1	87 HRE
Alumix 431			(2.78)		T1		300	5	100 HB
					T6		470	0.5	150 HB
01959					T1	420	510	10	

[a] *Heat treatment numerous approaches: T1—as-sintered naturally aged (at room temperature); T4—solution treated and naturally aged; T6—solution treated and artificially aged.*

Modified from Dobatkin VI, Elagin VI, Fedorov VM. Rapidly solidified aluminum alloys. Moscow: All-Russian Institute of Light Alloys Publishers; 1995 [in Russian] and Lall Ch, Bishop P. Conventional powder metallurgy aluminum alloys. In: ASM handbook, vol. 7. ASM International Publishers; 2015. p. 581–90

TABLE 16.13 Aluminum PM Alloys With Improved Tensile Ductility

Alloy	Sintered Density		Yield (MPa)	UTS (MPa)	Hardness HB	Elongation (%)
	g/cm^3	%				
Alumix 123, A-2014 (modified)	2.74	98.6	200	270	90	5
Alumix 231, A-4032 (modified)	2.66			220	80	3
Alumix 321, A-6061 (modified)	2.69	99,9	100	170	45	15
A-2618	2.71	99.7	207	322		10

All data derived as-sintered parts in the T1 condition.
Source: *Mais B, Müller A, Gradl J. Recent progress on standard PM aluminum premixes. In: Compiled by Russell A, Chernenkoff W, Brian J. Proceedings of 2014 Powder Metallurgy World Congress. Orlando (FL, U.S.A.): Metal Powder Industries Federation; 2014: p. 07-157–63;* Cooke RW, et al. Effect of Zr additions on the sintering response of an Al-Cu-Mg PM alloy. In: Proceedings of the 2012 international conference on powder metallurgy and particulate materials. Nashville (TN, U.S.A.): MPIF; 2014. p. 7155–69.

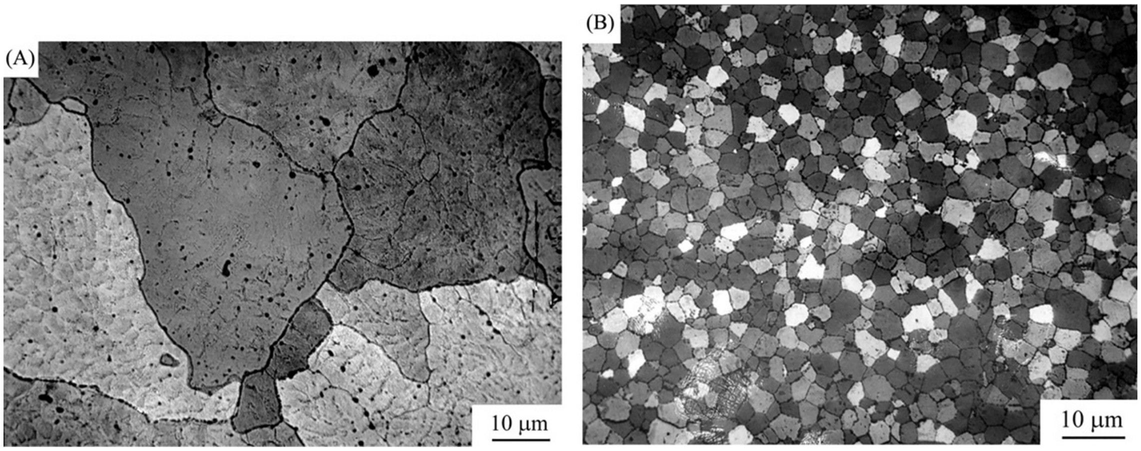

FIG. 16.12 Microstructure of Al-Zn-Mg type 1970 (Russian classification) aluminum alloy ingots poured by cooling rate about 125 K/s: without Sc addition (A); 0.2 wt% Sc (B).

grain size 20 μm and without dendrite forming, in contrast to the specimen without Sc (Fig. 16.12A) in possession of the inner grain dendrite structure and grain size in the 150 – 300 μm range.

Recently, in the Al-Zn-Mg system, the 1970 alloy (Al-5.4Zn-2.0Mg-0.3Cu-0.2Sc-0.1Zr) showed maximal strength with very good weldability (coefficient welding softening minimum 0.8) and possesses superplasticity. Characteristic mechanical properties of semiproducts from alloy 1970 in T6 condition data are shown in Table 16.14.

These exceptional advantages of alloying the aluminum alloys by scandium are explained by the unique properties of the Al_3Sc phase, which has a cubic lattice Ll_2 with a lattice spacing, exceeding the lattice spacing of Al approximately only on 1.3% [58]. Such a small difference in the size of lattice spacing provides a coherent bond between the Al_3Sc phase particles and the aluminum matrix. Maximal solubility of scandium in aluminum amounts to 0.3 wt%. After cooling with a rate about of 10^2 K/s, the cast alloy consists of α-Al and contains primary precipitates of Al_3Sc with sizes of 5–10 μm. During aging, the secondary dispersoids of Al_3Sc are precipitated with particle sizes generally below 20 nm, which very slowly grow by the increase of temperature and annealing time [57,59,60]. It was shown that zirconium dissolves in Al_3Sc with the formation of the $Al_3(Sc_{1-x}Zr)$ phase of variable composition, the coagulation kinetics of which substantially differ from Al_3Sc. Particle dimensions of the complex phase are substantially less and particles are slower to coagulate by elevation of temperature and annealing time during aging [61,62]; therefore, the considerable strengthening is preserved even after an hour-long annealing time at 773 K [62]. Thus, joint alloying by Sc and Zr is more effective for the increase of

TABLE 16.14 Characteristic Mechanical Properties of Semiproducts From Alloy 1970 in T6 Condition

	Along Fibers			Across Fibers			High Direction		
Semiproduct	UTS (MPa)	YS (MPa)	El (%)	UTS (MPa)	YS (MPa)	El (%)	UTS (MPa)	YS (MPa)	El (%)
Rolled plate, 32 mm	490	440	15	480	430	13	480	420	11
Forging	490	440	15	490	430	14	480	420	11
Sheet, 2 mm	520	490	11	520	490	11			

Source: Elagin VI, Zakharov VV, Filatov YuA, Rostova TD. Development of advanced aluminum alloys alloyed by scandium. In: Bannyh OA, et al., editors. Prospective technologies of light and special alloys. Moscow: Fismathgis; 2006. p. 181−93. (in Russian). https://books.google.com/books?isbn=5457966348.

recrystallization temperature [63]. A mechanism of formation and action of these phases is more particularly discussed in Chapter 24, in the paragraph "Scandium."

MELT SPINNING TECHNIQUE

The Al-based amorphous alloys with the combined properties of high mechanical strength and glass transition were obtained by a melt spinning technique [64]. Al-Ni-Y-TM (TM-transition metal: Zr, V, Nb, Cr, Mn, Fe, Co, Ni, or Cu) quaternary alloys were used in this study. Their ingots were prepared by arc melting a mixture of pure metals in an argon atmosphere. From the master alloy ingots, ribbons with a width of about 1 mm and different thicknesses ranging from 0.02 to 1 mm were made by a single roller melt spinning means in an argon atmosphere. An $Al_{85}Ni_5Y_8Co_2$ amorphous alloy showed the highest tensile strength (UTS) of 1250 MPa with 1.7% tensile fracture strain. The replacement of Y by 2 at % Co for $Al_{85}Ni_5Y_{10}$ was found to result in an increase of the critical ribbon thickness for formation of an amorphous phase (δ_c) from 120 to 900 μm, the heat of endothermic reaction due to glass transition (ΔH_g) from 143393 J/mole, and the tensile strength from 920 to 1250 MPa. Along with this, the heat of crystallization (ΔH_x) increases from 3.37 kJ/mole for $Al_{85}Ni_5Y_{10}$ to 3.60 kJ/mole for $Al_{85}Ni_5Y_8Co_2$. The authors [64] concluded that the simultaneous increase in the δ_c, ΔH_g, and UTS is presumably due to the change to the amorphous structure with a more dense random packing and larger bonding energy among the constituent atoms because the H_g is thought to reflect the integral of the atomic forces over the interatomic distance change in collapse from the amorphous to the crystalline phase.

In addition, it has been reported that nanocrystalline materials fabricated by crystallization of an amorphous phase exhibit useful characteristics, which are not obtained for amorphous and conventional crystalline alloys [65,66].

Kavamura et al. [67] developed a closed processing system to produce and consolidate amorphous $Al_{85}Ni_5Y_8Co_2$. alloy powders with the aim of making high-strength crystalline PM alloys. Mechanical properties of these bulky alloys were examined in comparison with those produced by the ordinary one in which the powder was once exposed in air. An $Al_{85}Ni_5Y_8Co_2$ ingot was prepared by arc melting a mixture of each pure metal in a purified argon atmosphere. Spherical amorphous alloy powder was produced by 9.8 MPa pressure helium atomization. Afterward, the amorphous powder less than 25 μm particle size was first cold pressed into a copper container up to the packing density of 75%, degassed at 773 K for 900 s, and then in such green compact condition extruded at 773 K (temperature much higher than the temperature crystallization of the $Al_{85}Ni_5Y_8Co_2$ amorphous alloy) with ex room-temperature extrusion ratios 2.5 and 10. Fig. 16.13 shows a schematic illustration of the closed PM processing system. About 500 g of the alloy ingot melted in the induction furnace is atomized using a helium or argon gas in the atomization chamber. The atomization apparatus is connected with a vacuum-type glove box, in which sieving of powder, green compact press forming by a vacuum press, sealing by spot-welding of the container with green compact, and green compact degassing are realized. The oxygen and moisture content in an argon atmosphere are controlled to be less than 1 ppm by a gas refiner in all closed PM systems.

As reported [67], the tensile strength of the ordinary processing bulky sample produced by the extrusion ratio of 10 is 900 MPa at room temperature and 480 MPa at 573 K. The tensile strength of the balks is improved by closed processing due to a decrease in the thickness and amount of the residual hydrate of the surface oxide layer on the powder particles. Therefore, the difference in oxygen content between the prealloyed ingot and the extruded alloys (Fig. 16.14) seems to correspond to the thickness of the layer on the powder particles.

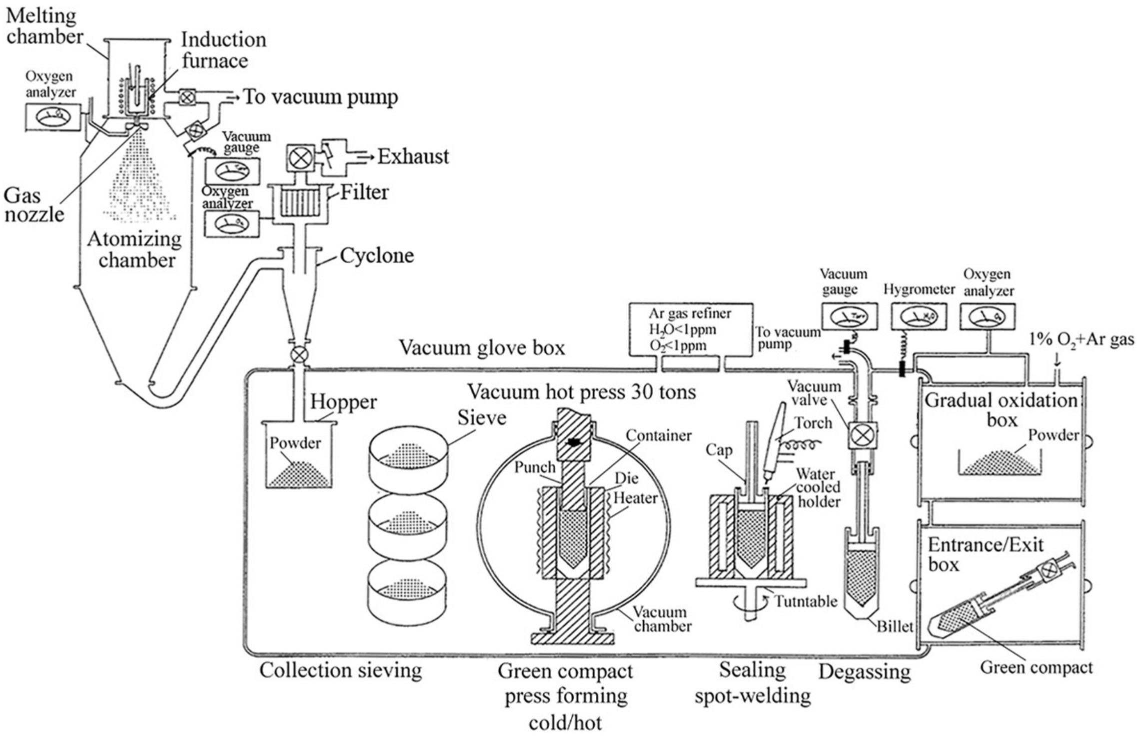
Melting chamber
Induction furnace
Oxygen analyzer
To vacuum pump
Vacuum gauge
Exhaust
Oxygen analyzer
Filter
Gas nozzle
Atomizing chamber
Cyclone
Vacuum gauge
Hygrometer
Oxygen analyzer
Ar gas refiner
H₂O<1ppm
O₂<1ppm
To vacuum pump
1% O₂+Ar gas
Vacuum glove box
Hopper
Vacuum hot press 30 tons
Sieve
Container
Punch
Die
Heater
Powder
Vacuum valve
Torch
Cap
Water cooled holder
Gradual oxidation box
Powder
Entrance/Exit box
Tutntable
Vacuum chamber
Billet
Green compact
Collection sieving
Green compact press forming cold/hot
Sealing spot-welding
Degassing

FIG. 16.13 Schematic of the close PM processing system.

FIG. 16.14 Oxygen and hydrogen contents in a prealloyed and its bulk alloys extruded at extrusion ratio of 10 and temperature 773 K in the closed and ordinary processings. The cold and not degassing treatments were realized for 900 s at room and 774 K, respectively.

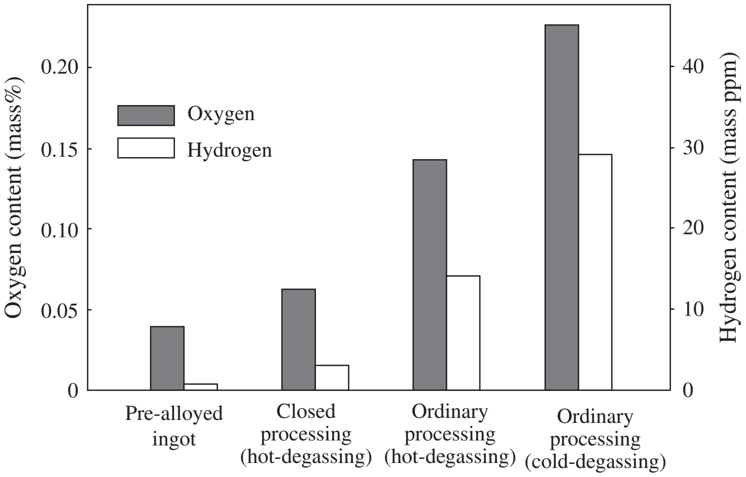

It was found that the tensile strength of the crystallized bulk produced by the extrusion ratio of 10 is 60 MPa higher at 573 K and the room-temperature tensile strength of the bulk prepared by extrusion at a small extrusion ratio of 2.5 is 240 MPa higher than that produced by ordinary processing. So long as the closed processing is effective for the decrease in the thickness of the oxide layer and the amount of hydration in the layer, the breakup and distribution of the surface oxide layer are made easy by the closed processing. This change seems to be the reason for the improvement of the mechanical strength for bulks extruded at a small extrusion ratio. However, the strength of the bulks extruded at the extrusion ratio of 10 is independent of the processing type because this extrusion ratio is large enough to break completely the oxide layer and distribute homogeneously its fragments.

Kawamura et al. [68] reported that the $Al_{93}Ti_{3.5}Fe_{3.5}$ PM alloys exhibited tensile strength of 786 MPa and plastic elongation of 3.2%. These alloys had high thermal stability up to 600 K, low density (2.90 g/cm^3), high Young's modulus (91 GPa), and low coefficient of thermal expansion ($20.2 \times 10^{-4}\ K^{-1}$). The powders were produced by helium gas atomization at a pressure of 9.8 MPa and a pouring molten alloy temperature of 1473 K. Subsequently, the separated powder fractions less 25 μm particle size were first cold pressed into a copper container up to the packing density of 75%, and then degassed for 900 s at the same temperature as the extrusion temperature. The extrusion was performed at an extrusion ratio of 5 or 10, temperatures ranging from 603 to 713 K, and a ram speed of 2.5 mm/s.

WATER ATOMIZATION

The well-known water-atomization (WA) process allows one to increase the cooling rate. This technology is widely used for the production of ferrous metals and some nonferrous ones (e.g., copper). However, the process has not found application to aluminum alloys for two main reasons: danger of explosion due to rapid hydrogen emission, and high reactivity of aluminum that can cause heavy oxidation of the surface of atomized powders as a result of interaction between aluminum and water.

The problem of the powder quality and safety in the course of WA aluminum alloy powder production was solved at the Institute for Problems of Materials Science (Kiev, UA) [69–72]. This solution consists of the following:

- By using water solutions with inhibitors from the group of weak electrolytes and stabilizers of dispersions-protective colloids as well as their mixtures.
- By hydrogen ion control.
- By the control of suspension temperature.
- By the hydraulic size classification of the atomized product.
- By means of a contact-convection drying process with disintegration of powder particle aggregates, continuous immixture, and even distribution of particles on a heat supplying surface.

Newly prepared aluminum powders strongly react with water at room and especially at elevated temperatures. During aluminum oxidation in water, multilayered films are forming on the metal surface, and they are mainly composed of aluminum hydrate $Al(OH)_3$ and aluminum oxide hydroxide (AlOOH), the structure of those considerably depending on oxidation temperature [73]. An aluminum oxide surface film is formed as follows:

A boehmite film forms as a result of dissolution of cell butts on the metal surface:

$$Al + 2H_2O = AlOOH + 3/2\,H_2$$

then, boehmite is dehydrated

$$2AlOOH = Al_2O_3 + H_2O$$

Thus the resulting reaction is

$$2Al + 3H_2O = Al_2O_3 + 3H_2$$

Evidently, the presence of structure defects such as grain and interparticle boundaries, pores, local chemical inhomogeneities, etc., accelerates the rate water-aluminum interaction.

The typical morphology of water-atomized, high-strength aluminum alloy powder particles is shown in Fig. 16.15. The powder particles have a very irregular shape and uneven surface (Fig. 16.15A). As the transmission electron microscopy shows, the surface oxide of water-atomized powders is nonuniform in its thickness (Fig. 16.15B). Rather, three-dimensional film islets with a typical thickness of 30 − 40 monolayers usually cover 30%−70% of the particle surface. The rest is covered with a thin oxide film of about three to a maximum of eight monolayers.

Typical profiles of several elements as a result of a study of depth distributions of electropositive elements with primary O_2^+ and secondary positive ions are shown in Fig. 16.16. Only Mg exhibits a pronounced enrichment of subsurface layers. Both Zn and Cu are distributed more or less homogeneously with some deviations from an ideal plane profile. The main metallic impurities, Fe and Ca, are typically enriched in subsurface layers, as is seen from Fig. 16.16A. However, Mg, which is enriched and oxidized on the powder surface, also appears in the surface oxide. The average thickness of the surface oxide film as well as the widths of the observed Mg, Fe, and Ca segregation zones are estimated on the basis of the available depth profiles and respective ion sputter rate data. These thicknesses are taken to be proportional to the sputtering times required for a 50% drop in the element profiles [74,75]. The average thickness of the surface oxide usually varies from 4 to 10 nm. The thicknesses of Mg, Ca, and Fe enrichment layers range from 30 to 70 nm.

This conclusion is of importance from the viewpoint of further processing of water-atomized powders. Because the surface oxide is nonuniform in thickness, separate thick film islands do not impede transport processes in the course of powder compacting and thus sufficient cohesion of the interparticle boundaries can be achieved during compacting.

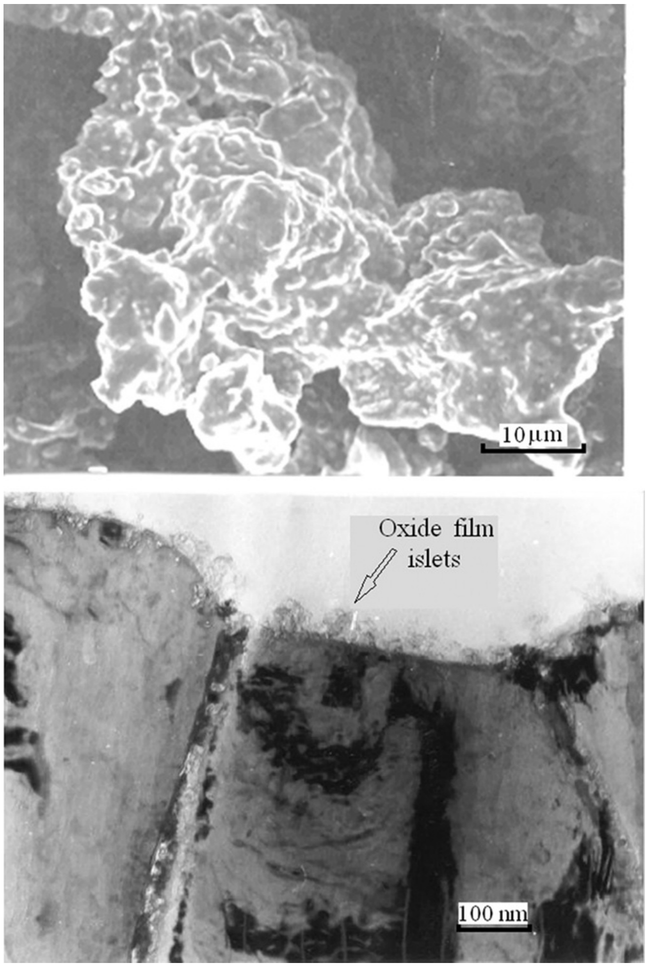

FIG. 16.15 SEM and TEM (microtome) micrographs illustrating irregular shape of particles and non-uniformity of the surface oxide film. *Courtesy of Krajnikov.*

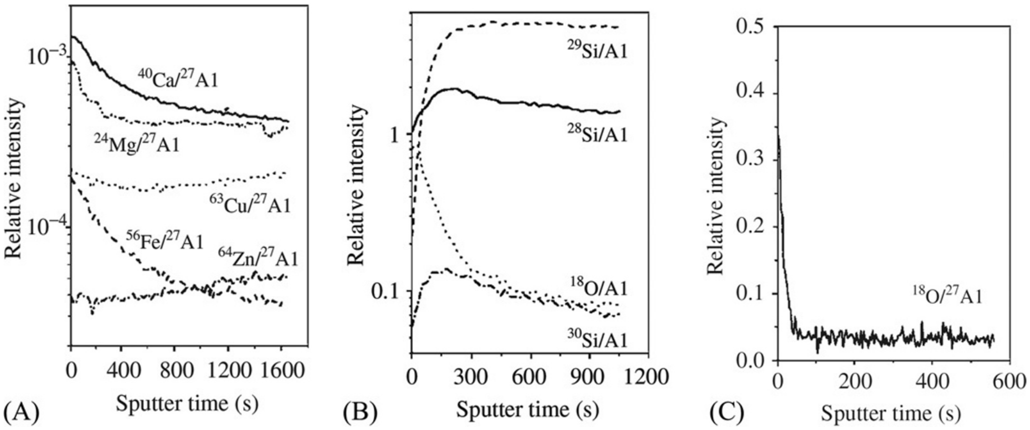

FIG. 16.16 Typical depth profiles for: (A) is Mg, Ca, Cu, Zn and Fe ions normalised to Al (primary O_2^+ and secondary positive ions), (B) is Si and ^{18}O ions normalised to Al (primary Cs^+ and secondary negative ions), (C) is $^{18}O/^{27}Al$ (primary O_2^+ and secondary negative ions). *Courtesy of Krajnikov.*

Microscopic kinetics emission as a result of the metallic powder particles reaction with water enables the explosion risk of the process to be characterized. The experimental investigation of gas emission kinetics is carried out by means of a laboratory appliance that consists of a reaction vessel, a measuring dome to collect generated gases, a gas pressure sensor, a unit for pressure compensation, and a recording device. The gas collected in the dome was analyzed by a chromatograph. This method is exact and permits gas emission to be measured with an accuracy within 1 mL per 1 kg of powder sample [76,77]. The samples for measurements are taken in a suspension state or wet-filtered powder condition, that is, just after the operation of melt atomization and before drying. Characteristics of gas emission are usually measured for commercially available or experimental dry powder samples when the surface oxide film already has been formed and thus the reactivity of the powder already has been lowered. Evidently, the results obtained on primary wet powders are more exact.

The typical gas emission dependences on reaction time for high strength aluminum alloys and elevated temperature ones at room temperature and at pH 4.0 and 6.0 are shown in Fig. 16.17. The rate of powder-water interaction strongly depends on the pH value. The nature of reaction kinetics abruptly changes with increasing pH to 6.0. The reaction activity of elevated temperature alloy powders with water is considerably lower in comparison with high-strength quaternary system Al-Zn-Mg-Cu alloys. But for both aluminum alloy types at pH 4.0, which depend on the composition and content of the inhibitor, in given conditions, gas emission does not pose a danger.

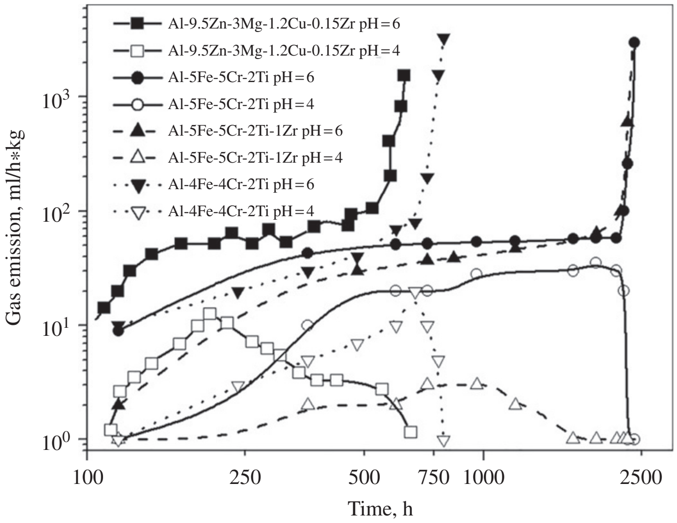

FIG. 16.17 Gas emissions as a function of reaction time in water for several powders at pH 4.0 and 6.0.

Fig. 16.18 represents the schematic diagram of the pilot plant of IPMS (Institute for Problems of Material Science) for the production of aluminum alloy powders by water atomization. The technological process consists of the following steps. The charge, which is prepared with the use of master alloys, containing all alloying elements, is melted in the induction furnace. Ready melt is poured into a tundish, where it flows out through a nozzle in the bottom. The melt stream is atomized by jets of the cooled high-pressure water in the atomizing chamber. An inhibitor is introduced into the cooled water reservoir. A water suspension of the atomized metal powder forms at the bottom of the chamber and then flows into the suspension reservoir. The suspension is continuously pumped out from the reservoir and is supplied to the hydraulic classifier (Fig. 16.19). The suspended powder is classified into various size fractions. The suspension with coarse fractions is returned into the suspension reservoir and is subjected to mechanical dehydration by filtering under vacuum. The filtering by means of a high-performance porous filter dehydrates the suspension with fine fractions. The classified powders are dried in a vacuum or by the contact-convection drying technique. The automatic control system controls the hydrogen ion exponent (pH) value and the temperature of the water and suspension.

Drying, that is evaporation of moisture from water-atomized powders and removal of vapors, is a process with high specific energy consumption. In this connection, mechanical dehydration is used to maximally reduce the moisture content of powder. Because aluminum alloy powders are reactive, the drying method and dryer must prevent thermal ignition and ensure explosion safety. Heat-and-mass transfer is hindered in wet particle aggregates and agglomerates. This may cause the drying agent not to have enough time to take away the released heat during the reaction of metal and moisture, which may accelerate the reaction and avalanche-like rise in temperature. Therefore, the disintegration of particle aggregates is an important requirement for the drying process.

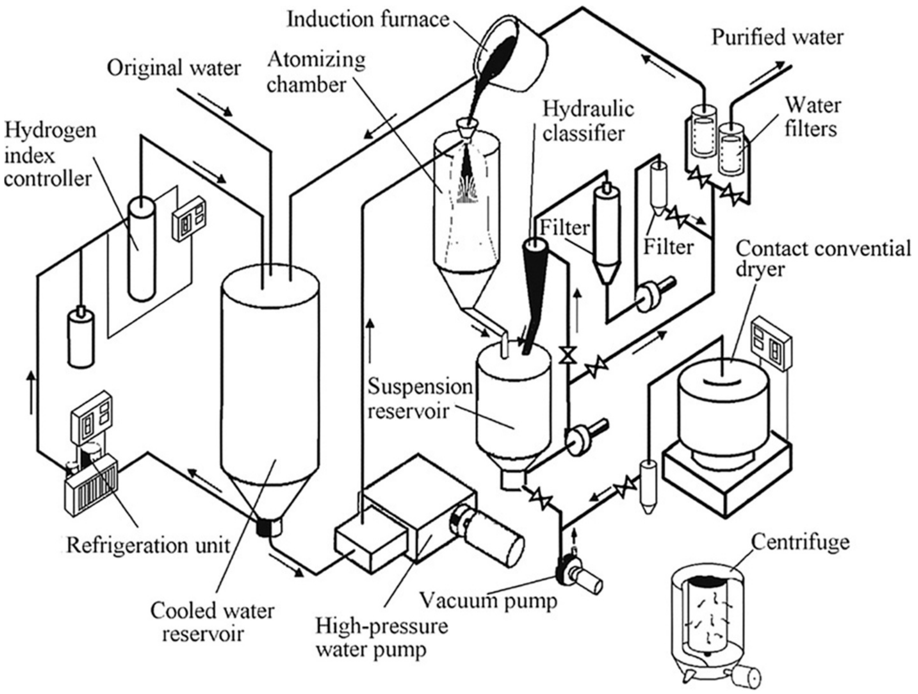
Induction furnace
Purified water
Original water
Atomizing chamber
Hydrogen index controller
Hydraulic classifier
Water filters
Filter
Filter
Contact convential dryer
Suspension reservoir
Refrigeration unit
Centrifuge
Vacuum pump
Cooled water reservoir
High-pressure water pump

FIG. 16.18 Scheme illustrating the developed water atomization technology.

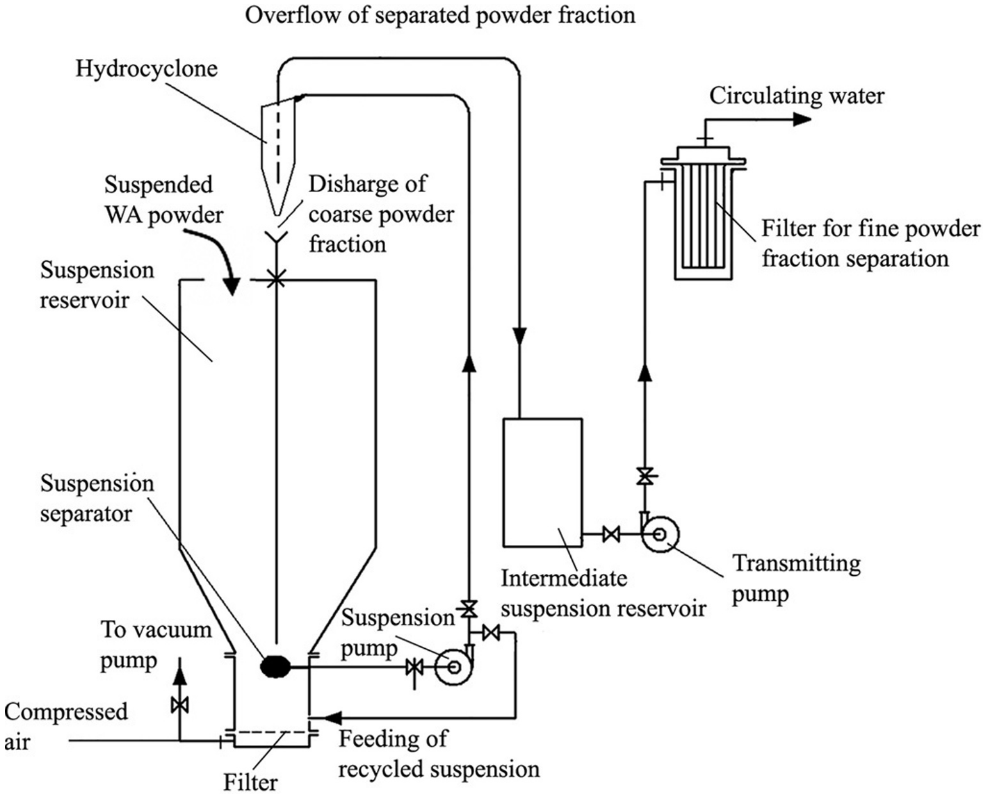
Overflow of separated powder fraction
Hydrocyclone
Circulating water
Suspended WA powder
Disharge of coarse powder fraction
Filter for fine powder fraction separation
Suspension reservoir
Suspension separator
Transmitting pump
Intermediate suspension reservoir
Suspension pump
To vacuum pump
Compressed air
Feeding of recycled suspension
Filter

FIG. 16.19 Schematic of the hydroclassification system on particle size fraction.

A dryer of the IPMS pilot plant enables contact-convection drying and conductive drying with vapor evacuation [78]. A schematic of the dryer in the contact-convection condition is presented in Fig. 16.20 and a general view of the dryer is shown in Fig. 16.21.

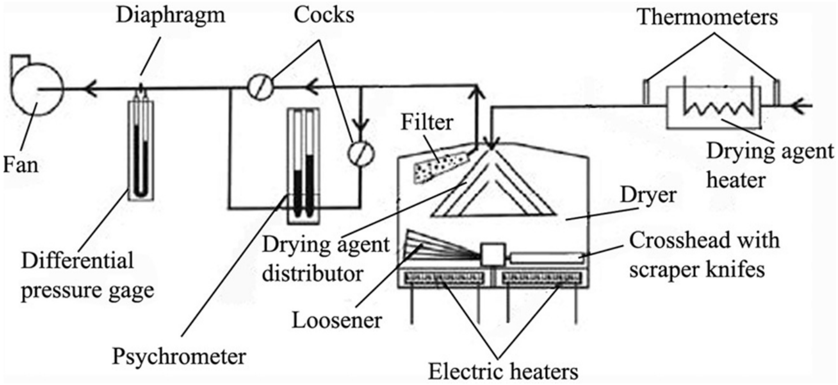
Diaphragm
Cocks
Thermometers
Fan
Filter
Drying agent
heater
Dryer
Crosshead with
scraper knifes
Differential
pressure gage
Drying agent
distributor
Loosener
Psychrometer
Electric heaters

FIG. 16.20 IPMS dryer in contact-convection condition.

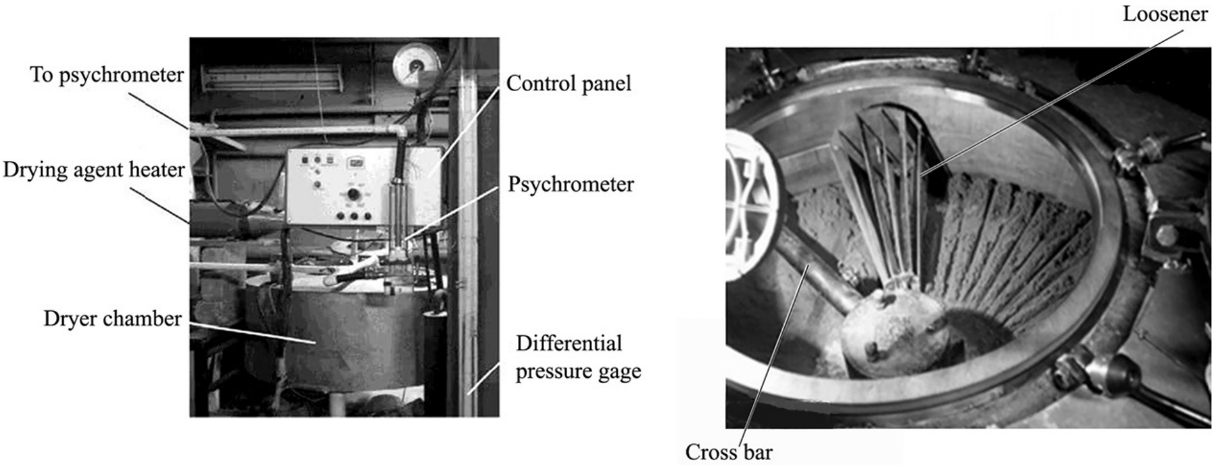
To psychrometer
Drying agent heater
Dryer chamber
Control panel
Psychrometer
Differential
pressure gage
Loosener
Cross bar

FIG. 16.21 General view of the dryer (*left*) and inside view of the dryer chamber (*right*).

The dryer is a cylindrical chamber with a metal plate at the bottom into which flat electric heaters are embedded. The heaters are arranged uniformly in a horizontal plane. The set temperatures of the metal plate and dried powder are controlled automatically by switching the on/off sections of the electric heaters. The chamber has a feeding opening in the cover and an unloading opening in the bottom. The former is equipped with two nozzles: one for feeding a drying agent into the chamber and the other for removing it together with the vapor. At the inlet of the latter nozzle, there is a filter to prevent fine particles leaving the chamber together with the drying agent and vapor. Both nozzles are used during the combined supply of heat (contact-convection drying), whereas during conductive vacuum drying, the feeding nozzle is shut off and the other is connected to the vacuum pump.

To disintegrate particle aggregates and maintain the uniform distribution of the dried powder over the metal plate, the particles adhered to the plate surface are separated by two scraper knives mounted on the crosshead and intended to raise the powder layer (Fig. 16.20). A loosener in the form of a drum with strip ribs following them breaks particle aggregates while rotating. The shape of the scraper knives and plates of the loosener as well as control of their orientation make it possible to break particle aggregates and maintain the uniform distribution of the dried powder over the plate (Fig. 16.21B).

Based on a study of the contact-convection drying of aluminum and Al-Fe-Cr, Al-Fe-V-Si and Al-Si alloy system powders, the process parameters of drying were optimized. The maximum permissible temperature values (T_{lim}) as a function of specific humidity (m) are presented in Fig. 16.22. The area over the graphic chart is prohibitive because of self-ignition danger. The initial temperature range of drying agent is $303-323$ K, depending on the specific humidity value.

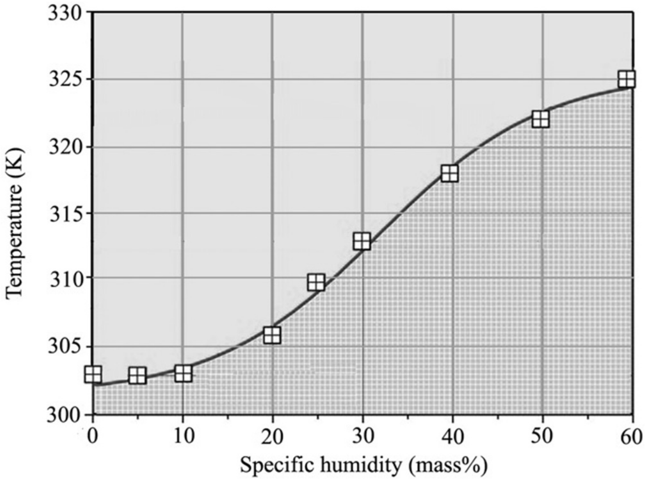

FIG. 16.22 Maximum permissible temperature (T_{lim}) as function of specific humidity (m)

The batch of initial humid powder for a dryer with 1.0-m chamber diameter amounts to 4–5 and 7–8 kg by up to 3 and 4–5 g/cm^3 alloy mass density, respectively.

The total concentration of gas impurities, such as adsorbed and chemisorbed oxygen and aqua, in as-dried powders ranges from 400 to 2000 ppm, depending on alloy composition and powder size distribution.

In common use, the classifier permits separating out sufficiently narrow particle fractions to be separated out if the separation regime is optimized. For example, for separation of fraction minus 20 μm of water-atomized $Al_{94}Fe_{3.0}Cr_{3.0}$ alloy powder, the most efficient hydroclassification regimes are obtained using suspension hydraulic pressure $p_s = 0.02$ MPa; the corresponding suspension velocity at the entry to the hydrocyclone amounts to 1.35 m/s (v_c). Oversized particles practically are absent in the conditions of optimal hydroclassification (Fig. 16.23). It is significant that in relatively narrow particle size ranges, the size distribution also obeys the normal logarithmic law. This weight distribution is characterized by median diameter $d_{50} = 12$ μm and standard (mean square) deviation $\sigma = 1.65$, while the initial nonclassified water-atomized $Al_{94}Fe_{3.0}Cr_{3.0}$ alloy powder contains up to 24 wt% of the fraction minus 20 μm.

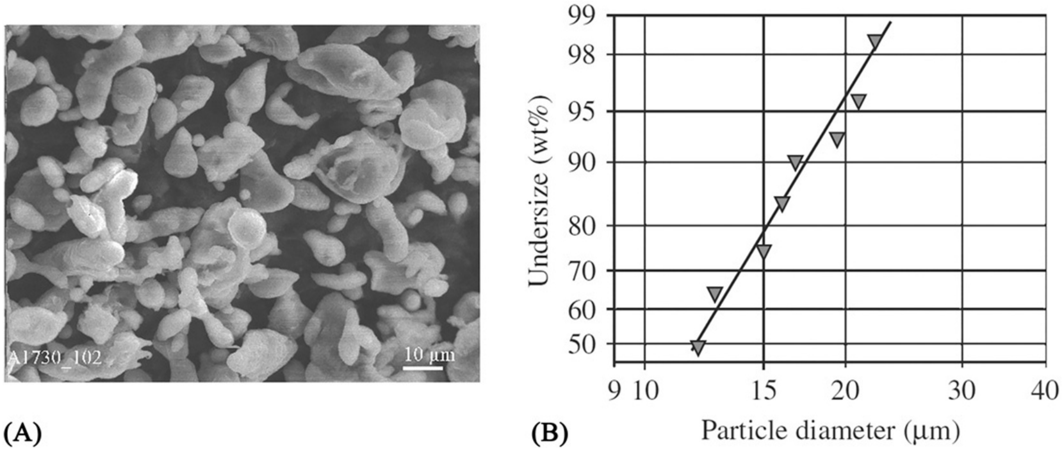

FIG. 16.23 Fraction less 20 μm of water atomized $Al_{94}Fe_{3.0}Cr_{3.0}$ alloy powder separated by hydroclassification: SEM micrograph of the powder (A); Particle size distribution plotted on the log-probability paper (B).

Typical particle section micrographs of the selected less than 20 μm fraction particles are shown in Fig. 16.24. The specimens of powder particles for structural investigations were prepared from cold-pressed briquettes with porosity about 30%, followed by electrolytic polishing. The cooling rate of melts was estimated with the use of the dendrite parameter, which is equal to the average size of the dendrite cells [18,27]. The average sizes of the structural grains in the microphotographs of the particles with the projected diameters of 9.5 μm (Fig. 16.24, left particle) and 13.5 μm (Fig. 16.24, right

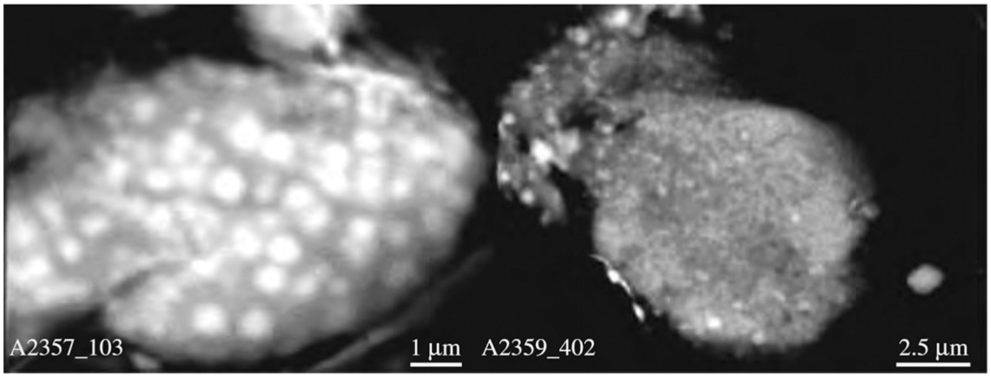

FIG. 16.24 Particle section micrographs of selected less 20 μm fraction particles of water atomized $Al_{94}Fe_{3.0}Cr_{3.0}$ alloy powder (Fig. 16.23, *left*).

particle) are 0.3 and 1.0 μm, respectively. Averaged melt cooling rates for the particles of such sizes of structural grains are 2.1×10^7 and 9.3×10^6 K/s respectively.

The technology used for powder compaction consists of two main stages, namely cold pressing followed by degassing and hot extrusion. Because the total concentration of water and hydrogen should not exceed 0.3 ppm to provide sufficiently dense billets [22], the main goal of degassing is the reduction of residual gas concentrations to a necessary level, followed by isolation of the degassed billets from the atmosphere. Compacting is aimed at the production of pore-free billets and conservation of the microstructure and phase composition of the RS powders.

At first, the powder is formed into green compacts in air at room temperature to a relative density of 30%, so that the particle surfaces remain accessible for vacuum outgassing and moisture removal. Further, the encapsulated in green billets aluminum containers are degassed under 0.1 Pa vacuum at 673 K. After degassing, the properly sealed containers are extruded in air at 673 K, with a velocity of die travel of ~0.3 mm/s and an extrusion ratio of about 12.8.

The use of rapid solidification (RS) allows one to increase the solubility of the insoluble impurities and alloying elements and thus to decrease the number and size of surplus phases [18]. As shown [72,79], the use of the newly developed technology based on high-pressure water atomization (WA) allowed producing a set of high-quality aluminum alloy powders that have been then consolidated for various applications. In particular, ultrahigh-strength, high-strength weldable, and elevated temperature PM alloys showed high mechanical properties exceeding those of cast alloys of similar compositions [79–81].

Recycling of Secondary Aluminum

One of the application areas of the new water-atomization process may be in the recycling of secondary aluminum. Contamination of aluminum scrap by iron and silicon is the important problem of recycling of secondary aluminum [82]. Both iron and silicon have limited solubility in the aluminum matrix. As a result, cast ingots of secondary aluminum contain coarse Fe and Si base precipitates with diameters of a few microns. Such hardly deformable inclusions are often located at grain boundaries or triple junctions and they usually have weak cohesion with the matrix [83]. Under load, cracks first of all nucleate at the interfaces of the matrix and the coarse precipitates. Therefore, such precipitates serve as principal fracture sources. As is known, if nucleation and propagation of the crack are connected with a single fracture source, then characteristics of the tensile strength and especially parameters of the fatigue strength decrease as compared with the opposite case when many cracks simultaneously arise from several sources. Coarse particles can in a similar manner influence corrosion resistance. Therefore, the use of cast secondary aluminum for production of high-quality alloys for crucial structural applications is hindered by the presence of coarse Fe and Si base precipitates in the microstructure [18].

In the work [84], the possible effects of iron and silicon on the structure and properties of PM produced on the basis of water-atomized powders were studied. The high strength Al-Zn-Mg-Cu system alloys were selected for investigation (Table 16.15). The total bulk concentration of all alloying elements lies between 13.4 and 14.55 mas%. Various combinations of Fe and Si with a maximum total concentration of 1.8 mas% were added to furnace charges during powder atomization in order to study their effect on the structure and mechanical properties.

The particle size distributions of the water-atomized Al-Zn-Mg-Cu alloys obey a lognormal law (Fig. 16.25). The water-atomization conditions were as follows: water pressure 10 MPa, superheat of the melt temperature equal to 150–200 K, and diameter of a gravity melt stream 7.0–7.5 mm. In these conditions, the median diameters of the mass distribution are in the

TABLE 16.15 Composition of High Strength Al-Zn-Mg-Cu System Alloys

	Alloying Elements (mas%)				Impurities (mas%)		
Alloy No.	Zn	Mg	Cu	Total: Zn+Mg+Cu	Si	Fe	Fe+Si
1	9.3	0	1.9	14.1	0	0	0
2	9.4	2.8	1.6	13.8	0	0.4	0.4
3	9.4	4	1.3	14.7	0.3	0.15	0.45
4	9.4	2.9	1.44	13.74	0	0.6	0.6
5	10.0	3.2	1.35	14.55	0.55	0.13	0.68
6	10.0	2.9	1.38	14.28	0	0.93	0.93
7	8.6	3.5	1.3	13.4	0	1	1
8	9.4	3.3	1.3	14	0.9	0.9	1.8

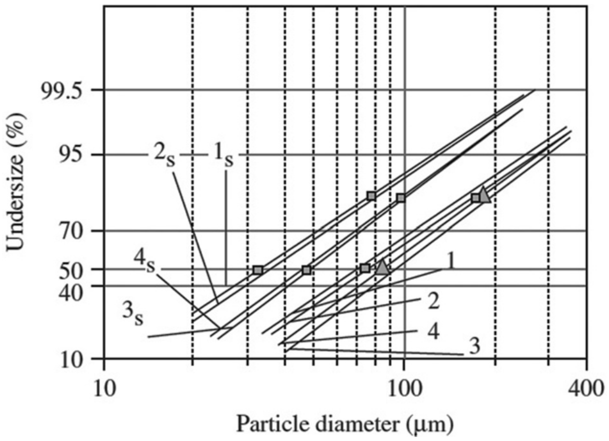

FIG. 16.25 Weight (3, 4, 7, and 8) and surface (3_s, 4_s, 7_s and 8_s) particle size distributions of Al-Zn-Mg-Cu system alloys (Table 16.15).

range 72–83 μm and of the surface one equal to 33–47 μm. The geometric standard deviation represented the slope of the curve, and the spread of particle size about the median value, respectively, is in the range 2.0–2.3.

The cooling rate of melts is estimated with the use of the dendrite parameter, which is equal to the average size of dendrite cells [18,27]. The correlation between particle size and cooling rate is shown in Fig. 16.26.

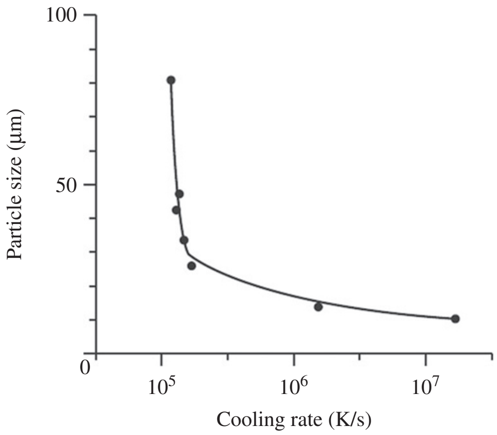

FIG. 16.26 Correlation between powder particle size and cooling rate.

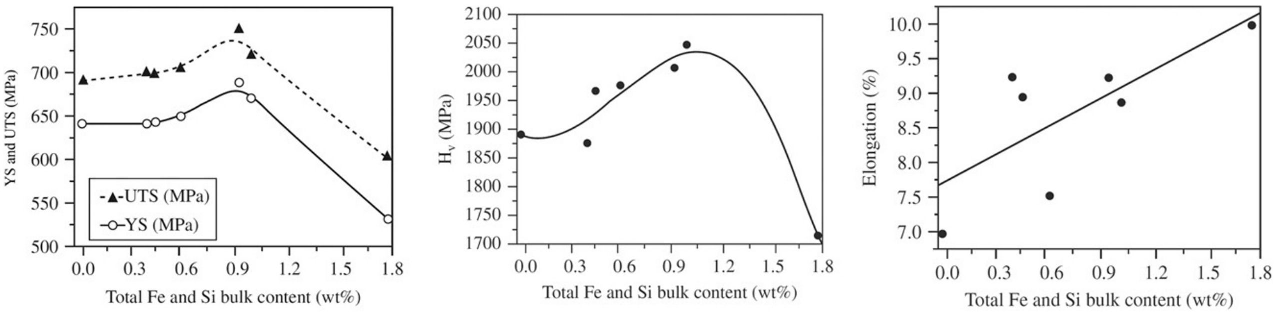

FIG. 16.27 Correlation between the mechanical property characteristics of Al-Zn-Mg-Cu system alloys and the common bulk concentration of Si, Fe additions.

PM Al-Zn-Mg-Cu system alloys based on WA powders generally show a high level of room temperature tensile strength (~700 MPa) with sufficient plasticity (elongation ~7%–9%). A correlation between the characteristics of mechanical properties and the common bulk concentration of impurities is shown in Fig. 16.27. The strength and hardness curves clearly demonstrate two regions. At lower impurity concentrations (up to 1%), both strength and hardness increase with impurity concentration without any evident loss of plasticity. A further increase of the impurity concentration, however, reduces the level of strength: If the common concentration of Fe and Si rises from 1% to 1.8%, then the strength goes down from approximately 700 to 600 MPa while plasticity is less sensitive to the impurity concentration. The hardness behavior generally correlates with the strength.

The use of RS allows one to dissolve impure atoms in the matrix. The atomization regimes used provide dissolution of at least 1.1 mas% Fe and Si. At higher impurity concentrations, coarse Fe and Si base particles precipitate and serve as fracture sources. As a result, the tensile strength of PM alloys decreases. Higher cooling rates (or finer powder fractions) should be used to restrain precipitation of the above precipitates [84].

Elevated Temperature Aluminum Alloys

The water-atomization process provides promising possibilities in advance of elevated temperature aluminum alloys. A comparative analysis of alloying principles for creating elevated temperate powder alloys shows the possibility of two approaches [18,80]. The first possibility is alloying with transition metals having some solubility in solid aluminum in accordance with equilibrium diagram. At moderately high cooling rates (10^3–10^4 K/s), these metals form the supersaturated solid solutions in aluminum, which, due to the influence of elevated temperatures and mechanical deformation during powder consolidation to semifinished products, decompose into a dispersion of intermetallic or quasicrystalline phases. Prospective alloying elements in this class include Cr, Mn, Zr, Ti, W, Mo, and Nb. The second approach is the heterogenization of the cast structure by alloying with metals practically insoluble in aluminum even at cooling rates of 10^6 K/s, such as Fe, Co, Ni, and rare earth elements. These elements precipitate upon crystallization in the form of dispersed intermetallics that are a part of the eutectic in the boundaries of dendrite cells, forming a framework.

The elevated temperature alloys with the highest properties include Al-Fe-Cr(Mn), Al-Cr-Zr(Mn), Al-Fe-V(Mo), and Al-Fe-Ce alloy systems. The chromium-based system is noteworthy among them. The Al-Cr alloys have higher thermal stability at elevated temperatures than the Al-Fe and Al-Fe-Zr alloys. Thus, the Al-8Cr alloy retains its strength after holding for 100 h at 573 K. The alloys in this system show good machinability [85] and somewhat lower density. High-temperature treatment of these alloys allows their mechanical properties to be improved.

Elevated temperature alloys of this nonequilibrium composition can be produced only by rapid melt solidification. Melt atomization with inert gas was used to make Al-4Cr-1Fe alloy powders [86]. The powder was compacted in two stages: (i) cold pressing and (ii) hot extrusion. The mechanical properties of the Al-7Cr-1Fe alloy are described in Ref. [87], where compacts were made from a mixture of 45 μm gas-atomized and 70 nm nanosized powders. To promote compaction, the powder mixture was subjected to 10 min pulsed treatment at 423 K. The powders were subsequently consolidated at 823 K and 40 MPa for 10 min. The mechanical properties of the compacts after treatment at 448 K showed the following mechanical properties at room temperature: elastic modulus $E = 71$ GPa, UTS $= 266$ MPa, YS $= 240$ MPa, and El $=$ 1.6%. The vapor-deposited Al-Cr-Fe alloys were studied in Ref. [88] at 5 to 9 wt% Cr and 0.6 to 3.0 at.% Fe. The highest strength was exhibited by Al-8.7Cr-1.5Fe [89]. Great amounts of the Al-8.5Cr-1.2Fe alloy powder were produced by the vapor deposition method [88]. Vapors of the elements condensed on a collector to form the alloy of desired composition.

The intermediate product as a 9-mm strip was rolled to a thickness of 1.7 mm. This resulted in a superfine fibrous material. This technology has not received wide commercial application for production of elevated temperature aluminum alloys. Therefore, the vapor deposition method is not economical, especially for high-temperature applications requiring expensive equipment and much energy to transfer the element into a vapor phase.

The Al-8Cr-1.5Fe alloys based on gas-atomized (GA) and water-atomized (WA) powders were developed [90]. Particles of the WA powder are irregular and have an uneven surface (Fig. 16.28A–B) while particles of the GA powder are spherical (Fig. 16.28C–D). Analysis showed that the equilibrium oxygen content in air in normal conditions was 0.05–0.06 wt% for the GA powders and about 0.2 wt% for the GA powders. However, the oxygen content of the compacted WA powders decreases to 0.02%–0.03% after degassing.

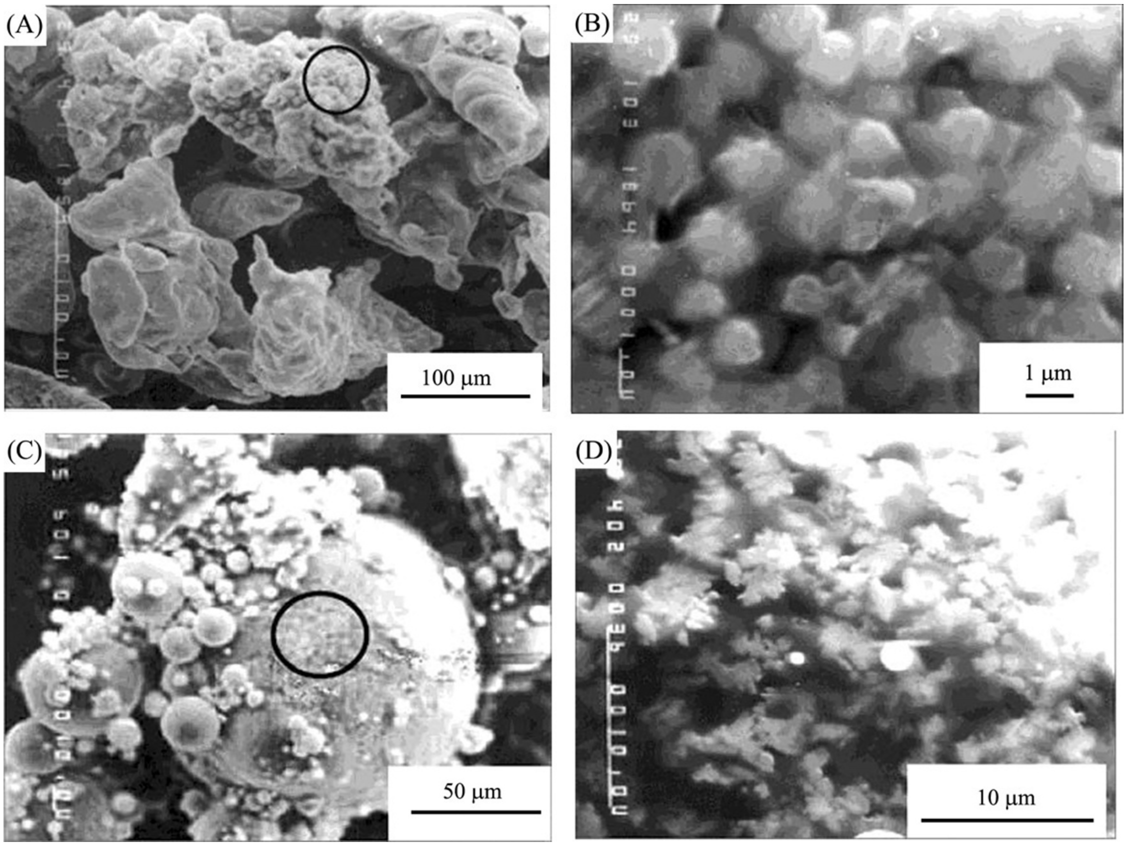

FIG. 16.28 SEM images of Al-8Cr-1.5Fe powder particles: general appearance of the WA (A) and GA (C) particles and surface of the separate particle WA (B) and GA (D).

Structural analysis shows that particles of the second phase in the WA powders are finer and their number in the aluminum matrix is greater than that in the GA powders (Fig. 16.29). The rods extruded from the water-atomized powders have much higher hardness, ultimate strength, and yield stress than those from the gas-atomized powders, with plasticity being acceptable at all temperatures (RT, 453, and 573 K). An additional powder metallurgy operation such as pulsed hot pressing does not increase the strength of billets from either the WA or GA powders. The alloy based on the water-atomized 0–63 μm powder shows the maximum ultimate tensile strength: 483, 332, and 261 MPa by (3.5%−4.0%)El at RM, 453, and 573 K, respectively.

The developed RS technology allows the production of high-quality alloys for elevated temperature applications. The excellent compressibility of WA powders simplifies the procedure of powder consolidation, which is based on hot extrusion of cold-pressed degassed powders. The level of property achieved here is comparable with that of other alloys of similar composition known from the literature and mainly exceeds them [91]. The data adduced in Table 16.16 have characterized the mechanical properties of elevated temperature aluminum alloys achieved by means of advanced water-atomization technology [29,90,91].

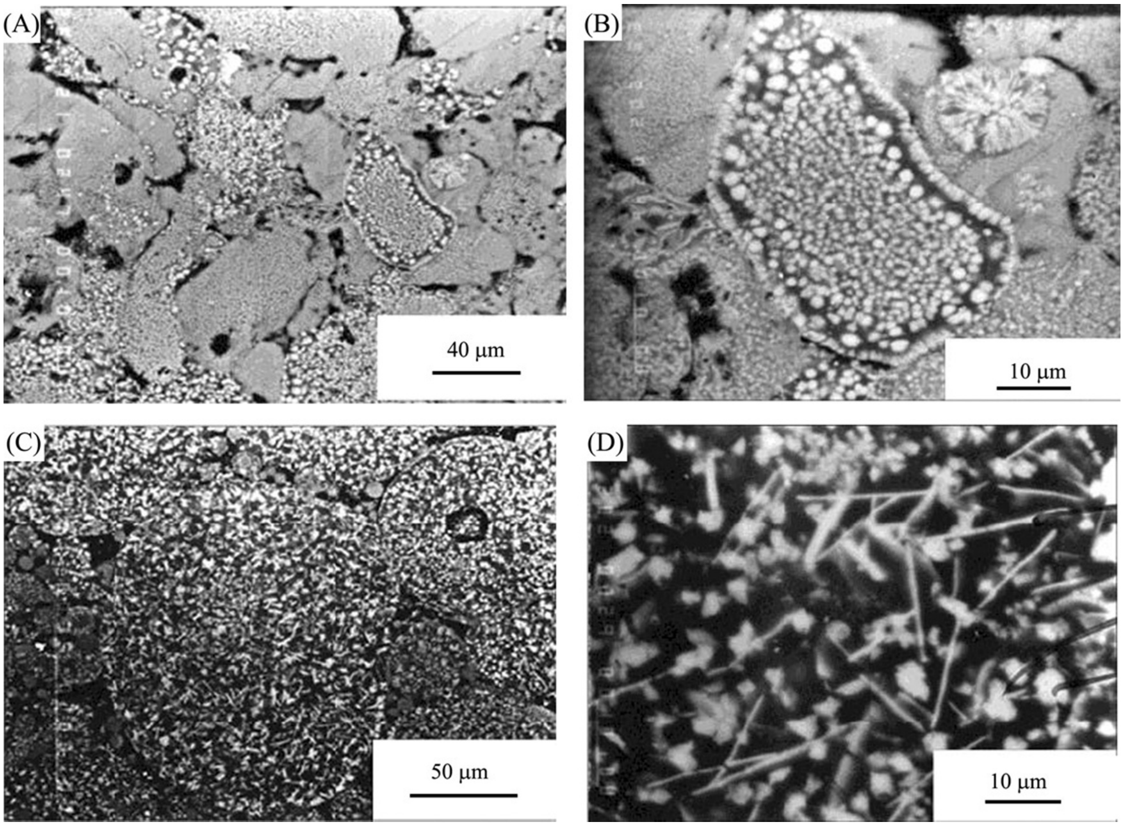

FIG. 16.29 SEM images of electrolytically polished metallographic sections of cold pressed briquettes with 30% porosity of the water-atomized (A), (B) and gas-atomized (C), (D) Al-8Cr-1.5Fe powder particles.

TABLE 16.16 Mechanical Properties of Elevated Temperature Aluminum Alloys Achieved by Means of Advanced Water-Atomization Technology

Alloy Composition (at%)	Semiproduct	Temperature (K)	Mechanical Properties			
			HV (MPa)	UTS (MPa)	YS (MPa)	El (%)
$Al_{94.9}Fe_{0.75}Cr_{4.35}$[a]	Rod, 6 mm in diameter	RT	…	483	402	4.5
		463	…	364	332	4.3
		573	…	261	236	4.7
$Al_{94.7}Fe_{2.6}Cr_{2.7}$[a]	Rod, 6 mm in diameter	RT	…	459	398	10.6
		463	…	359	328	7.4
		573	…	247	221	3.1
$Al_{94.3}Fe_{4.7}Ce_{1.0}$[a]	Rod, 7 mm in diameter	RT	…	590	524	10
		573	…	320	270	6.5
$Al_{92.83}Fe_{6.03}Ce_{1.14}$[a]	Rod, 7 mm in diameter	RT	…	500	460	11
		573	…	290	260	7
$Al_{94}Fe_{2.5}Cr_{2.5}Ti_{1.0}$[b]	Rod, 10 mm in diameter	RT	2717	633	590	5.2
		463	…	…	…	…
		573	…	310	291	3.0
		673	…	199	177	6.7

Continued

TABLE 16.16 Mechanical Properties of Elevated Temperature Aluminum Alloys Achieved by Means of Advanced Water-Atomization Technology—cont'd

Alloy Composition (at%)	Semiproduct	Temperature (K)	Mechanical Properties			
			HV (MPa)	UTS (MPa)	YS (MPa)	El (%)
$Al_{84.2}Fe_7Cr_{6.3}Ti_{2.5}$[b]	Rod, 10mm in diameter	RT	1910	620	581	5.0
		463	…	482	450	4.6
		573	…	355	335	3.0
$Al_{94}Fe_{2.5}Cr_{2.5}Ti_{0.7}Zr_{0.3}$[b]	Rod, 10mm in diameter	RT	1920	642	611	7.4
		573	…	365	322	1.9
		673	…	190	188	5.4
$Al_{94}Fe_{2.5}Cr_{2.5}Ti_{0.5}Nb_{0.5}$[b]	Rod, 10mm in diameter	RT	1880	647	597	2.7
		573	…	368	355	1.63
		673	…	202	171	4.7
$Al_{94.9}Cr_{4.35}Fe_{0.75}$	Rod, 7mm in diameter	PT		445	491	4.0
		463		332	368	2.8
		573		225	250	3.5

[a] *Particle size fraction 0–63 μm.*
[b] *Particle size fraction 0–40 μm; RT is the room temperature.*

Al-Mg System Alloys

The Al-Mg system represents the most popular nonheat treatment, strong, weldable alloys with high corrosion resistance. In the Al-Mg-Sc system, solid-solution hardening by Mg is combined with precipitation hardening by intermetallic Al_3Sc particles. Along with the merits of transition metals used for doping aluminum alloys [18], scandium is especially advantageous, as mentioned above in connection with the Al-Zn-Mg system because it forms intermetallic Al_3Sc with lattice parameter with a small difference from one of the aluminum matrix [58].

The additions of scandium, zirconium, and chromium influence the structure and mechanical properties of Al-Mg alloys produced by casting in a water-cooled copper mold and by the powder metallurgy methods are discussed [92,93]. A fraction of 0–40 μm of both alloys showed maximal tensile strength values (Fig. 16.30). With powder particle sizes decreasing up to 0–20 μm, the tensile strength values are lowered that can be interpreted by redundant increasing of oxidation level of powders. Fraction 40–63 μm of the Al-4Mg-1,0Sc alloy gave appreciable decreasing of tensile strength values. This results, evidently, from decreasing cooling rate and semiproduct structure coarsening, accordingly.

The strength of PM/WA alloys is much higher than that of cast alloys (Table 16.17). Alloying of Al-5Mg base alloy (#174) by 0.3 wt% zirconium (alloy #17, both of production technique, yields a small increase of strength while alloying by scandium in the same volume (alloy #178) brings about the substantial increase of strength). Increase of the content of zirconium (alloy #224p) and scandium (alloy #261p), especially the latter, gives rise to a considerable increase of strengthening effect, but also simultaneously the decline of their plasticity, from a 21.2% (base alloy #174p) to 7.8% (alloy #261p). Close to alloy #261p level strength, it is possible to attain by alloy with a lower content of scandium, but simultaneous alloying by zirconium (alloy #176p), due to formation of nanosized $Al_3(Sc_{1-x}Zr_x)$ phase. The most nearby composition alloy #261p to the Scalmalloy0.7 excels the latter by strength.

Al-Zn-Mg System Alloys

Aluminum commercial alloys in the Al-Zn-Mg system form a wide class of structural materials. They are wrought, heat-treatable alloys that show adequate strength, formability, good weldability, and high stress corrosion cracking resistance [18,96]. Improvement methods of Al-Zn-Mg system alloys produced by conventional casting technology as well granules

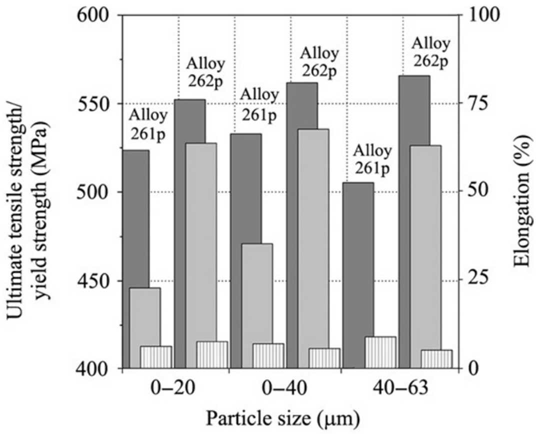

FIG. 16.30 Tensile strength data dependence on powder particles size fractions from which Al-4Mg-1,0Sc (#261p) and Al-5Mg-0.7Sc-0.3Zr (#262p) alloys are made.

TABLE 16.17 Room Temperature Tensile Strength of Semiproducts of Al-Mg System Alloys Made by Various Technologies

Alloy Number	Nominal Alloy Composition (wt%)	Parameters				Semiproduct	Technology
		HV (MPa)	YS (MPa)	UTS (MPa)	EL (%)		
174p[a]	Al-5Mg	928	242	370	21.2	6-mm rod[b]	PM/WA[c]
174c[d]	Al-5Mg	730	167	298	30.5	6-mm rod[b]	Casting[e]
182p	Al-5Mg-0.15Zr	924	255	383	19.2	6-mm rod[b]	PM/WA
182c	Al-5Mg-0.15Zr	788	205	318	23.0	6-mm rod[b]	Casting
175з	Al-5Mg-0.3Zr	932	255	383	19.2	6-mm rod[b]	PM/WA
178p	Al-5Mg-0.3Sc	1142	400	485	11.0	6-mm rod[b]	PM/WA
178c	Al-5Mg-0.3Sc	1171	366	470	12.5	6-mm rod[b]	Casting
224p	Al-4Mg-1.0Zr		403	449	8.1	6-mm rod[b]	PM/WA
261p	Al-5Mg-1.0Sc	1531	473	534	7;8	6-mm rod[b]	PM/WA
176p	Al-5Mg-0.3Sc-0.3Zr	1384	452	503	10.7	6-mm rod[b]	PM/WA
180p	Al-5Mg-0.3Sc-0.15Zr-0.2Cr	1326	438	506	12.4	6-mm rod[b]	PM/WA
180c	Al-5Mg-0.3Sc-0.15Zr-0.2Cr	1207	376	489	12.7	6-mm rod[b]	Casting
262	Al-5Mg-0.7Sc-0.3Zr	1680	538	562	5.9	6-mm rod[b]	PM/WA
Scalm alloy0.7	Al-4.3Mg-0.7Sc-0.3Zr-0.5Mn		460	490	16.0	Extrudate shapes[f]	Scalm [94]
1570[g]	Al-5.6Mg-0.25Sc-0.1Zr-0.39Mn		300	400	15.0	Pressed semiproducts	G/T [95]

p, denotes obtaining by PM technology.

[a] *IPMS alloy numeration.*

[b] *Extruded 6 mm rods by 12.8 extrusion ratio from 0 to 40 μm fraction of water-atomized powders.*

[c] *PM/WA Denotes the PM technology based on the water-atomized powders.*

[d] *c denotes the obtaining by casting technology.*

[e] *Casting denotes the casting of 55 mm in diameter subjected to two-step extrusion: from 55 to 25 mm (extrusion ratio 4.8) and from 25 to 6 mm in diameter (extrusion ratio 17.4).*

[f] *Extrudate shapes with maximal cross-section size 30 mm; Scalm, PM technology based on scaly powders.*

[g] *Classified by the Russian Federation; G/T, is the granular technology.*

technology (G/T) and ones based on (GA) powders were discussed above. Further advance is possibly by the increase of alloying elements content both of basic – Zn and Mg, in possession of greater solubility in aluminum as compared with other elements, and transitional refractory and rare earth metals, little or in general insoluble in an aluminum. This is feasible by increasing the rapid solidification of melt as compared with (G/T) and (GA), which are characterized by a cooling rate in 10^3–10^4 K/s range of the former and up to 10^5 K/s of the latter [18,22]. The total content of transition refractory metals by G/T is no more than 1.2%–1.4%, and the corrosion cracking point may shift to a total Zn + Mg content of 8%. For this total zinc and magnesium content, their optimum ratio is 5:3. Considering this and assuming that much more rapid cooling of PM alloys produced from water-atomized powders permitted an increase in the content of transition refractory metals, the total content of transition refractory metals was taken in the 1.2%−2.5% range [97].

The water-atomized powders were made at the pilot plant of IPMS (Fig. 16.18), according to the procedure described in Ref. [98]. The dried powder was pressed in air at room temperature to form briquettes with about 30% porosity. The briquettes were placed into a die, which was vacuumized under gradual heating in the chamber of a press for hot compaction. Pulsed forging of the briquettes was fulfilled at 673 K and a pressure to 1 GPa. Then the billets (25 mm in diameter and 50 mm in height) were subjected to rod extrusion (6 mm in diameter) at 673 K. For casting of the alloys, a melting plant consisting of a high-frequency generator and an induction furnace placed into a vacuum chamber with a controlled inert gas atmosphere was used. The plant is equipped with a device for stirring the molten metal and a temperature control system. The metal was melted in a ceramic crucible from which the melt was poured into a water-cooled copper mold. Argon was blown through the melt for its purification, and then it was poured through ceramic filters. Preformed rods were produced by hot extrusion of billets and subsequent heat treatment. The optimum extrusion temperature was 623–673 K. The samples were quenched from 743 K and aged at 393 K for 24 h.

A typical SEM microphotograph of water-atomized Al-5Zn-3Mg alloy powder is shown in Fig. 16.31. The particles are of irregular shape (Fig. 16.31A). The microstructure of the grains depends on the cooling rate and composition of the alloys. It is seen (Fig. 16.31B) that the size of nondendritic grains equivalent to the dendritic parameter [18] ranges between 0.5 and 2.5 μm, with average size of 1.0 μm corresponding to the cooling rate 10^6 K/s of the melt calculated with the procedure described in Ref. [18].

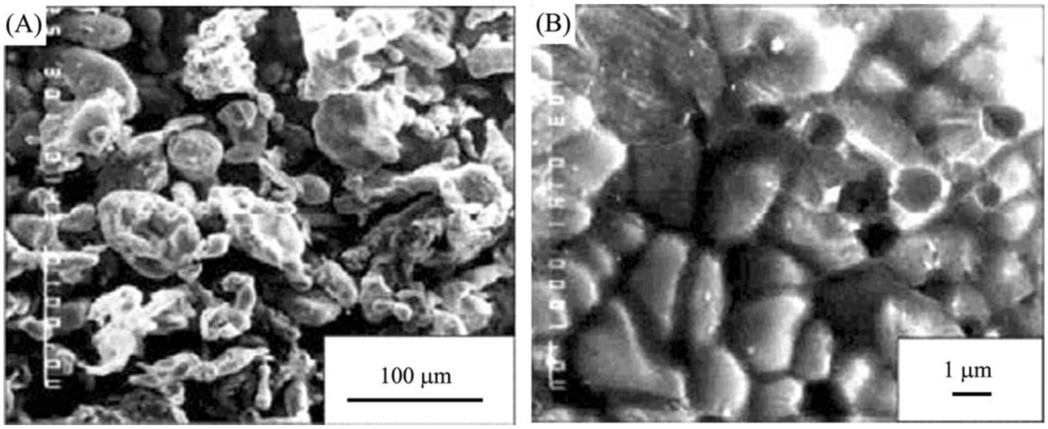

FIG. 16.31 Microstructure of the Al-5Zn-3Mg alloy: (A) powder, (B) surface of an individual grain.

Scanning electron microscopy and microanalysis revealed intergranular layers 0.2–0.5 μm in thickness, enriched with zinc and magnesium and less by scandium and zirconium (Fig. 16.32) while manganese is not observed along the cut line.

The tensile strength characteristics of the Al-5Zn-3Mg system alloy semiproducts produced by powder metallurgy, based on water-atomized powders, casting, and granular technologies, are shown in Table 16.18. The preforms made by PM/WA technology have considerably higher strength in comparison with casting and granular technologies by the same or close composition alloys. This alloy has the greatest mechanical properties currently attained by welding Al-Zn-Mg alloys.

The strength of G/T alloy 1970 in possession of the greatest mechanical properties currently attained by welding Al-Zn-Mg alloys is also lower than that of PM alloys of close composition.

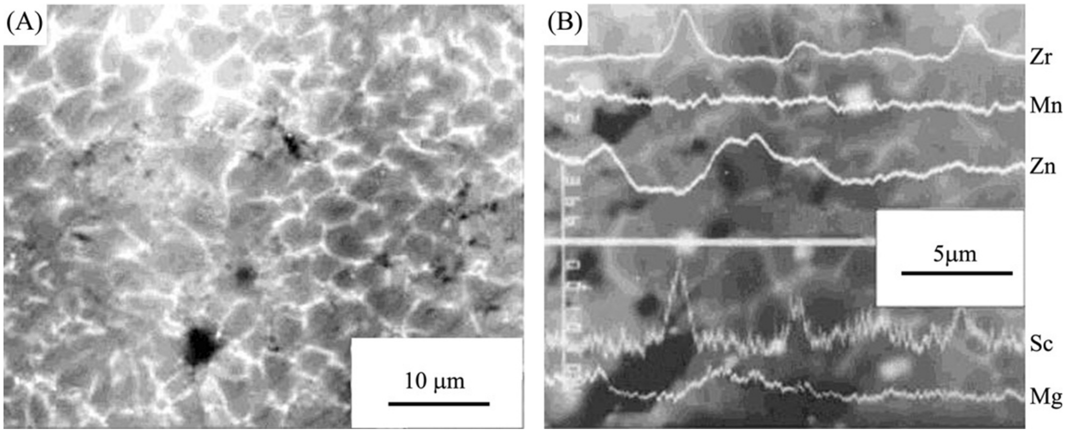

FIG. 16.32 Structure of the polished section of a cold-pressed briquette of the Al-5Zn-3Mg-0.5Mn-0.7Zr-0.3Sc alloy (A); distribution of elements along a cut line (B).

TABLE 16.18 Mechanical Characteristics of Al-5Zn-3Mg System Alloy Semiproducts Produced by Powder Metallurgy, Casting and Granular Methods

Alloy Number	Nominal Alloy Composition (wt%)	Parameters			Semiproduct	Technology
		YS (MPa)	UTS (MPa)	EL (%)		
1p[a]	Al-5Zn-3Mg	500	575	10.4	6-mm rod[b]	PM/WA[c]
1c[d]	Al-5Zn-3Mg	383	433	13.0	6-mm rod[b]	Casting[e]
2p	Al-5Zn-3Mg-0.7Zr	542	612	11.1	6-mm rod[b]	PM/WA
2c	Al-5Zn-3Mg-0.7Zr	452	495	13.7	6-mm rod[b]	Casting
3p	Al-5Zn-3Mg-0.85Zr-0.22Cr-0.17Ni-0.15Ti	530	608	9.9	6-mm rod[b]	PM/WA
3c	Al-5Zn-3Mg-0.85Zr-0.22Cr-0.17Ni-0.15Ti	356	427	15.5	6-mm rod[b]	Casting
4p	Al-5Zn-3Mg-0.7Zr-0.3Sc	596	651	7.7	6-mm rod[b]	PM/WA
4c	Al-5Zn-3Mg-0.7Zr-0.3Sc	531	590	10.3	6-mm rod[b]	Casting
5p	Al-5Zn-3Mg-0.85Zr-0.22Cr-0.17Ni-0.15Ti-0.3Sc	553	618	8.1	6-mm rod[b]	PM/WA
5c	Al-5Zn-3Mg-0.85Zr-0.22Cr-0.17Ni-0.15Ti-0.3Sc	532	570	6.3	6-mm rod[b]	Casting
6p	Al-5Zn-3Mg-0.7Zr-0.3Sc-0.15Cr-0.2Ni-0.15Ti-0.5Co	594	649	6.8	6-mm rod[b]	PM/WA
6c	Al-5Zn-3Mg-0.7Zr-0.3Sc-0.15Cr-0.2Ni-0.15Ti-0.5Co	566	608	9.0	6-mm rod[b]	Casting
1970[f]	Al-(5.0–5.8)Zn-(1.8–2.2)Mg-(0.2–0.45)Cu-0.3Mn-(0.05–0.12)Zr-(0.15–0.25)Sc-(≤0.2Fe, ≤0.1Si)	420–490	440–550	10–14		G/T
1949[f]	(4.5–5.5)Zn-(2.5–3.5)Mg-(0.7–1.0)Zr-(0.15–0.3)Cr-(0.1–0.2)Ti-(0.1–0.25)Ni-(0.0002–0.05)Be	500 420	540 520	8.0 8.0	20-mm strip 2-mm sheet	G/T [18] G/T [18]

p, denotes the obtaining by PM technology.

[a] *IPMS alloy numeration.*

[b] *Extruded 6 mm rods by 12.8 extrusion ratio from 0 to 40 μm fraction of water-atomized powders.*

[c] *PM/WA denotes the PM technology based on the water-atomized powders.*

[d] *c denotes the obtaining by casting technology.*

[e] *Casting denotes the casting of 55 mm in diameter subjected to two-step extrusion: from 55 to 25 mm (extrusion ratio 4.8) and from 25 to 6 mm in diameter (extrusion ratio 17.4).*

[f] *Classified by the Russian Federation; G/T, is the granular technology.*

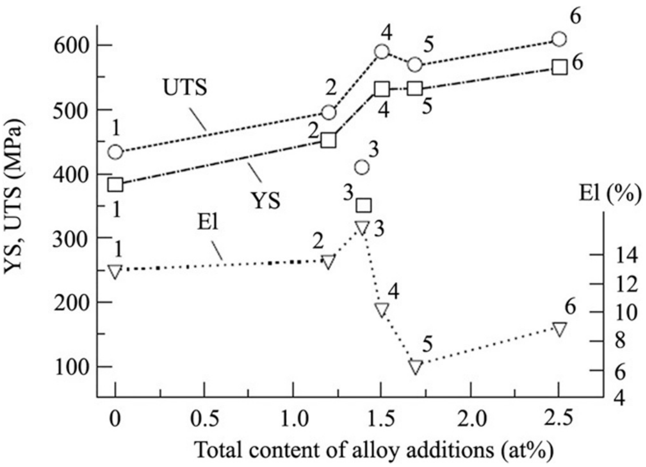

FIG. 16.33 Mechanical properties of extruded rods of PM/WS alloys in T1 state versus the total content of alloying elements: the numbers of points correspond to the numbers of alloys in Table 16.18.

Fig. 16.33 shows the mechanical properties of extruded rods of PM/WA alloys in a T1 state versus the total content of alloying elements. The ultimate strength and yield stress become higher when the amount of doping elements increases from 1.39% (alloy 3) to 1.5% (alloy 4). These characteristics grow approximately to the same extent as when the amount of doping elements increases from 0% to 1.2%. The better mechanical characteristics of alloy number 4 are due to the scandium addition, which leads to precipitation of the matrix-coherent $Al_3(Sc_{1-x}Zr_x)$ phase. Plasticity decreases yet remains at a level acceptable for wrought alloys. A further increase in the amount of doping refractory metals to 2.5% in the number 6 alloy does not improve strength but reduces plasticity. The lower strength of the number 5 alloy at 1.69% refractory metals is probably caused by chromium doping of the alloy, which results in increasing of the Guinier-Preston zones part [99].

The ultimate tensile strength ranges of the aluminum alloys made from water-atomized powders are shown in Fig. 16.34.

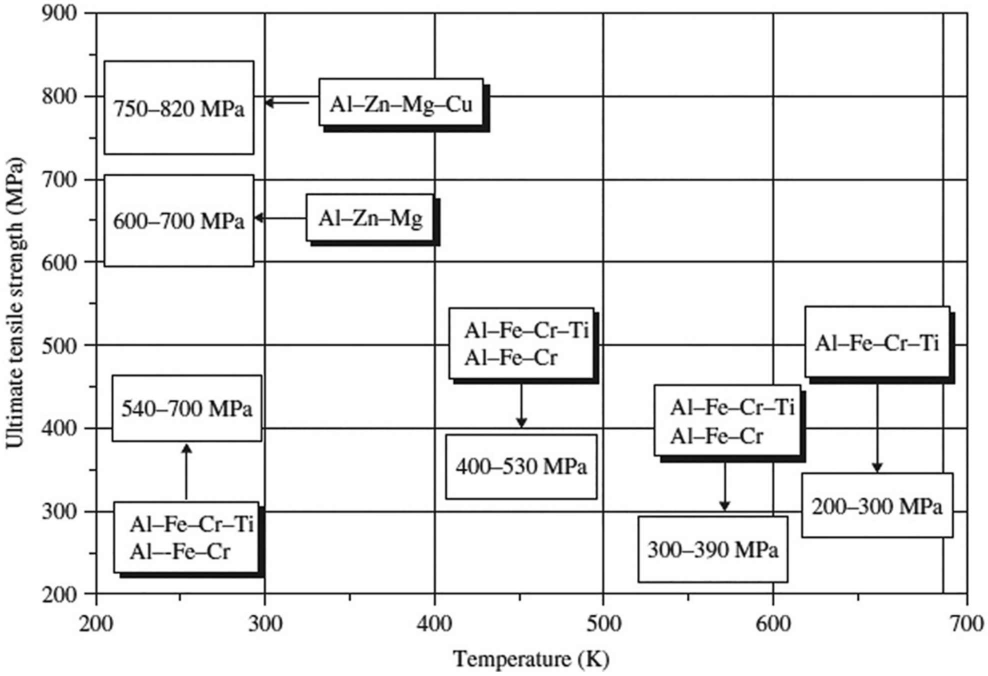

FIG. 16.34 Ultimate tensile strength ranges of the aluminum alloys made from water atomized powders.

SPRAY FORMING

Spray forming is a metal spraying process for the production of near-net shape parts. In this technique, the melt of metal is gas atomized to form a fine spray of molten particles that are deposited and sintered onto a stationary or moving substrate. Therefore, the powder metallurgical process is accomplished omitting a cold solid powder state.

In a typical spray-forming process, the metal melt is poured from the tundish into the atomization zone and is disintegrated by impinging high-energy inert gas jets. In the resulting spray cone, the molten metal droplets partly solidify at high cooling rates and are accelerated toward the substrate, where the mushy droplets are compacted to a solid preform. The principle of the spray-forming process is illustrated in Fig. 16.35.

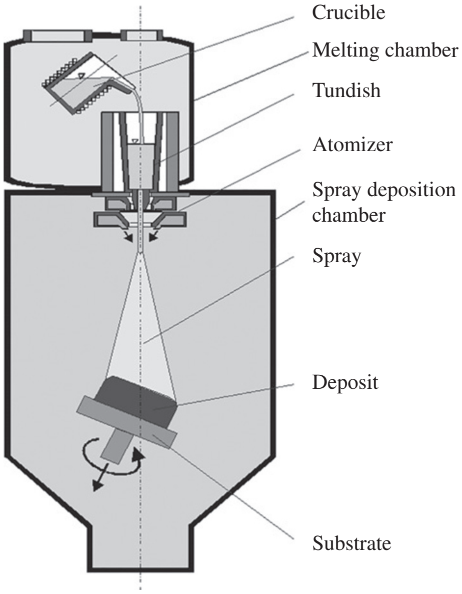

FIG. 16.35 Spray forming process principle.

The idea of spray forming was developed in the late 1960s by Singer [100] at the University of Swansea in Wales, the United Kingdom. The process of spray forming was further developed initially as an alternative to the production of thin metal sheets directly from the melt, which should replace the conventional metallurgical route of casting and subsequent metal forming of big slabs. For the first commercial application, scientists of Singer's group founded Osprey Metals Ltd. [101]. Starting from here, several scientific groups all over the world took an active part in the research and development of the fundamentals and application potentials of spray forming [102–108].

The specific advantages of different spray-formed materials as well as the properties of spray-formed, near-net shaped products and the state of the art of research and industrial application of the process are documented in the periodical international user conferences on spray forming ICSF and the International Conferences on Spray Deposition and Melt Atomization SDMA that took place in 2000, 2003, 2006, 2009 and 2013 at the University of Bremen as well as in the publication series of the scientific contributions on spray forming in the special research program at the University of Bremen.

Different setups and ways of description and combination of fundamental process stages can be found in the literature [102,109,110]. The starting point of an analysis is the subdivision of the spray-forming process into three main stages (Fig. 16.36) [111]:

- Preparation of the melt and atomization; this stage includes the preparation of the alloy composition and the delivery and disintegration of the liquid from the continuous melt flow to the resulting droplet size distribution.
- Particle transport in the spray cone; here, the spray cone behavior and development, described by the multiphase flow of metal droplets/particles and the gas, the momentum, and heat transport within phases and exchange between phases are in focus.
- Impact and deposition of droplets; the impact of the droplets and compaction to the resulting deposit in combination with the behavior of the product occurs in this stage.

Modeling and simulation of the spray-forming process is an essential tool for process understanding and development [111–114]. Integral spray-forming models, especially for the thermal behaviour in spray forming, have been derived by

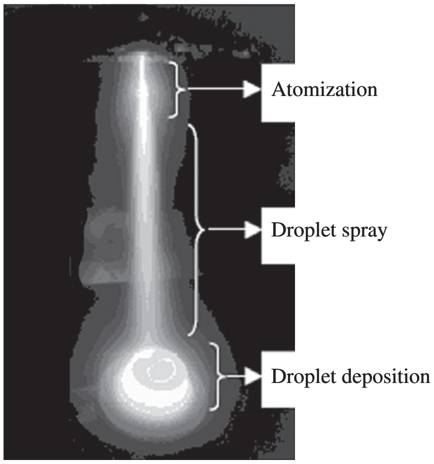

FIG. 16.36 Subdivision of the spray forming process into three main stages.

Bergmann et al. [115], Minisandram et al. [116], and Pedersen et al. [117,118]. Connection of various submodels is performed for transient temperature material behavior, from melt superheating in the tundish to room temperature in the preform via cooling and solidification.

In technical applications, the nonferrous metals that are used for the production of semifinished products by spray forming are:

- Conventional metals and alloys based on copper or aluminum.
- Metals and alloys that are difficult to cast (because they tend to segregate).
- Super alloys (e.g., on nickel basis) and titanium.
- Particle reinforced metal-matrix composites (MMCs) [119–123].

The spray-formed products are typically free from macrosegregation and prior-particle boundaries that occur in conventional PM products. The spray forming is helpful in increasing the maximum solute content of alloying elements and achieving a finer distribution of second-phase particles in an equiaxed fine-grain structure. Such homogeneous, low-segregation, fine-scale alloy microstructures are useful for extrusion, rolling, forging, and super plastic forming processes.

The main geometries that are produced by spray forming are illustrated in Fig. 16.37:

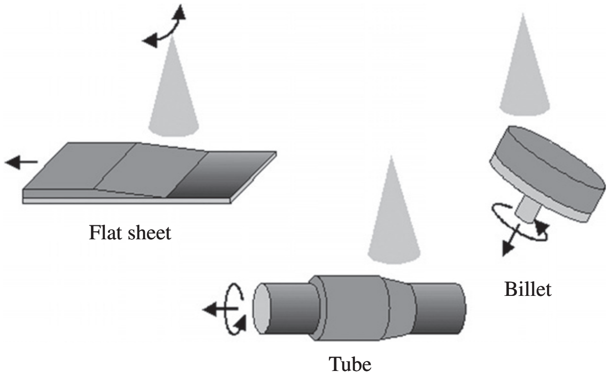

FIG. 16.37 A schematic of the production of flat sheet, billet, and tube by spray forming.

- Flat products (sheets) are manufactured either by scanning (oscillating) the atomizer or by using (linear) slit nozzles in order to spread the spray cone over a certain area and spraying onto a linear moving substrate.
- Tubes and rings are produced by directing the atomizer or stationary spraying onto a tube-shaped or cylindrical substrate. The core will be drilled out or remains in the form for realization of a two-layered product (with different properties on the inside and outside). Spray-formed tubes are used in the chemical industry while spray-formed rings will be used in big dimensions for applications in turbines and propulsion units (aeronautics and astronautics).

Billets are presently the most common manufactured geometries produced by spray forming. Cylindrical billets are commonly used as preform for a subsequent extrusion process. The manufacturing of a billet is realized by spraying at an inclined angle off-center on a rotating cylindrical substrate, which will be withdrawn during the process (commonly in a vertical direction for a standing billet, but sometimes in a horizontal direction, producing a laying billet). To increase the production rate and throughput, sometimes two atomization units are used simultaneously [124]. Spray-formed billets are presently produced up to a diameter of approximately 0.5 m and up to a height of 2 m. Typically billets are deformed (e.g., extruded or forged) to be used for applications in the automotive and aerospace industries.

Fig. 16.38 shows views of the equipment used in a pilot plant at the Research Center “Spray Forming” at the University of Bremen for obtaining spray-forming products. This processing line includes separately three different modeling areas (with different time scales): (a) melt flow in the tundish, (b) particle cooling in the spray, and (c) growth and cooling of the deposit. The melting capacities of the four spray-forming facilities available within the center differ from 1 to 20 L and the maximum melting temperatures from 1073 to 1873 K.

Contributions to fundamentals and applications of several nonferrous metal material groups are: copper-based materials [125], aluminum-based materials [126,127], titanium- and ceramic-free superalloys [128], compound materials and MMCs [129], and lightweight metals (e.g., magnesium) [130].

Examples of spray-formed Al-Li alloys are UL30 and UL40, having increased levels of lithium and zirconium in comparison with one of the most commonly used Al-Li alloys, 8090 (Al-2.5Li-1.0Cu-0.7Mg-0.12Zr). According to White et al. [131], UL30 (Al-3.0Li-1.0Cu-0.7Mg-0.3Zr) shows a 4.4% increase in specific modulus over 8090, and the strengthening is primarily by duplex particles Al_3Zr (β') and Al_3Li (δ') and copper and magnesium in solid solution. Palmer et al. [132] have spray formed UL40 (Al-4Li-0.2Zr) with lithium content reaching the limit of solid solubility at the eutectic temperature. They found the as-sprayed grain structure equiaxed with grain sizes in the range 40–50 μm.

A precipitation-hardened aluminum alloy with ultrahigh strength and high ductility has been developed by spray forming. The strength of the alloy lies in the range general cast alloys cannot achieve, and the ductility exceeds that of the alloys made by the powder metallurgy method that is classified in the same rapid solidification process as spray forming. In the spray-forming process, the additive amount of the strengthening alloying elements needed for precipitation hardening can be increased due to the inhibition of the coarse segregation during solidification. On top of that, during both the high-temperature deformation and the solution treatment after the spray forming, the authors have succeeded in further strengthening by the control of the precipitate growth. In comparison with the powder metallurgy method that can control the solidification segregation by rapid cooling as well as spray forming, further ductility has been achieved, attributed to low oxide inclusions due to the lack of powder handling. The relationship between the microstructural change and mechanical properties is reported in detail.

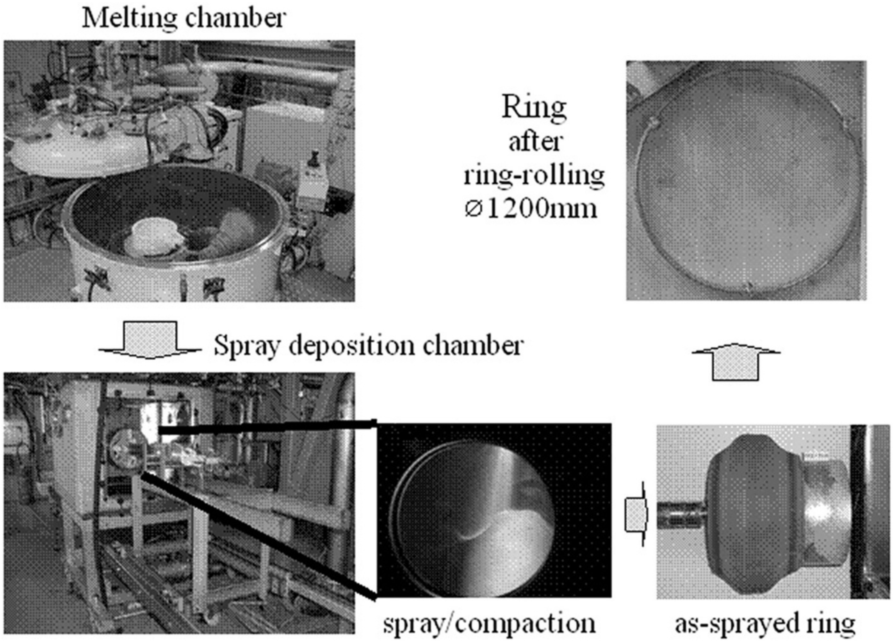

FIG. 16.38 Equipment views used in a pilot plant by Research Centre “Spray Forming” at the University of Bremen for obtaining of spray forming products. *Courtesy: University of Bremen, Germany.*

Kobelco group developed spray-formed Al-Zn-Mg-Cu system alloy with a tensile strength of 780 MPa and a breaking extension of 14% [133]. The manufacturing process of the alloy semiproducts comprises the following six steps:

- Spray forming; higher G/M ratio (gas/melt flow rates) with higher yield and lower density was chosen because of more rapid solidification and finer microstructure.
- Degassing; it was found that the degassing temperature of 743 K for 4 h gives the lowest residual gas pore ratio.
- Hot isostatic pressing (HIP): it was found that 763 K temperature and 120 MPa pressure are needed as an HIP condition.
- Long-term solution treatment: the removal means for the coarsened precipitates is a long-term solution treatment of 240 h after the HIP. With this treatment after HIP, the size of the precipitates was fine as well as the final material through T6 treatment without the HIP.
- Extruding: it was found that increasing the extrusion ratio from 10 to 20 degrades both the tensile strength and breaking elongation while the extrusion temperature should be less than 623 K.
- T6 treatment: it was found that the aging temperature of 383 K in comparison with 483 K tends to improve the tensile strength by 5% in exchange for degradation of the breaking elongation, also by 5%.

The authors [133] discussed the relationship between the microstructural change and mechanical properties.

The microstructures of spray-deposited and homogenized Al-10.8Zn-2.8Mg-1.9Cu-0.16Zr (wt%) alloy had been studied [134]. The melt was atomized using nitrogen gas at 0.6 MPa pressure; the atomizing temperature was 1073 K and the distance of the atomizing deposition was constant at 400 mm.

A high-strength Al-Zn-Mg-Cu alloy was prepared by the spray-deposition technique. The microstructures of spray-deposited and homogenized Al-Zn-Mg-Cu alloys were studied using scanning electron microscopy, transmission electron microscopy, and X-ray diffraction. The results indicate that the microstructure of the spray-deposited alloy mainly is composed of the Al matrix and the $Mg(ZnCu)_2$ compounds. The spray-deposition process has an obvious modification in size, morphology, and distribution of the secondary phases in the microstructure as well as reducing segregation. After homogenization, the coarsening of the grains in the microstructure is not obvious while a phase transformation of primary $Mg(ZnCu)_2$ particles to Al_2CuMg phase was found.

The natural aging behavior of the spray-formed Al-(11–13)Zn-(2.2–2.6)Mg-(1.0–1.3)Cu-(0.1–0.3)Zr-(0.2–0.6)Mn (wt%) alloy has been studied [135]. The time intervals of natural aging were 3, 6, 12, 24, 30, and 36 months. The results showed that the tensile strengths were increased and the elongations were decreased respectively during the first 24 months, the tensile strength increased from 710 MPa at the beginning to 810 MPa while the elongations decreased from 11% to 6% at the first 24 months. The tensile strength decreased to 740 MPa and the elongation increased to 10% when the natural aging time went to 30 months. When the natural aging time went to 36 months, the tensile strength increased to 800 MPa and the elongation decreased to 8%. The first aging peak appearance because of the precipitation of G.P zones and the second aging peak appearance because of the precipitation of η'($MgZn_2$) phases are explained.

Al-Cu-Fe-based stable quasicrystalline alloys were spray deposited in bulk (around 40 kg), with and without the addition of Sn [136]. The spray-deposited materials were characterized in terms of microstructure, hardness, and thermal stability. The results showed that the $Al_{62.5}Cu_{25}Fe_{12.5}$ alloy contains the single quasicrystalline icosahedral phase (i-phase) along with a minor λ-$Al_{13}Fe_4$ phase, whereas the $Al_{62.5}Cu_{25}Fe_{12.5}$ + 10(wt%)Sn alloy contains five phases: the major i-phase, β-Sn, θ-Al_2Cu, λ-$Al_{13}Fe_4$ and β-AlFe(Cu) phases. The hardness value of the Al-Cu-Fe alloy reached 10.5 GPa at 50 g load while that for Al-Cu-Fe-Sn alloy was somewhat lower. DSC analysis showed only one transformation peak at 1128.5 K for i-phase in $Al_{62.5}Cu_{25}Fe_{12.5}$, indicating the melting temperature.

An Al-Fe-Cr-Ti alloy has been spray formed in bulk [42]. Nominal composition alloy Al-Fe_3-Cr_2-Ti_2 was vacuum induction melted, solidified, and remelted under Ar for spray forming to produce a 19 kg billet. As-spray-formed material was hot isostatically pressed (HIPed) at either 723 K, 4 h at 100 MPa or 823 K, 2 h at 190 MPa. The 723 K HIPed material was then either hot forged at 673 K to a true strain or extruded at 748 K to a 7.5-mm bar at an extrusion ratio of 16:1. The authors discussed the structure, phase contents of the spray formed, and the subsequent consolidated materials and mechanical properties of the latter. Table 16.19 shows a summary of the mechanical properties of spray-formed Al-2.7Fe-1.9Cr-1.8Ti, along with nominally Al-3Fe-2Cr-2Ti produced by mechanical alloying and PM based on gas-atomized powder methods. UTS level of SF/HIP/F at RT and temperatures up to 473 K are higher in comparison with MA/E. SF/HIP/F and GA/E (<125 μm) properties at RT were broadly similar while the mechanical properties of similar $Al_{94}Fe_{2.5}Cr_{2.5}Ti_{1.0}$ alloy produced by PM technology based on water-atomized powder are much higher (Table 16.19).

TABLE 16.19 Mechanical Characteristics of Al-Fe-Cr-Ti System Alloy Semiproducts Produced by Spray Forming, GA/E[a] and MA/E[b] Technologies

Alloy Composition	Technology	Temperature (K)	Parameters YS (MPa)	UTS (MPa)	El (%)	Reference
$Al_{93.6}$-$Fe_{2.7}$-$Cr_{1.9}$-$Ti_{1.8}$	Spray formed 723 K/HIPed/forged at 673 K (SF/HIP/F)	RM 373 473 673	469 430 300 100	545 460 340 110	3.8	[42]
Al_{93}-Fe_3-Cr_2-Ti_2	Mechanical alloying/extruded	RM 473 573 673		430 305 200 120		[42]
Al_{93}-Fe_3-Cr_2-Ti_2 25 − 50 μm size powder	Gas-atomized/extruded	RM	500	600		[43]
Al_{93}-Fe_3-Cr_2-Ti_2 < 125 μm size powder	Gas-atomized/extruded	RM	470	540		[44]

[a] *GA/E, PM technology based on gas-atomized powder.*
[b] *MA/E, mechanical alloying/extruded.*

In another variation of the spray-forming technology, Siemers et al. [137] used a low-pressure plasma spray deposition (PSD) technique for producing metal-matrix composites (MMCs). In this process, plasma (near 9573–18873 K) is formed in the interior plasma gun by the discharge of a DC arc through a flowing gas mixture (argon or nitrogen with additions of 2–15% hydrogen or helium). Powder is injected into the plasma jet through one or more injector ports. Then, the powder is entrained in the high-velocity plasma jet (Mach 2–3), melted, transported, and impacted on a substrate where the molten droplets solidify at cooling rates of 10^5 to 10^6 K/s, according to [137]. Siemers et al. produced composites of metal-metal, metal-carbide, and metal-oxide combinations. They also produced graded layered structures of near-theoretical density to minimize the effects of interfacial stresses developed due to thermal mismatch between the constituents. Continuous as well as discontinuous composites can be fabricated by the PSD process. Continuous laminates, consisting of alternating layers of metal and reinforcement, are produced by first depositing metal, next depositing reinforcement, and repeating the sequence to build the desired final thickness. For fabricating discontinuous laminates of individual splattered particle lamellas (2–4 μm thick and 50–150 μm diameter), a powder blend of two or more different compositions can be injected into the plasma jet.

The PSD process is commonly used to apply a metal coating deposit onto engine components or protective ceramics for high-temperature service in the aerospace, automotive, and power-generation industries.

Many works have been performed in the fundamental study of the PSD process, including its simulation by means of computational fluid dynamics to model the plasma flow, particle dynamics, and heat transfer [138]. On the substrate part of the process, numerous studies have been carried out on the impact of the single liquid droplet on a solid surface. Both experimental and computational studies have been performed on materials such as zirconia [139], alumina [140], nickel [141], and tin [142] and on mild or stainless steel, glass, or other substrates.

A new strip-casting process, termed “spray rolling” (also “spray strip casting”), combines elements of spray forming and twin-roll casting [143,144]. Thus, the powder metallurgical process of a semiproduct in the form of strips is accomplished, omitting the cold solid powder state and billet compacts. In this process, molten metal is atomized with a high velocity inert gas, the resultant droplets are quenched in flight, and the spray is deposited onto mill rolls (Fig. 16.39). In-flight conventional heat transfer, extracting most of the metal’s latent heat and conduction heat transfer at the rolls rapidly removes the initial heat. Hot deformation of the semisolid material by the rolls completely consolidates the rapidly solidified product. The high solidification rates in spray rolling allow a wider range of alloys to be processed, and at higher production rates than is currently possible in commercial twin-roll casting practices [145–147].

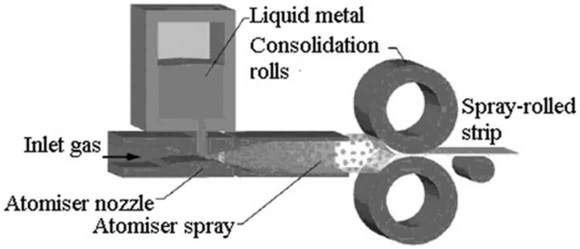

FIG. 16.39 Schematic of spray rolling principle. *Source: McHugh KM, Delplanque JP, Johnson SB, Lavernia EJ, Zhou Y, Lin Y. Spray rolling aluminum alloy strip. Mater Sci Eng A 2004;383(1):96–106.*

Direct strip-casting techniques are attractive because they improve the economics of manufacturing aluminum sheet products by eliminating the ingot casting, homogenization, and hot-rolling unit operations in conventional ingot processing while significantly reducing energy consumption. Tensile results for spray-rolled SR 2124 and SR7050 aluminum alloys, according to the data of the Idaho National Engineering and Environmental Laboratory (INEEL), [143,148] are summarized (Table 16.20).

TABLE 16.20 Tensile Properties of Spray-Rolled and Commercial 2124 and 7050 Aluminum Alloy Strips

				Tensile Properties		
Alloy	**Composition**	**G/M**	**Heat Treatment**	**UTS (MPa)**	**YS (MPa)**	**El (%)**
Commercial 2124	Al-4.4Cu-1.5Mg-0.6Mn	…	T851	483	448	6
SR 2124	Al-4.4Cu-1.5Mg-0.6Mn	0.15	T851	441	407	6
SR 2124	Al-4.4Cu-1.5Mg-0.6Mn	0.30	T851	483	469	7
Commercial 7050	Al-6.2Zn-2.3Cu-2.3Mg-0.6Mn-0.12Zr	…	T7651	510	448	12
SR 7050	Al-6.2Zn-2.3Cu-2.3Mg-0.6Mn-0.12Zr	…	ST·2h·A	545	496	10
SR 7050	Al-6.2Zn-2.3Cu-2.3Mg-0.6Mn-0.12Zr	…	ST·15h·A	545	503	7

SR is the spray rolled; ST is the solution treatment at 744K; A is the aging (398K, 12h + 439K, 15h).

Commercial 2124-T851 and 7050-T7651 plates are remelted and spray rolled. The alloys were induction melted under a nitrogen atmosphere, heated about 100K above the liquidus temperature, and pressure fed into an atomizer. Atomized droplets were directed horizontally and deposited into a roll gap of a 200 × 300 mm 2-HI Fenn rolling mill operating at a roll surface speed of 4.1 m/min to produce strips measuring about 100 mm wide and 2.5 mm thick. The mill had standard tool-steel mill rolls. An inert gas atmosphere within the spray apparatus minimized in-flight oxidation of the atomized droplets. Strips were made under gas-to-metal mass flow rates (G/M) of 0.15 and 0.3 while maintaining other constant processing conditions. The production rate was 4100 kg/(hm).

As shown in Table 16.20, for a spray-rolled 2124 strip, increasing G/M from 0.15 to 0.30 resulted in an increase in tensile properties. The tensile properties of spray-rolled 2124-T851 produced at G/M = 0.30 compare favorably with those of commercial conventional material. Overall tensile properties of the spray-rolled and heat-treated 7050 are similar to those of the commercial product.

OTHER TECHNOLOGIES

There are also other powder metallurgy processing techniques such as the XD process, solid free-from fabrication (SFF), and self-propagating high temperature synthesis (SHS), which one can regard as potential for developing high-performance aluminum alloys and composites, including functionally graded materials.

In the XD process, elemental components of the desired reinforcing phase are mixed with or incorporated into the metallic matrix material. The mixture is heated to a high temperature ($>T_m$) where a self-propagating reaction takes place. The elemental constituents react exothermally, forming a dispersion of ultrafine reinforcing particles in the matrix. As the particles of the reinforcing phase are formed by an exothermic reaction at an elevated temperature, they tend to be stable through subsequent processing at high temperatures. Larsen et al. [149] used the XD process to produce a master alloy material containing TBA-70 sponge: 70 wt% TiB_2 and 30 wt% Al, which was subsequently used for fabricating the discontinuously reinforced aluminum composites.

Solid free-form fabrication facilitates integrated manufacturing, from computer-aided design to finished parts, using only additive processing [150–152]. A solid or surface model is electronically sectioned into layers of predetermined thickness. Net-shape composite components can be directly produced from the elemental or prealloyed matrix powders, mixed with suitable reinforcement by sintering, layer by layer, under a scanning laser beam.

Self-propagating high temperature synthesis (SHS) is a process in which the synthesis reaction occurs through the reactant mixture in the form of a combustion wave [153]. Several advantages of the SHS process may include purity of the product, energy efficiency, formation of metastable phases, and simultaneous synthesis and densification. Therefore, the SHS process has the potential to be the available method for producing high-performance MMCs. Functionally graded materials including MMCs create a continuous transition from a substantially ceramic material usable to high temperatures to a partly or fully metallic material [154–156].

REFERENCES

[1] United Aluminum. www.unitedaluminum.com/chemical-composition-and-properties-of-aluminum-alloys.

[2] Buhl H, editor. Advanced aerospace materials. Berlin, Heildelberg: Springer-Verlag Publishers; 1992.

[3] Nembach E. Particle strengthening of metals and alloys. NY: John Wiley & Sons Publishers; 1997.

[4] Li PY, Yu HJ, Dai SL, Liu DB, Chai SC, Li YR. Development of high damping aluminum alloys and composites using rapidly solidified powder metallurgy process. Mater Sci Forum 2003;426–432:411–6.

[5] Sfat C, Vasile T, Vasilescu M. Researches focused on structure of aluminum alloys processed by rapid solidification, used in automotive industry. In: Proceedings of 15th international Plansee Seminar, vol. 4; 2001. p. 792–800.

[6] Bhagat RB. Advanced aluminum powder metallurgy alloys and composites. In: Eisen WB, Ferguson BL, German RM, editors. ASM handbook. vol. 7. ASM International Publishers; 1998. p. 841–58.

[7] Gomes LACM, et al. Production of MA956 alloy reinforced aluminum matrix composites by mechanical alloying. Mater Res 2015;18(2). https://doi.org/10.1590/1516-1439.346114.

[8] Fleck NA, Muller GM, Ashby MF, Hutchinson JW. Strain gradient plasticity: theory and experiment. Acta Metall Mater 1994;42(2):475–87. https://doi.org/10.1016/0956−7151(94)90502−9.

[9] Kamrani S, Simchi A, Riedel R, Seyed Reihani SM. Effect of reinforcement volume fraction on mechanical alloying of Al-SiC nanocomposite powders. Powder Metall 2007;50(3):276–82. https://doi.org/10.1179/174329007X189621.

[10] Torres B, Lieblich M, García-Escorial A. Effect of heat treatments at 753 K on an aluminium alloy matrix composite reinforced with Ni_3Al powder particles. Scr Mater 2006;54(8):1485–9. https://doi.org/10.1016/j.scriptamat.2005.12.052.

[11] Torres B, Lieblich M, Ibañez J, García-Escorial A. Mechanical properties of some PM aluminide and silicide reinforced 2124 aluminium matrix composites. Scr Mater 2002;47(1):45–9. https://doi.org/10.1016/S1359-6462(02)00095-7.

[12] Murakami Y. Aluminum-based alloys. Mater Sci Technol 1996;8:213–76.

[13] Bhaduri A, Gopinath V, Ramakrishnan P. SiC particulate reinforced aluminum matrix composites prepared by mechanical alloying. In: Proceedings of the 1996 World Congress on powder metallurgy & particulate materials, part 2. Princeton (NJ): Metal Powder Industries Federation; 1996. p. 3–12.

[14] Wang E, Hu L. Nanocrystalline and ultrafine grained materials by mechanical alloying. In: Proceedings of 2006 powder metallurgy World Congress. Busan (Korea): Korean Powder Metallurgy Institute; 2006. p. 911–2.

[15] Vitjaz PA, Lovshenko FG, Lovshenko GF. Mechanical alloyed alloys based on aluminum and copper. Minsk: Belaruskaja Nauka Publishers; 1998 [in Russian].

[16] Jones H. Rapid solidification of metals and alloys. London: Institute of Metallyrgists Publishers; 1982.

[17] Das SK. Rapidly solidified P/M aluminum and magnesium alloys–recent developments. Rev Part Mayer 1993;1:1–40.

[18] Dobatkin VI, Elagin VI, Fedorov VM. Rapidly solidified aluminum alloys. Moscow: All-Russian Institute of Light Alloys Publishers; 1995 [in Russian].

[19] Savage SJ, Froes FH. Production of rapidly solidified metals and alloys. J Meteorol 1984;36(4):20–8.

[20] Fleetwood MJ. Rapid solidification processing. Met Mater 1987;3(1):14–20.

[21] United Technologies Corporation. U.S. Patent 4,078,873, Mar. 14, 1978.

[22] Bondarev BI, Shmakov YV. Technology of rapidly solidified Al alloy production. Moscow: All-Russian Institute of Light Alloys Publishers; 1997 [in Russian].

[23] Lawley A. Atomization. Princeton (NJ): MPIF Publishers; 2003.

[24] Dunkley JJ. Atomization. In: Eisen WB, Ferguson BL, German RM, editors. ASM handbook. vol. 7. ASM International Publishers; 1998. p. 35–52.

[25] Dobatkin VI. Continuous casting and casting properties of alloys. Oboronizdat: Moscow; 1948 [in Russian].
[26] Ghuljaev BB. Solidification and steel heterogeneity. Moscow: Metallurgizdat Publishers; 1950 [in Russian].
[27] Eskin GI. Non-dendritic crystallization of light alloys. Technol Light Alloys 2000;2:17–25 [in Russian].
[28] Neikov OD, Milman YV, Miracle DB, Lotsko DV, Sirko AI, Yefimov NA. Effect of Sc alloying additions on structure and mechanical properties of PM and cast high-strength Al alloys of same composition. In: Proceedings of PM 2001 Congress & Exhibition. Nice: European Powder Metallurgy Association; 2001. p. 219–24.
[29] Neikov OD, Vasilieva GI, Sameljuk AV, Krajnikov AV. Water atomized aluminum alloy powders. Mater Sci Eng A 2004;383:7–13.
[30] Dobatkin VI, Belov AF, Eskin GI, Borovkina CI, Golder Yu.G. Crystallization regularities of metallic materials. Soviet Union scientific discovery #271, 1983.
[31] Elagin VI. Alloying of wrought alloys by transition metals. Moscow: Metallurgia Publishers; 1975 [in Russian].
[32] Dric ME, Bochvar NP, Kadaner ES, et al. Equilibrium diagrams of systems based on aluminum and magnesium. Nauka Publishers: Moscow; 1977 [in Russian].
[33] Dahl W, et al. Metallkunde 1977;68(2):121–9.
[34] Varich NI, Burov LM, Kolesnichenko KE. Izvestija VUZov. Non-ferrous Metalurgija 1967;3:111–4 [in Russian].
[35] Inoue A, et al. Sci Rep Res Inst Tohoku Univ A 1990;35(1):101–14.
[36] Novikov II, Zolotorevskiy VS. Dendritic liquation in alloys. Nauka Publishers: Moscow; 1966 [in Russian].
[37] Cox AR, Moore EC, Van Reuth EC. On the rapid solidification of superalloys. In: Proceedings superalloys: metallurgy and manufacture. Baton Rouge (LA): Claitor's Press; 1976. p. 45–9.
[38] Patterson RJ. Rotating disc atomization. In: Metals handbook. 9th ed. vol. 7. Metals Park (OH, USA): Powder Metallurgy. Publ.; 1984. p. 45–54.
[39] Anderson R. Powder metallurgy at Pratt and Whitney. Int J Powder Metall 1990;26(2):171–9.
[40] United Technologies Corp. U.S. Patent 4,343,750, Aug. 10, 1982.
[41] Schade CH, Dunkley JJ. Atomization. In: ASM handbook. vol. 7. ASM International Publishers; 2015. p. 58–71.
[42] Banjongprasert C, Hogg SC, Liotti E, Grant PS. Spray forming of bulk nanostructured Al-Fe-Cr-Ti. In: CD proceedings of the 4th spray deposition and melt atomization conference SDMA 2009. Bremen (Germany): Universität Bremen; 2009. p. 1–10.
[43] Todd I, et al. The influence of processing variables on the structure and mechanical properties of nano-quasicrystalline reinforced aluminium alloys. Mat Sci Eng A 2004;375 – 377:1235–8.
[44] Kimura HM, Sasamori K, Inoue A. Formation, microstructure and mechanical properties of Al–Fe base quasicrystalline alloys. Mat Sci Eng A 2000;294–296:168–72.
[45] Mamat O, Saleh MH, Ismail F. Gas atomization of aluminum alloy powder. In: Cherenkoff RA, Jandeska WF, editors. Proceedings of the 2000 international conference of PM aluminum and light alloys automotive applications; 2000.
[46] Schatt W, et al. Pulvermetallurgie: Technologien und Werkstoffe. 2nd ed. Berlin: Springer; 2007.
[47] Huo S, Daye W, Wolfe F. New generation PM Al-materials for automotive applications. In: Russell A, Chernenkoff W, Brian J, editors. Proceedings of 2014 powder metallurgy World Congress. Orlando (FL, U.S.A.): Metal Powder Industries Federation; 2014. p. 09-137–09-44.
[48] Khambekar J, Pittenger BH. Understanding and prevention metal-dust hazards. Int J Powder Metall, MPIF, NJ (USA) 2013; 49(4): 39-47.
[49] NEFA. Standard of the prevention of fire and dust explosions of the manufacturing, processing and handling of combustible particulate solids. NEFA Standard 654, 2013.
[50] Schatt W, et al. Pulvermetallurgie: Technologien und Werkstoffe. 2nd ed. Berlin: Springer; 2007.
[51] Schaffer GB, Huo SH. Sintering of aluminum in various atmospheres. In: Advances in powder metallurgy and particulate materials, part 5. New York: MPIF; 2008. p. 25–31.
[52] Huo SH, et al. The effect of hydrogen on the sintering of PM aluminum alloys. In: Advances in powder metallurgy and particulate materials, part 5. New York: MPIF; 2010. p. 1–8.
[53] Lall C, Bishop P. Conventional powder metallurgy aluminum alloys. In: ASM handbook. vol. 7. ASM International Publishers; 2015. p. 581–90.
[54] Pohl A. Wear resistant sintered aluminium parts for automotive applications. Powder Metall 2006;49(2):104–6, http://www.tandfonline.com/doi/abs/10.1179/174329006X115984.
[55] Mais B, Müller A, Gradl J. Recent progress on standard PM aluminum premixes. In: Russell A, Chernenkoff W, Brian J, editors. Proceedings of 2014 powder metallurgy World Congress. Orlando (FL, U.S.A.): Metal Powder Industries Federation; 2014. p. 07-157–07-63.
[56] Elagin VI, Zakharov VV, Petrova AA, Vyshegorodzeva EV. Influence of scandium on structure and properties of alloys Al-Zn-Mg. Izv AN SSSR Metals 1983;4:180–3 [in Russian].
[57] Elagin VI, Zakharov VV, Pavlenko SG, Rostova TD. Effect of zirconium additions on ageing Al-Zn alloys. Phys Metal Res 1985;60(1):97–100 [in Russian].
[58] Rechkin VN, Lamikhov LK, Samsonova TP. Crystal structure of scandium aluminides. Kristallografija 1964;9(3):405.
[59] Elanzev AV, Lushnikova TV. Ageing kinetics of high-strength aluminum alloy 01970 obtained by granulation technique. In: Proceedings of the VII International scientific and technical Ural school-workshop of the metallographer-young scientists. Yekaterinburg: UGTU-UPI; 2006. p. 30–1 [in Russian].
[60] Keiser MS, Datta S, Roychowdhury A, Banerjee MK. Effect of Scandium on the microstructure and ageing behaviour of cast Al-6Mg alloy. Mater Charact 2008;59:1661–6.
[61] Davydov VG, Elagin VI, Zakharov VV, et al. About alloying of aluminum alloys by scandium and zirconium additions. MiTOM 1996;8:25–30.
[62] Milman YuV, Lotsko DV, Sirko OI. "Sc effect" of improving mechanical properties in aluminium alloys. Mater Sci Forum 2000; 331–337(2): 1107–12. Trans. Tech. Publications, Switzerland.
[63] Kendig KL, Miracle DB. Strengthening mechanisms of an Al-Mg-Sc-Zr alloy. Acta Mater 2002;50:4165–75.

[64] Inoue A, Matsumoto N, Masumoto T. Al-Ni-Y-Co amorphous alloys with high mechanical strengths, wide supercooled liquid region and large glass-forming capacity. Mater Trans JIM 1990;31(6):493–500.

[65] Yoshizava Y, Oguma S, Yamauchi KJ. New Fe-based magnetic alloys composed of ultrafine grain structure. Appl Phys 1988;64:6044–6.

[66] Suzuki K, Kataoka N, Inoue A, Masumoto T. High saturation magnetization and soft magnetiv properties of the Fe-Zr-B alloys with ultrafine grain structure. Mater Trans JIM 1990;31(8):743–6.

[67] Kawamura Y, et al. High-strength crystalline aluminum alloys produced from amorphous powder by a closed P/M processing. Mater Trans JIM 1993;34(10):969–75.

[68] Kawamura Y, Liu H-B, Inoue A, Masumoto T. Rapidly solidified powder metallurgy Al-Ti-Fe alloys. Scr Mater 1997;37(2):205–10.

[69] Neikov OD. Rapidly solidified aluminum alloy powders. In: Proceedings of 1998 Powder Metallurgy World Congress. vol. 1. Shrewsbury (UK): European Powder Metallurgy Association; 1998. p. 129–34.

[70] Neikov OD. Water atomized powder technologies for advanced aluminum alloy production. In: Proceedings of 2000 powder metallurgy World Congress. Kyoto: Japan Society of Powder Metallurgy; 2000. p. 464–6.

[71] Neikov OD, et al. Russian Federation Patent No 2,078,427, Dec. 1994.

[72] Neikov OD, Krajnikov AV, Sameljuk AV, Vasilieva GI, Chaykina NG. An experimental study of water atomisation of aluminum alloys. In: Proceedings of 2002 powder metallurgy World Congress. vol. 3. Orlando (USA): Publ. Metal Powder Industries Federation; 2002. p. 74–85.

[73] Zhuravlev VA, Zakharov AP. Oxidation of aluminum in water at different temperatures. Dokl AN USSR 1980;252(5):1162–6 [in Russian].

[74] Krajnikov AV, Gastel M, Ortner HM, Likutin VV. Surface chemistry of water atomized aluminium alloy powders. Appl Surf Sci 2002;191: 26–42.

[75] Krajnikov AV, Gastel M, Ortner HM. Surface characterisation of water-atomized Al-Zn-Mg-Cu alloy powders by SIMS and AES. Microchim Acta 2002;138:1–12.

[76] Burykin AA, Neikov OD, Rabin PB, Sharova LC. Microencapsulation of metal powders for prevention of explosions and dust emissions during their production and processing. Sov Powder Metall Met Ceram 1991;6:98–103.

[77] Neikov OD, Rabin PB, Vasiliyeva GI. Mcrocapsulated aluminium powders. Mater Sci Forum 1997;242:219–22.

[78] Neikov OD, et al. Features of drying water-atomized aluminum alloys powders. Powder Metall Metal Ceram 2013;52(5-6):241–6.

[79] Neikov OD, et al. Properties of rapidly solidified powder aluminum alloys for elevated temperatures produced by water atomization. In: Proceedings of 2002 World Congress of PM & particulate materials. vol. 7. Orlando (USA): Metal Powder Industries Federation; 2002. p. 14–27.

[80] Neikov OD, Milman YV, Miracle DB, Lotsko DV, Sirko AI, Zakharova NP. Effect of powder size on mechanical properties of elevated temperature aluminum alloys. In: Proceedings of PM 2001 Congress & Exhibition. Nice: European Powder Metallurgy Association; 2001. p. 225–30.

[81] Neikov OD, et al. Production method of semiproducts from aluminum alloys. Russian Federation Patent No 2,238,172, Jul. 2003.

[82] Gjostein NA. Alternative materials for a new generation of vehicles. Mater Sci Forum 1997;242:51–61.

[83] Tsubakino H, Yamamoto A, Kato T, Suehiro A. Precipitation in deformed Al-Fe and Al-Fe-Si dilute alloys. Mater Sci Forum 2000;331–337:951–6.

[84] Neikov OD, et al. Advanced PM aluminum alloys produced by new rapid solidification technology. In: Proceedings of PM2004 World Congress. Wien (Austria): European Powder Metallurgy Association; 2004. p. 237–42.

[85] Li PY, Dai SL, Li CY, Liu BC. Some developments in rapidly solidified aluminum alloys for elevated temperature applications. Acta Metall Sin 1999;12(4):452–61.

[86] Sheppard T, Ioannidis EK. Powder metallurgy aluminum alloys: characteristics of an Al–Cr–Fe rapidly solidified alloy. J Mater Sci 1990;25(9):3965–75.

[87] Srivatsan TS, et al. The quasistatic fracture behavior of a bulk Al–Cr–Fe alloy made by consolidating micron- and nanosized powders. J Metastable Nanocryst Mater 2005;23:255–8.

[88] Bowen AW, Gilmore CJ. Texture development in a hot-rolled rapidly quenched Al–Cr–Fe alloy. Text Microstruct 1991;14–18:1049–54.

[89] Garder R. Vapor deposition aluminum alloys. Mater Des 1989;10(6):274–9.

[90] Neikov OD, et al. Effect of starting powder properties on the structure and mechanical characteristics of Al–8Cr–1.5Fe alloy for high-temperature applications. Powder Metall Metal Ceram 2013;52(3-4):144–53.

[91] Neikov OD, Milman YV, Sirko AI, Sameljuk AV, Krajnikov AV. Elevated temperature aluminum alloys produced by water atomization. Mater Sci Eng A 2008;477(1–2):80–5.

[92] Milman YV, et al. Structure and properties of Al–Mg alloys depending on scandium and zirconium additions and production methods. Powder Metall Metal Ceram 2010;49(7–8):429–37.

[93] Neikov OD, et al. Advanced high-strength nanostructured Al-Mg alloys produced by new rapid solidification technology. In: Proceedings of PM 2010 World Congress, Florence (Italy), vol. 4. Bellstone Shrewsbury, UK: European Powder Metallurgy Association; 2010. p. 25–32.

[94] Bosch AJ, Senden R, Entelman W, Knüwer M, Palm F. Nanostructured and high strength alloys: scalmalloy—a unique high strength and corrosion insensitive AlMgScZr material concept. Aluminium Alloys. Wiley-VCH 2009; 1: 2215 – 23.

[95] Elagin VI, Zakharov VV, Filatov YA, Rostova TD. Development of advanced aluminum alloys alloyed by scandium, In: Bannyh OA, et al., editors. Prospective technologies of light and special alloys. Moscow: Fismathgis; 2006. p. 181–93 [in Russian]. https://books.google.com/books?isbn=5457966348.

[96] Elagin VI. Issues of developing Al–Zn–Mg alloys. Technol Light Alloys 1999;3:7–13.

[97] Milman YV, et al. Effect of doping with refractory rare-earth metals on the structure and properties of Al-5Zn-3Mg alloys produced by powder metallurgy and casting methods. Powder Metall Metal Ceram 2013;52(1–2):58–66.

[98] Neikov OD, Krajnikov OV, Milman YuV, et al. Method of producing semifinished articles from aluminum alloys [in Ukrainian], Ukrainian Patent 66588, Sep. 2005.

[99] Milman YV. Scandium influence on structure, mechanical properties and corrosion resistance of aluminum alloys. In: Advanced materials and technologies. Kiev (Ukraine): Vydavnichiy Dim Akademperiodika; 2003. p. 335–60.
[100] Singer ARE. Recent developments and opportunities in spray forming. In: Kolloquium des SFB 372 1:Bremen: University Bremen; 1996. p. 123–40.
[101] Brooks RG, Moore C, Leatham AG, Coombs JS. The Osprey process. Powder Metall 1977;(2):100–2.
[102] Annavarapu S, Apelian D, Lawley A. Processing effects in spray casting of steel strip. Metall Trans A 1988;190:3077–86.
[103] Lavernia EJ, Wu Y. Spray atomization and deposition. Chichester: John Wiley & Sons; 1996.
[104] Leatham AG, Lawley A. The Osprey Process: principles and applications. Int J Powder Metall 1993;29(4):321–9.
[105] Mathur P, Apelian D, Lawley A. Analysis of the spray deposition process. Acta Metall 1989;37(2):429–43.
[106] Bauckhage K. Atomization of molten metals. In: Proceedings of the international conference liquid atomization and spraying systems ICLASS-91 Gaithersburg (USA); 1991.
[107] Tsao CYA, Grant NJ. Modeling of the liquid dynamic compaction spray process. Int J Powder Metall 1994;30(3):323–33.
[108] Reichelt W. Stand der industriellen Anwendung des Sprühkompaktierens. In: Kolloquium des SFB 372, 1. Bremen: University Bremen; 1996. p. 189–98.
[109] Lawley A, Mathur P, Apelian D, Meystel A. Spray forming: process fundamentals and control. Powder Metall 1990;33:109–11.
[110] Ottosen P. Numerical simulation of spray forming. Ph. D. Thesis. Technical University Denmark, 1993.
[111] Mi J, Grant PS, Fritsching U, Belkessam O, Garmendia I, Landaherea A. Multiphysics modelling of the spray forming process. Mater Sci Eng A 2008;477(1–2):2–8.
[112] Fritsching U. Spray simulation–modeling and numerical simulation of sprayforming metals. Cambridge (UK): Cambridge Univ. Press; 2004.
[113] Hattel JH. Mathematical modelling and numerical simulation of casting processes. Ph.D. Dissertation. Lyngby Technical University Denmark, 1999.
[114] Hattel JH, Pryds NH, Pedersen TB, Pedersen AS. Numerical modelling of the spray forming process: the effect of process parameters on the deposited material. In: Bauckhage K, Uhlenwinkel V, Fritsching U, editors. Proceedings of the spray deposition and melt atomization conference SDMA 2000. Bremen: University Bremen; 2000. p. 803–12.
[115] Bergmann, D., Modellierung des Sprühkompaktierprozesses für Kupfer- und Stahlwerkstoffe. Dissertation Universität Bremen, 2000.
[116] Minisandram RS, Forbes Jones RM, Kelkar KM, Patankar SV, Carter Jr WT. Prediction of thermal history of preforms produced by the clean metal spray. Mater Sci Eng A 2002;326(1):184–93.
[117] Petersen K, Pedersen AS, Pryds N, Thorsen KA, List JL. The effect of particles in different sizes on the mechanical properties of spray formed steel composites. Mater Sci Eng A 2002;326(1):40–50.
[118] Pryds N, Hattel JH, Pedersen TB, Thorborg J. An integrated numerical model of the spray forming process. Acta Mater 2002;50:4075–91.
[119] Singer ARE. Metal matrix composites made by spray forming. Mater Sci Eng A 1991;135:13–7.
[120] Lawley A, Apelian D. Spray forming of metal matrix composites. In: Wood JV, editor. Proceedings of the second international conference on spray forming (ICSF2). Swansea (UK): Woodhead Publishing; 1993. p. 267–73.
[121] Gupta M, Juarez-Islas J, Frazier WE, Mohamed F, Lavernia EJ. Microstructure, excess solid solubility and elevated-temperature mechanical behavior of spray-atomized and codeposited Al-Ti-SiCp. Metall Trans B 1992;23:719–36.
[122] Srivatsan TS, Lavernia EJ. Use of spray techniques to synthesize particulate-reinforced metal-matrix composites. J Mater Sci 1992;27(22):5965–81.
[123] Wo Y, Lavernia EJ. Interaction mechanisms between ceramic particles and atomized metallic droplets. Metall Trans A 1992;23(10):2923–35.
[124] Markus S, Fritsching U. Spray forming with multiple atomisation. In: Proceedings of 2nd spray deposition and melt atomization conference. Bremen: Universität Bremen; 2003. p. 8-3–8-16.
[125] Müller HR. Eigenschaften und Einsatzpotential Sprühkompaktierter Kupferlegierungen. In: Kolloquium des SFB 372. vol. 1. Bremen: Universität, Bremen; 1996. p. 33–56.
[126] Hummert K. Sprühkompaktieren von aluminumwerkstoffen im industriellen maßstab—Stand der Entwicklung. In: Kolloquium des 372. vol. 1. Bremen: Universität, Bremen; 1996. p. 199–215.
[127] Kozarek RL, León DD, Mansour A. An investigation of linear nozzles for spray forming aluminum sheets. In: Kolloquium des SFB 372. vol. 1. Bremen: Universität, Bremen; 1996. p. 141–60.
[128] Müller FG, Benz MG, Carter Jr. WT, Forbes RM, Leatham A. Neues Verfahren zur Herstellung von Pulver, Formteilen oder halbzeugen aus titan oder keramikfreien superlegierungen. In: Kolloquium des SFB 372. vol. 1. Bremen: Universität, Bremen; 1996. p. 169–88.
[129] Lavernia EJ. Spray atomization and deposition of metal matrix composites. In: Kolloquium des SFB 372. vol. 1. Bremen: Universität, Bremen; 1996. p. 63–122.
[130] Ebert T, Moll F, Kainer KU. Sprühkompaktieren von Magnesiumlegierungen. In: Proceedings of 3rd international conference on spray forming, Cardiff; 1996. p. 177–85.
[131] White J, Mingard K, Hughes IR, Palmer IG. Aluminum alloys with unique property combinations by spray casting. In: Proceedings of 2nd international conference on spray forming 1993, Swansea. Cambridge (UK): Woodhead Publ. Ltd; 1993. p. 355–64.
[132] Palmer IG, Chellman DJ, White J. Evaluation of a spray deposited low density Al-Li alloy. In: Proceedings of 2nd international conference on spray forming 1993, Swansea. Cambridge (UK): Woodhead Publ. Ltd; 1993. p. 385–92.
[133] Oda T, Hata H, Ehira M. Development of ultra high strength aluminum alloy by spray forming. In: CD proceedings of the 4th spray deposition and melt atomization conference SDMA 2009. Bremen (Germany): Universität Bremen; 2009. p. 1–12.
[134] Baiqing X, et al. On the microstructures of spray-deposited and homogenized Al-Zn-Mg-Cu alloys. In: CD proceedings of the 4th spray deposition and melt atomization conference SDMA. 2009. Bremen (Germany): Universität Bremen; 2009. p. 1–4.

[135] Guowei Z. The natural aging behavior of super-high strengths aluminum alloys by spray forming. In: CD proceedings of the 5th spray deposition and melt atomization conference SDMA 2013. Bremen (Germany): Universität Bremen; 2013. p. 1–8.

[136] Srivastava VC, et al. Development of bulk quasicrystalline materials by spray forming. In: CD proceedings of the 5th spray deposition and melt atomization conference SDMA. 2013. Bremen (Germany): Universität Bremen; 2013. p. 1–15.

[137] Siemers PA, Jackson MR, Mehan RI, Rairden III JR. Production of composite structures by low-pressure plasma deposition. Ceram Eng Sci 1985;6(7–8):896–907.

[138] Ng HW, Remesh K, Devasenapathi A, Yu SCM, Kang CW. Simulation on deposit topology in the plasma spray process. In: Proceedings of 2nd spray deposition and melt atomization conference. Bremen: Universität Bremen; 2003. p. 8-53–8-65.

[139] Planche MP, Normand B, Suzon E, Coddet C. The relationships between in-flight particle characteristics and coating properties under plasma spraying. In: Proceedings of international thermal spray conference; 2001. p. 771–7.

[140] Pershin L, Pasandideh-Fard M, Mostaghimi J, Chandra S. In: Effect of substrate properties on the formation of plasma sprayed alumina splats. In: Proceedings of international thermal spray conference; 2001. p. 813–20.

[141] Pershin L, McDonald A, Chandra S. Effect of substrate oxidation on the spreading of plasma-sprayed nickel. In: Proceedings of 3rd spray deposition and melt atomization conference. Bremen: Universität Bremen; 2006. p. 56-1–56-11.

[142] Pasandideh-Fard M, Bhola R, Chandra S, Mostaghimi J. Deposition of tin droplets on a steel plate: simulations and experiments. Int J Heat Mass Transf 1998;41:2929–45.

[143] McHugh KM, Delplanque JP, Johnson SB, Lavernia EJ, Zhou Y, Lin Y. Spray rolling aluminum alloy strip. Mater Sci Eng A 2004;383(1):96–106.

[144] McHugh KM, Lin Y, Zhou Y, Lavernia EJ, Delplanque JP, Johnson SB. Spray rolling aluminum alloy strip for transportation applications, materials processing and manufacturing division. In: Sixth global innovations proceedings: trends in materials and manufacturing technologies for the transportation industry and powder metallurgy research and development in the transportation industry. San Francisco (CA): TMS; 2005. p. 219–24.

[145] Gras C, Meredith M, Hunt JD. Microstructure and texture evolution after twin roll casting and subsequent cold rolling of Al-Mg-Mn aluminum alloys. J Mater Process Technol 2005;169:156–63.

[146] Sun N, Patterson Burton RB, Suni JP, Simielli EA, Weiland H, Allard LF. Microstructural evolution in twin-roll cast AA3105 during homogenization. Mater Sci Eng A 2006;416:232–9.

[147] Yun M, Lokyer S, Hunt JD. Twin roll casting of aluminum alloys. Mat Sci Eng A 2000;280:116–23.

[148] McHugh KM, Lin Y, Zhou Y, Johnson SB, Delplanque J-P, Lavernia EJ. Microstructure evolution during spray rolling and heat treatment of 2124 Al. In: Proceedings of 3rd spray deposition and melt atomization conference. Bremen: Universität Bremen; 2006. p. 51-1–51-12.

[149] Larsen DE, Adams ML, Kampe SL, Chritodoulou L, Bryant JD. Influence of matrix phase morphology on fracture toughness in a discontinuously reinforced XD titanium aluminide composite. Scr Metall 1990;24:851–6.

[150] Marcus HL, Bourell DL. Solid preform fabrication finds new application. Adv Mater Process 1993;144(3):28–35.

[151] Studt T. Rapid prototyping key to fast development. R&D Mag 1994;55–6.

[152] Belyavin K, Minko D, Bykov R, Kuanichik O. Investigation of pulse-periodical laser radiation power effect on stability of liquidmetallic contacts between powder particles by selective laser sintering. In: Proceedings of 2006 powder metallurgy World Congress. Busan (Korea): Korean Powder Metallurgy Institute; 2006. p. 911–2.

[153] Munir ZA. The synthesis and consolidation of powders by self-propagating combustion methods. Rev Part Mater 1993;1:41–74.

[154] Mortensen A, Koczak MJ. The status of metal matrix composite research and development in Japan. JOM 1993;45(3):10–8.

[155] Ford R. Recent developments in functionally gradient materials. Mater Process Rep 1992;1–6.

[156] Song DH, et al. Thermomechanical properties of functionally gradient Al-SiC$_p$ composites. In: Proceedings of 2006 powder metallurgy World Congress. Busan (Korea): Korean Powder Metallurgy Institute; 2006. p. 87–8.

FURTHER READING

[157] Herrera EJ, Gallardo JM, Rodriguez JA. New way to consolidate mechanically alloyed aluminum powder. In: Proceedings of 1998 Powder Metallurgy World Congress, compiled by European Powder Metallurgy Association (UK), vol. 1. ; 1998. p. 317–22.

[158] Powder metallurgy. In: Metals handbook. 9th ed. vol. 7. American Society for Metals; 1984.

[159] Aluminum and aluminum alloys. In: ASM speciality handbook. Metals Park (OH, USA): ASM International Publishers; 1993.

[160] Jung TK, Sung TJ, Kim MS, Kim WY. A comparative study of mechanical property in Al-8Fe-2Mo-2V-1Zr bulk alloys fabricated from an atomized powder and melt spun ribbon. In: Proceedings of 2006 Powder Metallurgy World Congress. Busan (Korea): Korean Powder Metallurgy Institute; 2006. p. 1105–6.

[161] Genkava T, Yamasaki M, Kavamura Y. Microstructure and mechanical properties of rapidly solidified powder metallurgy Al-Fe-V-Si-X. In: Proceedings of 2006 Powder Metallurgy World Congress. Busan (Korea): Korean Powder Metallurgy Institute; 2006. p. 1123–4.

[162] Cooke RW, et al. Effect of Zr additions on the sintering response of an Al-Cu-Mg PM alloy. In: Proceedings of the 2012 international conference on powder metallurgy and particulate materials. Nashville (TN, U.S.A.): MPIF; 2014. p. 7155–69.

[163] Zakharov VV, Rostova TD. High-strength weldable alloy 1970 on the Al–Zn–Mg system base. Metal Sci Heat Treatment Metals 2005;4:10–7.

Chapter 17

Production of Magnesium and Magnesium Alloy Powders

Oleg D. Neikov* and **Victor G. Gopienko**†

**Frantsevich Institute for Problems of Materials Science (IPMS), Kiev, Ukraine, †All-Russian Aluminum-Magnesium Institute, Saint Petersburg, Russia*

Chapter Outline

Introduction 533
Production Methods 533
  Mechanical Crushing 533
  Melt Atomization 535
  Production of Magnesium Granules 538
  Gas-Phase Method 539
  Electrolysis 540
  Plasma-Transferred Arc Melting Process 540
Applications 541
References 546

INTRODUCTION

Powders and granules of magnesium and their alloys find various applications in modern technology, such as modifying metallurgical properties of metals; manufacturing Grignard reagents [1] that are used in organic synthesis to produce pharmaceuticals, perfumes, and other fine chemicals; chemical reduction; additives in electric welding electrode flux; and manufacture of corrosion-resistant constructional purpose details.

Magnesium-based alloys are used in various applications in the aerospace, automotive, and 3C (computer, communication, and consumer electronics products) industries. These applications are driven largely because of a combination of low density, low melting point, good castability, and high specific stiffness of magnesium alloys. Further, high-strength, magnesium-based alloys also have the potential to be used as lightweight armor, which can provide superior protection against modern threats [2]. These applications demand high strength and high ductility that cannot be achieved by the traditional casting process.

Powder metallurgy offers a unique route to targeting novel compositions and unique microstructures leading to high-performance lightweight magnesium applications. Rapidly solidified powder and the use of nanostructured powder have been studied and reported in the literature with promising results [3–7].

Magnesium is a reactive material like aluminum and titanium (Table 17.1). The heat of formation, ΔH_0, of magnesium oxide equals of 603.2 kJ/mol. Magnesium is potentially explosive in the powder form. The lower explosive limit of the powder with particles smaller than 74 μm amounts to 10 g/m^3 and the rate of pressure rise equals 6.3 MPa/s (see Chapter 27). The development of the production methods should take into account these features of magnesium.

PRODUCTION METHODS

The basic methods of magnesium powder production are mechanical crushing (scratching of an ingot from magnesium card tape fixed on a rotating drum, milling of an ingot), atomization of molten metal, evaporation-condensation, and electrolysis.

Mechanical Crushing

The first industrial production of magnesium powder originated for pyrotechnic purposes in the early 20th century in Germany. The method consists of scratching a magnesium ingot by a card tape fastened on a rotating drum. The machine tool intended for this process, the "kratz machine," has been improved for a long time. Powder dispersivity is adjusted by the speed of magnesium plate feeding, the speed of drum rotation, and the diameter of the card tape needles. The drum

Handbook of Non-Ferrous Metal Powders. https://doi.org/10.1016/B978-0-08-100543-9.00017-8
© 2019 Elsevier Ltd. All rights reserved.

TABLE 17.1 Properties of Reactivity of Mg in Comparison With Al and Ti

				Heat of Fusion		Specific Heat Capacity		Combustion[a]	Heats of Formation Oxides		
										Heat of Formation (ΔH_0)[b]	
Material	**Density (g/cm^3)**	**Melting Point (Approximate) (K)**	**Boiling Point (K)**	**kJ/mol**	**cal/mol**	**J/g·K**	**cal/g·K**	**K**	**Oxide**	**kJ/mol**	**cal/mol**
Magnesium	1.74	922	1363	8.954	2.139	0.90	0.215	3373	MgO	−603.2	−144.090
Aluminum	2.70	933	2740	10.790	2.577	1.02	0.244	3773	Al_2O_3	−1691.5	−404.080
Titanium	4.51	1993	3560	15.450	3.690	0.52	0.124	3273	TiO_2	−955.9	−228.360

[a] *Source: Ref. [7].*

[b] *The adiabatic combustion temperature in oxygen at 100 kPa pressure.*

moved along its axis to enable the entire plane of the plate to be processed uniformly. Abrasion uniformity is provided by a continuous back and forth motion of the plate, which entered into the case of the machine tool through a special aperture. The card tape is reeled on a steel drum. The diameter of the drum is commonly 200 mm; the needle speed on the surface is about 1000 m/min. The thickness of the magnesium plate is usually 40 mm by 350 mm width. The minimal diameter of the card tape needles was 0.64 mm. To prevent sparking while the needles are falling out from the tape, the case of the kratz machine is manufactured of aluminum-magnesium alloy. The received powder gets into a box, which is installed in the casing of the kratz-machine. The finest magnesium powders—"suspended" (intangible by touch) were produced by additional crushing of the powder manufactured in the kratz machine in ball mills in the atmosphere of carbon dioxide.

Magnesium chips and grit are also produced by cutting cylindrical blanks 200–300 mm in diameter in a lathe using a special sawtooth cutter. The average particle size is 1 mm; the content of particles smaller than 0.75 mm in size is not higher than 35 wt%. The capacity of the machine tool is 8.8–15 kg/h.

Along with other methods, a method to produce magnesium powders by milling an ingot with subsequent crushing of the chips in a grinding machine and a hammer mill is applied in the United States. This method is more efficient than the above method of producing powders with the help of the card tapes. Special machine tools equipped with vertical and horizontal cutters are used. The produced chip-shaped powder is sucked into the collecting system, precipitates in a cyclone, and is divided by a screening machine to commodity fractions by particle size. The smallest fractions are caught by an oil filter placed in front of a ventilator. When necessary, powders are exposed to rolling in a ball mill for obtaining particles with a spherical shape (Fig. 17.1).

Characteristics of the powders produced by the method of mechanical grinding are given in Table 17.2. These powders commonly contain not <99.5% Mg and not >0.05% Fe, 0.005% Cl, and 0.1% of moisture (in weight).

Melt Atomization

Magnesium powders produced by inert gas atomization are polydisperse and have a particle size from several microns up to 0.5–1 mm. The hardware for the atomization is similar to that used for producing aluminum powders (see Chapter 15). Powders are classified into required fraction particle sizes.

The technology developed in VAMI (the Russian National Aluminum-Magnesium Institute) consists of atomization of the melt by jets of nitrogen with an oxygen additive of 3 ± 0.1 wt% while the melt temperature was 50–70°C higher than the melting point of magnesium or its alloy [8]. An optimum relation between the temperature of the melt and the atomizing gas, the pressure of the gas, the ratio of gas to metal mass flow, and other parameters as well as the optimum hardware-technological circuit of production provide fire and explosion safety for manufacture. Magnesium powders with the particle size smaller than 200 μm ranging from spherical (particles smaller than 50–100 μm) to oval (larger particles) are produced by this technology.

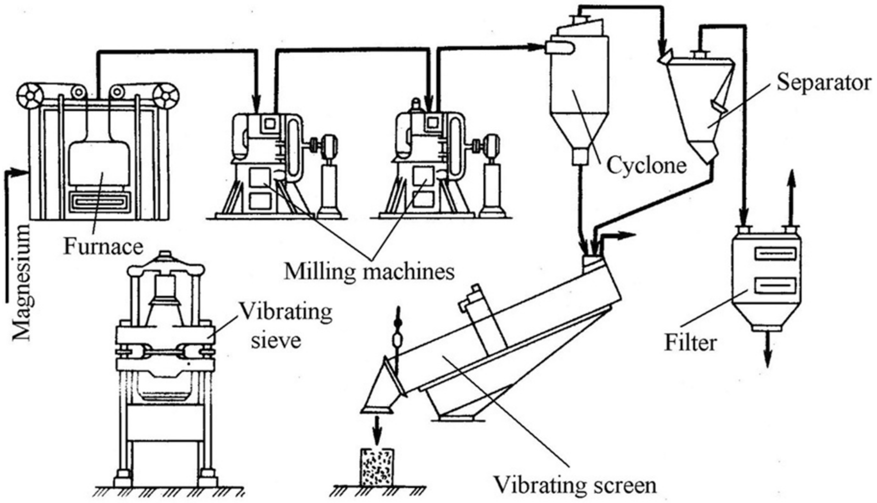

FIG. 17.1 The hardware-technological circuit of magnesium powder production.

TABLE 17.2 Properties of Typical Commercial Grades of Magnesium Powders

Type	Chemical Requirements (wt%) Max			Apparent Density (g/cm^3)	Particle Size Distribution (μm)	Source
	Mg	Alloying Elements	Admixture			
Turnings and chips						
LNR 11	99.5 min	…	…	0.4	1000–3000	ECKA
LNR 15	99.5 min	…	…	0.5	300–600	ECKA
LNR 16	99.5 min	…	…	0.6	3000–4000	ECKA
AZ91D	90	9Al-1.0Zn	…	0.6	1000–3000	ESKA
MG Turnings/ chips	…	…	…	…	(3–6 mm) × (<1 mm) × (5–15 mm) (<2 mm) × (1 mm) × (<8 mm)	JLM
MG Alloy scrap	…	…	…		+2.8 mm <2% −0.85 mm <5%	JLM
Powders						
PF 01/91	99 min	…	…	0.9	315–630	ECKA
PF 91/51 Type III	99.5 min	…	…	0.7	100–315	ECKA
PK 31 Type IV	97 min	…	…	0.5	<71	ECKA
Pure magnesium	99.8		Cu (0.02% max) Pb (0.01% max) Mn (0.1% max) Ni (0.001% max) Na (0.006% max) Sn (0.01% max)		A: +200 mesh: 0.5% max −325 mesh: 60% max B: + 200 mesh: 0% max −325 mesh: 95% min	MEP
Electron MAP+21	Bal.	2.7Nd, 1.3Gd, 0.3Zn, 0.6Zr/wt%	…	…	A: <150 μm; d_{50} = 90 μm B: <25 μm	MEP
Electron MAP+43	Bal.	4Y, 3Nd, 0.5Zr/wt%	…			ME
Electron MAP+91	Bal.	(8.5–9.5)Al, (0.45–0.9) Zn, (0.17–0.3)Mn/wt%				MEP
Electron MAP 21	Bal.	2.7Nd, 1.3Gd, 0.3Zn, 0.6Zr/wt%	…	…	(A) 80 × 325 size: +80 mesh: 5% max −325 mesh: 20% max (D) 325 × D size: +325 mesh: 5% max −325 mesh: balance	MEP
Electron MAP 43	Bal.	2.7Nd, 1.3Gd, 0.3Zn, 0.6Zr/wt%	…	…		MEP
Electron MAP 91	Bal.	(8.5–9.5)Al, (0.45–0.9) Zn, (0.17–0.3)Mn/wt%	…	…		MEP

Electron 21	Bal.	2.7Nd, 1.3Gd, 0.3Zn, 0.6Zr/wt%	…	…	−80 + 325 mesh size: +325 mesh: 5% max	MEP
AZ31 B	Bal.	3Al, 1Zn, 03Mn	…	…		MEP
AZ91 E	Bal.	(8.5–9.5)Al, (0.45–0.9) Zn, (0.17–0.3)Mn/wt%	…	…		MEP
WE43B	Bal.	4Y, 3Nd, 0.5Zr/wt%	…	…		
MG Powder	…	…	…	…	18–80 mesh (1.0 – 0.6 mm); 40–90 mesh (0.425–0.17 mm)	JLM
Passivation MG powder	…	…	…	…		JLM

Companies producing the commercial powders: ECKA, Eckart-Werke (trading companies: Eckart Austria and Eckart Switzerland); MEP, Hard Metals Inc. (Magnesium Electron Powders, PA, United States); Niagara Metallurgical Products Ltd. (Canada); JLM-Hebi City, Jiang Lang Metal Co. Ltd. (China).

Production of Magnesium Granules

Granulated magnesium is produced by atomization of the melt with the use of a salt flux for the protection of the metal against oxidation [8]. A flowchart of the spinning cup granulation process is represented in Fig. 17.2. The atomizing chamber, in which the magnesium melt atomization, cooling, and collection of the formed granules are carried out, has an internal diameter of 3.2 m. In the center of the chamber, a spinning cup with punched walls is placed; its rotation speed is in the range from 800 to 1600 rpm. The melted magnesium is introduced from the furnace into the spinning cup by a siphon. Simultaneously, the salt flux protecting magnesium from oxidation is brought into the spinning cup.

The flying out melt droplets through punched spinning cup walls under centrifugal force into the chamber are solidified in flight before colliding with chamber walls. With the help of a screw and pneumatic transport, the produced granules are removed from the chamber and sieved into size fractions. The fraction of 1.6–0.5 mm is a commercially useful fraction, the yield of which is higher than 90%–95%. The apparent density of granules is 0.85–0.95 g/cm^3. The granules consist of 90%–95% spheroidal particles while the content of the needle-shaped ones must not exceed 10% because, by their greater content, the flow rate deteriorates. A micrograph of spheroidal and needle-shaped magnesium granule particles is represented in Fig. 17.3. The capacity of the device is of 8000–10,000 tonnes/year.

Granules contain from 80 to 96 wt% of active magnesium while the rest is an oxide-salt film that can be separated from metal particles by abrasion, screening, or dissolution of the crushed salt phase. Afterward, the content of active magnesium in granules achieves 98.5–99.5 wt%. Application of such granulated magnesium is effective for desulfurization and modifying of pig iron, thermochemical and thermoacid processing of oil wells in the oil-extracting industry, and magnesium-organic synthesis of polyorganosiloxanes.

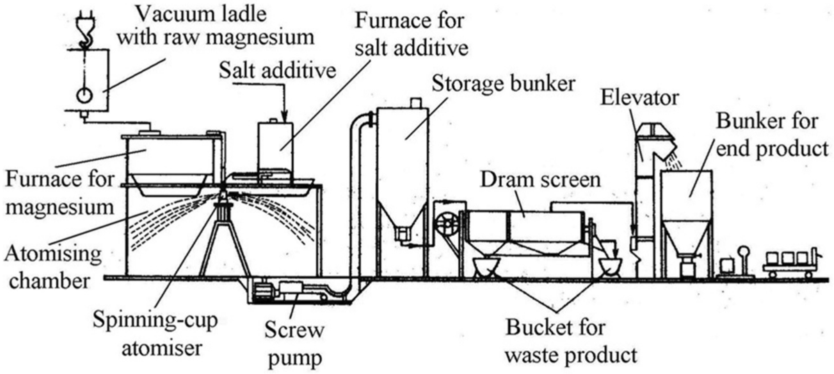

FIG. 17.2 Flowchart of the spinning cup magnesium granulation process.

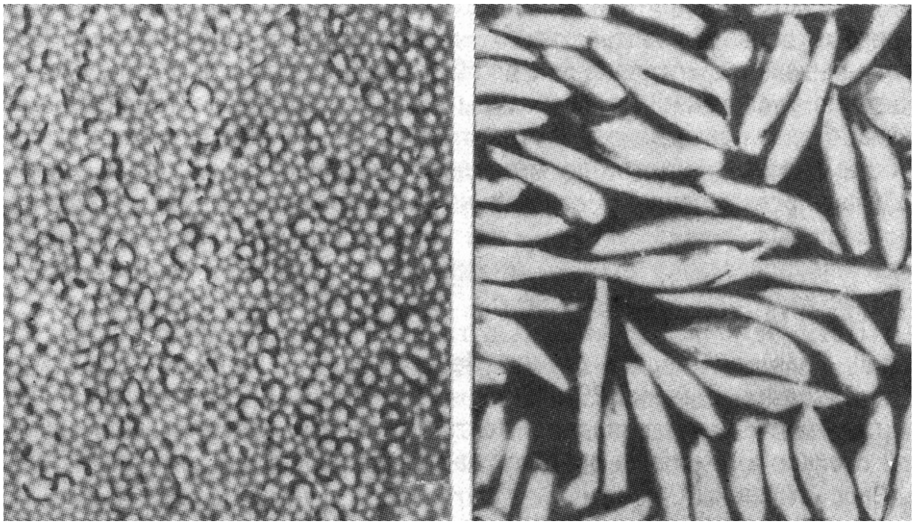

FIG. 17.3 Micrograph of spheroidal and needle-shaped magnesium granule particles with various magnification.

In Russia, devices for producing large granules (5–20 mm in diameter) by the atomization of molten magnesium in a fusible mix of alkaline chlorides and alkaline earth metals are used. The molten magnesium is atomized on the surface of a fusible salt melt at a temperature of 723–773 K. The metal drops solidify into granules from 3 to 25 mm in size and emerge on the melt surface, where, with the help of a scoop with a perforated bottom, they are separated from the salt melt and thrown into a rotating cooler drum. Granules at a temperature of 473–523 K are fed into a drum-type screening device for the separation of the commodity fraction (5–20 mm in diameter). The commodity fraction contains 1.5%–2.0% of salts.

The productivity of the device as a saleable fraction is from 1200 to 1500 kg/h with a yield of 90%–92%. It was found that the temperature of the molten salt (the temperature of the melted magnesium was maintained automatically in the interval 980 ± 10 K) exerts a principal influence on the saleable fraction yield. Its maximum is observed at temperatures of 773–823 K; when the salt melt temperature is raised to 873 K, the fraction of >15 mm consists almost completely of nonspherical particles. For manufacturing granules smaller in size, the installation with the spinning cup running at rotational speeds from 3000 to 10,000 rpm is used [9].

In the VSMPO-AVISMA Corporation (or metal-producing company of Verkhnyaya Salda, Russia), a granulated magnesium technique was developed consisting of magnesium melt or its alloys together with the salt mix and insertion into the melt of a dispersing agent (silicon oxide) with active stirring of the melt for metal dispersion. Then the melt is cooled to a temperature below the melting point of the metal, and granules are taken from the melt. The extracted granules are separated from solid chloride salts by screening. The granulated magnesium particles are roundish. The material is not caked and possesses good flowability that provides good pneumatic transport in the technological process. Granules are also produced from alloys of magnesium alloyed by aluminum, zinc, titanium, and other elements.

Coarse spherical granules of magnesium are produced by the technology based on the disintegration of liquid-metal magnesium jets in a molten salt. Molten metal in the form of the jets of the required diameter moving with a set speed is inserted into the salt melt, the temperature of which is lower than the temperature of magnesium crystallization. Fluctuations of internal pressure are created in metal jets with the help of the magneto-hydrodynamic method (MGD), and they are transformed into fluctuations of the jet surface, resulting in their disintegration into drops of equal size. Drops are cooled to ambient temperature and separated from molten salt as granules.

The technology allows the production of granules of magnesium and magnesium alloys of predetermined size in the range from 3 to 30 mm in diameter. The obtained granules are characterized by a dense structure; they contain up to 98% metallic magnesium and not >2% chloride. Apparent density of the product is 1.1 g/m^3.

Coarse spherical granules of magnesium of 5–15 mm in diameter are used for the production of organosilicon compounds by the method of continuous magnesium-organic synthesis. It is necessary to use large and heavy granules because granules of smaller sizes and thus a smaller weight are carried away with the products of synthesis. This increases the explosion hazard of the process due to secondary reactions with the formation of hydrogen. Such granules have a dense structure and a high content of the basic component—magnesium.

A method of producing fine spherical granules of magnesium was developed in the VSMPO-AVISMA Corporation. This method is based on capillary disintegration of magnesium jets under the action of regular fluctuations of the pressure created in the metal by the MGD method. In this technique, the inert atmosphere is used only during jet disintegration and drop spheroidization. Further, the drops get into the air atmosphere where they are finally crystallized and cooled down to the required temperature. The method is economical and does not demand a hermetic chamber. The method produces granules of the narrow size between 0.3 and 30 mm in diameter. Granules have a shining metal surface and a spherical shape. The apparent density of the granules is 1.0–1.1 g/cm^3. The content of metallic magnesium is 99.7% min.

A magnetic field facilitates a refining of a granule structure and hence expands the area of their usage not only as a chemical reagent (ferrous and nonferrous metallurgy, chemical industry, etc.), but also in powder metallurgy for producing high-strength materials by virtue of their low density. Such products are potentially suitable for mechanical engineering applications, including aviation and space technology.

The VSMPO-AVISMA Corporation developed a method of atomizing the molten magnesium by a magnetodynamic method in air. It is based on the discovery that magnesium droplets do not ignite in a strong magnetic field. The technology allows the production of monodisperse granules of equal size, shape, and weight with average characteristics varying within the ranges: weight of one granule, from 0.1 to 20 mg; size of granules (diameter of the head part), 0.3–3.0 mm; length of the granule, 1.5–15 mm; apparent density, 0.3–0.9 g/cm^3; content of metallic magnesium, >99.5% or >99.8%. The technology is used at the Solikamsk magnesium factory.

Gas-Phase Method

A high steam tension of magnesium vapor allows the use of the method of magnesium evaporation and vapor condensation for the production of fine magnesium powders. Two known types of gas-phase precipitation, physical vapor deposition

(PVD) and chemical vapor deposition (CVD), are described in Chapter 5. The PVD process includes melting the metal, vaporization of the melt, feeding the vapor into the zone of condensation, condensing the vapor into powder either in the free space or on a cooled surface (in a static or moving gas medium), and accumulating the powder in the cold part of the volume. The process is carried out in the presence of a neutral gas, sometimes with the addition of an oxidant or, on the contrary, of a passivating agent. The evaporation of the material is performed by an electron beam or a magnetron sputtering laser, either in a resistance or induction furnace.

Frishberg et al. reported about magnesium powder production by the gas-phase method on installation utilizing an induction furnace for the metal evaporation [10]. The vapor condensation in this installation is carried out in vacuum or in a rarefied atmosphere of inert gases. Vapor is condensed on a cooled brass drum 220 mm in diameter with its rotation speed being controlled; a knife cuts off the condensate. A graphite crucible containing the melt is closed by a cover with an adjustable tapping. Mixing vapor with the inert gas takes place in a special branch pipe. An end face of a branch pipe closely approaches the rotating surface of a crystallizer. Heating of the crucible is inductive. For producing magnesium powder with a particle size smaller than 1 μm, the temperature of the melt was 993 K, the gas pressure was 13.3 Pa, and the rotation frequency of the condenser was $0.75\,\mathrm{min}^{-1}$. Key process parameters consist of the temperature of metal evaporation and condensation, the nature and pressure of the inert gas, and the method and rate of condensate removal from the condensation zone.

Electrolysis

Crystalline magnesium in powder condition is precipitated on a cathode by electrolysis of the fusible melts down the magnesium melting point [8]. The melts contain magnesium chloride such as KCl-$MgCl_2$, KCl-NaCl-$MgCl_2$, KCl-Li; KCl-NaCl-$BaCl_2$, and $MgCl_2$ are usually used in the capacity of electrolytes. Soluble (magnesium, magnesium-based alloys) and insoluble (graphite) anodes are applied. The melt temperature is in the 673–793 K range, the current density on the anode is in the 0.1–0.5 $\mathrm{A/cm^2}$ range, and on the cathode is in the 0.4–2.0 $\mathrm{A/cm^2}$ range. The current yield reached 90%. The electrolytic magnesium powders are characterized by dendrite and acicular shapes and form the aggregates of 100–300 μm size while the sizes of separate crystals are from 5 to 60 μm. The dispersivity of powder particles is reduced with increasing temperature and duration of electrolysis and rises with current density increasing. The powders differ by high chemical purity.

Plasma-Transferred Arc Melting Process

For the purpose of improvement in alloying magnesium base alloys, Withers et al. applied a melting process with utilization of a plasma transferred arc (PTA), producing a mini melt pool [11]. The authors reported that mini pools of a 10–50 g size are small enough with rapid cooling to prevent density segregation and loss by volatilization. A PTA arc generates considerable stirring and oscillation in the mini pool that provides immediate solution of the additive alloying element. An illustration of a PTA torch that generates mini pools in the general size range of 10–20 mm diameter and 5–15 mm deep is shown in Fig. 17.4. An operating PTA system includes powder and wire feeders to add alloying elements to the basic mini melt pool of Mg, Al, or Ti.

FIG. 17.4 Schematic view of a plasma transferred arc (PTA) torch that produces a mini melt pool.

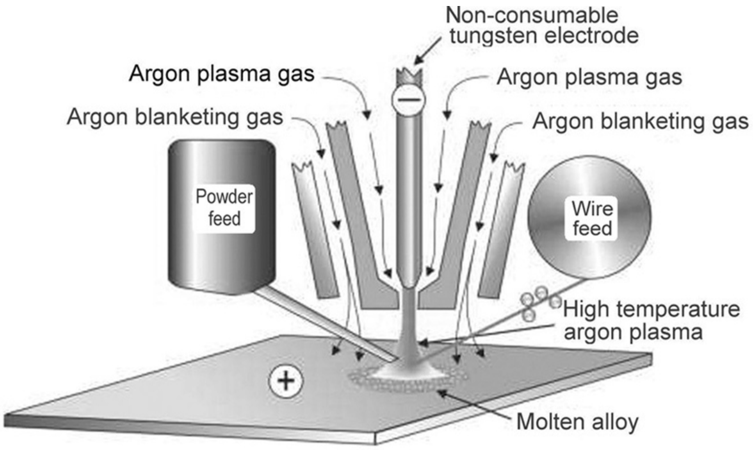

The alloy of nonequilibrium and immiscible constituents such as magnesium and titanium was synthesized as 50 Mg-50Ti by PTA mini pool processing. This alloy showed a flexure strength of approximately 500 MPa.

APPLICATIONS

Powders and granules of magnesium and their alloys find various applications in modern technology, including:

- Modifying metallurgical properties of metals, such as in the production of wrought steel and the removal of sulfur from hot iron products of blast furnaces.
- Manufacture of Grignard reagents, which are organometallic halides such as ethyl magnesium chloride (C_2H_5MgCl) that are used in organic synthesis to produce pharmaceuticals, perfumes, and other fine chemicals.
- Chemical reduction, as in the manufacture of beryllium and uranium.
- Additives in an electric welding electrode flux.
- Action as a light source in flares and photoflash bombs.
- Production of constructional purpose details in cases where only magnesium alloy powders and granules are applied.
- As an initial material for producing constructional products by the technique of the so-called thixotropic shaping, a new version of casting under pressure.

Nowadays, one of the basic consumers of granulated magnesium is ferrous metallurgy, where granulated magnesium in the pure state or as a mixture with lime and calcium carbide is applied for out-of-furnace pig-iron desulfurization. Granulated magnesium with a salt coating is applied in the pure state due to fire and explosion safety that provides the maximum effect.

Granulated magnesium is also applied in the structure of the so-called "powder" wire used for desulfurization of pig-iron by insertion of a wire into a ladle of melted pig-iron. Granulated magnesium with a salt coating is used in the production of high-strength spheroidal graphite cast iron.

Granulated magnesium with salt additives can be effectively used as a source of hydrogen production.

Granulated magnesium of various coarseness (from 1 to 20 mm) is used in the development of effective technologies for the synthesis of silicon-organic monomers.

There is expected to be a consumption growth for fine granules of magnesium alloys in the production of computers, mobile phones, and in the motor industry, where manufacture of thin-walled details by the method of thixomoulding is required. The efficiency of this method significantly depends on the method of granule production as well as their structure and size.

Spheroidal magnesium alloy powders of the three compositions (Table 17.2) for additive manufacturing technologies (trade name: Electron MAP+) are manufactured by HARD METALS Inc. (Magnesium Electron Powders). These powders are inert gas atomized and typically available in particle sizes as: (A) $<150\,\mu m$ ($d_{50}=90\,\mu m$) and (B) $<50\,\mu m$ ($d_{50}=25\,\mu m$). A micrograph of characteristic Electron MAP+ powder particles is represented in Fig. 17.5.

These powders are intended for use by selective laser sintering, direct laser sintering, electron beam melting, direct metal deposition, laser engineering net shapes, cold spray deposition, and other PM technologies.

The gas atomized powders (trade name: Electron MAP) with compositions such as Electron MAP+ powders are available in particle size as: (A) 80 × 325 size: +80 mesh (177 μm) of 5% max, −325 mesh (44 μm) of 20% max, and

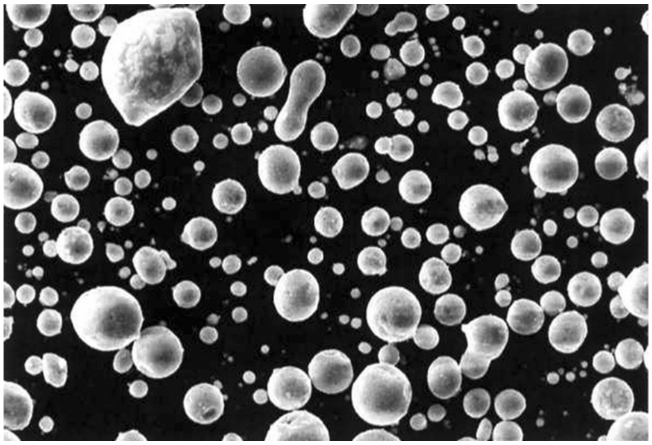

FIG. 17.5 Micrograph of characteristic Electron MAP+ magnesium alloy powder particles. *(Courtesy of Magnesium Electron Comp.)*

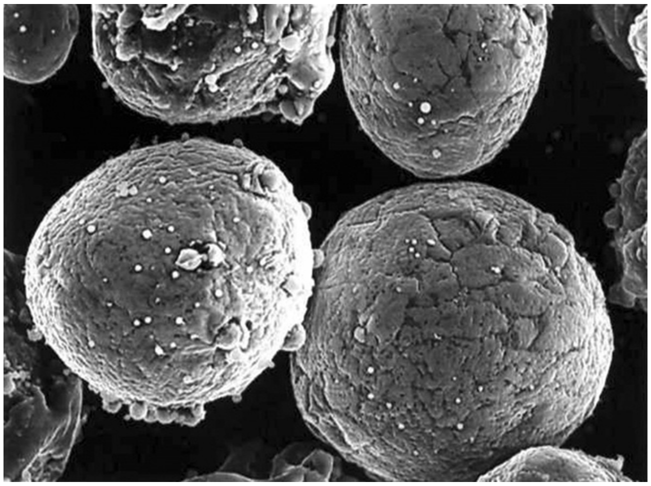

FIG. 17.6 Micrograph of Electron MAP magnesium alloy powder particles. *(Courtesy of Magnesium Electron Comp.)*

(B) 325 × D size: +325 mesh of 5% max, −325 mesh—balance. Fig. 17.6 illustrates the morphology of Electron MAP powder particles. The Electron MAP powders are assigned for use by powder forging, powder extrusion, hot and cold isostatic pressing, and equal channel angular extrusion.

Magnesium alloy powders of Elektron MAP43 (4 wt% Y, 3 wt% Nd, 0.5 wt% Zr, balance – Mg) and Elektron MAP 21 (2.7 wt% Nd, 1.3 wt% Gd, 0.3 wt% Zn, 0.6 wt% Zr, balance – Mg) were produced by Tandon and Madan [12] using the inert gas atomization process. The powders showed a fine dendritic microstructure (Fig. 17.7) resulting from rapid solidification due to the atomization process by a scalable gas atomizer [13]. The interdendritic spacing was between 1 and 3 μm for the −100/+325 mesh (150/44 μm) size. Apparent density, flow rate, and median diameter are for Electron MAP 43: 0.99 g/cm^3, 65 s/50 g, and 83 μm and for Electron MAP, 21: 0.99 g/cm^3, 65 s/50 g, and 83 μm, respectively. As the authors reported during the forging process, the powder was cold isostatically pressed into a preform and then subsequently heated and placed in a granular pressure transmitting media. A rapid application of large uniaxial pressure along with a smaller radial pressure resulted in rapid densification and full densification. The yield strength of the PM extruded Electron MAP 43 alloy was 260 MPa with a UTS of 290 MPa, and an elongation of approximately 20%, which compared favorably against commercially extruded cast Elektron 43 because the latter is characterized by yield strength of 170 MPa with a UTS of 220 MPa, and an elongation of approximately 2% [14].

The PM consolidated atomized Elektron MAP 21 showed higher strength as the yield strength of 350 MPa with a UTS of 360 MPa and an elongation of 10% while the commercial cast extruded Elektron 21 is characterized by a yield strength of 225 MPa with a UTS of 260 MPa, and an elongation of approximately 17% [15].

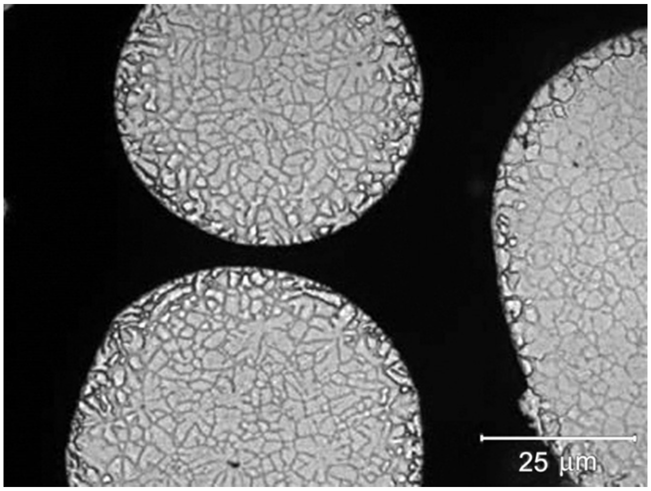

FIG. 17.7 Optical micrograph of Elektron MAP 43 size fraction −100/+325 mesh (150/44 μm). *(From Tandon R, et al. Influence of powder characteristics on the consolidation behavior of magnesium alloys for structural and energetic applications, In: Proceedings of the 2012 international conference on powder metallurgy and particulate materials. Basel (Switzerland): Metal Powder Industries Federation; 2012. p. 07-157–07-163.)*

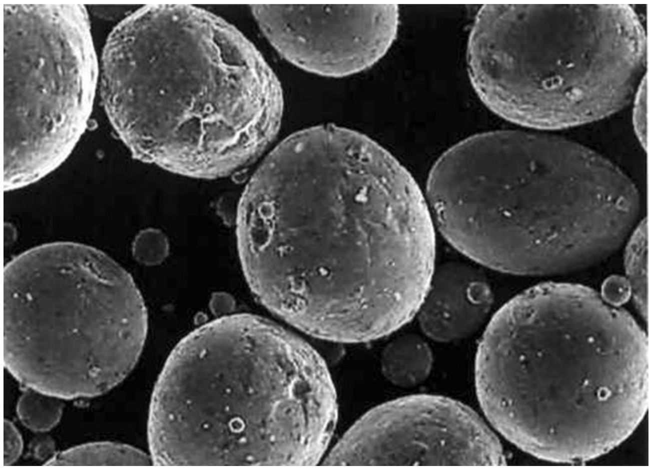

FIG. 17.8 Micrograph of Magnesium Electron pure magnesium powder. *(Courtesy of Magnesium Electron Comp.)*

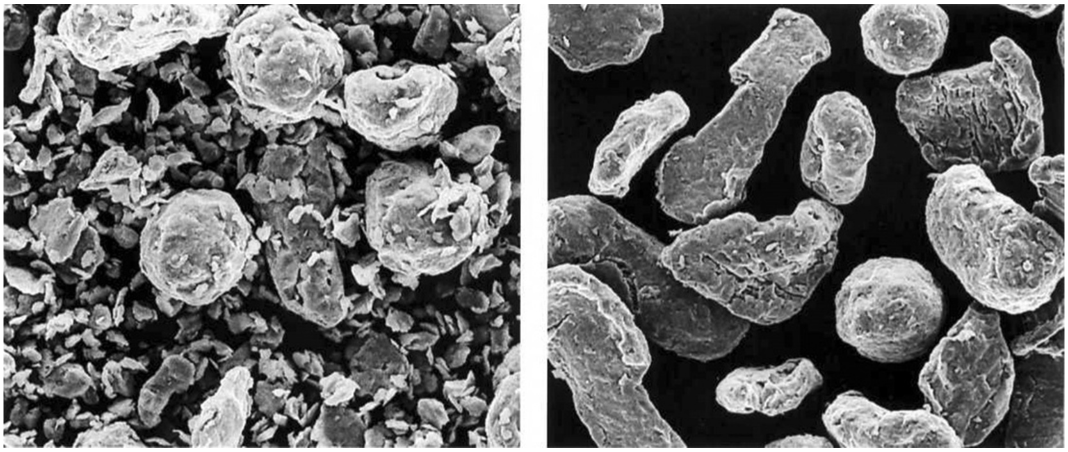

FIG. 17.9 Coarse and fine ground magnesium alloy powders of Magnesium Electron Comp. *(Courtesy of Magnesium Electron Comp.)*

The pure magnesium powders are made by the Magnesium Electron Company as blending additives for powder metallurgy parts and are available in particle size as: (A): +200 mesh (74 μm) of 0.5% max, −325 mesh (44 μm) of 60% min) and (B): +200 mesh of 5% max, −325 mesh of 95% min). The powders are spheroidal without satellites (Fig. 17.8).

Coarse and fine ground magnesium alloy powders of the three compositions (Table 17.2) are offered by the Magnesium Electron Company for PM applications. The particles of these powders have an irregular shape and uneven surface (Fig. 17.9).

Nanocrystalline $Mg_{97}Zn_1Y_2$ (at%) alloys having high specific tensile strength, high elevated temperature tensile strength, high plasticity, and using a rapidly solidified (RS) powder metallurgy process were developed by Kavamura and Inoue [3]. The RS raw material was prepared in ribbon form by a single roller melt spinning method at a circumferential velocity of 42 m/s. The RS ribbons were then annealed in a vacuum at 573 and 673 K for 1.2 ks. The RS powder metallurgy process was realized by a closed processing system in an argon gas (O_2, $H_2O < 0.5$ ppm) atmosphere on the laboratory installation. The details of the processing system are described in the article [16]. The RS $Mg_{97}Zn_1Y_2$ powder was produced by He-gas atomization at a gas-pressure of 9.8 MPa, and at a molten-alloy temperature of 1048 K. The powder, which was sieved to <32 μm, was used for the subsequent consolidation. The cooling rate of the sieved powder was estimated to be 1×10^5 K·s^{-1} or more. The sieved powder was first cold pressed in a copper can with an inner diameter of 20 mm and an outer diameter of 23 mm, and then degassed for 900 s at room temperature. To consolidate the RS powder, extrusion of the powder was performed at an extrusion ratio of 10, at temperatures ranging from 573 to 723 K, and at a ram speed of 2.5 mm/s.

The authors [3] reported that the RS $Mg_{97}Zn_1Y_2$ powder and its PM alloy consolidated at 573 K predominantly consist of a hexagonal closed packed (hcp) Mg phase. The alloy mainly consists of hcp-Mg grains with and without a high density of plane faults. The grain size was estimated to be about 180 nm. A small amount of fine rectangular $Mg_{24}Y_5$ precipitates with a grain size of about 7 nm was observed in the matrix grains.

The dimensions of the tensile specimens were a diameter of 2.5 mm and a gauge length of 16 mm for ambient temperature tests, and a diameter of 1.5 mm and a gauge length of 10 mm for elevated temperature tests [3]. As reported, the yield strength ($\sigma_{0.2}$) decreased from 610 to 430 MPa and the elongation increased from 5% to 16% with an increase in the extrusion temperature from 573 to 723 K. The Young's modulus was 45 GPa. The density of the alloy was 1.84 g/cm^3. The RS PM alloy extruded at 573 K exhibited higher yield strength (YS) of 610 MPa and an elongation of 5%. The specific tensile strength ($\sigma_{0.2}/\rho_m$, where ρ_m is the density of the alloy) was about four times as high as that of the commercial AZ91-T6 I/M alloys (83 MPa/ρ_m).

The study of the testing temperature dependence of the mechanical properties of the RS PM $Mg_{97}Zn_1Y_2$ alloys consolidated at 573 K [3] showed that the tensile yield strength decreased from 610 to 380 MPa with increasing the test temperature from room temperature to 473 K. It is significant that the alloy remained at high strength, exceeding 500 MPa even at a high temperature of 423 K while the elevated temperature strength of the commercial elevated temperature ingot WE54-T6 (Mg-Y-Nd) alloys was 200 MPa at temperatures below 473 K. The RS PM alloy exhibited a large elongation of 300% or more at a wide strain rate range from 10^{-2} to $10^{0}\,s^{-1}$. The elongation reached a maximum of 780% at a strain rate of $6 \times 10^{-2}\ s^{-1}$. At the same time, superplastic materials exhibited large in a uniaxial tension [17].

The AMX602 (Mg-6.0Al-0.5Mn-2.0Ca/mass%) and ZAXE1711 (Mg-l.0Zn-7.0Al-l.0Ca-l.0La/mass%) magnesium alloys indented for armor applications were developed collaboratively by the US Army Research Laboratory (ARL) and the Joining and Welding Research Institute (JWRI) of Osaka University [2]. These powders produced by the spinning water atomization process (SWAP) were used as raw initial materials [18,19]. The coarse Mg alloy powders were $1-5$ mm size. It was previously verified that the coarse Mg powders of these sizes were noncombustible. The α-Mg grain size of the raw powders was <0.5 μm. These raw powders were subjected by compaction and hot extrusion to fabricate the extruded bars. The bar had a cross-section of 24.5 mm × 40 mm × 1000 mm.

Jones and Kondoh [2] reported that by SWAP powder preparation, schematically illustrated in Fig. 17.10, noncombustive AMX602 magnesium alloy ingots were melted at 1053 K in the ceramic crucible in the inert gas environment. The effluent molten strickle through the nozzle in the crucible bottom is dispersed by the gas atomizer. Molten metal particles entered in the rotatable water stream on the inner surface of the chamber walls are rapidly crystallized. The chemical compositions of AMX602 alloy granules prepared by SWAP were the following: 6.01AI-0.26Mn-2.09Ca-0.038Si-0.004Cu-0.002Fe-0.007Zn-Mg Bal/mass%. The calcium is necessary because it promotes the noncombustive properties of the magnesium alloys. The impurity content of corrosive elements in magnesium alloys Fe and Cu is controlled to <0.005%. The coarse AMX602 granules prepared by SWAP were 1–5 mm in size with an irregular shape.

Fig. 17.11 shows the optical microstructures of the (A) AMX602 cast ingot, (C) granules, and (B) as-received powders prepared by SWAP. The cast ingot material consists of coarse α-Mg grains of 60–150 μm diameter. As shown in Fig. 17.11C, the powders revealed small dendrite structures that were formed during the rapid solidification of molten Mg alloy droplets. A mean dendrite arm spacing was 0.97 μm. The estimated solidification rate of SWAP Mg alloy powders is

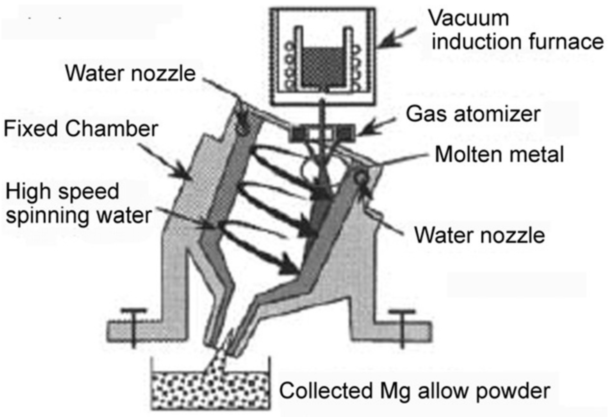

FIG. 17.10 Schematic illustration of spinning water atomization process (SWAP) installation to produce rapidly solidified Mg alloy granules. *(Modified from Sakamoto M, Akiyama S, Hagio T, Ogi K. Control of oxidation surface film and suppression of ignition of molten Mg-Ca alloy by Ca addition. J Jpn Foundry Eng Soc 1997; 69: 227–233.)*

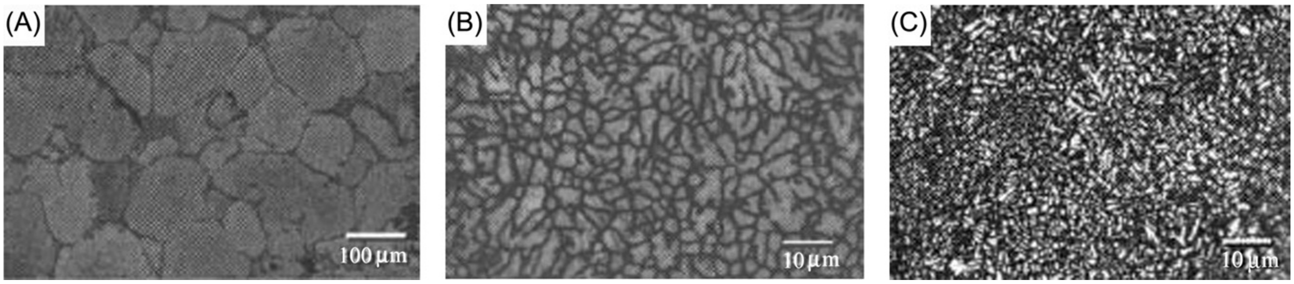

FIG. 17.11 Optical microstructures of AMX602 cast ingot (A), powders (B), and granules (C) prepared by SWAP. *(From Jones T, Kondoh K. Ballistic analysis of new military grade magnesium alloys for armor applications. In: Magnesium technology 2011. TMS (The Minerals, Metals and Materials Society); 2011. p. 425–30.)*

$1.1 \times 10^5\,\mathrm{K\,s^{-1}}$. The estimated solidification rate of SWAP Mg alloy granules is $1.1 \times 10^3\,\mathrm{K\,s^{-1}}$. The mean particle size of fine particles is 0.36 mm. The mean particle size of coarse powders is 1.87 mm.

According to data [2], the AMX602 magnesium alloy fabricated by extruding the green compacts of rapidly solidified granules showed α-Mg grains of 0.3–1.1 μm in diameter. Compared to the AMX602 extruded alloys using the cast ingot billets, the UTS and YS of the granule-extruded materials showed an increment of 30%–45%. The 422 MPa UTS and 14.2% elongation of samples are achieved by the preheating temperature at 623 K. Because of advanced powder metallurgy processing and chemical alloying, superior mechanical properties were achieved. The initial ballistic performance results of the Mg alloy AMX602 showed up to a 33% higher ballistic limit compared to the baseline Mg armor alloy AZ31B.

The additive friction stir (AFS) manufacturing process for metallic materials in which the added material can be in the form of powder or solid feedstock was applied by Kandasamy et al. [20] in the study of the mechanical properties of WE43 magnesium deposited by AFS using both gas-atomized powder and solid feed for their comparisons. The process is schematically explained in Fig. 17.12. The process principle is similar to friction stir welding processing, with the exception of the use of a filler feed. The filler metal is forced to flow between the rotating AFS tool and the substrate, whereby the filler material undergoes shear-induced severe plastic deformation, dynamic recrystallization, and deposition while the firmly clamped substrate is moving. The hydrostatic pressure and the heat generated from the adiabatic and frictional processes are crucial in obtaining sound bonding between the substrate and filler metal. The severe plastic deformation imparted into the filler and substrate interface yields a dense, homogenous, fine-grained wrought microstructure. The nominal chemical composition of the magnesium alloy WE43 substrate and the filler metal was Mg-4Y-3Nd-0.5Zr/mass%. The solid filler material was extracted from a rolled plate and used in the as-received and softened (798 K for 8 h) condition. The powder filler specimen sizes were 127 mm × 25.4 mm × 6.35 mm.

Kandasamy et al. [20] reported that the tensile strength, yield strength, and ductility of the base metal were 323 ± 3 MPa, 285 ± 1 MPa, and 12 ± 1%, respectively. The tensile strength of the deposit made using as-received filler in as-deposited condition was close to 300 MPa, which is 20 MPa lower than the base metal. A maximum tensile strength of 360 MPa and yield strength of 330 MPa with 11% ductility of the powder-deposited specimens were obtained upon aging at 273 K for 24 h. The authors are of the opinion that further optimization studies are needed to realize the full potential of powder-deposited samples.

Magnesium and its alloys are promising materials for biodegradable vascular stents, owing to their relatively low corrosion resistance to human body fluids and their good biocompatibility [21–23]. However, studies have also revealed that the rapid corrosion rate of conventional magnesium alloys causes premature loss of stent mechanical properties. The most

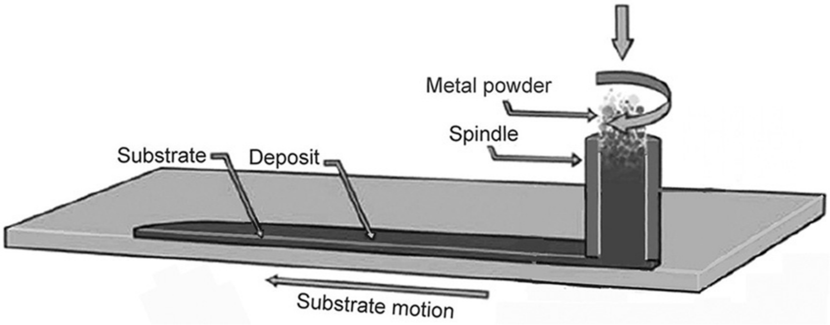

FIG. 17.12 Schematic representation of additive friction stir (AFS) process.

effective way to enhance both the mechanical properties and the corrosion resistance of engineering magnesium alloys is to add specific alloying elements such as rare earth elements [24–27]. However, the toxicity of these alloying elements in a biomaterial is still a controversial issue among biomedical scientists [22,26,28]. The studies by Alvarez-Lopez et al. [29] and Argade et al. [30] reported that in a AZ31 magnesium alloy, the best corrosion behavior in the phosphate-buffer solution could be achieved after extensive grain refinement by equal-channel angular pressing.

Ge et al. [31] concentrated their experimental investigation on a ZM21 magnesium alloy selected with the aim of exploring an alloy system preferentially formed by nontoxic elements, thus preserving the highest levels of biosafety and biocompatibility. It is reported that Ca, Zn, and Mn in fairly low concentrations do not produce harmful effects (these elements are actually essential for the human metabolism) [26,28,32], whereas elements such as Al, Zr, Y, and other RE elements that are used in other commercial Mg alloys to improve strength and corrosion resistance may give unwanted effects when released into the human body at high rates [22,23,26,33].

Wolff M, et al. reported [34] that significant enhancement of mechanical properties of Mg-based alloy biomedical implant parts was realized using 35 wt% of backbone polymer in the binder system of the feedstock.

REFERENCES

[1] Smith MB, March J. Advanced organic chemistry: reactions, mechanisms, and structure. 6th ed. New York: Wiley-Interscience; 2007.

[2] Jones T, Kondoh K. Ballistic analysis of new military grade magnesium alloys for armor applications. In: Magnesium technology 2011. San Francisco, CA: John Wiley & Sons, Inc.; TMS (The Minerals, Metals and Materials Society) 2011. p. 425–30.

[3] Kawamura Y, Inoue A. Rapidly solidified powder metallurgy Mg97Zn1Y2 alloys with tensile yield strength of 610 MPa and elongation of 5%. In: Kaplan HI, editor. Magnesium technology 2002. San Francisco, CA: John Wiley & Sons, Inc.; TMS (The Minerals, Metals and Materials Society) 2002. p. 227–32.

[4] Elsayed A, Umeda J, Kondoh K. The production of powder metallurgy hot extruded Mg-Al-Mn-Ca alloy with high strength and limited anisotropy. In: Magnesium Technology 2011. San Francisco, CA: John Wiley & Sons, Inc.; TMS (The Minerals, Metals and Materials Society) 2011. p. 475–80.

[5] Bettles CJ, Moss MH, Lapovok R. A Mg-Al-Nd alloy produced via a powder metallurgical route. Mater Sci Eng A 2009;515(1):26–31.

[6] Neikov O, et al. Advanced high-strength nanostructured Al-Mg alloys produced by new rapid solidification technology. Compiled by European powder metallurgy association, (Bellstone Shrewsbury, UK) proceedings of PM 2010 world congress. Florence; vol. 4. 2010. p. 25–32.

[7] Claeys S, Lampman S. Specialty applications of metal powders. In: ASM handbook. vol. 7. Materials Park, OH: ASM International Publishers; 1998. p. 1083–92.

[8] Naboychenko SS, editor. Handbook of nonferrous metal powders. Moscow: Metallurgia Publishers; 1997 (in Russian).

[9] Dunkley JJ. Atomization. In: ASM handbook. vol. 7. Materials Park, OH: ASM International Publishers; 1998. p. 35–52.

[10] Frishberg IV, Kvater LI, Kuzymin BP, Gribovskii SV. The gas-phase method of powder production. Moscow: Nauka Publishers; 1978 (In Russian).

[11] Withers J, Shapovalov V, Laughlin J, Loutfy R. Fabrication of Mg, Al and Ti advanced alloys and composites. Compiled by Russell A. Chernenkoff W, Brian J. Proceedings of 2014 powder metallurgy world congress. Orlando (FL, U.S.A.): Metal Powder Industries Federation; 2014. p. 09-145–09-50.

[12] Tandon R, Madan D. In: Gas atomized magnesium alloy powders: study of consolidation behavior. Compiled by Russell A. Chernenkoff W, Brian J. Proceedings of 2014 powder metallurgy world congress. Orlando (FL, U.S.A.): Metal Powder Industries Federation; 2014. p. 07-143–07-49.

[13] Tandon R, et al. In: Influence of powder characteristics on the consolidation behavior of magnesium alloys for structural and energetic applications. Proceedings of the 2012 international conference on powder metallurgy and particulate materials. Basel (Switzerland): Metal Powder Industries Federation; 2012. p. 07-157–07-63.

[14] Magnesium Elektron 43 Datasheet 467A & Datasheet 478, www.magnesium-elektron.com.

[15] Magnesium Elektron http://www.magnesium-elektron-powders.com/index.php/magnesium-alloy-powder-applications. [Accessed 31 January 2018].

[16] Kawamura Y, Inoue A, Masumoto T. Mechanical properties of amorphous alloy compacts prepared by a closed processing system. Scripta Metall Mater 1993;29:25–30.

[17] Sakuma T. A brief review on the project "towards innovation in superplasticity." Mater Sci Forum 1999;304–306:3–10.

[18] Sakamoto M, Akiyama S, Hagio T, Ogi K. Control of oxidation surface film and suppression of ignition of molten Mg-Ca alloy by Ca addition. J Jpn Foundry Eng Soc 1997;69:227–33.

[19] Nishida S, Motomura I. Estimation of heat transfer coefficient and temperature transition on melt drag process of AZ3I magnesium alloy by heat transfer and solidification analysis. J Jpn Inst Light Met 2008;58:439–42.

[20] Kandasamy K, et al. In: Effect of material feeding method on mechanical properties of additive friction stir deposited magnesium alloy. Compiled by Russell A. Chernenkoff W, Brian J. Proceedings of 2014 Powder Metallurgy World Congress. Orlando (FL, U.S.A.): Metal Powder Industries Federation; 2014. p. 07-138–07-42.

[21] Witte F. The history of biodegradable magnesium implants: a review. Acta Biomater 2010;6:1680–92.

[22] Gu XN, Zheng YF. A review on magnesium alloys as biodegradable materials. Front Mater Sci China 2010;4:111–5.

[23] Zeng R, Dietzel W, Witte F, Hort N, Blawert C. Progress and challenge for magnesium alloys as biomaterials. Adv Biomater 2008;10:B3–B15.

[24] Leeflang MA, et al. Long-term biodegradation and associated hydrogen evolution of duplex-structured Mg-Li-Al-(RE) alloys and their mechanical properties. Mater Sci Eng B 2011;176(20):1741–5.

[25] Feyerabend F, Fischer J, Holtz J, Witte F, Willumeit R, Drucker H, et al. Evaluation of short-term effects of rare earth and other elements used in magnesium alloys on primary cells and cell lines. Acta Biomater 2010;6:1834–42.

[26] Witte F, Hort N, Vogt C, Cohen S, Kainer KU, Willumeit R, et al. Degradable biomaterials based on magnesium corrosion. Curr Opin Solid State Mater Sci 2008;12:63–72.

[27] Wang YX, Guan SK, Zeng XQ, Ding WJ. Effects of RE on the microstructure and mechanical properties of mg-8Zn-4Al magnesium alloy. Mater Sci Eng A 2006;416(1–2):109–18.

[28] Hermawan H, Dube D, Mantovani D. Development in metallic biodegradable stents. Acta Biomater 2010;6:1693–7.

[29] Alvarez-Lopez M, Pereda MD, Del Valle JA, Fernandez-Lorenzo M, Garcia-Alonso MC, Ruano OA, et al. Corrosion behaviour of AZ31 magnesium alloy with different grain sizes in simulated biological fluids. Acta Biomater 2010;6:1763–71.

[30] Argade GR, Panigrahi SK, Mishra RS. Effects of grain size on the corrosion resistance of wrought magnesium alloys containing neodymium. Corros Sci 2012;58:145–51.

[31] Ge Q, Dellasega D, Demir A, Vedani M. The processing of ultrafine-grained mg tubes for biodegradable stents. Acta Biomater 2013;9(10):8604.

[32] Xu L, Yu G, Zhang E, Pan F, Yang K. In vivo corrosion behavior of Mg-Mn-Zn alloy for bone implant application. J Biomed Mater Res A 2007;83A:703–11.

[33] Yuen CK, Ip WY. Theoretical assessment of magnesium alloys as degradable biomedical implants. Acta Biomater 2010;6:1808–12.

[34] Wolff M, et al. In: Enhancement of thermal debinding and sintering of biodegradable MIM magnesium parts for biomedical applications. Compiled by European powder metallurgy association, (Bellstone Shrewsbury, UK) proceedings of PM 2016 world congress. Hamburg (Germany); 2016. p. 1–6.

Chapter 18

Production of Titanium and Titanium Alloy Powders

Oleg D. Neikov* and Victor G. Gopienko†
*Frantsevich Institute for Problems of Materials Science (IPMS), Kiev, Ukraine, †All-Russian Aluminum-Magnesium Institute, Saint Petersburg, Russia

Chapter Outline

Introduction 549
Chemical Reduction 550
- Sodium Reduction Method (Hunter Process) 550
- Armstrong Process 550
- Magnesium Reduction Method (Kroll Process) 551
- Calcium Hydride Reduction Process 553
- Hydrogenation/Dehydrogenation (HDH) Process 553

Plasma-Rotating Electrode Process (PREP) 554
Gas Atomization 555
Electrolysis of Titanium Compounds 558
- FFS-Cambridge Process 559
- MER Process 559
- Chinuka Process 560
- Electrolytic Refining of Titanium 561

Amalgam Metallurgy Technique 562
Other Methods 563
- TIRO Process 563
- Method of Disproportionation of Lower Titanium Halogenides 564
- CSIR Process 564
- Chemical Synthesis of Nanosized Titanium Powders 565
- Mechanical Alloying 565

Applications 565
- Titanium Powder Process Selection 567
- Titanium Powder-Based Materials Selection 567

References 568
Further Reading 570

INTRODUCTION

Titanium possesses an exclusive combination of low density, good mechanical properties at room and elevated temperatures, and good corrosion resistance. Titanium and its alloys are used extensively in the aerospace and biomedical industries as well as in other industrial applications. However, titanium ingots are expensive to produce and fabricate. Another problem is connected with segregation in highly alloyed titanium materials. The high cooling rate that PM technology makes possible ensures that significantly greater amounts of alloying elements remain in the solid solution compared with ingot metallurgy, and thus can substantially influence material phase composition and properties [1,2]. At the same time, PM processing permits articles that are close to their final shape. Therefore, this leads to reduced material loss during production as well as lower production costs.

There are many known processes of titanium and titanium alloy powder manufacture. Currently, chemical reduction, hydrogenation/dehydrogenation, gas atomization, plasma-rotating electrode, and plasma atomization processes are mainly used for commercial production. Small amounts of titanium powder are produced by electrolysis of titanium compounds ($TiC1_4$, $Ti0_2$) in melts, centrifugal atomization of the melt, amalgam metallurgy, and the disproportionation method of low titanium halogenides.

Development of new titanium production methods, such as the ITP/Armstrong, CSIRO (Commonwealth Scientific and Industrial Research Organization, Australia), and MER processes, is aimed at lowering the cost of PM titanium powder. However, these powders are not yet a commercial application.

Handbook of Non-Ferrous Metal Powders. https://doi.org/10.1016/B978-0-08-100543-9.00018-X
© 2019 Elsevier Ltd. All rights reserved.

CHEMICAL REDUCTION

Generally, the initial source of titanium powder is "sponge fines," so called owing to their appearance. Sponge fines are nodular particles (see Introduction, Fig. I2) of pure titanium produced during the chemical reduction process from titanium tetrachloride. The commercial manufacture of titanium metal includes the chlorination of natural or synthetically produced rutile, TiO_2 [1,3]. The obtained titanium tetrachloride is reduced to metallic titanium by the sodium reduction method known as the Hunter process, the magnesium reduction method known as the Kroll process, and the calcium hydride reduction process used in Russia.

In reduction processes of titanium tetrachloride, most of the residual chloride is removed by vacuum distillation or water leaching. The final sponge fines typically contain from 0.12 to 0.15 wt% Cl.

Sodium Reduction Method (Hunter Process)

This process invented in 1910 by Matthew A. Hunter was the first industrial process to produce pure ductile metallic titanium. Titanium tetrachloride is reduced with sodium to form pure metallic titanium (99.9%) by heating titanium tetrachloride with sodium at 973–1073 K:

$$4\text{Na(liq)} + \text{TiCl}_4\text{(g)} = 4\text{NaCl(liq)} + \text{Ti(s)}$$

Characteristic sponge fines manufactured by the Hunter process are shown in Fig. 18.1. A typical chemical analysis of commercial powders is given in Table 18.1. A screen analysis of sponge fines produced by sodium reduction is characterized by the content of the particle size fractions smaller than 105 μm in the amount of 78 wt% and fractions smaller than 64 μm and amount of 40.8 wt%.

Table 18.2 illustrates typical technological characteristics of titanium powders and tensile properties of Ti-6Al-4V compacts produced from sponge fines and an aluminum-vanadium master alloy.

Powder dispersivity grows at $TiCl_4$ bubbling through the melt, on the surface of which metallic sodium is supplied: the grain size of the basic mass of powder is lower than 20 μm. More finely dispersed powders are produced by low-temperature reduction of titanium's compounds in organic media by using alkaline metals or amalgams as reducing agents.

Though the Hunter process successfully produces very high-quality titanium, it was replaced by the more economical Kroll process. Currently, only a small facility uses the Hunter process to manufacture titanium sponge for high-purity sputtering targets [2].

Armstrong Process

Developed by Cristal Metals, formerly International Titanium Powders (ITP), the Armstrong process produces titanium powder by reduction of titanium tetrachloride with sodium, as the Hunter process does. However, this process is continuous in contrast to the batch mode of the Hunter process. The process begins with titanium tetrachloride that is reacted to form solid titanium powder and sodium chloride. The reaction is continuous and takes place in the titanium reactor.

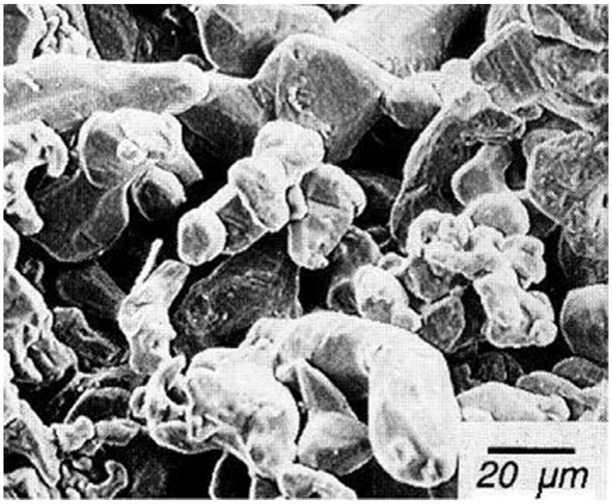

FIG. 18.1 Sponge fines produced by the sodium process.

TABLE 18.1 Typical Chemical Analysis of Chemical Reduction Process Titanium Sponge Fines, and Sinter-Compacted Ti-6Al-4V Produced From These Fines and Al-V Master Alloy Powders

Elements (Content, wt%)	Sodium Process			Calcium Hydride Reduction Process			Hydride/Dehydride Process		Electrolytic Process
	CP[a]	[b]	CP[c]	CP[a]	[d]	CP[e]	P6/4-3[f]	CP[g]	CP[g]
Al	…	6.2	…	…	4.65	…	5.09	…	…
V	…	4.1	…	…	3.80	…	4.17	…	…
O	0.13	0.24	0.05–0.30	0.19	0.20	0.25–0.30	0.131	0.15–0.30	0.05–0.30
N	0.03	0.016	0.02–0.03	0.06	0.06	0.05–0.06	0.006	0.03–0.05	0.02–0.03
H	0.07	0.002	0.02–0.03	0.34	0.30	0.20–0.40	0.0015	0.06–0.15	0.02–0.04
C	0.02	0.02	0.01 max	0.03	…	0.04–0.05	0.02	0.015–0.020	<0.02
Fe	0.02	0.18	0.01–0.02	0.11	…	0.15–0.20	0.1	0.07–0.10	0.02–0.08
Na	0.10	0.10	…	…	…	…	…	…	…
Cl	0.13	0.12	0.10–0.13	0.004	0.003	0.003–0.005	…	0.06–0.08	0.03–0.08
Si	…	…	0.006 max	0.05	…	0.06–0.07	0.02	0.01–0.02	<0.02
Ca	…	…	…	0.04	0.06	0.08	…	…	…
Ni	…	…	…	0.07	…	…	…	…	…
Cu	…	…	…	…	…	…	<0.01	…	…
Sn	…	…	…	…	…	…	0.01	…	…
Nb	…	…	…	…	…	…	1.17	…	…
Mo	…	…	…	…	…	…	0.01	…	…
W	…	…	…	…	…	…	0.01	…	…
Cr	…	…	…	…	…	…	0.02	…	…
Ti	Balance	Balance	Balance	Balance	Balance	Balance	Balance	Balance	Balance

[a] *Source: Ref. [2].*
[b] *Sinter compacted Ti-6Al-4V produced from these sponge fines and Al-V master alloy powder, source: Ref. [2].*
[c] *630+180 μm powder sizes, source: Ref. [1].*
[d] *Sinter compacted Ti-6Al-4V produced from these fines, source: Ref. [2].*
[e] *100 + 40 μm (25%), −40 μm (75%) powder sizes, source: Ref. [1].*
[f] *Composition of alloys synthesized from blends of CD and master alloy powders.*
[g] *640 + 180 μm powder sizes, source: Ref. [1].*
CP, commercially pure titanium.

Liquid sodium is pumped through a cylindrical chamber containing a centerline second tube. The $TiCl_4$ vapor is injected into the sodium stream through this inner tube/nozzle. The reaction occurs immediately downstream from the nozzle. The titanium powder is carried out in the excess sodium stream. Titanium, sodium, and sodium chloride are separated by filtration, distillation, and washing. The powder produced has a purity level near that of commercially pure grade 1 titanium, including a chlorine content of <50 ppm. By simultaneous reduction of other metal chlorides, it is possible to produce alloy powders.

Magnesium Reduction Method (Kroll Process)

This process occurs at 1073–1123 K:

$$2\mathrm{Mg(liq)} + \mathrm{TiCl_4(gas)} = 2\mathrm{MgCl_2(liq)} + \mathrm{Ti(s)}$$

Removing impurities from the sponge is realized by vacuum distillation. However, the sponge (Fig. 18.2) is very strong and cannot be easily crushed to size to eliminate the trapped $MgCl_2$. The main drawback of the Kroll process is that the time

TABLE 18.2 Technological Characteristics of Titanium Powders and Sintered Compacts Produced From These Powders

Technological Characteristics	Sodium Process			Calcium Hydride Reduction Process			Hydride/Dehydride Process		Electrolytic Process
	CP[a]	[b]	CP[c]	CP[a]	[d]	CP[e]	P6/4-3[f]	CP[g]	CP[h]
Tap density (g/cm^3)	…	…	0.9–1.2	…	…	0.95–1.40	…	1.35–1.70	1.4–1.8
Flow rate (s)	…	…	20 max	…	…	15 max	…	75 max	28 max
Yield strength (MPa)	…	868	…	…	865	…	868	…	…
Tensile ultimate strength (MPa)	…	945	…	…	966	…	965	…	…
Elongation (%)	…	15	…	…	13	…	14	…	…
Reduction of area (%)	…	25	…	…	32	…	31	…	…

[a] *Source: Ref. [2].*
[b] *Sinter-compacted Ti-6Al-4V produced from these fines and Al-V master alloy powder, source: Ref. [2].*
[c] *630–180µm powder sizes, source: Ref. [1]*
[d] *Sinter-compacted Ti-6Al-4V produced from these fines, source: Ref. [2].*
[e] *100–40µm (25%), −40µm (75%) powder sizes, source: Ref. [1].*
[f] *Composition of alloys synthesized from blends of CD and master alloy powders.*
[g] *630–180µm powder sizes, source: Ref. [1].*
[h] *180 µm powder size, source: Ref [1].*
CP, *commercially pure titanium.*

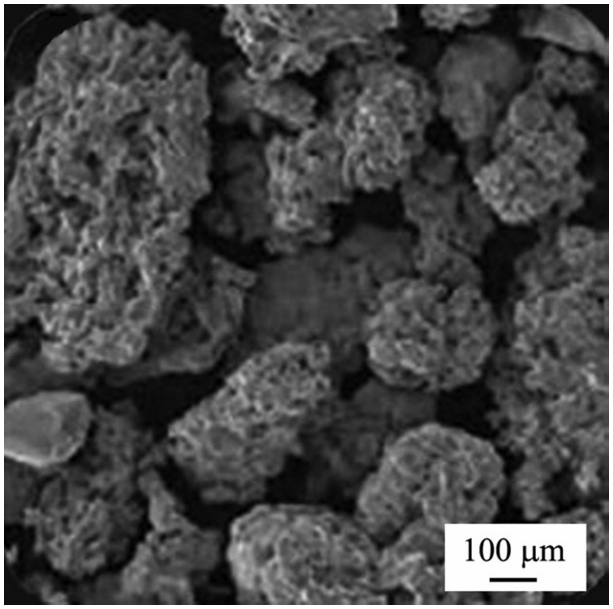

FIG. 18.2 SEM photomicrograph of sponge made by the Kroll process.

required for purification of the titanium sponge by vacuum distillation can exceed 4–5 days, depending on the titanium sponge block size.

When the sponge is crushed to a required size, the riddlings (particles finer than 2 mm) are of 3%–5% of the mass of the sponge produced. They are used in powder metallurgy, in anticorrosive coatings, and for the production of titanium carbides, nitrides, and other compounds. The yield of powder fractions of magnesium-thermal titanium essentially increases if vacuum separation of the reaction mass by hydrometallurgical processing is used. However, the quality of powders in this case is impaired.

Titanium powders can be produced by continuous reduction of $TiCl_4$ with gaseous magnesium in a stream of argon. In this process, the titanium powder and magnesium chloride are continuously carried out of the reaction zone.

To produce titanium powder, mechanical crushing of the titanium sponge is done. However, in this case there are some difficulties connected with the plasticity of high-purity titanium, therefore the titanium is preliminarily oxidized or hydrogenated to embrittle it. Such a method is especially interesting for crushing titanium alloys, Ti-Al alloys in particular, produced by an aluminothermic reduction of titanium dioxide.

Calcium Hydride Reduction Process

The reduction of titanium dioxide with calcium hydride is carried out at temperatures of 1423–1473 K:

$$Ti0_2 + 2CaH_2 = Ti + 2CaO + 2H_2$$

The reaction product is processed by a water solution of hydrochloric acid to remove CaO and $Ca(OH)_2$, then the powder is washed in distilled water, rinsed with alcohol, and dried at 333–343 K in vacuum.

Powder particles produced by the calcium hydride process have a spongy morphology similar to sponge fines produced by the sodium process, and consist of conglomerations of small particles fused together during the reaction process. The powder produced (size fraction lower than 200 μm) contains up to 90% of particles <10 μm in size and has an apparent density of 0.6–0.8 g/cm^3. The powder contains up to 0.05% of calcium as its oxide. The average particle size of commercially pure titanium powder is 41 μm [4].

Table 18.1 shows a typical chemical analysis of commercial powders produced by calcium hydride reductions. Table 18.2 gives typical technological characteristics of titanium powders and tensile properties of Ti-6Al-4V articles produced from calcium hydride-reduced titanium and aluminum-vanadium master alloy powders.

Hydrogenation/Dehydrogenation (HDH) Process

This method is based on the reaction of titanium with hydrogen at 623–973 K, the formation of fragile hydrides, and their mechanical crushing and subsequent dehydrogenation during 1–2 h at 973–1073 K to a powder-form product. A saturation of titanium by hydrogen achieves 2–3.5 wt%, depending on the purity of the initial material [1]. The hydrogenated titanium in possession of an angular shape (Fig. 18.3) is very brittle and can be simply ground to a fine powder. Mechanical crushing in ball mills allows manufacturing powders of the required grain size. The disadvantages of the method are difficulties of

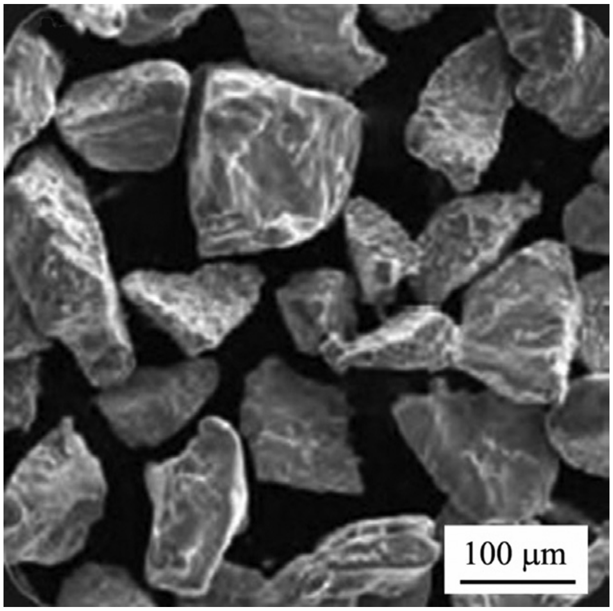

FIG. 18.3 SEM photomicrograph of angular hydrogenation/dehydrogenation (HDH) titanium powder.

hydrogen purification from oxygen and nitrogen as well as high sensitivity of titanium to the content of the residual hydrogen, causing fragility.

Typical chemical analysis and technological characteristics of titanium powders and sintered compacts are given in Tables 18.1 and 18.2.

Hydride of electrolytic titanium is distinguished by high purity and is used very effectively as a generator of hydrogen, in particular, in the annealing of watch fibers and as an additive to the charge of various metal powders that activates the process of sintering. Crushed titanium hydride can serve as a raw material in the production of materials such as titanium carbides, borides, nitrides, and silicides.

For reducing the titanium powder cost, the hydrogenation process followed by hydrometallurgical processing was suggested [5]. The processes of dehydration with complete or partial removal of hydrogen were developed.

Chemical reactions of continuous and semicontinous processes for manufacturing titanium hydride using titanium chlorides of different valences are listed in Table 18.3 [6]. Because reactions 3 and 10 under normal conditions have low yield and require either a high vacuum or special conditions (rapid quenching), magnesium is used for titanium dichloride reduction in industrial production.

The hydrogenated titanium powder produced at ADMA Product Inc. (https://www.admaproducts.com/) was used to manufacture titanium alloy parts for various applications, including aircraft and military, by the blended elemental PM process. The Ti-6Al-4 V bars were manufactured by cold isostatic pressing/sintering/rotary forging from TiH_2 powder [2].

PLASMA-ROTATING ELECTRODE PROCESS (PREP)

PREP is a centrifugal atomization process where the end of a consumable metal bar is melted while being rotated about its longitudinal axis. The molten metal is centrifugally atomized in the form of droplets that solidify in an inert gas atmosphere to spherical powder particles. The consumable electrode can be melted by various energy sources. For producing titanium-alloyed powders in the United States, helium plasma is used [3]. The electrodes are prealloyed bars of 60–65 mm in diameter and are rotated at speeds up to 15,000 rpm. Particle size depends on the alloy composition, the electrode diameter, and the rotation speed. Typical sizes for Ti-6Al-4V powders are between 100 and 300 μm with a median diameter of about 175 μm. The PREP powder is spherical (Fig. 18.4) while having good flow characteristics and a tap density about 65% of

TABLE 18.3 Chemical Reactions of Continuous and Semicontinuous Processes for Manufacturing Titanium Hydride Using Titanium Chlorides of Different Valency

No	Formula	Temperature (K)	Environment	Comments
1	$TiO_2+2C+4HCl=TiCl_4+2CO+2H_2$	1073–1273	Atmospheric	
2	$TiCl_4+Ti=2TiCl_2$	923–1000	Atmospheric	
3	$2TiCl_2=Ti+TiCl_4$	1073	Atmospheric or vacuum	The reaction rate at atmosphere pressure
4	$2TiCl_4+H_2=2TiCl_3+2HCl$	773–973	Atmospheric	
5	$TiCl_2+H_2=Ti+2HCl$	1273	Atmospheric	Excess of hydrogen
6	$2TiCl_3+H_2=2TiCl_2+2HCl$	773	Atmospheric	
7	$TiCl_4+H_2=TiCl_2+2HCl$	1072–1123	Atmospheric	Excess of hydrogen
8	$2TiCl_3=TiCl_2+TiCl_4$	723 773	Vacuum Atmospheric	
9	$TiCl_4$	1637	Atmospheric	Evaporation
10	$TiCl_4+2H_2=Ti+4HCl$	1273–2273	Atmospheric	Excess of hydrogen
11	$3TiCl_4+Ti=4TiCl_3$	923–1000	Atmospheric	
12	$Ti+H_2=TiH_2$	673–1023	Atmospheric	

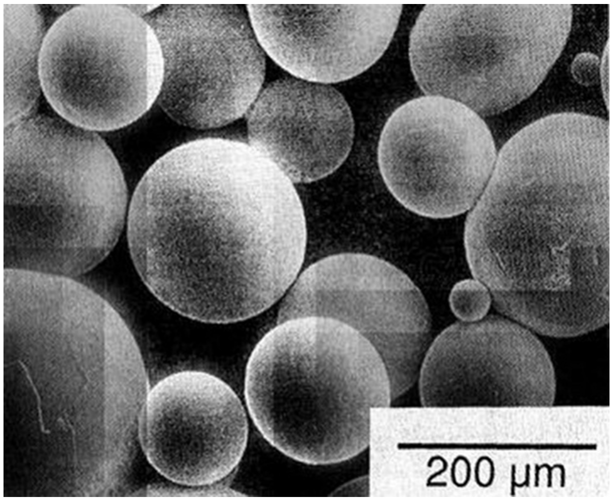

FIG. 18.4 Ti-6Al-4V powder produced by the plasma rotating electrode process.

solid substance. Various process modifications were investigated to produce finer powder [7]. In particular, the rotating electrode process (REP) was combined with gas atomization.

The rotating electrode process is also used by similar technologies in Russia, China, and Japan [1,3]. This process is discussed in more detail in Chapter 4. The PREP and REP powders are used to produce PM articles in aerospace, gas turbine engineering, environment control, and biomedical applications.

GAS ATOMIZATION

The plasma atomization process was developed to produce fine spherical titanium powder using titanium wire as the starting material [8]. In this process, the wire is fed into the apex of three plasma torches where it is melted and atomized in an argon atmosphere (Fig. 18.5). Droplets are then cooled during their flight in argon with a cooling rate in the range of 10^2–10^3 K/s. They are then solidified, forming spherical powder particles. Spherical titanium and Ti-6Al-4V alloy powders

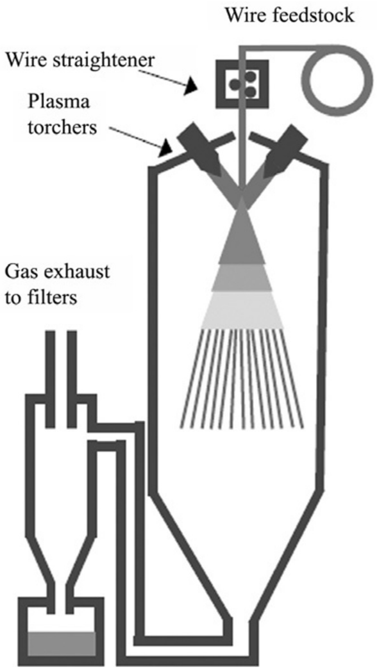

FIG. 18.5 Schematic of the plasma atomization process developed to produce fine spherical titanium powder from titanium wire.

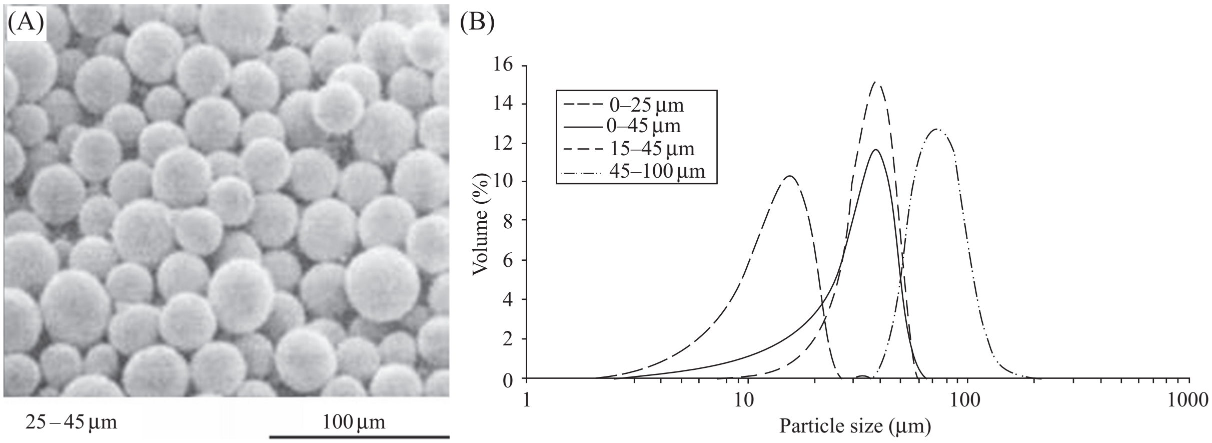

FIG. 18.6 Plasma-atomized powders (A) SEM photomicrograph of 25–45 µm size fraction, (B) Differential curves of particle size distribution of 4 size fraction.

with particle size from 0–25 to 0–180 µm have been commercialized in six size grades (Fig. 18.6) [9]. The oxygen content depends on particle size and is in the range 0.1–0.3 wt%. Apparent density depending on size fraction is in the 2.52–2.75 g/cm^3 range. The flow rate varies depending on particle sizes in the ranges from 23 to 200 s/(50 g). PyroGenesis Inc. proposes the use of plasma-atomized titanium powders for producing porous filters, applications in injection and thermal spray processes, and biomedical applications [8].

Plasma melting induction guiding gas atomization (PIGA) is another variation for producing ceramic-free Ti alloy powders using a gas atomization process developed by GKSS Research Centre in Geesthacht, Germany [10]. In this process, a prealloyed rod is introduced into a conical induction coil where the tip of the rod is heated. Once the melting temperature is reached, the melt drops down into the center of a nozzle. The obtained powder particles are predominantly in a spherical shape. The resulting finer 45 µm powders are used in metal injection molding (MIM) and other areas. The Leybold firm (Germany) has developed a technology to produce spherical powders of titanium and its alloys by melt atomization by inert gas [11]. The metal is melted in induction or electron-beam furnaces. Atomization is performed by argon or on a rotating disc.

The gas-atomized prealloyed Ti-6Al-4V alloy has a characteristic spherical shape (Fig. 18.7). For the purpose of decreasing the cost of argon-atomized powder manufacture, a premixed raw material consisting of titanium sponge and

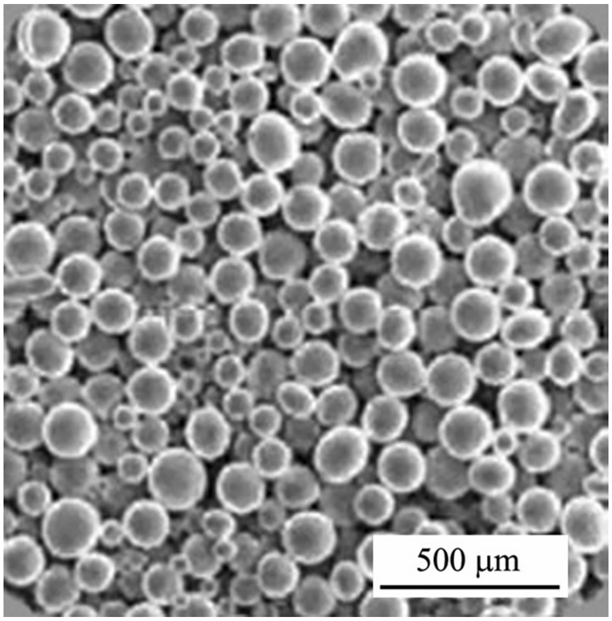

FIG. 18.7 SEM photomicrograph of a gas-atomized prealloyed Ti-6Al-4V. *(From Froes FH. Titanium powder metallurgy: developments and opportunities in a sector poised for growth. Powder Metall Rev 2013; 2(4): 29–42.)*

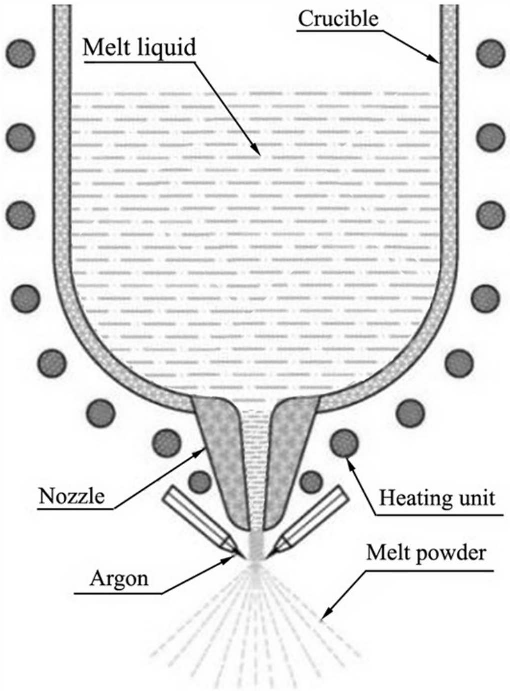

FIG. 18.8 Schematic of gas atomization process by experimental apparatus.

master alloy chips or granules is used [12]. Sintered MIM compacts using such Ti-6Al-4V alloy powder show that the tensile strength ranges from 810 to 880 MPa, and the tensile elongation is around 10%.

Vacuum induction gas atomizing (VIGA) is one of the gas atomization techniques to produce spherical titanium powders, including pure titanium, γ-TiAl, and titanium alloys. However, powders produced by VIGA commonly contain pores, which would be translated into the MIM and AM final products. In the work [13], the VIGA process was performed with high-purity argon gas. A schematic of the gas atomization process by experimental apparatus is shown in Fig. 18.8. The gas-atomized Ti-6Al-4V powders were mechanically sieved into two batches with various particle size ranges: ≥250 and ≤47 μm, respectively.

Fig. 18.9 shows the reconstructed X-ray computed tomography (CT) characteristic images of gas-atomized Ti-6Al-4 V powders. As is shown in Fig. 18.9A, there are pores with various sizes in the coarse powder. The biggest pore size is about 55 μm while the smallest is below 8 μm (Fig. 18.9A). The authors [13] reported that the total porosity for the coarse powder is about 1.68% after calculation using the software of VG Studio MAX 2.2. Any observed pores in the small particle are presented in Fig. 18.9B.

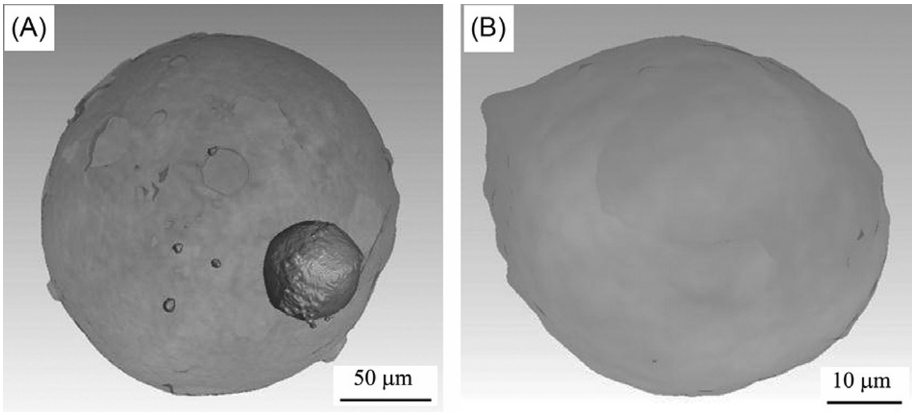

FIG. 18.9 Reconstructed X-ray computed tomography (CT) images of gas-atomized Ti-6Al-4V powders with the particle size of (A) ≥250 μm and (B) ≤47 μm; the navy-gray spheres in (A) indicate the pore defects in the coarse powder.

For more information, including fundamentals of gas atomization, see Chapter 4.

Numerous companies produce vacuum induction gas atomizing equipment. ALD Vacuum Technologies GmbH (Germany), ADMA Products Inc. (United States), SIMUWU Shanghai Gehand Vacuum Technology (China), SLT Zhuzhou Shuang Ling Technology Co. (China), etc., manufacture the vacuum induction gas atomization equipment in a wide capacity range. Thus, SLT Company produces such facilities of 1–1000 kg per batch capacity by vacuum pressure 0.05 Pa min. ALD Dynatech Furnace Pvt. Ltd. (India) manufactures VIGA from laboratory scale (1–8 L crucible volume) through pilot production (10–50 L crucible volume) up to large-scale atomization systems (with 300 L crucible volume). Fig. 18.10 shows a large-scale inert gas atomization system with a melting crucible maximum capacity of two tons, equipped with a double-door melting furnace chamber and a gas recycling system to recover the inert gas.

ELECTROLYSIS OF TITANIUM COMPOUNDS

In the 1960s and 1970s, great attention was paid all over the world to titanium production by electrolysis of titanium halogenides (mainly, chlorides and fluortantalates) and titanium oxides (TiO_2, Ti_2O_3, etc.). However, the obtained electrolytic powder had less purity than magnesium reduction powder, so it did not get commercial use. The studies were carried out by using chloride electrolytes based on chlorides of alkaline and alkaline-earth metals (KCl-NaCl, KCl-NaCl-$MgCl_2$). Difficulties of $TiCl_4$ and TiO_2 electrolysis (main kinds of Ti raw material) are connected with their low solubility in chloride solutions ($<1\%$). At the same time, it was possible to manufacture fine titanium powders on the cathode at low current yields due to special construction designs for $TiCl_4$ (bubbling) and TiO_2 (hashing) disintegration. The use of fluoride electrolytes allowed increasing the solubility of $TiCl_4$ and TiO_2 in the melt; however, in this case all the hardware-technological circuits of the electrolysis became very complicated and economically unprofitable.

A two-level method of electrolysis is considered as one of the prospective electrolysis techniques. In this method, at the beginning, the reduction of titanium tetrachloride in the melt to the tri- and bivalent condition at a low current density is carried out. Then the current density is raised, and titanium is precipitated on the cathode [14].

The new electrodeoxidation (EDO) titanium powder process is currently being developed and is based on a technique invented at Cambridge University known as the FFC Cambridge Process [15]. The EDO process uses molten salt electrolysis to convert metal oxide into the pure metal. Unlike conventional electrorefining, in the EDO process the metal oxide is not dissolved in the electrolyte but is instead sintered into a ceramic material that then becomes the cathode of the electrolytic cell. During electrolysis, oxygen is extracted from the cathode and given off through the molten calcium chloride electrolyte on the anode. As the anode is made of graphite, this is consumed in the process and mainly carbon monoxide is given off. At the end of the process cycle, the cathode is converted into oxygen-free metal.

The titanium alloys can also be made using the EDO process by means of adding oxides of the alloying additions to the initial oxide mixture used to make the cathode. These are mixed in the given quantities such that after reduction, the metals

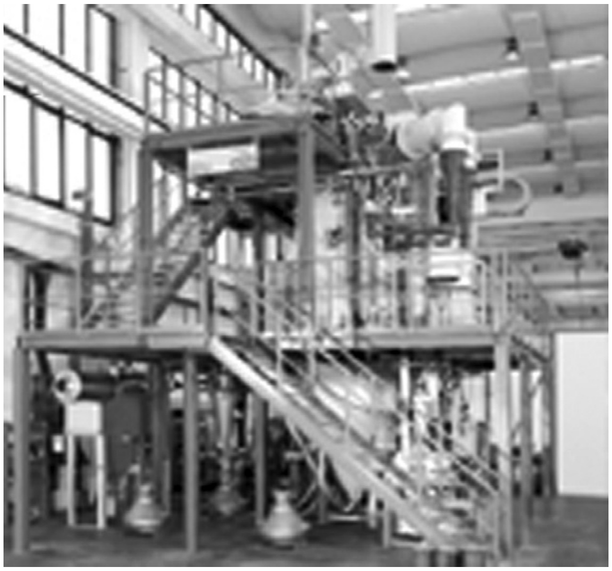

FIG. 18.10 Vacuum induction gas atomizing (VIGA) large-scale system with melting crucible maximum capacity of 2 tons. *(From ALD Dynatech Furnace Pvt. Ltd.)*

are in the correct proportions for the alloy. A large range of standard titanium alloy has now been made in this way. The process gives near-spherical titanium powder in the size ranges 20–250 μm in diameter. The powder particles are porous with a slightly irregular surface. The flowability of the dry powder is between that of atomized and HDH powders. Such a particle shape is favorable to give good green strength in processes such as pressing, sintering, or MIM.

FFS-Cambridge Process

In this process, solid titanium dioxide is cathodically reduced to titanium metal or titanium alloys in a molten salt (CaCl) (Fig. 18.11) [16]. The FFC process was developed by Fray, Farthing, and Chen at the University of Cambridge. It was realized by placing a metal oxide electrode in a molten salt bath heated to between 1073 and 1273 K and passing a current between it and an anode. At the interface between the current collector, the salt, and the metal oxide, the oxide ions leave the metal oxide and are carried across the salt to the anode, where they evolve as a gas.

The titanium dioxide is mixed with water to form a paste. It is then dried and pushed through an extrusion die to make the honeycomb or tablets. They are then fitted onto a wire, where they form the cathode in an electrolyte of molten salt with a graphite anode. Removal of a small amount of oxygen from the electrically insulating rutile phase converts it into the highly conducting Magnelli phase (Ti0$_2$-x). Continued electrolysis removes oxygen from the cathode, where it dissolves in the electrolyte and is then removed as oxygen, carbon monoxide, or carbon dioxide at the anode. At a voltage of 2.5–3.3 V, no calcium is deposited. Process time is between 24 and 48 h, with resulting oxygen levels below 1000 ppm and nitrogen of 5–20 ppm. Longer processing times allow lower oxygen levels. Reduction of several oxides has allowed production of Ti-6Al-4V [17].

MER Process

The MER process uses a composite anode of TiO_2, a reducing agent, and an electrolyte mixed with fused halides (Fig. 18.12). The composite anode approach containing stoichiometric carbon with the reduced TiO_2 is scaled to a daily output of 227 kg. The oxygen level of the batch products is below 500 ppm wt [18]. Predictions are for titanium production at a lower cost than the conventional Kroll process. Related background of the anode technology, applied to magnesium and aluminum, is provided in a set of expired patents [19–21]. Schematically, the process is shown in Fig. 18.12. The TiO_2 or rutile powders are mixed with carbonaceous material and binder, molded into electrode form, and heat-treated to form a composite anode. Ilmenite could be used for iron-containing alloys if the other impurities could be tolerated. The composite anode contains a reduced TiO_2 compound as TixOy-C. The Ti^{3+} ions are released into the electrolyte, further reduced, and deposed as titanium solid on the cathode. A CO/CO_2 mixture in bubble form is separated out at the anode. The titanium can be deposited as powder, flakes, or a solid deposit. Powder with particle size from 1 to 125 μm has been produced. The mean particle size can be controlled by process conditions.

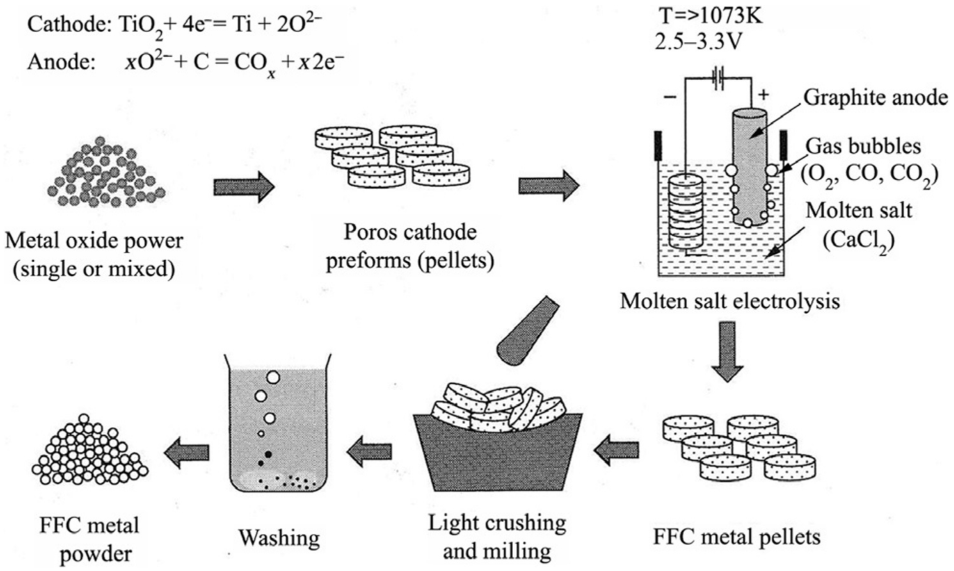

FIG. 18.11 The FCC Cambridge process.

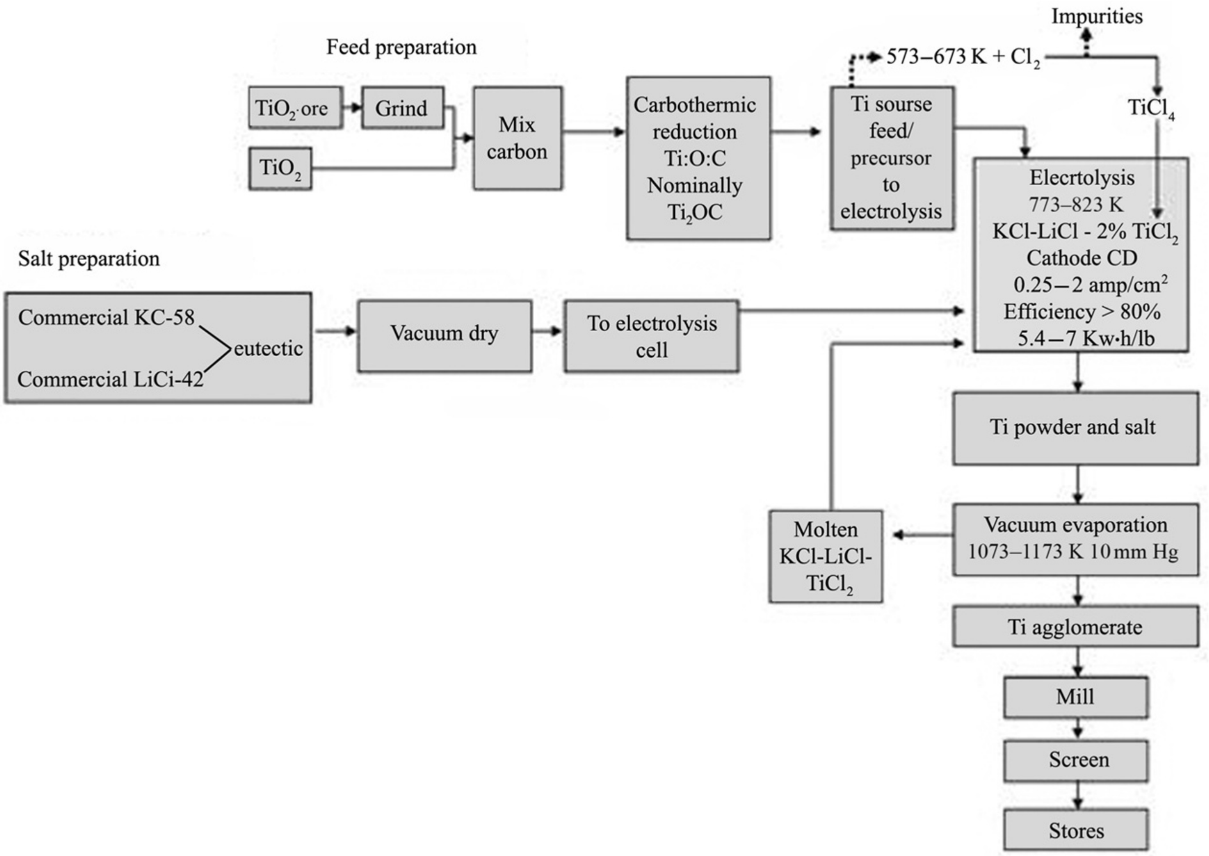
Feed preparation
Impurities
573–673 K + Cl$_2$
TiO_2 ore
Grind
Mix carbon
TiO_2
Carbothermic reduction Ti:O:C Nominally Ti_2OC
Ti sourse feed/ precursor to electrolysis
$TiCl_4$
Elecrtolysis
773–823 K
KCl-LiCl - 2% $TiCl_2$
Cathode CD
0.25−2 amp/cm^2
Efficiency > 80%
5.4−7 Kw•h/lb
Salt preparation
Commercial KC-58
Commercial LiCi-42
eutectic
Vacuum dry
To electrolysis cell
Ti powder and salt
Molten KCl-LiCl-$TiCl_2$
Vacuum evaporation
1073–1173 K 10 mm Hg
Ti agglomerate
Mill
Screen
Stores

FIG. 18.12 MER overall process to produce titanium powders from a TiO_2.

Chinuka Process

This process was invented at Cambridge University in 2005 [16]. It allows impure metal oxides to be reduced and refined to high-purity metals in a single process. The process (Fig. 18.13) is very similar to the MER process and has a main advantage that the broad range of titanium dioxide can be used. Compared to the FFC Cambridge process, a eutectic of NaCl:KCl is used as the electrolyte instead of $CaCl_2$, which reduces the operating temperature of the cell by approximately 200 K. The Chinuka process offers a number of specific advantages over existing technologies, including comparatively low operating temperatures; a cheap, water-soluble, nontoxic electrolyte; low power consumption; and the ability to directly treat impure ores.

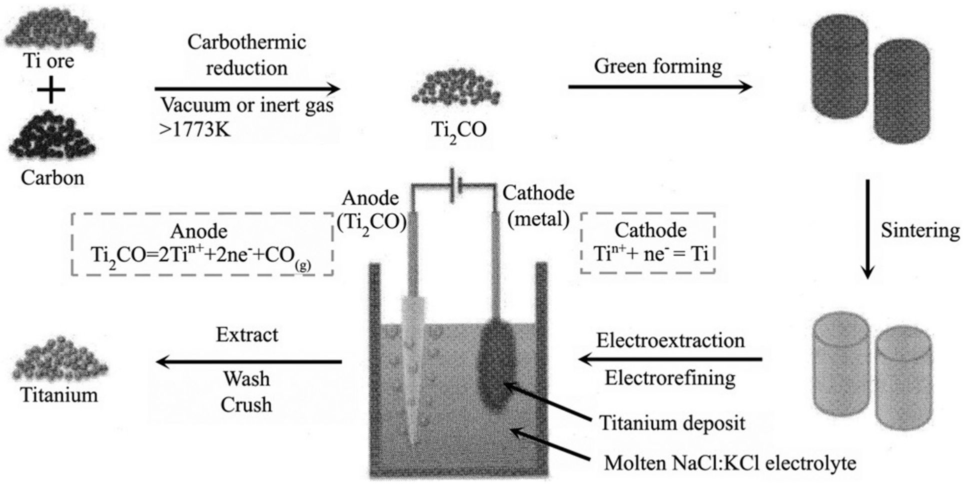
Ti ore
+
Carbon
Carbothermic reduction
Vacuum or inert gas
>1773K
Ti_2CO
Green forming
Sintering
Anode (Ti_2CO)
Cathode (metal)
Anode
$Ti_2CO=2Ti^{n+}+2ne^-+CO_{(g)}$
Cathode
$Ti^{n+}+ne^-=Ti$
Titanium
Extract
Wash
Crush
Electroextraction
Electrorefining
Titanium deposit
Molten NaCl:KCl electrolyte

FIG. 18.13 Schematical illustration of the Chinuka process.

Electrolytic Refining of Titanium

This electrolysis process with a soluble anode was developed by the VAMI Institute [22]. The technological circuit of the electrolytic refining process is shown in Fig. 18.14 [12].

By anode dissolution of titanium metal, utilizing waste products or alloys, and cathode sedimentation of crystalline titanium, a titanium powder characterized by low content of impurities (Fe, Si, C, O, N, etc.) is produced. There are conditions permitting us to obtain powders alloyed with aluminum, chromium, vanadium, manganese, zirconium, and other metals.

Raw materials for anodes include substandard titanium sponge, alloys based on titanium, and conducting products of titanium raw material reduction (oxycarbides, oxycarbonitrides, etc.). The electrolyte is the molten NaCl, or NaCl + KC1, or $NaCI + KC1 + MgCl_2$. The preparation of the electrolyte consists in the tetrachloride $TiCl_4$ reduction in molten NaCI and KCI using titanium scrap or sodium. Titanium ions are reduced to metal stepwise on the cathode; on the anode titanium is oxidized up to Ti^{2+} and Ti^{3+}. An average degree of oxidation (valency of titanium ions) in the electrolyte is 2.2–2.3. The process of titanium refining was carried out in electrolyzers of VAMI design (Fig. 18.15).

The electrolyzer is a two-cell device with a common heating furnace. Each cell consists of a retort with bulk anode containers and a cathode chamber hermetically connected with the retort. Both cells are electrically connected in parallel. The cathode chamber is supplied with mechanisms for moving the cathode and for cutting off the deposit as well as the device for additional loading of the anode material, which consists of bunkers with feeders and discharge spouts with shutters. The device for unloading the anode material in the form of a mobile tray with a folding bottom and the metal receiver is mounted on the retort. The cathode is freely suspended from a top bridge with a shear device, which is connected with the elevating screw mechanism.

During electrolysis, the cathode is immersed in the electrolyte; a current supplying unit placed in the chamber performs the current feed to it. For deposit removal, the cathode is raised to the extreme top position and then is stopped; the top bridge moves downward on the cathode and cuts off the deposit, which falls into the tray. Then the top bridge is raised, the cathode is released and restores into the retort, and the cathode current circuit is closed. Impurities not dissolved at the anode are collected in the anode slurry and are periodically removed from the electrolyzer by overspill through a taphole. During the whole cycle of processing metal waste products, starting from the loading of the initial raw material and finishing with the unloading of the end product, the leak tightness of the electrolyzer under a small excess pressure of the inert gas is controlled.

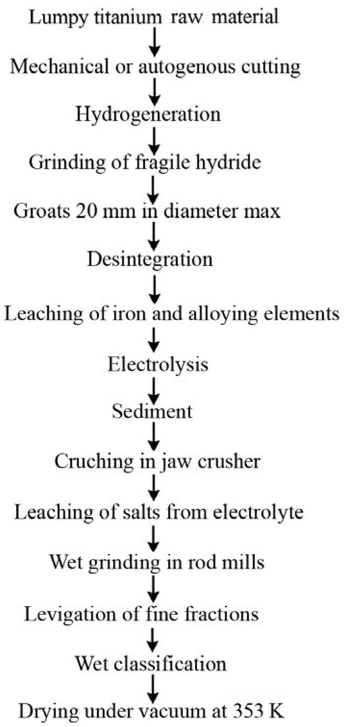
Lumpy titanium raw material
Mechanical or autogenous cutting
Hydrogeneration
Grinding of fragile hydride
Groats 20 mm in diameter max
Desintegration
Leaching of iron and alloying elements
Electrolysis
Sediment
Cruching in jaw crusher
Leaching of salts from electrolyte
Wet grinding in rod mills
Levigation of fine fractions
Wet classification
Drying under vacuum at 353 K

FIG. 18.14 Technological scheme of titanium powder production by the method of electrolysis with soluble anode (electrorefining).

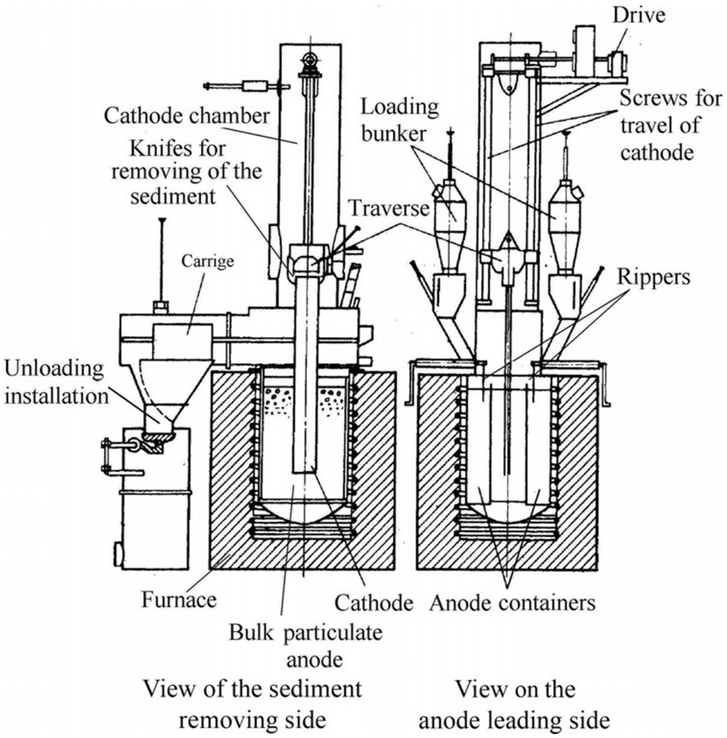

FIG. 18.15 VAMI electrolyzer with a bulk anode for producing titanium powder.

The current strength in the electrolyzers of VAMI is 10–15 κA. The capacity of the electrolyzer for titanium refining is 120–180 kg/day (of metal). When using melt based on the KCl-NaCl mix with a content of 2%–6% titanium and a temperature of 1073–1123 K, the cathode current density is maintained in the interval of 5–15 κA/m^2 while the anode current density is 4–8 times lower. Current yield counted as Ti^{2+} is 90%, and the specific charge of electric power is 10–11 kW h/kg. Titanium extraction under these conditions amounts to 95%–96% with the consumption of the electric power directly to electrolysis of 4.0–5.0 kW h/kg.

A high purity of powder purification is achieved with respect to iron, nickel, tin, molybdenum, silicon, nitrogen, oxygen, and carbon. The powders produced by electrolytic refining are more plastic than the powders produced by hydrogenation/dehydrogenation of the same titanium waste products. The method of electrolytic refining is realized at experimental industrial plants in Russia.

Physical and chemical characteristics and technological properties of the various kinds of titanium powders are shown in Tables 18.1 and 18.2. In working with powders of chemically active metals, their transport, storage, and processing carry a danger of ignition and explosion. To lower the reactivity of powders, various methods of passivation are used (Table 18.4).

AMALGAM METALLURGY TECHNIQUE

In this process, titanium tetrachloride is reduced by sodium amalgam obtained by electrolysis with a mercury cathode and a graphite anode (Fig. 18.16).

The process is carried out in a reactor in which the titanium tetrachloride is bubbled through the amalgam at a temperature of 361–377 K in an inert atmosphere (helium, argon, neon). The discharged chlorine is used for the chlorination of titanium dioxide, producing its tetrachloride:

$$TiCI_4 + 4Na\,(Hg) = Ti\,(Hg) + 4NaCl$$

The black powder formed is a mixture of titanium, mercury, sodium, and sodium and titanium chlorides. Mercury is removed in a vacuum furnace (vacuum of 1–10^{-2} Pa) or in inert atmosphere at 481–543 K. A mixture of titanium, its chlorides $TiCl_2$ and $TiCI_3$, and sodium chloride remains after distillation. NaCl is separated from the mixture in the inert atmosphere at 1088–1366 K. $TiC1_4$ reduction by a mixed sodium-potassium amalgam is carried out at 923 K. Low titanium chlorides decompose, and at a lowered pressure are removed. Sodium chloride is concentrated on walls and titanium

TABLE 18.4 Combustion Prevention for Titanium Powders

Manufacture	Branch of Industry	Technique of Powder Passivation
Production of refractory compositions and materials on their base	Nonferrous metallurgy, chemical and instrumental	Processing in acid solutions; high-temperature surface saturation; additives of aluminum oxide, nitrogen or carbon to argon plasma while dehydration
Production of friction materials by powder metallurgy	Engineering, petrochemical, etc.	Processing in aluminate solutions; processing by organosilicon composition liquids
Manufacturing of protective materials and coatings	Nonferrous metallurgy, food, and chemical	High-temperature oxidation (Combustion synthesis, consists in solid-phase reaction of titanium with titanium dioxide mixture). Use of epoxy resins for powder passivation
Production of sorbents and gas absorbers, and pyrotechnic compositions	Nuclear plant, electronics, pyrotechnics	Processing in acid solutions with addition of the spirits; surface metallization by cementation or electrochemical cooper plating; insertion of metals into argon plasma during dehydration
Manufacturing of sintered constructional and porous materials	Nonferrous metallurgy, mechanical engineering	Processing in acids and solutions of halogenides; electrochemical and plasma-chemical surface metallization

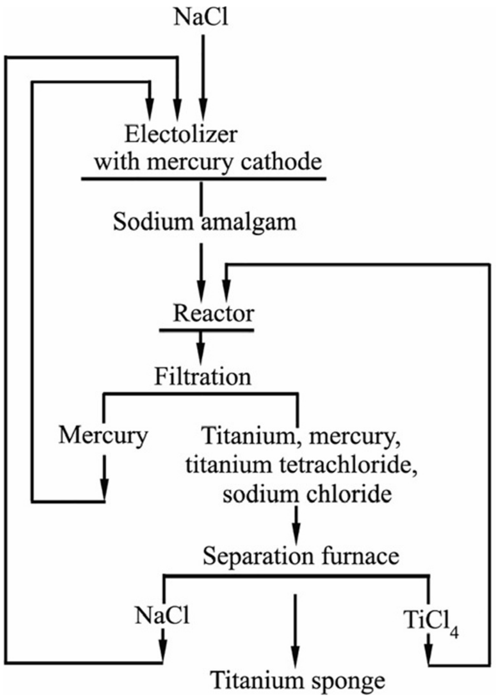
NaCl
Electolizer with mercury cathode
Sodium amalgam
Reactor
Filtration
Mercury
Titanium, mercury, titanium tetrachloride, sodium chloride
Separation furnace
NaCl
TiCl4
Titanium sponge

FIG. 18.16 Technological scheme of titanium powder production by the method of amalgam metallurgy.

crystals form a sponge. An advantage of the method is the production of particles of small size (1–10 μm) and the high purity of the titanium sponge.

The amalgam metallurgy fundamentals are discussed in Chapter 8.

OTHER METHODS

TIRO Process

This process uses Kroll chemistry for manufacturing commercially pure titanium powder (Table 18.5) in a continuous fluidized-bed reactor (Fig. 18.17). This process also uses continuous vacuum distillation.

TABLE 18.5 Chemical Composition of TIRO Process Commercially Pure Titanium Powder

Element Content (wt%)							
Ti	O	N	C	Fe	Na	Cl	Other, total
>99.70	<0.15	<0.01	<0.01	<0.02	<0.02	<0.02	<0.01

Source: Barnes JE, Williams J, Blue CA, Peter B. Titanium powder metallurgy—what's after Kroll process? In: International titanium association conference. Atlanta (GA, USA); 2012.

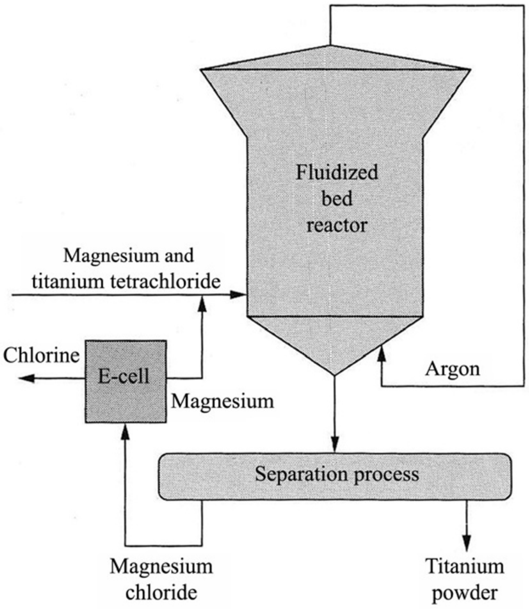

FIG. 18.17 Schematic of the TIRO process for manufacturing of commercially pure titanium powders. *(From Barnes JE, Williams J, Blue CA, Peter B. Titanium powder metallurgy – what's after Kroll process? In: International titanium association conference. Atlanta (GA, USA); 2012.)*

The advantages of the TIRO process include the following:

- Decreasing of specific energy consumption.
- Significant reduction of Kroll capital requirement.
- Low labor, high output, and continuity of the technological process.

This process developed by the Commonwealth Scientific and Industrial Research Organization (Australia) has been used for manufacturing thin sheets by direct powder rolling, extrusions, and cold-sprayed complex shapes.

Method of Disproportionation of Lower Titanium Halogenides

Low titanium halogenides ($TiCl_2$, $TiCl_3$) disproportionate with the formation of metal powder under certain conditions of atmosphere, temperature, and pressure. The process consists of transferring low titanium halogenides of scrap metal or ores to titanium tetrachloride ($TiCl_4$) at high temperatures. During the process, the formed low chlorides are condensed in the colder zone of the furnace. On heating, they disproportionate with the formation of highly dispersed titanium powder and titanium chloride, which is returned to the beginning of the process. The produced powder is suitable for powder metallurgy.

CSIR Process

CSIR is the abbreviation of the Council for Scientific and Industrial Research that devised a continuous process to produce titanium powder directly by the metallothermic reduction of $TiCl_4$ in molten salt, named the CSIR-Ti process. The authors

[23] described the experiments for this process. The initial continuous stirred tank reactor has the capacity to produce 400–500 g of titanium powder per experiment. The reactor was loaded with 3–4 kg of an alkali metal chloride salt. Because the salt can be very hydroscopic, it was predried at 423 K for >6 h. The reactor was placed in a furnace and heated to reaction temperature above the melting point of the relevant salt, after which the reducing alkali metal and titanium tetrachloride were added. Following an experiment, the reactor was allowed to cool to room temperature prior to opening. The solidified mass of salt was removed by aqueous leaching to recover the metal powder produced. Because a slight stoichiometric excess of reducing metal was added, caution was taken during leaching because alkali and alkali earth metals react intensively with water. The reactor headspace was flushed with argon, followed by the slow addition of leach liquor to limit the risk of fire and explosion. Following leaching, the titanium powder product was collected. The metal powder was washed repeatedly to remove as much residual salt as possible.

Chemical Synthesis of Nanosized Titanium Powders

A major concern with titanium-based materials is their high cost compared to the competing materials. This had led to investigations on various processes with potentially lower costs. One such route is the synthesis of nanosized titanium powders from ilmenite by chemical methods [24,25]. In this study, commercially available ilmenite and commercially available or LR grade TiO_2 of 99.5% purity was used for the synthesis of the titanium complexes. Titanium hydride was prepared by heating the titanium complex in a hydrogen atmosphere. The furnace containing titanium catecholate/gallate was evacuated to 10^{-6} Torr followed by flushing with argon, and then hydrogen gas. The process was repeated three times before heating the titanium complex in order to avoid the formation of unwanted products. The furnace was then heated to 873 K stepwise from room temperature and collected all by-products while hydrogen was passed through the furnace for another 3 h. The titanium hydride formed was cooled under an argon atmosphere and stored in the same atmosphere. The vacuum dehydrogenation was done for getting pure titanium powder of required size and purity. The length of dehydrogenation and control of temperature affected the size distribution of the powders. The process is a green route because all the reagents from the process can be recovered and reused.

Mechanical Alloying

The use of mechanical alloying to produce titanium-based alloys is relatively recent. The process is a simple technique to synthesize both equilibrium and nonequilibrium phases of materials starting with elemental powders where, generally, a mix of powders is processed in a high-energy ball mill [26]. Much of the work consists of the development of unique structural characteristics such as supersaturated solid solutions, metastable crystalline phases, amorphous phases, dispersion-hardened alloys, and nanostructured materials [26–28]. Mechanical alloying is also being studied as a technique for the manufacture of nanostructured intermetallic composites such as Ti-6Al-4V/SiC [29]. The mechanical alloying process was used to synthesize $Ti_{45}Zr_{38}Ni_{17}$ powders for plasma thermal spraying [30]. The elemental powders mechanically alloyed by a planetary ball mill are led to an amorphous state. This amorphous phase that primarily appeared in the thermally sprayed mechanically alloyed powders is transformed into the icosahedral quasicrystal phase after annealing at 828 K. The Vickers hardness for the quasicrystal layers was about 7 GPa.

APPLICATIONS

Titanium powders that have unique properties are used as alloying, refining, and modifying components in the production of metals and alloys in ferrous and nonferrous metallurgy. They have high chemical resistance to many organic and inorganic aggressive matters at normal and high temperatures. The high-temperature strength, good plasticity at low density, and high corrosion resistance of titanium surpass many constructional and composite materials. The properties of titanium are realized most fully, and with high economic efficiency, by PM technologies. They are used as a basis of charges for production of refractory and composite materials and catalysts.

Titanium powders are readily formed and sintered; products so made possess high corrosion resistance, strength, and relative lightness. They are used for producing constructional details in mechanical engineering, ceramic-metal porous filters, welding and smelting electrodes, and gas absorbers in various designs of electronic vacuum devices. Titanium powders are widely used as fillers of anticorrosive coatings based on epoxy resin, in the production of titanium carbide and nitride, and in other fields of industry. One application field for powders of titanium and its alloys is the aviation industry.

Cases and bracelets for watches, surgical tools, prostheses, frames of lenses, weapon details, etc., are produced from titanium powders by the powder metallurgy processes. Porous titanium with 40% porosity and high mechanical properties with compression yield strength of 85 MPa have been manufactured by a plasma-spray method [31]. Takemoto et al. [31] reported that a complex interconnected porous structure, together with bioactivity effectively provided by chemical and thermal treatment, produced enhanced bone in-growth and apposition.

In recent years, second generation low-modulus near β and β-type titanium alloys have been developed for bioapplications in order to avoid the "stress shielding" effect caused by the modulus mismatch between the implant and the bone [32,33]. In the work [34], the electrochemical properties and biocompatibility of injection-molded Ti-10Nb-10Zr powder were studied. A feedstock containing 55 vol% powder loading was molded in a standard mold. The binders were completely removed from molded components by solvent and thermal debinding at different temperatures. The debinded samples were sintered at 1773 K for 3 h at high vacuum. The sintered density, ultimate tensile strength, elongation, and hardness were 99%, 738 MPa, 14%, and 111.6 HRB, respectively. The authors [34] consider the Ti-10Nb-10Zr alloys due to their high strength and good bioactivity as promising for application as biomedical materials. Higher yield strength was achieved [35] by metal injection molding of Ti-13Nb-13Zr parts using a feedstock based on elemental powders. As-sintered material showed a density of 96.5% of theoretical density, a modulus of elasticity of about 85 GPa, and a yield strength of 842 MPa, but of low <1% elongation. Ti-29Nb-13Ta-4.6Zr alloy, usually called TNTZ alloy, specimens were made by the MIM process [36]. The injection-molded compacts were sintered in vacuum at various temperatures between 1423 and 1523 K for various holding times between 14.4 and 28.8 ks. The microstructure of the sintered alloy mainly consisted of β phase. The tensile strength and elongation of the alloy increased with elevating sintering temperature, and were around 650 MPa and 3% at a sintering temperature of 1523 K, respectively. The elasticity of the alloy was around 60 GPa, and was similar to that of the wrought alloy. The laser-engineered net shaping (LENS) technique was used for the preparation of biomedical Ti-6Al-7Nb alloy [37]. The surface of Ti-Al-Nb samples obtained by the LENS system was modified by electrochemical treatment. The anodization of titanium alloy was performed in glycol-based and glycerol-based 0.3 M ammonium fluoride solutions with the addition of 2 vol% of water. It was reported that the used electrolytes are able to form TiO_2 with nanoporous/nanotubular morphology on the surface of the titanium alloy with Nb content and that a stable oxide layer of thickness 10–11 μm was obtained by anodizing the alloy in a glycol-based solution.

Until recent years, commercialization of titanium implantable components via MIM was an academic endeavor and not feasible due to its inherent processing difficulties [38,39]. The technological commercialization and process capability of titanium MIM to ensure consistent chemistry and mechanical properties is reviewed in article [40].

Porous elements are applied as filters in various designs of cartridge filters, as aerators in devices of regeneration and flotation saturation, and as devices of biological purification of sewage [22]. They are used as filtering elements in drainage devices as well as as gas absorbers, fire resistors, dehumidifiers, and oil separators. Elements can be welded by argon-arc, contact, and diffusion welding and can be processed using metal-cutting machine tools.

Despite its high cost in comparison with traditional permeable materials, titanium elements are used with high economic efficiency due to high strength, exceptional corrosion resistance, biological inertness, and low density. Also, filters can easily be regenerated, do not adversely affect the solutions being filtered, reduce losses, and allow the pressure and rate of filtration or aeration to be increased.

Depending on the particle size of the initial powder and the parameters of pressing and sintering, permeable materials from titanium powders have a basic pore diameter between 25 and 200 μm, a porosity of 30%–50%, and the minimal factor of permeability for various groups of products ranges from 1.0 to 2.5 mm/s. Porous titanium sheets with well-defined thickness in the range of 150–600 μm and porosities in the range of 8%–53% were produced by tape casting of commercial titanium powders [41]. Gas-atomized and HDH powders with particle sizes below 45 μm were used as starting materials. Currently, the best compromise was achieved if HDH powders were used as starting materials, sheet thickness was adjusted below 400 μm, and the sintering was done at 1273 K, which leads to wide open porosity around 30%. It has been demonstrated by electrochemical tests that these sheets can be used as a porous transport layer (PTL) and current collector in polymer electrolyte membrane (PEM) electrolysis cells.

Additive manufacturing (AM) is, in addition to widespread manufacturing of functional prototypes, increasingly deployed for manufacturing of titanium alloy components for a wide range of applications, including use in the medical, dental, aerospace, and industrial fields.

In recent years, AM has gone from being a rapid prototyping technology for plastic and metal components to being a manufacturing process considered for its flexibility, design freedom, and weight saving. The principle is that components are built directly, layer by layer, from three-dimensional CAD data. Metal printing technology is dominated by selected melting processes. However, emerging technologies, for example, binder jetting, are gaining interest and are today applied for prototyping as well as serial production of components. Basically, all types of powders with suitable morphology and particle size can be applied to print green bodies. The subsequent sintering process is then optimized for each individual alloy. In the paper [42], the resulting properties from printing Ti-6Al-4V are presented. Digital metal technology, a two-step AM process, was applied for manufacturing Ti-6Al-4V components. Layer-wise precision binder jetting on a powder bed is followed by curing to develop the component's green strength. Subsequently, nonbonded powder is removed and component-sintered to develop density and strength. Process parameters are optimized for the alloy and physical properties examined in relation to material standard ISO 22068. In the study [43], the effects of titanium powder particle size on the mechanical properties and microstructures of AM parts manufactured by selective laser melting (SLM) were investigated. It is reported that the tensile strengths and elongations of the tensile specimens produced from different size powders (with median diameter 19.6, 22, 23.3, and 34.3 μm) by SLM at a laser power of 150 W and a scan speed of 200 mm/s vary in the ranges 610–470 MPa and 27%–11%, respectively. The technique of permeable coating production using a selective laser sintering method is described [44]. The coatings were made from titanium spherical powders using a layer-by-layer process from a metallurgical three-dimensional printer. The model of formation of the liquid metal necks between the powder particles by laser radiation for the effect of multiple reflections is reported.

The main mass of fine and medium titanium powders is used in the production of refractory compounds, particulate-reinforced titanium matrix composites, and metal-polymer anticorrosive compositions. Using self-propagating high-temperature synthesis (SHS process), it is possible to produce titanium carbide containing 79.3%–79.6% of titanium, 18.12%–19.42% of combined carbon, and 0.18%–0.28% of free carbon with high economic efficiency. The best results are achieved when using titanium powders finer than 0.1 mm. Powders of coarse fractions are used mainly as briquettes between 20 and 100 mm in diameter and 20–30 mm in height in ferrous metallurgy. Thus, only a part of the low-grade spongy titanium, which has not been converted to powders of average and fine fractions, is used in ferrous metallurgy. Besides, due to the high density of briquetted titanium and the small size of briquettes, the waste in their use is approximately 1.5 times lower than in direct use of spongy titanium. Batching and mechanization of briquette insertion into the molten steel is easily carried out.

Titanium Powder Process Selection

The characteristics of different types of titanium powders that are either available or under development at present are shown in Table 18.6.

In the powder process selection [45], the following aspects are considered:

- Cost of powder per unit weight. The powder that will approach most closely the price of titanium sponge is most likely to be high on the list for process selection.
- Powder process adaptability to scale up for powder production and for meeting major customer and market demands.
- Process controllability and lot reproducibility of the same product quality over many production lots as deliverables over time.
- Ability to satisfy the final processed product specification requirements given specific alloy chemistry, required product form, and so forth. Especially critical in this regard is the ability of the supplier to keep the production process under control and to satisfy the customer specifications for interstitial constituents.
- Minimizing the lead time. Powder producers must aim at greatly reducing that lead time to final deliverables.

The price of titanium sponge is usually used as the criterion for price comparisons for powder-based supply chain products. The two typifying different titanium PM technologies, namely blended elemental mixing powders of titanium with master alloy powders (BE) and the prealloyed (PA) methods, not only produce compacts with different sets of properties, but also with two different price ranges. At present, the most costly powders are those manufactured by PREP, REP, and GA methods. These technologies deliver powders at a price upward of $100 per kg. This is because PA spherical powders for high performance applications and near 100% densification require an expensive melt stock, ultraclean handling, and expensive compaction tools. Over the past decade, the emerging titanium powder technologies for the future of low-cost titanium production had been developed. The deciding factor of these new processes will be which one of them delivers titanium powder at a cost as close as possible to the current cost of the titanium sponge.

Titanium Powder-Based Materials Selection

Alloy selection is determined by the part design requirements and the design allowable for the intended application. The powder consolidation processing route is selected for the best balance of mechanical properties, including tensile strength, ductility (elongation), fracture toughness, and fatigue endurance limit as well as fatigue crack growth resistance.

TABLE 18.6 Characteristics of Different Types of Titanium Powders

Method/Process	Powder Type	Advantages	Conditions/Disadvantages
Sodium reduction method (Hunter process)	Elemental	High-quality titanium; excellent for cold press and sinter	Less economical regarding the Kroll process; limited availability
Magnesium reduction method (Kroll process)	Elemental	Lower cost; good compactability; readily available; low chloride	
Calcium hydride reduction process	Elemental	Lower cost; readily available	
Hydrogenation/dehydrogenation (HDH) process	Prealloyed	Readily available	High cost; fair compactability
Armstrong process	Elemental and prealloyed	Continuous process; moderate cost; compactable	Processibility/quality; production scale up
Plasma-rotating electrode process (PREP)	Prealloyed	High purity	High cost; not cold compactable
Inert gas atomization	Elemental and prealloyed	High purity; available	Not cold compactable
Mechanical alloying	Elemental	Simple technique; low cost	Powder contamination
MER process	Elemental and prealloyed	TBD	Developmental
FES-Cambridge process	Elemental and prealloyed	Available	Heightened oxygen; production scaling up
Chinuka process	Elemental and prealloyed	Operating temperature reduced; low power consumption	Developmental
Electrolytic refining process	Elemental	High purity	Pilot plant
TIRO process	Elemental	Low energy consumption; continuous	Commercialization planning stage
CSIP process	Elemental	Simple technique	Pilot plant
Method of disproportionation of lower titanium halogenides	Elemental	TBD	Developmental
Chemical synthesis of nano size titanium powders	Elemental and prealloyed	Low cost	Developmental

TBD, To Be Determined.

Modified from Froes FH. Titanium powder metallurgy: review—part 1. Adv Mater Process; 2012: 16–22.

Selection of the desired combination of processing steps must also be kept in mind in determining the final product cost. For preliminary guidance in making specific choices of powder-based titanium material selection, the designer is referred to the analysis and concluding remarks summarized previously in the current article for the tables covering processing-microstructure-property trends for given processing step sequences.

REFERENCES

[1] Naboychenko SS, editor. Handbook of non-ferrous metal powders. Moscow: Metallurgia Publishers; 1997 [in Russian].

[2] Duz V, Klevtsov A, Sukhoplyuyev V. Production of titanium powder. In: ASM handbook. Powder metallurgy, vol. 7. ASM International Publishers; 2015. p. 757–65.

[3] Froes FH, Eylon D. Powder metallurgy of titanium alloys. Int Mater Rev 1990;32(3):162–82.

[4] Moxson V, Senkov ON, Froes FH. Production and characterization of titanium powder products for environmental, medical and other applications. In: Froes FH, Hebeisen JC, editors. Proc. advanced particulate materials & processes. American Powder Metallurgy Institute; 1997. p. 387–94.

[5] Griga J, Petrunko A, Drozdenko V, Andreev A, Yatsenko A. New types of titanium powders: properties and applications, In: Proceedings of PM2004 world congress. vol. 1. Wien: Publ. European Powder Metallurgy Association; 2004. p. 249–53.

[6] Klevtsov AG, Nikishin AM, Shuvalov JV, Moxson VS, Duz VA. Continuous and semi-continuous processes for manufacturing titanium hydride using titanium chlorides of different valency. U.S. Patent 8,388,727 B2; March, 2013.
[7] Nachtrab WT, Roberts PR, Newborn HA. Powder metallurgy of advanced titanium alloys. Key Eng Mater 1993;77–78:115–40.
[8] Smagorinski ME, Tsantrizos PG. Production of spherical titanium powder by plasma atomization, In: Proceedings of 2002 world congress of PM and particulate materials. vol. 3. Orlando, FL: Metal Powder Ind. Fed; 2002. p. 3-248–60.
[9] Division of Raymor Industries Inc. Advanced powders & coatings. www.raymor.com.
[10] Limberg W, Aust E, Ebel T, Gerling R, Ogee B. Metal injection moulding of an advanced bone screw 7Nb alloy powder, In: Proceedings of PM2004 world congress. vol. 4. Wien: Publ. European Powder Metallurgy Association; 2004. p. 457–62.
[11] Hohman M, Ertl M, Choudhury A, Ludwig N. Experience with ceramic-free powder production methods. In: 1991-P/M in Aerospace and Defense Technologies. Princeton, NJ: Metal Powder Industries Federation; 1991. pp. 261–72.
[12] Fujita M, Arimoto N, Nishioka K, Miura H. New process for Ti alloy powder production by using gas atomisation. In: Proceedings of 2006 powder metallurgy world congress. Busan: Korean Powder Metallurgy Institute; 2006. p. 12–3.
[13] Chen G, Tan P, Wang J, He W, Tang H. Characteristics of Ti-6Al-4V powders by gas atomization, In: Compiled by European powder metallurgy association, (Bellstone Shrewsbury, UK) proceedings of PM 2016 world congress. Hamburg (Germany); 2016. p. 1–4.
[14] Ginatta MV, Orsello G, Perotti P, Beruti R. A newly designed plant for the electrowinning of titanium from molten salts, In: A newly designed plant for the electrowinning of titanium from molten salts. Proc. of sixth world conf. on titaniumSociete Francaise de Metallurgie; 1995. p. 753–7.
[15] Ward-Close CM, Godfrey AB, Thompson SR. Advances in titanium alloy powder, In: Proceedings of PM2004 world congress. vol. 1. Wien: European Powder Metallurgy Association; 2004. p. 261–6.
[16] Jewell D, Jiao S, Kurtanjek M, Fray D. Titanium metal production via oxide carbide electrorefining, In: Titanium 2012. International titanium association conference. Atlanta (GA, USA); 2012.
[17] Chen GZ, Fray DJ, Farthing TW. Direct electrochemical reduction of titanium dioxide to titanium in molten calcium chloride. Nature 2000; 407(Sept):361–4.
[18] Withers J, et al. Recent improvements for electrowinning titanium metal from composite anodes. www.francoiscardarelli.ca/PDF_Files/Article_Cardarelli_MER_Process [Accessed 30 March 2018].
[19] U.S. Patent 4,338,177 A; issued July 6, 1982.
[20] U.S. Patent 4,409,177 A; issued October 11, 1983.
[21] U.S. Patent 4,670,110 A; issued June 2, 1987.
[22] Gopienko VG, Ivanov AI, Ustinov VS, et al. Electrolytic refining of titanium, In: Proceedings of the third international titanium conference. vol. 1. Moscow: VILS; 1977. p. 77–83.
[23] van Vuuren DS, Oosthuizen SJ, Heydenrych MD. Titanium production via metallothermic reduction of $TiCl_4$ in molten salt: problems and products. J South Afr Inst Min Metall 2011;111(March):141–8.
[24] Sathyapalan A, Ramamohan TR, Ramakrishnan P. A novel chemical solution technique for the preparation of nano size titanium powders from titanium dioxide. Adv Powder Technol 2000;110(4):415–22.
[25] Sathyapalan A, Free ML. Titanium metal production via oxide carbide electrorefining, In: Compiled by Russell A. Chernenkoff W, Brian J. Proceedings of 2014 powder metallurgy world congressOrlando, FL: Metal Powder Industries Federation; 2014. p. 07-98–105.
[26] Froes FH, Suryanarayana C. Powder processing of titanium alloys. Rev Part Metals 1993;1:223–75.
[27] Ahn J, Lee K. Preparation of Ti-base intermetallic compounds by mechanical alloying. Mater Trans JIM 1995;36(2):297–304.
[28] Overcoglu ML, Senkov O, Srisukhumbowornchai N, Froes FH. Microstructural evolution of a nanocrystalline Ti-47.5Al-3Cr in the annealing range 725ºC–1200ºC produced by mechanical alloying and hot isostatic pressing, In: Proceedings of PM world congress. Granada: EPMA; 1998. p. 305–10.
[29] Chen X, Baburaj EG, Froes FH, Vassel A. Ti-6Al-4V/SiC composites by mechanical alloying and hot isostatic pressing, In: Proceedings of advanced particulate materials & processesChicago, IL: American Powder Metallurgy Institute; 1997. p. 165–92.
[30] Takasaki A, Uematsu S, Kelton KF. Ti-based quasicrystal layers produced by plasma thermal spraying, In: Proceedings of 2006 powder metallurgy world congressBusan: Korean Powder Metallurgy Institute; 2006. p. 51–2.
[31] Takemoto M, Fujibayashi S, Neo M, et al. Mechanical properties and osteoconductivity of porous bioactivity titanium. Biomaterials 2005;26:6014–23.
[32] Henriques VAR, Galvani ET, Petroni SLG, Paula MSM, Lemos TG. Production of Ti–13Nb–13Zr alloy for surgical implants by powder metallurgy. J Mater Sci 2010;45:5844–50.
[33] Zhao D, et al. Microstructure and mechanical behavior of metal injection molded Ti–Nb binary alloys as biomedical material. J Mech Behav Biomed 2013;28:171–82.
[34] Yemişci I, Gulsoy HO, Mutlu O, Gulsoy N. Powder injection molded of Ti10Nb10Zr alloy for bio-applications: electrochemical properties and biocompatibility, In: Compiled by European powder metallurgy association, (Bellstone Shrewsbury, UK) proceedings of PM 2016 world congress. Hamburg (Germany); 2016. p. 1–6.
[35] Bidaux JE, Comby F, Rodriguez-Arbaizar M, Girard H, Carreño-Morelli E. Powder injection moulding of low modulus Ti-13Nb-13Zr for implant application, In: Compiled by European powder metallurgy association, (Bellstone Shrewsbury, UK) proceedings of PM 2016 world congress. Hamburg (Germany); 2016. p. 1–6.
[36] Endo E, Nakayama H, Kyogoku H. Effect of sintering conditions on microstructures and mechanical properties of Ti-29Nb-13Ta-4.6Zr alloy fabricated by MIM process, In: Compiled by European powder metallurgy association, (Bellstone Shrewsbury, UK) proceedings of PM 2016 world congress. Hamburg (Germany); 2016. p. 1–5.
[37] Łazińska M, et al. Characterization of titanium oxide formed on biomedical Ti6Al7Nb alloy fabricated by laser engineered net shaping (LENS), In: Compiled by European Powder Metallurgy Association (Shrewsbury, UK), Proceedings of PM 2017 Euro Congress. Milan (Italy); 2017. p. 1–6.

[38] Grobowski JA, Piemme JC. Titanium MIM: technology for orthopedic devices, Queensbury, NY: Praxis Technology; 2014.https://praxisti.com/wp-content/uploads/2015/03/MPIF-2014-Titanium-MIM-Technology-for-Orthopedic-Devices_web.pdf. Accessed 30 March 2018.
[39] Dehghan-Manshadi A, Bermingham M, Dardusch M, St John D, Qian M. Metal injection moulding of titanium and titanium alloys: challenges and recent development. Powder Technol 2017: 1–46. https://doi.org/10.1016/j.powtec.2017.06.05 [Accessed 30 Aug. 2018].
[40] Piemme JC. Biocompatibility of components produced by titanium MIM, In: Compiled by European powder metallurgy association, (Shrewsbury, UK) proceedings of PM 2017 Euro congress. Milan (Italy); 2017. p. 1–6.
[41] Hackenmüller FJ, Bram M, Borgardt E, Panchenko O, Müller M. Porous titanium current collector for water electrolysis made by tape casting, In: Compiled by European powder metallurgy association, (Shrewsbury, UK) proceedings of PM 2017 Euro congress. Milan (Italy); 2017. p. 1–6.
[42] Persson M, et al. Properties of Ti-6Al-4V components produced by digital metal® binder jetting technology, In: Compiled by European Powder Metallurgy Association (Shrewsbury, UK), Proceedings of PM 2017 Euro Congress. Milan (Italy); 2017. p. 1–6.
[43] Mori S, et al. Effect of particle size on quality characteristics of pure titanium fabricated using metal additive manufacturing, In: Compiled by European Powder Metallurgy Association (Bellstone Shrewsbury, UK), Proceedings of PM 2016 World Congress. Hamburg (Germany); 2016. p. 1–6.
[44] Grigoriev E, Ilyuschenko A, Kuznechik O, Bykov R. Titanium-based permeable coatings produced by selective laser sintering spherical titanium powders, In: Compiled by European powder metallurgy association, (Bellstone Shrewsbury, UK) proceedings of PM 2016 world congress. Hamburg (Germany); 2016. p. 1–6.
[45] El-Soudani SM. Properties and selection of powder metallurgy titanium and its alloys. In: ASM handbook. Powder metallurgy, vol. 7. ASM International Publishers; 2015. p. 627–41.

FURTHER READING

[46] Froes FH. Titanium powder metallurgy: Developments and opportunities in a sector poised for growth. Powder Metall Rev 2013;2(4):29–42.
[47] Barnes JE, Williams J, Blue CA, Peter B. Titanium powder metallurgy – what's after Kroll process?, In: International titanium association conference. Atlanta (GA, USA); 2012.
[48] Froes FH. Titanium powder metallurgy: review–part 1. Adv Mater Process 2012;16–22.

Chapter 19

Production of Copper and Copper Alloy Powders

Oleg D. Neikov[*], **Stanislav S. Naboychenko**[†] **and Irina B. Murashova**[†]
[*]*Frantsevich Institute for Problems of Materials Science (IPMS), Kiev, Ukraine,* [†]*Ural State Technical University (UPI), Yekaterinburg, Russia*

Chapter Outline

Introduction 571
Atomization 572
  Atomization of Copper Powders 572
  Atomization of Copper Alloy Powders 576
Production of Copper Powder by Solid Phase Reduction of Copper Oxide 581
  Oxidation of Copper Powder 581
  Reduction of Copper Oxide 582
  Postreduction Procedure 583
  Recycling for Initial Materials 585
Production of Copper and Copper Alloy Powders by Electrolysis 585
  Electrodeposition of Copper Powders 585
  Electrolytic Powder Production 586
  Properties of Electrolytic Copper Powders 588
  Applications of Electrolytic Powders 592
Production of Copper Powders by Hydrometallurgical Processing 593
  Production of Copper Powders by the Reduction of Copper Oxide 594
  Copper Precipitation from Sulfuric Acid Media 595
  Copper Precipitation from Ammonia Media 599
  Copper Precipitation from Organic Phases 600
  Anhydride Process 601
  Cementation 601
  Electrowinning 602
Oxide Dispersion Strengthened (ODS) Copper Powder Production 603
  Manufacture 603
  Properties of ODS Copper Powders 604
  Applications of ODS Copper Powders 604
Applications of Copper and Copper Alloy Powders 607
Workplace Atmospheres Safety 612
References 613

INTRODUCTION

Copper-base powder metallurgy products rank third after iron and steel and aluminum-based powder-making (PM) products in terms of volume. Copper has high electrical and thermal conductivity and corrosion resistance. It can easily be wrought both hot and cold. Copper is exceeded only by silver among the materials used for electrical applications.

Copper-based powders are used to make self-lubricating bearings, the application of which in the PM industry dates back to the 1920s and still accounts for the major portion of PM copper and copper alloy applications. Other important uses for copper and copper-base PM materials include friction materials, electrical parts, filters, additives to iron, aluminum powder alloying, catalysts, paints, and pigments.

The copper-based PM products achieved a record 54,100 mt globally in 2000, as shown in Fig. 19.1 [1–4]. The shipment level of copper powders for PM use did not vary appreciably after 2013. Thus, the 2014 and 2015 shipments in Japan were 5025 and 4590 tons, respectively [3], and the 2016 shipments in North America were 16,272 tons [4]. The development of copper powder production is different from the ferrous powder sector. Copper-based products have achieved a global growth of <25% over the same period. One significant reason for this slowing down of growth has been the miniaturization of many products such as CD and DVD players, memory sticks, computers, etc., requiring ever smaller PM bearings.

Copper powders above 99% purity are commercially available. The four cardinal techniques of producing copper powders are atomization, oxide reduction, electrolysis, and hydrometallurgy. Of the above methods, atomization and oxide reduction are presently applied on a large global scale. Hydrometallurgical copper powders have not been manufactured in the United States since the early 1980s, but they are produced in Europe and Japan. A large portion of electrolytic powder

Handbook of Non-Ferrous Metal Powders. https://doi.org/10.1016/B978-0-08-100543-9.00019-1
© 2019 Elsevier Ltd. All rights reserved.

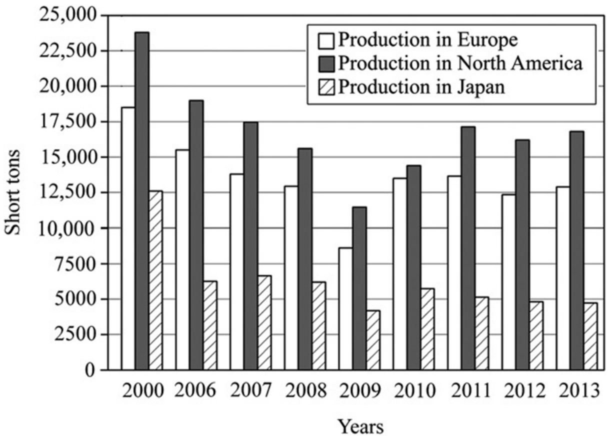

FIG. 19.1 Shipment of copper powders for PM usage. (Note: North America column in 2000 also includes the production in South America; the Japan column in 2000 consists of Asia and Oceania shipments [1]).

manufacture is in Russia, where the Uralelectromed Company, located in proximity to Yekaterinburg, annually produces about 6000 tons while its production facility for copper powder is estimated at a total of about 12,000 tons per annum. Electrolytic powder on a large scale is manufactured by the GGP Metalpowder AG company in Fürst, Germany.

ATOMIZATION

In this process, molten metal flows from a tundish through a refractory nozzle, and the liquid stream is disintegrated into droplets by the impact of water or gas jets. The droplets solidify into powder particles. Inert gas atomization produces spherical particles while the shape of water-atomized powders can be regulated from irregular to nearly spherical by controlling the interaction conditions between the water jet and the metal stream, including liquid flow rate, water pressure, and atomizer design. The particle shapes of gas and water-atomized copper powder are shown in Fig. 19.2.

Spherical copper powders have insufficient green strength for use in conventional PM. To give them compressibility, their particle shape and morphology may be transformed by means of mechanical processing and/or oxidation and reduction, as described below in this chapter under subtitle “Reduction of copper oxide.” Water is the preferred atomizing medium for producing copper and copper alloy powders. The copper powder of compacting-grade quality is produced from high-quality copper by water atomization. The obtained dried powder may be then subjected to an elevated temperature in a reducing atmosphere. Details of atomization, including fundamentals and atomizer design, are contained in Chapter 4.

Atomization of Copper Powders

Generally, the copper is superheated to 100–150 K above the melting point, providing flow rates of nearly 28 kg/min through one nozzle. Ordinarily, to produce powder with a particle size mainly <150 μm (100 mesh), water pressure must be in the range from 10 to 14 MPa.

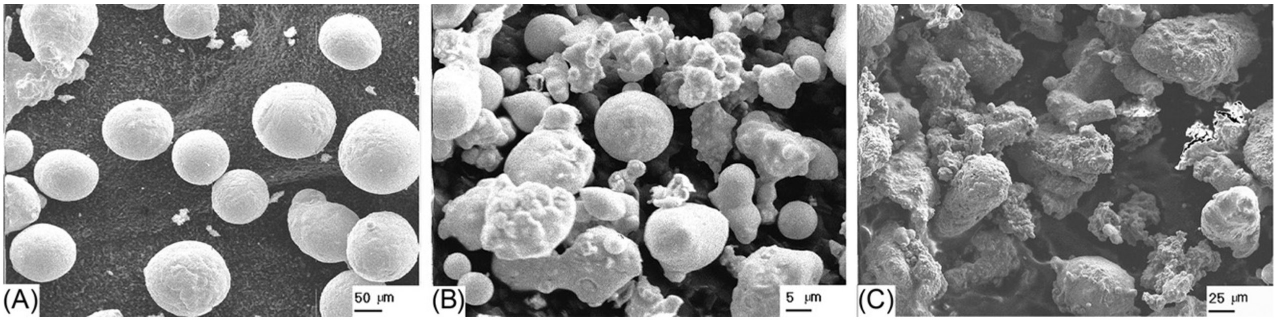

FIG. 19.2 Scanning electron micrographs of gas and water-atomized copper powders: (A) Nitrogen-atomized, (B) Water-atomized, apparent density of 3.95 g/cm^3, (C) Water-atomized, apparent density of 4.5 g/cm^3.

The conductivity of copper depends very strongly on the impurities. The effect of impurities in the solid solution on the electrical conductivity of oxygen-free copper is illustrated in Fig. 19.3. Therefore, it is very important to control the impurity content during melt preparation to achieve high conductivity and good fluidity.

The need for oxygen control at this stage of the process depends on the subsequent processing and end use of the powder. In the conventional refining of copper, poling and steam-generated hydrogen keep copper oxidation with the equilibrium curves shown in Fig. 19.4. Increasing oxygen content results in the production of a more irregular powder, and subsequent reduction of the atomized powder improves compatibility due to agglomeration and pore formation.

If the powder is used in the as-atomized state, a lower oxygen content is generally necessary because of the deleterious effects of oxygen in many applications. Oxygen is present partly as the surface oxide of copper particles and partly as the copper oxide within the particles. Removal of oxygen requires reduction temperatures of approximately 973 K or higher. At this temperature, some sintering takes place and it is necessary to mill the sinter cake to reduce it to powder.

In the reduction process, hydrogen readily diffuses through solid copper to react with oxygen and form steam. The large steam molecules, unable to diffuse through solid copper, break their way through grain boundaries, where a phenomenon known as hydrogen embitterment of copper reveals itself in the formation of blisters and cracks. These defects improve both compatibility and sintering rate during liquid-phase sintering of copper mixed with tin.

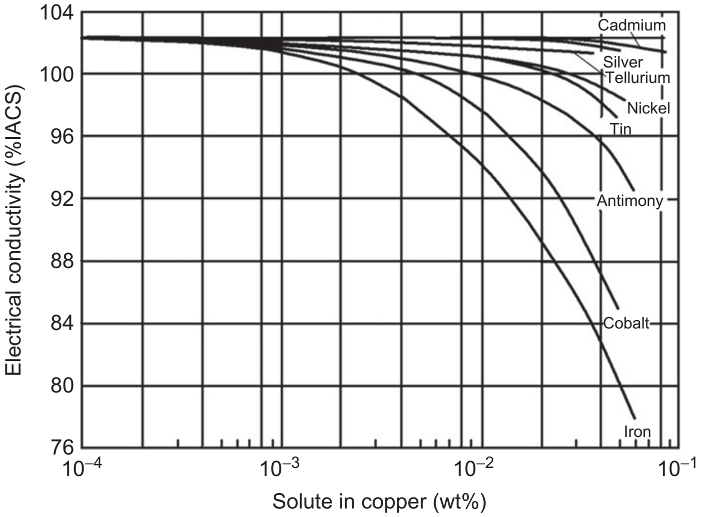

FIG. 19.3 Influence of impurities in solid solution on electrical conductivity of oxygen-free copper. (IACS is the abbreviation for International Annealed Copper Standard, is the percent of conductivity a material. has relative to copper, which is considered to be 100% conductivity). *(From Berry DF, Klar E. Production of copper powders. In: ASM Handbook, vol. 7. ASM International Publishers; 1998. p. 132–42.)*

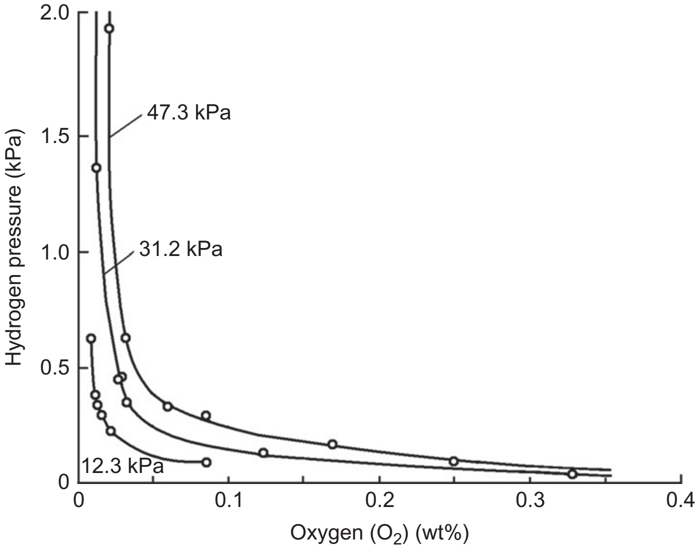

FIG. 19.4 Effect of partial pressures of hydrogen and steam on oxygen content of liquid copper at 1423 K. $Cu + H_2 \leftrightarrow 2Cu + H_2O$ reaction at various water vapor pressures.

Some applications of copper powders require apparent densities lower than those reachable with water atomization. These powders can be produced by the addition of negligible quantities, up to 0.2%, of certain elements such as magnesium, titanium, calcium, and lithium, to the copper melt prior to atomization. These metal additions decrease the surface tension of copper and/or form oxide films on the particle surface during atomization. Magnesium additions are usually used to produce PM grade such as design parts, filters, and additives for iron powders. Such powders may have apparent densities as low as 2 g/cm^3.

The addition of small amounts of phosphorous (0.1–0.3 wt%) to the molten copper before atomization allows the manufacture of a spherical powder very low in oxygen. During atomization, even by means of air, the phosphorus oxidizes and forms a protective gaseous phosphorus pentoxide (P_2O_5) compound. Such powders have apparent densities up to approximately 5.5 g/cm^3.

Spherical copper powders with controlled particle size are used in applications such as thermal spray coatings, metal impregnated plastics, and heat exchangers. Irregular copper powders are used in compacting applications such as bronze mixes for self-lubricating bearings, friction materials, electrical brushes, electrical parts requiring high strength and electrical/thermal conductivity, additions to iron mixes, and diamond cutting wheels. Irregular copper powders are also used in brazing compounds and various chemical applications such as catalysts and in the production of copper compounds.

The typical properties of commercial grades of water- and gas-atomized copper powders are given in Table 19.1.

A flow diagram of the water atomization process for copper and copper alloy powder production is shown in Fig. 19.5. Such a technological scheme with certain modifications is used at the Polena Metallurgical Works, in Tula, Russia, and was also used at the Alaverdsk Mining-Metallurgical Integrated Works, in Armenia.

The first stage in the atomization process is the preparation of charge material for melting. Copper cathodes are cut by shears into pieces suitable for charging into the furnace. Charge components are weighed, heated up to 423 K to exclude the moisture, and placed into boxes which are transferred to the melting zone. Then melting is carried out, usually with induction furnaces. They also may be used as holding for overheating and finishing a melt prepared in other furnaces, for instance, in an air furnace or resistance furnace. Such duplex melting processes improve the control of the melt preparation and decrease energy consumption.

The procedure is as follows. The copper is charged into the furnace and heated to 1290–1310 K. After melting, the remaining ingredients are added, the melt being covered by a layer of dry charcoal. The melt is then transferred to the holding furnace and the temperature raised to 1470 ± 10 K and held for 10 min. The slag is then removed and the melt "poled" with green wood and sampled for chemical analysis. The melt is superheated to approximately 1500–1550 K (144–194 K over the melting point) and then poured into the tundish preheated up to 1370–1420 K while the melt surface is covered by charcoal. Liquid copper flows out through a calibrated pipe in the bottom, forming a melt stream that is atomized by water jets. Thus, a "free fall" water atomization design is used [8]. Water pressure is 13–15 MPa and the water consumption is 14–17 L per kilogram. The temperature of the copper melt at the beginning of atomization is 1470 ± 10 K while at the end of atomization, it is not $<$1440 K.

The copper powder pulp in a weight ratio of solid to water at approximately 1–10 is dewatered in vacuum filters. Powder with water up to 15 wt% is accumulated on the filter surface. Wet powder is dried in a convective dryer in an upward flow of gases such as a combustion product of natural gas. Coarse powder particles above commercial powder size fall to the bottom of the container connected to the drier. Part of the commercial powder also falls into this container. This settling powder is then briquetted and in the form of briquettes is returned for remelting. Dried powder is separated in primary and secondary cyclones. The former separates powder fractions approximately coarser than 50 μm while the latter separates the fine particle fraction. Subsequent separation of coarser fractions into given size ranges is done on a sealed round vibrating screen. The moisture content in the dried powder is max 0.5 wt%.

To avoid moisture condensation in the duct of the drying unit, the system is preheated for about 15 min before being set in operation. The outside surfaces of the drying pipe, cyclones, and connecting ducts are thermally insulated.

Powders from storage bins in the required ratio (depending on commercial powder size distribution) are blended in a double-cone or a toroidal vibrating mixer. To prevent oxidation, the powder is covered by a passivating addition based on polymeric compounds. The powder is charged into the container, ensuring uniform descent of powder layers in the container cross-section during powder unloading, which prevents its segregation. A container with commercial powder is installed into a unit of proportioning and packing, and powder is poured into the polyethylene bags with capacity up to 20 kg, vacuum degassed, and the bags are sealed.

A study of the properties of water-atomized copper powder produced using a broad range of atomization pressures (0.2–40 MPa) and water-to-melt ratios, m_w/m_m (1.3–26.8), was conducted by Masip et al. [9]. The powders and granules were made by free-fall atomizers with two or four water fan jets. The authors reported that the median particle size (δ_{50}) decreases when the water-to-melt mass flow rate ratio increases. However, the importance of this effect goes down when

TABLE 19.1 Properties of Typical Commercial Grades of Copper Powders Produced by Atomization

Chemical and Physical Properties											Source
Copper (wt% min)	Acid (Insoluble, wt%, max)	Oxygen (wt%, max)	Apparent Density (g/cm^3)	Flow Rate (s/ 50 g)	Sieve Analysis (wt%)						
					Sieve Size (μm)						
					+250	+140	+100	+75	+45	−45	
99.0	…	…	4.5–5.5	…	…	20–50	30–60	10	trace	…	[5]
98.5 (a)	…	…	4.5–5.5	…	…	Trace	5 max	2 max	bal	60–90	[5]
99.0 (g.ph)	…	0.2 max	4.5–5.5	45 max	3 max	Nil	3 max	15–35	…	40–70	MMP
99.95 (g)	…	…	…	…	Mean size ranges from 22 to 5 μm depending on the grades						OSPR
99.0 (w)	…	0.25	2.7–3.1	35	Nil	1.0	…	20–40	20	35–50	MMP
99.3 (w)	0.1	…	2.5–2.7	…	…	0.8 max	…	70 max	bal	30 – 45	[5]
99.5 (w)	…	…	2.85–3.25	28	..	..	0.2	13	41	45.8	A-Ch
99.5 (w)	…	…	2.77–2.73	45 max	…	Nil	1 max	8 max	50 max	…	Pom
99.5 (w)	0.01	…	2.85	27	…	Trace	0.4	12	13	75	PYR
99.6 (w)	…	…	3.1–3.5	…		<0.1	<10	…	30–40	…	GGP
98.5 (w)	…	…	2.0–3.0	…			<0.1	≤1.0	bal	60–80	GGP
99.3 (w.s)	…	0.3	3.3–3.5	35–30	…	Less as 160 μm amounts 85 wt%					[6]
99.5 (w.t)	…	0.21	3.0–3.1	38	…	…	18.4	17.6	28.1	29	[7]
99.8 (w)	…	0.1	3.5	…	Mean diameter 5.1 μm						NIPP
99.0 (m)	0.1	…	2.1–2.5	…	..	..	1 max	3 max	14 max	85 min	[5]

(a) Air-atomized; (g) gas-atomized; (g.ph) gas-atomized with phosphorus addition; (w) water-atomized; (m) water-atomized aluminum with magnesium addition; (w.s) without reduction treatment; and (w.t) after reduction treatment. Companies producing the powders: Pom: Pometon; MMP: Makin Metal Powders Ltd.; OSPR: OSPREY Metals Ltd.; PYR: PYRON Metal Powders; A-Ch: American CHEMET Co.; NIPP: Nippon Atomized Metal Powders Co.; GGP: GGP Metalpowder AG.

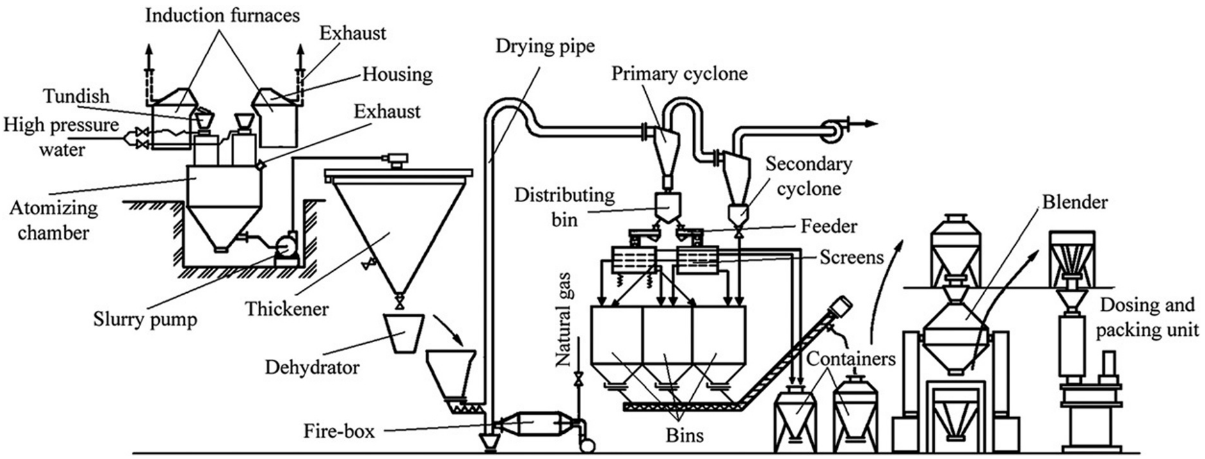

FIG. 19.5 A flow diagram of the water-atomization process for production of copper and copper alloy powders.

the m_w/m_m flow rate ratio goes up, being very important for values lower than 5, relevant in the range from 5 to 10, and negligible above 10. Thus, $\delta_{50}=220\,\mu\text{m}$ by 0.8 MPa water pressure and $m_w/m_m=3$ while $\delta_{50}=15\,\mu\text{m}$ at 40 MPa water pressure and $m_w/m_m=9$. Several empirical formulas for median particle size definition were compared.

Atomization of Copper Alloy Powders

Commercial copper alloy powders, including brasses, bronzes, and nickel silver, are manufactured in a similar way to copper. Usually, the same integrated manufacturing facilities are used to complete the melting process, atomization, dewatering, drying, particle size separation, and blending of a lot. High purity row materials are used. To ensure continuity and homogeneity, the molten batch is transferred to a second furnace with a greater holding capacity than the primary melting furnace. Induction heating is preferred for the final melting process to ensure the continuous induced liquid metal movement required for alloy homogeneity, including uniform heavy alloying element dispersion, such as lead in lead-bearing alloys.

Atomization is achieved by maintaining a constant flow of molten stream from the secondary furnace and by controlling the pressure of the atomizing medium. The adjustment of powder properties, including particle size distribution, apparent density, and the green strength of the compacts of each alloy is achieved by controlled variation of the atomizing process conditions comprising atomizing medium flow rate, molten metal superheating, atomizer design, etc. Subsequent reduction of oxides is not required for standard PM copper alloy grades.

Air-cooled, air-atomized powder is collected and passed over a primary screen to separate oversized particles. Usually, these are remelted during the processing of each alloy. In conclusion, the screened powder may be blended with dry organic lubricants, such as zinc stearate, for use in the manufacture of PM structural components.

Powder properties are maintained constant by periodically recording the atomizing parameters and evaluating the properties of representative samples from the in-process atomized product.

Atomization of Brass Powders

Brasses include the larger portion of copper-base alloy powders used for PM part fabrication. Typical copper-zinc brass powders have zinc content ranging from 10 to 30 wt%. Lead may be added in small amounts, from 1% to 2%, to improve the machinability of the sintered compacts. The melting temperature is lowered as the zinc content increases. Thus, the melting temperatures range from 1318 K for 90Cu—10Zn to 1233 K for 70Cu—30Zn. A superheat in excess of the melting point depends on heat losses within the manufacturing system and the physical property requirements of the atomized powders. Typical micrographs of water- and gas-atomized brasses are shown in Fig. 19.6. Particle morphology of both powders does not appreciably differ. The characteristic properties of commercial brass alloy powders are presented in Table 19.2.

For typical commercial brass, the compressibility at 414 MPa is 7.6 g/cm^3 and the green strength at 414 MPa is 10–12 MPa. Both compressibility and green strength data, which play a key role in PM processing, are determined on powders lubricated with 0.5% lithium stearate.

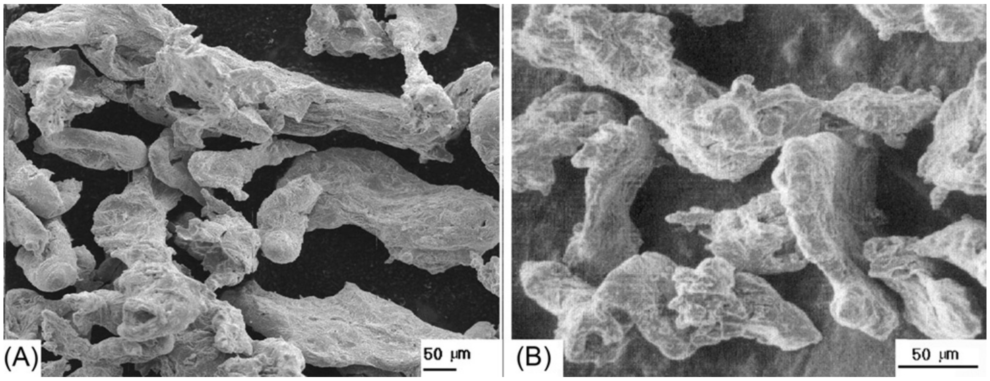

FIG. 19.6 Scanning electron micrographs of water and gas-atomized brasses: (A) Water-atomized brass (80%Cu-19%Zn-1%Pb), (B) Air-atomized brass (80%Cu-18%Zn-2%Pb).

Bronze Powders

Ordinary compositions are 90%Cu-10%Sn and 85%Cu-15%Sn, produced by the same technique as brass powder except that high purity copper and tin are used. As base powders for parts fabrication, the use of prealloyed atomized bronze compositions is hampered because of their modular particle form and high apparent density, both of which contribute to poor compacted green strength. The typical properties of the bronze alloy compositions are given in Table 19.2. Prealloyed bronze powders are made commercially by air as well by water atomizing. The 90/10 bronze powders, which are introduced in bronze premixes for bearing manufacture, find wide application. Low green strength owing to high apparent density (3.2–3.6 g/cm^3) is overcome by introducing lower apparent density copper powders and a choice of lubricants with a lower deleterious effect on green strength.

Fine bronze powder 80/20 (SF-BR8020) is produced by ultrahigh-pressure water atomization. Such powders, manufactured by Nippon Atomized Metal Powders, have an irregular shape with a mean diameter of 5, 10, and 15 μm for different powder grades. The tap density is 3.6 and 3.8 g/cm^3 for 5 and 10 μm mean size powders, respectively. Typical application of these powders is as a metal bond for diamond tools. The bronze powder 95/5 (SFB95) is also produced by the ultrahigh-pressure water atomization. It has an irregular shape and is highly porous. The apparent density is about 2.0 g/cm^3, and the flow rate is close to 34.9. It may be used for bearings requiring high precision.

Compressibility for typical bronze powder, such as 90/10 composition, is 7.4 g/cm^3 at 414 MPa and green strength 414 MPa is 10–12 MPa. Both compressibility and green strength data are for the powders lubricated with 0.5% lithium stearate.

Spherical 89/11 and 90/10 bronze powders are used to manufacture filters. These powders are usually made by horizontal air atomizing and dry collection and separation. The spherical shape is attained due to the addition of small amounts of phosphorus in the range from 0.2 to 0.45 wt%, which is introduced into the molten bronze in the form of a Cu-15%P alloy prior to atomizing. During air atomization, the oxygen predominantly reacts with phosphorus, forming phosphorus pentoxide, which is volatile at the atomizing temperature. As a result, the surface oxidation of the droplets, which would lead to an irregular shape on solidification, is avoided.

The spherical powders with particle size usually ranging from 45 to 850 μm are screened to produce a number of grades, each with a narrow particle size range. Thus, the commercial spherical bronze powders produced by Makin Metal Powder include 16 grades varying in size from 45/63 μm to 850/1180 μm. Each grade may contain up to 5% of particles above the upper size limit and up to 10% of particles below the lower size limit.

Properties of filter materials produced by loose powder sintering of spherical powders are strongly dependent on the particle size. Characteristically, a sintered filter made from spherical powder with a particle size between 180 and 125 μm with filter thickness 1.6 mm has a tensile strength of 33–35 MPa, a viscous permeability coefficient of 9×10^{-6} m^2, and the lowest dimensions of particles retained by the filter of 2.5 μm while a filter with a particle size between 850 and 600 μm with filter thickness 3.2 mm has a tensile strength of 20–22 MPa, a viscous permeability coefficient of 2.5×10^{-4} m^2, and the lowest dimensions of particles retained by a filter of only 50 μm [10].

A study on the effect of a gas recirculation system on the powder quality was carried out by Uhlenwinkel et al. [11]. At this plant, the gas recirculation is supported by the blower, behind which part of the gas could exit. The remaining gas is distributed to the top of the atomization chamber by a duct system. The atomization chamber outlet is connected by a pipe with a cyclone, the overflow branch pipe of which in turn is connected with the inlet side of the blower. The gas velocity was

TABLE 19.2 Properties of Typical Commercial Grades of Copper Alloy Powders Produced by Atomization

Grade chemical Composition (wt%)	Particle Shape	Oxygen (wt%, max)	Apparent Density (g/cm^3)	Flow Rate (s/ 50 g)	Sieve Analysis, wt%						Source
					Sieve Size. μm						
					+250	+150	+100	+75	+45	−45	
Brasses											
10–30 Zn, 1–2 Pb (a)	Irregular	…	3.0–3.2	24–26	…	2.0 max	…	17–37	34–72	60 max	[10]
16–21 Zn, 1–2 Pb (w)	Irregular	…	3.1–3.3	40	− 160 μm amounts 90 wt% min						[6]
212. (30 ± 1)Zn (a)	Irregular	…	2.9–3.5	45 max	0	…	…	…	10–25	60–90	Pom
212–63(w) (30 ± 1)Zn	Irregular	…	2.3–3.0	…	0	10 max	…	− 53 μm amounts 95 wt% min			Pom
Bronzes											
85–90 Cu, (a) 10–15 Sn	Irregular	…	3.3–3.5	…	…	2 max	…	17–37	32–72	60 max	[10]
86–88 Cu, 9–11 Sn (w)	Irregular	0.2	3.7–3.9	35 max	−160 μm amounts 90 wt% min						[6]
CuSn10 (a) 10 ± 1 Sn	Irregular	…	2.45–2.7	40 max	0	10 max.	10	…	75–85	…	Pom
CuSn 90/10 < 212 μm	Irregular	≤ 0.15	2.7–2.9	…	<0.1	7–15	…	…	52–85	Reminder	GGP
CuSn 90/10, < 75 μm	Irregular	≤ 0.15	3.0–3.5	…	…	…	< 0.1	0.5	25–45	Reminder	GGP
CuSn 85/15	irregular	≤0.15	3.0–3.6	…	…	…	< 0.1	2.0	10–40	Reminder	GGP
SBP (w) 87.5–91 Cu, 9–12 Sn 0.2–0.45 P	Spherical …	…	16 grades of spherical powders in narrow size range of 45/63 μm grade to 850/1180 μm grade								MMP
SFB95 (w) 4.5–5.5 Sn	Irregular, highly porous structure		1.8–2.2	30–45	…	10 max	25 max	30–50	40–75	20–70	NIPP
Leaded bronze powders											
CuPbSn 80/10/10 < 160 μm	Irregular		3.3–4.0	…	…	…	…	5–25	20–40	40–70	GGP

TABLE 19.2 Properties of Typical Commercial Grades of Copper Alloy Powders Produced by Atomization—cont'd

Grade chemical Composition (wt%)	Particle Shape	Oxygen (wt%, max)	Apparent Density (g/cm^3)	Flow Rate (s/50 g)	Sieve Analysis, wt%						Source
					Sieve Size. μm						
					+250	+150	+100	+75	+45	−45	
CuPbSn 80/10/10 < 80μ	Irregular		3.4–3.8				≤ 0.2	≤ 2.0	≤ 30	≤ 60	GGP
Premix bronze powders											
MP-0 9.5–10.5 Sn 0.5–0.75 lubricant	…	…	2.7–2.9	30 max	…	1.1 max	10 max	5–25	20–40	40–60	MMP
PM-020 9–11 Sn, 0.2C max 0.4 lubricant	…	…	2.75–2.95	35 max	0.2 max	1 max	2–6	20–35	31–46	25–35	GGP
Grades MM 90 Cu, 10 Sn	..	…	3.1	30	…	trace	0.5	2.0	4.5	93	PYR
Nickel silvers											
Nickel Silver P. 60–64 Cu 17–23 Zn 17–19 Ni	(a) Irregular		2.9–3.3	27–35	…	2 max	…	13–33	26–46	26–56	GGP
NS-2 64 Cu, 18 Zn, 18 Ni	(w) Irregular		…	…	Median diameter 10 μm						NIPP

(a) Air-atomized, (w) water-atomized; Companies producing the powders: Pom: Pometon; MMP: Makin Metal Powders Ltd.; GGP: GGP Metalpowder AG., PYR: PYRON Metal Powders; NIPP: Nippon Atomized Metal Powders Co; GGP: GGP Metalpowder AG.

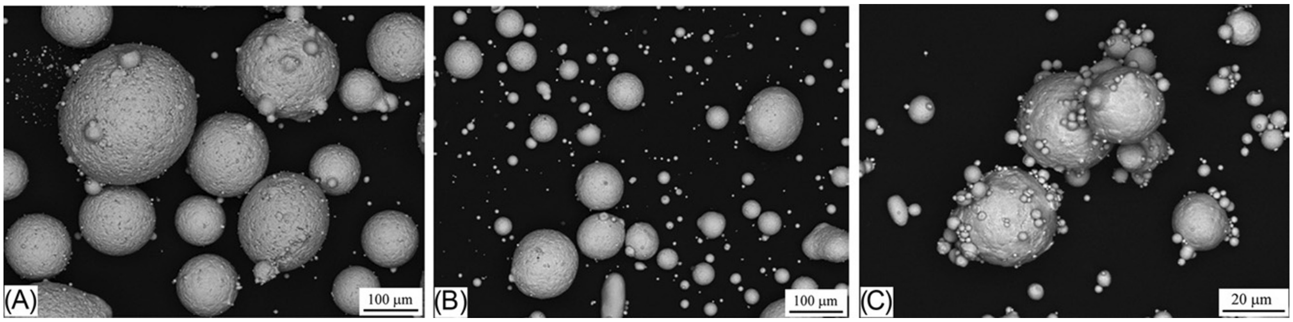

FIG. 19.7 SEM images of Cu—10Sn powder produced by free-fall atomizer without (A) and with (B) gas recirculation and produced by a close-coupled atomizer with gas recirculation (C).

19 m/s (without atomization gas), which represents a gas flow of about 840 m^3/h. The free-fall atomizer (ffa) and close-coupled atomizer (cca) were used. The alloy Cu—10Sn (10 wt% Sn) was melted in the crucible and superheated to a temperature of 1388 K for the ffa and 1638 K for the cca.

The powders generated with the ffa (Fig. 19.7A and B) are much larger than the cca powders (Fig. 19.7C). The ffa powder with gas recirculation has a mass median diameter of 82 μm and a geometric standard deviation $d_{84,3}/d_{50,3}$ of 1.72. Without gas recirculation, the mass median diameter increases to 102 μm but the geometric standard deviation is not affected significantly. The powders generated with the cca do not show a difference in the mass median diameter (22 μm) irrespective of whether gas recirculation is used [11]. In the case of cca, the powder satellite content increases.

Irregular Cu-Pb-Sn Powders

Several compositions as 70Cu—30Pb, 84Cu–8Pb–8Sn, and 80Cu–10Pb–10Sn are manufactured by water atomization. The apparent density is in range from 3.3 to 4.0 g/cm^3 for powders with a fraction size below 100 and 160 μm. These powders play an important role in the manufacture of friction and sliding materials.

Varied commercial bronze powders for diamond tools are produced by ultrahigh-pressure water atomization. These powder grades include: CuSnAl, contains 27–29 wt% Sn, 4.5–5.5 Al; SF-CuAl(80–20), contains 19–21 wt% Al, max 0.1 wt% Sn; SF-CuAg(80–20), contains 20 wt% Ag, max 0.1 wt% Sn; SF-CuNiSn, contains 9–11 wt% Sn, 19 to 21 wt% Ni; and others.

Nickel Silver Powders

Nickel-silver base alloy compositions (60–65)Cu–(17–19)Ni–(17–23)Zn are ordinarily used in the PM industry for sintered parts. These alloys can be modified by the addition of lead to improve machinability. The melting technique is similar to that used for brasses, except the melt temperature is 1366 K for superheat in excess of the melting point. Fine nickel silver powder consisting of 64Cu–18Ni–18Zn is produced by ultrahigh-pressure water atomization. Median diameter of this powder is 10 μm. Water-atomized Cu—Ni alloy powders consisting of 74–76 wt% Cu and 24–26 wt% Ni are also required for the manufacture of sintered parts. Table 19.2 shows the characteristic properties of water-atomized nickel silver powders. Compressibility for nickel silver powder at 414 MPa is 7.6 g/cm^3 and green strength at 414 MPa is 9.6–11 MPa. Both compressibility and green strength data are determined for powders lubricated with 0.5% lithium stearate.

Next to bronze bearings, nickel silvers along with brasses are the most widely used materials for structural PM parts. Typical applications include hardware for latch bolts and cylinders for locks and shutter components for cameras; gears, cams, and actuator bars in timing assemblies and in small generator drive assemblies; and decorative trims and medallions. In many of these applications, corrosion resistance, wear resistance, and artistic appearance play important roles.

Premix Bronze Powders

Currently, a number of companies manufacture premixed bronze powders in a "press ready" condition that is formulated to a customer' requirements (Table 19.2). Thus, a wide variety of powder types can be used for the production of sintered bronze 90/10, for example, mixed, partially prealloyed, or prealloyed powders. Each type has certain advantages and drawbacks, and every decision as to powder type and mixing technique is a compromise that can turn out well or not so well. The use of premixes leads to improved quality of the parts produced because of the constancy of the properties of the mixes produced in standard grades in specialized factories with large mixers are reliable quality control systems. Additionally, the

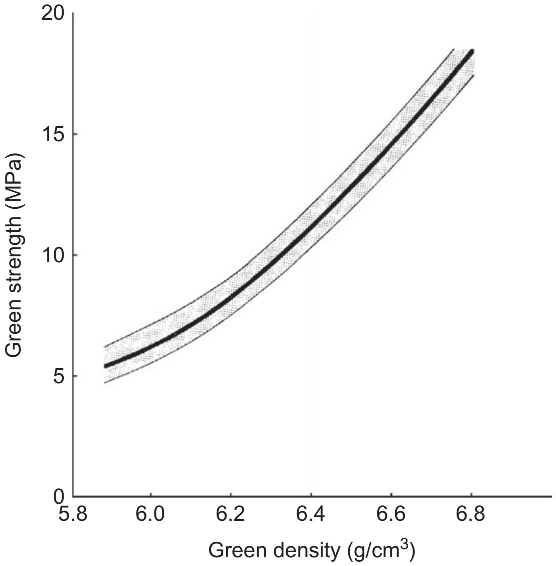

FIG. 19.8 Dependence between the green density and the green strength of premixes for sintered bronze 90/10: PM-020 (88.5–90.5 wt% Cu, 9–11 wt% Sn, max 0.2 wt% C, 0.4 wt% lubricant); PMC-020 (87.5–89.5 wt% Cu, 9–11 wt% Sn, 1.0–1.5 wt% C, 0.25 wt% lubricant).

parts manufacturers' costs are reduced as it is not required to buy, check, and store the separate ingredients; it also allows the manufacturer to avoid the cost of mixing and the associated risks.

Fig. 19.8 shows the dependence between the green density and the green strength of premixes for sintered bronze 90/10. The elevated green strength of the premixes allows trouble-free manufacture even in the case of extremely thin-walled or highly porous bearings. Partially prealloyed powders are added for better control of the sintering properties.

PRODUCTION OF COPPER POWDER BY SOLID PHASE REDUCTION OF COPPER OXIDE

Oxide reduction was the first large-scale production of copper powders. In the United States, it still remains one of the main commercial processes for copper powder manufacturing. In this process, particulate copper oxide is transformed to copper at elevated temperatures in reducing gases. The sintered porous cake produced is then ground to powder. Originally, the initial charge for reduction was copper mill scale or cement copper. However, as copper powder of higher purity was required, particulate copper of high purity (chopped scrap or atomized powder) as the starting material was oxidized to cuprous, cupric oxide, or a mixture of both.

Melting is usually carried out in either fuel-fired or induction furnaces. It is important to ensure a very low content of elements that form very stable oxides—such as aluminum and silicon which make the powders less compressible and very abrasive, while tin and lead additions cause difficulties in pouring the melt due to incrustation and clogging in the furnaces and nozzles. In the case of applications of copper powder for electrical and friction parts, it is important to remove the impurities with a harmful effect on electrical and thermal conductivity (see Fig. 19.2).

Large-scale atomization usually is run as a continuous process. Molten copper may be discharged through a tube in the side of the furnace wall and directly atomized, or through a tundish. Both air and water may be used as the atomizing medium, but horizontal air atomization into a rotating drum eliminates the need for dewatering and drying of the powder.

Micrographs of air-atomized and water-atomized powders are shown in Fig. 19.2. The water-atomized powder has a more irregular particle shape, and its oxide content is somewhat lower due to a higher cooling rate after atomization. At this stage in the process, particle shape is not particularly important. The coarse shot-type particulate copper produced by low-pressure air or water atomization (Fig. 19.9) is the typical starting material for the pure copper oxide process.

Oxidation of Copper Powder

There are two copper oxides: the red cuprous oxide, Cu_2O, and black cupric oxide, CuO. The oxidation of copper is a well-known process. At high temperatures, oxidation follows the parabolic, in which film thickness increases with the square root of time. At low temperatures, linear, logarithmic, and cubic oxidation rates have been observed, depending on the previous history of the oxide. The reaction of the copper oxide formation may be represented as follows:

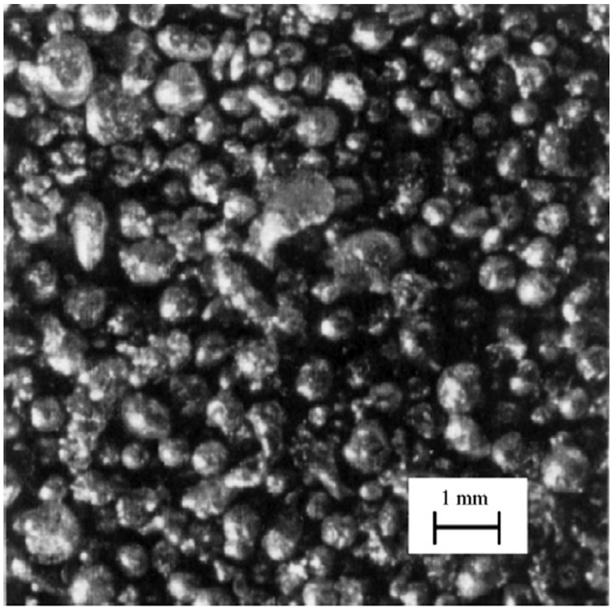

FIG. 19.9 Scanning electron micrographs of air granulated copper.

$$2(\mathrm{Cu}) + \tfrac{1}{2}(\mathrm{O_2}) = [\mathrm{Cu_2O}]\ \text{exothermic}$$

$$\Delta G = -41{,}166 - 1.27 \times 10^{-3} T \ln T + 3.7 \times 10^{-3} T^2 - 1.80 \times 10^{-7} T^3 + 27.881T$$

$$k = 957\mathrm{e} - 37^{100/RT},\ \mathrm{g}^2 \cdot \mathrm{cm}^{-4} \cdot \mathrm{h}^{-1}$$

where ΔG is the free energy in calories per gram mole; T is the absolute temperature, degrees Kelvin; R is the gas constant; and k is the a rate constant mathematically derived

$$[\mathrm{Cu}] + \tfrac{1}{2}(\mathrm{O_2}) = [\mathrm{CuO}]\ \text{exothermic}$$

$$\Delta G = -37{,}353 - 0.16 T \ln T - 1.69 \times 10^{-3} T^2 - 9 \times 10^{-8} T^3 + 25.082T$$

$$\Delta H = -38{,}170 + 1.30T + 0.99 \times 10^{-3} T^2 + 0.57 \times 10^5 T^{-1}$$

where ΔH is the heat in calories per gram mole;

$$[\mathrm{Cu_2O}] + \tfrac{1}{2}(\mathrm{O_2}) = 2[\mathrm{CuO}]\ \text{exothermic}$$

$$\Delta G = -33{,}550 + 0.95 T \ln T - 3.75 \times 10^{-3} T^2 + 22.340T$$

$$\Delta H = -35{,}710 + 3.28T - 0.40 \times 10^{-3} T^2 - 0.20 \times 10^5 T^{-1}$$

$$k = 0.0268\mathrm{e} - 20^{140/RT},\ \mathrm{g}^2 \cdot \mathrm{cm}^{-4} \cdot \mathrm{h}^{-1}$$

Oxidation or roasting of copper powder in commercial conditions is usually carried out in air at temperatures above 923 K. Oxidation in fluidized beds or in rotary kilns provides higher oxidation rates as a result of increasing the contact between the powder and the oxidizing gas. However, due to the strongly exothermic nature of the oxidation reaction, these operations are more difficult to control than roasting in a belt conveyer furnace.

Both oxides of powders, cuprous oxide and cupric oxide, are brittle and easy to grind to particle size below 150 μm. Furthermore, they are porous.

Reduction of Copper Oxide

Reducing atmospheres include hydrogen, dissociated ammonia, or other exothermic or endothermic gas mixtures. The typical reduction temperature ranges from 698 to 923 K. At temperatures of 973 K and above, sintering of the product may take place. Reduction of particulate copper oxide is generally accomplished in a continuous belt furnace with a stainless steel belt. The depth of the copper oxide bed is approximately 25 mm in which reduction happens gradually from top to bottom during motion of the conveyor belt in the countercurrent of the reducing atmosphere. Exothermic reduction processes especially need a careful control of reducing atmosphere content, oxide particle size, reduction temperature, and other processing parameters to optimize the reduction rate and to adjust the pore structure. Hydrogen is a more effective reducing agent than carbon monoxide, especially at low temperatures. However, at higher temperatures all reduction reactions in the presence of either hydrogen or carbon monoxide go to completion. In the simultaneous presence of cations of alkali metals and 0.03–0.05 wt% Se or Te, the reduction is accelerated significantly, the process can be carried out at a lower temperature, and the dispersivity and plasticity of powder particles increase [6].

The reaction of the copper oxide reduction with hydrogen and carbon monoxide can be written:

$$[\mathrm{Cu_2O}] + (\mathrm{H_2}) \leftrightarrow 2[\mathrm{Cu}] + (\mathrm{H_2O})\ \text{exothermic}$$

$$\Delta G = -16,260 + 2.21\,T\,\ln T + 1.28 \times 10^{-3} T^2 + 3.80 \times 10^{-7} T^3 - 24.768T$$

$$\Delta H_{298.1K} = -17,023$$

Temperature (K)	1173	1223	1273	1323
p_{H_2}, Pa (a)	1.39	2.0	2.76	3.77

$$[\mathrm{Cu_2O}] + (\mathrm{CO}) \leftrightarrow 2[\mathrm{Cu}] + (\mathrm{CO_2})\ \text{exothermic}$$

$$\Delta G = -27,380 + 1.47\,T\,\ln T - 1.4 \times 10^{-3} T^2 + 0.5 \times 0^{-6} T^3 - 7.01T$$

$$\Delta H = -27,380 - 1.47T + 1.4 \times 10^{-3} T^2 - 1.1 \times 0^{-6} T^3$$

Temperature (K)	1173	1323	1356
p_{CO}, Pa (a)	2.8	9.06	11.33

$$2[\mathrm{CuO}] + (\mathrm{H_2}) \leftrightarrow [\mathrm{Cu_2O}] + (\mathrm{H_2O})\ \text{exothermic}$$

$$\Delta G = -24,000 - 0.01\,T\,\ln T + 5.4 \times 10^{-3} T^2 + 3.7 \times 10^{-7} T^3 - 22.896T$$

$$\Delta H_{298.1K} = -23,543$$

$$[\mathrm{CuO}] + (\mathrm{H_2}) = (\mathrm{H_2O}) + [\mathrm{Cu}]\ \text{exothermic}$$

$$\Delta H_{290K} = -31,766$$

$$2[\mathrm{CuO}] + (\mathrm{CO}) \leftrightarrow [\mathrm{Cu_2O}] + (\mathrm{CO_2})\ \text{exothermic}$$

$$\Delta H = -33,300.$$

where ΔG is the free energy in calories per gram mole; T is the absolute temperature, degrees Kelvin; R is the gas constant; p_{H_2} is the partial pressure of hydrogen; p_{CO} is the partial pressure of carbon monoxide; the values of p_{H_2} and p_{CO} are given in Pascals; and (a) total pressure is 1 atm.

Regulation of the reduction process allows control of the particle porosity, pore size, and particle size distribution of the final powder over a wide range. As with other metal oxides, low reduction temperatures usually lead to the production of particles having fine porosity and a correspondingly high specific surface. High reduction temperatures lead to the production of particles containing large pores and low specific surface. High reduction temperatures generally result in more complete reduction and interparticle sintering.

Postreduction Procedure

The reduced copper oxide appears from the reduction belt furnace as a porous cake. It is usually disintegrated in two stages. Primarily, the cake is broken into smaller pieces in a jaw crusher or similar equipment, accompanied by fine grinding in hammer mills. Then, the reduced and milled powder is screened and, if necessary, blended and generally treated by proprietary antioxidants to stabilize it against oxidation. Without this treatment, copper powders, especially when exposed to moist air, usually tarnish with attendant detriment to green strength and other side effects. With increasing oxidation, the color of the powder changes from orange to purple to black. Oxygen content increases from a typical 0.1–0.2 wt% to several tenths of a percent, and may amount to 1 wt%. Powders with a large specific surface area are more sensitive to discoloration.

Complete lots of powder are subjected to a series of tests designed to ensure performance in various applications. Various combinations of the controlling parameters during melting, atomization, oxidation, reduction, and grinding permit the manufacture of powders with characteristics tailored to the requirements of all major applications.

Typical properties of a commercial copper powder produced by the solid phase reduction of copper oxide are shown in Table 19.3. The single most important application for copper powder is for self-lubricating bronze bearings. In the United States, these bearings are manufactured predominantly from elemental mixtures of copper and tin. From about 1960, premixed and lubricated blends of 90% copper and 10% tin that have controlled dimensional change characteristics during sintering have been increasingly in use. Apart from bronze bearings, applications of these powders include copper-base friction materials, electrical contacts and brushes, diamond wheels, and copper additions to iron mixes for structural parts [12]. Noncompacting applications include copper fillers in plastics, catalysts, and many chemical applications.

TABLE 19.3 Properties of Typical Commercial Grades of Copper Powders Produced by Oxide Reduction

		Copper powder purity, wt% min								
Property	**Unit**	**99.8[a] [10]**	**99.8[a] [10]**	**99.8[a] [10]**	**99.6[b] [10]**	**99.5[b] [10]**	**99.53 [11]**	**99.64 [11]**	**99.62 [11]**	**99.36 [11]**
Chemical composition:										
Hydrogen loss	wt% max	0.13	0.13	0.16	0.28	0.26	0.23	0.24	0.26	0.39
Acid insoluble	wt% max	0.03	0.04	0.04	0.10	0.10	0.04	0.03	0.05	0.12
Copper	wt%	bal	bal	bal	bal	bal	bal	bal	bal	bal
Sieve analysis:										
+150	μm	0.1	…	…	…	…	0.3	…	…	0.1
+100	μm	0.6	0.1	0.1	0.1	0.1	11.1	0.6	0.3	1.0
+75	μm	15.5	9.5	7.3	2.8	0.2	26.7	8.7	5.7	4.9
+45	μm	42.8	33.4	29.0	10.3	1.4	24.1	34.1	32.2	12.8
–45	μm	41.1	57.0	63.6	86.7	98.6	37.8	56.6	61.8	81.2
Apparent density	g/cm^3	3.00	2.83	2.73	1.61	0.94	2.99	2.78	2.71	1.56
Hall flow rate	s/50 g	22	23	24	…	…	23	24	27	…
Compacting properties at 165 MPa[c]:										
Green density	g/cm^3	6.15	6.12	6.03	6.0	5.9	6.04	5.95	5.95	5.76
Green strength[d]	MPa	8.6	9.7	10.4	20.0	29.0	6.15	7.85	9.3	21.4

[a] *For bronze self-lubricating bearings.*
[b] *For friction materials and electrical brushes.*
[c] *Masured with die wall lubrication only.*
[d] *Transverse rupture strength.*

Recycling for Initial Materials

When using copper mill scale as the starting material for making oxide-reduced copper powder, additional treatment to remove impurities is required before reduction. A typical copper scale contains 75–87 wt% Cu, 2–2.5 wt% SiO_2, 0.1–0.4 wt% Fe_2O_3, 1.0–1.2 wt% CaO; 1.0–1.3 wt% Al_2O_3, and contaminants of 1.0–1.5 wt% machine oils and 4%–4.5% moisture. The amount of copper oxide in the scale ranges from 25 to 30 wt%. The size fractions of the copper scale are generally below 150 μm.

The scale is normally annealed in air at temperatures above 900 K. Then, after accomplishment of the oxidation process, the copper oxide produced in the form of porous cake is ground fine. Before reduction, it is treated with a 10%–15% solution of sulfuric acid at 450 ± 5 K, at which powder yield is 60%–70%. However, etching solutions appear and sulfuric acid consumption is 0.9 ton per ton of finished powder. During the reduction of copper oxide, the copper scale-to-slag weight ratio is up to 1:1. The apparent density of reduced copper powder with size fractions below 75 μm ground in ball mills is 3.05 g/cm^3. Finished powder yield is 60%–65% of the initial copper scale weight.

A copper scale treatment technique is also known [6] where after oxidation, 5–6 wt% soda is added to copper oxide and the mixture is ground over 3–4 h. The ground product is then reduced at temperatures ranging from 1100 to 1150 K by converted gas. The sponge thus produced is wet ground using a liquid-to-solid ratio of 1 to 1 for a period of 3–3.5 h. It is then treated with a 3%–5% solution of hydrochloric acid and subsequently washed, dried, and finally further reduced. The reduced copper powder is of 98%–98.5% purity, the specific surface is 0.06 m^2/g, and the particle shape is angular.

If the feed material includes impurities, they are preliminarily eliminated by hydrochemical processes. Thus, processing of a low-grade scrap by the ammonia method–ammonium-carbonate leaching and distillation of the solution (120–160 g/L Cu, treatment with steam or at 380–400 K during 2.5–3.0 h)–results in precipitation of alkaline copper carbonate.

Depending on scrap composition, the precipitate can include nickel, cobalt, zinc, arsenic, and cadmium, that is, elements soluble in ammonia. The precipitate is washed, dried, and converted to copper by hydrogen reduction. Finished copper powder is 98.5–99.4 wt% pure and the contaminants contain max 0.03 wt% C and 0.05–0.15 wt% total volume of other elements, including S, Fe, Pb, Sn, Ca, and Mg.

PRODUCTION OF COPPER AND COPPER ALLOY POWDERS BY ELECTROLYSIS

In the electrolytic process, copper is electrodeposed to obtain a spongy powder deposit at the cathode rather than a smooth, adherent one. In this feature it differs from the process of copper refining, where a strongly adherent product is desired. Low copper ion concentration and high acid content in the electrolyte favor the formation of powder deposits. High cathode current density and use of an electrolytically refined copper anode also facilitate the formation of powder electrodeposition. Along with these conditions, the control of additional variables is necessary to produce powders that satisfy commercial requirements. These variable parameters include the quantity and type of addition agent, temperature and circulation rate of the electrolyte, size and type of the anode and cathode, electrode spacing, and brush-down interval. A technological scheme for the electrolytic process is shown in Fig. 19.9.

Electrodeposition of Copper Powders

Electrolyte Composition

Copper content in the electrolyte must be fairly low to prevent adherent deposits. In the desired range, current efficiency rises with increasing ion concentration, with a maximum to 92% in the range from 23 to 33 g/L copper, as shown in article [10]. Above approximately 33 g/L, current efficiency decreases and, simultaneously, the deposit becomes adherent instead of powdery. Apparent density and particle size also grow with a rise in copper ion concentration while a high acid content promotes the formation of powder. As shown in the work [13], current efficiency increases to a maximum at a concentration of 120 g/L of sulfuric acid, then gradually falls as the acid content increases. Apparent density decreases with increasing acid content.

Certain addition agents to the sulfate/sulfuric acid electrolyte are used to alter powder characteristics. It was reported [10] that the addition of surfactants led to the production of powder with a controlled particle size at a current density of 215 A/m^2, in contrast with the 700–1100 A/m^2 normally used, which results in a considerable reduction in power cost. The addition of sodium sulfate, as was reported [14], reduces cathode current density, and as the sulfate content is increased, the powder becomes finer. By contrast, replacement of the normal sulfuric acid electrolyte by a sulfamate electrolyte favors the formation of a coarse copper powder [15]. Small quantities of copper chloride have been added to the electrolyte to increase the dendritic structure of powder particles and to increase the yield of fine powder due to the polarizing effect of the chloride ions [16].

Processing Conditions

High current density accelerates the powder formation, but has a minor effect on current efficiency. An appreciable decrease in particle size takes place as current density is increased. Thus, in an electrolyte containing 25 g/L copper and 120 g/L free sulfuric acid, increasing the current density from 600 to 1000 A/m^2 raised the quantity of the particle under 53 μm from 20% to 96%.

Raising the operating temperature of the cell increases the current efficiency and reduces the cell voltage. However, cell operation is hindered at temperatures higher than 333 K, and powders produced at elevated temperatures are coarser than those obtained at lower temperatures. Therefore, electrolytic cells are operated at temperatures ranging from 298 to 333 K.

The method used to remove the powder deposit from the cathode and the brush-down intervals have a significant effect on powder properties. Commonly the powder is removed mechanically by means of brushing. The brush-down interval assists in control of the particle size of the deposit. As shown in article [10], the powder becomes coarser as the interval is increased from 15 to 60 min and the apparent density increases as the brush-down interval is extended. Processes to remove the deposit automatically from the cathode have been proposed. For this purpose, an organic extract was used in combination with sodium lauryl sulfate [17].

Details of operating conditions, including fundamentals of the electrolytic crystallization of dendrite deposits, are contained in Chapter 8.

Electrolytic Powder Production

As has been mentioned, the production of the electrolytic copper powder, as illustrated in Fig. 19.10, generally follows the processes used in electrolytic refining of copper but with different operating conditions, which are required to obtain a deposit of powder. Typical conditions for the production of electrolytic copper powder can be summarized as shown in Table 19.4.

Generally, the anodes are electrolytically refined copper and the cathodes are antimonial lead sheet. In a typical installation, the cathodes are 610 × 860 × 9.5 mm in dimension [10]. The electrodes are arranged parallel to one another in rubber-lined or plastic electrolysis baths with the electrolyte, which flows from the top to the bottom of the bath. Both anodes and cathodes are short to allow enough space at the bottom of the bath for the collection of the deposited powder. Typically, each cell is 3.4 m long by 1.1 m wide by 1.2 m high, and contains 18 cathodes spaced at 160 mm intervals and 19 anodes that are hung alternately. The general view of electrolytic cells at the electrolysis plant for precipitation of copper in sulfuric acid is presented in the Fig. 19.11.

Copper is deposited on the cathodes in the form of dendritic particles removed periodically by brushing. Regularly, after operating the bath for several days, the power is turned off. Most of the electrolyte is drained from the bath, and the powder

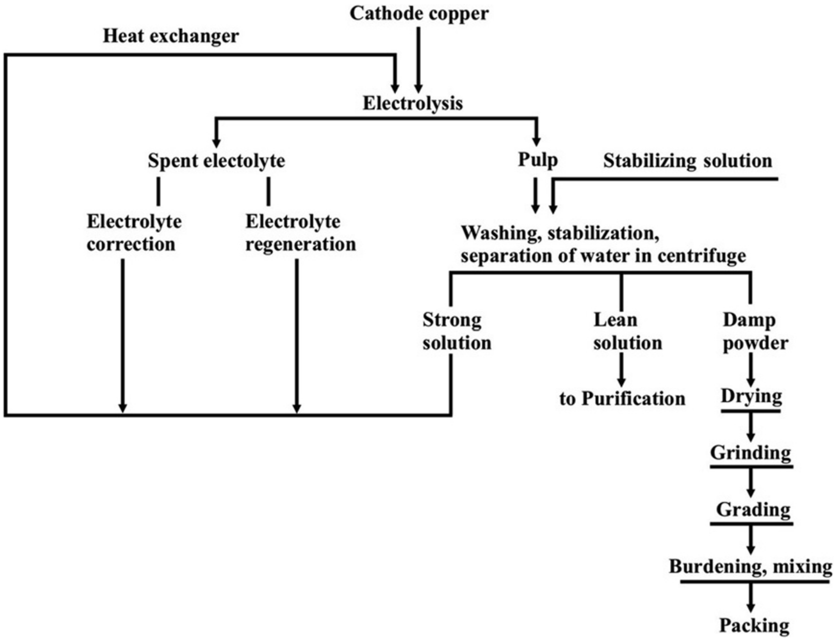

FIG. 19.10 Technological scheme of electrolytic process of copper powder production.

TABLE 19.4 Summary of Typical Conditions for the Production of Electrolytic Copper Powder

	Quantity	
Parameter	**Process by Ref [5]**	**Process by Ref [6]**
Copper content in electrolyte	5–15 g/L	10–20 g/L
Sulfuric acid content in electrolyte	150–175 g/L	120–175 g/L
Chlorine ion	…	0.5–1.5 mg/L
Temperature	298–333 K	320–330 K
Anode current density	430–550 A/m^2	390–450 A/m^2
Cathode current density	700–1100 A/m^2	2500–3100 A/m^2
Bath potential	1.0–1.5 V	1.1–1.9 V

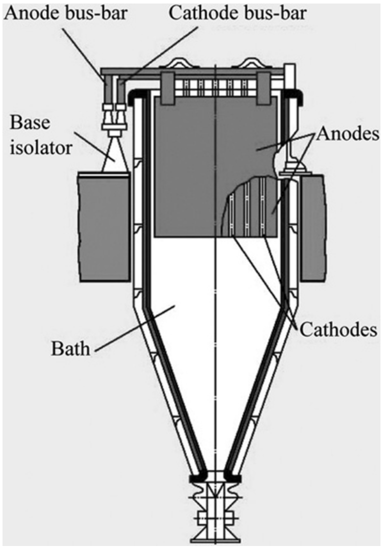

FIG. 19.11 Electrolytic cell for copper powder production.

slurry is removed. The powder is dewatered in a filter, washed several times, and again dewatered. A treatment, for example, with an aqueous solution of gelatin protects the powder from oxidation during subsequent operations.

Then, the damp powder is subjected to a furnace treatment. The furnace processing also alters certain properties, including particle size and shape, apparent density, and green strength of compacts made from the powder. Typically, an electric mesh belt furnace is used. To prevent the powder from spilling through the belt, a continuous sheet of high wet-strength paper is fed to the belt as undercoat for the powder. A roller compresses the powder to improve heat transfer. As it enters the furnace, water is vaporized and the paper burns, but not before the powder has been sintered enough to prevent it from spilling through the belt. The furnace atmosphere is produced in units in which natural gas and air are mixed to yield an atmosphere containing 17% H_2, 12% CO, and 4% CO_2, with the balance being nitrogen. By changing the furnace temperature between 750 and 1030 K and altering the exposure time, the particle size distribution and apparent density may be varied to suit requirements. Upon completion of the furnace treatment, the cake is subjected to grinding and classifying.

In another method [6], the cathodes are of electrolytically refined copper as well the anodes. In a typical installation of this kind, anodes are manufactured in the form of a sheet 880 by 900 by 50 mm and cathodes in the form of a rod (Fig. 19.12).

Such a technique is used at the copper-smelting plant of the Uralelectromed Company. The electrolyte (copper sulfate and sulfuric acid) circulates in a closed-loop system, passing through the electrolyzers, pressure tanks, and heat exchanger. The dendritic copper powder deposited on the cathodes is removed once per 2–3 h by shaking. On removal from the bath, the powder slurry is transferred to a centrifuge, where the electrolyte is removed and the powder washed. The addition of surface-active agents, such as certain fatty acid salts, during washing protects the powder from oxidation [18]. The damp

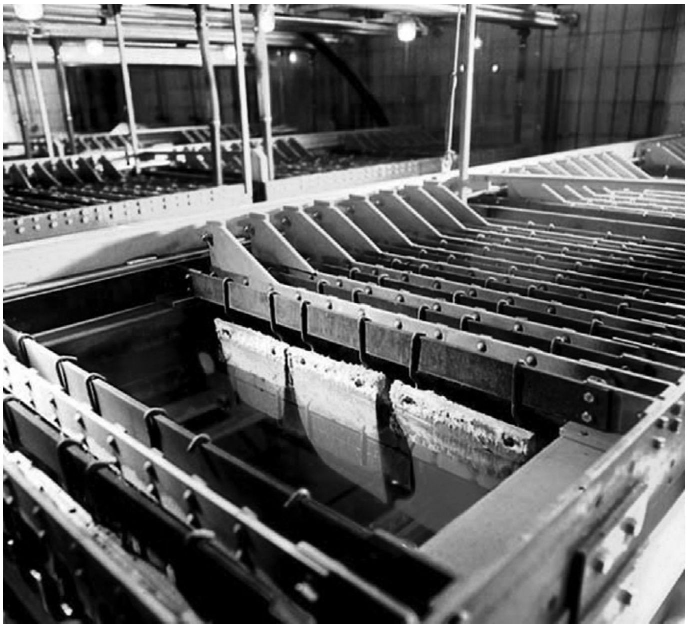

FIG. 19.12 Electrolytic cells at electrolysis plant for precipitation of copper in sulfuric acid. *(Courtesy: Ecka Granules).*

powder is dried in a flow drying pipe by furnace gases. The dried powder is subjected to grinding in ball mills and to subsequent particle size classifying in an air classifier.

Grinding is another operation in which powder properties can be altered. When fine grinding is performed at high speed, hammer mills, feed rate, mill speed, and discharge screen openings under the mill can be varied to obtain the powder characteristics desired. The powder leaving the hammer mills is delivered to screens, where the oversize is separated and returned for additional grinding. The undersize of the 150 μm powder is classified in an air classifier, and the fines are transferred to the blending operation. Oversize product is returned for regrinding or used as melting stock.

The finished powders are stored in the drams to which a drying agent such as silica gel or camphor is added to prevent further oxidation. In the case of high volume finished powder that meets customer specifications, powder is selected from various batches in appropriate proportions and mixed in a blender. The lot is sampled before being removed from the blender, and if required, corrections to the particle size distribution are made before the powder is packed in shipping drums.

Table 19.5 contains the technological parameters of electrolysis by production of copper and copper alloys powders, including copper-nickel, copper-lead, copper-tin, and copper-iron.

Properties of Electrolytic Copper Powders

The properties of electrolytic copper powder depend on various parameters of the operation and, therefore, can be adjusted by modification of certain process variables. Properties of typical commercial grades of electrolytic powders are shown in Table 19.6.

A feature of powder produced by the electrolytic process is high purity, with a copper content usually exceeding 99.5 wt%. A measure of the oxygen content is obtained by exposing a sample of powder to hydrogen flow at an elevated temperature, as specified in ISO 4491–2, ASTM E 159, MPIF 02, and GOST 29006–91 (For detailed information on this method, see the description in the paragraph "Determination of oxygen content by reduction methods," in Chapter 1). Usually, the hydrogen loss ranges from 0.1–0.5 wt%, depending mainly on the specific surface. Nitric acid insolubles are determined according to ISO 4496, ASTM E 194, and GOST 30550–98 standards (see Appendix A, at the end of book) and are usually <0.05 wt%.

Particle size distribution is selected to suit the application and can be varied over a wide range. Several combinations are shown in Table 19.6. Apparent densities of electrolytic powders are available usually from 0.65–3.2 g/cm^3. They differ in the quantity of apparent density of light and heavy. The powders with apparent densities below 1.2–1.3 g/cm^3 are generally referred to as light. In addition, the electrolytic powders with apparent density <0.45–0.60 g/cm^3 are ultralight (Cu CH-L5 and Cu CH-L7 of GGP Metalpowder AG manufacturer). The heavy powders are produced, as described above, by means of thermomechanical treatment of the former.

TABLE 19.5 Technological Parameters of Electrolysis and Powder Made Properties by Production of Copper and Copper Alloy Powders

Mode	Electrolyte Composition	Current Density (kA/m^2)	Temperature (K)	Electrolysis Parameters and Conditions
Copper				
WS	7–35 g/L Cu 50–100 g/L H_2SO_4	0.5–0.9	298–330	Current efficiency 80–99%, particle size 20–100 μm, brush-down interval 15–60 min
WS	4–24 g/L Cu 163 g/L H_2SO_4	1–2	313	Apparent density 0.8–2.2 g/cm^3, particle size 5–60 μm, current efficiency 75–96%
WS [19]	5–35 Cu 120–250 g/L H_2SO_4 0–6 g/m^3 Cl^-	0.5–6.0	315–333	Current efficiency 60–98%, apparent density 0.8–2.5 g/cm^3, specific surface 500–1800 cm^2/g
WS	25–30 g/L Cu 90 g/L NH_2HSO_3	1.5–4.0	…	Copper in the form of sulfamate; current efficiency 90–93%; circulation 1/(A·h), particle size 80 μm
WS [20]	6.4 g/L Cu 50 g/L H_2SO_4	–	287–323	Permanent overvoltage 0.3–0.7 V, particle size 2–200 μm
WS [21]	16–30 g/L Cu 160 g/L H_2SO_4	0.45–2.0	323	Permanent overvoltage 0.3–0.5 V; apparent density 2.7 g/cm^3; current efficiency 100%
WS [22]	12–15 g/L Cu 160 g/L H_2SO_4	0.02–4.7	323	Linear current variation; current. Efficiency 100%; particles size 20–100 μm in dependence of the current increasing rate
WS	6.4 g/L Cu 50 g/L H_2SO_4	–	298	Pulsing voltage with amplitude 600 mV; frequency 1–100 Hz; particle size 50–200 μm
WS	10–12 g/L Cu 150–200 g/L H_2SO_4	0.6	303–308	Pulse current; full period: pulse =10:1; particle size 50μm; current efficiency 98–99%; apparent density 1.5 g/cm^3
EDC	3.2 g/L Cu H_2SO_4; 0.02–1% oleic acid	2.5	293	Drum rotation 10–40 rpm; dendrite size 0.3–3 μm
EDC [23]	3.2 g/L Cu Solutions of carbon acids in toluene	2.5	293	Rotation 10–40 rpm; oleic acid is changed to stearine to decrease Cu_2O yield; current efficiency is 93%
RSP	5.3–10.6 g/L Cr Na_2CO_3	1.0	343	Raw material–CuO with particles 0.25 mm; cathode–copper; anode–coal; particle size to 0.5 mm; current efficiency 67–69%
M	0.2–10 wt% CuCl KCl–NaCl	0.01–20	720–1170	At 720–840 K there are formed two-dimensional twin dendrites (112); at 1170 K–three-dimensional (100)
C	H_2SO_4 to pH = 3.3–3.6; 12–15 g/L NaF	–	363–368	Drum rotation 3–5 rpm; cementing agent is aluminum
C	3–4 g/L Cu H_2SO_4	–	300–310	Cementing agent is Zn powder; mixing ($Re = 10^3$–10^4)
Copper-Nickel				
WS	1 g/L Cu; 4 g/L Ni; 40 g/L NaCit, (a); 30 g/L NaCl; 20 g/L NH_4Cl			Cathode–stainless steel; anode–graphite; average particle size is 2 μm
Copper-Lead				
WS [24]	13–35.6 g/L Cu + Pb; (pH 3)	2.5–3.0	313	(0.2–0.3) mole/L Cu + Pb; sulfamine solution; $(Cu/Pb)_{alloy} \cong (Cu/Pb)_{sol}$

Continued

TABLE 19.5 Technological Parameters of Electrolysis and Powder Made Properties by Production of Copper and Copper Alloy Powders—cont'd

Mode	Electrolyte Composition	Current Density (kA/m^2)	Temperature (K)	Electrolysis Parameters and Conditions
Copper-Tin				
WS [25]	Cu/Sn (3/1–1/3); Na_3Cit 40 g/L; (pH 2)	1.6	303	Alloy: 92Cu – 8Sn (solid solution) lattice constant–0.3665 nm
EDC	8 g/L Cu; 20 g/L Sn; 20 g/L HCl; 50 g/L NH_4Cl; (pH = 1.5); SAS 0.2%	1.5	293	Alloy: 90Cu – 10 Sn; current efficiency 88%; voltage 12 V; cathode–graphite; specific surface is 3.76 m^2/g; apparent density is 0.97 g/cm^3; resistance is 7.5×10^{-4} Ohm · cm; copper is in the form of sulfate, tin is in the form of chloride
WS	7 g/L Cu; 41.5 g/L Sn; (pH 6–8); natrium tripolyphosphate	1.5–2.5	303–314	Intensive mixing; yellow crystals
Copper-Iron				
EDC	(1.25–11.25) g/L Cu; (5.5–16.5) g/L Fe; 0.5% oleic acid	0.4–2.8	284–323	Organic lay–toluene

Production mode: WS: electrolysis of aqueous solution; RSP: reduction of solid phase; EDC: electrolysis from double-layered cell; M: melt electrolysis; C: cementation; SAS: surfactant; (a): NaCit–Sodium citrate; Information on RSP, EDC, M, C is contained in Chapter 8.

Generally, powders with a density of less than about 1.3 g/cm^3 do not flow, powders with apparent density ranges from 1.3–2.3 g/cm^3 have a poor flow rate, and powders with higher apparent densities flow freely. The flow rates of the common blends of electrolytic copper powder range from 25 to 40 s/50 g.

The green density is a function of the compacting pressure. Depending on particle distribution of the dendritic powder blends used, the green densities amount to 6.0–6.3 g/cm^3 at compacting pressure 100 MPa, as shown in Fig. 19.13, and rise to 7.7–8.0 as the compacting pressure is increased to 550 MPa. Green strength increases with the green density, and therefore with compacting pressure, as shown in Fig. 19.14. In this example, green strength for fine light copper powder such as the FS type (see Table 19.6) rises from 8 to 21 MPa as the green density is increased from 5.5 to 6.3 g/cm^3 and the green strength for heavy powder such as the SSM type (see Table 19.6) rises from 5 to 14 MPa as the green density is increased from 5.75 to 6.5 g/cm^3.

The particle shape of deposited electrolytic copper is generally dendritic, as shown in Fig. 19.15. However, during subsequent processing, including thermomechanical treatment, initial dendrites are enlarged due to welding together of small particles and rounding them somewhat (Fig. 19.16).

The compacting pressure is an important variable to take into account because the pressing and sintering conditions have an appreciable influence on the properties of sintered compacts. During sintering, the gases from the atmosphere, from the products of reduction, or from the lubricant must escape if conducting compacts are to be obtained. So, when the compacting pressure is too high, the flow through interconnected pores may be hindered, and gas cannot escape. Compacting pressures not higher than 275 MPa should be used in the production of large, thick parts from electrolytic copper powder, though higher pressures can be used for thin-walled parts [26].

The tensile strength and elongation of parts made from a typical powder blend in relationship to compacting pressure and sintering time are shown in Fig. 19.17 [27]. The powder was lubricated with lithium stearate, then pressed at 1273 K in an atmosphere of dissociated ammonia. It shows that good tensile properties can be achieved with short sintering times.

Powder metallurgy techniques have long been successful in the production of parts containing highly conductive copper. Even small amounts of impurities in the copper drastically reduce its conductivity. As conductivities above 90% IACS are required, only high purity copper powder can be considered as starting material. In this connection, the electrolytic copper powder provides the best conditions for this. However, high conductivity can be achieved only in

TABLE 19.6 Properties of Typical Commercial Grades of Copper Powders Produced by the Electrolytic Process

		Source: Standard Grades													
		GGP				ESP		UEM		MMP		Pom			
Properties	**Unit**	**FFL**	**FS**	**SSM**	**Cu CH-L10UF5**	**C100**	**C270**	**PML2**	**SA**	**SFG16–200**	**SFG22**	**LP0**	**SB**	[10]	[10]
Nominal composition:															
Hydrogen loss	wt%	0.17 max	0.12 max	0.10 max	0.07 max	0.15	0.08	0.2 max	0.2 max	0.2 max	0.20 max	0.40 max	0.15 max	0.15 max	0.20 max
Acid insoluble	wt%	…	…	…	…	0.02	0.02	0.04 max	0.04 max	…	…	…	…	0.06 max	0.06 max
Copper	wt%	99.7 min	99.75 min	99.8 min	99.85 min	99.7	99.9	99.6	99.7 min	99.4 min	99.4 min	99.5 min	99.8 min	99.8 min	99.7 min
Sieve analysis:															
+250	µm	…	…	0.2 max	…	…	…	…	nil	…	…	…	.nil	…	…
+150	µm	…	…	1 max	…	…	…	…	3–9	…	nil	…	5 max	1 max	…
+100	µm	…	…		…	…	…	…	25–35	nil	20 max	nil	15–25	6 max	…
+75	µm	0.2 max	0.2 max	23–29	…	…	…	…	…	3 max	10–25	0.2 max	38–48	…	trace
+45	µm	12 max	12 max	29–37	$\delta_{50} < 5$ µm	…	…	…	80–90	…	15–45	12 max	…	50–60	10 max
–45	µm	90 min	90 min	37–43	…	…	…	90 min	10–20	75–85	30–45	…	37–43	40–50	90 min
Apparent density	g/cm^3	1.0	1.75–1.95	2.30–2.50	1.0	1.0	2.7	0.90–1.10	2.25–2.55	1.501.70	2.10–2.40	0.65–0.75	2.35–2.55	2.3–2.5	0.9–1.1
Hall flow rate	s/50 g	none	none	40 max	…	none	26	none	40 max	45 max	45 max	none	40 max	37	none
Compacting properties at 165 MPa:															
Green density	g/cm^3	6.3	6.3	6.5	…	5.9	6.1	…	…	6.40	6.40	…	…	6.4	6.0
Green strength (d)	MPa	25	21	14	…	27.5	10.3	…	…	15 min	5 min	…	…	14	18

GGP: GGP Metalpowder AG; ECP: ElectroCopper Products Ltd.; UEM: Uralelectromed; PM: Pometon; MMP: Makin Metal Powders Ltd.

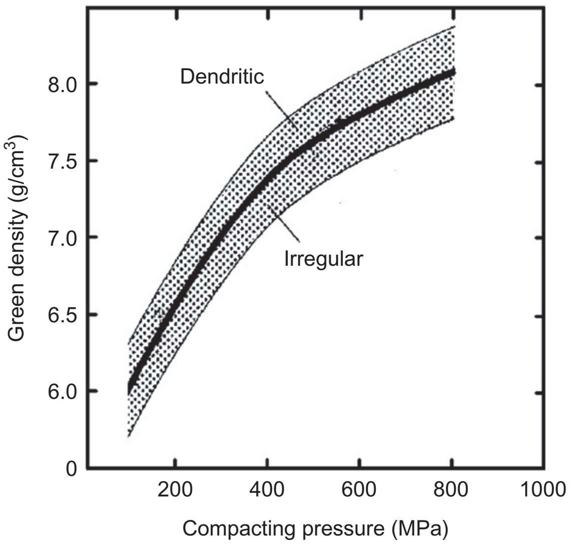

FIG. 19.13 Effect of compacting pressure on green density. *(Source: Peissker E. Metal powders, Norddeutsche Affinerie. Hamburg: Brillant-Offset Publ; 1986.)*

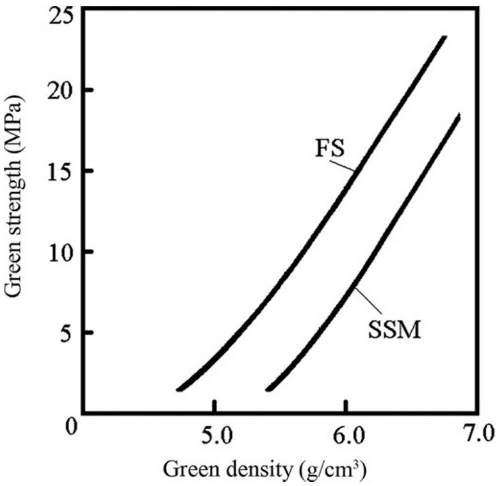

FIG. 19.14 Relationship between green density and green strength.

high-density compacts, as shown in Fig. 19.18, and the latter is generally possible only by means of recompacting and resintering [27,28].

The test data represent an example of such processing (Fig. 19.19). The starting material is electrolytic heavy copper powder of *K* grade produced by GGP Metalpowder AG [28], which differs from powder of the SSM grade (see Table 19.6) in a lower content of fine particle fractions, <40 µm.

Compression should not be too high during the first compacting because this would hinder the escape of the lubricant from the specimen to be sintered. Even small lubricant residues spoil the electrical conductivity.

Applications of Electrolytic Powders

Currently, electrolytic copper powder is produced in England, Germany, Italy, Russia, Japan, India, and Brazil, where it is used in most copper powder applications. The production of electrolytic copper powder has recommenced in the United States where, in the early 1980s, it was stopped and replaced by oxide reduction or water atomization.

Electrolytic copper powder is still the powder of choice in many electrical and electronic applications, where high electrical and thermal conductivity is required. Complex parts such as armature bearing blocks, contacts for circuit breakers, heavy-duty contacts for circuit breakers, high-duty vacuum contact materials for contact tubes and electrode caps for

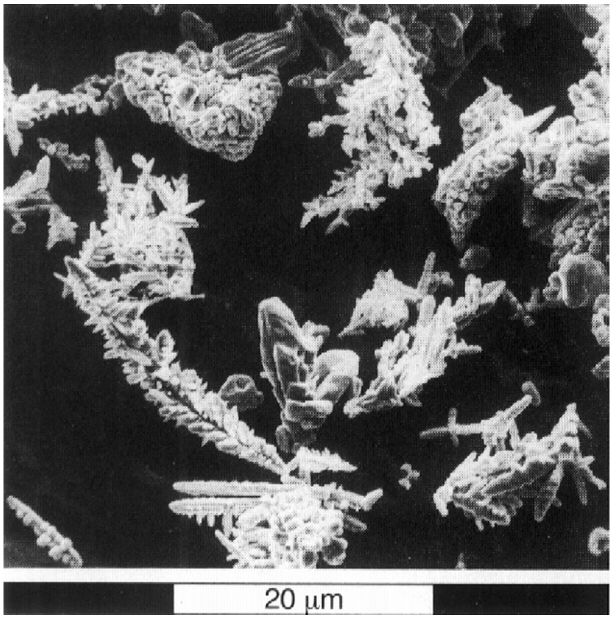

FIG. 19.15 Dendritic structure of fine light electrolytic copper powder.

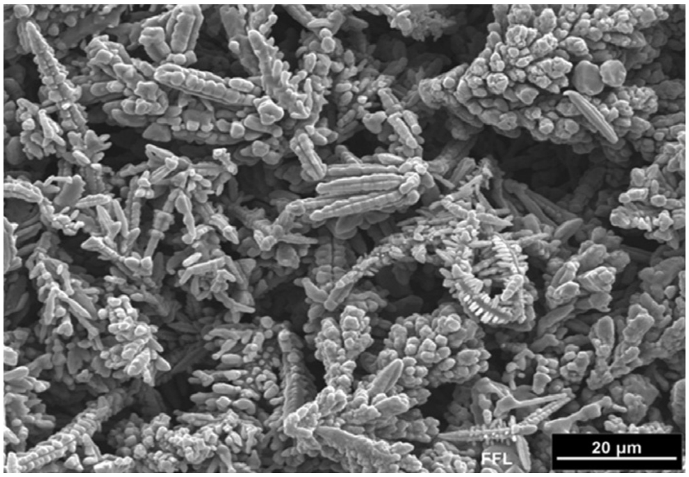

FIG. 19.16 Structure of heavy electrolytic copper powder.

welding, shading coils for contactors, switch gear components for use in switch boxes with capacities up to 600 A, and components for 150 and 250 A fuse blowouts are in regular production.

Electrolytic copper is still the preferred powder in the manufacture of electrical brushes due to the combination of purity, high electrical conductivity, high surface area, and particle dendritic shape, which allow a large volume of graphite to be accommodated in a copper matrix with high conductivity and high green strength.

Electrolytic copper powder is used with various nonmetallic materials to produce friction parts, such as linings for clutches and brakes. Premixes of iron-copper or iron-copper-carbon are utilized in various automotive applications (gears, sprockets, piston rings) and similar components.

PRODUCTION OF COPPER POWDERS BY HYDROMETALLURGICAL PROCESSING

The basic hydrometallurgical processing steps consist of leaching the raw material, accompanied by the precipitation of the metal from the solution. The most significant precipitation methods are cementation, reduction generally with hydrogen at normal or elevated atmospheric pressure, and electrolysis. The use of some leaching precipitation steps or the addition of solvent extraction, flotation, or ion exchange improves the purity of the final product.

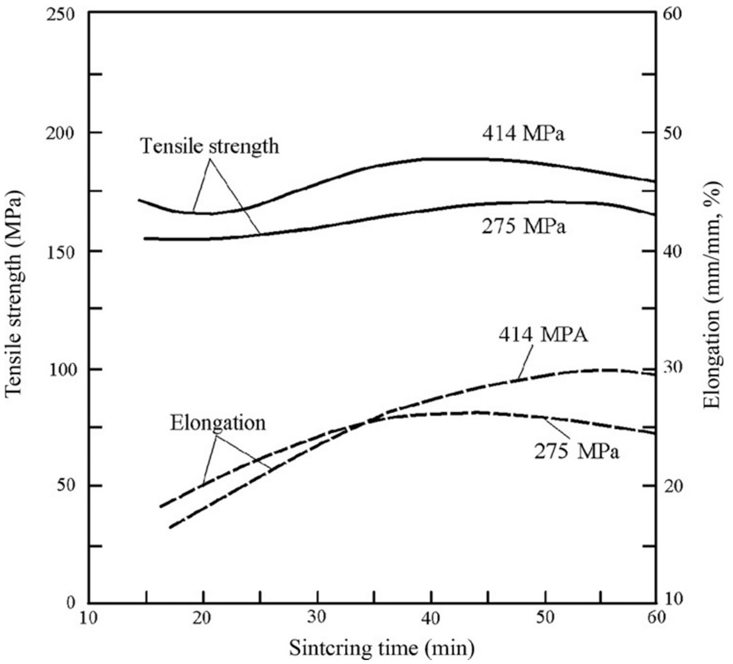

FIG. 19.17 Effect of compacting and sintering conditions on tensile properties. *(Source: Technical data from AMAX Metal Powders. AMAX Copper Inc.; 1968.)*

Production of Copper Powders by the Reduction of Copper Oxide

Leaching

The leaching of copper sulfide and copper oxide ores entails partial dissolution to cupric sulfate with sulfuric acid and iron sulfate. The presence of pyrites in many ore deposits, and its reaction with water and oxygen to form iron sulfate and sulfuric acid, creates an important source of acid. In dump leaching, the pH of the solution is maintained between 1.5 and 3.0, partly to preserve bacteria that promote and accelerate the oxidation of purity and copper sulfate minerals and also to prevent hydrolysis of iron salts. The copper content of the solution varies from <1 g/L to several grams per liter.

Another leaching method is ammonia leaching, which is used for certain copper oxide ores. These methods are called leach-precipitation-flotation and are applied to mixed sulfide ores. There are also leaching techniques involving the precipitation of the metal from organic phases [6].

Reduction Processes

Copper powders can be precipitated from ammoniacal, sulfurous, and organic media by reduction with hydrogen, carbon monoxide, and sulfur dioxide. The most effective reducer is hydrogen. Thermodynamic data for a number of reactions of copper precipitation under pressure are provided in Tables 19.7 and 19.8. The equilibrium residual concentration of Cu (II) ions depending on pH solution and hydrogen pressure p_{H2} may be represented in accordance with Nernst as:

$$-\lg\left[\mathrm{Cu}^{2+}\right]=\frac{E^{\mathrm{o}}_{\mathrm{Cu}^{2+}|\mathrm{Cu}}}{0.0296}+2\mathrm{pH}+\lg p_{\mathrm{H2}}$$

where $E^{\mathrm{o}}_{\mathrm{Cu}^{2+}|\mathrm{Cu}}$ is the standard potential of the system $\mathrm{Cu}^{2+}\leftrightarrow\mathrm{Cu}$; pH is the potential of hydrogen; and p_{H_2} is the hydrogen pressure.

The reduction of Cu (II) ions includes the stage of Cu (I) ion formation; their equilibrium concentration under the conditions (when temperature ranges from 313 to 473 K; and liquor contains 0.1–0.8 mol/L of Cu^{2+}; 0.3–2.0 mol/L of H_2SO_4) can be written:

$$[\mathrm{Cu}^{+}]=\left[\mathrm{Cu}^{2+}\right]_0^{0.5}-\exp\left\{\frac{5350}{T}-10.52\right\}$$

The kinetics of copper precipitation from sulfate and ammoniacal media have special features, as shown in the generalized equations given in Table 19.9.

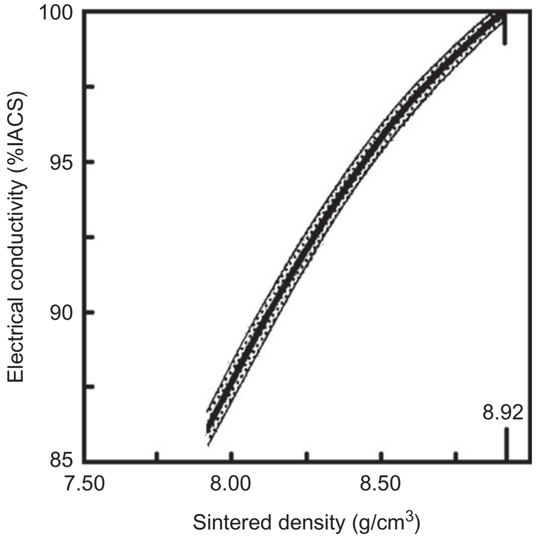

FIG. 19.18 Dependence of electrical conductivity on sintered density. *(Source: Peissker E. Metal powders, Norddeutsche Affinerie. Hamburg: Brillant-Offset Publ; 1986.)*

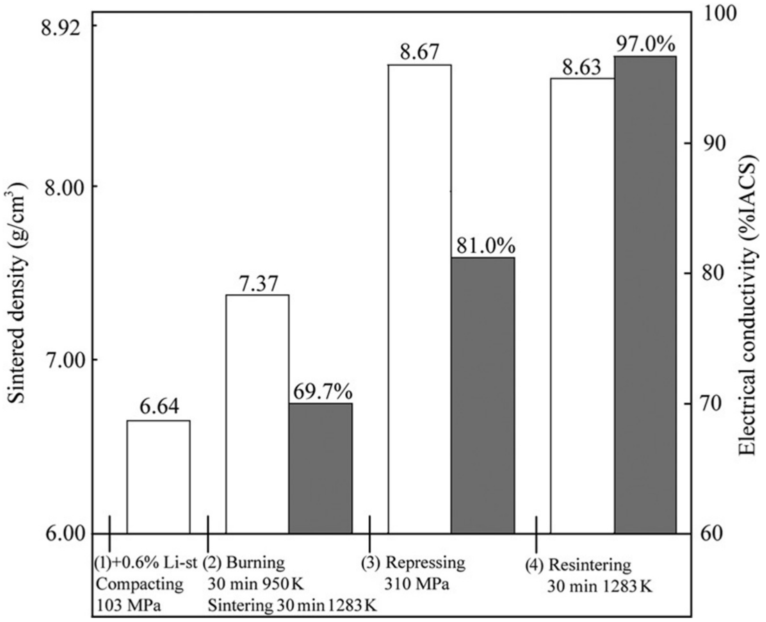

FIG. 19.19 Effect of recompacting and resintering on sintered density and electrical conductivity. *(Source: Peissker E. Metal powders, Norddeutsche Affinerie. Hamburg: Brillant-Offset Publ; 1986.)*

Copper Precipitation from Sulfuric Acid Media

The kinetics of Cu (I) ion formation are described by the equation:

$$\frac{d[\mathrm{Cu}^+]}{d\tau} = 4.3 \times 10^9 \left[\mathrm{Cu}^{2+}\right]_0 p_{\mathrm{H2}} \cdot \exp(-12900/T).$$

It is correct in the ranges: $T = 390-440$ K, $p_{\mathrm{H2}} = 1.0-3.5$ MPa, $[\mathrm{Cu}^{2+}] = (0.2-1.3)$ *mole*/*L*, $[\mathrm{H_2SO_4}]_0 < 0.2$ *mole*/*L*.

Due to Cu (I) ion formation, the accompanying ion impurities have great importance, which can lead to:

- The oxidation of Cu (I) ions (Fe^{3+}, Co^{3+}, $\mathrm{CrO_4^{2-}}$, etc.) that leads to slowing down of the process and the increase of hydrogen consumption;
- The formation of sparingly soluble compounds with Cu (I) ions, which thus pollute the powder (halides, thiocyanates, $\mathrm{TeO_3^{2-}}$ etc).

TABLE 19.7 Equation and Equilibrium Constant (C) Values for Reduction Reaction of Cu (II) Ions by Gaseous Reagents in Acidic and Ammonia Solutions

Reaction	$-\Delta H°$, kJ/(g·ion)	Equation of Equilibrium Constant, C	Dependence of C on Temperature T	Values of C, at Temperature	
				298 K	423 K
$Cu^{2+}+H_2=Cu+2H^+$	66.94	$C=\frac{a^2_{H^+}}{a_{Cu^{2+}}f_{H_2}}$	$\lg C=-0.24+\frac{3497}{T}$	3.15×10^{11}	1.06×10^{8}
$Cu^{2+}+CO+H_2O=Cu+CO_2+2H^+$	64.09	$C=\frac{a^2_{H^+}f_{CO_2}}{a_{Cu^{2+}}f_{CO}f_{H_2O}}$	$\lg C=3.78+\frac{3348}{T}$	1.025×10^{15}	4.95×10^{11}
$Cu^{2+}+SO_2+2H_2O=Cu+SO_4^{2-}+4H^+$	109.28	$C=\frac{a^4_{H^+}a_{SO_4^{2-}}}{a_{Cu^{2+}}f_{SO_2}f^2_{H_2O}}$	$\lg C=-12.74+\frac{5716}{T}$	2.78×10^{6}	5.6
$Cu(NH_3)_2^{2+}+H_2=Cu+2NH_4^+$	114.46	$C=\frac{a^2_{NH_4^+}}{a_{Cu(NH_3)_2^{2+}}f_{H_2}}$	$\lg C=-3.62+\frac{5984}{T}$	2.39×10^{16}	3.36×10^{10}
$Cu(NH_3)_2^{2+}+CO+H_2O=Cu+CO_2+2NH_4^+$	112.60	$C=\frac{a^4_{NH_4^+}f_{CO_2}}{a_{Cu(NH_3)_2{}^{2+}}f_{CO}f_{H_2O}}$	$\lg C=0.15+\frac{5882}{T}$	7.53×10^{19}	1.12×10^{14}
$Cu(NH_3)_2^{2+}+SO_2+2H_2O=Cu+SO_4^{2-}+2NH_4^++2H^+$	158.56	$C=\frac{a^2_{NH_4^+}a_{SO_4^{2-}}a^2_{H^+}}{a_{Cu(NH_3)_2^{2+}}f_{SO_2}f^2_{H_2O}}$	$\lg C=-17.15+\frac{8282}{T}$	4.36×10^{10}	2.69×10^{2}

a_i is the activity factor of an *i*-ion; f_j is the fugitivity of a *j*-component.

TABLE 19.8 Values lg$C$ of the Reducing Reaction of Several Copper Compounds With Gaseous Reagents Depending on Temperature

Reaction	lg$C$ at Temperatures (K)				
	600	700	800	900	1100
$CuO+H_2\leftrightarrow Cu+H_2O$	8.6	7.3	6.3	5.5	4.4
$Cu_2O+H_2\leftrightarrow 2Cu+H_2O$	6.9	5.8	5.0	4.4	3.4
$CuO+CO\leftrightarrow Cu+CO_2$	11.1	9.5	8.3	7.3	5.8
$CuCl_2+H_2\leftrightarrow Cu+2HCl$	2.9	3.1	3.4	3.7	4.4
$CuSO_4+2H_2\leftrightarrow Cu+SO_2+2H_2O$	8.2	7.0	6.0	5.2	4.1
$CuCO_3+Cu(OH)_2+2H_2\leftrightarrow 2Cu+CO_2+3H_2O$	14.1	11.8	10.0	8.6	6.4

Accumulated acid during precipitation equimolar to precipitated copper impairs the kinetics of the process and increases solution aggressivity. An expediency is to add ammonium sulfate or sulfates of the first-group metals (Na_2SO_4, K_2SO_4), which dilute the activity concentration of H^+ ions, but a more effective procedure is to introduce a slurry of oxides or copper hydroxides, or other soluble neutralizer.

Copper precipitation from sulfurous solutions is characterized by high selectivity toward the accompanying impurities. Coprecipitation of ions As (III), Bi (III), and Sb (III) occurs after precipitation of 90%–95% Cu. The noble metals are precipitated quantitatively.

The mechanism of Cu (II) reduction with hydrogen is heterolytic and includes the following stages:

1. Solution of gas and saturation by the aqueous phase.

TABLE 19.9 Kinetic Parameters of Copper Reduction

Reducer	Medium	Kinetics equation	ΔE, kJ/mol	Rate constant, MPa/s (*k*)	Interval of Examined Parameters			
					p, MPa	*T*, K	$[Cu^{2+}]$ (g-ion)/L	Solution Composition
H_2	Ammoniac	$kSp_{H_2}{}^{0.5}$	67.4	…	1.0–3.0	440–490	1.0–2.5	6.5 MNH_3 1.5 M$(NH_4)_2SO_4$
	Acetate	$k[Cu^{2+}]p_{H_2}$	86 ± 0.5	$(1.05 \pm 0.05) \times 10^7$ MPa/s	0.5–2.0	373–423	0.1–0.2	25–50% HAc[a]
	Sulfuric acid	$k[Cu^{2+}]p_{H_2}$	107 ± 2.0	8×10^9 MPa/s	1.0–2.5	403–423	0.3–1.3	$pH > 1.0$
		$k[Cu^{2+}]p_{H_2}^{0.5}[H_2SO_4]^{-0.5}$	107 ± 2.5	$8.7 \times 10^9\ MPa^{0.5} \times L^{-4.5}\ mol^{-1.5}$	1.5–4.5	403–423	0.3–1.3	$pH < 1.0$
SO_2	Sulfuric acid	$k[Cu^{2+}]^2\ p_{SO_2}^{0.5}[H_2SO_4]^{-0.5}$	66.2	2×10^5(g-ion)L^{-3}	0.25–1.0	393–453	0.05–0.2	0.1–0.6 M H_2SO_4
CO	Sulfate	$k[Cu^{2+}]^2p_{CO}$	140.0	2.56×10^{14} g-ion	1.0–4.0	423–463	0.1–0.8	buffer
	Acetate	$\frac{k_1[Cu^+][Cu^{2+}]}{[H^+]} + \frac{k_2[Cu^{2+}]^2p_{CO}}{[H^+]}$	109 ± 1.3	$k_1 = 1.84 \times 10^9$ MPa $k_2 = 4.\ 4 \times 10^6$	1.5–3.4	378–396	0.048–0.12	0.25 MNaAc 0.5 MHAc[b]

[a] *HAc is the acetic acid.*
[b] *NaAc is the sodium acetate; M is denote mole/L.*

2. Activation of hydrogen by Cu (II) and Cu (I) ions
   $Cu^{2}+H_2 \rightarrow (Cu\langle{}^{H}_{H})^{n+} \rightarrow CuH^{n-1}+H^{+}$
3. Formation and accumulation of Cu (I) ions
   $Cu(II) + CuH^{n-1} \rightarrow 2Cu(I) + (H \text{ or } H^{+})$
4. Disproportionation of excess Cu (I) ions in respect of the equilibrium concentration ones

Process parameters accelerating copper precipitation lead to the production of powder with more fine, dense, roundish particles. At $T > 420$ K, the agglomeration of dispersed particles is observed, resulting in decreasing of the flow rate, apparent density, and powder specific area. Variation of technological parameters within the limits that do not worsen the copper precipitation rate affects powder properties weakly.

An increase in inert sulfate content causes the formation of dispersed roundish powder particles that increase its flow rate and apparent density. The particle shape depends on the sulfate type: roundish with (ammonia or Fe (II) sulfates), elongated with (zinc sulfate 0.08–0.16 mol/L NH_3; 0.015–0.03 mol/L PO_4^{3-}; 0.01–0.05 mol/L Cl^{-}).

Varying by the type and surfactant consumption, the copper powder properties are changed within the following limits: specific surface area ranges 0.02–0.18 m^2/g, apparent density 0.9–2.2 g/cm^3, and particle size 20–42 µm. An increase in surfactant consumption increases the carbon content in powder.

An increase in the number of densifications from 1 to 6 results in an increase of powder apparent density and flow rate 1.6 times and powder size 1.67 times while powder surface decreases 2 times; conglomerates are formed, the sedimentation rate increases and dewatering becomes easier. The powder particle precipitation rate is 6–9.6 cm/min (particles size is 72–81 µm, apparent density is 0.6–0.84 g/cm^3, and specific surface is 1.9–2.3 m^2/g). On centrifuging (filtrational perchlorovinyl fabric, separation factor 200–300, temperature 310–320 K), the powder residual moisture content ranges from 10% to 15% and a maximum of 4.5% of the powder is entrained with centrifuge discharged filtrate. If water consumption for powder washing (water-to-powder mass ratios) is in the 3–5 range at temperatures that do not exceed the 300–310 K interval, the residual content of sulfate sulfur is max 0.03%–0.05%. Oxidation prevention is achieved by powder treatment of powder with 0.3%–0.4% naphthenate soap solution.

On reduction of product in the hydrogen current, the temperatures up to 520–670 K appreciably influence the powder properties: the particles become more round and solid, and the powder apparent density and flow rate increase to 7%–10%. At temperatures in the range from 870 to 1100 K, the particle fractions <74 µm are sintered. During annealing, 40%–60% of the sulfur, 60%–70% of the carbon, and up to 98% of the oxygen are removed; the residual impurities consist of 0.005–0.016 wt% S, 0.05–0.1 wt% C, and 0.03–0.05 wt% O_2. More complete elimination of impurities requires a primary content oxygen in the powder in the range from 2 to 3 wt% and annealing temperature in the range from 900 to 1200 K. However, in this case a cake forms that requires further grinding and particle size classifying. Such powder is characterized by higher apparent density and flow rate, though its yield is smaller due to screening out of coarse particles flattened during milling.

At compacting pressure p over 12 MPa, the useful green compacts are formed; the tensile strength of compacts made by pressing at $p > 500$ MPa from hydrogen-reduced powder and electrolytic powder are identical. Powder compactibility is described by the relationship $p/p_{max} = Q^{0,2}$ (Q–relative compact density). Compressibility of powders obtained from ground cake is 15%–20% worse.

By varying the parameters of the powder precipitation and its subsequent processing, the powder properties can be altered within the following limits: apparent density of 0.5–2.5 g/cm^3, flow rate of 0.0–3.5 g/s, and specific surface of 0.034–4.2 m^2/g. The powder chemical composition is similar to electrolytic powder. Compared with the latter, copper powder precipitated from sulfuric acid media is characterized by higher apparent density and flow rate, smaller specific surface area, dispersivity, and tendency to gas saturation and oxidation.

Copper as copper (I) chloride was precipitated from the chloride solutions (25 g/L Cu; 20 g/L HCl) at 373 K and $p_{H_2} = 1.0$ MPa in an hour but even at 437 K and $p_{H_2} = 2.0$ MPa, metallic copper is absent.

Organic reducing agents (sugar, glucose, starch, fructose, and sawdust of varied arboreal kinds) precipitate copper powder with density max 15–20 g/L at 433–443 K, during 1.0–3.0 h. However, incomplete copper precipitation, impurity of powder, and recycled solution with reducer destruction substances indicate inadaptability (low technological effectiveness) of the tested agents.

For hydroxide pulp processing (400–450 K, $p_{H_2} = 2.0–2.5$ MPa), medium pH and temperature are the governing process parameters: at pH > 4.5 and temperature lower than 413 K Cu(I) oxide forms; in a more acidic medium and at higher temperatures, copper powder is obtained.

Nanosized Cu powders from copper sulfate pentahydrate ($CuSO_4$ $5H_2O$) inside a nonionic polymer matrix, using a wet chemical reduction process, were synthesized in the laboratory scale by Kim et al. [29].

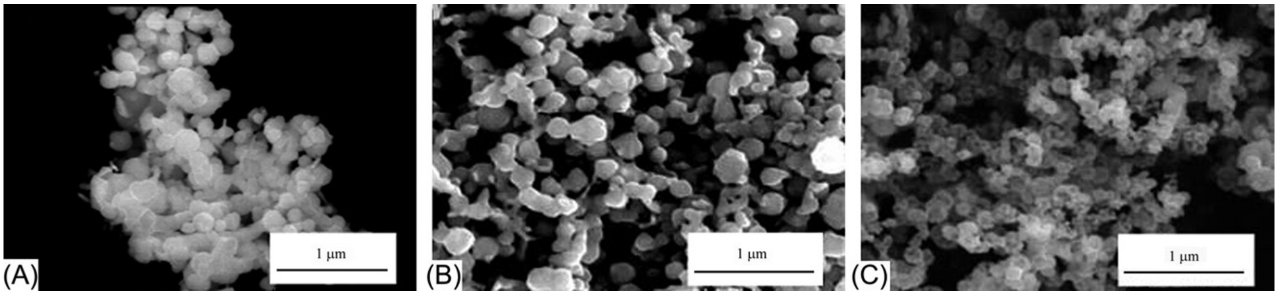

FIG. 19.20 SEM micrographs of the copper powders prepared at several sucrose contents: (A) without sucrose, (B) with 0.004 M, and (C) with 0.04 M sucrose content.

Copper sulfate ($CuSO_4{\cdot}5H_2O$), hydrazine hydrate ($N_2H_4{\cdot}H_2O$), sodium hydroxide, commercial sucrose as a dispersant, a pH control agent, and nonionic polymer network were used as the starting materials. An appropriate amount of copper sulfate was dissolved directly in distilled water with sucroses in the 0.004–0.04 M range. The resulting mixtures were heated at 343 K, 353 K, 363 K, and 363 K for 2 h, and then hydrazine hydrate (molar ratio of $N_2H_4{\cdot}H_2O/CuSO_4{\cdot}5H_2O = 7$) was slowly injected into the mixtures. After washing and filtration, the as-prepared products were dried at 298 K for 24 h.

Fig. 19.20 shows the SEM images of Cu powders prepared (A) without sucrose, (B) with 0.004 M, and (C) with 0.04 M sucrose content. In the former, the large particles arise due to the coalescence of primary particles in irregular shape agglomerates. On the contrary, by sucrose adding, the agglomeration of particles is prevented. The authors [29] reported that the Cu powder synthesized by the addition of 0.004, 0.02, and 0.04 M of sucrose shows the particle size decreasing with increasing sucrose content while the particle size increased by a reaction temperature in 333–363 K range. The lower value particle size of the 127 nm median diameter with standard deviation 1.9 was observed at the 0.04 M sucrose content.

Copper Precipitation from Ammonia Media

A process rate with a kinetics constant K does not depend on original copper concentration; it decreases with an increase in ammonia and ammonium sulfate concentration and increases with an increase of temperature, the seed surface, and hydrogen pressure raised to the 0.5 power:

$$d\left[\mathrm{Cu(NH_3)_n}\right]^{2+}/d\tau = KS \cdot p_{\mathrm{H_2}}^{0.5} \exp(-1860/T)$$

Optimal content of free ammonia should provide production of copper complexes $[\mathrm{Cu\ (NH_3)_n}]^{2+}$ where $n = 2.2$–2.5.

Ammonia media stimulate coreduction of nickel together with copper and powder contamination, especially where the ratio of Cu^{2+} to Ni^{2+} is between 3.5 and 5.0 and there is a deficiency of ammonia. Copper residue should be >10 g/L at $[\mathrm{Zn}]_0 \leq 50$ g/L.

Zinc is present in the powder as a result of zinc ammine hydrolysis (insufficient amount of total ammonia, elevated temperature); its hydroxide or alkaline carbonates are eliminated from the powder by means of a weak acid solution at the washing stage. Basic solution includes 150–160 g/L copper; if the copper content is higher, it becomes unstable during storage. Leaching of metallized feed yields a part of the copper in solution as Cu (I) ammoniate. It is significant for oxygen consumption reduction but does not influence the process rate. Usually, the ratio Cu (I) to Cu (II) is approximately 1.6–2.0.

If the temperature is raised from 436 to 477 K, for 45 min or 3.7 time less is required to reduce the residual copper to 1 g/L starting with a solution containing 135 g/L. The recommended temperature is 460–470 K; the hydrogen pressure must be not <2.1–2.5 MPa.

Surfactant additives of polyacrylic acid or ammonium polyacrilate base added in a quantity of 0.005–0.5 g/L reduce the amount of powder depositions, decreases the powder agglomeration, and insignificantly increases the copper precipitation rate. Densification cycles increase the copper precipitation rate while appreciably enlarging the size and density of powder. Powder particle shape is nonequiaxed.

The process includes the following steps:

$$\mathrm{Cu(NH_3)_n^{2+} + 0.5H_2 \rightarrow (NH_3)_n^{+} + H^{+}}$$

$$\mathrm{(NH_3)_n^{+} + 0.5H_2O \rightarrow 0.5Cu_2O + NH_4^{+} + (n-1)NH_3}$$

$$\mathrm{2\,Cu_2O + H_2 + 2H^{+} \rightarrow 3Cu + Cu^{2+} + 2H_2O}$$

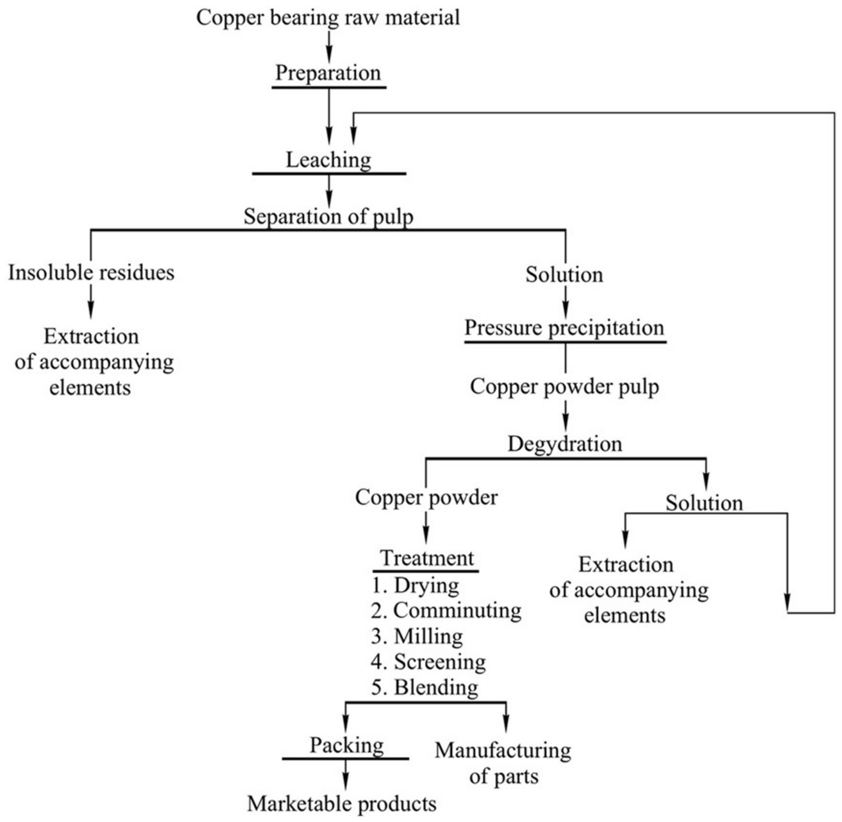
Copper bearing raw material
Preparation
Leaching
Separation of pulp
Insoluble residues
Extraction of accompanying elements
Solution
Pressure precipitation
Copper powder pulp
Degydration
Copper powder
Solution
Treatment
1. Drying
2. Comminuting
3. Milling
4. Screening
5. Blending
Extraction of accompanying elements
Packing
Manufacturing of parts
Marketable products

FIG. 19.21 Flowsheet of copper powder production by hydrometallurgical processing.

Copper content usually exceeds 99.5% and powder particle size ranges from 5 to 40 μm. Up to 90% of copper in powder form is precipitated from ethylenediamine copper solutions by hydrogen under pressure (393–413 K, $p_{H_2}=1.4-4.2$ MPa, during 1–3 h).

The flowsheet of copper powder production by hydrometallurgical processing from scrap copper, grout copper and copper concentrate, matte, and solutions supplied from adjacent fabrications is shown in Fig. 19.21. This production flowsheet is similar to the hydrometallurgical methods of cobalt and nickel powder production. The main features are the absence of a seed preparation stage and a limited number of densification cycles (does not exceed four).

Copper Precipitation from Organic Phases

Processing of lean ores by heap or underground leaching yields weak solutions from which copper is extracted using organic agents to form a saturated metal–organic solution containing 2–10 g/L Cu. The solution undergoes the reextract and then copper is precipitated from the obtained aqueous solution (30–40 g/L Cu) by electrolysis. Reduction of the saturated organic solution with hydrogen under pressure facilitates the production of copper powder without reextract.

Promising results are obtained by treatment of an organic solution (33% tertiary carbonic acid + kerosene +5–30 g/L Cu) with hydrogen at 403–493 K and $p_{H_2}=2.0$ MPa. The mixture of heptane acid with kerosene saturated with copper was treated at 413 K and $p_{H_2}=2.4$ MPa. This process passes through the Cu (I) ion formation stage and has an autocatalytic nature; the addition of seed enlarges powder particle size. Preliminary treatment of organic solution also enlarges powder particle size, especially with n increasing ratio of NH_3/Cu. The colloidal phase formation by the 0.1 ratio is eliminated. When the ratio amounts to 2.0, easy-filtered powder is produced.

From the copper-saturated extractants (LIX-64, LIX-65 N, SME-529, Acorgap-5100), the best results were observed by precipitation with extractant LIX-65 N. Treatment of the organic solution including 30% LIX-65 N, 20% decanol, 50% kerosene, and 9.0 g/L Cu in the presence of copper powder (30%–35% of total solution) at 470–500 K, $p_{H_2}=$ 1.7–2.8 MPa for 1.0–1.5 h yields >90% of precipitated copper.

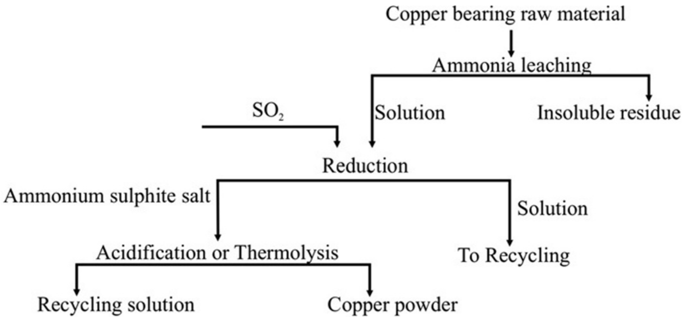

FIG. 19.22 Flowsheet of copper powder production by the anhydride method.

Anhydride Process

During processing of the ammoniacal solution by sulfur dioxide, the ammonium sulfate copper (I) salt is precipitated and decomposed hydrothermally (by treatment of aqueous solution at elevated temperature) or by acidation, the copper powder is made (Fig. 19.22).

Copper scrap and metal-bearing precipitates are used rather than other copper-bearing materials. By leaching of copper scrap and metal precipitate (at 310–330 K, and maintaining the weight ratio of NH_3 to Cu^+ at approximately 4.2–4.3, with aeration), solutions with enhanced content of Cu (I) ions are obtained, thus requiring less sulfur dioxide to precipitate the copper.

At 300–350 K and $p_{H_2} = 1.6$–2.0 MPa, about 70% of copper is precipitated selectively from the accompanying impurities (Zn, Ni, As, etc.):

$$2Cu(NH_3)_4SO_4 + 3SO_2 + 3H_2O \rightarrow 2Cu(NH_3)SO_3 + 3(NH_4)_2SO_3$$

Copper powder is produced by acidation of the slurry, which contains $Cu(NH_3)SO_3$, sediment, or by elevated temperature hydrolysis (at 413–443 K, and maintaining the weight ratio of liquid-to-solid at 1 to 1, during approximately 10–15 min):

$$2Cu(NH_3)SO_3 \rightarrow 2Cu + (NH_4)_2SO_4 + SO_2$$

Powder composition is as follows: 99.3–99.8 wt% Cu; 0.01–0.03 wt% S; 0.06–0.2 wt% O_2; 0.002–0.08 wt% Zn; and max 0.001% total Pb, Co, Ni, As, Sb, Bi, Fe, Mn, and Sn. Particle size ranges from 12 to 60 μm and roundish is the general particle shape; the apparent density is 1.3–3.0 g/cm^3 and the flow rate is 0,8 to1,6 g/s. The powder properties depend on acid consumption, ammonium sulfate amount, the presence of seed, treatment parameters, and process hydrodynamics.

A process where the copper salt is dissolved in acetonitrile (AN) is described as:

$$3Cu_2SO_3CuSO_4 \cdot 2H_2O + 5CuSO_4 \xrightarrow{AN} 7CuSO_4 + 2H_2SO_4 + 2SO_2$$

(330 K, 50% AN solution, 0.09 M SO_2, and 0.4 M H_2SO_4) the solution can be reduced in an autoclave (at 423 K) or by distillation (steam, 360 K, 0.5 h duration) to precipitate up to 50% of the Cu as powder and to regenerate AN. The particle size is below 53 μm; they are crystals and not inclined to agglomerate. Content of Mg, Zn, and Fe in the powder is max $(5–7) \times 10^{-4}$ mass% that is 60–70 times lower than by direct hydrolysis of ammonium sulfate salt.

The anhydride method uses simpler equipment, consumes less power, and production costs are lower in comparison with autoclave reduction under pressure. However, it is necessity to utilize the generated ammonium sulfate, the yield of copper directly extracted is less and their recirculating load increases.

Cementation

The precipitation of a metal from solution by the addition of another less noble metal is known as cementation. The fundamental equation for copper recovery from copper-bearing liquors using zinc is:

$$Cu^{2+} + Zn = Zn^{2+} + Cu$$

Sulfate solution contains 50 g/L of copper and 5–20 g/L of sulfuric acid. The latter hinders the hydrolysis of impurities ingressed in the solution. An additional factor providing high purity of copper powder (97.0%–98.5% Cu) is high residual content of copper in the solution (1–2 g/L). Consumption of zinc powder with particle size from 100 to 400 μm is determined by the stoichiometry of the above equation, taking into account the residual content of the copper in the solution.

The process is carried out at 323 K in the agitators with mechanic stirrers. The final slurry is filtered, then the powder is washed with water, stabilized with 0.05% soap solution, and dried.

The general precipitation reaction of copper recovery from cupric sulfate by the addition of iron is:

$$\mathrm{Fe} + \mathrm{CuSO_4} = \mathrm{Cu} + \mathrm{FeSO_4}$$

Practically, scrap iron, such as detinned and shredded cans, is used. Subsequent separation, washing, reduction, and pulverizing results in the production of a copper powder that contains considerable amounts of iron and acid insolubles, such as alumina and silica. For this process, chemical analyses of cement copper from different sources [10] show that total copper content ranges from 75 to 85 wt% and impurity content depending on scrap composition varies in the following ranges: 0.7–10.0 wt% iron, 0.5–1.1 wt% sulfur, 0.5–1.1 wt% nitric acid insolubles, 0.08 wt% calcium oxide, 0.5–1.2 wt% alumina, 0.4 wt% silicon dioxide, 0.2 wt% lead, and 9.5 wt% oxygen.

Electrowinning

Electrowinning is used to recover copper from leach solutions containing more than approximately 25 g/L of copper. The electrolytic cells are equipped with insoluble lead antimony anodes and 99% Ni cathodes. The copper powder deposits do not stick, and gravitate to the bottom of the cells. The temperature of the electrolyte is maintained at 333 K; cathode current varies from 1350 to 2700 A/m^2. When the copper concentration falls below 15 g/L, the electrolyte is drained and used for feed ore leaching. Particle size of the powder prior to heat treatment processing ranges from 1 to 25 μm. Copper content is excellent >99.9%. However, the power requirements for electrowinning of copper are approximately 10 times as large as those for electrowinning of copper using soluble anodes.

Copper may be precipitated from low content leach solutions by solvent extraction, followed by stripping with dilute sulfuric acid into an aqueous solution and electrowinning. Carboxylic acid and hydroxylamine-based compounds have been found to be selective solvents of low water solubility, to have good stability, and to be compatible with inexpensive diluents.

Another technique is used for obtaining copper powder with electrochemical regeneration of the reducer. Copper is reduced in the solution by titanium ions (III) in the anode space of an electrolyzer (Fig. 19.23) at room temperature [30]. The flow diagram of this process is shown in Fig. 19.24. Metallic copper is precipitated from solution by the following reaction:

$$\mathrm{Cu^{2+}} + 2\mathrm{Ti\,(III)} = \mathrm{Cu\,(powder)} + 2\mathrm{Ti\,(IV)}$$

Copper ions go to the anode space from the soluble anodes. Suspended powder in electrolyte permanently enters to filtering, then the filtered electrolyte is returned into the cathode space, where the reducer, namely titanium ions (III), is regenerated on the perforated lead cathode.

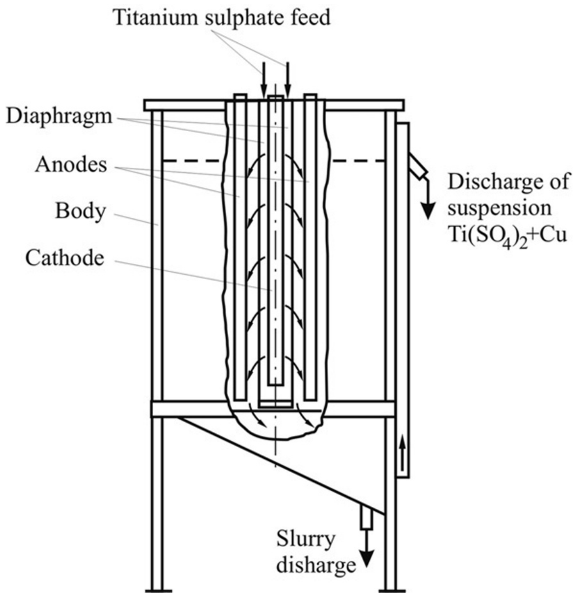

FIG. 19.23 Electrolytic cell for production of copper powder by electrochemical regeneration of reducer.

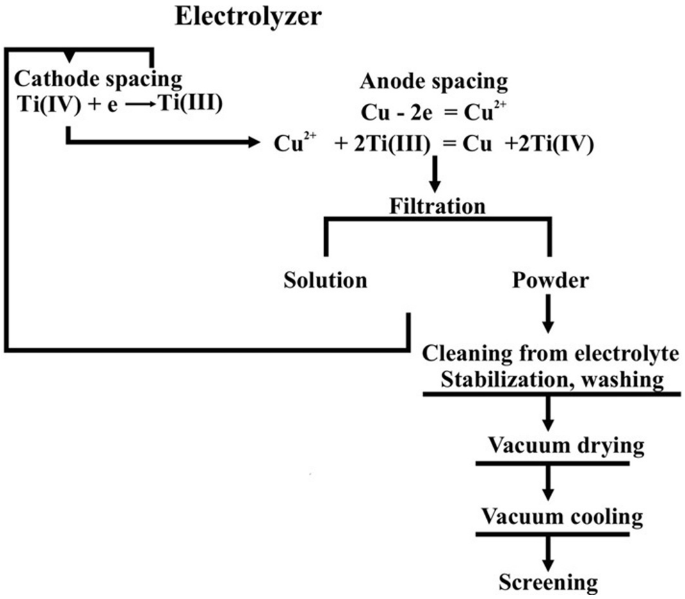

FIG. 19.24 Flowsheet to produce copper powder by electrochemical regeneration of reducer.

Anode space is separated from the cathode by a diaphragm made of chlorine fiber previously tightened by boiling in distilled water for 20 min. The level of the catholyte is higher than the anolyte level that ensures the electrolyte flow from the cathode space to the anode. The powder separated on the filter is washed with water to remove the electrolyte, stabilized with 0.05% soap solution, then washed again, dried under vacuum at 373–393 K, cooled under vacuum to room temperature, and classified. Electrolyte circulated with a rate of 22 L/h contains 184.2 g/L of $Ti_2 (SO_4)_3$ and 98 g/L of H_2SO_4. The cathode current density at 298 K is 50 A/m^2 and anode current density is 400 A/m^2. The made powder consists of particles of approximately 1.5 μm in size with a distinctive faceting shape.

Various characteristic methods for electrowinning copper and copper alloy powders from leach solutions can be found in Table 19.5.

OXIDE DISPERSION STRENGTHENED (ODS) COPPER POWDER PRODUCTION

Because of its high electrical and thermal conductivity, copper is widely used in industry; however, it has relatively low strength, especially at elevated temperatures. It can be strengthened by using stable oxides such as alumina, zirconia, titania, thoria, or yttria. For this, the PM technique is used. Because the above oxides are insoluble in molten copper, dispersion-strengthened copper cannot be made by conventional ingot metallurgy.

Manufacture

Oxide dispersion-strengthened copper can be produced by several methods [31]: simple mechanical mixing of the copper and oxide powders, coprecipitation from salt solutions, mechanical alloying [32], or by selective internal oxidation [33]. The latter produces the finest and most uniform dispersion. Size distribution and cost vary substantially among these methods. Alumina is a common strengthening phase used in the production of ODS copper.

The internal oxidation method is based on the principle that a copper-aluminum solid solution is internally oxidized at elevated temperature. For effective internal oxidation, oxygen must diffuse into the matrix (copper) several orders of value rather than the solute element (aluminum). Powder metallurgy possesses the advantage that powder particles can be internally rapidly oxidized and then consolidated into the required shape. Chapter 3 contains the mechanical alloying (MA) and ODS fundamentals.

The internal oxidation process involves the low aluminum addition in copper and atomizing the melt by means of a high-pressure inert gas such as nitrogen. The powder obtained is mixed with an oxidant that consists of fine copper oxide powder. Then, the mixture is heated to a high temperature at which the oxide dissociates and the oxygen produced diffuses into the particles of the copper-aluminum solid solution. Because aluminum forms oxide more readily than copper, the aluminum in the alloy is oxidized to aluminum oxide. After entire oxidation of the aluminum, surplus oxygen in the powder is reduced by heating the powder in hydrogen or in a dissociated ammonia atmosphere.

Three grades of ODS copper are commercially available, which are designated as C15715, C15725, and C15760 by the Copper Development Association [34]. The nominal compositions of these grades are: 99.7 wt% (99.3 vol%) Cu, 0.3 wt% (0.7 vol%) Al_2O_3, C15715 grade; 99.5 wt% (98.8 vol%) Cu, 0.5 wt% (1.2 vol%) Al_2O_3, C157215 grade; and 98.9 wt% (97.3 vol%) Cu, 1.1 wt% (2.7 vol%) Al_2O_3, C15760 grade.

The powder is consolidated into fully dense shapes by various techniques. Semiproducts, such as rod and bar, are made by sealing the powder in a suitable metal container, usually copper, and hot extruding it to the given size. Strip is manufactured either by rolling rods of extruded rectangular bars or by directly rolling powder with or without a container. Wire is produced by cold drawing of a rod. The HIP of powder sealed in a container is used when large pieces cannot be made by hot extrusion. Such shapes can also be made by forging sealed powder or green compacts.

Finished parts are made from semiproducts by machining, brazing, and soldering. Fusion welding is not applicable because it causes the aluminum oxide to precipitate from the liquid copper matrix, accompanied with the loss of dispersion strengthening. Flash welding, in which the liquid metal is squeezed out of the weld joint, and electron beam welding, in which a small heat-affected zone is created, have been used with success.

Properties of ODS Copper Powders

The properties of ODS copper strongly depend on aluminum oxide content. They can be altered to meet a wide range of design requirements by varying the aluminum oxide content and/or cold work. Typical for rod stock in the hot extruded condition, increasing the aluminum oxide content from 0.45 to 2.7 vol% increases the tensile strength from 360 to 670 MPa while elongation is decreased from 27% to 14%.

Physical properties of ODS copper closely resemble those of pure copper because the former contains small amounts of aluminum oxide as discrete particles in an essentially pure copper matrix. Table 19.10 shows properties of the commercial ODS coppers, comparing them with oxygen-free (OF) copper [30]. The melting point does not differ from that of copper because the matrix melts and the aluminum oxide particles are separated regarding the melt. Density, coefficient of thermal expansion, and modulus of elasticity are similar to those of pure copper.

The free or reducible oxygen content of the above three ODS coppers (Table 19.10), usually about 0.02–0.05 wt%, is present in the form of dissolved oxygen and cuprous oxide. Alloys in this state are inclined to hydrogen embrittlement at high temperatures. In these low-oxygen compositions, the reducible oxygen can be converted to nonreducible oxide by adding up to 0.02 wt% boron as an oxygen getter. These grades are then resistant to hydrogen embrittlement.

Electrical and thermal conductivities at room temperature range from 78% to 92% of those for pure copper. In combination with the high strengths of these materials, they enhance the electrical and heat conduction capabilities for a given section's size and structural strength. Therefore, they enable reduction of section size for component miniaturization without damage to structural strength or electrical and heat conduction capabilities. At elevated temperature, the decrease in electrical and thermal conductivities of ODS coppers does not differ from those of pure copper.

ODS copper has high resistance to softening, even after exposure to temperatures close to the melting point of copper because the aluminum oxide particles are stable at these temperatures and retain their original size and spacing. At typical brazing and glass-to-metal sealing temperatures (above 830 K), ODS coppers retain much of their strength while OF copper loses its strength. At above 870 K, the ODS coppers have a rupture strength comparable to or better than some stainless steels. ODS copper has high thermal stability at elevated temperatures because the aluminum oxide particles retain their initial particle size and spacing, even after prolonged heating, and prevent recrystallization of the matrix.

Applications of ODS Copper Powders

Oxide dispersion-strengthened copper has received wide market acceptance in series applications [31,34]. The main applications are enumerated below.

Lead Wires. ODS copper wire is used in lead for incandescent lamps. Its high-temperature strength retention capability allows glass-to-metal seals to be made without abnormal softening of the lead. This in turn eliminates the need for expensive molybdenum support wires. Superior strength of the lead enables a reduction in lead diameter to save material. ODS copper wire also can be used in leads for discrete electronic components such as diodes.

Relay Blades and Contact Supports. These parts involve current-carrying arms that connect fixed contact points with the electrical circuit. Generally, the relay blade and contact supports have silver contacts brazed or riveted to them. The strength-retention capability of ODS copper after exposure to elevated temperature allows brazing of contacts to the blade without perceptible strength loss. Due to the higher electrical conductivity of ODS copper, it has replaced conventional copper alloys, such as phosphor bronze and beryllium copper, in some relays.

TABLE 19.10 Properties of Oxide Dispersion-Strengthened (ODS) and Oxygen-Free (OF) Copper Powders

Property				Unit	Material			
					C15715	C15725	C15760	OF Copper
Cooper content				wt%/ vol%	99.7/99.3	99.5/98.8	98.9/97.3	99.9
Aluminum oxide content				wt%/ vol%	0.3/0.7	0.5/1.2	1.1/2.7	…
Melting point				K	1356	11,356	1356	1356
Density				g/cm^3	8.90	8.86	8.81	8.94
Electrical resistivity at 293 K				Ω·mm^2/m	0.0186	0.0198	0.0221	0.017
Electrical conductivity at 293 K				%IACS	92	87	78	101
Thermal conductivity at 293 K				W/(m·K)	365	344	322	391
Linear coefficient of thermal expansion for 293–1273 K				ppm/K	16.6	16.6	16.6	17.7
Modulus of elasticity				GPa	130	130	130	115
		Thickness or diameter (mm)	Temper or condition[a]					
Tensile strength	Flat products	10	AC	MPa	413	434	517	…
		2.5	CW 75%	MPa	…	…	627	…
		2.3	CW 78%	MPa	…	586	…	…
		1.3	CW 88%	MPa	579	…	…	…
		0.15	CW 98%	MPa	661	675	737	…
	Plate	Up to 130	AC	MPa	365	413	…	…
		25	CW 60%	MPa	476	496	…	…
		16	CW 75%	MPa	483	524	…	…
	Rod	38–14	AC	MPa	393	441	551	…
		19	CW 55%	MPa	427	…		…
		13	CW 14%	MPa	…	…	572	…
		7	CW 94%	MPa	496	…	…	…
		7	CW 74%	MPa	…	…	620	390
	Wire	1.3	CW 99%	MPa	524	…	…	…
		0.4	CW 99.9%	MPa	606	…	…	…
	Rounds	Up to 760	AC	MPa	365	413	469	…
Yield strength	Flat products	10	AC	MPa	331	345	413	…
		2.5	CW 75%	MPa	…	…	572	…
		2.3	CW 78%	MPa	…	544	…	…
		1.3	CW 88%	MPa	537	…	…	…

Continued

TABLE 19.10 Properties of Oxide Dispersion-Strengthened (ODS) and Oxygen-Free (OF) Copper Powders—cont'd

Property				Unit	Material			
					C15715	C15725	C15760	OF Copper
		0.15	CW 98%	MPa	613	613	655	…
	Plate	Up to 130	AC	MPa	255	296	…	…
		25	CW 60%	MPa	427	441	…	…
		16	CW 75%	MPa	455	467	…	…
	Rod	38–14	AC	MPa	324	358	517	…
		19	CW 55%	MPa	407	…	…	…
		13	CW 14%	MPa	…	…	544	…
		7	CW 94%	MPa	469	…	…	…
		7	CW 74%	MPa	…	…	599	…
	Wire	1.3	CW 99%	MPa	496	…	…	…
		0.4	CW 99.9%	MPa	579	…	…	…
	Rounds	Up to 760	AC	MPa	255	296	331	…
Elongation	Flat products	10	AC	%	20	21	13	…
		2.5	CW 75%	%	…	…	8	…
		2.3	CW 78%	%	…	8	…	…
		1.3	CW 88%	%	7	…	…	…
		0.15	CW 98%	%	6	6	6	…
	Plate	up to 130	AC	%	26	19	…	…
		25	CW 60%	%	10	9	…	…
		16	CW 75%	%	10	9	…	…
	Rod	38–14	AC	%	27	24	22	…
		19	CW 55%	%	18	…	…	…
		13	CW 14%	%	…	…	16	…
		7	CW 94%	%	9	…	…	…
		7	CW 74%	%	…	…	14	…
	Wire	1.3	CW 99%	%	2		…	…
		1.3	HT 923 K	%	10	…	…	…
		0.4	CW 99.9%	%	1	…	…	…
	Rounds	up to 760	AC	%	26	19	4	…
Hardness	Flat products	10	AC	HRB	62	72	81	…
		2.5	CW 75%	HRB	…	…	85	…
		2.3	CW 78%	HRB	…	83	…	…
	Plate	up to 130	AC	HRB	62	68		…

TABLE 19.10 Properties of Oxide Dispersion-Strengthened (ODS) and Oxygen-Free (OF) Copper Powders—cont'd

					Material			
Property				Unit	C15715	C15725	C15760	OF Copper
	Rod	38–14	AC	HRB	62	73	80	…
		19	CW 55%	HRB	68	…	…	…
		13	CW 14%	HRB	…	…	83	…
		7	CW 94%	HRB	72	…	…	…
		7	CW 74%	HRB	…	…	86	…
	Rounds	up to 760	AC	HRB	…	68	76	…

[a] *AC, as consolidated; CW: cold work % reduction in area; HT: heat treatment for 1 h.*

Sliding Electrical Contacts. ODS copper bars are used in overhead sliding electrical contacts for high-speed electric trains. Their high resistance to abrasive wear provides up to 10 times longer contact life and reduces the maintenance costs significantly. The higher the train speed, the greater the advantage of ODS copper over other copper-base materials.

Resistance Welding Electrodes. ODS copper electrodes are widely used for resistance welding in automotive, appliance, and other sheet metal processing industries. It is well known that sticking of the electrodes to the workpiece is a major problem when welding galvanized and other coated steel. This usually results in electrodes pulling off their holders and necessitates stopping the assembly line to change the electrodes. Such interruptions are very costly. ODS copper electrodes eliminate sticking to galvanized and other coated steel. Increasing use of coated steels in the automotive industry has predicted further wide usage of ODS copper electrodes.

Metal-Inert-Gas Welding Contact Tips. Resistance of ODS copper to abrasive wear from the steel wire enables the tips to maintain the bore diameter and minimizes the wandering of the arc. This is important in automated welding lines. The nonsticking property of ODS copper also minimizes the material build up.

X-ray and Microwave Tube Components. Another example of ODS copper applications is the stems for the rotating anodes in x-ray tubes where high strength retention after brazing and glass-to-metal sealing are important. The high thermal conductivity of ODS copper also enables more efficient heat removal, thus lowering the operating temperature and providing longer tube life and quieter tube operation.

Particle Accelerator Components. Oxide dispersion-strengthened copper plates and bars are used in mirrors and x-ray absorbers because of their high thermal conductivity, high strength, creep resistance, and vacuum integrity. The high-energy particle beams are shaped and focused by using mirrors, lenses, and prisms in large doughnut-shaped hollow rings,

Other Applications. Other various applications of ODS copper include anode stems in chloride cells, high field magnet coils, anode stems chlorine cells, electrodischarge machining electrodes, high-speed motor and generator components, commutators, and hybrid circuit package components.

APPLICATIONS OF COPPER AND COPPER ALLOY POWDERS

Basic applications for copper and copper-base PM materials are summarized in Table 19.11. These include bearings, electrical parts, friction materials, structural materials, brushes, filters, additives to iron powders (alloying as well as infiltration), catalysts, pigments, and paints.

An assortment of bearings and parts of sintered bronze are shown in Fig. 19.25. Bearings made from sintered bronze have a uniform interconnected porosity ranging generally from 18% to 30%. The pore volume is impregnated once only with oil, after which the bearing functions maintenance-free and self-lubricating. Because of these advantages, self-lubricated bearings account for a significant part of PM applications. There are also many applications for sintered bronze parts.

TABLE 19.11 Applications of Copper and Copper-Base Powders

Applications	Powder Type
Automotive and machinery	
Bearings	Bronze, copper-lead-tin, copper-lead, copper-lead-zinc, copper-nickel, ODS copper
Brake bands and linings	Copper, brass, copper-lead, copper-lead-tin, copper-tin-zinc-iron
Bushings	Bronze
Control panels, instruments	Nickel-silver
Counterweights	Copper-tungsten
Chemical	
Chemical catalysts	Copper
Filters	Bronze
Flame arresters	Bronze
Fungicide additive	Copper
Soil conditioning	Copper
Valves and pumps	Copper-nickel
Coatings and paints	
Conductive paints and plastics	Copper and brass
Antifouling paints	Copper
Decorative paints	Copper, brass, bronze
Lacquers	Brass, bronze
Mechanical plating	Copper, brass
Spray coating	Copper, brass
Vacuum metallising	Copper
Construction hardware	
Conductive and nonsparking floors	Copper
Decorative plastics	Copper, bronze, and brass
Dissimilar circuit package components	ODS Copper
Domestic water filters	Brass
Locks and keys	Brass, bronze, and ODS Copper
Fastening bolt	Brass
Pipe joint compounds	Copper, brass
Electrical and electronic	
Brushes	Copper, Copper-lead-tin-carbon
Brush holders	Nickel-silver
Contacts	ODS Copper
Heatsinks	Copper
Printed circuits	Copper
Semiconductor stud bases	Copper, ODS Copper
Telephone components	Brass, bronze
Particle accelerator components	ODS Copper

TABLE 19.11 Applications of Copper and Copper-Base Powders—cont'd

Applications	Powder Type
Switch and contactor components	Copper, brass
Incandescent lamps	ODS Copper
X-ray, microwave tube parts	ODS Copper
Antigalling pipe joint compounds	Copper
Copper lubricants	Copper
Plastic-filled metal	Copper, bronze
Self-lubricating (oil-filled) parts	Bronze
Manufacturing and machining	
Abrasive wheel bonding	Copper
Brazing compounds	Copper, brass, bronze
Electrodischarge machining	Copper
Electrochemical machining	Copper
Resistance welding electrodes	Copper, copper-chromium, ODS Copper
Metal-inert-gas welding contact tips	Copper,, ODS Copper
Ordnance	
Armor-piercing cores	Copper
Fuse parts	Brass
Projectile rotating bands	Copper, brass
Other equipment and uses	
Business machines	Brass
Coins, metals, medallions	Copper-nickel
Cordless devices	Copper
Fingemail polish	Copper
Lawn and garden equipment	Bronze
Metal bond for diamond tools	Bronze, copper-nickel
Photographic equipment	Bronze, brash, nickel-silver

Various configurations of carbon brushes suitable to conduct electrical current in sliding contacts are pictured in Fig. 19.26. Fine electrolytic copper powders form a durable matrix in which dispersed graphite serves as a dry lubricant and prevents seizing of the brushes. The dendritic particle shape ensures good mixability with graphite and high green strength.

Friction materials are required as linings for clutches and brakes. Typical arrangements are shown in Fig. 19.27. Friction linings have the property of converting mechanical energy of motion to heat by means of friction, the heat in turn having to be continuously dissipated to prevent overheating. Various types of friction materials are employed, depending on the amount of heat to be dissipated. In the capacity of friction components, silicon dioxide, aluminum oxide, silicon nitride, etc., are employed. Graphite, lead, molybdenum sulfide, and others play a part in lubricating components. In the case of smaller quantities of converted energy, it is sufficient to employ linings of the synthetic resin type, which may be reinforced with embedded metal particles, that is, so-called semimetallic linings. High-duty linings, on the other hand, contain continuous metallic solids that provide mechanical strength and good heat dissipation. In this matrix, seizure-preventing and friction-producing components are embedded.

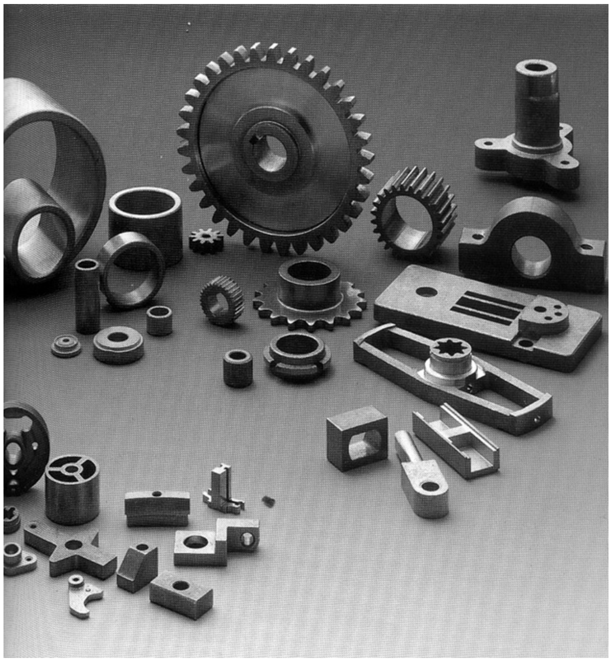

FIG. 19.25 Assorted bearings and parts made from PM bronze. *(Courtesy of Norddeutsche Affinerie Aktiengesellschaft. Nowadays "Aurubis AG.")*

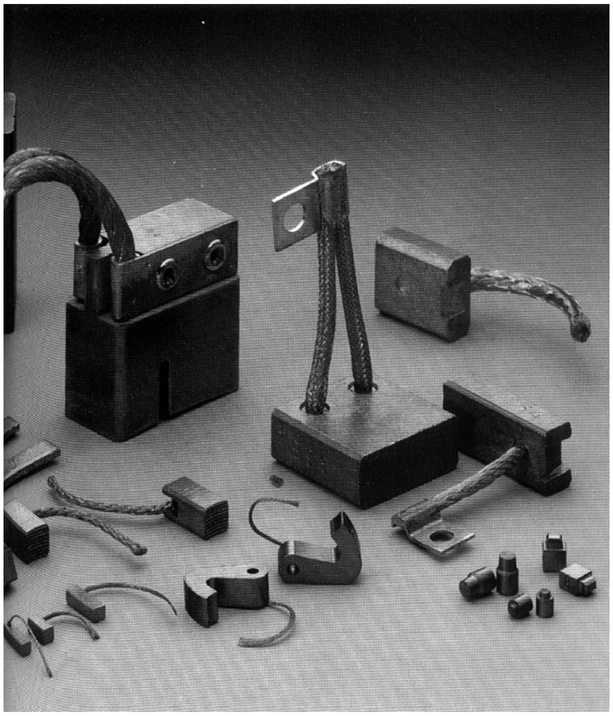

FIG. 19.26 Typical carbon bronze brushes. *(Courtesy of Norddeutsche Affinerie Aktiengesellschaft. Nowadays "Aurubis AG.")*

Formation and functional effectiveness of the supporting of the metallic matrix depend substantially on the metal powder used. Dendritic copper powders ensure high green strength, intensive bonding between particles, and high sintering activity, especially with the addition of elementary tin and liquid phase sintering.

Filters made of sintered bronze, exhibited in Fig. 19.28, have a porosity of between 30% and 50%. A uniform distribution of interconnected pores by almost equal size and shape is characterized. The size of the pores, and hence the permeability of the filter material, can be controlled by choosing suitable particle sizes in starting powder. Normally, the standard fractions used range from below 40 μm to 630–1000 μm.

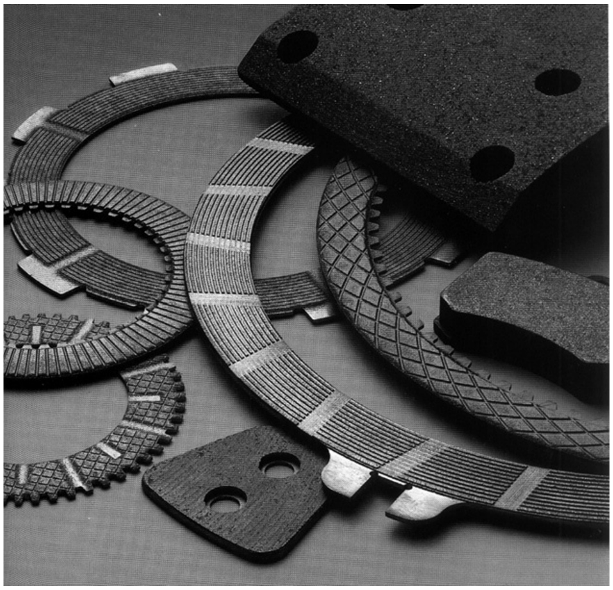

FIG. 19.27 Friction PM parts assortment. *(Courtesy of Norddeutsche Affinerie Aktiengesellschaft. Nowadays "Aurubis AG.")*

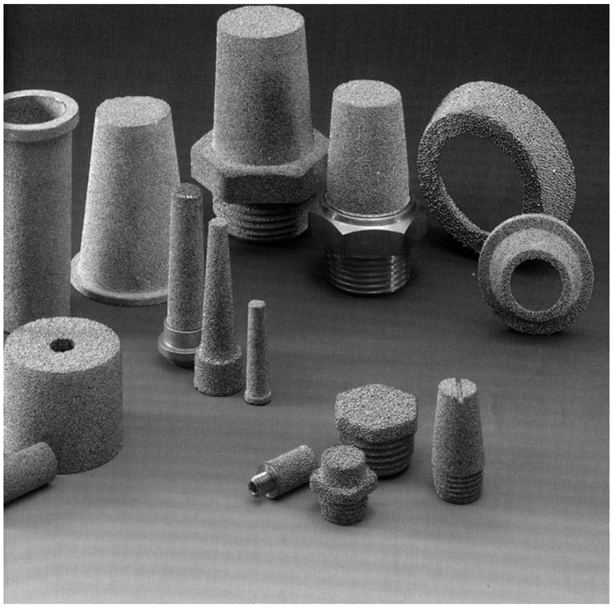

FIG. 19.28 Filters made of sintered bronze spherical powders. *(Courtesy of Norddeutsche Affinerie Aktiengesellschaft. Nowadays "Aurubis AG.")*

Generally, manufacture is by the loose powder sintering process, and sintering is done in graphite or steel dies, mostly under hydrogen or cracked ammonia. Sintering temperatures are about 1058 K with sintering times approximately 60 min. Spherical bronze powder contains about 0.35% phosphorus. The latter increases the surface tension of the melt to be atomized and so ensures a good spherical particle shape. The addition of phosphorus also reduces the solidus temperature of the tin bronze to about 973 K, which in turn allows the advantages of liquid phase sintering to be accomplished.

Recent advances in mobile electronics lead the trend toward smaller electronic systems, and effective heat dissipation becomes one of the critical issues. Therefore, the micro copper pipes show promise due to their high heat-removing properties. The micro heat pipe has been commonly manufactured by conventional machining processes or lithography processes [35–37]. As these processes require large amounts of time and cost, so the powder injection molding (PIM) process is introduced as an alternative manufacturing process in this research. Because the total thickness of the micro heat pipe in mobile electronics is required to be under 0.6 mm, the wall thickness of the pipe should be about 0.1–0.2 mm. Thus, in order to fabricate the pipe by using PIM, it is necessary to develop the PIM process for a thin-walled structure.

FIG. 19.29 Morphology of the pure copper powder.

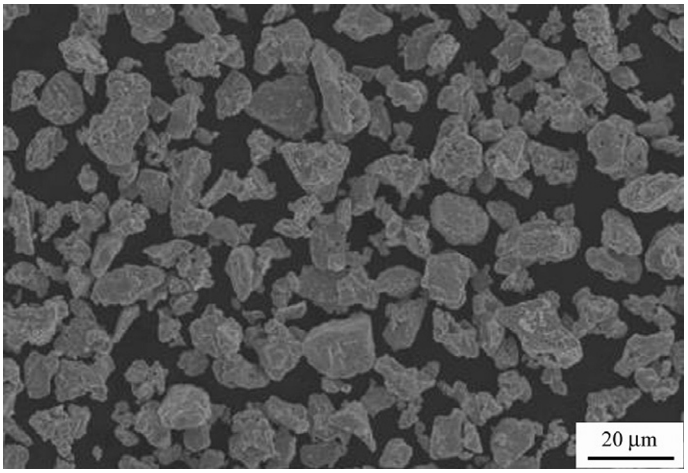

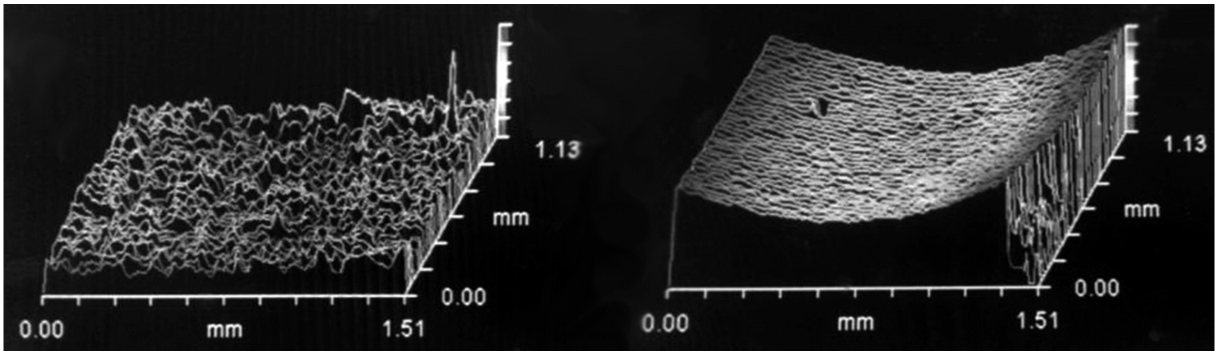

FIG. 19.30 Surface of the specimen without solvent debinding (left) and normal specimen (right).

Powder characteristics that enable metal injection molding of high conductivity copper heat sinks are investigated by Johnson et al. [38]. Gas-atomized, water-atomized, oxide-reduced, and jet-milled copper powders are compared in terms of particle size, packing density, mixing torque, and impurity content. The authors reported that densities near 95% of theoretical are achieved for all the powders. Overall impurity contents for typical powders are about 0.15 wt%, resulting in thermal conductivities of 280–320 $W \cdot m^{-1} \cdot K^{-1}$ for PIM copper. The thermal conductivity is decreased significantly for powders that contained 50 ppm or more iron. It is estimated that elimination of the remaining porosity allows increasing the thermal conductivity to 350 $W \cdot m^{-1} \cdot K^{-1}$.

Thin-walled structures, which have 0.19 μm thickness, were fabricated by using copper PIM technology [39]. In this work, pure copper powders with median diameter 10.9 μm, apparent density 3.05 g/cm^3, and pycnometer density 7.71 g/cm^3 were used. Their morphology looks irregular, is illustrated in Fig. 19.29.

Several binders were utilized. The mixing process was carried out with a twin extrude type mixer, with 30 rpm mixing speed, and at 423 K mixing temperature. A square plate mold cavity was used for the injection molding process. It had 12.5 mm of length and 700 μm of thickness. The thickness of the cavity was controlled by using a stainless steel mold insert. A two-step debinding process including solvent debinding and thermal debinding was carried out. Solvent debinding was conducted in a bath of N-hexane at 323 K. Ten minutes was enough to extract all the wax and SA except 1 wt% of the remaining content for the 700 μm of specimen thickness. Thermal debinding was fulfilled in a hydrogen atmosphere. The sintering was carried out in a hydrogen atmosphere at 1300 K for 1 h. The heating rate was 5 K/min. The shrinkage and final density were 0.181 and 0.995, respectively. As the authors [39] reported, warpage phenomena was observed. When the solvent debinding process was absent, the warpage was about twice larger than that of normal samples (Fig. 19.30).

WORKPLACE ATMOSPHERES SAFETY

Inspirable copper dust takes a predominantly fibrous effect. The long-term expose limit (8 h reference period) of copper (and copper compounds) dust and mists fumes, according to EH40 Workplace Exposure Limits [40], is 1.0 mg/m^3 while copper fume is 0.2 mg/m^3. The legal OSHA [41] airborne permissible exposure limit is 1.0 mg/m^{3}and 0.1 mg/m^3 as copper fume.

The ALV of copper aerosol in the workplace atmosphere as the shift time-weighted average concentration is 0.5 mg/m^3 while the threshold limit value (TLV) is 1.0 mg/m^3; it is placed in the second class of danger out of the four-class standard system, according to the Russian Federation Standard 12.1.005–88 [42]. The above standard standardizes the ALV of copper phosphide, copper sulfate, copper chloride, etc. The copper chromium phosphate is the most harmful inspirable substance among the standardized copper compounds and is placed in the first most dangerous class. Its ALV limit is 0.02 mg/m^3.

Copper in drinking water imparts a foul taste and is related to the third class of danger; the TLV is 1.0 mg/L, according to the Russian Federation Standard 4630–88 [43].

Copper powder <44 μm does not inflame in an aerogel state as well as in a suspended solid one in air. Data about combustibility of copper dust and some bronze and brass compositions as well as the prevention of inflammability can be found in Chapter 27.

REFERENCES

[1] Williams B. Powder metallurgy—a global market review. In: International Powder Metallurgy Directory & Yearbook, 12th ed. 1; 2006/2007. p. 5–16.

[2] Pfingstler R. State of the PM industry in North America. In: Compiled by Russell A, Chernenkoff W, Brian J. Proceedings of Powder Metallurgy World Congress. Orlando (FL, U.S.A.): Metal Powder Industries Federation; 2014, p. 1–12.

[3] Saito T. Global review overview of PM industry in Asia. In: Compiled by European Powder Metallurgy Association, (Bellstone Shrewsbury, UK) Proceedings of PM 2016 world congress. Hamburg (Germany); 2016: p. 1–7.

[4] McGeehan P. State of the PM industry in North America—2016. In: Compiled by European Powder Metallurgy Association, (Bellstone Shrewsbury, UK) Proceedings of PM 2016 World Congress. Hamburg (Germany); 2016. <file:///C:/Users/oleg/AppData/Local/Temp/Temp3_17-03-2017_00-01-35.zip/SOI-WorldCongress-Final.pdf>

[5] Berry DF, Klar E. Production of copper powders. In: ASM handbook, vol. 7. ASM International Publishers; 1998. p. 132–42.

[6] Naboychenko SS. Nonferrous metal powders. Handbook. Moscow: Publ. Metullurgiya; 1997 [in Russian].

[7] Sarkisyan NS, Nichiporenko OS, Kol'chinskii MZ, Pokotilo EP, Bondarenko BI, Karibyan AN. Production of copper powder at the Alaverdy mining and metallurgical integrated works. Sov Powder Metall Met Ceram 1991;30(3):432–5.

[8] Neikov OD. NonFerrous powder production technologies. In: International Powder Metallurgy Directory & Yearbook, 12th ed. 1; 2006/2007. p. 25–35.

[9] Masip Y, et al. Characteristics of water atomized particles produced using a broad range of atomization pressures and water-to-melt ratios. In: Compiled by Russell A. Chernenkoff, Brian J. Proceedings of 2014 Powder Metallurgy World Congress. Orlando (FL, U.S.A.): Metal Powder Industries Federation; 2014: p. 02–61–75.

[10] Pelletiers TW, Berry DF. Production of copper alloy powders. In: ASM handbook, vol. 7. ASM International Publishers; 1998. p. 143–5.

[11] Uhlenwinkel V, Schwenck D, Ellendt N. Gas recirculation affects the powder quality. In: Compiled by Russell A. Chernenkoff, W. Brian. Proceedings of 2014 Powder Metallurgy World Congress. Orlando (FL, U.S.A.): Metal Powder Industries Federation; 2014: p. 02–46–53.

[12] Klar E, Berry DF. Properties and selection: Nonferrous alloys and special-purpose materials. In: ASM handbook. 2:ASM International Publishers; 1990. p. 392–402.

[13] Kumar D, Gaur AK. Electrochemical studies on production of electrolytic copper powders. J Electrochem Soc India 1973;(July):211–6.

[14] Artamonov VP, Pomosov AV. Effect of foreign electrolytes on the production of copper by contact deposition. Izv VUZ Cvetn Metall 1976;2:30–4 [in Russian].

[15] Kotovskaya NL, Prosviryakova II, Pomosov AV, Kurvyakova LM. Manufacture of coarse copper powder from sulfamate electrolytes. Sov Powder Metall Met Ceram 1973;12(2):93–6.

[16] Gurevich LI, Pomosov AV. The effect of chlorides on electrodeposition of powdered copper precipitates. Sov Powder Metall Met Ceram 1969; 8(1):10–5.

[17] Singh SK, Akerkar DD. A continuous self-regulating method of making copper powder by electrolysis. NML Tech J 1975;17:23–6.

[18] Pomosov AV, Numberg MI, Krymakova EG. Protection of copper powder against corrosion during manufacture and storage. Sov Powder Metall Met Ceram 1976;15(3):175–7.

[19] Peissker T. Production and properties of electrolytic copper powder. Powder Met Powder Technol 1984;18(2):87–90. 92–8, 100–1.

[20] Popov K, Maksimovich M, Trnjancev J. Dendritic electrocrystallization and the mechanism of powder formation in the potentiostatic electrocrystallization of metals. J Appl Electrochem 1981;11:239–46.

[21] Murashova IB, Potapov OA, Pomosov AV. Electrodeposition of finely divided copper of uniform structure. Sov Powder Metall Met Ceram 1988; 27(8): 596–601.

[22] Murashova IB, Korkin SL, Pomosov AV, Nikol'skaya NY, Susloparov DG. Electrodeposition of finely divided copper under conditions of a linearly increasing current. Sov Powder Metall Met Ceram 1986;25(10):792–7.

[23] Balakina ML, Serpuchenko EA, Kurilenko OD. Production of copper powders in a two-layer electrolytic bath in the presence of higher fatty acids. Sov Powder Metall Met Ceram 1984;23(7):1–4.
[24] Fedyushkina YA, Pomosov AV. Conditions of preparation of copper-lead alloy powder. Sov Powder Metall Met Ceram 1971;10(8):610–3.
[25] Fedyushkina YA, Pomosov AV. Electrodeposition of copper-tin alloy powder from a sulfamine electrolyte. Sov Powder Metall Met Ceram 1971; 10(6):434–6.
[26] Taubenblat PW, Smith WE, Evans CE. Production of PM parts from copper powders. Precis Met 1972;(April):41.
[27] Technical data from AMAX Metal Powders. AMAX Copper Inc; 1968.
[28] Peissker E. Metal powders, Norddeutsche Affinerie. Hamburg: Brillant-Offset Publ; 1986.
[29] Kim TW, et al. Preparation and characterization of monodispersed and nano-sized Cu powders. Mater Sci Forum 2007;534–536(109):534–6.
[30] Kotovskaya NL, Pomosov AV. Study various factors influence upon crystallization and dispersivity of copper powder produced by reduction. J Appl Chem 1970;44(3):548–52 [in Russian].
[31] Nadkarni A. Copper powder metallurgy alloys and composites. In: ASM Handbook, vol. 7. ASM International Publishers; 1998. p. 859–73.
[32] Benjamin JS. The International Nickel Company Inc. US Patent 3,785,801, 1974.
[33] Nadkarni AV, Klar E. SCM Corporation. US Patent 3,779,714, 1973.
[34] Copper Development Association. https://alloys.copper.org/alloy/C15725?referrer=facetedsearch. Accessed 31 January 2018.
[35] Hopkins R. Flat miniature heat pipes with micro capillary grooves. ASME J Heat Transfer 1999;121(1):102–9.
[36] Lee M. Integrated micro-heat-pipe fabrication technology. J Microelectromech Syst 2003;12(2):138–46.
[37] Lim HT. Fabrication and evaluation of a copper flat micro heat pipe working under adverse-gravity orientation. J Micromech Microeng 2008;18(10): 105013 (1–8), https://doi.org/10.1088/0960-1317/18/10/105013.
[38] Johnson JL, et al. Evaluation of copper powders for processing heat sinks by metal injection moulding. Powder Metall 2005;48(2):123–8.
[39] Cho H, Lee J, Park SJ. Fundamental experiments for fabrication of copper micro heat pipe by powder injection molding. In: Compiled by European Powder Metallurgy Association, (Bellstone Shrewsbury, UK) Proceedings of PM 2016 world congress. Hamburg (Germany); 2016: p. 1–6.
[40] EH40-Update to EH40/2005 Workplace Exposure Limits. 2nd ed., published 2011 (as consolidated with amendments, December 2011).
[41] US New Jersey Department of Health and Senior Services. Hazardous Substance Sheet. Copper. Revision: September 2016. <http://www.nj.gov/health/eoh/rtkweb/documents/fs/0528.pdf>.
[42] GOST 12.1.005 – 88, Standard RU. Moscow: Publishers of Standarts; 1988 [in Russian]
[43] SanPiN 4630–88. Sanitary Regulation and Standards of surface waters from pollution. Publishers of MinZdrav: Moscow; 1988 [in Russian].

Chapter 20

Production of Zinc, Cadmium, and Their Alloy Powders☆

Irina V. Frishberg
Fine Metal Powders R & D Company, Yekaterinburg, Russia

Chapter Outline

Production of Zinc Powders **615**
Evaporation-Condensation Method 615
Melt Atomization 620
Electrochemical Method 621
Other Methods 624
Production of Cadmium Powders **625**
Production of Cadmium and Zinc Alloy Powders **625**
Safety Measures in Zinc and Cadmium Powder Production and Handling **626**
Applications **628**
Zinc Powders in Protective Zinc-Rich Coatings 628
Anticorrosive Zinc-Rich Coatings for Roll and Sheet Steel and Metal Wear 630
Sherardizing (Thermodiffusion Galvanizing) 630
Mechanical Plating 630
Recycling of Tungsten Carbide Powders 631
Implant Production 631
References 631

PRODUCTION OF ZINC POWDERS

There are different methods known for producing zinc powder, among them melt atomization, inert gas condensation, electrolysis of aqueous solutions, etc. Low melting and boiling points (692.5 and 1180 K, respectively) and the high chemical activity of zinc make the methods based on evaporation and condensation the most appropriate for the manufacture of zinc powder [1]. Due to a combination of high activity and high specific surface area, zinc powders find application in a variety of fields, including metallurgy, chemistry, medicine, electrical engineering, etc.

Evaporation-Condensation Method

The evaporation-condensation or physical vapor deposition (PVD) method comprises melting the zinc, evaporation of the melt, and condensation of the vapor in a neutral gas medium. In commercial production, the evaporation is carried out either in externally heated equipment or in electrothermal or induction furnaces. The continuous process of zinc powder production (Fig. 20.1) includes three sequentially arranged installations: a reverberating furnace for zinc melting and partial elimination of iron and lead, a rectification column, and a condenser.

The charge containing zinc of various grades is loaded into the gas-heated reverberating furnace that has three sections: a melting area, a liquation section, and a superheater. In the melting area, the charge is melted at about 820 K; in the liquation section, some of the iron precipitates at 740–770 K as a sediment of ferrous zinc and lead, which is periodically removed. The dross accumulating on the surface of the melt is skimmed once a day and sent for recycling in kilns or muffle furnaces. Zinc with an iron content of <0.1 wt% is fed into the superheater at a temperature of about 870 K. From the superheater, the molten zinc is fed by a chute to a rectifying column (Fig. 20.2) to one of the carborundum trays in the upper part of the column. The shaft of the column is lined with chamotte bricks and equipped with a gas supply duct and a waste gas flue. The shaft of the column consists of 20–24 W-shaped trays in the combustion section and 17–22 flat trays in the non-heated section.

☆ Expanded and updated by O.D. Neikov.

Handbook of Non-Ferrous Metal Powders. https://doi.org/10.1016/B978-0-08-100543-9.00020-8
© 2019 Elsevier Ltd. All rights reserved.

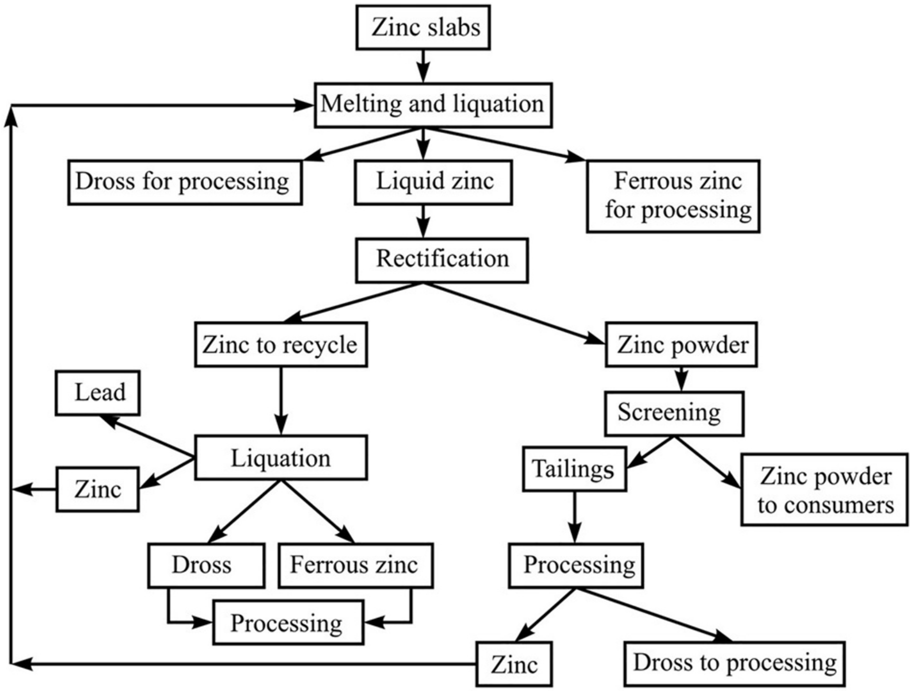
Zinc slabs
Melting and liquation
Dross for processing
Liquid zinc
Ferrous zinc for processing
Rectification
Zinc to recycle
Zinc powder
Lead
Liquation
Zinc
Screening
Tailings
Zinc powder to consumers
Dross
Ferrous zinc
Processing
Processing
Zinc
Dross to processing

FIG. 20.1 Flow-sheet of the process of producing zinc powder by rectification of the melt.

FIG. 20.2 Rectification column.

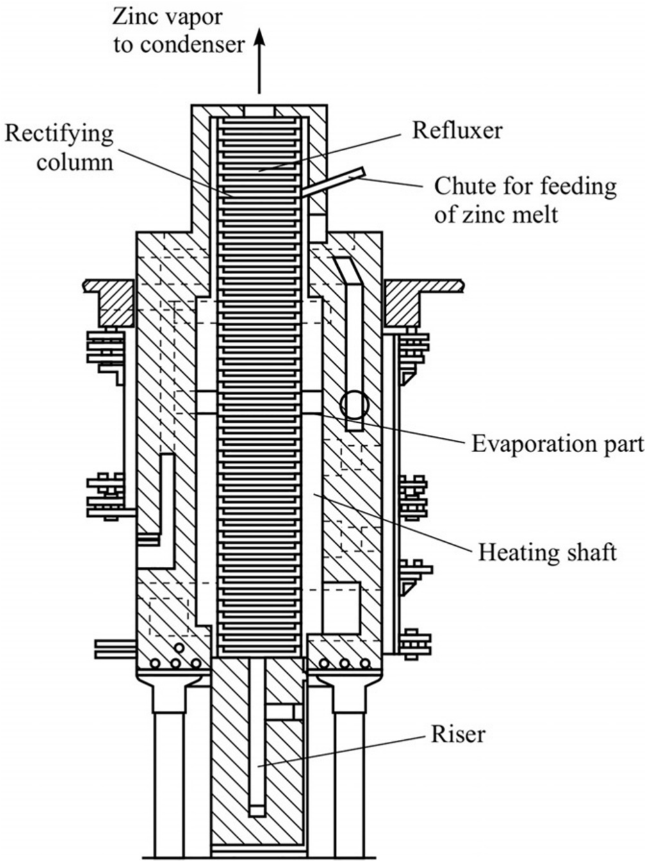
Zinc vapor to condenser
Rectifying column
Refluxer
Chute for feeding of zinc melt
Evaporation part
Heating shaft
Riser

Most of the zinc evaporates in the combustion chamber of the column at 1470–1570 K. The zinc vapor rises countercurrently to the metal melt flowing down from the top trays, gives up some heat to the melt, and reaches the condenser, where condensation of the vapor and the formation of solid particles of zinc take place at temperatures of 520–670 K. The target is a highly active polydisperse powder.

Condensation occurs according to one of two roads: vapor-liquid-crystal or vapor-crystal. The first road results in the generation of granules formative the coarse fraction. The condensation in accordance with the second road proceeds in two condensers at a significant temperature difference between the incoming gas and the condensation surface. Tables 20.1 and 20.2 present the condensation conditions and the basic parameters of the process.

The temperature within the condenser volume varies depending on the distance from the wall: 340–360 K at a distance of 25 mm; 450–500 K at 1000 mm; and 530–620 K at 1750 mm. The condensers are periodically cleaned by vibratory or mechanical methods. After leaving the condenser, zinc powder undergoes separation by sieving. The 0.3 mm tailings are recycled. The reflux part of the condensate amounting to up to 30% of the zinc charge, enriched in high-boiling components, passes from the lower trays of the column (see Fig. 20.2) through a hydroseal to a recirculating tank.

An interaction of silicon carbide and iron in the reflux flow occurs at 1370–1570 K, according to the reaction:

$$\mathrm{Fe_{Zn}} + n\mathrm{SiC} \leftrightarrow \mathrm{FeSi}_n + n\mathrm{C};\quad \Delta G^0_{1500} = -16{,}000\,\mathrm{J/mol}$$

The presence of iron in the zinc melt impairs the equipment; an increase of the iron content in the zinc from 0.04% to 0.06% reduces the service life of the column by 20%. Zinc is therefore subjected to liquation refinement in order to reduce the iron content to 0.02% or lower. Besides iron, the zinc charge usually also contains lead, cadmium, copper, and arsenic. The entire cadmium content passes to the zinc powder due to its lower boiling point. The lead content of the condensate, irrespective of its content in the zinc charge, can be reduced to a minimum under a certain temperature condition. Copper does not interact with silicon carbide. Due to its accumulation in the recycled zinc, the formation of brass occurs that is prone to precipitate on the lower trays of the column, thus hampering the process. Aluminum present in the charge in the amount of 0.01–0.05 wt% and concentrating in the reflux is useful for refining the zinc.

Zinc from the precipitation tank is fed into the reverberatory furnace. In the case where zinc oxide is to be separated, the reflux is taken out of the main cycle and processed in liquation and retort furnaces.

A process comprising evaporation of the melt with simultaneous refining can also be used. It allows the content of high boiling point metallic impurities such as iron, copper, etc., to be reduced as much as 30 times. The installation yields up to 12 t/day. Lowering the process temperature as well as using more pure source zinc also reduces the content of iron, copper, lead, tin, arsenic, and other impurities.

A technique has been developed that permits the condensation of zinc vapor to be carried out in a single water-cooled condenser. The content of the fraction <10 μm in the powder increases up to 30–45 wt%. The tightness of the equipment accounts for a lower risk of autoignition of zinc vapor in the condenser; the conditions of column maintenance are improved.

The following advantages are features of the rectification method:

1. Less pure, that is, a less expensive zinc source may be used, such as scrap.
2. Controllable powder properties.
3. Higher specific surface area of powder particles.
4. Powder particles of a regular spherical shape are produced.

Good technical performance and high economic indicators are features of the electrothermal process. The electrothermal furnace (Fig. 20.3) of $520 \times 520\,\mathrm{mm}^2$ in area is charged with blast-furnace coke sized between 380 and 20 mm. Graphite plates are connected to copper electrodes. The graphite electrode in the upper part of the furnace is sunk into the coke to a depth of 900 mm at a distance of 2550 mm from the lower graphite plates. Liquid metal is fed by metering ladles into the upper part of the furnace. The remaining metal melt is tapped through the tap hole while zinc vapor passes through a pipe connected with the condenser. The power rating of the transformer is 360 kVA.

The condensation plant (Fig. 20.4) consists of two main condensers with a surface area of $65\,\mathrm{m}^2$ and one additional condenser with a $37\,\mathrm{m}^2$ surface area. The gas from the additional condenser is directed into a cyclone cooler and further into the cyclone and a bag filter. The inert gas from the bag filter is recycled to the first condenser via the vapor line. The flow rate of the recirculating gas controls the particle size of the powder. The capacity of the blower is of $9.9\,\mathrm{m}^3$/min, pressure 17.4 kPa. The capacity of the installation amounts to 2000 t/year with power consumption 1000 kWh/t zinc powder; the consumption of coke is 2 kg/t of powder.

TABLE 20.1 Operating Modes of Rectification Columns (I, II) and Particle Size Distribution

	Temperature (K)			Composition of the Gas Phase in Condensers (wt%)						Particle Size Distribution (wt%)					
		In column condensers		I			II			Fraction (mm)					
Operating Mode	In Heating Shaft	I	II	CO	CH_4	H_2	CO	CH_4	H_2	+2.5	–2.5 +0.315	–0.315 +0.16	–0.16 +0.071	–0.071	Zinc Powder Yield (t/day)
1	1530–1540	660	630	1.9	–	–	1.7	–	–	0.8	4.2	0.1	2.1	92.8	14.1
2	1540–1545	630	600	1.7	0.32	23.6	1.4	0.33	21.0	2.4	5.2	0.3	2.4	89.7	14.7
3	1530–1540	630	640	7.0	0.78	13.5	8.0	1.2	18.0	6.9	1.5	0.3	2.7	88.6	14.5
4	1490–1530	630	690	2.3	0.32	18.0	2.0	0.33	13.0	3.9	15.2	3.2	7.1	70.6	13.8

Note: Mode 1, characteristic of normal operation of the condensers; mode 2, forced cooling of condenser walls; mode 3, supply of ~1 m^3/h carbon dioxide into condensers in counter flow to zinc vapor; mode 4, supply of water vapor into condenser (≈1 m^3/h).

TABLE 20.2 Typical Characteristic of Zinc Powders Produced by Rectification of the Melt

	Fraction Content (%)				Particle Size Analysis of the Fraction <0.071 mm						
	+0.16 mm		−0.16 mm		Content of Particles of Various Size (μm) wt%						
Mode	**Zn Total**	**Zn Met**	**Zn Total**	**Zn Met**	**>15**	**10–15**	**8–10**	**6–8**	**4–6**	**2–4**	**<2**
1	98.0	91.8	98.5	94.2	8.3	22.0	11.1	17.2	20.0	12.6	8.8
2	98.4	94.1	98.3	95.2	11.4	16.7	13.2	7.1	17.9	18.9	14.8
3	98.3	96.7	98.0	93.3	15.2	14.7	23.4	7.4	15.4	17.3	6.6
4	–	–	–	–	18.0	21.2	8.7	16.7	17.2	12.8	5.5

Note: See note to Table 20.1.

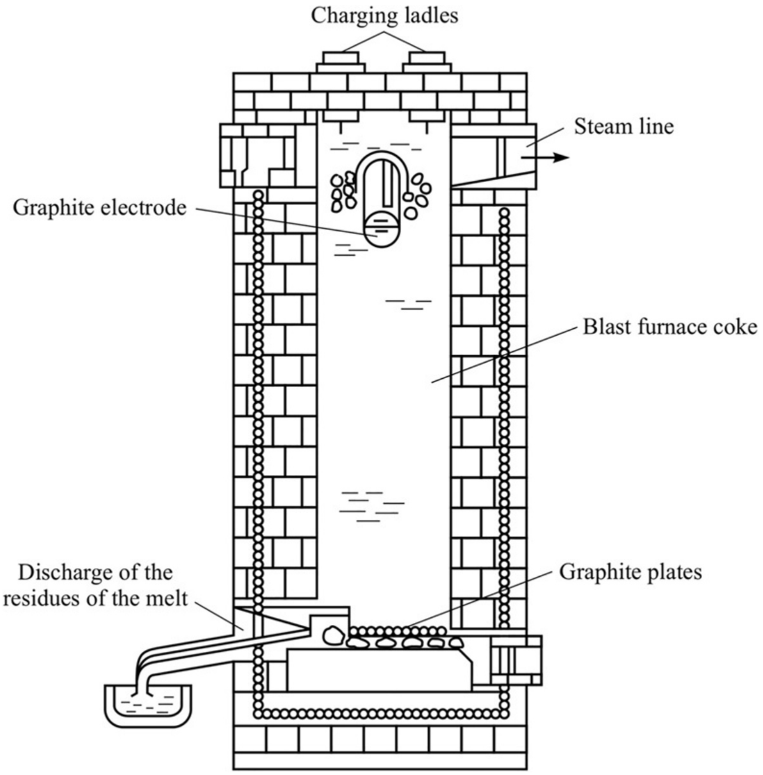

FIG. 20.3 Electrothermal furnace for production of zinc powder.

Depending on the flow rate of the recirculating gas, the powder yield amounts to 29.6%–32.4% from the first condenser, 30%–36% from the second, 12.5%–17.5% from the third, 9%–15% from the cyclone, and 5%–10% from the bag filter.

The electrothermal method does not ensure high purity of the zinc powder.

Inert Gas Condensation

A new method for producing fine zinc powder based on the inert gas condensation (IGC) process has been developed at the Institute of Metallurgy, Ural Branch of the Russian Academy of Science, and commercialized by the Fine Metal Powders Company in Yekaterinburg, Russia [2,3]. The "Tuman" ("Fog") installation of a modular type is the core of the process. The controlled process provides powders of a targeted particle size at a high yield. The total plant capacity in terms of zinc powder is up to 1500 t/year (Fig. 20.5).

The Tuman unit operates on a 12-h cycle. Chapter 5 contains more detailed information about this unit. The power consumption of the evaporator totals 46.5 kW, the consumption of the inert gas (argon) amounts to 56 m^3/month, and

FIG. 20.4 Electrothermal process flow-sheet.

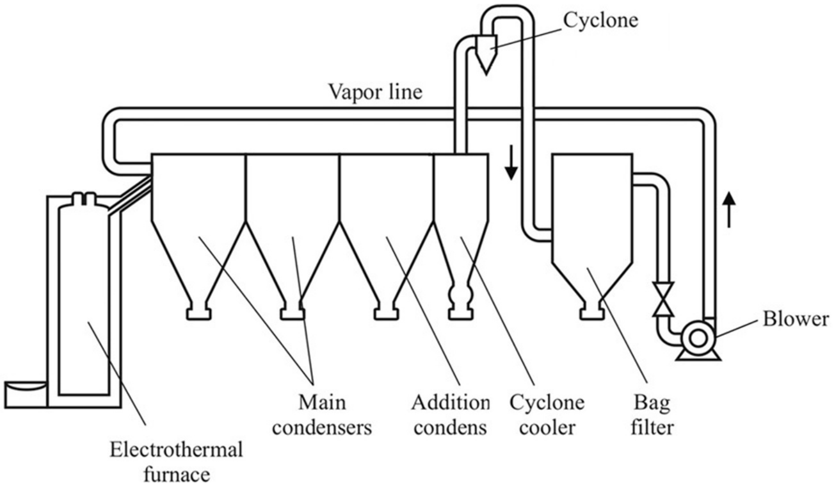

FIG. 20.5 The "Tuman" installations (the Fine Metal Powders Company's Advanced Technologies Plant).

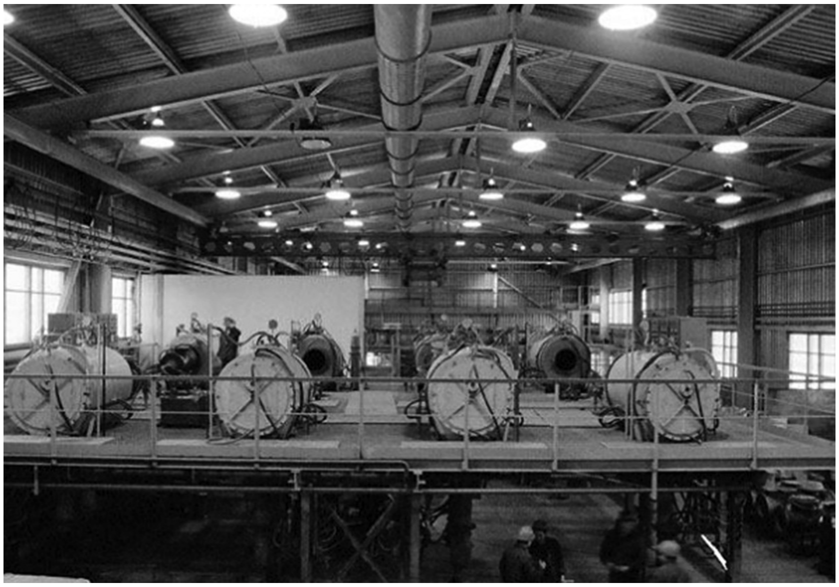

the consumption of the cooling water is 3.5 m^3 per one modulus per hour. The zinc content is Zn 99.98% while the trace impurities of Pb, Fe, Cu, Sn, and As amount to 76, 10, 6, 1, and 2 ppm, accordingly. Spherical powder produced by the IGS process is shown in Fig. 20.6.

Melt Atomization

As shown in Fig. 20.7, zinc melt is fed into the atomization nozzle via a tube made of quartz glass, graphite, or ceramic. Gas atomization can result in spherical or elongated particles (Fig. 20.8).

A flaky powder made by centrifugal atomization is illustrated in Fig. 20.9. The superheated melt is fed through a nozzle onto a dram having a corrugated surface, with the corrugation being made parallel to the axis of dram rotation.

To obtain fine powder by gas atomization, different measures can be used such as increasing the gas pressure and, appropriately, the gas flow rate; ultrasonic impact on the gas stream; heating the gas prior to feeding it into the nozzle [4]; and nozzles of special design [5,6]. Information about hot gas atomization and different designs is in Chapter 4.

As a rule, water atomization is not used for metals with a melting temperature below 773 K because of the formation of extremely irregular particle shapes due to extremely rapid solidification. Zinc is the lowest melting metal that is water atomized commercially. Thus, zinc powder for alkaline manganese batteries is produced by melt atomization under water pressure of about 5.5 MPa. The median mass particle size of this powder amounts to 180 μm with a geometric standard deviation about 2.34 [7].

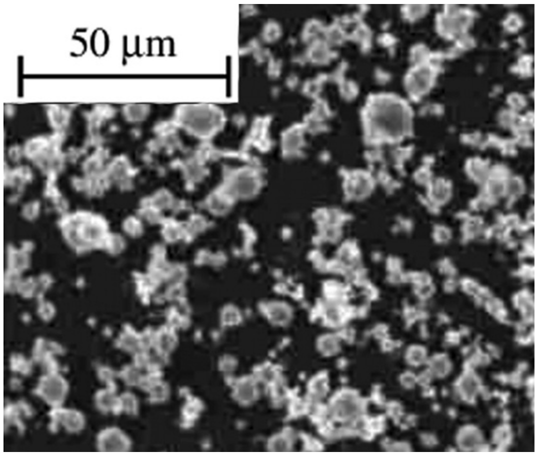

FIG. 20.6 Spherical powder produced by the ICG process.

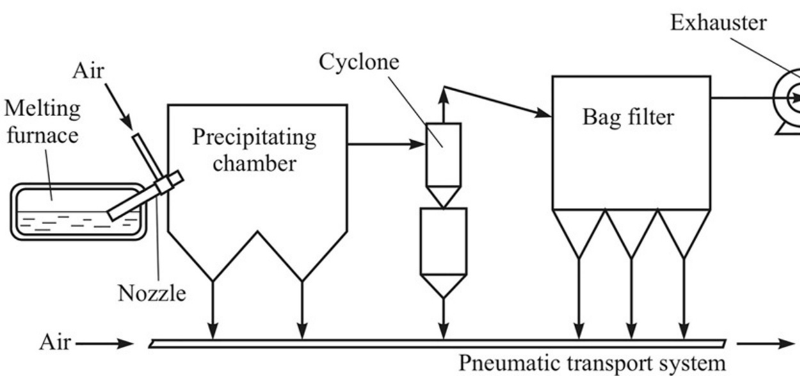
Exhauster
Cyclone
Air
Melting furnace
Precipitating chamber
Bag filter
Nozzle
Air
Pneumatic transport system

FIG. 20.7 Flow-sheet of producing zinc powder by the atomization process.

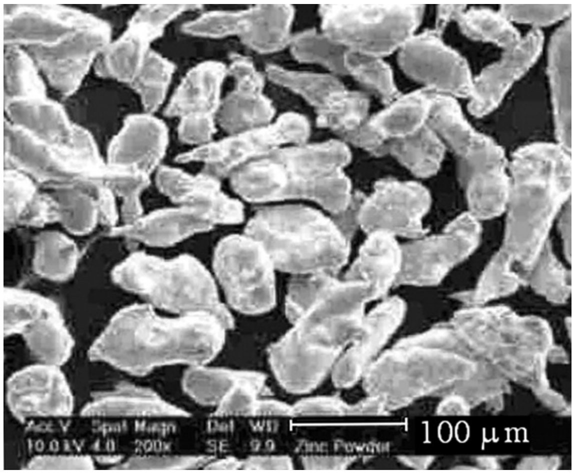
Acc.V Spot Magn Det WD
10.0 kV 4.0 200x SE 9.9 Zinc Powder
100 µm

FIG. 20.8 Elongated particles of powders produced by the gas-atomization process.

Electrochemical Method

The electrochemical method allows the production of high-purity powders.

Cathodic precipitates of various types can be obtained:

- Dense layers of flaky or crystalline particles; to obtain powder, these particles must be subjected to disintegration.
- Spongy soft precipitates easy for attrition.
- Loose precipitates of fine powder that do not require additional treatment.

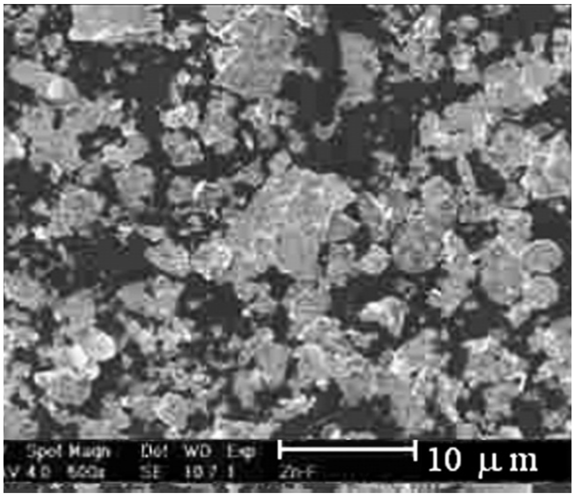

FIG. 20.9 Flaky powder produced by centrifugal atomization.

Zinc sponge is produced from alkaline zincate electrolytes (18 g/L Zn, 250 g/L NaOH) obtained either by leaching oxidized zinc-containing source material with an alkaline solution or from recycling wastes from the manufacture of benzidine, hydrosulfate, etc.

The cathodes are conventionally made of nickel, stainless steel, or magnesium. The electrolysis parameters are a voltage of 3.5–4.0 V, a current density of 2700 A/m^2, and a temperature of 293–323 K. The spongy cathodic precipitate easily slides down the cathode. After washing, it is used as a reducing agent in chemical processes. Dry powder contains 99.3% Zn [1].

A process is known that uses an electrolyte consisting of sodium hydroxide and sodium zincate, Na_2ZnO_3 [8]. A zinc content of about 55 g/L yields a deposit of the suitable particle size. The current density is about 1076 A/m^2. Under these conditions, the deposit is a loosely adherent sponge that can be easily scraped or brushed off the cathode and processed to powder.

In the production of zinc powder from industrial wastes, the latter are leached in a 6-M solution of sodium hydroxide at 330 K, bringing the zinc content of the solution to 30–40 g/L. Then the alkaline solution of the sodium zincate undergoes electrolysis at a temperature of 310–330 K and a current density of 2500–3000 A/m^2. The zinc sponge is removed by scraper blades. The precipitate is reduced to powder in an electrolyte medium by the disperser rotating at a speed of 1000–1500 rpm. The alkali residues are washed off the zinc powder.

The principal parameters of the electrochemical process are given in Table 20.3.

Dendritic deposits are formed if there are obstacles on the electrode that hinder the transfer of discharging ions to the electrode surface. They are created using various polarization methods.

The work [9] contains study results of the effect of the polarization conditions on the growth dynamics and structure of electrolytic dendritic zinc deposits obtained at room temperature from electrolyte with 0.3 mol/L zinc oxide and 4.0 mol/L of sodium hydroxide.

The following polarization modes were compared:

Galvanostatic mode by the maintenance of constant amperage of 1020 A/m^2 per the initial electrode surface.

Pulsed galvanostatic mode with congruent pulse amplitude to the amperage in the galvanostatic condition by at a ratio of pulse to pause lengths of 15/15 and 30/30 s.

Potentiostatic mode with constant polarization of –0.4 V relative to the nonpolarized zinc electrode in the solution.

Combined mode including the galvanostatic mode applied for 5 min and the pulsed potentiostatic mode with alternation of the pulse with amplitude –0.4 V and a pause in the 30/30 s ratio.

The deposit obtained in galvanostatic conditions has a typical dendritic structure (Fig. 20.10A). At high magnifications (Fig. 20.11A), it is shown that the real surface of dendrites is not flat but rather a honeycomb structure with crystallographic orientation, as in hexagonal lattices. The thickness of the cell walls is virtually constant over the whole field and is about 40–50 nm; these cells are not smooth and have a columnar structure. These honeycomb structures have extremely low packing density and high specific surface area.

During pulsed galvanostatic electrolysis, the concentration of discharging ions in the diffusion layer increases during pauses between pulses. When current is recurrently switched on, the overvoltage is not as high as it was at the beginning of the electrolysis because of the increase in the near-electrode ion concentration and deposit surface area due to the previous

TABLE 20.3 Specification of Electrolytic Methods of Manufacturing Zinc Powder

Process	Electrolyte Composition (kg/m^3)	Current Density (κA/m^2)	Temperature (K)	Process Characteristics
AS	$ZnCl_2$ of 15–80; pH = 4.4–5.8	0.1–0.8	293–363	Graphite anode; electrolyte is periodically adjusted by concentrated solution of $ZnCl_2$
AS	$ZnCl_2$ of 20–40; NaCl of 300	0.54	–	Current efficiency of 95%; chlorides are easily washed out of the sponge
AS	Zn of 15–22; NH_4NO_3 of 10; HNO_3 to 63	0.2–0.3	293	…
AS	Zn of 10; NaOH of 200	1.1–1.5	303	Nickel anode, magnesium cathode; spongy deposit; powder yield of 90%
AS	Zn of 8–16; NaOH of 100–200	0.5–1.0	293–323	Current efficiency of 75%–90%; deposit build-up time of 2–4 h; active zinc content of dry powder of 90%–97%
AS	$ZnSO_4$ of 20–40; NaOH of 230	0.5–2.5	298–318	Powder apparent density of 0.32–0.45 g/cm^3; specific surface area of 0.35–0.58 m^2/g
AS	$ZnSO_4$ of 0.5–200; NaCl of 20	1.8–20.8	308–343	–
RSPh	Na_2CO_3 of 159; ZnO	1.0	293	Raw material is ZnO; metallic zinc content of product of 90%; drying temperature of 333–338 K; particles are small, porous
AS	Zn of 40; NaOH of 220; oleate Na of 0.05; $CuSO_4$ of 0.5	3.0	333	Powder obtained in potentiostatic conditions ($E = -2.04$ V, normal hydrogen electrode) features elevated activity in the synthesis of rongalite
AS	$ZnSO_4$ of 60–65; NH_4Cl of 150; H_3BO_3 of 20; NH_3 of 20–25	0.3	290–293	Sedimentation of the powder at a potential of (−1.15 to −1.2) V, normal hydrogen electrode; pH = 10
RSPh	Na_2CO_3 of 159; ZnO	1.0	293	Raw material is ZnO; metallic zinc content of product of 90%; drying after washing and stabilization at 333–338 K; particles are porous

AS is aqueous solution; RSPh is the reduction from the solid phase.

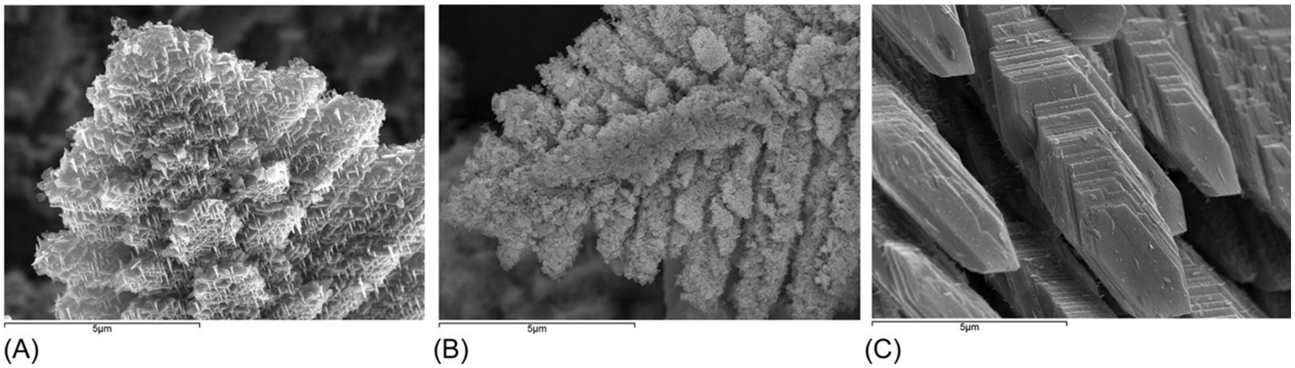

FIG. 20.10 Morphology of zinc dendritic depositions occurs in the following conditions: (A) galvanostatic, (B) combined, and (C) impulsive galvanostatic by impulse/pause equal to (15 s)/(15 s). *(Courtesy of Prof. T. Ostanina.)*

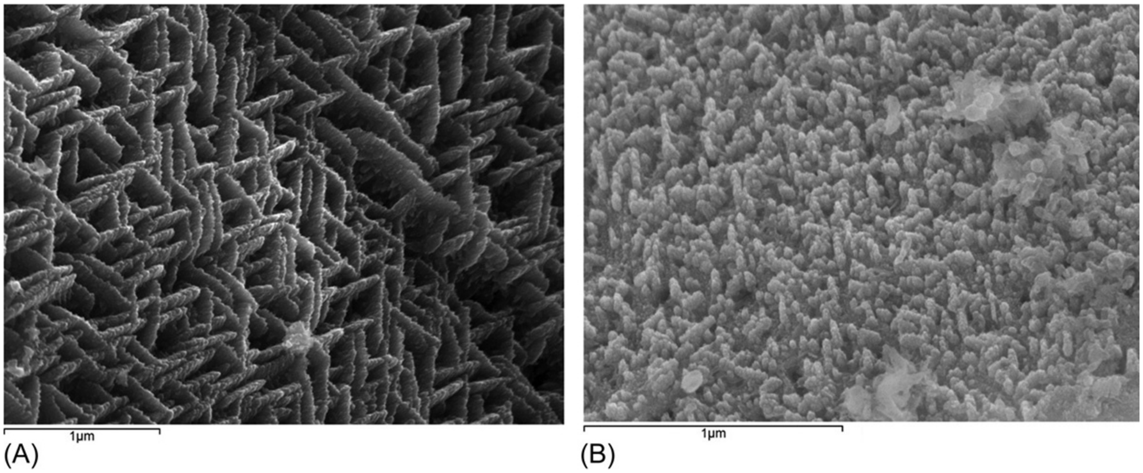

FIG. 20.11 SEM micrographs of zinc dendritic depositors occur in galvanostatic (A) and combined (B) conditions at high magnifications. *(Courtesy of Prof. T. Ostanina.)*

pulses. Therefore, the adatoms do not form new nuclei but are built into existing growth steps. In this case, a dendrite branch is of lamellar structure, in contrast to the honeycomb structure in the previous mode (Fig. 20.10C). This leads to a dramatic increase in the differential density of the deposit and a decrease in the specific surface area.

In the combined mode, there were alternating periods of growth and dissolution of the metal. A honeycomb structure forms at the stage of growth, and selective dissolution of the walls occurs during pauses. During the next potentiostatic pulse, the overvoltage remains high despite the considerable development of the surface, and the oversaturation of adatoms is sufficient for their crystallization on highly curved sites. This leads to the formation of a one-dimensional structure consisting of thin columns (with a diameter smaller than the thickness of the cell walls formed during the first stage) and measuring about 20–30 nm (Figs 20.10B and 20.11B). In the end, the volume is filled with interconnected columns forming a "vaulted" structure with an even lower filling factor than in the honeycomb structure.

The characteristics of zinc dendritic deposition at the end of the electrolysis cycle by various polarization modes are summarized in Table 20.4.

Other Methods

Mechanical grinding in various devices of ball, hammer, inertial, vibratory, jet type, etc., is one of the methods of obtaining fine zinc powder.

Air impact mills provide powders with a particle size in the range of 10–150 µm. The stability of the operation parameters and continuous recycled process are features of these plants.

TABLE 20.4 Characteristics of Zinc Dendritic Deposition at the End of the Electrolysis Cycle by Various Polarization Modes (Mean Value)

	Characteristic of Deposits			
Deposition Mode	y (cm^2)	S_m (cm^2/g)	ρ_{dep} (g/cm^3)	P (%)
Galvanostatic	0.11	302	0.18	97
Pulsed galvanostatic				
15/15 s	0.09	197	0.24	88
30/30 s	0.10	207	0.21	97
Potentiostatic	0.23	493	0.15	98
Combined	0.24	403	0.14	98

y is the length of dendrite; S_m is the specific surface of the deposition; ρ_{dep} is the deposition density; P is the porosity of the deposition; $P = 100 - \frac{100 m_{dep}}{V_{dep}\rho_{Zn}}$; m_{dep} is the mass of deposition; V_{dep} is the volume of the deposition; ρ_{Zn} is the zinc density.

Powders <1 μm in size can be produced by wet grinding in attritors in the presence of substances preventing autoignition of the powder such as nitrobenzene and salts of oleic or stearic acid. The addition of surfactants to the dispersing liquid will aid in reducing the particle size further.

Cryogenic methods enable fine and ultrafine powders to be produced. To obtain ultrafine powder, the powder is suspended in an aqueous medium and subsequently frozen under ultrasonic impact. The water is evaporated in a vacuum; the resulting product is a powder with a particle size <1 μm.

Zinc powder can be produced as a by-product by treatment of zinc-containing wastes. The surface of the zinc-containing melt is blown with an inert gas. Zinc vapor is condensed as a fine powder on the surface of a rotating water-cooled drum (a rotational speed of 0.5–10 rpm) located at a distance of 500–3000 mm from the surface of the melt. The average size of the resulting particles is <3 μm.

PRODUCTION OF CADMIUM POWDERS

All methods used for producing zinc powder are applicable to producing cadmium powder. Electrolytic deposition is the most common method (Table 20.5).

Cadmium powder can be obtained by cementation from a solution of copper-cadmium cake in waste electrolyte and the removal of copper from it. The composition of the solution is (kg/m^3): Cd 6–12; Ni 0.01–0.04; Fe 0.02–0.06; Cu $(0.2–0.3) \times 10^{-3}$; Co 0.08–0.12. Deposition is carried out in centrifugal reactor-separators using zinc dust. The thallium presence in the solution is precipitated together with cadmium but, after the bulk of the zinc dust is utilized, thallium goes back into the solution. The cementation of cadmium is finished when the concentration of thallium in the solution gets close to the initial level. Ions of silver and indium promote the cementation of cadmium. The duration of the operation is 35–40 min. The precipitate contains up to 95%–99% Cd. Power consumption is 1–2 kWh per solution volume of 1 m^3.

Cadmium powder with high electrochemical activity consisting of structurally uniform dendrite particles can be obtained from aqueous solutions on a horizontal cathode at varying current density. The composition of the electrolyte is (kg/m^3): Cd 5.6–20.2; acetic acid 90; potassium acetate 100–150; diethylenetriamine-penta-acetic acid 7.8–28 or diamine-cyclohexane-tetra-acetic acid 8.6–31. The current density rises with the duration of the process from a minimum value ($i_0 = 1.0–1.5\,\kappa A/m^2$) to a maximum of $i_\tau = 3.0\,\kappa A/m^2$. The duration of growth of the disperse layer approaches 0.3–0.5 h. The powder is washed with a 5% solution of acetic or sulfuric acid, deionized water, or acetone and dried in a vacuum. The cadmium anode without filler has a porosity of 60%–70% and ensures a discharge current efficiency of 90%.

PRODUCTION OF CADMIUM AND ZINC ALLOY POWDERS

Zinc- or cadmium-based alloys are conventionally produced by the electrochemical method (see Table 20.3) or by atomization (Table 20.6).

For producing an alloy with an atomic fraction of zinc of up to 40%, solutions of zinc and cadmium sulfate are used. Powders of targeted composition have been obtained by varying the composition of the solution and the current densities (Table 20.7). Alloys are precipitated at galvanostatic conditions.

The alloy powder corresponds to a conglomerate of particles of dendrite shape with their longitudinal dimension approaching twice the cross-sectional dimension. An increase in the current density from 1000 to 15,000 A/m^2 leads to a reduction in particle size by a factor of 1.5–2.0 (from 250×140 μm to 150×75 μm). A change in the composition of the solution does not affect the particle size significantly.

Zinc-copper alloy powders can be produced by electrolytic deposition from cyanide as well as from pyrophosphate, ammoniate, tartrate, citrate, and other solutions. For some alloys (Zn-Fe, Zn-Sn), there exists a nearly direct relation between the concentration of the metal in the solution and the ratio of the atomic fractions of the corresponding metals in the alloy. The composition of the alloy also depends on the current density, the temperature of the electrolyte, and the intensity of agitation.

Spherically shaped powders of zinc, cadmium, and their alloys can be produced by atomization of the melt that contains additives of alkali metals: Li, Na $\geq 0.001\%$ or K, Ce, Rb $\geq 0.01\%$. Atomization of a zinc melt containing 0.4% Na (the temperature of the melt is 770 K, air temperature is 320 K, and pressure is 0.3 MPa) provides a powder with up to 80% particles of spherical shape in the size range of 150–480 μm. The apparent density of the powder is 4.2 g/cm^3. Without the addition of sodium, particles obtained under the same conditions have an irregular shape, the metallic luster is less marked, and the apparent density is 3.2 g/cm^3.

TABLE 20.5 Specification of Electrolytic Methods of Manufacturing Powders of Cadmium and Its Alloys

Process	Electrolyte Formulation (kg/m^3)	Current Density (кA/m^2)	Temperature (К)	Process Characteristics
Cadmium				
EAS	$CdCl_2$; HCl	30–70	300	Sponge of fine two-dimensional dendrites; cadmium in the form of chloride
EAS	Cd of 0.11–11; H_2SO_4 of 50	0.05–0.2	300	Constant overvoltage of 80–150 mV; particle shapes dendrites and needles with a length in the range of 70–300 μm
EAS	$CdCl_3$	3–0.75	298	Replacement of cementation by electrolysis reduced cost due to dust retention by a factor of 5
EAS	$CdSO_4$	5–15	298	Current efficiency of 86%–93%; particle size of 50–80 μm; chemical cell capacity increases by 20%–30%, and their service life increases by a factor of 1.5–1.6
EAS	Cd_{start} of 100;Cd_{end} of 20; H_2SO_4 of 10	0.6	298–301	Zinc present in the solution to 30–40 kg/m^3 is admissible; current efficiency of 93%–96%; deposit building up time of 24 h
ENAS	Dimethylformamide-solvent; NH_4BF_4 of 210; $Cd(BF_4)_2$ of 28.6–114.4	4	298	Constant overvoltage of 0.1–0.25 V; rotating electrode; deposit is washed off; at a rotational speed of 20–270 s^{-1} and operating time of 60 min; average particle size is of 6–29 μm
RSPh	CdO in form of tablets, NaOH of 40	3–4	298	Raw material is CdO, nickel anode; drying for 90 min at 323 К; current efficiency of 96%; particles: dendrite, polydisperse, porous
Cadmium-zinc alloy				
AS	$CdSO_4$ of 8.4–37.5; $ZnSO_4$ of 2.4–48.3	1–15	293	Current efficiency of 90%–96%; powder composition depends on deposit build-up time and concentration of cadmium in the solution
Cadmium-iron alloy				
AS	Cd + Fe of 10; (NH_4) $2SO_4$ of 50; pH 2.7	35	293	Independent regulation of anodic currents of cadmium and iron; current efficiency of 65%–67%; average particle size of 5 μm
Cadmium-nickel alloy				
AS	$(CdSO_4 + NiSO_4)$ 0.2 mol/L; NH_4Cl of 5.4	3	293	Current efficiency of 65%; average particle size of 2 μm; phase composition-mechanical mixture of cadmium and nickel: (Cd/Ni) powder = (Cd/Ni) solution

EAS is electrolysis of aqueous solution; ENAS is electrolysis of nonaqueous solution; RSPh is the reduction from the solid phase; AS is aqueous solution.

A technique is known for producing zinc alloy powders by adding 5%–80% iron and 0.2%–5% aluminum or copper to the molten zinc. The melt is cooled and ground. The powder has elevated corrosion resistance and is hardly oxidized, owing to the protective cathodic action of iron. It is used as filler in resins.

SAFETY MEASURES IN ZINC AND CADMIUM POWDER PRODUCTION AND HANDLING

The high chemical activity of fine and, particularly, ultrafine, zinc, and cadmium powders accounts for their flammability and explosiveness. Due to this fact, fire and explosion safety measures are necessary in zinc and cadmium powder

TABLE 20.6 Typical Characteristics of Zinc Powder Produced by Ultrasonic Atomization of the Melt

		Fraction Yield (%)										
		Particle Size (μm)										
Medium	**Pressure (MPa)**	**+120**	**−120 +80**	**+100**	**−100 +50**	**−80 +63**	**−63 +40**	**−50**	**−40**	**Metal Consumption (kg/min)**	**Content of Oxygen in Fraction <63 μm (wt%)**	**Apparent Density (g/cm^3)**
Argon	–	10.6	20.3	–	–	10.4	51.1	–	7.6	–	0.02	–
Air	–	25.5	29.1	–	–	13.8	27.9	–	3.7	–	0.14	–
Vacuum	0.1	–	–	69.5	18.5	–	–	12	–	10.2	–	3.6
Vacuum	0.2	–	–	7.0	8.0	–	–	85	–	35.0	–	3.9

TABLE 20.7 Effect of Electrolyte Composition on Powder Composition and Cathode Potential (Current Density of 15,000 A/m^2)

Content in Solution (g-ion/L)		Atomic Fraction of Zn in Powder (%)		
Cd^{2+}	Zn^{2+}	Actual	Estimated	Cathode Potential (V)
0.18	0.15	6.9	6.5	–0.77
0.18	0.075	6.5	7.5	–0.78
0.18	0.03	5.6	6.2	–80
0.09	0.15	14.5	15.0	–78
0.07	0.15	20.6	22.3	–0.79
0.045	0.15	29.5	28.6	–0.81

production and handling. For powder with particles <74 m, the minimum spontaneous ignition temperature is 870 and 843 K and the minimum ignition energy is 640 and 4000 mJ for zinc and cadmium powders, respectively. The zinc sponge is removed by scraper blades. The lower explosive limit for zinc powder is 480 g/m^3 (see Chapter 27). The spontaneous ignition temperature depends on the chloride content (>0.05%); moisture stimulates the spontaneous ignition process.

The presence of zinc oxide determines the degree of toxicity of zinc powder. Inhalation or swallowing of zinc powder injures breathing organs and causes gastrointestinal disturbances. Under the workplace exposure limits, in the European PM industry the long reference period exposure limits (WELs) for zinc respirable dust is 4 mg/m^3. The threshold limit value (TLS) in the air at the workplace (in terms of zinc oxide) adopted by CIS 12.1.005–88 is 0.5 and 0.05 mg/m^3 [10]. The TLS in drinking water (in terms of metal zinc) is 1.0 mg/L [11]. Techniques for the prevention of exposure to hazards are described in Chapter 27.

APPLICATIONS

There are two basic sectors of application of zinc powders:

- Protective coatings, including zinc-rich primers and paints; powder coating; and sherardizing.
- Chemical processes: purification of zinc solutions before electrolysis at electrolytic zinc plants; manufacture of reducing agents (sodium and zinc hydrosulfite) for the paper and textile industries; in the mining industry (for the extraction of gold, silver, and other precious metals); and manufacture of alkaline batteries.

For manufacturing alkaline batteries and for other chemical applications, high-purity zinc powder is needed, which is produced using extra pure special high grade (SHG) zinc.

Zinc Powders in Protective Zinc-Rich Coatings

Zinc-rich coatings combine the advantages of metallic (cathodic protection) and paint (barrier, hydro insulating effect) coatings that make them perfectly suitable for "cold" galvanizing of metals.

The most important applications of zinc-rich primers and paints are coatings exposed to severe corrosion-hazardous conditions: offshore oil fields, the petroleum industry, power engineering, sea container production, shipbuilding, and ship repair. These materials are also widely used for protecting metal structures in the construction of buildings, bridges, etc.

Zinc-containing protective materials are divided into zinc primers containing 25%–75% zinc and zinc-rich primers (85%–92% Zn). They are also distinguished by the type of binding agent: (a) organic compounds (e.g., systems based on epoxy ethers and epoxy polyamides or moisture-curing systems based on polyurethane, vinyl, and vinyl chloride rubbers); and (b) inorganic compounds on the base of ethyl silicates and alkaline silicates. Inorganic compounds display higher density and greater abrasion resistance, but require a more careful pretreatment of the surface and perform lower flexural strength than organic zinc-rich compounds [12].

Zinc powders used as pigments in anticorrosive coatings should meet certain requirements. Thus, the metal zinc content in such powders should not be lower than 95% with a minimum of zinc oxide present. Limits are set on the content of lead (<0.15%) and iron (<0.004%); no moisture is admissible. Lead impairs the quality of the coating and threatens labor safety conditions while welding. Elevated iron content of the powder reduces the protective potential of the primer while moisture causes caking of the stored powder and creates a risk of emission of hydrogen prone to destroy the protective effect of the coating [13,14].

Zinc powders conventionally used in zinc-rich protective coatings have their particle size in the range of 3–12 μm (Table 20.8). The particle size of powders influences the density of particle packing. The maximum packing density of about 61% of the solids content (by volume) is peculiar to powders with an average particle size of 6 μm.

In recent years, powders with flaky particles (see Fig. 20.9), 0.2–0.4 μm thick and 20–30 μm long, have been used in primers and paints. When flaky powders are used, reliable corrosion protection is achieved at a powder content of 80% of the dry coating that reduces the consumption of zinc and increases the covering capacity and the elasticity of the coating.

TABLE 20.8 Specification of Zinc Powders for Protective Coatings

		Manufacturer, Grade, Manufacturing Technique			
Characteristics	**ASTM Standard for Zinc Dust Type III (For Use in Zinc Rich Coatings)**	**Umicore, Belgium. Zinc Dust Grade 4P16, (Distillation)[a]**	**Trident Alloy, United Kingdom Delaville Standard CP75 Zinc Dust (Electrothermal Furnace Technology)[b]**	**US Zinc, United States Grade USZ # 1 XL (Distillation)[c]**	**Fine Metal Powders Company, Russia Zinc Powder Grade PZHD-1 (IGC Technique)**
Total zinc, calculated as Zn, min.%	99.0	99.0	98.0	98.5	99.0
Metallic zinc, min.%	96.0	96.5	95.0	95	96.0
Lead, calculated as Pb, max.%, s	0.002 (20 ppm)	0.003	0.1	0.01	0.013
Cadmium, calculated as Cd, max.%	0.001 (10 ppm)	0.0005	0.005	0.01	0.004
Iron, calculated as Fe, max.%	0.002	0.002	0.003	0.02	0.003
Medium particle size, μm	–	3.4–3.9	–	5–8	4–12
Coarse particles μm max.%					
+150	0.1	0.00	0.01	Trace	0.00
+75	0.8	0.00	0.3	0.1	0.8
+45	3.0	0.7	5.0	4.0	3.0
Specific weight, g/cm^3	–	–	7.1	7.1	7.1

[a] *Source: http://www.jamesmbrown.co.uk/zincdust/zincdust.htm.*
[b] *Source: http://www.tridentalloys.com/Pigments.*
[c] *Source: http://www.uszinc.com/ZincDust/ProductSpecs/XL_.*

Anticorrosive Zinc-Rich Coatings for Roll and Sheet Steel and Metal Wear

Protective coatings for roll and sheet steel based on pure fine zinc powder have been developed. These are DACROMET, ZINCOMET, GEOMET, PLAS, etc.

DACROMET is an inorganic coating composed of zinc and aluminum flake in a binding matrix of chromium oxides. Zinc and aluminum platelets align in multiple layers forming a metallic silver gray coating. Applied as a liquid material, the coating becomes totally inorganic after curing at 594K. The corrosion resistance performances of DACROMET are particularly high at a low thickness (from 5 to 10 μm). DACROMET can serve as a base for most paints, including electrodeposited paint. Two DACROMET coating types are commonly used to meet the automobile industry's requirements:

Grade A: coating weight $>24\,\mathrm{g/m^2}$, average thickness of 5–7 μm.
Grade B: coating weight $>36\,\mathrm{g/m^2}$, average thickness 8–10 μm.

Coatings of greater thickness may be applied to increase the duration of the corrosion protection. Several application techniques are used industrially, among them immersion and pneumatic or electrostatic spray.

Sherardizing (Thermodiffusion Galvanizing)

Sherardizing is a very reliable and versatile method of coating steel surfaces and therefore giving high protection against corrosion and abrasion. The metal articles are heated in the presence of zinc powder (dust). The process is normally carried out in a slowly rotating closed container at temperatures ranging from 593 to 773K (Fig. 20.12). Several aftertreatments may be applied (chrome passivation, lubrication, etc.).

A sherardized coating forms two layers of zinc-iron alloy: a diffused gamma layer containing 21%–28% of iron and a compact delta layer containing 8%–10% of iron. The thickness of the coating may be in the range of 10–110 μm.

The main benefits of the sherardized coating are the thickness of the coating remains regular and uniform, even on irregular or complex shaped and recessed components; high adhesion due to the zinc-iron alloy diffusion; no hydrogen embrittlement; versatility; easy operation; and environmental friendliness.

Usage: anticorrosion treatment of metal articles (nails, bolts, screws, cast iron articles, metal pegs, medium-sized metal objects of irregular form, etc.).

An important feature of thermodiffusion galvanizing is that it does not impair the mechanical properties of heavy-duty fixing parts (bolts and nuts).

Mechanical Plating

Steel articles are placed in a drum with a mixture of a zinc powder, an activating solution, and glass beads. The drum is then tumbled and the beads impact zinc onto the surface of the steel. The thickness of the resulting zinc coating is 10–12 μm. Also, cadmium powders and mixtures of Zn and Cd powders may be used.

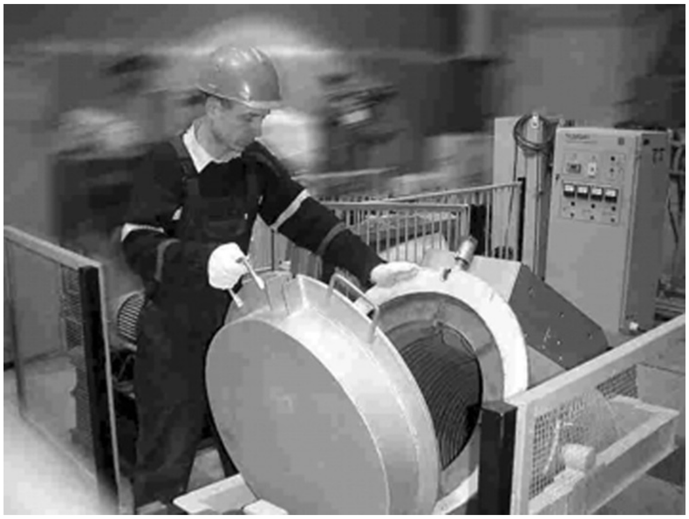

FIG. 20.12 An installation for thermodiffusion galvanizing (sherardizing): general view while container is being charged.

TABLE 20.9 Powder Characteristics and Light Element Content

Zn Powder	Undersize (μm)			Hall Funnel Flow (s)	Content of Impurities (ppm)		
	δ_{10}	δ_{50}	δ_{90}		Oxygen	Nitrogen	Hydrogen
Powder 1	10	29	58	No flow	2585 ± 71	17 ± 2	23 ± 1
Powder 2	26	39	60	20.98	2551 ± 81	17 ± 2	7.6 ± 0.8

Recycling of Tungsten Carbide Powders

The most important process for hardmetal scrap direct conversion into graded powder ready for pressing and sintering is the so-called "Zn process" [15–17]. The zinc process steps are as follows: (1) Sorted, cleaned, and crashed hardmetal scrap**;** (2) Reaction in molten zinc at 1173–1273 K in a protective atmosphere (Ar/H_2); (3) Vacuum distillation at 1273–1323 K; (4) Crushing, ball milling, and screening; (5) <75 μm powder ball mill, screen, blend, carbon adjust; and (6) Graded hard metal powder for use.

Implant Production

There is a long-term interest in biodegradable load-bearing implants in medical research in general, and thus also in medical laser-bed powder-bed fusion (PBF-L) research. The third group of alloys after magnesium and iron alloy groups to be considered promising for biodegradable implant production are Zn alloys [18–20]. The first peer-reviewed publication on this subject appeared in 2007 [21].

The main objective of the work [22] was the study and development of the direct metal printing (DMP) process for pure Zn. DMP is a commercial name that refers to the same basic process in which a laser is used to selectively fuse powder along a trajectory based on a computer-aided design (CAD) file. Two different Zn powders were used for this research. The first, P1, was produced by air atomization. The second, P2, was produced by nitrogen atomization. As Table 20.9 shows, P2 has a better flowability than P1. Both powders have some porosity and the amount of pores is similar for both powders.

This study has shown that it is possible to produce high-quality Zn parts by direct metal printing (DMP). Single track scans were used to estimate suitable process parameters. In the two-dimensional experiments, the hatch spacing was chosen to balance track overlap and smoke formation. The quality of the layers after DMP largely depended on the flowability of the powder. A relative density of $>99.70\%$ was obtained for a $10 \times 10 \times 10\,mm^3$ density cube. A vertical cross-section of this sample showed that elongated grains grow in the building direction across multiple layers.

REFERENCES

[1] Naboychenko SS, editor. Handbook of nonferrous metal powders. Moscow: Metallurgia Publishers; 1997 [in Russian].

[2] Frishberg IV, Yurkina LP, Subbotina OY, et al. Experience in development and commercial implementation of new zinc-rich coatings for protection of steel against corrosion. In: Proceedings of the EuroPM 98 international conference**:** European Powder Metallurgy Association, vol. 4; 1998. p. 825–6.

[3] Frishberg IV, Subbotina OY, et al. New Russian zinc-rich materials. In: Promyshlennaya Okraska; 2003. p. 8–15. 1. (in Russian).

[4] Dunkley JJ. Hot gas atomisation—economic and engineering aspects. In: Compiled by European powder metallurgy association, (Bellstone Shrewsbury, UK) proceedings of 2004 powder metallurgy world congress. Vienna: vol. 4; 2004. p. 101–5.

[5] Ünal A. Effect of processing variables on particle size in gas atomization of rapidly solidified aluminium powders. Mater Sci Technol 1987;3:1029–39.

[6] Rieken JR, Heidloff AJ, Anderson IE, Mullis A. In: Development of a close-coupled gas atomization for fine metal powder production. In: Compiled by Russell a. Chernenkoff, W. Brian James proceedings of 2014 powder metallurgy world congress. Orlando (FL, USA): Metal Powder Industries Federation; 2014. p. 02-54–02-60.

[7] Dunkley JJ. Atomisation of metal powders in powder metallurgy. In: An overview of Jenkins I, and Wood J: institute of metals; 1991. p. 2–21.

[8] Taubenblat PW. Chemical and electrolytic methods of powder production. In: ASM handbook. vol. 7. Materials Park, OH: ASM International Publishers; 1998. p. 67–71.

[9] Ostanina TN, Rudoj VM, Darintseva AB, Cheretaeva AO, Demakov SL, Patrushev AV. Effect of the polarization conditions on the structural properties of zinc dendritic deposits. Powder Metall Metal Ceram 2014;139(9):489–97.

[10] Occupational Safety Standards System. General sanitary requirements for working zone air. GOST 121.005 – 88 (in Russian).

[11] Sanitary regulations and standards of surface waters from pollution. SanPaN 4630–88 (in Russian).

[12] Zinc-rich paints for corrosion protection. PCE; 1997, 2 (11): 26–33.

[13] Karakasch N. Zinc coating review – 2000 and beyond. Corros Manage 2001;5.

[14] High-quality coatings for steel bridges. Tikkurila Coatings 1999; 1: 12–5.

[15] Kieffer BF, Lassner E. Tungsten recycling in today's environmet. Berg- und Hüttenmännische Monatshefte 1994;139(9):340–5.

[16] Kieffer BF. Processes for the recycling of tungsten carbide scrap. Int J Refract Met Hard Mater 1986;5(4):65–8.

[17] Kieffer BF, Baroch EF. In: Sohn HY, Carlson ON, Smith, editors. Extractive metallurgy of refractory metals. Proceedings of symposium. Chicago, IL: sponsored by the TMS-A1ME refractory metals committee and the physical chemistry of extractive metallurgy committee at the 110th AIME annual meeting; 1981. p. 273–94.

[18] Heiden M, Walker E, Stansiu L. Magnesium, iron and zinc the trifecta of bioresorbable orthopaedic and vascular implantation—a review. J Biotechnol Biomater 2015;5(178). https://doi.org/10.4172/biotechnology-biomaterials.1000178.

[19] Bowen PK, Drelich J, Goldman J. Zinc exhibits ideal physiological corrosion behavior for bioabsorbable stents. Adv Mater 2013;25:2577–82.

[20] Bowen PK, et al. Biodegradable metals for cardiovascular stents: From clinical concerns to recent Zn – alloys. Adv Healthc Mater 2016;5(10):1121–40.

[21] Wang X, Lu H, Li X, Li L, Zheng Y. Effect of cooling rate and composition on microstructures and properties of Zn-Mg alloys. Trans Nonferrous Metals Soc China 2007;17:122–5.

[22] Lietaert K, Baekelant W, Thijs L, Vleugels J. Direct metal printing of zinc: from single laser tracks to high density parts. In: Compiled by European powder metallurgy association, (Bellstone Shrewsbury, UK) proceedings of PM 2016 world congress. Hamburg (Germany); 2016: p. 1–6.

Chapter 21

Production of Nickel and Nickel-Alloy Powders

Oleg D. Neikov*, Stanislav S. Naboychenko† and Irina B. Murashova†

*Frantsevich Institute for Problems of Materials Science (IPMS), Kiev, Ukraine †Ural Federal University (UrFU), Yekaterinburg, Russia

Chapter Outline

Introduction 633
Carbonyl Process of Nickel Powder Production 633
Nickel Tetracarbonyl Formation and Decomposition 634
Commercial Technique 635
Health and Environmental Protection Measures in Carbonyl Nickel Production 638
Powder Properties and Applications 638
Hydrometallurgical Processing 644
Feed Processing 644
Leaching 645
Copper Removal 646
Oxidation and Hydrolysis 646
Hydrogen Reduction by Autoclave Processing 646
Sulfide Precipitation 649
Powders Covered by Nickel 650
Autoclave Processing of Nickel Hydroxide and Carbonate Pulps 651
Atomization 652
Hardfacing Powders 652
Superalloy Powders 654
Mechanical Alloying 657
Production of Nickel Powder by Reduction Processes 661
Solid-Phase Reduction 661
Reduction by Organic Reagents 662
Production of Nickel Powder by Electrolysis 663
Peculiarity of Nickel Alloy Powders by Using in Additive Manufacturing 664
References 667

INTRODUCTION

The two main processes for producing nickel powder are the carbonyl process, where nickel carbonyl is decomposed, and hydrometallurgical techniques, where the reduction of an aqueous solution of a nickel salt with hydrogen under pressure is realized (the Sherritt process). Nickel and nickel-alloy powders can also be produced by inert gas or water atomization, by the electrolytic method, by solid-phase reduction, and by mechanical alloying. All these technologies are discussed in this chapter.

CARBONYL PROCESS OF NICKEL POWDER PRODUCTION

The manufacture of nickel powders by the decomposition of nickel carbonyl dates back to a process developed in 1889 by Ludwig Mond, together with his collaborators Carl Langer and Friedrich Quincke. They found [1] that carbon monoxide at atmospheric pressure and at a temperature between 313 and 373 K reacts with active nickel to form a colorless gas, nickel tetracarbonyl:

$$\mathrm{Ni} + 4\mathrm{CO} \overset{323\,\mathrm{K}}{\leftrightarrow} \mathrm{Ni(CO)_4}.$$

They further showed that the reaction is easily reversible by heating the nickel tetracarbonyl to temperatures in the range 423–573 K:

$$\mathrm{Ni(CO)_4} \overset{503\,\mathrm{K}}{\leftrightarrow} \mathrm{Ni} + 4\mathrm{CO}.$$

Formed nickel that has been in contact with air does not react with carbon monoxide.

Handbook of Non-Ferrous Metal Powders. https://doi.org/10.1016/B978-0-08-100543-9.00021-X
© 2019 Elsevier Ltd. All rights reserved.

Mond built an experimental plant near Birmingham, England, and developed the Mond-Langer carbonyl process for separating nickel from Canadian matte containing 40% Ni. Opening in 1895, the plant produced 1.5 tons of nickel weekly. Mond afterward opened a refinery in Clydach, Wales, and during the 27 years the refinery operated, the factory processed >90,000 tons of nickel in the form of pellets. In this process, which in modified form is still used at the Clydach refinery, nickel oxide manufactured by roasting nickel sulfide is recovered to nickel sponge by hydrogen, activated by sulfiding, and sublimated as carbonyl in an atmospheric reactor. Nickel carbonyl manufactured in this way is decomposed directly in the powder and pellet condition as a section of a continuous process of refining.

Nickel Tetracarbonyl Formation and Decomposition

Conversion of nickel to a carbonyl at a fixed temperature depends primarily on the partial pressure of the carbon monoxide present. For given conditions of surface activity, the rate of gaseous or liquid formation is determined by the reaction temperature, and increases with increasing partial pressure of carbon monoxide. A feature of the dependence of system pressure and temperature on the reaction rate in the formation of nickel tetracarbonyl is a peak corresponding to optimal temperature, as shown in Fig. 21.1 [2].

The nickel tetracarbonyl formation reaction is highly exothermic:

$$\mathrm{Ni} + 4\mathrm{CO} \rightarrow \mathrm{Ni(CO)_4}$$

$$\Delta_{\mathrm{f}} H^{298} = +160.4\,\mathrm{kJ/(g\cdot mol)}\ \{38.4\,\mathrm{kcal/(g\cdot mol)}\}$$

Therefore, a high conversion-rate commercial nickel carbonyl process requires a large heat removal system.

At room temperature, nickel tetracarbonyl is a colorless volatile liquid with a high vapor pressure. It boils at about 316 K at atmospheric pressure and begins to decompose at 333 K or less, depending on the conditions. Its melting point is 256 K and the specific gravity amounts to 1.36135 at 273 K and 1.27132 at 309 K. Nickel tetracarbonyl is only weakly soluble in water (0.018 g/100 mL at 283 K), but is easily miscible with many organic solvents. The stability of metal carbonyls varies greatly. Nickel tetracarbonyl begins to liberate carbon monoxide and nickel at 273 K in a vacuum, and the decomposition becomes appreciable above 333 K in an inert gas under atmospheric pressure.

In the formation of powder particles from the gaseous phase, several joint phenomena act. They include the formation of complex nuclei, the secondary crystallization of nickel on the surface of the finest particles, and the interaction of particles in the crystallization process. At the specified temperature, the homogeneous part of the decomposition of nickel tetracarbonyl obeys the rate equation shown by Carlton and Goldberger in a work [3]:

$$r = \frac{K_0 p_{\mathrm{ca}}}{1 + K_{\mathrm{g}} p_{\mathrm{co}}}$$

where r is the decomposition rate in grams per cubic centimeter per hour, K_0 is the rate constant in grams per square centimeter per hour, K_{g} is the adsorption constant of carbon monoxide on metal in Torr^{-1}, p_{ca} is the partial pressure of carbonyl

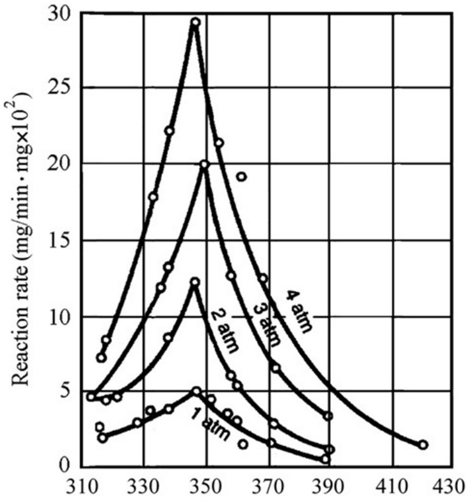

FIG. 21.1 Dependence of system pressure and temperature on reaction rate in the formation of nickel tetracarbonyl.

in Torr, and p_{co} is the partial pressure of carbon monoxide in Torr. The decomposition rate for nickel tetracarbonyl is directly proportional to the partial pressure of the carbonyl and inversely to the partial pressure of the residual carbon monoxide.

Conditions that affect the formation of the nickel particles during carbonyl decomposition (such as processing temperature, and the concentration and rate of the nickel tetracarbonyl feed to the decomposer) can vary significantly. These influence the physical and technical properties of the powders. Additions to nickel tetracarbonyl in the decomposer can change the mechanism of powder forming as well as particle morphology. Thus, hydroquinone sublimated with the carbonyl functions as a free radical trap in the formation of macroparticles of nickel metal.

The most important industrial application area of nickel tetracarbonyl is for refining nickel, where nickel pallets and powder products are manufactured. The plated products and a wide range of metallic and nonmetallic (for example, nickel-coated graphite) powders can be produced by making coatings of nickel on various surfaces by means of decomposition the carbonyl under special conditions. Nickel tetracarbonyl found application as a catalyst for organic synthesis as well as providing a means for the manufacture of several organonickel compounds. It also serves to form nickel molds for the glass industry and for vapor plating on smooth surfaces such as plastic and metal.

Commercial Technique

Currently, the largest producers of high-purity nickel powders manufactured by the thermal decomposition of nickel tetracarbonyl are factories in Clydach, Wales, the United Kingdom, Copper Cliff, Sudbury, Ontario, Canada, and the Norilsk Nickel Company, Russia.

The thermal decomposition of nickel tetracarbonyl processes is distinguished by pressure value as the low, atmospheric pressure carbonyl technique, as high pressure amounts to 20 MPa, and as average pressures ranging from 2 MPa to 7 MPa.

Spongy nickel (the product of the reduction of process wastes or natural nickel ores), copper-nickel converter mattes, natural ores, metallic nickel (metal-working cuttings), alloys of the copper-nickel-iron system, anode scrap, etc. are used as raw materials.

Low Pressure Carbonyl Technique

Vale's Clydach refinery in South Wales (formally Inco Ltd) still uses the basic concept of the Mond-Langer process and produces nickel powders using the atmospheric pressure carbonyl technique. The use of feed matte as the granular nickel oxide containing small amounts of copper, cobalt, iron, and siliceous matter make it possible to employ low pressure carbonyl processing. The latest innovations comprised the replacement of the many small hearth-type reducers and volatilizers of the original plant by large rotary kilns arranged in lines of two kilns with a smaller sulfiding unit. In the initial unit of each line, the nickel matte feed is reduced to metal by a countercurrent flow of preheated hydrogen at temperatures ranging from 670 to 770 K.

The reduced nickel matte is then activated by sulfiding with increasing sulfur concentration to 2 wt% and is sublimated in the final kiln at atmospheric pressure and temperature in the range from 320 to 340 K by a countercurrent flow of carbon monoxide. This horizontal rotary kiln (5 m in diameter, 40 m length) has a 200-ton capacity (Fig. 21.2). It is divided into two sections: the first is equipped with scrapers for material intermixing and in it the extraction of the main part of the nickel is accomplished; the second section completes the extraction of nickel. Collected dust is supplied into it by a screw conveyer. The carbon monoxide is injected along the whole reactor length. The duration of carbonyl processing is about 96 h; the nickel yield amounts to 95%. There is no necessity in the nickel carbonyl cleaning because the soft mode of metal carbonyl formation practically excludes the formation of impurities (iron and cobalt carbonyls).

The obtained nickel tetracarbonyl vapor is transferred to the decomposition device where seed (carbonyl nickel powder) is added (Fig. 21.3). A bucket elevator provides continuous circulation of formed pellets through the decomposer to achieve up to commercial size amounts of 5–10 mm.

Pellets (or powder) from the elevator are introduced into the top of a tubular heater (1.2 m in diameter, 6.7 m height) to separate the particles with commercial size. Commercial sized particles are additionally processed in a classifier and removed from the cycle. Underseeding fractions are returned to the elevator. Noncommercial size particles are heated to 470–500 K in heater. Then they are transferred into a heat-insulated decomposer, in which nickel tetracarbonyl vapor and carbon monoxide at 340 K are injected. Carbon monoxide containing 0.1% $Ni(CO)_4$ is removed from the top of the chamber and returned to the synthesis stage. Carbonyl content in the gas–vapor mixture is a max 15 wt% to prevent the pellets coalescencing by a high rate of nickel deposition. The carbonyl low pressure process is continuous, automated, and economical.

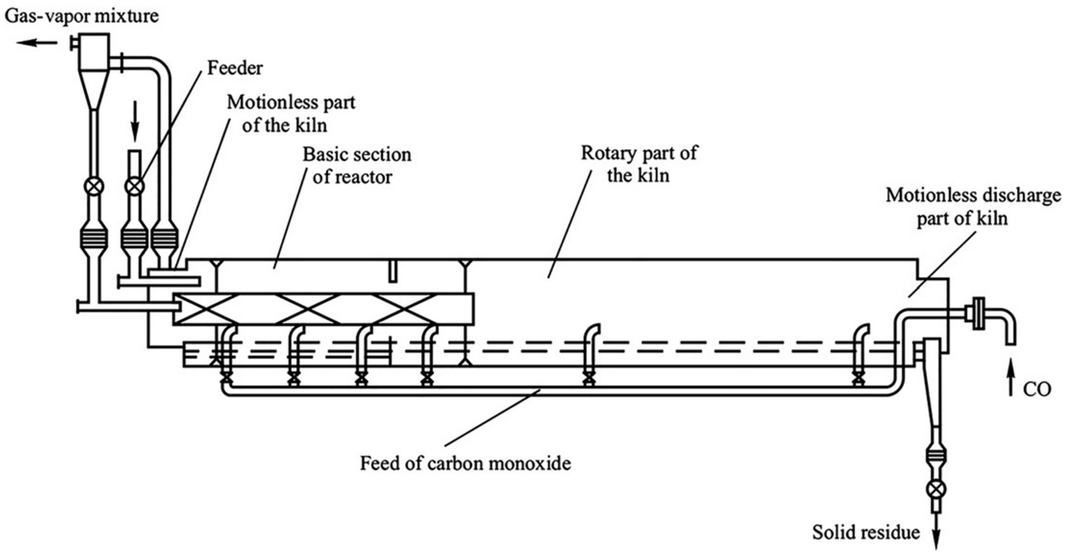
Gas-vapor mixture
Feeder
Motionless part of the kiln
Basic section of reactor
Rotary part of the kiln
Motionless discharge part of kiln
CO
Feed of carbon monoxide
Solid residue

FIG. 21.2 Rotary kiln for synthesis of nickel carbonyl at the Clydach refinery.

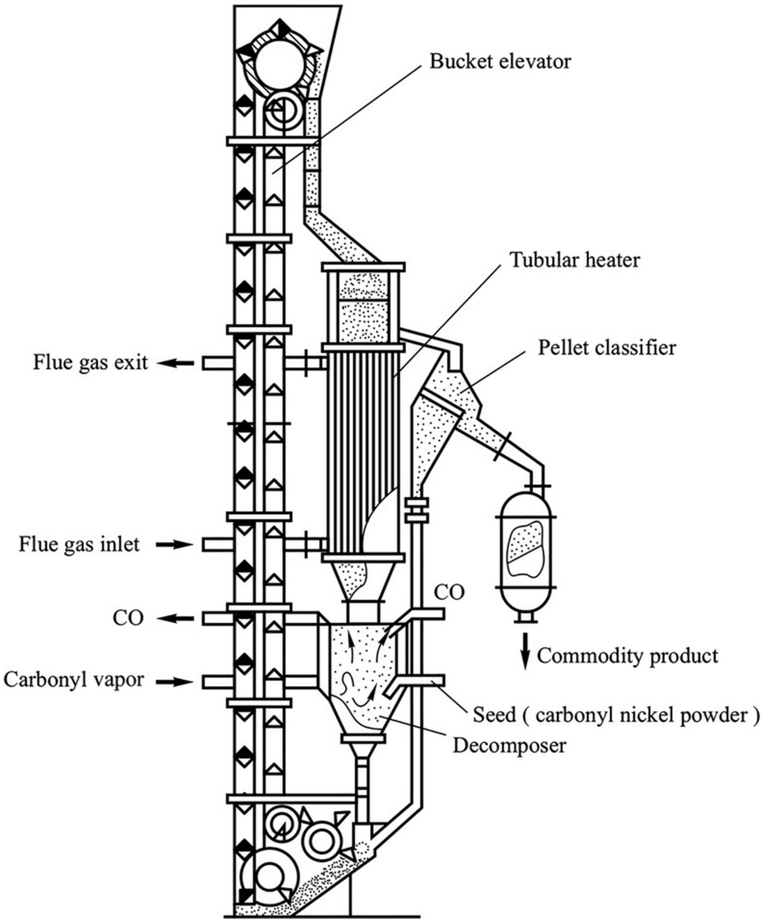
Bucket elevator
Tubular heater
Pellet classifier
Flue gas exit
Flue gas inlet
CO
CO
Carbonyl vapor
Commodity product
Seed (carbonyl nickel powder)
Decomposer

FIG. 21.3 Schematic of the decomposer for carbonyl nickel pellet production.

Average Pressure Carbonyl Technique

The Copper Cliff refinery uses the same basic process chemistries, but forms nickel tetracarbonyl at elevated pressure, which is necessary to extract nickel in the presence of a high copper concentration. The plant feed is a mixture of oxides and sulfides of nickel, copper, iron, cobalt, other crude metallics, and refinery residues that contain nickel.

This mixture is charged with coke into one of two 64 metric ton capacity, top-blown rotary converters (Fig. 21.4). In this process, silicates and some of the iron are slagged off and the liquid metal is then granulated by water atomization. In this condition, the granules contain 65–75 wt% Ni, 15–20 wt% Cu, 2–3 wt% Fe, and 3 wt% S represented as sulfides.

The dried metallic granules are batch fed into a 136-t capacity reactor (Fig. 21.5), where they are reacted with carbon monoxide at temperatures up to 450 K and pressures up to 7 MPa. Nickel and some iron are extracted as a crude carbonyl sublimate while copper, cobalt, precious metals, and impurities are retained in the residue. Iron removal is controlled to between 20% and 50% of the input volume. Cobalt does not form carbonyl compounds because they occur only when carbon monoxide pressures of 15 MPa are achieved. The reactors are water cooled because the nickel tetracarbonyl formation is exothermic.

Extracted carbonyl sublimates are condensed and stored at atmospheric pressure. The carbon monoxide carrier gas is recycled. The condensed product, containing both soluble nickel and iron carbonyls, is next pumped to fractionating columns, where it is separated into nickel tetracarbonyl vapor and iron-rich liquid carbonyl. Fractionating the raw carbonyl liquid is achieved easily, owing to the fact that the boiling points of the nickel and iron carbonyls are 316 K and 376 K, respectively. The purity of manufactured nickel tetracarbonyl vapor is 99.998%, by residue of nickel and iron carbonyls in a ratio of 1–7. From the top of the column, nickel tetracarbonyl vapor is exhausted off and fed into powder decomposers. A little below the top of the column, liquid nickel tetracarbonyl is taken off and either kept in storage or delivered to nickel pellet decomposers.

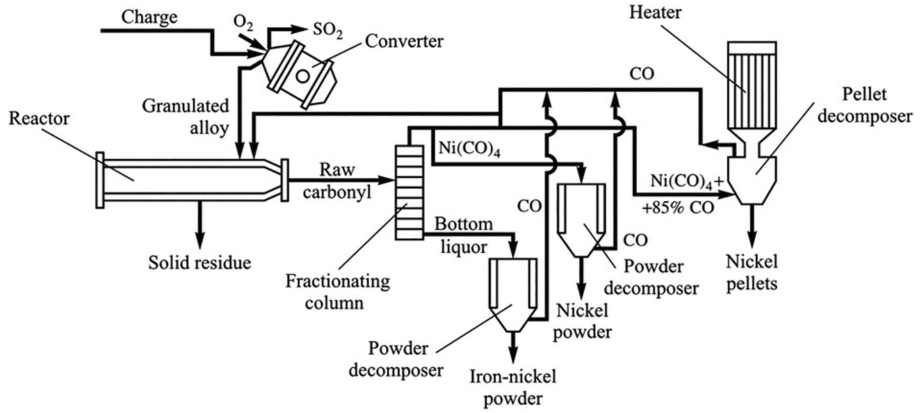
Charge
O_2
SO_2
Converter
Heater
CO
Pellet decomposer
Reactor
Granulated alloy
$Ni(CO)_4$
Raw carbonyl
$Ni(CO)_4$+ +85% CO
CO
Bottom liquor
CO
Solid residue
Fractionating column
Powder decomposer
Nickel pellets
Nickel powder
Powder decomposer
Iron-nickel powder

FIG. 21.4 Flow sheet of the Copper Cliff Nickel refinery process for the manufacture of nickel products using elevated pressure carbonyl processing.

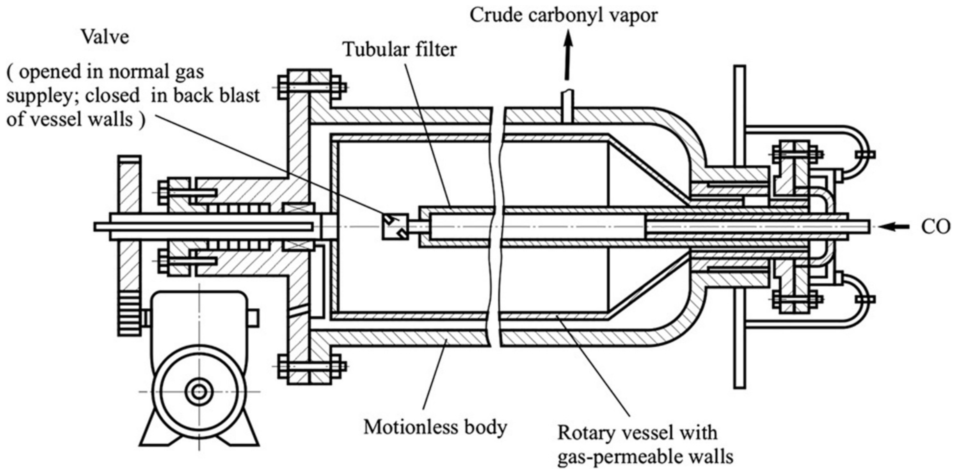
Crude carbonyl vapor
Valve
(opened in normal gas suppley; closed in back blast of vessel walls)
Tubular filter
CO
Motionless body
Rotary vessel with gas-permeable walls

FIG. 21.5 Reactor for synthesis of nickel carbonyl at elevated pressures.

The powder decomposers are steel cylinders with heated jackets. Nickel carbonyl vapor is introduced into the decomposer chamber slightly above atmospheric pressure, where it contacts the heated decomposer walls that are preset at a temperature between 520 and 620 K. The nickel tetracarbonyl decomposes into nickel powder with the release of carbon monoxide. The latter is recycled through filters and fed by a gas compressor to the pressure carbonyl reactors while the powder is collected, gas purged, stabilized by a surface oxide film, and transferred to storage, completely free from carbon monoxide and carbonyl.

High-Pressure Carbonyl Technique

High-pressure carbonyl processes are required when the feed concentrates contain high amounts of copper, cobalt, and other impurities, as in the case of one on the base of the Norilsk-Talnakh ore. The nickel deposits of Norilsk-Talnakh are the largest nickel-copper-palladium deposits in the world. The Norilsk Nickel Group of companies is the world's largest producer of nickel and palladium and one of the world's leading producers of platinum and copper. It also produces various by-products such as cobalt, rhodium, silver, gold, iridium, ruthenium, selenium, tellurium, and sulfur. Its largest operations are located in the Norilsk-Talnakh area near the Yenisei River in the Krasnoyarsk Territory of Russia.

A high-pressure carbonyl process was used at the Severonickel refinery in Zapolyarny, located approximately 200 miles from St. Petersburg, Russia, where commercial production of carbonyl nickel powder began in the early 1960s. The feed matte is based on the ores of nickel-copper-sulfide deposits (Zhdanovskoye, Zapolyarnoye, Kotselvaara, and Semiletka fields) located in the Murmansk region, near Russia's border with Norway. Currently, the producer of carbonyl nickel powders is the Kola MMC Company, the operational division of the Norilsk Nickel group.

The high-grade pyrite ores are ground in ball mills, and the milled material is processed in a smelter, then converted to matte. The latter is reacted with carbon monoxide at pressures up to 25 MPa at 470–520 K to produce a high purity nickel tetracarbonyl that is separated from the iron and other carbonyls as a result of condensation, distillation, and vaporization. The thermal shock decomposes nickel tetracarbonyl into nickel powder, with the release of carbon monoxide. The powder is discharged from the decomposers and packed in steel drums.

Health and Environmental Protection Measures in Carbonyl Nickel Production

Nickel carbonyl is a highly toxic agent; the threshold limit values (TLVs) of the nickel carbonyl in the workplace atmosphere by the RU Standard (GOST 12.1.005–88) [4] is 0.0005 mg/m^3; a lethal dose amounts to 0.1 mg/m^3. It causes acute and chronic intoxication and is a weak carcinogen. Fatalities due to intoxication during production have been reported.

Toxic carbon monoxide can be responsible for acute and chronic poisoning in the manufacturing process. Under the Legislation and Health and Safety in the European powder-making industry, the long- and short-term occupational exposure limits (OELs) for carbon monoxide in the workplace atmosphere are 50 vpm (60 mg/m^3) and 300 vpm (360 mg/m^3), respectively [5]. The long term TLV for carbon monoxide in the workplace atmosphere by the RU Standard (GOST 12.1.005–88) is 20 mg/m^3 (~17 vpm).

Nickel carbonyl dissolves in process water up to dangerous concentrations due to significant water solubility amounting to 180 mg/L at a temperature of 283 K. Its maximum allowable concentration in an aqueous medium is not officially stated, but the admissible concentration limit of nickel amounts to 0.001 mg/L, according to SanPiN 4630–88 [6]. The conditional admissible concentration limit of nickel carbonyl in water is 0.0003 mg/L, providing the OEL in the air equilibrium layer with a water surface.

Detailed information on health and environmental protection measures in the carbonyl industry can be found in Chapter 6.

Powder Properties and Applications

Powders properties depend on the conditions of nickel carbonyl decomposition and their extra processing. Light (2–4 μm) and heavy (3–10 μm) nickel powders and 5–10 mm pellets are mainly produced in the industry.

Generally, four types of nickel powders produced by thermal decomposition of nickel tetracarbonyl are differentiated: acicular powder particles, chain-like, high surface area powders, and high density semismooth particles. These powders exhibit uniform size, structure and high surface area, and the technique ensures a high degree of purity.

Basic characteristics of Inco types and Norilsk Nickel types of carbonyl nickel powders are shown in Table 21.1. Inco heavy powders are marked by "100" series and light powders by "200." Acicular particles are the characteristic type of

TABLE 21.1 Basic Characteristics of Inco and Norilsk Nickel Carbonyl Nickel Powders

Type	Average Particle Size (µm)	Particle Shape	Apparent Density (g/cm^3)	Angle of Repose (degree)	Content of Impurities (wt%)			
					O	C	Fe	S
Inco powders[a]								
210	0.5–1.0	Chain-like	<0.5	…	0.10	0.05–0.15	<0.01	0.002
255	2.6–3.4	Chain-like	0.45–0.6	72	0.10	0.05–0.15	<0.01	0.0002
287	2.9–3.6	Chain-like	0.8–1.0	66	0.10	0.05–0.15	<0.01	0.0002
100	3–5	Acicular	1.6–2.1	65	0.10	0.05–0.20	<0.01	0.0002
122	4–7	Acicular	1.9–2.5	60	0.10	0.05–0.10	<0.01	0.0002
128	7–9	Acicular	2.5–3.0	48	0.10	0.05–0.10	<0.01	0.0002
337	40–300	Semi smooth high density	3.5–4.0	…	0.25	0.08–0.10	0.01–0.05	< 0.001
Norilsk Nickel powders and pellets[b]								
S 20	1.85–2.2	Chain-like	0.51–0.64	…	…	0.09	0.0015	0.0007
S 30	2.91–3.5	Chain-like	0.6–0.8	…	…	0.28	0.002	0.001
1 L5	2.1–2.4	Acicular	1.01–1.4	…	…	0.28	0.002	0.001
1 L8	1.4–1.6	Chain-like	0.45–0.6	…	…	0.001	0.002	0.001
UT1	7–8.5	High density	3.0–3.5	…	0.02	0.1	0.003	0.0001
UT3	3–6	Quasicubic shape	1.91–2.5	…	0.02	0.072	0.003	0.0001
DNK-0	7–13 mm	Spheroidal	…	…	…	0.015	0.015	0.001

[a] *Content of other impurities, wt%: Zn, Zr < 0.01; Al, B, Mg < 0.005; Bi, Co, Cr, Cu, Mn, Mo, Pb, Si, Sn, Ti < 0.001.*

[b] *Content of other impurities <0.006 wt%; more information about Norilsk Nickel carbonyl products can be found on www.nornickel.ru.*

nickel powder produced by carbonyl decomposition (Inco types 120–123, and Norilsk Nickel type IL5). They are fine and regular in shape with rough surfaces (Fig. 21.6) [7].

The Inco powder typically contains 700–900 ppm (0.07–0.09 wt%) oxygen, 3–5 ppm (0.0003–0.0005 wt%) iron, max 1 ppm (0.0001 wt%) sulfur, and 600–700 ppm (0.06–0.07 wt%) graphitic carbon. The Fisher subsieve size is 3–7 µm, the apparent density is 1.8–2.7 g/cm^3, and the surface area amounts to 0.4 m^2/g (BET) [8].

Chain-like nickel powders (Inco types 255, 287, etc., Norilsk Nickel type 1 L7, 1 L8, etc.) are characterized by their acicular, chain-like structure of relatively fine particles, which make them fluffy in character with a low apparent density of 0.45–1.0 g/cm^3 and large specific surface area of 0.6–0.7 m^2/g (BET). The typical structure and chain-like shape of this powder type are shown in Fig. 21.7.

Ultrafine nickel powders (e.g., Inco type 210, Norilsk Nickel type S10 (Fig. 21.8)) also have chain-like morphology, but the particles are finer, the Fisher subsieve size is 0.5–1.0 µm, and specific surface areas range from 1.5–6 m^2/g, depending on the grade.

Semismooth, high-density nickel powders exist in fine and coarse sizes. The fine Inco type 337 ranges from 10 to 40 µm in diameter and the Norilsk Nickel type UT1 from 7 to 8.5 µm, respectively (Fig. 21.9); the coarse is 400–1000 µm in diameter. Powder apparent density ranges from 3.5 to 4.2 g/cm^3.

A large part of the carbonyl nickel product is manufactured in the form of pellets (i.e., spherical granules) in ranges from 5 to 13 mm in diameter. Pellets are characterized by lamination (shaped like an onion) structure (Fig. 21.10). This structure is formed as a result of multiple passing of particles through the decomposer to achieve the required pellet size. The

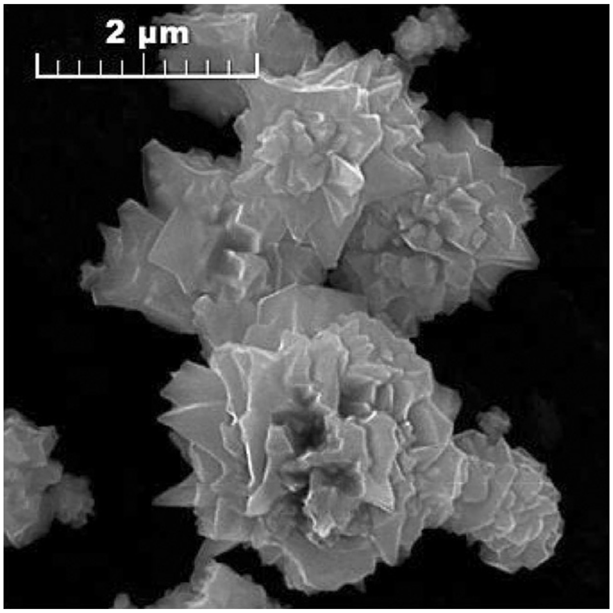

FIG. 21.6 Scanning electron micrograph of the ordinary type of nickel powder produced by carbonyl decomposition.

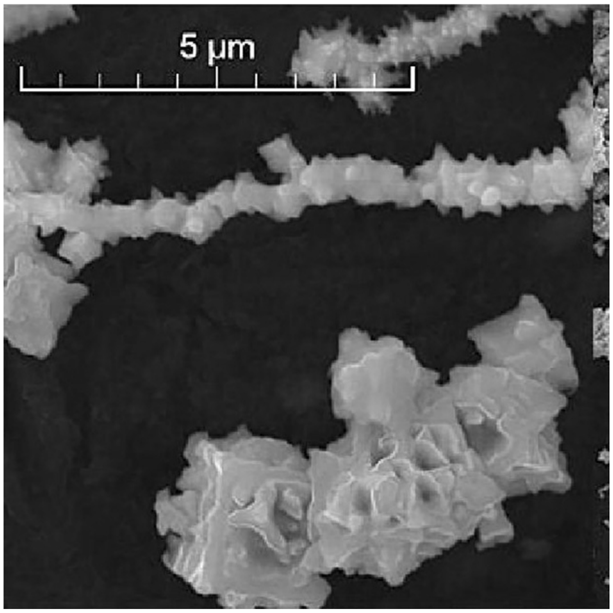

FIG. 21.7 Scanning electron micrograph of the chain-like type of nickel powder produced by carbonyl decomposition.

presence of iron carbonyl impurities in amounts of 1–2 wt% catalyzes the reaction of carbon monoxide thermal decomposition and influences the nickel powder particle shape formed at the stage of nickel carbonyl decomposition. Spherical nickel particles with an "onion-shaped" structure are formed due to carbon monoxide decomposition with a carbon content up to 1 wt%. Particle surfaces are transformed into an acicular shape (Fig. 21.6) during decomposition of nickel tetracarbonyl when the carbon monoxide content is approximately 0.05 wt%. Detailed information on the onion-shaped structure forming can be found in Chapter 6.

Chemical composition of commercial pellets (e.g., Norilsk Nickel type DNK) includes 99.95–99.98 wt% Ni, 0.015 wt% C, 0.015 wt% Fe, 0.001 wt% Cu, 0.001 wt% S, 0.0005 wt% Co, 0.0001 wt% Pb, and 0.0001 wt% As. The low melting-point elements and dissolved gas impurities in carbonyl pellets are higher than in all grades of electrolytic nickel products.

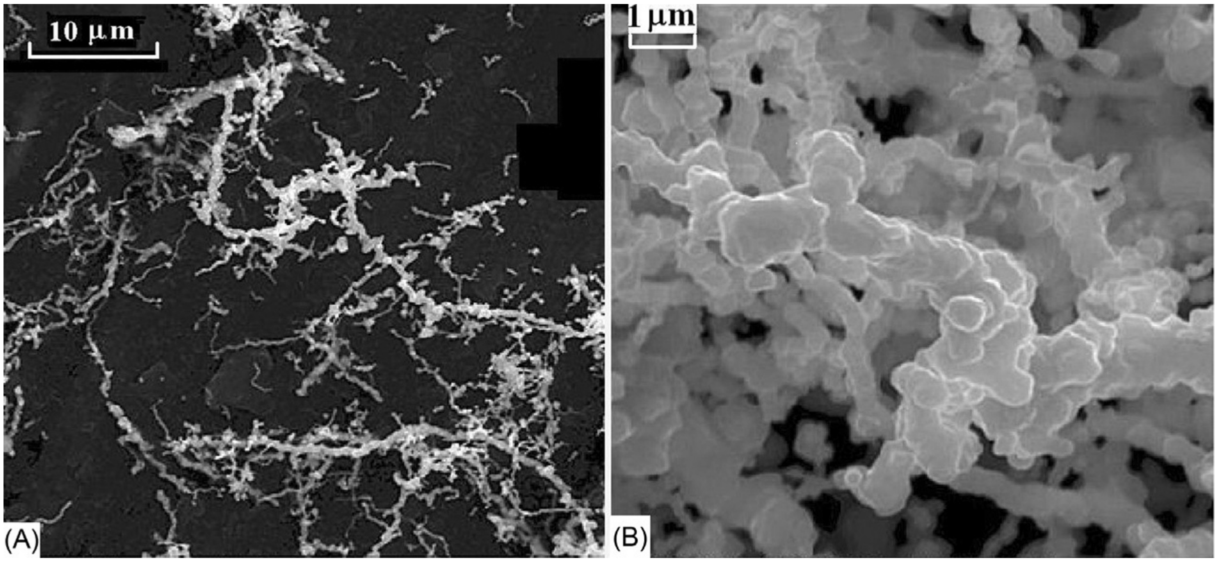

FIG. 21.8 Scanning electron micrograph at lower (A) and higher (B) magnifications of ultrafine powder particles connected in the chains produced by carbonyl decomposition.

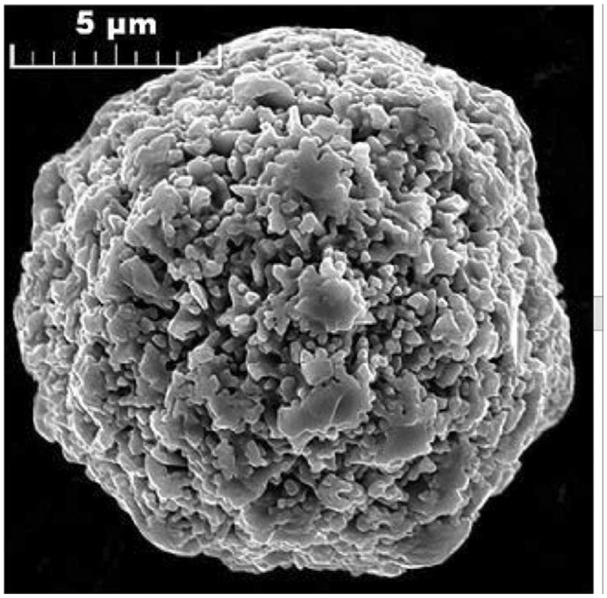

FIG. 21.9 Scanning electron micrograph of semismooth high-density nickel powder produced by carbonyl decomposition.

The Norilsk Nickel carbonyl powders are distinguished by high purity above 99.9 wt% metallic nickel, with a low level of oxidation and other impurities, especially, iron and cobalt. The properties of these high-purity nickel powders have been tailored to meet the demanding requirements of the chemical, energy, and metal industries. Currently, these products provide the basic nickel source for a wide range of specialized products.

RU Standard GOST 9722 (Appendix 1 in this Chapter) differentiates the four brands of carbonyl nickel powder depending on their chemical composition: PNK-U, PNK-0, PNK-1, and PNK-2. The nickel content in PNK-U and PNK-0 is a min 99.9 wt% and in PNK-1 and PNK-2, a min 99.7 wt%. The content of impurities is regulated in these powders. According to apparent density, the powders are divided as follows: T–heavy; L–light, and K–coarse. Each is subdivided by particle morphology and size. Apparent density classification of carbonyl nickel powders according to GOST 9722-97 is given in Table 21.2.

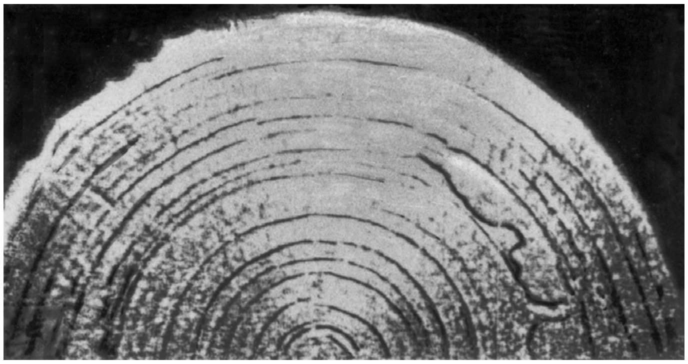

FIG. 21.10 Micrograph of the cross-section of a carbonyl nickel pellet.

TABLE 21.2 Apparent Density of Carbonyl Nickel Powders Accordingly With GOST 9722-97 (RUS)

Powder Type	Sub-group According to Apparent Density	Apparent Density (g/cm^3)
PNK-UT1, PNK-OT1, PNK-2T1	1	3.00–3.50
PNK-UT2, PNK-OT2, PNK-2T2	2	2.50–2.99
PNK-UT3, PNK-OT3, PNK-2T3	3	1.91–2.50
PNK-UT4, PNK-OT4, PNK-2T4	4	1.41–1.90
PNK-1L5, PNK-2L5	5	1.01–1.40
PNK-1L6, PNK-2L6	6	0.81–1.00
PNK-1L7, PNK-2L7	7	0.61–0.80
PNK-1L8, PNK-2L8	8	0.45–0.60
PNK-2K9	9	1.30–1.70
PNK-2K10	10	min 1.20

The carbonyl nickel powders and pellets have a wide application, including PM components, rechargeable batteries and fuel-cell electrodes, magnets, ferrites, hard alloys, chemicals and catalysts, welding products, pigments and coatings, electronic alloys, getters, conductive resins, and plastics. Application areas of the Inco type and Norilsk Nickel type of carbonyl nickel powders are given in Table 21.3.

The strongly linked chain morphology in combination with a low apparent density and a high surface area of ultrafine carbonyl nickel powders is favorable for the production of sintered plates with a porosity approaching 90%, which is strong enough to withstand the stresses during charging and discharging of the rechargeable batteries. Nickel powders (Norilsk Nickel types S) are characterized by their unique, chain-like, highly convoluted structure, with a low apparent density ranging from 0.52 to 0.56 g/cm^3 and a specific surface area ranging from 1.5 to 2.0 m^2/g (Fig. 21.11), which make them suitable for manufacturing rechargeable batteries. Ultrafine nickel powder Inco type 210 also answers the above demands.

Carbonyl nickel powders have the advantage of conventional lead-acid batteries, the electrical power of which decays rapidly at low temperatures. This is of paramount importance for reliable starter batteries in countries with cold winters.

Generally, the requirements of nickel containing composition powders for PM applications consist of high purity, high rate diffusion transfer by interaction with the surrounding particles of other powders, high specific surface area, and a reasonably narrow particle size distribution. These powders are fine and regular in a quasicubic shape with rough surface projections. Typical of such powders is the Norilsk Nickel type UT3 (Fig. 21.12).

Due to its purity, carbonyl nickel is used for the production of steel and special alloys, including cobalt-free steels and alloys for nuclear power, and refractory materials because the absence of volatile impurities is very important for materials used under load at high temperatures. In chemical and catalyst applications, the fine particle size and high specific surface area of carbonyl nickel powders promote their rapid dissolution in acid for the production of high purity nickel chemicals and catalysts. A particular interest is their use in the production of reformer catalysts in oil refining. During the reforming of

TABLE 21.3 Application Areas of Inco Type and Norilsk Nickel Type of Carbonyl Nickel Powders

	Carbonyl Nickel Powder Types	
Application Area	**Inco Type**	**Norilsk Nickel Type** [6]
Rechargeable batteries	210, 210, 255, 287	S10, S20
Fuel cells	210, 210H, 255, 287	S20, S27, S30, L5, L6, L7, L8
Domestic batteries	210	L5, L6, L7, L8
Powder metallurgy components	4SP	UT1. UT2, UT3-PM, UT4, US3-1CG, US3-1CGL, L5, L6, L7, L8
Chemicals and catalysts	110, 210	UT1. UT2, UT3-PM, UT4,US3-1CG, US3-1CGL, L5, L6, L7, L8
Magnets	HDNP, 525	US3-1CG, US3-1CGL, L5, L6, L7, L8
Hard metals	210, 210H	US3-1CG, US3-1CGL, L5, L6, L7, L8, UT1. UT2, UT4
Electronics	110, 525	S20, S27, S30, L5, L6, L7, L8
Paints, inks	110, 525	S10
Welding	4SP	UT1. UT2, UT3-PM, UT4,US3-1CG, US3-1CGL

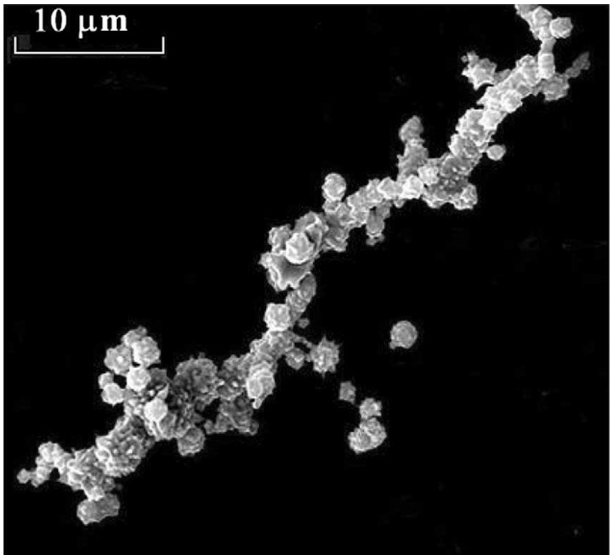

FIG. 21.11 Scanning electron micrograph of a linked particle nickel powder type produced by carbonyl decomposition.

crude oil, hydrogen is passed through a ceramic tube impregnated with nickel, and the process of converting crude oil to high octane fuel is appreciably accelerated.

In the area of paints and plastics, the inherent electromagnetic properties of nickel, coupled with its oxidation resistance, have enabled the carbonyl nickel powder to be used as a shield against electromagnetic interference (EMI). Currently, most electronic devices are enclosed in plastic casings to protect the components with an inexpensive, aesthetically pleasing design. Plastics, however, lack one essential feature: they are not conductive, and consequently, do not shield electronic equipment from unwanted EMI. Although nickel is not quite as good a conductor as copper and silver, it absorbs more EMI than most metals because its high magnetic permeability.

Generally, carbonyl powders are free flowing, easy sintering, and have good compressibility. Nickel-based alloys and compositions are characterized by high corrosion resistance and stability to high temperature oxidation. They are used for gaseous thermal spraying to provide a protective coating on components operating in corrosion environments, conditions of abrasive wear, and dry friction at high temperatures.

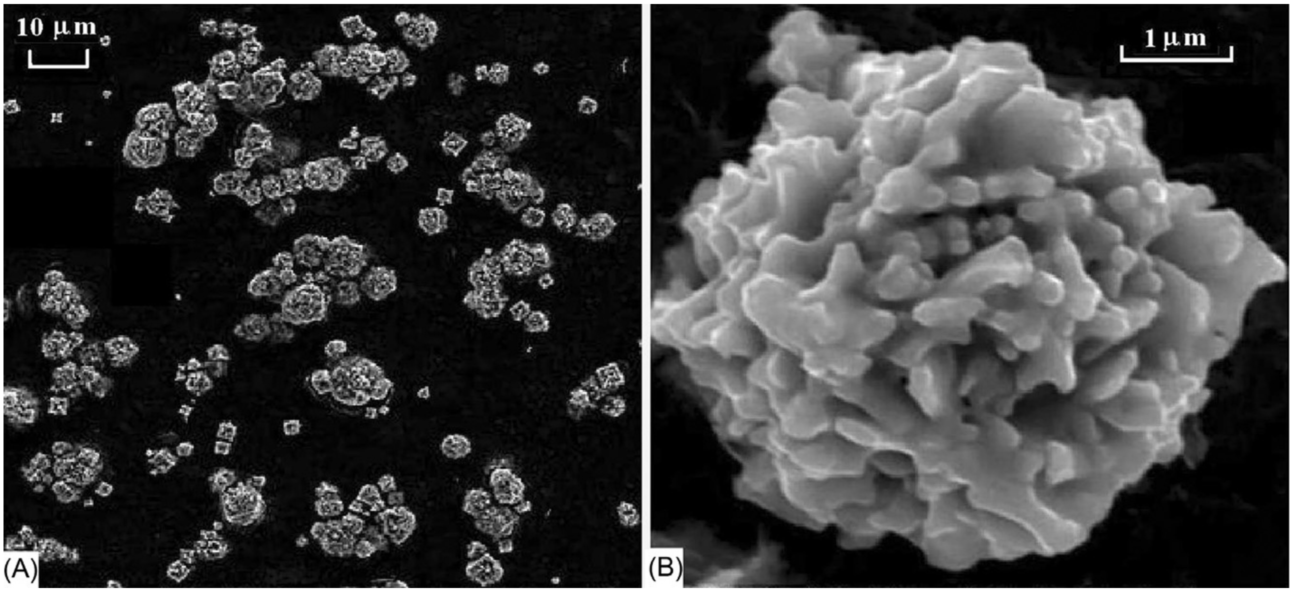

FIG. 21.12 Scanning electron micrograph at lower (A) and higher (B) magnifications of quasicubic shape powder produced by carbonyl decomposition.

The thermoresistant compositions nickel-metal (Ni-Al, Ni-Ti), nickel-carbide (Ni-WC), nickel-oxide (Ni-ZrO_2), and nickel-metal-oxide (Ni-Al-WO_3) are used for resistant wear-refractory coatings and heat insulating plasma coatings. The solid lubricant-nickel composition for antifriction coatings and friction units working at dry friction or in water (nickel-graphite, nickel-boron nitride) are produced by vapor-phase precipitation of nickel on powder particles (cladding).

Characteristic nickel-coated graphite (NCG) powders are of two types, containing nickel of 60 wt% and 75 wt%, respectively. The first clad type consists of a 95 wt% sieve size fraction 100–250 μm in diameter, and the apparent density of the powder ranges from 1.4 to 1.5 g/cm^3; the second clad type consists of a 90 wt% sieve size fraction 200–325 μm in diameter, and the apparent density ranges from 1.7 to 1.9 g/cm^3.

The combination of low-density graphite with a layer of conductive nickel results in a lightweight filler suited for conductive gaskets (extruded, molded, sheet), sealants, and plasma sprays. In silicone gasket rings, conductive fillers are used that are manufactured from carbon black, NCG, silver-plated materials (AgAl, AgCu, AgNi, Ag-glass), and pure silver. NCG is significantly better than carbon black, less effective than pure silver, and comparable to silver-coated materials. NCG is 3–4 times less expensive than silver-plated materials and pure silver.

Carbonyl powders are characterized by free flowing, good compressibility, and easy sintering. High porous electrodes (porosity in a range from 70% to 90%) for nickel-cadmium accumulators and hydrogen-oxygen fuel elements, elements of electronic equipment, sintered magnets, easy regenerated filters, and catalysts are made of them.

HYDROMETALLURGICAL PROCESSING

The production of nickel powders by hydrometallurgical processing involves leaching, solution purification, and metal recovery operations. As the recovery stage is accomplished in the autoclaves at elevated pressure and temperature processing, it is also called autoclave processing [9].

The Sherritt refinery in Fort Saskatchewan, Alberta, Canada, is an example of hydrometallurgical processing used in the manufacturing of nickel powders [10]. This process is adaptable to operate with a wide assortment of different feedstocks, predominantly the sulfide concentrates. A schematic diagram of the Sherritt process is shown in Fig. 21.13. This process has been also adopted by the Western Mining Corporation in a refinery at Kwinana, Western Australia.

Feed Processing

The main feed to the Sherritt refinery was a nickel and cobalt sulfide produced in Mao, Cuba [11]. The sulfide ore from Moa Bay deposits is high in iron along with cobalt. The processing of this ore is accomplished by means of high-pressure leaching with sulfuric acid. The key operation in this process is the separation of nickel and cobalt from iron, which typically constitutes 50 wt% of the ore. It is possible to achieve the selective dissolution of nickel and cobalt with <1 g/L iron in

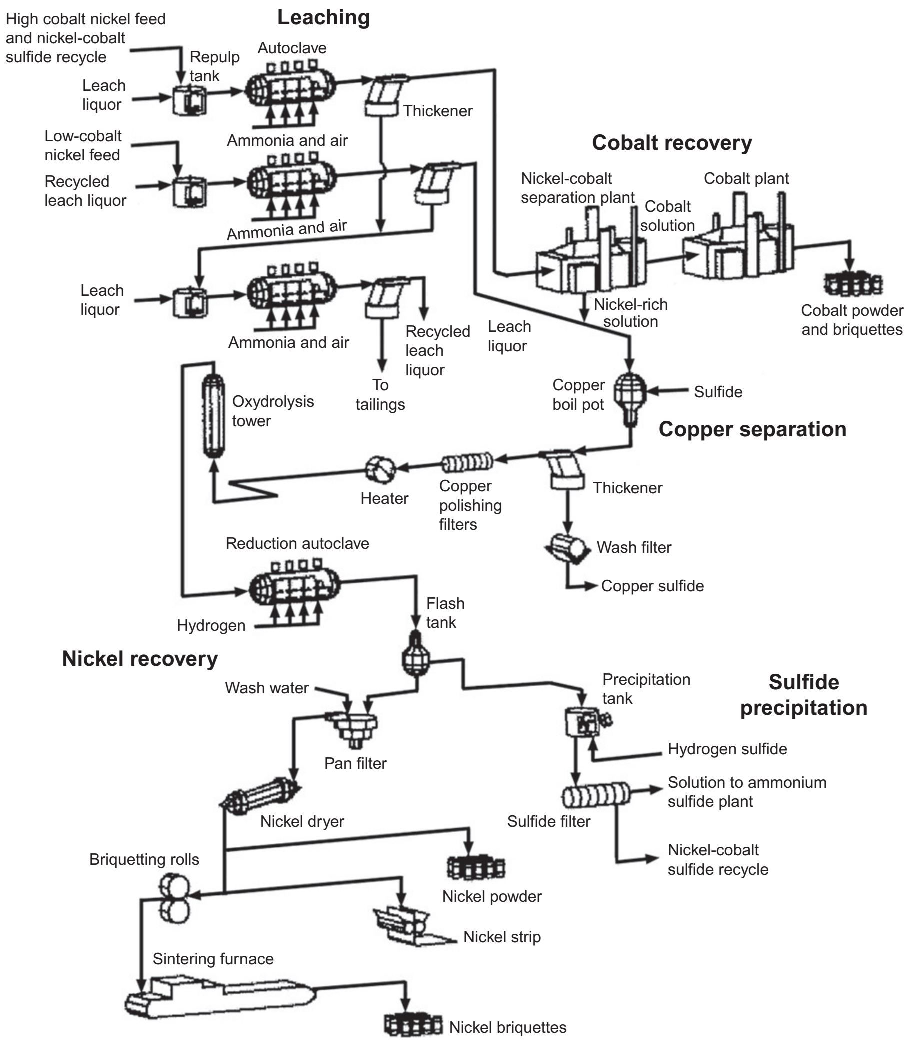
High cobalt nickel feed and nickel-cobalt sulfide recycle
Leaching
Repulp tank
Autoclave
Leach liquor
Thickener
Low-cobalt nickel feed
Ammonia and air
Recycled leach liquor
Ammonia and air
Cobalt recovery
Nickel-cobalt separation plant
Cobalt solution
Cobalt plant
Leach liquor
Ammonia and air
Recycled leach liquor
Leach liquor
Nickel-rich solution
Cobalt powder and briquettes
To tailings
Oxydrolysis tower
Copper boil pot
Sulfide
Copper separation
Heater
Copper polishing filters
Thickener
Wash filter
Copper sulfide
Reduction autoclave
Hydrogen
Flash tank
Nickel recovery
Wash water
Pan filter
Precipitation tank
Sulfide precipitation
Hydrogen sulfide
Solution to ammonium sulfide plant
Nickel dryer
Sulfide filter
Nickel-cobalt sulfide recycle
Briquetting rolls
Nickel powder
Nickel strip
Sintering furnace
Nickel briquettes

FIG. 21.13 Flow diagram of Sherritt's hydrometallurdical process. *(Modified from Freeman G. Production of nickel powders by hydrometallurgical processing. In ASM Handbook, vol. 7. ASM International Publishers; 1998. p. 171 – 174).*

the leach liquor. The typical chemical composition of nickel-cobalt sulfide produced in Moa includes 51–56 wt% Ni, 5.0–6.0 wt% Co, 0.5–0.8 wt% Fe, 0.1–0.2 wt% Cu, 1.0–1.3 wt% Zn, and 32–37 wt% S. This concentrate is packaged in the form of a wet filter cake.

Leaching

The first stage in the refining process is the leaching of the metal content from the sulfide feed. The leaching process is carried out at elevated temperature and pressure in continuous conditions during interaction between the fine sulfide concentrate and ammonium sulfate in the autoclaves. The typical conditions in the leach autoclaves are the following: temperature 363–368 K, pressure 0.77–0.84 MPa (110–120 psig), ammonia 80–110 g/L, and ammonium sulfate 150–200 g/L. The resulting leach reaction is the oxidative dissolution of the metal sulfides to soluble amine complexes with the simultaneous oxidation of sulfide to salts, including sulfate (SO_4^{2-}). The general equation for the ammoniacal leaching of the sulfides may be represented as:

$$\mathrm{MS} + n\mathrm{NH}_3 + 2\mathrm{O}_2 \rightarrow \mathrm{M}(\mathrm{NH}_3)_n^{2+} + \mathrm{SO}_4^{2-}$$

where M includes nickel, cobalt, iron, copper, and zinc; *n* ranges from 2 to 6.

The leaching process uses the differing stability of the amine complexes. The iron amine complex is hydrolyzed to a hydrated iron oxide, $Fe_2O_3{\cdot}H_2O$, because it is the least stable. The leach slurry is delivered to a thickener where the leach liquor is separated from the solid residue of the precipitated hydrated iron oxide.

In reality, the reaction chemistry of the leaching process is significantly more complicated due to the peculiar behavior of sulfur in alkaline solutions. The reaction order of the oxidation of sulfur to form sulfate, sulfamate, and a class of ammonium thiosalts may be described as follows:

$$S^{2-} \rightarrow S_2O_3^{2-} \rightarrow S_nO_6^{2-} \rightarrow SO_4^{2-} + SO_3NH_2^{-}$$

where n ranges from 2 to 6. The leach liquor contains sulfur in several forms, depending on the given time up to 4h. The leach solution typically contains 60–70 g/L Ni, 6–9 g/L Co, 1–2 g/L Cu, 130 g/L NH_3, 200 g/L $(NH_4)_2SO_4$, and a fluctuating quantity of other sulfur compounds.

Several solution purification steps must be accomplished before it is possible to reduce nickel, as a pure metal, from the leach solution.

The next step of the refining process is the cobalt separation at the nickel-cobalt separation plant, where the leach liquor is transported. The Sherritt cobalt refining process is described in Chapter 22. After the removal of cobalt, the nickel-rich solution is subjected to copper removal processing.

Copper Removal

Copper is removed from the leach liquor and nickel-rich solution in an apparatus named the "copper boil" (Fig. 22.13), where the combination of lowering the ammonia level by boiling to distill off the free ammonia and the addition of elemental sulfur and sulfur dioxide at elevated temperatures results in the precipitation of copper sulfide. The copper sulfide is a mixture of copper monosulfide (CuS) and cuprous sulfide (Cu_2S).

The removal of copper is achieved due to the fact that copper sulfide is less soluble than nickel sulfide. This copper sulfide as a by-product is filtered, washed, and dried for further utilization.

Oxidation and Hydrolysis

The solution remaining after copper elimination contains an appreciable quantity of sulfamate and other forms of unsaturated sulfur compounds. If they are not fully converted to sulfate, the nickel powder product would contain unacceptable high sulfur content. This is accomplished during hydrolyzing the sulfamate to sulfate at 518 K and oxidizing the thionates to sulfate with air at 4.8 MPa (700 psi) in one combined stage. Ammonium sulfamate ($NH_4OSO_2NH_2$) is a herbicide and must be hydrolyzed to sulfate to avoid contamination of the ammonium sulfate fertilizer. Ammonium sulfate is crystallized from the reduction end solution, following sulfide precipitation of the insignificant amounts of metal remaining in the solution after hydrogen reduction.

Hydrogen Reduction by Autoclave Processing

In the final stage of the Sherritt process, nickel is precipitated from the solution as a metal powder. The essence of this process is to precipitate the nickel ions in the solution to nickel powder using hydrogen as a reductant. The reduction of metal from the solution by hydrogen requires that the hydrogen potential of the system should exceed the electrode potential of the metal ions, in which case hydrogen will move into the solution and metal precipitates. The hydrogen potential is controlled by the pH of the solution and the pressure of hydrogen.

The hydrogen reduction of nickel develops on the base of the heterolytic mechanism; therefore, the process rate is proportional to the seed powder surface. Changing the type and quantity of seed powder make it possible to produce nickel powders with different particle size and shape, different compositions, and quasialloys (nickel coating of different materials stable under processing parameters).

The role of surfactant is important (typically, consisting of 0.001 mol/L thioacetamide, 0.01–0.005 g/L ethylene-malonic anhydride, 1 mg/gNi of anthraquinone, and derivatives on their base) due to which metal precipitates on the seed powder surfaces with a constant rate. This provides for the production of powder with a more equiaxed (close to spherical) shape of particles; simultaneously, the duration of the induction period is reduced and the process accelerates.

Anthrahydroquinone is a strong reducing agent, which is formed when antraquinone adsorbed on the solid surface interacts with activated hydrogen in the alkaline medium; as a result, the chemical reduction of nickel ions (II) occurs and anthraquinone is regenerated, according to the scheme given in Fig. 21.14.

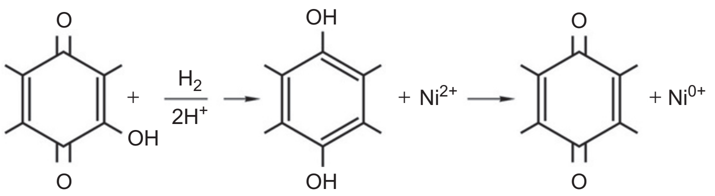

FIG. 21.14 Hydrogen reduction pattern of nickel ions by participation of anthraquinone.

For description the dependence nature of autoclave precipitation of a metal from ammonia solutions on the main parameters, there were proposed the kinetic equations:

by Makhov (Canada, 1957):

$$-\frac{d\left[\mathrm{Ni}^{2+}\right]}{d\tau}=k\left[\mathrm{Ni}^{2+}\right]\cdot p_{\mathrm{H}_2}\cdot S\cdot \exp\left(-\frac{5126}{T}\right)$$

by Dobrokhotov (USSR, 1962):

$$-\frac{d\left[\mathrm{Ni}^{2+}\right]}{d\tau}=k\left[\mathrm{Ni}^{2+}\right]\cdot p_{\mathrm{H}_2}^{0.5}\cdot S\cdot \exp\left(-\frac{8930}{T}\right)$$

$$k=4.2\cdot 10^{-12}s^{-1}\cdot \mathrm{MPa}^{-0.5}\cdot \mathrm{cm}^{-2}$$

in both equations, T is the temperature in K and S is the seed powder surface in cm^2;

by M. Sato (Japan, 1972):

$$-\frac{d\left[\mathrm{Ni}^{2+}\right]}{d\tau}=k_1\left[\mathrm{Ni}^{2+}\right]^{0.5}\cdot p_{\mathrm{H}_2}^{0.5}\cdot S-k_2\cdot\left(\left[\mathrm{H}^+\right]-\left[\mathrm{H}^+\right]^*\right)$$

where $[H^+]^*$ is concentration of hydrogen ions in a solution with $pH=4.3$, p_{H_2} is the pressure in atmospheres of hydrogen in the autoclave, S is the seed powder surface in cm^2, $k_1=5\times 10^{-10}\,mol\cdot cm^{-2}\cdot s^{-1}$; and $k_2=2.5\times 10^{-5}\,mol\cdot cm^{-2}\cdot s^{-1}$.

The reduction process is accomplished in mechanically agitated horizontal autoclaves at elevated pressures and temperatures. This batch process includes two separate stages: initial nucleation and subsequent densification. In the nucleation stage, fine nickel seed powder is formed in the autoclave. During the densification process, nickel from solution is reduced onto the seed powder particles, which then grow in size. The reduction process can be described as follows:

$$\mathrm{Ni}^{2+}+2\mathrm{NH}_3+\mathrm{H}_2\rightarrow \mathrm{Ni}^0+2\mathrm{NH}_4^+$$

The presence of free ammonia is necessary to neutralize the hydrogen ions arising during reduction. During the reduction process, the slurry in the autoclave is agitated by means of impellers.

The initial nucleation stage is carried out in the autoclave at a hydrogen partial pressure of 2.5 MPa, and the solution is heated to 380–400 K. Under the stated conditions, the seed powder in the form of fine particles of metallic nickel is produced in 30–40 min. Then, the hydrogen supply is terminated and impellers are stopped; in 5 min a clarified solution is carefully decanted through the submerged tube into a separate reservoir and returned to the stage of raw material leaching.

The autoclave with seed powder is refilled with fresh nickel solution, the agitators are restarted, hydrogen pressure is applied, and the subsequent densification stage of the reduction process is started. This batch reduction process is repeated 50–60 times to create successive coatings of nickel on the powder particles. The process is complete when the powder has reached the required size.

Depending on the number of densification operations, the hydrogen pressure ranges from 2.5 to 3.3 MPa (pressure is higher by the end of the whole precipitation operation); the solution temperature is supported at the level from 450 to 470 K; and the duration of a single densification operation ranges from 16 to 65 min. Typical densification operation parameters during nickel recovery using hydrogen are given in Table 21.4.

On the completion of the next recurrent operation (when the nickel content in the solution decreases to 1 g/L), the stirrers are switched off in sequence at regular intervals, beginning with the most remote from the discharge assembly. The settling duration amounts to 1–2 min and the solution is discharged into an evaporator. The fresh portion of solution is poured into the autoclave and, by analogy, the cycle is repeated in the presence of precipitated powder remaining from the preceding densification operation. The precipitated nickel powder is not discharged from the autoclave until the 15th densification cycle. Then, after every 3 or 4 cycles, part of the powder is downloaded to decrease the load on the autoclave drive. The

TABLE 21.4 Typical Densification Operation Parameters During Nickel Recovery Using Hydrogen

Serial Number of Operation	Hydrogen Pressure (MPa)	Temperature (K)	Duration (min)	Intermediate Discharges (min)
0 (Initial nucleation)	2.1	390	28	…
1	2.1	455	16	…
2	2.5	455	15	…
13	2.8	477	19	…
18	2.8	472	27	1
19	2.8	472	27	…
23	2.8	472	28	1
24	3.2	472	26	…
27	3.2	472	29	1
28	3.2	472	30	…
31	3.2	472	35	1
35	3.2	472	36	1
36	3.2	472	39	…
39	3.2	477	35	1
40	3.2	477	47	…
43	3.2	477	41	1
44	3.2	477	45	…
47	3.2	477	53	1
48	3.2	477	55	…
50	3.2	477	63	1
51	3.2	477	65	Complete

duration of the whole reduction process ranges from 70 to 80 h. While the stirrers are operated, the entire contents of the autoclave are downloaded into the evaporator. The autoclave is washed by circulating solutions for more complete powder removal.

With increasing densification cycles, their duration is increased (Table 21.4). Fig. 21.15 shows the increase of particle size (A) and apparent density (B) with the number of densification cycles in a commercial operation [10].

Up to 2 wt% of powder remains on the autoclave walls during precipitation, so to avoid clogging the apparatus, this deposit is removed by a solution containing 3–4 g/L NH_3 and 200 g/L $(NH_4)_2SO_4$. The autoclave is blown by gas consisting of 93 vol% nitrogen and 7 vol% oxygen. The operation seizes about 6–7 h at 380 ± 5 K, with a gas pressure of 2.8 MPa. The obtained nickel-containing solution is returned to the stage of initial nucleation for seed powder formation into the autoclave for the next running cycle.

The addition of various organic additives to the densification reduction can also be used to ensure the means of controlling the size, shape, and surface morphology of the powder manufactured.

The nickel feed solution also contains significant quantities of cobalt and zinc. Zinc is removed without a problem because it will not be reduced to the metallic state under the process conditions while cobalt has a similar standard reduction potential to that of nickel (−0.267 V for cobalt compared to −0.241 V for nickel). In order to achieve the complete reduction of nickel, the ammonia concentration is controlled in the reduction feed solution to give ammonia a total metal molar ratio of 1.9–1.0.

The slime consisting of nickel powder and reduction end solution is discharged from the autoclave and collected in evaporators. Then the powder is let out from the evaporator cone as a 90 wt% solid slurry and is filtered and washed

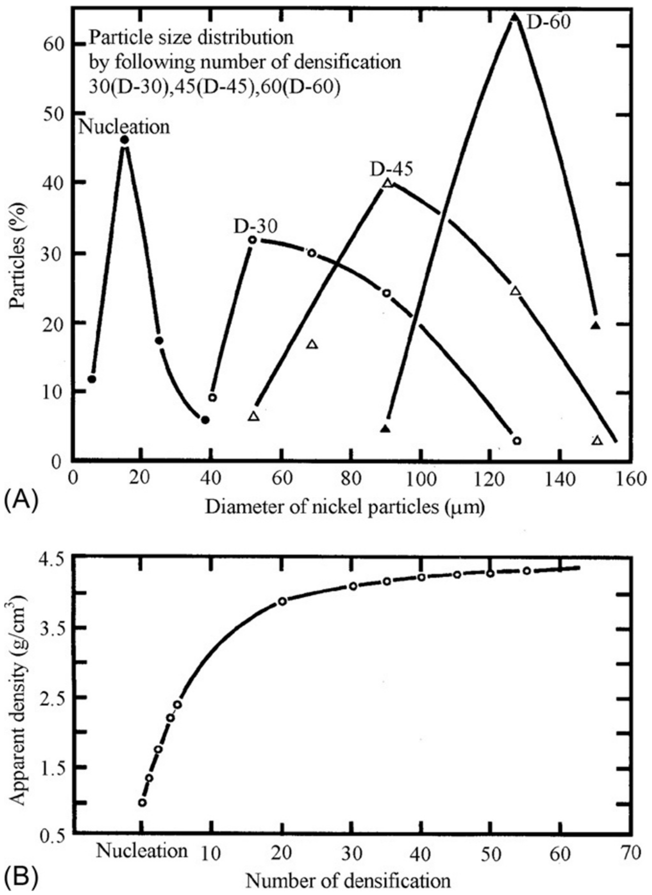

FIG. 21.15 Dependence of the particle size distribution (A) and apparent density (B) on the number of densification cycles.

on a rotary pan filter. From the pan filter, the wet powder with a moisture residue amount of 5 wt% is fed by a screw feeder into a rotary dryer, where it is dried at 400 K. Annealing in a current of hydrogen at 700 K over 2 h is carried out to remove carbon; dried gas is used for oxygen removal under the same conditions. Powder sintering is observed at temperature $>$ 1200 K. The dried powder is reloaded into the service reservoir by an elevator, where it is passed through vibrating screens, and then fractions are mixed to obtain the required powder brands. Next, nickel powder is either packed as a powder product or transferred to the briquetting operation.

Typical properties of Sherritt's standard grade nickel powder are chemical composition includes 99.9 wt% Ni, 0.08 wt% Co, 0.01 wt% Fe, 0.003 wt% Cu, 0.025 wt% S, and 0.006 wt% C; granulometric composition is characterized with the following data: 0–10 wt% +150 μm, 5–10 wt% (−150+100) μm, 20–45 wt% (−100+75) μm, 10–25 wt% (−75+63) μm, 10–35 wt% (−63+45) μm, and 5–25 wt% (−45) μm; and apparent density ranges from 3.5 to 4.5. Fig. 21.16 shows a scanning electron micrograph of a powder produced by Sherritt's hydrometallurgical processing.

For briquetting, the powder is first blended with an organic binder in a pug mill and then compacted on a briquetting rolls. Raw briquettes are sintered in an electric conveyor furnace for carbon and sulfur removal and, through sintering at a temperature of 1230–1240 K, structural integrity is imparted to the briquettes. The removal of carbon is achieved by oxidation in air and giving either carbon monoxide or carbon dioxide while the effect for sulfur removal depends on the maintenance of reductive conditions in the hydrogen atmosphere with the release of hydrogen sulfide. The sintering furnace therefore consists of three zones: the oxidizing zone for carbon removal, the reducing zone for sulfur removal, and finally a cooling zone.

Sulfide Precipitation

The liquor from hydrogen reduction contains residual nickel, cobalt, and zinc. These metal ions are precipitated using hydrogen sulfide and recovered as sulfide precipitates. The common precipitation reaction can be written:

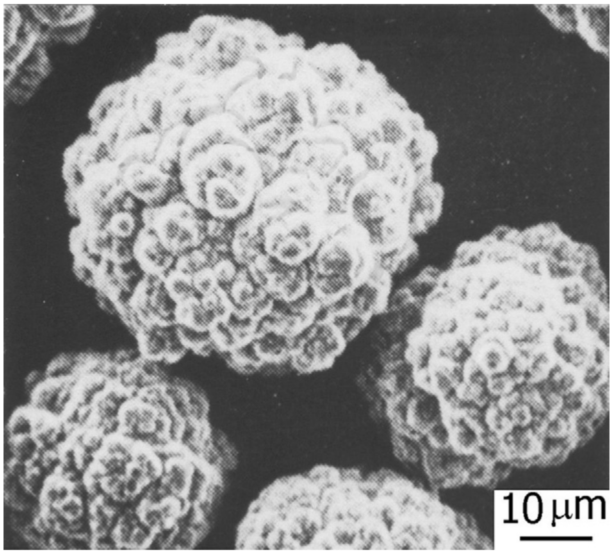

FIG. 21.16 Scanning electron micrograph of a powder produced by hydrometallurgical processing.

$$M^{2+}(aq) + H_2S \rightarrow MS(s) + 2H^+(aq)$$

where M includes nickel, cobalt, and zinc. Metals can be selectively removed from solution by controlling the pH of the sulfide precipitation reaction. The pH is controlled by the addition of ammonia to neutralize the acid generated in the precipitation reaction. The nickel and cobalt sulfides are then returned to leach, the zinc sulfide, which is precipitated separately, is sold as by-product, and the barren liquor (metal free ammonium sulfate solution) proceeds to ammonium sulfate recovery. The latter, after removal of the metal values as metal sulfide, consists only of ammonium sulfate, which is referred to as a "barren solution." This solution is then evaporated and ammonium sulfate, which is formed as a refinery by-product, is recovered in crystalline form. This crystalline ammonium sulfate recovery after centrifuging, drying, and screening is sold as fertilizer.

For the production of especially pure powder, ordinary powder was dissolved into sulfuric acid. The solution was refined from copper by means of cementation by nickel powder, from iron (oxidization by H_2O_2 while the neutralization was carried out using ammonia), and from cobalt by means of α-nitroso-β-naphthol. After that, the solution was thoroughly filtered; the residual content of each impurity was at most 0.5 mg/L. Fine nickel carbonate powder is used for seed powder, forming in the autoclave at a concentration of 5 g/L. The hydrogen reduction process is carried out at 550 K, and at hydrogen pressure 2.4 MPa. The ammonia concentration is adjusted in the nickel reduction feed to give an ammonia to metal molar ratio of 2.2. Produced powder is more pure nickel powder than that produced by the carbonyl or electrolytic nickel processes.

Most hydrometallurgically produced nickel powder is compacted into briquettes for consumption as an alloying additive in the steel industry. Smaller amounts of powder are roll compacted into nickel strips or dissolved to produce various nickel salts.

Powders Covered by Nickel

Hydrometallurgical processing makes it possible to precipitate nickel on the surface of different solid materials (powder, hollow granules, particles in the form of threads, etc.). The particle size of the powder produced is determined by the size of seed powder top-charged in the autoclave and ranges from 20 to 2000 μm. The particle size and shape is controlled during densification processing. Ammonium carbonate, ammonium sulfate solutions, aqueous pulps of nickel (II) hydroxide, or alkaline nickel carbonate is used.

The parameters ensuring a uniform layer of seed powder cladding by processing of the ammonium sulfate solutions are the following: 420 K, hydrogen pressure ≥ 1.5 MPa, ammonium sulfate to metal molar ratio above 1.8, and ammonia to metal molar ratio 2.5. The ammonium sulfate concentration should not be <115 g/L. If the ammonium sulfate content is >200 g/L, the solution viscosity increases, which results in a decrease of the process rate, reduced apparent density, powder fluidity, and degree of cladding, especially for seed powders with low specific density. The coarser the seed

TABLE 21.5 Properties and Application Areas of Nickel Composite Powders Covered by Nickel

Type	Ni (%)	Properties	Application Areas
Ni–C	50–85	Erosion resistance, increased strength, ease of handling by spraying	Coating of turbine buckets, evaporating surfaces by spraying method
Ni–Al	80–82	Spheroidal, heat resistance, wear resistant	Coating of parts working surfaces of rotary piston engines
Ni–carbides (borides, nitrides)	…	Corrosion resistance, high strength, compressibility is better than mechanical mixtures have	Spraying of working surfaces of plasma generators, production of cutting tools by PM technique
(Ni, Cr, Al)–betonyte	…	Erosion resistance, heat resistance, ease of handling by spraying	Valves, heater nozzles, nozzles of turbines operating under conditions of high temperatures and flow velocities

powder, the thicker the nickel cover layer must be; several densification cycles are necessary to provide cladding continuity. The layer continuity of seed powder cladding is achieved if the rate of nucleation is higher than the speed of their growth. The lower the nickel precipitation rate, the higher the probability of nonuniformity of thickness and cladding continuity.

The kinetic equation is correct in the interval of 370–460 K and hydrogen pressure in the range from 0.5 to 2.0 MPa:

$$= 48.6 \cdot 10^{-6} p_{H_2}^{0.94} \exp\left(\frac{1408}{T}\right)$$

where τ is the transient time, h; p_{H_2} is the hydrogen pressure, MPa; and T is the temperature, K.

When p_{H_2} is in the range from 1.5 to 1.8 MPa and T is 420–470 K, a processing duration of 6–8 min is required to produce a cladding thickness of 1–5 μm containing 98–99 wt% Ni.

Depending on hydrogen pressure and particle size, composite Ni—Al powders have apparent densities between 1.42 and 1.83 g/cm^3 and specific surface area ranging from 0.3 to 4.1 m^2/g. Table 21.5 presents the properties and application data of typical composite nickel-coated powders.

The coating with nickel of chromium powders, technical diamonds, fiberglass and glass powder, and red phosphorus was accomplished by hydrometallurgical processing [9].

Autoclave Processing of Nickel Hydroxide and Carbonate Pulps

In 1962, Dobrokhotov (Hypronickel, St. Petersburg, Russia) discovered [9] that during processing of a pulp containing 2–3 wt% nickel hydroxide at 470–520 K and hydrogen pressure in the range from 2 to 3.0 MPa, powder with nickel content up to 99.7 wt% is obtained in 1 h. It is characterized by increased dispersivity and low cementing activity in relation to copper.

An ordinary nickel powder is dissolved in an ammonium-carbonate solution and then distilled in order to produce a high purity powder with low apparent density (0.5–1.0 g/L) and a particle size of 2–3 μm. The feed to the autoclave process is a nickel carbonate with the following chemical composition: 46–47.5 wt% Ni, 12–14 wt% CO_2, 16.5 wt% OH^-, and 0.7 wt% NH_3; apparent density of the precipitate is 0.22 g/cm^3 and the specific surface area is 24.4 m^2/g.

The precipitate is diluted by an ammonium-carbonate solution to the following pulp composition: 75 g/L Ni, 29 g/L CO_2, and 11 g/L NH_3. Fine nickel seed powder is introduced into an autoclave to give a Ni concentration in the pulp of 2 g/L. The reduction process is fulfilled at 420–460 K and the hydrogen pressure in the range from 2.8 to 3.8 MPa. In order to effect the required properties of powder, the ammonia concentration is adjusted in the nickel reduction feed solution to give an NH_3/Ni molar ratio <1.0 or >4.0, and a CO_2/Ni molar ratio <0.5. The impurity content in the powder is max in wt%: 0.07Co; 0.01 Fe; 0.008Cu; 0.04C; 0.005S; 0.002 Al; 0. Ca; and 0.001 Si. By varying the process conditions, powder with apparent density of 0.3–3.6 g/cm^3 and a specific surface area in the range from 0.5 to 10.0 m^2/g can be produced.

The following conditions are recommended [9] for the reduction of aqueous carbonate pulp: hydrogen pressure 2.5–3.0 MPa, temperature 400–420 K, 0.01–0.05 g/L anthraquinone or palladium chloride as the catalyst; initial pH value

5.9–6.4; and <1.0 g/L Ni. The particle shape is hexagonal, the particle size is 1.0–2.0 μm, the powder specific surface area ranges from 1.0 to 6.0 m^2/g, and the apparent density is 1.0–2.0 g/cm^3. This powder is used in the production of nickel plates in alkaline accumulators.

The nickel hydroxide aqueous pulp typically contains 12–48 g/L nickel hydroxide, 1.5 mg/L $PdCl_2$, and 4 g/L NaOH (pH value amounts to 13). The reduction process in the autoclave is carried out at a temperature above 430 K and hydrogen pressure 2.5–3.0 MPa. Powder particles have a spherical shape; the average particle size is in the range of 50–70 nm. Powder is inclinable to agglomeration and oxidation (up to 2%–6% oxygen). Powder apparent density is 0.3–0.6 g/cm^3 and the specific surface area is 25 m^2/g.

The reduction by hydrogen of nickel hydroxide or alkaline carbonate is attractive because of the problem of nickel recovery from oxidized ores. In the acid leaching of ore, the metal is precipitated from the solution in the form of hydroxide by using magnesium oxide. In the ammonia technology, the oxidized ore is subjected by reducing roasting, ammonium-carbonate leaching, and solution distillation as a result of alkaline nickel carbonate producing.

ATOMIZATION

Atomized nickel alloy powders are used mainly for hardfacing, aerospace components, and electric power industry constituents. Nickel-based alloy powders are widely used in the manufacturing of PM superalloys.

Hardfacing Powders

Hardfacing is the application of hard, wear-resistant material to the surface of a component by welding, thermal spraying, or a similar process, mainly to reduce wear. Hardfacing is used on original equipment as well as for the repair of worn components. Hardfacing consumable materials are acceptable in different forms, such as powder, solid welding rods or wires, and tubular rods or wires.

Gas and water atomization are the most widely used techniques for manufacturing hardfacing powders. Particle size intervals of different grades of powder used for various hardfacing processes are found within the range from 10 to 150 μm. For instance, the plasma spray operation requires fine powders in the 10–45 μm range, but special dispensing devices are required to prevent powder flow problems. In some conditions, in the case of the plasma-transferred arc, the particle size in a range of 45–150 μm is preferable. The use of excessive fines is damaging to the coating because fines tend to have higher surface oxides and burn-off tendencies. Certain hardfacing techniques, such as the bulk welding process, require coarse powder in the 100–600 μm range.

Powder shape is also of great importance in any hardfacing operation. Spherical powders have the inside track to the service and solidity of the coating. Spherical powders flow better than irregular ones, which is important when using gravity powder-feed devices. Gas-atomized powders generally are spherical in shape but inclined to satellite formation. Water-atomized powders can be irregular or spherical, depending on the alloy type and the cooling rate. Irregular particle shape, numerous satellites, or narrow size distribution lower apparent density and decrease the flow rate of the powder. The oxygen content of these powders is still below 0.1 wt%.

Commercially available nickel hardfacing alloys can be subdivided into three groups: boride-containing alloys, carbide-containing alloys, and Laves phase-containing alloys. For the most part,nickel hardfacing powders are of the Ni-Cr-B-Si base and are self-fluxing during deposition because of the presence of boron and silicon. Additions of these elements influence the melting temperature range of nickel-base alloys, which is an important factor for hardfacing powders. Owing to the decrease of the melting point, an oxyacetylene torch can easily be used.

The elevated cooling rate makes it possible to form unstable intermetallic nickel-boron (Ni_3B, Ni_3B_4 and Ni_4B_3), nickel-chromium (CrB, Cr_2B, and Cr_5B), and other boride compound hard phases [12]. The unstable nickel-boron phases, the self-fluxing reactions, and the wetting properties during fusing lead to a much higher reaction rate with the oxides present on the substrate. The Laves phase is a somewhat topologically close-packed intermetallic compound, which has a hexagonal structure similar to M_7C_3 carbides, but the hardness value is less than that of carbides. Laves phase materials retain mechanical properties in a wide range of temperatures.

Generally, the finer structure produced by more rapidly cooling provides improved wear resistance in the final coating. These same features may also contribute to improved corrosion resistance.

Compositions and properties of several typical standard grades are given in Table 21.6. Deposit hardness of these alloys is as high as 60 HRC, depending on the chromium, boron, and silicon contents. Alloys containing large amounts of boron and chromium, such as Ni-15.5Cr-4Si-3.5B-0.8C (alloy No. 60), are extremely abrasion-resistant but have poor impact toughness.

TABLE 21.6 Chemical Composition and Hardnesses of Typical Nickel Hardfacing Alloys

		Source. Trade Name									
		Cabot Corp					ANVAL		Haynes International Inc.		
Property	**Unit**	**Alloy No 22**	**Alloy No 35**	**Alloy No 40**	**Alloy No 50**	**Alloy No 60**	**B-60C**	**625**	**C-22**	**Alloy C**	**Alloy 716**
Nominal composition											
B	wt%	1.5	1.6	1.7	2.4	3.5	3.5	…	…	…	0.5
C	wt%	0.2 max	0.3	0.35	0.45	0.8	0.65	0.1 max	0.22 max	0.12	1.1
Co	wt%	…	…	…	…	…	…	…	…	…	11
Cr	wt%	…	3.7	7.5	11.0	15.5	15.5	21.5	21.5	17	26
Cu	wt%	…	…	…	…	…	2.5	…	…	…	…
Fe	wt%	1 max	1.2	1.5	3.0	4.0	4.0	5.0 max	5.0	…	29.0
Mo	wt%	…	…	…	…	…	2.5	9.0	13.5	17.0	3.0
Nb	wt%	…	…	…	…	…	…	3.6	…	…	…
Ni	wt%	Bal	Bal	Bal	Bal	Bal	Bal	Bal	Bal	Bal	Bal
Si	wt%	2.8	3.1	3.5	4.0	4.3	3.8	…	…	…	…
V	wt%	…	…	…	…	…	…	…	0.15	…	…
W	wt%	…	…	…	…	…	…	…	3.0	…	3.5
Nominal deposit microhardness											
DPH	DPH	220–250	320–365	350–415	525–575	710–790	…	…	…	…	…
HRC	HRC	19–24	32–37	35–42	49–52	59–62	…	…	…	…	32
Melting range	°C	940–1240	…	994–1152	976–1063	964–1003	…	…	…	…	…

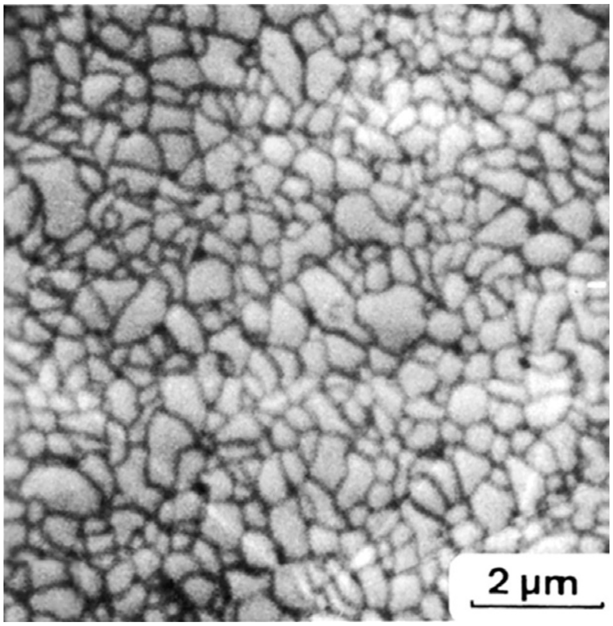

FIG. 21.17 Scanning electron micrograph of melt-spun ribbon on a polished and etched chill surface. *(Source: Duflos F, Stohr JF. Comparison of the quench rates attained in gas-atomized powders and melt-spun ribbons of Co- and Ni-base superalloys: influence on resulting microstructures. Journal of Materials Science 1982; 17(120): 3641–52).*

The low-melting point eutectic of self-fluxing Ni-Cr-Si-B alloys combines with the surface oxides of powders to form borosilicates, which promote wetting on the substrate. The most common use of these powders is in spray-and-fuse and manual torch applications in the glass industry. Additions of copper and molybdenum to self-fluxing alloys are introduced to improve corrosion and pitting resistance. These alloy powders have good abrasive and metal-to-metal wear resistance, although hot hardness and corrosion resistance are somewhat worse than those of the cobalt-based alloys. The use of carbide-containing nickel alloys has been confined. The most widely used in this group is the Ni-Cr-Mo-C system. Hastelloy Alloy C is a typical alloy in this system, which has good corrosion resistance and is normally deposited by the plasma spray technique. Carbide-containing alloys of the Ni-Cr-Mo-Co-Fe-W-C system are attractive as low-cost alternatives to cobalt-base alloys. A typical alloy in this system is Haynes Alloy 716, which contains M_7C_3- or M_6C-carbide phases.

At present, the maximum melt cooling rate has been achieved under heat abstraction from a melt by contact with the metallic substrate [13]. The phenomenon of heightened solubility by such cooling rates becomes possible. The cooling rate of liquid metals achieves 10^5–10^7 K/s, depending on ribbon thickness, which is changed from 20 to 80 μm; the roller circumferential speed is ~30 m/s and the output of the Al alloy is up to 4–6 kg/min. The phenomenon of heightened solubility by such cooling rates becomes possible.

Duflos and Stohr [14] discussed the quench rates attained in melt-spun ribbons of Ni-base alloy (5Co-4Cr-2Mo-6W-6Ta-1Ti-1.5Hf-7.5Al-0.1C-Bal. Ni.). The melt spinning was done in a purpose-built chamber under an inert atmosphere of pure argon or helium. The ribbon width was typically 4 mm and the thickness ranged from 27 to 40 μm, depending largely on the fluid flow conditions. The gradation of structure through the ribbon thickness at different levels within the ribbon thickness (40 μm) showed that the major part of the ribbon thickness is represented by a cellular structure (Fig. 21.17). The average cell size, which varied slightly from the chill zone across the cellular region, was of the order of 0.36 μm. The quench rate of such cell sizes, according to the authors' estimation [14], is about $10^5\,K{\cdot}s^{-1}$.

The melt spinning roller technique is widely used in laboratory investigations, but no commercial operator is known to use this method.

Superalloy Powders

The alloys with high strength at high temperature that are used primarily in turbine engines for aircraft and power generation are termed superalloys. These materials are predominantly nickel-base alloys that are alloyed with refractory elements including molybdenum, tungsten, cobalt, niobium, and tantalum. The PM superalloys are characterized by high homogeneous concentration of both solid solution strengthening elements and the γ'-forming aluminum and titanium intermetallic phases. The PM process makes it possible to form these structural features because of the high rate of crystallization.

The superalloys have been developed due to the need for progressively higher strength at higher temperatures for advanced aircraft engines. With ingot-based material, segregation associated with more complex alloying is a problem and it is aggravated by the need for larger billets for larger turbine discs. A solution to this problem was to minimize segregation through rapid solidification of the alloy by atomization to powder and subsequent consolidation by a technique that does not melt the powder particles while accomplishing full density. The PM process allows making superplastic and yielding to isothermal forging the consolidated products. Therefore, near-shape forgings could be made. Near-shape articles are also made by hot isostatic pressing (HIP). Although PM alloys cost more than conventional wrought alloys, they have the advantage of yield strength and tensile capability due to maintaining the expected cycle life of products. Table 21.7 gives typical compositions of several common grades.

All powders used to produce PM superalloys are prealloyed, which means that the powder is made from the molten state and each powder particle is a minibillet with the same composition as the molten alloy. Various methods are known to produce superalloy powders. Inert gas atomization and vacuum atomization are the most commercial superalloy powder-making processes.

In gas atomization, high-purity feed materials are vacuum induction melted and then atomized using inert gas. The liquid metal is atomized by high-pressure gas jets. Generally, the gas-atomized powder is solidified at a rate in the range from 10^3 to 10^4 K/s. It is collected in a bottom chamber and/or cyclone collector. The particle size distribution resulting from this process depends mainly on the surface tension, γ, viscosity, η, and density, ρ, of the melt as well as the velocity, v, of the atomizing gas and the atomizer design. Oxygen content is of the order of 100 ppm, depending on particle size. Argon is usually used for atomization of superalloys. The use of nitrogen gas normally requires some modifications in composition to accommodate the nitrogen increase during the atomization process.

Vacuum atomization is based on the rapid evolution of gas when a molten metal is supersaturated with gas under pressure and is then suddenly exposed to a lower pressure. An arrangement consists of two vertical chambers connected by a transfer tube. The atomized powder particles, which are solidified at a rate of about 10^3 K/s, fall to the bottom of the upper chamber. The cooled powder is collected under vacuum in another chamber, which is sealed and backfilled with an inert gas (Chapter 4 contains a more detailed description of this technique). This technique is capable of atomizing up to 1000 kg of superalloy spherical powder in one cycle. This technology has been employed for LC Astroloy, MERL 76, and IN-100 alloys.

Superalloy powder is also produced using the centrifugal atomization. One example of this technique is the rotating electrode process (REP) used in the early production of the IN-100 and René 95 powders. In this process, a bar of the specified composition, 15–75 mm in diameter, acts as a consumable electrode. The end of this rotating positive electrode is melted by a direct current electric arc between the consumable electrode and a stationary tungsten negative electrode. The process is carried out in helium gas. Centrifugal force causes spherical molten droplets to come off the high-speed rotating electrode. These droplets rapidly solidify and are collected at the bottom of the chamber.

The plasma rotating electrode process (PREP) is the modification of the REP process and differs from the former in that the plasma is used for melting the consumable electrode. Cooling rates amount to 10^5 K/s for IN-100 [16]. The use of the rotating electrode technique is restricted because of the problem in rapidly solidified superalloy consumable electrodes manufacturing.

Obtained powders are screened to remove oversized particles and then blended to produce a uniform size distribution. All the powder-handling processes are designed to eliminate the possibility of introducing foreign material into the powder. This involves the use of specially designed stainless steel containers, valves, and inert gas handling or air handling of powder in clean rooms.

Depending on the application, a powder size ranging from 250 to 45 μm is characteristic. Before being loaded into a die for consolidation, superalloy powders are evaluated for cleanliness by techniques such as water elutriation, which separates nonmetallic inclusions from the powder. During preparatory processing, the powder is heated in a vacuum to remove air and adsorbed moisture. This procedure can be accomplished before loading or after loading into the die. In the former case, outgassed powder is loaded from an evacuated container into an evacuated consolidation container and then sealed. In the latter case, powder is loaded in air into a consolidation container, which is next cold and hot outgassed and then sealed.

Superalloy powders are consolidated to full density using a combination of high pressure and high temperature. The primary consolidation methods for superalloys are HIP, extrusion, and a combination of the two. For HIP, the powder consolidation container can be a simple geometric shape or a complicated near-net shape. The product can be in the form of a billet ready for subsequent extrusion and/or forging. The HIP parameters usually used are 1310–1480 K at 105–205 MPa for

TABLE 21.7 Chemical Composition and Tensile Properties of Typical PM Superalloys

Property	Unit	Trade grade. Source								
		René 95 [15]	IN 100 [16]	LC Astroloy [17]	René 88DT [18]	Udimet 720, [19–21]	N 18 [22,23]	AF2-1DA-6 [19,24]	PA 101 [25,26]	MERL 76 [19,27,28]
Nominal composition										
Al	wt%	3.5	5.0	4.0	2.1	2.0	4.3	4.6	3.5	5.1
B	wt%	0.01	0.02	0.02	0.015	0.020	0.015	0.015	0.015	0.03
C	wt%	0.06	0.07	0.03	0.05	0.025	0.02	0.04	0.12	0.02
Co	wt%	8.0	18.5	17.0	13.0	14.7	15.5	10.0	9.0	18.6
Cr	wt%	13.0	12.4	15.0	16.0	16.0	11.5	12.0	12.6	12.4
Hf	wt%	0	0	0	0	0	0.5	0	0.95	0.35
Mo	wt%	3.5	3.2	5.0	4.0	3.0	6.5	2.8	1.9	3.3
Nb	wt%	3.5	0	0	0.7	0	0	0	0	1.4
Ta	wt%	0	0	0	0	0	0	1.5	4.0	0
Ti	wt%	2.5	4.3	3.5	3.7	5.0	4.3	2.8	4.1	4.3
Zr	wt%	0.05	0.06	0.04	0.04	0.03	0	0.1	0.04	0.06
V	wt%	…	0.8	0	0	0	0	0	0	0
W	wt%	3.5	0	0	4.0	1.25	0	6.5	4.1	0
Ni	wt%	bal	bal	bal	bal	bal	bal	bal	bal	bal
Tensile properties										
At RT										
UTS	MPa	1650	1591	1345	1232	1630	1580	1586	1472	1615
YS	MPa	1260	1102	930	1143	1194	1080	1138	945	1050
EL	%	18	26	22	20	22	20	12	15	…
At 427°C										
UTS	MPa	1557	…	…	…	1620	1570	…	…	…
YS	MPa	1109	…	…	…	1170	1070	…	…	…
EL	%	11	…	…	…	26	20	…	…	…
At 760°C										
UTS	MPa	1158	1267[a]	1068	1170	1170	1070	1550	1088	1060
YS	MPa	951	1068[a]	792	971	970	980	1100	875	990
EL	%	10	18[a]	22	13	20	6	21	11	…
At 900°C										
UTS	MPa	…	…	…	…	…	…	1200	…	…
YS	MPa	…	…	…	…	…	…	780	…	…
EL	%	…	…	…	…	…	…	10	…	…

UTS, ultimate tensile strength; YS, yield strength; EL, elongation; RT, room temperature.

[a] *At 700°C.*

3–5 h [17]. Extrusion of superalloy powder can be done either as the extrusion of powder in the loose state or extrusion of preconsolidated billets. Extrusion ratios used for direct extrusion of powder are at least 7 to 1. With extrusion of preconsolidated billets, the powder may be preconsolidated by HIP, a separate forging press, or in the extrusion press. Extrusion ratios for solid billet are normally of the order of 3 to 1.

Table 21.7 gives the compositions of PM superalloys. It is of interest to note that when PM superalloys were introduced in the 1970s, the strength and fatigue properties were clearly superior to those of cast/wrought alloys [29,30]. Since then, process improvements have led to a decrease in the size and number of inclusions that initiate low level fatigue fractures [31,32].

Fundamentals about atomization are described in Chapter 4, “Atomization and Granulation,”

MECHANICAL ALLOYING

Mechanical alloying (MA) is usually a dry, high-energy ball milling technique and has been employed to synthesize composite metallic powders with both equilibrium and nonequilibrium phases starting from elemental powders. This technique was developed by John Benjamin and his colleagues at Inco [33], combining the advantages of precipitation hardening and oxide-dispersion strengthening (ODS) in several nickel- and iron-base superalloys for service at temperatures of 1270 K and above.

Mechanism of alloying changes at different milling stages [34]. During high-energy milling, the powder particles are repeatedly flattened, fractured, and rejoined. Every time two steel balls collide, some powder is hit between them.

The force of the impact plastically deforms the particles, creates new surfaces, and causes the particles to weld together. The composite particles at this stage have a characteristic layered structure consisting of various combinations of the starting constituents. After milling for a certain length of time, the mechanical alloying process reaches the stage where each particle contains virtually all the starting ingredients in the proportion they were mixed together. At this stage, the steady-state equilibrium is achieved when a balance is attained between the rate of welding and the rate of fracturing.

The ratio of balls to powder most commonly used is in the range from 10:1 to 20:1. The balls themselves range usually from 8 to 10 mm in diameter and are made from through-hardening steel.

The feed powders generally used for the production of mechanically alloyed oxide dispersion-strengthened superalloys are widely accessible commercially pure powders with particle sizes in ranges from 1 to 200 μm. These powders fall into wide categories of pure metals, master alloys, and refractory compounds. The pure metals include nickel, chromium, tungsten, molybdenum, and tantalum. The master alloys, containing nickel-base alloys with relatively large quantities of aluminum, titanium, and zirconium, are quite brittle when cast and easily comminuted to powder. About 2 vol% of nanosize yttrium oxide, Y_2O_3 (25 nm), is added to form the dispersoid. This oxide, which is prepared by calcination of oxalate precipitates, consists of crystallites of about 50 nm agglomerated into pseudomorphous particles of about 1 μm. The yttrium oxide becomes entrapped along the interfaces between fragments in the composite metal powders. After completion of the powder milling, a uniform interparticle spacing of about 0.5 μm is achieved. For dispersion-strengthened superalloys, the amount of refractory oxide added ranges from about 0.4–1.5 wt%, in particular, yttrium oxide added is in the range from 1 to 2.7 vol% [35].

For mechanical alloying, several types of high-energy ball mills are used. They differ in capacity, efficiency of milling, appliances for cooling, mill kinetics controlling, etc. Shaker mills and planetary ball mills are popular mills for carrying out MA experiments, which mill about 10 g (shaker mill) and a few hundred grams (planetary ball mill) of the powder at a time. In attritors, a charge varying from a few kilograms to about 40 kg can be processed. Mechanical alloying accomplished in ball mills of up 1200 kg is widely used for commercial production of different superalloy powders. The milling time decreases with an increase in the energy of the mill. Therefore, a process that takes only a few minutes in the shaker mill such as SPEX (SPEX SamplePrep Mixer/Mill) can take hours in an attritor and a few days in a commercial ball mill.

Currently, several types of high-energy mills are used for mechanical alloying, including attritors, shaker mills, planetary ball mills, vibrating mills, rod mills, and new designs that have been developed in recent years for specialized purposes. Chapter 3 contains these data and fundamentals about mechanical alloying.

The characteristic mechanically alloyed nickel superalloy powder contains particles ranging from 10 to 500 μm with an average particle size between 50 and 200 μm. The internal structure of the powder is independent of particle size when the steady state during milling is achieved. A homogeneous distribution of ultrafine refractory oxide particles must be developed in a highly alloyed matrix by the production of ODS alloys.

Very high hardnesses up to 520 HV are reached in the powders because of the hard plastic deformation during mechanical alloying. In this connection, cold compaction as a consolidation method is not an option. The simple sintering process also is not available for consolidation of ODS alloys. The most generally used method of consolidation is hot compaction followed by hot extrusion, or by direct hot extrusion at temperatures greater than half the melting point. This process could be used if one is not concerned with the loss of the metastable condition, such as the crystallization of the amorphous phase in the powder. Several of the consolidation modes used for mechanical alloyed powders, both of laboratory and industrial scope, include hot isostatic pressing, powder rolling, plasma-activated sintering, and explosive compaction.

Powder contamination is an important problem in the mechanical alloying technique. Contamination of powders can be traced to the chemical purity of the feed powders, the milling equipment, the milling atmosphere, and the process control agents (PCA) added to the powders.

One way of minimizing contamination from the grinding medium and container is to use the same material for the container and grinding medium as the powder being milled. However, the problem is complex because the MA technique is applied to a variety of materials, and it is impossible to get the containers and grinding medium of all these materials. If a container of the material to be milled is not available, then a thin coating on the internal surface of the container of the material to be milled can be used to minimize the contamination. Parallel with this is a simple rule that could be followed to minimize contamination: the container and grinding medium should be harder then the powder being milled.

Contamination of powders is strongly dependent on the milling atmosphere. It has been ascertained that if the container is not properly sealed, the atmosphere surrounding the container contaminates the powder. It has also been observed that flushing with argon gas will not remove oxygen and nitrogen absorbed on the container's internal surfaces. Schemes have been proposed to reduce the leakage of the ambient atmosphere into the container. For instance, experiments showed that improvement of the pressurization and the use of high-purity argon (99.998 wt%) atmosphere resulted in the processing of high reactive metals such as high-quality titanium alloy powder with as little as 100 ppm oxygen and 15 ppm nitrogen [34]. This process, however, may not be economically viable and therefore may not be workable on a commercial scale.

The compositions and properties of several typical grades of commercially mechanically alloyed nickel-base superalloys are given in Table 21.8.

The ODS nickel-base superalloys continue to find applications in a wide variety of industries. Thus, the two production facilities of Inco have a combined annual powder capacity approaching 300,000 kg. The MA superalloys are intended mainly for three groups of applications, including gas turbine vanes, turbine blades, and sheets for use in corrosive atmospheres. Alloy MA 754 was the first mechanically alloyed nickel-base ODS superalloy to be produced on a large commercial scale. The largest application is as vanes and bands for aircraft gas turbine engines. This material is essentially an Ni-20Cr alloy strengthened by Y_2O_3 that results in higher strength and good resistance to thermal fatigue. Alloy MA 758 was developed for applications where its high chromium content is needed for greater oxidation resistance, in particular for internal combustion engine components, mainly in critical fuel injection parts. The alloy is also used in the glass industry for high temperature parts requiring both elevated temperature strength and resistance to extremely corrosive molten glass. The mechanical properties of this alloy are similar to those of MA 754. Superalloy MA 760 is supplemented by γ' age hardening. Its composition was designed to provide a combination of high-temperature strength, long-term structural stability, and oxidation resistance. The tensile strength properties of alloy MA 760 exceed those of MA 754 but are surpassed by those of MA 6000. Its primary application is expected to be for gas turbines. The MA 6000 is a more complex alloy developed as a material for advanced gas turbines, and is used for first and second turbine vanes and blades machined from a solid rod. Superalloy MA 6000 combines γ' hardening and oxide-dispersion strengthening from the yttrium oxide addition. Aluminum and chromium contents provide the oxidation resistance while titanium, tantalum, chromium, and tungsten jointly ensure sulfide resistance. The tungsten and molybdenum also function as solid-solution strengtheners. MA 6000 is a perfect alloy for gas turbine vanes and blades when exceptionally high temperature strength is required.

Recently, a rapid solidification process termed the gas atomization reaction synthesis (GARS) [40] was developed for production of precursor powders for ODS ferritic stainless steel that, by the following consolidation and heat treatment, formed stable nanometric oxide dispersoids [40,41]. Thus the GARS process enables decreasing the contamination of ODS-produced powders. This production method for the precursor powders involves disintegration of a molten metal stream by a high-velocity gas mixture containing mostly inert gas and a small controlled fraction of a reactive element; oxygen in this case. In situ, the nascent particles form a thin, kinetically favorable, metastable oxide phase upon solidification. This oxide phase can then be dissociated upon high temperature consolidation via an oxygen exchange reaction in which the prior particle boundary oxide behaves as a chemical reservoir supplying oxygen to react with a rare earth (RE) element, yttrium in this case, either a solute trapped in a solid solution or a phase segregated as an intermetallic within the particle. The aim of the process is to create highly stable nanometric oxide dispersoids of relatively homogenous size and spacing. This desired distribution is based on strengthening theories that describe high-temperature particle strengthening [42,43].

TABLE 21.8 **Compositions and Properties of Selected Typical ODS Mechanically Alloyed Nickel-Based Superalloys**

Property	Unit	Trade grade. Source					
		MA 754 [35,36]	MA 757 [37]	MA 758 [38]	MA 760 [35,36]	MA 6000 [39]	TMO-2 [35,36]
Nominal composition							
Al	wt%	0.3	4.0	0.3	6.0	4.5	4.2
B	wt%	…	…	…	0.01	0.01	…
C	wt%	0.05	…	0.05	0.05	0.05	…
Co	wt%	…	…	…	…	…	9.7
Cr	wt%	20	16	30	20	15	6
Mo	wt%	…	…	…	2.0	2.0	2.0
Ta	wt%	…	…	…	…	2.0	4.7
Ti	wt%	0.5	0.5	0.5	…	0.5	0.8
Zr	wt%	…	…	…	0.15	0.15	…
W	wt%	…	…	…	3.5	4.0	12.4
Y_2O_3	wt%	0.6	0.6	0.6	0.95	1.1	1.1
Ni	wt%	bal	bal	bal	bal	bal	bal
Mass density	g/cm^3	8.3	7.79	8.13	7.53	8.11	8.58
Melting point	^{0}C	1400	…	…	…	1296–1375	…
Tensile properties							
At RT							
UTS	MPa	965	…	949	…	1294	…
YS	MPa	586	…	560	…	1284	…
EL	%	21	…	27	…	4	…
At 871°C							
UTS	MPa	248	…	339[a]	…	1156[b]	…
YS	MPa	214	…	214[a]	…	781[b]	…
EL	%	31	…	47[a]	…	6[b]	…
At 982°C							
UTS	MPa	190	…	173[c]	…	407	…
YS	MPa	169	…	151[c]	…	344	…
EL	%	18	…	29[c]	…	12	…

UTS, ultimate tensile strength; YS, yield strength; EL, elongation; RT, room temperature.

[a] *At 800°C.*

[b] *At 760°C.*

[c] *At 1000°C.*

Latter, a GARS method was utilized to produce the precursor Ni-Cr-Y-Ti powder with a surface oxide and an internal rare earth (RE) containing an intermetallic [44]. Using close-coupled gas atomization, precursor powders of the following high Y/Ti ratio compositions (measured) $Ni_{81.40}Cr_{16.11}Y_{1.06}Ti_{1.20}Al_{0.16}$ – Alloy1, $Ni_{81.43}Cr_{18.32}Y_{0.05}Ti_{0.05}Al_{0.07}$ – Alloy2, and $Ni_{80.56}Cr_{18.23}Y_{0.20}Ti_{0.09}$ – Alloy3 are made. Inert Ar gas was used for the atomization and the reactive gas was injected slightly downstream (Fig. 21.18) in contrast with the earlier experiments of Rieken et al. [40], when melt stream was

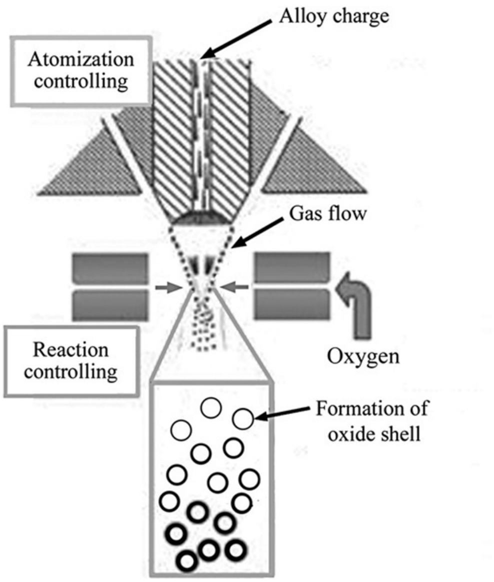

FIG. 21.18 Schematic production by gas atomization reaction synthesis (GARS) of ODS precursor powders with in situ formation an oxide shell.

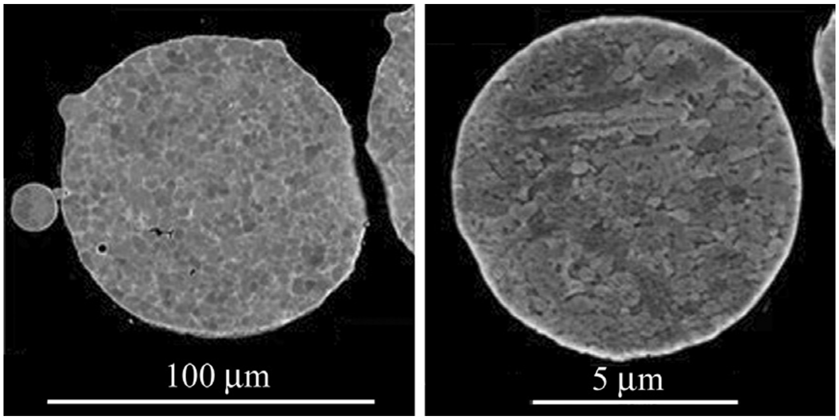

FIG. 21.19 SEM particle section micrographs of the high Y/Ti Alloy 1 – $Ni_{81.40}Cr_{16.11}Y_{1.06}Ti_{1.20}Al_{0.16}$: 100 μm particle size (left), 5 μm particle size (right).

atomized by a mixture containing mostly inert gas and a small controlled fraction of a reactive element. The mass gas/metal ratio was in the 0.97–1.09 range.

Meyer [44] reported that the oxygen content (at ppm) in Alloy 1, Alloy 2, and Alloy 3 was 35,800, 1620, and 6970, respectively. The lower oxygen content in Alloy 3 can be interpreted by lower aluminum content. Oxide thickness as a function of particle size is varied in the 3–240 nm range with particle size increasing from 3 to 100 μm. Powder larger than approximately 20 μm in diameter exhibited primarily dendritic microstructures. A transition in primary morphology occurred between particles of approximately 10 and 20 μm with powder particles <10 μm in diameter exhibiting a primarily equiaxed microstructure. SEM particle section micrographs of the high Y/Ti Alloy 1 are shown in Fig. 21.19. With decreasing particle size from 100 to 7 μm, the average dendritic parameter (or grain) size is decreased from 3 to 0.3 μm.

Consolidation and heat-treatment were performed to control the exchange of oxygen from the surface oxide to the RE intermetallic to form oxide dispersoids. Hot isostatic pressing (HIP) consolidation performed at 973 K and 310 MPa (45 ksi) for 4 h results in approximately 92%–93% density and contained continuous prior particle boundary oxides and internal intermetallic phases. The sample became fully dense after either 1 h or 2 h vacuum anneals at 1473 K and $\sim 10^{-4}$–10^{-5} Torr ($\sim 1.33 \times 10^{-2}$–1.33×10^{-3} Pa).

Gas turbines contribute a significant portion of the world's power demand as well as the majority of aircraft propulsion needs. Today's complex cooled gas turbine components would not be possible without continuous advances in both materials and manufacturing science and technology. The turbine hot gas part is the most costly portion of the engine and therefore, improvements in materials and manufacturing, especially those that enable better cooling, carry a high return

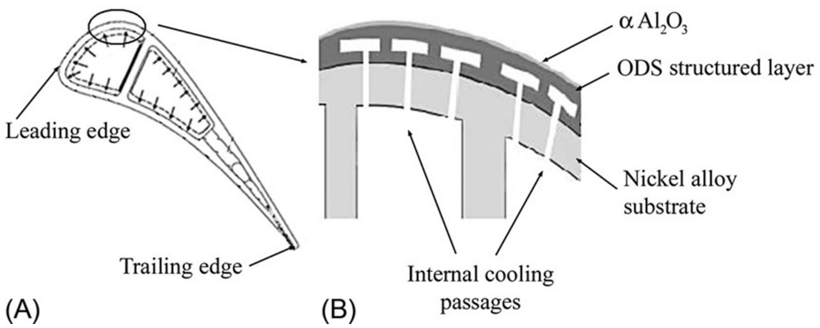

FIG. 21.20 Schematic of a turbine blade cooling: (A) cross-section of turbine blade; (B) near blade surface embedded microchannels.

on investment. Therefore, the development and integration of advanced material systems and airfoil cooling techniques are important directions for gas turbine progression [45–47].

Future land-based gas turbine engines are being designed to operate with inlet temperatures exceeding 1770 K. Recently, turbine parts have been fabricated from nickel-based superalloy materials, and may be coated with an insulating thermal barrier coating. Additionally, turbine blades and vanes often contain internal and film cooling features for reducing the likelihood of thermomechanically induced failure in order to prolong component life. Alvin et al. [47] reported that the NETL (National Energy Technology Laboratory) Regional University Alliance (RUA) devised advanced turbine airfoil architecture that included Ni-based superalloys that are coated with low-cost, oxidation-resistant, slurry, β-NiAl aluminide diffusion bond coat systems. These systems are subsequently coated with either commercially air plasma sprayed or electron beam physical vapor deposition the thermal barrier coatings, or with overlayers that are capable of providing thermal insulating properties up to temperatures approaching 1870–1970 K [48,49]. Fig. 21.20 illustrates a near-surface embedded microchannel concept that positions the internal cooling passages at the outer boundary of the alloy substrate, adjacent to or as a microchannels within an ODS layer.

PRODUCTION OF NICKEL POWDER BY REDUCTION PROCESSES

Solid-Phase Reduction

The basic raw materials are nickel oxide produced by roasting sulfide materials, or thermal decomposition of oxygen-containing compounds such as hydroxides and carbonates as well as salts and compounds of nickel thermally unstable at 1000–1200 K. The general equation for the solid-phase reduction may be represented as:

$$NiO + R \rightarrow Ni + RO$$

$$NiA + R \rightarrow Ni + RA$$

where R is the reducing agent and A is an acid radical.

Hydrogen, carbon monoxide, low-sulfur carbon-containing materials (wood charcoal, oil coke, graphite), and natural gas are used as reducing agents. While using hydrogen, the process is carried out at 773–823 K; the powder produced has high dispersivity and developed a (sponge) particle surface. At higher temperatures (above 823 K), structure recrystallization, partial sintering, and coarsening of particle size are observed. Reduction accelerates when reduced operation is carried out in a fluidized bed or under pressure of hydrogen.

Heating nickel oxalate in hydrogen at 503–673 K produces ultrafine powder. To prevent sintering, organic reagents are added to the initial charge, for instance, a mixture of silicone oil and tetrahydrofuran. The powder is cooled in a hydrogen current, washed with acetone for removal of organic traces, and dried in air. Particle size is 0.3–1.0 μm. Particles are needle-shaped. Sometimes nickel oxalate is converted to hydroxide by treatment of a precipitate by alkaline solution. Then this precipitate of $Ni(OH)_2$ is calcined in a hydrogen atmosphere at 820–1200 K for two h. Powders of magnetic alloys based on Fe-Ni-Co are produced by an analogous method at 570–690 K.

The nickel formates are reduced at 470–570 K with the formation of ultrafine powder with a specific surface of 10–14 m^2/g, an apparent density of 0.4–0.45 g/cm^3, and a particle size of 0.1–0.3 μm.

Reduction by producer gas is made at 830–870 K in multihearth or in fluidized bed furnaces. Obtained powder is used in hydrometallurgy for purification of nickel-cobalt solutions from copper by cementation. During reduction by solid carbon (970–1100 K), the powder is inevitably contaminated by inclusions of the reducing agent and carbide formation. The charge is preliminarily granulated for increasing layer gas-permeability. Powder sintering is avoided by the introduction of 0.5–1.0 wt% $CaCl_2/MgCl_2$ or by using fluidized bed furnaces.

Reduction by Organic Reagents

There are various methods of nickel powder production by reduction processes using organic reagents. The nickel powders, which are used as a catalyst in the process of oil hydrogenation, are produced by reduction by means of hydrazine from the following compositions:

- Nickel borate solution in the presence of a catalyst (platinum or palladium salts).
- Aqueous or ammoniacal solutions in the presence of platinum or palladium salts; in final product contents 96–97 wt% Ni.
- A mixture of nickel acetylacetonates in boiling ethanol.
- An aqueous solution with the addition of sodium borohydride at $p_{H_2} = (6\text{–}10)$MPa; $T = 300\text{–}360$ K; the powder is treated with glue, washed with alcohol, and dried.
- A nickel sulfate solution in the presence of Rochelle salt and platinum chloride; 96 wt% of the Ni was extracted in the colloid product contains 99% of the Ni.
- Nickel hydroxide (II) (the ratio of liquid to solid is 1 to 2, 3, temperature 293 K); in 46 h up to 99 wt% of the Ni in the form of powder with apparent density of 6.78 g/cm^3 was precipitated; typical powder particle size distribution is characterized by the following data: 5 wt% (+150) μm, 27.8 wt% (−150+100) μm, 14.1 wt% (−100+83) μm, 53.1 wt% (−83) μm.
- For the production of nickel powder, oxide dispersion strengthening by 2% zirconium dioxide, nickel salt is treated by alkali at 350–360 K, and disulfo-zirconium acid is added as well as 2.0–2.5 L hydrazine to 1 kg salt; the precipitate is filtered, washed, dried, and calcined in a hydrogen atmosphere at 720 K for 1 h.

In the treatment of nickel salts by hydrazine, it is possible to influence the particle shape and size by varying the type of solution (aqueous, ethyleneglycol, diethylamine, di-, tri- ethyleneamine) and the process conditions (metal concentration, composition and specific consumption of reagents, temperature). When particle agglomeration is excluded, nanosized powders of 0.1–1.25 μm are produced with narrow particle size distribution. The nickel content of the powder amounts to 99.8%.

During processing of basic nickel carbonate pulp using hydrazine-hydrate at 360 K, >96% of the nickel is precipitated as ultrafine powder (particle size is 40–70 nm, specific surface is 21 m^2/g). Particle agglomeration was avoided by a polyvinyl alcohol addition.

Nickel powder properties are remarkably improved if the nickel powder contains up to 1.0 wt% Mg or 0.1 wt% Ca. With this aim, the initial nickel solution containing alloying elements in the required amount is treated by sodium hydroxide and the precipitate obtained is processed with hydrazine.

Processing of alcaline nickel carbonate by sodium formate with phase transformations depending on temperature is given in the scheme below:

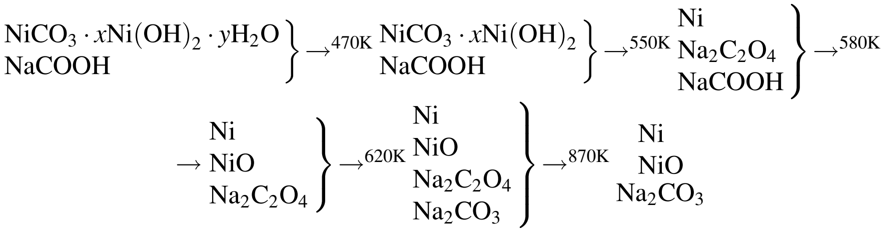

$$\left.\begin{matrix}\mathrm{NiCO_3\cdot \mathit{x}Ni(OH)_2\cdot \mathit{y}H_2O}\\\mathrm{NaCOOH}\end{matrix}\right\}\rightarrow_{470K}\left.\begin{matrix}\mathrm{NiCO_3\cdot \mathit{x}Ni(OH)_2}\\\mathrm{NaCOOH}\end{matrix}\right\}\rightarrow_{550K}\left.\begin{matrix}\mathrm{Ni}\\\mathrm{Na_2C_2O_4}\\\mathrm{NaCOOH}\end{matrix}\right\}\rightarrow_{580K}$$

$$\rightarrow\left.\begin{matrix}\mathrm{Ni}\\\mathrm{NiO}\\\mathrm{Na_2C_2O_4}\end{matrix}\right\}\rightarrow_{620K}\left.\begin{matrix}\mathrm{Ni}\\\mathrm{NiO}\\\mathrm{Na_2C_2O_4}\\\mathrm{Na_2CO_3}\end{matrix}\right\}\rightarrow_{870K}\begin{matrix}\mathrm{Ni}\\\mathrm{NiO}\\\mathrm{Na_2CO_3}\end{matrix}$$

The product is washed by water to remove sodium salts. It is then dried, annealed at 900–970 K in a hydrogen atmosphere, milled, and screened. Chemical composition of the powder produced includes 99.0 wt% Ni; 0.42 wt% Co; 0.003 wt% Cu; 0.09 wt% Fe; 0.02 wt% C; 0.02 wt% S; and 0.06 wt% O_2. Powder particle size ranges from 2 to 9 μm, the specific surface is 6–6.8 m^2/g, and the apparent density is 1.8–1.9 g/cm^3.

Nickel powder with a colloidal structure is produced when nickel salt is treated in an organic liquid (glycerol, silicone, and vaseline oil) at a temperature not <520 K. For example, nickel formate is mixed with silicone oil in mass relation 1:1 and treated at 480 K during 1 h. Powder is separated by centrifuge, washed with toluene and dried. It is monophase, the particles have an equiaxed shape, and their size depends on the dispersivity of initial nickel salt. The powder purity is determined by raw material composition; there are problems connected with the usage of wash solutions.

Processing of nickel formic precipitate by acetone (liquid-to-solid ratio of up to 6:1) is performed at the temperature 523 K in the presence of polyacrilamide oligomer that lyophilizes and protects powder particles from oxidation, thus excluding their pyrophoricity and permitting the production of powder with the following characteristics: mass density 8.4–8.6 g/cm^3, specific surface 8.0–9.6 m^2/g, and particle size is 2–5 μm.

The aqueous-spirit solution of hydroxide pulp and nickel formate (ratio of spirit to water in the range from 0.1 to 10) is processed in an autoclave at 430–520 K and hydrogen pressure 2.5–5.0 MPa by using surfactant (acrylonitrile, pyridine); powder particles are of spherical shape, and their size ranges from 0.07 to 0.2 μm. The choice of conditions depends on the requirements of powder properties. High hydrogen pressure, the proper surfactant, and an increased ratio of spirit to water promote production of fine powder.

For the production of powder with super-high specific surface, a process is known where nickel chloride and metallic aluminum (nickel-to-aluminum ratio of up to 1 to 1) are mixed and treated in alkaline melt in an inert gas atmosphere at 870 K for 4–5 h. A reactor of special construction with electrical heating and mixing of reacting components is used. The powder produced has a specific surface up to 100 m^2/g and is useful in the chemical industry for production of catalysts or polymer compositions.

Production of Nickel Powder by Electrolysis

Nickel powder is produced by electrolysis from a sulfate electrolyte with soluble anodes, which are produced by nickel refining (Fig. 21.21). Chloride ions as hydrochloric acid are injected into the solution to prevent passivation of the nickel anodes.

A temperature in the ranges of 320–330 K is maintained by the use of water-cooled cathodes. The electrolyte consists of 2–5 g/L nickel, 45–60 g/L sulfate-ions, and 0.05–0.15 g/L chloride-ions at pH ranging from 5.5 to 7. Approximation of anode current efficiency to cathode one by chloride-ion concentration control provides the electrolyte composition stability. Cell voltage is 12–15 V at cathode density 1.8–2.2 kA/m^2. The electrolyzer is a bin-type one with hollow disc cathodes rotated in reciprocating directions. The powder precipitate is removed by knives.

Table 21.9 contains the chemical composition of CIS standard grade electrolytic nickel powders (GOST 9722-79). The powders typically contain minimum 95.5 wt% nickel and max 0.2 wt% oxygen. The sieve content under 71 μm particle size of powder PNE-1 is 96 wt% minimum while under 45 μm it is 30 wt% minimum. Its apparent density is 3.4 g/cm^3. The powder PNE-3 is coarser: the sieve content <250 μm is a minimum 97 wt% and oversize is not >3 wt%. Its apparent density is 5.0 g/cm^3.

The electrolytic nickel powder is characterized by a coral-like dendritic structure formed by growing powder particles (Fig. 21.22A). At a magnification of 10,000 × (Fig. 21.22B), the growing particles, 0.5–3 μm in length and 0.5–1.0 μm in

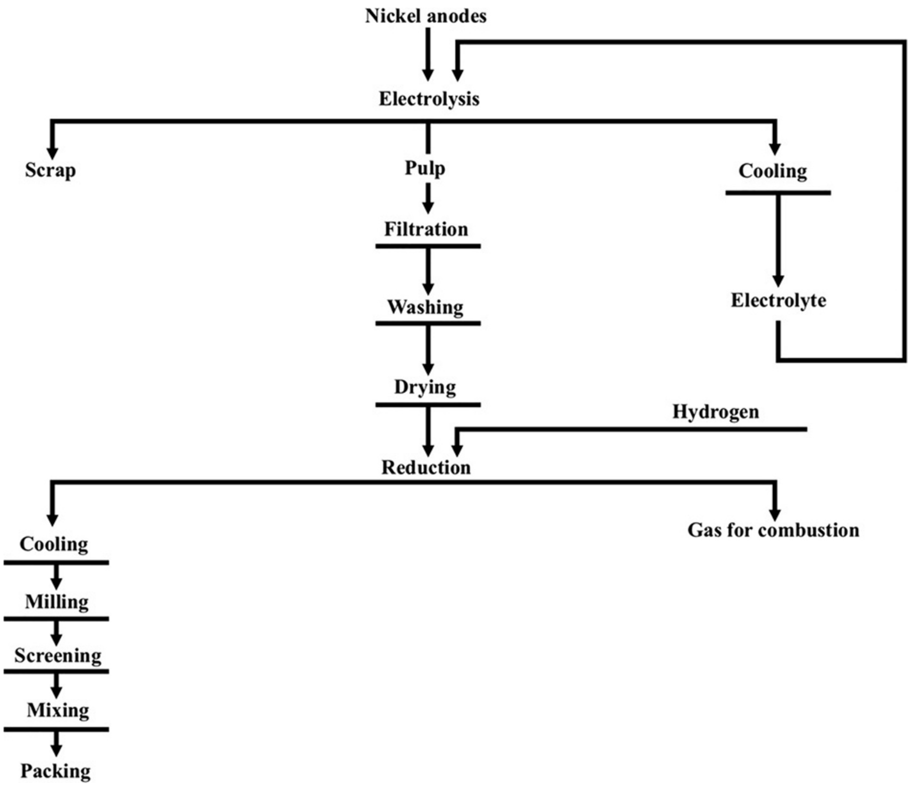

FIG. 21.21 Flow sheet for nickel powder production by electrolysis.

TABLE 21.9 Chemical Composition of CIS's Standard Grade Electrolytic Nickel Powders (GOST 9722-79)

		Impurities Maximum (wt%)					
Brand	**Nickel, Minimum (wt%)**	**O**	**Fe**	**Co**	**Si**	**C**	**S**
PNE-1	99.5	0.02	0.10	0.20	0.03	0.06	0.008
PNE-3	99.5	0.02	0.20	0.50	0.03	0.08	0.010

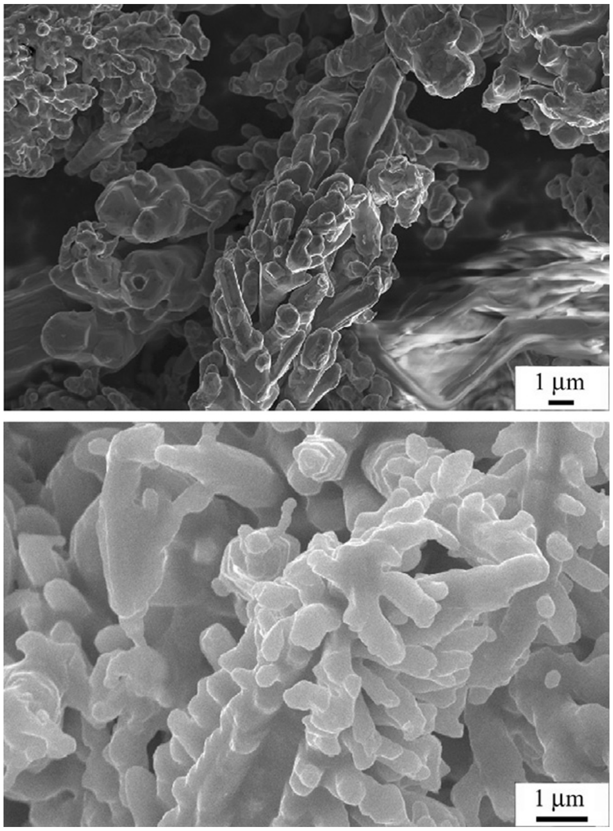

FIG. 21.22 SEM images of electrolytic nickel powder at various magnifications.

thickness, are seen to be arranged like needles on fir branches 10–15 μm in length. This powder was produced by electrolyzing a nickel sulfate solution in aqueous ammonia with a nickel anode serving as an additional source of Ni^{2+} ions [50].

There are various means of production of nickel and nickel-alloy powders by electrolytic processes. Several of them are summarized in Table 21.10. Currently, the largest producer of electrolytic nickel powder in Russia is the Norilsk Nickel Company [7].

PECULIARITY OF NICKEL ALLOY POWDERS BY USING IN ADDITIVE MANUFACTURING

One of the main problems occurring when Ni-based superalloys are used is their poor machinability. Such a problem can be solved by using powder metallurgy or additive manufacturing (AM) [54]. Additive manufacturing is an upcoming method for manufacturing of complex near-net-shaped products with a reduced need for expensive tooling and machining [55,56]. One of these methods is selective laser melting (SLM), which is using powder as the raw material. The process includes selective melting of powder according to a 3D-CAD file followed by applying new layers one by one; the component is created by building up [57]. Compared to more conventional methods such as casting, milling, and forging, AM creates parts in one single step without the need of molds, tools, and postmachining. Moreover, the application of AM allows the

TABLE 21.10 Production of Nickel and Nickel-Alloy Powders by Electrolysis

Method	Chemical Composition of Electrolyte	Current Density (kA/m^2)	Temperature (K)	Electrolysis Parameters
Nickel				
WS	20 g/L $NiSO_47H_2O$; 20 g/L $(NH_4)_2SO_4$; 10 g/L NaCl (pH = 4–4.5)	0.5–3.0	303–308	Current efficiency is 40–60%; particle size ranges 40–60 μm.
WS	50 g/L $NiCl_2$; 25 g/L NH_4Cl; HCl up to pH 1–1.5	…	293–313	Current efficiency is 66–75%
WS	20 g/L $NiCl_2$; 25 g/L NH_4Cl; 10 g/L NaCl (pH 5.2–7.3)	5	313	Powder consists of 55% of particles with size 60 μm; 30% of particles with size <25 μm; 20% of particles with size <10 μm
WS	15–25 g/L $NiSO_47H_2O$; 40 g/L NH_4Cl; 50–80 g/L NaCl; (pH 6.5–7.2)	5–10	293–303	Current efficiency is up to 65–70%; cell voltage is 7–12 V; easy removal of powder
WS [51]	35–57 g/L $NiSO_4$; 30–50 g/L NH_4Cl; 20–40 g/L K_2SO_4; (pH 4.4)	4–20	303	Current efficiency (*CE*) is 53%; soluble nickel and insoluble lead anodes are activated simultaneously $i_a^{Pb}/i_a^{Ni} = \frac{1}{CE} - 1$
WS [52]	47.8–57.4 g/L $NiSO_47H_2O$; 200 g/L NaCl; 50 g/L NH_4Cl;	1–10	323	Linear current time history; particles size 60–80 μm; specific current consumption 6.4–8 kW h/kg
WS	4–8 g/L Ni; 20 g/L NH_4Cl; 10 g/L NaCl; (pH 5.5–6.5)	$i_c = 3.6$; $i_a = 0.4–0.5$	303–313	Current efficiency is 70–80%; cell voltage is 8 V
WS	17 g/L Ni; 200 g/L NaCl; 50 g/L NH_4Cl; (pH 6.3)	3.0	323	Current efficiency is 95%; particle size is 60–80 μm.
WS	4–10 g/L Ni; 20 g/L H_3BO_3; 25 g/L Na_2SO_4; 20 g/L $(NH_4)_2SO_4$; 20–60 g/L urea	3.7–8.0	…	Current efficiency is 55–80%; air agitation; period of precipitation is 20–30 min; particle size is up to100 μm
Nickel-Cobalt				
WS	2–10 g/L $NiSO_4$; 2–8 g/L $CoSO_4$; 30–132 g/L $(NH_4)_2SO_4$; 12.4–24.8 g/L H_3BO_3; 10 g/L Na_2SO_4; (pH 2.1–9.6)	0.2–1.33	293	$[Ni/Co]_{alloy} = [Ni/Co]_{solution}$
Nickel-Tellurium				
WS	7 g/L Ni; 33 g/L $(NH_4)_2SO_4$; 20 g/L K_2SO_4; 0.02–0.156 g/L Te.	12	308	Current efficiency is 42%; average particle size is 50μm; Te content in powder is 0.25 wt%.

Continued

TABLE 21.10 Production of Nickel and Nickel-Alloy Powders by Electrolysis—cont'd

Method	Chemical Composition of Electrolyte	Current Density (kA/m^2)	Temperature (K)	Electrolysis Parameters
Nickel-Chromium				
WS	15 g/L $NiCl_2$; 94 g/L(Ni + Cr);	4–5	318	Current efficiency is 35%; $i_c = 10$ A/m^2 on auxiliary cathode
Nickel-Zink				
WS	5 g/L Ni; 16.2 g/L Zn; 20 g/L $(NH_4)_2SO_4$; 50 g/L NaCl;	8.9–20.8	298–343	Nickel as $Ni(NH_4)_2SO_4 \cdot 2H_2O$, zinc as sulfate; particle size is 5–10 μm; current efficiency is 34%.
WS	10–20 g/L Ni; 18.2 g/L Zn; 20 g/L$(NH_4)_2SO_4$; 50 g/L NaCl	1.8–20.8	298–343	Nickel as salt $Ni(NH_4)_2SO_4 \cdot 2H_2O$, zinc as sulfate; particles size is 15–20 μm; current efficiency is 21 to 70%.
WS	50–60 g/L Ni; 16.2 g/L Zn; 20 g/L $(NH_4)_2SO_4$; 50 g/L NaCl	1.8–13.3	298–323	Ni as salt $Ni(NH_4)_2SO_4 \cdot 2H_2O$, zinc as sulfate; dendrites 25–75 μm in size; current yield is 67–72%.
Nickel-Iron-Molybdenum				
WS	9.5 g/L Ni; 1.7 g/L Fe; 0.48–0.45 g/L Mo; 19.8 g/L $(NH_4)_2SO_4$; (pH 2.5–2.7)	$i_c = 2.3$ $i_a^{Ni} = 0.1–0.2$ $i_a^{Fe} = 0.1–0.2$ $i_a^{Pb} = 1–2$	298	$i_a^{Fe}/i_a^{Ni} = 5/27$; on net near Fe anode $i = 50–70$ A/m^2; Mo as $(NH_4)_2MoO_4$; Ni and Fe as sulfates; alloy is near permalloy
Nickel-Iron [53]				
WS	11.2–11.7 g/L (Ni + Fe); 50 g/L $(NH_4)_2SO_4$; 15 g/L KCl; 2.25 g/L NaF; (pH = 5)	3.0	303	Optimum [Ni]/Fe] = 1/1 (mole) $[Ni/Fe]_{alloy} = [Ni/Fe]_{solution}$ alloys are solid solutions; up to 76% Fe fcc lattice; over – bcc; current efficiency is 73%; size 40 μm max; density 2.8 to 3 g/cm^3

WS: electrolysis in aqueous solution; *CE*: current efficiency; i_a, i_c: anode and cathode current densities; i_a^{Pb}, i_a^{Ni}: current densities on insoluble (Pb) and soluble (Ni) anodes respectively.

TABLE 21.11 Nominal Chemical Composition of the Investigated Powders

Element	Cr	Fe	Mo	Co	W	Mn	Si	C	Ni
wt%	20.5–23	17–20	8–10	0.5–2.5	0.2–1	<1	<1	0.05–0.15	Bal.

production of complex-shaped components that was not possible before [54,57]. A majority of the AM processes use powders as a raw material, and in many cases the powder will be recovered. This means that the unmelted powder will be recycled and mixed with virgin powder and be used again. There is no standard on how this recycling process should be handled, what fraction of recycled powder can be used, how many times, etc. Exposure of the powder to the high temperature during the AM process, sieving, handling, etc., will inevitably result in formation, redistribution, and/or growing of surface oxide species in order to minimize the high surface energy of the powder.

The study [58] was focused on the evaluation of the surface oxide state of two Hastelloy X Ni-based superalloy powders, virgin and recycled after the SLM process. Table 21.11 contains the nominal chemical composition of the investigated powders. It was reported that a thin uniform nickel hydroxide layer covers the surfaces of the both HX Ni-based superalloy virgin and recycled powders with the presence of "islands" formed by fine particulate features of thermodynamically stable Al-Cr-Ti-Si oxides. The segregation of Al and Cr to the surface of the recycled powder was observed. Loss of silicon due to sublimation was also detected on the surface of recycled powder. The surface nickel hydroxide layer has an average thickness of about 1 nm for both virgin and recycled powder. HR SEM+EDX analysis showed that both powders consist preferably of spherical particles with clearly visible cellular to dendritic structure on the surface. The surface of recycled powder is much more contaminated with particulate oxides that have a complex oxide nature, in comparison with the virgin powder. The recycle ability of the HX Ni-based superalloy powder is limited by creation and growing of thermodynamically stable surface oxides due to the high content of alloying elements and exposure to high temperatures during the SLM process.

REFERENCES

[1] Mond L, Langer C, Quinke F. Action of carbon monoxide on nickel. Proc Chem Soc. 1890; 1: 749–53. Downloaded by University of Sussex on 08 January 2013. https://doi.org/10.1039/CT8905700749. [Accessed 31 Decmber 2017].

[2] W.M. Goldberger, D.F. Othmer, The kinetics of nickel carbonyl formation, Ind Eng Chem Process Des Dev (July) (1963) 202–209.

[3] H.E. Carlton, W.M. Goldberger, Fundamental consideration of carbonyl metallurgy, J Met 1965 (June) (1965) 611–615.

[4] GOST 12.1.005-88 [in Russian].

[5] Guide to legislation and health and safety in the European PM industry, Pub EPMA, Shrewsbury, 1997.

[6] Sanitary Regulations and Standards of Surface Waters from Pollution. SanPiN 4630-88 [in Russian].

[7] Norilsk Nickel, Carbonyl powder and pellets, Available from: www.nornickel.ru.

[8] J.H. Tundermann, Carbonyl vapormetallurgy, in: ASM handbook, vol. 7, ASM International Publishers, 1998, pp. 167–171.

[9] S.S. Naboychenko (Ed.), Nonferrous metal powders. Handbook, Publ. Metullurgiya, Moscow, 1997 [in Russian].

[10] G. Freeman, Production of nickel powders by hydrometallurgical processing, in: ASM handbook, vol. 7, ASM International Publishers, 1998, pp. 171–174.

[11] A. Ritter, The Sherritt – Cuba joint venture: uncertainties for both partners, Tag Archives: Sherritt International, http://thecubaneconomy.com/articles/tag/sherritt-international/, Sept 6, 2016. (Accessed 31 December 2017).

[12] P.A. Kammer, W. Simm, H.T. Steine, The influence of atomisation process and parameters on metallic powders and coating properties, in: Thermal Spray Research and Applications, Publ. ASM International, 1990, pp. 773–776.

[13] O. Hitoshi, O. Takashi, I. Nobuyki, N. Motonori, Development of safe production system for Mg-Zn-Re rapidly solidified powders, in: Proceedings of PM2004 World Congress, vol. 1, Publ. European Powder Metallurgy Association, UK, 2004, pp. 111–115.

[14] F. Duflos, J.F. Stohr, Comparison of the quench rates attained in gas-atomized powders and melt-spun ribbons of co- and Ni-base superalloys: influence on resulting microstructures, J Mater Sci 17 (12) (1982) 3641–3652.

[15] J.J. Conwey, M.S. Sperber, F.J. Rizzo, Enhanced properties of nickel-base superalloys using hot isostatic pressing (HIP) of powder metals, in: Proceedings of 2002 world congress on powder metallurgy & particulate materials, Princeton, Publ MPIF, 2002, pp. 8-123–8-137.

[16] J.E. Coyne, W.H. Couts, C.C. Chen, R.P. Roehm, Superalloy turbine components–which is the superior manufacturing process: As-HIP, HIP + iso-forge or gatorizing of extrusion, in: Proceedings of powder metallurgy superalloys–aerospace materials for the 1980s, vol. 1, Publ. MPR, 1980.

[17] J.H. Moll, B.J. McTiernan, Powder metallurgy superalloys, in: ASM handbook, vol. 7, ASM International Publishers, 1998, pp. 887–902.

[18] D.D. Krueger, R.D. Kissinger, R.G. Menzies, Development and introduction of a damage tolerant high temperature nickel-base disk alloy, Rene 88 DT, in: Superalloys, Publ. The Minerals, Metals and Materials Society, 1992.

[19] D. Furrer, H. Fecht, Ni-based superalloys for turbine discs, J Met (January) (1999) 14–16.

[20] H. Hattory, M. Takekawa, D. Furrer, R.J. Noel, Evaluation of U720 for gas turbine application, in: Superalloys, Publ. The Minerals, Metals and Materials Society, 1996, pp. 705–711.

[21] J.H. Moll, J.J. Conway, Characteristics and properties of As-HIP PM Alloy 720, in: Proceedings of conference of superalloys 2000. Seven Springs (PA), Publ. TMS, Wareendale, 2000, pp. 135–142.

[22] C. Ducrocq, A. Lasalmonie, Y. Honnorat, N18, a new damage tolerant PM superalloy for high temperature turbine discs, in: Proceedings of the sixth international symposium on superalloys 1988. Seven Springs (PA), Publ. The Metallurgical Society, Wareendale, 1988, pp. 63–72.

[23] M. Soucail, M. Marty, H. Octor, Development of coarse grain structures in a powder metallurgy nickel base superalloy, Scr Mater 34 (4) (1996) 519–525.

[24] D.F. Gray, Mechanical properties of thick section AF2-IDA-6 powder metal turbine rotors, in: Proceedings rapidly solidified materials, Publ. American Society for Metals, 1985, pp. 387–395.

[25] B. Ewing, F. Rizzo, C. ZurLippe, Powder metallurgy products for advanced gas turbine applications, in: Proceedings of the Second International Simposium of Superalloys Sept. 1972, Publ. TMS, Wareendale (PA), 1988, pp. BB1–BB20.

[26] B.A. Ewing, A solid-to-solid HIP-bond processing concept for the manufacture of dual-property turbine wheels for small gas turbines, in: Proceedings superalloys, Publ. American Society for Metals, 1980, pp. 169–178.

[27] R.L. Dreshfield, R.V. Miner, Application of superalloy powder metallurgy for aircraft engines, in: Proceedings of 1980 International Powder Metallurgy Conference, PM Supperalloy Technology and Applications. Publ, Washington (DC), 1980, pp. 123–141.

[28] D.J. Evans, R.D. Eng, Development of a high strength hot-isostatically-pressed disk alloy, MERL 76, in: Proceedings modern developments in powder metallurgy, vol. 14, Publ. Metal Powder Industries Federation, 1980, pp. 51–63.

[29] R.L. Athey, J.B. Moore, Development of IN100 powder metallurgy discs for advanced jet engine application, in: Proceedings of the Eighteenth Sagamore Army Materials Research Conference, Publ. Syracuse University Press, Syracuse (NY), 1972, pp. 281–301.

[30] D.R. Chang, D.D. Krueger, R.A. Sprague, Superalloy powder processing, properties and turbine disk applications, in: Proceedings of the fifth international symposium on superalloys, Publ. TMS, Wareendale (PA), 1984, pp. 245–273.

[31] G.S. Garibov, Current trends of PM superalloys discs production technology for gas turbine engines, in: Proceedings advanced in powder metallurgy and particulate materials—2001, Publ. MPIF, Princeton (NY), 2001, pp. 78–83.

[32] G.S. Garibov, R.N. Sizova, Y.A. Nozhnitski, K. MYe, L.S. Buslavski, Prospects of production of aerospace materials and techniques for their processing at the beginning of the 21 century, Technol Light Alloys 4 (2002) 106–113.

[33] J.S. Benjamin, Dispersion strengthened superalloys by mechanical alloying, Metall Trans 1 (1970) 2943–2951.

[34] C. Suryanarayana, Mechanical alloying, in: ASM handbook, vol. 7, ASM International Publishers, 1998, pp. 80–90.

[35] J. de Barbadillo, J. Fischer, Dispersion-strengthened nickel-base and iron-base alloys, in: ASM handbook, vol. 2, ASM International Publishers, 1990, pp. 722–729.

[36] P. Gilman, J.S. Benjamin, Nickel- and iron-based dispersion strengthened alloys, in: ASM handbook, vol. 7, ASM International Publishers, 1998, pp. 722–726.

[37] Inconel Alloy MA 754, Alloy Dig., ASM International, 1990 Rev. March 1990.

[38] Inconel Alloy MA 758, Alloy Dig., ASM International, 1990 Rev. May 1996.

[39] Inconel Alloy MA 6000, Alloy Dig., ASM International, 1980 Rev. July 1983.

[40] J.R. Rieken, I.E. Anderson, M.J. Kramer, Innovative powder processing of oxide dispersion strengthened (ODS) ferritic stainless steels, in: Advances in powder metallurgy & particulate materials, vol. 2, MPIF, San Diego (CA, USA), 2011, pp. 31–49.

[41] J.R. Rieken, et al., Reactive gas atomization processing for Fe-based ODS alloys, J Nucl Mater 428 (2012) 65–75.

[42] J. Roesler, E. Arzt, A new model-based creep equation for dispersion strengthened materials, Acta Metall Mater 38 (1990) 671–683.

[43] B. Reppich, On the dispersion strengthening mechanisms in ODS materials, Z Metallkd 93 (7) (2002) 605–613.

[44] J.L.L. Meyer, Advanced gas atomization production of oxide dispersion strengthened (ODS) Ni-base superalloys through process and solidification control, [Graduate thesis and dissertations]Iowa State University, Ames (Iowa, USA), 2013.

[45] R.S. Bunker, The role of materials and manufacturing technologies as enablers in gas turbine cooling for high performance engines, in: F. Dogan, N. Manjooran (Eds.), Advances in energy materials, Ceramic Transactions,, vol. 205, WILEY, Hobolken (NJ, USA), 2009, pp. 3–22.

[46] R.S. Bunker, Gas turbine cooling: moving from macro to micro cooling, in: Proceedings of ASME turbo expo 2013: turbine technical conference and exposition (GT2013,), 2013, pp. 1–17 San Antonio (Texas, USA).

[47] M.A. Alvin, et al., NETL research efforts on development and integration of advanced material systems and airfoil cooling configurations for future land-based gas turbine engines, in: Proceedings of ASME turbo expo 2014: turbine technical conference and exposition (GT2014), ASME, Düsseldorf (Germany), 2014, pp. 1–9. Available from: http://proceedings.asmedigitalcollection.asme.org/ on 04/28/2015 Terms of Use: http://asme.org/terms.

[48] M.A. Alvin, et al., Development and assessment of coatings for future power generation turbines, in: Proceedings of ASME turbo expo 2112 (GT2012), ASME, Copenhagen (Denmark), 2012, pp. 1–7. Available from: http://proceedings.asmedigitalcollection.asme.org/ (web archive link, 02 January 2016). (Accessed 2 January 2016) Terms of Use: http://www.asme.org/about-asme/terms-of-use.

[49] M.A. Alvin, et al., Extreme temperature coatings for future gas turbine engines, in: Proceedings of turbine technical conference and exposition ASME turbo expo 2013 (GT2013-94432), 2013, pp. 1–10 San Antonio (TX, USA).

[50] A.S. Kurlov, A.A. Rempel, V.I. Matrenin, A.S. Stikhin, Morphology and crystal-chemical characteristics of cobalt and nickel nanopowders prepared by thermochemical and electrolytic methods, Inorg Mater 49 (2) (2013) 153–158.

[51] S.V. Krupin, B.P. Yuriev, Reasonable solution composition of nickel powder production by electrolysis, Sov Powder Metall Met Ceram 1 (1975) 20–23.

[52] USSR Patent 1,257,120, September, 1986.

[53] I.B. Murashova, A.V. Pomosov, V.P. Artamonov, Electro precipitation of powder nickel-iron alloy, Sov Powder Metall Met Ceram 6 (1976) 1–4.

[54] T. DebRoy, et al., Additive manufacturing of metallic components—process, structure and properties, Prog Mater Sci 92 (2018) 112–224.

[55] K.S. Chan, M. Koike, R.L. Mason, T. Okabe, Fatigue life of titanium alloys fabricated by additive layer manufacturing techniques for dental implants, Metall Mater Trans A Phys Metall Mater Sci 44 (2) (2013) 1010–1022.

[56] L.E. Murr, Metallurgy of additive manufacturing: examples from electron beam melting, Addit Manuf 5 (2015) 40–53.

[57] M. Simonelli, et al., A study on the laser spatter and the oxidation reactions during selective laser melting of 316L stainless steel, Al-Si10-Mg, and Ti-6Al-4V, Metall Mater Trans A 46 (9) (2015) 3842–3851.

[58] R. Shvab, A. Leicht, E. Hryha, L. Nyberg, Characterization of the virgin and recycled nickel alloy HX powder used for selective laser melting, in: Compiled by European powder metallurgy association, (Bellstone Shrewsbury, UK) proceedings of PM 2016 world congress, 2016, pp. 1–7 Hamburg (Germany).

Chapter 22

Production of Cobalt and Cobalt-Alloy Powders

Oleg D. Neikov*, Stanislav S. Naboychenko† and Irina B. Murashova†
Frantsevich Institute for Problems of Materials Science (IPMS), Kiev, Ukraine, †Ural Federal University (UrFU), Yekaterinburg, Russia

Chapter Outline

Introduction 669
Hydrometallurgical Process 669
  Leach Autoclave Method 669
Solid-Phase Reduction 673
Atomization 674
Carbonyl Processing 676
Production of Cobalt and Cobalt-Alloy Powders by Electrolysis 678
Amalgam Techniques 681
Other Methods 681
Health and Environmental Protection Measures 683
References 684
Further Reading 684

INTRODUCTION

Like nickel, cobalt is found in the Earth's crust only in a chemically combined form, save for small deposits found in the alloys of natural meteoric iron. The free element, produced by reductive smelting, is a hard, lustrous, silver-gray metal. Currently, some cobalt is produced specifically from various metallic-lustered ores, for example cobaltite (CoAsS), but the main source of the element is as a by-product of copper and nickel mining. The copper belt in the Democratic Republic of the Congo, the Central African Republic, and Zambia yields most of the cobalt mined worldwide.

Cobalt and cobalt-alloy powders are used in the powder metallurgy (PM) industry predominantly in the production of permanent magnets, superalloys (high-temperature and creep-resistant alloys), and wear-resistant hardfacing alloys. Cobalt powder is also used as the allowing element in tool and die steels, and as a binder in cemented carbides. The cobalt-base alloys are the current materials for application in oral and orthopedic surgery. Cobalt is a significant material for the PM industry due to its capability to improve the high-temperature properties of superalloys, the cutting capability of sintered carbide and high-speed tool steels, and the toughness of high-strength steel.

In this chapter, the following methods of cobalt powder production are discussed: the hydrometallurgical technique, the reduction of oxides, atomization, carbonyl processing, the electrolytic method, the amalgam technique.

HYDROMETALLURGICAL PROCESS

The hydrometallurgical process of cobalt powder incorporates three main processing stages: chemical dissolution (leaching), solution purification, and metal recovery. Because the leaching stage is accomplished in the leach autoclaves, it is also called autoclave processing [1].

Leach Autoclave Method

The leaching autoclave process is based on the ammoniacal pressure leaching of the sulfides to produce soluble nickel and cobalt hexamine sulfate complexes. This process is described in detail in Chapter 21.

The Sherritt (Corefco) refinery in Fort Saskatchewan, Alberta, Canada, was the first successful commercialization of the hydrometallurgical process for the treatment of a nickel sulfide concentrate. This refinery commenced operation in 1954. At present, the primary feed to the Sherritt refinery is nickel and cobalt sulfides, which include 51–56 wt% Ni, 5.0–6.0 wt%

Handbook of Non-Ferrous Metal Powders. https://doi.org/10.1016/B978-0-08-100543-9.00022-1
© 2019 Elsevier Ltd. All rights reserved.

Co, 32–37 wt% S, and 1.0–1.3 wt% Zn. The first stage in the refining process is the leaching of the metal sulfides to soluble amine complexes with the simultaneous oxidation of sulfide sulfur (S^{2-}) to form a series of soluble thiosalts, including sulfate. The general equation for the ammoniacal leaching of sulfides may be represented as:

$$MS + nNH_3 + 2O_2 \rightarrow M(NH_3)_n^{2+} + SO_4^{2-}$$

where M includes nickel, cobalt, iron, copper, and zinc, and n is 2–6.

The typical conditions in the leach autoclaves are represented by the following data: temperature 363–368 K, pressure of 110–120 psig (7.7–8.4 atm), ammonia 80–100 g/L, and ammonium sulfate 150–200 g/L. Before the possibility of reducing the nickel from the leach solution as the pure metal, several solution purification steps are completed. The leach liquor is transferred to the nickel-cobalt separation plant, where cobalt is separated from the nickel as a pure crystalline cobaltic hexamine salt [2]. A flow diagram of this process is shown in Fig. 22.1. The nickel-rich solution remaining after the selective removal of cobalt is directed to the nickel plant for further solution purification processing and final nickel powder production.

Cobalt (III) hexamine sulfate, $[Co(NH_3)_6]_2(SO_4)_3$ is the basis for the separation and purification of cobalt from nickel. The initial step of this separation involves the precipitation of a cobalt-nickel hexamine salt. This precipitation is realized by the addition of ammonium sulfate and ammonia to the leach solution:

$$\left[Co(NH_3)_6\right]_2(SO_4)_3\,(aq) + 2\left[Ni(NH_3)_6\right](SO_4)\,(aq) + (NH_4)_2SO_4 \rightarrow 2(NH_4)\left[Co(NH_3)_6\right]Ni(NH_3)_6]\,(SO_4)_3\,(s)$$

FIG. 22.1 Flow diagram of the Sherritt cobalt refining process.

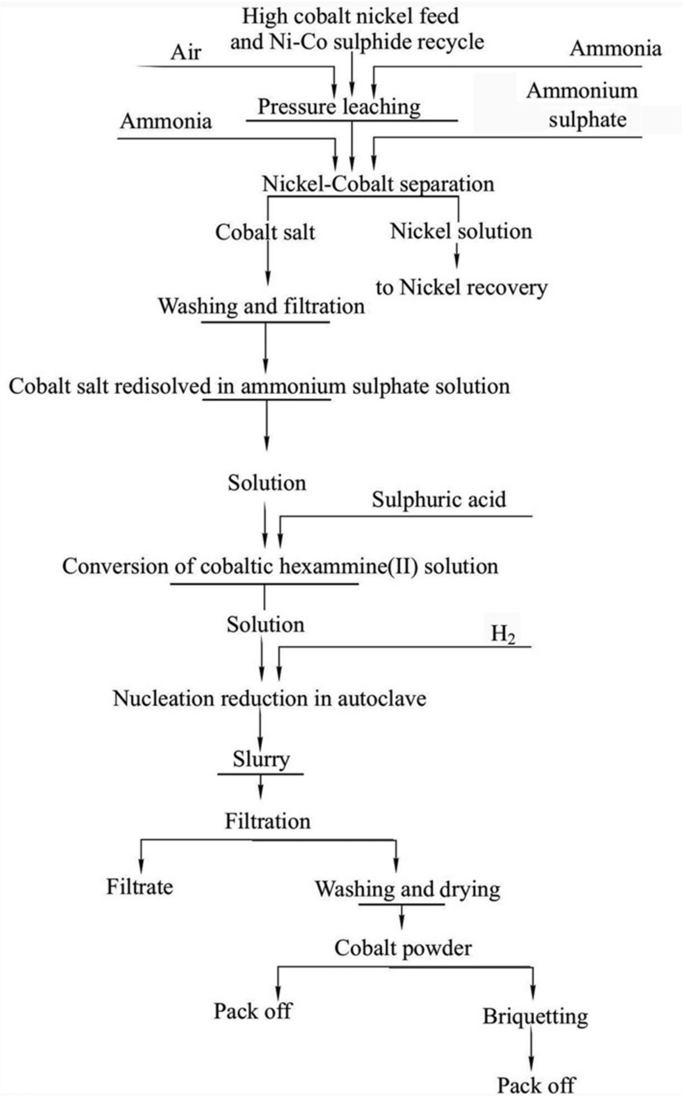
High cobalt nickel feed
and Ni-Co sulphide recycle
Air
Ammonia
Pressure leaching
Ammonia
Ammonium sulphate
Nickel-Cobalt separation
Cobalt salt
Nickel solution
to Nickel recovery
Washing and filtration
Cobalt salt redisolved in ammonium sulphate solution
Solution
Sulphuric acid
Conversion of cobaltic hexammine(II) solution
Solution
H2
Nucleation reduction in autoclave
Slurry
Filtration
Filtrate
Washing and drying
Cobalt powder
Pack off
Briquetting
Pack off

The relatively insoluble cobaltic hexamine sulfate precipitates in the cobalt-nickel salt while the more soluble nickel hexamine sulfate remains in the solution. This selective nickel removal from the cobalt-nickel hexamine salt results in the isolation of a purified cobalt salt:

$$2(\mathrm{NH_4})\left[\mathrm{Co(NH_3)_6}\right]\left[\mathrm{Ni(NH_3)_6}\right](\mathrm{SO_4})_3\,(\mathrm{s}) \leftrightarrow 2(\mathrm{NH_4})^{+}(\mathrm{aq}) + 2\left[\mathrm{Ni(NH_3)_6}\right]^{2+}(\mathrm{aq}) + 2\left[\mathrm{Co(NH_3)_6}\right]^{3+}(\mathrm{aq}) + 6(\mathrm{SO_4})^{2-}(\mathrm{aq})$$

and in the continued reaction

$$2\left[\mathrm{Co(NH_3)_6}\right]^{3+}(\mathrm{aq}) + 3(\mathrm{SO_4})^{2-}(\mathrm{aq}) \rightarrow \left[\mathrm{Co(NH_3)_6}\right]_2(\mathrm{SO_4})_3\,(\mathrm{s}).$$

The cobalt hexamine salt is then recrystallized to remove the remaining nickel contamination. After washing and filtration, the pure cobalt salt is dissolved in an ammonium sulfate solution.

A step referred to as "conversion" completes the reduction of the cobalt (III) present in the pure cobaltic hexamine solution to cobalt (II). The conversion of cobaltic hexamine to a cobaltous ammine is accomplished by the controlled addition of metallic cobalt powder, as determined by the following stoichiometry:

$$\left[\mathrm{Co(NH_3)_6}\right]_2(\mathrm{SO_4})_3 + \mathrm{Co}\,(\mathrm{powder}) \rightarrow 3\left[\mathrm{Co(NH_3)_4}\right]\mathrm{SO_4}.$$

The purpose of the reduction process is the chemical reduction of cobaltous ammine to cobalt powder. The reduction of cobalt is a batch operation that occurs in a reduction autoclave under hydrogen atmosphere at elevated pressure and temperature. Cobalt powder is produced in a cycle comprising one nucleation reduction, which refers to the hydrogen reduction process. By this process, fine cobalt seed powder is produced with the aid of a sodium sulfide/sodium cyanide catalyst. After the completion of the nucleation reduction, the solution is decanted from the seed powder, which remains in the autoclave to use as a catalyst. In the course of the cycle, the initially fine seed powder coarsens.

The purpose of the densification processing is to deposit reduced cobalt onto the seed particles until the desired powder density and particle size have been achieved. Every densification is an autoclave hydrogen reduction process, where metallic cobalt precipitates from the solution depositing on the seed powder, by the following reaction:

$$\left[\mathrm{Co(NH_3)_2}\right]\mathrm{SO_4} + \mathrm{H_2} \rightarrow \mathrm{Co}\,(\mathrm{metal}) + (\mathrm{NH_4})_2\mathrm{SO_4}.$$

The rate of the process and its completeness depend on several factors, including the ammonium sulfate concentration, the ratio of ammonia to cobalt, the hydrogen pressure, temperature, and the quantity of seed powder present. At the end of every densification, the powder is deposited, the spent solution is decanted, and the slurry is discharged from the autoclave to a flash tank, where the initial separation of cobalt powder from the end solution is accomplished. After washing the cobalt in a vacuum pan filter to remove ammonium sulfate and drying, the product is packaged as powder or compacted into briquettes and sintered. Typical properties of the Sherritt cobalt powder are shown in Table 22.1.

The kinetics of the reducing autoclave process were studied by Ratner and Dobrokhotov (Gipronickel, USSR, 1966) in the temperature (T) interval 420–520 K, hydrogen pressure $p_{\mathrm{H_2}}$ =7–45 atm, the ratio of ammonia to cobalt $\mathrm{NH_3/Co} = 3$–7, the concentration of cobalt (II), $[\mathrm{Co^{2+}}]_0 = 0.1$–0.8 mol/L, and at seed consumption 0.11–0.7 mol/L. The kinetic indexes are shown in the first-order autocatalysis equation:

$$\left[\mathrm{Co(NH_3)}_n\right]^{2+} + \mathrm{H_2} \rightarrow \mathrm{Co} + 2\mathrm{NH_4^+} + (n-2)\mathrm{NH_3}$$

$$-\frac{d[\mathrm{Co^{2+}}]}{d\tau} = K_0\frac{[\mathrm{Co^{2+}}]_\tau}{\left\{[\mathrm{Co^{2+}}]_0 - [\mathrm{Co^{2+}}]_\tau\right\}}\cdot\frac{p_{\mathrm{H_2}}}{1+0.9p_{\mathrm{H_2}}}S\cdot n\cdot 10^{-\frac{2695}{T}}$$

where τ is the time; S, $K_0 = 9.53\times10^{-2}\ \mathrm{L^{-1}\cdot mol\cdot s^{-1}\cdot cm^2}$; S is the surface of cobalt seed powder, $\mathrm{cm^2}$; n is the molar ratio of $\mathrm{NH_3}$ to Co(II), $[\mathrm{Co^{2+}}]_0$ is the initial concentration of $[\mathrm{Co^{2+}}]$, and $[\mathrm{Co^{2+}}]_\tau$ is the concentration of $\mathrm{Co^{2+}}$ at the moment τ.

The reduction mechanism is heterolytic, therefore a seed is very important and there is the possibility of the cladding of the introduced materials by cobalt as well as for making cobalt powders of a desired size, structure, apparent density, fluidity, and specific surface area. The function of the anthraquinone is not so significant; obviously, the ions Co (II) are not reduced to Co by generating anthrahydroquinone and the catalyst circle of anthraquinone functioning is broken down.

After solution treatment, a period of hydrogen induction is observed, the duration of which decreases with a decrease of the sodium sulfide consumption. Its optimal consumption for fine powder production is 0.01 M. Both the induction period and the treatment duration are decreased in the presence of sodium cyanide. As a result, more dispersed and less agglomerated particles are produced, especially in the presence of surfactant and at a high concentration of ammonium sulfate. The following parameters are operative for the nucleation stage: $T = 423$–473 K $p_{\mathrm{H_2}} = 1.5$–3.0 MPa; $(\mathrm{NH_4})_2\mathrm{SO_4} > 200$ g/L; and

TABLE 22.1 Properties of the Cobalt Powder by Hydrometallurgical Processing

		Factory, Company			
				Jedee	
Property	**Unit**	**Sherritt International Corp.**	**UMEX**	**Extrafine**	**Ultrafine**
Chemical					
Co	wt%	99.9	99.8[a]	99.9	99.9
Impurities max					
Ni	wt%	0.02	0.15	0.003	
Fe	wt%	0.005	0.001	0.005	0.005
Cu	wt%	0.005	0.0005	0.002	0.002
Ag	wt%	…	0.12	…	…
Al	wt%	…	0.0005	0.003	0.003
Na	wt%	…	0.001	0.005	0.005
Mg	wt%	…	0.0005	0.004	0.004
Mn	wt%	…	0.0005	0.002	0.002
Pb	wt%	…	0.002	0.005	0.005
S	wt%	0.03	0.006	0.005	0.005
C	wt%	0.05	0.18[b]	0.03	0.03
O_2	wt%	…	0.7[c]	…	0.50
Screen size (μm)					
+150	wt%	0–15	…		
−150+106	wt%	5–25	…		
−105+75	wt%	5–15	…		
−75+63	wt%	5–15	…		
−63+45	wt%	20−45	…		
–45	wt%	10–50	…	100	100
−38	wt%	…	99.98		
Average powder size (FSSS)	μm		0.9	1.01–1.50	0.8–1.00
Apparent density	g/cm^3	2.5–3.5	1.2	…	
Tap density	g/cm^3	…	2.5	…	

[a] *Determined by subtraction of nonorganic content from 100% (e.g. Cobalt = 100%–Ni–Cu–Ag–Fe–S).*
[b] *Carbon occurs in the form of residual organic material. 90% of the C is removed during treatment in hydrogen, vacuum, or an inert atmosphere at temperatures up to 673 K.*
[c] *Oxygen occurs in the form of residual organic material. During treatment in vacuum or inert atmosphere, up to 75% of the oxygen is removed at temperatures up to 673 K. During treatment in a hydrogen atmosphere, up to 90% of the oxygen is removed at similar temperatures.*

NH_3/Co = 2.3–2.5. From other surfactants, the compound containing 1–4 atoms of sulfur at 0.001–0.004 mol of S^{2-} per 1.0 L is of interest.

The main method of powder property variation is to increase the number of densification cycles. The rate of the densification reduction increases with increasing temperature, hydrogen pressure, and seed consumption. Addition of surfactant makes it possible to influence the particle grain size and produce monodisperse powders. However, they are a possible source of powder contamination by carbon and sulfur.

TABLE 22.2 Properties of Composite Powders on the Base of Metal Carbides (Seed Size is 44 μm)

Metal	Part of Coating (%)	Content (%)		Average Size (μm)	Bulk Density (g/cm^3)
		Co	S		
W	81.3	18.6	0.01	14.8	…
Mo	77.9	20.0	0.035	6	1.56
Ti	78.0	19.5	0.09	3.8	1.23
Cr	80.7	18.4	0.046	7.0	2.0

During the period from 1968 to 1982, Outokumpu (Finland) was producing through the leaching autoclave method up to 1500 t of cobalt powder per year from secondary raw materials, pyrite concentrate, and semifinished products. The typical conditions in the leach autoclaves were the following: temperature of 450 K and a total pressure of 4.0 MPa. The content of metallic cobalt in the powder produced was 99.8 wt% min.

In 1983, the Impala Platinum Company (Springs, South Africa) built a cobalt powder workshop on the basis of copper-nickel converter matte processing. Double sulfate ammonia salt $MSO_4(NH_4)_2SO_4\,6H_2O$ was precipitated from the solution after the autoclave extraction of nickel contained 1–3.0 g/L Ni; 0.5–1.0 g/L Co; 400–500 g/L $(NH_4)_2SO_4$. The composition of this salt includes 3.7 wt% Co, 11.2 wt% Ni, 0.025 wt% Fe, 0.004 wt% Cu, 0.015 wt% Mn; 60 wt% $(NH_4)_2SO_4$. It was dissolved in recycled ammonia solution, purified, and the ratio of ammonia to cobalt adjusted to $2.3-2.5$. The solution entering the cobalt precipitation contains 30 g/L Co, 500 g/L $(NH_4)_2SO_4$, 20 g/L NH_3; max 5 mg/L Ni, 3 mg/L Fe, 1.0 mg/L Cu; 1.0 mg/L Mn. The residual cobalt content in the solution after precipitation is 1–2 g/L.

The use of carbon monoxide as a reducer gas and the treatment of hydroxide suspensions and organic media by hydrogen have been investigated.

$$3\left[Co(NH_3)_6\right]^{2+} + 15CO + 6H_2O \rightarrow \left[Co(NH_3)_6\right]\left[Co(CO)_6\right]_2 + 3(NH_4)_2CO_3 + 6NH_4^+$$

Dobrokhotov (1962) showed the possibility of producing cobalt powder by processing cobalt (II) hydroxide pulp with a content of solid matter 2–3 wt% at 390–420 K, p_{H_2} =2.5–3.0 MPa; in 1 h, powder containing 99.7 wt% Co was produced.

Ultrafine powders (with particles less than 1 μm) are produced by the autoclave method due to the prevention of particle growth. For this purpose, the ammonium sulfate concentration is increased. The initial solution contains a sediment of basic cobalt sulfate as a seed, then the silver sulfate (catalyst) is added as well as an organic surfactant to prevent particle agglomeration. The composition of the powder produced is the following: 0.15 wt% C, 0.75 wt% O_2, 0.006 wt% S, 0.17 wt% Ni, and 0.15 wt% Ag. Apparent density is 1.1–1.6 g/cm^3. Specific surface area is 2.0–3.0 m^2/g. Such powder is used in the production of magnetic compounds and as a bond in solid alloy production based on carbides of high melting point metals and diamonds.

Properties of composite powders based on autoclave cobalt coating of different metal seed types are presented in Table 22.2.

SOLID-PHASE REDUCTION

One of the main applications of cobalt powder is its use as a binder in the production of hardmetals (tungsten carbides). The greater part of this powder is produced by the reduction of cobalt oxide with hydrogen at relatively low temperatures, generally below 1073 K, to obtain the necessary degree of powder fineness. At low reduction temperatures (523–653 K), pyrophorus powder is produced; this property disappears at temperatures above 973 K. To prevent powder from oxidation, it is cooled to 333–343 K in an inert or reducing atmosphere.

The reduction of cobalt salts to metal may be represented as follows:

$$Co(Hal_2) + H_2 \xrightarrow{623-673K} Co + 2H(Hal)$$

$$CoC_2O_4 + 2H_2 \xrightarrow{1023K} Co + 2CO + 2H_2O$$

$$\mathrm{Co(HCOO)_2 + H_2 \xrightarrow{973K} Co + 2CO + 2H_2O}$$

$$\mathrm{[Co(NH_3)_5]Cl_3 + 1.5H_2 \xrightarrow{973K} Co + 3NH_4Cl + 2NH_3}$$

where Hal is a halide anion.

In the work [3], cobalt powder was made through a single-step reduction of cobalt carbonate under a hydrogen atmosphere. SEM microphotographs of this powder (Fig. 22.2) show that the particles in the 0.5–1.0 μm size prevail along with smaller particles up to 100 nm. Particle shape is elongated with a length-to-thickness ratio of about 2 to 1 and their surface looks smoothed (Fig. 22.2A). At a magnification of 50,000 × (Fig. 22.2B), it may be seen that the particles that are 150–250 nm in length and 100 nm in thickness are the intergrowing of nanoparticles less than 100 nm in size.

Typical properties of cobalt powders produced by solid-phase reduction are shown in Table 22.3.

Cobalt powder can also be produced by the reduction of cobalt oxide with carbon, carbon monoxide, and methane [1]. However, this technology has not been commercialized. Reduction by these reagents occurs in the following way:

$$\mathrm{Co_3O_4 + 4C \xrightarrow{1203K} 6Co + 4CO_2}$$

$$\mathrm{Co_3O_4 + 4CO \xrightarrow{623-1103K} 3Co + 4CO_2}$$

$$\mathrm{Co_2O_3 + CH_4 \xrightarrow{723K} 2Co + 4CO + H_2O.}$$

The reduction temperature by carbon is 1203 K, by charcoal and carbon black 923 K, by methane 723 K, and by carbon monoxide from 623 to 1103 K. All processes are carried out in muffle electric furnaces during 1–2 h; powders are contaminated by carbon and contain cobalt carbide. In the case of metallothermic reduction of cobalt oxides, aluminum, boron, magnesium, and silicon are used at temperatures ranging from 2700 to 2900 K:

$$\mathrm{Co_nO_m + M \rightarrow nCo + MO_m}$$

$$\mathrm{3CoO + 2Al \xrightarrow{2773K} 3Co + Al_2O_3}$$

$$\mathrm{CoO + Mg \rightarrow Co + MgO.}$$

Cobalt of high purity (99.9% Co) in the form of fine scales or needles is obtained as a result of the treatment of cobalt chloride by aluminum at 903 K in molten NaCl – KCl.

ATOMIZATION

Atomized powders of cobalt-base alloys find a wide use for high-temperature applications. One of the major uses of these powders is hardfacing. This section discusses only hardfacing powders. Gas and water atomization are the most widely used methods for producing hardfacing powders.

The carbide-containing alloys and alloys containing the Laves phase are the two types of commercially effective cobalt-base hardfacing alloys. Typically, a carbide-containing alloy with a nominal composition of Co-28Cr-4W-1.1C is a eutectic alloy containing 16–17 vol% M_7C_3-type carbides in a cobalt-base matrix alloyed with chromium and tungsten. Laves phase is a kind of topologically close-packed intermetallic compound that has a hexagonal structure similar to

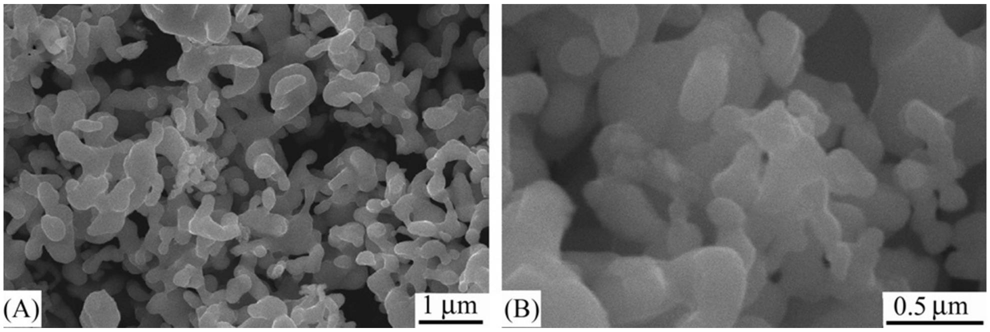

FIG. 22.2 SEM images, at (A) 10,000× and (B) 50,000× magnifications, of cobalt powder made by the solid-phase reduction process. *Source: Kurlov AS, Rempel AA, Matrenin VI, Stikhin AS. Morphology and crystal-chemical characteristics of cobalt and nickel nanopowders prepared by thermochemical and electrolytic methods. Inorg Mater 2013;49(2):153–8.*

TABLE 22.3 Typical Properties of Cobalt Powders Produced by the Solid-Phase Reduction Technique

Property	Unit	Value
Chemical		
Cobalt[a]	wt%	99.6
Impurities max		
Nickel	wt%	0.08
Iron	wt%	0.08
Silicon	wt%	0.035
Calcium	wt%	0.020
Manganese	wt%	0.020
Carbon	wt%	0.015
Zinc	wt%	0.010
Sulfur	wt%	0.008
Copper	wt%	0.001
Lead	wt%	0.003
Hydrogen loss	wt%	0.20
Screen analysis (μm)		
+150	wt%	0.01
−150+75	wt%	0.04
−75+45	wt%	0.15
−45+38	wt%	0.20
−38	wt%	99.60
Average particle size	μm	5
Apparent density	g/cm^3	1.8
Tap density	g/cm^3	3.0

[a] *Hydrogen loss not included.*

Source: Freeman G. Production of cobalt-base powders. In ASM handbook, vol. 7. ASM International Publishers; 1998. p. 179–81.

M_7C_3 carbides, but the hardness value is less than that of carbides and amounts to 1000–1200 HB [4]. Laves phase materials retain mechanical properties over a wide range of temperatures. Their main uses are for plasma spray hardfacing operations such as plasma spray coating of gas turbine blades. There are two different Laves phase-containing cobalt-base alloys available for hardfacing applications: Co-28Mo-8Cr-2Si and Co-28Mo-17Cr-3Si. These alloys contain at least 50 vol% of Laves phase.

In the microstructure of the carbide-containing alloys, the lightest colored phase is the matrix, which has a face-centered cubic (fcc) crystal structure. The dark phase is M_7C_3; the exact composition is $(Cr_{0.85}Co_{0.14}W_{0.01})_7C_3$, which has a hexagonal crystal structure. Generally, resistance to abrasive wear is imparted by the presence of carbides whereas the resistance to corrosion and/or elevated temperature hardness retention is imparted by the matrix. The matrix alloy similarly defines galling wear properties.

To minimize oxygen content, gas atomization is the most widely used technique for producing these powders. Some producers prefer vacuum melting and inert-gas atomization (typically nitrogen or argon) to air melting and air atomization. Oxygen content in these atomized powders is significantly below 1000 ppm while the nitrogen level may vary from 600 to 2000 ppm.

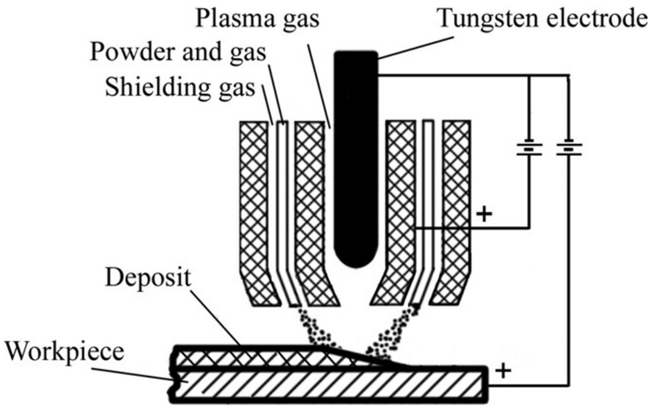

FIG. 22.3 Schematic of the plasma-transferred arc hardfacing process.

The plasma-transferred arc hardfacing process is schematically shown in Fig. 22.3. It is a welding process in which the powder is introduced into a combined arc/plasma stream to form a molten pool on the workpiece. The alloy is carried from a powder feeder to the plasma torch in a stream of argon gas, which forms the plasma and is directed from the torch into the arc effluent where it is melted and the fusion is bonded to the base metal. A direct current power source connecting the tungsten electrode and workpiece provides energy for the transferred arc. A second direct current power source connects the tungsten electrode and the arc-constricting orifice supports of the nontransferred arc, which adds the heat of the transferred arc and serves as a pilot arc to initiate the transferred arc.

Powder used for plasma-transferred arc hardfacing process generally [5] ranges from about 150 to 45 μm in size. Coarser powders can be also used because the transferred arc easily melts such powder. Deposits ranging from 0.64 to 3.2 mm thick can be produced rapidly in a single pass.

The composition and hardness of several typical alloys are presented in Table 22.4. The alloys in the Co-Cr-W-C system retain high hardness at elevated temperatures, mostly from carbide and solid-solution strengthening rather than precipitation hardening. As shown, the alloys RCoCrC and RCoCrB are higher hardness modifications of alloy RCoCrA because of higher carbon and tungsten contents. Alloy RCoCrC contains a primary M_7C_3, a eutectic M_7C_3 plus matrix, and a secondary M_6C. Alloy RCoCrB is similar to alloy RCoCrA, but it has more M_6C and, therefore, contains interdendritic eutectic carbide (chromium and tungsten rich).

Cobalt-base hardfacing powders are unsurpassable for use in combined wear-resistant, corrosion-resistant, and high-temperature applications.

Duflos and Stohr [5] discussed the comparison of the quench rates attained in gas-atomized powders and melt-spun ribbons of Satellite 6 (27.7Cr-4.0W-1.43Si-1.22C-Bal.Co): influence on resulting microstructures. Gas atomization with nitrogen as the atomizing gas used for Satellite 6 was conventional. Cobalt-base alloys were spun to ribbon by melt spinning with a copper roller as the rotating chill substrate. The melt spinning was done in a purpose-built chamber under an inert atmosphere of pure argon or helium. The ribbon width was typically 4 mm and the thickness ranged from 27 to 40 μm depending largely on the fluid flow conditions.

A cellular structure with cell dimension of 0.1–0.2 μm is observed in a 15 μm diameter particle of the gas-atomized powder (Fig. 22.4). The quench rate of such particle sizes, according to authors' estimation [6], is about 10^5 K·s^{-1}.

The gradation of structure through the ribbon thickness at different levels within the ribbon thickness showed that the major part of the ribbon thickness (20 μm) is represented by a cellular structure (Fig. 22.5). The cell diameter, which varied slightly from the chill zone across the cellular region, was typically of the order of 0.2 μm.

A gas-atomization technology for the production of cobalt-alloy fine powders is used by the Sandvik Osprey Company [7]. The commercial powders, depending on grades (Co 212, Co 502, and Co 90), contain 20–29.0 wt% chromium, 1.0–10 wt% nickel, 2.0–15.0 wt% tungsten, 0.75–3.0 wt% iron, and 0.02–2.0 wt% carbon. The particle shape is predominately spherical. The mean particle size ranges from 6.7 to 12.0 μm.

CARBONYL PROCESSING

At present, the carbonyl method for cobalt powder production is very restricted by low capacity and the unsatisfactory quality of powder [1]. Cobalt carbonyl $Co_2(CO)_8$ is produced by the action of the carbon monoxide on the fine powder of the freshly reduced cobalt-containing materials at 423–443 K and pressure up to 20 MPa. Reductions of cobalt carbonate

TABLE 22.4 **Chemical Composition and Hardness of Typical Cobalt Hardfacing Alloys**

		AWS Designation or Trade Name					
Property	**Unit**	**RCoCrA**	**RCoCrB**	**RCoCrC**	**Alloy 21**	**Alloy 20**	**Tribaloy T-800**
Nominal composition							
C	wt%	1.1	1.4	2.5	0.25	2.5	…
Co	wt%	bal	bal	bal	bal	bal	bal
Cr	wt%	28	29	30	27	32	17
Fe	wt%	3 max	3 max	3 max	2 max	…	…
Mo	wt%	1 max	1 max	1 max	5.5	…	…
Mn	wt%	1 max	1 max	1 max	1 max	…	…
Ni	wt%	3 max	3 max	3 max	2.8	…	…
Si	wt%	1	1.4	1	2 max	17	3
W	wt%	4	8	4	…		…
Nominal microhardness							
DPH	DPH	424	471	577	255	653	653
HRC	HRC	39–42	40–48	52–54	24–27	53–55	54–64
Approximate hardness of microconstituents							
Matrix	DPH	370	420	510	250	540	800[a]
Particles							
Alloy type		Eutectic	Eutectic	M_7C_3	Eutectic	M_7C_3 M_6C	Laves phase
Hard particles	DPH	900[b]	900[b]	900[b]	900	1700	1100

[a] *Matrix and Laves phase eutectic.*
[b] *Matrix and M_7C_3 eutectic.*

Source: Cabot Corp. AWS–American Welding Society.

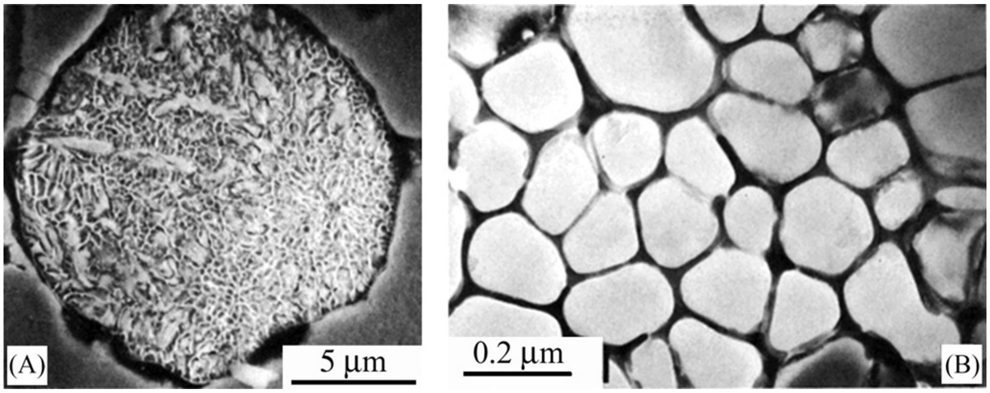

FIG. 22.4 Cellular structure observed in a 15 μm diameter gas atomized powder particle: (A) scanning electron micrograph on a polished section; (B) transmission electron micrograph on a thin foil. *From Duflos F, Stohr JF. Comparison of the quench rates attained in gas-atomized powders and melt-spun ribbons of co- and Ni-base superalloys: influence on resulting microstructures. J Mater Sci 1982;17(12):3641–52.*

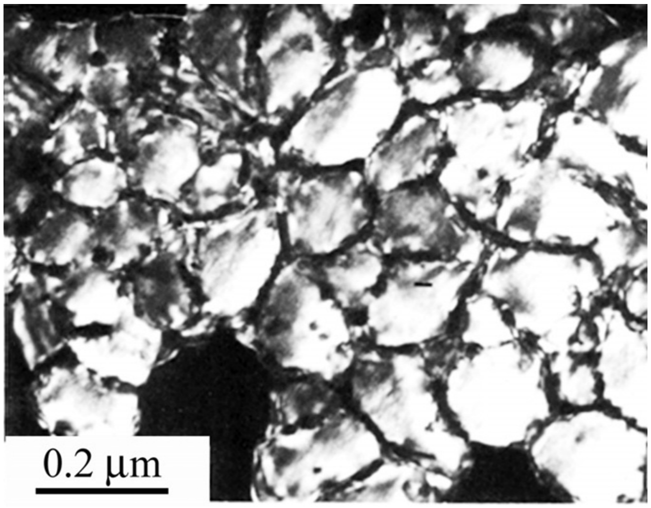

FIG. 22.5 Transmission electron microscopy in a Stellite 6 (27.7 Cr-4.0 W-1.43Si-1.22C-Bal.Co) ribbon section. *From Duflos F, Stohr JF. Comparison of the quench rates attained in gas-atomized powders and melt-spun ribbons of co- and Ni-base superalloys: influence on resulting microstructures. J Mater Sci 1982;17(12):3641–52.*

in benzene or hexane and synthesis from halide salts in the presence of metallic reducing agents are used. The joint synthesis of nickel and cobalt carbonyls from nickel-cobalt raw material followed by their separation is possible.

Fine black cobalt powder is produced by carbonyl decomposition in a current of carbon monoxide at 423–523 K with subsequent thermal treatment in a hydrogen atmosphere at temperatures ranging from 620 to 1200 K. Passivated fine powder containing approximately 99.99 wt% cobalt and 0.01 wt% carbon is produced by the decomposition of cobalt carbonyl in an inert organic solvent (decalin, silicone and vaseline oil, glycerol, etc.). Organic fluid prevents the contact of the colloid particles formed with air as well as their agglomeration. A protective film that prevents oxidation and powder inflammability is formed due to liquid adsorption on the metallic particle surface.

PRODUCTION OF COBALT AND COBALT-ALLOY POWDERS BY ELECTROLYSIS

Powder is produced from sulfate electrolyte at pH = 5.5–6.0 using soluble cobalt anodes (Fig. 22.6) [1]. Cobalt current efficiency is low (60%) due to low overvoltage of hydrogen on cobalt. A high value of pH solution is necessary to keep cobalt current efficiency above level. Equilibrium material balance in the electrolyzer is regulated by the pH value. The boric acid is introduced as a buffer addition agent. The cathode current efficiency is lower than the anode one so that cobalt concentration in the solution is increased with time. The electrolyte is diluted by condensate to maintain a given concentration of the electrolyte. In the case of solution depletion, the metal dissolution procedure is intensified by the addition of concentrated sulfuric acid.

The anodes are cast from electrolytic cobalt. Sulfate electrolyte is circulated through the electrolyzer in a closed system, including the heat exchanger supporting required temperature in the cells. Electrolysis is kept at current density ranges from 1800 to 2500 A/m^2 and temperature 333–343 K during about 2–3 h. Powder is precipitated on titanium disc cathodes and then a strippable deposit is gravitated on the tank bottom. The suspended solid is transferred to the settler after the accomplished electrolysis. The clarified electrolyte is returned for electrolysis after filtration while powder is treated by acid solution to wash out hydroxides; it is then washed with distilled water. Powder is dried at 673–683 K during about 3–4 h and reduced at 1173–1233 K during 10 h in a hydrogen atmosphere. After cooling of the vessel with powder in n air environment about 2–3 h and then in s cell with running water (3 h), the powder is milled in ball mills and screened.

The electrolyte is prepared by anode dissolution of cobalt in sulfuric acid solution (at concentrations in the range from 30 to 35 kg/m^3) at a current density of 250–300 A/m^2. Electrolysis is stopped when cobalt concentration has increased up to 18–20 kg/m^3, the solution is diluted down to 6–8 kg/m^3 of Co, then the pH of the solution is adjusted up to 5.5–6.0 by means of soda and boric acid is introduced as a buffer addition agent (5–10 kg/m^3).

Properties of the electrolytic cobalt powder are as follows:

- Chemical composition includes 99.25 wt% Co, max 0.4 wt% Ni, max 0.04 wt% Cu, max 0.2 wt% Fe, max 0.025 wt% S, max 0.02 wt% C, and max 0.1 wt% Cr.
- Granulometric composition consists of the particles max 4 wt% above 71 μm, min 30 wt% (–71 +45) μm, and min 66 wt% below 45 μm**.**

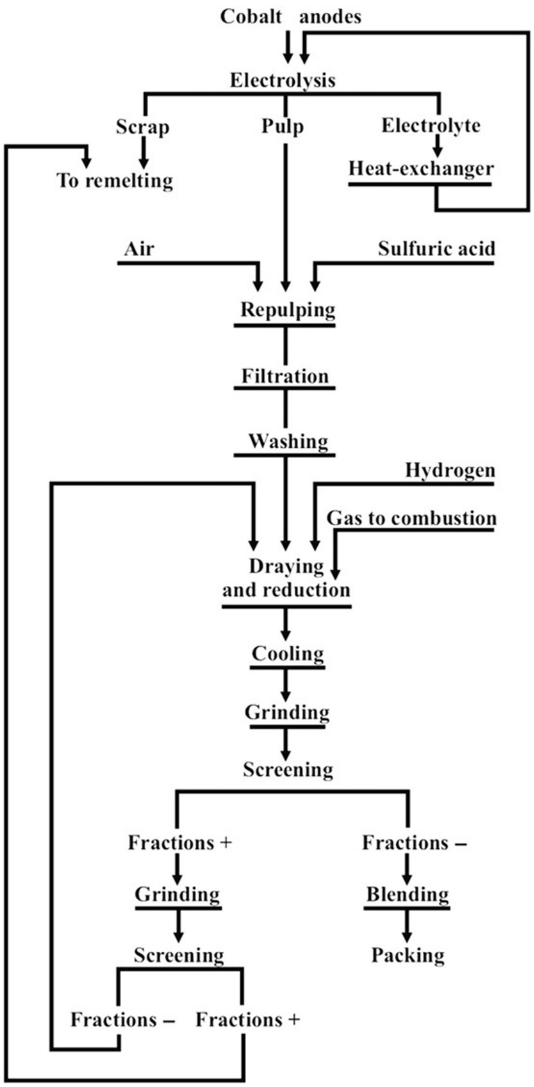
Cobalt
anodes
Electrolysis
Scrap
Pulp
Electrolyte
To remelting
Heat-exchanger
Air
Sulfuric acid
Repulping
Filtration
Washing
Hydrogen
Gas to combustion
Draying
and reduction
Cooling
Grinding
Screening
Fractions +
Fractions –
Grinding
Blending
Screening
Packing
Fractions –
Fractions +

FIG. 22.6 Flowsheet of cobalt powder production by electrolytic processes.

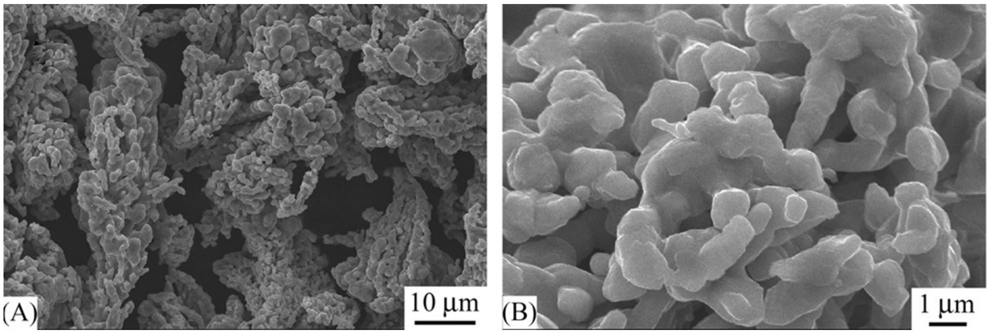

FIG. 22.7 SEM images of the electrolytically prepared cobalt powder.

SEM micrographs of the electrolytic cobalt powder prepared by electrochemical precipitation from an aqueous solution of cobalt and ammonium sulfates [3] showed that its particles were 2–5 μm in length and about 1 μm in thickness and formed a branched dendritic structure (Fig. 22.7A). At a magnification of 10,000 ×, the large particles are seen to be intergrowths of approximately equiaxed particles ~1 μm in size (Fig. 22.7B).

Comparison of the morphology of the cobalt powders demonstrates the following: at the microstructural level, the solid-phase reduction cobalt powder (Co_{spr}) consists of individual particles (Fig. 22.2A). In contrast, the electrolytic powder has a dendritic microstructure. At a magnification of 10,000 ×, the Co_{spr} (Fig. 22.2A) and electrolytic cobalt (Fig. 22.7A) powders are seen to be similar in particle shape, but the average particle size of the electrolytic powder is about twice that of the Co_{spr} powder. As Curlov et al. [3] discussed, a more in-depth SEM characterization of the electrolytical powder showed that its large particles, about 1 μm in size, were formed by tightly bonded nanoparticles 20–30 nm in size. Therefore, the electrolytic cobalt powder is nanostructured and has a larger specific surface area than the Co_{spr} powder. These differences in morphology suggest that the electrolytic cobalt powder is more attractive for use in the production of electrochemical power sources.

Various electrolytic techniques of cobalt and cobalt-base alloy powder production are given in Table 22.5.

TABLE 22.5 Production of Cobalt and Cobalt-Alloy Powders by Electrolysis

Method	Electrolyte Composition	Current Density (kA/m^2)	Temperature (K)	Electrolysis Parameters
Cobalt				
WS	$CoSO_4$; $(NH_4)_2\ SO_4$, Na_2SO_4, H_3BO_3;	1.0	300	Particle shapes are needle-like and fan-like dendrites
EDC	5–74 g/L Co, chloride solution, pH = 1–6	0.5–8.0	283–333	Coercive force ranges from 100 to 870 Oe; particle size ranges from 0.5 to 4 μm
EDC	23–24 g/L Co; max 25 g/L NaCl chloride solution	3.0–4.0	298	Cobalt current efficiency amounts to 85%−87%
EDC	5–74 g/L Co; chloride solution, pH = 1–6	4.5	298	$Cl^-/SO_4^{2-} = 1/5$; cobalt current efficiency amounts to 78%–85%; with increasing content of SO_4^{2-} the cobalt current efficiency decreases
SPR[a]	400 g/L NaOH	1.0	353	Raw material is Co_3O_4 or $CoCO_3 \cdot 2CuO \cdot 2H_2O$; particle size about 0.5–1 μm; electrolysis duration is minimum 4–5 times as large as t_{theory}[b] for cobalt oxide, and 7–8 times as large as t_{theory} for $CoCO_3$
Cobalt-Iron				
AM	62.4 g/L Co; 29.7 g/L Fe; HCl up to pH = 2	0.5	313	Anodes consist of 66.3 wt% Co, 33.3 wt% Fe; salts are the sulfates; after heat treatment at 462–473 K for 120–300 min: coercive force range 1700–1850 Oe; particle size is about 0.5–1.5 μm
AM	31.2 g/L Co; 59.4 g/L Fe; HCl up to pH = 2	0.5	40	Anodes consist of 33.3 wt% Co, 68.6 wt% Fe; salts are sulfates; heat treatment at 453 K during 60–240 min: coercive force range 1660–1930 Oe; particle size is 0.5–1.5 μm
Cobalt–Tungsten				
WS	21.2 g/L Co; 21.3 g/L Na_2SO_4; 5.7 g/L W; 29.0 g/L citric acid; 20.0 g/L $(NH_4)_2SO_4$; pH = 2	3.0	20–30	Co in the form of sulfate; W in the form of Na_2WO_4; cobalt current efficiency amounts to 60%–70%; cathode of Ni; $(Co/W)_{alloy} \sim (Co/W)_{solution}$ (in molar ratio); alloys up to 20% wt% W are solid solutions; particle shape is globular dendrites with size about 100 μm

[a] *Electrochemical reduction occurs in thin surface film of the dispersoids.*
[b] *Cobalt current yield in that system is low, so it is necessary to increase electrolysis duration in compared with t_{theory} – calculated in accordance with Faraday's law for known current.*
Production method: WS, aqueous solution electrolysis; EDC, electrolysis in two-layer cell; SPR, solid phase reduction; AM, amalgam metallurgy method (see Chapter 8).

TABLE 22.6 Coercive Force (Oe) at 203 K of the Heat-Treated Cobalt Powder Made by the Amalgam Technique

	Duration of Heat Treatment (min)				
Temperature of Heat Treatment (K)	0	20	40	60	Note
393	530	1080	1110	1110	Without tin addition
408	570	1050	1035	1040	Without tin addition
423	530	1135	1100	1055	Without tin addition
453	565	935	858	845	Without tin addition
303	…	1060	1100	1080	With tin addition
423	…	1116	1065	1065	With tin addition

AMALGAM TECHNIQUES

Electric precipitation of cobalt (or its alloys with iron and nickel) is realized at 313 K from sulfate electrolyte with a cobalt weight-part concentration amount of 94 g/L on agitated mercury cathode in a cell with a soluble cobalt anode (or proper composition alloy) at an interelectrode space that amounts to 1 cm. Anode and cathode current densities are equal at 500 A/m^2. The required value of pH = 2 is achieved by adding hydrochloric acid. Amalgam is heat treated after electrolysis. Thus cobalt particles change their shape from dendritic to needle, or thread-like. Metals (e.g., tin) for counteraction of the particle agglomeration and improving the magnetic properties of suspension are introduced into the amalgam (Table 22.6) [1].

After heat treatment, the amalgam is concentrated by means of filtration and is exposed to orientation in a magnetic field with strength above 50 V/m. This treatment provides mechanically compact forms of hard material. The final mercury removal is accomplished by distillation and the sintered mass is reduced to fine thread-like particles. The particle size ranges from 0.5 to 1.5 μm with the fiber stem diameter around 0.02 μm.

OTHER METHODS

The ultrafine powder is obtained by the reduction of cobalt formate in a vaseline medium (at temperature range 473–513 K during 1 h). This powder is separated by centrifuge, washed by solvent (toluene), and dried. The particle size of the powder ranges from 0.5 to 1.0 μm and the shape is close to spherical by using an ultrasonic field at a frequency about 44 kHz and an intensity of 750 kW/m^2. This method makes it possible to cover the cobalt particle surface by copper or silver films. For this purpose, the cobalt formate is mixed with glycerol, the silver or copper salts (e.g., nitrates, ammoniates) soluble in the organic phase are added, and the mixture is heated to 423–463 K. Cobalt powder with particle sizes about 0.2–0.5 μm clad with silver or copper is produced.

As powder properties are significantly dependent on the characteristics of the basic reduced solid phase, some decisions for the preparation of the basic raw material before its reduction are proposed [1]. Thus, ammonia salts of cobalt:

- Are evaporated at 353–373 K to obtain the dry salts.
- Are injected into the chamber at temperature 1173–1473 K to produce cobalt (III) oxide.
- Are treated by a sodium hydroxide solution that results in a precipitate of hydrated cobalt (II) oxide.
- Are treated by carbon dioxide at pressure $p_{CO_2} = 0.15–0.5$ MPa, a temperature up to 370 K, and a sediment of alkaline cobalt carbonate is precipitated.

Further, the solid phase obtained is washed, dried, and regrounded. The intermediate product is reduced in a hydrogen current at 670–900 K, and an ultrafine cobalt powder is obtained.

In the case, when cobalt is precipitated from solution in the form of oxalate, the sediment is treated by a sodium hydroxide solution. Prepared cobalt (II) hydroxide is either washed, dried, and reduced in hydrogen, or it is treated by hydrazine at 380 ± 5 K and pH = 9.0, or it is calcined and 0.2–2 wt% of tungsten carbide powder is added to the cobalt oxide to prevent powder sintering during reduction by hydrogen at 970–1020 K.

The ultrasonic spray pyrolysis (USP) is a versatile technique for producing various materials in a wide range of composition, size, and morphology [8,9]. Suh and Suslick [10] applied the USP technique to synthesize silica-encapsulated metal nanoparticles. Cobalt nanoparticles were produced by the hydrogen reduction of cobalt chloride in a multistage

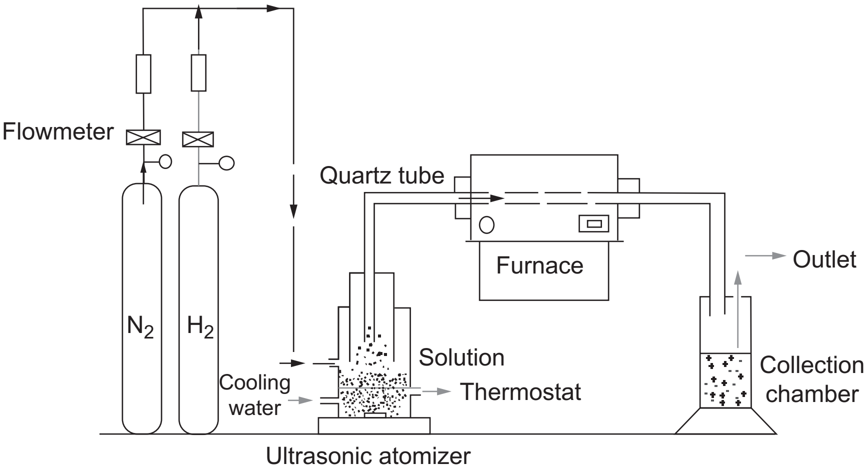

FIG. 22.8 Schematic of the laboratory installation for cobalt nanopowder synthesis.

tubular aerosol flow reactor by Jang et al. [11]. Reaction zone temperature, preheating temperature, the mole fraction of $CoCl_2$ and H_2, and residence time were considered as key process variables for the control of particle size and size distribution. Ranging from 50 to 78 nm in average diameter, cobalt nanoparticles with narrow size distribution were synthesized throughout the above-mentioned experiments.

Spherical cobalt powders were made by USP of cobalt nitrate aqueous solutions followed by thermal decomposition of generated aerosols in a hydrogen atmosphere [12]. The reaction for the formation of cobalt metal from cobalt nitrate can be described as

$$Co(NO_3)_2 + 2H_2 \rightarrow Co + 2NO_2 + 2H_2O.$$

Fig. 22.8 shows the schematic of the laboratory installation for cobalt nanopowder synthesis. A purified leach solution prepared from cemented tungsten carbide scrap using nitric acid was utilized as the starting material [13]. The hydrogen reduction was done at 973–1173 K starting from cobalt nitrate solutions with concentrations of 0.08 mol Co/L and 0.04 mol Co/L. A cobalt nitrate aerosol of about 4 μm was obtained in an ultrasonic atomizer with a frequency of 800 kHz. The liquid feed rate amounted to between 12 and 14 mL per hour. The aerosol was transported by H_2-carrier/reduction gas to an electrical heated furnace. Under spray pyrolysis conditions in a hydrogen atmosphere and at a flow rate of 1 L/min, the dynamic (continuous) reduction took place in the quartz tube reactor during about 1.0 s.

The recovery of cobalt powder and tungsten carbide from a cemented carbide scrap SEM micrograph of the synthesized cobalt powders at 1073 K by cobalt nitrate solution of 0.08 M Co/L is shown in Fig. 22.9. The cobalt powder particles are almost spherical with an uneven surface; some agglomeration of particles is particularly present.

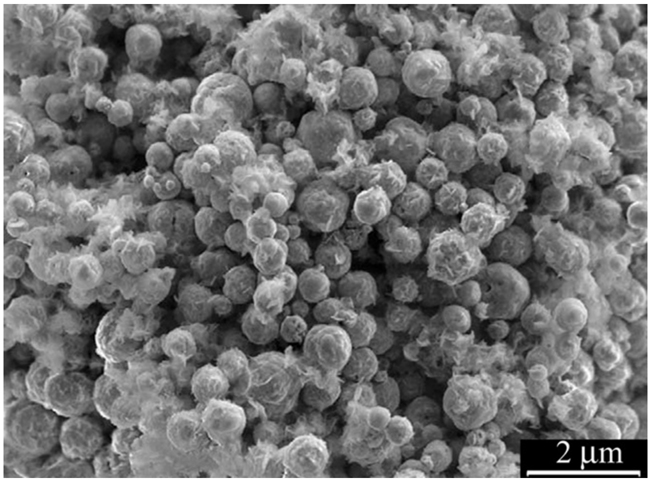

FIG. 22.9 SEM micrograph of the synthesized cobalt powders at 1073 K by a cobalt nitrate solution of 0.08 M Co/L. *From Sebahattin G, Srećko S, Bernd F. Synthesis of nanosized spherical cobalt powder by ultrasonic spray pyrolysis. Mater Res Bull 2006;41(10):1882–90.*

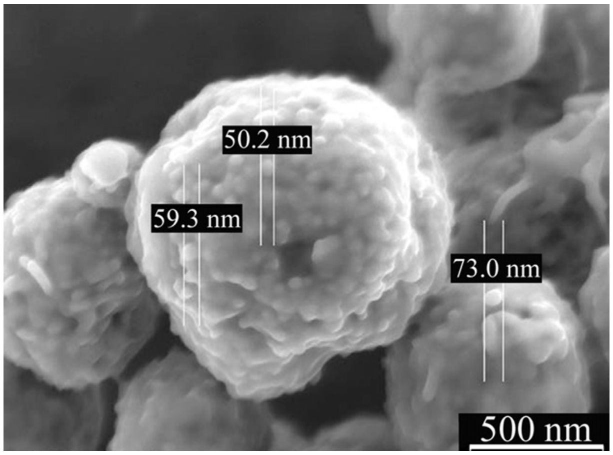

FIG. 22.10 SEM micrograph of ultrasonic spray pyrolysis cobalt powder obtained at 973 K with a precursor cobalt concentration of 0.08 mol/L (magnification 50,000×). *From Sebahattin G, Srečko S, Bernd F. Synthesis of nanosized spherical cobalt powder by ultrasonic spray pyrolysis. Mater Res Bull 2006;41(10):1882–90.*

The authors [12] discussed that, under the same conditions, the reduced concentration of cobalt in the precursor solution decreases the particle size and uniformity of the powder. The increase in the number of larger particles with cobalt concentration appears to indicate that they are produced by the coagulation, surface reaction, and sintering. However, smaller particles that seemed to be grown by the coagulation and surface reaction are observed at low cobalt concentrations. In difference to nonagglomerated particles by ultrasonic spray pyrolysis nanosized primary particles prepared in the gas phase [9] form aggregates because of interactive forces between particles. Such aggregates change into large particles when the temperature in the gas phase is high enough to sinter the aggregates. Thus, uniform nanoparticles can be produced by spray pyrolysis at proper conditions using uniform drops of precursor salts with low vapor pressure. Fig. 22.10 presents a scaled SEM picture of particles received from 973 K, 0.08 mol/L cobalt nitrate solution by USP. The particles between 50 and 73 nm seen in Fig. 22.10 constitute one big spherical particle of cobalt powder.

Mechanical alloying for the cobalt-alloy powder production of high-entropy alloys (HEAs) is predominantly used [14,15]. In recent times, high-entropy alloys (HEAs) have been the topic of extensive research as these materials are promising candidates for many challenging applications, including tools, molds, and functional coatings. Exceptional properties such as elevated temperature strength, corrosion, and wear resistance result from the unique microstructure [16].

Eißmann et al. [17] reported that the high-entropy alloy CoCrFeMnNi was produced by argon gas atomization. The resulting spherical powder with nearly ideal equimolar composition was subsequently divided. Selected powder fractions were then compacted by two different methods: spark plasma sintering and pressureless sintering. After spark plasma, sintering dense and homogeneous samples are obtained. No change in composition compared to the initial powder could be detected. The sample showed a single-phase microstructure with fcc structure. The density was up to 98% of theoretical value. Pressureless sintering led to samples with a maximum density of 87% for the finest fraction. The achieved hardness of the spark plasma sintering samples was approximately 169 HV and the elastic modulus 198 GPa. The tensile strength ranges from 571 MPa to 613 MPa and the elongation from 27% to 37%, depending on the sintering temperature, while the bending strength was determined to be approximately 920 MPa and the outer fiber strain more than 30%.

HEALTH AND ENVIRONMENTAL PROTECTION MEASURES

Cobalt metal fumes and dust can affect the body if they are inhaled or if they come in contact with eyes or skin. Therefore, they cause irritation of the nose and throat. The current OSHA standard for cobalt metal fumes and dust is 0.1 mg/m^3 averaged over an eight-hour work shift. The American Conference of Governmental Industrial Hygienists has recommended a threshold limit value (TLV) for cobalt metal fumes and dust of 0.05 mg/m^3. The long-term TLVs of the powders in a workplace atmosphere under the CIS Standard (GOST 12.1.005–88) are (in mg/m^3) for: Ni, 0.05; Co, 0.5; Mo metal, 0.5; and W, 6.0.

Metal carbonyls are toxic with volatile ones such as nickel and cobalt carbonyl being particularly dangerous. Nickel carbonyl is a carcinogen as well as being flammable and reactive. Details of nickel carbonyl dangers and measures for health and environmental protection are considered in Chapter 6.

Dicobalt octacarbonyl, $Co_2(CO)_8$, is especially dangerous in cobalt carbonyl processing. The major health hazards include a potentially fatality if inhaled, allergic reactions, decreased pulmonary function, and dyspnea.

The TLVs of the carbonyls in the workplace atmosphere under the CIS Standard (GOST 12.1.005–88) are (in mg/m^3): $Ni(CO)_4$, 0.0005 (≈0.0004 ppm);$Co_2(CO)_8$, 0.01; $Mo(CO)_6$, 1.0; and $W(CO)_6$, 2.0. The admissible concentration limit of cobalt salts in drinking water is 0.01 mg/L.

Contact of cobalt dust with strong oxidizers may cause fire and explosion. Dicobalt octacarbonyl $Co_2(CO)_8$ is a noncombustible solid, but by decomposing in air, it forms flammable carbon monoxide that is emitted during decomposition.

Mercury, involved in the amalgam technique, is a toxic chemical. Mercury can affect the body if it is inhaled or if it comes in contact with eyes and skin. It may enter the body through the skin. The current OSHA legal airborne permissible limit is 0.1 mg/m^3 averaged over an eight-hour work shift whereas the National Institute for Occupational Safety and Health (NIOSH) has recommended for cobalt metal fume and dust a TLV of 0.05 mg/m^3 for 10 h of work. According to the CIS Standard (GOST 12.1.005–88), the maximum permissible concentration of mercury fumes in the workplace during an eight-hour shift and ultimate nonrecurrent are 0.01 and 0.05 mg/m^3, respectively.

Implementation of enclosed operations, local exhaust ventilation, and general ventilation must be done to meet the requirements of ensuring the workplace exposure limit. A complex of measures for health and environment protection contains personal protective equipment. Details of safety engineering in the production of powders are considered in Chapter 27.

REFERENCES

[1] Naboychenko SS, editor. Handbook of nonferrous metal powders. Moscow: Metallurgia Publishers; 1997 [in Russian].

[2] Kerfoot DGE. U.S. Patent 5,468,281; 1995.

[3] Kurlov AS, Rempel AA, Matrenin VI, Stikhin AS. Morphology and crystal-chemical characteristics of cobalt and nickel nanopowders prepared by thermochemical and electrolytic methods. Inorg Mater 2013;49(2):153–8.

[4] Powder AP, editor. Handbook of metal powders. Reinhold Publ.; 1966.

[5] Madan DS, Winter FW. Metal and metal alloy powders for welding, hardfacing, brazing, and soldering. In: ASM handbook. vol. 7, ASM International Publishers; 1988. p. 1065–82.

[6] Duflos F, Stohr JF. Comparison of the quench rates attained in gas-atomized powders and melt-spun ribbons of co- and Ni-base superalloys: influence on resulting microstructures. J Mater Sci 1982;17(12):3641–52.

[7] Sandvik Osprey Company. Cobalt alloy metal powder. https://www.materials.sandvik/en/products/metal-powder/list-of.../cobalt-alloys/ [Accessed 31 January 2018].

[8] Kodas T. United States Patent 6,316,100; 2001.

[9] Tsai SC, et al. Ultrasonic spray pyrolysis for nanoparticles synthesis. J Mater Sci 2004;39:3647–57.

[10] Suh WH, Suslick KS. J Am Chem Soc 2005;127(34):12007–10.

[11] Jang HD, et al. Mater Res Bull 2004;39:63–70.

[12] Sebahattin G, Srećko S, Bernd F. Synthesis of nanosized spherical cobalt powder by ultrasonic spray pyrolysis. Mater Res Bull 2006;41(10):1882–90.

[13] Gürmen S, Stopic S, Friedrich B. Recovery of cobalt powder and tungsten carbide from cemented carbide scrap. World Metall Erzmetall 2004;57(6):321–6.

[14] Fu WJZ, Wang W, Wang H, Zhang J, Wang Y, Zhang F. Mechanical alloying synthesis and spark plasma sintering consolidation of CoCrFeNiAl high-entropy alloy. J Alloys Compd 2014;589:61–6.

[15] Wang C, Ji W, Fu Z. Mechanical alloying and spark plasma sintering of CoCrFeNiMnAl high-entropy alloy. Adv Powder Technol 2014;25(4):1334–8.

[16] Tsai MH, Yeh JW. High-entropy alloys: a critical review. Mater Res Lett 2014;2(3):1–17.

[17] Eißmann N, et al. High-entropy alloy CoCrFeMnNi produced by powder metallurgy, In: Compiled by European Powder Metallurgy Association, Proceedings of PM 2016 world congress, Hamburg (Germany); 2016. p. 1–7.

FURTHER READING

[18] Freeman G. Production of cobalt-base powders. In: ASM handbook. vol. 7. ASM International Publishers; 1998. p. 179–81.

Chapter 23

Production of Refractory Metal Powders

Oleg D. Neikov*, Stanislav S. Naboychenko†, Irina B. Murashova† and Nicholas A. Yefimov*
*Frantsevich Institute for Problems of Materials Science (IPMS), Kiev, Ukraine, †Ural State Technical University (UPI), Yekaterinburg, Russia

Chapter Outline

Introduction 685
Production of Tungsten and Tungsten Carbide Powders 686
Tungsten Metal Powders 686
Tungsten Carbide Powders 707
Tungsten Carbide Electrical Contacts 712
Diamond Tools 714
Hardfacing 714
Cemented Carbides 717
Production of Cemented Carbide Powders 717
Cemented Carbide Compaction 719
Sintering and Secondary Operations 721
Recycling 721
Molybdenum Metal Powders 723
Production of Molybdenum Powders 723
Properties of Molybdenum and Molybdenum Alloy Powders 725
Workplace Atmospheres Safety 733
Niobium and Tantalum 734
Niobium and Niobium Alloys 734
Tantalum 742
Tantalum Carbide 744
Workplace Atmosphere Safety 747
Rhenium 747
Production of Rhenium Powder 747
Rhenium Alloys 750
Applications 750
References 751

INTRODUCTION

Tungsten, molybdenum, niobium, tantalum, and rhenium, classified as the refractory metals, are distinguished by several general characteristics, including high melting point, high density, and superior resistance to wear and corrosion. With the exception of two of the platinum-group metals, osmium and iridium, they have the highest melting temperatures and lowest vapor pressures of all metals. Tungsten has a melting point of 3683 K, the highest of all metals, and has a density more than twice that of iron. However, they are also subject to heavy oxidation above 773 K, and they must be protected for service at elevated temperatures using coatings or non-oxidizing atmospheres. These metals have body-centered cubic crystal structures (except for rhenium, whose crystal form is hexagonal).

Powder metallurgy is the only production route for commercial tungsten, rhenium, and their alloys, because melting technology is costly and results in a coarse-grained microstructure, which negatively affects both further processing and the properties of the final product. Selection of a specific refractory metal alloy is often based on fabricability rather than strength or corrosion resistance. Special attention must be taken during the processing and use of refractory metals because of their ductile-to-brittle transition temperatures (DBTTs) and their reactions with gases [1].

Niobium, tantalum, and their alloys are the most easily fabricated refractory metals. They are ductile in the pure state and have high interstitial solubility for carbon, nitrogen, oxygen, and hydrogen. Both niobium and tantalum adsorb hydrogen and form hydrides at moderate temperatures. Niobium and tantalum begin oxidizing at 473 K and 673 K, respectively. Below 1643 K, the oxides are non-volatile, but the ductility of the parent material is reduced because of oxygen absorption.

Molybdenum, molybdenum alloys, tungsten, and tungsten alloys have limited solubility for carbon, nitrogen, oxygen, and hydrogen. Molybdenum begins to oxidize at approximately 773 K. At temperatures above 1053 K, the eutectic temperature of MoO_2 and MoO, oxides become partly volatile, and the oxidation rate accelerates rapidly with increasing temperature.

Extrusion (or hot forging) is used for transformation the arc-cast refractory metal ingots into rounds or rectangular bars. These bars, as well as PM-sintered products, are processed into sheets, plates, foil, tubing, and rods. When the refractory

Handbook of Non-Ferrous Metal Powders. https://doi.org/10.1016/B978-0-08-100543-9.00023-3
© 2019 Elsevier Ltd. All rights reserved.

products are involved and cannot be fabricated from standard mill products, they require machining or pressing and sintering to near-net shape. Many refractory metals and alloys are available as wire. Tungsten wire, which is produced in diameters as small as 0.01 mm, is used extensively for lighting, electronic devices, and thermocouples. Tantalum wire is used widely in capacitor manufacturing and in surgical applications. Molybdenum mill product forms, such as sheets and foil, can be stamped into simple shapes. Molybdenum is also machined with ordinary tools and can be gas tungsten arc and electron beam welded or brazed.

The refractory metals are extracted from ore concentrates, transformed by processing into intermediate products, and then reduced to the metal. Except for niobium, they are produced exclusively as metal powders, which are consolidated by sintering and/or melting. The process for niobium differs only in that the metal is generally reduced by aluminothermic reduction of oxide.

PRODUCTION OF TUNGSTEN AND TUNGSTEN CARBIDE POWDERS

Tungsten was adopted in industry at the beginning of the 20th century due to its application as an alloying element in high-speed steels and as filament wire in incandescent lamps. In both applications, pure tungsten was manufactured in powder form.

At the end of the 19th century, very hard tungsten carbides, WC and W_2C, were studied by Henri Moissan [2,3]. However, for a long time, all attempts to compact tungsten carbide powders resulted in porous and brittle products. In 1922, researchers of the OSRAM study group combined the brittle tungsten carbide with a ductile metal binder. After sintering such powder mixtures, a material of both high strength and toughness was obtained. Sintered hardmetals, based on tungsten carbide bonded with cobalt, were first commercially produced by WIDIA in Germany in 1926. The global hardmetal industry is estimated to have totaled 32,250 mt in 2002 with a sales value of over $8.5 billion followed by further rises to 51,900 mt in 2006, with sales at an estimated $43 billion. Of these production quantities, around 60% is for sintered cutting tool materials used for machining all types of metallic components, for woodworking, mining tools, drilling tools used in oil exploration, etc., and the remainder is used for components such as rolls used in steel mills, metal forming dies, and structural components for severe wear resistance applications [4].

Western Europe once led the market in this sector, but its share diminished to 39% in 2006, while China's market share increased to 33%, the United States' share is at around 13%, and Japan accounts for 12%, with others at 3%.

Since 1993, the global production of tungsten, which is the main raw material used in sintered hardmetal products, has fluctuated in a narrow range between 30,000 mt and 35,000 mt. China is the predominant tungsten producer accounting for almost 85% of global output in 1999. The usages of tungsten scrap as a raw material is estimated to be as high as 30% in some countries, with the incentive to use scrap increasing as tungsten prices increase. As a result, annual global consumption of tungsten has been in the range of 40,000–50,000 t [5], and over half of the tungsten consumption is for tungsten carbide powder for hardmetal production. Along with this, important products are based on tungsten alloy powders, such as:

- Heavy metal alloys (W-Fe-Cu-Ni-Co) typically comprising 90–98 wt% tungsten
- Electrical contacts (W-Cu, W-Ag)
- Ductile tungsten, including lamp filaments.

Tungsten, as an alloying element for steels and superalloys, is predominantly used as ferro-tungsten, or as melting base alloys, which are prepared from either ore concentrates or tungsten-bearing scrap. An insignificant part of the tungsten consumption is used in the form of various chemical products, such as catalysts, pigments, solid lubricants, and heavy liquids.

Tungsten Metal Powders

Production of Tungsten Powder by Hydrogen Reduction

Feed to Process: Industrial raw materials to process tungsten-bearing minerals are wolframite ([Mn, Fe]WO_4), scheelite ($CaWO_4$), ferberite ($FeWO_4$), and hübnerite ($MnWO_4$). The lower limit of workable tungsten concentration ranges from 0.1 to 0.3 wt% WO_3. Concentrations of >2 wt% are infrequent. The average WO_3 content is usually about 0.5 wt% [6,7]. Recently, Wolfram Bergbau and Hütten GmbH (WBH) in Austria, a world-leading producer of tungsten oxide, tungsten metal, and tungsten carbide, mined about 400,000 t of scheelite ore, with a 536,306 t peak in 1986, with an average WO_3 content of 0.55 wt% [8]. Depending on the mineral type, different techniques, such as gravity methods and flotation, are used to concentrate the ore to reduced WO_3 contents of about 40–60 wt%. Tungsten-bearing scrap, which usually has a high tungsten content, is a considerable alternative tungsten source to the natural mineral resources.

Process: The main process steps from concentrates or scrap through the formation of high purity ammonium paratungstate (APT: $(NH_4)_{10}$ $(H_2W_{12}O_{42})\cdot 2H_2O$) intermediate to tungsten metal powder [6] are shown schematically in Fig. 23.1.

In the dissolution step, the tungsten-bearing feed materials (wolframite concentrate and oxidized tungsten scrap) are treated with NaOH, or scheelite concentrate is treated with Na_2CO_3 to form water-soluble sodium tungstate $NaWO_4$.

The purification steps include:

- Removal of aluminum, arsenic, fluorine, phosphorus, and silicon by precipitation.
- Substitution of sodium by NH_4 forms an ammonium solution $(NH_4)_2WO_4$. This is ordinarily done by solvent extraction, which is a liquid ion exchange process, in which tungsten is extracted by means of an aliphatic amine dissolved in isodecanol and kerosene. This process is followed by re-extraction into an aqueous ammonia solution.
- Crystallization of APT by evaporation of ammonia and water. APT is the intermediate product of highest purity for metallic tungsten and tungsten carbide powder production.

The calcination step includes heating the APT to 673–1173 K, predominantly in rotary furnaces, for ammonia and water elimination. If accomplished in an excess of air, the resulting oxide is WO_3 yellow tungsten oxide. Under exclusion of oxygen, a slightly reduced, blue-colored tungsten oxide is formed ($WO_{3\text{-}x}$ tungsten blue oxide). WO_3 is the most stable α-oxide with a homogeneity range of WO_3-$WO_{2.96}$; it has three crystalline modifications: monoclinic modification stable at temperatures lower than 1000 K, tetragonal modification in the range from 1000 K to 1370 K, and cubic modification at temperatures higher than 1370 K. It sublimes noticeably at 1070–1120 K and exists in the form of polymer molecules in the vapor phase.

Reduction step with hydrogen reducer: The reduction of the oxide to metal proceeds through several intermediate oxide phases. Generally, two furnace designs for the reduction process are used industrially: a multitube pusher type and rotary furnaces. During the reduction process, the sequence in which oxides occur depends on the applied temperature and on the

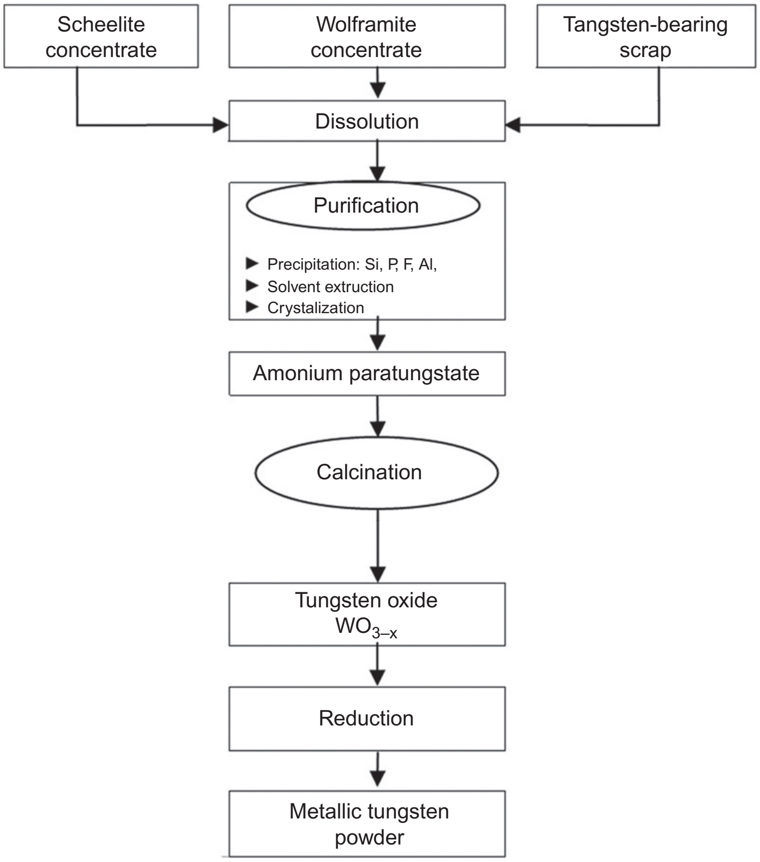

FIG. 23.1 Tungsten metal powder production flowsheet.

moisture within the powder bed, accordingly, which are static in pusher-type popular furnaces and dynamic in rotary furnaces.

Tungsten reduction by hydrogen includes four steps:

$$WO_3 + 0.1H_2 \leftrightarrow WO_{2.9} + 0.1H_2O, \quad K_{eq} = -3792.0/T + (4.8286)$$

$$WO_{2.9} + 0.18H_2 \leftrightarrow WO_{2.72} + 0.18H_2O, \quad K_{eq} = -142.5/T + 1.684$$

$$WO_{2.72} + 0.72H_2 \leftrightarrow WO_2 + 0.72H_2O, \quad K_{eq} = -801.7/T + 0.8615$$

$$WO_2 + 2H_2 \leftrightarrow W + 2H_2O, \quad K_{eq} = -2219/T$$

$$WO_3 + 3H_2 \leftrightarrow W + 3H_2O$$

The numerical value of summary equilibrium constant $K_{eq,sum}$ may be calculated as a composition of four previous equilibrium constants for preceding stages. It measures for temperature T, K

$$K_{eq.sum} = \frac{9.61 \times 10^{11}}{T^4} - \frac{1.26 \times 10^{10}}{T^3} + \frac{2.67 \times 10^7}{T^2} - \frac{1.55 \times 10^4}{T}$$

In the pusher furnace, tungsten oxide is loaded into flat metal "boats," which are pushed through the horizontal furnace tubes (Fig. 23.2). Increased demand for tungsten products made it possible for WHB Company to modernize the reaction stage by replacing the manually operated pusher furnaces by automated furnaces (Fig. 23.3). The powder layer preserves its static state throughout the whole reduction process. Typical reduction temperatures range from 873 K to 1373 K. The boats are pushed at a rate usually in the range of 5 to 30 mm/min. The hydrogen flow is commonly in the countercurrent direction. Water vapor formed during reduction is carried away by the hydrogen flow. The cooler is located on the discharge end of the tube. Electrolytic hydrogen (collected in gas holders and freed from oxygen) and steam are used. As the hydrogen supply is greatly in excess of that required for the reduction (the efficiency is not $>20\%$), the outgoing gas passes through a regeneration plant and returns to the process after drying. The boats are shifted in the direction of higher temperatures and less-damp water concentrations. Reduction rate is controlled by water vapor diffusion through the layer of WO_3 powder, and then, transformation throughout the all layer section $WO_3 \rightarrow WO_{2.9} \rightarrow WO_{2.72} \rightarrow WO_2 \rightarrow W$ is accomplished.

The pusher-type furnace is very adaptable to the manufacture of different particle size powders and can quickly be adapted to produce the desired powder properties.

By variation of reduction parameters such as temperature, powder layer depth in the boats, and boat speed, the particle size of the metallic tungsten powder can be controlled. Grain size of the WO_2 particles depends significantly on the tungsten

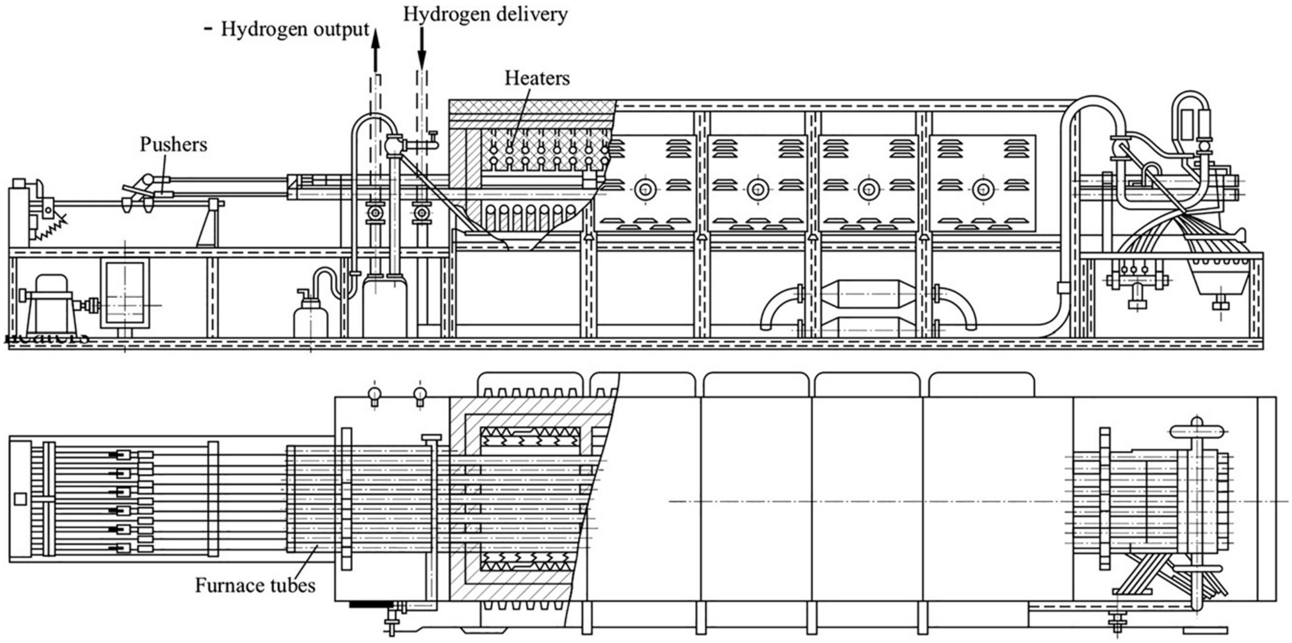

FIG. 23.2 Multitube push type furnace.

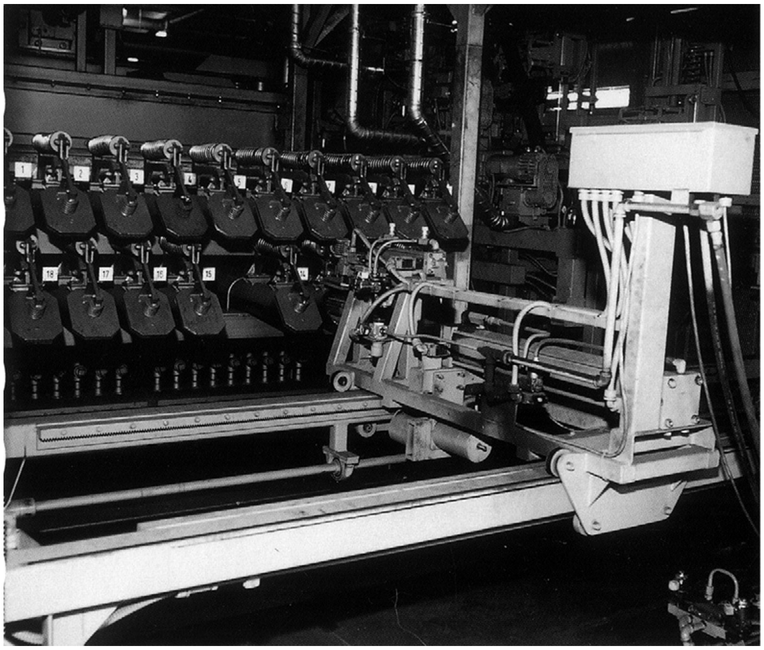

FIG. 23.3 Automatic push type furnace. *(Courtesy: Wolfram Bergbau- und Hütten-GmbH.)*

particle size. Increase of the tungsten powder particle size is encouraged by high temperature and quick temperature increase along the furnace tube, high push rate, large depth of the powder layer, low hydrogen flow rate, and its high humidity.

By using rotary furnaces, the tungsten oxide is directly introduced into the rotating furnace tube. An overall view of a rotary furnace used at the refining plant of WBH Company is shown in Fig. 23.4.

The rotating furnace tube has, as a consequence, not a static but a dynamic powder layer. The depth of the layer is influenced by the feed rate, rotational speed, incline, and lifters inside the tube. The temperature range is comparable to that of pusher-type furnaces, and the hydrogen flow direction is also usually countercurrent. With respect to changes in particle size, the rotary furnace is not as flexible as the pusher furnace. A characteristic of application is the continuous production of powders, with medium size ranging from 1 to 3 μm.

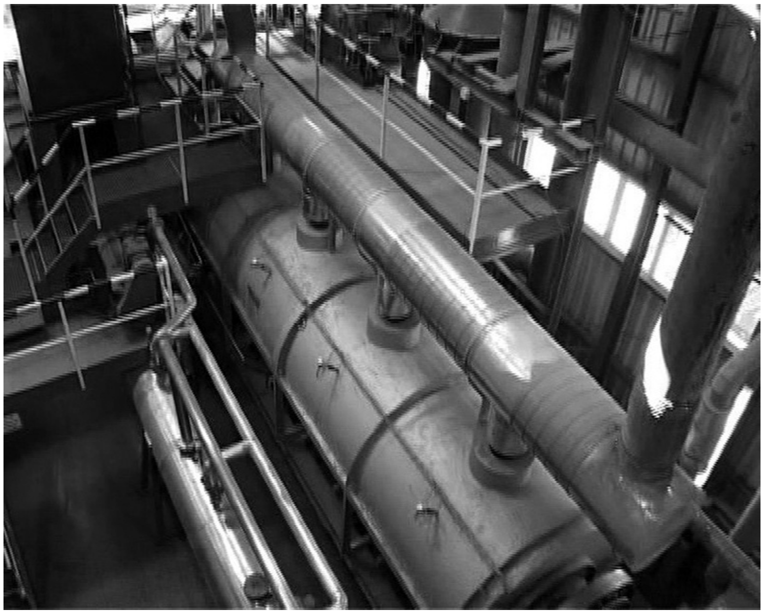

FIG. 23.4 Rotary furnace. *(Courtesy: Wolfram Bergbau- und Hütten-GmbH.)*

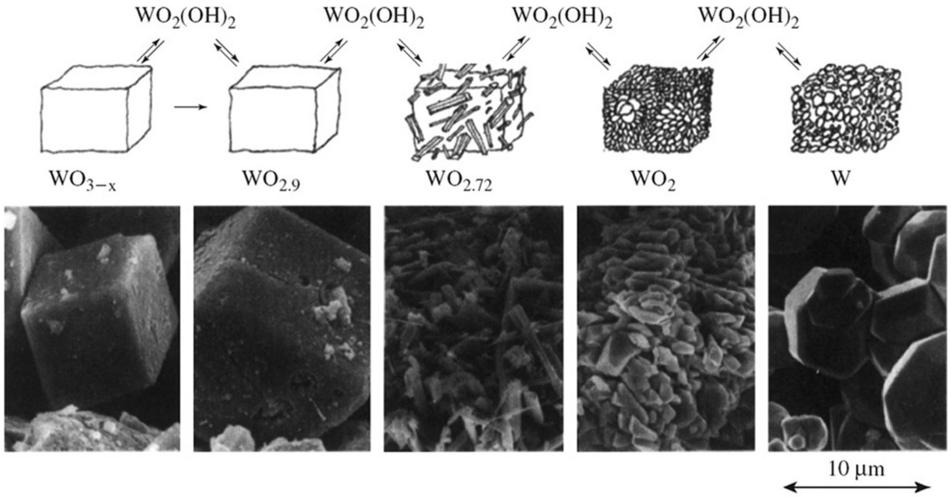

FIG. 23.5 Morphological transformations of tungsten oxides during reduction at 1273 K. *(Source: Spross M. Berg- und Huettenmaennische Montashefte. J Min Metall Mater Geotech Plant Eng 1996;141 (8):359–362.)*

The intermediate oxides differ as regards both color and morphology. The latter is illustrated in Fig. 23.5. The cause of these morphological changes is the transport of tungsten via the gas phase, that is, chemical vapor transport (CVT) during the reduction sequence. Tungstic acid, $WO_2(OH)_2$, has been identified as the most volatile compound in the system W-O-H and is responsible for the CVT. If the partial pressure ratio p_{H_2O}/p_{H_2} is low enough, the reduction from WO_2 to tungsten starts. From a thermodynamic point of view, $WO_2(OH)_2$ may form from both WO_2 and tungsten, but the equilibrium pressure is lower above tungsten, which causes the CVT of $WO_2(OH)_2$ from WO_2 to tungsten, where this vapor deposits as metallic tungsten, thus leading to growth of the tungsten crystal. The CVT mechanism permits the control of the metallic tungsten particle size through the interaction of temperature and humidity (partial pressure ratio p_{H_2O}/p_{H_2}), which is shown schematically in Fig. 23.6 for the pusher furnace [6,9,10].

Reduction by Solid Carbon

Reduction follows the relationship shown in Fig. 23.7 and can be written:

$$\begin{array}{l} WO_3 + 3CO = W + 3CO_2 \\ 3(CO_2 + C = 2CO) \\ \hline WO_3 + 3C = W + 3CO, \quad K_{eq} = P_{CO}^{-3} \end{array}$$

where K_{eq} is equilibrium constant.

Relation temperature/humidity	Process parameters in push furnace	Tungsten transport via gas phase	Tungsten deposition W powder formation $WO_2(OH)_2 + 3H_2 = W + 4\,H_2O$
Low temperature → Low humudity →	• Low temperature • High H_2 flow rate • Low oxide boatload	$WO_2(OH)_2$ → → →	Fine tungsten metal powder
High temperature → High humidity →	• High temperature • Low H_2 flow rate • High oxide boatload		Coarse tungsten metal powder

FIG. 23.6 Control of the metallic tungsten particle size in the push furnace.

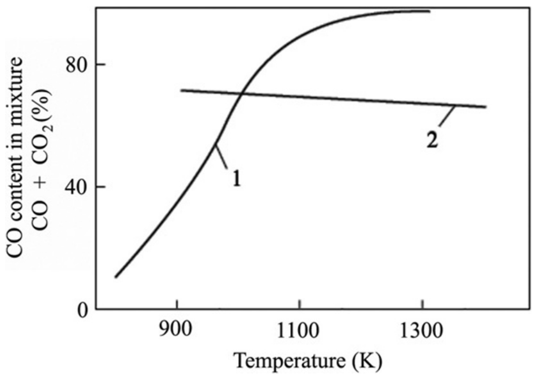

FIG. 23.7 Equilibrium compositions of gaseous mix of CO and CO_2 depending on temperatures for CO–CO_2 and CO–CO_2–WO_2–W systems. 1: C+CO_2 ↔ 2CO; 2: WO_2+2CO ↔ W+2CO_2.

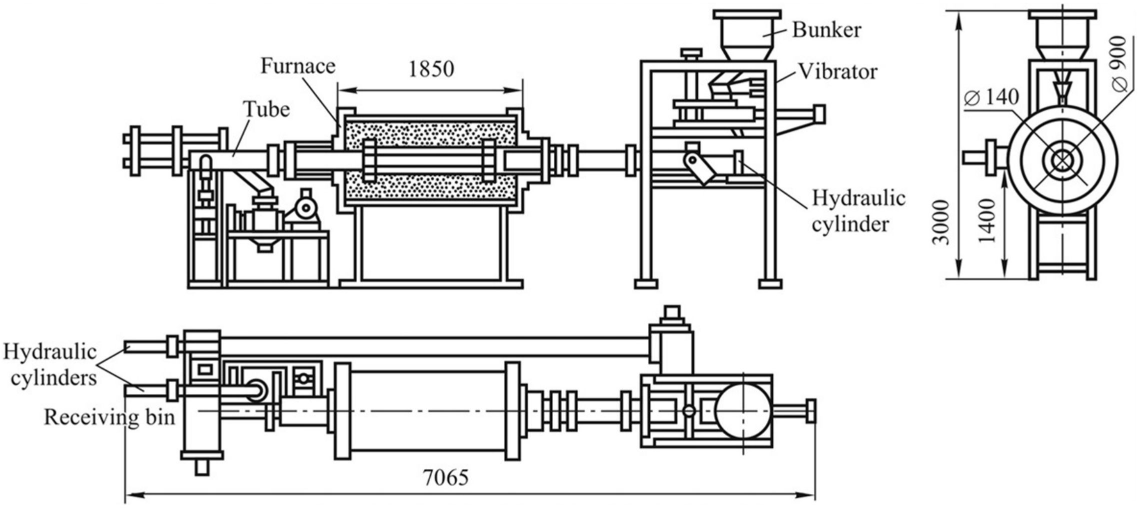

FIG. 23.8 Push type furnace for tungsten anhydride reduction by carbon.

At temperatures lower than 1000K, the oxide is not reduced because of insufficient partial pressure of CO. The temperature necessary to accelerate the process is above 1470K. Reduction is accomplished in pusher type furnaces with carbon tubes (Fig. 23.8). Maximum temperature in the furnace is 2100K; consumption power is 25kW, daily yield is 350–380kg [11].

To produce fine powders, the temperature is maintained in the range from 1670K to 1770K, the boats are moved through the high temperature zone rather faster, or some excess of black is injected. The powder produced contains inclusions of carbides and is friable. These powders are used for the production of tungsten carbide powders.

Precipitation from Gaseous Phase of Tungsten Hexafluoride and Tungsten Hexachloride

The powder is produced from gaseous substances:

- at low temperature by dissociation of tungsten hexafluoride or tungsten hexachloride in hydrogen;
- by decomposition of tungsten hexachloride in inert gas (argon or nitrogen);
- by high temperature decomposition of tungsten hexafluoride in hydrogen fluoride.

The melting point of tungsten hexafluoride is 276K, and its boiling point is 290.1K. The melting and boiling points of tungsten hexachloride are 554.5K and 623K, respectively. Reduction of tungsten hexafloride takes place according to the reaction (HHal) formation:

$$\mathrm{WHal}_x + 0.5\,x\mathrm{H}_2 = \mathrm{W} + x\mathrm{HHal},$$

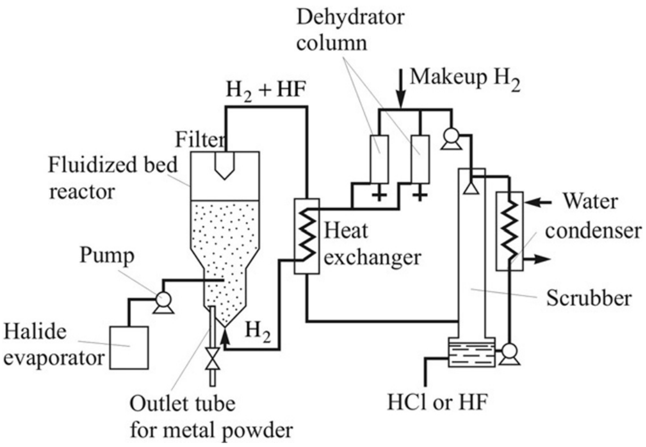

FIG. 23.9 Flow diagram of the reduction process by precipitation from gaseous phase of tungsten hexafluoride and tungsten hexachloride in fluidized bed.

$$K_{eq} = p^{x}_{\mathrm{HHal}} \Big/ \left(p^{0.5x}_{\mathrm{H_2}} p_{\mathrm{MHal}_x}\right)$$

A flow diagram of the reduction process by precipitation from the gaseous phase of tungsten hexafluoride and tungsten hexachloride is shown in Fig. 23.9. The plant consists of a halide evaporator, reactor of fluidized bed and devices for regeneration and gaseous product collection, and a porous bottom made of sintered coarse tungsten powder, replaced sometimes by a layer of tungsten small fragments (1–5 mm) or a metal grate placed in the lower part of the reactor. Tungsten halide vapor from the evaporator, together with hydrogen and argon, is supplied by pump to the lower part of the preheated reactor where, at the bottom, tungsten fine powder (20–60 μm) as seed is found. During reduction, the seed is converted into granules which are discharged periodically or continuously. The hydrogen chloride or fluoride is collected in a scrubber. After discharge of the hydrogen and argon mixture from the desiccant, the hydrogen is absorbed by heated titanium sponge, and argon is returned to the cycle. The sponge is dehydrogenated periodically, and purified hydrogen is also returned to the cycle. The temperature in the reactor influences the degree of metal precipitation. However, increasing the temperature above 1170 K leads to eventual sintering of seed particles and, as a result, to the failure of the fluidized bed.

Tungsten reduction from tungsten hexachloride is carried out at 1020–1070 K and from tungsten hexafluoride at 820–870 K. In the first case, the molar ratio of hydrogen to tungsten hexachloride in the gas-vapor mixture is maintained at approximately 30–40 to 1; while the molar ratio of hydrogen to argon is approximately 1.75 to 1; tungsten recovery amounts to 90%–99% and degree of precipitation on powder is 96%–97%. In the second case, the molar ratio of hydrogen to tungsten hexafluoride, maintained at 15–18 to 1, provides full recovery of tungsten. The gaseous flow rate must be in the range of 5–10 cm/s for fluidized bed formation.

For the production of tungsten powders with a spherical particle shape, the metal is reduced from concentrated solutions of salts, oxides, or hydroxides. Spheroidizing takes place in the high temperature zone where powder is transferred by carrier gas.

High purity tungsten nanopowders are produced from fluorine-containing compounds according to the following scheme: tungsten metal ion extraction from aqueous solutions (fluorine organic acids, ethers, amines, carbonyl acids, ketones and others), re-extraction by solutions of fluorine compounds (hydrogen fluoride, ammonium fluoride, ammonium hydrogen fluoride), and reduction of tungsten fluoride and tungsten oxyfluoride in hydrogen current. Metal powder particle size is approximately 30 nm. Similar powders are also produced by evaporation of volatile chlorides and hydrides in a reaction gas atmosphere (hydrogen, ethane, ammonia), heating being done by high-frequency induction or laser beam.

Production of Tungsten Powder by a Plasma Process

The plasma process is realized at temperatures much higher than the boiling point of the basic materials. Tungsten is produced in a vaporous state. Powder is formed by condensation, coagulation, or crystallization accompanied by polymorphous transformations. Complete reduction to tungsten is achieved by processing tungsten trioxide in an argon-hydrogen plasma (by the molar ratio of argon to hydrogen at 1 to 1) at temperatures ranging from 4270 K to 5270 K.

A two-stage scheme is used for the production of powder with a narrow range of granulometric composition (0.6–2 μm) preserving its properties by storing in air. In the first step, the tungsten trioxide is preliminarily reduced at 2270 K to a

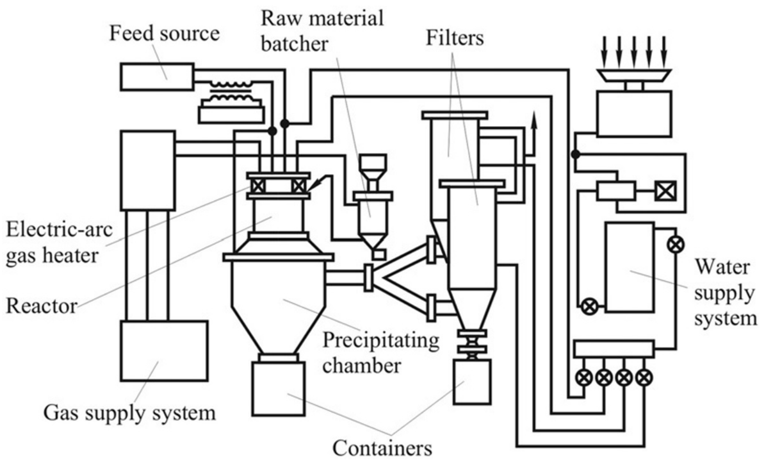
Feed source
Raw material batcher
Filters
Electric-arc gas heater
Reactor
Gas supply system
Precipitating chamber
Containers
Water supply system

FIG. 23.10 Electric arc device for tungsten and molybdenum oxides reduction by hydrogen.

residual oxygen content in the powder of 8%; in the second step, annealing at 1020–1070 K in reduction furnaces is carried out.

Plasma plant (Fig. 23.10) contains a consumable tungsten electrode inside a chamber, in which is a direct current arc (200 A, 30 V). The powder particles formed with average size about 0.05 μm are carried to a bag filter by a stream of hydrogen-argon mixture. The capacity up to 60 kg/h of tungsten powder with particle size 0.03–0.05 μm is provided for by control of jet temperature and reaction area geometry. Tungsten powder produced in compound current of arc and radio-frequency plasmas has average particle size about 10 nm and impurities content not >33 ppm Fe, 23 ppm Mo, 17 ppm Si and 280 ppm carbon.

Amalgam Method

Tungsten and molybdenum powders can be produced by reducing their pentachlorides by 2–5 wt% zinc amalgam (Fig. 23.11). The reduction reactions may be represented as follows:

$$2\mathrm{MoCI_5} + 5\mathrm{Zn(Hg)} = 2\mathrm{Mo(Hg)} + 5\mathrm{ZnC1_2} + (\mathrm{Hg})$$

$$2\mathrm{WCl_5} + 5\mathrm{Zn(Hg)} = 2\mathrm{W(Hg)} + 5\mathrm{ZnCl_2} + (\mathrm{Hg})$$

Amalgam consumption is 110%–200% of stoichiometry reactions. The process temperature is a little bit lower than the boiling point of the zinc chloride formed (591 K). After metal reduction, the temperature is increased to 623 K and maintained for 30 min for growth of the crystals. Molten zinc chloride is floated on the amalgam surface, cooled, and then a

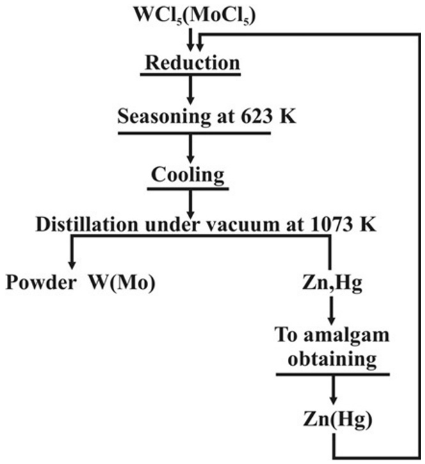
WCl5(MoCl5)
Reduction
Seasoning at 623 K
Cooling
Distillation under vacuum at 1073 K
Powder W(Mo)
Zn,Hg
To amalgam obtaining
Zn(Hg)

FIG. 23.11 Flow sheet of molybdenum and tungsten powder production by amalgam method.

solidified cake of zinc chloride is separated from the amalgam surface. Excess zinc and mercury are distilled off in a vacuum by increasing the temperature to 1073 K.

Carbonyl Technique

Tungsten and molybdenum carbonyl powders are produced by carbon monoxide action on their compounds (salts) at high pressures and elevated temperatures with metal carbonyl formation, and subsequently, its thermal decomposition with emission of dispersed metal. This process has been developed on enlarged laboratory and semi-industrial scales.

Synthesis of carbonyls is done in liquid media. Fig. 23.12 shows a flow diagram of this process. The basic materials for this process are the following: higher metal chlorides ($MoCI_5$ and WCl_6), produced from ore concentrates, zinc powder as reducer, and dichlorethane or ether as solvent. After solvent cleaning, basic materials are fed into an autoclave in the following sequence: dichlorethane, metal chloride, zinc, and ether. For tungsten carbonyl production, the reaction components are charged in a weight ratio of tungsten hexachloride to zinc powder of 1 to 0.667 and volumetrical ratio of tungsten hexachloride to ether of 1 to 25. The process is carried out at 320–350 K and under 4–6 MPa of carbon monoxide pressure.

On completion of the synthesis, carbon monoxide is removed from the autoclave, and the reaction mass is taken to the still where first, the solvents are distilled off, and then, carbonyl is evaporated off by live steam. Solvents then go to a regeneration unit and, after purifying, are returned to the process. Carbonyl is supplied to a water spraying capacitor, and the suspension is delivered to a nutsche filter and the filtrate exhausted to the collector by vacuum pump. Squeezed carbonyl is fed to the topping still, cleaned from iron pentacarbonyl ($Fe(CO)_5$) by 1% aqueous solution of sodium hydroxide, and is distilled once more using live steam. Cleaned carbonyl is filtered in the nutsche filter, washed with distilled water and dried in a vacuum oven. The plant capacity is 200–500 kg per day; autoclave volume is 1–15 L, with carbonyl efficiency amounts to 80%–90%.

There is also a method of dry synthesis from chlorides. The process uses iron swarf as the reducing agent and is conducted under carbon monoxide at a pressure up to 28 MPa and a temperature of 550 K. The advantage of this process is the absence of inflammable solvents.

Tungsten and molybdenum powders are also produced by carbonyl decomposition under atmospheric pressure and at temperature ranges from 620 K to 1470 K in a gas current (hydrogen, nitrogen, and others). Sometimes, it is decomposed at reduced pressure without using a carrier gas. Powder efficiency is about 90%. The flow sheet of powder production in hydrogen is shown in Fig. 23.13. Crystalline carbonyl is charged into a horizontal sublimator of the "pipe-in-pipe" type with exterior heating. After sealing, the system is cleaned out using pure nitrogen. In the sublimator, carbonyl is heated up to temperatures ranging from 330 K to 400 K, and its vapor is carried by preheated and purified hydrogen to a decomposition unit provided with electroheating. Carbonyls are decomposed at temperatures ranging from 620 K to 670 K. The powder is collected in a container. Tungsten powder efficiency is 94%; molybdenum powder efficiency is 86%.

More detailed information on the carbonyl process is contained in Chapter 6.

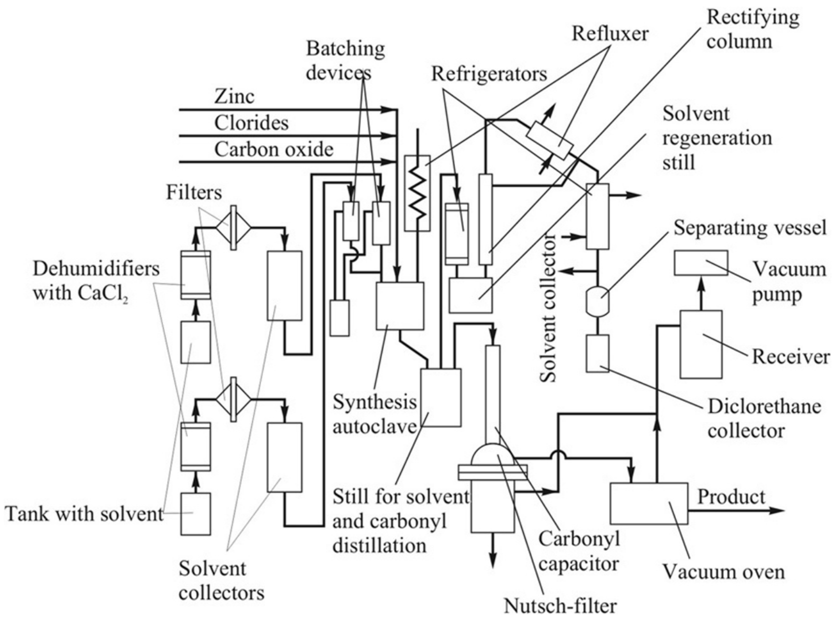
Batching devices
Refluxer
Rectifying column
Refrigerators
Zinc
Clorides
Carbon oxide
Solvent regeneration still
Filters
Separating vessel
Dehumidifiers with $CaCl_2$
Solvent collector
Vacuum pump
Receiver
Synthesis autoclave
Diclorethane collector
Product
Tank with solvent
Still for solvent and carbonyl distillation
Carbonyl capacitor
Vacuum oven
Solvent collectors
Nutsch-filter

FIG. 23.12 Diagram of plant for tungsten and molybdenum carbonyl synthesis in solvent media.

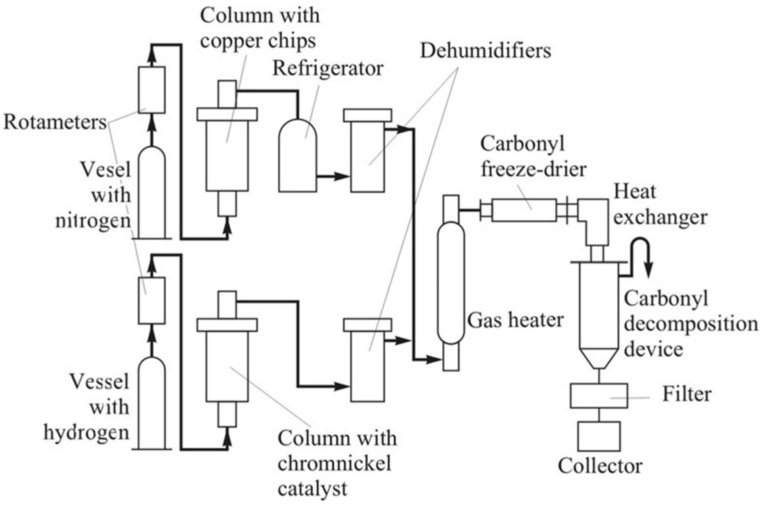

FIG. 23.13 Flow sheet of powder production by carbonyl decomposition in hydrogen current.

Properties of Tungsten Powders

Tungsten has two outstanding properties: the highest melting point of all metals at 3683 K and a very high density of 19.25 g/cm^3 at 293 K. It cannot be shaped using traditional casting techniques. Consolidation of tungsten powders is based almost exclusively on powder metallurgical methods [12,13]. Therefore, definite and detailed powder specifications are very important in order to obtain the required final properties of a consolidated tungsten product. These specifications include physical and chemical properties. The basic physical properties are particle size, flow rate, and different powder density values. All the powder sizes, from ultrafine to hundreds of microns, are produced on an industrial scale, but the bulk of the powder used at present is in the size range 2–5 µm.

Particle sizes in the range of 1–10 µm are measured by Fisher subsieve sizer (FSSS) (ASTM B 330 and MPIF 32 standards) [14] and correspond to particle sizes observed directly by optical microscopy (OM) (MPIF E 20 and GOST 23402-78 standards) and by scanning electron microscopy (SEM). SEM and OM are also the best ways to estimate the overall particle morphologies. Particle size distributions can be measured by light scattering techniques (ASTM B 822 standard) or by sedimentation based on X-ray monitoring of gravity sedimentation scattering (sedigraph) (ASTM B 761 standard). Controlling the reduction parameters make it possible to produce either narrow or wide size distribution and to provide any specific requirement on tungsten powders for various applications.

Apparent density (ISO 3923 standard, and in accordance with it ASTM B 212, MPIF O4, and GOST 19440 standards), tap density (ISO 3953 standard, and in accordance with it, is accepted in ASTM B 527, MPIF 46, and GOST 25279 standards) as well as green density and green strength have great importance for determining the behavior of a powder during subsequent consolidation steps, including pressing and sintering.

A feature of tungsten powder is a relatively high purity, in comparison with most other metal powders used for powder metallurgical products. Table 23.1 contains analytical data of typical tungsten powders produced by hydrogen reduction. Trace elements, including molybdenum, aluminum, arsenic, silicon, phosphorus, sodium, potassium, calcium, magnesium, and sulfur, are removed during ammonium paratungstate manufacture. The contaminants, such as nickel, chromium, iron, and cobalt, characteristic alloying elements of reduction boats or furnace tubes, have to be avoided.

Physical analyses of typical medium sized tungsten metal powders are presented in Table 23.1. The characteristic morphology of the tungsten powders produced by hydrogen reduction is shown in Fig. 23.14. The particles have angular prismatic shape in either coarse or submicron sizes.

In the powders reduced by solid carbon with stoichiometric carbon black consumption, the carbon content is decreased to 0.5 wt% and oxygen to 0.10–0.15 wt. Apparent density of these powders ranges between 3 and 7 g/cm^3 by 1–10 µm powder particles size. Such powders may be used in hard alloy manufacture to produce tungsten carbide.

Tungsten powders obtained by precipitation from the gaseous phase of tungsten hexafluoride and tungsten hexachloride (reduction of highest halides) with particle sizes between 0.05 and 0.80 µm and roundish shape are of high purity (Table 23.2) and differ significantly from tungsten powder reduced from oxides.

Tungsten powders produced from WF_6 in hydrofluoric medium and by WO_x decomposition in hydrogen current are finer than particles produced by high-temperature WF_6 dissociation or by high-temperature treatment of preliminary chlorinated wastes. High oxygen content in some "gas-phased" powders is caused by their high absorption properties in wet air.

TABLE 23.1 Properties of Typical Tungsten Powders Produced by Conventional Calcination/Reduction Process

		Source: Standard Grades								
		WBH		OSRAM						
Property	**Unit**	**1 μm**	**Coarse**	**W 06**	**W 10**	**W 15**	**W 25**	**W 35**	**W 45**	**W 65**
Particle sizes FSSS										
As supplied	μm	1	48	0.6±0.1	1.0±0.1	1.5±0.2	2.5±0.3	3.5±0.3	4.5±0.3	6.5±1.0
Lab milled	μm	…	…	0.5±0.1	0.8±0.1	1.4±0.2	2.4±0.3	3.3±0.3	4.2±0.3	3.5±1.0
Scott density	g/cm^3	…	…	2.0±0.2	2.5±0.3	2.8±0.3	3.3±0.3	4.0±0.3	4.5±0.4	4.7±0.5
Tap density	g/cm^3	…	…	3.8±0.3	4.4±0.3	4.8±0.3	5.2±0.4	6.0±0.4	6.3±0.5	6.5±0.8
Tungsten min. Excluded oxygen	wt%			99.98		99.95				
				Typ. Virgin[a]	Guar. Virgin	Typ. reclaimed[b]	Guar. Reclaimed			
Trace impurities:										
Aluminum	ppm	<5	<5	<20	<25	<20	<20			
Calcium	ppm	<2	<2	<5	<10	<10	<15			
Carbon	ppm	…	…	…	…	…	…			
Chromium	ppm	…	…	<5	<5	<5	<5			
Cobalt	ppm	<5	<5	<5	<20	<100	<100			
Copper	ppm	…	…	<5	<5	<10	<15			
Iron	ppm	<5	<5	<20	<25	<20	<30			
Lead	ppm	…	…	<5	<5	<5	<5			
Magnesium	ppm	…	…	<5	<5	<5	<5			
Manganese	ppm	…	…	<5	<5	<5	<5			
Molybdenum	ppm	<20	<20	<50	<100	<150	<200			
Sodium	ppm	…	…	<5	<10	<10	<15			
Nickel	ppm	<5	<5	<10	<15	<5	<15			
Oxygen	ppm	2650	250	800	800	800	800			
Phosphorus	ppm	…	…	…	…	…	…			
Potassium	ppm	…	…	<5	<5	<5	<10			
Silicon	ppm	<10	<10	<20	<20	<30	<30			
Sulfur	ppm	<5	<5	<10	<10	<20	<20			

[a] *Tungsten powder made from tungsten ore.*

[b] *Tungsten powder made by recycling sintered carbide scrap; Companies: WBH: Wolfram Bergbau- und Hütten- GmbH; OSRAM: OSRAM Bruntál spol. s r. o.*

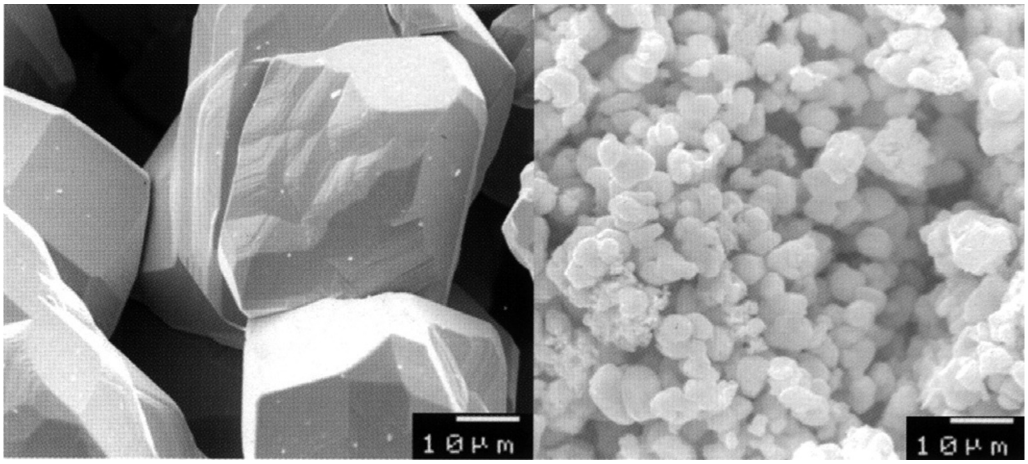

FIG. 23.14 Scanning electron micrographs of coarse and submicron tungsten powders produced by hydrogen reduction.

TABLE 23.2 Composition of Typical Tungsten Powders Produced by Reduction of Highest Halides

Property	Unit	Technique [7]		
		LTF	LTHL	HTF
Average particle size	µm	0.8	0.1	0.2
Trace impurities:				
Aluminum	ppm	…	…	14
Arsenic	ppm	…	…	80
Calcium	ppm	30	…	12
Chromium	ppm	…	7	…
Fluorine	ppm	130	…	900
Iron	ppm	1500	600	130
Magnesium	ppm	10	20	…
Manganese	ppm	30	5	…
Molybdenum	ppm	…	320	1300
Oxygen	ppm	200	6500	…
Silicon	ppm	10	60	300
Titanium	ppm	100	…	…

LTF: Low temperature dissociation by reduction of tungsten hexafluoride in hydrogen; LTHL: Low temperature dissociation by reduction of tungsten hexachloride in hydrogen; HTF: high temperature decomposition of tungsten hexafluoride in hydrogen fluoride medium.

Properties of carbonyl powders are shown in Table 23.3. Tungsten and molybdenum powders produced at decomposition temperature 620–670 K in hydrogen are represented by 60%–70% of particles with round shape with rough and sharp spurs on the surface with mean particle sizes of 2–4 µm (Fig. 23.15). Tungsten powders contain 1.4–2.2 wt% carbon and up to 2.0 wt% of oxygen, while molybdenum powders contain 3.4–3.9 wt% carbon and up to 5.8 wt% of oxygen.

Particles of tungsten and molybdenum powders reduced at temperatures in the range from 670 K to 1170 K in an argon current are spherical and non-uniform in size, especially at low decomposition temperatures. The surface of molybdenum particles is comparatively smooth, while the surface of tungsten particles is uneven and includes some separate spheroids <1 µm in size. The particles become significantly smaller in size, and specific surface increases on increase of the

TABLE 23.3 Variation of Properties With Decomposition Temperature for Carbonyl Tungsten Powders

Decomposition Temperature in Current of Argon (K)	Color of Powder	Average Particle Size (μm)	Specific Surface Area (m^2/g)	Carbon Content (wt%)	Lattice Spacing (nm)
673	Gray	1.2	0.18	1.08	0.4178
773	Gray	1.0	0.21	1.00	0.4172
873	Dark-gray	0.74	0.30	1.50	0.4167
700	Black	0.12	1.56	1.83	0.4163
973	Black	0.07	3.00	1.82	0.4159
1073	Black	0.03	8.20	…	…
2273–4243	Black	0.01–0.03	…	0.50–1.00	…

(a) SHF: discharge in nitrogen current.

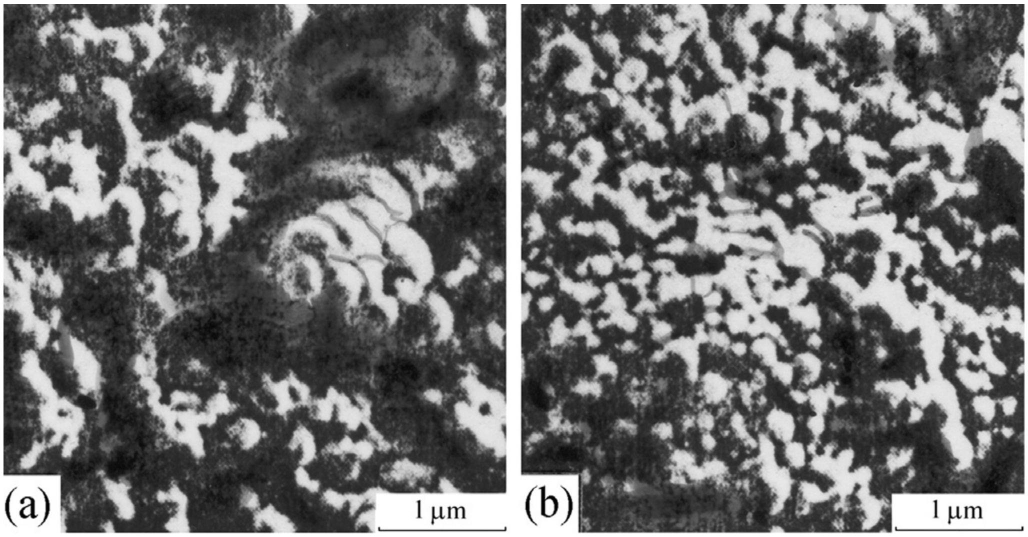

FIG. 23.15 Scanning electron micrographs of carbonyl tungsten (A) and molybdenum (B) powders.

decomposition temperature from 670 K to 1170 K; for example, for tungsten powders, the average size decreases from 1.2 μm to 0.03 μm, and the specific surface increases from 0.18 m^2/g to 8.2 m^2/g, respectively. Carbon content in tungsten powders obtained in argon is 1.9 wt%, while in molybdenum powders, it amounts to 3.5 wt%. The addition of an oxidizing component to the carrier gas decreases the carbon content in the powder.

Sintering temperatures of carbonyl tungsten and molybdenum powders are some hundreds of degrees lower than that of powder produced by other methods. They are used for the production of porous and compact parts by powder metallurgy.

Metal carbides, for example, ZrC and other abrasive materials such as boron nitride, can be coated with tungsten or molybdenum by thermal decomposition of their carbonyls resulting in improved of service performance. For example, the hardness of cutting wheels of cubic boron nitride metallized by tungsten is increased twofold. Diamond grains metallized by tungsten increase their cohesion in instrument assembly, preventing diamond chipping. Other methods of abrasives metallization are not effective enough because they do not provide good coating cohesion.

The quantity of carbon and oxygen in the powder depends, first of all, on the process conditions in its production. Peak of carbon content is observed at about 970 K connected with free amorphous carbon formation because of catalytic decomposition of the carbon oxide. Carbon content can be decreased by a process of carbonyl $W(CO)_6$ decomposition in super-high-frequency discharge at temperatures ranging between 3043 K and 4000 K in a nitrogen current. The particles have a spherical shape and their size ranges from 12 nm to 30 nm; nitrogen content is 0.3 wt%, and oxygen content is not >1 wt%. The content of other impurities does not exceed the value 1.0×10^{-4} wt%.

Carbonyl tungsten powders are metastable carbides with a face-cantered cubic lattice. Their properties change with increasing temperature; thus, lattice spacing decreases (see Table 23.3).

Powders obtained by plasma-chemical reduction are characterized by high dispersivity; particles of an average size of about 0.07 μm form weak conglomerates with a developed specific surface and a very low apparent density of 0.25 g/cm^3. When first produced, a large quantity of hydrogen chloride is absorbed on the powder surface, which volatilizes during storage in air, while the oxygen concentration is increased to 4%–8%.

Nanopowders of approximately 20 nm average particle size are produced by melt atomization in arc argon plasma. Tungsten particles of 510 nm sizes have face-cantered or hexagonal close-packed lattice in comparison with typical body-centered for solid state.

Tungsten powders obtained through high-temperature reduction in argon-hydrogen plasma represent double component systems consisting of α-W (body-centered lattice) and β-W (A-15) with main peaks (210) of β-phase and (110) of α-phase.

Tungsten Powder Applications

Ultrahigh purity powders are used for manufacturing semiconductors and high-performance electrodes of high-intensity discharge (HID) lamps to avoid outgassing of impurities and guarantee a consistent lamp quality with increased lifetime. In particular, the incorporation of alpha emitters such as uranium and thorium is extremely crucial and must be held below 1 ppb [15]. The mobile alkali ions (for instance, sodium and potassium) have to be held below 0.1 ppm. Purification of APT by means of multiple extraction and crystallization steps ensures the required purity, so all production steps must be carried out in clean room conditions [6,16].

In the work [17], a method based on ammonium paratungstate (APT) row material, used for the production of ultrahigh-purity tungsten powder (6N W), was developed. The APT was reduced by hydrogen to high-purity tungsten metal powder (Fig. 23.16). Two types of high purity tungsten material for electrodes in HID were prepared. One was a tungsten rod with a diameter in the range of 12–40 mm, which was processed by powder compaction with cold isostatic pressing (CIP), sintering at a temperature higher than 2273 K in an induction heating furnace under a hydrogen protection atmosphere, and hot forging. The other was a tungsten wire with a diameter in the range of 0.02–12 mm, which was fabricated by powder compaction by CIP, self-resistance sintering at a temperature approximately 2970–3070 K, swaging, and wire drawing.

The Fisher subsieve sizer (FSSS) particle size of the produced 6N W powder is in the range of 2.2–3.2 μm, and the apparent density is approximately 2.5 g/cm^3. The SEM image of the powder morphology is shown in Fig. 23.17. The δ_{10}, δ_{50}, and δ_{90} of the tungsten powder (analyzed using a laser particle size distribution analyzer) are 2.027 μm, 5.161 μm, and 15.816 μm, respectively. The flowablility of the 6 N W powder is suitable for producing tungsten rods, wires, and targets. The purity (excluding the gaseous ingredients) of the tungsten rods and wires is 5 N or higher (Table 23.4).

Tungsten is currently the most promising material for the first wall in demonstration fusion reactors (DEMO) and as a plasma facing material (PFM) in future fusion reactors [18]. Feasibly utilizing tungsten in the next generation of fusion reactors will require components with a thin tungsten layer. Coating technologies such as vacuum plasma spray (VPS), physical vapor deposition (PVD), and chemical vapor deposition (CVD) have been studied in recent years [19–21]. High purity (>99.9999%), full density (19.23 g/cm^3) tungsten parts and coatings were manufactured with chemical vapor deposition (CVD) method with a deposition rate higher than 0.6 mm/h [22]. The thermal conductivity of the CVD-W material with a columnar grain structure is higher than that of forged tungsten, but the coefficient of thermal expansion (CTE) of both types of tungsten is very similar. Thermal shock tests show that the threshold energy of CVD-W for crack initiation is between 1.5 and 2.25 MJ/m^2, while that of forged tungsten is lower than 1.1 MJ/m^2, because the pyramidal shapes of the surface of CVD-W coating can withstand a greater level of distortion, preventing the appearance of cracks. The high melting point (3683 K) of all metals, low tritium retention, high thermal conductivity, and the high low erosion rate under plasma loading makes tungsten a suitable PFM.

Pure tungsten powders: Pure tungsten powders are made into rods by pressing and sintering. In order to achieve high densification, a high temperature in the range of 2273–3373 K is required [2,6]. The sintered tungsten bars thus obtained are forged or rolled at elevated temperatures in order to produce rods (which are subsequently drawn to manufacture wires) or sheets. Such pure tungsten materials are widely used for high temperature applications, for example, in high-temperature furnace parts [2,6]. For these materials, powders produced by the highest halide reduction can be used.

Non-sag tungsten wires: To prevent sagging of tungsten filaments in incandescent lamps during high temperature operation, doping elements—aluminum, silicon, and potassium—are included in the powder [3,23]. The present technique consists of adding an aqueous solution of compounds containing aluminum, silicon, and potassium into the tungsten oxide

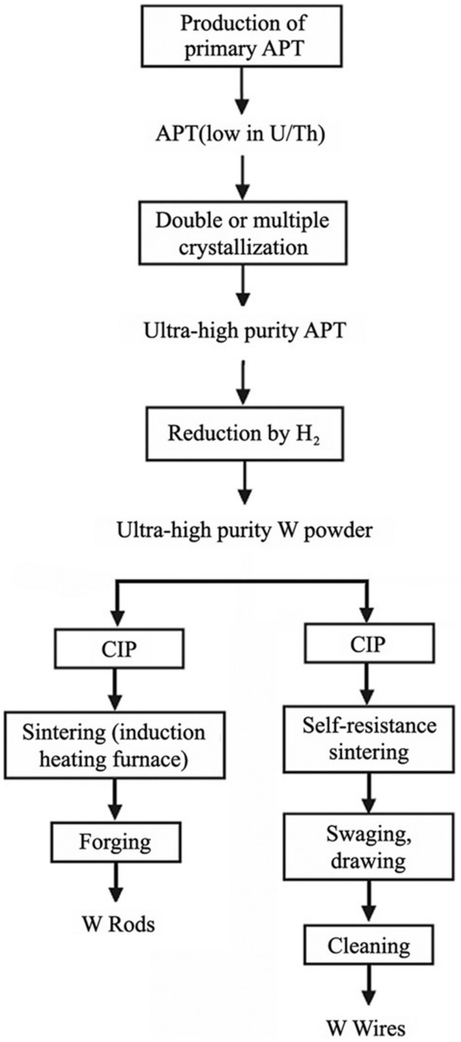
Production of primary APT
APT(low in U/Th)
Double or multiple crystallization
Ultra-high purity APT
Reduction by H_2
Ultra-high purity W powder
CIP
Sintering (induction heating furnace)
Forging
W Rods
CIP
Self-resistance sintering
Swaging, drawing
Cleaning
W Wires

FIG. 23.16 Flow sheet of the process of ultrahigh purity tungsten products.

FIG. 23.17 SEM micrograph of the ultrahigh purity tungsten (6NW) powder.

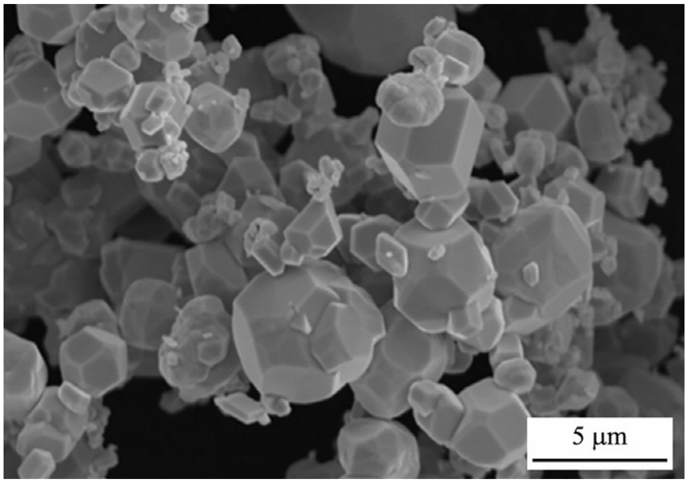

TABLE 23.4 Purity of the High Purity Tungsten products

Product	Tungsten Powder	Tungsten Rod	Tungsten Wire
Purity (tungsten element content, wt%)	99.999931	99.99989	99.999922

powder before reduction to tungsten metal. During this reduction, a portion of the above trace elements is incorporated into the tungsten metal powder particles. During the sintering of the pressed tungsten powder, aluminum and silicon evaporate, while the potassium atom is too big to diffuse through the tungsten lattice.

This process results in the incorporation of potassium droplets as inclusions. During wire drawing, the small potassium droplets are elongated and finally break into a multitude of little tiny potassium bubbles in lines along the wire axis, which results in an elongated interlocked grain structure. During recrystallization at elevated temperatures, the tiny potassium bubbles effectively stabilize through an effect similar to dispersion hardening, the movement of dislocations, and thus, the migration of the grain boundaries perpendicular to the wire axis. Large inclusions in the metal particles generate large potassium pores in the sintered ingot from which long bubble rows are formed in the wire. This characteristic structure explains the non-sag properties of the tungsten filaments in incandescent lamps [2,6,23–26].

Spheroidization of tungsten powders: The spherical tungsten powders exhibit outstanding properties such as excellent flowability, high bulk density, and low sintering shrinkage, making them suitable for abroad range of applications such as thermal spraying, additive manufacturing, etc. The thermal plasma technique has been proven effective for preparing spherical tungsten powders because of its high temperature and high enthalpy [27–29]. Plasma spheroidization of tungsten powders consists of two main processes: first, the raw tungsten powder, injected into the high temperature region of radio frequency (RF) thermal plasma, is heated and melted to form spherical droplets (due to surface tension), and then, the melted droplets solidify into spherical particles due to rapid quenching when they spurt out of the plasma. However, not all powder particles can be melted completely, despite the plasma temperature being much higher than the melting point of tungsten. Possible reasons for this incomplete melting could be that the powder particles cannot absorb sufficient plasma energy due to the non-uniform temperature inside the plasma torch, the local cooling effect of plasma by the cold carrier gas and flow of powder particles [28], or insufficient optimization of experimental parameters.

The paper [30] describes a study of the spheroidization of tungsten powders by radio frequency thermal plasma, including the melting, solidification, and growth behavior of the tungsten powder particles during the spheroidization process. The flight time and melting time of tungsten powder particles in the plasma were estimated, and the growth behavior of the particles, specifically, the change in the average tungsten powder particle size before and after plasma spheroidization, was analyzed. The flight time and melting time for tungsten powder particles with radius of 7.8 μm were calculated to be 9.3 ms and 2.9 ms, respectively. The particle size distribution before and after spheroidization were determined (Table 23.5). It can be seen (Fig. 23.18A) that the raw powder particles are irregular, and the particles after RF processing (Fig. 23.18B) possess a spheroidal shape with few satellites present on the rough particles' surfaces. The authors reported [30] that the change in powder particle size during the process showed that growth of tungsten powder particles was mainly caused by the coalescence of droplets in the thermal plasma system. The experimental results demonstrated that the spheroidization rate could reach up to 95% under the operating conditions used.

Tungsten composite materials: Tungsten metal powder blended with other powders, such as copper, iron, cobalt, and nickel, form so-called "tungsten heavy alloys" (WHAs), which typically contain 90–98 wt% W and can be liquid phase sintered at about 1773 K. Their properties include high density (17–19 g/cm^3) and ductility, and energy penetration and

TABLE 23.5 Particle Size Distribution of the Tungsten Powders Before and After Spheroidization

	Undersize (μm) of Cumulative Distribution			
Powder Condition	δ_5	δ_{10}	δ_{50}	δ_{90}
Raw powder	5.78	7.09	15.60	29.02
In-flight particles	…	…	20	…
Spheroidized powder	4.52	7.11	28.79	68.02

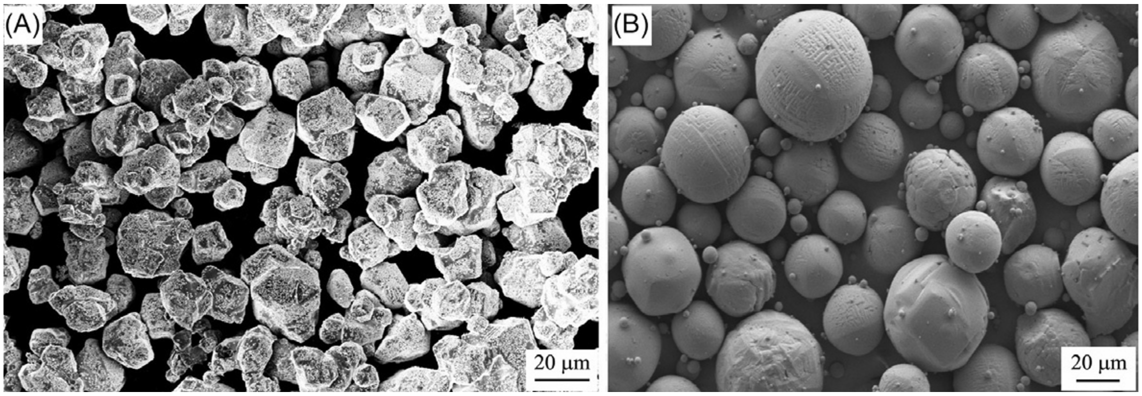

FIG. 23.18 Field emission SEM images of tungsten powders: (A) raw powder, (B) spheroidized powder.

radiation shields are the application fields of these tungsten materials [6]. WHAs are typically formulated from elemental powders with mean particle sizes in the range of 1 μm to 7 μm. Because of exclusive high melting temperature of tungsten, PM manufacturing methods are predominantly used for such materials.

Infiltration (INF) is used exclusively for making tungsten-based composite contact materials. Refractory metal powder is first blended to the desired composition with or without a small amount of binder to impart green strength, then it is pressed and sintered into a skeleton of the required shape. Silver or copper is next infiltrated into the pores of the skeleton. This technique produces the highest density composites, generally 97% or more of theoretical density. Because of the presence of some closed pores in the sintered skeleton, complete densification is not possible.

The press-sinter method can be used for small refractory metal parts (not exceeding about 25 mm in diameter). A high density material is obtained by pressing a blended powder of the exact final composition into shape and then sintering it at the melting point of the low-melting-point component (liquid-phase sintering). In some cases, an activating agent such as nickel, cobalt, or iron is added to improve the sintering effect on the refractory metal particles. For this process, powders of much finer particle size are preferable to enable more bonding surface. However, material formed by this process is weaker compared that formed via the infiltration process.

The press-sinter-re-press (PSR) process is used for all categories of contact materials, especially silver-based materials. Blended powders are compacted to the desired shape and then sintered. The materials are further densified by a second pressing (re-pressing). Sometimes, the properties can be modified by a second sintering or annealing. The flexibility of this process makes it applicable to parts of any configuration and of any material. Material thus produced may also have weaker bonding between particles.

The first heavy alloy developed was a W-Ni-Cu alloy. Alloys of this ternary system are still used occasionally, mainly for applications in which ferromagnetic character and resistance must be minimized. However, the present industry standard W-Ni-Fe exceeds the above alloy in corrosion resistance and mechanical properties. Most of the current purposes for WHAs are best satisfied by the W-Ni-Fe system. Alloys such as 93W-4.9Ni-2.1Fe and 95W-4Ni-1Fe represent common compositions. Mechanical properties depend on the nickel-to-iron ratio. They are sensitive to hydrogen embrittlement due to the body-centered cubic (bcc) structure of the principal tungsten phase [31]. By means of the nickel-to-iron ratio selection and post-sinter heat treatment, optimal mechanical properties are obtained. There are two common post-sinter heat treatments for WHAs. Vacuum heat treatment is useful for the reduction of hydrogen embrittlement, as is resolution and quench for reduction of segregation-induced embrittlement. If alloys are subjected to vacuum heat treatment, nickel-to-iron ratios in the range of 2.3–4 should be chosen, as better mechanical properties are generated [32,33]. For example, 91W-6.3Ni-2.7 Fe alloy ensures an ultimate tensile strength of 940 MPa, elongation of 35%, and hardness of 29 HRC.

The addition of cobalt to a W-Ni-Fe alloy is a common approach for a slight increase of both strength and ductility. The presence of cobalt provides solid solution strengthening of the binder and slightly enhanced tungsten-matrix interfacial strength. Even higher mechanical properties are attainable from the W-Ni-Co system with nickel-to-cobalt ratios ranging from 2 to 9 [34]. These alloys provide high static tensile strength, ductility and hardness, for example, for 91W-6Ni-3Co alloy, ultimate tensile strength is 960 MPa, elongation is 40%, and hardness is 31 HRC. The use of such alloys is generally limited to defense applications requiring advanced mechanical properties.

A number of other special WHAs are known, too. An example is an addition of molybdenum to the W-Co-Ni-Fe quaternary alloy to restrict tungsten dissolution and spheroid growth, resulting in higher strength, but reduced ductility, in the sintered state [35]. The addition of boron in the form of NiB and FeB to W-Ni-Fe system alloys leads to a small increase of hardness in some cases, in particular, for W-7NiB-3Fe and W-7NiB-3FeB compositions [36]. The sintering temperature selected for these alloys was 1773 K.

The structural and mechanical properties of 90W-7Ni-3Fe alloy compacts produced using a high-voltage electric pulse sintering technique were studied [37]. High-voltage electric pulse consolidation (HVEPC) involves passing a high-voltage discharge passage (30 kV) with a high current density (≈ 100 kA·cm^{-2}) and short pulse duration ($<300\,\mu$s). This current pulse is passed through a powder filling during the application of external pressure. The rapid increase in temperature at the areas of contact of the powder particles leads to their instantaneous welding. In this study, the average particle size of selected heavy alloy was equal to 6.03 μm; powder density was equal to 17.13 g/cm^3. The value of the applied voltage varied from 4.5 kV to 5.8 kV. The pressure applied to the filling was equal to 45 MPa. It was reported [37] that the relative density of the sintered compacts is in the range of 94.9%–95.9% of theoretical density. The highest density increase values and increased microhardness of compacts are achieved at the maximum value of discharge 5.8 kV, although stabilized density values were obtained at 5.6 kV. Further increase in the microhardness by increasing discharge voltage leads to embrittlement of the material. The microstructure of the cylindrical shape samples is shown in Fig. 23.19. The average grain size is approximately 10 μm; that is, high-voltage sintering contributes to maintaining a fine-grained structure, more uniform distribution of iron-nickel binder, and almost total absence of porosity.

Porous skeletons of pressed tungsten metal powder infiltrated with copper alloys or silver forming W-Cu as well as W-Ag composites are widely used as electrical contacts [38–40] due to their high electrical conductivity, low thermal coefficient of expansion, and their resistance to damage caused by electrical arc formation.

Many researchers have tried to obtain W-Cu alloys of full density without sintering additives by use of fine tungsten powder and increasing the homogeneity of the W-Cu powder in order to facilitate rearrangement of tungsten particles in liquid copper during liquid-phase sintering [41,42]. Through mechanical alloying of W/Cu or tungsten oxide and copper oxide, homogeneous W-Cu composite powders with nanosized tungsten particles can be produced, and fully densified specimens can be fabricated.

W-(25/30)Cu composite powders were fabricated by the sol-spray drying and subsequent hydrogen reduction, then pressed and directly sintered [43]. The authors reported that when sintering time (ranging from 15 min to 120 min) and temperature (between 1573 and 1693 K) are increased, relative densities of W-(25/30)Cu increase. When sintered at 1693 K for 120 min, relative densities of W-25Cu and W-30Cu composite materials are 98.09% and 99.13%, respectively. According to kinetic characteristics during sintering, the first stage of W-Cu liquid sintering finishes at some time from 0 to 30 min into the process. During the sintering process, spherical tungsten grains grow and uniformly distribute into the matrix Cu phase. According to liner fitting of W grain sizes, grain growth of W-25/30Cu composite materials conforms to the dissolve-precipitation mechanism during liquid phase sintering. BE-SEM images of W-30Cu sintered at 1693 K for 30–120 min show (Fig. 23.20) that nearly spherical tungsten particles are uniformly distributed by copper phase, and with sintering going on, tungsten particles grow.

In the work [44], W-30 wt% Cu alloys were fabricated using cold pressing and infiltration sintering methods from two types of powders, that is, mixed copper-tungsten (abbreviated name: M-Cu-W) powders and newly developed copper-coated tungsten composite (abbreviated name: Cu@W) powders. The latter were prepared using the thermo-electroless method [45]. Tungsten-copper mixed powders with an average particle size of tungsten 6–8 μm and copper-coated tungsten powders with an average particle size 4–10 μm were used to fabricate bulk W-30Cu alloys through infiltration sintering at

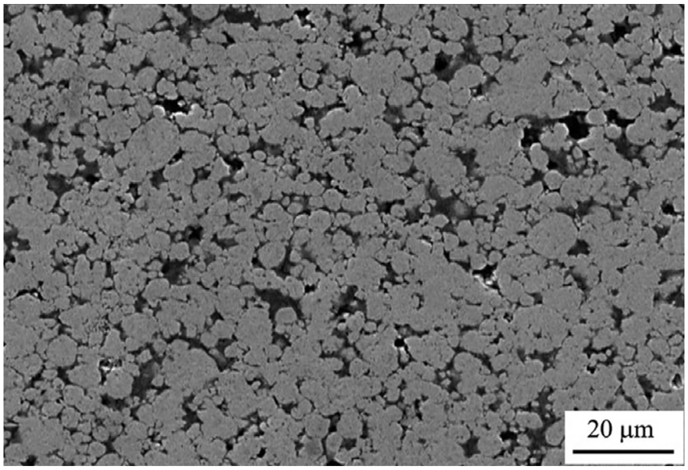

FIG. 23.19 Microstructure of the cylindrical shape sample of 90W-7Ni-3Fe alloy compacted by high-voltage electric pulse consolidation.

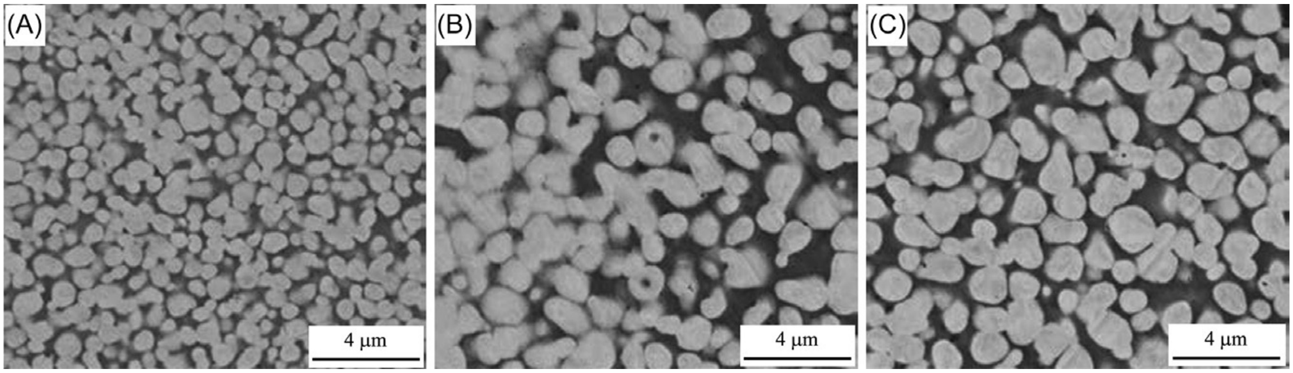

FIG. 23.20 SEM images of W-30Cu composite sintered at 1653K for 30–120min: (A) 30min, (B) 60min, (C) 120min.

1623K for 90min under a hydrogen atmosphere. The polyhedral structures of tungsten particles are observed (Fig. 23.21A), while the surface of roundish copper particles appears rough (Fig. 23.21B). The cross-section image of the coated powder (Fig. 23.21C) shows that the copper phase is coated onto the surface of tungsten particle with coating thickness in the 2–6μm range.

Microstructures of W-30Cu alloys fabricated by the infiltration sintering method are shown in Fig. 23.22, in which the gray-white particles are tungsten phase, and the black ones are copper phase. It can be seen in Fig. 23.22A that the copper

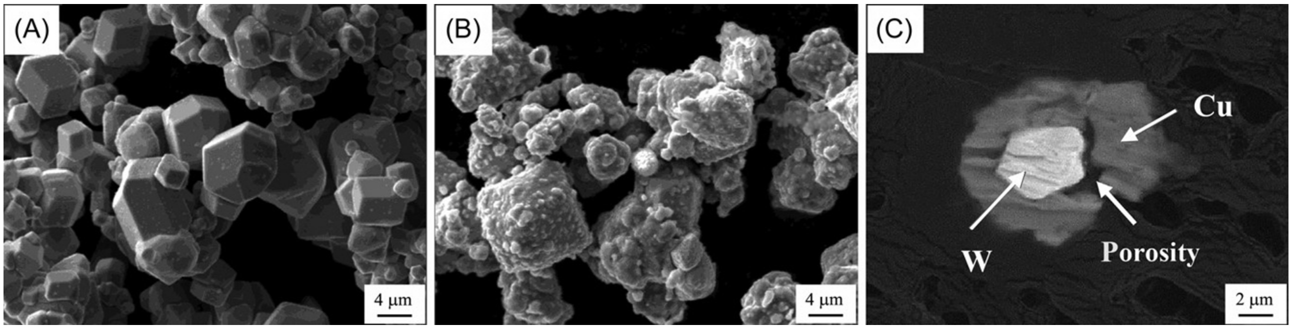

FIG. 23.21 The morphology of copper coated tungsten composite powders: (A) pure tungsten powders, (B) copper coated tungsten powders, (C) cross section of the coated powder. *(Modified from Chen W, et al. Infiltration sintering of WCu alloys from copper-coated tungsten composite powders for superior mechanical properties and arc-ablation resistance. J Alloys Compd 2017; 728(25 Dec): 196–205.)*

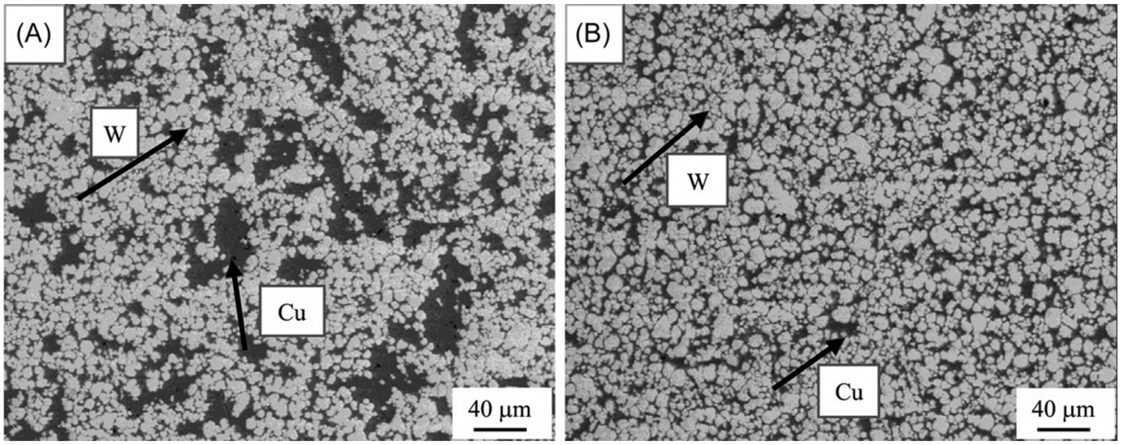

FIG. 23.22 Microstructures of W-30Cu alloys fabricated by the infiltration sintering method: (A) mixed copper-tungsten powder; (B) copper-coated tungsten composite. *(Source: Chen W, et al. Infiltration sintering of WCu alloys from copper-coated tungsten composite powders for superior mechanical properties and arc-ablation resistance. J Alloys Compd 2017; 728(25 Dec): 196–205.)*

phase in the (M-Cu-W) alloy has a certain segregation (denoted by arrow). The copper particles are distributed among the tungsten particles with size distribution in the 40–100 μm range. In contrast, in the (CuW) alloy (Fig. 23.22B), the tungsten particles are distributed more homogeneously, and no obvious agglomerates can be observed.

Chen et al. [44] reported that the arc-erosion resistance of the CuW alloy is better than that of the (M-Cu-W) alloy. The ablation area of the former was larger, and its ablation crater was shallower, and the arc erosion is mainly attributed to the evaporation of the low melting point of copper. For the (M-Cu-W) alloy, arc erosion was mainly attributable to the sputtering of copper.

A mechanothermochemical process using the liquid solution as starting material and a grinding process using salt-free oxide powder enables the production of ultrafine, homogeneous W-Cu composite powders [46]. The spheroidal composite W-Cu oxide powder is produced by spray drying an aqueous solution of tungsten and copper salts, and subjecting it to subsequent oxidation. The spheroidal structure of the oxide powder is destroyed during ball milling, and W-10 wt% Cu composite with nanosized particles is produced through reduction of the ground oxide powder at 974 K in hydrogen. But as the copper content in W-Cu composite powder decreases, densification of W-Cu powder compacts is difficult due to pore formation by local densification in agglomerated powders. W-10 wt% Cu-based oxide powders with tungsten trioxide addition before reduction sintered at 1673 K in hydrogen can achieve a sintered density of 17.05 g/cm^3, which amounts to 98.5% of theoretical density. The thermal and electrical conductivities of such a composite are 203 W/(m·K) and 36.5%IACS, respectively [46].

To fabricate tungsten-copper nanocomposite powder, the tungsten-copper oxide mixture ball-milled in argon was reduced at a low temperature of 573 K [47]. The reduced W-Cu nanocomposite powder was consolidated at 1473 K for 1 h with a heating rate of 10 K/min.

It has been shown recently that porous tungsten can be obtained at approximately 1473 K, a much lower temperature than the 2273 K used in the conventional process. This has been achieved by employing reactive sintering. Reactive sintering method makes use of the addition of aluminum, the low melting phase of which decreases the process temperature while acting as a potential sintering aid. As a result, higher homogeneity and uniform porosity distribution have been obtained [48].

High-energy ball milling is a well-known technique for producing oxide-dispersion strengthened materials. Due to activation of a material during grinding without oxide and metal powder admixtures, this method has essential advantages [49–51]. It makes the sintering stage easier, resulting in both higher rate and lower temperature. The reduced size of mechanically ground particles and their high density in lattice defects promote the sintering transport phenomena. It also leads to finer and more homogeneous oxide dispersion. This latter feature, together with the nanocrystalline structure of the ground powders, results in a small grain size after sintering. As reported [52], long milling times on the order of 30 h of W-1 vol% Y make it possible to reach a relative density of 96.5% after sintering for 4 h in vacuum at 2073 K, while within a milling time of 80 min, the relative density amounts only to 76.5%.

Recent developments [53,54] define the production of W/Cu composite powders which can be directly pressed to shape and sintered, being produced without infiltration or machining, which is of particular importance with respect to their application as heat sinks in the semiconductor industry.

Tungsten with oxide dispersions is manufactured with the addition of thorium-containing compounds, such as thorium oxide or thorium nitrate. The mixtures consisting of tungsten metal powder and the above additives are pressed, sintered, and further processed into wires or sheets. The main application of this material is welding electrodes, which, due to the high electron emission ability of thorium, ensure easier arc formation, and offer stabilization and improved physical properties arising from dispersion hardening in sheets and wires, particularly for vibration-resistant automotive lamps [2,6]. Because of the radioactive danger of thorium, alternatives have been developed. Cerium and lanthanum have been tried as potential candidates to replace thorium in welding electrodes.

Properties of typical tungsten based composites are shown in Table 23.6.

Recovery of Metallic Tungsten

Virtually almost all types of tungsten products, if available in large enough amounts and workable, are presently recycled [4,6]. Even unselected, low-quality scrap containing enough tungsten can be used as a feed material for the chemical ammonium paratungstate production process, electrochemical recovery, or for alloying in steel. But any possible, practicable use for selected tungsten scrap is, of course, desirable for economic reasons. Typical kinds of tungsten scrap include:

- Selected manufacturing scrap of pure tungsten can easily be crushed in high energy mills and directly re-used for applications with lower quality demands.

TABLE 23.6 Properties of Typical Tungsten Base Composites

Nominal Composition (%)	Manufacturing Method[a]	Density (g/cm^3)		Electrical Conductivity (% IACS)	Hardness	Tensile Strength (MPa)	Modulus of Rupture (MPa)	Data Source [b]	Application Examples
		Calculated	Typical						
Tungsten-silver									
85Ag-15W	PSR	11.27	10.60–11.30	85–90	25–38 HRB	…	…	A	Current-carrying contacts in circuit breakers' light-duty contactors
70Ag-30W	PSR	12.16	12.00	72–80	40–47 HRB	…	…	A	Automotive starting switches, circuit breakers
60Ag-40W	PSR	12.84	12.10–12.60	60–65	50–60 HRB	…	…	A	
35Ag-65W	INF	14.92	14.20–14.77	45–53	80–93 HRB	…	827	C	
	PSR	14.92	14.65–14.74	47–50	55–65 HRB	…	572	C	
27.5Ag-72.5W	INF	…	15.56	49	90 HRB	483	896	C	Motor starters, aircraft equipment, circuit breakers, contactors, computers, arcing tips
10Ag-90W	PSR	17.81	17.25	29–35	95–105 HRB	379	758	C	Motor governor, semiconducting material
Tungsten-copper									
50Cu-50W	INF	11.39	11.90–11.96	45–63	60–81 HRB	…	…	A	Arcing tips, vacuum interrupter, oil circuit breakers
44Cu-56W	INF	12.87	12.76	55	79 HRB	434	827	C	Circuit breaker runners, arcing tips, tap change arcing tips
30Cu-70W	INF	14.45	13.85–14.18	36–51	86–96 HRB	…	1000	C, A	
Ternary alloys									
91W-6.3Ni-2.7Fe	PSR	…	…	…	29 HRC	940[c]	…	[34]	Defense applications
91W-6Ni-3Co	PSR	…	…	…	31 HRC	960[d]	…	[34]	

[a] INF, press-sinter-infiltrate; PSR, press-sinter-repress (blended powder of the desired composition are compacted to the required shape and then sintered. Afterwards, the material is further densified by a second pressing. Sometimes the properties can be modified by a second sintering or annealing).

[b] A: Advance Metallurgy Inc., McKeesport, PA. C: Contacts, Materials, Welds, Inc., Indianapolis, IN.

[c] Elongation 35%.

[d] Elongation 40%.

- Chips of heavy metal, obtained during the shaping operations, can be transformed into re-usable powder by means of oxidation and subsequent reduction. Large solid pieces can be machined into smaller pieces to enable subsequent recycling. The oxidation step leads to a total disintegration of the chips into oxide powder containing tungsten trioxide and tungstates of iron, nickel, or cobalt. Hydrogen reduction results in a metal powder, in which all the components (W/Fe/Co/Ni) of the initial heavy metal are presented.
- Composite scrap mixtures, such as W/Cu, are difficult to oxidize, and are, therefore, not suitable for chemical recycling. Also, re-using in the steel industry cannot be realized due to the deleterious effect of copper in steel. A possible option is salt melt digestion with sodium nitrate, sodium nitrite, and sodium carbonate mixtures. However, this process presents environmental problems due to the nitrogen oxide formation. An alternative would be the electrochemical recovery of the tungsten.
- The slimes recovered from grinding high-speed tool steel, such as those containing up to 6 wt% tungsten, are de-watered by hot air and oxidized in a tube furnace in oxygen (0.05 m/s) with self-heating up to 1220 K. The oxides are vaporized at a temperature higher than 1670 K and condensed on cold screens. Tungsten extraction yield reaches up to 86% after 6 h at 1620 K. The condensate from tungsten and molybdenum oxides is reduced in hydrogen for 2 h at 1173 K. This results in powders with an average particle size of 15 μm and the following element content: 50 wt% tungsten, 50 wt% molybdenum, 0.02 wt% vanadium, 0.02 wt% chromium, and 0.1 wt% iron.
- The recovery process for tungsten bearing wastes includes the following steps: oxidation in hot air; milling of formed mixture of tungsten oxide and cobalt-tungsten oxide; and reduction at $T < 947\,°C$ in endogas or dissociated ammonia with an addition of natural gas.
- The recycling of composites of tungsten with thorium-containing compounds has problems due to radioactivity. Therefore, direct recycling in the steel industry is impossible. Chemical recovery in the conventional process leads to inadequate separation of thorium, and consequently is also inapplicable. At present, the only possible way to recycle this material is by electrolysis, such as through the method based on the electrolytic dissolution of tungsten in ammonia [55]. The difficulty is carrying out the process in such a way as to prevent dissolution of any of the radioactive products.

Accident Prevention When Working with the Tungsten Powder

Metallic tungsten dust is not toxic and is ranked in the fourth category according to State Standard 12.1.005-88 under the legislation in the Commonwealth of Independent States (CIS) [56]. Tungsten inspirable dust takes a predominantly fibrous effect. The limit for dust in the atmosphere of the work place unhealthy is 6 mg/m3. Under the Workplace exposure limits in the European PM industry, the long- and short-term (15-min reference period) workplace exposure limits (WELs) for tungsten and insoluble compounds (as W) in the workplace atmosphere are 5 mg/$m^3$and 10 mg/m^3, respectively [57]. Tungsten in drinking water is also unhealthy and falls into the second category. A limit of 0.05 mg/L is specified in CIS State Standard 4630-88 [58].

Fine oxidizable powder mixed with air can constitute an explosion hazard, but the risk with tungsten powder is minimal even with powder fraction <74 μm; a minimal ignition temperature of powder deposits (self-ignition temperature) is 583 K. The products with such characteristics of inflammability and explosion risk are relegated to the "low explosion hazard" class of danger according to the Guide to Legislation and "Health and Safety" in the European PM Industry [59].

Common techniques are mainly used for pollution prevention and environmental control during powder manufacture and its processing. Detailed information on health and environment protection measures and on the prevention of inflammability risk in such conditions can be found in the Chapter 27.

Tungsten Carbide Powders

Tungsten carbide powder is the basis for the production of cemented carbides, the vast class of hard, wear-resistant, refractory materials, in which the hard carbide particles are bound together, or cemented, by a soft and ductile metal binder. Conventional manufacturing of tungsten carbide powders accounts worldwide for the bulk of the tungsten carbide powder produced. This technique permits the production of tungsten carbide powders with particle sizes ranging from 0.15 μm to 50 μm [60]. This field offers all industrial applications and is described below, along with other methods.

Production of Tungsten Carbide Powders

Conventional technique: There are two methods [15,61] by which tungsten carbide powders are produced from pure tungsten powder. In the first method, fine tungsten powders are blended with high purity carbon black, filled into graphite boats, and pushed through a high temperature furnace under hydrogen at temperatures between 1673 K and

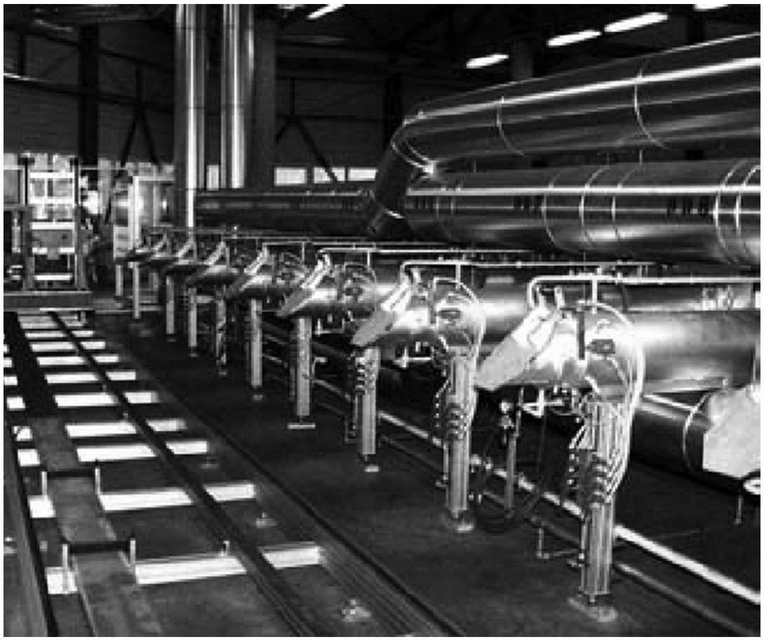

FIG. 23.23 Single tube push type furnace for tungsten carbide powder production. *(Courtesy: Wolfram Bergbau- und Hütten-GmbH.)*

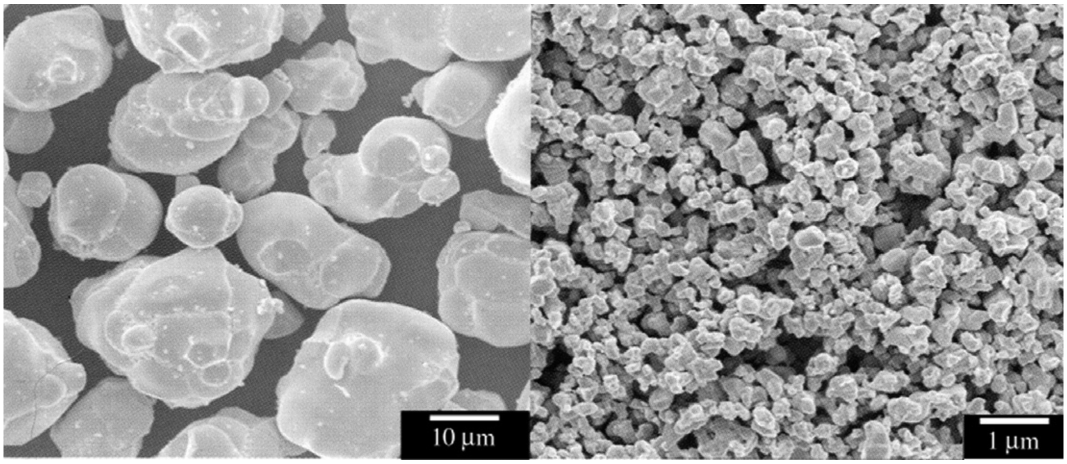

FIG. 23.24 Scanning electron micrographs of coarse and ultrafine tungsten carbide powders. *(Courtesy: Wolfram Bergbau- und Hütten-GmbH.)*

1773 K. Compared to the reduction step for tungsten, temperatures are much higher, and single tube pusher type furnaces (Fig. 23.23) are used. Each particle is composed of numerous tungsten carbide crystals. The particle size of the tungsten carbide powder (Fig. 23.24), for the most part, preserves the particle size of the submicron tungsten metal powder (see Fig. 23.14). Further, cooled caked tungsten carbide powder is de-agglomerated. This step just separates particles from sticking to each other and is not used to change the particle size. This process, including the ore-processing steps, is also called the conventional calcination-reduction-carburization (CRC) process and offers the potential to manufacture commercial WC ultrafine powders with median grain sizes below 0.5 μm. Strict process control and a high degree of automation permits greater uniformity and batch-to-batch reliability [62].

This process is unsuitable for the production of coarse-grained powder. Techniques of the former conventional tungsten carbide production are usually limited during carburization to temperatures around 2270 K. At these temperatures, carburization with tungsten powder with particles <100 μm can be achieved, but the resulting product is polycrystalline.

By the latter, the increase of tungsten carbide single crystals is realized by the use of a liquid phase, which is able to dissolve both tungsten and carbon. The formation of tungsten carbide within the melt of solvent metal, such as iron, is the basis of the Menstruum process, also called “macro process.” [63] The powder mixtures of tungsten ore concentrates, iron oxide, aluminum, calcium carbide, and/or carbon react exothermally (after ignition by a detonator) to generate tungsten carbide, iron, calcium oxide, and aluminum oxide. A high temperature exothermic reaction ($2Al+3FeO \leftrightarrow Al_2O_3+3Fe$) at about 2770 K produces a molten mass that, when solidified, consists of tungsten carbide crystals dispersed in iron and a slag containing impurities. This technique permits complete reduction and carburization of a batch of about 22 t of tungsten carbide, which is achieved in 60 min. To get the tungsten carbide in powder form, the solidified solvent metal is dissolved, which is ordinarily done with hot hydrochloric acid. The obtained tungsten carbide powder is separated according to desired particle size by sieving. Menstruum tungsten carbide powders have a high yield of well-faceted single crystal particles with sizes of 400 μm and below.

Production of fine grained powder: Recently, the demands for tungsten carbide powders finer than 1 μm are increasing, as material for precision tools such as drills and end mills for metal cutting, printed circuit boards, cutters and precision pins, and so on. This increased demand, together with conventional techniques’ efficiency limitations in producing fine-grained metal powders [64], creates a strong motivation to develop alternative techniques.

Tokyo Tungsten Co., Ltd. has developed [65] the direct carburizing process, in which tungsten trioxide and carbon black react in the following steps:

$$WO_3 \rightarrow (WO_{2.9}) \rightarrow (WO_{2.72}) \rightarrow WO_2 \rightarrow W \rightarrow W_2C \rightarrow WC$$

At the $(WO_{2.72}) \rightarrow WO_2$ step, ultrafine particles are generated and then transformed into tungsten carbide without grain growth. The starting material is prepared in the form of pellets from a mixture of tungsten oxide with carbon black. Subsequent reaction is accomplished in rotary furnaces in two steps: the direct reduction of the WO3 to tungsten by carbon under nitrogen, followed by carburization under hydrogen at temperatures up to 1873 K to tungsten carbide powder. This method permits the production of ultrafine powder with particle sizes ranging from 0.1 μm to 0.7 μm. Vickers hardness, HV (50 kg), decreases from 2150 to 1900 as particle size increases from 0.1 μm to 0.3 μm.

Another direct carburization process has been developed by Dow Chemical Company [66,67]. A mixture of tungsten trioxide and carbon black falls through a vertical reactor at temperatures of approximately 2270 K. Accordingly, the reaction time is a few seconds and results in the formation of an intermediate mixture of W, W_2C, WC, and C. This product must be subjected to a second, more conventional carburization step. Particle sizes were reduced by controlling the milling time, carbon content, inhibitor addition, and sintering temperature. The characteristic particle size range for this process is between 0.1 μm and 0.8 μm, which is identical to the lowest limits of the conventional process [64].

The spray conversion process has been developed for Nanodyne Inc. [68] to produce nanopowders. Aqueous solutions of tungsten and cobalt salts are spray dried, then subsequently reduced and carburized with a gas mixture such as hydrogen and ammonia or carbon dioxide and carbon monoxide in a fluidized bed reactor. The product obtained is relatively large (about 75 μm) hollow WC-Co composite powder particles that consist of tungsten carbide crystallites with a grain size of about 30 nm. This product is milled in order to obtain a powder suitable for consolidation.

Another technique to produce tungsten carbide nanopowders is a chemical vapor reaction process [69]. This process is based on the gas phase reaction of metal halides with different gas mixtures to produce nanosized powder ranging from 5 nm to 50 nm. Production of tungsten carbides is possible in principle; however, the process seems better adapted to the production of nitrides or carbides of other group IV and V refractory metals.

Properties of Tungsten Carbide Powders

High hardness is one of the most important properties of pure tungsten carbide and is the basis for the application in hardmetals, also called “cemented carbides.” As of 2014, >50% of the 30,000 tons of tungsten produced annually was used in the production of cemented carbides [70].

A number of physical and technological characteristic values are quite similar to those for tungsten metal powders. Tungsten carbide powders may have powder particle structures which are either single or polycrystalline. SEM and bright field TEM images (Fig. 23.25) show the typical morphology and physical constitution of ultrafine tungsten carbide [62]. The grain boundaries within a single particle are revealed by dotted lines.

Recent developments in the field of standard ultrafine grades were driven, above all, by the need to control the sinter activity and grain growth tendency of ultrafine carbides. Table 23.7 shows the basic characteristics of standard ultrafine powder grades. Abbreviation CRC symbolizes the milestones of conventional process from tungsten concentrate to tungsten carbide through calcination, reduction, and carburization.

The values obtained using a Fisher subsieve sizer (FSSS), based on the air permeability method of measuring the average particle size of powders, are not absolute and irreproducible in the range of ultrafine powders. It could be

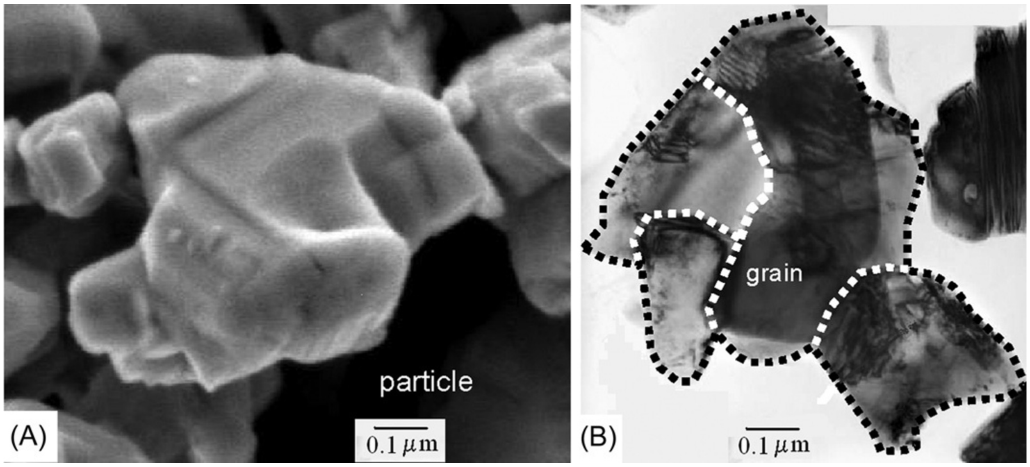

FIG. 23.25 Morphology and physical constitution of ultrafine tungsten carbide. (A) Scanning electron micrograph of powder particles; (B) transmission electron microscopy image of single particle. *(Courtesy: Wolfram Bergbau - und Huttengesellschaft mbH NfG KG, Austria.)*

TABLE 23.7 Properties of Ultrafine Tungsten Carbide Powder Grades

		Standard Grades				
Property	**Unit**	**CRC025**	**WC O6**	**CRC020**	**WC 05**	**CRC015**
FSSS[a] grain size	μm	0.63	0.64	0.55	0.56	0.49
BET specific surface area (S_{BET})	m^2/g	1.71	1.52	2.03	1.95	2.43–2.83
BET calculated particle size[b]	μm	0.22	0.25	0.19	0.20	0.16–0.14
FESEM particle size d_{SEM}[c]	μm	…	0.30	…	0.25	0.18
Total carbon	wt%	6.12	6.17	6.09	6.19	6.11–6.15
Free carbon	wt%	0.03	0.03	0.03	0.02	0.01–0.05
VC	wt%	Undoped	0.1–0.5	Undoped	0.3–1.0	0.3–1.0
$Cr_3 C_2$	wt%	Undoped	0.1–0.5	Undoped	0.3–1.0	0.3–1.0
Oxygen	ppm	900	1030	1080	1450	1810–2800

[a] *Fisher Sub-Sieve Size.*
[b] *BET particle size calculated, based on measurement of minimum 300 particles, according equation:* $d_{BET} = \frac{6}{15.6 S_{BET}}$ μm.
[c] *FESEM particle size according equation:* $d_{SEM} = \sum_{d_i}^{d_j} d / \sum_{d_i}^{d_j} N$ μm, where $\sum_{d_i}^{d_j} d$ is sum of diameter of all particles in range from d_i to d_j; $\sum_{d_i}^{d_j} N$ is total number of particles in range from d_i to d_j.
VC, vanadium carbide.

demonstrated using scanning electron microscopy that obtained FSSS particle sizes are overstated by two to three times in comparison with reality [64,71]. With field emission secondary electron microscopy (FESEM), particle sizes are slightly higher than calculated by BET (Table 23.7) because the surface roughness may give a high surface area measurement, leading to the wrong conclusion that they are finer. In turn, an arithmetic mean FESEM particle size, calculated according to Eq. (c) in Table 23.7 used for particle size distribution:

$$\varphi(d) = \frac{\sum_{d_i}^{d_j} d}{\sum_{d_1}^{d_N} d}$$

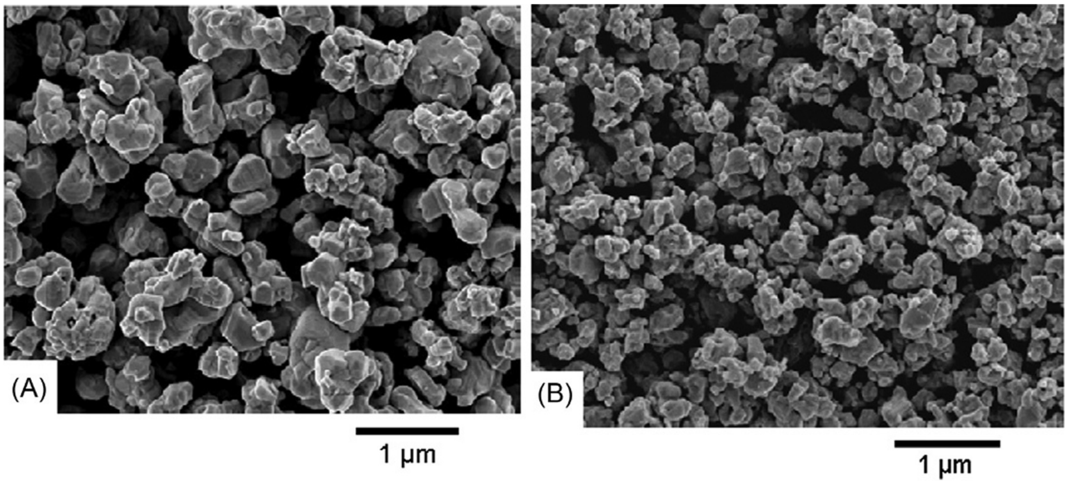

FIG. 23.26 Scanning electron micrographs of standard tungsten carbide powder grades CRC025 (A) and CRC015 (B).

where $\sum_{d_1}^{d_N} d$ is sum of particle diameter of all measured particles N (µm) does not represent reliable weight particle distribution. In consequence of cubic dependence of particle volume on its size, the weight distribution will be leveled by FESEM particle size distribution calculated by the sum of particle diameters. In reality, for example, if powder particle size boundaries ranged from 0.05 to 1.0, the linear particle sizes would differ by 20 times, while their volumes would differ by 8000 times. Thus, the average FESEM particle size may be understated.

A higher fines yield can be advantageous in order to increase the sinter activity/densification rate (at low sintering temperatures during solid state sintering) or to enable a slight rise in hardness due to maximum grain growth inhibition. Special applications (in particular, in the area of wear parts) set the demand for carbide grades with BET specific surface areas higher than 2.4 m^2/g. Developed CRC 015 grade satisfies these requirements (see Table 23.7). These carbides with calculated BET particle sizes of 0.15 µm are produced in full-scale units by the conventional CRC process. Powder grades CRC 025 and CRC 015 differ appreciably in their particle sizes (Fig. 23.26).

Added chromium plays an important role in grain growth inhibition during sintering. Energy dispersion analysis provides evidence [61] that chromium added during powder processing is preferentially present at WC/WC grain boundaries, even in the interior of polycrystalline particles or in necks between carbide particles. 10 wt% Co alloys produced by conventional liquid phase sintering at 1693 K and doped with chromium carbide (0.3–1.0 wt% $Cr_3\,C_2$) and vanadium carbide (0.3–0.6 wt% VC) resulted in coercitivity values ranging from 440 Oe to 560 Oe with a corresponding increase in BET specific surface area from 1.5 to 2.8 m^2/g. Additionally, the increase in maximum coercitivity is directly proportional to the BET surface area.

The most important chemical component of tungsten carbide powder is its carbon content. Stoichiometric pure tungsten carbide has a total carbon content (C_t) of 6.135 wt%. From the point of view of thermodynamic equilibrium, WC has a very narrow stability range [2]. Thus, not even a small carbon shortage leads to W_2C to the formation of free carbon (C_f). In commercial WC powders, there is always a small portion of free carbon present, about 0.03% at a stoichiometric C_t level. Even when the total carbon is below the stoichiometric level, the coexistence of traces of W_2C and C_f can occur. The carbon balance is important for hardmetal manufacturing, because a shortage of carbon leads to the formation of the brittle phases, for instance, Co_2W_3C, and any excess in carbon leads to graphite precipitation. Thus, both cases result in a detrimental effect on the mechanical properties of the final product [2,61].

The role of carbon source in the production of WC powders starting from metal tungsten (W) and tungsten oxide (WO_3) has been studied [72]. Those conclusions follow.

In the $W + C \rightarrow WC$ process conditions, inert atmospheres are recommendable for the synthesis of WC when metallic tungsten powders are used as precursors. In these conditions, fine WC powders can be obtained at 1373 K using either graphite or carbon black powders. The resulting WC powders consist of agglomerates of submicron particles with irregular platelet morphology.

In the $WO_3 + 4C \rightarrow WC + 3CO$ process conditions, is possible to synthesize WC directly from WO_3 powders. In this case, atmospheres containing hydrogen are needed to activate reduction of oxides at lower temperatures, whereas, at higher temperatures, reduction is promoted by the presence of carbon. Carburization in Ar-50%H_2 of mixes containing WO_3 + carbon black is complete at 1373 K, whereas, for WO_3 + graphite powders, complete transformation to WC is achieved at higher temperatures (1573 K). High energetic milling of WO_3 + graphite allows the complete carburization at 1373 K. The resulting WC powders have spherical morphology, submicron particle size, and crystalline grain sizes below 30 nm.

Nanoscale WC-η composite powder was synthesized by in situ reaction of tungsten oxide, cobalt oxide, and carbon black mixtures for fabricating a nanostructured WC-based coating in which the conventional Co matrix was substituted for η phases (Co_6W_6C, Co_3W_3C, Co_2W_4C, etc.) [73]. WC-η nanocomposite powder with a particle size of 50–200 nm was prepared by in situ reaction of metal oxides and carbon, based on which, the nanostructured, WC-based coating was then fabricated by high-velocity, oxy-fuel thermal spraying. Song, et al. [73], based on fulfilled studies, reported the following:

(a) Above 1170 K, the synthesized composite powder contains only WC and η phases. At lower temperatures, the $CoWO_4$ phase preferentially forms in the synthesized powder and then transforms into W_2C, W, Co_6W_6C, and Co_3W_3C phases as the temperature increases.

(b) The amount of η phases of the obtained WC-η composite powder depends largely on the carbon addition of the raw materials. The appropriate carbon content was estimated as 3.9%–4.2% for the WC-Co thermal spray feedstock powder resulting in no metallic Co phase.

(c) The thermal spraying feedstock prepared using the WC-η nanocomposite powder has a homogeneous WC particle size distribution with a mean size of about 260 nm. In contrast, the conventional powder consists of WC particles of $3-5\,\mu m$ (Fig. 23.27).

Elements such as vanadium, chromium, tantalum, and niobium, due to their grain-growth inhibiting effect during hardmetal sintering, are added to tungsten carbide powder in amounts around 0.1–1.5 wt%. Such elements can be introduced as carbide to the tungsten carbide powder, or as oxide or carbide prior to the carburization step. Trace elements similar to nickel, iron, and cobalt can be admitted in amounts around 100 ppm. At the same time, there are other impurities that should be limited in the very low ppm range because of their detrimental action on hardmetal properties. Calcium, sulfur, silicon, and phosphorus are typical of such elements [74,75]. Compositions and properties of several standard tungsten carbide powders are given in Table 23.8.

Tungsten Carbide Electrical Contacts

Tungsten carbide analogous to other refractory metals and their carbides is distinguished by high melting and boiling points and very high hardness at both room and elevated temperatures, but also by poor electrical and thermal conductivities and poor oxidation resistance. Forming a composite can compensate for these drawbacks. The development of composite contact materials involving silver with tungsten or molybdenum or their carbides has resulted in materials that can withstand higher currents and more arcing than other contact materials, without experiencing sticking or rapid erosion. Refractory metals, the content of which can vary from 10% to 90%, offer good mechanical wear resistance and resistance to arcing. Silver provides good electrical and thermal conductivities.

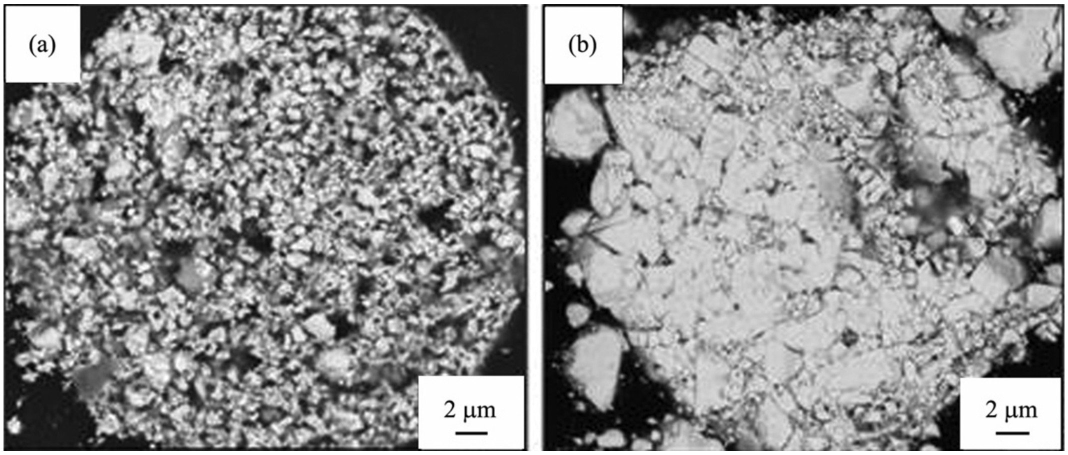

FIG. 23.27 Cross-sectional microstructures of the feedstock particles prepared with the WC-η composite powder (A) and (B) the conventional powder. *(Source: Song X, Wang H, Yang T, Liu X, Wang X. In situ synthesis of nanoscale WC-η composite powder and its application in cermet coating. In: Compiled by European Powder Metallurgy Association. Proceedings of PM 2016 world congress. Hamburg (Germany); 2016: p. 1–6.)*

TABLE 23.8 Properties of Typical Tungsten Carbide Powders

		Source: Standard Grades								
		WBH		OSRAM						
Property	**Unit**	**WC 05D [3]**	**WC 06**	**BC04U**	**BC10U**	**BC45S**	**BC65S**	**BC75H**	**WC-TiC 70/30[a]**	**WC-Ti 50/50[a]**
FSSS[b]	μm	0.53	0.64	0.5–0.7	0.91–1.20	4.31–5.00	11.01–15.00	> 30	2.0 ± 0.3	2.0 ± 0.3
BET specific surface area	m^2/g	1.90	1.52	…	…	…	…	…	…	…
Nominal composition:										
Total carbon	wt%	6.23	6.17	6.13 ± 0.05	6.13 ± 0.05	6.13 ± 0.05	6.13 ± 0.05	6.13 ± 0.05	9.7–10.2	12.6 ± 0.2
Free carbon	wt%	0.04	0.03	max 0.08	max 0.08	max 0.06	max 0.06	max 0.06	max 0.25	max 0.4
VC	wt%	0.32	0.1–0.5	…	…	…	…	…	…	…
Cr_3C_2	wt%	0.64	0.1–0.5	…	…	…	…	…	…	…
Trace elements:										
Aluminum	ppm	10	<5	…	…	…	…	…	…	..
Calcium	ppm	3	<2	…	…	…	…	…	max 0.01	max 0.01
Chromium	ppm	…	…	100	100	50	50	75	…	…
Cobalt	ppm	<5	<5	…	…	…	…	…	…	…
Copper	ppm	<2	…	…	…	…	…	…	…	…
Iron	ppm	46	20	350	350	500	500	500	max 0.05	max 0.05
Magnesium	ppm	<1	…	…	…	…	…	…	…	…
Molybdenum	ppm	<20	<20	…	…	…	…	…	…	…
Nickel	ppm	<5	<5	150	150	100	100	100	…	…
Oxygen	ppm	1440	1030	3000	2500	500	500	500	…	…
Phosphorus	ppm	<20	…	…	…	…	…	…	…	…
Potassium	ppm	<4	…	…	…	…	…	…	max 0.01	max 0.01
Sulfur	ppm	6	<5	…	…	…	…	…	max 0.01	max 0.01
Silicon	ppm	<10	<10	…	…	…	…	…	max 0.005	max 0.005
Density	g/cm^3			14.72	14.91	14.94	14.94	14.94	…	…
Hardness	HV30			2000	1650	1380	1220	<1050	…	…
Coercivity	O_e			500	260	122	80	<60	…	…

[a] *Fine-grained Grade; WBH: Wolfram Bergbau- und Hütten Company (Sankt Martin im Sulmtal, Austria); OSRAM: OSRAM Sulvanias, North America (Wilmington, MA, United States).*

[b] *Fisher Sub-Sieve Size.*

Silver does not alloy with tungsten, molybdenum, or their carbides. Therefore, PM processes are used in their manufacture. Depending on the composition, contact materials are accomplished either by pressing and sintering or by the press-interinfiltrate method. At temperatures rise above the melting point of the infiltrant, the liquid metal penetrates and fills the interconnecting voids of the pressed and sintered compact. Densities that are 96%–99% of the theoretical density can be achieved by this technique. Infiltrated contact materials find use as current-carrying contacts in air- and oil-immersed circuit breakers, heavy-duty relays, automotive starters, and switches. Copper infiltrant, which costs less but has very poor corrosion resistance, is used for parts that operate in non-corrosive environments such as oil, vacuum, or inert atmospheres. Table 23.9 contains data on typical tungsten and carbide electrical contact grades published by manufacturers, which usually include density, hardness, and electrical conductivity.

Diamond Tools

Tungsten carbide powder, together with certain metal powders, can be used to adjust the characteristics of alloys in which diamonds are embedded [76].

HARDFACING

Hardfacing is the application of hard, wear-resistant material to the surface of a component by welding, thermal spraying, or a similar process for the main purpose of reducing wear. Carbide/metal mixtures very like hardmetal compounds are applied to machine parts to improve their resistance. This can be realized by flame or plasma spraying of powders or by welding techniques. The detonation gun spray process is also used. The extremely high particle velocities achieved in this process result in coating with higher density, greater internal strength, and superior bond strength than can be achieved with conventional plasma spraying or single-step flame spraying.

Another category of hardfacing techniques is cladding. Hardfacing materials can be clad onto substrates by furnace fusing prearranged layers of loosely bonded hardmetal onto the substrate. Thus, the Conforma Clad Process (Conforma Clad, Inc.) uses a flexible cloth made of polytetrafluoroethylene and a hardfacing powder of the desired composition. The main benefit from this technique is that the cloth can be cut into any required size and placed on the surface to be coated, regardless of the profile of the workpiece. During subsequent furnace sintering, polytetrafluoroethylene is vaporized, and the hardfacing powder forms the deposit layer [77].

Sintered tungsten carbide powders are widely used for thermal spray coatings and torch welding hardfacing. Powder can be a product of crushing bulk WC-Co alloys or specifically made spherical shaped pellets. Tungsten carbide powders for thermal spray coatings usually contain from 6% to 18% cobalt. Particle sizes of WC-Co for thermal spray coatings range from 5 μm to 150 μm. Powder particle sizes for torch welding hardfacing range from 20 μm to 100 μm.

Macrocrystalline tungsten carbide powders are a special kind of tungsten carbide powder manufactured by a high-temperature thermit process during which ore concentrate is converted directly to tungsten carbide. This product maintains the correct stoichiometric carbon content of 6.13 wt%. Macrocrystalline tungsten carbide is grown in crystals ranging from 1 μm to 5 mm. Coarse mesh sizes of macrocrystalline carbide are extensively used in abrasion erosion protection applications. The finer size powder is employed as wear rate modifier. Coarse tungsten carbide powder can also be obtained by conventional carburization method. Commercial grade powders are manufactured by H. C. Starck GmbH (Munich, Germany), Kennametal India Ltd. (Bengaluru, India), etc.

Cast tungsten carbide is another category of carbide that also finds wide applications in hardfacing. Cast carbide refers to eutectic of WC and W_2C that can range in carbon content from 3.5 to 4.5 wt%. It is manufactured by melting compounds of metallic tungsten, tungsten carbide, and carbon at a temperature above 3270 K. The melt is cast into billets, which are then crushed to the size range of powder. The cast is crushed to powder <850 μm and as fine as below 45 μm. Cast carbide, mostly used in torch welding hardfacing, is often used in combination with sintered tungsten carbide and other carbides to enhance wear resistance. At the same time, the addition of cast carbide tends to produce coatings with lower toughness.

A relatively new spherical cast tungsten carbide product has all the basic characteristics of crushed cast carbide. However, this material has extremely high wear resistance and higher resistance to chipping and cracking in comparison with crushed cast carbide due to its spherical shape. Spherical cast carbide is manufactured by a technique ensuring rapid solidification of molten eutectic carbide droplets [78].

Diamond-like carbon (DLC) coatings technology due to their surface smoothness, hardness, and chemical inertness in combination with a low friction coefficient against most metals make DLC films interesting for wear-protective purposes. However, DLC films present high compressive internal stress and low chemical interaction between films and their metal

TABLE 23.9 Properties of Typical Tungsten Carbide Electrical Contact Grades

Nominal Composition (%)	Manufacturing Method[a]	Density (g/cm^3)		Electrical Conductivity (% IACS)	Hardness	Tensile Strength (MPa)	Modulus of Rupture (MPa)	Data Source[b]	Application Examples
		Calculated	Typical						
Tungsten carbide-silver									
65Ag-35WC	INF	11.86	11.53–11.85	55–60	50–65 HRB	272	483	C, A	Aircraft contactors, lighting relays, low-voltage switches, Circuit breakers
60Ag-40WC	PSR	12.09	11.40–11.92	46–55	60–70 HRB	…	…	A	
50Ag-50WC	INF	12.56	12.12–12.50	43–52	75–83 HRB	276	793	C, A	
40Ag-60WC	INF	13.07	12.0–12.92	40–47	90–100 HRB	379	827	C, A	Heavy-duty
38Ag	INF	13.18	12.92–13.29	35–38	90–100 HRB	552	…	C	Circuit breakers
20Ag-80WC	PSR	14.23	13.2	19	400 HV (c)	…	…	M	Semiconducting material
Tungsten carbide-copper									
50Cu	INF	11.39	11.0–11.27	42–47	90–100 HRB	…	1103	C, A	Arcing contacts in oil, wiping shoes in power transformers
44Cu	INF	11.77	11.64	43	99 HRF	…	1241	C	
30Cu	INF	12.78	12.65	30	38 HRC	…	…	…	

[a] *INF, press-sinter-infiltrate; PSR, press-sinter-repress (blended powder of the desired composition are compacted to the required shape and then sintered. Afterwards, the material is further densified by a second pressing. Sometimes the properties can be modified by a second sintering or annealing).*

[b] *A: Advance Metallurgy, Inc., McKeesport, PA. C: Contacts, Materials, Welds, Inc., Indianapolis, IN. M: Metz Degussa, South Plainville, NJ.*

FIG. 23.28 Schematic of the magnetron sputtering system.

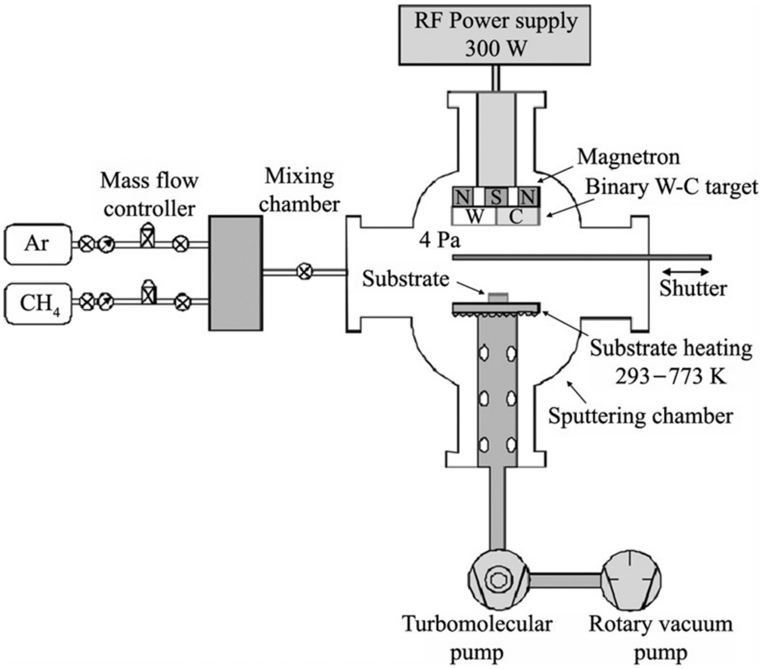
RF Power supply
300 W
Magnetron
Binary W-C target
N S N
W C
Mass flow
controller
Mixing
chamber
Ar
CH4
4 Pa
Substrate
Shutter
Substrate heating
293−773 K
Sputtering chamber
Turbomolecular
pump
Rotary vacuum
pump

substrates. Now, the most general approach to solve the adhesion problem is to use metal or silicon interlayers between steel and DLC.

In work [79], a physical vapor deposition (PVD) method for the deposition of tungsten carbide and DLC multilayer coatings by using a single sputtering target comprised of two equal halves (one half carbon, the other tungsten) was realized. A set of coatings were deposited by means of a RF (radio frequency) (13.56 MHz) magnetron sputtering system (Fig. 23.28).

The different layers are obtained by the variation of the argon and methane/argon sputtering gas composition. The pressure of both argon an argon/methane mixture was 4 Pa. Using this deposition method, researchers prepared multilayer coatings onto steel substrates. The coatings are formed by a multilayer stack of different WC layers and an upper DLC layer. The DLC thickness was approximately 0.3 µm, and the total thickness was approximately 1.0 µm. Fig. 23.29 shows the SEM cross-section morphology of a WC/DLC multilayer.

As reported [79], the structure of this multilayer stack consists of cubic WC_{1-x} polycrystalline layers separated by carbon rich narrow interlayers. The upper DLC layer has been obtained in the same process by increasing the methane concentration in the gas mixture. The experiments have demonstrated that multilayer coatings improve the adhesion and wear resistance of the DLC coatings on steel substrates while keeping their low friction properties.

FIG. 23.29 SEM micrograph of cross-section of a WC/DLC multilayer coating. *(Source: Rincón C, Zambrano G, Carvajal A, Esteve J. Tungsten carbide/diamond-like carbon multilayer coating on steel for tribological applications. Surf Coat Technol 2001; 148(2–3): 277–83.)*

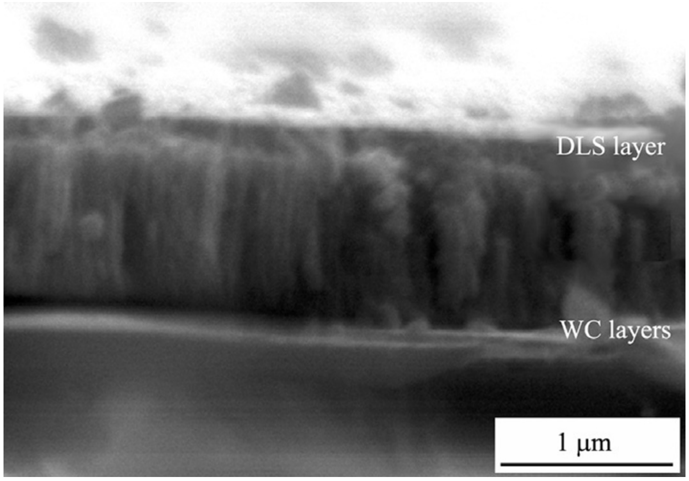
DLS layer
WC layers
1 µm

The paper [80] presents the results of abrasive wear resistance, microhardness, and adhesive wear resistance tests conducted on AISI 1020 commercial steel when it is standardized, heat treated through a process of quenching-tempering, and when a coating of tungsten carbide in powder form of nanometric size is deposited on it. This had been reported as follows:

Knoop microhardness tests allowed researchers to conclude that thermally treated specimens with a quenching-tempering process improve this property by 5.5%, while the WC coatings have a more significant increase, reaching a value of 124.2% compared to standard steel. The average loss of material per unit of covered length during abrasive wear resistance tests on AISI 1020 standard steel, thermally treated with a quenching-tempering process and coated with nanometric-sized WC is of 0.0382 mm^3/m, 0.0291 mm^3/m, and 0.0151 mm^3/m, respectively. The average loss of material per unit of covered length during adhesive wear resistance tests on AISI 1020 standard steel, thermally treated with a quenching-tempering process and coated with nanometric-sized WC is of 0.0827 mm^3/m, 0.0736 mm^3/m, and 0.0271 mm^3/m, respectively.

CEMENTED CARBIDES

Production of Cemented Carbide Powders

Optimal interfacial bonding in hardmetals is achieved by means of optimization of balance between the high hardness of the tungsten carbide and the high toughness of a ductile binder metal, such as cobalt, nickel, or iron [76,81]. The steps of hardmetal manufacture include: blending of grade powders, milling, powder consolidation, liquid phase sintering, post-sintering operations, and post-sinter forming. The excellent wetting of tungsten carbide by cobalt is one of its key properties. By variation of the tungsten carbide particle size and the percentage of cobalt, desired properties of the hardmetals can be obtained [76,81,82].

Fig. 23.30 illustrates, in diagram form, that tungsten carbide particles with equal particle size may differ concerning the size of the individual crystals within the particles, which, depending on the powder manufacturing process, can either be single or polycrystalline. This characteristic has a strong influence on the behavior of the powder during the manufacturing of the cemented carbide. Generally, the higher the number of subgrains per WC particle, the finer the microstructure of a hardmetal can be [3].

A general rule, moreover, is the finer the carbide and the lower the cobalt content, the harder, but less tough, the composite is. But, higher binder content at a certain hardness (combined with a lower average WC grain size) does not necessarily mean a higher toughness. In particular, in the lower hardness range, this relationship does not hold. At the higher hardness range, however, a higher binder can reduce the carbide contiguity, and thus, improve the hardness to toughness relationship. However, the improvements which can be obtained at a high hardness are obviously limited for hardness above 2000 HV30 [83], while the basic WC-Co material has been modified to produce a variety of hardmetals, which are used in a wide range of applications, including metal cutting, mining, construction, rock drilling, metal forming, structural components, and wear parts.

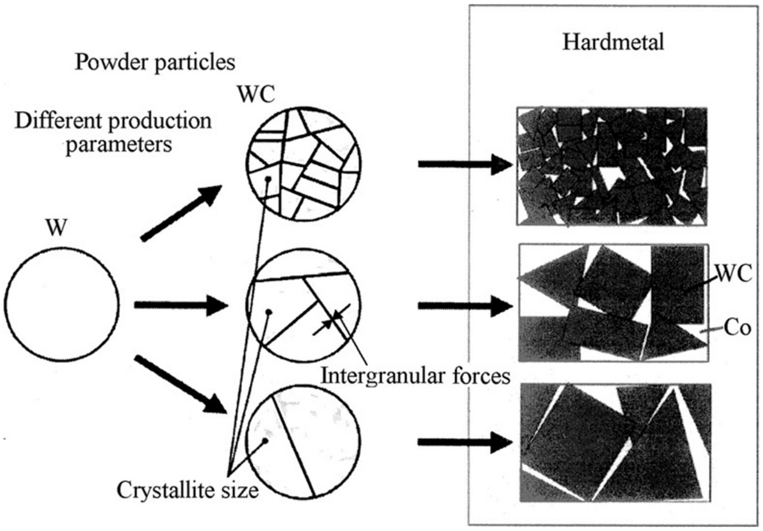

FIG. 23.30 Influence of crystalline size of tungsten carbide particles on the microstructure forming of hard metal.

Additions of other carbides such as titanium, tantalum and niobium, or titanium carbonitrides are used in steel cutting grades and are produced from metal oxides of titanium, tantalum and niobium. These oxides in particulate form are mixed with metallic tungsten powder and carbon black. The oxides are reduced under a hydrogen atmosphere or vacuum at elevated temperatures and form solid solution carbides WC-TiC, WC-TiC-TaC, or WC-TiC-(Ta, Nb)C. The Menstruum process can be used to produce a WC-TiC solid solution. In this method, both carbides are dissolved in liquid nickel, which functions as a contributory metal. Solid solution carbides are then precipitated during cooling.

The cemented carbide powders may consist of tungsten carbide mixed with a finely dispersed metallic binder (cobalt, nickel, or iron) or with additions of other above-named cubic carbides, depending on the desired properties and application of the tool. Intensive milling is necessary to disintegrate the initial carbide crystallites and to blend all components so that every carbide particle is coated with binder material. This process is accomplished in ball mills, vibratory mills, or attritors using carbide balls. The mills are usually lined with carbide sleeves; however, mills lined with low-carbon steel or stainless steel are also used.

Grinding is carried out under an organic liquid such as heptane or acetone to prevent oxidation of the powder. After milling, the liquid is distilled off, and the powder is dried. A solid lubricant, such as paraffin wax, is added to the powder mix in the final stage of the milling or subsequently in a blender. The lubricant protective coating prevents or greatly reduces the oxidation of the powder and imparts strength to the powder mix during its consolidation.

In the spray drying process commonly used in the hardmetals industry, a hot inert gas such as nitrogen impinges on a stream of carbide particles. Thus, a product in the form of spheroidal powder aggregates is produced.

The favorable mechanical properties of WC-Co-based cemented carbides are significantly deteriorated at elevated temperatures or in corrosive environment [84]. In order to overcome these shortcomings, the introduction of ordered fcc_L$1_2\gamma'$ precipitates [85] into a Co-binder is a way to strengthen the binder phase and improve its high temperature properties or corrosion resistance, similar to that in cobalt-base superalloys [86]. Thus, it offers new possibilities for development of novel WC-Co-Ni-Al cemented carbide that possesses both high-temperature strength and environmental resistance. Long et al. [87] recently developed a type of WC-Co-Ni-Al cemented carbides with novel $\gamma+\gamma'$ Co-based binder. The abnormal WC grain is much larger than average, and this greatly worsens the mechanical properties of the alloys because these abnormal grains act as initiation points for cracking and breakage [88]. Thus, suppression of abnormal grain growth (AGG) becomes an important issue for the preparation of ultrafine or nanocrystalline WC-Co cemented carbide [89]. However, the mechanism for AGG is not fully understood. Park et al. [90] considers the AGG behavior to be related to two-dimensional (2-D) nucleation. Recently, Long et al. [91] considered the 2-D nucleation of WC grains in ultracoarse WC-Co-Ni-Al alloys in connection with solid-liquid interfacial energy and solubility of tungsten in the binder phase.

In the work [92], the growth behavior of WC grains in WC-Co-Ni-Al alloys with different Co-Ni-Al binder phase compositions was studied. Powder mixtures of WC-18(Co-Ni-Al) samples were milled in ethyl alcohol in a ball mill at the ball-to-powder ratio of 6:1 for 48 h. Powder mixtures of WC-8Co like WC-8Ni_3Al were milled in ethyl alcohol in a ball mill at the ball-to-powder ratio of 15:1 for 96 h. These powder mixtures were then dried under vacuum at 358 K. These samples were uniaxially cold pressed into bars of 25 × 8 × 6.7 mm at a pressure of 150 MPa and then sintered at 1723 K under the 6 MPa pressure for 1 h and cooled with a furnace. Then, WC grains in the as-sintered samples were extracted by removing the binder matrix with saturation hydrochloric and Fe_3Cl solution in supersonic cleaner. Fig. 23.31 shows the morphology of cemented carbide grains extracted from the WC-18(Co-Ni-Al) alloys sintered at 1723 K for 1 h. It can be seen that, as the Ni_3Al content increases, WC grain size is significantly reduced, especially the size of the coarse WC grains.

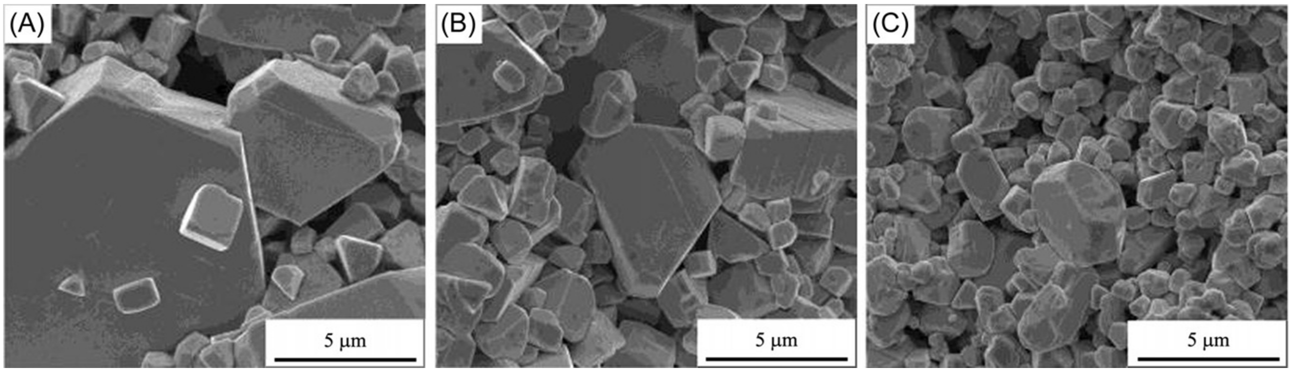

FIG. 23.31 Morphology of cemented carbide grains extracted from the WC–18 (Co-Ni-Al) alloys obtained by various Ni_3Al content: (A) without Ni_3Al, (B) 5.3 wt% Ni_3Al, (C) 11.3 wt% Ni_3Al.

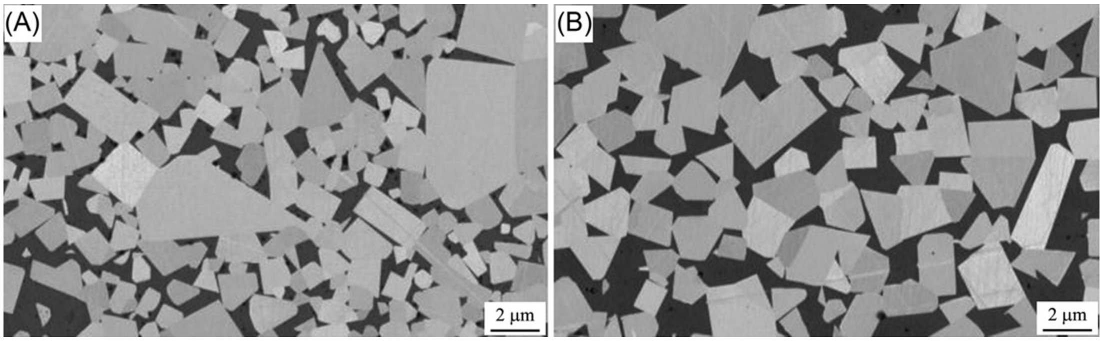

FIG. 23.32 Microstructure of binder jet printed and sintered parts with 12 wt%Co (A) and 17 wt%Co (B).

It was concluded [92] that with the increase of Ni_3Al content in Co-Ni-Al binder, the increasing interface energy slows the growth rate of WC; therefore, with the increase of Ni_3Al content in Co-Ni-Al binder, the AGG of the alloy is appreciably inhibited.

Additive manufacturing (AM) of polymer, metal, and ceramic materials has become more and more common. For hardmetals however, very little work has been reported so far. Yet, the implementation of additive manufacturing in the field of hardmetals would enhance the possibility of producing complex shaped parts, which cannot be produced by conventional means, and allowing the production of parts within hours instead of days because of the tool-free production technology.

Binder jetting of cemented carbide green parts was first published by Kelley in 1998 [93]. Like select selective laser sintering (SLS), it is a powder-bed-based AM technique. In contrast to SLS, the particles are not selectively "sintered" but "glued" together by organic binder, which is applied layer-by-layer using a special print head. Thus, the printed parts are green parts, and their green density is mainly based on the powder density of the used starting material. During a post-printing debinding step, the organic materials used during printing must be removed, and the samples must be sintered.

Using this technique, in the work [94], the samples with cobalt contents between 12 wt% and 20 wt% were produced by sintering temperatures between 1673 K and 1743 K. Densities achieved are above 99.8% of theoretical density and hardness as well as fracture toughness are comparable to standard hardmetal grades with the same composition. The 17wt%Co samples showed homogeneous microstructure, while samples with 12wt%Co showed some larger WC grains, which can be avoided by using a composition with grain growth inhibitors such as Cr_3C_2 or vanadium carbide (Fig. 23.32).

A suspension-based method of thermoplastic 3D printing (T3DP) has been developed as an AM technology within the last 10 years. As reported [94], using T3DP showed promising results for cemented carbides. WC-10wt%Co samples were produced with nanosize WC powders of very fine cobalt powder. The hardmetal content in the organic suspension was 67 vol% which results in a quite high green density compared to conventional hardmetal fabrication. Samples were debindered under standard conditions with hydrogen and sinter-HIPed at 1623 K with 6 MPa argon HIP pressure. The results showed that by T3DP, total density of parts was 14.23 ± 0.01 g/cm^3 above full density, and the properties were comparable to conventional (via uniaxial pressing) produced samples.

Uhlmann et al. [95] showed that cemented carbide with a content of 17 wt% Co with a density of 96% theoretical density and different geometries could be produced by additive manufacturing selective laser melting process.

Cemented Carbide Compaction

A variety of techniques is used to compact hardmetal powders to the desired green density and shape before they can be sintered to full density. Powder consolidation methods include uniaxial pressing, cold isostatic pressing (CIP), extrusion, and injection molding. Processes such as uniaxial pressing and CIP are performed using powders directly after their creation, whereas extrusion and injection molding require extra processing by binders. Consolidation and shaping of cemented carbide powders are described in several publications [96–100].

Pressing

Pressing involves compaction of powder under pressure by constraining it between die walls and rams to increase green density to a required level. In uniaxial pressing, powder in a die is pressed between top and bottom rams. Pressing is a one-step process, combining consolidation of the powder to required green density and achieving required shape. Compaction force ranges from 165 MPa to 331 MPa. Pressing is often used to produce near-net shape carbide parts, which requires optimization of various processes and powder properties, like controlling the relationship between pressing pressure and shrinkage factor (green dimension/sintered dimension or green-sintered dimension/green dimension). Simple metal-cutting insert shapes are typically round or polygonal with straight walls, with or without a central hole. Rods are also produced in straight-walled dies with curved upper and lower punches by length pressing, with the length perpendicular to the pressing axis. These are used to make blanks for drills and end mills. Parts with clearance angles are also pressed in single-action tooling with an angled die wall. Multiplaten tooling is used to create shapes with significant steps in height or changes in cross-section. For geometries that contain undercuts, cross holes, and other geometries that prevent removing the part from the die, moving side die elements are used in side pressing.

Extrusion

Rods, end mills, boring bars, and wires are formed by extrusion. Components having internal structures, such as internal holes for delivering coolant to the cutting edge, are also made using extrusion. The extrusion process is accomplished in an extrusion press, using either a piston-type or screw-type mechanism to push a powder-binder mix through a nozzle. Batch and continuous extrusion presses are used. The most common nozzle shape is round, but a variety of cross-sections can be extruded. Optimal powder-binder mix content and good mixing are required. Generally, powder properties, binder type and amount, as well as extrusion temperature, determine extrusion pressure and speed. Powder compaction is required to remove porosity and achieve sufficiently high green density so that full density is achieved on sintering. Poor mixing of powder and binder results in binder pools, which create imperfections and microstructural defects. Binder content and temperatures that are too high can cause a high rate of extrusion without sufficient powder compaction. Too low a binder content results in excessively high pressing pressures, which can cause surface cracks and damage to tooling and press.

Cold Isostatic Pressing

Cold isostatic pressing (CIP), in which the powder is subjected to equal pressure from all directions, followed by machining, is also in general use for wear and metal forming tools. Cold isostatic pressing is commonly used for parts that are too large to be pressed in uniaxial presses and that do not require high precision in the sintered state. Dry-bag and wet-bag cold isostatic presses are used. In this process, an impervious moldable bag placed in pressure chamber is filled with powder and subjected to an isostatic pressure of 69 MPa to 207 MPa using a water-based liquid medium at ambient temperature. Shaped bags with cores are used to obtain near-net shapes. Powders with no or low wax are used in cold isostatic pressing. Dimensional tolerances for parts produced by CIP are relatively large, so size and shape control are not as critical as in uniaxial pressing. Parts are machined in the green, or presintered, state, and after sintering.

Injection Molding

Injection molding of carbide powders is similar to injection molding metal powders and is used for high-volume production of relatively complex-shaped parts. Fig. 23.33 shows a schematic representation of the injection molding process. Carbide injection molding is achieved by mixing additional waxes, polymers, and surfactants with a dried powder to attain the

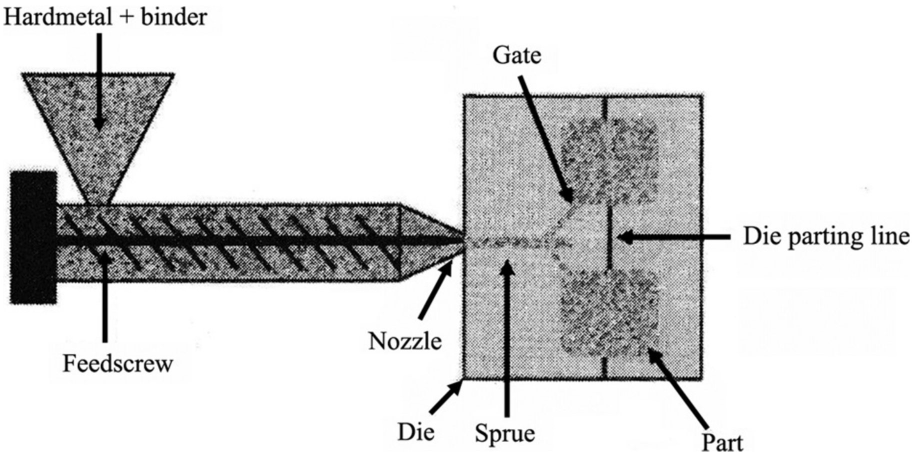

FIG. 23.33 Schematic of injection molding process.

desired solids loading, injecting the thermoplastic feedstock into a die, removing from the die, and debinding in one or more stages prior to sintering. Large parts with wall thicknesses less than about 15 mm are produced by low-pressure systems, while smaller geometries with higher dimensional control and surface finish requirements are generally produced by high-pressure systems. The differences in high- and low-pressure systems are usually the polymer versus wax content and solids loading. Due to the angular shape of carbide grains, the attainable solid loading in high-pressure systems is usually limited to 53%–58% by volume.

Binder systems must minimize shrinkage on cooling in the die, and avoid carbon and oxygen pickup. Polymers must be selected for their clean burning during thermal debinding to avoid addition of impurities into the system. Surfactants are required to reduce molding pressure and to reduce tool wear. It is important that binder components are compatible with each other and bonded to powder to avoid separation. Mixing of additional lubricants into the powder to form a feedstock is performed in sigma and continuous mixers. Carbides are more sensitive to porosity than metallic systems; therefore, avoidance of air traps in the molding process is very important.

The additional steps of mixing and debinding, as well a longer cycle time in molding, add to the cost as compared with traditional die pressing.

Sintering and Secondary Operations

Hardmetals (cemented tungsten carbide, cemented carbide) are two-phase materials consisting of hard carbide phases and binder materials. The binder phase is primarily cobalt, but can also contain other binders including nickel, iron, vanadium, chromium, and molybdenum, or a combination of these. Successful application of these materials in metal cutting, oil drilling, mining, construction, metal forming, and shaping dies depends on achieving low levels of residual porosity with uniform, homogenous microstructure and desired chemical composition. Generally, there are two major sintering methods: pressureless sintering and pressure-assisted sintering. Pressureless sintering techniques include vacuum and partial-pressure, hydrogen, and microwave sintering. Pressure-assisted techniques include overpressure sintering (sinter-HIP), sintering followed by postsinter HIP, hot pressing, and several rapid hot consolidation techniques. The sintering of carbide materials is comprehensively considered in several publications [98,101–103].

The first step in the sintering process is the removal of the lubricant from the powder compact. Then, by the pressureless sintering method, the compacts are usually set on graphite trays coated with graphite paint. Using a semicontinuous or batch type graphite furnace, the compacts are first heated to about 770 K in a hydrogen atmosphere or vacuum. Subsequent to lubricant removal, the compacts are sintered in a vacuum of 0.1 Pa (or 10^{-3} Torr) at a final sintered temperature ranging from 1623 K to 1873 K, depending on the content of the cobalt binder and the desired microstructure. This leads the cobalt to melt and binds the carbide particles together. Shrinkage of the compact ranges from 17% to 25% on a linear scale and provides a practically pore-free, fully dense material.

The sinter-HIP process was developed in the early 1980s [104]. In this process, low-pressure hot isostatic pressing (up to about 7 MPa) is combined with vacuum sintering, and pressure is maintained at the sintering temperature while the metallic binder is still molten. This technique facilitates the production of pore-free products at costs only slightly higher than those of vacuum sintering green compacts.

In the 1970s, the hardmetal industry took advantage of hot isostatic pressing (HIP), in which vacuum-sintered material is re-heated under a gas (argon or helium) pressure of 100–150 MPa. The temperatures of this process are 278–323 K below the sintering temperature. Sintering plus HIP is used to further reduce porosity and improve part durability. Acceptable levels, distribution, and sizes of porosity depend on the applications, and their measurement method is described in the article [105]. The high temperatures and pressures employed in the HIP autoclave improve the nearly perfect properties of hardmetal parts by removing any residual internal porosity and pits.

A large number of hardmetal parts are machined after sintering because of surface finish, geometry and tolerance requirements. This operation is both time-consuming and expensive. The sintered parts can undergo many secondary operation including processing by means of metal-bonded diamond or silicon carbide wheels, turned with a single-point tool, or lapped with diamond-containing slurries, electrical discharge machining, and brazing to achieve desired condition, such as shape, specified size, edge state, and surface finish.

RECYCLING

Hardmetal scrap containing tungsten carbide can be divided into two groups:

- Soft scrap, such as hardmetal grinding sludge, filter dusts, broken green parts, and floor sweepings

- Hard scrap, which represents sintered parts consisting of either used parts or fragments.

The contamination of the scrap with impurities is another criterion for classification. While particulate scrap contains impurity levels that cannot be admitted for direct reuse, hard scrap, even if heavily contaminated, can be classified, thus making direct reuse easier. Hardmetal recycling processes can be subdivided into the following kinds:

- Direct conversion of sorted hard scrap into graded powder ready for pressing and resintering.
- "Zinc process" is the most significant process used [106]. It includes the following main processing steps: sorted, cleaned, and crushed hardmetal scrap; reaction in molten zinc at 1173–1273 K in argon or hydrogen atmosphere; vacuum distillation at 1273–1323 K; obtained cake is consecutively crushed, and ball milled, and the resultant powder is screened; then, oversize product ($>75\,\mu m$) is returned to melting, undersize product ($<75\,\mu m$) is ball milled, and blend carbon adjusted, resulting in graded hardmetal powder.
- Also used on a commercial scale is the so-called "coldstream process," a high-velocity process. The cleaned, sorted, and previously crushed hardmetal scrap is entrained in a gas stream (7 MPa) and projected against a stationary baffle plate. After the material has struck the target and shattered, it is removed from the impact chamber by suction. Material is then subjected to screening. The oversize product is returned into a feed vessel for subsequent impact against the baffle plate. Further classification of undersize material and mixing of different size fractions result in graded hardmetal powder ready for use.
- Removing the binder by means of leaching is another method of hardmetal recycling. The composition of the hardmetal scrap used for the leaching process determines the quality of the resulting carbide residue.
- The chemical conversion process can be used for all contaminated scraps, either soft or hard, to recover primary powders of the hardmetal components. Fig. 23.34 schematically shows the process from the contaminated and unsorted scrap via the conventional WC powder manufacturing route, which involves calcination, reduction, and carburization intermediate to tungsten carbide powder.

Due to the intrinsic value of the hardmetal components, and due to the increasingly more severe legislation concerning waste disposal and the preservation of natural resources, today, recycling has considerable significance, which will increase in the future.

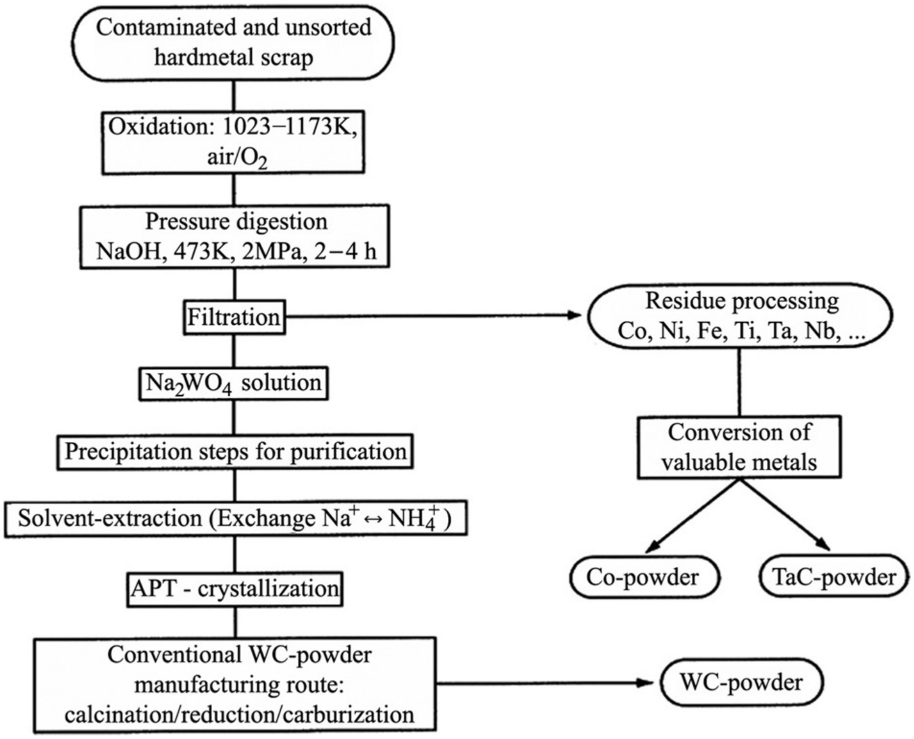
Contaminated and unsorted hardmetal scrap
Oxidation: 1023–1173K, air/O_2
Pressure digestion NaOH, 473K, 2MPa, 2–4 h
Filtration
Residue processing Co, Ni, Fe, Ti, Ta, Nb, ...
Na_2WO_4 solution
Conversion of valuable metals
Precipitation steps for purification
Solvent-extraction (Exchange $Na^+ \leftrightarrow NH_4^+$)
Co-powder
TaC-powder
APT - crystallization
Conventional WC-powder manufacturing route: calcination/reduction/carburization
WC-powder

FIG. 23.34 Flowsheet for the chemical conversion process. *(Source: Lux B, Zeiler B. Production of tungsten and tungsten carbide powders. In: ASM handbook, vol. 7. ASM International Publishers; 1998 p. 188–201.)*

MOLYBDENUM METAL POWDERS

Molybdenum powders find application in different fields of technique. The major use for molybdenum is as an alloying element for alloy and tool steels, stainless, and nickel- or cobalt-based superalloys to increase hot strength, toughness, and corrosion resistance. Molybdenum ingots, produced by melting PM electrodes, are extruded, rolled into sheets or rods, and subsequently worked to other mill product shapes, such as wire and tubing.

Molybdenum has outstanding electrical and heat conducting capabilities. The latter is approximately 50% higher than that of steel, iron, and nickel alloys. It finds wide usage as a heat sink. The coefficient of thermal expansion of molybdenum plots almost linearly with temperature over a wide range. This characteristic, in combination with its heat conducting capabilities, accounts for its use in bimetal thermocouples. Methods of doping molybdenum powder with potassium aluminosilicate to obtain a non-sag microstructure comparable to that of tungsten have also been developed [107]. In the electrical and electronic industries, molybdenum is used in cathodes and cathode supports, for radar devices, as current leads for thoria cathodes, and cores for winding tungsten filaments. Molybdenum plays a significant role in the rocket industry, where it is used for high-temperature structural parts. Molybdenum alloys satisfy the requirements for use in airframes because of their retention of mechanical properties after thermal cycling due to high recrystallization temperatures and good creep strength. Molybdenum has been also effective in the nuclear, chemical, glass, and metallizing industries.

Production of Molybdenum Powders

Molybdenum powder is produced by a technique similar to that used for tungsten powder. Molybdenum disulfide (MoS_2) is the major source of raw material. Molybdenum disulfide is concentrated by flotation and transformed to an impure technical molybdenum trioxide (MoO_3) by means of roasting, which oxidizes the sulfur and removes it as gaseous sulfur dioxide [108].

Subsequent purification takes advantage of the sublimation characteristics of molybdenum trioxide. Above 820 K, it sublimes easily and can be distilled from its impurities and condensed again as pure molybdenum trioxide. Solvent extraction processes are also acceptable. Additional purification can also be achieved by dissolving molybdenum trioxide in ammonia to form ammonium molybdate, $(NH_4)_2MoO_4$. The pure molybdenum trioxide or ammonium molybdate is reduced in tube push type or rotary furnaces similar to those used for tungsten reduction. Typical purification reduction reactions can be written:

$$MoS_2 + 7/2O_2 = MoO_3 + 2SO_2 \text{ endothermic (reaction)}$$

$$MoO_3 + 3H_2 = Mo + 3H_2O$$

$$MoO_3 + 2NH_4OH = (NH_4)_2MoO_4 + H_2O$$

$$(NH_4)_2MoO_4 + 3H_2 = Mo + 2NH_4OH + 2H_2O$$

Reduction of molybdenum trioxide by dry hydrogen involves two steps: $MoO_3 \rightarrow MoO_2 \rightarrow Mo$ [11]. The bond strength metal-oxygen in MoO_3 is less than in WO_3, and in MoO_2, is larger than in WO_2. The magnitudes of the equilibrium constants for the two steps of Mo reduction ($K_{eq} = p_{H_2O}/p_{H_2}$) are given in Table 23.10.

The first step is fulfilled at temperatures ranging from 670 K to 920 K to realize slow increase of temperature in order to accomplish the formation of MoO_2 at 770–820 K and not to form molten material at 820–870 K (low-melting eutectic Mo_4O_{11}-MoO_2). The second reduction step is carried out at 920–1220 K. The reduction parameters like temperature, reduction time, and powder layer thickness (oxide load of the boats in push type furnace) are chosen so that the residual oxygen content does not exceed 1000 ppm after the second reduction step.

TABLE 23.10 Magnitudes of the Equilibrium Constants for the Two Steps of Molybdenum Reduction

Temperature (K)	670	700	870	915	1070	1200
K_{eq}, 1st step (n-d)	5.0×10^7	…	1.7×10^6	…	1.58×10^5	…
K_{eq}, 2nd step (n-d)	…	0.076	…	0.234	0.389	0.55

n-d, Non-dimensional.

TABLE 23.11 Properties of Typical Molybdenum Metal Powders Produced by Hydrogen Reduction

		Sources		
		[3]	SIC Standards	
Property	**Unit**	**1–6 µm**	**TU48-19-316**	**TU48-19-313**[a]
Particle sizes	µm	1–6[b]	<5	40–150
Nominal composition				
Molybdenum	wt%	99.9[c]	99.5	99.9
Trace elements:				
Aluminum	ppm	5–25	50	…
Calcium	ppm	3–15	70	70
Carbon	ppm	10–50	…	…
Chromium	ppm	5–25	…	…
Cobalt	ppm	…	…	…
Copper	ppm	5–10	…	…
Iron	ppm	10–100	140	…
Lead	ppm	5–10	…	…
Magnesium	ppm	1–10	30	30
Nickel	ppm	5–50	50	200
Oxygen + water	ppm	500–1000	3000	…
Potassium	ppm	…	500	…
Silicon	ppm	…	50	…
Sodium	ppm	…	150	150
Tin	ppm	15–50	…	…
Tungsten	ppm	100–300	400	…
NVM (summation of Ca, Na, K, S)	ppm	500–1000	…	…

[a] *Coarse powder for plasma spraying, CIS: Commonwealth of Independent States' standards.*
[b] *Particle size FSSS.*
[c] *Metallic molybdenum content, exclusive of gases.*

Properties of typical molybdenum metal powders produced by reduction of molybdenum trioxide by hydrogen are shown in Table 23.11.

To produce high-purity molybdenum powder, an aqueous solution of ammonium molybdate is mixed with a solution of iron chloride (III); formed precipitate of iron molybdate is separated from the solution containing some of the impurities. A solution is acidified to make molybdic acid (H_2MoO_4); that is separated and then dissolved in an aqueous solution of ammonia (NH_4OH). At the second stage of purification, the obtained solution of refined ammonium molybdate is mixed with a solution of iron chloride (III), and the cycle is repeated; formed precipitate of iron molybdate is separated, washed, and, after acidifying the molybdic acid, is dissolved in an aqueous solution of ammonia. The solution is separated by filtration, and finally, pure ammonium molybdate is cooled. The crystals of pure ammonium molybdate are separated and reduced in a hydrogen atmosphere at 1170–1220 K.

Reduction of low boiling point molybdenum chlorides and fluorides also allows production of high-purity molybdenum powder. The melting point of molybdenum pentachloride ($MoCI_5$) is 467 K, and its boiling point is 541 K. A fluidized bed unit for reduction is described in Chapter 4, where molybdenum pentachloride is being supplied at temperatures ranging from 470 K to 570 K ($MoCI_3$ is decomposed at higher temperature). Optimal conditions providing metal precipitation of

88% and reduction degree of 98% are as follows: temperature range from 870 K to 1070 K, $MoCI_5$ concentration in gas vapor phase of 4–5 vol%, and a molar ratio of hydrogen to molybdenum pentachloride NLE 30 to 1. Obtained fine powder contains: 40–60 wt% fraction minus 0.6 μm, 20–23 wt% fraction 0.6–1.2 μm, 10–20 wt% fraction 1.6–1.8 μm, and 1–3 wt% fraction 1.8–2.4 μm.

If a rotating reaction chamber is used, where ammonia paramolybdate is reduced by hydrogen, porous conglomerates of dispersed powders are obtained which are narrow in size and shape. Powders are characterized by high bulk mass and good flow, and their dispersivity depends on temperature condition. Highly dispersed (3–5 μm) powders of rhenium and molybdenum alloy (1:1) are produced by treatment of $ReOMoO(OCH_3)_7$ in two steps: calcinations in oxygen (523–573 K, 1–2 h) and reduction by hydrogen (1073–1173 K, 2–3 h).

The carbonyl process for molybdenum powder production is based on the decomposition of carbonyl molybdenum $(Mo(CO)_6)$. The powder particle sizes are around 1 μm, and the surface of the particles is rather smooth. Having increased the temperature of carbonyl decomposition, there have been changes in powder color, carbon content, apparent density, and lattice spacing (Table 23.12). Carbonyl molybdenum powders enriched by carbon represent the metastable carbides with face-centered lattice. The increasing decomposition temperature leads to the extension of lattice spacing.

Impurities of carbon and oxygen are typical for molybdenum powders, and the content of sulfur, phosphorus, and arsenic does not exceed 1 ppm.

By execution of the carbonyl process in a hydrogen and nitrogen current, a peak of carbon (amorphous) content is observed at 970 K as a result of catalytic decomposition of its dioxide. Addition of oxidizing components into a gas-carrier leads to decreasing carbon content. For instance, the powder obtained in nitrogen with 2.2% of oxygen at 670 K contains 0.27 wt% carbon. To remove impurities, it is effective to heat treat powders at 1170 K and above. The carbon amount goes down by a digit factor, while carbonyl decomposition in ultrahigh frequency discharges.

Properties of Molybdenum and Molybdenum Alloy Powders

The high boiling and melting points of molybdenum (4912 K and 2890 K, respectively) are second only to those of tungsten, rhenium, and osmium. Molybdenum is not used as widely as tungsten because it oxidizes more readily and erodes faster on arcing than tungsten. Nevertheless, due to the density of molybdenum (10.2 g/cm^3), which is about half that of tungsten (19.3 g/cm^3), use of the former is advantageous where mass limitation is important. The cost of molybdenum is also lower. In addition to its use in make-(before-) break contacts, molybdenum is widely used for mercury switches because it is not attacked, but only wetted, by mercury.

Like tungsten, molybdenum strips and sheets are made by swaging or rolling sintered powder compacts. Table 23.13 shows the physical properties of pure molybdenum and tungsten metals. Temperature effects on the physical and mechanical properties of molybdenum and tungsten rods are illustrated in Fig. 23.35.

The mechanical properties of molybdenum and molybdenum alloys greatly depend on the amount of working treatment below their recrystallization temperature and on the ductile-to-brittle transition temperature. The minimum recrystallization temperature is 1173 K. The metal maintains superior strength and hardness at elevated temperatures. However, when hot strength is required, a molybdenum alloy (rather than elemental material) is the material of choice. Titanium and zirconium additions to molybdenum create alloys with hot strength and recrystallization temperatures above those of unalloyed molybdenum.

TABLE 23.12 Dependence of Carbonyl Molybdenum Powder Properties on Decomposition Temperature

Decomposition Temperature in Current of Argon (K)	Color of Powder	Apparent Density (g/cm^3)	Carbon Content (wt%)	Lattice Spacing (nm)
670	Gray	0.5	2.36	…
770	Gray	…	3.28	0.42019
870	Dark-gray	…	3.38	0.42030
970	Black	…	3.53	0.42100
1070	Black	2.50	3.48	0.42220
2970–3970	Black	…	0.10–0.20	…

TABLE 23.13 Typical Properties of Molybdenum and Tungsten

Property	Unit	Molybdenum	Tungsten
Density	g/cm^3	10.22	19.3
Crystal structure			
Hardness HB	GPa	1500	70
Modulus of elasticity		bcc	bcc
At 293 K	GPa	325	405
At 1273 K	GPa	220	325
Melting point	K	2890	3410
Boiling point	K	4912	5660
Specific heat			
At 293 K	J/kg·K	251	134
Thermal conductivity at 293 K	W/m·K	138	154
Coefficient of linear thermal expansion at 293 K	μm/m·K	5.53	4.43
Electrical resistivity at 293 K	nΩ·m	53.4	55
Electrical conductivity at 293 K	%IACS	33	31

Some of the physical properties of molybdenum and tungsten vary considerably with cross-sectional and grain structure.

Table 23.14 gives basic mechanical property data for 0.38 mm wire fabricated from pure molybdenum and several of the advanced molybdenum alloys.

The TZM molybdenum alloy is a high-strength, high-temperature material. This material is manufactured either by the PM or arc-melting processes. The composition of TZM consists of: (0.01–0.04) wt% carbon, (0.40–0.55) wt% titanium, (0.06–0.12) wt% zirconium, <0.0005 wt% hydrogen, <0.010 wt% iron, <0.002 wt% nickel, <0.002 wt% nitrogen, <0.0025 wt% oxygen, <0.008 wt% silicon, and the balance of molybdenum. At 1273 K, its strength is about 720 MPa, which is approximately twice that of unalloyed molybdenum. The alloy is excellent for structural applications under conditions where unalloyed molybdenum is normally used [109].

In comparison with unalloyed molybdenum, TZM has a higher recrystallization temperature and higher strength and hardness at room and elevated temperatures. Its advanced mechanical properties are due to the dispersion of composite carbides in the molybdenum matrix. Basic application fields of TZM include:

- Die inserts for casting metals
- Die bodies and punches for hot stamping
- Tools for metalworking
- Heat shields and linings for furnaces, structural parts and heating elements
- Rocket nozzles.

To improve the elevated temperature strength of PM TZM alloys, titanium and zirconium carbides have been replaced by hafnium carbide. An alloy containing 1% Hf and 0.06% C has a tensile strength of 580 MPa at 1588 K, in comparison with 480 MPa for TZM. Creep rate at 1478 K at a stress of 330 MPa is 0.038%/h, compared to 0.05%/h for TZM [110].

Table 23.15 presents the compositions and properties of various molybdenum-silver composites for electrical make-break contacts [109].

To improve the mechanical properties, including ductility and creep resistance of structural molybdenum-base materials, doped molybdenum alloys were developed addition a small amount of aluminum, potassium, silicon, or rare-earth oxides [111]. Recently, high-toughness molybdenum alloys have been developed with fine grains and finely dispersed titanium carbide particles by mechanical alloying (MA) and hot isostatic pressing (HIP) processes, followed by hot forging and hot and warm rolling. The high toughness of the alloy may be due mainly to grain-boundary strengthening by fine carbide particles having semi-coherency with the adjacent matrix, and the particles have the beneficial effects of increasing

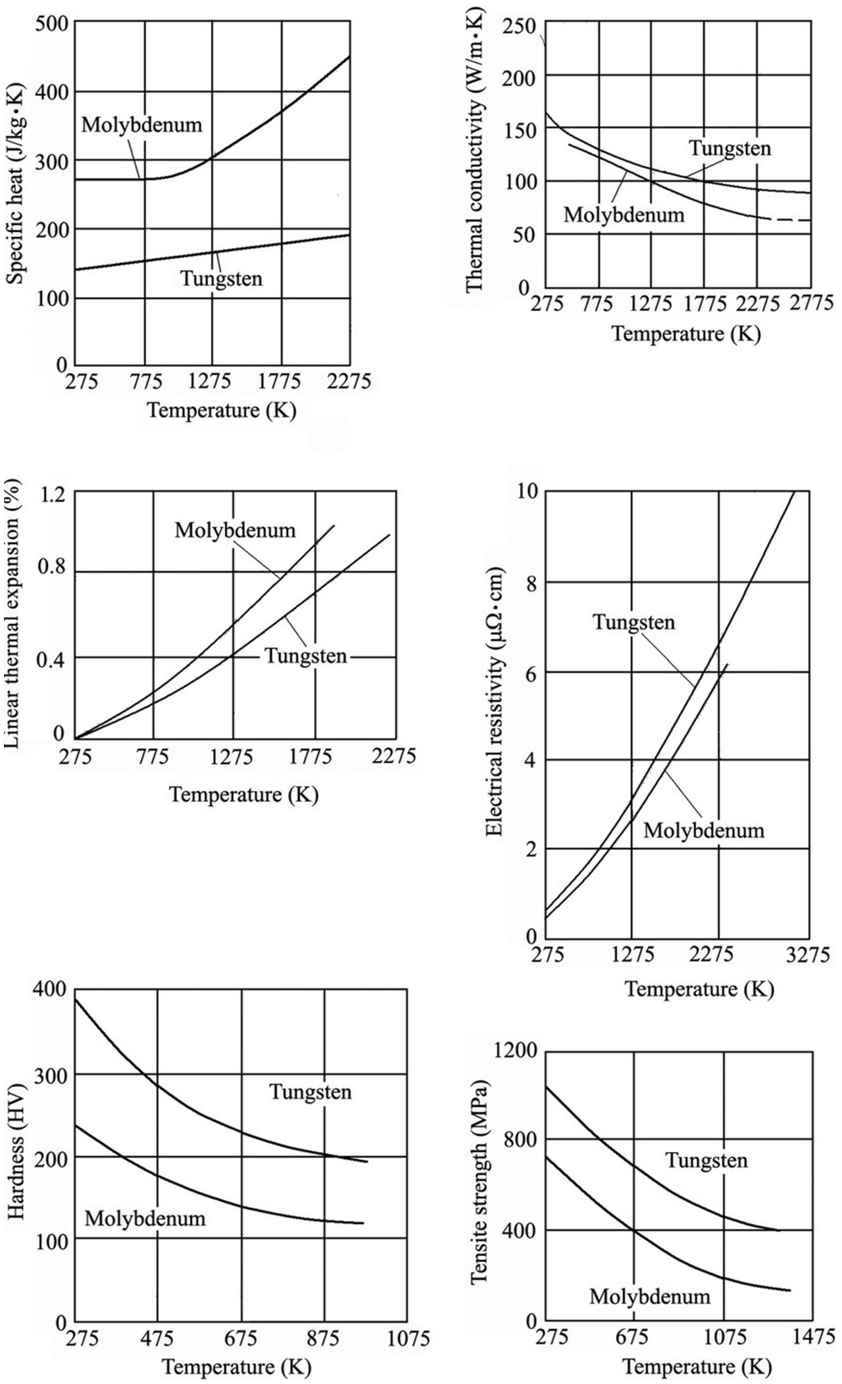

FIG. 23.35 Physical and mechanical properties of molybdenum and tungsten rods depending on the temperature. *(Adopted from Shen Y-S, Lattari P, Gardner J, Wiegard H. Electrical contacts. In: ASM Handbook, vol.2. Novelty (OH, USA): ASM International Publishers; 1990. p. 840–68.)*

the recrystallization temperature and hindering grain growth. However, in both cases, a large amount of plastic working was required. Such working may limit the products available to thin sheets or thin wires shapes, which are inapplicable as structural materials.

Data regarding the mechanical properties for carbide-dispersed molybdenum alloys are given in Table 23.16. Because the properties of materials with the same composition depend on manufacturing methods, the manufacturing methods are also referenced in these tables. These common methods of producing composite electrical contact materials are described in subparagraph "tungsten powder applications" (see above).

Molybdenum alloys with 0.8 mol% zirconium carbide (ZrC) or tantalum carbide (TaC) as dispersed particles were fabricated by mechanical alloying and HIP or spark plasma sintering (SPS) [112]. Powders of pure molybdenum (average

TABLE 23.14 Tensile Properties of 0.38 mm Molybdenum Wire at Room and Elevated Temperatures

Material Sign	Composition	Temperature (K)	Ultimate Tensile Strength (MPa)	Elongation (%)
Unalloyed molybdenum	Mo	293	1350	4.1
		1273	305	2.4
		1373	140	10.3
		1473	115	12.5
MT-104	Mo-0.5Ti-0.08Zr-0.01C	293	1565	3.1
		1273	1020	2.7
		1373	795	3.2
		1473	675	2.8
Mo+45W	Mo-45W	293	1980	3.6
		1273	1095	2.3
		1373	950	2.3
		1473	745	2.2
HCM	Mo-1.1Hf-0.07C	293	1795	2.9
		1273	1270	3.4
		1373	1185	3.3
		1473	1035	3.0
HWM-25	Mo-25W-1.0Hf-0.035C	293	1935	3.2
		1273	1350	3.3
		1373	1250	3.1
		1473	1075	4.6
HWM-45	Mo-45W-0.9Hf-0.03C	293	2135	3.6
		1273	1460	3.3
		1373	1295	2.6
		1473	1170	2.4

Source: Adopted from Lambert JB et al. Refractory metals and alloys. In: Properties and selection: nonferrous alloys and special-purpose materials. ASM Handbook, vol. 2. Novetly (OH, USA): ASM International Publishers; 1990. p. 558–85.

particle size 4.1 μm), ZrC (2 μm) and TaC (1.1 μm) were mixed to obtain the target composition in an argon atmosphere. These blended powders were subjected to mechanical alloying for 108 ks in a planetary type ball mill with lining and balls made of a cemented carbide (WC-Co). HIP and SPS were conducted at 1573 K and 147 MPa for 10.8 ks in argon, and at 2073 K and 74 MPa for 0.3 ks in a vacuum of 10 Pa, respectively. These alloys were annealed in a vacuum of 2.7×10^{-4} Pa at 1873–2473 K for 3.6 ks. Yield strength, ultimate tensile strength and elongation at 300 K and high temperature for Mo-0.8 mol% ZrC, Mo-0.8 mol% TaC, and pure Mo conducted with tensile specimens in form of bar 4 mm wide, 25 mm long, and 1 mm thick are shown in Table 23.16. The superplastic behavior was investigated on a gauge section 3 mm wide, 8 mm long, and 2 mm thick. In both MA with HIP and MA with SPS specimens of Mo-08 mol% ZrC as sintered, the tensile strengths are 1.8 times higher than that of pure molybdenum; however, no plastic behavior is found. While both MA with HIP and MA with SPS specimens of annealed Mo-08 mol%ZrC are superior in terms of room temperature strength, their yield and tensile strengths are about 3 and 2.1 times higher, respectively, than that of pure molybdenum.

TABLE 23.15 Properties of Typical Molybdenum-Silver Composites for Electrical Make-Break Contacts

Nominal Composition (%)	Manufacturing Method[a]	Density (g/cm^3)		Electrical Conductivity (% IACS)	Hardness	Tensile Strength (MPa)	Modulus of Rupture (MPa)	Data Source[b]	Application Examples
		Calculated	Typical						
90Ag-10Mo	PSR	10.47	10.38	65–68	35–40 HRB	…	…	A	Air conditioner control
80Ag-20Mo	PSR	10.44	10.36	59–62	38–42 HRB	…	…	A	Light- and medium-duty applications, automotive circuit breakers switches, circuit breakers
75Ag-250Mo	PSR	10.42	10.33	58–61	44–47 HRB	…	…	A	
50Ag-50Mo	INF	10.35	10.10–10.24	45–52	70–80 HRB	…	758	C, A	Air- and oil-circuit breakers, arcing tips, traffic signal relays, home circuit breakers
	PSR	10.35	10.14	50	65	…	552	C, A	
45Ag-55Mo	INF	13.33	10.10–10.32	44–58	75–82 HRB	…	…	A	
40Ag-60Mo	INF	10.32	10.10–10.32	42–49	80–90 HRB	…	…	C, A	Aircraft switches, breaker arcing tips, electric raisers, air- and oil-circuit breakers
	PSR	10.32	10.12	45	50–68	…	676	C, A	
30Ag-70Mo	INF	10.29	10.00–10.31	35–45	85–95	414	931	C, A	Air-circuit breakers. Low-erosion arcing tips
25 Ag-75Mo	INF	10.27	10.27	31–34	93–97	414	938	C, A	
20 Ag-80Mo	INF	10.26	10.23–10.26	28–32	96–98	407	965	C, A	Arcing contacts, heavy-duty electrical applications
15 Ag-85Mo	INF	10.24	10.18	28–31	97–102	…	…	G	
10 Ag-90Mo	INF	10.23	10.13	27–30	97–102	…	…	G	Semiconducting material

[a] *INF, press-sinter-infiltrate; PSR, press-sinter-repress (blended powder of the desired composition are compacted to the required shape and then sintered. Afterwards, the material is further densified by a second pressing. Sometimes the properties can be modified by a second sintering or annealing).*

[b] *A: Advance Metallurgy, Inc., McKeesport, PA. C: Contacts, Materials, Welds, Inc., Indianapolis, IN. G: Gibson Electric Inc., Delmont, PA.*

TABLE 23.16 Mechanical Properties at 300 K for Carbide Dispersed Molybdenum Alloys

	Analyzed Composition (wt%)										
Alloy	**Metal**	**C**	**N**	**O**	**Manufacturing Method**	**Relative Density (%)**	**Condition**	**Grain Size (μm)**	**Yield Strength (MPa)**	**Ultimate Tensile Strength (MPa)**	**Elongation (%)**
Mo-0.8ZrC	0.70Zr	0.100	0.022	0.140	MH	99.9	As sintered	0.3	…	827	0.0
							Annealed	1.8	1015	1053	0.6
Mo-0.8ZrC	0.69Zr	0.117	0.032	0.138	MS	99.9	As sintered	2.7	…	838	0.0
							Annealed	2.8	1038	1077	9.0
M0–0.8TaC	1.2Ta	0.110	0.019	0.137	MS	99.9	As sintered	10.9	559	707	12
							Annealed	11.2	547	639	38
Pure Mo	…	0.001	0.001	0.001	MH	100	Recrystallized	53.8	344	469	54

MH: Mechanical alloying and hot isostatic pressing, MS: Mechanical alloying and spark plasma sintering.

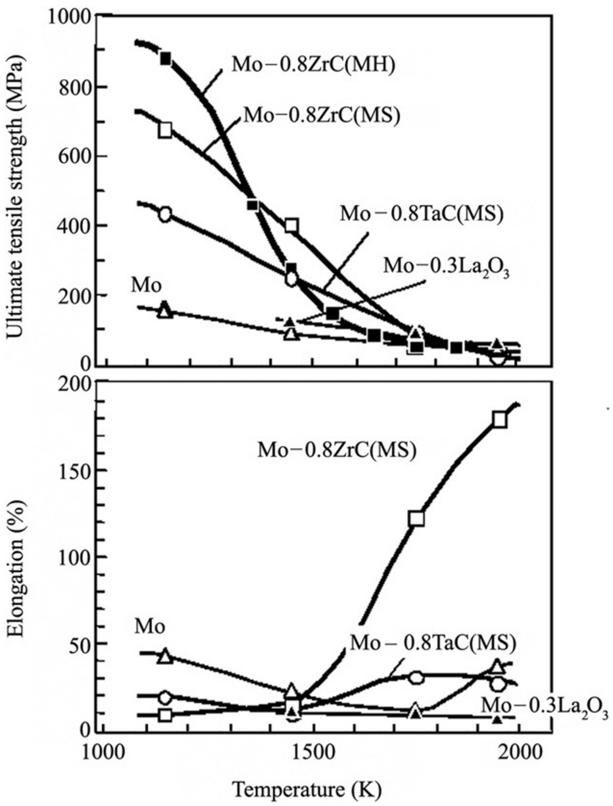

FIG. 23.36 Dependence of ultimate tensile strength and elongation of the carbide dispersed molybdenum alloys on temperature: (MH) corresponds to HIP with MA powders, (MS) corresponds to SPS with MA powders. *(Source: Takida T, Kurishita H, Mabuchi M, Igarashi T, Doi Y, Nagae T. Mechanical properties of fine-grained sintered molybdenum alloy processed by mechanical alloying. In: Kneringer G. editor. Proceedings of 15th international Plansee seminar, vol. 1. Reutte (Tirol, Austria): Plansee Holding AG; 2001. p. 293–304.)*

The carbide dispersed molybdenum alloys exhibit excellent strength up to 1373 K. Their tensile strengths are 3–5 times higher below 1473 K (about 0.5 melting point), and 1.5–2 times higher at 1773 K, than those of pure molybdenum and Mo-0.8 mol%TaC (Fig. 23.36). The elongation of Mo-08 mol%ZrC with grain size of 3.0 μm obtained by means of SPS with MA increased rapidly in the temperature range over 1773 K, and a superior limit elongation of 180% is attained at 1973 K.

Variations in the nature of the oxide and consolidation method have been shown to have a significant effect on the mechanical properties of oxide dispersion strengthened (ODS) molybdenum material [113]. Comparison of the effect of doping technique species on tensile properties of ODS molybdenum-lanthana and ODS molybdenum-yttria alloys illustrates that, for both oxide species, the wet doping technique results in a much finer dispersion of oxide particles ranged from 0.08 to 0.12 μm. The wet doping process uses an aqueous tantalum nitrate solution to dope the molybdenum dioxide (MoO_2) precursor before its reduction to molybdenum metal powder [114]. At ambient temperature, the alloy's strength is not strongly sensitive to either doping technique, but, at high temperatures, the wet doping technique produces superior material for a given oxide. Lanthana-doped material is also superior to yttria-doped material at elevated temperature. The ODS molybdenum material contains nominally 2 vol% La_2O_3 that corresponds to a lanthanum (La) content of 1.09 wt%.

The addition of a small amount of group VIII transition metals, such as nickel and palladium, can lower the activation energy of sintering and decrease the sintering temperature from >1970 to <1570 K [115]. However, such activation-sintered compacts have no ductility, and thus, have restricted application in industry [116]. Through activated liquid phase sintering, the addition of 1.5 wt% Ni to molybdenum was shown to improve the sintered density significantly to 97% at 1573 K, while the pure molybdenum only reached 82% theoretical density. But, this impairs ductility. This embrittlement appears to be caused by a grain boundary layer of a Ni-Mo compound about 2 nm thick formed during sintering [117]. Due to the brittle nature of this compound, the Ni-containing molybdenum fractures through this thin compound layer.

There are several grades of ODS Mo alloys available for commercial use. The most popular doping levels of lanthana (La_2O_3) to molybdenum are: 0.3% by weight, 0.6% by weight and 1.1% by weight. In work [118], the thin sheets, that is,

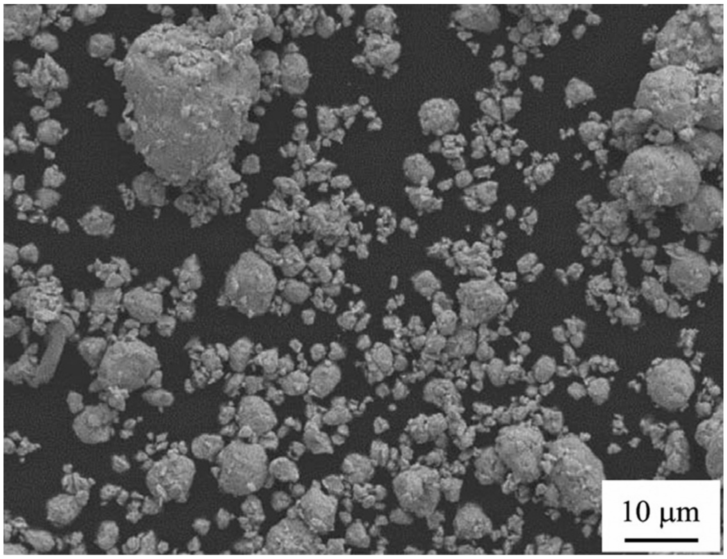

FIG. 23.37 SEM image of molybdenum powder with 1 at.% Na after ball milling for 75 h. *(Source: Bergk B, Mühle U, Kieback B, Koutná N, Holec H, Clemens H. Nanocrystalline alloys of molybdenum with sodium and yttrium obtained by mechanical alloying. In: Compiled by European Powder Metallurgy Association. CD/USB proceedings of PM 2017 euro congress. Milan (Italy); 2017: p. 1–6.)*

0.5 mm and 0.2 mm thick, of these alloys were studied. The ingots were made by cold-isostatic pressing of the Mo-lanthana (MoLa) powders with subsequent sintering. The ingots were subsequently thermo-mechanically processed, first into plates during hot rolling, then into sheets. It was concluded [118] that the annealed 0.6 wt% and 0.3 wt% lanthana MoLa sheets exhibited deep drawability with a 900–1020 MPa UTS range, 800–920 MPa YS range, and about 25%–27% elongation, and can be considered the best material for the majority of furnace components applications, while the thin MoLa sheets, that is, 0.2 mm thick, exhibited ideal isotropy of bendability under annealed condition with no regard to lanthana content. There was also reported that hardness is not a reliable differentiating factor among lanthana-content MoLa sheets.

Molybdenum alloys with low contents of immiscible sodium and yttrium elements made by mechanical alloying were studied [119]. The alloys were produced by high-energy ball milling utilizing a Retsch SM 200 mill placed inside an argon glove box to guarantee high purity conditions and to avoid uptake of oxygen and nitrogen. Fig. 23.37 shows a SEM image of an alloy with 1.0 at.% Na after milling for 75 h. The particle sizes distribute in 1–20 μm range. As reported, the nominal concentration of 1 at.% Na or Y the solute content remains constant up to temperatures of 1173 K. For higher temperatures, the solute content starts decreasing until at 1473 K almost no sodium like yttrium is left. The alloy's structure is characterized by the following: the grains have been grown to about 150 nm and are reduced to about one tenth of the value for the as milled samples; it is revealed that sodium (as well as yttrium) adapts itself to the molybdenum lattice.

Because the conventional sintering of molybdenum requires high temperatures and long holding times, which leads to large grain growth, much research has been focused on the enhancement of the sinterability of Mo using spark plasma sintering (SPS) technique [120–122].

In the work [123], molybdenum nanopowder was sintered by SPS technique under various temperatures, pressures, heating rates, and holding times in order to decrease the grain size. Nanosized molybdenum powder from US Research Nanomaterials, Inc., (TX, United States) with a purity of 99.9% (metal basis) has been used in this study. The powders correspond to agglomerates of roundish particles with a size range of about 50–200 nm (Fig. 23.38).

The SPS device was set to apply the periodic sequence of 12 ms of DC pulses followed by a pause of 2 ms. For 60 MPa or 120 MPa SPS pressure levels, measured initial green (after pre-cold compaction) densities of the Mo powder compacts were ∼ 58% and ∼ 67%, respectively. Sintering conditions of the conducted SPS tests included heating rates of 100 K/min or 200 K/min from 873 K to the maximum temperature (1473, 1573, 1873, or 2073 K) with dwell times of 0 or 10 min.

The grain sizes of Mo pellets showed large dependence on sintering temperature. Fig. 23.39 shows the grain size of SPSed Mo pellets sintered under different temperatures with the same conditions of 60 MPa, 100 K/min, and 0 min holding time. As shown in Fig. 23.39A, 1573 K conditions are related to a small grain size of 2 μm, while grain size increased to ∼37 μm or ∼ 54 μm when the sintering temperature was over 1873 K (Fig. 23.39B and C). At sintering temperatures between 1573 K and 1873 K, the Mo oxide phase melted and moved to the grain boundary regions.

In this study [123], the highest achieved microhardness was 435 kgf/mm^2 (∼4.266 GPa). Relative density of 95.77% was achieved with 1473 K, 60 MPa, 100 K/min, and 10 min holding time. Optimal conditions for Mo pellet processing that resulted in small grain size, high density, and high hardness are determined to be 1473 K, 60 MPa, 100 K/min, and 10 min holding time under vacuum.

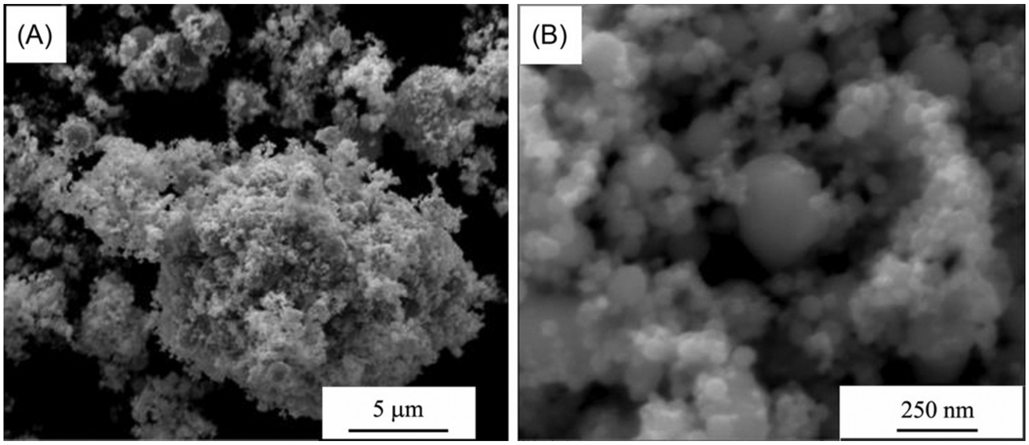

FIG. 23.38 SEM images of molybdenum nanopowders at two magnifications. *(Source: Lee G, Olevsky E, McKittrick J. Spark plasma sintering of molybdenum nanopowders. In: Compiled by European Powder Metallurgy Association. CD/USB proceedings of PM 2016 world congress. Hamburg (Germany); 2016: p. 1–6.)*

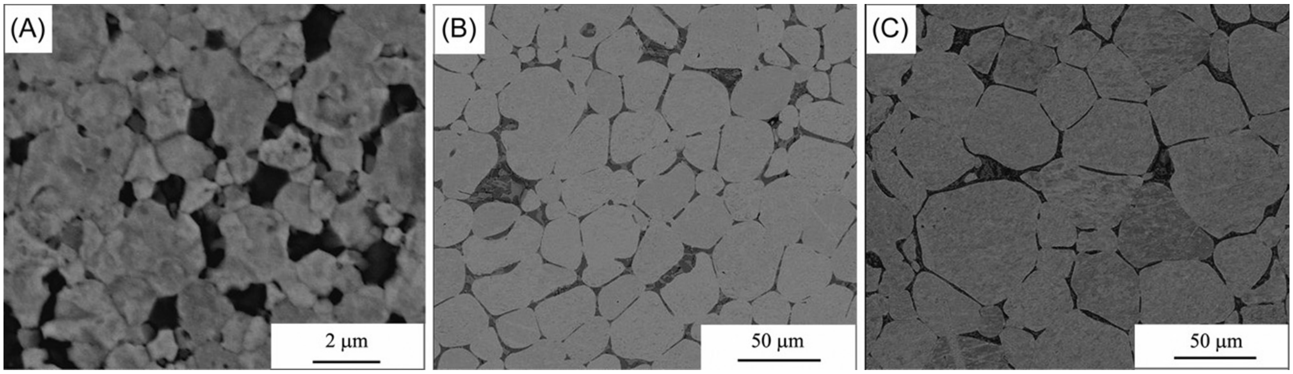

FIG. 23.39 SEM phase images of spark plasma sintering (SPS) pellets consolidated at different temperatures: (A) 1573 K, (B) 1873 K, and 1973 K; white regions indicate Mo, black regions indicate Mo oxide. *(Source: Lee G, Olevsky E, McKittrick J. Spark plasma sintering of molybdenum nanopowders. In: Compiled by European Powder Metallurgy Association. CD/USB proceedings of PM 2016 world congress. Hamburg (Germany); 2016: p. 1–6.)*

The elaboration possibilities of the refractory Mo_3Al intermetallic compound by self-propagating high-temperature synthesis (SHS) starting from a near stoichiometric mixture of powder components were considered [124].

High-purity fine powders of molybdenum and aluminum (MO006021 and AL006031 grades) had been used as staring materials. Appropriate amounts of them, corresponding to 76:24 (Mo:Al) atomic ratio (a near stoichiometric), had been preliminarily homogenized in a Turbulla blender for 30 min. To facilitate SHS reaction, ahead of time, researchers carried out an intimate homogenization and an energetic activation of the component powder mixture by a controlled mechanical alloying-mechanical disordering (MA + MD), by milling for 3 h in a planetary ball mill under argon atmosphere. An SEM image of Mo-Al powder mixture subjected by 3 h (MA + MD) processing is shown in Fig. 23.40.

As reported [124], by subjecting compacts realized from the above powder mixture by SHS in thermo-explosion mode under pressure, cylindrical compacts of a microstructure similar to superalloys, consisting of a multitude of submicron Mo_3Al crystallites embedded in a Mo-Al alloy matrix, density of 73.26%, and higher Vickers hardness than of Mo (1742 MPa, vs. ~ 1400 MPa) have been obtained.

Workplace Atmospheres Safety

Under the Workplace exposure limits in the European PM industry the long- and short-term (15-min reference period) workplace exposure limits (WELs) for soluble molybdenum compounds (as Mo) are 5 mg/m^3 and 10 mg/m^3, accordingly, and the limits for insoluble compounds (as Mo) in the workplace atmosphere are 10 mg/m^3 and 20 mg/m^3, respectively [57]. According to US New Jersey Department of Health and Senior Services. Hazardous Substance Sheet, the legal OSHA airborne permissible exposure limit for molybdenum is 15 mg/m^3.

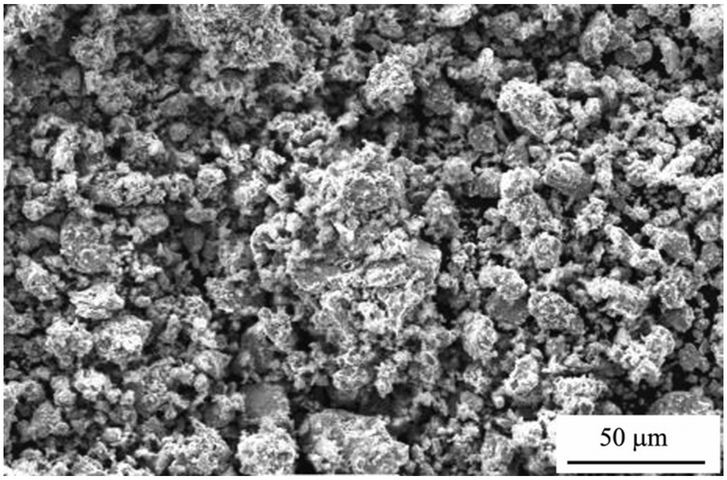

FIG. 23.40 SEM image of Mo-Al powder mixture subjected by 3h mechanical alloying- mechanical disordering (MA+MD) processing. *(Source: Orban RL, Salomie D, Orban M, Neamţu B, Sechel N, Lung T. SHS synthesis from mechanical activated powdered components mixture of molybdenum aluminade Mo_3Al for use at extremely high temperatures. In: Compiled by European Powder Metallurgy Association. CD/USB proceedings of PM 2016 world congress. Hamburg (Germany); 2016: p. 1–6.)*

The aerosols of metallic molybdenum, either soluble or insoluble molybdenum compounds and molybdenum silicide, have a predominantly fibrous effect and are related to the third class of danger according to State Standard 12.1.005-88 under the legislation in the CIS [56]. The stated average limit value (ALV) of the metallic molybdenum aerosol in the workplace atmosphere as the shift time-weighted average concentration is $0.5\,mg/m^3$, while the threshold limit value (TLV) is $3\,mg/m^3$. The ALVs of the insoluble and soluble molybdenum compounds and molybdenum silicide in dust form are 1.0, 4.0 and $4.0\,mg/m^3$, respectively, while the ALV of soluble molybdenum compounds in the form of condensed aerosols is $2.0\,mg/m^3$. Molybdenum content in potable water has a toxicological effect and is related to the second class of danger, and the TLV is 0.25 mg/L according to CIS State Standard 4630-88 [58].

Molybdenum powder, even with particle sizes at a fraction $\leq 74\,\mu m$, is not explosive in the air; the minimum ignition temperature of powder deposits (self-ignition temperature) is 583 K. The products with such characteristics of inflammability and explosion risk are related to the “low explosion hazard” class of danger according to the Guide to Legislation and “Health and Safety” in the European PM Industry [59].

Common techniques are mainly used to prevent pollution and environmental damage during powder manufacture and processing. Detailed information on health and environment protection measures in such conditions can be found in Chapter 27.

NIOBIUM AND TANTALUM

Niobium and tantalum are often found in close combination in their ores. The most important niobium-tantalum-bearing minerals are columbite and tantalite, which form isomorphous series $FeNb_2O_6$-$MnNb_2O_6$ and $FeTa_2O_6$-$MnTa_2O_6$, and the ores are variations of the compound $(Fe, Mn)(Nb, Ta)_2O_6$. Tantalum and niobium are separated from ore and from one another by digestion in aqueous hydrofluoric acid, followed by solvent extraction with methyl isobutyl ketone (MIBK), as illustrated in Fig. 23.41 [125]. In the first contact, only the niobium and tantalum fluorides are soluble in the MIBK. Thus, they are separated from the contaminants iron, manganese, titanium, and zirconium, which remain in aqueous solution. The fact that the solubility of tantalum in MIBK is high over an extensive range of acidity, while niobium is soluble only at high acidity, is used for separation of tantalum fluoride and niobium fluoride. This is accomplished in a series of subsequent steps, where MIBK contacts aqueous solutions of varying acidity.

Commercially, deposits of niobium are found also in the pyrochlore $[(Na, Ca)_2(Nb, Ta, Ti)_2O_4(OH, F)H_2O]$, which is mined in Canada and Brazil. These ores are mostly tantalum free and are enriched to concentrates containing 55%–60% niobium pentoxide by means of a series of operations including grinding, flotation, and leaching. The extraction of niobium by high-temperature chlorination of the ore is also an appropriate technique for niobium powder production [126].

Niobium and Niobium Alloys

Niobium is used in commercial applications as an alloying element in steels. Nearly 75% of all niobium metal is used as a minor alloying addition in low-alloy steel. About 20%–25% is used as an alloy addition in nickel-base superalloys and heat-

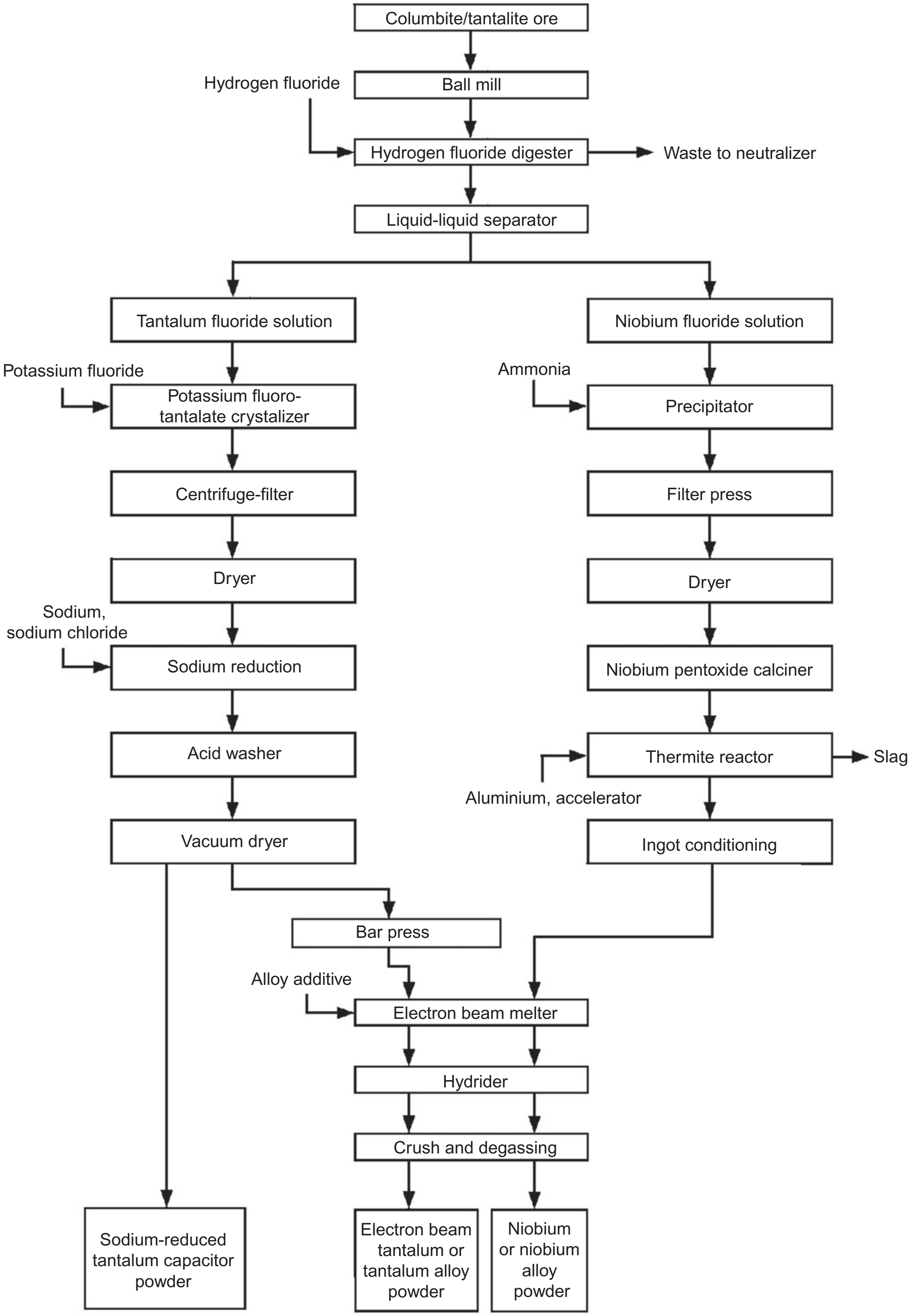
Columbite/tantalite ore
Hydrogen fluoride
Ball mill
Hydrogen fluoride digester
Waste to neutralizer
Liquid-liquid separator
Tantalum fluoride solution
Niobium fluoride solution
Potassium fluoride
Potassium fluoro-tantalate crystalizer
Ammonia
Precipitator
Centrifuge-filter
Filter press
Dryer
Dryer
Sodium, sodium chloride
Sodium reduction
Niobium pentoxide calciner
Acid washer
Thermite reactor
Slag
Aluminium, accelerator
Vacuum dryer
Ingot conditioning
Bar press
Alloy additive
Electron beam melter
Hydrider
Crush and degassing
Sodium-reduced tantalum capacitor powder
Electron beam tantalum or tantalum alloy powder
Niobium or niobium alloy powder

FIG. 23.41 Niobium and tantalum production flowchart. *(Source: Kirk RE, Othmer DF, editors. Encyclopedia of chemical technology, vol. 22, 3rd ed. John Wiley & Sons; 1983.)*

resisting steel. Only 1%–2% of all niobium used is in the form of niobium base alloys and pure niobium metal including super-conducting niobium-titanium alloy, which accounts for over one half of all niobium alloys produced [127].

Production of Niobium Powders

Metallothermic Reduction: Initially, niobium metal was produced by PM methods, which involved high-temperature vacuum sintering and carbon reduction. However, in the early 1960s, aluminothermic reduction and electron beam purification came into general use. At present, the basic process for the recovery of niobium, along with recovery from columbite and tantalite ores shown in Fig. 23.41, is the aluminothermic reduction of pyrochlore concentrates to ferroniobium. Niobium metal is purified by a chlorination process, where volatile niobium pentachlorate ($NbCl_5$) is distilled and then hydrolyzed to the oxide. The metal is next recovered by a second aluminothermic reduction

$$3Nb_2O_5 + 10Al \rightarrow 6Nb + 5Al_2O_3.$$

During the exothermic reaction, oxide impurities are slagged and removed from the molten niobium. Calcium and magnesium have also high reactivity for the reduction of niobium oxide to niobium. However, magnesium has an advantage over calcium in that it has a high vapor pressure (0.078 bar), even at a moderate boiling temperature of 1363 K. Therefore, niobium metal powders can be also prepared by using a magnesiothermic reduction process [128–131]. Okabe reported a preforms reduced process (PRP) for niobium metal using a magnesiothermic reduction process [129]. Using a cyclone separator assembly, niobium is prepared by the reaction between the magnesium vapor and niobium oxide [128]. However, preparing niobium metal using the cyclone reduction techniques resulted in high concentration of oxygen (7.68%) [128]. In the work [132], an attempt was made to prepare the niobium metal powder with lower oxygen content using the magnesium vapor reduction process. The influence of various factors in the magnesium vapor reduction of niobium oxide and deoxidation of niobium metal powder in a two-stage reduction process is discussed. Prepared by magnesium vapor reduction at 1123 K for 5 h, niobium powder contained about 8 mass% oxygen. After second stage reduction, the oxygen concentration decreased to 0.65 mass%. An SEM micrograph of the niobium powder after second stage reduction is shown in Fig. 23.42. As it appears, fine particles of niobium powder less 1.0 μm form agglomerates from 5 μm to 10 μm in size.

Carbothermic Reduction: Carbothermic reduction is also practiced [133]. Reduction is conducted in two steps involving the formation of niobium carbide:

$$Nb_2O_5 + 7C = 2NbC + (5CO)$$

$$Nb_2O_5 + 5NbC = 7Nb + 5CO$$

It is not desirable to conduct carbothermic reduction in one stage. Stock of Nb_2O_5 contains only 57.2% of niobium, and even in briquette form, it has low density ($\approx 1.8\,g/cm^3$). High volumes of CO ($\approx 0.34\,m^3$) are consumed per 1 kg of stock leading to the reduction process' low capacity. Therefore, the first step is carried out in graphite-tube resistance push-type furnaces in a hydrogen atmosphere at a temperature of 2070 K. The graphite cartridge with the stock ($Nb_2O_5 + 7C$) is pushed through the furnace for 1–1.5 h. Lightly sintered niobium carbide is ground to powder and blended with Nb_2O_5 in a surplus of 3%–5% against the stoichiometric ratio. Then, this mixture is pressed into briquettes at a pressure of 100 MPa and calcined in a

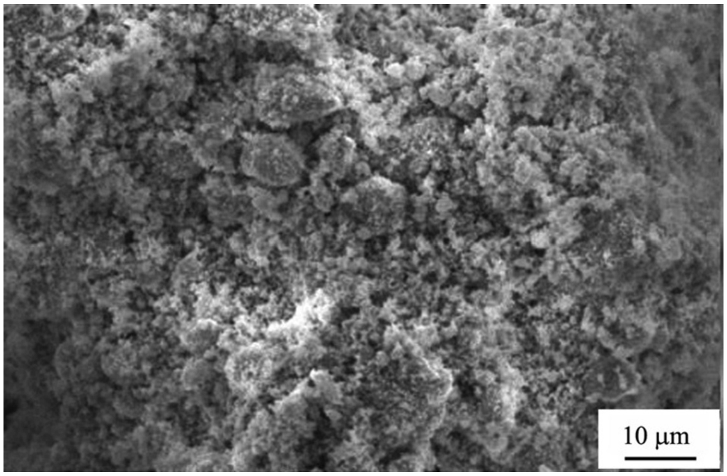

FIG. 23.42 SEM micrograph of the niobium powder made by magnesium vapor reduction. *(Source: Kumar TS, Kumar SR, Rao ML, Prakash TL. Preparation of niobium metal powder by two-stage magnesium vapor reduction of niobium pentoxide. J Metallurgy 2013; (Article ID 62934): 1–6.)*

vacuum furnace at 2070 K and a residual pressure of 1.3–0.13 Pa for 6 h. The niobium reduction goes by intermediary stages of lower oxide formation (NbO_2 and NbO). It is important that at temperatures above 900 K, a part of Nb_2O_5 is evaporated, while NbO_2 and NbO evaporate at higher temperatures. Niobium oxide vapor is adsorbed on the carbon and niobium carbide particles, where niobium is reduced. The second step goes with higher capacity, therefore, the mixture Nb_2O_5+5NbC has 82.4% niobium in briquettes with a density of about 3 g/cm^3.

Reduction by Sodium: The reduction of potassium fluorine niobate (K_2NbF_7) by sodium may be represented as follows:

$K_2NbF_7+5Na=Nb+2KF+5NaF$

This process is realized in a shaft furnace using a layerwise loaded charge in a steel crucible. Sodium surplus (15%–20%) in the form of sodium chloride layer is poured onto the top of the charge; the crucible is placed into the preheated furnace (up to 870 K) and kept for 1.0–1.5 h at 1170–1270 K. Niobium powder is washed, first in cold then in hot water, and is next washed with dilute nitric or hydrochloric acid (to eliminate iron, titanium and other impurities) and 2.5% cold hydrofluoric acid for 5–15 min to decrease the niobium oxide content.

Electrolysis of Melt: Electrolysis of melt is also used. Refined salts are melted in a nickel crucible (cathode), and Nb_2O_5 is introduced into the melt; the anode is a graphite rod, and the electrolyte temperature is 1020 K. Voltage on the cell is 2.5 V; cathode current density ranges from 5 to 6 kA/m^2, and current efficiency is not >30%. The niobium deposit is coarse-grained and contaminated with the lowest niobium oxides. Two types of electrolyte are used K_2NbF_7-KCl-Nb_2O_5 and K_2NbF_7-KCl-NaCI (for refining). In liquid melt of the former, before Nb_2O_5 is introduced, the following reactions take place:

$K_2NbF_7+KF=K_3NbF_8$ and/or $K_2NbF_7+KCl=K_3NbF_7Cl$

Having added niobium pentoxide in surplus of KF, the reaction can be written:

$K_2NbF_7+13KF+2Nb_2O_5=5K_3NbO_2F_4$

Complex niobium containing ions hypothetically NbF_8^{3-}, NbF_7^{2-} and $NbO_2F_4^{3-}$ are present in the electrolyte. At temperatures in the range from 970 K to 1020 K and cathode current density ranging from 1 to 8 kA/m^2, it is possible to obtain niobium powder, in which, compared to anode material, the impurities content is less by an order of magnitude: for iron, 1–3, for silicon, 1–1.5, for carbon, 1–1.5, and for oxygen, 1.0.

Niobium sponge can be produced also by electrodeposition from halide melts. Electrolysis of bromide and iodide melts (4%–6% Nb) is carried out with addition of alkali metal chlorides at 973 K and cathode current density of 5 kA/m^2. Current efficiency is about 40%. The obtained sponge is lightly milled to powder. For niobium reduction from halide melts, the starting material is niobium produced by carbothermic reduction and the electrolyte is a mixture of NaCl and K_2NbF_7, with 10%–40% of the latter. In an argon atmosphere, niobium is oxidized on the anode and reduced on the cathode using a cathode current density of 32–41 kA/m^2 and temperature between 1100 K and 1200 K.

The electrolysis cell (Fig. 23.43) made of nickel is put into the furnace with graphite heaters and a heat shield. On the furnace cover, a water-cooled chamber for charging is erected, in which the cathode is vertically moved. Current efficiency,

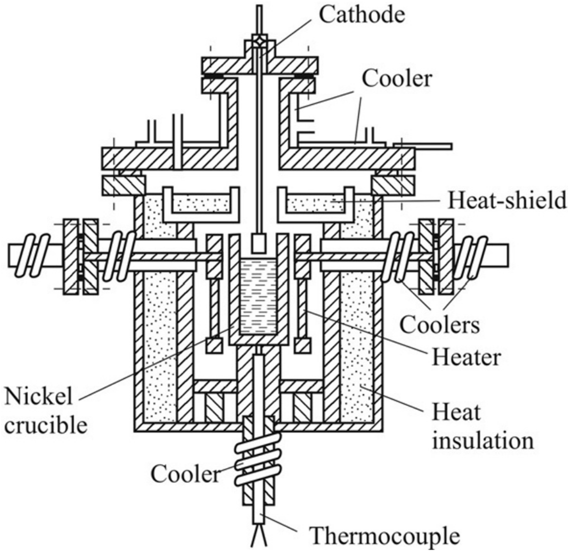

FIG. 23.43 Elecrolyzer for niobium refining.

TABLE 23.17 Compositions of Contaminant Elements in Anodes and Electrolytic Niobium Powder

Elements	Unit	Anode	Powder
Aluminum	ppm	10	10–20
Calcium	ppm	50	50
Chromium	ppm	20	10
Copper	ppm	10	1
Iron	ppm	30	70–150
Lead	ppm	…	10
Magnesium	ppm	10	10
Manganese	ppm	…	10
Nickel	ppm	10	100–500
Silicon	ppm	30	4–5
Tin	ppm	…	10
Titanium	ppm	1000	100
Vanadium	ppm	…	10
Zirconium	ppm	5000	100

calculated to Nb^{2+}, ranges from 23.1% to 34.6%. Compositions of contaminant elements in electrolytic refined niobium powders and in anodes are given in Table 23.17. The powders (cathode product) consist of modified coarse dendrites.

Hydride-Dehydride Process: Powders are produced from ingots by means of hydriding, crushing, and subsequent dehydriding of electron beam (EB) melted ingots. These melt-grade powders have higher purity than the sodium-reduced types and have better dielectric properties. However, unit capacitance is usually lower for EB-powder. Although the dielectric properties of niobium oxide are inferior to those of tantalum oxide, niobium has been evaluated as a means of manufacturing low-cost capacitors. Considerable niobium powder development work is required before niobium capacitors will be offered commercially. Usually, powders are crushed to pass a 180 μm (80-mesh) screen and a mean particle size of 10–15 μm is typical.

Niobium Alloys

Typical compositions of niobium and niobium alloy powders are given in Table 23.18.

Niobium powder is frequently used as the starting material to blend with other alloying powders. The blend is pressed to bars and melted. Niobium metal scrap, which is reduced to powder by the hydride-dehydride process, can also be incorporated into the alloy blends.

Some efforts [127] have been directed to producing complex metastable alloy powders, such as niobium-aluminum and niobium-silicon alloys, by liquid metal atomization and rapid solidification.

Most commercial niobium alloys are in wrought form. Primary (bulk) processing is generally done by high temperature extrusion or forging. Secondary working manufactures a variety of mill products such as rods, sheets, wire, foil, and tubing. Powder metallurgy methods have been evaluated for common niobium alloys, such as C-103 (Nb-10Hf-1Ti) and Nb-30Hf-9W. It has been found that the high production cost of atomization prevents economical manufacturing of net shape parts. However, hydride-dehydride niobium powders are used to produce commercial quantities of hot working preforms of alloy Nb-30Hf-9W [127].

The NbCu composite is used to produce electric contacts, resistances, welding electrodes, microwaves absorbers, and heat sinks. Some studies of the Nb-Cu composite with varying (5–20 wt%) copper content were carried out [134–136]. In the work [137], the Nb-Cu composites with 12.5 wt% and 25 wt% Cu content where produced by mechanical alloying using planetary ball milling. Niobium powder made by hydride-dehydride technique (HDH) and copper powder made by carbonyl process were used in this work. The characteristic morphology of these powders is shown in Fig. 23.44.

TABLE 23.18 Typical Compositions of Niobium and Nb-10Hf-1Ti Alloy Powders Made by the Hydride-Dehydride Process

Property	Unit	Analysis		
		Niobium		Nb-10Hf-1Ti (C-103 Niobium Alloy) Source: Fansteel Inc
		Source: Fansteel Inc	GOST 26252–84 I-grade	
Elements:				
Niobium	wt%	≥99.7%	balance	≥87.2%
Hafnium	ppm	<20	…	9.8 wt%
Titanium	ppm	<20	<10	0.91 wt%
Aluminum	ppm	<20	<10	<20
Boron	ppm	<1	…	<10
Carbon	ppm	500	<50	194
Cobalt	ppm	<10	<10	<10
Copper	ppm	<40	<30	<40
Hydrogen	ppm	150	<20	50
Iron	ppm	100	<30	200
Magnesium	ppm	…	<10	…
Manganese	ppm	…	<10	…
Molybdenum	ppm	<20	<30	100
Nickel	ppm	<20	<10	<20
Oxygen	ppm	1820	<2000	1980
Nitrogen	ppm	197	<200	62
Silicon	ppm	30	<30	<20
Tantalum	ppm	800	<600	2800
Tin	ppm	…	<10	…
Tungsten	ppm	<50	<30	1100
Zirconium	ppm	<20	<10	1800
Other elements[a]	ppm	<20	…	<20
Physical properties:	ppm			
Apparent density	g/cm^3	…	0.7	…
Average particle sizes,	(μm)[b,c,d]	…	1.0; 1.1; 1.3	…
Surface area	m^2/g	…	0.76	…

[a] *Other elements include cadmium, chromium, magnesium, manganese, lead, tin, vanadium.*
[b] *Method of particle sizes determination: BET particle size calculated.*
[c] *Mercury porosimetry.*
[d] *FESEM particle size.*

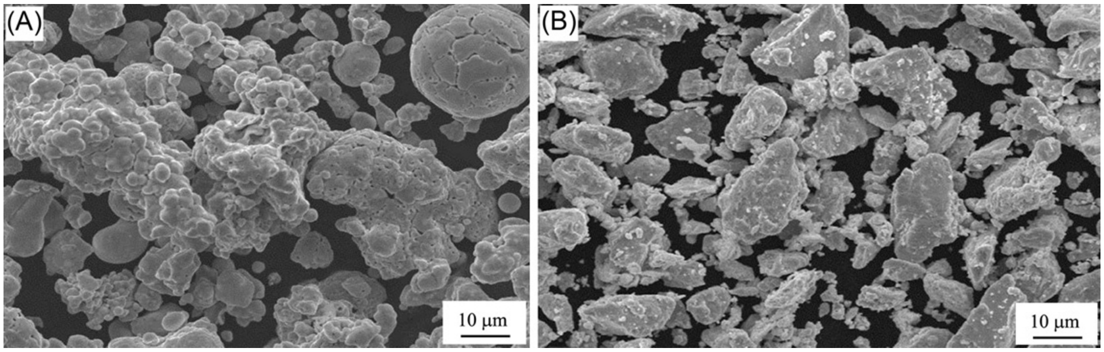

FIG. 23.44 Morphology of (A) carbonyl cooper powder and (B) HDH niobium powder. *(Source: Dias A, Grossi J, Muterlle PV. Production of NbCu composite by powder metallurgy. In: Completed by European powder metallurgy association. CD/USB proceedings of PM2017 euro congress. Milan (Italy): EPMA; 2017: p. 1–6.)*

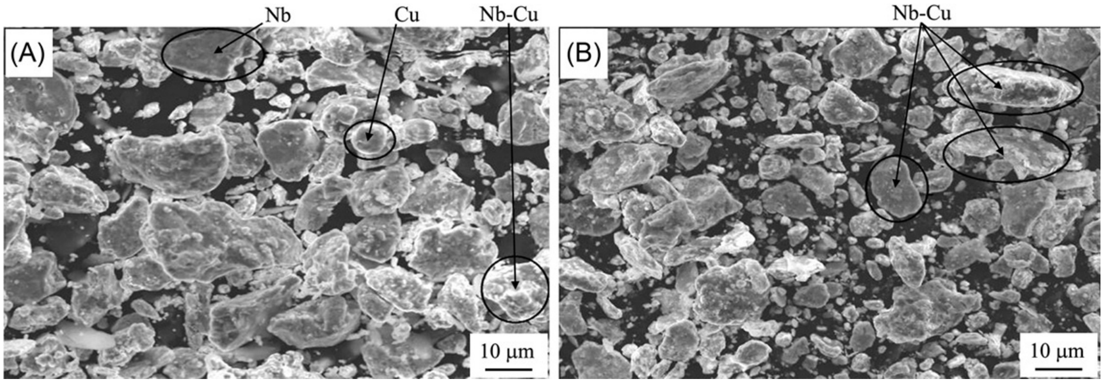

FIG. 23.45 Morphology of Nb-Cu composite powders with 12.5 wt% of cooper content (A) after two and (B) eight hours milling for the samples. *(Source: Dias A, Grossi J, Muterlle PV. Production of NbCu composite by powder metallurgy. In: Completed by European powder metallurgy association. CD/USB proceedings of PM2017 euro congress. Milan (Italy): EPMA; 2017: p. 1–6.)*

Fig. 23.45A and B exhibit the morphology of powders with 12.5 wt% of copper after two and eight hours milling for the samples, respectively. Two hours of milling was not effective to obtain the NbCu composite by mechanical alloying, because the powders still preserve their elementary conditions. Milling for eight hours shows that the elementary powders are not yet visible.

After milling, the powders were compacted at 400 MPa using a uniaxial mechanical press. The sintering of green samples was carried out in a tubular furnace with an argon atmosphere at a 1373 K temperature. As reported, all samples presented higher than 75% of full density, and in the samples with 25wt%Cu, the densification was higher than 80%.

Nb-Si intermetallic composites feature is high-temperature strength at rather low densities. They have a density of around 7 g/cm^3, which is significantly lower than the density of nickel-based superalloys with about 9 g/cm^3 [138,139]. For high-temperature resistant components in the high-pressure section of aircraft and land-based turbines, nickel-based superalloys are currently applied. The efficiency of these turbine engines can be further improved by increasing the service temperature. Currently, heat-resistant nickel alloys (HRNAs) for casting monocrystalline GTE blades have reached the limiting operating temperatures of 1370–1420 K for the material, which is 80%–85% of their melting point. Therefore, refractory alloys such the niobium-based silicide intermetallic composites (Nb-Si) are a promising material group for these applications. Until now, the utilized processing technologies to develop Nb-Si alloys were mainly casting, directional solidification, arc melting plus subsequent extrusion, physical vapor deposition, and hot extrusion of gas-atomized powders [140,141]. The challenge remains to find a processing technique that achieves a homogeneous microstructure and allows the production of near net shape Nb-Si components for industrial production [139,140].

The paper [142] reports the development of several metal injection molding (MIM) test geometries by utilizing gas-atomized powder. The same powder was processed by hot isostatic pressing (HIP) as well. After sintering, some MIM samples were subjected to subsequent HIPing to achieve further densification. Residual porosity, microstructure, phase distribution, and density achieved by these three processing techniques (MIM, HIP and MIM+HIP) are compared. Mechanical properties at ambient and elevated temperatures are assessed for both the sintered MIM samples and HIP

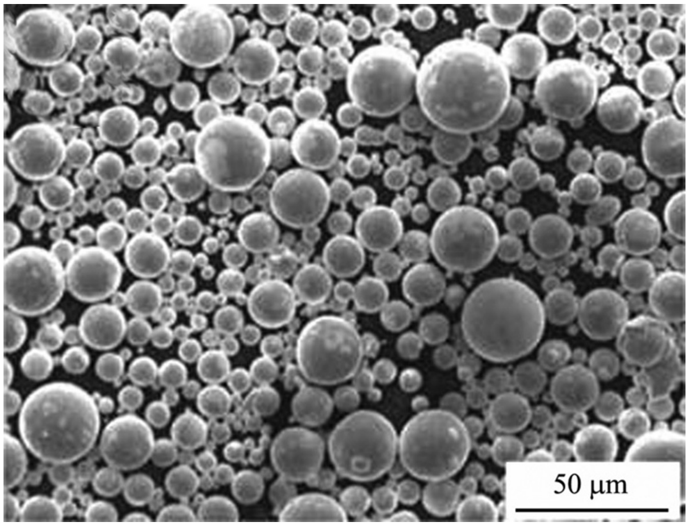

FIG. 23.46 SEM of the gas atomized Nb-Si powder <25 μm size fraction. *(Source: Mulser M, Hartwig T, Seemüller C, Heilmaier M, Adkins N, Wickins M. Influence of the processing technique on the properties of Nb-Si intermetallic composites for high-temperature applications processed by MIM and HIP. In: Compiled by Russell A, Chernenkoff W, Brian J. Proceedings of 2014 powder metallurgy world congress. Orlando (FL, USA): Metal Powder Industries Federation; 2014: p. 04-8-16.)*

material. Powder of the nominal composition Nb-20Si-23Ti-3Cr-6Al-4Hf (at.%) was produced by gas atomization in an argon atmosphere by electrode induction melting. A scanning electron micrograph of materials gas-atomized in an argon atmosphere by electrode induction melting is shown in Fig. 23.46. The powder particles are spherical with a smooth surface and limited satellites.

Compared with an HIP sample of powder <25 μm size fraction (Fig. 23.47A), the MIM sample of the same powder size fraction (Fig. 23.47B) shows a higher porosity with pores up to 10 μm in diameter.

As reported [142], the microstructure achieved by MIM reveals a much finer grain structure and more homogeneously distributed silicide particles compared to HIP. However, the MIM samples show larger HfO_2 precipitates and a higher residual porosity. By subsequent HIP processing, the residual porosity was reduced, increasing the density to 99.2%. The mechanical properties at RT and elevated temperatures of the as-sintered condition are significantly lower than those achieved by HIP material.

In the work [143], the alloying behavior and properties of Nb_5Si_3 were studied. The study used data for the silicide parameters as valence electron concentration (VEC) and electronegativity ($\Delta\chi$) and for the silicide solubility range, which were determined using the concentration $X = Al + B + Ge + Si + Sn$ in $(Nb,TM)_5X_3$). Actual chemical compositions of tetragonal Nb_5Si_3 in developmental Nb-silicide based alloys were used to calculate VEC, $\Delta\chi$ and X. Relationships between solvent and solute additions in Nb_5Si_3 and its parameters VEC and $\Delta\chi$ were found. Changes in the hardness and creep of tetragonal Nb_5Si_3 were related to the parameters VEC and $\Delta\chi$.

The influence of the technological regimes of vacuum induction melting and oriented crystallization melting on the content of alloying elements and the structure of an in-situ composite of the Nb-Si system alloyed with titanium, hafnium, aluminum, chromium, molybdenum, tungsten, and zirconium was studied [144]. The following conclusions were made:

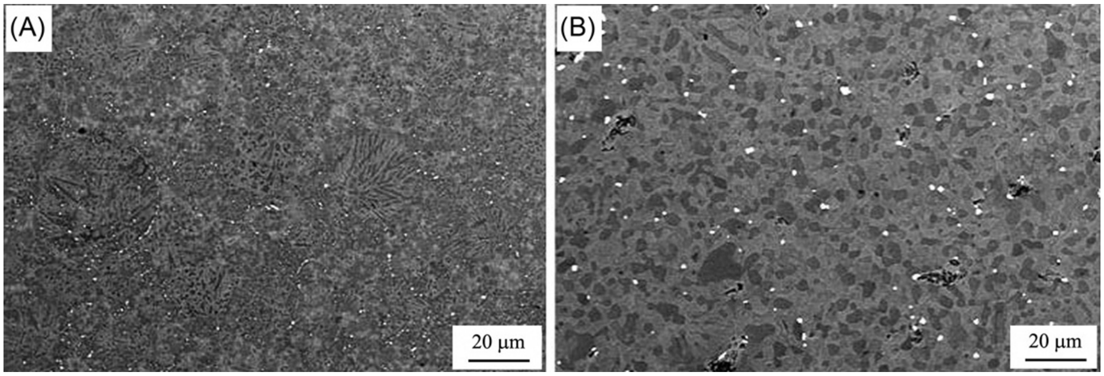

FIG. 23.47 Scanning electron micrographs of (A) HIP and (B) MIM of <25 μm size powder fraction of the Nb-Si intermetallic composite. *(Source: Mulser M, Hartwig T, Seemüller C, Heilmaier M, Adkins N, Wickins M. Influence of the processing technique on the properties of Nb-Si intermetallic composites for high-temperature applications processed by MIM and HIP. In: Compiled by Russell A, Chernenkoff W, Brian J. Proceedings of 2014 powder metallurgy world congress. Orlando (FL, USA): Metal Powder Industries Federation; 2014: p. 04-8-16.)*

- The microstructure of samples of a composite based on Nb-Si is represented by eutectic cells oriented along the direction of crystallization. The phase composition contains the Nb solid solution (matrix) with the bcc lattice, niobium silicide γ-Nb_5Si_3 with the hexagonal lattice, and hafnium oxide HfO_2 with the bcc lattice. Niobium silicide γ-Nb_5Si_3 has an orientation close to I100I along the direction of the growth axis, while the Nb matrix is oriented along the direction I110I.
- In cast material, an inhomogeneous distribution of alloying elements in the solid solution is observed. The titanium, chromium, and aluminum concentrations at the cell boundaries are higher than in the center, while the molybdenum, niobium, and tungsten concentrations are lower. Exposure at a temperature of 1773 K for 20 h contributes to leveling the concentration of alloying elements in the solid solution, but leads to the intensified formation of hafnium oxides.
- The tensile strengths of niobium composites at 1473 K are almost two times higher than those for heat-resistant nickel alloy (HRNA) single crystals; with consideration of the lower density of composites (7.386 g/cm^3 compared to 8.9–9.1 g/cm^3 for HRNAs), the advantage in the specific strength is even more significant.

Tantalum

Several methods for reducing tantalum compounds to tantalum metal have been developed, but sodium reduction of the double salt, potassium tantalum fluoride (K_2TaF_7), to produce tantalum metal powder is the most commonly used. The general equation for the reduction with sodium may be represented as:

$$K_2TaF_7 + 5Na = Ta + 5NaF + 2KF$$

The reaction is carried out in a stirred reactor containing molten sodium chloride diluent under an inert atmosphere. The reaction is exothermic and accompanied by heat evolution amounting to 1500 kJ/mol (2 kJ per 1 g of molten sodium). After cooling, the resulting salt cake is removed from the reactor and crushed. The tantalum powder is recovered by thoroughly washing with hot distilled water with an addition of hydrochloric acid and subsequently dried at 380–400 K. Particles are usually rounded in shape, with a tendency to form grape-like clusters during reduction. Individual particles in such clusters range in size from 1 μm to 10 μm, depending on reduction variables, including temperature, agitation, and salt purity.

Electronic capacitor applications generally require fine particles with high surface area. In one modification of the process, potassium tantalum fluoride, sodium chloride, and sodium metal are mixed into a paste and reacted without pre-melting [145]. Flake-shaped tantalum particles are produced by this technique. Because flakes have a higher surface-to-volume ratio than spheres, they are suitable for capacitor applications. In another modification of the process, tantalum powder with a highly developed surface can be produced by conducting the process in the presence of small amounts of boron, phosphorus, sulfur, and silicon. An even more appreciable effect is achieved by additions ranging from 0.002% to 0.5% of halides, oxides, or sulfides of Ti, Zr, and Hf.

Generally, a wide range of sodium reduced capacitor powders is currently available, with unit capacitances ranging from 5000 μF·V/g to >25,000 μF·V/g. Capacitor powders are also manufactured by the HDH process. The electron beam (EB) melting step allows improvement of the purification of tantalum metal powders. In this process, sodium-reduced powders are pressed into bars which are subsequently EB melted. The resulting ingot is placed in a furnace with a hydrogen atmosphere. The tantalum is fully hydrided on slow cooling from 1070 K under hydrogen. The brittle hydride is crushed, ground, and classified to yield powder with average particle sizes ranging from 3 μm to 6 μm. The particles have an angular shape.

Additions of small amounts (10–100 ppm) of sintering inhibitors, such as phosphorus, are frequently employed. These agents allow finer powders to be used than would be possible in the absence of an inhibitor. Alternatively, higher sintering temperatures can be used without loss of surface area, thereby aiding vaporization of undesirable impurities. Dielectric properties are thus improved.

Because capacitance is directly proportional to the tantalum surface area accessible to an electrolyte, a porous structure is desirable. Thus, it is desirable to press the powders to as low a density as possible, while retaining sufficient green strength for handling. In general, sodium-reduced powders can be pressed to lower densities than EB melted, degassed hydride powders. The former material is used in high-capacitance devices at lower voltage ratings (<50 V). However, because of the higher purity of the latter powders, they allow operation at higher voltage. Thus, comparing the two basic types of tantalum powders when used for capacitor manufacture shows that the sodium-reduced powder material has a higher capacitance per gram of powder and better green strength for pressed compacts, while electron beam melted, degassed hydride powder material has higher purity, better flow characteristics and higher voltage capability in capacitor devices. Currently, sodium-reduced tantalum powders are generally used for 80%–90% of capacitor applications.

There is an electrolytic process for producing tantalum using an electrolyte containing potassium fluorotantalate (K_2TaF_7), potassium (sodium) chloride and/or fluoride in which tantalum pentoxide is dissolved. Carbon dioxide and carbon monoxide are formed at the anode. An anode effect arises during electrolysis of the K_2TaF_7 melt. Potassium chloride and fluoride provide easy fusibility, fluidity, and conductivity of the electrolyte, while the tantalum pentoxide improves wettability of the graphite anode. The cathode can be made of molybdenum, nickel, nichrome, or steel.

Thus, the oxide-fluoride-chloride electrolytes contain ions of K^+, Cl^-, F^-, TaF_8^{3-}, $TaOF_6^{3-}$ (when the content of Ta_2O_5 in the electrolyte is <5%) or $TaO_2F_4^{3-}$ (when content of Ta_2O_5 in the electrolyte is 5% and more).

The discharge of Ta^{5+} ions occurs on the cathode:

$Ta^{5+} + 5e \rightarrow Ta$

Scheme of the anode process can be written:

$$TaOF_6^{3-} - 2e = TaF_5 + F^- + 0.50_2$$
$$TaF_5 + 3K^+ + 3F^- = K_3TaF_8$$
$$0.5O_2 + C = CO\,(O_2 + C = CO_2)$$

Thus, Ta_2O_5 undergoes an electrolysis treatment after finally being introduced into the melt. Precipitation of tantalum on the cathode and oxygen on the anode can be described:

$$4Ta^{5+} + 20e \rightarrow 4Ta \text{ and } 10O^{2-} - 20e \rightarrow 5O_2$$

Reaction of graphite oxidation on the anode accompanied by evolution of energy leads to its depolarization, so that the amount of energy necessary to decompose of Ta_2O_5 is decreased.

The electrolyte contains 2.5–8.5 wt% Ta_2O_5, 8.5–32.5 wt% K_2TaF_7, 27.5–57.5 wt% KF, and 25.5–55 wt% KC1; its melting temperature is about 920–970 K, depending on electrolyte composition. Electrolysis is accomplished at 970–1020 K. An advanced electrolyte containing 3–3.5 wt% Ta_2O_5, K_2TaF_7, 66.5–72 wt% (NaCl + KC1) with a reduced melting point of 270 K allows electrolysis to be conducted at 970 K.

There are two types of electrolyzers. In the first type, a graphite crucible serves as an anode, and a metal bar located in the center of the crucible is the cathode. The second type includes a metal crucible as the cathode and a graphite rod or a hollow perforated graphite tube as an anode disposed in the center of the crucible (Fig. 23.48). The latter is preferable. In this electrolyzer, Ta_2O_3 is loaded into the cell through the hollow anode, and the gases are eliminated through the orifice in the side of the electrolyzer. Electrolysis is performed at a current density 5 kA/m^2 on the cathode and 1.2–1.6 kA/m^2 on the anode. Tantalum dendrites are deposited on the bottom and the sides of the crucible. The process is terminated as soon as the

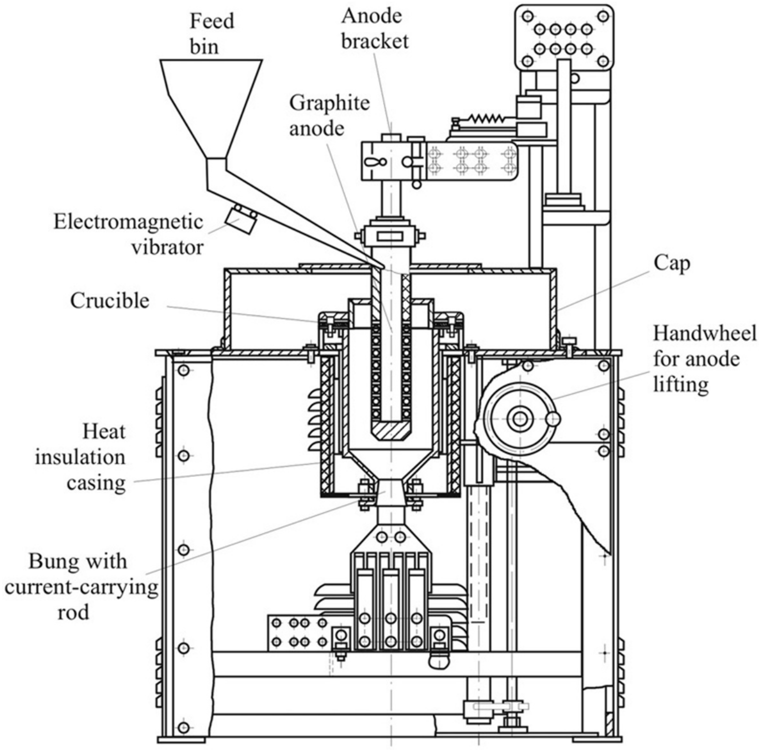

FIG. 23.48 Elecrolyzer for tantalum production.

cathode deposit fills two-thirds of the crucible capacity. Tantalum powder particles are imbedded in the solidified electrolyte that protects the metal from oxidation on cooling. The powder particle sizes range from 30 μm to 120 μm.

The cathode product is milled in a ball mill that operates in a closed cycle with an air separator. The electrolyte phase is separated and returned to the cell for electrolysis. The tantalum powder is washed on shaking tables in water jets to eliminate electrolyte, treated with a hot mixture of hydrochloric acid and nitric acid in porcelain reactors to eliminate molybdenum and iron, washed with water again, and dried.

A vacuum heating process is also available in which the cathode crucible is heated in argon to 1270 K to melt the electrolyte. The vessel is then evacuated and the electrolyte sucked out. The metallic tantalum in form of weakly fritted dendrites in 100–120 μm sizes precipitated on the crucible walls is scraped off and ground. Current efficiency is 80%–83%; power consumption is 2300 kWh per ton.

Tantalum powder can be produced by electrolysis of melts containing tantalum pentachloride ($TaCl_5$). The liquid or vapor $TaCl_5$ ($\leq$ 10% of tantalum) is introduced into the melt (NaCl + NaF, NaCl + KCl, or NaCl + KCl + KF) at temperature ranges from 1020 K to 1220 K, by voltage in the cell 6–8 V, cathode current density 5 kA/m^2, and anode current density of 10–20 kA/m^2; current efficiency amounts to 85%–88%.

The method of tantalum refining in chloride-fluoride and fluoride melts is still attractive, as the majority of impurities are eliminated completely; iron content is decreased 10–50 times, oxygen and hydrogen contents are decreased 10–100 times, and molybdenum and tungsten content is decreased 10^4–10^5 times, but it is difficult to eliminate niobium.

The electrochemical method for producing tantalum powder based on reducing electrochemically dissolved tantalum ions (Ta^{n+}) by dysprosium divalent ions (Dy^{2+}) in molten salt was investigated [146]. A tantalum rod (anode) was immersed in the NaCl-36 mol%KCl-4 mol%$MgCl_2$-6 mol%$DyCl_2$ molten salt at 1000 K, and it was anodically dissolved in this salt. The electrochemically dissolved Ta^{n+} ions were reduced in situ by Dy^{2+} ions in the molten salt to produce tantalum powder. After completion of the electrolysis process, tantalum powder mixed with salt was recovered by leaching the mixture with acids. The salt and some metallic impurities were dissolved in an acetic acid solution. The resulting tantalum powder was rinsed in aqueous HCl at room temperature; it was then rinsed with distilled water, alcohol, and acetone, and subsequently dried under vacuum. Fig. 23.49 shows the SEM images of the tantalum powders obtained at various currents. As shown, the particles are loosely agglomerated to form a porous structure; the average particle size of the powder successively increased by a small amount when the currents were increased to 2.0 A and 4.0 A,

As reported, tantalum powder with a purity of around 97 mass% and an average primary particle size of around 0.1 μm was obtained by this electrochemical method in the NaCl-36 mol%KCl-4 mol%$MgCl_2$-6 mol%$DyCl_2$ molten salt at an applied current of 1.0 A.

Typical impurity compositions of sodium-reduced tantalum powder, electron beam melted, degassed hydride powder, electrolytic powder, and purified electrolytic powder are given in Table 23.19.

Tantalum Carbide

The conventional technique for tantalum carbide powder production is similar to methods by which tungsten carbide powders are produced. Stoichiometric tantalum carbide can be used as an additive to WC-Mo grade powder attritions to enhance the physical properties of sintered material. It can be also used as a grain growth inhibitor preventing the formation of large grains, resulting in increased hardness of the sintered parts. Additions from a tenth of 1%–30% are common

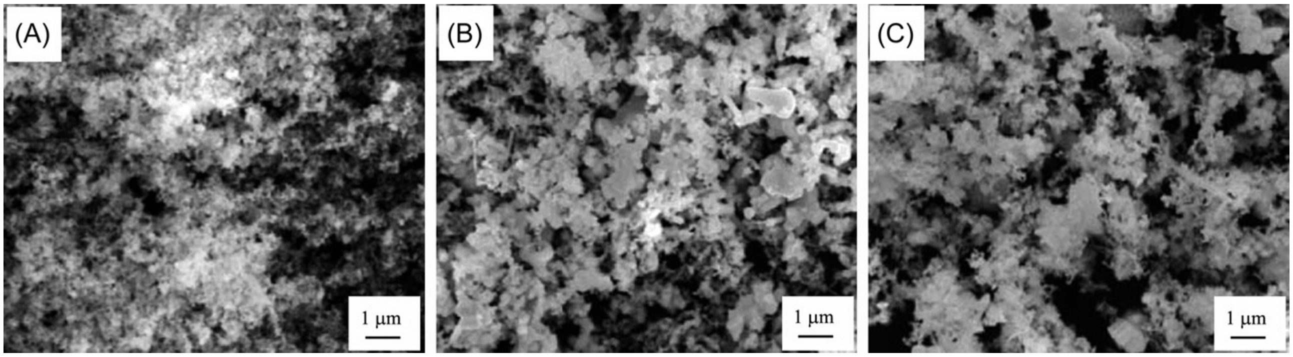

FIG. 23.49 SEM images tantalum powder obtained by the electrochemical method in NaCl–36 mol%KCl–4 mol%$MgCl_2$–6 mol%$DyCl_2$ molten salt at various currents: (A) $i = 1A$; (B) $i = 2A$; (c) $i = 4A$.

TABLE 23.19 Typical Compositions of Tantalum Powders Manufactured by Different Methods

Element	Powder Analysis (ppm)			
	Sodium-Reduced[a]	Electron Beam Melted Degassed-Hydride	Electrolytic from Oxide Chloride or Oxide Fluoride-Chloride Melts	Purified from Fluoride-Chloride or Fluoride Melts With K_2TaF_7
Aluminum	10	5	..	…
Calcium	10	5	…	…
Carbon	100	45	200–300	20–30
Chromium	25	5	…	…
Cobalt	10	5	…	…
Copper	10	5	…	…
Fluorine	…	…	10	…
Hydrogen	30	30	…	…
Iron	50	30	…	20–30
Iron +Nickel	…	…	300–1000	…
Lead	10	5	…	…
Magnesium	10	5	…	…
Manganese	10	10	…	…
Nickel	50	5	…	…
Niobium	50	20	…	…
Nitrogen	90	40	…	…
Oxygen	2400	1650	1000–2000	100–200
Silicon	25	10	1000	…
Sodium	10	5	…	…
Tin	10	5	…	…
Titanium	10	5	1000	…
Tungsten	25	25	…	…
Vanadium	10	5	…	…
Zirconium	10	5	…	…

[a] *Source: Fansteel Inc.*

and completely dependent on the particular application. Typical composition of commercial tantalum carbide powder, produced by OSRAM Sylvania Company, is given in Table 23.20. It also makes tantalum-niobium carbide (TaNbC) of several compositions, such as 90/10, 80/20, and 60/40.

In the work [147], the hydrate ammonium tantalate was selected as precursor of the tantalum carbide. The reactions between precursor ($(NH_4)TaO(C_2O_4)_3H_2O$) and mixture of methane and hydrogen were carried out at relatively low temperature of 1270 K in a resistive furnace, consisting of an alumina fixed bed reactor. As shown, the precursor powder obtained in this work has large particles composed of irregular shape agglomerates consisting of small crystallites (Fig. 23.50A), while the tantalum carbide powder particles preserve configuration, but their surface looks somewhat fitted (Fig. 23.50B).

TABLE 23.20 Typical Properties of Tantalum Carbide Powder

Property	Range	Typical
Particle size FSSS	0.5–2.0 μm	0.8–1.5 μm
Chemical analyses	Maximum percent	Typical percent
Total carbon	6.15–6.30	6.20–6.30
Free carbon	0.15	0.07
Calcium	0.02	0.005
Iron	0.05	0.04
Niobium	0.25	0.10
Oxygen	0.15	0.13
Silicon	0.02	0.01
Titanium	0.02	0.01

Source: OSRAM Sylvania.

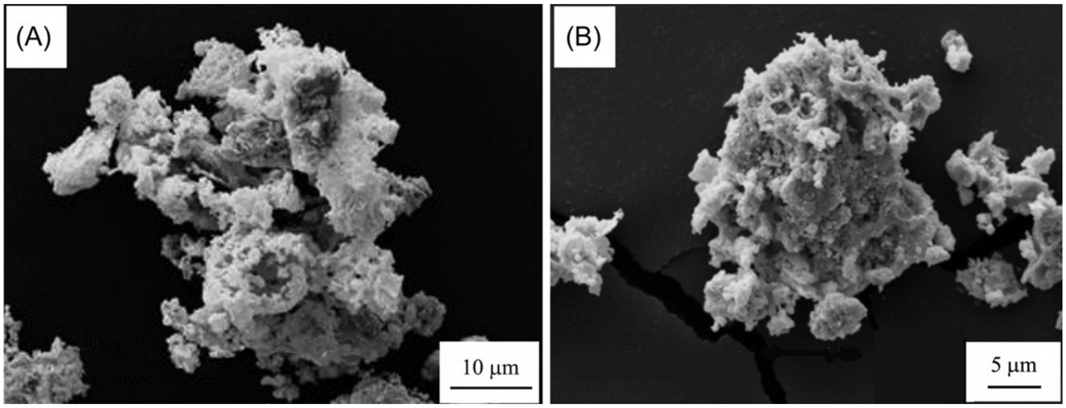

FIG. 23.50 SEM images of the (A) precursor powder and (B) and tantalum carbide powder.

As concluded [147], this precursor can be used in TaC synthesis at much lower temperatures and reaction times compared to those used in conventional synthesis. For the conventional method, the tantalum carbide is obtained at temperatures ranging from 1570 K to 1770 K; however, for good homogeneity in the final product, high temperatures around 2270 K throughout the reaction are necessary. The method using hydrate ammonium tantalate precursor allowed production of tantalum carbide at 1273 K and an isotherm of two hours. The results presented for TaC revealed the formation of pure phase with characteristics different from those conventionally obtained such as particle size and average crystallite size in the nanometer order, reaching 12.05 nm.

Consolidation and Manufacturing of Semi-Products

Powder metallurgy semiproducts of tantalum and its alloys are commonly made by cold isostatic pressing the powders into bars. The bars are then resistance sintered in a vacuum furnace at 1.33×10^{-2} Pa. Heating occurs due to the passage of an electric current. For tantalum, temperatures above 2570 K are required to achieve full density and sufficient purification as a result of removal of interstitial impurity elements. Sintered bars are then rolled or drawn at room temperature, with suitable intermediate vacuum anneals.

Models of initial stage sintering that consider the starting particle morphology have been applied to tantalum to develop higher energy capacitors [148,149]. An example of the agreement is shown in [150] for nonisothermal sintering of agglomerated tantalum flakes.

Powder metallurgy products differ from those produced from cast materials primarily because surface oxides are present in the initial powders. These oxides are contained in the microstructure of the consolidated PM material. Recrystallization is inhibited, and finer grained metal is obtained. The material is usually harder and has higher yield and tensile strength, but it is somewhat less ductile.

Microalloying additions, such as thoria and yttria, are sometimes added to control grain size and strength after recrystallization. Small quantities of silicon are also added, particularly to bars that are subsequently drawn to capacitor wire. Silicon promotes the retention of ductility of the wire by preventing embrittlement of the tantalum lead wire embedded in the capacitor pellet. During vacuum sintering, oxygen diffuses from the surrounding powder into the embedded wire, which has lower oxygen, and collects at grain boundaries, thereby stimulating embrittlement. Silicon operates as a getter for the excess oxygen. A part of the silicon vaporizes harmlessly in the form of volatile silicon monoxide.

Tungsten and hafnium are the alloying additions commonly added to improve the strength properties of tantalum. Typical properties for commercially produced tantalum and tantalum PM alloys and for comparison cast alloys are given in Table 23.21.

Ta-2.5%W is used for the fabrication of corrosion-resistant heat exchangers, valves, and other chemical equipment. Less ductile Ta-10%W alloy is a harder, stronger, and more wear-resistant alloy and is especially suited for the manufacture of furnace hardware, missile parts, nozzles, and fasteners. A Ta-7.5%W alloy, made by powder metallurgy, is useful for springs, siphons, and leaf springs in severe corrosion environments, such as hydrochloric acid, bromine, or dry chlorine. Because the yield strength of the PM product is higher than that of ingot material of the same composition, its modulus of resilience is also considerably higher, as illustrated in Table 23.21.

Workplace Atmosphere Safety

The aerosols of metallic niobium and tantalum are not toxic and relegated to the fourth, lowest class of danger according to State Standard 12.1.005-88 under the legislation in the Commonwealth of Independents States (CIS) [56]. Inspirable dust of both metals predominantly has a fibrous effect. The stated average limit value (ALV) of the aerosols of tantalum and its alloys in the workplace atmosphere, as the shift time-weighted average concentration, is 10 mg/m^3. As for niobium, the State Standard 12.1.005-88 standardizes only niobium nitride ALV, which amounts to 10 mg/m^3 (as the shift time-weighted average concentration). Under the workplace exposure limits in the European PM industry the long- and short-term (15-min reference period) workplace exposure limits (WELs) for tantalum are 5 mg/m^3 and 10 mg/m^3, accordingly [57].

Niobium in potable water has a toxic effect and is placed into the second class of danger and the TLV is 0.01 mg/L (for the inorganic compounds, including transition metals, subject to summation of all form contents) according to CIS State Standard 4630-88 [58].

The low concentration ignition limit (LCIL) of the metallic tantalum powder with particle sizes below 44 μm in the air is 200 g/m^3; minimum ignition temperatures of powder aerosols and aerogels (self-ignition temperature) are 903 K and 563 K, respectively. The products with such characteristics of inflammability and explosion risk are placed in the "moderate explosion hazard" class of danger according to the EPMA Guide to Legislation and "Health and Safety" in the European PM Industry [59].

Common techniques are mainly used for pollution prevention and environmental control by powder manufacturing and its processing. Detailed information on health and environment protection measures and also on prevention of inflammability and explosion risk in such conditions can be found in Chapter 27.

RHENIUM

Except for tungsten and carbon, among the elements, rhenium has the highest melting point, which is 3453 K. Its density is exceeded only by osmium, iridium, and platinum. Rhenium has the highest modulus of elasticity among the refractory metals. A ductile-to-brittle transition temperature does not exist in pure rhenium. Rhenium is one in refractory metals that does not form carbides.

Production of Rhenium Powder

The main method for rhenium powder production is reduction of ammonium perrhenate (NH_4ReO_4) by hydrogen. The reduction can be written:

TABLE 23.21 Typical Properties for Commercially Tantalum and Tantalum Alloys

		Standard Grades						
		Commercial Pure Tantalum			Ta-7.5W, PM		Ta-7.5W, Sheet[b]	
Property	**Unit**	**EB Melted[a]**	**PM**	**Ta-10W, EB Melted[a]**	**Wire**	**Sheet**	**Ingot**	**PM**
Density, at RT	g/cm^3	16.9	16.6	16.8	16.8	16.8	…	…
Melting point	°C	3000	3000	3030	3025[c]	3025[c]	…	…
Hardness, HV	HV	110	120	245	325	400	…	…
Hardness, DPH	DPH	…	…	…	…	…	150	291
Tensile strength:								
At 293 K	MPa	205	310	550	1035	1165	…	…
473 K	MPa	190	…	515	…	…	…	…
1023 K	MPa	140	…	380	…	…	…	…
1273 K	MPa	90	…	305	…	…	…	…
Yield strength								
At 293 K	MPa	165	220	460	1005	875	483	676
473 K	MPa	69	…	400	…	…	…	…
1023 K	MPa	41	…	275	…	…	…	…
1273 K	MPa	34	…	205	…	…	…	…
Elongation								
At 293 K	%	40	30	25	6	7	…	…
473 K		30	…	…	…	…	…	…
1023 K		45	…	…	…	…	…	…
1273 K		33	…	…	…	…	…	…
Modulus of elasticity								
At 293 K	GPa	185	185	205	200	200	196	196
1023 K	GPa	160	…	150	…	…	…	…
Modulus of resilience (U_R)[d]								
At RT	MPa	…	…	…	…	…	593	1172

[a] *EB, electronic beam.*
[b] *Measured for 2.1 mm thick, annealed and recrystallized sheet.*
[c] *Estimated.*
[d] $U_R = \sigma_0^2/2E$; σ_0^2 *is the yield strength;* E *is Young's modulus.*

Source: Adapted from Lambert JB et al. Refractory metals and alloys. In: Properties and selection: nonferrous alloys and special-purpose materials. ASM Handbook, vol. 2. Novelty (OH, USA): ASM International Publishers; 1990. p. 558–85.

$$NH_4ReO_4 + 2H_2 = Re + 1/2\,N_2 + 4H_2O$$

Typical impurity composition of hydrogen reduced powders is: $\leq \cdot 5$ ppm (Al + Fe + Cu + Mo), ≤ 10 ppm (Ca + Si + P + Na), ≤ 20 ppm (Mg + Ni + S), ≤ 50 ppm K, ≤ 1 ppm Mn, and Cu ≤ 0.5 ppm.

Raw material is milled in rubber-lined drums, then reduced in pusher type furnaces. The ammonium perrhenate is loaded into flat molybdenum boats that are pushed through the furnace. Reduction takes place in two stages. At

TABLE 23.22 Typical Chemical Composition of ≤74 μm and ≤44 μm Rhenium Powders

	Analysis (ppm)	
Elements	**≤74 μm (−200 mesh)**	**≤44 μm (−325 mesh)**
Aluminum	1.4	1.4
Boron	0.1	0.1
Calcium	0.2	0.2
Carbon	<10	<10
Chromium	1.5	1.5
Copper	0.5	0.5
Hydrogen	56	56
Iron	2.3	2.3
Manganese	0.1	0.1
Molybdenum	0.4	0.4
Nickel	1.7	1.7
Nitrogen	22	22
Oxygen	898	898
Silicon	0.2	0.2
Tantalum	<5	<5
Tungsten	0.33	0.33
Vanadium	<0.005	<0.005
Zinc	0.1	0.1

616–636 K, RO_2 is formed, and a final reduction to metal is done at 1220–1240 K. The boats' time in the hot zone of furnace is 1–2 h. Average size of powder particles ranges from 1 μm to 3 μm. Apparent density ranges from 1.5 g/cm^3 to 1.9 g/cm^3. Typical chemical compositions of ≤74 μm and ≤ 44 μm rhenium powders are shown in Table 23.22.

Among the refractory metals, rhenium has the highest tensile strength (Fig. 23.51). Rhenium has high electrical resistivity. It typically exhibits higher resistivity than tungsten. This feature, associated with a low vapor pressure, makes it

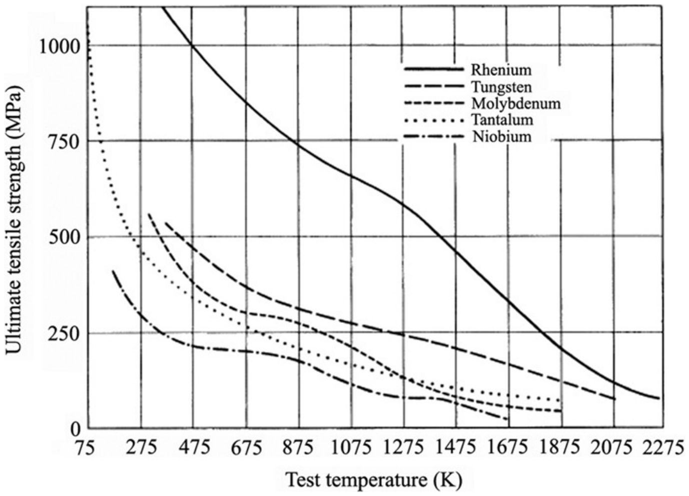

FIG. 23.51 Dependence of ultimate tensile strength for pure refractory metals on temperature. *(Source: Lambert JB et al. Refractory metals and alloys. In: Properties and selection: nonferrous alloys and special-purpose materials. ASM Handbook, vol. 2. Novelty (OH, USA): ASM International Publishers; 1990. p. 558–85.)*

perfectly suited for filament applications; parallel with this, it preserves ductility and is not affected by the oxidation/reduction cycle experienced in these applications, as is tungsten. Rhenium does not react with molten copper, silver, tin, or zinc.

Rhenium is resistant to hydrochloric acid and sea-water corrosion and to the mechanical effects of electrical erosion. At elevated temperatures, rhenium resists reaction in hydrogen and inert atmospheres.

Rhenium bars are produced by uniaxial pressing, while tubes are produced by cold isostatic pressing. Compaction pressures are typically 200 MPa to 250 MPa [151]. Green parts are presintered at 1470 K to 1670 K for 30 min in hydrogen to increase their handling strength. Final sintering at about 2970 K can be performed either in hydrogen or high vacuum. Typical densities are 80%–90% of theoretical density, and mill powders are cold worked with frequent annealing because of rhenium's rate of work hardening. Net-shape rhenium components can be sintered at temperatures of about 2570 K to near-full density [152].

Rhenium Alloys

Rhenium is used in combination with platinum in catalysts, especially for selective hydrogenation and crude oil reforming. Rhenium catalysts show high resistance to poisons, such as nitrogen oxides, sulfur, and phosphorus.

Rhenium is an advantageous alloying addition with other refractory metals. It greatly enhances the ductility and tensile strength of refractory metals and their alloys. This tendency is retained on heating above the recrystallization temperature. For example, alloys of molybdenum and rhenium are more ductile than pure molybdenum. An alloy with 35% Re can be rolled at room temperature to >95% reduction in thickness before cracking. For economic reasons, molybdenum-rhenium alloys are not widely used commercially. Alloys of molybdenum with 5% and 41% Re are used for thermocouple wires.

Applications

Rhenium alloys are used in nuclear reactors, semiconductors, thermocouples, electronic tube components, gyroscopes, parts for rockets, electrical contacts, thermionic converters, and various parts for high temperature aerospace applications.

Recent developments in the production of net shapes by powder metallurgy, rhenium manufacturing techniques have generated significant saving in both time and budget. For instance, the thrusters of different and unique types of aerospace components (rhenium combustion chambers) were manufactured by means of near-shape technique [153]. Near-net shapes are produced using elastometric molds with and without hard tooling inserts. The mold cavity is dimensioned so that, after CIP and sintering, final dimensions require only a minimum amount of finish machining [154]. The use of this technique allows the making of parts with a density of 95%–98% after sintering and 98.5%–99.9% on subsequent hot isostatic pressing [155]. The typical microstructure of the initial rhenium metal powders is shown in Fig. 23.52. The production of near-shape PM rhenium combustion chambers has reduced the manufacturing cost to 35%, and shortened the manufacturing time by 30%–40%. The quantity of rhenium metal powder used to produce a chamber is reduced by

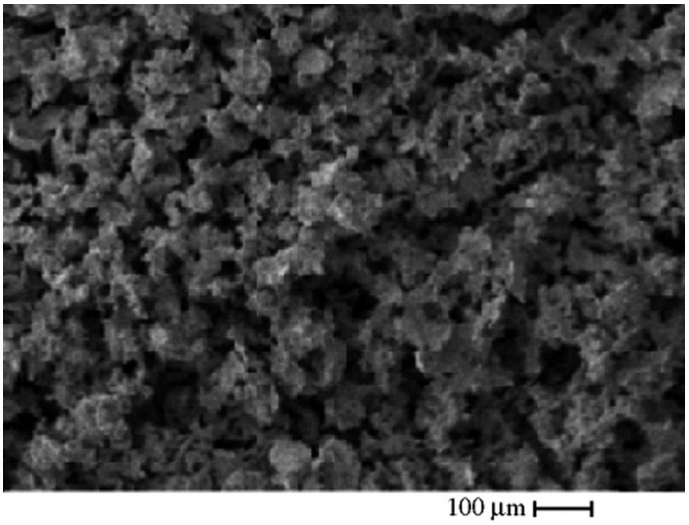

FIG. 23.52 Scanning electron micrograph of the rhenium metal powder. *(Source: Leonhard T, Downs J. Near net shape of powder metallurgy rhenium parts In: Infringer G, editor. Proceedings of 15th International Plan see Seminar, vol. 1. Reutter (Tirol, Austria): Plansee holding AG; 2001. p. 647–57.)*

approximately 70%, and subsequent reduction in machining costs is nearly 50%. Thus, cold isostatic pressing to near-net shape has provided significant cost savings and increased the quality and density of rhenium parts.

Tungsten-rhenium alloys, applied by vapor deposition, are used to coat the surface of molybdenum targets in X-ray tube manufacture. Other rhenium alloys, with tungsten and molybdenum, are used for filaments, grid heaters, cathode cups, and ignitor wires in photoflash bulbs. One of the largest applications for rhenium is for mass spectrometer filaments. These are available in commercial (99.99%) and zone-refined (99.95%) purities.

REFERENCES

[1] Hu P, et al. Preparation and ductile-to-brittle transition temperature of the La-TZM alloy plates. Int J Refract Met Hard Mater 2015;52:131–6.

[2] Yih SWH, Wang CT. Tungsten sources, metallurgy, properties, and applications. New York and London: Plenum Press; 1979.

[3] Lux B, Zeiler B. Production of tungsten and tungsten carbide powders. In: ASM Handbook. vol. 7. ASM International Publishers; 1998. p. 188–201.

[4] Williams B. Powder metallurgy—a global market review. In: International Powder Metallurgy Directory & Yearbook. 12th ed., vol. 1; 2005/2006. p. 5–11.

[5] Technical data, International Tungsten Industry Association.

[6] Lassner E, Schubert WD, Lüderitz E, Wolf HU. Tungsten, tungsten alloys, and tungsten compounds. In: Ullmann's Encyclopedia of Industrial Chemistry. vol. A27. VCH Verlagsgeselshaft GmbH; 1992.

[7] Spross M. Berg- und Huettenmaennische Montashefte. J Min Metall Mater Geotech Plant Eng 1996;141(8):359–62.

[8] Wolfram, 1975–2000. Wolfram Bergbau und Hütten GmbH.

[9] Haubner R, Schubert WD, Lassner E, Lux B. Mechanism of technical reduction of tungsten: Part 1 literature review. Int J Refract Met Hard Mater 1983;2:108–15.

[10] Haubner R, Schubert WD, Hellmer H, Lassner E, Lux B. Mechanism of technical reduction of tungsten: Part 2 hydrogen reduction of tungsten blue oxide to tungsten powder. Int J Refract Met Hard Mater 1983;2:156–63.

[11] Naboychenko SS, editor. Handbook of Non-Ferrous Metal Powders. Moscow: Metallurgia; 1997 [in Russian].

[12] Refractory metals. In: ASM Handbook. vol. 7. ASM International Publishers; 1998. p. 903–13.

[13] Ciulik JR, Shields JA, Kumar P, Leonhardt T, Johnson JL. Properties and selection of powder metallurgy refractory metals. In: ASM Handbook. vol. 7. ASM International Publishers; 2015. p. 593–8.

[14] Method for determination of average particle size of metal powders using the fisher subsieve sizer. In: MPIF Standard 32. Princeton: MPIF Publishers; 2003. p. 45–7.

[15] Lassner E, Schubert WD. Tungsten: properties, chemistry, technology of the element alloys and chemical compounds. New York (NY): Kluwer Academic/Plenum Publishers; 1999.

[16] Wilhartitz P, Ortner HM, Krismer R. Analytical characterization of ultrapure refractory metals—a critical comparison of techniques. In: Bildstein H, Ortner HM, editors. Proceedings of 12th International Plansee Seminar. vol. 3. Reutte (Tirol, Austria): Metallwerk Plansee GmbH; 1989. p. 576–86.

[17] Yu Y, Bai F, Zheng A, Song J, Peng F. Ultrahigh purity tungsten and its applications. In: Compiled by Bose A. Dowding RJ, Johnson JL. Proceedings of the 9th Tungsten, Refractory & Hardmaterials Conference. Orlando (FL, USA): Metal Powder Industries Federation; 2014: p. 313–20.

[18] Philipps V. Tungsten as material for plasma-facing components in fusion devices. J Nucl Mater 2011;415:52–9.

[19] Liu X, Tamura S, Tokunaga K, et al. High heat flux properties of pure tungsten and plasma sprayed tungsten coatings. J Nucl Mater 2004;329–333:687–91.

[20] Pintsuk G, Smid I, Döring J-E, Hohenauer W, Linke J. Fabrication and characterization of vacuum plasma sprayed W/Cu-composites for extreme thermal conditions. J Mater Sci 2007;42:30–9.

[21] Hirai T, Kreter A, et al. Critical heat flux loading experiments on CVD-W coating in the TEXTOR tokamak. Fusion Eng Des 2006;81:175–80.

[22] Lv Y, Song J, Liu J, Yu Y, Yan B. The properties and applications of tungsten prepared via chemical vapor deposition. In: Compiled by Bose A, Dowding RJ, Johnson JL. Proceedings of the 9th Tungsten, Refractory & Hardmaterials Conference. Orlando (FL, USA): Metal Powder Industries Federation; 2014: p. 345–50.

[23] Pink E. In: Bartha L, editor. The Metallurgy of Doped/Non-Sag Tungsten. Netherlands: Springer; 1989.

[24] Bartha L, Lassner E, Schubert WD, Lux B, editors. The chemistry of non-sag tungsten. Int J Refract Met Hard Mater 1995;13 [special issue].

[25] Harmat P, Grósz T, Rosta L, Bartha L. A novel method for shape analysis: deformation of bubbles during wire drawing in doped tungsten. In: Kneringer G, editor. Proceedings of 15th International Plansee Seminar. vol. 4. Reutte (Tirol, Austria): Plansee Holding AG; 2001. p. 108–17.

[26] Horacsek O, Bartha L. Potassium incorporation into tungsten by entrapment of dopant particles formed on the surface of AKS-doped TBO. In: Kneringer G, editor. Proceedings of 15th International Plansee Seminar. vol. 1. Reutte (Tirol, Austria): Plansee Holding AG; 2001. p. 658–68.

[27] Wang JJ, Hao JJ, Guo ZM, Wang YM. Preparation of spherical tungsten and titanium powders by RF induction plasma processing. Rare Metals 2015;34:431–5.

[28] Proulx P, Mostaghimi J, Boulos MI. Heating of powders in an RF inductively coupled plasma under dense loading conditions. Plasma Chem Plasma Process 1987;7:29–52.

[29] Jiang XL, Boulos MI. Induction plasma spheroidization of tungsten and molybdenum powders. Trans Nonferrous Metals Soc China 2006;16:13–7. https://doi.org/10.1016/s1003-6326(06)60003-4.

[30] Zhu H, Tong H, Cheng C, Liu N. Study on behaviors of tungsten powders in radio frequency thermal plasma. Int J Refract Met Hard Mater 2017;66(August):76–82.

[31] Dudder GB, Gurwell WE. Hydrogen embrittlement effects on tensile properties of tungsten heavy alloys. In: Proceedings. Tungsten and Tungsten Alloys–Recent Advances. The Minerals, Metals, and Minerals Society; 1991. p. 161–7.

[32] Caldwell SG. Variation of Ni/Fe ratio in W-Ni-Fe heavy alloys: a current perspective. In: Proceedings 'Tungsten and Tungsten Alloys–1992'. Metal Powder Industries Federation; 1993. p. 89–96.

[33] Rabin BH, Moyer RM. Microstructure and tensile properties of tungsten-nickel-iron compositions. Metall Trans A 1998;19:1523–32.

[34] Spencer JR, Mullendore JA. Relationship between composition, structure, properties, thermo-mechanical processing, and ballistic performance of tungsten heavy alloys. Report MTL TR 91–44, Watertown: U.S. Army Materials Technology Laboratory; 1991.

[35] Caldwell SG. Tungsten heavy alloys. In: ASM Handbook. Powder Metallurgy, vol. 7. ASM International Publishers; 1998. p. 914–21.

[36] Debata M, Upadhyaya A. Sintering of tungsten-based heavy alloys with NiB and FeB additives. In: Compiled by European Powder Metallurgy Association. Proceedings of 2004 Powder Metallurgy World Congress. Vienne (Austria): EPMA; 2004. vol. 4, p. 825–30.

[37] Ermakova NS, Bashlykov SS, Grigoriev EG, Golstev VI. The mechanical properties of tungsten heavy alloys produced by high-voltage consolidation process. In: Compiled by European Powder Metallurgy Association, (Shrewsbury, UK). CD/USB Proceedings of PM 2017 Euro Congress. Milan (Italy); 2017: p. 1–4.

[38] Sebastian KV. Properties of sintered and infiltrated tungsten-copper electrical contact material. Int J Powder Metal Powder Techn 1981; 17(4):297–302.

[39] German RM, Hens KS, Johnson JL. Powder metallurgy processing of thermal management materials for microelectronic application. Int J Powder Metall 1994;30(2):205–15.

[40] Wang WS, Hwang KS. The effect of tungsten particle size on the properties of infiltrated-Cu compacts. In: Compiled by Mckotch RA, Webb R. Proceedings "Advances in Powder Metallurgy and Particulate Materials". vol. 1. Chicago (USA): MPIF-APMI; 1997. p. 757–64.

[41] Kim JC, Ryu SS, Kim YD, Moon IH. Densification behavior of mechanically alloyed W-Cu composite powders by the double rearrangement process. Scr Mater 1998;39(6):669–76.

[42] Yu JH, Kim TH, Lee JS. Particle growth during liquid phase sintering of nanocomposite W-Cu powder. Nanostruct Mater 1997;9:229–32.

[43] Fan J, Guo Y, Liu T, Zhu S. Densification and microstructure of nanocrystalline W-(25/30)Cu powders. In: Proceedings of the 9th Tungsten, Refractory & Hardmaterials Conference. Orlando (FL, USA): Metal Powder Industries Federation; 2014. p. 426–30.

[44] Chen W, et al. Infiltration sintering of WCu alloys from copper-coated tungsten composite powders for superior mechanical properties and arc-ablation resistance. J Alloys Compd 2017; 728(25 Dec): 196–205.

[45] Park YS, An CY, Kannan PK, Seo N, Zhuo K. Fabrication of dendritic silver-coated copper powders by galvanic displacement reaction and their thermal stability against oxidation. Appl Surf Sci 2016;389:865–73.

[46] Hong S-H, Kim T-H, Kim B-K. Fabrication of W-10Cu alloy with high thermal conductivity. In: Compiled by Arnold V, Chu C-L, Jandeska WF, Sanderow HI, Proceedings of 2002 Powder Metallurgy World Congress. Orlando (FL, USA): MPIF; 2002. p. 7-180–7-190.

[47] Kim DG, Lee KW, Kim YD. Fabrication of nanostructural W-Cu powder using W-CuO mixture. In: Compiled by Arnold V, Chu CL, Jandeska WF, Sanderow HI. Proceedings of 2002 Powder Metallurgy World Congress. Orlando (FL, USA): MPIF; 2002. p. 7-165–7-170.

[48] Selcuk C, Morley N, Wood JV. Effect of post-sintering heat treatment on porous tungsten in relation to sintering swelling. In: Compiled by European Powder Metallurgy Association. Proceedings of 2004 Powder Metallurgy World Congress. Vienne (Austria): EPMA; 2004. vol. 2, p. 152–8.

[49] Ivanov E, Wickersham Jr CE. Compaction of mechanically milled pure nanocrystalline tungsten. In: Kneringer G, editor. Proceedings of 14th International Plansee Seminar. vol. 1. Reutte (Tirol, Austria): RWF Werbegesellschaft; 1997. p. 207–16.

[50] Öveçoglu ML, Ozkal B, Suryanarayana C. A composition of the sintering characteristics of ball milled and attritor milled W-Ni-Fe heavy alloys. J Mater Res 1998;11(7):1673–82.

[51] Povarova KB, Makarov PV, Luk'yanchikova SS, Zavarina EK. Effect of high-energy ball milling on structure and some properties of powder tungsten alloys. Izvest Ross Akad Nauk, Metally 1994;6:113–23 [in Russian].

[52] Taillard RA, Avettand-Fènoel M-N, Dhers J, Foct J. Ball-milling and sintering of blends of tungsten and yttrium-reach powders. In: Compiled by Arnold V, Chu C-L, Jandeska WF, Sanderow HI, Proceedings of 2002 Powder Metallurgy World Congress. Orlando (FL, USA): MPIF; 2002. p. 6-188-202.

[53] US Patent 5,686,676. Nov 1997.

[54] Bose A, Walker D, Timmons R, Graham M. Complex shaped hardmetals by PM. In: Compiled by European Powder Metallurgy Association. Proceedings of 2004 Powder Metallurgy World Congress. Vienne (Austria): EPMA; 2004. vol. 3, p. 400–9.

[55] Austrian AT-Patent AT 403,060, 1997.

[56] Commonwealth of Independents States Standard GOST 12.1.005-88 [in Russian].

[57] EH40-Update to EH40/2005 Workplace Exposure Limits. 2nd ed., published 2011 (as consolidated with amendments, December 2011).

[58] Sanitary Regulation and Standards of surface waters from pollution. SanPiP 4630-88.

[59] Guide to Legislation and 'Health and Safety' in the European PM Industry. Publ. EPMA; 1997.

[60] Zeiler B. The potential of conventional tungsten carbide powder manufacturing. In: Kneringer G, editor. Proceedings of 14th International Plansee Seminar. vol. 4. Reutte (Tirol, Austria): RWF Werbegesellschaft; 1997. p. 265–76.

[61] Brooks KJA. World directory and handbook of hard metals and hard materials. 6th ed. International Carbide Data: East Barnet (England); 1996.

[62] Bock A, Zeiler B. Production and characterization of ultrafine WC powders. In: Kneringer G, editor. Proceedings of 15th International Plansee Seminar. vol. 4. Reutte (Tirol, Austria): Plansee Holding AG; 2001. p. 229–44.

[63] US Patent 3,379,503. Apr. 1968.

[64] Schubert WD, Bock A, Lux B. General aspects and limits of conventional ultrafine WC powder manufacture and hard metal production. In: Bildstein H, Eck R, editors. Proceedings of 13th International Plansee Seminar. vol. 4. Reutte (Tirol, Austria): Plansee Metall AG; 1993. p. 283–305.
[65] Yamamoto Y, Matsumoto A, Doi Y. Properties of ultrafine tungsten carbide and cemented carbide by direct carburization. In: Kneringer G, editor. Proceedings of 14th International Plansee Seminar. vol. 2. Reutte (Tirol, Austria): RWF Werbegesellschaft; 1997. p. 596–608.
[66] US Patent 5,380,688. Jan 1995.
[67] Carroll DF. Processing and properties of ultrafine WC/Co hard materials. In: Kneringer G, editor. Proceedings of 14th International Plansee Seminar. vol. 2. Reutte (Tirol, Austria): RWF Werbegesellschaft; 1997. p. 168–82.
[68] US Patent 5,230,729. Jul 1993.
[69] EU Patent EP 0 568861 B1, 1993.
[70] Wolfe TA, Johnson JL, Mehrotra PK. Production of carbide powders. In: ASM Handbook. vol. 7. ASM International Publishers; 2015. p. 711–4.
[71] Fang Z. Wear resistance of powder metallurgy alloys. In: ASM Handbook. vol. 7. ASM International Publishers; 1998. p. 965–77.
[72] Gilardi R, Alzati L. The role of carbon source in the production of WC powders. In: Compiled by Bose A, Dowding RJ, Johnson JL. Proceedings of the 9th Tungsten, Refractory & Hardmaterials Conference. Orlando (FL, USA): Metal Powder Industries Federation; 2014: p. 37–44.
[73] Song X, Wang H, Yang T, Liu X, Wang X. In situ synthesis of nanoscale WC-η composite powder and its application in cermet coating. In: Compiled by European Powder Metallurgy Association. Proceedings of PM 2016 World Congress. Hamburg (Germany); 2016: p. 1–6.
[74] Schubert WD, Kübel E. Mechanical testing of specimens and impact of trace elements on properties of hard. In: Bildstein H, Ortner HM, editors. Proceedings of 12th International Plansee Seminar. vol. 2. Reutte (Tirol, Austria): Metallwerk Plansee GmbH; 1989. p. 869–909.
[75] Uhrenius B, Brandrup-Wognsen H, Gustavson U, Lethinen B, Manninen H. On the formation of impurity-containing phases in cemented carbides. In: Bildstein H, Ortner HM, editors. Proceedings of 12th International Plansee Seminar. vol. 2. Reutte (Tirol, Austria): Metallwerk Plansee GmbH; 1989. p. 71–96.
[76] Schedler W. Hardmetall für den Praktiker. VDI-Verlag GmbH; 1988.
[77] Hu B. Metal and alloy powders for welding, hardfacing, brazing, and soldering. In: ASM Handbook. vol. 7. ASM International Publishers; 2015. p. 769–82.
[78] US Patent 5,089,182. Feb 1992.
[79] Rincón C, Zambrano G, Carvajal A, Esteve J. Tungsten carbide/diamond-like carbon multilayer coating on steel for tribological applications. Surf Coat Technol 2001;148(2–3):277–83.
[80] Santos A, Gonzalez C, Ramirez ZY. Characterization of tungsten carbide coatings deposited on AISI 1020 steel. J Phys 2017;786(012011):1–7. https://doi.org/10.1088/1742-6596/786/1/012011. Conference Series.
[81] Oyana ST, editor. The Chemistry of Transition Metals Carbides and Nitrides. Blacky Academic and Professional; 1996.
[82] Brookes KJA. World Directory and Handbook of Hardmetals and Hard Materials. 6th ed. Hertfordshire (UK): International carbide data; 1996.
[83] Schubert WD, Neumaster H, Kinger G, Lux B. Hardness to toughness relationship of fine-grained WC-Co hard metals. In: Kneringer G, editor. Proceedings of 14th International Plansee Seminar. vol. 4. Reutte (Tirol, Austria): RWF Werbegesellschaft; 1997. p. 249–64.
[84] Zhang K, et al. Microstructure and composition of the grain/binder interface in WC–Ni_3Al composites. Int J Refract Met Hard Mater 2014;44:88–93.
[85] Almond E, Roebuck B. Identification of optimum binder phase compositions for improved WC hard metals. Mater Sci Eng A 1988;105:237–48.
[86] Sato J, Omori T, Oikawa K, Ohnuma I, Kainuma R, Ishida K. Cobalt-base high-temperature alloys. Science 2006;312:90–1.
[87] Long J, et al. A new type of WC–Co–Ni–Al cemented carbide: Grain size and morphology of γ'-strengthened composite binder phase. Scr Mater 2017;126:33–6.
[88] Mannesson K, Borgh I, Borgenstam A, Agren J. Abnormal grain growth in cemented carbides — Experiments and simulations. Int J Refract Met Hard Mater 2011;29:488–94.
[89] Yang DY, Kang SJL. Suppression of abnormal grain growth in WC–Co via pre-sintering treatment. Int J Refract Met Hard Mater 2009; 2009(27):90–4.
[90] Park Y, Hwang N, Yoon D. Abnormal growth of faceted (WC) grains in a (Co) liquid matrix. Metall Mater Trans A 1996;27:2809–19.
[91] Long J, et al. Microstructure evolution of WC grains in WC–Co–Ni–Al alloys: effect of binder phase composition. J Alloys Compd 2017;710:338–48.
[92] Long J, Chen F, Du Y, Yi M. Growth behavior of WC-Co-Ni-Al alloys. In: Completed by European Powder Metallurgy Association. Proceedings of PM2017 Euro Congress. Milan (Italy); 2017: p. 1–6.
[93] Kelley A. Tungsten-carbide by three dimensional printing, Releigh (NC, USA): NC State University; 1998, https://pdfs.semanticscholar.org/01e8/33b179d50f58158d5a0f9407062b8fee13bd.pdf. Accessed April 2018.
[94] Pötschke J, Berger C, Richter H-J. Additive manufacturing of hardmetals. In: Compiled by European Powder Metallurgy Association, (Shrewsbury, UK). CD/USB Proceedings of PM 2017 Euro Congress. Milan (Italy); 2017: p. 1–6.
[95] Uhlmann E, Bergmann A, Gridin W. Investigation on additive manufacturing of tungsten carbide-cobalt by selective laser melting. Proc CIRP 2015;35:8–15.
[96] Cermets and cemented carbides. In: ASM Handbook. vol. 7. ASM International Publishers; 1998. p. 922–40.
[97] German RM. Powder metallurgy & prticxulate materials processing. Metal Powder Industries Federation; 2005.
[98] Bose A. A earliest perspective on the commercial PM metal-ceramic composite: cemented tungsten carbide. Int J Powder Metall 2011;47(2):31–50.
[99] Roediger H, van den Berg H, Dreyer K, Kassel D, Ortths S. Near-net-shaping in the hardmetal industry. Int J Refract Met H 2000;18:111–20.
[100] Mehrotra PK. Powder processing and green shaping. In: Sarin VK, Mari D, Llanes L, editors. Comprehensive Hard Materials. Amstelsevier: Elsevier; 2014. p. 213–35.

[101] Brookes KJA, editor. World Directory and Handbook of hardmetals and hard materials. 5th ed. International Carbide Data; 1992.

[102] Bose A, Eisen WB. Hot consolidation of powders and particulates. Metal Powder Industries Federation; 2003.

[103] Bose A, Sadangi R, Mehrotra PK. Sintering of hardmetals. In: ASM Handbook. vol. 7. ASM International Publishers; 2015. p. 720–3.

[104] Hellman PM. Review of HIP development, hot isostatic pressing—theories and application. Centek Publishers; 1988.

[105] Runyon G, Sargent B. Cemented carbide quality control. In: ASM Handbook. vol. 7. ASM International Publishers; 2015. p. 729–32.

[106] Kieffer BF, Baroch EF. Extractive metallurgy of refractory metals. AIME Publishers; 1981.

[107] Bewlay BP, Briant CL, Murray ML. Molybdenum-tungsten interdiffusion and the influence on potassium bubbles in tungsten lamp wire. Metall Mater Trans A 1998;29(12):2933–9.

[108] Dorfler RR, Laferty JM. Review of molybdenum recovery process. J Met 1981;33(4):48–54.

[109] Shen Y-S, Lattari P, Gardner J, Wiegard H. Electrical contacts. In: ASM Handbook. vol. 2. Novetly (OH, USA): ASM International Publishers; 1990. p. 840–68.

[110] Lambert JB, et al. Refractory metals and alloys. In: Properties and Selection: Nonferrous Alloys and Special-Purpose Materials. ASM Handbook, vol. 2. Novetly (OH, USA): ASM International Publishers; 1990. p. 558–85.

[111] Endo M, Kimura K, Udagava T, Tanabe S, Seto H. The effects of doping molybdenum wire with rare earth elements. In: Bildstein H, Ortner HM, editors. Proceedings of 12th international plansee seminar. vol. 1. Reutte (Tirol, Austria): Metallwerk Plansee GmbH; 1989. p. 37–52.

[112] Takida T, Kurishita H, Mabuchi M, Igarashi T, Doi Y, Nagae T. Mechanical properties of fine-grained sintered molybdenum alloy processed by mechanical alloying. In: Kneringer G, editor. Proceedings of 15th International Plansee Seminar. vol. 1. Reutte (Tirol, Austria): Plansee Holding AG; 2001. p. 293–304.

[113] Mueller AJ, Shields JA, Buckman RW. The effect of thermo-mechanical processing on the mechanical properties of molybdenum–2 vol% lanthana. In: Kneringer G, editor. Proceedings of 15th International Plansee Seminar. vol. 1. Reutte (Tirol, Austria): Plansee Holding AG; 2001. p. 485–97.

[114] US Patent 5,868,876. Feb 1999.

[115] German RM, Labombard CA. Sintering molybdenum treated with Ni, Pd and Pt. Int J Powder Metall Powder Tech 1982;18(2):147–56.

[116] Hwang KS, Huang HS. The liquid phase sintering of molybdenum with Ni und Cu addition. Mater Chem Phys 2001;67:92–100.

[117] Huang HS, Hwang KS. Embrittlement of activation sintered molybdenum. In: Proceedings of 2002 Powder Metallurgy World Congress, compiled by Arnold V, Chu C-L, Jandeska WF, Sanderow HI, Princeton (New Jersey, USA): MPIF Publishers; 2002. p. 6-77-88.

[118] Winnicka MB. The effect of lanthana content on the mechanical properties and formability of ODS Mo alloys. In: Compiled by Bose A, Dowding RJ, Johnson JL. CD/USB Proceedings of the 9th Tungsten, Refractory & Hardmaterials Conference. Orlando (FL, USA): Metal Powder Industries Federation; 2014: p. 501–12.

[119] Bergk B, Mühle U, Kieback B, Koutná N, Holec H, Clemens H. Nanocrystalline alloys of molybdenum with sodium and yttrium obtained by mechanical alloying. In: Compiled by European Powder Metallurgy Association. CD/USB Proceedings of PM 2017 Euro Congress. Milan (Italy); 2017: p. 1–6.

[120] Ohser-Wiedemann R, Martin U, Seifert HJ, Müller A. Densification behavior of pure molybdenum powder by spark plasma sintering. Int J Refract Met Hard Mater 2010;28:550–7.

[121] Park HK, Ryu JH, Youn HJ, Yang JM, Oh IH. Fabrication and property evaluation of Mo compacts for sputtering target application by spark plasma sintering process. Mater Trans 2012;53:1056–61.

[122] Mouawad B, et al. Full densification of molybdenum powders using spark plasma sintering. Metall Mat Trans A 2012;43:3402–9.

[123] Lee G, Olevsky E, McKittrick J. Spark plasma sintering of molybdenum nanopowders. In: Compiled by European Powder Metallurgy Association. CD/USB Proceedings of PM 2016 World Congress. Hamburg (Germany); 2016: p. 1–6.

[124] Orban RL, Salomie D, Orban M, Neamţu B, Sechel N, Lung T. SHS synthesis from mechanical activated powdered components mixture of molybdenum aluminade Mo_3Al for use at extremely high temperatures. In: Compiled by European Powder Metallurgy Association. CD/USB Proceedings of PM 2016 World Congress. Hamburg (Germany); 2016: p. 1–6.

[125] Kirk RE, Othmer DF, editors. Encyclopedia of chemical technology. 3rd ed. vol. 22. John Wiley & Sons; 1983.

[126] US Patent 3,294,482. 1966.

[127] Wojcik CC. Processing, properties, and applications of high-temperature niobium alloys. In: Proceedings of 1994 Symposium, High Temperature Silicides and Refractory Alloys. vol. 322; 1994. p. 519–30. Mater Res Soc.

[128] Luidold S, Antrekowitsch H, Ressel R. Production of niobium powder by magnesiothermic reduction of niobium oxides in a cyclone reactor. Int J Refract Met Hard Mater 2007;25(5–6):423–32.

[129] Okabe TH, Iwata S, Imagunbai M, Maeda M. Production of niobium powder by magnesiothermic reduction of feed preform. ISIJ Int 2003; 43(12):1882. –9, 2003.

[130] Park I, Okabe TH, Waseda Y, Yu HS, Lee OY. Semi-continuous production of niobium powder by magnesiothermic reduction of Nb_2O_5. Mater Trans 2001;42(5):850–5.

[131] Orlov VM, Kryzhanov MV. Production of tantalum powders by the magnesium reduction of tantalates. Russian Metallurgy (Metally) 2015; 2015(7):590–3.

[132] Kumar TS, Kumar SR, Rao ML, Prakash TL. Preparation of niobium metal powder by two-stage magnesium vapor reduction of niobium pentoxide. J Metallurgy 2013;1–6 (Article ID 62934).

[133] Zelikman AN, Korshunov BG. Metallurgy of rare metals. Moscow: Metallurgiya Publisher; 1991 [in Russian].

[134] Nikolaev AK, Rozenberg VM. Heat resistant steels and alloys. Properties of Cu-Nb alloys. Met Sci Heat Treat 1972;14(10):888–90.

[135] Torrobla JM, Costa CE, Velasco F. P/M aluminum matrix composites: an overview. J Proc Technol A 2003;133:203–6.

[136] Sharma IG, Chakraborty S, Majumdar S, Suri AK. A study on preparation of copper-niobium composite by aluminothermic reduction of mixed oxides. J Alloys Compd 2002;336(1):247–52.

[137] Dias A, Grossi J, Muterlle PV. Production of NbCu composite by powder metallurgy. In: Completed by European powder metallurgy association. CD/USB Proceedings of PM2017 Euro Congress. Milan (Italy): EPMA; 2017: p. 1–6.

[138] Zhao JC, Westbrook JH. Ultrahigh-temperature materials for jet engines. MRS Bull 2003;28(09):622–30. Cambridge University Press.

[139] Bewlay BP, Jackson MR, Zhao JC, Subramanian PR, Mendiratta MG, Lewandowski JJ. Ultrahigh-temperature Nb-silicide-based composites. MRS Bull 2003;28(09):646–53. Cambridge University Press.

[140] Jehanno PM, et al. Assessment of a powder metallurgical processing route for refractory metal silicide alloys. Metall Mater Trans A 2005; 36A(3):515–23.

[141] Seemüller HCM. Evalution of powder metallurgical processing routes for multi-components niobium silicide-based high-temperature alloys. Doctor dissertation. Karlsruhe (Germany): Kalsruher Instituts für Technolgie; 2016.

[142] Mulser M, Hartwig T, Seemüller C, Heilmaier M, Adkins N, Wickins M. Influence of the processing technique on the properties of Nb-Si intermetallic composites for high-temperature applications processed by MIM and HIP. In: Compiled by Russell A, Chernenkoff W, Brian J. Proceedings of 2014 Powder Metallurgy World Congress. Orlando (FL, USA): Metal Powder Industries Federation; 2014: p. 04-8–16.

[143] Tsakiropoulos P. On the alloying and properties of tetragonal Nb_5Si_3 in Nb-silicide based alloys. Materials 2018;11(69):1–19.

[144] Kablov EN, Svetlov IL, Karpov MI, Neiman AV, Min PG, Karachevtsev FN. High-temperature composites based on the Nb-Si system reinforced with niobium silicides. Inorg Mater Appl Res 2017;8(4):609–17.

[145] Borchwes P, et al. Extractive metallurgy of refractive metals. Publ. Metallurgical Society of the American Institute of Mechanical Engineers; 1981.

[146] Yuan B, Okabe TH. Production of fine tantalum powder by electrochemical method. Mater Trans 2007;48(10):2687–94.

[147] Lima MJS, Souto MVM, Silva AS, Gomes UU, de Souza CP. Nanometric tantalum carbide production at low temperature and characterization. Tecnol Metal Mater Miner, São Paulo 2015;12(4):304–9.

[148] German RM. Computer modeling of sintering processes. Int J Powder Metall 2002;38(2):48–66.

[149] German RM. History of sintering; empirical phase. Powder Metall 2013;56(2):117–23.

[150] Dubois SG, Ganesan R, German RM. Sintering of high surface area tantalum powder. In: Compiled by Chen, et al. Tantalum. Warrendalle (PA, USA): The Minerals, Metals and Materials Society; 1996; p. 319–23.

[151] Trybus CL, Wang C, Pandheeradi M, Meglio CA. Powder metallurgical processing of rhenium. Adv Mater Process 2002;23–6 (No. December).

[152] Leonhardt T, Moore N, Downs J, Hamister M. Advances in powder metallurgy rhenium. In: Compiled by Eisen WB, Kassam S. Advances in Powder Metallurgy and Particulate Materials. Princeton (NJ, USA): Metal Powder Industries Federation; 2001: p. 193–203.

[153] Leonhard T, Hamster M, Carlen JC. Near-net shape powder metallurgy rhenium thruster. AIAA paper 2000-3132, 2000.

[154] Price PE. Cold isotactic pressing. In: ASM Handbook. vol. 7. ASM International Publishers; 1998. p. 382–8.

[155] Leonhard T, Downs J. Near net shape of powder metallurgy rhenium parts. In: Infringer G, editor. Proceedings of 15th International Plan see Seminar. vol. 1. Plansee Holding AG, Reutter (Tirol, Austria); 2001. p. 647–57.

Chapter 24

Production of Rare Metal Powders

Oleg D. Neikov*, Stanislav S. Naboychenko† and Irina B. Murashova†
*Frantsevich Institute for Problems of Materials Science (IPMS), Kiev, Ukraine †Ural State Technical University (UPI), Yekaterinburg, Russia

Chapter Outline

Introduction 758
Vanadium 758
  Workplace Atmospheres Safety 765
Zirconium 766
  Reduction of Zirconium Tetrachloride by Magnesium 767
  Reduction of Potassium Hexafluorozirconate by Sodium 768
  Reduction by Calcium or Calcium Hydride 768
Production of Zirconium Powders by Electrolysis 768
  Amalgam Method 770
  Combustion Synthesis of Zirconium Nitrides 771
  Other Methods 771
  Lead Zirconate Titanate (PZT) Ceramics 772
  Workplace Atmospheres Safety 773
Indium 774
  Workplace Atmospheres Safety 776
Thallium 776
  Workplace Atmospheres Safety 776
Ruthenium 776
  Workplace Atmospheres Safety 778
Production of Rare Earth Metal-Alloy Powders 778
  Physical Properties 779
  Chemical Properties 781
  Sources of Raw Material 781
  Methods of RE Elements Separation 782
  Initial Compounds for Metals Production 785
  Electrochemical Methods 787
  Metallothermic Methods 787
  Lanthano-Thermic Method 788
  Carbothermic Method 788
  Refinement of RE by Distillation 788
  Workplace Atmospheres Safety 789
  Range of Applications 789
Beryllium 798
  Physical Properties 811
  Beryllium Compounds 800
  Sources of Raw Material 812
  Magnesium-Thermal Reduction of Beryllium Fluoride 800
  Electrolysis From Beryllium Chloride Electrolyte 801
  Production of Leafed Beryllium by Electrorefining From Melts 801
  Beryllium Powder Production 801
  Beryllium Oxide Powder Production 804
  Powder Consolidation and Production of Wrought Products 804
  Wrought Product Forms 807
  Applications of Beryllium 807
  Workplace Atmosphere Safety 810
Scandium 810
  Physical Properties 811
  Sources of Raw Material 812
  Scandium Production 813
  Applications 824
Radioactive Metals: Thorium and Uranium 819
  Physical and Chemical Properties 820
  Thorium Powder Production 820
  Uranium Powder Production 822
  Applications 824
  Safety Engineering 824
References 825
Further Reading 829

Handbook of Non-Ferrous Metal Powders. https://doi.org/10.1016/B978-0-08-100543-9.00024-5
© 2019 Elsevier Ltd. All rights reserved.

INTRODUCTION

"Rare metals," listed in Table 24.1 [1], is a phrase dating from the beginning of the 20th century to denote elements for which extraction had not yet been commercially realized or which had found little application; less common was another term in use. The majority of the rare metals (RM) are, in fact, widely distributed in the earth's crust, but their extraction from rocks and refining present complicated technical problems. With improved extraction processes and increasing consumption, the phrase "rare metals" is losing its original significance.

In Table 24.1, the rare metals are divided into several classes, but this convention is of limited significance, as many of the elements could be included in more than one group. For example, rubidium and cesium can be light or trace elements, while rhenium, a typical trace element, is simultaneously a refractory metal, and titanium is a refractory metal as well as a light metal. Thus, the rare metals group is not distinguished on some kind of scientific classification of the elements but was formed historically.

Information on powder production of refractory metals, including tungsten, molybdenum, niobium, tantalum, and rhenium is given in Chapter 23, while information on titanium powders is contained in Chapter 18.

VANADIUM

Of the rare elements, vanadium is one of the most common. The content of vanadium in the earth's crust exceeds that of copper, zinc, or lead. A brittle metallic vanadium powder was first obtained by the English chemist Roscoe in 1869, but it was only in 1927 that Marden and Rich succeeded in producing ductile vanadium in the form of granules and beads. However, even today, vanadium is regarded as one of the most difficult metals to produce in pure form because of its non-homogeneous composition and high impurity content, especially interstitial impurity. In this connection, and because of the high cost, vanadium has mainly been used as an alloying addition [2].

TABLE 24.1 Classification of Rare Metals

Group of Periodic Table	Elements	Group by Techniques Classification
I	Lithium, rubidium[a], cesium[a]	Lightweight
II	Beryllium	
IV	Titanium, zirconium, hafnium[b]	Refractory
V	Niobium, tantalum, vanadium	
VI	Molybdenum, tungsten	
VII	Rhenium[b]	
III	Gallium, indium, thallium	Trace elements
IV	Germanium	
VI	Selenium, tellurium	
VII	Rhenium	
VIII	Ruthenium	
III	Scandium, yttrium, lanthanum, and lanthanides (14 elements from cerium to lutetium)	Rare-earth
II	Radium	Radioactive elements
III	Actinium and actinides (thorium, protactinium, uranium, and transuranium elements)	
V	Polonium	

[a] *Rubidium and cesium are the trace elements, but by their properties may be related also to light rare metals.*
[b] *Hafnium and rhenium are typical trace elements, but by their properties may be related also to refractory metals.*

As a base for heat-resisting alloys, vanadium is of interest because of such properties (Table 24.2) as high strength at elevated temperatures up to 873–1073 K, relatively low density 6.1 g/cm^3, good corrosion resistance (approximately the same as that of titanium and chromium), resistance to attack by liquid alkali metals (nuclear reactor coolants), small thermal neutron capture cross-section ($(4.5 \pm 0.9) \times 10^{-28}$ m^2/at) and negligible capture cross-section of fast neutrons with energies of 100–1000 keV in the region of the maximum of the energy spectrum of sodium-cooled fast breeder reactors [3]. Vanadium has potential as a construction material for reactors. The metal (and particularly its alloys), being resistant to corrosion by carbon dioxide, shows great promise as a jet engine material.

According to [4], at temperatures above 873 K, vanadium and carbon dioxide vigorously react with each other, which manifests itself in an increase in the weight of specimens, a rise in their carbon content and a change in their surface phase composition (formation of oxides, following by carburization at temperature above 1073 K). Thus, in carbon dioxide, vanadium base materials should not be used at temperatures exceeding 873 K.

Of the numerous methods of producing metallic vanadium, the following, usually yielding a sponge or powder product, can be cited:

- Reduction of vanadium pentoxide by aluminum and subsequent vacuum treatment (aluminothermic process),
- Reduction of pentoxide or trioxide by carbon or vanadium carbides in a vacuum (carbothermic process),
- Reduction of various vanadium oxides by calcium in the presence of a halide flux (calciothermic process),
- Reduction or decomposition of vanadium halides by hydrogen or metals (magnesium or sodium), and
- Electrolytic refining in a salt bath or precipitation out of a salt bath, using chloride and bromide melts.

Aluminothermic reduction of the pentoxide (V_2O_5) is the simplest and cheapest method of manufacture of a crude product for subsequent refining and for the production of ferro-vanadium and titanium-vanadium-aluminum alloys [5].

Calciothermic reduction is widely used for obtaining vanadium powder from vanadium trioxide [6]. A better than 99% pure metal can be produced (Table 24.3). A high concentration of impurities and variation of impurity content both within

TABLE 24.2 Typical Properties of Vanadium

Property	Unit	Value
Density	g/cm^3	6.11
Crystal type[a]		bcc
Atomic diameter	nm	0.266
Brinell hardness	MPa	600
Melting point	K	2173 ± 25
Boiling point	K	3650
Specific heat at 0–373 K	J/(kg·K)	480
Heat of fusion	kJ/mol	18.0
Heat of vaporization	kJ/mol	460
Thermal conductivity at 373 K	W/(m·K)	30.9
Coefficient of linear thermal expansion at temperature ranges from 20 to 1373 K	μm/(m·K)	9.53
Specific electrical resistance at RT	μΩ·m	0.26[b]
Volume diffusion	m^2/s	4×10^{-5}
Volume diffusion activation energy	kJ/mol	317
Grain boundary diffusion	m^2/s	5×10^{-14}
Grain boundary diffusion activation energy	kJ/mol	209
Section capture of heat neutrons $n \times 10^{24}$	cm^2	5.1 ± 0.2

[a] *Crystal type: bcc, body-centered cubic.*
[b] *After cold treatment.*
RT, room temperature.

each batch and from batch to batch, which are linked with the specific nature of the calciothermic reduction process, constitute major obstacles to the use of calciothermic powder in powder metallurgy.

The magnesiothermic process, in which the complex physicochemical behavior of vanadium chlorides during reduction is of special interest, has potential for the manufacture of metal of low oxygen and nitrogen content at reduced cost. Vanadium containing 60–90 ppm oxygen was manufactured by magnesiothermic reduction [7].

Carbothermic reduction of oxides in a vacuum is the most economical method of producing vanadium intended for electrolytic refining. However, to obtain pure ductile vanadium containing, to say, 0.06% oxygen and 0.12% carbon, it is necessary to perform additional operations such as hydrogenation, crushing, milling, and composition correction, which decrease productivity [8]. This method would appear to be the most suitable for the production of carbon containing vanadium alloys by the simultaneous reduction of oxides with carbon or certain carbides.

Thermal decomposition of vanadium diiodide is an excellent laboratory method of vanadium refining, but, because of low productivity, it is not suitable for commercial production.

So far, electrolytic refining is the only method of producing vanadium powder with an interstitial impurity content low enough to enable high-density ductile metal to be obtained by powder metallurgy techniques. Vanadium of various origins (reduced by the carbothermic, calciothermic, and other processes) is electrolytically refined in a chloride bath. A single refining increases the purity of metal from 99.4% to 99.98% and a second to 99.99%. Such characteristics of the electrolytic process as continuity, precise control and regulation of parameters and modest purity requirements for starting materials which do not an adverse effect on the quality of the end product, ensure a uniform impurity content and particle size distribution. These properties are particularly important in the production of materials by powder metallurgy.

Numerous companies manufacture the vanadium powders (Stanford Advanced Materials (CA, United States), All-Chemie, Ltd. (SC (United States), Changsha Langfeng Metal Materials Co., Ltd. (China) et al.). American Elements Company (CA, United States) produced high-purity vanadium powders containing from 99 to 99.999 wt% vanadium (V-M-02-P, V-M-03-P, V-M-04-P, and V-M-05-P products codes, respectively). The powder particle average sizes are in the range 10 − 50 μm (−100 mesh) and <1 μm (−325 mesh).

TABLE 24.3 Nominal Chemical Composition of Vanadium Powders Produced by Different Methods

		Method			
			Electrolysis, Grade[a]		
Element	Unit	Calciothermic Reduction	VEL-1[b]	VEL-2	Carbothermic Reduction[c]
Vanadium	wt%	99.00	99.99	99.40–99.92	98.00
Trace impurities:					
Aluminum	ppm	200	<100	<100	…
Calcium	ppm	1000	…	…	…
Carbon	ppm	400–2300	<100	<100	1200
Iron	ppm	200	<100	<1000	…
Hydrogen	ppm	20–50	...	…	…
Molybdenum	ppm	100	…	…	…
Nickel	ppm	…	<100	<400	…
Nitrogen	ppm	60–500	<500	<400	…
Silicon	ppm	…	<100	<100	…
Sulfur	ppm	…	<50	<50	…
Oxygen	ppm	200–1400	<500	<1000	600

[a] *CIS (Commonwealth of Independents States) TU 48-4-335-86 standard.*
[b] *After second refining.*
[c] *Carbothermic reduction with subsequent refinement.*

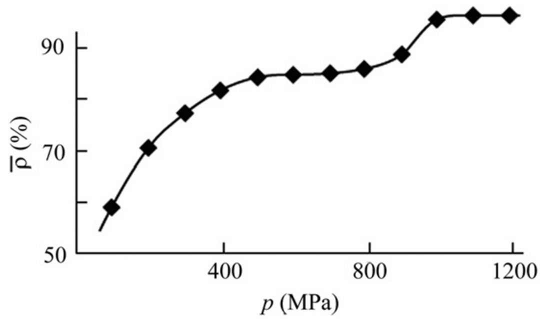

FIG. 24.1 Variation of relative density ($\overline{\rho}$) of compacts of VEL1 and VEL2 powders depending on the pressing pressure (p).

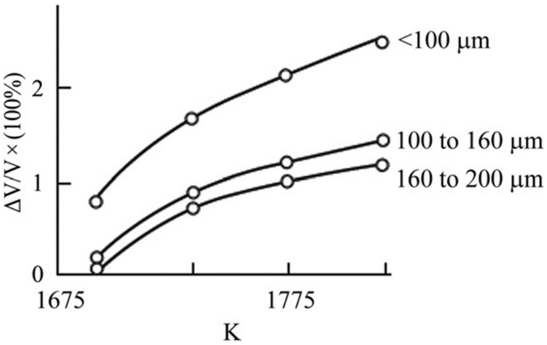

FIG. 24.2 Variation of volume shrinkage of compacts from several fractions of VEL1 and VEL2 powders depending on the sintering temperature.

Vanadium powders VEL2 and VEL3 below 150 μm in size exhibit good compressibility. Double-ended pressing in steel dies under pressure of 1.0 to 1.2 GPa enables relative compact densities of 92% to 93% to be attained (Fig. 24.1) [7].

Vacuum sintering at a residual pressure of 1.33 MPa is accompanied by a slight shrinkage of the compacts. Powder particle sizes below 200 μm do not affect the general character of the volume shrinkage sintering (Fig. 24.2), but a powder of particle size less than 100 μm exhibits greater activity during sintering, which leads to a higher degree of densification, as compared with coarser powder fractions.

A well-known Ti-6Al-4V alloy is widely used for various industrial applications in aerospace, chemical plants, and so on, because of its high strength, good ductility, high corrosion resistance, and low density. In order to improve its machinability and reduce the cost of producing parts with complicated shapes, the metal injection molding (MIM) technique was used [9]. The starting material consisted of pure titanium powder with the particles below 45 μm and 10 wt% of coarse or fine 60Al-40V powder of particle sizes less than 40 μm and 20 μm, respectively. The powder mixtures were then kneaded with binder (30 wt% polypropylene, 40 wt% polymethyl methacrylate, 29 wt% paraffin wax, and 1 wt% stearic acid) by means of a pressure-type kneading machine at 443 K for 8 ks. The powder loading was 65 vol%. The feedstock produced was then injection molded into compacts. After injection molding, extraction debinding, which vaporized the solvent, was conducted at 343 K for 21.6 ks in n-hexane, to remove partially the wax and polymethyl methacrylate. Final thermal debinding was performed from room temperature to 703 K in reduced pressure of argon gas, and continuous sintering was accomplished in a vacuum (of the order of 10^{-2} Pa) with various sintering conditions.

The relative density of the compacts for both coarse and fine 60Al-40V powder types increases with increasing sintering temperature and reaches 97%–98% at 1623 K. The relative density of the compacts using fine 60Al-40V powders is about 1% higher than that of the compacts using the coarse one (Fig. 24.3). The tensile strength of the compacts increases with increasing sintering temperature, but it abruptly decreases at sintering temperatures above 1523 K (Fig. 24.4). The behavior of the elongation as a function of sintering temperature is similar to that of the tensile strength.

Vanadium and vanadium alloys are widely used in powder metallurgy tool steels. PM processing of tool steels (also named "particle metallurgy tool steel") was first introduced commercially by the Crucible Materials Corporation in 1970, and is currently the primary manufacturing method used for the development and production of high-performance, high-alloy tool steel and tooling composites [10]. Generally, the basic PM process consists of induction melting of pre-alloyed material (with or without secondary refining), gas atomization to produce a rapidly solidified spherical powder, screening

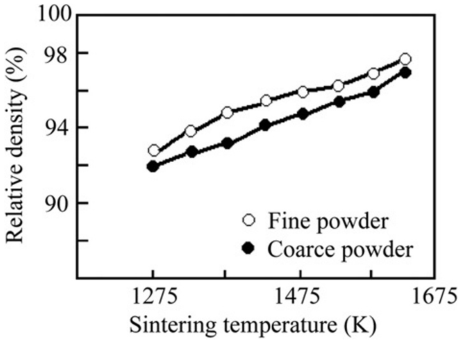

FIG. 24.3 Influence of sintering temperature on the relative density of Ti-60Al-40V alloy compacts for two granulometric composition of 60Al-40V powders (coarse and fine powders with particle sizes <45 and <20 µm, respectively). *Source: Itoh Y, Harikou T, Sato K, Miura H. Improvement of ductility for injection moulding Ti-6Al-4V alloy. In: Compiled by European Powder Metallurgy Association, Bellstone (Shrewsbury, UK), Proceedings of 2004 powder metallurgy world congress, vol. 4; 2004. p. 445–50.*

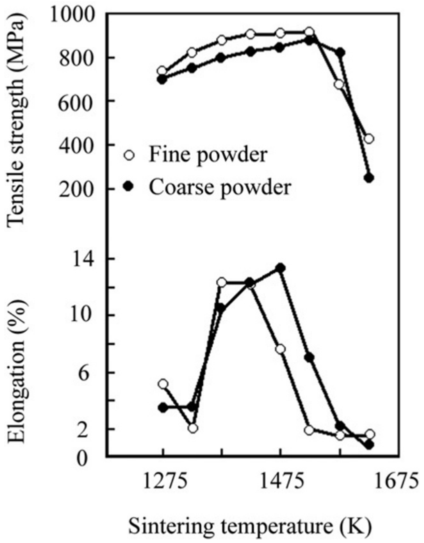

FIG. 24.4 Influence of sintering temperature on the tensile properties of Ti-60Al-40 V alloy compacts in the form of strip with a length 75 mm, a width 5 mm, and a thickness 2 mm for two granulometric compositions of 60Al-40V powders (coarse and fine powders with particle sizes <45 and <20 µm, respectively). *Source: Itoh Y, Harikou T, Sato K, Miura H. Improvement of ductility for injection moulding Ti-6Al-4V alloy. In: Compiled by European Powder Metallurgy Association, Bellstone (Shrewsbury, UK), Proceedings of 2004 powder metallurgy world congress, vol. 4; 2004. p. 445–50.*

and encapsulation of the powder, and consolidation by HIP. There are a few select applications where it may be practical or technically necessary to use the HIP product directly, while the more common practice is to HIP a large cylindrical compact that is then hot-worked to round or rectangular billets for subsequent hot rolling and finishing to round bar, flat bar, or plate and sheet products. These are the same product forms in which conventionally produced tool steels are stocked for sale to tooling or equipment component manufacturers. Consolidation by hot extrusion or other forging techniques is technically feasible, but usually not workable due to size limitations. It is also possible to produce near-net shapes using HIP technology, but it is commonly more economical to machine directly from semi-finished products.

The distinguishing characteristic of wrought PM high-alloy tool steels, compared to conventionally ingot cast and wrought materials of similar composition, is the uniform distribution and small size of the primary carbides that form in the PM tool steels due to rapid solidification of the particles obtained by atomization. Fig. 24.5 shows the primary carbide distribution observed in the heat-treated microstructures of 51 mm diameter wrought PM and conventional T15 alloy (1.5C-12W-5V-5Co), where the primary carbides are a combination of vanadium-rich MC and tungsten-rich M_6C types.

Many of the PM high-speed steels are also used in cold work operations, where a combination of good wear resistance and high hardness are required. PM M3 and PM M4 (Table 24.4) are particularly well-suited for cold working application because of their excellent combination of wear resistance, toughness, and grinding characteristics over a wide range of hardness.

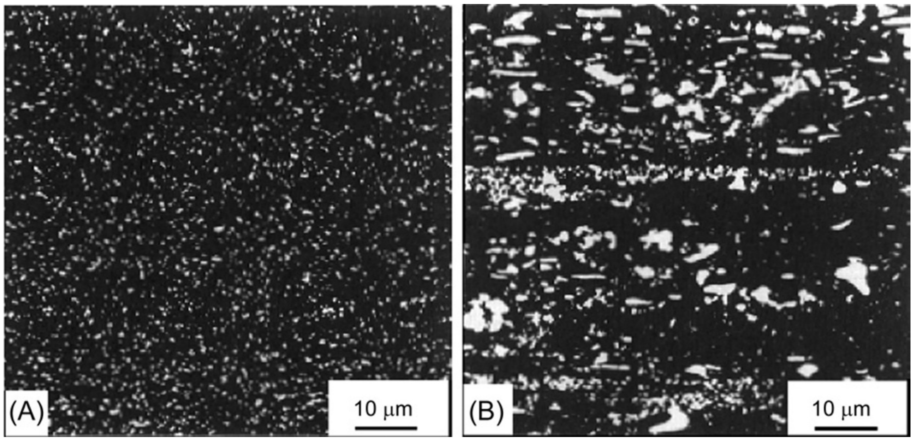

FIG. 24.5 Primary carbides in heat treated PM (A) and conventional cast (B) 1.5C-12W-5V-5Co high speed steel alloys. *Source: Dixon RB, Stasko W, Pinnow KE. Particle metallurgy tool steels. In: ASM handbook, vol. 7. ASM International Publishers; 1998. p. 786–802.*

TABLE 24.4 Nominal Compositions for Several of the Commercially Available PM High Speed Steels and PM Cold-Work Tool Steels

		Special Steels						
		High Speed Steels[a]			Cold-Work Tool Steels, Grades[b]			
Property	**Unit**	**M3**	**M4**	**T15**	**PM 3V CPM 3V**	**PM 8Cr4V Vanadis 4**	**PM 8Cr10V Vanadis 10**	**PM 18V CPM 18V**
Nominal chemical composition:								
Carbon	wt%	1.3	1.4	1.6	0.80	1.50	2.90	3.90
Chromium	wt%	...	…	…	7.50	8.00	8.00	5.25
Cobalt	wt%	…	…	5.0	…	…	…	…
Manganese	wt%	<0.30	<0.30	<0.30	…	…	…	…
Molybdenum	wt%	5.0	5.0	…	1.00	1.00	1.50	1.30
Silicon	wt%	<0.50	<0.50	<0.50	…	…	…	…
Sulfur	wt%	<0.03	<0.03	<0.03	…	…	…	…
Tungsten	wt%	6.25	5.75	15.0	…	…	…	…
Vanadium	wt%	3.0	4.0	5.0	2.75	4.00	9.80	17.50
Carbide content:								
MC	vol %	...	…	…	4.7	6.6	13	30.5
M_7C_3	vol %	...	…	…	0.4	5.7	14	…
Total	vol %	...	…	…	5.1	12.3	27	30.5
Hardness	HRC	65–67	65–67	66–68	60[c]	60[d]	60[e]	62[f]

[a] *Commercial equivalent grade.*
[b] *In denominator it is given commercial equivalent grade.*
[c] *Heat treatment 1394 K/30 min + air cool + 797 K temper (3 × 2 h).*
[d] *Heat treatment 1294 K/30 min + air cool + 797 K temper (2 × 2 h).*
[e] *Heat treatment 1333 K/30 min + air cool + 825 K temper (2 × 2 h).*
[f] *Heat treatment 1394 K/30 min + oil quench + 825 K temper (2 × 2 h).*
Company suppliers of PM high-alloy tool steels (their names, location, and trade name prefixes): Bohler/Uddeholm Corporation (Austria, Vanadis/Isomatrix PM); Hitashi Metals (Japan, HAP); Daido Steel (Japan, DEX); Nachi Fujikoshi (Japan, FAX); Erasteel Kloster AB (Sweden, ASP); Bodycote Powdermet AB (Sweden, APM); Crucible Materials Corporation (United States, CPM); Carpenter Technology Corporation, (United States, Micromelt PM).
Sources: Dixon RB, Stasko W, Pinnow KE. Particle metallurgy tool steels. In: ASM handbook, vol. 7. ASM International Publishers; 1998 p. 786–802, Haswell WT, Stasko W, Dax FR. Cobalt-free CPM high speed steels. In: Processing and properties of high speed tool steels. Publishers TMS/AIME; 1980. p. 147–58, Riedl R, Karagöz S, Fischmeister H, Jeglitsch F. Developments in high speed tool steels. Steel Res 1987; 58(8): 339–52, Westin L, Wisell H. Powder metallurgy high speed steels. Scand J Metall 1996; 25(1): 41–6.

Recent PM tool steel development has tended to focus on the following: (a) even more wear-resistant vanadium compositions containing 15%–18% vanadium with up to 30% by volume of primary MC-type carbides; (b) low-to-intermediate carbide volume fraction materials moderately alloyed with vanadium and chromium to optimize their toughness by maintaining good wear resistance; and (c) high vanadium and high chromium compositions for wear applications that also require good corrosion resistance.

Table 24.4 lists the nominal compositions for several of the commercially available PM high speed steels and PM cold-work tool steels. All of the tool steels listed in the table are capable of attaining 60–62 HRC during heat treatment, which is the typical application hardness range for cold work tooling.

Much work has been done to develop the potential of cemented carbides where a substantial amount of the tungsten carbide of conventional WC-Co alloys has been replaced by vanadium carbide (i.e., WC-(V,W)C_x alloys, with x always <1). To optimize the composition, 15V-W-C-Co alloys varying in composition were examined. They were prepared by mechanical alloying [11]. The cobalt content of the alloys was kept constant at 50 at%. The high cobalt content was selected to permit favorable formation of each phase. The carbon content was 27.8 at% in seven of the alloys (high-carbon or HC alloys) and 22.8 at% in eight of the alloys (low-carbon or LC alloys, so that the (V + W)/C ratio would be 0.8 and 1.2, respectively, and the substitution of vanadium for tungsten in VC_x was systematically increased. The lattice parameter of (V, W) C_x decreases with increasing V/(V + W) ratio (i.e., with decreasing W content) (Fig. 24.6). It is also shown that for V/(V + W) ratio the lattice parameters of (V, W)C_x in carbon rich (HC) alloys are consistently larger than in carbon-depleted (LC) alloys.

Fig. 24.7 shows that the microhardness of (V, W)C_x, measured at 50 g, varies with the V/(V + W) ratio value. The scatter in the microhardness results is large (mean standard deviations ± 150HV0.05) because the measurements were carried out on random cross-sections of (V, W)C_x particles. In spite of the scatter, the results show that the microhardness appears to reach a maximum value at V/(V + W) between 0.8 and 0.88. It is also shown that the microhardness of LC is consistently

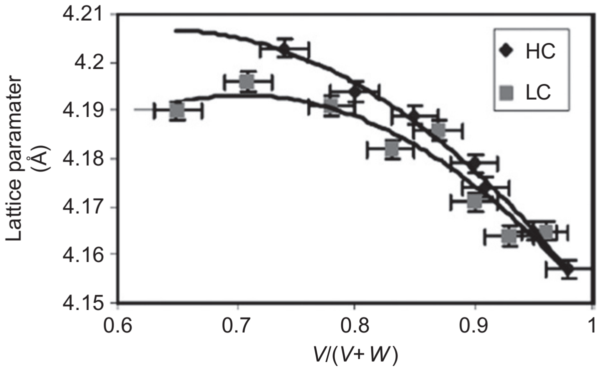

FIG. 24.6 Dependence of the lattice parameter of (V,W)C_x on the V/(V + W) ratio in (V,W)C_x. HC stands for "high carbon V-W-C-Co alloys" with nominal carbon content 27.8 at% and LC stands for "low carbon V-W-C-Co alloys" with nominal carbon content 22.8 at%. *Source: Zinyana J, et al., Effect of composition on the (V,W)C in V-W-C-Co alloys. In: Proceedings of 15th international Plansee seminar. vol. 4. Plansee: Publishers Plansee Holding AG; 2001. p. 291–9.*

FIG. 24.7 Dependence of the micro hardness (HV0.05) of (V,W)C_x on the V/(V + W) ratio in (V,W)C_x. HC and LC have the meaning as in Fig. 24.6. *Source: Zinyana J, et al., Effect of composition on the (V,W)C in V-W-C-Co alloys. In: Proceedings of 15th international Plansee seminar. vol. 4. Plansee: Publishers Plansee Holding AG; 2001. p. 291–9.*

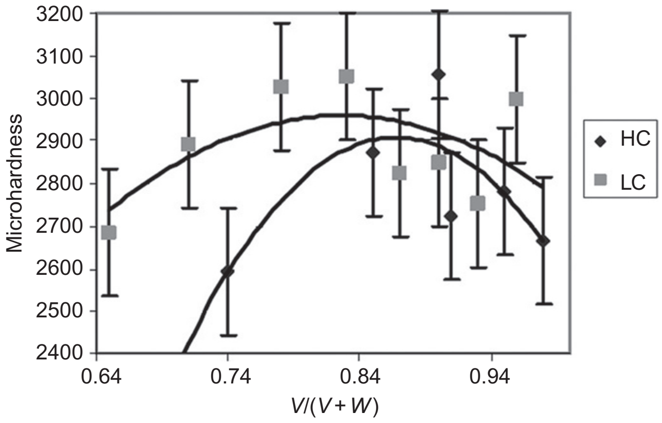

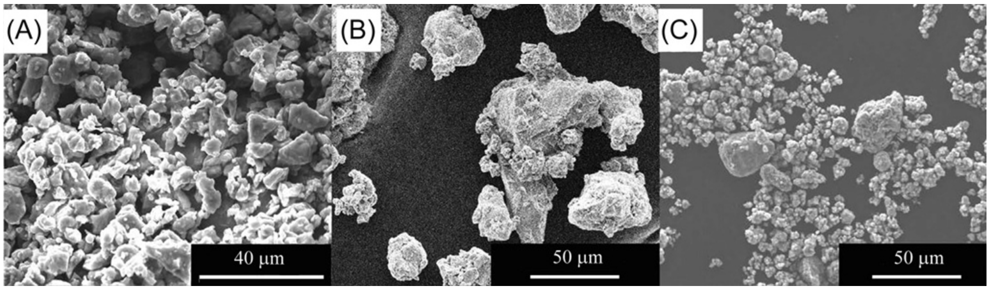

FIG. 24.8 Scanning electron microscopy images of vanadium powders milled with different surfactants (A) stearic acid, (B) KCl and (C) NaCl.

higher than the microhardness of HC alloys, while the lattice parameter in low carbon alloys has been found to be consistently smaller than in high carbon alloys.

Vanadium metal powders, ball milled with different surfactants, namely, stearic acid, KCl, and NaCl, had been studied [12]. Vanadium powder with a purity of 99.99% and particle size ~50 μm was mechanically milled (10 h) using a high-energy planetary ball mill (Retsch, PM 400). The powder was milled with 0.5 wt% above different surfactants. The powder was handled inside a glove box under an argon (99.99% pure) environment. Ball milling was performed using tungsten carbide (WC) vials and balls, with a milling speed of 250 rpm and a milling cycle comprised of 10 min run and 20 min idle. Surfactant-induced morphological characteristics of the ball-milled vanadium powders are shown in Fig. 24.8.

It shows that surfactants essentially alter both the morphology and the particle size distribution of the powders. Vanadium powder milled with NaCl yields homogenously distributed spherical particles with a particle size distribution of ~5 μm, while milling with KCl results in irregularly shaped particles with a particle size distribution of ~25 μm. Powders milled with stearic acid show a uniform distribution of irregularly shaped particles with a particle size distribution of ~10 μm. Scanning electron microscopy images indicate the domination of fracturing phenomenon when vanadium powders are milled with NaCl, while KCl and stearic acid promote cold welding during milling. It was found that vanadium powders milled with NaCl have nanostructure, while those milled with stearic acid and KCl yield amorphous and nanocomposite vanadium powders, respectively.

Effects of annealing temperature on the microstructure and properties of pure vanadium manufactured by hot isostatic pressing (HIP) were studied [13]. The results show that the microstructure of pure vanadium in the annealing process presented three obvious phases of recovery, recrystallization, and grain growth. With increasing annealing temperature, the quantity of band martensite and tensile strength decreased gradually, and band martensite was diminished completely over 1223 K; the ductility of pure vanadium increased first, and then decreased, reaching maximum after annealed at 1223 K. The ultimate strength, elongation, and reduction in area of pure vanadium annealed at 1223 K reached 380 MPa, 35.2%, 64%, respectively.

Tungsten-based vanadium alloys had been fabricated by powder metallurgy and consolidated by spark plasma sintering (SPS) at temperature of 1873 K for 3–5 min at 50 MPa [14]. Four different concentrations of vanadium ranging from 1 to 10 wt% were used to investigate the behavior of the developed alloys. SPS constrains the grain growth of tungsten and fine grains of 1 μm are obtained for W-7V alloy. The micro-hardness illustrates its dependence on density and fine grain structures of tungsten vanadium alloy. The variations of vanadium concentration has not only shown an obvious impact on the microstructures, but also improved the densification and mechanical properties of the tungsten based materials. The maximum relative density of 98.5% was achieved for the highest concentration (10 wt%) of vanadium alloy with micro-hardness of 507 HV and bending strength of 692.5 MPa.

Workplace Atmospheres Safety

Inspirable dust of vanadium compounds has a predominantly carcinogenic effect. The British workplace exposure limit (WEL) in a long-term (8 h) period of vanadium pentoxide is 0.05 mg/m^3. The European occupational exposure limit stated as Indicative Occupational Exposure Limit Values (IOELVs) is identical to the British limits. Data of the stated average limit value (ALV) of the aerosols of vanadium compounds in the workplace atmosphere, as the shift time-weighted average concentration, and the classes of danger according to the Commonwealth of Independents States Standard GOST 12.1.005-88 [15], are given in Table 24.5. As for vanadium, the State Standard 12.1.005-88 standardizes ALV of vanadium pentoxide, vanadium trioxide, ferrovanadium, and vanadium containing slags. The vanadium

TABLE 24.5 Average Limit Value (ALV) of the Aerosols of Vanadium Compounds in the Workplace Atmosphere

Vanadium Compound	Condition of Harmful Agent	ALV (mg/m^3)	Class of Danger
Vanadium pentoxide	Fume	0.1	I
Vanadium trioxide	Dust	0.5	II
Vanadium pentoxide	Dust	0.5	II
Ferrovanadium	Dust	1.0	II
Vanadium containing slags	Dust	4.0	III

pentoxide fume is the most harmful inspirable substance and is related to the first most dangerous class according to above Standard.

Vanadium in potable water takes toxicological action and is related to the third, next-to-last class of danger, and the TLV is 0.1 mg/L according RUS Standard GOST 4630-88 [16].

The flammability and explosivity of metallic vanadium are characterized by the following data. Solid vanadium becomes brittle on heating above 573 K and intensive oxidation occurs at 873–973 K with vanadium pentoxide formation; at 973 K it reacts with nitrogen, forming a yellow-bronze vanadium nitride. A powder containing 86.4 wt% vanadium, with particle size below 74 μm forms a settled dust (aerogel) with a self-ignition temperature of 763 K; minimum aerogel ignition energy is 8 mJ; self-ignition temperature of suspended solid in air is 773 K; the low concentration ignition limit of suspended powder in air is 220 g/m^3; the explosion pressure of suspended solid concentration in air is 350 kPa; maximum rate of pressure rise is 6.9 MPa/s; maximum explosion-proof oxygen content in suspension of matter in gas with diluted carbon dioxide is 10 vol%; minimum suspended solid ignition energy in air is 60 mJ [17].

The products with such characteristics of inflammability and explosion risk are placed in the "moderate explosion hazard" class of danger according to Guide to EU Legislation and "Health and Safety" in the European PM Industry [18].

Voluminal quenching of burning vanadium can be done by special powder compounds, but argon is the best medium [17]. Common techniques are mainly used to prevent pollution and for environmental control during powder manufacture and processing. Detailed information on health and environment protection measures and also on prevention of inflammability and explosion risk in such conditions can be found in Chapter 27.

ZIRCONIUM

Zirconium powders find wide application in electronics, pyrotechnics, engineering, steel production, nuclear power industry, refractory, ceramics, enamels, and in casting. The ability of zirconium powder to absorb gases ensures the keeping of a high vacuum; to this effect, it is plated on the surface of anodes, grids, and other parts in electronics.

Zirconium powders are characterized by low temperature of inflammability and high rate of pressure rise. Due to these properties, they are used as the igniter in detonators, photoflashes, and in manufacturing smokeless powder.

Zirconium is used for steel deoxidation and denitriding and for alloying in armor and gun steels, as well corrosion-resistant and heat-resistant steels. Zirconium improves the strength characteristics of copper (0.1–6.0 wt% addition); it imparts fine grain structure to magnesium alloys and prevents lead segregation in leaded bronze.

The zirconium content in the earth's crust is relatively high, about 0.025 wt%, and exceeds that of copper, zinc, and lead. There are nearly 20 zirconium-containing known minerals but, at present, only two minerals, zircon (zirconium orthosilicate) and baddeleyite (with up to 98 wt% ZrO_2) are the main commercial sources.

The zircon ores are enriched by gravitational technique in combination with magnetic and electrostatic separation. High-purity zirconium dioxide is used as the initial product for zirconium powder production.

Physical properties and diffusion factors for zirconium are given in Table 24.6.

The production of zirconium powders is accompanied by considerable technological difficulties because of their high chemical activity. Reaction of zirconium with oxygen, nitrogen, carbon, carbon oxides, and water vapor is followed by a large decrease of Gibbs' energy. Zirconium is more easily ignited than aluminum because its oxide is a less protective coating than Al_2O_3, therefore aluminum melts before it ignites, while zirconium particles ignite before they melt.

TABLE 24.6 Typical Properties of Zirconium

Property	Unit	Value
Density	g/cm^3	6.52
Crystal type[a]		bcc
Atomic diameter	nm	0.316
Brinell hardness	MPa	640–670
Melting point	K	2125 ± 10
Boiling point	K	4650
Specific heat at 273–373 K	J/(kg·K)	264
Heat of fusion	kJ/mol	23.0
Heat of vaporization	kJ/mol	567
Thermal conductivity at 373 K	W/(m·K)	30.9
Coefficient of linear thermal expansion in the temperature ranges from 293 to 1373 K	μm/(m·K)	8.9
Specific electrical resistance resistivity at 293 K	μΩ·m	0.41
at 1073 K	μΩ·m	1.43
Volume diffusion	m^2/s	1.3×10^{-4}
Volume diffusion activation energy	kJ/mol	272
Grain boundary diffusion	m^2/s	6×10^{-16}
Grain boundary diffusion activation energy	kJ/mol	184
Section capture of heat neutrons, $n \times 10^{24}$	cm^2	0.18

[a] *Crystal type: bcc, body-centered cubic.*

Sources: Zelikman AN, Korshunov BG. Metallurgy of rare metals. Moscow: Metallurgiya Publisher; 1991 [in Russian] and German RM. Sintering theory and practice. New York: John Wiley & Sons Publishers, 1996.

Methods of producing zirconium powder or sponge can be classified into five groups:

- Reduction of zirconium tetrachloride by magnesium or sodium,
- Reduction of zirconium fluoride (ZrF_4) by calcium or of potassium hexafluorozirconate (K_2ZrF_6) by sodium,
- Reduction of zirconium dioxide by calcium or calcium hydrate,
- Electrolytic methods for production or refining of zirconium powders, and
- Iodide method of zirconium refining.

Some of the methods for zirconium powder and sponge production are discussed below.

Reduction of Zirconium Tetrachloride by Magnesium

Reduction of zirconium tetrachloride by magnesium named the Kroll process [19] is commercially the most widely used [20,21]. Zircon is generally used as precursor for the manufacture of zirconium tetrachloride feedstock for the Kroll process. The zircon ($ZrSiO_4$) is carbochlorinated to produce zirconium tetrachloride ($ZrCl_4$), silicon tetrachloride ($SiCl_4$), and carbon monoxide (CO) according to equation:

$$ZrSiO_4 + 4C + 4Cl_2 \rightarrow ZrCl_4 + SiCl_4 + 4CO$$

The relatively impure $ZrCl_4$ separated from the $SiCl_4$ during the carbochlorination process, still contains hafnium. In one of several methods to separate hafnium and zirconium [20], hydrolysis of $ZrCl_4$ is followed by liquid-liquid extraction as the oxychloride ($ZrOCl_2$), followed by precipitation as $Zr(OH)_4$ and thermal decomposition to ZrO_2. The ZrO_2 is then again carbochlorinated, and the resulting $ZrCl_4$ used as a feedstock in the Kroll process. In this process, the $ZrCl_4$ is reduced with magnesium metal in a sealed batch reactor at about 1123 K. Zirconium metal and magnesium chloride are formed in an exothermic reaction:

$$ZrCl_4 + 2Mg \rightarrow Zr + 2MgCl_2$$

The magnesium chloride and any excess magnesium used in the reaction are removed from the reaction mixture by high-temperature vacuum distillation. The pyrophoric zirconium sponge so obtained is crushed, sorted, and purified by vacuum arc remelting to yield the metal as ingots. The metal can also be purified by the Van Arkel-De Boer process [20], where it is allowed to react with a halogen (e.g., iodine), and the metal halide vapor is then decomposed on a white-hot (1673 K) tungsten wire to yield so-called crystal bar:

$$Zr + 2I_2 \rightarrow ZrI_4$$

$$ZrI_4 \rightarrow Zr + 2I_2$$

Reduction of Potassium Hexafluorozirconate by Sodium

This reaction requires external heating:

$$K_2ZrF_6 + 4Na = Zr + 4NaF + 2KF$$

The specific reaction heat effect amounts to 1110 kJ per 1 kg of (K_2ZrF_6+4Na) mixture.

The process is performed in a sealed steel reactor in a vacuum or in an argon atmosphere at 1073–1173 K with sodium excess of 15%–20%. After cooling, the cake is knocked out from the reactor and treated with water or NH_4CI-solution to remove sodium skulls, then it is ball milled and the fluorides leached with water in the reactors with an agitator. To eliminate iron, the powder is treated with hydrochloric acid, washed with water, filtered, and dried in a vacuum at 330 K.

Reduction by Calcium or Calcium Hydride

Reduction of zirconium dioxide by calcium or calcium hydride is accomplished in an argon atmosphere at temperatures from 1273 to 1373 K. Reduction by calcium hydride is a modified calciothermic process because the calcium is the main reducing agent. The calcium hydride is obtained as a result of action by dry hydrogen on calcium at 673–873 K. The reduction of zirconium dioxide by calcium and calcium hydride may be represented by the following reactions:

$$ZrO_2 + 2Ca = Zr + 2CaO$$

$$ZrO_2 + 2CaH_2 = ZrH_2 + 2CaO + H_2$$

Reaction heat is insufficient for a self-sustained process. It requires continuous heat admission. The process is carried out in sealed heat-resistant steel reactors, where a briquetted mixture of zirconium dioxide and dry pure calcium is charged. Calcium chloride is added to the feed to regulate the grain size of the zirconium powder. The reactor atmosphere is evacuated and replaced by argon. The reduction process is continued for 1 h at 1273–1373 K. The reduced product after cooling is ground, washed with a large volume of water for calcium oxide removal, treated by dilute hydrochloric acid, washed by water, and dried in a vacuum at 313–323 K.

In the case of reduction by calcium hydrate, a briquetted mixture of zirconium dioxide and calcium hydride is charged into a reactor. As calcium hydrate decomposes in moist air, it is preserved in sealed containers, while grinding and blending are kept in leakproof grinders and blenders under argon. After exhausting, the reactor is filled with dry hydrogen and reduction is accomplished at 1173–1273 K. In contrast to the calciothermic process, as a result of reduction by calcium hydrate, zirconium hydride (ZrH_2) is obtained. This gives a certain advantage, because zirconium hydride is less oxidized by washing from calcium oxide, in comparison with zirconium powder.

Typical properties of zirconium powders produced by calciothermic and natriothermic processes are given in Table 24.7.

PRODUCTION OF ZIRCONIUM POWDERS BY ELECTROLYSIS

Zirconium can be obtained by electrolysis of zirconium halides in a salt melt. The best results are obtained with electrolytes containing K_2ZrF_6 in a melt of KCl or NaCl. Potassium chloride is preferable because its decomposition voltage is higher

TABLE 24.7 Properties of Zirconium Powders Produced by Different Methods

Property	Unit	Method				
		Calciothermic Reduction, Grade[a]		Natriothermic Reduction, Grade[b]		
		PZrC1	PZrC2	PZrN-A	PZrN-B	PZrN-V
Chemical composition:						
Zirconium:						
Active	wt%	≥96	≥96	73.0–76.9	71.1–73.5	67.2–71.1
Whole	wt%	…	…	93–94	92.5–93.1	91.5–92.5
Calcium	ppm	500	500	≤1500	≤1500	≤1500
Carbon	ppm	≤500	≤500	≤2500	…	1000–3000
Chlorine	ppm	≤30	≤30	≤30	≤30	≤30
Fluorine	ppm	…	…	≤100	≤100	≤100
Hydrogen	ppm	≤1500	≤2000	≤2000	…	1000–3000
Iron	ppm	≤500	≤500	≤3000	≤3000	≤3000
Magnesium	ppm	…	…	≤1500	≤1500	≤1500
Sulfur	ppm	…	…	≤7000	≤7000	≤7000
Moisture	wt%	…	…	≥14	≥14	≥14
Granulometric composition:						
10 μm under seeding	wt%	≥50	≥50	44–58	44–50	43–47
from 10 to 20 μm	wt%	…	…	20–47	29–39	31–38
from 20 to 50 μm	wt%	…	…	10–22	17–21	19–22
50 μm oversize	wt%	≤ 1.0	≤ 1.0	≤ 0.5	≤ 1.0	≤ 2.0
Specific surface	m^2/g	0.19–0.25	0.15–0.19	…	…	…

[a] *CIS TU 48-4-234-84 standard.*
[b] *CIS TU 48-4-376-76 standard.*

than that of sodium chloride and an anode effect on the graphite anodes occurs only at high current density. A mixture of 70% KC1 + 30% K_2ZrF_6 melts at 1000 K, so that the electrolysis can be conducted at 1020–1070 K. Solubility of the KF obtained during electrolysis is better than that of NaF which simplifies separation of electrolyte from the cathode precipitate (zirconium powder). The major reactions taking place on the cathode in the electrolyzer are:

$$ZrF_6^{2-} \leftrightarrow Zr^{4+} + 6F^-$$

$$Zr^{4+} + e \rightarrow Zr^{3+} + e \rightarrow Zr^{2+} + 2e \rightarrow Zr^0$$

Chlorine is formed on the anode (current density is 4 kA/m^2):

$$4F^- + 4KCl(4NaCl) - 4e \rightarrow 4KF(4NaF) + 2Cl_2\uparrow$$

During the electrolysis, the electrolyte is enriched with fluorine ions that interact with the carbon of graphite anodes forming CF_4. Optimum cathode current density for an electrolyte of 25%–30% K_2ZrF_6 + 75%–70% KC1 composition ranges from 3.5 to 4.5 A/m^2. The cathode deposit includes 30% of zirconium powder with particle size ranging from 50 to 200 μm; the remainder is electrolyte salts. Current efficiency amounts to 60%–65%.

A scheme of a typical electrolyzer for zirconium powder production is shown in Fig. 24.9. Four graphite electrodes (two anodes and two alternating current electrodes for electrolyte melting) are sited in a stainless steel vessel with water-cooled walls. The cathodes are made of steel.

FIG. 24.9 Scheme of typical electrolyzer for zirconium powder production.

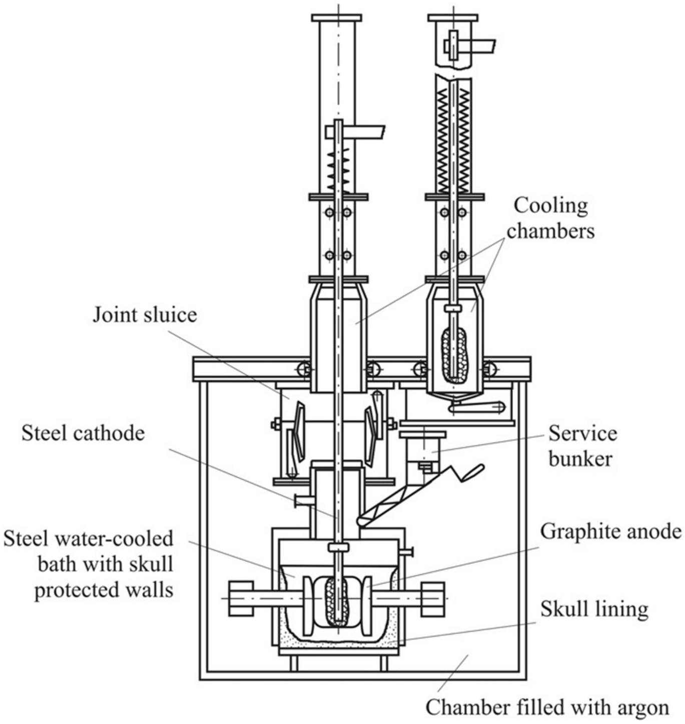

After the electrolyte has been melted by alternating current, the cathode is submerged into the melt, and direct current is applied. Electrolysis is performed in an argon atmosphere. A wall accretion of solidified electrolyte is formed on the bath walls and protects the electrolyte from iron contamination and the walls from a corrosive electrolyte. On completion of the electrolysis, the cathode with precipitate passes to the cooling chamber; the sluice and cooling chamber are evacuated and filled with argon. The precipitate is cooled in the argon atmosphere, then it is separated from the cathode, jaw-crushed into pieces of 8–10 mm and followed by wet grinding (in order to avoid of zirconium oxidation and combustion in the air). The salts are removed by washing at 330 K, then the powder is washed with 10% solution of hydrochloric acid, subsequently with distilled water, next by alcohol or acetone and finally dried in a vacuum at 323–333 K. Fine fractions are used in powder metallurgy; coarse particles are either remelted or reground.

Typical contaminants of the obtained powder are: 60 ppm oxygen, 30 ppm nitrogen, 500 ppm carbon, 1 ppm copper, 130 ppm iron, 700 ppm nickel, 200 ppm titanium; $\leq$20 ppm manganese, 30 ppm chromium, 500 ppm cobalt; 20 ppm chlorine; 100 ppm magnesium, and 500 ppm silicon.

Amalgam Method

Zirconium powder can be produced by an amalgam method. Zirconium tetrachloride is reduced by potassium-lithium amalgam:

$$\mathrm{KLi(Hg)} + \mathrm{ZrCl_4} \rightarrow \mathrm{Zr(Hg)} + \mathrm{KCl} + \underset{\mathrm{melt}}{\mathrm{LiCl}}$$

The amalgam concentration amounts to 0.8%, with the potassium-to-lithium ratios of up to 4 to 1 and excess metal-reducer 1%–4%. Reduction is performed in a column at 673 K in the lower part, while the upper part of the column is water cooled. The mixture of zirconium tetrachloride, lithium amalgam and potassium amalgam is pumped continuously to the heated area where it is kept for several minutes to ensure 100% reduction of the tetrachloride. The reduction is performed in the column under pressure to prevent evaporation of mercury at 673 K. In the cold part of the column, the salt melt solidifies and floats up, while amalgam enriched with zirconium accumulates under the mercury layer. The amalgam is filtered through porous partitions. Residues of mercury, potassium, and lithium are sublimated under vacuum at 1673 K. Zirconium is obtained in the form of sponge. The sublimation products are returned to the reaction zone.

Combustion Synthesis of Zirconium Nitrides

This method was discovered in the late 1960s in the former Soviet Union [22]. Zirconium nitride (ZrN) has been produced by combustion synthesis with phosphorus [23, 24]. This powder can be used to form refractory corrosion-resistant coatings and conducting materials in electronic applications. Depending on the nitrogen pressure, zirconium nitrides with a wide range of nitrogen compositions have been synthesized, ranging from solid solution with a minimum amount of nitrogen ($ZrN_{0.1}$) to single-phase supersaturated solutions ($ZrN_{0.34}$ $ZrN_{0.45}$), as well as stoichiometric ZrN. Full conversion to the stoichiometric compound can be achieved by dilution of the initial metal powder with the corresponding nitride product [25,26].

Other Methods

Plasma-Assisted Reduction of Zirconium Tetrachloride by Magnesium

A continuous process in which $ZrCl_4$ is reduced with magnesium in a plasma reactor to produce finely divided zirconium metal powder is discussed [27]. At the plasma process pilot plant (Fig. 24.10), a 30-kW direct-current power supply provides power to a water-cooled non-transferred arc plasma torch. The plasma is started with argon and then switched over to run on nitrogen. Both the argon and nitrogen are minimum 99.99% pure. The reactor consists of a high-temperature reaction zone and a separation zone fitted with a ceramic filter. The reaction zone is 300 mm long and has an inside diameter of 40 mm. Both sections of the reactor are water-cooled. Gas suspension passes through a water-cooled elbow to a tube and shell heat exchanger, where it is finally cooled to near room temperature. The particles are removed from the off-gas stream by a cyclone and bag filter. The off-gas is scrubbed by 20% (m/v) KOH solution before being released to the atmosphere.

Anhydrous low-hafnium $ZrCl_4$ and Mg metal were fed continuously to the plasma reactor at a rate of 0.31 kg/h. Due to losses in the system, the recovery of crude product was 77.5%. After purification to remove unreacted feed material and $MgCl_2$ by leaching, greater than 98% pure zirconium metal powder was obtained. The overall recovery of purified Zr was 74%. The conversion efficiency of the process was 95%. The particle sizes of manufactured powders are generally less 10 μm (Fig. 24.11A), and their shape (along mainly with roundish) is oblong, while numerous particle agglomerates are observed.

There are several different known ways of plasma technique application for metallic zirconium powder manufacturing. So, the preparation of metallic Zr nanoparticles by ultrafast laser ablation of a zirconium rod in isopropyl alcohol has been discussed [28]. This process produces a colloidal solution of zirconium nanoparticles. Moreover, it was shown that the size distribution of nanoparticles could be greatly reduced by employing femtosecond laser pulses for ablation. A plasma induced cathodic discharge electrolysis under Ar gas in molten salt has also been used for fabricating 50 nm metallic zirconium nanoparticles [29].

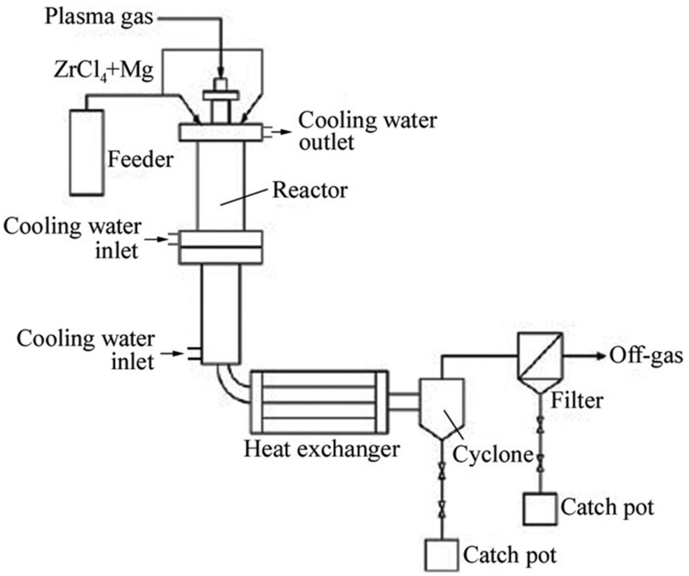

FIG. 24.10 The plasma process pilot plant.

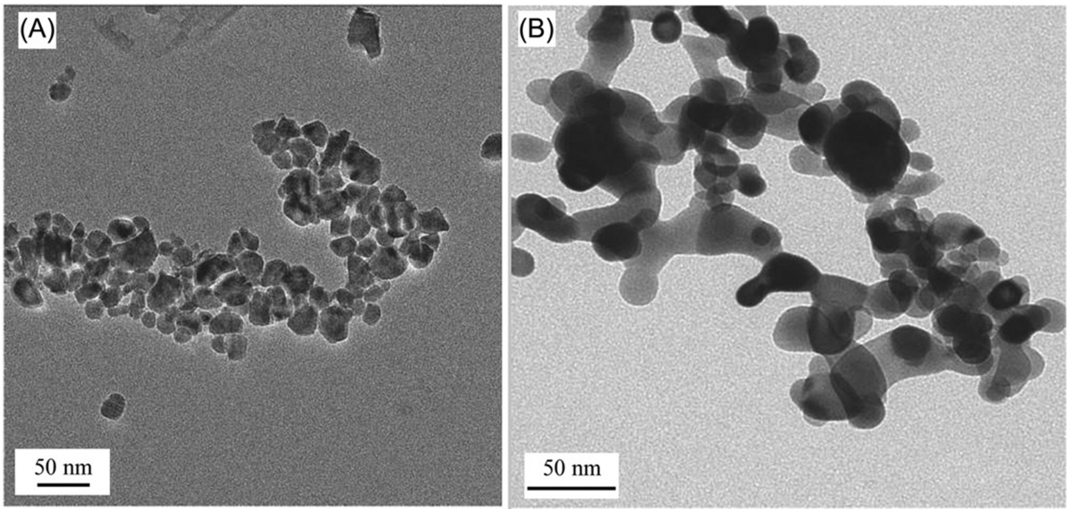

FIG. 24.11 A scanning electron micrograph of the zirconium powder made by plasma-assisted reduction of zirconium tetrachloride by magnesium.

Reduction of Zirconium Dioxide by Magnesium using Autoclave Processing

This method, which its developers [30, 31] called the RAPET method (Reaction under Autogenic Pressure at Elevated Temperatures) was realized in laboratory conditions. The reaction is carried out by reacting zirconium dioxide with magnesium at 1023 K in a closed Let-Lok cell. In general, a stainless steel cell is filled with a single reactant (or a combination of reactants) and heated at an appropriate temperature under its autogenic pressure. The pressure is generated by the thermal dissociation of reactants and the Let-Lok apparatus as an autoclave with a relief valve at 160 atm. On completion of the reaction, the additionally formed MgO is removed by treatment with acid. It is reported [31] that the product involves pure metallic zirconium, without any traces of the MgO by-product. The average size of metallic Zr made is around 63 ± 6 nm. These numbers show that there is no appreciable change in the particle size of the precursor, zirconium dioxide, during the reduction. Though the agglomeration, the size of individual particles can be discerned (Fig. 24.12).

Lead Zirconate Titanate (PZT) Ceramics

Lead zirconate titanate (PZT) ceramics have been widely used for a sensor and actuator due to its strong piezoelectric property. The manufacturing process for PZT powder was developed using powder technology including powder injection molding (PIM) and press-sinter method [32]. In this study, the $Pb(Al_{0.5}Nb_{0.5})O_3$-$Pb(Zr_{0.52}Ti_{0.48})O_3$ powder was used, which morphology of the agglomerated and irregularly shaped particles with 2.13 μm median diameter is shown in Fig. 24.13.

FIG. 24.12 TEM image of metallic zirconium powder, final product produced by RAPET method.

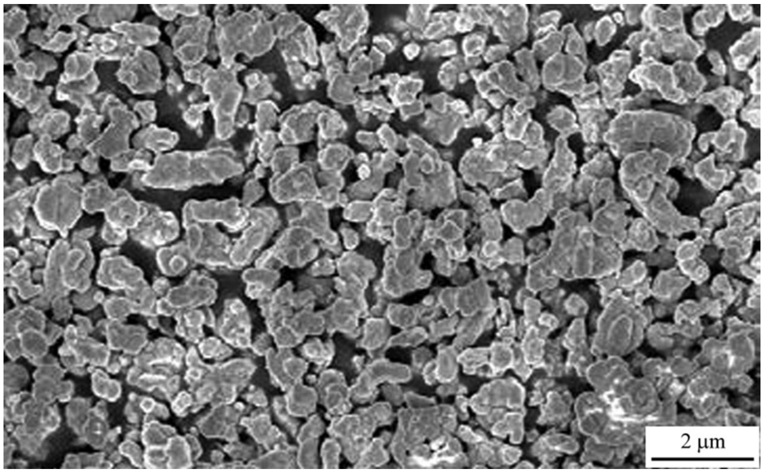

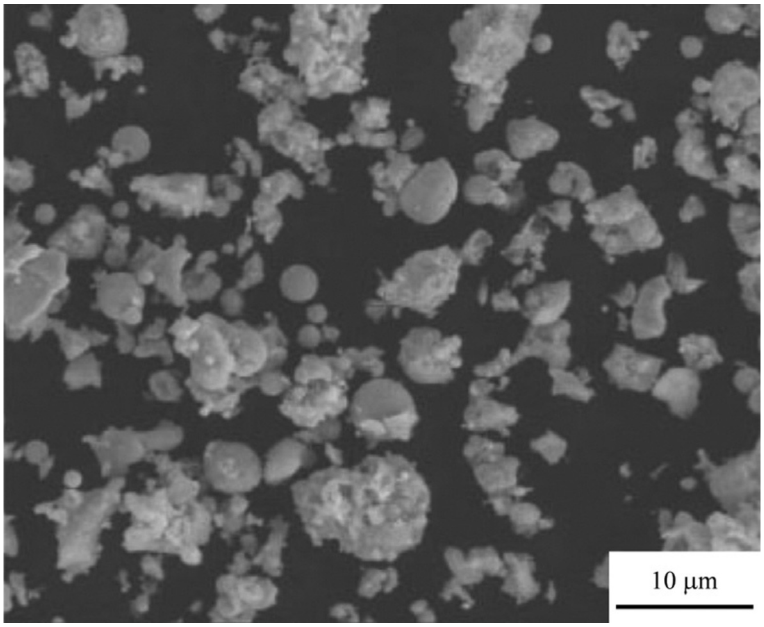

FIG. 24.13 SEM image of $Pb(Al_{0.5}Nb_{0.5})O_3$-$Pb(Zr_{0.52}Ti_{0.48})O_3$ powder.

Press-sinter method including compaction, sintering and the PIM process including mixing, injection molding, debinding, and sintering were developed. Using the developed PIM process, micro PZT structure for application of PZT polymers composite was fabricated. The micro PZT pattern with 110 μm lateral dimension and 300 μm height was fabricated.

Workplace Atmospheres Safety

Inspirable dust of zirconium metals and zirconium compounds takes a predominantly fibrous effect. The British workplace exposure limit (WEL) in long-term (8 h) period of zirconium compounds (as Zr) is 5.0 mg/m^3. The OSHA (Occupational Safety and Health Administration) legal airborne permissible exposure limit is 5.0 mg/m^3 averaged over 8-h workshift. Data of the stated average limit value (ALV) of the aerosols of zirconium and its compounds compounds in the workplace atmosphere, as the shift time-weighted average concentration, and the classes of danger according to the RUS Standard GOST 12.1.005-88 [15], are given in Table 24.8. The above State Standard standardizes ALV of metallic zirconium, zirconia, zirconium dioxide, zirconium carbide, zirconium nitride, and zirconium fluoride. Zirconium fluoride is the most harmful inspirable substance among the standardized zirconium compounds and is placed in the second danger class of the four-class Standard system.

Metallic zirconium is characterized by the following data of flammability and explosivity. Zirconium is a combustible metal. Solid zirconium in the air at room temperature is stable. On heating to less than 673–773 K, it develops a protective film. At higher temperatures, simultaneously with increasing oxidation rate, solution of oxygen occurs that markedly

TABLE 24.8 Average Limit Value (ALV) of the Aerosols of Zirconium and Its Compounds in the Workplace Atmosphere

Denomination	Condition of Harmful Agent	ALV (mg/m^3)	Class of Danger
Zirconium metallic	Aerosol	6	III
Zirconia	Aerosol	6	IV
Zirconium dioxide	Aerosol	6	IV
Zirconium carbide	Aerosol	6	IV
Zirconium nitride	Aerosol	4	III
Zirconium fluoride	Aerosol	1	II

decreases the ductility. An aerogel of powder below 74 μm in size has a self-ignition temperature of 463 K; the low concentration ignition limit of suspended solid (airborne powder) is 40–64 g/m^3; maximum explosion pressure by suspended solid concentration in air is 630 kPa; maximum rate of pressure rise is 28.4 MPa/s; maximum explosion-proof oxygen content in suspended matter in argon gas is 4 vol%; minimum suspended solid ignition energy in air is 5 mJ.

The products with such characteristics of inflammability and explosion risk are placed in the "high explosion hazard" class of danger according to the Guide to Legislation and "Health and Safety" in the European PM Industry [18]. Voluminal quenching methods and special powder compounds are used for quenching of burning zirconium powders. Talc is a better medium for voluminal quenching [17].

Zirconium hydride (ZrH_2). Powder with particle size below 74 μm displays self-ignition temperature an aerogel at 543 K; the low concentration ignition limit of suspended solid in air about 85 g/m^3; maximum explosion pressure by suspended solid concentration in air is 630 kPa; maximum explosion-proof oxygen content of a suspended solid in argon is 6 vol%; minimum suspended matter ignition energy in air is 60 mJ.

Zirconium carbide. Powder with particle size below 53 μm exhibits self-ignition temperature of an aerogel at 615 K; the low concentration ignition limit of airborne powder is about 142 g/m^3. Common techniques are mainly used to prevent pollution and environmental control during powder manufacture and its processing. Detailed information on health and environment protection measures and also on prevention of inflammability and explosion risk in such conditions can be found in Chapter 27.

INDIUM

The content of indium in the earth's crust amounts to 1.5×10^{-5}%. Indium-only minerals are very rare and do not have commercial significance. The greatest indium concentrations are found in the minerals kilindrite $Pb_6Sb_2Sn_6S_2$ (from 0.1 to 1.0 wt% In), franckeite $Pb_5Sn_3Sb_2S_{14}$ (under 0.1 wt% In), stannite $Cu_2FeSn\ S_4$ (under 0.1 wt% In the sphalerites, indium content ranges from 0.1 to 0.0001 wt%. Indium content is higher in zinc ores with high concentration of iron and stibium.

Indium is distinguished for its high capture cross-section for thermal neutrons (Table 24.9) and so can be used in control rods in nuclear reactors.

TABLE 24.9 Typical Properties of Indium and Thallium

Property	Unit	Value	
		Indium	Thallium
Density	g/cm^3	7.362	11.83
Crystal type[a]		fct[a]	H[b]
Atomic diameter	nm	0.322	0.342
Hardness HB	MPa	10	30
Melting point	K	429	576
Boiling point	K	2353	1730
Specific heat at 273–423 K	J/(kg·K)	243	137
Heat of fusion	kJ/mol	3.3	4.3
Heat of vaporization	kJ/mol	226	163
Thermal conductivity from 273 to 373 K	W/(m·K)	25.1	38.9
Coefficient of linear thermal expansion at RT	μm/(m·K)	24.8	28
Specific electrical resistance	μΩ·m	0.082 (273 K)	0.18 (RT)
Section capture of heat neutrons, $n \times 10^{24}$	cm^2	190	3.3

[a] *fct, face-centered tetragonal.*
[b] *H, hexagonal for α modification, stable under 500 K; fcc, face-centered cubic, by above 500 K temperatures β modification is stable.*

Sources: Zelikman AN, Korshunov BG. Metallurgy of rare metals. Moscow: Metallurgiya Publisher; 1991 [in Russian] and German RM. Sintering theory and practice. New York: John Wiley & Sons Publishers, 1996.

Various waste and semi-finished products of zinc and lead manufacture are the main sources of indium. As well as indium, these products often contain other trace elements: cadmium, gallium, thallium and germanium. In zinc pyrometallurgy, the dust of coking furnaces and lead obtained as a result of rectifying purification of preliminary indium can serve as a source of indium. In zinc hydrometallurgy, the sublimation of rotary-kiln or fuming processes and copper-cadmium cakes may be used for indium sources. In lead production, the refinement of lead products and various waste products (for example, dust and copper removing slags of reverberatory process) can also serve as sources of indium.

Indium recovery technique usually includes two steps:

- Obtaining indium concentrate with indium content over 1 to 2 wt%.
- Production of preliminary indium.

Black indium is recovered from a solution by cementation on zinc or aluminum sheets. Low standard indium potential (−0.34 V) allows purification of the solution from impurities of the elements with less negative standard potentials such as copper, arsenic and antimony (Table 24.10), while it is shown that indium and a number of other metals can be precipitated by cementation on zinc and aluminum.

A feature of indium powder production by electrolysis is low yield (10%) of powder fraction under 50 μm. A cementation technique has the advantage for indium sponge production, where the indium is precipitated from sulfate solutions as sponge by zinc dust cementation on aluminum sheets at 330 K. In solution with excess of sulfate ions, complete deposition of indium is made difficult because of its tendency to form complex ions $[In(SO_4)_2]^-$; therefore, hydrochloric acid is introduced on the basis of 10–20 mL per 1 L of solution. From chloride solutions, indium is precipitated by cementation on zinc sheets. The sponge is separated easily from the metal precipitator; it is washed with water, dried and ground.

Production of powder by air atomization of a melt allows an increase in productivity and yield of powder fraction below 50 μm, but this process has the problem of nozzle freezing owing to the low melting temperature. Reduction or avoidance of nozzle freezing is possible by means of hot gas atomization. Simultaneously, such a technique also contributes to reducing the energy consumption [33].

At air pressure 1.2–1.3 MPa, the yield of below 45 μm powder exceeds 80 wt%. In powder PIR grade (TU 48-0213-5/0-86 Standard), the 160 μm oversize does not exceed 1 wt%, while in the 45 μm product there is not less than 70%.

The main application for high-purity indium is in semi-conductor techniques. As was referred to above, indium has a remarkably high cross-section capture for thermal neutrons. Due to this, indium is used in alloys containing 19% In, 71% Ag and 10% Cd and 54%–62% In, 8%–18% Cd and balance B for the control rods in nuclear techniques. Wear-resistant coatings of indium are used for protection of bearings from corrosive action of hot lubricants in powerful engines (for example, in aviation and automotive industry). Indium coatings possess high reflecting ability and do not grow dim. Therefore, they are used as reflectors.

Alloys In-Sn-Cd-Bi and In-Pb-Sn are used as solders for joining of metals, glass, quartz and ceramics. In vacuum techniques, solders of indium alloy with tin (50% In and 50% Sn) serve for joining glass with glass or metal. They ensure vacuum-tight joins. Powders are also use in any application where high surface areas are desired such as water treatment and in fuel cell and solar applications.

Numerous companies manufacture the indium powders (Sigma-Aldrich, Inc., Reade International Corp., American Elements Company, et al.). American Elements Company produced high purity indium powders contain from 99 (IN-M-02-P) up to 99.999 wt% indium (IN-M-07-P, product code). The powder particle average sizes are in the range 10–50 μm (−100 mesh) and <1 μm (−325 mesh).

TABLE 24.10 Standard Potential Valuations of Series Metals

Element	Standard Potential, V	Element	Standard Potential, V	Element	Standard Potential, V
Al^{3+}/Al	−1.53	Cd^{2+}/Cd	−0.40	Ge^{4+}/Ge	−0.15
Zn^{2+}/Zn	−0.76	In^{3+}/In	−0.34	Sn^{2+}/Sn	−0.136
Ga^{3+}/Ga	−0.52	Ti^{+}/Ti	−0.336	As^{3+}/As	+ 0.247
Fe^{2+}/Fe	−1.53	Pb^{2+}/Pb	−0.126	Cu^{2+}/Cu	+ 0.34

Workplace Atmospheres Safety

The Europe occupational exposure limits in long-term (8 h) period of indium compounds (as In) is 0.1 mg/m^3, in short-term exposure period (15-min reference period) is 0.3 mg/m^3 [34]. The NIOSH (National Institute for Occupational Safety and Health) recommended airborne exposure limit is 0.1 mg/m^3 averaged over a 10-h workshift. Commonwealth of Independents States (CIS) Standard GOST 12.1.005 − 88 [15] lays down the admissible content of indium oxide (In_2O_3) in workplace atmospheres. Its occupational exposure limit (OEL) of the inspirable fraction of dust in the work-place atmosphere is 4 mg/m^3. Indium oxide is not toxic and is relegated to the third class of danger according to the above standard.

THALLIUM

The thallium weight content in the earth's crust amounts to 3×10^{-4}%. Thallium-only minerals are very rare and, in general, thallium is widely dispersed. The greatest thallium concentrations are found in iron sulfides (pyrites and marcasites), where its content reaches 0.1% to 0.5%. At present, waste and semi-finished products serve as major raw material sources.

Crude thallium is usually recovered from sulfate solution by cementation on zinc sheets (standard potential Tl^+/Tl is −0.336 V). This process allows the removal from solution of impurities of the series elements such as zinc, lead, chromium and others. Cementation with subsequent alkali refinement makes it possible to produce metal not less than 99.96% pure which is suitable for use in alloys or for the manufacture of salts for infra-red optics. Typical physical properties of thallium are given in Table 24.9.

Ultrafine thallium powder is produced by electrolysis. Electrolyte composition is: 0.005–0.020 mol/L $TlSO_4$, 0.1–0.23 mol/L $(NH_4)_2SO_4$, 0.1 mol/L H_3PO_3; 0.07 mol/L $Na_2SO_4 \cdot 10H_2O$. Current efficiency amounts to 17% at current density 0.667 kA/m^2. Decreasing the thallium sulfate content leads to a fall in the current efficiency. Powder is precipitated in the form of dendrites. The lower the concentration of thallium ions and ammonia sulfate and the lower the pH, the smaller the grain size of the deposit. Powder contains small amounts of thallium oxides Tl_2O and Tl_2O_3. Quantity of oxides in the deposit is minimal at ammonia sulfate concentration 0.1 mol/L and pH 2.4 [35].

American Elements Company (CA, United States) produced high purity thallium powders contain from 99 up to 99.999 wt% thallium (TL-M-02-P, TL-M-03-P, TL-M-04-P, and V-M-05-P products codes, respectively). The powder particle average sizes are in the range 10–50 μm (−100 mesh) and <1 μm (−325 mesh).

Thallium powder is used as an alloy addition to alloys with the object of decreasing the alloy grain size. Powders are also useful in any application where high surface areas are desired, such as water treatment and in fuel cell and solar applications.

Workplace Atmospheres Safety

The Europe occupational exposure limits in long-term (8 h) period of thallium soluble compounds (as Tl) is 0.1 mg/m^3; the danger concerns absorption through the skin. The OSHA (Occupational Safety and Health Administration) legal airborne permissible exposure limit is 0.1 mg/m^3 averaged over 8-h workshift. CIS Standard GOST 12.1.005-88 [15] refers only to the admissible content of thallium bromide and thallium iodide in workplace atmospheres. Their occupational exposure limits (OEL) of the inspirable fraction dust in workplace atmosphere are 0.01 mg/m^3. Thallium is placed in the highest, first class of danger according to the above standard.

Thallium content in potable water takes sanitary- toxicological effect and is in the exceedingly dangerous (First) class. The TLV is 0.0001 mg/L (for the inorganic compounds, including transition elements subject to summation of all form gross contents) according to CIS State Standard 4630-88 [16].

RUTHENIUM

Ruthenium is one of the platinum group metals. Solid metallic ruthenium is silvery-white, while the powder has a grey color. Ruthenium is an extremely rare and very scattered element. Its weight content in the earth's crust amounts to 5×10^{-7}%. It appears in the form of isomorphous admixture in the minerals of the osmium-iridium group, together with other platinum minerals. Ruthenium is also contained in copper-nickel sulfide ores and concentrated in the process of nuclear reactor work. Physical properties and diffusion factors for ruthenium are given in Table 24.11.

In the form of solid metal, it is not soluble in acids, including aqua regia, though it is attacked by solutions of alkali metal hypochlorites, alkali melts, and peroxides. Ruthenium is not oxidized at room temperature, while at elevated temperatures it

TABLE 24.11 Typical Properties of Ruthenium

Property	Unit	Value
Density at RT	g/cm^3	12.45
Crystal type[a]	…	H
Atomic diameter	nm	0.268
Brinell hardness	MPa	250–350[b]
Melting point	K	2577 ± 10[c]
Boiling point	K	4373
Heat of vaporization	kJ/mol	619
Specific heat at 298 K	J/(kg·K)	238
Steam saturated pressure at 2273 K	mm Hg	1×10^{-4}
Thermal conductivity at PT	W/(m·K)	105
Coefficient of linear thermal expansion at 298 K	μm/(m·K)	6.4
Specific electrical resistance at 298 K	μΩ·m	0.074

[a] *Crystal type: H hexagonal.*
[b] *Value ranges are determined by anisotropy.*
[c] *Monocrystalline purity 99.98%.*

Sources: Fedorchenko IM (ed.), Encyclopedia of inorganic materials. Glavnaja Redakcija Ukrainskoy Sovetskoy Encycpopedii, Kiev, 1977 [in Russian].

is oxidized to ruthenium dioxide, RuO_2. Fine powdered ruthenium readily absorbs hydrogen (ruthenium niello can absorb 1500 times its own volume of hydrogen).

The semi-finished product of the platinum metals refining process contains ruthenium and is the principal its source. Ruthenium concentrate is melted with a mixture of alkali and niter or heated with either sodium or barium peroxides, sublimated in the form of ruthenium tetroxide. This is dissolved in hydrochloric acid and the ruthenium precipitated in the form of ruthenium ammonium hexachloride. This is reduced in a hydrogen current. The resulting ruthenium powder is 99.9% pure [36].

Ruthenium additions appreciably increase hardness, strength and corrosion resistance of various alloys. One likely field of application is in hard metals based on tungsten carbide with a cobalt binder [37]. The effect of the ruthenium is a modification of the liquid phase during sintering which restricts grain growth. This leads to increased strength and hardness and, thus, improved cutting performance. Recently, several compositions of hard metal have been studied [38, 39]. The starting

TABLE 24.12 Nominal Composition (wt%) of WC/Co, (WC-Cr_3C_2-VC)/Co, and WC/(Co-Fe-Ni) Systems and Grain Size After Sintering (d_g)

WC/Co				(WC-Cr_3C_2-VC)/Co				WC/(Co-Fe-Ni)			
WC	Co	Ru	d_g (μm)	WC-Cr_3C_2-VC	Co	Ru	d_g (μm)	WC	Co-Fe-Ni	Ru	d_g (μm)
94.0	6.0	…	2.5	94.0	6.0	…	0.70	88	12	…	1.48
94.0	5.2	0.8	1.55	94.0	5.2	0.8	0.70	88	10	2	0.87
90.8	9.2	…	2.09	90.8	9.2	…	0.79				
90.8	8.0	1.2	1.26	90.8	8.0	1.2	0.65				
87.4	12.6	…	2.31	87.4	12.6	…	0.79				
87.4	11.0	1.6	0.73	87.4	11.0	1.6	0.65				

materials for the powder mixtures containing tungsten carbide, cobalt, vanadium carbide, chromium carbide, Co-Fe-Ni alloy and ruthenium powders were tried in different combinations (Table 24.12). The powders were mixed and milled by the ball mill with surfactant addition. After milling, the mixtures were granulated. Pressing under 300 MPa pressure produces samples of 55 × 10 × 5 mm. The ratio of green density to theoretical density was 0.52 and the flexural strength of obtained specimens amounts to 4 MPa. Sintering was done using three different cycles depending on cobalt and ruthenium content and at temperatures ranging from 1688 to 1743 K.

For all the alloy types, it appears that ruthenium acts as a grain growth inhibitor. The reduction in the particle size of tungsten carbide is noticeable for the compounds only doped with ruthenium (see Table 24.12). Addition with other inhibitors of grain growth, such as the vanadium and chromium carbides, has only a weak effect on the grain size. The increase is approximately 20%. At the same time, it has an influence comparable with the other inhibitors on the mechanical properties. Typical microstructures of WC/Co and (WC-Cr_3C_2-VC)/Co systems without and with ruthenium addition are shown in Fig. 24.14.

The effect of Ru addition on physical and mechanical properties of selected compositions based on WC-Co was discussed [40]. Addition of Ru expanded the allowable carbon range of WC-Co alloys without formation of undesirable eta-phase or C-porosity. Major mechanical properties showed some change due to the addition of Ru at levels examined in the current study. Thermal conductivity of Ru alloyed WC-Co alloys were lower than unalloyed WC-Co alloy, but Ru containing alloys showed higher hot hardness than unalloyed WC-Co alloy, and the difference remained the same up to a temperature of 1273 K investigated in this study.

Doping with ruthenium improves the flexural strength in particular for grades with vanadium and chromium carbides. The increase is particularly high, above 20%, for the (WC-Cr_3C_2-VC)-11Co-0.16Ru system. Ruthenium additions improve the performances in machining over the conventional hard metals. Effect of Ru addition on the corrosion behavior of WC-Co alloys has been reported to show improvement in corrosion resistance in sulfuric acid environment [41].

Ruthenium is introduced into platinum and palladium base alloys used for manufacturing wear-resistant parts of various measuring instruments, electrical make-break contacts and jewelry. Thermocouples for use at temperatures up to 2273 K are made of iridium-ruthenium alloys. Metallic ruthenium, its alloys and metallo-organic compounds are used as catalysts in the synthesis of organic and inorganic products.

Workplace Atmospheres Safety

CIS Standard GOST 12.1.005-88 [15] contains only a requirement as to admissible content of ruthenium dioxide in workplace atmospheres. The occupational exposure limit (OEL) of the respirable fraction dust in workplace atmosphere is 1 mg/m^3. It is placed in the second class of danger according to the above standard.

PRODUCTION OF RARE EARTH METAL-ALLOY POWDERS

The collection of 14 elements with ordinal numbers from 58 (cerium) to 71 (lutetium) disposed in group III of the periodic table behind lanthanum and with similar properties are called rare earth (RE) elements. Therefore, lanthanum is usually included in this group and the elements are named lanthanides (Ln) (i.e., similar to lanthanum). In addition, elements of the third group, yttrium and scandium, are chemical analogs of lanthanides. In its properties, yttrium is closer to the lanthanides than is scandium. In view of the fact that scandium essentially differs from lanthanides and has little geochemical connection with them, scandium is considered below in a separate subsection.

Due to their physicochemical properties, lanthanides are similar. This is explained by features of their electron shells: with growth of the atomic nucleus (growth of the ordinal numbers), the structure of the two outer electron levels of lanthanide atoms remains the same, as because by transition from element to element the electrons appear in the deep underlying electron level 4*f*. The maximum possible electron number in the 4*f*-level is 14 and determines the number of lanthanide elements.

Bond strength of the electrons is increased as the 4*f*-level is filled by half (to seven electrons) or full to the complete 14 electrons. Therefore, the gadolinium and lutetium atoms are distinguished by the most stable configuration of the 4*f*-level. Oxidation level +4 is shown by cerium and praseodymium (due to the easy passage of first *f*-electrons on the 5*d*-level) and by terbium and dysprosium, following after gadolinium. Oxidation level +2 is observed in samarium, europium and ytterbium, that is, by elements with electron number on the *f*-level near to 7 and 14.

Rare earth elements (REE) are divided into two subgroups: “light” or cerium [(La), Ce, Pr, Nd, Pm, Sm, and Eu] (LREEs) and “heavy” or yttrium [Gd, Tb, Dy, Ho, Er, Tm, Yb, Lu, and (Y)] (HREEs). This division was originally based on the difference in the solubility of the double sulfates formed by lanthanides with sodium or potassium sulfates.

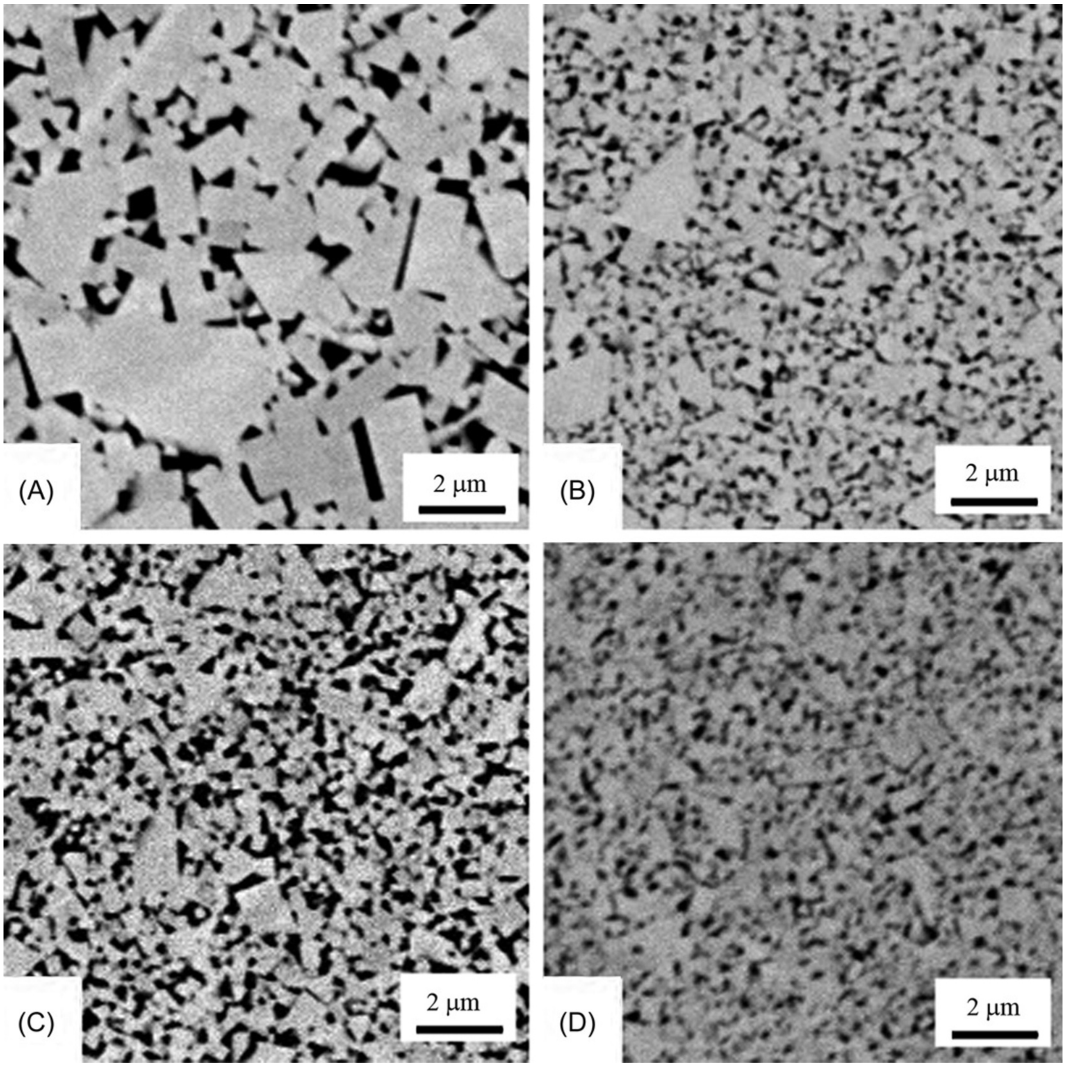

FIG. 24.14 Typical microstructures of WC/Co (A, C) and (WC-Cr_3C_2-VC)/Co (B, D) with binder content 9.2%Co (A, B) and 8%Co+1.2%Ru (C, D). *Source:* Bonjour, Chr., Actis-Data, A., Effects of ruthenium additions on the properties of WC-Co ultra micrograins. In: Proceedings of PM2004 World Congress. Wien (Austria): European Powder Metallurgy Association; 2004. vol. 3, pp. 515–21.

In succeeding years, periodicity of variation of several properties was ascertained within the collection of lanthanides, corresponding to their division into two subgroups.

Contrary to the above enumerated properties, some properties of elements are changed continuously. Thus, as the ordinal number is increased, the radii of atoms and ions are continuously decreased. This fact, called "lanthanide compression," explains the gradual basicity reduction of elements from cerium to lutetium and stipulates the distinctions in dissolubility of lanthanide salts and the stability of their composite compounds.

Physical Properties

Lanthanides are silvery-white metals. Some of them (for example, praseodymium and neodymium) have a slightly yellow color. Physical properties of the lanthanides are given in Table 24.13.

The melting points of elements of the cerium subgroup are lower than those of elements of the yttrium subgroup. It is notable that the boiling points of samarium, europium and ytterbium, indicated valence 2+, are considerably lower than for the other lanthanides. Also notable is the high capture cross-section for thermal neutrons of gadolinium, samarium, and europium.

TABLE 24.13 Physical Properties of Lanthanides and Yttrium

Element	Atomic Number	Atomic Diameter (nm)	Crystal Type[a]	Density (g/cm^3)	Melting Point (K)	Boiling Point (K)[b]	Specific Electrical Resistance (μΩ·m)	Capture Cross Section of Thermal Neutron, Capture Cross Section, $n \times 10^{24}$ (cm^2)	E (GPa)
Lanthanum	57	0.374	H	6.162	1153	3743	0.57	8.9	39.15
Cerium	58	0.365	fcc	6.768	1068	3706	0.75	0.70	30.58
Praseodymium	59	0.3656	H	6.772	1208	3485	0.68	11.2	35.92
Neodymium	60	0.3642	H	7.007	1297	3303	0.64	44	38.6
Promethium	61	0.524	H	7.26	1308	3473	…	…	…
Samarium	62	0.3604	R	7.563	1345	2067	0.92	6500	34.80
Europium	63	0.398	bcc	5.245	1095	1800	0.81	4500	…
Gadolinium	64	0.358	H	7.886	1586	3539	1.34	44000	57.3
Terbium	65	0.356	H	8.258	1629	3503	1.16	44	58.64
Dysprosium	66	0.3546	H	8.559	1685	2840	0.91	1100	64.33
Holmium	67	0.3552	H	8.779	1747	2973	0.94	64	68.50
Erbium	68	0.3514	H	9.062	1802	3141	0.86	166	74.74
Thulium	69	0.3492	H	9.318	1818	2223	0.90	118	…
Ytterbium	70	0.388	feck	6.943	1097	1469	0.28	36	18.15
Lutetium	71	0.3468	H	9.849	1936	33675	0.68	108	…
Yttrium	39	0.3602	H	4.472	1795	3609	0.53	1.38	67

[a] *Crystal types:* H, *hexagonal;* feck, *face centered cubic;* R, *rhombohedral;* bcc, *body-centered cubic.*
[b] *Approximately.*

The high pure lanthanides are plastic and easily yield to deformation (forging and rolling). The mechanical properties are strongly dependent on impurity content, particularly hydrogen, sulfur, nitrogen, and carbon. Values of ultimate strength and modulus of elasticity of the yttrium subgroup metals (except for ytterbium) are higher than those of metals of the cerium subgroup.

All lanthanides, including lanthanum, are paramagnetic; some of them (gadolinium, dysprosium and holmium) reveal ferromagnetic properties. α-lanthanum is transformed into a superconductivity state at 4.9 K and into β-lanthanum at 5.85 K. Other lanthanides do not show superconductivity even at temperatures below 10 K.

Chemical Properties

The lanthanides are distinguished by high chemical activity. They form stable oxides, halogenides, and sulfides, and react with hydrogen, carbon, hydrocarbons, carbon monoxide and dioxide, nitrogen, and phosphorus. Metals decompose water (slowly in the cold, more rapidly at elevated temperature) and readily dissolve in hydrochloric, sulfuric, and nitric acids.

At temperatures above 453–473 K, the metals are rapidly oxidized in air.

The lanthanide oxides are characterized by chemical stability and high melting points. Thus, cerium dioxide melts at about 2800 K and lanthanum oxide at above 2300 K.

The lanthanide hydroxides, $Ln(OH)_3$, have an alkaline nature and are weakly soluble in water and alkalis. The pH at which they are precipitated decreases from 7.62 for cerium to 6.82 for lutetium, corresponding to decreasing basicity in the lanthanides' row from cerium to lutetium. Chlorides, sulfates, and nitrates of the trivalent lanthanides are soluble in water and crystallized for the most part in the different form of crystallohydrates.

Fluorides and oxalates are weakly soluble in water and in dilute mineral acids. Fluorides are precipitated in the form of crystallohydrates of $LnF_3 \cdot 0.5H_2O$ composition or non-aqueous salts (for example, Pr and Nd salts). For oxalates, the most typical composition is $Ln_2\,(C_2O_4)_3\;10H_2O$. Solubility in water of oxalates of the yttrium subgroup elements is higher than that of the cerium subgroup elements. On heating to 773–873 K, the oxalates are decomposed with the formation of Ln_2O_3 type oxides.

Phosphates, carbonates, and ferrocyanides are also weakly soluble in water. Most single lanthanide salts are inclined to form double or composite salts with alkali metals and ammonia as well with bivalent elements.

Lanthanides form composite compounds with many organic substances. Among them the compounds with citric acid and series of aminopolyacetic acids are of great importance. Stability of composite compounds with organic acids is generally increased in series from lanthanum to lutetium and that is widely used in some methods for separation of lanthanides.

Sources of Raw Material

The lanthanides content in the earth's crust is about 0.01 wt%, which equals the copper content. There are more than 250 known minerals containing RE, 60–65 of them can be classed as RE minerals, which contain RE oxides in amounts more than 5%–8%. As regards their chemistry, phosphates, fluorides, silicates, silicotitanates, titanium silicates, niobium tantalates, and titanium niobates are the main minerals.

The following minerals have the largest commercial importance:

- monazite, (Ce, La, …)PO_4 contains 50%−60% La_2O_5 and 4%−7% ThO_2
- bastnaesite, (Ce, La, …)FCO_3 contains 73%−77% $Ln_2\,O_3$
- loparite, (Na, Ca, Ce, …)$_2$ (Ti, Nb, Ta)$_2O_6$ contains 39.2%–40% TiO_2; 32%–34% (Ce, La, …)$_2O_3$, and 8%–10% (Nb, Ta)$_2O_5$
- parisite, Ca(Ce, La, …)$_2$ $[CO_3]_2O_6$ contains 53%–64.5% RE_2O_3, and from traces to 8% yttroparisit
- euxenite, (Y, Ce, Ca, …) (Ti, Nb, Ta)$_2O_6$ contains 18.2%–27.7% (Y, Er, …)$_2O_3$, 0.2%−4.3% (Ce, La, …)$_2O_3$, 16%–30% TiO_2, 4.3%–1.4% Nb_2O_5 and 1.3%–23% Ta_2O_5
- xenotime, YPO_4 contains 52%–62.6% Y_2O_3.

One of the basic sources of cerium subgroup elements is monazite, which is commonly found in gravel deposits together with ilmenite, zirconia, lodestone, and other minerals. Using gravitational and magnetic enriching methods, monazite concentrates with 58%–65% Ln_2O_3 are obtained. From them, simultaneously with thorium, the lanthanides are eluated.

The largest ore deposits are in India, Brazil, the United States, Australia, Madagascar, and Sri Lanka. Commercial deposits of bastnaesite are located in the United States and Burundi. Concentrates, containing nearly 60% Ln_2O_3, bare produced from such ores by means of flotation. Combination of concentrate roasting with subsequent acid processing enables the production of a concentrate with 90% of Ln_2O_3.

In Russia, laporite is an important commercial source of RE, deposits of which are situated on the Kolsky peninsula. Laporite ores are easily reduced, yielding concentrates containing 80%–90% mineral. During the process, the lanthanides are simultaneously reduced along with niobium, tantalum and titanium.

Euxenite, xenotime, as well the tailing of certain uranium-containing ore processing, are important raw materials for the recovery of yttrium subgroup elements.

Whatever the RE raw material, the metals are recovered in the form of oxide and hydroxide which must then be separated to obtain the individual elements. Scrap in the form of (RE)Co_5 or (RE_2)Co is also used. Scrap is heated up to 1070 K in air to remove organic impurities. The oxygen content is reduced to 0.07% during the following treatment with metallic calcium at 1370 K. The scrap then is ground and washed with acid solution to free it from calcium oxide. Produced powder is added to material for the production of magnets. Rare-earth metal scrap cobalt magnets are treated with hydrochloric or oxalic acid. As a result, the RE elements are precipitated, while cobalt is taken into solution.

Methods of RE Elements Separation

As a consequence of the similarity of lanthanides properties, their separation is a complicated problem. Earlier separation methods were mainly based on difference in solubility of lanthanide compounds. As a result of numerous separate crystallizations or precipitations, the individual elements of different purity were obtained. For separation of certain elements, their ability to be oxidized to the tetravalent state (Ce, Pr, and Tb) or to 2+ valence state (Sm, Eu, and Yb) was used. In this case, the separation is facilitated by the appreciable differences in properties of lanthanide compounds with oxidation level +4 and +2 in comparison with lanthanide compounds with oxidation level +3.

Recent lanthanide separation schemes are based on using more effective methods: liquid extraction and ion exchange. In some separation schemes, selective oxidation and reduction are applied.

Separation of REE by Extraction

At present, the extraction methods have become the main ones in REE separation schemes. In commercial production, organophosphorus extracting agents are mainly used: tributylphosphate (TBP), diethyl hexyl phosphoric acid and carbonic acids [1]. Separation is based on regular variation of distribution coefficient values along the lanthanides row. In commercial production, the REE separation by TBP extraction is, for the most part, done from nitric acid solutions containing RE nitrates. The extraction proceeds with trisolvate formation:

$$\mathrm{Ln}^{3+}_{(\mathrm{aqu})} + 3\mathrm{NO}^{-}_{3(\mathrm{aqu})} + 3\mathrm{TBP}_{(\mathrm{org})} \leftrightarrow \mathrm{Ln}(\mathrm{NO}_3)_3{\cdot}3\mathrm{TBP}_{(\mathrm{org})}$$

$$D = K_c\left[\mathrm{NO}_3^-\right]^3_{(\mathrm{aqu})} \cdot [\mathrm{TBP}]^3_{(\mathrm{org})}$$

where K_c is the equilibrium constant of the extraction reaction and D is the distribution coefficient.

The D values in the TBP-HNO_3 system at high concentrations of HNO_3 in the 11–15 mol/L range increase continuously with increase of lanthanide atomic number. However, in solutions with HNO_3 concentrations lower 5 mol/L, the inversion of regularity variation of distribution coefficients for the europium-lutetium row occurs (Fig. 24.15). This is explained by hydration energy growth along the heavy RE elements row, becoming apparent at low acidity that makes difficult the displacement of aqueous molecules from hydrates.

At high acidity (more than 12 mol/L), the average value of the division coefficient β of the adjoined elements from lanthanum to terbium $\beta = D_{z+1}/D_z$ amounts to 1.9. For elements from terbium to lutetium, this value is lower. Therefore, for all the RE group, one can accept on average β = 1.5. By using TBP extraction for division of RE on subgroups, the process is carried out in nitrate solutions with HNO_3 concentration ranging from 7 to 10 mol/L. In this process, yttrium falls into the heavy RE subgroup (Dy–Lu).

In the RE separation by extraction, the process is usually conducted in a cascade of the mixer-clarifier type. A countercurrent system is used, consisting of extraction, flushing and re-extraction sections. The total number of cascade steps ranges from 50 to 90.

In 2013, Lee et al. [42] reported the leaching of NdFeB magnet scrap with HCl, HNO_3, H_2SO_4, or NaOH. The processes were optimized with regard to temperature, leaching time, concentration of leaching reagent, and solid-to-liquid ratios. HCl and H_2SO_4 showed the best performance. Neodymium was recovered from an optimized H_2SO_4 leaching solution with 75.41% yield by precipitation. The optimal conditions were a solid-to-liquid ratio of 20 g/L, 15 min leaching time, and 3 M hydrochloric acid or 1.5 M sulfuric acid.

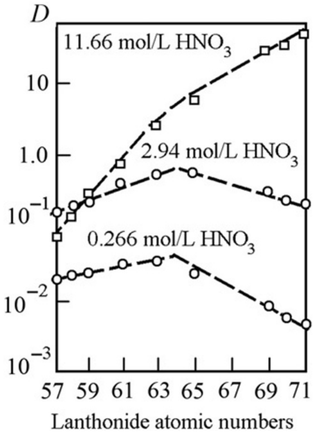

FIG. 24.15 Dependence of distribution coefficient *D* on lanthanide atomic number for europium-lutetium row. *Source: Zelikman AN, Korshunov BG. Metallurgy of rare metals. Moscow: Metallurgiya Publisher; 1991 [in Russian].*

Yoon et al. [43] carried out a similar investigation and reported that increasing the leaching temperature gave an increased leaching effect of H_2SO_4 when leaching the NdFeB magnetic scrap. The optimal leaching conditions were determined to be 4h leaching time at 343K using 3M H_2SO_4. The main obstacle in leaching of the NdFeB magnet scrap is leaching the iron, which usually makes up around two-thirds of the NdFeB magnet, into the solution.

Results obtained by Önal and co-workers [44] showed that powdered NdFeB magnets can be selectively leached, with iron remaining in the solid residue. The powdered samples were transformed into a sulfate mixture by mixing the powder with sulfuric acid in alumina crucibles with the acid: magnet ratios (g/g) of 2.15 (12M), 3.2 (13.5M), 4.3 (14.5M), and 8.6 (16M). The mixtures obtained were then dried in a muffle furnace at 383K for 6–24h. The dried samples were then treated at 923–1073K for 15–120min, resulting in a selective roasting process. The obtained calcines were later leached with demineralized water for 15min to 24h at 225 rpm on a shaker. This process led to 95%–100% extraction efficiencies for Nd, Pr, Dy, and Gd, while Fe remained in the residue after leaching.

RE Separation by Ion-Exchange Chromatography

At present, ion-exchange chromatography is a complementary method usable for obtaining individual high purity RE, mainly heavy ones.

For separation of lanthanides by ion-exchange chromatography, various cationite resins are used. Separation is usually accomplished by elution chromatography. Lanthanide ions' affinity to a resin is diminished from La^{3+} to Lu^{3+}, that is, in order of decreasing hydrated ion size. However, RE ions' affinity to resin is very close and does not ensure sufficiently effective division. Better separation is achieved by using eluting solutions containing organic compounds which form various stability complexes with RE ions.

The feasibility of using salmon milt for RE elements recovery and separation was studied [42]. The comparison of REE adsorption pattern between the milt system and other adsorbent systems (cellulose phosphate, Ln-resin, bacteria, and DNA-filter hybrid) showed that salmon milt has a sufficiently high affinity to adsorb REEs and the adsorption capacity of the milt is 1.04mEq/g, which is comparable with that of commercial cation exchange resin. Milt powder can be used for batch-type recovery and separation. There is discussed its application to Nd magnet, separation of Fe and RE elements (Nd or Dy) by adsorption on milt at pH 4 and subsequent RE elements desorption from the milt at pH 2. Considering that milt, an industrial waste from fishery industries, is a low-cost material, its ion-exchange capacity has a substantial potential for use in different fields such as the separation of RE elements.

Washing out efficiency corresponds to the durability of anion lanthanide complexes. With the motion of washing-out solution along a column (or connected in-series columns), the composite of cations is divided on the separate sorption zones (stripes) moving with certain rates to the column exit. For the washing out, various organic compounds, forming complexes with lanthanides, are used. Ethylenediaminetetraacetic acid (EDTA) is widely employed for chromatography RE division. EDTA is one of the α-amino-acids. It is a tetrabasic acid with two nitrogen atoms and is denoted H_4V. With triple-charged ions of lanthanides, EDTA forms the chelate compounds, in which nitrogen atoms are connected with the lanthanide ion by coordinating bonds.

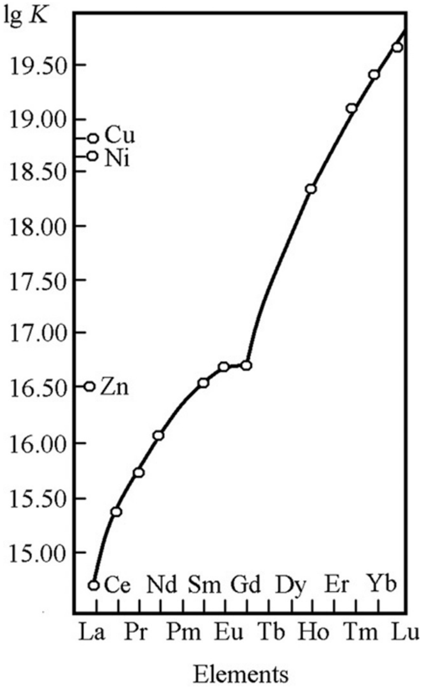

FIG. 24.16 Dependence of stability constant of lanthanide complexes with EDTA on lanthanide atomic number from lanthanum to lutetium. *Source: Zelikman AN, Korshunov BG. Metallurgy of rare metals. Moscow: Metallurgiya Publisher; 1991 [in Russian].*

The stability constant of these complex compounds is defined by the equation:

$$Ln^{3+} + HV^{3-} \leftrightarrow H(LnV)$$

$$K = \frac{[H(LnV)]}{[Ln^{3+}] \cdot [HV^{3-}]}$$

As is obvious from Fig. 24.16, the stability constants of lanthanide complexes with EDTA increases from lanthanum to lutetium, that is, with rise of lanthanide atomic number. The stability complex constants of two adjoined elements differ from each other on average by 2.4 times. This determines the conditions for highly selective action of EDTA for using elevation RE cations from a resin.

Schemes of Complete Separation

Various schemes are used for complete separation of RE, in which the methods described above are combined. By way of illustration, Fig. 24.17 shows a scheme for the separation of the cerium subgroup elements. A mixture of hydroxides is usually fed for separation. Initially, from the mixture, cerium can be extracted by oxidation. Then separation by means of countercurrent extraction is performed on three fractions: light RE (lanthanum, cerium, praseodymium, and neodymium), middle RE (praseodymium, neodymium, samarium, and europium) and enriched fraction by gadolinium and elements of the yttrium subgroup (neodymium, samarium, europium, gadolinium, and ytterbium). From the second and third fractions, samarium and europium, one can proceed by sodium amalgam reduction and separate as described above. The separation of elements in each of the separate fractions is accomplished by extraction and ion-exchange chromatography methods.

During separation of yttrium subgroup elements (for example, using extraction in chloride-thiocyanate system), a fraction containing Gd, Tb and Dy, and a fraction containing Ho, Er, Tb, Tm, and Lu, are obtained. Subsequent separation is done using extraction and ion-exchange chromatography. Ytterbium is produced by reduction from nitrate solutions using sodium amalgam.

The work [45] was focused on the extractions of the cerium (LREEs) and the yttrium (HREEs) REE subgroups from a real leachate from a neodymium magnet leachate in sulfuric acid media. The extracting agent D2EHPA (di-(2-ethylhexyl) phosphoric acid) diluted in Solvent 70, hexane, octane, cyclohexanone, chloroform, 1-octanol, and toluene was used.

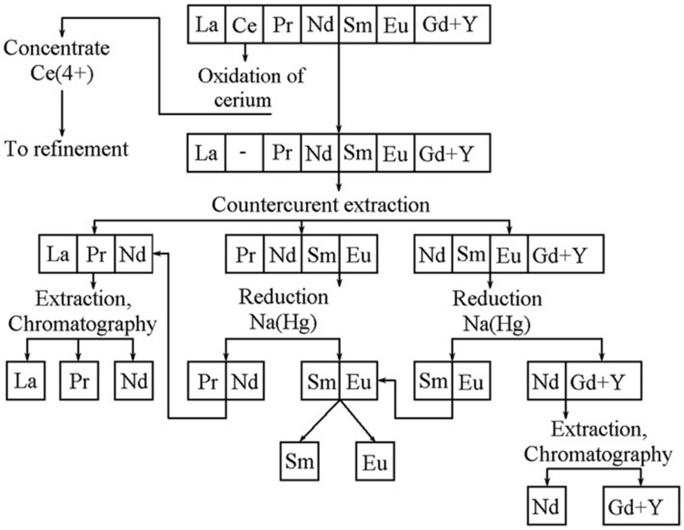

FIG. 24.17 Principle circuit of cerium sub-group elements separation

The concentrations of D2EHPA in the used diluents were 0.3, 0.6, 0.9, and 1.2 M for the investigation of the effects of using different diluents on the extraction of REEs and the separation between the light and the heavy REEs.

It was concluded that the most suitable diluents for the solvent extraction of REEs with D2EHPA (where aliphatic diluents were used) were hexane, octane, and Solvent 70. The slightly polar diluents, that is, cyclohexanone, chloroform, and 1-octanol, showed the lowest distribution ratios for the extracted REEs. Toluene was found to be somewhere between the two subgroups REEs. According to the obtained distribution ratios for the REEs, the best separation factors between the HREEs and the LREEs were obtained by extracting with 0.3 M D2EHPA in hexane. Under such conditions, almost all the Dy and Gd were extracted from the solution, while around half of the amount (50%) of the LREEs were extracted. The stripping studies were performed using the organic phases after the extraction with 0.3 M D2EHPA in hexane and 1.2 M D2EHPA in octane. It has been shown that the complete stripping of the elements back into the aqueous phase is achieved at 2 M HCl or higher.

Molecular Recognition Technology

Molecular recognition technology (MRT) corresponds with selective transport of metal ions in the developed solid supported SuperLig systems by selection a good match of cavity radius of this system with cation ionic radius of separated individual metal. SuperLig products consist of small (0.5 mm) particles packed into fixed-bed columns [46].

Izatt, et al. [47] had described the application of molecular recognition technology to separation of the rare earth elements. A leach solution from Bokan-Dotson Ridge (Alaska) feedstock was the feed material for the separations. The entire set of sixteen REE (Pm excluded) was initially separated from the non-REE gangue metals present. This initial separation, accomplished at the >99% level, is an important step in the process. Separation of the set of sixteen REE into individual elements at >99% purities was achieved in a three-step process. In Step 1, Sc and Ce are separated from the REE group. In Step 2, light REE (Y, La, Pr, Nd) are separated from heavy REE (Sm through Lu). In Step 3, individual members in the light and heavy subgroups are separated from each other. Individual REE were collected as carbonates. In Table 24.14, the purity of each individual, separated REE as a carbonate salt, or in solution prior to salt production, is given.

The MRT process has significant advantages due to processing without organic solvents and decreasing of waste, therefore reduces the use and generation of hazardous substances.

Initial Compounds for Metals Production

In view of the high chemical durability of lanthanide compounds (oxides and halogenides), pure metals and their alloys are obtained by thermal reduction or electrolysis of melts. The initial compounds for metals production are mainly chlorides or fluorides.

Production of Chlorides

Dehydration of $RECl_3 \cdot nH_2O$ crystallohydrate or the oxide chlorination “dry” method is applied for the chlorides.

TABLE 24.14 Purity Levels of 16 Rare Earth Elements Separated by Molecular Recognition Technology (MRT)

Rare Earth Element	Purity of Carbonate Salt, %	Rare Earth Element	Purity of Carbonate Salt, %
lanthanum	99.9	Dysprosium	99.9
Cerium[a]	99.5	Holmium	99.5
Praseodymium	99.9	Erbium	99.9
Neodymium	99.9	Thulium	99.6
Samarium[a]	99.2	Ytterbium	99.0
Europium	99.9	Lutetium	99.2[a]
Gadolinium[a]	99.2	Yttrium	99.4
Terbium	99.1	Scandium	99.1[a]

[a] *Purity reported for solution prior to salt production.*

Source: Izatt SR, et al. Molecular recognition technology: a green chemistry process for separation of individual rare earth metals. IBC; White paper on separation of rare earth elements 2016; p. 1–12. http://ucore.com/documents/WhitePaper_REE_Separations.pdf.

In order to prevent the formation of oxychlorides, LnOCl, as a result of hydrolysis, the dehydration of crystallohydrates is done in dry hydrogen chloride at temperatures ranging from 673 to 723 K. In this way, oxychlorides are converted into chlorides:

$$LnOCl + 2HCl = LnCl_3 + H_20$$

Dry methods are based on the interaction of RE oxides with various chloridizing agents: chlorine in the presence of carbon, ammonium chloride, and hydrogen chloride. Chlorine in the presence of carbon and carbon tetrachloride reacts with RE oxides at temperatures ranging from 973 to 1073 K and as a result the molten chlorides are obtained. The interaction with ammonium chloride at 473–573 K is represented by the equation:

$$Ln_2O_3 + 6NH_4Cl = 2LnCl_3 + 6NH_3 + 3H_20$$

After the reaction has ended, the NH_4Cl excess is sublimated by heating at temperatures from 573 to 593 K. Anhydrous RE chlorides are hygroscopic. Therefore, it is necessary to avoid their contact with moist air during processing and to keep them in a dry inert gas atmosphere.

Production of Fluorides

RE fluorides are obtained by dehydration of hydrated salts, precipitated from solutions, or by the action of hydrogen fluoride on RE oxides. RE fluorides are precipitated from nitrate or muriatic solutions by hydrofluoric acid. Some of the RE (lanthanum, cerium and others) are precipitated in the form of semi-hydride $LnF_3 \cdot 0.5H_2O$, the others (praseodymium, neodymium) without crystal water. By heating a solution with fluoride residues by an infra-red source, the hydrated fluorides are transformed into anhydrous ones. The precipitates are then washed with alcohol and dried at 673 K in a dry argon atmosphere. Fluorides produced in this way contain impurities of oxyfluorides, LnOF. It is possible to remove them by drying in a current of hydrogen fluoride.

Pure fluorides are obtained by the action of hydrogen fluoride on oxides at 823–848 K:

$$Ln_2O_3 + 6HF = 2LnF_3 + 3H_20$$

Fluoridation of oxide pellets is fulfilled in push type tube furnaces through which boats with oxides are pushed in a gas countercurrent. It is possible to perform the fluoridation of oxides in a fluidized bed. Fluorides, in contrast to chlorides, are less hygroscopic, which makes processing easier.

Electrochemical Methods

A number of methods of producing lanthanides by the electrolysis of molten salts have been developed. Among them, electrolysis of non-aqueous RE chlorides in molten alkali and alkaline-earth metal chlorides is more widespread. This technique is used on a commercial scale mainly for the production of cerium subgroup, mischmetal and individual metals.

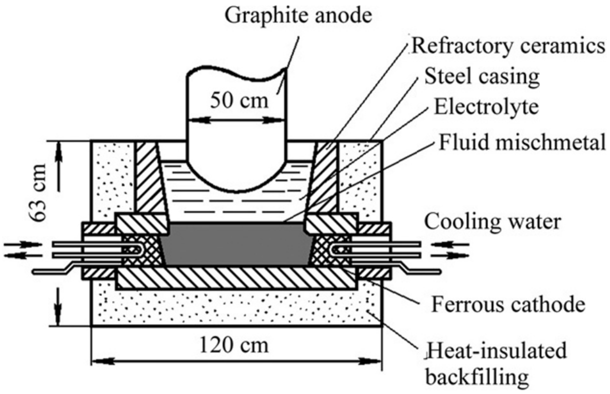

FIG. 24.18 Scheme of typical electrolyzer usable for producing mischmetal

During electrolysis, these metals are precipitated on the cathode in the molten state due to their comparatively low melting points.

The production of the yttrium subgroup metals by electrolysis is more difficult because, with the exception of ytterbium, they have comparatively high melting points (from 1586 to 3609 K). Because of the evaporation of the halogen salts, as well as difficulty in selecting suitable materials for the salt bath, and for the electrodes, the production of the yttrium subgroup metals by electrolysis is practically impossible and is, therefore, not used.

The electrolytes used for mischmetal or cerium subgroup metals usually contain 50% KCl+50% $CaCl_2$, corresponding to the eutectic with melting point 933 K or 50% KCl+50% NaCl, melting at 931 K. In melts of these salts, the lanthanide chlorides are readily soluble. The electrolyzer bath contains approximately 58%–60% $LnCl_3$ and the rest alkali and alkaline-earth metal chlorides with a small addition of calcium fluoride. The scheme of a typical electrolyzer usable for mischmetal is shown in Fig. 24.18. Electrolyte temperatures range from 1073 to 1173 K. The process is carried out at a tension of 10–15 V and a current of 1000–2000 A depending on electrolyzer size. Current efficiency ranges from 50% to 70%.

The mischmetal or cerium produced contains 94%–99% RE and impurities: <1% silicon, 1%–2.5% iron, also carbon, calcium, aluminum and others. It is possible to increase the RE purity by applying metals, such as tantalum, non-interacting with lanthanides, for electrodes, high purity magnesia and beryllia for crucible linings, as well as by accomplishing the electrolysis in inert gas.

Metallothermic Methods

The metallothermic methods can be used to obtain all lanthanides, except europium and ytterbium. The process is applicable only to the lower halogenides, and for the other metals reduction of oxide with lanthanum or carbon and sublimation in a vacuum are developed. Reduction of fluorides or chlorides by calcium is also used. Otherwise, the production of the heavier RE and yttrium is done using calcium.

Lanthano-Thermic Method

Reduction of samarium, europium, and ytterbium from their oxides by lanthanum is implemented in a vacuum simultaneously with distillation of the metals formed, which have higher vapor pressure than lanthanum:

$$Sm_2O_3 + 2La = 2Sm^{\uparrow} + La_2O_3$$

Typically, the process is carried out in a tantalum crucible. The unit includes an assembled condenser in its upper part. A mixture of oxide and 20% surplus lanthanum chips is placed in the crucible, which is heated in a vacuum induction furnace to about 1673 K. During heating, the vacuum is maintained at not lower than 1.33×10^{-2} Pa. The sublimation is accompanied by abrupt pressure fall to 1.33×10^{-5} Pa, because the evaporated metals actively absorb the residual gases. Condensation takes place at temperatures from 573 to 673 K. In this case, metal is obtained in the form of a coarse-crystalline crust. At lower temperatures metal powder is produced. The samarium, europium and ytterbium so produced are practically free from Ta and Ln. Impurities content of carbon, nitrogen, hydrogen, and oxygen do not exceed 0.01%. Cerium or mischmetal, instead of lanthanum, can serve in the capacity of reducing agent.

Carbothermic Method

This technique includes two steps:

- Reduction of Ln_2O_3 by carbon at temperatures between 1875 and 1975 K as a result of lanthanide carbide producing:

$$Ln_2O_3 + 7C = 2LnC_2 + 3CO$$

- Dissociation of the carbide in vacuum with sublimation of the lanthanide:

$$Ln_2C_2 = 2Ln^{\uparrow} + 2C$$

This method is used for the production of samarium, europium and ytterbium, which have relatively low boiling temperatures, 2067, 1800, and 1469 K, respectively.

The process is led in a graphite crucible where a briquette mixture of oxide with 10% surplus carbon (black) is placed into the crucible which is heated in a vacuum induction furnace. The first step is led by pressure in the furnace of 13.3 Pa at temperatures 1873–1973 K for about 3 h. As a result lanthanide carbide is obtained. The second step is accomplished by pressure of 0.13 Pa and temperatures ranges from 1873 to 2173 K. Lanthanide sublimates arise from carbide dissociation and are precipitated on a cooled condenser made from tantalum or molybdenum. Samarium obtained by this method contains the following impurities: 0.05% carbon, 0.1% oxygen, 0.035% hydrogen, and <0.1% nitrogen.

Refinement of RE by Distillation

Refinement of rare earth metals, obtained by one of the methods described, is accomplished by distillation in a vacuum. This method is particularly effective for refining of refractory metals of the yttrium subgroup, including yttrium.

Metal is placed in a tantalum crucible conjoined with a tantalum condenser and both are connected to a vacuum system. The crucible is heated by induction. The fusion is led by vacuum $\leq$0.0013 Pa. During fusion of dysprosium, holmium and erbium, the temperatures in the crucible are maintained in the range 1873–1973 K, while in the condenser from 1173 to 1273 K. For more refractory yttrium, terbium and lutetium, the temperatures in the crucible is kept at 2273–2473 K and 1573–1673 K, respectively.

Workplace Atmospheres Safety

Workplace exposure limits [15] contains requirements as to the admissible content of cerium dioxide, cerium fluoride, and yttrium oxide in workplace atmospheres.

The stated average limit value (ALV) of the cerium dioxide aerosol in the workplace atmosphere as the shift time-weighted average concentration is 5 mg/m^3. It is placed in the third class of danger according to the above standard. The ALV of cerium fluoride aerosol in the workplace atmosphere as the shift time-weighted average concentration is 0.5 mg/m^3, while the threshold limit value (TLV) is 2.5 mg/m^3. It is placed in the third class of danger, next to the last, according to the above standard. Yttrium oxide aerosol is also placed in the third class of danger. Its ALV is 2 mg/m^3 in the workplace atmosphere.

Cerium is a combustible metal. Cerium powder in suspended solid state in air is explosive. A powder with particle sizes finer than 80 μm exhibits: self-ignition temperatures in aerogel and in suspended solid state in air states of 373 and 421 K, respectively; the minimum explosion concentration of suspended solid in air is 36 g/m^3 [15] The products with such characteristics of inflammability and explosion risk are placed in the "high explosion hazard" class of danger according to the Guide to Legislation and "Health and Safety" in the European PM Industry [18]. Argon and special powder compounds are used for quenching of burning cerium powder [15].

Yttrium powder is a combustible substance. Milled yttrium with particles ranging from 50 μm to 400 μm is characterized by following combustibility parameters: self-ignition temperatures in aerogel state is 586 K, while by radiation heating, it is 428 K; self-ignition temperature suspended solid in air is 705 K. The low concentration of ignition limit of suspended solid in air was not found up to 1000 g/m^3 [17]. Yttrium powder with particle sizes finer than 80 μm, obtained by means of milling in argon, has an ignition temperature of 443 K and minimum explosion concentration of suspended solid in air is 36 g/m^3. Consequently, the latter product can also be placed in the "high explosion hazard" class of danger.

As for cerium powder, the voluminal quenching method by argon and special powder compounds are used for quenching of burning yttrium powder [17].

Samarium hexaboride (SmB_6). Samarium hexaboride is a combustible material. Powder with particles less than 56 μm has a self-ignition temperature of 938 K.

Range of Applications

Rare earth elements in the form of metals, alloys, and chemical compounds have found wide application in metallurgy, glass and ceramic production, nuclear power, lighting, television and laser techniques, chemical industry, medicine, and agriculture.

The powder metallurgy technique discovers new possibilities in the creation of materials containing rare earth elements with properties unachievable by traditional metallurgy. Rapid solidification processes and mechanical alloying permit the synthesis of a variety of stable and metastable phases including supersaturated solid solutions, fine crystalline and quasi-crystalline intermediate phases, and amorphous alloys.

Refractory and Elevated Temperature Alloys

The 2 vol% lanthana- and 2 vol% yttria-doped molybdenum materials exceed appreciably in mechanical properties of arc-melted and cast molybdenum and Z6 grade, a commercial zirconia-doped material [48, 49]. The creep rupture strength values of oxide dispersion strengthened (ODS) 2 vol% lanthana-doped molybdenum material [26] is twice that of arc-melted and cast and of Z6 zirconia-doped materials.

Variations in oxide kind and consolidation method have been shown to have a significant effect on the mechanical properties of ODS molybdenum material [49]. Comparison of the effect of doping technique and species on tensile properties of ODS molybdenum-lanthana and ODS molybdenum-yttria alloys illustrates that, for both oxide species, the wet doping technique results in a much finer dispersion of oxide particles ranging from 0.08 to 0.12 μm. The wet doping process is based on using an aqueous lanthanum nitrate solution to dope the molybdenum dioxide (MoO_2) precursor before its reduction to molybdenum metal powder [50]. At ambient temperature, the alloy's strength is not strongly sensitive to either doping technique but, at high temperatures, the wet doping technique produces superior material for a given oxide kind. Lanthana-doped material is also superior to yttria-doped material at elevated temperatures. The ODS molybdenum material contains nominally 2 vol% La_2O_3 that corresponds to a lanthanum (La) analyzed content of 1.09 wt%. The tensile properties of this material as a function of temperature are shown in Fig. 24.19. The total amount of product in the final material forms varied from 92% to 99.6% relative density (RD). Flat sheet was produced by cold isostatic pressing (CIP). The 4.8-mm diameter rod was processed from a 70-mm diameter CIPed billet, which was sintered, and then processed to a final condition by a combination of rolling and swaging at elevated temperature. The 38-mm rod was consolidated by CIPing nominal 280 mm diameter billet which was sintered and then hot extruded to bar at 4 to 1 ratio. A section of the bar was then turned to a 70-mm diameter round and then rod rolled to final diameter. After a high temperature (>1873 K) annealing treatment, a highly elongated interlocking grain microstructure, typical of an oxide dispersion strengthened material, is obtained [51].

So as to synthesize several yttria dispersed tungsten alloys resistant to high temperature metal corrosion and with improved mechanical behavior at rather high temperatures, the ODS process by ball milling and sintering of tungsten and yttria powders was developed [52, 53].

The W-Y system by the ODS process with yttrium content in the range from 1 to 17 vol% was studied [54]. Long milling times on the order of 30 h are necessary to reach a significant reduction of particle size, a grain size of a few tens of nanometers, and the finest microscopic distribution of yttrium. The milled powders were axially compacted into green pellets at pressure of 1.2 GPa. The resulting pellets were then sintered using a 300 K/h heating rate. Four hours at 2073 K vacuum sintering treatment may give rise to a 96.5% relative density. Vacuum sintering is much to be preferred to a treatment under hydrogen. The vacuum sintered samples may exhibit levels of micro hardness up to 840 HV_{100}. Comparison of the evolution of relative density with variation of microhardness of the W-1.0vol%Y vacuum sintered samples is shown in Fig. 24.20.

Molybdenum disilicide is a promising material for high temperature structural applications because of its high thermal conductivity, high melting point, lower density and elevated oxidation resistance. However, its use is limited by poor toughness and poor creep strength at elevated temperatures. Attempts have been made to improve it by synthesizing RE-$MoSi_2$ composites [55]. The mixtures of 99.9% pure molybdenum with particle size ranging from 2 to 4 μm, 99.5% pure silicon less than 45 μm in size and 99.9% pure RE with nearly 1 μm particle sizes were used for preparation of composites. The RE content in the composites was 0.2, 0.4, 0.6, 0.9, or 1.2 wt%, respectively. The composites were synthesized by mechanical alloying (MA) and self-propagating high-temperature synthesis (SHS). The resulting powders were then hot pressed in a graphite die at 1573–1673 K for 20 min. The hardness and fracture toughness of molybdenum

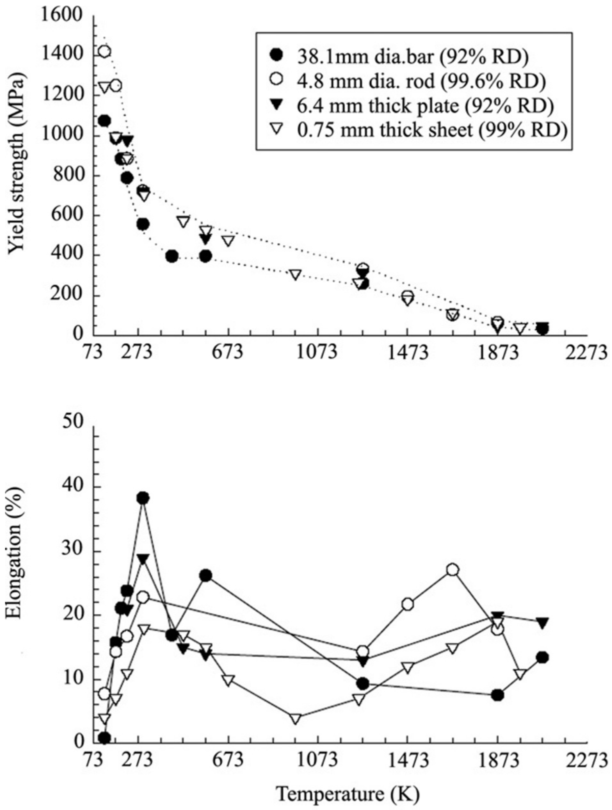

FIG. 24.19 The tensile properties of ODS molybdenum-2 vol% lanthana specimens as a function of temperature. *Source: Mueller AJ, Shields JA, Buckman RW. The effect of thermo-mechanical processing on the mechanical properties of molybdenum–2 vol% lanthana. In Proceedings of 15th international Plansee seminar. Plansee Holding AG, vol. 1, 2001, p. 485–97.*

FIG. 24.20 Comparison of the evolution of relative density with variation of microharness of the W-1.0vol%Y vacuum sintered samples

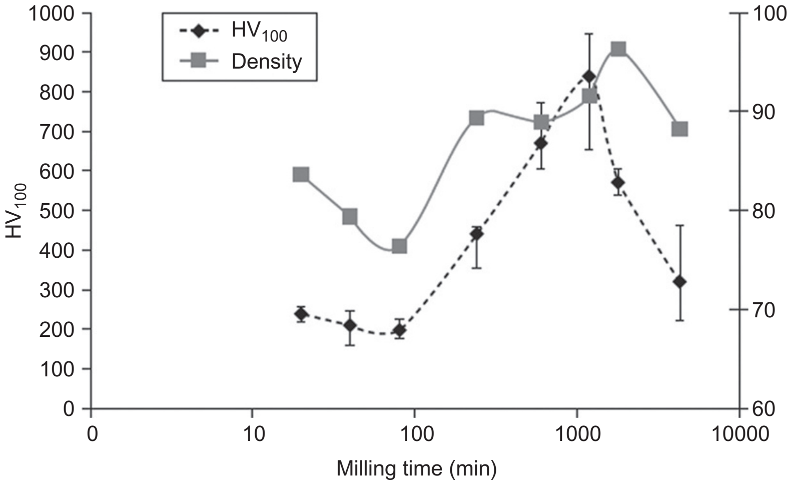

disilicide material at elevated temperatures in the range from 1073 to 1673 K were improved by the addition of rare earth elements. They are increased nearly by 50%, when adding the optimum amounts, 0.9 wt%.

Rare earth elements are used as alloying additions in aluminum and magnesium alloys to improve mechanical properties, particularly, at elevated temperatures [56–58].

One such alloy, aluminum with 8% of iron and 4% of cerium is of interest. It is obtained on the basis of powders made by high pressure gas atomization of a melt composed of high purity 99.999 aluminum, 99.99 iron and 99.9 cerium. This atomization process [59] produces a powder with a relatively thin oxide film compared to current commercial atomization.

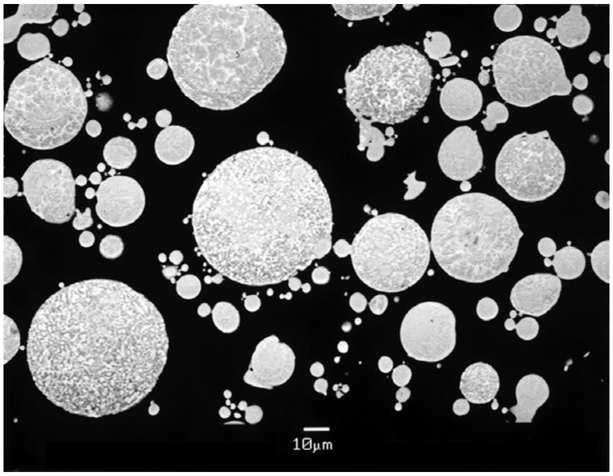

FIG. 24.21 Scanning electron micrographs of atomized Al-8 wt%Fe-4 wt%Ce alloy powder. *Source: Foley JC, Hunt WH, Barnard DJ, Laabs FC. Simple powder metallurgy processing of Al-8Fe-4Ce alloys. In: Proceedings of 2002 Powder Metallurgy World Congress. Orlando (FL, USA): MPIF; 2002. p. 1-103–114.*

A scanning electron micrograph of as atomized powder is shown in Fig. 24.21. The gas atomized powder composition determined by chemical analysis contained: 8.06 wt% iron, 3.84 wt% cerium, 45 ppm nitrogen, 676 ppm oxygen, 176 ppm carbon, balance aluminum. The minus 75 μm powder was poured into a copper can which was then evacuated and sealed before extrusion. The latter is done at 643 K with a 9-to-1 extrusion ratio. The extruded material in the form of a 10 mm rod was then machined into miniature tensile specimens. Three replicate tensile specimens were tested at room temperature, 523 and 598 K. In addition, separate tensile specimens were annealed at 523 and 598 K for 100 h and subsequently tested at room temperature. The use of cleaner powders simplifies the process by eliminating the degassing and hot pressing of the compacts that are required with the commercial RS process [56]. According to the authors [58], although the cost of producing the cleaner powder will be higher than current atomization costs, the overall costs should be much less in comparison with the commercial process because of the elimination above mentioned processing steps. However, high pure aluminum and cerium powder processing relates to technical difficulties owing to explosion risk of such powders.

The Al-Fe-Ce system alloys where produced on the base of modified water atomization technology [60] Details of this process, including design of the pilot plant, are described in Chapter 16. The technology used for powder compacting consists of two main stages. At first, the powder is formed into green compacts by cold pressing in air at room temperature to a relative density of 30% so that the particle surface remains accessible for vacuum outgassing and moisture removal. Further, the encapsulated in aluminum containers green billets are degassed under 0.1 Pa vacuum at 673 K. After degassing, the properly sealed containers are extruded in air at 673 K, with a velocity of die travel of ~0.3 mm/s and an extrusion ratio of about 12.8 to produce rods of 7 mm diameter.

The microstructures of polished section of cold powder briquette of two typical metallographic sections of Al-Fe-Ce alloy are shown in Fig. 24.22. Individual particles or even different grains within a powder particle differentiate in

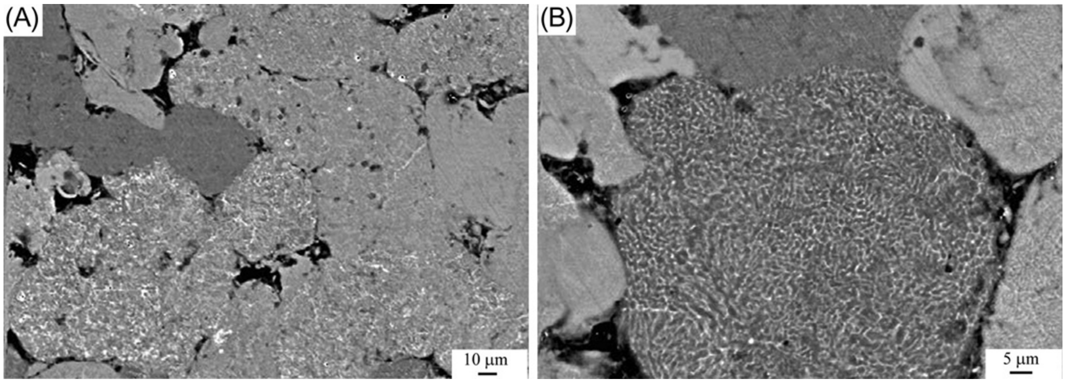

FIG. 24.22 Microstructures of polished section of cold powder briquette of two typical metallographic sections of Al-Fe-Ce alloy in backscattering electrons of various magnifying.

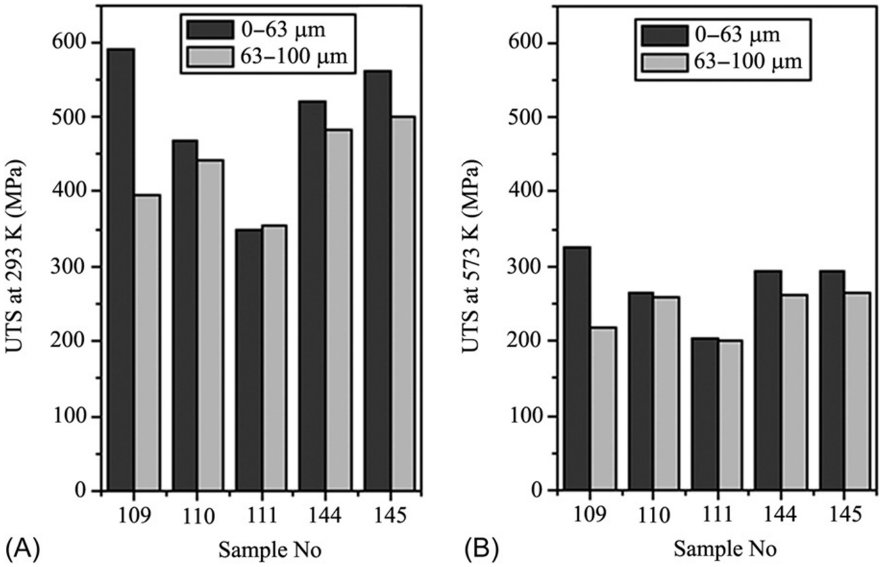

FIG. 24.23 Ultimate tensile strength at room temperature (A) and at 573 K (B) for alloys:

Alloy No	Fe	Ce	Al
109	9.0	4.9	Balance
110	9.3	4.8	Balance
111	8.3	4.8	Balance
144	11.2	5.3	Balance
145	9.5	4.78	Balance

microstructure (Fig. 24.22A) that is caused by differences in solidification behaviors of the solidifying fronts growing into the melt and of primary intermetallic phases distributed in the melt. Most of particles exhibit a cellular, or subdendritic, dendritic-like structure with an arm spacing of a few hundred nanometers in colonies of a few microns in diameter (Fig. 24.22B). The non-dendritic and subdendritic cell sizes are different for different particles. For example, the calculated cell size values shown in Fig. 24.22B range from 1.2 to 0.94 μm, that in accordance with Eq. (10) (Chapter 4), corresponds to cooling rates 5.7×10^5 to 1.2×10^6 K/s.

The values of UTS at RT and 573 K plotted for various compositions of alloys made from powder fractions 0–63 μm and 63–100 μm are represented in Fig. 24.23. As is seen, almost all alloys produced from fine powders show 25–200 MPa higher ultimate tensile strength at room temperature than corresponding alloys produced of coarse powders. The only exception is alloy No 111 where UTS for both size fractions is almost the same. The difference in UTS values decreases to 5 to 100 MPa at 573 K temperature.

Stability of alloy structure and properties at elevated temperatures follows from the results of measurements of Vickers hardness as a function of exposure time at 573 K (Fig. 24.24). The hardness is a rather weak function of exposure time for all studied alloys because variation of the hardness value lies within 2% of the average.

The tensile properties of PM Al-8 wt% Fe-4 wt% Ce are given in Table 24.15. For comparison, data for commercial alloys of similar composition are also included in this table. As is obvious, the PM specimens retain quite high mechanical properties at temperatures up to 588–598 K.

Manufacture of Electrodes

Thorium oxide is added to tungsten electrodes because of its high electron emission and easy arc formation. Environmental control and safety regulation associated with the use of radioactive thorium, have led to the development of alternatives.

Since the 1970s, tungsten electrodes activated by rare earth metal oxides to avoid thorium radioactivity have been researched and developed in China, the Soviet Union, Japan, and elsewhere. It was reported that in the case of low current

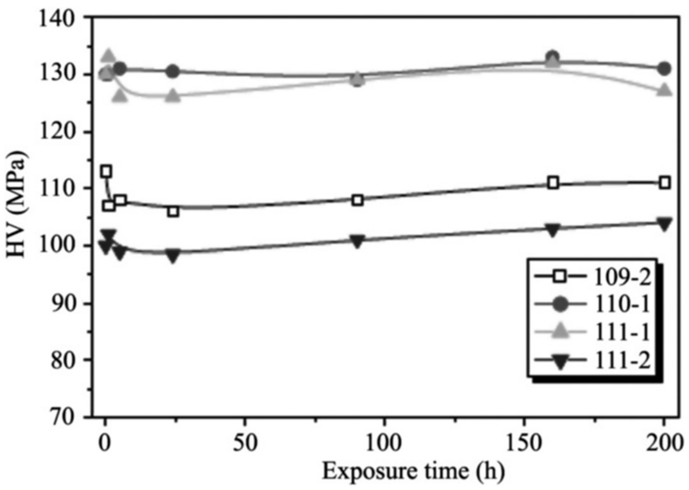

FIG. 24.24 Vickers hardness at room temperature as a function of exposure time at 573 K of alloys made from 0 to 63 μm powder fraction (1) and 63–100 μm powder fraction (2).

TABLE 24.15 Tensile Properties of Elevated Temperature Alloys Doped by Cerium

Property	Unit	Alloy (Source)				
		CU78 [61][a]	CZ42 [56][a]	Al-Fe-Ce [56][a,b]	Modified CU78 [58][a]	Alloy 109[c] [60]
Nominal composition						
Iron	wt%	8.3	7.0	8.0	8.0	9.0
Cerium	wt%	4.0	6.0	7.0	4.0	4.9
Aluminum	wt%	Balance	Balance	Balance	Balance	Balance
Tensile strength at room temperature	GPa	428	448	484.9	447 ± 13	580
at 439 K	GPa	…	365	…	…	…
at 523 K	GPa	…	…	…	391 ±14	
at 533 K	GPa	…	283	…	…	
at 589 K	GPa	…	221	193.8	…	
at 598 K	GPa	…	…	…	362 ± 23	320
Yield strength at room temperature	GPa	352	379	418.9	325 ± 15	395
at 439 K	GPa	…	345	…	…	
at 523 K	GPa	…	…	…	300 ± 15	
at 533 K	GPa	…	262	…	…	
at 589 K	GPa	…	200	178.1	275 ± 25	220
at 598 K	GPa	…	…	…	…	…
Modulus of elasticity at room temperature	GPa	…	78.6	…	…	…
At 166°C	GPa	…	68.9	…	…	…
At 232°C	GPa	…	64.1	…	…	…
At 260°C	GPa	…	62.1	…	…	…
At 316°C	GPa	…	56.5	…	…	…
Elongation at room temperature	%	…	5.0	7.0	3.0	11.0
at 589 K	%	…	…	7.6	5.7	6.0

[a] *Supplier: Alcoa.*
[b] *Thin-sheet specimens.*
[c] *Made by technology based on water atomized powders.*

welding W-CeO_2 electrodes can replace W-ThO_2 electrodes. Subsequently, it was reported [62] that tungsten electrode properties can be improved by adding combined rare earth oxides to tungsten and W-ThO_2 electrodes can be replaced by tungsten electrodes activated by combined rare earth oxides, namely La_2O_3, CeO_2, and Y_2O_3.

As an alternative to ThO_2 cathodes, La_2O_3-Mo cathodes were appeared in the middle 1970s. However, because of their poor emission stability, La_2O_3-Mo cathodes have not been used commercially [63]. Attempts have been made to improve them by means of cathode carburization, that is, forming of a porous carbide layer on the cathode surface. As it is shown, the porous carbide layer can store active substances and carry them to the surface. The bulk diffusion of lanthanum atoms increases after carburization as carbon reduces the bonding between lanthanum atoms and the molybdenum surface [64,65]. Mo_2C formed in the carburization process can reduce La_2O_3 to metallic La which is favorable for emission. According to [63], the carburization process of La_2O_3-Mo cathodes can be divided into three steps:

- Carbon, formed by the decomposition of benzene, is absorbed on the surface of carbide layer,
- Carbon diffuses to the Mo-Mo_2C interface through the carbide layer, and
- Carbon has a chemical reaction with Mo at the interface to form Mo_2C.

The secondary electron emission property and microstructure of La_2O_3-Y_2O_3-Mo cermet cathode were discussed [66]. It had been shown that the cathode prepared by the sol-gel doping method has fine microstructure containing rare earth oxide (RE_2O_3) nanoparticles and uniform distribution of different substances. An RE_2O_3 layer about 28 nm in thickness was formed on the cathode surface. The secondary emission property of electrodes is improved by their activation. The secondary emission yield by activation at 1373 K reached 5.24, about 1.8 times higher than that of the cathode activated at 1873 K.

Carburized La_2O_3 doped Mo filament cathodes were prepared by two carburization methods [67]. One was prepared with carbon powder in which the filaments were embedded. Another was produced from plain La-Mo cathodes by subjecting the formed and mounted filaments to a heat treatment in a hydrogen atmosphere consisting of benzene vapor, which was carried to the treating chambers by a stream of hydrogen under controlled flow conditions. The carburized filament prepared with carbon powder is composed of MoC, which has a dense structure whereas that prepared with mixed gas of hydrogen and benzene possesses loose structure due to the formation of Mo_2C.

It was reported [67] that the carburization enhances thermionic emission property, thus the emission current density increases from 0.03 to 5.06 A/cm^2 at 1673 K. The thermionic emission obtained from the filament cathode is correlated with the carburization method and the carburized product. The carburized filament prepared with carbon powder is composed of MoC, which has a dense structure, exhibiting the emission property about 4/5 lower than that prepared with mixed gas of hydrogen and benzene because the carburized product Mo_2C possesses loose structure.

Patented tungsten cathode material includes finely dispersed particles of a rare earth oxide and tungsten carbide [68]. As a result of such structure, diffusion of the rare earth oxide is accelerated, and supply of rare earth elements to a cathode surface is ensured, thereby improving discharge characteristics. Application area of the patented tungsten cathode material is as a discharge cathode material for tungsten-arc inert-gas welding (TIG), plasma spraying, plasma cutting, electrical discharge machining, and discharge lamps.

Permanent Magnets

Rare earth alloys magnets are characterized by a high coercive force (H_c) and residual induction (B_r). These alloys are processed to provide the maximum energy product, which is the numerical value of energy product $H_c \cdot B_r$ in the second quadrant (top left) of the hysteresis curve (Fig. 24.25). The energy product is measured by approximation of the largest rectangle to the demagnetization curve, found in the second quadrant of the hysteresis loop.

The high coercivity of the rare earth elements is based on nucleation and pinning of domain walls at surfaces and at grain boundaries. Generally, the blended fine particles are compacted in a magnetic field, sintered, heat treated, machined to size, coated and magnetized. Typical energy products range from 130 to 160 kJ/m^3 by conventional processing. $SmCo_5$ single phase magnets are widely used. In precipitation hardened $Sm(Co, Cu)_{7.5}$, copper is substituted for some of the cobalt. This produces a fine, coherent precipitate, about 10 nm in size, when aged at 673–773 K.

Recently, neodymium-iron-boron permanent magnets are widely used, accounting for the majority revenue of over 60% in 2015 [69]. In the main, the NdFeB permanent magnets are produced in China (Table 24.16). The neodymium is more abundant and less costly than other rare earth metals. Commonly, an alloy close to the composition of $Nd_{15}Fe_{77}B_8$ is melted and then rapidly solidified by pouring a stream of molten metal on to a rotating cold disk. This rapid solidification process produces a thin, amorphous ribbon. The ribbon, in turn, is chopped and crushed into 200 μm particles. The particles can be bonded with polyamides and injection molded to form magnets.

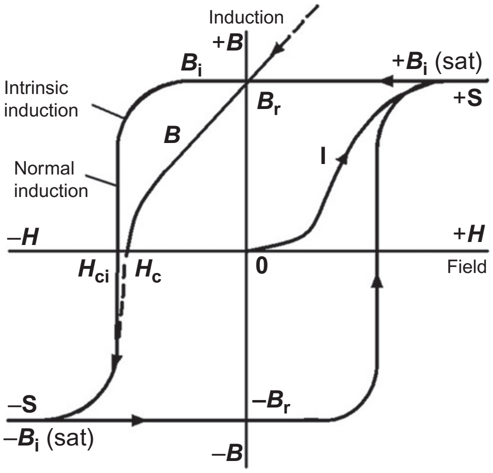

FIG. 24.25 Typical hysteresis loop for a permanent magnet material

TABLE 24.16 The NdFeB Permanent Magnets Market, Metric Tons

Production by Country/Region	2012	2015
China	50,000	65,000
Europe	1000	1000
Japan	10,000	8000
United States	…	2000
All other	2000	2000
Total	63,000	78,000

Source: Benecki WT. The permanent magnet market—2015. Magnetics 2013 conference, Orlando (FL, U.S.A.); 2013.

The technique is known for preparing compacts by hot pressing. The $Nd_{13.6}Fe_{73.7}Co_{6.6}Ga_{0.6}B_{5.5}$ ribbon powder was hot pressed and the fully dense compacts were subsequently hot deformed [70]. Minimum deformation required to achieve good texture was around 50%. Deformation temperatures, in the range from 873 to 1273K, enabled useful anisotropy to be achieved. With the optimum processing parameters, a maximum energy product ($H_c \cdot B_r$) as high as 409kJ/m^3 was achieved.

The influence of heat treatment on properties of Nd-Dy-Fe-Co-Nb-Al-Cu-B sintered magnets is shown in publication [71]. The alloys were prepared by vacuum induction melting of 99.9% to 99.99% purity elements. In three initial alloy types, the rare earth element nominal contents were in the following ranges: from 13.8 to 12.0at% Nd, 0.75at% Dy, and 3.4at% Tb. For comparison, different compacting techniques were used: sintering at temperatures 1235 and 1373K and hot isostatic pressing at temperatures in the range from 1073 to 1350K, and pressure from 60 to 180MPa at exposures from 3 to 10ks. Optimized heat treatment parameters depend on various alloying elements; for example, on alloying with the optimized treatment temperatures range from 800 to 850K (3.6ks), while with copper the optimized temperature interval ranges from 725 to 775K (3.6ks). The maximum energy product ($H_c \cdot B_r$) values for given magnet compositions are in range 320–360kJ/m^3.

The Nd-Fe-B magnets were produced from gas atomized powders (GA) [72]. The neodymium content in five initial alloys ranged from 14.5 to 16at%. There were included additions of terbium, dysprosium, titanium, molybdenum, boron, vanadium, and aluminum. Alloys were prepared by induction melting of raw materials with purity above 99.9% under high purity argon. The magnets were sintered at 1323K for 1h. The main phases of rapidly solidified alloys are tetragonal $Nd_2Fe_{14}B$ and the rest is $Nd_{1.11}Fe_4B_4$ and a solid solution on an Nd base. The dendrite structure is typical for all five investigated alloy compositions. Isothermal annealing of GA magnets at 1073 K leads to formation of an optimum structure. Heavy rare earth elements, dysprosium and terbium, enhance the main magnetic $Nd_2Fe_{14}B$ type phase lattice that leads to an increase of magnetic properties. The best coercivity achieved for GA magnets was $H_c = 800$kA/m.

In order to examine the compacting of the Nd-Fe-B magnetic powder as well as the applied technology on the physical properties of the Nd-Fe-B dielectromagnets, two powder types were used [73]. Both types were manufactured by the company Magnequench Inc. and are marketed under the names MQP-B and MQP-S-11-9. The MQP-B powder is produced from Nd-Fe-B alloy by the melt spinning technique. The average size of particles in ribbon form of this powder is about 200 μm. The MQP-S-11-9 powder is manufactured by atomization. The average size of particles for this type of powder ranges from 35 to 50 μm. Both powder types are used for manufacturing of compression-molded as well as injection-molded magnets.

The injection-molded dielectromagnet manufacturing process consisted of injection of a mix composed of magnetic powder and polystyrene as a binder agent. The injection molding process was accomplished at temperatures in the range from 433 to 513 K and under injection pressures of either 100 MPa or 130 MPa. The compression-molded dielectromagnets consisted of compression molding the magnetic powder bound by Epidian100 heat-hardening resin, which contributed 2.5% of the total weight of powder and resin mixture. Fig. 24.26 shows microscope photographs of cross-sections of the injection-molded dielectromagnets made from powders. Magnetic properties of the atomized powder magnets are lower than the ones of the ribbon powder magnets (Table 24.17). The advantage of the former consists of better technological features: preparation of the atomized powder is easier; the mold is more densely filled with the material and manufacturing of injection-molded magnets with a higher content of hard magnetic powder (about 62% volume ratio) is possible.

New metastable nanocrystalline multicomponent systems prepared by mechanical alloying or by mechanochemical methods show an enhanced remanence or improved high temperature properties [74]. For isotropic magnets, high energy ball milling is used as a versatile technique for the preparation of nanocomposites in the (PrNd)FeB system. Alloy

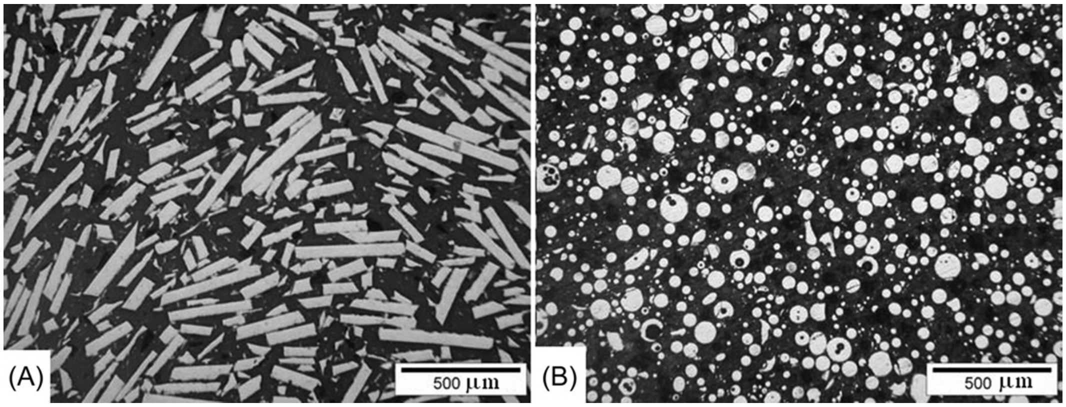

FIG. 24.26 Photographs of cross section of the injection molded Nd-Fe-B dielectromagnets from ribbon (A) and from atomized (B) powders. *Source: Ślusarek B, Paszkowski L, Biało D. The influence of kind of powder on physical properties of Nd-Fe-B dielectromagnets. Microstructure and properties of Nd-Fe-B dielectromagnets, produced from gas-atomized powders. In: Proceedings of PM2004 world congress. Wien (Austria): European Powder Metallurgy Association; 2004, vol. 4. p. 555–60.*

TABLE 24.17 Magnetic Properties of the Nd-Fe-B Dielectromagnets

Powder Grade	Powder Obtaining Process	Particle Shape	Magnet Production Process	Magnetic Properties		
				B_r (T)	H_c (kA/m)	$(H_c \cdot B_r)_{max}$ (kJ/m^3)
MQP-B	Melt spinning	Ribbon	Compression molded	0.71	735	82.72
MQP-S-11-9	Melt atomization	Spheroidal	Compression molded	0.572	796	51.17
MQP-B	Melt spinning	Ribbon	Injection molded	0.467	829	40.71
MQP-S-11-9	Melt atomization	Spheroidal	Injection molded	0.363	812	24.03

B_r is the residual magnetic induction; H_c is the high coercive force; $(H_c \cdot B_r)_{max}$, is the energy product measured by fitting the largest rectangle to the demagnetization curve, found in the second quadrant of the hysteresis loop (Fig. 24.25).

composition optimization and mixing with iron lead to hard magnetic multiphase powders with improved corrosion resistance suitable for high performance bonded magnets. The high values of maximum energy product $(H_c{\cdot}B_r)_{max}$ and magnetic induction are due to the presence of α-Fe and an exchange coupling effect resulting in effectively single-phase demagnetization curves (see Fig. 24.25).

Due to the increasing demand for REEs [69] and the uncertainty in the supply of virgin REEs, the possibilities of recovering and reusing them from spent products are presently being investigated [75–77]. Some products are rich in materials containing significant amounts of REEs. One such material is neodymium-iron-boron (NdFeB) magnet scrap, which could be a source of neodymium and dysprosium, added to increase the Curie temperature of the magnet, and some other REEs, depending on the type of magnet. Recycling of discarded magnets requires removal of the magnet from the device where it has been in use, demagnetization, size reduction, and a hydrometallurgical (leaching and separation from the liquid phase) or pyrometallurgical (high-temperature processes and separation in molten salts) separation of the constituent elements [45,77–79].

Solvent extraction, or liquid-liquid extraction, is a commonly used hydrometallurgical method for the recovery and removal of metal ions from aqueous solutions [45, 79]. The aqueous phase, that is, the leachate obtained by acid dissolution of the waste, in this case containing dissolved REEs along with cobalt and other contaminating metals, is mixed with an organic phase containing ligand molecules ("extractants") designed to selectively transfer the chosen ions to the organic phase. The combination of solvent and ligand can be varied in order to optimize the properties of the organic phase for a certain separation process. In some cases, a third component, called a modifier, can be added in order to modify an important property of the organic phase [80]. However, it is difficult to separate the REEs from each other due to their chemical similarity [77,79].

Generalized typical magnetic properties of the bonded and of the sintered magnets, made from rare earth alloys as well as from ferrites for comparison, are given in Fig. 24.27.

Rare earth magnets are used in electronic watches and traveling wave tubes. Direct-current and synchronous motors and generators include rare earth magnets for size reduction. The reasons for usage comprise high flux density, high coercive field, high energy size value, and temperature stability. Rare earth magnets are also used in medical devices, such as thin motors in implant pumps and valves, and in aiding eyelid motion. It is significant that more than thirty parts of a present-day car (for example, door locks, oil pump, windows, seat supports, wipers, headlight direction, brakes, steering, etc.) include rare earth alloy magnets.

The market is segmented by application into automotive, electronics, medical, aerospace, energy, and industrial sectors [69]. The electronics segment is expected to grow at a CAGR of more than 9.0% over the period 2016 to 2024, driven by increasing demand for smartphones, sensors, and electrodynamic speakers. In addition, a significant reduction in the size of the product is expected to result in an increasing use of the product in small size electronic devices. Energy generation segment is expected to witness a growth rate of over 9.0% over the period 2016 to 2024 owing to increasing use of high-strength magnets in wind turbine generators is expected to drive market growth over the forecast period. Furthermore,

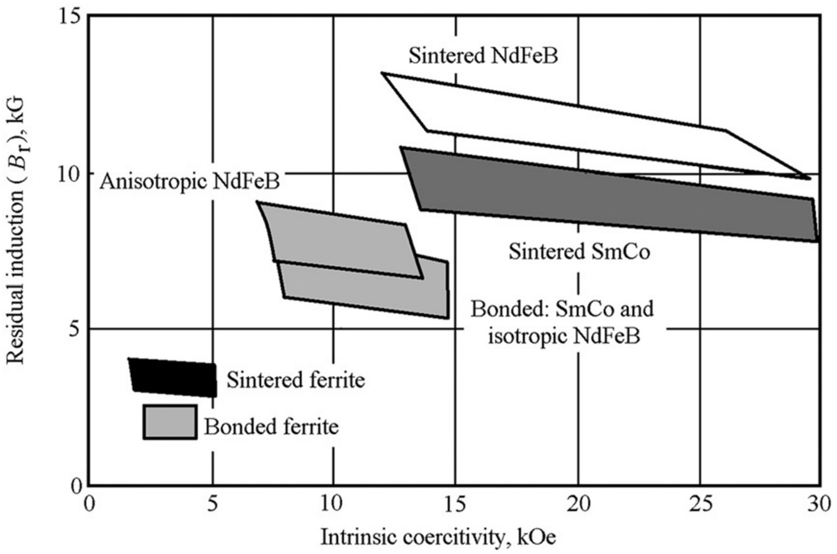

FIG. 24.27 Generalized typical magnetic properties of bonded and of sintered magnets. *Source: Ormerod J, Constantinides S. PM Magnetic materials and applications, short course, 22–23 June 1993 Metal Powder Industries Federation Publishers; 1993.*

growing awareness for the non-conventional source of energy coupled with favorable governmental regulations for wind energy generation systems is expected to act as prime drivers for industry demand.

Cemented Tungsten Carbides

The study of RE-doped cemented carbide was started in the early 1960s in China, and intensive investigations in this field have been reported lately [81–83]. Recently, an enrichment effect of RE metal on the sinter skin was observed during the sintering process of high activity mischmetal (mainly containing lanthanum and cerium) doped cemented carbides with low and medium carbon levels [84].

BERYLLIUM

Beryllium is a light grey metal and has the lowest density among the construction metals. This metal, due to its unique mechanical and physical properties, is used in various nuclear, aerospace, space, optical, medical, X-ray, and consumer fields.

Cast beryllium usually has a coarse crystalline structure and, because of its high crystal anisotropy, wrought processing is not feasible. Therefore, powder metallurgy is the only acceptable technique for manufacturing strong homogeneous beryllium billets.

Physical Properties

Beryllium is a light metal with a combination of physical properties that is not found in any other metal (Table 24.18). A close packed hexagonal crystal structure α-modification (with $a = 0.2286\,\text{nm}$ and $c = 0.3584\,\text{nm}$ and c/a ratio of 1 to 1.56) at above 1523–1533 K, near to melting point is transformed into cubic β-form. The value c/a of beryllium crystal structure is low compared with other metals such as titanium (1 to 1.58).

Beryllium has a relatively high melting point, high modulus of elasticity, relatively high electrical conductivity (35%–45% IACS), high specific heat, low coefficient of thermal expansion and highest among metals of heat capacity; beryllium is distinguished by very small capture cross-section for thermal neutrons and high ability to scatter them. Beryllium penetrability by X-rays is 16–17 times as large as aluminum penetrability. Beryllium is non-magnetic.

Wrought beryllium has the highest strength-to-weight ratio of all construction metals and retains durability at elevated temperatures up to 873 K. However, mechanical properties strongly depend on the processing technique and subsequent thermal and mechanical processing. Extrusion and rolling lead to anisotropic properties caused by orientation of hexagonal beryllium crystals in a certain direction. Consequently, for example, the tensile strength of extruded rod or rolled bar in the longitudinal direction is one and a half to twice that in the transverse direction. Anisotropic mechanical properties are not observed in articles obtained by PM (usually by hot pressing), because of the random orientation of the crystals.

In dry air, beryllium does not oxidize significantly at temperatures up to about 870 K because it forms a protective oxide film, similar to that of aluminum, formed in air. Rapid oxidation is observed at 1173–1273 K. Above 973 K, beryllium slowly reacts with nitrogen, forming beryllium nitride (Be_3N_2). Hydrogen does not react with beryllium right up to melting point. Halogens react with beryllium at elevated temperatures, beginning at 573 K forming BeX_2 (X is halogen). High-purity beryllium is stable in pure water up to 373 K, but the presence of inclusions of chlorides and/or carbides in the metal and of chloride, sulfate, etc., ions in the water accelerates corrosion.

Beryllium is dissolved in hydrochloric and sulfuric acids, slowly reacts with dilute nitric acid in the cold, but is dissolved on heating. It is dissolved by caustic alkali solutions forming the beryllate ($MeBeO_2$).

At temperatures down to 770–970 K, beryllium is stable in contact with melted metals and alloys that can be used as a heat-transfer medium in nuclear reactors. Bismuth, Bi-Pb alloys, Bi-Pb-Sn alloys, sodium, potassium, Na-K alloys, and lead are relevant in this context.

Molten beryllium reacts with carbon with the formation of beryllium carbide (Be_2C) and reacts with such durable and refractory oxides as magnesium oxide, aluminum oxide, calcium oxide, and zinc peroxide, due to high beryllium affinity for oxygen.

Beryllium Compounds

Only one oxide, BeO, also named beryllia, is known in the beryllium-oxygen system. It is a refractory compound with a melting point of 2780 K and high chemical stability (enthalpy formation is 599 kJ). Beryllium oxide is remarkable for high heat conductivity that ensures heat resistance. Burned at 2073 K, beryllium oxide is virtually insoluble in acids and does not react with fused metals (uranium, iron, nickel, calcium, and others).

TABLE 24.18 Typical Properties of Beryllium

Property	Unit	Value
Density	g/cm^3	1.847
Crystal type[a] [1]		HCP
Atomic diameter	nm	0.228
Vickers hardness	MPa	1670
Modulus of elasticity	GPa	275–300
Melting point	K	1560
Boiling point	K	2742
Specific heat at room temperature	kJ/(kg·K)	1.88
Heat of fusion [85]	kJ/mol	12.2
Heat of vaporization [85]	kJ/mol	292
Thermal conductivity	W/m·K)	190
Coefficient of linear thermal expansion at temperature ranges [86]:		
At 298 to 373 K	μm/(m·K)	11.6
At 373 to 573 K	μm/(m·K)	14.5
At 573 to 873 K	μm/(m·K)	16.5
At 873 to 1273 K	μm/(m·K)	18.4
Electrical conductivity [85]	% IACS	40
Electrical resistivity	nΩ·m	36 (at RT)
Volume diffusion [85]	m^2/s	6×10^{-5}
Volume diffusion activation energy [85]	kJ/mol	161
Capture cross section of heat neutrons $n \times 10^{24}$	cm^2	0.009
Transmits sound [86]	m/s	12,600
Reflects light [86]:		
Optical reflectivity	%	50
Ultraviolet reflectivity	%	55
Infrared (10.6 μm)	%	98

[a] *Crystal type: H, hexagonal.*

Beryllium fluoride, BeF_2, is a colorless crystalline material and is very hygroscopic. It is highly soluble in aqua (about 18 mol/L). Beryllium fluoride with alkali metal fluorides and ammonium forms composite salts. The salts, Na_2BeF_4 and $(NH_4)_2BeF_4$, play an important part in technology. Beryllium fluoride is obtained by thermic decomposition of ammonium fluoroberyllate at 1173 K.

Beryllium hydroxide, $Be(OH)_2$, precipitated from beryllium salt solutions in the pH interval from 6 to 8, possesses amphoteric properties: beryllium salt solutions are formed by dissolving in acids, while beryllates (Me_2BeO_2) are formed by dissolving in alkalis. Beryllium hydroxide is dissolved in ammonium carbonate, forming a carbonate complex, $(NH_4)_2[Be(CO_3)_2]$. Solutions of the latter are decomposed on boiling, a slightly soluble basic carbonate $BeCO^3 \cdot nBe(OH)^2 \cdot mH_2O$ being precipitated.

Beryllium forms alkaline salts with a series of organic acids with general formula $Be_4O(RCOO)_6$, which are produced by the action of organic acids on beryllium hydroxide. In technology, compound $Be_4O(CH_3COO)_6$ is used. Salt is sublimed without decomposition at temperatures 630–670 K.

Beryllium forms intermetallic compounds with a series metals, differing by infusibility, low density and oxidation resistance up to 1770–1870 K. Of greatest interest are the following: beryllides $ZnBe_{13}$, $TaBe_{17}$, and $MoBe_{12}$ with melting temperatures about 2200, 2250, and 1970 K, respectively.

Sources of Raw Material

The beryllium content in the earth's crust is about 6×10^{-4} wt%. Nearly 40 beryllium minerals are known, mainly various complicated silicates. The following minerals have the largest commercial importance: beryl, chrysoberyl, phenacite, helvine, bertrandite, and donalite.

Beryl ($Be_3Al_2(Si_6O_{18})$) is the most prevalent beryllium mineral. It contains up to 14.1 wt% BeO and often admixtures of alkaline metals. The hardness of beryl is 7.5–8 on the Mohs scale.

Phenacite or phenakite (Be_2SiO_4) is the richest mineral as regards beryllium content 46 wt%. The hardness of phenacite is 7.5. At present, phenacite, along with beryl, has a large commercial significance.

The commercial beryllium ore deposits are confined to pegmatitic and hydrothermal-pneumatolytic types. At present, the hydrothermal-pneumatolytic type ore deposits contain mainly phenacite, chrysoberyl, helvine, and bertrandite, opened at the beginning of the 1950s in the United States, are becoming commercially important.

Beryllium ores are usually lean: BeO content ranges from 0.03% to 2%. They are difficult to concentrate because of their similarity to the rocks with which they occur in association. The major ore concentration methods are the following:

- Selective grinding is used for ores, which contain soft rocks (soft slates, talc, and others). The hard beryllium minerals are separated from barren rock minerals on screens or in separators;
- Flotation is used for disseminated beryl ores. Beryl is floated with fatty acids (rapic acid). For concentrating phenacite and bertrandite ores, the concentration schemes include gravitation in heavy liquids (for medium-and coarsely crushed ores) and flotation for finely crushed disseminated ores.

Standard beryllium flotation concentrates in Russia contain from 9.7% to 6.12% BeO.

Beryllium concentrates are usually processed to beryllium oxide or beryllium hydroxide, from which beryllium fluoride or chloride is produced—the initial materials for beryllium production. The fluoride and sulfate methods are used in commercial practice for processing beryllium concentrates.

The fluoride technique is based on beryllium conversion by means of complex fluorides, Na_2SiF_6 and Na_3FeF_6. As a result of the interaction of beryl with complex fluorides at temperatures ranging from 1020 to 1070 K, sodium tetrafluoroberyllate (Na_2 BeF_4), which is soluble in aqua, is formed. Compounds of other elements have low solubility.

The sulfate technique is based on conversion of beryllium together with aluminum and iron into a sulfate solution, while the main bulk of silicon dioxide remains as an insoluble residue. As long as beryllium slowly reacts with concentrated sulfuric acid, even at 470–520 K, preparatory operations of concentrate alloying with lime or thermal activation of beryllium are conducted.

At present beryllium is obtained by two methods:

- Reduction of beryllium fluoride by magnesium;
- Electrolysis from chloride electrolyte.

Magnesium-Thermal Reduction of Beryllium Fluoride

Magnesium is used as a reducing agent, because it does not form compounds in solid solution with beryllium:

$$BeF_2 + Mg = Be + MgF_2; \Delta G^0_{1000K} = -118\,kJ$$

The redundant BeF_2 is introduced in a flux composition. Reduction is done in graphite crucibles in induction furnaces. A mixture of magnesium fluoride and beryllium fluoride, not avoiding additional impurities, is used as flux for protection from oxidation. Magnesium is introduced in 75% stoichiometric quantity. Reduction is carried out in an inert atmosphere at temperatures ranging from 1170 to 1270 K. Next, the temperature is raised to 1570 K (higher than beryllium melting point). The prills float to the surface and are assembled in an ingot ("lens"). During cooling, beryllium solidifies before the flux, which allows the ingot to be withdrawn from fused flux. The ingots obtained contain to 1.5% Mg, about 0.1% BeO, 0.1% Fe and Al, and other impurities. They are refined by remelting at 1770 K.

Electrolysis From Beryllium Chloride Electrolyte

The electrolyte contains $BeCl_2$ and NaCl in weight ratio 1 to 1. It is close to eutectic composition (58.7%$BeCl_2$+41.3% NaCl) with melting point 488 K, that permits electrolysis to be carried out at low temperatures around 620 K. Beryllium is deposited on the nickel electrodes; chlorine is evolved on the graphite anode:

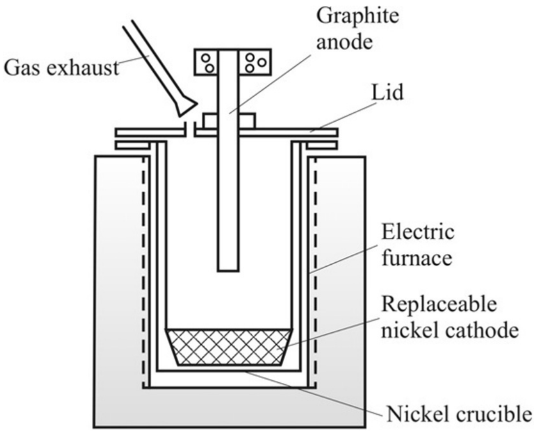

FIG. 24.28 Scheme of electrolyzer for flake beryllium production.

$$Be^{2+} + 2e = Be$$

$$2Cl^{-} - 2e = Cl_2$$

An electrolytic cell made of nickel is put into a furnace (Fig. 24.28). Replaceable cathodes are perforated nickel crucibles. Chlorine evolved on the graphite anode is removed by the exhaust system.

Originally, the electrolyte is refined from impurities of more electropositive metals as compared with Be (such as Cu, Fe, Ni, and others) at voltage of about 1.5 V. Then the cathode is replaced and the voltage increased to 2.08 V. Cathode current density is 1 kA/m^2, anode current density is 4 kA/m^2. Electrolysis is conducted at 693 K. Current efficiency is 60%–65%.

The cathode, with precipitated beryllium, is removed from the electrolyzer while still hot. On cooling, the beryllium flake is removed from the cathode and sequentially washed by water, alkali solution, diluted nitric acid, and again with water, and then it is centrifuged and dried.

Dried beryllium flakes are pressed into briquettes, which are vacuum remelted and cast into ingots. Typical impurity contents of electrolytic beryllium after vacuum remelting are 30 ppm Al, 30 ppm Ca, 20 ppm Cl, 20 ppm Cu, 70 ppm Fe, 30 ppm Ni, and 20–30 ppm Si.

Production of Leafed Beryllium by Electrorefining From Melts

The feed is preliminary beryllium in disks. The electrolyte consists of 40–50 wt% $BeCl_2$ and 50–60 wt% NaCl. Temperature ranges from 590 to 600 K. Cathode current density is 830 A/m^2, anode current density is 3000 A/m^2. The electrolyzer has a construction similar to the one for beryllium recovery with insoluble anodes (see Fig. 24.28). Preliminary beryllium disks are set on the graphite rod. Another type of electrolyzer is equipped with a gradually extending anode made of refined beryllium. After extraction, cathode deposits are washed with 10% solution of ammonium carbonate, oxalic acid and ethyl alcohol. The impurity content in the final product is as follows: 60–100 ppm Fe, 80–300 ppm Ni; and 6–20 ppm Mn. Current efficiency is up to 80%, beryllium recovery amounts to 80%.

Beryllium Powder Production

The vacuum remelted beryllium ingots are cut into chips by lathe turning. But chips produced in this way are relatively coarse and must be reduced to fine particle sizes before consolidation into homogeneous, fine grained billets.

Grinding

Until recently, ball milling and attrition grinding were the only processes used to reduce machining chips to powder. Attrition milling is accomplished by impact and shear forces which may be classified as a high energy ball milling process [87], where the rotating charge of balls and milling product form a vortex by means of a rotating impeller.

This milling process results in basal plane cleavage. Thus, the powder particles produced by attrition technique tend to form flakes (Fig. 24.29A) with flat corresponding to {0002} basal planes. Ball milled powders have a similar shape. As a result of their particle shape and crystallographic texture, consolidated billets reveal anisotropy of both physical and

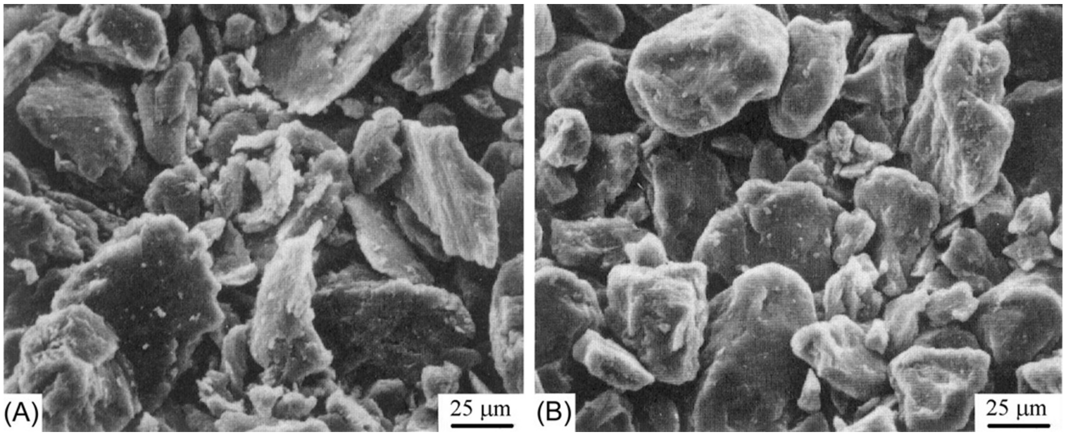

FIG. 24.29 Scanning electron micrographs of flake like attritional (A) and blocky impact ground (B) powders. *Source: Marder JM, Wellman B. Production of beryllium powders. In: ASM handbook, vol. 7. ASM International Publishers; 1998. p. 202–5.*

mechanical properties. During vibratory die loading for consolidation, the flat faces of many particles align, forming extended volumes with a common crystallographic feature. The basal plane corresponds to the flat faces. Impact grinding is used to minimize anisotropic effects. Resultant particles are blocky, rather than flake like (Fig. 24.29B).

Milling chips in a water-cooled disk grinder with a beryllium lining in a dry inert gas atmosphere is also used. Another known process is ball milling in an aqueous medium, the powder being subsequently washed with dilute nitric acid and, to prevent oxidation, organic liquid(s) [6]. These powders have also particles tending to flake shape.

The coldstream impact process is used to reduce anisotropy. Chips and powder are entrained in a high speed gas stream and are impacted against a stationary beryllium target. Rapidly expanding gases leaving the nozzle create a strong cooling effect by adiabatic gas cooling, which is greater than the heat generated by pulverization. Therefore, the process occurs at well below room temperature. The high speed pulverization process, coupled with the latter, activates the secondary and tertiary non-basal cleavage systems. The resultant particles have roundish, rather than flake-like, facets.

After the material has struck the target and shattered, it is removed from the impact chamber by suction. It is then transported to a primary classifier, which allows the oversize to return to the feed hopper for subsequent impact against the target. The finished product is separated by the secondary classifier and transported to collection containers. More detailed information on coldstream impact grinding as well as on other grinding technique can be found in Chapter 2.

The particle shape and crystallographic texture, obtained by impact grinding leads to substantially reduced correlation between crystallographic basal planes and flat powder particle faces, leading to decreased anisotropy and an improvement in longitudinal tensile elongation. The transverse-to-longitudinal ductility ratio for attrition milled powder is about 3 to 1. For impact ground powder, this value is approximately 1.6 to 1.

The strength of beryllium is related directly to grain size which is primarily a function of the particle size, oxide content and consolidation temperature of the powder used. Because oxides are a primary grain-boundary pinning agent, fine particle size enhances oxide content and, therefore, strength. The strength imparted by fine grain size and the potential embrittlement effect of excessively high oxide content must be balanced against each other. Characteristics of beryllium powders used to manufacture billets are given in Table 24.19. American Elements Company (CA, United States) produced high purity beryllium powders contain from 99 to 99.999 wt% vanadium (BE-M-02-P, BE-M-03-P, BE-M-04-P, and BE-M-05-P products codes, respectively). The powder particle average sizes are in the following range: −325 mesh, −100 mesh, 10–50 μm, and <1 μm.

Gas Atomization of Beryllium

Inert gas atomization enables beryllium powder to be produced in semi-manufactured condition without a chip-forming step [88]. Parallel with this, the major advantage of this process over conventional impact ground powder technique is the increased isotropy of the consolidated material. This is especially important in optical systems, where isotropy is a primary factor in component performance, particularly in cryogenic systems in which thermal constructions can cause distortion in anisotropic components. Economic benefits may also be obtained if this process is used on a commercial production scale.

Gas atomization beryllium was developed in the mid-1980s. Further development in the 1990s created aluminum-beryllium alloys containing 40–62 wt% Be. Vacuum induction melting is used to prepare the melts of beryllium and

TABLE 24.19 Characteristics of Beryllium Powders Used to Manufacture of the Billets

		Grade				
Property	**Unit**	**S-65**[a,b]	**S-200F**[a]	**IP-70**[a]	**IP-220**[a]	**O-30**[c]
Elements:						
Beryllium	wt% min	99.2	98.5	99.0	98.0	Balance
Beryllium oxide	wt% max	0.9	1.5	0.7	2.2	0.5
Aluminum	wt% max	0.05	0.1	0.07	0.10	0.07
Calcium	wt% max	0.005	…	…	…	…
Carbon	wt% max	0.09	0.15	0.07	0.15	0.12
Chromium	wt% max	0.01	…	…	…	…
Cobalt	wt% max	0.005	…	…	…	…
Copper	wt% max	0.025	…	…	…	…
Iron	wt% max	0.08	0.13	0.10	0.15	0.12
Lead	wt% max	0.005	…	…	…	…
Magnesium	wt% max	0.01	0.08	0.07	0.08	0.07
Manganese	wt% max	0.005	…	…	…	…
Molybdenum	wt% max	0.005	…	…	…	…
Nickel	wt% max	0.025	…	…	…	…
Silicon	wt% max	0.045	0.06	0.07	0.08	0.07
Silver	wt% max	0.005	…	…		…
Titanium	wt% max	0.025	…	…	…	…
Uranium	wt% max					
Zinc	wt% max	0.005	…	…	…	…
Zirconium	wt% max	0.025	…	…	…	…
Other metallic impurities[c]	wt% max	…	0.04	0.04	0.04	0.04
Particle sizes 45 μm under seeding	wt% min	98	98	98	98	…

[a] *Impact ground.*
[b] *Nominal composition of nuclear grade of beryllium powder.*
[c] *Inert gas atomized.*

Sources: Refs Hashiguchi DH, Svilar M, Sayer AB, Morales AL. Beryllium and aluminum-beryllium alloys. In: ASM handbook, vol.7, Powder metallurgy. ASM International Publishers; 2015: p. 757–65 and Marder JM, Wellman B. Production of beryllium powders. In: ASM handbook, vol. 7. ASM International Publishers; 1998. p. 202–5.

aluminum-beryllium alloys. Beryllium oxidizes at melt temperature, while vacuum is used to protect the melt. Melting an alloy consisting of high melting temperature beryllium (1570 K) and lower temperature aluminum (933 K) in a vacuum does not result in a melt boiling problem, because both elements have similar vapor pressures under the melt conditions. A vapor pressure of 1.3 mbar (1 mm of Hg) is reached at a temperature 1793 K for beryllium and 1803 K for aluminum [89]. The melt chamber is backfilled with inert gas prior to atomization. The melt is poured into a tundish where through a funnel in bottom the melt flows out. The melt stream is atomized by high-pressure jet of inert gas (argon, helium or nitrogen). A small amount of oxygen in the inert gas passivates the powder to minimize pyrophorisity [90].

Hashiguchi et al [90] reported that the microstructure of inert gas atomized aluminum-beryllium alloys consists of a dendritic eutectic structure of aluminum and beryllium. Beryllium secondary arm spacing is about 5 μm, which is 1 to 2 orders of magnitude finer than for static-cast alloy.

The typical chemical composition of inert gas atomized beryllium powder is given in Table 24.19.

Microalloying Influences

The impurity elements that have an influence on the beryllium properties include aluminum, cobalt, copper, iron, magnesium, nickel, silicon, oxygen and carbon.

Aluminum and iron can cause deleterious effects in beryllium. The presence of aluminum at the grain boundaries leads to reduced ductility in components for elevated temperature applications. Iron forms the compound $FeBe_{11}$, which results in precipitation hardening. Yield point feature observed in beryllium has been attributed to the pinning of dislocations by $FeBe_{11}$ precipitates [51]. If it persists until the ultimate strength is reached, the beryllium fractures with little plastic deformation. Aluminum and iron, when present together in beryllium, can form the compound $FeAlBe_4$. The appropriate balancing of aluminum and iron content eliminates the embrittlement action of aluminum or $FeBe_{11}$ precipitation without the use of ultra-high purity.

Silicon acts as a sintering assistant in the consolidation of beryllium powder. In practice, the hot pressing of beryllium powder with silicon content is difficult because of the pressure limitation when using graphite dies. The high pressure capability of hot isostatic pressing is often used for the consolidation of low-silicon, high-purity electrolytic powder. A variant is to dope the material with trichlorosilane at the vacuum hot pressing (VHP) stage. In general, aluminum, iron and silicon cause agglomeration and growth of beryllium oxide and also act on recrystallization, grain growth and creep strength of beryllium. Copper, cobalt and nickel show extensive solubility in beryllium.

Among the non-metallic impurities, only carbon and oxygen are observed to any appreciable extent. Both have minimal solubility in beryllium. Carbon occurs as the cubic refractory beryllium carbide compound, which is usually found within the grains. This carbide accelerates the corrosion of beryllium, as it slowly hydrolyzes in the presence of moisture.

Oxygen forms stable beryllium oxide, which is principally a grain-boundary constituent. However, it may also be found in the matrix. Typical concentrations of beryllium oxide in beryllium powders in commercial billets range from 0.7% to about 2.0%.

Beryllium Oxide Powder Production

Beryllium hydroxide ($Be(OH)_2$) is used as feedstock to produce beryllium oxide (BeO) [90]. The hydroxide is dissolved in sulfuric acid to form beryllium sulfate ($BeSO_4$) crystals, which is calcined in air at a temperature between 1420 and 1720 K before decomposing into high purity BeO powder. Calcining produces agglomerates of particles 0.1 to 0.2 μm in size. Typical tap density at this stage 20% to 25% of solid. The agglomerates are spray dried with binders to increase tap density and flowability and is pressed into green parts, machined and sintered. Beryllia ceramic possesses by unique combination of high electrical resistivity (2×10^{14} to $1.3 \times 10^{15}\,\Omega \cdot m$) with high conductivity (250 to 330 W/m·K).

Powder Consolidation and Production of Wrought Products

The most common powder consolidation methods are vacuum hot pressing and hot isostatic pressing. Other methods, such as cold pressing and sintering and vacuum sintering, have also been used to consolidate beryllium and beryllium alloy powders.

Vacuum Hot Pressing

This technique was most frequently used for manufacturing commercial beryllium billets. Graphite dies are commonly used due to a low coefficient of thermal expansion, which simplifies removal of the beryllium billet after cooling. Graphite is available in sufficiently large sizes to produce vacuum hot pressings above 560 mm in diameter. Pressings that are too large in diameter for graphite dies are accomplished in nickel alloy (IN-100) up to 1830 mm in diameter.

Beryllium powder is vibratory loaded into the dies to achieve a density of about 55%. The assembly is then placed in a vacuum hot pressing chamber. Typical pressing temperatures range from 1270 to 1370 K and compacting pressure ranges from 3.5 to 14 MPa. Properties of vacuum hot-pressed billets are given in Table 24.20.

Hot Isostatic Pressing (HIP)

Improved isotropy of both microstructure and mechanical properties is a major advantage of isostatic pressing. This is achieved because the pressure is applied from all sides, shrinkage is uniform in all directions and directionality originating from the pressing operation is prevented.

In the HIP process, the powder is loaded into a mild steel container, degassed at elevated temperature to remove air and vapor, and the container is sealed. Hot isostatic consolidation at pressures of about 103 MPa and at temperatures from 1070 to 1300 K. Dry, low-oxygen-containing argon is used as the pressure medium. These process conditions are the only

TABLE 24.20 Properties of Beryllium Hot Pressed Block Billets

		Grade				
Property	**Unit**	**S-200F**	**S-65B**	**I-70A**	**I-220-H**	**EP**[a]
Chemical composition:						
Beryllium	% min	98.5	99.2	99.0	98.0	Balance
Beryllium oxide	% max	1.5	1.0	0.7	2.2	…
Aluminum	% max	0.10	0.06	0.07	0.10	0.03
Carbon	% max	0.15	0.12	0.07	0.15	…
Iron	% max	0.13	0.12	0.10	0.15	0.10
Magnesium	% max	0.06	0.08	0.07	0.08	0.05
Silicon	% max	0.06	0.06	0.07	0.08	0.03
Other metal impurities	% max	0.04	0.04	0.04	0.04	0.03
Powder type		Impact ground	Impact ground	Impact ground	Impact ground	Flakes
Minimum density	g/cm^3	1.84	1.84	1.84	1.84	…
Theoretical density	%	99	99	99.3	99	…
Average grain size	µm max	25	15	20	25	…
Ultimate strength (min)	MPa min	324	289.6	241.3	379	…
Yield strength (min)	MPa min	241	206.8	172.3	275	…
Elongation (min)	% min	2	2	2	2	…

Note: Pressing sizes can range from 188 to 1830 mm in diameter and 150 to 1680 mm in length, depending on grade and compositions.
[a] *Electrolytic beryllium flakes are pressed in briquettes, which are vacuum remelted and cast into ingots.*
Sources: Refs Zelikman AN, Korshunov BG. Metallurgy of rare metals. Moscow: Metallurgiya Publisher; 1991 [in Russian] and Marder JM, Wellman B. Production of beryllium powders. In: ASM handbook, vol. 7. ASM International Publishers; 1998. p. 202–5.

effective means of reliably consolidating high purity beryllium powders to full theoretical density. While ordinary purity beryllium powder, which contains sufficient concentration of impurity elements such as aluminum and silicon that act as sintering aids in the hot pressing, can be vacuum hot pressed to nearly theoretical density by pressing at about 7 MPa at 1300 K. Consolidation of aluminum-beryllium alloys is carried out at a temperature between 720 and 900 K. The HIP capsule is removed machining or chemical etching techniques after consolidation. Uniform processed densities greater than 99.7 % of solid are produced within blocks and NNS (near-net shape) blanks.

The mechanical properties of three grades of hot isostatic consolidated beryllium powder are compared to their vacuum hot pressed parallel parts in Table 24.21. Isostatic consolidation of high purity powder material improved physical and mechanical properties, including fine grain size, well distributed oxide content, a high degree of isotropy, good compression creep properties, good elevated temperature properties, and no grain growth up to 1530 K.

TABLE 24.21 Mechanical Properties for VHP and HIP Beryllium

		Grade					
		S-200F		I-70		I-220	
Property	**Unit**	**HIP**	**VHP**	**HIP**	**VHP**	**HIP**	**VHP**
Ultimate tensile strength	MPa	414	324	345	241	448	379
Yield strength	MPa	296	241	207	172	345	275
Elongation	%	3	2	2	2	2	2

Source: Marder JM, Wellman B. Powder metallurgy beryllium. In: ASM handbook, vol.7, powder metallurgy ASM International Publishers; 1998. p. 941–6.

Beryllium powders are consolidated to near theoretical density also by:

- Cold isostatic pressing (CIP) followed by vacuum hot pressing,
- CIP followed by pressure-less sintering,
- CIP followed by hot isostatic pressing, and
- Direct hot isostatic pressing.

Cold Isostatic Pressing and Sintering

Cold isostatic pressed beryllium is vacuum sintered at temperatures between 1270 and 1490 K. Vacuum is required to prevent oxidation of the green preforms. Densities greater than 99% of theoretical are achieved. Heat sinks and nuclear limiter tiles for the JET reactor are made using CIP and sinter and are sometimes coined (compressed between two closed-die surfaces) for tighter dimensional tolerance control. Cold isostatic press and sinter is also used to make three-dimensional parts for electro-optical mirrors, gimbals, and system parts. A latex bag or polyurethane bags are designed to compact the NNS green compacts. The latex bag is fixed in a quick-disconnect vacuum mold to hold the shape of the bag. The bag is vibratory loaded with powder. Filled and de-aired bags are fixed and placed inside the CIP unit. Water is pumped into a CIP chamber to pressure between 140 and 415 MPa to isostatically compact the powder into a green body. The polymer bag is stripped from the green preform.

Cold Isostatic Pressing and Extrusion

CIP and extrusion is the commercial process used to produce extruded AlBeMet rod and bar. Cold isostatic pressing is used to compact powder into a cylindrical shape, which is encapsulated in copper mold. The copper serves as low-abrasive lubricant when it slides against the extrusion die tooling. The encapsulated billet is degassed at an elevated temperature in a vacuum in a similar manner to that in HIP consolidation. Otherwise, powder is extrusion consolidated without a CIP step. The sealed billet is preheated to a temperature low enough to avoid incipient melting of the copper-aluminum interface phase of the aluminum-beryllium powder (698–813 K). Extrusion is performed using a taper die. The fully dense, semi-product (rod, bar, tube) is chemically etched or machined to remove the copper skin. Extruded aluminum-beryllium alloys are annealed at a temperature of 860 K.

Wrought Product Forms

After beryllium powder consolidation, it is easily processed by conventional metalworking techniques. Wrought forms of beryllium with optimum properties are produced from vacuum hot pressed billets by conventional hot-working techniques. Wrought products show improved mechanical properties in the predominant direction of metal flow. Mechanical properties of wrought products depend greatly on crystallographic orientation. Biaxial or triaxial deformation procedures are often used to produce semi-products with balanced directional properties.

Sheet, plate and foil are the most commonly manufactured wrought forms of beryllium. These flat products are produced by encasing beryllium billets in steel jackets, followed by cross rolling at moderate temperature. Beryllium foil is available in thicknesses from 0.025 to 0.5 mm and panel sizes up to 125 × 300 mm.

Rod, tubing, and structural shapes are available by beryllium extrusion. Their mechanical properties in the direction of metal flow are superior to the mechanical properties of hot pressed billets in the direction of metal flow. Input billets for extrusion are usually machined from hot pressed blocks. Extrusion billets are jacketed in low-carbon steel containers that have been shaped during extrusion through a steel draw plate at 1173–1340 K. Then, the steel jackets are chemically removed from the extrusions.

Conventional rod is produced in sizes from 9.5 to 135 mm in diameter. Tubing is available from 6.4 mm outside diameter by 1 mm wall thickness up to 150 mm outside diameter by 3.2 mm wall thickness. Typical tensile properties of beryllium sheet and extrusions are listed in Table 24.22.

Components of beryllium and aluminum-beryllium alloys are successfully joined by brazing and welding. Typically, silver- aluminum-base braze is used for beryllium. Aluminum-beryllium sheet is by tungsten inert arc welding. Both materials are welded by electron beam welding, which minimizes heat input into the join design. Process AlBeWeld [90] conditions were developed to specifically electron beam weld aluminum-beryllium alloys processed by HIP into lightweight optical and heat-sink structures. Diffusion HIP adhesive bonding are also used.

Machining practices for beryllium typically requiring a tungsten carbide tool to minimize insert wear during long machining steps. While beryllium is not a hard metal, it is abrasive and easily forms a discontinuous chip. Beryllium

TABLE 24.22 Typical Tensile Properties of Beryllium Wrought Specimens

Product	Manufacturing Method	Test Orientation	Ultimate Tensile Strength (MPa)	Yield Strength (MPa)	Elongation[a] (%)
Block					
Ordinarily purity[b]	VHP	L T	370 390	266 273	2.3 3.6
Hugh purity	HIP	L T	455 455	287 287	3.9 4.4
High-oxide instrument grade	VHP	L T	476 511	406 413	1.5 2.7
Fine grain size	HIP	L T	580 587	407 407	3.7 4.2
Sheet (1 to 6.4 mm, thick)	Hot rolled	…	531	372	16
Ordinarily purity powder					
Ordinarily purity ingot	Hot rolled	…	352	172	7
Extrusion					
Ordinarily purity powder	Hot extrusion	…	655–690	345–518	8–13
Ordinarily purity ingot	Hot extrusion	…	628–655	345518	8–13
Forgings	…	…	483–600	435–600	0–4.5
Ordinarily purity					

[a] *Elongation in 50 mm.*
[b] *Structural grade contains about 1.8%BeO.*
L, *longitudinal;* T, *transverse.*
Source: Floyd DR, Lowe JN. Beryllium science and technology, vol. 2. New York: Plenum Press; 1979.

machine chip is easily recycled by introducing it into the production stream. For protection from contamination, beryllium is dry machined when economically practical. Over the last few decades, machining practices have evolved with new tool coatings, computer-aided design, and more numerical control (CNC) machining being used to produce high-precision parts. Aluminum-beryllium alloys are also easily machined at feeds and speeds using CNC techniques approaching conventional aluminum machining procedures and almost using a water-based coolant. Typical speeds for aluminum-beryllium alloys are 91 to 300 surface m/min using feed rates of 0.08 to 0.10 mm/rev. Beryllium is machined at speeds of 60 to 215 surface m/min using similar feed rates.

Electrical discharge machining, or spark machining, uses a high-voltage spark to burn and melt through a conductive metal workpiece. A high-conductivity, high-strength, thin brass (copper-zinc) wire is used as the electrode when fine, detailed features are required. The electrical discharge machining process machines beryllium with significantly less microstructural strain compared with conventional chip machining methods at an acceptable production rate using CNC technology. Cutting rates range from 5 to 0.25 mm/min.

Applications of Beryllium

Nuclear and X-Ray Applications

Beryllium is used as a reflector material, in research and fast reactors, as well as in power reactors, for moderators, reflectors and fuel cladding material. S-65 beryllium structural grade (Table 24.20) is a premium material lower in oxide and other elements, which is important characteristic in nuclear applications, including neutron multipliers and reflectors.

Exclusive combination of properties of beryllium greatly improves the control of nuclear fusion energy reactors such as the Joint European Torus (JET). The excellent oxygen gathering performance of beryllium with its low atomic number eliminates plasma density disruption, increases the time scale of magnetohydrodynamic effects and reduces runaway photoneutron production.

Because of excellent transparency to soft X-rays and other radiation such as gamma rays, beryllium is used in X-ray tube windows. Owing to its low density, beryllium passes X-rays 17 times better than an equivalent thickness of aluminum. Most of this equipment requires disks thinner than 0.25 mm and are cut from sheet or machined from vacuum hot pressed blocks. Sheet and foil, depending on grade, are produced to a thickness ranging from 8 μm to 6.3 mm. Larger plate thickness is also produced. Mechanical properties of grades PF-60, SR-200, PS-200 grades [91] within the plane of the sheet are typically higher than those for the input material due to crystallographic orientation that occurs during the metalworking operation.

In medical radiation detection devices such as axial tomographic scanners and other related equipment with pressurized detection chambers, the transparency of beryllium to X-rays and its stiffness are combined. A stiff beryllium window resists the internal gas pressure with minimum deflection.

Optical Beryllium Grades

Optical beryllium grades are used in applications that require highly isotropic properties, including three-dimensional thermal expansion. Mirrors and optics subject to thermal cycling must maintain their condition. Two optical grades are I-220-H, made of high-purity impact-ground beryllium, and O-30, made from inert gas atomized powder [92]. Both materials can be used in the as-polished condition, or they can be coated before polishing.

Aerospace Applications

The unique combination of low density, high modulus of elasticity and dimensional stability of beryllium makes it an ideal choice for structural parts in aerospace components. In particular, a beryllium structure as well as beryllium optical system was applied in the Hughes MODIS satellite; a beryllium thrust tube assembly was used in the Japanese CS-2 satellite.

The development of higher ductility grades of beryllium in various wrought forms, including sheet metal, has increased the potential application of beryllium in the aerospace sphere.

High Temperature Conditions

Beryllium has the highest specific heat among all the structural materials, good thermal conductivity, relatively high melting point and resistance to oxidation up to about 970 K. It is a highly efficient heat sink, heat shield and airplane and automobile brake material. Beryllium is also used for making thrust chambers and nozzles of rocket engines.

Apparatus Applications

Beryllium is used in components in inertial guidance systems. It is used in precision navigational aids for aircraft, spaceship, missiles, ships and submarines. The high modulus, high precision elastic limit and dimensional stability under high g-forces make beryllium the elect material for these conditions. The material I-220-H [92] is used in such applications.

Beryllium Alloys

AlBeMet and Aluminum-Beryllium-Lithium Alloys. An alloy of 68 wt% beryllium with aluminum is known under the commercial alloy name AIBeMet 162. The physical properties and mechanical properties of the three commercial available forms (extrusions, sheet and hot isostatic pressed block) are presented in Table 24.23.

In comparison with unalloyed beryllium, fabrication such as welding and joining of AIBeMet can be easier. This makes AIBeMet an alternative when the properties of beryllium are well in excess of required values. The properties of AIBeMet make it a candidate for many applications in which aluminum or titanium could also be used. In commercial products, AIBeMet served as the voice coil actuator in high-performance hard disk drives in the early 1990s due to its light weight and high stiffness. Along with this, the brake calipers of Formula I automobiles had been made from AIBeMet and used by many racing teams. The solid solubility limit of beryllium in aluminum is low (0.3 at%). This alloying limit can be extended by rapid solidification PM technology. Lewis et al. at Lockheed Corporation have examined Al-Be-Li alloys by RS-PM and have attained values of specific modulus that are significantly higher than those attained in conventional aluminum alloys [93]. They used melt spinning to examine Al-Be-Li and Al-Be alloys designed to be age hardenable and to have ultralow density. Al-20.5Be-2.4Li and Al-29.6Be-1.3Li alloys illustrated the best properties.

TABLE 24.23 Properties of AlBeMet 162 and Aluminum-Beryllium-Lithium Alloys

Property	Unit	Alloy		
		AlBeMet 162	Al-20.5Be-2.4Li	Al-29.6Be-1.3Li
Nominal chemical composition:				
Beryllium	wt%	68.0	20.5	29.6
Lithium	wt%	…	2.4	1.3
Aluminum	wt%	Balance	Balance	Balance
Physical properties:				
Density	g/cm^3	2.01	2.298	…
Elastic modulus at 298 K	GPa	200	123	142
Elastic modulus at 473 K	GPa	195	…	…
Linear coefficient of thermal expansion at 298 to 373 K	μm/(m·K)	16.35	…	…
Thermal conductivity at 298 K	W/(m·K)	212	…	…
Specific heat	kJ/(g·K)	1.5	…	…
Electrical resistivity	μΩ·cm	3.43	…	…
Solidus temperature	K	917	…	…
Mechanical properties:				
Ultimate tensile strength:				
As-quenched	MPa	…	451	…
Under-aged	MPa	…	…	494
Peak aged	MPa	…	531	536
AMS 7911, HIPed block	MPa	262	…	…
AMS 7913, sheet	MPa	386	…	…
AMS 7912, extrusion (longitudinal)	MPa	358	…	…
Yield strength				
As-quenched	MPa	…	321	…
Under-aged	MPa	…	…	434
Peak aged	MPa	…	483	497
AMS 7911, HIPed block	MPa	193	…	…
AMS 7913, sheet	MPa	276	…	…
AMS 7912, extrusion (longitudinal)	MPa	276	…	…
Elongation				
As-quenched	%	…	6.4	…
Under-aged	%	…	…	5.0
Peak aged	%	…	3.3	2.6
AMS 7911, HIPed block	%	2	…	…
AMS 7913, sheet	%	5	…	…
AMS 7912, extrusion (longitudinal)	%	7	…	…

Sources: Aluminum and aluminum alloys. In: Davis JR, editor. ASM speciality handbook. ASM International Publishers; 1990, and Marder JM, Wellman B. Powder metallurgy beryllium. In: ASM handbook, vol.7, powder metallurgy ASM International Publishers; 1998. p. 941–6.

E-Material Metal-Matrix Composite. E-materials are metal-matrix composites made by consolidating a mixture of beryllium and beryllium oxide. They are used in applications where thermal management, controlled coefficient of thermal expansion, and high modulus are critical. E-materials are used in printed wiring boards, electronic modules, and high-performance avionic surface-mounted devices.

Workplace Atmosphere Safety

Inspirable dust of beryllium and its compounds are both carcinogens and able to cause allergic illnesses. European workplace exposure limits (WELs) of beryllium and beryllium compounds (as Be) are 0.002 mg/m^3 over an 8-h time-weighted average (TWA) reference period [94]. The OSHA (Occupational Safety and Health Administration) legal airborne beryllium permissible exposure limit (PEL) is 0.002 mg/m^3 averaged over an 8-h workshift; 0.005 mg/m^3 as a ceiling limit not to be exceed during any 15-min work period [95]. According to State Standard 12.1.005-88 under the legislation in the Commonwealth of Independents States (CIS) [15], the occupational stated average limit value (ALV) of the beryllium and its compounds in the workplace atmosphere, as the shift TWA concentration is 0.001 mg/m^3. There are classed with the extremely dangerous powders, the first class of danger class according to the above State Standard.

Because of the high toxicity of beryllium and its compounds, a complex of industrial safety measures at the beryllium manufacturers is provided. The processes are especially dangerous where beryllium and its compound powders are used and processed, solutions are filtered, evaporated and decanted, molten and volatile compounds are sublimated. These industrial safety measures include maximum encapsulation of all units and interoperational transport, maximum mechanization and automation of the processes, remote control units, conducting of manual operations by means of manipulators in airproof boxes. In vented chambers, where equipment is located, an under pressure is maintained, in order to prevent an escape of beryllium suspended solid. The beryllium containing suction gases are subjected to high-performance cleaning. Beryllium trace concentrations are continuously controlled in workplace atmospheres and in factory ambient air.

The combustibility of metallic beryllium is characterized by the following data. Solid beryllium is noncombustible. Self-ignition temperatures of beryllium powders in air range from 810 to 970 K, in water vapor from 620 to 720 K, in carbon dioxide at 840 K and in nitrogen above 1570 K. In humid gases, self-ignition temperatures for all cases are lower, than in dry ones. A suspended solid with particles coarser than 100 μm in air is explosion-proof. The burning temperature of beryllium amounts to 2273 K. The diffusion burning rate front on the powder surface amounts to 0.64 mm/s.

The products with such characteristics of inflammability and explosion risk are placed in the "moderate explosion hazard" class of danger according to the Guide to Legislation and "Health and Safety" in the European PM Industry [18].

To extinguish burning beryllium it is necessary to use calcium fluoride powder (with consumption about 150 kg per 1 m^2) or dry sand. For luminal quenching method, argon is used in concentration 35 vol% min in burning zone. Fire-fighting water foam, carbon dioxide and fire-extinguishing refrigerants must not be used [17].

As regards permissible beryllium concentration in potable water, the harmfulness limiting sign of beryllium threshold limit values (TLV) in potable water is sanitary-toxicological effect. Beryllium is, therefore, classed as an extremely dangerous substance, in the first class of danger according to the State Standard 4630-88 [16]. Its TLV is 0.0002 mg/L (subject to summation of all form contents).

SCANDIUM

Physical Properties

The atomic number of scandium is 21. Among the light metals, scandium is unique in its combination of low density with high melting point. Typical physical properties of scandium are given in Table 24.24.

Compact scandium is a silvery-white metal. It reacts with oxygen, halogens, sulfur and carbon. The surface film formed in air prevents further oxidation. With nitrogen, scandium reacts at temperatures above 770 K with nitride, ScN, formation. Scandium is easily dissolved in mineral acids, except for chromic and hydrofluoric acids and it reacts slowly with concentrated sodium hydroxide. The ion radius Sc^{3+} (0.083 nm [1]) is less than Y^{3+} (0.097 nm) and triple-charged RE ions (0.088–0.103 nm). Therefore, in scandium compacts the tendency to hydrolysis is greater than in similar rare earth compounds.

With metals of I, II, VII, VIII, and VI by-subgroups and II, III, IV, and V main subgroups of the periodic table, scandium forms intermetallic compounds ScMe, Sc_2Me, $ScMe_2$, and $ScMe_3$, and other types. The elements of III, IV, V and VI by-subgroups form eutectics with scandium.

TABLE 24.24 Typical Properties of Scandium

Property	Unit	Value
Molecular weight	g/mol	44.9559
Density	g/cm^3	2.989
Crystal type[a]: α-Sc (till 1610 K) lattice parameters β-Sc (above 1610 K)	nm	c-p H $a=0.33083$ $c=0.52680$ bcc
Atomic diameter	nm	0.328
Brinell hardness	MPa	390
Melting point	K	1814
Boiling point	K	3109
Specific heat		
at 298 K	J/(mol·K)	25.52
at 1773 K	J/(mol·K)	39.80
Heat of fusion	kJ/mol	14.1
Heat of vaporization	kJ/mol	377.8
Thermal conductivity at 373 K	W/(m·K)	15.7
Coefficient of linear thermal expansion at in the temperature ranges from 293 to 1373 K	μm/(m·K)	10.2
Specific electrical resistance at 298 K (polycrystalline specimen)	μΩ·m	410

[a] *Crystal type:* c-p H, *close-packed hexagonal;* bcc, *body-centered cubic.*

Sources: Refs Zelikman AN, Korshunov BG. Metallurgy of rare metals. Moscow: Metallurgiya Publisher; 1991 [in Russian] and Alexandsandrovsky SV, Siziakov VM, Kucenko DV, Ratner AH. Metallothermic obtaining methods of heightened purity scandium and its alloys. Moscow: Ore and Metals Publishers: 2004 [in Russian].

Scandium forms compounds with oxidation level of element+3. Others element oxidation levels are not characteristic for scandium.

Sources of Raw Material

Scandium is a typical trace element of rocks. Its content in the earth's crust is about 6×10^{-3} wt%. Scandium does not form its own deposits. Scandium minerals, thortveitite ($Sc_2[Si_2O_7]$) and sterrettite ($ScPO_4 \cdot 2H_2O$), are very uncommon and have no commercial significance. Minerals, in which scandium is present in the form of isomorphous admixtures with concentration of Sc_2O_3 ranging from 0.005% to 0.3%, are more extensive.

Scandium mineral raw materials are concentrated in Australia, China, Kazakhstan, Norway, Russia, Ukraine, the United States and Madagascar. In Australia, scandium mineral reserves are contained in nickel and cobalt ore deposits, in Kazakhstan in uranous deposits, in Madagascar and Norway in pegmatite rocks. In Ukraine, scandium is contained in iron ores. In China, scandium mineral reserves are contained in tin, tungsten and iron ore deposits.

Because scandium is a trace element, currently it is usually obtained by means of extraction from waste and middling of metallurgical production, uranium-containing phosphorites, hydrolytic sulfuric acid, scandium-vanadium ores, mine waters and aluminum-scandium alloys.

Scandium content in processing products of raw material amounts to 1–10 ppm. Therefore, starting with the material, initial concentrates are obtained, which are further processed into scandium compounds. Scandium-containing materials are taken into solution by treatment with acids, sodium hydroxide or by chlorination followed by washing with water or acid. To recover scandium from solution, the following basic methods are used: precipitation of low-solubility compounds, extraction by organic solvents and ion exchange.

TABLE 24.25 Distribution of Scandium in Various Minerals

Raw Source	Raw Processing Scope (10^3 tons per year)	Sc Content (ppm)	Sc_2O_3 Year Yield (Tons Per Year)
Bauxites	71,000	1–20	710–1420
Uranic ores	50,000	1–10	50–500
Ilmenites	2000	10–20	20–40
Wolframites and cassiterites	200	100	20
Zircons	100	50–100	5–10

Sources: Alexandsandrovsky SV, Siziakov VM, Kucenko DV, Ratner AH. Metallothermic obtaining methods of heightened purity scandium and its alloys. Moscow: Ore and Metals Publishers: 2004 [in Russian] and Korshunov BG, Reznik AM, Semenov SA. Scandium. Moscow: Metalurgija Publishers; 1987 [in Russian].

At present, the largest quantity of scandium is mined together with bauxites. Methods of its extraction from the red slime of alumina production are based on direct opening by mineral acids. The distribution of scandium in various minerals is shown in Table 24.25.

Scandium Production

Currently, metallic scandium is produced mainly by metallothermic reduction of non-aqueous scandium fluoride or scandium chloride by magnesium or calcium in an inert gas atmosphere:

$$2ScF_3 + 3Ca = 3CaF_2 + 2Sc$$

The starting material is pure scandium oxide. Scandium oxide grade compositions according to CIS (Commonwealth of Independents States) TU 48-4-335-86 standard are illustrated in Table 24.26.

A technological line diagram of high-purity metallic scandium production is shown in Fig. 24.30. Pure scandium oxide is heated in a current of hydrogen fluoride at 873 K. Reduction is conducted in tantalum or molybdenum crucibles.

The scandium fluoride thus produced is reduced at 1123 K, rising to 1870 K, after which scandium and the slag separate and the reduction is complete. Then, the metal is remelted under vacuum 10^{-3} Pa to eliminate the volatile residual impurities. At a temperature of 1973 K, scandium is sublimed. In order to reduce contamination by tantalum, it is recommended to add metals, which alloy with the scandium and allow reduction to be carried out at a lower temperature. As calcium does not alloy with scandium, zinc is added and, in order to lower the melting point of the slag, lithium fluoride is introduced. In this case, the scheme of reduction process may be represented as follows:

$$2ScF_3 + 3Ca + 8Zn + 12LiF = 2(Sc \cdot 4Zn) + 3(CaF_2 \cdot 4LiF)$$

The process is carried out in argon at 1373 K. After reduction, zinc and calcium admixtures are sublimed from sponge scandium in a vacuum. The initial calcium-thermic scandium is refined to high purity by one of following methods:

- vacuum fusion; duration of processing is over 10 h; metal is manufactured in the form of ingot
- vacuum distillation at temperatures above 1812 K; high purity scandium in fine crystalline form results. Aluminum sublimes first of all, iron the last, which complicates the process during refining of a high purity residuum. Contamination of scandium occurs due to interaction with the material of the container
- zone melting; produces a monocrystalline ingot with perfect structure, but productivity is low as it is necessary to repeat the process 15–20 times
- electrorefining; the refinement coefficient amounts to 100–1000 times. This process is effective for purification from RE, aluminum, calcium, copper, iron, magnesium, silicon and radioactive elements.

The metallothermic scandium is a silvery-white powder with a golden tint. The minimum scandium contents for ScM-1, ScM-2 and ScM-3 grades are 99.85%, 99.74% and 99.65%, respectively, according to CIS TU 48-4-483-87 standard (Table 24.26). The scandium purity reaches 99.998% and higher by calcium-thermic process with a highly effective distillation technique.

TABLE 24.26 Chemical Composition of Scandium Oxide and Metallothermic Metallic Scandium Grades

		Grades					High Refined Scandium	
		Scandium Oxide[a]		Metallic Scandium[b]				
Elements	**Unit**	**OS-99.9**	**OS-99.0**	**ScM-1**	**ScM-2**	**ScM-3**	**D**[c]	**E**[d]
Scandium oxide	wt% min	99.9	99.0	…	…	…	…	…
Scandium	wt% min	…	…	99.85	99.74	99.65	99.998	99.996
Impurities:								
Aluminum	ppm max	30	100	100	100	100	9.00	0.7
Calcium	ppm max	100	500	300	200	200	0.08	3.0
Chromium	ppm	…	…	…	…	…	0.3	1.0
Cobalt	ppm max	…	…	…	…	…	0.10	1.0
Copper	ppm max	50	100	100	100	100	0.10	1.0
Iron	ppm max	50	500	300	600	1000	4.00	2.0
Magnesium	ppm max	30	100	100	200	200	0.01	2.0
Manganese	ppm max	30	100	…	…	…	0.20	1.0
Nickel	ppm max			…	…	…	0.01	1.00
Phosphorous	ppm max	100	200	…	…	…	…	…
Potassium	ppm max	…	…	…	…	…	0.05	0.5
Silicon	ppm max	100	500	200	500	600	0.1	3.0
Titanium	ppm max	50	500	100	200	200	0.4	1.00
Vanadium	ppm max	…	…	…	…	…	0.05	2.00
Ytterbium	ppm max	50	500	100	100	100	…	…
Yttrium	ppm max	50	500	100	100	100	…	…
Zirconium	ppm max	50	1000	100	100	100	…	…
Impurities total	wt% max	0.1	1.0	…	…	…	…	…

[a] *CIS TU 48-4-335-86 Standard.*
[b] *CIS TU 48-4-483-87 Standard.*
[c] *D, Calcium-thermic scandium produced by distillation refining technique at "Giredmet" pilot plant (Moscow).*
[d] *E, Calcium-thermic scandium obtained by electrorefining in halogenide melts.*

Applications

One of the major scandium application areas is the development of high strength aluminum alloys. Scandium influences the alloy structure, promotes formation of a subgrain structure and prevents the recrystallization due to the following features:

- Scandium interacts with aluminum under the eutectic type phase diagram with variable solubility. It is inclined to form supersaturated solid solutions in non-equilibrium conditions even at low solidification rate.
- Crystalline lattice of intermetallic Al_3Sc, formed by interaction of scandium with aluminum, almost coincides with structural lattice of aluminum under dimensionally structural parameters. This property is the basis of its strongest influence on the properties of alloys.

Due to these features, a small scandium addition (0.15–0.25 wt%) produces aluminum alloys and welds with non-dendritic structure and, as a result, improved performance.

Maximum scandium solubility in solid aluminum amounts to approximately 0.24 wt% [96], while even at solidification rates above 373 K per second, scandium levels up to 0.6 wt% are retained in Al solid solution [97]. According to [98], at

FIG. 24.30 Technological line diagram of the production process for high-purity metallic scandium.

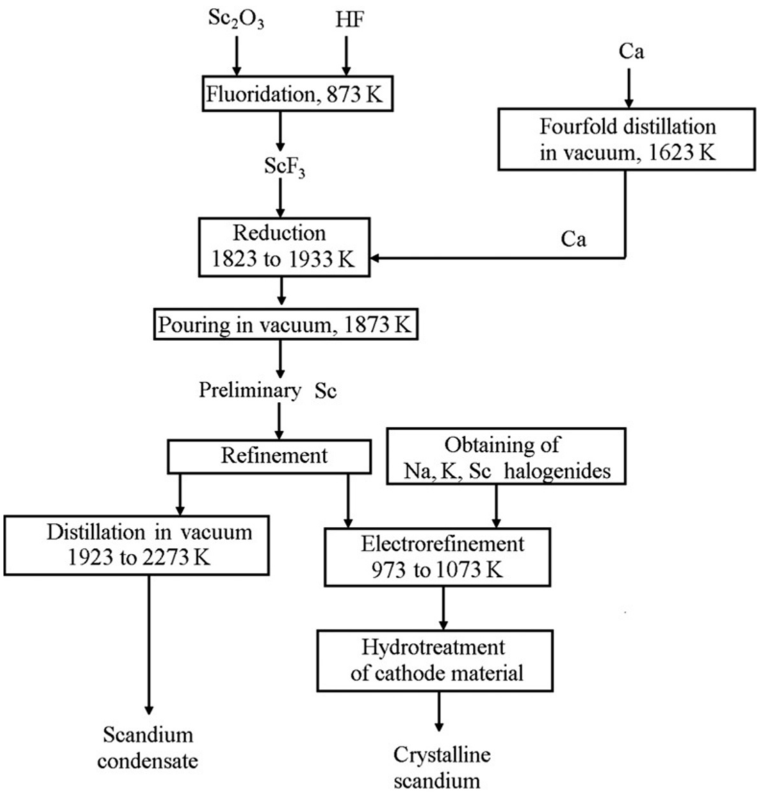
Sc_2O_3
HF
Fluoridation, 873 K
ScF_3
Ca
Fourfold distillation in vacuum, 1623 K
Reduction 1823 to 1933 K
Ca
Pouring in vacuum, 1873 K
Preliminary Sc
Refinement
Obtaining of Na, K, Sc halogenides
Distillation in vacuum 1923 to 2273 K
Electrorefinement 973 to 1073 K
Hydrotreatment of cathode material
Scandium condensate
Crystalline scandium

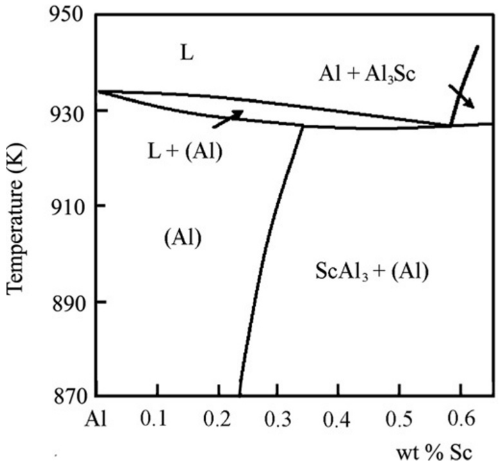

FIG. 24.31 Al-Sc system phase diagram at the aluminum rich end.

573 K per second, scandium levels up to 1 wt% are preserved in Al, Al-Mg, Al-Mg-Ag and Al-Zn-Mg alloys. In accordance with reference [97] at a cooling rate of 10^7 K/s, scandium concentration in solid solution can be retained at 5.0 wt%.

According to aluminum-scandium phase diagram (Fig. 24.31), the eutectic reaction $L \leftrightarrow \alpha\text{-Al} + Al_3Sc$ is observed at Al-0.55 wt% Sc alloy [99]. In this case, after solidification and aging, the alloy contains α-Al and dispersed precipitate of AI_3Sc. With scandium concentrations above 0.55 wt%, primary precipitation of AI_3Sc occurs and this leads to a decrease of grain size in the solid. However, this concentration is decreased by the presence of other alloying elements (in particular titanium, zirconium and hafnium) [100].

Aluminum alloys alloyed with scandium are usually classified [96] into four groups:

- Thermally non-strengthened weldable Al-Mg base alloys,
- Thermally strengthened high-strength weldable Al-Zn-Mg base alloys,

- Thermally strengthened ordinary and high-strength weldable Al-Li base alloys, and
- Thermally strengthened high-strength Al-Zn-Mg-Cu base alloys.

Alloys based on the Al-Zn-Mg system have a favorable combination of mechanical properties and corrosion resistance and technological effectiveness (good weldability, plastic deformability and ability to self-quench). However, they yield to Al-Zn-Mg-Cu base alloys as regards tensile strength. Thus, the cast alloys 7178 (US specification) and its analogue B96 (Russian specification) have ultimate tensile strength (in T6 condition) at room temperature of 605 and 660 MPa, respectively, while the ultimate tensile strength of advanced ternary alloys, as an example, 7039 amounts only to 450 MPa [56].

Further increase of properties of Al-Zn-Mg alloys is impossible by traditional ingot technology, because increasing the main alloying elements (Zn + Mg) content reduces corrosion resistance and the addition of refractory transition metals is usually limited by their low solubility in solid alloys at low cooling rates.

Powder metallurgy opens the possibilities for additional alloying of aluminum alloys by crystallization with high cooling rates.

Rapidly solidified Al-Zn-Mg alloys (with total Zn + Mg content of 8–10 wt%) have been produced by high pressure water atomization of the melt, providing cooling rates up to 10^6 K/s. Advanced technology of aluminum and aluminum alloy powders is described in Chapter 16. The alloys were doped with scandium, zirconium and other transition metals. After hot degassing in a vacuum of porous green powder briquettes, they are direct hot extruded to the rods and sheets. Under another consolidation scheme, the degasified porous green powder briquettes were hot pulse pressed in vacuum at a pressure 1.0 GPa. Then, these compacts are extruded as in the former scheme. Both scheme products are subsequently subjected to thermal treatment [101].

Typical water-atomized powder particles of ternary Al-Zn-Mg base alloy are shown in Fig. 24.32, including their morphology (a) and surface microstructure of the individual particle (b). The size of individual particle grains ranges from 0.5 to 2.0 μm, with an average 1.0 μm (Fig. 24.32B), which corresponds to a cooling rate of the melt of 10^6 K/s [102]. The compositions of PM Al-Zn-Mg base alloys are given in Table 24.27. For comparison, similar cast alloys were also made in parallel. For the PM alloys, minus 100 μm powder was selected. Samples of PM and cast alloys were subjected to similar thermomechanical treatment.

Rapid solidification of the melt ensures a fine, non-dendritic structure without participation of scandium in contrast to slow solidification processes, where scandium plays the main role in grain and non-dendritic structure formation. A dislocation cellular structure, with a cell size of about 1 μm, was evident in all PM alloy rods after T6 treatment (Fig. 24.33). A polygonal cell structure was observed in all PM alloys. The dislocation density is increased in the cell walls. A disorientation of the cells is observed, which facilitates improvement of mechanical properties.

Two types of the secondary dispersoids in Al-Zn-Mg base extruded rods, $Al_3(Sc_{1-x}Zr_x)$ and $MgZn_2$, are seen in transmission electron microscopy images (Fig. 24.34). Comparison of the contributions of both phases to alloy strengthening is possible, based on the present concept of precipitation strengthening in Al-Zn-Mg alloys [103, 104]. Essentially, there are two different types of dislocation movement in particle strengthened crystals (Fig. 24.35), the cutting in Guinier-Preston zones by small sized second phase particles and the Orowan mechanism by precipitated particle sizes increasing amounts to d_{cr}, where dislocations bypass the generally incoherent and unshearable particles to form a ring-shaped dislocation loop (Orowan loop). However, according to both theories, the strengthening by particles depends on their volume fractions.

Thus, the strengthening contribution of $Al_3(Sc_{1-x}Zr_x)$ is significantly smaller than that of $MgZn_2$, because of its appreciably reduced volume fraction and increased size, while an additional strengthening effect is connected with $Al_3(Sc_{1-x}Zr_x)$

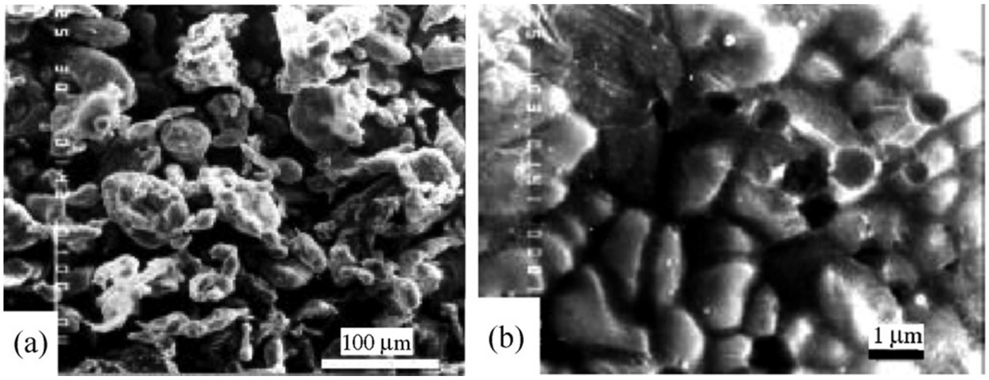

FIG. 24.32 Typical scanning electron micrographs of the particles (A) and surface microstructure of a separate particle (B).

TABLE 24.27 Typical Tensile Properties of Al-Zn-Mg Extruded Rods

		Alloy						
Property	**Unit**	**3P**[a]	**3C**	**5P**	**5C**	**7P**	**23P**	**24P**
Nominal chemical composition								
Aluminum	wt%	Balance	Balance	Balance	Balance	Balance	Balance	Balance
Zinc	wt%	5.0	5.0	5.0	5.0	5.8	5.5	5.5
Magnesium	wt%	3.0	3.0	3.0	3.0	4.0	3.0	3.0
Scandium	wt%	0.3	0.3	0.3	0.3	0.3	…	0.3
Zirconium	wt%	0.5	0.5	0.85	0.85	0.3	0.8	0.3
Cobalt	wt%	…	…	…	…	…	…	…
Copper	wt%	…	…	…	…	0.6	0.6	0.6
Chromium	wt%	…	…	0.22	0.22	…	0.3	…
Manganese	wt%	0.5	0.5	…	…	0.5	0.5	0.5
Nickel	wt%	…	…	0.17	0.17	…	0.15	…
Titanium	wt%	…	…	0.22	0.22	…	0.15	…
Tensile properties[b]								
Hardness	MPa	1860	1710	1770	1400	1980	…	…
Ultimate tensile strength	MPa	651	590	618	427	719	655	700
Yield strength	MPa	596	531	553	356	652	614	656
Elongation	%	7.7	10.3	8.1	15.5	9.4	8.8	7.1

[a] *The PM and cast alloys are denoted by the letters "P" and "C," accordingly.*

[b] *Samples of PM and cast alloys were subjected to similar thermomechanical treatments. They were hot extruded in the air at 673 K, with the rate of die travel in ranges 0.3 to 1.2 mm/s and extrusion ratio about 17 to 1 (ratio of sample initial cross section to final one); rods of 6 mm diameter are tensile tested in condition T6.*

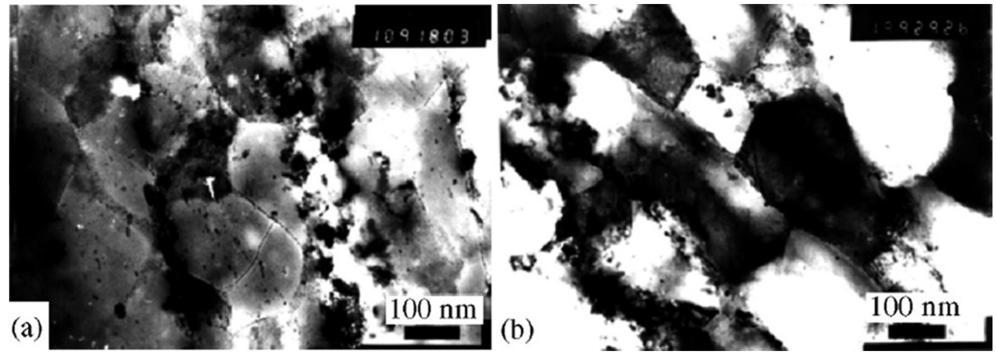

FIG. 24.33 Transmission electron micrographs of PM rods in T6 condition in the longitudinal section: (A) Al-5Zn-3Mg-0.7Zr-0.3Sc-0.5Mn alloy and (B) Al-5.5Zn-3Mg-0.3Zr-0.3Sc-0.5Mn-0.6Cu alloy.

or Al_3Zr. These particles precipitate within the grains from the supersaturated solid solution during heating prior to quenching. The particle dimensions do not exceed 4–5 nm and increase only on lattice defects. The main role of $Al_3(Sc_{1-x}Zr_x)$ and other intermetallics is in preventing recrystallization and the preservation of the cellular structure.

The maximum strength and the strong age-hardening of Al-Zn-Mg alloys are considered to be associated with precipitation of the metastable η'-phase. Its hexagonal structure, similar to the equilibrium η-phase, is plausible with the following precipitation sequence for alloys of relatively high Zn to Mg ratio: solid solution → GP zones → η'-phase → η-phase. The equilibrium phase is the binary intermetallic of composition $MgZn_2$, while η' is the corresponding metastable phase.

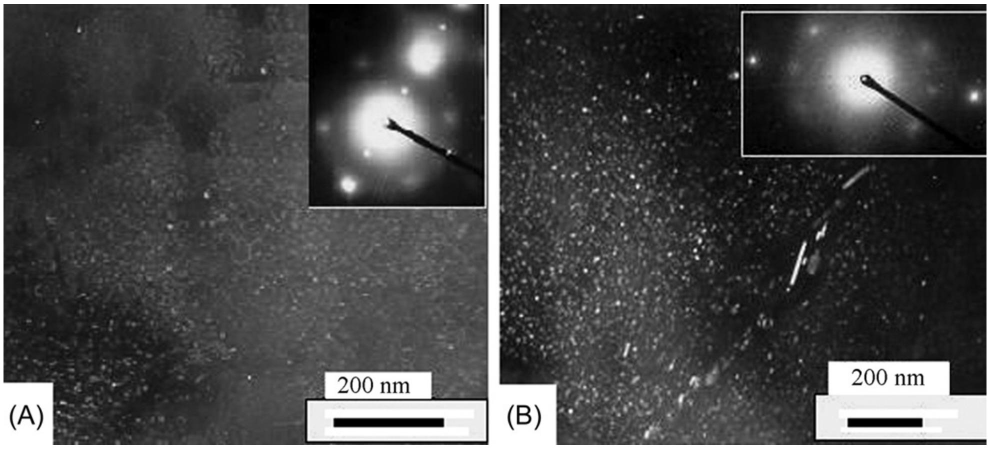

FIG. 24.34 Secondary dispersoids in the PM rod longitudinal section of ternary Al-Zn-Mg base alloy doped with scandium and zirconium: (A) dark-field images in reflection (001) of the phase $Al_3(Sc_{1-x}\ Zr_x)$; (B) dark-field images in reflection (201) of the phase $MgZn_2$.

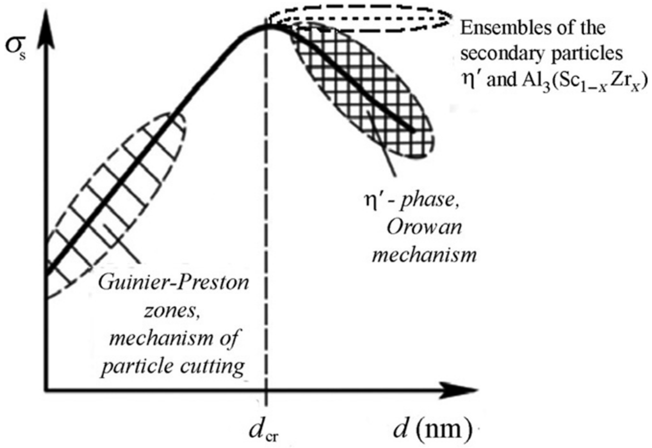

FIG. 24.35 Scheme illustrating dependence of yield strength σ_s on the average size of second phase particles in Al-Zn-Mg alloys doped with scandium and zinc.

As was found experimentally, a simultaneous increase of the strength and plasticity can be achieved for wrought semi-finished products alloyed with Sc in combination with other TM and RE metals after T6 treatment. A principal explanation of this effect was found [104, 105] by analyzing the dependence of yield strength as a function of particle size (see Fig. 24.35). Sc increases the size of η'-particles. In this case, the size of η'-particles, $2r$, can exceed the critical size d_{cr}, which leads to a transition from the mechanism of cutting the particles by dislocations to the mechanism of detour according to the Orowan model. Under such a transition, the plasticity of an alloy increases. At the same time, the strength can decrease. However, by alloying with Sc, a second ensemble of dispersed particles of $Al_3(Sc_{1-x}Zr_x)$ is formed that eliminates the loss of strength. Thus, the alloying with Sc can, in principle, lead to the simultaneous increase in strength and plasticity.

Ultimate tensile strength (UTS), yield stress (YS), elongation (EL) and Vickers hardness (HV) of PM and cast alloy rod specimens of Al-Zn-Mg alloys in T6 condition at room temperature are summarized in Table 24.27. Tensile strength comparison with cast alloys shows that PM alloys based on WA-N powder technology have considerably higher strength characteristics. These products are characterized by excellent weldability. The welding seam has fine crystallized equiaxial microstructure without columnar crystallites, while no recrystallization took place in a heat-affected zone. Tensile strength ratio of sheet to weld ranges from 0.85 to 0.89.

The features of scandium effect on ternary Al-Zn-Mg base alloys as discussed above are similar for thermally strengthened high-strength Al-Zn-Mg-Cu base alloys and also depend on the melt solidification rate.

The Al-Mg system represents the most popular non-heat treatment, strong, weldable alloys with high corrosion resistance. In the Al-Mg-Sc system, solid-solution hardening by Mg is combined with precipitation hardening by intermetallic Al_3Sc particles [104].

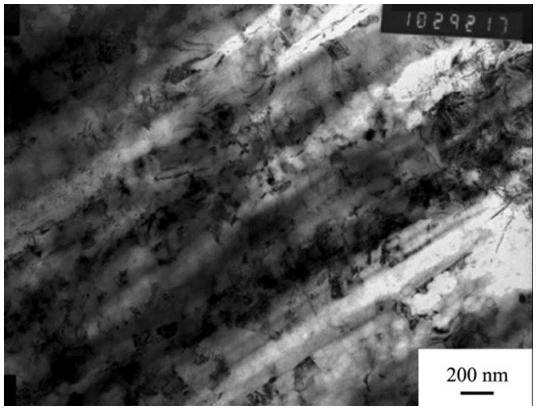

FIG. 24.36 TEM microstructure of extruded Al-4Mg-0.7Sc-0.3Zr alloy in longitudinal section of a 7-mm rod.

The Al-Mg-Sc system alloys using PM technology based on water atomized powders are developed [106, 107]. Fusion in an induction furnace was superheated in the range 150–200 K (above of melting point). Metal fusion was water atomized under pressure 15 MPa with pH of 3.5–4.0, by the control of suspension temperature, which should not exceed 298 K. The atomized powders classified into three size fractions, namely 0–20, 0–40 and 40–63 μm. Fraction of 0–20 μm was separated from batches of powders by means of hydroclassification. The remainder fractions after drying are separated by sieving method. The technology used for powder consolidation consists of two main stages, degassing of cold pressed green compacts and their hot extrusion. The paper [106] analyses mechanical behavior and microstructure of some Al-Mg base alloys. The oxide films on the WA powder surface are comminuted during extrusion into ultrafine particles that are disposed, as TEM local X-ray spectrometry analysis showed, along the boundaries of fibers and cells (Fig. 24.36). The presence of nanoparticles of intermetallides in the structure hinders growth and confluence of fibers and cells that prevents the recrystallization.

The developed Al-5Mg system alloys alloyed by scandium and zirconium showed the highest level strength. The highest ultimate tensile strength of the developed alloys is on a level up to 524–562 MPa at sufficient plasticity. The composition and mechanical properties of PM Al-Mg-Sc system alloys are more in detail described in Chapter 16.

However, there is no known big commercial use of scandium, and the global yearly demand for the metal is relatively very small, around 20 tons. The reason for this is usually found in scandium's low concentration and its difficulty in separating it from the ore, pushing costs to elevated levels (around US $7000/kg of concentrate [108]), thereby hampering its commercial use. Inherently, in spite of a growing interest from the automotive industry, among others, the price of Al-Sc master alloys is still too high for most commercial applications.

The development of efficient technologies of scandium recovery from red mud is one of the major direction in decreasing the scandium cost. Therefore, developed by US RUSAL technological process, based on carbonization leaching of scandium, is a promising work [109, 110]. Alumina production by Bayer process [111] involves formation of considerable red mud yield (1.5–3.0 tons of red mud per 1 ton of alumina). The advantage of those sources along with huge yield is high content of scandium and other rare earth metals up to 120 g/t and 1500 g/t, respectively. Annual producing of two RUSAL refineries in Russia is more than 2 million tons of red mud with scandium content 240 g/t [109].

The study of scandium recovery from red mud with incidental partial sodium bicarbonate (caustic) removal was carried out using red mud slurry produced after processing of Timan bauxite deposit at Ural refinery (Russia). Chemical composition of slurry solid phase was following (wt%): 10.0SiO_2, 12.0Al_2O_3, 46.0Fe_2O_3, 4.5TiO_2, 8.0CaO, Na_2O; (90.0 g/t)Sc, (650 g/t)Zr. The block flow diagram of the pilot unit for scandium concentrate production from red mud is presented in Fig. 24.37 and includes the carbonization leaching and two hydrolytic precipitation stages of scandium concentrate with removal of main impurities (Fe, Ti, Zr). Scandium carbonization leaching is intensified by the gassing of slurry by carbon dioxide under pressure.

The authors [109] reported that the increasing of carbon dioxide pressure from 0.1 to 0.6 MPa results in considerably augment the scandium recovery from 17.0% to 25.8%. It was also noted that pressure scandium leaching tends to the partial sodium bicarbonate removal from red mud with its recycling to the process.

Another route of decreasing the scandium cost is the scale production mining of the deposits with elevated scandium content. Newly, thortveitite deposits were discovered in Australia, in the South-eastern state of New South Wales (NSW) and North-eastern state of Queensland, which possess a significant quantity of scandium oxide (around 30%–40%).

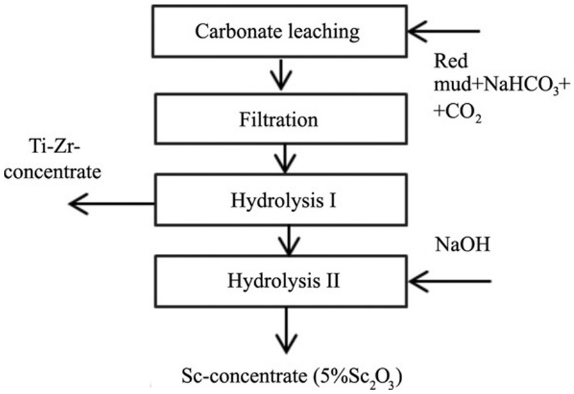

FIG. 24.37 Block process diagram of the pilot unit for production the scandium concentrate from red mud.

According the prognoses [108], the work started on three new mines will be able to produce together 112 tons every year of scandium oxide.

Australia's mining projects are advancing fast and soon will be able to produce first quantities of scandium. The Nyngan project in NSW will be able to produce 80,000 tons of high-grade scandium ore and 95,000 tons of low-grade ore per year, which translates to around 40 tons of scandium oxide annually—the primary form of refined scandium. The second project in NSW, the Syerston project, has an estimated life of 20 years, and aims to produce 78,000 tons of thortveitite ore per year, enough to extract about 42 tons of scandium oxide per year. Finally, the third NSW mine, which has only recently started, is called Owendale. It will produce around 30 tons/year of scandium oxide for over a 70 years period.

RADIOACTIVE METALS: THORIUM AND URANIUM

Physical and Chemical Properties

Thorium is a soft silvery-white metal when freshly cut. Two crystalline forms exist: α-thorium with face centered cubic lattice is stable up to 1670 K and above 1670 K β-thorium has body centered cubic lattice.

Uranium is a plastic gray steel-blue metal. Three uranium crystal modifications are known: α-uranium is in the orthorhombic system, which is stable up to 835 K, β-uranium with tetragonal lattice is stable in the range from 835 to 1042 K, γ-uranium with face-centered cubic lattice is stable at temperatures above 1042 K. Typical physical properties of thorium and uranium are given in Table 24.28.

In air at room temperature thorium as well as uranium are slowly oxidized, giving a black oxide film, which retards the corrosion but does not prevent it. Uranium at temperatures above 423 K and thorium above 673 K are rapidly oxidized.

In the thorium-oxygen system only one oxide, thorium dioxide (ThO_2) exists. Its melting point is 3669 K, and it possesses a high chemical stability. In the uranium-oxygen system there are six known oxides, UO_2, U_2O_8, and UO_3 being the most important. Oxygen solubility in thorium and uranium is insignificant. Thorium and uranium actively react with hydrogen to form hydrides (ThH_2, $ThH_{3.75}$, and UH_3).

Both metals react with nitrogen at 870–1070 K, forming nitrides. Uranium nitrides are not readily soluble in acids and are inactive to alkali solutions. Thorium nitrides are decomposed by water with the emission of ammonia. Uranium and thorium form carbides with carbon, which are decomposed by water producing hydrocarbons.

With fluorine, uranium and thorium react in the cold, while with other halogens on heating. The most important uranium fluoride is the hexafluoride, UF_6, which is used in the separation of the isotopes, while the tetrafluoride, UF_4, is the starting material for the production of uranium metal.

Both metals slowly corrode in water up to 273 K, while in steam above 473 K, uranium and thorium strongly oxidize, forming UO_2 and ThO_2. At room temperature, thorium slowly dissolves in nitric, sulfuric and hydrofluoric acids, but is readily soluble in hydrochloric acid. Alkali solutions react slowly with thorium.

Hydrofluoric acid reacts slowly with uranium. At room temperature, the metal does not react with dilute sulfuric acid and, on heating, the corrosion rate is the same as in water. Hydrochloric acid rapidly dissolves uranium; in nitric acid the dissolution rate is moderate.

TABLE 24.28 Typical Properties of Thorium and Uranium

		Value	
Property	**Unit**	**Thorium**	**Uranium**
Density at 293 K	g/cm^3	11.72	19.10
Crystal type		fcc[a]	O[b]
Atomic diameter	nm	0.360	0.312[c]
Hardness HB	MPa	530–1500[d]	2350–3850[d]
Modulus of elasticity at 298 K	GPa	79	190
Melting point	K	2023	1405
Boiling point	K	5060	4404
Specific heat	J/(kg·K)	100	117
Heat of fusion	kJ/mol	13.81	9.14
Heat of vaporization	kJ/mol	514	423
Thermal conductivity at 293 K	W/(m·K)	29.3	26.7
Thermal expansion at 298 K	μm/(m·K)	11.0	13.9
Electrical resistivity at 293 K	μΩ·m	0.13	0.30
Section capture of heat neutrons, $n \times 10^{24}$	cm^2	7.31	7.68

[a] *fcc, face-centered cubic for α-thorium crystal modification at temperatures up to 1670 K.*
[b] *O, orthorhombic for α-uranium crystal modification at temperatures up to 835 K.*
[c] *Empirical.*
[d] *Depending on annealing conditions of wrought metal.*

Sources: Zelikman AN, Korshunov BG. Metallurgy of rare metals. Moscow: Metallurgiya Publisher; 1991 [in Russian] and German RM. Sintering theory and practice. New York: John Wiley & Sons Publishers, 1996.

Thorium Powder Production

Commercially, thorium is produced by metallothermic reduction of its compounds (thorium dioxide and halogenide) or by electrolysis of melts. To produce particularly high purity thorium (predominantly for research purposes) thermo-dissociation of thorium iodide is used.

In view of the high melting point, thorium is produced in powder or sponge form, which is then transformed into compact metal by PM method or by melting.

Reduction of Thorium Dioxide by Calcium

High purity thorium dioxide is for the most part obtained by thermal decomposition of thorium oxalate at 870–920 K. Calcium is used to reduce the oxide to metal:

$$\mathrm{ThO_2 + 2Ca = Th + 2CaO}$$

$$\Delta H^0_{1300\mathrm{K}} = -60\,\mathrm{kJ}; \Delta \mathrm{G}^0_{1300\mathrm{K}} = -24.7\,\mathrm{kJ}$$

Reaction heat is insufficient for out-of-furnace processing. Reduction is conducted in a pure argon atmosphere in an apparatus of the form shown in Fig. 24.38. The charge (a mixture of thorium dioxide with calcium chips) is fed into a steel crucible, lined with molybdenum sheet or calcium oxide.

The reduction is accomplished in an argon atmosphere at temperatures ranging from 1273 to 1373 K. After cooling, the reaction product is leached by water and dilute hydrochloric acid for the elimination of calcium and calcium oxide. For the separation of fine fractions, thorium powder is washed on a concentration table. For eliminating thorium dioxide films from the surface of particles, the powder is washed in turn by 15% nitric acid and water, and then dried under vacuum.

To produce coarse particles, calcium chloride is included in the charge. This chloride is molten at the reduction temperature and takes part of the calcium oxide into solution and this reduces the influence that the CaO has in retarding the growth of the thorium powder particles. For better use of crucible volume, the charge ($\mathrm{ThO_2 + Ca + CaCl_2}$) is preliminarily

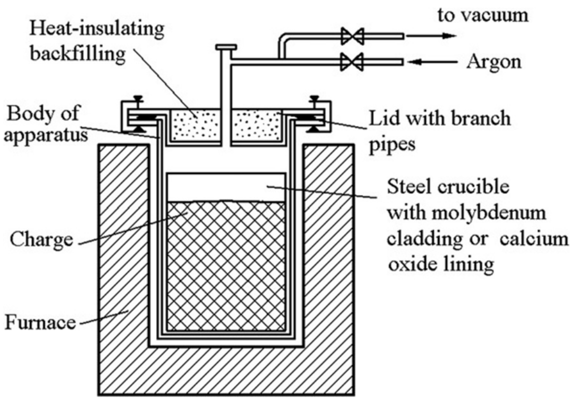
Heat-insulating backfilling
to vacuum
Argon
Body of apparatus
Lid with branch pipes
Steel crucible with molybdenum cladding or calcium oxide lining
Charge
Furnace

FIG. 24.38 Scheme of apparatus for thorium dioxide reduction by calcium.

briquetted. In this case, for complete reduction, a 25% calcium excess against its stoichiometric content is enough. The yield of thorium recovery yield in powder amounts to 90%. Its purity ranges from 99.6% to 99.8%.

Electrolysis of Melts

Thorium is electro-refined from chloride-fluoride melts containing 30%–45% $ThCI_4$ and eutectic KC1 + LiCl. The process is performed at 840–920 K, at current density 1.5 kA/m^2 and cell voltage 2.0 V. Thorium is oxidized stepwise to Th^{4+} on the anode and is reduced to metal on the cathode.

The electrolyzer is placed into a resistance furnace quartz vessel with an inside diameter of 67 mm and height of 432 mm, sealed with a rubber plug through which a molybdenum cathode, thorium anode and a tube for argon entrance are interposed. Electrolysis is complete in 6–8 h; the cathode with powder precipitate is taken out, submerged in cold water and subsequently washed in water, 10% nitric acid, distilled water, acetone, ethyl alcohol and dried. The product is in the form of coarse dendrites. Their size decreases with increase of cathode current density.

There is also known hydride process, as well as saw chips and lathe turnings means of thorium powder making [112]. In making thorium powder by the hydride process, cleaned lathe chips were used as feed material. In this method, ThH_4 is produced at between 523 and 558 K and is decomposed to the dihydride at 773 K. Finally, the dihydride is decomposed at 973 K with the formation of thorium powder (Fig. 24.39).

Production of Thorium Compacts

Thorium powders possess high plasticity and allow high compacting pressure. The pressure levels for calcium thermic and electrolytic thorium powders range from 0.8 to 1.2 GPa and 0.6 to 0.8 GPa, respectively.

Pressed billets are sintered in a vacuum 0.1–0.6 Pa at temperatures from 1370 to 1670 K for 30–60 min. Sintered billets have density 11.5–11.6 g/cm^3 (about 98.3% theoretical). Their Brinell hardness ranges from 520 to 700 MPa, while ultimate tensile strength ranges from 170 to 220 MPa.

It is also possible to produce dense material by melting. Thorium powders or sponge are melted in electric-arc furnaces or in vacuum induction furnaces. In the latter case, thorium is melted in beryllium oxide crucibles, which are heat-resistant to thorium up to 2070 MPa. The beryllium crucible is inserted into a graphite one, which is heated by induction. Melting is conducted under vacuum 0.133 Pa and lower.

Uranium Powder Production

Metallic uranium can be produced by the following methods:

- Reduction of uranium oxides by calcium or calcium hydride.
- Reduction of uranium tetrafluoride or uranium tetrachloride by calcium or magnesium.
- Electrolysis of halogen salts in molten media.

As a result of uranium oxide reduction as well as electrolysis of melts, metallic uranium powders are obtained which are separated from the oxides and salts by treatment with water and acids. On the other hand, metallothermic reduction of halogen salts produces uranium in the form of ingots which readily separate from the slag. The advantage of this explains why this process is widely used.

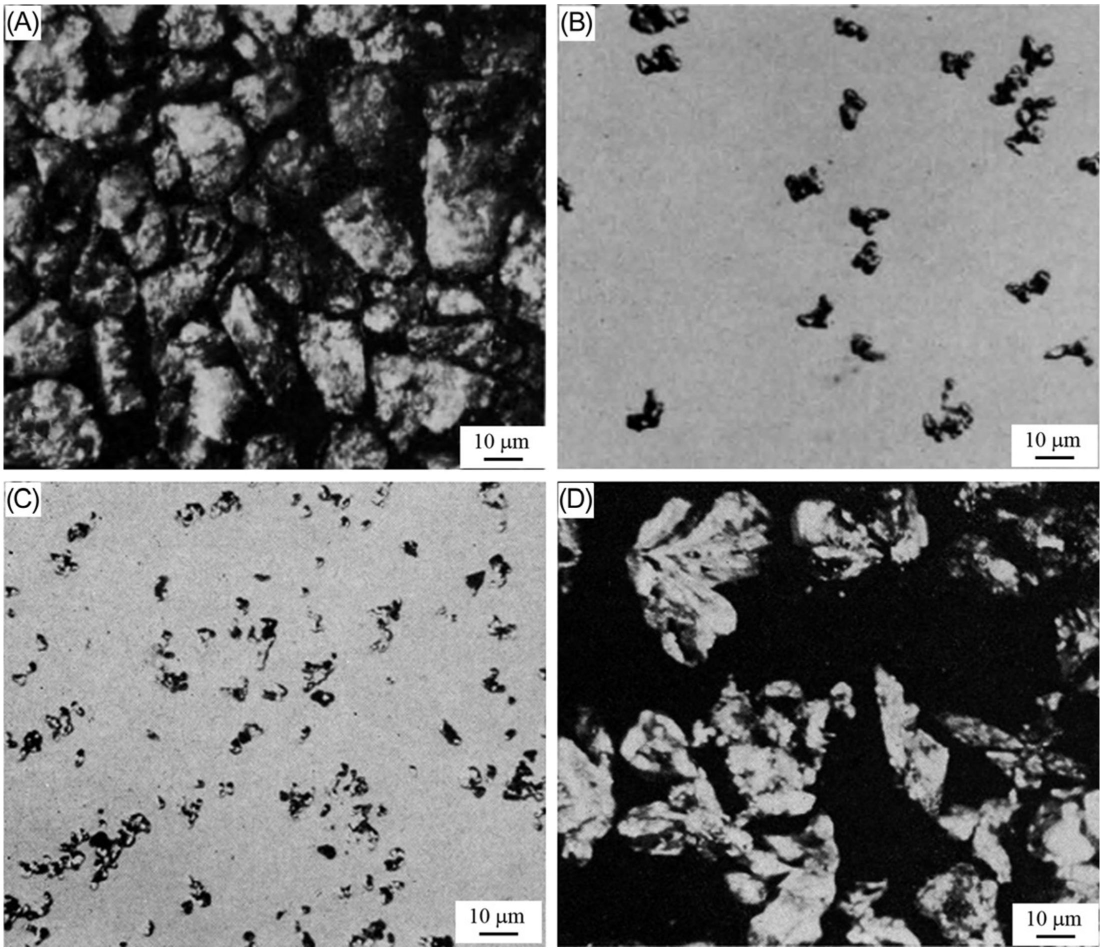

FIG. 24.39 Thorium powder fabricated by various methods: comminuted chips (A), hydride process powder (B), calcium reduced powder (C), electrolytic flake (D). *From Beaver WW, Wikle KG, Klein JG. Fabrication of thorium powders. J Met 1956;445–54.*

Uranium tetrachloride in contrast to fluoride is very hygroscopic, which makes it difficult to work with. Additionally, the chloride boils at 1070 K, which causes further difficulties. Therefore, production of uranium is based predominantly on reduction of uranium tetrafluoride.

Atomization, while common for most production metals, is seldom used in the production of uranium or other radioactive elements [113]. Of the commercially common atomization methods, the rotating disk method for atomization of uranium has been developed by the Korean Atomic Energy Research Institute [114].

The hydride-dehydride process has been used since the 1950s as a uranium powder production method [115]. It is considered as good method for producing very fine (often under 38 μm). At moderate temperatures (typically under 570 K), the uranium reacts with hydrogen. The uranium hydride has a much lower density than the uranium metal (10.9 vs. 19 g/cm^3) and it emerges off the ingot surface as hydride powder. After the hydriding step is completed, the uranium hydride is reduced by heating the hydride powder under a vacuum. The hydrogen slowly dissociates from the powder leaving only the uranium alloy in powdered form. The process is expressed by the following reversible equation:

$$3H_2 + 2U \leftrightarrow 2UH_3$$

The morphology of uranium powders made by hydride-dehydride process and inert gas atomization are represented in Fig. 24.40.

Applications

A potential use of thorium is in nuclear power engineering. Under the action of thermal neutrons, natural thorium (isotope 232 Th) is converted to fissionable isotope 233 U. However, at present, consumption of thorium in this direction is restricted owing to sufficient resources of uranium.

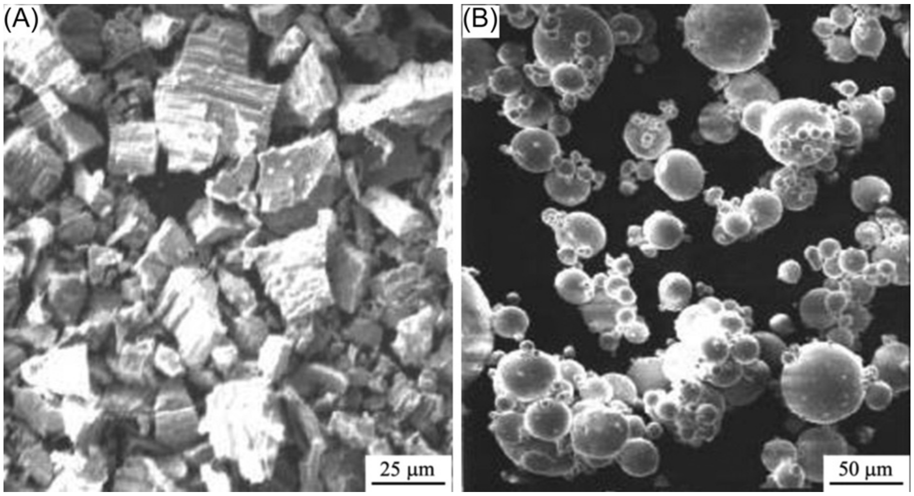

FIG. 24.40 The morphology of uranium powders made by (A) hydride-dehydride process and (B) inert gas atomization.

Many applications of thorium are becoming obsolete due to environmental concerns largely limitations from the radioactivity of thorium and its decay products. Thorium is thus being phased out of many of its uses [116, 117]. Most thorium applications use its dioxide, rather than the metal. One particular characteristic of this compound is its high melting point, 3660 K – the highest of all known oxides. In particular, that helps the compound remain solid when introduced into a flame, and when it is, it considerably increases the luminance of the flame; this is the main reason thorium is used in gas mantles [118]. Light emitted by thorium is almost exclusively located in the visible spectrum, which explain the brightness of thorium mantles [119]. Thorium in mantles, though still common, have been being replaced with a different rare-earth element, yttrium, since the late 1990s. During the production of incandescent filaments, recrystallization of tungsten is significantly lowered by adding small amounts of thorium dioxide to the tungsten sintering powder before drawing the filaments [118]. A small addition of thorium to tungsten thermocathodes considerably reduced the work function of electrons; as the result, electrons are emitted at considerably lower temperatures [116]. Since the 1920s, thoriated tungsten wires have been used in electronic tubes and in the cathodes and anticathodes of X-ray tubes and rectifiers. Due to the reactivity of thorium with atmosphere oxygen and nitrogen, thorium also marks impurities in the evacuated tubes. Introduction of transistors in the 1950s significantly diminished this use, though not entirely [118]. Thorium dioxide is used in gas tungsten arc welding to increase the high-temperature strength of tungsten electrodes and improve arc stability. Nevertheless, because of safety concerns, thorium oxide is being replaced in this use with other oxides, such as those of zirconium, cerium, and lanthanum [120].

Thorium dioxide is a material for heat-resistant ceramics, as used in high-temperature laboratory crucibles, as a main material or as an addition to zirconium dioxide. An alloy of 90% platinum and 10% thorium is an effective catalyst for oxidizing ammonia to nitrogen oxides, but this has likewise been replaced by an alloy of 95% platinum and 5% rhodium because of its better mechanical properties and greater durability [118].

When added to glass, thorium dioxide helps increase refractive index and decrease dispersion. Such glass finds application in high-quality lenses for cameras and scientific instruments [121]. Yellowed lenses may be restored to their original colorless state with lengthy exposure to intense ultraviolet radiation. Thorium dioxide has since been replaced by rare earth oxides in this application, as they provide similar effects and are not radioactive [118].

Thorium tetrafluoride is used as an antireflection material in multilayered optical coatings. It has an optical transparency in the range of 0.35–12 µm, and its radiation is primarily due to alpha particles, which can be easily stopped by a thin cover layer of another material [122]. Replacements for thorium tetrafluoride are being developed as of the 2010s [123].

Thorium and its compounds were used for alloying in alloys based on nickel, cobalt, magnesium and aluminum. Due to high electron emission capability of thorium, it is used to create tungsten based material with an oxide dispersed phase. This material is produced by means of PM. Tungsten metal powder and thorium-containing compounds (such as thorium dioxide or thorium nitrate) are mixed, pressed, sintered and further processed to wire or sheet [124, 125]. Commercially produced mechanically alloyed TD-Ni alloy is an elevated temperature nickel-base alloy, containing 2.0 wt% thorium oxide. Its ultimate tensile strength at 970 K amounts to 150 MPa (Source: Inco Alloys International [126]). However, at present, thorium and thorium dioxide are being replaced in these applications by other rare and rare earth elements, as well their oxides.

Metallic thorium, thorium dioxide, as well as other thorium compounds are used in catalyst compositions in organic synthesis in the chemical industry.

Uranium serves as basic nuclear fuel. Two isotopes ^{235}U and ^{233}U are able to maintain a chain reaction with slow neutrons. The former is contained in natural uranium; therefore, it is the primary nuclear fuel. The latter fissile isotope is obtained by radiation of thorium with thermal neutrons.

Safety Engineering

The International Atomic Energy Agency (IAEA) is authorized to establish and adopt standards of safety for protection of health and minimization of dander to life and property, and to provide for the application of these standards [127]. In the IAEA safety standards series are Safety Fundamentals, Safety Requirements and Safety Guides.

Safety Requirements standards include Governmental, legal and regulatory framework for safety [128], Leadership and Management for Safety [129]. Radiation protection and safety of radiation sources: International Basic Safety Standards [130], etc.

In addition to the development of a system of radiological protection that is used as the basis for regulations and practices worldwide, the International Commission on Radiological Protection (ICRP) also provides information essential to the implementation of the system. Central to the application of the system is the use of the protection quantities "equivalent dose" and "effective dose." ICRP has provided sets of dose coefficients (dose per unit exposure) to allow users to calculate equivalent and effective doses for intakes of radionuclides or exposure to external radiation for comparison with dose limits, constraints, and reference levels [131].

Table 24.29 contains the committed effective dose per unit intake *e*(g) via inhalation and ingestion (Sv/Bq) by working with radioactive thorium and uranium.

Thorium is a combustible metal, thorium powder is pyrophorus. Thorium is characterized by the following data of flammability and explosibility [17]. The self-ignition temperatures of aerogel and suspended solid in air are 553 and 543 K, respectively; the low concentration ignition limit of suspended solid in air is 75 g/m^3; explosion pressure is 630 kPa

TABLE 24.29 Workers: Committed Effective Dose Per Unit Intake *e*(g) via Inhalation and Ingestion (Sv/Bq) for Radioactive Thorium and Uranium

			Inhalation			Ingestion	
Radionuclide	Physical Half-Life (Years)	Type Materials[a]	f_1[b]	e (Sv/Bq) (1 µm)[c]	e (Sv/Bq) (5 µm)	f_1	e(g)
^{230}Th	7.7×10^{4}	M S	5.0×10^{-4} 2.0×10^{-4}	4.0×10^{-5} 1.3×10^{-5}	2.8×10^{-5} 7.2×10^{-6}	5.0×10^{-4} 2.0×10^{-4}	2.1×10^{-7} 8.7×10^{-8}
^{232}Th	1.4×10^{10}	M S	5.0×10^{-4} 2.0×10^{-4}	4.2×10^{-5} 2.3×10^{-5}	2.9×10^{-5} 1.2×10^{-5}	5.0×10^{-4} 2.0×10^{-4}	2.2×10^{-7} 9.2×10^{-8}
^{234}U	2.44×10^{5}	F M S	0.020 0.020 0.002	5.5×10^{-7} 3.1×10^{-6} 8.5×10^{-6}	6.4×10^{-7} 2.1×10^{-6} 6.8×10^{-6}	0.020 0.002	4.9×10^{-8} 8.3×10^{-9}
^{235}U	7.04×10^{8}	F M S	0.020 0.020 0.002	5.1×10^{-7} 2.8×10^{-6} 7.7×10^{-6}	6.0×10^{-7} 1.8×10^{-6} 6.1×10^{-6}	0.020 0.002	4.6×10^{-8} 8.3×10^{-9}
^{238}U	4.47×10^{8}	F M S	0.020 0.020 0.002	4.9×10^{-7} 2.6×10^{-6} 7.3×10^{-6}	5.8×10^{-7} 1.6×10^{-6} 5.7×10^{-6}	0.020 0.002	4.4×10^{-8} 7.6×10^{-9}

[a] *Type F materials are the deposited materials that are readily absorbed into blood from the respiratory tract (fast rate of absorption), Type M materials are the deposited materials that have intermediate rates of absorption into blood from the respiratory tract (moderate rate of absorption), Type S materials are the deposited materials that are relatively insoluble in the respiratory tract (slow rate of absorption).*

[b] *The f_1 value is the fraction of an ingested element absorbed directly into body fluids.*

[c] *The activity median aerodynamic diameter.*

Source: Vienna International Centre (Austria). Radiation protection and safety of radiation sources: International Basic Safety Standards. Series No GSR Part 3. IAEA Safety Standards, 2014 (in English, also available in French, Spanish, Russian, Arabic, Chinese). http://www-pub.iaea.org/MTCD/publications/PDF/Pub1578_web-57265295.pdf and Eckerman K, Harrison J, Menzel H-G, Clement CH. ICRP Publication 119: Compendium of dose coefficients based on ICRP Publication 60. In: Clement CH, editor. Ann ICRP, 4(4). Elsevier; 2013. p. 1–130 max; maximum rate of pressure rise is 84 MPa/s; explosion-proof oxygen content in inert gas is 4 vol% max; minimum suspended solid in air ignition energy is 5 mJ. The products with such characteristics of inflammability and explosion risk are placed in the "high explosion hazard" class of danger according to the Guide to Legislation and "Health and Safety" in the European PM Industry [18].

Methods used to extinguish thorium-fires include: high volume carbon dioxide (12 kg/m^3 for 2–5 min); special powder mixes based on potassium and sodium chlorides, and voluminal quenching by argon [17].

Uranium flammability and explosibility are characterized by the following data. Fine uranium powder is energetically oxidized and can easily ignite spontaneously. A powder with particle size below 74 μm exhibits: self-ignition temperatures of aerogel and suspended solid in air of 373 and 293 K, respectively; the low concentration ignition limit of suspended solid in air is 60 g/m^3; explosion pressure is 480 kPa max; maximum rate of pressure rise is 35 MPa/s; explosion-proof oxygen content in nitrogen is 1.5 vol% max, in helium 2.5 vol%, in argon 2.0% and in carbon dioxide 0 vol%; minimum suspended solid in air ignition energy is 45 mJ. The products with such characteristics of inflammability and explosion risk are placed in the "high explosion hazard" class of danger [18]. Uranium spontaneous ignition is possible under water and even in a moist argon atmosphere. Steam reacts with uranium at 423–523 K and interaction occurs more readily than with oxygen. At 1023 K, uranium readily reacts with carbon dioxide. There are known cases of spontaneous ignition in carbon dioxide [1]. Uranium chips burn in nitrogen oxide at 673–773 K.

Extinguishing facilities of uranium are the same as for thorium and consist of the voluminal quenching method by argon (more efficient than carbon dioxide) and fire extinguishing powders which are represented by mixtures of potassium and sodium chlorides.

REFERENCES

[1] Zelikman AN, Korshunov BG. Metallurgy of rare metals. Moscow: Metallurgiya Publisher; 1991. in Russian.

[2] Eisen WB. PM tool and high speed steel—a comprehensive review. In: Proceedings of 5th international conference on advanced particulate materials and processes. Metal Powder Industries Federation; 1997. p. 55–63.

[3] Trefilov VI, Moiseev VF. Fine particles in refractory metals. Kiev: Naukova Dumka Publishers; 1978. in Russian.

[4] Vlasyuk RZ, VYa K, Lyapunov AP, Radomysel'skii ID. Interaction of titanium and vanadium with carbon dioxide on heating. Sov Powder Metall Met Ceram 1986;25(1):54–7.

[5] Wang CT, Baroch EF, Worcester SA, Shen YS. Preparation and properties of high-purity vanadium and V–15 Cr–5 Ti. Metall Trans A 1970;1 (6):1683–9.

[6] Naboychenko SS, editor. Handbook of non-ferrous metal powders. Moscow: Metallurgia Publishers; 1997. in Russian.

[7] Radomysel'skii ID, Solntsev VP, Evtushenko OV. Powder metallurgy of vanadium and its alloys (Review). Sov Powder Metall Met Ceram 1987;26 (5):367–72.

[8] HA Wilhelm, JK Mcclusky. US Patent 3,463,634. 1969.

[9] Itoh Y, Harikou T, Sato K, Miura H. Improvement of ductility for injection moulding Ti-6Al-4V alloy, In: Compiled by European Powder Metallurgy Association, Bellstone (Shrewsbury, UK). Proceedings of 2004 Powder Metallurgy World Congress vol. 4; 2004. p. 445–50.

[10] Consemüller K, Hribernik B, Schneider G. Tool steels present and future. In: Proceedings of 4th international conference on tooling. Bochum: Ruhr University Publishers; 1996. p. 3–16.

[11] Zinyana J, et al. Effect of composition on the (V,W)C in V-W-C-Co alloys. In: Proceedings of 15th international Plansee seminar. vol. 4. Plansee: Publishers Plansee Holding AG; 2001. p. 291–9.

[12] Krishnan VK, Sinnaeruvad K. Synthesis of nanostructured vanadium powder by high-energy ball milling: X-ray diffraction and high-resolution electron microscopy characterization. Philos Mag 2016;96(10):402–8.

[13] Donghua X, Kezhao L, Xiaobin X, Ye L, Yangping C. Effect of annealing temperature on the microstructure and properties of pure vanadium. Rare Metal Mater Eng 2008;37(9):1566–9.

[14] Arshad K, et al. Effects of vanadium concentration on the densification, microstructures and mechanical properties of tungsten vanadium alloys. J Nucl Mater 2014;455(1–3):96–100.

[15] RUS Standard GOST 12.1.005 – 88. Intergovermental Standard. Overall hygiene and sanitary requirements of air workplace exposure limits. Standards, Moscow, 2000 [in Russian].

[16] MinZdrav. Sanitary regulation and standards of surface waters from pollution. SanPiP 4630–88. Moscow: Publishers of MinZdrav; 1988. in Russian.

[17] Baratov AN, Korolychenko AJ editors. Handbook. Fire- and explosion-proof of matters and materials and means for their quenching. Moscow: Chimia Publishers; 1990 [in Russian].

[18] EPMA. Guide to EU legislation and 'environmental health and safety' in the European PM Industry. 2009.

[19] Ishizuka H. Process for producing metallic zirconium. US Patent 4242136, 1980.

[20] Benedict M, Pigford TH, Levi HW. Nuclear chemical engineering. New York: McGraw-Hill; 1981.

[21] UX Consulting services. Nuclear zirconium alloy market outlook. 2017. https://www.uxc.com/p/products/rpt_zirc.aspx.

[22] Merzhanov, A.G., Shkiro, V.M., Borovinskaya, I.P., Soviet Union Certif. [Patent], 255221, 1971.

[23] Merzhanov AG, Borovinskaya IP. Self-propagating high-temperature synthesis of refractory inorganic compounds. Dokl Akadem Nauk USSR 1972;204(2):366–9. in Russian.

[24] Muchnik SV, Lomnitskaya YF, Chernogorenko VB, Lynchak KA. Interaction under combustion in powder mixtures of copper-zirconium-phosphorus. Sov Powder Metall Met Ceram 1993;11–12:670–865.

[25] Borovinskaya IP, Loryan VE. Self-propagating synthesis of solid solution in zirconium-nitrogen system. Dokl Akadem Nauk USSR 1976;231 (4):911–4. in Russian.

[26] Borovinskaya IP, Loryan VE. Self-propagating high-temperature synthesis of titanium nitrides under high pressure of nitrogen. Sov Powder Metall Met Ceram 1978;11–12:655–851.

[27] Nel JT, Havenga JL, Makhofane MM, Jansen AA. The plasma-assisted manufacture of zirconium metal powder from zirconium tetrachloride. J South Afr Inst Min Metall 2012;112(1):63–8.

[28] Golightly JS, Castleman AW. Synthesis of zirconium nanoparticles by ultrafast laser ablation. Z Phys Chem 2007;221:1455–68. https://doi.org/10.1524/zpch.2007.221.11-12.1455.

[29] Tokushige M, Nishikiori T, Ito Y, Russ J. Plasma induced cathodic discharge electrolysis to form various metal/alloy nanoparticles. Electrochemistry 2010;46:619–26. https://doi.org/10.1134/S1023193510060042.

[30] Pol SV, Pol VG, Gedanken A. Reactions under autogenic pressure at elevated temperature (RAPET) of various alkoxides: formation of metals/metal oxides-carbon core-shell structures. Chem Eur J 2004;10:4467–73. https://doi.org/10.1002/chem.200400014.

[31] Eshed M, Pol S, Gedanken A, Balasubramanian M. Zirconium nanoparticles prepared by the reduction of zirconium oxide using the RAPET method. Beilstein J Nanotechnol 2011;2:198–203. https://doi.org/10.3762/bjnano.2.23.

[32] Han JS. Investigation of PZT ceramics produced by powder processing. In: Compiled by Russell A, Chernenkoff W, Brian J. Proceedings of 2014 powder metallurgy world congress. Orlando (FL, U.S.A.): Metal Powder Industries Federation; 2014: p. 04-28–34.

[33] Dankley JJ. Hot gas atomization—economic and engineering aspects. In: Proceedings of PM2004 world congress. vol. 1. Wien (Austria): European Powder Metallurgy Association; 2004. p. 13–8.

[34] CHCS. EH40/2005 Workplace exposure limits. Europe occupational exposure limits. 2nd ed. HSE, 2011.

[35] Abd El-Halim AM, Khalil KM. Electrolytic production of thallium powder in sulphate bath. Surface Texhnol 1984;23(4):215–23.

[36] Fedorchenko IM, editor. Encyclopedia of inorganic materials. Kiev: Glavnaja Redakcija Ukrainskoy Sovetskoy Encycpopedii; 1977. in Russian.

[37] Shing TL, Luycks S, Northrop IT, Wolff I. The effect of ruthenium additions on the hardness, toughness and grain size of WC-Co. Int J Refract Met Hard Mater 2001;19:41–4.

[38] Bonjour C, Actis-Data A. Effects of ruthenium additions on the properties of WC-Co ultra micrograins. In: Proceedings of PM2004 world congress. vol. 3. Wien (Austria): European Powder Metallurgy Association; 2004. p. 515–21.

[39] Bonjour C. Effects of ruthenium additions on the properties and machining behaviour of WC-Co hard metals. In: Proceedings of PM2004 world congress. vol. 3. Wien (Austria): European Powder Metallurgy Association; 2004. p. 528–34.

[40] Mehrotra P, et al. Recent advances in ruthenium containing hardmetals, In: Compiled by European Powder Metallurgy Association, Bellstone Shrewsbury. UK Proceedings of PM 2016 World Congress, Hamburg (Germany); 2016. p. 1–6.

[41] Potgieter JH, et al. Influence of Ru additions on the corrosion behavior of WC-Co cemented carbide alloys in sulphuric acid. Int J Refract Met Hard Mater 2011;29:478–87.

[42] Lee C, Chen Y, Liao C, Popuri SR, Tsai S, Hung C. Selective leaching process for neodymium recovery from scrap Nd-Fe-B magnet. Metall Mater Trans A 2013;44(13):5825–33.

[43] Yoon H-S, et al. Leaching kinetics of neodymium in sulfuric acid from E-scrap of NdFeB permanent magnet. Korean J Chem Eng 2014;31 (4):706–11.

[44] Önal MAR, Borra CR, Guo M, Blanpain B, Van Gerven T. Recycling of NdFeB magnets using sulfation, selective roasting, and water leaching. J Sustain Metall 2015;1(3):199–215.

[45] Gergoric M, Ekberg C, Steenari B-M, Retegan T. Separation of heavy rare-earth elements from light rare-earth elements via solvent extraction from a neodymium magnet leachate and the effects of diluents. J Sustain Metall 2017;3(3):601–10.

[46] Izatt SR, Bruening RL, Izatt NE. Status of metal separation and recovery in the mining industry. J Met 2012;64:1279–84.

[47] Izatt SR, et al. Molecular recognition technology: a green chemistry process for separation of individual rare earth metals. IBC; White paper on separation of rare earth elements 2016; p. 1–12. http://ucore.com/documents/WhitePaper_REE_Separations.pdf

[48] Conway JB, Flagella PN. Creep-rupture data for the refractory metals to high temperatures. New York: Gordon & Breach Science Publishers; 1971.

[49] Mueller AJ, Shields JA, Buckman RW. The effect of thermo-mechanical processing on the mechanical properties of molybdenum–2 vol% lanthana. In: Proceedings of 15th international Plansee seminar. vol. 1. Plansee Holding AG; 2001. p. 485–97.

[50] Bianco R; Buckman, R.W; Geller, C.B. High strength, creep-resistant molybdenum alloy and process for producing the same. US Patent 5,868,876 (1999).

[51] Bianco R, Buckman RW. Mechanical properties of oxide dispersion strengthened (ODS) molybdenum. In: Proceedings "Molybdenum and Molybdenum Alloys". The Minerals, Metals & Materials Society; 1998. p. 125–42.

[52] Povarova KB, Makarov PV, Luk'yanchikova SS, Zavarina EK. Effect of high-energy ball milling on structure and some properties of powder tungsten alloys. Izv Ross Akad Nauk Met 1994;6:113–23.

[53] Itoh Y, Ishivata Y. Strength properties of yttrium–oxide–dispersed tungsten alloys. JSME Int J Ser A 1996;39(3):429–34.

[54] Taillard RA, Avettand-Fènoel M-N, Dhers J, Foct J. In: Ball-milling and sintering of blends of tungsten and yttrium-rich powders. In: Proceedings of 2002 Powder Metallurgy World Congress, Princeton. New Jersey, U.S.A.: MPIF Publishers; 2002. p. 6-188–202.

[55] Zhang H, Liu X, Ning A. Microstructures and properties of rare earth-particles reinforced $MoSi_2$ composites. In: Proceedings of 15th International Plansee Seminar. vol. 1. Plansee: Publishers Plansee Holding AG; 2001. p. 339–52.

[56] Davis JR. Aluminum and aluminum alloys. In: ASM speciality handbook. ASM International Publishers; 1990.

[57] Anderson IE, Foley JC, Flumerfelt JF. Simplified aluminum powder metal processing routes for automotive applications. In: Proceedings of First International conference on powder metallurgy aluminum & light alloys for automotive applications. Princeton (New Jersey, USA): MPIF Publishers; 1998. p. 75–82.

[58] Foley JC, Hunt WH, Barnard DJ, Laabs FC. Simple powder metallurgy processing of Al-8Fe-4Ce alloys. In: Proceedings of 2002 powder metallurgy world congress. Orlando (FL, USA): MPIF; 2002. p. 1-103–114.

[59] Kim YW. Processing, microstructure, properties of Al-Fe-Ce alloys. In: Proceedings 'Dispersion strengthened aluminum alloys'. Warrendale (PA): TMS Publishers; 1988. p. 157–80.

[60] Neikov OD, et al. Elevated temperature Al alloys produced by water atomization. Mater Sci Eng A 2008;477:80–5.

[61] Lee DY, Zupon DY. High temperature performance of dispersion strengthened PM aluminum alloys. In: Proceedings 'Dispersion strengthened aluminum alloys'. Warrendale (PA): TMS Publishers; 1988. p. 265–81.

[62] Nie Z, Chen Y, Zhou M, Zuo T. Research and development of tungsten electrodes added with rare earth oxides. In: Proceedings of 15th International Plansee Seminar. vol. 1. Plansee: Publishers Plansee Holding AG; 2001. p. 568–74.

[63] Wang J, Zhou M, Zuo T, Zhang J, Nie Z. Carbonization kinetics of La_2O_3–Mo cathode materials. In: Proceedings of 15th international Plansee seminar. vol. 1. Plansee: Publishers Plansee Holding AG; 2001. p. 684–94.

[64] Sreenivasa RG, Dhamadhikari CV, Nigavekar AS. Effect of carburization on diffusion and desorption properties of La–Mo system. J Vac Sci Technol 1989;A7(6):3269–72.

[65] Sreenivasa RG, Dhamadhikari CV, Nigavekar AS. Some aspect of adsorption, diffusion, and thermal desorption properties of a La–Mo system. J Vac Sci Technol 1989;A6(5):3005–12.

[66] Wang J, et al. Characteristics of La_2O_3–Y_2O_3–Mo cermet cathode with RE_2O_3 nano particles. Curr Appl Phys 2011;11(3):667–72.

[67] Wang J, et al. Characterization of carborized La_2O_3 doped Mo filament cathode. Phys Status Solidi 2012;C9(1):26–31.

[68] A Matsuo, Y Ueno, Y Kai. US Patent, US 20140017114 A1, 2014.

[69] Benecki WT, Claggett TK, Trout SR. Permanent magnets 2010–2020. Walter T. Benecki LLC; 2010.

[70] Leonowicz M, Derewnicka D, Krzton H, Panchanathan V. Structural anisotropy in Nd-Fe-B magnets processed by hot working of melt-spun ribbon powder. In: Proceedings of 2002 powder metallurgy world congress. Princeton (New Jersey, USA): MPIF Publishers; 2002. p.14-1–10.

[71] Lukin A, Matveyenkov A. Influence of heat treatment parameters on properties of Nd-Dy-Fe-Co-Nb-Al-Cu-B sintered magnets. In: Proceedings of PM2004 world congress. vol. 4. Wien (Austria): European Powder Metallurgy Association; 2004. p. 511–34.

[72] Vystavkina V, Brecharya G, Vasilyeva E. Microstructure and properties of Nd-Fe-B magnets, produced from gas-atomization powders. In: Proceedings of PM2004 world congress. vol. 4. Wien (Austria): European Powder Metallurgy Association; 2004. p. 539–44.

[73] Ślusarek B, Paszkowski L, Biało D. The influence of kind of powder on physical properties of Nd-Fe-B dielectromagnets. Microstructure and properties of Nd-Fe-B dielectromagnets, produced from gas-atomized powders. In: Proceedings of PM2004 world congress. vol. 4. Wien (Austria): European Powder Metallurgy Association; 2004. p. 555–60.

[74] Schultz L, Gutfleisch A, Kirchner A, et al. Keynote: high performance nanocrystalline functional materials. Microstructure and properties of Nd-Fe-B magnets, produced from gas-atomized powders. In: Proceedings of PM2004 world congress. vol. 4. Wien (Austria): European Powder Metallurgy Association; 2004. p. 569–75.

[75] Polyakov EG, Sibilev AS. Recycling rare-earth-metal wastes by pyrometallurgical methods. Metallurgist 2015;59(5):368–73.

[76] Bandara HMD, Apelian JW, Emmert D, Marion H. Rare earth recycling: forecast of recoverable Nd from shredder scrap and influence of recycling rates on price volatility. J Sustain Metall 2015;1(3):179–88.

[77] Tunsu C, Petranikova M, Gergorić M, Ekberg C, Retegan T. Reclaiming rare earth elements from end-of-life products: a review of the perspectives for urban mining using hydrometallurgical unit operations. Hydrometallurgy 2015;156:239–58.

[78] Binnemans K, Jones PT, Blanpain B, Van Gerven T, Yang Y, Walton A, Buchert M. Recycling of rare earths: a critical review. J Clean Prod 2013;51:1–22.

[79] Xie F, Zhang TA, Dreisinger D, Doyle F. A critical review on solvent extraction of rare earths from aqueous solutions. Miner Eng 2014;56:10–28.

[80] Kuipa PK, Hughes MA. Diluent effect on the solvent extraction rate of copper. Sep Sci Technol 2002;37:1135–52.

[81] Ji X, Jian-gao Y, Xing-hua G. Application of rare earth elements in cemented carbide inserts, drawing dies and mining tools. Mater Sci Eng A 1996;209:287–93.

[82] Xu C, Xing Y, Huang C. Research and development of rare-earth cemented carbides. Int J Refract Met Hard Mater 2001;19(3):159–68.

[83] Zhang L, Schubert W-D, Huang B, Chen S, Zhang C. Cerium enrichment phenomena on the sinter skin of cemented carbide. In: Proceedings of 2004 powder metallurgy world congress. vol. 4. Bellstone (Shrewsbury, UK): European Powder Metallurgy Association; 2004. p. 443–9.

[84] Zhang L, Schubert WD, Huang B, et al. Surface observation of rare earth doped cemented carbide. PM Sci Tech Briefs 2003;5(3):17–23.

[85] German RM. Sintering theory and practice. New York: John Wiley & Sons Publishers; 1996.

[86] Marder JM, Wellman B. Powder metallurgy beryllium. In: ASM handbook, vol.7, powder metallurgy. ASM International Publishers; 1998. p. 941–6.

[87] Courtney TH. Modeling of mechanical milling and mechanical alloying. In: Particulate materials 2. Metal Powder Industries Federation Publishers; 1994.

[88] Marder JM, Wellman B. Production of beryllium powders. In: ASM handbook. vol. 7. ASM International Publishers; 1998. p. 202–5.

[89] Weast RC, editor. Handbook of chemistry and physics. 64th ed. Boca Raton (FL, USA: CRC Press, Inc; 1984.

[90] Hashiguchi DH, Svilar M, Sayer AB, Morales AL. Beryllium and aluminum-beryllium alloys. In: ASM handbook, vol.7, Powder metallurgy. ASM International Publishers; 2015. p. 757–65.

[91] Materion Electrofusion. Fremont (CA, U.S.A.). https://materion.com/products/beryllium-products/beryllium-x-ray, 2018 (Accessed 31 January 2018).

[92] Materion Brush Beryllium and Composites. Elmore (OH, U.S.A.). https://materion.com/-/media/files/pdfs/corporate/bubrochures/beryllium_0311.pdf, 2018 (Accessed 31 January 2018).

[93] Lewis RE, Yaney DL, Tanner LE. The effect of lithium in Al-Be alloys. In: Proceedings 'aluminum-lithium alloys V'. ASM International Publishers; 1990. p. 731–40.

[94] EH40-Update to EH40/2005 Workplace Exposure Limits. 2nd ed., 2011 (as consolidated with amendments, December 2011).

[95] US New Jersey Department of Health and Senior Services. Hazardous substance sheet. Nickel carbonyl. Revision: February 2001.

[96] Alexandsandrovsky SV, Siziakov VM, Kucenko DV, Ratner AH. Metallothermic obtaining methods of heightened purity scandium and its alloys. Moscow: Ore and Metals Publishers; 2004. in Russian.

[97] Driz ME, Kadaner ES, Dobatkina TV, Turkina NI. Interaction of scandium with aluminum on the aluminum rich part of Al–Sc system. Izv AN USSR Metals 1973;4:213–7. in Russian.

[98] Parker BA, Zhou ZF, Nolle P. The effect of small additions of scandium on the properties of aluminium alloys. J Mater Sci 1995;30:452–8.

[99] Driz ME, Toropova LS. Bykov YuG, et al. Al–Sc metastable phase diagram of the aluminum-rich part. Izv AN USSR Metals 1983;1:179–82. in Russian.

[100] Hyde AF, Norman AF, Prangnell PB. The effect of cooling rate on the morphology of primary AI_3Sc intermetallic particles in Al–Sc alloy. Acta Mater 2001;49:1327–37.

[101] Neikov OD, Lotsko DV, Sirko AI, Sameljuk AV, Thompson GE, Zakharova NP, Yefimov NA. Properties of rapidly solidified powder alloys of the Al-Zn–Mg system. Mater Sci Forum 2002;396–402:1223–8.

[102] Eskin GI. Non-dendritic crystallization of light alloys. Technol Light Alloys 2000;2:17–25. in Russian.

[103] Lendvai J. Precipitation and strengthening in aluminium alloys. Mater Sci Forum 1996;217–22:43–56.

[104] Milman Yu V. Influence of scandium on structure, mechanical properties, and corrosion resistance of aluminum alloys. In: Proceedings 'advance materials and technologies'. Kyiv: National Academy of Sciences of Ukraine Publishers; 2003. p. 335–60.

[105] Milman YV, Sirko AI, Lotsko DV, Senkov ON, Miracle DB. Microstructure and mechanical properties of cast and wrought Al-Zn–Mg–Cu alloys modified with Zr and Sc. Mater Sci Forum 2002;396–402:1217–22.

[106] Milman YV, et al. Structure and properties of Al–Mg alloys depending on scandium and zirconium additions and production methods. Powder Metall Met Ceram 2010;49(7–8):429–37.

[107] Neikov OD, et al. In: Advanced high-strength nanostructured Al-Mg alloys produced by new rapid solidification technology. Proceedings of PM 2010 world congress, Florence (Italy), vol. 4. European Powder Metallurgy Association; 2010. p. 25–32.

[108] Djukanovic G. Are aluminium-scandium alloys the future? Aluminium Insider, 2017. http://aluminiuminsider.com/aluminium-scandium-alloys-future/.

[109] Petrakova OV, Panov AV, Gorbachev SN, Milshin ON. Improved efficiency of red mud processing through scandium oxide recovery. In: Proceedings of Bauxite Residue Valorization and Best Practices. vol. 4. Leuven (Belgium): Kuleuven; 2015. p. 355–62.

[110] Aluminium Insider. Rusal produces first batch of scandium oxide. 2016. http://aluminiuminsider.com/rusal-produces-first-batch-of-scandium-oxide.

[111] Hobashi F. Bayer's process for alumina production: a historical perspective. Bull Hist Chem 1996;17/18:15–9.

[112] Beaver WW, Wikle KG, Klein JG. Fabrication of thorium powders. J Met 1956;445–54.

[113] Clark CR, Meyer MK. In: Strauss JT, editor. Fuel powder production from ductile uranium alloys. Transactions of the 1998 international meeting on reduced enrichment for research and test reactors, Sao Paulo (Brazil); 1988. p. 1–9.

[114] Kim KW, et al. Characterization of U-2 wt% Mo and U-10 wt% Mo alloy powders prepared by centrifugal atomization. J Nucl Mater 1997;24:179–84.

[115] Mueller WM, Blackledge JP, JP LGG, editors. Metal hydrides. Academic Press; 1968.

[116] Wickleder MS, Fourest B, Dorhout PK. The chemistry of the actinide and transactinide elements. In: Morss LR, Edelstein NM, Fuger J, editors. Thorium. 3rd ed. vol. 3. Springer-Verlag; 2006. p. 52–160. https://doi.org/10.1007/1-4020-3598-5_3.

[117] Furuta E, Yoshizawa Y, Aburai T. Comparisons between radioactive and non-radioactive gas lantern mantles. J Radiol Prot 2000;20(4):423–31.

[118] Stoll W. Thorium and thorium compounds. In: Ullmann's encyclopedia of industrial chemistry. Wiley-VCH; 2005. https://doi.org/10.1002/14356007.a27_001.

[119] Ivey HF. Candoluminescence and radical-excited luminescence. J Lumin 1974;8(4):271–307. https://doi.org/10.1016/0022-2313(74)90001.

[120] Uttrachi J. Weld like a pro: beginning to advanced techniques. CarTech Inc.; 2015, ISBN: 978-1-61325-221-5.

[121] Hammond CR. The Elements. In: Handbook of chemistry and physics. CRC Press; 2004. 81st ed.

[122] Rancourt JD. Optical thin films. Bellingham (WA, U.S.A): SPIE Press; 1996.

[123] Kaiser N, Pulker HK, editors. Optical interference coatings. Springer; 2013, ISBN: 978-3-540-36386-6.

[124] Yih SWH, Wang CT. Tungsten sources, metallurgy, properties, and applications. Plenum Press Publishers; 1979.

[125] Lassner E, Schubert WD, Lüderitz E, Wolf HU. Tungsten, tungsten alloys, and tungsten compounds. In: Ulmann's encyclopedia of industrial chemistry. vol. A27. VCH Verlagsgesellshaft GmbH Publishers; 1992.

[126] Suryanarayana C. Mechanical alloying. In: ASM handbook. vol. 7. ASM International Publishers; 1998. p. 80–90.

[127] Vienna International Centre (Austria). Fundamental safety principles. Series No, SF-1. IAEA Safety Standards, 2006 (in English, also available in French, Spanish, Russian, Arabic, Chinese).

[128] Vienna International Centre (Austria). Governmental, legal and regulatory framework for safety. Series No GSR Part 1. IAEA Safety Standards, 2016 (in English, also available in French, Spanish, Russian, Arabic, Chinese).

[129] Vienna International Centre (Austria). Leadership and Management for Safety. No GSR Part 2. IAEA Safety Standards, 2016 (in English, also available in French, Spanish, Russian, Arabic, Chinese).

[130] Vienna International Centre (Austria). Radiation protection and safety of radiation sources: International Basic Safety Standards. Series No GSR Part 3. IAEA Safety Standards, 2014 (in English, also available in French, Spanish, Russian, Arabic, Chinese). http://www-pub.iaea.org/MTCD/publications/PDF/Pub1578_web-57265295.pdf.

[131] Eckerman K, Harrison J, Menzel H-G, Clement CH. ICRP Publication 119: Compendium of dose coefficients based on ICRP Publication 60. In: Clement CH, editor. Ann ICRP, vol. 4(4). Elsevier; 2013. p. 1 – 130.

FURTHER READING

[132] Dixon RB, Stasko W, Pinnow KE. Particle metallurgy tool steels. In: ASM handbook. vol. 7. ASM International Publishers; 1998. p. 786–802.

[133] Westin L, Wisell H. Powder metallurgy high speed steels. Scand J Metall 1996;25(1):41–6.

[134] Takahashi Y, et al. Recovery and separation of rare earth elements using salmon milt. PLoS One 2014;12:1–9. https://doi.org/10.1971/journal.pone.0114858.

[135] Benecki WT. The permanent magnet market—2015. In: Magnetics 2013 conference, Orlando (FL, U.S.A.). 2013.

[136] Ormerod J, Constantinides SPM. Magnetic materials and applications, short course, 22–23 June 1993. Metal Powder Industries Federation Publishers; 1993.

[137] Floyd DR, Lowe JN. Beryllium science and technology. vol. 2. New York: Plenum Press; 1979.

[138] Korshunov BG, Reznik AM, Semenov SA. Scandium. Moscow: Metalurgija Publishers; 1987. in Russian.

[139] Meija J, et al. Atomic weight of the elements. Pure Appl Chem 2016;88(3):265–91.

Chapter 25

Production of Noble Metal Powders

Oleg D. Neikov*, Stanislav S. Naboychenko† and Irina B. Murashova†
**Frantsevich Institute for Problems of Materials Science (IPMS), Kiev, Ukraine, †Ural Federal University (UrFU), Yekaterinburg, Russia*

Chapter Outline

Introduction 831
Production of Silver Powders 832
Chemical Processes 832
Atomization 833
Mechanical Comminution Processes 833
Production of Silver Powder From Solution by Electrolysis 834
Production of Silver Powder by Chemical Reduction With Electrochemical Regeneration of the Reducer 835
Production of Fibrous Dendritic Silver Residue From Molten Electrolytes 835
Production of Gold Powders 835
Production of Platinum-Group Powders 837
Powders of Platinum Metals 837
Chemical Reduction 839
The Carbonyl Process 840
Autoclave Precipitation 841
Production of Noble Metal Alloys Powders 842
Production of Platinum Black Deposit (Niello) 844
Synthesis of Palladium Nanopowders by Methods of Zone Electrochemistry 845
Producing of Noble Nanoparticles in Metal-Organic Frameworks Pores 845
Noble Metals Application in Implantable Medical Devices 845
References 846

INTRODUCTION

The properties of noble metals including silver, gold, and platinum-group metals are listed in Table 25.1.

Chemical precipitation, thermolysis, electrolysis, hydrogen reduction, and melt atomization are often used for the production of powders of these metals. The basic materials are solutions, salt pulps, and hydroxides; in the latter case, solid-phase properties significantly influence the properties of the powder produced, complicating the reproducibility of a number of its characteristics (particle size, bulk mass, surface).

Among organic reagents, such as formaldehydes, alcohols, oxalic and formic acids and their salts, and glycerin, and among nonorganic ones, such as hydrazine and its derivatives, borates of alkali and alkaline-earth metals, hypophosphites, Ti (III), Cr (III), and V (III) salts, are used most often. Organic reducers are safe, available, and allow carrying out the process at low temperatures. The produced powders have a developed surface; they are also dispersed (1.0–10 μm), but are gas-saturated and require a special finishing procedure. Formic acid and its salts, sodium formate in particular, are used most often. This is an available, nontoxic, and easily soluble reagent. The precipitation factors depend on temperature, pH value, and reagent consumption, but there is a problem of washing the powder free from sodium ions resulting in high water consumption (up to 160–200 L per 1 kg of precipitate). The particle size of the produced residue is between 0.05 and 0.5 μm.

Reney's method is based on producing the alloy, followed by selective leaching of the less noble component by acid or alkali solutions. The produced precipitates of metals or their alloys have a large specific surface (80–100 m^2/g), but the residues of the leached metal contaminate them, so they need to be passivated.

Thermolysis means the thermal decomposition of metal salts (nitrates, halides, ammoniates, carbonates, formates), which form volatile products upon heating. The powders produced are distinguished by a nonuniform granulometric composition, a small specific surface, and contamination by thermolysis products.

Electrochemical methods (extraction from solutions, processing of salt pulp and hydroxides, electrolysis of wastes and recycled raw materials) are widely used in the production of noble metal powders. Powder properties depend on the electrolyte content, the current density, the hydrodynamic conditions, and the cathode shape.

A solid-phase reduction of salts and oxides of noble metals by hydrogen at 500–700 K is possible; however, the powders produced (especially palladium powders) are inclined hydrogenetion and contain up to 0.1% of adsorbed hydrogen. Indices

Handbook of Non-Ferrous Metal Powders. https://doi.org/10.1016/B978-0-08-100543-9.00025-7
© 2019 Elsevier Ltd. All rights reserved.

TABLE 25.1 Basic Properties of Noble Metals

Characteristic	Metals							
	Ag	Au	Ru	Rh	Pd	Os	Ir	Pl
Serial number	47	79	44	45	46	76	77	78
Atomic mass, g/mole	107.9	197	101.1	102.9	106.4	190.2	192.2	195.1
Relevant oxidation rates			3, 4, 6–8	3	2	4,6–8	3–4	2,4
Density, g/cm^3	10.49	19.32	12.45	12.41	12.02	22.61	22.65	21.45
Temperature, K:								
of melting	1234	1337	2856	2239	2098	3306	2739	2041
of boiling	2485	3080	4423	4000	4516	5285	4701	4098
Specific heat capacity, J/(K·mole)	25.4	25.2	24.0	25.1	26.0	24.8	25.1	25.9
Thermal conductivity, W/(K·m), at 298 K	433	318	117	152	75.2	87.6	147	74.6
Specific electrical resistivity, nΩ·m, at 293 K	16.1	22.1	71	43.3	105.1	81.2	47.1	105

of hydrogen reduction (purity and physical properties of the powder) are significantly improved when the hydrothermal method is used, by precipitation of metals from an organic aqueous medium at elevated temperature (380–450 K).

PRODUCTION OF SILVER POWDERS

Basic methods of production are solid-phase reduction, chemical precipitation from solutions or pulp, electrolytic precipitation, and electrolysis.

Chemical Processes

Most silver salts are easily reduced from the solution, with the only limitation being their solubility. The most common compounds are silver nitrate and silver oxide. Organic reducing agents such as alcohol, sugar, or aldehydes are used to manufacture silver powder from silver oxide. For example, dextrose can be used to produce a very fine silver powder:

$$2AgNO_3 + 2NaOH \rightarrow Ag_2O_{(s)} + 2NaNO_3 + H_20$$

$$12Ag_2O + C_6H_{12}O_6 \rightarrow 24Ag_{(s)} + 6CO_2 + 6H_20$$

Organically precipitated silver powders have particle sizes ranging from 5 µm to less than 0.1 µm. However, these silver powders tend to agglomerate into aggregates 10 µm in size or larger. To avoid agglomeration, the powder can be precipitated in the presence of a surfactant or deagglomerated after the precipitation using a mechanical technique.

Silver powders are produced by mixing an acidified solution with a solution of tin (II) salts in the presence of anion-type surfactants, controlled pH values, and temperature.

To produce submicron particles of silver and palladium, their concentrated nitrate solutions are used, aerosol forming and drop separation by size are provided, and then drying and conversion of aerosol particles to the metallic condition are performed in a reducing atmosphere at elevated temperature.

Particles 7–10 µm in size are produced by the evaporation of silver at 1270 K with subsequent condensation in a nitrogen atmosphere.

Metal-ceramic contacts of heightened wear resistance are produced from silver-based compositions (Ag–oxides of cadmium, copper, zinc, tin, or lead, and Ag-Ni) from nitric-acid solutions of appropriate composition; the metals are jointly precipitated in the form of hydrates and carbonates. Powder mixtures with a particle size of 0.1–0.4 µm are produced after separation of precipitates, followed by their washing, drying, and calcination at 670–770 K. To provide a heightened flow rate, an agglomeration is carried out; the size of the produced particles is 200–400 μm. Removal of cadmium oxide proceeds during sintering of products containing cadmium oxide at $T > 970$ K; a contact film of silver, which excludes oxidation, is formed in the surface layer.

A composition for the products that retains their electrical conductivity and wear resistance at low temperatures (for example, electrical contacts) and in a vacuum is produced by mechanical stirring of dispersed silver powders with additives of 2%–49% of rhenium or molybdenum disulfide in water or alcohol.

Silver powder is produced by processing a solution of silver nitrate (0.05 M) and 4-(methylamino)phenol sulfate in the ratio of $[(C_7H_9ON)]\cdot H_2S0_4/AgNO_3 = 1.05$. The precipitate is washed by a 3% solution of sodium nitrite, by hot water (330–340 K), and dried at 373±5 K; the powder contains not less than 98.7% of Ag. The particle shape is regular polyhedrons 0.5–20 μm in size or ovals 0.3–4.5 μm in size. The powder surface is 0.19–0.21 m^2/g, the apparent density is 2.4 g/cm^3. The powder is used for film covering production (70% of Ag) with specific electric resistance not higher than $1.2 \times 10^{-7}\ \Omega\cdot m$.

Silver powder is also produced by processing hydroxide pulp with a solution of sodium formate; the precipitate is washed by water and dried. Powder properties (specific surface, S, apparent density, ρ, median mass diameter, d_m) significantly depend on the reduction conditions:

	S (m^2/g)	ρ (g/cm^3)	d_m (μm)
Production conditions			
without surfactants	4.9	0.98	Aggregates
with surfactants	0.45–1.25	1.6–2.6	0.5–2.5
$L{:}S = 10$ (relation of liquid to solid)	1.3	…	10
$L{:}S = 1$	0.8	2.9	17

The consumption of the reducing agent is 1.1%–2.4% of the precipitated powder mass with a content of 99.9% of Ag.

It is possible to produce silver powder by a self-propagating low temperature reaction of precipitated silver chloride with zinc. In this process, powder of silver or a "silver-zinc" alloy of the Ag_nZn_m type is produced by means of chemical reactions considered as the kind of contact displacement:

$$2AgCl + H_20 \leftrightarrow Ag_2O + 2HCl$$

$$2AgCl + Zn \rightarrow Ag + ZnCl_2$$

$$\Delta G = -150\,\mathrm{kJ/mole}$$

Zinc consumption is stoichiometric; the duration of the process is 15–20 min, the transformation level is close to 100%. Powder surface area is 0.8 m^2/g, the particle size is 1–2 μm, and their shape is round.

Atomization

Silver powder is produced by the atomization of a molten silver stream with gas or liquid. Average particle sizes generally are within the range of 10–50 μm. The gas-atomized powder generally approaches a spherical shape with a smooth surface, minimal porosity, and a high powder density [1].

The spray pyrolysis technique for the manufacture of silver powders is also used. This process involves spraying a silver nitrate solution into a flame formed by a coaxial burner. Control of the flame temperature and spray conditions allows for the control of particle size and shape [2].

Spray pyrolysis produces solid spherical dense silver powders. An aerosol of silver nitrate solution is heated to temperatures as low as 873 K in nitrogen to decompose the silver salt and to produce a fully dense silver powder. The particle size of the powder is 5 μm and smaller.

Mechanical Comminution Processes

Mechanical milling is used to change the properties of silver powders, including disintegration of particle aggregates, particle shape, and particle surface characteristics. This process can be used for most types of silver powders with techniques such as ball milling, vibratory milling, or attrition milling.

A feature of these processes is that they are time consuming and require special precautions to prevent contamination from the mill and milling medium. Various types of milling media can be used, including zirconia balls (ZrO_2), metallic balls, and glass balls. Continued milling produces two-dimensional silver flakes. The sizes of the milling media is between 10 and less than 1 mm, depending on the sizes of the initial powder and the size of the resulting silver flake required. Generally, an organic surfactant is introduced during the milling process to prevent the agglomeration of particles with each other while grinding and to control the size and shape of the silver flake.

Production of Silver Powder From Solution by Electrolysis

The basic raw material is Dore's alloy that contains: 87%–95% of Ag; 2%–14% of platinoids and gold; 1%–4% of Cu; 0.06%–0.01% of Ni; 0.005%–0.01% of As; 0.01%–0.05% of Sb; 0.1%–0.2% of Fe; 0.001%–0.005% of Pb; 0.002%–0.01% of Se; 0.005%–0.1% of Te; and silver-containing materials (80%–84% of Ag; 16%–20% of Cu). In according with State Standard 28595-90, silver of three brands (CpA-1, CpA-2, and CpA-3) is used in the cells with soluble anodes (respectively 99.99%, 99.98%, and 99.9% of Ag).

Silver is precipitated on the cathode as a loose needle-like deposit that is easily stripped from the cathode. The current efficiency in the nitrate solution is approximately 100%. The cause of electric loss is short circuits of silver dendrites and simultaneous reduction of NO_3^- anions to HNO_2, NO_2^-, NO_2 (gas), or NO (gas).

The respective O/R potentials are 0.94, 1.01, 0.77, and 0.95 V (nhe). Therefore the concentration of the free acid is decreased.

Fine silver powder is precipitated at the silver anode due to the $Ag_2^+ = Ag + Ag^+$ reaction. Practically all impurities except gold and platinoids pass into the solution. Part of the palladium can pass into the solution from platinoids. Selenium and tellurium should be eliminated from the anode material during fire refining.

The powder is produced in cells with vertical or horizontal cathodes (Table 25.2) as well as on a rotating cylindrical cathode. Vertical cathodes in cells are sheets of silver, high-clean aluminum, or stainless steel. The intercathode space is 16–20 cm. The anodes are put into a diaphragm box with stretched bags from polyvinyl chloride (PVC) to collect the anode sludge. The ends of the cathode rods are pushed into slots welded to a bus. Vertical plates that perform reciprocal movements are installed for deposit removal. The silver deposit is stripped into a box with a filter bottom. A telfer for lifting the frame and the box with silver powder is installed above cells. The powder is removed by knives from the cylindrical rotating cathode, and a bottom knife transfers the deposit to the sloping conveyor.

Cells with a horizontal location of electrodes are manufactured of plastic or ceramics and lined with acid-proof tiles. A graphite dalle (cathode) is embedded into the cell bottom. Half the cell bottom length is splayed to provide powder deposit discharge. An anode box with the bottom made of fire bars, on which a filtration nylon material, plastic grid, and some layers of anode plates are placed, is installed above the horizontal part of the cell. The current is supplied by heavy contacting leads, to which the ends of a flexible cable are soldered. Anodic contacts are manufactured of 50% Ag+50% Au alloy; cathodic contacts are fabricated from silver. Once every day, the deposit is discharged by knives on the filtration frame that is brought to the cell by a car. The deposit is washed by hot water acidified by nitric acid

TABLE 25.2 Electrolysis Conditions and Process Parameters

Parameters	Cell With Vertical Electrodes	Cell With Horizontal Electrodes
Electrolyte concentration, kg/m^3:		
Silver	10–20	40–50
Nitric acid	10–15	15–25
Cathodic current density, A/m^2	1500	400–500
Temperature, K	313–343	313–323
Deposit growth time, min	2–10	1440
Cell voltage, V	2–2.8	3.2–3.8
Current efficiency, %	95–97	87–90

(1 kg/m^3). Cleaning the solution includes the elimination of lead and copper. Lead is precipitated by sulfuric acid. To eliminate copper, at first silver cementation from the solution is performed by copper plates, then the deposit is removed, and copper cathodes and insoluble magnetite anodes are put into the cell; the copper concentration is decreased to 10 kg/m^3 during electrolysis.

It is possible to produce silver powder in the cells with insoluble anodes. Titanium sheets are covered by a thin platinum layer. Anode current density is twice as high compared with the cathode one. The nitric acid concentration increases during electrolysis whereas the silver ion concentration decreases. Periodically, a part of the electrolyte is vented away for regeneration and removal of platinum metals and gold.

Silver powder produced by electrolysis meets the following requirements: >99.9% of Ag, not less than 0.02% of Cu; 0.04% of the sum (Fe, Pb, Al, Bi), 0.001% of NO_3^-, 0.005% of SO_4^{2-}, 0.08% of moisture (over 100%); particle size for PS1 brand: 97% of the size fraction of (−56) μm, for PS2 brand: and 96% of the size fraction of (−160) μm.

Production of Silver Powder by Chemical Reduction With Electrochemical Regeneration of the Reducer

Fine silver powder is produced in the anodic space of the electrolyzer close to the surface of soluble silver anodes by chemical reduction with titanium (III) ions:

$$Ag^+ + Ti(III) = Ag + Ti(IV)$$

The composition of the solution is 10% of $Ti_2(SO_4)_3$ and 10%–15% of H_2SO_4. The electrolysis is carried out at 298 K, providing cathode and anode current densities of 50–100 and 250 A/m^2, respectively. The fine powder formed with a particle size of 1 μm is precipitated on the bottom of the electrodes. The solution of titanium sulfate goes to the cathodic space where titanium (IV) ions are reduced to Ti (III) ions. The powder is washed on a filter by 5% solution of sulfuric acid to eliminate titanium and then by water to eliminate sulfate ions. The water residue is eliminated by alcohol or acetone washing. The final drying of the powder is performed under vacuum at 315–325 K.

The several ways of production of electrolytic silver and silver-alloy powders are shown in Table 25.3.

Production of Fibrous Dendritic Silver Residue From Molten Electrolytes

Electrolysis is carried out using a silver nitrate melt based on the potassium-sodium eutectic (15–33 wt% of silver) at a temperature of 523–563 K in an open cell without additional stirring [8]. A flat anode in the form of a silver bar with insulated silver current supply is placed on the cell bottom. The cathode is a silver wire ($d = 1.5$ mm) clamped at the top between rolls of the lifting device. Prior to turning on the main current, a current of 0.1–0.2 A is applied for 1–2 min to provide stronger adherence of the fibrous deposit to the cathode. Without current interruption, the fibrous deposit is precipitated on the sublayer, simultaneously providing cathode lifting (v) and current (i_a) regulation to the required level (in the range of 0.5–10 A). The speed of cathode lifting (from 0.25 to 12 cm/min) is controlled with the help of a gearbox and by changing the voltage applied to the motor from the electric power supply. Electrolysis conditions have to provide a part of the electrode of a constant length to be submersed into the electrolyte. After electrolysis, a tow of silver threads is washed to remove any adhering salt. Proper combinations of current and cathode lifting rate allow producing fibers with a length up to 30 cm and various structures (Fig. 25.1).

PRODUCTION OF GOLD POWDERS

Gold-bonding conductors, owing to their high reliability and conductivity, find a variety of applications in electronics and communication systems. The bonding behavior of gold as well as its electrical conductivity make it desirable in hybrid microcircuitry. A special reliability of gold is connected with its superior resistance to oxidation. The primary cost of using gold is rather high, but lost operating time and repair expenses as a result of the deterioration of electrical properties of nongold elements due to the formation of oxide or sulfide films on contact surfaces are much higher [9].

Production of particles 3–180 μm in size is realized by gold vaporization in an inert gas atmosphere and condensation in ethanol. Ultrafine gold powder particles are produced from the solution based on organic complexes by thermolysis of its aerosols (drop diameter is of 1–5 μm) in an inert medium at temperatures higher than 770 K.

Many processes for manufacturing gold powder use an aqueous solution of $HAuCl_4$. This gold chloride solution is produced by dissolving gold grain or shot in aqua regia followed by heating to decompose and remove the nitric acid. A variety of reducing agents can be used to reduce gold to gold powder, including other metal powders (zinc, magnesium, aluminum,

TABLE 25.3 Electrolysis Conditions and Process Parameters of Noble Metal Powder Production

Method	Electrolyte Composition (Content of Components, kg/m^3)	Current Density, kA/m^2	Temperature, K	Electrolysis Parameters
Palladium				
WS	10 of Pd (pH 9)	0.5–7.0	293	Electrolyte: $Pd(NO_3)_2+NH_4OH$; current efficiency is of 40%
Platinum				
WS	3–5 of $Pd(NH_3)_2(NO_2)_2$ 100 of $K_4P_2O_7 \cdot 3H_2O$; 50 of NH_4OH; (pH 10.5)	1.0	333	Current efficiency is of 19%–20%; deposit is black powder; apparent density is of 5 g/cm^3
Silver				
WS	32–48 of $AgNO_3$; 3–5 of HNO_3; 50–100 of $NaNO_3$	i_k =1.2; i_a=0.3–0.4	313–323	Current efficiency is of 85%–96%; voltage is 2 V
WS	15–20 of Ag; 10–15 of HNO_3	1.5	313–323	Time for deposit growth is 2 min, interelectrode space is 50 mm, voltage is 2–2.8 V; electric power consumption is 0.6 kW h/kg
WS [3]	20 of $AgNO_3$; 10 of $NaNO_3$; up to pH 1 of HNO_3	i_k=2.0; i_a=0.5	298	Current efficiency is 97%–100%; particle size is 2–3 μm
WS	20–300 of H_2SiF_6	0.3–5.0	293–323	Silver anodes, stainless steel cathodes; 40%–80% of particles with size 60 μm, apparent density is 1.1–2.5 g/cm^3
WS [4]	15–20 of Ag; 100–200 of NH_2SO_3H; (pH 0.5–1.5)	0.6–0.8	291–298	Current efficiency is 90%–100%; particle size is 50–100 μm; mass use ratio is 60%–70%
EDC	50 of $AgNO_3$; 0.5% of oleic acid; (pH 1–2)	1.2	293	Graphite disc is used for cathode; rotation is 60 rpm; precipitation time is 1 h; voltage is of 10 V; current efficiency is 99.8%; powder surface is 15–18 m^2/g
Palladium-Silver				
WS [5]	10 of Pd+Ag (pH 9)	0.5–7.0	293	Current efficiency (42%) depends on total metal concentration. Particle size is of 1–20 μm $(Pd/Ag)_{powder=}(Pd/Ag)_{solution}$
Palladium-Platinum				
WS [6]	10–100 of Pd+Pt; (pH 2.5–2.7)	0.5–4.0	293	Particles size is 1–10 μm; alloys are solid solutions; salts are chlorides; $(Pt/Pd)_{powder=}(Pt/Pd)_{solution}$
Platinum-Cobalt				
WS [7]	3–5 of $Pt(NH_3)_2(NO_2)_2$; 5–8 of $CoSO_4 \cdot 7H_2O$; 100 of $K_4P_2O_7 \cdot 3H_2O$; 50 of NH_4OH; (pH 10.5)	1.0–2.0	333	Black powder, current efficiency is 20%; $(Pt+Co)_{sum}=5$–10 kg/m^3; at $(Pt/Co)_{solution}=2/1$ $(Pt/Co)_{alloy}$ 1:1 (at); residue is absent under $i \leq$ 100–200 A/m^2
Silver-Nickel				
WS	30 of Ag+Ni; 5–10 of Ag; 20–25 of Ni; (pH 4–6)	2.5–3.0	291–298	Sulfamic electrolyte; in solution Ni:Ag=5:1; current efficiency is 40%; anodes–Ag: Ni=1:4, the higher temperature, the richer the silver alloy

TABLE 25.3 Electrolysis Conditions and Process Parameters of Noble Metal Powder Production—cont'd

Method	Electrolyte Composition (Content of Components, kg/m^3)	Current Density, kA/m^2	Temperature, K	Electrolysis Parameters
Palladium-Nickel				
WS	4–14 of Pd+Ni; 20 of NH_4Cl; (pH 9.5)	10–15	293	[Pd/Ni]=2/1; solid solutions; $(Pd/Ni)_{powder}=(Pd/Ni)_{solution}$; particles size is 85–107 µm; current efficiency is 65%
Palladium-Copper				
WS	5–13.5 of Pd+Cu; 30 of NaCl; 60 of NH_4Cl; (pH 0.5)	3–4	293	$(Pd/Cu)_{powder}=(Pd/Cu)_{solution}$; particle size is 90–220 µm; current efficiency is 65%; alloys are hard solutions

WS: water solution electrolysis; EDC—electrolysis from double-layer cell (see Paragraph "Reduction from solution through film of surfactants" of Chapter 8).

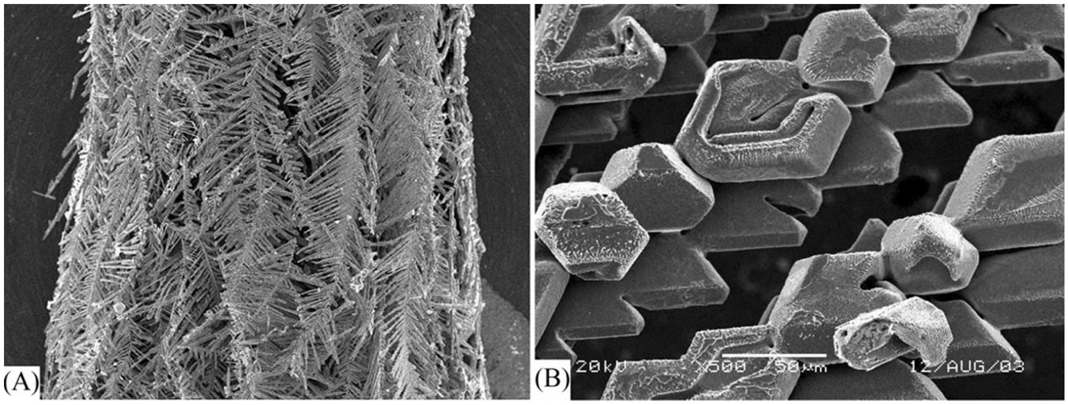

FIG. 25.1 Silver fibrous deposits (current (i_a), A; velocity of electrode lifting (v), cm/min): (A) $i_a=1$ A, $v=5$ cm/min; (B) $i_a=5$ A, $v=3$ cm/min.

and iron), sulfur compounds (sulfur dioxide, sodium sulfite, potassium sulfite, and ferrous sulfate), hydrazines, aldehydes, oxalates, hydrogen peroxide, and others.

Potassium sulfite or sodium sulfite can be directly added to an aqueous gold chloride solution to produce spherical gold particles [10]:

$$2HAuCl_4 + 3Na_2SO_3 + 3H_2O = 2Au_{(S)} + 3\,H_2SO_4 + 6NaCl + 2HCl$$

Gold powder can also be produced by mechanical comminution. Sheets of gold are reduced by rolling to produce a foil between 10 and 20 µm thick, followed by beating to produce a gold foil of 0.2–0.5 µm thick. These foils are subjected to mechanical comminution, ensuring an ultrafine gold powder production. Larger gold powders and gold flake can be manufactured by ball milling [11].

PRODUCTION OF PLATINUM-GROUP POWDERS

Powders of Platinum Metals

The chemical composition is shown in Table 25.4. Powders with metal content not lower than 99.9% are produced according to special specifications. Each lot of powder corresponds to one brand of metal; foreign mechanical inclusions are not allowed.

Indium powder. Particle size of the powder is not greater than 0.8 mm. The powder is used for the manufacture of alloys, special coverings, and other products. The powder is supplied in lots of 250 kg.

TABLE 25.4 Chemical Composition of Refined Powders of Platinum Metals

Chemical Composition, wt%												
Metal, Brand[a]	Basic Metal Content, Min	Platinum Metals, Total	Impurities, Max									
			Pb	Fe	Si	Ba	Mg	Au	Al	Volatile Matters	Sn	Total
Iridium												
IA-1	99.95	0.02	0.005	0.01	0.002	0.002	0.001	0.002	0.005	0.01	–	0.05[b]
IA-2	99.90	0.045	0.01	0.02	0.005	0.005	0.003	0.002	0.005	0.01	–	0.10
Palladium												
Pd AP-1	99.95	0.025	0.005	0.01	0.005	–	–	0.005	0.005	–	0.001	0.05
Pd AP-2	99.90	0.050	0.005	0.02	0.005	–	–	0.010	0.005	–	0.005	0.10
Platinum												
PL AP-0	99.98	0.015	–	0.003	0.002	–	–	–	–	–	–	0.02[c]
PI AP-1[d]	99.95	0.025	0.005	0.010	0.005	–	–	0.005	0.005	–	0.001	0.05
PI. AP-2[e]	99.90	0.050	0.005	0.010	0.005	–	–	0.005	0.005	–	0.005	0.10
Rhodium												
Rh-Al	99.95	0.02	0.005	0.01	0.005	0.005	0.001	0.002	–	0.01	–	0.05[f]
Rh-A2	99.90	0.03	0.005	0.02	0.005	0.005	0.003	0.002	0.002	0.02	–	0.10
Osmium												
OsA-0	99.97	–	–	0.01	–	–	–	0.002	–	–	–	0.03[g]
Os A-l	99.95	–	–	0.01	–	–	–	0.002	–	–	–	0.05
OsA-2	99.90	–	–	0.03	–	–	–	0.002	–	–	–	0.10
Ruthenium												
Ru A-0	99.97	–	0.003	0.003	0.003	0.002	–	0.002	0.002	–	–	0.03[h]
Ru A-l	99.95	–	0.005	0.01	0.005	0.005	–	0.002	0.005	–	–	0.05
Ru A-2	99.90	–	0.01	0.02	0.0!	0.005	–	0.002	0.005	–	–	0.10

[a] *In CIS classification.*
[b] *Including Ag, Ni, and Cu.*
[c] *Including Ag, Mg, Cu, Ni, and volatile matters.*
[d] *Including 0.00l of Sb.*
[e] *Including 0.005 of Sb.*
[f] *Including Ag, Cu, Ni, Ti, and Al.*
[g] *Including Pt, Pd, Rh, Ir, Ag, Cu, and Ni.*
[h] *Including Pt, Pd, Rh, Ir, Ag, Cu, Ni, Mg, O, and the volatile matter Si, Al, Mg, Ba, Na including.*

Palladium powder. Particle size of powder is not greater than 1.6 μm. The powder is supplied in lots of not more than 350 kg. It is used for the the manufacture of contacts, alloys, chemicals, catalysts, special coatings, and other products.
Platinum powder. Particle size of the powder is less than 1.6 μm; a content of the size fraction larger than 1.6 μm up to 2% is allowed. The mass of a powder lot is not larger than 350 kg. The powder is used for the manufacture of special units, alloys, coatings, semifinished items, and chemicals.
Rhodium powder. Particle size of powder is not greater than 0.8 μm; it is packed into plastic cans (net weight 25–5000 g) or in welded glass capsules (net weight 0.1–25 g). The mass of the powder lot is not greater than 350 kg. It is used for the manufacture of alloys, products, and chemicals.
Osmium powder. Particle size of the powder is less than 1.0 μm; inclusions of the size fraction larger than 1.0 μm (up to 2%) are allowed. The powder is packed into glass containers (25–5000 g) and capsules (0.1–25 g). It is used for the manufacture of alloys, semifinished items, special products, coatings, and chemicals.
Ruthenium powder. Particle size of powder is below 1.0 μm; inclusions of the size fraction larger than 1.0 μm (up to 2%) are allowed. The powder is packed into plastic containers (25–5000 g) and glass capsules (0.1–25 g). It is used for the manufacture of alloys, semifinished items, special products, coatings, and chemicals.

Chemical Reduction

The precipitation of platinum oxide at the interaction of H_2PtX_6 (where X is Cl^-, Br^-, I^-) with $NaNO_3$ and the processing of the oxide in a hydrogen atmosphere is the oldest method of platinum niello production. Dispersivity is controlled at the stage of platinum oxide precipitation by variations of the salt nature and the inclusion of halides of alkali-earth metals (the latter are typical additions).

The process of reducing $[PtCl_6]^{2-}$ ion by sodium formate includes a number of consecutive stages: Pt (IV)→Pt(II)→Pt; the higher the (Cl^-) ion concentration, the slower the process rate. The activation energy for the interval of 95–60°C is 105 kJ/mole.

The fractional conversion of the metal to powder achieves 99.9% in processing of chloro-amine compounds of platinum and palladium in a sodium hydroxide solution by reducing agents (sodium formate, aluminium, hydrazine salts).

Platinum niello is produced by the reaction of ammonium hexachlorplatinate with a 2.5-M solution of formic acid or sodium formate at 375 ± 5 K; a pH of 6.0–6.5 is supported with the help of NaOH (or NH_3).

Metallic palladium powder is formed (without reducer) in the process of boiling dichloridiamminpalladium salt in a saturated alkali solution. If this salt is treated slowly (3 h at 375 ± 5 K) in a sodium hydroxide solution and sodium formate (0%–20% of stoichiometric consumption) is used as the reducer, we can get palladium niello. An increase of sodium formate consumption from 10% to 80% of the stoichiometrically necessary level results in a decrease of palladium niello specific surface from 32 to 3 m^2/g. Palladium precipitation from chloride solutions by sodium formate is performed in accordance with the following scheme:

$$[PdCl_4]^{2-}\xrightarrow[Cl^-]{H_2O}[Pd(H_2O)Cl_3]^-\xrightarrow[\text{slowly}]{HCOO^-}[Pd(HCOO)Cl_3]^{3-}\rightarrow Pd+CO_2+H^++3Cl^-$$

The greatest influence on the increase of the process rate is exerted by an increase of temperature, sodium formate concentration, and seed consumption. The process rate decreases at high pH and especially if chloride ions are introduced. It is explained by the enhanced resistance of metal chloride components to the activation:

$$\left[M(NH_3)_2Cl_2\right]+H_2O\leftrightarrow\left[M(NH_3)_2H_2OCl\right]^++Cl^-$$

With the appearance of the metallic niello, the process becomes autocatalytic.

Palladium powder is produced by processing its ammonium complexes with a mixture of formic acid and with its ammonium salt prepared in the following manner: (CH_2O_2:$NH_4OH \geq 1.0$:0.3) at 350–360 K.

Cladding of powders of various metal oxides by platinum or palladium is achieved by the thermolysis method.

Powders of platinum, palladium, ruthenium, and iridium are precipitated from an acid-salt solution by cementation with zinc, copper, magnesium, aluminum, or cadmium. The powder surface area is 0.1–1.0 m^2/g. A possible formation of intermetallics with the precipitator used reduces the powder quality.

Fine powders of platinum group metals are precipitated from aqueous or nonaqueous solutions of salts by radiation by an election beam in doses of 10–30 mrad.

The Carbonyl Process

Powders of platinum group metals can be precipitated by the use of carbon monoxide:

$$MCl_x^{n-} + yCO \rightarrow M(CO)_y Cl_{x-y}^{y-n} + yCl^-$$

$$M(CO)_y Cl_{x-y}^{y-n} + yH_2O \rightarrow M + yCO_2 + 2yH^+ + (x-y)Cl^-$$

$$MCl_x^{n-} + yCO + yH_2O \rightarrow M + yCO_2 + 2yH^+ + xCl^-$$

There are several platinum carbonyl compounds:

$$Pt(CO)_2Cl_2, PtCOCl_2, Pt_2(CO)_3Cl_4, Pt(CO)_2Cl_6$$

High carbonylchlorides are hydrolyzed to monocarbonylchloride; the latter is decomposed by interaction with water forming the platinum powder:

$$[PtCOCl_3]^- + H_2O \rightarrow Pt + CO_2 + 3Cl^- + 2H^+$$

Platinum metals may exist in chloride solutions in different ion forms according to the concentration of chloride ions.

$$PdCl_2 + CO \rightarrow PdCOCl_2$$

$$PdCOCl_2 + H_2O \rightarrow Pd + CO_2 + 2HCl$$

Palladium complexes with maximal coordinate number 4 are formed in concentrated chloride solutions. In accordance with the above mentioned mechanism:

$$[PdCl_4]^{2-} + 2CO \rightarrow \left[Pd(CO)_2Cl_4\right]^{2-}$$

$$\left[Pd(CO)_2Cl_4\right]^{2-} + 2H_2O \rightarrow Pd + 2CO_2 + 4HCl$$

This process includes a number of subsequent transformations with complex ions of different structures as the participants. The reduction is performed from the solutions (100–120 g/L of Pd; 1–2 M of HC1) or the H_2PdCl_4 salt solution, which is neutralized by alkali to a pH of 6–8 and precipitated at 340–345 K.

The rate of palladium precipitation decreases in the presence of organic compounds (acetone, ethanol, butane). When the organic phase concentration is increased, the fine fractions output is increased also, and practically monodispersed powder can be produced. Palladium powder with a particle size of 1.2–1.7 μm was reduced in the system palladium salt solution + about 10% of metal; the particle shape is nonequiaxed, and the structure is porous.

The properties of palladium powders used for the manufacture of thin-walled ceramic condensers are presented in Table 25.5.

Characteristic properties of palladium powders are homogeneity of phase and chemical composition, high particle size dispersity (0.3–3.5 μm), and insignificant pyrophorisity, though of large specific surface (3.5–16.0 m^2/g). Apparent density

TABLE 25.5 Properties of Palladium Powders Used for the Manufacture of Thin-Walled Ceramic Condensers

Property	Palladium	Alloy
Palladium content (min %)	97	96
Chlorine-ion content (%)	0.01	0.04
Tap density (g/cm^3)	0.8–1.0	3.0–4.0
Specific surface (m^2/g)	10–16	3.5–6.0
Average particle size (μm)	0.3–0.6	2.0–3.5
Beginning of oxidation (K)	470–490	820–870
Phase composition	Pd	Pd + (5–10)% of PdO
Degree of transformation to oxide (%)	100	15–20

rises with the increase of the concentration of palladium salt, hydrochloric acid in the solution and the temperature and amounts to 0.8–2.8 g/cm^3. The specific surface is most significantly influenced by the content of palladium and acid in the solution, and the temperature as well. To precipitate 1 kg of palladium, 262 g of carbon monoxide with an 80% level of usage is required.

Osmium powder is produced from platinum containing 0.6%–1.0% of Os in two steps, according to the scheme OsO_4 oxide sublimation–electrolysis. Melting is done in an oxidizing atmosphere, and sublimates are collected in a 20% NaOH solution. Osmium-bearing powder (50%–70% of Os) is produced after the first stage by electrochemical precipitation. It is retreated in the same way; the final cathode residue is washed free from impurities, dried, and calcinated in a hydrogen atmosphere.

Autoclave Precipitation

Complex compounds are stable forms of noble metal ions in aqueous solutions. The thermodynamic probability of their autoclave reduction by hydrogen is sufficient significant. The development of the process of metal powder precipitation processes is determined by the kinetic parameters and courses at less rigid parameters than the precipitation of copper, nickel, and cobalt powders.

The precipitation of gold from its thiosulfate, chloride, and bromide complexes with 3+ charge proceeds at 330–340 K.

V.V. Ipatyev (1926) had first revealed the possibility of platinum precipitation from the chloride complex. He carried out this process at 293–303 K, $p_{H_2} = 2.5$–4.0 MPa within 18–40 h. A positive influence of a seed was established, and the precipitation rate increased in the series Pt, Ir, Rh, and Pd. In general, this process can be described by the following reactions:

$$H_yMCl_x + \frac{y}{2}H_2 \rightarrow M + xCl^- + 2yH^+$$

Similar reactions for actual platinum metals are presented below:

$$H_2PtCl_3 + 0.5H_2 \rightarrow Pt + 3Cl^- + 3H^+ \quad E_0 = 1.47V$$

$$H_2IrCl_3 + 0.5H_2 \rightarrow Ir + 3Cl^- + 3H^+ \quad E_0 = 1.02V$$

$$H_2PtCl_4 + H_2 \rightarrow Pt + 4Cl^- + 4H^+ \quad E_0 = 0.73V$$

$$H_2PdCl_4 + H_2 \rightarrow Pd + 4Cl^- + 4H^+ \quad E_0 = 0.62V$$

$$H_2RhCl_6 + 2H_2 \rightarrow Rh + 6Cl^- + 6H^+ \quad E_0 = 0.44V$$

Palladium and rhodium were reduced from the solutions containing 15–25 ppm (parts per million) of metal and 1 M of HC1 at a hydrogen pressure of 0.1 MPa at 293–313 K, and platinum and ruthenium were reduced at 343–353 K. The effect of increasing p_{H_2} to 0.35 MPa is established only for platinum and ruthenium.

In processing the acetate sulfate solutions. The reduction of Rh (III), Pt (IV), and Ru (III) to metal proceeded rather quickly, and the process rate did not depend on the anion concentration and the ionic force of the solution. Cl^-, I^-, NH_3 ligands at their content higher than 3N decelerate platinum metal precipitation, and the process stops in the presence of CN^- ($p_{H_2} = 0.01$ MPa, 353 K). There is an induction period in kinetic curves: the process rate is described by the equation of the first order of $-d[M]/d\tau = k[M^{n+}]\cdot[H_2]$ type. Experimental rate constants k (c^{-1}) of reduction are as follows:

$$k: \text{for} RuCl_6^{3-} = 1.0; \quad \text{for} RhCl_6^{3-} = 0.18;$$
$$\text{for} PdCl_4^{2-} = 0.33; \quad \text{for} PtCl_4^{2-} = 5 \times 10^{-4}$$

The precipitation of palladium from the solution bearing 2 g/L of Pd as H_2PdCl_4 requires the following: 303 K, $p_{H_2} = 0.3$ MPa; $\tau = 1$ h; the process is not developed in the presence of Cu (II) or Fe (III) ions.

Iridium can be reduced only to Ir (III) during the processing of chloride solutions bearing Ir (VI) ions at 303 K. Iridium metal is precipitated from the solution (64 mg/dm^3, 20 g/L of HC1) only at 413 K, $p_{H_2} = 0.3$ MPa within 1 h. Platinum metals are precipitated at 353–420 K within 0.5–1.0 h with sufficient stirring. Selective precipitation can be carried out depending on temperature and hydrochloric acid concentration.

Homogeneously sized silver powder with a bulk weight of 0.3–3.0 g/cm^3 is produced by processing silver oxide pulp bearing 10–200 g/L of solid, $T = 330$–390 K, and $p_{H_2} = 0.5 - 2.5$ MPa within 10–40 min. Ammonia or silver salt is added to the pulp to increase the bulk weight, and alkaline-earth metal sulfides or silver powders are added to decrease it. The powder produced is used for the manufacture of products, compositions, and catalysts.

Noble metal powders can be precipitated by carbon monoxide in the interval of pH ≤7.0, at temperature 293–473 K, and $p_{CO} \geq 0.1$ MPa.

PRODUCTION OF NOBLE METAL ALLOYS POWDERS

The key condition of alloy production is phase composition uniformity achieved by alignment of the precipitation rate of components and their joint crystallization.

The most popular methods are chemical, contact displacement, and electrochemical precipitation.

Silver-palladium powders used, in particular, as metallized paste fillers in capacitor production have to meet the following requirements: 70% of Ag and 30% of Pd, surface of not lower than 1.5–2.3 m^2/g, apparent density of 0.7–1.0 g/cm^3, content of the fraction with the particles of size ≥90 μm not higher than 15%, and a homogeneous phase composition.

For their production, the basic raw material is dissolved in nitric acid, then the solution (80–100 g/L of Ag and Pd) is neutralized by alkali to pH 4.5–5.0, and the powder is precipitated by sodium formate to the residual content Σ(Pd, Ag) < 1 mg/L at 340–350 K. The reducer consumption is 1.5–2.0-times the stoichiometric composition. The produced powder is annealed in a reducing atmosphere and screened. Due to a developed surface (>5–7 m^2/g) and the presence of residual nitrates, the oxygen content in the powder can rise to 1.5%–2.0%, which is intolerable.

Powders with an average particle size of 0.6 μm were produced using hydrazine as a reducer (320–330 K, six times the consumption of stoichiometric quantity). According to another method, the silver-palladium composition is produced by stirring nitrate solutions (17 g/L of Ag, 3 g/L of Pd) with a reagent-precipitator (hydrazine + surfactants) at 326 ± 5 K. The surface of the produced powder is 2–7 m^2/g.

The Pd-Cu alloy (55% of Pd) is produced from the solution of chlorides of these metals by reduction with hydrazine-sulfate. Two-three component alloys are produced by precipitation from hydroxy-ammonia and chloride ammonia complexes (the latter to provide the phase composition uniformity) of the $(NH_4)_2MCl_4$ type where M is Pt (IV), Pd (IV), Os (IV), and Ir (IV) with further treatment of the powder in hydrogen at 670 K.

A local reduction, first of all of palladium, is possible when using a pulp of salts of metals, which are constituents of the produced alloy, and its precipitation by an organic reducer (most often sodium formate). Further, this results in a nonhomogeneous distribution of solid solution components in the volume of a unit particle and a formation of up to 2%–5% of individual metal inclusions.

Powders of Pt-Pd alloy are produced by joint precipitation by treatment of a solution of chloride complexes of these metals with a sodium formate solution:

at pH <3

$$H_2[PdCl_4] + HCOONa \rightarrow Pd + 3HCl + NaCl + CO_2; \Delta G = -158\ \mathrm{kJ/mole}$$

at pH >3

$$[PdCl_4]^{2-} + HCOO^- \rightarrow Pd + H^+ + 4Cl^- + CO_2$$

$$[PtCl_6]^{2-} + 2HCOO^- \rightarrow Pt + 2H^+ + 6Cl^- + 2CO_2$$

The process includes: (1) induction, (2) precipitation and growth of nuclei, and (3) desorption and withdrawal into the solution of reaction products:

1. The induction stage is the diffusion of complex ions of the metal and the reducer to the seed surface.
2. The stage of precipitation and growth of nuclei is adsorption and an oxidation-reduction reaction:

$$[PdCl_4]^{2-}_{ads} + 2e \rightarrow Pd + 4Cl^-_{ads}$$

$$HCOO^-_{ads} - 2e \rightarrow CO_{2(ads)} + H^+_{ads}$$

accompanied by the growth of nuclei.

3. The stage of reaction product desorption and their diffusion into the solution.

In the case of multiple crystallization, the limiting stage is diffusion of Pt (Pd) (II) compounds to crystal surfaces. With the increase in pH, a part of aqua and hydroxo forms in the composition of the metal complex ions as well as the probability of niello precipitate formation.

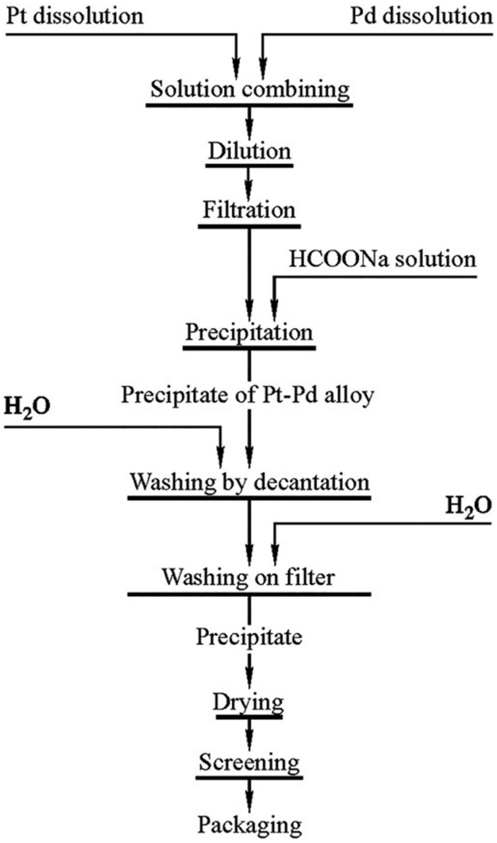

FIG. 25.2 Flow-sheet of Pt-Pd chemical precipitation from solutions.

The basic diagrams of alloy chemical precipitation are shown in Figs. 25.2 and 25.3. They differ according to the type of basic raw material: a slurry of metal salts or a solution. The proportion of components in the material that takes part in the precipitation provides further production of the alloy with a predetermined composition. It is adjusted in the starting material: for example, when producing the alloy PtPd-40p (in Russian classification) the proportion $[Pt]_0$:$[Pd]_0=1.4\pm0.1$ is kept in the solution. The precipitation is performed by a sodium formate solution ($\gamma=1.25$) at 435 ± 2 K, pH >7. The precipitate is filtered out and thoroughly washed for complete elimination of Cl (I) and Na (I) ions. The precipitate is dried for 4–6 h at 342 K and for 20–24 h at 393 K. It is then screened and packed.

The composition of the alloy of PtPd-40p brand (in CIS classification) is: Σ(Pt, Pd)>96.5 wt% including 58–61 wt% of Pt; not more than 0.04 wt% of Cl; 0.03 wt% of Na; 0.5 wt% of moisture; and 0.05–1.0 wt% of volatile matter (O_2, H_2, CO_2, CO).

This alloy is a single-phase alloy; its bulk density is of 1.4–1.9 g/cm^3. For example, per 1 kg of PtP-90 niello precipitate produced from metal, the consumption (in kg) is the following: 2.4 of $HN0_3$; 9.0 of HC1; 2.4 of Na_2CO_3; 3.0 of HCOONa; 200 of H_2O; and 100 kW h of electric energy. In particular, this alloy is, like platinum, suitable for the metallization of pottery surfaces bearing bismuth or titanium. In the processing of ammonium complexes of platinum and palladium (pH 12–13; 420–430 K; L: $S=2$; τ =0.5–1.0 h), the latter are precipitated fully as powder.

The technique provides a quick and complete procedure with the minimum consumption of alkali and without an external reducer. The particles have a spherical form, their size is 0.3–0.4 μm, and the specific surface of the powder is 2–4.5 m^2/g [11]. The size of the particles decreases when the temperature of the process increases, and the specific surface of the powder increases slightly.

Pt-Pd-Rh alloy is produced by thermolysis of a mixture of complex salts of $[M\ (NH_3)_4]NH_4(RhCl_6)]$, $M(NH_3)_4[RhH_2OCl_5]$ type where M is Pt (II), Pd (II). The products are solid solutions with compositions preset in the stage of mixture preparation; the powder particles have a spherical shape and the particle size is ≥10 μm.

A powder with apparent density of 0.7–1.9 g/cm^3 and a porous structure of particle conglomerates 30–40 μm in size is produced by thermolysis of platinum and palladium glycine complexes.

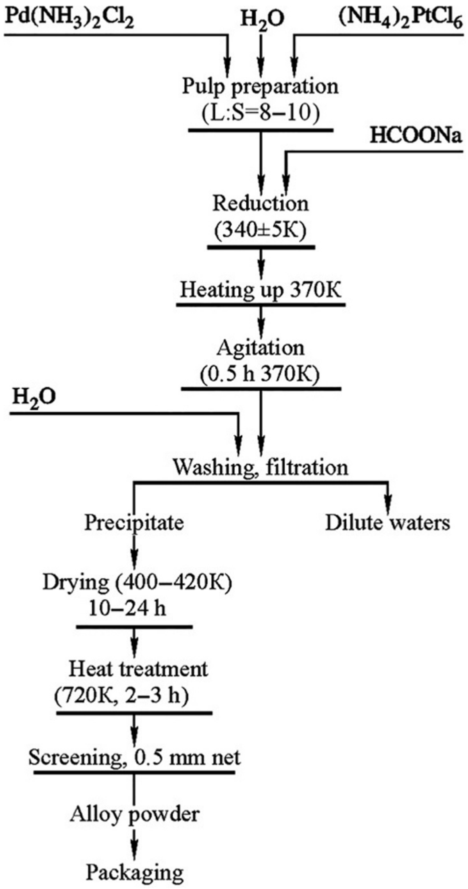
Pd(NH3)2Cl2
H2O
(NH4)2PtCl6
Pulp preparation
(L:S=8–10)
HCOONa
Reduction
(340±5K)
Heating up 370K
Agitation
(0.5 h 370K)
H2O
Washing, filtration
Precipitate
Dilute waters
Drying (400–420K)
10–24 h
Heat treatment
(720K, 2–3 h)
Screening, 0.5 mm net
Alloy powder
Packaging

FIG. 25.3 Method of Pt-Pd chemical precipitation from pulp.

Powders of palladium-based compositions were produced by thermolysis of aminooxalate complexes of $[Pd(NH3)_4]$ $[M(C_2O_4)_2]$ type where M is Zn, Cu, Ni, Co. An intermetallic was produced in the Pd-Zn system while, in other cases, the solutions were mixed with the metal in the ratio of 1:1. The powder particle size for all compositions is not larger than 1μm.

An isomorphic solution of platinum in palladium is precipitated by hydroformulation of a solution bearing platinum and palladium. The larger the palladium content, the greater the process rate. Platinum is precipitated sufficiently completely at the atomic proportion Pt/Pd=(1–2)/1. The procedure is performed at 343K, $[HCl]_0=0.75$ M, $[NaCl]_0=1.25$ M. Increasing the Cl (I) ion concentration decelerates the process, but increasing acidity accelerates it; the powder particle size is 1.8–2.7μm. Temperature and duration are governing factors for Pt-Pd-Rh mixture precipitation: 26% of the metal was precipitated at 370K within 3h while 97% was precipitated in 8h.

PRODUCTION OF PLATINUM BLACK DEPOSIT (NIELLO)

Before platinization, the electrodes are carefully cleaned in a chrome mixture or by SiO_2 powder, then calcinated. Platinization is carried out in the solution containing 30 kg/m^3 of H_2PtCl_6 and 0.2–2.3 kg/m^3 of $Pb(CH_3COO)_2$ at a current density that provides a moderate gassing on the electrodes ($\approx$50 A/m^2) and at 295K within 15min. In the case of simultaneous platinization of two electrodes (for example, for application in cells of electrical conductivity measurement), the current is commutated from time to time.

After platinization, the electrodes are put into a 10% solution of sulfuric acid and polarized cathodically within 5min with an auxiliary platinum electrode as the anode. The current strength in this case is adjusted also by gassing intensity. The adsorbed chlorine is reduced and eliminated more easily while washing as chloride ions. The electrodes are washed in running warm water and then in cold distilled water. The platinized electrodes have to be stored under a water layer as they loose wettability in air. Replatinization is performed in 1–2 min.

Synthesis of Palladium Nanopowders by Methods of Zone Electrochemistry

Palladium powder with a particle size of 5–15 nm is characterized by specific catalytic properties. Nanoparticles and their dendrite-shaped aggregates are produced from palladium chloride by means of cetyltrimethylammonia bromide (CTAB). The cylindrical part of the titanium rod is protected by plastic, and rectangular pulses of direct current and ultrasound are supplied alternatively to the electroactive disc part of the electrode. A predominant size of spherical particles (nuclei stripped from the electrode surface during ultrasound supply) is increased from 5 to 11–13 nm as the current density decreases from 130 to 80 A/m^2 in the solution with a palladium salt concentration of 10 mol/m^3. A preferred concentration range of palladium salt is 5–50 mol/m^3, and the interval between adjacent ultrasound pulses is 5–10 s. The CTAB content can vary within a range from 20 to 30 kg/m^3. Dendrite aggregates from nanoparticle chains are formed with increasing electrolysis duration to 2.5 h [12].

Manufacturing methods for electrolytic platinum-group powders and electrolytic platinum-group alloy powders are shown in Table 25.3.

Producing of Noble Nanoparticles in Metal-Organic Frameworks Pores

Metal-organic frameworks or porous coordination polymers continue to attract much attention in new emerging areas, particularly those related to energy use and environmental protection. The ZIF-8 framework ($Zn(mim)_2$, mim is 2-methylimidazole) has become popular for use as a support of select metal nanoparticles (M-NPs) for heterogeneous catalysis [13–15].

Zhang et al. [16] reported that an integral part of a porous framework and uniformly distributed throughout the internal pore space, the high density of the exposed B–H bond in zeolite-like porous BIF-20 (BIF = boron imidazolate framework) showed an effectively produce nanoparticles within its confined pore space. Small noble-metal nanoparticles (silver and gold) are directly synthesized into its pores without the need for any external reducing agent or photochemical reactions, and the resulting Ag@BIF-20 (or Au@BIF-20) samples show high catalytic activities for the reduction of 4-nitrophenol. The weight percentage of the silver nanoparticles in BIF-20 is 3.01%.

Noble Metals Application in Implantable Medical Devices

Implantable medical devices (cardiac defibrillators, cochlear implants, or neuromuscular micro stimulators) have been used worldwide to restore body functions, improve the quality of life, and save lives. Implantable medical devices are implanted long term and contain electronic circuits and batteries. In addition, for a safe and sustainable implantation in the human body without the release of toxic products and device degradation by body fluids, a hermetic housing is required. Generally, conductive pads that are surrounded by a biocompatible insulating material [17] ensure the communication between an electronic system located in hermetic packaging and sensors on the human body. A hermetic electrical feedthrough is thus essential for a safe and functional active implantable biomedical device. It needs to be as small as possible for patient comfort and safety reasons.

To bond metal and ceramic materials, brazing is so far the most widely used technique when a mechanically reliable gas tight bonding is required. However, for implantable devices, a high content of expensive noble metals is often added into the brazing paste, such as gold. The commonly used ceramic/metal feedthrough is made of pure platinum pins surrounded by alumina [17]. This kind of complex multimaterial component fabrication by a conventional process needs complex and expensive steps due to the dimensional accuracy required by each part and the brazing process.

Powder injection molding (PIM) can open new opportunities to manufacture hermetic feedthroughs between metal electrodes, ceramic insulators, and metal rings for packaging welding. The process allows manufacturing complex multimaterial and gas tight components in a reduced number of producing steps. Moreover, it allows, with an appropriate choice of materials and treatment conditions, bonding ceramic and metal without brazing. This work proposes to explore the PIM potential to carry out a hermetic feedthrough without brazing.

Two feedthroughs for medical implantable devices were carried out by PIM [18]. The metal-ceramic interfaces formed, Pt/Al_2O_3 and Al_2O_3/Ti-6Al-4 V, were investigated. Pure platinum wires with 0.33 mm diameter are used. Wires were cut to obtain 25 mm length pins. Then, the pins were cleaned in an ethanol/acetone bath. An alumina feedstock (a mixture of ceramic powder and binder) was supplied by Inmatec GmbH, Germany. CT1200 alumina in the feedstock with a 99.8% purity was used.

The leakage measurements performed on a circular feedthrough show that, for parts sintered under argon or vacuum, the rate of leakage is lower than 1.10^{-9} mbar. After alumina sintering, the leakage rate measurement on the Pt pin/alumina interface was lower than 1.10^{-9} mbar. To simulate the second thermal treatment, pin/alumina parts were heated at 1523 K under vacuum or argon. The leakage rate was also found to be below 1.10^{-9} mbar. The same gas tightness measurement was also performed on parts used for tensile tests with the same results. All results show that the bonding between the platinum pin and alumina is strong enough to obtain a hermetic interface, fulfilling the feedthrough requirements.

REFERENCES

[1] Butts A, Coxe CD, editors. Silver–economics, metallurgy, and use. Malabar: Krieger Publishing; 1975.
[2] Glicksman HD. Production of precious metal powders: silver, gold, palladium, and platinum. In: ASM Handbook, vol. 7. ASM International Publishers; 1998. p. 182–7.
[3] Baimakov YV, Zhurin AI. Electrolysis in hydrometallurgy. Moscow: Metallurgiya Publisher; 1977 [in Russian].
[4] Tomiltseva AK, Vyacheslavov PM, Burkat GK, Tsoi ZN. Silver powders electroprecipitation from sulphamine electrolyte. Soviet J Appl Chem 1978;51(9):2094–7 [in Russian].
[5] Yurev BP, Shkuryakova SP. Electrolytic preparation of fine Pd-Ag powders of any given chemical composition. Soviet Powder Metall Metal Ceram 1973;12(1):443–6 [in Russian].
[6] Shkuryakova SP, Yurev N. Production of fine platinum-palladium alloy powders. Soviet Powder Metall Metal Ceram 1974;13(12):953–5 [in Russian].
[7] Zayats AI, Perekhrest NA. Dispersed Pt-Co alloys precipitation. Soviet J Appl Chem 1972;45(10):2248–50 [in Russian].
[8] Ivanovskiy LE, Rozanov IG, Zotin IV, Khramov AP. Production of dendrite metals deposits by ionic melt electrolysis and their application. Liquid Melts 1997;2:51–9.
[9] Davies RR. New development in electronics and communications. In: RO MG, Bradley AG, editors. Precious Metals. Pergamon Publ.; 1981.
[10] Short, O.A., U.S. Patent 3,771,996, 1973.
[11] Collier N. Advanced in gold powder technology. Gold Bull 1977;10(3):62–6.
[12] Qiu XF, Xu JZ, Zhu JM, Zhu JJ, Xu S, Chen HY. Controllable synthesis of palladium nanoparticles via a simple soundoelectrochemical method. J Mater Res 2003;18(6):1399–404.
[13] Moon HR, Kim JH, Suh MP. Redox-active porous metal-organic framework producing silver nanoparticles from Ag^{I} ions at room temperature. Angew Chem Int Ed 2005;44:1261–5.
[14] Suh MP, Moon HR, Lee EY, Jang SY. A redox-active two-dimensional coordination polymer: preparation of silver and gold nanoparticles and crystal dynamics on guest removal. J Am Chem Soc 2006;128:4710–8.
[15] Zlotea C, et al. Pd nanoparticles embedded into a metal-organic framework: synthesis, structural characteristics, and hydrogen sorption properties. J Am Chem Soc 2010;132:2991–7.
[16] Zhang HX, Liu M, Bu X, Zhang J. Zeolitic BIF crystal directly producing noble-metal nanoparticles in its pores for catalysis. Sci Rep 2014;4(3923) https://doi.org/10.1038/srep03923, http://www.nature.com/articles/srep03923 (Accessed 31 December 2017).
[17] Jiang G, Zhou DD. Technology advances and challenges in hermetic packaging for implantable medical devices. New York: Springer; 2010.
[18] Vincenti D, Delette G, Laucourne R. A Gas tight platinum-alumina-TA6V feedthrough for implantable medical devices without brazing by powder metal injection. In: compiled by European Powder Metallurgy Association, (Bellstone Shrewsbury, UK) Proceedings of PM 2017 European Congress, Milan (Italy); 2016: p. 1–6.

Chapter 26

Production of Powders of Lead, Tin, Bismuth, and Their Alloys

Oleg D. Neikov*, Stanislav S. Naboychenko† and Irina B. Murashova†

Frantsevich Institute for Problems of Materials Science (IPMS), Kiev, Ukraine, †Ural Federal University (UrFU), Yekaterinburg, Russia

Chapter Outline

Introduction 847
Lead Powder Production 847
Atomization 847
Ball Milling 848
Electrolysis 850
Tin Powder Production 850
Bismuth Powder Production 854
Health and Environment Protection 854
Applications 858
References 860
Further Reading 861

INTRODUCTION

Lead, tin, and bismuth are distinguished by a low melting point. Their typical physical properties are represented in Table 26.1.

Due to this low melting point, the atomization process is simplified, and there are fewer problems with the selection of the refractory material for manufacturing melting furnaces, fused metal tubes, and atomizers [1–4]. An opportunity for hot gas atomization (above the melt temperature) that increases the stability of the atomization process due to melt drops welding on the atomizer is presented. This allows the use of close-coupled atomizers with the formation of a melt film on the nozzle edge [2–5] (see Chapter 4).

Currently, most lead, tin, and bismuth powders are produced by atomization because it is a convenient and cost-effective technique for the production of large powder batches while ball milling is popular for lead oxide manufacturing and bismuth contains thermoelectric material production.

LEAD POWDER PRODUCTION

Atomization

A typical lead powder production process based on hot gas atomization is described in book [1]. The bars of lead brands (CO and C1 brands in Russian Standard GOST 16138) serve as the raw material. Superheating the molten lead above 820 K noticeably decreases the surface energy and viscosity, resulting in fine powder making. However, the growing sublimation and high toxic lead vapor confine the superheat up to 720 K.

Lead bars are melted in a crucible. The melt is superheated up to 770 K and poured into a tundish, where a constant melt level is maintained. From the tundish, through a calibrated bottom orifice of 4–5 mm in diameter, metal flows into the atomization action zone, where it is atomized by an atomizer with an annular jet. The air blast at 0.6–0.8 MPa range pressure is heated in order to provide the temperature in the atomization zone in the 470–520 K range. To prevent drops sticking to the chamber walls, the vertical metal gas stream is deflected in a horizontal direction by auxiliary airflow. Air consumption for atomization ranges from 1.8 to 2.2 m^3 air per 1 kg melt. Powder from the chamber is transferred to sieving and the used air is subjected to dedusting in a cyclone and bag filter.

Table 26.2 gives the chemical and sieve analysis data for several commercially available lead powders produced by atomization. Air-atomized lead particles are roundish in shape. Fig. 26.1 illustrates typical particle shapes and surface topography.

Handbook of Non-Ferrous Metal Powders. https://doi.org/10.1016/B978-0-08-100543-9.00026-9
© 2019 Elsevier Ltd. All rights reserved.

TABLE 26.1 Typical Properties of Lead, Tin, and Bismuth

Property	Unit	Value		
		Lead	Tin	Bismuth
Physical properties				
Density[a]	g/cm^3	11.10	7.30	9.8
Crystal type[b]		fcc	Tetra.	R
Atomic diameter	nm	0.350	0.316	0.326
Melting point	K	601	505	544.2
Boiling point	K	2013	2543	1833
Specific heat	kJ/(kg·K)	130	226	120
Heat of fusion	kJ/mol	5.0	7.2	11.3
Heat of vaporization	kJ/mol	178	290	105
Solid-vapor surface energy	J/m^2	0.61	0.68	…
Elastic modulus at 298 K	GPa	200	55	32
Linear coefficient of thermal expansion from 298 to 373 K	μm/(m·K)	27.56	22.4	13.3
Thermal conductivity at 298 K	W/(m·K)	35.3	66.6	7.8
Electrical resistivity	μΩ·m	0.207	0.115	1.07
Mechanical properties				
Ultimate tensile strength	MPa	12–13	10–50	5–20
Hardness HB	MPa	30–40	50	93
Elongation	%	55	40	…

[a] *At room temperature.*
[b] *Crystal type: fcc, face-centered cubic (polymorphic at temperatures below 286.2 K);* Tetra, *tetragonal;* R, *rhombohedral.*

From Fedorchenko IM. Encyclopedia of inorganic materials. Kiev: Glavnaja Redakcija USE; 1977 [in Russian], German RM. Sintering theory and practice. New York: John Wiley & Sons Publishers; 1996.

Ball Milling

Two main methods, the Barton pot process and the ball mill method, are used for the production of lead oxide, also called lead monoxide, as the key component of automotive lead-acid batteries [6–8]. There are three lead oxides with commercial applications: lead suboxide (2PbO, Pb), also known as gray/lead oxide (battery oxide); litharge (PbO) red lead oxide (Pb_3O_4); or lead ortho-plumbate (PbO_4^{4-}).

The Barton pot process uses a cast iron pot with an upper and lower stirrer rotating at different speeds. Molten lead is fed through a port in the cover into the pot, where it is broken up into droplets by high-speed blades. Heat is supplied initially to develop an operating temperature from 643 to 753 K [7]. The exothermic heat from the resulting oxidation of the droplets is usually sufficient to maintain the desired temperature. The oxidized product is removed from the pot by an air stream. Automatic shaker-type fabric filters, often preceded by cyclone mechanical collectors or settling chambers, are the common choice for collecting lead oxides.

The ball mill method is based on the initiation of lead oxidation in air by heat generated during milling. Lead is fed into the rotating drum in the form of small cylinders. The feed rate is controlled automatically to maintain optimum lead quantities inside the drum. The lead oxide, produced by abrasion between the lead cylinders in a stream of air, is removed and transported to the baghouse by the same airflow. The aspiration system is specifically designed to take out only those particles within the usable size range (fine and very fine). Coarser particles remain in the drum until further oxidation; no screening or return of excessively large particles to the mill is required. The technical data of the SOVEMA "S" Series lead oxide mills [8] are represented in Table 26.3.

TABLE 26.2 Properties of Commercially Available Lead Powders Produced by Atomization

Property	Unit	Standard Grades		
		ПСА [a]	63 [b]	CSC [c]
Nominal composition				
Lead	wt%	99.7 min	99.7 min	99.6 min
Trace elements				
Antimony	ppm	5 max	…	…
Arsenic	ppm	5 max	…	…
Bismuth	ppm	50 max	…	…
Copper	ppm	10 max	…	…
Iron	ppm	20 max	…	…
Oxygen	wt%	0.3 max	…	…
Total impurities	wt%	0.3 max	…	…
Calcined residue after treatment by nitric acid	wt%	0.01 max	…	…
Sieve analysis				
–106 + 80 μm	wt%	…	…	5 max
–80 + 75 μm	wt%	1.0 max	nil	
–75 + 63 μm	wt%	1.5 max	0.2 max	15 max
–63 + 45 μm	wt%	…	10 max	
–45 μm	wt%	75–90	…	85 min
Apparent density	g/cm^3	5–6	4.5 ± 0.5	4.5–6.0

[a] *The requirements of CIS Standard GOST 16138.*
[b] *Pometon S.p.A. Standard grade.*
[c] *Chang Sung Corporation.*

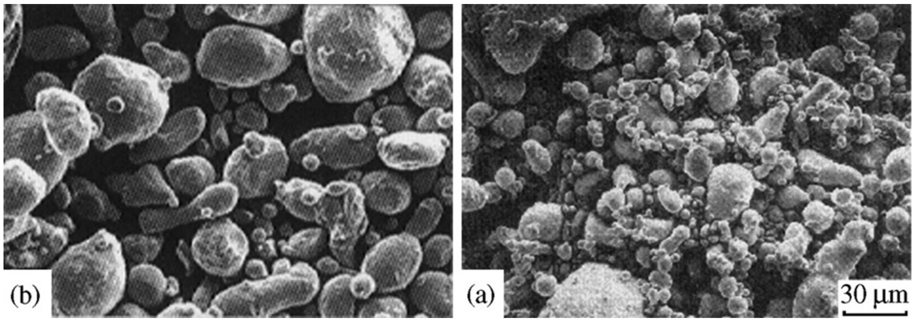

FIG. 26.1 Scanning electron micrographs of atomized (A) tin and (B) lead powders.

Comparison between the reactivity and productivity of the two production processes is characterized as the reactivity of lead oxide. In terms of battery performance, the ball mill method has an undeniable advantage. Therefore, the powder produced by this method is much more active due to the larger specific surface of the powder and also to the absence of orthorhombic (yellow) lead. In terms of productivity and production costs, the Barton pot method has a considerable advantage.

TABLE 26.3 Technical Data of the SOVEMA "S" Series Lead Oxide Mills

Components and Characteristics	Unit	Mill Type		
		S 300 (8 T)	S 600 (14 T)	S 1000 (24 T)
Lead oxide features				
Rate of oxidation	%	60%–80% (metallic lead content 40%–20%)		
Apparent density	g/cm^3	1.4–1.6		
Acid adsorption	mg/g	240–280 mg H_2SO_4/(g lead oxide)		
Particle size: typical distribution by 70% lead oxide content	µm	50% of the sample < 2.0µm; 75% of the sample below <5.0µm; 90% of the sample below <7.0 µm		
Electric requirements				
Mill				
• Exhaust fan	kW	37	75	132
• Feed conveyer	kW	0.75	0.75	0.75
• Return conveyer	kW	0.55	0.55	1.1
Filter				
• Exhaust fan	kW	13.2	18.4	26
• Cleaning fan	kW	5.5	7.5	9
• Extraction conveyer and valve	kW	0.75	0.75	0.75
• Air flow control shutters	kW	0.15	0.15	0.15
Water requirement				
Flow rate	L/min	30 L/min at 0.2 MPa		
Average consumption	L/h	300	200	300
Compressed air	MPa	0.6 MPa max – 0.4 MPa min		
Machine weight (Mill + filter)	kg	8500	15,000	23,000

Electrolysis

Methods of lead powder production by electrolysis render possible the manufacture of high purity powders. Electrolysis process parameters are adduced in Table 26.4.

Ultrafine lead powders, usable in lubricant compositions for formation of a protective layer against radiation, are produced by thermolysis. Alkylamide of oleic acid is mixed with lead formate in proportions ensuring 20% lead content in the mixture, which is then processed at 510 K for 1 h. As a result, powder with roundish particles and sizes ranging from 0.2 to 0.8 µm is produced.

TIN POWDER PRODUCTION

For tin powder production, the horizontal cross-jet air atomization technique is often used [13]. Pressures commonly employed range from 345 to 1725 kPa. Compressed air is preheated in a gas-fired heat exchanger to prevent freezing of the tin within or around the nozzle orifice arising from the chilling effect of the expanding air as it is streaming through the nozzle. The air stream with atomized particles enters the horizontal atomization chamber, where it is sucked by a fan into a cyclone where the powder is collected. The finest particles, which have not separated in the cyclone, are then retained on a filter.

TABLE 26.4 Production of Electrolytic Powders of Bismuth, Tin, Lead, Antimony, and Their Alloys

Method	Electrolyte Composition	Current Density (A/m^2)	Temperature (K)	Electrolysis Conditions and Ready Powder Properties
Bismuth [9]				
EDC	59.5 g/L Bi, 100 g/L NH_4Cl; 65.0 g/L glycerin; (pH from 0.2 to 2); 0,2% oleic acid	3.0	278	Cathode rotation 70 rpm; upper layer is mixture of cyclohexane and toluene; particle sizes: 0.05–0.1 μm
EDC	59.5 g/L Bi; 20.0 g/L HCl; 150 g/L NH_4Cl; oleic acid 0.5% in toluene	3.0–4.0	288–298	Cathode rotation 60 rpm; ready particulate product is aggregates of small particles.
Tin [10]				
EDC [10]	31.3–62.6 g/L Sn 0.5% Oleic acid	0.5–8.0	278–333	Top layer solvent is toluene; powder particle sizes: 0.2–0.5 μm
CED	12–119 g/L Sn	…	293–333	Substituting metal: Zn; solution: $SnCl_4$; drum rotation 12 rpm; particle sizes <300 μm; apparent density 1.51 g/cm^3
CED	12–119 g/L Sn	…	300	Substituting metal: Zn; solution: $SnCl_2$; rate of solution depletion 39.7 g/(L·h); average size of particles 222 μm; apparent density 0.67 g/cm^3
CED	12–119 g/L Sn	…	300	Substituting metal: Al; solution $SnCl_2$; rate of solution depletion 53 g/(L·h); average size of particles 249 μm; apparent density 0.56 g/cm^3
CED	Sn saturation	–	300	Substituting metal: Zn; solution $SnSO_4$; rate of solution depletion 10.7 g/(L·h); average size of particles 154 μm ; apparent density 1.08 g/cm^3
Lead				
WS	20–30 g/L Pb; 100–160g/L NaOH; 26.7–40 g/L NaCl; KCl up to 50.0 g/L	0.2–1.5	293	Solution on the basis of $PbCl_2$; lead anodes; current efficiency: approx. 100%
WS	7.5 g/L Pb; 200 g/L NaCl; 130 g/L NaOH	0.4–1.5	293	Current efficiency: 70–82%; precipitate deposition time is 5 min
WS	40 g/L Pb; 300 g/L NaCl	0.5–2.0	318	Current efficiency: 80.6–89.1%; voltage on the cell: 3–4.7V
WS	28 g/L Pb; 100 g/L NaOH; 29 g/L Na_2CO_3	3.0–4.0	291–296	Precipitate deposition time: 40–60 min
M	0.2–0.9 g/L Pb; NaOH	5.0–12.0	613–643	Lead in the melt is in form of Na_2PbO_2; nickel anodes
Lead-Tin				
M	10 g/L Pb; 59.6 g/L $SnCl_2$; 26.4 g/L KCl	5.0–6.0	510–550	Lead is contained in the melt as $PbCl_2$; current efficiency: 75%; 93–95% Pb contains in ready product; average size of particles 100 μm
Lead-Bismuth [11]				
EDC	35 g/L (Pb+Bi); 50 g/L NH_4NO_3; 30 mL/L HNO_3	2.0	293	Top layer: 0.03% oleic acid solution in toluene; ratio Pb to Bi is 10 to 1 in ready powder; current efficiency: 45–50%; particle sizes: 0.1–5 μm

Continued

TABLE 26.4 Production of Electrolytic Powders of Bismuth, Tin, Lead, Antimony, and Their Alloys—cont'd

Method	Electrolyte Composition	Current Density (A/m^2)	Temperature (K)	Electrolysis Conditions and Ready Powder Properties
Bismuth-Tin [12]				
EDC	(30–60) g/L (Bi + Sn); 50 g/L $(NH_4)NO_3$; 30 mL/L HNO_3 conc.	2.0	293	Alloys contains 70 to 90% Bi; particle sizes: 0.1–5 μm
EDC	33.2 g/L Bi; 31.4 g/L Sn; 100 g/L NH_4Cl; 30 g/L HCl	1.5	298	Cathode rotation 60 rpm; upper layer: toluene with 0.5% oleic acid; current efficiency: 50%; alloy consists about 80% Bi; salts: chlorides
Tin-Antimony				
EDC	(63–200) g/L (Sn + Sb) (80–100) g/L NH_4F (pH = 3.54)	0.2–0.6	298	Ratio $SnCl_2$ to $SbCl_3$ is 1.0 to 1.0; alloys: mixture of tin and intermetallides; current efficiency: 60%–85%; particle sizes: 0.1–2 μm

Technique: WS, water solution electrolysis; EDC, electrolysis from double-layer cell (see section "Reduction from solution through film of surfactants" in Chapter 8); CED, contact electrolytic displacement (see section "Contact displacement method (Cementation)" in Chapter 8); M, electrolysis from the melt [composition–% (by mass)].

The vertical melt atomization technique also finds application for tin powder production. One such unit is shown in Fig. 26.2 [14]. It consists of a reservoir to which molten metal is fed by gravity. From the reservoir, the metal flows into the tundish. The flow is controlled by an electromagnetic arrangement device so as to maintain a constant level in the tundish and, therefore, a constant flow rate to the atomizer. The reservoir, tundish, batcher, atomizer, and the fused metal tubes connecting them are provided by electric heaters. The atomizer is mounted on the lid of the cylindrical atomization chamber into which a jet of melt is atomized by an annular air jet, forming a metal-air stream. Cold air is fed into that stream with directed jets formed by an exhaust manifold with apertures placed under the chamber lid.

The additional cooling by means of air jets increases the turbulence of the metal-air stream, raises the cooling rate of the particles, and decreases the adhesion of powder on the chamber walls. Atomized powder accumulates in the container at the bottom of the atomization chamber. The finest particles, which have not separated in the chamber, are then retained on a filter.

The closed nozzle design [14] has been used (Fig. 26.3). The atomizer was equipped with changeable parts, nozzles, and sleeve to ensure various operating modes. The nozzles differ by arrangement of the discharges and their diameters: one central discharge for melt out flow (a) and three radial discharges with axes perpendicular to the outside wall (b) of the nozzle. Table 26.5 contains the technological parameters of tin powder production by means of a vertical melt atomization technique.

The physical properties of tin powder depend on atomization conditions and sieving procedures. Coarse grades are atomized by larger metal streams using lower air pressures. The finer grades of powder require higher pressures and a small molten metal stream. Sieving is an independent means of controlling the size of the largest particles in the powder.

Table 26.6 contains data about properties of commercially produced tin powders. Impurities in the tin melt stock carry over to the powder. The tin powder purity is directly related to the purity of the ingot melted.

The production of active powder used as a catalyst is based on the transformation of white tin (β) into gray tin (α) at a temperature below 286.2 K. The gray tin modification has a cubic diamond-type structure with lattice spacing $a = 6.4891$ Å. This conversion process takes place at temperatures below 256.4 K with significant volumetric expansion ($\Delta V = 26.6\%$) and depends on temperature and metal purity. Powder particles have an irregular fission-fragment shape with a rather developed surface, which is 30–40 times that of the atomized powder.

By means of electric explosion of tin wire in an ethyl alcohol medium, a powder with particle sizes from 13 to 20 μm is produced. The powder particle sizes were decreased still further two to three times by including 1.0 wt% cadmium or 0.56 wt% bismuth in the melt.

Ultrafine tin powders with particle size ranging from 0.3 to 0.8 μm are produced by electrochemical precipitation from a double layer bath consisting of an aqueous phase represented by chloride/fluoride electrolyte (150 g/L $SnCl_2{\cdot}2H_2O$

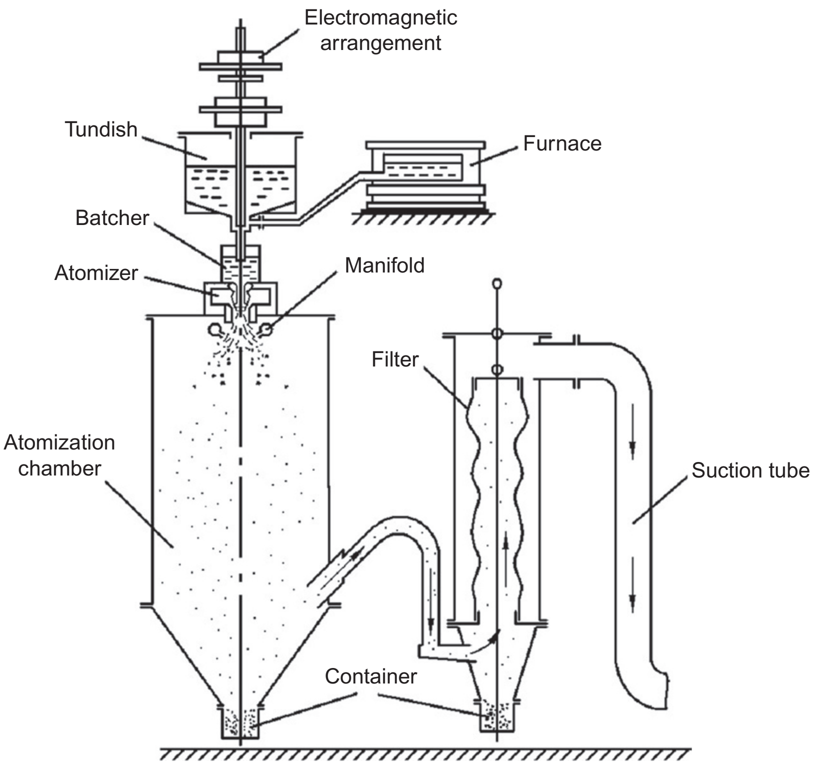
Electromagnetic arrangement
Tundish
Furnace
Batcher
Atomizer
Manifold
Filter
Atomization chamber
Suction tube
Container

FIG. 26.2 Vertical melt atomization technique of tin powder production.

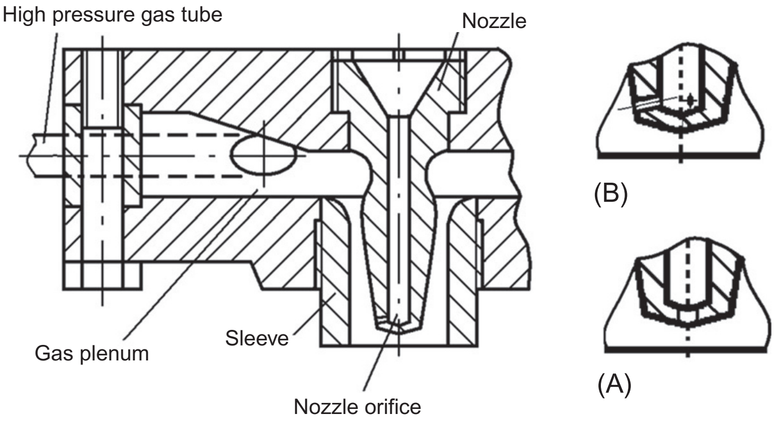
High pressure gas tube
Nozzle
Gas plenum
Sleeve
Nozzle orifice
(B)
(A)

FIG. 26.3 Close-coupled atomizer with changeable nozzles and sleeves: (A) nozzle with three radial discharges with axes perpendicular to the outside nozzle wall; (B) nozzle with one central orifice for melt outflow.

and 60 g/L NH_4F) and an organic medium—a solution of oleic acid in toluene [10]. At current density in the range from 50 to 500 A/m^2 and temperature ranging from 293 to 333 K, tin is reduced from complex anions $[SnClF_2]^-$ and appears in the form of black powder with particles being distributed uniformly in the organic layer of the bath. Sodium salts are not desirable due to possible formation of sodium oleate. After electrolysis, the powder is extracted from the organic phase, separated from the organic liquid by centrifugation, and washed free from the electrolyte by hot distilled water (360 K) and an aqueous solution of acetone or ethyl alcohol in relation 1.0–1.0. Washed powders are dried under vacuum at room temperature to constant mass. Oxide phases are absent due to adsorption by oleic acid. Current efficiency reaches 100%. The shape of particles is dendritic with short branches of the second order axes (Fig. 26.4). The structure of powders also depends on the cathode material. Comparison of silver, nickel, stainless steel, and aluminum cathodes shows that coarser particles are formed on silver cathodes, which have the most positive potential, while the finest particles are observed on deposition on the aluminum cathode, which has the most negative potential.

TABLE 26.5 Technological Parameters of Tin Powder Production by Means of Vertical Melt Atomization Techniques

Atomizer Type	Melt Mass Flow (kg/h)	Discharge Time of 1.0 kg Melt (s)	Melt Temperature (K)	Operating Gas Pressure in Atomizer (MPa)	Temperature of Operating Gas in Atomizer (K)	Pressure of Cooling Gas (MPa)	Powder Yield (%)[a]
3w/3.0[b]	498.3	7.2	623	0.55	623	1.8	87.1
3w/2.8	478.8	7.5	623	0.53	593	1.4	93.2
3w/2.0	264.6	13.0	623	0.50	603	3.0	93.9
1/3.0[c]	361.2	10.0	623	0.51	593	1.5	83.7
1/2.5	297.4	12.1	623	0.50	633	2.5	66.7
1/2.0	198.7	15.1	623	0.52	658	2.5	94.6
1/1.5	185.0	19.5	623	0.50	658	2.2	98.8

[a] *Percentage of expended raw material for the various nozzle types.*
[b] *Fraction numerator signifies "three radial discharges with axes perpendicular to the outside nozzle wall," in denominator is value of the orifice diameters, mm.*
[c] *Fraction numerator signifies "the nozzle with one central orifice for melt outflow," in denominator is value of the orifice diameters, mm.*

BISMUTH POWDER PRODUCTION

Bismuth powder can be produced by such processes as the mechanical comminution of bulk bismuth, electrolysis of nitrate and sulfate solutions at high current densities, electrolysis of $BiCl_3$ in methyl alcohol and glacial acetic acid, electrolysis of $BiBr_3$ in molten $A1Cl_3$, reduction of aqueous solutions of bismuth salts with various agents, and cathodic reduction of bismuth oxide.

Electrolytic bismuth powder is produced by the same method as tin powder in a two-layer bath with rotating cathode and soluble anode [9]; electrolyte composition: aqueous phase of 59.5 g/L Bi, 20 g/L HCl and 150 g/L NH_4Cl; organic phase toluene, and 5% oleic acid. The process is carried out at current density 3–4 kA/m^2 and at temperature ranging from 288 to 298 K; current efficiency is between 65% and 70%. Ultrafine powder modified by oleic acid is separated from the organic phase by centrifugation, then freed from the electrolyte by hot distilled water (360 K) and an aqueous solution of acetone or ethyl alcohol 1.0–1.0. Powders are dried under vacuum at room temperature to constant mass. Powders produced have particle sizes in the range from 0.1 to 0.5 μm. Other electrolytic production methods for bismuth, tin, and lead powders as well as their alloys [9–12] are given in Table 26.4.

A reduction method of bismuth powder production was described by the authors [15]. Bismuth powder was produced from freshly prepared α-Bi_2O_3 by reduction with a mixture of molecular and atomic hydrogen at 543 K. The reduction process $\alpha\text{-}Bi_2O_3 \rightarrow Bi$ makes possible the synthesis of bismuth powder without any intermediate phases. Up to 573 K, the reduction occurs due to a diffusion mechanism while at higher temperatures, it occurs through a diffusion-kinetic mechanism, resulting in increasing the reaction rate up to six times.

American Elements Company [16] specializes in producing high-purity bismuth powder (up to 99.9999 of BI-M-06-P brand) for use in preparation of pressed and bonded sputtering targets as well as in chemical vapor deposition (CVD) and physical vapor deposition (PVD) processes by thermal and electron beam evaporation, low temperature organic evaporation, atomic layer deposition, and metallic-organic and chemical vapor deposition. Commercially available powder comes in the following particle sizes: <44 μm, <150 μm, 10–50 μm, and submicron (<1 μm).

HEALTH AND ENVIRONMENT PROTECTION

Lead and the manufacture of its inorganic compounds carry grave dangers and harmful conditions. Lead is a highly toxic agent. According to US New Jersey Department of Health and Senior Services, the OSHA (Occupational Safety and Health Administration) legal airborne permissible exposure limit is 0.05 mg/m^3 averaged over 8-hour workshift. The occupational exposure limits (OEL) in the workplace atmosphere under legislation in the CIS Standard [17] amounts to 0.005 mg/m^3 as

TABLE 26.6 Properties of Commercial Tin Powders

		Standard Grades									
		ASTM Grade, sample			GOST 9723[a]			MMP[b]		Pom[c]	Bel[d]
Properties	**Unit**	**A**	**B**	**C**	**PO1**	**PO2**	**PO3**	**–100**	**–600**	**106**	**M Tin**
Nominal composition											
Tin	wt%	99.8 min	99.8 min	99.8 min	99.1 min	99.0 min	99.0 min	99.85 min	99.85 min	99.7 min	99.85 min
Trace elements, max											
Antimony	wt%	0.04	0.04	0.04	0.05	0.05	0.05	…	…	..	0.04
Arsenic	wt%	0.05	0.05	0.05	0.015	0.015	0.015	…	…	..	0.05
Bismuth	wt%	0.015	0.015	0.015	0.05	0.05	0.05	…	…	…	0.03
Cadmium	…	…	…	…	…	…	…	…	…	…	0.001
Copper	wt%	0.04	0.04	0.04	0.03	0.03	0.03	…	…	…	0.04
Iron	wt%	0.015	0.015	0.015	0.02	0.02	0.02	…	…	…	0.01
Lead	wt%	0.05	0.05	0.05	0.15	0.25	0.215	…	…	…	0.05
Nickel	…	…	…	…	…	…	…	…	…	…	0.01
Oxygen	wt%	…	…	…	0.5	0.5	…	0.15	0.15	…	…
Sulfur	wt%	0.1	0.1	0.1	0.016	0.016	0.016	…	…	…	0.01
Zinc	…	…	…	…	…	…	…	…	…	…	0.005
Sieve analysis											
+150 µm	wt%	48.0	0.3 max	…	…	…	…	0,5 max	…	…	1.0
+125 µm	wt%	…	…	…	…	…	…	…	…	nil	…
+100 µm	wt%	46.5	3 max	…	…	…	…	15. max	…	0,1 max	
+80 µm	wt%	…	…	…	0.5 max	0.5 max	…	…	…	…	…
+75 µm	wt%	4.0	3–8	…	…	…	…	15–35	nil	…	3.0
+71 µm	wt%	…	…	…	2.0 max	2.0 max	…	…	…	…	…
–63 µm	wt%	…	…	…	…	…	100	…	…	…	…
+53 µm	wt%	…	…	…	…	…	…	10–30	0.5 max	…	…
+45 µm	wt%	1.0	12–25	…	…	…	…	10 max	2.0 max	15–45	…

Continued

TABLE 26.6 Properties of Commercial Tin Powders—cont'd

		Standard Grades									
		ASTM Grade, sample			GOST 9723			MMP		Pom	Bel
Properties	**Unit**	**A**	**B**	**C**	**PO1**	**PO2**	**PO3**	**–100**	**–600**	**106**	**M Tin**
–45 μm	wt%	0.5	70–85	98 min	85–95	80 min	95 min	35–55	98 min	…	96.0
Fisher subsieve size, average size of particles	μm	…	10–15	1–3	…	…	…	…	…	…	…
Apparent density	g/cm^3	3.35	3.7–4.2	1.3–2.0	3.0–4.0	3.2–4.2	3.2–4.2	…	…	3.8±0.4	3.3

[a] *Russian Federation Standard.*
[b] *MMP—Makin Metal Powders Ltd (GB).*
[c] *Pometon. S.p. A., Metal powders and granules (Italy).*
[d] *Bel—Belmont metals Inc. (USA).*
ASTM—*American Society for Testing and Materials.*

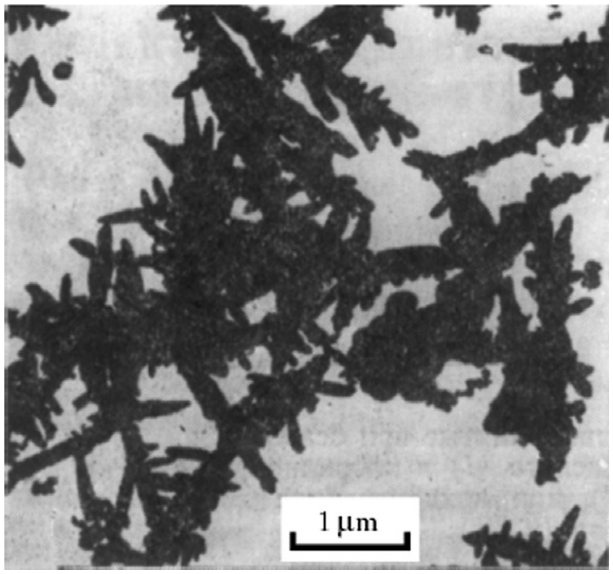

FIG. 26.4 Typical scanning electron micrograph of powder produced by electrochemical precipitation from a double-layer bath.

the shift time weighted average concentration and 0.01 mg/m^3 as peak concentration. It is classed with the extremely dangerous powders, the first class according to the above state Standard.

Because of the high toxicity of lead and its inorganic compounds, a complex of the industrial safety measures of lead powder manufacture is provided. These industrial safety measures include maximum encapsulation of all units and interoperational transport, maximum mechanization and automation of the processes, remote control of units, and conducting manual operations by means of manipulators in airtight boxes. In vented chambers where equipment is located, an underpressure is maintained in order to prevent an escape of airborne lead. The lead-containing suction gases are subjected to high-performance cleaning. Lead trace concentrations are continuously controlled in the workplace atmosphere and in the ambient factory air.

The admissible concentration limit of lead in an aqueous medium per toxicological indication is 0.03 mg/L. It is classified as a highly dangerous agent in the second dangerous class according to SanΠiN 4630-88 Standard [18].

The occupational exposure limit in the workplace atmosphere of bismuth and its inorganic compounds is 0.5 mg/m^3. It is placed in the second class of danger, according to the RF Standard [17].

The admissible concentration limit of bismuth in an aqueous medium per toxicological indication is 0.1 mg/L (for the inorganic compounds, including transition elements, subject to total contents of all forms). It is classified as a highly dangerous agent in the second dangerous class, according to SanΠiN 4630–88 Standard [18].

The vapors of toluene used for the electrochemical precipitation of tin powder in a double-layer bath process are classed as a third-class danger. Its occupational exposure limit in the workplace atmosphere amounts to 50 mg/m^3. Toluene is a substance with pencil-beam action demanding the automatic monitoring of its content in air. It is capable of causing allergic illnesses in working conditions. The admissible concentration limit of toluene in an aqueous medium per organoleptic indication, changing the smell, is 0.5 mg/L. It is classed as a moderately dangerous agent in the fourth dangerous class.

Metallic tin in particulate form is a combustible material while solid metal is noncombustible. The self-ignition temperatures of tin powder, containing 98 wt% with particles below 74 μm in size in aerogel and suspended solid conditions, are 793 and 933 K, respectively. The low concentration ignition limit (LCIL) is 220 g/m^3; the maximum explosion-proof oxygen content in airborne powder (LOC) diluted by carbon dioxide is 15 vol%. The combustibility and explosiveness of tin alloy with 2 wt% lead is characterized by the following data. Self-ignition temperatures of the powder with particles below 74 μm in size in aerogel and suspended solid conditions are 703 and 903 K, respectively [19]; the LCIL is 190 g/m^3; the maximum explosion pressure by airborne powder content 1000 g/m^3 is 340 kPa; the maximum rate of pressure rise is 12 MPa/s; the minimum airborne powder ignition energy is 80 mJ; and the LOC diluted by carbon dioxide is 16 vol%.

Products with such characteristics of inflammability and explosion risk are placed in the "moderate explosion hazard" class of danger,according to the Guide to Legislation and Health and Safety in the European powder-making industry [20].

To extinguish burning tin powder, it is necessary to use a mix of potassium and sodium chloride powder (with consumption about 15–50 kg per one square meter), or dry sand. For the voluminal quenching method, argon is used, consuming about 12.0 kg/m^3 in the burning zone.

Lead in particulate form is difficult to ignite. Self-ignition temperatures of lead powder with particles below 53 μm in size in aerosol and suspended solid conditions are 473 and 983 K, respectively.

Oleic acid, used for electrochemical precipitation of tin, bismuth, and their alloy powders in the double-layer bath process, is a combustible liquid. Its properties are characterized by the following data. The melting point is 287 K, the boiling point is 653 K, and the heat of combustion 10,370 kJ/mol. Oleic acid is insoluble in water. Its self-ignition and ignition temperatures are 553 and 453 K, respectively. To extinguish burning oleic acid, it is necessary to use bicarbonate of soda powder or the voluminal quenching method by means of carbon dioxide, consumption of about 0.7 kg/m^3 in the burning zone.

The cyclohexane, which is also used in the electrochemical precipitation of tin, bismuth, and their alloy powders in the double-layer bath process, is a highly inflammable liquid. Its properties are characterized by the following data. The melting point is 279.5 K, the boiling point is 353.7 K, and the heat of combustion is 3689 kJ/mol. Cyclohexane is insoluble in water. Its self-ignition temperature is 532 K. The lower and upper flame propagation limits in air are 1.3 and 7.8 vol%, respectively. The maximum explosion pressure is 858 kPa, the maximum rate of the flame propagation is 0.436 m/s, the minimum ignition energy is 0.22 mJ, and the burning temperature amounts to 2270 K. The means of extinguishing burning cyclohexane are the same as for oleic acid [19].

Techniques for the prevention of exposure to hazards are described in Chapter 27.

APPLICATIONS

The largest commercial application of lead and lead oxide, key components of lead-acid batteries, is the automotive industry. According to the "Global Automotive Battery Market–Analysis of Growth, Trends, Progress, and Challenges (2015–2020)" report, issued in August 2016, the automotive battery market is expected to grow at a CAGR of 5.29% to a market size of USD XX billion by the year 2020. Automobiles have a large number of functions these days. The new features have put great pressure on car batteries, which have to take on higher loads. The new fuel-saving technologies such as microhybrid systems are also leading to higher battery usage.

Tin powders are used extensively in the production of porous, self-lubricating bronze bearings and as constituents in soldering and brazing powders and pastes. Tin powders are also used in powder metallurgy structural parts, friction disks, clutches, brake linings, bonded resin friction materials, metal graphite brushes, diamond abrasive grinding wheels, bronze filters, peen plating, plasma arc spraying, chemical formulations, additives for rubber and plastics, chemical manufacturing, smokeless powder for pyrotechnics, foams, and tin flake.

The requirements for powders utilized for soldering paste production are a high content of fine particles and a low oxygen content. Some typical solder alloy powder grades used in soldering pastes and creams are listed in Table 26.7.

Because copper and lead have limited solubility in each other, they are difficult to alloy by conventional ingot metallurgy. Copper-lead powder mixtures have excellent cold-pressing properties. They can be compacted at pressures as low as 76 MPa to densities as high as 80% of theoretical density. After sintering, they can be repressed at pressures as low as 152 MPa to become practically nonporous bearings.

Cu-Pb-Sn PM materials are also used to replace solid bronze bearings. They are produced by spreading the powder in a predetermined thickness on a steel strip, sintering, rolling to theoretical density, resintering, and annealing. The end product has a residual porosity of about 0.25%. These materials include Cu-25Pb-0.5Sn, Cu-25Pb-3.5Sn, Cu-10Pb-0.5Sn, and Cu-50Pb-0.5Sn.

Tin, lead, and bismuth powders are used as compacted metal powders in the production of metallic foams. The metal powders are mixed with foaming agents to give a completely homogeneous mixture. The result of the subsequent densification step is a foamable material that, upon heating to temperatures within the range of the melting point, expands into a highly porous cellular solid with a closed pore structure. The typical structure of lead foam is shown in Fig. 26.5. More information about metallic foam technology can be found in Chapter 11.

As is known, **t**he conversion of thermal energy to electrical energy is named as a thermoelectric (TE) conversion [21]. The TE effect can be used for both power generation and electronic refrigeration. Thermoelectric technology and solid-state devices based on the TE effect have a number of advantages, including having no moving parts as well as being reliable and scalable. The technology has therefore aroused worldwide interest in many fields, including waste heat recovery and solar heat utilization (power generation mode) as well as temperature-controlled seats, portable picnic coolers, and thermal management in microprocessors (active refrigeration mode)**.**

TABLE 26.7 Typical Solder Alloy Powder Grades

		Standard Grades													
		ASTM Grade, Samples						GOST 1499, Samples[a]						Nippon AMP	
Property	**Unit**	**10 B**	**30 B**	**50 B**	**63 B**	**62 P**	**96.5TS**	**ПОС 10** [b]	**ПОС 40** [b]	**ПОС 61** [b]	**ПОС 90** [b]	**ПОССу 61-0.5** [c]	**ПОССу 95-5** [d]	**80-20**	**60-40**
Composition															
Main components															
Tin	wt%	8–12	28–32	48–52	61–65	61.5–67.5	95–96	9–10	39–41	60–62	89–91	60–62	94–96	80	60
Antimony	wt%	0.2–0.5	0.2–0.5	0.2–0.5	0.2–0.5	0.3–0.5	0.2–0.5	…	…	…	…	0.2–0.5	4.0–5.0	…	…
Lead	wt%	bal	bal	bal	bal	bal	bal	bal	bal	bal	bal	bal	bal	20	40
Trace elements, max															
Aluminum	wt%	0.005	0.005	0.005	0.005	0.005	0.005	0.002	0.002	0.002	0.002	0.002	0.002	…	…
Antimony	wt%	…	…	…	…	…	…	.0.05	.0.05	.0.05	.0.05	…	…	…	…
Arsenic	wt%	0.02	0.02	0.02	0.02	0.02	0.02	0.03	0.03	0.03	0.02	0.03	0.05	…	…
Bismuth	wt%	0.25	0.25	0.25	0.25	0.25	0.25	0.1	0.1	0.1	0.1	0.1	0.2	…	…
Copper	wt%	0.08	0.08	0.08	0.08	0.08	0.08	0.05	0.05	0.05	0.05	0.08	0.1	…	…
Iron	wt%	0.02	0.02	0.02	0.02	0.02	0.02	0.02	0.02	0.02	0.02	0.02	0.02	…	…
Lead	wt%	…	…	…	…	…	…	…	…	…	…	…	…	…	…
Nickel	wt%	…	…	…	…	…	…	0.02	0.02	0.02	0.02	0.02	0.08	…	…
Silver	wt%	…	…	…	…	1.75–2.25	3.3–3.7	…	…	…	…	…	…	…	…
Sulfur	wt%	…	…	…	…	…	…	0.02	0.02	0.02	0.02	0.02	0.02	…	…
Zinc	wt%	…	…	…	…	…	…	0.002	0.002	0.002	0.002	0.002	0.002	…	…
Particle sizes	μm	…	…	…	…	…	…	≤50	≤50	≤50	≤50	≤50	≤50	5[e]	10[e]
Solidus temperature	K	541	456	456	456	452	494	…		…	…	…	…	…	…
Liquidus temperature	K	572	528	489	456	452	494	…		…	…	…	…	…	…
Soldering range	K	602–642	558–598	486–555	485–526	482–531	524–564	…		…	…	…	…	…	…

[a] *CIS Standard.*
[b] *Antimonousless.*
[c] *Low- antimonous.*
[d] *Antimonous.*
[e] *Median diameter.*
Nippon AMP: Nippon Atomized Metal Powders CO.

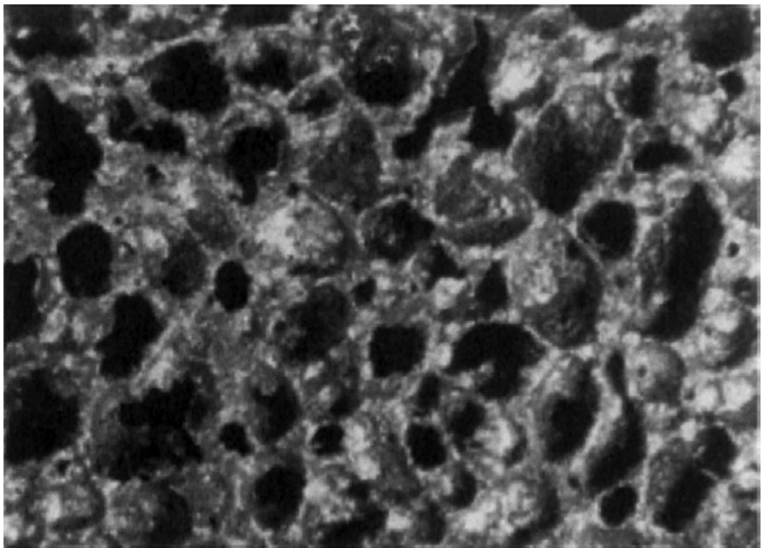

FIG. 26.5 Optical micrograph of cross-section of lead foam. *From Banhart J, Baumeister J, Weber M. Metallic foam. In: ASM handbook, vol. 7. ASM International Publishers; 1998. p. 1043–7.*

Li et al. [22] focused on thermoelectric conversion of Bi-Te alloys, skutterudite compounds, and Ag-Pb-Sb-Te quaternary systems. A novel method for rapid preparation of Bi_2Te_3 nanosized powders with an average particle size of about 70 nm was developed by Chen et al. [23]. A starting Bi_2Te_3 particulate material of ~5 mm average size was subjected by cryogenic grinding in the liquid nitrogen. For comparison, the conventional high-energy ball milling was used to prepare the Bi_2Te_3 nanosized powders. It was found that Bi_2Te_3 does not transform into a nonequilibrium amorphous phase or decomposes during the cryogenic grinding process. Spark plasma sintering was used for powder consolidation. The authors reported that spark plasma sintering showed that cryogenic grinding can produces much finer and good sinterability Bi_2Te_3 powders in comparison with high-energy ball milling.

REFERENCES

[1] Naboychenko SS, editor. Handbook of nonferrous metal powders. Moscow: Metallurgia Publishers; 1997 [in Russian].

[2] Strauss JT. Close-coupled gas atomization using elevated temperature gas. In: Proceedings of 1999 powder metallurgy international conference, vol. 1, San Diego, CA: Metal Powder Industries Federation; 1999. p. 22–33.

[3] Wolf G, Till K, Scholz R. Hot gas atomisation. In: Proceedings of 2002 powder metallurgy world congressPrinceton: MPIF Publishers; 2002 p. 3-163–3-177.

[4] Dunkley JJ, Aderhold D. The fourth dimension in gas atomisation and the influence of gas density on the atomisation of melts. In: Proceedings of the 4th International Conference on Spray Deposition and Melt Atomization, SDMA2009Bremen: Universität Bremen; 2009. p. 1–8.

[5] Rieken JR, Heidloff AJ, Anderson IE, Mullis A, Chernenkoff RA, Brian W. Development of a close-coupled gas atomization process for fine metal powder production. In: Proceedings of 2014 Powder Metallurgy World CongressOrlando, FL: Metal Powder Industries Federation; 2014 p. 02-54–60.

[6] Pavlov D. Lead-acid batteries. Amsterdam: Elsevier; 2011.

[7] Gravita India Ltd. http://www.gravitagroup.com/Lead-Oxide-Manufacturing.asp.

[8] SOVEMA “S” Series lead oxide mills, di Verona (Italy). //sovema_lead_oxide_mill.pdf.

[9] Zhelibo EP, Grechanjuk VG. On bismuth fine powders deposition on passivated electrodes. Sov Powder Metall Met Ceram 1978;6:1–6.

[10] Zhelibo EP, Grechanjuk VG. Electrodeposition of tin fine powders from cloride-fluoride electrolytes. Sov Powder Metall Met Ceram 1978;7:4–7.

[11] Fil’ TN, Khimchenko EI, Isaj VN, Romanova AV. Electrodeposition and X-ray diffraction examination of high-disperse lead–bismuth alloy. Sov Powder Metall Met Ceram 1977;3:12–9.

[12] Zhelibo EP, Grechanjuk VG. Effect of electrolyte composition on conditions of tin–bismuth highdispersed alloy formation. Sov Powder Metall Met Ceram 1978;8:5–9.

[13] Ullrich WJ. Production of tin powders. In: ASM handbook. vol. 7. ASM International Publishers; 1998. p. 146–7.

[14] Adamchik LV, Bondarenko SG, Koval’chuk VG, Pavlenko DV, Statsenko ID. Gas-sprayed tin powders. Sov Powder Metall Met Ceram 2003;42 (1–2):100–4.

[15] Chernogorenko VB, Lynchak KA. Production of bismuth powder by the reduction of bismuth oxide with a mixture of molecular and atomic hydrogen. Sov Powder Metall Met Ceram 1973;12(5):360–2.

[16] American Elements Company. https://www.americanelements.com/bismuth-particles-7440-69-9 [Accessed 31 January 2018].

[17] CIS Standard GOST 12.1.005-88. Moscow: Publishers of Standards; 1988 [in Russian].

[18] Sanitary Regulation and Standards of surface waters from pollution. SanΠiN 4630-88. Moscow: MinZdrav; 1988 [in Russian].

[19] Baratov AN, Korolychenko AJ, editors. Handbook Fire- and explosion-proof of matters and materials and means for their quenching. Chimia: Moscow; 1990 [in Russian].
[20] Guide to Legislation and 'Health and Safety' in the European PM Industry. EPMA; 1997.
[21] Bechnia K. Fundamentals of Thermoelectrocity. Oxford: University Press; 2015.
[22] Li JF, et al. High-performance nanostructured thermoelectric materials. NPG Asia Mater 2010;2:152–8.
[23] Chen X, et al. Preparation of nano-sized Bi_2Te_3 thermoelectric material powders by cryogenic grinding. Prog Nat Sci Mater Int 2012;22(3):201–20.

FURTHER READING

[24] Fedorchenko IM, editor. Encyclopedia of inorganic materials. Kiev: Glavnaja Redakcija USE; 1977 [in Russian].
[25] German RM. Sintering theory and practice. New York: John Wiley & Sons Publishers; 1996.
[26] Lawley A. Atomization. Metal Powder Industries Federation Publishers: Princeton; 2003.
[27] Banhart J, Baumeister J, Weber M. Metallic foam. In: ASM handbook. vol. 7. ASM International Publishers; 1998. p. 1043–7.

Chapter 27

Safety Engineering in the Production of Powders

Oleg D. Neikov
Frantsevich Institute for Problems of Materials Science (IPMS), Kiev, Ukraine

Chapter Outline

Introduction 865
Dangerous and Harmful Manufacturing Factors 866
  Dust, Gaseous, and Vapor Emissions 866
  Ambient Noise and Vibration 866
  Heat Radiation 866
  Electrostatic Electricity 866
Properties of Powders 868
  Adhesion 868
  Hygroscopicity and Wettability 868
  Abrasiveness 869
  Inflammability and Explosivity of Powders 869
  Thermophysical Properties 875
Technique for the Prevention of Exposure Hazards 879
  Workplace Exposure Limits 879
  Common Demands to Production Area, Equipment, and Processes 881
  Explosion and Fire Safety 885
  Quenching Means 886
  Dust Explosion Protection Systems 887
  Localization of Powder-Gas Emissions 892
  Definition of the Local Exhaust Capacity 901
Clarification of Recirculated Water 918
  Mechanical Clarification Methods 918
  Chemical Treatment Methods 919
  Ion-Exchange Method 920
  Sorption, Evaporation, and Flotation Methods 922
Dust and Gas Cleaning 923
Waste Products Utilization, Storing, and Transportation 924
  Waste Utilization 924
  Storing and Transportation of Hazardous Powders 925
References 927
Further Reading 928

INTRODUCTION

The production of metal powders results in various dangerous and harmful manufacturing byproducts; the means for their prevention and mitigation of their action are considered in this chapter.

Open flames, heat radiation, molten metal, flammable and explosive dusts and gases, dusts and gases which cause harm through inhalation, and eye and skin contact, elevated temperatures in the workplace atmosphere, elevated temperatures of equipment surfaces, noise and vibration, voltage in electric circuits, electrostatic electricity, movable mechanisms, and mobile parts of equipment are dangerous and harmful agents inherent to the production of powders.

Generally, the dangerous and harmful factors in powder production, and in subsequent powder processing, are classified as chemical and physical agents. The latter include:

- the risks to health from exposure to noise,
- hand transmitted mechanical vibrations and whole-body vibrations, and
- the effects of electric and magnetic fields.

Chemical agents are classified by the properties of the substances concerned. Their action results in health risks in the form of suspended matter which becomes harmful upon inhalation, and contact with eyes or skin.

The physical-chemical properties of these dusts are characterized by their chemical composition, particle size distributions, specific surface, flammability, explosive properties, oxidizability, relative density, specific electrical resistance, adhesion property, wettability, abrasivity, solubility, etc.

Handbook of Non-Ferrous Metal Powders.. https://doi.org/10.1016/B978-0-08-100543-9.00027-0
© 2019 Elsevier Ltd. All rights reserved.

DANGEROUS AND HARMFUL MANUFACTURING FACTORS

Dust, Gaseous, and Vapor Emissions

The main sources of dust and emission of gas and vapor are melting furnaces for atomization, stands for heating the crucibles and tundishes, powder drying, classification, loading and unloading units, dosing, and packing. The heating of crucibles and tundishes by means of natural gas forms combustion gas containing approximately 12 vol% carbon dioxide, to about 2 vol% carbon monoxide and 2 vol% hydrogen, and maximum 0.2 vol% nitrogen oxides. The fusion of metals and atomization of melts are accompanied mainly by emission of metal oxides (Table 27.1). Thus, during copper melting in a 0.4-tn induction crucible furnace, the concentration of copper oxides in the convection current of sublimates over the melt amounts to 250 mg/m^3, in brass melting, between 830 and 2700 mg/m^3; while during the pouring of the melt into the tundish, the concentration amounts to 5700 mg/m^3, and in the pouring of bronze, to 7500 mg/m^3. The sublimates contain up to 90 wt% of particles with sizes below 2.5 μm.

Typical data of dust concentration and particle sizes distribution in aspiration exhausts by copper and copper alloys atomized powder production are given in Table 27.2.

The content of vapor in aspiration gas is determined by the intensity of vapor emission with assignment per mass flow of aspiration gas. Thus, during drying in the vibrodryer of water-atomized copper alloy powder with initial 8 wt% and residual 0.5 wt% water content with gas mass flow 1500 m^3/h, after 5 minutes drying, the vapor concentration in the aspiration gas is 21.4 g/m^3.

Ambient Noise and Vibration

The furnaces, atomizing installations, high-pressure pumps, equipment for crushing, comminution, and sieving, and lifting-transport equipment are noise sources. Data about characteristic levels noise created by certain operations are given in Table 27.3. The measures for reduction of general noise level and pressure levels in octave bands up to admissible sizes are requested by standard acts [1–3].

Vibrosieves are the major vibration source in powder production. Their levels of common vibration by geometric mean frequencies are characterized by following data: 89.5, 82.5, and 75 dB along 16, 31.5, and 63 Hz, respectively, while the admissible limit is 92 dB.

Heat Radiation

Molten metal, furnace equipment, and burning torches used for heating crucibles and tundishes are the main sources of heat radiation. Thus, in the tundishes heating zone at 1 m from the torch, the heat radiation amounts to 2250 J/(m^2·h), while the melting area near an induction furnace achieves about 12,880 J/(m^2·h). In such zones, protection from heat radiation is necessary.

Electrostatic Electricity

The electrical conductivity of dust is characterized by the resistivity value of the dust layer. Resistivity values are subdivided into good (below 10^2 Ω·m), medium (from 10^2 to 10$^{8–9}$ Ω·m), and high ohmic resistance (above 10$^{8–9}$ Ω·m). For resistivity determination, a dust layer is formed, and its electrical resistance measured.

TABLE 27.1 Typical Composition of the Sublimates Formed During Melting and Atomization

	Content of Elements (wt%)					
Metal	Copper	Zinc	Lead	Tin	Carbon	Oxygen and Other
Copper	92–96	…	…	…	…	5–8
Brass 63	9	24	…	…	38.4	28.6
Bronze	34	45.4	0.41	15.7	4.3	0.2
Zinc	…	77.0	…	…	…	23.0

TABLE 27.2 Typical Data of Dust Concentration and Particle Sizes Distribution in Aspiration Exhausts by Copper and Copper Alloys Atomized Powder Production

Technological Operation	Dust Concentration in Aspiration Exhausts (g/m^3)	Weight Powder Distribution by Particle Size (μm) Fractions (%)						
		<4	4–6.3	6.3–10	10–16	16–25	25–40	>40
Melt preparation:								
In induction furnace:		All particles are finer than 2.5 μm						
Copper	0.007							
Bronze (Cu-5Sn-5Zn-5Pb)	0.009							
Brass (Cu-20Zn)	0.031							
In reverberatory furnace:								
Zinc	2.56	90 wt% particles are finer than 2.5 μm						
Water atomization of melt:		All particles are finer than 10 μm						
Copper	0.02							
Bronze (Cu-5Sn-5Zn-5Pb)	0.03							
Brass (Cu-20Zn)	0.15							
Drying by vibrodryer[a]:		38.0	22.0	26.0	10.0	4.0	…	…
Copper	0.1							
Bronze (Cu-5Sn-5Zn-5Pb)	0.12							
Brass (Cu-20Zn)	0.15							
Sieving of powders	0.05–1.2	36.5	8.0	12.5	15.0	18.3	4.8	4.9
Blending in mixers:								
Double-cone mixers	0.36	24.1	22.6	20.9	1.6	0.8	24.0	16/0
Impeller mixers	3.2	16.0	24.0	0.8	1.6	2.9	22.6	14.1
Dry continued mills (discharge places)	4.5	4.1	1.8	3.2	2.2	6.4	15.8	66.7
Weight batchers	0.05	38.0	22.0	26.0	10.0	0.4	…	…
Unloading from conveyor into bin or technological apparatus	1.0	14.8	6.8	…	9.0	31.8	16.8	20.0
Loading-unloading of powder from conveyor to conveyor	2.7	13.9	5.3	3.2	8.9	31.9	16.1	20.7
Elevators (charge places)	2.96	6.5	39.3	32.1	11.6	6.6	4.0	…

[a] *Chapter 14 contains data of drying by vibrodryer.*

TABLE 27.3 Characteristic Noise Levels by Fulfilment Certain Operations

Manufacturing Process	Common Noise Level (dB)	Pressure Level (dB) in Octave Bands (Geometric Mean Frequencies, Hz)							
		63	125	250	500	1000	2000	4000	8000
Shears cutting of copper bars	84	93	88	84	81	80	78	76	72
Fusion in induction furnace	101	77	74	80	76	91	70	70	61
Water atomization	86	80	80	83	80	82	71	70	68
Sieving of the powders	92	87	87	87	90	87	81	76	70

The movement of powder and dust streams is accompanied by their electrization; here, the value of charge depends on both the nature of the dust and the material of the contacting surface. The lowest specific charge value for bronze and brass powder and dust is observed by using copper as the contacting material. The movement of bronze and brass powder streams leads to the appearance of specific charge 3.35 C per 1 g bronze powder and 2.99 C per 1 g brass powder. On a surface of an aluminum alloy or chromium, the electrostatic electricity charges for bronze and brass particle are 5.5 and 3.5 C/g, respectively, and on a steel-contacting surface, 6.35 and 3.88 C/g, respectively [4].

PROPERTIES OF POWDERS

Adhesion

The ability of particles to form aggregates and adhere to apparatus walls is a function of autohesion and adhesion interaction. Autohesion is the interaction of particles with each other, and adhesion is of the interaction of particles with the monolayer of surfaces. The tensile strength of a dust layer characterizes its dust autohesion. Under autohesion, the dust is classified into three groups: nonagglutinated dust with tensile strength below 60 Pa, weakly agglutinated with tensile strength ranging from 60 to 300 Pa, and strongly agglutinated—higher than 600 Pa.

For examples, bronze powders are referred to as weakly agglutinating with tensile strength from 60 to 244 Pa depending on their particle sizes distribution. A brass powder coarser than 160 μm is placed into non-agglutinating group, having the breaking strength of 44 Pa. The powder-like portions of brass powders are referred to as weakly agglutinating, with breaking strength on the order of 200 Pa.

Powder flowability is characterized by the angle of repose. The static and dynamic angles of repose are differentiated. The former refers to the angle, at which the side surface of particulate material is located after removal of a supporting wall. The dynamic angle is the angle between the basis and element cone, obtained by free-fall of powder onto a flat horizontal surface. More detailed interpretation of flowability and angle of repose is contained in Chapter 1 of this book.

Hygroscopicity and Wettability

Hygroscopicity, that is, the ability to absorb moisture from the environment, influences powder properties such as autohesion and adhesion interaction, flowability, and the electrical conductivity of the dust layer, making it necessary to take into account when designing aspiration installations.

The so-called equilibrium specific humidity of powder is its moisture content which corresponds to the current gas moisture. The hygroscopic moisture content is determinated by drying a sample to constant weight. This method is most widely used, but is not applicable to substances with decomposition or fusion temperatures below 383 K.

The wettability of dust is determined by the interaction of molecules on the boundary of solid, liquid, and gaseous phases and leads to a liquid film forming on the surface of the particles. The wetting of dust particles by water droplets is the base of the wet-dedusting process.

The tendency of the dust toward wetting is evaluated by the film floatation method, which consists of determination of the weight of a powder placed on the surface of water that sinks in a specified time. At wettability, the dust is divided into three groups: bad, medium, and good wettability, for which the percentage of particles that sink is 30, 30–80, and greater than 90 wt%, respectively.

Abrasiveness

The abrasive properties of dust depend on the hardness, particle shape, density, and particle sizes and can be expressed as abrasive coefficient K_a. A laboratory method of K_a determination for their values, exceeding 0.5×10^{-12} m^2/kg, is based on determination of the degree of wear of a plate, located at an angle of 45 degrees by a stream of the powder investigated.

Inflammability and Explosivity of Powders

Metals which have the potential to combine with oxygen have the further potential to ignite or explode when in their dispersible condition. Powders in layer or dust deposits are not exploded, but by action of applicable ignition source, they can catch fire and burn. A local initial explosion usually breaks up the deposit and leads to dust cloud formation. Here, the flame is able to expand throughout the cloud, and can generate an explosion of large-scale destructive strength.

Inflammation and explosion can occur not only due to oxygen, but also via other exothermic reactions, for example, as a result of the interaction of magnesium with nitrogen and aluminum and magnesium with freon.

The evaluation of combustibility of the powder in layer or dust deposit consists of minimal ignition temperatures, smoldering temperature, and combustibility group.

The tests for an explosion assessment of powder or dust in suspended solid state are follows:

- Low concentration ignition limit
- Minimum ignition and self- ignition temperatures
- Maximum explosion pressure
- Maximum rate of pressure rise
- Minimum ignition energy
- Limiting oxygen concentration to prevent ignition

Conditions for explosion to occur include the following criteria:

- The powder must be combustible,
- The powder must be capable become suspended solid state,
- The concentration of airborne powder particles in the dust cloud must be within the critical ignition limit range,
- The suspended solid in contact with an ignition source in air must be capable of initiating and sustaining flame propagation, and
- The atmosphere into which the dust is suspended must contain sufficient oxygen to support combustion.

Combustibility is the ability of a material to burn; the materials can be divided into combustible, difficult, and incombustible. Depending on the material combustibility group, an appropriate category of manufacture is accepted, as well as the technical decisions, providing the fire explosion safety of powder production, storage, and transportation are designed.

Ignition of Dust Deposits and Powder Layers by Self-heating or Hot Surfaces

Smoldering combustion, or glow fires, in powder or dust deposits can give rise to explosions in several ways. Smoldering combustion can start as a slow process in the powder deposit at quite low temperatures, in some cases, even at normal room temperature. Smoldering combustion can also be initiated by a hot object that is either fully embedded in the dust deposit or on which the deposit lies.

Smoldering temperature (T_{sm}, K) is the temperature during self-heating at which the exothermic reaction rate increase leads to the appearance of smoldering.

Minimum ignition temperature (T_i, K) is the minimum temperature of powders at which, in the presence of an external ignition source, the temperature increases through the exothermic reaction, ending in spontaneous flame appearance. According to the size of T_i, the material is classified on combustibility grade and fire hazard of equipment and technological processes. In the test originally used by the U.S. Bureau of Mines and described by Dorsett et al. [5], a small basket of metal gauze is filled with the powder and placed in a furnace through which air of constant, known temperature flows at a slow, specified rate. The temperature within the powder bed is monitored continuously, and by increasing the air temperature in steps, a level is reached at which the temperature in the powder sample begins to rise above that of the surrounding air. This critical air temperature is taken as the minimum ignition temperature of the powder. However, this temperature is not a true powder constant but depends on the experimental conditions, in particular, the size of the powder sample tested. Grewer [6] developed a more refined version of the original U.S. Bureau of Mines test. The furnace has six vertical cylindrical cavities into which small metal gauze baskets are placed. One of the baskets contains an inert reference sample, while the other five hold test samples. The furnace can be programmed to give a specific rate of temperature rise, such as 1 K/min. The temperature at which a test sample temperature starts to rise faster than that of the inert reference sample is taken as the minimum ignition temperature of that sample.

Self-ignition temperature (T_{si}, K) is the minimum temperature of dust deposits or powder layers at which the exothermic reaction rate abruptly increases, ending in spontaneous flame production. A reacting chamber containing a powder sample is heated. The powder heating occurs from wall heat transfer or during rapid mixing of previously heated components of a mixture. The knowledge of T_{si} is necessary for temperature heating limitations of equipment surfaces and combustible mixtures. A hot-plate test for ignition temperature determination is used. The test procedure is specified in detail by the International Electrotechnical Commission [7].

Minimum Explosive Dust Concentration

The earlier U.S. Bureau of miners (USBM) method was based on the 1.2 liter Hartmann tube with its top opening covered by a paper diaphragm. A comparatively weak continuous induction spark source was used for ignition. The dust concentration was defined as the quantity of dust dispersed, divided by the 1.2 liter volume of the tube: This is probably because the effect of some of the sources of error partly cancel each other. However, data from the early USBM method, such as that obtained by empirical correlation, must be regarded as indicative only. In the standard test used in the United States and United Kingdom for a number of years and described by Dorsett et al. [5], a known quantity of the powder was dispersed as a cloud in a slim, vertical, cylindrical container of 1.2 liter volume and exposed to a continuous spark ignition source. Starting with very small powder quantities and repeating the test with steadily increasing amounts, a critical quantity was reached at which the dust cloud ignited. The critical mass of dust, divided by the volume of the test container, was taken as the minimum explosive dust concentration.

The International Electrotechnical Commission [8] evaluated a test method based on the 20 liter Siwek [9] sphere (Fig. 27.1). Nordtest [10] and the 1 m^3 vessel (Fig. 27.2) of the International Standards Organization (ISO) [11] are alternative methods. The explosion criterion of ISO standard is that the maximum explosion pressure should be at least 0.15

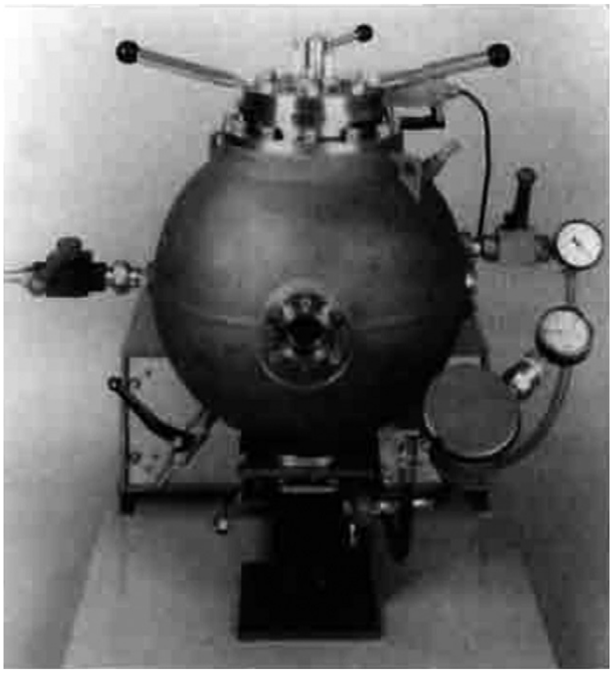

FIG. 27.1 A view of 20 liter Siwek sphere to determine pressure development in dust explosions. *Source: Siwek R (1988, November). Reliable determination of safety characteristics in 20 litre apparatus. In: Proceedings of the conference on flammable dust explosions. St. Louis (MO, USA); 1988. p. 1–2.*

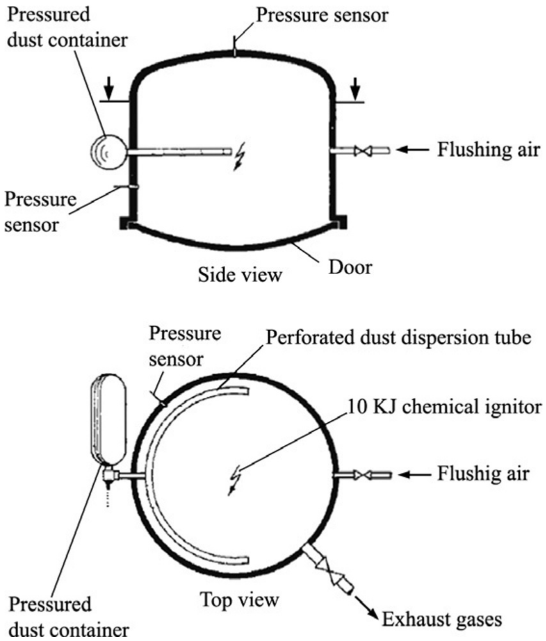
Pressured
dust container
Pressure sensor
Flushing air
Pressure
sensor
Door
Side view
Pressure
sensor
Perforated dust dispersion tube
10 KJ chemical ignitor
Flushig air
Pressured
dust container
Top view
Exhaust gases

FIG. 27.2 The 1 m^3 closed vessel of the International Standards Organization (ISO). *Source: International Standards Organization. Explosion Protection Systems. Part 1: Determination of explosion indices of combustible dusts in air. International Standard ISO/DIS 6184/1. Geneva: ISO; 1985.*

MPa. This includes the pressure of 0.11 ± 0.01 MPa generated by the powerful chemical 10 kJ ignitor only, without dust. Tests are conducted with successively decreasing dispersed dust masses in steps of 0.2 g until a mass is reached at which the maximum pressure is lower than 0.15 MPa in three consecutive tests with the same dispersed dust mass. The minimum explosive concentration is then assumed to lie between the highest nominal concentration (dispersed mass divided by vessel volume) at which the maximum explosion pressure was less than 0.15 MPa in three successive tests.

The 1 m^3 IS0 vessel would be expected to yield the most reliable assessment of the minimum explosive concentration. Because of the large volume of the dust cloud, even a very strong ignition source of 10 kJ would not interfere with the main phase of dust cloud propagation. However, just because of its large size, the 1 m^3 test is not very suitable for routine testing, and smaller, laboratory-bench-scale methods are needed.

The 4.0-liter installation of Institute for Problems of Material Science (IPMS) [12,13] involves the creation of a rather uniform dust cloud, the control of particle concentration in the explosion chamber and the regulation the parameters of powder atomization and ignition (Fig. 27.3). In a state of suspended solid sampling for definition of particle concentration distribution in the chamber inside, the IPMS unit is schematically shown in Fig. 27.4.

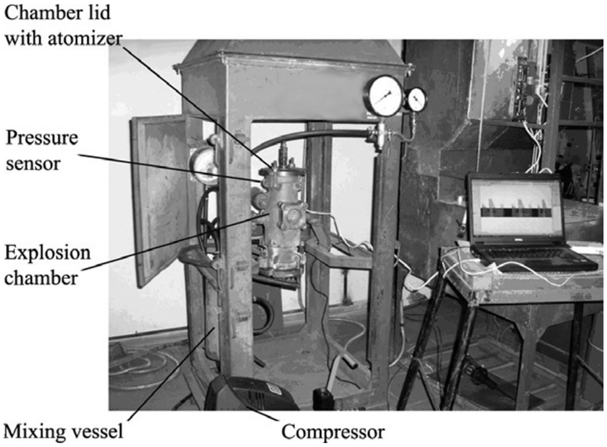
Chamber lid
with atomizer
Pressure
sensor
Explosion
chamber
Mixing vessel
Compressor

FIG. 27.3 A view of the 4.0 liter IPMS unit. Courtesy of IPMS

FIG. 27.4 Scheme of the 4.0 liter IPMS unit in state of suspended solid sampling: (A) unit top part with atomizer; (B) sampler during suspended solid in explosion chamber.

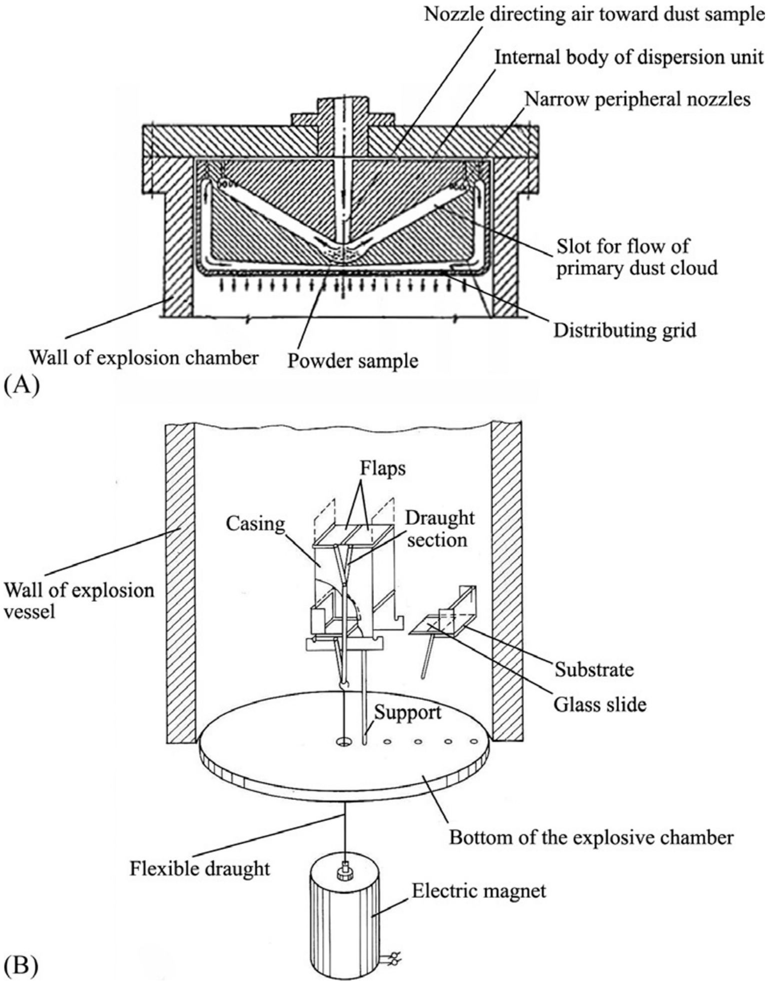
Nozzle directing air toward dust sample
Internal body of dispersion unit
Narrow peripheral nozzles
Slot for flow of primary dust cloud
Distributing grid
Wall of explosion chamber
Powder sample
(A)
Flaps
Casing
Draught section
Wall of explosion vessel
Substrate
Glass slide
Support
Bottom of the explosive chamber
Flexible draught
Electric magnet
(B)

Minimum Ignition Temperature of Dust Clouds

Hot surfaces capable of igniting dust clouds exist in a number of situations in industry, such as in furnaces, burners, dryers, and inter-stage transport of various kinds. In addition, hot surfaces can be generated accidentally by overheating bearings and other mechanical parts. If an explosible dust cloud is generated in some uncontrolled way in the proximity of a hot surface with a temperature above the actual minimum ignition temperature, a dust explosion can result. It is important, therefore, to know the actual minimum ignition temperature and take adequate precautions to ensure that temperatures of hot surfaces in areas where explosible dust clouds can occur do not rise to this value. However, the minimum ignition temperature is not a true constant for a given dust cloud, but depends on the geometry of the hot surface and the dynamic state of the cloud.

The ignition temperature of dust clouds in contact with a hot surface was traditionally determined in the United States and the United Kingdom by the Godbert-Greenwald furnace [5]. In this apparatus, the internal surface of a vertical cylindrical ceramic tube, open at the lower end, is kept at a specified, constant temperature, and a sample of the powder is dispersed as a dust cloud into the tube from above by a blast of air. The automatically controlled temperature of the internal wall of the tube is changed in steps, and the experiment repeated until the minimum temperature for ignition has been identified. The resulting, improved Godbert-Greenwald furnace test was proposed as a standard for determining minimum ignition temperature of dust clouds. The essential details concerning both apparatus and procedure are given in the standard produced by the IEC [7].

Minimum Electrical Spark Ignition Energy of Dust Clouds

It is known that explosible dust clouds can be ignited by electric sparks and arcs that occur in switches and motors and in short-circuiting caused by damaged cables. In addition, some categories of electrostatic discharges may initiate dust

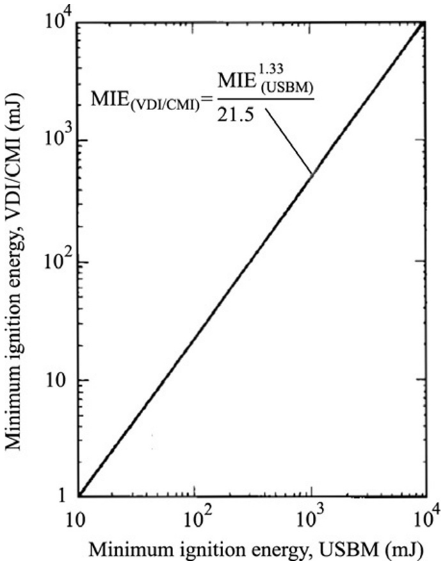

FIG. 27.5 Approximate empirical correlation between the minimum ignition energies measured by the earlier USBM method and values generated by the more recent methods described by Eckhoff [14] and Berthold [15], and the method being evaluated by the IEC.

explosions in industry. Hazardous electrostatic discharges include capacitive sparks, propagating brush discharges, and discharges by dynamic interaction of powder gravitation flow with gaseous medium, and by motion, the powders in the shuts.

The original USBM method for determining minim electrical spark ignition energy (w_{min}) of dust cloud (MIE) definition is based on the 1.2-liter Hartmann tube with its top opening covered by a paper diaphragm [5]. An appropriate quantity of dust was placed in the dispersion cup at the bottom of the 1.2-liter plastic cylinder and dispersed by a blast of air deflected by a conical "hat," as indicated. A spark was discharged across the electrodes synchronously with the transient appearance of the dust cloud in the spark gap region. However, due to the design of the electric spark generator used earlier by the USBM, part of the stored capacitor energy $1/2CV^2$ (where C is the capacitance, V is the initial capacitor voltage) was lost in a high-voltage transformer, and therefore, the net spark energy was smaller than the nominal '$1/2CV^2$ quoted as the spark energy. However, when comparing MIE data for similar dusts, determined by the earlier USBM method and the more recent methods described by Eckhoff [14] and Berthold [15] (VDI/CMI), an approximate empirical correlation is indicated, as shown in Fig. 27.5. However, Eckhoff [16] noted that the correlation must be used as an indication only and must not be extrapolated.

Maximum Explosion Pressure at Constant Volume

Maximum explosion pressure (p_{max}, MPa) is the maximum pressure, emergent by explosion of airborne powder in a closed vessel with initial pressure 101.325 kPa. These data are necessary for strength design of the equipment.

The Hartmann bomb, described by Dorsett et al. [5] has been used throughout the world for nearly half a century to assess the maximum explosion pressure of dust clouds. This apparatus, which is illustrated in Figs. 27.6, consists of a closed vertical 1.2 liter stainless steel cylinder into which a known quantity of dust is dispersed as a cloud by a vertically upward blast of air and exposed to an ignition source. The ignition sources used include continuous trains of electric sparks, single synchronized sparks, synchronized chemical ignitors, and glowing resistance wire coils.

Because of the small volume of the Hartmann bomb, the heat loss to the vessel wall during the explosion is significant. Therefore, the maximum pressures measured are generally somewhat lower, typically by 25%–30%, than those generated with the same dusts in larger vessels, such as the 1 m^3 IS0 vessel and various 20-liter vessels [16]. This occurs even though the pressures measured in the Hartmann bomb are not corrected for the increased initial pressure due to the dust dispersion air.

The 1 m^3 standard ISO vessel to determine maximum explosion pressure and maximum rates of pressure rise of dust clouds in air at constant volume is illustrated in Fig. 27.2. A container of approximately 5 liters capacity and capable of being pressurized with air to 2.0 MPa is attached to the explosion chamber. The container is fitted with a 19- mm diameter opening valve of 10 ms opening time. The container is connected to the explosion chamber via a 19-mm diameter perforated semicircular spray pipe. The diameter of the holes in the pipe should be in the range of 4–6 mm. The number of holes is

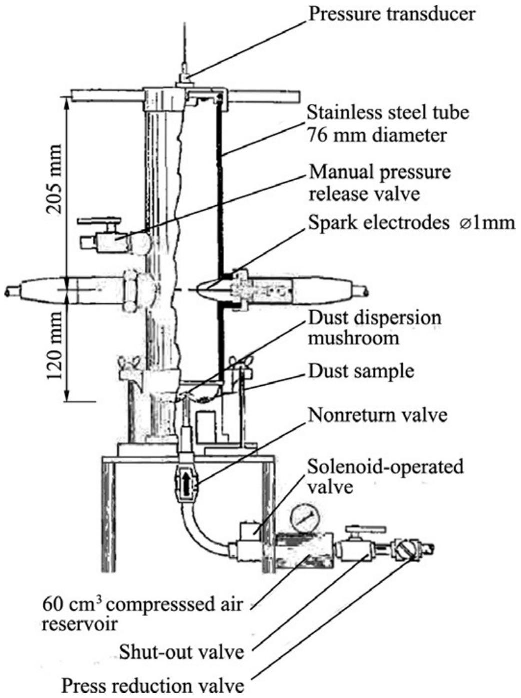

FIG. 27.6 The 1.2-L Hartmann bomb to determine pressure development in dust explosion of constant volume.

chosen such that their total cross-sectional area is approximately 300 m^2. The ignition source is a pyrotechnical ignitor with a total energy of 10 kJ and arranged to fire after a fixed delay of 0.6 s after onset of dust injection. The mass of the pyrotechnical ignition source is 2.4 g, and it consists of 40% zirconium, 30% barium nitrate, and 30% barium peroxide. An electric fuse head activates it. The ignitor is located at the geometric center of the explosion chamber. Two pressure sensors, linked to a recorder, are fitted to measure the explosion chamber pressure development.

The Siwek 20-liter sphere apparatus (Fig. 27.1) was developed primarily to obtain maximum explosion pressures and explosion rates in agreement with data from the 1 m^3 IS0 vessel. The sphere substantially is a small-scale version of the 1 m^3 IS0 vessel. The original dust dispersion system was of the same type as that of the 1 m^3 IS0 vessel, consisting of a pressurized dust reservoir, from which the dust was injected into the main vessel through a perforated tube, as illustrated in Fig. 27.2. The experimental conditions required to obtain agreement with the 1 m^3 IS0 vessel were specified in a standard issued by the American Society for Testing and Materials [17]. The ignition source has to be the same type of 10 kJ chemical ignitor as used in the 1 m^3 IS0 test. The ignition delay is, however, shorter (60 ms) because of the smaller vessel size. Maximum explosion pressures measured with this apparatus are relatively close to the 1 m^3 vessel (Table 27.3)

The measuring of maximum explosion pressures by 4 liter IPMS unit shows magnitudes of this parameter, though less volume of explosion chamber, close to the Siwek 20-liter sphere apparatus, like the 1 m^3 vessel for the same powders (Table 27.6). This can explain by higher dispersivity and more even distribution of particles in dust cloud. The dependence of the maximum explosion pressure on suspended solid concentration determined by the 4-liter IPMS unit is illustrated in Fig. 27.7. One can see that maximum explosion pressure increases parabolically with the growth of suspended solid concentration reaching its maximum.

Maximum Rate of Explosion Pressure Rise at a Constant Volume

Maximum rate of pressure rise (explosion violence) is the relation of an increment pressure, developed during explosion in a closed vessel, to time interval in the course of which this increment occurs. Magnitude of K_{St} (MPa m/s) is necessary for design of the equipment and design of devices, and explosion venting.

The method for determining K_{St}, values of dusts specified by the International Standards Organization [11] is the same as for measurement of maximum explosion pressure. Because the standard vessel has a volume of 1 m^3, the K_{St}, values in MPa·m/s are numerically identical with the maximum rate of pressure rise in MPa/s. A considerable number of nonstandardized closed vessels have been used to assess explosion violence. Nagy et al. [18] performed experiments in vessel

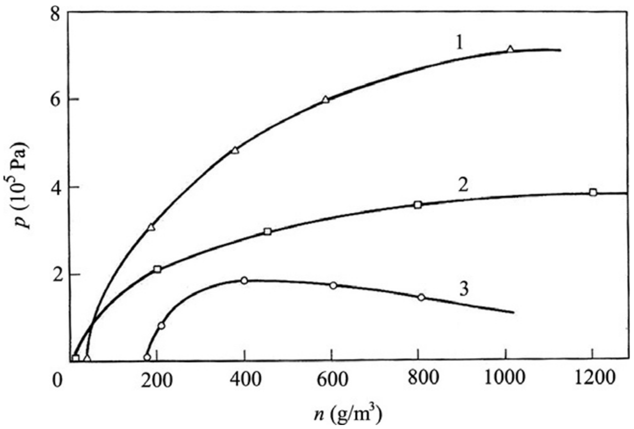

FIG. 27.7 Dependence of the maximum explosion pressure on suspended solid concentration determinate by 4 liter IPMS unit: (1) aluminum powder; (2) titanium powder, (3) titanium carbide powder.

volumes ranging from the 1.2 liters of the Hartmann bomb to 14 m^3. They normalized their results by multiplying all the measured maximum rates of pressure rise by the cube root of the vessel volume.

Combustibility and explosibility values of non-ferrous powders are given in Table 27.4.

Dependence the Ignitability and Explosibility of the Gas-Suspended Solid Mixture on the Oxygen Content in Oxidizing Gas

Limiting oxygen concentration (LOC) to prevent ignition is minimum oxygen concentration in combustible gas-suspended solid mixture, below which the ignition and combustion become impossible whatever the fuel content in the mixture. LOC size is used for determination of the explosion-proof regimes of the technological processes, pneumatic transport, and design of explosion-suppression and fire-quenching systems and installations.

In the United States, as described by Dorsett et al. [5], two standard test methods were used. The apparatus used in these tests is similar to the Godbert-Greenwald furnace [5] mentioned above in sub-paragraph, “Minimum ignition temperature in dust clouds.” In the first test, the ignition source was an electric spark; in the second test, the hot tube wall. Usually, the limiting gas compositions for flame propagation obtained for the same dust from the two tests differed significantly, with the hot surface test yielding lower critical permissible oxygen contents than the spark test.

Characteristic explosion pressure dependences of gas-suspended aluminum flakes on the oxygen content in similar oxidizing gases determinate by 4 liter IPMS unit are shown in Fig. 27.8. The aluminum flakes concentration was 870 g/m^3 in all tests. As is seen, the dependence of p on the oxygen content in the gas is parabolic in all cases. As for effectiveness of explosion suppression, the above listed inert gases (Fig. 27.8) can be placed in the following order: helium, nitrogen, argon, carbon dioxide. The greater effectiveness nitrogen in comparison to argon results from nitrogen’s higher heat conductivity. The influence of heat conductivity is seen in cases of helium and argon, both of which have the same specific heat, but which differ in heat conductivity by a factor of 10. In addition, nitrogen is significantly cheaper than helium. Therefore, nitrogen is preferable as protective gas.

The explosion pressure dependences of gas-suspended aluminum flakes differing by solid phase content on oxygen content in nitrogen-oxygen mixture are shown in Fig. 27.9. These tests were made at a 4 liter IPMS installation. As seen, the limiting oxygen concentration decreases with the increase of suspended solid content, therefore, the LOC was defined at a maximum explosible suspended aluminum flakes concentration [13].

Thermophysical Properties

Thermophysical properties comprises specific heat capacity, thermal conductivity, coefficient of linear thermal expansion, heat of vaporization, and heat of combustion. Thermophysical magnitudes of the materials are given above, in sections where powder production is described.

The combustion heat (enthalpy) of a material (ΔH) is a change of enthalpy during combustion reaction of the material weight unit with equivalent oxygen amount. ΔH quantity (Table 27.5) is used for determination of manufacturing areas and building categories for explosion and fire hazard. ΔH quantity of composite materials is calculated on ΔH quantities of elements contained in them.

TABLE 27.4 Combustibility and Explosibility Values of Non-Ferrous Powders

Material	Particle Sizes (μm)	Powder			Suspended Powder in Air					Combustibility Group
		T_i (K)	T_{si} (K)	$T_{s.sp}$ (K)	w_{min} (mJ)	LCIL (g/m^3)	p_{max} (MPa)	K_{St} (MPa·m/s)	LOC (vol %)[a]	
Magnesium[BM]	<74	763	693	723	0.025	10	0.66	6.3	0Ar[b]; +C; +N	CB[c]
Magnesium, spheroidal[13]	<280	…	…	873	…	20	0.67	12.3	2N	CB
Magnesium, milled[13]	<100	…	…	793	…	40				
Magnesium[19]	280[d]	…	…	1033		200	0.7	1.2	3N	CB
Zirconium(e)	<75	…	463	…	5	40–64	0.63	9.1	3N; 5Ge; +Ar; +C	CB
Zirconium[BM]	3–6	453	463	…	0.0004	40	0.45	4.45	3N; 5Ge; +Ar; +C	CB
Uranium[BM]	<10	…	373	293	25	60	0.37	23.8	+C; 1N; 2Ar; 2Ge	CB
Titanium, calcium hydride[13]	<50	…	…	793	10[d]	13	0.39	11.8.	2.5N	CB
Titanium, electrolytic[13]	<50	…	…	613	…	40	0.39	9.8	3N	CB
80Ti–20Ni alloy[e]	<50	…	423	…	…	10	…	…	…	CB
Aluminum dust[e]	<27	593	793	683[f]	…	40	1.3	6.86	3N	CB
Aluminum flakes[13]	<20	…	...	793	…	45	0.78	6.87	8N	CB
Aluminium powder[19]	29[d]	>723[f]	…	983		30	1.24	41.5	5N	CB
Aluminum, spheroidal[13]	<50	…	…	1023	…	45	0.72	3.5	8N	CB
85Al–15Li alloy[e]	149	…	933	…	140	100	0.66	25.5	…	CB
50Al–50Mg alloy	<71	…	933	…	…	90	0.49	6.37	2.5N	CB
50Al–50Cu alloy[e]	44	…	1103	…	100	100	0.468	17.9	…	CB
58Al–42Ni alloy[e]	44	…	813	…	80	190	0.544	…	14N	CB
Thorium[e]	7	…	553	543	5	75	0.57	…	2Ar; 2N; 5He; 7C	CB
Yttrium, milled[e]	<80	…	443	…	…	36	…	…	…	…
Silicocalcium[13]	<50	…	…	763	…	42	0.66	20	8N	CB
Sulfur[19]	20[d]	…	..	553	…	…	0.68	15.1	…	CB
Silicon[e]	<74	…	1033	1053	80	100	0.75	8.4	11Ar; 12C	CB
Silicon[19]	<10	…	1123	>723	…	125	1.02	12.6		
80Si–20Zr alloy[d]	<53	…	819	…	…	104	…	…	…	CB

TABLE 27.4 Combustibility and Explosibility Values of Non-Ferrous Powders—cont'd

		Powder			Suspended Powder in Air					
Material	Particle Sizes (µm)	T_i (K)	T_{si} (K)	$T_{s.sp}$ (K)	W_{min} (mJ)	LCIL (g/m^3)	p_{max} (MPa)	K_{St} (MPa·m/s)	LOC (vol%)	Combustibility Group
Boron[BM]	<44	…	673	743	60	100	0.63	1.7	11N	CB
Chromium[BM]	<74	…	673	…	140	190	0.4	…	14C	CB
Hafnium[e]	<180	…	523	663	…	210	…	…	…	…
Tantalum[e]	<44	…	573	903	120	200	0.35	3.03	…	CB
Zinc[e]	<74	…	583	873	913	480	0.490	1.8	10C	CB
Zinc (from zinc coating)[19]	19[d]	>723[f]	…	1073	…	…	0.6	8.5		CB
Vanadium[e]	<74	…	763	773	60	220	0.35	0.69	10C	CB
Bronze[BM]	<53	…	463	643	…	1000	0.3	0.9	…	CB
Bronze powder[19]	21[d]	533[f]		663		750	0.41	3.1	…	CB
Tin[BM]	<53	…	703	…	80	190	0.26	0.9	16C	dCB
96Sn–2Pb alloy[e]	<74	…	703	903	80	190	0.340	1.2	16C	dCB
Antimony[BM]	<74	…	603	693	1920	420	0.056	0.7	16C	dCV
Cadmium[BM]	<74	…	523	843	4000	…	0.05	0.7	…	dCB
Lead[BM]	<53	…	543	983	…	…	…	…	…	dCB
Tellurium[BM]	<44	…	613	823	…	…	…	…	…	dCB
Molybdenum[BM]	<74	530	583	993	…	…	…	…	…	dCB
Cobalt[BM]	<44	…	643	1033	…	…	…	…	…	dCB
Tungsten[BM]	<74	…	703	990	…	…	…	…	…	dCB
Nickel	<50	…	743	…	…	220	…	…	…	dCB
Beryllium[BM]	1	…	813	1183	…	…	…	…	…	dCB
Copper	<44	Does not inflame								iCB
Copper dust	80 wt% <40 µm 14 wt% <10 µm	743	466	Does not inflame in airborne state						dCB
Brass (87Cu–10.9Zn)	27 wt% <10 µm	Does not inflame in layer as well as in airborne state								iCB
Brass dust (88.1Cu)	88 wt% <10 µm	723	478	Does not inflame in the airborne state						dCB
Bronze(Cu–5Sn–5Zn–5Pb)	80 wt% <100 µm	893	888	Does not inflame in the airborne state						dCB

(+) in LOC column, is designated that suspended powder is fired in pure inert gas.

[a] *Ciphers in LOC column is designated an oxygen explosion-proof content by used protective gas, in vol%.*

[b] *Abbreviation of the gas-diluted: Ar, argon; C, carbon dioxide; N, nitrogen; He, helium.*

[c] *Abbreviation of the material combustibility group: CB: combustible, dCB: difficult by combustible, iCB: incombustible.*

[BM] *Source: Report of Investigation Bureau of Mines, V.S. GPO, 1964, 6516.*

[d] *Median diameter.*

[e] *Baratov AN, Korolychenko AJ, editors. Fire- and explosion-proof of matters and materials and means for their quenching. Moscow: Chimia; 1990.*

[f] *Smoldering temperature.*

$T_{s.sp}$ *is the self-ignition temperature of suspended solid.*

[13] *The cipher located overhead, at the right top of material name is the reference source.*

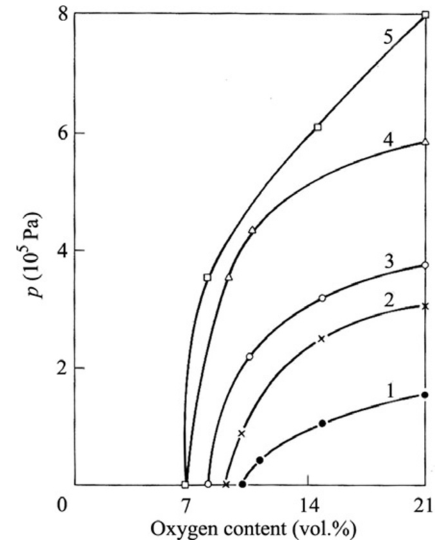

FIG. 27.8 Explosion pressure dependences of gas-suspended aluminum flakes on the oxygen content in several oxidizing gases by different inert gas component: (1) carbon dioxide; (2) argon; (3) nitrogen; (4) helium.

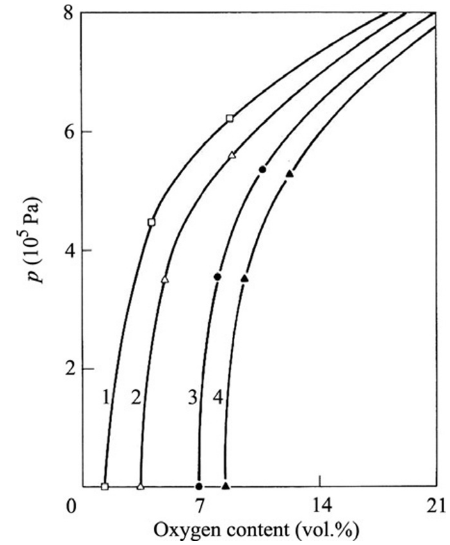

FIG. 27.9 Explosion pressure dependences of gas-suspended aluminum flakes different by solid phase content on oxygen content in nitrogen-oxygen mixture: (1) carbon dioxide; (2) argon; (3) nitrogen; (4) helium.

TABLE 27.5 Heat of Oxide Formations and Combustion of Materials

Element	Oxide	Heat of Oxide Formation (kJ/kg)	Heat Combustion of Element (kJ/kg)
Aluminum	Al_2O_3	16470	34170
Barium	BaO	3620	4040
Calcium	CaO	11340	15900
Carbon	CO_2	8970	32860
Magnesium	MgO	15050	25080
Silicon	SiO_2	15200	32550

TABLE 27.6 Explosion-Proof Characteristics of Gaseous Reducing Agents and Easily Combustible Liquids

Substance	Concentration Limits of Flame Propagation (vol%)	Maximum Explosion Pressure (MPa)	Rate of Pressure Rise (MPa/s)[a]
Hydrogen	4–75	0.65	64/70
Ammonia	18–28	0.60	…
Dissociated ammonia with hydrogen content (vol%):			
75	5.4–73.1	…	…
40	10.6–75.1	…	…
20	21.5–76.1	…	…
Endogas with hydrogen content (vol%):			
40	8.8–71.8	…	…
20	16.2–69.2	…	…
Ethyl alcohol	3.6–19.0	0.62	10/16
Methyl alcohol	6.34–7.0	0.63	10.55/21.3
Isopropyl alcohol	2–12	0.69	8.3/12.3
Benzine	1.2–6.9	…	…

[a] *Average rate of pressure rise/Maximum rate of pressure rise.*

Explosion-proof characteristics of the gaseous reducing agents and easily combustible liquids, used in the production of non-ferrous powders, are given in Table 27.6. Combustibility and explosibility values of non-ferrous powders are given above in Table 27.4 (the powders are placed in decreasing order of activity).

Fig. 27.10 illustrates the dependence of LCIL, $p_{\max}$, and average rate of pressure rise $K_{St(mid)}$ on the particle sizes for water-atomized aluminum alloy powder [19]. The values of LCIL increase and $K_{St(mid)}$, decrease continuously with increasing particle size in ranges from 50 μm to 130 μm. The $p_{\max}$, quantities show a weak dependence on particle size in the range from 50 μm to 80 μm followed by a stronger decrease of $p_{\max}$, for coarser powders.

A feature of aluminum and aluminum-based alloy powders is the risk of powder ignition resulting from either exothermal reactions with air or formation of hydrogen on contact with water. They lightly react at room temperature with aqueous alkali solution accompanied by hydrogen evolution. The mixing of aluminum powder with alkali solution might lead to an explosion. Such powders react strongly with many metalloids. Thus, aluminum chips burn in bromine, forming aluminum bromide. On heating, aluminum reacts with sulfur. Finely ground aluminum reacts with halogenated hydrocarbons; if present in small amounts, aluminum chloride (which forms during this reaction) acts as catalyst, which accelerates the reaction, leading to explosion in some cases. Such an occurrence is observed on heating aluminum powder with methyl chloride, carbon tetrachloride, and mixture of chloroform with carbon tetrachloride up to a temperature of about 423 K. Mixture of aluminum powder with copper oxide, silver oxide, and especially, lead dioxide burns with blast. A mixture with carbon or nitro-compounds is explosive.

Guide to EU Legislation [20] includes recommendation to categories high, moderate, or low hazard, depending on minimum ignition temperature, explosion limits, and oxygen content (Table 27.7).

TECHNIQUE FOR THE PREVENTION OF EXPOSURE HAZARDS

Workplace Exposure Limits

The proportion of total particulate matter which is inhaled into a human body depends on the properties of the particles, on the speed and direction of air movement near the body, on breathing rate, and whether breathing is through the nose or

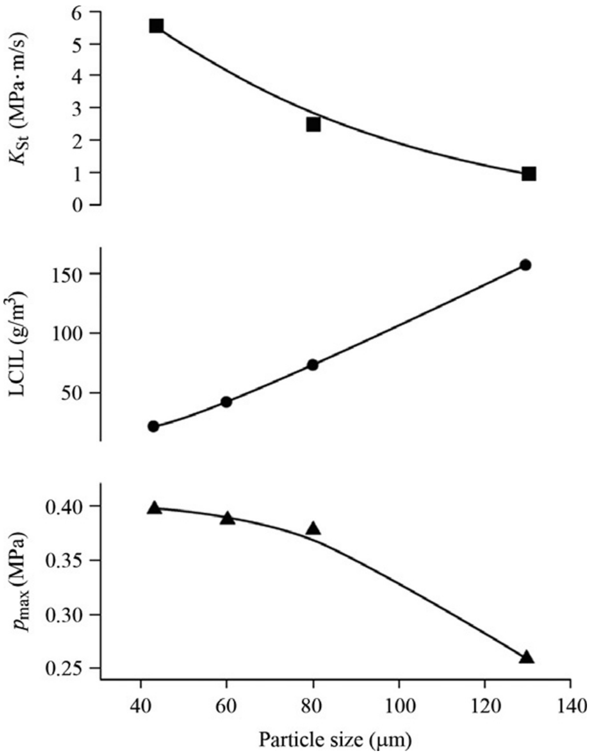

FIG. 27.10 Dependence of low concentration ignition limit (LCIL), maximum explosion pressure (p_{max}) and average rate of pressure rise on the particle sizes for water atomized aluminum alloy powder.

TABLE 27.7 Explosion Assessment of Metals According to Guide to EU Legislation [20]

	Explosion Hazard Category		
Explosion-Proof Characteristics	**High Explosion Hazard**	**Moderate Explosion Hazard**	**Low Explosion Hazard**
Minimum oxygen requirement	<3 vol%	>3 wt%	…
Minimum ignition concentration	<873 K	From 573 to 1073 K	>973 K
Explosion concentration limit	From 20 to 50 g/m^3	From 100 to 500 g/m^3	…
Examples	Zirconium, magnesium, and aluminum	Copper, silicon, tin, and zinc	Cobalt, lead, molybdenum

mouth. Inhaled particles can then deposit somewhere in the respiratory tract or can be exhaled. The site of deposition, or probably of exhalation, depends on the properties of the particle, respiratory tract, breathing pattern, and other factors.

The European Standard EN/481/1993 on "Workplace Atmospheres. Size fraction definitions for measurement of airborne particles" includes the planning and performing of measurements [21]. The introduction to this standard states that there is a wide variation from one person to another in the probability of particle inhalation, deposition, reaction to deposition, and clearance. Nevertheless, it is possible to define conventions for size selective sampling of airborne particles when the purpose of the sample is health related. These conventions are relationships between aerodynamic diameter and the fractions to be collected or measured, which approximate the fractions penetrating to the regions of the respiratory tract under average conditions. A view of the penetration of respirable particle fractions in a human body is typically determined in the following way: particles finer than 100 μm penetrate to the larynx, particles with average size 11.64 ± 1.5 μm penetrate to the bronchi, and particles with average size 4.25 ± 1.5 μm penetrate to the alveolus.

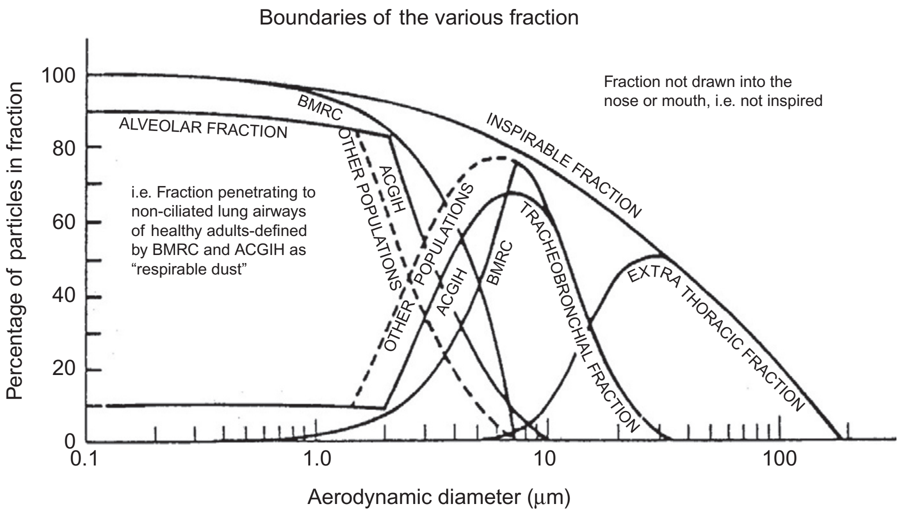

FIG. 27.11 Recommended values of size ranges for occupational and environmental health related air sampling.

Recommended values of size ranges for occupational and environmental health related air sampling are represented in Fig. 27.11. There are three optional boundaries between the tracheobronchial and alveolar components of the thorax fraction. Two of these are the traditional recommendations for working adults, of the British Medical Research Council (BMRC) and the American Conference of Governmental Industrial Hygienists (ACGIH). The third, labeled "other populations," corresponds to sensitive members of the general public who have constricted bronchial airways (from American Industrial Hygiene Association Journal, May 1981).

The workplace exposure limits values of harmful materials related to non-ferrous powder production, their classification, and prior phase conditions enacted in European Union [22], the United States [23], and the Commonwealth of Independent States (CIS) [24] are contained in Table 27.8. Differing abbreviations for the same sense of workplace exposure limits are used: WEL (workplace exposure limit) in EU, PEL (permissible exposure limit value) and TLV (threshold limit value) in the United States, TLV in CIS. Depending on the degree of danger of the substances and materials, the four danger classes are listed as: highest danger Class I, down to Class IV. These values are accepted by the Commonwealth of Independent States (CIS) Standard, GOST 12.1.005-88 [24], while the numbering of hazard rating in reverse order is used in the United States, New Jersey Department, standards.

According to EU Directives, the chemical elements and their compounds as they occur in the natural state or as produced by industry, including any additives required for the purpose of placing them on the market, or any impurity deriving from the production process/materials used are classified. There are two different types of "substances" which may be classified as dangerous: those already listed in Annex I of Directive 67/548/EEC (European Inventory of Existing [Commercial] Chemical Substances [EINECS]), or new substances not listed in EINECS which will need classification by the producer or importer. The procedure for classifying new substances is given in Annex V of Directive 67/548/EEC. The Annex I contains literature references and data banks with limit values, including Ref. [21].

Most of these substances are able to cause fibrogenesis and allergic diseases; beryllium, nickel, its compounds, and vanadium chloride are carcinogenic. The systematic contact with metallic powder aerosols is able to lead to occupational diseases.

A danger level of metallic dusts for humans' health depends on chemical composition and their oxidation level, particle size, concentration, action duration, penetration routes into organs, presence of impurities, etc.; by means of suitable control, the dust concentration in the workplace atmospheres must be maintained below TLV level. Table 27.9 gives the main data about the biological influence of metallic powders on the human organism [24].

Common Demands to Production Area, Equipment, and Processes

The workplace atmosphere parameters must be in conformity with the standards. The European Standard is related to the requirements of Directive 80/1107/EEC and its 88/642/EEC. The United States' exposure limits are defined by US New Jersey Department of Health and Senior Services. Hazardous Substance Sheet. Commonwealth of Independent States (CIS) follows the GOST 12.1.005-88, GOST 12.1.003-83, and GOST 12.1.012-78.

TABLE 27.8 Workplace Exposure Limits

		Regional Standards					
		EU		United States		CIS	
Substance	Phase State	WEL (mg/m^3)	Comments[a]	PEL (mg/m^3)	Hazard Rating[b]	TLV (mg/m^3)	Danger Class[c,d]
Aluminum oxide (alumina, electrolytically produced corundum)	Aerosol	10.0	…	5.0	2	6.0	IV
Aluminum alloys, on aluminum basis	Aerosol	4.0	…	5.0	…	2.0	IV
Antimony	Aerosol	0.5	…	0.5	2	0.2/0.5[d]	II
Arsenic nonorganic compounds (on As basis):							
Arsenic content below 40 wt%	Aerosol	…	…	…		0.01/0.04[d]	II
Arsenic content more than 40 wt%	Aerosol	0.1	Carc	0.01	4	0.01/0.04[d]	I
Barium	Aerosol	0.5	…	0.5	2	6.0	IV
Beryllium and its compounds on beryllium basis	Aerosol	0.002	Carc	0.002/0.005[d]	CAR	0.001	I
Bismuth	Aerosol	…	…	0.5	2	0.5	II
Cadmium	Aerosol	0.025	Carc	0.01	4	0.01/0.05[d]	I
Chromate, bichromate (on Cr_2O_3 basis)	Aerosol	…	…	…	…	0.01	I
Chromium oxide (on Cr^{+3} basis)	Aerosol	…	…	…	…	1.0	III
Cobalt	Aerosol	0.1	Carc, Sen	0.5	CAR	0.5	II
Copper	Aerosol	1.0/2.0[d]	…	1.0	2	0.5/1.0[d]	II
Copper	Fume	0.2	…	0.1	…	…	…
Lead and its inorganic compounds	Aerosol	…	…	0.05	4[e]	0.005/0.01[d]	I
Magnesium	Aerosol	…	…	15	1		
Magnesium chlorate	Aerosol	…	…	…	…	5.0	III
Manganese oxides (on MnO_2 basis)							
Mechanically ground	Aerosol	0.5	…	…	…	0.3	II
Condensation aerosol	Aerosol	…	…	…	…	0.05	I
Mercury metallic	Mist	0.2	…	0.05[f]	3	0.006/0.01[d]	I
Molybdenum metallic	Aerosol	5/10[d]	…	10.o	1	0.5/3.0[d]	III
Molybdenum pentochloride	Aerosol	…	…	5.0	2		
Molybdenum silicide	Aerosol	…	…	…	…	4.0	III
Molybdenum sulfide	Aerosol	…	…	…	…	6.0	IV
Molybdenum trioxide	Aerosol	…	…	5.0	…	…	…
Nickel	Aerosol	0.1	Sk, Carc, Sen	1.0[g]	3	0.05	I

TABLE 27.8 Workplace Exposure Limits—cont'd

		Regional Standards					
		EU		United States		CIS	
Substance	**Phase State**	**WEL (mg/m^3)**	**Comments**	**PEL (mg/m^3)**	**Hazard Rating**	**TLV (mg/m^3)**	**Danger Class**
Nickel ammonium sulfate	Aerosol	0.1	Sk, Carc, Sen	0.1[h]	CAR		
Nickel carbonyl	Aerosol	…	…	0.001 ppm	CAR	0.0005[i]	I
Silicon dioxide by its contain in dust, wt%:							
>60	Aerosol	…	…	…	…	1.0	II
10–60	Aerosol	…	…	…	…	2.0	II
2–10	Aerosol	…	…	…	…	4.0	III
Titanium and its oxides	Aerosol	4.0	…	15	2	10	IV
Titanium sulfide	Aerosol	…	…	…	…	6.0	IV
Titanium tetrachloride (on HCl basis)	Mist	…	…	…	…	1.0	II
Thorium	Aerosol	…	…	…	…	0.05	I
Tungsten, tungsten carbide, tungsten silicide	Aerosol	5/10[d]	…	5/10[d]	…	6.0	IV
Vanadium containing slag dust	Aerosol	…	…	…	…	0.5	II
Vanadium oxide dust	Aerosol	…	…	…	…	0.5	II
Vanadium oxide fume	Aerosol	…	…	…	…	0.5	II
Vanadium pentoxide	Aerosol	0.05	…	0.05[h]	3	…	…
Vanadium tetrachloride	Aerosol	…	…	0.05	…	…	…
Yttrium	Aerosol	1.0/3.0[d]	…	1.0	…	…	…
Yttrium oxide	Aerosol	…	…	…	…	2.0	III
Zinc chloride	Fume	1.0/2.0[d]	..	1.0	3	… …	
Zinc oxide	Aerosol	…	…	5.0	…	0.5	II
Zinc sulfide	Aerosol	…	…	… …		5.0	III
Zirconium and its compounds	Aerosol	5.0/10.0[d]	…	…	…	…	…
Zirconium dioxide	Aerosol					6.0	III
Zirconium metallic	Aerosol					6.0	III
Zirconium nitride	Aerosol					4.0	III

[a] *The Carc/CAR (capable of causing cancer and/or heritable genetic damage), Sen (capable of causing occupational asthma) and Sk (can be absorbed through the skin) notations are not exhaustive. Notations have been applied to substances identified in IOELV Directions [22].*

[b] *Hazard rating: 0—minimal, 1—slight, 2—moderate, 3—serious, 4—severe.*

[c] *Highest dangerous class I reducing down to class IV.*

[d] *Numerator is the long-term exposure limit (8-h time-weighted average),; denominator is the short-term exposure limit (15 minute reference period).*

[e] *Data of NJDHSS (New Jersey Department of Health and Senior Services).*

[f] *Data of NIOSH (National Institute for Occupational Safety and Health).*

[g] *Data of OSHA (is the federal Occupational Safety and Health Administration).*

[h] *Data of ACGIH (American Conference of Governmental Industrial Hygienists).*

[i] *0.0005 $mg/m^3 \approx$ 0.0004 ppm.*

WEL is the workplace exposure limit; PEL is the permissible exposure limit.

TABLE 27.9 Biological Influence of Metallic Powders on Human Organism

Material	Danger Class	TLV (mg/m^3)	Influence on Human Organism
Copper	II	0.5/1.0[a]	It tends to cause diseases of the breathing organs, cardiovascular system, and gastrointestinal tract
Chromium chromate, bichromate (on Cr_2O_3 basis)	I	0.01	It causes allergic rash, and appearance of the pits on skin and nose cavity; chromate, bichromate are probable carcinogen in humans
Lead	I	0.005/0.01	It is toxic and tends to cause acute and chronic poisoning with lesions in many human systems and organs
Manganese oxides (on MnO_2 basis) mechanical ground	II	0.3	Toxic and causes acute and chronic poisoning with lesion of many human systems and organs
Nickel	I	0.05	Evidence of common toxic effect. It causes acute and chronic poisoning with preemptive lung lesions
Zinc oxide	II	0.5	Fever condition
Aluminum	IV	2.0	Moderate fibrogenesis and weak common toxic influence
Magnesium	IV	2.0	Moderate fibrogenesis and weak common toxic influence
Titanium	IV	10.0	Weakly toxic

[a] *Numerator is short-term maximal value; denominator is average during shift value.*

For powder production, there are no special requirements regarding buildings, construction, or production area with respect to air environment, harmful impurity contents, sonic level, or vibration.

The common recommendations for preventing and controlling exposure hazards [20] include:

For preventing exposure

- Change the process to eliminate the unnecessary operations.
- Modify the process to eliminate the hazardous substances.
- Substitute a less hazardous substance or the same substance in a less hazardous form.

For controlling exposure hazards

- Totally enclose the process.
- Design the plant or system to operate so as to minimize generation of gravitational spills, and in the event of spills minimize the area of contamination.
- Design the plant to minimize powder transfers and overcharging.
- Provide for partial enclosure with local exhaust ventilation (aspiration).
- Provide for local exhaust ventilation.
- Design the transfer units and local exhaust to minimize powder entrainment and suction rate.
- Provide for sufficient general ventilation by dilution.
- Reduce the number of employees exposed.
- Exclude non-essential access.
- Reduce the period of exposure.
- Exclude contacts of powders with substances leading to oxidation, combustion, or explosion.
- Regularly clean contamination from walls, surfaces, etc.
- Provide for safe means of storage and disposal of hazardous substances.
- Provide for adequate facilities for washing, changing, storage of clothing, including laundering of contaminated items
- Prohibit eating, drinking, smoking, etc., in contaminated items.
- Where the above measures do not prevent exposure hazards or provide adequate control then, in addition, use suitable personal protective equipment.

Equipment in which there are places in which explosive mixtures could form must be equipped with a safety valve or diaphragm. Explosion parameters are basic data for the calculation of safety valves and diaphragms [16]. For apparatus and pipelines destined for liquid and gaseous toxic and explosive products, the arrangements for blow-through must be provided.

In order to avoid entry of explosive or toxic gases from technological pipelines in water, air, and steam communications, it is necessary to provide check valves or hydroseals. The apparatus and communications for toxic, combustible, and aggressive liquids must have emergency capabilities permitting full removal of liquids contained within by self-draining. It is necessary provide for techniques to eliminate the generation of a pressure in an enclosure, or to minimize it, if the maintenance of overpressure is not conditioned by a technological requirement.

It is necessary to provide in the design of reloading units and local exhaust systems (aspiration) minimizing of powder entrainment and suction rate by means of decreasing the number and height of the reloadings and final velocity of gravitational powder stream, elimination of possibility of "free pass" through the bins, and the provision for powder delivery through sealed feeders.

In crushing and grinding equipment in which overpressure and directed flows are formed, it is necessary to provide for tight sealing of charge and unloading units, eliminating aerodynamic connections with ambient air and conjugated equipment; along with this, for decreasing overpressure, the zones under such pressure are connected with underpressure zones by means of bypasses [25].

Surfaces of walls, ceilings, and floors of production areas and storage facilities must be smooth with minimum quantity of ledges, and moisture-resistant to allow wet mechanized cleaning.

Explosion and Fire Safety

The classification of production areas and buildings as regards to explosion-fire and fire risk is given in the Commonwealth of Independent States (CIS) according to Technological Designing Standard ONTP-24–86 [26]. The categories are determined for the most disadvantageous conditions subject to types of combustible substance and materials, their quantity, fire-danger, and features of technological processes (Table 27.10). The category of risk is indicated by a letter—A (higher) down to D (lower).

The quantity of substances which come into production areas and can form the explosive gas-air or steam-air mixtures needs to be assessed, starting from a possible emergency on the basis of the largest amount of substances or materials which are the most hazardous with respect to explosion consequence. In production areas where the emissions of explosive gases or vapor in workplace atmospheres is possible, it is necessary provide for automatic control of their content.

Thermoprocessing equipment is widely used for manufacturing non-ferrous metal powders. The safety of such equipment and the controlled atmospheres often used as part of the manufacturing process are, therefore, of paramount importance to the PM technique. The European Standard (EN 746) contains common safety requirements for industrial

TABLE 27.10 Categories of Production Areas and Buildings on Explosion-Fire and Fire Risk

Building Category	Substance and Material Characteristics Situated (Circulating) in Production Areas
A (explosion-fire risk)	Combustible gas, highly inflammable liquids with flash temperature up to 3001 K in such quantity that they can form steam-air explosive mixtures, by which ignition, the calculated explosion overpressure in the building develops, exceeds 5 kPa. The substance and materials able to burst and burn by interaction with water, air oxygen, or with each other in such quantity that the calculated explosion overpressure in the building exceeds 5 kPa
B (explosion-fire risk)	The combustible dust and fibers, highly inflammable liquids with flash temperature above 301 K, and combustible liquids in such quantity that can form air-dust or steam-air explosive mixtures, by which ignition the calculated explosion overpressure in the building develops exceeds 5 kPa
V (fire-risk)	The combustible and difficult combustible liquids, solid combustibles, difficult combustible substances and materials (including dusts and fibers), and substances and materials able by interaction with water or/and air oxygen only burn, on conditions that the buildings, in which they are positioned or circulate, do not fall into A and B categories
G	Incombustible substances and materials in hot, glowing, or fused condition, processing of which is accompanied by emission of radiant heat, sparks, and flame; burning gases, liquids, and solid substances which are burned or used as fuel
D	Incombustible substances and materials in the cold condition

thermoprocessing equipment (Part 1) and safety requirements for combustion and fuel handling systems (Part 2), including the safety of persons and property during commissioning, start-up, maintenance periods, and dismantling, as well as in the event of foreseeable faults or malfunctions which may occur.

Furnaces with annealing atmospheres must be equipped with a control system of gas reburning torch presence, which must prevent spontaneous breakage and extinction of the torch; this system must be assembled with a gas supply system and emergency ventilation. Furnaces operating with hazardous atmospheres must also be equipped with a purging system which is actuated (automatically as far as possible) in case of danger, for example, by decreasing hazardous atmosphere pressure, in order to bring the equipment to a safe condition by replacing the hazardous atmosphere with an inert gas.

According to [20,21], the European Development Center, in Sheffield, UK, has available Material Safety Data Sheets (MSDS) for industrial gases and gas mixtures in printed form or on CD-ROM.

Quenching Means

As quenching means for combustible metallic powders, gases, and liquids, fire-extinguishing refrigerants, powders, and combined compositions are used. Typical physico-chemical properties of fire-extinguishing refrigerants which are used in Commonwealth of Independent States countries are given in Table 27.11. The aliphatic hydrocarbons (alkanes) are the basis of the refrigerants.

Fire-extinguishing powders are finely ground mineral salts with various additions that obstruct caking. For their basis, phosphorus-ammonium salts (mono-, diammoniumphosphates, and ammophos), sodium carbonate and bicarbonate, sodium and potassium chlorides, and others are used. As additions, organosilicon compounds, metal stearates, nepheline, talc, and others are used. A mechanism of the extinguishing effect is the inhibition of burning as a result of chain reaction active centers binding. A heterogeneous recombination of these centers occurs on powder surface, as well as a homogeneous interaction of sublimation products with active centers.

The extinguishing ability of powders depends not only on the chemical nature of powders but also on their fineness. The finer the powder particles are, the larger their surface, and the higher their effectiveness. However, the possibility of ultrafine powder production and use is restricted. Optimal particle sizes of commonly used powders range from 40 μm to 80 μm. Typical data about fire extinguishing powders used in Independent States countries are given in Table 27.12.

In combined compositions, the properties of several fire extinguishing means are associated. The compositions which represent the combinations of a carrier with intense burning inhibitor are the most effective, for example, aqueous-refrigerant emulsions and combinations of air-based foam with refrigerants related to them.

For voluminal quenching, nitrogen-refrigerant and carbon dioxide-refrigerant compositions have been developed. These compositions ensure a 4 to 5 times decrease in the specific rate of expensive bromine refrigerants. The composition containing 85 wt% carbon dioxide and 15 wt% 114B2 refrigerant is especially advantageous. The reciprocal solubility of

TABLE 27.11 Typical Physicochemical Properties of Fire-Extinguishing Refrigerants

Physicochemical Properties	CF_3Br	$C_2F_4Br_2$	CF_3Br
Refrigerant sign	13B1	114B2	12B1
Molecular mass	148.93	259.89	165.4
Temperature (K):			
Boiling point	215.2	320.5	269
Freezing point	105	261.5	112.5
Steam pressure at 293 K (kPa)	1753	311	539
Density of liquid (g/cm^3)	1.575	2.18	1.83
Viscosity at 293 K (Pa·s)	160	762	520
Self ignition temperature (K)	968	815	…
Fire-extinguishing concentration (kg/cm^3)	220 to 250	195 to 220	255
For petroleum product (vol%)	(14–16)	(9–10)	(14)

TABLE 27.12 Fire-Extinguishing Powders

Powder Trademark[a]	Main Component	Area Application (Fire Class)	Fire-Extinguishing Ability (kg/m^2)
ПСВ-3	Sodium bicarbonate	B, C, E	1.6
ПФ	Diammonium phosphate	A, B, C, E	1.4
ПС	Sodium carbonate	D	40
П-2АП	Ammophos	A, B, C, E	1.8
Пirant A	Ammophos	A, B, C, E	1.8
ПГС-М	Mixture potassium and sodium chlorides	B, C, D	26D
CI-2	Silica gel saturated by 114B2 refrigerant	D (metal-organic compounds and metal hydrides)	20–32D
PC	Swelling graphite	D (potassium alloys sodium alloys)	6.0 9.0
МГС	Graphite with lowered density	D, for sodium	3.0
		for lithium	10.0

[a] *Data about fire-extinguishing powders used in Independent States countries; Fire classes: A, combustion of solid matters; B, combustion of liquid matters; C, combustion of gaseous matters; D, combustion of metals and metal containing matters.*

components in the ratio cited in the condensed state contribute its merits. For this reason, the possibility of joint composition storage is simplified, and the cost of using it is reduced. By voluminal quenching, the calculated composition weight m (in kg) amounts to:

$$m = KVq_n$$

where K is the coefficient taking into account the unsealed production area; V is the volume of production area, m^3; q_n is supply rate of quenching composition amounts to 0.27 kg/ m^3 for supply duration $\tau = 30$ s, and 0.4 kg/m^3 by $\tau = 60$ s.

Recommended quenching means are given in Table 27.13 with the parameters being taken as reference values.

The most effective quenching means for alkaline metals are МГС and ПС powders and voluminal quenching by means of gaseous mixture nitrogen and carbon dioxide. The best quenching compositions for alkaline-earth metals are ПГС-М powders and argon for voluminal quenching. For polar hydrocarbon liquids (alcohols, acetone, either, etc.), the best quenching means for large spillages are water spray, foam, and ПСВ powder, and for little fire—water and carbon dioxide. The most effective quenching means for hydrogen and hydrocarbon gases, including liquefied gases, are cooling by water and voluminal quenching.

For fire quenching on combustible gas supply systems, high pressure water, inert gas, steam, or air delivery are provided for flame break, followed by filling of the system with inert gas.

Dust Explosion Protection Systems

Explosion protection techniques include venting, flameless venting, suppression, and isolation—either separately or in combination.

Dust Explosion Venting

Dust explosion venting is a well-established method of protecting against damaging explosion overpressures and is by far the most popular explosion protection technique, extensively described in commonly accepted engineering literature and standards [27–29]. Venting enables pressure developed during an explosion inside a vessel to be safely released in the environment, thus preventing the vessel from bursting. The sizing cases of pressure venting devices set up [30] for the following conveying condition: 10 m^3 $\leq$ V $\leq$ 250 m^3 enclosure volume ranges; 2500 m^3/h maximum flow rate; maximum explosion overpressure $p_{\max} \leq 0.9\,\text{MPa}$; $5\,\text{m}\cdot\text{MPa}\cdot\text{s}^{-1} \leq K_{\text{st}} \leq 30\,\text{m}\cdot\text{MPa}\cdot\text{s}^{-1}$ maximum rate of pressure rise.

TABLE 27.13 Recommended Quenching Means

Quenching Means		Substances and Materials							
Composition	Parameters	NP-HCL	P-HCL	H-CM	HC-G	Hydrogen	AM	AEM	AOrg
Water	I,(L/(m^2·s)) τ=30–60 min	0.2	0.25	0.2	0.1[d]	0.08[d]	…	…	0.3
Air-mechanical mean multiplicity foam	I, L/(m^2·s), τ=30–60 min	0.08	…	0.05	…	…	…	…	…
Voluminal quenching									
Carbon dioxide	G (kg/m^3), τ=2 min	0.7	0.7	0.7	…	…	…	12[i] τ=2–5	…
Refrigerants[a]	G (kg/m^3), τ=0.2 min	0.22[b]	0.22	0.22[c]	0.32 τ=0.5	1.16 τ=0.5	…	…	…
85 wt%CO_2+15 wt% $C_2F_4Br_2$ (CF_3Br)	G (kg/m^3), τ=0.5 min	0.27	0.27	0.27 (c)	0.4	0.57	2.0–2.5[f] τ=0.5–5.0	…	…
Powder									
ПСВ-3	G (kg/m^2)	0.66	0.66	…	4.0[e]	…	…	…	…
П-2АП, Пirant A, ПФ	G (kg/m^2) G (kg/m^2) G (kg/m^2)	0.89 0.65 0.47	0.89 0.65 0.47	0.4 0.31 0.23	5.0[e]	…	…	…	…
ПГС-М, ПС, МГС, PC, ПФК	G (kg/m^2) G (kg/m^2) G (kg/m^2) G (kg/m^2) G (kg/m^2)	… … … … …	… … … … …	… … … … …	… … … … …	… … … … …	… 40–60 10[g] 9[h] …	15–50[j] … … … 100[k]	… … … … …
CI-2	G (kg/m^2)	…	…	…	…	…	…		20–32

[a] *114B2 and 12B1 are the refrigerants.*
[b] *$G=0.37\,kg/m^3$ for work categories A and B.*
[c] *For glowing materials the G is increased to twice.*
[d] *For cooling the equipment adjacent to burning center.*
[e] *Powder rate on 1 kg of effluent gas.*
[f] *Mixture 94 vol% nitrogen and 6 vol% carbon dioxide.*
[g] *For quenching of sodium and lithium.*
[h] *For quenching of sodium and sodium-potassium alloy.*
[i] *Argon.*
[j] *For quenching of magnesium and aluminum.*
[k] *For quenching of calcium and beryllium by means of calcium fluoride powder (ПФК).*
Symbols: I is the supply rate of quenching means; τ is the quenching time; Substances and materials: NP-HCL is the nonpolar hydrocarbon liquids (including petroleum products); P-HCL is the polar hydrocarbon liquids (alcohols, acetone, either, etc.); H-CM is the hard carbonic products; HC-G is the hydrocarbon gases, including liquefied gases; AM is the alkaline metals (sodium, potassium, etc.); AEM is the alkaline-earth metals (magnesium, aluminum, etc.); AOrg is the organoaluminum compounds. Quenching compositions:
Source: Baratov AN, Korolychenko AJ, editors. Fire- and explosion-proof of matters and materials and means for their quenching. Moscow: Chimia; 1990.

Dust filters are the most common type of dust/air separation equipment. Dust filters will typically have a dirty air volume and a clean air volume. The clean air volume includes the inner volume of filter bags, cartridges and envelopes if the dust is separated from the air at the outer surface of the filter (Fig. 27.12A). The preferred location of the vent is below the filter elements. When filter elements (partially) block the vents, either completely remove the filter elements in front of the vent or shorten them so that they do not extend below the top of the vent. In addition, bars should be installed to refrain the filter elements from obstructing the venting process. The distance X between the first arrays of filter elements and the venting device should be such that the passage area directly in front of the venting device at least equals that of the venting device.

For calculating the explosion venting device of a cyclone (Fig. 27.12B), it is necessary to take into account the entire cylindrical volume, V_1 (without subtracting the air outlet pipe), the conical volume, V_2, as well as the volume of the settling chamber, V_3. Typically, the explosion vent is located on top of the air outlet pipe, implying that the vent area equals the total

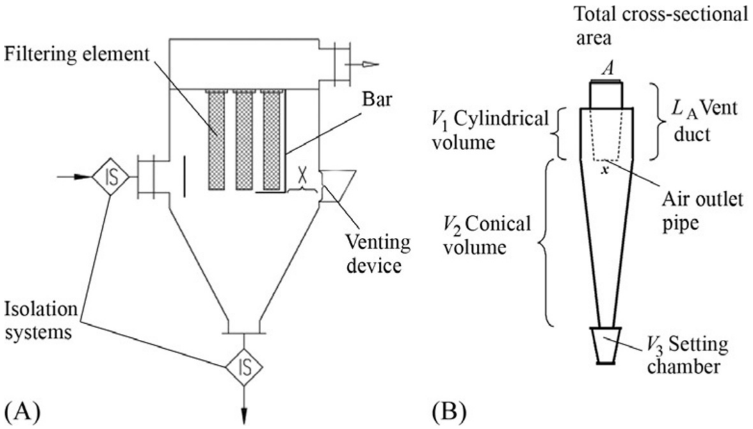

FIG. 27.12 Schematically images of dust explosion protection of dust separation equipment: (A) bag filter, (B) cyclone.

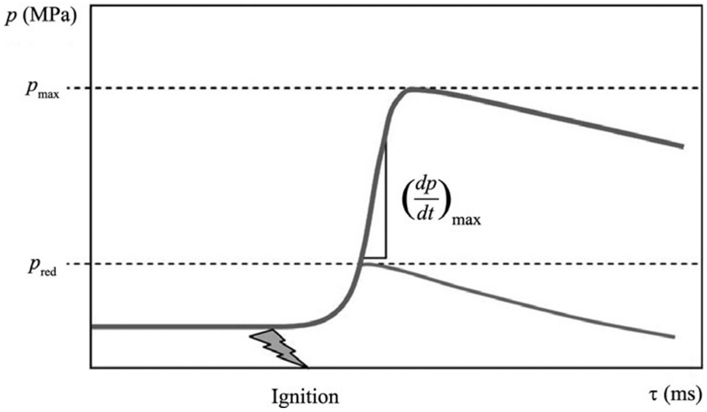

FIG. 27.13 Explosion pressure curve in closed vessel.

cross-sectional area, A, of the air outlet pipe. For the venting design, the air outlet pipe should be considered as a vent duct with length, L_A. Should the air outlet pipe be tapered inside, use the smaller cross-sectional area, X, for the calculation of p_{red}. If additional vents are required, these will be preferably located on top of the cyclone (shoulders), around the air outlet pipe.

A rupture diaphragm is placed on the vessel and designed to open at a static burst pressure (p_{stat}) well below the pressure at which the vessel would be destroyed or damaged (Fig. 27.13). The area of the rupture diaphragm (A) is calculated to be large enough to allow fast discharge of pressure [31]. EN 14491 [27] and NFPA 68 [30] contain the calculation methods of explosion venting devices. The calculation of rupture diaphragm area can be made using the following equation:

$$A = 10^{-4} \times \left(1 + 1.54 p_{\text{stat}}^{4/3}\right) K_{\text{st}} V^{3/4} \sqrt{\frac{p_{\max}}{p_{\text{red}}}}$$

where p_{stat} is the vent nominal static burst pressure (bar), K_{st} is the maximum rate of pressure rise (m·bar·s^{-1}), V is the volume of the vessel, p_{red} is the reduced pressure after deflagration (bar).

Explosion Flameless Venting

While venting allows the control of the pressure developed inside an enclosure, it does not mitigate the hazards of the flame exiting from the vent [32]. It is therefore not recommended to apply conventional venting for enclosure located indoors because of the secondary dust explosion hazards. In this case, vent ducts can be added to redirect the flame (and pressure) outside the building. However, adding a vent duct can largely increase the reduced pressure (p_{red}) inside the enclosure, making it difficult to apply effectively. Another option is flameless venting [33,34].

The principle of a flameless venting device typically includes an explosion vent panel and a flame-quenching unit enclosing layers of stainless steel mesh (Fig. 27.14). The flame-quenching unit may be cylindrical, rectangular, or segmented (Fig. 27.14B). Flameless venting mitigates flame hazards, and significantly reduces the pressure effects outside the process vessel, compared to a conventional venting device, thus reducing the exclusion zones. It offers a compact

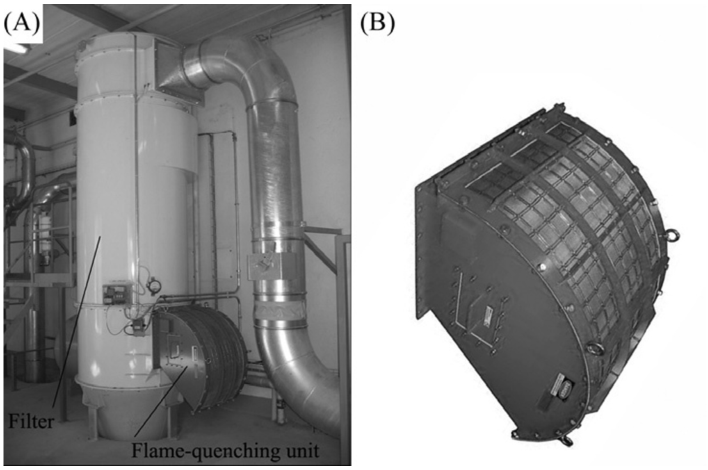

FIG. 27.14 Filter (A) equipped by flame-quenching unit (B).

alternative to vent ducting, with a much better venting efficiency. However, flameless venting does not fit all situations. It may sometimes be preferable to consider suppression technique, especially when there is not enough space to install vents or when the processed material is toxic.

Explosion Suppression

An explosion suppression system typically consists of pressure sensors, high rate discharge (HRD) suppressor with appropriate dispersion nozzles, and control panel. After ignition of a dust cloud, the flame front expands and pressure waves are emitted. The pressure sensor detects the pressure increment and sends a signal to the control panel, which, in turn, initiates the suppressant discharge. Both nitrogen and suppressant agent are rapidly released into the vessel and extinguish the fireball by reducing the temperature of the combustible material below a level necessary to sustain combustion. Suppression is an active technique that has several advantages compared to conventional venting: there is no release of pressure, flame, or potentially toxic material in the environment, as the explosion is "contained" within the enclosure. It also reduces the damage to the equipment and mitigates the potential fire hazards, which can arise after an explosion. On the other hand, suppression systems typically are more expensive than vents. Suppression is also more difficult to achieve in small enclosures (typically $< 1\ \text{m}^3$), as pressure rates of rise are usually very high (i.e., the time to reach a certain pressure level is shorter than in a large enclosure).

Explosion Isolation

Process equipment usually is connected to other parts of a facility by pipes. A dust explosion originating in an enclosure, even vented, will likely propagate through these pipes and potentially reach other process equipment. By propagating, the flame front will accelerate and stronger pressure effects will be produced. This means that the resulting explosion in the secondary vessel can be much more violent than the initial event. This emphasizes the need to carefully consider explosion isolation. The objectives of isolation are multiple:

- to prevent flame propagation to a secondary enclosure
- to prevent pressure piling and flame jet ignition in the secondary enclosure
- to prevent deflagration to detonation transition in pipes (high L/D)

Isolation can be achieved in two different ways: either passive or active. Passive systems are activated by the explosion itself and include diverters, float valves, and flap valves (Fig. 27.15). In the example of a flap valve, the pressure generated by the explosion will push a gate and close the pipe, thus avoiding propagation of the flame to the protected area. Passive systems are simpler and typically require less maintenance.

While active systems require tripping by a sensor for activation, upon triggering, they will close a mechanical valve ahead of the flame front or inject an extinguishing agent in the pipe to stop further flame propagation. Active systems include chemical barriers, gate valves, and pinch valves (Fig. 27.16).

Placement of the device must assign on the assumption of following: if an isolation device is placed too far from the ignition, the deflagration can transit into a detonation prior to reaching the device and damage it; if it is placed too close to

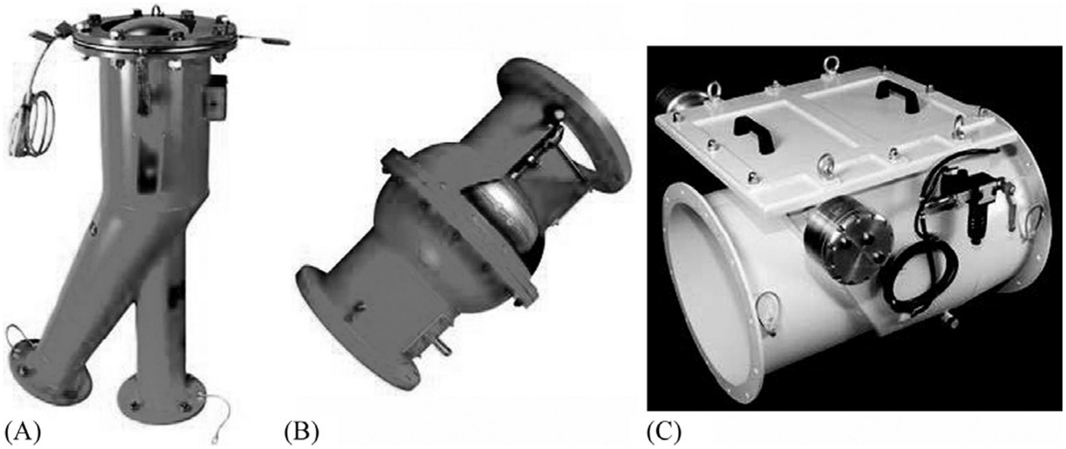

FIG. 27.15 Passive explosion isolations systems of Fike Corpoiration: (A) diverter, (B) float valve, (C) flap volve.

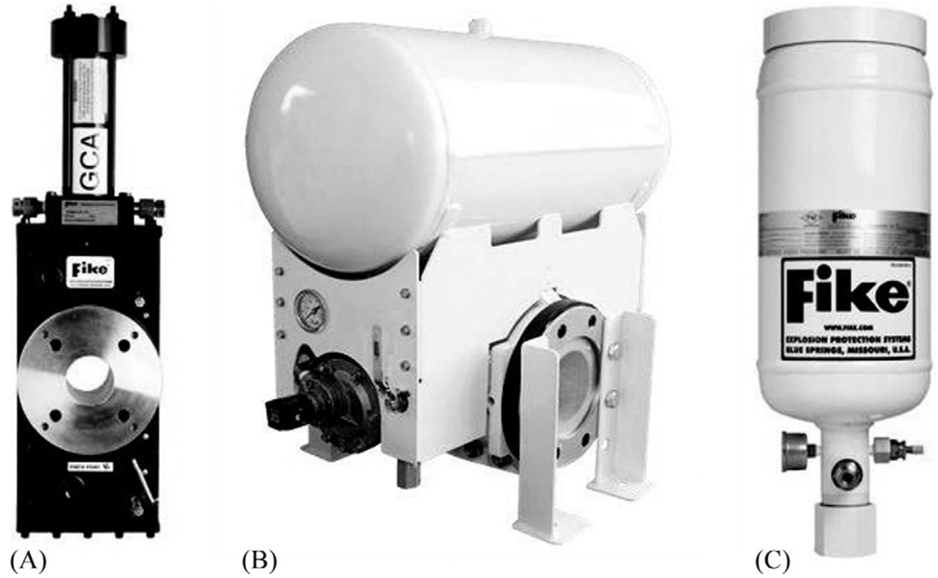

FIG. 27.16 Active explosion isolations systems of Fike Corporation: (A) explosion isolation valve, (B) explosion isolation pinch valve, (C) chemical barrier standard rate discharge (SRD) device.

the ignition, then it may not be entirely closed and able to block the passage of flame when it arrives. The components that make up the total time for isolation are:

- Time for the pressure growth to exceed the activation pressure of the detector, or for the optical detector to see a flame (T_{act})
- Time for the electronics (detector and control panel) to respond (T_{elec})
- Time for the mechanical barrier to close, or for the chemical barrier to form (T_{bar}) is described by the formula:

$$T_{\text{iso}} = T_{\text{act}} + T_{\text{elec}} + T_{\text{bar}} + T_{\text{bar}}$$

The total time for the isolation process should always be less than the time for the flame T_{flame} to travel to the barrier's location: $T_{\text{iso}} = T_{\text{flame}}$.

Localization of Powder-Gas Emissions

Aspiration involves the isolation of the powder-gas emission origin, removal of these emissions via an exhaust, and separation of particles from aspirated gas before its ejection into the environment. It is also possible in certain conditions that aspiration can provide heat removal and prevent overheating of the material being processed.

There are opened-loop and closed-loop aspiration systems. The latter is much more complicated and requires the provision of protective gas and a leak-tight construction. Resorting to closed-loop systems in the case of suspended solid with low values of LCIL and limiting oxygen concentration (LOC) is favorable.

Dust or harmful gases formed as a result of mechanical and thermal processes or chemical reactions in the equipment and aspiration covers flow out when overpressure arises in nonhermetic systems. The main processes responsible for such pressure formation are the following:

- Dynamic interaction of particle gravitation flow with the gaseous medium causes ejection pressure, p_e
- When closed chambers and volumes are filled with particulate materials, excess pressure, p_v appears as a result of a decrease the empty volume and redistribution of pressure in the loading apparatus as ejection pressure acts
- In equipment with moving parts, a high peripheral velocity accounts for an excess pressure, p_{eq}, and directed air flows result
- As a result of heat exchange during the processing of heated materials, the density of gaseous media in the equipment and covers differs from the density of the surrounding air and, hence, the pressure of the gaseous medium is re-distributed: heat pressure p_t appears
- Mass transfer as a result of chemical transformations or vaporization causes pressure p_{mt}

Ejection Pressure p_e

During the movement of particulate materials in closed chutes of non-hermetic units, a directed flow of ejected air is created. This is typical for numerous operations: reloading from one conveyor to another, feeding of materials by conveyors into units, and discharge of material from units onto conveyors or into adjacent equipment.

During transportation of powder, it is necessary to provide sloping chutes with minimum inclination (under conditions of powder motion), in order to decrease harmful emission.

The interaction with air of the surface of moving powder on the bottom chute is described in Ref. [35] by the equation:

$$F\Sigma\zeta v_2^2\rho_2 = \int_0^l c_\tau b|v_1 - v_2|(v_1 - v_2)\rho_2 dx \tag{27.1}$$

where F is the square of the chute cross-section; $\Sigma\xi$ is the sum of local resistance to motion of the ejected air; v_1 is the velocity of the moving powder, v_2 is the ejected air velocity; c_τ is the coefficient of dynamic interaction of surface of the moving powder surface with gaseous medium/air; b is the width of chute; l is the length of chute; ρ_2 is the air density; here and below by lower index "1" the magnitudes characterizing the material movement are denoted, and by lower index "2"—the air.

The left part of above (Eq. 27.1) shows the resistance force to the ejected air motion, while the right part describes the force causing this motion as a result of interaction between the moving material free surface and the gas medium. With the decrease of v_1, l, and b and the increase of $\Sigma\zeta$, the force causing ejection decreases, as well as the ejected air rate, and, therefore, the value of the required suction capacity L_a. The decrease of v_1 and l is achieved by decreasing the height of fall. Decrease of v is also possible at the expense of the sloping chutes with minimum inclination (under conditions of powder movement); however, as a result Fv_2 is decreased, because Fv_2 depends more strongly on v_1 than on l.

The aspiration cover with double walls (Fig. 27.17) has an aerodynamic advantage. Such a design ensures the removal of the over pressure focuses from leak-stop-sealing systems and equalizing pressures on the inner surface of the outer walls of the aspiration covers. Typical parameters of the belt conveyor reloading unit are given in Table 27.14.

Reloading units that maintain powder in quasi-interconnected motion condition unchanged during changes in powder-consumption rate have been designed. These units achieve a considerable decrease of the free powder surface during powder gravitation flow for interaction with the gaseous medium. Such conditions are achieved in chutes in the form of three-edged prism with one of ribs directed down [36]. The use of such a device during processing of metallic powder decreased aspirated air consumption by 1.7–2.3 times, and reduced powder loss by 2.5–3 times.

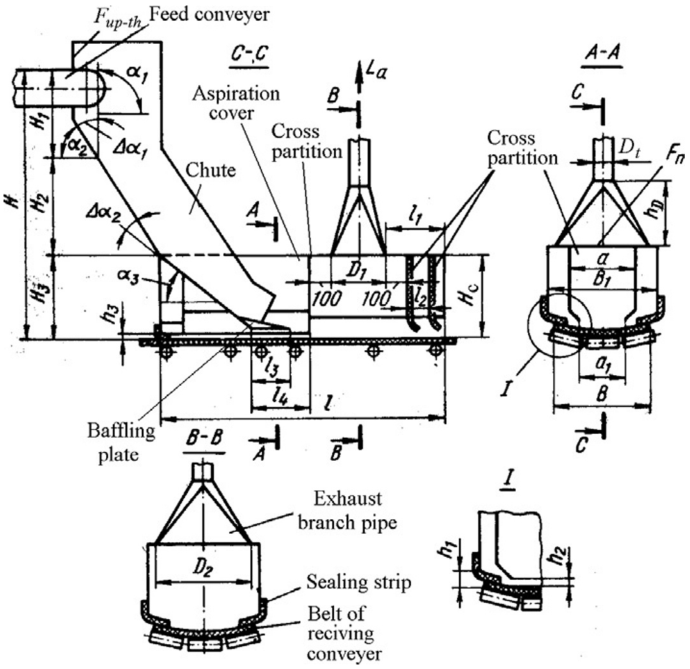

$F_{up\text{-}th}$
Feed conveyer
C-C
Aspiration cover
Cross partition
Chute
L_a
B
A-A
C
Cross partition
D_t
F_n
h_D
α_1
α_2
$\Delta\alpha_1$
$\Delta\alpha_2$
α_3
H
H_1
H_2
H_3
h_3
A
l_1
D_1
100
100
l_2
H_C
l_3
l_4
l
a
B_1
a_1
B
I
Baffling plate
B-B
A
B
C
Exhaust branch pipe
D_2
Sealing strip
Belt of reciving conveyer
I
h_1
h_2

FIG. 27.17 Diagram of the belt conveyor reloading unit.

TABLE 27.14 Typical Parameters of the Belt Conveyor Reloading Unit

B	B_1	a	a_1	H_C	l	l_1	l_2	l_3	l_4	h_1	h_2	h_3
400[a]	520	300	280	300	1400	250	100	200	400	2.5δ	1.5δ	3.5δ
500	650	375	350	380	1500	250	100	250	500	2.5δ	1.5δ	3.5δ
630	820	485	455	500	1820	325	100	330	630	2.5δ	1.5δ	3.5δ
800	1040	600	560	600	2200	400	100	400	800	2.5δ	1.5δ	3.5δ

[a] *All dimensions are given in millimetres, δ is the belt thickness.*

Overpressure in Closed Chambers

When closed chambers and volumes are filled with particulate material, excess pressure p_Σ appears as a result of a decrease in the unoccupied volume p_v, and re-distribution of pressure in the loading apparatus as ejection pressure acts

$$p_\Sigma = p_v + p_e \tag{27.2}$$

Diagrams of various filling units are shown in Fig. 27.18. In the case where a closed sagger is filled from a pressurized batcher (Fig. 27.18A), during the process the forced-out air is displaced, moves in the chute and further through the powder layer in consumed volume. Then, in the chute, at the site of its junction with the consumed volume, the maximum pressure corresponds to pressure p_v necessary for overcoming of powder layer resistance to forced out air flow

$$p_v = G_1 g \rho_2 H_m / K_f \, \rho_1 F_m \tag{27.3}$$

where G_1 is a material mass flow during sagger filling (kg/s), ρ_1 is the material density (kg/m^3), H_m is the highest material level in the consumed volume (m), F_m is the horizontal square occupied by material in the consumed volume (m^2), K_f is the filtration coefficient whose values are given in Directive for designing and computation of aspiration in metallic powder production including combustible and explosive [36].

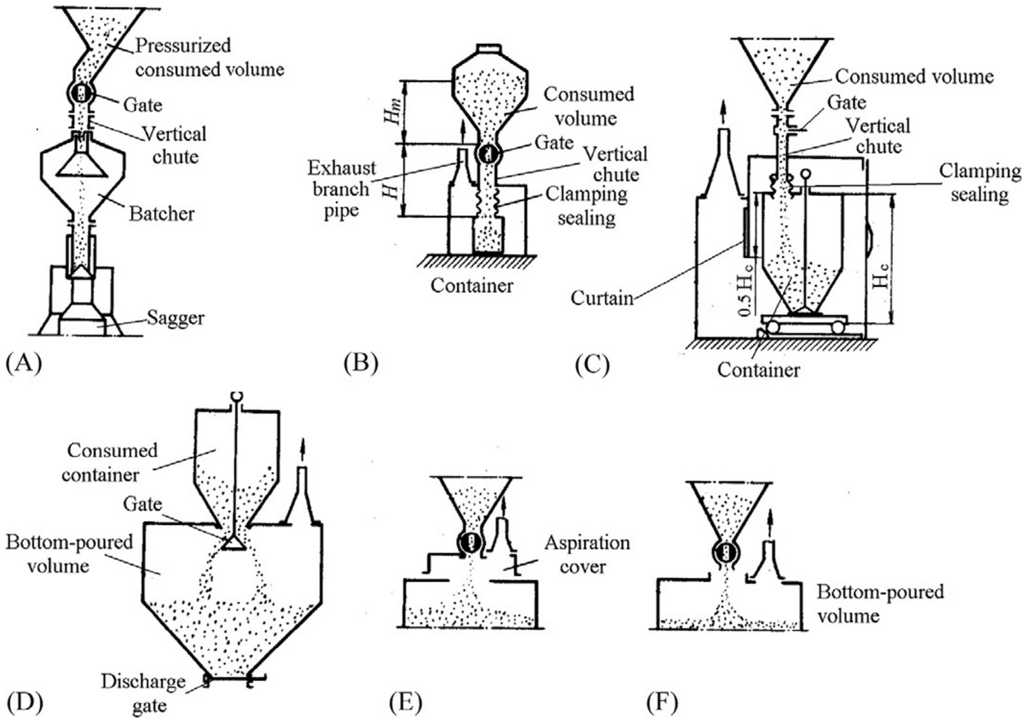
Pressurized consumed volume
Gate
Vertical chute
Batcher
Sagger
(A)
Hm
H
Exhaust branch pipe
Consumed volume
Gate
Vertical chute
Clamping sealing
Container
(B)
Consumed volume
Gate
Vertical chute
Clamping sealing
Curtain
0.5 Hc
Hc
Container
(C)
Consumed container
Gate
Bottom-poured volume
Discharge gate
(D)
Aspiration cover
(E)
Bottom-poured volume
(F)

FIG. 27.18 Diagrams of various filling units: (A) closed sagger filled from pressurized batcher; (B, C) loading of container in cabin type aspiration covers; (D) bottom-poured volume from container; (E, F) loading of movable containers.

At the inlet to the chute, the site of its joining to the consumed volume, the overpressure (Eq. 27.2) is minimal dangerous and harmful agents

$$p_{\Sigma_{\min}} = p_v - p_e$$

while, at the outlet end, the sagger entrance, the summarized pressure (Eqs. 27.2 and 27.3) amounts to

$$p_{\Sigma_{\max}} = p_v + p_e$$

$$p_e = 145\psi G_1 \rho_2 v_{1k}^3 (gF\rho_1 d_a)^{-1} \qquad (27.4)$$

where ψ is an aerodynamic resistance coefficient of the particles, v_{1k} is the material velocity in the chute outlet, and d_a is the average particle size.

A design for joining and the sort of sealant material are selected depending on the value of $p_{\Sigma_{\max}}$.

In the case of nonhermetic receiving volume the required suction capacity is determined by the equation:

$$L_a = L_v + L_n$$

where L_v is the air flow displaced from the receiving volume during filling, L_n is the air flow (Eq. 27.5), which is sucked through the non-compactnesses in the receiving volume or aspiration cover. The value of the discharge coefficient through the openings amounts to 0.65:

$$L_n = 3300F_n (p_c/\rho_2)^{0.5}, \mathrm{m}^3/\mathrm{h} \qquad (27.5)$$

where p_c is the normalized underpressure in the cover (Pa).

In case of the suction connection directly to the loading volume (Fig. 27.18E) the required suction capacity L_a. must be calculated subject to flow rate value ejected by powder gravitation flow.

To decrease p_v in powder-filled chambers, pressurized chambers and loading devices should be used. At the same time, if suction is connected to the casing of the charging unit (but not to the volume being loaded), the influence of p_e on the required suction capacity L_a. is absolutely excluded, because $\Sigma\zeta \rightarrow \infty$. Using pressurized chambers and loading devices, the air being displaced as a result of the powder coming in content best of all is realized by means of the bypasses connecting the bottom-poured vessel with the receiving one, or a combination of discharge nipple with ejection exhaust (Fig. 27.19).

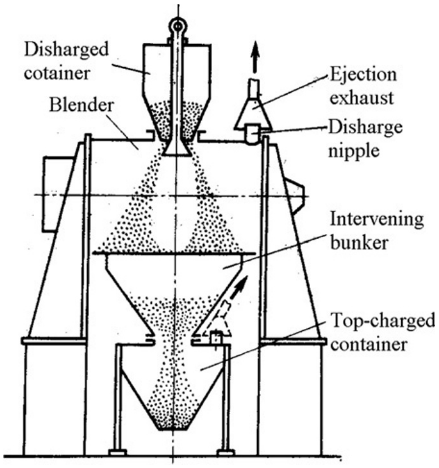

FIG. 27.19 Diagram of the feeding and unloading of a blender equipped by ejection exhaust.

Pressure Created by Equipment Moving Parts

The most effective means of eliminating the action of excess pressure p_{eq}, created by moving parts, is pressurized filling of loading and unloading units, isolated from the environment and from other equipment. Pressurized packing should withstand maximum pressure. Bypass pipes should be used to discharge excess pressure. They should connect zones of over pressure with under-pressure zones.

The maximum pressure p_{eq}, created by moving parts of a hammer crusher (Fig. 27.20), is determined from the equation:

$$p_{eq}^{*} = c_h\left(1.5\frac{c_m G_1}{c_h \rho_1 d_a} + nF_{h1}i\right)\frac{\rho_2 l_R}{4F}\bar{v} \tag{27.6}$$

where c_h is coefficient of dynamic interaction of the rotating parts with air, G_1 is a material mass flow, c_m is coefficient of dynamic interaction of the particulate material with air in the crusher chamber, ρ_1 is material density, d_a is root-mean-square diameter of material after collision with hammers and bumper slabs, $F_{h.1}$ is the sum area of one row of rotating parts, F is the cross-section of the hammer body, in which the parts revolve (the section is orientated normally to root-mean-square air velocity vector in inner crusher), n is the rotation velocity of hammers, l_R is the trajectory length of the active part rotor center diameter D_{ac} from the material entrance site in hammers action zone and the end of the separation grate, i is a number of hammer rows, $\bar{v}$ is a root-mean-square peripheral velocity of the active rotating parts D_{ac}

$$D_{ac} = \frac{2\sum_{i=1}^{n} F_{h.a} \times r}{\sum_{i=1}^{n} F_{h.a}} \tag{27.7}$$

where r is the distance from the hammer mill axis to the mass center of the corresponding constituent of the active rotor parts; $F_{h.a}$ is the constituent cross-section area of the active rotor parts.

In crushing conditions in comparison with running without a material feeding, the created pressure is appreciably higher.

Heat Pressure p_t

The gaseous medium pressure in apparatus cascade with aspiration covers is re-distributed if its density differs from the environment as a result of heat exchange during processing of the elevated temperature materials. The value of p_t is determined by the equation:

$$p_t = 0.5g\left(\rho_{2_{env}} - \rho_{2_{r.v}}\right)H \tag{27.8}$$

where $\rho_{2_{env}}$ is the density of the environment medium, $\rho_{2r.v}$ is the density of the gaseous medium in the lower aspiration cover, H is maximum value of the difference between the apparatus (cascade) cross sections levels which are aerodynamically connected.

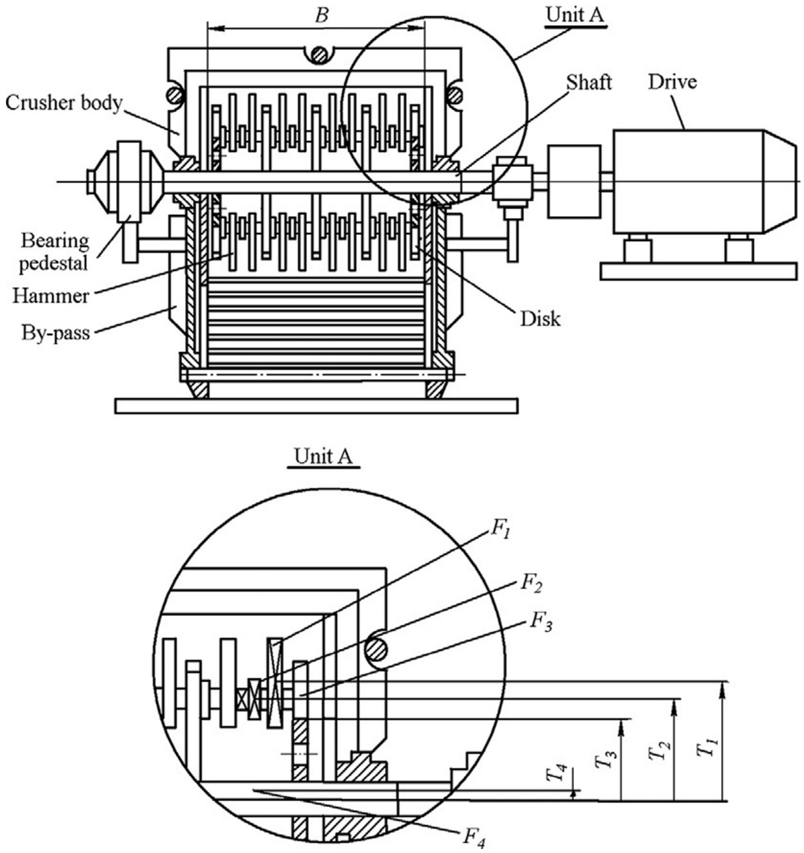

FIG. 27.20 Hammer mill with built-in bypass pipes.

Pressure p_{mt}*—Mass Transfer Result*

Pressure p_{mt} arising from the mass transfer is the result of chemical transformations or vaporization. Emergent overpressure in pressurized capacity during phase transfer with gas (vapor) volume yield J (kg/(m^3·s)), with density ρ_2 (kg/m^3) during τ (s) may be represented as follows:

$$p_{\mathrm{mt}} = (p_{\mathrm{mt}_\tau} - p_{\mathrm{mt}_0}) = p_{\mathrm{mt}_0}\left(e^{J\tau/\rho_2} - 1\right)$$

where p_{mt_τ} and p_{mt_0} are the pressure in pressurized capacity at τ and the starting moment, respectively.

Capacity of Local Suctions

In practice, one of the above mechanisms may function independently, but, more often than not, they occur in combination.

The mass balance equation is the initial one for determination of the required suction capacity:

$$\sum_{i=1}^{N} L_{\mathrm{a_i}} = \sum_{j=1}^{n} L_{\mathrm{d_j}} \tag{27.9}$$

where $L_{\mathrm{a_i}}$ and $L_{\mathrm{d_j}}$ are air flow arriving in the cover through j-th channel (chute, opening) and receding from cover by i-th suction (or going off through i-th channel), respectively.

The value of the gaseous component deleted is determined by the difference of pressure (Eqs. 27.3, 27.4, 27.6, and 27.8) and hydraulic resistance of the chute and leakinesses (openings). Generally, by the simultaneous action of several above-mentioned mechanisms, flow rates through the chute L_{c} and leakinesses L_{n} are described by equations:

$$L_c = F_c \sqrt{\frac{2\left(p_e - p_t \pm p_{eq} + p_v + \Delta p\right)}{\rho_2 \Sigma \zeta}} \tag{27.10}$$

$$L_n = \sum_{i=1}^{n} F_{o_i} \sqrt{\frac{2p_c}{\zeta_i \rho_{2_{env}}}} \tag{27.11}$$

where $\Sigma\zeta$ is a sum of resistance coefficients to gaseous component motion, ζ_i is the resistance coefficient of i-th opening to suction air, p_c is a normalized underpressure in aspiration cover, Δp is a pressure difference determined by action of local exhausts, ρ_2 is the air density in the chute, F_{o_i} is the area of i-th opening.

If gas emission occurs and its density differs from that of the gas filling the unit, it is more convenient to operate by flow mass values G_a but not by the volumes of aspiration gas. In the case, when pressure arises only as a result of gas emission

$$G_a = \sum_{i=1}^{n} F_{o_j} \sqrt{\frac{2p_c \rho_{2_{env}}}{\zeta}} \frac{(1 + m_c)}{(1 + m_{env})}$$

where m_c and m_{env} are the emission gas content in cover and environment, respectively.

Aspiration in Combustible Powder Conditions

The use of aspiration for controlled heat removing, to prevent excessive heating of the processed material, can be used in conditions of material grinding with relatively high energy activation of the oxidation reaction (50 to 60 kJ/mole and higher). The critical temperature $t_{1_{cr}}$ of the ground material coming from the mill is considered that at which glowing particles appear in them. In work [37], the heating process of the material during milling is described and an account of $t_{1_{cr}}$ is given.

During mechanical processing of materials with low energy activation values, fire/explosion-safety can be ensured by the use of controlled protective atmospheres. The method for production of powders, granules, and briquettes of chemically active metals and their alloys is described in source [38]. This technique comprises the comminution of initial bulky material in a shielding gas over a film-forming composition, followed by sieving size classification, blending, and subsequent compacting (Fig. 27.21).

This processing line includes vibro jaw crusher unit (A) (in this flowchart, the unit boundaries are marked by dotted lines), cone inertia crusher unit (B), vibro size separator unit (C), vibro blender unit (D), briquetting press unit (E), film-forming composition generation unit (F), and closed-loop shielding gaseous change system (Q). Each unit is developed as autonomous with cascade equipment location and is connected with the delivery and returning pipes by means of pipe-bends. The transportable containers (Fig. 27.22) serve the consumed volumes. The containers are equipped with gas distributing design and bypass which allow to maintain the controlled protective atmospheres.

The introduction of film forming composition comprises an organosilicon compound and surfactant increases the explosion safety, capacity, and finished powder yield [39]. Reducing the dust-like powder fraction emission by means of film formation contributes to increased explosion safety. During the comminution, the film forming composition covers the freshly formed surface of the particles, and dust-like fractions form particle aggregates. By means of the available controlled comminution process parameters, it is possible to obtain powders with specified improved properties. Table 27.15 shows typical conditions of process parameters for silico-calcium powder production. As shown, the treatment of the initial particulate material by the organosilicon compound and surfactant ensures increasing the finished powder yield, decreasing the temperature of the ground material, and explosion safety improvement. In the given case, the acceptable size fraction yield ranges from 1.0 to 0.05 mm with improved explosion safety and capacity. The developed technique (Table 27.15) allows such requirements to be met.

Melt Atomization Units

An aspiration cover over an induction melting furnace in the form of a housing located above the crucible and hingedly connected with the furnace frame and exhaust duct (Fig. 27.23) is recommended. Such a design ensures cover location above dust-gas emission source in whatever furnace position, and highly effective aspiration during the whole technological cycle, including melt preparing and pouring [40]. Position of the aspiration cover during melt pouring into tundish is shown in Fig. 27.24.

Typical data of dust concentration and volume of aspiration gas from induction furnaces are given in Table 27.16.

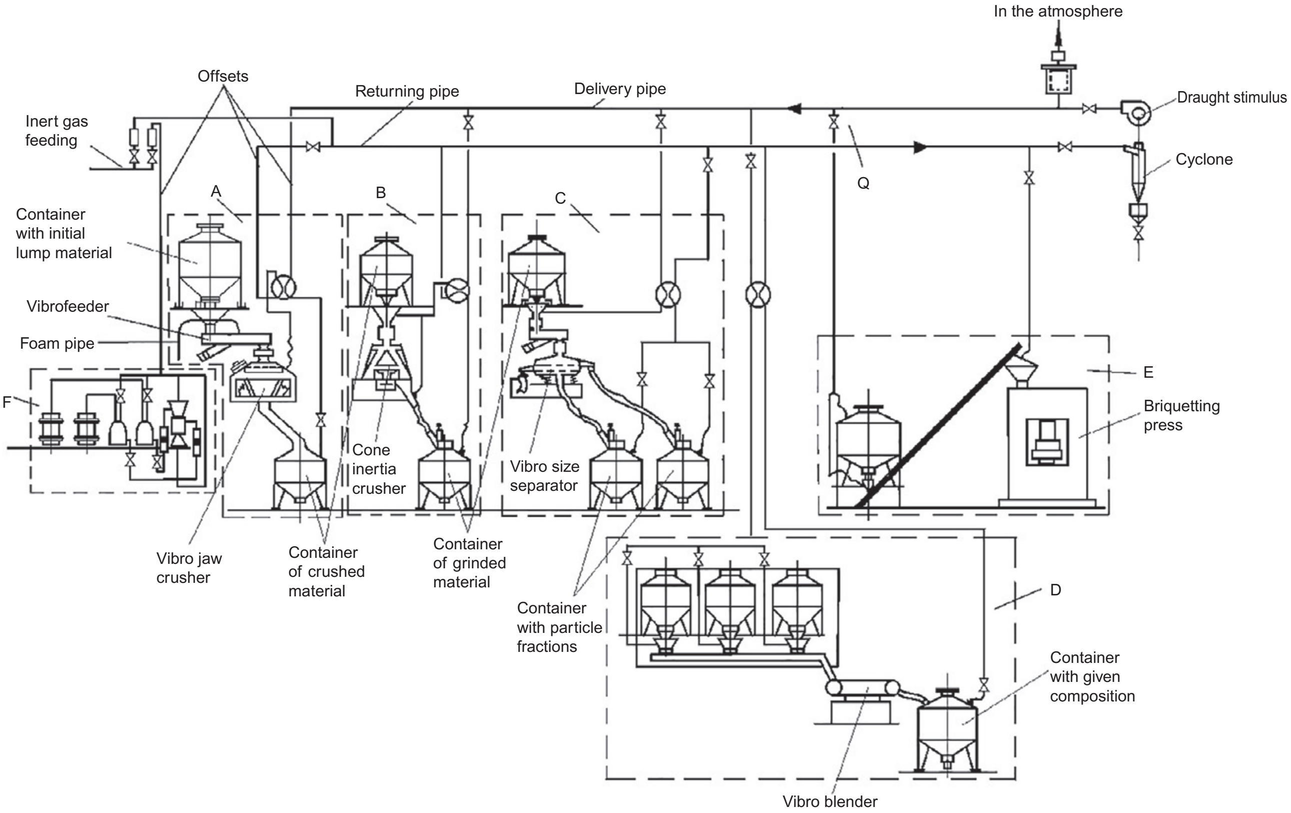
In the atmosphere
Offsets
Returning pipe
Delivery pipe
Draught stimulus
Inert gas feeding
Cyclone
Q
A
B
C
Container with initial lump material
Vibrofeeder
Foam pipe
E
F
Briquetting press
Cone inertia crusher
Vibro size separator
Vibro jaw crusher
Container of crushed material
Container of grinded material
D
Container with particle fractions
Container with given composition
Vibro blender

FIG. 27.21 Flowchart of the process of production of powders, granules, and briquettes of chemical active metals and their alloys.

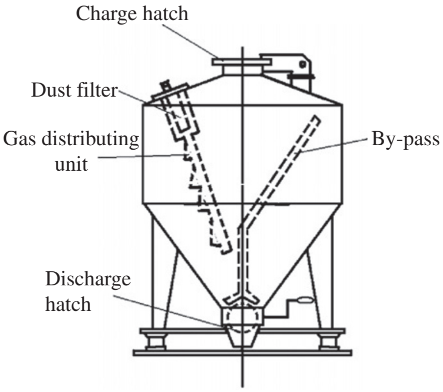
Charge hatch
Dust filter
Gas distributing unit
By-pass
Discharge hatch

FIG. 27.22 Transportable container.

Grinding Units

During the operation of some kinds of equipment pulsating motion occurs. For example, in drum mills, pulsations can appear as a result of displacement of milled bodies. In such cases, dust emissions are effectively localized through the employment of covers with inside and outside chambers [41] (Fig. 27.25).

The use of such devices [42] during grinding copper shot in tumbling mills (Fig. 27.26) decreased the required suction capacity L_a by 1.3 times in comparison to ordinary aspiration covers, and powder loss to the aspirated air was decreased by 7 times.

There are numerous designs of reloading units for minimizing the aspiration volume and powder carryover with aspirating air [35,43]. One of these designs consists of improving the unloading section of reloading unit (Fig. 27.27). In this design, expanding unloading part of chute and longitudinal baffle result in the formation of a closed-circuit air circulation.

TABLE 27.15 Process Parameters for Silicocalcium Powder Production

			Dust Content (g/m^3)		Particle Size (mm)		Fraction Content (wt%)			Explosibility	
FFC (wt %)	G_m (kg/h)	T_m (K)	C_1	C_2	+ 1.0	−1.0 +0.4	−0.4 +0.1	−0.1 +0.05	− 0.005	LCIL, g/m^3	LOC, vol%
0.0	230	353	6.29	16.6	9.9	24.1	30.2	15.3	20.5	150	14
0.2	418	318	6.09	13.3	11.2	34.1	24.3	18.2	12.2	370	14
0.3	969	308	5.29	4.55	9.3	37.3	29.5	16.3	7.6	400	16
0.5	983	308	4.70	1.15	0.5	57.0	21.2	15.5	5.8	400	16
0.6	971	318	4.40	1.87	1.1	44.7	29.7	19.3	5.2	400	16

FFC is the film forming composition content, G_m, is the finished powder yield, T_m, is the temperature of powder on discharge from cone inertia crusher, C_1 is the dust content in air in aspiration cover of the vibro jaw crusher, C_2 is the dust content in air in aspiration cover of the cone inertia crusher, LOC is an oxygen explosion-proof content of nitrogen in gas-diluted protective atmospheres.

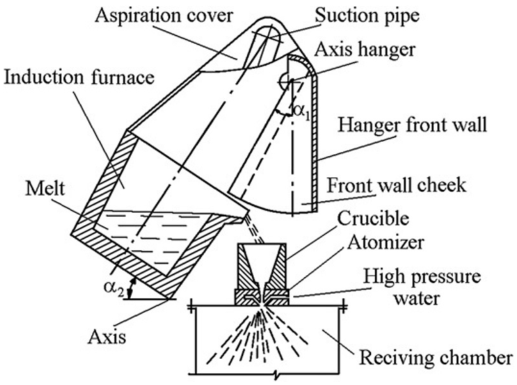
Aspiration cover
Suction pipe
Axis hanger
Induction furnace
α_1
Hanger front wall
Melt
Front wall cheek
Crucible
Atomizer
High pressure water
α_2
Axis
Reciving chamber

FIG. 27.23 Aspiration cover of an induction melting furnace.

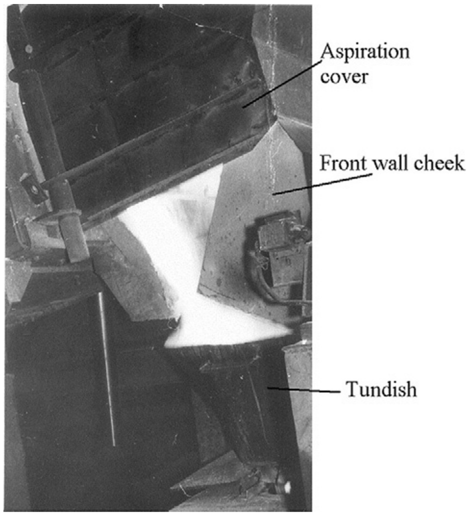
Aspiration cover
Front wall cheek
Tundish

FIG. 27.24 Position of the aspiration cover during melt pouring into tundish.

TABLE 27.16 Dust Concentration and Aspiration Gas Volume from Induction Furnaces

Induction Furnace Type (ISC)	Powder Commercial Grade (ISC)	Aspiration Gas Volume at 313 K (m^3/h)	Average Dust Concentration (mg/m^3)
Copper powder[w]			
IST—0.16[a]	PMR	1000	2.7
ILK—0.4[b]	PMR	3000	7.0
IST—0.4	PMR	3000	7.0
IST—1.0	PMR	4500	18.0
Brass powders[w]			
IST—0.16	PLS – 60[c]	1100	9.0
ILK—0.4	PLS – 60	3000	31.0
IST—0.4	PLS – 60	3000	31.0
IST—1.0	PLS – 60	5000	72.0
Bronze powders			
IST—0.16[w]	Cu-5Sn-5Zn-5Pb	1100	3.4
ILK—0.4[w]	Cu-10Sn	3000	10.0
IST—0.4[w]	Cu-5Sn-5Zn-5Pb	3000	10.0
IST—1.0[g]	Cu-10Sn-0.3P	5000	9.0
Aluminum powder[g]			
IAT—0.4	PA-5[d]	4000	12.0

(ISC) Independent States Countries grades.
[a] *IST is the brand of crucible induction furnace, while the quantity—the metric ton capacity of charge with iron.*
[b] *ILK is the brand of channel induction furnace.*
[c] *(30± 1)wt%Zn.*
[d] *99 wt% Al.*
[w] *Water atomized powder.*
[g] *Gas atomized powder.*

FIG. 27.25 Aspiration of the ball mill with peripheral milled powder discharge. Modifications: (A) with ejection suction device; (B) with bypass pipe. Source: Ref 17

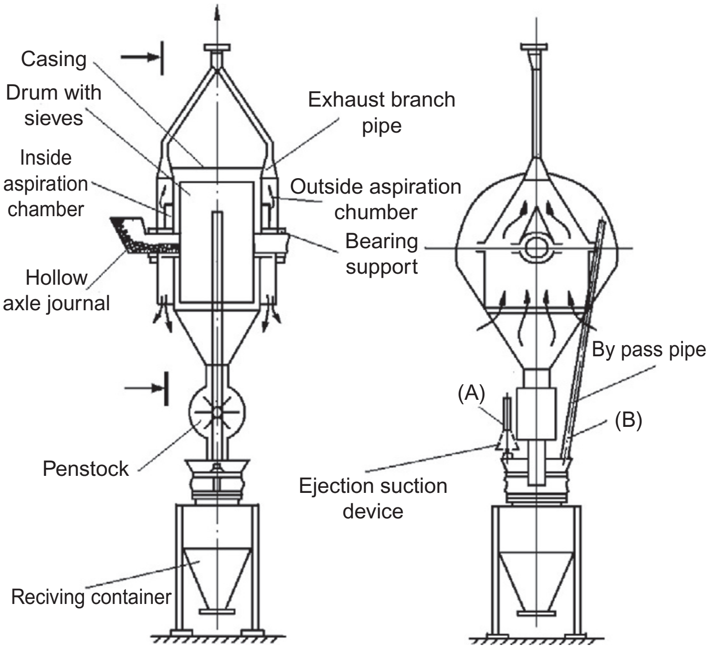
Casing
Drum with sieves
Exhaust branch pipe
Inside aspiration chamber
Outside aspiration chumber
Bearing support
Hollow axle journal
By pass pipe
(A)
(B)
Penstock
Ejection suction device
Reciving container

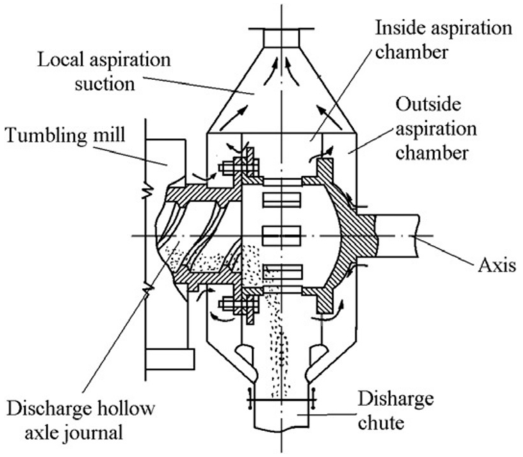
Local aspiration suction
Inside aspiration chamber
Tumbling mill
Outside aspiration chamber
Axis
Discharge hollow axle journal
Disharge chute

FIG. 27.26 Discharge unit of a tumbling mill.

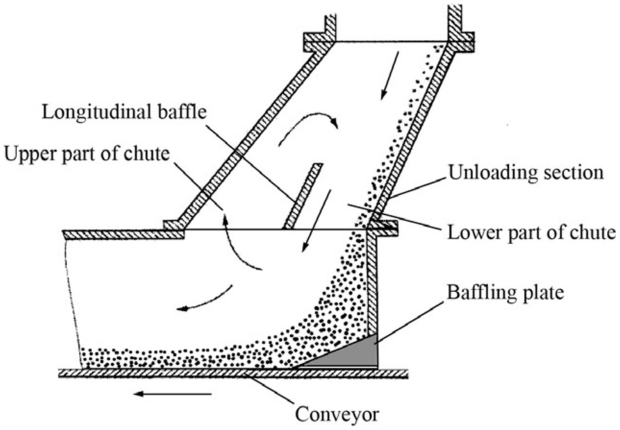
Longitudinal baffle
Upper part of chute
Unloading section
Lower part of chute
Baffling plate
Conveyor

FIG. 27.27 Unloading section of reloading unit

Because air circulation processes in such chutes still have not been described analytically, therefore, the choice of design parameters for handling facilities is hindered.

Definition of the Local Exhaust Capacity

Aspiration for Particulate Material Reloading in Closed Gravity Chutes

Unsealed and pressurized reloading units are distinguished. To decrease the dust emission, air exhaust capacity, and loss of the particulate material, the following are recommended:

- To provide sloping chutes with minimum inclination (that allows material movement), it is necessary to avoid the vertical end of the chute leading to the entrance to the cover of receiving unit
- To minimize the decrease in the fall height of the gravitational material flow, in case of necessity, the turns in vertical flat perform (Fig. 27.28) according to scheme (A), except for scheme (B).
- the aspiration covers of the belt conveyer loading locations perform with double walls (Fig. 27.17) for various particulate materials, or with single concave walls (Fig. 27.29) mainly for powder reloading.
- in the case of powder reloading, the chutes are rather in the form of a three-edged prism with one of the ribs directed down (Fig. 27.29).
- in the case of the pressurized receiving volume capacity, the local exhaust must be attached to the feed conveyer unloading head cover

FIG. 27.28 Scheme of the chute turns in vertical flat: admissible (A); undesirable (B).

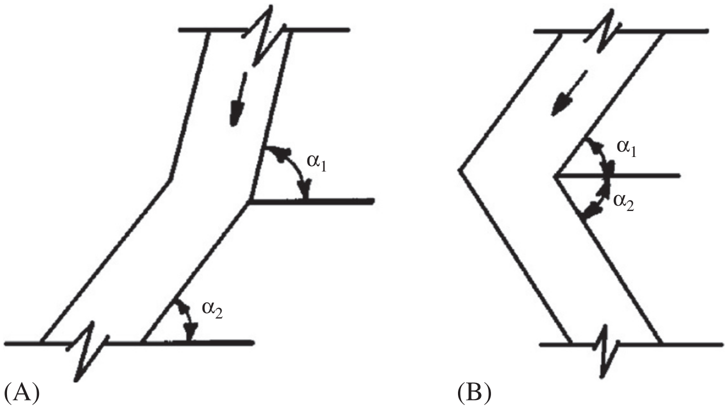
α1
α2
(A)
α1
α2
(B)

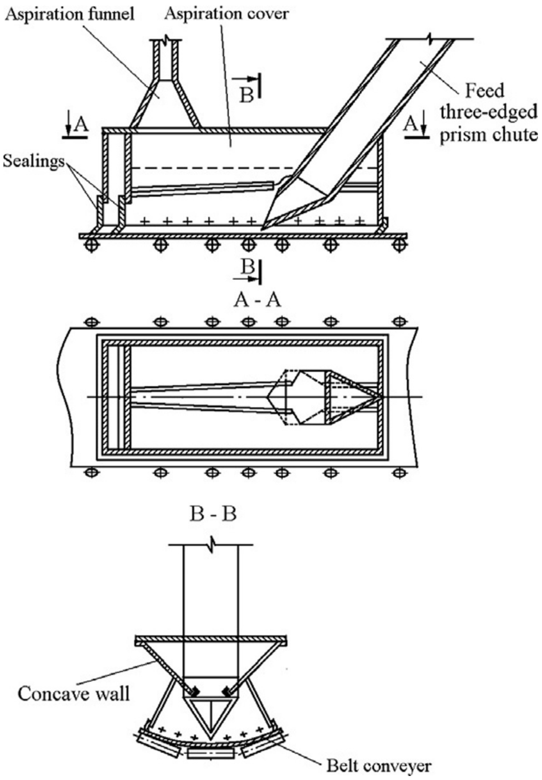
Aspiration funnel
Aspiration cover
B
A
Sealings
A
Feed three-edged prism chute
B
A - A
B - B
Concave wall
Belt conveyer

FIG. 27.29 Receiving belt conveyer cover with single concave walls.

- the air velocity in the exhaust branch pipe inlet attached to the conveyer cover: for the materials either of average particle sizes in the range from 0.2 to 3 mm by $\rho_1 \geq 2{,}000\ \mathrm{kg/m^3}$ and average particle sizes in the range from 0.2 to 7 mm by $\rho_1 \geq 1200\ \mathrm{kg/m^3}$, at most 1 m/s; for the materials containing particles with diameters of to 0.3 mm and above 50% yield by maximum size particles 3.0 mm with ρ_1 ranges from 1,200 to 4,500 $\mathrm{kg/m^3}$ and with $\rho_1 > 4{,}500\ \mathrm{kg/m^3}$, up to 0.4 and 0.7 m/s, respectively.

The determination of the local exhaust device comprises the following steps:

(1) For the local exhaust definition the following initial data (Table 27.17) and basic calculated magnitudes (Table 27.18) are used.

(2) The entrance rate into the receiving apparatus cover v_{1f} is calculated by means of step-by-step definition of rates for rectilinear chute lengths over formulas or nomogram (Fig. 27.30).

TABLE 27.17 Initial Data for the Definition of the Local Exhaust Capacity of Particulate Material Reloadings by Closed Gravity Chutes

Parameter	Symbol	Unit	Note
Material mass flow	G_1	kg/s	
Density of the material	ρ_1	kg/m^3	
Temperature of the material	t_1	K	
Granule composition	$g(d)$	%	
Belt width of receiving conveyer	B	m	See Fig. 27.17
Material fall height from feed conveyer to entrance to the receiving conveyer cover	H	m	In case of sectional chutes with bends it is taken into account the fall height of every chute part (see Fig. 27.17)
Length of the inclined chute	l_{ch}	m	In case of sectional chutes, the length of every section
Inclination of the chute to the horizontal plane	α	grade	By chutes with bends, the inclinations of every chute part
Angle changing of chute inclination at a bend location	$\Delta\alpha$	grade	See Fig. 27.28
Cross-section area of the chute at site entrance of the material in receiving conveyer cover	F_{ch}	m^2	
Width of the chute cross-section area	b	m	
Height of the chute cross-section area	h	m	
Air density	ρ_2	kg/m^3	

For the vertical initial length

$$v_{1\mathrm{v},\mathrm{i}=1} = \sqrt{19.6H_\mathrm{i}} \tag{27.12}$$

For the incline lengths

$$v_{1\mathrm{ch},\mathrm{i}} = \sqrt{(v_{1\mathrm{f},i-1}k_{\mathrm{tn}})^2 + 19.6H_\mathrm{i}(1-0.9f_{\mathrm{fr}}\mathrm{ctg}\,\alpha_\mathrm{i})} \tag{27.13}$$

where $v_{1\mathrm{f},\,\mathrm{i}}$ is the material moving rate at the length end of the previous chute section, m/s; f_{fr} is the friction coefficient of particulate material moving along the steel bottom chute (it is accepted 0.625 for coarse and 0.9 for fine powders; k_{tn} is the rate reduction coefficient of material flow turn (due to change of the inclination of the chute), which magnitudes are given in Table 27.19.

The initial material rate on the first chute length, on feed conveyer level is taken to equal zero.

(3) The average diameter of the material particles is calculated by the formula

$$d_\mathrm{m} = 0.01\sum_{i=1}^{n} d_\mathrm{i} m_\mathrm{i} \tag{27.14}$$

where d_i is the average diameter of particles in the i- interval, mm; m_i is the mass part of particles in i- interval, wt%; n is number of intervals.

(4) The size of ζ_{en} is calculated from the formula

$$\zeta_{en} = 2.4\,(F_{\mathrm{ch}}/\mathrm{F}_{\mathrm{n.f}})^2 \tag{27.15}$$

TABLE 27.18 The Basic Calculated Magnitudes for the Definition of the Local Exhaust Capacity for Particulate Material Reloadings on Closed Gravity Chutes

Parameter	Symbol	Unit	Note
Material rate at the first inclined chute	v_{1c}	m/s	Eq. (27.12)
Material rate under entrance receiving conveyer cover	v_{1r}	m/s	
Material rate under meeting with bottom of receiving unit (conveyer belt)	v'_{1r}	m/s	
Relation of initial material rate to the final one in the chute	n	d/l (a)	
Average material particle size	d_m	mm	Eq. (27.13)
Local resistance coefficient:			
Of entrance in the feed conveyer cover	ζ_{en}		Eq. (27.15)
Of the chute	ζ_{ch}		Eq. (27.16)
Of the cross partition in receiving conveyer cover	ζ_{par}		Table (27.20)
Underpressure on the inside surface of the outer receiving conveyer cover walls	$p_{c.r}$	Pa	Eq. (27.17)
Underpressure on the inside surface of the outer feed conveyer cover walls	$p_{c.f}$	Pa	Table (27.21)
Area of the non-compactnesses in cover:			
Of the feed conveyer	$F_{n.f}$	m^2	
Of the receiving conveyer	$F_{n.r}$	m^2	Eq. (27.18)
Heat pressure originating from overload of the heated materials	p_t	Pa	is taken into account, when $t_1 \geq 323$ K Eq. (27.19), Eq. (27.20), Eq. (27.21)
Coefficient of dynamic interaction of the moving material surface in the sloping chute with air	c_τ		Eq. (27.22), Eq. (27.23)
Ejection coefficient	φ		Eq. (27.25)
Local exhaust capacity of pressurized covers of the receiving apparatuses, volumes, and conveyers	$L_{a.f}$	m^3/h	Eq. (27.26)
Local exhaust capacity of unpressurized covers of the receiving apparatuses, volumes, and conveyers	$L_{a.r}$	m^3/h	Eq. (27.27)
Air flow volumes, which are sucked through the leakinesses of a feed conveyer head unloading cover	$L_{n.f}$	m^3/h	Eq. (27.28)
Local exhaust capacity of unpressurized covers of the receiving apparatuses, volumes, and conveyers (heated material at temperature above 323 K)	$L_{a.r}$	m^3/h	Eq. (27.29)
Air flow volumes, which are sucked through the leakinesses of a receiving conveyer cover	$L_{n.r}$	m^3/h	Eq. (27.30)
Air flow volumes ejected by particle gravitation flow	L_{ej}	m^3/h	Eq. (27.31)

The sum of the local resistances to the covers and chute $\Sigma\zeta$ is determined from the equation:

$$\Sigma\zeta = \zeta_{en} + \zeta_{ch} + \zeta_{par} \tag{27.16}$$

For vertical chutes $\zeta_{ch} = 1.5$; for the inclined chutes and chutes with turns $\zeta_{ch} = 2.5$.

The value of the local resistance coefficient of the cross partition in receiving conveyer cover ζ_{par} (see Figs. 27.17 and 27.31) is determined from Table 27.20 depending on the relations $F_{ch}/F_{f.cr}$ and $F_{f.pr}/F_{f.cr}$, where $F_{r.pr}$ is the cross-section

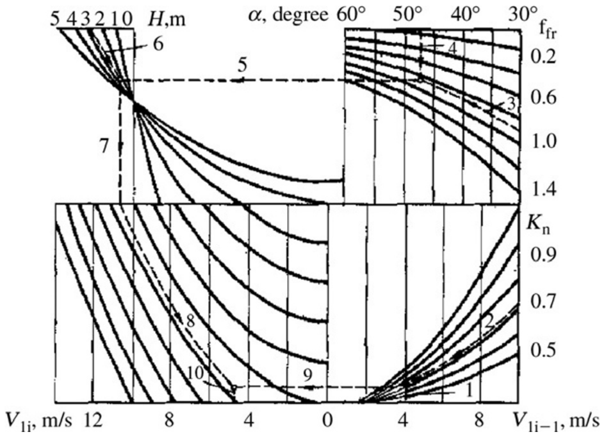

FIG. 27.30 Nomogram for definition of the material rate under entrance of receiving conveyer cover, $v_{1.i}$. Example: it is given $v_{1(i-1)}$; $k_{tn}=0.72$; $f_{fr}=0.9$; $\alpha_i = 47^0$; $H_i=2.9$ m. Answer: $v_{1.i}=4.76$ m/s.

TABLE 27.19 Values of the Rate Reduction Coefficient k_{tn} Depending on Change of the Chute Inclination

$\Delta\alpha = \|\alpha_{i-1} - \alpha_i\|$ (degree of arc)	k_{tn}	$\Delta\alpha = \|\alpha_{i-1} - \alpha_i\|$ (degree of arc)	k_{tn}
60	0.47	30	0.85
50	0.64	20	0.93
45	0.70	10	0.97
40	0.75	0.00	1.00

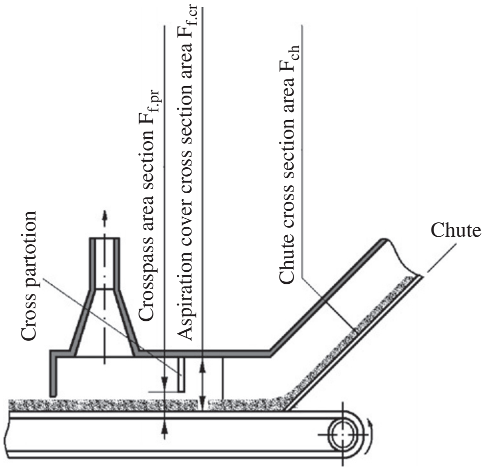
Cross partotion
Crosspass area section F_f.pr
Aspiration cover cross section area F_f.cr
Chute cross section area F_ch
Chute

FIG. 27.31 Scheme to the calculation of ζ_{par} for cover with double walls and solid cross partition.

area of passing under the partition wall, m^2; $F_{r.cr}$ is cross section area of receiving conveyer cover, m^2. The advisable value of $F_{f.pr}/F_{f.cr} = 0.25$–0.3.

(5) The underpressure on the inside surface of the outer receiving unit cover walls is defined by the formula (Eq. 27.17)

$$p_{c.r} = 0.163 k_{c.r} \left(v'_{1r}\right)^2 \tag{27.17}$$

TABLE 27.20 Dependence ζ_{par} on the Relations $F_{ch}/F_{f.cr}$ and $F_{f.pr}/F_{f.cr}$

	ζ_{par} values by $F_{f.pr}/F_{f.cr}$ Relation				
$F_{ch}/F_{f.cr}$	**0.1**	**0.2**	**0.3**	**0.4**	**0.5**
1.0	193	44.5	17.8	8.12	4.02
0.8	124	28.5	11.4	5.19	2.57
0.6	69.5	16.0	6.41	2.92	1.45
0.4	30.9	7.12	2.84	1.30	0.64
0.2	7.72	1.78	0.71	0.32	0.16

where v'_{1r} is the material rate on meeting with the bottom of the receiving unit (conveyer belt), which is determined by the formula (Eq. 27.13), here H must be increased by the fall height of material in the receiving unit cover; $k_{c.r}$ is the correction coefficient, which is taken from Table 27.21.

(6) The area values of the non-compactnesses in the cover of the feed conveyer $F_{n.f}$ and of the receiving conveyer $F_{n.r}$ are accepted on the constructive data:
$F_{n.f}$ amounts 0.3 and 0.5 m^2 for belt width in the range from 0.5 to 0.8 m and 1.0 m, respectively;
under the stipulation that $F_{n.r}$ must be not exceed the values, calculated from the formula

$$F_{n.r} = 2(l + B_1)\delta \tag{27.18}$$

where l and B_1 are the length and width of cover in its part lower (Fig. 27.17); δ is width of a conditional opening, 0.015 m.

(7) The heat pressure p_t is determined from Eq. (27.8) reduced to the form

$$p_t = p_{t.m}H \tag{27.19}$$

where $p_{t.m}$ is the specific heat pressure (by $H = 1.0$ m), as shown in Table 27.22, which is constituted by the formulae (27.20) and (27.21) for various technological parameters.

$$p_{t.m} = 4.905\left(\rho_{2.a} - \rho_{2.d}\right) \tag{27.20}$$

where $\rho_{2.a}$ and $\rho_{2.d}$ and air density at ambient air temperature $t_{2.a} = 289$ K and air temperature in receiving conveyer cover $t_{2.d}$.

$$t_{2.d}. = 0.5k_t\left(t_1 - t_{2.a}\right) \tag{27.21}$$

where k_t is the correction factor.

(8) The dynamic interaction coefficient with air of the material surface, as it moves along an inclined chute, is determined by formulae (27.22) and (27.23) or nomogram (Fig. 27.32)

$$c_\tau = 0.09\alpha^{-1}\left(d_m c_\tau^*\right)^{0.4} \tag{27.22}$$

where α is chute angle of slope in radians

$$c_\tau^* = 3.26m_v - 3.6m_v^2 + m_v^3 \tag{27.23}$$

$$m_v = 10^3 G_1/\rho_1 b$$

b is a size, which characterizes the material moving stream contact surface with air in the chute, m;
b is the chute width for rectangular cross section chutes;
$b = 0.5d_c\sqrt{\pi}$ for round cross section chutes with d_c diameter;

TABLE 27.21 Correction Coefficient, $k_{c.r}$ Values

Reloading Unit Type	Cover Design	Cover Parameters		Correction Coefficient $k_{c.r}$	
		H_c/B_1	l_1/B_1.	Initial Particulate Material	Metallic Powders
Reloading from feed conveyer to receiving conveyer	Receiving conveyer cover:				
	- Nonthrough-pass with single flat walls	From 0.4 to 0.75 ≤ 0.75 0.4	From 0.4 to 0.75 From 0.75 to 1.0 ≤ 0.45	0.65 0.55 1.3	0.75 0.65 1.35
	- Nonthrough-pass with double flat walls (Fig. 27.17)	From 0.75 to 1.0	From 0.4 to 0.75	0.45	0.50
	- Nonthrough-pass with single concave walls (Fig. 27.29)	From 0.8 to 1.0	…	0.45	0.560
	- Through-pass with single flat walls	From 0.4 to 0.75	…	4.0	4.5
Elevator or other equipment, which is loaded by gravitation chute:	Single cover	…	…	3.5	4.5
Elevator	Casing type cover of the elevator stretching station	…	…	3.0	4.0
Load by gravitation chute of a nonpressurized bin	The local exhaust is attached to bin covering	…	…	2.0	2.5
Load by gravitation chute of a pressurized bin	The local exhaust is attached to the feed conveyor head cover	…	…	0.8	1.2

H_c is the height of the receiving conveyer cover; B_1 is the width of the receiving conveyer cover; l_1 is the spacing between the converging cone of local exhaust and exit from cover (Fig. 27.17).

$$b = \sqrt{\frac{4G_1 \operatorname{tg}(0.5\gamma_{rib})}{\rho_1 \beta_1 v_1}} \tag{27.24}$$

for the chutes in the form of a three-edged prism with one of ribs directed down (Fig. 27.29) γ_{rib} is the angle between facets convergent to the rib directed down, degree; β_1 is the solid volumetrical concentration in quasi-interconnected motion, in the chute, m^3/m^3 (it is accepted in range from 0.035 to 0.05 m^3/m^3).

(9) The ejection coefficient φ is defined by Eq. (27.25) or nomograms (Figs. 27.33, 27.34, and 27.35)

$$\varphi = \frac{\sqrt{0.44(1-n^3)^2 + 2(1-n^2)^2(A-1)[B+0.25(1+n^2)] - 0.67(1-n^3)}}{(1-n^2)(A-1)} \tag{27.25}$$

where $A = \frac{h\Sigma\zeta}{c_\tau l_{ch}}$; $B = \frac{AC}{\Sigma\zeta v_{1f}^2}$; $C = \frac{p_{c.r} - p_t}{\rho_2}$.

(10) The formulae for calculation of the reloading unit local exhausts with various degrees of pressurization of the covers and temperature of materials are given in Table 27.23.

TABLE 27.22 Specific Heat Pressure (Values $H = 1$ m) p_t for Various Temperatures of Incoming Particulate Material t_1 and Aspirated Air $t_{2.d}$

t_1		$t_{2.d}$				
(°C)	(K)	(°C)	(K)	k_t	$\rho_{2.d}$ (kg/m^3)	p_t (Pa)
50	323	32	305	1.0	1.16	0.29
75	348	43	316	0.95	1.11	0.49
100	373	52	325	0.90	1.08	0.69
150	423	62	335	0.75	1.05	0.88
200	473	75	348	0.70	0.99	1.08
250	523	87	360	0.65	0.98	1.18
300	573	95	368	0.60	0.96	1.28
350	623	104	377	0.57	0.94	1.37
400	673	114	387	0.55	0.92	1.47
450	723	122	395	0.52	0.90	1.57
500	773	128	401	0.50	0.88	1.67
600	873	138	411	0.45	0.86	1.77

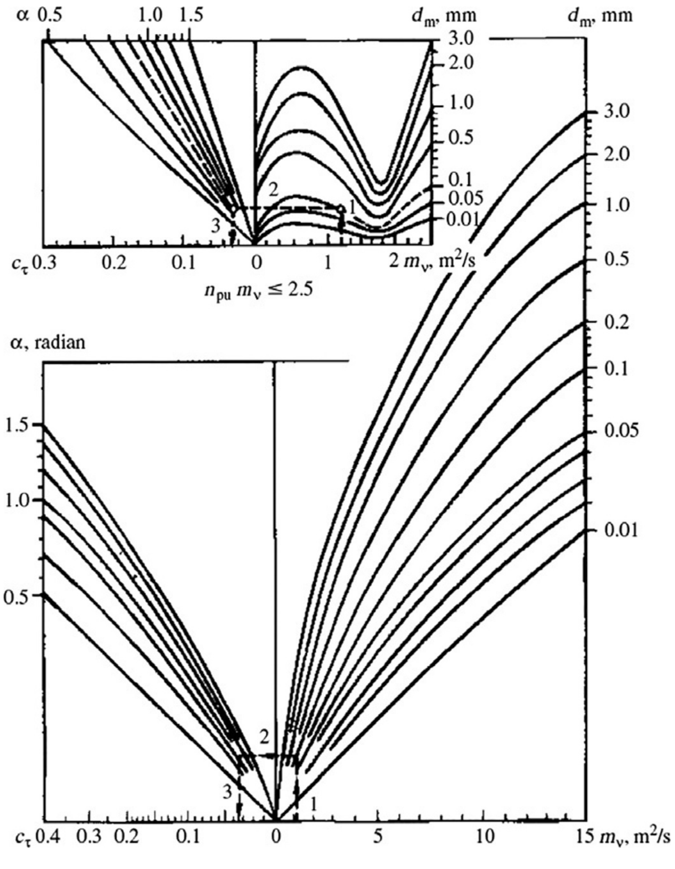

FIG. 27.32 Nomogram for the c_τ definition. Example: it is given $G_1 = 1.945$ kg/s; $\rho_1 = 7800$ kg/m^3; $b = 0.2$ m; $d_m = 0.11$ mm; $\alpha = 0.82$ radian. Answer: $m_v = 10^3 \frac{1.945}{7800 \times 0.2} = 1.248$ m^2/s; $c_\tau = 0.031$.

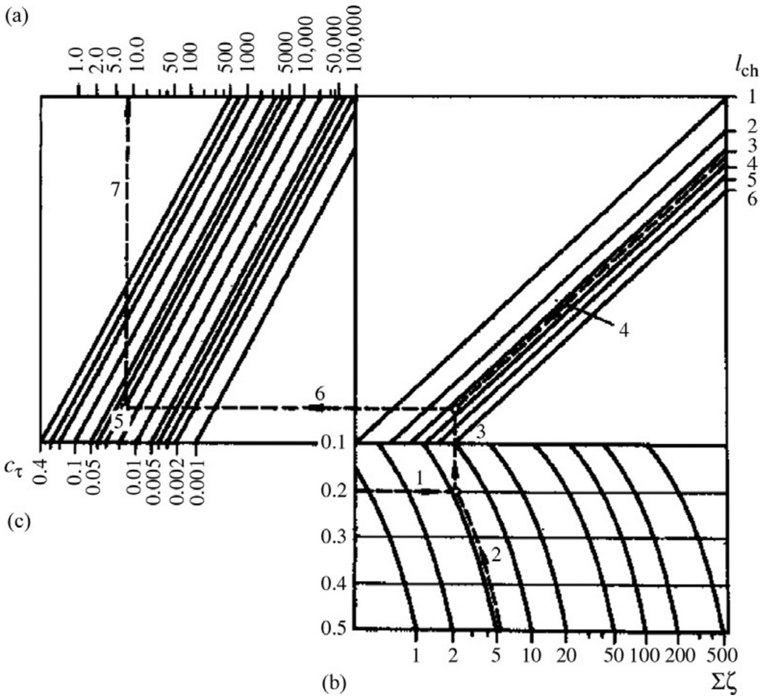

FIG. 27.33 Nomogram for the *A* definition. Example: it is given $h=0.2$ m; $\Sigma\zeta=5.2$; $c_\tau=0.031$; $l_{ch}=3.28$. Answer: $A=8.65$.

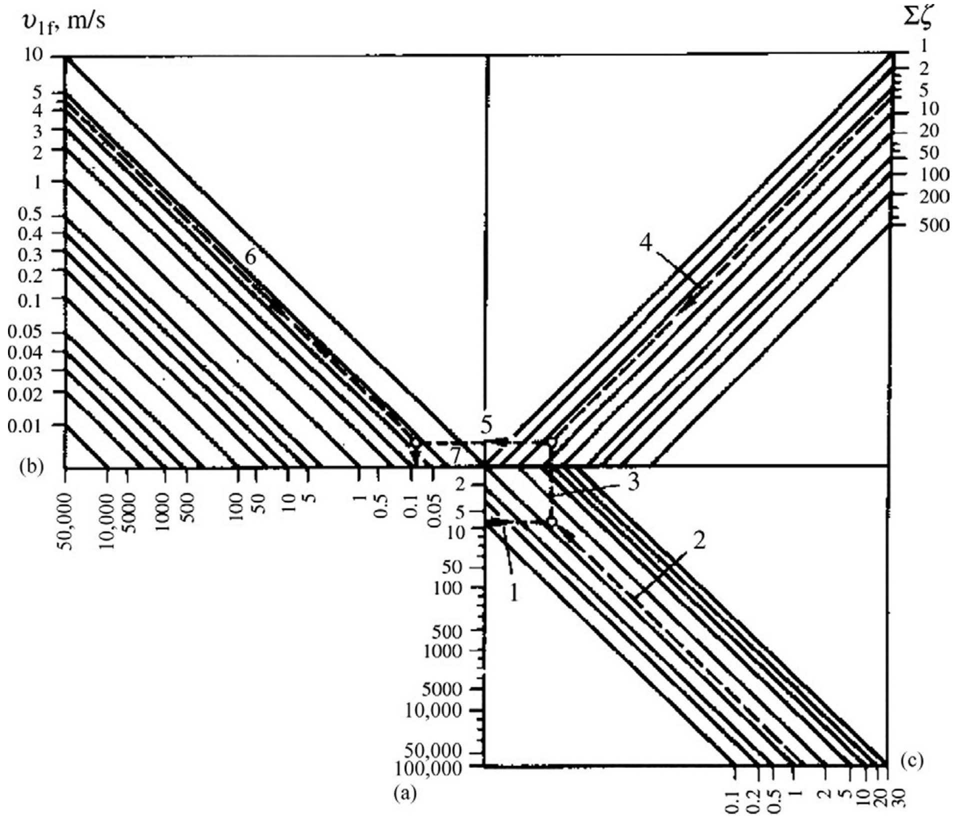

FIG. 27.34 Nomogram for the *B* definition. Example: it is given $A=8.65$; $p_{c.r}=1.64\,\text{Pa}$; $p_t=0$; $t_{2.d}=293\,\text{K}$ ($\rho_2=1.2\,\text{kg/m}^3$); $\Sigma\zeta=5.2$; $v_{1.r}=4.71\,\text{m/s}$; $C=\frac{p_{c.r}-p_t}{\rho_2}=\frac{1.64-0}{1.2}=1.37$; Answer: $B=0.09$.

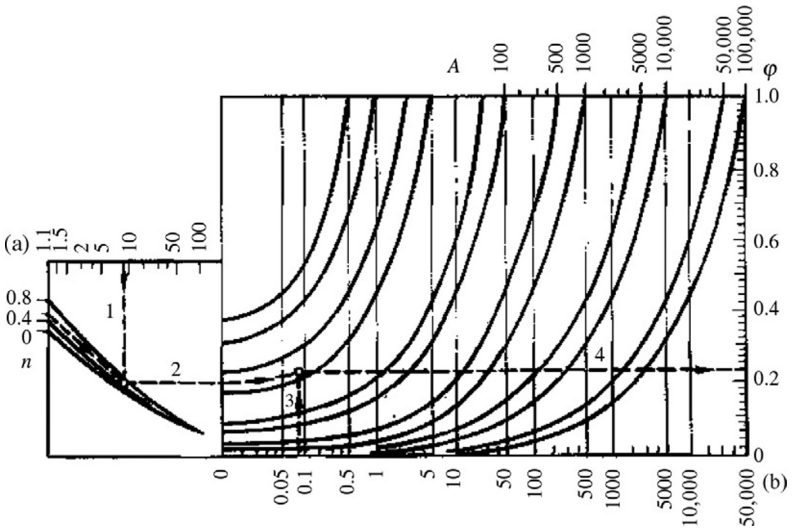

FIG. 27.35 Nomogram for the φ definition. Example: it is given $A=8.65$; $n=0.6$; $B=0.09$. Answer: 0.247. Note: For $A>100$ the n quantity does not take part in the φ definition.

TABLE 27.23 Formulas for the Determination of the Local Suctions (m^3/h)

Cover Characteristic	Attaching Location of the Local Suction	Symbol	Formula	
Pressurized	To the cover of the unloading head of feed conveyer	$L_{a.f}$	$L_{af}=L_{nf}=3300F_{nf}\sqrt{\frac{\rho_{cf}}{\rho_2}}$	(27.26)
Unpressurized for:				
Unreheated materials (temperature below 323 K)	To the receiving unit cover	$L_{a.r}$	$L_{a.r}=L_{n.r}+L_{ej}$	(27.27)
Heated materials (temperature above 323 K)	Both to the receiving unit cover and to the unloading head of feed conveyer	$L_{a.r}$, $L_{a.f}$	$L_{a.f}=400B_{c.f}$ where $B_{c.f}$ is the width of head feed unit cover (m)	(27.28)
			$L_{a.r}=(L_{n.r}+L_{ej})$ where	(27.29)
			$L_{n.r}=3300F_{n.r}\sqrt{\frac{\rho_{c.r}}{\rho_2}}$	(27.30)
			$L_{ej}=3600F_{ch}\varphi v_{1f}$	(27.31)

Examples of the Computation

Belt conveyer reloading: The calculation of the local exhaust capacity of the belt conveyer reloading unit with double flat walls cover of receiving conveyer (Fig. 27.17) is illustrated. The initial data by selected $F_{n.f}$, $F_{n.r}$, and F_{ch} values: $G_1=1.945$ kg/s; $\rho_1=7800$ kg/m^3; $t_1=293$ K; $F_{ch}=0.0258$ m^2; $d_m=0.11$ mm; $F_{n.f}=0.04$ m^2; $F_{n.r}=0.02$ m^2; $H_1=0.8$ m; $H_2=0.8$ m; $H_1=H_{c.r}=0.38$ m; $\alpha_1=90°$; $\alpha_2=47°$; $\alpha_3=40°$; $b=0.2$ m; $l_{ch}=3.88$ m; $p_t=0$; $F_{c.r}=0.09$ m^2.

Solution:

The powder gravitational movement rate at the end of the initial vertical tract of the chute is determined by formula (27.12)

$$v_{1v,i=1}=\sqrt{19.6\times0.8}=3.96\ \mathrm{m/s}$$

The powder movement rate at the end of the inclined part of the chute at the site entrance in the receiving conveyer cover is defined by formula (27.13) or nomogram (Fig. 27.30):

$$v_{1\mathrm{sh,i}}=\sqrt{(3.96\times0.72)^2+19.6\times2.9(1-0.9\times0.9\times0.93)}=4.71\ \mathrm{m/s}$$

where $f_{f.r}=0.9$, $k_t=0.72$ by $\Delta\alpha=43°$ (it is found from Table 27.19).

The sum of the local resistances per formulas (27.15) and (27.16) amounts to

$$\Sigma\zeta = 2.4\,(0.0258/0.09)^2 + 2.5 + 1.7 = 5.2$$

here ζ_{par} is found from Table 27.20 by $F_{\text{f.pr}}/F_{\text{f.cr}} = 0.3$ and $F_{\text{ch}}/F_{\text{f.cr}} = 0.286$.

The coefficient c_τ is determined by formulae (27.22) and (27.23) or nomogram (Fig. 27.32):

$$m_v = 10^3 \frac{1.945}{7800 \times 0.2} = 1.247\ \text{m}^2/\text{s}$$

$$c_\tau^* = 3.26 \times 1.247 - 3.6 \times 1.247^2 + 1.247^3 = 0.4$$

$$c_\tau = 0.09\,(0.82)^{-1} \cdot (0.11 \cdot 0.4)^{0.4} = 0.031$$

$$\alpha_2 = 47^\circ = 0.82\,\text{radian}.$$

The powder movement rate at the end of the inclined chute on meeting the bottom of the receiving unit (conveyer belt) is defined according to Eq. (27.13) or nomogram (Fig. 27.30):

$$v'_{1r} = \sqrt{(4.71 \times 0.98)^2 + 19.6 \times 0.38(1 - 0.9 \times 0.9 \times 1.19)} = 4.64\ \text{m/s}$$

The underpressure on the inside surface of the outer receiving unit cover walls, defined by formula (27.17), and amounts to

$$p_{\text{c.r}} = 0.163 k_{\text{c.r}} \left(v'_{1.\text{r}}\right)^2 = 0.163 \times 0.5 \times 4.64^2 = 1.64\text{Pa}$$

The ejection coefficient φ is defined by Eq. (27.25) or nomograms (Figs. 27.33, 27.34, and 27.35)

$$\varphi = \frac{\sqrt{0.44\left(1 - 0.6^3\right)^2 + 2\left(1 - 0.6^2\right)^2 (8.65 - 1)\left[0.1 + 0.25\left(1 + 0.6^2\right)\right]} - 0.67\left(1 - 0.6^3\right)}{\left(1 - 0.6^2\right)(8.65 - 1)} = 0.25$$

where

$$n = \frac{3.96 \times 0.72}{4.71} = 0.6; A = \frac{0.2 \times 5.2}{0.031 \times 3.88} = 8.65; B = \frac{8.65 \times 1.37}{5.2 \times 4.71^2} = 0.1; C = \frac{1.64}{1.2} = 1.37$$

Air flow volumes ejected by particle gravitation flow in the receiving conveyer cover per Eq. (27.31) at Table 27.23 amount to:

$$L_{\text{ej}} = 3600 \times 0.25 \times 4.71 \times 0.0258 = 110\ \text{m}^3/\text{h}$$

The air flow volumes, which are sucked through the porosity of the receiving conveyer cover, are defined by Eq. (27.29)

$$L_{\text{n.r}} = 3300 \times 0.02 \sqrt{\frac{1.64}{1.2}} = 78\ \text{m}^3/\text{h}$$

The local exhaust capacity according to Eq. (27.27) amounts to

$$L_{\text{a.r}} = 110 + 78 = 188\,\text{m}^3/\text{h}.$$

Discharge of Containers

The pressurized performance of the container discharge unit and receiving vessel allows the effective use of bypass pipes to reduce excess pressure by means of connection zone of excess pressure with thinning zone that leads the flow of dust-laden gas from receiving vessel into the container, in the space above the falling powder level (Fig. 27.36).

The taper conjunction in the abutment of the container delivery cell to the receiving bin checkerwork provides air-tightness. The entrance to the bypass tube is cleared by container placing on the receiving bin. Such a design is favorable for powder processing in air as well in protective atmospheres for combustible and explosion-risk powders. Table 27.24 contains the necessary data for designing the bypass pipes.

The gas volume being displaced from receiving vessel during powder discharge amounts to

$$L_{\text{b-p}} = \frac{G_1}{\rho_{\text{ap}}}\ \ \text{m}^3/\text{s}$$

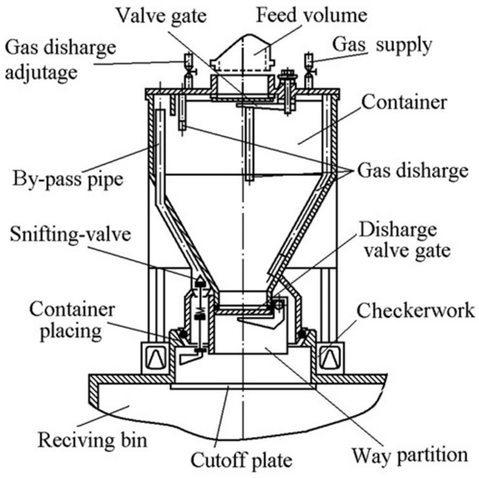
Valve gate
Feed volume
Gas disharge adjutage
Gas supply
Container
By-pass pipe
Gas disharge
Snifting-valve
Disharge valve gate
Container placing
Checkerwork
Reciving bin
Cutoff plate
Way partition

FIG. 27.36 Container at discharge position by pressurized mating with a pressure sealed receiving vessel.

TABLE 27.24 Necessary Data for Designing of Bypass Pipes

Parameter	Symbol	Unit
Density of materials	ρ_1	kg/m^3
Apparent density	ρ_{ap}	kg/m^3
Material mass flow	G_1	kg/s
Atmosphere underpressure in the space above the lowering powder level in volume which is unloaded	p_f	Pa
Atmosphere overpressure in receiving volume (bin)	p_r	Pa
Cross-section of the bypass pipe	$F_{\text{b-p}}$	m^2
Diameter of the bypass pipe	$D_{\text{b-p}}$	m
Sum of the local hydraulic resistances of the bypass pipe	$\Sigma\zeta_{\text{b-p}}$	
Gas volume being displaced from receiving bin	$L_{\text{b-p}}$	m^3/s

The cross-section of bypass pipe

$$F_{\mathrm{b-p}} = \frac{L_{\mathrm{b-p}}}{v_{2(\mathrm{b-p})}}\,\mathrm{m}^2$$

where

$$v_{2(\mathrm{b-p})} = \sqrt{\frac{2(p_{\mathrm{r}} - p_{\mathrm{f}})}{\rho_2 \Sigma\zeta_{\mathrm{b-p}}}}\,\mathrm{m/s}.$$

Single Rotary Hammer Mills

The most effective means of eliminating the effect of excess pressure, created by moving rotary parts, has been noted before, is pressurized performance of loading and unloading units, isolating from the equipment installation in the order in which it must function. It is effective to provide the hammer mill with bypass pipes to reduce excess pressure. They connect the mill cavity, situated at underpressure, with the discharge unit, situated at overpressure (Fig. 27.37). The initial data that are necessary for the determination of the capacity of the suction devices are enumerated in Table 27.25.

The determination of the basic calculated magnitudes includes the following steps.

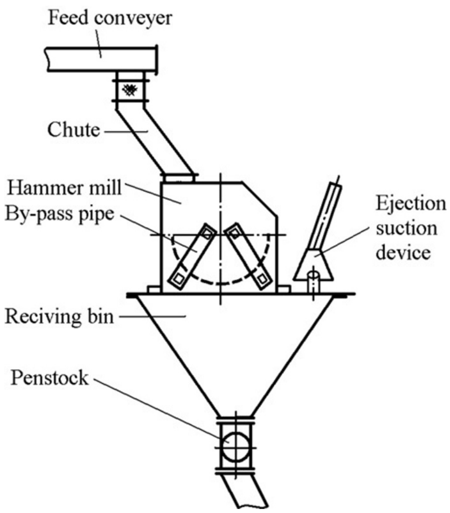

FIG. 27.37 Scheme of a hammer mill installation.

TABLE 27.25 Data for the Determination of the Capacity of Hammer Mill Suction Devices

Parameter	Symbol	Unit	Note
The installation scheme and initial data			
Maximum pressure, when tightness is retained	p	kPa	
Material mass flow	G_1	kg/s	
Material density	ρ_1	kg/m^3	
Type of the hammer mill			
Number of the hammer rows	i		
Rotation velocity of hammers	n	s^{-1}	
Root-mean-square diameter of crushed material particles	d_m	m	Eq. (27.14)
Area cross-section of the feed chute	F_f	m^2	
Area cross-section of the discharge chute	F_{des}	m^2	
The basic calculated magnitudes			
Sum area of the one row of rotating parts	$F_{h.1}$	m^2	Calculated by summation of the constituents
Constituent cross-section area of the active rotor parts	$F_{h.a}$	m^2	See Fig. 27.20
Distance from the hammer mill axis to mass center of the corresponding constituent of the active rotor parts	$r_1, \dots r_n,$	m	See Fig. 27.20
Conditional diameter circle describable by mass center of the active rotor part	D_{ac}	m	Eq. (27.7)
Root-mean-square rotary velocity of hammers	$\bar{v}_h$	m/s	Eq. (27.32)
Trajectory length of active part rotor center diameter D_{ac} from the material entrance site in hammers action zone and the end of separation grate	l_D	m	Eq. (27.33)
Cross-section of hammer mill chamber, orientated normally to the D_{ac} trajectory, in the zone of flow components movement	F	m^2	See Fig. 27.20
Sum of the local aerodynamic resistances to the gas movement in hammer mill	ζ_h		Receptee amounts to 10
Hydraulic characteristic of the bypass pipes	$R_{b.p}$		Eq. (27.34)

Continued

TABLE 27.25 Data for the Determination of the Capacity of Hammer Mill Suction Devices—cont'd

Parameter	Symbol	Unit	Note
Sum of the local hydraulic resistance coefficients of feed section of the hammer mill installation	$\Sigma\zeta_f$		Eq. (27.35)
Sum of the local hydraulic resistance coefficients for the discharge section of the hammer mill	$\Sigma\zeta_d$		Eq. (27.36)
Sum of the local hydraulic resistance coefficients for the bypass pipes	$\Sigma\zeta_{b.p}$		Eq. (27.37)
Local resistances to the gas entrance from the bypass pipe to mill chamber	$\zeta_{en.h}$		
Sum of the local hydraulic resistance coefficients to the gas movement in bypass pipes	$\sum_{i=2}^{i=N}\zeta_{b.p_i}$		Eq. (27.38)
Sum of the local hydraulic resistance coefficients of the gas movement in the mill installation net	$\Sigma\zeta_{net}$		
Maximum gas medium pressure originating by hammer mill	$p_{h\text{-}m}$	Pa	Eq. (27.39)
Coefficient of dynamic interaction			
Of the rotating parts with mill chamber atmosphere	c_h		Eq. (27.40)
Of the material pieces with mill chamber atmosphere	c_m		Eq. (27.41)
Hydraulic characteristic of the net	R_{net}	kg/m^7	Eq. (27.42)
Underpressure in zone around of the hammer shaft close to the inside surface of body side walls (position of bypass attachment)	p_h	Pa	Eq. (27.43)
Diameter of the ejection suction device discharge socket	D_{ds}	m	Eq. (27.44)
Gas volume flow through the ejection suction device socket	$L_{d.s}$	m^3/s	Eq. (27.45)

(1) The root-mean-square diameter of crushed material particles is defined on sieve analysis data base by formula (27.14):

$$d_m = 0.01\sum_{i=1}^{n} d_i m_i$$

(2) The conditional diameter of circle describable by mass center of the active rotor part rotation is calculated from Eq. (27.7):

$$D_{ac} = \frac{2\sum_{i=1}^{n} F_{h.a}\times r}{\sum_{i=1}^{n} F_{h.a}}$$

Here (see Fig. 27.20)

$$\sum_{i=1}^{n} F_{h.a}\times r = F_{h.a(1)}\times r_1 + F_{h.a(2)}\times r_2 + \ldots + F_{h.a(n)}\times r_n$$

$$\sum_{i=1}^{n} F_{h.a} = F_{h.a(1)} + F_{h.a(2)} + \ldots + F_{h.a(n)}$$

where $F_{h.a(1)}$, $F_{h.a(2)}$, … $F_{h.a(n)}$, are constituent cross-section area of the active rotor parts; r_2, r_1,…r_n, are the distance from the hammer mill axis to the mass center of the corresponding constituents of the active rotor parts.

(3) The root-mean-square circumferential speed of the hammers equals

$$v_{\mathrm{h}} = 3.14 D_{\mathrm{ac}} n \tag{27.32}$$

(4) Trajectory length of active part rotor center of diameter D_{ac} from the material entrance site in hammers action zone and the end of separation grate is

$$l_{D_{\mathrm{ac}}} = 8.72 \times 10^{-3} D_{\mathrm{ac}} \alpha_{\mathrm{i}} \tag{27.33}$$

where α_{i} is the angle between the particulate material entrance in the action zone of the hammers and conventional plane passing through the shaft center and the grate end measured in the course of shaft rotation.

(5) The cross-section of the hammer mill body cavity, orientated normal to the D_{ac} trajectory, in the zone of the flow components movement is determined as the product of the mill cavity width and the distance between the driving shaft surface up to fire-grate in radius course (Fig. 27.20).

(6) Hydraulic characteristic of the bypass pipes $R_{\mathrm{b.p}}$

$$R_{\mathrm{b.p}} = 0.5 \Sigma \zeta_{\mathrm{b.p}} \rho_2 (F)^{-2} \tag{27.34}$$

where $\Sigma\zeta$ is sum of the local hydraulic resistance coefficients to the gas flow in the bypass pipes; F is the cross-section of the hammer mill cavity, in which the parts rotate (the section is orientated normally to root-mean-square air velocity vector in inner crusher).

(7) The sum of the local hydraulic resistance coefficients is defined in the following way:

(a) for the feed section of the hammer mill installation including feed conveyer unpressurized cover with non-compactnesses in the form of slots and gravitational chute

$$\Sigma \zeta_{\mathrm{f}} = \zeta_{\mathrm{en}} + \zeta_{\mathrm{f\text{-}ch}} \tag{27.35}$$

where ζ_{en} is the local hydraulic resistance coefficient of the slot determined by the formula

$$\zeta_{\mathrm{en}} = 2.4 \left(\frac{F}{F_{\mathrm{en}}} \right)^2$$

F_{en} is the cross-section of the slots; $\zeta_{\mathrm{f\text{-}ch}}$ is the local hydraulic resistance coefficient of the feed chute: for inclined chutes and chutes with corners $\zeta_{\mathrm{en}} = 2.5 \left(\frac{F}{F_{\mathrm{f}}} \right)^2$, F_{f} is the cross-section of the feed chute, while for vertical chutes $\zeta_{\mathrm{en}} = 1.5 \left(\frac{F}{F_{\mathrm{ch}}} \right)^2$, respectively;

(b) For the discharge section

$$\Sigma \zeta_{\mathrm{d}} = \zeta_{\mathrm{fun}} + \zeta_{\mathrm{d-ch}} + \zeta_{\mathrm{d-f}} \tag{27.36}$$

where $\Sigma\zeta_{\mathrm{fun}}$ is the local hydraulic resistance coefficient of the receiving funnel; $\Sigma\zeta_{\mathrm{d\text{-}ch}}$ is the local hydraulic resistance coefficient of the discharge chute; $\Sigma\zeta_{\mathrm{d\text{-}f}}$ is the local hydraulic resistance coefficient of the unit feed of the adjoining inter-operational transport or processing apparatus.

Using an unpresserized receiving bin, in which it is necessary to support the underpressure,

$$\Sigma \zeta_{\mathrm{d}} = (\zeta_{\mathrm{fun}} + \zeta_{\mathrm{en.b}}) \left(\frac{F}{F_{\mathrm{en.b}}} \right)^2$$

durante absentia of funnel $\zeta_{\mathrm{fun}} = 0$.

By mounting the hammer mill direct on the bin equipped with ejection suction device (Fig. 27.37),

$$\Sigma \zeta_{\mathrm{d}} = \zeta_{\mathrm{en.b}} \left(\frac{F}{F_{\mathrm{en.b}}} \right)^2 + \zeta_{\mathrm{d.s}} \left(\frac{F}{F_{\mathrm{d.s}}} \right)^2$$

TABLE 27.26 Values of the Hydraulic Resistance Coefficient of the Entrance Flow from Bypass Pipe into the Hammer Mill Chamber Dependence on Design Geometry

	$\zeta_{en.h}$ Values by Relation $\Delta/D_{b.p}$[b]						
Relation $r/D_{b.p}$[a]	**0.05**	**0.07**	**0.10**	**0.15**	**0.20**	**0.25**	**0.30**
0.1	5.6	3.7	2.3	0.62	0.57	0.76	0.93
0.2	4.5	2.3	0.9	0.52	0.51	0.62	0.75

[a] *r is the rounding radius in the location of the connection of bypass pipe with mill chamber by gas flow entrance into it.*
[b] *Δ is the gap between the bypass pipe plane opening by gas flow entrance into mill chamber and mill rotating body flank.*

TABLE 27.27 Values of the Bypass Pipe Flow Friction Coefficient ($\zeta_{fr\text{-}b.p}$) in Dependence on Pipe Cross-Section Area ($F_{b.p}$)

$F_{b.p}$	$\zeta_{fr\text{-}b.p}$	$F_{b.p}$	$\zeta_{fr\text{-}b.p}$	$F_{b.p}$	$\zeta_{fr\text{-}b.p}$
0.005	0.474	0.02	0.350	0.04	0.260
0.0078	0.463	0.03	0.310	0.05	0.200
0.01	0.420	…	…	…	…

where $\zeta_{en.b}$ and $\zeta_{d.s}$ are the hydraulic resistance coefficients of the entrance in the receiving bin and its exit to the socket, respectively; $F_{en.b}$ and $F_{d.s}$ are the cross-section areas of the entrance to the bin and the discharge socket, respectively. The $\zeta_{en.b}$ and $\zeta_{d.s}$ values for conditions (Fig. 27.22) can be received equal to 0.5 and 1.0, respectively;

(c) For the bypass pipes

$$\Sigma\zeta_{b..p} = \left(\zeta_{en.h} + \zeta_{en-b.p} + \zeta_{fr-b..p}\right)\left(\frac{F}{F_{b.p}}\right)^2 \tag{27.37}$$

where $\zeta_{en.h}$ in the hydraulic resistance coefficient at the entrance from bypass pipe to the hammer mill cavity (Table 27.26); $\zeta_{fr\text{-}b.p}$ is the hydraulic resistance coefficient at the entrance the flow to the bypass pipe, equals 0.5; $\zeta_{fr\text{-}b.p}$ is the flow friction coefficient of the bypass pipe (Table 27.27); $F_{b.p}$ is cross-sectional area of the bypass pipe.

In the case of several bypass pipes $\sum_{i=2}^{i=N}\zeta_{b.p_i}$is determined from a relation:

$$\sum_{i=2}^{i=N}\zeta_{b.p_i} = \left[\sum_{i=2}^{i=N}\left(\frac{N_{b.p_i}}{\sum\zeta_{b.p_i}}\right)\right]^{-1} \tag{27.38}$$

where $N_{b.p_i}$ and $\sum\zeta_{b.p_i}$ are numbers of the parallel i-type bypass pipes and sum of the hydraulic resistance coefficients of each of them, respectively.

For the cover permeability

$$\sum\zeta_n = 2.4\left(\frac{F}{F_n}\right)^2$$

(8) The gas pressure created by the hammer mill ($p_{h.m}$, Pa) in the absence of bypass pipes (see also Eq. 27.6)

$$p_{h.m} = \left(\frac{B_{h.m} - \sqrt{B_{h.m}^2 - 4A_{h.m}}}{2A}\right)^2 \tag{27.39}$$

TABLE 27.28 Values of the c_h^* and c_m^* Coefficients

Dynamic Interaction Coefficients	Coefficient Values by F_h/F		
	0.4–0.6	**0.6–0.65**	**0.65–0.7**
c_h^*	0.04	0.1	0.18
c_m^* for different σ (MPa)			
19.6	5.5	13.7	24.7
36.0	6.46	16.1	29.0
96.0	11.2	28.7	…

σ is the compressive strength of grinding material.

where

$$B_{h.m} = \sqrt{\frac{k_r}{v_h}}$$

$$A_{h.m} = \frac{k_r}{v_h^2} - \frac{\rho_2 \zeta_{h.m} k_r}{2k_{h.m}} - \frac{1}{k_{h.m}}$$

$$k_{h.m} = c_h \left(1.5\frac{c_m G_m}{c_h \rho_1 d_m} + nF_h i\right) \frac{\rho_2 l_D v_h}{4F}$$

$$k_r = \frac{2}{\rho_2 \Sigma \zeta_{net}}$$

where $\Sigma\zeta_{net}$ is sum of the net hydraulic resistance coefficient related to area F (the net contains feed and discharge units up to entrance into the aspiration funnel); $\zeta_{h.m}$ is the hammer mill hydraulic resistance coefficient, which is accepted as equal to 10.

The c_h and c_m values in the absenceof the bypass pipes are accepted as $c_h = c_h^*$ and $c_m = c_m^*$ (Table 27.28).

(9) The dynamic interaction coefficients in the presence of the bypass pipes are defined by the formulae:

$$c_h = 1.07\left(c_h^*\right)^{0.94}\left(\frac{R_{net}}{R_{b.p}}\right)^{0.01} \tag{27.40}$$

$$c_m = 1.07\left(c_m^*\right)^{0.94}\left(\frac{R_{net}}{R_{b.p}}\right)^{0.01} \tag{27.41}$$

where R_{net} is the hydraulic characteristic of the net

$$R_{net} = 0.5\rho_2 \sum \zeta_{net} (F)^{-2} \tag{27.42}$$

(10) Underpressure in the zone around of the hammer shaft close to the inside surface of body side walls (position of bypass attaching) (Pa)

$$p_h = 1.93 p_{h.m}^{0.88} \left(\frac{\sum \zeta_{b.p}}{\sum \zeta_{net}}\right)^{0.11} \left(\frac{F}{F_h}\right)^{3.27} \tag{27.43}$$

(11) The diameter of the ejection suction device discharge socket

$$D_{d.s} = 0.905\left(\frac{G_1}{\rho_1}\right)^{0.5}\left(\frac{\zeta_{d.s}\rho_2}{p_{d.r}}\right)^{0.25} \tag{27.44}$$

where $p_{\mathrm{d.r}} = p_{\mathrm{h.m}}$ for direct discharge of the milled material into technological apparatus (or inter-operation transport); $p_{\mathrm{d.r}} = p_{\mathrm{h.m}} + p_{\mathrm{ej}}$ for discharge of the milled material via a chute; p_{ej} is calculated from Eq. (27.4).

(12) The diameter of the ejection suction funnel entrance

$$D_{\mathrm{f.en}} = (10 - 15)D_{\mathrm{d.s}}$$

(13) The gas volume flow through the ejection suction device discharge socket under the action of the overpressure in the receiving cover

$$L_{\mathrm{d.s}} = 1.11 D_{\mathrm{d.s}}^2 \sqrt{\frac{p_{\mathrm{d.r}}}{\rho_2 \zeta_{\mathrm{d.s}}}} \tag{27.45}$$

CLARIFICATION OF RECIRCULATED WATER

The clarification of recirculated water and waste waters depends on the extent of their pollution and are therefore subjected by different treatments:

- Mechanical clarification methods consist in removal of suspended solid by separation under the action of gravity, centrifugal forces, or on filtration membranes.
- Chemical treatment methods are based on the use of the processes and reagents, producing the insoluble precipitates. For chemical purification processes, oxidation, neutralization, and other chemical reactions are used. For treatment, slaked lime, limestone, calcium chloride, calcium hypochloride, ferric sulfate, and other substances are used.
- Of the physical-chemical methods, sorption, coagulation, electrolysis, ion-exchange, extraction, crystallization, and decontamination are used.
- Biochemical methods are based on processes providing mineralization.

Mechanical Clarification Methods

The gravity precipitation is accomplished in the precipitators, while the separation under action of the centrifugal forces in the hydrocyclones and precipitation centrifuges (information about details can be found in Chapter 14).

During the powder production by water atomization it is usually enough to clean the recirculated water by mechanical means. The flow chart of the recycling of the water during the water atomization of copper alloy powder is shown in Fig. 27.38. The water from the initial water reservoir is fed by high pressure pump to the atomizer. The sludge (typically having water-to-solid ratio up to 8:10) from the atomization chamber is delivered by a slurry pump into the thickener (see Fig. 14.3 in Chapter 14). The dewatered material is loaded into a vacuum cartridge filter chamber (see Fig. 14.7 in Chapter 14). The vacuum pump sucks off the water. The clarified waters from the thickener and loosened in the water-drop eliminator condensed moisture are collected and pumped to a cartridge filter from which refined water goes, via a cooler if necessary, to the initial water reservoir.

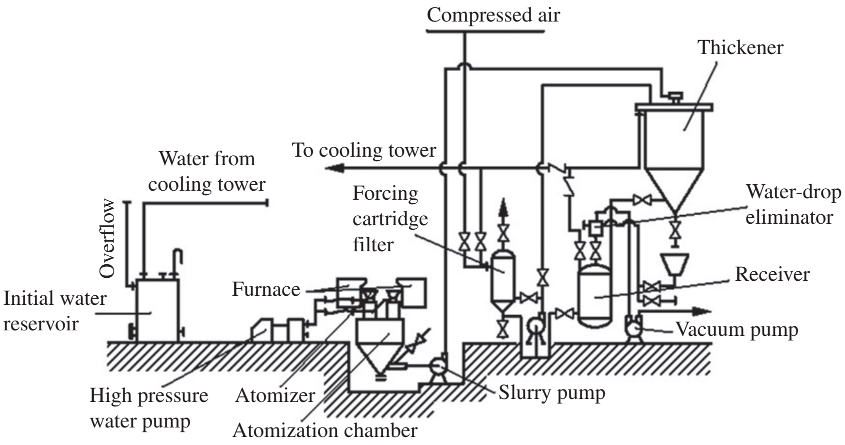

FIG. 27.38 Flow chart of the water recycling in water atomized copper alloy powders production.

TABLE 27.29 Changing of the Hydrogen Ion Exponent (pH) During Deposition from Acid and Neutral Solutions

	Hydrogen Ion Exponent in Waste Waters Inclusive of Metal Cations					
Deposition Process Advance	Cu^{2+}	Ni	Zn^{2+}	Pb	Co	Cd
At the start of deposition	5.3	6.7	5.4	6.0	6.7	7.2
When deposition is complete	8.0–9.0	9.0–9.5	8.0–9.0	8.5	8.0	8.5–9.0

Chemical Treatment Methods

Water with high acidity is neutralized with lime. This can be crushed lime, chalk, dolomite, or marble filters. The filter layer with 3–8 cm size fragments is from 0.8 to 1.2 m thick. The filtering rate does not exceed 5 $m^3/(m^2 \cdot h)$. In acidic waste water comprising metal cations, the acid neutralization by lime enables the recover copper, nickel, zinc, lead, cobalt, cadmium, and other metals. During deposition from acid and neutral solutions, the hydrogen ion exponent (pH) changes as shown in Table 27.29. For 1 m^3 of water with elevated acid content, 0.5–1 kg of quicklime is consumed.

The cementation of copper on broken iron is the basic and simplest technique for copper extraction; in this case, the iron cations proceed into solution, while copper is precipitated on the scrap as metal. The acid waste waters, saturated with iron cations, are treated with lime and passed to a thickener. The clarified water is returned to the process. The best reagent is low-grade lime including calcium carbonate. The waste water refinement from nickel ions is realized by reagent method with nickel precipitation as hydroxide or carbonate salt compositions. The wastewater refinement from zinc and its extraction is produced by lime milk, prepared from the third-grade lime. During processing the deposition is precipitated in form of hydroxide and basic salt. Lead can be recovered by analogous processes. Mercury is usually extracted either by precipitation in the form of sulfide, or by means of filtering through a highly alkaline as sodium. In the former the mercuric sulfide is in the colloidal state; therefore, it is coagulated with aluminum sulfate $Al_2(SO_4)_3 \cdot 18H_2O$, iron sulfate $FeSO_4 \cdot 7H_2O$, lime or a mixture of these reagents. Cyanide in cyanide-containing waste is converted by oxidation into non-toxic insoluble ferro-cyanides or oxidized by hypochlorite, followed by sedimentation and filtration.

A typical flow chart of the refinement from the heavy metal cations is shown in Fig. 27.39. The waste water in the reactor is mixed with slaked lime, a precipitate is formed in the thickener, and the treated water is reused. The lime suspension is made by the wet grinding in the mill, in close circuit with hydrocyclone. The lime quantity is determined based on the nature and concentration of the impurities.

The sizeable lime expenditures and large volumes of the obtained metal oxides hydrates are features of the imperfections of the chemical treatment methods. Furthermore, the precipitation of the oxides hydrates demands the maintaining of pH outlets exactly in the given ranges.

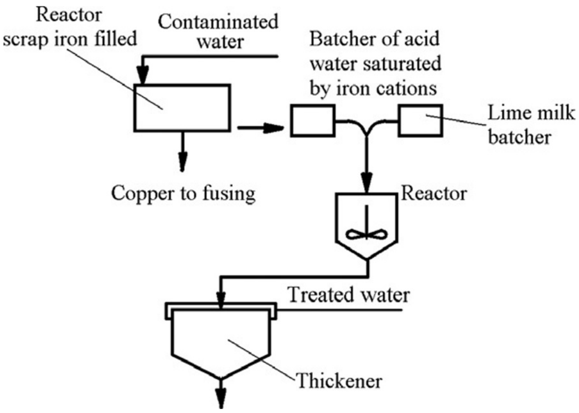

FIG. 27.39 Scheme of the contaminated water purification from copper cations by the cementation technique.

Ion-Exchange Method

Ion exchange is a more recent technique. By means of the ion-exchange resins the following metals are extracted: zinc, copper, nickel, silver, chromium, and others. The synthetic ion-exchange in aqua resin-ionites are extended. Also used are the strong-acid sulfonic cationics KY-1 and KY-2, subacid carboxyl cationic KB-4, and anionites, AB-17, EDE-10Π, and AN-31 (RUS commercial grades).

The absorption capacity of 1 g ionite amounts to 6–10 mg-eq/h. The ion-exchange rate depends on the rate of ion diffusion from solution into ionite, chemical reaction of double ion exchange in ionite, and displaced ion diffusion from ionite into the solution.

By ion-exchange on the sulfonic cationic KY-2, the ions are disposed in the following order of displacement energy: $H^+ < Na^+ < Mg^{2+} < Zn^{2+} < Co^{2+} < Cu^{2+} < Cd^{2+} < Ni^{2+} < Ca^{2+} < Sr^{2+} < Pb^{2+} < Ba^{2+}$. The cations, to the right, are absorbed less readily than those on the left. For instance, calcium is adsorbed from equimolar solution 2–2.25 times greater than sodium.

The weak acid anions CO_3^{2-} and SiO_3^{2-} are removed only by strong alkaline anionite such as AV-17 (in the absence of the strong acid anions), while the strong acid anions are removed by weak alkaline anionite such as AN-31. During the anion exchange process, the anions are removed in following order: $SO_4^{2-} > Cl^- > NO_3^- > NO_2^- > CO_3^{2-} > SiO_3^{2-}$.

The filtering rate through the fixed-bed or fluidized layer of the ionite is about 16 m per minute. The latter is more effective. The purification process is accomplished in absorption columns. Of the known designs, columns with grates and downpipes are the most efficient. In such columns, along the height the without fall-through grates are placed and at the bottom fall-through grate are located. On the column top, the annular overflow chute and ionite feed funnel are placed.

The waste water is fed into the column bottom and during upward flow it creates a fluidised layer on the fall-through grates. The treated water is descharged through the annular overflow, while the saturated ionite is discharged from the column bottom and by air-lift is fed from above into a regeneration column, into which the regeneration solution is fed from below. Washed regenerated ionite is returned in the ion-exchange column.

The ion-exchange technique is used also for desalting the recirculating water used for melt atomization, washing of the powders and equipment, and for powder cooling. The process of partial desalting includes two basic stages: cation exchange (i.e., removal of cations) and anion exchange (i.e., removal of anions).

The cation exchange is done by passing the processed liquid through the hydrogen-cation-exchange filters. On the hydrogen-cation-exchange filters, the cations are exchanged for hydrogen, and the equivalent amount of acid is generated in the filtrate. The subsequent acid filtrate pass through the anion-exchange filters leads to the retention of the acid anions by the anionite. As a result, desalted water, from which cations and anions are eliminated, is obtained.

The operating exchange capacity of cationite is defined by the equation:

$$E_c = \alpha_{ef-c} E_{f-c} - 0.5q_c\,(h_W + C_{Na})$$

where $\alpha_{ef\text{-}c}$ is the coefficient of regeneration efficiency, in the range 0.9–0.93; $E_{f\text{-}c}$ is the total dynamic exchange capacity of cationite, (g-eq)/m^3; q_c is the specific consumption of water, m^3 per one wastewater m^3; h_W is the total water hardness, (g-eq)/m^3; C_{Na} is the sodium content in the treated water, (g-eq)/m^3.

Table 27.30 includes data for the hydrogen-cation-exchange filters calculation.

By countercurrent cation exchange with total salt content in the treated wastewater of 20 mg-eq/L and specific acid consumption 110 g/(g-eq), the full softening is obtained with simultaneous removal of the Na^+ cation up to a residual of about 0.08 mg-eq/L.

The anionite-exchange filters, designed for the elimination of strong acid anions, contain a weak basic anionic, for example, AN-31 (trademark), while for the elimination of weak acids (CO_3^{2-} and SiO_3^{2-}), strong basic anionic AB-17 types are used.

The operating exchange capacity of anionic AN-31 (trademark) is defined by the equation:

$$E_a = \alpha_{ef-a} E_{f-a} - 0.8q_a\,C_a$$

where $\alpha_{ef\text{-}a}$ is the coefficient of the anionite regeneration efficiency dependent on the alkali discharge intensity (by its discharge intensity 60 g on 1 g-eq of the absorbed sulfates and chlorides, the $\alpha_{ef\text{-}a}$ is taken up amount to 0.8–09); $E_{f\text{-}a}$ is the total anionite dynamic exchange capacity, (g-eq)/m^3 (in accordance with Table 27.31); q_a is the specific consumption of washing water m^3 per one wastewater m^3 (it takes 20 m^3 water per 1 m^3 of the anionic); C_a is anion concentrations of strong acids in the water fed to the anionic filters. The technological data for calculation of the anionite filters in desalting circuits are given in Table 27.31.

TABLE 27.30 Data for the Calculation of Hydrogen–Cation-Exchange Filters

Parameters	Unit	Normative Values
Cationite type		Sulfonated coal CK–1, cationite KY–2
Grain size:		
CK–1	mm	1.0 – 1.1
KY–2	mm	1.0 – 1.25
Allowable bed height	m	up to 3.3
Apparent density of commercial cationic material:		
CK–1	kg/m^3	550
KY–2	kg/m^3	690
Temperature of treatment water	K	288–313
Number of as-maintained filters	pcs	not less as 3 operational and 1 reserve
Advisable filtering rate, at water hardness, mg-eq/L:		
Under 5	m/h	20 (30)[a]
Under 10	m/h	15 (25)
Under 15	m/h	10 (20)
Hydraulic resistance of filters according to cationite type:		
CK–1 by filtering rate. m/h		
10	m-Water column	20
20	m-Water column	24
30	m-Water column	28

[a] *Maximum at the time when one of the filters is in regeneration regime.*

TABLE 27.31 Technological Data for Calculation of the AN-31 Brand Anionic Material Filters

Parameters	Unit	Normative Values
Moisture load	%	15
Apparent density	g/cm^3	0.72–0.75
Grain sizes in turgid condition	mm	0.4–2.0
Anionic yield	%	5–10
Total anionic dynamic exchange capacity	(g-eq)/m^3	>800
Number of as-maintained filters	pcs	Not less as 3 operational and 1 reserve
Advisable filtering rate, taking into account full $E_{f\text{-}a}$ using	m/h	15–20
Regeneration of anionic material with alkali:		
Specific consumption	g/(g-eq)	60
Solution strength	%	4
Passage rate	m/h	20
Washing of anionic material:		
Specific water consumption	m^3/m^3	20
Passage rate of washing water	m/h	8–10

Sorption, Evaporation, and Flotation Methods

Sorption Method

Sorption method is used for wastewater purification from phenols, acetone, trichloroethylene, and others solvents, which are used in the electrochemical methods of powder production. As adsorbents, activated carbon, breeze coke, peat, chalk, and limestone in the form of irregular shaped grains from 1.5 to 5 mm in diameter are used. Reduction of adsorbent is done by chemical dissolvents, steam, or via heat treatment. Motionless as well as fluidized bed of adsorbent in adsorbers are used. The design of the former is simpler; but, the adsorbers with fluidized beds are more effective.

Commercial plants usually contain a column (Fig. 27.40) with a larger diameter in the upper section head part, equipped with an overflow chute for venting of the treated water. The waste water is fed into the conic end, over which the distributive grating with 5–10 mm diameter apertures is located. A 2.5–2.7 m activated carbon layer is formed on the grating. The activated carbon is fed into the column by a batcher through the vertical pipe. The flow rate is such as to maintain the carbon in the fluidised state. Part of the treated water containing spent carbon is removed through a discharging branch to the carbon catcher. The treated water from column is discharged in the overflow chute and is vented with water from discharge branch. The activated carbon is subjected to regeneration, after which is returned to the adsorber. The adsorbed substances are taken out during regeneration by means of organic solvents, steam distillation, and evaporation with a heated gas current.

Evaporation Method

Evaporation represents the distillation with water steam the volatile matter, contaminating the water. This technique can be used for the removal of phenols. Here the waste water is not polluted by chemical reagents. Evaporators of varios evaporation rate are commercial available. So, Lakeview Engineering Products Inc. (IN, United States) produces the evaporators including 8gph (18.9 Lph) to 500 gph (1,892.5 Lph) and 150 L to 3,360 L tank capacity.

Flotation Method

Flotation is used for the removal of surfactants, fats, and oil products. The process is based on the floating-up of air blebs with particles polluting the waste water.

Numerous companies specialize in the area of waste water treatment and recirculation: Rochen UF System, Germany, designs & assembles the water-purifying equipment; National Water storage, PIK group Companies, Russia, deal with the treatment of waste water and water conditioning; Jurby Water Tech International, Great Britain, produces decarburization, reverse osmosis, and demineralization installations, and chemical reagents for water treatment technologies; H2K Technologies, Inc. – Corcoran (MN, United States) carbon adsorption, sand and multi-media filters manufacturer; (KWI Co., Russian branch, produces flotation equipment for waste water treatment; Kreal-water purification and conditioning Co., Russia, builds waste water treatment installations, purification filters, and water conditioning equipment; and OY LABKO AB, Finland, produces equipment for waste waters treatment, etc.

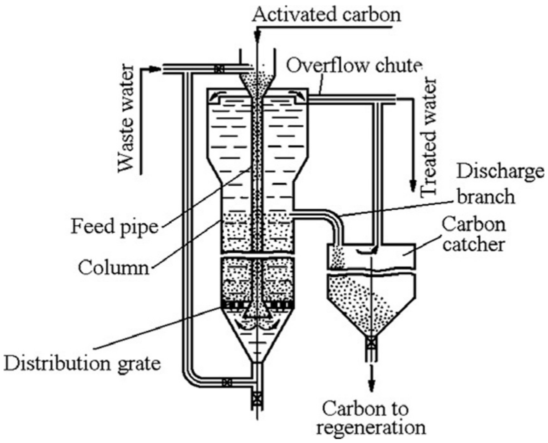

FIG. 27.40 Sorption technique for the waste water purification.

DUST AND GAS CLEANING

The selection of equipment for dust removal is based on the following criteria:

- the degree of dust removal required
- the physical and chemical properties of the dust
- temperature, moisture content, chemical reactivity, dust concentration, and the volume of the gas to be treated
- the operating regime of the equipment.

The dedusters are subdivided into coarse, medium, and fine cleaning, depending on their gas cleaning efficiency. The coarse dedusters collect efficiently particles bigger than 10 μm, while particles smaller than 2 μm are not collected. The medium cleaning plants collect efficiently up to 2 μm, and fine cleaning plants collect particles in the range below 2 μm.

Depending on the dust collecting mechanism, dedusters are subdivided into mechanical (dry and wet), porous and fibrous filters, electrical precipitation, and plants, based on some other effects (such as acoustical and condensation coalescence of the particles). Such coagulated particles are collected further in some coarse or medium cleaning plants. A magnetic effect, thermophoresis, and other mechanisms have been explored. However, such processes are still in the experimentation stage.

The gas cleaning plants, KP type (Table 27.32) are intended for cleaning the exhaust gas emissions from carbon monoxide and organic compositions with weight concentration up to 10 mg/m^3. The apparatus (Fig. 27.41) consists of a vertical cylindrical body, within which, the basket with catalyst, dividing sidewalls, and shell-and-tube circular heat exchanger are coaxially assembled. Under the basket, the jet burner and turbulence promoter are located. The basket consists of the two concentrically situated cylinders. The space between cylinders is filled with catalyst.

Preliminary heating of the exhaust gas emissions is realized by the heat of the refined gases in the shell-and-tube circular heat exchanger. The turbulence promoter ensures temperature uniformity in front of the catalyst layer. The exhaust gas emissions come via the intertubular space of the heat exchanger to the jet burner, which warms them up with admixtures

TABLE 27.32 Gas Cleaning Plants

		Plant Type[a]				
Parameter	**Unit**	**KP-1.6-2Y-01**	**KP-3.15-2Y-01**	**KP-1.6-2Y-01**	**KP-1.6-2Y-01**	**KP-1.6-2Y-01**
Capacity (max)	m^3/h	1600	3150	6300	12500	25000
Heat transfer area (min)	m^2	35	39.4	110	400	715
Hydraulic resistance (max)	kPa	10	10	10	10	10
Catalyst total volume (min)	m^3	0.2	0.36	0.65	0.86	1.6
Temperature of exhaust gas emissions:						
Before catalyst layer, not more than	K	723	723	723	723	723
Maximum in apparatus	K	773	773	773	773	773
Maximum concentration of impurities in gases:						
Carbon monoxide and organic Compositions (converting to carbon)	g/m^3	10	10	10	10	10
Dusts	g/m^3	0.01	0.01	0.01	0.01	0.01
Purification efficiency, minimum	%	95	95	95	95	95
Consumption of fuel gas, maximum	m^3/h	10.1	22.1	38.9	64.8	118.0
Specific power consumption, maximum	kW·h/(1000 m^3)	58.6	65.2	57.5	48.4	44.7
Weight (max)	ton	2.62	3.13	5.85	13.63	24.82

[a] *CIS Standards.*

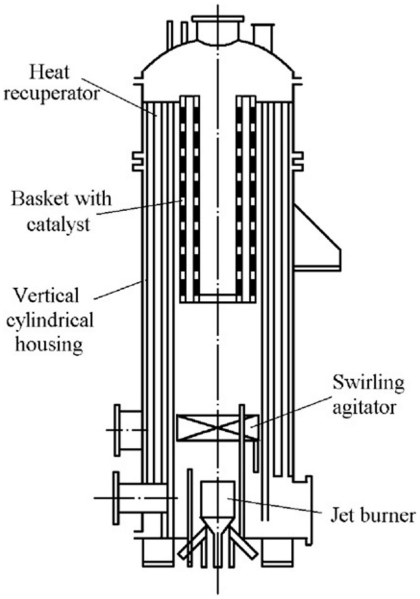

FIG. 27.41 Type KP apparatus for the purification from carbon monoxide and organic compounds of effluent gas.

of oxidizers to the temperature range from 523 K to 723 K, whereupon the gases through the turbulence promoter reach the catalyst layer. The catalyst type and operating temperature are chosen depending on the exhaust gas emissions composition and the concentration of impurities. As a result of the catalytic oxidation of the impurities, carbon dioxide and water are formed. The characteristics of the exhaust gas emissions cleaning apparatus are given in Table 27.32.

The operating details and special features of dust and gas cleaning equipment can be found in respective brochures available from the manufactures. So, the Suomen Imurikeskus Oy specializes in the area of gas cleaning from ultrafine dust.

WASTE PRODUCTS UTILIZATION, STORING, AND TRANSPORTATION

Waste Utilization

The hazardous waste products legislation in the EU as well as in International becomes increasingly important for the metals and alloys industry [21,44]. It is also an area in which end users must try to eliminate or restrict the use of such metals or alloys because they are classified, prompted by fear of downstream disposal problems, or because they fear damaging the company's "green" image.

It is accepted that waste products can be subdivided into three main areas: scrap for recycling, scrap for disposal (waste), and scrap components within assemblies.

Scrap for recycling is not "waste," and therefore, is not subject to waste regulations. This type of scrap should return to the producer, or it can be sold to authorized scrap dealers.

The off-size waste products are pressed into briquettes and returned to the technological process, if they correspond with the composition conditions, or transferred to processing as secondary raw materials. In that case, the safety requirements are regulated by corresponding statutory acts, as GOST 12.2.055-81, and OST 4 GO.091.266-87 in Russian Federation.

Scrap for disposal (waste) is defined within the framework Directive 91/156/EES if it cannot be recycled and must be disposed of. It is important to establish whether the scrap or waste meets the Special Waste definition. This can be established by the following conditions:

- if it is a listed waste (this includes waste arising from surface treatment of metals; liquid waste or sludge containing metal or compounds; dust or waste powder containing metal compounds)
- if it contains a listed substance (this includes many metals and/or their compounds)
- if it falls into either of the above categories, does it also have dangerous properties.

Such scrap is classified as a special waste, and the waste generator has the duty of care in the disposal of the waste. It must also be handled by an authorized waste disposal agent and disposed of in an authorized landfill site.

Scrap components within assemblies. Here, the scrap producer first has to establish whether it is economically feasible to extract the components made from the classified material for recycling. There is, however, no legal requirement to remove the

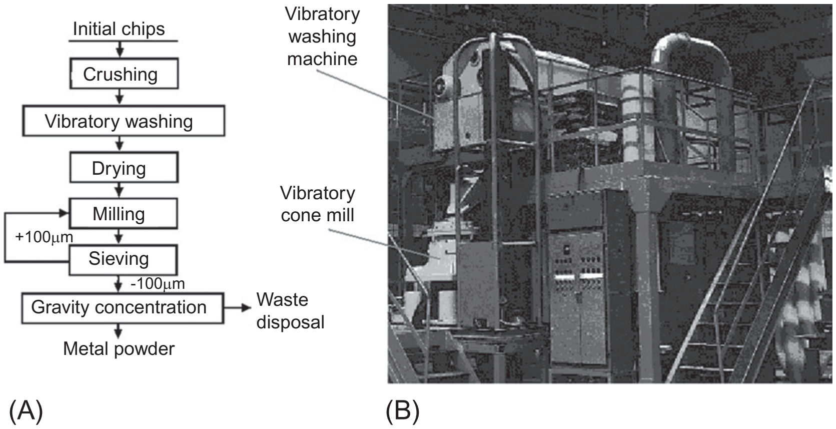

FIG. 27.42 Metal chip waste recycling: (A) scheme of process, (B) overview of the installation. *Courtesy of the Mekhanobr Institute, Saint Petersburg.*

components prior to disposal. In disposing of the equipment with the components still in it, the scrap producer must carry out a risk assessment as to whether the waste falls under Special Waste Regulation to determine the technique of disposal.

A typical metal machining scrap recycling process is schematically shown in Fig. 27.42. The initial chips (includes copper, brass, tin, or titanium) with size up to 500 mm are fed to a hammer crusher. Crushed chips less than 5 mm are cleaned in a vibratory washing machine, followed by drying and subsequent milling in vibratory cone mill. The milled product is divided by means of vibratory sieve into fractions +100 µm and −100 µm. The former is returned for further milling, while the latter is subjected to gravity concentration.

Waste disposal as related to the metals and alloys industries will be affected by a new EU legislation which will require ecotoxicology classification.

Directive 2008/98/EC on waste [44] contains a new and wider definition of hazardous waste which extends to metallic dusts and powder as well as liquid or sludges containing metals or metal compounds. Components of wastes which render them hazardous include nickel compounds.

Demands of this directive include:

- competent authorities to draw up hazardous waste management plans and to make these public
- Member states to identify and record all hazardous waste being disposed of within their borders
- inspection of hazardous waste collection and transport activities must, in particular, cover the origin and destination of the waste
- operators who dispose, recover, and collect or transport hazardous waste must not mix different categories of waste or mix hazardous waste with non-hazardous waste
- wastes must be suitably packaged and labelled in accordance with international and community standards in force.

The European Waste Catalogue is a non-exhaustive list of wastes [45], which unconditionally includes waste containing nickel and its compounds, intended to provide a common terminology for waste management activities throughout the EU. The Catalogue represents a list of waste, which the EC was required to produce under Article 1 of the Waste Framework Directive 75/442/EEC, as amended by 91/156/EEC.

Storing and Transportation of Hazardous Powders

The storing and transport of dangerous goods are governed by a large number of international treaties and national legislation. The principal regulations, based on the “Recommendations on the transport of dangerous goods” (as published in the nineteenth revised addition [46]) addressed to governments and to the international organizations concerned with safety in the transport of dangerous goods are the following:

- The European Agreement concerning the international carriage of dangerous goods by road (ARD) which applies to the international (as well as in some cases also to the national) transport of harmful substances in Europe. The agreement has been signed by most European countries.
- The agreements concerning the carriage of dangerous goods by rail (RID) which are part of the Treaty on the International carriage by rail (COTIF), which has been signed by most European states.
- The International Maritime Dangerous Goods code (IMDG Code) is applicable worldwide and applies to ships carrying dangerous goods in packaged form or in solid form in bulk.

- The International Air Transport Association (IATA) dangerous goods regulations which are applicable worldwide to all airlines which are members or associate members of IATA [47].

In addition, International Civil Aviation Organization had submitted a development of recommendation for amendments to the Technical Instructions for the Safe transport of dangerous goods for incorporation in the 2019–20 edition [48].

The Standards GOST 12.2.055-81 and OST 4 GO.091.266-87 stipulate in CIS the safety regulations by storing, transportation, and using active and harmful materials. The categories of production areas and buildings on explosion-fire and fire risk are determined in Commonwealth of Independent States (CIS) in according to Technological Designing Standard ONTP-24–86 [26].

Dangerous goods are products which can represent a significant risk to health, safety, or property during transportation. They are assigned to one or more of the nine UN hazard classes by descending order of danger and where applicable to one of three UN packing groups. The flammable solids are placed in Class 4, while flammable liquids are in Class 3, and corrosives in Class 8. The criteria for classification and packaging of dangerous goods are based on the Recommendations of the United Nations Committee of Experts on the Transport of Dangerous Goods [46].

The packing groups include:

- Packing Group I: Great Danger
- Packing Group II: Medium Danger
- Packing Group III: Minor Danger

For metal powders, the main classification area is for flammability (Class 4). This class is subdivided as follows:

- Division 4.1: flammable solids are solids, other than those classed as explosive, which, under conditions encountered in transport, are readily combustible, or may cause or contribute to fire through friction.
- Division 4.2: pyrophorics are the substances liable to spontaneously combust or self-heat under normal conditions encountered in transport, or to heating up in air, which are then liable to catch fire.
- Division 4.3: emission of the flammable gases covers the substances which, on contact with water, are liable to become spontaneously flammable or to give off flammable gases in dangerous quantities.

Some examples of tests undertaken by EPMA members on the classification for transportation of metal and alloy powders [20] are given in Table 27.33.

TABLE 27.33 Classification for Transportation of a Range of Metal and Alloy Powders

Metal Powders	Class 4.1	Class 4.2	Class 4.3	Thermal Stability	Conclusions
Lead <40 µm	Packaging group III	Packaging group II	…	High reactive	Class 4.2 Packaging group II
Lead <63 µm	…	…	…	High reactive	…
Coarse copper	…	…	…	Low reactive	…
Copper <63 µm	…	…	…	Reactive	…
Bronze <40	…	…	…	Low reactive	…
Brass <63 µm	…	…	…	Low reactive	…
Phosphor-copper <80 µm	…	…	…	Reactive	…
Copper flake <40 µm	…	Packaging group II	…	High reactive	Class 4.4 Packaging group II
Tungsten <2 µm	Packaging group II	…	…	Reactive	Class 4.1 Packaging group II
Zinc <63 µm	…	…	Class 4.3	Low reactive	…
Tin <40 µm	…	…	…	Low reactive	…
Bronze premix with lubricant	…	…	…	High reactive	..

Source: Guide to Legislation and 'Health and Safety' in the European PM Industry. Publ. EPMA; 1997.

The EC criteria for classification, choice of symbols, and indication of danger with risk (R) phrases are given in Directive 67/548/EES. Thus, R10 is Flammable, R12 is Extremely Flammable, R11 is Highly Flammable (idem Class F), R15 is contact with water liberates extremely flammable gases, and R17 is spontaneously flammable in air.

REFERENCES

[1] Commonwealth of Independent States Standard GOST 12.1.003-83. Occupational Safety Standards System. Noise. General Requirements of Safety (in Russian).
[2] Commonwealth of Independents States Standard SNiP II-12-77. Occupational Safety Standards System. Protection away from the Noise. Designing Standards (in Russian).
[3] ANSI. Noise Control Safety Standards. ISO 9001: 2015, https://webstore.ansi.org/safety_standards/noise_safety/noise_control.aspx. Accessed June 2018.
[4] Naboychenko SS, editor. Handbook of Non-Ferrous Metal Powders. Moscow: Metallurgia Publishers; 1997 [in Russian].
[5] Dorsett HG, Jacobson M, Nagy J, et al. Laboratory equipment and test procedures for evaluating explosibility of dusts. Report Inv. 5624, Washington (DC, USA): US Bureau of Mines; 1960.
[6] Grewer IF. (1971) Zur selbstentzundung von abgelagertem staub. Staub-Reinhalt, Luff 1971;31:97–101.
[7] International Electrotechnical Commission. Electrical apparatus for use in the presence of combustible dust. Part 2: Test methods. In: Section 1: Method for determining ignition temperatures of dust (International standard). Geneva: Central Office of IEC; 1994.
[8] International Electrotechnical Commission. Electrical apparatus for use in the presence of ignitable dust. Part 2: Test Methods. In: Sheet 2-5: Method for determining the minimum explosible Concentration of dust/air mixtures (Draft). Geneva: Central Office of IEC; 1990.
[9] Siwek R. (1988, November) Reliable determination of safety characteristics in 20 litre apparatus. In: Proceedings of the Conference on flammable Dust Explosions. St. Louis (MO, USA); 1988. p. 1–2.
[10] Nordtest. Dust clouds: minimum explosible dust concentration. Nordtest Method NT Fire 011, 2nd ed. Espoo, Finland: Nordtest; 1989.
[11] International Standards Organization. Explosion Protection Systems. Part 1: Determination of explosion indices of combustible dusts in air. International Standard ISO/DIS 6184/1, Geneva: ISO; 1985.
[12] Nedin VV, Neikov OD, Alekseev AG, Krivtsov VA. Explosion risk of metallic powders. Kiev: Naukova Dumka; 1971.
[13] Alekceev AG, Neikov OD. The explosion risk of metal powders. Staub 1990;50:245–50.
[14] Eckhoff RK. Towards absolute minimum ignition energies for dust clouds? Combust Flame 1975;24:53–64.
[15] Berthold W. Bestimmung dev mindestziindenevgie von staub/luft-gemischen. Vortschrittberichte Series 3, no. 134. Düsseldorf (Germany): VDI, Düsseldorf VDI-Verlag; 1987.
[16] Eckhoff RK. Dust Explosions in the Process Industries. 3rd ed. Amsterdam: Gulf Professional Publishing; 2003.
[17] American Society for Testing and Materials. ASTM standard E 1226-88 for pressure and rate of pressure rise for combustible dust. In: Annual Book of ASTM Standards. vol. 14.02. Philadelphia: ASTM; 1988. p. 688–98.
[18] Nagy JE, Seiler C, Conn JW, et al. Explosion development in closed vessels. Report Inv. 7507, Washington (DC, USA): US Bureau of Mines; 1971.
[19] Neikov OD, et al. Explosion-security of manufacture processes of advanced water atomized aluminium alloy P/M technology. In: Compiled by Arnold V, Chu C-L, Jandeska WF, Sanderow HI. Proceedings of 2002 powder metallurgy world congress. Orlando (FL, USA): MPIF; 2002. p. 7-60–9.
[20] Guide to Legislation and 'Health and Safety' in the European PM Industry. Publ. EPMA; 1997.
[21] Commission of the European communities. Practical guidelines of a non-binding nature on the protection of the health and safety of workers from the risks related to chemical agents at work. Brussels; 2004.
[22] EH40-Update to EH40/2005 Workplace Exposure Limits. second ed., published 2011 (as consolidated with amendments, December 2011).
[23] US New Jersey Department of Health and Senior Services. Hazardous Substance Sheet. Nickel carbonyl, Revision: February 2001, http://nj.gov/health/eoh/rtkweb/documents/fs/1343.pdf. Accessed 31 January 2018.
[24] Commonwealth of Independent States Standard GOST 12.1.005-88. Occupational Safety Standards System. General sanitary requirements for working zone air (in Russian).
[25] Soviet Union Patent 1,044,328. Jun 1981.
[26] Technological Designing Standard ONTP-24-86 (in Russian).
[27] British Standard BS EN 14491: 2006. Dust explosion venting protective systems. [Accessed June 2018].
[28] European and NFPA Standard: EN 14373:2005 Explosion suppression systems. [Accessed June 2018].
[29] British Standard BS EN 14797:2006 EN. 2006 Explosion venting devices. [Accessed June 2018].
[30] NEFA 68: Standard on explosion protection by deflagration venting. Edition. 2018.
[31] Siwek R, Cavallin S. New revised European norm on dust explosion venting protection systems EN 14491. Chemical Engineering Transactions 2012;26:387–92.
[32] Taveau J. Application of dust explosion protection systems. Procedia Engineering 2014;84:297–305.
[33] Snoeys J. Dust explosion protection using flameless venting. Herentals (Belgium): Fike Corporation. <www.fike.com/wp-content/uploads/2015/10/Flameless_Venting_White_Paper.pdf>.
[34] Snoeys J, Going JE, Taveau JR. Advances in dust explosion protection techniques: flameless venting. Procedia Engineering 2012;45:403–13.
[35] Neikov OD, Logachev IN. Aspiration and air dedusting during manufacture of powders. Moscow: Metallurgija Publishers; 1981 [in Russian].

[36] Directive for designing and computation of aspiration in metallic powder production including combustible and explosive. Kiev: IPMS Publishers; 1995.
[37] Neikov OD. Ignition prevention during the comminution of reduced sponge iron. Sov Powder Metall Met Ceram 1977;16(11):901–4.
[38] RU Patent 2,122,926. May 1997.
[39] Soviet Union Patent 1,436,341. Feb 1987.
[40] Soviet Union Patent 1,460, 831. Jan 1987.
[41] Soviet Union Patent 1,131,536. Mar 1983.
[42] Soviet Union Patent 413,990. Mar 1972.
[43] Logachev I, Logachev K, Averkova O. Local exhaust ventilation. Boca Raton (FL, USA): CRC Press; 2016.
[44] European Commission. Guidance on the interpretation of the key provisions of Directive 2008/98/EC on waste. [Accessed June 2018].
[45] Environmental Protection Agency. European waste catalogue and hazardous waste list. From 1 June 2015, http://www.epa.ie/waste/municipal/wasteclass/. Accessed June 2018.
[46] United Nations. Transport of dangerous goods. vol. 1; 2015. New York and Geneva.
[47] IATA Dangerous Goods Regulations. 59th ed. Effective 1 January 2018.
[48] International Civil Aviation Organization. Development of recommendation for amendments to the Technical Instructions for the Safe transport of dangerous goods. Working group Meeting. Montreal (Canada): 2017.

FURTHER READING

[49] BHA. Brenn- und explosions-kenngrössen von staüben. Berufsgenossenschaftliches Institut für Arbeitssicherheit. Bergbau-Versuchsstrecke. In: Institut für Explosionsschutz und Sprengtechnik. Bielefeld (Germany): Erich Schmidt Verlag GmbH & Co; 1987.
[50] Soviet Union Patent 485928. Otkrytiya, Izobbreteniya; 36: 1975.

Appendix 1

Methods of Powder Characterization and Testing

Standard Title	Origin				
	ISO	ASTM	MPIF	CIS	Other
Metallic powders—determination of apparent density—Part 1: Funnel method	3923/1	B 212	04	GOST 19440-94	…
Density, apparent of metal powders using the Arnold meter	…	B 703	48	…	…
Density, apparent of non-free-flowing metal powders	…	B 417	28	…	…
Metallic powder—determination of apparent density—Part 2: Scott volumeter method	3923/2	B 329	…	GOST 19440-94	
Test method for metal powder skeletal density by helium or nitrogen pycnometry	…	B923	…	…	…
Flow rate of metal powders	4490	B 213	03	GOST 20899-75	…
Test methods for flow rate of metal powders using the Carney funnel	…	B964	…	…	…
Measuring dimensional change of metal powder specimens due to sintering	4492	B 610	44	GOST 29012-91	…
Metallic powders—determination of oxygen content by reduction methods—Part 1, part 2, part 3, part 4	4491-1, 2, 3, 4	E159	02	GOST 29006-91 GOST 27417-87 GOST 18897-73	…
Standard test method for loss of mass in a reducing gas atmosphere for cobalt, copper, tungsten, and iron powders (hydrogen loss)	4491/2	E159	02	GOST 29006-91	…
Test method for determination of hydrogen in aluminum and aluminum alloys by inert gas fusion	…	E2792	…	…	…
Test method for determination of hydrogen in titanium and titanium alloys by inert gas fusion thermal conductivity/infrared detection method	…	E1447	…	…	…
Test method for analysis of titanium and titanium alloys by direct current plasma and inductively coupled plasma atomic emission spectrometry	…	E2371	…	…	…
Test method for analysis of Ni-base alloys by wavelength dispersive X-ray fluorescence spectrometry	…	E2465	…	…	…
Test method for analysis of nickel alloys by inductively coupled plasma atomic emission spectrometry (performance-based method)	…	E2594	…	…	…

	Origin				
Standard Title	**ISO**	**ASTM**	**MPIF**	**CIS**	**Other**
Test method for determination of carbon in refractory and reactive metals and their alloys by combustion analysis	…	E1941	…	…	…
Metallic powders—determination of envelope—specific surface area from measurements of the permeability to air of a powder bed under study-state flow conditions	10070	…	…	GOST 23401-90	…
Metallic powders—determination of particle size distribution by gravitational sedimentation in a liquid and attenuation measurement	10076	…	…	…	…
Metallic powders—determination of acid insoluble content in iron, copper, tin, and bronze powders	4496	E194	6	GOST 30550-98	…
Terminology relating to sieves, sieving methods, and screening media	…	E1638	…	…	…
Metallic powders—determination of particle size by dry sieving	4497	B 214	05	GOST 18318-94	MIL-STD-1233
Particle size analysis—laser diffraction methods—Part 1: General principles	13320-1				
Metallic powders. determination of particle shape	…	…	…	GOST-25849-83	…
Test method for determination of oxygen in tantalum powder by inert gas fusion technique	…	E1569	…	…	…
Metallic powders, excluding powders for hardmetals—determination of compatibility (compressibility) in uniaxial compression	3927	B 331	45	GOST 25290-90	…
Metallic powders—determination of Green strength by transverse rupture of rectangular compacts	3995	B 312	15	GOST 25282-93	…
Particle size distribution of metal powders and related compounds by light scattering	…	B 822	…	…	…
Particle size distribution of refractory metals and their compounds by X-ray monitoring of gravity sedimentation	…	B 761	…	…	…
De-agglomeration of refractory metal powders and their compounds prior to particle size analysis	…	B 859	…	…	…
Particle size distribution of refractory metals-type powders by turbidimetry	…	B 430	…	…	…
Particle size, average, of metal powders by fisher subsieve sizer	…	B 330 C 721	32	…	MIL-STD-1233
Particle size analysis of particulate substances by optical microscopy		E 20	…	GOST 23402-78	…
Standard test methods for determining average grain size	…	E112	…	…	…
Permeable sintered metal materials—determination of bubble test pore size	4003	…	…	GOST 26849-86	…
Pore volume distribution of catalysts by mercury intrusion porosimetry	…	D 4284	…	…	…
Bulk density and porosity of granular refractory materials by mercury intrusion porosimetry	…	C 493	…	…	…
Standard test method for apparent porosity in cemented carbides	…	B276	…	…	…

Standard Title	Origin				
	ISO	**ASTM**	**MPIF**	**CIS**	**Other**
Sampling and sample preparation procedures	3082	…	…	GOST 23148 …	
Sampling and testing aluminum powder and paste	…	D 480	…	…	…
Sampling finished lots of metal powders	3954	B 215	01	GOST 23148-78	
Standard shear testing method for bulk solids using the Jenike shear cel	…	D 6128	…	…	…
Subsieve analysis of granular metal powders by air classification	…	B 293	12	…	…
Tap density of metal powders	3953	B 527	46	GOST 25279-93	MIL-STD-1233
Tension test specimens for pressed and sintered metal powders	2740	E 8	10	…	…
Testing copper-base infiltrating powders	…	…	49	…	…
Terms used in powder metallurgy	3252	B 243	9	GOST 17359-82	
British Standards 2955 glossary of terms relating to powders	…	…	///	…	British Standards 2955
Wire-cloth sieves for testing purposes, specification	565 3310/1	E 11		GOST 3584	RR-S-366

Standards referenced include the following: American Society for Testing and Materials (ASTM); International Organization for Standardization (ISO); Metal Powder Industries Federation (MPIF); Commonwealth of Independents States (CIS); MIL—Superintendent of Documents, US Government Printing Office, Washington, DC 20402.

Appendix 2

Standards and Metal Powder Specifications

Standard Title	Designation		
	ASTM	CIS	Other
Materials standards for metal injection-molded parts	…	…	MPIF Standard 35
Materials standards for PM self-lubricating bearings	…	…	MPIF Standard 35
Materials standards for PM structural parts			MPIF Standard 35
Standard for the prevention of fire and dust explosion from the manufacturing, processes, and handling of combustible particulate solids	…	GOST 12.1.005-88	NEFA 654
Standard guide for characterizing properties of metal powders used for additive manufacturing processes	F3049—14	…	…
Standard specification for bronze-base powder metallurgy (PM) bearings	438	…	…
Standard terminology of powder metallurgy	B243—13	…	…
aluminum pigment, powder and paste, for paint	D 962	GOST 5494-95	TT-P-320B
Aluminum powder, flaked, grained, and atomized	…	…	MIL-A-512A
Aluminum lumpy pigment	…	GOST 10096-76	…
Antimony, powdered, technical	…	…	MIL-A-10841B
Brass powder (for sintering)	…	…	MIL-B-11552B
Bronze powder, gold	D 267	…	TT-P-340
Copper powder	…	GOST 4960	…
Copper powder (for use in ammunition)	…	…	JAN-C-768
copper electrolytic powder, ultrafine, stabilized	…	TU 17911-368-094-96	…
Copper reduced powder, stabilized	…	TU 48-O318-O83-94	…
Copper powder for use in antifouling paints	D 964	…	…
Cobalt powder	…	GOST 9721-79	…
Iridium, powdered	…	GOST 12338-81	…
Magnesium-aluminum alloy, powdered	…	…	JAN-M-454
Magnesium powder (for use in ammunition)	…	…	JAN-M-382A
Manganese, powdered (for use in ammunition)	…	…	JAN-M-476A
Nickel powder	…	GOST 9722-79	…
Nickel powder (for use in ammunition)	…	…	JAN-N-412A
Niobium powder	…	GOST 26252-84	…

Standard Title	Designation		
	ASTM	CIS	Other
Palladium, powdered	…	GOST 14836-82	…
Powders, metal, atomized (aluminum, magnesium, magnesium-aluminum)	…	…	MIL-P-14067B
Rhodium, powdered	..	GOST 12342-81	…
Tin powder	…	GOST 9723-79	…
Tin, pulverized	…	…	JAN-T-458
Titanium, powdered	…	…	MIL-T-13405
Tungsten, powdered	…	…	MIL-T-13827
Zinc powder	…	GOST 12601-76	…
Zinc dust (for use in pyrotechnics)	…	…	JAN-Z-365
Zinc dust (metallic zinc powder); dry (paint pigment)	D 520	…	TT-P-460 No. 1
Zirconium-nickel alloy powder (for use in delay compositions)	…	…	MIL-Z—11410A
Zirconium powder (calciothermic)	…	TU 48-4-234-84	…
Zirconium powder (natriothermic)	…	TU 48-4-376-76	…
Zirconium, powdered (for use in ammunition)	…	…	JAN-Z-399A
Miscellanea			
Brushes, electrical contacts, and carbon stock, electrical contact brush			
Precision electroformed sieves, specification	E 161	…	…

Standards referenced include the following: American Society for Testing and Materials (ASTM), Commonwealth of Independents States (CIS), MIL—Superintendent of Documents, U.S. Government Printing Office, Washington, D.C. 20402, Metal Powder Industries Federation (MPIF), The National Fire Protection Association.

Abbreviations and Symbols

A	ampere
Å	angstrom
ABC	activity-based costing
ac	alternating current
ACGIH	American Conference of Governmental Industrial Hygienists
AES	Auger electron spectroscopy
AMS	Aerospace Material Specification
ANSI	American National Standards Institute
ASTM	American Society for Testing and Materials
at.%	atomic percent
atm	atmosphere (pressure)
bal	balance
bcc	body-centered cubic
BEI	back scattering electron image
bet	body-centered tetragonal
Btu	British thermal unit
CIP	cold isostatic pressing
cm	centimeter
CMC	ceramic-matrix composite
CNC	computer numerical control
CP	commercial pure
cpm	cycles per minute
cps	cycles per second
CSA	Canadian Standards Association
cSt	centiStokes
CTE	coefficient of thermal expansion
CVD	chemical vapor deposition
CVI	chemical vapor infiltration (impregnation)
d_a	project area diameter of the particle
dB	decibel
Dc	direct current
DC arc	direct current arc
DCA	differential calorimetric analysis
diam	diameter
DIN	Deutsche Institut fur Normung
d_p	perimeter diameter of the particle
DTA	differential thermal analysis
e	charge of an electron; natural log base, 2.71828
E	modulus of elasticity; Young's modulus; potential
E_S	secant modulus
EDM	electrical discharge machining
EIMAC	European Industry Metals and Alloys Classification Group
El	elongation
emf	electromotive force
EMI	electromagnetic interference
Eq	equation
EPMA	European Powder Metallurgy Association

ESC	environmental stress cracking
esu	electrostatic units
et al.	and others
eV	electron volt
F	Faraday constant; force
fcc	face-centered cubic
FCGR	fatigue crack growth rate
fct	face-centered tetragonal
Fig.	figure
FM	figure of merit
ft	foot
g	gram
G	gauss
GA	gas atomized
gal	gallon
GPa	gigapascal
gpd	grains per denier
gr	grain
h	hour
h	thickness
H	henry
H	change in height; degree of homogenization; enthalpy; hardness; height; magnetic field
HB	Brinell hardness
hcp	hexagonal close-packed
HDT	heat-deflection temperature
HDVC	hot dynamic non-capsule vacuum compacting
HE	hot extrusion
HERF	high-energy-rate forging
HIP	hot isostatic pressing
hp	horsepower
HPWA	high pressure water atomization
HR	Rockwell hardness
HV	Vickers hardness
Hz	hertz
i	current (measure of number of electrons)
I	current; emergent intensity
IACS	International annealed copper standard
IATA	International air transport association
IC	integrated circuit
ID	inside diameter
IEC	International Electrotechnical Commission
IMDG Code	International maritime dangerous goods code
in.	inch
INTER	International thermonuclear experimental reactor
IPD	integrated product development
IPMD	International Powder Metallurgy Directory
IPMS	Institute for Problems of Materials Science
IPPC	integrated pollution prevention and control
IPTS	International Practical Temperature Scale
IR	infrared (radiation)
ISAO	International Civil Aviation Organization
ISO	International Organization for Standardization
ITS	International Temperature Scale
IV	intrinsic viscosity
J	joule
JIS	Japanese Industrial Standard
JWRL	Welding Research Institute of Osaka University
k	karat

k	Boltzmann constant; notch sensitivity factor; thermal conductivity; wave number
K	Kelvin
K	bulk modulus of elasticity; coefficient of thermal conductivity; empirical constant; interface reaction; mean integrated thermal conductivity
K_{I}	stress-intensity factor
K_{Ic}	mode I critical stress-intensity factor; plane-strain fracture toughness
K_{Id}	dynamic fracture toughness
K_{Iscc}	threshold stress intensity for stress-corrosion cracking
K_{c}	plane-stress fracture toughness
K_{f}	stress-concentration factor
kg	kilogram
km	kilometer
kN	kilonewton
kPa	kilopascal
ksi	kips (1000 lb) per square inch
kV	kilovolt
kW	kilowatt
l	mean free path; length
L	liter; longitudinal direction; liquid
lb.	pound
lbf	pound force
LCA	life cycle analysis (or assessment)
LCIL	low concentration ignition limit
L/D	length-to-diameter ratio
LED	light-emitting diode
LEFM	linear-elastic fracture mechanics
LOC	explosion proof limit oxygen content
ln	natural logarithm (base e)
log	common logarithm (base 10)
m	matrix; meter
m	ion mass; Weibull modulus
M	metal atom
M	molecular weight
MA	mechanical alloying
mA	milliampere
MeV	megaelectronvolt
NDT	nondestructive testing
mg	milligram
Mg	megagram
MIM	metal injection molding
min	minimum; minute
MJ	megajoule
mL	milliliter
MLCCs	multilayer ceramic capacitors
MILT	marketing lead time
mm	millimeter
MMC	metal-matrix composite
mod	modified
mol%	mole percent
MOR	modulus of resilience; modulus of rupture
mPa	millipascal
MPa	megapascal
mpg	miles per gallon
mph	miles per hour
MPIF	Metal Powder Industrial Federation
ms	millisecond
MS	megasiemens
MSDS	material safety data sheets

mT	millitesla
MTBT	mean time between failures
MTTF	mean time to failure
mV	millivolt
MV	megavolt
MW	molecular weight
n	growth exponent
n	integral number
N	Newton
N	fatigue life (number of cycles)
NAERG	North American Emergency Response Guidebook
NASA	National Aeronautics and Space Administration
NBS	National Bureau of Standards
NC	numerical control
NDE	nondestructive evaluation
NDI	nondestructive inspection
mg	milligram
Mg	megagram
MIM	metal injection molding
NFPA	National Fire Protection Association
NIOSH	National Institute for Occupational Safety and Health
NIST	National Institute of Standards and Technology
NJDHSS	New Jersey Department of Health and Senior Services
nm	nanometer
No.	number
NSS	near-net shape
OD	outside diameter
ODS	oxide-dispersion strengthened
Oe	oersted
OELs	occupational exposure limits
OHA	operating hazards analysis
ORNL	Oak Ridge National Laboratory
OSHA	Occupational Safety and Health Administration
oz	ounce
p	page
p	pressure
Pa	pascal
PCA	process control agent
PCE	pyrometric cone equivalent
PDS	product design specification
PDT	product design team
PEL	permissible exposure limit
P/F	powder forging
pH	negative logarithm of hydrogen-ion activity
PM	powder metallurgy
ppb	parts per billion
ppba	parts per billion atomic
ppm	parts per million
ppt	parts per trillion
Pr	Prandtl number
psi	pounds per square inch
PTC	positive temperature coefficient
PVD	physical vapor deposition
QC	quality control; quasicrystals
QLD	quality loss function
r	radius vector in a plane normal to the axis
r	particle radius; radius of curvature; rate of reaction; reflectivity; spherical particle radius
R	roentgen

R	average particle radius; gas constant; radius; ratio of the minimum stress to the maximum stress; resistance; reliability
$\mathrm{R_a}$	surface roughness in terms of arithmetic average
RA	reduction of area rad absorbed radiation
rad	absorbed radiation dose; radian
Re	Reynolds number
REM	rare earth metal
Ref	reference
rem	remainder
rf, RF	radio frequency
RH	relative humidity
rms, RMS	root mean square
rpm	revolutions per minute
RS	rapid solidification
RT	room temperature
RTI	relative thermal index
s	second
S	siemens
S	distance traveled
SAE	Society of Automotive Engineers
scfm	standard cubic foot per minute
SCOEL	Scientific Committee on Occupational Exposure Limits
SEM	scanning electron microscopy
sfm	surface feet per minute
SG	standard grade
SI	Système International d'Unités
sineh	sine hyperbolic
S/N	signal-to-noise (ratio)
S-N	stress-number of cycles
SPC	statistical process control
sp gr	specific gravity
SPF	superplastic forming
std	standard
STEM	scanning transmission electron microscopy
STM	scanning tunneling microscopy
t	thickness; time
T	Tesla; transverse direction
T	absolute temperature; temperature; tenacity; total dispersion; transmittance
T_m	melt temperature
TEM	transmission electron microscopy
TGA	thermogravimetric analysis
TLVs	threshold limit values
TM	threshold limit values; transition metal
TMA	thermomechanical analysis
TMS	The Minerals, Metals, and Materials Society
TP	thermoplastic
TQM	total quality management
TWA	time-weighted average
USBM	US Bureau of Mines
NJDHSS	US New Jersey Department of Health and Senior Services
UTS	ultimate tensile strength
UV	ultraviolet
v	velocity; workpiece
V	volt
VAMI	Russian National Aluminum-Magnesium Institute
VD	vacuum degassing
VHP	vacuum hot pressing
V_f	volume fraction of fiber
V_m	volume fraction of matrix

V_v	volume fraction of void content
VI	viscosity index
vol	volume
vol%	volume percent
W	watt
W	total radiation; width
WA	water atomization, water atomized
WELs	workplace exposure limits
wt%	weight percent
x	axial distance
X	neck diameter
XRD	X-Ray diffraction
Y	scale of microstructural segregation
yr	year
YS	yield strength
z	ion charge
Z	atomic number; impedance
0	angular measure; degree
^{0}**C**	degree Celsius (centigrade)
^{0}**F**	degree Fahrenheit
0^{0}	fiber direction
90^{0}	perpendicular to fiber direction
α	coefficient of thermal expansion
γ	shear strain; surface energy; surface tension
γ_b	interfacial energy
δ	an increment; a range; change in quantity; grain boundary width; median diameter
Δ	an increment; a range; change in quantity
ΔT	temperature difference or change
ε	strain
$\dot{\varepsilon}$	strain rate
ζ	local resistance to flow of gas (air)
η	loss coefficient; viscosity
θ	angle; geometrical constant
θ_i	angle of incidence
θ_r	angle of refraction
κ	dielectric constant
λ	thermal conductivity
μ	friction coefficient; linear attenuation coefficient; magnetic permeability
μin	microinch
μm	micrometer (micron)
μs	microsecond
ν	Poisson's ratio; velocity
π	pi (3.141592)
ρ	density; resistivity
σ	Stefan-Boltzmann constant; strength; stress; tensile stress; tensile strength
σ_a	applied stress
σ_f	applied axial load
Σ	summation of
τ	shear stress
ϕ	angle of internal friction; dihedral angle; porosity; power
Φ	reaction rate (kinetic function); volume concentration of impurity ions
ψ	damping; geometrical constant
ω	frequency
Ω	atomic volume; electrical conductivity; molecular volume of solute; ohm
∂	partial derivative
$\partial\eta/\partial t$	kinetic function
$\leftrightarrow$	direction of reaction
$=$	equals

≈	approximately equals
≠	not equal to
≡	identical with
>	greater than
>>	much greater than
≥	greater than or equal to
∞	infinity
∝	is proportional to; varies as
∫	integral of
<	less than
<<	much less than
≤	less than or equal to
±	maximum deviation
−	minus; negative ion charge
×	diameters (magnification); multiplied by
·	multiplied by
/	per
%	percent
+	plus; positive ion charge
√	square root of
~	approximately; similar to

GREEK ALPHABET

Α, α	alpha
Β, β	beta
Γ, γ	gamma
Δ, δ	delta
Ε, ε	epsilon
Ζ, ζ	zeta
Η, η	eta
Θ, θ	theta
Ι, ι	iota
Κ, κ	kappa
Λ, λ	lambda
Μ, μ	mu
Ν, ν	nu
Ξ, ξ	xi
Π, π	pi
Ρ, ρ	rho
Σ, σ	sigma
Τ, τ	tau
Υ, υ	upsilon
Φ, φ	phi
Χ, χ	chi
Ψ, ψ	psi
Ω, ω	omega

Index

Note: Page numbers followed by *f* indicate figures and *t* indicate tables.

A

Acoustic properties of metallic foam materials
  pressure fluctuation, 345
  sound absorption, 345
  sound dissipation, 345
  vibration, 345
Additive manufacturing (AM)
  additive manufacturing processes, 377*t*, 379*t*
  applications of additive manufacturing, 384–395
  direct energy deposition (DED), 375–376
  heat source:nomenclature for electron beam (EB), 363
  heat source:nomenclature for gas metal arc (GMA), 363
  heat source:nomenclature for laser (L), 363
  heat source:nomenclature for plasma arc (PA), 363
  powder bed fusion (PBF), 375–376
  powders for additive manufacturing processes, 376–383
  principles for additive manufacturing, 374–375
  selective laser melting (SLM), 375
  standard guide for characterizing properties of metal powders used for additive manufacturing processes, 933–934*t*
ADMA Product Inc., 558
Admissible concentration limit of lead in aqueous medium, 857
All-Russian Light Alloys Institute (VILS), 490
Aluminized explosives
  air blast, 478
  “Alex$^{®}$”, 477
  aluminothermic reduction, 478
  ammonal, 477
  ammonium perchlorate, 478
  antidetonants, 478
  aquarium tests, 477
  bubble energies, 477
  detonation pressure, 477–478
  detonation products, 477–478
  detonation temperature, 478
  energetic materials, 477
  explosion fireball, 478
  expanding detonation products, 478
  expansion of gases, 477
  exploding wires in nitrogen atmosphere, 477–478
  explosive transformation, 477
  flame temperature, 477
  high chemical activity, 477–478
  high-energy carrier, 477
  high explosives, 477–478
  incendiary effects, 477
  industrial explosives, 477
  nanometric aluminum powder, 477
  PBX compositions, 477
  plasmochemical method, 477–478
  plastic-bonded explosives, 477
  plate dent depth tests, 477
  pyrotechnic flakes, 477
  reducing agent, 478
  rock ammonites, 477
  rocket propellants, 477
  shock compressibility, 477
  shock wave loading, 477
  shock wave reflection, 477
  small-scale performance testing, 477
  spherical particles, 477
  surface of Al particles, 477
  surface temperature, 478
  thermite mix, 478
  trinitrotoluene (TNT), 477–478
  velocity of detonation, 477
  ultrafine aluminum powder, 477
  underwater weapons, 477
Aluminothermic reduction
  burning temperature, 478
  polymerization of ethyls, 478
  production of aluminum alkyls, 478
  thermite mix containing, 478
Aluminum
  aluminum groats, 478
  high-purity aluminum, 478
  porous aluminum, 478
  technical-purity aluminum, 478
Aluminum alloy powder production by water atomization
  aluminum hydrate, 505
  Al–Mg system alloys, 516–520
  aluminum oxide hydroxide, 505
  aluminum oxide surface film, 505
  Al–Zn–Mg system alloys, 518
  boehmite film, 505
  contact-convection drying process, 505, 507, 509–510
  conduction–convection drying, 505, 507, 509–510
  conductive drying, 509
  conductive vacuum drying, 509
  elevated temperature aluminum alloys, 513–515
  gas emission kinetics, 507
  high-strength aluminum alloy, 505
  high-strength quaternary system, 507
  hydraulic size classification, 505
  hydroclassification, 508*f*, 510
  hydrogen ion control, 505
  inhibitors from the group of weak electrolytes, 505
  interparticle boundaries, 505
  oxide film, 505, 507
  pilot plant of IPMS, 507, 518
  recycling of secondary aluminum, 511–513
  surface oxide film, 505, 506*f*
  suspended powder, 507
  suspension temperature, 505
Aluminum and magnesium alloys (applications of additive manufacturing)
  building direction, 385
  built part, 384–385, 386*f*
  cell size, 385
  cell spacing, 385
  cooling rate, 385
  Elektron MAP+43, 386
  energy density, 387
  evaporation temperature, 386
  gas pore, 385
  heat input, 387
  laser beam machining process, 385
  laser powder bed processing, 385
  laser power, 386–387
  laser scanning speed, 387
  layer height step, 386
  layer thickness, 386–387
  Magnesium Elektron powder grade, 386
  near-eutectic composition, 385
  powder flow rate, 386
  powder particles sphericity, 384–385
  laser pulsed input, 387
  rapidly solidified, 385–386
  scan speed, 386
  select laser melting (SLM), 386–387
  shielding gas, 386, 390
  solidification range, 385
  stereological effect, 385
  thermal conductivity, 385
  transition metals, 385–386
  travel speed, 386
  thin layers of metal powder, 385–386
  ytterbium fibre laser, 385–386

Aluminum based composite
  accumulative roll bonding (APB) process, 364
  alumina nanofibres, 364
  aluminum carbide phase, 364
  aluminum matrix composites, 364
  aluminum metal composites (AMCs), 363–364
  aluminum titanium dioxide composites, 364
  ball milling, 364
  introduction of nanodiamond, 364
  reinforcing particles, 364
  repetitive press roll bonding (RPRB), 364
  severe plastic deformation (SPD), 364
  titanium dioxide (TiO_2) particles, 364
Aluminum based composite powders
  aluminum matrix composite powders, 352
  aluminum oxide films, 354
  boron carbide, 353
  cells, 352–353
  cryomilling technique, 353
  gas and water atomized powders, 352
  hot extrusion, 352
  interfacial debonding, 353
  mechanical alloying (MA), 352
Aluminum oxide surface film
  boehmite film, 505
  interparticle boundaries, 505
  main metallic surfaces, 505
  non-uniform in thickness, 506*f*
  particles surface, 505
  interparticle boundaries, 505
  segregation zones, 505
  three-dimensional film islets, 505
  uneven surface, 505
Aluminum scrap recycling
  crushing in cutting units, 474
  dry crushing, 474
  foil processing, 474
  grit, 474
  processing of recycled aluminum to granules, 477
  production of powder products from waste aluminum foil, 474
  recycling of aluminum scrap, 474
  waste aluminum foil, 474–476
  waste products, 474
  wet crushing, 474
Al–Mg system alloys
  additions of scandium, zirconium, chromium, 516
  mechanical properties, 516
  non-heat treatment alloys, 516
  PM/WA alloys, 516, 520
  precipitation hardening, 516
  Scalmalloy 0.7, 516
  solid–solution hardening, 516
  transition metals, 516
  weldable alloys, 516
Al–Zn–Mg system alloys
  cooling rate, 516–518
  corrosion cracking point, 516–518
  corrosion cracking resistance, 516–518
  chromium doping, 520
  formability, 516–518
  doping elements, 520
  doping refractory metals, 520
  G/T alloy 1970, 518
  Guinier–Preston zones, 520
  heat-treatable alloys, 516–518
  hot extrusion of billets, 518
  mechanical properties, 518
  non-dendritic grains, 518
  rod extrusion, 518
  pulsed forging, 518
  rare earth metals, 516–518
  rod extrusion, 518
  scandium addition, 520
  structural materials, 516–518
  transitional refractory metals, 516–518
  PM/WA technology, 518
  weldability, 516–518
  wrought alloys, 520
Amalgam metallurgy methods
  amalgam cementation of a more negative metal, 263
  electrolyzer with amalgam bipolar electrodes, 266
  mercury electrode, 263
  Nernst equation, 263–265
  nuclei crystallization, 265
  oversaturated amalgams, 263
  standard potential, 265*t*
Amalgam metallurgy technique (production of titanium and titanium alloy powders)
  black powder, 562–563
  electrolysis with mercury cathode, 562
  inert atmosphere, 562
  mercury, 562–563
  mercury cathode, 562
  sodium amalgam, 562
  sodium chloride, 562–563
  titanium chlorides, 562–563
  titanium crystals, 562–563
  titanium sponge, 562–563
  vacuum furnace, 562–563
Amalgam techniques
  agitated mercury cathode, 681
  anode and cathode current densities, 681
  electric precipitation of cobalt, 681
  soluble cobalt anode, 681
  sulfate electrolyte, 681
Angle of repose
  factors influencing on angle of repose, 56
  measuring the angle, 55
  ultimate angle, 55
Anticorrosive zinc-rich coatings for roll and sheet steel metal ware
  DACROMET, 630
  GEOMET, 630
  PLAS, 630
  ZINCOMET, 630
Anthrahydroquinone, 646, 671
Anthraquinone, 228, 646, 651–652, 671
Apparent density, 3, 47, 49–51, 50*t*, 53*t*, 119, 555–556, 577, 585, 588, 598, 642*t*
Apparatuses for powder analysis
  Analisette 22 Nano Tec Plus, 60*t*
  ASAP 2020, 60*t*
  AutoPore IV 9500, 60*t*
  FlowSorb III, 60*t*
  Master Tech 052 Autosampler, 60*t*
  Microtrac S3500 particle size analyser, 60*t*
  Multisizer 4 Coulter Counter, 60*t*
  Multivolume pycnometer 1305, 60*t*
  Tristar 1000, 60*t*
  Saturn Digisizer 5205, 60*t*
  Sedigraph III PLUS particle size analyzer, 60*t*
Application fields for aluminum powders
  aluminum alloy powders, 478
  aluminum alloys, 478
  aluminum-based elevated temperature alloys, 513–515
  aluminum-based high strength alloys, 478
  aluminum granules, 478
  aluminothermic reduction, 478
  automobile tires, 479
  cold solder, 479
  constructional materials, 478
  energetic materials, 477
  explosives, 477–478
  ferrous metallurgy, 478
  filler material in plastics, 479
  increase the thermal resistance and mechanical strength of refractory material, 479
  lubricant in producing ceramic details, 479
  production of high density refractory materials, 479
  production of porous adsorption materials for cryogenic equipment, 479
  production of a welding wire and cutting emulsions, 479
  protective rubber, 479
  pyrotechnic, 477
  rocket propellants, 477
Applications of additive manufacturing
  aluminum and magnesium alloys, 384–387
  nickel base alloys, 392–395
  titanium alloys, 387–392
Applications of beryllium, 807–810
  aerospace applications, 808
  apparatus applications, 808
  beryllium alloys, 808–810
  high temperature conditions, 808
  optical beryllium grades, 808
  nuclear and x-ray applications, 807–808
Applications of chemically reduced powders and sols
  catalyst, 225
  chemically reduced metal, 225
  colloid adsorption, 225
  metal colloid, 225
  metallized dispersed carrier, 225
  preliminary activation, 225
  reducer solution, 225
  salt, 225
  selective precipitation, 225
Applications of nanomaterials
  cemented carbides, 300–302
  electrical storage systems, 306–307
  fibre-reinforced material, 302
  gradient materials, 302–303

  miniaturized systems, 307
  nanopowder–polymer composites, 303–304
  semiconductors, 305–306
  thin film technique, 304–305
  vapor deposition in vacuum, 297–300
Applications of thorium
  antireflection material, 823
  alloying in alloys, 823
  catalyst compositions, 824
  electronic tubes, 823
  gas mantles, 823
  gas tungsten arc welding, 823
  heat-resistant ceramics, 823
  high-quality lenses, 823
  Incandescent filaments, 823
  organic synthesis, 824
  TD–Ni alloy, 823
  thoriated tungsten wires, 823
  thorium dioxide, 823–824
  tungsten thermocathodes, 823
Aqueous solution method
  photoluminescence (PL), 306
  photoluminescent nanoparticles, 306
  surfactants, 306
  syntheses of highly photoluminescent semiconductor nanoparticles, 306
  thioglycerol, 306
  thioglycole acid, 306
Archimedes' law, 42–43
Armstrong process
  continuous process, 550–551
  Cristal Metals Inc., 550–551
  International Titanium powders (ITP) process, 550–551
  liquid sodium, 550–551
  reduction of titanium tetrachloride with sodium, 550–551
  sodium chloride, 550–551
  sodium stream, 550–551
  solid titanium powder, 550–551
Aspiration in combustible powder conditions
  cascade equipment location, 897
  chemically active metals, 897
  closed-loop shielding gaseous change system, 897
  controlled protective atmospheres, 897
  film-forming composition, 897
  organosilicon compound, 897
  shielding gas, 897
  silico calcium powder, 897
  surfactant, 897
  transportable containers, 897
Atomic adsorption spectrometry (AAS)
  flame atomic absorption spectrometry, 36
  flame atomic emission spectrometry, 36
  flame atomic fluorescence spectrometry, 36
Atomic-force microscopy (AFM)
  cantilever, 275–276
  contact mode, 275–276
  frequency modulation, 276
  measuring the tip-to-sample distance, 276
  non-contact mode, 276
  oscillation, 276
  tapping mode, 276
  tip (probe), 276
Atomization
  centrifugal atomization, 167–172
  explosive atomization, 176–177
  flame spray pyrolysis, 176–177
  gas atomization, 143–167
  impact atomization, 173
  impulse atomization method, 173–174, 174*t*
  hot gas atomization, 165–166
  melt drop orifice technique, 173–175
  melt drop vibrating orifice method, 174
  oil atomization, 142
  plasma atomization process, 175
  pulsated orifice ejection method, 174–175
  roller atomization, 175
  vacuum-dynamic atomization, 167
  vibrating electrode atomization, 173
  water atomization, 128–142
Atomization and granulation
  atomization, 125–177
  granulation, 177–181
Atomization mechanism
  models of gas atomization, 149–158
  water atomization mechanism, 128–142
Atomization of copper alloy powders, 576–581
Atomization of copper powder, 572–576
Atomized nickel alloy powders
  gas atomization, 655
  hardfacing powders, 652–654
  hardfacing process, 652
  Haynes alloy 176, 654
  water atomization, 652
Atomized powders of cobalt-base alloys
  atomization, 674–676
  carbide-containing alloys, 674–675
  cellular structure, 676, 677*f*
  cobalt-base matrix, 674–675
  elevated temperature hardness, 675
  gas atomization, 675–676
  hardfacing applications, 674–675
  hardfacing powders, 674
  interdendritic eutectic carbide, 676
  Laves phase, 674–675
  melt spinning, 676
  nontransferred arc, 676
  plasma transferred arc, 676
  plasma transferred arc hardfacing process, 676, 676*f*
  plasma spray coating, 674–675
  plasma spray hardfacing, 674–675
  solid–solution strengthening, 676
Attritors
  attritor in horizontal performance, 97–98, 98–99*f*
  batch attritors, 97
  circulation attritor system, 102
  continuous mode, 101–102
  dry grind attritors, 101–102, 103*f*
  high speed attritors (HAS), 101–102
  laboratory Simoloyer attritors, 99*f*
  Netzsch attritors, 98, 98*t*, 101
  Union process attritors, 98, 99*f*
  vertical attritors, 97, 97*f*
Auger electron spectroscopy (AES)
  Auger effect, 30–31
  Auger electrons, 31
  electron transition process, 31
Autoclave(s)
  discharging units, 231
  double-pipe heat exchanger, 230–231
  horizontal autoclaves, 230
  mechanical stirring, 230
  powder pulp transportation, 231
  process characteristics control, 230
  protective cladding, 230
  safety fittings, 230
  self-evaporator, 230–231
  thermal protection, 230
  vertical autoclaves, 230
Autoclave precipitation of metal powders
  autoclave, 226–227
  autoclave precipitations of metal powders from organic phases, 230
  autoclave processing of hydroxide and metal carbonate pulps, 229
  hydrodynamics, 227
  hydrogen reduction, 225
  reaction gas pressure, 227
  safety engineering, 231
  seed, 228
  Sherritt process, 225
  solution composition, 228
  surfactants, 228–229
Autoclave precipitations of metal powders from organic phases
  contamination, 230
  extraction-precipitation cycle, 230
  fire-risk, 230
  leaching-extraction process, 230
  organic phase, 230
  organometallic phases, 230
  power-consumption, 230
Autoclave processing of nickel hydroxide and carbonate pulps
  alkaline accumulators, 651–652
  ammonia–carbonate leaching, 652
  ammonium–carbonate solution, 651
  aqueous carbonate pulp, 651–652
  nickel hydroxide aqueous, 652
  nickel seed powder, 651
  palladium chloride, 651–652
  reduction of aqueous carbonate pulp, 651–652
Autoclave processing of hydroxide and metal carbonate pulps
  catalytically active powders, 229
  dissolved hydrogen concentration, 229
  hydrothermal conditions, 229
  metal hydroxide, 229
  metal hydroxide solubility, 229
  narrow size distribution, 229
  roundish shape particles, 229
Average pressure carbonyl technique
  carbon monoxide carrier gas, 637
  carbonyl sublimates, 637
  Copper Cliff refinery, 637, 637*f*
  elevated pressure, 637, 637*f*
  high copper concentration, 637

Average pressure carbonyl technique *(Continued)*
  nickel pellet, 637
  nickel tetracarbonyl vapor, 637
  slightly above atmospheric pressure, 638
  sulfides of nickel, 637

B

Beryllium
  applications of beryllium, 807–810
  beryllate ($MeBeO_2$), 798–799
  beryllium carbide, 798, 804
  beryllium compounds, 798–799
  beryllium nitride, 798
  beryllium oxide, 798
  beryllium oxide powder production, 804
  beryllium powder production, 801–804
  electrolysis from chloride electrolyte, 800–801
  gas atomization, 802–803
  grinding, 801–802
  hexagonal beryllium crystals, 798
  magnesium thermal reduction of beryllium fluoride, 800
  microalloying influences, 804
  powder consolidation and production of wrought products, 804–806
  production of leafed beryllium by electrorefining of melts, 801
  sources of raw material, 800
  workplace atmosphere safety, 810
  wrought beryllium, 798, 807*t*
  wrought product forms, 806–807
Beryllium alloys
  AlBeMet, 808
  aluminum–beryllium–lithium alloys, 808, 809*t*
  E-material metal-matrix composite, 810
Beryllium oxide powder production, 804
  beryllia ceramic, 804
  beryllium hydroxide, 799–800, 804
  beryllium sulfate crystals, 804
  calcining in air, 804
Beryllium powder production
  beryllium oxide powder production, 804
  gas atomization, 802–803
  grinding, 801–802
  microalloying influences, 804
Biomedical implants, 328, 346, 546
Brass powders, 576
Bronze powders, 324, 577–581
Bubble test of pore size
  air bubbles discharge, 46
  first air bubble, 46
Bulk analysis
  atomic adsorption spectroscopy (AAS), 36–38
  determination of oxygen content by reduction methods, 38
  inductively coupled plasma atomic emission spectroscopy (ICP-AES), 36
  inert gas fusion, 35
  x-ray fluorescence spectrometry, 35–36
  x-ray powder diffraction (XRPD), 33–35
Bulk density
  apparent density, 49–50
  Funnel method, 51
  Scott volumeter, 51–52
Bulk properties of powders
  angle repose, 55–56
  bulk density, 49–52
  flow rate, 54
  fluidization, 55
  frictional properties, 48–49
  multiaimed powder tester, 57
  screening model (also called sifting phenomenon), 54
  segregation of particles, 54
  sliding at impact point, 54
  tap density, 52–53
  trajectory effect, 54
Bayer process
  alumina production, 818
  high content of scandium, 818
  red mud, 818

C

Cadmium powder, 625–628
Calcination-reduction-carburization (CRC) process, 707–709, 711
Calcium hydride reduction process, 550, 553, 568*t*
Capacity of local suctions
  mass balance equation, 896
  leakinesses (openings), 896–897
  local exhaust, 896–897
  resistance coefficients, 896–897
  underpressure in aspiration cover, 896–897
Carbon nanotube (CNT) reinforced metal composite powders
  acid-treated CNTs (ATCNTs), 357
  aluminum alloy matrix, 357
  aluminum carbide (Al_4C_3) crystals, 357
  carbon nanotubes (CNTs), 357
  dispersion of CNTs, 357
  multiwalled carbon nanotubes MWCNT, 357
Carbonyl method for cobalt powder production
  black cobalt powder, 678
  carbon monoxide, 678
  carbonyl decomposition, 678
  cobalt carbonyl, 678
  halide salts, 676–678
  hydrogen atmosphere, 678
Carbonyl process of nickel powder production
  average pressure carbonyl technique, 637–638
  Clydach refinery, 634–635, 636*f*
  health and environment protection measures in carbonyl nickel production, 638
  high pressure carbonyl technique, 638
  low pressure carbonyl technique, 635–636
  Ludwig Mond, 633
  Mond–Langer process, 635
  nickel tetracarbonyl, 633
  nickel tetracarbonyl formation and decomposition, 634–635
  Norilsk Nickel Company, Russia, 635
  powder properties an applications, 638–644
Carbothermic method (production of RE metal-alloy powders)
  cooled condenser, 788
  dissociation of carbide in vacuum, 788
  lanthanide carbide, 788
  reduction of lanthanide oxide by carbon, 781
  sublimation of lanthanide, 788
  surplus carbon, 788
Carney funnel, 51–52
Cemented carbides
  gas phase carburization, 301
  grain growth preventing, 301
  high energy milling, 301
  mechanochemical synthesis, 301
  Nanodyne Process, 301
  nanostructured cemented carbides, 301
  WC–Co powders, 301–302
Cemented tungsten carbides
  cemented carbides with low and medium carbon levels, 798
  mischmetal, 798
  RE-doped cemented carbides, 798
Centrifugal atomization methods, 169–172
  melt spinning centrifugal atomization, 125
  melt spinning roller technique, 171–172
  models of centrifugal atomization, 167–169
  rapid solidification rate (RSR) process, 171
  spinning disc atomization, 169–171
Centrifugal pumping system
  analyze agglomerating samples, 21
  rapid flow rate, 21
  rotating electrode atomization, 172
Chemical precipitation from solution
  chemical precipitation, 221
  coexistence with water, 221
  oxidation–reduction reaction, 221
Chemical reduction
  application of chemically reduced powders and sols, 225
  chemical precipitation from solutions, 221
  kinetics of solid phase formation in solution, 223–225
  thermodynamic peculiarities of metal chemical reduction, 221–222
Chemical reduction (production of titanium and titanium alloy powders)
  Armstrong process, 550–551
  calcium hydride reduction process, 553
  hydrogenation/dehydrogenation (HDH) process, 553–554
  magnesium reduction method (Kroll process), 551–553
  sodium reduction method (Hunter process), 550
Chemical synthesis of nano size titanium powders
  argon atmosphere, 565
  chemical methods, 565
  hydrogen atmosphere, 565
  ilmenite, 565
  titanium catecholate/gallate, 565
  titanium hydride, 565
  vacuum dehydrogenation, 565

Chemical vapor deposition (CVD) process
  aerosol assisted CVD (AACVD), 197
  aluminum and copper deposited by CVD, 198
  atmospheric pressure CVD (APCVD), 197
  chemical vapor infiltration, 302
  CVD for refractory metals, including molybdenum, tantalum, niobium, and rhenium, 198
  direct liquid injection CVD (DLICVD), 197
  installation for deposition by CVD technique, 198*f*
  metal carbonyl gas, 198
  microwave plasma-assisted CVD (MPCVD), 197
  low-pressure CVD (LPCVD), 197–198
  parallel-plate reactor of plasma enhanced CVD process, 199*f*
  plasma-enhanced CVD (PECVD), 197–198
  refractory metal foams, 198
  remote plasma-enhanced CVD (RPECVD), 197
  tungsten hexafluoride, 197–198
  ultrahigh vacuum CVD (UHVCVD), 197
  volatile precursors, 197
  wear-resistant and thermostable covering, 198
Chinuka process
  cheap, 560
  directly treat impure ores, 560
  high-purity metals, 560
  impure metal oxides, 560
  low operating temperature, 560
  low power consumption, 560
  nontoxic electrolyte, 560
  single process, 560
Classification in centrifugal field
  Bahco classifier, 17
  cyclone classifier, 17–18
Classification in gravitational field, sedimentation method, 13–16
Closed-cell materials, 338–346
Closed-cell metallic foams, 330–333
  foaming of ingots containing blowing agents (Formgrip/Foamcast), 332
  foaming of melts by gas injection (Hydro/Alcan), 331–332
  foaming of melts with blowing agents (Alporas), 330–331
  solid–gas eutectic solidification (Gasar), 332
Coating steel products
  enamels, 478
  paints, 478
  plasma spraying, 478
  protect products, 478
  protective pigment, 478
  thermal diffusion, 478
  silvery color, 478
  spray deposition, 478
  varnishes, 478
Cobalt
  amalgam techniques, 681
  atomization, 674–676
  carbonyl processing, 676–678
  cobalt-alloy powders, 678–680, 680*t*
  coating, 673
  electrolytic techniques, 678–680
  hardmetals, 673
  health and environment protection measures, 683–684
  hydrometallurgical process, 669–673
  leach autoclave method, 669–673
  production of cobalt and cobalt alloy powders by electrolysis, 678–680
  ultrasonic spray pyrolysis (USP), 681–683, 683*f*
Cohesive strength
  arch form, 47–48
  consolidation pressure, 47–48
  hollow form, 47
  Jenike apparatus, 47–48, 48*f*
  shear normal stress, 48
  shear stress, 48
  shear tester, 47–48
  stagnant zones, 47
  yield locus, 48
Cold isostatic pressing and extrusion (beryllium and beryllium comprising alloy powders)
  copper mold, 806
  cylindrical shape, 806
  extruded AlBeMet rod and bar, 806
  taper die, 806
Cold isostatic pressing and sintering (beryllium powder)
  CIP chamber, 806
  cold isostatic pressing (CIP), 806
  green preforms, 806
  latex bag, 806
  near-net shape (NNS), 806
  nuclear limiter tiles, 806
  vacuum mold, 806
  vacuum sintered, 806
Coldstream process, 722
Combustion synthesis of zirconium nitrides
  conducting materials, 771
  electronic application, 771
  phosphorus, 771
  refractory corrosion-resistant coatings, 771
  single-phase supersaturated solutions, 771
  stoichiometric compound, 771
Compaction methods
  centrifugal slurry casting, 326
  cold welding, 325
  die compaction, 325
  direct typing method, 326
  extrusion, 326
  gravity sintering process, 325
  isostatic pressing, 325
  laser deposition by direct typing, 326
  lower compaction forces, 325
  roll compaction, 325–326
  wet powder spraying, 326
Composite manufacturing methods
  coprecipitation, 363
  hybrid consolidation nanotube (CNT), 363
  internal oxidation, 363
  powder metallurgy methods, 363
  press sinter-extrude, 363
Compressibility
  compacting pressure, 57–58
  lubricants, 57–58
  lubrication techniques, 57–58
  powder lubrication method, 57–58
  theoretical density, 57
  wall lubrication, 57–58
Compressibility and compactibility of metal powders
  compactibility, 57
  compressibility, 57–58
  green strength, 58–59
  dendrite deposit, 238
  dendrite growth rate, 238
  specified green density, 57
  unsintered ("green") compacts, 57, 59, 59*f*
3D Computer-added design (CAD), 375, 566–567, 664–666
Conforma Clad Process, 714
Consolidation and manufacturing of molybdenum semi-products
  alloying additions, 747
  cold isostatic pressing, 746
  corrosion-resistant heat exchangers, 747
  nonisothermal sintering, 746
  interstitial impurity elements, 746
  microalloying additions, 747
  preventing embrittlement, 747
  volatile silicon monoxide, 747
Contact displacement method (cementation)
  cementing metal (precipitator), 254–256
  chemical treatment, 258
  complexing ligands, 257–258
  diffusion control, 255–257
  electrolytic precipitation, 254–258
  flat growth front, 257–258
  heterogeneous reaction, 254
  potential of reduction reaction, 255
  precipitable metal, 255–256
  precipitation rate, 256
  spherical diffusion on the tips, 256
  tangential growth, 255–256
  tangentially spread film, 256
  tip radius, 255, 257
Contact displacement reactions
  combustion reaction, 108–109
  conjugated dissolution, 108
  critical milling time, 108
  diffusion process, 108
  fracturing of powder particles, 108
  gradual conversion, 108
  high surface defects, 108
  ignition time, 108–109
  interparticle welding, 109
  preventing the risk of explosion, 108
  reactive reductant, 108–109
  self-propagating combustion reactions, 109
  welding of powder particles, 108
Contact-convection drying process
  conductive vacuum drying, 509
  dryer, 507, 509, 509*f*
  drying agent, 507, 509–510
  explosion safety, 507
  heat-and-mass transfer, 507
  loosener, 509

Contact-convection drying process *(Continued)*
  maximum permissible temperature, 509–510, 510*f*
  particle aggregates, 507, 509
  self-ignition danger, 509–510
  specific humidity, 509–510, 510*f*
Copper alloy powders, 571–612
Copper based composite powders
  carbon nanostructures, 364–365, 365*f*
  carbon nanofibres (CNFs), 364–365
  carbon nanotubes (CNTs), 364–365
  chemical vapor deposition (CVD), 365
  copper-based metal matrix composites (MMCs), 364
  copper-graphite composites, 364–365
  copper matrix composites, 354, 366
  copper powder, 365
  copper reinforcement, 353–354
  dispersed oxides particle, 354
  high energy ball milling, 354, 354*f*
  internal oxidation, 366
  mechanical alloying, 366
  nanocrystalline alloy, 353–354
  reinforcing component, 364–365
  sliding electrical contacts, 364–365
Copper powder, 571–612
Copper precipitation
  from ammonia media, 599–600
  from organic phases, 600
  from sulfuric acid media, 595–599
Copper precipitation in industrial electrolysis
  advanced control method, 245
  cathode rod, 245
  cell section, 245
  cell voltage, 248
  commercial electrolytic cell, 245, 248
  crusting effect, 245
  dendritic copper powder, 245
  dendritic copper sediment, 245
  deposition period, 245–248
  electrolysis efficiency, 245
  electrolysis process, 245
  electrolyte, 248
  formation of copper sediment, 245
  galvanostatic conditions, 245
  globular tips, 245
  growth front, 245–248
  hydrogen bubbles, 245
  kinetics of electrolysis process, 245
  near-electrode space, 245, 249–250
  overpotential, 245–248, 247*f*
  patentiostatic conditions, 245–248
  spherulite, 245
  structural parameter, 245, 247*f*
  Uralélektromed' Joint Stock Company, 245
  video recording of copper deposit growth, 245
Coulter counter
  aperture format, 21–22, 22*f*
  aperture sizes, 22
  continuous sample analysis, 22
  flow cell format, 21
  flow channel, 22
  orifice in electric field, 21–22
  particle traversing the orifice, 21
  suspended particles, 21
  suspension vessel, 21
  voltage pulses, 21
Counting and sizing of particles by indirect measures
  coulter counter, 21–22
  Fisher subsieve sizer, 18–19
  light scattering, 20–21
  turbidimetry, 19–20
Crystallization centers, 224, 260, 468
Crushers
  jaw crusher, 74
  gyratory crushers, 74
  hammer crushers, 74–75
Crushing and grinding. *See* Mechanical crushing and grinding
Cryogenic methods (production of zinc powder)
  frozen aqueous medium, 625
  ultrafine powder, 625
  ultrasonic impact, 625
Crystal defects
  dislocations, 104–105
  stacking faults, 104–105
  vacancies, 104–105
CSIR process
  alkali metal chloride salt, 564–565
  continuous process, 564–565
  CSIR-Ti process, 564–565
  leach liquor, 564–565
  metallothermic reduction, 564–565
  reaction temperature, 564–565
  reactor, 564–565
  relevant salt, 564–565
  residual salt, 564–565
  solidified mass, 564–565
  stirred tank reactor, 564–565

D

Dangerous and harmful manufacturing factors
  abrasiveness, 869
  adhesion, 868
  ambient noise and vibration, 866
  dust, gaseous, and vapor emissions, 866
  heat radiation, 866
  hydroscopic and wettability, 868–869
  inflammability and explosivity of powders, 869–875
  thermophysical properties, 875–879
Dependence the ignitability and explosibility of the gas−suspended solid mixture on the oxygen content in oxidizing gas
  combustible gas−suspended solid mixture, 875
  electric spark, 875
  Four liter IPMS unit, 875
  Godbert–Greenwald furnace, 875
  ignition source, 875
  limiting oxygen concentration (LOC), 875
  minimum oxygen concentration, 875
  permissible oxygen content, 875
Determination of oxygen content
  Karl Fisher's reagent, 38
  reducing tube with closed end, 38
  reduction in hydrogen, 38
  running reducing tube, 38
  stream of pure dry hydrogen, 38
Direct energy deposition (DED)
  computer aided design (CAD), 375
  DED processes, 375
  electric arc, 375
  electron beam, 375
  feedstock material, 375–376
  filler wire, 375
  fusion welding, 375
  laser beam (L), 375–376
  layer-by-layer deposition, 375
  molten pool, 375
  powder stream, 375
  shielding gas, 375
  substrate plate, 375
  3D parts, 375
Dispersing units
  dry dispersing units, 21
  liquid dispersing units, 21
  suspension preparation, 21
  vibratory feeder, 21
  ultrasonic bath, 21
Dust explosion venting
  calculation of rupture diaphragm, 889
  explosion flameless venting, 889–890
  Fike Corpoiration, 891*f*
  flame-quenching unit, 889–890, 890*f*
  flap volve, 890, 891*f*
  float valve, 890, 891*f*
  location of the vent, 888
  maximum explosion overpressure, 887
  passive explosion isolations systems, 891*f*
  pressure venting devices, 887
  rupture diaphragms, 889
  vent, 888–889

E

EDS apparatus
  analyzer, 29
  electron beam/x-ray beam, 29
  Peltier cooling systems, 29
  pulse processor, 29
  Si(Li) detector, 29
  X-ray detector, 29
  X-ray fluorescence spectrometer, 29
Ejection pressure
  aspirated air consumption, 892
  aspiration cover, 892
  aspiration cover with double walls, 892
  belt conveyor reloading, 892, 893*t*, 893*f*
  closed chutes, 892
  ejected air motion, 892
  ejected air velocity, 892
  non-hermetic units, 892
  quasi-interconnected motion, 892
  powder gravitation flow, 892
  reloading from one conveyor to another, 892
  reloading units, 892, 893*t*, 893*f*
Electrical explosion
  electrical explosion of wires technology (EEW), 176, 291–292
  electroexplosive powders, 291, 292*f*
  explosion of aluminum wires in water, 292

- high-voltage pulse, 291
- installation for producing electroexplosive powders, 291, 292*f*
- metal wire, 291
- spherical particles shape, 292

Electrical explosion of wires technology, 176, 291–292
- explosive destruction, 176, 291
- time of explosion, 176, 291
- velocity of product recession, 291

Electrical storage systems
- electric driven vehicles, 306
- gel polymer electrolytes, 307
- large-scale lithium-ion-batteries, 306
- polymer composite electrolytes, 307
- portable electronic devices, 306
- primary batteries, 306
- secondary batteries, 306
- solvent-free polymer electrolytes, 307

Electrochemical methods
- amalgam metallurgy method, 263–267, 265–266*f*
- contact displacement method (cementation), 254–258, 255*f*
- copper precipitation in industrial electrolysis, 245–248, 258*t*
- electrolysis of aqueous solution, 240–254
- physical and chemical principles of electrolytic crystallization of dendrite deposit, 236–240
- production of multicomponent alloy powders, 252–254
- production of powders by electrolysis from melts, 258–262
- reduction from solution through film of surfactants, 248–250

Electrochemical methods (production of RE metal-alloy powders)
- alkaline-earth metal chlorides, 787
- cerium subgroup, 786–787
- electrolysis of molten salt, 786–787
- electrolyte temperatures, 787
- lanthanide chlorides, 787
- mischmetal, 786–787, 787*f*
- non-aqueous RE chlorides, 786–787

Electrochemical methods (production of zinc powders), 621–624
- adatoms, 622–624
- alkaline zincate electrolytes, 622
- cathodic precipitates, 621–622
- columnar structure, 622
- combined mode, 622, 624
- crystalline particles, 621
- dendritic structure, 622
- dendritic zinc deposits, 622, 623–624*f*, 624, 624*t*
- flaky particles, 621
- galvanostatic mode, 622
- honeycomb structure, 622–624
- lamellar structure, 622–624
- polarization modes, 622, 624, 624*t*
- potentiostatic mode, 622
- pulsed galvanostatic mode, 622
- spongy soft precipitates, 621

Electrodeoxidation (EDO) titanium powder process, 558

Electrolysis from beryllium chloride electrolyte, 800–801
- beryllium flakes, 801
- electrolytic cell, 801
- graphite anode, 800–801
- impurities of more electropositive metals, 801
- nickel electrodes, 800–801

Electrolysis of aqueous solution, 235–237, 240–254
- anode current efficiency, 242
- cathode current efficiency, 241–243
- copper precipitation in industrial electrolysis, 245–248
- current density, 240–242
- current load on the electrolyzer, 242–243
- depletion factor, 240–241, 254
- deposit resistivity, 240–241
- diffusion coefficient, 236
- diffusion layer, 241
- electrode potential, 256
- electrolyzer, 240, 242, 243–244*f*
- equilibrium potential, 241
- exchange current density, 237–238
- Faraday constant, 236
- galvanodynamic electrolysis, 241
- galvanostatic, 245
- hydrogen emission, 240
- mechanism of diffusion-limited aggregation of metal particles, 240
- metal ion charge, 241–242
- overpotential, 245
- patentiostatic, 245–248
- polarization, 240–241
- radius of dendrite tip, 241
- rate of dendrite elongation, 260
- solution resistivity, 240–241
- specific surface energy, 241
- tip radius, 239
- transfer factor, 258

Electrolysis of melts (thorium powder production), 821
- chloride–fluoride melts, 821
- hydride process, 821
- lathe turning, 821
- molybdenum cathode, 821
- saw chips, 821
- thorium anode, 821
- thorium chloride, 821
- thorium dihydride, 821
- thorium powder, 821, 822*f*

Electrolysis of titanium compounds, 558–562
- Chinuka process, 560, 560*f*
- electrolytic refining process, 561–562, 561*f*
- FFC-Cambridge process, 559, 559*f*
- MER process, 559, 560*f*

Electrolytic deposition process, 337
- catalytic devices, 337
- deposition, 337
- dissolution, 337
- electrode, 337
- electrically conductive, 337
- electrolytic deposition, 337
- ionic deposition ionic deposition, 337
- Ni–metal hydride batteries, 337
- polymer template cathode, 337
- sputtering, 337

Electrolytic methods for production/refining of zirconium powders
- argon atmosphere, 770
- cathode deposit, 769
- electrolyzer, 768–769, 770*f*
- fluorine ions, 769
- graphite electrodes, 769
- potassium chloride, 768–769
- production of zirconium powders by electrolysis, 768–770
- sodium chloride, 768–769
- sodium dioxide, 768–769
- solidified electrolyte, 770
- zirconium halides, 768–769

Electrolytic refining of titanium, 561–562
- capacity of electrolyzer, 562
- content of impurities, 561
- crystalline titanium, 561

Electrolytic refining process
- electrolyzer of VAMI design, 561
- high purity, 562
- powder purification, 562
- soluble anode, 561, 561*f*
- tetrachloride reduction, 561
- titanium extraction, 562
- titanium scrap, 561
- titanium sponge, 561
- valency of titanium ions, 561
- VAMI institute, 561

Electron beam directed vapor deposition, 337
- axial electron beam gun, 337
- deposition template, 337
- He carrier gas jet, 337
- nickel based superalloy, 337
- polymer foam templates, 337
- thermal decomposition, 337

Electron beam installation, 297–298, 297*f*
- all-purpose electron beam installation UE-209, 297, 297*f*
- electron beam guns, 298
- gun chambers, 298
- working chamber, 298

Electron probe x-ray microanalysis (EPMA), 29–30
- beam of accelerated electrons, 29
- electron microprobes, 29
- energy dispersive spectrometry (EDS), 29
- wavelength dispersive x-ray spectroscopy (WDS), 29–30

Electrons generated by electron beam, 28, 28*f*
- Auger electrons, 28
- backscattered electrons, 28
- elastically scattered electrons, 28, 28*f*
- inelastically scattered electrons, 28, 28*f*
- secondary electrons, 28

Elevated temperature aluminum alloys, 513–515
- alloying with transition metals, 513
- heterogenization, 513
- high-temperature applications, 513–514
- insoluble in aluminum, 513

Elevated temperature aluminum alloys *(Continued)*
  intermetallic phases, 513
  mechanical properties, 513–514, 515–516*t*
  nonequilibrium composition, 513–514
  oxygen content, 514
  pulsed hot pressing, 514
  quasicrystalline phases, 513
  supersaturated solid solutions in aluminum, 513
  vapor deposition method, 513–514
  water-atomized (WA) powders, 514, 515*f*
Energy absorption of metallic foams, 345
  aluminum face sheets, 345
  aluminum foam core, 345
  damping capacities, 345
  elastic modulus, 345
  sandwiches, 345
  stress–strain curve, 345
  vibrational bending test, 345
Energy dispersive spectrometer (EDS), 29
  EDS apparatus, 29
  electron hole, 29
  electron shell bound, 29
  energy dispersive x-ray analysis, 29
  high-energy beam, 29
EO Paton Electric Welding Institute, 281, 297
Evaporation–condensation method (production of zinc powders), 615–620
  combustion chamber, 617
  condensation of zinc vapor, 617
  condensation conditions, 617
  condenser, 617, 619
  electrothermal process, 617, 620*f*
  rectification column, 615, 616*f*, 618*t*
  rectification method, 617
  reverberating furnace, 615
  zinc vapor, 617
Evaporation–condensation process
  adiabate expansion of gas medium, 189
  condensation in vapor jet, 189
  cooled substrate surface, 189
  diffusion condensation, 189
  growth of condensation nuclei, 190
  precipitating of the particles, 189
  rate of condensation, 191
  supercooling, 189
  thermo- and diffusion-phoretic forces, 189
Evaporation means
  electron beam, 195
  hollow cathode, 195
  induction heating, 195
  laser beam heating, 195
  low-voltage arc, 195
Explosion flameless venting, 889–890
  cylindrical flame-quenching unit, 889–890
  flame-quenching unit, 889–890, 890*f*
  layers of stainless steel mesh, 889–890
  rectangular flame-quenching unit, 889–890
  segmented flame-quenching unit, 889–890
  vent duct, 889–890
  venting efficiency, 889–890
Explosion isolation, 890–891
  active explosion isolations systems, 891*f*
  chemical barrier standard rate discharge, 891*f*
  explosion isolation pinch valve, 891*f*
  explosion isolation valve, 891*f*
  extinguishing agent, 890
  flame front, 890
  flame propagation, 890
  gate valves, 890
  pinch valves, 890, 891*f*
  prevent deflagration, 890
  prevent detonation transition in pipes, 890
  prevent flame propagation, 890
  time for mechanical barrier to close, 891
  time for pressure growth, 891
  total time for the isolation process, 891
Explosion suppression, 890
  dispersion nozzles, 890
  dust cloud, 890
  high rate discharge suppressor, 890
  pressure sensors, 890
  suppressant agent, 890
  suppression system, 890
Explosive atomization, 176–177
  electrical explosion of wires technology, 176
  steam explosion method, 176, 176*f*

F

Factors influencing on angle of repose, 56
Features of nanoparticles, 272–274
  electromagnetic properties, 274
  mechanical properties, 274
  optical properties, 274
  structural characteristics, 272
  thermodynamic data, 273–274
FFC-Cambridge process, 559, 559*f*
  extrusion die, 559
  graphite anode, 559
  Magnelli phase, 559
  metal oxide electrode, 559
  molten salt bath, 559
  oxide ions, 559
  process time, 559
  solid titanium dioxide, 559
  titanium dioxide, 559
  University of Cambridge, 559
Fisher subsieve seizer, 18–19, 695, 699, 709–711
  air permeability, 19
  constant sample packing, 19
  Fisher subsieve numbers, 19
  Kozeny–Carman equation, 18–19
  Kozeny constant, 18–19
  mean particle size, 19
  packed bed, 19
  pore structure, 19
  permeability of powder bed, 19
  quality control process, 19
  Subsieve Auto Sizer, 19
Flame atomic emission spectrometry (AES), 37*f*
  atomizer, 36
  background signal values, 36
  hot flame gases, 36
Flame atomic fluorescence spectrometry (AFS), 37*f*
  atomic emission signals, 36
  emission method, 36
  excite analyte atoms radiatively, 36
  external light beam, 36
  light signal, 36
Flame spray pyrolysis, 176–177
  cluster formation, 176
  coalescence, 176
  droplet evaporation, 176
  finally agglomeration, 176
  flamelets feed, 176
  hexamethyldisiloxane, 176
  liquid fuel, 176
  metallic precursors, 176
  nucleation, 176
  permanent ignition of the spray, 176
  pressure swirl nozzle, 176–177, 177*f*
  two-substance nozzle, 176
  xylene, 176
Flow rate, 21, 47, 130–131, 133, 135, 145–146, 148, 153, 158, 162, 164–166, 168–171, 173–175, 205, 207, 287, 287*f*, 386, 408–409, 423–424, 446, 449, 493–494, 538, 555–556, 572, 574–576, 598, 601, 617, 620, 652, 682, 692, 852, 887, 896–897, 922
  die cavity, 54
  flow through the orifice, 54
  Hall funnel, 54
  non-free flowing powder, 54
  standard funnel, 54
Fluidization, 378
  air entrainment, 55
  airborne fine particles, 55
  funnel flow patterns, 55
  interparticle motion, 55
  mass flow pattern, 55
  trajectory effect segregation, 55
  wide particle size distribution, 55
Foaming agents, 330, 339–340, 342, 858
  calcium carbonate, 334–336
  decomposition, 334–337
  decomposition temperature, 334–337
  dolomite, 335
  foamable precursors, 335
  foaming process, 334–335
  liquidus temperature, 335–336
  magnesium carbonate, 335–336
  magnesium hydroxide, 335
  titanium hydride, 334–335
  zirconium hydride, 334
Foaming of ingots containing blowing agents (Formgrip/Foamcast)
  aluminum melt, 332
  gas release, 332
  heating rates, 332
  pore structures, 332
  precursors, 332
  reinforced metals, 332
  titanium–hydride particles, 332
Foaming of melts by gas injection (Hydro/Alcan)
  direct-foaming process, 332
  gas bubbles, 331–332
  impeller, 331–332
  injecting gases, 331–332
  metal-matrix composite, 331

  mixing techniques, 331
  vibrating nozzles, 331–332
  viscous mixture, 331–332
Foaming of melts with blowing agents (Alporas)
  blowing agent, 330–331
  calcium metal, 330–331
  foaming process, 331
  titanium hydride, 331
  viscous liquid, 331
Foaming of powder compacts (Foaminal/Alulight), 333
  blowing agent, 333
  heat treatment, 333
  metal matrix, 333
  mixing of metal powders, 333
  powder blends, 333
Foaming process, 331–332, 334–335, 345
  accumulative roll bonding process, 336, 336*f*
  cell structures, 335–336
  cell wall, 335–336
  decomposition, 334–337
  decomposition gas, 335–336
  decomposition temperature, 334–337
  released gas, 335–336
  rounded cell structure, 335–336
  spherical cell structure, 335–336
Frictional properties, 54
  angle of internal friction, 48–49
  coefficient of sliding friction, 48–49
  effective angle, 48–49
  external friction, 48–49
  internal friction, 48–49
  shear cell, 48–49, 48–49*f*
  shear tester, 48–49
  sliding friction, 48–49
  wall friction angle, 48–49, 49*f*
Funnel method, 378
  Carney funnel, 51
  discharge opening, 51
  Hall funnel, 51, 51*f*

G

Gas adsorption, 59–61
  adsorbed layers, 39
  adsorbate pressure, 39
  Brunauer–Emmet–Teller (BET) model, 39–40, 40*f*
  closed pores, 39
  isotherm of nitrogen adsorption, 39–40
  multilayer adsorption theory, 39
  pressure transducers, 40–41
  specific surface area, 39–41, 40*f*
Gas atomization, 169, 172, 324, 340–341, 381–385
  gas atomized powders, 158–162, 317
  gas atomizing units, 144–147
  hot gas atomization, 165–166
  internal mixing nozzles, 162–163, 162*f*
  models of gas atomization, 149–158
  other gas atomization methods, 162–167
  powder cleanliness, 161–162
  process parameters, 148–149
  ultrasonic gas atomization, 163–165
  vacuum-dynamic atomization, 167, 167*f*
Gas atomization (production of titanium and titanium alloy powders)
  argon atmosphere, 555–556
  ceramic-free Ti alloy, 556
  electron-beam furnaces, 556
  gas atomization process, 556–557, 557*f*
  plasma atomization process, 555–556, 555*f*
  plasma melting induction guiding gas atomization (PIGA), 556
  pre-mixed raw material, 556–557
  spherical titanium powder, 555–557, 555*f*
  vacuum induction gas atomizing (VIGA), 557–558, 558*f*
Gas atomization beryllium
  anisotropic components, 802
  dendritic structure, 803
  increased isotropy of consolidated material, 802
  high pressure jet of inert gas, 802–803
  inert gas atomization, 802–803
  optical systems, 802
  vacuum induction melting, 802–803
Gas atomization of aluminum powders
  Alcoa process, 461, 462*f*
  annular gas jet, 463
  atomizer, 462, 465*f*
  atomizing nozzle, 461
  atomizing torch, 460
  chiller chamber, 461–462
  ejection nozzle, 462, 465*f*
  heated gas, 463
  horizontal aspirating installations, 460
  microstructure of powder particles, 460
  RUSAL PM manufacturing plant, 462, 465*f*
  spraying torch, 463
  suction (ejection) effect, 461, 463
  top–down atomization, 462
  tundish, 463
  vertically upward aspirating plants, 460–461
  Volgograd Aluminum plant, 466
Gas atomized powders, 142, 148, 317, 385–386, 462, 466, 496, 514, 524, 541–542, 545, 652, 655, 676, 677*f*, 740, 791, 795, 808, 833
  cellular structure, 160–161
  cooling rate during solidification, 160
  dendritic morphology, 160
  internal porosity, 161
  Lubanska's formula, 158, 159*f*
  microstructure, 160–161, 161*f*
  model for solidification time, 159–160
  particle size, 158–161
  solidification time, 159–160
  specific gas consumption, 158
  spheroidization time, 160
  surface morphology, 158–161
  Weber number, 158–159
Gas atomizing units, 144–147
  confined nozzle designs, 145, 145*f*
  free fall design, 145*f*
  Nanoval nozzle design, 146, 147*f*
  prefilming hybrid atomizer, 146–147, 147*f*
  prefilming nozzle design, 145–146, 146*f*
  pressure-swirl hybrid prefilming atomizer, 146, 147*f*
  ultrasonic gas atomizer, 158, 163–165
  VAMI aspirating nozzle design, 144, 144*f*
  WIDEFLOW confined linear nozzle design, 145
Gas-phase method of metal powder production
  application of gas-phases processes, 194–199
  chemical vapor deposition (CVD) process, 197–198
  controlled condensation process, 194
  evaporation means, 195
  formation of alloy powders, 193
  gas-phase precipitation, 198
  health and environment protection, 198–199
  inert gas condensation (IGC), 187, 194
Gleiter's installation, 280, 280*f*
Gold alloy powders, 29
Gold brazing alloy powders, 142
Gold–platinum powder, 835, 838*t*
Gold powder production
  apparent density, 832*t*
  aqueous gold chloride solution, 837
  ball milling, 837
  gold chloride solutions, 835–837
  gold flake, 837
  gold foil, 837
  gold powder production, 835–837
  gold vaporization, 835
  mechanical comminution, 837
  physical properties, 832*t*, 835
  sheets of gold, 837
  spherical gold particles, 837
  thermolysis, 835
Gradient materials
  coated cutting tools, 302
  combination of different layers, 302
  core–coat type, 302–303
  functionally different materials, 302
  parallel layers, 302–303
Graphene oxide composite powders
  aluminum composites reinforced with graphene nanosheets, 360
  cetyl trimethyl ammonium bromide (CTAB), 360
  graphene oxide sheets, 360–361
  high lithium-ion diffusion rate, 362
  lithium-ion batteries (LIBs), 360–361
  metal oxide–RGO composite powder, 360–361
  reduced graphene oxide (GO), 360–361
  spray pyrolysis, 360–362
  zinc sulfide RGO composite powder, 361–362, 361–362*f*
Gravity filling of shaped molds, 326
Green strength, 57, 141, 160, 211, 325, 558–559, 566–567, 572, 576–577, 581, 581*f*, 590, 592*f*, 609, 702, 742
  bending stress, 59
  device for testing of green strength, 59*f*
  green specimen, 58–59

- Green strength *(Continued)*
  - non-sintered material, 59, 59*f*
  - plastic deformation, 58–59
  - sample strength, 59
- Grinding (production of RE powders)
  - adiabatic gas cooling, 802
  - anisotropic effect, 801–802
  - attrition milling, 801
  - ball milling, 801–802
  - characteristics of beryllium powders, 802, 803*t*
  - coldstream impact process, 802
  - embrittlement effect, 802
  - grain size, 802
  - high energy ball milling process, 801
- Grinding in attritors (production of zinc powders)
  - addition of surfactants, 625
  - salts of oleic acid, 625
  - salts of stearic acid, 625
  - substances preventing autoignition, 625
  - wet grinding, 625
- Grinding medium
  - agate, 103*t*
  - high-density media, 102
  - media hardness, 103
  - powder contamination, 103
  - silicon nitride, 103*t*
  - sintered corundum, 103*t*
  - stainless steel, 103*t*
  - tungsten carbide, 103*t*
  - zirconium oxide, 103*t*
- Grinding techniques
  - ball mills, 75–78, 76–78*f*
  - ball-to-powder weight ratio (BPR), 108–110, 119, 482
  - batch attrition mills, 82
  - circulation attrition mills, 82, 84
  - cold stream process, 85
  - colliding balls, 75
  - cone inertia crusher, 80, 81*f*, 83*t*
  - conical ball mills, 77–78, 78*f*
  - continuous attrition mills, 84, 84*f*
  - cylindrical ball mills, 78–79, 79*f*
  - fluidized bed jet mill, 85, 85–86*f*, 86*t*
  - Fritsch planetary ball mill Pulverisette, 79*f*, 87–88*t*
  - grinding kinetics, 75
  - grinding media, 78–82
  - high-energy milling methods, 85–88
  - jet mills, 85, 85–86*f*, 86–87*t*
  - medium agitating mills, 81–84
  - other high-energy milling methods, 85–88
  - planetary mills, 79, 79*f*
  - rod mills, 78
  - shaker mill, 88
  - tumbling ball mills, 75–78
  - vibrating grinders, 80–81, 82*t*, 82*f*
  - vibratory ball mills, 80, 80*f*
- Grinding units
  - covers with inside and outside chambers, 898
  - pulsating motion, 898
  - suction capacity, 898
  - tumbling mills, 898, 901*f*
- Guinier–Preston zones, 520, 815

H

- Hall funnel, 51, 51*f*, 54
- Hardfacing, 714–717
- Hardfacing process, 653*t*, 674
  - carbide-containing alloys, 652, 654
  - cobalt-base hardfacing alloys, 676
  - plasma transferred arc hardfacing process, 676, 676*f*
  - laves phase, 652, 674–675
- Health and environment protection, 198–199, 209–210, 638, 683–684
  - admissible concentration limit in aqueous medium, 857
  - encapsulation, 857
  - extinguishment by burning, 858
  - explosion pressure, 857–858
  - explosion risk, 857
  - flame propagation limit, 858
  - heat of combustion, 858
  - high-performance cleaning, 857
  - industrial safety measures, 857
  - inflammability, 857
  - occupational exposure limits in the workplace atmosphere, 854–857
  - self-ignition temperature, 857–858
  - toxic agent, 854–857
  - voluminal quenching method, 858
  - workplace atmosphere, 854–857
- Health and environment protection (cobalt and cobalt alloy powders)
  - allergic reactions, 684
  - amalgam techniques, 684
  - carbon monoxide, 684
  - cobalt carbonyl processing, 684
  - cobalt metal fume and dust, 684
  - dicobalt octacarbonyl, 684
  - enclose operations, 684
  - environment protection, 684
  - general ventilation, 684
  - health hazards, 684
  - irritation, 683
  - legal airborne permissible limit, 684
  - local exhaust ventilation, 684
  - mercury, 684
  - nickel carbonyl, 683
  - personal protective equipment, 684
  - safety engineering, 684
  - workplace atmosphere, 683–684
- Health and environment protection measures in carbonyl nickel production
  - nickel carbonyl dangerous, 638
  - nickel carbonyl dissolves, 638
  - toxic carbon monoxide, 638
- Heat pressure, 906, 908*t*
  - aspiration cover, 895
  - density of environment medium, 895
  - density of gaseous medium in lower aspiration cover, 895
  - elevated temperature materials, 895
  - heat exchange during processing, 895
- Hertz–Knudsen equation, 188, 281
- High-energy milling process
  - HE (high-energy) ball mill, 85, 88, 91, 354, 354*f*, 357–358, 482, 565, 657, 705, 732, 860
  - large-diameter tumbling ball mills, 85, 289
- High pressure carbonyl techniques
  - carbon monoxide, 638
  - condensation, 638
  - distillation, 638
  - feed concentrates, 638
  - high-grade pyrite ores, 638
  - nickel–copper–palladium deposits, 638
  - Norilsk Nickel group companies, 638
  - Norilsk–Talnakh ore, 638
  - Severonickel refinery, 638
  - thermal shock, 638
  - vaporization, 638
- High-strength aluminum alloys
  - alloying elements, 511
  - aluminum matrix, 511
  - aluminum scrap, 511
  - Al–Zn–Mg–Cu system alloys, 511, 512–513*f*, 512*t*
  - corrosion resistance, 511
  - fatigue strength, 511
  - grain boundaries, 511
  - hardly-deformable inclusion, 511
  - high-strength quaternary system, 507
  - impurity concentration, 513
  - mechanical properties, 511, 513, 513*f*
  - particle size distributions, 511–512, 512*f*
  - PM Al–Zn–Mg–Cu system alloys, 513
  - recycling of secondary aluminum, 511–513
  - secondary aluminum, 511–513
  - superheat of melt temperature, 511–512
  - water atomized powders, 511–512
- Hot gas atomization
  - closed-coupled atomizer, 165–166
  - effect of gas temperature, 165
  - glass-forming alloys, 165–166
  - nozzle freezing, 165
- Hot isostatic pressing (HIP) (beryllium powders)
  - fine grain size, 805
  - full theoretical density, 804–805
  - high degree of isotropy, 805
  - high purity beryllium powders, 804–805
  - low-oxygen containing argon, 804–805
  - near-net shape, 804–805
  - nearly theoretical density, 804–805
  - pressure medium, 804–805
- Hybrid core/shell nanoparticles
  - encapsulation, 303–304
  - magnetic encapsulated polymer, 303
  - microsphere composite, 303–304
  - microwave plasma synthesis, 303–304
  - inorganic core, 303
  - polymer matrix, 303
  - polymerizable organic shell, 303
  - Sn-nanoparticles encapsulated, 303
- Hydraulic size classifications
  - classified powders, 507
  - suspended powder, 507
  - suspension reservoir, 507

  hydraulic classifier, 434*t*
  various size fractions, 507
Hydrogen reduction by autoclave processing (production of nickel powders)
  alkaline medium, 646
  autoclave precipitation, 647
  briquetting operation, 648–649
  densification cycles, 647–648, 649*f*
  heterolytic mechanism, 646
  hydrogen ions, 647
  hydrogen potential, 646
  hydrogen pressure, 647
  kinetic equations, 647
  nucleation stage, 647
  powder formation, 648
  reducing agent, 646
  seed powder, 646–647
  Sherritt's hydrometallurgical processing, 649
  surfactant, 646
Hydrometallurgical processing (production of nickel powders)
  cobalt separation, 646
  copper removal, 646
  elevated pressures and temperatures processing, 647
  feed processing, 644–645
  hydrogen reduction by autoclave processing, 646–649
  leaching, 645–646
  Moa Bay deposits, 644–645
  metal recovery operations, 644
  nickel–cobalt sulfide, 644–645
  oxidation and hydrolysis, 646
  selective dissolution, 644–645
  separation of nickel and cobalt, 646
  Sherritt process, 644
  Sherritt refinery, 644–645
  solution purification, 644, 646
  sulfide precipitation, 649–650
  sulfuric acid, 644–645, 650
Hydrometallurgical process of cobalt powder
  chemical dissolution (leaching), 669
  leach autoclave method, 669–673
  metal recovery, 669
  solution purification, 669–670
Hydrophobization
  corrosion resistance, 445–446
  electrolytic copper powder, 446
  electrolysis kinetics, 446
  stability of powder, 446
  surfactant and organic compounds, 445
  volatile inhibitors, 446
Hysteresis mercury
  contact angle hysteresis, 46, 46*f*
  connectivity model, 46
  extrusion curves, 46
  ink-bottle theory, 46
  intrusion curves, 46

I

Ignition of dust deposits and powder layers by self-heating or hot surfaces
  dust deposits, 869–870
  exothermic reaction rate, 869–870
  external ignition source, 869–870
  glow fires, 869
  hot-plate test, 870
  ignition temperature, 869–870
  International Electrotechnical Commission, 870
  minimum ignition temperature, 869–870
  powder deposit, 869
  reacting chamber, 870
  self-ignition temperature, 870
  smoldering combustion, 869
  smoldering temperature, 869
  spontaneous flame production, 870
  U.S. Bureau of Mines test, 869–870
Impact atomization
  heat of evaporation, 173
  heat of solidification, 173
  impeller, 173
  molten metal feed rate, 173
  powder yield, 173
  superheat, 173
  vaporization, 173
  volatile liquid coolant, 173
Impact point, 54
Impulse atomization method, 174*t*
  gas atmosphere, 173
  gravity impulse mode, 173
  impulse generator, 173
  impulse mode, 173–174
  mass throughput, 173–174
  melt superheat temperature, 173
  monosized granules, 173
  narrow particle size distribution, 173
  nozzle plate complete with orifices, 173
  orifice shape, 173
  orifice size, 173
  thermal model of melt droplets cooling, 174
Inconel alloy 625 nickel based superalloy, 337
Indium
  air atomization of melt, 775
  black indium, 775
  cementation technique, 775
  control rods in nuclear techniques, 775
  franckeite, 774
  high cross-section capture for thermal neutrons, 774–775
  hot gas atomization, 775
  indium concentrate, 774–775
  indium powders, 775
  indium recovery technique, 775
  indium sponge production, 775
  kilindrite, 774
  production of preliminary indium, 775
  semi-conductor technique, 775
  solders for joining of metals, glass, quartz and ceramics, 775
  source of indium, 775
  sphalerites, 774
  wear-resistant coatings of indium, 775
Inductively coupled plasma atomic emission spectroscopy (ICP-AES)
  atomic emission spectroscopy, 36
  excitation source, 36
  highly ionized gas, 36
  inductive coupled plasma, 36
  multi-element analysis, 36
Inert gas condensation (production of zinc powders)
  spherical powder, 619–620, 621*f*
  'Tuman' ('Fog') installation, 619, 620*f*
Inert gas fusion
  fusion area, 35
  gas/metal bonding, 35
  inert carrier gas, 35
  physical and chemical bonding, 35
Infiltration (INF), 842
Inflammability and explosivity of powders
  dependence the ignitability and explosibility of the gas suspended solid mixture on the oxygen content in oxidizing gas, 875
  ignition of dust deposits and powder layers by self-heating or hot surfaces, 869–870
  maximum explosive pressure at constant volume, 873–874, 875*f*
  maximum rate of explosion pressure rise at a constant volume, 874–875
  minimum electrical spark ignition energy of dust clouds, 872–873, 873*f*
  minimum explosive dust concentration, 870–871
  minimum ignition temperature of dust clouds, 872
Initial compounds for metals production (production of RE metal alloy powders)
  production of chlorides, 785–786
  production of fluorides, 786
Institute for Problems of Materials Science (Kiev, UA), 318, 505
Instrumental indentation
  Berkovich indenter, 276
  impression, 276
  indentation depth, 276
  indentation load, 276
  indentation load-depth curve, 276
  indenter, 276–278, 277*t*
  local strength, 276
  plastic deformation, 276
  Poisson's ratio, 276–278
  residual stress, 276
  unloading process, 276–278, 277*f*
  specimen holder, 278
  Young's modulus, 276–278
Internal mixing nozzles, 162*f*
  nozzle exit, 162–163
  prefilming spin nozzle, 162–163
  pressure swirl hybrid prefilming atomizer, 162–163
  ring gas atomizer, 162–163
  tangential inlet, 162–163
International Center for Electron Beam Technology (ICEBT), 297, 297*f*
Inter-stage transport
  belt conveyors, 452
  bucket elevator, 453
  bypass tube, 452
  cone valve system, 452, 452*f*
  containers, 452
  continuous inter-stage transports, 452

Inter-stage transport *(Continued)*
  discontinuous inter-stage transports, 452
  dustproof performance, 452–453
  gravel pumps, 452
  loading devices, 452
  material handling equipment, 452
  pneumatic transport, 454
  processing equipment, 452
  spiral conveyors, 452–453, 453*f*
  transportation of dry mixtures, 452
  unloading devices, 452
  vibrating conveyors, 452–453
  vertical spiral vibrating conveyors, 452
  worm conveyors, (Not found)
Ion guns, 31
  cesium gun, 33
  duoplasmatron, 33
  electron ionization, 33
  liquid metal ion gun, 33
  surface ionization source, 33
Iridium
  chemical composition, 838*t*
  particle size, 841
  precipitated from acid-salt solution, 839
  property, 841
  surface area, 839
Isostatic compaction
  cold isostatic pressing (CIP), 325
  hot isostatic pressing (HIP), 325
  near-net shapes, 325
  sintering, 325
  uniform density, 325

J
Jaw crusher, 65, 74, 74*f*, 583–584, 897
JCPDS International Centre for diffraction data, 34
Jenike AM
  Jenike shear cell, 48–49, 48*f*
Jet mills, 85, 85–86*f*, 86–87*t*, 289, 289–290*f*, 612
JET reactor, 806
Joining, powder metallurgy materials, 341
Joining, refractory metal powders
  brazing, 721
  fusion welding, 375

K
Kinetics and mechanism of the process (solid-phase reduction)
  adsorption-autocatalytic theory, 212–213
  active surface centers, 214
  chemisorption of reducing gas, 214
  crystal chemical transformation, 214
  diffusion conditions, 213
  diffusion-kinetics range of the reduction process, 214
  indirect reaction, 212
  kinetic equation, 214
  multistage mechanism, 214
Kinetics of solid phase formation in solution
  aqueous solution, 224
  autocatalytic effect, 223, 225
  chemical reagents, 225
  cluster, 223–224
  constant of process rate, 223
  crystallization centers, 224
  induction period, 223–224
  kinetic factors, 223
  kinetic reduction curve, 224
  ligand, 225
  metal ions, 224–225
  metallic colloids, 225
  nucleation rate, 224–225
  oxidation–reduction potential, 223–225
  particle shape, 224–225
  particle size, 223–225
  protective colloids, 225
  reduced metal rate, 224
  reduction reaction, 224
  Rostovtsev kineic equation, 214
Kozeny–Carman equation, 18–19, 41

L
Laboratory mills for mechanical alloying, 100–101
  attritors, 99*f*
  HE (high-energy) mill, 100, 100*f*
  laboratory ball mill, 100*f*
  planetary mills, 101
  SPEX mill, 100
  Uni-Ball mill, 101
  vertical rod mill, 101
Langmuir formula, 281
Lanthano-thermic method
  reducing agent, 787
  reduction by lanthanum, 787
  samarium oxide, 787
  tantalum crucible, 787
Laves phase, 652, 674–675
Leaching (first stage in refining process)
  ammonium sulfate, 645
  cobalt separation, 646
  elevated temperature and pressure, 645
  leach liquor, 646
  leaching process, 645–646
  metal sulfides, 645
  oxidative dissolution, 645
  refining process, 645–646
  sulfide feed, 645
Leaching autoclave process
  ammonium sulfate, 670–673
  autoclave cobalt coating, 673
  cobalt hexamine sulfate complexes, 669
  cobalt–nickel hexamine salt, 670–671
  cobalt sulfate, 673
  densification reduction, 672
  hydrometallurgical process, 669–673
  kinetics of the reducing autoclave process, 671
  metal carbides, 673*t*
  nickel sulfide concentrate, 669–670
  nucleation reduction, 671
  pure crystalline cobaltic hexamine salt, 670
  purification steps, 670
  refining process, 669–670, 670*f*
  Sherritt cobalt refining process, 670*f*
  Sherritt refinery, 669–670
  soluble amine complexes, 669–670
Lead-acid batteries, 642, 848
  automotive industry, 858
  fuel saving technologies, 858
  Global Automotive Battery Market, 858
  micro hybrid systems, 858
Lead oxide powder production
  acid adsorption, 850*t*
  apparent density, 850*t*
  automotive lead-acid batteries, 848
  ball milling, 848–849
  Barton pot process, 848
  grey/lead oxide, 848
  heat generating during milling, 848
  high-speed blades, 848
  lead ortho-plumbate, 848
  lead oxidation in air, 848
  lead oxide powder production, 848
  particle size, 848
  rate of oxidation, 850*t*
  red lead oxide, 848
Lead powder production, 847–850, 849*t*, 849*f*
  apparent density, 849*t*
  electrolysis, 850
  electrolyte composition, 851–852*t*
  health and environment protection, 854–858
  hot gas atomization, 847
  lead-acid batteries, 848
  lead–bismuth, 851–852*t*
  lead oxide, 848, 850*t*
  lead–tin, 851–852*t*
  lubricant compositions, 850
  nominal composition, 849*t*
  properties, 849*t*
  roundish particles, 850
  sieve analysis, 847, 849*t*
  standard grades, 849*t*
  superheat, 847
  thermolysis, 850
Lead zirconate titanate (PZT) ceramics
  piezoelectric property, 772
  press-sinter method, 772–773
  PZT polymers composite, 773
  PZT powder, 772
  sensor, 772
Light scattering, 695
  centrifugal pumping system, 21
  dispersing units, 21
  laser light, 20–21
  laser particle sizer, 21
  Mie theory, 20–21
  parallel laser beam deflect, 20
  scattering angle, 20
  sensor elements, 20
  unified scatter technique, 21
Localization of powder-gas emissions
  aspiration for particulate material reloading in closed gravity chutes, 901–909
  aspiration in combustible powder conditions, 897
  capacity of local suctions, 896–897
  definition of the local exhaust capacity, 901–918
  ejection pressure, 892
  grinding units, 898–901

  heat pressure, 895
  melt atomization units, 897
  overpressure of closed chambers, 893–894
  pressure created by equipment moving parts, 895
  pressure − mass transfer result, 896
  single rotary hammer mills, 912–918
Low pressure carbonyl technique
  atmospheric pressure carbonyl technique, 635
  circulation of formed pellets, 635
  decomposition device, 635
  extraction of nickel, 635
  heat-insulated decomposer, 635
  Inco Ltd, 635
  Mond–Langer process, 635
  nickel carbonyl cleaning, 635
  nickel matte feed, 635
  nickel tetracarbonyl vapor, 635
  nickel yield, 635
  pellets coalescence, 635
  preheated hydrogen, 635
  synthesis stage, 635

M

Magnesium
  magnesium alloy powders, 533–541
  magnesium alloys, 384–387, 491*f*, 539, 541, 545–546, 766, 790
  magnesium chips, 535
  magnesium grit, 535
  magnesium granules, 173–174, 538–539, 538*f*
  magnesium powder, 171, 386, 533–535, 535*f*, 536–537*t*, 539–540, 543, 543*f*
  production of magnesium granules, 538–539
  production of magnesium and magnesium alloy powders, 533–541
  production of magnesium powders, 533–535
Magnesium alloy powders
  AMX602, 544–545, 545*f*
  AZ31B, 536–537*t*, 545
  AZ91E, 536–537*t*
  Electron MAP 21, 536–537*t*, 542
  Electron MAP 43, 536–537*t*, 542
  Electron MAP 91, 536–537*t*
  Electron MAP+ 21, 536–537*t*
  Electron MAP+ 43, 536–537*t*
  Electron MAP+ 91, 536–537*t*
  ground magnesium alloy powders, 543
  nanocrystalline $Mg_{97}Zn_1Y_2$ (at%), 543
  WE43B, 552*t*
  ZAXE1711, 544
  ZM21, 546
Magnesium granules
  active magnesium, 538
  apparent density, 538–539
  applications, 538–539
  coarse spherical granules, 539
  content of metallic magnesium, 539
  dense structure, 539
  granule structure, 539
  monodisperse granules, 539
  oxide-salt film, 538
  particle shape, 539
  production of magnesium granules, 538–539
  shining metal surface, 539
  size of granules, 539
  spherical granules, 539
Magnesium reduction method (Kroll Process), 550–553, 568*t*
Magnesium-thermal reduction of beryllium fluoride
  beryllium fluoride BeF2, 800
  flux composition, 800
  inert atmosphere, 800
  magnesium fluoride, 800
  reducing agent, 800
Magneto-hydrodynamic method (MGD), 539
Manufacture of composite(s)
  aluminum-based composites, 363–364
  composite manufacturing methods, 363
  copper-based composites, 364–366
  refractory metal and carbide-based composites, 366–368
  silver-based composites, 363
Manufacture of composite powders
  aluminum-based composite powders, 352–353
  carbon nanotube (CNT)-reinforced metal composite powders, 357–360
  copper-based composite powders, 353–354
  graphene oxide composite powders, 360–363
  nickel–clad aluminum powders, 351–352
  refractory-based composite powders, 355
  titanium-based composite powders, 355
Manufacture of electrodes (RE comprising)
  carburization process of La_2O_3–Mo cathodes, 794
  carburized filament, 794
  carburized La_2O_3 doped Mo filament cathodes, 794
  discharge lamps, 794
  electrical discharge machining, 794
  La–Mo cathodes, 794
  La_2O_3–Mo cathodes aluminum-based composite, 794
  La_2O_3–Y_2O_3–Mo cermet cathode, 794
  plasma cutting, 794
  plasma spraying, 794
  RE_2O_3 layer, 794
  thermionic emission, 794
  ThO_2 cathodes, 794
  tungsten-arc inert-gas welding (TIG), 794
  tungsten cathode material, 794
  W–CeO_2 electrodes, 792–794
  W–ThO_2 electrodes, 792–794
Manufacturing technique of quasicrystalline powders
  argon atmosphere, 315
  argon atomization, 317
  atomization in helium atmosphere, 316
  centrifugal atomization, 316
  cooled copper crucible, 315
  cooling rate, 316–318
  crushing of ingots, 315
  evaporated powders, 315
  extrusion of water atomized powder, 318–319
  faceted shape, 314
  flake shape, 315
  gas atomized powders, 317
  high-frequency furnace, 315
  high-speed-rotating disc, 316
  icosahedral QC phase, 314–315, 316*t*, 317
  mechanical alloying, 314
  nanocrystalline structure, 314
  nozzle atomizer, 316
  oxygen content, 317
  pulse energy, 315
  polyhedral shape, 315
  QC structure, 313–314
  rotating target, 315
  spherical shape, 317
  tumbling ball mill, 315
  vaporization by laser beam, 315
  water atomized powders, 318–319
  wave length, 315
  Young modulus of QC, 319
Mass analyzer
  electrostatic analyzer, 33
  magnetic analyzer, 33
  quadrupole mass analyzer, 33
  sector instrument, 33
  time of flight mass spectrometry, 33
Material selection (Porous materials)
  bronze, 324, 324*f*
  nickel, 324, 325*f*
  nickel alloys, 324
  nonferrous metals, 324
  prealloyed powders, 324
  premixed elemental powder, 324
Maximum explosive pressure at constant volume
  American Society for Testing and Materials, 874
  closed vessel, 873
  electric sparks, 873, 875
  explosion chamber, 872*f*, 873–874
  explosion of airborne powder, 873
  glowing resistance wire coils, 873
  Hartmann bomb, 873, 874*f*
  ignition sources, 873
  IS0 vessel, 873–874
  maximum explosion pressure of dust clouds, 873
  pyrotechnical ignitor, 873–874
  Siwek 20-liter sphere apparatus, 874
  synchronized chemical ignitors, 873
Maximum rate of explosion pressure rise at a constant volume
  closed vessel, 874–875
  explosion violence, 874–875
  International Standards Organization, Explosion Protection Systems, 874–875
  maximum rate of pressure rise, 874–875
Measuring angle of repose
  base cone, 55
  circular method, 55
  crater method, 55
  dynamic angle of repose, 56
  height cone, 55
  ledge method, 55
  powder heap, 55
  rotating cylinder, 55
  titling table, 55

Mechanical activation, 87–88, 94–96, 108, 121, 290
Mechanical alloying
  aluminum-base alloys, 107, 113–118
  applications, 112–119
  attritors, 94, 97–99
  brittle–brittle component systems, 107
  commercial mills, 101–102
  consolidation, 94
  contact displacement reactions, 108–109
  cobalt-base alloys, 113
  copper-base alloys, 119
  ductile–brittle component systems, 92, 104–106
  ductile–ductile component systems, 105, 106*f*
  equilibrium materials, 91
  friction effect, 94
  grinding medium, 92, 97, 102–104
  high-energy milling process, 91, 104
  high-energy mills, 100, 113–114
  impact effect, 94
  laboratory mills, 100–101
  mechanical alloying fundamentals, 104–107
  mechanical alloying process, 92–94, 114*f*, 119
  milling equipment, 94–104
  nickel-base alloys, 112–113
  nonequilibrium alloys, 91
  oxide dispersion strengthened (ODS) alloys, 107
  powder contamination, 94, 103, 109–111, 111*t*
  prealloyed powders, 91–92, 107
  precipitation strengthened, 91
  process control agent (PCA), 92–93
  Rehbinder's effect, 92
  selection of grinding medium, 102–104
  shaker mills, 94, 96–97, 100
Mechanical alloying (production of titanium and titanium alloy powders)
  amorphous phases, 565
  dispersion-hardened alloys, 565
  elemental powders, 565–566
  equilibrium phases, 565
  high-energy ball mill, 565
  metastable crystalline phases, 565
  nanostructured intermetallic composites, 565
  nanostructured materials, 565
  non-equilibrium phases, 565
  planetary ball mill, 565
  simple technique, 565
  supersaturated solid solutions, 565
  titanium based alloys, 565
Mechanical alloying fundamentals
  agglomeration, 104–105, 113–114
  diffusion distances, 105, 108
  dislocation, 104–105
  chemical conversion, 104
  cold welding, 104–105, 113–114
  convoluted lamellae, 104–105
  crystal defects, 104–105
  fatigue failure mechanism, 104
  flattened particles, 105
  fracture, 104
  fragile flakes, 104
  grain boundaries, 104–105
  interatomic forces, 104
  plastic deformation, 104, 107
  structural refinement, 104–105
  surface deformation, 107
  work hardened, 104–105
Mechanical crushing and grinding
  Bong's Work Index, 72
  brittle materials, 66, 74
  comminution, 65, 70
  crushers, 74–75
  disintegration process, 66
  disruption, 66
  ductile metal, 66–68
  grindability, 70–72
  grinding techniques, 75–81
  hardgrove grindability index, 71
  mechanism of the ductile metal deformation, 66–68
  regularities of milling, 68–73
  temperature rise during milling, 72–73
Mechanical plating
  activating solution, 630
  cadmium powder mixtures of Zn and Cd powders, 630
  glass beads, 630
  mixtures of Zn and Cd powders, 630
  zinc powder, 630
Mechanical properties of metallic foam materials, 338–346
  cell wall, 344
  collapse, 344
  densification, 344
  elastic buckling, 344
  fracture, 344
  plastic collapse stress, 344
  roughly constant stress plateau, 344
  tetrakaidecahedral unit, 344
  x-ray tomography, 344
  yield strength, 344
  yielding, 344
Mechanical properties of porous materials, 323–328, 328*f*
Mechanism of ductile metal deformation
  accumulation of dislocations, 66–67
  Griffith's relation, 67–68
  Griffith–Irwin–Orovan's relation, 67
  microcracks, 66–67
  multiphase disintegration, 66
  Rehbinder effect, 67
  shear stress, 67
Melt atomization (production of zinc powders))
  centrifugal atomization, 620
  gas atomization, 620, 621*f*
  gas pressure, 620
  hot gas atomisation, 620
  irregular particle shape, 620
  rapid solidification, 619*f*, 620, 622
  ultrasonic impact, 620, 625
  water atomization, 620
Melt atomization units
  aspiration cover, 897, 899*f*
  crucible, 897
  dust-gas emission source, 897
  exhaust duct, 897
  induction furnace, 897, 900*t*
  tundish, 897, 899*f*
Melt drop orifice techniques
  impulse atomization method, 173–174
  melt drop vibrating orifice method, 174
  pulsated orifice ejection method, 174–175, 175*f*
Melt spinning centrifugal atomization
  melt spinning roller technique, 171–172
  rapid solidification rate (RSR) process, 171
  rotating electrode atomization, 172
  spinning cup, 169, 179
  spinning disc atomization, 169–171
Melt spinning roller techniques
  centrifugal force, 171
  cooling rate, 171
  copper roller, 171
  flakes, 171
  flaky magnesium powder, 171
  flaky powders, 171, 172*f*
  heat abstraction, 171
  heat contact, 171
  nonequilibrium solubility, 171
  ribbon thickness, 171
  ribbons, 171
  roller circumferential speed, 171
  rotating roller, 171
  spinning roller technique, 171, 172*f*
Melt spinning techniques
  Al-based amorphous alloys, 503
  closed processing system, 503
  helium gas atomization, 504–505
  high-strength crystalline PM alloys, 503
  vacuum-type glove box, 503
MER process
  anode technology, 559
  batch products, 559
  bubble form, 559
  carbonaceous material, 559
  composite anode, 559
  fused halides, 559
  rutile powders, 559
  solid deposit, 559
Mercury porosimetry
  capillary radius, 43–44
  hysteresis mercury, 44
  mercury intrusion porosimetry, 43, 46
  mercury meniscus, 43–44
  penetrometer unit, 44
  pressure transducer, 44
  sessile drop mode, 44
  shadowgraph, 44
  surface area determination, 45
  surface tension, 45
  x-ray and ultrasonic flow-detection, 44
  Young–Laplace–Washburn equation, 43–44
Metal injection molding (MIM), 165–166, 283, 307, 326, 343, 556, 566, 612, 740–741, 761
Metallic foams. *See also* Porous powder and metallic foams
  cellular materials, 328–330
  closed-cell materials, 330–333
  foaming agents, 334–336

  - metallic foams materials, 338–346
  - open-cell materials, 338
  - open-cell metallic foams, 336–338
- Metallic foams (materials for functional application)
  - biomaterials, 343
  - acetabular system, 343
  - bone cement, 343
  - buoys, life buoys, 346*t*
  - dental implants, 343
  - electrodes for NiMH and NiCd batteries, 346
  - encapsulating of noise sources, 346*t*
  - filler material, 343
  - fuel cells, 343
  - high temperature filtration, 342
  - high temperature resistant materials, 342
  - hip implants, 343
  - Inconel-alloy-based foams, 342
  - lightweight molybdenum foam, 343
  - nickel foam strip, 343
  - orthopedic applications, 343
  - soot-filter, 343
  - space holder, 343
  - space holder mixtures, 343
  - thin porous bead coatings, 343
  - vertebra fusion, 343, 346
- Metallic foams (materials for structural application)
  - biporous metallic foams, 340–341
  - diffusion welding technique, 341
  - heat exchangers, 341
  - high pressure molding, 340
  - liquid metal matrix composites, 340
  - metallic hollow sphere structures, 340
  - nozzle system, 340
  - sandwich foam production, 341
  - spray coating process, 340
- Metallic foams materials
  - materials for functional applications, 342–344
  - materials for structural applications, 338–342
- Metallographic microscopy
  - automatic image analysis, 10
  - coating thickness measurement, 10
  - failure analysis, 10
  - glass plate, 10
  - grain size analysis, 10
  - grain structure analysis, 10
  - pore morphology, 10
  - powder particles surface, 10
  - transmission principle, 10
- Metallothermic methods (production of RE metal-alloy powders)
  - carbothermic method, 788
  - lanthano-thermic method, 787
  - sublimation in vacuum, 787
- Method of disproportionation of lower titanium halogenides
  - high temperatures, 564
  - low chlorides, 564
  - ores, 564
  - scrap metal, 564
  - titanium chloride, 564
  - titanium tetrachloride, 564
- Method of RE elements separation
  - molecular recognition technology, 785
  - RE separation by ion-exchange chromatography, 783–784
  - separation of REE by extraction, 782–783
  - schemes of complete separation, 784–785
- Method of weight samples
  - Andreasen's pipette, 16
  - Andreasen–Esenwein's pipette, (AU: Not found)
  - IPMS pipette, (AU: Not found)
  - pipette method, 16
  - residual weight, 16, 20
  - suspended powder, 16
- Microalloying influences (beryllium properties)
  - act on recrystallization, 804
  - compound FeAlBe$_4$, 804
  - embrittlement action, 804
  - growth of beryllium oxide, 804
  - impurity elements, 804
  - non-metallic impurities, 804
- Microanalysis
  - electron probe x-ray microanalysis (EPMA), 29–30
  - scanning electron microscopy (SEM), 27–29
- Microencapsulation
  - chemical methods, 446
  - film-forming material, 446
  - fluidized bed, 446
  - physical methods, 446
  - polycondensation, 446
- Microencapsulation of nanoparticles
  - glyoxal, 293
  - hydrophobic protective layer, 293
  - low-molecular-weight organic substances, 293
  - metal content, 294
  - mono either, 293
  - oxidation rate, 293–294
  - oxide layers, 293–294
  - polymers, 293
  - protective coatings, 293
  - stearic acid, 293
  - storage period, 294
  - surface of metal nanoparticles, 293
  - thickness of layer, 294
  - water vapor, 293–294
- Micromerograph
  - micrograph apparatus, 15–16
  - particle size distribution analysis, 15–16
  - sediment accumulation, 15–16
  - sediment weight, 15–16
- Milling equipment
  - grinding medium, 102–104, 110
  - milling containers, 110
- Minimum electrical spark ignition energy of dust clouds
  - electric sparks and arcs, 872–873
  - explosible dust clouds, 872–873
  - Hartmann tube, 873
  - hazardous electrostatic discharges, 872–873
  - paper diaphragm, 873
  - powder gravitation flow, 872–873
  - spark energy, 873
  - stored capacitor energy, 873
  - USBM method, 873
- Minimum explosive dust concentration
  - continuous induction spark source, 870
  - critical mass of dust, 870
  - dust cloud, 870
  - empirical correlation, 870
  - explosion chamber, 871, 872*f*
  - explosion criterion of ISO standard, 870–871
  - four liter installation IPMS, 871
  - Hartmann tube, 870
  - International Electrotechnical Commission, 870–871
  - International Standards Organization (ISO), 870–871, 871*f*
  - minimum explosive concentration, 870–871
  - one cubic meter ISO vessel, 870–871
  - standard test, 870
  - suspended solid sampling, 871, 872*f*
  - U.S. Bureau of miners (USBM) method, 870
- Minimum ignition temperature of dust clouds
  - dust cloud, 872
  - Godbert–Greenwald furnace, 872
  - hot surface, 872
  - internal surface, 872
  - minimum ignition temperature, 872
  - standard for determining minimum ignition temperature of dust cloud, 872
  - vertical cylindrical ceramic tube, 872
- Models of centrifugal atomization
  - angular velocity, 168
  - centrifugal acceleration, 169
  - direct drop formation (DDF) mode, 167
  - formation disintegration, 168
  - ligament formation mode, 167
  - protuberances, 167
  - rotating electrode process, 167–168
  - rotating speed, 167
  - size distribution, 167
  - surface tension forces, 167–168
- Models of gas atomization
  - above WCP atomization, 154
  - aspiration pressure, 154–155, 154*f*
  - below WCP atomization, 153–154
  - Bradley's mathematical model, 149
  - capillary wave model, 149–150
  - close-coupled gas atomization, 152–153, 152*f*
  - closed wake, 152–155, 152*f*
  - criterial dependences, 149
  - droplet diameter definition, 150–151
  - film hollow cone, 151
  - hysteresis type aspiration behavior, 155
  - Ingebo equation, 150
  - Large–Eddy simulation, 155–156
  - Mach number, 149–150
  - Mach shock disc, 153
  - melt film formation, 152, 156
  - model of droplet formation, 149
  - model of pressure-swirl atomization, 151, 151*f*, 152*t*
  - model for disintegration of liquid sheet, 150*f*
  - Newtonian fluids, 149
  - open wake, 152–153, 152*f*
  - pulsatile gas atomization model, 153

Models of gas atomization *(Continued)*
  Reynolds number, 150
  subambient pressure region, 153
  wake closure effect, 153
  wake-closure pressure (WCP), 153
  wave length, 149
  wave models of Ingebo, 150
  Weber number, 149
Molecular recognition technology
  carbonate salt, 785
  cation ionic radius, 785
  selective transport of metal ions, 785
  supported SuperLig products, 785
  three step process, 785
Molybdenum and molybdenum alloy powders
  cold-isostatic pressing, 731–732
  composite carbides, 726
  creep resistance, 726–727
  die bodies, 726
  die inserts, 726
  ductility, 726–727, 731
  electrical make-break contacts, 726, 729*t*
  hafnium carbide, 726
  heat shields, 726
  heating elements, 726
  high-energy ball milling, 732
  linings for furnaces, 726
  immiscible sodium and yttrium elements, 732
  mechanical alloying, 726–728, 732
  mechanical alloying-mechanical disordering, 733, 734*f*
  microhardness, 732
  molybdenum–lanthana alloy, 731
  molybdenum–silver composites, 726, 729*t*
  molybdenum–yttria alloy, 731
  near stoichiometric mixture of powder components, 733
  punches for hot stamping, 726
  recrystallization temperature, 725–727
  rocket nozzles, 726
  self-propagating high-temperature synthesis (SHS), 733
  sintering temperature, 731–732
  spark plasma sintering (SPS), 727–728, 732, 733*f*
  structural parts, 726
  thermo-explosion mode, 733
  thin sheets, 726–727, 731–732
  titanium carbide, 726–727
  TZM molybdenum alloy, 726
  wet doping technique, 731
  zirconium carbides, 726–728
Multiaimed powder tester FT4
  basic flow energy, 57
  downward traverse, 57
  Freeman Technology, 57
  FT4 equipment, 57
  force signal, 57
  torque signal, 57
  upwards traverse, 57

N

Nanopowder(s)
  applications, 296–307
  cemented carbides, 300–302, 301*t*
  electrical storage systems, 306–307
  features of nanoparticles, 272–274
  fibre-reinforced material, 302
  microencapsulation of nanoparticles, 293–294
  miniaturized systems, 307
  nanopowder chemical passivation, 293
  nanopowder–polymer composites, 303–304
  powder processing methods, 294–295
  production methods, 278–292
  semiconductors, 305–306
  testing of nanopowders, 275–278
  thin film technique, 304–305
  safety aspects of nanopowders production, 295–296
Nanopowder-polymer composities
  composite nanoparticles, 303
  microsphere composite nanoparticles, 303–304
  polymer-matrix composites, 303
Netzsch attritors, 98*t*, 101, 102*f*
Nickel, 119, 162, 173, 204–209, 208*f*, 216, 221, 225, 235–236, 236*f*, 252, 287*f*, 325–326, 352, 633–657, 645*f*, 661–667
Nickel-alloy powders
  atomizated nickel alloy powders, 652–657
  autoclave processing of nickel hydroxide and carbonate pulps, 651–652
  carbonyl process of nickel powder production, 633–644
  hardfacing powders, 652–654
  hydrometallurdical processing, 644–652, 645*f*
  mechanically alloyed nickel superalloy powders, 657
  powder covered by nickel, 650–651
  production of nickel powder by electrolysis, 663–664
  production of nickel powder by reduction processes, 661–663
  production of nickel and nickel-alloy powders, 633–667
  superalloy powders, 654–657
Nickel base alloys (related to applications of additive manufacturing)
  DED-L (direct energy deposition by laser heat source), 392
  DED-PA (direct energy deposition by plasma arc heat source), 392
  direct energy deposition (DED) process, 392
  electron beam melting (EBM), 392
  elevated temperatures, 392
  functionally graded system, 392
  Inconel 625, 392, 394*t*
  Inconel 718, 392, 394*t*
  Intermetallides, 392
  Invar 36, 392–393, 393*f*, 394*t*
  laser scanning speed, 393, 393*f*
  laser scanning tracks, 393
  Ni-base superalloys, 392
  NiCr superalloy enriched by titanium, 392
  nickel chrome superalloy matrix, 392
  PBF-EB (powder bed fusion by electron beam heat source), 392, 394*t*
  PBF-L (powder bed fusion be laser heat source), 392, 394*t*
  powder bed fusion (PBF) process, 392, 394*t*
  powder bed layers, 392
  Rene 142, 392
  selective laser melting (SLM), 392–393, 393*f*
  3D layerwise laser cladding, 392
  turbine blades, 392
  turbine engines, 392
Nickel–clad aluminum powders, 351–352, 474
  carbonyl process, 351
  compounds clad by nickel, 351, 474
  Co-base superalloys, 392
  EBM scanning, 392
  melt pool, 392
  nickel coating, 474
  plasma coatings, 474
  properties of nickel–clad aluminum powders, 474
  spraying of coatings, 474
  thickness of the coating layer, 474
  vibro-fluidized bed, 351
Nickel powders, 208–209, 208*f*, 287, 294, 325*f*, 378, 380*f*, 385–386, 600, 633, 635, 638–639, 640–641*f*, 641–642, 643*f*, 644, 646–651, 662–664, 663–664*f*, 670
Niobium alloys, 162, 290, 734–742
  arc melting, 740
  direction of crystallization, 742
  directional solidification, 740
  electric contacts, 738
  electrode induction melting, 740–741
  hot extrusion, 740
  hot isostatic pressing, 740–741
  microwaves absorber, 738
  niobium composites, 742
  niobium–aluminum alloys, 741–742
  niobium-based silicide intermetallic composites, 740
  niobium–copper alloys, 738
  niobium powders, 73, 736–738, 736*f*, 738*t*, 740*f*
  niobium–silicon alloys, 740–742
  oriented crystallization melting, 741–742
  physical vapor deposition, 740
  production of niobium powders, 734, 736–738
  silicide parameters, 741
  valence electron concentration, 741
  welding electrodes, 738
Nitriding and oxide formation
  nitride film, 446
  nitriding treatment, 446
  nitrogen-containing compound, 446
  oxide film, 446
Noble metal powders
  gold powders, 835–837
  iridium powder, 837
  osmium powder, 839
  palladium powder, 839
  platinum powder, 839
  platinum-group powders, 837–842
  production of noble metal powders, 842–844
  rhodium powder, 839

  ruthenium powder, 839
  silver powders, 832–835
Nontransferred arc, 447–448, 448*f*, 676
Non-sag tungsten wires
  doping elements– aluminum, silicon, potassium, 699–701
  elongated interlocked grain structure, 701
  incandescent lamp, 699–701
  potassium bubbles, 701
  tungsten filaments, 699–701
  tungsten lattice, 699–701
  tungsten metal powder particles, 699–701
Norilsk Nickel Concern, 351, 474
Nucleation stage, 647, 671–672

O

Occupational exposure limits of bismuth in workplace atmosphere, 854–857
Occupational exposure limits of lead in workplace atmosphere, 854–857
Occupational Safety and Health Administration (OSHA), 209, 612–613, 683–684, 773, 776, 810
Open-cell materials
  nickel alloys, 338
  nickel foams, 338
  supercapacitor, 338
Open-cell metallic foams
  catalysts, 336–337
  diffusion process, 338
  flow fluids, 336–337
  heat transfer, 336–337
  high-temperature supports, 336–337
  electrochemical cells, 336–337
  multifunctional load supporting, 336–337
  synthesis of open-cell metal foams, 336–337
  ultralightweight metal foams, 337
Optical microscopy, 6–7, 38
  automatic counting devices, 8
  bank register, 9
  contiguity and overlap, 9
  dispersing fluid, 8
  dissolving collodion, 9
  eyepiece graticules, 9, 9*f*
  filar micrometer eyepiece, 9
  particle images, 9
  particle photographs, 9
  preparation techniques of slides, 8
  recognition of the particles, 9
  recording micrometer eyepiece, 9
  segregation of particle sizes, 8
  slit scanning method, 9
  spot scanning devices, 9
  Vigdorchik's denumerably-measuring, 9
Orowan loop, 815
Orowan mechanism, 815
OSHA. *See* Occupational Safety and Health Administration (OSHA)
Osmium
  chemical composition, 841
  particle size, 839
Oxide dispersion strengthened alloys, 112–113, 179, 482
  corrosion resistance, 107
  elevated temperature strength, 107
  extrusion, 107
  high oxidation resistance, 107
  homogenization of the powders, 107
  hot corrosion resistance, 107
  inhibit the recovery process, 107
  inhibit the recrystallization, 107
  prealloyed powders, 107
  stable oxides, 107
  tumbling ball mills, 107
  uniform dispersion, 107

P

Packaging
  proportioning and packaging of powders, 451
  rotary table, 451–452
  vibrating densification, 452–453
  volume batching, 451
  weight batching, 451
Palladium powder
  autoclave precipitation, 841–842
  average particle size, 833, 840*t*
  beginning of oxidation, 840*t*
  carbonyl process, 840–841
  chemical reduction, 839
  chemical precipitation from pulp, 844*f*
  chemical precipitation from solution, 832, 843*f*
  palladium–copper, 836–837*t*
  palladium–nickel, 836–837*t*
  palladium–platinum, 836–837*t*
  palladium–silver, 836–837*t*
  particle size, 831–833, 837
  production of powders of alloys based on noble metals, 831
  properties of palladium powders, 840–841, 840*t*
  silver–palladium composition, 842
  specific surface, 833, 839–841
  synthesis of palladium nanoparticles by methods of zone electrochemistry, 845
  tap density, 840*t*
  water solution electrolysis, 845
Particle image analysis
  chemistry analysis, 6–7
  morphological analysis, 6–7
  particle shape, 6–8
  size measurements, 7
Particle shape
  acicular, 7
  angular, 7
  crystalline, 7
  dendritic, 7
  fibrous, 7
  film boiling conditions, 137–139
  flaky, 7
  granular, 8
  irregular, 8
  lamellar, 8
  shape factors, 8
  spherical, 8
  spheroidization time, 137–139, 141
Particle size distribution analysis
  classification in centrifugal field, 16–18
  classification in gravitational field, 13–16
  classification in inertia force field, 18
  counting and sizing of particles by indirect measures, 18–21
  metallographic microscopy, 10
  optical microscopy, 8–9
  regularities of granulometric composition, 22–26
  scanning electron microscopy, 10
  sieve analysis, 11–13
  transition electron microscopy, 10–11
Passivation methods
  inhibition of cathode processes, 444
  reduction of the degree of thermodynamic instability, 444–445
  rising of ohmic resistance, 444–445
Passivation techniques
  hydrophobization, 445–446
  inhibition of cathode processes, 444
  microencapsulation, 446
  nitriding and oxide formation, 446
  passivation methods, 444–446
  thermodynamic instability, 442, 444–445
Permanent magnets
  binder agent, 796
  compression molded, 796
  coercive force, 794
  direct-current motors, 797
  electronic watches, 797
  electronics segment, 797–798
  gas atomized powders, 795
  generators, 797
  hydrometallurgical method, 797
  hysteresis loop, 794
  injected molded magnets, 796
  mechanical alloying, 796–797
  medical devices, 797
  melt spinning technique, 796
  nanocrystalline multicomponent systems, 796–797
  Nd–Dy–Fe–Co–Nb–Al–Cu–B sintered magnets, 795
  NdFeB permanent magnets, 794
  $Nd_{13.6}Fe_{73.7}Co_{6.6}Ga_{0.6}B_{5.5}$ ribbon powder, 795
  (PrNd)FeB system, 796–797
  ribbon powder magnets, 796
  rare earth alloys magnets, 794
  residual induction, 794
  single-phase demagnetization curves, 796–797
  $SmCo_5$ single phase magnets, 794
  synchronous motors, 797
  traveling wave tubes, 797
Permeability of metallic foams
  fluid velocity, 345
  gas diffuses, 345
  perforation, 345
  porous media, 345
  pressure drop, 345
  surface modification, 345
  wettability, 345
Permeametry
  gas permeability, 41

- Permeametry *(Continued)*
  - Kozeny–Carman equation, 41
  - pressure drop, 41
  - specific surface area, 41
  - Tovarov's apparatus, 41
  - velocity of fluid flow, 41
- Permissible exposure limit (PEL), 209, 612–613, 773, 776, 810, 881
- Physical and chemical principles of electrolytic crystallization of dendrite deposits
  - cathode overvoltage, 236
  - crystal-spherulite, 238
  - diffusion limitations, 237
  - dendrite deposit growing, 238–239, 241
  - dendrite growth, 236–238
  - electric precipitation, 236
  - electrochemical reaction, 237
  - Faraday constant, 236
  - galvanostatic electrolysis, 237
  - metal deposition, 236
  - ohmic control, 240
  - Pomosov depletion factor, 237
  - potentiostatic conditions, 237–238
  - Runge–Kutt method, 239
  - smooth spheroidal spherulite-globules, 236
  - spherical diffusion rate, 238
  - tip shape, 238
  - transfer control, 240
- Physical and chemical properties (thorium, uranium)
  - face centered cubic lattice, 819
  - orthorhombic system, 819
  - thorium oxide, 819
  - thorium hydride, 819
  - thorium nitrides, 819
  - uranium hexafluoride, 819
  - uranium hydride, 819
  - uranium nitrides, 819
  - uranium–oxygen system, 819
  - uranium tetrafluoride, 819
- Physical vapor deposition (PVD)
  - arc-vapor deposition, 337
  - evaporation–condensation process, 195
  - evaporation means, 195
  - metal spray deposition, 337
  - powder formation, during vapor condensation, 189–192
  - properties of powders, 196
  - PVD process installations, 195
  - reactive sputtering, 337
  - theoretical basis, 194
  - thermal evaporation, 337
- Pycnometry
  - Archimedes' law, 42–43
  - bulk volume, 42
  - density of PM materials, 42
  - displacement principle, 42–43
  - gas pycnometry, 42–43
  - helium-filled sample system, 43
  - liquid pycnometry, 42–43
  - pycnometer, 43
  - porosity, 42
  - powder density, 43
  - pressure/volume relationship, 43
  - specific volume, 42
  - submerged powder, 43
- Plasma atomization process
  - argon atmosphere, 175
  - cooling rate, 175
  - plasma torch, 175
  - spherical titanium powder, 175
  - wire feedstock, 175
- Plasma-rotating electrode process (PREP)
  - centrifugal atomization process, 554–555
  - consumable metal bar, 554–555
  - helium plasma, 554–555
  - rotating electrode process (REP), 554–555
  - spherical powder particles, 554–555
- Plasma transferred arc hardfacing process, 676, 676*f*
- Platinum alloy powders, 845
- Platinum powders
  - apparent density, 833, 840–841
  - autoclave precipitation, 841–842
  - black powder, 844–846
  - chemical composition, 838*t*
  - chemical precipitation, 831–832
  - particle size, 831–832
  - platinization, 844
  - platinum black powder, 844–846
  - platinum carbonyl compounds, 840
  - platinum–cobalt, 836–837*t*
  - platinum electrode, 844
  - platinum niello production, 839
  - platinum oxide, 839
  - water solution electrolysis, 836–837*t*
- Poisson's ratio, 68, 276–278
- Porosimetry
  - bubble test of pore size, 46
  - capillary rise phenomenon, 43–44
  - contact angle, 43–44, 44*f*
  - gas porosimetry, 43
  - mercury porosimetry, 43–44
- Porous aluminum
  - aluminum powder slurry, 478
  - boiling cooling system, 478
  - boiling heat transfer, 478
  - boiling heat transfer coefficient, 478
  - ebullient cooling system, 478
  - fin heat sink, 479
  - heat conductivity, 478
  - heat removal from the electronic equipment, 478
  - heat sink, 478
  - heat sink cooling materials, 478
  - polyvinyl alcohol water solution, 478
  - powder injection molding, 479
  - technology of foil processing, 474
  - vacuum heat-treatment furnace, 478
  - ultrasonic treatment, 478
- Porous materials
  - battery electrodes, 323, 326
  - bearings, 323–324
  - biomedical implants, 328
  - diesel soot filters, 329–330*t*
  - filters, 323–324, 326
  - flexible porous sheet material, 327
  - fuel cells, 328
  - volumetric-flow-restricting devices, 328
- Porous PM materials. Application areas
  - boundary layer control, 323, 328
  - filtration/separation technology, 326
  - flow control devices, 323, 328
  - gas–liquid contacting, 328
  - reservoirs and capillary attraction, 329–330*t*
  - surface area devices, 329–330*t*
- Porous powders.. *See also* Porous powder and metallic foams
  - compaction methods, 325–326
  - material selection, 324
  - mechanical properties, 326
  - porous aluminum, 334*f*
  - powder preparation, 324–325
  - sintering, 326
- Porous powders and metallic foams
  - cellular PM materials, 323
  - compaction methods, 325–326
  - metallic foams, 328–346
  - material selection, 324
  - metal sponge, 323
  - porous aluminum, 334*f*
  - porous powders, 323–328
  - powder preparation, 324–325
- Powder bed fusion (PBF)
  - formation of the powder bed, 376
  - laser beam heat source (L), 375–376
  - printing process, 375–376
  - packing density, 376
  - part's cross-section, 375–376
  - powder bed, 375–376
  - powder packing, 376
- Powder characterization and testing
  - bulk properties of powders, 47–57
  - particle image analysis, 6–8
  - particle shape, 7–8
  - particle size distribution analysis, 8–26
  - sampling of powders, 4–6
  - size measurements, 7
  - surface area and porosity of powders, 38–46
  - techniques of chemical analysis for powders, 26–38
- Powder cleanliness
  - atomization nozzle design, 162
  - atomizing gas, 162
  - carbon, oxygen, nitrogen, and hydrogen impurities, 162
  - ceramic-free pouring nozzle, 162
  - crucible- and ceramic-free, 162
  - electrode induction melting gas atomization process, 162
  - EIGA process, 162
  - electroslag remelting, 162
  - impurity control, 161
  - inclusion capture, 162
  - inductively melted without crucible, 162
  - inert gas jet, 162
  - initial charge impurities, 162
  - interstitial impurity, 162
  - non-metallic inclusions, 161
  - melting atmosphere, 162
  - oxygen level, 162

  prealloyed rods, 162
  primary sources of intermediate impurities, 162
  refractory ceramics, 162
  vapor pressure, 162
Powder characteristics (water atomized powders)
  Bramley's formula, 138
  bubble boiling conditions, 137–138
  cellular structure, 142
  dendrite parameter, 139
  effect of pouring temperature, 135, 136*f*
  film boiling conditions, 137–139
  film-bubble heat emission conditions, 138
  first critical heat current density, 137–138
  heat transfer coefficient, 135, 137–138, 139*f*
  heat transfer process, 137
  irregular shape, 134, 138–141
  liquid drop cooling process, 137–138
  liquidus temperature, 137, 139
  log normal size distribution, 135
  melt drop cooling time, 137
  melt drop size, 139–141
  melt strand, 137
  non-dendrite grain, 138
  non-dendritic structure, 142
  oxide film, 141–142
  particle shape, 136–141, 137*f*, 139–140*f*
  particle size distribution, 135–142
  particle structure, 138
  pouring melt temperature, 138–141, 140*f*
  second critical heat current density, 137–138
  spherical shape, 137
  spheroidization time, 137–139, 141
  standard deviations, 135
  steam film, 137–138
  unevenness surface, 238
  water boiling, 137
Powder consolidation and wrought products (beryllium and beryllium alloy powders)
  cold isostatic pressing and sintering, 806
  hot isostatic pressing (HIP), 804–806, 805*t*
  vacuum hot pressing (VHP), 804, 805*t*
  wrought product forms, 806–807, 807*t*
Powder contamination
  chemical purity, 110
  flushing by argon, 110
  grinding medium, 109–110
  magnitude contamination, 109–110
  milling atmosphere, 110
  milling equipment, 110
  minimizing powder contamination, 110
  nitrogen, 110, 111*t*
  oxygen, 110, 111*t*
  proper cleaning, 110
  reactive metals, 110
  sealing quality, 110
Powder preparation
  blending, 325
  centrifugal separation, 324
  cleanliness, 325
  narrow size distributions, 324
  particle size distributions, 324
  secondary processing, 324
  separation, 324
  ultrasonic sieve screening, 324
  vibratory sieve screening, 324
Powder production by PVD
  bronze powder, 196*t*
  copper powder, 195, 196*t*
  lead powder, 195, 196*t*
  zinc powder, 195–196, 196*t*
Powder production using the method of zone electrochemistry
  current impulse, 254
  electrochemical impulse, 254
  electrolysis duration, 254
  ultrasonic (zone) impulse, 254
Powder properties and applications (carbonyl nickel powders)
  acicular powder particles, 638
  apparent density classification, 641, 642*t*
  catalysts, 642–643, 643*t*
  chemical industry, 641
  coatings, 642–644
  conductive resins and plastics, 642
  electronic alloys, 642
  ferrites, 642
  filamentary chain-type nickel, 324
  fuel-cell electrodes, 642
  getter, 642
  hard alloys, 642
  high density semi-smooth particles, 638
  high surface area powders, 638
  Inco types of carbonyl nickel powders, 638–639, 639*t*, 642, 643*t*
  lamination structure, 639–640
  magnets, 642
  Norilsk Nickel types of carbonyl nickel powders, 638–640, 639*t*, 642, 643*t*
  pigments, 642
  rechargeable batteries, 642
  shaped like an onion, 639–640
  spherical granules, 639–640
  welding products, 642
Powder sample preparation (for SEM and TEM)
  automatic image analyzer, 10
  carbon film, 10
  carbon substrate grid, 10
  dispersing agent, 10
  electron microscope grid, 10
  ethylene glycol sublimates, 10
  fused metal, 11
  particle thicknesses, 11
  precipitation of carbon vapor, 10
  shadowing particle dispersions, 11
  smooth substrate, 10
  substrate, 10
  viewing screen, 10
  viscous liquid, 10
Powders for additive manufacturing
  angle of repose, 378
  avalanche angle, 378, 380*f*, 385
  avalanche surface fractal, 378
  composition, 385–386
  computed tomography (CT), 377
  feedstock material, 373, 375–377
  flowability, 377–378, 379*t*, 382, 385
  gas atomization (GA), 377, 381–385
  gas metal arc welding processes, 376–377
  microhardness testing, 392
  multiple reuse cycles, 381
  plasma rotating electrode process (PREP), 377, 383, 384*f*
  porosity, 377*t*, 379*t*, 383–385, 387, 390, 393, 393*f*
  powder characterization and testing, 377–381, 379*t*, 380–381*f*
  powder feeding rate, 376–377
  powder properties, 381–383, 381*t*, 382–384*f*
  revolution powder analyzer, 378, 380*f*, 385–386
  rheological measurements, 395
  ring shear cell tester, 378, 380*f*
  rolled sheet, 375–377
  rotary atomization, 383
  shape, 377–381, 379*t*, 381*f*
  size distribution, 377–378, 379*t*, 380*f*
  surface morphology, 377–381, 381*f*
  Vickers microindentation hardness, 392
Powders for composites
  composite manufacturing methods, 363
  manufacture of composite powders, 351–352
  manufacture of composites, 363–368
Powder spheroidization by thermal plasma processes
  DC thermal plasma treatment, 448
  densification of particles, 446–447
  direct current (DC) arc plasma torches, 446–447
  inductively coupled plasma (ICP) technology, 446–447
  laser cladding process, 448
  non-transferred arc DC torche, 447–448, 448*f*
  plasma gas, 447
  radio frequency (RF), 447
  recycling of nickel based powders, 448
  RF induction plasma systems, 447–448, 447*f*
  spheroidization of particles, 446–447
  spheroidization of titanium powders, 448, 448*t*
  Tekna inductively coupled plasma torch, 448
  Tekna Systems Incorporated, 447–448
  thermal plasmas, 446–448
Powders with quasicrystalline structure
  discovery and structure of quascrystalline materials, 313–314, 314*f*
  manufacturing technique of quasicrystalline powders, 314–319
  properties and applications of quasicrystalline materials, 313–314, 315*t*
Precipitation from gaseous phase of tungsten hexafluoride and tungsten hexachloride
  decomposition of tungsten hexachloride, 691
  dissociation of tungsten hexafluoride in hydrogen, 691
  gaseous substances, 691
  halide evaporator, 692
  high temperature decomposition, 691
  reactor of fluidized bed, 692
  spherical particle shape, 692
  tungsten hexafluoride, 691–692, 692*f*

Precipitation from gaseous phase of tungsten hexafluoride and tungsten hexachloride *(Continued)*
  tungsten oxyfluoride, 692
  tungsten reduction, 692
Preparation techniques of slides
  Canada balsam, 9
  cover slip, 8
  glass slide, 8
  permanent slide, 8–9
  shearing action, 8
  staircase effect, 374
  thin films, 9
Press-sinter method, 702, 772–773
Press-sinter-re-press (PSR) process, 702
Principles of additive manufacturing
  computer-aided design (CAD), 374
  fusing, 374
  layer processing time, 374
  rapid prototyping, 374
  recoating time, 374
  selective laser melting (SLM), 375
  sintering, 374, 374*f*
  thickness of layer, 374
  work platform, 374
Process control agent (PCA)
  dispersion strengthening, 92–93
  embrittling the powders, 92–93
  interstitial compounds, 92–93
  organic compounds, 92
  surfactant, 92–93
Processing of powders and processing equipment
  dehydration, 403–413, 405*t*
  interstage transport, 452–454
  mixing, 435–441
  packaging, 451–452
  passivation techniques, 442–446
  powder classification by size, 424–435
  proportioning, 449–451
  thermal drying, 413–424
Processing of recycled aluminum to granules
  aluminum scrap, 477
  chips, 477
  drink cans, 477
  ferrous metallurgy, 477
  impurities, 477
  mechanical impurities, 477
  processing of aluminum scrap, 477
  recycled aluminum, 477
  remelting, 477
  remelting–casting technologies, 477
  steel deoxidation, 477
Production methods
  chemical precipitation from solutions, 282–285
  condensation technique, 278–282
  high-energy disintegration, 289–292
  plasma chemical synthesis, 286–288
  spray conversion method, 285
Production of cadmium powders
  cementation (contact displacement) method, 625
  centrifugal reactor-separators, 625
  copper–cadmium cake, 625
  electrolysis of aqueous solution, 626*t*
  electrolysis of non-aqueous solution, 626*t*
  electrolytic deposition, 625
  reduction from the solid phase, 626*t*
  waste electrolyte, 625
Production of chlorides (RE chlorides)
  ammonium chloride, 786
  anhydrous RE chlorides, 786
  carbon tetrachloride, 786
  dehydration of lanthanide crystallohydrate, 785
  hydrogen chloride, 786
  oxide chlorination, 785
  oxychlorides, 786
Production of cobalt and cobalt alloy powders by electrolysis
  alkaline cobalt carbonate, 681
  ammonium sulfates, 670–673, 679
  anode dissolution of cobalt, 678
  cobalt current efficiency, 678, 680*t*
  cobalt formate, 681
  current density, 678, 680*t*
  dendritic microstructure, 680
  electrochemical precipitation, 679
  electrolytic cobalt powder, 679–680
  electrolyzer, 678
  metal dissolution, 678
  properties of the electrolytic cobalt powder, 678–679
  soluble cobalt anodes, 678, 681
  sulfate electrolyte, 678, 681
  suspended solid, 678
  titanium disc cathodes, 678
Production of flakes, pigments, paints and pastes
  aluminum flake pigments, 470
  aluminum flake production, 472
  aluminum flakes, 468, 470, 471*t*, 472–473
  aluminum pastes, 472–473, 472*f*, 473*t*
  aluminum pigments, 470
  cold welding, 470
  fatty additive, 470
  lamellar particle shape, 470
  leafing aluminum pastes, 472, 473*t*
  leafing paste, 472
  leak-tight mill working, 470
  liquid hydrocarbons, 472
  lumpy flakes, 470, 471*t*
  melt stream, 466
  metallic shine, 472, 473*t*
  non-leafing aluminum pastes, 472, 473*t*
  production of pastes, 472
  porous aluminum, 478, 479*f*
  roof coatings, 472
  slurry, 472
  stearin acid, 472
  varnish film, 472
  volatile liquids, 472
Production of fluorides (RE fluorides)
  anhydrous fluoride, 786
  dehydration of hydrated salts, 786
  fluoridation, 786
  hydrofluoric acid, 786
  hydrogen fluoride, 786
  muriatic solution, 786
  nitrate solution, 786
  precipitates, 786
Production of granules
  aluminum granulation, 465–468, 468*f*
  aluminum granules, 466, 468, 469*t*
  automotive coatings, 472
  centrifugal atomization, 466, 467*t*, 468*f*
  cold welding, 470
  cooling in gas atmosphere, 466, 468*f*
  cooling in liquid, 466, 468*f*
  cooling on cold surface, 466, 468*f*
  drop casting, 466
  drop-shaped granules, 466
  dry grinding, 472
  fatty additive, 470, 472
  free casting into water, 466, 468*f*
  gallium cementation, 466
  gas forming agent, 473
  granulated alloys, 466, 468
  granulated aluminum, 465–466
  granulated aluminum alloys, 466
  granule size, 466
  impulse atomization, 468
  melt centrifuging, 466–468
  melt stream, 466
  monodisperse droplets, 468
  needle-shaped granules, 466
  nozzle plate, 468
  orifice size, 468
  orifice shape, 468
  polychromatic effect, 472
  protection of particle surface, 466
  spherical granules, 466
  spinning cup, 466
  Volgograd Aluminum plant, 466
  wet grinding, 472
  water-cooled metal disk, 466
  water-filled explosives, 473
  water paste, 473
Production of leafed beryllium by electrorefining from melts
  cathode deposits, 801
  gradually extending anode, 801
  insoluble anodes, 801
  preliminary beryllium disks, 801
  refined beryllium, 801
Production of magnesium and magnesium alloy powders
  production of magnesium granules, 538–539, 538*f*
  production of magnesium powders, 533–541, 535*f*, 536–537*t*
Production of magnesium granules, 538–539, 538*f*
Production of molybdenum powders
  ammonium molybdate, 723–724
  calcinations in oxygen, 725
  carbonyl molybdenum, 725, 725*t*
  carbonyl process for molybdenum powder, 725
  iron chloride, 724
  molybdenum chlorides, 724–725
  molybdenum disulfide, 723

  molybdenum pentachloride, 724–725
  molybdenum trioxide, 724
  reduction by hydrogen, 725
  rotary furnaces, 723
  solvent extraction processes, 723
  tube push furnace, 723
Production of multicomponent alloy powders
  chemical compounds, 254
  combined anodes, 253
  constant solution composition, 253
  dendrite tips, 252–253
  diffusion control, 252–253
  growing depletion factor, 254
  kinetics of electrochemical reduction, 254
  metal ions, 252–254
  metal salt, 253
  soluble anodes, 253
  spherical diffusion, 253
Production of nickel alloy powders by mechanical alloying
  contamination of powders, 658
  close-coupled gas atomization, 659–660
  dispersion-strengthened superalloys, 657
  gas atomization reaction synthesis (GARS), 658, 660*f*
  gas turbine engines, 658
  grinding medium, 658
  high-energy ball milling technique, 657
  high-temperature particle strengthening, 658
  highly alloyed matrix, 657
  hot isostatic pressing (HIP), 657–658, 660
  mechanism of alloying, 657
  milling atmosphere, 658
  minimizing contamination, 658
  nanometric oxide dispersoids, 658
  Ni-based superalloys, 661
  ODS layer, 661
  Oxide dispersion strengthening (ODS), 657–658
  plasma activated sintering, 657–658
  powder rolling, 657–658
  precursor Ni–Cr–Y–Ti powder, 659–660
  precursor powders, 658
  superalloy MA 754, 658
  superalloy MA 760, 658
  superalloy MA 6000, 658
  turbine blades and vanes, 658
Production of nickel powder by electrolysis
  anode current, 663
  aqueous ammonia, 663–664
  chloride-ions, 663
  coral-like dendritic structure, 663–664
  electrolyte composition, 663
  electrolytic nickel powder, 663–664, 664*t*, 664*f*
  fir branches, 663–664
  hollow disc cathodes, 663
  hydrochloric acid, 663
  powder precipitate, 663
  soluble anodes, 663
  sulfate electrolyte, 663
Production of nickel powder by reduction processes
  reduction by organic reagents, 662–663
  solid phase reduction, 661
Production of niobium powders
  carbothermic reduction, 736
  electrolysis of melt, 737, 737*f*, 738*t*
  hydride–dehydride process, 738
  metallothermic reduction, 736, 736*f*
  reduction by sodium, 737
Production of niobium powders by carbothermic reduction
  graphite cartridge, 736–737
  graphite-tube, 736–737
  hydrogen atmosphere, 736–737
  lower oxide formation, 736–737
  niobium carbide, 736
  niobium carbide particles, 736–737
  niobium oxide vapor, 736–737
  push type furnaces, 736–737
  reduction in two-steps, 736
Production of niobium powders by electrolysis of melt
  alkali metal chlorides, 737
  cathode current density, 737
  cathode product, 737–738
  electrolysis cell, 737–738
  electrolysis of bromide, 737
  electrolyte temperature, 737
  graphite rod, 737
  nickel crucible (cathode), 737
  niobium pentoxide, 737
  niobium sponge, 737
Production of niobium powders by metallothermic reduction
  aluminothermic reduction, 736
  chlorination process, 736
  columbite ore, 736
  cyclone separator assembly, 736
  electron beam purification, 736
  exothermic reaction, 736
  magnesiothermic reduction process, 736
  magnesium vapor reduction process, 736, 736*f*
  moderate boiling temperature, 736
  niobium pentachlorate, 736
  oxygen content, 736
  pyrochlore concentrates, 736
  tantalite ore, 736
  vapor pressure, 736
Production of platinum-group powders
  alloys based on noble metals, 842–844, 843–844*f*
  autoclave precipitation, 841–842
  carbonyl process, 840–841
  chemical reduction, 839
  electrolysis, 835
  electrolysis from double-layer cell, 836–837*t*
  water solution electrolysis, 836–837*t*
Production of powder products from waste aluminum foil
  aerated concrete, 474
  aluminum flake powders, 474–476, 475–476*f*
  aluminum foil scraps, 474–476
  ball milling, 474–476
  crushing in cutting units, 474
  dry crushing, 474
  fingerprint detection, 474, 476
  foil thickness, 474–476, 475–476*f*
  foil waste products, 474
  grinding in mills, 474
  grit, 474
  inks, 474, 476
  inorganic solvent, 474, 476
  laminated flake powder, 475
  milling time, 475
  mineral spirits, 474, 476
  oleic acid, 476, 476*f*
  paints, 474, 476
  paste manufacturing industry, 474, 476
  recycling, 474
  recycling of aluminum scrap, 474–477
  saving material, 474
  technology of foil processing, 474
  wet crushing, 474
Production of powders by electrolysis from melts
  chloride and fluoride salts of metals, 260
  dendrite crystallization, 262
  dendrite length, 265–266
  dendrite precipitate, 262
  electronegative metal powders, 258
  flat growth front, 258
  metal chlorides, 260
  soluble anode, 260, 262
Production of rare earth metal alloy powders
  electrochemical methods, 786–787, 787*f*
  initial compounds for metal production, 785–786
  metallothermic methods, 787
  methods of RE elements separation, 782–785, 783–784*f*
  refinement of RE by distillation, 788
  sources of raw material, 781–782, 800
Production of silver powders
  atomization, 833
  chemical processes, 832–833
  chemical reduction with electrochemical reduction of the reducer, 835
  electrolysis from double-layer cell, 836–837*t*
  evaporation of silver, 832
  fibrous dendritic silver residue from molten electrolytes, 835, 837*f*
  mechanical comminution, 833–834
  silver anode, 834–835
  spray pyrolysis technique, 833
  water solution electrolysis, 836–837*t*
Production of thorium compacts
  calcium thermic thorium powder, 821
  electric-arc furnace, 821
  electrolytic thorium powder, 821
  pressed billets, 821
  vacuum induction furnace, 821
Production of titanium and titanium alloy powders
  amalgam metallurgy technique, 562–563, 563*f*
  chemical reduction, 550–554
  chemical synthesis of nano size titanium powders, 565
  CSIR process, 564–565

- Production of titanium and titanium alloy powders *(Continued)*
  - electrolysis of titanium compounds, 558–562
  - gas atomization, 555–558, 555–558*f*
  - mechanical alloying, 565
  - method of disproportionation of lower titanium halogenides, 564
  - plasma-rotating electrode process (PREP), 554–555, 555*f*
  - TIRO method, 563–564, 564*t*, 564*f*
  - titanium, 549
  - titanium alloy powders, 549
  - titanium powder-based materials selection, 567–568
- Production of tungsten carbide powders
  - calcination– reduction–carburization (CRC) process, 707–708
  - carbon black, 707–709
  - carburization, 708–709
  - chemical vapor reaction process, 709
  - direct carburizing process, 709
  - gas phase reaction, 709
  - Menstruum process, 708–709
  - Menstruum tungsten carbide powders, 708–709
  - production of fine grained powder, 709
  - pure tungsten powder, 707–708
  - single tube pusher type furnaces, 707–708
  - spray conversion process, 709
  - tungsten carbide crystallites, 709
  - tungsten ore concentrates, 708–709
  - vertical reactor, 709
- Production of tungsten powder by a plasma process
  - boiling point, 692
  - coagulation, 692
  - condensation, 692
  - crystallization, 692
  - direct current arc, 693
  - polymorphous transformations, 692
  - radio-frequency plasma, 693
  - two stage scheme, 692–693
  - vaporous state, 692
- Production of zinc and cadmium alloys powders
  - atomization of melt, 625
  - cyanide solutions, 625
  - dendrite shape, 625
  - electrochemical method, 625
  - reduction from the solid phase, 626*t*
  - zinc–copper alloy powders, 625
- Production of zinc, cadmium, and their alloy powders
  - production of cadmium and zinc alloy powders, 625–626, 627–628*t*
  - production of cadmium powders, 625, 626*t*
  - production of zinc powders, 615–625
  - safety measures in cadmium and zinc powders production and handling, 626–628
- Production of zinc, cadmium, and their alloy powders, applications
  - anticorrosive zinc-rich coatings for roll and sheet steel metal ware, 630
  - cathodic protection, 628
  - manufacture of reducing agents, 628
  - mechanical plating, 630
  - pigments in anticorrosive coatings, 628–629
  - powder coating, 628
  - powders with flaky particles, 629
  - protective coatings, 628–629, 629*t*
  - purification of zinc solutions, 628
  - recycling of tungsten carbide powders, 631
  - sherardizing, 630, 630*f*
  - zinc-rich compounds, 628
  - zinc-rich paints, 628
  - zinc-rich primers, 628–629
- Production of zinc powders
  - cryogenic methods, 625
  - electrochemical methods, 621–624, 623*t*
  - evaporation-condensation method, 615–620, 616*f*, 618–619*t*, 619–620*f*
  - inert gas condensation, 619–620, 620–621*f*
  - mechanical grinding, 624
  - melt atomization, 620, 621–622*f*
  - rectification of the melt, 616*f*
  - reduction from the solid phase, 623*t*
- Properties and applications of quasicrystalline materials
  - CRISTOME quasicrystalline powders, 317, 318*t*
  - electric resistivity, 313–314
  - electronic structure of QC, 313–314
  - Fermi surface, 313–314
  - hardness, 314, 315*t*
  - icosahedral QC phases, 314–315, 316*t*, 317
  - mechanical alloying, 314, 316*t*
  - mechanical properties, 314, 315*t*
  - nanoquasicrystalline strengthening, 319, 320*t*
  - Peierls stress, 314
  - phason defects, 314
  - phonon and phason components, 314
  - polyamide composite reinforced by QC particles, 317
  - polymer-matrix composites reinforced with QC particles, 317
  - QC Al–Cu–Fe coatings, 319
  - QC interatomic bonds, 313–314
  - quasicrystals (QC), 313–314
  - rapid solidification, 316*t*
  - selective laser sintering (SLS), 317
  - semiconductors, 313–314
  - specific electric resistance, 313–314
  - surface hardened composite layers, 319
  - thermal conductivity, 313–314, 315*t*, 318*t*, 319
  - thermal diffusivity, 318*t*
  - thermal dilatation coefficient, 318*t*
  - ultrasonic impact processing, 319
  - yield strength, 314
  - Young's modulus, 314
- Properties of tungsten powders
  - alpha emitters, 699
  - ammonium paratungstate, 695, 699
  - apparent density, 695, 699
  - carbon content, 695, 697–699, 698*t*
  - carbonyl tungsten powders, 698*t*, 699
  - chemical properties, 695
  - chemical vapor deposition (CVD), 699
  - decomposition, 695, 697–699, 698*t*
  - demonstration fusion reactor (DEMO), 699
  - Fisher subsieve sizer (FSSS), 699
  - flowablility, 699
  - gravity sedimentation scattering, 695
  - green density, 695
  - green strength, 695, 702
  - hexagonal close-packed lattice, 699
  - high density, 695, 701–702
  - high intensity discharge (HID) lamps, 699
  - hydrofluoric medium, 695
  - light scattering techniques, 695
  - morphology of tungsten powders, 695, 699, 704*f*
  - particle size distributions, 695, 699, 701, 701*t*
  - physical properties, 695
  - physical vapor deposition (PVD), 699
  - plasma facing material, 699
  - properties of carbonyl powders, 697
  - pure tungsten powders, 699
  - semiconductor manufacture, 699
  - sintering temperature, 698, 702–703
  - spherical shape, 698–699
  - surface of tungsten particles, 697–698
  - thermal conductivity, 699
  - thermal decomposition, 698
  - trace elements, 695, 699–701
  - tungsten hexafluoride, 695
  - ultrahigh purity powders, 699
  - vacuum plasma spray, 699
- Proportioning
  - annular slot, 450
  - Auger dosing system, 451
  - automatic dosing machines, 451
  - feeder-activator design, 450
  - feed hopper, 449
  - feed rate, 451
  - fluidized state, 450
  - funnel flow mode, 450
  - milled product dosing, 451
  - powder feeders, 449
  - semi-automatic powder filling machines, 451
  - wheel feeder, 451
- Pulsated orifice ejection method
  - driving device, 174–175
  - mono-sized spherical particles, 174–175
  - narrow particle size distribution, 174–175
  - rectangular waves, 174–175
- Pure tungsten powders, 699, 704*f*, 707–708
- PVD process installations
  - physical sputtering, 195
  - plate-type rectifying columns, 195
  - powder production by PDV, 195–196
  - reactant gas medium, 195
  - "Tuman" unit, 195–196, 196*f*
  - zinc powder manufacturing, 195, 195*f*
- Pyrophorus, 673, 824–825

Q

- Quantum confinement effects
  - Bohr radius, 305
  - conduction band, 305
  - electron energy band, 305
  - valence band, 305
  - wavelength of the electron, 305

Quasicrystalline films
  annealing, 304–305
  flash evaporation method, 304
  heat treatment, 304
  low thermal conductivity, 305
  magnetron sputtering, 304
  multilayer films, 304
  nanosized quasicrystalline films, 304
  thermal barrier coating, 305
Quasicrystalline materials
  applications of quasicrystalline materials, 313–314, 315*t*
  crystallographic structure, 313
  decagonal QC structure, 313
  discovery of quasicrystals, 313–314
  five-fold symmetry, 313, 314*f*, 319, 319*f*
  icosahedron geometric figure, 313
  low electric and thermal conductivity, 313–314
  manufacturing technique of quasicrystalline powders, 314–319
  metastable, 313
  rapid crystallization, 313
  rapid solidification, 313, 316*t*
  rotational symmetries, 313
  semiconductors, 313–314
  Shahtman, 313
  specific electric resistance, 313–314
  structure of the quasicrystals (QC), 313
Quenching
  electrical contact materials, 726
  hardfacing, 714–717
  refractory metal powders, 702

R

Radioactive metals:thorium and uranium
  applications, 822–824
  physical and chemical properties, 819, 820*t*
  production of thorium compacts, 821
  thorium powder production, 820–821
Range of applications (RE metals, alloys, compounds)
  agriculture, 789
  cemented tungsten carbides, 798
  chemical industry, 789
  glass and ceramic production, 789
  laser technique, 789
  lighting technique, 789
  manufacture of electrodes, 792–794
  medicine, 789
  nuclear power, 789
  permanent magnets, 794–798, 795–797*f*, 795–796*t*
  refractory and elevated temperature alloys, 789–792
  television technique, 789
  traditional metallurgy, 789
Rapid prototyping
  built platform, 374
  infrared (IR) laser, 374
  polymer resin, 374
  selective laser sintering (SLS), 374
  stereolithography (SLA), 374
  thermoplastic materials, 374
  UV light, 374
Rapid solidification process
  cooling rate, 488–490, 489*t*, 491*f*, 492
  crystallization process, 490
  dendrite parameter, 488–489
  equilibrium diagram, 489*t*, 491*t*, 492, 492*f*
  eutectic systems, 492
  extension of solubility limits, 487
  hyperbolic equation, 488
  metastable equilibrium diagram, 492, 492*f*
  metastable process, 487
  non-dendritic grains, 488–490, 491*f*
  nucleation, 488–491
  peritectic systems, 492
  precrystallization undercooling, 490–491
  rapid crystallization, 491
  solidification, 487–492, 489*t*
  supersaturated solid solution, 492
Rare earth (RE) elements
  cerium, 778–779, 780*t*, 781, 784, 786*t*, 788
  cerium subgroup, 779, 781, 784, 786–787
  ferromagnetic properties, 781
  'heavy' (HREEs) elements, 778–779, 784–785
  'lanthanide compression', 779
  lanthanide elements, 778
  lanthanide hydroxides, 781
  lanthanum, 778, 780*t*, 781–782, 784, 784*f*, 786, 786*t*
  'light' (LREEs) elements, 778–779, 784–785
  lutetium, 778–779, 780*t*, 781–782, 783–784*f*, 784
  paramagnetic, 781
  yttrium, 778–779, 780*t*, 782
  yttrium subgroup, 779, 781–782, 784, 787–788
Rare metal powders
  bastnaesite, 781
  chlorides, 759, 781, 785–787, 798, 800, 820–821
  composite compounds, 779, 781
  euxenite, 781–782
  fluorides, 768, 781, 786–787, 800
  initial compounds for metals production, 785–786
  loparite, 781
  methods of RE elements separation, 782–785
  monazite, 781
  niobium tantalates, 781
  nitrates, 781–782, 784, 786
  oxalates, 781
  parisite, 781
  phosphates, 781
  production of rare earth metal-alloy powders, 778–798
  sources of raw material, 781–782, 800, 811–812
  sulfates, 775–776, 781, 783, 798, 800
  titanium niobates, 781
  vanadium, 758–766, 758–760*t*, 766*t*, 773, 778, 786, 795, 813*t*
  xenotime, 781–782
Recycling of tungsten carbide powders
  ball milling, 631
  crushing, 631
  graded powder, 631
  hardmetal scrap direct conversion, 631
  protective atmosphere, 631
  reaction in molten zinc, 631
  screening, 631
  vacuum distillation, 631
  Zn process, 631
Reduction by organic reagents (production of nickel powders)
  alcaline nickel carbonate, 662
  catalysts, 662–663
  colloidal structure, 662
  hydrazine–hydrate, 662
  narrow particle size distribution, 662
  nickel borate solution, 662
  nickel carbonate pulp, 662
  nickel sulfate solution, 663–664
  phase transformations, 662
  polyacrilamide oligomer, 662
  polymer compositions, 663
  roasting of sulfide materials, 661
  sodium formate, 662
  thermal decomposition, 661
Reduction from solution trough film of surfactants
  absorbed surfactant layer, 249
  bottom electrolyte layer, 248–249
  electrocrystallization process, 249
  ferromagnetic particles, 249–250
  hydrogen emission, 249
  organic liquid, 249–250
  running magnetic field, 249–250
  two-layer electrolyte, 248–249
  ultrafine elongated whiskers, 249
  upper layer, 248–249
Reduction methods of powder production
  application of chemically reduced powders and salts, 225
  autoclave precipitation of metal powders, 225–231, 226*f*
  carbochlorination process, 767–768
  chemical reduction, 221–225
  metallothermy, 221
  solid-phase reduction of metal oxides and salts, 211–218
Reduction of thorium dioxide by calcium
  calcium chips, 820
  calcium oxide, 820–821
  concentration table, 820
  dilute hydrochloric acid, 820
  furnace processing, 820
  molybdenum sheet, 820
  separation of fine fractions, 820
  thermal decomposition, 820
  thorium dioxide, 820, 821*f*
  thorium oxalate, 820
  thorium recovery yield, 820–821
Reduction of tungsten oxide by solid carbon
  carbon tube, 691
  high temperature zone, 691
  pusher type furnaces, 691

- Reduction of zirconium dioxide by calcium or calcium hydride
  - briquetted mixture, 768
  - calcium thermic process, 768
  - reduction process, 768
  - self-sustained process, 768
- Reduction of zirconium dioxide by magnesium using autoclave processing
  - Let–Lok apparatus, 772
  - pure metallic zirconium, 772
  - RAPET method, 772
  - reacting zirconium dioxide with magnesium, 772
  - reaction under autogenic pressure at elevated temperatures, 772
  - thermal dissociation of reactants, 772
- Reduction of zirconium tetrachloride by magnesium
  - high-temperature vacuum distillation, 768
  - Kroll process, 767–768
  - magnesium chloride, 767–768
  - pyrophoric zirconium sponge, 768
  - vacuum arc remelting, 768
  - Van Arkel–De Boer process, 768
  - zirconium tetrachloride, 767
- Refinement of RE by distillation
  - distillation in vacuum, 788
  - tantalum condenser, 788
  - tantalum crucible, 788
  - yttrium subgroup, 788
- Refractory and elevated temperature alloys (alloying RE elements)
  - Al–Fe–Ce system alloys, 791
  - alloying addition RE elements, 790
  - aluminum alloys, 790
  - aqueous lanthanum nitrate solution, 789
  - gas atomized powder, 791
  - magnesium alloys, 791
  - modified water atomization technology, 791
  - ODS molybdenum–lanthana alloys, 789, 790*f*
  - ODS molybdenum–yttria alloys, 789
  - RE–molybdenum disilicide composites, 789–790
  - RE–$MoSi_2$ composites, 789–790
  - self-propagating high-temperature synthesis (SHS), 789–790
  - W-Y system, 789
  - yttria-doped material, 789
  - zirconium doped material, 789
- Refractory-based composite powders
  - ball milling, 355
  - chemical synthetic, 355
  - composite refractories, 355
  - freeze–drying technique, 355
  - high-temperature applications, 355
  - mechanochemical methods, 355
  - non-oxide refractories, 355
  - oxide co-reduction, 355
  - oxide refractories, 355
  - tungsten–copper alloy powders, 355
- Refractory metal and carbide-based composites
  - acid treated carbon nanotubes (ATCNTs), 366, 367*f*
  - composite contact material, 366
  - infiltrated composite contacts, 366
  - molybdenum–silver composites, 366
  - press-sinter-infiltrate method, 366
  - suspension based technique, 366
- Refractory metal foams
  - aircraft wing, 337
  - catalytic filtration devices, 337
  - fuselage structures, 337
  - nozzle flaps, 337
  - thermal insulation, 337
- Refractory metal powders
  - accident prevention when working with the tungsten powders, 707
  - cemented carbides, 717–721
  - hardfacing, 714–717
  - molybdenum, 723–734
  - niobium, 734–742
  - production of refractory metal powders, 686–714, 717–721, 723–751
  - production of tungsten and tungsten carbide powders, 686–714
  - recovery of metallic tungsten, 705–707
  - recycling, 721–722
  - rhenium, 747–751
  - tantalum, 742–744
  - tungsten, 686–707
  - tungsten carbide powders, 707–712
  - tungsten metal powders, 686–707
  - tungsten powder applications, 699–705
- Regularities of granulometric composition
  - log-normal distribution, 23
  - normal distribution, 23
  - Rosin–Rammler distribution, 23
- Regularities of milling
  - agglomeration, 70
  - agglomeration of particles, 70
  - bonding by welding, 68–69
  - cold welding, 70
  - impacting force, 68, 69*f*
  - impact process by colliding balls, 68–70, 69–71*f*
  - particle fragmentation, 70
  - particle size growth, 65
  - particle size reduction, 65
- RE-separation by ion-exchange chromatography
  - anion lanthanide complexes, 783
  - cationite resins, 783
  - elution chromatography, 783
  - elution solutions, 783
  - ethylenediaminetetraacetic acid (EDTA), 783–784, 784*f*
  - hydrated ion size, 783
  - ion-exchange capacity, 783
  - REE adsorption, 783
  - RE elements desorption, 783
  - RE ions, 783
  - RE magnet, 783
  - salmon milt, 783
  - separation of lanthanides, 783
  - separation of RE elements, 783
- Restriction and limitation
  - pressure limitation, 804
  - mercury penetration, 45
- Rhenium powders
  - electrical contacts, 750
  - electrical resistivity, 749–750
  - electronic tube components, 750
  - gyroscopes, 750
  - isostatic pressing, 750–751
  - near-shape technique, 750–751
  - nuclear reactors, 750
  - pusher type furnaces, 748–749
  - reduction of ammonium perrhenate, 747–748
  - resistant to hydrochloric acid, 750
  - rubber-lined drums, 748–749
  - semi-conductors, 750
  - thermionic converters, 750
  - thermocouples, 750
  - uniaxial pressing, 750
- Rhodium powder
  - autoclave precipitation, 841–842
  - chemical composition, 748–749, 749*t*
  - filament applications, 749–750
  - low vapor pressure, 749–750
  - properties, 749*f*
  - thermolysis of mixture of salts, 843
- Roll compaction
  - connected pores formation, 325–326
  - honeycomb-like structure, 325–326
  - porous nickel sheet materials, 325–326
  - titanium porous plates, 325–326
- Roller atomization
  - acicular, 175
  - conductive heat transfer, 175
  - contra-rotated rolls, 175
  - epoxy coatings, 175
  - flaky particles, 175
  - irregular, 175
  - phenolic resin coatings, 175
  - ribbon particles, 175
  - roll coatings, 175
  - spheroidal particles, 175
  - twin rollers, 175
- Rotating electrode atomization
  - anode rotational speeds, 172
  - arc plasma, 172
  - consumable rotating bar, 172
  - plasma rotating electrode process (PREP), 172
  - rapidly rotating impeller, 173
  - rotating electrode process (REP), 172
  - rotational speed, 172
  - tungsten tipped device, 172
- RSR (rapid solidification rate) process
  - atomizer rotor, 493–494
  - closed-loop helium recirculation, 493–494
  - cooling helium jets, 493–494
  - helium gas, 493–494
  - high thermal conductivity gas, 494
  - narrow size distribution powders, 494
  - nickel base superalloys, 494
  - specialty aluminum alloy, 494
- Ruthenium
  - copper–nickel sulfide ores, 776
  - minerals of the osmium–iridium group, 776
  - platinum group metals, 776
  - ruthenium concentrate, 777

- Ruthenium powder
  - alkali metal hypochlorites, 776–777
  - autoclave precipitation, 841–842
  - catalysts in the synthesis of organic and inorganic products, 778
  - chemical composition, 777–778, 777*t*
  - iridium–ruthenium alloys, 778
  - particle size, 778
  - reduction in hydrogen current, 777
  - refining process, 777
  - ruthenium additions, 777–778, 777*t*, 779*f*
  - ruthenium ammonium hexachloride, 777
  - ruthenium dioxide, 776–777
  - ruthenium niello, 776–777
  - ruthenium tetroxide, 777
  - thermocouples, 778
  - wear-resistant parts, 778

S

- Safety engineering in production of powders
  - clarification of recirculated water, 918–922
  - dangerous and harmful manufacturing factors, 866–868
  - dust and gas cleaning, 923–924
  - technique of the prevention exposure hazards, 879–918
  - waste products utilization, storing and transportation, 924–927
- Safety measures in cadmium and zinc powders production and handling
  - fire and explosion safety measures, 626–628
  - ignition temperature, 626–628
  - inhalation zinc powder, 628
  - lower explosive limit, 626–628
  - toxicity of zinc powder, 628
  - zinc oxide, 628
- Sampling of powders
  - chute splitting, 6
  - composite sample, 4
  - conical pouring, 6
  - free-flowing powders, 4
  - keystone sampler, 4
  - point samplers, 4
  - quartering, 6
  - rotary sample divider, 4, 4*f*
  - sample preparation procedures, 5
  - sampling flowing powder streams, 4
  - scoop sampling, 6
  - selected samples, 4
  - stream sampling ladles, 4
  - travers cutter, 4
  - weight of powders, 6
- Scandium
  - applications, 813–819
  - physical properties, 810–811
  - scandium production, 812
  - sources of raw material for scandium production, 811–812
- Scandium applications
  - additional strengthening effect, 815–816
  - Al–Mg–Sc system, 817
  - Al–Sc master alloys, 818
  - aluminum alloys, 814–815
  - concept of precipitation strengthening, 815
  - control of suspension temperature, 818
  - corrosion resistance, 815
  - crystalline lattice, 813
  - dislocation cellular structure, 815
  - dislocation movement, 815
  - equiaxial microstructure, 817
  - Guinier–Preston zones, 815
  - high cooling rate, 815
  - hot degassing, 815
  - intermetallic AI_3Sc, 813
  - intermetallic $Al_3(Sc_{1-x}\ Zr_x)$, 815–816
  - intermetallic $MgZn_2$, 815
  - melt solidification rate, 817
  - nanoparticles of intermetallides, 818
  - non-dendritic structure, 813, 815
  - Orowan mechanism, 815
  - oxide films, 818
  - polygonal cell structure, 815
  - refractory transition metals, 815
  - ring-shaped dislocation loop, 815
  - secondary dispersoids, 815, 817*f*
  - structural lattice, 813
  - supersaturated solid solutions, 813, 815–816
  - surface microstructure, 815, 815*f*
  - thermally non-strengthened weldable Al–Mg base alloys, 814
  - thermally strengthened high-strength Al–Zn–Mg–Cu base alloys, 815
  - thermally strengthened high-strength weldable Al–Zn–Mg base alloys, 814
  - thermal treatment, 815
  - water atomized powders, 815, 818
  - weldability, 817
- Scandium production
  - electrorefining, 812
  - high-purity metallic scandium, 812, 814*f*
  - inert gas atmosphere, 812
  - lithium fluoride, 812
  - metallic scandium, 812
  - metallothermic reduction, 812
  - metallothermic scandium, 813*t*
  - monocrystalline ingot, 812
  - scandium chloride, 812
  - scandium fluoride, 812
  - scandium oxides, 812
  - sponge scandium, 812
  - vacuum distillation, 812
  - vacuum fusion, 812
  - volatile impurities, 812
  - zone melting, 812
- Scanning electron beam instruments, 29–30, 30–31*t*, 35
- Scanning electron microscopy (SEM)
  - automatic image analyzer, 10
  - backscattered detector, 27–28
  - chemical analysis of micron-size area, 27–28
  - crystallographic orientations, 27–28
  - electron beam instruments, 28
  - electrons generated by the electron beam, 28
  - magnifications, 30*t*
  - polydisperse granulometric composition, 10
  - powder sample preparation, 29
  - secondary electron detector, 27–28
- Scanning tunneling microscope
  - map of heights, 275
  - needle (probe), 275
  - surface topography, 275
  - tracking loop, 275
- Scheme of complete separation (RE separation)
  - cerium subgroup elements, 784, 785*f*
  - chloride-thiocyanate system, 784
  - countercurrent extraction, 784
  - extracting agent, 784–785
  - extracting agent D2EHPA (di-(2-ethylhexyl) phosphoric acid), 785
  - extraction, 784–785
  - ion-exchange chromatography, 784
  - light RE, 784
  - middle RE, 784
  - neodymium magnet leachate, 784–785
  - nitrate solution, 784
  - separation of cerium subgroup, 784
  - three fractions, 784
  - yttrium subgroup, 784
- Scintillation detectors, 36
- Scott volumeter
  - density cup, 52
  - gravitational powder jet, 51–52
- Screening model, 54
- Secondary ion mass spectrometer
  - ion beam, 32–33
  - ion column, 33
  - ion gun, 33
  - mass analyzer, 33
  - ratio ion detection unit, 33
  - vacuum sample chamber, 33
- Secondary ion mass spectroscopy (SIMS)
  - impinging primary ions, 32
  - impurity analysis, 32
  - in-depth concentration profile, 32
  - ion bombardment, 32
  - mass spectrometer, 32–33
  - primary beams, 32–33
  - quadrupole mass spectrometer, 32
  - secondary ion mass spectrometer, 33
  - secondary ions, 32–33
  - sputtering rates, 32
- Sedimentation method
  - accumulation of the sediment, 15
  - dispersion suspension, 14
  - liquid for suspension, 14*t*
  - method of weight samples, 16
  - micromerograph, 15–16
- Segregation of particles, 54
  - heterogeneity, 54
- Selective laser melting (SLM)
  - basic principles, 375
  - deposition, 375
  - fiber laser scan, 375
  - inert gas atmosphere, 375
  - laser technology, 375
  - layer of powder, 375
  - loose powder, 375
  - melting machine, 375
  - molten pool, 375
  - substrate platform, 375
  - 3D functional system, 375

Self-propagating combustion reactions, 108–109
Self-propagating high temperature synthesis (SHS)
  combustion wave, 527
  functionally graded materials, 526
  metastable phases, 527
  reactant mixture, 527
Semiconductor nanostructures
  de Broglie wavelength, 305
  0D, 1D, 2D, 3D, 305
Semiconductors
  aqueous solution method, 306
  classification of semiconductor nanostructures, 305
  photoluminescent semiconductor, 306
  quantum confinement effects, 305
  sol-gel method, 306
Separation of REE by extraction
  countercurrent system, 782
  extraction methods, 782
  extraction reaction, 782
  heavy RE elements row, 782
  lanthanides row, 782
  leaching conditions, 783
  nitrate solutions, 782
  organophosphorus extracting agents, 782
  RE nitrates, 782
  TBP extraction, 782
  tributylphosphate (TBP), 782
  trisolvate, 782
Shape factors
  bulkiness factor, 8
  elongation factor, 8
  surface factor, 8
Sherardizing (thermo-diffusion galvanizing)
  anti-corrosion treatment of metal articles, 630
  coating steel surfaces, 630
  compact delta layer, 630
  diffused gamma layer, 630
  protection against corrosion and abrasion, 630
Sieve analysis
  sieve shaker, 11
  variations, 13
Signals used in scanning electron beam instruments
  Auger electron, 31*t*
  backscattered plasmon, 31*t*
  elastically backscattered electrons, 31*t*
  inelastically backscattered electrons, 31*t*
  secondary electrons, 31*t*
Silver alloy powders, 835
Silver-nickel, 836–837*t*, 852–853
Silver powders
  apparent density, 833
  fibrous dendritic silver, 835, 837*f*
  particle size, 832–833
  production of silver powders, 832–835
Single rotary hammer mills
  active rotor part rotation, 914
  by-pass pipes, 915–917
  dynamic interaction coefficient, 913–914*t*, 917, 917*t*
  ejection suction, 915–917
  excess pressure, 912
  hammers action zone, 913–914*t*, 915
  hydraulic resistance coefficient, 915–917
  moving rotary parts, 912
  underpressure, 912, 915, 917
  unpresserized receiving bin, 915
Sintering of porous metal
  bond growth, 326
  melting temperature, 326
  sintering temperature, 326
  surface energy, 326
Size measurement
  Feret's diameter, 7
  longest diameter, 7
  Martin's diameter, 7
  maximum horizontal intercept diameter, 7
  perimeter diameter, 7
  project area diameter, 7
  two-dimensional particle size images, 7
Sliding at impact point
  chute angle, 54
  constrained moving, 54
  impact point, 54
  suspension state, 54
Sodium reduction method (Hunter process)
  aluminum–vanadium master alloy, 550
  ductile metallic titanium, 550
  metallic titanium, 550
  sponge fines, 550, 550*f*
  temperature reduction, 550
  titanium tetrachloride, 550
Solder alloy powders, 858, 859*t*
Sol-gel method
  agglomeration of the nanoparticles, 306
  CdTe nanoparticles, 306
  glass phosphors, 306
  layer-by-layer (LbL) self-assembly method, 306
  semiconductor nanoparticles, 306
  ZnSe nanoparticles, 306
Solid–gas eutectic solidification (Gasar)
  elongated pores, 332
  eutectic system, 332
  gas-reinforced, 332
  high pressure, 332
  hydrogen atmosphere, 332
Solid phase reduction (production of nickel powder)
  fluidized bed, 661
  hydrogen atmosphere, 661
  hydrogen current, 661
  needle shaped, 661
  nickel oxalate, 661
  producer gas, 661
  purification of nickel–cobalt solutions, 661
  reducing agents, 661
  roasting of sulfide materials, 661
  sponge particle surface, 661
  thermal decomposition, 661
Solid phase reduction of cobalt oxide
  binder in production of hardmetals, 673
  cobalt carbide, 674
  metallothermic reduction, 674
  reduction by carbon, 674
  reduction by hydrogen, 674
  reduction of cobalt oxide, 673–674
  reduction of cobalt salts, 673–674
  reduction temperature, 673–674
  treatment of cobalt chloride, 674
Solid-phase reduction of metal oxides and salts
  application of chemically reduced powders and salts, 225
  conveyor furnaces, 219
  drum furnaces, 219
  feed stock and reagent-reducers, 215–218
  kinetics and mechanism of process, 212–215
  powder production, 218–219
  push type furnaces, 218
  safety engineering, 220–221
Soluble gas atomization process
  argon hydrogen mixture, 163
  droplets solidify, 163
  gas-saturated molten metal, 163
  powder collection tank, 163
  rapid expansion, 163
  spherical powder, 163
  vacuum atomization, 163
Sources of raw material (beryllium comprising)
  bertrandite, 800
  beryl, 800
  beryllium concentrates, 800
  concentration methods, 800
  disseminated ores, 800
  electrolysis from beryllium fluoride, 800
  flotation, 800
  fluoride technique, 800
  phenacite, 800
  reduction of beryllium fluoride by magnesium, 800
  selection grinding, 800
  sulfate technique, 800
Sources of raw material for scandium production
  alumina production, 812, 818
  aluminum–scandium master alloys, 811
  Australia's mining, 819
  bauxites, 812
  Bayer process, 818
  carbon dioxide pressure, 818
  carbonisation leaching, 818
  elevated scandium cotent, 818–819
  extraction by organic solvents, 811
  ion exchange, 811
  iron ores, 811
  metallic scandium, 812, 813*t*
  metallothermic reduction, 812
  mine waters, 811
  precipitation of low-solubility compounds, 811
  red mud of alumina production, 818
  RUSAL technological process, 818
  scandium chlorides, 812
  scandium concentrate, 818
  scandium fluoride, 812
  scandium recovery, 818
  scandium–vanadium ores, 811
  slurry solid phase, 818
  sterrettite, 811
  thortveitite deposits, 818–819
  Timan bauxite diposit, 818

- trace element of rocks, 811
- Ural refinery, 818
- waste and middling of metallurgical production, 811

Special methods of production of metal powders recovered from spent solutions
- coaxially located anode, 250–251
- conducting particles, 251
- eco-cell, 250–251
- hammering rods, 251–252
- horizontally rotating cylinder, 250–251
- ion-change membrane, 250–251
- pump-cell, 251
- rotating cylindrical layer, 251–252

Spheroidization of tungsten powders
- carrier gas, 701
- plasma spheroidization of tungsten powders, 701
- plasma temperature, 701
- plasma torch, 701
- radio frequency (RF) thermal plasma, 701
- rapid quenching, 701
- raw tungsten powder, 701
- spherical droplets, 701
- surface tension, 701
- thermal plasma technique, 701

Spinning cup granulation process, 494, 496, 538

Spinning cup water granulation process
- annular wall of water, 179
- atomizing chamber, 179
- centrifugal force, 179
- cup wall apertures, 179
- mobile layer of water, 179
- nozzle plug, 179
- overflow apertures, 179
- rotating cup, 179
- rotating disc, 179
- spinning cup water granulator, 179
- suspended granules discharge, 179

Spinning disc atomization
- argon atmosphere, 170*t*, 171
- battery applications, 169
- chiller chamber, 169
- electronic applications, 169
- free fall melt feeding, 169
- helium atmosphere, 169–171
- hollow cone melt film, 169–171
- melt film, 169–171
- melt flow rate, 169
- narrow size distribution, 169
- needle shaped powder, 169
- prefilming nozzle, 169, 170*t*
- pressure-centrifugal-atomizer, 169
- roller circumferential speed, 171
- running speed, 169
- satellite-free, 169
- solder powder electronic applications, 169, 170*f*
- solder powder particle size, 169–171, 170*t*

Spinning water atomization process (SWAP)
- gas atomizer, 179
- irregular shape, 544
- non-combustive properties, 179
- nozzle plug, 179
- rotatable water stream, 179

Spray drying
- agglomerate size distribution, 178
- antifoaming agents, 178
- binders for agglomeration, 178
- bulk density, 178
- control of powder properties, 178
- deflocculating agents, 179*t*
- defoamers, 178
- free-flowing agglomerates, 178
- frothing agents, 178
- plasticizers, 178
- rapid evaporation, 178
- slurry, 178, 419
- spray-dried slurries, 178
- spray dryer, 419, 420*f*
- suspending agents, 178
- wetting agents, 179*t*

Spray forming
- aluminum based materials, 523
- compound materials, 523
- copper based materials, 523
- cylindrical billets, 523
- flat products, 522
- gas atomization, 521
- impact and deposition of droplets, 521
- integral spray-forming models, 521–522
- lightweight metals, 523
- metal spraying process, 521
- moving substrate, 521–522
- multiphase cone, 521
- plasma spray deposition (PSD), 525
- precipitation hardened aluminum alloy, 523
- quasicrystalline alloys, 524
- spray cone, 521–522
- spray deposited materials, 524
- spray formed rings, 522
- spray formed tubes, 522
- substrate, 521, 525
- titanium superalloys, 522–523

Spray granulation
- binding liquid, 177
- direct current plasma-heated fluidized bed, 177
- fluidized bed, 177, 178*f*
- formation of agglomerates, 177
- granule size, 177
- hot gaseous fluidized bed, 177
- nanophase composite powders, 177
- porous non-homogenous shell structure, 177
- scalable technologies, 177
- two-fluid spray nozzle, 177

Spray rolling (spray strip casting)
- atomized droplets, 526
- direct strip-casting techniques, 526
- inert gas atmosphere, 526
- liquidus temperature, 526
- roll gap, 526
- rolling mill, 526, 526*f*
- roll surface speed, 526
- spray-rolled strip, 526, 526*t*

Standards, development of
- ASTM International, 929–931*t*
- CIS (Commonwealth of Independents States)–GOST, 410, 426–427*t*, 765–766, 776, 778, 881
- France, 426–427*t*
- Germany–DIN, 426–427*t*
- International Standards Organization (ISO), 3, 870–871, 874–875
- ISO, Technical Committee, 870–871
- Japan, 54
- Metal Powder Industries Federation (MPIF), 929–931*t*
- Russian Federation–GOST, 849*t*, 854–857
- United Kingdom–BSI, 870

Standard terminology of powder metallurgy. ASTM, Designation: B243–13, 271

Standard test methods for metal powders and powder metallurgy products, 59

Steam explosion method
- CANOPUS method, 176, 176*f*
- explosive formation of steam, 176
- stream of cooled water, 176

Storing and transportation of hazardous powders, 925–927
- dangerous goods, 925–926
- IATA dangerous goods regulations (DGR), 926

Surface analysis
- Auger electron spectroscopy (AES), 30–32
- secondary ion mass spectroscopy (SIMS), 32–33
- x-ray photoelectron spectroscopy (XPS), 32

Surface area and porosity of powders
- gas adsorption, 39–41
- permeametry, 41–42
- picnometry, 42–43
- porosimetry, 43–46

Surface area determination (by mercury)
- mercury porosimetry, 45
- specific pore geometry, 45

Surface tension of mercury, 45

Surfactants, 228–229, 248–250, 721

Surfactants (by autoclave processing)
- anthraquinone, 228
- carboxyl containing surfactant, 229
- covering, 228
- mechanism of anti- skull formation, 229
- organic substances, 228
- polyacrylic salts, 228
- powder dispersity, 228
- skull formation, 228

Synthesis of open-cell metal foams
- catalysts, 336–337
- chemical vapor deposition, 337
- electrochemical cells, 336–337
- open-cell mold, 336–337
- physical vapor deposition, 337
- PM route, 336–337

T

Tantalum
- consolidation and manufacturing of semi-products, 746–747
- tantalum carbide, 744–747

Tantalum *(Continued)*
  tantalum compounds, 742
  tantalum metal powders, 742
Tantalum carbide
  grain growth inhibitor, 744–745
  hydrate ammonium tantalate, 745
  precursor of the tantalum carbide, 745, 746*f*
  tantalum carbide powder, 744–745, 746*f*
  tantalum–niobium carbide, 744–745
Tantalum metal powders
  electrochemical method, 744
  electrolytic process, 742–743
  HDH process, 742
  molten sodium chloride, 742
  sodium reduction, 742
Tantalum powder producing by electrolytic process
  anode current density, 744
  cathode crucible, 744
  cathode current density, 744
  electrolyte, 744
  potassium (sodium) chloride, 742–743
  potassium fluorotantalate, 742–743
  tantalum dendrites, 743–744
  tantalum pentachloride, 744
  tantalum pentoxide, 742–743
  tantalum refining, 744
Tantalum powder production by hydride–dehydride (HDH) process
  brittle hydride, 742
  electron beam (EB) melting, 742
  porous structure, 744
  sintering inhibitors, 742
  slow cooling, 742
Tantalum powder production by sodium reduction
  capacitor powders, 742
  electronic capacitor applications, 742
  flake-shaped tantalum particles, 742
  potassium tantalum fluoride, 742
Tantalum refining
  chloride–fluoride melt, 744
  fluoride melt, 744
  molten salt, 744, 744*f*
  reducing electrochemically dissolved tantalum ions, 744
  tantalum rod anode, 744
Tap density
  graduated glass cylinder, 52
  tapped powder, 52
  vibrated powder, 52
Technique for prevention of exposure hazards
  common demands to production area, equipment, and processes, 881–885
  dust explosion protection systems, 887–891
  localization of powder-gas emissions, 892–901
  workplace exposure limits, 879–881
Techniques of chemical analysis for powders
  bulk analysis, 33–38
  microanalysis, 27–30
  surface analysis, 30–33
Temperature rise during milling, 72
  bulk temperature, 73
  contact temperature, 72–73
  Hertz's theory of elastic impact, 72–73
Testing of nanopowders
  instrumental indentation, 276–278
  testing of nanopowder structures and chemistry, 275–276
Testing of nanopowder structures and chemistry
  atomic adsorption spectroscopy (AAS), 275
  atomic force microscopy, 275
  auger electron spectroscopy (AES), 275
  bulk analysis, 275
  electron probe x-ray microanalysis (EPMA), 275
  energy dispersive spectrometry (EDS), 275
  inductively coupled plasma atomic emission spectroscopy (ICP-AES), 275
  magnetic force microscopy, 275
  scanning electron microscopy (SEM), 275
  scanning tunneling microscopy, 275
  secondary ion mass spectroscopy (SIMS), 275
  surface analysis, 275
  transmission electron microscopy (TEM), 275
  wavelength dispersive x-ray spectrometry (WDS), 275
  X-ray powder diffraction (XRPD), 275
Thallium
  alkali refinement, 776
  alloy addition, 776
  crude thallium, 776
  decreasing the alloy grain size, 776
  electrolysis, 776
  electrolyte composition, 776
  fuel cell application, 776
  marcasites, 776
  pyrites, 776
  solar application, 776
  thallium ions, 776
  thallium oxides, 776
  thallium powder, 776
  thallium sulfate, 776
  ultra-red optics, 776
  water treatment, 776
Thermal properties of metallic foams
  cell connectivity, 345
  cell wall structures, 345
  gaseous reducing agents, 879
  heat conduction, 345
  heat exchangers, 345
  heat pipes, 345
  heat sinks, 345
  ligament structures, 345
  modelling of heat transfer and thermal exchanges, 345
  pore size distribution, 345
  surface roughness, 345
  tortuosity, 345
  water atomized aluminum alloy powder, 346
Thermodynamic peculiarities of metal chemical reduction
  difference of oxidizer and reducer potentials, 221
  oxidation–reduction potentials, 222–223*t*
  oxidation–reduction reaction, 221
  thermodynamic data, 221
Thermophysical properties
  aluminum bromide, 879
  aluminum chloride, 879
  aqueous alkali solution, 879
  building categories, 875
  carbon tetrachloride, 879
  coefficient of linear thermal expansion, 875
  combustibility and explosibility values, 879
  combustible liquids, 879, 879*t*
  combustion heat (enthalpy), 875
  combustion reaction, 875
  copper oxide, 879
  exothermal reactions, 879
  explosion and fire hazard, 875
  explosion limits, 879
  explosion-proof characteristics, 879, 879*t*
  Guide to EU Legislation, 879
  halogenated hydrocarbons, 879
  heat of combustion, 875
  heat of vaporization, 875
  hydrogen evolution, 879
  manufacturing areas, 875
  methyl chloride, 879
  minimum ignition temperature, 879
  nitro-compounds, 879
  rate of pressure rise, 879, 879*t*
  silver oxide, 879
  specific heat capacity, 875
  thermal conductivity, 875
  thermophysical magnitudes, 875
Thin film technique
  diamagnetic matrix, 304
  electric arc evaporation, 304
  ion deposition technology, 304
  ion-plasma deposition, 304
  magnetron sputtering, 304
  metallic cathodes, 304
  multi-layer, 304
  nanosized quasicrystalline films, 304
  paramagnetic matrix, 304
  platinum filament, 304
  quasicrystalline films, 304
Thorium powder production
  electrolysis of melts, 821
  reduction of thorium dioxide by calcium, 820–821
Tin powder
  apparent density, 855–856*t*
  applications, 858
  fisher subsieve size, 855–856*t*
  nominal composition, 855–856*t*
  properties, 852, 855–856*t*
  sieve analysis, 855–856*t*
  trace elements, 855–856*t*
Tin powder production
  atomization, 852
  bismuth–tin, 851–852*t*
  close-coupled atomizer, 853*f*
  cooling gas, 854*t*
  cooling rate, 852
  current density, 852–853
  electrolysis, 852–853
  electrolysis from double-layer cell, 851–852*t*
  electrolyte composition, 851–852*t*

  horizontally cross-jet air atomization technique, 850
  lead–tin, 851–852*t*
  melt temperature, 854*t*
  powder yield, 854*t*
  pressure of cooling gas, 854*t*
  tin-antimony, 851–852*t*
  tin powder applications, 852
  vertical melt atomization technique, 852
  water solution electrolysis, 851–852*t*
Titanium alloys (applications of additive manufacturing)
  build geometry, 387
  build platform, 390
  columnar microstructures, 390
  corrosion resistance, 387
  electron beam melting, 387–390
  longitudinal direction, 390
  melt pool, 387–390
  powder bed fusion, 387–390
  spot size, 390
  strength-to-weight ratio, 387
  transverse direction, 390
Titanium-based composite powders
  ceramic slurry approach, 355
  metal–ceramic composite powders, 355
  metallic biomaterials, 355
  metal matrix composites (MMCs), 355
  nano-carbon materials, 355
  rare earth oxides, 355
  titanium alloy–hydroxyapatite, 355
  titanium matrix composites, 355
Titanium powder-based materials selection
  balance of mechanical properties, 567–568
  desired combination of processing steps, 567–568
  final product cost, 567–568
  powder consolidation processing route, 567–568
  processing step sequences, 567–568
Titanium powder process selection, 567
  cost of powder per unit weight, 567
  current cost titanium sponge, 567
  master alloy powders, 567
  minimizing the lead time, 567
  powder process adaptability, 567
  prealloyed (PA) methods, 567
  process controllability, 567
Tovarov's apparatus, 41*f*
Trajectory effect
  chute, 54
  frictional drag, 54
  pile surface, 54
Transition electron microscopy (TEM)
  counting particles, 10
  electron microscope grid, 10
  powder sample preparation, 10
  vacuum unit, 11
Transportable containers
  by-pass tube, 452, 911
  discharge of containers, 911–912
  excess pressure, 911
  explosion-risk powders, 911
  pressurized performance, 911
  protective atmospheres, 911
  receiving vessel, 911, 912*f*
  thinning zone, 911
Tumbling ball mills
  large tumbling ball mills, 107
  stainless steel balls, 73
Tungsten-arc inert-gas welding (TIG), 794
Tungsten carbide powder
  diamond tools, 714
  production of tungsten carbide powder, 707–709
  properties of tungsten carbide powder, 709–712
  tungsten carbide electrical contacts, 712–714
Tungsten composite materials
  addition of molybdenum to quaternary alloy, 702–703
  body-centered cubic (bcc) structure, 702
  copper-coated tungsten composite, 703–704, 704*f*
  copper–tungsten powder, 703–704, 704*f*
  corrosion resistance, 702
  dissolve-precipitation mechanism, 703
  electrical contacts, 703
  elemental powders, 701–702
  high-voltage electric pulse consolidation, 703, 703*f*
  infiltration sintering, 704–705, 704*f*
  iron–nickel binder, 703
  liquid-phase sintering, 702
  mechanical alloying, 703
  mechano–thermo–chemical process, 705
  pores of the skeleton, 702
  press-sinter method, 702
  press-sinter-re-press process, 702
  sol-spray drying, 703
  thermo electroless method, 703–704
  thorium-containing compounds, 705
  tungsten–copper nanocomposite powder, 705
  tungsten heavy alloys (WHAs), 701–702
  tungsten powder infiltrated with copper alloys, 703
  tungsten with oxide dispertions, 705
  vacuum heat treatment, 702
  welding electrodes, 705
Tungsten metal powders
  amalgam technique, 693–694, 693*f*
  carbonyl technique, 694, 694–695*f*
  precipitation from gaseous phase of tungsten hexafluoride and hexacloride, 691–692, 692*f*
  production of tungsten powder by a plasma process, 692–693, 693*f*
  production of tungsten powder by hydrogen reduction, 9*f*, 686–690, 687–690*f*
  properties of tungsten powders, 695–699, 696–698*t*, 697–698*f*
  reduction by solid carbon, 690–691, 691*f*
Tungsten powder applications
  non-sag tungsten wires, 699–701
  pure tungsten powders, 699
  spheroidization of tungsten powders, 701, 701*t*, 702*f*
  tungsten composite materials, 701–702
  ultrahigh purity powders, 699
Tungsten powder production by carbonyl technique
  autoclave, 694
  carbon monoxide action, 694
  carbonyl decomposition, 694, 695*f*
  compounds (salts), 694
  dry synthesis from chlorides, 694
  elevated temperatures, 694
  high pressures, 694
  horizontal sublimator, 694
  metal carbonyl formation, 694
  reducing agent, 694
  synthesis of carbonyls, 694
  tungsten hexachloride, 694
Tungsten powder production by hydrogen reduction
  ammonium paratungstate (APT), 687
  calcination step, 687
  chemical vapor transport, 690
  dissolution step, 687
  dynamic powder layer, 689
  hydrogen reducer, 687–688
  purification step, 687
  pusher furnace, 688–689, 688–689*f*
  reduction step, 687–688
  rotary furnaces, 687–689
  tungsten-bearing minerals, 687
  tungsten-bearing scrap, 686–687
  wolframite concentrate, 686–687

U

Ultrahigh purity powders, 699
Ultrasonic additive manufacturing (UAM) process
  adhesively joined parts, 375
  brazing, 375
  diffusion bonding, 375
  laser welding, 375
  metallic sheet, 376
  resistance welding, 375
  sheet lamination process, 375
  swelling effects, 375
  ultrasonic consolidation, 375
  ultrasonic vibration, 375
Ultrasonic gas atomization
  capillary wave atomization model, 164
  capillary wavelength, 163
  cavitational phenomena, 163
  confined ultrasonic atomizer, 164, 164*f*
  Hartman tube principle, 164
  HEVs ultrasonic atomization, 164
  maximum entropy formalism, 125–126
  pneumo-acoustic atomizers, 164
  Sono–Tek ultrasonic nozzle, 164–165
  ultrasonic atomization technology, 164–165
  ultrasonic frequency, 163
  ultrasonic nozzles, 164–165
Ultrasonic spray pyrolysis (USP)
  cemented carbide scrap, 682
  cobalt nanopowder synthesis, 682

Ultrasonic spray pyrolysis (USP) *(Continued)*
  cobalt nitrate aerosol, 682
  cobalt nitrate aqueous solutions, 682
  cobalt oxide, 681
  hydrogen reduction, 681–682
  narrow size distribution, 681–682
  non-agglomerated particles, 683
  precursor solution, 683
  silica-encapsulated metal nanoparticles, 681–682
  spherical cobalt powders, 682
  ultrafine cobalt powder, 681
  ultrasonic atomizer, 682
Uranium powder production
  electrolysis of halogen salts, 821
  hydride–dehydride process, 822
  metallic uranium, 821
  metallothermic reduction, 821
  reduction of uranium tetrachloride, 821
  reduction of uranium tetrafluoride, 821–822
  uranium hydride, 822
  uranium oxide, 821

V

Vacuum hot pressing (VHP) (beryllium powders)
  graphite dies, 804
  manufacturing commercial beryllium billets, 804
  nickel alloy dies, 804
  vacuum hotpressed billets, 804, 805*t*
  vacuum hot pressing chamber, 804
Vanadium
  aluminothermic reduction process, 759
  calciothermic reduction, 759–760, 760*t*
  carbothermic reduction, 759–760, 760*t*
  content of vanadium, 758
  decomposition of vanadium halides, 759
  ductile vanadium, 758, 760
  electrolytic refining, 759–760
  magnesiothermic reduction, 760
  spark plasma sintering, 765
  tungsten based vanadium alloys, 765
  vanadium alloys, 760–762, 765
  vanadium carbides, 759, 764
  vanadium compositions, 764
  vanadium dioxide, 759
  vanadium oxides, 759
  vanadium pentoxide, 759
  vanadium powders, 759–761, 760*t*, 765, 765*f*
  vanadium refining, 760
  vanadium trioxide, 759–760
Vapor deposition in vacuum
  combine production and processing, 297
  condensation of metallic vapor, 279
  crystallizer, 279
  electron beam installation, 297–298, 297*f*
  electron beam technologies (ICEBT), 297–298, 297–298*t*
  evaporating of metal, 278–279, 279*f*
  gas-phase technique, 297
  inert gas condensation process (IGS), 297
  microlaminate coating, 298
  nucleation centers, 279
  prevention of oxidation, 297
  supersaturation, 279, 491
VSMPO-AVISMA Corporation, 539

W

Waste aluminum foil recycling, 474–476, 475–476*f*
Waste products utilization, storing, and transportation
  storing and transportation of hazardous powders, 925–927, 926*t*
  waste utilization, 924–925, 925*f*
Waste utilization
  European Waste Catalogue, 925
  hazardous waste, 924–925
  metal machining scrap, 925
  scrap components, 924–925
  scrap for disposal, 924
  scrap for recycling, 924
  waste disposal, 924–925
Water atomization
  powder characteristics, 134
  water atomization mechanism, 132–134
  water atomization technique, 128–132
Water atomization mechanism
  bubble boiling conditions, 137–138
  cooling rate, 132, 137–138
  cooling time, 137–139
  droplet formation model, 133–134
  energy carrier, 132, 134*f*, 138–139, 139–140*f*
  film boiling conditions, 137–139
  film-bubble heat emission, 138
  first critical heat current density, 137–138
  Grandzol and Tallmadge, 132–133
  heat transfer, 132, 135, 137–138
  heat transfer coefficient, 135, 137–138, 139*f*
  liquid melt drop formation, 132
  liquidus temperature, 137, 139
  melt drop cooling time, 137
  melt superheat, 133
  second critical heat current density, 137–138
  spheroidization time, 137–139, 141
  steam film, 132, 137–138
  steam formation, 132
  superheated compressed steam, 132
  Ternovoy’s formula, 133–134
Water atomization technique
  annular jet, 129*f*
  annular ring nozzles, 130
  binary water cone configuration, 131–132, 131*f*
  closed V-jets, 129*f*, 132
  conical water swirl jet atomizer, 130–131, 130–131*f*
  IPMS atomizer, 132
  open V-jets, 129*f*
Water granulation
  atomizing chamber, 179
  cup wall apertures, 179
  overflow apertures, 179
  pouring molten metals, 179
  rotating cup, 179
  spinning cup water granulation process, 179
  spinning cup water granulator, 179
  spinning water atomization process, 179
  SWAP installation, 179
  water quenching, 179
Wavelength dispersive x-ray spectroscopy (WDS)
  angular position of the crystal, 35
  charge carriers, 29
  crystal-monochromators, 35
  energy-dispersive spectrometer, 29
  gas-filled proportional detectors, 36
  radiation current, 35
Workplace exposure limits
  airborne particles, 880
  American Conference of Governmental Industrial Hygienists (ACGIH), 881
  American Industrial Hygiene Association Journal, 881
  British Medical Research Council (BMRC), 881
  chemical substances (EINECS), 881
  commonwealth of Independent States (CIS) Standard, GOST 12.1.005-88, 881
  danger classes, 881
  dust concentration in the workplace atmospheres, 881
  occupational and environmental health, 881, 881*f*
  permissible exposure limit value (PEL), 881
  threshold limit value (TLV), 881
  tracheobronchial and alveolar components, 881
  workplace atmospheres, 880–881
Wrought product forms (RE powders)
  beryllium extrusion, 806
  biaxial or triaxial deformation procedures, 806
  cross rolling at moderate temperature, 806
  crystallographic orientation, 806
  direction of metal flow, 806
  encasing beryllium billets in steel jackets, 806
  foil, 806
  hot-working technique, 806
  numerical control (CNC), 806–807
  plate, 806
  process AlBeWeld, 806
  sheet, 806, 807*t*

X

XD-process
  exothermic reaction, 527
  metallic matrix material, 527
  reinforced aluminum composites, 527
  reinforcing phase, 527
  self-propagating reaction, 527
  ultrafine reinforcing particles, 527
X-ray diffraction (XRD), 27, 34, 38, 78–79, 378–381, 524
X-ray fluorescence spectroscopy (XRF)
  element-wise decomposition, 36
  excitation of atoms, 35
  fluorescent signal, 35
  secondary fluorescent emission, 35
  X-ray beam, 35
  X-ray spectrometers, 35

X-ray photoelectron spectroscopy (XPS)
  average surface chemistry, 32
  electron energy analyzer, 32
  electron multiplier, 32
  ion gun as x-ray source, 32
  pulse-counting detector, 32
  quantitative spectroscopic technique, 32
  ultrahigh vacuum conditions, 32
X-ray powder diffraction (XRPD)
  automated powder diffractometers, 34
  crystallites, 33, 35
  determination of crystallinity, 33
  high-temperature studies, 33
  lattice-parameters determinations, 33
  monochromatic x-ray beam, 35
  pattern-recognition methods, 34
  phase identification and analysis, 33
  Rietveld method, 35
  thin film characterization, 33
  Wulf–Bragg's law, 34

Y

Yield strength
  aluminum alloys, 498, 500–501*t*
  properties of AlBeMet, 809*t*, 810
  tensile properties of alloys doped by cerium, 792, 793*t*
  tensile properties of molybdenum wire, 725–726, 728*t*
  tensile properties of PM superalloys, 655, 656*t*
  titanium powders and sintered compacts, 550, 552*t*
Young–Laplace– Washburn equation, 43–44
Young's modulus, xx, 276–278, 314, 357, 360, 504–505, 544

Z

Zinc powder, 128, 143–144, 169, 195–196, 196*t*, 357, 601–602, 615, 616*f*, 617, 619–620, 619*f*, 621*f*, 622, 623*t*, 625–630, 627*t*, 629*t*, 694. *See also* Production of zinc, cadmium, and their alloy powders
Zinc process, 631, 722
Zinc-rich composite powders
  aluminum pigment, 356–357, 356*f*
  cathodic protection properties, 355–356
  coating cathodic protection, 355–356
  epoxy zinc-rich coating, 356–357, 356*f*
  inorganic zinc-rich coating, 355–357
  lamellar aluminum, 356–357
  lamellar-type pigment, 356–357
  lamellar zinc, 357
  sacrificial pigment, 357
  zinc-rich coating, 355–357
Zirconium powder
  deoxidation and denitriding of steel, 766
  zirconium baddeleyite, 766
  zirconium dioxide, 766
  zirconium ortho-silicate, 766
  zirconium powder production, 766
Zirconium powder applications
  armor and gun steels, 766
  corrosion-resistant steels, 757
  electronics, 766
  elevated temperature alloys, 789–792
  igniter in detonators, 766
  nuclear power industry, 766
  photoflashes, 766
  pyrotechnics, 766
  refractory, 766
  smokeless powder, 766
  steel production, 766
Zirconium powder production
  amalgam method, 770
  combustion synthesis of zirconium nitrides, 771
  electrolytic methods for production or refining of zirconium powders, 767
  iodide method of zirconium refining, 767
  lead zirconate titanate (PZT) ceramics, 772–773, 773*f*
  plasma-assisted reduction of zirconium tetrachloride by magnesium, 771, 771–772*f*
  reduction of zirconium dioxide by calcium or calcium hydrate, 768
  reduction of zirconium dioxide by magnesium using autoclave processing, 772, 772*f*
  reduction of zirconium fluoride (ZrF_4) by calcium or of potassium hexafluorozirconate (K_2ZrF_6) by sodium, 768
  reduction of zirconium tetrachloride by magnesium or sodium, 767–768
  zirconium powder applications, 766